



Analysis of pesticide and veterinary drug residues in baby food by liquid chromatography coupled to Orbitrap high resolution mass spectrometry

María Luz Gómez-Pérez, Roberto Romero-González, José Luis Martínez Vidal, Antonia Garrido Frenich*

Research Group "Analytical Chemistry of Contaminants", Department of Chemistry and Physics, Research Centre for Agricultural and Food Biotechnology (BITAL), University of Almería, Agrifood Campus of International Excellence, ceIA3, E-04120 Almería, Spain

ARTICLE INFO

Article history:

Received 10 April 2014
Received in revised form
18 July 2014
Accepted 21 July 2014
Available online 31 July 2014

Keywords:

Exactive-Orbitrap
Pesticide
Veterinary drug
Baby food
Matrix effect
Representative matrix

ABSTRACT

Pesticide and veterinary drug residues have been simultaneously determined in several baby foods as meat, fish and vegetable-based baby food. A generic extraction method without clean-up step was applied. Moreover, the use of a representative matrix for proper quantification of all target compounds was studied and the best results were obtained when vegetable-based baby food was used as representative matrix, allowing the reliable quantification of more than 300 compounds. The method was validated and good recoveries were obtained for most of compounds at concentrations higher than $50 \mu\text{g kg}^{-1}$. Limits of detection (LOD) ranged from 0.5 to $50 \mu\text{g kg}^{-1}$, whereas limits of quantification (LOQ) were established between 10 and $100 \mu\text{g kg}^{-1}$. Limits of identification (LOIs) ranged from 0.5 to $50 \mu\text{g kg}^{-1}$. This method was applied to the analysis of 46 different baby food samples and no positive samples were found.

© 2014 Elsevier B.V. All rights reserved.

1. Introduction

There are significant economic benefits associated with the use of pesticides and veterinary drugs (VDs), but the inadequate use of these substances can provoke a transfer to the food chain, producing negative consequences in the consumer health [1]. Special attention must be paid to children and infants because they are a vulnerable risk group [2] due to their poor immunologic system and low weight [3–5].

The European Commission only has set up maximum residue levels (MRLs) for some chemicals and contaminants, such as pesticides and mycotoxins in processed cereal-based baby food and infant formulae, at $10 \mu\text{g kg}^{-1}$ or even at lower concentrations ($4\text{--}8 \mu\text{g kg}^{-1}$) [6]. This Directive (Commission Directive 2006/141/EC) put emphasis on the control of pesticides or transformation products (including metabolites) of pesticides with a maximum acceptable daily intake of $0.5 \mu\text{g kg}^{-1}$ body weight. Moreover, some pesticides shall not be used in agricultural production intended for the production of baby foods [7]. Regarding MRLs of pharmacologically active substances (including antibiotics) general MRLs are established for foodstuffs of animal origin [8] and the "zero tolerance" principle

should be applied to those pharmaceuticals and foodstuffs for which MRLs have not been established [9].

The wide variety of infant food matrices and their complexity, as well as the high number of compounds that should be monitored, requires the application of reliable, high-throughput and efficient analytical methods [10]. There are studies related to the determination of several classes of VDs [2,5,9,10] and pesticides [11–15] in baby food, and one work focused on the development of a multiresidue method, where VDs and pesticides are analysed simultaneously by quadrupole (Q)-Orbitrap-MS [16] has been recently published. For that purpose, the development and application of generic extraction procedures are necessary. Moreover, the quantification process should be as fast and reliable as possible. In this sense, the use of high performance liquid chromatography coupled to Orbitrap mass spectrometry (UHPLC-Orbitrap-MS) [17] is sufficient to enable the detection, quantification and accurate mass measurement of a wide range of residues in complex matrices as baby food. However it is well-known that when electrospray ionization (ESI) is employed, matrix effect must be taking into account [18,19] and precision, linearity and sensitivity of the results are significantly affected, because matrix compounds can be responsible for the modification of the analytes behaviour into the electrospray source. This matrix effect can decrease (suppression) or increase (enhancement) the instrumental response of the analyte, and therefore, the analysis of a real

* Corresponding author. Tel.: +34950015985; fax: +34950015008.
E-mail address: agarrido@ual.es (A. Garrido Frenich).

sample or a pure analyte standard solution does not provide the same instrumental response [20]. Moreover, post-interface signal suppression has sometimes been observed when Orbitrap analyser is used, and this is mainly due to a high abundance of matrix multiple charged proteins in the C-trap located before the analyser [21].

The most commonly strategies used to compensate this matrix effect are based on several calibration procedures as matrix-matched calibration, standard addition method or isotopically labelled standards [22], being matrix-matched calibration the most widely used in routine laboratories. Other approaches to minimize matrix effect are the development of efficient extraction procedures, which can decrease the extraction of interferents [23], or the use of the dilution of the sample. In this sense, and despite the simultaneous extraction of other compounds present in the matrix, “dilute and shoot” method could be an interesting approach because of the dilution of the extracted compounds [24], minimizing matrix effect [25].

On the other hand, there is a wide variety of baby food with different compositions (i.e. meat or fish-based baby food, etc), and therefore, different matrix-matched calibrations should be performed for each type of baby food in order to achieve a reliable quantification. This is time-consuming, especially for routine laboratories, and thus, the use of a representative matrix is desirable in order to minimize the quantification process and associated quality controls [26].

The aim of this study was the analysis of more than 350 pesticides and VDs in several types of baby food based on a variety of raw materials (meat, fish and vegetables) evaluating matrix effect in all matrices, as well as the possibility of using a representative matrix for quantification, decreasing time-consuming.

2. Materials and methods

2.1. Chemicals and reagents

Pesticides and VDs analytical standards were purchased from Sigma-Aldrich (Madrid, Spain), Riedel-de-Haën (Seelze, Germany), Fluka (Steinheim, Germany), Dr. Ehrenstorfer GmbH (Ausburg, Germany), Witega (Berlin, Germany), Santa Cruz (Santa Cruz, CA, USA) and European Pharmacopoeia (Strasbourg, France). Individual stock standard solutions (100–450 mg L⁻¹) were prepared in methanol, acetone or acetonitrile, and they were stored at 5 °C or –18 °C (VDs). LC–MS grade methanol, acetonitrile and acetone were obtained from Fluka. VDs were grouped in families and a solution for each of them was prepared from corresponding individual stock standard solutions in methanol or acetonitrile, whereas two multi-pesticide solutions (corresponding to typical LC and GC-amenable compounds) were prepared in acetone or methanol. Then, a multi-compound working solution containing all the analytes (0.41 mg L⁻¹) was prepared by combining suitable aliquots of each individual standard stock solution and diluting them with LC–MS-grade methanol. This solution was kept at –18 °C. Formic acid (purity >98%) and ammonium formate (purity >99%) were obtained from Panreac (Barcelona, Spain). LC–MS water was provided by Scharlau (Barcelona, Spain). Extra-Bond Florisil cartridges (500 mg, 3 mL) were purchased from Scharlau (Barcelona, Spain). For accurate mass calibration, a mixture of caffeine, Met-Arg-Phe-Ala acetate salt (MRFA) and Ultramark 1600 (Proteo Mass LTQ/FT-Hybrid ESI positive mode calibration mix) and a mixture of acetic acid, sodium dodecyl sulphate, taurocholic acid sodium salt hydrate and Ultramark 1621 (fluorinated phosphazines) (ProteoMass LTQ/FT-Hybrid ESI

negative mode calibration mix) from Thermo Fisher Scientific (Rockford, IL, USA) were used in the Orbitrap analyser.

2.2. Apparatus

For the extraction procedure, a rotary agitator from Heidolph (Schwabach, Germany) and an analytical AB204-S balance (Mettler Toledo, Greifensee, Switzerland) were used. Centrifugations were performed in a Consul 21 high-volume centrifuge from Olto Alresa (Madrid, Spain).

2.3. UHPLC-Orbitrap-MS analysis

The separation of the analytes was carried out using a Transcend 600LC (Thermo Scientific Transcend™, Thermo Fisher Scientific, San Jose, CA, USA) equipped with an analytical column Hypersil GOLD aQ C18 column (100 mm × 2.1 mm, 1.7 μm particle size) from Thermo. The mobile phase consisted of 0.1% (v/v) formic acid and ammonium formate 4 mM in water (eluent A) and 0.1% (v/v) formic acid and ammonium formate 4 mM in methanol (eluent B). The analysis started with 95% of eluent A. After 1 min, this percentage was linearly decreased to 0% in 7.0 min. This composition was held during 4.0 min and increased again up to 95% in 0.5 min, followed by a re-equilibration time of 1.5 min (total running time=14.0 min). The flow rate was 0.3 mL min⁻¹ and the column temperature was set at 30 °C. Aliquots of 10 μL of the sample extract were injected into the chromatographic system.

The UHPLC system was coupled to a single stage Orbitrap mass spectrometer (Exactive™, Thermo Fisher Scientific, Bremen, Germany) operating with a heated electrospray interface (HESI-II, Thermo Fisher Scientific, San Jose, CA, USA), in positive (ESI+) and negative ionization mode (ESI-) using the previously developed parameters [27]. Mass spectra were acquired using four alternating acquisition functions: (1) full MS, ESI+, without fragmentation (the higher collisional dissociation (HCD) collision cell was switched off), mass resolving power=25000 FWHM; scan time=0.25 s; (2) all ions fragmentation (AIF), ESI+, with fragmentation (HCD on, collision energy=30 eV), mass resolving power=10000 FWHM; scan time=0.10 s; (3) full MS, ESI- using the settings explained for (1); and (4) AIF, ESI- using the settings explained for (2). Mass range in the full scan experiments was set at *m/z* 70–1000. All the analyses were performed without lock mass. Mass accuracy was carefully monitored as follows: checked daily with the calibration mix solution (see Section 2.1); evaluated (once a week) and calibrated when necessary (every two weeks at least). Data were acquired using matrix-matched external calibration mode and they were processed using Xcalibur™ version 2.2.1 (Thermo Fisher Scientific, Les Ulis, France) with Qual and Quant browser. Genesis peak detection was applied. ToxID™ 2.1.1 (automated compound screening software, Thermo Scientific) was used for screening and LCQuan™ 2.6 software (Thermo Scientific) was used for quantification during method validation and sample analysis.

2.4. UHPLC-QqQ-MS analysis

These analyses were carried out using an Agilent series 1290 RRLC instrument (Agilent, Santa Clara, CA, USA) equipped with a binary pump (G4220A), a high-performance autosampler (G4226A), an autosampler thermostat (G1330B) and a column compartment thermostat (G1316C). The system was coupled to an Agilent QqQ mass spectrometer (6460A) with a Jet Stream ESI ion source (G1958-65138). For the chromatographic separation of the extracts, a Zorbax Eclipse Plus C18 column (100 mm × 2.1 mm, 1.8 μm particle size) from Agilent was used. Column temperature was set at 30 °C and injection volume was 5 μL. Chromatographic

separation was performed using the same gradient profile described in [27]. The flow rate was set at 0.3 mL min^{-1} . Jet Stream Ion Source parameters: drying gas temperature and sheath gas temperature were $325 \text{ }^\circ\text{C}$ and $400 \text{ }^\circ\text{C}$ respectively; drying gas flow and sheath gas flow were 7 and 12 mL min^{-1} respectively; nebulizer pressure was 40 psi ; capillary voltage was set at 4000 V in positive acquisition. Multiple reaction monitoring (MRM) mode was used. Agilent Mass Hunter Quantitative analysis (Agilent Technologies, Inc.) was used for data acquisition and quantification of samples.

2.5. Sample preparation

For the extraction of all compounds, a method used in a previous study [27] was selected. The procedure was carried out as follows: 2.5 g of baby food was weighed into a 50 mL -propylene tube and 2.5 mL of water was added and mixed using a vortex. Then, 7.5 mL of acetonitrile containing formic acid ($1\% \text{ v/v}$) was added, and the sample was shaken end-over-end for 1 h using a rotary agitator. The tube was centrifuged (12 min , 4500 rpm , 2264 g) and 1 mL of extract was transferred into a vial and injected onto the chromatographic system.

The addition of a clean-up step was evaluated in order to minimize matrix effect, using one procedure previously tested [28]. Briefly, after centrifugation step, 3 mL of the extract was passed through a Florisil cartridge (by gravity), and 1 mL was transferred into a vial and injected onto the chromatographic system.

2.6. Baby food samples and matrix-matched calibration curves preparation

A total of 46 different baby food samples based on a variety of raw materials (meat, fish and vegetables) were analysed. Although nowadays there is a huge variety of baby food in the market, the selection was based on the most popular samples among consumers. A detailed explanation of the composition of each sample is shown in the Electronic Supplementary Data (ESD, Table S-1). As it can be observed, the composition is very similar within each type of raw material (meat, fish or vegetables), existing few variations depending on the rest of the components. For that, it can be guaranteed that the matrix chosen to develop the experiments is representative enough of all samples within the same group (meat, fish or vegetables). These samples were purchased from different local markets (Almería, Spain), and all of them were analysed following the procedure described above. Those samples, showing the absence of the target compounds, were used as blank samples in the preparation of standards and recovery studies. For this aim, a sample of each type of raw material (meat, fish and vegetables) was used. In order to avoid errors and ensure the reliability of the results, an internal quality control (IQC) was carried out. This IQC was based on the use of a blank extract that eliminated false positives caused by a contamination in the extraction procedure or by the presence of an interference; a reagent blank (obtained by performing the whole procedure without sample) that removed any possibility of a false positive due to contamination in the instruments or reagents used; a spiked blank sample at $50 \mu\text{g kg}^{-1}$ to assess the extraction efficiency; and a calibration curve to check linearity and sensitivity.

For matrix effect evaluation, blank samples were extracted following the procedure explained in Section 2.5 and the obtained extracts were spiked at different concentration levels that ranged from 2.5 to $100 \mu\text{g L}^{-1}$ (matrix-matched calibration) before chromatographic analysis. A solvent calibration was also prepared at the same concentration levels.

3. Results and discussion

A high number of compounds belonging to different families of pesticides and VDs were selected. Information of molecular formula, accurate mass, retention time and characteristic ions of the compounds analysed is shown in Table S-2. Fragments were obtained using a solvent-standard at $500 \mu\text{g kg}^{-1}$.

Matrix effect was evaluated in several types of baby food as meat-based, fish-based and vegetable-based. In all cases, matrix effect was calculated by comparison of the slope obtained for each compound when matrix-matched and solvent calibrations were performed. Signal suppression or matrix enhancement was considered tolerable in the range 0.80 – 1.20 (comparison of matrix-matched and solvent slopes). The values outside this range indicated a strong matrix effect, and matrix-matched standard calibration must be used for quantification purposes [29].

3.1. Influence of the extraction procedure on matrix effect

Generic extraction methods, used in order to extract a wide range of compounds, can provide low selectivity and other substances that can interfere in the ionization process could also be extracted, being the addition of a clean-up procedure a good option to minimize this matrix effect. However, it is also well-known that during these clean-up steps, some compounds can interact with the sorbent and therefore, recovery could also be affected [30].

In order to evaluate this, recovery and matrix effect were studied when a clean-up step was added to the extraction procedure developed by Gómez-Pérez et al. [27], using Florisil, because it provided suitable results in previous studies [28]. For recovery studies, the three types of baby food were spiked at $50 \mu\text{g kg}^{-1}$ (three replicates), and recovery was estimated using matrix-matched calibration, showing the results in Fig. 1.

First, it can be observed that without clean-up (Fig. 1a), more than 350 compounds had recoveries between 70 and 120% for meat, fish and vegetable-based baby food. However, when a clean-up step was included (Fig. 1a), the number of compounds with suitable recoveries was lower. Thus, for fish and vegetable-based food, the number of extracted compounds was 283 and 288 respectively, whereas for meat-based baby food, the number decreased till 189 . Therefore, the results in Fig. 1a indicate that the use of the Florisil clean-up step causes a reduction in the number of compounds demonstrating acceptable recovery (70 – 120%) for all three types of baby food, and the greatest reduction was observed for meat-based baby food. This fact indicates that the use of a clean-up step depends on the type of matrix evaluated, and the interactions between target compounds, matrix and sorbent should be considered. Therefore, fish and vegetable-based baby food are less influenced by the addition of a clean-up step, while the results are different in meat when this step is added.

For the evaluation of matrix effect, calibration curves at five concentration levels (ranged from 2.5 to $100 \mu\text{g L}^{-1}$) were prepared in solvent and in extracts from the three matrices, analyzing three replicates of each level.

It can be seen (Fig. 1b) that in general, suppression effect was observed for most of the target compounds in the three matrices evaluated (Table S-3). When a clean-up step was used, it can be noted that the number of compounds without matrix effect increased. However, some differences can be observed between the matrices evaluated. For instance, vegetables and fish-based baby food reduced the number of compounds showing matrix effect (see Fig. 1b). This could be explained considering that some of the coextractives substances in vegetables and fish products, which could affect the ionization of the selected analytes, are retained by the sorbent, reducing the matrix effect when a clean-up step is

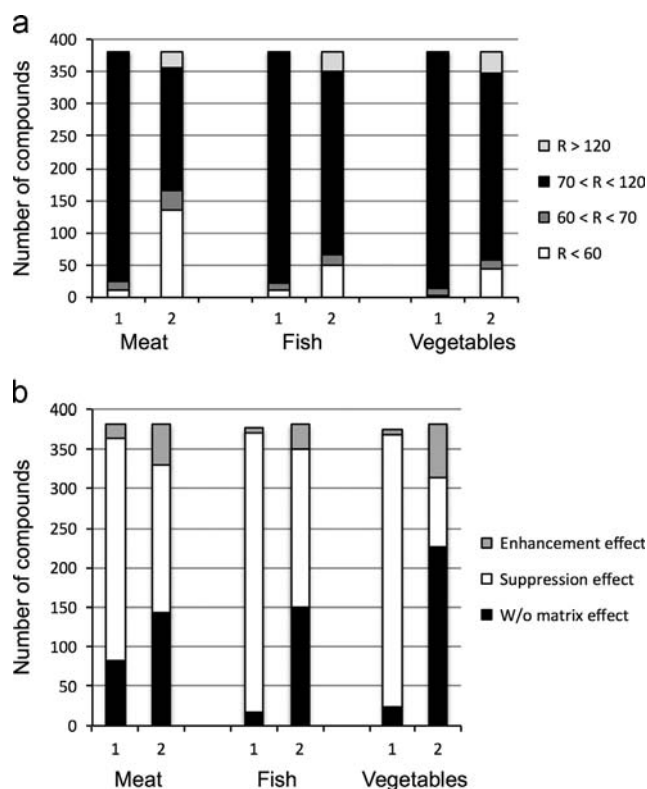


Fig. 1. Effect of the addition of a clean-up step on: (a) the recovery and (b) matrix effect in the three matrices evaluated. Number codes: 1: without clean-up; 2: with clean-up. (Note: W/o: without).

added. On the other hand, in the case of meat-based baby food, the percentage of protein is higher than in the other matrices, and this could explain the differences in the obtained results, comparing with fish and vegetable-based baby food. Nevertheless, sample clean-up was not used in further experiments, bearing in mind that it did not lead to significant reduction of matrix effect in some of the matrices evaluated, as well as it did not improve the recovery of the target compounds.

3.2. Selection of a representative matrix

Bearing in mind the existence of matrix effect, matrix matched calibration can be used in order to perform reliable quantification. However, this is time-consuming in routine laboratories, because different commodities must be analysed, and therefore, the use of a representative matrix is interesting in order to perform one matrix-matched calibration per batch.

First, signal variation was evaluated, comparing the slopes (calibration curve between 2.5 and 100 $\mu\text{g L}^{-1}$) obtained for the three matrices evaluated. Thus, if the slope ratio ranged from 0.8 to 1.20, it was considered that the slope observed for both matrices was similar. However, if the ratio is lower than 0.8 it means that there is a signal suppression in relation to the proposed representative matrix, whereas if the ratio is higher than 1.20, a signal enhancement is observed. The obtained results are shown in Fig. 2. It can be noted that when meat was used as representative matrix, more than 300 compounds showed similar signal when they were analysed in fish, whereas for vegetables, less than 250 compounds provided the same signal. The same conclusions were obtained if fish matrix was used as representative matrix. However, when vegetable-based baby food was used as representative matrix, similar values were obtained in the other three matrices (approximately 250 compounds in each one), showing similar slope.

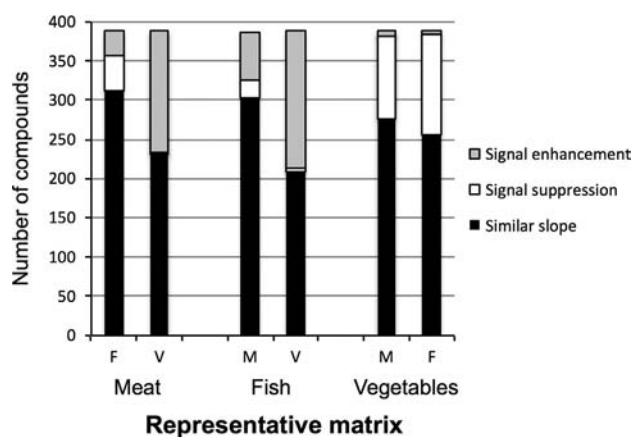


Fig. 2. Evaluation of matrix effect in the three matrices studied, using several matrices as candidates as representative matrices. Codes: F: Fish; M: Meat; V: Vegetable.

Table 1

Number of extracted compounds with acceptable recovery values (70–120%) obtained with the different matrices and using a representative matrix.

Representative matrix	Spiked matrix		
	Meat	Fish	Vegetables
Meat	366	315	316
Fish	314	368	309
Vegetables	323	312	375

In a second step, the obtained calibration curves were used to estimate the recoveries of the target compounds in the other matrices included in this study. For that, one fortification level (50 $\mu\text{g kg}^{-1}$) was evaluated and the obtained results are shown in Table 1. Good recoveries for spiked compounds in fish and vegetable samples were obtained if meat matrix was used for quantification purposes and the number of extracted compounds in relation to the maximum value (using the same matrix for quantification purposes) was lower than 17%. The same results were obtained if spiked matrices were quantified using fish or vegetables as representative matrices, indicating that one of these three matrices could be used in routine analysis as representative matrix. In this case, vegetables-based baby food could be used as representative matrix for the three matrices evaluated, bearing in mind that more than 300 hundred compounds could provide suitable recoveries using this matrix for calibration/quantification purposes.

According to these results, vegetable-based baby food was chosen as representative matrix. An advantage arising from the choice of this matrix is related to its low fat content. This provokes a decrease in maintenance procedures, which is important in routine laboratories. As it can be observed in Electronic Supplementary Data (ESD, Table S-1), the composition is very similar within each type of raw material (meat, fish or vegetables), presenting few variations among them. Therefore, this particular vegetable-based sample can be considered as representative for the other types of baby food evaluated in this study.

3.3. Method validation

A validation protocol was developed to establish the performance characteristics of the method. Several parameters such as linearity, intra-day precision, inter-day precision, recovery, limits of detection (LODs), limits of quantification (LOQs) and limits of

identification (LOIs) were studied, showing the obtained results in Table S-4 and S-5.

Linearity was evaluated in the range 2.5–100 $\mu\text{g L}^{-1}$, obtaining determination coefficients (R^2) higher than 0.9900 for most of compounds in all matrices. Moreover, deviation of the residuals of each calibration point was evaluated, checking that it was lower than 20%.

Recoveries were evaluated at three different concentration levels (10, 50 and 100 $\mu\text{g kg}^{-1}$). Five blank samples were spiked at each level and the results are indicated in Table S-4 and S-5. They were very similar for meat, fish and vegetable-based baby food, observing that at the lowest studied concentration (10 $\mu\text{g kg}^{-1}$) the number of recovered compounds with acceptable values (70–120%) [31] ranged from 40% (fish) to 60% (vegetables), considering that 391 compounds were included in this study. At 50 $\mu\text{g kg}^{-1}$, the results were very homogeneous, with acceptable recoveries between 94% (meat) and 96% (vegetables) of the target compounds. Finally, at 100 $\mu\text{g kg}^{-1}$ the number of recovered compounds ranged between 96% (fish) and 100% (vegetables). It must be highlighted that there were several compounds that presented anomalous values: cinerine I (not extracted in meat and fish), dichlofuanid, tolufluamide and thiodiocarb (recoveries below 60% in meat and fish), ethoxyquine, naled, nicarbazin, vinclozoline and pyrethine I (they were not extracted in meat and fish), fenthion (it presented unacceptable recovery values in fish and high relative standard deviation (RSD) values), flufenamic acid and threolandomycin (not extracted in fish), hexythiazox (not extracted in meat and only extracted at the lowest studied concentration in fish), maduramycin (it was not extracted in fish and the recovery value at the highest concentration was above 120%), minocycline (not extracted in fish), penicillin V (only presented adequate recovery values at 50 $\mu\text{g kg}^{-1}$ in fish), pymetrozine (RSD values were high in meat and it was not recovered in fish) and pyrethrin II (not extracted in meat). For these compounds, a specific extraction procedure should be applied instead of the generic approach used in this study in order to achieve suitable recoveries.

Precision was studied by performing repeatability (intra-day precision) and reproducibility (inter-day precision) studies. Repeatability was evaluated by analysing five spiked blank samples at the fortification levels evaluated in the recovery study (10, 50 and 100 $\mu\text{g kg}^{-1}$) and extracted during the same day. In this case, RSDs were lower than 25% for most of compounds in all matrices. Inter-day precision (reproducibility) was only studied in vegetable-based baby food by analysing three spiked blank samples at 50 $\mu\text{g kg}^{-1}$ and extracted in 5 consecutive days. In this case, RSDs were lower than 25% for all the compounds.

LODs (Table S-4) were estimated by analysing spiked blank samples at different concentration levels (0.5, 1, 2.5, 5, 10, 12.5, 25, 50 and 100 $\mu\text{g kg}^{-1}$). The criteria used for determining these limits were the retention time window (RTW), isotopic pattern and mass error (< 5 ppm) of the characteristic ion. Most of compounds had LODs of 0.5 $\mu\text{g kg}^{-1}$.

LOQs (Table S-4) were determined according to the minimum concentration that provides suitable recovery (70–120%) and RSD values ($< 25\%$). It can be observed that LOQ value was 10 $\mu\text{g kg}^{-1}$ for most of compounds included in this study (60%), whereas it was higher for the rest of compounds (50 or 100 $\mu\text{g kg}^{-1}$).

LOIs were established as the minimum concentration for which the accurate mass error was < 5 ppm for the characteristic ion and one fragment ion, according to the established criteria in the Commission Decision 2002/657/EC for identification purposes [32]. They were estimated by analysing spiked blank baby food samples at different concentration levels (0.5, 1, 2.5, 5, 10, 12.5, 25, 50 and 100 $\mu\text{g kg}^{-1}$). They were calculated following the procedure developed in a previous work [33]. This means a time

consuming evaluation of the data for each compound, and they ranged from 0.5 to 50 $\mu\text{g kg}^{-1}$ in most cases. As it can be seen in Table S-4, many compounds had LOIs higher than LOQs. Because of the low sensitivity obtained for the fragments, these compounds could only be unambiguously identified with at least one fragment (apart from the characteristic ion) at concentrations higher than LOQ [30].

Comparing these results with a recent published work [16], some points must be highlighted. First of all, there are some differences in the extraction procedure. The method applied in the present study presents multiple advantages: simplicity, rapidity, minimal use of solvents and reagents, as well as the final extract is collected from the original tube, avoiding possible external contamination. Secondly, run-time analysis is slightly shorter, being this parameter an important factor that must be taking into account in routine laboratories, due to the high amount of samples that have to be analysed every day. On the other hand, in the work developed by Jia et al. [16], LOD values are lower than in the present study, due to the improvements in sensitivity provided by Q-Orbitrap-MS instruments.

3.4. Sample analysis

A total of 46 different baby food samples based on a variety of raw materials (meat, fish and vegetables) were analysed. These samples were purchased from different local markets and all of them were manufactured in Spain. The workflow followed to detect and identify positive samples was: detection of negative and non-negative samples (using the screening software ToxID); identification of non-negative samples by the use of fragment ions; and quantification of the identified compounds [27].

When ToxID was used for screening purposes, default tolerances for retention time (RT) and mass accuracy of molecular ions were established ($\text{RT} \pm 30$ s and mass accuracy ± 5 ppm). About 8% of compounds were detected as false positives (not considering fragment information). Then, to confirm non-negative samples, isotopic pattern and characteristic fragments were monitored, using the same default tolerances for retention time and mass accuracy of the fragments. Only a possible positive of 6 α -methylprednisolone in a meat-based baby food sample was found (Fig. 3a) after the analysis of the samples. According to SANCO guidelines [31], the (quasi) molecular ion and one fragment are necessary for a reliable identification/confirmation of a compound. In spite of the fact that UHPLC-Orbitrap-MS is sufficient to enable detection and accurate mass measurement of a wide range of residues at low concentration levels in complex sample matrices, sometimes fragments present low sensitivity or the signal is not reproducible, so the identification process is difficult. In this particular case, and due to the low response provided by the fragment, triple quadrupole (QqQ) was used to guarantee the reliability of the results. The transitions monitored for this compound were 375.1 $>$ 357.1 (fragmentor 80 V, collision energy 10 eV) and 357.1 $>$ 161.1 (fragmentor 80 V, collision energy 10 eV). However this compound was not detected when QqQ was used (Fig. 3b). Therefore no residues of the target compounds were detected in the samples analysed.

4. Conclusions

Matrix effect has been studied in different types of baby food based on a variety of raw materials (meat, fish and vegetables), using matrix-matched calibration approach. This undesirable effect has been observed during the determination of more than 350 compounds in this kind of matrices. The influence of a clean-up step has been evaluated, obtaining that the addition of a clean-up stage in the

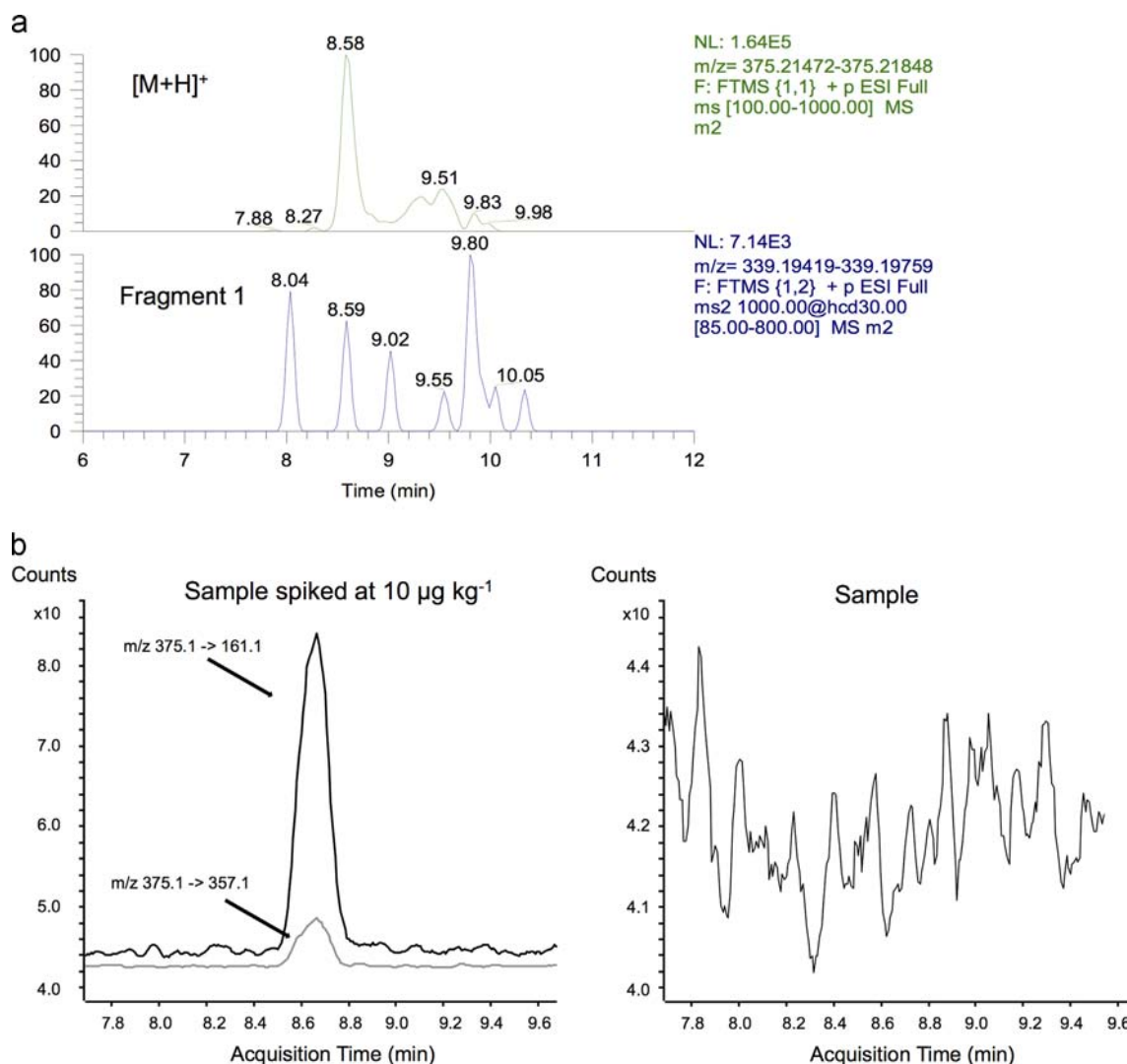


Fig. 3. (a) Extracted ion chromatogram of the characteristic ion of 6 α -methylprednisolone (m/z 375.21660) and fragment (m/z 339.19589) in a meat-based baby food sample, and (b) UHPLC-QqQ-MS/MS chromatograms of the sample analysed by QqQ.

extraction procedure reduces significantly matrix effect, when Exactive-Orbitrap is used, but also the number of recovered compounds. The application of a representative matrix for proper quantification of all the target compounds, using only one matrix-matched calibration and minimizing time analysis, has also been evaluated, obtaining that vegetable-based baby food could be used as a representative matrix for proper quantification of several types of baby food. This procedure could be desirable for routine analysis, when a huge number of different samples must be analysed each day. However, the determination of the selected compounds at lower concentrations would be desirable, improving the developed methodology.

Acknowledgments

The authors gratefully acknowledge the Spanish Ministry of Economy and Competitiveness (MINECO) and FEDER for financial support (Project Ref. AGL2010-21370). M.L.G.P. acknowledges her grant (F.P.I) (MINECO, Ref. AGL 2010-21370) and Spanish Society of Mass Spectrometry (SEEM) for financial support. R.R.G. is also grateful for personal funding through the “University Research Plan” (Almería University) and Cajamar.

Appendix A. Supporting information

Supplementary data associated with this article can be found in the online version at <http://dx.doi.org/10.1016/j.talanta.2014.07.066>.

References

- [1] J. Wang, D. Leung, *J. Agric. Food Chem.* 57 (2009) 2162–2173.
- [2] A. Gentili, D. Perret, S. Marchese, M. Sergi, C. Olmi, R. Curini, *J. Agric. Food Chem.* 52 (2004) 4614–4624.
- [3] A.V. Herrera-Herrera, J. Hernández-Borges, M.A. Rodríguez-Delgado, M. Herrero, A. Cifuentes, *J. Chromatogr. A* 1218 (2011) 7608–7614.
- [4] G. Vukovic, D. Shtereva, V. Bursic, R. Mladenova, S. Lazi, *Food Sci. Technol.* 49 (2012) 312–319.
- [5] M.M. Aguilera-Luiz, J.L. Martínez Vidal, R. Romero-González, A. Garrido Frenich, *Food Chem.* 132 (2012) 2171–2180.
- [6] Commission Directive 2006/141/EC of 22 December 2006 on infant formulae and follow-on formulae and amending Directive 1999/21/EC. *Off. J. Eur. Union*, L 401 (2) 30.12.2006. (available on <http://eur-lex.europa.eu/LexUriServ/LexUriServ.do?uri=OJ:L:2006:401:0001:0001:EN:PDF>, last accessed April 2014).
- [7] Commission Directive 2003/13/EC of 10 February 2003 amending Directive 96/5/EC on processed cereal-based foods and baby foods for infants and young children. *Off. J. Eur. Union*, L 41 (33) 10.02.2003. (available on <http://eur-lex.europa.eu/LexUriServ/LexUriServ.do?uri=OJ:L:2003:041:0033:0036:EN:PDF>, last accessed April 2014).
- [8] Commission Regulation (EU) No 37/2010 of 22 December 2009 on pharmacologically active substances and their classification regarding maximum residue limits in foodstuffs of animal origin. *Off. J. Eur. Union*, L 15 (1) 20.01.2010. (available on

- (<http://eur-lex.europa.eu/LexUriServ/LexUriServ.do?uri=OJ:L:2010:015:0001:0072:EN:PDF>), last accessed April 2014).
- [9] E. Rodríguez, F. Navarro Villoslada, M.C. Moreno-Bondi, M.D. Marazuela, *J. Chromatogr. A* 1217 (2010) 605–613.
- [10] E. Rodríguez, M.C. Moreno-Bondi, M.D. Marazuela, *Food Chem.* 127 (2011) 1354–1360.
- [11] C.C. Leandro, P. Hancock, R.J. Fussell, B.J. Keely, *J. Chromatogr. A* 1103 (2006) 94–101.
- [12] C. Przybylski, C. Segard, *J. Sep. Sci.* 32 (2009) 1858–1867.
- [13] L. Hollosi, K. Mittendorf, H.Z. Senyuva, *Chromatographia* 75 (2012) 1377–1393.
- [14] B. Gilbert-López, J.F. García-Reyes, J.F. Molina-Díaz, *Food Chem.* 135 (2012) 780–786.
- [15] U. Kapoor, M.K. Srivastava, A.K. Srivastava, D.K. Patel, Z. Garg, L.P. Srivastava, *Environ. Toxicol. Chem.* 32 (2013) 723–727.
- [16] W. Jia, X. Chu, Y. Ling, J. Huang, J. Chang, *J. Chromatogr. A* 1347 (2014) 122–128.
- [17] A. Makarov, E. Denisov, A. Kholomeev, W. Balschun, O. Lange, K. Strupat, S. Horning, *Anal. Chem.* 78 (2006) 2113–2120.
- [18] J. Zhan, Y. Zhong, X. Yu, J. Peng, S. Chen, J. Yin, J. Zhang, Y. Zhu, *Food Chem.* 138 (2013) 827–834.
- [19] B. Huerta, A. Jakimska, M. Gros, S. Rodríguez-Mozaz, D. Barceló, *J. Chromatogr. A* 1288 (2013) 63–72.
- [20] S. Kittlaus, J. Schimanke, G. Kempe, K. Speer, *J. Chromatogr. A* 1218 (2011) 8399–8410.
- [21] A. Kaufmann, M. Widmer, K. Maden, *Rapid Commun. Mass Spectrom.* 24 (2010) 2162–2170.
- [22] A. González-Antuña, J.C. Domínguez-Romero, J.F. García-Reyes, P. Rodríguez-González, G. Centineo, J.I. García Alonso, A. Molina-Díaz, *J. Chromatogr. A* 1288 (2013) 40–47.
- [23] A. Gerssen, M.A. McElhinney, P.P.J. Mulder, R. Bire, P. Hess, J. de Boer, *Anal. Bional. Chem.* 394 (2009) 1213–1226.
- [24] D.G. Beach, W. Gabryelski, *Anal. Chem.* 85 (2013) 2127–2134.
- [25] H.G.J. Mol, P. Plaza-Bolaños, P. Zomer, T.C. de Rijk, A.A. Stolker, P.P.J. Mulder, *Anal. Chem.* 80 (2008) 9450–9459.
- [26] J.L. Martínez Vidal, A. Garrido Frenich, T. López López, I. Martínez Salvador, L. Hajjaj el Hassani, M. Hassan Benajiba, *Chromatographia* 61 (2005) 127–131.
- [27] M.L. Gómez-Pérez, P. Plaza-Bolaños, R. Romero-González, J.L. Martínez-Vidal, A. Garrido-Frenich, *J. Chromatogr. A* 1248 (2012) 130–138.
- [28] M.M. Aguilera-Luiz, R. Romero-González, P. Plaza-Bolaños, J.L. Martínez Vidal, A. Garrido Frenich, *Anal. Bioanal. Chem.* 405 (2013) 6543–6553.
- [29] B. Kmellar, P. Fodor, L. Pareja, C. Ferrer, M.A. Martínez Uroz, A. Valverde, A.R. Fernández-Alba, *J. Chromatogr. A* 1215 (2008) 37–50.
- [30] M. Anastassiades, S.J. Lehotay, D. Stajnbaher, F.J. Schenk, *J. AOAC Int.* 86 (2003) 412–431.
- [31] Guidance Document on Analytical Quality Control and Validation Procedures for Pesticide Residues Analysis in Food and Feed. Document No. SANCO/12571/2013, 01/01/2014.
- [32] Commission Decision of 12 August 2002 implementing Council Directive 96/23/EC concerning the performance of analytical methods and the interpretation of results. *Off. J. Eur. Commun.* 2002, L 221(8) 12.8.2002 (available on, (<http://eur-lex.europa.eu/LexUriServ/LexUriServ.do?uri=OJ:L:2002:221:0008:0036:ES:PDF>), last accessed April 2014).
- [33] M.M. Aguilera-Luiz, R. Romero-González, P. Plaza-Bolaños, J.L. Martínez-Vidal, A. Garrido Frenich, *J. Agric. Food Chem.* 61 (2013) 829–839.



Detection of trace microcystin-LR on a 20 MHz QCM sensor coated with in situ self-assembled MIPs

Hao He^{a,b,c}, Lianqun Zhou^{a,*}, Yi Wang^{d,*}, Chuanyu Li^a, Jia Yao^a, Wei Zhang^a, Qingwen Zhang^e, Mingyu Li^f, Haiwen Li^a, Wen-fei Dong^a

^a CAS Key Lab of Bio-Medical Diagnostics, Suzhou Institute of Biomedical Engineering and Technology, Chinese Academy of Sciences, Suzhou 215163, Jiangsu, China

^b Changchun Institute of Optics, Fine Mechanics and Physics, Chinese Academy of Sciences, Changchun 130033, Jilin, China

^c University of Chinese Academy of Sciences, Beijing 100049, China

^d Centre for Biomimetic Sensor Science, School of Materials Science and Engineering, Nanyang Technological University, Singapore 637553, Singapore

^e Key Laboratory of Cluster Science of Ministry of Education, Beijing Institute of Technology, Beijing 100081, China

^f State Key Laboratory of Modern Optical Instrumentation, Zhejiang University, Hangzhou 310027, Zhejiang, China

ARTICLE INFO

Article history:

Received 26 May 2014

Received in revised form

19 July 2014

Accepted 21 July 2014

Available online 30 July 2014

Keywords:

Molecularly imprinted polymers

In situ self-assembly

Quartz crystal microbalance

Microcystin-LR

High frequency QCM

ABSTRACT

A 20 MHz quartz crystal microbalance (QCM) sensor coated with in situ self-assembled molecularly imprinted polymers (MIPs) was presented for the detection of trace microcystin-LR (MC-LR) in drinking water. The sensor performance obtained using the in situ self-assembled MIPs was compared with traditionally synthesized MIPs on 20 MHz and normal 10 MHz QCM chip. The results show that the response increases by more than 60% when using the in situ self-assembly method compared using the traditionally method while the 20 MHz QCM chip provides four-fold higher response than the 10 MHz one. Therefore, the in situ self-assembled MIPs coated on a high frequency QCM chip was used in the sensor performance test to detect MC-LR in tap water. It showed a limit of detection (LOD) of 0.04 nM which is lower than the safety guideline level (1 nM MC-LR) of drinking water in China. The low sensor response to other analogs indicated the high specificity of the sensor to MC-LR. The sensor showed high stability and low signal variation less than 2.58% after regeneration. The lake water sample analysis shows the sensor is possible for practical use. The combination of the higher frequency QCM with the in situ self-assembled MIPs provides a good candidate for the detection of other small molecules.

© 2014 Elsevier B.V. All rights reserved.

1. Introduction

Water bloom is a phenomenon wherein various kinds of alga proliferate rapidly as a result of water eutrophication. As water bloom occurs, some alga produce harmful cyclic peptide toxins such as microcystins [1,2]. The chemical and physical properties of microcystins are studied by many researchers [3]. Drinking water contains small amounts of microcystins that could cause harm to human health [4]. More than 50 different kinds of microcystins have been isolated. Among the different kinds of microcystins, microcystin-LR (MC-LR) is the most harmful and widespread one [5].

Currently, the qualitative and quantitative analyses of microcystins are mainly based on high-performance liquid chromatography (HPLC) [6] and thin layer chromatography (TLC) [7]. Immunological methods, such as enzyme-linked immunosorbent

assay (ELISA) [8] and protein phosphatase inhibition assay (PPIA) [9], are also used in the detection of microcystins. They are highly specific, simple and suitable for large number of samples. However, these technologies are time-consuming and rely on bulky instruments that require well-trained operators and costly chemical procedures. Furthermore, the widespread use of plastic additives can interfere the HPLC results [10]. Therefore, more stable, easy-to-use, rapid and specific methods for microcystins detection have been developed [11].

A biosensor typically relies on an active recognition element and a transducer [12]. Of most transducers used in biosensors, the quartz crystal microbalance (QCM) is a simple, inexpensive, portable and sensitive gravimetric sensor [13]. Due to its high sensitivity down to mass change of nanogram level, it has been widely used for detection of drugs [14], nucleic acids [15], peptides [16] and so on [17].

In most studies, AT-cut 5 MHz or 10 MHz crystal chips are often used [14,18]. Based on the Sauerbrey equation [19], a higher resonant frequency of the QCM increases the sensitivity of the sensor. However, studies on the use of QCM with frequency higher

* Corresponding authors. Tel.: +86 51269588061, +06583129060.

E-mail addresses: zhoulq@sibet.ac.cn (L. Zhou), yiwang@ntu.edu.sg (Y. Wang).

than 10 MHz for sensors are scarce [20]. The lack of studies on the use of QCM with frequency higher than 10 MHz is attributed to the requirement of extremely fragile thin quartz chips. In this study, the sensor performance of the sensor with the AT-cut 20 MHz quartz crystals is compared with that with the normal 10 MHz ones.

In addition, the recognition element of the sensor is a key factor for the specificity of the sensors. In the past few decades, immunoassay techniques based on antibody have been widely used in the active sensing unit because of its high specificity and sensitivity for target molecules [21,22]. However, poor stability, high cost and time-consuming production still pose problems for the use of immunoassay techniques. Therefore, the development of a synthetic alternative that can mimic the recognition elements of target molecules with high stability and competitive specificity are needed [23].

Molecular imprinting is an attractive technique for the development of artificial receptors [24,25]. It is a promising technique for the preparation of polymers with pre-designed recognition sites which have the right shape and functionality to specifically capture template molecules [26,27]. To achieve this, the template, functional monomer, cross-linker and initiator are copolymerized into three-dimensional cross-linked polymers followed by removal of the template molecules to form the recognition cavities of the templates. Molecularly imprinted polymers (MIPs) provides comparable affinity and specificity to the recognition of target molecules, thus MIPs has been widely applied for the development of biosensors [28–30] and other areas [31,32].

So far, two major approaches have been utilized to integrate MIPs with transducers. One of the common methods includes the immobilization of pre-synthesized MIPs particles on a transducer by physical entrapment [14,18], which forms rather a thick film thus reduces the sensitivity of the biosensor. The in situ self-assembly method, however, is more favorable in the development of the sensor surface [33]. The in situ self-assembly method could obtain an extremely thin film with controllable thickness and good homogeneity. In addition, this method performed better sensitivity than physical entrapment [34]. To the best of our knowledge, no research has been reported on the development of MIPs based on the in situ self-assembly method for highly sensitive detection of microcystins.

The detection of MC-LR using normal AT-cut 10 MHz crystal and physical entrapment method was previously reported [18, 35].

In Chianella's work, the author synthesized MIPs using the traditional physical entrapment method. The MIPs were used as a material for solid-phase extraction (SPE) and as a sensing element used to coat the QCM sensor. With the help of SPE, which provides up to 1000-fold pre-concentration, the limit of detection (LOD) of his work was 0.35 nM. Without the use of MIPs-SPE, the sensor may not achieve the detection limit for MC-LR of 1 nM indicated in China's drinking water safety guideline. With this step added, the measurement of MC-LR was still time-consuming and complex. In reality, there is an urgent need for sensor to detect MC-LR of 1 nM directly without any pre-operation.

The higher frequency QCM coated with in situ self-assembled MIPs has the potential to detect MC-LR of 1 nM directly without any pre-operation. However, there is no report on the combination of high frequency QCM and in situ self-assembled MIPs in one biosensor. In this study, a 20 MHz QCM sensor coated with in situ self-assembled MIPs was firstly studied for the detection of MC-LR in water. The sensitivity of the sensor system are investigated and compared with other reported results. The control experiments on the investigation of the sensor response to analogs indicate a good specificity and reproducibility of the sensor system.

2. Material and methods

2.1. Reagents

MC-LR, microcystin-RR (MC-RR), microcystin-YR (MC-YR) and nodularin were purchased from Taiwan Algal Science Inc. (Taiwan, China). Methacrylic acid (MAA), ethylene glycol dimethacrylate (EGDMA) and 11-mercaptoundecanoic acid (MUA) were purchased from Sigma-Aldrich (Schnelldorf, Germany). 2,2'-Azobisisobutyronitrile (AIBN) and dimethyl sulfoxide (DMSO) were purchased from Sinopharm Chemical Reagent Co. Ltd (Shanghai, China). All other reagents were of analytical grade and purchased from Sinopharm Chemical Reagent Co. Ltd (Shanghai, China).

2.2. QCM system

The QCM system (Fig. 1) was composed of a homemade detection cell, a network analyzer (E5061B, Agilent, USA) and a PC. AT-cut quartz crystals (12.5 mm diameter, Chenjing Electronic Co. Ltd., Beijing, China) resonating at 10 MHz with Au electrodes

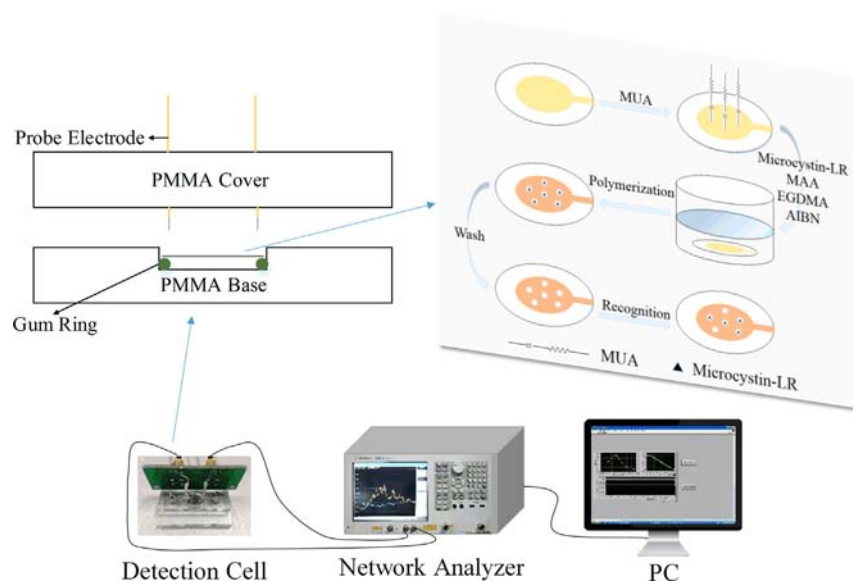


Fig. 1. The MC-LR detection system and the synthesis progress of MIPs on the chip.

(6 mm diameter) on each side and AT-cut quartz crystals (6.5 mm diameter, Chenjing Electronic Co. Ltd., Beijing, China) resonating at 20 MHz with Au electrodes (3.5 mm diameter) on each side were used. The Sauerbrey equation was established for the AT-cut shear mode QCM [19], which relates the mass change per unit area at the crystal surface to the observed change in oscillation frequency of the crystal

$$\Delta f = -2.26 \times 10^{-6} f^2 \Delta m / A \quad (1)$$

where Δf is the frequency change in Hz; f is the resonant frequency of the crystal in Hz; Δm is the mass change on the surface of the crystal in g; and A is the piezoelectric active crystal area in cm^2 . For the 10 MHz and 20 MHz quartz crystals used, Eq. (1) shows that a mass increase of 1 ng/cm on the electrode resulted in a frequency change of 0.226 Hz and 0.904 Hz respectively.

2.3. MIPs film synthesis

For the preparation of pre-polymerization solution, 1 mg of MC-LR and 0.86 mg of functional monomer MAA were dissolved in 500 μL of DMSO and kept at room temperature for 3 h. Afterward, 1.98 mg of cross-linker EGDMA and 0.2 mg of AIBN as initiator were added into the solution.

Prior to use the chip was cleaned in the Oxygen Plasma Cleaner for 3 min, followed by rinsing with absolute ethanol and deionized water sequentially. The chip was then dried using nitrogen. The freshly cleaned chip was dipped into 10 mL of 50 mM MUA-ethanol solution, and kept at room temperature for 12 h. The chip was washed with absolute ethanol and deionized water, dried by nitrogen, and a self-assembled monolayer (SAM) was formed on the chip. The chip was then dipped into 10 mL of 200 mM AIBN-ethanol solution, and kept at room temperature for 3 h and dried by nitrogen; the chip was finally dipped into the pre-polymerization solution. The pre-polymerization solution was purged with nitrogen for 10 min, and the container was covered. Polymerization was carried out at 60 $^{\circ}\text{C}$ for 15 h in a hot-air oven. After the polymerization process, the chip was rinsed by an ethanol-acetic acid solution (9/1, v/v) to remove the template and other possible residual chemicals. Finally, the chip was washed by deionized water and dried by nitrogen. In addition, a non-imprinted polymers (NIPs) film was prepared without the presence of template molecules to be used as a control sample for the investigation on sensor specificity.

2.4. QCM measurement

First, the MIPs film coated chip was placed into the homemade detection cell and stabilized for several minutes. This step was

repeated three times and the average frequency was recorded. Secondly, the chip was taken out and dipped into different concentrations of standard solution of MC-LR. The chip was subsequently washed with deionized water and dried by nitrogen. Finally, the chip was returned into the cell and stabilized for several minutes. This step was also repeated three times and the average frequency was recorded. The frequency change for each solution was calculated and recorded. After each measurement, the chip was rinsed with an ethanol-acetic acid solution (9/1, v/v), followed by deionized water, and then dried using nitrogen.

Detections were taken in air and detection conditions were maintained constantly throughout the experiment.

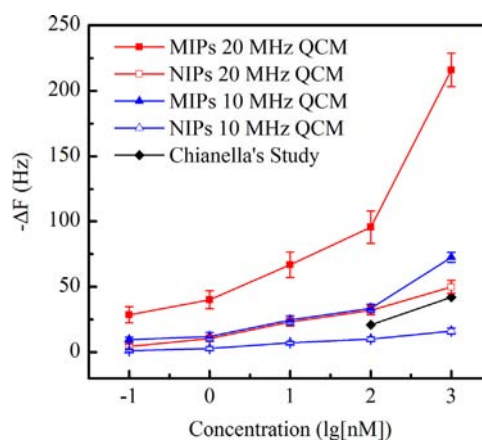


Fig. 3. Sensor responses of MIPs and NIP film coated chips at resonant frequency of 10 MHz and 20 MHz, respectively, for the detection of different concentration of MC-LR ($n=3$), in comparison with Chianella's study [18].

Table 1

Sensor response of MIPs film coated sensor chip (20 MHz) to different concentrations of MC-LR.

Concentration (nM)	Signal (Hz)	Noise (Hz)	S/N	S/3N
0.1	28.61	6.88	4.16	1.39
1	40.15	6.90	5.82	1.94
10	66.85	9.70	6.89	2.30
100	95.63	10.43	9.17	3.06
1000	215.88	17.75	12.16	4.05

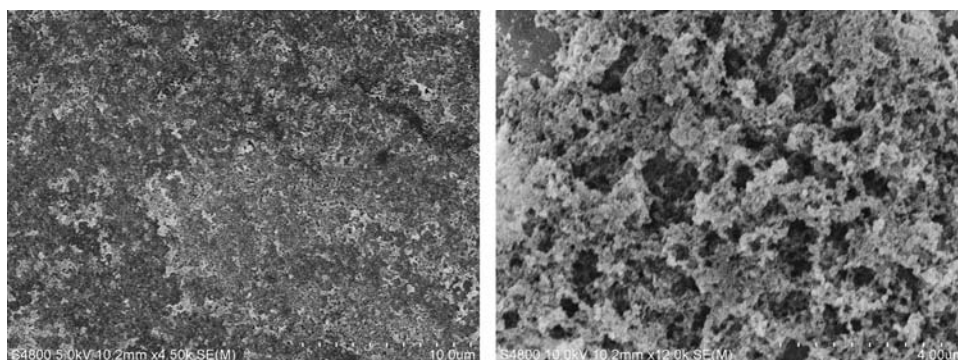


Fig. 2. SEM image of the MIPs film on the chip with a 10 μm scale (left) and a 4 μm scale (right).

2.5. Sample preparation

Tap water was collected from the Gaoxin District, Suzhou, China. The water samples were analyzed by HPLC (Agilent

1260LC), and the concentration of the original MC-LR was less than 0.01 nM. The tap water was first filtered using a 0.22 μm filter. 10 mL of tap water was placed into a 20 mL tube, and then spiked with different concentrations of MC-LR and other analogs.

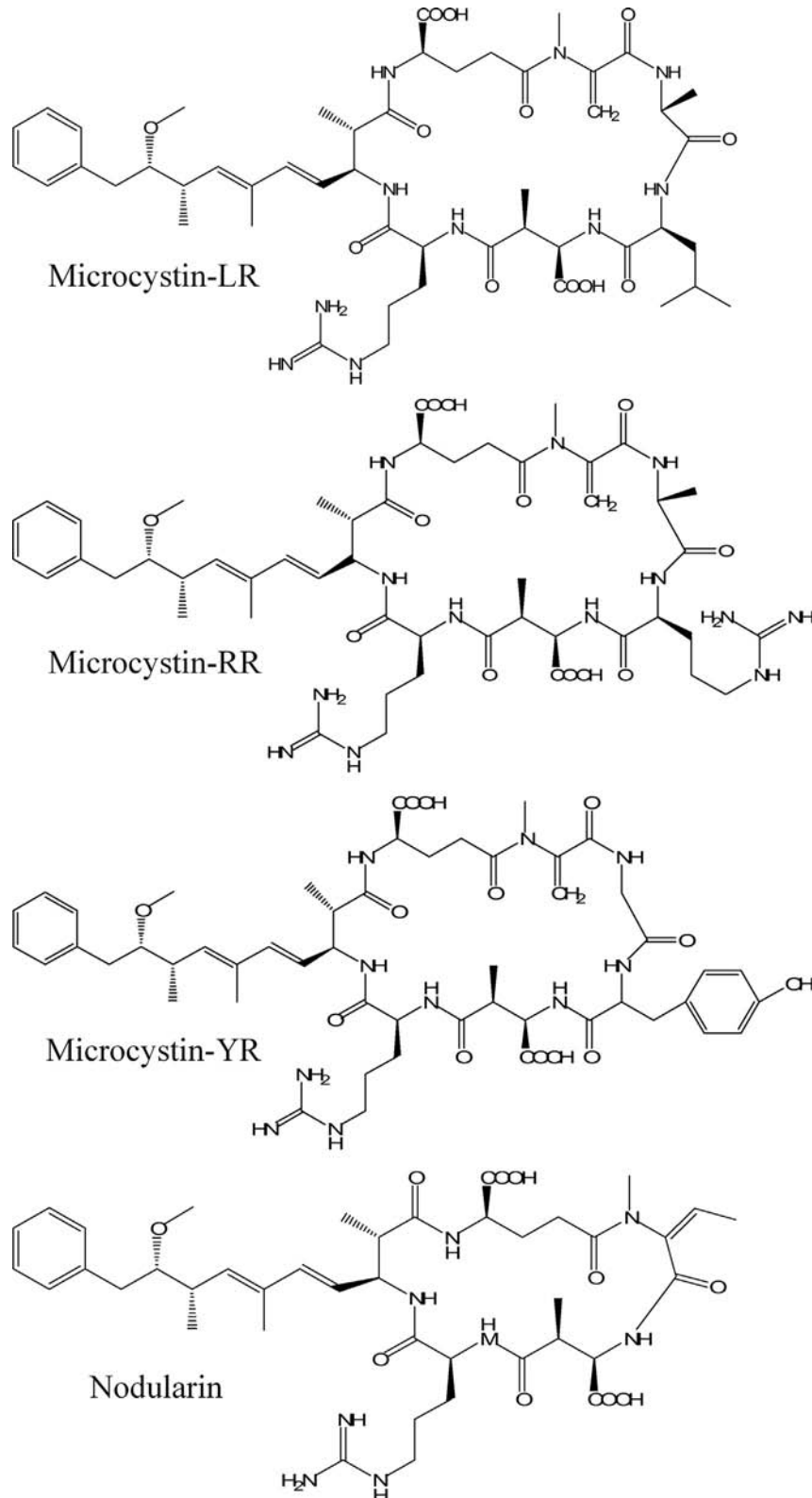


Fig. 4. Chemical structures of MC-LR and its analogs.

3. Results and discussion

3.1. QCM sensor

A layer with porous structure was observed after forming the MIPs on the sensor chip, as indicated in the SEM imaging (Fig. 2). After the deposition of MIPs, the 10 MHz chip had a resonant frequency drop of 967 Hz. According to the Sauerbrey equation, the mass per unit area of the MIPs was $4.3 \mu\text{g cm}^{-2}$. Assuming that the density of the film is 1.5 g cm^{-3} , the thickness of the MIPs film was estimated to be approximately 29 nm.

The responses of the MIPs and NIPs film coated sensor chips at resonant frequency of 10 MHz and 20 MHz, respectively, in the sample solution with different concentrations of MC-LR from 0.1 to 1000 nM were showed in Fig. 3. We compared the results of our study with other work in which the QCM sensor chip was modified with MIPs by physical entrapment [18]. With the same QCM working frequency (10 MHz), our sensor coated with the in situ self-assembled MIPs shows about 60% and 70% higher response at a concentration of 100 and 1000 nM of MC-LR, respectively.

In the traditional physical entrapment method used by Chianella, polymer was first synthesized and then ground into particles. The particles were then added into polyvinyl chloride polymer (PVC)–tetrahydrofuran solution and spread onto QCM chips. After the complete evaporation of solvent, the polymer film was immobilized on the QCM chips. The grind step is complex and inevitably destroys some recognition sites. The size of the obtained particles is highly dispersed. Additionally, some recognition sites embedded in the particles are inaccessible. Using the physical entrapment method, the film is thick and inhomogenous because of the highly dispersed particles. The thickness of the film is more than hundreds of nanometers. And PVC may block some recognition sites. The thick film and the limited availability of the recognition sites reduced the efficiency of the MIPs film [36]. Using the in situ self-assembly method, we synthesized the MIPs film on the chip directly. This can avoid some disadvantage encountered when using the physical entrapment method. And the synthesized film is ultra-thin [37]. The thickness of our film was about 29 nm, which is thinner than the film synthesized using the physical entrapment method. Given that the thickness is one of the most important factors that influence the sensitivity of the MIPs film coated sensor [34], the response of our sensor was much better.

Based on Eq. (1), the sensor with 20 MHz should have a quadruple signal compared with the sensor with 10 MHz. At concentrations ranging from 0.1 nM to 1000 nM MC-LR, the sensor signal on 20 MHz QCM was three to four times higher than the sensor with 10 MHz.

The MIPs coated sensor working at the resonant frequency of 20 MHz showed a high response of 40.1 Hz frequency shift ($S/N=5.8$), at a concentration of 1 nM. To determine the LOD of the sensor, we linearly fitted the signal to triple noise ratio ($S/3N$) with the concentration of MC-LR (Table 1)

$$S/3N = 5.773 + 0.6453 \lg(c) \quad (2)$$

where c is the concentration of MC-LR in nM. The LOD of 0.04 nM was deduced as the concentration of MC-LR at which the signal response is three times of the noise.

3.2. Specificity of the sensor

To investigate the specificity of the sensor, analogs of MC-LR such as MC-RR and MC-YR and a potential interferent such as nodularin (Fig. 4 shows the structure of them) were used to evaluate the specificity of the MIPs film.

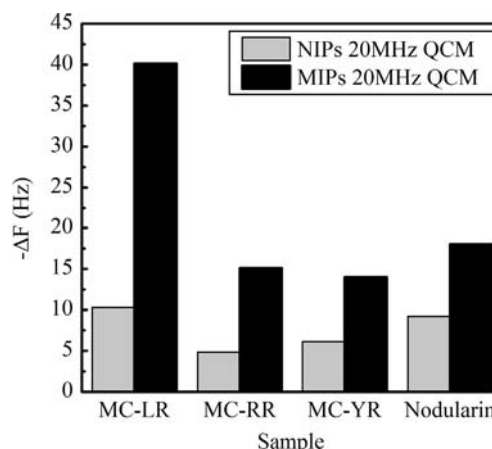


Fig. 5. Sensor response of MIPs and NIPs coated sensors chip (20 MHz) to MC-LR and its analogs at a concentration of 1 nM.

Table 2

Sensor response of MIPs film coated sensor chip (20 MHz) to standard samples and real samples of MC-LR.

Samples	Signal (Hz)		
	1 nM	10 nM	100 nM
Standard sample ^a	44.08	63.21	101.75
Lake water ^b	40.12	69.56	110.35
50% Diluted lake water ^c	46.08	70.97	100.89

Signal is reported as mean of three experimental results.

^a MC-LR standard sample with different concentrations (1 nM, 10 nM and 100 nM).

^b Lake water sample spiked with MC-LR to form final concentrations of 1 nM, 10 nM and 100 nM.

^c Lake water sample was diluted 50%, with deionized water and then spiked with MC-LR to form final concentrations of 1 nM, 10 nM and 100 nM.

Results shown in Fig. 5 indicate that the sensor was not sensitive to these analogs at a concentration of 1 nM. In contrast to the MIPs film, the NIP film showed similar response to all the compounds indicating non-specific response. All the results strongly demonstrated that the sensor in our study had high selectivity for MC-LR.

3.3. Reproducibility of the sensor

To evaluate the reproducibility of the MIPs film, the sensor chip was incubated with the same concentration of MC-LR solution for several times under the same conditions to record the sensor responses. After each measurement, the chip was regenerated by an ethanol–acetic acid solution (9/1, v/v) and deionized water sequentially, and then dried using nitrogen. After the regeneration, the signal variation was less than 2.58%. Using SAM between the electrode and the film, the film was grafted to the electrode by covalent bonding and did not fall off easily. Therefore, the sensor had good reproducibility.

3.4. Lake water sample analysis

To show the possibility of the MIP–QCM detection for practical use, we analyzed environment water spiked with MC-LR. The real sample was collected from the Taihu Lake near the Suzhou National New & Hi-tech Industrial Development Zone, China. There was no obvious water bloom in this area and the water from this area of the lake was clear. The sample was filtered using a 0.22 μm filter. By using HPLC, the concentration of MC-LR in this

sample was estimated to be 0.49 nM. 10 mL of sample was placed into a 20 mL tube, and then spiked with MC-LR to form final concentrations of 1, 10 and 100 nM, respectively. All the samples were analyzed with our 20 MHz QCM–MIP sensor system. Results in Table 2 showed that there was no significant variation between the standard sample and real sample responses. This indicated that our sensor was possible for practical use.

4. Conclusion

In combination of a higher frequency QCM and the in situ self-assembled MIPs, a MC-LR biosensor has been developed with a low LOD of 0.04 nM. This result demonstrates the feasibility of direct MC-LR detection in water. With the quartz crystals working at the same resonant frequency of 10 MHz, the in situ self-assembled MIPs showed 60% higher response than the traditional physical entrapped MIPs. The sensor with 20 MHz chip shows three to four times higher response than the 10 MHz sensor chip, which is comparable with the theoretical results. The low sensor responses to the analogous indicate good specificity to MC-LR. The sensor is stable, and the signal variation is less than 2.58% after regeneration. The lake water sample analysis shows the possibility of the sensor for practical use. The combination of the high frequency QCM with in situ self-assembled MIPs provides a good candidate for the detection of other molecules.

Acknowledgment

This work was financially supported by the National Natural Science Foundation of China under Grant nos. (51202154, 51205268 and 91123029), the National High Technology Research and Development Program of China (863 Program, Grant no. 2012AA063302), the Natural Science Foundation of Jiangsu Province under Grant nos. (BK2013116, BK2012190), National 863 Key Project under Grant no. 2012AA040503, the Science Technology development program of Suzhou city under Grant no. ZXY2012011, the Nano-technology for special project of Suzhou city under Grant no. ZXG2013038, and the SRF for ROCS, SEM.

References

- [1] W.W. Carmichael, *J. Appl. Bacteriol.* 72 (1992) 445–459.
- [2] K.L. Rinehart, K. Harada, M. Namikoshi, C. Chen, C.A. Harvis, M.H. Munro, J.W. Blunt, P.E. Mulligan, V.R. Beasley, *J. Am. Chem. Soc.* 110 (1988) 8557–8558.

- [3] J.R. Bagu, F.D. Sönnichsen, D. Williams, R.J. Andersen, B.D. Sykes, C. Holmes, *Nat. Struct. Biol.* 2 (1995) 114–116.
- [4] S. Pouria, A. de Andrade, J. Barbosa, R.L. Cavalcanti, V.T.S. Barreto, C.J. Ward, W. Preiser, G.K. Poon, G.H. Neild, G.A. Codd, *Lancet* 352 (1998) 21–26.
- [5] N.A. Robinson, G.A. Miura, C.F. Matson, R.E. Dinterman, J.G. Pace, *Toxicol.* 27 (1989) 1035–1042.
- [6] E.C. Agüete, A. Gago-Martínez, J.M. Leao, J.A. Rodríguez-Vázquez, C. Menard, J.F. Lawrence, *Talanta* 59 (2003) 697–705.
- [7] A. Pelander, I. Ojanperä, K. Sivonen, K. Himberg, M. Waris, K. Niinivaara, E. Vuori, *Water Res.* 30 (1996) 1464–1470.
- [8] F.S. Chu, X. Huang, R.D. Wei, *J. Assoc. Off. Anal. Chem.* 73 (1990) 451–456.
- [9] L.H. Xu, P.K.S. Lam, J.P. Chen, J.M. Xu, B.S.F. Wong, Y.Y. Zhang, R.S.S. Wu, K.I. Harada, *Chemosphere* 41 (2000) 53–58.
- [10] M. Ikawa, N. Phillips, J.F. Haney, J.J. Sasner, *Toxicol.* 37 (1999) 923–929.
- [11] Z. Lin, H. Huang, Y. Xu, X. Gao, B. Qiu, X. Chen, G. Chen, *Talanta* 103 (2013) 371–374.
- [12] I.K. Anthony, P.F. Turner, George S. Wilson, *Biosensors: Fundamentals and Applications*, Oxford University Press, 1987.
- [13] R.L. Bunde, E.J. Jarvi, J.J. Rosentreter, *Talanta* 46 (1998) 1223–1236.
- [14] A. Gültekin, G. Karanfil, M. Kuş, S. Sönmezöglü, R. Say, *Talanta* 119 (2014) 533–537.
- [15] K. Feng, J. Li, J.-H. Jiang, G.-L. Shen, R.-Q. Yu, *Biosens. Bioelectron.* 22 (2007) 1651–1657.
- [16] A.S. Afonso, B.F. Zanetti, A.C. Santiago, F. Henrique-Silva, L.H. Mattoso, R.C. Faria, *Talanta* 104 (2013) 193–197.
- [17] F. Salam, Y. Uludag, I.E. Tothill, *Talanta* 115 (2013) 761–767.
- [18] I. Chianella, S.A. Piletsky, I.E. Tothill, B. Chen, A.P. Turner, *Biosens. Bioelectron.* 18 (2003) 119–127.
- [19] G. Sauerbrey, *Z. Phys.* 155 (1959) 206–222.
- [20] Y. Okahata, M. Kawase, K. Niikura, F. Ohtake, H. Furusawa, Y. Ebara, *Anal. Chem.* 70 (1998) 1288–1296.
- [21] U. Bilitewski, A. Turner, *Biosensors in Environmental Monitoring*, Taylor & Francis, 2004.
- [22] D. Lepage, A. Jiménez, J. Beauvais, J.J. Dubowski, *Light: Sci. Appl.* 2 (2013) e62.
- [23] F.L. Dickert, P. Lieberzeit, M. Tortschanoff, *Sens. Actuators, B* 65 (2000) 186–189.
- [24] O. Ramström, R.J. Ansell, *Chirality* 10 (1998) 195–209.
- [25] M.J. Whitcombe, M.E. Rodriguez, P. Villar, E.N. Vulfson, *J. Am. Chem. Soc.* 117 (1995) 7105–7111.
- [26] J. Matsui, T. Kato, T. Takeuchi, M. Suzuki, K. Yokoyama, E. Tamiya, I. Karube, *Anal. Chem.* 65 (1993) 2223–2224.
- [27] G. Wulff, *Angew. Chem. Int. Ed.* 34 (1995) 1812–1832.
- [28] M.L. Yola, L. Uzun, N. Özaltın, A. Denizli, *Talanta* 120 (2014) 318–324.
- [29] Q. Zhang, L. Jing, J. Zhang, Y. Ren, Y. Wang, Y. Wang, T. Wei, B. Liedberg, *Anal. Biochem.* (2014). 10.1016/j.ab.2014.06.014.
- [30] K. Haupt, K. Mosbach, *Chem. Rev.* 100 (2000) 2495–2504.
- [31] R.J. Krupadam, G.P. Patel, R. Balasubramanian, *Environ. Sci. Pollut. Res.* 19 (2012) 1841–1851.
- [32] D. Kriz, O. Ramström, K. Mosbach, *Anal. Chem.* 69 (1997) 345A–349A.
- [33] M. Lotierzo, O.Y.F. Henry, S. Piletsky, I. Tothill, D. Cullen, M. Kania, B. Hock, A.P. F. Turner, *Biosens. Bioelectron.* 20 (2004) 145–152.
- [34] N. Gao, J. Dong, M. Liu, B. Ning, C. Cheng, C. Guo, C. Zhou, Y. Peng, J. Bai, Z. Gao, *Analyst* 137 (2012) 1252–1258.
- [35] I. Chianella, M. Lotierzo, S.A. Piletsky, I.E. Tothill, B. Chen, K. Karim, A.P. Turner, *Anal. Chem.* 74 (2002) 1288–1293.
- [36] M. Yan, *Molecularly Imprinted Materials: Science and Technology*, CRC Press, 2004.
- [37] T. Panasyuk-Delaney, V.M. Mirsky, M. Ulbricht, O.S. Wolfbeis, *Anal. Chim. Acta* 435 (2001) 157–162.



Quantitative evaluation by attenuated total reflectance infrared (ATR-FTIR) spectroscopy of the chemical composition of decayed wood preserved in waterlogged conditions



Benedetto Pizzo^{a,*}, Elisa Pecoraro^a, Ana Alves^{b,c}, Nicola Macchioni^a, José Carlos Rodrigues^{b,c}

^a CNR-IVALSA, Istituto per la Valorizzazione del Legno e delle Specie Arboree, via Madonna del Piano 10, Sesto Fiorentino (FI), Italy

^b Tropical Research Institute of Portugal (IICT), Forest and Forest Products Centre, 1349-017 Lisboa, Portugal

^c Centro de Estudos Florestais, Instituto Superior de Agronomia, 1349-017 Lisboa, Portugal

ARTICLE INFO

Article history:

Received 18 March 2014

Received in revised form

16 July 2014

Accepted 21 July 2014

Available online 1 August 2014

Keywords:

Partial least square (PLS) regression

Multivariate analysis

Wet wood chemistry

Infrared spectroscopy

Archaeological wood

Lignin

Holocellulose

ABSTRACT

This paper reports on the assessment of lignin and holocellulose by means of ATR-FTIR analysis and multivariate PLS regression. The analysis was conducted on 59 samples coming from different excavations where wood had been preserved in waterlogged conditions. A range of results from different wood species (*Alnus* sp.p., *Cupressus sempervirens*, *Larix decidua*, *Picea abies*, *Pinus* sp.p., *Quercus* sp.p., *Ulmus* sp.p.), states of preservation, waterlogged environments, and burial times are presented.

A calibration model was selected after comparing different reference data (samples extracted and not-extracted, and ash-rich and ash-free bases of calculation for the calibration values), and two different post-acquisition spectroscopic manipulations (both in terms of normalisation procedures and of spectral ranges used for the calibration). Results showed that the best models were different depending on which considered component (lignin or holocellulose) was measured and to which data set (softwood or hardwood) the samples belonged. It is shown that the predictive ability of the models is affected by high ash content (too contaminated samples had to be excluded in order to attain good results, because of excessive overlapping of bands related to the inorganic fraction) but not by the preliminary extraction of sample. Furthermore, the stability of best models is also demonstrated and a procedure of external validation carried out on an external set of samples confirmed the general validity of the identified models.

© 2014 Elsevier B.V. All rights reserved.

1. Introduction

The structural modifications which wood undergoes during burial in waterlogged conditions [1–3] require that an effective treatment to be carried out on artefacts after their discovery, to ensure their safe conservation. However, after consolidation, some changes may still occur in artefacts both in short and long term, even when they are kept in well-controlled conditions such as those found in a museum. For instance, this occurrence could be related to some kind of interaction between the selected consolidant product and the maintenance environment [4–6]. In this perspective, a diagnostic evaluation of a piece should be carried prior to the application of any kind of conservation treatment, because it would provide the opportunity to check for the presence of potential interactions between the applied treatment

and the remaining wood components. Moreover, the evaluation of the extent of decay prior to conservation allows the grading of the same decay, and potentially, therefore, the tailoring of a treatment to the specific state of preservation of the find.

Within this framework, a quantitative, reliable and quick measurement of the residual structural chemical components constituting cell walls of the archaeological wood material represents an important step towards the broad applicability of a systematic approach intended to evaluate the state of preservation of archaeological wooden objects at the time of their discover. Conventional wet chemical analyses are accurate but they have major limitations especially with regard to the amount of material required for the test and the fact that they are not very quick. A previous work [7] has already shown how ATR-FTIR analysis can be reliably used as a very good alternative for the quantitative estimation of the structural biopolymers constituting archaeological wood (namely, lignin and holocellulose). That approach made use of a preliminary calibration procedure able to establish a correlation between the spectra obtained on some archaeological samples and the values obtained by the conventional wet chemical

* Corresponding author.

E-mail address: pizzo@ivalsa.cnr.it (B. Pizzo).

analysis carried out on the same samples. A good way of proceeding is through spectra processing via multivariate analysis, which involves the simultaneous observation and analysis of more than one output at the same time. It is known that this procedure can obtain reliable values after calibration, that is, it produces smaller errors (usually quantified by the coefficient of determination, R^2 , and by the root mean square error of cross validation, RMSECV) compared to univariate analysis, thanks to the overcoming of the possible nonlinear relationships between absorption and concentration that may be encountered in the infrared (IR) signal [8]. In fact, univariate analysis is often inadequate to perform consistent evaluations, due to several reasons: high variability in terms of chemical structure of the decayed ancient material; considerable content of inorganic components (the ash, due to the sediment that permeates wood during burial), which can disturb the interpretation of analyses [9]; the overlap of signals attributable to non-structural compounds, such as extractives, to the structural ones [10,11].

However, in Ref. [7] only samples belonging to selected softwoods and which were still in waterlogged conditions (and hence without any preliminary preparation) were analysed. Such an approach highlights some possible limitations, the most important one being related to the presence of extractives. It is well known how both the quantity and the quality of extractives in wood are highly variable and mostly depending on wood species [12–14], and that some signals related to these substances can influence the intensity of the vibrations of structural cell wall components, such as lignin [15]. As a consequence, it can be hypothesised that the calibration model obtained from non-extracted material could depend on the considered wood species. Therefore, a research effort is still required before proposing the techniques based on infrared spectroscopy as a routine protocol for diagnostic evaluations in the analysis of archaeological wood. On the other hand, this further investigation must necessarily be carried out on dry wood meal, in order to allow the preliminary extraction of the material with solvents.

The aim of present work is to quantitatively evaluate the structural chemical components constituting the cell walls of a series of archaeological wood samples coming from different excavation sites in Italy by means of ATR-FTIR spectroscopy. The purpose of these evaluations was to assess how the various parameters which usually characterise waterlogged archaeological wood may affect the calibration models for this material. More specifically, the considered parameters were: the preliminary extraction of samples, the effect that ash has on the values obtained after wet analyses (used to calibrate the model), and the subdivision of species to which the samples belonged.

2. Materials and methods

2.1. Wood material

This study reports on the analysis of 59 archaeological wood samples from several excavations carried out in Italy. The essential information of these samples can be seen in Table 1. All the samples

are different from those described in Ref. [7] and they are representative of the different waterlogged environments, burial times, wood species and states of preservation that are often found in excavations. In the majority of cases, small blocks (approximately $4 \times 2 \times 1 \text{ cm}^3$ edges) were carefully taken from the centre of the various findings, in order to limit the heterogeneity in the extent of decay which usually characterises waterlogged wood. No specific orientation was chosen for the blocks because they were milled after drying.

All samples were analysed by means of both, wet chemistry methods and ATR-FTIR spectroscopy.

2.2. Wet chemical analyses

Conventional wet chemical analyses were carried out using specific standards, on the 40–60 mesh fraction obtained after sieving the meal. The following parameters were measured for all samples: (a) organic extractive content, by means of Soxhlet extraction [16], by using a mixture of toluene and ethanol, 2:1 v/v, as the extracting solvent; (b) aqueous extractive content, by means of Soxhlet extraction, carried out on the same meal previously extracted with organic solvents; (c) lignin content, measured in the extracted meal according to the Klason method [17]; (d) ash content [18]. The holocellulose amount was calculated by arithmetic difference with the sum of the other chemical components (in practice, as complement to 100%). In fact, it was previously shown that the direct measurement of the holocellulose content, instead of its calculation, is unreliable in archaeological material [9].

For the calibration phase, the results of wet analyses were referred to 2 different bases of calculation

1. ash-free anhydrous weight of woody mass (values were calculated to exclude the ash amount) (series W),
2. the anhydrous weight of the whole sample, i.e. also including the ash amount (series S).

2.3. ATR-FTIR analyses

ATR-FTIR spectra were acquired both before and after solvent extraction. Spectra were recorded on a Bruker FT-IR spectrometer (Alpha) with the following settings: 42 scans per sample, spectral resolution of 4 cm^{-1} , wavenumber range of $4000\text{--}400 \text{ cm}^{-1}$, using a diamond single reflection attenuated total reflectance (ATR) accessory and a zero filling of 2. Post spectroscopic manipulation was kept to a minimum. Atmospheric compensation and offset-correction to the minimum between 1920 and 1880 cm^{-1} was applied to the ATR-FTIR spectra (Software OPUS 6.5 from Bruker).

2.4. Data analysis

Spectra were normalised in the spectral range of $700\text{--}1800 \text{ cm}^{-1}$, by means of two different procedures, namely Min-Max (MMN) and Vector Normalisation (VN). The Min-Max normalisation procedure sets the absorbance to zero at the selected minimum (1800 cm^{-1}),

Table 1

Number and essential information of the analysed archaeological wood samples. All were preserved in waterlogged conditions. The acronym MWC stands for Maximum Water Content, and it is usually considered to represent the decay of waterlogged archaeological wood (the higher it is the more decayed is the wood).

Analysed wood species	Age (min–max)	Burial environment	Total number of samples	Range of MWC (min–median–max)
<i>Alnus</i> sp.p.	XIV–XVIII c. A.D.	Lagoon	9	173–248–475
<i>Cupressus sempervirens</i>	I–IIc.A.D.	Coastal	7	120–204–258
<i>Larix decidua</i>	I–XVIIIc.A.D.	Coastal, lagoon	8	131–145–372
<i>Picea abies</i>	I–IIc.A.D.	Coastal	4	194–339–413
<i>Pinus</i> sp.p.	VIIc.B.C.–II c.A.D.	Coastal, river	10	238–333–587
<i>Quercus</i> sp.p.	VIIc. B.C.–XVIIIc. A.D.	Coastal, river, lagoon	8	231–354–590
<i>Ulmus</i> sp.p.	VIIc.B.C.–XVIIIc.A.D.	Coastal, deltaic, river, lagoon	13	134–359–751

whereas the highest value is set to 2 at the selected maximum (between 1015 and 1035 cm^{-1}).

The VN calculates the average y -value of the spectrum. The average value is subtracted from the spectrum decreasing the mid-spectrum to $y=0$. The sum of the squares of all y -values is calculated and the spectrum is divided by the square root of this sum. The vector norm of the result spectrum is 1.

Selection of the calibration models were based on R^2 and RMSECV [7,8,19]; additionally, the number of PLS components (Rank) was also considered, since higher Rank may correspond to adding more spectral noise to the model, which deteriorates the analysis (as shown previously in Ref. [19]).

3. Results and discussion

The samples analysed had a broad variation in the state of preservation; some samples were still rich in polysaccharides and others were enriched in lignin (which implies a significant depletion of structural carbohydrates) (Fig. 1). Furthermore, Fig. 2 shows the comparison between the spectra related to a sample of fresh elm wood and two elm archaeological samples (Pp B17 and Cm 5 in Fig. 2). It can be seen how bands with maxima at 1733, 1370, 1158, 1104, 1027, and 895 cm^{-1} , which are attributable to polysaccharides [20], have high absorbance in the fresh sample, and are greatly reduced in sample Cm 5 and practically non-existent in sample Pp B17. In contrast, maxima at 1266 and 1217 cm^{-1} , due to CO groups in lignin, are clearly visible in sample Pp B17, whereas in sample Cm 5 they are dominated by the polysaccharides, as is normally the case for spectra obtained from fresh wood (Fig. 2). It is also worth to note that bands with maxima at 1593 cm^{-1} , 1506 cm^{-1} , and 1422 cm^{-1} , all attributable to the aromatic skeletal vibrations, remained almost unchanged among the three samples. These data are consistent with those reported in literature for archaeological wooden material [7,10,21].

The validation and model optimisation procedure was carried out on normalised spectra by using two different approaches:

- A single spectral range (SSR). In this case, the same spectral range (700–1800 cm^{-1}) was used for the quantification of both wood components to be determined (lignin and holocellulose);
- A differentiated spectral range (DSR). In this case, 4 different spectral ranges were used for the quantification of either lignin

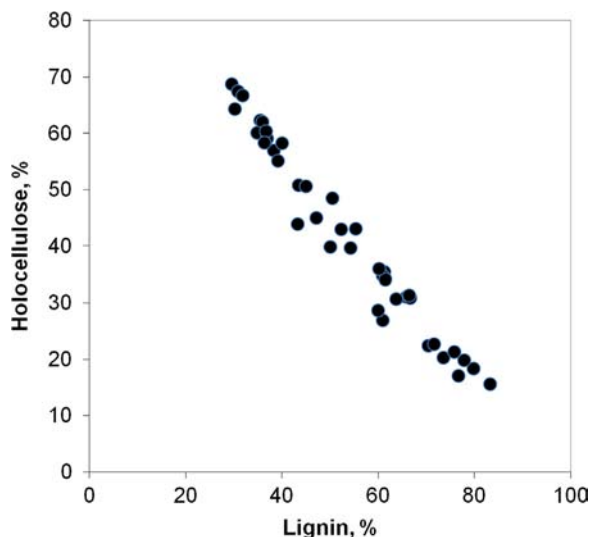


Fig. 1. Graph of holocellulose vs. lignin values as obtained after conventional wet analyses for all the considered samples. It can be seen how they cover a broad calibration range (from approximately 26.5% to 83.4% for lignin, and from 15.6% to 69.7% for holocellulose), and are uniformly distributed within this range.

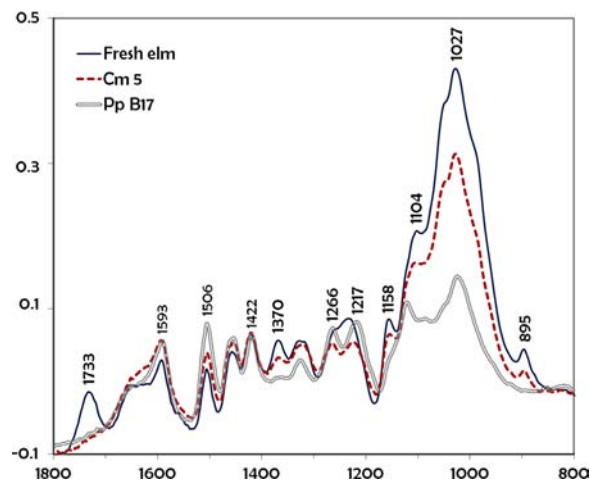


Fig. 2. Comparison between the spectra of fresh elm wood and two archaeological elm samples, showing the difference between a material in good condition (Cm 5) and one in a bad state of preservation (Pp B17). Spectra were Vector normalised in the range 1200–1800 cm^{-1} .

or holocellulose. More specifically, the ranges used for lignin were

- 1185–1295 cm^{-1} + 1480–1540 cm^{-1} in the case of softwoods,
 - 1185–1350 cm^{-1} + 1480–1540 cm^{-1} in the case of hardwoods.
- Instead, for holocellulose the following intervals were used:
- 700–1200 cm^{-1} + 1300–1400 cm^{-1} + 1650–1800 cm^{-1} in the case of softwoods,
 - 700–1200 cm^{-1} + 1350–1400 cm^{-1} + 1650–1800 cm^{-1} in the case of hardwoods.

The intervals in DSR calibration were selected because most vibrations related to groups present in lignin and holocellulose fall in the same regions [7–11].

Possible outliers in the data were identified in the set of data by applying the Cross Validation process, which is an internal validation routine. This is an important step in constructing the model, because the presence of anomalous samples may create distortions in the models, thus increasing the prediction error. Therefore, a procedure was adopted where possible outliers, as identified by the software, were removed one by one, in progression. Each time, the parameters associated to errors into the model (R^2 and RMSECV) and of Rank were evaluated, and this procedure was repeated in: (a) both SSR and DSR calibration regions; (b) both Mini-Max (MMN) and Vector (VN) normalisation procedures; (c) both ash-free (W) and ash-rich (S) series; (d) both extracted and not-extracted meal; (e) both lignin and holocellulose wood components.

An example of the outcomes of this procedure is shown in the Supplementary section (Supplementary data S1–S4), whereas the optimal values obtained for the various considered data sets (softwoods, hardwoods and softwoods plus hardwoods) are reported in Table 2.

The results show how, depending on the considered data set, the combinations optimising the model parameters for lignin and holocellulose were not always the same between them (Table 2). For example, while in the case of softwoods the model was the same for lignin and holocellulose (in both cases: S/Not-extr/MMN/DSR), for hardwoods it was different (W/Extr/VN/DSR and S/Not-extr/VN/DSR for holocellulose and lignin, respectively). Analogously, the model was also different when the data set was constituted by both softwoods and hardwoods (S/Not-extr/MMN/DSR and S/Extr/VN/SSR for holocellulose and lignin, respectively) (Table 2).

Table 2

Optimal values of model parameters for the various considered datasets (softwoods, hardwoods and softwoods plus hardwoods). In the Table, the calibration region 'SSR' means: 700–1800 cm^{-1} ; the calibration region 'DSR' indicates the differentiated spectral ranges specified in Section 3, from (a) to (d) (different for either lignin or holocellulose and for either softwoods or hardwoods). A detailed description is also given in the caption of Supplementary data S2–S4 in the Supplementary section.

Data set	Wood component	Optimal series	Rank	R^2 (%)	RMSECV (%)	Excluded samples
Softwoods	Holocellulose	S/Not-extr/MMN/DSR	4	92.87	3.79	6
	Lignin	S/Not-extr/MMN/DSR	3	94.22	3.20	6
Hardwoods	Holocellulose	W/Extr/VN/DSR	5	97.99	2.89	6
	Lignin	S/Not-extr/VN/DSR	4	96.43	3.82	5
Hardwoods + Softwoods	Holocellulose	S/Not-extr/MMN/DSR	7	94.19	3.97	8
	Lignin	S/Extr/VN/SSR	3	91.04	4.67	7

Therefore, a unique model could not be identified, but a different combination of parameters must be adopted in modeling, depending on either the considered wood components (lignin or holocellulose) or the considered data set (softwoods or hardwoods).

In most cases the optimal values of model parameters were related to the Not-extr series (except for holocellulose with the data set constituted by hardwoods and for lignin with the data set constituted by both hardwoods and softwoods, Table 2). Moreover, the series S always gave the best results (except again for the hardwoods' holocellulose). Considering that samples of Not-extr series were not extracted before acquiring spectra, and that the numerical differences in the calibration values between S and W series are related to the ash amount (in W series this amount was excluded in fact, and the other values recalculated to take account of this exclusion), it would seem at first that neither the extractives nor the ash amount have a negative impact on the prediction of wood cell wall structural components by means of ATR spectra and PLS analysis.

However, for both the hardwood and the softwood data sets, some of the outlier values excluded from the calibration model were those that had ash contents higher than 10% (there were 2 for the softwoods and 3 for the hardwoods), whereas the average value of ash in not-excluded samples was 3.0% for softwoods and 3.8% for hardwoods (data not shown). Therefore, contrariwise to what seemed initially, the ash amount plays a very important role for the quality of the calibration model, and too contaminated samples had to be excluded by the multivariate analysis process in order to attain good results. The reason of such a behaviour has been already explained previously [9], and it is due to the overlapping of bands related to the inorganic fraction with specific signals attributable to the organic matrix. Therefore, the present outcome that the S series produced better model parameters than for the W series, only reliably applies to samples within a relatively low ash content.

The effect of extractives on the quality of the models has been rarely investigated in a systematic way for PLS calibration modeling. Usually extracted material is preferred [8,19,20,22–24], but several works can be found in the scientific literature where preliminary extraction of wood powder is not considered [25–27]. Occasionally, where both extracted and not-extracted meal has been considered, the influence of extractives has been regarded as unfavourable in PLS-based calibrations [28]. In the present case, instead, models based on non-extracted material performed better than those based on extractive-free powder in the case of softwoods and in the case of hardwood lignin (instead, preliminary extraction was preferable for hardwood holocellulose). This occurrence is related to the large calibration range used in present case (26.5–83.4% for lignin, and 15.6–69.7% for holocellulose, values for the W series, Fig. 1). This minimises the effect of the additional vibrations coming from the extractives that

overlap those from the structural wood cell compounds (lignin and holocellulose), even though the organic extractive content was as high as 11.5% for the softwoods, and 9% for the hardwoods (data not shown). It is worth to note that none of the samples where these maximum values were obtained have been excluded from the model.

Furthermore, whereas no specific trends were associated to the normalisation procedure (MMN behaved better for softwoods and for holocellulose when the data set was constituted by hardwoods and softwoods taken together, VN gave better results in the other cases), the model parameters associated to the differentiated spectral range (DSR) were better than those for SSR (except in the case of lignin when the data set was constituted by both hardwoods and softwoods). Thus the use of ranges differentiated for lignin and holocellulose resulted in a more precise calibration compared to using a same region for both components; a similar outcome was also found in the case of softwood samples analysed at the completely wet state [7]. This occurrence also proves how important it is to select a suitable spectral range for the calibration model.

It is worth noting that, in the case of both holocellulose and lignin, the optimal model parameters obtained when the softwood data set was used were worse than when the hardwood dataset was used (Table 2). This means that the estimated values obtained by the present methods are more reliable in the case of hardwood species compared to the softwood ones, that is, softwoods are more difficult to process than hardwoods.

It also appears from Table 2 that trying to calibrate softwoods with a data set also based on hardwoods is an unreliable procedure: the specific softwood model better predicted the softwood samples than the mixed (hardwoods plus softwoods) model (Table 2). This occurrence was also confirmed when the values of structural components in softwoods were predicted according to the two different data sets considered (namely, only softwoods and softwoods plus hardwoods): the better fit of the predicted data with the softwood dataset is clear in the case of lignin, whereas the holocellulose values are more similar (Fig. 3). This implies that holocellulose and lignin predicted values are more reliable when either softwoods or hardwoods are predicted with their specific data set (softwoods with softwoods, and hardwoods with hardwoods).

It is also worth noting that the values of the model parameters obtained in present work are comparable with other values achieved by employing ATR-PLS or DFRIFT-PLS calibration: Zhou et al. [24] reported of a R^2 value of 80.6% for the cross-validation procedure carried out on poplar lignin, and Tucker et al. [23] a R^2 of 98.7% for the lignin amount of steam-exploded material obtained from whole-tree forest thinning. With DRIFT, Ferraz et al. [22] found a coefficient of determination of 96% for pine lignin and of 93% for eucalyptus lignin, whereas Meder et al. [26] found for pine lignin a R^2 of 84% also with DRIFT, and of 95% in

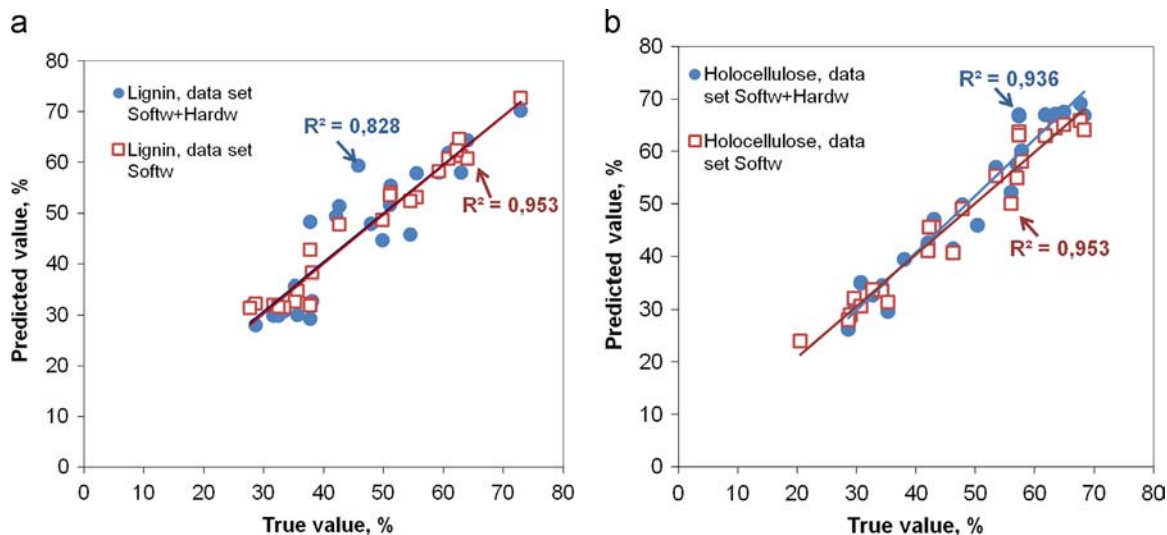


Fig. 3. Predicted vs. measured values for lignin (a) and holocellulose (b) with the softwood or the combined softwood-hardwood datasets. The value of R^2 is the determination coefficient as defined in Microsoft Excel[®]. The models used to predict the values are those reported in Table 2.

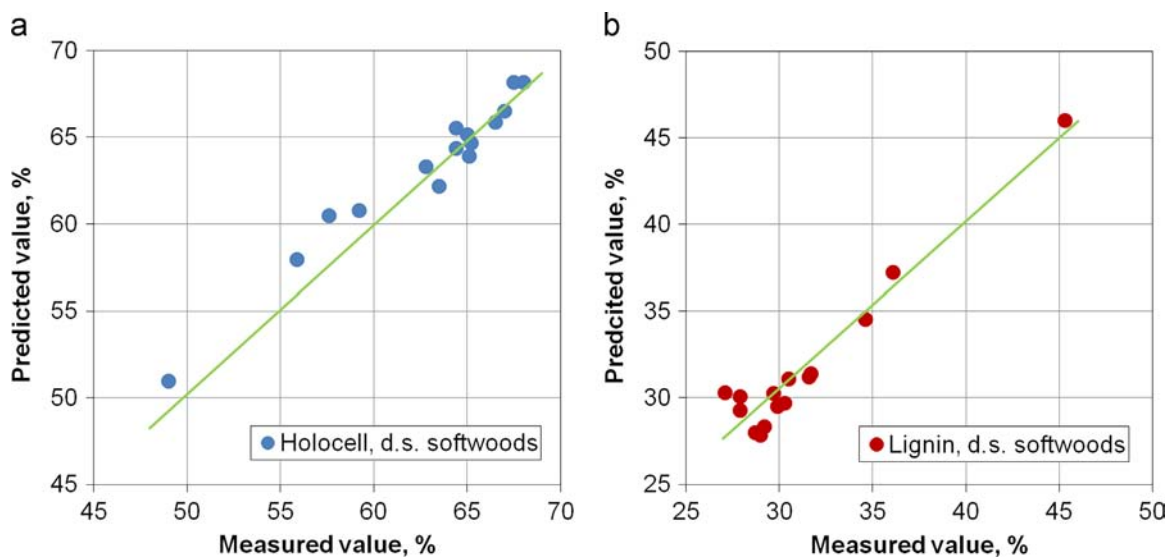


Fig. 4. Predicted vs. measured holocellulose (a) and lignin (b) values for the softwood samples taken from the excavation in Venice. Predicted values were calculated according to the model S/Not-extr/MMN/DSR, that is, the optimal one with the softwood dataset. In each graph, the straight-lines are those related to the calibration model (e.g. the same as those reported in Fig. 3 for softwoods).

transmission mode (with KBr pellets). The model parameters with holocellulose found in the research presented in this paper are appreciably better than those obtained by Meder et al. [26] for total carbohydrate (58% with DRIFT and 72% in transmission).

The stability of the proposed model was also evaluated by using the leave-more-out (LMO) method. According to this method, one sample is progressively left out in the Cross Validation routine, and each time the related prediction error is assessed. The limited variation in error values obtained in the model when n samples are consecutively eliminated gives a good estimation for the stability of the achieved prediction model [23,29,30]. For the data presented here, with either softwood or hardwood datasets, the LMO method was performed by excluding up to 7 samples, for both lignin and holocellulose. This amount represented approximately 25% of the whole set of samples considered for each data set (see Supplementary data S5 in the Supplementary section). In the case of holocellulose, values of R^2 diminished by a maximum of 7% (from 92.9% to 85.8%) with the softwood dataset (the Rank kept constant at 3, except in one case where it was 5, data not shown),

and of less than 5% (from 98% to 93%) with the hardwood dataset (in this case, the Rank varied from 4 to 6, data not shown). The calibration of lignin was even more stable: values of R^2 diminished by less than 6% (from 94.2% to 88.4%) with the softwood dataset (the Rank kept constant at 3, data not shown), and of maximum 2% (from 96.4% to 94.3%) with the hardwood dataset (in this case, the Rank varied from 4 to 3, data not shown). In all cases, the variations in the error parameters were very limited, and the stability of the model is therefore demonstrated.

A true validation was also performed by using an external set of samples taken from an excavation carried out subsequently to those used to set-up the model. In this case, 30 additional specimens (15 hardwoods, *Alnus*, and 15 softwoods, *Pinus*) were collected from some foundation piles in Venice, and processed according to the best methods reported in Table 2 for each related data set (e.g. softwoods were processed according to the S/Not-extr/MMN/DSR model for both holocellulose and lignin). Then, the predicted values were compared to those measured on the same material by means of the wet analyses (Fig. 4 and Fig. 5). Results

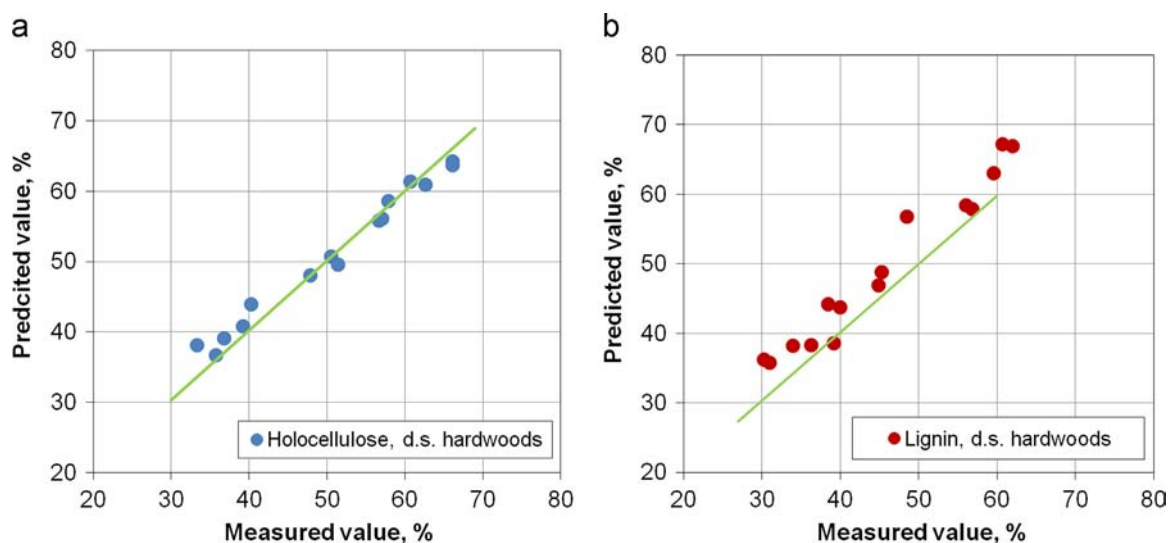


Fig. 5. Predicted vs. measured holocellulose (a) and lignin (b) values for the hardwood samples taken from the excavation in Venice. Predicted values were calculated according to the models W/Extr/VN/DSR and S/Not-extr/VN/DSR for holocellulose and lignin, respectively. The straight-line are those related to the calibration models.

Table 3

Values of the determination coefficient of prediction (R_p^2) and of the root-mean square error of prediction (RMSEP) for the additional samples constituting the validation dataset (15 softwoods and 15 hardwoods).

	R_p^2 (%)	RMSEP (%)
Lignin, softwoods	95.17	1.21
Holocellulose, softwoods	93.43	1.29
Lignin, hardwoods	91.50	3.13
Holocellulose, hardwoods	96.73	1.99

from all the considered models had very good agreement between predicted and true values, as also confirmed by the values of the prediction errors associated to the utilised models (Table 3).

4. Conclusion

The results presented in this work show that it is possible to use ATR-mid FTIR for a reliable and quantitative evaluation of the residual amount of lignin and holocellulose in waterlogged decayed wood. In fact, in the identified calibration procedure, the values of the error parameters associated to the best models were very good (R^2 as high as 97.99%, RMSECV as low as 2.89%), and they were also stable (as confirmed by the leave-more-out procedure). However, different combinations of parameters had to be adopted in predictions depending on either the considered wood components (lignin, holocellulose) or the considered data set (softwoods or hardwoods) and, in this perspective, the use of a differentiated range (DSR) in the calibration procedure is demonstrated to be a good approach in order to improve the accuracy of the model (this also demonstrated the importance of spectral range choice for calibration via multivariate PLS analysis). It was also observed that the estimated values were more reliable in the case of hardwoods compared to softwoods. The good predictive ability of selected models was also proved by a procedure of external validation, carried out on an external set of samples.

However, it is shown that an excessive ash content in the archaeological samples can affect the predictive ability of the models; highly contaminated samples had to be excluded in order to attain good quality calibration models. Preliminary extraction of samples did not seem to provide any appreciable reduction of the error parameters, thanks to the large calibration range used in

present case which minimised the disturbing effects related to the presence of extractives.

Acknowledgements

This work has been carried out within the framework of the agreement CNR-GRICES (FCT) of a Bilateral Project between IVALSA (Italy) and IICT (Portugal). Samples from Venice have been collected within the framework of a specific project on the foundation piles of the City, CORILA and the other project partners are gratefully acknowledged. Authors want to thank Luigi Fiorentino, who carried out wet chemical analyses, and Dr. Mark Irle, Ecole Supérieure du Bois, Nantes, who revised the language.

Appendix A. Supplementary material

Supplementary data associated with this article can be found in the online version at <http://dx.doi.org/10.1016/j.talanta.2014.07.062>.

References

- [1] C. Capretti, N. Macchioni, B. Pizzo, G. Galotta, G. Giachi, D. Giampaola, *Archaeometry* 50 (2008) 855–876.
- [2] J.I. Hedges, G.K. Cowie, J.R. Ertel, R.J. Barbour, P.G. Hatcher, *Geochim. Cosmochim. Acta* 49 (1985) 701–711.
- [3] P. Hoffmann, M.A. Jones, in: R.M. Rowell, R.J. Barbour (Eds.), *Archaeological Wood: Properties, Chemistry and Preservation*, American Chemical Society, Washington DC, 1990, pp. 35–65.
- [4] G. Almkvist, *The chemistry of the Vasa: iron, acids and degradation*, department of chemistry, Swedish university of agricultural sciences, Uppsala, 2008.
- [5] S. Braovac, H. Kutzke, *J. Cult. Herit.* 13 (2012) S203–S208.
- [6] E. Hocker, G. Almkvist, M. Sahlstedt, *J. Cult. Herit.* 13 (2012) S175–S182.
- [7] B. Pizzo, E. Pecoraro, N. Macchioni, *Appl. Spectrosc.* 67 (2013) 553–562.
- [8] J. Rodrigues, J. Puls, O. Faix, H. Pereira, *Holzforschung* 55 (2001).
- [9] B. Pizzo, A. Alves, N. Macchioni, A. Alves, G. Giachi, M. Schwanninger, et al., Characterization of waterlogged wood by infrared spectroscopy, in: J. Gril (Ed.), *Proceedings of the International Conference Held COST Action IE0601 Wood Science for Conservation of Cultural Heritage*, 5–7 November, 2008, Braga Port, University Press, Firenze, 2010: pp. 236–241.
- [10] G. Giachi, B. Pizzo, I. Santoni, A Chemical characterization of the decay of waterlogged archaeological wood, in: K. Strætkvern, D.J. Huisman (Eds.), *Proceedings of the 10th ICOM Groupon on Wet Organic Archaeological Materials Conference WOAM, 2007*, Rijksdienst voor Archeologie, Cultuurlandschap en Monumenten, Amersfoort, 2009: pp. 21–33.
- [11] A.K. Moore, N.L. Owen, *Appl. Spectrosc. Rev.* 36 (2001) 65–86.
- [12] B. Pizzo, C.L. Pometti, J.-P. Charpentier, N. Boizot, B.O. Saidman, *Ind. Crops Prod.* 34 (2011) 851–859.

- [13] C.L. Pometti, B. Pizzo, M. Brunetti, N. Macchioni, M. Ewens, B.O. Saidman, *Bioresour. Technol.* 100 (2009) 1999–2004.
- [14] I. Santoni, B. Pizzo, *Int. J. Adhes. Adhes.* 31 (2011) 743–753.
- [15] K.K. Pandey, *Polym. Degrad. Stab.* 87 (2005) 375–379.
- [16] TAPPI, T204-cm07, Solvent Extractives of Wood and Pulp, Standards Technical Association of Pulp and Paper Industry, 360 Lexington AM, New York 17, N.Y-7, 2007.
- [17] TAPPI, T222-om02, Acid-Insoluble Lignin in Wood and Pulp, Standards Technical Association of Pulp and Paper Industry, 360 Lexington AM, New York 17, N.Y-7, 2002.
- [18] TAPPI, T211-om02, Ash in Wood, Pulp, Paper and Paperboard: Combustion at 525 °C, Standards Technical Association of Pulp and Paper Industry, 360 Lexington AM, New York 17, N.Y-7, 2002.
- [19] J. Rodrigues, O. Faix, H. Pereira, *Holzforschung* 52 (1998) 46–50.
- [20] M. Schwanninger, J.C. Rodrigues, H. Pereira, B. Hinterstoisser, *Vib. Spectrosc.* 36 (2004) 23–40.
- [21] J. Gelbrich, C. Mai, H. Militz, *Int. Biodeterior. Biodegrad.* 61 (2008) 24–32.
- [22] A. Ferraz, J. Baeza, J. Rodriguez, J. Freer, *Bioresour. Technol.* 74 (2000) 201–212.
- [23] M.P. Tucker, Q.A. Nguyen, F.P. Eddy, K.L. Kadam, L.M. Gedvilas, J.D. Webb, *Appl. Biochem. Biotechnol.* 91–93 (2001) 51–61.
- [24] G. Zhou, G. Taylor, A. Polle, *Plant Methods* 7 (2011) 1–10.
- [25] H. Chen, C. Ferrari, M. Angiuli, J. Yao, C. Raspi, E. Bramanti, *Carbohydr. Polym.* 82 (2010) 772–778.
- [26] R. Meder, S. Gallagher, K.L. Mackie, H. Böhler, R.R. Meglen, *Holzforschung* 53 (1999) 261–266.
- [27] S. Raiskila, M. Pulkkinen, T. Laakso, K. Fagerstedt, M. Löija, R. Mahlberg, et al., *Silva Fenn.* 41 (2007) 351–371.
- [28] G.G. Allison, S.C. Thain, P. Morris, C. Morris, S. Hawkins, B. Hauck, et al., *Bioresour. Technol.* 100 (2009) 1252–1261.
- [29] J. Rodrigues, A. Alves, H. Pereira, D. da Silva Perez, G. Chantre, M. Schwanninger, *Holzforschung* 60 (2006) 402–408.
- [30] P.C. Williams, D.C. Sobering, Comparison of commercial Near-Infrared Transmittance and Reflectance Instruments for analysis of whole grains and seeds, *J. Infrared Spectrosc.* 1 (1993) 25–32.



An air carrier flow system for the spectrophotometric determination of water in biodiesel exploiting bleaching of the cobalt chloride complex



Andréia C. Pereira, Boaventura F. Reis, Fábio R.P. Rocha*

Centro de Energia Nuclear na Agricultura, Universidade de São Paulo, P.O. Box 96–13400-970, Piracicaba – SP, Brazil

ARTICLE INFO

Article history:

Received 30 May 2014

Received in revised form

16 July 2014

Accepted 19 July 2014

Available online 27 July 2014

Keywords:

Flow analysis

Multicommutation

Water

Biodiesel

Humidity

Spectrophotometry

Cobalt chloride

ABSTRACT

Water content is an important parameter in biodiesel quality control, as excess of this substance may lead to biofuel hydrolysis, microorganism proliferation, and alterations in the oxidative stability of the biofuel. The threshold limit is established as 200 mg kg^{-1} and the determination is usually based on Karl Fischer titration. In this work, a simple, reliable and environmentally friendly procedure is proposed for water determination in biodiesel by exploiting a multicommutated flow system with air carrier stream. The method relies on the color fading of the cobalt chlorocomplex in the presence of the analyte, which is monitored by spectrophotometry. A linear response was observed from 100 to 5000 mg kg^{-1} water, with detection limit, coefficient of variation ($n=20$) and sampling rate estimated as 25 mg kg^{-1} , 0.7% and 30 h^{-1} , respectively. The procedure consumes only $3.5 \text{ }\mu\text{g}$ of CoCl_2 and generates $750 \text{ }\mu\text{L}$ of waste per determination. Results obtained by using the standard additions method agreed with those attained by the Karl Fischer titration at the 95% confidence level.

© 2014 Elsevier B.V. All rights reserved.

1. Introduction

Use of biodiesel fuel has increased worldwide due to its low impact on the environment and as a source of renewable energy to replace diesel and other petroleum derivatives. As such, this biofuel should meet the recommended parameters to ensure its quality for both use and storage [1] as well as to avoid emission of toxic substances.

Water determination is important for the quality control of biodiesel. The biofuel contains water as a result of the production process (washing to remove excess of alcohol and glycerol byproducts) and the absorption of atmospheric humidity. Excess of water may cause biodiesel hydrolysis yielding free fatty acids, which increases acidity and favors proliferation of microorganisms and corrosion of storage tanks [2]. Moreover, water may increase the formation of oxidation products during storage of the biofuel, which can damage the vehicle injection system and engine. In view of these aspects, water content in biodiesel is limited to 200 mg kg^{-1} [3,4] and this parameter should be monitored in the final product and during storage, which requires a fast and reliable procedure.

Water has been determined in different sample matrices by chromatography [5,6], spectrophotometry [7], fluorimetry [8], and mainly electroanalysis [9,10]. The Karl Fischer (KF) titration, the

most widespread method, has also been recommended for biodiesel analysis [11,12]. However, it presents some drawbacks such as the need for specialized equipment, rigorous sample manipulation, and the use of toxic reagents. Furthermore, biodiesel often contains additives and impurities that may favor side reactions during the coulometric KF titration [13].

Batch spectrophotometric procedures using alternative reagents, such as cobalt chloride [14], potassium dichromate [15], dithizone [16], and acridine orange [17] have been proposed for determination of water in various organic solvents. These procedures are time-consuming and involve several steps, thus impairing sample throughput and increasing the risks of systematic errors. Moreover, they are highly susceptible to sample contamination due to absorption of atmospheric humidity. Flow-based analytical procedures exploiting the KF reagent have been proposed to circumvent some disadvantages of the batch analogues [18–24]. In this sense, side reactions were minimized and sample throughput was increased by reducing the reaction time, while contamination from atmospheric humidity and contact of the analyst with the toxic reagents were diminished by sample processing in a closed system. On the other hand, sensitivity is usually worse than that achieved in the batch procedure and some interferences were not circumvented. The performance of flow injection spectrophotometric procedures for water determination in acetone exploiting different reagents was also evaluated [7].

In spite of the availability of some alternatives and the previously mentioned drawbacks, the KF method prevails in the analysis of biodiesel. This emphasizes the need for the

* Corresponding author. Fax: +55 19 3429 4610.

E-mail address: frprocha@cena.usp.br (F.R.P. Rocha).

development of rapid, reliable, and environmentally friendly procedures for biofuel analysis. The goal of the present work was therefore to develop a flow system with air carrier stream for the spectrophotometric determination of water in biodiesel based on discoloration of the cobalt chloride complex in ethanolic medium.

2. Materials and methods

2.1. Reagents and solutions

All solutions were prepared daily with anhydrous ethanol (99.9%, Merck, Germany) and analytical grade chemicals. The working standards were prepared within 100–5000 mg kg⁻¹ water, and a 5.25 × 10⁻³ mol L⁻¹ cobalt chloride solution was used as reagent. Air was used as a carrier to minimize the ethanol consumption and to avoid dispersion of the sample zone. Anhydrous ethanol was also used in the washing step.

Biodiesel samples were analyzed by the standard additions method. Solutions were prepared from 3.75 mL of biodiesel with the addition of 10–50 μL of water (two spikes per sample). Volumes were made up to 5.00 mL with anhydrous ethanol, which is miscible with both water and biodiesel. Samples with the same dilution in ethanol, but without water addition, were taken as reference.

2.2. Apparatus

The flow system was built up with four three-way solenoid valves (NResearch, USA), a Teflon[®] confluence connector, and 0.8-mm i.d. polyethylene tubes. A peristaltic pump (model CP 78017-10, Ismatec IPC, Switzerland) was equipped with Tygon[®] and Viton[®] tubes for propelling aqueous and ethanolic solutions, respectively. The solenoid valves were computer-controlled through a parallel interface coupled to a current drive based on the ULN2803 integrated circuit [25]. The detection system consisted of a multi-channel CCD spectrophotometer (USB 2000, Ocean Optics, Dunedin, FL) with a tungsten-halogen light source and optical fibers for radiation transport. A lab-made glass flow-cell (30-cm optical path and 1.7 mm i.d.) with glass waveguides [26] was used for the spectrophotometric measurements. The control software was developed in Visual Basic 6.0 (Microsoft, USA), and data acquisition was performed with the software supplied by the spectrophotometer manufacturer.

2.3. Flow system

The flow diagram showed in Fig. 1 was operated according to the switching course in Table 1. The multicommutation approach was exploited for solutions management by binary sampling [27] and air was used as the carrier stream [28]. The fluids were propelled at 0.6 mL min⁻¹ (S, R and E) and 1.0 mL min⁻¹ (air). In the position showed in Fig. 1, all liquids are recycled to the corresponding vessels and only air is flowing to the system. Each solution is sampled by switching the corresponding valve simultaneously to V₄, aiming to interrupt the air flow through the manifold and avoid segmentation of the sample zone. Volumes are defined by the flow rate and the switching times (see Table 1). The analytical cycle started (steps 1 and 2) by inserting 10 sample and reagent aliquots alternately (i.e. 10 sampling cycles). This corresponds to total sample and reagent volumes of 600 and 100 μL, respectively. The sample zone was transported by air through to reaction coil toward the detection cell (step 3). The analytical path was washed with ethanol by the actuation of valve V₃ before sample replacement (step 4).

The coiled reactor and the reagent solution were maintained inside a water bath with temperature controlled at 25.0 ± 0.1 °C

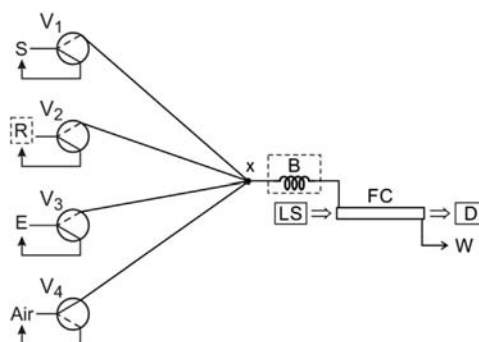


Fig. 1. Flow diagram of the proposed procedure. S=sample; R=reagent (5.25 × 10⁻³ mol L⁻¹ CoCl₂ in anhydrous ethanol); E=anhydrous ethanol; Air=carrier stream; V₁-V₄: three-way solenoid valves; x=Teflon[®] joint point; B=50-cm coiled reactor; LS=tungsten-halogen light source; FC=30-cm long flow cell (1.7 mm i.d.); D=detector; W=waste. Dashed lines indicate components inserted in a temperature-controlled water bath (25.0 ± 0.1 °C).

Table 1
Valve switching course for water determination in biodiesel.

Step	Description	Valves	Time (s)	Volume (μL)
1 ^a	Sample insertion	V ₁ ,V ₄	6.0	60
2 ^a	Reagent insertion	V ₂ ,V ₄	1.0	10
3	Measurement	0	10	–
4 ^b	Washing	V ₃ ,V ₄	5.0	50

^a Ten sampling cycles.

^b Step required only for sample replacement.

due to the thermochromic properties of the reagent [29]. Off-set adjustment of the detection system was performed with ethanol inside the flow cell. Absorbance values were measured as peak height at 650 nm; all measurements were carried out in triplicate. The analytical signal was based on the difference between reference and sample signals, measured in the absence and presence of water, respectively.

2.4. Reference procedure

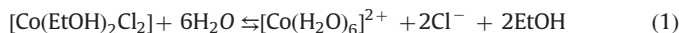
Coulometric KF titration for determining the water content in engine fuels, as recommended by ASTM [3], was employed as the reference procedure for accuracy assessment. A biodiesel aliquot was injected into the titration vessel of a KF apparatus in which iodine was coulometrically generated at the anode for the KF reaction. After titration of the water content, excess of iodine indicated the end point.

3. Results and discussion

The proposed procedure was based on discoloration of the CoCl₂ complex, which shows thermochromic and solvatochromic properties [29], i.e., the solution color is affected by the temperature and solvent nature. The aqueous solution of cobalt chloride is pink due to the formation of the octahedral hexa-aquacobaltate complex, [Co(H₂O)₆]²⁺. On the other hand, anhydrous CoCl₂ is a blue solid and its solutions in different organic solvents (e.g. ethanol) are also blue due to the formation of chlorocomplexes. The reversible changes in color of this system caused by temperature are also known [29]. Despite being widely investigated, bleaching of the cobalt chloride complex was not still exploited for water determination.

The addition of low amounts of water into a CoCl₂ ethanolic solution causes fading of the blue color, simultaneously with the formation of the pink aquocomplexes. Thus, the hexa-aquacobaltate

and chlorocomplexes coexist, and the equilibrium between them is shifted by increasing the amount of water in ethanolic medium (Eq. (1)). The tetrachlorocobaltate complex presents higher molar absorptivity than the hexaaquacobaltate, and thus the fading of the blue complex can yield higher sensitivity than the formation of the pink complex.



The solvent polarity affects the absorption spectrum of the cobalt chloride and blue solutions are also formed in other organic solvents, such as acetone [30]. Aiming to evaluate the effect of the solvent on the color fading in the presence of water, absorption spectra were obtained for $1.3 \times 10^{-3} \text{ mol L}^{-1}$ CoCl_2 solutions with and without 3000 mg kg^{-1} water in ethanol, acetone and a 1:1 ethanol/acetone mixture at room temperature (Fig. 2). Low water amounts effectively decrease the solution absorbance in anhydrous ethanol due to the displacement of the equilibrium (Fig. 2a). It was observed that the molar absorptivity of the reagent was higher in acetone ($294 \text{ L mol}^{-1} \text{ cm}^{-1}$) and in the solvent mixture ($346 \text{ L mol}^{-1} \text{ cm}^{-1}$) than in ethanolic medium ($126 \text{ L mol}^{-1} \text{ cm}^{-1}$), but the absorption spectra did not significantly change with water addition (Figs. 2b and c), thus indicating that formation of the octahedral complex is not favored in these media. Indeed, the blue complex formed in aprotic solvents, such as acetone, is quite stable to chromotropic changes [30]. Aiming to improve sensitivity, the reagent was prepared in ethanol for the implementation of the flow-based procedure.

In preliminary experiments with a 1-cm optical path cell, a linear response was observed from 1000 to 10000 mg kg^{-1} water ($A = 0.05 + 0.06 C_{\text{H}_2\text{O}}$, $r = 0.994$). Although the quantification limit was five-fold better than that reported previously for water determination in acetone [7], it is still unsuitable for biodiesel analysis, by considering the

threshold limit of 200 mg kg^{-1} [3,4]. Therefore, a 30-cm optical path flow cell was selected to improve sensitivity of the proposed procedure.

The blue color of the CoCl_2 ethanolic solution did not change significantly upon heating [29]. However, the measurement repeatability was affected by temperature changes. Coefficients of variation (500 mg kg^{-1} water, $n=20$) with and without temperature control were 0.7% and 3.6%, respectively. The reagent solution and the reaction coil were then kept in a temperature-controlled water bath to improve precision.

Procedure optimization was carried out by the univariate method aiming to improve analytical sensitivity. Both the magnitude of the reference signal relative to the cobalt chloride complex and that after bleaching by water were taken into account.

The effect of the reagent concentration (Fig. 3a) was evaluated by keeping the total volumes of sample and reagent at $350 \mu\text{L}$ (divided in 35 sampling cycles, i.e., 35 pairs of $10 \mu\text{L}$ aliquots of sample and reagent). This volume was required to completely fill the long path-length cell, whose internal volume was ca. $700 \mu\text{L}$. The analytical response increased up to 1.5 mmol L^{-1} , which is five-fold lower than that used in the flow system for water determination in acetone [7].

The influence of sample volume was evaluated by keeping CoCl_2 concentration in the sample zone to avoid reagent dilution due to changes in the volumetric fractions. Reagent volume was maintained at $10 \mu\text{L}$, and its concentration was varied from 1.5 to 6.8 mmol L^{-1} while the sample volume was varied from 10 to $80 \mu\text{L}$ (Fig. 3b). The analytical response increased with the sample volume up to $60 \mu\text{L}$, and then the sample:reagent volumetric fraction of 6:1 was selected for further experiments. The corresponding cobalt chloride concentration was 5.25 mmol L^{-1} to assure the same amount established in the previous study. Under these conditions, 10 sampling cycles ($70 \mu\text{L}$ each) were enough to

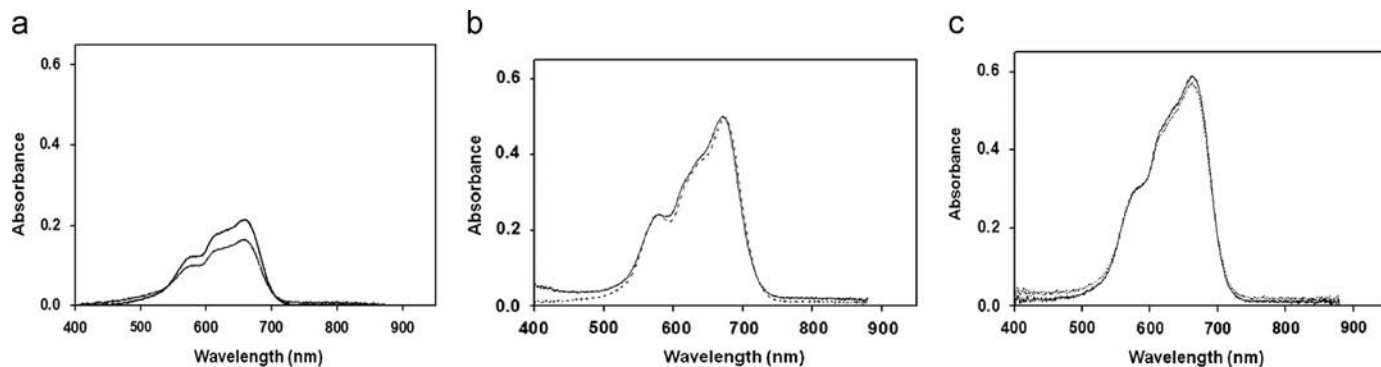


Fig. 2. Absorption spectra of $1.3 \times 10^{-3} \text{ mol L}^{-1}$ CoCl_2 in (a) ethanol, (b) acetone, (c) 1:1 ethanol:acetone solutions in the absence (upper curve) and presence (lower curve) of 3000 mg kg^{-1} water.

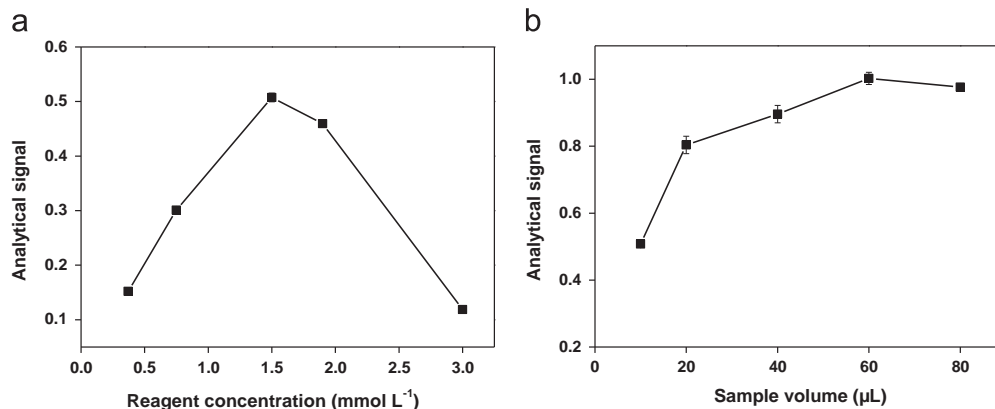


Fig. 3. Influence of (a) reagent concentration and (b) sample volume on the analytical signal. Error bars refer to the estimative of standard deviations from triplicate measurements.

completely fill the flow cell. As the reaction (Eq. (1)) is relatively fast (steady state is achieved in less than 5 s) and suitable mixing conditions were provided by the binary sampling approach, the reactor was maintained as short as possible (50 cm).

Under optimized conditions, a linear response was observed from 100 to 5000 mg kg⁻¹ water described by the equation $A=0.007+0.118C_{H_2O}$ ($r=0.998$, $n=5$), with sensitivity 20-fold higher than that achieved with a 1-cm optical path flow cell. The discrepancy in relation to the theoretical value expected from Beer's law is due to the higher relative response provided by lower reagent concentration used in the experiments with the 1-cm cell. The coefficient of variation and sampling rate were estimated at 0.7% ($n=20$; 1000 mg kg⁻¹) and 30 h⁻¹, respectively. The detection limit (25 mg kg⁻¹) was estimated as the lowest concentration that yielded an absorbance value significantly different of the reference signal at the 95% confidence level. For one determination, 60 µg of CoCl₂ and 600 µL of sample were required.

Comparison of the analytical features of the proposed procedure with those achieved in previously described flow-based ones is presented in Table 2. All procedures were applied to water determination in pure organic solvents, and the present work is the first application for determining this parameter in biodiesel, which is a considerably more complex sample. In spite of the lower sampling rate, the proposed procedure stands out because of better precision, lower detection limit, and by avoiding the use of toxic, expensive or hazardous reagents. For comparison, the coulometric Karl Fischer procedure designed for petroleum products, lubricating oils, and additives allowed water determination from 10 to 25000 mg kg⁻¹ [3]. As previously mentioned, the main drawbacks of this procedure are consumption of toxic reagents and solvents as well as risks of interferences by side reactions.

The analytical features obtained with the proposed procedure allowed for determination of water in biodiesel without any

sample pretreatment. However, the slopes of the analytical curves obtained in the presence of biodiesel were from 25 to 75% lower than that attained in ethanol, thus indicating a matrix effect. The standard addition method was then applied for sample analysis and the results (Table 3) agreed with those obtained by the Karl Fischer titration recommended by ASTM at the 95% confidence level. Results obtained by both procedures also showed comparable variances at 95% of significance.

4. Conclusions

A simple, precise and sensitive flow-based procedure was developed for the spectrophotometric determination of water in biodiesel, based on an inexpensive and low-toxic reagent. Sample and reagent consumptions, as well as waste generation, were minimized. The low detection limit achieved is an attractive aspect, as this parameter tends to become increasingly restrictive in biodiesel quality control (e.g. Brazilian legislation has reduced the threshold limit from 500 to 200 mg kg⁻¹ with a perspective to reduce to 100 mg kg⁻¹ in the near future). In addition, the achieved analytical features indicate that the proposed procedure can be applied to other kinds of samples, such as organic solvents. Moreover, contamination caused by atmospheric humidity was minimized by sample processing in a closed system. The proposed procedure is thus an inexpensive and reliable alternative for water determination in routine analysis of biodiesel.

Acknowledgments

This is a contribution of the National Institute of Advanced Analytical Science and Technology (INCTAA) and Núcleo de Pesquisa em Tecnologia e Inovação para Sustentabilidade na Agricultura. The authors acknowledge the fellowships and financial support from the Brazilian funding agencies CNPq and FAPESP (proc. 2011/23498-9). E.A.G. Zagatto is thanked for critical comments.

References

- [1] I.P. Lôbo, S.L.C. Ferreira, R.S. Cruz, *Quim. Nova* 32 (2009) 1596–1608.
- [2] M.R. Monteiro, A.R.P. Ambrozini, L.M. Lião, A.G. Ferreira, *Talanta* 77 (2008) 593–605.
- [3] ASTM D6304: Standard Test Method for Determination of Water in Petroleum Products, Lubricating Oils and Additives by Coulometric Karl Fisher Titration, Pennsylvania, United States.
- [4] ANP Resolution No. 14, from 11.5.2012 – DOU 18.5.2012.
- [5] O.F. Bennett, *Anal. Chem.* 36 (1964) 684 (684).
- [6] M.J. Egovalle, E.S. Dellamonica, *J. Chromatogr.* 717 (1981) 121–125.
- [7] M. Guzman, J.L.P. Pavón, E.R. Gonzalo, C. Hatfield, J. Ruzicka, G.D. Christian, *Analyst* 116 (1991) 1043–1049.
- [8] C. Niu, L. Li, P. Qin, G. Zeng, Y. Zhang, *Anal. Sci.* 26 (2010) 671–674.
- [9] R. Karlsson, *Talanta* 19 (1972) 1639–1644.
- [10] A. Cedergren, *Talanta* 21 (1974) 367–375.
- [11] G. Knothe, *J. Am. Oil Chem. Soc.* 83 (2006) 823–833.
- [12] P.B.L. Fregolente, L.V. Fregolente, M.R.W. Maciel, *J. Chem. Eng. Data* 57 (2012) 1817–1821.
- [13] S. Grunke, *Food Control* 12 (2001) 419–426.
- [14] G.H. Ayres, B.V. Glanville, *Anal. Chem.* 21 (1949) 930–934.
- [15] C.L. Luke, *Anal. Chim. Acta* 54 (1971) 447–459.
- [16] G.D. Christian, C.E. Matkovich, *Anal. Chim. Acta* 60 (1972) 319–324.
- [17] E. Sabadini, R.A. Baricatti, F.B.T. Pessine, T.D.Z. Atvars, *Quim. Nova* 17 (1994) 27–30.
- [18] A.F. Taylor, R.E. Escott, *Analyst* 110 (1985) 847–849.
- [19] C. Liang, P. Vácha, W.E. van der Linden, *Talanta* 35 (1988) 59–61.
- [20] I. Kagevall, O. Astrom, A. Cedergren, *Anal. Chim. Acta* 132 (1981) 215–218.
- [21] I. Nordin-Anderson, O. Astrom, A. Cedergren, *Anal. Chim. Acta* 162 (1984) 9–18.
- [22] N. Dantan, S. Kroning, W. Frenzel, S. Kuppers, *Anal. Chim. Acta* 420 (2000) 133–142.
- [23] I. Kagevall, O. Astrom, A. Cedergren, *Anal. Chim. Acta* 114 (1980) 199–208.
- [24] E.V. Aquino, J.J.R. Rohwedder, C. Pasquini, *Talanta* 71 (2007) 1288–1293.

Table 2

Analytical features of flow-based procedures for the spectrophotometric determination of water in different samples.

Sample	Reagent	Linear Range (mg kg ⁻¹)	LD (mg kg ⁻¹)	CV (%)	SR (h ⁻¹)	Reference
Acetone	K ₂ Cr ₂ O ₇	500–50,000	300	2.4	–	7
Fugacillin	Karl Fischer	100–50,000	–	0.5	120	20
Organic solvents	Karl Fischer	100–50,000	–	0.5	120	21
Methanol	Karl Fischer	100–10,000	20	3.0	120	22
Organic solvents	Karl Fischer	100–2,000	–	1.0–2.0	120	23
Ethanol	Karl Fischer	200–5,000	–	3.0–9.0	–	24
Biodiesel	CoCl ₂	100–5,000	60	0.7	30	This work

LD: limit of detection; CV: coefficient of variation; SR: sampling rate.

Table 3

Mean values and uncertainties ($n=3$) for determination of water in biodiesel by the proposed and reference procedures.

Sample	Water (mg kg ⁻¹)	
	Proposed procedure	Reference procedure [3]
1	118 ± 1	112 ± 1
2	272 ± 2	285 ± 3
3	337 ± 3	323 ± 5
4	197 ± 2	184 ± 2
5	214 ± 2	213 ± 2
6	296 ± 3	294 ± 3

- [25] E. Rodenas-Torralba, F.R.P. Rocha, B.F. Reis, A. Morales-Rubio, M. Guardia, *J. Autom. Meth. Manag.* 2006 (2006) 1–9.
- [26] T.R. Dias, M.A.S. Brasil, M.A. Feres, B.F. Reis, *Sensors Actuat. B* 198 (2014) 448–454.
- [27] F.R.P. Rocha, B.F. Reis, E.A.G. Zagatto, J.L.F.C. Lima, R.A.S. Lapa, J.L.M. Santos, *Anal. Chim. Acta* 468 (2002) 119–131.
- [28] K. Peterson, P.K. Dasgupta, *Talanta* 36 (1989) 49–61.
- [29] K. Sone, Y. Fukada, *Inorganic Thermochemistry*, Springer, Berlin (1987) 13–20 (and 32–34).
- [30] E. Wagner-Czauderna, A. Boron-Cegielkowska, E. Orłowska, M.K. Kalinowski, *Transit. Metal Chem.* 29 (2004) 61–65.



Combination of electrochemistry with chemometrics to introduce an efficient analytical method for simultaneous quantification of five opium alkaloids in complex matrices

Mohammad-Bagher Gholivand^{a,*}, Ali R. Jalalvand^{a,b}, Hector C. Goicoechea^b, Raimundo Gargallo^c, Thomas Skov^d, Giti Paimard^a

^a Faculty of Chemistry, Razi University, Kermanshah 671496734, Iran

^b Laboratorio de Desarrollo Analítico y Quimiometría (LADAQ), Cátedra de Química Analítica I, Universidad Nacional del Litoral, Ciudad Universitaria, CC 242 (S3000ZAA) Santa Fe, Argentina

^c Solution Equilibria and Chemometrics Group, Department of Analytical Chemistry, University of Barcelona, Diagonal 645, E-08028 Barcelona, Spain

^d Quality & Technology, Department of Food Science, Faculty of Science, University of Copenhagen, Copenhagen, Denmark

ARTICLE INFO

Article history:

Received 9 June 2014

Received in revised form

19 July 2014

Accepted 20 July 2014

Available online 26 July 2014

Keywords:

Ant colony optimization

Genetic algorithm

Sample selection

Multivariate calibration

Opium alkaloids

Simultaneous determination

ABSTRACT

For the first time, an analytical methodology based on differential pulse voltammetry (DPV) at a glassy carbon electrode (GCE) and integration of three efficient strategies including variable selection based on ant colony optimization (ACO), mathematical pre-processing selection by genetic algorithm (GA), and sample selection (SS) through a distance-based procedure to improve partial least squares-1 (PLS-1, ACO-GA-SS-PLS-1) multivariate calibration (MVC) for the simultaneous determination of five opium alkaloids including morphine (MOP), noscapine (NOP), thebaine (TEB), codeine (COD), and papaverine (PAP) was used and validated. The baselines of the DPV signals were modeled as a smooth curve, using P-splines, a combination of B-splines and a discrete roughness penalty. After subtraction of the baseline we got a signal with a two-component probability density. One component was for the peaks and it was approximated by a uniform distribution on the potential axis. The other component was for the observed noise around the baseline. Some sources of bi-linearity deviation for electrochemical data were discussed and analyzed. The lack of bi-linearity was tackled by potential shift correction using correlation optimized warping (COW) algorithm. The MVC model was developed as a quinary calibration model in a blank human serum sample (drug-free) provided by a healthy volunteer to regard the presence of a strong matrix effect which may be caused by the possible interferents present in the serum, and it was validated and tested with two independent sets of analytes mixtures in the blank and actual human serum samples, respectively. Fortunately, the proposed methodology was successful in simultaneous determination of MOP, NOP, TEB, COD, and PAP in both blank and actual human serum samples and its results were satisfactory comparable to those obtained by applying the reference method based on high performance liquid chromatography-ultraviolet detection (HPLC-UV).

© 2014 Published by Elsevier B.V.

Abbreviations: DPV, differential pulse voltammetry; GCE, glassy carbon electrode; ACO, ant colony optimization; GA, genetic algorithm; SS, sample selection; PLS, partial least squares; MOP, morphine; NOP, noscapine; TEB, thebaine; COD, codeine; PAP, papaverine; HPLC-UV, high performance liquid chromatography-ultraviolet detection; CCD, central composite design; PSO, particle swarm optimization; PBS, phosphate buffered solution; MVC, multivariate calibration; OLS, ordinary least squares; EJCR, elliptical joint confidence region; CE, capillary electrophoresis; GC-MS, gas chromatography-mass spectrometry; RMSEP, root mean square errors of prediction; REP, relative error of prediction; DDW, doubly distilled water

* Corresponding author. Tel.: +98 831 4274557; fax: +98 831 4274559.

E-mail addresses: mbgholivand2013@gmail.com, mbgholivand@yahoo.com (M.-B. Gholivand).

<http://dx.doi.org/10.1016/j.talanta.2014.07.053>
0039-9140/© 2014 Published by Elsevier B.V.

1. Introduction

Opium is partially dried latex obtained from opium poppy cultivated mainly in Asia, South America and part of Europe [1]. Opiate and their derivatives are very potent analgesics commonly used as therapeutic agents. Some of these compounds are also frequently abused as illicit drugs [2]. Opiates can be classified into the three following series: the first one is constituted of the poppy alkaloids, including morphine (MOP), noscapine (NOP), thebaine (TEB), codeine (COD), and papaverine (PAP); the second category mainly included semi-synthetic or synthetic derivatives of MOP such as pholcodine, ethylmorphine (codethyline) and dextromethorphan which are used in therapy as antitussives and analgesics; the third class is composed of narcotic compounds

including diacetylmorphine (heroin), buprenorphine and methadone [3], usually employed as substitutes in the treatment of addiction.

Many techniques such as gas chromatography–mass spectrometry (GC–MS) [4–7], high performance liquid chromatography (HPLC) [8–10], capillary electrophoresis (CE) [11–14] and electrochemical [15,16] analysis are already available for the quantification of opiates and their derivatives. Among these methods, electrochemical techniques have gained much more attention for their high sensitivity, high accuracy, simple operation mode and low cost. However, no electrochemical methodologies have been developed for simultaneous determination of MOP, NOP, TEB, COD, and PAP, probably due to their similar structural patterns and electrochemical responses showing dramatic overlapping when using conventional electrodes. Recently, voltammetric methods have been reported for the determination of some of these drugs using modified electrodes [17–19], but the treatment involved is time-consuming and the associated cost is high. Thus, it is important to develop new methodologies for the simultaneous determinations of these drugs. An attractive possibility is the use of chemometric and multivariate calibration methods.

In multivariate calibration, variable selection chooses those potentials from the whole available voltammogram which have maximum information regarding the analyte of interest while discards those carrying irrelevant information (noise, saturation regions) or those heavily overlapped with other sample components which are not of interest [20,21]. Variable selection can also be applied to any multivariate technique where some sensors can in principle be more selective as to the analyte or property of interest, while others may give negligible signals. Improvement of analytical performance of partial least squares (PLS) has been reported upon variable selection, which supports the continuing interest in this chemometric activity [22,23]. Mathematical pre-processing techniques exist for removing variations in voltammograms from run to run, which are unrelated to analyte concentration changes [24,25]. The removal of these unwanted effects leads to more parsimonious PLS models requiring less latent variables than those based on raw data, and often produce better statistical indicators. Sample selection is another important activity in PLS regression analysis of complex samples and is intended to provide representativeness to the set of samples used for model building [26]. Outlier detection has been extensively discussed in the literature, and several diagnostics have been proposed [27]. From a formal point of view, an outlier is a value which is not representative for the rest of the data [28]. In the context of PLS calibration, the main objective is to identify samples with features which make them significantly different from the remaining ones. Recently, Allegrini et al. [29] have combined all the above procedures into a single algorithm (ACO-GA-SS-PLS-1) whose aim was to find the best PLS calibration model within a Monte Carlo-type philosophy. For variable selection, they have used ant colony optimization (ACO) [30,31] instead of GA. The former

algorithm resembles the behavior of ant colonies in the search of the best path to food sources. It has been recently implemented with success in the field of variable selection, showing better performances than other approaches such as GAs [32–34] and particle swarm optimization (PSO) [35]. For an understanding of details and conditions necessary to successfully apply ACO-GA-SS-PLS-1 the reader is referred to Ref. [29].

In this work, we present the development of an electroanalytical methodology based on DPV at a GCE and the ACO-GA-SS-PLS-1 [29] for the simultaneous determination of MOP, NOP, TEB, COD, and PAP in human serum samples of both healthy and patient volunteers (Scheme 1). Finally, the accuracy of the proposed method in simultaneous determination of MOP, NOP, TEB, COD, and PAP in human serum samples will be compared with the reference method based on HPLC-UV. Literature survey revealed that no attempt has been made till date to the simultaneous voltammetric determination of MOP, NOP, TEB, COD, and PAP with the aid of Chemometrics.

2. Experimental

2.1. Chemicals and solutions

MOP, NOP, TEB, COD, and PAP were purchased from Sigma-Aldrich. A phosphate buffered solution (PBS, 0.1 mol L⁻¹) of pH 3.0 was prepared from chemicals (analytical grade) including NaH₂PO₄ and Na₂HPO₄ from Merck. All other chemicals used in the investigation were of analytical grade obtained from regular sources and used without further purification. Stock standard solutions of MOP, NOP, TEB, COD, and PAP were prepared by exact weighing and dissolving of their solid powder in Methanol (5.0 mL) with a concentration level of 0.1 mol L⁻¹ and were stored at dark in a refrigerator until analysis time. Working solutions were prepared by appropriate dilution of the stock standard solutions with PBS (0.1 mol L⁻¹, pH 3.0). All the solutions were prepared by doubly distilled water (DDW).

2.2. Apparatus and softwares

Electrochemical experiments were performed using an Autolab (Eco Chemie BV, Netherlands) controlled by the NOVA software (Version 1.8). A conventional three-electrode cell was used with a saturated Ag/AgCl as reference electrode, a Pt wire as counter electrode and a GCE as working electrode. The pH of the solutions was adjusted using a JENWAY-3510 pH meter equipped by a combined glass electrode. HPLC-UV analyses reported in this study were carried out by a Medical Diagnostic Laboratory in Kermanshah, Iran whose HPLC system consisted of a Younglin ACME 9000.0 (Seoul, Korea) equipped with a quaternary pump, online degasser, column heater, autosampler and UV detector. Data collection and analyses were performed using Autochro 2000.0



Scheme 1. Schematic representation of the methodology employed to simultaneous quantification of MOP, NOP, TEB, COD, and PAP.

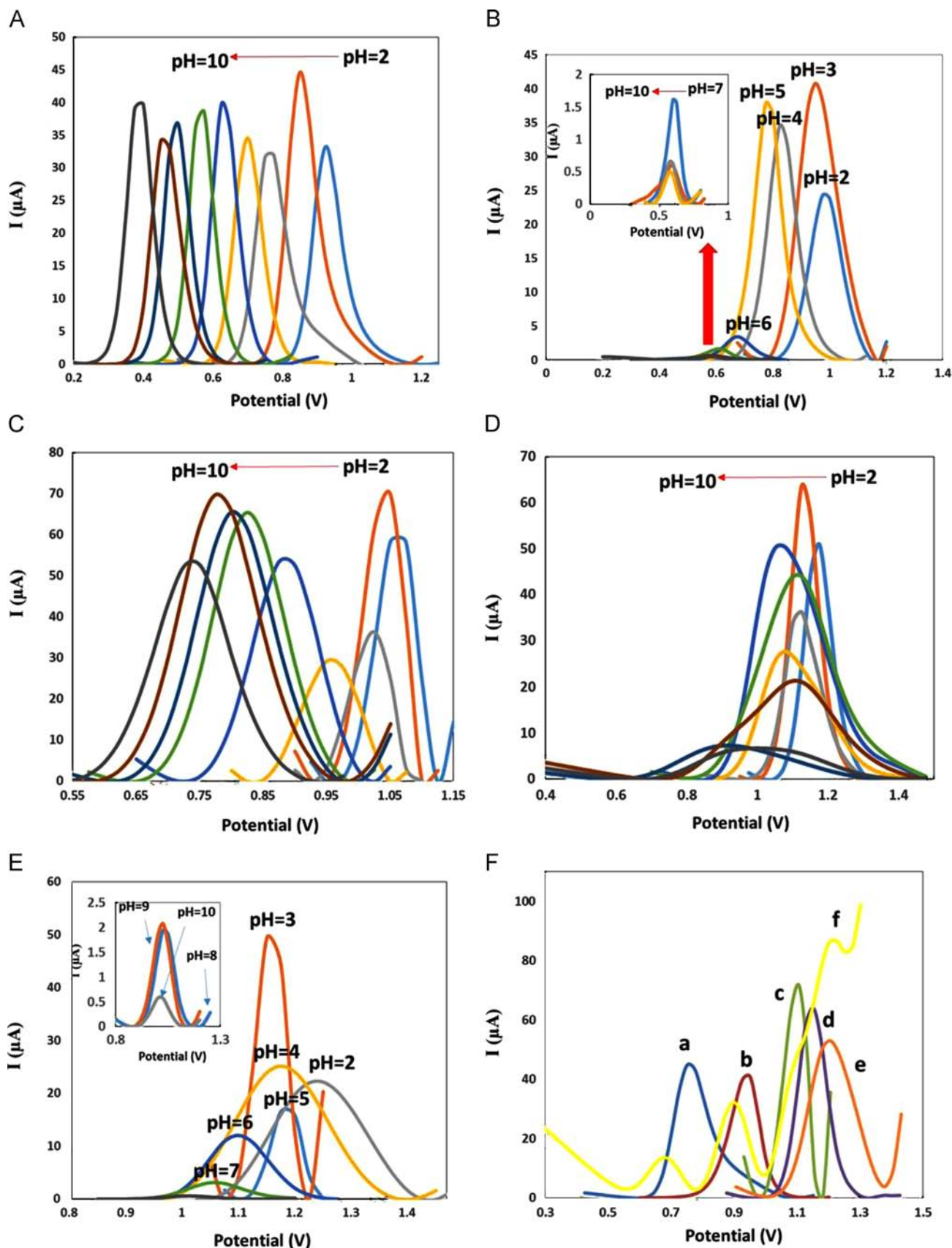


Fig. 1. Differential pulse voltammograms of (A) MOP (360 × 10⁻³ mol L⁻¹), (B) NOP (0.1 × 10⁻³ mol L⁻¹), (C) TEB (0.1 × 10⁻³ mol L⁻¹), (D) COD (0.1 × 10⁻³ mol L⁻¹), and (E) PAP (130 × 10⁻³ mol L⁻¹) in 0.1 mol L⁻¹ PBS at different pHs. (F) Differential pulse voltammograms of (a) MOP (360 × 10⁻³ mol L⁻¹), (b) NOP (0.1 × 10⁻³ mol L⁻¹), (c) TEB (0.1 × 10⁻³ mol L⁻¹), (d) COD (0.1 × 10⁻³ mol L⁻¹), (e) PAP (130 × 10⁻³ mol L⁻¹) and (f) a mixture of MOP (360 × 10⁻³ mol L⁻¹), NOP (0.1 × 10⁻³ mol L⁻¹), TEB (0.1 × 10⁻³ mol L⁻¹), COD (0.1 × 10⁻³ mol L⁻¹), and PAP (130 × 10⁻³ mol L⁻¹) in PBS (0.1 mol L⁻¹, pH 3.0).

software (Younglin). Separation was achieved on C-18 column, Perfectsil Target ODS3 (150.0 mm × 4.6 mm, 5.0 μm) with a 10.0 mm × 4.0 mm, 5.0 μm guard column (MZ-Analysentechnik, Mainz, Germany). The elution was isocratic with mobile phase of acetonitrile and 10.0 mmol L⁻¹ potassium phosphate buffer adjusted to pH 6.0 with orthophosphoric acid (83/17, v/v). The flow rate was 1.0 mL min⁻¹ and yielded a backpressure of about 740.0 psi. The column temperature was maintained at 35 °C, the detection was monitored at a wavelength of 285.0 nm and injection volume was 20.0 μL. All the recorded electrochemical data was smoothed, when necessary, and converted to data matrices by the use of several home-made m-files in MATLAB environment (Version 7.14, MathWorks, Inc.). All the computations for baseline correction, data alignment and multivariate calibration (MVC) were performed in MATLAB environment. All the computations were performed on a DELL XPS laptop (L502X) with Intel Core i7-2630QM 2.0 GHz, 8 GB of RAM and Windows 7-64 as its operating system.

2.3. Preparation of the serum samples

A blank human serum sample (drug-free) was provided by a healthy volunteer who not exposed to any drug or opium for at least 10.0 months. Actual human serum samples were collected from two patients, a patient under PAP treatment (Serum 1) and a cancerous patient under NOP treatment (Serum 2), kindly provided by a Medical Diagnostic Laboratory in Kermanshah, Iran. The following methodology was used to prepare all the serum samples: according to the method of Shu et al. [36], to eliminate protein and other substances, 5.0 mL of human serum sample was placed in a 10.0 mL glass tube and 5.0 mL of 15.0% (w/v) Zinc Sulfate solution-Acetonitrile (50/40, v/v) was added. The glass tube was vortexed for 20.0 min, maintained at 4.0 °C for 15.0 min followed by centrifugation at 4000.0 rpm for 5.0 min. Then, the supernatant was collected in the same tube and this solution was used for subsequent analyses.

2.4. Model efficiency estimation

Whether a model can be applied to analysis of human serum samples or not, model validation is possibly the most important step in the model building sequence. In order to evaluate the performance of MVC models, each model was validated for the prediction of validation and test sets, evaluating root mean square errors of prediction (RMSEP), and relative error of prediction (REP).

$$\text{RMSEP} = \sqrt{\frac{\sum_{i=1}^n (y_{\text{pred}} - y_{\text{act}})^2}{n}} \quad (1)$$

$$\text{REP}(\%) = \frac{100}{y_{\text{mean}}} \sqrt{\frac{1}{n} \sum_{i=1}^n (y_{\text{pred}} - y_{\text{act}})^2} \quad (2)$$

where y_{act} and y_{pred} are actual and predicted concentrations of each component, respectively, and n is the number of samples in validation or test set.

2.5. Electrochemical procedure

Prior to electrochemical experiments, the GCE was successively polished to a mirror using 0.3 and 0.05 μm Alumina slurry. Afterward, the electrode was washed thoroughly with Ethanol and DDW and dried at room temperature. All electrochemical experiments were carried out at room temperature. The DPV measurements were carried out at the following operating conditions for the five studied analytes: step potential 0.025 V, modulation

amplitude 0.055 V, modulation time 0.05 s, interval time 0.5 s, and scan rate 0.05 V s⁻¹.

3. Results and discussion

3.1. Electrochemical studies

3.1.1. pH dependence study

To select the best pH for the simultaneous determination of MOP, NOP, TEB, COD, and PAP, the effect of pH on the peak current of the anodic differential pulse voltammograms (DPVs) of MOP, NOP, TEB, COD, and PAP was investigated. Fig. 1A–E shows the influence of the pH of the PBS (0.1 mol L⁻¹), in the range of 2.0–10.0, on the signal intensities of 0.1 mM MOP, NOP, TEB, COD, and PAP. As can be observed in Fig. 1A–E, all peak currents of the studied analytes have a maximum value at pH 3.0. Taking into account that for analytical purposes both maximal and stable currents are necessary, a pH value of 3.0 was selected for further experiments. The oxidation peak potential of all studied analytes shifted to less positive values as the pH of the buffer solution was increased (Fig. 1A–E).

3.1.2. Effect of scan rate

The influences of scan rate (ν) on the peak current (I_p) of MOP, NOP, TEB, COD, and PAP at the GCE in PBS (0.1 mol L⁻¹, pH 3.0) were studied by cyclic voltammetry (not shown). In the range of 10.0–800.0 mV s⁻¹, a linear relationship was established between I_p and $\nu^{1/2}$, for all of the studied analytes, indicating the diffusion controlled mechanism. The linear regression equations are $I_{p, \text{MOP}} (\mu\text{A}) = 1.0906 + 127.66\nu^{1/2} \text{ V s}^{-1}$ ($R^2 = 0.9941$), $I_{p, \text{NOP}} (\mu\text{A}) = 30.372 + 36.421\nu^{1/2} \text{ V s}^{-1}$ ($R^2 = 0.9911$), $I_{p, \text{TEB}} (\mu\text{A}) = 21.123 + 174.09\nu^{1/2} \text{ V s}^{-1}$ ($R^2 = 0.9908$), $I_{p, \text{COD}} (\mu\text{A}) = 17.535 + 156.24\nu^{1/2} \text{ V s}^{-1}$ ($R^2 = 0.9950$), and $I_{p, \text{PAP}} (\mu\text{A}) = 12.342 + 143.12\nu^{1/2} \text{ V s}^{-1}$ ($R^2 = 0.9986$).

3.2. Chemometric studies

3.2.1. A glance to necessity of MVC

Fig. 1F shows the DPVs of MOP (curve a), NOP (curve b), TEB (curve c), COD (curve d), PAP (curve e) and their mixture (curve f) in PBS (0.1 mol L⁻¹, pH 3.0). In all conditions evaluated, a strong signal overlapping was observed for the simultaneous analysis of MOP, NOP, TEB, COD, and PAP at the GCE (see Fig. 1F, curve f). Thus, the quantification of any of these analytes will be biased if univariate calibration is used as analytical method, and for tackling this problem it was necessary to use MVC.

3.2.2. Calibrations

3.2.2.1. Univariate calibrations. Prior to multivariate calibration experiments, univariate calibration experiments were performed (Fig. 2A–E) and calibration curves were constructed with several points as peak current versus analyte concentration in the range 0.02–7.41 and $7.41\text{--}360.0 \times 10^{-3} \text{ mol L}^{-1}$ for MOP (inset of Fig. 2A), $1.0\text{--}600.0 \times 10^{-6} \text{ mol L}^{-1}$ for NOP (inset of Fig. 2B), $5.0\text{--}500.0 \times 10^{-6} \text{ mol L}^{-1}$ for TEB (inset of Fig. 2C), $1.2\text{--}250.0 \times 10^{-6} \text{ mol L}^{-1}$ for COD (inset of Fig. 2D), and $0.3\text{--}135.0 \times 10^{-3} \text{ mol L}^{-1}$ for PAP (inset of Fig. 2E), and evaluated by linear regression which were the limiting assayed concentrations in subsequent analyses. All analytes showed linear dependences between peak current and concentration at different concentrations intervals.

3.2.2.2. Multivariate calibrations. When the analytes are analyzed in the presence of interferences, the electrochemical profile revealed additional changes to those observed in the absence of interferences. The main changes observed were minor alterations in the baseline and displacement of peak potential, probably due

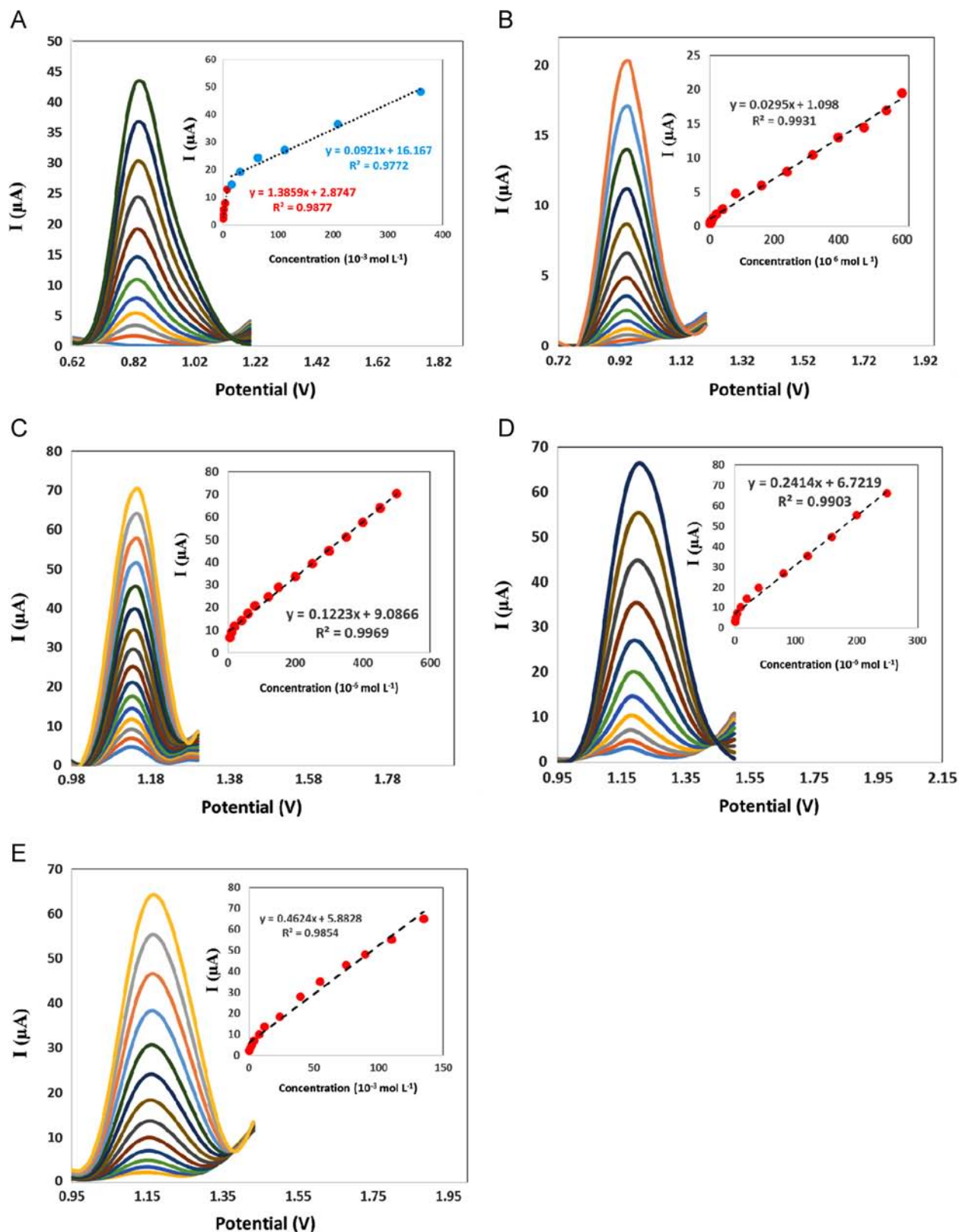


Fig. 2. Representative differential pulse voltammograms of (A) MOP, (B) NOP, (C) TEB, (D) COD, and (E) PAP PBS (0.1 mol L^{-1} , pH 3.0) at different concentrations. Insets: dependence of I_p with concentration.

to modification in viscosity of the solution and consequently the diffusion coefficient of the analytes. This effect produces alterations in the chemometrics responses and for this reason, the calibration and validation sets were prepared in a blank human serum sample (drug-free).

3.2.2.3. Calibration set. The human serum has a complex matrix and may contain a lot of unexpected interferences therefore, if the presence of these interferences was not considered during calibration, a first-order MVC model would give biased predictions of the concentration of the analytes of interest. Therefore, the

calibration set was prepared in a blank human serum sample (drug-free) which was collected from a healthy volunteer to regard the complex matrix of the serum sample which may contain a lot of unexpected interferences. This strategy was applied in order to provide PLS-1 enough information concerning the signals of the analytes when they are embedded into the real background. All the calibration mixtures (the compositions of the calibration mixtures were selected according to a central composite design (CCD), Table 1) were prepared in the blank human serum sample spiked with an appropriate amount of each analyte of interest considering the linear calibration ranges (previously established from univariate calibrations for each analyte). All samples were diluted with PBS (0.1 mol L⁻¹, pH 3.0) to adjust the pH and then appropriate amounts of these diluted samples were transferred to the electrochemical cell, and the solutions were measured in random order. Final concentration of each analyte was obtained by multiplying the detected value by the appropriate dilution factor.

3.2.2.4. Validation set. To check the prediction ability of the model after optimizing all calibration parameters, a validation set of fifteen quinary mixtures (Table 1) was prepared in the blank human serum sample (drug-free). The concentrations of five analytes were selected at random from the corresponding calibration ranges. All samples were diluted with PBS (0.1 mol L⁻¹, pH 3.0) to adjust the pH and then appropriate amounts of these diluted samples were transferred to the electrochemical cell, and the solutions were measured in random order. Final concentration of each analyte was obtained by multiplying the detected value by the appropriate dilution factor.

3.2.2.5. Test set. With the purpose of evaluating the proposed method in a very interfering environment such as human serum, a test set of fifteen quinary mixtures (Table 1) was prepared in Serum 1 (see Section 2.3.) with random amount of each analyte of interest in the same concentration range used for calibration. All samples were diluted with PBS (0.1 mol L⁻¹, pH 3.0) to adjust the pH and then appropriate amounts of these diluted samples were transferred to the electrochemical cell, and the solutions were measured in random order. Final concentration of each analyte was obtained by multiplying the detected value by the appropriate dilution factor. It should be noted that all the samples related to the test set were prepared in the Serum 1 (see Section 2.3) which contains PAP therefore, the exact concentrations of the spiked PAP were computed by a previous knowledge about the initial amount of PAP in the Serum 1 which was obtained by analyzing the Serum 1 with HPLC-UV method prior to analyzing by the proposed method in this study.

3.2.3. Pretreatment and data arrangement

Besides the problem arising from the presence of severely overlapping analyte profiles, in the present study two additional complications may occur: (1) interactions among analytes and the background interferences present in the serum, which may cause signal changes in comparison with pure analyte profiles, and (2) sample-to-sample potential shifts in the analyte profiles, which are common in voltammetric studies. For tackling the first problem, it was necessary to include the possible interferences in the calibration set in order to allow PLS-1 to model the analyte-background interactions before prediction on new samples. Concerning the second commented problem, some preprocessing alternatives were independently applied on the electrochemical responses before PLS-1 model building and validation.

In our previous work [37] we pointed out that voltammetric performance can be enhanced by eliminating noise and background components therefore, baseline elimination is a crucial

step for reducing both complexity and number of the unexpected components. Moreover, it was demonstrated that the use of signal pre-treatments such as baseline and potential shift corrections improve the quality of first-order voltammetric signals and, as a consequence, the performance of resolution by first-order algorithms [37]. In the subsequent sections, some strategies are examined for achieving the mentioned aims.

3.2.3.1. Baseline correction. A variety of instruments deliver signals that consist of a series of more or less isolated peaks. The physical or chemical information is in the positions and the heights of the peaks. Ideally the baseline should be flat, but this is seldom the case. In practice slow, but strong, fluctuations are seen, which are known as background, drift, or baseline. The aim of this section was to estimate a baseline from a data series, exploiting two characteristic properties: the baseline changes smoothly, while all peaks have the same sign, either positive or negative. After estimation, the baseline is subtracted, and peak analysis can follow. Baseline correction was performed based on an adaptation of the method described in de Rooi et al. [38]. The baseline was modeled as a smooth curve, using P-splines, a combination of B-splines and a discrete roughness penalty [39]. After subtraction of the baseline we got a signal with a two-component probability density. One component was for the peaks and it was approximated by a uniform distribution on the positive axis. The other component was for the observation noise around the baseline; it was assumed to be normal. For an understanding of the assumptions and conditions necessary to successfully apply baseline correction the reader is referred to Ref. [38].

3.2.3.2. Potential shift correction. For chemometric model building, several strategies have been proposed to align shifted signals such as chromatograms, electropherograms or NIR spectra. One of the most popular ones is correlation optimized warping (COW) [40,41]. However, this situation has been scarcely described for electrochemical signals [37]. According to the literature, the shift in electrochemical responses can be originated from adsorptive phenomena on the electrode surface, pH variations in the cell or fluctuations in the composition of cell solution, among others [42].

A basic assumption for application of a MVC model is the data bi-linearity, which may be compromised by the above commented potential shifts. Therefore, the DPV signals were aligned towards a target signal using COW. The COW algorithm was introduced by Nielsen et al. [40] as a method to correct for shifts in discrete data signals. It is a piecewise or segmented data preprocessing technique that uses dynamic programming to align a sample signal towards a reference signal by stretching or compression of sample segments using linear interpolation. First, the segment and slack were optimized using a simplex-like optimization routine and then mean voltammogram was selected as target “signal”.

The results of baseline and shift corrections are shown in Fig. 3. Fig. 3A shows the raw DPV data recorded for the calibration set. Fig. 3B shows the results of baseline-corrected data, and as can be seen the baseline is satisfactorily corrected. Fig. 3C shows the results of applying COW for data alignment and it confirms the capability of COW for aligning the data. Fig. 3D and E shows baseline- and shift-corrected DPV data for validation and test sets, respectively.

3.3. Performance evaluation of the developed MVC model in blank and actual serum samples

In PLS calibration, it is usual to have two data sets: a calibration set, employed to build the regression model, and a validation set to check the prediction ability of the PLS model

Table 1
Concentration data of calibration set (C₁–C₃₀), validation set (V₁–V₁₅), and test set (T₁–T₁₅).

Sample	MOP (10 ⁻³ mol L ⁻¹)	NOP (10 ⁻⁶ mol L ⁻¹)	TEB (10 ⁻⁶ mol L ⁻¹)	COD (10 ⁻⁶ mol L ⁻¹)	PAP (10 ⁻³ mol L ⁻¹)	Sample	MOP (10 ⁻³ mol L ⁻¹)	NOP (10 ⁻⁶ mol L ⁻¹)	TEB (10 ⁻⁶ mol L ⁻¹)	COD (10 ⁻⁶ mol L ⁻¹)	PAP (10 ⁻³ mol L ⁻¹)
C ₁	90	150	125	62.5	101.25	V ₁	50	2	7.5	1.5	0.5
C ₂	90	150	125	187.5	33.75	V ₂	100	350	420	132	120
C ₃	90	150	375	62.5	33.75	V ₃	0.4	1.5	132	241	21
C ₄	90	150	375	187.5	101.25	V ₄	15	400	178	77	76
C ₅	90	450	125	62.5	33.75	V ₅	245	280	298	45	54
C ₆	90	450	125	187.5	101.25	V ₆	320	140	15	53	33
C ₇	90	450	375	62.5	101.25	V ₇	12	27	45	89	25
C ₈	90	450	375	187.5	33.75	V ₈	0.5	33	121	131	100
C ₉	270	150	125	62.5	33.75	V ₉	135	95	150	178	77
C ₁₀	270	150	125	187.5	101.25	V ₁₀	45	210	210	55	29
C ₁₁	270	150	375	62.5	101.25	V ₁₁	20	375	280	33	25
C ₁₂	270	150	375	187.5	33.75	V ₁₂	85	410	320	21	61
C ₁₃	270	450	125	62.5	101.25	V ₁₃	190	51	390	78	89
C ₁₄	270	450	125	187.5	33.75	V ₁₄	280	38	22	120	95
C ₁₅	270	450	375	62.5	33.75	V ₁₅	150	455	14	199	41
C ₁₆	270	450	375	187.5	101.25	T ₁	2.4	3.6	10	5	130
C ₁₇	0.02	300	250	125	67.5	T ₂	31	450	456	56	97
C ₁₈	360	300	250	125	67.5	T ₃	243	567	341	77	66
C ₁₉	180	1	250	125	67.5	T ₄	321	552	23	87	54
C ₂₀	180	600	250	125	67.5	T ₅	176	21	245	98	88
C ₂₁	180	300	5	125	67.5	T ₆	131	18	55	43	120
C ₂₂	180	300	500	125	67.5	T ₇	189	187	67	42	128
C ₂₃	180	300	250	1.2	67.5	T ₈	55	32	123	78	76
C ₂₄	180	300	250	250	67.5	T ₉	63	540	32	122	55
C ₂₅	180	300	250	125	0.3	T ₁₀	29	41	65	134	41
C ₂₆	180	300	250	125	135	T ₁₁	88	25	198	66	34
C ₂₇	180	300	250	125	67.5	T ₁₂	192	66	234	22	73
C ₂₈	180	300	250	125	67.5	T ₁₃	44	91	66	157	51
C ₂₉	180	300	250	125	67.5	T ₁₄	51	75	76	198	67
C ₃₀	180	300	250	125	67.5	T ₁₅	55	70	65	180	60

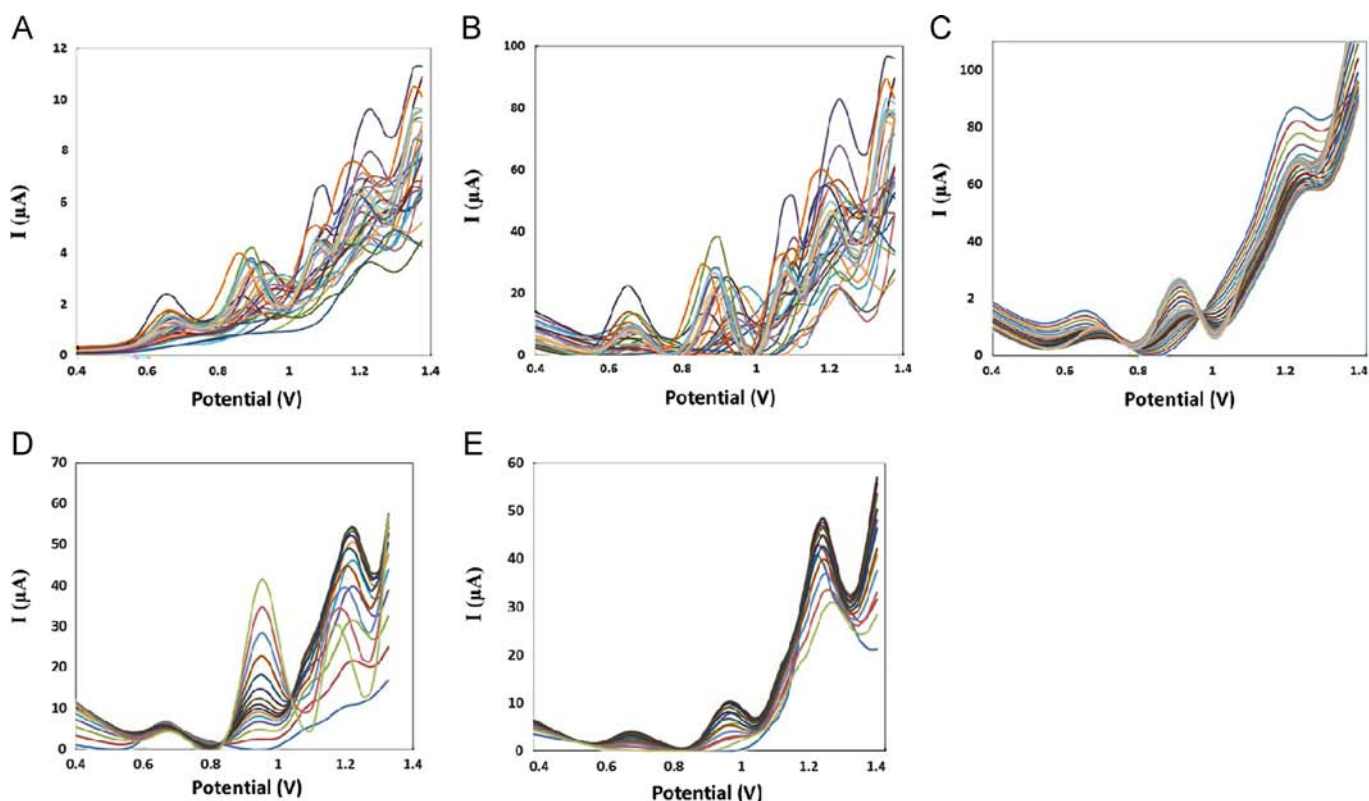


Fig. 3. Differential pulse voltammograms corresponding to: (A) raw data of the calibration set, (B) baseline-corrected data of the calibration set, (C) baseline- and shift-corrected data of the calibration set, (D) baseline- and shift-corrected data of the validation set, and (E) baseline- and shift-corrected data of the test set.

Table 2
Specific ACO-GA-SS-PLS-1 parameters.

Parameter	MOP	NOP	TEB	COD	PAP
Number of ants	30	30	30	30	30
Blind proportion	0.5	0.5	0.5	0.5	0.5
Minimum number of variables	3	3	3	3	3
Maximum number of variables	8	8	8	8	8
Number of chromosomes	40	40	40	40	40
Mutation frequency	0.1	0.1	0.1	0.1	0.1
Cycles	40	40	40	40	40
Epochs	40	40	40	40	40
Sensor window	10	10	10	10	10
Tolerance	0.3	0.3	0.3	0.3	0.3
Latent variables	6	5	7	5	6

after all calibration parameters have been optimized, but in this study we are going to determine the analytes' concentrations in actual human serum samples which have a very complex matrix due to the presence of many interferences present in the serum therefore, with the purpose of evaluating the method in the presence of interferences, a test set was also prepared in an actual human serum sample.

Before calibration, it is usual to assess the optimum number of latent variables in order to avoid overfitting, by applying the well-known cross-validation method described by Haaland and Thomas [43]. With the purpose of estimating the number of optimum latent variables for ACO-GA-SS-PLS-1 leave-one-sample-out cross-validation was performed. The optimum number of factors is estimated by calculating the ratios $F(A) = \text{PRESS}(A < A^*) / \text{PRESS}(A)$, where $\text{PRESS} = \sum (c_{i,\text{act}} - c_{i,\text{pred}})^2$, A is a trial number of factors, A^* corresponds to the minimum PRESS, and $c_{i,\text{act}}$ and $c_{i,\text{pred}}$ are the actual and predicted concentrations for the i th sample left out of the calibration during cross validation, respectively. Then, the

Table 3
Figures of merit obtained by ACO-GA-SS-PLS-1 in validation and test data sets.

	MOP	NOP	TEB	COD	PAP
Full voltammogram					
RMSEP _{Validation}	0.51	1.16	0.99	1.54	1.95
RMSEP _{Test}	0.89	1.77	2.13	0.96	1.45
REP% _{Validation}	4.32	3.11	3.08	2.22	2.11
REP% _{Test}	2.14	1.96	2.66	1.31	2.09
$R^2_{\text{Validation}}$	0.8911	0.9110	0.9087	0.9031	0.9321
R^2_{Test}	0.9341	0.9213	0.8976	0.9123	0.9040
No. of latent variables	6	5	7	5	6
After ACOGASS selection					
RMSEP _{Validation}	0.08	0.15	0.11	0.08	0.16
RMSEP _{Test}	0.11	0.09	0.08	0.11	0.07
REP% _{Validation}	0.97	0.88	0.75	0.91	0.68
REP% _{Test}	0.07	0.11	0.07	0.06	0.13
$R^2_{\text{Validation}}$	0.9765	0.9802	0.9888	0.9901	0.9795
R^2_{Test}	0.9981	0.9706	0.9900	0.9898	0.9805
No. of latent variables	4	4	5	4	5
Pre-processing	None	None	None	None	None

number of factors leading to a probability of less than 75% that $F > 1$ is selected.

The ACO-GA-SS-PLS-1 algorithm was run on the calibration, and validation sets using the parameters shown in Table 2. According to the results presented in Table 3, with very satisfactory values for RMSEPs and REPs for the five analytes of interest it is apparent that the ACO-GA-SS-PLS-1 approach has found the correct answer. The results indicated that the RMSEPs_{Validation} and REPs_{Validation} found by ACO-GA-SS-PLS-1 were apparently smaller than those with no selection.

With the purpose of analyzing the potentiality of the evaluated methodology based on DPV data processed by ACO-GA-SS-PLS-1, a test set of fifteen quinary mixtures (see Table 1) was prepared

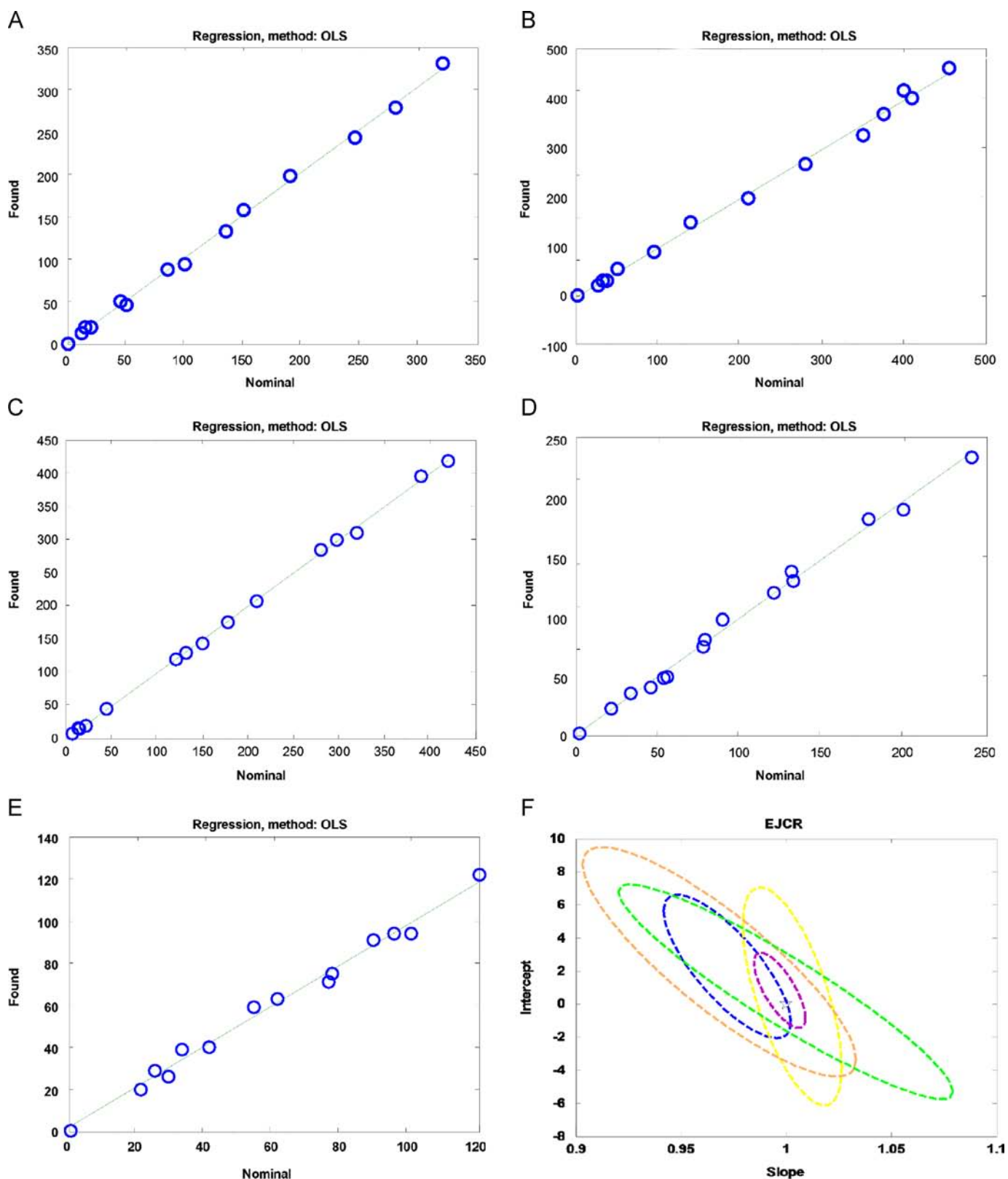


Fig. 4. Plots for predicted concentrations as a function of nominal values for (A) MOP, (B) NOP, (C) TEB, (D) COD, and (E) PAP in validation set. (F) Elliptical joint regions (at 95% confidence level) for the slopes and intercepts of the regressions for MOP (blue ellipse), NOP (yellow ellipse), TEB (purple ellipse), COD (orange ellipse), and PAP (green ellipse) in validation set. Star point marks the theoretical (0,1) point. (For interpretation of the references to color in this figure legend, the reader is referred to the web version of this article.)

in Serum 1 (see Section 2.3.) with random amount of each analyte of interest in the same concentration range used for calibration. All samples were diluted with PBS (0.1 mol L^{-1} , pH 3.0) to adjust the

pH and then appropriate amounts of these diluted samples were transferred to the electrochemical cell. Final concentration of each analyte was obtained by multiplying the detected value by the

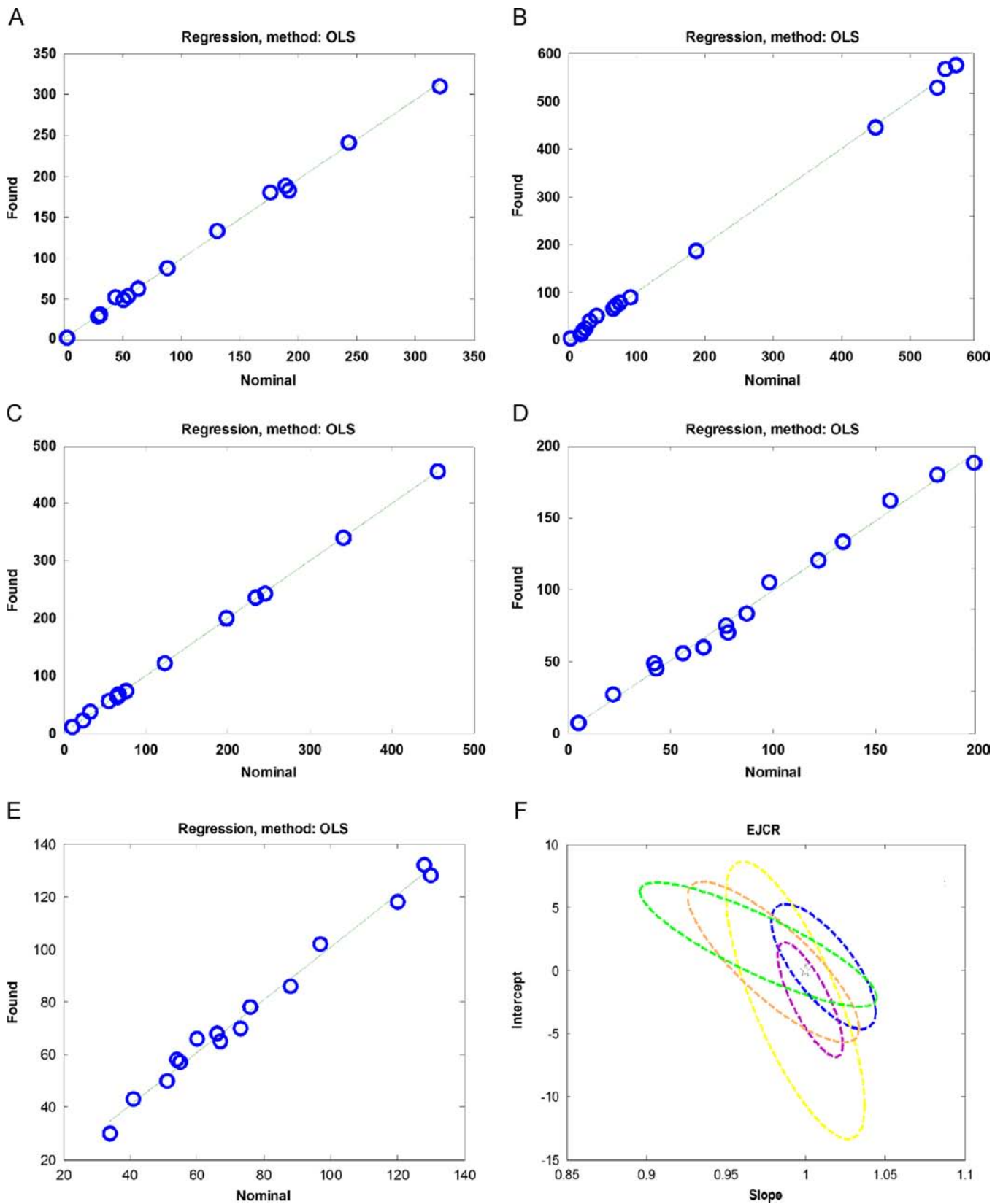


Fig. 5. Plots for predicted concentrations as a function of nominal values for (A) MOP, (B) NOP, (C) TEB, (D) COD, and (E) PAP in test set. (F) Elliptical joint regions (at 95% confidence level) for the slopes and intercepts of the regressions for MOP (blue ellipse), NOP (yellow ellipse), TEB (purple ellipse), COD (orange ellipse), and PAP (green ellipse) in test set. Star point marks the theoretical (0,1) point. (For interpretation of the references to color in this figure legend, the reader is referred to the web version of this article.)

appropriate dilution factor. According to the results presented in Table 3 for the test set, with very satisfactory values for $RMSEPs_{Test}$ and $REPs_{Test}$ for the five analytes of interest it is apparent that the ACO-GA-SS-PLS-1 approach has found the correct answer. The results indicated that the $RMSEPs_{Test}$ and $REPs_{Test}$ found by ACO-GA-SS-PLS-1 were apparently smaller than those with no selection.

For the sake of a further investigation into the accuracy of the proposed method, the predicted concentrations of both validation (Table S1, Supplementary Information) and test (Table S2) sets were regressed on the nominal concentrations. In this case an ordinary least squares (OLS) analysis of predicted concentrations versus nominal concentrations was applied [44]. The calculated intercept and slope were compared with their theoretically expected values (intercept=0, slope=1), based on the elliptical joint confidence region (EJCR) test. If the ellipses contain the values 0 and 1 for intercept and slope (ideal point), respectively, showing the predicted and nominal values do not present significant difference at the level of 95% confidence and the elliptic size denotes precision of the analytical method, smaller size corresponds to higher precision [45]. Figs. 4A–E and 5A–E show the regression of predicted concentrations on nominal values based on OLS method corresponding to the validation and test sets, respectively, and Fig. 4F and Fig. 5F show the corresponding ellipses of the EJCR analyses. As can be concluded from Figs. 4A–E and 5A–E, the predictions for MOP, NOP, TEB, COD, and PAP in both validation and test sets are in good agreement with the nominal values. If the EJCRs for validation set are analyzed (Fig. 4F), it is notable that while the ellipses for NOP, TEB, COD, and PAP include the theoretically expected point (ideal point), indicating accuracy of the developed methodology for these analytes while the ideal point falls on the MOP ellipse, denoting slightly poorer prediction accuracy for MOP. But all the ellipses in the test set contain the ideal point (Fig. 5F) which shows the accurate determination of all analytes in test set by the developed methodology. The statistical results shown in Table 3, with adequate values for $RMSEPs_{Test}$ and $REPs_{Test}$ for all analytes, do also support this conclusion.

3.4. Comparison of the performance of the proposed methodology with the reference method (HPLC-UV)

When a new analytical method is introduced it is necessary to check its results with those of a well-known reference method. Regarding this important point, we extended our study for comparing its accuracy for simultaneous determination of MOP, NOP, TEB, COD, and PAP in another actual human serum sample (Serum 2, see Section 2.3) with the reference method based on HPLC-UV. Table 4 compares the results obtained by the proposed method with those obtained by HPLC-UV. Although, the results indicate that the accuracy of the HPLC-UV methods is slightly better than that of the proposed method but it may be concluded that the results obtained using the proposed method are in an acceptable agreement with those obtained by the HPLC-UV method.

Taking into account the good results obtained by applying both proposed and HPLC-UV methods, either of them can be recommended for the simultaneous determination of MOP, NOP, TEB, COD, and PAP in human serum samples. Recommendation of the proposed method will depend on the analyst's knowledge about the theoretical considerations on the chemometric methods. If the analyst suffers from instrumental limitations for applying HPLC-UV, it is better to use the proposed method. However, this option needs having a background about the theoretical aspects of chemometric methods. But for a person who does not have enough knowledge about chemometric methods and is not face

Table 4

Results of analysis of Serum 2 by the proposed methodology in this study and reference method (HPLC-UV).

Opium alkaloid	Proposed methodology in this study			Reference method (HPLC-UV)	
	Added (mol L ⁻¹)	Found	Recovery (%)	Found	Recovery (%)
MOP	None	N.D ^a	–	None	N.D
	5×10^{-3}	4.8	96.0	5	100.0
	50×10^{-3}	53	105.6	51	101.9
	21×10^{-3}	20.5	97.6	22	104.5
NOP	None	2	–	1.8	–
	60×10^{-6}	64	103.2	62.5	100.8
	4×10^{-6}	6.2	104.8	6.1	102.4
TEB	100×10^{-6}	108	105.7	99	97.0
	None	N.D	–	0.02	–
	10×10^{-6}	9.5	95.0	9.9	99.0
	250×10^{-6}	260	103.8	248.5	99.4
COD	100×10^{-6}	96	96.0	101.2	101.2
	None	N.D	–	N.D	–
	140×10^{-6}	135.3	96.6	139.1	99.3
	75×10^{-6}	78	103.8	74	98.7
PAP	12×10^{-6}	13	107.7	11.6	96.7
	None	N.D	–	N.D	–
	67×10^{-3}	70	104.3	67.1	100.1
	31×10^{-3}	29.8	96.1	30.8	99.3
	42×10^{-3}	44.2	104.9	41	97.6

^a Not detected.

to instrumental limitations it is recommended to use HPLC-UV method.

4. Concluding remarks

In the present article, combination of electrochemistry with chemometrics led us to introduce an efficient analytical method for simultaneous determination of MOP, NOP, TEB, COD, and PAP at a GCE in very complex matrices. The five studied analytes exhibited a similar anodic behavior, all of irreversible character and pH-dependent. A strong voltammetric overlapping was observed for the simultaneous analysis of these compounds. The overlapping was successfully resolved using ACO-GA-SS-PLS-1. This is the newest example of the power of implementation of three of the main optimization methods in partial least-squares calibration for processing electrochemical data. Because of the non-bilinear behavior of the experimental data, the potential shift correction was carried out by COW as an efficient chemometric algorithm. The baseline of the DPV signals was successfully removed by an efficient chemometric algorithm. To regard the presence of a strong matrix effect which may be caused by the possible interferences present in the human serum sample, the MVC model was built and validated in a blank human serum sample (drug-free) provided by a healthy volunteer which allowed us to exploiting first-order advantage for the simultaneous determination of the five studied analytes in very interfering media such as human serum samples. Finally, the application of the developed method to simultaneously assay the concentrations of MOP, NOP, TEB, COD, and PAP in an actual human serum sample allowed to obtain satisfactory results which were in accordance with the HPLC-UV reference method. This study allows one to propose the present method as a promissory, cheap and accessible alternative for routine determination of the concentrations of MOP, NOP, TEB, COD, and PAP in human serum samples.

Acknowledgments

The financial supports of this project by Razi University Research Council, UNL, CONICET and ANPCyT are gratefully acknowledged. We would also like to thank the reviewers for their insightful comments which led us to an improvement of the work.

Appendix A. Supplementary information

Supplementary data associated with this article can be found in the online version at <http://dx.doi.org/10.1016/j.talanta.2014.07.053>.

References

- [1] S. Li, C. He, H. Liu, K. Li, F. Liu, J. Chromatogr. B 826 (2005) 58–62.
- [2] R. Dams, T. Benijts, W.E. Lambert, A.P. De Leenheer, J. Chromatogr. B 773 (2002) 53–61.
- [3] J. Pothier, N. Galand, J. Chromatogr. A 1080 (2005) 186–191.
- [4] K. Lachenmeier, F. Musshoff, B. Madea, Forensic Sci. Int. 159 (2006) 189–199.
- [5] T. Saito, H. Mase, S. Takeichi, S. Inokuchi, J. Pharm. Biomed. Anal. 43 (2007) 358–363.
- [6] Y.H. Wu, K.L. Lin, S.C. Chen, Y.Z. Chang, Rapid Commun. Mass Spectrom. 22 (2008) 887–897.
- [7] A. Spasic, V. Lukic, M. Spasic, Toxicol. Lett. 180 (2008) S163.
- [8] P. Fernandez, L. Morales, C. Vazquez, A.M. Bermejo, M.J. Taberero, Forensic Sci. Int. 161 (2006) 31–35.
- [9] J.W. Costin, S.W. Lewis, S.D. Purcell, L.R. Waddell, P.S. Franis, N.W. Barnett, Anal. Chim. Acta 597 (2007) 19–23.
- [10] S. Pichini, R. Pacifici, M. Pellegrini, E. Marchei, E.P. Alarcon, C. Puig, O. Vall, O.G. Algar, J. Chromatogr. B 794 (2003) 281–292.
- [11] M.M. Reddy, V. Suresh, G. Jayashanker, B.S. Rao, R.K. Sarin, Electrophoresis 24 (2003) 1437–1441.
- [12] M.L. Agui, C.C. Blanco, A.M.G. Campana, J. Chromatogr. B 877 (2009) 833–836.
- [13] A.R. Fakhari, S. Nojavan, S.N. Ebrahimi, C.J. Evenhuis, J. Sep. Sci. 33 (2010) 2153–2159.
- [14] F. Wei, M. Zhang, Y.Q. Feng, Electrophoresis 27 (2006) 1939–1948.
- [15] J.M.P.J. Garrido, C.D. Matos, F. Borges, T.R.A. Macedo, A.M.O. Brett, Anal. Lett. 37 (2004) 831–844.
- [16] B. Rezaei, S. Damiri, J. Solid State Electrochem. 14 (2010) 1079–1088.
- [17] A. Navae, A. Salimi, H. Teymourian, Biosens. Bioelectron. 31 (2012) 205–211.
- [18] B. Rezaei, S. Zohreh Mirahmadi Zare, Sens. Actuators, B 134 (2008) 292–299.
- [19] M.H. Pournaghi-Azar, A. Saadatirad, J. Electroanal. Chem. 624 (2008) 293–298.
- [20] R.K.H. Galvão, M.C.U. Araújo, in: S.D. Brown, R. Tauler, B. Walczak (Eds.), Comprehensive Chemometrics, 3, Elsevier, Amsterdam, 2009 (p. 233).
- [21] H.W. Siesler, Y. Ozaki, S. Kawata, H.M. Heise (Eds.), Near-infrared Spectroscopy: Principles, Instruments, Applications, Wiley-VCH, Weinheim, Germany, 2002.
- [22] D. Broadhurst, R. Goodacre, A. Jones, J.J. Rowland, D.B. Kell, Anal. Chim. Acta 348 (1997) 71–86.
- [23] J.-P. Gauchi, P. Chagnon, Chemom. Intell. Lab. Syst. 58 (2001) 171–193.
- [24] P. Geladi, D. MacDougall, H. Martens, Appl. Spectrosc. 39 (1985) 491–500.
- [25] R.J. Barnes, M.S. Dhanoa, S.J. Lister, Appl. Spectrosc. 43 (1989) 772–777.
- [26] A. Lorber, B.R. Kowalski, J. Chemom. 2 (1988) 67–79.
- [27] D.L. Massart, B.G.M. Vandeginste, L.M.C. Buydens, S. De Jong, P.J. Lewi, J. Smeyers-Verbeke, Handbook of Chemometrics and Qualimetrics: Part A, Elsevier, Amsterdam, 1997 (p. 202).
- [28] D.L. Massart, B.G.M. Vandeginste, L.M.C. Buydens, S. De Jong, P.J. Lewi, J. Smeyers-Verbeke, Handbook of Chemometrics and Qualimetrics: Part A, Elsevier, Amsterdam, 1997 (p. 109).
- [29] F. Allegrini, A.C. Olivieri, Talanta 115 (2013) 755–760.
- [30] M. Shamsipur, V. Zare-Shahabadi, B. Hemmateenejad, M. Akhond, J. Chemom. 20 (2006) 146–157.
- [31] F. Allegrini, A.C. Olivieri, Anal. Chim. Acta 699 (2011) 18–25.
- [32] H.C. Goicoechea, A.C. Olivieri, J. Chem. Inf. Comput. Sci. 42 (2002) 1146–1153.
- [33] C.E. Boschetti, A.C. Olivieri, J. NIR Spectrosc. 12 (2004) 85–91.
- [34] H.C. Goicoechea, A.C. Olivieri, J. Chemom. 17 (2003) 338–345.
- [35] N. Sorol, E. Arancibia, S.A. Bortolato, A.C. Olivieri, Chemom. Intell. Lab. Syst. 102 (2010) 100–109.
- [36] J.H. Suh, Y.Y. Lee, H.J. Lee, M. Kang, Y. Hur, S.N. Lee, D.H. Yang, S.B. Han, J. Pharm. Biomed. Anal. 75 (2013) 214–219.
- [37] M.B. Gholivand, A.R. Jalalvand, H.C. Goicoechea, T.h. Skov, Talanta 119 (2014) 553–563.
- [38] J.J. de Rooi, P.H.C. Eilers, Chemom. Intell. Lab. Syst. 117 (2012) 56–60.
- [39] P.H.C. Eilers, B.D. Marx, Stat. Sci. 11 (1996) 89–121.
- [40] N.-P.V. Nielsen, J.M. Carstensen, J. Smedsgaard, J. Chromatogr. A 805 (1998) 17–35.
- [41] G. Tomasi, F. Van den Berg, C. Andersson, J. Chemom. 18 (2004) 231–241.
- [42] A.J. Bard, L.R. Faulkner, Electrochemical Methods: Fundamentals and Applications, 2nd ed., John Wiley & Sons, Inc., New York, 2001.
- [43] D.M. Haaland, E.V. Thomas, Anal. Chem. 60 (1988) 1193–1202.
- [44] A.G. Gonzalez, M.A. Herrador, A.G. Asuero, Talanta 48 (1999) 729–736.
- [45] J.A. Arancibia, G.M. Escandar, Talanta 60 (2003) 1113–1121.



Degradation of phenolic compounds by laccase immobilized on carbon nanomaterials: Diffusional limitation investigation



Ran Pang, Mingzhu Li, Chengdong Zhang*

College of Environmental Science and Engineering, Ministry of Education Key Laboratory of Pollution Processes and Environmental Criteria, Tianjin Key Laboratory of Environmental Remediation and Pollution Control, Nankai University, Tianjin 300071, China

ARTICLE INFO

Article history:

Received 8 June 2014

Received in revised form

11 July 2014

Accepted 16 July 2014

Available online 27 July 2014

Keywords:

Carbon nanoparticles

Laccase

Immobilization

Degradation

Phenolic compounds

ABSTRACT

Carbon nanoparticles are promising candidates for enzyme immobilization. We investigated enzyme loading and laccase activity on various carbon nanoparticles, fullerene (C₆₀), multi-walled carbon nanotubes (MWNTs), oxidized-MWNTs (O-MWNTs), and graphene oxide (GO). The loading capacity was highest for O-MWNTs and lowest for C₆₀. The activity of laccase on various nanomaterials using 2,2'-azino-bis(3-ethylbenzothiazoline-6-sulfonic acid) (ABTs) as a substrate decreased in the following order: GO > MWNTs > O-MWNTs > C₆₀. We speculated that aggregation of the nanoparticles influenced enzyme loading and activity by reducing the available adsorption space and substrate accessibility. The nanoparticle-immobilized laccase was then used for removal of bisphenol and catechol substrates. Compared to free laccase, the immobilized enzymes had significantly reduced reaction rates. For example, the reaction rate of GO-laccase conjugated with bisphenol or catechol substrates was only 10.28% or 12.33%, respectively, of that of the free enzyme. Considering that there was no obvious structural change observed after enzyme immobilization, nanomatrix-induced diffusional limitation most likely caused the low reaction rates. These results demonstrate that the diffusional limitation induced by the aggregation of carbon nanoparticles cannot be ignored because it can lead to increased reaction times, low efficiency, and high economic costs. Furthermore, this problem is exacerbated when low concentrations of environmental contaminants are used.

© 2014 Elsevier B.V. All rights reserved.

1. Introduction

Enzymes catalyze many chemical reactions in living systems under mild conditions. The immobilization of enzymes is a useful tool that can reduce costs by enabling efficient recovery, recyclability, enhanced stability under harsh conditions, and continuous use in enzymatic processes in analytical and medical applications [1,2]. The challenges of using immobilized enzymes are identifying new matrix materials with appropriate structural characteristics, such as morphology and surface functionality, and compositions, in addition to understanding enzyme–matrix interactions to improve the catalytic efficiency [3,4].

Recently, nano-structured materials, such as carbon nanomaterials, nano-sized polymer beads, and metal nanoparticles, have been utilized as immobilization matrices for enzymes. The use of nanoparticles offers many advantages, such as effective enzyme loading, large surface area, and increased mechanical strength [5,6]. Among the nano-structured materials, carbon nanomaterials

are the most promising candidates for enzyme immobilization because of their chemical inertness, biocompatibility, and electrical conductivity [7,8]. Ren et al. [9] reported that single-wall carbon nanotubes enhanced the activity of horseradish peroxidase (HRP) by binding to the enzyme close to the active site and participating in the electron transfer process. Graphene oxide (GO)-immobilized HRP showed improved thermal stability and was active over a wide pH range, resulting in higher removal efficiency with several phenolic compounds when compared to soluble HRP [10].

However, the properties of a nanomaterial, such as its surface chemistry, morphology, and size, can influence the adsorption, conformation, and activity of immobilized enzymes. Yang showed [11] that GO greatly enhanced peroxidase activity by unfolding cyt c by electrostatic interactions, whereas reduced GO inhibited cyt c activity via hydrophobic interactions, resulting in decreased substrate accessibility to the heme active site. Boncel et al. [12] demonstrated that different chemical functionalizations of the nano-matrix led to various types of catalytic activity and enantioselectivity. They determined that lipase immobilized onto multi-walled carbon nanotubes (MWNTs) exhibited exceptionally high activity, whereas lipase immobilized onto oxidized MWNTs (O-MWNTs) exhibited low activity with high enantioselectivity.

* Correspondence to: College of Environmental Science and Engineering, Nankai University, 94 Weijin Road, Tianjin 300457, China. Tel.: +86 22 6229517.

E-mail address: zhangchengdong@nankai.edu.cn (C. Zhang).

However, the effects of the properties of the nanomaterial, nature of the interface between the enzyme and nanomaterial, and nature of the substrate environment on enzyme activity have not been fully elucidated. Many enzymes denature when immobilized on nanostructured surfaces, resulting in lower enzyme activity and weaker substrate binding, and various, sometimes contradictory, mechanisms have been suggested [13,14]. Therefore, more insightful studies are needed to investigate the interactions between enzymes and nanomaterials.

Laccases are extracellular enzymes that catalyze the four one-electron oxidation of electron-rich compounds with a simultaneous four-electron reduction of molecular dioxygen to water [3]. Immobilized laccase has a wide range of commercial applications in the oxidation of dyes and lignins and in ethanol production, waste water treatment, and degradation of toxic polycyclic aromatic hydrocarbons [15]. Laccases have been successfully immobilized onto different nanomaterials, such as a MWNT paste electrode [16], nanocomposites formed by chitosan and carbon nanotubes [17], meso-structured silica materials [18], platinum nanoparticles, and reduced graphene composites deposited onto screen printed electrodes [19]. However, most studies on nanoparticles have focused on the improvement of enzyme activity, loading, and catalytic efficiency rather than reaction rates because nanoparticles offer significantly reduced mass transfer resistance as a result of the shortened diffusional path of substrates compared to large-sized porous materials [20]. However, these studies have not considered that the aggregation of nanoparticles may change their exposure surface, porosity, and stability, leading to altered diffusional paths and substrate accessibility to the immobilized enzyme.

The aim of the present study was to assess laccase immobilized on different carbon nanomaterials, MWNTs, O-MWNTs, GO, and fullerene (C₆₀) as a biocatalyst for the degradation of bisphenol A (BPA) and catechol as model phenolic contaminants. To immobilize the laccase, physical adsorption was used rather than covalent bonding because changes in enzyme structure and activity directly reflect the surface-induced non-specific interactions between the enzyme and nanomatrix. To the best of our knowledge, no reports have systematically evaluated the effects of the carbon nanomaterial on the activity of immobilized laccase and how these interactions affect the degradation of phenolic substrates.

2. Materials and methods

2.1. Materials

Sublimed C₆₀ powder (purity > 99.5%) was purchased from SES Research (Houston, TX). MWNTs and O-MWNTs were purchased from Chengdu Organic Chemical Company (Sichuan Province, China). GO (purity > 99%) was purchased from Plannano Technology Company (Tianjin, China). Laccase (EC 1.10.3.2, from *Trametes versicolor*), BPA (purity > 97%), catechol (purity > 99%), and 2,2'-azino-bis-(3-ethylbenzthiazoline-6-sulfonic acid) (ABTs, purity > 98%) were purchased from Sigma-Aldrich (China). All other chemicals and solvents used were of analytical grade or higher.

The surface elemental compositions of nanoparticles were determined by X-ray photoelectron spectroscopy (PHI-5000 Versa Probe, Japan). The ζ potentials were measured by electrophoretic mobility using a ZetaPALS (Brookhaven Instruments, Holtsville, USA). The Brunauer Emmere Teller (BET) surface areas were measured using an ASAP 2010 Accelerated Surface Area and Poresimetry System (Micromeritics Co., USA), and the surface area was calculated using the multipoint adsorption and desorption data of N₂ at 77 K in the relative pressure range of 10⁻⁷–1. The

Table 1

Elemental compositions, zeta potentials, and Brunauer–Emmett–Teller (BET) surface areas of various nanoparticles.

Nanoparticles	Elemental composition ^a		Zeta potential ^b (mV)	BET surface area (m ² /g) ^c
	C%	O%		
C ₆₀	98.91	1.09	–12.73	10.96
GO	65.50	32.88	–12.53	145.16
MWNTs	97.40	2.60	–19.05	113.71
O-MWNTs	96.11	3.89	–16.93	165.64

^a Analyzed by X-ray photoelectron spectroscopy.

^b Measured by electrophoretic mobility using a zetasizer.

^c Determined by N₂ adsorption using the BET method.

physicochemical properties of the carbon nanoparticles are listed in Table 1.

2.2. Adsorption experiments

Nanoparticles were added to 0.1 M potassium phosphate buffer (pH 7.0) to a final concentration of 1000 mg/L. To increase the dispersion of the nanoparticles, each suspension was ultrasonicated (150 W, 40 kHz) for 6 h. Then, 1 mL of the sonicated sample was dispensed into a microcentrifuge tube and exposed to 50 μ L of freshly prepared enzyme solution with final concentrations of 0.5 mg/mL, 1 mg/mL, 1.5 mg/mL, 2.0 mg/mL, and 2.5 mg/mL. The mixture was shaken for 1 h at 160 rpm at room temperature, as adsorption equilibrium is achieved after 30 min of incubation. The samples were subsequently centrifuged at 7100g for 5 min, and the supernatants were removed. Three washes with 1 mL of phosphate buffer (0.1 M, pH 7.0) were performed to remove unbound enzyme. All supernatants were analyzed for protein content using the bicinchoninic acid method (BCA) [14]. The amount of enzyme loaded onto the nanoparticles was determined by measuring the difference in the concentration of enzyme in solution before and after exposure to the nanoparticles.

2.3. TEM study

After the adsorption experiments, 1 mg of the nanoparticle–laccase conjugate was resuspended in 1 mL of phosphate buffer and diluted with 50 mL of distilled water. The samples were prepared by air-drying a drop of suspension onto a copper TEM grid (Electron Microscopy Sciences, USA). The morphology of the samples was examined using a JEOL-2010 transmission electron microscope (JEM-2010 FEF, JEOL, Japan).

2.4. Enzyme activity assays

Laccase activity was determined by monitoring the oxidation of ABTs to the cation radical (ABTs^{•+}) at 420 nm [21]. The assay mixture contained 0.5 mM ABTs prepared in 0.1 M potassium phosphate buffer at pH 7.0, and the temperature was set at 25 °C; 50 μ L of free laccase solution (10 mg/mL) was added to 1 mL of assay mixture in quartz cuvettes and immediately mixed by inversion. The change in absorbance was examined every 5 s over a period of 60 s at 420 nm using a UV–vis spectrometer (TU-1810, Persee Co., China). One unit (U) of laccase activity was defined as the amount of ABTs^{•+} produced by 1 g of enzyme per minute.

To immobilize laccase, 1.5 mg of nanoparticle–laccase conjugate (enzyme loading of 0.5 mg laccase/mg nanoparticle) was immersed into a 1.5 mL assay mixture. After 60 s, the reaction was terminated by the addition of 10 μ L of concentrated hydrochloric acid (12 M). Then, the assay mixture was centrifuged at

11,100g for 5 min. The absorbance of the supernatant was measured at 420 nm using a UV-vis spectrophotometer (ΔA). Because of the adsorption of ABTs⁺⁺ by nanoparticle-enzyme conjugates, the immobilized enzyme activity was adjusted using the following equation:

$$\Delta A_{\text{real}} = \Delta A / (1 - A\%) \quad (1)$$

$$A\% = (A_0 - A_1) / A_0 \quad (2)$$

where $A\%$ is the percentage of ABTs⁺⁺ adsorbed by the nanoparticle-laccase conjugate and A_0 and A_1 are the optical densities before and after addition of nanoparticle-laccase conjugates, respectively. ΔA_{real} was used to calculate the ABTs⁺⁺ concentration based on a standard curve of optical density against ABTs⁺⁺ concentration (SI). The activity of immobilized enzyme was determined using the definition above.

To measure the adsorption of ABTs⁺⁺ by the nanoparticle-laccase conjugate, 1.5 mL of 0.5 mM ABTs was catalyzed by free enzyme (0.5 mg) for 60 s, and the reaction was then terminated by adding 10 μL of concentrated hydrochloric acid (12 M). The optical density was recorded as A_0 . Then, 1.5 mg of the nanoparticle-laccase conjugate (enzyme loading of 0.5 mg laccase/mg nanoparticle) was added to the solution as an adsorbent. After 60 s, the solution was centrifuged at 11,100g for 3 min, and the optical density of the supernatant was recorded as A_1 .

2.5. Kinetic studies

Kinetic studies of the free and immobilized laccase were conducted at various concentrations (0.1 mM, 0.2 mM, 0.5 mM, 1 mM, and 2 mM) of the ABTs substrate in 0.1 M phosphate buffer at pH 7.0. Nanoparticle-conjugate (1.5 mg) containing 0.5 mg of laccase was added to the substrate solution (1.5 mL) and reacted for 60 s. For a control, 0.5 mg of free enzyme was used.

The Michaelis-Menten kinetics were evaluated, and the data were fit to the following equation:

$$v = \frac{V_{\text{max}}[S]}{[S] + K_m} \quad (3)$$

where v is the reaction rate (mmol/min), $[S]$ is the concentration of the substrate (mM), V_{max} (mmol/min) is the maximum rate achieved by the system at maximum (saturating) substrate concentrations, and K_m (Michaelis-Menten constant, mM) is the substrate concentration at which the reaction rate is half of V_{max} . K_m and V_{max} were determined from the Lineweaver-Burk double reciprocal plots that fit the following equation:

$$\frac{1}{v} = \frac{K_m}{V_{\text{max}}} \frac{1}{[S]} + \frac{1}{V_{\text{max}}} \quad (4)$$

The turnover number (also termed k_{cat}) is defined as the maximum number of molecules of substrate that an enzyme can convert to product per catalytic site per unit of time and can be calculated using the following equation:

$$k_{\text{cat}} = \frac{V_{\text{max}}}{[E]_{\text{T}}} \quad (5)$$

where $[E]_{\text{T}}$ is the total concentration of enzyme (mM).

2.6. Enzymatic degradation of phenolic compounds

Laccase solution (1 mL) containing approximately 0.5 mg of free laccase or 1.5 mg of nanoparticle-laccase conjugate (enzyme loading of 0.5 mg laccase/mg nanoparticle) was added to 20 mL of BPA (10 mg/L) or catechol (10 mg/L) solution. ABTs was added as a mediator at a concentration of 0.5 mM. The mixtures were shaken at 160 rpm at 25 °C. An aliquot (1.5 mL) of the reaction was removed at 0 h, 0.25 h, 1, 3 h, 6 h, 9 h, 12 h, 18 h, and 24 h, and

10 μL of concentrated hydrochloric acid was added to terminate the reaction. The samples were centrifuged at 11,100g for 5 min, and the concentrations of BPA and catechol in the supernatants were determined using high-performance liquid chromatography (Alliance 2695, Waters, USA) with a symmetry reversed-phase C18 column (3.5 μm , 4.6 mm \times 150 mm) and Waters 2489 UV/visible detector. For BPA analysis, 50 μL of the solution was injected and eluted from the column at a flow rate of 0.8 mL/min using a mobile phase consisting of a 11:9 mixture of acetonitrile:water. BPA was detected at 224 nm. For catechol analysis, the sample was eluted with a 3:7 mixture of acetonitrile:water at a flow rate of 1 mL/min and detected at 206 nm. The reliabilities of HPLC methods for analysis of bisphenol and catechol were established through its linearity and limits of quantization (LOQs). The validation parameters are provided in Table S1. The chromatograms of the BPA and catechol analyses are shown in Fig. S1.

To detect adsorption of BPA/catechol onto nanoparticle-laccase conjugates 24 h after enzymatic incubation, the mixture was centrifuged at 11,100g for 5 min. The quantity of BPA/catechol in the supernatant was determined to be Q_L . Ethyl acetate (5 mL) was added to the solid precipitate, which was extracted for 15 min with an efficiency of $100 \pm 5\%$. The BPA/catechol in the ethyl acetate extracts was determined by HPLC as Q_E . The initial content of BPA/catechol was Q_0 ; therefore, the content that had been degraded (Q_D) would be equal to the following: $Q_D = Q_0 - Q_E - Q_L$.

2.7. Adsorption of BPA, catechol, and ABTs⁺⁺ on nanoparticle-laccase conjugates

Phosphate buffer (1 mL, 0.1 M) containing 1.5 mg of nanoparticle-laccase conjugate (enzyme loading of 0.5 mg laccase/mg particle) was inactivated by addition of 10 μL of concentrated hydrochloric acid (12 M). Deactivated nanoparticle-laccase conjugates were obtained by centrifugation at 11,100g for 5 min and resuspended in phosphate buffer (1 mL). The deactivated enzyme conjugate solution was then added to 20 mL of substrate solution containing 10 mg/L BPA or catechol or 0.5 mM ABTs⁺⁺. The mixtures were shaken at 160 rpm at 25 °C for 24 h. After centrifugation at 11,100g for 5 min, the concentrations of BPA and catechol in the supernatant were determined by HPLC, and the concentration of ABTs⁺⁺ was calculated based on the standard curve described in Supplementary material. Here, we investigated the adsorption of ABTs⁺⁺ on conjugates rather than ABTs because of the undetectable feature of ABTs on UV-vis spectrophotometry. The adsorption of ABTs⁺⁺ onto negatively charged conjugates (both laccase and nanoparticles were negatively charged at pH 7.0) was similar to or higher than that of ABTs because of electrostatic attraction.

2.8. Statistical analysis

Each experiment was performed in triplicate under each tested condition, and the values represent the means \pm standard deviation of three experiments. Significant differences ($P < 0.05$) between treatments were determined using one-way ANOVA. All statistical analyses were conducted using Statistical Packages for the Social Sciences (SPSS) Version 19.0.3.

3. Results and discussion

3.1. Adsorption isotherms of laccase on various carbon nanomaterials

The adsorption results of laccase on the four carbon nanomaterials are shown in Fig. 1. The adsorption data were fitted to the Freundlich isotherm, $q = K_F C_w^n$, where q (mg/mg) is the equilibrium

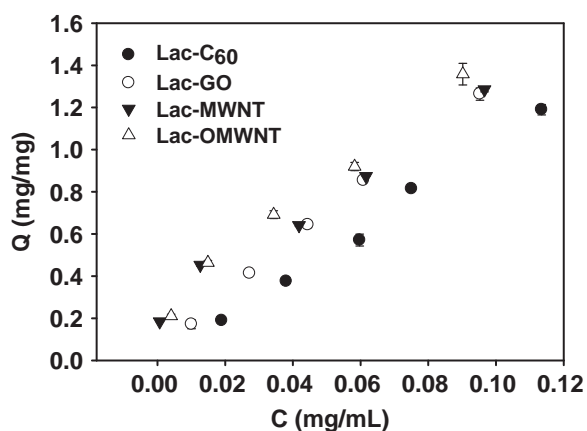


Fig. 1. Adsorption isotherms plotted as immobilized concentration (q) versus the aqueous phase equilibrium concentration (C) of laccase in the presence of 1000 mg/L of various nanoparticles at pH 7.0 in 0.1 M phosphate buffer. Error bars, in some cases smaller than the symbols, represent the standard deviations of three measurements.

Table 2
Summary of fitting parameters of adsorption isotherms.

NPs	K_F ($\text{mg}^{-n} \text{mL}^n/\text{mg}$) ^a	n ^a	R^2
C ₆₀	11.89 ± 1.64	1.06 ± 0.06	0.99
GO	10.20 ± 0.11	0.89 ± 0.00	1.00
MWNTs	4.44 ± 1.54	0.56 ± 0.12	0.94
O-MWNTs	5.93 ± 0.99	0.63 ± 0.06	0.99

^a K_F and n were fitting parameters from the Freundlich model.

concentration of laccase on the nanomatrix, C_w (mg/mL) is the equilibrium concentration of laccase in aqueous solution, K_F ($\text{mg}^{-n} \text{mL}^n/\text{mg}$) is the Freundlich affinity coefficient, and n (unitless) is the linearity index. The fitting parameters are summarized in Table 2. In general, the Freundlich model provided reasonably good fits to the data, confirming that laccase exhibited non-ideal adsorption onto heterogeneous surfaces in addition to multilayer sorption. The relative positions of the isotherms in Fig. 1 indicate that the loading capacity was the highest for O-MWNTs and lowest for C₆₀, and the same trend was observed for the surface area (Table 1). Interestingly, the surface area of O-SWNTs was almost 16 times higher than that of C₆₀, whereas the enzyme loading onto O-SWNTs was only 1.6 times higher than that of C₆₀ at the same initial concentration (0.06 mg/mL). Therefore, in addition to the surface area, other factors may influence the adsorption process.

The differences in adsorption capacity may be caused by different aggregation properties. For instance, carbon nanotubes (CNTs) tend to aggregate as bundles (Fig. 2A and B) because of Van der Waals interactions, the available sorption sites of CNT bundles include the surface area, the interstitial and groove areas formed between the CNTs [22]. GO has a large specific surface area (two accessible sides), and the abundant oxygen-containing surface functionalities (indexed by high oxygen content in Table 1), such as epoxide, hydroxyl, and carboxylic groups [23], and high water solubility increase the dispersibility of GO sheets (Fig. 2C). Nevertheless, Fig. 2D shows that C₆₀ exhibited extensive agglomeration, with the agglomerates ranging from several hundred nm to several μm based on TEM images. Aggregation of spherical C₆₀ resulted in closed interstitial spaces, prohibiting the entrance of the enzyme.

In comparison with MWNTs, because of the introduction of polar carboxylic and hydroxyl groups (indexed by Fourier transform infrared transmission analysis in Fig. S2), O-SWNTs tend to

form large agglomerates because of hydrogen bonding interactions (Fig. 2A). This bundling process results in a decrease in the exposed effective surface for adsorption, which explains the slight increase in adsorption capacity observed for O-MWNTs relative to C₆₀. Notably, no clear tubular-like structure was visible in TEM images (Fig. 2A) because O-MWNTs were shortened and thinned as a result of the oxidation treatment [12].

The heterogeneity index (n) for each isotherm also reflected the heterogeneous properties of the adsorption space resulting from aggregation. For C₆₀ agglomerates, the available adsorption space is the external surface, which is relatively homogeneous, and the value of n was thus close to 1.0. For MWNT and O-MWNT aggregates, in addition to the external surface, the interstitial and groove areas are also available for adsorption; thus, the adsorption surface was more heterogeneous and the values of n were much lower than 1.0. Based on the flat surface and good dispensability of GO, the value of n was determined to be 0.89 for the adsorption isotherm.

3.2. Residual activities and kinetic study of the immobilized enzyme

After immobilization, the residual activity of laccase decreased in the following order: GO > MWNTs > O-MWNTs > C₆₀. Nearly 65.6% of the activity was retained for GO-laccase conjugates relative to free laccase, whereas only 10.64% of the activity was retained for the C₆₀-immobilized enzyme (Fig. 3). We measured the kinetics to evaluate the affinity of the substrate towards immobilized laccase. Fig. S3 shows the Lineweaver-Burk plots of the immobilized laccase-catalyzed oxidation of the ABTs substrate. The calculated kinetic parameters from Fig. S3 are listed in Table 3.

K_M represents the affinity of the enzyme to its substrate, and when the K_M value is low, the affinity for the substrate is high. The K_M value for C₆₀ immobilized-laccase was almost ten times higher than that of free laccase, whereas the K_M value for GO-immobilized laccase was similar to that of free laccase. The K_M values of nanoparticle-laccase conjugates increased in the following order: C₆₀ > O-MWNTs > MWNTs > GO. In the present study, the K_M values of laccase immobilized to nanomaterials were on the same order of magnitude as those reported for nanoporous gold-immobilized laccase [24].

k_{cat} Corresponds to the oxidation rate, specifically the effective first-order rate constant for the breakdown of the enzyme-substrate complex (catalytic rate constant or turnover number). The k_{cat} to K_M ratio represents the catalytic efficiency of the enzyme [25]. The k_{cat} values of laccase immobilized to the four different nanoparticles were lower than those of free laccase, and the catalytic efficiencies were 5.93%, 59.53%, 33.30%, and 26.55% for C₆₀-, GO-, MWNT-, and O-MWNT-immobilized enzymes, respectively, compared to that of free laccase (Table 3).

The increase in K_M values and decrease in k_{cat} and k_{cat}/K_M values relative to free laccase were caused by either of the following: (1) conformational changes of the enzyme, resulting in a lower possibility of forming a substrate-enzyme complex, or (2) lower accessibility of the substrate to the active site of the immobilized enzyme [26]. The secondary structure of laccase was first investigated using circular dichroism spectroscopy. Fig. S4 shows that the secondary structures of laccase did not significantly change in the presence of various nanoparticles. Although many studies have reported the structural changes of enzymes during interactions with nanoparticles [14,27], the extent of the structural change may be affected by the nature of the enzyme and nanomaterial, the incubation conditions, and the interactions. Thus, in our study, substrate accessibility is a major concern. Compared to the porous and irregular surface of CNTs and C₆₀ aggregates, the flat surface and two accessible sides of GO, in addition to its high dispersibility, would be favorable for substrate

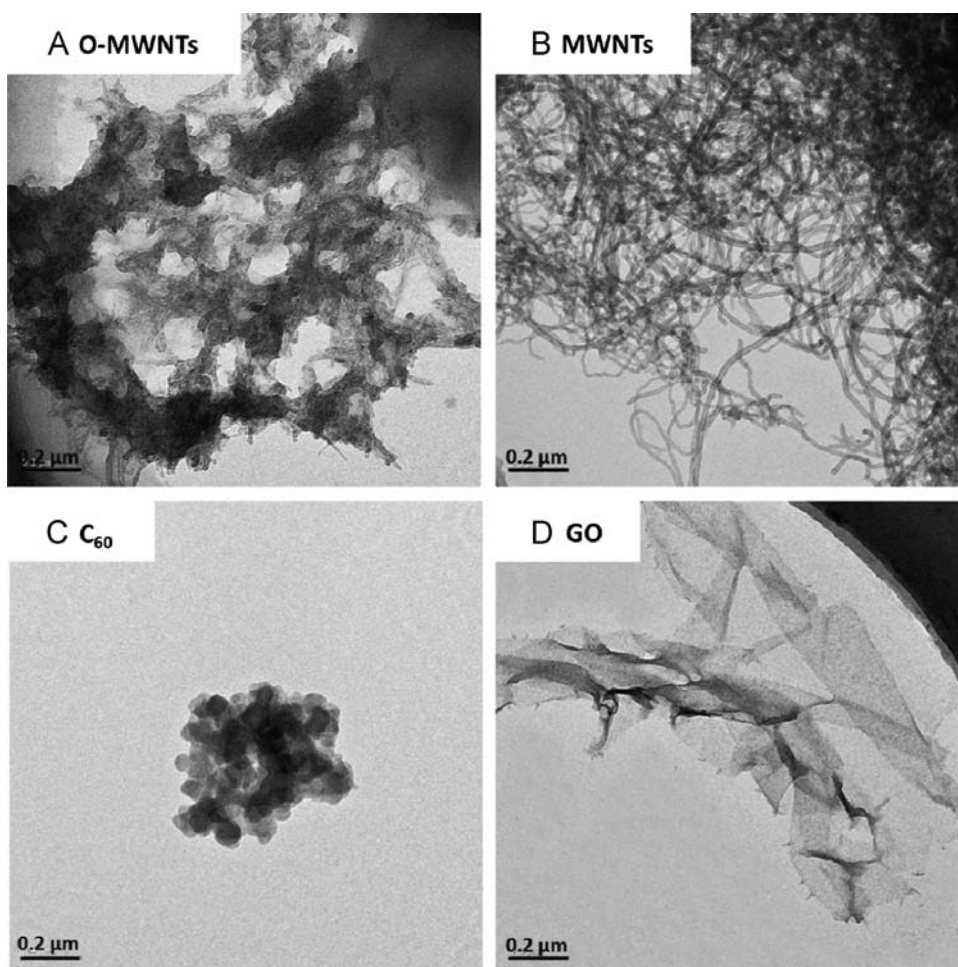


Fig. 2. Transmission electron microscope images of the following nanoparticle–laccase conjugates: (A) O-MWNTs; (B) MWNTs; (C) C₆₀; and (D) GO.

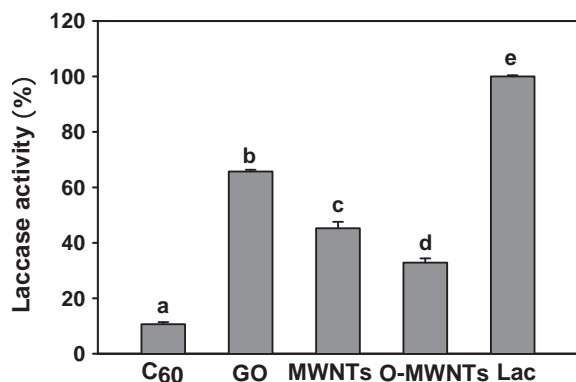


Fig. 3. Residual activities after immobilization on various carbon nanomaterials. The amount of enzyme loaded was 0.5 mg protein/mg nanoparticles, and ABTS (0.5 mM) was used as a substrate. The different letters indicate significant differences between mean values ($p < 0.05$).

access. Additionally, substrate accessibility can also be influenced by the orientation of the active site of the enzyme. If the active site is oriented towards a surface that prevents the substrate from accessing the active site, then decreased enzyme activity (reduced rate of product formation) will be observed. Based on the similar K_M values of the GO-immobilized and free enzyme, we can infer that the binding pocket was not perturbed or blocked by GO. Moreover, GO was shown to facilitate electron transfer in metalloprotein-catalyzed oxidative reactions [28]. In general, the observation of the highest catalytic efficiency for laccase

Table 3

Turnover number (k_{cat}), Michaelis–Menten constant (K_M), and catalytic efficiency (k_{cat}/K_M) of free and immobilized laccase.

Enzyme form	k_{cat}^a (s ⁻¹)	K_M (mmol)	k_{cat}/K_M (mmol ⁻¹ s ⁻¹)	k_{cat}/K_M (%)
Lac-C ₆₀	8.46	0.51	16.60	5.93
Lac-GO	13.33	0.08	166.60	59.53
Lac-MWNTs	11.18	0.12	93.20	33.30
Lac-O-MWNTs	10.40	0.14	74.29	26.55
Lac	15.39	0.055	279.85	100.00

^a The molecular mass of laccase is 96 kDa.

immobilized onto GO mainly resulted from the high accessibility of the substrate.

For C₆₀, the k_{cat} value decreased to 50%, whereas the K_M value almost increased 10-fold, which may be the result of crowding. Using the same enzyme loading rate (0.5 mg laccase/mg nanoparticle), protein molecules were attached to the C₆₀ surface in a more crowded manner because of its smaller surface area (less than 10% of that of other carbon nanomaterials). The binding pocket of the enzyme may have been blocked by other enzyme molecules, which would explain the significantly reduced substrate affinity compared to that of other carbon nanomaterials.

3.3. Removal of phenolic compounds by immobilized enzymes

The catalytic properties of laccase immobilized onto various carbon nanoparticles were further investigated using BPA and catechol as reducing substrates. The enzymatic degradation is

Table 4
Kinetic parameters of BPA and catechol removal by free and immobilized laccase. ^a

Enzyme form	BPA		Catechol	
	k^b	R^2	k^b	R^2
Lac-C ₆₀	0.0070 ± 0.0007	0.9515	0.0104 ± 0.0012	0.9449
Lac-GO	0.1097 ± 0.0030	0.9981	0.1877 ± 0.0294	0.9634
Lac-MWNTs	0.0966 ± 0.0084	0.9807	0.1073 ± 0.0135	0.9667
Lac-O-MWNTs	0.0434 ± 0.0025	0.9862	0.0598 ± 0.0074	0.9609
Lac	1.0714 ± 0.0577	0.9932	1.5364 ± 0.1382	0.9826

^a Because of rapid adsorption, the first 15 min of data were excluded from model fitting.

^b Obtained from the following first-order kinetic model: $y = ae^{-kx}$.

shown in Fig. S5, and the results from the kinetic models confirmed that the degradation of phenolic compounds obeyed the first-order rate kinetic model based on the high regression coefficient values (R^2 , Table 4). The degradation rates (k) for both BPA and catechol exposed to various nanoparticles decreased in the following order: GO > MWNTs > O-MWNTs > C₆₀. These results are consistent with previously reported residual laccase activity with the ABTs substrate. However, to our surprise, even for GO-immobilized laccase, which retained 65.69% activity (Fig. 3) compared to the free enzyme, the kinetic rate was only approximately 10% of that of the free enzyme irrespective of the phenolic compound used as a substrate. The rate ratio ν_{imm}/ν_{free} (effectiveness factor η) is regarded as the extent of diffusional limitation, where ν_{imm} and ν_{free} are the rates of the reaction catalyzed using the same enzyme concentrations with immobilized and free enzyme under identical conditions [2]. Using BPA as substrate, the η values were 0.93%, 10.28%, 9.34%, and 3.73% for C₆₀-, GO-, MWNT-, and O-MWNT-immobilized laccase, respectively, which were much lower than those of the ABTs substrate. A similar trend was observed when catechol was used as a substrate. Therefore, diffusional limitation was a significant problem when nanoparticle-laccase conjugates were used to remove phenolic contaminants.

Mass diffusion includes both the external diffusion from the bulk solution to the surface of nanoparticle conjugates and the intraparticle diffusion inside porous supports. The external diffusion may be similar for ABTs and phenolic substrates because of continuous shaking. Intraparticle diffusion may be influenced by the adsorptive forces of solutes of low concentration interacting with carrier materials and porous diffusion. We first investigated the adsorption affinity of various substrates onto nanoparticle-laccase conjugates. Surprisingly, the adsorption of ABTs on GO-laccase conjugates was similar to that of BPA, and the adsorption of ABTs on MWNT-laccase conjugates was even higher than that of BPA (Fig. 4). The adsorption of catechol onto the four nanoparticle-laccase conjugates remained similar. The difference in the affinity of the substrate to the nanomaterial may not be primarily responsible for the significant reduction in the η value with phenolic substrates. Therefore, porous aggregates of nanoparticles with high heterogeneity may create a tortuous pathway for the substrate inside the matrix, significantly contributing to the nanoparticle-induced diffusional limitation. This phenomenon is particularly pronounced at low substrate concentrations because porous diffusion can lead to different concentrations inside and outside the matrix.

The slow transfer of active intermediates and release of products may also lead to diffusional limitation. The degradation/removal of phenolic compounds by laccase is described using the following equations:

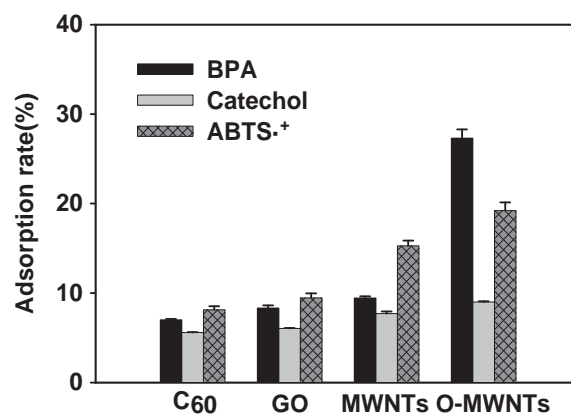
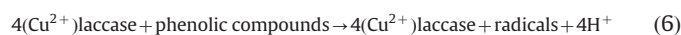


Fig. 4. Comparisons of the adsorbing affinities of various substrates on 1.5 mg of nanoparticle-laccase conjugates. The amount of enzyme loaded was 0.5 mg protein/mg nanoparticles. The substrate concentrations were 10 mg/L BPA, 10 mg/L catechol, and 0.5 mM ABTs⁺.

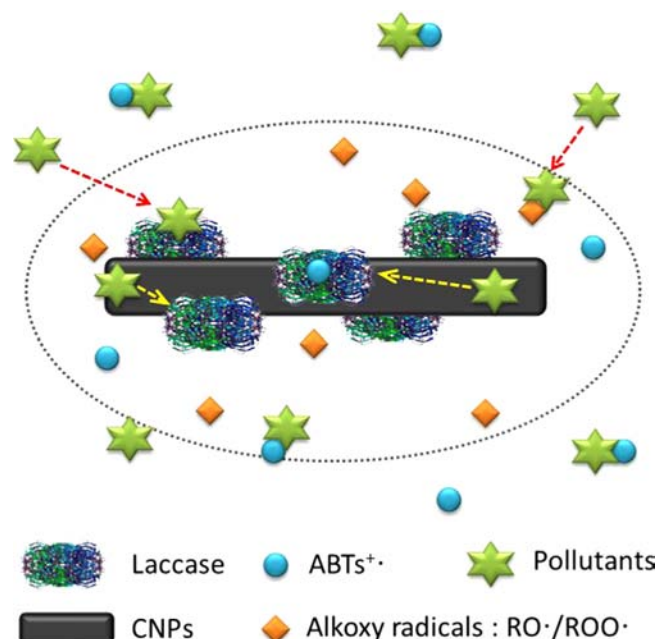
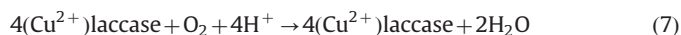


Fig. 5. Schematic illustration of diffusional limitation resulting from immobilization and the mechanism of increasing the reaction rates using ABTs as a mediator.



The phenoxy radicals attack other phenolic compounds or couple with other phenoxy radicals to form other biodegradation products and/or oligomers [29]. These phenoxy radicals are short-lived and only effective close to the location where they are generated. To react with phenoxy radicals, the mass transfer of phenolic compounds from the bulk solution to the nanomaterial surface will govern the reaction rate (Fig. 5). Other factors, such as product inhibition, which occurs when the insoluble products generated via coupling reactions block the active site of enzyme, may also influence the reaction rate.

In contrast, ABTs is directly oxidized by laccase to the corresponding cation radical (ABTs⁺), which is detected as the reaction product. Hence, when using ABTs as a substrate, no further chain reactions occur and the diffusional limitation of intermediates is minimized. The ABTs cation radical is highly stable and has been speculated to function as a diffusible oxidant of the enzyme

[15]. We also tested the assumption that the addition of ABTs as a diffusible mediator accelerates BPA removal as illustrated in Fig. 5; the kinetic parameters are summarized in Table 5, and the degradation data are shown in Fig. S6. As predicted, the values of the effectiveness factor η increased to 1.96%, 22.55%, 11.76%, and 8.82% for C₆₀-, GO-, MWNT- and O-MWNT-immobilized laccase, respectively. In the presence of ABTs, the reaction rate for free laccase slightly decreased, which may have resulted from competition of ABTs with BPA for the active site. Interestingly, although 0.5 mM ABTs was added as a mediator in the presence of 10 mg/L BPA substrate, the reaction rates only increased by approximately 1 to 2-fold. Arboleda showed that the removal efficiency of free laccase increased from approximately 30% to 100% in the presence of 0.01 mM ABTs and 5 mg/L BPA [30]. These results suggest that

Table 5
Kinetic parameters of BPA removal by free and immobilized laccase with ABTs as a mediator. ^a

Enzyme form	BPA + ABTs		Ratio of $k_{\text{BPA+ABTs}}/k_{\text{BPA}}$
	k^b	R^2	
Lac-C ₆₀	0.0215 ± 0.0010	0.9850	3.07
Lac-GO	0.2337 ± 0.0227	0.9837	2.13
Lac-MWNTs	0.1203 ± 0.0063	0.9923	1.25
Lac-O-MWNTs	0.0909 ± 0.0051	0.9893	2.09
Lac	1.0167 ± 0.1293	0.9809	-0.05

^a Because of rapid adsorption, the first 15 min of data were excluded from model fitting.

^b Obtained using the following first-order kinetics model $y = ae^{-kx}$.

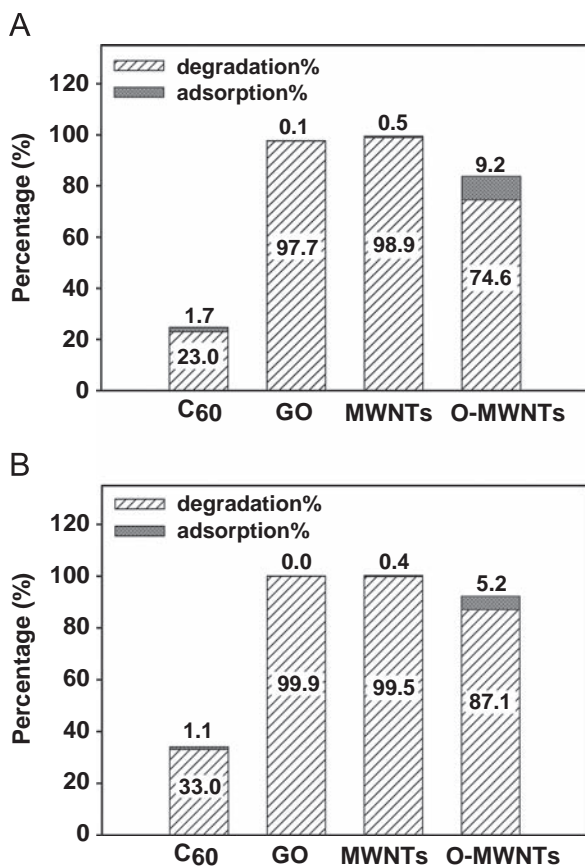


Fig. 6. The degradation and adsorption efficiency of 10 mg/L (A) BPA and (B) catechol by 1.5 mg of different nanoparticle–laccase conjugates (enzyme loaded with 0.5 mg protein/mg nanoparticles) after incubation for 24 h.

the carbon nanomatrix may also involve an electron mediator system, such as diffusional limitation induced by the adsorption of the ABTs cation radical onto the negatively charged nanoparticle surface, thereby providing a radical scavenger effect [31] for the carbon nanoparticles. Further investigation is required in this area.

Notably, although low reaction rates were detected for nanoparticle–laccase conjugates, the overall removal efficiency was not affected. In our study, after 24 h, the overall transformation efficiencies for BPA (excluding adsorption by matrix) were 97.7% and 98.9% in GO- and MWNT-immobilized systems, respectively (Fig. 6). Almost 100% of catechol was enzymatically transformed in the same two systems. Even for laccase-O-MWNTs, only 26.6% catalytic efficiency was observed in terms of ABTs oxidation, whereas the efficiency was 74.6% and 87.1% overall for transformation of BPA and catechol, respectively, after 24 h. These results suggest that laccase immobilized onto carbon nanomaterials can be active for long periods of time and that the reduced reaction rates did not lead to decreased efficiency when sufficient time was given.

4. Conclusion

Carbon nanomaterials have emerged as promising candidates for enzyme immobilization. Our results suggest nanoparticle-mediated effects on substrate accessibility and diffusional limitation need to be carefully considered, which may result in extended reaction times, low efficiency, and high economic cost. In particular, this problem is exacerbated when low concentrations of environmental contaminants are used.

However, nanoparticle-immobilized enzymes continue to be of great scientific and commercial interest because of their wide range of applications resulting from their unique advantages. Therefore, it is necessary to gain insight into the interface between the protein, the nanomaterial, and the bulk substrate solution. By manipulating the particle size, aggregation status, and enzyme density, the wealth of nano-immobilization techniques can be exploited.

Acknowledgments

We appreciate the useful suggestions of Professor Wei Chen at Nankai University. This work was supported by the Ministry of Science and Technology of the People's Republic of China (Grant 2014CB932001), the National Natural Science Foundation of China (Grant 81373039), and the Tianjin Municipal Science and Technology Commission (Grant 13JCZDJC35900).

Appendix A. Supplementary material

Supplementary data associated with this article can be found in the online version at <http://dx.doi.org/10.1016/j.talanta.2014.07.045>.

References

- [1] N. Laurent, R. Haddoub, S.L. Flitsch, Trends Biotechnol. 26 (2008) 328–337.
- [2] W. Tischer, V. Kasche, Trends Biotechnol. 17 (1999) 326–335.
- [3] M. Asgher, M. Shahid, S. Kamal, H.M.N. Iqbal, J. Mol. Catal. B: Enzym. 101 (2014) 56–66.
- [4] N. Carlsson, H. Gustafsson, C. Thörn, L. Olsson, K. Holmberg, B. Åkerman, Adv. Colloid Interface Sci. 205 (2014) 339–360.
- [5] S.A. Ansari, Q. Husain, Biotechnol. Adv. 30 (2012) 512–523.
- [6] J. Kim, J.W. Grate, P. Wang, Trends Biotechnol. 26 (2008) 639–646.
- [7] W. Feng, P. Ji, Biotechnol. Adv. 29 (2011) 889–895.
- [8] R.V. Munda, X. Wu, J. Sauer, J.S. Dordick, R.S. Kane, Curr. Opin. Biotechnol. 28 (2014) 25–32.
- [9] L. Ren, D. Yan, W. Zhong, Carbon 50 (2012) 1303–1310.

- [10] F. Zhang, B. Zheng, J. Zhang, X. Huang, H. Liu, S. Guo, J. Zhang, *J. Phys. Chem. C* 114 (2010) 8469–8473.
- [11] X. Yang, C. Zhao, E. Ju, J. Ren, X. Qu, *Chem. Commun.* 49 (2013) 8611.
- [12] S. Boncel, A. Zniszczoł, K. Szymańska, J. Mrowiec-Białoń, A. Jarzębski, K.Z. Walczak, *Enzyme Microb. Technol.* 53 (2013) 263–270.
- [13] M.F. Cabral, L.F. Sgobbi, E.M. Kataoka, S.A.S. Machado, *Colloids Surf. B: Biointerfaces* 111 (2013) 30–35.
- [14] C. Zhang, S. Luo, W. Chen, *Talanta* 113 (2013) 142–147.
- [15] M. Dastban, H. Schraft, T.A. Syed, W. Qin, *Int. J. Biochem. Mol. Biol.* 1 (2010) 36–50.
- [16] T.M.B.F. Oliveira, M. Fátima Barroso, S. Morais, P. De Lima-Neto, A.N. Correia, M.B.P.P. Oliveira, C. Delerue-Matos, *Talanta* 106 (2013) 137–143.
- [17] M. Diaconu, S. Litescu, G. Radu, *Microchim. Acta* 172 (2011) 177–184.
- [18] L. Fernando Bautista, G. Morales, R. Sanz, *Bioresour. Technol.* 101 (2010) 8541–8548.
- [19] I. Cesarino, H.V. Galesco, F.C. Moraes, M.R.V. Lanza, S.A.S. Machado, *Electroanalysis* 25 (2013) 394–400.
- [20] E.P. Cipolatti, M.J.A. Silva, M. Klein, V. Feddern, M.M.C. Feltes, J.V. Oliveira, J. L. Ninow, D. de Oliveira, *J. Mol. Catal. B: Enzym.* 99 (2014) 56–67.
- [21] R. Bourbonnais, M.G. Paice, *FEBS Lett.* 267 (1990) 99–102.
- [22] B. Pan, B.S. Xing, *Environ. Sci. Technol.* 42 (2008) 9005–9013.
- [23] J. Zhang, F. Zhang, H. Yang, X. Huang, H. Liu, J. Zhang, S. Guo, *Langmuir* 26 (2010) 6083–6085.
- [24] H. Qiu, C. Xu, X. Huang, Y. Ding, Y. Qu, P. Gao, *J. Phys. Chem. C* 113 (2009) 2521–2525.
- [25] M. Auriol, Y. Filali-Meknassi, C.D. Adams, R.D. Tyagi, T.-N. Noguero, B. Piña, *Chemosphere* 70 (2008) 445–452.
- [26] P. Ciaurriz, E. Bravo, K. Hamad-Schifferli, *J. Colloid Interface Sci.* 414 (2014) 73–81.
- [27] D.W. Horn, K. Tracy, C.J. Easley, V.A. Davis, *J. Phys. Chem. C* 116 (2012) 10341–10348.
- [28] X. Zuo, S. He, D. Li, C. Peng, Q. Huang, S. Song, C. Fan, *Langmuir* 26 (2009) 1936–1939.
- [29] Q. Huang, W.J. Weber, *Environ. Sci. Technol.* 39 (2005) 6029–6036.
- [30] C. Arboleda, H. Cabana, E. De Pril, J.P. Jones, G.A. Jiménez, A.I. Mejía, S.N. Agathos, M.J. Penninckx, *ISRN Biotechnol.* 2013 (2013) 1–12.
- [31] M.J. Martínez-Morlanes, P. Castell, P.J. Alonso, M.T. Martínez, J.A. Puértolas, *Carbon* 50 (2012) 2442–2452.



Determination of acrylamide and glycidamide in various biological matrices by liquid chromatography–tandem mass spectrometry and its application to a pharmacokinetic study



Tae Hwan Kim^{a,1}, Soyoung Shin^{b,1}, Kyu Bong Kim^c, Won Sik Seo^d, Jeong Cheol Shin^d, Jin Ho Choi^d, Kwon-Yeon Weon^d, Sang Hoon Joo^d, Seok Won Jeong^d, Beom Soo Shin^{d,*}

^a School of Pharmacy, Sungkyunkwan University, Suwon, Gyeonggi-do, Korea

^b Department of Pharmacy, Wonkwang University, Iksan, Jeonbuk, Korea

^c School of Pharmacy, Dankook University, Cheonan-si, Chungnam, Korea

^d College of Pharmacy, Catholic University of Daegu, Gyeongsan-si, Gyeongbuk, Korea

ARTICLE INFO

Article history:

Received 5 May 2014

Received in revised form

14 July 2014

Accepted 15 July 2014

Available online 24 July 2014

Keywords:

Acrylamide

Glycidamide

LC–MS/MS

Pharmacokinetics

Tissue distribution

ABSTRACT

Acrylamide (AA) is a heat-generated food toxicant formed when starchy foods are fried or baked. This study describes a simple and sensitive liquid chromatography–tandem mass spectrometry assay for the simultaneous quantification of AA and its active metabolite, glycidamide (GA) in rat plasma, urine, and 14 different tissues. The assay utilized a simple method of protein precipitation and achieved a lower limit of quantification of 5, 10 and 25 ng/mL of AA and 10, 20 and 100 ng/mL of GA for plasma, tissues and urine, respectively. The assay was fully validated to demonstrate the linearity, sensitivity, accuracy, precision, process recovery, and stability using matrix matched quality control samples. The mean intra- and inter-day assay accuracy was 91.6–110% for AA and 92.0–109% for GA, and the mean intra- and inter-day assay precisions were $\leq 10.9\%$ for AA and $\leq 8.60\%$ for GA. The developed method was successfully applied to a pharmacokinetic study of AA and GA following intravenous and oral administration of AA in rats. Tissue distribution characteristics of AA and GA were also determined under steady-state conditions.

© 2014 Elsevier B.V. All rights reserved.

1. Introduction

Acrylamide (AA) is a white and highly water-soluble chemical that has been used in various fields such as oil, cosmetic, water treatment, and textile industries since mid-1950s [1]. AA has shown to cause a variety of tumors in experimental animals. The carcinogenicity of AA has been extensively studied and increased incidences of tumors in mammary gland, thyroid, and skin have been documented [2–4]. Based on the animal studies, AA is classified as a probable human carcinogen by the United States Environmental Protection Agency [1] and International Agency for Research on Cancer [5]. Various other toxicities have been reported, including neurotoxicity in animals [6,7] and humans [8–10], reproductive toxicity in rodents [11,12], and mutagenicity in somatic cells in vitro [13] and in vivo [14], as well as in germ cells in vivo [15].

* Correspondence to: College of Pharmacy, Catholic University of Daegu, 13-13 Hayang-ro, Hayang-eup Gyeongsan-si, Gyeongbuk 712-702, Korea.
Tel.: +82 53 850 3617; fax: +82 53 850 3602.

E-mail address: bsshin@cu.ac.kr (B.S. Shin).

¹ Authors contributed equally to this work.

In 2002, it has been reported that AA is formed by the Maillard reaction during cooking of carbohydrate-rich foods at high temperature [16,17]. Significant levels of AA were found in certain fried, baked, and deep-fried foods such as potato chips (318 ppb), ground coffee (205 ppm), crackers and snack (169 ppb), and bakery products (34 ppb) [16–19]. Since the hazardous effects of AA as an industrial chemical are well known, the discovery of AA in the daily diet renewed the interests in its potential health effects and raised considerable concern [20].

AA toxicities are known to be mediated by its epoxide metabolite, glycidamide (GA). GA is predominantly formed by CYP2E1 [21–24]. GA-induced genotoxicity and mutagenicity have been reported in rodents [14,25], rodent germ cells [15,26], and *Salmonella typhimurium* [27]. GA reacts with DNA to form DNA adducts with even higher affinity than AA [28–30], which appears to be the major cause of mutagenicity and carcinogenicity by AA exposure [5,31,32].

To assess the potential risks of AA exposure on human health, it is essential to determine AA and GA concentrations in biological fluids. While many analytical methods have been described for the determination of AA in drinking water [33–36] and food stuffs [37–39], few bioanalytical methods are available that can be used

for *in vivo* pharmacokinetic or toxicokinetic studies. The first reported method to determine AA in biological samples was the radioactivity assay of labeled AA (2,3-¹⁴C AA) [40]. Later, assays utilizing high pressure liquid chromatography (HPLC) and liquid chromatography–tandem mass spectrometry (LC–MS/MS) have been developed. These assays include an HPLC/UVD with protein precipitation for determination of AA in rat plasma [41], an LC–MS/MS assay with solid phase extraction (SPE) for determination of AA and GA in mouse serum [42] and an LC–MS/MS assay with protein precipitation to determine AA and GA in human placenta [43]. However, the HPLC/UVD and LC–MS/MS methods utilizing protein precipitation lack sufficient sensitivity (LLOQ=500 ng/mL) [41,43]. The only bioanalytical method which achieves sufficient sensitivity is the LC–MS/MS assay with SPE sample preparation (LLOQ=0.71 ng/mL for AA, 8.7 ng/mL for GA) [42]. To date, most of the pharmacokinetic studies of AA [31,32,44,45] rely on this LC–MS/MS assay with SPE which is complicated, time consuming, and less cost efficient. A simple and rapid assay which is adaptable to various biological samples with high sensitivity is not yet available.

In the present study, a simple and sensitive LC–MS/MS method using single-step protein precipitation sample preparation was developed and validated for the simultaneous determination of AA and GA in biological matrices including plasma, urine, and various tissues. The method was applied to an *in vivo* study to characterize the absorption, tissue distribution and disposition pharmacokinetics of AA and GA after intravenous (i.v.) injection, i.v. infusion, and oral administration in rats.

2. Experimental

2.1. Materials

AA, acrylamide-D₃ standard solution (500 mg/L, internal standard, IS) and formic acid were purchased from Sigma-Aldrich (St. Louis, MO, USA). GA was purchased from Toronto Research Chemicals (Toronto, ON, Canada). Acetonitrile, methanol, and distilled water (all HPLC grade) were purchased from Mallinckrodt Baker (Phillipsburg, NJ, USA).

2.2. Preparation of standard solutions

Primary stock solutions of AA and GA were prepared by dissolving 10 mg each of AA and GA separately in 10 mL of distilled water. The working standard solutions were prepared by further dilution of the primary stock solutions with acetonitrile. The acrylamide-D₃ standard solution (100 µL) was diluted to 10 mL with acetonitrile.

2.3. Calibration standards and quality control (QC) samples

All calibration curves consisted of at least seven calibrator concentrations, a blank sample (without IS) and a zero sample (with IS). The calibrator and QC samples were prepared by spiking 5 µL of the working standard solution to 45 µL of the blank rat biological matrices. Various blank biological samples were obtained from at least 10 rats by collecting blood, urine, and tissues of liver, kidney, spleen, lung, heart, testis, stomach, small intestine, large intestine, fat, skin, muscle, brain, and thyroid. Tissue samples were homogenized in isotonic saline. Four different levels of low QC, medium QC, high QC, and lower limit of quantification (LLOQ) samples were prepared for AA and GA in each biological matrix. Different calibration ranges were constructed depending on the biological matrices of plasma, urine, and tissue samples. The calibration standards and QC samples for AA and GA in different biological matrices are presented in Table 1. The QC samples were prepared once, and aliquots (50 µL each) were stored at –20 °C until analysis.

2.4. Sample preparation

The working standard solutions of IS (500 ng/mL for plasma and tissue samples, and 2000 ng/mL for urine samples) were added to 50 µL of the biological samples. Blank acetonitrile (50 µL for plasma and tissue samples and 650 µL for urine samples) was used as the protein precipitating solvent. The mixture was mixed on a vortex mixer for 1 min and centrifuged at 16,060g for 10 min (Biofuge Fresco; Kendro, Osterode, Germany). For all tissue samples except thyroid, the supernatant (75 µL) was diluted with the same volume of acetonitrile and centrifuged at 16,060g for 10 min. Finally, 75 µL of the diluted supernatant was mixed with 25 µL of distilled water, and a portion (7.5 µL) was injected into the LC–MS/MS.

2.5. LC/MS/MS instruments and conditions

A model 1200 HPLC coupled with a model 6430 LC–MS/MS system (Agilent, Santa Clara, CA, USA) was used for sample analysis. Samples were separated on a dC₁₈ column (150 × 2.10 mm² i.d., 3 µm; Atlantis, Milford, MA, USA) with a Security Guard column (Phenomenex, Torrance, CA, USA). The mobile phase was a mixture of acetonitrile and 0.05% of formic acid (10:90 v/v). The flow rate was 0.1 mL/min, and the column oven temperature was 30 °C for all samples.

The electro spray ionization source was operated in a positive mode and samples were detected in the multiple reaction monitoring (MRM) mode with a dwell time of 200 ms per MRM channel. Gas temperature, gas flow rate, and nebulizer gas pressure was set at 300 °C, 10 L/min, and 20 psi, respectively. The MRM transition of precursor to product ion pairs were m/z 71.9→55.0 for AA, m/z

Table 1

Concentrations of calibrators and QC samples for acrylamide and glycidamide in various biological samples.

Compound	Matrix	Concentration (ng/mL)	
		Calibrator	QC samples
Acrylamide	Plasma	5, 10, 50, 100, 500, 1000, 2000, and 5000	5, 20, 500, and 4500
	Urine	25, 50, 100, 500, 1000, 2000, 5000, and 10,000	25, 300, 1000, and 9000
	All tissues*	10, 20, 50, 100, 500, 1000, 2000, and 5000	10, 40, 500, and 4500
Glycidamide	Plasma	10, 50, 100, 500, 1000, 2000, and 5000	10, 20, 500, and 4500
	Urine	100, 150, 500, 1000, 2000, 5000, and 10,000	100, 300, 1000, and 9000
	All tissues*	20, 50, 100, 500, 1000, 2000, and 5000	20, 40, 500, and 4500

* The lowest concentration in the calibrator and QC samples for thyroid was 5 ng/mL for acrylamide and 10 ng/mL for glycidamide."

87.9→44.2 for GA, and m/z 75.0→58.0 for acrylamide-D₃. The fragmentor voltage was set at 90 V for AA and acrylamide-D₃ and 35 V for GA. The collision energy was set at 2 V for AA and acrylamide-D₃ and 5 V for GA. Data acquisition was performed with MassHunter Quantitative Analysis (Agilent).

2.6. Assay validation

2.6.1. Specificity, linearity and sensitivity

Specificity was assessed by analyzing blank matrix and the blank matrix spiked with AA, GA, and IS. The linearity of the method was evaluated over the concentration ranges described for different biological matrices (Table 1). All calibration curves were constructed by the weighted regression method ($1/x$) of the peak area ratios of AA and GA to the internal standard vs. theoretical concentrations. The LLOQ was defined as the lowest concentrations of AA and GA of the calibration curves that yielded a signal-to-noise (S/N) ratio > 20 with acceptable accuracy and precision ($\leq 15\%$).

2.6.2. Accuracy and precision

Intra- and inter-day accuracy and precision were determined by assaying five replicates of LLOQ, low QC, medium QC, and high QC samples in each matrix each day for 5 consecutive days. Acceptable criteria for accuracy and precision were within $\pm 15\%$ relative error from the nominal values and within $\pm 15\%$ relative standard deviation except at LLOQ, where it should not deviate by more than 20%.

2.6.3. Recovery

Process recoveries were evaluated by comparing the LC–MS/MS responses of reference and test samples using five replicates of the low and high QC samples. Reference samples and test samples were prepared by dissolving AA, GA, and IS in distilled water and biological matrix, respectively. The sample preparation procedures were the same as described. The recovery was calculated by dividing the analyte peak area of the test sample by that of the reference sample.

2.6.4. Stability

The stability of AA and GA was examined under four different conditions using five replicates of low and high matrix-matched QC samples. The short term stability was determined by analyzing low and high QC samples left at room temperature for 4 h. The long-term stability was determined by analyzing low and high QC samples left at $-20\text{ }^\circ\text{C}$ for 2 weeks. The auto sampler stability was determined by analyzing low and high QC samples left in the auto sampler at $4\text{ }^\circ\text{C}$ for 24 h. Lastly, the freeze and thaw stability was determined by analyzing QC samples subject to three freeze-thaw cycles. All stability data are expressed as the percentage of the mean calculated vs. actual concentrations.

2.7. In vivo pharmacokinetic study

Male Sprague-Dawley rats (8–10 weeks, 230–290 g; Hyochang Science, Daegu, Korea) were kept in plastic cages with free access to standard diet (Cargill Agri Purina, Seong-nam, Korea) and water. The animals were maintained at a temperature of $23 \pm 2\text{ }^\circ\text{C}$ with a 12 h light–dark cycle and relative humidity of $50 \pm 10\%$. The animal study was approved by the Ethics Committee for the Treatment of Laboratory Animals at Catholic University of Daegu (IACUC 2012-07) and conducted following standard operating procedures.

AA was dissolved in distilled water at a concentration of 1 mg/mL and administered by penile vein injection ($n=4$) and

oral gavage ($n=4$) at a dose of 2 mg/kg. Rats were fasted 12 h prior to the AA dose. Approximately 0.2 mL of the jugular venous blood samples were collected at 5, 10, 15, and 30 min, 1, 2, 4, 6, 8, 10, 12, 14, and 15 h post-dose. Plasma samples were harvested by centrifugation of the blood samples at 16,060g for 5 min. Urine samples were collected for over 24 h.

Tissue distribution of AA and GA were examined under steady-state conditions after i.v. infusion of AA. The rats were anesthetized by intraperitoneal injection of Zoletil 50[®] (20 mg/kg; Virbac Laboratories, Carros, France) and surgically cannulated with polyethylene (PE) tubing (0.58 mm i.d. and 0.96 mm o.d.; Natume, Tokyo, Japan) in the right jugular vein for blood sampling and femoral vein for i.v. injection and infusion. After 2 days of recovery, AA dissolved in distilled water was administered by i.v. injection as a loading bolus dose (0.236 mg/kg) and i.v. infusion (2 $\mu\text{g}/\text{min}/\text{kg}$) for 12 h. The loading dose was calculated as the volume of distribution (0.589 L/kg) multiplied by the target steady-state plasma concentration (400 ng/mL), while the infusion rate was calculated as the clearance (5.13 mL/min/kg) multiplied by the target steady-state plasma concentration (400 ng/mL). The volume of distribution and clearance of AA were obtained from the i.v. injection study. Blood samples were collected at 1, 2, 4, 6, 8, 10, and 12 h during infusion and centrifuged at 16,060 g for 5 min. At the end of the infusion, rats were sacrificed with diethyl ether and the tissues of liver, kidney, spleen, lung, heart, testis, stomach, small intestine, large intestine, fat, skin, muscle, brain, and thyroid were excised and immediately homogenized in normal saline (T10 basic; IKA, Wilmington, DE, USA). All samples were stored at $-20\text{ }^\circ\text{C}$ until analysis.

2.8. Data analyses

The plasma concentration–time data were analyzed by a non-compartmental method using the WinNonlin 2.1 nonlinear least squares regression program (Pharsight, Cary, NC, USA) to obtain pharmacokinetic parameters. The terminal elimination half-life ($t_{1/2}$) was calculated as $0.693/\lambda_z$. The area under the serum concentration–time curve from time zero to the last observation time point (AUC_{all}) was calculated using the trapezoidal rule and AUC to infinity time (AUC_{inf}) was obtained by adding C_n/λ_z to AUC_{all} . The systemic clearance (CL) was calculated as dose/AUC . Apparent volume of distribution during the terminal phase (V_z) and steady state volume of distribution (V_{ss}) were calculated as CL/λ_z and $\text{CL} \cdot \text{MRT}$, respectively. The peak serum concentration (C_{max}) and the time to reach C_{max} (T_{max}) were read directly from the observations. The fraction of dose excreted into urine ($F_{\text{e,urine}}$) was calculated by dividing the amount excreted into urine ($A_{\text{e,urine}}$) by dose. The absolute bioavailability (F) after oral dosing was calculated as $F = (\text{Dose}_{\text{iv}} \cdot \text{AUC}_{\text{oral}}) / (\text{Dose}_{\text{oral}} \cdot \text{AUC}_{\text{iv}})$. The tissue-to-plasma partition coefficients (K_p) were expressed as the tissue-to-plasma concentration ratios. Obtained data were statistically tested by unpaired t -test between the two means for the unpaired data. The statistical significance level was set at $p < 0.05$.

3. Results and discussion

3.1. Optimization of sample preparation and chromatography

The present assay employed a simple protein precipitation procedure for the determination of AA and GA in biological samples. Protein precipitation has advantages over other sample preparation methods such as SPE [42], liquid–liquid extraction [46], and column switching [47] in that it is rapid, simple, and may be adaptable to high-throughput screening. It also allows a high process recovery by minimizing the chances to loss of analytes

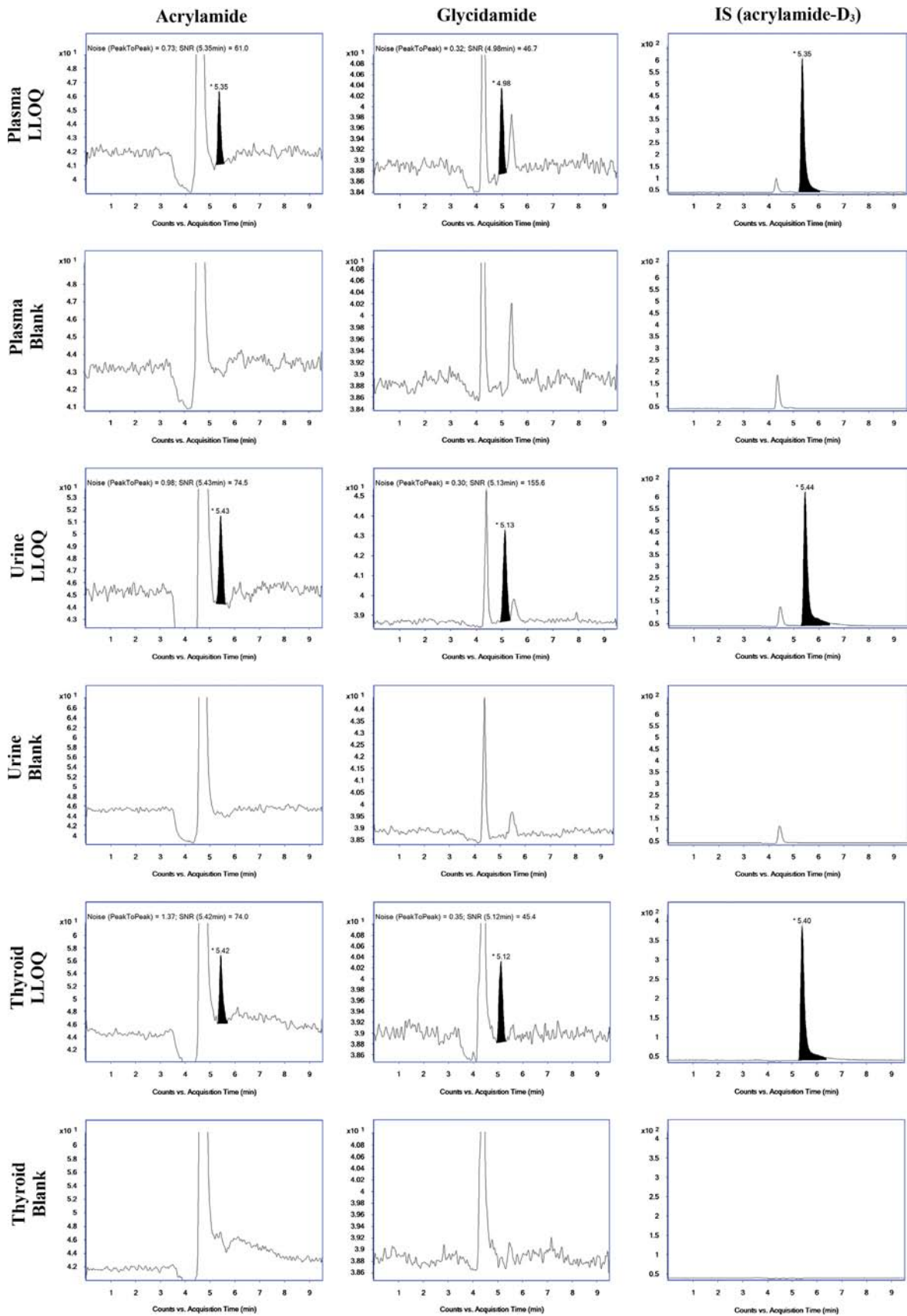


Fig. 1. Representative MRM chromatograms of acrylamide, glycidamide and acrylamide-D₃ (IS) obtained at LLOQ in plasma, urine and thyroid.

during the sample clean-up process. In contrast, protein precipitation may be more susceptible to endogenous interferences or matrix effects because the efficacy of removing endogenous

interference may be lower than other complicate methods. Concerning AA and GA, which both have a low molecular weight and high hydrophilicity, polar endogenous components may possibly

Table 2
Intra- and inter-day accuracy and precision of acrylamide and its active metabolite, glycidamide in various biological matrices ($n=5$).

Matrix	Conc (ng/mL)	Acrylamide				Glycidamide				
		Intra-day (%)		Inter-day (%)		Conc (ng/mL)	Intra-day (%)		Inter-day (%)	
		Accuracy	Precision	Accuracy	Precision		Accuracy	Precision	Accuracy	Precision
Plasma	5	105	3.67	106	1.34	10	103	4.21	101	6.96
	20	99.8	3.83	95.7	2.70	20	101	4.65	102	5.75
	500	96.0	2.30	97.0	1.52	500	98.3	3.74	98.2	3.76
Urine	4500	106	3.04	103	1.36	4500	106	2.12	100	7.63
	25	102	4.28	103	5.68	100	102	5.66	98.2	7.90
	300	103	3.85	103	3.66	300	97.5	4.56	98.8	5.40
Liver	1000	103	2.00	102	1.95	1000	97.9	3.74	98.2	4.71
	9000	102	0.86	96.8	3.62	9000	103	1.44	99.5	3.65
	10	105	4.55	97.0	9.03	20	105	5.36	104	4.14
Kidney	40	95.3	4.68	99.2	6.76	40	100	5.29	102	5.55
	500	94.2	4.58	98.3	4.26	500	96	3.51	101	4.37
	4500	104	2.01	106	2.50	4500	103	1.61	104	2.75
Spleen	10	107	3.29	103	5.53	20	92.0	3.93	96.0	8.58
	40	94.7	4.55	96.5	3.27	40	93.7	4.82	95.4	5.14
	500	92.6	4.86	95.7	4.79	500	94.9	3.02	93.2	3.60
Lung	4500	101	2.63	103	4.16	4500	100	1.84	99.8	1.76
	10	97.8	7.92	102	4.95	20	102	7.00	101	7.17
	40	99.8	7.45	98.6	4.41	40	99.3	6.56	96.5	5.76
Heart	500	102	5.52	99.7	5.82	500	98.9	5.11	95.3	4.54
	4500	106	3.71	108	1.46	4500	104	1.04	100	2.74
	10	101	7.05	109	4.07	20	105	4.55	103	5.89
Testis	40	96.7	6.21	99.3	4.57	40	102	4.93	103	3.30
	500	94.1	2.84	99.9	5.04	500	94.6	3.43	94.0	3.11
	4500	101	1.64	102	2.38	4500	99.5	2.56	101	1.79
Stomach	10	107	3.21	105	5.58	20	97.5	4.89	94.3	3.38
	40	99.8	3.86	97.0	5.63	40	96.5	4.19	98.1	4.29
	500	94.6	1.92	93.7	2.24	500	99.1	5.59	98.1	3.33
Small intestine	4500	106	2.68	107	2.99	4500	103	3.79	106	3.21
	10	105	4.41	105	4.52	20	104	3.68	105	4.79
	40	95.5	6.28	96.9	3.57	40	98.5	1.47	97.9	3.97
Large intestine	500	97.3	1.55	97.5	6.57	500	93.1	1.95	94.7	2.42
	4500	105	1.70	105	2.40	4500	104	1.24	102	1.86
	10	105	4.89	105	4.62	20	102	5.44	98.7	5.44
Fat	40	101	4.77	96.8	4.18	40	96.2	2.56	95.1	3.80
	500	103	4.65	99.4	7.28	500	101	1.85	97.8	4.61
	4500	105	2.70	98.2	4.96	4500	108	1.24	102	6.91
Skin	10	99.6	6.52	99.0	5.76	20	103	4.86	104	6.86
	40	99.2	3.40	98.0	5.05	40	95.0	4.81	99.1	4.28
	500	99.6	4.03	98.9	5.24	500	99.5	6.92	100	6.35
Muscle	4500	101	4.69	101	6.00	4500	106	3.33	106	2.94
	10	100	4.05	99.4	6.81	20	97.4	5.35	100	7.87
	40	91.7	1.31	95.0	5.49	40	97.1	4.74	103	5.07
Brain	500	94.7	3.82	96.1	8.14	500	94.8	1.56	98.1	3.93
	4500	96.2	3.05	99.5	5.38	4500	104	2.92	103	1.42
	10	102	10.9	107	6.51	20	97.7	7.45	103	6.63
Thyroid	40	100	3.90	97.8	3.30	40	101	5.57	98.1	5.85
	500	102	6.57	94.1	4.99	500	106	4.63	99.9	3.04
	4500	97.9	3.38	101	3.38	4500	108	2.43	105	4.68
Muscle	10	102	6.24	98.3	4.35	20	101	3.86	104	8.12
	40	98.9	1.36	96.6	5.10	40	97.0	5.25	98.2	5.29
	500	94.1	3.44	99.3	4.80	500	102	3.29	97.0	1.50
Brain	4500	105	3.10	105	2.51	4500	101	2.01	105	3.30
	10	110	4.90	102	6.87	20	105	3.13	103	5.41
	40	97.9	5.12	93.7	3.47	40	101	3.44	97.8	7.52
Thyroid	500	91.6	1.01	92.7	1.61	500	97.2	2.14	102	4.03
	4500	101	1.74	101	4.23	4500	101	2.03	105	7.92
	10	104	5.77	103	5.69	20	101	7.74	103	5.53
Muscle	40	92.6	1.49	96.5	4.57	40	94.0	2.98	97.9	5.07
	500	93.9	2.15	99.4	7.63	500	101	4.21	104	2.90
	4500	106	0.93	106	1.45	4500	105	3.28	109	1.55
Brain	5	98.1	4.34	99.8	5.46	10	107	3.54	100	7.79
	40	93.9	2.51	97.3	3.37	40	98.5	5.03	98.1	3.61
	500	93.7	1.02	97.0	5.69	500	95.4	3.74	97.4	2.30
Thyroid	4500	105	1.24	102	1.03	4500	104	2.83	102	1.53

be co-eluted leading to low resolution or matrix effect. Thus, separation of the target analytes from endogenous compounds is challenging during assay development.

To separate the target analytes from polar endogenous components and achieve a sufficient retention, highly aqueous compositions of the mobile phase (> 90%, 0.05% formic acid) were initially adapted with a high resolution Kinetex C₁₈ column. However, the recovery of AA and GA was > 150% for plasma and < 20% for urine with high variability, suggesting the possibility of signal enhancement or suppression caused by a matrix effect. The peak shape of the IS was split and endogenous interferences peaks were also observed. Other columns specially designed for the separation of polar analytes under reverse phase conditions (e.g., Luna CN column, Atlantis HILIC column, and Atlantis C₁₈ column) were then tested. The CN column resulted in unsatisfactory recovery (< 10%) and the HILIC column resulted in highly unstable baselines. Acceptable separation and recovery were achieved using the Atlantis C₁₈ column. With the mobile phase composition of acetonitrile and 0.05% formic acid in water (10:90 v/v), AA, GA, and IS peaks were well separated from endogenous interferences in all tested biological samples (Fig. 1).

To optimize the sample preparation, methanol and acetonitrile were evaluated as the protein precipitating solvents with different dilution factors. Acetonitrile showed stable baselines with less endogenous interferences and was selected as the protein precipitation agent. The dilution factor was also optimized by analyzing peak intensities with different volumes of the protein precipitating solvent. Optimal recoveries were obtained with 3-, 15-, and 6-fold dilution for plasma, urine, and tissue samples, respectively.

Representative MRM chromatograms of AA, GA, and IS obtained by analyzing blank biological matrices and the matrices spiked with each compound yielding concentrations of LLOQ are shown in Fig. 1. The retention time for AA, GA, and IS was 5.4, 5.0, and 5.4 min, respectively. Examination of blank sample, zero sample, and other calibrators showed no interfering peaks at the retention times corresponding to the target analytes.

3.2. Method validation

3.2.1. Linearity, sensitivity, precision, and accuracy

Calibration ranges were determined depending on the analytes and matrices. The calibration curves were linear over AA concentration ranges of 5–5000 ng/mL for plasma and thyroid,

25–10,000 ng/mL for urine, and 10–5000 ng/mL for all tissues except thyroid, and over GA concentrations ranges of 10–5000 ng/mL for plasma and thyroid, 100–10,000 ng/mL for urine, and 20–5000 ng/mL for all tissues except thyroid, with correlation coefficients > 0.999. At LLOQ of each analyte in various matrices, the signal-to-noise ratio was > 20 (range 41.0–145), and accuracy and precision were acceptable. While the LLOQ for AA in the rat plasma is higher than the LLOQ from the reported assay which was determined in the mouse serum [42], the LLOQ for GA is comparable.

Table 2 shows the intra- and inter-day accuracy and precision determined at the LLOQ, low QC, medium QC, and high QC matrix matched samples with five replicates each day on 5 consecutive days. The intra- and inter-day accuracies were 91.6–110% for AA and 92.0–109% for GA. The precision of AA and GA was ≤ 10.9% and ≤ 8.58%, respectively.

3.2.2. Recovery and matrix effect

The recoveries of AA and GA at low and high QC samples and IS in each biological matrix are presented in Table 3. The process recovery was calculated by comparing the peak area of the analyte obtained from the standard solution spiked in matrices followed by protein precipitation process to that of the analyte obtained from the matrix free solvent. Since no extraction step was involved, the process recovery directly reflected the matrix effect. The process recovery of AA in all tested matrices ranged from 37.1 ± 2.0% (small intestine) to 77.3 ± 3.2% (fat). The highest process recovery of GA was observed for kidney (68.7 ± 3.6%) and the lowest recovery was observed for urine (39.9 ± 0.3%). For IS, the recovery was highest for fat (75.5 ± 2.9%) and lowest for thyroid (44.9 ± 1.6%). Even if the recovery of target compounds was not high mainly due to the matrix effects, the process recoveries were consistent and reproducible in all tested batches (Table 3) with minimal variation (CV 1.3–8.9%).

3.2.3. Stability

The stability tests were conducted by using low and high matrix matched QC samples. Table 4 summarizes the results of the auto sampler stability, freeze–thaw stability, short-term, and long-term stability of AA and GA in each biological matrix as the mean percentages of the calculated vs. theoretical concentrations. No significant deviations were observed compared to the theoretical concentrations, indicating that AA and GA were stable under all tested conditions.

Table 3

Process recovery of acrylamide, glycidamide, and the internal standard (acrylamide-D₃) in rat biological matrices (n=5, mean ± S.D.).

Matrix	Acrylamide		Glycidamide		Acrylamide-D ₃ (IS) 500 ng/mL
	Low QC	High QC	Low QC	High QC	
Plasma	63.3 ± 1.3	60.8 ± 0.8	59.3 ± 3.1	56.6 ± 0.5	58.7 ± 3.2
Urine	46.5 ± 0.9	42.6 ± 2.0	45.4 ± 1.5	39.9 ± 0.3	46.0 ± 0.9*
Liver	45.0 ± 1.0	44.9 ± 1.0	47.0 ± 2.2	46.0 ± 0.6	45.6 ± 1.4
Kidney	66.4 ± 1.2	69.4 ± 3.9	68.7 ± 3.6	65.9 ± 0.7	70.3 ± 3.2
Spleen	56.6 ± 0.9	56.3 ± 0.5	57.9 ± 2.5	56.2 ± 0.6	64.0 ± 3.0
Lung	42.7 ± 1.2	44.3 ± 0.7	50.7 ± 2.6	43.5 ± 0.6	45.1 ± 2.0
Heart	56.6 ± 1.1	54.4 ± 0.2	59.3 ± 3.5	59.9 ± 0.4	58.2 ± 2.8
Testis	55.9 ± 0.9	57.0 ± 0.6	58.7 ± 3.1	59.6 ± 0.3	61.9 ± 2.5
Stomach	64.2 ± 1.3	56.1 ± 1.9	55.4 ± 2.3	55.8 ± 0.8	63.4 ± 2.0
Small intestine	37.1 ± 2.0	39.6 ± 3.1	49.8 ± 2.0	48.7 ± 0.6	51.6 ± 1.8
Large intestine	56.3 ± 0.8	56.1 ± 0.7	56.6 ± 1.7	60.5 ± 0.5	59.1 ± 1.0
Brain	47.9 ± 2.5	42.7 ± 0.8	47.4 ± 2.3	43.5 ± 0.4	46.1 ± 1.8
Fat	74.7 ± 2.0	77.3 ± 3.2	60.3 ± 0.8	60.9 ± 0.5	75.5 ± 2.9
Thyroid	44.4 ± 1.2	46.6 ± 0.7	52.4 ± 2.5	57.4 ± 0.5	44.9 ± 1.6
Skin	72.5 ± 3.4	69.5 ± 0.4	63.3 ± 2.6	63.9 ± 0.8	74.1 ± 2.5
Muscle	62.8 ± 1.3	59.3 ± 0.6	65.2 ± 2.6	64.1 ± 0.6	64.5 ± 1.7

* The process recovery of acrylamide-D₃ (IS) in urine samples was determined at 2000 ng/mL.

Table 4
Stability of acrylamide and glycidamide in various biological matrices ($n=5$, mean \pm S.D.).

Matrix	Auto sampler		Freeze-thaw		Short-term		Long-term	
	Low QC	High QC	Low QC	High QC	Low QC	High QC	Low QC	High QC
Acrylamide								
Plasma	98.5 \pm 2.9	97.3 \pm 4.4	95.5 \pm 1.0	101 \pm 6	101 \pm 2	95.1 \pm 1.1	100 \pm 3	96.2 \pm 1.3
Urine	99.2 \pm 2.5	101 \pm 1	97.6 \pm 2.1	99.7 \pm 1.6	101 \pm 2	103 \pm 1	98.7 \pm 2.6	102 \pm 1
Liver	102 \pm 3	99.5 \pm 5.9	102 \pm 2	101 \pm 5	103 \pm 4	101 \pm 6	101 \pm 3	96.9 \pm 2.7
Kidney	101 \pm 3	99.1 \pm 3.7	99.3 \pm 2.3	98.2 \pm 3.3	102 \pm 4	97.2 \pm 3.9	101 \pm 3	100 \pm 5
Spleen	95.2 \pm 4.1	100 \pm 4	94.5 \pm 4.3	97.4 \pm 3.9	96.3 \pm 2.8	104 \pm 2	98.5 \pm 4.3	95.9 \pm 3.6
Lung	103 \pm 2	96.1 \pm 3.8	104 \pm 2	95.4 \pm 2.6	105 \pm 2	102 \pm 4	103 \pm 2	104 \pm 6
Heart	103 \pm 3	95.9 \pm 1.7	96.3 \pm 3.0	94.9 \pm 2.4	104 \pm 2	95.7 \pm 2.3	98.7 \pm 0.7	96.6 \pm 2.3
Testis	93.8 \pm 1.9	102 \pm 5	96.0 \pm 4.1	99.3 \pm 4.2	90.4 \pm 2.7	99.2 \pm 5.6	92.1 \pm 1.3	102 \pm 4
Stomach	99.2 \pm 3.1	105 \pm 2	98.4 \pm 5.6	104 \pm 1	96.7 \pm 4.7	104 \pm 3	95.5 \pm 3.8	102 \pm 2
Small Intestine	92.6 \pm 2.1	102 \pm 1	98.3 \pm 1.5	103 \pm 1	94.0 \pm 3.2	103 \pm 3	95.3 \pm 3.3	101 \pm 0
Large intestine	105 \pm 7	99.1 \pm 1.0	101 \pm 7	99.7 \pm 1.6	101 \pm 2	99.2 \pm 1.4	102 \pm 6	99.2 \pm 2.8
Fat	99.7 \pm 1.3	104 \pm 4	100 \pm 2	102 \pm 1	100 \pm 2	102 \pm 3	100 \pm 1	104 \pm 4
Skin	98.1 \pm 5.4	101 \pm 4	94.3 \pm 3.7	98.0 \pm 3.8	97.8 \pm 5.3	104 \pm 2	95.8 \pm 3.0	105 \pm 5
Muscle	97.2 \pm 4.2	102 \pm 4	98.2 \pm 4.3	103 \pm 5	95.3 \pm 3.8	101 \pm 3	95.4 \pm 4.5	102 \pm 3
Brain	98.7 \pm 1.6	103 \pm 2	96.9 \pm 3.8	103 \pm 1	96.9 \pm 1.8	102 \pm 3	98.8 \pm 2.0	101 \pm 1
Thyroid	92.9 \pm 2.8	98.5 \pm 4.7	93.8 \pm 2.0	104 \pm 3	93.0 \pm 3.3	101 \pm 6	92.6 \pm 2.1	102 \pm 4
Glycidamide								
Plasma	101 \pm 6	103 \pm 3	99.7 \pm 3.3	102 \pm 2	104 \pm 6	107 \pm 2	103 \pm 5	105 \pm 2
Urine	97.7 \pm 7.0	96.4 \pm 4.8	96.2 \pm 4.1	94.3 \pm 1.9	100 \pm 6	97.7 \pm 4.1	98.0 \pm 5.2	99.7 \pm 1.6
Liver	94.3 \pm 1.3	101 \pm 5	94.4 \pm 2.3	103 \pm 5	95.0 \pm 1.5	97.9 \pm 5.7	98.2 \pm 4.2	101 \pm 3
Kidney	101 \pm 3	107 \pm 1	101 \pm 3	106 \pm 2	101 \pm 5	106 \pm 2	101 \pm 3	107 \pm 1
Spleen	97.2 \pm 3.1	98.3 \pm 5.9	92.7 \pm 2.7	96.7 \pm 5.9	97.9 \pm 3.2	105 \pm 3	98.5 \pm 3.4	92.7 \pm 3.6
Lung	101 \pm 5	100 \pm 7	98.4 \pm 3.7	95.5 \pm 1.2	101 \pm 5	103 \pm 5	99.9 \pm 3.8	108 \pm 3
Heart	102 \pm 3	95.3 \pm 7.1	101 \pm 3	90.8 \pm 1.1	104 \pm 5	105 \pm 4	103 \pm 3	91.4 \pm 2.6
Testis	98.2 \pm 5.1	101 \pm 7	105 \pm 5	105 \pm 5	95.5 \pm 1.4	98.9 \pm 6.5	103 \pm 3	105 \pm 2
Stomach	98.8 \pm 5.2	105 \pm 4	96.6 \pm 4.3	102 \pm 1	97.3 \pm 5.1	107 \pm 3	96.2 \pm 3.9	105 \pm 1
Small Intestine	99.5 \pm 4.0	99.5 \pm 5.0	100 \pm 3	99.3 \pm 4.6	96.3 \pm 4.9	101 \pm 5	93.8 \pm 4.5	93.9 \pm 1.5
Large intestine	103 \pm 6	101 \pm 2	107 \pm 6	104 \pm 3	96.7 \pm 4.7	100 \pm 2	100 \pm 4	100 \pm 2
Fat	99.2 \pm 7.6	106 \pm 5	100 \pm 6	106 \pm 4	94.7 \pm 3.7	106 \pm 3	97.7 \pm 4.3	111 \pm 2
Skin	98.4 \pm 7.1	106 \pm 4	97.1 \pm 4.9	108 \pm 3	102 \pm 6	101 \pm 3	98.4 \pm 7.8	104 \pm 1
Muscle	103 \pm 5	108 \pm 2	103 \pm 4	108 \pm 2	103 \pm 5	105 \pm 1	93.7 \pm 3.5	105 \pm 4
Brain	97.2 \pm 3.8	105 \pm 2	98.2 \pm 5.4	105 \pm 2	99.4 \pm 7.2	104 \pm 3	98.3 \pm 6.6	106 \pm 1
Thyroid	104 \pm 7	107 \pm 3	102 \pm 7	109 \pm 4	98.9 \pm 7.5	105 \pm 5	99.0 \pm 4.5	106 \pm 4

3.3. Application to pharmacokinetic study

3.3.1. Pharmacokinetics of AA and GA

The developed method was applied to monitor the plasma concentration-time profiles and the urinary excretion of AA and its metabolite GA in rats after i.v. injection and oral administration of AA. The pharmacokinetics of AA is known to be linear over the dose of 1.0–100 mg/kg in rats [40]. In our study, the administered dose for both i.v. injection and oral administration were 2 mg/kg which is within the dose range of the linear pharmacokinetics in rats. The average plasma concentration-time profiles are shown in Fig. 2 and the obtained pharmacokinetic parameters of AA and GA are summarized in Table 5. After i.v. injection, plasma levels of AA declined in a mono-exponential manner. AA was converted to GA, which also declined in a mono-exponential manner. While the elimination half-lives ($t_{1/2,\lambda z}$) of AA and GA were independent of the administration routes, the $t_{1/2,\lambda z}$ of GA was significantly longer than that of AA for both routes of administration ($p < 0.05$, Table 5). Orally administered AA was rapidly and extensively absorbed; the time to reach the maximum concentration (T_{max}) of AA was 0.50 ± 0.00 h and the oral bioavailability was $80.5 \pm 6.3\%$. Following AA dose at 2.0 mg/kg in this study, the $AUC_{0-\infty}$, which is based on the last observed plasma concentration, was over 99.6% and 93.8% of the extrapolated AUC_{inf} for AA and GA, respectively. This data indicate that the assay was sensitive enough to evaluate the full pharmacokinetic profiles of AA and GA.

Interestingly, metabolic conversion of AA to GA was more rapid and extensive after oral administration than after i.v. injection. The T_{max} of GA was significantly faster after oral administration than after i.v. injection (2.50 ± 1.00 vs. 6.00 ± 0.00 h, $p < 0.05$).

The metabolite-to-parent compound area under the curve (AUC) ratio (AUC_{GA}/AUC_{AA}) was higher after oral administration than after i.v. injection (0.64 vs. 0.12). This observation suggests that orally administered AA is subject to a significant pre-systemic first-pass metabolism. Urinary excretion of AA and GA was minimal ($< 1\%$ of the administered dose).

3.3.2. Tissue distribution of acrylamide and glycidamide

The developed assay was applied to characterize the tissue distribution characteristics of AA and GA in rats under steady-state conditions. Since AA is frequently found in the daily diet, humans may be exposed to AA continuously. Thus, it may be useful to characterize the tissue distribution of AA under steady-state conditions. The plasma concentration-time profiles of AA and GA during i.v. infusion and the steady-state tissue concentrations are shown in Fig. 3 and Table 6. Plasma concentrations of AA and GA reached their steady-states within 2 h after initiation of infusion. The observed steady-state plasma AA concentrations (mean 347 ± 45 ng/mL) appeared to be comparable to the target concentration of 400 ng/mL. The average steady-state plasma GA concentration was lower (113 ± 37 ng/mL) than the parent compound. The steady-state tissue concentrations and the tissue-to-plasma partition coefficients (K_p) for AA and GA are presented in Fig. 3 and summarized in Table 6. This is the first report on the steady-state distribution of AA and its metabolite GA in a total of 14 tissues, including spleen, lung, heart, stomach, intestine, fat, and thyroid. Consistent with the hydrophilic nature of AA and its small volume of distribution, AA concentrations in tissues were lower than the plasma concentrations. The highest concentration of AA was

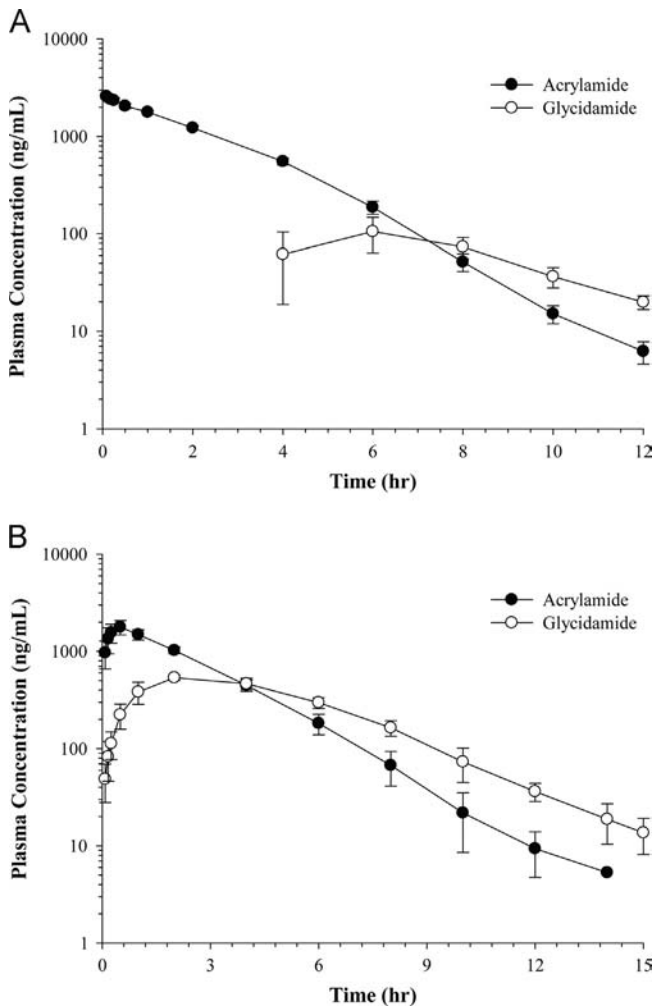


Fig. 2. Average plasma concentration–time profiles of acrylamide and glycidamide after (A) intravenous injection and (B) oral administration of acrylamide at a dose of 2 mg/kg in rats ($n=4$ each). Each point represents the mean \pm S.D.

Table 5
Pharmacokinetic parameters of acrylamide and glycidamide following i.v. injection and oral administration of acrylamide at a dose of 2 mg/kg to rats (mean \pm S.D.).

Compound	Parameters	Route of administration		
		i.v. ($n=4$)	p.o. ($n=4$)	
Acrylamide	$t_{1/2}$ (h)	1.33 ± 0.06	1.32 ± 0.08	
	T_{max} (h)	NA	0.50 ± 0.00	
	C_0 or C_{max} (ng/mL)	2760 ± 170	1780 ± 300	
	AUC_{all} (ng · h/mL)	6490 ± 250	5220 ± 410	
	AUC_{inf} (ng · h/mL)	6500 ± 250	5240 ± 410	
	V_z or V_z/F (L/kg)	0.589 ± 0.038	0.730 ± 0.039	
	CL or CL/F (mL/min/kg)	5.13 ± 0.19	6.40 ± 0.51	
	V_{ss} (L/kg)	0.642 ± 0.031	NA	
	F (%)	NA	80.5 ± 6.3	
	$A_{e,urine}$ (μ g)	5.21 ± 2.36	1.51 ± 0.63	
	$F_{e,urine}$ (%)	0.961 ± 0.495	0.299 ± 0.131	
	Glycidamide	$t_{1/2}$ (h)	$2.31 \pm 0.33^*$	$1.93 \pm 0.28^*$
		T_{max} (h)	6.00 ± 0.00	$2.50 \pm 1.001;^\#$
C_{max} (ng/mL)		105 ± 41	541 ± 32	
AUC_{all} (ng · h/mL)		775 ± 349	3310 ± 300	
AUC_{inf} (ng · h/mL)		826 ± 329	3350 ± 310	
$A_{e,urine}$ (μ g)		4.61 ± 1.60	7.28 ± 3.21	

* $p < 0.05$ vs. acrylamide.

^\# $p < 0.05$ vs. i.v.

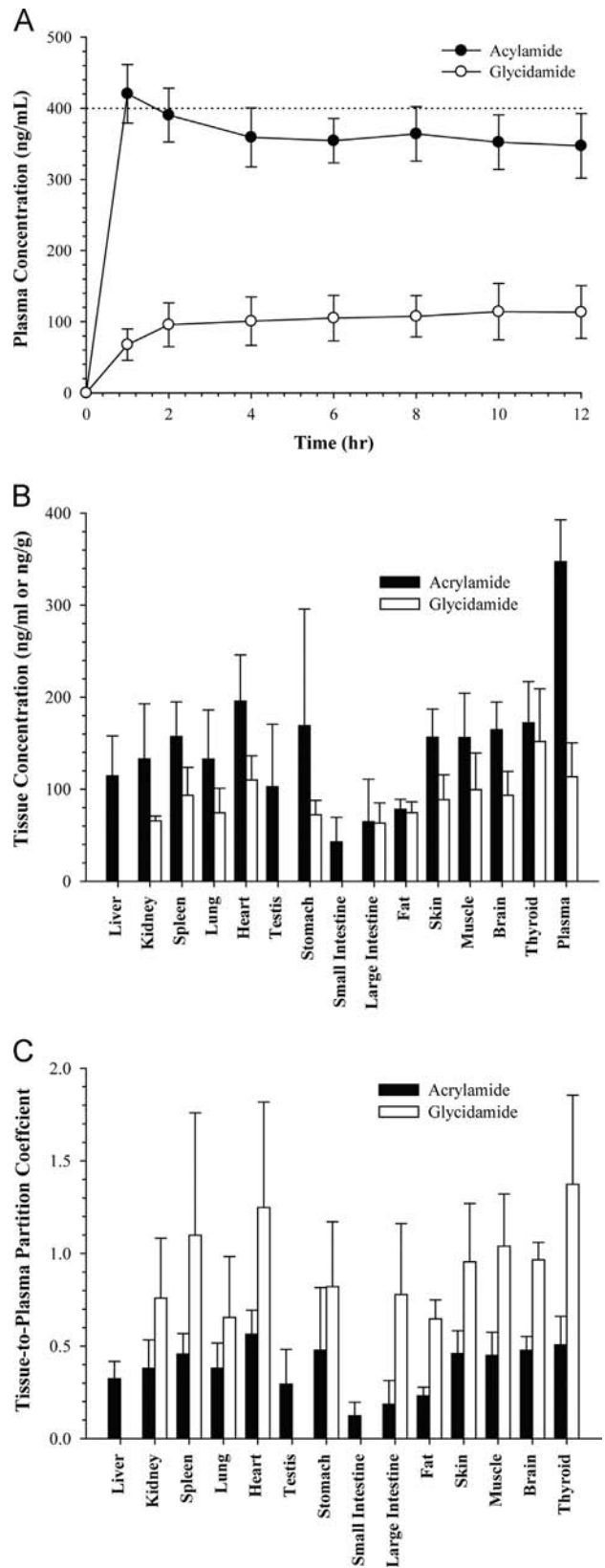


Fig. 3. (A) Average plasma concentration–time profiles of acrylamide and glycidamide during intravenous infusion of acrylamide, (B) the steady-state concentrations of acrylamide and glycidamide in various tissues and (C) their steady-state tissue-to-plasma partition coefficients in rats ($n=4$).

observed in heart followed by thyroid, stomach, brain, spleen, skin, muscle, kidney, lung, liver, testis, fat, large intestine, and small intestine. GA concentration was the highest in thyroid followed by

Table 6
Steady-state tissue concentrations and tissue-to-plasma partition coefficients (K_p) of acrylamide and glycidamide in rats ($n=4$, mean \pm S.D.).

Matrix	Acrylamide		Glycidamide	
	Concentration (ng/g)	K_p	Concentration (ng/g)	K_p
Plasma	347 \pm 45	NA	113 \pm 37	NA
Liver	115 \pm 43	0.324 \pm 0.093	BLOQ	NA
Kidney	133 \pm 60	0.380 \pm 0.153	65.6 \pm 5.3	0.661 \pm 0.281
Spleen	157 \pm 38	0.456 \pm 0.112	93.3 \pm 30.4	0.956 \pm 0.575
Lung	133 \pm 54	0.381 \pm 0.136	74.4 \pm 26.5	0.570 \pm 0.286
Heart	196 \pm 50	0.564 \pm 0.130	110 \pm 26	1.09 \pm 0.50
Testis	103 \pm 68	0.295 \pm 0.188	BLOQ	NA
Stomach	169 \pm 127	0.477 \pm 0.339	72.2 \pm 15.7	0.714 \pm 0.305
Small intestine	42.9 \pm 26.8	0.124 \pm 0.073	BLOQ	NA
Large intestine	64.7 \pm 46.1	0.187 \pm 0.128	63.4 \pm 21.7	0.677 \pm 0.334
Fat	78.2 \pm 10.8	0.231 \pm 0.046	74.5 \pm 11.8	0.562 \pm 0.090
Skin	157 \pm 30	0.459 \pm 0.125	88.6 \pm 27.0	0.831 \pm 0.274
Muscle	156 \pm 48	0.450 \pm 0.125	99.5 \pm 39.6	0.905 \pm 0.245
Brain	165 \pm 30	0.476 \pm 0.076	93.3 \pm 25.8	0.840 \pm 0.082
Thyroid	172 \pm 45	0.506 \pm 0.154	152 \pm 57	1.20 \pm 0.42

heart, spleen, muscle, brain, skin, stomach, large intestine, kidney, lung, and fat. Distribution of GA into liver and small intestine was minimal. Although tissue concentrations of GA were mostly lower than AA concentrations, relatively high concentrations of GA were observed in thyroid, fat and large intestine, which were comparable with AA concentrations. It was of particular interest to observe the significant distribution of AA and GA in representative target tissues of carcinogenicity and neurotoxicity, such as thyroid, brain, and skin.

4. Conclusions

A specific and sensitive LC–MS/MS assay was developed and validated for the simultaneous determination of AA and its active metabolite GA in various biological matrices of rat plasma, urine, and 14 different tissues. The method was successfully applied to determine the oral bioavailability in rats after i.v. and oral administration of AA. In particular, tissue distribution characteristics of AA and GA were evaluated under steady-state conditions. The developed assay may be useful in risk assessment studies of AA and GA.

Acknowledgment

This work was supported by Grant 12162MFDS722 from the Korea Food and Drug Administration and National Research Foundation of Korea (NRF) Grant No. 2012R1A2A2A02044997 and 22A2013000073 (BK21 Plus).

References

- [1] U.S. Environmental Protection Agency (EPA), EPA 749-F-94-005a: Chemical Summary for Acrylamide, 1994.
- [2] M.A. Friedman, L.H. Dulak, M.A. Stedham, *Fundam. Appl. Toxicol.* 27 (1) (1995) 95–105.
- [3] K.A. Johnson, et al., *Toxicol. Appl. Pharmacol.* 85 (2) (1986) 154–168.
- [4] R.J. Bull, M. Robinson, J.A. Stober, *Cancer Lett.* 24 (2) (1984) 209–212.
- [5] International Agency for Research on Cancer (IARC), IARC Monographs on the Evaluation of Carcinogenic Risks to Humans, 1994, p. 389.
- [6] P.S. Spencer, H.H. Schaumburg, *Can. J. Neurol. Sci.* 1 (2) (1974) 143–150.
- [7] P.S. Spencer, H.H. Schaumburg, *Can. J. Neurol. Sci.* 1 (3) (1974) 152–169.
- [8] C.J. Calleman, et al., *Environ. Health Perspect* 99 (1993) 221–223.
- [9] L.O. Goffeng, et al., *Neurotoxicol. Teratol.* 30 (3) (2008) 186–194.
- [10] J.W. Donovan, T. Pearson, *Vet. Hum. Toxicol.* 29 (1987) 462 (Abstract).
- [11] K.L. Dearfield, et al., *Mutat. Res.* 330 (1–2) (1995) 71–99.
- [12] R.W. Tyl, M.A. Friedman, *Reprod. Toxicol.* 17 (1) (2003) 1–13.
- [13] A. Besaratinia, G.P. Pfeifer, *J. Natl. Cancer Inst.* 95 (12) (2003) 889–896.
- [14] M.G. Manjanatha, et al., *Environ. Mol. Mutagen* 47 (1) (2006) 6–17.
- [15] B.I. Ghanayem, et al., *Biol. Reprod.* 72 (1) (2005) 157–163.
- [16] D.S. Mottram, B.L. Wedzicha, A.T. Dodson, *Nature* 419 (6906) (2002) 448–449.
- [17] E. Tareke, et al., *J. Agric. Food Chem.* 50 (17) (2002) 4998–5006.
- [18] J. Rosen, K.E. Hellenas, *Analyst* 127 (7) (2002) 880–882.
- [19] U.S. Environmental Protection Agency (EPA), EPA/635/R-07/009F: Toxicological Review of Acrylamide, 2010.
- [20] WHO, Joint FAO/WHO Consultation on Health Implication of Acrylamide in Food, 2002, 33 pp.
- [21] E. Bergmark, C.J. Calleman, L.G. Costa, *Toxicol. Appl. Pharmacol.* 111 (2) (1991) 352–363.
- [22] E. Bergmark, et al., *Toxicol. Appl. Pharmacol.* 120 (1) (1993) 45–54.
- [23] T.R. Fennell, et al., *Toxicol. Sci.* 85 (1) (2005) 447–459.
- [24] S.C. Sumner, et al., *Chem. Res. Toxicol.* 12 (11) (1999) 1110–1116.
- [25] B. Paulsson, et al., *Mutat. Res.* 535 (1) (2003) 15–24.
- [26] W.M. Generoso, et al., *Mutat. Res.* 371 (3–4) (1996) 175–183.
- [27] K. Hashimoto, H. Tani, *Mutat. Res.* 158 (3) (1985) 129–133.
- [28] J.J. Solomon, et al., *Cancer Res.* 45 (8) (1985) 3465–3470.
- [29] G. Gamboa da Costa, et al., *Chem. Res. Toxicol.* 16 (10) (2003) 1328–1337.
- [30] D.R. Doerge, et al., *Mutat. Res.* 580 (1–2) (2005) 131–141.
- [31] D.R. Doerge, et al., *Toxicol. Appl. Pharmacol.* 202 (3) (2005) 258–267.
- [32] D.R. Doerge, et al., *Toxicol. Appl. Pharmacol.* 208 (3) (2005) 199–209.
- [33] S. Cavalli, S. Polesello, G. Saccani, *J. Chromatogr. A* 1039 (1–2) (2004) 155–159.
- [34] A. Hashimoto, *Analyst* 101 (1209) (1976) 932–938.
- [35] U.S. Environmental Protection Agency (EPA), EPA Method 8316: Acrylamide, Acrylonitrile and Acrolein by High Performance Liquid Chromatography (HPLC), 1994.
- [36] U.S. Environmental Protection Agency (EPA), EPA Method 8032A: Acrylamide by Gas Chromatography, 1996.
- [37] L.S. Bologna, et al., *J. Chromatogr. Sci.* 37 (7) (1999) 240–244.
- [38] K. Takata, T. Okamoto, *J. Environ. Chem.* 1 (3) (1991) 559–565.
- [39] Y. Zhang, et al., *J. Chromatogr. A* 1142 (2) (2007) 194–198.
- [40] M.J. Miller, D.E. Carter, I.G. Sipes, *Toxicol. Appl. Pharmacol.* 63 (1) (1982) 36–44.
- [41] D.S. Barber, et al., *J. Chromatogr. B. Biomed. Sci. Appl.* 758 (2) (2001) 289–293.
- [42] N.C. Twaddle, et al., *Cancer Lett.* 207 (1) (2004) 9–17.
- [43] K. Annola, et al., *J. Chromatogr. B Anal. Technol. Biomed. Life Sci.* 876 (2) (2008) 191–197.
- [44] E.K. Kopp, W. Dekant, *Toxicol. Appl. Pharmacol.* 235 (2) (2009) 135–142.
- [45] D.R. Doerge, et al., *Toxicol. Lett.* 169 (1) (2007) 34–42.
- [46] F. Sorgel, et al., *Chemotherapy* 48 (6) (2002) 267–274.
- [47] E.K. Kopp, et al., *J. Agric. Food Chem.* 56 (21) (2008) 9828–9834.



Short communication

Determination of *cmc* of imidazolium based surface active ionic liquids through probe-less UV–vis spectrophotometry



Mudasir Ahmad Rather, Ghulam Mohammad Rather, Sarwar Ahmad Pandit,
Sajad Ahmad Bhat, Mohsin Ahmad Bhat*

Department of Chemistry, University of Kashmir, Srinagar-190006, J&K, India

ARTICLE INFO

Article history:

Received 29 May 2014

Received in revised form

15 July 2014

Accepted 18 July 2014

Available online 29 July 2014

Keywords:

Surface active ionic liquids

Probe-less UV–visible spectrophotometry

Tensiometry

Micellization

ABSTRACT

In the first of its kind we herein report the results of our studies undertaken on the micellization behaviour of imidazolium based surface active ionic liquids (SAILs) to prove that their critical micelle concentration (*cmc*) can be estimated through ultraviolet–visible (UV–vis) spectroscopy without using any external probe. Tensiometric and spectrophotometric investigations of a series of freshly prepared SAILs viz. 1-octyl-3-methylimidazolium chloride ([OMIM][Cl]), 1-octyl-3-methylimidazolium dodecyl-sulphate ([OMIM][DS]), 1-octyl-3-methylimidazolium benzoate ([OMIM][Bz]), 1-octyl-3-methylimidazolium salicylate ([OMIM][Sc]), 1-octyl-3-methylimidazolium acetate ([OMIM][Ac]) are presented as a case study in support of the said claim. The *cmcs* estimated through spectrophotometric method were found to be close to the values estimated through tensiometry for the said SAILs. The *cmcs* for the investigated SAILs were found to vary in order of [OMIM][Cl] > [OMIM][Ac] > [OMIM][Bz] > [OMIM][Sc] > [OMIM][DS]. To the best of our knowledge the present communication will be the first report about the synthesis, characterization and micellization behaviour of [OMIM][Bz] and [OMIM][Sc].

© 2014 Elsevier B.V. All rights reserved.

1. Introduction

Ionic liquids (ILs) are a class of organic molten electrolytes with melting point close to or below 100 °C [1,2]. In addition to being environmentally benign, inherent physico-chemical properties of ILs like high thermal stability, wide liquidus range, high conductivities, large electrochemical window, tuneable solubility and mixing properties make them promising materials for diverse applications like catalysis [3,4], electrochemistry [5,6] and separations [7–9] etc.

Very recently ILs bearing long alkyl chains have been reported to exhibit amphiphilic properties. This new category of ILs named as surface active ionic liquids (SAILs) which are supposed to offer combined desired features of ILs and surfactants [10], have started attracting considerable attention from solution chemists. On account of their eco-friendly and amphiphilic nature, the SAILs can be explored as promising substitutes of conventional surfactants in applications like micellar catalysis [11], solubilisation [12,13,14], protein folding [15,16] and drug delivery [17] etc. An important advantage of working with SAILs is that their hydrophobic and

hydrophilic character can be fine-tuned through easily achievable structural/functional alterations in their cationic and anionic substituent groups [18,19]. SAILs based on 1-alkyl-3-methyl imidazolium cation have become a focus of recent investigations in colloid and interface science [20–24].

In solution chemistry the critical micelle concentration (*cmc*) is considered as one of the important parameters used for evaluation/comparison of efficiency of surface active agents for their desired applications. Hence the designing of safe, cost effective, rapid and reliable methods for estimation of *cmc* has been an attractive area of research in colloidal chemistry. The presently used methods for estimation of *cmc* rely on changes in the nature of functional dependence of some physical properties with concentration on account of micelle formation by a surfactant in its solution [25]. The simplest and quickest among these are the spectroscopic methods which rely on the change in absorption behaviour upon aggregation. However, a disadvantage attributed to spectrophotometric *cmc* estimation of conventional surfactants is that the method requires the use of an organic dye or some other species, with a characteristic UV–vis absorption behaviour, as a probe to reflect the onset of micellization [26,27]. These additives in turn may alter the micellization characteristics of the surfactants and hence lead to estimation of an apparent and not the actual *cmc*. Moreover, these probes may alter the structure and

* Corresponding author. Tel./fax: +91 194 2414049.

E-mail address: mohsinch@kashmiruniversity.ac.in (M.A. Bhat).

the stability of micelles in an undeterminable way, thereby making spectrophotometry a less reliable and less preferred method for CMC estimations in surface chemistry laboratories.

The peculiar inherent structural features in certain class of surfactants abrogate the need for use of any foreign probe for the estimation of their *cmc* through spectrophotometry [28]. After a keen assessment of available literature about spectroscopic studies on imidazolium based ILs, it was concluded that the presence of imidazolium ring makes them to absorb significantly in the entire UV region [29–31]. In view of the presence of UV–vis active imidazolium in SAILS and expected variations in the environment around this ring during micellization, some questions do arise about the solution behaviour of this new class of amphiphilic ionic liquids: Should UV–vis spectra of such SAILS show a deviation or transition from usual behaviour near CMC? How sharp shall this deviation be and how close match the range representing the said transition in absorption behavior will be to the *cmc* estimated through other reliable methods for such SAILS? Can the imidazolium ring of SAILS act as an intrinsic chromophore for estimation of their *cmc* spectrophotometrically? In search for an answer to these questions we investigated the micellization behaviour of a series of freshly prepared SAILS viz 1-octyl-3-methylimidazolium chloride ([OMIM][Cl]), 1-octyl-3-methylimidazolium dodecyl sulphate ([OMIM][DS]), 1-octyl-3-methylimidazolium benzoate ([OMIM][Bz]), 1-octyl-3-methylimidazolium salicylate ([OMIM][Sc]) and 1-octyl-3-methylimidazolium acetate ([OMIM][Ac]). To the best of our knowledge the synthesis of [OMIM][Bz] and [OMIM][Sc] is yet to be reported in the literature. Although micellization behaviour of [OMIM][Cl] has been reported [32] there is no such report about [OMIM][DS], [OMIM][Bz], [OMIM][Sc] and [OMIM][Ac]. The *cmc*s of aforesaid SAILS were determined using probe-less UV–vis spectrophotometry and tensiometry.

2. Experimental section

Spectroscopic grade imidazolium based surface active ionic liquids (SAILS) were synthesised through the reported procedures [31,33–37] with slight modifications for obtaining better yields. The details of the synthetic procedures are given in the supplementary information. For the estimation of the CMCs of these SAILS, tensiometric and spectrophotometric techniques were employed. Tensiometric measurements were carried out on a Kruss K9 Tensiometer connected to a HAAKE GH bath that maintained the temperature at the desired value (within ± 0.1 °C). The spectrophotometric measurements were carried on Evolution 201 Thermo scientific UV–visible Spectrophotometer equipped with a Peltier system for temperature control from 0 to 100 °C (within ± 0.1 °C).

3. Results and discussion

In our spectrophotometric study, the concentration effect on absorbance behaviour of each SAIL in UV–visible range (200–360 nm) was monitored. Fig. 1 depicts sets of UV–vis spectra recorded at different concentrations of [OMIM][DS] in water at 298 K. The absorption behaviour is typical of imidazolium based ILs. The inset in Fig. 1, represents a magnification of the recorded spectra in the wave length range of 240–360 nm. The absorption behaviour in this range is attributed to aggregates of imidazolium ions [31,38]. A typical absorption versus concentration plot for wavelengths in this range reveals that upto a certain SAIL concentration the absorbance varies linearly with concentration in accordance with Beer–Lambert law. But above this SAIL specific concentration the rate of the increase, though linear, is very different from the rate before. Absorbance versus concentration

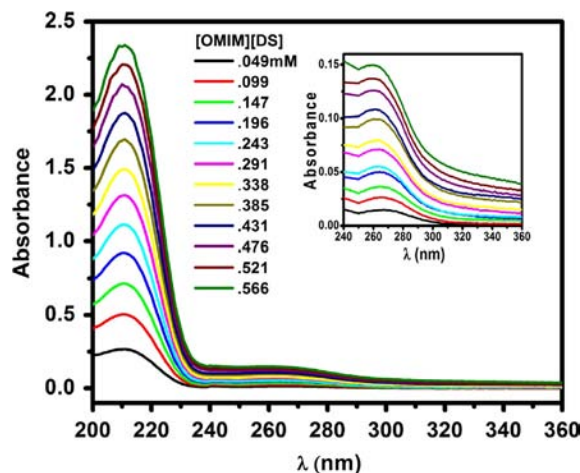


Fig. 1. UV–vis spectra recorded for changing concentrations of [OMIM][DS] in water at 298 K. The inset shows magnified version of the spectra in the wavelength range 240–360 nm.

plots (Fig. 2) as recorded in the present study fit to two straight line segments making a sharp intersect. The concentration corresponding to the point of intersection was found to be specific to each SAIL and seems to represent the onset of micellization process. The concentrations corresponding to the break points observed in the Beer plots are tabulated in Table 1. Surface tension measurements were also performed to evaluate the *cmc* of the investigated SAILS in their aqueous solutions. Fig. 3 presents surface tension versus log C profiles at 298 K showing a linear decrease of surface tension with log C for all the investigated solutions up to a SAIL specific concentration beyond which the surface tension remains almost constant. The absence of minima around the breakpoints is a clear indication of absence of impurities in the SAILS. The breakpoint concentrations representing the *cmc* values of the SAILS are presented in Table 1.

As seen from the entries in Table 1, the break point concentrations observed in the Beer plots are a close match to those observed in the tensiometric plots for the investigated SAILS, clearly establishing that the former correspond to their *cmc*s. Hence the *cmc* of imidazolium based SAILS can be estimated through spectroscopic methods without involving use of any probe as required for conventional surfactants. Needless to mention that the *cmc* obtained for [OMIM][Cl] through both the techniques in the present study is found to be in good agreement with the value already reported for the said SAIL through conductometry and tensiometry [32].

The *cmc*s obtained through tensiometry as well as spectrophotometry follow the same trend and vary in the order of [OMIM][Cl] > [OMIM][Ac] > [OMIM][Bz] > [OMIM][Sc] > [OMIM][DS]. However, as evident from Fig. 2, the Beer plots of [OMIM][Cl] and [OMIM][Sc] exhibit different behaviour after *cmc* with small increase in absorbance in contrast to a sharp increase in others. Both the observations can be explained on the basis of the extent to which the presence of counter ions at micellar surface stabilizes or screens the electrostatic repulsion between head groups and how the resulting stabilization alters the aggregation behaviour of the particular SAIL. The micelle stabilization ability of counterions has been observed to be a collective result of factors like their hydrated radius, polarizability, hydrophobicity, bulkiness and position in Hofmeister series [15,39–41]. Generally it is observed that the average aggregation number of micelles increases with increasing hydrophobicity of counterions. This implies that ions with stronger hydrophobicity can bind their counterions more strongly and hence reduce the repulsive interaction between similarly charged head groups thereby stabilizing the micelle with consequent reduction of *cmc*. In line with this argument and as

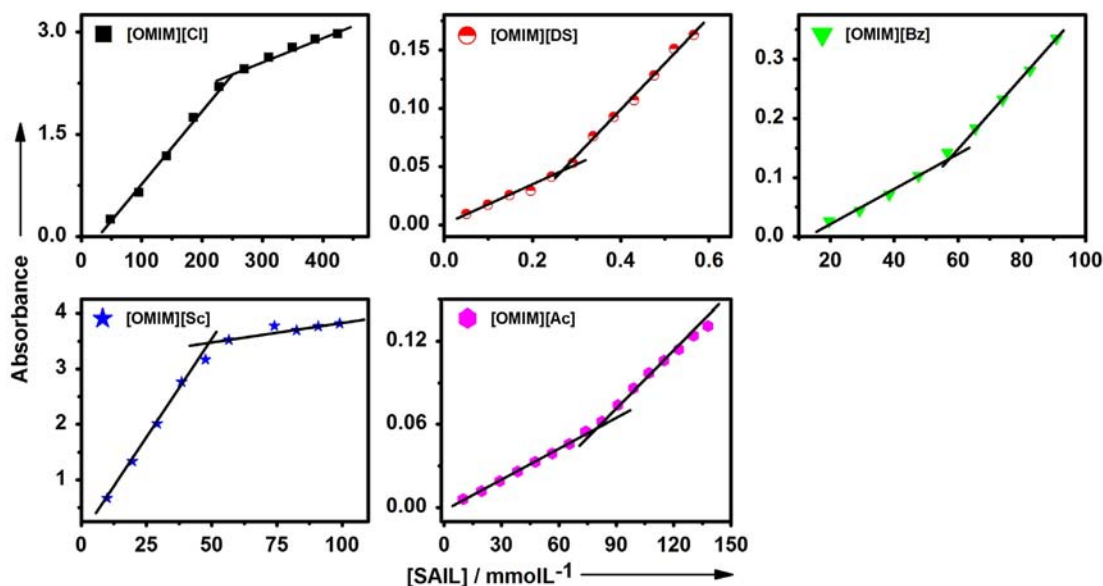


Fig. 2. Variation of absorbance with concentration of Imidazolium based surface active ionic liquids [SAIL] in water in the wavelength range of 240–360 nm.

Table 1

*cmc*s Of various of Imidazolium based surface active ionic liquids [SAILs] in water as estimated through tensiometry and UV–visible spectrophotometry at 298 K. Surface excess (Γ_{\max}) and minimum surface area per head group (A_{\min}) estimated from tensiometric plots (Fig. 3) are included.

[SAIL]	<i>cmc</i> (mM) Tensiometry	<i>cmc</i> (mM) UV–visible spectrophotometry	Γ_{\max} ($\times 10^3 \text{ mol m}^{-2}$)	A_{\min} (\AA^2)
[OMIM][DS]	0.23	0.26	2.072	0.080
[OMIM][Sc]	52.50	49.50	1.723	0.096
[OMIM][Bz]	69.40	62.10	2.243	0.074
[OMIM][Cl]	247.20	248.10	1.927	0.086
[OMIM][Ac]	87.30	80.80	1.866	0.089

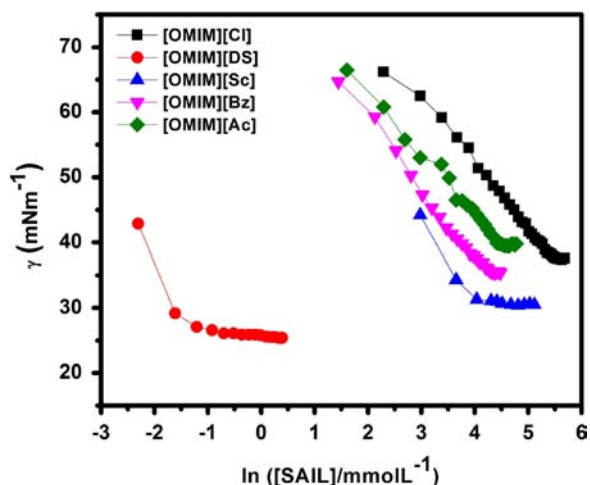


Fig. 3. Variation of surface tension with concentration of Imidazolium based surface active ionic liquids ([SAIL]) in water as recorded at 298 K.

reasoned by Jiao et al. [42] for the lower *cmc* of [BMIM][DS], the *cmc* of [OMIM][DS] with long alkyl chains associated with both the cation and anion was observed to be the lowest among the investigated SAILs. The low *cmc*s of [OMIM][Sc] and [OMIM][Bz] in comparison to [OMIM][Cl] and [OMIM][Ac] can be attributed to presence of hydrophobic phenyl ring in the counter anions in both the cases. Presence of these hydrophobic rings which intersperse into the palisade layer stabilizes the micelle leading to lowering of *cmc*. However, the *cmc* of [OMIM][Sc] is observed to be less than

that of [OMIM][Bz] which can be attributed to the presence of an extra –OH group in salicylate which might stabilize the micelle to a greater extent. Similar observation has been reported by Akram et al. [43] in their studies related to impact of counter anions on the micellization behaviour of Gemini surfactants. In the observed *cmc* sequence, [OMIM][Bz] is followed by [OMIM][Ac], with [OMIM][Cl] having the highest *cmc* value, perhaps due to higher hydrated size of chloride than acetate ion, owing to which the counter ion binding shall be less effective in the former case.

Besides *cmc*, parameters like surface excess and minimum area occupied per head group were calculated from the tensiometric plots (Fig. 3) and the estimated values are included in Table 1. Surface excess together with minimum area occupied by a head group decide the extent of packing at the air/water interface. Higher surface excess and hence lower A_{\min} indicate close packing at air/water interface [42,43]. As clear from the entries in Table 1, the surface excess values are in the order [OMIM][Bz] > [OMIM][DS] > [OMIM][Cl] > [OMIM][Ac] > [OMIM][Sc], and expectedly the A_{\min} values follow the reverse trend. The observed trend reflects the extent of stabilization of monolayer through various possible interactions, at air/water interface, of the surface active ions with their respective counter ions. The possible interactions include π – π , cation– π , hydrogen bonding and electrostatic interactions. The highest surface excess of [OMIM][Bz] may be due to the extra stabilization of monolayer by hydrophobic benzoate ions, which might reside closer to the interface. Comparatively the lower surface excess of [OMIM][DS] may be attributed to the competitive adsorption between its cation and anion, both being amphiphilic and hence expected to lead to steric crowding at the interface. Next to [OMIM][DS] in the observed sequence is [OMIM][Cl]

which has higher surface excess than [OMIM][Ac] followed by [OMIM][Sc]. The negative charge on acetate as well as salicylate is delocalized over their large sizes, the result being a weaker interactions with the imidazolium cation and hence their lower surface excess compared to [OMIM][Cl] [38].

4. Conclusions

Tensiometric and UV–visible spectrophotometric measurements of the aqueous solutions of imidazolium based surface active ionic liquids (SAILs) were carried out. These studies establish that the *cmc* of imidazolium based SAILs can be estimated spectrophotometrically from Beer plots without involving any external probe which is required in case of conventional surfactants. The results clearly demonstrate that SAILs show sensitivity to counter ions like other conventional surfactants for their micellization and surface activity in aqueous media.

Acknowledgement

MAB thanks Department of Science and Technology, New Delhi, India, for the research grant no. SR/S1/PC-11/2009. MAR thanks CSIR for the financial assistance. Authors would like to thank Prof. Khaliqz Zaman Khan for his support in correcting the grammar and editing of long sentences for the revised MS.

Appendix A. Supporting information

Supplementary data associated with this article can be found in the online version at <http://dx.doi.org/10.1016/j.talanta.2014.07.046>.

References

- [1] J. Dupont, R.F. de Souza, Paulo A.Z. Suarez, *Chem. Rev.* 102 (2002) 3667–3692.
- [2] T. Welton, *Chem. Rev.* 991 (1999) 2071–2084.
- [3] R. Sheldon, *Chem. Commun.* (2001) 2399–2407.
- [4] T. Welton, *Coord. Chem. Rev.* 248 (2004) 2459–2477.
- [5] S.F. Wang, T. Chen, Z.L. Zhang, X.C. Shen, Z.X. Lu, D.W. Pang, K.Y. Wong, *Langmuir* 21 (2005) 9260–9266.
- [6] B.M. Quinn, Z. Ding, R. Moulton, A.J. Bard, *Langmuir* 18 (2002) 1734–1742.
- [7] J. Gui, Y. Deng, Z. Hu, Z. Sun, *Tetrahedron Lett.* 45 (2004) 2681–2683.
- [8] A. Arce, M.J. Earle, H. Rodríguez, K.R. Seddon, *Green Chem.* 9 (2007) 70–74.
- [9] J. Fliieger, A. Siwek, M. Pizon, A.C. zajkowska-Zelazko, *J. Sep. Sci.* 36 (2013) 1530–1536.
- [10] O.A. E. Seoud, P.A. R. Pires, T.A. Moghny, E.L. Bastos, *J. Colloid Interface Sci.* 313 (2007) 296–304.
- [11] K. Bica, P.G. Philipp, J. Gritsch, A.K. Rössmann, C. Schröderb, R. Zirbsc, *Chem. Commun.* 48 (2012) 5013–5015.
- [12] M. Markiewicz, C. Jungnickel, H.P.H. Arp, *Environ. Sci. Technol.* 47 (2013) 6951–6958.
- [13] M. Amin, O.A. Chat, M.H. Najar, G.M. Rather, A.A. Dar, *J. Colloid Interface Sci.* 364 (2011) 163–169.
- [14] P.A. Bhat, A.A. Dar, G.M. Rather, *J. Chem. Eng. Data* 53 (2008) 1271–1277.
- [15] H. Weingärtner, C. Cabrele, C. Herrmann, *Phys. Chem. Chem. Phys.* 14 (2012) 415–426.
- [16] N. Gul, M.A. Mir, J.A. Khan, R.H. Khan, G.M. Rather, A.A. Dar, *J. Colloid Interface Sci.* 364 (2011) 157–162.
- [17] S. Mahajan, R. Sharma, R. Kumar Mahajan, *Langmuir* 28 (2012) 17238–17246.
- [18] H. Wang, J. Wang, S. Zhang, X. Xuan, *J. Phys. Chem. B* 112 (2008) 16682–16689.
- [19] T. Singh, A. Kumar, *J. Phys. Chem. B* 111 (2007) 7843–7851.
- [20] J. Jiao, B. Han, M. Lin, N. Cheng, L. Yu, M. Liu, *J. Colloid Interface Sci.* 412 (2013) 24–30.
- [21] M. Blesic, M.H. Marques, N.V. Plechkova, K.R. Seddon, L.P. N. Rebelo, A. Lopes, *Green Chem.* 9 (2007) 481–490.
- [22] K. Srinivasa Rao, T. Singh, T.J. Trivedi, A. Kumar, *J. Phys. Chem. B* 115 (2011) 13847–13853.
- [23] P. Brown, C.P. Butts, J. Eastoe, D. Fermin, I. Grillo, H.-C. Lee, D. Parker, D. Plana, R.M. Richardson, *Langmuir* 28 (2012) 2502–2509.
- [24] N. Cheng, P. Yu, T. Wang, X. Sheng, Y. Bi, Y. Gong, L. Yu, *J. Phys. Chem. B* 118 (2014) 2758–2768.
- [25] M.A. Bhat, A.A. Dar, A. Amin, P.I. Rashid, G.M. Rather, *J. Chem. Thermodyn.* 39 (2007) 1500–1507.
- [26] A. Beyaz, W.S. Oh, V.P. Reddy, *Colloids Surf., B* 35 (2004) 119–124.
- [27] A. Beyaz, W.S. Oh, V.P. Reddy, *Colloids Surf., B* 36 (2004) 71–74.
- [28] F. Ysambertt, F. Vejar, J. Paredes, J.L. Salager, *Colloids Surf., A* 137 (1998) 189–196.
- [29] A. Paul, P.K. Mandal, A. Samanta, *Chem. Phys. Lett.* 402 (2005) 375–379.
- [30] A. Paul, P.K. Mandal, A. Samanta, *J. Phys. Chem. B* 109 (2005) 9148–9153.
- [31] M.A. Bhat, C.K. Dutta, G.M. Rather, *J. Mol. Liq.* 181 (2013) 142–151.
- [32] C. Junnickel, J. Luczak, J. Ranke, J.F. Fernandez, A. Muller, *J. Thoming, Colloids Surf., A* 316 (2008) 278–284.
- [33] (a) J. Dupont, C.S. Consorti, P.A. Z. Saurez, R.F. deSouza, *Org. Synth.* 79 (2002) 236–243;
(b) J. Dupont, C.S. Consorti, P.A. Z. Saurez, R.F. deSouza, *Org. Synth.* 10 (2004) 184–188.
- [34] M.J. Earle, C.M. Gordon, N.V. Plechkova, K.R. Seddon, T. Welton, *Anal. Chem.* 79 (2007) 758–764.
- [35] J.G. Huddleston, A.E. Visser, W.M. Reichert, H.D. Willauer, G.A. Broker, R.D. Rogers, *Green Chem.* 3 (2001) 156–164.
- [36] J.M. Obliosca, S.D. Arco, M.H. Huang, *J. Fluoresc.* 17 (2007) 613–618.
- [37] S.D. Arco, R.T. Laxamana, O.D. Giron, J.M. Obliosca, *Philippine J. Sci.* 138 (2009) 133–139.
- [38] H. Zhang, H. Liang, J. Wang, Kun Li, *Z. Phys. Chem.* 221 (2007) 1061–1074.
- [39] M.A. Bhat, A.A. Dar, A. Amin, G.M. Rather, *J. Dispersion Sci. Technol.* 29 (2008) 514–520.
- [40] M. Jan, A.A. Dar, G.M. Rather, *Colloids Surf., A* 335 (2009) 114–120.
- [41] S. Manet, Y. Karpichev, D. Dedovets, R. Oda, *Langmuir* 29 (2013) 3518–3526.
- [42] J. Jiao, B. Dong, H. Zhang, Y. Zhao, X. Wang, R. Wang, L. Yu, *J. Phys. Chem. B* 116 (2012) 958–965.
- [43] M. Akram, S. Yousuf, T. Sarwar, Kabir ud-din, *Colloids Surf., A* 441 (2014) 281–290.



Label-free detection of exonuclease III by using dsDNA-templated copper nanoparticles as fluorescent probe



Hao Zhang^{b,a}, Zihan Lin^a, Xingguang Su^{a,*}

^a Department of Analytical Chemistry, College of Chemistry, Jilin University, Changchun 130012, China

^b Key Laboratory for Chemical Cleaner Production Technologies of The Education Department of Jilin Province, Jilin University of Chemical Technology, Jilin 132000, China

ARTICLE INFO

Article history:

Received 9 April 2014

Received in revised form

17 July 2014

Accepted 21 July 2014

Available online 30 July 2014

Keywords:

DNA

Copper nanoparticles

3'-5' exonuclease

Exonuclease III

Fluorescent sensor

ABSTRACT

3'-5' Exonuclease activities play key roles in maintaining genome stability, so the detection of 3'-5' exonuclease activity is very important for diseases diagnosis and drug development. In this paper, we established a simple, sensitive, low-cost and label-free method to detect the activity of exonuclease III (Exo III) by using double-strand DNA (dsDNA)-templated copper nanoparticles as fluorescent probe. Fluorescent Cu nanoparticles (NPs) with maximum emission wavelength of 575 nm are formed by using double-strand DNA (dsDNA) as templates. Upon the addition of Exo III, the dsDNA templates would be digested from 3' to 5', and the formation of fluorescent Cu NPs would be inhibited. Thus, the fluorescence intensity of dsDNA-Cu NPs would decrease. This method exhibits a low detection limit of 0.02 U mL⁻¹ for Exo III. Compared with the previous reports, this method does not need complex DNA sequence design, fluorescence dye label and sophisticated experimental techniques.

© 2014 Elsevier B.V. All rights reserved.

1. Introduction

Exonucleases are DNA degrading enzymes, which can digest DNA sequences from 3'-termini or 5'-termini. Exonuclease that contains 3'-5' exonuclease activity can remove nucleotides from the 3'-termini at DNA strands. The 3'-5' exonuclease plays important roles in several key cellular and physiological processes, such as repair of DNA double-strand breaks [1], contribution to the fidelity of DNA synthesis [2], promotion of genetic recombination [3] and prevention of genome instability [4]. The lack of 3'-5' exonuclease activity will cause serious diseases. For example, a major 3'-5' exonuclease TREX 1 shows DNA-editing roles in DNA replication or gap filling during DNA repairs [5]. Mutations in TREX 1 have been linked to four distinct diseases, Aicardi-Goutières syndrome, Systemic Lupus Erythematosus, Familial Chilblain Lupus and Retinal Vasculopathy and Cerebral Leukodystrophy [6]. WRN exonuclease is involved in DNA repair, which encodes a 3'-5' exonuclease. WRN exonuclease has been identified in an autosomal recessive genetic disorder Werner syndrome [7]. Therefore, the detection of 3'-5' exonuclease activity is important for diseases diagnosis and drug development.

The traditional methods for detecting 3'-5' exonuclease activity are commonly based on gel-based and/or require the use of radioisotopes labeled DNA [8–10]. However, these methods are costly, unwieldy, time-consuming and necessary security arrangement to control radiographic exposure. Recently, alternative methods for 3'-5' exonuclease activity detection have been developed such as fluorescence methods. For example, Leung et al. developed a label free and G-quadruplex-based fluorescence assay method for the detection of 3'-5' exonuclease activity [11]. Lee et al. reported a new assay platform for DNA exonuclease activity detection based on the preferential binding of single-stranded DNA (ssDNA) over double-stranded DNA (dsDNA) to graphene oxide [12]. By using molecular beacons, Wu et al. developed an ultrasensitive and rapid turn-on fluorescence assay for the detection 3'-5' exonuclease activity of exonuclease III [13]. These assay methods showed great advantages over the traditional methods. However, these methods suffered from costly fluorescence dye labeled DNA probes and rigorous design of the DNA sequence. Therefore, the development of a simple, sensitive and low-cost detection method for detecting 3'-5' exonuclease activity is important and would be useful.

Recently, ultrasensitive fluorescent metal nanoparticles have attracted special research interest in the field of biochemical analysis due to their remarkable optical properties, good biocompatibility and facile surface modification. For example, a simple fluorescence method for cysteine detection has been developed

* Corresponding author. Tel.: +86 431 85168352.

E-mail address: suxg@jlu.edu.cn (X. Su).

based on fluorescent silver clusters [14]. Glutathione-bound gold nanoclusters have been used as the fluorescence probe for detection of glutathione S-transferase-tagged proteins [15]. Silver and thioflavin T hybrid nanoclusters with extra bright and photostable emissions showed a new tool for biological imaging [16]. Lately, Mokhir et al. reported that fluorescent copper nanoparticles (Cu NPs) could be formed by using double-strand DNA as templates, whereas single strand DNA templates could not support the formation of Cu NPs [17]. The obtained dsDNA-templated Cu NPs exhibited low-toxicity, excellent fluorescence properties, good water solubility and high biocompatibility. Thus the dsDNA-Cu NPs had been used as fluorescence probes in some biological assays [18–20].

Herein, we designed a simple, sensitive, low cost and label-free strategy to detect the 3′–5′ exonuclease activity based on the formation of fluorescent Cu NPs by using dsDNA as templates. The dsDNA was used as both template for Cu NPs formation and substrate of the 3′–5′ exonuclease. The exonuclease could digest dsDNA probe to decrease the concentration of dsDNA templates, which would inhibit the formation of fluorescent Cu NPs. Hence, the 3′–5′ exonuclease activity could be detected through the changes of the fluorescence intensity of the system. Compared with the previous reported works, this strategy does not need any complex DNA sequence design or fluorescence dye label. Meanwhile, it exhibits high sensitivity and selectivity for detecting the 3′–5′ exonuclease activity.

2. Experimental

2.1. Apparatus and instruments

Fluorescence measurements were carried out on a Shimadzu RF-5301 PC spectra fluorophotometer. A quartz fluorescence cell with an optical path length of 1.0 cm was used. The fluorescence spectra were obtained with the excitation wavelength of 350 nm. All pH measurements were made with a Starter-2C pH meter (Ohaus Instruments Co. Ltd., Shanghai, China). Transmission electron microscope (TEM) images were obtained with Tecnai G2 F20 S-Twin.

2.2. Reagents

DNA oligomers were purchased from Sangon Biotech (Shanghai) Co., Ltd. The sequences of the DNA oligonucleotides were as follows:

DNA1, 5′-AATAATAAGCTATAATAATT-3′
DNA2, 5′-AATTATTATAGCTATTATT-3′

Exonuclease III (Exo III), sodium ascorbate were purchased from Sangon Biotech (Shanghai) Co., Ltd. Glucose, $\text{CuSO}_4 \cdot 5\text{H}_2\text{O}$, $\text{MgCl}_2 \cdot 6\text{H}_2\text{O}$, sodium dehydrogenized phosphate (NaH_2PO_4) and disodium hydrogen phosphate (Na_2HPO_4) were purchased from Aldrich Chemical Co. The water used in all experiments had a resistivity higher than $18 \text{ M}\Omega \text{ cm}^{-1}$. Self-made 10 mmol L^{-1} PBS buffer (pH 7.4, 10 mmol L^{-1} NaH_2PO_4 – Na_2HPO_4) was used as the medium for the detection process.

2.3. Fluorescence assay

Typically, in order to prepare dsDNA templates, two ssDNA strands (DNA1, DNA2) were mixed together in $80 \mu\text{L}$ 10 mmol L^{-1} PBS buffer (pH 7.4) with 5 mmol L^{-1} Mg^{2+} and reacted for 20 min at 25°C to form the stable dsDNA. Then, various concentrations of $10 \mu\text{L}$ Exo III were added to the dsDNA solution. After incubation of

1 h at 37°C , a mixed solution containing 10 mmol L^{-1} PBS buffer (pH 7.4), sodium ascorbate and 250 mmol L^{-1} NaCl was introduced. After vibrating for 1 min, $10 \mu\text{L}$ CuSO_4 solutions were added to the mixture solution with the final concentrations of 500 nmol L^{-1} DNA, $120 \mu\text{mol L}^{-1}$ Cu^{2+} and 1.5 mmol L^{-1} sodium ascorbate. The mixed solution was kept for 10 min at room temperature, and then the fluorescent Cu NPs were formed. All experiments were repeated for three times.

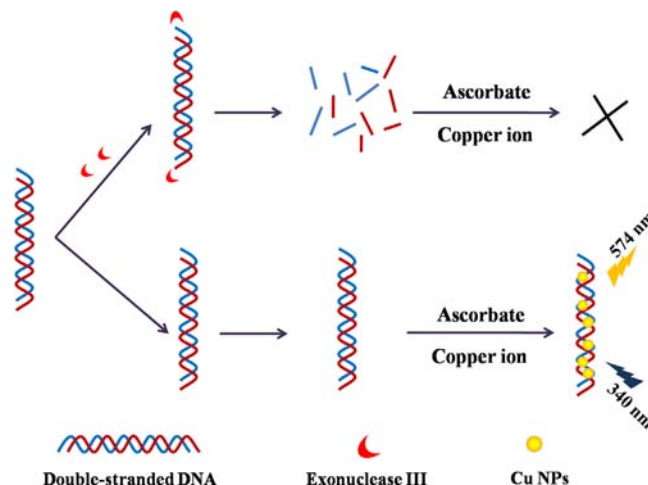
2.4. Serum sample assay

Human blood samples were collected from local hospital. All the blood samples were obtained through venipuncture and centrifuged at $10,000 \text{ rpm}$ for 10 min after stored for 2 h at room temperature. 0.4 mL serum sample was mixed with 0.6 mL acetonitrile. After vigorously shaking for 2 min, the mixture was centrifuged at $10,000 \text{ rpm}$ for 10 min. The obtained supernatant was diluted by 10 times with deionized water and the Exo III activity assay was done as described above.

3. Results and discussion

3.1. Sensor design

Exonuclease III (Exo III) is well known as a sequence-independent 3′–5′ exonuclease, which has been widely used in biochemical analysis [21,22]. Exo III can catalyze the stepwise removal of mononucleotides from DNA duplexes in the direction from blunt or recessed 3′-termini to 5′-termini, while it is unable to catalyze the removal of bases from single stranded DNA or DNA duplexes with a protruding 3′ end [23]. Scheme 1 shows the design of the label-free fluorescent probe for Exo III activity detection. The sensing system contains two completely complementary nucleic acid strands, which are simply designed based on DNA hybridization. The hybridized dsDNA was introduced to act as both templates for Cu NPs formation and substrate of Exo III. In the absence of Exo III, the DNA1 and DNA2 would hybridize to form stable DNA duplexes. Upon the addition of Cu^{2+} ions and sodium ascorbate, the formed dsDNA-templated Cu NPs are clustered on dsDNA through the reduction of copper(II) to copper(I) followed by the disproportionation of copper(I) into copper(II) and copper(0) [17]. The formed stable Cu nanoparticles show strong fluorescence. However, in the presence of the Exo III, the stable DNA duplexes will be cleaved into fragments due to the high exodeoxyribonuclease activity



Scheme 1. Schematic illustration of the Exo III detection based on the dsDNA-templated fluorescent Cu NPs.

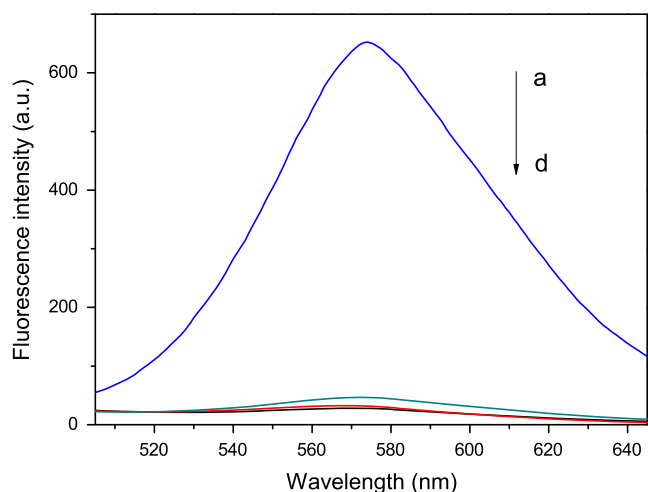


Fig. 1. Fluorescence spectra of obtained Cu NPs under different conditions. (a) DNA1 strand + DNA2 strand, (b) DNA1 strand + DNA2 strand + Exo III, (c) DNA1 strand and (d) DNA2 strand. Conditions: 500 nmol L^{-1} DNA1, 500 nmol L^{-1} DNA2, 3 U mL^{-1} Exo III, 1.5 mmol L^{-1} sodium ascorbate, $120 \text{ }\mu\text{mol L}^{-1}$ Cu^{2+} ; PBS 10 mmol L^{-1} , pH 7.4.

of Exo III on DNA duplexes. Hence, the introduction of Cu^{2+} ions and ascorbate cannot form the fluorescent Cu NPs due to the lack of the dsDNA templates. Accordingly, low fluorescence intensity is observed. Thus, the Exo III activity can be detected via the changes of the fluorescence intensity in the system.

To demonstrate the feasibility of our new strategy for detecting 3'-5' exonuclease activity, fluorescence emission spectra of the sensing system under different conditions were recorded. As shown in Fig. 1, the dsDNA successfully worked as templates for the formation of fluorescent Cu NPs and high fluorescence intensity could be observed (Fig. 1 curves a). However, when Exo III was added into the system, the dsDNA would be digested into fragments from the 3'-termini. For the lack of dsDNA templates, the formation of Cu NPs would not happen, resulting in low fluorescence intensity (Fig. 1 curves b). In addition, by using either DNA1 strand (Fig. 1, curves c) or DNA2 strand (Fig. 1, curves d), no fluorescent signal could be detected, which proved that the ssDNA would not be used as effective templates for the formation of Cu NPs. In other words, in the absence of dsDNA or only in the presence of ssDNA templates, fluorescent Cu NPs would not be formed. The results indicated that our proposed strategy could be used to detect Exo III activity.

Since it has been reported that whether Cu NPs are emissive or not is dependent on their sizes [24], the TEM images of the CuNPs before and after the addition of Exo III have been investigated. As shown in Fig. 2, the addition of Exo III will inhibit the formation of the dispersive Cu NPs, which indicates that the DNA duplexes will be cleaved into fragments due to the addition of Exo III, and the introduction of Cu^{2+} ions and ascorbate cannot form the fluorescent Cu NPs due to the lack of the dsDNA templates.

3.2. Optimization of sensor

To obtain the optimal experimental conditions for Exo III activity assay, we investigated the effects of double-stranded DNA concentrations, the concentrations of Cu^{2+} and sodium ascorbate, and the reaction time on the fluorescence intensity of dsDNA-Cu NPs.

Because dsDNA acted as the templates for the formation of fluorescent Cu NPs, we firstly studied the effect of dsDNA concentrations on the fluorescence intensity of Cu NPs. As shown in Fig. S1, the fluorescence intensity of dsDNA-Cu NPs increased with

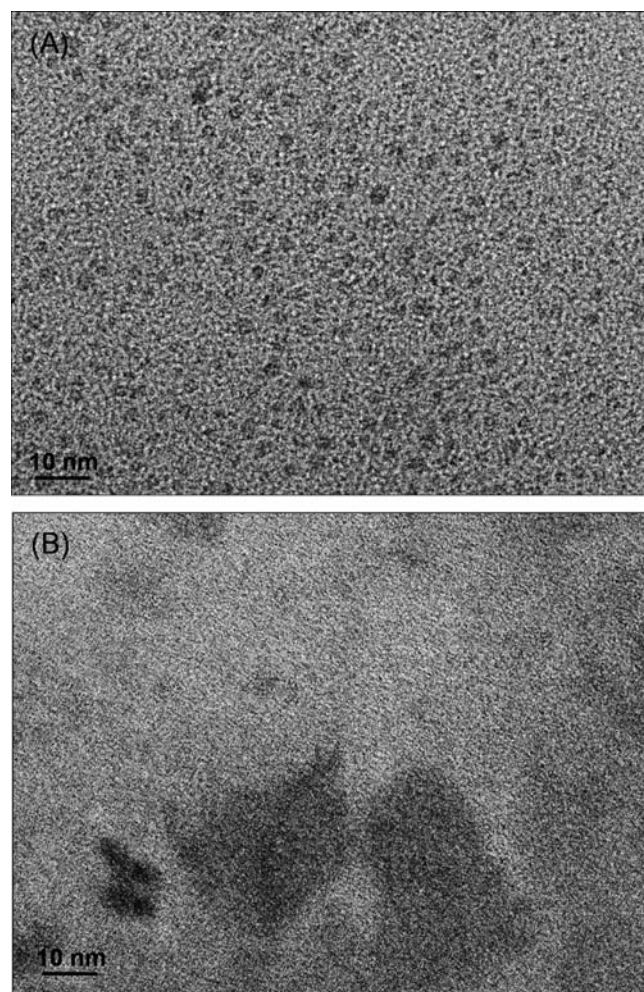


Fig. 2. The TEM images of the CuNPs before (A) and after (B) the addition of 5 U mL^{-1} Exo III.

the increase of dsDNA concentration, and there was a good linear correlation between the fluorescence intensity and dsDNA concentrations in the range of 100 nmol L^{-1} to 1000 nmol L^{-1} (Fig. S1 inset). It indicated that the formation of Cu NPs specifically depended on the concentration of dsDNA with the other conditions fixed. In the further experiments, we used a dsDNA concentration of 500 nM , because the corresponding fluorescence intensity could satisfy the detection requirements.

As the source of the formed fluorescent Cu NPs, Cu^{2+} was an important factor in influencing the fluorescence intensity of the probe. To form Cu NPs effectively, a certain high Cu^{2+} ion/dsDNA ratio was necessary. The effect of the concentrations of Cu^{2+} was investigated in this paper. As shown in Fig. S2A, the fluorescence intensity of the Cu NPs sharply increased with the increase of Cu^{2+} ion concentration. At low Cu^{2+} ion concentration, Cu^{2+} ions preferred to bind to the backbone phosphate negative groups through nonspecific electrostatic attraction [25]. When Cu^{2+} ion concentration was further increased, with much higher affinity than the phosphate negative groups, the Cu^{2+} ion began to interact with DNA bases [26], and could be reduced by ascorbate to form stable fluorescent Cu nanoparticles. Hence, the enhancement of fluorescence intensity was observed. When the concentration of Cu^{2+} ion was higher than $120 \text{ }\mu\text{mol L}^{-1}$, the fluorescence intensity decreased gradually. It might be due to the decreasing of the dsDNA templates with the destruction of the DNA double helix by the generated hydroxyl radicals at the higher

Cu^{2+} concentration [27]. Hence, the $120 \mu\text{mol L}^{-1}$ of Cu^{2+} concentration was used in the further experiments. Considering high concentrated Cu^{2+} /ascorbate mixture would degrade the dsDNA templates via the produced hydroxyl radicals, the concentration of sodium ascorbate was also optimized. It could be seen in Fig. S2B, the fluorescence intensity increased remarkably with the increasing of ascorbate concentrations, indicating that the ascorbate efficiently acted as a reducing agent and stabilizing ligand in the formation of Cu NPs [28]. When the concentrations of ascorbate exceeded 1.5 mmol L^{-1} , the fluorescence intensity was decreased. The reason of high ascorbate concentrations influencing the formation of the Cu NPs would be similar with that of high concentration of Cu^{2+} ion. So, we chose 1.5 mmol L^{-1} of sodium ascorbate in further experiment.

Finally, the effect of reaction time was studied. Without the addition of Exo III, the reaction time was recorded after starting the reduction reaction between Cu^{2+} ions and ascorbate in the presence of dsDNA. As shown in Fig. S3A, the fluorescence intensity of dsDNA–Cu NPs increased with the increase of reaction time and achieved a plateau within 10 min, which indicated that the formation of Cu NPs by the reduction of Cu^{2+} with ascorbate was nearly complete in 10 min. So the reduction time of 10 min was used in the following experiments.

For using the dsDNA–Cu NPs as fluorescent probe to detect the Exo III activity, the effect of incubation time was investigated with the addition of 5 U mL^{-1} Exo III. It could be seen in Fig. S3B, the fluorescence intensity of dsDNA–Cu NPs decreased quickly and reached the plateau after 30 min. It had been reported that the DNA digestion proceeded faster with higher concentration of Exo III [12]. That is to say, at the lower concentration of Exo III, more time was required for the complete digestion of dsDNA. Considering the complete digestion of dsDNA by Exo III, we used 60 min of incubation time in this study.

3.3. Exo III detection

Under the optimal conditions, the formed dsDNA–Cu NPs were used as fluorescent probe for Exo III detection. As shown in Fig. 3, when a series of different concentrations (0.05 U mL^{-1} to 5 U mL^{-1}) of Exo III were introduced to the dsDNA–Cu NPs system,

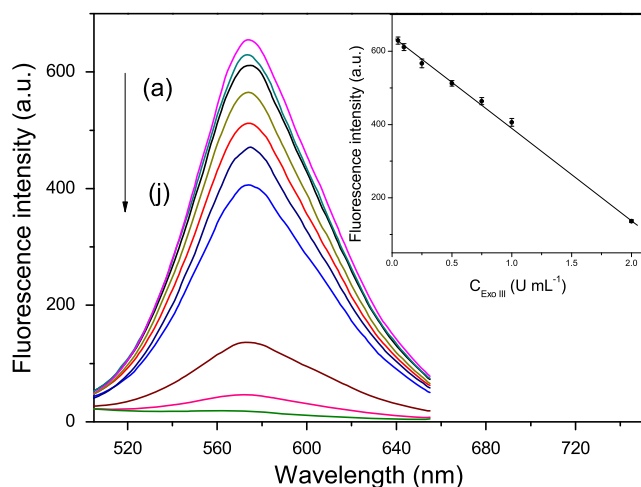


Fig. 3. Fluorescence spectra for the determination of Exo III at different concentrations: (a) 0 U mL^{-1} , (b) 0.05 U mL^{-1} , (c) 0.1 U mL^{-1} , (d) 0.25 U mL^{-1} , (e) 0.5 U mL^{-1} , (f) 0.75 U mL^{-1} , (g) 1 U mL^{-1} , (h) 2 U mL^{-1} , (i) 3 U mL^{-1} , (j) 5 U mL^{-1} . Inset: the linear relationship between the fluorescence intensity and the Exo III concentrations. Conditions: 500 nmol L^{-1} dsDNA; 1.5 mmol L^{-1} sodium ascorbate; $120 \mu\text{mol L}^{-1}$ Cu^{2+} ; PBS 10 mmol L^{-1} , pH 7.4.

the fluorescence intensity of the formed dsDNA–CuNPs gradually decreased with the increasing concentrations of Exo III. Fig. 3 inset described the relationship between the Exo III concentration and the fluorescence intensity of dsDNA–Cu NPs at the maximum emission wavelength. A linear correlation existed between the fluorescence intensity and the concentration of Exo III in the range of 0.05 U mL^{-1} to 2 U mL^{-1} . The regression equation was $F = -251.72[\text{Exo III}] + 641.04$ with a correlation coefficient of 0.999. The limit of detection (LOD) for Exo III was 0.02 U mL^{-1} . The LOD was calculated by the equation $\text{LOD} = (3\sigma/s)$, where σ was the standard deviation of nine blank signals and s was the slope of the calibration curve. This LOD was much lower than that of the reported G-quadruplex-based label-free fluorescence method [11] and comparable to the labeled fluorescent method [13]. The relative standard deviation (RSD) was 2.2% for the determination of 1 U mL^{-1} Exo III ($n=6$), which indicated a good reproducibility.

To demonstrate the selectivity of the present method, we investigated the effect of a series of 15 U mL^{-1} nonspecific enzymes on the fluorescence intensity of Cu NPs, including lysozyme, Exo I, EcoRI and Hind III. Exo I belongs to a similar exonuclease family to Exo III, which could catalyze the removal of mononucleotides on single-stranded DNA from the 3' to 5' direction. EcoRI and Hind III belong to the restriction endonuclease, which could cleave the DNA within a defined sequence. Lysozyme belongs to neither exonuclease nor endonuclease. As shown in Fig. 4, under the same conditions for Exo III detection, only Exo III caused an obvious fluorescence decrease. These results indicated that the proposed method has good selectivity for Exo III detection.

We further studied the practical application of the proposed method by detecting Exo III activity in human serum samples. The results are listed in Table 1. Results show that the concentrations of Exo III in human serum can be detected with RSD lower than 3.2% and the average recoveries of Exo III in the human serum samples were in the range of 96.8–101%. We use UV–vis method [29] as a contrast method to detect Exo III in the human serum samples. It can be seen that the results obtained by the proposed method were in good agreement with those provided by UV–vis method. The results demonstrate that our proposed label-free fluorescence sensing platform is feasible for detecting Exo III activity in human serum sample.

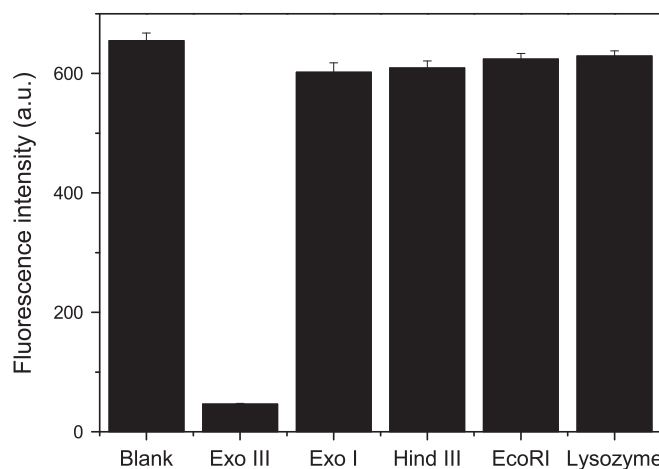


Fig. 4. Selectivity of dsDNA–Cu NPs sensing system for Exo III detection. The concentrations of all the interferents are fixed on 15 U mL^{-1} and the concentrations of Exo III is 3 U mL^{-1} . Conditions: 500 nmol L^{-1} dsDNA; 1.5 mmol L^{-1} sodium ascorbate; $120 \mu\text{mol L}^{-1}$ Cu^{2+} ; PBS 10 mmol L^{-1} , pH 7.4.

Table 1
Detection of Exo III activity in human serum sample.

Samples	UV–vis method Found ($\mu\text{mol L}^{-1}$)	Our label-free fluorescence sensing platform				
		Found ($\mu\text{mol L}^{-1}$)	added ($\mu\text{mol L}^{-1}$)	Found ($\mu\text{mol L}^{-1}$)	Recovery (%)	RSD (%, $n=3$)
1	0.49	0.51	0.25	0.74	97.4	2.6
2	0.98	0.99	0.5	1.02	101	1.0
			0.25	1.20	96.8	3.2
			0.5	1.47	98.7	1.3

4. Conclusion

In this paper, we established a simple, sensitive, low-cost and label-free method to detect Exo III. The design of dsDNA sequence is simply based on DNA hybridization, which could be digested by Exo III. For the dsDNA acting as templates for Cu NPs formation, the digestion of dsDNA would cause the decrease of the formed Cu NPs, resulting in the decreased fluorescence intensity. Hence, the concentration of Exo III can be detected through the changes of the fluorescence intensity in the sensor system. Compared with the previous reported works, this strategy does not need any complex DNA sequence design, fluorescence dye label, and sophisticated experimental techniques. At the same time, this method exhibits high sensitivity and selectivity for the detection of Exo III.

Acknowledgments

This work was financially supported by the National Natural Science Foundation of China (No. 21075050, No. 21275063) and the science and technology development project of Jilin province, China (No. 20110334).

Appendix A. Supporting information

Supplementary data associated with this article can be found in the online version at <http://dx.doi.org/10.1016/j.talanta.2014.07.065>.

Reference

- [1] T.T. Paull, M. Gellert, *Mol. Cell* 1 (1998) 969–979.
- [2] L.P. Song, M. Chaudhuri, C.W. Knopf, D.S. Parris, *J. Biol. Chem.* 279 (2004) 18535–18543.
- [3] D.B. Gammon, D.H. Evans, *J. Virol.* 83 (2009) 4236–4250.
- [4] Y.H. Jin, R. Obert, P.M.J. Burgers, T.A. Kunkel, M.A. Resnick, D.A. Gordenin, *Proc. Natl. Acad. Sci.* 98 (2001) 5122–5127.
- [5] Y.G. Yang, T. Lindahl, D.E. Barnes, *Cell* 131 (2007) 873–886.
- [6] D. Kavanagh, D. Spitzer, P.H. Kothari, A. Shaikh, M.K. Liszewski, A. Richards, J.P. Atkinson, *Cell Cycle* 7 (2008) 1718–1725.
- [7] J.-C. Shen, L.A. Loeb, *Trends Genet.* 16 (2000) 213–220.
- [8] D.A. Lehtinen, S. Harvey, M.J. Mulcahy, T. Hollis, F.W. Perrino, *J. Biol. Chem.* 283 (2008) 31649–31656.
- [9] M. Brucet, J. Querol-Audí, K. Bertlik, J. Lloberas, I. Fita, A. Celada, *Protein Sci.* 17 (2008) 2059–2069.
- [10] A.V. Nimkar, A.Z. Özsoy, J. Genschel, P. Modrich, S.C. Kowalczykowski, *Proc. Natl. Acad. Sci.* 105 (2008) 16906–16911.
- [11] C.H. Leung, D.S.H. Chan, B.Y.W. Man, C.J. Wang, W. Lam, Y.C. Cheng, W.F. Fong, W.L.W. Hsiao, D.L. Ma, *Anal. Chem.* 83 (2011) 463–466.
- [12] J. Lee, D.H. Min, *Analyst* 137 (2012) 2024–2026.
- [13] X. Wu, J. Chen, J.X. Zhao, *Analyst* 139 (2014) 1081–1087.
- [14] L. Shang, S. Dong, *Biosens. Bioelectron.* 24 (2009) 1569–1573.
- [15] C.-T. Chen, W.-J. Chen, C.-Z. Liu, L.-Y. Chang, Y.-C. Chen, *Chem. Commun.* (2009) 7515–7517.
- [16] N. Makarava, A. Parfenov, I.V. Baskakov, *Biophys. J.* 89 (2005) 572–580.
- [17] A. Rotaru, S. Dutta, E. Jentzsch, K. Gothelf, A. Mokhir, *Angewandte Chemie Int. Ed.* 49 (2010) 5665–5667.
- [18] Z. Zhou, Y. Du, S. Dong, *Anal. Chem.* 83 (2011) 5122–5127.
- [19] L.L. Zhang, J.J. Zhao, H. Zhang, J.H. Jiang, R.Q. Yu, *Biosens. Bioelectron.* 44 (2013) 6–9.
- [20] L.L. Zhang, J.J. Zhao, M. Duan, H. Zhang, J.H. Jiang, R.Q. Yu, *Anal. Chem.* 85 (2013) 3797–3801.
- [21] R. Miranda-Castro, D. Marchal, B. Limoges, F. Mavre, *Chem. Commun.* 48 (2012) 8772–8774.
- [22] G. Wang, G. Xu, Y. Zhu, X. Zhang, *Chem. Commun.* 50 (2014) 747–750.
- [23] X.H. Zhao, Q.J. Ma, X.X. Wu, X. Zhu, *Anal. Chim. Acta* 727 (2012) 67–70.
- [24] G. Liu, Y. Shao, J. Peng, W. Dai, L. Liu, S. Xu, F. Wu, X. Wu, *Nanotechnology* 24 (2013) 345502.
- [25] V. Andrushchenko, J.H. van de Sande, H. Wieser, *Biopolymers* 72 (2003) 374–390.
- [26] X.F. Jia, J. Li, L. Han, J.T. Ren, X. Yang, E.K. Wang, *ACS Nano* 6 (2012) 3311–3317.
- [27] C.F. Monson, A.T. Woolley, *Nano Lett.* 3 (2003) 359–363.
- [28] J.H. Chen, J. Liu, Z.Y. Fang, L.W. Zeng, *Chem. Commun.* 48 (2012) 1057–1059.
- [29] I. Locke, M. Ramsey, S. Hill, B. Carpenter, *J. Anal. Methods Chem.* 15 (1900) 65–70.



Synthesis of a mixed-model stationary phase derived from glutamine for HPLC separation of structurally different biologically active compounds: HILIC and reversed-phase applications



Tarık Aral^{a,*}, Hayriye Aral^{a,*}, Berrin Ziyadanoğulları^b, Recep Ziyadanoğulları^b

^a University of Batman, Faculty of Science and Art, Department of Chemistry, Batman, Turkey

^b University of Dicle, Faculty of Science, Department of Chemistry, Diyarbakır, Turkey

ARTICLE INFO

Article history:

Received 5 April 2014

Received in revised form
18 July 2014

Accepted 21 July 2014

Available online 31 July 2014

Keywords:

Mixed-model stationary phase

Polar stationary phase

Nucleotides and nucleosides

Phytohormones

Phenolic compounds

HILIC

ABSTRACT

A novel mixed-mode stationary phase was synthesised starting from *N*-Boc-glutamine, aniline and spherical silica gel (4 μm, 60 Å). The prepared stationary phase was characterized by IR and elemental analysis. The new stationary phase bears an embedded amide group into phenyl ring, highly polar a terminal amide group and non-polar groups (phenyl and alkyl groups). At first, this new mixed-mode stationary phase was used for HILIC separation of four nucleotides and five nucleosides. The effects of different separation conditions, such as pH value, mobile phase and temperature, on the separation process were investigated. The optimum separation for nucleotides was achieved using HILIC isocratic elution with aqueous mobile phase and acetonitrile with 20 °C column temperature. Under these conditions, the four nucleotides could be separated and detected at 265 nm within 14 min. Five nucleosides were separated under HILIC isocratic elution with aqueous mobile phase containing pH=3.25 phosphate buffer (10 mM) and acetonitrile with 20 °C column temperature and detected at 265 nm within 14 min. Chromatographic parameters as retention factor, selectivity, theoretical plate number and peak asymmetry factor were calculated for the effect of temperature and water content in mobile phase on the separation process. The new column was also tested for nucleotides and nucleosides mixture and six analytes were separated in 10 min. The chromatographic behaviours of these polar analytes on the new mixed-model stationary phase were compared with those of HILIC columns under similar conditions. Further, phytohormones and phenolic compounds were separated in order to see influence of the new stationary phase in reverse phase conditions. Eleven plant phytohormones were separated within 13 min using RP-HPLC gradient elution with aqueous mobile phase containing pH=2.5 phosphate buffer (10 mM) and acetonitrile with 20 °C column temperature and detected at 230 or 278 nm. The best separation conditions for seven phenolic compounds was also achieved using reversed-phase HPLC gradient elution with aqueous mobile phase containing pH=2.5 phosphate buffer (10 mM) and acetonitrile with 20 °C column temperature and seven phenolic compounds could be separated and detected at 230 nm within 16 min.

© 2014 Elsevier B.V. All rights reserved.

Abbreviations: HPLC, high-performance liquid chromatography; RPLC, reversed-phase liquid chromatography; NPLC, normal-phase liquid chromatography; HILIC, hydrophilic interaction chromatography; DCC, dicyclohexylcarbodiimide; DCM, dichloromethane; H, hexane; EtOAc, ethyl acetate; TFA, trifluoroacetic acid; GPTMS, 3-glycidyloxypropyltrimethoxysilane; Boc, *tert*-butoxycarbonyl; SP, stationary phase; TLC, thin layer chromatography; THF, tetrahydrofuran; AcOH, acetic acid; ACN, acetonitrile

* Corresponding authors.

E-mail addresses: tarik.aral@batman.edu.tr (T. Aral), hayriye.aral@batman.edu.tr (H. Aral).

<http://dx.doi.org/10.1016/j.talanta.2014.07.060>

0039-9140/© 2014 Elsevier B.V. All rights reserved.

1. Introduction

Hydrophilic interaction liquid chromatography (HILIC) is a powerful alternative for normal-phase liquid chromatography (NPLC) and reversed-phase liquid chromatography (RPLC) modes for separation of polar compounds with a polar stationary phase [1,2]. The surface of polar stationary phase is generally modified by polar functional groups such as –NH₂, –CN, –CH(OH)CH₂OH. Developing new and special separation materials has received considerable interest in recent years [3]. HILIC can be used to separate peptides, carbohydrates and other lower molecular weight polar compounds [4]. Typically, the order of elution in HILIC is the opposite of that seen in RP-HPLC. However, while

retention in RP-HPLC is usually dependent on hydrophobicity of an analytes, retention in HILIC is more dependent on the presence of hydrophilicity of an analyte [5].

The stationary phase is very important in all types of chromatography [6]. As it is well known, the chemical characteristics of a stationary phase affect the separation of any group compounds. Because the separation efficiency of a stationary phase depends on its separation mechanism [7,8]. Most stationary phases only provided single separation mechanism [9,10] and were applied in single chromatographic mode. Mixed-mode approach emerged due to a need for better retention control for both polar and non-polar molecules. Multiple mechanisms of interactions allow the use of one stationary phase for a much wider range of applications as compared to RP or HILIC approach. Simultaneous analysis of polar and non-polar, ionisable and neutral, and organic and inorganic compounds and other complex mixtures is possible. This kind of stationary phase can reduce the cost of analysing and improve work efficiency to a great extent. It deserves wide and further investigations. Several kind of stationary phases with mixed-mode performance have been investigated such as phenylpropanolamine [8], phenylamine [11,12], 8-quinolinol [13], poly(1-allylimidazole) [14], imidazole [15,16], pyridine [17,18] and dipyrindine [19] functional silicas. These stationary phases were tested mixed-mode chromatography, to separate organic compounds and ions on the same column.

One of the most important properties of a stationary phase is that it should have a wide application area for a wide range of analyte class. Therefore, to design a new stationary phase that can be used to separate a wide range of analyte class from non-polar to highly polar is very important. In this study, we focused on synthesis a new mixed-model stationary phase bearing non-polar groups such as, aliphatic chain and aromatic ring beside of highly polar amide, amine and hydroxyl groups. The synthesis of the stationary phase involves the synthesis of a new amide compound and the surface modification of spherical silica particles (4 μm , 60 \AA) via the attachment of this new compound to the silica surface. Influences of different separation conditions, such as the mobile phase, pH, flow rate and temperature, on the separation and retention behaviours of four nucleotides and five nucleosides were also studied. Furthermore, in order to see the efficiency of new stationary phase in RP conditions, eleven phytohormones and seven phenolic compounds were separated.

2. Experimental

2.1. Reagents and materials

Silica gel 60 (Merck, 0.040–0.063 mm) and silica gel/TLC cards (F254), used for column chromatography and TLC, respectively, were purchased from Merck. The solvents used in HPLC were of HPLC grade and purchased from Merck. All of the selected analytes (Scheme 1) and all other reagents and solvents were purchased from Sigma–Aldrich or Merck. All reagent used in the synthesis were reagent grade unless otherwise specified. Melting points were determined by an Electrothermal 9300 apparatus with open capillaries. Infrared spectra were recorded on a Mattson 1000 FTIR spectrometer. Elemental analyses were performed with a Thermo Scientific FLASH 2000 instrument. Deionised water was purified using a Millipore Milli-Q water system. ^1H (400 MHz) and ^{13}C (100 MHz) NMR spectra were recorded on a Bruker AV400 high-performance digital FT-NMR spectrometer. The chemical shifts (δ) and coupling constants (J) are expressed in parts per million (ppm) and hertz, respectively.

2.2. HPLC conditions

The chromatographic equipment consisted of an Agilent 1260 HPLC system, including a quaternary pump, degasser, autosampler, DAD detector and thermostated column compartment (Agilent, Waldbronn, Germany). The column (250 \times 4.6 mm, stainless steel) was packed with modified silica gel using the slurry packing technique under high pressure. Standard solutions of each analyte (1 mg mL^{-1}) were prepared in acetonitrile, whereas kinetin (K) and *N*-benzylaminopurine (BAP) were prepared in a 30:70 acetonitrile–0.1 N NaOH mixture. All solutions were stored at $-25\text{ }^\circ\text{C}$. The solutions were further diluted with water to obtain a final concentration of 100 ppm per analytes. The detection wavelengths were between 230 and 280 nm. The chromatographic conditions different from the conditions given in this section are described in the figures or tables.

2.3. Synthesis

2.3.1. *N*-Boc-*N'*-phenylglutamide (**1**)

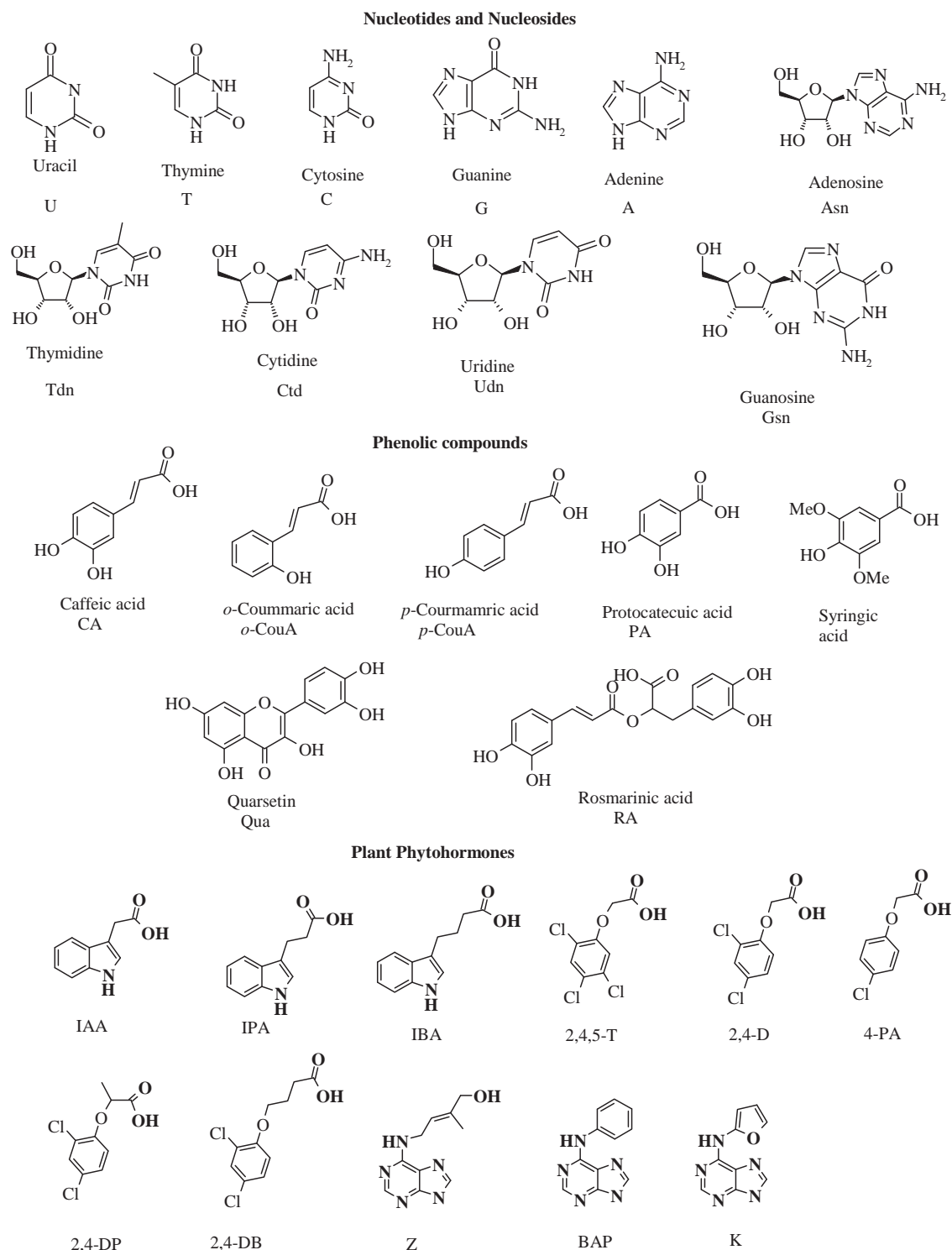
Dicyclohexylcarbodiimide (DCC, 1.71 g, 8.3 mmol) dissolved in THF (15 mL) was added to a stirred solution of *N*-Boc-phenylglutamine (1.86 g, 7.55 mmol) and aniline (7.22 mg, 8.3 mmol) in THF (15 mL) at $0\text{ }^\circ\text{C}$ for 1 h. After stirring overnight at room temperature, the mixture was filtered and evaporated. The residue was purified by column chromatography on silica gel (H:EtOAc=1:6) to afford *N*-boc-*N'*-amide (**1**) as a white solid. Yield: 1.44 g, 60%. Mp: 178–179 $^\circ\text{C}$. ^1H NMR (CDCl_3): δ (ppm); 1.98 (s, 9H), 1.74–1.94 (m, 2H), 2.08–2.22 (m, 2H), 4.02–4.07 (m, 1H), 6.81 (s, 1H), 7.02–7.61 (m, 7H), 9.67 (s, 1H). ^{13}C NMR (CDCl_3): δ (ppm); 28.08, 28.65, 32.04, 55.32, 78.59, 119.70, 123.73, 129.16, 139.42, 155.87, 171.44, 174.16. IR ν (cm^{-1}): 3423, 3386, 3329, 3251, 3195, 3132, 3037, 2979, 2931, 2851, 1698, 1659, 1606, 1558, 1510, 1446, 1367, 1251, 1172, 1027, 756.

2.3.2. Deprotection of *N*-Boc group (**2**)

TFA/AcOH (1:1) (1.2 mL) was added to a stirred solution of *N*-Boc-*N'*-amide (**1**) (1.0 g, 2.1 mmol) in dichloromethane (5 mL) at $0\text{ }^\circ\text{C}$. After stirring overnight at room temperature, the solvent was evaporated and 1 N NaOH (5 mL) was added to the residue. The mixture was extracted with THF (3 \times 20 mL) and toluene (3 \times 10 mL), respectively, dried over Na_2SO_4 , filtered and evaporated under vacuum to afford a pure amide (**2**) as a white solid. Yield: 500 mg, 72%. Mp: 185–186 $^\circ\text{C}$. ^1H NMR (CDCl_3): δ (ppm); 2.00–2.55 (m, 7H), 4.02 (m, 1H), 7.05–7.09 (m, 1H), 7.30–7.34 (m, 2H), 7.60–7.63 (m, 2H), 7.89 (s, 1H). ^{13}C NMR (CDCl_3): δ (ppm); 25.80, 29.71, 56.88, 119.84, 123.98, 129.22, 139.24, 152.01, 171.75, 178.06. IR ν (cm^{-1}): 3326, 3256, 3197, 3139, 3093, 3047, 2929, 2850, 1698, 1662, 1623, 1564, 1498, 1444, 1309, 1244, 1087, 1044, 893, 755, 666.

2.3.3. Amide-bonded stationary phase (**3** and **4**)

N'-amide (500 mg, 2.25 mmol) was dissolved in ethanol (5 mL) and (3-glycidyloxypropyl)trimethoxysilane (GPTMS, 1.0 g, 4.2 mmol) was added to the mixture. The mixture was stirred and refluxed for 2 days. The solvent was removed by evaporation, and the solid part was washed with dichloromethane and hexane successively, to remove GPTMS residue. The solid part was dissolved in toluene (60 mL) and HPLC-quality spherical silica gel (4 μm , 60 \AA) (4 g) was added to the mixture. The mixture was refluxed for 4 days. The solvent was removed by evaporation, and the amide-bonded silica was washed with chloroform by Soxhlet extraction overnight and dried under vacuum for 7 h to afford white powders (**4**). Elemental Analysis: C 9.36, H 1.38, N 1.63 (0.39 mmol of loaded amide/g SP).



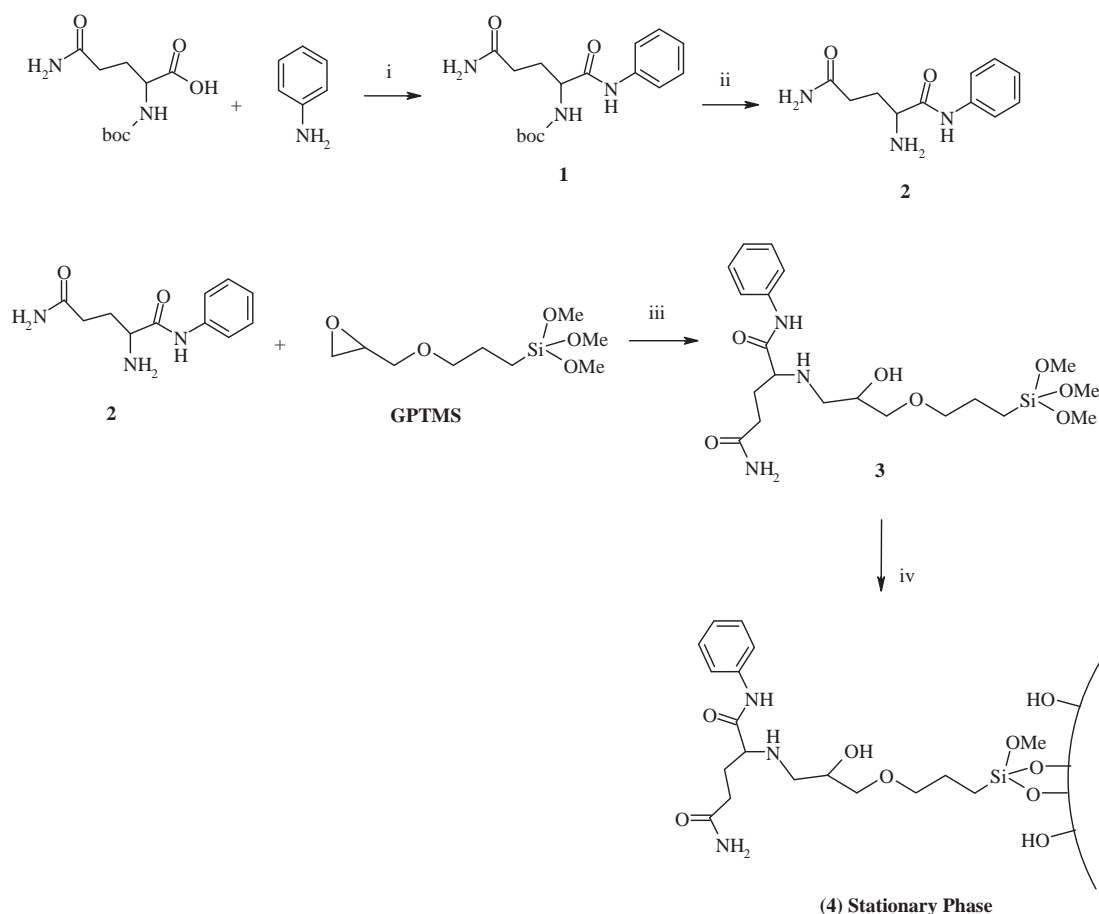
Scheme 1. Chemical structures of model test compounds separated by a new amide-silica column.

3. Results and discussion

3.1. Synthesis

The new amide-functionalised silica gel was prepared as outlined in [Scheme 2](#). This polar stationary phase bears two different amide polar groups, one of which is the polar head and the other one is embedded into aromatic phenyl ring, and an amino alcohol group. The stationary phase also includes aliphatic and aromatic groups. Therefore, it can well interact with polar compounds and

can show selectivity towards moderately polar and non-polar analytes. To obtain the stationary phase, first, the amide ligand was synthesised in two steps ([Scheme 2](#)). *N*-Boc-*N'*-amide (**1**) was obtained in 60% yield by the reaction of *N*-boc-glutamine with aniline. The deprotection of **1** gave amide ligand **2** in 72% yields. Then, (3-glycidyloxypropyl)trimethoxysilane (GPTMS) was attached to amide ligand **2** to obtain amid ligand bonded to the linker (**3**). After **3** was washed by hexane and dichloromethane to remove the unreacted GPTMS, the HPLC-quality spherical silica gel (4 μm , 60 \AA) was added to the mixture and refluxed in toluene for



Scheme 2. Reagents and conditions. (i) DCC, room temperature, 24 h (ii) TFA/AcOH (1:1, v/v), DCM, (iii) EtOH, reflux, 2 days, (iv) Spherical silica gel, Toluene, reflux, 4 days.

4 days. Ligand bonded silica was washed by Soxhlet extraction using 150 mL of chloroform overnight and dried under vacuum to obtain the novel stationary phase (4).

3.2. Characterisation of the stationary phase

The novel amide-silica stationary phase was characterised by FT-IR and elemental analysis. Table 1 shows the elemental analysis of blank silica (Si) and amide-bonded silica (4). The resulting bonded stationary phase consists of 0.39 mmol of the amide ligand on each gram of the stationary phase.

The IR spectrum of Si showed a strong silanol (SiOH) band at 3484 cm^{-1} . This peak was weakened in the spectrum of 4. The functional group C–OH also formed by the epoxide ring opening. Hence, this band may belong to both C–OH and Si–OH groups. The band at 1636 cm^{-1} was absent, the band at 963 cm^{-1} was also very weak and new weak bands appeared at $2983\text{--}2938\text{ cm}^{-1}$ and 1650 cm^{-1} . Therefore, the FT-IR spectra of the solid samples confirmed the reactions on the surface of the silica. Thus, synthesis of a new amide stationary phase from the spherical silica gel was confirmed by elemental analysis and FT-IR.

3.3. HPLC evaluations

The HPLC separation studies were performed with a column packed with the new mixed-mode stationary phase using a standard test mixture composed of four nucleotides: thymine, uracil, adenine and cytosine and five nucleosides: thymidine, uridine, adenosine, guanosine and cytidine under HILIC condition (Scheme 1). The effects of the separation conditions, such as mobile phase, pH and

Table 1
Elemental analysis results of blank silica and ligand bonded silica.

Structure	C (%)	H (%)	N (%)
Blank silica gel (Si)	0	0.03	0
Stationary phase (4)	9.36	1.38	1.63

temperature, on the separation and retention behaviours of nucleotides and nucleosides in this system were studied, and four nucleotides and five nucleosides were separated with isocratic elution. The best separation was achieved using an isocratic elution with an aqueous mobile phase and acetonitrile with a $20\text{ }^{\circ}\text{C}$ column temperature and detected at 265 nm within 14 min for the four nucleotides (Fig. 1) and using a isocratic elution with an aqueous mobile phase containing 10 mM potassium phosphate buffer, pH=3.25, and acetonitrile with a $20\text{ }^{\circ}\text{C}$ column temperature and detected at 265 nm within 14 min for the five nucleosides (Fig. 2). The results were also compared with four commercially available HILIC columns for separation of nucleotides and nucleosides mixture (Figs. 3 and 4). The effects of some conditions, such as mobile phase, pH and temperature on the separation of nucleosides were discussed in Figs. 5 and 6 and Tables 2 and 3.

Gua and Gaiki were studied retention behaviour of nucleotides and nucleosides mixture in HILIC mode on four different commercially available HILIC columns using acetonitrile/water (85/15, v/v) containing 10 mM ammonium acetate, $30\text{ }^{\circ}\text{C}$ column temperature, 1.5 mL/min flow rate at 248 nm [20]. In this study, five or six analytes were separated between 7 and 12 min as shown in Fig. 3. To compare the performance of our new column, the test mixture

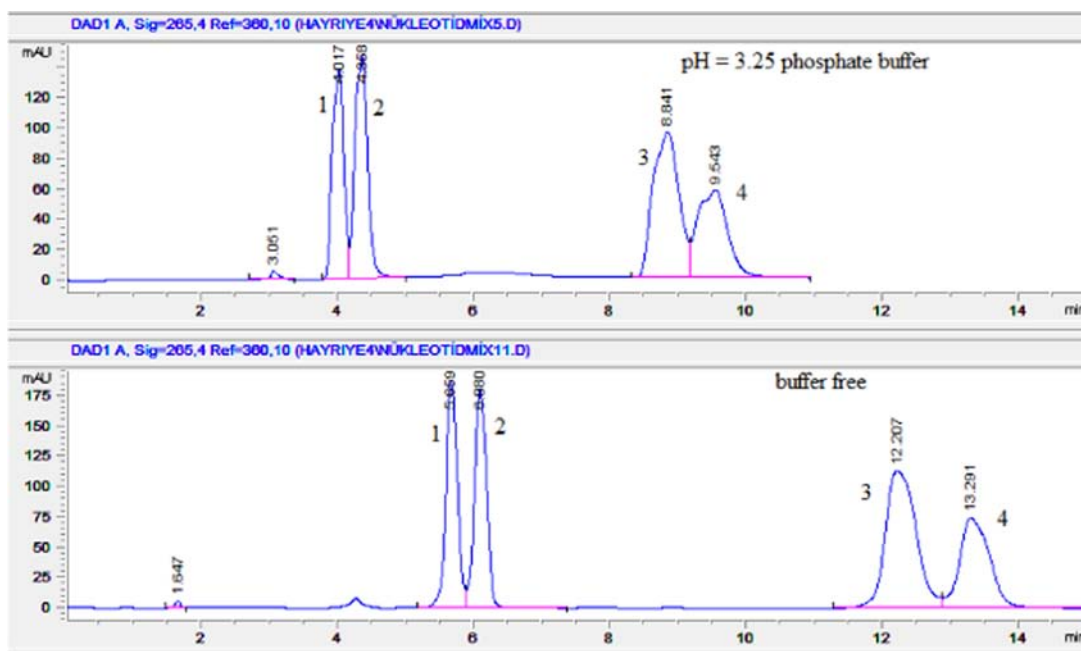


Fig. 1. Separation of nucleotides on the new mixed-model column. Isocratic elution: ACN in water: 80%, flow rate: 0.7 mL/min., temp: 20 °C. Injection volume: 5 μ L. Detection: 265 nm. Analytes: 1: thymine, 2: uracil, 3: adenine, 4: cytosine.

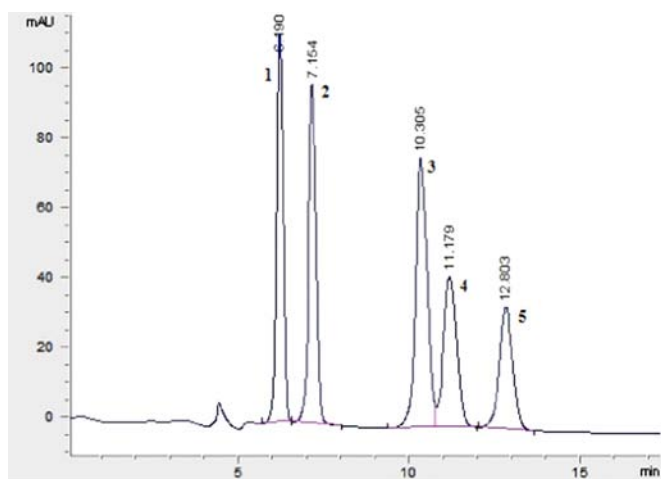


Fig. 2. Separation of nucleosides on the new mixed-model column. Isocratic elution: ACN in phosphate buffer (pH 3.25, 10 mM): 80%, flow rate: 0.7 mL/min., temp: 20 °C. Injection volume: 5 μ L. Detection: 265 nm. Analytes: 1: thymidine, 2: uridine, 3: adenosine, 4: guanosine, 5: cytidine.

composed of four nucleotides and five nucleosides was the employed the column under same condition except for buffer. Because of bad peak resolution was observed with ammonium acetate, phosphate buffer (pH 3:25) was preferred and six analytes were separated in 10 min (Fig. 4). From comparison of the results, in terms of both selectivity and analysis time, the new column gave very good results as shown in the figures. Although, the new column has shown similar activity with ZIC-HILIC column in terms of selectivity and analysis time, elution order of the analytes are different for all type of columns.

The effect of the stationary phase on RP condition was tested for eleven phytohormones: indole-3-acetic acid (IAA), indole-3-propionic acid (IPA), indole-3-butyric acid (IBA), abscisic acid (ABA), zeatin (Z), 6-benzylaminopurine (BAP), kinetin (K), 1-naphthaleneacetic acid (NAA), 2,4,5-trichlorophenoxyacetic acid (2,4,5-T), 2,4-dichlorophenoxypropionic acid (2,4-DP), 2,4-dichlorophenoxybutyric acid (2,4-DB), 4-chlorophenoxyacetic acid (4-PA),

and 2,4-dichlorophenoxyacetic acid (2,4-D) and seven phenolic compounds: *p*-coumaric acid, *o*-coumaric acid, protocatechuic acid, caffeic acid, syringic acid, rosmarinic acid and quercetin (Scheme 1). The eleven phytohormones were separated using a gradient elution with an aqueous mobile phase containing 10 mM potassium phosphate buffer, pH=2.5, and acetonitrile with a 20 °C column temperature and detected at 230 and/or 270 nm within 12 min (Fig. 7). The best separation for the seven phenolic compounds was achieved using a gradient elution with an aqueous mobile phase containing 10 mM potassium phosphate buffer, pH=2.5, and acetonitrile with a 20 °C column temperature and detected at 230 nm within 16 min (Fig. 8).

3.3.1. Separation of nucleotides and nucleosides on HILIC conditions

3.3.1.1. Influence of pH on the separation process. The mobile phases in HILIC play an important role on the retention process. The pH conditions are generally controlled by buffer solutions with a 5–20 mM salt concentration [21]. Whether pH of the buffer is above or below the pKa of the analyte determines its charge state, which in turn affects the hydrophilicity of the analyte and likewise the interaction with the stationary phase [22–24]. At a higher buffer pH, the ionization of weak bases was suppressed, reducing ionic retention, leading to further opportunities to manipulate selectivity [25]. Acidic or neutral mobile phase pH is commonly used due to the instability of silica-based columns at high pH [26]. In this study, the effect of the mobile phase pH on HILIC separation was investigated using buffer solutions with different pH. A 10 mM phosphoric acid/potassium dihydrogen phosphate buffer was selected for pH 2–4 (2.5, 3.25 and 4.03) (Fig. 5, pH=2.5 was not shown). A stock solution of 10 mM, pH=2 phosphate buffer was first prepared, and then the pH of the stock solution was adjusted to desired pH values (2.5, 3.25 and 4.03). The retention time of guanosine decreased with the mobile phase pH increased from 3.25 to 4.03. Therefore, as seen in Fig. 5, adenosine and guanosine cannot be separated at pH 4.03. Furthermore, the other analytes cannot be separated at the pHs above 4.03 and below 3.25 (not shown here). Hence, the best separation was observed at pH 3.25.

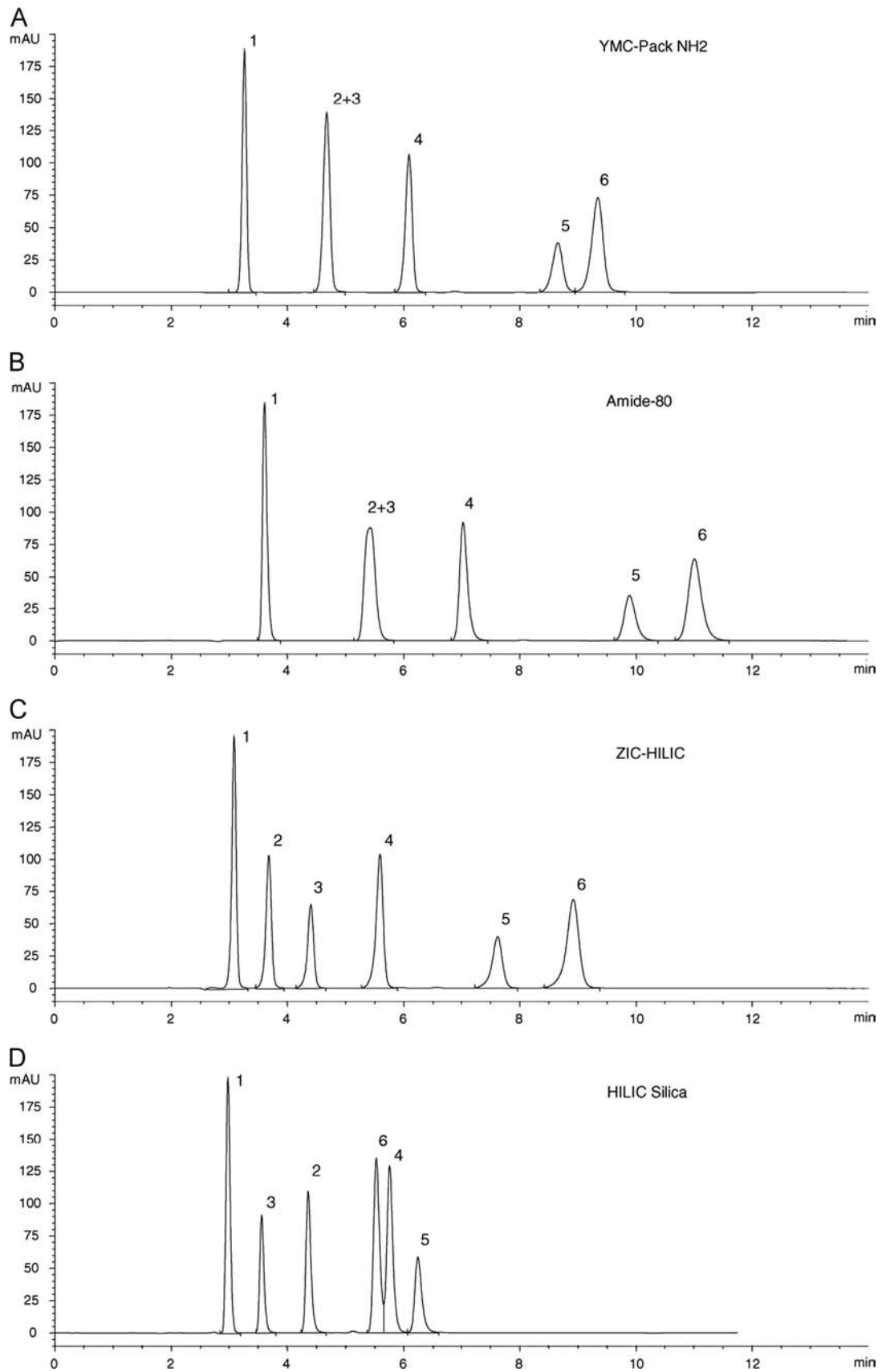


Fig. 3. Separation of nucleotides and nucleosides on: (A) YMC-Pack NH₂, (B) TSKgel Amide-80, (C) ZIC-HILIC, and (D) HILIC Silica columns. Mobile phase: acetonitrile/water (85/1, v/v) containing 10 mM ammonium acetate. Column temperature: 30 °C. Flow rate: 1.5 mL/min. UV detection at 248 nm. Compounds: (1) uracil, (2) adenosine, (3) uridine, (4) cytosine, (5) cytidine, and (6) guanosine. [20].

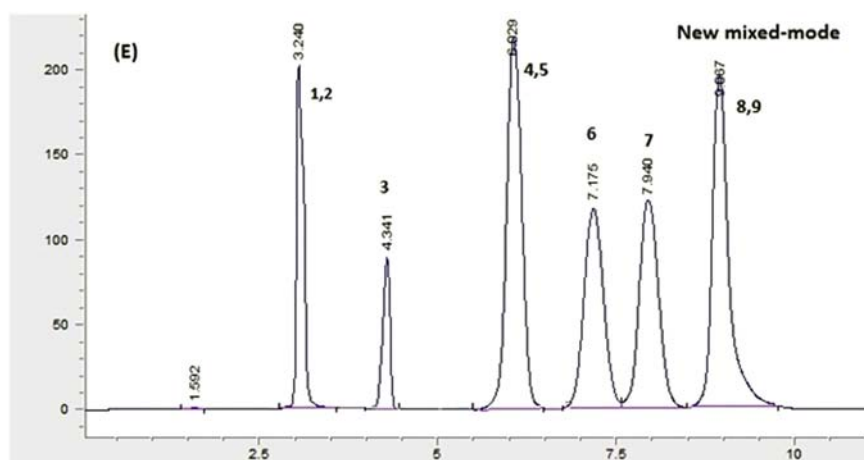


Fig. 4. Comparison of the new mixed-model column with commercial available HILIC columns for separation of nucleotides and nucleosides mixture on (E) the new mixed-model columns. Mobile phase: Isocratic elution: ACN in phosphate buffer (pH 3.25, 10 mM): 85 %. All other conditions are same as the Fig. 3. Compounds: (1) thymine, (2) uracil, (3) thymidine, (4) uridine, (5) adenine (6) adenosine (7) guanine (8) guanosine and (9) cytidine.

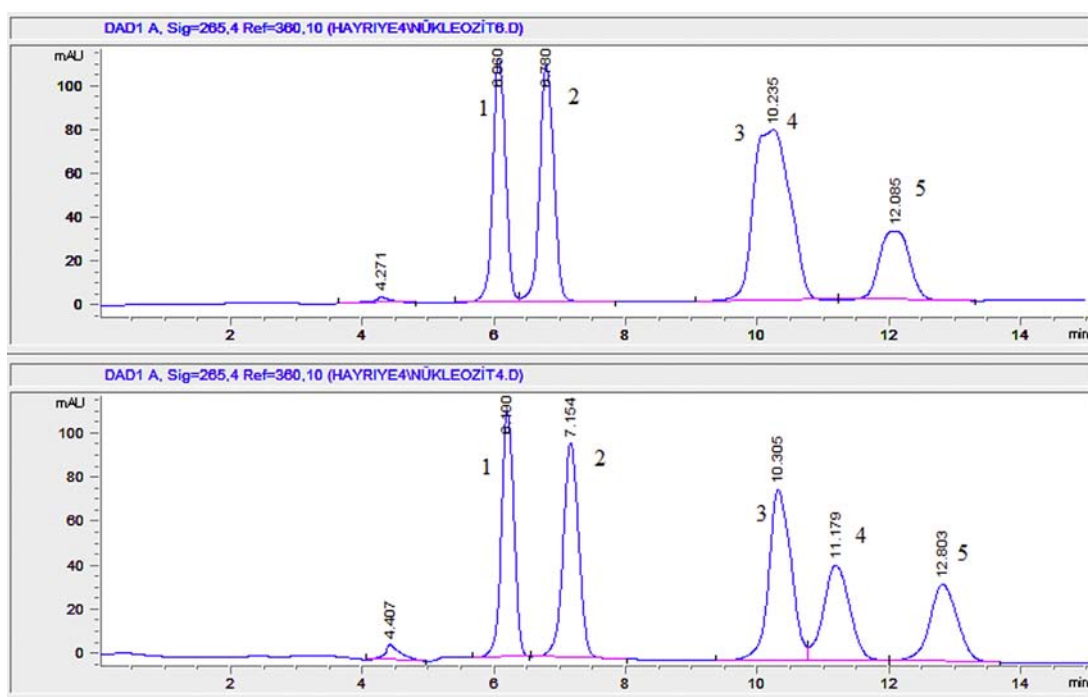


Fig. 5. Effect of pH=3.25–4.03 on nucleoside separation. All other conditions are the same as the optimum conditions (Fig. 2).

3.3.1.2. Influence of the mobile phase on the separation process. Different organic modifiers, such as alcohols, THF and ACN, are used in mobile phase mixtures in HILIC or RPLC separations but better results have been reported for ACN [27]. In fact, the mobile phase used in the HILIC mode usually contains water and ACN mixtures. Thus, all chromatographic studies were performed using isocratic elution with acetonitrile and water or an aqueous mobile phase containing potassium phosphate buffer.

The influence of the buffer concentration on retention was investigated using 0, 10 and 20 mM of aqueous potassium phosphate buffer at the optimum pH, 3.25 (Fig. 5), and it was found that the best separation is achieved by 10 mM buffer. Suitable separation could not be achieved when buffer-free (0 mM) aqueous ACN was used; a long analysis time, bad peak shape and low selectivity were observed. The separation was improved when using 10 mM buffer. The separation selectivity of the all analytes was increased by increasing the buffer concentration from 0 to

10 mM. With increasing buffer concentration, the elution of the analytes from the column accelerated as shown in Fig. 6. The higher concentration (20 mM) led to the merging of the peaks separated by the 10 mM buffer. This may be caused by acidic buffer and alkaline analytes. Thus, one can conclude that the best separation is obtained by 10 mM buffer.

The influence of aqueous phase containing a constant phosphate buffer (pH: 3.25) concentration at 10 mM content on retention was also investigated. Although all of five analytes could be separated at 17% and 20% buffer content, only four analytes were separated at 25% buffer content. Furthermore, the retention times were decreased by increasing the water content in the mobile phase, which is a typical behaviour for HILIC columns. Chromatographic data (retention factor, theoretical plate number and peak asymmetry) for separation of nucleosides on this condition were given in Table 2. As shown in the figure, the best theoretical plate number values and peak asymmetry factors were

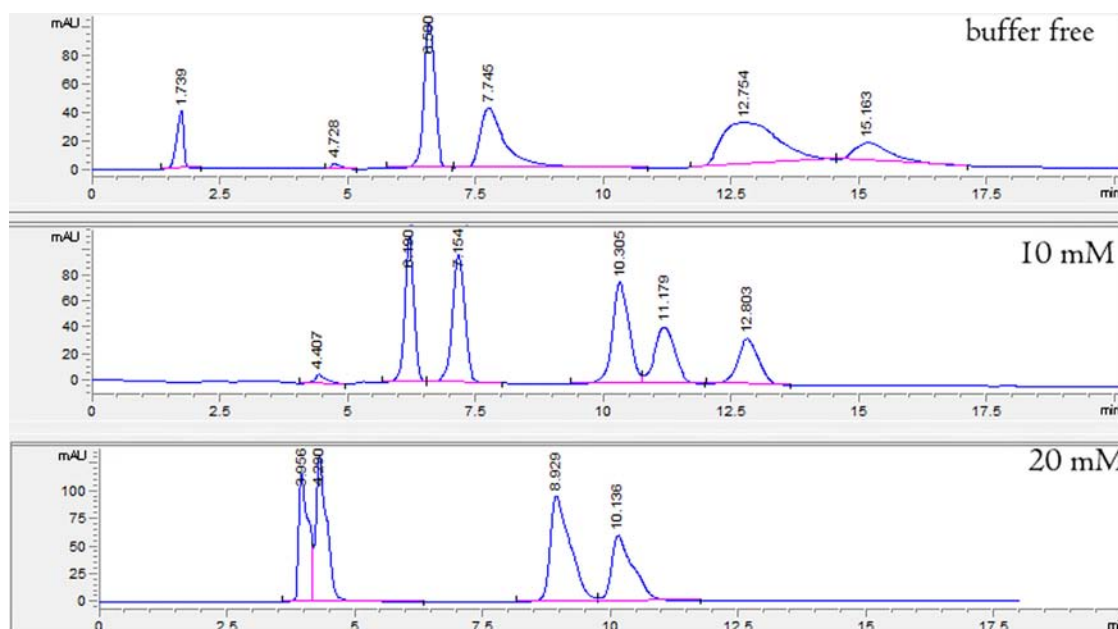


Fig. 6. Effect of the buffer concentration in the isocratic elution on nucleoside separation. All other conditions are the same as the optimum conditions (Fig. 2).

Table 2

Effect of the buffer content (water content) on chromatographic parameters for separation of nucleosides.

Anlyte	17%					20%					25%				
	tR	k	N	A _f	α	tR	k	N	A _f	α	tR	k	N	A _f	α
1	6.61	0.35	1977.74	1.15	1.71	6.19	0.50	5311.57	1.09	1.64	5.46	0.48	4829.96	1.06	1.29
2	7.99	0.60	2451.48	1.16	2.45	7.15	0.82	4921.43	1.08	2.21	5.98	0.62	4496.40	1.11	1.94
3	12.36	1.47	2068.13	1.41	1.18	10.30	1.81	5401.92	1.24	1.16	8.15	1.20	N.D	N.D	1.00
4	13.64	1.73	2231.07	1.32	1.14	11.18	2.10	5347.86	1.06	1.13	8.15	1.20	N.D	N.D	1.24
5	14.86	1.97	1866.25	1.30		12.80	2.38	5404.48	1.18		9.21	1.49	5226.11	1.01	

Chromatographic conditions: 250 × 4.6 mm I.D. column packed with the new mixed-model phase; all other conditions are the same as the optimum conditions (Fig. 2). k, retention factor; N, theoretical plate number; A_f, peak asymmetry factor; α = k₂/k₁, k₃/k₂, k₄/k₃ and k₅/k₄ as selectivity.

Table 3

Effect of the temperature on chromatographic parameters for separation of nucleosides.

Anlyte	10 °C					20 °C					30 °C				
	tR	k	N	A _f	α	tR	k	N	A _f	α	tR	k	N	A _f	α
1	6.25	0.44	4094.55	1.19	1.45	6.19	0.50	5311.57	1.09	1.64	6.16	0.43	4351.52	1.17	1.45
2	7.11	0.64	4146.62	1.32	2.23	7.15	0.82	4921.43	1.08	2.21	7.00	0.63	4019.30	1.25	2.21
3	10.53	1.43	1707.87	1.14	1.08	10.30	1.81	5401.92	1.24	1.16	10.28	1.39	4280.40	1.10	1.08
4	11.01	1.54	3042.85	1.22	1.47	11.18	2.10	5347.86	1.06	1.13	10.78	1.51	3485.00	1.19	1.26
5	12.67	1.92	3422.27	1.36		12.80	2.38	5404.48	1.18		12.46	1.90	4251.21	1.13	

Chromatographic conditions: 250 × 4.6 mm I.D. column packed with the new mixed-model phase; all other conditions are the same as the optimum conditions (Fig. 2). k, retention factor; N, theoretical plate number; A_f, peak asymmetry factor; α = k₂/k₁, k₃/k₂, k₄/k₃ and k₅/k₄ as selectivity.

obtained with 20% of water content which is chosen as optimum condition.

3.3.1.3. Influence of column temperature on the separation process. The column temperature is an important parameter in the separation process. An increase in column temperature reduces the analysis time in typical RP chromatographic systems [28]. This change in selectivity as a function of column temperature is dependent on the functional groups of both the analyte and the stationary phase as well as the composition of the mobile phase [29–31]. It is widely accepted that a mobile phase becomes more hydrophobic at high temperatures [32], reducing the retention of analytes in RPHPLC. But the opposite phenomenon

should occur in HILIC based on this theory: the retention of hydrophilic compounds should increase as a function of the temperature because the strength of the mobile phase decreases. Nevertheless, both increasing and decreasing retention have been documented in the literature as a consequence of increasing temperature. Thus, these findings prove that the nature of both the analyte and the stationary phase and their mutual interactions influence the overall retention [32].

In this study, the effect of temperature on the retention and separation of nucleosides was investigated by varying the column temperature from 10 to 30 °C under the optimum conditions using isocratic elution. Chromatographic data (retention factor, theoretical plate number and peak symmetry) for separation of nucleosides on this condition were given in Table 3. Both increasing and

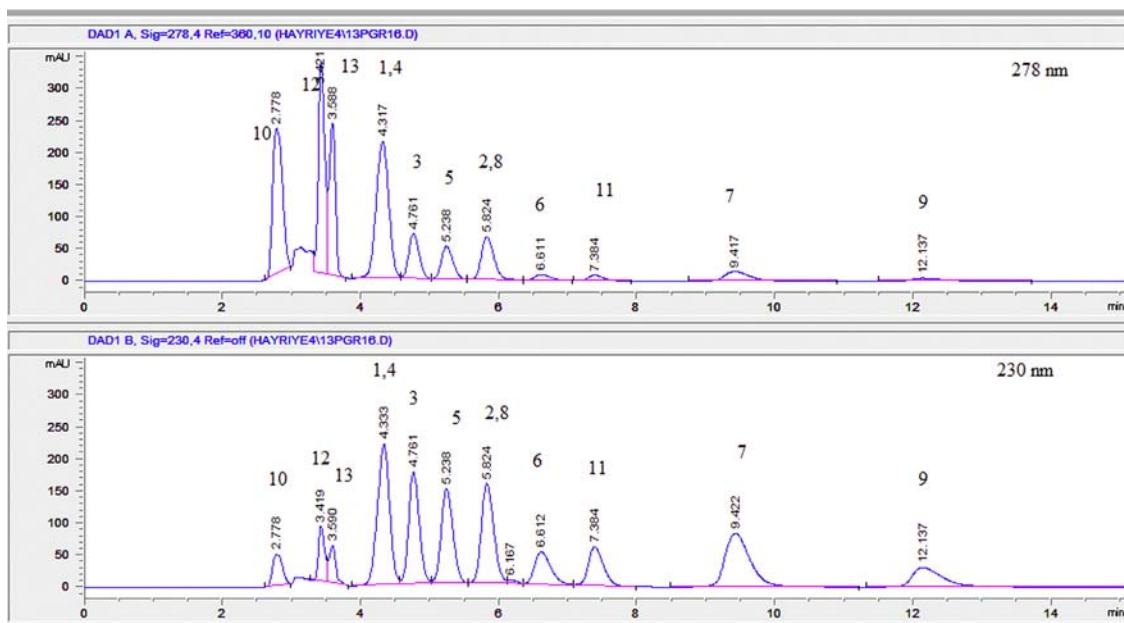


Fig. 7. Separation of plant phytohormones on the new mixed-model column. Gradient elution: ACN in phosphate buffer (pH 2.5, 10 mM), 0–30 min; 10–30%, Flow rate: 1 mL/min., Temp: 20 °C. Injection volume: 5 μ L. Detection: 230–278 nm. Analytes: 1: IAA, 2: 4-PA, 3: IPA, 4: IBA, 5: 2,4-D, 6: 2,4-DP, 7: 2,4,5-T, 8: Z, 9: 2,4-DB, 10: K, 11: BAP.

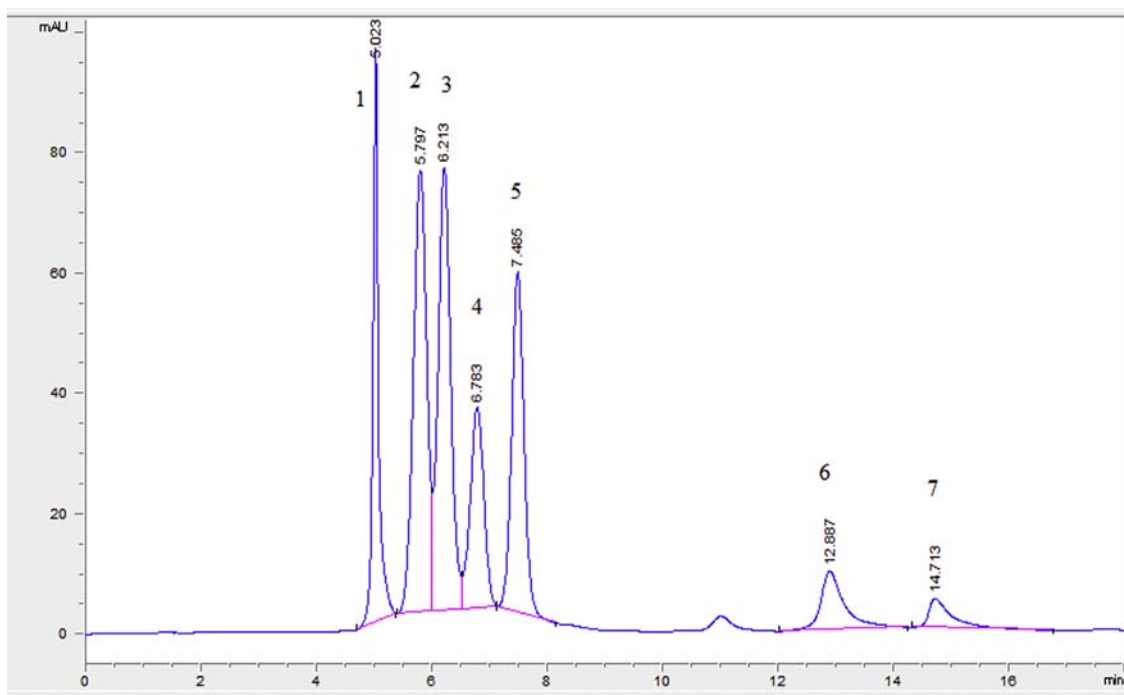


Fig. 8. Separation of phenolic compounds on the new mixed-model column. Gradient elution: ACN in phosphate buffer (pH 2.5, 10 mM), 0–7 min; 3%, flow rate: 0.7 mL/min., 8–20 min; 3–30, %, flow rate: 1 mL/min., temp: 20 °C. Injection volume: 3 μ L. Detection: 230 nm. Analytes: 1: PA, 2: CA, 3: p-CouA, 4: SA, 5: o-CouA, 6: RA, 7: Qua.

decreasing retention have been documented in the table as a consequence of increasing temperature. While the retention time of adenosine was decreased with increasing temperature from 10 to 30 °C, retention time of guanosine was increased from with increasing temperature 10 to 20 °C and decreased with increasing temperature 20 to 30 °C. The selectivity factors between adenosine (3) and guanosine (4) (α_{3-4}) were 0.92, 1.16 and 1.08 for 10, 20 and 30 °C respectively, as shown in Table 3. The highest selectivity was obtained with 20 °C. Further, the highest theoretical plate number was obtained with 20 °C. Therefore, we can conclude that the optimum temperature was 20 °C.

3.3.1.4. Reversed-phase applications of the new stationary phase: Separation of phytohormones and phenolic compounds. In our previous study, we have synthesised a new polar-embedded stationary phase and used for separation of phytohormones [33] and several different classes of small polar and non-polar compounds [34] successfully. The results were compared with those of ODS-C18 column. In those studies, twelve phytohormones were separated in 26 min and eleven phenolic compounds were separated in 40 min. In current study, we have made investigation to see whether or not RPLC applications are suitable with this new stationary phase. For this purpose, phytohormones and phenolic

compounds were chosen because they are more soluble in ACN than water and can be separated in RP conditions. Eleven phytohormones and seven phenolic compounds were studied and separated in a short analysis times as shown in Figs. 7 and 8, respectively. The retention times of all analytes were decreased by increasing ACN content in the mobile phase. Consequently, eleven phytohormones were separated in 12 min and seven phenolic compounds were separated in 15 min under RP conditions. These results are much better than our previous works [33,34]. It can be seen that this new column has a high selectivity for separation of phytohormones and phenolic compounds in RP mode. In conclude, this new stationary phase can be successfully used not only in HILIC applications but also in RPLC applications.

3.3.1.5. Column stability tests. The new stationary phase was tested in low and high pH condition. The chromatographic conditions for the tests were as follows: mobile phase for low pH: ACN/40 mM, pH=2.40 aqueous potassium phosphate buffer (50/50), mobile phase for high pH: ACN/40 mM, pH=8.80 aqueous borate buffer (50/50); flow rate, 1 mL/min; temperature, 40 °C; detection, 280 nm; probe, adenine.

The column was continuously purged with the mobile phase at a rate of 1 mL/min, and periodically tested by recording of retention time of adenine. After about 1000 column volumes of mobile phase with low pH, there was essentially no change in the retention for adenine. Therefore, we found that the column is stable at pH=2.40 which is below the lowest pH studied in this work. Therefore, we found that the column is stable at pH=2.40 which is below the lowest pH studied in this work. On the other hand, the same column was also used for the stability tests in high pH condition. After about 500 column volumes of mobile phase with high pH, there was no considerable change in the retention for adenine. But after 1000 volumes, there was just about 10% change in the retention time of adenine, and peak shape and symmetry were also reduced. Consequently, although this column seems to be quite stable in high pH, care should be taken when working in high pH. Because the column stability is limited in high pHs.

4. Conclusion

A new mixed-mode stationary phase containing several polar and non-polar groups was prepared by modification of spherical silica gel. Initial chromatographic tests show that this phase can be used under HILIC conditions to separate nucleotides and nucleosides and reversed-phase conditions to separate phytohormones and phenolic compounds. The new polar stationary phase may possess several retention mechanisms, such as hydrogen-bonding and electrostatic interaction. The effects of several parameters, such as pH, buffer and acetonitrile concentration and temperature on retention were studied. This new type of polar stationary phase

could efficiently separate four nucleotides, five nucleosides, nucleotides and nucleosides mixture, eleven plant hormones and seven phenolic compounds under isocratic and gradient eluent conditions. The new mixed-model stationary phase can be successfully used in both HILIC and RPLC applications and has potential application to the separation of complex analytes with different physicochemical properties. Further investigations of this new stationary phase in other application fields are in progress.

Appendix A. Supporting information

Supplementary data associated with this article can be found in the online version at <http://dx.doi.org/10.1016/j.talanta.2014.07.060>.

References

- [1] Q.W. Yu, B. Lin, Y.Q. Feng, F.P. Zou, J. Liq. Chromatogr. Related Technol. 31 (2008) 64–78.
- [2] T.Y. Guo, P. Liu, Y.Q. Xia, M.D. Song, J. Appl. Polym. Sci. 116 (2010) 1611–1616.
- [3] H. Qiu, X. Liang, M. Sun, S. Jiang, Anal. Bioanal. Chem. 399 (2011) 3307–3322.
- [4] A.J. Alpert, M. Shukla, A.K. Shukla, L.R. Zieske, S.W. Yuen, M.A.J. Ferguson, A. Mehlert, M. Pauly, R. Orlando, J. Chromatogr. A 676 (1994) 191.
- [5] A.J. Alpert, Adv. Chromatogr. 44 (2006) 317.
- [6] M.R. Gama, R.G.C. Silva, C.H. Collins, C.B.G. Bottoli, Trends Anal. Chem. (2012).
- [7] M.A. Strege, Am. Pharm. Rev. 2 (1999) 53.
- [8] M.A. Strege, Anal. Chem. 70 (1998) 2439.
- [9] B.Y. Zhu, C.T. Colin, R.S. Hodges, J. Chromatogr. 548 (1991) 13.
- [10] T. Saga, Y. Inoue, K. Yamaguchi, J. Chromatogr. 625 (1992) 151.
- [11] A.S. Feste, I. Khan, J. Chromatogr. 630 (1992) 129.
- [12] A.J. Alpert, M. Mukta, A.K. Shukla, L.R. Zieske, S.W. Yuen, M.A.J. Ferguson, A. Mehlert, M. Pauly, R. Orlando, J. Chromatogr. A 676 (1994) 191.
- [13] S.C. Churms, J. Chromatogr. A 720 (1996) 75.
- [14] S.C. Lin, W.C. Lee, J. Chromatogr. A 803 (1998) 302.
- [15] A.R. Oyler, B.L. Armstrong, J.Y. Cha, M.X. Zhou, Q. Yang, R.I. Robinson, R. Dunphy, D.J. Burinsky, J. Chromatogr. A 724 (1996) 378.
- [16] T. Yoshida, Anal. Chem. 69 (1997) 3038.
- [17] C.T. Mant, L.H. Kondejewski, R.S. Hodges, J. Chromatogr. A 816 (1998) 79.
- [18] T. Yoshida, T. Okada, T. Hobo, R. Chiba, Chromatographia 52 (2000) 418.
- [19] T.J. Higley, T. Yoshida, LCGC N. Am. Suppl. (2003) 20.
- [20] Y. Guo, S. Gaiki, J. Chromatogr. A 1074 (2005) 71–80.
- [21] Y. Kawachi, T. Ikeami, H. Takubo, Y. Ikeami, M. Miyamoto, N. Tanaka, J. Chromatogr. A 1218 (2011) 5903–5919.
- [22] B. Buszewski, S. Noga, Anal. Bioanal. Chem. 402 (2012) 231–247.
- [23] P. Hemström, K. Irgum, J. Sep. Sci. 29 (2006) 1784–1821.
- [24] W. Naidong, J. Chromatogr. B 796 (2003) 209–224.
- [25] D.V. McCalley, J. Chromatogr. A 1171 (2007) 46–55.
- [26] M. Liu, E.X. Chen, R. Ji, D. Semin, J. Chromatogr. A 1188 (2008) 255–263.
- [27] T.L. Ascah, K.M.L. Kallury, C.A. Szafranski, S.D. Corman, F. Lui, J. Liq. Chromatogr. Related Technol. 19 (1996) 3049–3073.
- [28] J.W. Li, P.W. Carr, Anal. Chem. 69 (1997) 837–843.
- [29] J.W. Li, P.W. Carr, Anal. Chem. 69 (1997) 2202–2206.
- [30] Y. Mao, P.W. Carr, Anal. Chem. 73 (2001) 4478–4485.
- [31] Z.G. Hao, B.M. Xiao, N.D. Weng, J. Sep. Sci. 31 (2008) 1449–1464.
- [32] R. Kucera, P. Kovarikova, M. Klivicky, J. Klime, J. Chromatogr. A 1218 (2011) 6981–6986.
- [33] H. Aral, T. Aral, B. Ziyadanoğulları, R. Ziyadanoğulları, Talanta 116 (2013) 155–163.
- [34] H. Aral, T. Aral, K.S. Çelik, B. Ziyadanoğulları, R. Ziyadanoğulları, Chromatographia 77 (2014) 771–781.



Analyzing the biosensor signal in flows: Studies with glucose optrodes



K. Kivirand^a, A. Floren^b, M. Kagan^a, T. Avarmaa^b, T. Rincken^a, R. Jaaniso^{b,*}

^a Institute of Chemistry, University of Tartu, Ravila 14a, Tartu 50411, Estonia

^b Institute of Physics, University of Tartu, Ravila 14c, Tartu 50411, Estonia

ARTICLE INFO

Article history:

Received 6 April 2014

Received in revised form

15 July 2014

Accepted 21 July 2014

Available online 30 July 2014

Keywords:

Modeling

Dual-optrode biosensor

Flow regime

Glucose

Pre-steady state calibration

ABSTRACT

Responses of enzymatic bio-optrodes in flow regime were studied and an original model was proposed with the aim of establishing a reliable method for a quick determination of biosensor signal parameters, applicable for biosensor calibration. A dual-optrode glucose biosensor, comprising of a glucose bio-optrode and a reference oxygen optrode, both placed into identical flow channels, was developed and used as a model system. The signal parameters of this biosensor at different substrate concentrations were not dependent on the speed of the probe flow and could be determined from the initial part of the biosensor transient phase signal, providing a valuable tool for rapid analysis. In addition, the model helped to design the biosensor system with reduced impact of enzyme inactivation to the system stability (20% decrease of the enzyme activity lead to only a 1% decrease of the slope of the calibration curve) and hence significantly prolong the effective lifetime of bio-optrodes.

© 2014 Elsevier B.V. All rights reserved.

1. Introduction

Biosensors are analytical devices incorporating a bio-recognition element and a physical transducer for the detection of target compounds. The transducer converts the recognition event into a measurable signal and can be of different type: electrochemical, optical, thermal or piezoelectrical. Most enzymatic biosensors are based on electrochemical transducers [1], which, in case of catalytic red-ox reactions, sense directly the charge transfer or detect the consumption of O₂ or generation of H₂O₂ in the reaction. At the same time, there is an increasing interest in optical transducers [2–4], in particular those detecting O₂ and H₂O₂ in solutions. Optical sensors have several advantages: they are resistant to electrical and electrochemical interferences, allow non-contact sensing or transmission of parallel sensor signals over a single optical fiber, and have relatively long service interval [5].

Irrespective of the specific nature of bio-recognition processes and signal transduction mechanisms, biosensors are ideally expected to perform as the regular physical sensors – that is to operate continuously, reversibly and rapidly, giving accurate information in real or near real-time and facilitating on site applications. This implies that all the sensor components (platform, bio-recognition entities, transducer, signal conditioning unit) are

carefully engineered and the transfer function of the sensor is described by adequate model.

The basic tool for modeling enzymatic biosensors is the convection–diffusion–reaction equation (or a system of such equations), which is numerically solved for given boundary and initial conditions [6–14]. These conditions depend on several aspects: the geometry of the sensor, location of the enzyme (immobilized or distributed in solution), transducer type, and mode of liquid motion (batch or flow-through regime). Flow-through systems, e.g. those used for flow injection analysis (FIA), are advantageous as allowing high sample throughput and overall reduction of the analysis time [15,16]. Whereas most of the recent modeling efforts are devoted to describing the sensor performance in flow regime, all these efforts are still made (and valid) only for amperometric transducers. Therefore, for optimizing the construction of optical biosensors and for detailed signal analysis of such sensors specially targeted studies have to be undertaken.

In the present work, we are investigating the flow-through enzymatic biosensor with fiber-optic optrodes (or optodes) based on luminescence quenching by oxygen. Such bio-optrodes have been introduced in Ref. [17] and further developed in Refs. [18–25] in parallel with industrial [26], biological [27], and medical [21,28,29] applications. In order to analyze correctly the signal of such biosensor, one has to know the actual level of dissolved oxygen in the probe, and therefore the dual-optrode sensing has been introduced [19–21], which uses an enzyme-activated optrode together with a reference optrode for oxygen.

The main goal of the present work was to develop a simple but sufficiently accurate model for describing the response of optical

* Corresponding author. Tel.: +372 7374731.

E-mail address: raivo.jaaniso@ut.ee (R. Jaaniso).

enzymatic biosensor operating in flow regime. To achieve this, we constructed a stable dual-optrode biosensor; carried out experiments with glucose optrodes, using glucose oxidase for glucose detection; developed a model for describing the sensor response, and fitted the experimental data with the theoretical curves. The development of the model was aimed for obtaining the analytical transfer functions for the sensor, which could be used for calibration and signal processing in practical devices.

2. Experimental

2.1. Dual-optrode biosensor system with flow cell

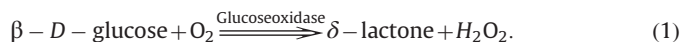
The scheme of the dual-optrode biosensor is shown in Fig. 1. The system consists of two optrodes, flow cell, heater, opto-electronic unit, and control unit. The glucose and reference optrodes were placed into isolated identical flow channels ($l=50$ mm; $\varnothing=3$ mm) of the carefully thermostated flow cell. The opto-electronic unit provided optical excitation (wavelength 405 nm) of luminescence, as well as the detection and amplification of luminescence signals (wavelength 690 nm) from optrodes. The optrodes were connected to the unit through plastic coated quartz fibers ($\varnothing=1$ mm, NA=0.37) supplied with SMA connectors.

As the analytical performance of the biosensor was anticipated to be greatly dependent on temperature [21,30], the stabilization of the cell temperature was one of the most crucial issues of the experimental setup: so a high-precision temperature sensor (RTD, class A) was placed into a similar flow channel and connected with the control device of the Kapton[®] (polyimide film) insulated flexible heater surrounding the flow cell. The control unit was connected to PC via USB interface and included ADCs for signal conversion, I/O ports for switching the LEDs for luminescence excitation, and PID regulator for heater.

The bio-optrode and reference optrode were placed into identical flow channels, which allows to make precise differential or ratiometric measurements and hence minimize the influence of experimental noise like occasional oxygen fluctuations in the flow,

caused by adverse effects such as bacterial growth; temperature fluctuations; or pressure fluctuations of the peristaltic pump.

The oxidation of glucose, catalyzed by glucose oxidase was studied as a model reaction:



2.2. Preparation of the bio-optrodes

The oxygen optrodes used were based on optical quartz fibers, which were dip-coated with oxygen-sensitive films. The detection of oxygen was based on measuring the phosphorescence quenching of Pd-tetraphenylporphyrin molecules, encapsulated into a polymethyl methacrylate (PMMA) film [31]; the latter covering the cylindrical surface of a 30 mm long optical fiber with diameter of 1 mm. Pd-porphyrin (Porphyrin Systems) and PMMA polymer (molar mass 40,000 g/mol, Sigma-Aldrich) were dissolved in chloroform or tetrahydrofuran, the solutions were treated on ultrasonic bath and filtered through a teflon filter with 1 μm pore size. After dip-coating, the fiber-tips were dried at room-temperature for some hours and aged at 60 °C for ~ 1 month [31,32].

Glucose oxidase (GOD, EC 1.1.3.4. from *Aspergillus niger*, 17,300 U/g protein, Sigma-Aldrich) was immobilized onto the threads made of nylon-6,6, according to a previously published protocol [33] with some minor modifications. Nylon threads (consisting of 60 filaments with a diameter of 25 μm twisted together) were immersed into 98% (w/w) dimethyl sulfate for 10 h at 50 °C, washed several times with ice-cold methanol and 0.1 M phosphate buffer (PB) (pH 6.50) and immersed into 12.5% glutaraldehyde solution (in 0.1 M PB, pH 6.50) for 1 h at room temperature. The activated threads were washed with 0.1 M PB (pH 6.50) and incubated in GOD solution (100 U/ml), first for 2 h at room temperature and then overnight at 4 °C. Finally, the threads were thoroughly washed and stored in 0.1 M PB (pH 6.50) at 4 °C.

For the preparation of a glucose optrode, 19 cm of GOD-containing thread with initial catalytic activity 0.016 U/cm was cut and coiled around the oxygen-sensitive surface of the oxygen optrode, where it formed a bio-recognition layer for glucose

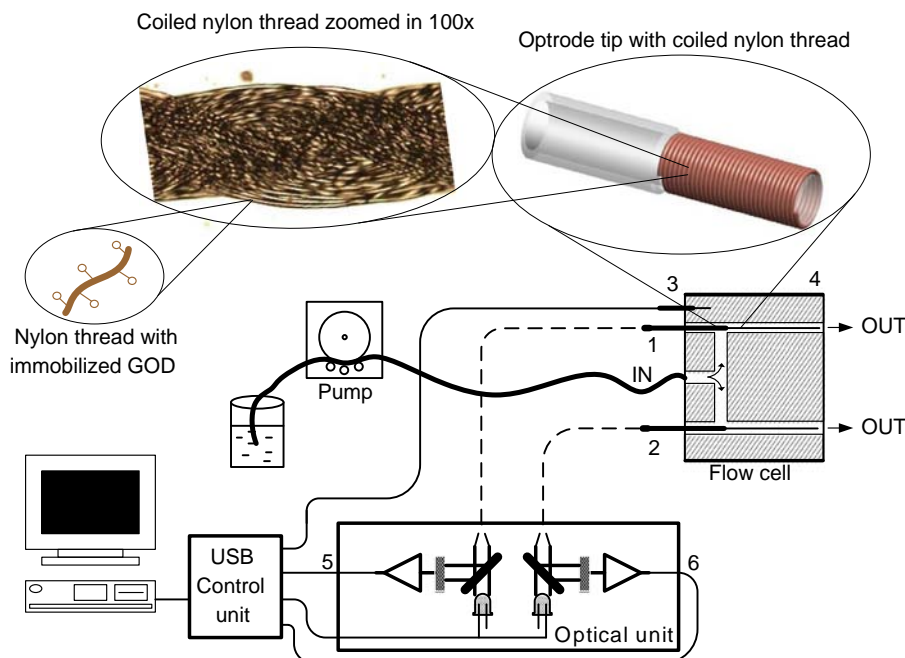


Fig. 1. Scheme of dual-optrode biosensor system: 1—glucose bio-optrode; 2—reference optrode; 3—temperature sensor; 4—Kapton flexible heater; 5 and 6—electronic signals from two detection channels. Optical fibers are shown with dashed lines. Insets show magnified scheme and image of optrode.

[34,35]. The catalytic activity of the thread was tested before each series of measurements. If the activity dropped below 80% of its initial value, the GOD-containing thread was replaced. The reference oxygen optrode was covered with 19 cm of identical “blank” thread.

2.3. Measurement procedures and data acquisition

Glucose stock solutions were prepared in 0.1 M phosphate buffer (PB) (pH 6.50) and allowed to mutarotate overnight along with their aeration with air at 37 °C; glucose solutions were prepared into air-saturated PB (at 37 °C) immediately prior to use. All reagents used were of analytical grade.

To minimize the influence of bubble forming on the biosensor signal, the inflow of the solution was in the bottom and the outflow in the upper part of the cell. The flow rate of the measurements was varied from 0.8 ml/min to 13.0 ml/min. The average flow velocities in the channels of the flow cell were estimated to be between 0.3 to 4.8 cm/sec, taking into account the free cross-section of a channel (4.5 mm²). After each measurement the system was washed with 0.1 M PB (pH 6.50) until the sensor signals reached their initial values.

The flow cell was thermostated at 37.0 ± 0.1 °C. This temperature was optimal to gain the highest biosensor sensitivity at reasonable dissolved oxygen concentration (DOC) levels in the studied solutions. The dual-sensor response for glucose was found as the ratio of DOC at bio-optrode and reference optrode at every time moment measured, so minimizing the impact of experimental noise.

The sensor signal was recorded with the interval of 1 s between the consecutive data points; each experimental curve consisted of at least 300 data points. The dissolved oxygen concentration was calculated on the basis of Stern–Volmer relationship [36], using original software Oxysens 2.0. The software also controlled the system and allowed automated measurements. In particular, it allowed to set and record the measurement temperature, and took into account the temperature corrections, required for accurate determination of DOC. The temperature dependence of Stern–Volmer coefficient, determined earlier in Ref. [31], was used.

3. Model

In the flow cell, there are generally two processes governing the oxygen concentration at the optrode surface:

- 1) enzyme-catalyzed reaction in the enzyme containing layer;
- 2) transport of oxygen and the second substrate into and in the flow cell.

The studied reaction (1) is of ping-pong type [37] and can be described in the quasi-steady-state approximation as following:

$$\frac{ds(t)}{dt} = \frac{dc(t)}{dt} = -\frac{V_{MAX}}{1 + \frac{K_S}{s(t)} + \frac{K_{O_2}}{c(t)}} \quad (2)$$

where $s(t)$ is the substrate concentration, and $c(t)$ is DOC at time moment t ; K_S and K_{O_2} are Michaelis' constants for substrate and oxygen, respectively; and V_{MAX} is the ultimate reaction speed.

If the following condition is fulfilled:

$$\frac{K_S}{s} \gg 1 + \frac{K_{O_2}}{c} \quad (3)$$

Eq. (2) can be simplified to:

$$\frac{ds(t)}{dt} = \frac{dc(t)}{dt} = -k_R s(t), \quad (4)$$

where

$$k_R = \frac{V_{MAX}}{K_S} \quad (5)$$

For glucose oxidation $K_S \gg K_{O_2}$ [37], and therefore condition (3) is fulfilled in a quite wide range of β -D-glucose and oxygen concentrations. The upper limit of oxygen concentration is generally determined by its saturated value ($c_0 \sim 0.2$ – 0.3 mM at temperatures 20–40 °C). In what follows, we will assume the reaction to be described by first order kinetics (4), and as we will see below, this approach is justified even at substrate concentrations exceeding several times the value of c_0 .

Regarding the transport processes, the addition of substrate and oxygen into the vicinity of sensor surface will be described in the model with linear kinetic terms. Then the overall process can be modeled by two kinetic equations:

$$\frac{ds(t)}{dt} = -k_R s(t) + k_S [s_0 F(t) - s(t)] \quad (6)$$

$$\frac{dc(t)}{dt} = -k_R s(t) + k_{O_2} [c_0 - c(t)] \quad (7)$$

The rate constants k_S and k_{O_2} characterize the exchange speed of the concentrations of substrate and oxygen, respectively, between the flowing liquid and sensor surface (see Fig. 2). We note that similar phenomenological description of transport has been previously successfully used, for example, in modeling of BIACORE experiments [38].

It is assumed here, that oxygen concentration in the flowing liquid entering the cell is always c_0 , and after passing the initial front, the substrate carried by liquid flow has constant concentration s_0 . The function $F(t)$ describes the arrival front of the substrate into the cell. When the passage of the front is fast compared to the reaction and transport processes, then $F(t)$ can be approximated by Heaviside function:

$$F(t) = H(t) = \begin{cases} 0, & t < 0 \\ 1, & t \geq 0 \end{cases} \quad (8)$$

We also assume that there is no substrate present in the cell before $t=0$. Under these conditions the solutions of Eqs. (6) and (7) are:

$$s(t) = s_0 k_S \int_0^t dt' \exp[(k_R + k_S)(t' - t)], \quad (9)$$

$$c(t) = c_0 - k_R \int_0^t dt' s(t') \exp[k_{O_2}(t' - t)]. \quad (10)$$

After inserting Eq. (9) into (10) and evaluating the integrals one obtains:

$$c(t) = c_0 - s_0 \frac{k_R k_S}{k_{SR} k_{O_2}} \left\{ 1 - \exp(-k_{O_2} t) + \frac{k_{O_2}}{k_{O_2} - k_{SR}} [1 - \exp(-k_{SR} t)] \right\}, \quad (11)$$

where we used the notation

$$k_{SR} = k_S + k_R. \quad (12)$$

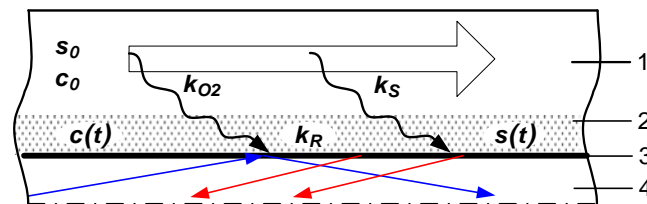


Fig. 2. Cross-section of the flow cell and scheme of model processes. 1- flowing liquid; 2 - flossy coating containing immobilized enzyme molecules; 3 - oxygen sensitive coating; 4 - core of optical fiber. The arrows inside the fiber represent the light involved in optical oxygen sensing.

The stationary solution for DOC is:

$$c_f = \lim_{t \rightarrow \infty} c(t) = c_0 - s_0 \frac{k_R k_S}{k_{SR} k_{O_2}} \quad (13)$$

The Eq. (11) can be rewritten in a following form:

$$\frac{c(t)}{c_0} = 1 - A \cdot f(t), \quad (14)$$

where

$$f(t) = 1 - \frac{k_{SR}}{k_{SR} - k_{O_2}} \exp(-k_{O_2} t) + \frac{k_{O_2}}{k_{SR} - k_{O_2}} \exp(-k_{SR} t) \quad (15)$$

is the normalized function describing the temporal evolution of relative DOC. It is easy to verify that it is a monotonic function changing from zero to unity i.e. $f(0) = 0$ and $\lim_{t \rightarrow \infty} f(t) = 1$.

Parameter A gives the relative difference between the initial (c_0) and final stationary (c_f) oxygen concentrations and can be easily determined experimentally as a normalized change of DOC between the initial and final steady states:

$$A = \frac{c_0 - c_f}{c_0} = \frac{s_0 k_R k_S}{c_0 (k_S + k_R) k_{O_2}}. \quad (16)$$

4. Comparison of sensor response with the model

A series of sensor responses, recorded at different glucose concentrations in two flow channels are shown in Fig. 3. At constant saturated DOC, the response of the reference sensor was not dependent on glucose concentration, while the response of the glucose biosensor decreased due to consumption of oxygen according to reaction (1). One can see five pairs of response and recovery curves taken successively at a flow rate of 2.7 ml/min. The arrows mark the time moments, when the substrate was added. The duration of substrate injection was 300 s and thereafter the signal was restored in the flow of pure buffer solution to the initial level.

In Fig. 4, a closer look at the (normalized) response curves at four different glucose concentrations is given together with the model curves obtained by fitting with Eqs. (14), (15). For each curve, the parameter A and two rate constants, k_{O_2} and k_{SR} , were determined. The application of the model for the characterization of the biosensor output signal resulted in good correlation ($R^2 = 99\%$, standard deviations from the model 0.00077, p -value < 0.0001). As one can see in Fig. 4, at the beginning of the response curves the signal decreases relatively slowly, whereas

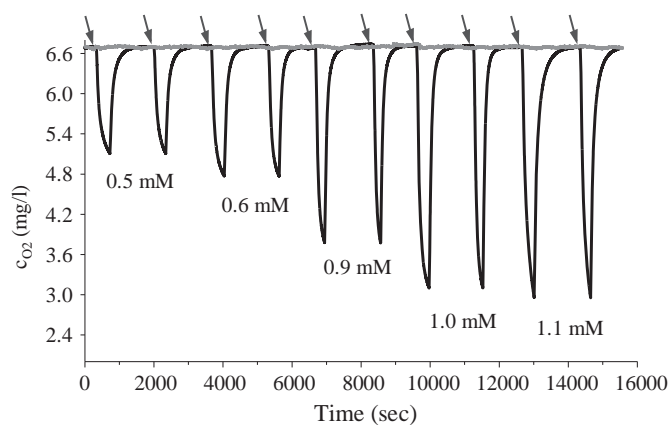


Fig. 3. Response curves of glucose bio-optrode (black line) and the reference optrode (gray line) of consecutive measurements at different glucose concentrations (two measurements at each concentration). Measurements were carried out at 37 °C in 0.1 M phosphate buffer (pH 6.50) at flow rate 2.7 ml/min. Arrows indicate the time of adding the substrate solution.

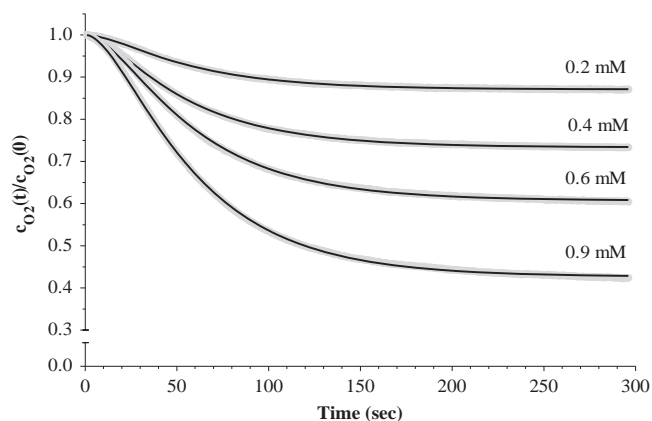


Fig. 4. Fitting the experimental curves (gray) obtained at different glucose concentrations (0.2 mM; 0.4 mM; 0.6 mM; 0.9 mM) with the proposed model. Theoretical approximations are shown as solid black lines. Measurements were carried out at 37 °C in 0.1 M phosphate buffer (pH 6.50) at flow rate 2.7 ml/min.

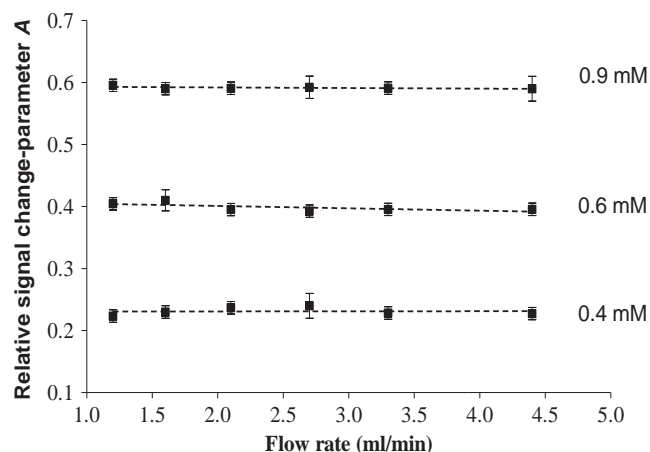


Fig. 5. The relative signal change parameter at different glucose concentrations and flow rates. Measurements were carried out at 37 °C in different glucose solutions in 0.1 M phosphate buffer (pH 6.50).

this change is accelerating. Such behavior is caused by the lack of substrate in the enzyme-containing layer at the initial moment and is accurately described by the model.

Parameter A characterizes the biosensor steady-state response (see Eq. (16)), which is the most common information used in biosensor studies [39]. It can be simply estimated by recording the initial and final steady state signals. Such procedure – determining the change of steady state signal (or the presumed 95% of it) versus substrate concentration – is the most common way of calibrating and using the biosensors. However, the fitting of temporal response curves, as demonstrated in Fig. 4, provides not only more accurate way of determining parameter A , but also valuable information included in rate constants.

For characterizing the processes in the flow system, the dependence of parameter A on flow rate at different glucose concentrations was studied (Fig. 5). As one can see, the value of parameter A was practically independent on the flow rate in the studied range of 0.8 to 13.0 ml/min. This result has an important practical consequence: it allows constructing universal calibration curves, not dependent on the flow rate in the system. We will discuss the interpretation of this result later; at this point we note in addition, that it was not possible to carry out experimental measurements at small flow rates (under 0.8 ml/min) due to the accumulation of air bubbles in the cell. In what follows, the results

obtained at a medium flow rate of 2.7 ml/min are mainly used as examples.

The determined values of parameter A were used for biosensor calibration. The slope of the calibration curve was calculated separately for every studied flow rate and no statistically significant differences in the slope values at different flow rates were detected. The glucose calibration curve at flow rate 2.7 ml/min possessing a linear dependence with the slope $(0.701 \pm 0.008) \text{ mM}^{-1}$ ($R^2 = 0.997$) is shown as an example in Fig. 6. The absence of constant term in this dependence indicates the lack of systematic errors in the results.

Let us now remind that in addition to parameter A , two rate constants were determined from each response curve. For example, fitting the experimental curves shown in Fig. 3 with Eq. (15) resulted the values 0.023 s^{-1} and 0.068 s^{-1} for two rate constants. One of these values characterizes the oxygen transport (k_{O_2}) and the second one the combined effect of reaction and substrate transport (k_{SR}). However, because the Eq. (15) is symmetric with respect of two rate constants (formula remains the same at the interchange $k_{O_2} \leftrightarrow k_{SR}$), one requires additional information for assigning the determined rate values to one or another particular process.

Furthermore, the procedure of evaluating the rate parameters of individual processes, k_S and k_R , should be established. Inserting k_R from Eq. (12) into Eq. (16) one gets a quadratic equation for k_S . The solution of this equation is:

$$k_S = \frac{k_{SR}}{2} \pm \sqrt{\left(\frac{k_{SR}}{2}\right)^2 - A \frac{C_0}{S_0} k_{SR} k_{O_2}}, \quad (17)$$

which allows to calculate the substrate transport rate k_S from the values of parameters (A , k_{O_2} and k_{SR}) obtained from fitting the experimental data. For this calculation only such assignment of k_{O_2} and k_{SR} values is reasonable, which results positive (or zero) value of the expression under the square root in Eq. (17). In case of our experimental data this condition was found to be satisfied only when $k_{SR} > k_{O_2}$. This condition solves the problem due to Eq. (15) symmetry and allows fixing the value of k_{O_2} . Still, as Eq. (17) gives two solutions (with plus and minus signs, respectively), one should define an additional criterion for the determination of unique set of rate parameters k_S and k_R .

At this point, it should be reminded that the values of A (as well as the values of k_{O_2} and k_{SR}) were independent on the flow rate. This fact indicates that in the studied flow rate range the mass transfer was entirely limited by the transport (diffusion) in the

layer of enzyme carrier. As the diffusion rates are inversely proportional to the molecular dimensions (Stokes radii), the following condition should hold for oxygen and glucose: $k_{O_2} > k_S$. This condition is satisfied only for the solution of Eq. (17) with minus sign and hence assures unique determination of parameters.

Following the rules, established above for the relative magnitude of the rate parameters, we calculated the transport rates for oxygen and glucose, k_{O_2} and k_S respectively, for every biosensor response curve. These coefficients were not dependent on the glucose concentration or the flow rate of the analytes and their mean values, calculated from different measurements were not significantly different. The mean values of k_{O_2} and k_S were found to be 0.022 (SD=0.003) s^{-1} and 0.0030 (SD=0.0004) s^{-1} , respectively. Finally, the reaction rate was obtained from Eq. (11), which resulted $k_R = 0.065$ (SD=0.004) s^{-1} . The value of the ratio k_{O_2}/k_S , supposedly indicating the relationship of molecular radii of glucose and oxygen molecules, was between 5.9 and 7.9. This result is in a good correlation with the ratio of van der Waals' radius of oxygen (1.52 Å) and molecular size of glucose (10 Å), equaling to 6.6.

To conclude, we demonstrated that the model describes the sensor responses adequately and allows: (1) clear interpretation of underlying processes; (2) easy biosensor calibration from pre-steady-state data. In this final paragraph of the section we explore the last feature further: we demonstrate how and in which limits the pre-steady-state data can be used for shortening the measurement time. For this purpose we fitted the temporal responses (shown in Fig. 4) within different time intervals (the curves were fitted between $t=0$ and $t=t_F$, whereas t_F was varied from 300 s to a minimal value of ~ 20 s). This allowed simulating the situation, where the sensor output value is determined from shorter and shorter measurements. The results for parameter A , determined at three different substrate concentrations, are presented in Fig. 7. It is evident, that in all cases the parameter A is practically constant down to the measurement time $t_F \sim 60$ s. In Fig. 7, the data for two fitting procedures are presented. The filled dots present the data obtained when all parameters (A , k_{SR} , and k_{O_2}) in Eqs. (14,15) were freely varied, whereas the empty dots present the data obtained when the rate parameters were fixed (as determined at previous calibration) and only parameter A was varied. As one can see, by using the fixed set of pre-calibrated rate parameters, the measurement time can even be as short as 20 s. In other words, for

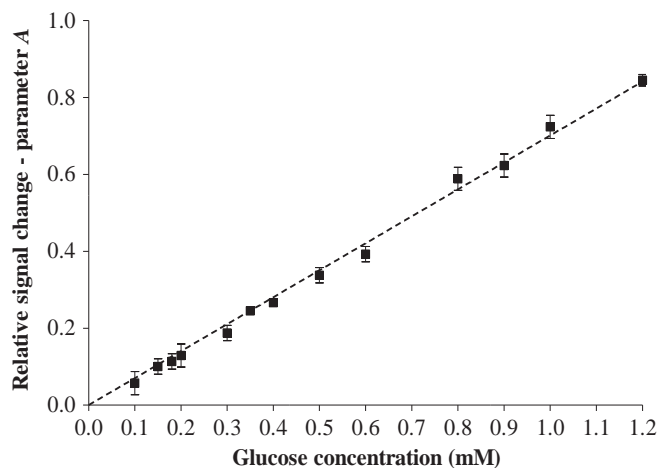


Fig. 6. The dependence of the relative signal change parameter A on glucose concentration. Measurements were carried out at 37°C in 0.1 M phosphate buffer (pH 6.50) at flow rate 2.7 ml/min.

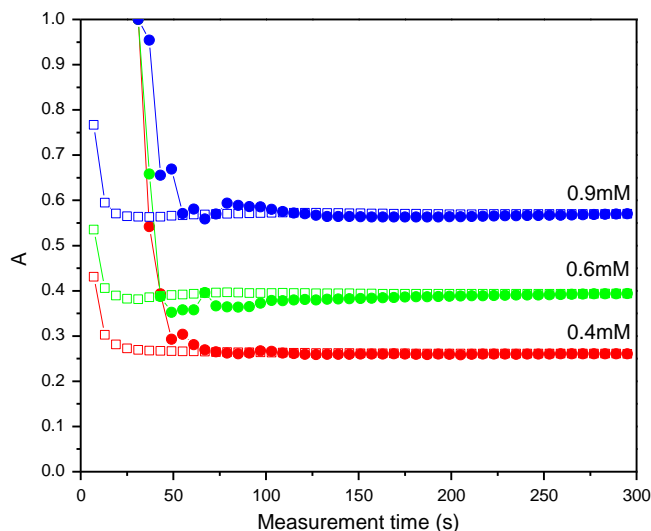


Fig. 7. The dependence of parameter A on the measurement time. Measurements were carried out at 37°C in 0.4 mM, 0.6 mM, and 0.9 mM glucose solutions in 0.1 M phosphate buffer (pH 6.50) at flow rate 2.7 ml/min. At fitting, all three parameters (filled dots) or only parameter A (open dots) was freely varied.

obtaining the parameter A (and then the substrate concentration from the calibration curve presented in Fig. 6) there is no need to record the signal up to 300 s but the recording time can be as short as 20 s. Note that these concrete values of characteristic times are related to concrete bio-optrodes and may hence vary between different systems, e.g. the optrodes with higher enzyme activity will have higher reaction rate, which leads to shorter characteristic times as well. If we look at the fitting results in Fig. 7 and at the signal changes in Fig. 4 in parallel, more general criterion may be formulated. In Fig. 4 one observes that the relative signal dropped at 20 and 60 s by $\sim 20\%$ and $\sim 50\%$, respectively. In conclusion, one can determine the substrate concentrations by measuring the signal until it has dropped only by 20–50% of its maximal (steady-state) change, and not waiting until the signal change has reached the 95% level of the presumed final change. This presents a significant advantage, as the measurement time can be shortened more than by one order in magnitude.

5. Discussion

Modeling of biosensor signals in flows is usually based on the diffusion-advection-reaction equation, which can be generally solved only by numerical methods [7–14]. Analytical solutions have been found only in few special cases [40]. In case of two-substrate reactions (1), one has even more complicated situation, described by a system of two coupled diffusion-advection-reaction equations.

As it is described in previous sections, a more simple approach based on ordinary rate equations allowed to evaluate the biosensor signals well not only qualitatively (providing clear interpretation of the response curves as well as such basic characteristics as sensitivity and stability, see below) but also quantitatively (providing enough precision even for pre-steady-state data). For understanding the success of this approach, an analogy with thermal transport problems can be drawn. Thermal problems are generally governed by an analog of diffusion equation but frequently a more simple approach with ordinary differential equation is used with rate parameters determined by thermal conductance and capacity. The advantage of rate equations is similar in both problems: simple analytical solutions provide clear and transparent interpretation and easy calculation procedure. Of course, the simplified description of the problem can be used only within certain parameter limits, which guarantee required precision for a given practical application. In the present case, for example, the model is valid until the processes of advection and diffusion in the solution outside the layer of enzyme carrier start to play a bigger role. This means that the model cannot be applied at very low flow rates or for describing the measurements in the stopped-flow regime. However, in the flow regime the model was completely adequate in a wide range of the flow rates.

The independence of model parameter A (describing the relative signal change) from the flow rate indicated that the transport is limited by diffusion in the layer of enzyme carrier and the advection in the flow channel is relatively fast. Previously we gave a coarse estimate of the ratio of diffusion rates based on molecular sizes. More precisely, the diffusion rates are given by the inverse values of characteristic diffusion times through a layer with thickness d :

$$\begin{aligned} k_{O_2} &= D_{O_2}/d^2 \\ k_S &= D_S/d^2 \end{aligned} \quad (18)$$

Here D_{O_2} and D_S are the diffusion coefficients of oxygen and substrate, respectively, in the enzyme carrier. Therefore we have

$$k_{O_2}/k_S = D_{O_2}/D_S \quad (19)$$

From the literature one can find that in the water at 37 °C $D_{O_2} = 2.7 \times 10^{-5} \text{ cm}^2/\text{s}$ [41] and $D_S = 0.9 \times 10^{-5} \text{ cm}^2/\text{s}$ [42]. These values lead to the ratio of diffusion coefficients equal to 3, whereas higher value has been found from our experiments – about 7. This discrepancy can be explained by somewhat preferential deceleration of glucose diffusion inside the flossy nylon thread. For example, in hydrogels [43] both the oxygen and glucose diffusion become slower as compared to water environment, whereas the effect is about twice stronger for glucose. This results in a similar ratio of diffusion rates as found in our study. Taking into account the thickness of the thread $d = 0.3 \text{ mm}$, one can estimate the diffusion coefficients in the buffer-filled nylon threads at 37 °C: after inserting the experimental transfer rates ($k_{O_2} = 0.022 \text{ s}^{-1}$ and $k_S = 0.003 \text{ s}^{-1}$) into Eq. (18) one obtains $D_{O_2} = 2.0 \times 10^{-5} \text{ cm}^2/\text{s}$ and $D_S = 0.27 \times 10^{-5} \text{ cm}^2/\text{s}$.

The most crucial parameter of a sensor is its sensitivity. In the present case the maximal (initial) sensitivity follows from Eq. (16), and is given by

$$S = \left| \frac{dc_f}{ds_0} \right| = \frac{k_R}{k_S + k_R} \frac{k_S}{k_{O_2}} \quad (20)$$

This can be compared with the sensitivity of a system, where the reaction takes place in a closed volume with distributed enzyme and fast mixing of components. Then a simple equation $c_f = c_0 - s_0$ holds for the reaction (1), and the sensitivity $S = 1$. It follows from Eq. (20), that the sensitivity is generally lower for a flow system. The maximal sensitivity of the latter can be achieved if $k_R \gg k_S$ and is then determined by the ratio k_S/k_{O_2} . The latter ratio is given by Eq. (19) i.e. it is determined by the ratio of diffusion coefficients, and therefore can hardly be increased by the design of the sensor. The only way to maximize the sensitivity is to fulfill the condition $k_R \gg k_S$ i.e. by increasing the reaction rate (enzyme activity) above a certain limit. Note that in our system the activity of the immobilized enzyme was high enough to gain sufficiently high bio-optrode activity and reaction rate (k_R was 20 times bigger than k_S). This can be estimated as an optimal situation, as at too high reaction rates the condition set by Eq. (8) becomes invalid, in other words – a more realistic description of arrival front has then to be included into the model. In our studies the passage time of the solution's initial front was 1–3 s, which was short enough to be neglected as compared to the characteristic reaction time $1/k_R = 15 \text{ s}$.

The condition $k_R \gg k_S$ also assures high stability of the sensor. For example, if the enzyme activity and accordingly the reaction rate decreases by 20% (from 0.065 s^{-1} to 0.052 s^{-1}), the sensitivity (Eq. (20)) and equally the slope of the calibration curve in Fig. 6 change just by 1%. Furthermore, the system sensitivity does not drop below 90% of the initial one even in the case only 30% of the initial enzymatic activity is remaining. Consequently, the actual design of the flow-through biosensor enables to prolong the effective lifetime of optrodes, commonly quite limited due to the inactivation of the bio-selective material and the consequent loss of system sensitivity. Finally, it is worth to remind that the signal stability of the current biosensor design is also warranted (further improved) by the lack of flow-rate dependence and elimination of drifts common to sensing and reference channels.

The model can be applied to other set-ups as well as far as two general conditions are fulfilled: (i) exponential reaction law, resulting from Eq. (3); (ii) diffusion-limited transport of substrates. If these conditions are met, the model can be directly applied for other 2-substrate enzymes, immobilized on other carriers with different procedures as well. The concrete parameters, k_R , k_S , and k_{O_2} , will have different values of course, for each particular set-up, and have to be determined by due calibration. Moreover, these parameters are generally temperature dependent and when the sensor is to be used at different temperatures, the calibration should be performed in the full actual temperature range.

The validity of condition (i) depends on the values of Michaelis' constants K_S and K_{O_2} , and can be estimated for each particular enzyme, whereas the immobilization may change the situation in some degree [1]. The condition (ii) requires the presence of a substrate-permeable layer (thread, gel [18], sol-gel [20], or polymer [21] coating) between the probe liquid and enzymes. Note that with this layer one can engineer the sensitivity, stability and dynamic range of the biosensor.

6. Conclusions

Dual-channel biosensor with fiber-optical oxygen transducers was constructed and used as a model system for studying the biosensor transfer (sensing) functions in flows on the example of glucose oxidase catalyzed reaction. The transducers and the flow cell of the sensor system were designed to match the thread-type enzyme carriers. A mathematical model involving two-substrate reaction (e.g. oxidase-catalyzed reactions, glucose oxidation in particular) and mass transport of substrates was developed for describing the sensor signal. The model is based on a system of rate equations and has a relatively simple analytical solution. This facilitated the interpretation of the experimental sensor data and allowed to develop a method for determining the biosensor output from early pre-steady state signals. It was demonstrated that the sensor reading could be obtained when the signal was changed only by 20% towards its final steady state value, which reduces the detection time about 10-fold as compared to standard procedures (requiring at least 95% signal change). It was established that the sensor parameters did not depend on the flow rate in a relatively wide range (0.8–13 ml/min or 0.3–4.8 cm/s), which showed that the mass transport was determined by diffusion in a flossy layer of substrate carrier. The application of the model to the experimental data also enabled to optimize the biosensor system. It allowed predicting optimal biosensor parameters for obtaining maximal sensitivity and high stability, on one hand, and for achieving fast determination of substrate concentration from pre-steady state data, on the other hand.

Acknowledgments

This work was supported by Estonian Science Foundation Grant no. 9061, Estonian Research Council Grant IUT 20-17, and by the European Regional Development Fund Project "Mesosystems: theory and applications", 3.2.0101.11-0029.

References

- [1] N.J. Ronkainen, H.B. Halsall, W.R. Heineman, *Chem. Soc. Rev.* 39 (2010) 1747–1763.
- [2] J.C. Pickup, F. Hussain, N.D. Evans, O.J. Rolinski, D.J.S. Birch, *Biosens. Bioelectron.* 20 (2005) 2555–2565.

- [3] S. Borisov, O.S. Wolfbeis, *Chem. Rev.* 108 (2008) 423–461.
- [4] M.-S. Steiner, A. Duerkop, O.S. Wolfbeis, *Chem. Soc. Rev.* 40 (2011) 4805–4839.
- [5] M.W. Johnston, J.S. Williams, U.S. Geological Survey Open-File Report 2006-1047, 11 p, 2006, (<http://pubs.usgs.gov/of/2006/1047/pdf/ofr2006-1047.pdf>).
- [6] C.D. Mell, J.T. Maloy, *Anal. Chem.* 47 (1975) 299–307.
- [7] J.K. Leypoldt, D.A. Gough, *Anal. Chem.* 56 (1984) 2896–2904.
- [8] S. Bacha, A. Bergei, M. Comtat, *Anal. Chem.* 67 (1995) 1669–1678.
- [9] J.J. Gooding, *Electrochem. Commun.* 1 (1999) 119–123.
- [10] R. Baronas, F. Ivanauskas, J. Kulyš, *J. Math. Chem.* 32 (2002) 225–237.
- [11] J. Lammertyn, P. Verboven, E.A. Veraverbeke, S. Vermeir, J. Irudayaraj, B.M. Nicolai, *Sens. Actuators B* 114 (2006) 728–736.
- [12] V. Flexer, K.F.E. Pratt, F. Garay, P.N. Bartlett, E.J. Calvo, *J. Electroanal. Chem.* 616 (2008) 87–98.
- [13] D. Baronas, F. Ivanauskas, R. Baronas, *J. Math. Chem.* 49 (2011) 1521–1534.
- [14] M.R. Romero, A.M. Baruzzi, F. Garay, *Sens. Actuators B* 162 (2012) 284–291.
- [15] M.I. Prodromidis, M.I. Karayannis, *J. Flow Inject. Anal.* 21 (2004) 5–10.
- [16] M. Bäcker, D. Rakowski, A. Poghossian, M. Biselli, P. Wagner, M.J. Schöning, *J. Biotech.* 163 (2013) 371–376.
- [17] W. Trettnak, M.J.P. Leiner, O.S. Wolfbeis, *Analyst* 113 (1988) 1519–1523.
- [18] M.C. Moreno-Bondi, O.S. Wolfbeis, M.J.P. Leiner, B.P.H. Schaffar, *Anal. Chem.* 62 (1990) 2377–2380.
- [19] L. Li, D.R. Walt, *Anal. Chem.* 67 (1995) 3746–3752.
- [20] O.S. Wolfbeis, I. Oehme, N. Papkovskaya, I. Klimant, *Biosens. Bioelectron.* 15 (2000) 69–76.
- [21] A. Pasic, H. Koehler, I. Klimant, L. Schaupp, *Sens. Actuators B* 122 (2007) 60–68.
- [22] V.I. Ogurtsov, J. Hynes, Y. Will, D.B. Papkovsky, *Sens. Actuators B* 129 (2008) 581–590.
- [23] G. Ozturk, S. Timur, S. Alp, *Anal. Lett.* 41 (2008) 608–618.
- [24] S. Nagl, M.I.J. Stich, M. Schäferling, O.S. Wolfbeis, *Anal. Bioanal. Chem.* 393 (2009) 1199–1207.
- [25] C. Zhou, Y. Shi, X. Ding, M. Li, J. Luo, Z. Lu, D. Xiao, *Anal. Chem.* 85 (2013) 1171–1176.
- [26] P.J. Scully, L. Betancor, J. Bolyo, S. Dzyadevych, J.M. Guisan, R. Fernandez-Lafuente, N. Jaffrezic-Renault, G. Kuncova, V. Matejec, B. O'Kennedy, O. Podrazky, K. Rose, L. Sasek, J.S. Young, *Meas. Sci. Technol.* 18 (2007) 3177–3186.
- [27] D.M. Cochran, D. Fukumura, M. Ancukiewicz, P. Carmeliet, R.K. Jain, *Ann. Biomed. Eng.* 34 (2006) 1247–1258.
- [28] Z. Zhou, L. Qiao, P. Zhang, D. Xiao, M.M.F. Choi, *Anal. Bioanal. Chem.* 383 (2005) 673–679.
- [29] A. Pasic, H. Koehler, L. Schaupp, T.R. Pieber, I. Klimant, *Anal. Bioanal. Chem.* 386 (2006) 1293–1302.
- [30] D. Peedel, T. Rincken, *Proc. Estonian Acad. Sci.* 61 (2012) 306–313.
- [31] K. Öige, T. Avarmaa, A. Suisalu, R. Jaaniso, *Sens. Actuators B* 106 (2005) 424–430.
- [32] R. Jaaniso, T. Avarmaa, A. Suisalu, A. Floren, A. Ruudi, K. Öige, *Proc. SPIE* 5946 (2005) 150–159.
- [33] K. Kivirand, T. Rincken, *Sens. Lett.* 7 (2009) 580–585.
- [34] T. Rincken, J. Järv, A. Rincken, *Anal. Chem.* 79 (2007) 6042–6044.
- [35] K. Kivirand, R. Rebane, T. Rincken, *Sens. Lett.* 9 (2011) 1794–1800.
- [36] M. Quaranta, S.M. Borisov, I. Klimant, *Bioanal. Rev.* 4 (2012) 115–157.
- [37] Q.H. Gibson, B.E.P. Swoboda, V. Massey, *J. Biol. Chem.* 239 (1964) 3927–3934.
- [38] D.G. Myszka, X. He, M. Dembo, T.A. Morton, B. Goldstein, *Biophys. J.* 75 (1998) 583–594.
- [39] D.A. Baker, D.A. Gough, *Anal. Chem.* 68 (1996) 1292–1297.
- [40] J. Crank, *The Mathematics of Diffusion*, 2nd ed., Clarendon Press, Oxford, 1975.
- [41] A.C.F. Ribeiro, O. Ortona, S.M.N. Simoes, C.I.A.V. Santos, P.M.R.A. Prazeres, A.J. M. Valente, V.M.M. Lobo, H.D. Burrows, *J. Chem. Eng. Data* 51 (2006) 1836–1840.
- [42] P. Han, D.M. Bartels, *J. Phys. Chem.* 100 (1996) 5597–5602.
- [43] S.A.M. Van Strooe-Biezen, F.M. Everaerts, L.J.J. Janssen, R.A. Tacken, *Anal. Chim. Acta* 273 (1993) 553–560.



An innovative approach to the recovery of phenolic compounds and volatile terpenes from the same fresh foliar sample of *Rosmarinus officinalis* L.



Maria Bellumori^a, Marco Michelozzi^b, Marzia Innocenti^a, Federica Congiu^a, Gabriele Cencetti^b, Nadia Mulinacci^{a,*}

^a Dipartimento di Neuroscienze, Psicologia, Area del Farmaco e Salute del Bambino (NEUROFARBA), Sezione di Farmaceutica e Nutraceutica e Centro Interdipartimentale di Ricerca per la Valorizzazione degli Alimenti (Ce.R.A), Università degli Studi di Firenze, via U. Schiff 6, 50019 Sesto Fiorentino, Firenze, Italy

^b Istituto Bioscienze e BioRisorse, CNR, via Madonna del Piano, 50019 Sesto Fiorentino, Firenze, Italy

ARTICLE INFO

Article history:

Received 31 March 2014

Received in revised form

21 July 2014

Accepted 23 July 2014

Available online 1 August 2014

Keywords:

Sequential extraction

Rosmarinic acid

Volatile terpenes

Enzymatic oxidation

ABSTRACT

Rosmarinus officinalis L. is a plant of relevant commercial interest because of its volatile fraction and also its phenolic constituents which are both well known for their numerous properties. Nevertheless, an extractive method suitable to recovering both the aromatic and phenolic fractions from the same fresh foliar tissue has not yet been reported. In this work we have optimized a two-step procedure able to recover first the phenolic compounds and successively the volatile terpenes from the same foliar sample. The recovery of the whole phenolic fraction, partially degraded using a traditional extractive method, was guaranteed and we observed a significant increment in the amount of volatile terpenes compared to a traditional extraction procedure. We also highlight crucial information on the enzymatic activity of the endogenous oxidases that rapidly transform the phenolic substrates, mainly the rosmarinic acid.

Our results suggest that this extractive procedure could also be used for other aromatic plants, thus providing a useful tool for more complete analyses of the main phytochemicals available in fresh foliar samples and creating the possibility of incrementing yields of volatile compounds.

© 2014 Elsevier B.V. All rights reserved.

1. Introduction

The Mediterranean basin is endowed with a rich wealth of aromatic plants such as rosemary, (*Rosmarinus officinalis* L. from Labiatae), a small evergreen shrub whose health benefits from its essential oil and properties of food preservation have been recognized since antiquity. It is known that rosemary leaves contain both volatile components that characterize its essential oil, and antioxidant phenolic compounds belonging to different chemical classes and having varying polarity and solubility.

Essential rosemary oil contains mainly monoterpenes and their derivatives (95–98%), the remainder (2–5%) being sesquiterpenes [1]. Volatile mono- and sesquiterpenes are the main constituents of the essential oil which has been used as flavor and fragrance throughout history in the ancient civilizations of Egypt, India, Greece and Rome. Today rosemary extracts are used not only to obtain essential oils but also to prepare phenolic extracts that are increasingly employed to provide natural alternatives to synthetic

antioxidant and artificial preservatives for foodstuffs [2,3] or as components of cosmetics [4]. The antioxidative property and part of the antimicrobial activity of fresh and dried rosemary leaves are related to the non-volatile phenolic compounds such as carnosic acid, carnosol, rosmarinic acid and a group of minor flavonoids. As reported in the ESCOP monograph [5] and in the dictionary of phytotherapy (Campanini, 2004) [6], rosemary leaf extracts are commonly used in traditional medicine against dyspepsia, dysmenorrhea and rheumatic diseases. Among the numerous activities of the phenolic rosemary extracts we can highlight their hepatoprotective [7,8], antihyperglycemic [9,10], antiulcerogenic [11] and antibacterial properties [12].

To the best of our knowledge, a chemical characterization both in terms of volatile and phenolic compounds from the same fresh foliar sample of rosemary has not yet been reported in the literature. Since it would be useful to have a suitable method for extracting the main secondary metabolites from a foliar sample for integrated studies on numerous samples, we decided to explore this possibility. Our aims were: a) to optimize a unique procedure for extracting the phenolic compounds and volatile terpenes from a sample of fresh rosemary leaves; b) to apply specific GC/MS and

* Corresponding author. Tel.: +39 0554573773; fax: +39 0554573737.
E-mail address: nadia.mulinacci@unifi.it (N. Mulinacci).

HPLC/DAD/MS analyses to determine respectively the volatile terpenes and the antioxidant phenolic fraction; c) to compare different sequential methods and highlight the advantages of the optimized extractive procedure.

2. Materials and methods

2.1. Plant material

Numbers of mature leaves were randomly sampled in May 2011 from adult plants of a single clone of *Rosmarinus officinalis* L. growing in the plant nursery of the National Research Council in Florence, Italy.

2.2. Composite sampling

About 30 g of fresh foliar tissue representing the plant leaf population of the rosemary clone were thoroughly mixed and grounded with liquid nitrogen to form a composite which was then subsampled for the GC and HPLC analyses. Some grounded leaf powder (EtC 20 m) was then freeze-dried.

2.3. Traditional extractive method

The first extractive step was designed to recover the volatile fraction. Rosemary samples were frozen in liquid nitrogen and ground in a porous ceramic mortar (grinding time about 1 min). The grinding is performed to allow breakdown of cellular structures containing terpenic constituents, avoiding the loss of these substances which are extremely volatile.

For each sample, 0.5 g of ground material were extracted with 3 mL of *n*-pentane or 3 mL of *n*-hexane, using tridecane as internal standard. The extraction process was performed for 24 h in a shaker at 1000 rpm at 24 °C. The *n*-pentane or *n*-hexane extracts were filtered through 0.45 µm filters, stored in vials at –20 °C before GC/FID analysis (Fig. 1, Pen or Hex samples). The solid residue was subjected to further extraction, according to a previously described procedure [13], for recovery of the phenolic compounds. In particular, leaves were extracted with ethanol (two steps) by alternation of magnetic stirring and sonication with ultrasounds. The ethanolic extract obtained after filtration was submitted to a liquid/liquid extraction with pentane or hexane (1:1, v/v) to remove part of the chlorophyll. The residual ethanol solution was analyzed directly by HPLC (Fig. 1, EtC sample).

To prevent phenolic oxidation, different amounts of vitamin C (5–20% w/w) were added to some samples before grinding (Fig. 1, EtC+VitC samples).

2.4. Innovative extractive method

The volatile terpenes were extracted in a second step after ethanol extraction of phenolic compounds (Fig. 2). Applying this method, 0.5 g of ground material were extracted with 10 mL of ethanol according to Mulinacci et al. [13]. The ethanol extract obtained after filtration was submitted to liquid/liquid extraction with pentane or hexane (1:1, v/v) and then analyzed by HPLC (Fig. 2, Et-REF); the *n*-pentane/*n*-hexane solutions were analyzed by GC/MS (Fig. 2; Def-Pen, Def-Hex). At the same time, the solid residue was recovered and volatile terpenes were extracted. The resulting pentane/hexane solutions were analyzed by GC/MS (Fig. 2; Et-Pen, Et-Hex samples).

2.5. GC/FID analyses

The analyses were performed with the Perkin-Elmer AutoSystem XL gas chromatograph equipped with an automatic sampler for liquid injections.

To obtain the separation of the enantiomeric monoterpenes an Elite-Betacydex betacyclodextrin capillary column 30 m long and 0.25 mm diameter (Perkin-Elmer) was used. GC analysis was carried out using H₂ as carrier gas at 2.0 mL min⁻¹ by a flame ionization detector at 250 °C and at an injector temperature of 230 °C. The oven temperature program was started at 40 °C for 3 min and increased to 200 °C, at 1 °C min⁻¹; the final temperature of 200 °C was maintained for 10 min.

2.6. GC/MS analyses

The analyses were performed on a GC/MS system from Perkin-Elmer Technologies composed of a Perkin-Elmer AutoSystem XL gas chromatograph equipped with an automatic sampler for liquid injections coupled to a TurboMass mass spectrometer. The gas chromatograph was equipped with the column described above, operating with helium as carrier gas at a constant flow of 3 mL/min⁻¹. The oven temperature program was the same as described above. The mass spectrometer operated with an electron ionization of 70 eV, scanning the mass range from 35 to 350 m/z. Ion source temperature was 200 °C. The GC/MS control and data elaboration were performed by Perkin-Elmer Technologies TurboMass 5.4.2.1617 ver. Chemstation software. The mass spectrometer was calibrated using perfluorotributylamine as the calibration standard with the Chemstation software.

The analysis of pure standards in the same analytical condition allowed attribution of some GC/MS signals and when a pure standard was not available, identification was attempted by comparing the recorded mass spectra with a MS spectral database (Wiley library) and taking into account the chromatographic order of elution.

2.7. HPLC/DAD/ESI/MS analyses

The analyses were carried out using an HP 1100 L liquid chromatograph coupled with a DAD detector and an HP 1100 MSD mass spectrometer with an API/electrospray interface (all from Agilent Technologies, Palo Alto, CA, USA).

A 150 mm × 2 mm i.d., 4 µm Fusion, RP18 column (Phenomenex, USA) equipped with a precolumn of the same phase was used. The mobile phases were (A) 0.1% formic acid/water and (B) CH₃CN; the following multistep linear solvent gradient was applied: in 0–15 min from 15 to 25% B; at 25 min with 35% B; at 35 min with 50% B; at 40 min with 100% B and a final plateau of 8 min. Equilibration time 10 min, flow rate 0.2 mL/min⁻¹, oven temperature 26 °C and injection volume 5 µL.

2.8. Quantitative evaluation

Absolute amounts of volatile terpenes were determined by comparison with the tridecane internal standard, and expressed as mg/g fresh weight (FW).

The quantitative evaluation of the main phenolic constituents was performed by using two external standards, rosmarinic acid at 330 nm and carnosic acid at 284 nm. According to a previous study [13], rosmarinic acid was also used to quantify all the flavonoids while carnosic acid to determine the non-volatile diterpenoids (carnosic acid and derivatives). The calibration curve of rosmarinic acid (Sigma-Aldrich) was in a linearity range between 0.1 µg and 9.4 µg with a *r*² 0.9999; the calibration curve of carnosic acid

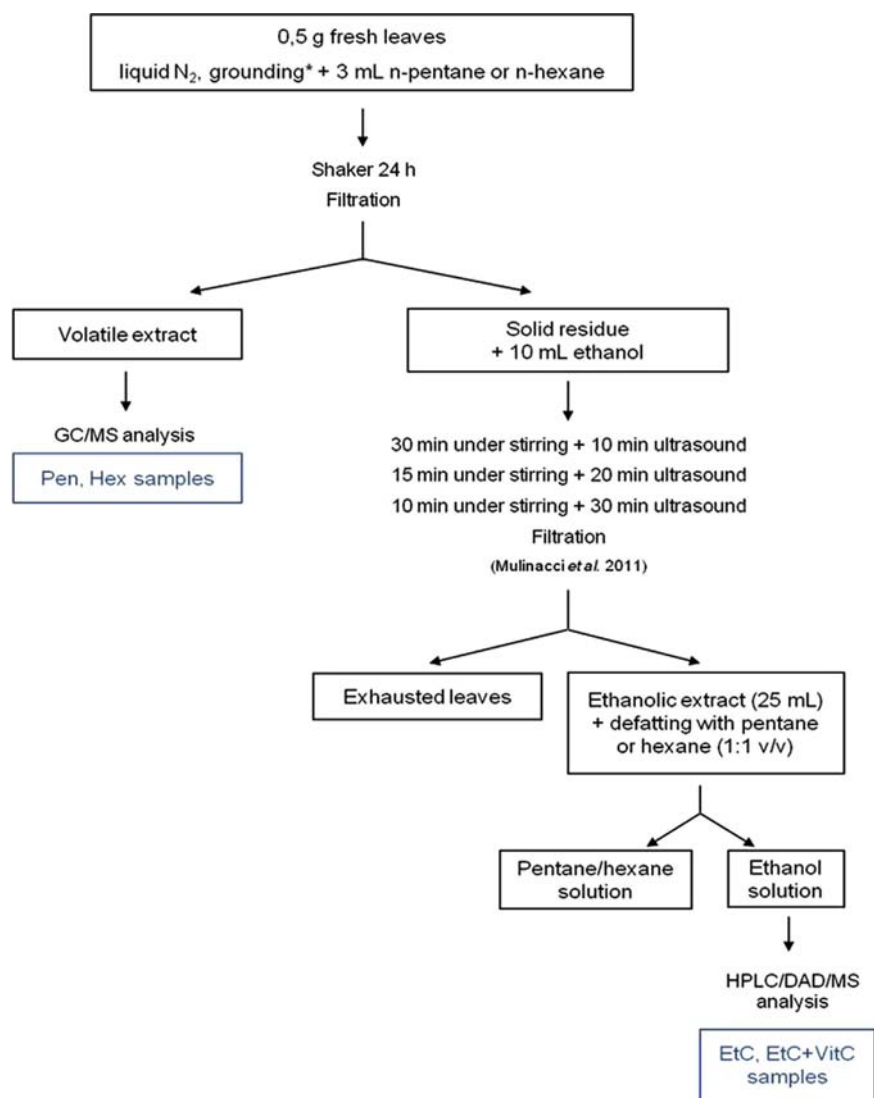


Fig. 1. Traditional extractive method. *Different amounts of vitamin C (from 5% to 20% w/w) were tested.

(Sigma-Aldrich) was in the linearity range between 0.05 μg and 3.4 μg , with r^2 0.9998.

2.9. Statistical analyses

Data were not normally distributed (Kolmogorov–Smirnov one sample test) and were analyzed by the non-parametric Kruskal–Wallis ANOVA followed by the Mann–Whitney U-test for multiple comparisons using SYSTAT 12.0 software (Systat Software Inc., Richmond, CA, USA). Differences were accepted as significant at the 5% level.

3. Results and discussion

Our goal was to get a more complete biological picture of the same foliar tissue by sequentially extracting the volatile terpenes and phenolic compounds from a single fresh sample, using a unique procedure. This extractive approach is a useful tool for analyzing numerous samples, particularly when available in small amounts. We have evaluated this strategy by working on fresh rosemary leaves and applying two different methods.

A traditional extraction method was firstly used to recover the volatile fraction and subsequently the antioxidant phenolic

compounds. A method suitable for characterizing and quantifying all the phenolic constituents of the leaves [13] was used to obtain the reference samples (Fig. 2, Et-REF) and to evaluate the percentage of recovery of these compounds through the traditional method.

The traditional extraction method indicated that a pretreatment of rosemary leaves with lipophilic solvents such as *n*-pentane or *n*-hexane for 1 to 24 h of contact induced a strong decrease of the major phenols, mainly rosmarinic acid (Fig. 3a, EtC sample). Furthermore, HPLC/DAD analysis of this extract showed a considerable decrease in carnosic acid with a corresponding increment in its typical oxidized products, carnosol and rosmanol. Such behavior can be related to the presence of the native H_2O in the leaf that allows oxidation of carnosic acid as previously demonstrated [13].

The strong decrease in rosmarinic acid was highlighted after only 20 min of contact of the fresh leaves with *n*-pentane or *n*-hexane (Fig. 3a, EtC 20 min sample). In addition, the fast degradation of the phenolic components after the preliminary extraction of the volatile compounds, was clearly confirmed by foliar browning, indicating the formation of oxidized compounds frequently produced in damaged vegetables. Consequently, an enzymatic reaction involving endogenous phenol oxidases was hypothesized. Nevertheless it was unclear how the enzymatic activity was

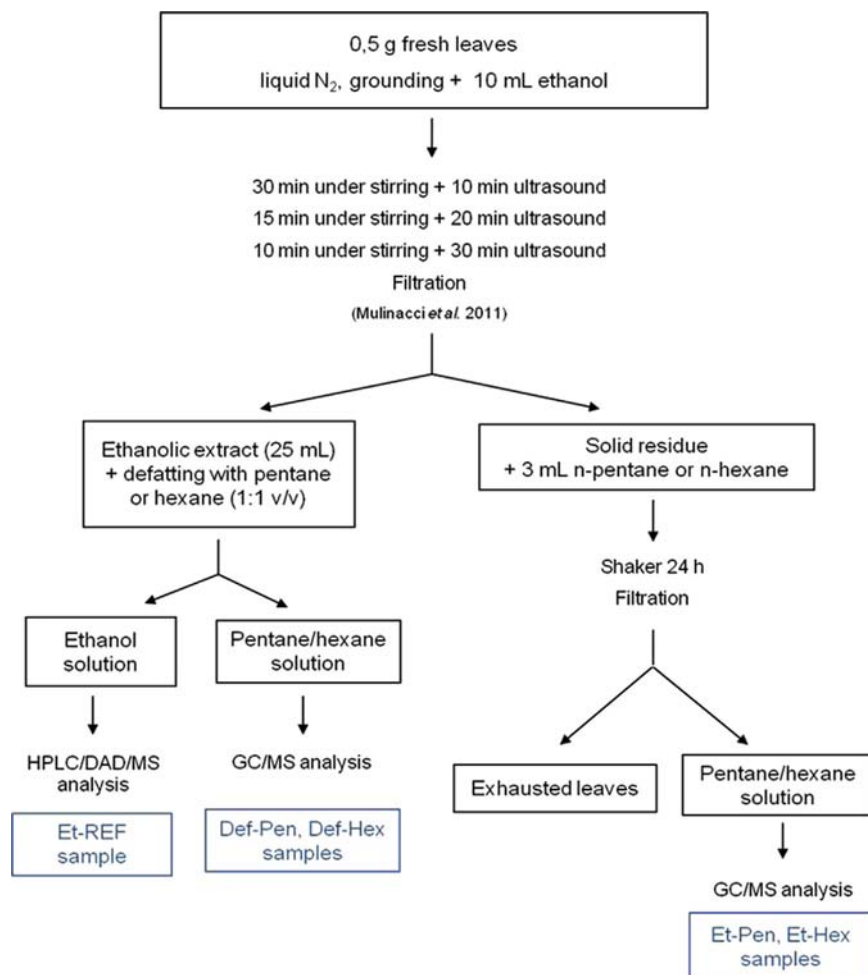


Fig. 2. Innovative extractive method.

possible in the presence of lipophilic organic solvents and to explain this phenomenon, the possible role of the native H₂O in the fresh leaves was considered. The presence of water during the extraction of the volatile compounds allowed us to obtain a two-phase system in which the aqueous phase, even if in small amount, was adequate to allow oxidative enzyme activity and to promote the conversion of carnosic acid into carnosol, as previously demonstrated [14].

To confirm this hypothesis an extraction on dried rosemary leaves was carried out (Fig. 3b). The results of the chromatographic analyses confirmed the crucial role of the water since no reduction in rosmarinic acid content was observed; nevertheless, a loss in the total terpenoid and flavonoid content appeared one more time. These data confirmed that enzymatic oxidation of rosmarinic acid in the fresh leaves, not observed in the correspondent dried samples, was rapidly obtained in the presence of the native water (about 50–60% of the fresh weight) that provided a microenvironment where the enzyme can act, despite the presence of pentane or hexane in the upper layer.

The next tests were aimed at inhibiting the phenol oxidases by using strong inorganic acids (HCl and H₂SO₄ 0.1 N as final concentration) added immediately after grinding during the traditional extraction method. Despite the strong acidic medium, the enzymatic oxidation of rosmarinic acid was almost complete within a short time, suggesting rapid degradation kinetics of these enzymes, already present during the grinding of the leaves.

These results indicate the complexity of operating on the same fresh foliar tissue of rosemary for extracting sequentially the volatile

and phenolic components, without significant loss of rosmarinic acid and terpenoid content.

A successive test carried out to prevent phenolic oxidation during the traditional extraction method was to add different amounts of powdered vitamin C (5%–20% w/w) to rosemary leaves before the grinding. Vitamin C was chosen because of its high solubility in water and its ability to act as a strong antioxidant, as conformed by its same use in preventing browning of freshly-cut fruit.

The results concerning the volatile fraction obtained by GC/MS analysis showed that vitamin C does not cause significant differences in the concentration of volatile terpenes, compared to the profiles obtained by conventional extraction with pentane or hexane (Fig. 1, Pen and Hex samples). Even at very high doses (20% w/w) vitamin C was only partially protective against rosmarinic acid oxidation (Fig. 4).

Traditionally, it is common practice for sequential extractions to start with more lipophilic solvents such as ether or hexane and successively apply more polarized media such as ethanol or methanol water mixtures for the phytochemical screening of a plant sample [15]. Nevertheless, in light of the results we obtained with the traditional procedure, we decided to hypothesize an innovative extraction method for treating the fresh leaves. We reversed the conventional approach and the samples were first extracted with ethanol to recover the phenolic compounds and secondly with pentane or hexane (Fig. 2) to obtain the volatile fraction.

An unexpected result was the significant increment in the extraction yields for the volatile terpenes when we applied this innovative method (Fig. 5, Et-Pen, Et-Hex extracts) compared to

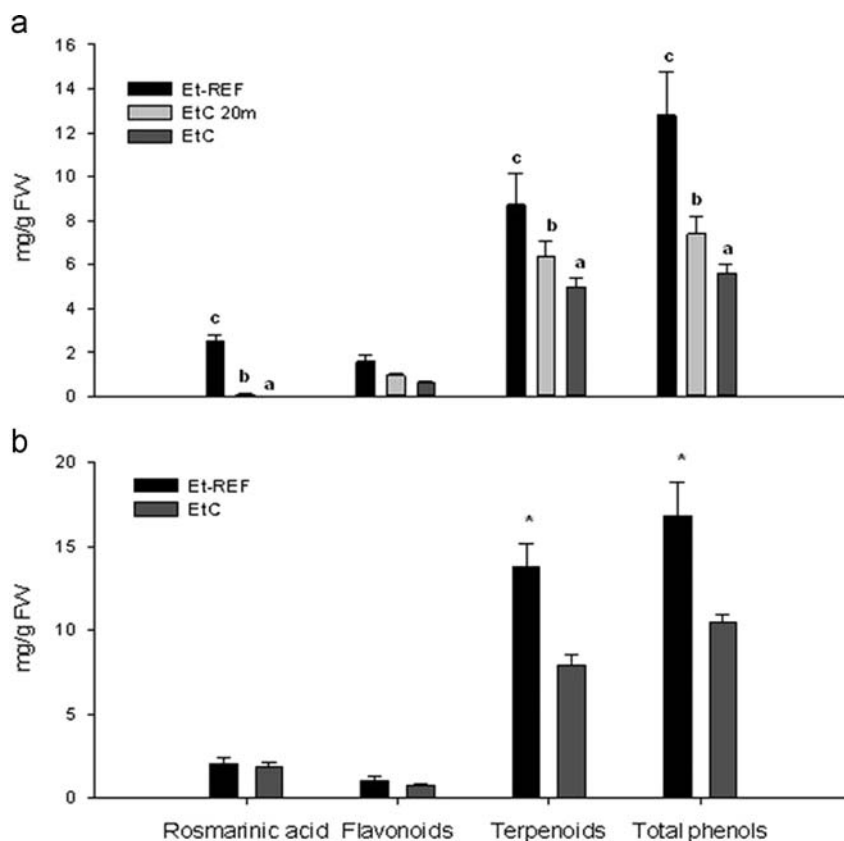


Fig. 3. Comparison of phenolic content among different extracts (Et-REF, EtC, EtC 20 m) obtained with the traditional extraction method on fresh (a) and on freeze-dried (b) leaves. Bars represent means \pm SD of 3 measurements; bars not visible indicate SD smaller than the symbol. Different letters and an asterisk indicate significant differences between different extracts respectively in fresh (Kruskal–Wallis ANOVA, $p < 0.05$) and freeze-dried (Mann–Whitney U test, $p < 0.05$) leaves.

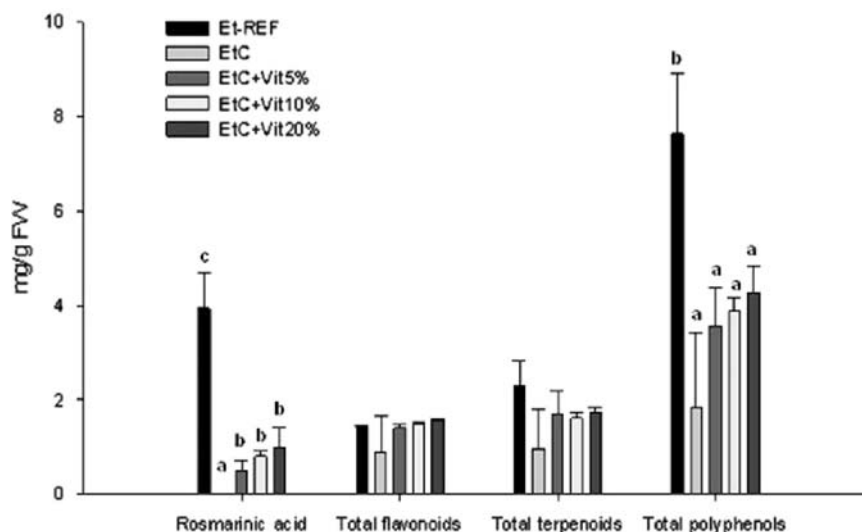


Fig. 4. Effect of vitamin C on phenolic content in the extracts obtained according to Fig. 1. Bars represent means \pm SD of 3 measurements; bars not visible indicate SD smaller than the symbol. Different letters indicate significant differences between different extracts (Kruskal–Wallis ANOVA, $p < 0.05$).

the traditional approach (Fig. 5, Pen and Hex samples). This result was particularly interesting when considering that higher extractive yields were obtained despite the small amount of volatile terpenes removed by the ethanol extraction (Fig. 2 and Fig. 5; Def-Pen, Def-Hex samples). Presumably the ethanol pretreatment combined with a physical treatment with ultrasounds for about 2 h, helped to break down the cellular structures and promote the subsequent penetration of the lipophilic solvent into the leaf tissue [16,17].

The qualitative composition of the volatile terpenic fractions obtained with these two approaches (the traditional versus the innovative extraction methods) was evaluated to verify if the increased yields had similar or different GC profiles. Fig. 6 compares the amounts of the main volatile terpenes in the two extracts obtained using the traditional and innovative methods, respectively. The first result was that all the samples treated with *n*-pentane provided higher yields than the samples extracted with *n*-hexane (Fig. 6; Pen, Et-Pen and Def-Pen). The *n*-pentane,

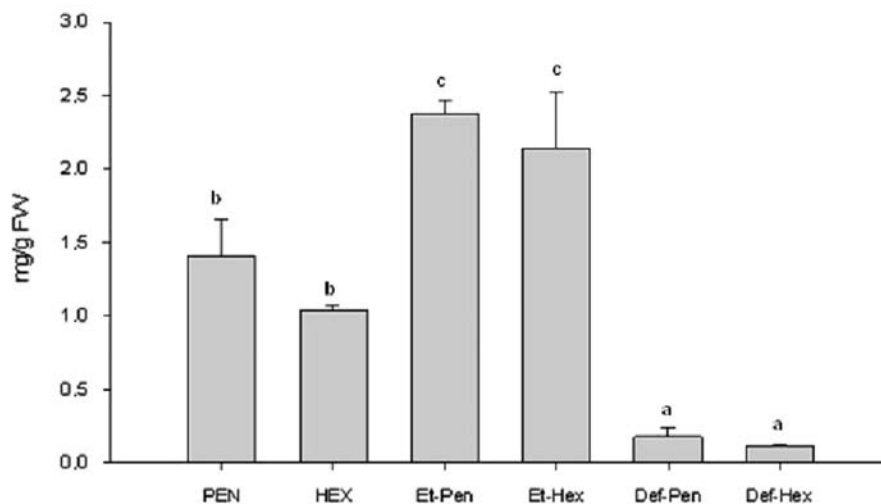


Fig. 5. Comparison of the total terpene content in the extracts obtained by the traditional and innovative extraction methods. Bars represent means \pm SE of 3 measurements; bars not visible indicate SE smaller than the symbol. Different letters and an asterisk indicate significant differences between different extracts (Kruskal–Wallis ANOVA, $p < 0.05$).

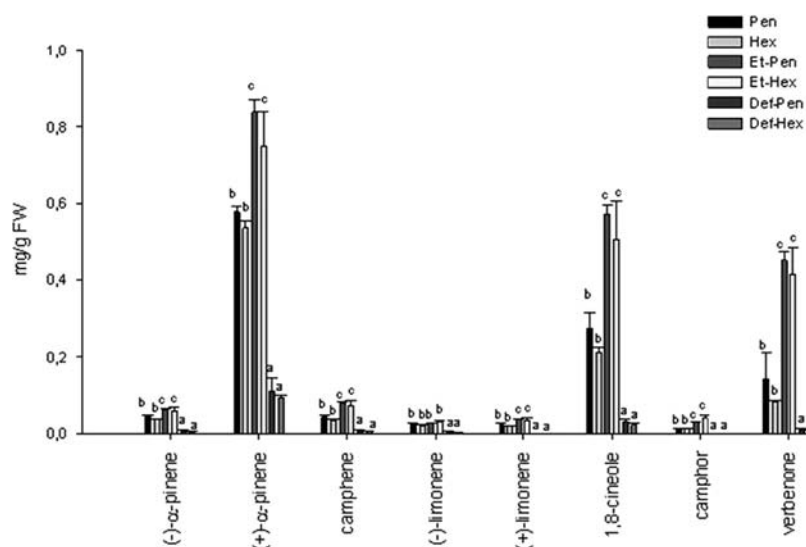


Fig. 6. Content of the main terpenes in the extracts obtained by the traditional and innovative extraction methods. Bars represent means \pm SE of 3 measurements; bars not visible indicate SE smaller than the symbol. Different letters and an asterisk indicate significant differences between different extracts (Kruskal–Wallis ANOVA, $p < 0.05$).

because of its greater extractive capacity, proved to be the most suitable solvent for the extraction of the volatile fraction from rosemary. The three compounds (+)- α -pinene, 1,8-cineole and verbenone were proved to be the most abundant of the analyzed extracts.

4. Conclusions

Although the traditional approach to phytochemical investigations of plant samples suggests the use of a lipophilic solvent and only subsequently of more polar media, we found that this approach was not suitable for our purposes. Unexpectedly, we found that an extraction procedure, in which a more polar solvent (ethanol) is applied and successively a very lipophilic media such as *n*-hexane or *n*-pentane is used, proves to be the best approach for analyzing fresh rosemary leaves.

The conventional method was not able to guarantee the complete recovery of the native phenolic compounds, even with the use of a potent antioxidant such as vitamin C to prevent

enzymatic oxidation. On the other hand, our proposed innovative approach not only ensured the recovery of all the main phenolic components but it also provided a consistently higher extraction yields of the volatile fraction. Moreover, the low standard errors of the means indicate the good repeatability of this new procedure. Our study's innovative findings can be taken into account when planning a suitable process for the analysis of rosemary leaves, or to avoid anomalous and unexpected results during sample treatment. Further studies should be performed to evaluate the applicability and efficacy of this method for other aromatic plants.

Acknowledgments

This research was supported by the Regione Toscana, Agenzia Regionale Sviluppo e l'Innovazione nel Settore Agricolo, project "Olio essenziale di rosmarino toscano - OLIROTO". Our thanks to Dr Sandra Gallori for her technical assistance in preparing the manuscript and Dr. Mary Forrest for final English editing of the manuscript.

References

- [1] A. Angioni, A. Barra, E. Cereti, D. Barile, J.D. Coisson, M. Arlorio, S. Dessi, V. Coroneo, P. Cabras, L. J. Agric. Food Chem. 52 (2004) 3530–3535.
- [2] Scientific Opinion of the Panel on Food Additives, Flavourings, Processing Aids and Materials in Contact with Food on a request from the Commission on the use of rosemary extracts as a food additive, EFSA J. 721 (2008) 1–3.
- [3] S. Moreno, T. Scheyer, C.S. Romano, A.A. Vojnov, Free Rad. Res. 40 (2) (2006) 223–231.
- [4] C.J. Lee, L.G. Chen, T.L. Chang, W.M. Ke, Y.F. Lo, C.C. Wang., Food Chem. 124 (2011) 833–841.
- [5] Rosmarini Folium, ESCOP Monographs, The Scientific Foundation for Herbal Medicinal Products, second edition, Publisher: ESCOP, the European Scientific Cooperative on Phytotherapy, Exeter, UK (2009) 429–436.
- [6] E. Campanini, Dizionario di Fitoterapia e Piante Medicinali, second ed., Tecniche Nuove., Milano, Italy, 2004.
- [7] J. Sotelo-Felix, D. Martinez-Fong, P. Mureil De la Torre, Eur. J. Gastroen. Hepat. 14 (2002) 1001–1006.
- [8] R. Gutiérrez, J.L. Alvarado, M. Presno, O. Pérez-Veyna, C.J. Serrano, P. Yahuaca, Phytother. Res. 24 (4) (2009) 595–601.
- [9] A. Al-Hader, Z. Hasan, M. Aqel, J. Ethnopharmacol. 43 (1994) 217–221.
- [10] T. Bakirel, U. Bakirel, O.Ü. Keles, S.G. Ülgen, H. Yardibi, J. Ethnopharmacol. 116 (2008) 64–73.
- [11] P. Dias, M. Foglio, A. Possenti, J. Ethnopharmacol. 69 (2000) 57–62.
- [12] O.Y. Celiktas, E.E.H. Kocabas, E. Bedir, F.V. Sukan, T. Ozek, K.H.C. Baser, Food Chem. 100 (2007) 553–559.
- [13] N. Mulinacci, M. Innocenti, M. Bellumori, C. Giaccherini, V. Martini, M. Michelozzi, Talanta 85 (2011) 167–176.
- [14] T. Masuda, Y. Inaba, T. Maekawa, Y. Takeda, H. Tamura, H. Yamaguchi, J. Agric. Food Chem. 50 (21) (2002) 5863–5869.
- [15] I. Morelli, G. Flamini, L. Pistelli, Manuale dell'Erborista – Biosintesi, estrazione e identificazione delle sostanze vegetali, Tecniche Nuove, Milano, Italy, 2005.
- [16] M. Toma, M. Vinatoru, L. Paniwnyk, T.J. Mason, Ultrason. Sonochem 8 (2) (2001) 137–142.
- [17] F. Chemat, K.K. Zill-e-Huma, Ultrason. Sonochem 18 (2011) 813–835.



A novel fluorescence probing strategy for the determination of parathion-methyl

Xu Yan^a, Hongxia Li^b, Xinyan Wang^c, Xingguang Su^{a,*}

^a Department of Analytical Chemistry, College of Chemistry, Jilin University, Changchun 130012, China

^b School of Pharmacy, Jilin University, Changchun 130021, China

^c Changchun Institute of Applied Chemistry, Chinese Academy of Sciences, Changchun 130022, China

ARTICLE INFO

Article history:

Received 13 May 2014

Received in revised form

9 July 2014

Accepted 10 July 2014

Available online 31 July 2014

Keywords:

Quantum dots

Electron transfer

Parathion-methyl

Organophosphorus hydrolase

Agricultural samples

ABSTRACT

A sensitive fluorescence probing strategy for parathion-methyl (PM) detection was developed based on electron transfer (ET) between *p*-nitrophenol (the hydrolysate of PM) and CdTe quantum dots (QDs) in cetyltrimethylammonium bromide (CTAB). PM was hydrolyzed by organophosphorus hydrolase (OPH) to form *p*-nitrophenol. *P*-nitrophenol is a typically electron-deficient compound due to the strong electron-withdrawing effect of the nitro groups. The positive charge of CTAB which make it assemble with electronegative mercaptopropionic acid-capped QDs, could be used as an absorbent for *p*-nitrophenol due to the strong hydrophobic interaction between the long alkyl chain of CTAB and aromatic ring of *p*-nitrophenol. Thus, the fluorescence intensity of CdTe QDs/CTAB probe could be quenched by *p*-nitrophenol due to the ET mechanism. The fluorescence intensity of the QD/CTAB system was proportional to PM concentration in the range of 25–3000 ng mL⁻¹, with a detection limit of 18 ng mL⁻¹. Furthermore, the proposed method was simple in design and fast in operation, and has been successfully used for PM detection in environmental and agricultural samples with satisfactory recovery.

© 2014 Elsevier B.V. All rights reserved.

1. Introduction

Organophosphorous (OP) compounds are a broad group of chemicals widely used as pesticides in agriculture, as antihelmintics in medicine, and as chemical warfare agents in the airline industry [1–5]. Parathion-methyl (PM), one of the important OPs, has been widely used to protect crops and vegetables for defending sucking and chewing insect infestation [6–8]. While, the inhibition of acetylcholinesterase activity by PM can lead to a disturbance of neuronal function and even death [9]. Public concern for its adverse effects on human reproduction has increased because of its genotoxic effect on somatic and sperm cells [10–13]. Therefore, it is significant to detect the PM residues in environmental and agricultural samples.

Many methods for OPs detection have been reported, including the Association of Official Analytical Chemists methods [14,15], and enzyme-linked immunosorbent assays [16]. These assays require expensive instrumentation, complex sample preparation or purification procedures, and costly bio-molecular reagents. As an alternative to the expensive instrumental and laborious antibody methods, fluorescence measurements have been successfully

developed as a qualitative and quantitative screening tool for OPs detection [17]. Quantum dots (QDs) owing to the quantum-size confinement effects, have unique spectral and electronic properties such as narrow emission spectra, water solubility and high light stability, resulting in being widely used for biological detection [18–21]. Recently, QDs has been applied to pesticides detection, such as, Liang et al. developed a sensitive biosensor based on graphene nanosheets, CdTe QDs and acetylcholinesterase enzymatic reaction for OPs sensing [22]. QDs-based molecularly imprinted polymer composite nanospheres are prepared to detect diazinon [23]. Bi-enzymes of acetylcholinesterase and choline oxidase combined with QDs are used as biological receptors to analyze OPs [9,24]. Though these fluorescent methods have been reported for pesticides detection, they need complex technologies (graphene nanosheets, molecularly imprinted polymer, or bi-enzymes system) to capture the analyte or amplify signal. Organophosphorus hydrolase (OPH), which exhibits the special capability to hydrolyze OPs without the addition of other substrates, has been widely used in recent years [25,26]. Lan et al. developed a novel biosensor by using OPH to detect PM [27]. The OPH-based methods have many advantages such as high selectivity and fast response time [28,29]. So QDs associated with OPH provided a potential application in OPs detection.

In this work, we reported a high sensitive probing strategy for PM detection based on CdTe QDs and OPH. The probing strategy

* Corresponding author. Tel.: +86 431 85168352.

E-mail address: suxg@jlu.edu.cn (X. Su).

was based on electron transfer (ET) between CdTe QDs and *p*-nitrophenol (the hydrolysate of PM by OPH) in cetyltrimethylammonium bromide (CTAB). The positive charge of CTAB which make it easily assembled with electronegative mercaptopropionic acid (MPA)-capped QDs, could be used as an absorbent for *p*-nitrophenol due to the strong hydrophobic interaction between the long alkyl chain of CTAB and aromatic ring of *p*-nitrophenol [30–32]. In this case, when *p*-nitrophenol was assembled around CdTe QDs, the fluorescence intensity of CdTe QDs was quenched due to the ET mechanism. The established fluorescence sensing system has high selectivity and sensitivity for PM detection. And this sensing system has been successfully applied to detect PM in environmental and agricultural samples with good precision and accuracy.

2. Experiment section

2.1. Reagents and instruments

All reagents and solvents were at least analytical grade. The water used in all experiments had a resistivity higher than $18 \text{ M}\Omega \text{ cm}^{-1}$. 3-Mercaptopropionic acid (MPA) (99%) was purchased from J&K Chemical Co. and tellurium powder (~ 200 mesh, 99.8%), CdCl_2 (99%) and NaBH_4 (99%) were purchased from Aldrich Chemical Co. Cetyltrimethylammonium bromide (CTAB) was obtained from Beijing Dingguo Changsheng Biotechnology Company. Sodium hydroxide (NaOH), hydrogen chloride (HCl) and ethanol were purchased from Beijing Chemical Works. Parathion-methyl (PM) was purchased from Sigma-Aldrich Corporation. Organophosphorus hydrolase (OPH) was obtained from Beijing singin biya Biological engineering Ltd.

The fluorescence spectra were recorded by using a RF-5301 PC spectrofluorophotometer (Shimadzu, Japan) equipped with a xenon lamp using right-angle geometry. Ultraviolet spectra were obtained on a Shimadzu UV-1700 UV-vis spectrophotometer (Shimadzu Co., Kyoto, Japan). All pH measurements were made with a PHS-3C pH meter (Tuopu Co., Hangzhou, China). In both experiments, a 1 cm path-length quartz cuvette was used.

2.2. Syntheses of CdTe QDs

Water compatible CdTe QDs used in this study were synthesized by refluxing routes with mercaptopropionic acid (MPA) as stabilizer [33]. Briefly, sodium hydrogen telluride (NaHTe) was produced in an aqueous solution by the reaction of sodium borohydride (NaBH_4) with tellurium powder at a molar ratio of 2:1. Later, fresh NaHTe solution was added to 1.25 mmol L^{-1} CdCl_2 solutions at pH 11.2 in the presence of MPA with N_2 protection, and the molar ratio of $\text{Cd}^{2+}/\text{MPA}/\text{HTe}^-$ was fixed at 1:1.5:0.2. The CdTe precursor solution was subjected to a reflux at 250°C under open-air conditions with condenser attached. The stable water-compatible CdTe QDs showed emission peaks at 658 nm upon the excitation of 380 nm. The slit width of excitation and emission was 5 and 5 nm, respectively. According to William Yu et al. [34], the concentration of CdTe QDs solution was calculated to be $8.77 \times 10^{-6} \text{ mol L}^{-1}$.

2.3. Detection of PM

100 μL CdTe QDs solution, 200 μL CTAB (500 ng mL^{-1}) and 150 μL PBS (0.1 mol L^{-1} , pH 8.5) were successively added into a 2.0 mL calibrated test tube, shaken thoroughly and equilibrated for 1.0 min. Then, different amounts of *p*-nitrophenol solutions were added, and the test tube was diluted to the mark with deionized water, shaken thoroughly for 2 min until the solution was fully mixed. The fluorescence spectra were recorded in the wavelength

range of 560–760 nm upon the excitation at 380 nm, and the fluorescence intensity at 668 nm was used for quantitative analysis.

2.4. Real sample detection

The proposed method was used for PM detection in environmental and agricultural samples, including water and rice. Tap water was collected from our laboratory and rice samples were purchased from a local supermarket. The spiked samples were prepared according to previous report [8,35].

The water samples (10 mL), which were filtered with filter paper (9 cm), were spiked with 50, 100 and 5000 ng mL^{-1} PM, respectively. The samples were directly detected by the proposed method.

Rice samples (10 g) were ground, spiked with PM standards of 50, 100 and 5000 ng mL^{-1} , respectively. The samples were thoroughly homogenized and then allowed to stand overnight. The samples were mixed with 20 mL acetonitrile and 4 mL water, ultrasonic extraction for 30 min and centrifuged for 10 min at 4000 rpm. Then, 1 g sodium chloride was added in the above extracted liquid. 15 mL the supernatant was transferred and evaporated at 40°C under a nitrogen stream. The dry residue was dissolved and diluted with 2 mL of OPH solution (40 mg mL^{-1}) containing 10% ethanol and detected by the proposed methods. The experiment of each sample was conducted in triplicate.

3. Results and discussion

3.1. Design of the sensing strategy

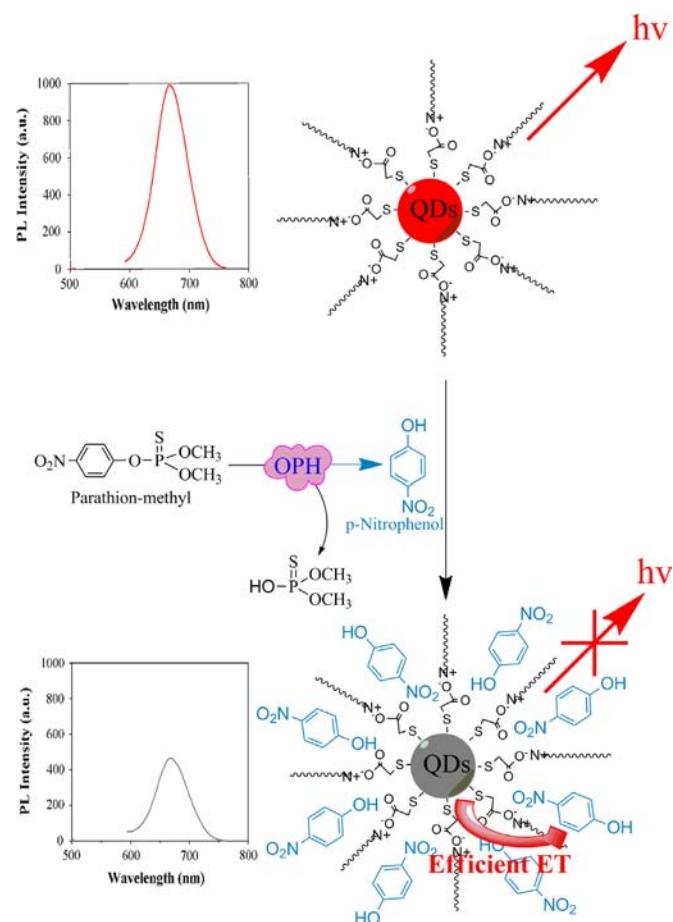
In this work, a high sensitive probing strategy for PM detection based on CdTe QDs and OPH was developed. The sensing principle was based on ET between CdTe QDs and *p*-nitrophenol (the hydrolysate of PM by OPH). As shown in Scheme 1, the positive charged CTAB could be easily assembled with negative charged MPA-capped CdTe QDs based on electrostatic self-assembly technology [31]. Due to the strong hydrophobic interaction between aromatic ring of *p*-nitrophenol and the long alkyl chain of CTAB, *p*-nitrophenol was easily assembled around CdTe QDs [30–32]. Furthermore, *p*-nitrophenol, a typically electron-deficient compound, could quench the fluorescence of CdTe QDs due to the ET quenching mechanism [36–38], which could be used for PM detection.

3.2. Characteristic of CdTe QDs/CTAB probe

Fig. 1A shows the zeta potentials of CdTe QDs and CTAB. It is significant to note that the zeta potentials of CdTe QDs and CTAB are -32.69 mV and 5.17 mV , respectively. The zeta potentials demonstrate that the electrostatic interaction could make CdTe QDs and CTAB close to each other. The UV-vis absorption spectra and photoluminescence (PL) emission spectra of MPA-capped CdTe QDs and the CdTe QDs/CTAB mixture were shown in Fig. 1B and C. With the addition of CTAB, the UV-vis absorption peak around 610 nm became gentle (Fig. 1B). From Fig. 1C, it also could be seen that the PL emission peak of MPA-capped CdTe QDs around 658 nm was narrow and symmetrical. After the addition of CTAB to CdTe QDs solution, the surface capped layer of the CdTe QDs was changed from MPA to CTAB which existed long alkyl chain, as a result, the PL emission peak of the CdTe QDs/CTAB mixture exhibited a significant red shift to 668 nm. Thus, the above results indicate the successful CTAB-functionalized modification on the surface of CdTe QDs.

3.3. Feasibility of PM detection

In order to test the feasibility of the proposed method, we first investigated the effect of *p*-nitrophenol on the PL intensity of CdTe QDs/CTAB probe. Fig. S1A shows that the PL intensity of CdTe QDs/CTAB probe could be obviously quenched by *p*-nitrophenol. The results confirmed that the proposed method for PM detection based on the fluorescence quenching of CdTe QDs/CTAB was feasible. Then, the effect of CTAB was evaluated, we compared the fluorescence quenching of CdTe QDs by *p*-nitrophenol in the presence and absence of CTAB. As shown in Fig. S1, when the



Scheme 1. The schematic illustration of the principle of CdTe QDs/CTAB probing strategy for PM detection.

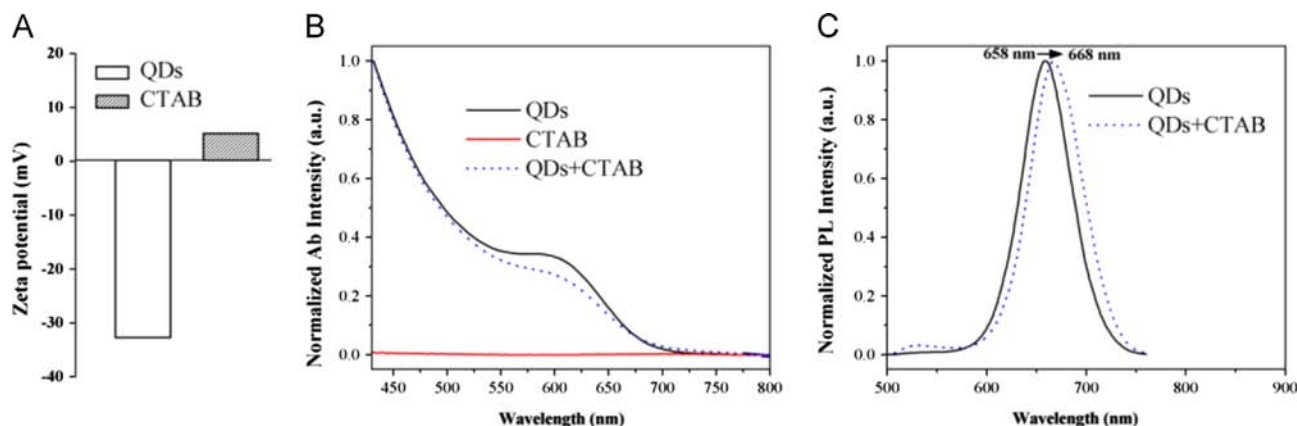


Fig. 1. (A) The zeta potentials of CdTe QDs and CTAB. (B) The UV-vis absorption spectra of CdTe QDs, CTAB and the CdTe QDs/CTAB mixture. (C) The fluorescence emission spectra of CdTe QDs and the CdTe QDs/CTAB mixture.

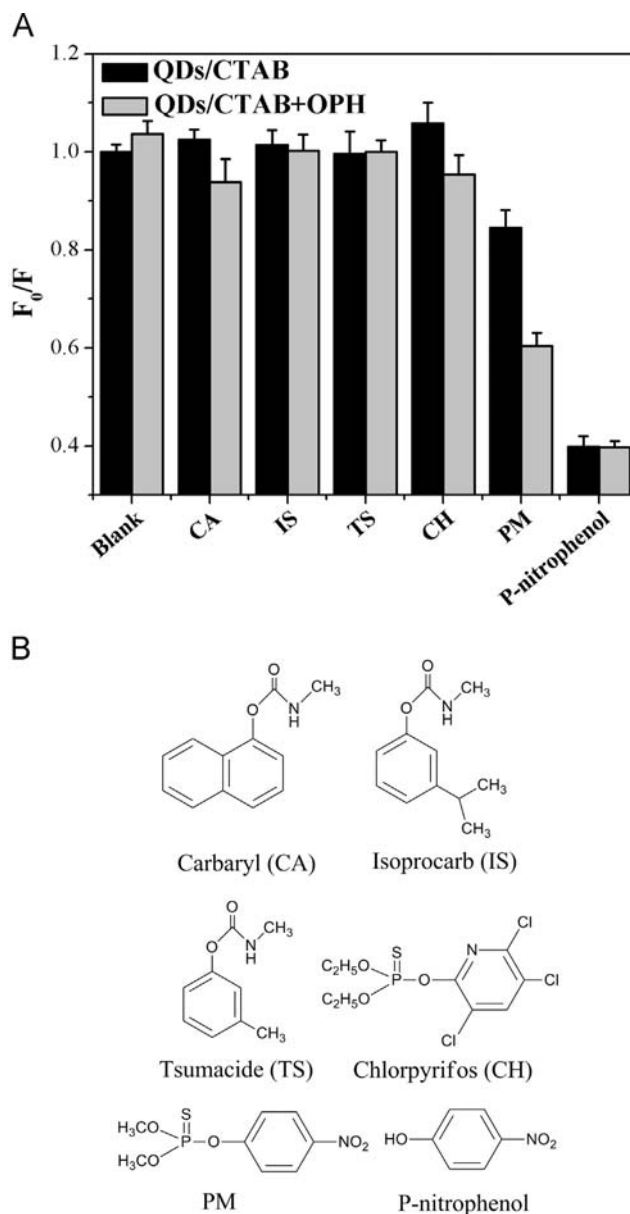


Fig. 2. (A) The effect of pesticides on the PL intensity of CdTe QDs/CTAB and CdTe QDs/CTAB-OPH system. (B) The chemical structure of analytes. PM: parathion-methyl; CA: carbaryl; CH: chlorpyrifos; IS: isoprocarb; TS: tsumacide. The concentration of CdTe QDs, CTAB, pesticides and OPH is $0.44 \mu\text{mol L}^{-1}$, 75 ng mL^{-1} , 2000 ng mL^{-1} and 15 U mL^{-1} , respectively.

concentration of *p*-nitrophenol was increased to 3000 ng mL⁻¹, 26% of the PL intensity of CdTe QDs was quenched, while 72% of the PL intensity of CdTe QDs was quenched in the presence of CTAB. These results demonstrated that CTAB, the binding “bridges”, could absorb *p*-nitrophenol and improve the ET efficiency between *p*-nitrophenol and CdTe QDs. Furthermore, the proposed method was also evaluated by adding different analytes (chlorpyrifos, isoprocarb, tsumacide, carbaryl, PM and *p*-nitrophenol) [17,39] (Fig. 2). As shown in Fig. 2A, when these pesticides were added to CdTe QDs/CTAB and CdTe QDs/CTAB-OPH system, there is little influence on the fluorescence intensity ratio F_0/F (F_0 and F are the PL intensity of QDs/CTAB in the absence and presence of analyte) except for PM and *p*-nitrophenol. The OPH could not obvious affect the fluorescence intensity ratio F_0/F of CdTe QDs/CTAB probe. But when PM was added to the CdTe QDs/CTAB-OPH system, the fluorescence intensity ratio F_0/F was decreased to 60% of the original intensity. And the quenching efficiency of PM on the CdTe QDs/CTAB-OPH system is more remarkable than that on the CdTe QDs/CTAB system. It could be concluded that the presence of OPH could improve the sensitivity and increase the specificity of CdTe QDs/CTAB system for PM detection.

3.4. Optimization for PM detection

The positive charge of CTAB could easily assemble with electro-negative MPA-capped QDs, making the distance between the CdTe QDs and *p*-nitrophenol closer to improve the ET efficiency between *p*-nitrophenol and CdTe QDs. If the CTAB concentration was lower, the binding “bridges” between CdTe QDs and *p*-nitrophenol were not enough, the ET efficiency would be lower. When the concentration of CTAB was higher, the PL intensity of CdTe QDs would decrease due to the formation of precipitate, which would make the CdTe QDs unstable [40,41]. So, the effect of the CTAB concentration was studied first. As shown in Fig. 3, the PL intensity of CdTe QDs with different concentration of CTAB decreased to 49.45, 48.03, 61.67 and 50.97% when 3000 ng mL⁻¹ of PM was added in CdTe QDs/CTAB system. The PL intensity and the ET efficiency reached a maximum when the concentration of CTAB reached 50 ng mL⁻¹. Therefore, 50 ng mL⁻¹ CTAB was chosen for the further experiments.

The effect of pH on the PL intensity of CdTe QDs/CTAB and CdTe QDs/CTAB-PM-OPH system were investigated in the pH range of 6.0–9.0 (Fig. 4). As shown in Fig. 4A, the fluorescence intensity of

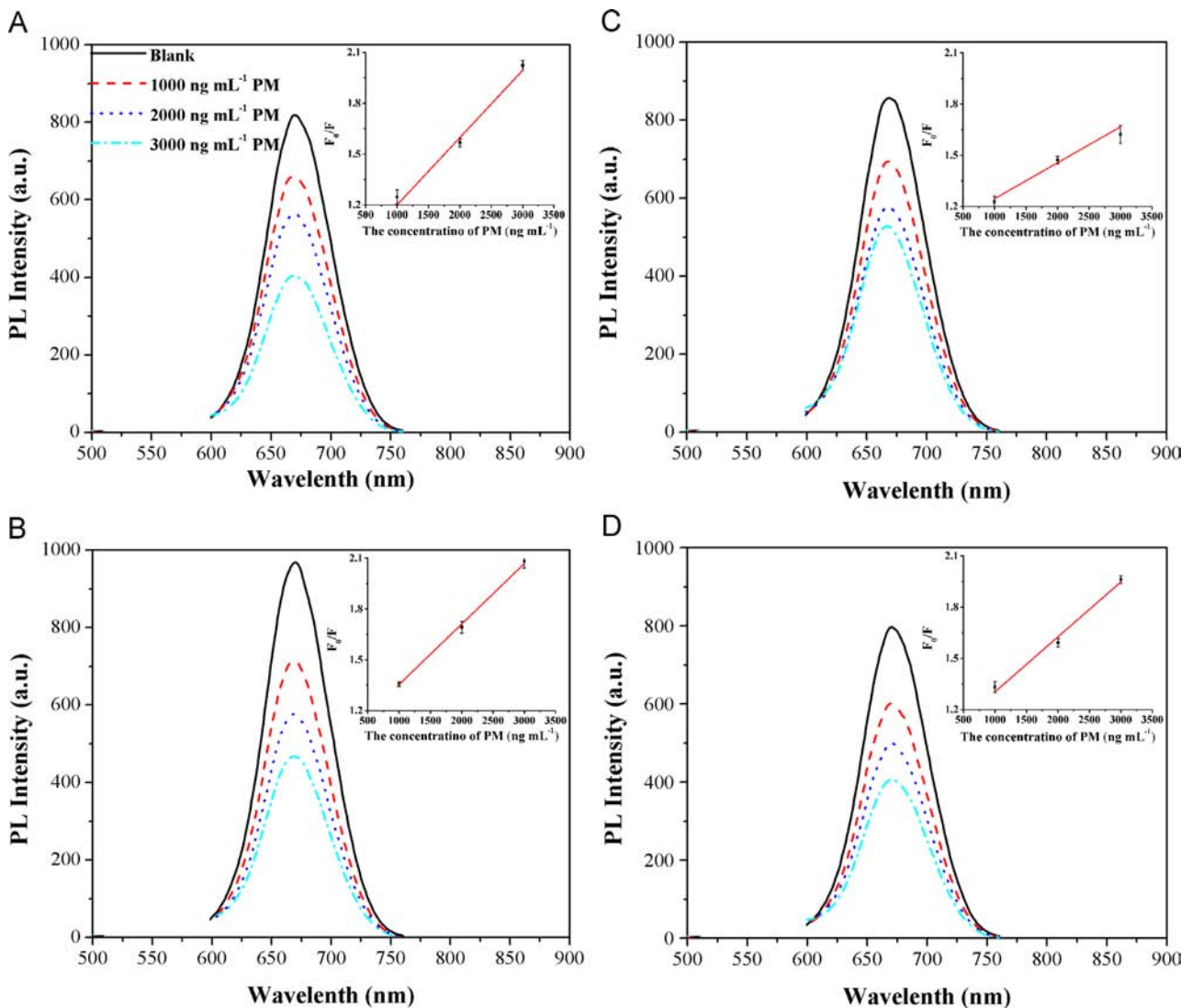


Fig. 3. Effect of CTAB concentration on the PL intensity of CdTe QDs system. CTAB: (A) 37.5; (B) 50; (C) 62.5; (D) 75 ng mL⁻¹. Inset: plot of fluorescence intensity ratios F_0/F versus the concentration of PM. F_0 and F are the PL intensity of CdTe QDs/CTAB system with OPH in the absence and presence of PM. The concentration of CdTe QDs and OPH is 0.44 $\mu\text{mol L}^{-1}$ and 15 U mL⁻¹, respectively.

both systems increased with the increase of the pH. The higher ET efficiency was observed when pH was 8.5. It can be seen from Fig. 4B, the fluorescence intensity ratio F_0/F (F_0 and F are the PL intensity of CdTe QDs/CTAB system in the absence and presence of PM-OPH) increased with the increase of pH value (from 6.0 to 8.5). When the pH value further increased from 8.5 to 9.0, the F_0/F was almost unchangeable. Therefore, pH 8.5 was selected in the further experiments. Then, the effect of OPH concentration (0–50 U mL⁻¹) on the ET process was studied. The result in Fig. 5 shows that the fluorescence intensity ratio F_0/F of QDs/CTAB system was increased obviously by the addition of OPH in the range of 0–10 U mL⁻¹. When the OPH concentration further increased from 10 to 50 U mL⁻¹, there are little influence on the fluorescence intensity ratio F_0/F of QDs/CTAB system. So, 10 U mL⁻¹ of OPH was selected in this study. The effect of ionic strength on the fluorescence intensity ratio F_0/F was studied. As shown in Fig. S2, ionic strength (0–11.25 mg mL⁻¹) has little effect on the fluorescence intensity ratio F_0/F . Thus, the CdTe QDs/CTAB probe has high salt tolerance.

3.5. Detection of PM

The PL spectra of the CdTe QDs–CTAB system upon addition of different concentrations of PM (from 0 to 3000 ng mL⁻¹) were shown in Fig. 6. It can be seen that the PL intensity of CdTe QDs/CTAB system decreased with the increasing concentration of PM, and the fluorescence quenching ratios F_0/F (F_0 and F are the fluorescence intensity of CdTe QDs/CTAB system in the absence and presence of PM) was proportional to the PM concentration in the concentration range of 25–3000 ng mL⁻¹ (inset in Fig. 6).

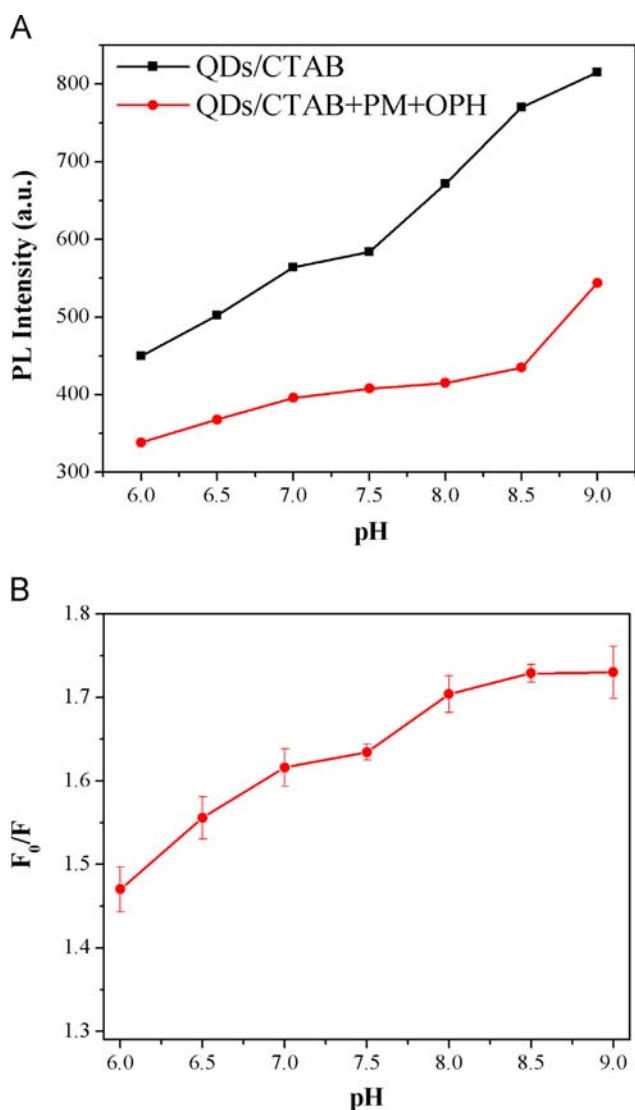


Fig. 4. (A) Effect of pH on the PL intensity of CdTe QDs/CTAB system in the absence and presence of PM-OPH. (B) Effect of pH on the PL intensity ratio F_0/F . F_0 and F are the PL intensity of CdTe QDs/CTAB system in the absence and presence of PM-OPH. The concentration of CdTe QDs, CTAB, PM and OPH is $0.44 \mu\text{mol L}^{-1}$, 50 ng mL^{-1} , 2000 ng mL^{-1} and 15 U mL^{-1} , respectively.

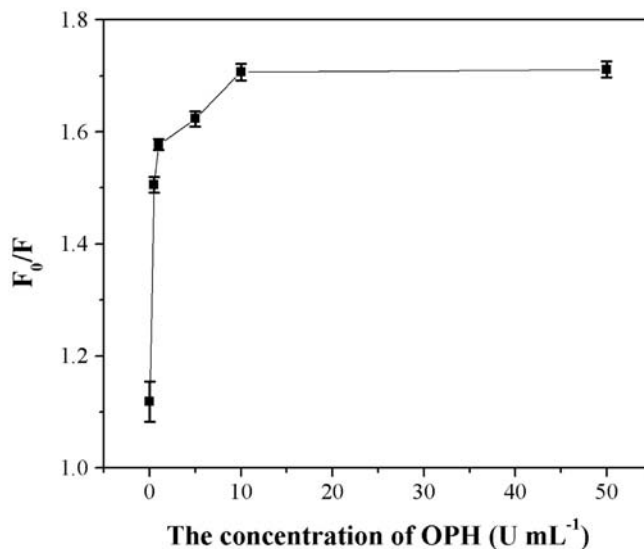


Fig. 5. Effect of OPH concentration on the PL intensity of CdTe QDs/CTAB system. F_0 and F are the PL intensity of CdTe QDs/CTAB system in the absence and presence of PM-OPH. The concentration of CdTe QDs, CTAB, and PM is $0.44 \mu\text{mol L}^{-1}$, 50 ng mL^{-1} , and 2000 ng mL^{-1} , respectively. PBS: 10 mmol L^{-1} buffer solution (pH 8.5) at room temperature.

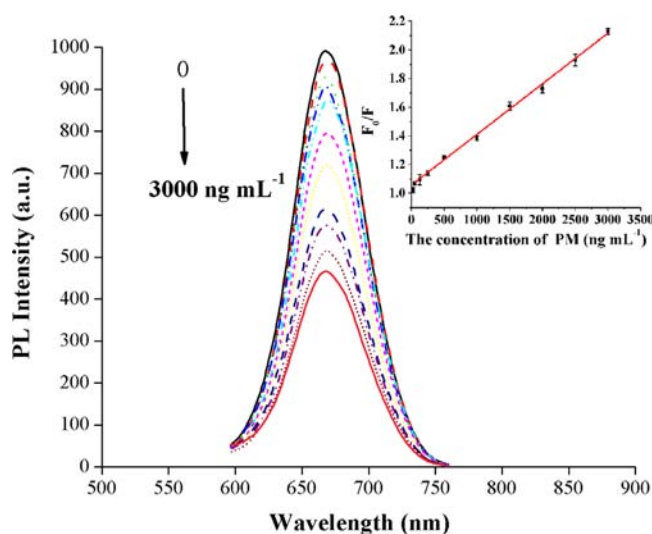


Fig. 6. The fluorescence spectra of CdTe/CTAB system upon the addition of different concentrations of PM in the range from 0 to 3000 ng mL^{-1} . Inset: plot of fluorescence quenching ratios F_0/F versus the concentration of PM. F_0 and F are the PL intensity of CdTe QDs/CTAB system in the absence and presence of PM-OPH. The concentration of CdTe QDs, CTAB and OPH is $0.44 \mu\text{mol L}^{-1}$, 50 ng mL^{-1} and 10 U mL^{-1} , respectively. PBS: 10 mmol L^{-1} buffer solution (pH 8.5) at room temperature.

The regression equation could be described as follow:

$$F_0/F = 3.532 \times 10^{-4} (\pm 6.643 \times 10^{-6}) [\text{PM}] + 1.03725 (\pm 0.0076), (\text{ng mL}^{-1}) \quad (1)$$

The corresponding regression coefficient $R^2=0.993$, and the detection limit ($S/N=3$) for PM was 18 ng mL^{-1} . The maximum residue limit (MRL) of PM is 100 ng mg^{-1} in rice sample set by the Ministry of Agriculture of the People's Republic of China [47]. Therefore, the above results demonstrated that the CdTe QDs/CTAB fluorescence probe could be used for PM detection in rice samples. A comparison between this work and other reported methods for PM detection in detection limit (LOD) and linear range were summed up in Table 1. The sensitivity of this method was obviously better than most of the reported methods.

3.6. Interference study

The selectivity of this novel sensing strategy for PM detection was further evaluated with commonly coexisting substances. Table 2 showed that the tolerable concentration ratios of coexisting substances to 1000 ng mL^{-1} PM was 100-fold for K^+ , citrate, sodium tartaric acid and glucose, 50-fold for Zn^{2+} , Fe^{3+} and NO_2^- , and 40 U mL^{-1} pepsin, trypsin and glucose oxidase. It can be seen that the common metal ions, inorganic ions and enzymes have no obvious interference on PM detection. Furthermore, some common phenol derivatives, including phenol, 4-aminobenzene-sulfonic acid, *p*-chloronitrobenzene, disodium phenyl phosphate, *o*-nitrophenol and resorcinol were investigated. As shown in Fig. S3, compared with the phenol derivatives (3000 ng mL^{-1}), only PM+OPH could obviously quench the fluorescence intensity of CdTe QDs/CTAB probe (F_0 and F are the PL intensity of CdTe QDs/CTAB probe in the absence and presence of analyte, respectively). Therefore, this proposed method has high selectivity and excellent resistance to interference.

3.7. Real samples detection

In order to evaluate the feasibility of the proposed method in real samples detection, the developed method was applied to PM detection in tap water and rice samples. The results obtained by standard addition method were shown in Table 3. The fluorescence method proposed in this paper was compared with the conventional method (UV spectrophotometry). From Table 3, the results obtained by the proposed method were in good agreement with those provided by the conventional method. It can be seen that the recoveries in the real samples was between 97 and 118% and the RSD was lower than 5.1%. The above results demonstrated the potential applicability of the QDs/CTAB probe for PM detection in real samples.

Table 1
Comparison of performance of different PM probing strategy.

Method	Linear range (ng mL^{-1})	LOD (ng mL^{-1})	References
Biosensor using MPH enzyme	0–26,312	1052.8	[27]
Amperometric biosensor based on OPH	1,316–10,528	18.4	[42]
HPLC	27–20,000	100.0	[14]
Optical microbial biosensor	1,053–21,057	78.9	[43]
Electrochemical sensor	5–3000	5.7	[44]
Fe_3O_4 imprinted polymers	15–2500	5.2	[45]
Enzyme-linked immunosorbent assay	44–1380	18.9	[46]
CdTe QDs/CTAB system	25–3000	18.0	This work

Table 2
Effect of coexistence substances on the detection of PM (PM is 1000 ng mL^{-1} , OPH is 10 U mL^{-1}).

Coexisting substance	Tolerable concentration	Molar ratio	$\Delta F/F$ (%)
KCl	$1 \times 10^5 \text{ ng mL}^{-1}$	100	0.19
ZnCl_2	$5 \times 10^4 \text{ ng mL}^{-1}$	50	1.78
FeCl_3	$5 \times 10^4 \text{ ng mL}^{-1}$	50	–2.32
NaNO_2	$5 \times 10^4 \text{ ng mL}^{-1}$	50	8.15
Sodium citrate	$1 \times 10^5 \text{ ng mL}^{-1}$	100	–0.56
Sodium tartaric acid	$1 \times 10^5 \text{ ng mL}^{-1}$	100	5.97
Glucose	$1 \times 10^5 \text{ ng mL}^{-1}$	100	7.38
Pepsin	40 U mL^{-1}		–1.54
Trypsin	40 U mL^{-1}		–5.16
Glucose oxidase	40 U mL^{-1}		–4.27

^a $\Delta F = F_0 - F$, where F_0 and F are the fluorescence intensity of CdTe QDs/CTAB-PM-OPH system in absence and presence of interfering species.

Table 3
Determination of PM in tap water and rice samples.

Sample	Spiked concentration (ng mL^{-1} , ng mg^{-1})	Found PM		Recovery (%)	RSD ($n=3$, %)
		UV	This methods		
Tap water	50	/	48.9	97.80	2.19
	100	94.77	96.48	96.48	2.91
	500	483.29	514.85	102.97	3.40
Rice	50	/	48.34	96.69	5.37
	100	112.34	113.78	113.78	4.35
	500	524.86	585.65	117.13	5.09

4. Conclusion

In summary, this work has developed a highly sensitive CdTe QDs/CTAB fluorescence probe for PM detection through the strong hydrophobic interaction between *p*-nitrophenol (the hydrolysate of PM) and CTAB, and *p*-nitrophenol could quench the PL intensity of QDs due to the ET process. The proposed method is more applicable and convenient without the need of costly antibodies and complicated surface modification. Furthermore, the CdTe QDs/CTAB system has been successfully used for PM detection in environmental and agricultural samples with satisfactory results.

Acknowledgments

This work was financially supported by the National Natural Science Foundation of China (Nos. 20875036, 21075050) and the Science and Technology Development Project of Jilin Province, China (No. 20110334).

Appendix A. Supporting information

Supplementary data associated with this article can be found in the online version at <http://dx.doi.org/10.1016/j.talanta.2014.07.032>.

References

- [1] J.E. Storm, K.R. Karl, J. Doull, *Toxicology* 150 (2000) 1–29.
- [2] B. Piña-Guzmán, M. Sánchez-Gutiérrez, F. Marchetti, I. Hernández-Ochoa, M.J. Solís-Heredia, B. Quintanilla-Vega, *Toxicol. Appl. Pharmacol.* 238 (2009) 141–149.
- [3] B.C. Giordano, G.E. Collins, *Curr. Org. Chem.* 11 (2007) 255–265.
- [4] R.G. Hendrickson, J.R. Hedges, *Crit. Care Clin.* 21 (2005) 641–652.
- [5] S. Young, L. Balluz, J. Malilay, *Sci. Total Environ.* 322 (2004) 3–20.

- [6] R. Arjmandi, M. Tavakol, M. Shayeghi, *Int. J. Environ. Sci. Technol.* 7 (2010) 175–182.
- [7] L.G. Wang, Y.C. Liang, X. Jiang, *Bull. Environ. Contam. Toxicol.* 81 (2008) 377–382.
- [8] X. Yan, X.J. Tang, H.X. Li, E.Z. Sheng, D.D. Yang, M.H. Wang, *Food Anal. Methods* 7 (2013) 1186–1194.
- [9] H. Liang, D. Song, J. Gong, *Biosens. Bioelectron.* 53 (2014) 363–369.
- [10] D.S. Rupa, P.P. Reddy, O.S. Reddi, *Hum. Exp. Toxicol.* 9 (1990) 385–387.
- [11] G. Mathew, K.K. Vijayalaxmi, M.A. Rahiman, *Mutat. Res./Genet. Toxicol.* 280 (1992) 169–173.
- [12] K. Narayana, N. Prashanthi, A. Nayanatara, H.H. Kumar, K. Abhilash, K.L. Bairy, *Mutat. Res./Genet. Toxicol. Environ. Mutagen.* 588 (2005) 28–34.
- [13] B. Piña-Guzmán, M.J. Solís-Heredia, A.E. Rojas-García, M. Urióstegui-Acosta, B. Quintanilla-Vega, *Toxicol. Appl. Pharmacol.* 216 (2006) 216–224.
- [14] G.M. Huang, J. Ouyang, W.R.G. Baeyens, Y.P. Yang, C.J. Tao, *Anal. Chim. Acta* 474 (2002) 21–29.
- [15] C.K. Zacharis, C. Christophoridis, K. Fytianos, *J. Sep. Sci.* 35 (2012) 2422–2429.
- [16] X. Yan, H.Y. Shi, M.H. Wang, *Anal. Methods* 4 (2012) 4053–4057.
- [17] K. Zhang, Q.S. Mei, G.J. Guan, B.H. Liu, S.H. Wang, Z.P. Zhang, *Anal. Chem.* 82 (2010) 9579–9586.
- [18] X. Gao, G.C. Tang, X.G. Su, *Biosens. Bioelectron.* 36 (2012) 75–80.
- [19] V. Bagalkot, L. Zhang, E. Levy-Nissenbaum, S. Jon, P.W. Kantoff, R. Langer, O.C. Farokhzad, *Nano Lett.* 7 (2007) 3065–3070.
- [20] X.H. Gao, Y.Y. Cui, R.M. Levenson, L.W.K. Chung, S.M. Nie, *Nat. Biotechnol.* 22 (2004) 969–976.
- [21] C.Y. Zhang, H.C. Yeh, M.T. Kuroki, T.H. Wang, *Nat. Mater.* 4 (2005) 826–831.
- [22] H. Liang, D.D. Song, J.M. Gong, *Biosens. Bioelectron.* 53 (2014) 363–369.
- [23] Y.Y. Zhao, Y.X. Ma, H. Li, L.Y. Wang, *Anal. Chem.* 84 (2011) 386–395.
- [24] Z.Z. Zheng, X.Y. Li, Z.F. Dai, S.Q. Liu, Z.Y. Tang, *J. Mater. Chem.* 21 (2011) 16955–16962.
- [25] E.I. Rainina, E.N. Efremento, S.D. Varfolomeyev, A.L. Simonian, J.R. Wild, *Biosens. Bioelectron.* 11 (1996) 991–1000.
- [26] X.J. Ji, J.Y. Zheng, J.M. Xu, V.K. Rastogi, T.C. Cheng, *J. Phys. Chem. B* 109 (2005) 3793–3799.
- [27] W.S. Lan, G.P. Chen, F. Cui, F. Tan, R. Liu, M. Yushupujiang, *Sensors* 12 (2012) 8477–8490.
- [28] N. Jaffrezic-Renault, *Sensors* 1 (2001) 60–74.
- [29] B. Prieto-Simón, M. Campàs, S. Andreeescu, J.L. Marty, *Sensors* 6 (2006) 1161–1186.
- [30] A. Khenifi, B. Zohra, B. Kahina, H. Houari, D. Zoubir, *Chem. Eng. J.* 146 (2009) 345–354.
- [31] J.J. Li, X. Li, R. Yang, L.B. Qu, P.D.B.C. Harrington, *Anal. Chim. Acta* 804 (2013) 76–83.
- [32] J.J. Pan, B.H. Guan, *J. Hazard. Mater.* 183 (2010) 341–346.
- [33] C. Wang, Q. Ma, X.G. Su, J. Nanosci. *Nanotechnol.* 8 (2008) 4408–4414.
- [34] W. William Yu, L.H. Qu, W.Z. Guo, X.G. Peng, *Chem. Mater.* 15 (2003) 2854–2860.
- [35] X.D. Hua, L.M. Wang, G. Li, Q.K. Fang, M.H. Wang, F.Q. Liu, *Anal. Methods* 5 (2013) 1556–1563.
- [36] H.B. Li, C.P. Han, *Chem. Mater.* 20 (2008) 6053–6059.
- [37] R. Freeman, T. Finder, L. Bahshi, I. Willner, *Nano Lett.* 9 (2009) 2073–2076.
- [38] L. Jia, J.P. Xu, D. Li, S.P. Pang, Y. Fang, Z.G. Song, J. Ji, *Chem. Commun.* 46 (2010) 7166–7168.
- [39] J.W. Sun, T.T. Dong, Y. Zhang, S. Wang, *Anal. Chim. Acta* 666 (2010) 76–82.
- [40] Y.L. Wang, J.P. Lu, Z.F. Tong, L. Chen, *Acta Chim. Sin.* 67 (2009) 2222–2226.
- [41] G.C. Tang, L.P. Du, X.G. Su, *Food Chem.* 141 (2013) 4060–4065.
- [42] A. Mulchandani, P. Mulchandani, W. Chen, *Anal. Chem.* 71 (1999) 2246–2249.
- [43] J. Kumar, S.K. Jha, S.F. D'Souza, *Biosens. Bioelectron.* 21 (2006) 2100–2105.
- [44] H. Parham, N. Rahbar, *J. Hazard. Mater.* 177 (2010) 1077–1084.
- [45] S.Y. Xu, C.J. Guo, Y.X. Li, Z.R. Yua, C.H. Wei, Y.W. Tang, *J. Hazard. Mater.* 264 (2014) 34–41.
- [46] Z.L. Xu, H. Deng, X.F. Deng, J.Y. Yang, Y.M. Jiang, D.P. Zeng, F. Huang, Y.D. Shen, H.T. Lei, H. Wang, Y.M. Sun, *Food Chem.* 131 (2012) 1569–1576.
- [47] <http://www.chinapesticide.gov.cn/mprlsv/mprls.html>.



Determination of L-canavanine and other free amino acids in *Vicia disperma* (Fabaceae) seeds by precolumn derivatization using diethyl ethoxymethylenemalonate and reversed-phase high-performance liquid chromatography



Cristina Megías, Isabel Cortés-Giraldo, Julio Girón-Calle, Javier Vioque, Manuel Alaiz*

Instituto de la Grasa (C.S.I.C.), Avda. Padre García Tejero 4, 41012 Sevilla, Spain

ARTICLE INFO

Article history:

Received 25 April 2014

Received in revised form

23 July 2014

Accepted 26 July 2014

Available online 2 August 2014

Keywords:

HPLC

Vicia disperma

L- α -amino- γ -(guanidinoxy)-*n*-butyric acid

L-canavanine

Free amino acids

Diethyl ethoxymethylenemalonate

ABSTRACT

A method for determination of the non-protein amino acid L- α -amino- γ -(guanidinoxy)-*n*-butyric acid (L-canavanine) and other free amino acids in *Vicia disperma* is presented. Seed extracts were derivatized by reaction with diethyl ethoxymethylenemalonate and analyzed by reverse-phase high-performance liquid chromatography. Calibration curves showed very good linearity of the response. The limit of detection and quantification were 0.15 and 0.50 μ M, respectively. The method has a high intra- (RSD=0.35%) and inter-repeatability (RSD=2.86%), and a remarkable accuracy with a 99% recovery in spiked samples. The method is very easy to carry out and allows for ready analysis of large number of samples using very basic HPLC equipment because the derivatized samples are very stable and have very good chromatographic properties.

© 2014 Elsevier B.V. All rights reserved.

1. Introduction

Plants produce and accumulate a great number of secondary metabolites to avoid being eaten by herbivores, including glucosinolates, alkaloids, polyphenols, terpenoids, and free amino acids. Many plants belonging to the *Fabaceae*, including some crops, accumulate high amounts of free amino acids in their seeds [1]. L-canavanine (L- α -amino- γ -(guanidinoxy)-*n*-butyric acid) is a non-protein amino acid very rich in nitrogen and it appears that it accumulates in the seeds not only as a defensive measure against herbivores, but also as a form of nitrogen storage for embryo growth [2]. A taxonomic survey has led to the discovery of 1500 species and 246 genera of legumes containing L-canavanine as a free amino acid, including *Canavalia*, *Dioclea*, *Colutea*, *Robinia*, and *Vicia* [1,3,4]. Some of these legumes store very high amounts of L-canavanine [5], e.g. 13% of the seed dry weight representing more than 95% of the nitrogen in free amino acids [6].

Vicia disperma (*Fabaceae*) belongs to section *Cracca* subgenus *Cracca*, which includes most of the *Vicia* species rich in L-canavanine [1]. It is an annual climbing herb with stems up to 100 cm long and very abundant fruits that most frequently contain two seeds, which is the reason of its common name, two-seeded vetch. *V. disperma* is a drought-resistant plant very abundant in siliceous soils in the Mediterranean Region, especially in the Iberian Peninsula, Italy, south of France, and north of Africa. In spite of its abundance in the Mediterranean region, there are no reports on the use of the seeds for human consumption or for feeding animals. Nevertheless, these seeds have good nutritional properties concerning protein [7] and fatty acid composition [8], and are rich in polyphenols with high antioxidant activity [9].

L-canavanine is an arginine analog and antagonist that has been shown to be toxic to herbivores by replacing arginine in protein synthesis, leading to the production of aberrant proteins [3]. Animal experiments have shown a number of deleterious effects following consumption of legumes containing L-canavanine, e.g. decreased feed intake and growth, a significant reduction in plasma concentration of basic amino acids [10,11], and a reduction in plasma arginine, lysine, and histidine. Nevertheless, health-promoting and even therapeutics properties have been reported for canavanine, especially in relation with the inhibition of the growth of tumors and with cardiovascular health [12,13].

Abbreviations: HPLC, high-performance liquid chromatography; DEEMM, diethyl ethoxymethylenemalonate; I.S., internal standard; LOD, limit of detection; LOQ, limit of quantification; RSD, relative standard deviation

* Corresponding author. Tel.: +34 954 61 15 50; fax: +34 954 61 67 90.

E-mail address: alaiz@ig.csic.es (M. Alaiz).

<http://dx.doi.org/10.1016/j.talanta.2014.07.077>

0039-9140/© 2014 Elsevier B.V. All rights reserved.

Colorimetric [14], spectrophotometric [15] and high-performance liquid chromatography (HPLC) methods have been used for the analysis of L-canavanine [16–18]. Chromatographic separation in the HPLC methods that have been described so far provides a much higher selectivity, but these methods in general are time consuming and are also hampered by the limited stability of reagents or derivatized amino acid. The goal of this research was to determine whether HPLC chromatography of the ethoxymethylenemalonate (DEEMM) derivatives of free amino acids can be used for determination of L-canavanine as well as other free amino acids in the seeds of *V. disperma*. DEEMM is a universal reagent for amino groups and has been used in amino sugar [19] and amino acid [20] chemistry, as well as for amino acid analysis [21,22].

2. Materials and methods

2.1. Plant material

Seeds were collected from two *V. disperma* populations at the Sierra de Aracena y Picos de Aroche Natural Park, in Huelva province (Spain). Seeds were collected at full maturity and were allowed to dry at room temperature before storage at -20°C in falcon tubes. The GPS data for the two locations were: sample 1: N: 37.930591, W: 6.720131, and sample 2: N 37.887668, W 6.617276. Seeds (30 g) were ground using a MM 301 mill (Retsch, Haan, Germany).

2.2. Reagents

DEEMM, L-canavanine sulfate salt, DL-2-aminobutyric acid (internal standard, I.S.), amino acid standards, water (HPLC grade), and acetonitrile (HPLC grade) were purchased from Sigma-Aldrich (St. Louis, MO, USA).

2.3. Chromatographic system

The HPLC system (Beckman-Coulter) consisted of a 126 solvent module, 166 detector, and IBM personal computer. Data acquisition and processing were carried out using 32 Karat 7.0 version software (Beckman-Coulter). Samples (20 μL) were injected in a reversed-phase column (Novapack C18, 300×3.9 mm i.d., 4 μm , Waters).

Mobile phase A consisted of 25 mM glacial acetic acid and 0.02% sodium azide in water (w/v) adjusted to pH 6.0. Mobile phase B was acetonitrile. Mobile phases were filtered through a 0.45 μm membrane filter. For binary gradient elution, the program is shown in Table 1. The column was maintained at 18°C and operated at a flow-rate of 0.9 mL/min.

Table 1
Elution gradient for the HPLC analysis of L-canavanine and other amino acids.

Time (min)	Eluent A ^a	Eluent B ^b
0	96	4
3	88	12
13	88	12
30	69	31
35	69	31
40	96	4

^a 25 mM glacial acetic acid, 0.02% (w/v) sodium azide pH 6.0.

^b Acetonitrile.

2.4. Preparation of sample

Samples (2.0 mg in 1.5 ml eppendorf tubes) were stirred in ethanol:water (3:7 v/v, 1 ml) for 30 min at room temperature using a vortex mixer at full speed equipped with a tube holder (Labnet Biotecnica S.L., Madrid, Spain), and centrifuged at 8850g for 10 min using an Eppendorf 5415R microcentrifuge (Hauppauge, NY, USA). Pellets were reextracted twice more, and the resulting supernatants were pooled and dried under nitrogen.

2.5. Precolumn derivatization

Internal standard (24 μL , 0.424 g/L) and DEEMM (2 μL) were added to a solution of samples in 1 M borate buffer pH 9.0 (3 ml). The solution was thoroughly mixed and incubated at 50°C for 50 min. Samples were filtered through 0.22 μm membranes before injection into the HPLC system (20 μL).

2.6. Evaluation of the method

Evaluation was carried out by determination of linearity, limit of detection (LOD), limit of quantification (LOQ), repeatability, and accuracy (recovery) [23]. Calibration curves were drawn by plotting the peak area ratio of analyte/internal standard against reference analyte concentrations (determined in triplicate). LOD is the lowest concentration of analyte that is detectable by an analytical method and LOQ is the lowest solute concentration that can be determined with acceptable precision and accuracy. LOD and LOQ were calculated by injecting diluted standard solutions to determine the concentrations corresponding to a signal/noise ratio (S/N) of 3 and 10, respectively. The repeatability of the method was determined by the same analyst from the relative standard deviation (RSD) of the peak area based on 8 runs of a solution of the standard over 1 day (intra-day repeatability), and from the RSD of the peak area based on 8 runs of a solution of the standard on independent days (inter-day repeatability). Accuracy was tested by the standard procedure of adding three increasing concentrations of L-canavanine stock solution (10, 20 and 40 μM) to a seed sample. Non-spiked sample replicates (blanks) were used to determine the initial L-canavanine contents of the seed. The percentage recovery at each concentration was calculated as $[(\text{amount found in the spiked sample}) - (\text{amount found in the blank})] / (\text{amount added}) \times 100$.

2.7. Statistical analysis

The RSD was calculated according to the formula $\text{RSD} = s / \mu \times 100$, where s is the standard deviation and μ is the average value. It was expressed as a percentage. The Microsoft Office Excel 2003 data analysis package was used for statistical analysis.

3. Results and discussion

Determination of L-canavanine in plant seeds is of interest because although this amino acid was at first better known because of its antinutritional properties, it is currently recognized as a potential health-promoting and therapeutic agent. Some negative effects in humans caused by prolonged consumption of alfalfa seeds have been attributed to the presence of L-canavanine in the seeds [24]. Nevertheless, the antagonistic activity only occurs at low arginine concentrations [25]. L-canavanine has health-promoting and therapeutic properties that could justify its use in foods and pharmaceuticals. Most importantly, it has shown anti-cancer properties in cell cultures and experiments

with animals [13,26,27], and may also have applications as a modulator of nitric oxide synthesis [12,28,29].

Precolumn derivatization of L-canavanine and standard amino acids by reaction with DEEMM resulted in stable derivatives with a very good chromatographic behavior in reversed-phase HPLC. These derivatives were readily detected at 280 nm with no interference from the reagent and with low detection limits. Twenty-four amino acids were separated and identified in the *V. disperma* extracts by comparison with authentic standards in less than 35 min (Fig. 1A). The DEEMM derivative of L-canavanine eluted at 12.1 min, and the peak did not overlap with any other amino acid. L-canavanine was the major free amino acid in the seeds (Fig. 1B).

Analysis of 0.50–200 μM L-canavanine showed linear response ($r=0.9993$), low LOD (0.15 μM), and low LOQ (0.50 μM). Peak area for the L-canavanine DEEMM derivative was essentially unchanged for at least one week at room temperature as indicated by a very low inter-day repeatability (RSD=2.86%), indicating that the derivative is stable enough to allow for storage for several days at room temperature before analysis. The intra-day repeatability was excellent, as indicated by an RSD of 0.35%. The accuracy of the method was also supported by a 99% recovery (RSD=1.00–1.80%) of L-canavanine from seed extracts to which 10, 20 or 40 μM L-canavanine were added.

This method was applied to the determination of L-canavanine in the seeds of two populations of *V. disperma* (Table 2). The L-canavanine content was 2.792% (sample 1) and 2.079% (sample 2), which represents more than 90% of the nitrogen in free amino acids. The analysis also showed much lower amounts of aspartic acid, glutamic acid, asparagine, histidine, treonine, and arginine in both samples.

As compared to other methods reported for determination of L-canavanine, the major advantages of this method are its simplicity and the stability of reagents and derivatized amino acids, which allows for accurate, easy determination of L-canavanine in a large number of samples using unsophisticated equipment such as a basic HPLC system with an UV detector. Other HPLC methods,

Table 2

Contents (g/100 g seed dry weight) of L-canavanine and other free amino acids in *V. disperma* seeds. Data are the mean \pm standard deviation of three determinations.

Amino acid/sample	1	2
L-canavanine	2.792 \pm 0.031	2.059 \pm 0.063
Asp	0.036 \pm 0.001	0.105 \pm 0.006
Glu	0.111 \pm 0.004	0.059 \pm 0.005
Asn	0.043 \pm 0.002	0.027 \pm 0.001
Ser	0.003 \pm 0.000	0.006 \pm 0.001
Gln	0.000 \pm 0.000	0.000 \pm 0.000
His	0.098 \pm 0.003	0.059 \pm 0.004
Gly	0.009 \pm 0.001	0.012 \pm 0.001
Thr	0.142 \pm 0.003	0.126 \pm 0.012
Arg	0.109 \pm 0.006	0.022 \pm 0.001
Ala	0.014 \pm 0.001	0.015 \pm 0.001
Pro	0.000 \pm 0.000	0.000 \pm 0.000
Try	0.004 \pm 0.001	0.008 \pm 0.001
Val	0.006 \pm 0.001	0.007 \pm 0.001
Met	0.021 \pm 0.002	0.000 \pm 0.000
Cys–Cys	0.000 \pm 0.000	0.000 \pm 0.000
Ile	0.006 \pm 0.000	0.005 \pm 0.000
Trp	0.000 \pm 0.000	0.000 \pm 0.000
Leu	0.011 \pm 0.000	0.015 \pm 0.001
Phe	0.007 \pm 0.001	0.005 \pm 0.000
Cys	0.000 \pm 0.000	0.000 \pm 0.000
Lys	0.009 \pm 0.000	0.009 \pm 0.000

which are in general superior to earlier spectrophotometric methods [14,15], require more sophisticated equipment and are more time consuming. Pre-column derivatization using dansyl chloride and fluorescence detection has been applied for the HPLC analysis of L-canavanine in plant tissues [16], but elution time was too long and injection of one sample takes 110 min. A linear response in the range 15–500 μM , LOQ of 15 μM and LOD of 5 μM was described, with no R^2 provided [16]. Instability of the dansyl derivatives caused a rapid decline in fluorescence [17]. Dansyl chloride has also been used as a pre-column derivatization reagent for HPLC determination of L-canavanine with detection in the visible wavelength region [18]. In this case, time for analysis was similar to ours, but the canavanine standard was shown as two peaks that eluted at 16 and 26 min. The standard curve was based on the peak eluting at 26 min due to the better resolution of this peak. A linear relationship ($R^2=0.9941$) between peak area and canavanine concentration was observed over a range of 50–50,000 μM , and LOQ of 50 μM and LOD of 5–10 μM were described [18].

4. Conclusions

Reverse phase HPLC of DEEMM derivatives allows for determination of L-canavanine and other free amino acids in the seeds of *V. disperma*. As compared to other methods, this procedure has a number of advantages that taken together prove the value of this new approach. Thus, this method is easy to carry out in any standard HPLC device, does not use any toxic reagent, and can be used to easily process a high number of samples because the derivatized amino acids are stable even at room temperature. The analysis is based on the very good chromatographic and absorption characteristics of the DEEMM derivatives, which allow for very good resolution of the peaks, as well as very good sensitivity and repeatability.

Acknowledgments

This work was carried out with the financial support of the Junta de Andalucía (Spain) to the Laboratory of Bioactive and

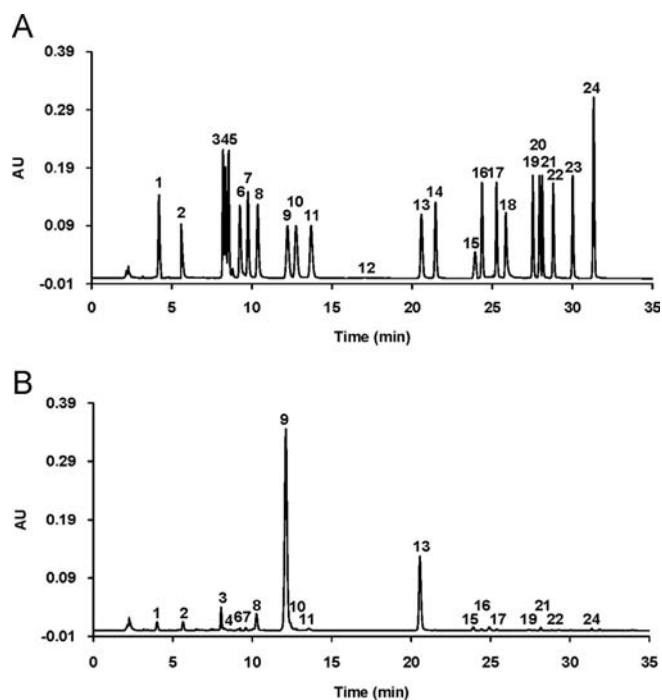


Fig. 1. HPLC analysis of the DEEMM derivatives of amino acid standards (A) and seed extracts (B). 1 = Asp; 2 = Glu; 3 = Asn; 4 = Ser; 5 = Gln; 6 = His; 7 = Gly; 8 = Thr; 9 = L-canavanine; 10 = Arg; 11 = Ala; 12 = Pro; 13 = I.S.; 14 = Tyr; 15 = ammonium ion; 16 = Val; 17 = Met; 18 = Cys–Cys; 19 = Ile; 20 = Trp; 21 = Leu; 22 = Phe; 23 = Cys; and 24 = Lys.

Functional Components of Plant Products (Instituto de la Grasa, C.S.I.C.). Cristina Megías and Isabel Cortés-Giraldo are respectively recipients of a JAE-Doc (C.S.I.C.) contract and a JAE-Pre (C.S.I.C.) fellowship from the “Junta para la Ampliación de Estudios” program (cofinanced by the European Social Fund). Thanks are due to María Dolores García Contreras for technical assistance.

References

- [1] E.A. Bell, A.S.L. Tirimanna, *Biochem. J.* 97 (1965) 104–111.
- [2] G.A. Rosenthal, *Plant Physiol.* 46 (1970) 273–276.
- [3] G.A. Rosenthal, *Amino Acids* 21 (2001) 319–330.
- [4] J.B. Harbone, *Phytochemistry* 6 (1967) 863–866.
- [5] G.A. Rosenthal, P. Nkomo, *Pharm. Biol.* 38 (2000) 1–6.
- [6] G.A. Rosenthal, *Biochem. Syst. Ecol.* 5 (1977) 19–20.
- [7] E. Pastor-Cavada, R. Juan, J.E. Pastor, M. Alaiz, J. Vioque, *J. Food Sci.* 76 (2011) C1118–C1124.
- [8] E. Pastor-Cavada, R. Juan, J.E. Pastor, M. Alaiz, J. Vioque, *J. Am. Oil Chem. Soc.* 86 (2009) 977–983.
- [9] E. Pastor-Cavada, R. Juan, J.E. Pastor, M. Alaiz, J. Girón-Calle, J. Vioque, *J. Food Biochem.* 35 (2011) 1373–1380.
- [10] G. Herzberg, H. Sheerin, J. Lerner, *Comp. Biochem. Physiol.* 40A (1971) 229–247.
- [11] D.A. Thomas, G.A. Rosenthal, *Toxicol. Appl. Pharmacol.* 91 (1987) 406–414.
- [12] A. Hrabak, T. Bajor, A. Temesi, *Biochem. Res. Commun.* 198 (1994) 206–212.
- [13] D.A. Thomas, G.A. Rosenthal, D.V. Gold, K. Dickey, *Cancer Res.* 46 (1986) 2898–2903.
- [14] G.A. Rosenthal, *Anal. Biochem.* 77 (1977) 147–151.
- [15] J. Cacho, G. Angeles, F. Ignacio, *Analyst* 114 (1989) 965–968.
- [16] C. Oropeza, L. Alpizar, M. Victo, L. Vargas, J. Quiroz, K.N. Scorer, *J. Chromatogr.* 456 (1988) 405–409.
- [17] V. Bianchi, L. Mazza, *J. Chromatogr.* 665 (1995) 295–302.
- [18] S. Ekanayake, K. Skog, N.-G. Asp, *Food Chem. Toxicol.* 45 (2007) 797–803.
- [19] A. Gómez-Sánchez, P. Borrachero, J. Bellanato, *Carbohydr. Res.* 135 (1984) 101–116.
- [20] M. Alaiz, J. Girón, F.J. Hidalgo, M.P. Maza, F. Millán, R. Zamora, J. Vioque, *Synthesis-Stuttgart* 7 (1989) 544–547.
- [21] M. Alaiz, J.L. Navarro, J. Girón, J. Vioque, *J. Chromatogr. A* 59 (1992) 181–186.
- [22] R. Begoña, V. Ladero, I. Cuesta, J.R. Álvarez-Buylla, M.C. Martín, M. Fernández, M.A. Álvarez, *Food Chem.* 139 (2013) 1029–1035.
- [23] I. Taverniers, M. De Loose, E.V. Bockstaele, *TrAC-Trends Anal. Chem.* 23 (2004) 535–552.
- [24] A. Montanaro, E.J. Bardana, *Rheum. Dis. Clin. N. Am.* 17 (1991) 323–332.
- [25] D.S. Swaffar, C.Y. Ang, P.B. Desai, G.A. Rosenthal, *Cancer Res.* 54 (1994) 6045–6048.
- [26] B.O. Vynnytska, O.M. Mayevska, Y.V. Kurlishchuk, Y.P. Bobak, O.V. Stasyk, *Anti-Cancer Drugs* 22 (2011) 148–157.
- [27] B. Vynnytska-Myronovska, Y. Bobak, Y. Garbe, C. Dittfeld, O. Stasyk, L.A. Kunz-Schughart, *Int. J. Cancer* 130 (2012) 2164–2175.
- [28] X. Li, R.N. Atkinson, S.B. King, *Tetrahedron* 57 (2001) 6557–6565.
- [29] D.M. Teale, A.M. Atkinson, *Eur. J. Pharmacol.* 271 (1994) 87–92.



Preparation and application of sulfaguanidine-imprinted polymer on solid-phase extraction of pharmaceuticals from water



Dragana Mutavdžić Pavlović^{a,*}, Korana Nikšić^a, Sara Livazović^a, Ivan Brnardić^b, Alojz Anžlovar^c

^a Department of Analytical Chemistry, Faculty of Chemical Engineering and Technology, University of Zagreb, Marulićev trg 19, 10000 Zagreb, Croatia

^b Faculty of Metallurgy, University of Zagreb, Aleja narodnih heroja 3, 44103 Sisak, Croatia

^c National Institute of Chemistry, Hajdrihova 19, SI-1000 Ljubljana, Slovenia

ARTICLE INFO

Article history:

Received 15 January 2014

Received in revised form

24 June 2014

Accepted 27 June 2014

Available online 1 August 2014

Keywords:

Sulfaguanidine

Molecularly imprinted polymers

Pharmaceuticals

Production wastewater

ABSTRACT

The molecularly imprinted polymers (MIPs) with sulfaguanidine as a template, methacrylic acid, 4-vinylpyridine, and 2-hydroxyethyl methacrylate as functional monomers, ethylene glycol dimethacrylate as a cross-linker and 2,2'-azobis-isobutyronitrile as an initiator have been prepared through the cross-link reaction of polymerization. Solid-phase extraction (SPE) procedure for the extraction of sulfaguanidine from water samples using the prepared MIPs and non-imprinted (NIPs) was evaluated. The best MIP in combination with commercial sorbents was applied for simultaneous extraction of eight pharmaceuticals. New SPE cartridges were prepared by combination of optimal produced MIP and Oasis HLB in 6 mL of polypropylene SPE reservoir.

The developed method which includes new SPE cartridge (MIP_{MAA}-Oasis HLB, 400 mg/6 mL) and thin-layer chromatography was validated. The method provides a linear response over the concentration range of 0.5–150 µg/L, depending on the pharmaceutical with the correlation coefficients > 0.9843 in all cases except for norfloxacin (0.9770) and penicillin G procaine (0.9801). Also, the method has revealed low limits of detection (0.25–20 µg/L), good precision (intra and inter-day), a relative standard deviation below 15% and recoveries above 95% for all eight pharmaceuticals. The developed method by using newly prepared SPE cartridge has been successfully applied to the analysis of production wastewater samples from pharmaceutical industry.

© 2014 Elsevier B.V. All rights reserved.

1. Introduction

In recent years, there has been growing concern about the occurrence of pharmaceuticals in the aquatic system [1,2]. As analytical techniques become more sensitive and more widely deployed, an increasing number of drugs are being detected. Several investigations have gathered evidence that substances of pharmaceutical origin are often not eliminated during the wastewater treatment and also not biodegraded in the environment [3]. Their incomplete removal by the wastewater treatment plants (WWTPs) is referred to as the major source of their release into the environment [4–6].

Consequently, a very sensitive research method is required for the study of the presence of pharmaceutical residues in the environmental samples, particularly wastewater. Simultaneous

analysis of several groups of compounds with quite different physico-chemical characteristics generally requires a compromise in the selection of experimental conditions, which in some cases, means failing to obtain the best performance for each compound. However, developing a multi-group method is rewarding as it can be applied in routine analysis, providing a large amount of data [7]. Several chromatographic methods have been developed for the pharmaceutical analysis in the environmental samples [7–13].

Solid-phase extraction (SPE) is routinely used in many laboratories for preconcentration and/or clean-up steps in the analysis of complex samples due to the advantages of simplicity, rapidness and little consumption of organic solvents. Despite to the popularity of SPE, new solid sorbents have appeared as an alternative to the conventional sorbents with the aim of achieving a more selective preconcentration of target analytes. Thus, immunosorbents and molecularly imprinted polymers (MIPs) appear as excellent candidates to accomplish this requirement [14].

* Corresponding author. Tel.: +385 1 4597204; fax: +385 1 4597250.

E-mail address: dmutavdz@fkit.hr (D. Mutavdžić Pavlović).

Molecularly imprinted polymers (MIPs) are an artificially produced macromolecular material, which has prearrangement of structure and specific molecular recognition ability [15] as a result of MIPs synthesis in the presence of target molecules named templates. After the template is removed from the resulting polymer matrix, binding sites having the size and shape complimentary to the template are generated [16].

Except template the components involved in the production of a MIP are functional monomer, cross-linking agent and initiator of radical polymerization. To obtain the highest affinity of the MIP towards the target analyte, careful selection of the monomer composition used in the production of the MIP is crucial. Choosing the right functional monomer is very important because this will determine, on one hand, the stability of the complex formed before and during the polymerization process and, on the other hand, the subsequent ability of the MIP to interact selectively with the target molecule [17]. In the last few years MIPs have been increasingly exploited as selective sorbents in molecularly imprinted solid-phase extraction (MISPE). To date, the main application of MIPs has been the extraction of analytes from biological samples [18–23] and environmental samples [1,2,16,24–31]. Biofluids such as plasma, serum and urine have been the most analysed biomatrices [18–21,23] with only few studies performed to the extraction of compounds from tissue samples [22]. Water is also a “leader” in environmental samples [1,2,16,24,25,27–31] unlike the soil [25,26] and sediments which also present unexplored area of MIPs application [32]. For example, in papers differently prepared MIPs for different purpose and for different type of analytes; sulfonamides (SAs) and methacrylic acid (MAA) for quantification of SAs in aquaculture product [33], organophosphorus pesticides (OPPs) and MAA for use in MIP-SPE sample enrichment of selected OPPs in fruit sample [34], acidic pharmaceutical and EDGMA for the selective extraction of a group of structurally related compounds such as acidic pharmaceuticals [35], methandrostenolone (MA) and chitosan for extraction of MA [36], and emodin with MAA and multiwall carbon nanotubes for purification and enrichment of emodin from kiwi fruit root [37] could be found. The reason for such a big growth of the interest in preparation of different MIPs is in the fact that they can be synthesized easily with high yields and low cost.

Sulfonamides are among the most widely used antimicrobials in human and veterinary medicine, and several SPE methods have been developed for their extraction from water and clean-up from biological matter [38–42]. Although sulfonamides are often analysed a group of antibiotics in the environment, most reported MIPs of SAs were prepared using sulfamethazine [14,43] or sulfamethoxazole [1,43,44] as the template molecule. Sulfaguanidine (SGUA) belongs to a sulfonamide group of antibiotic which are widely used in medicine, animal husbandry and veterinary practice. But many authors [39,40] when developing methods for sulfonamides do not include sulfaguanidine in it. Other authors [13,42], during the optimization procedure dropped sulfaguanidine from further study due to recoveries less than 10%. Reason for that probably lies in its physico-chemical properties. Namely, the structures in sulfaguanidine contain a strong basic group (pK_a 12.1) and are positively charged at most conditions, which make SPE extraction difficult by HLB cartridges [13].

In this paper, sulfaguanidine was used as template molecule based on previously published literatures [13,41,42,45] where it is evident that sulfaguanidine makes a problem during extraction procedure from water. According to our knowledge, preparation of MIP with SGUA template has not been published yet. Sulfaguanidine-imprinted polymers were synthesized using three different kinds of functional monomers (methacrylic acid (MAA),

4-vinylpyridine (4-VPy), 2-hydroxyethyl methacrylate (HEMA)) in a polar organic solvent acetonitrile. The recognition abilities of the synthesized polymers were studied. The goal of this work was not only to develop and apply the prepared MIPs to selective analysis of SGUA and its analogues from water sample but to apply the best MIP in the combination with the commercial sorbents for simultaneous analysis of different pharmaceutical classes from the water samples. According to that, new SPE cartridges were prepared in order to achieve the best extraction recovery for eight investigated pharmaceuticals, not only for SGUA. Investigated pharmaceuticals belong to the antibiotic group.

Extraction efficiency experiments were checked by thin-layer chromatography (TLC).

After the optimal combination of sorbents was selected, the performance of the MISPE-TLC method was validated and the method was successfully applied to the determination of pharmaceutical presence in the production wastewater samples from pharmaceutical industry.

2. Experimental

2.1. Pharmaceuticals, standards and reagents

The studied pharmaceuticals are as follows: trimethoprim (TMP), oxytetracycline (OTC), enrofloxacin (ENRO), norfloxacin (NOR), sulfaguanidine (SGUA), sulfamethazine (SMETH), sulfadiazine (SDIAZ) and penicillin G/procaine (PGP). All pharmaceutical standards were of analytical grade (> 99%) and obtained from Veterina Animal Health Ltd. (Kalinovica, Croatia). The chemical structures of the pharmaceuticals included in this study are shown in Fig. 1.

A stock standard solution of the eight pharmaceutical compounds was prepared by dissolving accurately weighed amounts of powdered standards in methanol. The mass concentrations of pharmaceutical compounds in the mixture were 5 mg/L for NOR, 10 mg/L for ENRO, and 100 mg/L for SMETH, SDIAZ, TMP, OTC, PGP, and SGUA. The standard working solution (2.5 mg/L for NOR, 5 mg/L for ENRO, and 50 mg/L for the others) was obtained by dilution of the stock standard solution with methanol.

Standard solutions of three (SGUA, SDIAZ, SMETH) and four pharmaceuticals (SGUA, SDIAZ, SMETH, TMP) were prepared in the same way but concentrations of all pharmaceuticals in mentioned solutions were 50 mg/L. Concentration of SGUA in standard solution of sulfaguanidine was 50 mg/L also.

All mentioned standard solutions were stored protected from light at 4 °C and all used solvents were HPLC-grade supplied by Kemika (Zagreb, Croatia).

Chemicals for the polymer syntheses were methacrylic acid (MAA), 4-vinylpyridine (4-VPy), 2-hydroxyethyl methacrylate (HEMA), ethylene glycol dimethacrylate (EDGMA) all of them from Sigma-Aldrich. The initiator 2,2'-azobis-isobutyronitrile (AIBN) was supplied by AKZO Chemie (Delfzijl, The Netherlands), and before use was recrystallized repeatedly from cold methanol and dried in a vacuum oven.

In this work chromatographic plates HPTLC silica gel 60 F₂₅₄ 10 × 20 cm² and HPTLC CN F₂₅₄ 10 × 10 cm² or 10 × 20 cm², purchased from Merck (Darmstadt, Germany) were used. For solid-phase extraction 200 mg Oasis HLB (Waters, Milford, Massachusetts) and Strata X (Phenomenex, Torrance, USA) cartridges were used. The polypropylene SPE empty reservoir (3 mL) and adequate 20 μm polyethylene frits (PTFE) were purchased from Agilent (Santa Clara, CA, USA).

Water sample free of antibiotics was taken from the wellspring near Borčec, north-west Croatia.

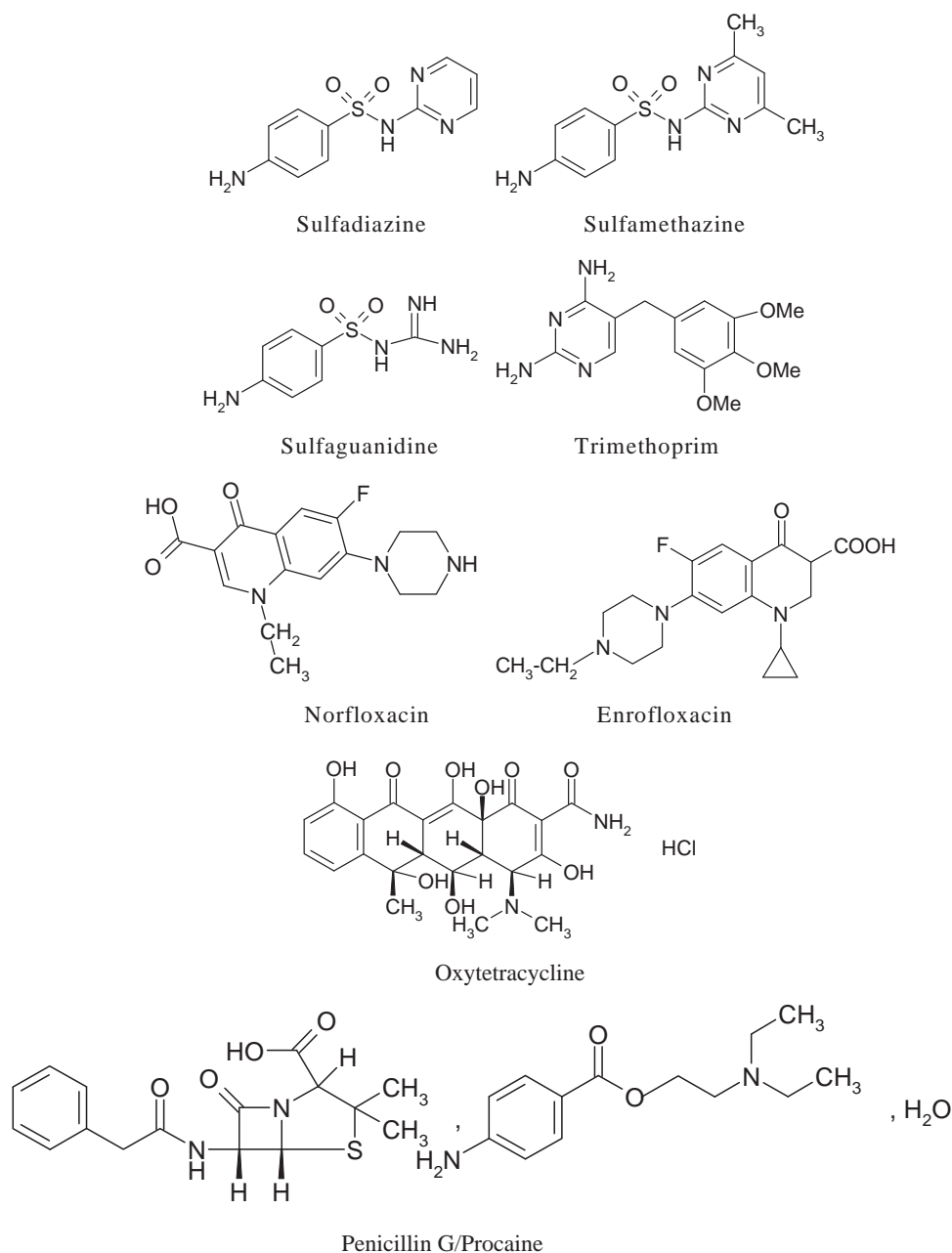


Fig. 1. Chemical structure of the studied pharmaceuticals.

2.2. Preparation of molecular imprinted polymers

The template molecule (SGUA, 107.1 mg, 0.5 mmol) was dissolved in 6 mL of acetonitrile and placed in a glass tube. Then, the functional monomer (MAA, 2.0 mmol, 0.175 mL, or 4-VPy, 2.0 mmol, 0.225 mL, or HEMA, 2.0 mmol, 0.240 mL), the cross-linking monomer (EDGMA, 10.0 mmol, 1.920 mL) and the initiator (AIBN, 0.12 mmol, 24.0 mg) were added. The polymerization mixture was degassed with stream of He for 5 min under sonication, and cured at 58 °C for 24 h. A non-imprinted polymer (NIP) containing no template was also prepared using the same procedure. The tubes were crushed and the polymer was ground. Powder polymer sorbent was placed in the empty SPE column. PTFE frits were placed above and below the polymer particle sorbent bed. Retained SGUA was then eluted with adequate volumes of MeOH: HAc (9:1) and after that with pure methanol. The presence of SGUA in eluate was tested by a determination with 3-aminophenol [46]. The 3-aminophenol solution was added

to the eluate and an orange-yellow azo product was formed. This experiment indicates SGUA in the eluate and also indicates the successful washing of MIPs.

2.3. Structural characterization of imprinted polymers

The morphology and microstructure of prepared MIP_{MAA} and NIP were investigated with a scanning electron microscope (SEM, Supra 35LV) operating at 1.5 kV. Powder of MIPs was used for microstructure investigations. For SEM investigations the surface of MIPs were coated with gold by vapour deposition using a vacuum sputter.

The infrared spectra of investigated MIP_{MAA} and NIP were recorded by a Fourier transform infrared (FTIR) spectrometer (Bruker Vertex 70) equipped with an attenuated total reflection (ATR) accessory with a diamond crystal. Sixteen scans were collected for each measurement over the spectral range of 400–4000 cm⁻¹ with a resolution of 4 cm⁻¹.

2.4. Sample preparation and extraction

Water samples were collected in amber glass bottles. Prior to extraction, wellspring water and wastewater used in this study were filtered through a Büchner funnel on black Whatman filter paper to eliminate the suspended matter and then filtered with the 0.45 µm nylon membrane filter. The samples were stored at 4 °C until SPE extraction, which was performed within 24 h in order to avoid any degradation.

The recovery studies were performed using spiked wellspring water samples. The spiked wellspring water samples were prepared from pre-filtered wellspring water by addition of 1 mL of working standard solutions of pharmaceuticals mixture to 100 mL of water.

The studied pharmaceuticals were extracted from the water samples and preconcentrated at one of the used cartridges using methanol as eluent on the apparatus for SPE. Before water application, the cartridges were conditioned with 5 mL of each methanol, and water. Based on the previous work [47], the pH of samples and water for preconditioning and washing steps was adjusted to 4.0 (HCl, 0.1 M). A sample volume of 100 mL was applied to the cartridge and the flow was kept at no greater than 4 mL/min. A wash step with 2 mL methanol (2%) was applied after the sample loading. The cartridge was allowed to dry for about 10 min using vacuum to remove excess water. The analytes retained were eluted with 2 × 5 mL of methanol. Following elution, the filtrates were evaporated on a rotary evaporator at 40 °C to dryness and redissolved with 1 mL of methanol obtaining 100-fold preconcentration.

2.5. Thin-layer chromatography

The samples were applied to the plates as bands by means of Linomat IV (Camag, Muttenz, Switzerland): volume 15 µL, band-width 5 mm, distance between middle of the bands 10 mm, speed 10 s/µL. In case when the extraction efficiency was determined on HPTLC CN F₂₅₄ plates, 0.05 M H₂C₂O₄:methanol=81:19 was used as a mobile phase. Chloroform:methanol=89:11 (v/v) was used as mobile phase in combination with HPTLC silica gel 60 F₂₅₄ chromatographic plates.

After development the plates were air-dried and the chromatograms were visualized under UV light at λ=254 nm in both cases and at λ=366 nm in case of HPTLC CN F₂₅₄ chromatographic plates by previously described procedures [47,48].

In the first set of experiments, the extraction efficiency of SGUA was checked using a different type of MIPs and NIPs sorbents. Based on these experiments, the best MIP was chosen. The obtained extraction efficiencies were compared with the extraction efficiency of SGUA achieved using commercial extraction sorbents Oasis HLB and Strata X.

In the second set of experiments, the extraction efficiency of three, four and eight pharmaceuticals from water samples were checked using the best prepared MIP (from the first set of experiments), MIP_{MAA} (500 mg/3 mL). Based on all of the aforementioned experiments and available literature [13,45], MIP_{MAA} cartridges were used in the last set of experiments in tandem with commercial sorbents Oasis HLB and Strata X. In one case, the commercial sorbent was in front in the sequence while in the second tandem, the order was reverse. The sorbent mass of all of the sorbents used in these experiments were the same (200 mg), so the total sorbent mass amounted to 400 mg. By means of the aforementioned experiments, optimal SPE cartridges were prepared in one column by adding the second sorbent to the existing one in an optimal sequence with a frit inserted between them.

3. Results and discussion

SGUA was selected as a template molecule. Other pharmaceuticals (Fig. 1) are excluded from the elections for a template molecule because they do not present a problem during extraction procedure [13].

3.1. Preparation of sulfaguanidine-imprinted polymers

3.1.1. Selection of a functional monomer

The structure of SGUA (Fig. 1) shows basic centres, one in the anilinium rest and the other in the guanidine group. SGUA is unusual compared to other sulfonamides because it does not possess a sulfonamide proton of appropriate acidity and therefore, unlike other sulfonamides, it has no acidic functional group (pK_{a3}=12.1). Its aniline amino group is rather basic with respect to other sulfonamides (pK_{a2} 2.8), but its guanidine group appears only as a very weak base (pK_{a1} 0.5) [49]. Consequently, SGUA is a potentially adequate template molecule to interact with MAA. In order to optimize the MIP preparation procedure, three different functional monomers capable of forming hydrogen bonds were tested: a acidic monomer such as MAA, a basic monomer such as 4-VPy, and a neutral monomer such as HEMA. In all three cases, EDGMA was used as a cross-linker and acetonitrile as a porogen solvent. In this work, EDGMA was chosen as a cross-linker due to its higher hydrophilic properties, which was beneficial to the synthesis of the water-compatible polymer [19]. Therefore, acetonitrile, which is miscible with water, can be used in either purely organic or aqueous solvent mixtures. The presence of the porogen in the aqueous load was expected to enable the polymer to interact selectively with the target [21].

NIPs were prepared in the same way but without SGUA as a template molecule. Once the imprinted polymer was prepared, the SGUA as a template must be removed from the polymer particles, leaving free cavities complementary in size, shape and functionality and ready for analytes recognition.

For that purpose, adequate volumes of MeOH: HAc (9:1) were used. This solvent mixture was chosen based on literature data [14,43,50,51] showing that the mentioned mixture was used to efficiently extract template molecules from the sulfonamide MIPs. In terms of the SGUA, the downloading was tested by spectrophotometric reagent 3-aminophenol [46]. A 3-aminophenol solution was added to the eluate after the washing and an orange-yellow azo product was generated. This experiment was suitable for quantitative template removal indicating presence of SGUA in the eluate, which justified its rinsing.

Regarding all the prepared polymers, the distribution coefficient *k* of SGUA by MIPs and NIPs as well as imprinting factors were calculated as follows[32,51,52]:

$$k^{SGUA} = \frac{(c_0 - c) V}{c m} \quad (1)$$

$$IF = \frac{k_{MIP}^{SGUA}}{k_{NIP}^{SGUA}} \quad (2)$$

where *c*₀ and *c* represent the initial and final concentrations, *V* represents the volume (mL) of the solution and *m* is the mass (g) of the tested polymer.

Based on these values, it was concluded that the MIP_{MAA} showed higher affinity for SGUA than the adequate NIP_{MAA} polymer and other prepared polymers pursuant to other functional monomers. The obtained imprinting factors (IF_{MAA}=3.43; IF_{HEMA}=1.90; IF_{4-VPY}=0.80) concerning the mentioned MIP_{MAA} represented an indication of a good imprinting effect.

The results of obtained imprinting factors could be explained through the structures of MIPs obtained with different monomers.

Structures of MAA, HEMA, 4-VPY cross-linked with EDGMA could be found in the literature [53–55]. Prepared cross-linked MIPs differ in their free molecules that enable interaction with SGUA (MAA-carboxylic, HEMA-hydroxyl and 4-VPY-pyridine groups). Anyway, MAA is a very good example of acidic functional monomers, which are suitable for hydrogen-bonding or proton accepting templates and are normally used for basic templates as SGUA, whereas 4-VP are used for acidic templates. Complexes between MAA and SGUA present strong interactions, especially between the carboxylic group of the methacrylic acid and sulfaguanidine molecule. Structures of MAA and SGUA interact in two points through H-bonding with carboxylic acid of MAA with the S=O and NH sulfonamide moieties or/and H-bonding with carboxylic acid of MAA with the sulfonyl O-atom and NH of central amide moieties and/or guanidine group. This can be attributed to the fact that MAA can act as both hydrogen bond donor and acceptor and can therefore interact with the template at one or two points of interaction as well as form MAA dimers. On the other hand, interaction with other investigated functional monomer would give a more homogeneous binding site by the fewer possible modes of interaction [56]. These observations suggest that the imprinted polymer of sulfaguanidine is likely to have heterogeneous binding sites when interacting with MAA which is the reason of better imprinting effect and selectivity for SGUA than MIPs obtained with other functional monomers. Moreover, the best results are achieved when templates attached to more than one binding site to functional monomer [57] and this is the case with MAA as functional monomer.

The above results for the polymer which was prepared using the MAA as a functional monomer had been expected. In addition, there is the fact that MAA was the most hydrophilic molecule among all of the used functional monomers that ensured the best retention of the SGUA by hydrogen bonds inside the pore of the incurred polymeric sorbents. Theoretically, SGUA is a basic compound due to its amino and amidine (guanidine) groups which may easily interact with MAA. MAA has a carboxylic acid group serving in this study as a hydrogen bond and proton donor as well as a hydrogen bond acceptor [24,58]. Also, relatively good results were obtained for HEMA what could be explained through polarity of free hydroxyl groups and SGUA. The lowest imprinting factor was obtained for 4-VPY as basic and non-polar molecule which theoretically seems to be, a non-ideal compound to interact with molecules such as sulfaguanidine and produce non-significant retention of an unspecific type. Taking into account the differences observed with NIPs, the MAA monomer was selected for further work.

3.1.2. Characterization of prepared polymers

The MIP as well as the NIP based on MAA were analysed by FTIR spectroscopy. The infrared spectra confirmed the presence of SGUA in the MIP-polymer sorbent. After washing the MIP_{MAA} with the methanol/acetic acid mixture (9:1), the pure methanol characteristic bands of the SGUA in the polymer sorbent disappeared. This indicates that washing was complete.

The morphology and microstructure of optimal polymers based at MAA were investigated with a scanning electron microscope. The SEM images of the prepared MIP_{MAA} and NIP_{MAA} polymers for solid-phase extraction are shown in Fig. 2a and b.

On the basis of SEM images, the polymer has polymerized in a network form creating irregular shapes with a high surface area. Both samples showed a similar structure. Furthermore, it can be noticed that the imprinted MIP_{MAA} has a rougher surface that corresponds to the increase in the surface area and therefore has bigger cavities in comparison to the NIP_{MAA}. The obvious reason for that is the presence of imprinted molecules [16]. The size of cavities is directly linked to the adsorption capacities, mass transfer and diffusion resistance. They can increase adsorption capacity, facilitate mass

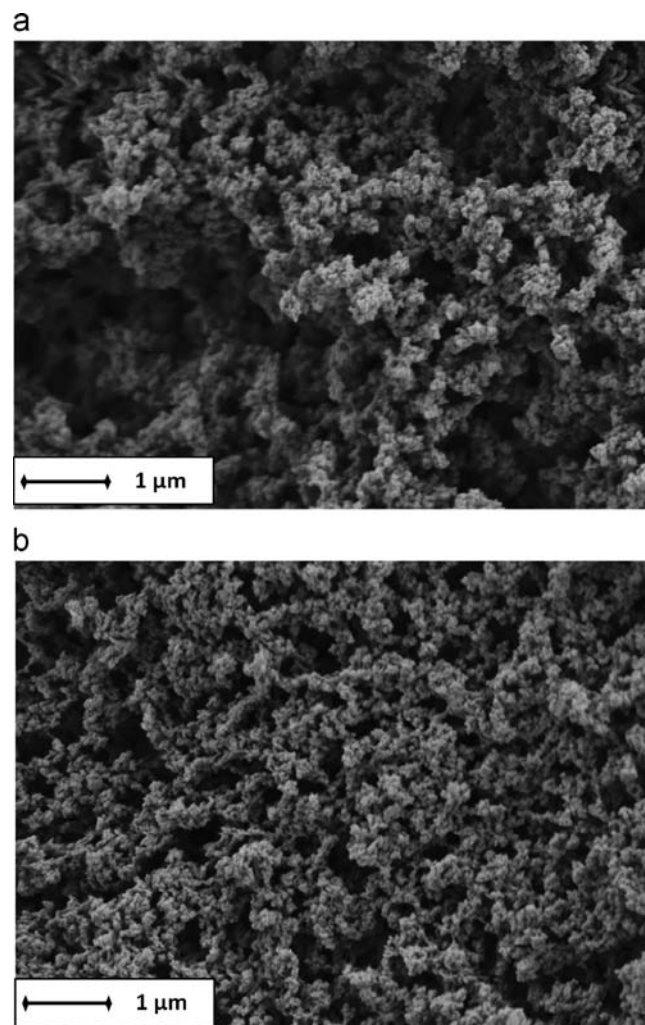


Fig. 2. SEM images of (a) MIP_{MAA} and (b) NIP_{MAA}.

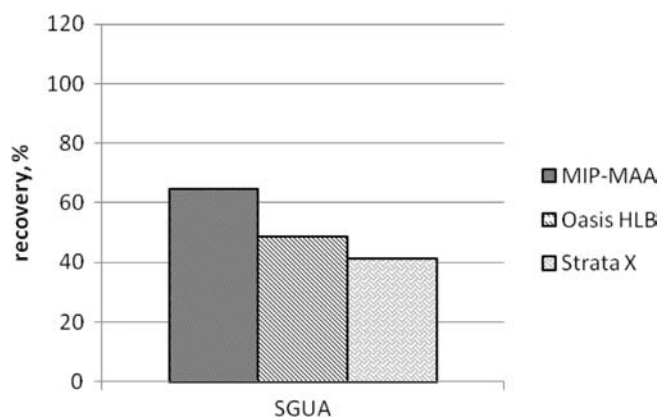


Fig. 3. Extraction efficiencies of SGUA obtained from the analysis of spiked water samples on prepared MIP_{MAA} sorbent and commercial sorbents same sorbent mass (200 mg).

transfer and decrease diffusion resistance [22]. The results comply with better retention of the SGUA with MIP as mentioned previously.

3.2. Solid-phase extraction of pharmaceuticals from water samples

In order to verify the effectiveness of the chosen-MAA based molecularly-imprinted polymers, the obtained extraction efficiencies

were compared with the extraction efficiency of SGUA achieved using commercial extraction sorbents Strata X and Oasis HLB. The results of these experiments are shown in Fig. 3.

The presented results suggest that it is obvious that the prepared MIP_{MAA} polymer was a better option for extraction of SGUA than the used commercial sorbents although the retention differences between them were not so high.

Some of our previous papers [45,59] demonstrated that commercial sorbents Strata X and Oasis HLB was not so good choice for extraction of SGUA especially in case of multicomponent analysis. So the next step was to apply the previously prepared MIP_{MAA} for the extraction of SGUA from water samples which contained other pharmaceuticals besides sulfaguanidine.

According to the prior cognition about MIPs, it could be presumed that the prepared MIP_{MAA} retained other sulfonamides as molecules of a similar structure like SGUA. Since MIPs are not completely specific sorbents i.e. they do not retain only one molecule, one could not suppose the probability of the retention of other pharmaceuticals, except for sulfonamides. Whereas MIP_{MAA} were prepared only because of SGUA, it could be expected that SGUA would have priority in retention over other pharmaceuticals. Extraction of three, four and eight pharmaceuticals from water samples using 500 mg of MIP_{MAA} was performed. The obtained results clearly confirm the previous hypothesis, recovery of SDIAZ 82.5%, SMETH 80.7% and SGUA 80.7% i.e. except sulfonamides the MIP_{MAA} retained TMP (42.7%) and PGP (38.2%). These results were in line with the expectations since TMP is a small molecule as well as PGP which contains two smaller molecules. Both molecules could enter the pores of the prepared polymeric surface but not in the right way (*key-lock* way), which suggests relatively low extraction efficiency (around 40%).

Regarding the extraction efficiencies of other investigated pharmaceuticals (ENRO, NOR and OTC was not detected), the commercial sorbents [13,45] provided better extraction results especially for fluoroquinolones which is not retaining at all by MIP_{MAA}. Based on these findings, MIP_{MAA} were used in the following set of experiments in tandem with commercial sorbents Oasis HLB and Strata X. In the first case, the commercial sorbent came first in the sequence while in the second tandem, the order was reverse. The sorbent mass of all sorbents used in these experiments were the same (200 mg), so the total sorbent mass amounted to 400 mg. Based on the aforementioned combination of sorbents, high extraction efficiencies were expected for all eight pharmaceuticals since these tandems facilitate resolution of the problem related to SGUA without significant impact on the extraction efficiencies of other seven pharmaceuticals. The results are shown in Table 1a.

Table 1
Comparison of the extraction recovery percentages obtained from the analysis ($n=3$) of spiked water samples by: (a) MIP_{MAA} sorbent in different tandem with commercial sorbents, (b) MIP_{MAA}-Oasis HLB (400 mg/6 mL) cartridge.

Pharmaceutical	(a)		(b)		MIP _{MAA} -Oasis-HLB
	sorbents tandem		1. MIP _{MAA}	1. Oasis HLB	
	1. MIP _{MAA}	1. Strata X	1. MIP _{MAA}	1. Oasis HLB	
	2. Strata X	2. MIP _{MAA}	2. Oasis HLB	2. MIP _{MAA}	
	Recovery, % ($n=3$)				
ENRO	38 ± 23	80 ± 7	92 ± 5	82 ± 7	97 ± 8
NOR	24 ± 24	51 ± 2	95 ± 0	70 ± 0	96 ± 6
OTC	93 ± 13	95 ± 6	100 ± 1	81 ± 5	96 ± 3
TMP	100 ± 0	72 ± 2	94 ± 7	92 ± 6	99 ± 3
SDIAZ	96 ± 2	94 ± 2	98 ± 1	95 ± 1	98 ± 3
SMETH	93 ± 1	100 ± 2	100 ± 4	98 ± 1	98 ± 3
PGP	86 ± 4	102 ± 2	100 ± 3	92 ± 9	98 ± 5
SGUA	88 ± 2	95 ± 2	98 ± 1	92 ± 6	100 ± 4

The presented results show fairly good extraction efficiencies for all of the used sorbent combinations. Extraction efficiencies of SGUA above 90% were reached but the extraction efficiencies of other pharmaceuticals were not so good in all cases. The worst extraction results were achieved with tandem MIP_{MAA}-Strata-X cartridges. Generally, the tandem between MIP_{MAA} and commercial sorbent Strata X could not be deemed as a good option for fluoroquinolones, especially for NOR. On the other hand, the highest extraction efficiencies for investigated pharmaceuticals, including the SGUA, were achieved using MIP_{MAA} in tandem with commercial sorbent Oasis HLB, when the HLB column was located below the MIP_{MAA}. The reason for that probably lies in the fact that the pharmaceuticals from the water samples were first to reach the MIP_{MAA} among all the members of the mentioned sequence. Thereat, the SGUA and other sulfonamides were retained but the fluoroquinolones and OTC passed through the sorbent unretained. That way, the active centres of the Oasis HLB sorbent stayed free primarily for retention of ENRO, NOR and OTC and then for retention of all the other pharmaceuticals which were not completely retained on the MIP_{MAA}. The above sorbent combinations prefer SGUA, because SGUA is a pharmaceutical which retained to Oasis HLB as the last in the investigated pharmaceutical mixture owing to its physico-chemical properties described above. The presented results encourage the assumption that commercial sorbent Oasis HLB is the better commercial option concerning the eight investigated pharmaceuticals than Strata X is.

With regard to the previously obtained results, the next goal was to prepare the aforementioned sorbent combinations in one cartridge reservoir. Whereas 200 mg of the Oasis HLB sorbent is the only sorbent (between all of used SPE material) in the 6 mL column, the newly prepared sorbent combination would be located in the same 6 mL column. The obtained results are displayed in Table 1b.

The obtained results reveal slightly higher values than those presented in Table 1a. Namely, in these sets of experiments, the losses of pharmaceuticals during the passage of the water samples through the cartridges was reduced since the water samples got in contact with only one wall of the used cartridges, which does resemble the previous experiments (Table 1a). Presented results make it obvious that the extraction efficiencies of all pharmaceuticals exceeded 95%. Still, the most important thing is the fact that the extraction efficiency of SGUA totalled 100%, particularly for the reason that SGUA seemed to be a big problem during the whole extraction procedure [13,36,37]. Taking these conclusions into consideration, MIP_{MAA} in tandem with Oasis HLB (400 mg/6 mL) was selected as the optimal new extraction cartridge for the investigated pharmaceuticals from the water sample.

3.3. Validation

The performance characteristics of the developed MISPE-HPTLC method were established by a validation procedure for a quantitative purpose. Selectivity, linearity, limits of detection (LOD) and quantification (LOQ), precision and recovery were studied.

For qualitative purpose, the method was evaluated by taking into the account the precision in the retention factor (R_f -value) and selectivity. The absence of false positive results for blank samples and a good separation were considered acceptable for selectivity.

Linear relationship between peak area and mass concentration of antibiotics was found. The linearity in the concentration range was assessed for each pharmaceutical in water samples in concentration range of 0.5–150 µg/L, depending on a pharmaceutical using the six standard solutions at concentrations in the working range from 0.025 to 0.75 mg/L for NOR, 0.05 to 1.5 mg/L for ENRO, and from 0.5 to 15 mg/L for SGUA, SDIAZ, SMETH, OTC, PGP

and TMP. Calibration curves were prepared for each compound from the spiked water samples by plotting the peak area versus the analytes concentration. The results were analysed by the linear regression method. The coefficients of correlation exceeded 0.9843, except for norfloxacin (0.9770) and for penicillin G procaine (0.9801), thus confirming the linearity of the method (Table 2).

The limits of detection (LODs) and quantification (LOQs) calculated by signal-to-noise ratio (S/N) of 3 and 10 for each pharmaceutical in the mixture are reported in Table 2.

To ensure correct quantification, precision of the method was studied by analysing nine loadings of the extracts obtained by adding the mixed standard solution with concentration level in the middle of linearity range (5 µg/L for NOR, 10 µg/L for ENRO and 100 µg/L other pharmaceuticals in water sample). Obtained results

Table 2
Results of quantitative determination of pharmaceuticals in water by MISPE–HPTLC.

Pharmaceutical	R^2	LOD (µg/L)	LOQ (µg/L)	Concentration level (µg/L)	Recovery, % (n=3)
ENRO	0.9843	0.5	1	1	96 ± 11
				5	97 ± 9
				15	93 ± 9
NOR	0.9770	0.25	0.5	0.5	104 ± 17
				2.5	94 ± 5
				7.5	95 ± 7
OTC	0.9921	5	10	10	106 ± 9
				50	94 ± 11
				150	93 ± 2
				10	n.d.;
TMP	0.9887	20	50	< LOQ	
				50	93 ± 11
				150	95 ± 10
SDIAZ	0.9997	5	10	10	92 ± 4
				50	92 ± 6
				150	101 ± 8
SMETH	0.9916	5	10	10	140 ± 10
				50	94 ± 6
				150	95 ± 6
PGP	0.9801	5	10	10	130 ± 12
				50	96 ± 2
				150	95 ± 11
SGUA	0.9950	5	10	10	108 ± 8
				50	108 ± 3
				150	99 ± 5

Table 3
Comparison of several solid-phase extraction methods for SGUA determination in water samples.

Matrix	SPE	Determination	LOD, µg/L	LOQ, µg/L	Recovery, %	Detected levels, µg/L	Reference
Surface water, lagoon wastewater, WWTP influent and effluent	Oasis HLB (500 mg/6 mL), pH 3	LC-MS/MS	–	–	< 10	–	[13]
Surface water, ground water, WWTP influent, WWTP effluent	Oasis HLB, Hysphere C18-EC, PLRP	LC-MS/MS	–	–	< 10	–	[41]
Ground, surface and lysimeter water	Oasis HLB (200 mg/6 mL), pH 4	LC-MS/MS	–	–	5	–	[42]
Production wastewater	Strata X (500 mg/3 mL), pH 4	LC-MS/MS	0.001	0.010	26–38	2.2–10.5	[45]
Production wastewater	Strata X (500 mg/3 mL), pH 4	TLC-HPTLC CN F ₂₅₄ plates	50 ^a	100 ^a	81	> > 250.0	[47]
	Oasis HLB (60 mg/3 mL), pH 4	TLC-HPTLC silica gel F ₂₅₄ plates	50 ^b	100 ^b	9–16	–	[48]
Production wastewater	Oasis HLB (60 mg/3 mL), pH 4	HPLC-DAD	40	60	11	211.1	[59]
Production wastewater	Strata X (500 mg/3 mL), pH 4	HPLC-DAD	10	15	76	–	[60]
Production wastewater	Oasis HLB (60 mg/3 mL), pH 4	TLC-HPTLC CN F ₂₅₄ plates	200	300	6–27	> 1100.0	[61]
Production wastewater	MIP _{MAA} -Oasis HLB (400 mg/6 mL), pH 4	TLC-HPTLC CN F ₂₅₄ plates	5	10	100	76.–520.0	This work

^a Calculated from ng/spot to µg/L based on 5 µL of volume per spot and 100 mL of water samples.

^b Calculated from µg/spot to µg/L based on 10 µL of volume per spot and 100 mL of water samples.

indicated very good precision of the MISPE–HPTLC method; the intra-day precisions were up to 10% and inter-day precision up to 15%. The recoveries data were calculated by comparison of the extracted analyte amounts with appropriate working standard solutions. The untreated water samples were fortified at three different concentrations from the linearity range, depending on pharmaceuticals and results are also presented in Table 2. Each recovery experiment was repeated 3 times. From presented results it could be seen that for all eight investigated pharmaceuticals very high extraction recoveries (> 90%) were achieved over the investigated concentration range. Also, it is obvious that the extraction recovery was not sample concentration dependent which is a very positive characteristic of the developed method.

The MISPE–HPTLC method proposed in this work showed high sensitivity for all the pharmaceuticals. Application of a combination of MIP_{MAA} and the commercial Oasis HLB sorbent make this method unique and provide for high sensitivity, especially when this method is compared with previously developed methods listed in Table 3. Anyway, its biggest advantage is a very successful extraction of SGUA.

3.4. Application to wastewater samples

The developed method MISPE–HPTLC was used for determination of SMETH, SDIAZ, SGUA, TMP, OTC, ENRO, NOR, and PGP in two production wastewater samples from the pharmaceutical industry (PWWS1 and PWWS2). Wastewater treatment consists of only a primary settlement and plant receive only industrial wastewater. Chemical synthesis processes of the veterinary pharmaceutical industry produce wastewaters which vary in character depending on production. Mentioned PWWS1 and PWWS2 samples were collected during 2 months.

Chromatograms obtained from PWWSs were visualized under UV light of $\lambda=254$ and 366 nm (Fig. 4).

Identification of the target compounds was achieved by comparison of R_F values of pharmaceutical compound standards with those of the compounds in wastewater samples. Except these, some of the target compounds assigned unique colour of spot as red spot of OTC or spot of fluoroquinolones (ENRO and NOR) as fluorescent at 366 nm. SDIAZ, SMETH and SGUA were identified in both wastewater samples. SDIAZ, SMETH and SGUA were detected in PWWS1 at very high concentrations, out of linearity range, especially SMETH. Their concentrations in PWWS2 were

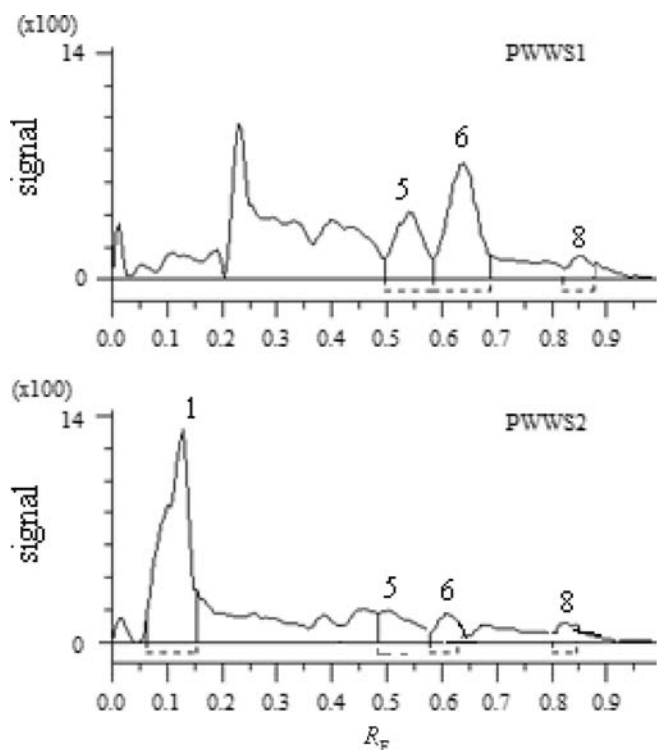


Fig. 4. HPTLC-videodensitometry chromatograms of wastewater samples, $\lambda = 366$ nm; 1-ENRO, 5-SDIAZ, 6-SMETH and 8-SGUA.

Table 4
Results of wastewater samples analysis.

Pharmaceuticals	Standards	PWWS1		PWWS2	
		R_F	Concentration ($\mu\text{g/L}$)	R_F	Concentration ($\mu\text{g/L}$)
ENRO	0.11	n.d.	n.d.	0.13	6264.0
SDIAZ	0.50	0.53	512.2	0.51	109.8
SMETH	0.61	0.63	1969.2	0.61	53.1
SGUA	0.85	0.85	520.0	0.86	76.8

n.d. – not detected.

significantly lower than in PWWS1. Besides these three pharmaceuticals, ENRO was identified in PWWS2 in very high concentration, much higher than the linearity range. Because of that, to determine a real concentration of detected compounds, both obtained extracts had to dilute a few times. NOR, OTC, PGP, and TMP were not detected in the PWWS analysed. Qualitative and quantitative results from analysis of the wastewater samples are summarized in Table 4.

Table 4 shows that sample PWWS2 contains more of the pharmaceutical compounds of interest than sample PWWS1. The concentrations of the pharmaceutical compounds in sample PWWS1 exceed the linear range of the method as well as ENRO in sample PWWS2.

4. Conclusion

MIPs are broadly applied to concentrate and separate molecules from different matrixes. A MIP was successfully synthesized using MAA and EDGMA as a functional monomer and cross-linker,

respectively. MIP_{MAA} exhibited good characteristics for extracting and concentrating SGUA from water samples.

This developed multi-class method, based on MISPE and followed by TLC determination has been proposed for simultaneous analysis of eight pharmaceutical compounds with a variety of structures and different physico-chemical properties. The recoveries obtained for all the investigated pharmaceuticals, using prepared MIP_{MAA} in tandem with commercial cartridge Oasis HLB, were higher than 90% (at three concentration levels), which is always very significant and desirable.

Several techniques were compared for their ability to concentrate and separate SGUA in real samples. The prepared new cartridge (MIP_{MAA}-Oasis HLB, 400 mg/6 mL) showed better recoveries with respect to other methods. Those results clearly indicate the need for thorough testing of the commercially available sorbents intended for use in wide-range screening methods for identification of unknown organic micropollutants in water. The MISPE-HPTLC method was successfully applied to analysis of production wastewater samples from pharmaceutical industry, so it can be a useful tool to determine the amount of pharmaceuticals discharged from WWTPs to an aquatic environment and to evaluate the effect of conventional WWTPs.

Acknowledgement

This study is a part of the research projects: 125-1253008-1350 and 125-1252970-3005, supported by the Ministry of Science, Education and Sports in the Republic of Croatia.

The authors would like to thank Waters, Instrumentalia, Zagreb, Croatia, for providing free samples of the 200 mg/6 mL Oasis HLB cartridges.

References

- [1] M. Valtchev, B.S. Palm, M. Schiller, U. Steinfeld, J. Hazard. Mater. 170 (2009) 722–728.
- [2] Z. Sun, W. Schüssler, M. Sengl, R. Niessner, D. Knopp, Anal. Chim. Acta 620 (2008) 73–81.
- [3] T. Heberer, Toxicol. Lett. 131 (2002) 5–17.
- [4] K. Polestra, W.W. Bakker, P.A. Klok, J.A. Kamps, M.J. Hardonk, D.K. Mijer, Am. J. Pathol. 151 (1997) 1163–1169.
- [5] M. Carballa, F. Omil, J.M. Lema, M. Llopart, C. Garcia-Jares, I. Rodriguez, M. Gomez, T. Ternes, Water Res. 38 (2004) 2918–2926.
- [6] D. Daughton, T.A. Ternes, Environ. Health Perspect. 107 (1999) 907–938.
- [7] M. Gros, M. Petrović, D. Barceló, Talanta 70 (2006) 678–690.
- [8] S. Castiglioni, R. Bagnati, D. Calamari, R. Fanelli, E. Zuccato, J. Chromatogr. A 1092 (2005) 206–215.
- [9] M. Petrović, M. Gros, D. Barceló, J. Chromatogr. A 1124 (2006) 68–81.
- [10] M.J. Gómez, M. Petrović, A.R. Fernández-Alba, D. Barceló, J. Chromatogr. A 1114 (2006) 224–233.
- [11] S. Grujić, T. Vasiljević, M. Laušević, J. Chromatogr. A 1216 (2009) 4989–5000.
- [12] R. López-Serna, M. Petrović, D. Barceló, Chemosphere 85 (2011) 1390–1399.
- [13] L.J. Zhou, G.G. Ying, S. Liu, J.L. Zhao, F. Chen, R.Q. Zhang, F.Q. Peng, Q.Q. Zhang, J. Chromatogr. A 1244 (2012) 123–138.
- [14] A. Guzmán-Vázquez de Prada, P. Martínez-Ruiz, A.J. Reviejo, J.M. Pingarrón, Anal. Chim. Acta 539 (2005) 125–132.
- [15] X. Jiang, W. Tian, C. Zhao, H. Zhang, M. Liu, Talanta 72 (2007) 119–125.
- [16] R.J. Krupadam, M.S. Khan, S.R. Wate, Water Res. 44 (2010) 681–688.
- [17] A. Beltran, F. Borruil, P.A.G. Cormack, R.M. Marce, Trends Anal. Chem. 29 (2010) 1363–1375.
- [18] M. Soleimani, S. Ghaderi, M. Ghahraman Afshar, S. Soleimani, Microchem. J. 100 (2012) 1–7.
- [19] H. Suna, F. Qiao, G. Liu, S. Liang, Anal. Chim. Acta 625 (2008) 154–159.
- [20] B. Okutucu, S. Önal, Talanta 87 (2011) 74–79.
- [21] C. Chassaing, J. Stokes, R.F. Venn, F. Lanza, B. Sellergren, A. Holmberg, C. Berggren, J. Chromatogr. B 804 (2004) 71–81.
- [22] L. Chen, J. Liu, Q. Zeng, H.A. Yu, H. Zhang, L. Ding, J. Chromatogr. A 1216 (2009) 3710–3719.
- [23] B. Rezaei, M.T. Jafari, R. Khademi, Talanta 79 (2009) 669–675.
- [24] Q. Feng, L. Zhao, J.M. Lin, Anal. Chim. Acta 650 (2009) 70–76.
- [25] M.J. García-Galán, M.S. Díaz-Cruz, D. Barceló, J. Hydrol. 383 (2010) 30–38.
- [26] E. Turiel, A. Martín-Esteban, J.L. Tadeo, J. Chromatogr. A 1172 (2007) 97–104.
- [27] C. Cacho, E. Turiel, C. Pérez-Conde, Talanta 78 (2009) 1029–1035.

- [28] E. Caro, R.M. Marcé, P.A.G. Cormack, D.C. Sherrington, F. Borrull, J. Chromatogr. A 1047 (2004) 175–180.
- [29] T. Alizadeh, M.R. Ganjali, P. Nourozi, M. Zare, Anal. Chim. Acta 638 (2009) 154–161.
- [30] C. Yu, X. Li, B. Hu, J. Chromatogr. A 1202 (2008) 102–106.
- [31] S. Zorita, B. Boyd, S. Jönsson, E. Yilmaz, C. Svensson, L. Mathiasson, S. Bergström, Anal. Chim. Acta 626 (2008) 147–154.
- [32] E. Caro, R.M. Marcé, P.A.G. Cormack, D.C. Sherrington, F. Borrull, Anal. Chim. Acta 552 (2005) 81–86.
- [33] X. Shi, Y. Meng, J. Liu, A. Sun, D. Li, C. Yao, Y. Lu, J. Chen, J. Chromatogr. B 879 (2011) 1071–1076.
- [34] M.M. Sanagi, S. Salleh, W.A.W. Ibrahim, A.A. Naim, D. Hermawan, M. Miskam, I. Hussain, H.Y. Aboul-Enein, J. Food Compos. Anal. 32 (2013) 155–161.
- [35] Y.-P. Duan, C.-M. Dai, Y.-L. Zhang, L. Chen, Anal. Chim. Acta 758 (2013) 93–100.
- [36] Y. Wang, E. Wang, Z. Wu, Z. Zhu, X. Zhu, Y. Dong, Carbohydr Polym 101 (2014) 517–523.
- [37] X. Yang, Z. Zhang, J. Li, X. Chen, M. Zhang, L. Luo, S. Yao, Food Chem. 145 (2014) 687–693.
- [38] W. Hela, M. Brandtner, R. Widek, R. Schuh, Food Chem. 83 (2003) 601–608.
- [39] B. Shao, D. Dong, Y. Wu, J. Hu, J. Meng, X. Tu, S. Xu, Anal. Chim. Acta 546 (2005) 174–181.
- [40] N.T. Malintan, M.A. Mohd, J. Chromatogr. A 1127 (2006) 154–160.
- [41] M.J. García-Galán, M.S. Díaz-Cruz, D. Barceló, Talanta 81 (2010) 355–366.
- [42] W.L. Shelver, H. Hakk, G.L. Larsen, T.M. DeSutter, F.X.M. Casey, J. Chromatogr. A 1217 (2010) 1273–1282.
- [43] N. Zheng, Q. Fu, Y. Li, W. Chang, Z. Wang, T. Li, Microchem. J. 69 (2001) 153–158.
- [44] X. Liu, C. Ouyang, R. Zhao, D. Shangguan, Y. Chen, G. Liu, Anal. Chim. Acta 571 (2006) 235–241.
- [45] S. Babić, D. Mutavdžić Pavlović, D. Ašperger, M. Periša, M. Zrnčić, A.J.M. Horvat, M. Kaštelan-Macan, Anal. Bioanal. Chem. 398 (2010) 1185–1194.
- [46] P. Nagaraja, H.S. Yathirajan, C.R. Raju, R.A. Vasantha, P. Nagendra, M.S. Hemantha Kumar, Il Farmaco 58 (2003) 1295–1300.
- [47] D. Mutavdžić, S. Babić, D. Ašperger, A.J.M. Horvat, M. Kaštelan-Macan, J. Planar Chromatogr. 19 (2006) 454–462.
- [48] S. Babić, D. Ašperger, D. Mutavdžić, A.J.M. Horvat, M. Kaštelan-Macan, J. Planar Chromatogr. 18 (2005) 423–426.
- [49] A. Białk-Bielińska, S. Stolte, M. Matzke, A. Fabiańska, J. Maszkowska, M. Kołodziejka, B. Liberek, P. Stepnowski, J. Kumirska, J. Hazard. Mater. 221–222 (2012) 264–274.
- [50] M.P. Davies, V. De Biasi, D. Perrett, Anal. Chim. Acta 504 (2004) 7–14.
- [51] N. Zheng, Y. Li, W. Chang, Z. Wang, T. Li, Anal. Chim. Acta 452 (2002) 277–283.
- [52] P. Luliński, M. Dana, D. Maciejewska, Talanta 119 (2014) 623–631.
- [53] B. Podkościelna, A. Bartnicki, B. Gawdzik, Express Polym. Lett. 6 (2012) 759–771.
- [54] N. Sahiner, Turk. J. Chem. 33 (2009) 23–31.
- [55] H. Yan, L. Jin, K.H. Row, Korean J. Chem. Eng. 23 (2006) 625–630.
- [56] C. Isarankura-Na-Ayudhya, C. Nantasenamat, P. Buraparungsang, T. Piacham, L. Ye, L. Bülow, V. Prachayasittikul, Molecules 13 (2008) 3077–3091.
- [57] N. Masqué, R.M. Marcé, F. Borrull, Trends Anal. Chem. 20 (2001) 477–486.
- [58] O. Brüggemann, A. Visnjevski, R. Burch, P. Patel, Anal. Chim. Acta 504 (2004) 81–88.
- [59] S. Babić, D. Ašperger, D. Mutavdžić, A.J.M. Horvat, M. Kaštelan-Macan, Talanta 70 (2006) 732–738.
- [60] D. Mutavdžić Pavlović, S. Babić, D. Dolar, D. Ašperger, K. Košutić, A.J.M. Horvat, M. Kaštelan-Macan, J. Separat. Sci. 33 (2010) 258–267.
- [61] S. Babić, D. Mutavdžić, D. Ašperger, A.J.M. Horvat, M. Kaštelan-Macan, Chromatographia 65 (2007) 105–110.



Novel flow injection analysis methods for the determination of total iron in blood serum and water



S.A.A. Elsuccary^{a,*}, Alaa A. Salem^b

^a Department of Chemistry, Faculty of Science, Beni-Suef University, Beni-Suef, Egypt

^b Department of Chemistry, College of Science, United Arab Emirates University, Al-Ain, UAE

ARTICLE INFO

Article history:

Received 20 April 2014

Received in revised form

21 July 2014

Accepted 21 July 2014

Available online 31 July 2014

Keywords:

Spectrophotometry

Iron in blood serum

Iron in water

ABTS

nFIA

rFIA

ABSTRACT

This work describes rapid, sensitive and highly precise methods for the determination of total iron in blood serum and water samples, using batch, nFIA and rFIA techniques. The proposed methods are based on the selective oxidation of 2,2'-azino-bis(3-ethylbenzothiazoline-6-sulfonate) (ABTS) by iron(III). The absorbance of the resultant green solution of radical cation (ABTS^{•+}) was monitored spectrophotometrically at $\lambda_{\max}=415$ nm. The reaction is stoichiometric with a ratio of 1:1 (Fe(III):ABTS) as determined by Job's and molar ratio methods. The proposed methods allow for the determination of Fe(III) in the ranges 0–4.5 mg L⁻¹ (LOD 25.5 $\mu\text{g L}^{-1}$, %RSD 0.97%, $n=7$); 0 to 4.5 mg L⁻¹ (LOD 370 $\mu\text{g L}^{-1}$, %RSD 1.28%, $n=7$) and 0 to 2.7 mg L⁻¹ (81.6 $\mu\text{g L}^{-1}$, %RSD 0.76%, $n=6$) for batch, nFIA and rFIA techniques, respectively. The proposed methods show high selectivity to Fe(III), as indicated by the high tolerance limits for common interfering ions. The nFIA method was applied in total iron assay in camel blood serum, whereas batch and rFIA methods were successful in the determination of total iron in municipal pipeline water and spiked groundwater. Statistical analysis indicated insignificant differences in accuracy and precision between the results obtained by the developed methods and ICP-AES or phenanthroline methods.

© 2014 Elsevier B.V. All rights reserved.

1. Introduction

Iron is one of the most abundant elements on Earth. It is an essential element for biological processes, including photo-synthetic and respiratory electron transport, nitrate reduction, chlorophyll synthesis, detoxification of reactive oxygen species in plants [1] and oxygen transport in humans [2]. In industry, iron is used in the construction of water pipes, while iron oxides are used as pigments in paints and plastics. Other iron compounds are used as food colors and for the treatment of iron deficiency in humans [3].

Iron oxides and hydroxides are the most common iron compounds found in nature, because of the high reactivity of Fe(II) and Fe(III) with oxygen. Other common natural iron compounds include carbonates, sulfates and sulfides [3]. Rainfall seeping through soil dissolves iron, leaching it into the groundwater, where it finds its way into wells and aquifers used to supply drinking water. In groundwater, iron concentration ranges typically between 0.5 and 10 mg L⁻¹, but concentrations up to 50 mg L⁻¹ may locally be found [3,4]. Iron concentration in drinking-water is normally less than 0.3 mg L⁻¹ but may be higher when various iron salts are used as coagulating agents in water-treatment plants, and when cast iron,

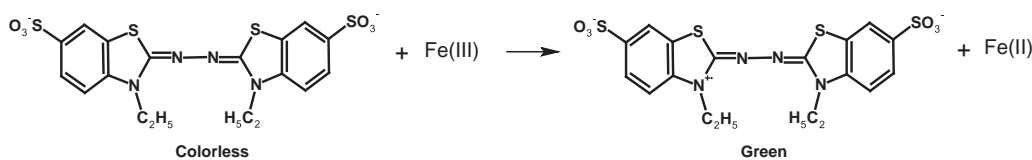
steel, and galvanized iron pipes are used for water distribution. In river waters the median iron concentration has been reported to be 0.7 mg L⁻¹ [3].

High iron concentration within water pipelines promotes undesirable bacterial growth (iron bacteria), resulting in the deposition of a slimy coating on the pipelines [5]. Excess ingestion of iron through polluted water can result in acute and/or chronic poisoning [6,7]. The average lethal dose of iron is 200–250 mg kg⁻¹ of body weight, but death may occur with doses as low as 40 mg kg⁻¹ of body weight [5]. On the other hand, an appreciable number of human diseases are related to iron deficiency. According to the World Health Organization (WHO), an extraordinarily large number of people (4–5 billion) are suffering from some form of iron deficiency, and up to 2 billion of them are clinically anemic [3,7].

Great concerns about the environmental impacts of iron on water resources and human health have spurred the development of sensitive and selective analytical techniques for its determination in various matrices. A variety of well-established methods, such as AAS, ICP-OES, ICP-MS, ion chromatography, capillary electrophoresis, stripping voltammetry, spectrofluorometry, chemiluminescence, and UV-vis spectrophotometry have been reported [8–10]. UV-vis spectrophotometric methods have received considerable attention and wide application due to their versatility, simple operation and low instrumentation cost. Most of these latter methods are based on the reaction of Fe(II) or Fe(III)

* Corresponding author.

E-mail address: saberelsuccary@yahoo.com (S.A.A. Elsuccary).



Scheme 1. Oxidation of ABTS to ABTS⁺ by Fe(III).

with a wide range of chromogenic reagents, or the catalytic activity of Fe(II) in some redox systems [8–10]. However, some of these methods suffer from poor sensitivity and/or selectivity and some are time consuming due to slow reaction rate. Moreover, in most of these methods, a prior reduction of iron(III) to iron(II) is required.

ABTS is a colorless reagent that can be oxidized to produce a radical cation (ABTS⁺) which has a stable green color with a broad absorption spectrum containing several maxima with a relatively high molar absorptivity at 415 nm. It has been used for the determination of nitrite [11], ferrate [12], reactive bromine and chlorine species [13], and as a substrate for enzymatic peroxide tests and percarboxylic acid analysis [14,15]. In addition, ABTS⁺ is a well-known reagent for the determination of antioxidant capacity [16,17].

In the present study, among many metal ions tested, Fe(III) was found to instantaneously and selectively oxidize ABTS with 1:1 stoichiometric ratio, through one-electron transfer reaction (Scheme 1). These unique characteristics, in addition to the high molar absorptivity of ABTS⁺, meet with the requirements for the development of fully automated, highly selective and sensitive method for the determination of iron.

Flow injection analysis (FIA) offers many advantages, such as high sample throughput, high reproducibility and minimum interference [18–20]. Among FIA techniques, reverse flow injection analysis (rFIA) is used to minimize reagent consumption, decrease sample dispersion, improve mixing efficiency and enhance sensitivity. Moreover, it is preferable in water analysis where a plenty of sample is available [21].

This paper introduces novel rapid and highly sensitive flow injection analysis methods for the determination of iron in biological and water samples, without the need for prior reduction of iron(III) to iron(II). The experimental conditions were carefully optimized and a detailed assessment of the possible interferences was carried out. The results of applying these new methods to the measurement of iron in blood serum, groundwater and pipeline water are presented. The results are shown to be in good agreement with those obtained by previously utilized methods.

2. Experimental

2.1. Materials and reagents

All reagents used were of analytical grade and all solutions not otherwise stated were prepared in deionized water. Standard iron (III) solution (0.01 mol L⁻¹) was prepared by dissolving the appropriate amount of Fe(NO₃)₃ · 9H₂O in 0.1 mol L⁻¹ HNO₃ followed by standardization by EDTA titration. The 2,2'-azino-bis(3-ethylbenzothiazoline-6-sulfonate)-diammonium salt reagent (ABTS), HCl, HNO₃, HClO₄, H₂SO₄ and H₃PO₄ were all purchased from Sigma-Aldrich.

2.2. Equipment

All absorbance measurements were made using a Varian Cary 50 UV-vis spectrophotometer equipped with a quartz cell with 1.00 cm light path length.

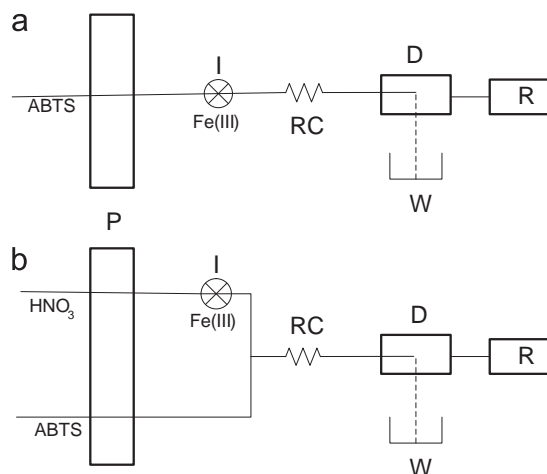


Fig. 1. FIA manifolds designed for iron determination. P=peristaltic pump; I= injection valve; RC= reaction coil; D= detector; R= recorder and W= waste.

2.3. Flow injection setup

Two arrangements of the FI manifold were designed: simple one-line and two-line manifolds, as depicted in Fig. 1. The parameters, namely, injection volume, flow rate, length of mixing coil, concentrations of ABTS and HNO₃ acid were optimized in both normal and reverse modes. Tygon tubing (0.8 mm i.d.) was used for the flow lines.

The flow injection setup consisted of a peristaltic pump (Masterflex model 7519-20, Cole Parmer Inc.) connected to a rotary injection valve (Rheodyne, P/N 7125) through a 30-cm Tygon tubing, coiled on a 2.5-cm diameter reel. The outlet of the valve was connected to the reaction coil. In the normal flow mode, the distance between the injection valve and the spectrophotometric cell was set at 80-cm, including a 15-cm reaction coil (0.8 mm i.d.). In the reverse flow mode this distance was 145-cm, including an 80-cm reaction coil (1.0 mm i.d.). A 390 μL flow cell (Hellma, 176.700-QS) was used with 10-mm light path length. The data were obtained using Varian UV-vis spectrophotometer and the output signals were recorded using Cary Win software. In the normal flow mode, the sample or iron(III) standard solution was injected via a plastic syringe into a merged stream of the ABTS solution. In the reverse flow mode, the ABTS reagent was injected into a merged stream of a standard or a sample solution.

2.4. Procedure

Parameter optimization was carried out using the univariate method, in which a parameter is modified while maintaining the other parameters at constant values. Then, whilst maintaining the first parameter at its optimum value, the next parameter is experimentally modified. This procedure was repeated for all parameters.

2.5. Water samples treatment

Groundwater (collected from Ras Al-Khaimah, UAE) and municipal pipeline water (collected from Al-Ain city) samples were acidified with dilute HNO_3 acid to $\text{pH} \sim 2.0$, and adjusted to $0.1 \text{ mol L}^{-1} \text{KNO}_3$ immediately after collection. Samples were allowed to equilibrate for 1 day, the pH was then adjusted to ~ 2.3 using dilute NaOH before analysis.

2.6. Serum sample treatment

Camel serum (0.75 mL) was transferred to a 15-mL centrifuge tube, diluted with 1.5 mL of deionized water and acidified with 3 mL of 1.0 mol L^{-1} nitric acid to precipitate proteins. The mixture

was agitated vigorously on a vortex-mixer for 3 min. The precipitate was allowed to stand for 5 min and centrifuged for 20 min at 3000 rpm, then the supernatant solution was decanted into a beaker. In order to prevent occlusion of iron within the precipitate, the precipitate was further twice washed with water and nitric acid, vortex-mixed and centrifuged, then the three supernatants were combined. The resultant solution was extracted twice with 30 mL of diethyl ether. The aqueous extract was diluted to 20 mL with water and analyzed by ICP-AES. A 15 mL portion of the aqueous extract was evaporated until dry, then dissolved in a mixture of $0.1 \text{ mol L}^{-1} \text{KNO}_3$ and $5 \times 10^{-3} \text{ mol L}^{-1} \text{HNO}_3$ acid, before being diluted with water to 6 mL. This diluted sample was divided into two equal portions, to one of them a standard Fe (III) solution was added. The two portions were sequentially injected into the ABTS carrier stream using the nFI mode. The iron concentration was calculated by the standard addition method.

3. Results and discussion

Preliminary investigations of Fe(III) and more than twenty other metal cations showed that only Fe(III) has the capacity to oxidize ABTS to a radical cation in acidic medium (Fig. 2). The oxidation reaction was virtually instantaneous (within ~ 6 s) and the reaction product was stable under these conditions for several hours (Fig. 3). This fast and selective oxidation of ABTS by Fe(III), along with the stability and the high molar absorptivity of the reaction product, encouraged us to use these properties in the development of rapid, sensitive and selective methods for the determination of iron using batch and FI techniques.

3.1. Batch measurements

3.1.1. Effects of acid species, its concentration and ionic strength

The effect of acid type on the reaction progress was investigated using 0.01 mol L^{-1} of HNO_3 , HClO_4 , HCl , H_2SO_4 or H_3PO_4 . For HNO_3 , HCl and HClO_4 media, the reaction was immediate and reached completion within a few seconds (~ 6 s). For H_2SO_4 medium, the reaction was slow and did not reach completion, perhaps due to the

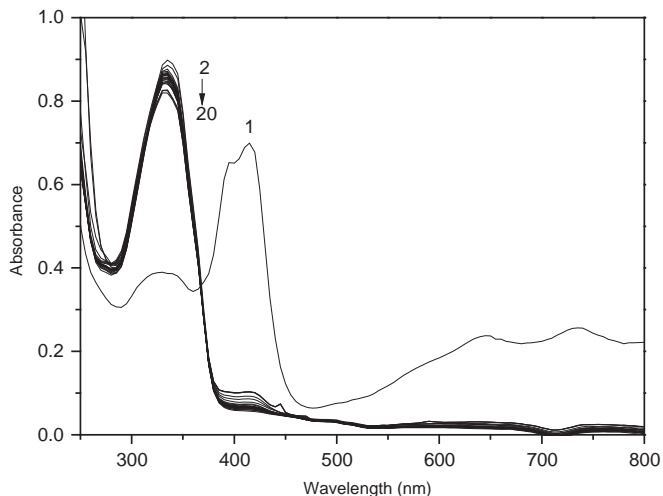


Fig. 2. Absorption spectra of ABTS ($2.5 \times 10^{-4} \text{ mol L}^{-1}$) treated with some metal ions in HNO_3 acid ($5 \times 10^{-3} \text{ mol L}^{-1}$), spectrum (1) is for Fe(III) ($2.5 \times 10^{-5} \text{ mol L}^{-1}$), spectrum (2) is for ABTS alone, and spectra (3–20) are for $1 \times 10^{-3} \text{ mol L}^{-1}$ Li^+ , Cs^+ , Rb^+ , Tl^+ , Ca^{2+} , Mg^{2+} , Sr^{2+} , Pb^{2+} , Hg^{2+} , Zn^{2+} , Cu^{2+} , Co^{2+} , Ni^{2+} , Cd^{2+} , Cr^{3+} , La^{3+} , Ce^{3+} , Al^{3+} . Measurements performed with deionized water as a blank.

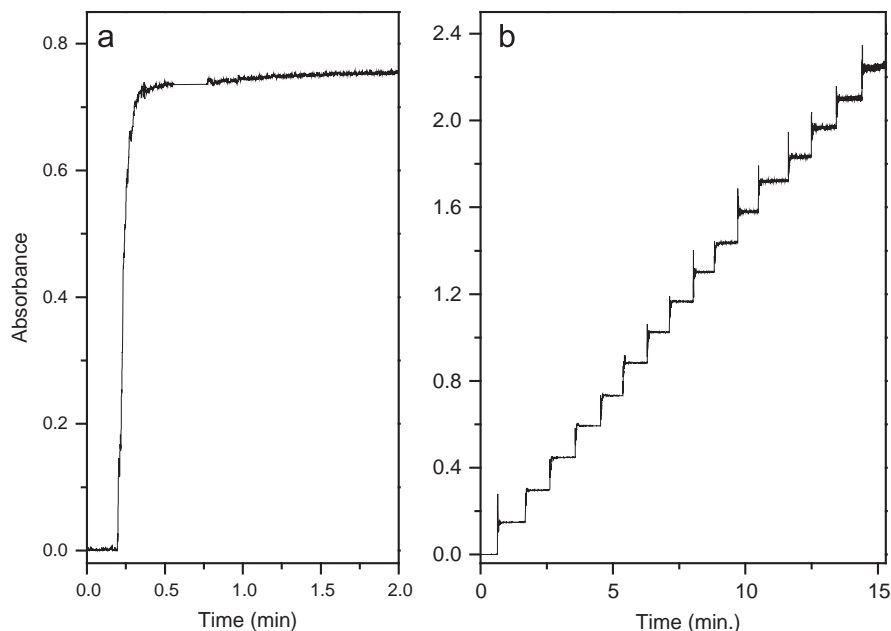


Fig. 3. Addition of Fe(III) standards to ABTS solution. (a) single addition, and (b) successive additions.

interaction of sulfate with the reduced form of ABTS. For H_3PO_4 medium, the reaction was very slow due to the formation of FeHPO_4^+ complex which stabilizes the Fe(III) state. Consequently, HNO_3 was chosen for subsequent experiments as it could oxidize Fe(II) into Fe(III) and did not show any oxidation effect on ABTS.

The effect of HNO_3 concentration was investigated over the range (1×10^{-3} – 0.1 mol L^{-1}) (Fig. 4). Maximum and constant absorbance readings were obtained in the concentration range (2.5×10^{-3} – $1.0 \times 10^{-2} \text{ mol L}^{-1}$). However, the absorbance readings were lower at higher acid concentrations, so $5 \times 10^{-3} \text{ mol L}^{-1} \text{ HNO}_3$ (pH=2.3) was chosen as the optimum.

The effect of ionic strength was assessed using KNO_3 (Fig. 4). Slightly lower absorbance readings were observed with increasing concentration up to $0.2 \text{ mol L}^{-1} \text{ KNO}_3$. Therefore, $0.1 \text{ mol L}^{-1} \text{ KNO}_3$ was used throughout.

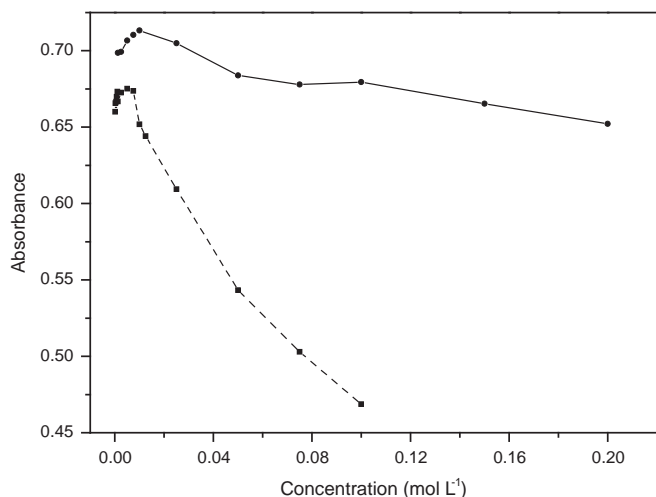


Fig. 4. Effect of HNO_3 acid (dashed line) and KNO_3 concentrations (solid line) on the oxidation of ABTS by Fe(III).

3.1.2. Effect of ABTS concentration

The stoichiometric ratio, as determined by the molar ratio and Job's methods, was 1:1. As the concentration of ABTS should be greater than that is required by stoichiometry for complete color development, ABTS concentrations up to an order of magnitude higher than the Fe(III) concentration were tested using $2.2 \text{ mg L}^{-1} \text{ Fe(III)}$ solution. A $6 \times 10^{-5} \text{ mol L}^{-1} \text{ ABTS}$ concentration (1.5 equivalent) was found to be sufficient for complete color development. A plateau absorbance reading was obtained with higher concentrations. Therefore, $2 \times 10^{-4} \text{ mol L}^{-1} \text{ ABTS}$ was chosen as the optimum concentration to extend the linear range to 4.5 mg L^{-1} .

3.2. Flow injection analysis

To obtain a reliable assay of iron, the FIA parameters, including the design of the FI manifold, injection volume, mixing coil length, flow rate of solutions and ABTS concentration were optimized to obtain the highest possible sensitivity and reproducibility based on the optimal experimental conditions for batch measurements.

3.2.1. Design of FI manifold

For the one line manifold arrangement using nFIA, the Fe(III) solution was injected into a stream of ABTS solution acidified with HNO_3 acid ($5 \times 10^{-3} \text{ mol L}^{-1}$). In the two-line manifold, the Fe(III) solution was injected into a stream of HNO_3 acid ($5 \times 10^{-3} \text{ mol L}^{-1}$) and was merged at a T-piece with the ABTS stream. The FIA peaks obtained by the one-line manifold were found to be more sensitive than the two-line manifold, so the former was used throughout.

3.2.2. Normal flow injection measurements

3.2.2.1. Effect of flow rate. The effect of flow rate of ABTS solution was investigated by measuring the peak height in the range of 1.2 – 5.1 mL min^{-1} (Fig. 5(a)). Intense and broad signals with long baseline recovery times were obtained for low flow rates up to 1.9 mL min^{-1} . This resulted in lowering the sample throughput.

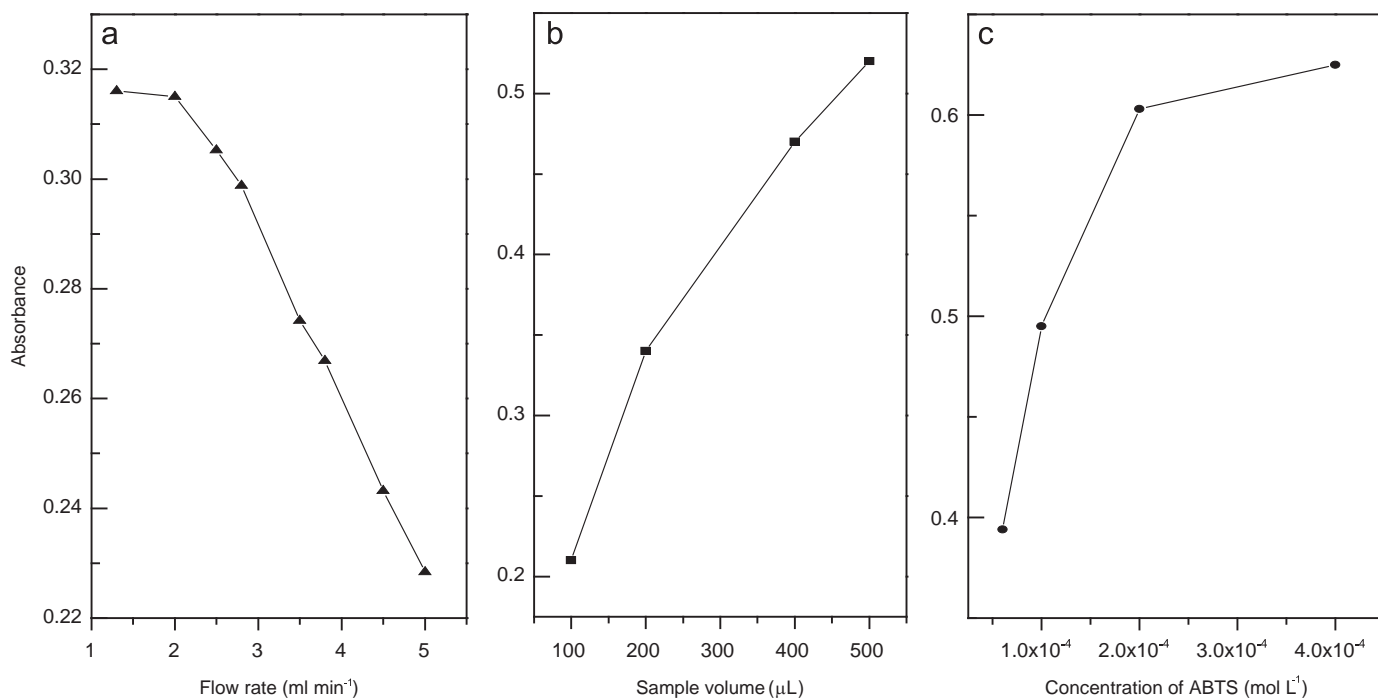


Fig. 5. (a) Effect of flow rate. Experimental conditions: ABTS $1 \times 10^{-4} \text{ mol L}^{-1}$ and Fe(III) 2.2 mg L^{-1} , both adjusted to $5 \times 10^{-3} \text{ mol L}^{-1} \text{ HNO}_3$ and $0.1 \text{ mol L}^{-1} \text{ KNO}_3$, no reaction coil, sample volume $500 \mu\text{L}$. (b) Effect of sample volume. Experimental conditions: ABTS $2 \times 10^{-4} \text{ mol L}^{-1}$, reaction coil length 15-cm, flow rate 2.8 mL min^{-1} , remaining conditions as for (a). (c) Effect of ABTS concentration. Experimental conditions: as for (b) using $500 \mu\text{L}$ sample volume and variable ABTS concentration.

Further increase in the flow rate led to a decrease in the peak height, but an increase in the sample throughput and reagent consumption. A flow rate of 2.8 mL min^{-1} was considered optimal, as it provided an acceptable compromise sensitivity, relatively high sample throughput and low consumption of reagent.

3.2.2.2. Effects of reaction coil length and injection volume. The length from the injector to the flow cell was optimized alternatively in the presence or absence of the reaction coil under the experimental conditions: ABTS ($2 \times 10^{-4} \text{ mol L}^{-1}$), Fe(III) (2.2 mg L^{-1}), both of them adjusted to $5 \times 10^{-3} \text{ mol L}^{-1}$ HNO_3 and 0.1 mol L^{-1} KNO_3 , flow rate (2.8 mL min^{-1}) and injection volume ($500 \mu\text{L}$). Reaction coil lengths of 0, 15 and 30 cm gave peak heights of 0.49, 0.52, 0.52, respectively. An 80-cm distance between the injector and flow cell, including a 15-cm reaction coil length was considered optimal and used for subsequent investigation.

The effect of the injection volume was investigated by injecting volumes ranging from 100 to $500 \mu\text{L}$ of 2.2 mg L^{-1} Fe(III). The peak height increased with increasing injection volume. A $500 \mu\text{L}$ injection volume gave the best sensitivity and was applied throughout (Fig. 5(b)).

3.2.2.3. Effect of ABTS concentration. The effect of varying ABTS concentration in the range 5×10^{-5} to $4 \times 10^{-4} \text{ mol L}^{-1}$ for the determination of 2.2 mg L^{-1} ($3.94 \times 10^{-5} \text{ mol L}^{-1}$) Fe(III) was explored. ABTS concentration up to $2 \times 10^{-4} \text{ mol L}^{-1}$ (5 equivalent) progressively increased the peak height. Further increase in the ABTS concentration resulted in a slight increase in the peak height (Fig. 5(c)). Thus, a concentration of $4 \times 10^{-4} \text{ mol L}^{-1}$ ABTS was chosen to obtain the highest sensitivity and to extend the linear range up to 4.5 mg L^{-1} .

3.2.3. Reverse flow injection analysis

3.2.3.1. Effect of flow rate. The effect of flow rate on rFIA signals was examined over the range 2.5 – 9.0 mL min^{-1} using the optimal conditions for nFIA. As shown in Fig. 6, an undesirable double peak was obtained. This pattern is more prone to occur in rFIA when large injection volumes are used [22]. Increasing the flow rate sharpened the peaks, however, the double peak pattern remained unchanged. The peak heights did not significantly change when the flow rate was increased, however, less precise peaks were obtained at higher flow rates.

The effect of flow rate on the measured signal depends on the kinetics of the chemical reaction. If the chemical reaction is not at equilibrium, as in many FIA systems, increasing the flow rates reduces the time available for the reaction to proceed toward equilibrium. Therefore, a lower signal will be observed because the

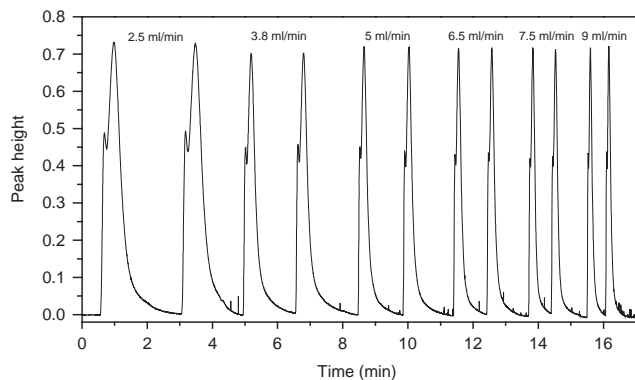


Fig. 6. Effect of flow rate on the peak height. Conditions: Fe(III) 2.2 mg L^{-1} , ABTS $2 \times 10^{-4} \text{ mol L}^{-1}$, both adjusted to $5 \times 10^{-3} \text{ mol L}^{-1}$ HNO_3 and 0.1 mol L^{-1} KNO_3 , injection volume $500 \mu\text{L}$, mixing coil length 80-cm.

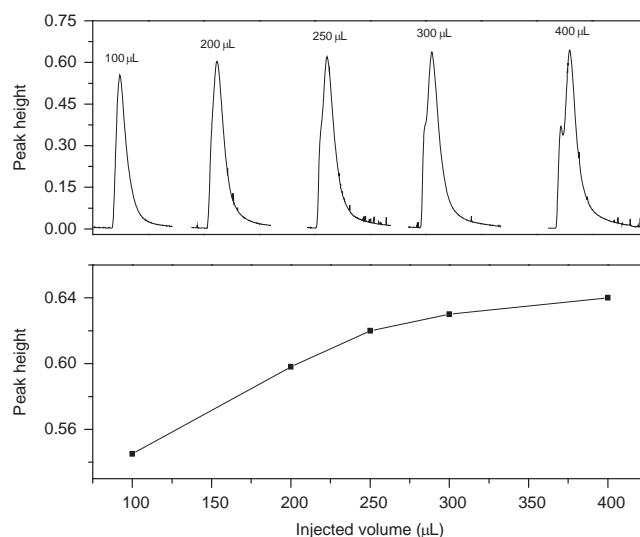


Fig. 7. Effect of injection volume on the peak height. Conditions: Fe(III) $4 \times 10^{-5} \text{ mol L}^{-1}$ in $5 \times 10^{-3} \text{ mol L}^{-1}$ HNO_3 , flow rate 6.5 mL min^{-1} , ABTS $2 \times 10^{-4} \text{ mol L}^{-1}$ in $5 \times 10^{-3} \text{ mol L}^{-1}$ HNO_3 , mixing coil length 76.5-cm.

formation of product is reduced [20]. Since the reaction between Fe(III) and ABTS has very fast kinetics, and the dispersion in rFIA is less than in nFIA [21], the measured signal in rFIA is minimally influenced by flow rate variations within a wide range. A flow rate of 6.5 mL min^{-1} was chosen to obtain the highest precision and a compromise sample throughput.

3.2.3.2. Effect of injection volume. The effect of injection volume on the peak height was investigated in the range 100– $400 \mu\text{L}$. The peak height linearly increased as the injection volumes increased up to $250 \mu\text{L}$. Furthermore, injection volumes up to $300 \mu\text{L}$ gave well defined single peaks, while double peaks were obtained at higher injection volumes (Fig. 7). Therefore, a $300 \mu\text{L}$ injection volume was used in subsequent investigations.

3.2.3.3. Effect of mixing coil length and its inner diameter. Reaction coil lengths from 0–110 cm were tested (Fig. 8). The maximum peak height was obtained with an 80-cm reaction coil length. The inner diameter of the reaction coil was also investigated, increasing the inner diameter from 0.8 mm to 1.0 mm led to a 15% increase in the peak height. A total distance of 145 cm between the injector and the flow cell including an 80-cm coil length of 1.0 mm i.d. was considered optimal and was used for further investigations.

3.2.3.4. Effect of ABTS concentration. The effect of ABTS concentration on rFIA signal is shown in Fig. 8. ABTS concentration of 10 times the Fe(III) concentration was found to be optimal. An $8 \times 10^{-4} \text{ mol L}^{-1}$ ABTS provided an upper detection limit of 2.7 mg L^{-1} Fe(III).

3.3. Calibration curves, reproducibility and sample throughput

Table 1 summarizes the figure of merits for the proposed methods. Compared with the widely used phenanthroline method [23], the proposed methods are more sensitive. Furthermore, although rFIA utilized smaller injected volumes than nFIA, it proved to be a more sensitive method than nFIA. This is due to the fact that the dispersion in rFIA is lower than in nFIA, so that the dilution of analyte is minimized [21].

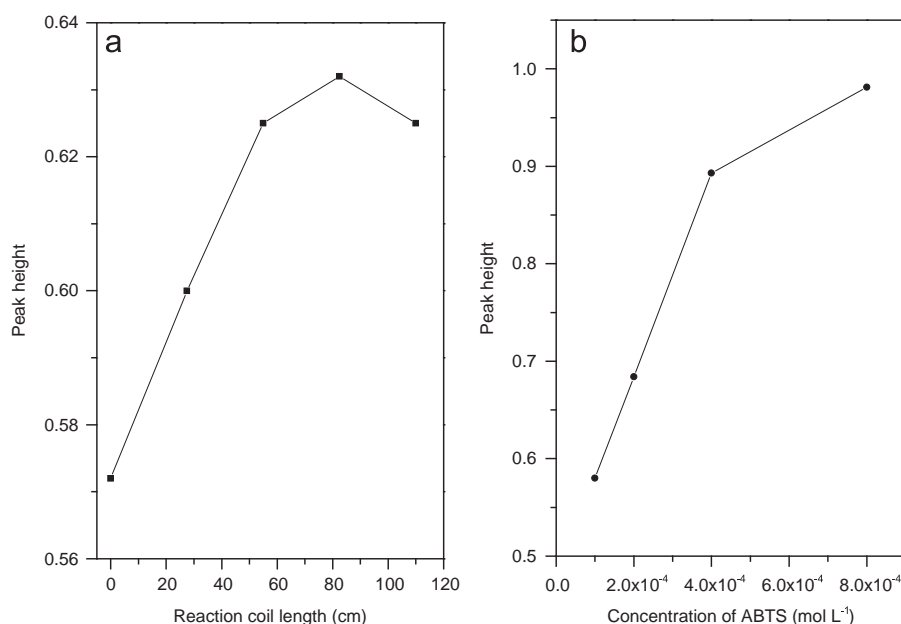


Fig. 8. (a) Effect of mixing coil length on the peak height. Conditions: Fe(III) 4×10^{-5} mol L $^{-1}$ in 5×10^{-3} mol L $^{-1}$ HNO $_3$, flow rate 6.5 ml min $^{-1}$, ABTS 2×10^{-4} mol L $^{-1}$ in 5×10^{-3} mol L $^{-1}$ HNO $_3$, injection volume 300 μ L. (b) Effect of ABTS concentration on the peak height. Conditions: as for (a) but with an 80-cm reaction coil length of 1.0 mm i.d. and varying of ABTS concentration.

Table 1

Analytical figure of merits of the proposed methods.

Technique	Batch	Normal flow	Reverse flow
Regression equation	$A = 30317.4 [\text{Fe}^{3+}] + 8.73 \times 10^{-4}$	$A = 13225 [\text{Fe}^{3+}] - 0.0292$	$A = 24090.1 [\text{Fe}^{3+}] + 0.021$
Regression coefficient	0.9998	0.9994	0.998
Dynamic range	$0 - 8.0 \times 10^{-5}$ mol L $^{-1}$ (0–4.5 mg L $^{-1}$)	$0 - 8.0 \times 10^{-5}$ mol L $^{-1}$ (0–4.5 mg L $^{-1}$)	$0 - 4.8 \times 10^{-5}$ mol L $^{-1}$ (0–2.7 mg L $^{-1}$)
Detection limit	4.6×10^{-7} mol L $^{-1}$ (25.5 μ g L $^{-1}$)	6.62×10^{-6} mol L $^{-1}$ (370 μ g L $^{-1}$)	1.46×10^{-6} mol L $^{-1}$ (81.6 μ g L $^{-1}$)
Quantification limit	1.53×10^{-6} mol L $^{-1}$ (85.3 μ g L $^{-1}$)	2.2×10^{-5} mol L $^{-1}$ (1.23 mg L $^{-1}$)	4.87×10^{-6} mol L $^{-1}$ (272 μ g L $^{-1}$)

Table 2

Interference of some alkali, alkaline earth and transition metal ions and anions on the determination of 1.12 mg L $^{-1}$ Fe(III).

Ion	Ratio [ion]/[Fe]	Relative error (%)	Ion	Ratio [ion]/[Fe]	Relative error (%)
K $^{+}$	5000	-3.7	Pb $^{2+}$	50 ^a	+4.8
Na $^{+}$	5000	-4.7	Cr $^{3+}$	50 ^a	+5.9
NH $_4^{+}$	5000	-4.7	Al $^{3+}$	300 ^a	+0.5
Li $^{+}$	5000	-3.7	La $^{3+}$	50 ^a	-0.5
Cs $^{+}$	3650	-5.9	NO $_3^{-}$	5000	-4.7
Rb $^{+}$	3650	-0.5	ClO $_4^{-}$	500	-3.4
Tl $^{+}$	50	+5.9	Cl $^{-}$	5000	-4.3
Ca $^{2+}$	3650	-0.5	I $^{-}$	50	-1.9
Ba $^{2+}$	50 ^a	+1.1	Br $^{-}$	500	+2.2
Sr $^{2+}$	500 ^a	-1.9	F $^{-}$	5	-2.1
Mg $^{2+}$	3650	-0.5	SCN $^{-}$	500	-5.3
Co $^{2+}$	3650	-1.9	CH $_3$ COO $^{-}$	100	-4.7
Ni $^{2+}$	500	-3.2	SO $_3^{2-}$	500	-3.2
Cu $^{2+}$	3650	-5.9	SO $_4^{2-}$	500	-8.5
Cd $^{2+}$	500	+2.1	PO $_4^{3-}$	50	-4.7
Hg $^{2+}$	3650	+4.8	N $_3^{-}$	2000	-4.3
Zn $^{2+}$	3650	+3.5	NO $_2^{-}$	500 ^b	-4.5

^a Higher concentration led to formation of precipitate with ABTS.

^b After treatment with sodium azide.

The proposed methods are highly precise, the obtained %RSD values for the determination of 1.12 mg L $^{-1}$ Fe(III) by the batch method, and 2.2 mg L $^{-1}$ Fe(III) by the nFIA and rFIA methods, were 0.97% ($n=7$), 1.28% ($n=7$) and 0.76% ($n=6$), respectively. Sample

throughputs of 35 and 45 h $^{-1}$ were obtained for the nFIA and rFIA, respectively.

3.4. Interference study

The potential interfering effects of common interfering ions on the accuracy of the determination of 1.12 mg L $^{-1}$ Fe(III) were assessed using the batch technique. The results listed in Table 2 show that, with the exception of NO $_2^{-}$ and F $^{-}$, all tested ions have insignificant effect on the determination of iron. Nitrite forms many oxidizing radical and peroxide species in acidic medium that oxidize the ABTS progressively, as shown in Fig. 9(a) [11]. The interference from nitrite can be effectively eliminated by converting nitrite into the unreactive molecular nitrogen through its reaction with sodium azide in acidic medium [24]:



Sodium azide up to 4×10^{-2} mol L $^{-1}$ was found to adequately remove nitrite ion up to 500 times the Fe(III) concentration, within 5 min of stirring in acidic conditions, before the addition of ABTS (Fig. 9(b)). After the treatment with sodium azide, the pH should be readjusted to ~ 2.3 . Attempts to eliminate the fluoride interference by addition of some common fluoride masking agents such as Ca $^{2+}$, Be $^{2+}$, Al $^{3+}$, La $^{3+}$ or Zr $^{4+}$ were not successful. Ba $^{2+}$, Sr $^{2+}$, Pb $^{2+}$ and trivalent cations concentrations higher than the tolerated ones interfere by forming precipitates with ABTS. Generally,

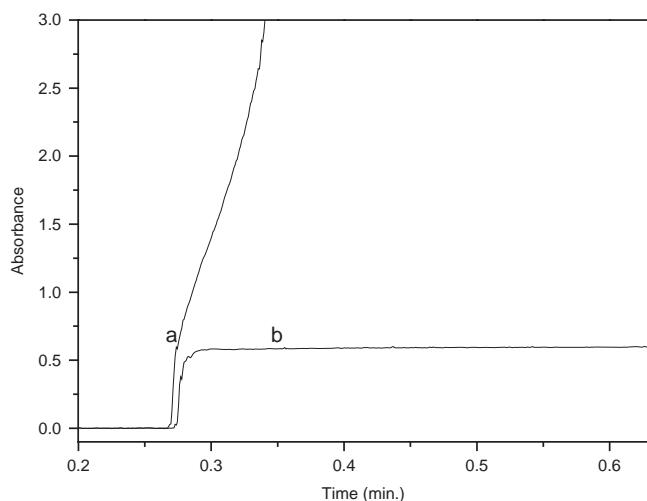


Fig. 9. Reaction of Fe(III) 1.12 mg L^{-1} with ABTS in the presence of $500 \text{ mg L}^{-1} \text{ NO}_2^-$: (a) untreated, and (b) treated with sodium azide $4 \times 10^{-2} \text{ mol L}^{-1}$.

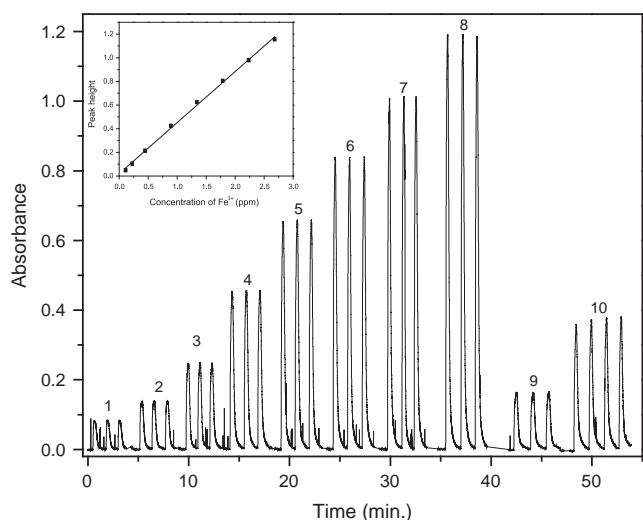


Fig. 10. Reverse flow injection signals of Fe(III) standard solutions (1)–(8), water sample (9), water sample spiked with standard solution (10), under the optimum conditions. (Insert – corresponding calibration curve).

the results show that the selectivity of the proposed methods is relatively better than other reported methods [25–32].

3.5. Applications

The proposed batch and rFIA methods were applied to the determination of total iron in municipal pipeline water and groundwater samples. Iron was not detected in either the municipal pipeline or groundwater. However, a pipeline water sample that was collected after council maintenance work was found to contain traces of iron. The rFI signals for the latter water sample and Fe(III) standards are depicted in Fig. 10. The results obtained were comparable with those obtained by the phenanthroline method [23] (Table 3). Statistical *t*- and *F*-tests indicated insignificant differences in accuracy and precision between the results obtained by the proposed methods and the phenanthroline method.

Groundwater samples spiked with $0.56 \text{ mg L}^{-1} \text{ Fe(III)}$ and analyzed using the rFIA procedure gave acceptable recoveries (90–100.7%) and excellent precision (Table 4). The recoveries may be correlated with the TDS and SO_4^{2-} concentrations. The

Table 3

Determination of iron in pipeline water sample using batch and rFIA methods.

Method	Iron, found (ppm) ^a	SD	% RSD	<i>F</i> -Test ^c	<i>t</i> -Test ^e
Batch technique:					
Direct calibration	0.271	0.013	4.8	6.76	1.50
Standard addition	0.260 ^b	0.0019	0.73	6.93 ^d	0.33 ^f
Reverse flow:					
Direct calibration	0.254	0.002	0.79	6.25	1.61
Standard addition	0.249	0.008	3.21	2.56	1.84
Phenanthroline					
Direct calibration [22]	0.259	0.005	1.94		

^a Average of three replicate measurements.

^b Average of five replicate measurements.

^c The tabulated *F*-value at 95% confidence level, $F_c(0.05, 2, 2)=19.00$.

^d The tabulated *F*-value at 95% confidence level, $F_c(0.05, 2, 4)=6.94$.

^e The tabulated *t*-value at 95% confidence level, $t_c(0.05, 4)=2.78$.

^f The tabulated *t*-value at 95% confidence level, $t_c(0.05, 6)=2.45$.

Table 4

Determination of iron in spiked groundwater using rFIA technique.

Sample	Iron, added (mg L^{-1})	Iron, found ^a (mg L^{-1}) $\pm tS/\sqrt{N}$	Recovery (%)
S1–S4	–	N.D.	–
S1	0.56	$0.564 \pm 9.05 \times 10^{-4}$	100.7
S2	0.56	$0.528 \pm 2.14 \times 10^{-3}$	94.3
S3	0.56	$0.516 \pm 9.02 \times 10^{-3}$	92.2
S4	0.56	$0.505 \pm 8.76 \times 10^{-3}$	90.2

^a Average of three determinations, *t*-value at the 95% confidence level ($df=2$)=2.92.

TDS and SO_4^{2-} concentrations for the four samples analyzed (S1–S4) were respectively, 789.2, 1802.3, 3182.5, 2103.8 for TDS, and 197.76, 460.8, 86.4, 345.6, for SO_4^{2-} . Generally, samples with high TDS and/or SO_4^{2-} gave low recovery values. This observation correlates with the effect of H_2SO_4 (section; effect of acid species) and the relatively high error (8.5%) for SO_4^{2-} in the interference study.

The applicability of the proposed nFIA method was tested by the determination of total iron in two camel serum samples. Although the normal iron concentration in camel serum is in the range $0.54\text{--}2.14 \text{ mg L}^{-1}$ [33], higher results were obtained; 5.35 and 3.88 mg L^{-1} . However, these results are in good agreement with those obtained by ICP-AES (5.48 ppm and 4.50 ppm), with recovery values of 97.63% and 86.3%. The high iron contents may be attributed to the fact that the animals were dehydrated.

4. Conclusion

In this work, new proposed batch, normal and reverse flow injection methods for the determination of total iron have been developed and optimized. The methods utilize the selective oxidation of ABTS by Fe(III) in acidic medium. They were shown to be very sensitive, as indicated by the detection limits: 25.5, 370, $81.6 \mu\text{g L}^{-1} \text{ Fe(III)}$ for batch, nFIA and rFIA methods, respectively. The methods have been applied to the determination of iron in groundwater, municipal pipeline water and camel serum samples. The results obtained were found to be in good agreement with those obtained by the phenanthroline method and ICP-AES. The batch technique is simple and facilitates the determination of iron in field analysis, as many types of portable colorimeters are now

available. On the other hand, the nFI and rFI techniques provide good sampling frequencies, that are commonly required for routine analyses in environmental and clinical laboratories.

Acknowledgments

We are very grateful to Beni-Suef and UAE universities for providing the laboratory facilities.

References

- [1] W.G. Sunda, S.A. Huntsman, *Mar. Chem.* 50 (1995) 189–206.
- [2] E.S. Gurzau, C. Neagu, A.E. Gurzau, *Ecotoxicol. Environ. Saf.* 56 (2003) 190–200.
- [3] World Health Organization (WHO), Iron in drinking-water, in: Background document for development of WHO guidelines for drinking-water quality, WHO/SDE/WSH/03.04/08, 2003.
- [4] NRC, National Research Council, Iron, University Park Press, Baltimore (MD), 1979.
- [5] Department of National Health and Welfare, nutrition recommendations, The Report of the Scientific Review Committee, Ottawa, Canada, 1990.
- [6] S. Ohno, N. Teshima, T. Sakai, K. Grudpan, M. Polasek, *Talanta* 68 (2006) 527–534.
- [7] A.D. Sheftel, A.B. Mason, P. Ponka, *Biochim. Biophys. Acta* 2012 (1820) 161–187.
- [8] V.K. Gupta, R. Dobhal, A. Nayak, S. Agarwal, D.P. Uniyal, P. Singh, B. Sharma, S. Tyagi, R. Singh, *Crit. Rev. Anal. Chem.* 42 (2012) 245–256.
- [9] S. Khan, R. Dashora, A.K. Goswami, D.N. Purohit, *Rev. Anal. Chem.* 23 (2004) 1–74.
- [10] E.P. Achterberg, T.W. Holland, A.R. Bowie, R.F.C. Mantoura, P.J. Worsfold, *Anal. Chim. Acta* 442 (2001) 1–14.
- [11] A.A. Salem, A.A. Soliman, I.A. El-Haty, *Anal. Chem. Insights* 6 (2011) 37–44.
- [12] Y. Lee, J. Yoon, U. von Gunten, *Water Res.* 39 (2005) 1946–1953.
- [13] U. Pinkernell, B. Nowack, H. Gallard, U. Gunten, *Water Res.* 34 (2000) 4343–4350.
- [14] H.U. Bergmeyer, *Methods of enzymatic analysis*, Verlag Chemie Weinheim, 2nd ed., Academic Press, Inc., New York and London, 1974.
- [15] U. Pinkernell, H.J. Lueke, U. Karst, *Analyst* 122 (1997) 567–571.
- [16] M. Ozyurek, K. Guclu, E. Tutem, K.S. Baskan, E. Ercag, S.E. Celik, S. Baki, L. Yildiz, S. Karaman, R. Apak, *Anal. Methods* 3 (2011) 2439–2453.
- [17] L.M. Magalhães, M. Santos, M.A. Segundo, S. Reis, J.L.F.C. Lima, *Talanta* 77 (2009) 1559–1566.
- [18] J. Ruzicka, E.H. Hansen, *Flow Injection Analysis*, NewYork, 2nd ed., Wiley, 1988.
- [19] M. Trojanowicz, *Flow Injection Analysis: Instrumentation and Applications*, World Scientific, London, 2000.
- [20] B. Karlberg, G.E. Pacey, *Flow Injection Analysis: A Practical Guide*, Elsevier, Amsterdam, 1989.
- [21] F.R. Mansour, N.D. Danielson, *Trends Anal. Chem.* 40 (2012) 1–14.
- [22] A.G. Fogg, X. Wang, J.F. Tyson, *Analyst* 114 (1989) 1119–1123.
- [23] L.S. Clesceri, A.E. Greenberg, A.D. Eaton, *Standard methods for the examination of water and wastewater*, 20th ed., American Public Health Association, Washington, 1998.
- [24] G.T.F. Wong, *Mar. Chem.* 130–131 (2012) 28–32.
- [25] T. Yamane, H. Yamada, *Anal. Chim. Acta* 308 (1995) 433–438.
- [26] K.-W. Cha, K.-W. Park, *Talanta* 46 (1998) 1567–1571.
- [27] T. Pojanagaroon, S. Watanesk, V. Rattanaphani, S. Liawrungrath, *Talanta* 58 (2002) 1293–1300.
- [28] A. Waseem, M. Yaqoob, A. Nabi, *Luminescence* 19 (2004) 333–338.
- [29] S. Ohno, N. Teshima, T. Sakai, K. Grudpan, M. Polasek, *Talanta* 68 (2006) 527–534.
- [30] S. Lunvongsa, M. Oshima, S. Motomizu, *Talanta* 68 (2006) 969–973.
- [31] W. Ruengsitagoon, *Talanta* 74 (2008) 1236–1241.
- [32] R.B.R. Mesquita, R. Suárez, V. Cerdà, M. Rangel, A.O.S.S. Rangel, *Talanta* 108 (2013) 38–45.
- [33] Y.E. Eltahir, H.M. Ali, M.H. Mansour, O. Mahgoub, *J. Anim. Vet. Adv.* 9 (2010) 764–770.



A new label-free and turn-on strategy for endonuclease detection using a DNA–silver nanocluster probe



Xue Tian, Xiang-Juan Kong, Zi-Mao Zhu, Ting-Ting Chen, Xia Chu*

State Key Laboratory for Chemo/Biosensing and Chemometrics, College of Chemistry and Chemical Engineering, Hunan University, Changsha 410082, PR China

ARTICLE INFO

Article history:

Received 19 June 2014

Received in revised form

25 July 2014

Accepted 30 July 2014

Available online 6 August 2014

Keywords:

Endonuclease

Silver nanocluster

Endonuclease inhibitor

Label-free

ABSTRACT

Endonuclease plays a vital role in a variety of biological processes and the assay of endonuclease activity and inhibitors is of high importance in the fields ranging from biotechnology to pharmacology. However, traditional techniques usually suffer from time intensive, laborious, and cost-expensive. This work aims to develop a facile and sensitive method for endonuclease activity assay by making use of the fluorescence enhancement effect when DNA–silver nanoclusters (DNA–Ag NCs) are in proximity to guanine-rich DNA sequences. The system mainly consists of block DNA (B-DNA), G-DNA and Ag-DNA. B-DNA serves as the substrate of the endonuclease (S1 nuclease as the model enzyme). G-DNA, which is pre-designed entirely complementary to B strand, contains a guanine-rich overhang sequence and hybridization part at the 5'-end. Ag-DNA involves a sequence for Ag NCs synthesis and a sequence complementary to the hybridization part of the G-DNA. In the "off" state, B-DNA plays the role as a blocker that inhibit the proximity between Ag NCs and guanine-rich DNA sequences, resulting in a low fluorescence readout. However, if S1 nuclease is introduced into the system, B-DNA was cleaved into mono- or short-oligonucleotides fragments, which could not hybridize with G-DNA. As a result, the subsequent addition of DNA–Ag NCs could bring guanine-rich DNA sequences close to the Ag NCs, accompanied by a significant fluorescence enhancement. Therefore, endonuclease activity could be successfully quantified by monitoring the variation in fluorescence intensity. In addition, this approach can also be applied for inhibitor screening of endonuclease. This label-free and turn-on fluorescent assays employing the mechanism proposed here for the detection of nuclease and inhibitors turn out to be sensitive, selective, and convenient.

© 2014 Elsevier B.V. All rights reserved.

1. Introduction

Endonucleases are a family of nucleases that are capable of hydrolyzing the phosphodiester linkages in the nucleic acid backbone. They play a vital role in a variety of biological processes involving replication, recombination, DNA repair, molecular cloning, genotyping, and mapping [1–5]. Moreover, the assay of endonuclease activity and inhibitors is of high importance in the fields ranging from biotechnology to pharmacology. Hence, development of sensitive assays for endonucleases activity are in great demand for clinical diagnostics, drug discovery, nanoscience, and biosensing. Traditional techniques, such as gel electrophoresis (PAGE), high-performance liquid chromatography (HPLC), radioactive labeling, and enzyme-linked immunosorbent assay (ELISA) have been established [6–9]. However, these conventional

protocols suffer from time intensive, laborious, cost-expensive, isotope labeling, and lack of sufficient sensitivity which restrict their widespread use. Recently, fluorescence-based bioanalytical methods have received intense research interest because of their remarkable features, such as high sensitivity, fast analysis speed, and simple instrumentation. A variety of fluorescent probes have been reported to sensitively detect endonuclease activity [10–12]. Although promising, these reported methods usually require complex labeling or sophisticated synthesis processes, leading to a high cost and time consuming. Therefore, it still remains a challenge to develop efficient, facile, sensitive, label-free, and amenable strategies to assay nuclease activity.

Few-atom noble-metal nanoclusters, such as Au, Ag and Pt nanoclusters, have attracted particular attention in the past decades due to the wide range of potential applications with their unique physical, electrical, and optical properties [13–16]. As promising alternatives to organic dyes and quantum, fluorescent Ag nanoclusters, in particular, are gaining much interest and have been successfully produced using various templates, such as DNA,

* Corresponding author. Tel./fax: +86 731 88821916.

E-mail address: xiachu@hnu.edu.cn (X. Chu).

polymers, small molecules, peptides, and proteins [17–21]. Among them, DNA stabilized silver nanoclusters (Ag NCs) have recently been the subject of intense research owing to their fascinating features including subnanometer size, ease of synthesis, good water solubility, excellent fluorescence property, and low toxicity. So far, many DNA–Ag NC-based biosensors have been successfully built to detect various biologically important targets [22–24]. Lately, Werner and colleagues discovered a new DNA–Ag NCs light-up system through placing NCs close to guanine-rich DNA sequences [25]. On the basis of this finding, a series of fluorescent turn-on methods have been developed for the detection of DNA, protein, small molecule, and cancer cell [25–29]. For instance, Ye et al. developed a fluorescence molecular beacon involving a guanine-rich DNA sequences, an aptamer, and Ag nanoclusters for the detection of adenosine triphosphate, and adenosine deaminase [26]. Wang et al. designed a new approach to light up DNA–Ag NCs-based beacons for the detection of DNA and protein by strand displacement reactions [28]. Yin and coworkers developed a label-free and turn-on aptamer strategy for cancer imaging [29]. While the exploration of fluorescence enhancement effect of Ag NCs upon guanine proximity in biochemical application is still in its infancy, such fluorescent probes are fascinating because of their simple design, “one-step” preparation, low cost, separation-free, and outstanding spectral and photophysical properties.

Inspired and encouraged by the above facts, based on the tremendous fluorescence enhancement effect of DNA–Ag NCs upon guanine proximity, a novel label-free and turn-on fluorescent DNA–Ag NCs probe for endonuclease detection was proposed in this work. To demonstrate the proof-of-concept of our design, S1 nuclease was selected as a model enzyme. The S1 nuclease is a widespread single strand DNA(ssDNA)-specific endonuclease, which can digest ssDNA into mono- or oligo-nucleotide pieces [30,31]. In this sensing process, B-DNA plays the role as a blocker that inhibit the proximity between Ag NCs and guanine-rich DNA sequences, resulting in a low fluorescence readout. However, if S1 nuclease is introduced into the system, B-DNA was cleaved into mono- or short-oligonucleotides fragments, which could not hybridize with G-DNA. As a result, the subsequent addition of DNA–Ag NCs could bring guanine-rich DNA sequences close to the Ag NCs, accompanied by a tremendous fluorescence enhancement. Therefore, the fluorescence response of Ag NCs is dependent on the concentration of S1 nuclease. Then, endonuclease activity could be successfully quantified by monitoring the fluorescence change.

2. Experimental

2.1. Materials

All oligonucleotides were synthesized and purified by Sangon Biotechnology Co., Ltd. (Shanghai, China) and their sequences are listed in Table 1. Silver nitrate (AgNO_3) and sodium borohydride (NaBH_4) were supplied by Sigma Aldrich (St. Louis, MO, USA). S1 nuclease ($100 \text{ U } \mu\text{L}^{-1}$) was obtained from Thermo Fisher Scientific Inc. The S1 nuclease buffer (20 mM NaAc, 150 mM NaCl, and 1 mM ZnSO_4 , pH 4.5) was used to dilute S1 nuclease and enzymatic

digestion reaction. All other chemicals were at least analytical grade and were used without further purification. All aqueous solutions were prepared using ultrapure water, which was purified with a Millipore Milli-Q water purification system (Billerica, MA, USA), and had an electric resistance $> 18.3 \text{ M}\Omega$.

2.2. Apparatus and characterization

All fluorescence measurements were carried out by using a Fluoromax-4 spectrofluorometer (HORIBA Jobin Yvon, Inc., NJ, USA). Both Ex and Em slits were set at 5.0 nm with a 950 V PMT voltage. The fluorescence emission spectra of each system were collected from 590 to 750 nm at the excitation wavelength of 570 nm. All fluorescence measurements were recorded at room temperature unless otherwise stated. The sizes and morphologies of the DNA-templated silver nanoclusters (DNA–Ag NCs) were obtained using a JEOL JEM-2100 transmission electron microscope with an acceleration voltage of 200 kV. The sample used for TEM imaging was prepared as follows: 5 μL of dilute colloid solution of the DNA–Ag NCs dispersed in water was drop-cast on thin, carbon formvar-coated copper grids and air dried before imaging.

2.3. Synthesis of DNA–Ag NCs

In this work, DNA–Ag NCs were synthesized based on a previous literature report with minor modification [18]. Briefly, DNA strand was first dissolved in ultrapure water and subsequently mixed with 120 μM AgNO_3 by vortexing in 20 mM sodium phosphate buffer, pH 7.0. After incubation for twenty minutes in an ice bath, the solution was reduced by adding freshly prepared NaBH_4 (120 μM) quickly with vigorous shaking for two minutes. The obtained solution was then stored at 4 $^\circ\text{C}$ in the dark for 12 h before fluorescence measurement.

2.4. Assay of S1 nuclease activity and inhibition

For measurement of S1 nuclease activity, 20 μL aliquot of reagent solution containing 5 μM B-DNA and S1 nuclease of various concentrations was used to perform the enzymatic digestion reaction. After incubation for 30 min at 37 $^\circ\text{C}$, the cleavage reaction was ended by heating at 95 $^\circ\text{C}$ for 10 min. Then 10 μL G-DNA of 10 μM and sodium phosphate buffer (pH 7.0) were added to mixed with the prepared solutions. The above mixture was heated at 80 $^\circ\text{C}$ for 20 min, and gradually cooled down to room temperature. Finally, the fluorescent DNA–Ag NCs probe was added into the system and allowed to react for 60 min at room temperature. Then the resulting solution was subjected to fluorescence measurements.

For the inhibition experiments, the inhibitor ATP of various concentrations was first introduced into the solution containing B-DNA, and then S1 nuclease was added. All other procedures were the same as the aforementioned assay of S1 nuclease activity.

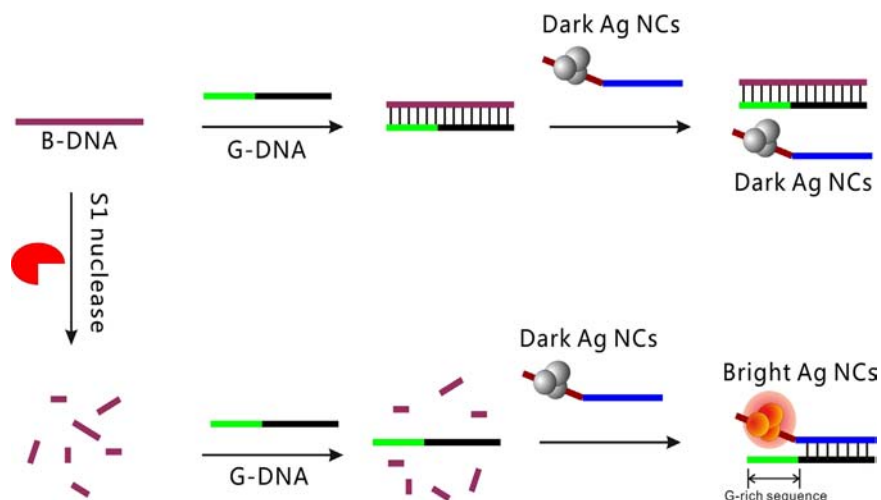
3. Results and discussion

3.1. Sensor design

The design of the label-free and turn-on fluorescent assay of S1 nuclease was displayed in Scheme 1. The system mainly contains block DNA (B-DNA), G-DNA and Ag–DNA. B-DNA, serving as the substrate of the endonuclease (S1 nuclease as the model enzyme), could be digested to mono- or oligo-nucleotide fragments. G-DNA, which is predesigned entirely complementary to B strand, contains a guanine-rich overhang sequence (green part in Scheme 1) and hybridization part (black domain in Scheme 1) at the 5'-end.

Table 1
Names and sequences of the oligonucleotides.

Name	Sequence
B-DNA	5'-CCCCACCCACCCACCCAGCACATCTGATAGTTC-3'
G-DNA	5'-GAACTATCAGATGTGCTGGGTGGGGTGGGGTGGG-3'
Ag–DNA	5'-CCTTAATCCCCAGCACATCTGATAGTTC-3'



Scheme 1. Schematic illustration of the label-free strategy for endonuclease assay based on the fluorescence enhancement effect of DNA–silver nanoclusters (DNA–Ag NCs) in proximity to guanine-rich DNA sequences.

Ag–DNA involves a sequence for Ag NCs synthesis (red domain in Scheme 1) and a sequence (blue domain in Scheme 1) complementary to the hybridization part of the G–DNA. In this sensing process, the Ag NCs prepared with Ag–DNA as the synthesis template displayed very weak fluorescence. However, great fluorescence enhancement occurred through placing the dark Ag NCs close to the guanine-rich DNA sequences. In the absence of S1 nuclease, the B–DNA kept its original state, which could effectively hybridizes with the G–DNA. As a result, the Ag NCs–template–segment failed to get close to guanine-rich DNA sequences and accordingly low fluorescence intensity was observed. When S1 nuclease was introduced into the system, the B–DNA was cleaved into fragments. In such case, B–DNA and G–DNA can not form the double-stranded DNA duplex. The resulting G–DNA could hybridize with the signal probe which will bring the Ag NCs close to guanine-rich sequences, thus resulting in the fluorescence enhancement. Therefore, endonuclease can be successfully quantified by monitoring the fluorescence changes.

3.2. Characterization of Ag NCs

In this label-free and turn-on strategy for endonuclease detection, the enhancement in fluorescent intensity of DNA–Ag NCs upon proximity of guanine-rich sequences was used as a signal readout. So, to demonstrate such sensing concept, we first investigated the fluorescence emission of the Ag–DNA templated Ag NCs before and after hybridized with G–DNA. As can be seen from Fig. 1A, before hybridization, only weak fluorescence emission at 510 nm was observed with 465 nm excitation (curves a and b in Fig. 1A). However, tremendous enhancement of fluorescence emission of the Ag–DNA templated Ag NCs occurred when G–DNA was added. We also found that the excitation and emission peaks changed to 570 nm and 625 nm respectively after hybridization (curves c and d in Fig. 1A). As can be seen from Fig. 1B, the fluorescence enhancement was fast and was completed within 60 min after the G–DNA was introduced into the solution. The results indicated that the fluorescence enhancement effect of the Ag–DNA templated dark Ag NCs could be produced through the hybridization between Ag–DNA and G–DNA which leads to the proximity of the Ag NCs and guanine rich sequences. As characterized by Transmission electron microscopy (TEM), the as-prepared DNA–Ag NCs were shown to be spherical and uniform with an average diameter of 2 nm (Fig. 1C).

3.3. Assay of S1 nuclease activity

To verify the application of the established strategy for endonuclease assay, fluorescence spectroscopy was then carried out. Upon being excited at 570 nm, only very weak fluorescence was observed of the formed DNA–Ag NCs (curve a, Fig. 2). However, the fluorescence emission was enhanced greatly upon guanine proximity (curve e, Fig. 2). When the B–DNA was introduced into the system, B–DNA hybridized with G–DNA and the subsequent addition of Ag NCs probe could not be brought close to the guanine-rich DNA sequences, leading to no enhancement in the fluorescence intensity (curve b, Fig. 2). The obtained result indicated that the introduction of B–DNA could effectively prevent the fluorescence enhancement caused by the proximity of G-rich sequences and the Ag NCs. However, in the presence of S1 nuclease, after B–DNA first incubated with S1 nuclease for 30 min at 37 °C, the fluorescence intensity increased obviously (curve d, Fig. 2). The result indicated that the B–DNA was cleaved into mono- or oligo-nucleotide fragments, which could not effectively hybridize with G–DNA, thus leading to the hybridization of G–DNA and Ag–DNA, accompanied by a tremendous fluorescence enhancement due to the proximity of G-rich sequences and the Ag NCs.

To validate whether the fluorescence enhancement was due to the digestion of B–DNA by S1 nuclease, control experiment was further carried out. S1 nuclease was first heated for 10 min at 95 °C. The denatured S1 nuclease was then incubated with B–DNA instead of the active S1 nuclease. It turned out to be a low fluorescence response, confirming the fluorescence change was really from the cleavage reaction of B–DNA by S1 nuclease (curve c, Fig. 2).

To depict the dynamic response range and detectable minimum concentration of endonuclease using the strategy, fluorescence response of DNA–Ag NCs upon adding different amounts of S1 nuclease into the system was recorded (Fig. 3A). It was found that the fluorescence signals were continually increased as the concentration of S1 nuclease increased from 0.01 to 50 U mL⁻¹. This indicated a gradual degradation of B–DNA. Fig. 3B outlines the relationship between the fluorescence signal and the concentration of S1 nuclease. A good linear relationship ($R^2=0.985$) in the concentration range from 2 to 20 U mL⁻¹ was showed as the inset in Fig. 3B. Besides, it should be emphasized that the strategy was sensitive to S1 nuclease with 0.01 U mL⁻¹ S1 nuclease can be detected.

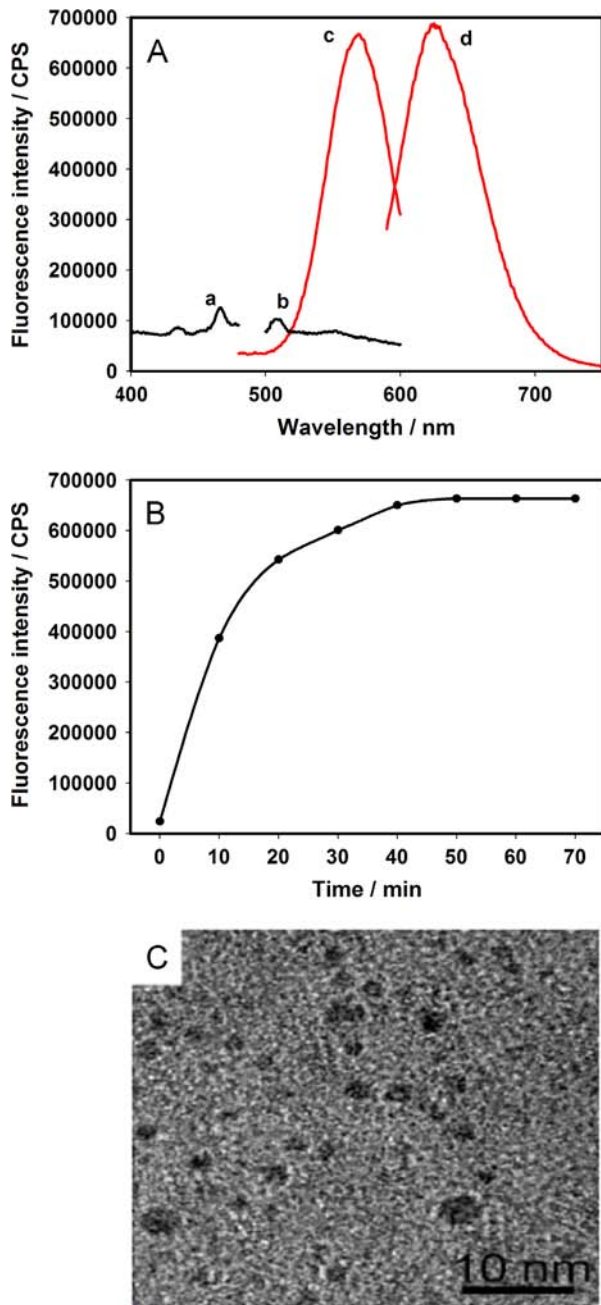


Fig. 1. (A) Excitation and emission spectra of the fluorescent Ag NCs obtained before (curves a and b) and after (curves c and d) addition of G-DNA. (B) The fluorescence intensity changes of DNA–Ag NCs upon addition of G-DNA as a function of incubation time at room temperature. (C) TEM image of DNA–Ag NCs.

3.4. Specificity of the assay

To examine the specificity of the DNA-based Ag NCs probes towards S1 nuclease, some other types of enzymes and proteins were added in place of S1 nuclease. Under the same experimental procedures and conditions as S1 nuclease, only S1 nuclease caused a dramatic fluorescence enhancement whereas other proteins resulted in nearly negligible fluorescence intensity change (Fig. 4). These results clearly indicated that the proposed method could be applied in the detection of S1 nuclease with high sensitivity and specificity.

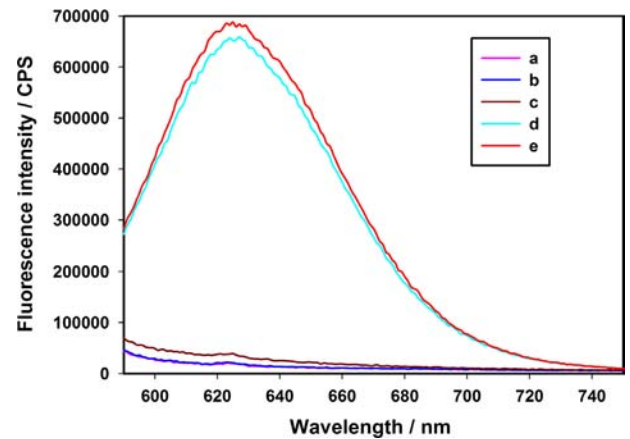


Fig. 2. The fluorescence emission spectra of DNA–Ag NCs in the presence of (a) no added reagent, (b) B-DNA and G-DNA, (c) B-DNA with denatured S1 nuclease, G-DNA, (d) B-DNA with S1 nuclease and G-DNA, and (e) G-DNA. The concentration of all DNA used was all $1.0 \mu\text{M}$. The concentration of S1 nuclease was 50 U mL^{-1} .

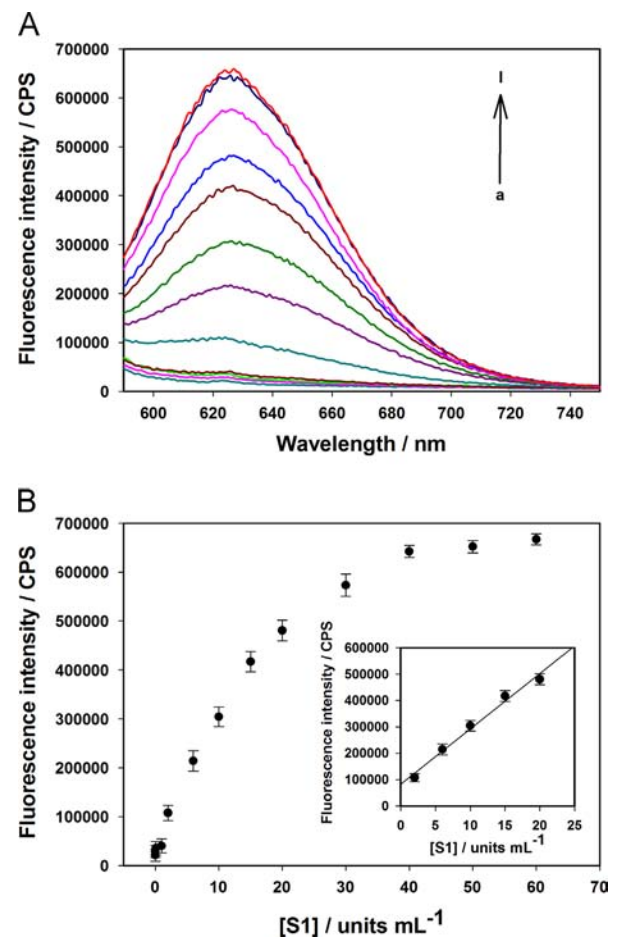


Fig. 3. (A) The fluorescence emission spectra of the assay system at various concentrations of S1 nuclease (from a to l): 0, 0.01, 0.1, 1, 2, 6, 10, 15, 20, 30, 40, 50 U mL^{-1} . (B) The relationship between the fluorescence intensity and the concentration of S1 nuclease. Inset shows a linear response of the assay system to S1 nuclease. The concentration of DNA used here was all $1.0 \mu\text{M}$. Error bars represented standard deviations from three repeated experiments.

3.5. S1 nuclease inhibition assay

The utility of this established strategy for screening potential inhibitors of S1 nuclease was also studied. ATP, a known S1 nuclease inhibitor [32], was selected here to investigate its

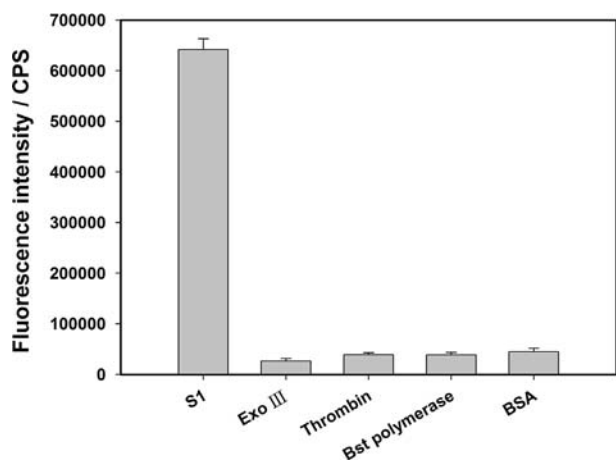


Fig. 4. Specificity analysis of the assay system. The concentration of S1 nuclease and ExoIII were 50 U mL^{-1} . All the other enzymes and proteins: Bst polymerase and thrombin were 500 U mL^{-1} . BSA was at a concentration of 1 mg mL^{-1} . Error bars represented standard deviations from three repeated experiments.

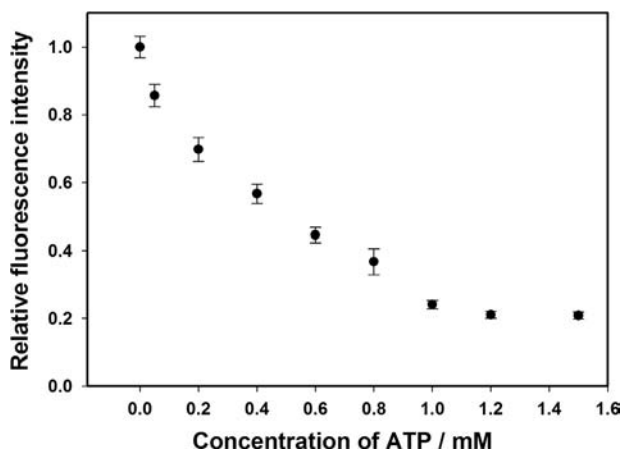


Fig. 5. Inhibitory effect of ATP on the activity of S1 nuclease. The concentration of S1 nuclease was 50 U mL^{-1} . Error bars represented standard deviations from three repeated experiments.

inhibition effect on the endonuclease through the proposed detection method. Fig. 5 depicts the effect of ATP concentrations on the endonucleases activity. The image demonstrated the fluorescence intensity changes of the Ag NCs when the system containing 50 U mL^{-1} S1 nuclease and different amounts of ATP. The result clearly showed that the activity of S1 nuclease became weaker with the increase in inhibitor concentration. This result obtained was in fair agreement with the fact that ATP has been reported to one of the inhibitors of S1 nuclease. Taken together, our proposed method showed great performance not only in the assay of endonucleases activity but also in screening of endonucleases inhibitors, which is of great importance in modern drug discovery.

4. Conclusions

In conclusion, we have succeeded in demonstrating a sensitive, facile, label-free and turn-on strategy for detecting endonuclease activity based on the fluorescence enhancement effect when place

DNA–silver nanoclusters (DNA–Ag NCs) in proximity to guanine-rich DNA sequences. Compared with some known assay methods, our proposed strategy belongs to the fluorescence turn-on model, which reduces the possibility of a false positive signal and improves the detection sensitivity. In addition, this strategy avoids oligonucleotide labeling or fluorescent compound synthesis, which offers the advantages of facile and cheap operation. Furthermore, our method can also be used to investigate the S1 nuclease inhibitor and employed for nuclease inhibitor screening. Finally, the synthesis of DNA–Ag NCs is simple, low cost and accessible to numerous labs. This innovative approach provides a successful paradigm in exploring fascinating properties of functional DNA–Ag NCs and a new opportunity for extending their applications in a wide range of fields, such as biology, biomedicine, and more bio/chemo sensing.

Acknowledgment

This work was supported by the National Natural Science Foundation of China (No. 21275045), NCET -11-0121, and Hunan Provincial Natural Science Foundation of China (Grant 12JJ1004).

References

- [1] M.R. Lieber, *BioEssays* 19 (1997) 233–240.
- [2] S.C. West, *Nat. Rev. Mol. Cell Biol.* 4 (2003) 435–445.
- [3] T.M. Marti, O. Fleck, *Cell. Mol. Life Sci.* 61 (2004) 336–354.
- [4] P. Norberg, T. Bergstrom, J.A. Liljeqvist, *J. Clin. Microbiol.* 44 (2006) 4511–4514.
- [5] N.D.F. Grindley, K.L. Whiteson, P.A. Rice, *Annu. Rev. Biochem.* 75 (2006) 567–605.
- [6] L.W. McLaughlin, F. Benseler, E. Graeser, N. Piel, S. Scholtissek, *Biochemistry* 26 (1987) 7238–7245.
- [7] S. Spitzer, F. Eckstein, *Nucleic Acids Res.* 16 (1988) 11691–11704.
- [8] A. Jeltsch, A. Fritz, J. Alves, H. Wolfes, A. Pingoud, *Anal. Biochem.* 213 (1993) 234–240.
- [9] K. Hiramatsu, H. Miura, S. Kamei, K. Iwasaki, M. Kawakita, *J. Biochem.* 124 (1998) 231–236.
- [10] J.J. Li, R. Geyer, W.H. Tan, *Nucleic Acids Res.* 28 (2000) e52.
- [11] P.C. Ray, A. Fortner, G.K. Darbha, *J. Phys. Chem. B* 110 (2006) 20745–20748.
- [12] F. Pu, D. Hu, J. Ren, S. Wang, X. Qu, *Langmuir* 26 (2010) 4540–4545.
- [13] J.P. Wilcoxon, B.L. Abrams, *Chem. Soc. Rev.* 35 (2006) 1162–1194.
- [14] H. Xu, K.S. Suslick, *Adv. Mater.* 22 (2010) 1078–1082.
- [15] S.I. Tanaka, J. Miyazaki, D.K. Tiwari, T. Jin, Y. Inouye, *Angew. Chem. Int. Ed.* 50 (2011) 431–435.
- [16] T. Chen, Y. Hu, Y. Cen, X. Chu, Y. Lu, *J. Am. Chem. Soc.* 135 (2013) 11595–11602.
- [17] J. Zheng, R.M. Dickson, *J. Am. Chem. Soc.* 124 (2002) 13982–13983.
- [18] J.T. Petty, J. Zheng, N.V. Hud, R.M. Dickson, *J. Am. Chem. Soc.* 126 (2004) 5207–5212.
- [19] T. Vosch, Y. Antoku, J.C. Hsiang, C.I. Richards, J.J. Gonzalez, R.M. Dickson, *Proc. Natl. Acad. Sci. U.S.A.* 104 (2007) 12616–12621.
- [20] J. Yu, S.A. Patel, R.M. Dickson, *Angew. Chem. Int. Ed.* 46 (2007) 2028–2030.
- [21] C. Guo, J. Irudayaraj, *Anal. Chem.* 83 (2011) 2883–2889.
- [22] S.W. Yang, T. Vosch, *Anal. Chem.* 83 (2011) 6935–6939.
- [23] J. Yin, X. He, K. Wang, Z. Qing, X. Wu, H. Shi, X. Yang, *Nanoscale* 4 (2012) 110–112.
- [24] L. Zhang, J. Zhu, S. Guo, T. Li, J. Li, E. Wang, *J. Am. Chem. Soc.* 135 (2013) 2403–2406.
- [25] H.C. Yeh, J. Sharma, J.J. Han, J.S. Martinez, J.H. Werner, *Nano Lett.* 10 (2010) 3106–3110.
- [26] M. Zhang, S.M. Guo, Y.R. Li, P. Zuo, B.C. Ye, *Chem. Commun.* 48 (2012) 5488–5490.
- [27] J. Li, X. Zhong, H. Zhang, X.C. Le, J.J. Zhu, *Anal. Chem.* 84 (2012) 5170–5174.
- [28] L. Zhang, J. Zhu, Z. Zhou, S. Guo, J. Li, S. Dong, E. Wang, *Chem. Sci.* 4 (2013) 4004–4010.
- [29] J. Yin, X. He, K. Wang, F. Xu, J. Shangguan, D. He, H. Shi, *Anal. Chem.* 85 (2013) 12011–12019.
- [30] F. Harada, J.E. Dahlberg, *Nucleic Acids Res.* 2 (1975) 865–872.
- [31] J.L. Butour, A.M. Mazard, C. Vieussens, N.P. Johnson, *Chem. Biol. Interact.* 73 (1990) 195–205.
- [32] P. Wrede, A. Rich, *Nucleic Acids Res.* 7 (1979) 1457–1467.



Electrochemical OFF–ON ratiometric chemodosimeters for the selective and rapid detection of fluoride

Veerappan Mani^a, Wen-Yung Li^a, Jiun-An Gu^a, Chun-Mao Lin^b, Sheng-Tung Huang^{a,*}

^a Department of Chemical Engineering and Biotechnology, National Taipei University of Technology, Taipei 10608, Taiwan (ROC)

^b Department of Biochemistry, College of Medicine, Taipei Medical University, No. 250, Wu-xing Street, Taipei 110, Taiwan (ROC)

ARTICLE INFO

Article history:

Received 27 May 2014

Received in revised form

23 July 2014

Accepted 24 July 2014

Available online 4 August 2014

Keywords:

Hydroquinone

Latent redox ratiometric probe

Chemodosimeters

Sensor

Fluoride

Selectivity

ABSTRACT

We have described two “OFF–ON electrochemical latent ratiometric redox chemodosimeters”, 1,4-Bis(tert-butyl dimethylsiloxy)benzene (H_2Q') and 1,4-Bis(tert-butyl dimethylsiloxy)-2-methoxybenzene (MH_2Q') for the selective detection of inorganic fluoride. The electrochemical signals of hydroquinone (H_2Q) and *o*-methoxy hydroquinone (MH_2Q) within this latent redox probes (H_2Q' and MH_2Q') were completely masked by protecting their hydroxyl group as silylether (OFF state). The externally added fluoride ions triggered the deprotection of H_2Q' and MH_2Q' and unmasked the electrochemical properties of H_2Q and MH_2Q respectively. The electrochemical reporters (H_2Q and MH_2Q) presented a pair of redox peaks at the electrode surface (ON state) and the peak currents are linearly dependent with the concentration of fluoride which leading to the ratiometric detection of fluoride. The limit of detection (signal-to-noise ratio=3) observed for the probes are $23.8 \mu M$ and $2.38 \mu M$ for H_2Q' and MH_2Q' respectively. The deprotection is highly selective for fluoride over other anions investigated. The probes are highly stable and the proposed approach offers rapid response time and promising practical applicability. The proposed strategy holds great promise for the commencement of new H_2Q based electrochemical probes by tuning the electrochemical behavior of H_2Q .

© 2014 Elsevier B.V. All rights reserved.

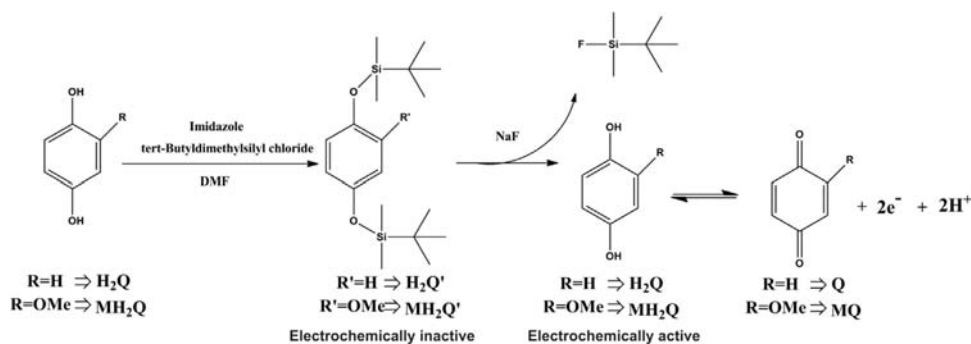
1. Introduction

Fluoride is widely used as the active ingredient in toothpaste formulations for the prevention of dental caries and other health benefits. In addition, fluorides are one of the essential trace elements required to form bones and teeth in human [1]. However, fluorides are potentially toxic, if their concentrations exceed levels that cause severe health risks such as dental fluorosis and bone diseases [2,3]. Therefore, the permissible overall quantity of fluoride present in toothpaste is regulated within the concentration range of 0.50 – 1.50 mg g^{-1} , while US Environmental Protection Agency's (US EPA) has recommended the upper allowed limit of 2 ppm ($105 \mu M$) fluorides in drinking water to prevent dental fluorosis [4]. Therefore, determination of fluorides is of great significance [5–9]. In the past years, several analytical methods have been developed for the determination of fluoride such as chromatography [10], ion selective electrodes [11–13], anion recognition [14], fluorimetry [15], spectrophotometry [16], and colorimetry methods [17]. But, most of these traditional ana-

lytical methods involve time-consuming and tedious procedures. Recently, several research groups have published optical chemodosimeters for the determination of fluoride; in this case, the detection approach involves typical fluoride triggered cleavage of Si–O bond in the designed probes with concomitant release of the optical reporters [8,17–21]. These optical chemodosimeters are able to provide excellent selectivity for the determination of fluoride attributed to the strong chemical affinity between fluoride and silicon. Compared with optical techniques, electrochemical techniques have relatively better performances in terms of short reaction time, high sensitivity, simplicity of the voltammetric instrumentation, simple operating protocols, direct use in point-of-care assays, potential for miniaturization and portability [22]. In the present work, we incorporated the similar concept of optical chemodosimeters into electrochemical redox probes for the simple and selective detection of fluoride at electrode surface.

The schematic representation for the mechanistic pathway of the designed “OFF–ON electrochemical latent ratiometric redox chemodosimeters” is given as Scheme 1: (1) Masking the electrochemical signal of hydroquinone (H_2Q) through silylation to obtain the probe, 1,4-Bis(tert-butyl dimethylsiloxy)benzene (H_2Q' , OFF state), (2) fluoride triggered cleavage of Si–O bond, and subsequent removal of silyl protecting group through quinone type

* Corresponding author. Tel.: +886 2271 2171 2525; fax: +886 02 2731 7117.
E-mail address: ws75624@ntut.edu.tw (S.-T. Huang).



Scheme 1. Schematic representation for the electrochemical determination of fluoride via fluoride induced electrochemical “ON–OFF” ratiometric latent redox switch.

rearrangement with concomitant release of electrochemical reporter (H_2Q), and (3) H_2Q readily undergoes electrochemical redox reaction and presented its redox peaks at the electrode surface. The deprotection is highly specific for sodium fluoride and the amount of released H_2Q is quantitative to the concentration of fluoride. The same “latent redox probe approach” of $\text{H}_2\text{Q}'$ was extended to 1,4-Bis (tert-butyl dimethylsilyloxy)-2-methoxybenzene ($\text{MH}_2\text{Q}'$), which is a methoxy derivative of $\text{H}_2\text{Q}'$. Preparation of the probes ($\text{H}_2\text{Q}'$ and $\text{MH}_2\text{Q}'$) involves very simple silylation reaction and the assay pathway involves rapid and quantitative determination of fluoride.

The aim of the present work is to develop a new electrochemical platform for the selective determination of fluoride. To the best of our knowledge, there is no report available in the literature employing H_2Q as the “Electrochemical OFF–ON Ratiometric Chemodosimeters” for the determination of fluoride. Considering the advantages of electrochemical methods and the need for the development of novel electrochemical approaches to selectively detect fluoride, herein we have designed two “electrochemical ratiometric redox probes”, by incorporating HQ and o-methoxy hydroquinone (MH_2Q) as the electrochemical reporters. The limit of detection (LOD) observed for these probes (23.8 μM for $\text{H}_2\text{Q}'$ and 2.38 μM for $\text{MH}_2\text{Q}'$) are within the upper allowed limit mandated by the US EPA.

2. Experimental

2.1. Materials and methods

H_2Q , sodium fluoride, and all the other chemicals were purchased from Sigma-Aldrich and used without further purification. Electrochemical measurements were recorded in a conventional three electrode cell employing BAS glassy carbon electrode (GCE) as the working electrode (area 0.071 cm^2), saturated Ag/Ag^+ (AgNO_3) filled with acetonitrile containing tetra-n-butylammonium bromide (TBAP) as the reference electrode and Pt wire as the counter electrode. 1 mM of TBAP dissolved in DMF was used as the supporting electrolyte. The determination of fluoride was carried out in DMF containing TBAP (1 mM), HEPES buffer (0.05 M, pH 7.8) (DMF–TBAP–HEPES solution), and probe (1 mM). The solutions were deoxygenated with pre-purified nitrogen for 5 min before performing each electrochemical experiment.

2.2. Preparation of $\text{H}_2\text{Q}'$ and $\text{MH}_2\text{Q}'$

$\text{H}_2\text{Q}'$ and $\text{MH}_2\text{Q}'$ was prepared in accordance to the procedure reported in the literature [23,24]. H_2Q (1.67 g, 15.2 mmol) was treated with TBDMS chloride (11.4 g, 75.3 mmol) and imidazole (10.2 g, 150 mmol) in DMF (5 ml) for overnight to yield $\text{H}_2\text{Q}'$ as a colorless solid (4.64 g, 90%). 2-methoxybenzene-1,4-diol (2.13 g,

15.2 mmol) was treated with TBDMS chloride (11.4 g, 75.3 mmol) and imidazole (10.2 g, 150 mmol) in DMF (7 ml) for overnight to yield the $\text{MH}_2\text{Q}'$ as a colorless solid (4.784 g, 85%). ^1H NMR data of the $\text{H}_2\text{Q}'$ and $\text{MH}_2\text{Q}'$ were in good agreement with those reported in the literature.

3. Results and discussion

3.1. Determination of fluoride using $\text{H}_2\text{Q}'$

The cyclic voltammogram (CV) acquired at GCE in DMF–TBAP–HEPES solution containing $\text{H}_2\text{Q}'$ (1 mM) (curve b, Fig. 1A) did not exhibit any characteristic redox peaks in the absence of fluoride, indicating the complete masking of $\text{H}_2\text{Q}'$ redox sites. However, the CV obtained in the presence of 0.24 mM NaF (curve c, Fig. 1A) exhibited well defined quasi reversible redox peaks related to the characteristic redox reaction of H_2Q . The redox reaction involves two electrons and two protons and occurred via semiquinone formation which was established fabulously in the literature [25]. The oxidation peak corresponding to the oxidation of H_2Q to p-benzoquinone (Q) was observed at the potential of +0.10 V, whereas the reduction peak corresponding to the reduction of Q to H_2Q was observed at the potential of –0.71 V. Thus, the CV results clearly indicating that the addition of fluoride triggered the silyl deprotection and uncloaks the redox active center of $\text{H}_2\text{Q}'$. Moreover, we observed that short time (5 min) is sufficient to complete the deprotection; thus our assay platform involves short reaction time allowing rapid detection of fluoride. CV obtained at GCE in DMF–TBAP–HEPES solution containing 1 mM of pristine H_2Q has been carried out to correlate the electrochemical behavior of pristine H_2Q (inset to Fig. 1A) and regenerated H_2Q from $\text{H}_2\text{Q}'$ (curve c, Fig. 1A). CV obtained for the pristine H_2Q is quite consistent with that of released H_2Q from $\text{H}_2\text{Q}'$ in terms of peak potentials and peak shapes supports the proposed protection/deprotection mechanistic pathway.

The effect of scan rate (ν) on the redox behavior of H_2Q was examined in DMF–TBAP–HEPES solution containing 1 mM $\text{H}_2\text{Q}'$ and 0.24 mM of NaF at the scan rates from 0.1 to 1.2 V s^{-1} (Fig. 1B). Both the anodic (I_{pa}) and cathodic peak current (I_{pc}) increased linearly with increase in scan rates from 0.1 to 1.2 V s^{-1} . A plot of square root of scan rates ($\nu^{1/2}$) and anodic peak current (I_p) exhibited linear relationship indicating that the redox reaction of released H_2Q occurred at the GCE is a diffusion controlled electron transfer process (inset to Fig. 1B).

Fig. 2A shows the CVs obtained at GCE in DMF–TBAP–HEPES solution containing $\text{H}_2\text{Q}'$ (1 mM) and different concentrations of NaF ($a=0.024$, $b=0.12$, $c=0.24$, $d=0.48$, $e=0.72$, $f=0.96$, and $g=1.19$ mM). As evident from the figure, a pair of well-defined redox peaks of H_2Q was present for the 0.024 mM addition of fluoride. Moreover, both I_{pa} and I_{pc} were increased linearly

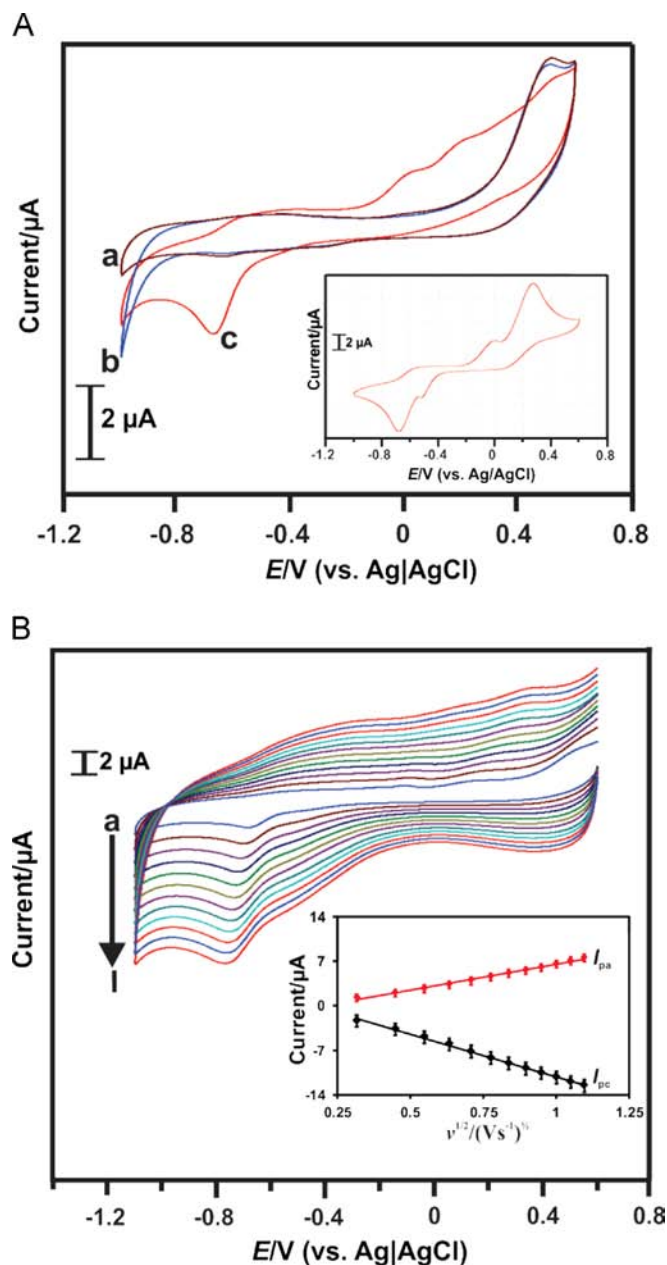


Fig. 1. (A) CVs obtained at GCE in DMF-TBAP-HEPES solution (a) containing H_2Q (1 mM) in the absence (b) and presence of 0.24 mM NaF (c) and 1 mM pristine H_2Q (inset). (B) CVs obtained at GCE in DMF-TBAP-HEPES solution containing H_2Q (1 mM) in the presence of 0.24 mM NaF at different scan rates from 0.1 to 1.2 V s^{-1} (curves a–i). Inset: $\nu^{1/2}$ vs. I_{pa} and I_{pc} .

upon increase in the concentration of fluoride. A plot of I_{pa} and I_{pc} vs. concentration of fluoride exhibited a linear relationship (Fig. 2B) with the slope of $7.153 \mu\text{A mM}^{-1}$ and $-8.586 \mu\text{A mM}^{-1}$ respectively. The linear range was observed between $23.8 \mu\text{M}$ and 1.19 mM , while limit of detection (LOD) was found to be $23.8 \mu\text{M}$ ($S/N=3$) which is sufficiently enough to detect the US EPA mandated upper limit of fluoride concentration in drinking water [4]. Monitoring I_{pc} of the H_2Q redox peaks offers more sensitivity than I_{pa} and therefore we choose I_{pc} for the determination of fluoride.

3.2. Determination of fluoride using MH_2Q

MH_2Q also follows similar electrochemical protection/deprotection pathway as H_2Q (Scheme 1). No redox peaks were observed in the

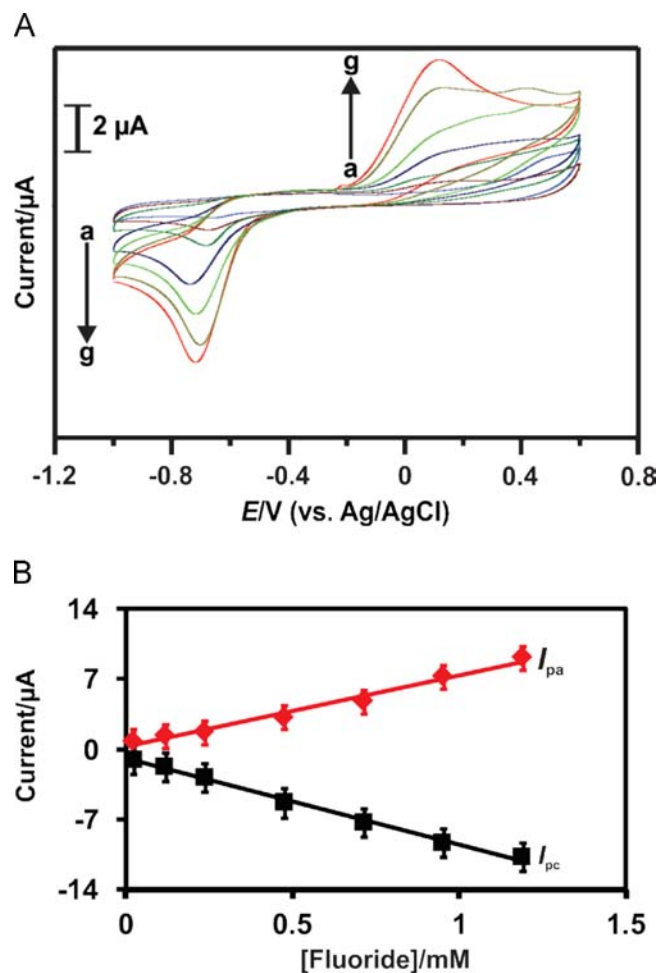


Fig. 2. (A) CVs obtained at GCE in DMF-TBAP-HEPES solution containing H_2Q (1 mM) with different concentrations of fluoride; 0.024 (a), 0.12 (b), 0.24 (c), 0.48 (d), 0.72 (e), 0.96 (f), and 1.19 mM (g). (B) Plot of [fluoride] vs. I_{pa} and I_{pc} .

absence of fluoride (protected, OFF) (curve a, Fig. 3A), whereas well defined redox peaks were observed in the presence of 0.24 mM NaF (deprotected, ON) (curve b, Fig. 3A). Here, the redox peaks are ascribed to the redox conversion between MH_2Q and MQ (*o*-methoxy benzoquinone). The CV obtained at the pristine MH_2Q (inset to Fig. 3A) is quite consistent with that obtained at the regenerated MH_2Q from MH_2Q .

MH_2Q follows concentration-dependent increase in I_{pc} with different concentrations of fluoride (Fig. 3B) and exhibited linear concentration range from $2.38 \mu\text{M}$ to 0.96 mM (inset to Fig. 3B). LOD ($S/N=3$) of MH_2Q was calculated to be $2.38 \mu\text{M}$ which is 10 fold lower than that observed at H_2Q . The probable reason for the lower LOD of MH_2Q might be the chelating effect caused by the formation of stable five membered chelating ring when sodium fluoride approaches MH_2Q which brings the fluoride anion more closer to silicon (Scheme 2). As a result, the removal of silyl ether become more easy even at low concentration of fluoride, whereas formation of this kind of chelating effect is not possible in H_2Q . Perhaps, this result indicating that any substituent on the ring of H_2Q may influence the analytical performance of the fluoride detection. Therefore the OFF/ON switching ability of the H_2Q can be tuned by different substituents to boost the performance of the resulting sensor. The sensor performance of the probes were listed in Table 1. It is evident from the table that, LOD and linear range of these probes are within the US EPA mandated upper limit of fluoride concentration in drinking water.

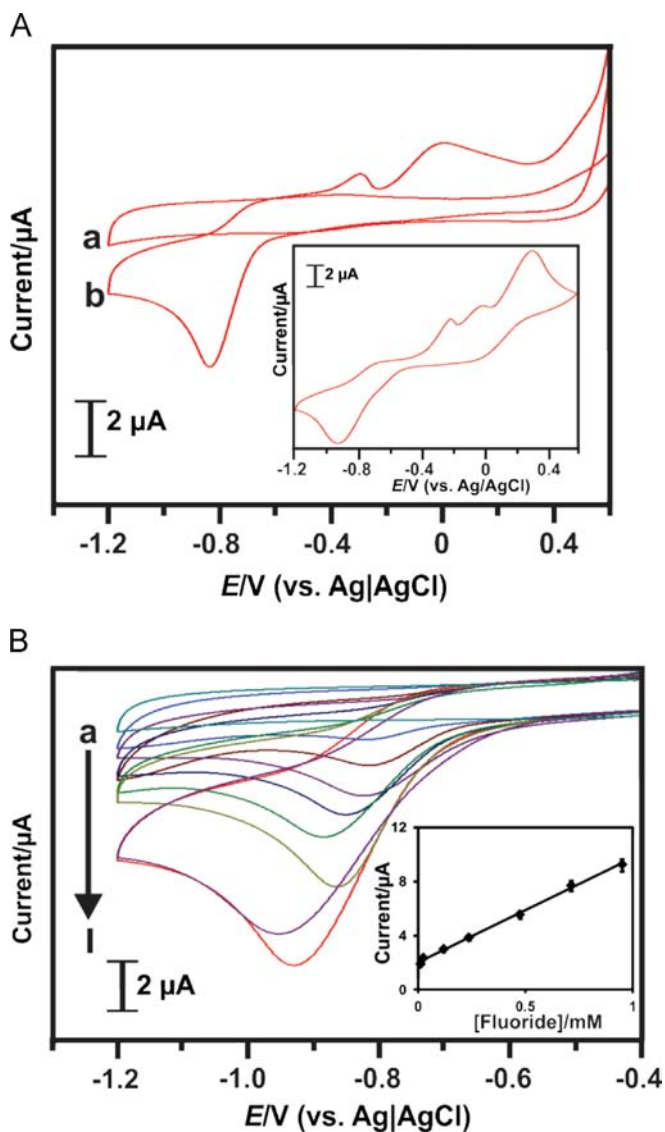
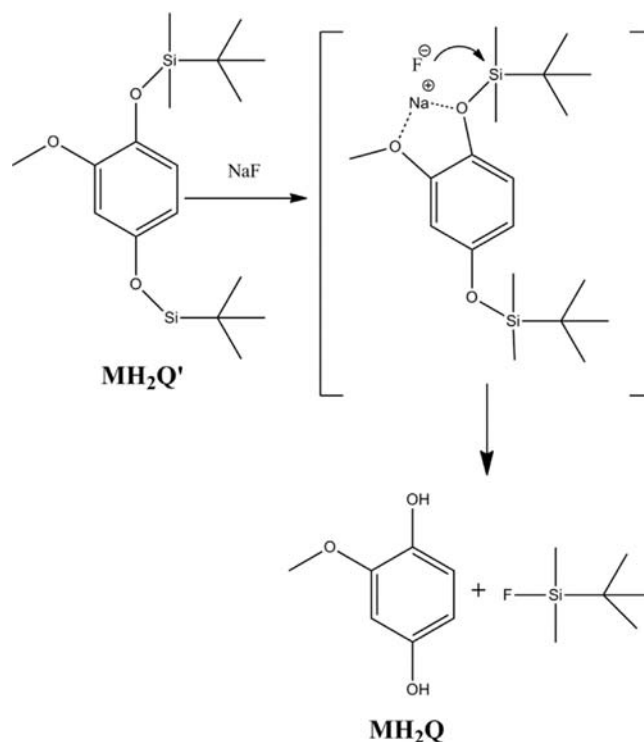


Fig. 3. (A) CVs obtained at GCE in DMF-TBAP-HEPES solution containing $\text{MH}_2\text{Q}'$ (1 mM) in the absence (a) and presence of 0.24 mM NaF (b) and 1 mM pristine MH_2Q (inset). (B) CVs obtained at GCE in DMF-TBAP-HEPES solution containing $\text{MH}_2\text{Q}'$ with different concentrations of fluoride: 0 (a), 2.38×10^{-3} (b), 11.9×10^{-3} (c), 23.8×10^{-3} (d), 0.12 (e), 0.24 (f), 0.48 (g), 0.72 (h), and 0.96 mM (i). Inset: [fluoride] vs. I_{pc} .

3.3. Selectivity

In order to study the selectivity of $\text{H}_2\text{Q}'$ towards fluoride detection, CV studies were carried out in the presence of variety of likely anionic interferences such as NaI, NaCl, NaBr, KH_2PO_4 , Na_2HPO_4 , LiClO_4 , NaOAc, NaNO_3 , KCN and NaN_3 . The CV obtained at GCE in DMF-TBAP-HEPES solution containing $\text{H}_2\text{Q}'$ (1 mM) exhibited well defined I_{pc} response towards addition of 2 mM NaF (a), whereas no noteworthy responses were observed for the addition of 2 mM of NaI (b), NaCl (c), NaBr (d), KH_2PO_4 (e), Na_2HPO_4 (f), LiClO_4 (g), NaOAc (h), NaNO_3 (i), KCN (j) and NaN_3 (k) (Fig. 4A). The selectivity studies clearly revealed that only fluoride was able to unmask the redox active sites of H_2Q from $\text{H}_2\text{Q}'$ among all the anions tested (Fig. 4B). This must be ascribed to the special chemical affinity between fluoride and silicon [5]. Thus, $\text{H}_2\text{Q}'$ is a highly selective redox probe for the determination of fluoride even in the presence of other common interferences. Similar to $\text{H}_2\text{Q}'$, $\text{MH}_2\text{Q}'$ has also found to be insensitive to other



Scheme 2. Schematic representation for the chelating effect observed in $\text{MH}_2\text{Q}'$.

Table 1

Electroanalytical parameters and sensor performance of the probes $\text{H}_2\text{Q}'$ and $\text{MH}_2\text{Q}'$.

Probes	$\text{H}_2\text{Q}'$	$\text{MH}_2\text{Q}'$
Limit of detection	23.8 μM	2.38 μM
Linear range	23.8 μM –1.19 mM	2.38 μM –0.96 mM
Repeatability	2.53%	2.72%
Reproducibility	3.22%	3.44%

anions tested and selective for the determination of fluoride (Figure not shown).

3.4. Stability, repeatability and reproducibility

To investigate the stability of the probes, DMF-TBAP-HEPES solutions containing 1 mM of each probe ($\text{H}_2\text{Q}'$ and $\text{MH}_2\text{Q}'$) were treated under thermal (60 °C) and ultrasonic conditions for 1 h and their respective CVs were recorded. Under these conditions, no characteristic redox peaks of their corresponding redox reporters (H_2Q and MH_2Q) were observed in the absence of fluoride. On the other hand, the redox reporters were liberated from the probes within few seconds in the presence of fluoride (Figs. 1B and 3B). Therefore, we concluded that both the probes are highly stable under thermal and ultrasonication conditions, while fluoride ions only able to trigger the deprotection. Both the two probes exhibited appreciable repeatability and reproducibility with acceptable recoveries for five experiments. Repeatability experiments were carried out using single electrode, while reproducibility experiments were carried out with five different electrodes (Table 1).

3.5. Real sample analysis

We demonstrated the practical feasibility of the proposed approach towards determination of fluoride present in water

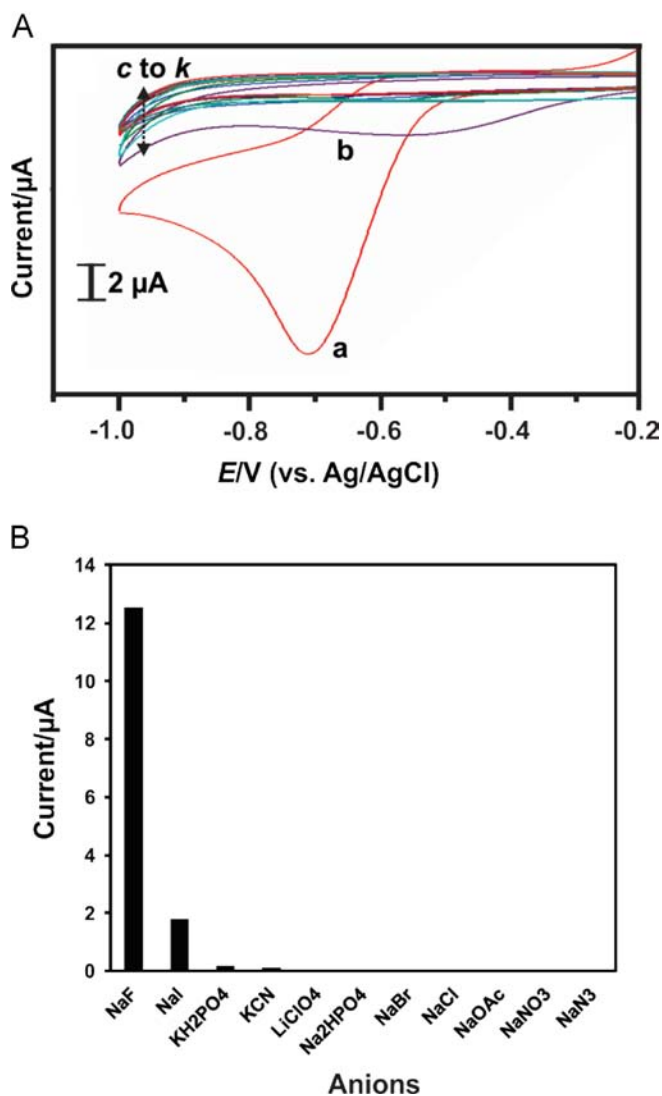


Fig. 4. (A) CVs obtained at DMF-TBAP-HEPES solution containing $\text{H}_2\text{Q}'$ (1 mM) with the presence of 2 mM of NaF (a) and NaI (b), NaCl (c), NaBr (d), KH_2PO_4 (e), Na_2HPO_4 (f), LiClO_4 (g), NaOAc (h), NaNO_3 (i), KCN (j), and NaN_3 (k). (B) Plot between various anions and their response towards NaF.

samples. The spiked fluoride concentrations are 25 μM and 250 μM . The found and recovery values are given in Table 2. As evident from the table, both the probes presented acceptable recoveries in tap and river water samples revealed the practical feasibility of the proposed approach.

3.6. Comparison of the proposed “latent ratiometric redox probe approach” with other methods

In the past decades, several optical probes have been reported which are relying on hydrogen bonds or Lewis acid coordination of fluoride with the probes, and most of these probes could only be operated in organic solvents to detect tetrabutylammonium (TBA^+) fluoride rather than inorganic fluoride salts which limited the application of sensing fluoride in the biological sample [26,27]. Furthermore, the LOD of this probe was in the upper mg/L range and transferring the sensing results electronically required additional optical sensing equipment. Nevertheless, the detection of low concentrations of fluoride in polar and aqueous solutions remains challenging without expensive analytical equipment. The electrochemical fluoride recognition strategies based on the Lewis acid coordination with arylboronic acids/esters incorporating

Table 2
Real sample analysis in water samples.

Probes	Tap water			River water		
	Added (μM)	Found (μM)	Recovery (%)	Added (μM)	Found (μM)	Recovery (%)
$\text{H}_2\text{Q}'$	25	24.2	96.8	25	26	104
	250	256	102.4	250	258	103.2
$\text{MH}_2\text{Q}'$	25	25.83	103.3	25	24.13	96.52
	250	245.1	98	250	244	97.6

ferrocenyl compounds as receptors are facing difficulties in the detection of aqueous fluoride ions [28–33]. On the other hand, electrochemical techniques based on the modified electrodes often lack selectivity. Most recently, a potentiometric sensor based on poly(3-aminophenylboronic acid) modified graphite rod electrode was reported for the determination of fluoride [34], however its detection range was beyond the upper limit imposed by US EPA. In the present work, we established a highly selective electrochemical inorganic fluoride sensing platform which allowed the direct transferring of sensing signal electronically and applicable for sensing fluoride in the biological sample. The LOD observed for the probes (23.8 μM for $\text{H}_2\text{Q}'$ and 2.38 μM for $\text{MH}_2\text{Q}'$) are within the relevant window of US EPA's mandated upper limit [4]. H_2Q is a potential electrochemical reporter attributed to its stable, predictable, and tailorable electrochemical properties, and its electrochemical signal could be easily measured by simple electrochemical methods such as cyclic voltammetry [25,35]. To the best of our knowledge, this is the first report demonstrating “latent redox ratiometric probe” approach through simple selective protection/deprotection strategy for the detection of fluoride.

4. Conclusions

A facile electrochemical “latent ratiometric redox probe” approach has been developed for the detection of fluoride employing H_2Q as the electrochemical reporter. The selectivity studies revealed that the deprotection is highly specific for fluoride. Both $\text{H}_2\text{Q}'$ and $\text{MH}_2\text{Q}'$ are highly stable and exhibited rapid response time. Real sample analysis revealed the practical applicability of the sensor. LOD of both the probes (23.8 μM for $\text{H}_2\text{Q}'$ and 2.38 μM for $\text{MH}_2\text{Q}'$) are within the upper limit prescribed by US EPA. Undoubtedly, the developed H_2Q based latent ratiometric approach holds great promise for the commencement of potential electrochemical probes for the detection of fluoride.

Acknowledgments

This work was supported by the National Science Council of Taiwan (NSC 103-2811-M-027-002 and 102-2113-M-027-002-MY3).

References

- [1] I.C. Guimaraes, C.C. Rezende, J.A.F. da Silva, D.P. de Jesus, *Talanta* 78 (2009) 1436–1439.
- [2] F.L. Cerklewski, *Nutrition*, Burbank, Los Angeles County, California (1998) 475.
- [3] M. Kaykhahi, M.H. Ghalehno, *Anal. Methods* 5 (2013) 5622–5626.
- [4] U. EPA, Total Coliforms (Including Fecal Coliforms and E. Coli), 54, 2009.
- [5] J. Du, M. Hu, J. Fan, X. Peng, *Chem. Soc. Rev.* 41 (2012) 4511–4535.
- [6] R. Perry-Feigenbaum, E. Sella, D. Shabat, *Chem. – Eur. J.* 17 (2011) 12123–12128.
- [7] M.S. Baker, S.T. Phillips, *Org. Biomol. Chem.* 10 (2012) 3595–3599.
- [8] S.Y. Kim, J.I. Hong, *Org. Lett.* 9 (2007) 3109–3112.

- [9] Y. Michigami, Y. Kuroda, K. Ueda, Y. Yamamoto, *Anal. Chim. Acta* 274 (1993) 299–302.
- [10] J.J. Potter, A.E. Hilliker, G.J. Breen, *J. Chromatogr. A* 367 (1986) 423–427.
- [11] R.A. Durst, *Ion-selective electrodes: proceedings, US National Bureau of Standards; for sale by the Supt. of Docs, US Govt. Print. Off, Washington, 1969.*
- [12] E. Kissa, *Clin. Chem.* 33 (1987) 253–255.
- [13] D.A. Skoog, *Fundamentals of Analytical Chemistry*, Grupo Editorial Norma, USA, 2004.
- [14] M. Cametti, K. Rissanen, *Chem. Commun.* (2009) 2809–2829.
- [15] H.C. Huang, K.L. Wang, S.T. Huang, H.Y. Lin, C.M. Lin, *Biosens. Bioelectron.* 26 (2011) 3511–3516.
- [16] T.L. Marques, N.M. Coelho, *Talanta* 105 (2013) 69–74.
- [17] J.A. Gu, Y.J. Lin, Y.M. Chia, H.Y. Lin, S.T. Huang, *Microchim. Acta* 180 (2013) 801–806.
- [18] K. Ghosh, D. Kar, R. Fröhlich, A.P. Chattopadhyay, A. Samadder, A.R. Khuda-Bukhsh, *Analyst* 138 (2013) 3038–3045.
- [19] L. Fu, F.L. Jiang, D. Fortin, P.D. Harvey, Y. Liu, *Chem. Commun.* 47 (2011) 5503–5505.
- [20] H. Lenormand, J.P. Goddard, L. Fensterbank, *Org. Lett.* 15 (2013) 748–751.
- [21] J. Wang, L. Yang, C. Hou, H. Cao, *Org. Biomol. Chem.* 10 (2012) 6271–6274.
- [22] L. Hu, S. Han, Z. Liu, S. Parveen, Y. Yuan, G. Xu, *Electrochem. Commun.* 13 (2011) 1536–1538.
- [23] T. Greene, P. Wuts, *Protecting groups in organic synthesis*, Wiley Interscience, New York, 1999.
- [24] J.P. Willis, K.A. Gogins, L.L. Miller, *J. Org. Chem.* 46 (1981) 3215–3218.
- [25] B. Eggins, J. Chambers, *J. Electrochem. Soc.* 117 (1970) 186–192.
- [26] S. Rivadehi, E.F. Reid, C.F. Hogan, S.V. Bhosale, S.J. Langford, *Org. Biomol. Chem.* 10 (2012) 705–709.
- [27] Y. Qu, J. Hua, H. Tian, *Org. Lett.* 12 (2010) 3320–3323.
- [28] C.R. Wade, A.E. Broomsgrove, S. Aldridge, F.P. Gabbai, *Chem. Rev.* 110 (2010) 3958–3984.
- [29] Q. Tan, L. Wang, H. Yu, L. Deng, *J. Phys. Chem. B.* 111 (2007) 3904–3909.
- [30] C. Dusemund, K.S. Sandanayake, S. Shinkai, *J. Chem. Soc. Chem. Commun.* (1995) 333–334.
- [31] H. Yamamoto, A. Ori, K. Ueda, C. Dusemund, S. Shinkai, *Chem. Commun.* (1996) 407–408.
- [32] F. Otón, A. Tárraga, M.D. Velasco, A. Espinosa, P. Molina, *Chem. Commun.* (2004) 1658–1659.
- [33] J. Xiong, L. Cui, W. Liu, J.E. Beves, Y.Y. Li, J.L. Zuo, *Tetrahedron Lett.* 54 (2013) 1998–2000.
- [34] H. Çiftçi, Y. Öztekin, U. Tamer, A. Ramanavicius, A. Ramanavicius, *Talanta* 126 (2014) 202–207.
- [35] M. Rafiee, D. Nematollahi, *Electroanalysis* 19 (2007) 1382–1386.



Acrylamide-modified graphene for online micro-solid-phase extraction coupled to high-performance liquid chromatography for sensitive analysis of heterocyclic amines in food samples



Qianchun Zhang^{a,b}, Gongke Li^{a,*}, Xiaohua Xiao^{a,*}

^a School of Chemistry and Chemical Engineering, Sun Yat-sen University, Guangzhou 510275, China

^b School of Biology and Chemistry, Xingyi Normal University for Nationalities, Xingyi 562400, China

ARTICLE INFO

Article history:

Received 19 June 2014

Received in revised form

23 July 2014

Accepted 26 July 2014

Available online 12 August 2014

Keywords:

Acrylamide-modified graphene

Online

Micro-solid-phase extraction

Heterocyclic amines

Food samples

ABSTRACT

Heterocyclic amines (HAs) are considered as potential mutagens and carcinogens, and are found in trace quantities (ng/g level) in food samples. Therefore, it is important to develop a selective and effective method to determine trace HAs in complex matrices. In this study, acrylamide-modified graphene (AMG) was successfully synthesised and showed good stability and permeability in aqueous and organic phases. AMG was used as an efficient adsorbent in the online micro-solid-phase extraction (μ -SPE) of trace HAs. The enrichment factors of the AMG μ -SPE column were determined as 78–166 for six HAs. An online method based on AMG μ -SPE coupled to high-performance liquid chromatography was developed. The limits of detection ranged from 0.70 to 2.5 ng/L. Trace HAs in spicy salted duck, baked fish, and fried chicken samples were determined and the concentrations of 2-amino-3-methylimidazo[4,5-f]quinoine, 2-amino-3,4-dimethylimidazo[4,5-f]quinoine, and 2-amino-3,8-dimethylimidazo[4,5-f]quinoxaline in these samples were 4.7–37.3, 8.1–15.4, and 43.3–109 ng/g, respectively. The recoveries for the six HAs ranged from 65.9% to 118%, and the relative standard deviation (RSDs) were less than 10.8%. The proposed online method was sensitive, reliable, and convenient for the analysis of trace HAs in food samples.

© 2014 Elsevier B.V. All rights reserved.

1. Introduction

Heterocyclic amines (HAs), found in cooked meat products, are considered as highly potential mutagens and carcinogens [1,2]. They are formed mainly during the frying, baking, grilling, roasting, and smoking of meat and fish, which are cooked at 150–250 °C [3]. The food safety issues of HAs are receiving increasingly more attention. To date, chromatographic techniques, including high-performance liquid chromatography (HPLC) with various detectors [4–12], gas chromatography–mass spectrometry [13,14] and capillary liquid chromatography [15–17], have been commonly used to identify and quantify HAs in different matrices. However, the concentration of HAs is normally in the relatively low ng/g range in complex matrices and a large number of matrix interferences can be present [18,19]. Efficient sample pretreatment and a sensitive analytical method are very important in HAs analysis. To date, several sample preparation techniques have been employed to preconcentrate HAs in different matrices such as

liquid–liquid extraction [20], dispersive liquid–liquid microextraction [4], solid-phase extraction (SPE) [21], hollow-fibre supported liquid membrane extraction [22], solid-phase microextraction (SPME) [23,24], supercritical fluid extraction [25], and tandem SPE [13,15,26]. However, the above methods were operated in the off-line mode; consequently, they are labour-intensive, tedious, and time-consuming. Online sample preparation techniques were improved in recent years, through miniaturisation and automation. These techniques show better sensitivity with good reproducibility, less solvent and sample consumption, and fewer analytical errors [27,28]. Micro-solid-phase extraction (μ -SPE), reported by Basheer and co-workers [29], is a promising alternative to the multi-step μ -SPE method, which is a simple and efficient sample preparation method for complex samples [30–32]. Thus, the implementation of suitable extraction media and online SPE procedures is an important strategy to establish sensitive and environment-friendly methods for complex sample analysis.

Various media were used in the past, such as C_{18} [3], ionic liquids [4–6], diatomaceous earth [21], carbowax [23], Oasis MCX [33], and a propylsulphonyl silica gel [34]. Although some conventional sorbents, or a coupling of different eluents in tandem were successfully used for the analysis of HAs, the sorbent is critical for improving the enrichment performance. Thus,

* Corresponding authors. Tel.: +86 20 84110922; fax: +86 20 84115107.

E-mail addresses: cesgkl@mail.sysu.edu.cn (G. Li), xiaoxhua@mail.sysu.edu.cn (X. Xiao).

developing an effective sorbent remains a great challenge for HAs analysis in meat samples. Graphene has received increasing interest and has become one of the most prominent topics of research over the last decade. As the graphene is a one-atom-thick planar sheet of sp^2 -bonded carbon atoms densely packed in a honeycomb crystal lattice, graphene exhibits a high theoretical surface area of close to $2630 \text{ m}^2/\text{g}$ [35]. The surface area is the characteristic that makes graphene a promising material for use in sample pretreatment [36], including matrix solid-phase dispersion [37], SPME [38], and SPE [39,40]. As a low-polarity material, graphene is incompetent to polar HAs extraction in the aqueous phase. Therefore, functional graphene sheets are crucial. Recently, ammonia, hydrazine hydrate, *n*-butyl amine [41], polydopamine [42], and benzylamine [43]-modified graphene have been used as sorbents in SPE for the effective enrichment of pesticides, phosphopeptide, pentachlorophenol, bisphenol A, and polyfluorinated analytes in different matrices.

In the present work, acrylamide-modified graphene (AMG) was successfully synthesized and used as an efficient adsorbent in a μ -SPE column to enable the online enrichment of trace HAs. Moreover, a novel analytical methodology based on AMG μ -SPE online coupled to HPLC was developed for the trace analysis of six HAs, namely IQ, IQX, MeIQ, MeIQX, 4,8-DiMeIQx, and 4,7,8-TriMeIQx, in spicy salted duck, baked fish, and fried chicken samples.

2. Experimental

2.1. Chemicals and materials

The compounds studied were as follows: 2-amino-3-methylimidazo[4,5-*f*]quinoine (IQ), 2-amino-3-methylimidazo [4,5-*f*] quinoxaline (IQX), 2-amino-3,4-dimethylimidazo [4,5-*f*] quinoine (MeIQ), 2-amino-3,8-dimethylimidazo [4,5-*f*] quinoxaline (MeIQX), 2-amino-3,4,8-trimethylimidazo [4,5-*f*] quinoxaline (4,8-DiMeIQx), and 2-amino-3,4,7,8-tetramethyl-3*H*-imidazo [4,5-*f*] quinoxaline (4,7,8-TriMeIQx). They were purchased from Toronto Research Chemicals (Toronto, Canada) and their chemical structures are shown in Fig. 1. Stock standard solutions of $100 \mu\text{g}/\text{L}$ in methanol were prepared and used for further dilutions. Acrylamide was purchased from Damao Chemical Reagent Company (Tianjin, China). Thionyl chloride was supplied from Chemical Industry Corporation (Guangzhou, China). Graphite powder (particle size $30 \mu\text{m}$) was purchased from Alfa Aesar. HPLC-grade acetonitrile was used for the mobile phase and

obtained from Dikma (Beijing, China). Ultrapure water was used throughout and was obtained from the MILLI-Q gradient A10 system (Millipore, UK). All the solutions were filtered through a $0.45\text{-}\mu\text{m}$ filter before being injected into the HPLC system. All the other reagents mentioned above were of analytical grade.

2.2. Instruments

An Esca lab 250 spectrometer with an Al $K\alpha$ X-ray source was employed for X-ray photoelectron spectroscopic (XPS) analysis. X-ray diffractometry (XRD) was carried out using a Rigaku diffractometer. Raman spectra were measured with Laser Micro-Raman Spectrometer (Renishaw, UK). Scanning electron microscopy (SEM) images were recorded on a 4300 SEM instrument (Hitachi, Japan). Transmission electron microscopic (TEM) characterization was performed on a Tecnai 10 TEM instrument (Philips, Netherlands). Fourier transform infrared (FT-IR) spectra were measured by Nicolet Avatar 330. All chromatographic measurements were obtained using Shimadzu (Japan) instruments, consisting of two high-pressure gradient pumps (LC-10 ATvp), a SPD-10Avp UV detector, a system controller (SCL-10 A vp), and a CLASS-VP chromatographic workstation.

2.3. Synthesis of AMG

Graphene oxide (GO) was synthesised from natural graphite according to published methods [44,45]. In brief, 3.81 g of graphite powder was treated with a mixture of concentrated 18.5 mL of H_2SO_4 , 3.87 g of P_2O_5 , and 3.88 g of $\text{K}_2\text{S}_2\text{O}_8$ at 80°C . The obtained preoxidized graphite was placed into cold concentrated H_2SO_4 , and KMnO_4 was slowly added. H_2O_2 and distilled water were then added to terminate the reaction. The resulting solution was centrifuged and washed with HCl solution, and finally dried to generate a brown solid. Then, 670 mg of GO was added to 35 mL of a SOCl_2 solution and ultrasonicated for 20 min, followed by stirring and reflux at 69°C for 30 h. Subsequently, the reactant was distilled at 92°C and added to 100 mL of *N,N*-dimethyl formamide (DMF) and 1.82 g of acrylamide under ultrasonication for 20 min. This mixture was stirred at 26°C for 24 h. The product was filtered through a $0.45\text{-}\mu\text{m}$ filter and washed thoroughly with deionised water until its filtrate became neutral. The AMG was dried at 80°C for 24 h in vacuum.

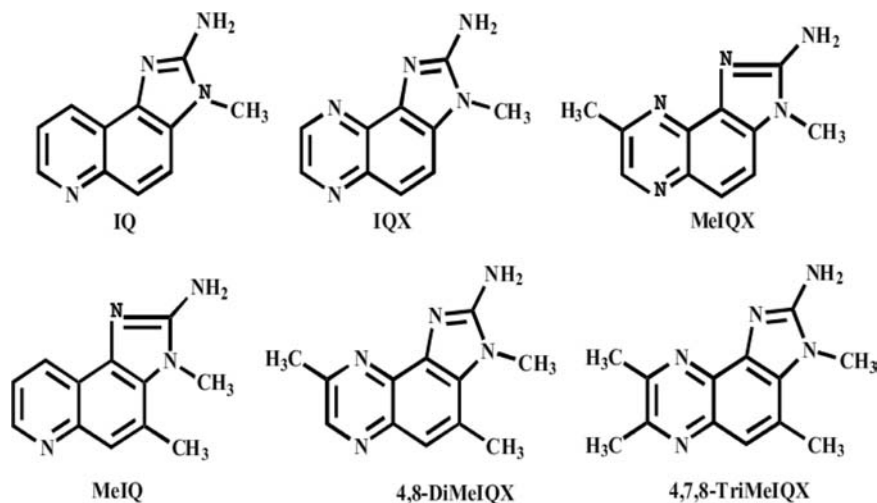


Fig. 1. Molecular structures of HAs compounds.

2.4. Preparation of AMG μ -SPE column

A polyetheretherketone (PEEK) rod (12 mm \times 7.2 mm o.d.) was drilled to produce a hole (10 mm \times 2.0 mm i.d.). Then, sieve plates were attached on both ends of the resulting PEEK tubing. The AMG was immediately pumped into the PEEK tube. Afterwards, the microcolumn was flushed with methanol, water, acetonitrile, and acetonitrile/water (pH 3.0 adjusted with 1.0 mmol/L ammonium acetate and acetic acid, 5:95, v/v) to adequately remove the unreacted reagents.

2.5. μ -SPE–HPLC online coupling system setup

The procedure for HAs enrichment was established (Fig. 2). The extraction process was divided into four steps and described as follows. (a) Sample loading and precondition. Valves 1 and 2 were switched to the LOAD position. The μ -SPE column was cleaned at a flow rate of 500 μ L/min by the mobile phase, and then flushed by water for 5 min until valve 1 was set to the INJECT position. At the same time, the sample loop was filled with 12.0 mL of the sample solution using a syringe. (b) Extraction. Valve 2 was switched to the INJECT position. The sample solution was driven by water to flow through the μ -SPE column at a flow rate of 600 μ L/min. (c) Cleaning up. Valve 2 was switched to the LOAD position. The μ -SPE column was cleaned with water to eliminate the residual sample solution and avoid its entry into the analytical column after the sample-solution loading. (d) Desorption procedure. Valve 1 was set to the LOAD position. The extracted HAs were desorbed from the μ -SPE column to the analytical column with the mobile phase at a flow rate of 200 μ L/min.

2.6. Adsorption experiments

The HAs extraction amount in the μ -SPE column was quantitatively estimated using linear regression equations obtained by plotting its calibration curve over a range of concentrations. The adsorption kinetic experiments were investigated. The HAs-adsorption capacities of adsorbent were determined at time intervals between 5.0 and 35.0 min at room temperature. Control

experiments were performed by using graphene, foloril, and C₁₈ as adsorbents for comparison.

2.7. Sample preparation

Spicy salted duck, baked fish, and fried chicken were shredded and 200 mg of thinly sliced tissue of each sample was used. The extraction was performed in 2.0 mL of *n*-butyl alcohol, 25 μ L of triethylamine, and 25 μ L of 25% ammonia water with an ultrasonic instrument (Kunshan, Suzhou, China) at 40 °C for 10 min. The extraction process was repeated after centrifuging the solution for 5 min at 8000 rpm. Subsequently, the extraction solutions were dried with reduced pressure evaporation, and then dissolved in the presence of 4 mL of acetonitrile as the solvent, 10 μ L of 10.3% potassium ferrocyanide (w/v), and 10 μ L of 21.9% zinc acetate (w/v) were added. The solution was then centrifuged for 10 min at 8000 rpm. The acetonitrile solution was shifted to a 15-mL centrifuge tube, and then 1 mL of dichloromethane, 2.5 mL of 1% sodium chloride aqueous solution (v/v), and 6 mL of *n*-hexane were added, and the resulting solution was oscillated and acetonitrile/dichloromethane was collected. Then, 4 mL of dichloromethane and 1 mL of dichloromethane were repeatedly added to extract the water phase. The acetonitrile/dichloromethane solutions were combined and dried with a reduced pressure distillation. Then, the residue was dissolved with 20.0 mL of water for the AMG sorptive extraction. The concentrations of each HA for the spiked sample solutions were 10.0, 30.0, and 50.0 ng/g, respectively.

2.8. Chromatographic conditions

All chromatographic separations were performed on an Atlantis T3 C₁₈ column (150 mm \times 4.6 mm i.d., 5 μ m) from Waters (Shanghai, China), and a 7.5-mm C₁₈ security guard column from Phenomenex (Torrance, Canada) was attached to the analytical column. The mobile phase used was acetonitrile/water (pH 3.0 adjusted with 1.0 mmol/L of ammonium acetate and acetic acid). The acetonitrile phase was increased from 5% to 25% (v/v) during 0–20 min. Its flow

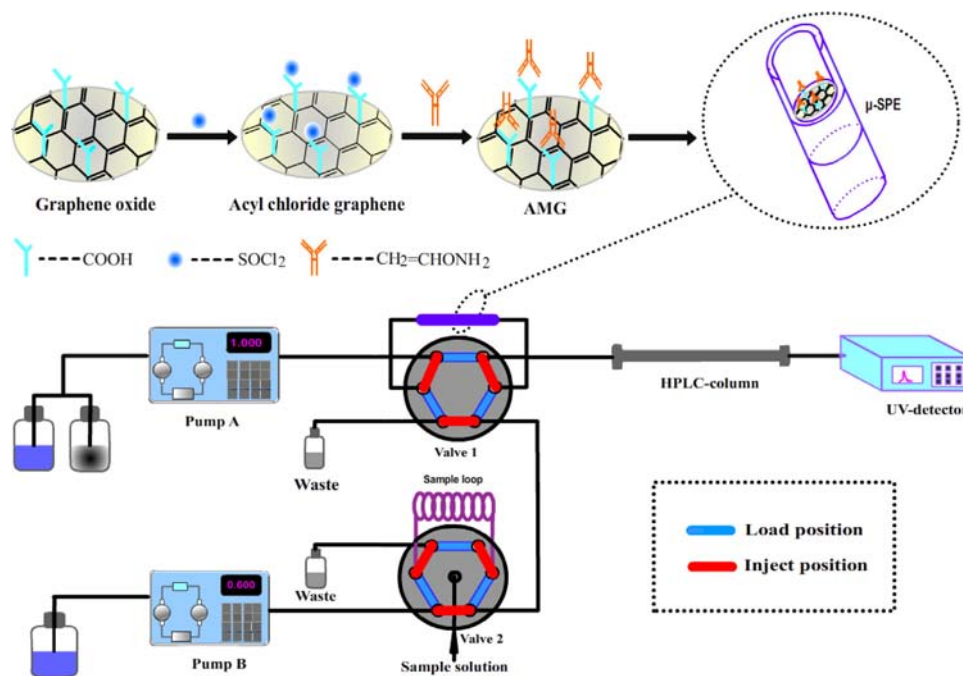


Fig. 2. Fabrication scheme of AMG-packed microcolumn and online μ -SPE–HPLC system.

rate was 1.0 mL/min and an ultraviolet detection wavelength was monitored at 263 nm.

3. Results and discussion

3.1. Synthesis of AMG

Although graphene exhibits a high surface area, it is ineffective to enrich polar compounds because of its low polarity. Acrylamide has two crucial functional amino groups: $-\text{NH}_2$ and $-\text{NH}-$, which can form strong hydrogen bonds with polar compounds. AMG can enhance the polarity of graphene while maintaining the large surface area and good adsorption performance. The synthesis process of AMG is shown in Fig. 2. GO was synthesised from natural graphite according to published method [44,45]. The grafting of acrylamide onto the GO surface can be accomplished by activating the carboxyl functionality of GO using thionyl chloride (SOCl_2). Functionalisation occurs through the formation of an amide linkage bond between the $-\text{COCl}$ functional groups of the activated GO and the $-\text{NH}_2$ functional groups of acrylamide [46].

3.2. Characterisation of AMG

The chemical composition of both the GO and AMG were analysed by XPS. Fig. 3 shows the presence of C–C, C–O, and C=O–O for GO and AMG. After reduction with acrylamide, the oxygen content decreased from 36.6% to 11.8%, while the N 1s XPS spectra of the AMG showed the presence of both $-\text{C}(\text{O})\text{NH}$ and $-\text{NH}_2$ functionalities at 399.8 and 401.9 eV, respectively. The C 1s XPS spectra were obviously reduced in C–O and C=O–O, indicating that the AMG has been successfully synthesised.

To verify the chemical bond formation, the structures of the synthesised material were characterised by FT-IR (Fig. 4). For GO, the peaks at 1724 and 1055 cm^{-1} show the presence of the C=O and epoxy C–O groups. For AMG, the characteristic peaks of the $=\text{CH}_2$ group stretching was observed at around 2917 cm^{-1} , that of

the C–N group at 1117 cm^{-1} , and those of the N–H group at 1584 cm^{-1} , and 712 cm^{-1} . It was confirmed that acrylamide was successfully bonded to the GO surface.

The XRD patterns of GO and AMG are shown in Fig. 5 a. For GO, the presence of the characteristic diffraction peak at ca. 11.0° indicated the successful oxidation of graphite. After amidation, GO was reduced to graphene and restored to the ordered crystal structure. The broad peak at ca. 24° corresponding to the (0 0 2) reflection of graphene indicated the poor order of graphene sheets along their stacking direction, suggesting that the graphene was composed of a few layers of stacked graphene sheets [47]. Fig. 5b shows the Raman spectra of the GO and AMG. Both the spectra showed the existence of a G band ($\sim 1580 \text{ cm}^{-1}$) and a D band ($\sim 1350 \text{ cm}^{-1}$). The intensity ratio of the D band to G band can also be used to evaluate the degree of disorder [48]. The intensity ratio for AMG (1.13) shows an enhanced value compared to that for

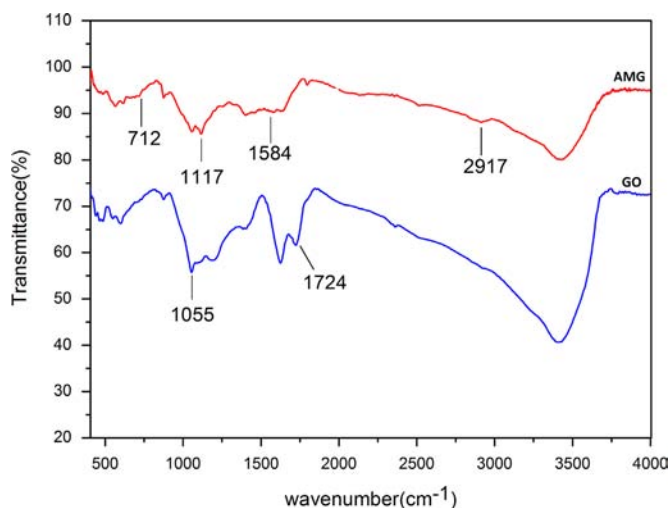


Fig. 4. FT-IR spectra of GO and AMG.

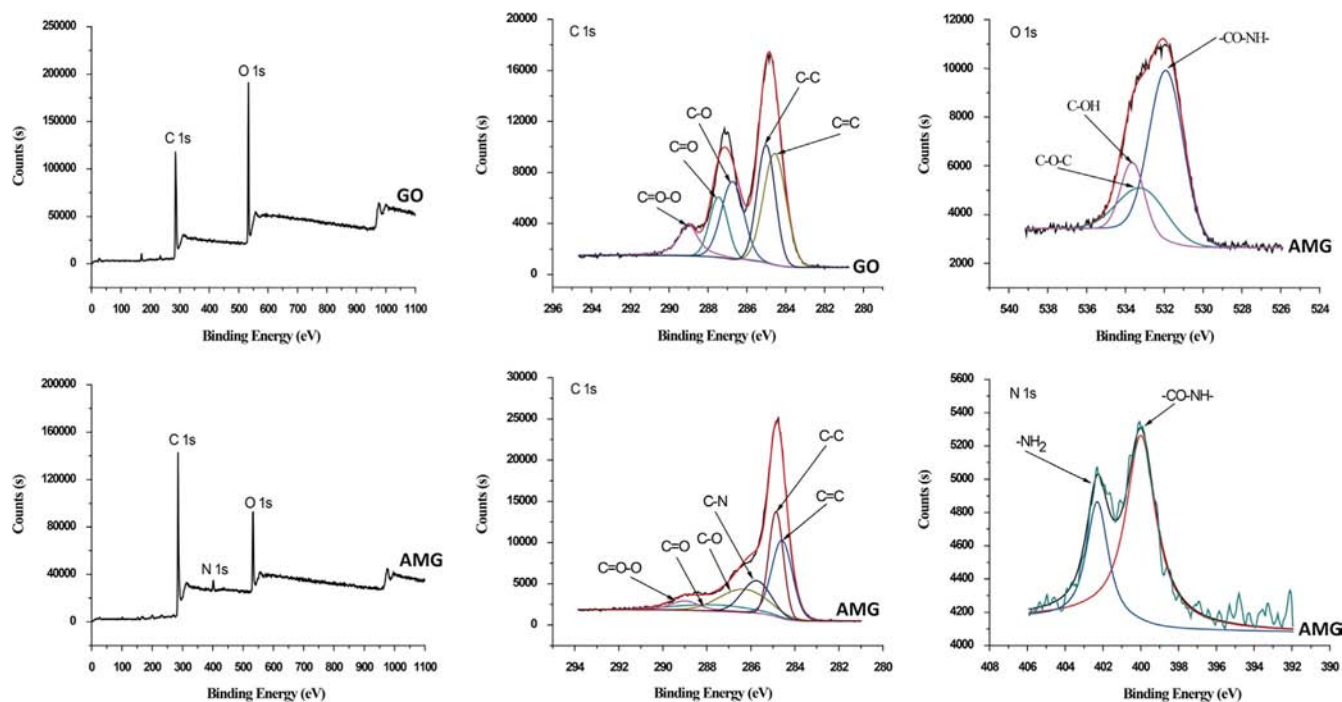


Fig. 3. XPS spectra of GO and AMG.

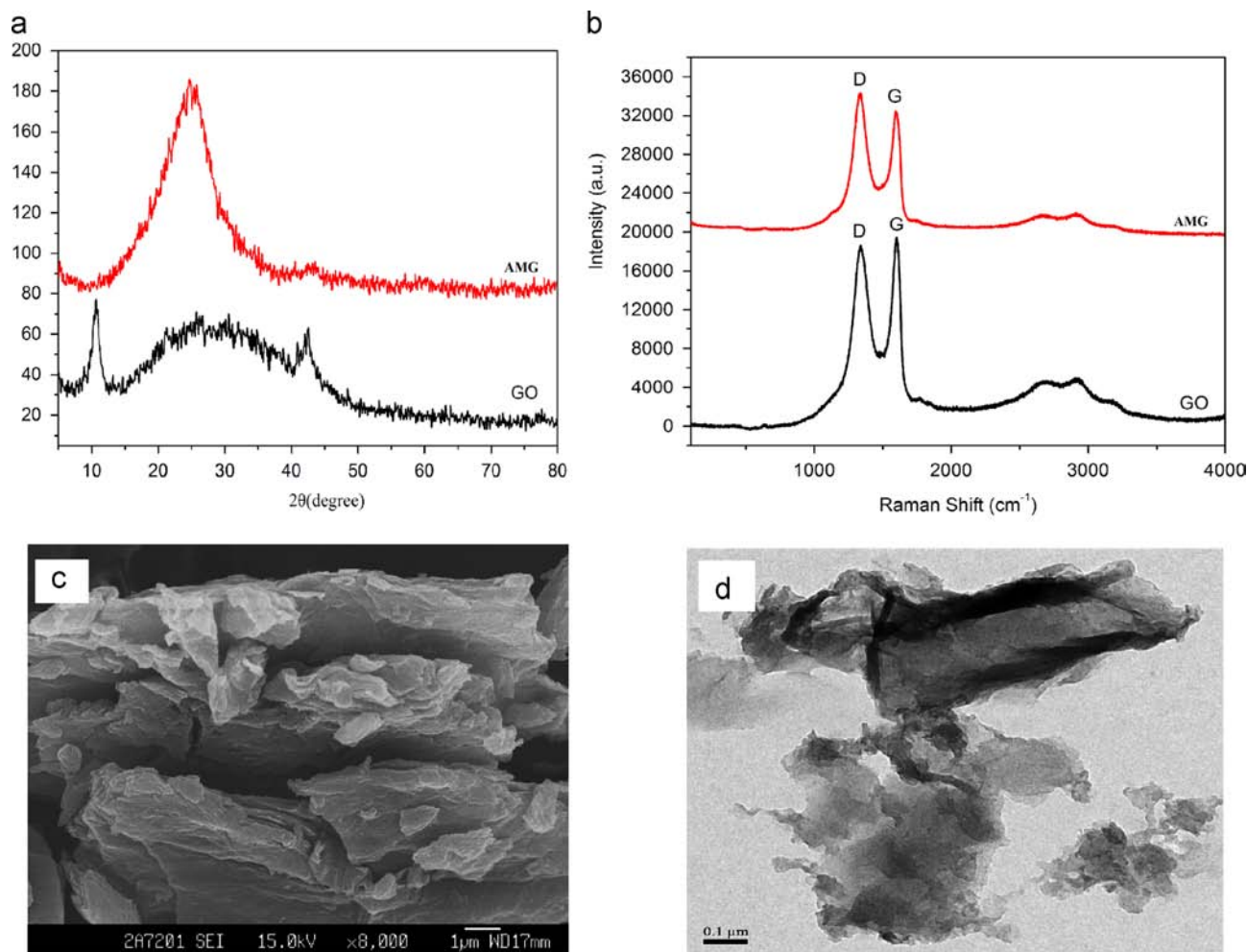


Fig. 5. (a) Wide-angle XRD pattern of GO and AMG, (b) Raman spectra of GO and AMG, (c) scanning electron microscope images of AMG with a magnification of $\times 8000$, and (d) a TEM image of AMG.

GO (0.88), indicating the presence of localised sp^3 defects within the sp^2 carbon network upon reduction of the exfoliated GO.

To observe the AMG surface, the prepared material was characterised by SEM and TEM. It can be clearly seen that crumpled silk wave-like carbon sheets exist, and that the AMG was loose and had multilayers. The morphology is essential to ensure good permeability (Fig. 5c), and is a characteristic feature of single-layer graphene sheets (Fig. 5d). It was important to increase the adsorption sites as well as improve the kinetics of the extraction process and extraction efficiency.

3.3. Adsorption performance of AMG for HAs

3.3.1. Enrichment capacity, stability and reproducibility

The enrichment capacity for the μ -SPE column of AMG was evaluated by the online extraction of six polar HAs (IQ, IQX, MeIQ, MeIQX, 4,8-DiMeIQx and 4,7,8-TriMeIQX). It was compared with the μ -SPE column of graphene, florisil, and C_{18} . The results are shown in Fig. 6a. Graphene, florisil, and C_{18} exhibited low adsorption towards all the six polar HAs, while the μ -SPE column of AMG showed better adsorption affinity towards these HAs. This was probably because of the selectivity adsorption caused by a strong affinity of the amide linkage to the polar HAs. Taken together, the results demonstrated that the AMG can be used as an excellent μ -SPE sorbent towards HAs in the aqueous phase.

In this work, the proposal method was done with the same AMG μ -SPE column, the working life of AMG μ -SPE column was

more than three months. It showed high stability and it could be used for extraction more than 100 times with no significant changes in extraction efficiency. Moreover, the repeatability of batch-to-batch synthesized AMG μ -SPE column was satisfied, the relative standard deviation (RSD, $n=5$) of peak area for extraction of six HAs was lower than 6.0%.

3.3.2. Adsorption kinetics studies

Adsorption kinetics has an important characteristic that governs the solute-uptake rate: it represents the adsorption efficiency of the adsorbent. The Lagergren pseudo-first-order kinetic model is one of the most widely used adsorption rate equations for the dynamic adsorption of a solute from a liquid solution. This model has been used to investigate the adsorption kinetics of HAs onto AMG. The Lagergren pseudo-first-order kinetic model can be expressed by the following equation [49, 50]:

$$\frac{dq_t}{dt} = k(q_e - q_t) \quad (1)$$

where q_t and q_e refer to the amount of HAs adsorbed (pmol) at any time, t (min), and at equilibrium, respectively; and k is the equilibrium rate constant of the pseudo-first-order sorption (min^{-1}). Eq. (1) can be integrated to obtain Eq. (2):

$$\log \frac{q_e}{q_e - q_t} = \frac{kt}{2.303} \quad (2)$$

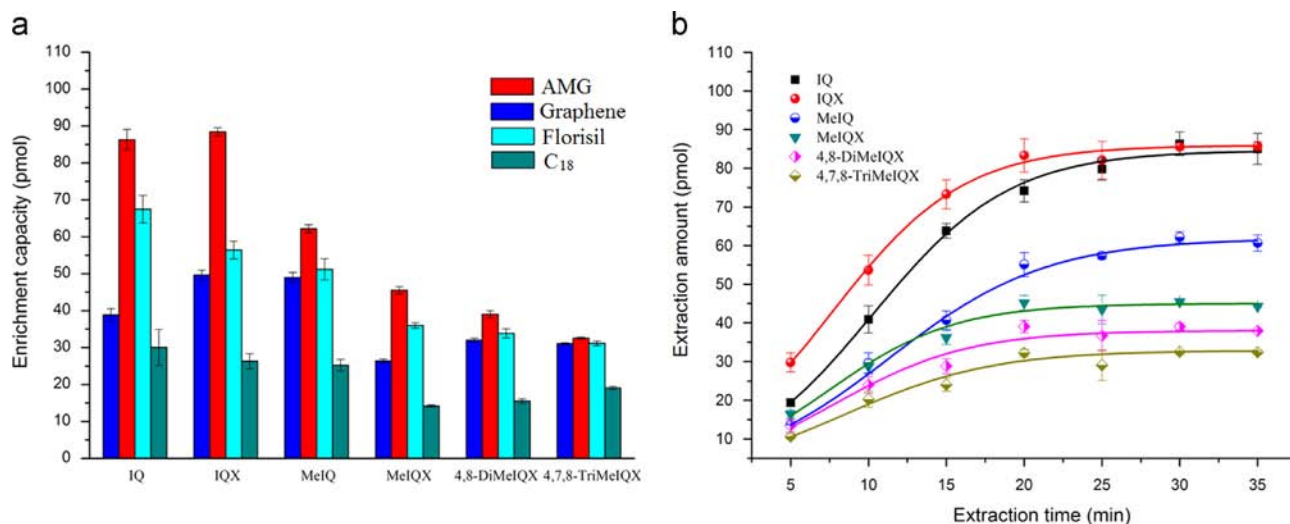


Fig. 6. (a) Extraction performance of HAs on different adsorbents at 25 °C, and (b) pseudo-first-order kinetic models for the adsorption of HAs from aqueous solution.

Table 1
Kinetic constants for HAs adsorption onto the AMG in water phase^a.

Compounds	$q_{e(\text{exper})}$	$q_{e(\text{calcu})}$	k	R_e
IQ	86.33	84.62	0.5255	0.9978
IQX	85.52	85.94	0.5480	0.9988
MeIQ	62.17	61.86	0.4568	0.9986
MeIQX	45.50	45.00	0.5693	0.9587
4,8-DiMeIQX	39.03	38.01	0.5348	0.9535
4,7,8-TriMeIQX	32.55	32.86	0.4890	0.9792

^a Online extraction time: 30 min, pH:7.0, ($q_{e(\text{exper})}$ /pmol, ($q_{e(\text{calcu})}$ /pmol, k /min⁻¹).

Eq. (2) can be rearranged to obtain the following nonlinear form (Eq. (3)):

$$\log(q_e - q_t) = \log(q_e) - \left(\frac{k}{2.303}\right)t \quad (3)$$

The $\log(q_e - q_t)$ versus t plot is used to determine the pseudo-first-order rate constant, k . The k , q_e , and coefficients of determination (R_e) with different amounts of HA were calculated and are shown in Table 1. It was found that the correlation coefficient (R_e) had good values for the adsorption of the HAs and a very little difference existed between $q_{e(\text{exper})}$ (experimental) and $q_{e(\text{calcu})}$ (calculated). It is a good pseudo-first-order fit to the experimental data; this indicates that the HAs in the AMG adsorption system obey the pseudo-first-order kinetic model for the entire sorption period.

The relationship between the extraction amount and time is shown in Fig. 6b. It was clearly indicated that the extraction equilibrium of the six HAs was 30 min. The enrichment factors were calculated by comparing the peak areas obtained before and after AMG μ -SPE. In comparison with the direct-injection chromatogram, a significant enhancement in the peak area was observed after extracted by the μ -SPE column. The enrichment factors were measured as 78–166 for the selected six HAs, indicating the remarkable preconcentration ability of the column.

3.4. Effect of experimental conditions

It is more convenient to directly connect the μ -SPE column with an HPLC system by a six-port valve to obtain an online μ -SPE-HPLC. This connection is preferred not only because of its relatively high strength and high pressure resistance but also because it is easier to assemble and work with an online port. This

eliminates the dead volume and avoids the residue of the sample from getting trapped in the valve between consecutive injections. In the present work, six HAs were selected as models to demonstrate the enrichment efficiency of the AMG μ -SPE. Some parameters greatly affected the extraction efficiency of the AMG μ -SPE, which included the pH of the sample solution, extraction flow rate, desorption solvent, desorption flow rate, and desorption volume. Each was systematically studied by using HAs standard solution of 5.00 μ g/L. Moreover, the type of desorption solvent can also significantly affect the adsorption efficiency. The desorption solvent was also studied and the mobile phase showed good desorption efficiency. Using the mobile phase as desorption solvent can simplify the manipulation of the microextraction, and therefore, the analytes were desorbed directly by the mobile phase.

3.4.1. Sample solution pH

The solution pH affects both the aqueous chemistry and the surface-binding sites of the adsorbents. The effect of pH on the sample solution was investigated for pH values 5.0–9.0 with 0.01 mol/L of sodium hydroxide and acetic acid. The extraction volume used was 2.5 mL, the extraction flow rate was 200 μ L/min, the desorption volume was 400 μ L, and the desorption flow rate was 100 μ L/min. The results are shown in Fig. 7a. The pH of the sample solution between 6.0 and 8.0 had little influence on the extraction efficiency of AMG, chiefly because the polarity of both the AMG and HA molecules was not obviously affected by the neutral sample solution. To simplify the sample preparation procedures, the pH of the sample solution was not adjusted and the samples were directly prepared with distilled water for further studies.

3.4.2. Extraction flow rate

The enrichment factor and analytical time of the μ -SPE procedure mainly depend on the extraction flow rate. Generally, the enrichment factor is a key parameter and a higher extraction flow rate is desirable for rapid analysis. The extraction flow rate is limited by the efficiency of sorbents and a decrease in the extraction efficiency. In this work, the extraction flow rate of μ -SPE was investigated from 200 to 800 μ L/min. The results are shown in Fig. 7b. It can be seen that the extraction efficiencies of the HAs were affected by the extraction flow rate; the largest peak area was achieved when the extraction flow rate was 600 μ L/min.

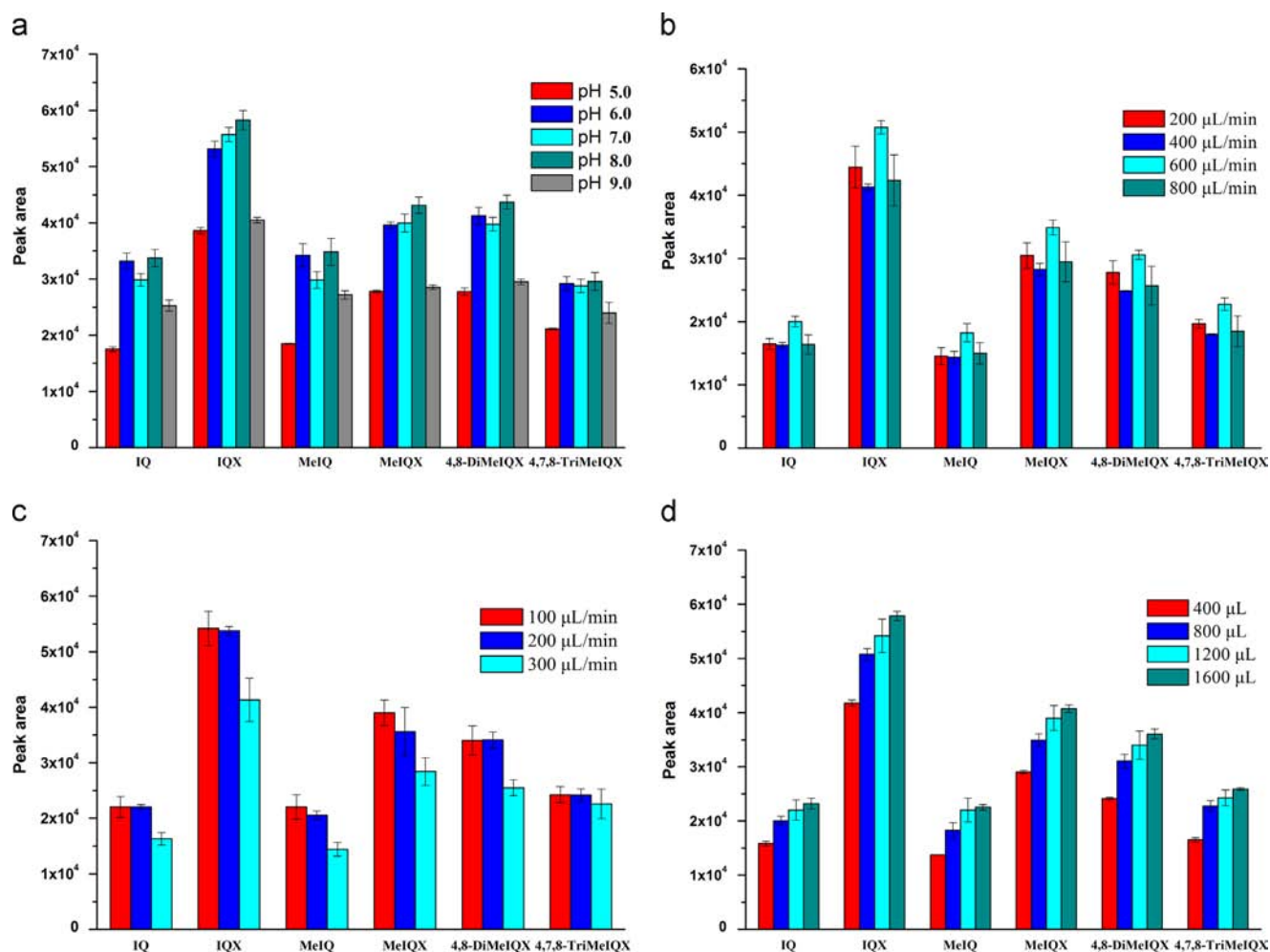


Fig. 7. Effect of experimental conditions on the extraction efficiency. (a) pH of the sample solution, (b) extraction flow rate, (c) desorption flow rate, and (d) desorption volume.

The μ -SPE column was also stable at this flow rate after consecutive injections. Therefore, the extraction flow rate of 600 $\mu\text{L}/\text{min}$ was selected.

3.4.3. Desorption flow rate

The effects of the desorption flow rate in the range 100–300 $\mu\text{L}/\text{min}$ were also investigated (Fig. 7c). The experimental results showed that 100 and 200 $\mu\text{L}/\text{min}$ of flow rates had no obvious effect on the total extraction amounts of the six HAs, while the analyte peak area is decreased when the flow rate was 300 $\mu\text{L}/\text{min}$. This might be attributed to the fact that the mass transfer of analytes from the solution to the AMG is a medium mass process; a flow rate faster than 200 $\mu\text{L}/\text{min}$ has no benefit for the equilibrium of analytes and sorbents. The desorption flow rate of 200 $\mu\text{L}/\text{min}$ was selected for the following experiments.

3.4.4. Desorption volume

As can be observed in Fig. 7d, desorption volume was also investigated from 400 to 1600 μL . The results indicated that desorption efficiencies were enhanced by increasing the desorption volume. The concentrated HAs could be efficiently transferred to the analytical column by 1200 μL of the desorption solvent; the peak shapes of all the analytes did not display any broadening or trailing. However, when the desorption volume was enlarged to 1600 μL , the peak shape of the IQ showed peak

broadening as well as a small increase in the desorption efficiency. Therefore, a 1200- μL desorption volume was selected for further studies.

3.5. Method validation

3.5.1. Analytical method

An online method based on the AMG μ -SPE coupling with HPLC was developed. The validation of the method was performed with the final optimum parameters; the results are shown in Table 2. The linear ranges were 0.020–5.0 $\mu\text{g}/\text{L}$ for IQX; 0.025–5.0 $\mu\text{g}/\text{L}$ for IQ, MeIQX, and 4,7,8-TriMeIQX; and 0.050–5.0 $\mu\text{g}/\text{L}$ for MeIQ and 4,8-DiMeIQX. The limits of detection (LODs) were within the range 0.70–2.5 ng/L, the limits of quantity (LOQs) were in the range 2.7–8.7 ng/L, LOD and LOQ were estimated on the basis of 3:1 and 10:1 signal to noise ratios, respectively, and the RSDs were achieved in the range 4.3–8.7% ($n=5$). The present work showed lower LODs and good precision. Moreover, the values of recovery (R) were estimated by the following equation.

$$R = \frac{A-b}{a(C_s \times V_s)} \times 100\% \quad (4)$$

where A is the peak area, a is the slope of calibrated curve, b is the intercept of calibrated curve, C_s is the spiked concentration, V_s is the spiked volume.

Table 2
The linear range, LOD, LOQ and RSD of AMG μ -SPE coupled to HPLC for HAs.

Compounds	Equation of linearity	Range ($\mu\text{g/L}$)	R^2	LOD (ng/L)	LOQ (ng/L)	RSD ^a (%) ($n=5$)
IQ	$Y=1.87 \times 10^4 X+6.84 \times 10^2$	0.025–5.00	0.9920	2.5	8.7	4.4
IQX	$Y=3.09 \times 10^4 X+2.49 \times 10^2$	0.020–5.00	0.9996	0.70	2.7	7.5
MeIQ	$Y=1.97 \times 10^4 X+8.82 \times 10^2$	0.050–5.00	0.9900	0.90	3.2	8.7
MeIQX	$Y=2.30 \times 10^4 X+3.30 \times 10^2$	0.025–5.00	0.9988	1.0	3.6	4.4
4,8-DiMeIQX	$Y=2.31 \times 10^4 X+5.39 \times 10^2$	0.050–5.00	0.9967	2.0	7.1	4.3
4,7,8-TriMeIQX	$Y=1.71 \times 10^4 X+7.43 \times 10^2$	0.025–5.00	0.9906	1.8	6.3	5.9

^a The method precision was monitored with 1.0 $\mu\text{g/L}$ mixed standard solution and the RSD of extraction amounts of six HAs.

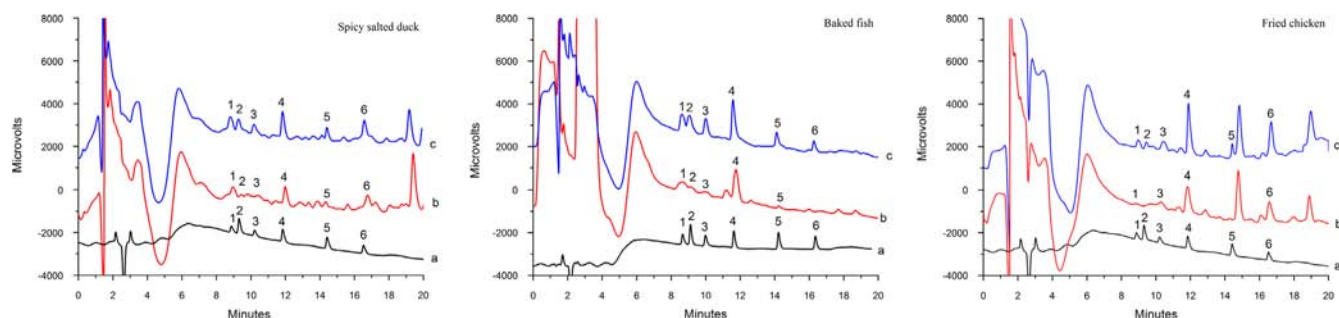


Fig. 8. Chromatograms of spicy salted duck, baked fish, and fried chicken samples with (a) a direction injection of the standard solution at 25.0 $\mu\text{g/L}$, (b) a sample solution extracted by AMG μ -SPE, and (c) a 30.0 ng/g of spiked sample solution extracted by AMG μ -SPE. The peaks are: 1. IQ, 2. IQX, 3. MeIQ, 4. MeIQX, 5. 4,8-DiMeIQX, and 6. 4,7,8-TriMeIQX.

Table 3
The analysis of HAs in food samples by AMG μ -SPE coupled to HPLC ($n=3$).

Samples	Analytes	Original amount (ng/g)	RSD (%)	Spiked concentration (ng/g)					
				10.0		30.0		50.0	
				Re ^a (%)	RSD (%)	Re (%)	RSD (%)	Re (%)	RSD (%)
Spicy salted duck	IQ	28.1	1.9	69.0	2.6	74.1	6.7	75.3	1.7
	IQX	2.0	8.0	91.6	3.3	73.8	2.0	89.2	8.6
	MeIQ	8.1	7.2	71.3	3.5	76.8	6.0	107	6.0
	MeIQX	43.3	7.3	94.0	4.2	91.5	10.2	113	8.7
	4,8-DiMeIQX	9.2	6.1	77.6	2.7	72.9	1.8	118	3.6
	4,7,8-TriMeIQX	55.2	9.5	102	10.3	112	1.5	114	3.7
Baked fish	IQ	37.3	1.5	72.4	1.9	70.9	2.8	73.6	3.8
	IQX	4.2	6.5	79.0	5.2	90.8	1.6	76.0	2.8
	MeIQ	13.0	3.8	107	3.8	104	1.7	116	8.7
	MeIQX	109	3.0	81.6	2.2	78.8	1.4	78.7	2.7
	4,8-DiMeIQX	4.1	3.6	87.4	5.9	89.9	3.0	89.3	4.6
	4,7,8-TriMeIQX	N.D. ^b	–	81.0	8.5	87.8	3.0	99.9	2.4
Fried chicken	IQ	4.7	4.5	65.9	3.3	75.1	1.5	81.1	2.2
	IQX	N.D.	–	73.9	10.8	85.4	3.0	82.9	5.6
	MeIQ	15.4	2.9	83.9	7.2	84.5	3.5	91.6	5.4
	MeIQX	104	5.2	95.5	3.3	96.4	4.7	103	3.9
	4,8-DiMeIQX	N.D.	–	75.6	8.6	89.2	5.7	97.6	5.3
	4,7,8-TriMeIQX	83.6	2.0	97.9	7.9	108	6.5	103	4.3

^a Re: recovery.

^b N.D.: not detected.

3.5.2. Application of HAs analysis in real samples

The present method was applied to determine trace amounts of HAs in spicy salted duck, baked fish, and fried chicken samples; the chromatograms of the samples extracted by the μ -SPE are illustrated in Fig. 8. The results demonstrated that all the six HAs could be accurately analysed in real samples. The μ -SPE column showed maximal elimination of the matrix interferences and enhancement of the sensitivity. The amounts of IQ, MeIQ, and MeIQX in these samples ranged within 4.7–37.3, 8.1–15.4, and 43.3–109 ng/g, respectively. IQX, 4,8-DiMeIQX, and 4,7,8-TriMeIQX

were also detected in some samples; the results are shown in Table 3. To evaluate the matrix effect on the established method, which was selected for spiking analysis at three concentrations 10.0, 30.0 and 50.0 ng/g with IQ, IQX, MeIQ, MeIQX, 4,8-DiMeIQX, and 4,7,8-TriMeIQX, chromatograms of the spiked samples of 30.0 ng/g are also shown in Fig. 8. As shown in Table 3, the recoveries for the six HAs in spicy salted duck, baked fish, and fried chicken samples were 69.0–118%, 70.9–116%, and 65.9–108%, respectively, with RSDs of 1.4–10.8%, indicating that the online AMG μ -SPE–HPLC method was sensitive and accurate.

4. Conclusions

In this work, AMG was successfully synthesised and fabricated in a PEEK tube to achieve online coupling to HPLC. The fabricated microcolumn can efficiently enrich the target compounds, and the enrichment factors were 78–166 for the six selected HAs. The LODs were in the range 0.70–2.5 ng/L, as was determined for the analysis of the HAs at the ng/g level in complex matrices. The proposed online method based on the AMG μ -SPE-HPLC was successfully applied to the analysis of HAs in spicy salted duck, baked fish, and fried chicken samples. The developed method demonstrated good linearity, satisfactory LODs, and repeatability, and was proven to be sensitive, convenient, and reliable in determining HAs in food samples.

Acknowledgements

This study was supported by the National Natural Science Foundation of China (no. 21127008), the Specialised Research Fund for the Doctoral Program of Higher Education (20120171110001), the Guangdong Provincial Natural Science Foundation of China (no. S2012010010787), and the Natural Science Foundation of the Guizhou Provincial Education Department (no. 2012070).

References

- [1] K.I. Skog, M.A.E. Johansson, M.I. Jägerstad, *Food Chem. Toxicol.* 36 (1998) 879–896.
- [2] A. Shin, M.J. Shrubsole, R.M. Ness, H.Y. Wu, R. Sinha, W.E. Smalley, Y. Shyr, W. Zheng, *Int. J. Cancer* 121 (2007) 136–142.
- [3] D. Natale, M. Gibis, M.T. Rodríguez-Estrada, J. Weiss, *J. Agric. Food Chem.* 62 (2014) 279–287.
- [4] L.B. Agudelo Mesa, J.M. Padró, M. Reta, *Food Chem.* 141 (2013) 1694–1701.
- [5] A. Martín-Calero, J.H. Ayala, V. González, A.M. Afonso, *Anal. Bioanal. Chem.* 394 (2009) 937–946.
- [6] A. Martín-Calero, V. Pino, J.H. Ayala, V. González, A.M. Afonso, *Talanta* 79 (2009) 590–597.
- [7] F. Oz, M. Kizil, *Food Anal. Methods* 6 (2013) 1370–1378.
- [8] F. Oz, *Food Chem.* 126 (2011) 2010–2016.
- [9] M. Costa, O. Viegas, A. Melo, C. Petisca, O. Pinho, I.M.P.L.V.O. Ferreira, *J. Agric. Food Chem.* 57 (2009) 3173–3179.
- [10] Y. Zhang, C.P. Lin, G.Z. Fang, J.B. Mei, X. Wang, S. Wang, *Eur. Food Res. Technol.* 234 (2012) 197–205.
- [11] H. Kataoka, T. Inoue, K. Saito, H. Kato, K. Masuda, *Anal. Chim. Acta* 786 (2013) 54–60.
- [12] Y.F. Fu, G. Zhao, S. Wang, J.J. Yu, F.W. Xie, H. Wang, J.P. Xie, *J. Chromatogr. A* 1333 (2014) 45–53.
- [13] B. Janoszka, U. Blaszczyk, L. Warzecha, M. Strózyk, A. Damasiewicz-Bodzek, D. Bodzek, *J. Chromatogr. A* 938 (2001) 155–165.
- [14] S. Casal, E. Mendes, J.O. Fernandes, M.B.P.P. Oliveira, M.A. Ferreira, *J. Chromatogr. A* 1040 (2004) 105–114.
- [15] S. Sentellas, E. Moyano, L. Puignou, M. Teresa Galceran, *J. Chromatogr. A* 1032 (2004) 193–201.
- [16] R. Gonzalo-Lumbreras, N. Rosales-Conrado, M.E. León-González, L.V. Pérez-Arribas, L.M. Polo-Díez, *J. Chromatogr. A* 1217 (2010) 6778–6784.
- [17] J.R. Soglia, R.J. Turesky, A. Paehler, P. Vouros, *Anal. Chem.* 73 (2001) 2819–2827.
- [18] M. Murkovic, *Anal. Bioanal. Chem.* 389 (2007) 139–146.
- [19] M.R. Khan, R. Busquets, J. Saurina, S. Hernández, L. Puignou, *Chem. Res. Toxicol.* 26 (2013) 1014–1022.
- [20] Y.S. Gu, I.S. Kim, J.K. Ahn, D.C. Park, D.M. Yeum, C.I. Ji, S.B. Kim, *Mutat. Res.* 515 (2002) 189–195.
- [21] Ö. Özdeştan, E. Kaçar, H. Keşkekoğlu, A. Üren, *Food Anal. Methods* 7 (2014) 116–126.
- [22] F.U. Shah, T. Barri, J.Å. Jönsson, K. Skog, *J. Chromatogr. B* 870 (2008) 203–208.
- [23] L. Cárdenes, J.H. Ayala, A.M. Afonso, V. González, *J. Chromatogr. A* 1030 (2004) 87–93.
- [24] A. Martín-Calero, J.H. Ayala, V. González, A.M. Afonso, *Anal. Chim. Acta* 582 (2007) 259–266.
- [25] H.P. Thiebaud, M.G. Knize, P.A. Kuzmicky, J.S. Felton, D.P. Hsieh, *J. Agric. Food Chem.* 42 (1994) 1502–1510.
- [26] G.A. Gross, A. Grüter, *J. Chromatogr. A* 592 (1992) 271–278.
- [27] E. Rodríguez, F. Navarro-Villoslada, E. Benito-Peña, M.D. Marazuela, M.C. Moreno-Bondi, *Anal. Chem.* 83 (2011) 2046–2055.
- [28] C.C. Acebal, M. Grünhut, I. Šrámková, P. Chocholeuš, A.G. Lista, H. Sklenářová, P. Solich, B.S. Fernández Band, *Talanta* 129 (2014) 233–240.
- [29] C. Basheer, A.A. Alnedhary, B.S. Madhava Rao, S. Valliyaveettil, H.K. Lee, *Anal. Chem.* 78 (2006) 2853–2858.
- [30] L. Guo, H.K. Lee, *J. Chromatogr. A* 1300 (2013) 24–30.
- [31] W.P. Zhang, Z.L. Chen, *Talanta* 103 (2013) 103–109.
- [32] L. Guo, H.K. Lee, *J. Chromatogr. A* 1218 (2011) 9321–9327.
- [33] H. Keşkekoğlu, A. Üren, *Meat Sci.* 96 (2014) 1446–1451.
- [34] K. Puangsombat, P. Gadgil, T.A. Houser, *Meat Sci.* 90 (2012) 739–746.
- [35] A.A. Balandin, S. Ghosh, W.Z. Bao, I. Calizo, D. Teweldebrhan, F. Miao, C.N. Lau, *Nano Lett.* 8 (2008) 902–907.
- [36] R. Sitko, B. Zawisza, E. Malicka, *TrAC-Trends Anal. Chem.* 51 (2013) 33–43.
- [37] Q. Liu, J.B. Shi, J.T. Sun, T. Wang, L.X. Zeng, N.L. Zhu, G.B. Jiang, *Anal. Chim. Acta* 708 (2011) 61–68.
- [38] S.L. Zhang, Z. Du, G.K. Li, *Anal. Chem.* 83 (2011) 7531–7541.
- [39] W.N. Wang, R.Y. Ma, Q.H. Wu, C. Wang, Z. Wang, *Talanta* 109 (2013) 133–140.
- [40] Y.B. Luo, G.T. Zhu, X.S. Li, B.F. Yuan, Y.Q. Feng, *J. Chromatogr. A* 1299 (2013) 10–17.
- [41] W.B. Guan, Z.N. Li, H.Y. Zhang, H.J. Hong, N. Rebeyev, Y.Q. Ma, Y.Y. J. *J. Chromatogr. A* 1286 (2013) 1–8.
- [42] Y.H. Yan, Z.F. Zheng, C.H. Deng, Y. Li, X.M. Zhang, P.Y. Yang, *Anal. Chem.* 85 (2013) 8483–8487.
- [43] H. Kawasaki, K. Nakai, R. Arakawa, E.K. Athanassiou, R.N. Grass, W.J. Stark, *Anal. Chem.* 84 (2012) 9268–9275.
- [44] W.S. Hummers, R.E. Offeman, *J. Am. Chem. Soc.* 80 (1958) 1339 (1339).
- [45] N.I. Kovtyukhova, P.J. Ollivier, B.R. Martin, T.E. Mallouk, S.A. Chizhik, E.V. Buzaneva, A.D. Gorchinskiy, *Chem. Mater.* 11 (1999) 771–778.
- [46] S. Niyogi, E. Bekyarova, M.E. Itkis, J.L. McWilliams, M.A. Hamon, R.C. Haddon, *J. Am. Chem. Soc.* 128 (2006) 7720–7721.
- [47] C.N.R. Rao, K. Biswas, K.S. Subrahmanyama, A. Govindaraj, *J. Mater. Chem.* 19 (2009) 2457–2469.
- [48] V. Chandra, J. Park, Y. Chun, J.W. Lee, I.C. Hwang, K.S. Kim, *ACS. Nano* 4 (2010) 3979–3986.
- [49] M. Ghaedi, A. Hassanzadeh, S. Nasiri Kokhdan, *J. Chem. Eng. Data* 56 (2011) 2511–2520.
- [50] L. Eskandarian, M. Arami, E. Pajootan, *J. Chem. Eng. Data* 59 (2014) 444–454.



Application of curcumin nanoparticles in a lab-on-paper device as a simple and green pH probe



Nahid Pourreza*, Hamed Golmohammadi

Department of Chemistry, College of Science, Shahid Chamran University, Ahvaz, Iran

ARTICLE INFO

Article history:

Received 19 May 2014

Received in revised form

20 July 2014

Accepted 21 July 2014

Available online 30 July 2014

Keywords:

Lab-on-paper

Curcumin nanoparticle

pH Sensor

Mean color intensity

ABSTRACT

This article describes the design and fabrication of a novel lab-on-paper device for pH sensing using curcumin nanoparticles (CURNs). In order to fabricate the lab-on-paper, the wax dipping method was used. The color of loaded paper with CURNs changed from yellow to orange and red to brown in the pH range of 7–13. The image of the lab-on-paper was taken by a digital camera and the picture was processed and analyzed using Adobe Photoshop software. The change in mean color intensity with pH was recorded and employed as an analytical signal for quantitative sensing of pH. The parameters affecting the pH sensor were optimized to enhance the selectivity and sensitivity of the method. Under optimum conditions, the mean color intensity was linearly proportional to the pH in the range of 8–13. The relative standard deviations of 10 replicate measurements of pH 9 and pH 12 were 2.3% and 1.5%, respectively. The developed sensor was successfully applied to the determination of pH in different water samples with satisfactory results.

© 2014 Elsevier B.V. All rights reserved.

1. Introduction

Paper-based devices have been developed for providing portable, low-cost and disposable platforms for detecting various analytes and clinical diagnosis [1–3]. The pioneering work on “Lab-on-paper” was carried out by Whitesides's group at Harvard University in 2007 [4]. This method presents a wide range of applications including biochemical analysis, health diagnostics, food quality control, environmental monitoring and forensic analysis [5–8]. Colorimetric [9–16], electrochemical [17–19], chemiluminescence [20,21], electrochemiluminescence [22], and electrical conductivity [23] detections are main quantifying approaches in the lab-on-paper method although other techniques such as mass spectrometry [24] and surface enhanced Raman spectroscopy [25] have also been applied. Among these methods, colorimetric detection is the most useful method because of its simplicity and easy performance by applying inexpensive and non-sophisticated image analysis software such as Photoshop and also instruments such as a digital camera, scanner or even a mobile phone camera [14,15]. Lab-on-paper devices have many advantages including cost-effective, portability, ease of fabrication and using minimum required reagent and sample [5,14,26]. Paper as a flexible and porous matrix is composed of hydrophilic cellulose fibers with an intrinsic capillary property which causes the flow of liquid without any external

forcing power [7,13]. On the other hand, having the advantages of low cost, high availability, biodegradability, portability, porous matrix and hydrophilic surface are making paper a suitable candidate for loading and absorbing the reagents such as suspensions of nanoparticles [12,27,28]. A variety of techniques have been developed to design and fabricate the lab-on-paper devices including photolithography, inkjet printing, plasma etching, paper cutting, wax printing, analog plotting, screen printing, and laser treatment [2,4,26].

The pH sensing has received great attention because of the importance of pH measurement in different scientific research fields and practical applications [29–31]. Many examples of pH sensors have been reported [29–36] in literature but only a few attempts have been made to pH sensing using paper devices [37–39]. Abe et al. have reported the simultaneous sensing of pH, total protein and glucose in urine samples using an inkjet printed microfluidic multianalyte chemical sensing paper device. They used a mixture of four different colored pH indicators comprising of thymol blue, methyl red, bromothymol blue and phenolphthalein in order to monitor pH in the range of 5–9 in urine samples [38,39]. In a different approach, Lei et al. proposed a carbon nanotube (CNT) based sensor on paper for the determination of pH in the range of 5–9. In the research of this group, pH measurement was based on decreasing of the resistance change with increasing the pH of the solution [37]. Various types of nanoparticles have been used in paper-based devices [12]. In particular, gold and silver nanoparticles as the two metal nanoparticles with surface plasmon resonance (SPR) characteristic

* Corresponding author. Tel.: +98 611 3331044; fax: +98 611 3337009.
E-mail address: npourreza@scu.ac.ir (N. Pourreza).

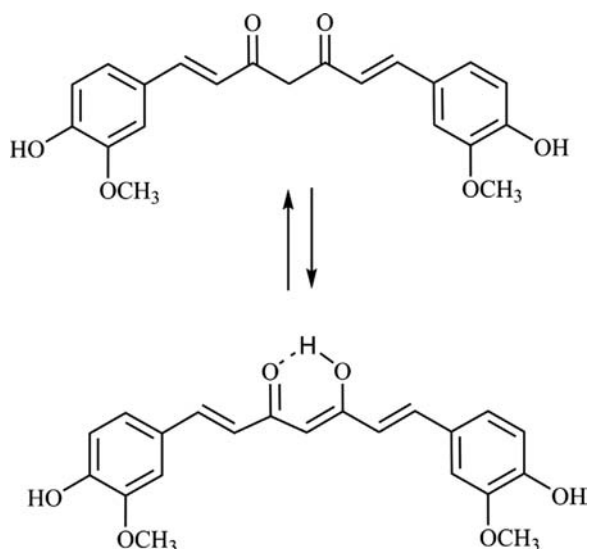


Fig. 1. Bis-keto (top) and enolate (bottom) tautomeric forms of curcumin.

have attracted much attention in paper based devices for colorimetric sensing of several chemical and biological compounds [40–42]. Hydroxy pyrene trisulfonate encapsulated as a microcapsule prepared by assembly of silica nanoparticles has also been used for fluorescence sensing of pH in the range of 5.8–8.0 [43].

Curcumin [(E, E)-1,7-bis (4-hydroxy-3-methoxy-phenyl)-1,6-heptadiene-3,5-dione] is a hydrophobic polyphenol compound which has been recognized as a naturally occurring yellow pigment and component of the spice, turmeric. It is extracted from the dried root of the rhizome *Curcuma longa*. As shown in Fig. 1 Curcumin demonstrates keto–enol tautomerism [44–46]. At basic mediums; the enolate form is prevailed form of curcumin and in the pH range of 3–7, curcumin demonstrates the H-atom donor characteristic because of its keto form. Curcumin bears properties such as antioxidant, anti-inflammatory, anticarcinogenic, antibacterial, wound healing and can readily chelate the metal ions to form the complexes [44]. Apart from these benefits, curcumin has low solubility in aqueous solutions and nanonization can help to overcome this drawback [45,46]. An alternative approach to improve the aqueous solubility is encapsulation of curcumin in micelle or surfactant solutions. Patra and Barakat studied the role of ionic liquid on solubilization of curcumin in the micellar system using various surfactants and determined the critical micelle concentration (cmc) values of aqueous CTAB, SDS and TX100 solutions in the presence and absence of ionic liquid [47]. Curcumin has been also applied as a fluorescence probe for sensing o-nitrophenol [48], DNA [49], protein [50] and estimation of phase transition temperature of liposomes [51]. The application of CUR-NPs as a probe for detection of analytes was reported by Pendya et al. [52]. They demonstrated that CURNs aggregate in the presence of trinitrotoluene (TNT) as an explosive compound and surface plasmon intensity of CURNs is changed. They have found that this property can be employed for selective, ultra-sensitive and simple recognition of TNT in aqueous media. We have recently reported the application of curcumin nanoparticle in a micelle mediated system for colorimetric sensing of sulfide [53].

The glass electrode which is the most widely used pH sensor suffers from alkaline error in basic solutions. This limitation of glass electrode is due to its sensitivity towards alkali metal ions at pH values above 9 [54]. However, determination of pH in strong alkaline industrial solutions and wastewater samples is of significant importance [55].

This research work presents the application of CURNs in fabrication of a novel lab-on-paper device for pH measurement in alkali solutions.

The CURNs were spotted into the lab-on-paper device followed by the addition of solutions with different pH values in the test zone, which subsequently changed the color of the test zone. An image of the test zone was recorded by a digital camera and the picture was processed and analyzed using Adobe Photoshop software and the mean color intensity in gray mode for each test zone was determined. The mean color intensity was decreased upon increasing the pH. The decrease in mean color intensity was proportional to the pH of solutions and was applied as an analytical signal for pH monitoring.

2. Experimental

2.1. Apparatus

Absorption spectra were recorded by a GBC UV–visible spectrophotometer model Cintra 101 (Sidney, Australia) using 1 cm glass cells. TEM image was performed with a transmission electron microscope (Zeiss-EM10C-80 KV, Germany). SEM images were obtained by a scanning electron microscope (Leo 1455 VP, Germany). A Metrohm digital pH-meter model 632 (Switzerland) with a combined glass electrode was used for pH measurements. An ultrasound bath (DSA 100-SK₂, 100 W power, 40 kHz Frequency, China) was used for fabrication of the nanoparticles ultrasonically. A rotary evaporator (Labrota 4000, Heidolph, Germany) was used for removing the solvent. Photographic images were taken with a digital camera (Power Shot SX230 HS, 12.1 megapixels, Canon, Japan).

2.2. Reagents and materials

Analytical grade chemicals and doubled distilled water was used. Britton–Robinson buffer solutions in the pH range of 7–12 were prepared from a mixture of phosphoric acid (Merck), boric acid (Merck) and citric acid (Merck) (0.04 mol L⁻¹ each). Buffer solutions in the pH range of 12–13 were prepared from 0.2 mol L⁻¹ KCl (Merck). The pH of the buffer solutions was adjusted to the exact value by the addition of 0.2 mol L⁻¹ NaOH (Merck) and using a pH meter. 1.0 mol L⁻¹ of NaCl was prepared by dissolving 5.844 g of sodium chloride (Merck) in water and diluting to 100 mL in a volumetric flask. 5% (v/v) of Triton X-100 (Merck) was prepared by diluting 5 mL of the reagent to 100 mL. Filter paper (Whatman No.1) was purchased from Whatman International, Ltd (England). Solid white beeswax was purchased from an herbaceous pharmacy (Ahvaz, Iran). Permanent magnets (circle shaped with 6 mm diameter and 1 mm thickness) were purchased from a local magnet shop (Ahvaz, Iran).

2.3. Synthesis of curcumin nanoparticles

The CURNs were fabricated by our previously reported method for the modification of the technique described by Bhawana et al. [45,53]. The fabrication procedure was performed as follows: the organic phase was prepared by dissolving 125 mg of curcumin in 25 mL of dichloromethane. For preparation of aqueous phase, 10 mL of Triton X-100 5% (v/v) was added to 90 mL of boiling water. Then 2 mL of organic phase was added dropwise to the aqueous phase (about 10 drops/min) under ultrasonic conditions, with an ultrasonic power of 100 W and a frequency of 40 kHz. The sonication was continued for 20 min followed by stirring on a magnetic stirrer at room temperature for 20 min until a yellow color was obtained. This solution was placed in a rotary evaporator in order to ensure the complete removal of dichloromethane. This solution was then stored in a brown bottle. The total concentration of CURNs solution was 0.271 mmol L⁻¹. The prepared CURNs are stable for more than 6 months. The TEM image of the CURNs after fabrication using the above approach can be observed in Fig. 2.

2.4. Fabrication of lab-on-paper

The wax dipping method recommended by Songjaroen et al. was used for fabrication of lab-on-paper device with some modification [2]. A typical fabrication procedure was depicted as follows: the solid beeswax was placed in a Pyrex beaker and melted on a hot plate. The temperature was maintained in the range of 100 ± 5 °C throughout the experiment using a thermometer. A piece of filter paper Whatman No.1 ($2.5 \text{ cm} \times 7.5 \text{ cm}$) was cut and placed on a glass slide. Then 10 circle shaped permanent magnets (6 mm diameter and 1 mm thickness) were put onto the paper and temporarily attached by means of magnetic force using an iron piece ($2.5 \text{ cm} \times 10 \text{ cm}$) which was placed on the backside of the glass slide. The assembly was soaked in melted wax for 1 s to allow molten wax to penetrate into the depth of the paper to form the hydrophobic walls and allowed to cool at room temperature. It was then removed from the glass slide, and the magnets were separated out from the paper.

2.5. Recommended procedure

The colorimetric assays were accomplished by the following steps: $1.0 \mu\text{L}$ volumes of CURNs solution were spotted into the middle of hydrophilic test zones on the lab-on-paper and allowed to dry for 15 min at room temperature. Then $1 \mu\text{L}$ volumes of different pH solutions were added to each test zone separately. After 30 min, an image of each test zone was captured by a digital camera. The picture was then processed and analyzed using Adobe Photoshop CS8 and the mean color intensity in gray mode for each test zone was determined. The color of the loaded lab-on-paper using the CURNs changed from yellow to orange and red to brown upon changing of pH from 8 to 13. The mean color intensity change with pH was recorded and employed as an analytical signal for pH sensing.



Fig. 2. TEM image of synthesized CURNs.

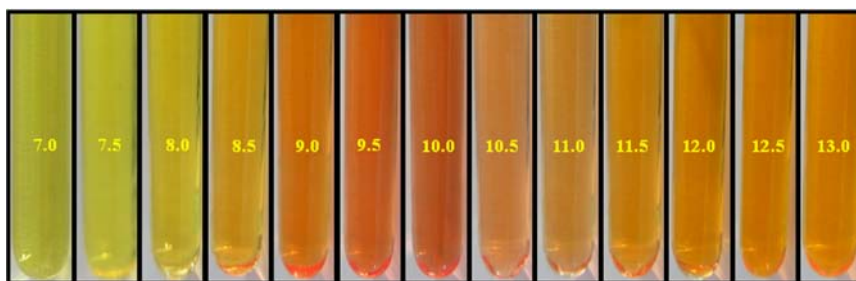


Fig. 3. Photographical images of the CURNs solutions with various pH values in the pH range of 7–13. The pH values from left to right are 7.0, 7.5, 8.0, 8.5, 9.0, 9.5, 10.0, 10.5, 11.0, 11.5, 12.0, 12.5 and 13.0. (For interpretation of the references to color in this figure legend, the reader is referred to the web version of this article.)

3. Results and discussion

3.1. Characteristics of CURNs at different pH values

Curcumin acts as a potent H-atom donor at pH 3–7, because of its keto form and above pH 8, the enolate form predominates, and curcumin acts mainly as an electron donor [44]. It has been shown that curcumin is completely deprotonated at pH 13 to form the highly negatively charged species Cur^{3-} . At pH 13, Cur^{3-} in water shows absorption maxima at 468 nm that is shifted to 457 nm in the presence of liposomes. Studies have also shown that the degradation of curcumin in aqueous solution is linked to the hydrolysis that occurs rapidly above neutral pH [56].

Based on the above discussions the pH dependence of the CURNs color was also investigated by changing the pH of solution from neutral to high alkaline solutions. The color changing and absorption spectra of the CURNs at different pH values in aqueous medium are shown in Fig. 3 and Fig. 4, respectively. As shown in Fig. 4, the absorption intensity of CURNs, initially decreased at $\lambda = 423 \text{ nm}$ in the pH range of 7.0–9.5 with a change of color from yellow to red, and new red shifted absorption bands appeared at $\lambda = 460 \text{ nm}$ in the pH range of 10–13 and absorption intensity at this wavelength increased from pH 10 to 13 with a change of color from red to brown.

However the behavior was different on the paper and the obtained mean color intensity for lab-on-paper test zones was decreased upon increasing of the pH values. Therefore, this decrease in mean color intensity which is proportional to the pH of the solutions was applied as an analytical signal for pH monitoring. In order to evaluate the change in optical properties of CURNs by increasing the pH values from neutral to alkali, the test zones of lab-on-paper at different pH values were characterized by SEM. The resulting SEM images presented in Fig. 5 indicate that there is a decrease in the number of CURNs and yet an increase the particle size of CURNs by changing the

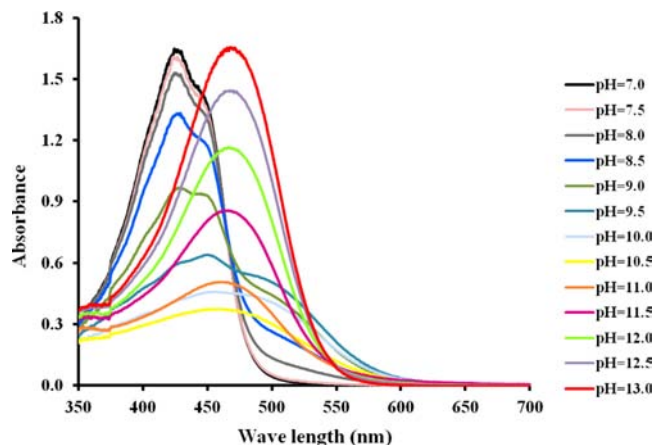


Fig. 4. UV-vis spectra of the CURNs solutions with various pH values in the range of 7–13 after 30 min. (For interpretation of the references to color in this figure legend, the reader is referred to the web version of this article.)

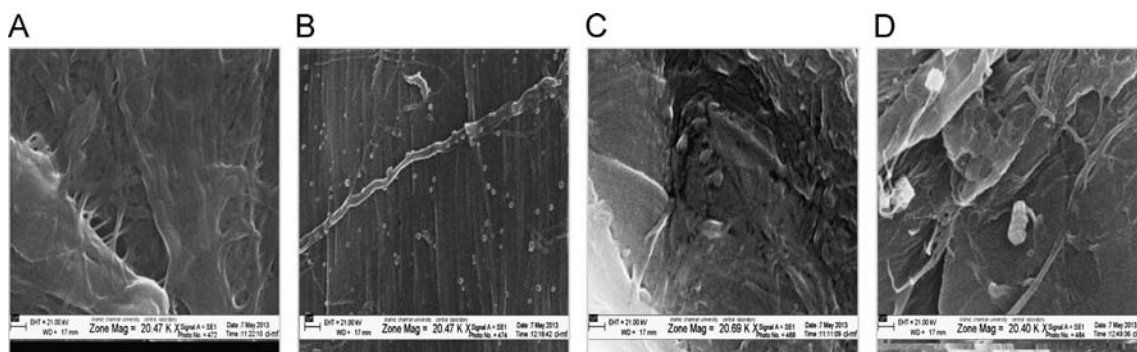


Fig. 5. SEM images (20,000 × magnification) of the test zone after (A) dropping the 1 μL solution with pH=7 and (B) dropping the 1 μL solution of CURNs followed by dropping 1 μL solutions with pH 7, (C) pH 10 and (D) pH 13, respectively.

pH from 7 to 13. On the other hand studies have shown that curcumin molecules are unstable and suffer rapid hydrolytic degradation at neutral–basic pH conditions [57]. It has also been suggested that micelles might suppress alkaline hydrolysis to some extent [58]. Thus, by increasing pH from 7 to 13 it is possible that both aggregation and degradation of CURNs are taking place and these phenomena could probably be responsible for the color change of CURNs under these conditions.

3.2. Influence of CURNs concentration and multiple addition of CURNs

In lab-on-paper devices the color intensity can be increased using multiple additions of the reagents on the test zone. Hence, to

obtain the maximum analytical signal, the effect of CURNs concentration and multiple additions of CURNs as reagent were investigated. To accomplish this goal the dropped reagent (1 μL of CURNs at each addition) was allowed to air dry (about 15 min) before the next addition. Then, after the final addition of the reagent, 1 μL of the solutions with specified pH values were placed on the test zone. As can be ascertained from Fig. 6, the maximum analytical signal (decrease in mean color intensity) was achieved when four times addition of CURNs was applied for all pH values.

3.3. Influence of electrolytes

High concentrations of salts often affect the response of the pH sensor. In order to appraise the electrolyte impact on the current sensor, the experiments were carried out by adding different salts such as NaCl, KCl, NaNO₃, KNO₃, and Na₂SO₄. The results indicate that the addition of up to 0.25 mol L⁻¹ of NaCl, KCl and Na₂SO₄ and 0.1 mol L⁻¹ of NaNO₃ and KNO₃ did not have significant effect on the performance of the pH probe.

3.4. Analytical performance

The analytical figures of merit for the developed sensor were evaluated using the recommended procedure under the optimum conditions. As shown in Fig. 7 the calibration graph for pH sensing was linear in the range of 8–13 with a correlation coefficient (*r*) of 0.9991 and the linear regression equation was $A = -14.075C + 282.64$.

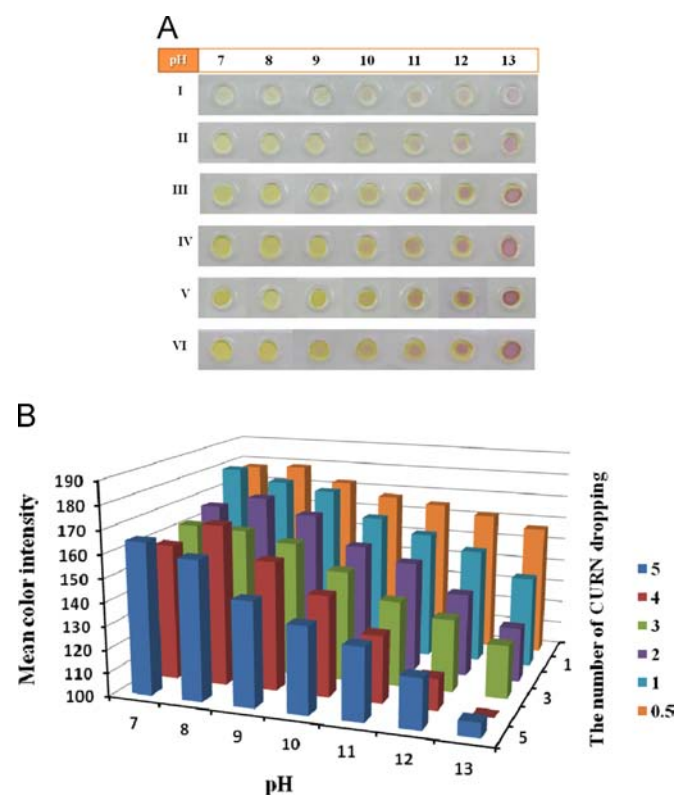


Fig. 6. (A) Color changes of the test zones after (I) one time dropping the 1 μL of the CURNs (1.35×10^{-3} mol L⁻¹) and (II) one (III) two (IV) three (V) four and (VI) five times dropping of the 1 μL of the CURNs (2.71×10^{-3} mol L⁻¹) followed by dropping of 1 μL of the solutions with pH values of 7, 8, 9, 10, 11, 12, 13 respectively, (B) Mean color intensity changes corresponding to observed color changes in part (A) of this figure. (For interpretation of the references to color in this figure legend, the reader is referred to the web version of this article.)

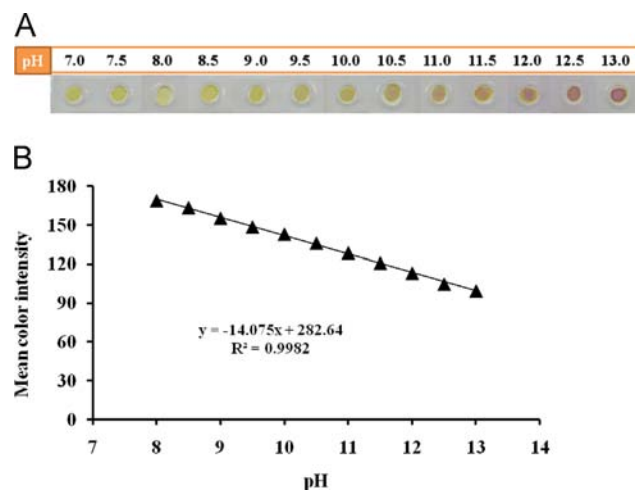





Fig. 7. Color changes of the test zones (A) and the corresponding calibration graph (B) for pH sensing using CURNs incorporated lab-on-paper. (For interpretation of the references to color in this figure legend, the reader is referred to the web version of this article.)

Table 1
The influence of interfering ions on the measurement of pH 10.

Interfering ion	Tolerable concentration (mg L ⁻¹)
Na ⁺ , Cl ⁻ , Ca ²⁺ , K ⁺ , PO ₄ ³⁻ , SO ₄ ²⁻ PO ₄ ³⁻ , borate, NO ₃ ⁻ , acetate, NH ₄ ⁺	1000
CO ₃ ²⁻ , HCO ₃ ⁻ , citrate, Mg ²⁺	500
Tartarate, Ba ²⁺	250
Br ⁻ , C ₂ O ₄ ²⁻ , F ⁻ , I ⁻	50
Pb ²⁺ , Co ²⁺ , Zn ²⁺	25
Cd ²⁺ , Al ³⁺ , Mn ²⁺ , Ni ²⁺	10
Ag ⁺ , Bi ³⁺	5
Cr ²⁺ , Fe ³⁺	2
Cu ²⁺ , Hg ²⁺	1

Table 2
Determination of pH in various water samples.

Water samples	pH Meter	Lab-on-paper ^a	Relative error (%)	Color
Mahshahr refinery wastewater	12.31 ± 0.36	12.72 ± 0.36	3.33	
Karoon River	10.02 ± 0.30	10.22 ± 0.15	1.99	
Ahvaz tap water	9.52 ± 0.26	9.75 ± 0.27	2.41	

^a $x \pm ts/\sqrt{n}$ at 95% confidence ($n=3$).

The relative standard deviations for 10 replicate measurements of pH 9 and pH 12 were 2.3% and 1.5%, respectively.

3.5. Interferences

In this study, the competitive experiments were carried out by adding different anions and cations and measuring the pH under the optimum experimental conditions. Any relative error equal or greater than $\pm 5\%$ from the analytical signal value was considered as interference. The pH of the solutions was adjusted at 10 (midpoint of linear range) and then measuring the analytical signal before and after adding the interfering ion. The results of this study summarized in Table 1 show the good selectivity of the sensor.

3.6. Application for pH sensing in water samples

The performance of the developed lab-on-paper sensor was validated by determining the pH values in water samples from various sources (Mahshahr refinery wastewater, Karoon River and Ahvaz tap water samples). The collected water samples were filtered to eliminate impurities and suspended solids and the pH of the samples was measured using the recommended procedure. Three measurements were performed at each pH. The results were compared with those obtained by a pH meter. The results of these assays presented in Table 2 indicate that there was a good agreement between the obtained pH values of both methods. The results also reveal that the matrices of the analyzed water samples have no significant influence on the performance of the method.

4. Conclusion

The above results illustrate the novel and effective application of CURNs in a lab-on-paper device for pH sensing. The change in optical characteristics of the CURNs was followed by changing the pH in the range of 8–13 and monitoring this phenomenon in solution by UV–vis

absorption spectra and in the paper medium by SEM. The color change of CURNs at different pH values could probably be as a consequence of degradation and aggregation of CURNs by increasing the pH of the solution. The developed pH sensor offers advantageous features of being entirely environmental friendly due to utilizing the CURNs as a safe and green nanoparticle, paper and beeswax for fabrication of sensor, minimal required reagent and sample and not requiring sophisticated instrumentation.

Acknowledgments

The authors are sincerely grateful to Shahid Chamran University, Research Council for the financial support of this project (Grant 1392). The financial support of the Iranian Nanotechnology Initiative Council is also appreciated.

References

- [1] A.W. Martinez, S.T. Phillips, E. Carrilho, S.W. Thomas, H. Sindi, G.M. Whitesides, *Anal. Chem.* 80 (2008) 3699–3707.
- [2] T. Songjaroen, W. Dungchai, O. Chailapakul, W. Laiwattanapaisal, *Talanta* 85 (2011) 2587–2593.
- [3] H. Sharma, D. Nguyen, A. Chen, V. Lew, M. Khine, *Ann. Biomed. Eng.* 39 (2011) 1313–1327.
- [4] A.W. Martinez, S.T. Phillips, M.J. Butte, G.M. Whitesides, *Angew. Chem. Int. Ed.* 46 (2007) 1318–1320.
- [5] D.D. Liana, B. Raguse, J.J. Gooding, E. Chow, *Sensors* 12 (2012) 11505–11526.
- [6] D.R. Ballerini, X. Li, W. Shen, *Microfluid. Nanofluid.* 13 (2012) 769–787.
- [7] C. Parolo, A. Merkoci, *Chem. Soc. Rev.* 42 (2013) 450–457.
- [8] X. Li, J. Tian, W. Shen, *Anal. Bioanal. Chem.* 396 (2010) 495–501.
- [9] S.A. Klasner, A.K. Price, K.W. Hoeman, R.S. Wilson, K.J. Bell, C.T. Culbertson, *Anal. Bioanal. Chem.* 397 (2010) 1821–1829.
- [10] A. Apilux, W. Siangproh, N. Praphairaksit, O. Chailapakul, *Talanta* 97 (2012) 388–394.
- [11] A.W. Martinez, S.T. Phillips, Z. Nie, C.-M. Cheng, E. Carrilho, B.J. Wiley, G.M. Whitesides, *Lab Chip* 10 (2010) 2499–2504.
- [12] Y.H. Ngo, D. Li, G.P. Simon, G. Garnier, *Adv. Colloid Interface Sci.* 163 (2011) 23–38.
- [13] A.K. Ellerbee, S.T. Phillips, A.C. Siegel, K.A. Mirica, A.W. Martinez, P. Striehl, N. Jain, M. Prentiss, G.M. Whitesides, *Anal. Chem.* 81 (2009) 8447–8452.
- [14] W. Dungchai, O. Chailapakul, C.S. Henry, *Anal. Chim. Acta* 674 (2010) 227–233.
- [15] A.K. Yetisen, M.S. Akram, C.R. Lowe, *Lab Chip* 13 (2013) 2210–2251.

- [16] X. Li, P. Zwanenburg, X. Liu, *Lab Chip* 13 (2013) 2609–2614.
- [17] P. Rattanarat, W. Dungchai, W. Siangproh, O. Chailapakul, C.S. Henry, *Anal. Chim. Acta* 744 (2012) 1–7.
- [18] Z. Nie, F. Deiss, X. Liu, O. Akbulut, G.M. Whitesides, *Lab Chip* 10 (2010) 3163–3169.
- [19] L.Y. Shiroma, M. Santhiago, A.L. Gobbi, L.T. Kubota, *Anal. Chim. Acta* 725 (2012) 44–50.
- [20] Sh. Wang, L. Ge, X. Song, J. Yu, Sh. Ge, J. Huang, F. Zeng, *Biosens. Bioelectron.* 31 (2012) 212–218.
- [21] J.L. Delaney, C.F. Hogan, J. Tian, W. Shen, *Anal. Chem.* 83 (2011) 1300–1306.
- [22] M. Zhang, L. Ge, Sh. Ge, M. Yan, J. Yu, J. Huang, S. Liu, *Biosens. Bioelectron.* 41 (2013) 544–550.
- [23] A. Arena, N. Donato, G. Saitta, A. Bonavita, G. Rizzo, G. Neri, *Sens. Actuators B* 145 (2010) 488–494.
- [24] H. Wang, N.E. Manicke, Q. Yang, L. Zheng, R. Shi, R.G. Cooks, Z.H. Ouyang, *Anal. Chem.* 82 (2010) 2463–2471.
- [25] W.W. Yu, I.M. White, *Anal. Chem.* 82 (2010) 9626–9630.
- [26] W. Liu, J. Luo, Y. Guo, J. Kou, B. Li, Z. Zhang, *Talanta* 120 (2014) 336–341.
- [27] X. Chen, J. Chen, F. Wang, X. Xiang, M. Luo, X. Ji, Z. He, *Biosens. Bioelectron.* 35 (2012) 363–368.
- [28] P.N. Nge, C.I. Rogers, A.T. Woolley, *Chem. Rev.* 113 (2013) 2550–2583.
- [29] D. Aigner, S.M. Borisov, F.J. Orriach Fernandez, J.F. Fernandez Sanchez, R. Saf, I. Klimant, *Talanta* 99 (2012) 194–201.
- [30] J. Lin, *Trends Anal. Chem.* 19 (2000) 542–552.
- [31] Y. Hiruta, N. Yoshizawa, D. Citterio, K. Suzuki, *Anal. Chem.* 84 (2012) 10650–10656.
- [32] H.-X. Chen, X.-D. Wang, X.-H. Song, T.-Y. Zhou, Y.-Q. Jiang, X. Chen, *Sens. Actuators B* 146 (2010) 278–282.
- [33] E. El-Deen, M. El-Giar, D.O. Wipf, *J. Electroanal. Chem.* 609 (2007) 147–154.
- [34] S. C-Cuevas, M.P. Cuellar, I.D. O-Paya, M.C. Pegalajar, L.F. C-Vallvey, *Anal. Chim. Acta* 681 (2010) 71–81.
- [35] Ch-F. Lin, G.-B. Lee, Ch-H. Wang, H.-H. Lee, W.-Y. Liao, T.-Ch. Chou, *Biosens. Bioelectron.* 21 (2006) 1468–1475.
- [36] P. Hashemi, R.A. Zarjani, *Sens. Actuators B* 135 (2008) 112–115.
- [37] K.F. Lei, K.-F. Lee, Sh.-I. Yang, *Microelectron. Eng.* 100 (2012) 1–5.
- [38] K. Abe, K. Suzuki, D. Citterio, *Anal. Chem.* 80 (2008) 6928–6934.
- [39] K. Abe, K. Kotera, K. Suzuki, D. Citterio, *Anal. Bioanal. Chem.* 398 (2010) 885–893.
- [40] P. Preechakasedkit, K. Pinwattana, W. Dungchai, W. Siangproh, W. Chaicumpa, P. Tongtawe, O. Chailapakul, *Biosens. Bioelectron.* 31 (2012) 562–566.
- [41] N. Ratnarathorn, O. Chailapakul, C.S. Henry, W. Dungchai, *Talanta* 99 (2012) 552–557.
- [42] W. Zhao, M.M. Ali, S.D. Aguirre, M.A. Brook, Y. Li, *Anal. Chem.* 80 (2008) 8431–8437.
- [43] A.J. Amali, N.H. Awwad, R.K. Rana, D. Patra, *Anal. Chim. Acta* 708 (2011) 75–83.
- [44] R.A. Sharma, A.J. Gescher, W.P. Steward, *Eur. J. Cancer* 41 (2005) 1955–1968.
- [45] Bhawana, R.K. Basniwal, H.S. Buttar, V.K. Jain, N. Jain, *J. Agric. Food Chem.* 59 (2011) 2056–2061.
- [46] F.-L. Yen, T.-H. Wu, Ch.-W. Tzeng, L.-T. Lin, Ch.-Ch. Lin, *J. Agric. Food Chem.* 58 (2010) 7376–7382.
- [47] D. Patra, C. Barakat, *Spectrochim. Acta Part A* 79 (2011) 1823–1828.
- [48] Y. Wang, K.M. Wang, G.L. Shen, R.Q. Yu, *Talanta* 44 (1997) 1319–1327.
- [49] D. Patra, R. Aridi, K. Bouhadir, *Microchim. Acta* 180 (2013) 59–64.
- [50] F. Wang, W. Haung, Y. Zhang, M. Wang, L. Sun, B. Tang, W. Wang, *J. Fluoresc.* 21 (2011) 25–34.
- [51] D. Patra, E. El Khorury, D. Ahmadieh, S. Darwish, R.M. Tafech, *Photochem. Photobiol.* 88 (2012) 317–327.
- [52] A. Pandya, H. Goswami, A. Lodha, Sh.K. Menon, *Analyst* 137 (2012) 1771–1774.
- [53] N. Pourreza, H. Golmohammadi, *Talanta* 119 (2014) 181–186.
- [54] D.A. Skoog, D.M. West, F.J. Holler, S.R. Crouch, *Fundamentals of Analytical Chemistry*, 5th ed., Thomson Learning Inc., USA, 2004.
- [55] M. Hecht, W. Kraus, K. Rurack, *Analyst* 138 (2013) 325–332.
- [56] E.D. El Khoury, D. Patra, *J. Phys. Chem. B* 117 (2013) 9699–9708.
- [57] Y.J. Wang, M.H. Pan, A.L. Cheng, L.I. Lin, Y.S. Ho, C.Y. Hsieh, J.K. Lin, *J. Pharm. Biomed. Anal.* 15 (1997) 1867–1876.
- [58] M.H. Leung, H. Colangelo, T.W. Kee, *Langmuir* 24 (2008) 5672–5675.



Graphene packed needle trap device as a novel field sampler for determination of perchloroethylene in the air of dry cleaning establishments

Mahmoud Heidari^{a,*}, Abdolrahman Bahrami^b, Ali Reza Ghasvand^c,
Maryam Rafiei Emam^a, Farshid Ghorbani Shahna^b, Ali Reza Soltanian^d

^a Department of Occupational Health, School of Health, Guilan University of Medical Sciences, Rasht, Iran

^b Department of Occupational Health, School of Health, Hamadan University of Medical Sciences, Hamadan, Iran

^c Department of Chemistry, Faculty of Science, Lorestan University, Khoramabad, Iran

^d Department of Biostatistics and Epidemiology, School of Health, Hamadan University of Medical Sciences, Hamadan, Iran

ARTICLE INFO

Article history:

Received 1 May 2014

Received in revised form

12 July 2014

Accepted 15 July 2014

Available online 24 July 2014

Keywords:

Needle trap device

Nano-platelets graphene

Perchloroethylene

Dry cleaning

ABSTRACT

In this paper we describe the application of a needle trap microextraction device packed with graphene nanoplatelets for the sampling and analysis of perchloroethylene in dry cleaning. The study was carried out in two phases. First the parameters for the sampling and analysis of perchloroethylene by NTD were evaluated and optimized in the laboratory. Then the sampler was used to determine the levels of perchloroethylene in a dry-cleaning shop. In the laboratory phase of the study the performance of the NTD packed with the proposed sorbent was examined in a variety of sampling conditions to evaluate the technique. The technique was also compared with NTDs packed with PDMS as well as SPME with Carboxen/PDMS-coated fibers. Both the NTDs and SPME performed better at lower sampling temperatures and relative humidity levels. The post-sampling storage times for a 95% recovery of the analyte were 5, 5 and 3 days for NTD-graphene, NTD-PDMS and SPME-CAR/PDMS respectively. The optimum desorption time was 3 min for NTDs packed with either graphene or PDMS and 1 min for SPME-CAR/PDMS. The limits of detection for the GC/MS detection system were 0.023 and 0.25 ng mL⁻¹ for NTDs packed with graphene and PDMS and 0.014 ng mL⁻¹ for SPME coated with CAR/PDMS. In the second stage of the study the evaluated technique was applied to the sampling and analysis of perchloroethylene in dry cleaning. In this environment the performance of the NTD-graphene as a field sampler for PCE was similar to that of the SPME-CA/PDMS, and better than the NIOSH 1003 method which had greater measurement variations. The results show that a NTD packed with carbonic graphene nanoplatelets and used as an active exhaustive sampling technique is effective for determination of VOC and HVOC occupational/environmental pollutants in air.

© 2014 Elsevier B.V. All rights reserved.

1. Introduction

Perchloroethylene (PCE or PERC) also called tetrachloroethylene, is a volatile, nonflammable, and colorless liquid with a sweet odor. It has been commercially available since the early 1900s and is now one of the most widely used chlorinated solvents worldwide. It is the solvent of choice in dry cleaning facilities. In 1994 its usage in this industry reached 90% within the European Union [1]. PCE is currently also used as a degreaser of metal parts, as an extraction solvent in chemical processing, as a heat-exchange fluid, and as a typewriter correction fluid. Those working in the

degreasing of metals are most heavily exposed to PCE contamination, primarily by inhalation [2].

PCE has been detected in the air, water and soil, as well as in food and in animal tissues. The United States Environmental Protection Agency (USEPA) ranks PCE as a hazardous air pollutant because of its toxicity and resultant impact on health [3]. The International Agency for Research on Cancer (IARC) classified PCE as a probable human carcinogen (Group 2A) [4,5]. In occupational studies, chronic exposure to PCE has been shown to adversely affect the kidneys, liver, central nervous system, and reproductive system. PCE can remain stored in fat tissue.

The OSHA method for determination of PCE in the workplace involves the use of adsorbent tubes for sample collection and GC-FID for sample analysis [6]. In the case of outdoor atmospheric samples, PCE as well as other VOCs are determined by the USEPA TO-14 method [7], which involves sampling in canisters and

* Corresponding author. Tel.: +98 9113203058; fax: +98 1313228843.

E-mail address: Heidari@gums.ac.ir (M. Heidari).

GC–MS analysis. The development of rapid screening methods is becoming increasingly important in analytical chemistry. Conventional methods used in analytical laboratories are usually not compatible with the need for routine and extensive monitoring [8,9].

In recent years there has been a growing demand for rapid, single-step and solvent-free microextraction sampling and analysis methods for volatile organic compounds. Solid-phase microextraction (SPME) and needle trap microextraction (NTME) with a needle trap device (NTD) sampler are examples of solventless sample preparation and introduction methods being developed today. SPME, first reported by Pawliszyn et al. in the early 1990s, is a simple, time-efficient, and solvent-free sample preparation technique [10]. It has been successfully applied to the extraction of various compounds at trace levels such as organic pollutants in environmental, food, biological, pharmaceutical, and clinical samples.

Despite its advantages SPME has some drawbacks. One of these is that, when applied to air samples, the extraction capacity is limited and normally based on equilibrium. In contrast the NTD technique combines the concept of miniaturized exhaustive active sampling and passive diffusive sampling with new microextraction concepts first introduced by Pawliszyn et al. [11]. For extraction, the sample is drawn inside the needle through the sorbent bed. Direct desorption is then facilitated by inserting the needle inside the GC injection port [12]. The NTD can be used for both active and passive sampling and its extraction capacity can easily be augmented by increasing the quantity of sorbent inside the needle. Another drawback of SPME is the fragility of the fibers. The NTD is more robust because the extraction phase is protected inside a stainless steel shield [13].

Until now the NTD technique has been used with commercial sorbents such as polydimethylsiloxane (PDMS), divinylbenzene (DVB) and Carboxen 1000 [14,15], Carboxen X and Tenax [16–18] and Porapak Q [19]. Combining NTD with new nano-material sorbents was first introduced by Heidari et al. [20,21]. Among the new nano-material sorbents, graphene, a single-atom-thick, two dimensional carbon material, is considered as the basic building block of all graphitic forms (including carbon nanotubes, graphite and fullerene (C₆₀)) [22].

In sampling techniques with an adsorption mechanism, the specific surface area of the sorbent plays an important role in the sampling process. The high surface area to weight (2630 m² g⁻¹) ratio of graphene is, therefore, an outstanding advantage. Other advantages of graphene include its remarkable thermal and chemical stability, ultra-high mechanical strength and low production cost [23–24]. These advantages make graphene a good candidate to use as a sorbent in modern microextraction techniques such as SPME [25] and NTD.

The aim of this study is to introduce a novel and powerful field sampler for the occupational and/or environmental assessment of trace elements in air. In this paper we describe the application of needle trap microextraction devices packed with graphene nanoplatelets for sampling and analysis of perchloroethylene in the laboratory and the field. This study was carried out in two phases. In the first the laboratory parameters for sampling and analysis of perchloroethylene by NTD sampler were evaluated and optimized. Then the sampler was used for determination of perchloroethylene in dry cleaning.

2. Experimental

2.1. Reagents and standards

Multi-layer graphene nanoplatelets (Fig. 1) with fewer than 30 layers, a purity higher than 95.5 wt%, a thickness of 4–20 nm, and

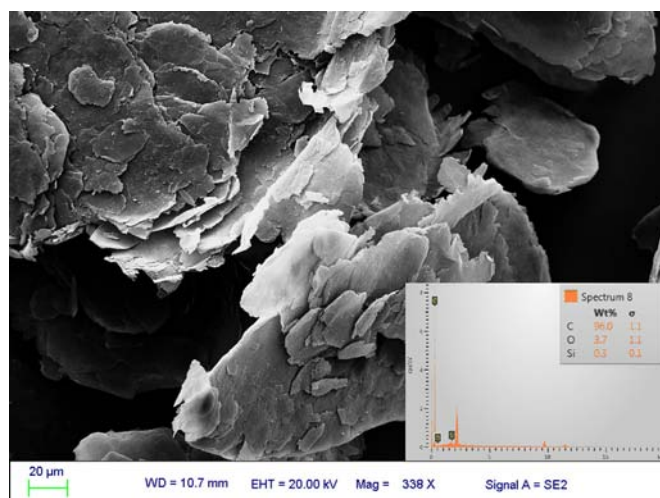


Fig. 1. Scanning electron micrograph and EDS analysis of the graphene nanoplatelets which used as sorbent in NTD.

a particle diameter 5–10 μm were obtained from the Chinese Academy of Sciences (Chengdu Organic Chemicals, Chengdu, China). Perchloroethylene in analytical grade was purchased from Sigma-Aldrich (Munich, Germany).

2.2. Instrumentation

Chromatography was performed using a Varian 3800 GC with a capillary column (VOCOL with 60 m × 0.25 mm × 0.25 μm) equipped with a Saturn 2200 MS system and a split-splitless injector. The column was initially set at 40 °C. This temperature was maintained for 4 min and then increased at a rate of 6 °C per min to 160 °C, for a total run time of 24 min. Injection of the NTDs was performed in splitless mode at a GC injector temperature of 300 °C. The flow rate of the Helium (99.999%) carrier gas was 1 mL min⁻¹. A home-made narrow-neck glass liner with a 1.5 mm I.D. and a 0.5 mm neck diameter was used in the GC injector for conducting the carrier gas into the NTDs via the hole in the side of the needle. The glass liner also ensured the efficient delivery of the analyte of interest to the GC column and served to prevent peak broadening. A home-made chamber was used to accurately adjust the analyte concentration, temperature and humidity of the sample matrix. A 21-gauge needle (10.5 cm length × 510 μm I.D. × 820 μm O.D.) was purchased from Kosan LTD. (Tokyo, Japan). A syringe pump (JMS SP-510, Hiroshima, Japan) was used to inject a predetermined measure of pure PCE into the standard sampling chamber thus providing the desired concentration of analyte. The manual SPME holder with 100 μm polydimethylsiloxane (PDMS) was purchased from Supelco (Bellefonte, PA, USA). For use of PDMS in NTD, a predetermined amount of sorbent packed inside the needle. PDMS purchased from Sigma-Aldrich (Munich, Germany). When sampling with NTDs, a low volume sampling pump (SKC 222 series, PA, USA) with a flow rate range of 1–200 mL min⁻¹ was used to draw accurate quantities of air into the needles and through the sorbent bed.

2.3. Preparation of the needle trap device

Each NTD was prepared by filling a 21-gauge stainless steel needle with sorbent material. To allow the sorbent to be packed inside the needle the internal metal plunger was shortened by 26 mm. The end of the shortened internal plunger determined the position of the first glass wool layer inside the needle. Three more plungers were cut so as to be 3, 18 and 21 mm shorter than the

distance between the tip of the inside head plunger and tip of the needle. There were used to position a first 3 mm layer of glass wool, followed by a 15 mm layer of sorbent and then a second 3 mm layer of glass wool in the space between the tip of the internal metal plunger and the tip of the needle. The glass wool packing before and after the sorbent served to position the sorbent firmly and prevent bleeding. This glass wool was expected to cause negligible flow restriction. Finally the needle trap was conditioned in a GC injector at 290 °C for 3 h by drawing Helium carrier gas through the sorbent bed. This procedure enabled the preparation of NTDs of consistent geometry. It also avoided the use of epoxy glue for packing the sorbent inside the needle. This glue, previously used by other researchers, leads to significant levels of impurities in ultra-trace analysis [14].

2.4. Sampling by NTD

First the performance characteristics of the NTD packed with graphene as sorbent were investigated for the sampling and analysis of PCE in the laboratory. The effects of temperature, relative humidity, breakthrough volume and sampling flow rate on the sampling phase were examined. The capability of the NTD sampler and its sorbent to store the sampled analyte was also assessed. The GC desorption time and temperature parameters, and carryover were studied. After optimizing the performance parameters of the NTD and its nanostructural sorbent for use as an exhaustive active sampler, the device was applied to the determination of PCE in dry cleaning.

A home-made standard chamber (50 cm × 10 cm × 5 cm) was prepared for laboratory testing inside of which a 1 ng mL⁻¹ concentration of PCE was maintained. To provide a dynamic standard concentration of analyte inside the chamber a predetermined amount of PCE was injected by syringe pump to a flow line connected to the sampling chamber. For exhaustive sampling, air was drawn inside the needle by means of a low volume sampling pump. After sampling, analysis was performed by inserting each NTD into the GC injector for thermal desorption of the adsorbed analytes. The Fig. 2 shows the sample peak of PCE obtained by the NTD–GC/MS system.

2.5. Performance parameters of NTD packed with nanoplatelets graphene

2.5.1. Investigation of sampling temperature and relative humidity

Sampling temperatures were set at 10, 25 and 35 °C with a thermostat-controlled radiation lamp placed in a heat-control chamber upstream of the standard chamber. Using a dimmer, different intensities of lighting energy and resulting temperatures were achieved. In order to adjust the relative humidity inside the standard chamber, the air flow to the chamber was supplied by two lines. Dry air was drawn from one line and saturated air from the other. The ratio of air flow from these two lines was adjusted via a control valve until the hygrometer inside the standard chamber indicated the desired relative humidity.

2.5.2. Storage time

Because of lack of analytical instruments in the field and hence the need to ship samplers to laboratories, the use of a NTD as a field sampler requires investigation of the device's capability to store the sampled analytes. For this reason, after sampling from a constant concentration of 1 ng mL⁻¹ of PCE at optimum conditions (10 °C and 20% RH), the NTDs were disconnected from the pump and prepared for storage. The two ends and side hole of the needles were covered by a Teflon cap, and the NTDs were placed into a glass container at 25 °C. The storage times investigated varied from 1 to 7 days, after which the response (peak area) of the analyte of interest was compared with the simultaneous NTD analysis to determine of amount of analytes lost.

2.6. Analytical performance parameters (Desorption time and temperature, carryover)

Desorption time and temperature are important performance parameters of the NTD technique with the proposed sorbent since they have significant effects on the peak response of the GC instrument. Longer desorption times can help complete the delivery of analytes to the GC column but may reduce the lifespan of the sorbent. Higher temperatures can cause better desorption with less carryover on the sorbent surface but this is limited by the thermal stability of both the sorbent and the compounds of interest. For these reasons, optimum desorption time and temperature should be carefully selected.

To determine the most efficient desorption time and temperature for the NTD, samples were analyzed at 1 min increments for times ranging from 1 to 5 min and at 10 °C intervals for temperatures ranging from 260 to 310 °C. Initial sampling was carried out at optimum conditions at a PCE concentration of 1 ng mL⁻¹. Three consecutive analyses were done for each desorption time and temperature. The results of the analysis were plotted against the peak area of GC responses. For each desorption time and temperature, the lowest levels that caused the highest peak responses were selected as the preferred values.

The percentage of carryover also depends on desorption time and temperature therefore these GC parameters should be selected so that quantitative desorption occurs with the least amount of carryover. To select the optimum desorption time and temperature, carryover and possible memory effect were investigated in a second desorption cycle two minutes after the first. For desorption times ranging from 1 to 4 min, the peak area acquired in the second desorption process was plotted as the amount of carryover accrued and the resulting graph was used to determine the optimum time required for conditioning the NTD between sampling cycles.

2.7. Field sampling by NTDs packed with nanoplatelets graphene

After optimizing all aspects of NTD sampling in the laboratory, NTDs packed with graphene nanoplatelets were used to determine

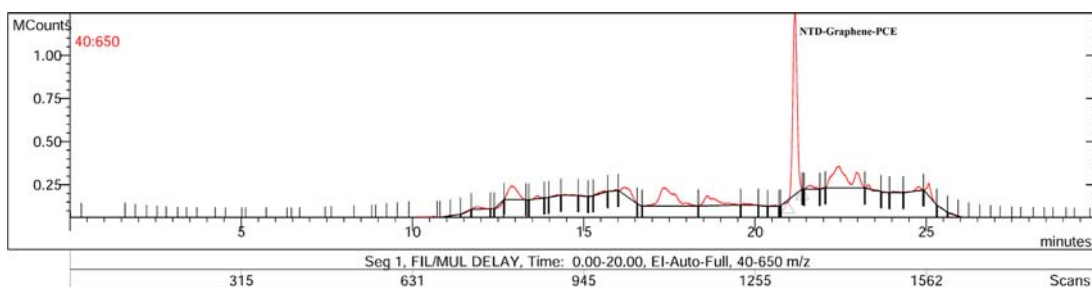


Fig. 2. GC/MS peak response of PCE after sampling by NTD packed with graphene as extraction media.

the concentration of perchloroethylene in a dry-cleaning shop. This was done by connecting NTDs to calibrated low-volume personal sampling pumps. Sampling flow rates of 3 mL/min and sampling volumes of 30 mL were used. These sampling sets were attached to workers in the respiratory zone of the dry-cleaning shop to estimate their exposure to PCE.

2.8. Method validation and comparative study

Validation of the NTD technique was performed under the optimized conditions determined previously in this study for the quantitative analysis of the target compound in a standard chamber. Calibration-curve samples were prepared over a 0.01–100 ng mL⁻¹ concentration range. Predetermined concentrations were achieved by using a syringe pump to inject calculated amounts of analytes into the standard chamber. To ensure precise results three consecutive extractions of each predetermined concentration of PCE were taken from the standard chamber. The calibration curves were arrived at by plotting the peak area of analytes against the corresponding concentrations. Linearity was evaluated in terms of the correlation coefficients of the regression equations of the calibration curves, which covered the 10 points at high, medium, and low concentrations of analyte drawn into the standard chamber. Linearity was also verified by determining the calculated (F_{cal}) and critical (F_{crit}) value of Mandel's fitting test. The limit of detection (LOD), based on an estimated signal-to-noise ratio (S/N) of 3, and the limit of quantitation (LOQ) of the method were determined by calculating the concentration corresponding to a signal-to-noise ratio of 10 for PCE.

The method was also validated with comparative studies both in the laboratory and in the field. In the laboratory phase of the study, inter-NTD comparison was done using NTDs packed with the proposed sorbent and NTDs packed with a commercial PDMS sorbent. The analytical performance of the NTD packed with the proposed sorbent was also compared to SPME with Carboxen/PDMS coated fiber. In the field the analytical performances of the NTD containing graphene nanoplatelets and SPME coated with CAR/PDMS were further compared to the NIOSH 1003 method for sampling and analyzing PCE in a dry-cleaning environment.

3. Results and discussion

3.1. Parameters related to the laboratory phase of the study

To use the NTD as a field sampler, it is necessary to investigate environmental parameters such as temperature and relative humidity. Furthermore the ability of the NTD with nanostructured

sorbent to store the sampled analyte and the possible effects of these environmental parameters on the sampling efficiency of the NTD and the proposed sorbent should also be determined.

3.1.1. Sampling temperature and relative humidity

In the laboratory phase of study sampling was done at temperatures of 10, 25 and 35 °C and at relative humidity levels of 20 and 80% to evaluate the effect of these environmental parameters on sampling efficiency. This sampling was carried out from a predetermined concentration of 1 ng mL⁻¹ of perchloroethylene in a standard chamber. The results demonstrated that an increase in either environmental parameter can lead to a decrease in sampling efficiency (Fig. 3).

The effect of temperature on the adsorption mechanism of an analyte onto any adsorbent media, and hence the sampling efficiency, is well-known and understood. As to relative humidity, the decrease in peak area of PCE in humid conditions can be attributed to a decrease in the specific sorbent area. The surface area of the graphene nanoplatelets used as sorbent may be reduced due to the moisture in the air causing the sorbent particles to stick together. This effect intensifies with increasing relative humidity. The problem may occur more frequently when using a NTD as a sampler for extracting analytes from the headspace above an aquatic media especially when the sample is heated by an increase in partitioning of analytes from aquatic matrix to headspace. A combination of high relative humidity (greater than 90%) and lengthy sampling time can cause the NTD to become choked with cohering sorbent particles which reduce the sorbent pore size. Because the relative humidity in a dry-cleaning environment is close to 80%, a small reduction of peak area and sampling efficiency of PCE is inevitable. Sampling time should be limited to prevent choking of the sorbent inside the NTD.

3.1.2. Storage time

The NTD technique is a single-step sampling and analyzing technique whereby determination of the sampled analytes can be performed by introducing the sampler directly to an analyzing instrument. In field sampling, however, it is often necessary to ship the NTD sampler to a laboratory. For this reason the effect of 1–7 days of sample storage time was investigated and the results compared to NTDs analyzed immediately after sampling from a constant concentration of 1 ng mL⁻¹ of PCE. The results showed that after 5 days of storage analyte recovery from the NTD sample is still greater than 95%. The performance characteristics of the NTD packed with graphene was similar to SPME coated with CAR/PDMS and better than the NTD packed with PDMS (Fig. 4).

The superior analyte storage performance of the NTD is due to the structure of the sampler since there is very little dead volume

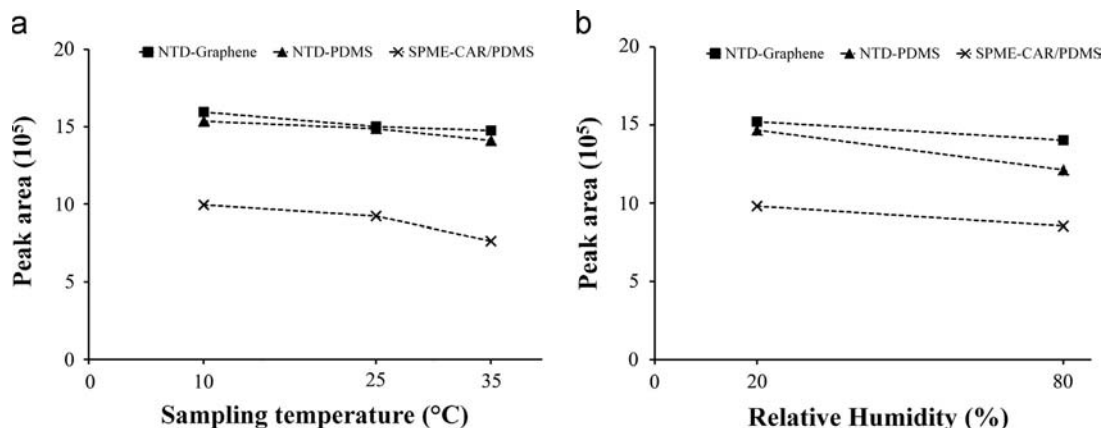


Fig. 3. Effect of environmental parameters of temperature (a) and relative humidity (b) on sampling efficiency of NTD-graphene, NTD-PDMS and SPME-CAR/PDMS for sampling of perchloroethylene in laboratory.

on each side of the sorbent packed inside the needle. By plugging the entrance and exit of the NTD with a septum cap after sampling, analyte loss can only occur as a result of the decomposition or migration of analyte to the dead volume inside the NTD. In other techniques, such as the use of a sorbent tube recommended by NIOSH for sampling VOCs and HVOCs (NIOSH 1501 and 1003), analytes that have migrated to the dead volume of sorbent tube can be lost during the extraction process when the glass tube is broken in order to transfer the charcoal granules to the solvent media. But with the NTD technique analysis can be performed by introducing the sampler directly into the GC injection port. Moreover analytes that have migrated to the dead volume of the NTD can be injected into the GC column by passing carrier gas through the needle. As a result the recovery of analytes from a NTD can remain high even up to 7 days after sampling.

3.1.3. Desorption time and temperature

Time and temperature both play a role on the desorption of analytes from a NTD and its sorbent bed. Because this was the first time that graphene nanoplatelets were used as a sorbent media with the NTD technique, the desorption characteristics of this sampler needed to be investigated. Clearly higher desorption temperatures and longer desorption times can result in the complete desorption of analytes with less carryover and memory effect, but this limits the lifespan of the sorbent bed. Desorption times and temperatures were assessed for NTDs packed with graphene and PDMS in five and six levels of 1–5 min and 260–310 °C respectively. The results were compared to SPME coated with CAR/PDMS subjected to desorption times of 30–150 s and desorption temperatures between 220 and 270 °C. The results revealed that the minimum desorption time and temperature with maximum peak response of PCE are 3 min at 280 °C for NTD-graphene and 3 min at 290 °C for NTD-PDMS. Optimum desorption time and temperature for SPME-CAR/PDMS were 60 s at 250 °C. Table 1 and Fig. 5 show the results for the desorption parameters.

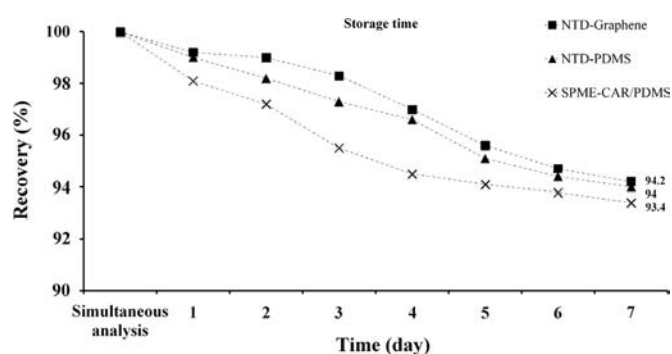


Fig. 4. The trend of analyte recovery and storage time analysis of NTD-graphene, NTD-PDMS and SPME-CAR/PDMS in the period of 1–7 days.

Table 1

Percentage of recovery after 1st desorption for optimum desorption time (D.T.) and 2nd desorption for carryover (C.O.) analysis of PCE for NTD and SPME.

Sampling technique	Percentage of analyte recovered at allocated time of 1–5 min for NTD and 30–150 s for SPME									
	1 (min)		2 (min)		3 (min)		4 (min)		5 (min)	
	D.T. (SD)	C.O. (SD)	D.T. (SD)	C.O. (SD)	D.T. (SD)	C.O. (SD)	D.T. (SD)	C.O. (SD)	D.T. (SD)	C.O. (SD)
NTD-Graphene	86.2 (1.82)	0.54 (0.018)	94.87 (1.12)	0.06 (0.001)	99.81 (1.79)	n.d. ^a	101.3 (1.36)	n.d.	100 (1.43)	n.d.
NTD-PDMS	83.19 (2.31)	0.72 (0.023)	95.02 (1.94)	0.34 (0.017)	99.77 (2.11)	0.12 (0.007)	98.47 (1.71)	n.d.	100 (2.28)	n.d.
SPME-CAR/PDMS	86.92 (1.14)	0.12 (0.007)	99.54 (1.96)	0.03 (0.001)	100.72 (2.33)	n.d.	99.89 (2.05)	n.d.	100 (1.67)	n.d.

^a n.d., not detected.

3.1.4. Carryover and memory effect investigation

Each NTD prepared with the proposed nanostructured sorbent can be used more than 100 times for the sampling and analysis of PCE so inter-sampling preparation and conditioning of the sampler is very important. After establishing the optimum desorption parameters for the NTD and proposed sorbent, carryover was investigated to determine the possible memory effect and the time required for the conditioning and preparation of the sorbent media between sampling cycles.

Table 1 shows the results for the carryover analysis of three microextraction samplers. From these it can be seen that for both NTD-graphene and NTD-PDMS, 3 min after inserting the sampler into the GC injection port there was no peak response greater than LOD. For SPME-CAR/PDMS no peak responses were observed for PCE after 1 min of conditioning and hence this duration was selected for conditioning and the prevention of carryover and memory effect.

3.1.5. Comparative study

Since this is the first report on the use of graphene nanoplatelets with a NTD the performance aspects of the proposed sampler needed to be evaluated by comparing it to some more established sampling techniques. For this reason, in the laboratory phase of this study the performance of the NTD containing graphene nanoplatelets was compared to that of a NTD packed with PDMS and to SPME coated with Carboxen/PDMS. Carboxen/PDMS was selected as the extraction sorbent for the SPME because previous research had emphasized the good performance of this sorbent for the sampling and analysis of VOCs and HVOCs [26–28]. The laboratory-phase comparative study between the NTD and SPME techniques was performed using analytical parameters such as LOD, LOQ, linearity of responses and LDR. In the field study, the solvent-less NTD-graphene extraction technique was compared to the SPME coated with CAR/PDMS and the NIOSH 1003 method

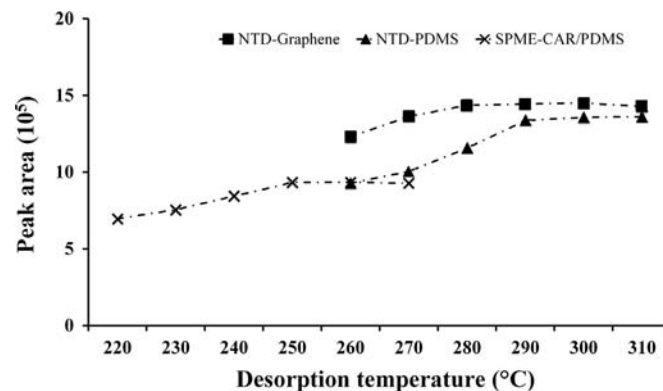


Fig. 5. Analytical performance for desorption temperature of NTD-graphene, NTD-PDMS and SPME-CAR/PDMS in GC injection port.

Table 2

Comparative study for analytical performances of NTD contained two sorbents of graphene and PDMS and SPME coated with CAR/PDMS for sampling and analysis of PCE verified with the coefficients of determination (r^2), calculated (F_{cal}) and critical ($F_{crit, 95\%}=5.59$) value of Mandel's fitting test.

Sampling technique	Range (ng mL ⁻¹)	LDR	r^2	F_{cal}	RSD (%)	LOD (ng mL ⁻¹)	LOQ (ng mL ⁻¹)
NTD-Graphene	0.01–100	0.01–70	0.9831	4.78	6.1	0.023	0.08
NTD-PDMS	0.01–100	1–60	0.9725	5.37	11.4	0.25	0.75
SPME-CAR/PDMS	0.01–100	0.01–80	0.9916	4.46	4.76	0.014	0.045

Table 3

Comparative study for performances of NTD packed with graphene and SPME coated with CAR/PDMS on PCE sampling in dry cleaning. The results compared to the NIOSH 1003 method recommended for sampling and analysis of HVOCs in air.

Quantitation	No. 1 ^a			No. 2 ^b			No. 3 ^c			No. 4 ^d			No. 5 ^e		
	NTD	SPME	NIOSH	NTD	SPME	NIOSH	NTD	SPME	NIOSH	NTD	SPME	NIOSH	NTD	SPME	NIOSH
Number of samples	5	5	5	5	5	5	5	5	5	5	5	5	5	5	5
Average concentration of PCE (mg/m ³)	43.34	37.17	56.56	34.14	29.43	41.65	27.12	25.46	33.53	1.91	1.76	4.3	1.34	1.11	3.17
RSD (%)	3.7	4.43	11.32	5.32	2.9	8.6	3.8	3.3	10.43	4.4	5.1	17.43	5.72	4.16	14.32
Percentage above TLV ^f	0.0%	0.0%	0.0%	0.0%	0.0%	0.0%	0.0%	0.0%	0.0%	0.0%	0.0%	0.0%	0.0%	0.0%	0.0%

^a Sampling performed at 1 m distance from washing machine in the dry cleaning shop at respiratory zone of the workers.

^b Sampling performed at 2 m distance from washing machine in the dry cleaning shop at respiratory zone of the workers.

^c Sampling performed at 5 m distance from washing machine in the dry cleaning shop at respiratory zone of the workers.

^d Sampling performed in the ironing room at respiratory zone of the workers.

^e Sampling performed in reception room at respiratory zone of the workers.

^f NIOSH recommended threshold limit value for PCE = 169.56 mg/m³.

which uses a solid sorbent tube and requires the use of a solvent for extraction.

The results of the comparative study in the laboratory show that the NTD packed with proposed sorbent has similar responses to the SPME technique. Both techniques produce fairly similar correlation coefficients from the regression analysis of their calibration curves. Also the resulting analyses of PCE from a standard chamber were close and with similar RSD. But in the field study the NTD containing graphene nanoplatelets produced better results than the NIOSH method 1003 for the sampling and analysis of PCE in a dry-cleaning environment. The variations in results for the NIOSH 1003 method were higher than the two other microextraction techniques. This may have been due to a loss of analytes during the solvent desorption process possibly resulting from the post-sampling migration of analytes to the dead volume inside the sorbent tubes and to incomplete extraction by the CS₂ extraction solvent. In contrast, the solvent-less NTD technique enables the total mass of analytes to be delivered without losses resulting in more accurate concentration readings. The results for the comparative field study are shown in Tables 2 and 3.

3.2. Field sampling of PCE in dry cleaning

Additionally to technique comparison, field sampling was also performed to monitor the levels of PCE in a work environment. The aim was to test an inexpensive and rapid method for sampling VOCs and HVOCs in air. Perchloroethylene was selected as a representative compound of the HVOC group and a dry-cleaning shop was chosen as an appropriate work environment in which to monitor the occupational exposure to PCE. Sampling was done at five stations in the shop's respiratory zone using NTD, SPME and NIOSH 1003 techniques. One sampling station was located in the reception, three more were placed 1, 2 and 5 m from the washing machine and a 5th station was located in the ironing room. The results demonstrated that NTD and SPME had smaller variations in responses compared to the NIOSH 1003 technique which had a greater RSD. At all the stations in the dry-cleaning store the concentrations of PCE were lower than those recommended by

NIOSH as a threshold limit value (169.56 mg/m³). The results for assessment of exposure to PCE are shown in Table 3.

4. Conclusions

This study was designed to develop a needle trap microextraction technique as a new and in-progress method that can be used for the sampling and analysis of different compounds in air. NTD is an inexpensive microextraction technique which can be used for the sampling and determination of a wide range of compounds in a single-step. This is the first report on the use of graphene nanoplatelets used with a NTD for determination of perchloroethylene in air. The study consisted of a laboratory and field phase. In the laboratory phase sampling and analytical performances of NTD-contained nanostructured sorbent was compared to the SPME technique. In the field NTDs were used for the environmental and occupational monitoring of PCE in dry cleaning and compared with the NIOSH 1003 method for HVOCs. The results demonstrated that the proposed nanoplatelets sorbent performed well when compared to the SPME sorbent coating most recommended for VOCs and HVOCs. In the dry-cleaning environment NTDs packed with the proposed sorbent performed better than the NIOSH 1003 method. Results showed that preparing a NTD with the new nanostructure sorbent and coupling this microextraction sampler to sensitive analyzing instrument like GC/MS can provide a powerful technique for the sampling and analysis of different environmental/occupational pollutants in air.

References

- [1] European Chemicals Bureau, European Union Risk Assessment Report Tetrachloroethylene (EUR 21680 EN). United Kingdom, 2005. pp. 1–164.
- [2] International Agency for Research on Cancer (IARC), Dry cleaning, some chlorinated solvents and other industrial chemicals, IARC Monogr. Eval. Carcinog. Risks Hum., vol. 63, Lyon, 1995, pp. 75, 159.
- [3] U.S. Environmental Protection Agency, Toxicological review of Tetrachloroethylene (Perchloroethylene). In Support of Summary Information on the Integrated Risk Information System (IRIS). 2012.

- [4] WHO (World Health Organization), Dry cleaning, some chlorinated solvents and other industrial chemicals. IARC Monograph Eval Carcinog Risk Hu., vol. 63, 1995. pp. 159.
- [5] WHO (World Health Organization), Tetrachloroethylene. WHO Guidelines for indoor air quality: selected pollutants, 2010. pp. 415–454.
- [6] Organic Method #1001, Occupational Safety and Health Administration (OSHA), (<http://www.osha-slc.gov/dts/sltc/methods/mdt/mdt1001/1001.html>).
- [7] Center for Environmental Research, US. EPA, Compendium of Methods for the Determination of Toxic Organic Compounds in Ambient Air, second ed., EPA/625/R-96/01b, January 1999.
- [8] M. Valcarcel, S. Cardenas, M. Gallego, Trends Anal. Chem. 18 (1999) 685–694.
- [9] M. Valcarcel, S. Cardenas, Anal. Bioanal. Chem. 381 (2005) 81–83.
- [10] C.L. Arthur, J. Pawliszyn, Anal. Chem. 62 (1990) 2145–2148.
- [11] J.A. Koziel, M. Odziemkowski, J. Pawliszyn, Anal. Chem. 73 (2001) 47–54.
- [12] V.H. Niri, I.Y. Eom, F.R. Kermani, J. Pawliszyn, J. Sep. Sci. 32 (2009) 1075–1080.
- [13] S. Bigham, J. Medlar, A. Kabir, C. Shende, A. Alli, A. Malik, Anal. Chem. 74 (2002) 752–761.
- [14] A. Wang, F. Fang, J. Pawliszyn, J. Chromatogr. A 1072 (2005) 127–135.
- [15] I.Y. Eom, A.M. Tugulea, J. Pawliszyn, J. Chromatogr. A 1196–1197 (2008) 3–9.
- [16] H. Jurdakova, R. Kubinec, M. Jurcisinova, Z. Krkosova, J. Blasko, I. Ostrovsky, L. Sojak, V.G. Berezkin, J. Chromatogr. A 1194 (2008) 161–164.
- [17] M. Mieth, S. Kischkel, J.K. Schubert, D. Hein, W. Miekisch, Anal. Chem. 81 (2009) 5851–5857.
- [18] J.D. Crom, S. Claeys, A. Godayol, M. Alonso, E. Antico, J.M. Sanchez, J. Sep. Sci. 33 (2010) 2833–2840.
- [19] P. Prikryl, R. Kubinec, H. Jurdakova, J. Sevcik, I. Ostrovsky, L. Sojak, V. Berezkin, J. Chromatogr. 64 (2006) 65–70.
- [20] M. Heidari, A. Bahrami, A.R. Ghiasvand, F.G. Shahna, A.R. Soltanian, Talanta 101 (2012) 314–321.
- [21] M. Heidari, A. Bahrami, A.R. Ghiasvand, F.G. Shahna, A.R. Soltanian, Anal. Chim. Acta 785 (2013) 67–74.
- [22] C.N.R. Rao, A.K. Sood, K.S. Subrahmanyam, A. Govindaraj, Angew. Chem. Int. Ed. 48 (2009) 7752–7777.
- [23] M.D. Stoller, S. Park, Y. Zhu, J. An, R.S. Ruoff, Nano Lett. 8 (2008) 3498–3502.
- [24] H.Q. Chen, M.B. Muller, K.J. Gilmore, G.G. Wallace, D. Li, Adv. Mater. 20 (2008) 3557–3561.
- [25] J. Chen, J. Zou, J. Zeng, X. Song, J. Ji, Y. Wang, J. Ha, X. Chen, Anal. Chim. Acta 678 (2010) 44–49.
- [26] A. Alonso, M.A.F. Torroba, M.T. Tena, B. Pons, J. Chromatogr. 57 (2003) 369–378.
- [27] C.M.M. Almeida, L. VilasBoas, J. Environ. Monit. 6 (2004) 80–88.
- [28] P.M.S. Juan, J.D. Carrillo, M.T. Tena, J. Chromatogr. A 1139 (2007) 27–35.



Determination of atropine sulfate using a novel sensitive DNA–biosensor based on its interaction on a modified pencil graphite electrode



Ali A. Ensafi^{a,*}, Parisa Nasr-Esfahani^a, Esmail Heydari-Bafrooei^b, B. Rezaei^a

^a Department of Chemistry, Isfahan University of Technology, Isfahan 84156–83111, Iran

^b Department of Chemistry, Faculty of Science, Vali-e-Asr University of Rafsanjan, Rafsanjan, P.O. Box 518, Iran

ARTICLE INFO

Article history:

Received 13 June 2014

Received in revised form

25 July 2014

Accepted 26 July 2014

Available online 12 August 2014

Keywords:

DNA–biosensor

Atropine detection

Modified pencil graphite electrode

Voltammetry

ABSTRACT

A novel, selective, rapid and simple electrochemical method is developed for the determination of atropine sulfate. UV–Vis and differential pulse voltammetry are used to study the interaction of atropine sulfate with salmon sperm ds-DNA on the surface of salmon sperm ds-DNA modified–pencil graphite electrode (PGE). For this purpose, a pencil graphite electrode (PGE) modified with multiwall carbon nanotubes (MWCNTs), titanium dioxide nanoparticles (TiO₂NPs), and poly-diallyldimethylammonium chloride (PDDA) decorated with ds-DNA is tested for the determination of atropine sulfate. The electrochemical oxidation peak current of adenine and guanine bonded on the surface of ds-DNA/PDDA–TiO₂NPs–MWCNTs/PGE is used to obtain the analytical signal. Decreases in the intensities of guanine and adenine oxidation signals after their interaction with atropine sulfate are used as indicator signals for the sensitive determination of atropine sulfate. Using ds-DNA/PDDA–TiO₂NPs–MWCNTs/PGE and based on the guanine signal, linear calibration curves were obtained in the range of 0.6 to 30.0 μmol L⁻¹ and 30.0 to 600.0 μmol L⁻¹ atropine sulfate with low detection limits of 30.0 nmol L⁻¹. The biosensor shows a good selectivity for the determination of atropine sulfate. Finally, the applicability of the biosensor is evaluated by measuring atropine sulfate in real samples with good accuracy.

© 2014 Elsevier B.V. All rights reserved.

1. Introduction

Drug analysis is an important branch of analytical chemistry for its role in drug quality control and wide impact on public health. Developing sensitive, simple, rapid, and reliable methods for the determination of active ingredients is, therefore, valuable and necessary.

Atropine (C₁₇H₂₃NO₃), the tropane alkaloid is widely found in solanaceae plants, such as *Flos daturae*, *Atropa*, and *Hyoscyamus* [1] and it is generally used as antispasmodic, anticholinergic, and antidote effects [2]. The drug has found wide clinical applications because of its strong parasympatolytic and anticholinergic actions [3]. Atropine, the racemic mixture of (S)-hyoscyamine and (R)-hyoscyamine, acts pharmacologically via blocking acetylcholine receptors of the muscarine subtype, which causes not only peripheral symptoms such as tachycardia, dilated pupils, and decreased gastrointestinal motility, but also affects the central nervous system and causes agitation, disorientation, and hallucination [4]. The most common atropine compound used in medicine is atropine sulfate

((C₁₇H₂₃NO₃)₂·H₂SO₄·H₂O) or sulfate monohydrate. Atropine sulfate, an alkaloid extracted from belladonna herb, is a classic cholinergic drug that is widely used in all kinds of viscera colic and administered as the medicine given before systemic anesthesia, as an anti-arrhythmic medicine [5,6], or for organophosphate poisoning treatment [7]. An inadequately low dosage fails to yield perfect remedial effects, while blindfold over-commitment may cause atropism [8]. Many cases of atropism have been reported [9,10] with an occurrence rate of up to 40–60% and a mortality rate of around 18.3% [11]. Since most alkaloids have special and distinct physiological properties in addition to toxicity, the determination of atropine sulfate is of great importance not only in clinical applications but also for pharmaceutical analysis.

A variety of methods are employed for the determination of atropine such as spectrophotometry [11], ion-selective electrode [12] and liquid chromatography [13]. However, spectrophotometry suffers from low sensitivity while liquid chromatography, although more sensitive, requires expensive apparatus, long and time-consuming procedures and different chemicals. In ion-selective electrode, the response is affected by electrical properties of the film and electric double-layer capacitance while it also suffers from low sensitivity. Electroanalytical techniques, however, have been shown to be excellent for the determination of pharmaceutical compounds in

* Corresponding author. Tel.: +98 311 3912351; fax: +98 311 3912350.

E-mail addresses: Ensafi@cc.iut.ac.ir, aaensafi@gmail.com (A.A. Ensafi).

different matrices. The advances made in the experimental electrochemical techniques used in the field of drug analysis owe much to their simplicity, low cost, and relatively short analysis time compared to other techniques [14,15]. As yet, there is only one electrochemical method reported in the literature for the determination of atropine, which used multiwall carbon nanotube electrode with a linear calibration curve of 0.014 to 0.094 $\mu\text{mol L}^{-1}$ [16]. However, the method does not enjoy adequate selectivity for the determination of atropine in real samples.

Over the last two decades, intense research has been devoted to DNA biosensors as useful tools for monitoring hybridization and DNA–molecule interactions [17–20]. The transduction of these events into measurable information has a great importance for pharmacological, medical, and environmental analyses [19,21,22]. Electrochemical DNA–biosensors have attracted attention among the DNA biosensors because they allow for rapid and inexpensive detection of ingredients [23–27]. While different types of electrode materials such as carbon paste [28], glassy carbon [29], carbon fiber [30], and graphite [23–27] have been used in their construction, pencil graphite electrode (PGE) was selected in this study for its cost effectiveness, commercial availability, and disposability.

A key issue with electrochemical DNA–based biosensors is achieving enhanced DNA immobilization on the substrates. DNA immobilization on the surface plays an important role in the performance of DNA biosensors as the amount of immobilized DNA probe will directly influence the sensor's accuracy, sensitivity, selectivity, and effective life [31]. In this study, a mixture of nanomaterials (MWCNTs and titanium dioxide nanoparticles (TiO_2NPs)) and positively charged polyelectrolytes (poly dialyldimethylammonium chloride, PDDA) were immobilized on the surface of a pencil graphite electrode (PGE) to improve the immobilization of ds-DNA on the surface.

A PGE modified with MWCNTs, TiO_2NPs , and PDDA decorated with a ds-DNA was fabricated (ds-DNA/PDDA– TiO_2NPs –MWCNTs/PGE) and the oxidation signals of adenine and guanine were obtained using differential pulse voltammetry (DPV). The decreases in the current intensities of guanine and adenine oxidation signals after interaction with atropine sulfate were used as indicators for the sensitive determination of atropine sulfate. The presence of both MWCNTs and TiO_2NPs was found to dramatically improve the immobilization rates by covalent and electrostatic immobilization. The new biosensor exhibited a better sensitivity for trace analysis than those reported previously. The new method is inexpensive, highly selective, rapid, and sensitive method for the direct determination of atropine sulfate in real samples.

2. Experimental

2.1. Chemicals

All solutions were prepared using reagent grade chemicals and doubly distilled water were used through.

Atropine sulfate was purchased from Aldrich Chemicals. Double stranded salmon sperm DNA (ds-DNA, catalog No. D8899) was purchased from Sigma-Aldrich (St. Louis, USA). Reagent grade Tris–HCl, CH_3COOH , CH_3COONa , H_3PO_4 , EDTA, NaCl, and NaOH were purchased from Aldrich Chemicals (Milwaukee, USA). PDDA (low molecular weight) was purchased from Sigma-Aldrich Chemicals (Milwaukee, USA).

Aqueous solution of PDDA was prepared with 0.5 mol L^{-1} NaCl. Multiwall carbon nanotubes (MWCNTs, diameter of 70–100 nm and length of 5–9 μm) was purchased from Fluka. Titanium dioxide nano particles (TiO_2NPs) powder (30 nm) was purchased

from Fluka. The suspensions were prepared in PDDA solution after sonication for 3 h to obtain a homogeneous suspension.

2.2. Apparatus

Electrochemical measurements were performed using an Autolab PGSTAT 12, potentiostat/galvanostat connected to a three electrode cell, Metrohm, Model 663 VA stand, with a GPES 4.9 software package (Eco Chemie, The Netherlands). The raw data was treated using the Savitzky and Golay filter (level 2) of the GPES software, followed by the GPES software moving average baseline correction with a “peak width” of 0.01. The reference electrode was Ag/AgCl (3 mol L^{-1} KCl) and the counter electrode was a platinum wire. A standard one-compartment three-electrode cell of 20 mL capacity was used in all experiments. PGE and/or modified–PGE was the working electrode. A Noki pencil was used as a holder for Pentel graphite leads. Electrical contact with the lead was obtained by soldering a metallic wire to the metallic part. The pencil was held vertically with 12 mm of the lead extruded outside (9 mm was immersed in the solution). The pencil leads were used as received. All the electroanalytical measurements were performed at room temperature.

Electrochemical impedance spectroscopy was carried out in the presence of 5.0 mmol L^{-1} $\text{K}_3[\text{Fe}(\text{CN})_6]/\text{K}_4[\text{Fe}(\text{CN})_6]$ as a redox probe in 0.1 mol L^{-1} KCl (0.1 mol L^{-1} PBS pH 4.0) at a polarization potential of 0.15 V in the frequency range of 0.005 to 10^5 Hz and at amplitude of 10 mV.

The differential pulse voltammetry was performed by employing a positive-going differential pulse potential scan (from 0.40 to 1.40), using a pulse amplitude of 50 mV, a pulse width of 50.0 ms and a scan rate of 10 mV s^{-1} . The oxidation signals of guanine and adenine were recorded. The raw data were treated using the Savitzky and Golay filter (level 2) of the GPES software, followed by the GPES software moving average baseline correction, using a “peak width” of 0.01.

UV–vis spectra were recorded with a double beam spectrophotometer, Jasco Model V–750, using 1.0 cm quartz cells.

Metrohm pH–meter (Model 827) with a glass electrode (Corning) was used to measure the solutions pH.

2.3. Functionalization and purification of MWCNTs

MWCNTs were purified and functionalized as described elsewhere [32]. A mass of 120 mg of MWCNTs was stirred in 10 mL of a 3 mol L^{-1} nitric acid solution for 20 h. The solid product was collected on a filter paper and washed several times with distilled water until the filtrate solution became neutral (pH 7). The functionalized MWCNTs thus obtained were then dried in an oven at 80 °C for 24 h. Nitric acid usually causes a significant destruction in carbon nanotubes and introduces –COOH groups at the ends or at the sidewall defects of the nanotube structure.

2.4. Preparation of free DNA and DNA modified–PGE

Initially, the surface of PGE was pretreated by applying +1.40 V for 300 s in a quiescent solution of 0.5 mol L^{-1} acetate buffer containing 0.02 mol L^{-1} NaCl (pH 4.8). Then, 5.0 mg of MWCNTs and 5.0 mg of TiO_2NPs were dispersed into 5.0 mL of 1.0 mg mL^{-1} PDDA solution. The mixture was sonicated for 3 h to obtain a homogeneous suspension. PGE was dipped into this composite for 2 h. To prepare the DNA–modified electrode, the modified PGE (PDDA– TiO_2NPs –MWCNTs/PGE) was immersed into the ds-DNA solution (1.0 mg mL^{-1} buffered with Tris–HCl, pH 7.0) for approximately 30 min and allowed to dry for 1 h at room temperature. This modified PGE was designated as ds-DNA/PDDA– TiO_2NPs –MWCNTs/PGE.

2.5. Interaction between ds-DNA and atropine sulfate at the ds-DNA-modified ds-electrode

In order to investigate the interaction between atropine sulfate and ds-DNA, the PDDA-TiO₂NPs-MWCNTs/PGE and/or ds-DNA/PDDA-TiO₂NPs-MWCNTs/PGE was initially placed in a quiescent solution (20 mL) of 0.5 mol L⁻¹ acetate buffer containing 0.02 mol L⁻¹ NaCl (pH 4.8). The DP voltammograms were recorded to get the blank signals of the electrodes. Then, the PDDA-TiO₂NPs-MWCNTs/PGE and/or ds-DNA/PDDA-TiO₂NPs-MWCNTs/PGE was immersed into the Tris-buffer solution (pH 7.0) containing different concentrations of atropine sulfate while the solution was stirred at 200 rpm for 25 min in an open circuit system. After accumulation of atropine sulfate, the ds-DNA/PDDA-TiO₂NPs-MWCNTs/PGE was rinsed and placed in the acetate buffer solution (pH 4.8) containing 0.02 mol L⁻¹ NaCl. Finally, differential pulse voltammograms were recorded to get the sample signals.

2.6. Preparation of real samples

Written informed consent was obtained from all participants prior to the collection of the blood and urine samples.

Blood serum and urine samples were obtained from hospitalized patients, stored at -20 °C pending analysis, and allowed to thaw at ambient temperature prior to use. Different amounts of atropine sulfate were spiked into the samples before the treatment. Acetonitrile was added to the samples, to separate any present proteins, before they were centrifuged and filtered. An amount of 2.0 mL of the filtered solution was mixed thoroughly with 8.0 mL of the Tris-buffer solution. The atropine sulfate content was measured according to the recommended procedure.

3. Results and discussion

3.1. SEM characterization

The surface topographies of the stepwise DNA biosensor fabrication processes were investigated using SEM (Fig. 1). The surface roughness of the unmodified PGE can be clearly seen in Fig. 1A, in which the graphite layers are also seen. The electrode coverage morphology also reveals that the effective surface area of the modified working electrodes is significantly increased as a result of using highly conductive MWCNTs and TiO₂NPs, which were well dispersed in the PDDA solution (Fig. 1B). The surface morphology, however, changed when ds-DNA was immobilized on the surface of MWCNTs-TiO₂NPs-PDDA/PGE (Fig. 1C).

3.2. Electrochemical impedance spectroscopy

Electrochemical impedance spectroscopy (EIS) is a valuable technique to investigate the interfacial characterization of an electrode surface, such as charge transfer resistance (R_{ct}) during the oxidation process. The value of the electron transfer resistance (semicircle diameter) depends on the dielectric and insulating features at the electrode-electrolyte interface. An increase in R_{ct} value indicates a resistance or hindrance of electron flow due to the addition of a substance on the surface of the electrode, which leads to an increase in R_{ct} value. A solution containing 5.0 mmol L⁻¹ Fe(CN)₆^{3-/4-} in 0.1 mol L⁻¹ KNO₃ (pH 4.0, phosphate buffer) was used as a probe. Fig. 2 displays Nyquist plot of the imaginary impedance (Z_{im}) vs. the real impedance (Z_{re}) of the EIS obtained from an unmodified PGE (curve a), PDDA-MWCNTs-TiO₂NPs/PGE (curve b) and dsDNA/PDDA-MWCNTs-TiO₂NPs/PGE (curve c). As shown in Fig. 2 (curve b), the R_{ct} (the diameter of the semicircle) decreases after modification of PGE by PDDA-MWCNTs-TiO₂NPs, which is due to the acceleration of electron transfer. It was found that the impedance of the electrode drastically decreased in the presence of PDDA-MWCNTs-TiO₂NPs. It may be due to promotion of electron transfer rate between [Fe(CN)₆]^{3-/4-} and the electrode surface. Furthermore, as shown in Fig. 2 (curve c) by addition of ds-DNA at the surface of PDDA-MWCNTs-TiO₂NPs, the amount of R_{ct} was increased, because the DNA reduces conductivity of PDDA-MWCNTs-TiO₂NPs and therefore the R_{ct} increases.

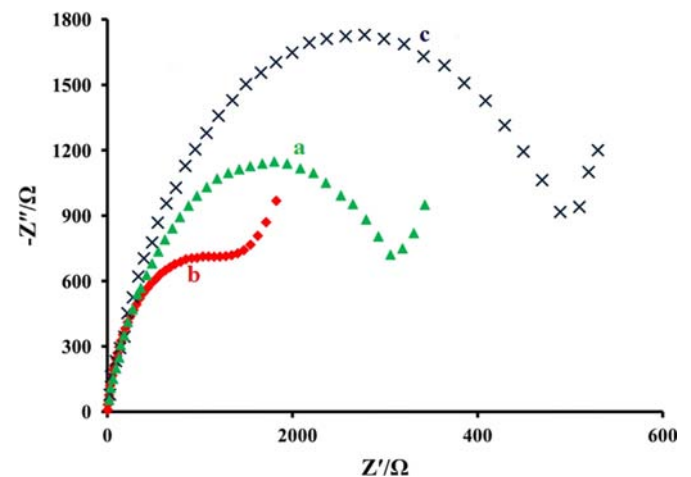


Fig. 2. Impedance spectra of a) bare PGE, b) PDDA-MWCNTs-TiO₂NPs/PGE, and c) dsDNA/PDDA-MWCNTs-TiO₂NPs/PGE in 5.0 mmol L⁻¹ Fe(CN)₆^{3-/4-} containing 0.10 mol L⁻¹ KCl.

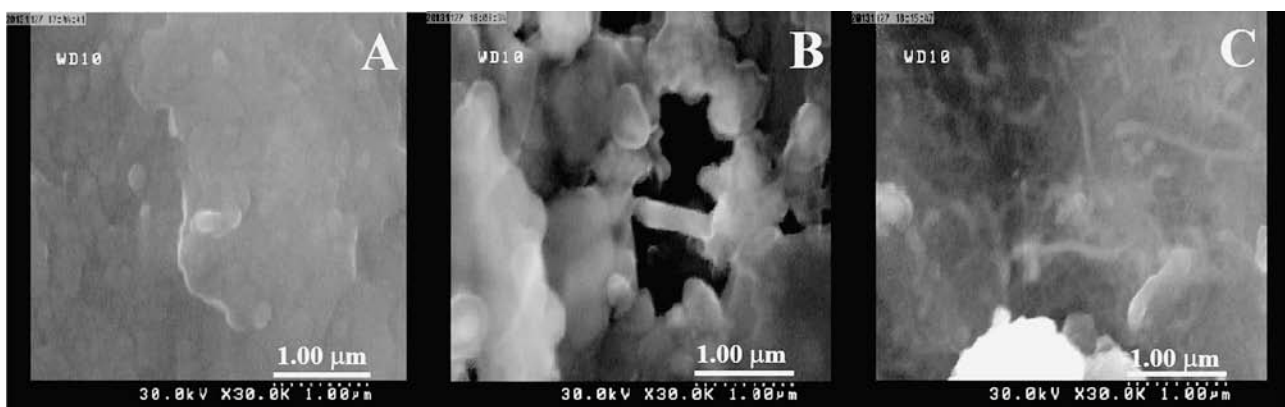


Fig. 1. SEM images of a) unmodified PGE, b) PDDA-MWCNTs-TiO₂NPs/PGE, and c) ds-DNA/PDDA-MWCNTs-TiO₂NPs/PGE.

3.3. Interaction between ds-DNA and atropine sulfate at ds-DNA/PDDA-TiO₂NPs-MWCNTs/PGE

DPV oxidation signals of guanine and adenine at the ds-DNA/PDDA-TiO₂NPs-MWCNTs/PGE before and after interaction with atropine sulfate are shown in Fig. 3. Different concentrations of atropine sulfate (0 to 600 $\mu\text{mol L}^{-1}$) were used to interact with guanine and adenine at the surface of ds-DNA/PDDA-TiO₂NPs-MWCNTs/PGE. It was found that the oxidation peaks current decreased with increasing atropine sulfate concentration. To investigate the electroactivity of atropine sulfate, the DNA free modified-PGE (PDDA-TiO₂NPs-MWCNTs/PGE) and/or unmodified PGE were immersed into a 100.0 $\mu\text{mol L}^{-1}$ of atropine sulfate solution while the solution was being stirred at 200 rpm for 25 min in an open circuit. No remarkable oxidation signal of atropine sulfate was obtained at the PDDA-TiO₂NPs-MWCNTs/PGE and/or unmodified PGE in the potential range of +0.40 and +1.40 V (dash lines, Fig. 3). Thus, it was concluded that atropine sulfate was not able to interact with the electrode surface to produce an oxidation signal. The decreases in the oxidation signals of guanine and adenine bases were attributed to the binding of atropine sulfate to these electroactive DNA bases. This could be explained as a possible damage to, or shielding of, the oxidizable groups of guanine and adenine bases while atropine sulfate interacted with the ds-DNA at the PGE surface. The results obtained showed that ds-DNA modified PGE might be used for the detection of atropine sulfate interaction with the ds-DNA.

3.4. UV-vis spectrophotometric study for the interaction of atropine sulfate and ds-DNA

UV-vis absorption spectrophotometry is a technique generally employed to investigate drug-DNA interactions. The UV-vis absorption peak positions of atropine sulfate are around 275 and 390 nm (Fig. 4b), and that of ds-DNA is at 285 nm (Fig. 4a). As is evident from Fig. 4c, the absorbance of atropine sulfate decreases at 390 nm and vanishes at 275 nm as a result of adding ds-DNA. These results reveal that there is a strong interaction between atropine sulfate and the ds-DNA. The intercalative binding of molecules to the ds-DNA helix has been characterized by an

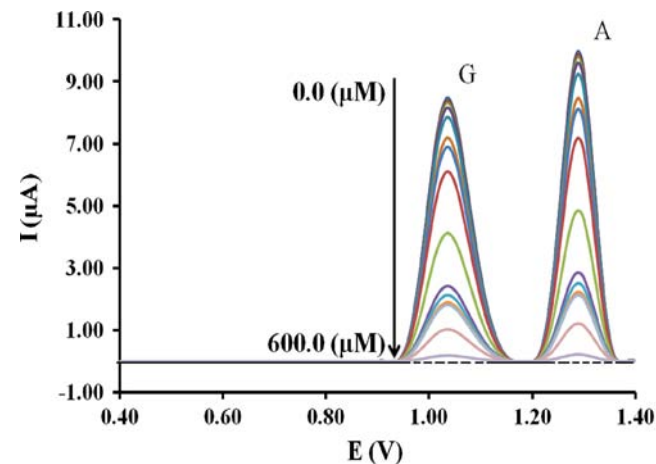


Fig. 3. Differential pulse voltammograms for the interaction of atropine sulfate with ds-DNA/PDDA-MWCNTs-TiO₂NPs/PGE; Oxidation signals of guanine and adenine after interaction with atropine sulfate at the surface of ds-DNA/PDDA-MWCNTs-TiO₂NPs/PGE (from up to down) 0.0, 0.6, 0.8, 1.0, 3.0, 6.0, 8.0, 10.0, 20.0, 30.0, 60.0, 80.0, 100.0, 300.0, 500.0, and 600.0 $\mu\text{mol L}^{-1}$ atropine sulfate. Dash lines show the unmodified PGE and PDDA-MWCNTs-TiO₂NPs/PGE signal in 100.0 $\mu\text{mol L}^{-1}$ atropine sulfate (pH 4.8). Conditions: scanning potential between +0.40 and +1.40 V in acetate buffer (pH 4.8).

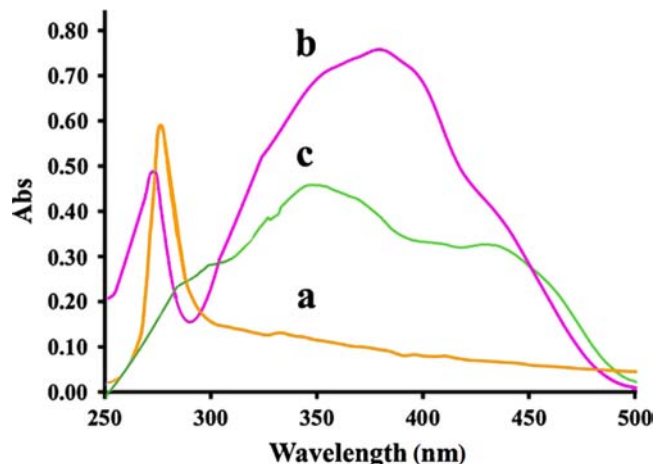


Fig. 4. UV-vis spectrogram of 100.0 $\mu\text{mol L}^{-1}$ atropine sulfate before (a) and after (c) the interaction with 1.0 mg mL^{-1} ds-DNA and (b) ds-DNA (1.0 mg mL^{-1}).

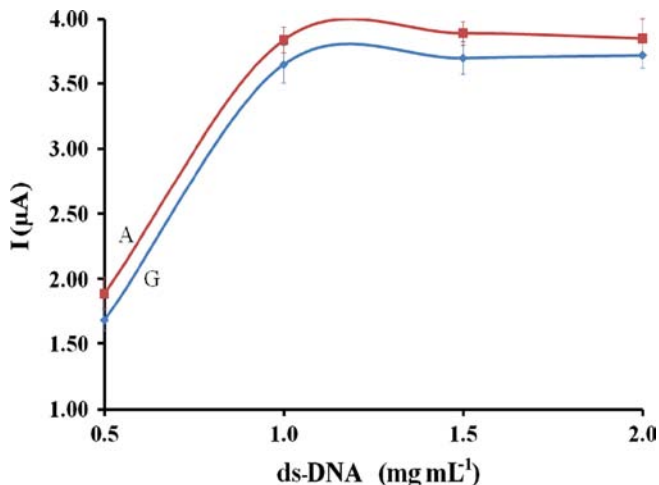


Fig. 5. Effect of the ds-DNA concentration on the guanine and adenine oxidation signals at the surface of ds-DNA/PDDA-MWCNTs-TiO₂NPs/PGE. Conditions are as in Fig. 3.

appreciable shift in wavelength (red shift ≥ 15 nm) due to the interaction of a ds-DNA π stack with the ligand, while the outside binders (groove binders) display a smaller red shift (red shift ≤ 8 nm) [33]. The red shift for absorption peaks at 390 nm is about 40 nm. UV-vis spectrophotometry combined with DPV is used to propose the most plausible mechanism for the interaction between atropine sulfate and ds-DNA. The decrease in the UV-vis absorption spectrum of atropine sulfate after interaction with ds-DNA, and the decrease in the DPV oxidation signal intensity of ds-DNA at PGE after interaction with atropine sulfate provide potent evidence for possible intercalation of atropine sulfate.

3.5. Effect of ds-DNA concentration on immobilization at PGE surface

The DNA biosensor was prepared by immobilizing salmon sperm ds-DNA on the PGE surface (Fig. 5). A linear relationship was observed between ds-DNA concentration and DVP signals of guanine and adenine bases in the concentration range of 0.05 to 1.0 mg mL^{-1} , beyond which it leveled off. Therefore, 1.0 mg mL^{-1} of ds-DNA was selected and used in all the further experiments.

3.6. Effect of accumulation time on immobilization of ds-DNA at the PGE surface

One important parameter for the immobilization of ds-DNA at an electrode surface is the accumulation time. It can be seen in Fig. 6 that the oxidation peaks current of guanine and adenine bases (of ds-DNA) on the ds-DNA/PDDA-TiO₂NPs-MWCNTs/PGE surface increased up to 30 min before they leveled off over longer times. At this accumulation time, the sites on the film surface were filled with the ds-DNA such that no more ds-DNA diffused onto the film surface. Therefore, 30 min was considered as an optimum accumulation time of ds-DNA for preparing the ds-DNA/PDDA-TiO₂NPs-MWCNTs/PGE.

3.7. Effect of incubation time of atropine sulfate on guanine and adenine signals

Binding of atropine sulfate to ds-DNA depends on their incubation time. Therefore, the incubation time for the interaction of atropine sulfate with the ds-DNA/PDDA-TiO₂NPs-MWCNTs/PGE surface was optimized. For this purpose, electrochemical detection was obtained and assessed for an incubation time of atropine

sulfate in the range of 5–40 min. The results (Fig. 7) showed dramatic decreases in the oxidation signals of guanine and adenine with increasing interaction time up to 25 min beyond, which the signals almost leveled off for longer incubation times. Accordingly, 25 min was selected as an optimum time for the interaction of atropine sulfate with the ds-DNA/PDDA-TiO₂NPs-MWCNTs/PGE.

4. Figures of merit

DPV was used at a pulse amplitude of 50 mV, a pulse width of 50.0 ms, and a scan rate of 10 mV s⁻¹. A linear dependency was observed between the analytical signals (considered as the decrease in guanine and adenine signals before and after interaction with atropine sulfate) and atropine sulfate concentrations. Using DPV and following the changes in the oxidation signal intensity of guanine after interaction with atropine sulfate concentration, the linear dependency was detected in the two regions in the ranges of 0.6–30.0 and 30.0–600.0 μmol L⁻¹. The regression equations were $I(\mu\text{A}) = 0.2054(\pm 0.0028)C_{\text{Atropine}} + 0.0594(\pm 0.0364)$ with $R^2 = 0.9982$ and $I(\mu\text{A}) = 0.0043(\pm 0.0004)C_{\text{Atropine}} + 6.1364(\pm 0.1251)$ with $R^2 = 0.9952$, respectively, where C is concentration of atropine sulfate in μmol L⁻¹.

The detection limit (3 S_b/m, three times of the standard deviation of the blank divided by the slope of the calibration curve) and the limit of quantitation (10 S_b/m) of the proposed method were found to be 0.03 and 0.10 μmol L⁻¹ of atropine sulfate. Fig. 8 shows the calibration curve obtained by plotting the changes in the oxidation signal of guanine after interaction of atropine with the sulfate of ds-DNA/PDDA-TiO₂NPs-MWCNTs/PGE with respect to atropine sulfate concentration.

To check the reproducibility of the biosensor, changes in the oxidation peak current of guanine after interaction of ds-DNA/PDDA-TiO₂NPs-MWCNTs/PGE with atropine sulfate (at concentrations of 1.0 and 100.0 μmol L⁻¹) were measured by repeating the tests within several days using the same biosensor. Between the measurements, the sensor was stored in dry conditions in an open air at room temperature. The biosensor's stability was tested during a period of 20 days by measuring guanine signals every 4th day and characterized by relative standard deviation (RSD%) values of the guanine peak currents. The RSD values for guanine signals after interaction with 1.0 μmol L⁻¹ atropine sulfate on interval times of 4-day were recorded as 3.9%, 3.1%, 3.6%, 4.1%, and 3.5% (n=5) and with an atropine sulfate concentration of 100.0 μmol L⁻¹, they were 4.2%, 3.4%, 3.8%, 3.3%, and 3.7% (n=5).

5. Interference study

Interference studies were carried out with several species prior to the application of the proposed method for the assay of atropine sulfate in real samples. Potential interfering substances were chosen from the group of substances commonly found with atropine sulfate in pharmaceuticals and biological fluids. Tolerance limit was defined as the maximum concentration of the potential interfering substance causing an error less than 5% in the determination of 20.0 μmol L⁻¹ atropine sulfate. The atropine sulfate was measured in the absence and presence of the potential interfering compounds, based on the recommended procedure. A substance was considered not to interfere if the variation in the peak current of atropine sulfate was less than 5%. The results are shown in Fig. 9 and are also presented in Table 1, indicating the high selectivity of the proposed method for atropine sulfate determination.

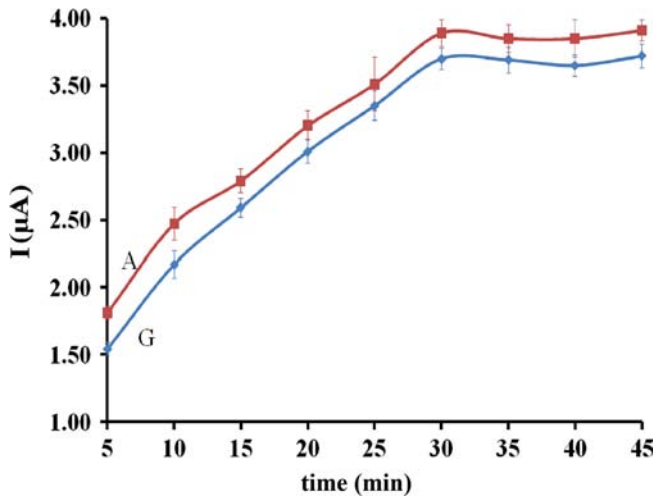


Fig. 6. Effect of accumulation time for immobilization of ds-DNA at PDDA-MWCNTs-TiO₂NPs/PGE on the guanine and adenine oxidation signals. Conditions are as in Fig. 3.

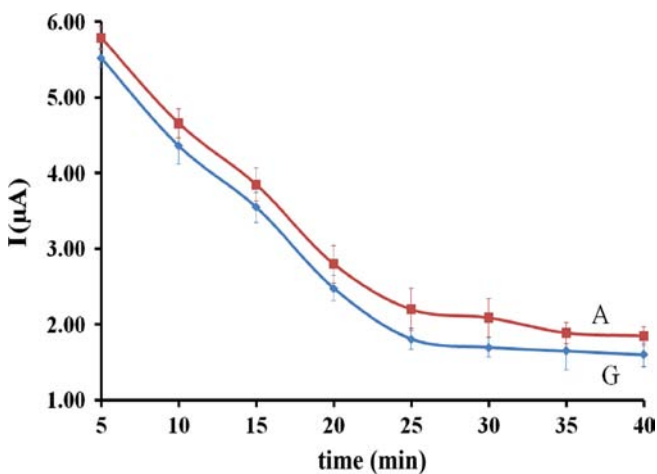


Fig. 7. Effect of incubation time of atropine sulfate at ds-DNA/PDDA-MWCNTs-TiO₂NPs/PGE surface on the guanine and adenine oxidation signals. Conditions are as in Fig. 3.

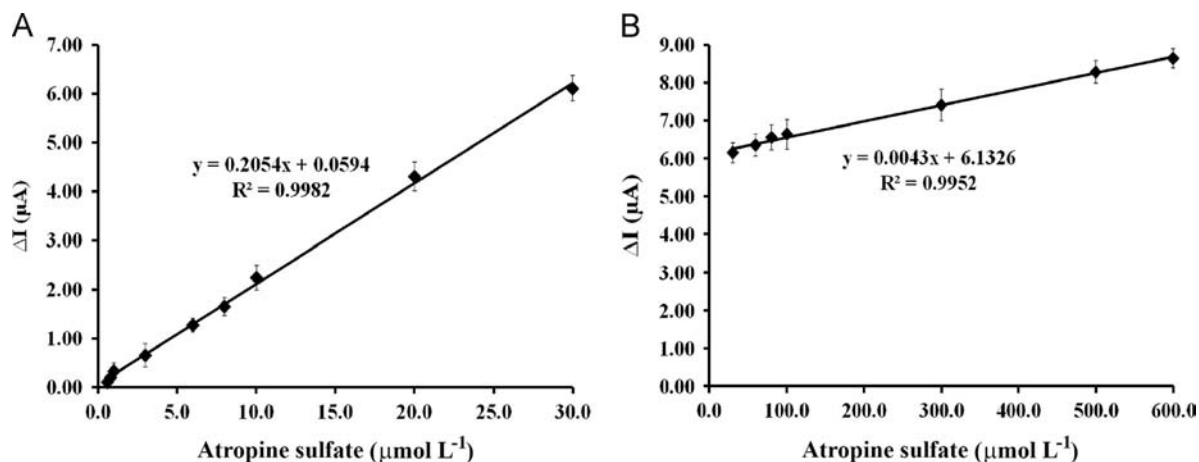


Fig. 8. Calibration curve for determination of atropine sulfate based on the changes of the oxidation signal of guanine after interaction with atropine sulfate. Conditions are as in Fig. 3.

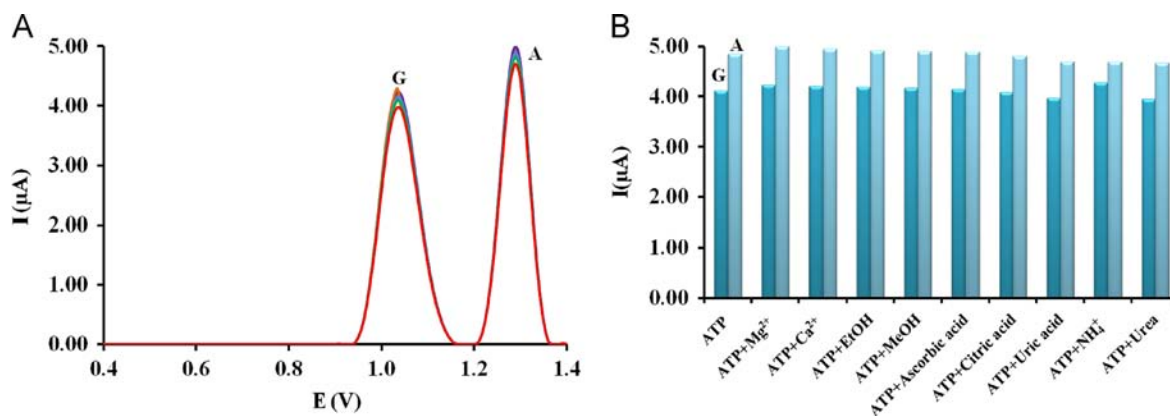


Fig. 9. A): Differential pulse voltammograms of 20.0 $\mu\text{mol L}^{-1}$ atropine sulfate (alone) and the atropine sulfate (APS) containing (from up to down) 10.0 mmol L^{-1} Mg^{2+} , 10.0 mmol L^{-1} Ca^{2+} , 10.0 mmol L^{-1} ethanol, 10.0 mmol L^{-1} methanol, 10.0 mmol L^{-1} ascorbic acid, 5.0 mmol L^{-1} citric acid, 2.0 mmol L^{-1} uric acid, 10.0 mmol L^{-1} NH_4^+ , and 2.0 mmol L^{-1} urea. B): Schematic diagram of the selectivity study. Conditions are as in Fig. 3 in acetate buffer (pH 4.8).

Table 1
Interference study for determination of 20.0 $\mu\text{mol L}^{-1}$ atropine sulfate.

Species	Tolerance limit (w/w)
Lactose, fructose, glucose, sucrose, methanol, ethanol, Ca^{2+} , Mg^{2+} , NH_4^+ , ascorbic acid	500*
Citric acid	250
Urea, uric acid	100

* maximum ratio checked.

6. Analytical performance

In order to evaluate the performance of the proposed method for real sample analysis, blood serum and urine samples were used for atropine sulfate analysis after preparation as described above. Five ds-DNA/PDDA-TiO₂NPs-MWCNTs/PGEs were also prepared to determine the recovery of atropine sulfate in blood serum and urine samples. The oxidation signals of guanine and adenine were obtained using DPV at the optimized conditions. A new ds-DNA/PDDA-TiO₂NPs-MWCNTs/PGE was prepared, immersed in the real sample solutions containing atropine sulfate, and stirred at 200 rpm for 25 min in an open circuit. The differential pulse voltammogram was then recorded. The peaks current of guanine and adenine were compared before and after interaction with the samples containing atropine sulfate to obtain the analytical signal.

The results are given in Table 2. In addition, the accuracy of the biosensor was checked using a standard HPLC method. Student t-test and F-test were used to evaluate the accuracy and precision of the proposed method. As can be seen in Table 2, the biosensor exhibited a good accuracy and precision for the determination of atropine sulfate.

7. Conclusion

In the present work, a sensitive DNA-biosensor was developed for the determination of atropine sulfate. The interaction of atropine sulfate with ds-DNA was initially investigated using electrochemical and UV-vis spectroscopy. The decreases observed in the intensities of the oxidation signals of guanine and adenine before and after interaction with atropine sulfate were used for the determination of atropine sulfate. PDDA as a polycation and MWCNTs plus TiO₂NPs of small sizes provide a surface with positive charges and a high surface area for the immobilization of ds-DNA as a polyanion. Using the ds-DNA/PDDA-TiO₂NPs-MWCNTs/PGE electrode, we were able to detect the interaction of atropine sulfate with ds-DNA, which allowed us to apply the DNA-modified electrode for the determination of atropine sulfate. The advantages of the proposed method are low limit of detection, wide linear dynamic range, ease of application, sensitivity, and its selectivity.

Table 2
Recovery of atropine sulfate in blood serum and urine samples (n=5).

Sample	Sample No	Atropine added ($\mu\text{mol L}^{-1}$)	Found by biosensor* ($\mu\text{mol L}^{-1}$)	Recovery (%)	Found by HPLC* ($\mu\text{mol L}^{-1}$)	$t_{\text{calculated}}^{**}$	$F_{\text{calculated}}^{**}$
Blood serum	1	–	< Detection limit	–	–	–	–
	2	3.00	2.90 ± 0.15	96.7	2.95 ± 0.19	1.02	2.98
	3	8.00	7.82 ± 0.40	97.7	7.89 ± 0.48	1.33	3.44
Urine	1	–	< Detection limit	–	–	–	–
	2	6.00	5.88 ± 0.22	98.0	5.82 ± 0.31	1.24	3.20
	3	10.00	9.60 ± 0.69	96.0	9.67 ± 0.63	1.49	3.65

* Average of five replicate measurements.

** Theoretical value of t-student test=2.78 (for $n=5$, $p=0.05$) and theoretical value for F-test=6.39 (for $n=5$, $p=0.05$).

Acknowledgment

The authors wish to thank the Research Council of Isfahan University of Technology (IUT), the Center of Excellence in Sensor and Green Chemistry, and the Iranian Nanotechnology Initiative Council for their support.

References

- [1] L. Mateus, S. Cherkaoui, P. Christen, K.M. Oksman-Caldentey, *Phytochem* 54 (2000) 517–523.
- [2] L. Meng, P. Meng, B. Tang, Q. Zhang, Y. Wang, *Forensic Sci. Int.* 231 (2013) 6–12.
- [3] J.G. Li, Y. Chun, H.X. Ju, *Electroanalysis* 19 (2007) 1569–1574.
- [4] J. Beyer, O.H. Drummer, H.H. Maurer, *Forensic Sci. Int.* 185 (2009) 1–9.
- [5] N.F. Atta, A. Galal, R.A. Ahmed, *Int. J. Electrochem. Sci.* 7 (2012) 10365–10379.
- [6] H. Peng, C. Liang, A. Zhou, Y. Zhang, Q. Xie, S. Yao, *Anal. Chim. Acta* 423 (2000) 221–228.
- [7] S. Sun, J. Lu, *Anal. Chim. Acta* 580 (2006) 9–13.
- [8] F. Ricard, E. Abe, C. Duverneuil-Mayer, P. Charlier, G. Grandmaison, J.C. Alvarez, *Forensic Sci. Int.* 223 (2012) 256–260.
- [9] L. Zhimei, L. Meng, Z. Huangdan, *J. Pharm. Pract* 4 (2004) 230–232.
- [10] E. Kozler, A. Mordel, S.B. Haim, *J. Pediatr.* 146 (2005) 41–44.
- [11] C. Xuefeng, F. Zuogang, *Chin. J. Mod. Appl. Pharm* 6 (2003) 514–516.
- [12] Y. Long, L. Lei, W. Li, D. He, L. Nie, S. Yao, *Analyst* 124 (1999) 1629–1634.
- [13] I. Papadoyannis, A. Zotou, V. Samanidou, M. Georganakos, *Instrum. Sci. Technol.* 22 (1994) 83–103.
- [14] N.F. Atta, A. Galal, R.A. Ahmed, *Electroanalysis* 23 (2011) 737–746.
- [15] N.F. Atta, A. Galal, R.A. Ahmed, *J. Electrochem Soc.* 158 (2011) F52–F60.
- [16] R.A. Dar, P.K. Brahman, S. Tiwari, K.S. Pitre, *Colloids Surface. B* 91 (2012) 10–17.
- [17] S.R. Mikkelsen, *Electroanalysis* 8 (1996) 15–19.
- [18] E. Palek, M. Fojta, *Anal. Chem.* 73 (2001) 74A–83A.
- [19] G. Chiti, G. Marrazza, M. Mascini, *Anal. Chim. Acta* 427 (2001) 155–164.
- [20] F. Lucarelli, G. Marrazza, A.P.F. Turner, M. Mascini, *Biosens. Bioelectron.* 19 (2004) 515–530.
- [21] J. Wang, M. Chicharro, G. Rivas, X. Cai, N. Dontha, P.A.M. Farias, H. Shiraishi, *Anal. Chem.* 68 (1996) 2251–2254.
- [22] M.S. Ibrahim, *Anal. Chim. Acta* 443 (2001) 63–72.
- [23] A.A. Ensafi, B. Rezaei, M. Amini, E. Heydari-Bafrooei, *Talanta* 88 (2012) 244–251.
- [24] A.A. Ensafi, E. Heydari-Bafrooei, M. Amini, *Biosens. Bioelectron.* 31 (2012) 376–381.
- [25] B. Dogan-Topal, B. Uslu, S.A. Ozkan, *Biosens. Bioelectron.* 24 (2009) 2358–2364.
- [26] L. Mirmoghtadaie, A.A. Ensafi, M. Kadivar, P. Norouzi, *Mater. Sci. Eng. C* 33 (2013) 1753–1758.
- [27] E. Mirmomtaz, A.A. Ensafi, S. Soleimani-Zad, *Electrochim. Acta* 54 (2009) 1141–1146.
- [28] J. Wang, X. Cai, G. Rivas, H. Shiraishi, P.A.M. Farias, N. Dontha, *Anal. Chem.* 68 (1996) 2629–2634.
- [29] M.L. Pedano, G.A. Rivas, *Biosens. Bioelectron.* 18 (2003) 269–277.
- [30] D.J. Caruana, A. Heller, *J. Am. Chem. Soc.* 121 (1999) 769–774.
- [31] K. Xu, J. Huang, Z. Ye, Y. Ying, Y. Li, *Sensors* 9 (2009) 5534–5557.
- [32] M.E. Ghica, R. Pauliukaite, O. Fatibello Filho, C.M.A. Brett, *Actuators B* 142 (2009) 308–315.
- [33] Y.J. Guo, J.B. Chao, J.H. Pan, *Acta Part A* 68 (2007) 231–236.



Electrochemical magnetoimmunosensing platform for determination of the milk allergen β -lactoglobulin



V. Ruiz-Valdepeñas Montiel, S. Campuzano*, F. Conzuelo, R.M. Torrente-Rodríguez, M. Gamella, A.J. Reviejo, José M. Pingarrón*

Departamento de Química Analítica, Facultad de CC. Químicas, Universidad Complutense de Madrid, E-28040 Madrid, Spain

ARTICLE INFO

Article history:

Received 7 May 2014

Received in revised form

23 July 2014

Accepted 27 July 2014

Available online 5 August 2014

Keywords:

β -Lactoglobulin

Amperometric magnetoimmunosensors

Magnetic beads

Milk

ABSTRACT

A very sensitive magnetoimmunosensor for the determination of β -lactoglobulin (β -LG) is reported in this work. A sandwich configuration involving covalent immobilization of the capture antibody (anti β -LG) onto activated carboxylic-modified magnetic beads (HOOC-MBs) and incubation of the modified MBs with a horseradish peroxidase labeled antibody (HRP-anti β -LG), is used. The resulting modified MBs are captured by a magnet placed under the surface of a disposable carbon screen-printed electrode (SPCE) and the amperometric responses are measured at -0.20 V (vs. Ag pseudo-reference electrode), upon addition of hydroquinone (HQ) as electron transfer mediator and H_2O_2 as the enzyme substrate. The β -LG magnetoimmunosensor exhibited a wide range of linearity (2.8 – 100 ng mL $^{-1}$) and a low detection limit of 0.8 ng mL $^{-1}$ (20 pg in 25 μ L sample). The magnetoimmunosensing platform was successfully applied for the detection of β -LG in different types of milk without any matrix effect after just a sample dilution. The results correlated properly with those provided by a commercial ELISA method offering a truthful analytical screening tool. These features make the developed methodology a promising alternative in the development of user-friendly devices for on-site determination of β -LG in dairy products.

© 2014 Elsevier B.V. All rights reserved.

1. Introduction

Food allergy has become one of the major health concerns nowadays. So far, there is no effective treatment for food allergens suffers and the only way to manage the health hazards resulting from allergens is to avoid the specific allergen containing food [1]. Milk is one of the most common sources of food allergies [2,3], affecting between 2% and 3% of infants [4]. β -LG is the major whey protein of cow and sheep's milk (2 – 3 g L $^{-1}$) and it is present also in other mammalian species but not in humans. It belongs to the lipocalin protein family and is considered the most important milk allergen especially for children, affecting about 3% of the population in the first year of life. Although milk is one of the food components which should be listed on the label of commercial food products, most of the allergenic reactions on insensitive consumers occur due to unexpected exposure of milk proteins in a product where milk is not included in the ingredients list. β -LG may be also an important marker in the detection of milk

adulteration, especially in case of replacement of goat's or sheep's milk by cow's milk [5]. Therefore, reliable detection methods are needed for regulatory agencies and food industry both in terms of milk protein allergy and milk and dairy product adulteration [6].

Although several analytical methods have been reported for β -LG detection including HPLC [7], capillary electrophoresis (CE), methods with laser-induced fluorescence (LIF) detection [8], enzyme linked immunoaffinity chromatography (ELIAC) [9], size exclusion chromatography [10], methods based on the resonance enhanced absorption (REA) effect [11] and surface plasmon resonance (SPR) [12] as well as commercially available and routinely used enzyme-linked immunosorbent assays (ELISAs) [13], there is still an urgent need to develop alternative methods with lower cost, higher sensitivity, selectivity and faster response. In the recent years, electrochemical biosensors have been perceived to be one of the most promising analytical tools with wide applicability in various biomedical and environmental fields because of their low cost, simple use, fast response, sensitivity as well as their capability for automation and miniaturization. To the best of our knowledge only one label-free electrochemical immunosensor, constructed by immobilization of the capture antibodies using glutaraldehyde on graphene-modified SPCEs has been reported earlier for the detection of β -LG [6]. Although the achieved sensitivity is very good, the fabrication procedure required multiple and complex steps for functionalizing the commercial graphene-modified SPCEs making it difficult to do for untrained people.

* Corresponding authors. Tel.: +34 913944315; fax: +34 913944329.

E-mail addresses: victor_lega90@hotmail.com (V. Ruiz-Valdepeñas Montiel), susanacr@quim.ucm.es (S. Campuzano), felipecf@quim.ucm.es (F. Conzuelo), rebeca.magnolia@gmail.com (R.M. Torrente-Rodríguez), mariagam@quim.ucm.es (M. Gamella), reviejo@quim.ucm.es (A.J. Reviejo), pingarro@quim.ucm.es (J.M. Pingarrón).

The use of magnetic beads (MBs) for the development of electrochemical immunosensors has demonstrated to be a useful tool to improve their sensitivity, reduce the time of analysis and minimize matrix effects [14–20]. Electrochemical magnetoimmunosensors allow the analysis of complex samples with no need for pre-enrichment or purification steps due to the “extraction” of the target analyte from the complex matrix and the measurement of the electrochemical signal in a “clean” environment [21]. These characteristics make functionalized MBs a particularly relevant tool for designing immunosensors to be used in complex real sample matrices. In this paper, we propose an amperometric magnetoimmunosensor for the determination of β -LG, the main milk allergenic protein, using a sandwich configuration, SPCEs and HOOC-modified MBs (HOOC-MBs). The developed methodology involved the immobilization of the capture antibody on the HOOC-MBs, and successive incubation steps of the modified MBs with the analyte and a specific HRP-labeled detector antibody. The electrochemical detection of the enzyme reaction product was carried out at disposable SPCEs using HQ as electron transfer mediator and H_2O_2 as the enzyme substrate. The magnetoimmunosensor was successfully applied to the analysis of different milk samples, demonstrating its potential role in food safety and consumer protection.

2. Materials and methods

2.1. Apparatus and electrodes

Amperometric measurements were performed with a CHI812B potentiostat (CH Instruments) controlled by software CHI812B. All measurements were carried out at room temperature. The electrochemical transducers employed were screen-printed carbon electrodes (SPCEs) (DRP-110, DropSens) consisting of a 4-mm diameter carbon working electrode, a carbon counter electrode and a Ag pseudo-reference electrode.

Homogenization of the solutions was facilitated by a Bunsen AGT-9 Vortex. A Thermomixer MT100 constant temperature incubator shaker (Universal Labortechnik) was also used. Magnetic separation steps for incubation/washing processes were performed using a Dynal MPC-S (product No. 120.20, Dynal Biotech ASA) magnetic particle concentrator. A neodymium magnet (AIMAN GZ) was used to control the attraction of the modified-MBs to the SPCE surface.

2.2. Reagents and solutions

Carboxylic acid-modified MBs (HOOC-MBs, 2.8 μm \varnothing , 10 mg mL^{-1} , Dynabeads[®] M-270 Carboxylic Acid) were purchased from Dynal Biotech ASA. NaCl, KCl, sodium di-hydrogen phosphate, di-sodium hydrogen phosphate, and Tris-HCl were purchased from Scharlab. Tween[®]20, *N*-(3-dimethylaminopropyl)-*N*'-ethylcarbodiimide (EDC), *N*-hydroxysulfosuccinimide (sulfo-NHS), ethanolamine, hydroquinone (HQ), hydrogen peroxide (30%, w/v), casein, alkaline phosphatase (from bovine intestinal mucosa), catalase (from bovine liver) and bovine β -LG were purchased from Sigma-Aldrich. 2-(*N*-morpholino)ethanesulfonic acid (MES) and bovine serum albumin (BSA, Type VH) were purchased from Gerbu. Ascorbic acid was purchased from Fluka.

The rabbit anti-bovine β -LG capture antibody (A10–125A) and the HRP conjugated rabbit anti-bovine β -LG detector antibody (A10–125P), components of the β -LG ELISA Kit, were purchased from Bethyl Laboratories, Inc. The kit was also used for validation purposes.

The following solutions prepared in deionized water were employed: 0.05 M phosphate buffer, pH 6.0; 0.1 M phosphate

buffer, pH 8.0; phosphate-buffered saline (PBS) consisting of 0.01 M phosphate buffer solution containing 137 mM NaCl and 2.7 mM KCl, pH 7.5; 0.025 M MES buffer, pH 5.0; 0.01 M sodium phosphate buffer solution consisting of PBS with 0.05% Tween[®]20 (pH 7.5, PBST), and 0.1 M Tris-HCl buffer, pH 7.2.

Activation of the HOOC-MBs was carried out with an EDC/sulfo-NHS mixture solution (50 mg mL^{-1} each in MES buffer, pH 5.0). The blocking step was accomplished with a 1 M ethanolamine solution prepared in a 0.1 M phosphate buffer solution of pH 8.0.

All chemicals used were of analytical-reagent grade, and deionized water was obtained from a Millipore Milli-Q purification system (18.2 $\text{M}\Omega$ cm).

2.3. Modification of MBs

A 3- μL aliquot of the HOOC-MBs commercial suspension was transferred into a 1.5 mL Eppendorf[®] tube. Then, the MBs were washed twice with 50 μL MES buffer solution during 10 min under continuous stirring (950 rpm, 25 $^\circ\text{C}$). Between each step the particles were concentrated using a magnet and, after 4 min, the supernatant was discarded. The MBs carboxylic groups were activated by incubation during 35 min in 25 μL of the EDC/sulfo-NHS mixture solution. The activated MBs were washed twice with 50 μL of MES buffer and re-suspended in 25 μL of a 10 $\mu\text{g mL}^{-1}$ anti- β -LG solution (in MES buffer). The anti- β -LG was captured onto the activated beads during 30 min at 25 $^\circ\text{C}$ under continuous stirring (950 rpm). Subsequently, the anti- β -LG-modified MBs were washed twice with 50 μL of MES buffer solution. Thereafter, the unreacted activated groups on the MBs were blocked by adding 25 μL of the 1 M ethanolamine solution (in 0.1 M phosphate buffer, pH 8.0) and incubating the suspension under continuous stirring (950 rpm) for 60 min at 25 $^\circ\text{C}$. After two washing steps with 50 μL of 0.1 M Tris-buffer (pH 7.2) and another one with 50 μL of PBST (pH 7.5), the anti- β -LG-coated MBs were re-suspended in 25 μL of a variable concentration of the target antigen (in PBST, pH 7.5) and incubated during 30 min (950 rpm at 25 $^\circ\text{C}$). Then the modified MBs were washed twice with 50 μL of PBST (pH 7.5) and immersed in 25 μL of a solution containing 0.75 $\mu\text{g mL}^{-1}$ HRP-anti- β -LG solution (in PBST, pH 7.5) during 30 min (950 rpm at 25 $^\circ\text{C}$). After two washing steps with the same buffer, the modified-MBs were re-suspended in 45 μL of 0.05 M sodium phosphate buffer solution (pH 6.0).

2.4. Amperometric measurements

The final resuspended modified MBs were captured on the SPCE surface according to the procedure described earlier [19]. The magnet holding block with the SPCE where the modified MBs were captured, was immersed into an electrochemical cell (see reference [19] for details) containing 10 mL 0.05 M phosphate buffer pH 6.0 and 1.0 mM HQ (prepared just before the electrochemical measurement). Amperometric measurements in stirred solutions were performed by applying a detection potential of -0.20 V vs. Ag pseudo-reference electrode upon addition of 50 μL of a 0.1 M H_2O_2 solution until the steady-state current was reached (approx. 1 min).

The amperometric signals given through the manuscript corresponded to the difference between the steady-state and the background currents. Unless otherwise indicated, each data point represents three independent measurements and the error bars show the standard deviations of measurements.

2.5. Analysis of milk samples

The developed SPCEs-based magnetoimmunosensors were applied to the determination of β -LG in different milk samples:

raw, UHT and pasteurized cow milk and human milk. The sample treatment consisted only of an appropriate dilution (between 2500 and 250,000, see Table 2) with the PBST (pH 7.5) buffer. Given the absence of matrix effect after performing the dilution required to fall the β -LG concentration in the milk matrices within the linear part of the calibration graph constructed with standards, the determination of β -LG was performed by interpolating the amperometric signals obtained with the diluted samples into that calibration plot. The anti β -LG-modified MBs were re-suspended in a 25 μ L-aliquot of the PBST diluted milk sample and incubated at 25 °C for 30 min with vigorous stirring (950 rpm). Thereafter, separation, washing and measurement protocols were similar to those described above for β -LG standard solutions.

For comparison purposes, the same milk samples were also analyzed by an ELISA methodology involving the use of the same immunoreagents.

3. Results and discussion

The fundamentals of the immunosensor configuration as well as of the electrochemical transduction are displayed in Fig. 1. Briefly, the specific capture antibody (anti β -LG) was covalently immobilized onto the HOOC-MBs previously activated with an EDC/sulfo-NHS solution. After a blocking step with ethanolamine of the unreacted activated groups of the commercial MBs, the anti β -LG-MBs were incubated in the sample solution and the target protein was sandwiched with the HRP-labeled detector antibody (HRP-anti β -LG).

The MBs bearing the sandwich immunocomplexes were magnetically captured on the electrode surface by placing the SPCE on a homemade magnetic holding block, and the biorecognition event was monitored by amperometric measurement of the reduction current generated with the HQ/H₂O₂ system. Using this methodology, the SPCE acted only as the electrochemical transducer while all the immunoreactions occurred on the surface of the MBs.

Table 1
Optimization of the different experimental variables involved in the preparation and functioning of the electrochemical magnetoimmunosensor for β -LG.

Experimental variable	Tested ranges	Selected values
[HOOC-MBs] (μ L)	2–10	3
[anti β -LG] (μ g mL ⁻¹)	1–50	10
[HRP-anti β -LG] (μ g mL ⁻¹)	0.1–10	0.75
Incubation time with anti β -LG (min)	15–60	30
Incubation time with β -LG (min)	15–120	30
Incubation time with HRP-anti β -LG (min)	15–60	30
Number of incubation steps	1 or 2	2

Table 2

Determination of the β -LG concentration (in μ g mL⁻¹) in different milk samples using the developed amperometric magnetoimmunosensor and comparison with the results obtained by a commercial ELISA spectrophotometric kit.

Milk samples	Dilution factor	ELISA	Magnetoimmunosensor
UHT whole milk	50,000	$(9 \pm 1) \times 10^2$ RSD _{n=3} =4.7%	$(8.7 \pm 0.7) \times 10^2$ RSD _{n=3} =3.0%
UHT whole milk (Ca ²⁺ enriched)	50,000	$(9.3 \pm 0.8) \times 10^2$ RSD _{n=3} =3.6%	$(9.3 \pm 0.3) \times 10^2$ RSD _{n=3} =1.4%
Semi-skimmed pasteurized milk	100,000	$(2.0 \pm 0.1) \times 10^3$ RSD _{n=3} =1.9%	$(2.0 \pm 0.3) \times 10^3$ RSD _{n=3} =6.8%
Raw milk	250,000	$(3.70 \pm 0.05) \times 10^3$ RSD _{n=3} =0.6%	$(3.8 \pm 0.3) \times 10^3$ RSD _{n=3} =3.5%
Human milk	–	ND	ND

ND: non detectable.

3.1. Optimization of the working variables

The non-specific binding of the enzymatic tracer on the functionalized MBs surface was evaluated. This was done by comparison of the amperometric signals obtained for a 50 ng mL⁻¹ β -LG standard solution with SPCEs capturing MBs prepared with and without immobilized anti β -LG. The obtained results (not shown) demonstrated low non-specific adsorption of β -LG or HRP-anti β -LG on the anti β -LG-free MBs leading to amperometric responses 35 times lower than those produced using the anti β -LG-HOOC-MBs. These results confirmed the successful and effective blocking of the remaining EDC/sulfo-NHS-activated HOOC-MBs with ethanolamine with no need for further blocking steps or solutions to perform the electrochemical immunoassay. In fact, experiments performed using buffer supplemented with 1 M NaCl or common blocking agents such as BSA did not produce a further minimizing of the non-specific adsorption of β -LG or HRP-anti β -LG.

Subsequently, all the experimental variables involved in the analytical performance of the magnetoimmunosensors were optimized. The selection criterion for the different variables was the largest current ratio obtained at -0.20 V (vs. Ag pseudo-reference electrode) for 50 and 0 ng mL⁻¹ β -LG (signal-to-blank, *S/N*, ratio). This detection potential was optimized previously for the HQ/H₂O₂ system [22]. Table 1 summarizes the variables checked and the values selected for the preparation and functioning of the magnetoimmunosensor. The results obtained in the optimization of anti β -LG and HRP-anti β -LG loadings are displayed in Fig. 2a and b, respectively. As expected, the current measured at -0.20 V for 50 ng mL⁻¹ β -LG increased significantly with the anti β -LG loading (Fig. 2a). However the current obtained in the absence of β -LG also increased with the anti β -LG loading above 10 μ g mL⁻¹ probably due to some interaction between the capture and detector antibodies used. As a consequence the *S/N* ratio increased until 10 μ g mL⁻¹ anti β -LG and then levelled off, this value being chosen for further work. Regarding the HRP-anti β -LG concentration, the amperometric signals obtained increased with the concentration of detector antibody. However, the non-specific adsorptions of the HRP-labeled antibody (in the absence of β -LG) increased to a greater extent than the specific ones (in the presence of 50 ng mL⁻¹ β -LG) above 0.75 μ g mL⁻¹ of HRP-anti β -LG. Consequently the resulting *S/N* ratio diminished above this value (Fig. 2b). Considering the best discrimination obtained, 0.75 μ g mL⁻¹ was selected as the optimal detector antibody concentration for further studies.

3.2. Analytical characteristics

The reproducibility of the amperometric responses for 50 ng mL⁻¹ β -LG was evaluated with 10 different magnetoimmunosensors

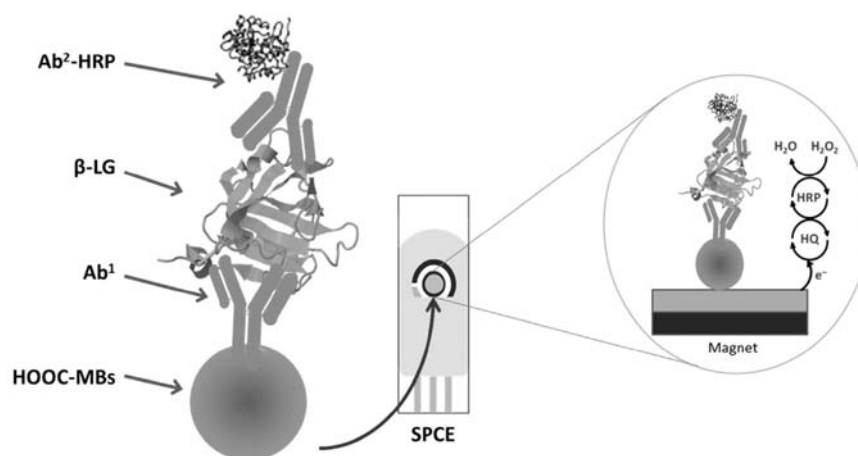


Fig. 1. Schematic display of the developed β -LG sandwich magnetoimmunosensor. The enzyme and electrode reactions involved in the amperometric detection of the mediated reduction of H_2O_2 with HQ at the SPCE are also shown.

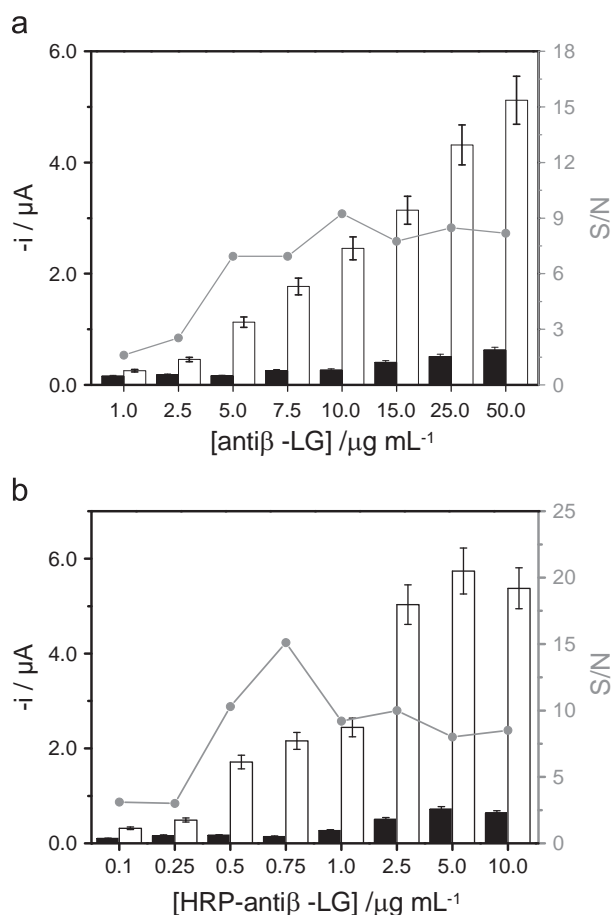


Fig. 2. Amperometric responses measured with the β -LG sandwich magnetoimmunosensor for 0 (black bars) and 50 ng mL^{-1} β -LG (white bars) as well as the corresponding S/N ratios, as a function of the anti β -LG (a) and HRP-anti β -LG (b) loadings. Error bars estimated as a triple of the standard deviation ($n=3$).

prepared on the same day and also with 6 magnetoimmunosensors prepared on different days. The relative standard deviation (RSD) values were 8.4% and 9.1%, respectively, suggesting an acceptable reliability in the whole procedure involving both the magnetoimmunosensors fabrication protocol (MBs modification and magnetic capture on the SPCE surface) and the amperometric transduction.

Under the optimized experimental conditions, a calibration plot for β -LG was constructed in PBST (Fig. 3). A range of linearity ($r=0.999$) between the measured current and the β -LG

concentration was found between 2.8 and 100 ng mL^{-1} , with a slope value of $(69.3 \pm 0.8) \text{ nA mL ng}^{-1}$ and an intercept of $(0.27 \pm 0.09) \mu\text{A}$. The values for the limits of detection (LOD) and quantification (LQ) were calculated according with the $3 s m^{-1}$ and $10 s m^{-1}$ criteria, respectively, where m is the slope of the linear calibration plot, and s was estimated as the standard deviation of the amperometric signals obtained without target β -LG. The LOD and LQ values were 0.8 and 2.8 ng mL^{-1} , respectively. These low values make it possible to remove strong matrix effects associated to real samples with an appropriate dilution without compromising the required sensitivity of the assay.

The employed methodology implied the immunoreactions to proceed only on the MBs and not on the electrode surface. Therefore, the storage stability of the anti β -LG-MBs conjugates, once the blocking step with ethanolamine was performed, was checked. Anti β -LG-MBs were stored at 4°C in Eppendorf[®] tubes containing $50 \mu\text{L}$ of filtered PBS. Each working day, a couple of the prepared conjugates were incubated into fresh solutions of HRP-anti β -LG supplemented with 0 or 50 ng mL^{-1} β -LG, according to the protocol described in the Experimental Section. No significant differences in the measured S/N ratio were apparent for 12 days, indicating an acceptable storage stability of the antibody-modified MBs conjugates which can be prepared and stored until the β -LG determination is required.

Although the LOD achieved is not as low as that reported by Eissa et al. (0.85 pg mL^{-1}) [6], it should be remarked that the sensitivity achieved is more than sufficient for the determination of β -LG in milk samples as it will be demonstrated below. Furthermore the inherent simplicity of the approach reported here can be claimed as an important practical advantage with respect to the immunosensor reported by Eissa et al., which required multiple reagents and complex and time consuming substrate and nanomaterial modification protocols, thus making it difficult to be considered as a suitable tool for the development of user-friendly devices for on-site quality control of dairy products.

3.3. Selectivity of the magnetoimmunosensor

The selectivity of the electrochemical magnetoimmunosensor toward β -LG was evaluated against various non-target proteins (BSA, alkaline phosphatase, catalase and LPO) at the concentration levels that can be commonly found in cow's milk as well as ascorbic acid. The tests were performed by comparing the current values measured with the magnetoimmunosensor for 0 and 50 ng mL^{-1} β -LG both in the absence and in the presence of these

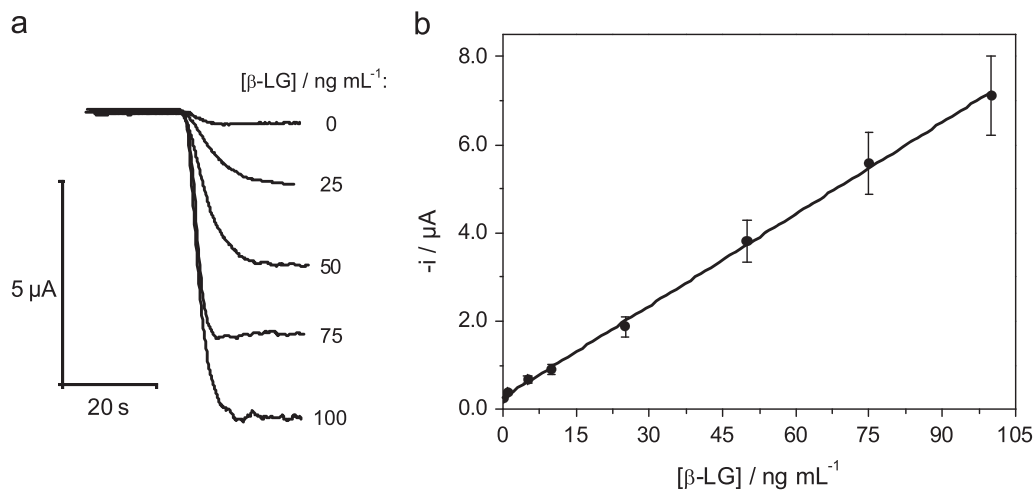


Fig. 3. Amperometric traces recorded with the β -LG sandwich magnetoimmunosensor for five different concentrations of β -LG (PBST buffer, pH 7.5) (a) and calibration plot constructed for β -LG. Error bars estimated as a triple of the standard deviation ($n=3$) (b).

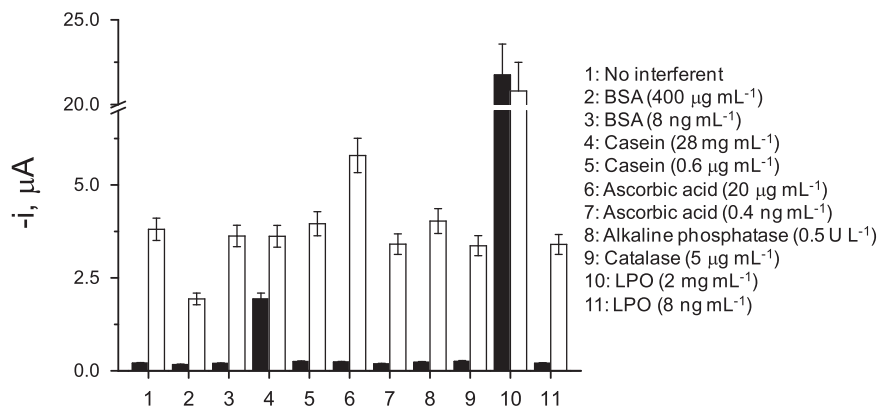


Fig. 4. Current values measured with the magnetoimmunosensor for 0 (black bars) and 50 ng mL^{-1} of β -LG (white bars) in the absence and in the presence of the indicated compounds at the specified concentrations. Error bars estimated as a triple of the standard deviation ($n=3$).

potential interfering compounds. Fig. 4 shows that no significant interference was found in the presence of alkaline phosphatase and catalase. However the presence of BSA (bar 2) produced a noticeable decrease in the measured current which was attributed to a partial blocking of the MBs active surface. Moreover, casein and LPO also interfered significantly in the β -LG determination at their usual high concentrations found in milk samples (bars 4 and 10, respectively). While the high response observed for casein in the absence of β -LG suggested an important cross-reactivity with the capture and detector antibodies, LPO was reported to be non-specifically adsorbed on the carboxylated MBs and catalyzes the H_2O_2 oxidation similarly to HRP [23,24]. Nevertheless, as it is shown below, a large sample dilution will be necessary to fit the target analyte concentration into the linear range of the calibration graph. Therefore, similar experiments were repeated upon performing the required dilutions applied to the milk samples ($\sim 50,000$ – $250,000$ times, see Table 2). As it can be seen (bars 3, 5, 7 and 11 in the figure), as expected, once the dilution was carried out no significant interference was apparent in all cases (Fig. 4).

3.4. Application to the analysis of milk samples

The developed magnetoimmunosensor was applied to the determination of β -LG in different milk samples. The possible existence of a matrix effect was tested by constructing a calibration plot from the samples adequately diluted with PBST and

spiked with growing amounts of a standard β -LG solution up to 100 ng mL^{-1} β -LG. All the slope values obtained for the respective calibration plots in the different samples assayed were statistically similar to that obtained for buffered standard β -LG solutions and, therefore, it could be concluded that no significant matrix effect was apparent once the large sample dilution factors required to perform the analysis, were made. Accordingly, β -LG quantification could be accomplished by simple interpolation of the measured current obtained for the samples diluted with PBST buffer solution into the calibration plot constructed with buffered β -LG standards (Fig. 3). The respective dilution factors for each analyzed milk sample, needed to fit the target analyte into the linear range of the calibration graph, are specified in Table 2.

The β -LG content found in the raw cow milk sample (Table 2) was within the ranges reported previously: 3–4 g L^{-1} [25], 2–4 g L^{-1} [26], 3.83 g L^{-1} [27] and 4.10 g L^{-1} [5]. Although the lack of data in the literature avoids to perform a thorough comparison, the lower content obtained in pasteurized and UHT milk samples could be attributed to the changes in the native structure of bovine β -LG caused by heat treatments. These structural changes become irreversible at temperatures beyond 80 $^\circ\text{C}$ [28] and may alter the target protein recognition by the antibodies. As the denaturation process progresses, the intra-chain disulphide bridges begin to break and the free sulphhydryl groups can now react with each other and aggregation of β -LG can take place [29–31]. As expected, no detectable β -LG content was observed for human milk which appears to be devoid of this protein (Fig. 5a).

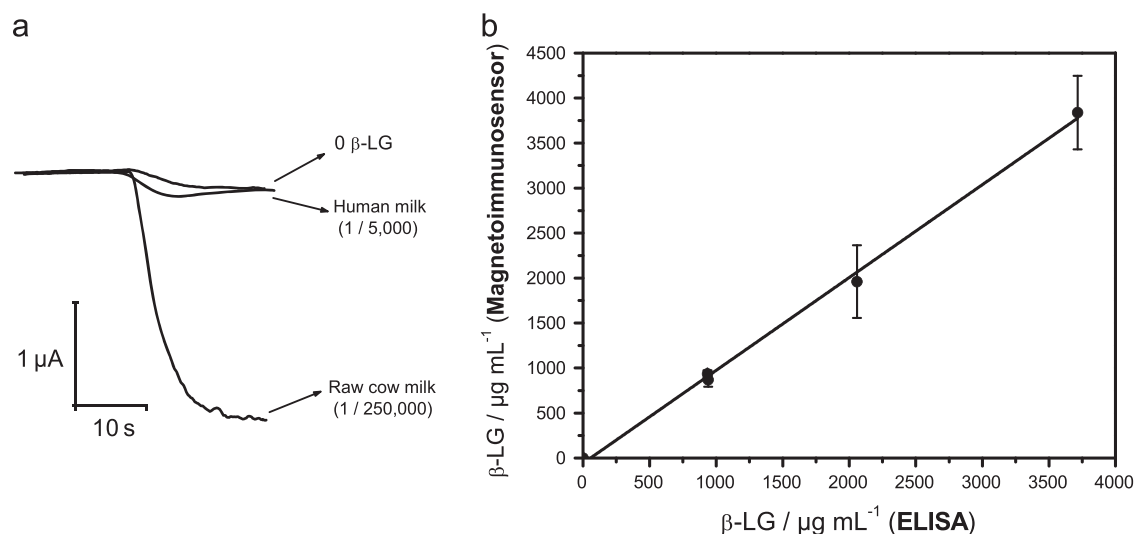


Fig. 5. Amperometric traces recorded with the magnetoimmunosensor in the absence of β -LG (PBST buffer, pH 7.5) and for 1/5000 PBST diluted human milk and 1/250,000 PBST diluted raw cow milk samples (a) and comparison of the results obtained with the magnetoimmunosensor and the ELISA (b). Error bars estimated as a triple of the standard deviation ($n=3$).

The results obtained in the analysis of all these samples with the magnetoimmunosensor were compared with those provided by a commercial ELISA kit using the same immunoreagents (see Table 2). It is important to remark that the same sample dilution step was needed when the protocol recommended for the ELISA was applied. By plotting the mean contents obtained with the magnetoimmunosensor versus those provided with the ELISA kit (Fig. 5b), the resulting linear least-squares regression graph ($r=0.999$) showed a slope value of (1.03 ± 0.03) and an intercept of (-58 ± 72) . As can be observed, the correlation found was highly satisfactory since the confidence intervals (at a significance level of $\alpha=0.05$) for the slope and intercept included the unit and the zero values, respectively, indicating that the methodology involving the use of the magnetoimmunosensor method exhibited no systematic errors and can be successfully used for the reliable determination of β -LG in milk samples.

A thorough comparison of the magnetoimmunosensor analytical performance against the commercial ELISA spectrophotometric kit allows the following conclusions to be attained: apart from the 10 times lower LOD (20 vs. 195 pg of β -LG) achieved (which is not a very relevant characteristic for milk analysis), the electrochemical immunosensor methodology is remarkably faster, the whole detection process lasting about 60 min (once the anti- β -LG-MBs are prepared), than the commercial kit (4 h). Moreover, the spectrophotometric method is difficult to be automated and hence hardly used in situ and not recommended to monitor routinely the milk quality. Conversely, the use of the magnetoimmunosensor simplified largely the whole analytical procedure, requiring smaller sample volumes, and can be easily automated and performed with portable and cost-effective instrumentation which makes it a very attractive and user-friendly tool to determine routinely the milk quality and to perform decentralized analysis. Furthermore, it is important to remark also that approximately 4000 assays can be made with the electrochemical magnetoimmunosensor using the reagents supplied by the ELISA kit, while only approximately 1000 assays are possible following the ELISA spectrophotometric methodology.

4. Conclusions

In this work, a disposable amperometric magnetoimmunosensor for quantification of β -LG in milk samples is reported. The

magnetoimmunosensor possesses an excellent analytical performance in terms of sensitivity, selectivity and reliability of the measurements even in raw milk with no need for complex or time-consuming pretreatment steps, after just a dilution with the appropriate buffer. The applicability of the developed magnetoimmunosensor was demonstrated by the analysis of different milk samples and the results were successfully validated against a commercial ELISA spectrophotometric kit. The magnetoimmunosensor performance compares advantageously with such ELISA kit in terms of rapidity, sensitivity, simplicity, and low cost and, therefore, it can be considered as a useful analytical tool to screen the presence of β -LG in the dairy industry. Moreover, the use of disposable mass-produced biosensors and the simplicity and easy automation and miniaturization of the required instrumentation constitute important advantages for an easy integration of the developed methodology into portable, reliable and user-friendly devices for milk quality control.

Acknowledgments

The financial support of the Spanish Ministerio de Economía y Competitividad Research Projects, CTQ2012-34238, and the AVANSENS Program from the Comunidad de Madrid (S2009PPQ-1642) are gratefully acknowledged. R. M. T.-R. and F. C. acknowledge FPI and FPU fellowships, respectively, from the Spanish Ministry of Education.

References

- [1] S. Eissa, L. L'Hocine, M. Sijaj, M. Zourob, *Analyst* 138 (2013) 4378–4384.
- [2] A. Høst, S. Halken, *Allergy* 45 (1990) 587–596.
- [3] A. Høst, *Asthma Immunol.* 89 (2002) 33–37.
- [4] L.A. Lee, A.W. Burkes, *Annu. Rev. Nutr.* 26 (2006) 539–565.
- [5] L. Ruprichová, M. Králová, I. Borkovcová, L. Vorlová, I. Bedáňová, *Acta Vet. Brno* 83 (2014) 067–072. <http://dx.doi.org/10.2754/avb201483010067>.
- [6] S. Eissa, C. Tlili, L. L'Hocine, M. Zourob, *Biosens. Bioelectron.* 38 (2012) 308–313.
- [7] Y. Ren, Z. Han, X. Chu, J. Zhang, Z. Cai, Y. Wu, *Anal. Chim. Acta* 667 (2010) 96–102.
- [8] C. Pelaez-Lorenzo, J.C. Diez-Masa, I. Vasallo, M. de Frutos, *Anal. Chim. Acta* 649 (2009) 202–210.
- [9] A. Puerta, J.C. Diez-Masa, M. de Frutos, *Anal. Chim. Acta* 537 (2005) 69–80.
- [10] J.A.P.P. van Dijk, J.A.M. Smit, *J. Chromatogr. A* 867 (2000) 105–112.
- [11] V. Hohensinner, I. Maier, F. Pittner, *J. Biotechnol.* 130 (2007) 385–388.

- [12] J.M. Billakanti, C.J. Fee, F.R. Lane, A.S. Kash, R. Fredericks, *Int. Dairy J.* 20 (2010) 96–105.
- [13] R. de Luis, M. Lavilla, L. Sánchez, M. Calvo, M.D. Pérez, *Food Control* 20 (2009) 643–647.
- [14] J.M. Nam, C.S. Thaxton, C.A. Mirkin, *Science* 301 (2003) 1884–1886.
- [15] A. Bange, H.B. Halsall, W.R. Heineman, *Biosens. Bioelectron.* 20 (2005) 2488–2503.
- [16] N.L. Rosi, C.A. Mirkin, *Chem. Rev.* 105 (2005) 1547–1562.
- [17] H. Zhang, X. Cheng, M. Richter, M.I. Greene, *Nat. Med.* 12 (2006) 473–477.
- [18] I. Willner, R. Baron, B. Willner, *Biosens. Bioelectron.* 22 (2007) 1841–1852.
- [19] F. Conzuelo, M. Gamella, S. Campuzano, A.J. Reviejo, J.M. Pingarrón, *Anal. Chim. Acta* 737 (2012) 29–36.
- [20] B. Esteban-Fernández de Ávila, V. Escamilla-Gómez, S. Campuzano, M. Pedrero, JM Pingarrón, *Electroanalysis* 25 (2012) 51–58.
- [21] E. Zacco, M.I. Pividori, S. Alegret, R. Galve, M.P. Marco, *Anal. Chem.* 78 (2006) 1780–1788.
- [22] M. Gamella, S. Campuzano, F. Conzuelo, A.J. Reviejo, J.M. Pingarrón, *Electroanalysis* 24 (2012) 2235–2243.
- [23] P. Resmini, C. Tripiciano, M. Rampilli, R. Lodi, *Riv. Soc. Ital. Sci. Aliment.* 14 (1985) 187–196.
- [24] F. Conzuelo, V. Ruiz-Valdepeñas Montiel, S. Campuzano, M. Gamella, R.M. Torrente-Rodríguez, A.J. Reviejo, J.M. Pingarrón, *Anal. Chim. Acta* 820 (2014) 32–38.
- [25] L. Monaci, V. Tregoat, A.J. van Hengel, E. Anklam, *Eur. Food Res. Technol.* 223 (2006) 149–179.
- [26] H.M. Farrell Jr., R. Jiménez-Flores, G.T. Bleck, E.M. Brown, J.E. Butler, L. K. Creamer, C.L. Hicks, C.M. Hollar, K.F. Ng-Kwai-Hang, H.E. Swaisgood, *J. Dairy Sci.* 87 (2004) 1641–1674.
- [27] Z. Sztankóová, *Náš chov* 4 (2006) 78–79.
- [28] H.L. Casal, U. Köhler, H.H. Mantsch, *Biochim. Biophys. Acta* 957 (1998) 11–20.
- [29] S.P. Roefs, K.G. de Kruif, *Eur. J. Biochem.* 226 (1994) 883–889.
- [30] L.K. Creamer, A. Bienvenue, H. Nilsson, M. Paulsson, M. van Wanroij, E.K. Lowe, S. G. Anema, M.J. Boland, R. Jimenez-Flores, *J. Agric. Food Chem.* 52 (2004) 7660–7668.
- [31] J. Rytönen, Effect of Heat Denaturation of Bovine Milk Betalactoglobulin on its Epithelial Transport and Allergenicity. *Acta Universitatis Ouluensis D Medica* 883. ISSN 1796-2234, 2006.



Determination of α - and β -boldenone sulfate, glucuronide and free forms, and androstadienedione in bovine urine using immunoaffinity columns clean-up and liquid chromatography tandem mass spectrometry analysis



Luca Chiesa^a, Radmila Pavlovic^a, Guglielmo Dusi^b, Elisa Pasquale^a, Alessio Casati^c, Sara Panseri^a, Francesco Arioli^{c,*}

^a Department of Veterinary Science and Public Health, University of Milan, Milan, Italy

^b Istituto Zooprofilattico Sperimentale della Lombardia ed Emilia Romagna "B. Ubertini", Brescia, Italy

^c Department of Health, Animal Science and Food Safety, University of Milan, Milan, Italy

ARTICLE INFO

Article history:

Received 8 May 2014

Received in revised form

9 July 2014

Accepted 11 July 2014

Available online 12 August 2014

Keywords:

Boldenone sulphate

Boldenone glucuronide

Boldenone

Androstadienedione

Bovine urine

Food safety

ABSTRACT

The debate about the origins of boldenone in bovine urine is ongoing for two decades in Europe. Despite the fact that its use as a growth promoter has been banned in the European Union (EU) since 1981, its detection in bovine urine, in the form of α -boldenone conjugate, is considered fully compliant up to 2 ng mL^{-1} . The conjugated form of β -boldenone must be absent. In recent years, the literature about boldenone has focused on the identification of biomarkers that can indicate an illicit treatment. β -boldenone sulfate is a candidate molecule, even if the only studies currently available have taken place in small populations. In this study, a method for the determination of sulfate and glucuronate conjugates of β -boldenone was developed and validated according to the European Commission Decision 2002/657/EC and applied to α -boldenone sulfate and glucuronide, α - and β -boldenone free forms and androstadienedione (ADD), too. The clean-up with immunoaffinity columns enabled the direct determination of the conjugates and free forms and allowed specific and sensitive analyses of urine samples randomly selected to verify this method. The decision limits ($\text{CC}\alpha$) ranged between 0.07 and 0.08 ng mL^{-1} , the detection capabilities ($\text{CC}\beta$) between 0.08 and 0.1 ng mL^{-1} . Recovery was higher than 92% for all the analytes. Intra-day repeatability was between 5.8% and 17.2%, and inter-day repeatability was between 6.0% and 21.8% for the studied free and conjugated forms. This method has been developed as a powerful tool with the aim to study the origin of boldenone in a trial on a significant number of animals.

© 2014 Elsevier B.V. All rights reserved.

1. Introduction

The use of substances that have hormonal activity for growth promotion in farm animals has been prohibited in the European Union (EU) since 1981 [1]. The bans on the use of such substances, on the trade of treated animals and their meat within the EU, and also on the import from third countries was confirmed in 1988 [2,3]. A typical substance with hormonal action is 17β -boldenone (1-dehydrotestosterone or androsta-1,4-dien-17 β -ol-3-one) (β -bold), an anabolic steroid that differs from testosterone only by the double bond between carbons 1 and 2 of the steroid A ring as

shown in Fig. 1. Arts et al. [4] reported the natural occurrence in calf urine of 17α -boldenone (α -bold) at concentrations ranging from <0.1 to 2.7 ng mL^{-1} . Since then, a number of studies and regulations followed, aiming to explain the presence of boldenone (bold) in bovine urine, to indicate a biomarker metabolite for illicit treatment, and to establish levels of the hormonal substance that could exclude administration to the animal [5,6]. In particular, in September 2003, the thesis of the natural production of this steroid was proposed by the experts within the EU, who stated that scientific knowledge was sufficient to conclude that the presence of α -bold in urine and faeces of bovine animals has a natural origin. They set the 'natural threshold' of 2 ng mL^{-1} in the urine of veal calves below which α -bold conjugate (boldenone conjugates are water soluble forms of boldenone bound to e.g. glucuronic acid formed by metabolism in the animals) come from sources other than illegal treatment. The presence of β -bold

* Correspondence to: Department of Health, Animal Science and Food Safety, University of Milan, Via Celoria, 10 - 20133 Milan, Italy. Tel.: +390250317877; fax: +390250317890.

E-mail address: francesco.arioli@unimi.it (F. Arioli).

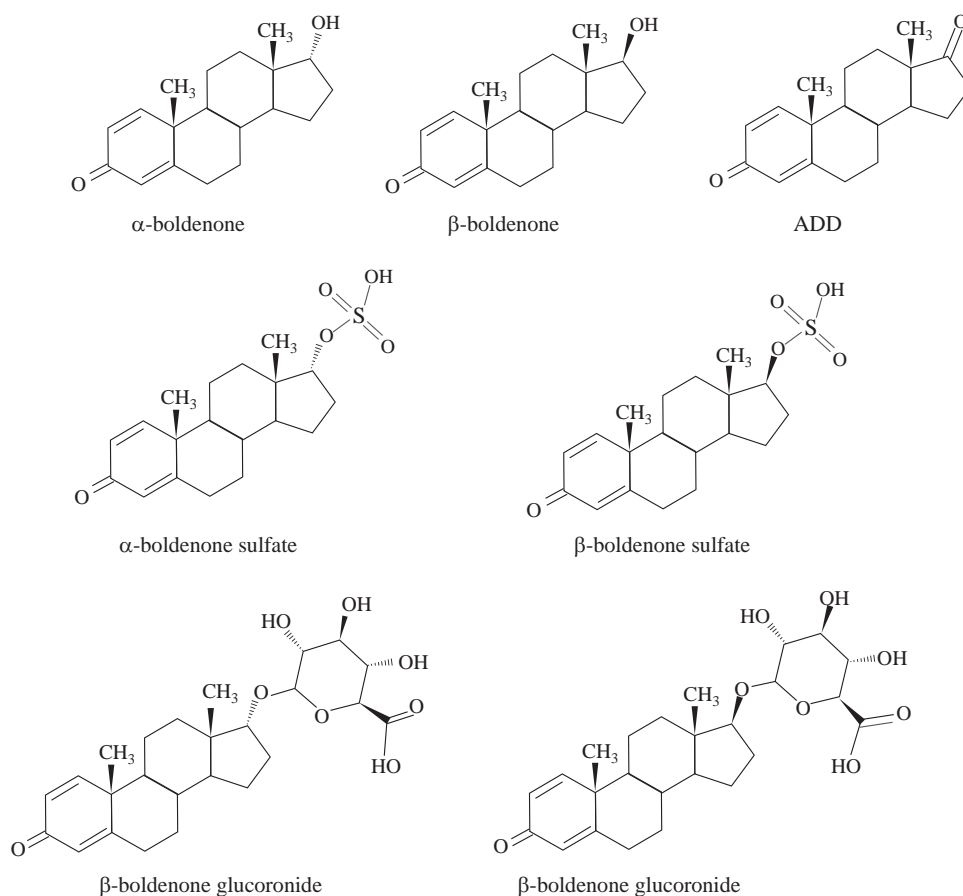


Fig. 1. Chemical structures of the seven analytes.

conjugates at any concentration in the urine of veal calves was indicated as the result of an illegal treatment [7]. The presence of conjugates of α - and β -bold, without specifying the nature of the ionized group (sulphate, glucuronide) is not the only option considered by the scientific community. Biddle [8] performed a study on beef cattle treated with three preparations of bold: intra-muscular bolus administration of β -bold, followed by oral administration of the supplement androstadienedione (1,4-androstadiene-3,17-dione) (ADD), and finally intra-muscular administration of β -bold undecylenate. He concluded that highly sensitive methods would be required to detect the abuse of bold using β -bold glucuronic acid conjugate as a marker; they could not confirm the EU recommended level of 2 ng mL^{-1} for α -bold glucuronic acid conjugate due to the lack of the reference standard. Finally, two markers, present in the glucuronate fraction regardless of route of administration, were specially indicated in this study: 6β -hydroxy- 17α -bold and $5z$ -androst-1-ene- $3z$ -ol-17-one (the letter 'z' indicates position α or β , due to the lack of the reference standard). Another study [9] investigated the metabolites of bold in treated cattle after intramuscular and oral treatment with bold, bold esters and ADD. The authors showed that the majority of metabolites, analysed by GC-MS, were glucuronide conjugates and that β -bold sulfate was present only in urine from treated animals (this last result obtained by LC-MS/MS). They therefore suggested to use β -bold sulfate as an indicator of bold administration, after larger scale studies. However, the study was conducted in a predominantly qualitative way, the analytical limits in the LC-MS/MS were not reported; therefore, the question: "Who is to say that as analytical limits decrease, (particular steroids) will not be discovered as endogenous at a lower concentration?" [6] has a fundamental importance. Destrez et al. [10] performed a study on treated male calves with oral administration

of ADD or with intra-muscular injection of bold undecylenate. The analytical limits for β -bold sulfate were set by both LC-MS/MS (negative ESI, SRM acquisition, triple quadrupole) and LC-HRMS (negative ESI, R 30,000, OrbitrapTM): the decision limits ($CC\alpha$) were 0.2 and 0.1 ng mL^{-1} and detection capability ($CC\beta$) 0.4 and 0.2 ng mL^{-1} , respectively. The authors concluded that once again β -bold sulfate demonstrated to be the candidate marker of a treatment. In an effort to develop a study on an extended population, deemed necessary also by the authors cited above, we developed an LC-MS/MS method with triple quadrupole technology that had the lowest analytical limits possible for the detection of β -bold sulfate in bovine urine. The method was also developed for α -bold sulfate, α - and β -bold glucuronide, ADD, α -bold and β -bold (Fig. 1). The validation was made according the Decision of Commission 2002/657/EC [11].

2. Materials and methods

2.1. Materials

All solvents were of HPLC or HPLC-MS grade quality and supplied by Fluka (Sigma-Aldrich, St. Louis, MO, USA). Formic acid (98–100%) was from Riedel-de Haën (Sigma-Aldrich, St. Louis, MO, USA). The chemicals for the preparation of artificial urine were from Sigma-Aldrich (St. Louis, MO, USA). β -bold sulfate (triethylamine salt), β -bold glucuronide, and α -bold were from LGC Standards (Teddington, UK), and ADD and β -bold were from Fluka (Sigma-Aldrich, St. Louis, MO, USA). The sulfate and glucuronide forms of α -bold, provided by research partners, were prepared by a two-step synthesis: the epimerization of β -bold (Steroid SpA, Cologno Monzese, Milan, Italy) using a modified Mitsunobu

protocol, according to Dodge and Lugar [12]; and sulphation, according to Sanaullah and Bowers [13] or glucuronation, according to Casati et al. [14], of α -bold. Internal standards were β -bold sulfate-d3 for sulfate forms, β -Bold-d3 for free forms (LGC Standards, Teddington, UK) and epitestosterone (EpiT) glucuronide-d3 for α - and β -bold glucuronide (National Measurement Institute, Pymble, NSW, Australia). Stock solutions of each analyte and of the internal standards were prepared in methanol at a concentration of 1 mg L^{-1} , and stored at -40°C . Working solutions were prepared daily by diluting the stock solutions. Immunoaffinity columns (IAC) were from Randox. Concentrated wash and storage buffers were supplied with the columns and diluted following the manufacturer's instructions before use (DM 2185, Randox Laboratories, Antrim, UK).

2.2. Artificial urine preparation

We were unable to find bovine urine samples in which all analytes were totally absent. Artificial urine was prepared in our laboratory for the validation studies, as described by Fabregat et al. [15]. Briefly, 0.1 g of lactic acid, 0.4 g of citric acid, 2.1 g of sodium bicarbonate, 10 g of urea, 0.07 g of uric acid, 0.8 g of creatinine, 0.37 g of calcium chloride $\cdot 2\text{H}_2\text{O}$, 5.2 g of sodium chloride, 0.0012 g of iron II sulfate $\cdot 7\text{H}_2\text{O}$, 0.49 g of magnesium sulfate $\cdot 7\text{H}_2\text{O}$, 3.2 g of sodium sulfate $\cdot 10\text{H}_2\text{O}$, 0.95 g of potassium dihydrogen phosphate, 1.2 g of dipotassium hydrogen phosphate, and 1.3 g of ammonium chloride were dissolved in 1 L of ultrapure water.

2.3. Urine sampling and storage

Urine samples were collected from untreated, under veterinary control, Charolaise or Limousine young bulls. Urine (about 100 mL) was collected into long-handled sterile containers. A visual inspection was made to check the urine clarity, in order to exclude the presence of raw materials or faecal contamination [16]. Only clear urine was put in 150-mL containers, cooled to 4°C and taken to the laboratory for storage at -40°C until extraction and analysis.

2.4. Sample preparation, extraction and purification

Five millilitres of centrifuged urine was added of internal standard to a final concentration of 2 ng mL^{-1} . The IAC was washed with 5 mL ethanol:water (70:30, v/v) and equilibrated with $3 \times 5 \text{ mL}$ wash buffer (flow rate $\leq 3 \text{ mL min}^{-1}$, i.e. about one drop per second). After adjusting the pH to 8 with 0.1 N NaOH, the urine was loaded (gravity flow). Wash buffer ($2 \times 5 \text{ mL}$) and water ($1 \times 5 \text{ mL}$) were used to wash the column. The elution of the bound analytes was then made by the application of 4 mL ethanol:water (70:30, v/v) (flow rates $\leq 3 \text{ mL min}^{-1}$) collected in a 15-mL polypropylene tube. The eluate was evaporated in a rotary evaporator. The dried extract was reconstituted in $500 \mu\text{L}$ of methanol:water (50:50; v/v) and transferred to an autosampler vial. The injection volume was $10 \mu\text{L}$. The IAC could be again used,

Table 1

Gradient timetable. A: 0.1% aqueous formic acid; B: methanol.

Time (min)	Eluent A%	Eluent B%
0	40	60
1	40	60
12	5	95
13	5	95
15	40	60
22	40	60

beginning from the equilibration described above, after a wash step with $2 \times 5 \text{ mL}$ ethanol:water (70:30, v/v).

2.5. LC-MS/MS analysis

LC analysis was carried out with an HPLC system (Thermo Fisher Scientific, San Jose, CA, USA), consisting of a Surveyor MS quaternary pump with a degasser, a Surveyor AS autosampler with a column oven, and a Rheodyne valve with $20\text{-}\mu\text{L}$ sample loop. Chromatographic separation was achieved by using a Synergi Hydro RP reverse-phase HPLC column ($150 \times 2.0 \text{ mm}$, i.d. $4 \mu\text{m}$), with a C18 guard column ($4 \times 3.0 \text{ mm}$) (Phenomenex, Torrance, CA, USA), kept at 30°C . The flow rate was $200 \mu\text{L min}^{-1}$, and the mobile phase consisted of 0.1% aqueous formic acid (solvent A) and methanol (solvent B). The gradient program is reported in Table 1. The overall run time was 22 min. The mass spectrometer was a triple quadrupole TSQ Quantum (Thermo Fisher Scientific, San Jose, CA, USA) equipped with an electrospray interface (ESI) set both in the positive (ESI+) and in the negative (ESI-) ionization mode. Acquisition parameters were optimized in the ion spray mode by direct continuous pump-syringe infusion of standard solutions of the analytes at the concentration of $1 \mu\text{g mL}^{-1}$, a flow rate of $20 \mu\text{L min}^{-1}$ and flow rate of the MS pump of $100 \mu\text{L min}^{-1}$ in the ion source of the mass spectrometer. Conditions were as follows: capillary voltage 3.5 kV; ion transfer capillary temperature 340°C ; nitrogen as sheath and auxiliary gas at 30 and 10 arbitrary units, respectively; argon as collision gas at 1.5 mTorr; and peak resolution 0.70 Da FWHM. The scan time for each monitored transition was 0.1 s, and the scan width was 0.5 amu. Four diagnostic product ions were chosen for each analyte and internal standard. The acquisition was made in the multiple reaction monitoring (MRM). The selected diagnostic ions, one of which chosen for the quantification, and collision energies are reported in Table 2. In Fig. 2, the LC-MS/MS reconstructed chromatogram of an artificial urine sample spiked with 0.1 ng mL^{-1} of each analyte is shown together with the ion spectra; on the right the internal standards (2 ng mL^{-1}) are also reported. Acquisition data were recorded and elaborated using Xcalibur™ software from Thermo.

2.6. Method validation

The developed method was validated according to Commission Decision 2002/657/EC [11]. Parameters taken into account were as follows: instrumental linearity, precision, recovery, decision limit ($\text{CC}\alpha$), and detection capability ($\text{CC}\beta$). The instrumental linearity was evaluated by drawing six points calibration curves in solvent, containing analytes concentrations corresponding to 0.25–0.5–1.0–2.0–3.0–4.0 ng mL^{-1} and a fixed amount of ISTDs corresponding to 20 ng mL^{-1} . The validation study was done using artificial

Table 2

MS/MS condition for the MRM acquisitions of analytes and internal standards. Ions for quantification are in bold. CE (eV): collision energy.

Analyte	Precursor ion $[\text{M}-\text{H}]^-$	Product ions _{CE} (m/z)	ESI
α -Bold sulfate	365	97 ₄₇ , 177 ₃₉ , 349 ₄₀ , 350₃₀	(-)
β -Bold sulfate	365	97 ₄₇ , 177 ₃₉ , 349 ₄₀ , 350₃₀	(-)
β -Bold sulfate-d3	368	98 ₅₄ , 180 ₄₁ , 352 ₄₀ , 353₃₁	(-)
α -Bold glucuronide	463	121 ₃₂ , 135 ₂₁ , 269₁₃ , 287 ₁₂	(+)
β -Bold glucuronide	463	121 ₃₂ , 135 ₂₁ , 269₁₃ , 287 ₁₂	(+)
EpiT glucuronide-d3	468	109 ₃₇ , 256 ₂₃ , 274 ₁₆ , 292₁₁	(+)
ADD	285	121₂₂ , 147 ₁₃ , 151 ₁₄ , 267 ₁₁	(+)
α -Bold	287	121₂₃ , 135 ₁₄ , 173 ₁₆ , 269 ₁₀	(+)
β -Bold	287	121₂₃ , 135 ₁₄ , 173 ₁₆ , 269 ₁₀	(+)
β -Bold-d3	290	91 ₄₈ , 121₂₇ , 138 ₁₄ , 272 ₁₀	(+)

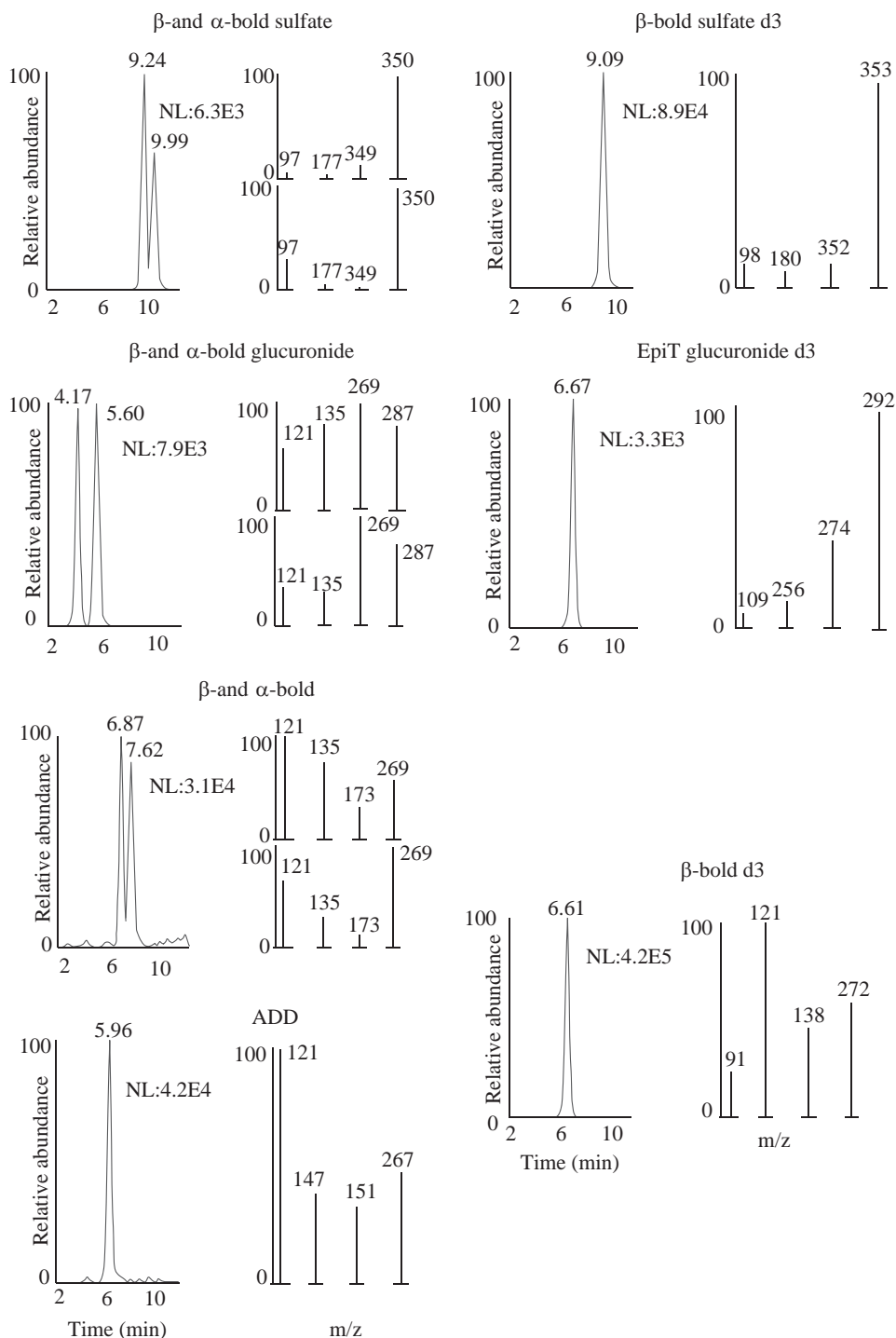


Fig. 2. Reconstructed LC-MS/MS chromatograms of a spiked artificial urine sample with the respective ion spectra. Left side: standard analytes (concentration=0.1 ng mL⁻¹). Right side: relative internal standards (concentration=2 ng mL⁻¹).

urine as explained in 2.2, so the evaluation of specificity could not be made. Matrix calibration curves were obtained by spiking urine samples with the seven analytes, resulting in three analytical series, each series with three concentration levels (0.05–0.1–0.2 ng mL⁻¹) and six samples per concentration level (6 samples × 3 concentration levels × 3 series=54 analyses). Method recovery and precision were evaluated using these matrix curves results; recovery was expressed in terms of percentage of measured concentration-to-fortified concentration ratio and precision as the coefficient of variability (CV). The same results were used to calculate the decision limit (CC_α) and detection capability (CC_β)

according to the matrix calibration curve procedure described in the Commission Decision 2002/657/EC as clarified in the document SANCO/2004/2726-revision 4 [17].

2.7. Evaluation of artificial urine suitability

Three curves were prepared to evaluate the suitability of artificial urine. One curve with low doses (0.05; 0.1; 0.2 ng mL⁻¹) of the seven analytes in artificial urine, two curves with high doses (0.5; 1.0; 2.5 ng mL⁻¹) in artificial and bovine urine, respectively.

The slopes and the Y-intercepts for each analyte of each curve were then compared with the unpaired *t*-test.

3. Results and discussion

The presence in bovine urine of α -bold and, primarily, β -bold in their free forms or as II phase metabolites, is a matter of debate in Europe. The need to study the conjugated metabolites of boldenone in urine as well as the development of a method that can distinguish the different conjugated forms, appears mandatory to distinguish between illicit treatment and the natural origin of boldenone in bovine urine. The developed method uses a simple extraction step with IAC and allows for the determination of ADD, sulfate, glucuronate, and free forms of α - and β -boldenone in only one chromatographic run at concentration levels suitable for research purposes.

3.1. Sample preparation, extraction and purification

The need for an analysis that directly determined the free sulfate and glucuronate forms of bold led us initially to direct our efforts on clean-up methods like liquid/liquid extraction. Unfortunately, some results were achieved only for bold sulfate but not for bold glucuronide, while a different extraction altogether had to be made to detect the free forms. Direct determination methods of bold sulfate with good analytical limits are present in literature, as already stated [10]; a unique method that could together determine sulfate, glucuronate and free α - and β -bold has not been developed even if Buiarelli et al. [18], in 2005 proposed a method for β -bold free and conjugate forms, free α -bold and 5β -androst-1-en-17 β -ol-3-one in bovine and human urine. The use of the IAC was, at least initially, due to a casual occurrence. Briefly, the IACs used in this study are in fact intended for the clean-up of urine and serum in order to detect the corticosteroids dexamethasone, betamethasone and flumethasone. In the course of the development of a method for the determination of these corticosteroids with bovine urine through IAC extraction and LC-MS/MS analysis with the full mass monitoring, we noticed the presence of interfering compounds. We hypothesized, because of the *m/z* values and due to the similarities in the chemical structures of anabolic steroids to corticosteroids, the compounds were the conjugate forms of boldenone. Subsequent trials performed by IAC clean-up of urine fortified with the standards confirmed previous suppositions and gave surprising results in terms of analytical limits. Therefore, we decided to refine the method as described in 2.4 and 2.5 and to validate it. IAC extraction is considered expensive, so we also considered the possibility that not all ten runs recommended by the manufacturer could be made, accounting for the different use from that indicated. We observed a constant response for the first eight runs, a tolerable decline in accuracy in the next two runs (that we roughly evaluated lower than 9%) and, subsequently, a variable and unpredictable fall in the column performance. Using a column for 10 cycles before discarding it is therefore advisable and keeps the cost per sample comparable to other techniques.

3.2. LC-MS/MS

Data acquisitions were performed on the pure standard compounds in full scan (*m/z* range 50–500) using the first quadrupole to choose the precursor ion. In MS/MS experiments *m/z* product ion scans were recorded between *m/z* 50 and 500 and the four product ions with the higher signal-to-noise ratio (*s/n*) for each analyte or internal standard were then chosen for analysis, performed in the MRM mode, because of its high sensitivity and

specificity. The precursor ions, the four diagnostic product ions and the collision energies are reported in Table 2. The four ions fulfilled the requirements provided by the Decision of Commission 2002/657/EC [11] for the group A substances as defined in Annex I of Directive 96/23/EC [19]. A minimum number of 3 ions (the precursor and 2 product ions) and of 4 identification points (IPs) are in fact required: as each one of the four product ions is equal to 1.5 IPs and the precursor is equal to 1.0 IP, the abundant value of 7 IPs was reached. The relative ion intensities also always complied with the maximum tolerances permitted. The ion for quantification was the most abundant of the four diagnostic ions.

3.3. Method validation

The instrumental linearity for the seven analytes was evaluated with calibration curves in solvent in a concentration range from 0.25 to 4.0 ng mL⁻¹ using standard solutions in methanol:water (50:50; v/v), containing a fixed amount of ISTDs (20 ng mL⁻¹ each). Regression coefficients of curves indicated a good fit for all analytes (α -bold sulfate, $r^2=0.982$; β -bold sulfate, $r^2=0.991$; α -bold glucuronide, $r^2=0.978$; β -bold glucuronide, $r^2=0.988$; ADD, $r^2=0.988$; α -bold, $r^2=0.995$; β -bold, $r^2=0.991$).

The matrix calibration curves built for each analyte were linear in the range from 0.05–0.2 ng mL⁻¹. The regression lines, obtained using the least square method, had good fit for all analytes (α -bold sulfate, $r^2=0.977$; β -bold sulfate, $r^2=0.995$; α -bold glucuronide, $r^2=0.985$; β -bold glucuronide, $r^2=0.990$; ADD, $r^2=0.995$; α -bold, $r^2=0.982$; β -bold, $r^2=0.994$).

Specificity and matrix effect were not evaluated; the presence of at least one of the studied analytes in any bovine urine sample required the use of artificial urine, as already specified in 2.2. Some bovine urine samples randomly selected were however checked, and the presence of one peak at the analyte retention times was shown not to be due to an interfering substance, i.e. the peak had all the characteristics of the analyte as provided by the Decision of Commission 2002/657/EC [11]. Precision, calculated by applying the one-way analysis of variance (ANOVA), was expressed as CVs, in terms of intra-day and inter-day repeatability. The results reported show that the intra- and inter-day repeatabilities for all the analytes were below 17.2% and 21.8%, respectively. These CVs

Table 3
Method trueness and precision.

Analyte	Concentration level (ng mL ⁻¹)	Recovery % (n = 18)	Repeatability	
			Intra-day (CV; n = 6)	Inter-day (CV; n = 18)
α -Bold sulfate	0.05	96	16.2	21.1
	0.1	103	17.2	20.4
	0.2	99	11.0	11.1
β -Bold sulfate	0.05	97	10.1	15.4
	0.1	102	9.8	13.2
	0.2	100	12.8	12.9
α -Bold glucuronide	0.05	106	15.2	21.8
	0.1	96	10.1	15.4
	0.2	101	11.0	11.2
β -Bold glucuronide	0.05	109	14.7	17.0
	0.1	93	10.5	12.3
	0.2	101	10.2	10.2
ADD	0.05	95	7.5	14.4
	0.1	104	6.6	11.3
	0.2	99	7.9	8.1
α -Bold	0.05	110	16.9	19.4
	0.1	92	9.8	12.1
	0.2	101	11.2	11.2
β -Bold	0.05	100	11.1	15.8
	0.1	100	8.1	11.7
	0.2	100	5.8	6.0

were lower than 22% as proposed by Thompson [20]. The high values were probably due to the low concentrations used for the method validation: The levels chosen were addressed to a subsequent research aimed to understand if conjugated bold in bovine urine have a natural or endogenous origin of and to eventually set a natural threshold. The mean recoveries ranged between 96% and 103% for α -bold sulfate, 97% and 102% for β -bold sulfate, 96% and 106% for α -bold glucuronide, 93% and 109% for β -bold glucuronide, 95% and 104% for ADD, 92% and 110% for α -bold, and 99% and 100% for β -bold. The data for all the analytes are reported in Table 3. $CC\alpha$ was calculated as described in the document SANCO/2004/2726 revision 4 [17] using parallel extrapolation to the x -axis at the lowest experimental concentration. $CC\alpha$ and $CC\beta$ values are reported in Table 4, which shows the low analytical limits obtained.

3.4. Evaluation of artificial urine suitability

After the first preliminary tests, we realized that we could not find bovine urine samples where all the studied analytes were totally absent. At least one peak for each 'blank' bovine urine at the retention times of the analytes was found. The estimated concentrations were moreover not much lower than 0.05 ng mL^{-1} , the lowest concentration considered in the validation study. In order to avoid errors in the parameter calculation, we could not

therefore simply subtract the peak areas to the corresponding ones that resulted in the spiked sample because of the similar values. The use of artificial urine was thus mandatory, even if an evaluation of its suitability was required. In a first step, we built two curves with high doses (0.5 ; 1.0 ; 2.5 ng mL^{-1}) in artificial and bovine urine, respectively. The choice of this concentration range was made taking into account the estimated concentrations of the peaks found in bovine "blank" urine. We therefore considered it satisfactory to use a range the minimum concentration of analyte which was at least 10 times higher than the estimated concentrations in the "blank" bovine urine. The correlation coefficients of all the curves so prepared were higher than 0.99. The slopes and Y intercepts of each analyte in the two different matrices, compared with an unpaired t -test, did not result in significant differences. However, we could not yet consider the two matrices similar, as we were using doses higher than those used for validation. As a second step, we compared the slopes and Y intercepts of the high dose and low dose curves of each analyte in artificial urine. In this case, too, no difference was found. Therefore, we verified that high and low doses of each analyte, if combined, belonged to the same curve and subsequently that artificial urine was suitable for method validation. Slopes and Y intercepts of this "wide range" curves were compared with the slopes and Y intercepts of the high and low concentration curves. No difference was found for each analyte. Accordingly, these curves were used as calibration curves for quantification of the samples described in 3.4.

Table 4
 $CC\alpha$ and $CC\beta$ validation data.

Analyte	$CC\alpha$ (ng mL^{-1})	$CC\beta$ (ng mL^{-1})
α -Bold sulfate	0.08	0.10
β -Bold sulfate	0.07	0.09
α -Bold glucuronide	0.08	0.1
β -Bold glucuronide	0.07	0.09
ADD	0.07	0.08
α -Bold	0.07	0.09
β -Bold	0.07	0.08

3.5. Application of the method

In order to verify the developed method in real conditions, we analysed four urine samples, randomly collected from the young bulls under veterinary control, for the detection of the seven studied molecules. The reconstructed chromatograms and ion spectra relative to one sample are shown in Fig. 3. The concentration values found in the four sample ranged from 0.15 to 0.63 ng mL^{-1} for α -bol sulfate (3 positives); from 0.09 to 0.26 ng

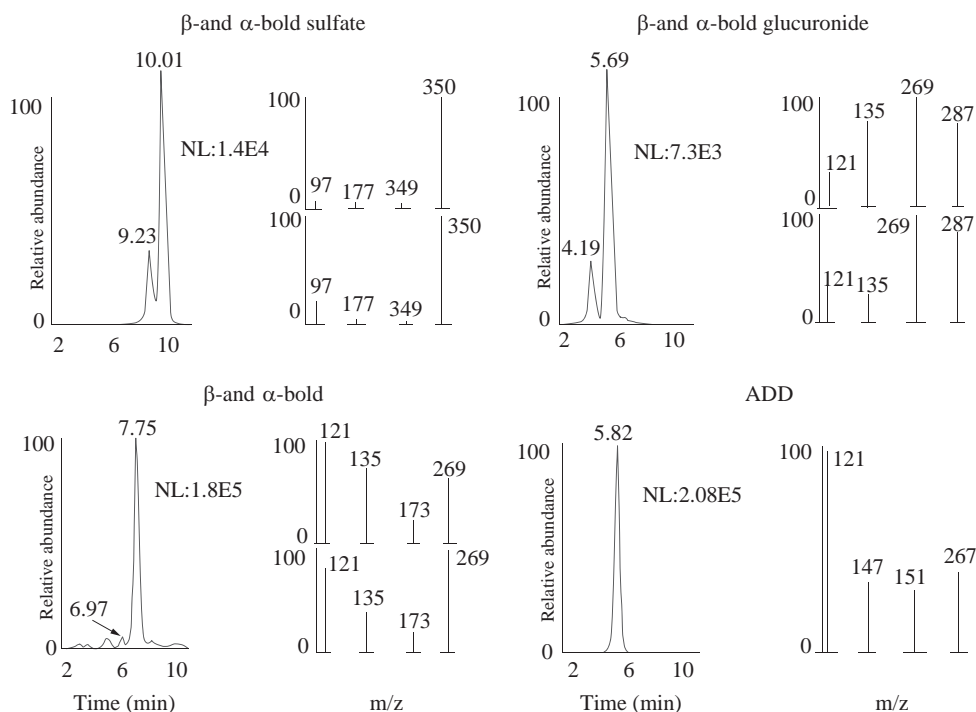


Fig. 3. Reconstructed LC-MS/MS chromatograms and respective ion spectra of the analytes detected in a urine sample.

Table 5

Results of the comparison between the IAC extraction plus LC–MS/MS analysis and the SPE extraction after hydrolysis plus LC–MS/MS analysis.

Urine sample	Described method (ng mL ⁻¹)		Comparison method (ng mL ⁻¹)
	β-bold sulfate	β-bold glucuronide	β-bold conjugate
1	0.14	0.19	nd
2	nd	0.34	0.25
3	nd	0.55	0.50
4	0.14	0.44	0.82
5	0.21	0.58	1.52

nd: Not detected.

mL⁻¹ for β-bol sulfate (3 positives); from 0.12 to 0.58 ng mL⁻¹ for α-bol glucuronide (4 positives); from 0.08 to 0.48 ng·mL⁻¹ for β-bol glucuronide (4 positives); and from 0.47 to 2.1 ng mL⁻¹ for ADD (4 positives); α-bol was found in one only sample (0.53 ng mL⁻¹) where β-bol was detected, too, at a concentration lower than CCβ.

For further confirmation of our results, we asked the Drug Residue Laboratory of the official organization Istituto Zooprofilattico Sperimentale della Lombardia e dell'Emilia Romagna (IZSLER) to test five other urine samples already analysed by us for the presence of only β-bol conjugates. The method used by IZSLER was a fully validated method according to the Commission Decision 2002/657/EC with SPE extraction [21]. It must be stressed that the method involved deconjugation with β-glucuronidase and indirect and non-specific determination of conjugate forms by LC–MS/MS: the differences in the sample preparation and analysis only permitted a qualitative comparison. The method outlined in this paper always detected β-bol glucuronide and three times it detected β-bol sulfate, while the method used for comparison found β-bol conjugate four times out of five. The possibility that incubation with β-glucuronidase could cause inter-transformations of steroids [22] and that β-boldenone could be neo-formed or metabolized cannot be discarded. It must be highlighted however that, when the samples were ordered by increasing concentrations found by the two different methods, the sequence was significantly the same as shown in Table 5.

4. Conclusions

A simple method that uses an IAC extraction and LC–MS/MS triple quadrupole analysis in the MRM mode, for the simultaneous determination of α- and β-bol sulfate, α- and β-bol glucuronide, α- and β-bol, and ADD in bovine urine was developed and validated according to EU Decision 2002/657/EC [11]. The method was verified on real samples. A further qualitative confirmation by a different laboratory on five urine samples that we had already analysed was made just for the conjugated forms of β-bol. The results were also satisfying in actual conditions and demonstrated

that IAC clean up can be used for the subsequent direct analysis of α- and β-bol and their sulfate and glucuronide conjugates, and for ADD for research purposes. The next step will be the study of the bold II phase metabolites as biomarkers of an illicit treatment 'to unambiguously distinguish treated from non-treated animals' [9] on a representative number of animals.

Acknowledgments

The authors wish to thank Nicola Brina and Piero Giorgi whose involvement allowed 'Coop Italia Società Cooperativa' to fund the study.

Elisa Pasquale is the recipient of a Cariplo Ph.D. fellowship in Animal Production in the Laboratory of Inspection of Food of Animal Origin at the University of Milan.

References

- [1] European Union, Off. J. Eur. Commun. L222 (1981) 32–33.
- [2] European Union, Off. J. Eur. Commun. L70 (1988) 16–18.
- [3] European Union, Off. J. Eur. Commun. L128 (1988) 36–38.
- [4] C. Arts, R. Schilt, M. Schreurs, L. Van Ginkel, Boldenone is a naturally occurring (anabolic) steroid in cattle. In: N. Haagsma, A. Ruiters, editors, in: Proceedings of the EuroResidue III Conference. Utrecht, The Netherlands: University of Utrecht, 1996, pp. 212–217.
- [5] H.F. De Brabander, S. Poelmans, R. Schilt, R.W. Stephany, B. Le Bizet, R. Draisci, S.S. Sterk, L.A. van Ginkel, D. Courtheyn, N. Van Hoof, A. Macri, K. De Wasch, Food Add. Contam. 21 (2004) 515–525.
- [6] J. Scarth, C. Akre, L. van Ginkel, B. Le Bizet, H. De Brabander, W. Korth, J. Points, P. Teale, J. Kay, Food Addit. Contam. Part A 26 (2009) 640–671.
- [7] European Union, European Commission, Health & Consumer Protection, Directorate General, Directorate D, Food Safety: Production and Distribution Chain D3, Chemical and Physical Risks; Surveillance, Boldenone Control In: Veal Calves—Draft Proposal, Brussels, 30 September 2003.
- [8] S. Biddle. Unpublished Studies on the Natural Occurrence of Boldenone in Bovine Urine and the Metabolism of Boldenone after Administration (HFL study HFL1382). (2005) Fordham: HFL Ltd. (http://randd.defra.gov.uk/Document.aspx?Document=VM02143_5287_FRP.pdf) (04 February 2014).
- [9] B. Le Bizet, F. Courant, I. Gaudin, E. Bichon, B. Destrez, R. Schilt, R. Draisci, F. Monteau, F. André, Steroids 71 (2006) 1078–1087.
- [10] B. Destrez, E. Bichon, L. Rambaud, F. Courant, F. Monteau, G. Pinel, J.-P. Antignac, B. Le Bizet, Steroids 74 (2009) 803–808.
- [11] European Union, Off. J. Eur. Commun. L221 (2002) 8–36.
- [12] J.A. Dodge, C.W. Lugar, Bioorg. Med. Chem. Lett. 6 (1996) 1–2.
- [13] L.D. Bowers Sanaullah, J. Steroid Biochem. Mol. Biol 58 (1996) 225–234.
- [14] S. Casati, R. Ottria, P. Ciuffreda, Steroids 74 (2009) 250–255.
- [15] A. Fabregat, O.J. Pozo, J. Marcos, J. Segura, R. Ventura, Anal. Chem. 85 (2013) 5005–5014.
- [16] C.A. Sgoifo Rossi, F. Arioli, A. Bassini, L.M. Chiesa, V. Dell'Orto, Food Addit. Contam 21 (2004) 756–762.
- [17] European Union, European Commission, Health & Consumer Protection, Directorate General Directorate E, Safety of the Food Chain, Document SANCO/2004/2726-revision 4, December 2008, Guidelines for the Implementation of Decision 2002/657/EC.
- [18] F. Buiarelli, G.P. Cartoni, F. Coccioli, L. Giannetti, M. Merolle, B. Neri, A. Terracciano, Anal. Chim. Acta 552 (2005) 116–126.
- [19] European Union, Off. J. Eur. Commun. L125 (1996) 10–32.
- [20] M. Thompson, Analyst 125 (2000) 385–386.
- [21] M. Gasparini, W. Assini, E. Bozzoni, N. Tognoli, G. Dusi, Anal. Chim. Acta 586 (2007) 154–162.
- [22] R. de la Torre, X. de la Torre, C. Alía, J. Segua, T. Baro, J.M. Torres-Rodríguez, Anal. Biochem. 289 (2001) 116–123.



Multilevel analysis of temperature dependent near-infrared spectra

Ruifeng Shan, Yue Zhao, Mengli Fan, Xiuwei Liu, Wensheng Cai, Xueguang Shao*

Collaborative Innovation Center of Chemical Science and Engineering (Tianjin), State Key Laboratory of Medicinal Chemical Biology, Research Center for Analytical Sciences, College of Chemistry, Nankai University, Tianjin 300071, China

ARTICLE INFO

Article history:

Received 14 June 2014

Received in revised form

23 July 2014

Accepted 26 July 2014

Available online 12 August 2014

Keywords:

Near-infrared spectra

Temperature

Multilevel simultaneous component analysis

Quantitative spectra-temperature relationship

Composition of solvent

ABSTRACT

Quantitative spectra-temperature relationship (QSTR) between near-infrared (NIR) spectra and temperature has been used for quantitative determination of the compositions in mixtures. In this work, QSTR is studied using multilevel simultaneous component analysis (MSCA) and the spectral data of the samples with different concentrations measured at different temperatures. MSCA model contains a between-individual model describing the differences between the individuals and a within-individual model capturing the differences within the data of all the individuals. NIR spectra of five different compositions (water-ethanol-isopropanol) measured at seven temperatures were analyzed. A between-temperature model describing the effect of temperature and a within-temperature model describing the variation of concentration were obtained, from which QSTR model is established and quantitative analysis is achieved. Furthermore, the difference between the between-temperature or within-temperature models of different mixtures is used to study the composition of the solvent.

© 2014 Elsevier B.V. All rights reserved.

1. Introduction

Near-infrared (NIR) spectra show not only isolated molecular structure and functional groups but also inter- or intra-molecular hydrogen bonds [1]. Variations of temperature change the extent of hydrogen bonding [2], and therefore the NIR spectra measured under different temperatures can reflect these changes. In order to investigate water structure, the dynamic behavior of water was studied using NIR spectra measured under different temperatures [3–5]. Structural analysis of proteins was performed based on the effect of temperature on NIR spectra [6,7]. These studies proved that the technique is helpful to understand the influence of water in biological systems. Moreover, NIR spectra have been adopted to study the interactions in hydrogen bonds based on temperature-induced spectral variations for aqueous solutions of alcohols [8–11]. Temperature dependent NIR spectra were also used to quantitative analysis using the three-way spectral dataset and high order chemometric approach [12]. The temperature of polyamide 66 was predicted based on the temperature-induced spectral variations [13]. In our previous works, a quantitative spectra-temperature relationship (QSTR) model between NIR spectra and temperature was established using partial least squares (PLS) regression and applied

to the quantitative determination of the compositions in mixtures, including water, methanol, ethanol and ethylenediamine [14,15].

Multilevel simultaneous component analysis (MSCA) was proposed by Timmerman to analyze the multivariate data at different levels [16]. The method was developed based on simultaneous component analysis (SCA) that can simultaneously analyze data of the samples belonging to multiple populations [17]. However, SCA model is focused on the variations within the populations but discards the variation between the populations [18–20]. Therefore, MSCA is developed to give a summary of the different types of variation at different levels in the data. A two-level MSCA model of multiple individuals contains a between-individual (the first level) model and a within-individual (the second level) model. According to the degree of the differences between individuals, MSCA-P, MSCA-PF2, MSCA-IND and MSCA-ECP models have been developed [16]. Among the models, MSCA-P model is computationally simpler, and thus it has been successfully applied in different fields, such as psychology [21,22], metabolomics [23–25], and process data analysis [26–28], etc. These applications proved that the model can give a view on different types of variation in the data and increase interpretability of the data.

In this work, MSCA was used to investigate temperature-induced and concentration-induced spectral variations in NIR spectra. QSTR was established by the temperature coefficients in the between-temperature model, and quantitative analysis was achieved by the concentration coefficients in the within-temperature model. Furthermore, the difference between both the temperature and concentration coefficients of different mixtures was used to study the composition of

* Corresponding author at: College of Chemistry, Nankai University, Tianjin 300071, China. Tel.: +86 22 23503430; fax: +86 22 23502458.

E-mail address: xshao@nankai.edu.cn (X. Shao).

solvent. The mixture of isopropanol–ethanol–water was used in this paper because different hydrogen bonds exists in the system.

2. Experimental

2.1. Reagents and sample preparation

Ethanol and isopropanol (Concord Technology Co., Ltd. Tianjin, China) are of analytical grade. Double distilled water was used. Five groups of mixture solutions were prepared. In each group, water–ethanol of different volume ratio was used as the solvent and isopropanol of different volume fraction was used as the solute. The volume ratios of water–ethanol are 8:2, 7:3, 5:5, 3:7 and 2:8 for the five groups, respectively, and volume fraction of isopropanol for each group of samples changes from 10% to 90% with a step of 10%.

2.2. Temperature control and spectral measurement

The temperature in the experiment was controlled by a Premium Heated Immersion Circulator (Thermo Fisher Scientific, New Hampshire, USA). The precision of the equipment for temperature control is ± 0.01 °C. In each experiment, the temperature changes from 60 to 30 °C with a step of -5 °C. The spectrum at each temperature was measured when the temperature does not change for 30 min.

All NIR spectra were measured from 4000 to 12000 cm^{-1} by a Vertex 70 spectrometer (Bruker Optics Inc, Ettlingen, Germany). The spectrometer was furnished with a transmittance optical fiber probe (Bruker Optics Inc, Ettlingen, Germany) of optical path 2 mm. A tungsten–halogen light source and InGaAs detector were used. The spectra are digitalized with ca. 4 cm^{-1} interval in Fourier transform. In the calculations, the variables from 5500 to 7803 cm^{-1} (598 data points) were used. To increase signal to noise ratio, both air reference and the spectra were measured with scan number 64.

As examples, Fig. 1(a) shows the measured NIR spectra of pure water, ethanol, isopropanol and their mixture under three different temperatures, and Fig. 1(b) shows the spectra of five water–ethanol–isopropanol mixtures with different water–ethanol volume ratio and 40% (v/v) isopropanol under seven temperatures. Clearly, the difference between the spectra measured at different temperatures can be seen from Fig. 1(a). Moreover, an isosbestic point can be found in the spectra of each sample and the isosbestic points of ethanol, isopropanol and the mixture appear at lower

wavenumbers compared to that of water. In Fig. 1(b), a regular change can be found and the isosbestic points of the five mixtures shift to low wavenumber as the water content decreases. Therefore, both temperature- and concentration-induced spectral variation are included in the spectra. Method for extracting the two kinds of variations is needed to analyze the samples.

3. Calculations

3.1. Organization of the data

In MSCA, the structure of data determines the information obtained from the model. In this study, for investigating the effect of temperature and concentration on the spectra, the spectra of a group samples measured at each temperature were taken as an individual, including the spectra of the samples with nine isopropanol concentrations from 10% to 90%. Therefore, the data of each group contains seven individuals, and each individual includes nine spectra. Five such data were obtained for the five groups of samples. In the following description, \mathbf{X}_{raw} denotes the spectra of a group, and $\mathbf{X}_{raw, i}$ represents the spectra of an individual, where $i=1\dots I$, I is the number of individual. The individual includes $K_i \times J$ spectra, where K_i is the number of spectra and J is the number of variables in the spectra.

3.2. Multilevel simultaneous component analysis

MSCA can be used if the variation in the data occurs on different levels simultaneously. A two-level MSCA model contains two models to explain the between-individual and within-individual difference in the data. The model for an individual i can be represented by [16,22]

$$\mathbf{X}_{raw, i} = \mathbf{1}_{K_i} \mathbf{m}^T + \mathbf{1}_{K_i} \mathbf{t}_{b, i}^T \mathbf{P}_b^T + \mathbf{T}_{w, i} \mathbf{P}_w^T + \mathbf{E}_{MSCA, i} \quad (1)$$

subjecting to the following constraints:

$$\begin{cases} \sum_{i=1}^I K_i \mathbf{t}_{b, i}^T = \mathbf{0} \\ \mathbf{1}_{K_i}^T \mathbf{T}_{w, i} = \mathbf{0} \end{cases} \quad (2)$$

where $\mathbf{1}_{K_i}$ denotes a column vector of ones with size K_i , \mathbf{m}^T is the overall mean of $\mathbf{X}_{raw, i}$, $\mathbf{t}_{b, i}^T$ and $\mathbf{T}_{w, i}$ represent the between-individual and within-individual scores, \mathbf{P}_b and \mathbf{P}_w are the between-individual and within-individual loadings, respectively, $\mathbf{E}_{MSCA, i}$ denotes the matrix of residuals, and $\mathbf{0}$ represents a zero vector. By imposing the constraints on the scores, the three parts of the

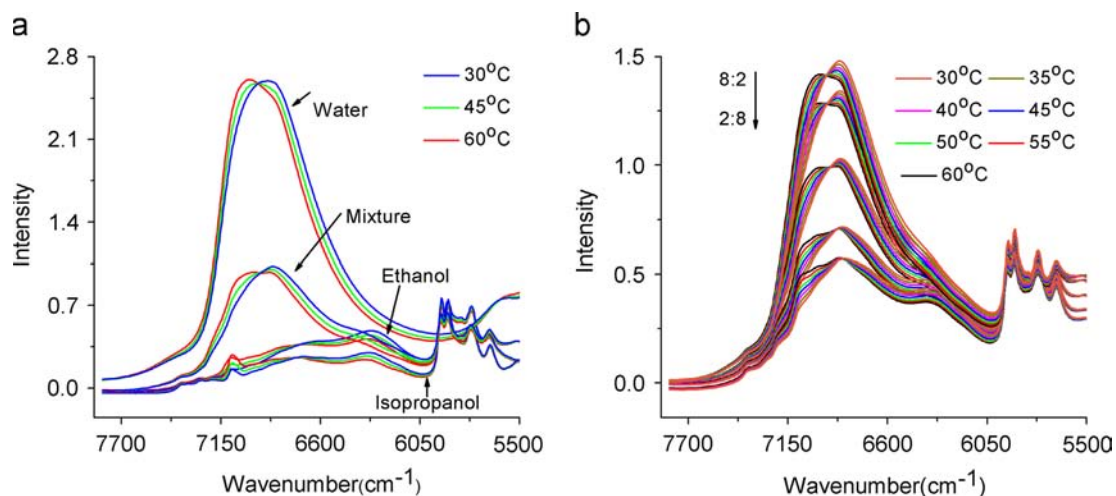


Fig. 1. Measured NIR spectra of pure water, ethanol, isopropanol and their mixture at three temperatures (a) and five groups of mixtures at seven temperatures (b).

MSCA model are forced to be orthogonal to each other [16], i.e., the model at different level can separately describes the different types of variation in the data.

In this study, a two-level MSCA model was built for the data \mathbf{X}_{raw} of each group of samples, i.e., the samples with a volume ratio of water–ethanol and nine isopropanol concentrations from 10% to 90%. In each \mathbf{X}_{raw} , the spectra measured at seven temperatures were included, forming seven individuals, $\mathbf{X}_{\text{raw},i}$ ($i=1\dots7$). Following the MSCA model in Eq. (1), \mathbf{X}_{raw} is mean-centered at first, and then the first level MSCA model can be obtained by performing a PCA on the mean spectra of the individuals. Therefore, the model explains only the variance between individuals or between temperatures. It can be named as a between-temperature model, in which the effect of temperature is described regardless of the influence of concentration. Thus, the score in the model is named as temperature coefficient. The relationship between the spectra and temperature, i.e., QSTR, can be obtained by the variation of the coefficients with temperature.

For calculating the second level MSCA model, the mean-centered individuals, in which the effect of temperature was eliminated, were used for performing the PCA. Therefore, the model describes only the difference induced by concentration. It can be named as a within-temperature model, in which the effect of concentration is described regardless of temperature. The score in the model is named as concentration coefficient. The calibration curve for quantitative analysis, i.e., the quantitative spectra-concentration relationship (QSCR), can be established by the variation of the coefficients with concentration.

For removing the variant background and noise in the spectra, continuous wavelet transform (CWT) was adopted, which has been proved to be an efficient tool for processing analytical signals [29–33]. In the calculation, Haar wavelet with a scale parameter 20 was used.

4. Results and discussion

4.1. Quantitative spectra-temperature relationship

Fig. 2 shows the relationship between the coefficients in the between-temperature model and temperature for the five groups of the mixture solutions, respectively. In the figure, each symbol denotes the coefficients in a model for a group of solutions. Each straight line, i.e., QSTR model, was obtained by least squares fitting of the coefficients. The parameters of the QSTR models were listed in Table 1. Fig. 2 clearly shows the linearity between the coefficient and temperature and the linearity can also be indicated by the

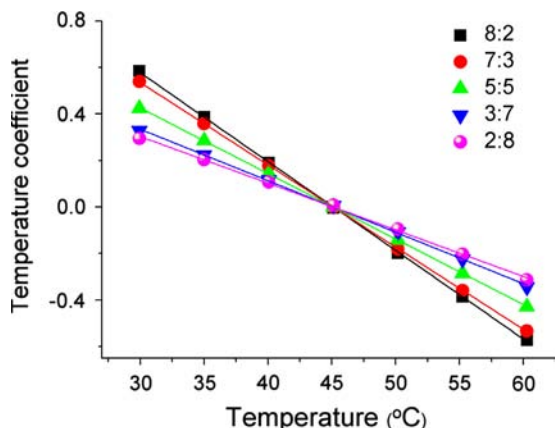


Fig. 2. Variation of the temperature coefficient with the increase of temperature in the between-temperature model.

Table 1

QSTR models for the five group mixture solutions and the squared correlation coefficients (R^2).

Sample group	QSTR model ^a	R^2
1	$y = -0.382x + 1.72$	0.9999
2	$y = -0.354x + 1.60$	0.9999
3	$y = -0.282x + 1.27$	0.9999
4	$y = -0.0222x + 0.991$	0.9993
5	$y = -0.020x + 0.906$	0.9986

^a y is the temperature coefficient and x is the temperature.

squared correlation coefficients (R^2) in Table 1. The results show that QSTR models obtained by MSCA can effectively describe the relationship between temperature and NIR spectra. Therefore, NIR spectroscopy can be used to predict the temperature of solutions with the QSTR model. Compared with the QSTR model built with PLS regression in our previous works [14,15], almost the same results were obtained. The results demonstrate that the QSTR model can be obtained by MSCA using the data of the samples with different concentration.

The changes of the molecular structures with the temperature may be used to explain the QSTR model. The interactions in the molecules and between the molecules will be affected by the temperature, and thus will be reflected in the NIR spectra. The influence of temperature on inter- or intra-molecular hydrogen bonds has been well studied [5,8–11]. Generally, different sizes of clusters are formed by hydrogen bonding in alcohols and water [1]. The increase of temperature will weaken the inter-molecular hydrogen bonds and strengthen the covalent O–H bonds. This makes the cluster size decrease and the relative absorbance of free groups increase [34]. Consequently, the band shifts towards higher energies (higher wavenumber) will occur in the spectra [3]. The band shifts can be clearly seen in Fig. 1 for both the pure water, ethanol, isopropanol and their mixtures. Because MSCA captures the spectral changes and the concentration-induced spectra changes are minimized in the model of the first level, the temperature-induced changes can be reflected in the model. The linearity of the models in Fig. 2 may be a proof of the gradually structural changes with temperature.

4.2. Effect of solvent composition

The results above clearly indicate that the slope of the QSTR model varies with the composition of the solvent. This demonstrates that the effect of temperature on the spectra changes for the samples with different composition. From Fig. 2, it can be seen that the slope gradually decreases with the increase of water content. The result indicates that the temperature variations have more strong influence on the spectra of the mixtures with high water content. The reason may be that water–water interactions are the dominant factor in the variation of the spectra with temperature, but the water–water interactions change with the content of ethanol in the mixtures because of the interactions between water and ethanol. The existence of ethanol weakens the aggregation of water molecules, and thus more free OH groups are obtained with the increase of temperature. Additionally, the structure transformation can be proved from the NIR spectra of pure water and ethanol at different temperatures in Fig. 1(a). In the figure, the existence of the isosbestic point in the spectra of water, ethanol, isopropanol and their mixture measured at different temperatures is offered as an evidence that there are two structural species, i.e., free molecules and hydrogen-bond molecules in the solutions [5]. This demonstrates that structural changes occur with increase of the temperature. Moreover, Fig. 1(b) shows that the isosbestic point of different mixtures shifts to low energy as

the water content decreases. The result is a further indication of the interaction between water and ethanol and the interaction becomes stronger with the increase of ethanol content [35]. Furthermore, the variation of the isosbestic point in Fig. 1(b) is almost linear with the content of ethanol. This is consistent with the fact that the isosbestic point is temperature independent and concentration dependent, and thus the variation can be used for quantitative determination.

In order to quantitatively investigate the relationship between the slope and the composition, the variation of the slope with the volume ratio of water–ethanol in the five groups of mixtures was plotted in Fig. 3. From the figure, it can be clearly seen that the slope has a linear decrease with the increase of water–ethanol volume ratio. A straight line with the squared correlation coefficients (R^2) 0.9944 is obtained by least square fitting of these points. Therefore, the curve in Fig. 3 can be used as the calibration curve for investigating the volume ratio of water–ethanol in the solvent. This further proved that MSCA does effectively extract the information of spectra. QSTR model obtained by the MSCA can not only predict the temperature but also contain the information of the composition of solvent. The method may provide a new way to study the composition of solvents for NIR spectroscopy.

4.3. Quantitative information

MSCA contains a between-temperature model describing the effect of temperature and a within-temperature model describing the concentration variation. In the within-temperature model, the temperature-induced spectra changes are minimized, and the concentration-induced changes can be reflected. Therefore, quantitative analysis can be achieved by the coefficients in the model. In order to investigate the effect of elimination of temperature influence, Fig. 4 displays the coefficients for a group of mixture solutions at seven temperatures in the within-temperature model. In the figure, the balls of different colors denote the coefficients for the nine isopropanol concentrations from 10% to 90%, respectively. From the figure, it can be seen that coefficients of each sample under seven temperatures are nearly on a straight line, i.e., almost exactly equal. The result indicates that the effect of temperature on spectra was eliminated for the mixtures with different concentrations. This proved that the within-temperature model does eliminate the influence of temperature, and a temperature insensitive model for quantitative analysis can be obtained.

Fig. 5 shows the relationship between the coefficients and isopropanol concentrations under seven temperatures for the five groups of mixture solutions. A symbol was used to denote the coefficients for a temperature, and the symbols in a color were used to denote the coefficients for a group of samples, respectively.

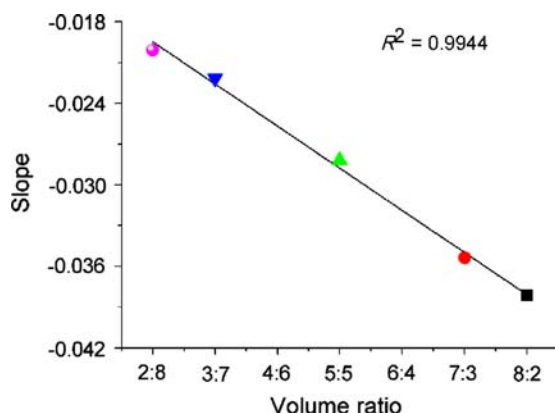


Fig. 3. Relationship of water–ethanol volume ratio and the slope of the QSTR models.

Clearly, the coefficients of each group of samples linearly ascend with the increase of isopropanol concentration. Seven calibration curves can be obtained by fitting the coefficients at each temperature for each group of samples. Because the effect of temperature on the spectra was eliminated, the calibration curves under different temperatures for each group of samples completely overlap into a straight line in Fig. 5. The calibration curves for five groups and the squared correlation coefficients (R^2) were summarized in Table 2. All the values of R^2 are higher 0.99, indicating that the curves can be used for quantitative determination of isopropanol concentration in the different solvents. In our previous works [14,15], quantitative analysis was obtained using the QSTR model established by PLS regression. The temperature of a solution was predicted by the model of the solvent at first, and then, the variation of intercept in the relationship of the predicted and measured temperature was used to determine the concentration. Compared with the previous method, quantitative determination can be achieved in one step by MSCA. Multi-step modeling and prediction are avoided.

Examining the calibration curves for the mixtures of the different solvents in Fig. 5, it can be found that the slope of curve varies with the composition of the solvent. This demonstrates that the effect of composition on the spectra can be reflected by the difference between calibration curves. Clearly, the slope of curve gradually ascends with the increase of water content in the solvent. Fig. 6 shows the variation of the slopes with increase of the volume ratio of water–ethanol. Clearly, there is also a good linearity between the

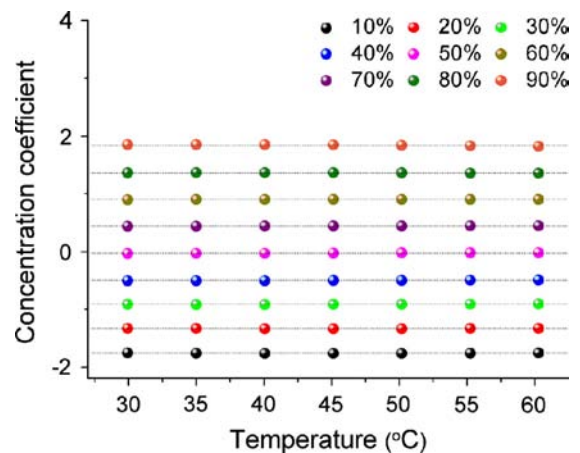


Fig. 4. Variation of the concentration coefficient with temperature for a group of mixture with different isopropanol concentration.

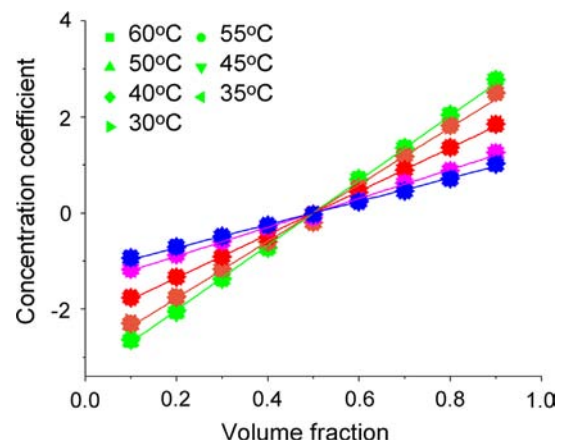


Fig. 5. Calibration curves of isopropanol concentration under different temperatures in the within-temperature model.

Table 2

Calibration curves of isopropanol concentration for the five group mixture solutions and the squared correlation coefficients (R^2).

Sample group	Calibration curve ^a	R^2
1	$y = 6.74x - 3.37$	0.9990
2	$y = 5.91x - 2.96$	0.9957
3	$y = 4.50x - 2.25$	0.9992
4	$y = 3.01x - 1.50$	0.9967
5	$y = 2.42x - 1.21$	0.9979

^a y is the concentration coefficient and x is the isopropanol concentration.

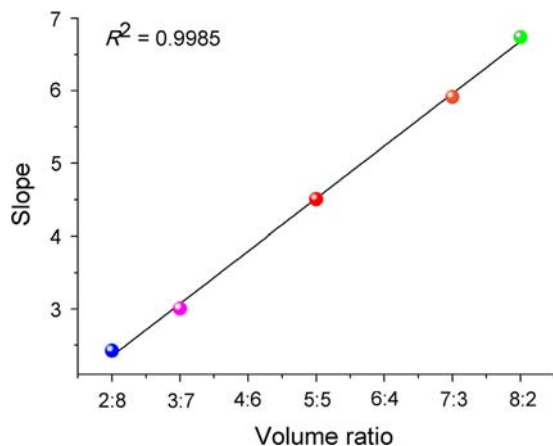


Fig. 6. Relationship of water–ethanol volume ratio and the slope in the relationship of the concentration coefficient and temperature.

slopes and the volume ratios as shown in Fig. 3. The squared correlation coefficient (R^2) is 0.9985, indicating that the slope of the calibration curve can also reflect the composition of the solvent. In the figure, the slope of the calibration curve is the reflection of sensitivity of quantitative analysis, and therefore the sensitivity can be improved by changing the composition of solvent. The result indicates that the method may provide an alternative for improving the sensitivity of quantitative analysis.

5. Conclusions

Temperature dependent NIR spectra were analyzed using MSCA. MSCA model that contains a between-temperature model and a within-temperature model was built. The between-temperature model describes the effect of temperature and within-temperature model describes the variation of concentration. For NIR spectral datasets of water–ethanol–isopropanol with five different compositions measured at different temperatures, QSTR was established by the temperature coefficients in the between-temperature model, and quantitative analysis was achieved by concentration coefficients in the within-temperature model. Furthermore, the composition

of water–ethanol was investigated by the difference between both the QSTR models and calibration curves for the mixtures with the different solvents. Therefore, the method may be a powerful tool for investigating the effect of temperature and quantitatively analysis. Moreover, it provides a new way to study the composition of solvent and improve the sensitivity of quantitative analysis for NIR spectroscopy.

Acknowledgements

This study was supported by National Natural Science Foundation of China (no. 21175074) and MOE Innovation Team (IRT13022) of China.

References

- [1] F. Wulfert, W.T. Kok, A.K. Smilde, *Anal. Chem.* 70 (1998) 1761–1767.
- [2] Y. Ozaki, Y. Liu, I. Noda, *Appl. Spectrosc.* 51 (1997) 526–535.
- [3] V.H. Segtnan, S. Sasic, T. Isaksson, Y. Ozaki, *Anal. Chem.* 73 (2001) 3153–3161.
- [4] B. Czarnik-Matusewicz, S. Pilorz, *Vib. Spectrosc.* 40 (2006) 235–245.
- [5] A.A. Gowen, J.M. Amigo, R. Tsenkova, *Anal. Chim. Acta* 759 (2013) 8–20.
- [6] Y.Q. Wu, B. Czarnik-Matusewicz, K. Murayama, Y. Ozaki, *J. Phys. Chem. B* 104 (2000) 5840–5847.
- [7] B. Yuan, K. Murayama, Y.Q. Wu, R. Tsenkova, X.M. Dou, S. Era, Y. Ozaki, *Appl. Spectrosc.* 57 (2003) 1223–1229.
- [8] Y.J. Chen, Y. Ozaki, M.A. Czarnecki, *Phys. Chem. Chem. Phys.* 15 (2013) 18694–18701.
- [9] M.A. Czarnecki, D.J. Wojtkow, *Phys. Chem. A* 108 (2004) 2411–2417.
- [10] M.A. Czarnecki, *Vib. Spectrosc.* 36 (2004) 237–239.
- [11] D. Wojtkow, M.A. Czarnecki, *J. Phys. Chem. A* 109 (2005) 8218–8224.
- [12] A.C. Peinado, F. van den Berg, M. Blanco, R. Bro, *Chemom. Intell. Lab. Syst.* 83 (2006) 75–82.
- [13] C.P.S. Kuda-Malwathumullage, G.W. Small, *J. Appl. Polym. Sci.* 131 (2014) 40476–40484.
- [14] X.G. Shao, J. Kang, W.S. Cai, *Talanta* 82 (2010) 1017–1021.
- [15] J. Kang, W.S. Cai, X.G. Shao, *Talanta* 85 (2011) 420–424.
- [16] M.E. Timmerman, *Br. J. Math. Stat. Psychol.* 59 (2006) 301–320.
- [17] H.A.L. Kiers, J.M.F. ten Berge, *Psychometrika* 54 (1989) 467–473.
- [18] H.A.L. Kiers, J.M.F. ten Berge, *Br. J. Mathemat., Stat. Psychol.* 47 (1994) 109–126.
- [19] H.A.L. Kiers, J.M.F. ten Berge, R. Bro, *J. Chemom.* 13 (1999) 275–294.
- [20] M.E. Timmerman, H.A.L. Kiers, *Psychometrika* 68 (2003) 105–121.
- [21] P. Kuppens, E. Ceulemans, M.E. Timmerman, E. Diener, C.Y. Kim-Prieto, *J. Cross-Cult. Psychol.* 37 (2006) 491–515.
- [22] J. Stouten, E. Ceulemans, M.E. Timmerman, A. Van Hiel, *J. Appl. Psychol.* 41 (2011) 357–380.
- [23] J.J. Jansen, H.C.J. Hoefsloot, J. van der Greef, M.E. Timmerman, A.K. Smilde, *Anal. Chim. Acta* 530 (2005) 173–183.
- [24] C.J. Xu, H.C.J. Hoefsloot, M. Dijkstra, K. Havenga, H. Roelofsen, R.J. Vonk, A.K. Smilde, *Anal. Chim. Acta* 661 (2010) 20–27.
- [25] A.L.M. Grootveld, C.J.L. Silwood, R.G. Brereton, *Metabolomics* 8 (2012) 64–80.
- [26] O.E. de Noord, E.H. Theobald, *J. Chemom.* 19 (2005) 301–307.
- [27] D.L.S. Ferreira, S. Kittiwachana, L.A. Fido, D.R. Thompson, R.E.A. Escott, R.G. Brereton, *Analyst* 134 (2009) 1571–1585.
- [28] O.E. de Noord, *J. Chemom.* 26 (2012) 340–344.
- [29] X.G. Shao, A.K.M. Leung, F.T. Chau, *Acc. Chem. Res.* 36 (2003) 276–283.
- [30] R.F. Shan, W.S. Cai, X.G. Shao, *Chemom. Intell. Lab. Syst.* 131 (2014) 31–36.
- [31] Y.N. Ni, Y. Wang, S. Kokot, *Talanta* 78 (2009) 432–441.
- [32] Y.N. Ni, R.M. Song, S. Kokot, *Spectrochim. Acta, Part A* 96 (2012) 252–258.
- [33] Y.H. Lai, Y.N. Ni, S. Kokot, *Vib. Spectrosc.* 56 (2011) 154–160.
- [34] I. Noda, Y. Liu, Y. Ozaki, M.A. Czarnecki, *J. Phys. Chem.* 99 (1995) 3068–3073.
- [35] B.S. Berlett, R.L. Levine, E.R. Stadtman, *Anal. Biochem.* 287 (2000) 329–333.



Atmospheric pressure solid analysis probe coupled to quadrupole-time of flight mass spectrometry as a tool for screening and semi-quantitative approach of polycyclic aromatic hydrocarbons, nitro-polycyclic aromatic hydrocarbons and oxo-polycyclic aromatic hydrocarbons in complex matrices



Daniel Carrizo^a, Celia Domeño^a, Isabel Nerín^b, Pilar Alfaro^a, Cristina Nerín^{a,*}

^a Aragon Institute of Engineering Research (I3A), EINA, Department of Analytical Chemistry, University of Zaragoza, María de Luna 3, 50018 Zaragoza, Spain

^b Smoking Cessation Unit, Department of Medicine, Psychiatry and Dermatology, Faculty of Medicine, University of Zaragoza, Domingo Miral s/n, 50009 Zaragoza, Spain

ARTICLE INFO

Article history:

Received 25 April 2014

Received in revised form

9 July 2014

Accepted 11 July 2014

Available online 22 July 2014

Keywords:

Direct analysis

Polycyclic aromatic hydrocarbons

Screening

Organic pollutants

Ambient ionization mass spectrometry

Tobacco

Cancer

ABSTRACT

A new screening and semi-quantitative approach has been developed for direct analysis of polycyclic aromatic hydrocarbons (PAHs) and their nitro and oxo derivatives in environmental and biological matrices using atmospheric pressure solid analysis probe (ASAP) quadrupole-time of flight mass spectrometry (Q-TOF-MS). The instrumental parameters were optimized for the analysis of all these compounds, without previous sample treatment, in soil, motor oil, atmospheric particles (ashes) and biological samples such as urine and saliva of smokers and non-smokers. Ion source parameters in the MS were found to be the key parameters, with little variation within PAHs families. The optimized corona current was 4 μ A, sample cone voltage 80 V for PAHs, nitro-PAHs and oxo-PAHs, while the desolvation temperatures varied from 300 °C to 500 °C. The analytical method performance was checked using a certified reference material. Two deuterated compounds were used as internal standards for semi-quantitative purposes together with the pure individual standard for each compound and the corresponding calibration plot. The compounds nitro PAH 9-nitroanthracene and oxo-PAH 1,4-naphthalenedione, were found in saliva and urine in a range below 1 μ g/g while the range of PAHs in these samples was below 2 μ g/g. Environmental samples provided higher concentration of all pollutants than urine and saliva.

© 2014 Elsevier B.V. All rights reserved.

1. Introduction

The quality control requirements are more and more demanding, especially in areas of food and health, where consumers have a high concern about the likely contamination or affection to their health. The number of samples requiring analysis has increased dramatically in the last years as well as the required sensitivity of the current analytical procedures [1]. These characteristics imply a high cost of the analysis. For this reason, fast screening procedures are gaining importance, as they permit the evaluation of the presence or absence of specific compounds in the samples that may require a further analysis in depth. These screening methods, most of them based on mass spectrometry (MS), are now promoted in a wide variety of areas.

Ambient mass spectrometry (Ambient MS) analysis has experienced a very rapid development during the last 7 years. This technique is defined as mass spectrometric analysis with minimal or no sample preparation using direct sampling and ionization at ambient conditions [2] and it represents the ideal tool for screening analysis. With the introduction of direct analysis in real time (DART) [3] and desorption electrospray ionization (DESI) [4], the analysis of samples without any prior treatment became possible for the first time [2]. In the DART technique, the sample is placed in a stream of helium that contains ionized atmospheric gases (such as water vapor and oxygen), and the analytes in the sample are ionized in open air in the laboratory environment. Desorption electrospray ionization (DESI) is carried out by directing charged droplets produced from a pneumatically-assisted electrospray onto a surface to be analyzed at atmospheric conditions. Ions of chemical species present on the surface, usually a paper impregnated in the sample, are produced through the interaction of charged droplets and the sample. DART and DESI are mainly

* Corresponding author. Tel.: +34 976 761873.

E-mail address: cnerin@unizar.es (C. Nerín).

qualitative techniques where the main purpose is to identify the presence of specific compounds present at the surface of the sample, i.e. targeted analysis. The development of these techniques creates an awareness of the power of Ambient MS and a new sub-field in mass spectrometry. DART and DESI techniques usually coupled to time of flight (TOF) detectors have been widely applied as direct screening techniques to a wide variety of samples [5–10].

Atmospheric-pressure solid-analysis probe (ASAP) was developed in 2005 [11]. The sample, usually introduced into the ionization chamber with a glass rod dipped either in the powdered or liquid sample or rubbing the surface, is vaporized and ionized at atmospheric pressure inside a small chamber, thus providing the ions, which arrive at the MS detector [12–13]. The major difference between DART and ASAP is the ionization mode. While DART is open to the environment allowing for water to be part of the chemical ionization process, ASAP takes place in dry atmosphere. DESI, DART and ASAP can be considered as screening techniques to take rapid decision about the further analysis in depth. Their major advantages are the absence of sample treatment, which is usually a tedious, expensive and time consuming step. None of them have a chromatographic separation before detection. This means that all the analytes present in the sample matrix, or formed during the ionization step, reach the source and all of them can be analyzed, thus minimizing any analyte losses. Thus, these techniques are mainly focused on target analysis and constitute powerful tools for screening the absence or presence of target compounds. In a few minutes the sample is injected and processed.

In ASAP, several key parameters, such as corona current, sample cone voltage and gas desolvation temperature need optimization, because they condition the total number of ions arriving at the detector. Important features, like the temperature of the ion source chamber where the sample is volatilized, remain constant (120 °C) to ensure the maximum volatilization. This technique can be applied to volatile or semi-volatile compounds in solid or liquid complex matrices, without previous sample treatment. The presence or absence of specific compounds at low concentration, and in some cases the order of magnitude of their concentration in the sample, are shown as very interesting characteristics of this technique. However, it is not possible to estimate toxicity from the presence of single compounds by using this method, because too similar compounds in environmental samples superimpose. Using ASAP for screening and semi-quantitative simultaneous analysis of several pollutants, such as polycyclic aromatic hydrocarbons (PAHs) and their nitro and oxo derivatives in complex matrices, can be very useful in health and environmental areas. This is the main purpose of the present paper.

PAHs, nitro-PAHs and oxo-PAHs derivatives are organic compounds listed as priority pollutants by international environmental protection agencies due to their carcinogenic, mutagenic, and toxic effects [14–20]. There are a few applications of Ambient MS methods for direct analysis of PAHs and related compounds [21–26]. However, the possibility of having a semi-quantitative approach using ASAP has not been explored yet. For this reason, the main objective of this work is to evaluate the performance of ASAP-Q-TOF-MS as a screening tool and semi-quantitative approach for PAHs, nitro-PAHs and oxo-PAHs in several liquid and solid complex samples, such as car exhaust, oil, atmospheric dust, urine and saliva. As far as we know, this article represents the first study using direct analysis in one single run through ASAP-Q-TOF-MS for this large series of priority organic pollutants. It is also the first time that a semi-quantitative approach has been proposed using a direct ASAP-MS-Q-TOF in very different complex matrices. A solid certified reference material (CRM) for PAHs was run in parallel with the samples, in order to check the method performance and the semi-quantitative data. The results obtained are shown and discussed.

2. Materials and methods

2.1. Chemicals and reagents

Certified standards of PAHs (naphthalene, acenaphthylene, acenaphthene, fluorene, phenanthrene, anthracene, pyrene, cyclopenta[cd]pyrene, benzo[a]anthracene, chrysene, benzo[k]fluoranthene, benzo[a]pyrene, dibenzo[a,h]anthracene and benzo[ghi]perylene), Nitro-PAHs (1-nitronaphthalene, 2-methyl-1-nitronaphthalene, 1,5-dinitronaphthalene, 2-nitrofluorene, 9-nitroanthracene, 2-nitrofluoranthene, 1-nitropyrene and 6-nitrocrysene) and Oxo-PAHs (1,4-naphthalenedione, benzophenone, 9-fluorenone, anthrone, 9,10-anthracenedione, 7H-benz[de]anthracen-7-one, benzo[a]anthracene-7,12-dione and naphthacene-5,12-dione) were supplied by Sigma-Aldrich (Madrid, Spain). Acenaphthene-d10 (99 atom% D) and benzo[a]pyrene-7,8-d2 (98 atom% D) for being used as internal standards were purchased from Sigma-Aldrich (Madrid, Spain). Detailed information about the molecular weight, chemical formula, CAS number and molecular structure for each of the analyzed compounds of the three families can be found in Table 1 and Figs. S1, S2 and S3 in the Supplementary information material. All the standard solutions were prepared in methanol reagent grade purchased from Scharlab (Barcelona, Spain). Combined solutions of the three families (PAHs, nitro-PAHs and oxo-PAHs) containing different concentrations of each standard were also used to check the performance of the mixtures in ASAP. A sediment as certified reference material (RTC-CRM104-50G, RT-Corp, WY, USA) containing PAHs was supplied by Sigma-Aldrich (Madrid, Spain). The amount of deuterated compounds added to both the standard mixture solution and the samples was in each case in the required final concentration of 10 ng/g IS in the sample. All standards were under gravimetric control and all concentrations are expressed as w/w basis.

2.2. ASAP-Q-TOF-MS instrument

The atmospheric solids analysis probe (ASAP) was coupled to a quadrupole-time of flight-mass spectrometer (QToF-MS), Xevo G2 QTOF (Waters Corporation, Manchester, UK). The instrument has a mass range up to m/z 100 000 and a resolving power of > 22,500 full width at half maximum (FWHM). In the ion source atmospheric pressure chemical ionization was used and the chamber temperature is constant at 120 °C. The key ion source parameters to be optimized were: corona current (μA), sample cone voltage (V) and desolvation gas temperature (°C). Acquisition mode used was MS full-scan data from 70 to 800 amu. Nitrogen was used as desolvation gas at 400 Lh⁻¹ flow. Cone flow was not needed for this technique. Currently, ASAP requires manual injection and can neither be processed unattended nor automatically.

2.3. ASAP-Q-TOF-MS analysis

As this technique is for target analysis, the first step is to analyze the individual compounds under the optimal experimental conditions. Variables such as cone voltage, desolvation gas temperature and corona current were optimized using standard solutions of pure compounds. Voltage of sampling cone was varied from 20 V to 80 V and voltage of the extraction cone was fixed at 0.1 V. The parameters of acquisition were as follows: a scan time of 1 s and mass range of m/z 70–800 to cover all PAH, nitro-PAH and oxo-PAH standards [27]. For each MS spectrum, the characteristic masses were selected and this information was used for searching the presence or absence of each compound in the real samples. Positive identification of the compounds was done using pure standards for all analyzed compounds, using several ions for each compound.

Table 1
Chemical characteristics and optimized parameters of the PAHs, nitro-PAHs and oxo-PAHs analyzed.

Compounds	Abbreviation	CAS	MW	Formula	Corona (μA)	Desolvation temperature ($^{\circ}\text{C}$)
Naphthalene	NAP	91-20-3	128.0626	C_{10}H_8	4	500
Acenaphthylene	ACN	208-96-8	152.0626	C_{12}H_8	4	500
Acenaphthene	ANA	83-32-9	154.0782	$\text{C}_{12}\text{H}_{10}$	4	500
Fluorene	FL	86-73-7	166.0782	$\text{C}_{13}\text{H}_{10}$	4	500
Phenanthrene	PH	85-01-8	178.0782	$\text{C}_{14}\text{H}_{10}$	4	500
Anthracene	ANTH	120-12-7	178.0782	$\text{C}_{14}\text{H}_{10}$	4	500
Fluoranthene	FLAN	206-44-0	202.0782	$\text{C}_{16}\text{H}_{10}$	4	500
Pyrene	PY	129-00-0	202.0782	$\text{C}_{16}\text{H}_{10}$	4	500
Cyclopenta [cd] pyrene	CPY	27208-37-3	226.0782	$\text{C}_{18}\text{H}_{10}$	4	500
Benzo[a]anthracene	BANTH	56-55-3	228.0782	$\text{C}_{18}\text{H}_{12}$	4	500
Chrysene	CH	218-01-9	228.0782	$\text{C}_{18}\text{H}_{12}$	4	500
Benzo[k]fluoranthene	BFLAN	207-08-9	252.0939	$\text{C}_{20}\text{H}_{12}$	4	500
Benzo[a]pyrene	BAP	50-32-8	252.0939	$\text{C}_{20}\text{H}_{12}$	4	500
Dibenzo[a,h]anthracene	DAN	53-70-3	278.1096	$\text{C}_{22}\text{H}_{14}$	4	500
Benzo[ghi]perylene	BPERY	191-24-2	276.0939	$\text{C}_{22}\text{H}_{12}$	4	500
1-Nitronaphthalene	1-N-NAP	86-57-7	173.0477	$\text{C}_{10}\text{H}_7\text{NO}$	6	500
2-Methyl-1-nitronaphthalene	2-m-1-N-NAP	881-03-8	187.0633	$\text{C}_{11}\text{H}_9\text{NO}_2$	6	500
1,5-Dinitronaphthalene	1,5-dN-NAP	605-71-0	218.0328	$\text{C}_{10}\text{H}_6\text{N}_2\text{O}_4$	6	500
2-Nitrofluorene	2-N-FL	607-57-8	211.0633	$\text{C}_{13}\text{H}_9\text{NO}_2$	6	500
9-Nitroanthracene	9-N-ANTH	602-60-8	223.0633	$\text{C}_{14}\text{H}_9\text{NO}$	6	500
2-Nitrofluoranthene	2-N-FLAN	892-21-7	247.0633	$\text{C}_{16}\text{H}_9\text{NO}_2$	6	500
1-Nitropyrene	1-N-PY	5522-43-0	247.0633	$\text{C}_{16}\text{H}_9\text{NO}_2$	6	500
6-Nitrochrysene	6-N-CH	08-02-7496	273.079	$\text{C}_{18}\text{H}_{11}\text{NO}_2$	6	500
1,4-Naphthalenedione	1,4-O-NAP	130-15-4	158.0368	$\text{C}_{10}\text{H}_6\text{O}_2$	6	300
Benzophenone	BENPHO	119-61-9	182.0732	$\text{C}_{13}\text{H}_{10}\text{O}$	6	300
9-Fluorenone	9-O-FL	486-25-9	180.0575	$\text{C}_{13}\text{H}_8\text{O}$	6	300
Anthrone	ANTHR	90-44-8	194.0732	$\text{C}_{14}\text{H}_{10}\text{O}$	6	300
9,10-Anthracenedione	9,10-O-ANT	84-65-1	208.0524	$\text{C}_{14}\text{H}_8\text{O}_2$	6	300
7H-Benzo[de]anthracene-7-one	7H-BANT	82-05-3	230.0732	$\text{C}_{17}\text{H}_{10}\text{O}$	6	300
Benzo[a]anthracene-7,12-dione	7,12-BANT	2498-66-0	258.0681	$\text{C}_{18}\text{H}_{10}\text{O}_2$	6	300
Naphthacene-5,12-dione	NAP-5,12-O	1090-13-7	258.0681	$\text{C}_{18}\text{H}_{10}\text{O}_2$	6	300

The samples were analyzed in continuous mode (3 min), with a cone voltage of 80 V. The desolvation gas temperature was manually varied from 200 $^{\circ}\text{C}$ to 500 $^{\circ}\text{C}$ to ensure the progressive volatilization of all the compounds and thus facilitate the target analysis of the sample. In this way, the three families of compounds were analyzed in only one acquisition. The ions from the lighter compounds appeared first and those from the heavier compounds arrived later at the detector. This procedure facilitated the identification of the compounds, as the corresponding ions were coming progressively according to their size. The ratio between ramp temperature and time scan can be seen in Fig. 1. The maximum intensity of each target ion together with the comparison versus the pure individual standards was used for further identification. Atmospheric pressure ionization (API) in positive polarity was selected.

For the analyzed samples, the same scan time was used (1 s) and the mass range was from m/z 70 to 800 to cover all the likely present compounds. A new glass rod was used for each sample. Before the analysis the glass rod was inserted into the source chamber at high temperature for 2 min to remove any contamination from the tip. The rod was then removed, cooled and then dipped into the sample for ten seconds. Solid samples (powdered) stucked to the glass rod, while liquid samples wet the rod. All samples were previously spiked with two deuterated internal standards, as above described, to check the sampling load and the performance of the whole process. In liquid samples the IS were dissolved giving a homogeneous solution. Solid samples (1 g) spiked with IS (10 μL of methanol solution) were homogenized in a vortex and a homogeneous slurry was obtained. Sample load was controlled through these IS, as previous calibration plot under the same experimental conditions was carried out with the IS. Calibration plots were previously obtained for both IS in standard

solution. This plot was further used to analyze the sample load and facilitate the semiquantitative approach.

Three replicates of each sample were analyzed. The accuracy and reproducibility (referred to mass accuracy) of all analyses was guaranteed by using a Lockspray. Leucine-enkephalin, generating $[\text{MH}]^+$ ions at 556.2771 Da was employed as the lock mass at a concentration of 2 ng mL^{-1} in water/acetonitrile with 0.1% formic acid. Blanks were obtained without loading any sample in the glass rod during the first 30–40 s of the acquisition, while applying the same temperature ramp as in the sample acquisition. Serial diluted solutions (0.1, 0.5, 1, 5, 10, 20 ng/ml) of individual standards at different concentrations were used to establish the limit of detection (LOD) and limit of quantitation (LOQ) under the same experimental conditions as the samples. LOD and LOQ were calculated as three times or ten times respectively the standard deviation of the blank at the same characteristic mass as each compound. The three standard solutions containing the three chemical groups were independently processed. Data were collected and processed using MassLynx software (Waters Corporation). Confirmation with the pure standards processed under the same conditions was carried out. Mass spectra shown in the figures are based on the average of several mass spectra.

2.4. Reference material and standards

A solid sediment as CRM for PAHs was used without previous sample treatment to demonstrate the performance of the semiquantitative approach in direct analysis by ASAP-Q-TOF-MS. The CRM was analyzed under the same experimental conditions as the samples. The glass rod was dipped into the powdered CRM sample and then introduced into ASAP. In order to know the amount of sample loaded into the system as well as to detect any problem

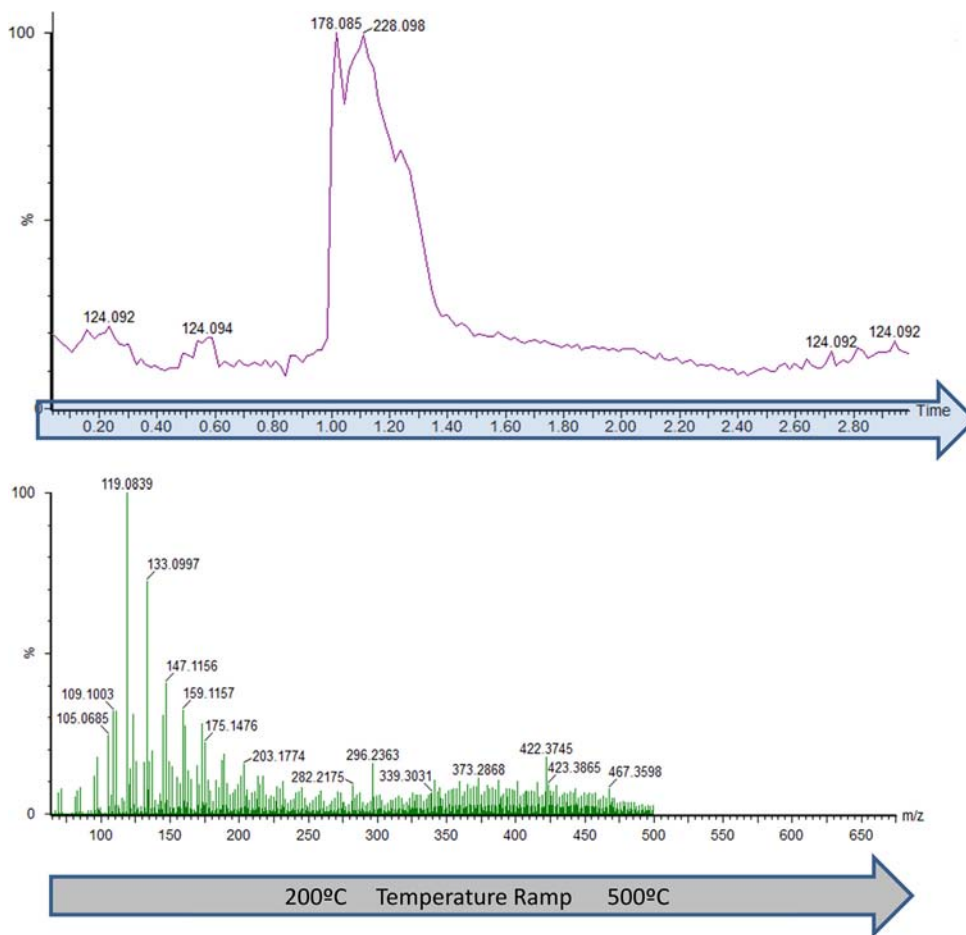


Fig. 1. Ramp temperature effect on the obtained mass spectra in an oil sample.

related with the matrix effect or ion suppression phenomena, 1 g of all samples was spiked with 10 μL of methanolic solution containing two deuterated PAHs (acenaphthene d10 and benzo[a]pyrene 7,8-d2) to get a final concentration of 10 ng/g of each IS. After spiking, the sample was shaken in a vortex and homogenized before the analysis. The IS were analyzed and taken into account for semi-quantitative purposes.

2.5. Samples

After optimization of the instrumental parameters for the three PAH families (PAHs, nitro-PAHs and oxo-PAHs), different types of samples with complex matrices (motor oil, soil, combustion particles, urine and saliva) were directly analyzed by ASAP-Q-TOF-MS in order to demonstrate the performance of the method. The glass rod was dipped into the solid or liquid sample and directly introduced into the ASAP chamber. As was above mentioned, fine powdered sample or small drops of liquid samples were stucked to the glass rod. The MS spectra acquired by MS-Q-TOF were registered and the abundance (response) of each ion referred to the internal standards was used for semi-quantitative purposes in all cases.

The description of the analyzed samples is as follows:

- Mineral motor oil from an automatic generator set.
- Soil from a parking lot heavily contaminated with vehicle exhaust and carburants.
- Combustion particles from the exhaust pipe of a diesel central heating system of a building.
- Biological fluids: (a) saliva from a heavy smoker (more than 20 cg/day) taken in the morning before smoking the first

cigarette of the day and 1 h after smoking 1 cigarette and (b) urine from a heavy smoker and from a non-smoker.

3. Results and discussion

3.1. ASAP analysis

The sample treatment is usually the bottle neck of any analytical procedure. Working with solid samples, materials or biological samples is always time consuming, as the dissolution, often derivatization and clean-up step are required before the analysis. All these sample treatment steps are usually manually managed, as automatic devices required loading the samples to process them in the right way. The whole analytical procedure (sample treatment+analysis) has to be done for qualitative and quantitative analysis. In this frame, ASAP is an excellent tool for target analysis, as the absence or presence of target compounds can be immediately achieved. This way, the further analysis in depth can be applied to only those samples with positive response from ASAP-MS-Q-TOF. Of course this technique cannot substitute the whole analytical procedure for quantitative analysis, but having the identification/presence of a compound and the idea of order of magnitude for the analyte is very useful to pass/fail criteria.

Due to no sample pre-treatment, direct injection and no chromatographic run, sample and blank are acquired in 3 min. This time can be considered as “fast” analysis.

With the identification of the compounds of interest, the absolute ion intensity can be quantified with respect to the internal standards added to the sample, and the values are later used for semi-quantitative purposes.

3.1.1. Optimization of ion source parameters

Following, key parameters were explored: corona current (μA), that affects the ionization; sample cone voltage (V), that influences fragmentation and desolvation gas temperature ($^{\circ}\text{C}$), that affects volatilization. Also different values for desolvation gas flow were tested. However, desolvation gas flow was found to have a minor influence for the ASAP generated spectrum, so a fixed value was used for the PAH families. The main purpose was to carry to the detector as much ions as possible, thus diminishing the in-source fragmentation what facilitates the further identification. To achieve this, one key parameter was changed while maintaining the others fixed. As expected, cone voltage was the unique parameter affecting the fragmentation. Three different optimization sets were carried out, one for each family of pollutants (PAHs, nitro-PAHs and oxo-PAHs). Optimal values for each family of analyzed compounds can be seen in Table 1. The target samples were analyzed for about 3 min, applying a desolvation temperature ramp and running a blank before and after each of the running samples.

The gas desolvation temperatures (300, 400 and 500 $^{\circ}\text{C}$) had no effect on the resulting spectra of the PAHs and nitro-PAHs, neither in fragmentation nor in the signal response (i.e., sensitivity). A different trend was found for the oxo-PAH family, where a higher sensitivity/response was found at a lower temperature (300 $^{\circ}\text{C}$) for the lighter and medium weight compounds, but not for the heaviest ones (m/z 258.0681 benzo[*a*]anthracene-dione/naphthalene-5,12-dione). For these two congeners the highest sensitivity was obtained at 500 $^{\circ}\text{C}$.

With a fixed gas desolvation temperature (500 $^{\circ}\text{C}$ for PAHs/nitro-PAH and 300 $^{\circ}\text{C}$ for oxo-PAH) the cone voltage was varied from 20, 40, 60 and 80 V for each compound family. Changing the cone voltage had a minor effect on the intensity of the spectra obtained for the nitro-PAH. Signal and fragmentation increased in parallel as the cone voltage increased. Sampling cone voltages between 20 V and 30 V can be considered typical for small compounds, causing minimal fragmentation. However for oxo-PAHs a similar signal and fragmentation pattern were found between 20 V and 80 V (data shown in Fig. 2). As can be seen, the minimum fragmentation and signal were obtained at 20 V, while the maximum was at 80 V. This indicates that oxo-PAHs are more resistant to fragmentation, even at cone voltages as high as

80 V and consequently the relationship between cone voltage and fragmentation of oxo-PAHs cannot be anticipated as a general performance.

3.1.2. Mass spectra for each PAH families

For PAHs, nitro-PAHs and oxo-PAHs, corona current (μA) was investigated over the range from 3 to 6, sample cone (V) at 20, 40, 60 and 80, and desolvation gas temperature ($^{\circ}\text{C}$) from 300 to 500. Fig. 3 shows the mass spectra obtained in optimum conditions for the analytical standards of PAHs (corona current 4 μA , sample cone at 80 V and desolvation gas temperature 500 $^{\circ}\text{C}$).

As there is no previous chromatographic separation, this technique is not capable to differentiate between several PAH isomers (e.g., m/z 202.0782 pyrene/fluoranthene, m/z 228.0782 benzo[*a*]anthracene/chrysene, etc.), since they have the same mass, which is a drawback of this direct technique. As can be seen in Fig. 3, the dominant ion sequence corresponds to the molecular ion (\blacktriangle) and to the protonated ion (\bullet , MH^+), except for naphthalene. The protonated ion (MH^+) was the most abundant in all the analyzed compounds with the only exception of naphthalene and fluorene. The protonated ion (MH^+) was used for semi-quantitative purposes (except for naphthalene, in which M^+ was used). The ratio between both species depends on sample conditions (e.g., humidity content) and this ratio was stable over the time experiment. According to Ray et al. [27], who worked with ASAP and steroids, the analysis of steroids by ASAP generally results in the formation of the product ion as either the radical cation $\text{M}^{+\bullet}$ or the protonated molecule (MH) $^+$. The formation of the protonated molecule is a result of proton transfer from ionized water clusters in the source. However, if the source is dry, as in ASAP, the formation of the radical cation is the primary ionization mechanism. The same behavior can be observed with PAHs. The mass spectrum from ASAP-MS-QTOF in optimum conditions of a mixture of eight nitro-PAHs is shown in Fig. 4. The molecular ion (\blacktriangle) and the protonated ion (\bullet) were the dominant ion series and again the charged ion series (MH^+) was the most abundant for all the compounds. This performance with Q-TOF-MS has been observed in other works [28].

Fig. 5 shows the mass spectrum of a mixture of eight oxo-PAHs from ASAP-MS-QTOF. In a similar fashion as that for the parent

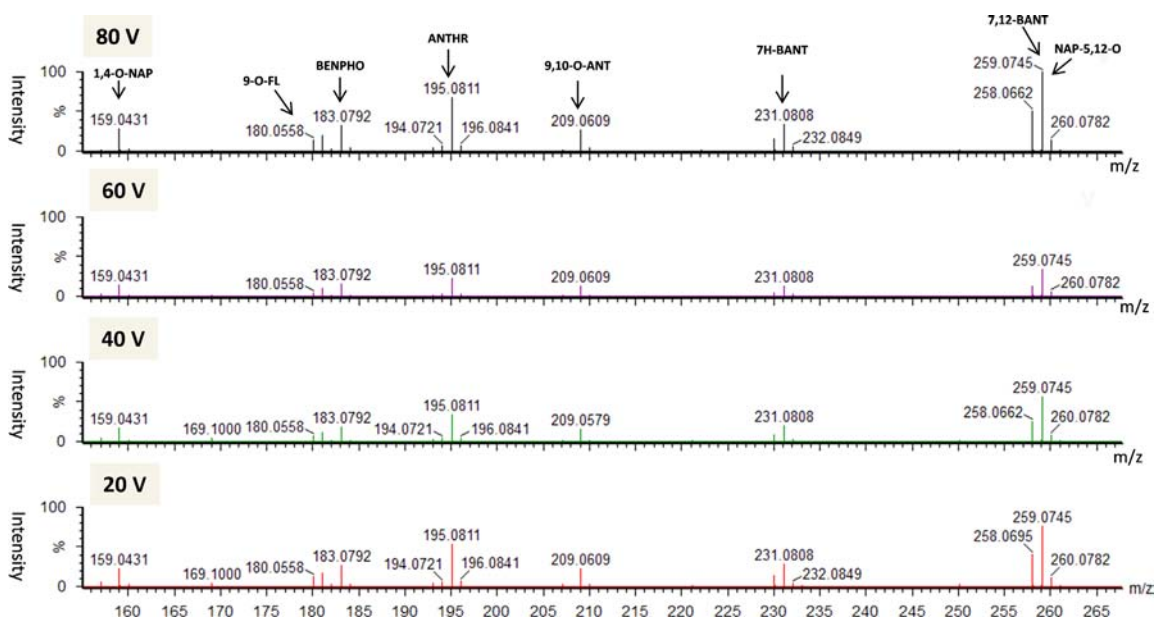


Fig. 2. Cone voltage effect on oxo-PAHs standard solution of 6 ng/ml (20, 40, 60, 80 V) (Abbreviations Table 1). Desolvation temperature: 300 $^{\circ}\text{C}$.

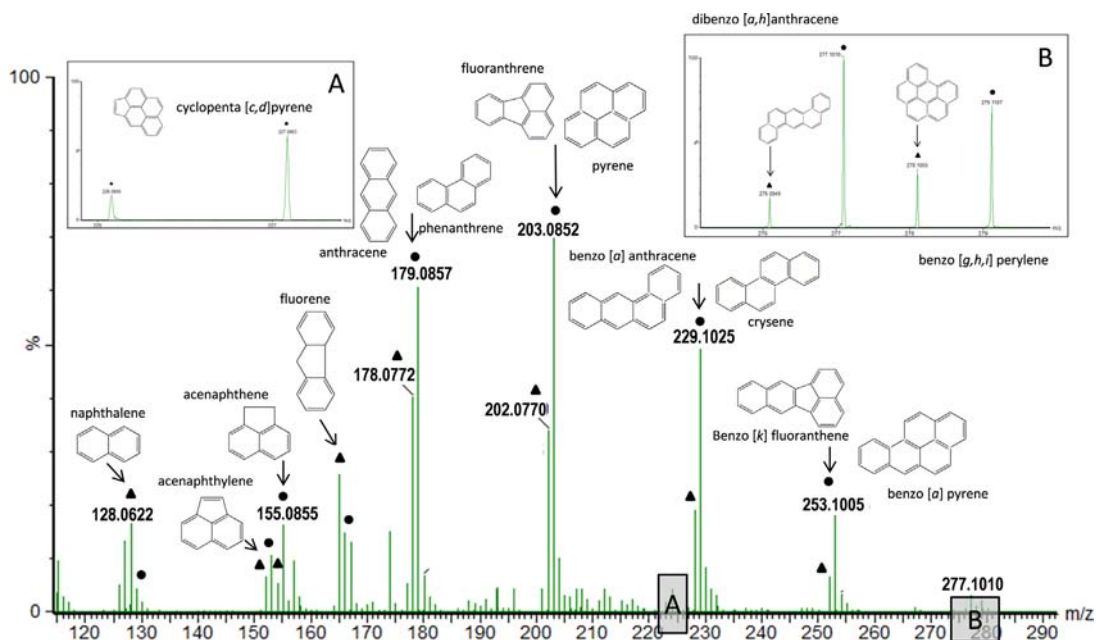


Fig. 3. ASAP-Q-TOF-MS spectrum (absolute response) of a standard solution of 18 ng/ml of each PAHs obtained at optimum conditions. (\blacktriangle denotes the molecular ion M^+ and \bullet the MH^+ ion series).

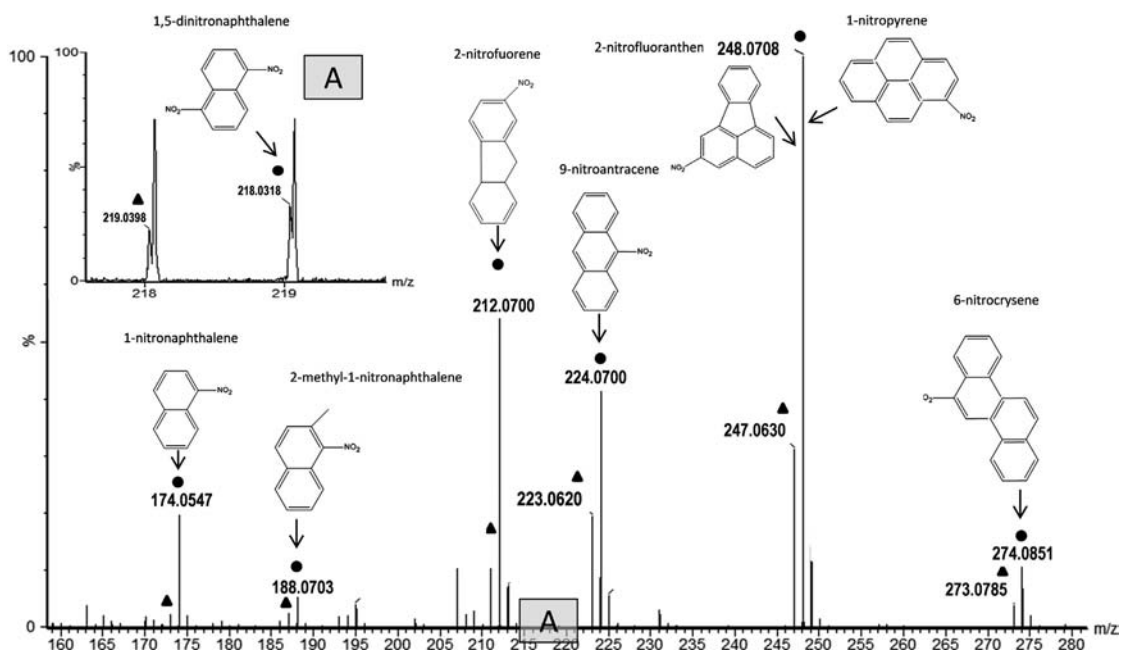


Fig. 4. ASAP mass spectrum (absolute response) of a standard solution (eighteen ng/ml) of eight nitro-PAHs (\blacktriangle denotes the molecular ion M^+ and \bullet the MH^+ ion series).

PAHs and nitro-PAHs, the molecular ion (\blacktriangle) and the protonated ion (\bullet , MH^+) were the dominant ion series and again the ion sequence was the most abundant for all the compounds.

Limits of detection, established with the pure compounds in methanol solution, as above described, were found to be around 20 ppb (ng/g) for PAHs and nitro-PAHs and only 5 ppb (ng/g) for the oxo-PAHs in the methanol solution of the standards. This difference in sensitivity could be explained by the higher ability or affinity of oxygen atoms in oxo-PAHs than in other PAHs to accept protons. The mass resolution and mass accuracy (ppm error) for the three families are shown in Table S3 of the Supporting information material.

Matrix influence and ion suppression phenomena can be a serious problem in any conventional analysis. Direct ASAP can be also affected by matrix influence. To investigate this potential problem, two different deuterated internal standards were added to both the samples and the CRM. From the results obtained it can be confirmed that matrix influence was observed but with very low intensity in all samples under study, probably because the analyzed samples were volatilized in the ASAP chamber and the ionization took place without problems (Figs. 6 and S4 SI material). Matrix influence and/or ion suppression phenomena can be the reason why some of the analyzed compounds display a higher standard error in the

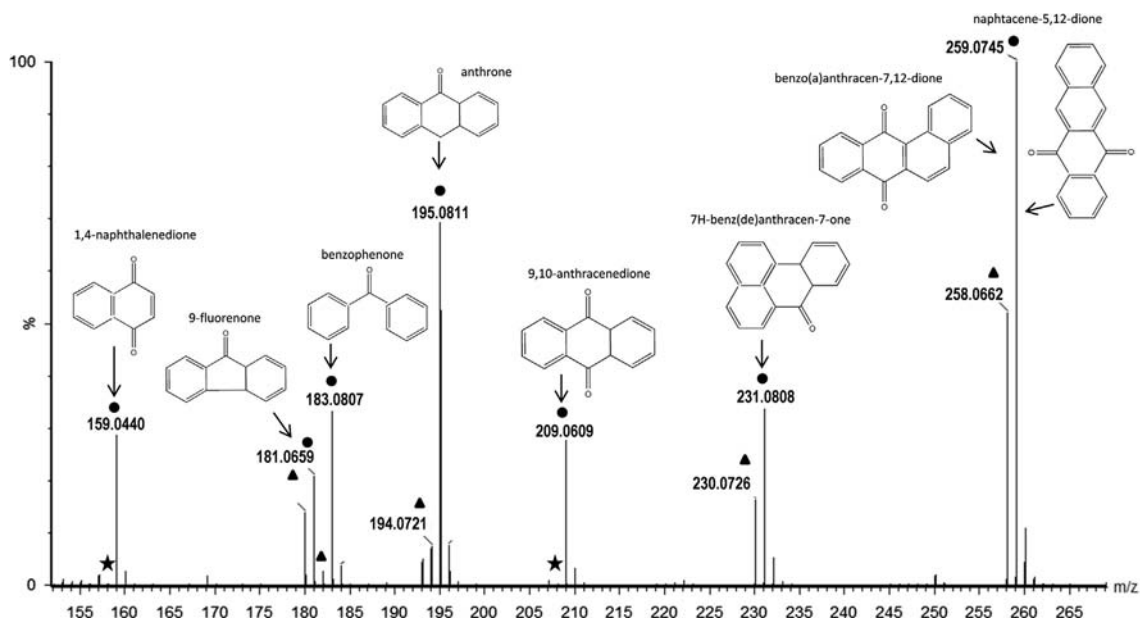


Fig. 5. ASAP-Q-TOF-MS mass spectrum (absolute response) of a standard solution (6 ng/ml each) of eight oxo-PAHs (★ denotes the molecular ion M^+ , • the MH^+ ion series and ▲ no M ion).

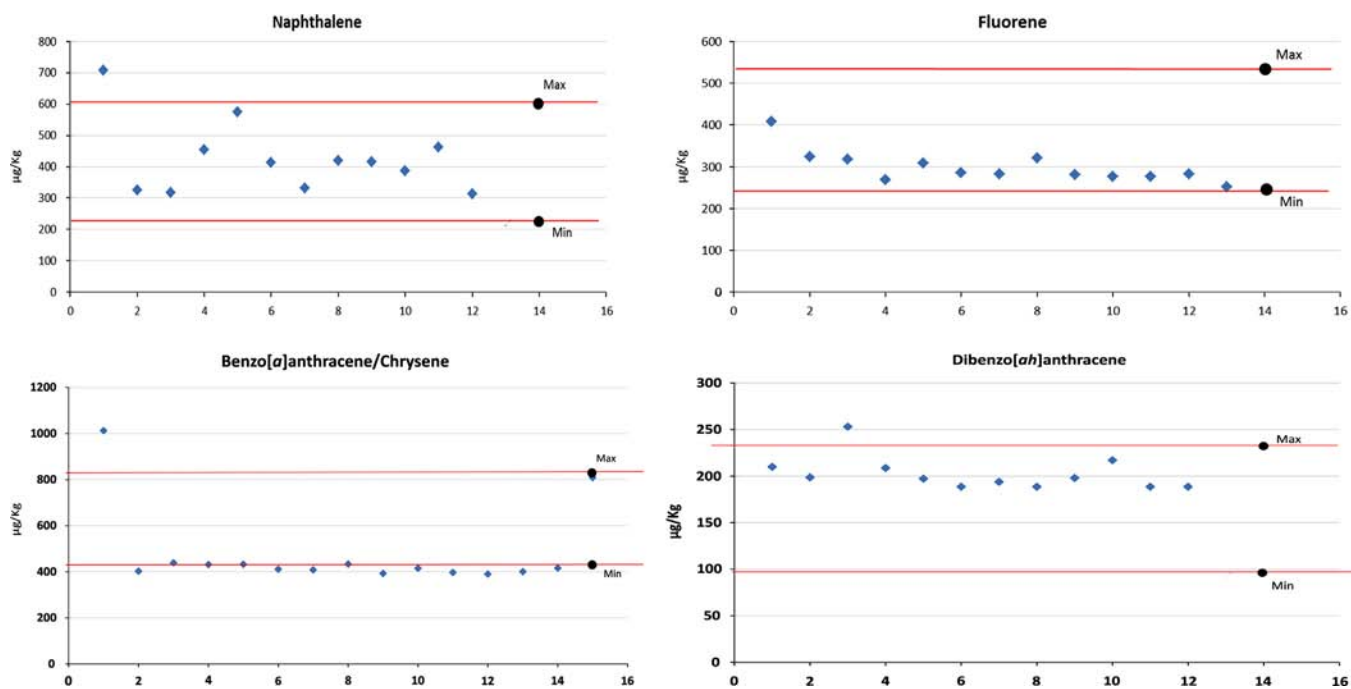


Fig. 6. Repetitive “analysis” of CRM (e.g., loads), with minimum and maximum prediction interval values (red line) for different PAHs congeners analyzed. (For interpretation of the references to color in this figure legend, the reader is referred to the web version of this article.)

repetitive injections of the oil sample (i.e., m/z 154.0782 acenaphthene) (Fig. S4).

3.1.3. Qualitative analysis of samples

An important advantage of the ASAP-Q-TOF-MS technique is the accurate mass obtained for the compounds of interest, so that the identification of compounds in complex matrices (i.e., oil, soil or saliva) without any prior treatment is much easier. The confirmation with the pure standards of each compound is usually required to confirm the identification.

Direct analysis using ASAP-MS-QTOF provides the exact masses of all the compounds present in the sample. As there is not

chromatographic separation those isomers having exactly the same m/z values cannot be confirmed. However, the presence of specific m/z value confirms the presence of some of the isomers. Several examples can be highlighted such as m/z 178.0782, which is common to phenanthrene and anthracene. For this reason several compounds have been included in Table 2 for each m/z value when required.

In the biological samples (i.e. saliva and urine from smokers), three families of contaminants were identified. Urine and saliva samples had constant conditions of humidity, as they are aqueous samples. In these conditions the protonation is improved and better results can be found. PAHs were the most abundant with at least three congeners (m/z 154.0782 acenaphthene, m/z 178.0782

Table 2
Identified and semi-quantitation range values ($\mu\text{g/g}$ or $\mu\text{g/ml}$) compounds in complex matrices analyzed in this work (+: 0–0.1; ++: 0.1–1; +++: 1–10; ++++: > 10; $\mu\text{g/g}$ or $\mu\text{g/ml}$).

Compounds	Oil	Soil	Ash	Saliva	Urine
Naphthalene	+++	+++	+++		
Acenaphthylene	+++	++	+++		
Acenaphthene		++	++	++	+++
Fluorene	+++	+++	+++		
Phenanthrene/Anthracene	+++		+++	+++	
Fluoranthene/Pyrene	+++	++++	+++		
Cyclopenta [cd] pyrene					
Benzo[a]anthracene/Chrysene	++	++	+	+	++
Benzo[k]fluoranthene/Benzo[a]pyrene	++	++			
Dibenzo[a,h]anthracene					
Benzo[ghi]perylene					
1-Nitronaphthalene					
2-Methyl-1-nitronaphthalene	+++	++			
1,5-Dinitronaphthalene					
2-Nitrofluorene	+++	++			
9-Nitroanthracene				+	
2-Nitrofluoranthene/1-nitropyrene					
6-Nitrocrysene					
1,4-Naphthalenedione					++
Benzophenone					
9-Fluorenone					
Anthrone					
9,10-Anthracenedione	+++		+++		
7H-Benzo[de]anthracen-7-one					
Benzo[a]anthracene-7,12-dione/ Naphthacene-5,12-dione					

phenanthrene/anthracene, m/z 228.0782 benzo[a]anthracene/chrysene) in both types of samples. These results are in accordance with the literature [29,30]. Meanwhile, only one congener of the nitro-PAH family was found (m/z 223.0633 probably, 9-nitroanthracene) in the saliva sample and only one oxo-PAH congener (m/z 158.0368 probably, 1,4-naphthalenedione) in the urine sample. In both cases these compounds were found in a heavy smoker just after smoking and not in a non-smoker. These results agree with those anticipated, i.e. that the parental compounds (PAHs) were more abundant than their reaction products (nitro or oxo-PAHs). However, it is important to note that 9-nitroanthracene was present already in the tobacco smoke, probably formed from anthracene during the smoking process, while 1,4-naphthalenedione was the result of oxidation of naphthalene in the human body and therefore excreted in the urine.

Fig. S5 shows the spectra for the PAH standards and saliva sample after smoking. The highly carcinogenic aromatic compounds (m/z 252.0939 either benzo[a]pyrene or benzo[k]fluoranthene or both) can be seen in saliva samples, together with many other compounds (e.g. m/z 152.0626 acenaphthylene, m/z 154.0782 acenaphthene or m/z 166.0782 fluorene), from a heavy smoker immediately after smoking [29]. However, benzo[a]pyrene is diluted with time in the mouth and disappears, indicating that it is swallowed and assimilated by the body. None of these compounds were found in a non-smoker saliva sample. This finding also confirms that these pollutants are coming from tobacco and not from environmental atmosphere. All these compound groups related to the sample from a heavy smoker are in good agreement with other studies related to the tobacco smoke exposure [31].

The analysis of urine samples also showed many possible PAHs congeners (e.g., m/z 154.0782 acenaphthene, m/z 178.0782 phenanthrene/anthracene or, m/z 228.0782 benzo[a]anthracene/chrysene), which were correlated with the congeners found in saliva, as well as an oxo-PAHs congener (m/z 158.0368 1,4-naphthalenedione).

A large number of PAH-like pollutants was found in the analyzed environmental samples, as expected and in accordance with the literature [32–35]. The highest number of congeners was

found in the soil sample (16) followed by the oil sample (15) and the ash sample with 9 compounds. Within the analyzed chemical families, PAHs account for the vast majority of congeners (14), followed by nitro-PAHs (4) and then oxo-PAHs (2). Fig. 7 shows the overlapped spectra of the nitro-PAHs and a polluted soil sample, in which highly toxic nitro-PAH compounds were found (i.e., m/z 211.0633 2-nitrofluorene). This compound is a well-known environmental pollutant and has been found as a major component in diesel exhaust [35].

3.1.4. Semi-quantitative approach

A semi-quantitative approach was attempted in order to gain information about the target analyte concentration in the samples. As discussed above, this technique is a powerful tool for the identification of a wide range of target compounds without any prior sample treatment. It can therefore be used as an exploratory approach for unknown samples. If there is evidence of the presence of target compounds, after this screening step, a further sample treatment step may be carried out if necessary. Two internal standards were added to all samples before the analysis, in order to have a better knowledge of sample loaded by the glass rod. The standard solutions used for calibration curves were handled and analyzed in the same manner as the samples, this means by direct analysis by ASAP-Q-TOF-MS, hence the results can be interpolated. This way, semi-quantitative values of these pollutants in the different sample matrices (i.e. solid and liquids) were obtained. It is important to point out that there is a difference between the direct load of a solid sample (the soil or sediment in this case) and the load of target compounds in a methanol solution of standards or in a liquid sample. For this reason only the order of magnitude of each compound can be obtained and not an accurate individual concentration.

The method performance was checked with the analysis of a sediment CRM for PAHs (used as a solid matrix with a “known” target analyte concentration) under the same experimental conditions as the samples. Also a known amount of two deuterated internal standards was added to CRM. The powdered sample was

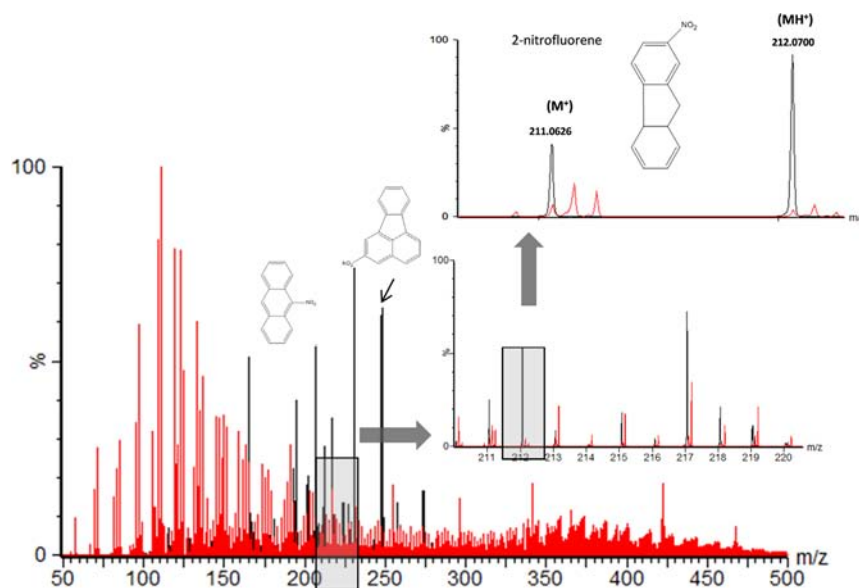


Fig. 7. Overlay mass spectrum (absolute response) of nitro-PAHs standard at 6 ng/ml each and a polluted soil sample, in which a highly toxic nitro-PAH compounds was found (i.e., nitrofluorene).

directly analyzed by ASAP-Q-TOF-MS and the semi-quantitative results were in the range given by the certified concentration values for some of the PAHs analyzed (Table S2, Fig. 6). Only in some cases (i.e., m/z 228.0782 benzo[*a*]anthracene/chrysene) a lower concentration compared with the minimum reference value was obtained (Fig. 6). Probably the volatilization step from the solid sediment sample affected the heaviest compounds more than the lighter ones. PAHs standard calibration curves are shown in Table S1 (SI material). Table S2 and Fig. 6 show the data obtained for the method performance for the sediment CRM. Fig. S4 (Supplementary information material) shows the data obtained for semi-quantitative analysis of five replicates of oil samples with the internal standards. Twelve replicates of the CRM were analyzed and certified values and prediction interval values (min/max), obtained by interpolation in the calibration graph using the IS, were compared. The prediction values are the maximum and minimum value (interval) provided by the certified material. The mean value plus min/max obtained for the CRM by ASAP-Q-TOF-MS were plotted. As can be seen in the graphs (Fig. 6) more than 90% of the values were within the prediction interval values. It can be emphasized that the recommended sample amount for using the CRM is 10 g when applying the sample treatment and further quantitative analysis. However in this case, the sample amount taken for the analysis was much lower, as there is neither sample treatment nor chromatographic separation. Thus, a semi-quantitative approach can be claimed for and the predicted intervals are useful for comparison.

Semi-quantitative analysis (Table 2) of biological samples allowed us to find values below 2 $\mu\text{g/g}$ for PAHs, and about 0.1 $\mu\text{g/g}$ for nitro-PAH and oxo-PAHs. Environmental samples (e.g. oil or contaminated soil) showed higher values of PAHs contamination, with values about 10 $\mu\text{g/g}$ for the lighter compound (i.e. naphthalene) and below 1 $\mu\text{g/g}$ for the heaviest ones such as benzo[*k*]fluoranthene and benzo[*a*]pyrene. For the four nitro-PAH congeners the values found were below 10 $\mu\text{g/g}$, and below 5 $\mu\text{g/g}$ for the oxo-PAH congeners. Unfortunately, as was above mentioned, several common ions are produced from different congeners of each family under study. Thus the semi-quantitative value in these cases cannot be assigned to only one compound and the total value has been provided, following the same system used in already published studies (e.g., Bamford et al.) [36].

4. Conclusions

A simultaneous analysis and semi-quantitative approach of PAHs, nitro-PAHs and oxo-PAHs in different matrices, in one single acquisition by direct analysis either in solid or liquid state, without any sample treatment, has been achieved by a new ASAP-Q-TOF-MS technique. The soft ionization and the mass accuracy, together with the high resolution provided by the Q-TOF-MS detector, allowed us to identify a large number of PAHs (15 compound groups), nitro-PAHs (4 congeners) and oxo-PAHs (2 congeners) in complex matrices. Saliva and urine were also directly introduced and analyzed and some nitro-PAHs and oxo-PAHs were found respectively. The method performance was checked for semi-quantitative approach through the analysis of a sediment CRM for PAHs congeners. The addition of two internal standards (deuterated PAHs) with known concentration to the target samples provided information about the sample load and analysis. Semi-quantitative approach of these compounds in soil, oil, car exhaust particles, saliva and urine has been optimized using ASAP-Q-TOF-MS, which represents a new valuable achievement for direct screening and evaluation of these contaminants in many different samples. This method can be used as a first exploratory approach in complex matrices for target compounds. The total analysis only takes some minutes and represents a powerful tool for screening of many samples in environmental and health areas.

Acknowledgments

This work has been financed by Gobierno de Aragón and Fondo Social Europeo (Spain) through the GUIA Group T-10 Grupo Consolidado de Investigación.

Appendix A. Supporting information

Supplementary data associated with this article can be found in the online version at <http://dx.doi.org/10.1016/j.talanta.2014.07.034>.

References

- [1] M. Porta, *Prev. Med.* 55 (2012) 560.
- [2] A. Venter, M. Nefliu, R.G. Cooks, *TrAC* 27 (2008) 284.
- [3] R.B. Cody, J.A. Laramée, H.D. Durst, *Anal. Chem.* 77 (2005) 2297.
- [4] Z. Takáts, J.M. Wiseman, B. Gologan, G. Cooks, *Science* 306 (2004) 471.
- [5] S.X. Yu, E. Crawford, J. Tice, B. Musselman, J.T. Wu, *Anal. Chem.* 81 (2009) 193.
- [6] H.W. Chen, A. Wortmann, W.H. Zhang, R. Zenobi, *Angew. Chem. Int. Ed.* 46 (2007) 580.
- [7] G. Corso, G. Paglia, D. Garofalo, O. D'Apolito, *Rapid Commun. Mass Spectrom.* 21 (2007) 3777.
- [8] J.F. García-Reyes, A.U. Jackson, A. Molina-Díaz, R.G. Cooks, *Anal. Chem.* 81 (2009) 820.
- [9] I. Cotte-Rodríguez, C.C. Mulligan, G. Cooks, *Anal. Chem.* 79 (2007) 7069.
- [10] K. Bentayeb, L.K. Ackerman, T.H. Begley, *J. Agric. Food Chem.* 60 (2012) 1914.
- [11] C.N. McEwen, R.G. McKay, B.S. Larsen, *Anal. Chem.* 77 (2005) 7826.
- [12] J.P. Smith, N.R. Cameron, J.A. Mosely, *Analyst* 137 (2012) 4524.
- [13] C. Petucci, J. Diffendal, *J. Mass Spectrom.* 43 (2008) 1565.
- [14] Directive 2005/69/EC of the European Parliament and Council of 16 November 2005.
- [15] P. Fernández, R.M. Vilanova, C. Martínez, P. Appleby, J.O. Grimalt, *Environ. Sci. Technol.* 34 (2000) 1906.
- [16] IARC, *Monographs on the Evaluation of Carcinogenic Risks to Human*, International Agency for Research on Cancer, Lyon, France, 2010.
- [17] J.N. Pitts, K.A. Van Cauwenberghe, D. Grosjean, J.P. Schmid, D.R. Fitz, W.L. Belsler, G.P. Knudson, P.M. Hynds, *Science* 202 (1978) 515.
- [18] M. Strandell, S. Zakrisson, T. Alsberg, R. Westerholm, L. Winquist, U. Rannug, *Environ. Health Perspect.* 102 (1994) 85.
- [19] F. Hernández, T. Portolés, E. Pitarch, F.J. López, *J. Mass Spectrom.* 44 (2008) 1.
- [20] L.C. Bosch, C.M. White, *Nitrated polycyclic aromatic hydrocarbons*, Dr. Alfred Huethig Verlag, Heidelberg (1985) 376.
- [21] E.A. Burns, V. Perraud, J. Greaves, B. Finalyson-Pitts, *Anal. Chem.* 82 (2010) 5922.
- [22] L. Xue, F. Xiaowei, Z. Yu, S. Guoying, M. Wu, J. Fu, F. Yan, H. Chen, *Anal. Methods* 4 (2012) 1212.
- [23] S. Guan, A.G. Marshall, S.E. Scheppele, *Anal. Chem.* 68 (1996) 46.
- [24] J.M. Purcell, R.P. Rodgers, C.L. Hendrickson, A.G. Marshall, *J. Am. Soc. Mass Spectrom.* 18 (2007) 1265.
- [25] C.S. Hsu, C.L. Hendrickson, R.P. Rodgers, A.M. McKenna, A.G. Marshall, *J. Mass Spectrom.* 46 (2011) 337.
- [26] F. Zydell, J.R. Smith, V.S. Pagnotti, R.J. Lawrence, C.N. McEwen, B.R. Capacio, *Drug Test. Anal.* 4 (2012) 308.
- [27] A.D. Ray, J. Hammond, H. Major, *Eur. J. Mass Spectrom.* 16 (2010) 169.
- [28] C. Domeño, E. Canellas, P. Alfaro, A. Rodríguez-Lafuente, C. Nerín, *J. Chromatogr. A* 1252 (2012) 146.
- [29] N.J. Aquilina, J.M. Delgado-Saborit, C. Meddings, S. Baker, R.M. Harrison, P. Jacob III, M. Wilson, L. Yu, M. Duan, N.L. Benwitz, *Environ. Int.* 36 (2010) 763.
- [30] Y.S. Ding, J.S. Trommel, X.J. Yan, D. Ashley, C.H. Watson, *Environ. Sci. Technol.* 39 (2005) 471.
- [31] U.S. Department of Health and Human Services, *How Tobacco Smoke Causes Disease: The Biology and Behavioral Basis for Smoking-Attributable Disease: A Report of the Surgeon General*. Atlanta, GA: U.S. Department of Health and Human Services, Centers for Disease Control and Prevention, National Center for Chronic Disease Prevention and Health Promotion, Office on Smoking and Health, 2010.
- [32] N. Tang, T. Hattori, R. Taga, K. Igarashi, X. Yang, K. Tamura, H. Kakimoto, V.F. Mishukov, A. Toriba, R. Kizu, K. Hayakawa, *Atmos. Environ.* 39 (2005) 5817.
- [33] B.A.M. Bandowe, J. Sobocka, W. Wilcke, *Environ. Pollut.* 159 (2011) 539.
- [34] Y. Kojima, K. Inazu, Y. Hisamatsu, H. Okochi, T. Baba, T. Nagoya, *Polycycl. Aromat. Compd.* 30 (2010) 321.
- [35] O. Ueda, S. Kitamura, Y. Huruse, T. Saito, Y. Kanzaki, Y. Yano, K. Tatsumi, S. Ohta, *Bull. Environ. Contam. Toxicol.* 66 (2001) 371.
- [36] H.A. Bamford, D.Z. Besabeh, M.M. Schantz, S.A. Wise, J.E. Baker, *Chemosphere* 50 (2003) 575.



Dispersive liquid–liquid microextraction for the determination of flavonoid aglycone compounds in honey using liquid chromatography with diode array detection and time-of-flight mass spectrometry



Natalia Campillo, Pilar Viñas, Gema Férrez-Melgarejo, Manuel Hernández-Córdoba*

Department of Analytical Chemistry, Faculty of Chemistry, Regional Campus of International Excellence Campus Mare Nostrum, University of Murcia, E-30100 Murcia, Spain

ARTICLE INFO

Article history:

Received 6 June 2014

Received in revised form

23 July 2014

Accepted 27 July 2014

Available online 12 August 2014

Keywords:

Honey

Flavonoids

Dispersive liquid–liquid microextraction (DLLME)

Liquid chromatography (LC)

Diode array detection (DAD)

Time-of-flight mass spectrometry (ToFMS)

ABSTRACT

A rapid approach for the determination of eight flavonoid aglycone compounds, baicalein, hesperitin, fisetin, naringenin, chrysin, myricetin, quercetin and kaempferol, in honey samples and related products has been optimized and validated. The enriched extracts obtained by dispersive liquid–liquid microextraction (DLLME) were analyzed by liquid chromatography with diode array detection coupled to electrospray ionization and time-of-flight mass spectrometry (LC–DAD–ESI–ToFMS). For DLLME, using acetonitrile and chloroform as disperser and extractant solvents, respectively, a Taguchi experimental method was applied to find the optimal combination of following six factors: disperser and extractant solvent volumes, sodium chloride concentration, pH of the aqueous phase, honey mass and centrifugation time. The sedimented organic phase obtained after centrifugation was evaporated, reconstituted in acetonitrile and submitted to LC. The matrix effect was evaluated, and it was concluded that sample quantification can be carried out against aqueous external standards when using DAD and by matrix-matched calibration in the case of ToFMS. Detection limits in the ranges of 0.4–4 and 0.01–0.5 ng g⁻¹ were obtained for DAD and ToFMS, respectively. Satisfactory recovery values between 80 and 111% were obtained for three spiked samples. Honeys and related products were analyzed and flavonoids were found within a wide range.

© 2014 Elsevier B.V. All rights reserved.

1. Introduction

The growing interest in functional foods has changed the way in which nutrition is regarded. Functional foods may be natural or be obtained by adding nutrients to foods and drinks to cover dietetic recommendations and to solve deficiencies in a specific nutrient [1,2]. Honey, which was initially used because of its sweetening power, is now widely consumed because of its other important properties, which, together with those of propolis and royal jelly, have led all of them to be considered as natural functional foods [3]. The antioxidant, antibacterial, antiviral, anti-inflammatory, anti-thrombotic and anti-allergic capacities of honey, propolis and royal jelly are attributed to many factors such as their pH, sugar content, hydrogen peroxide levels and phenolic compounds content, most of which are present as flavonoids [3]. The beneficial effects of flavonoids for human health are due to their hydrogen-donating

antioxidant activity and their capacity to complex the divalent transition metal cations involved in processes forming radicals. Flavonoids have two aromatic rings enclosing a heterocyclic six-membered ring with oxygen. Modifications of this central C-ring divide flavonoids into different classes: flavones, flavonols, flavanones, isoflavonoids, anthocyanins, flavanols, chalconoids, dihydrochalcones and aurones. The most widespread flavonoids are flavonols and flavanols [4]. The relation between the phenolic compound composition of honey and its botanical and geographical origin has been the object of many studies [5], especially since labeling of the botanical origin is legally protected.

The analysis of flavonoids in honey and related products has been reviewed previously [6–8]. The literature shows a very reduced number of gas chromatographic (GC) methods for these determinations because of the low volatility of flavonoid compounds, which makes it necessary to include a derivatization reaction [9–12], although some analyses have been carried out without this step [13]. Capillary electrophoresis (CE) [14] has also been proposed, although by far the most widely used technique for flavonoid quantification in honey and related products is liquid

* Corresponding author. Fax: +34 868 887682.

E-mail address: hcordoba@um.es (M. Hernández-Córdoba).

chromatography (LC) coupled to UV/visible [15–28], electrochemical [29], mass spectrometry (MS) detectors [30–33] or combination of two detection systems [34–41], where in many cases MS is used only for identification purposes [34–36,41].

The complexity of honey samples, which are rich in polar compounds such as sugars and in minor concentration proteins, means that sample treatment prior to LC analysis is necessary. The literature mentions different sample preparation methods, one being the widely applied method based on that described by Ferreres et al. [42], which combines filtration through the non-ionic polymeric resin Amberlite XAD-2 to remove polar compounds and extraction with ethyl ether as an additional clean-up to totally remove interferences [14–18,22–26,33,37]. Polymeric reversed-phase sorbents have also been used to isolate flavonoids from honey samples [19,21,32,34–36,38,39] in procedures that are straightforward because the liquid–liquid extraction step after filtration through Amberlite is omitted. Liquid–liquid extraction has been used by other authors as the only clean-up stage [20,31]. Very simple honey sample treatments involving dissolution in aqueous medium and filtration to remove solid particles without eliminating sugars and proteins, have been proposed with different detectors for LC [27,29,30].

In recent years, miniaturized preconcentration methodologies, in keeping with the principles of green analytical chemistry, have revolutionized many sample treatment steps in several aspects. Thus, liquid-phase microextraction techniques (LPME) have become an interesting alternative to traditional sample treatment methods, because they are faster, cheaper and more environmental friendly [43]. Dispersive liquid–liquid microextraction (DLLME) has been used for the preconcentration of a wide number of compounds from different samples including foods [44]. Only two bibliographic references have been found dealing with polyphenol determination in honey samples using DLLME to preconcentrate quercetin [27] and phenolic acids and flavonoids [41]. Both of the above mentioned references use DAD coupled to LC for quantitation purposes. The present work deals with the quantification of eight aglycone flavonoids, two flavones (baicalein and chrysin), two flavanones (hesperetin and naringenin) and four flavonols (fisetin, myricetin, quercetin and kaempferol), in honey and related products using DLLME combined with LC–DAD–ESI–ToFMS.

2. Experimental

2.1. Chemicals and reagents

Analytical-reagent grade ethanol, methanol, acetonitrile (ACN), dichloromethane, chloroform, carbon tetrachloride, 1,2-dichloroethane, 1,1,2,2-tetrachloroethane, tetrachloroethylene, 1-octanol, 1-undecanol, 1-dodecanol, toluene, hexane, isooctane, 2-octanone and 2-undecanone were obtained from Sigma (St. Louis, MO, USA). Deionized water was obtained from a Milli-Q water purification system (Millipore, Bedford, MA, USA). Sodium chloride, sodium acetate, formic acid (98%) and concentrated acetic acid were obtained from Fluka (Buchs, Switzerland).

Baicalein (5,6,7-trihydroxyflavone, $C_{15}H_{10}O_5$, 98%), naringenin (4',5,7-trihydroxyflavanone, $C_{15}H_{12}H_5$, $\geq 95\%$), myricetin (3,3',4',5,5',7-hexahydroxyflavone, $C_{15}H_{10}O_8$, $\geq 96\%$) and kaempferol (3,4',5,7-tetrahydroxyflavone, $C_{15}H_{10}O_6$, 97%) were supplied by Sigma. Hesperetin (3',5,7-trihydroxy-4'-methoxyflavanone, $C_{16}H_{14}O_6$, $\geq 98\%$), fisetin (3,3',4',7-tetrahydroxyflavone, $C_{15}H_{10}O_6$, $\geq 98\%$), chrysin (5,7-dihydroxyflavone, $C_{15}H_{10}O_4$, $\geq 98\%$) and quercetin (3,3',4',5,6-pentahydroxyflavone, $C_{15}H_{10}O_7$, 98%) were provided by Fluka. Standard stock solutions of each compound at 500 mg L⁻¹ were prepared in methanol and stored in darkness at 4 °C. Working standard mixture solutions were prepared daily by diluting the stock solutions with pure water.

2.2. Instrumentation

The LC system consisted of an Agilent G1312A (Agilent, Waldbronn, Germany) pump operating at a flow-rate of 0.8 mL min⁻¹. The solvents were degassed using an on-line membrane system (Agilent G1379B). The column was maintained at ambient temperature in a thermostated compartment (Agilent G1316A). Separation was performed on a Discovery HS PEG column (Supelco, Bellefonte, PA, USA) (150 mm × 4.6 mm, 5 μm), while injection (20 μL) was performed using an autosampler (Agilent G1367A). Autosampler vials of 2 mL capacity provided with 250 μL microinserts with polymeric feet were used. The mobile phase used consisted of a gradient program: 5 min linear from 30:70 to 33:67 ACN/formic acid (0.1% v/v), then a linear gradient from 33% to 45% ACN in 10 min, with this mobile phase being maintained for 3 min.

The LC system was first coupled to a diode array multiple wavelength detector (Agilent 1100 G1315C) operating at 280 and 370 nm. The time-of-flight mass spectrometry device (Agilent G6220A) was equipped with an electrospray ionization (ESI) source. Data were collected in negative mode by scanning a m/z 100–1000 range using the following operation parameters: capillary voltage, 2500 V; nebulizer gas pressure, 60 psi; drying gas flow, 12 L min⁻¹; drying gas temperature, 350 °C; fragmentor voltage, 180 V; skimmer voltage, 65 V; octapole RF, 250 V. Applied Biosystems/MDS-SCIEX Analyst QS software (Frankfurt, Germany) was used for data processing. Accurate mass measurements of each peak from the total ion chromatograms were obtained by means of an automated calibrant delivery system, to provide mass correction. The ToF mass spectrometer carried out the internal mass calibration automatically, using a dual-nebulizer electrospray source with an automated calibrant delivery system, which introduces the flow from the outlet of the chromatograph, together with small amounts (about 5 μL min⁻¹) of a calibrating solution, ES–TOF tuning mix reference (Agilent). Ten reference masses were used between 112.985587 and 966.000725 m/z . Mass Hunter software, version B-02-00, was used for autocalibrating and continuously recording the results of internal reference masses and the raw data.

Analyses were carried out using the extracted ion chromatogram of the deprotonated molecule of each analyte. The exact theoretical masses based on the formula were calculated using the molecular weight calculator tools of Mass Hunter software, these data being shown in Table 1. The accurate mass spectrum of the analytes was obtained by subtracting the background of the extracted ion chromatogram. The accurate mass of the deprotonated molecule was used for both quantitation and confirmation purposes. The peak areas were used as analytical signals for quantitation.

An EBA 20 (Hettich, Tuttlingen, Germany) centrifuge was used for collecting the sedimented phases obtained from the DLLME process.

Table 1
Mass spectral data of the analytes obtained by DLLME–LC–ESI–ToFMS.

Compound	Elemental composition	Theoretical mass (m/z)	Calculated mass (m/z)	Error (ppm)	DL ^a (ng g ⁻¹)
Baicalein	$C_{15}H_{10}O_5$	270.0528	270.0523	-1.89	0.06
Hesperetin	$C_{16}H_{14}O_6$	302.0790	302.0795	1.44	0.08
Fisetin	$C_{15}H_{10}O_6$	286.0477	286.0478	0.28	0.40
Naringenin	$C_{15}H_{12}O_5$	272.0685	272.0689	1.39	0.09
Chrysin	$C_{15}H_{10}O_4$	254.0579	254.0586	2.68	0.05
Myricetin	$C_{15}H_{10}O_8$	318.0376	318.0376	0.49	0.91
Quercetin	$C_{15}H_{10}O_7$	302.0427	302.0427	0.24	0.22
Kaempferol	$C_{15}H_{10}O_6$	286.0477	286.0478	0.28	0.13

^a Calculated for a signal-to-noise ratio of 3.

2.3. Samples and analytical procedure

A total of eight honey samples were obtained from different suppliers. The samples had been marketed as lavender, orange blossom, rosemary, heather, eucalyptus, chesnut, thyme and flowers, but no verification of the floral origin was made. Three samples of commercial liquid propolis (one of them blended with orange juice: propolis 3) and one of royal jelly were also analyzed.

One gram of honey was dissolved in 10 mL of acetate buffer solution (0.01 M, pH 3) and placed in a 15 mL screw-cap glass centrifuge tube with conical bottom. Next, a mixture containing 1.5 mL of acetonitrile (disperser solvent) and 150 μ L of chloroform (extractant solvent) was rapidly injected into the aqueous mixture by means of a syringe. A cloudy solution, resulting from the dispersion of the fine organic droplets in the aqueous solution, was formed. After a few seconds of extraction, the mixture was centrifuged for 1 min at 3400 rpm, and the dispersed chloroform droplets settled at the bottom of the conical tube. The sedimented phase (volumes in the 110–125 μ L range, depending on the sample) was collected by means of a microsyringe and evaporated to dryness using a mild nitrogen stream. The residue was reconstituted in the minimum volume of acetonitrile necessary to inject by means of the autosampler (50 μ L) and a 20 μ L aliquot was injected in the LC system.

Recovery experiments were carried out using honey sample masses of about 20 g spiked with a standard mixture of the flavonoids at concentration levels roughly corresponding to 10- and 100-fold the quantification limit obtained for the LC–DAD of each compound. The samples were left to equilibrate at room temperature for at least 30 min before proceeding with the optimized procedure, which was applied to 1 g aliquots of samples. The fortification procedure was applied to three different honey samples at two concentration levels, and three replicates were analyzed in each case.

3. Results and discussion

3.1. Liquid chromatographic separation

Reversed phase chromatography was used. Preliminary experiments were carried out using a Tracer Spherisorb C18 ODS2 column and different mixtures (ACN:water and ACN:formic acid) as the mobile phase in the both isocratic and gradient modes. Nevertheless, no efficient separation of the analytes was achieved. The optimal separation conditions were established by injecting 20 μ L of an aqueous standard solution containing the analytes at a concentration level of 1 μ g mL⁻¹, into the Discovery HS PEG column. The mobile phase was initially composed of 30:70 ACN:1% (v/v) formic acid. The concentration of ACN was then linearly increased to 33% in 5 min and then to 45% in 10 min, a mobile phase composition that was maintained for 3 min. All the analytes eluted during the second linear gradient, except for kaempferol, which eluted while the ACN percentage was maintained at 45%. Different experiments were carried out in order to eliminate the first linear gradient, but lower resolution was always obtained for the analytes. Several formic acid concentrations in the 0.1–1% (v/v) range were assayed and no significant differences were observed in the retention times and chromatographic peak shape; therefore, a concentration of 0.1% was adopted for the acid. Despite assaying different ramps of between 33% and 45% of ACN, hesperetin and fisetin coeluted. Nevertheless, this was not a problem because these compounds were monitored at very different wavelengths in the DAD system and with different values of [M–H]⁻ in the ToFMS. The mobile phase flow rate was 0.8 mL min⁻¹, and the elution order and the retention times for the analytes were (1) baicalein (t_R =8.97 min); (2) hesperetin (t_R =9.97 min); (3) fisetin (t_R =10.07 min); (4)

naringenin (t_R =11.61 min); (5) chrysin (t_R =12.46 min); (6) myricetin (t_R =12.87 min); (7) quercetin (t_R =14.52 min) and (8) kaempferol (t_R =16.02 min). Separation factors (α) in the 1.1–1.2 range and resolution (R_s) between 1.45 and 2.51 were obtained for those analytes monitored at 280 nm (baicalein, hesperetin, naringenin and chrysin), and in the 1.1–1.3 and 2.1–4.8 for those detected at 370 nm (fisetin, myricetin, quercetin and kaempferol).

The exact mass measurements and mass errors obtained in the ToFMS for molecular ions are shown in Table 1.

3.2. Optimization of the DLLME conditions

The first step in the DLLME optimization procedure was to select the most appropriate disperser and extractant solvents. For this purpose, 1 g of a spiked honey (at 1 μ g g⁻¹ concentration level for all compounds) was dissolved in 10 mL of water and 150 μ L of different organic solvents were assayed using 1 mL of ACN as disperser solvent. Lower extraction efficiencies were attained for solvents of lower density than water (1-undecanol, 1-dodecanol, 1-octanol, 2-octanone, 2-undecanone, toluene, hexane and iso-octane) than those obtained with organic solvents denser than water. Carbon tetrachloride, tetrachloroethane, chloroform, tetrachloroethylene, 1,2-dichloroethane and dichloromethane were the extractants assayed. Dichloromethane was discarded because no settled phase was obtained owing to its high water solubility. Tetrachloroethylene was also discarded because of the long time required to evaporate the sedimented phase and carbon tetrachloride because no preconcentration of the analytes was attained. As shown in Fig. 1, chloroform extracted all the analytes with higher efficiency than 1,2-dichloroethane and tetrachloroethane, and so it was selected as extractant solvent. The main parameter considered for the selection of the disperser solvent was its miscibility in the extraction solvent and the aqueous phase. ACN, methanol and ethanol have this property, and were tested in this study using 1.0 mL of each solvent and 150 μ L of chloroform as the extractant solvent. ACN provided the best discernible settled phase and so was selected; moreover, it was in close consonance with the mobile phase.

The Taguchi experimental method, an orthogonal array design, was applied to study the possible influence on DLLME of six factors (each at three levels) which might influence the dispersion, extraction and collection efficiency namely, organic extractant

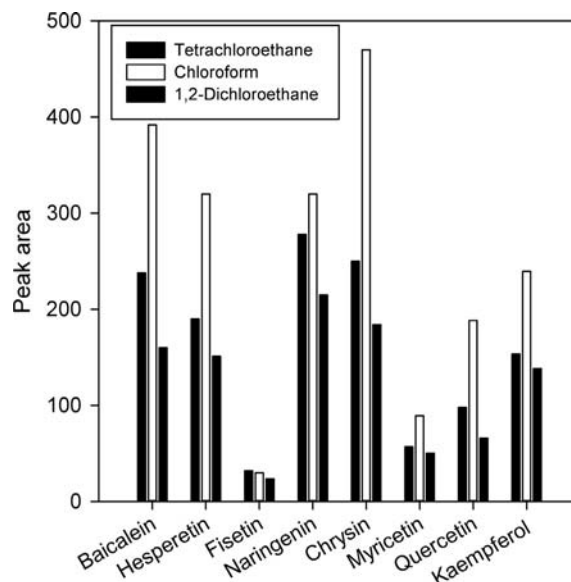


Fig. 1. Selection of extractant solvent for DLLME. Aqueous phase volume, 10 mL; organic solvent volume, 150 μ L; and disperser solvent, 1 mL ACN.

volume, disperser solvent volume, honey sample mass, centrifugation time, pH and sodium chloride concentration of the aqueous phase. For this purpose, 10 mL of an aqueous solution containing different masses, in the 0.5–1.5 g range, of a fortified honey at concentration levels of $1 \mu\text{g g}^{-1}$, was used. The volumes of the extractant and disperser solvents were varied between 50–150 μL and 0.5–1.5 mL, respectively. The effect of ionic strength was studied with NaCl concentrations between 0% and 5% m/v and the pH of the aqueous solution between 3 and 6. Centrifugation times, applied to disrupt the dispersion of the organic droplets, of 1, 3 and 5 min at 3400 rpm were studied. In all cases, the sedimented phase was evaporated and the residue reconstituted in 50 μL of ACN. When the honey mass was increased from 0.5 to 1.0 g, the mean response increased and then was practically constant with a 1.5 g sample mass, so a sample mass of 1.0 g was selected. The highest extraction efficiencies were obtained with 1.5 mL of ACN and 150 μL of chloroform. Varying the pH between 3 and 6 with 0.01 M buffer solutions showed that optimal results were obtained at pH 3, which was selected. Extraction efficiency was higher for all the analytes in the absence of salt and, thus, its addition to the extraction solution was discarded. The centrifugation time necessary to disrupt the cloudy solution was not seen to be a significant factor for extraction efficiency, and so 1 min was adopted for this step at the maximum speed supported by the centrifugal tubes used.

A statistical analysis of variance (ANOVA) test was performed to discriminate which parameters significantly affected extraction efficiency (Table 2). From the calculated variance ratios, F , it was deduced that only one factor considered in the experimental design was statistically significant, at a 95% confidence level (in all cases the calculated F was greater than the critical value). This variable was the extractant volume. The contribution of the residual error to the signal variability indicates the goodness of the experimental design used. It is noteworthy that the application of the ANOVA test showed that the disperser volume was not a variable of statistically significant effect on the DLLME extraction efficiency, nevertheless its contribution of the residual error to the signal is not negligible.

3.3. Analytical characteristics of the method

To study the relevance of any matrix effect, an ANOVA test was used to compare the slopes of aqueous standards calibration graphs and those obtained when the standard additions method was applied to three different honey samples (eucalyptus, thyme and orange blossom). The absence of a matrix effect when using LC–DAD confirmed as the “ p ” values were higher than 0.05 for the eight analytes in the three samples. Consequently, quantification of the samples by DLLME combined with LC–DAD was carried out against external aqueous standards; the corresponding analytical

characteristics are shown in Table 3. The repeatability was calculated using the relative standard deviation for ten successive analyses of heather honey fortified at a concentration level of 300 ng g^{-1} for all compounds (Table 3) and values lower than 11% were obtained. Fig. 2 shows the DLLME combined with LC–DAD elution profiles obtained in the analysis of a standard solution mixture.

In contrast, a matrix effect was detected when LC–ESI–ToFMS was used, aqueous standard calibration providing higher slopes for all the analytes than standard additions. Nevertheless, the application of a one-way ANOVA test to the slopes obtained for the different matrices pointed to the absence of significant differences at 95% confidence level, p values varying in the 0.05–0.808 range depending on the compound (Table 4). Therefore, a matrix-matched calibration method

Table 3

Analytical characteristics of the DLLME combined with the LC–DAD method.

Compound	λ (nm)	Slope ^a (mL ng^{-1})	Correlation coefficient	DL ^b (ng mL^{-1})	RSD ^c (%)
Baicalein	280	3.50 ± 0.10	0.9958	0.4 (4)	5.1
Hesperetin	280	3.10 ± 0.08	0.9951	0.5 (5)	6.2
Fisetin	370	0.35 ± 0.02	0.9963	3.9 (39)	11
Naringenin	280	2.83 ± 0.11	0.9984	0.8 (8)	7.3
Chrysin	280	4.84 ± 0.18	0.9970	0.4 (4)	4.9
Myricetin	370	0.44 ± 0.03	0.9959	4.1 (41)	11
Quercetin	370	1.42 ± 0.06	0.9984	1.3 (13)	8.3
Kaempferol	370	2.81 ± 0.10	0.9978	0.7 (7)	6.0

Values in brackets are ng g^{-1} .

^a Mean value \pm standard deviation ($n=5$).

^b Calculated for $S/N=3$.

^c Calculated at a concentration level of 300 ng g^{-1} for each compound ($n=10$).

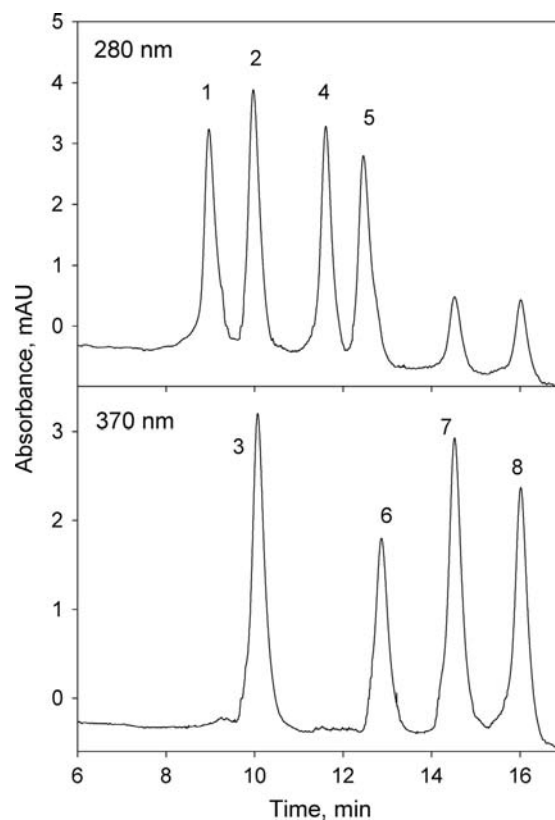


Fig. 2. Elution profiles obtained for an aqueous standard solution using the DLLME combined with LC–DAD optimized procedure. The concentrations of the compounds were (1) Baicalein, 15 ng mL^{-1} ; (2) hesperetin, 20 ng mL^{-1} ; (3) fisetin, 150 ng mL^{-1} ; (4) naringenin 20 ng mL^{-1} ; (5) chrysin, 10 ng mL^{-1} ; (6) myricetin, 60 ng mL^{-1} ; (7) quercetin, 40 ng mL^{-1} and (8) kaempferol, 20 ng mL^{-1} .

Table 2

Results of the analysis of variance for mean response.

Variation source	Degrees of freedom	Sum of squares	Mean of squares	F	P	Contribution (%)
Sample mass	2	30,773	15,386	0.32	0.733	3.7
Dispersant volume	2	217,756	108,878	2.25	0.142	26.4
Extractant volume	2	510,370	255,185	5.27	0.020	61.9
pH	2	54,481	27,240	0.56	0.582	6.6
Ionic strength	2	4717	2358	0.05	0.953	0.6
Centrifugation time	2	6437	3219	0.07	0.936	0.8
Error	14	677,814	48,415			
Total	26	1,502,348				

was adopted for quantification by LC–ESI–ToFMS. The comparison of the standard deviations of the different slopes for each compound did not show significant differences (F values of 0.366–2.92). The regression coefficients obtained under the selected conditions showed a directly proportional relationship between the amount of analyte extracted and the corresponding peak area, being in all cases higher than 0.997. Detection limits (DLs) and quantification limits (QLs) were calculated on the basis of three and ten times the signal-to-noise ratios, respectively. The data obtained for DLs appear in Table 4, while QLs in the 0.035–1.6 ng g⁻¹ range were obtained. When comparing the DLs obtained using DAD and ESI–ToFMS, an increase in sensitivity of between 4.5 and 10 was observed in favor of ToF, depending on the compound. When the DLs obtained by DLLME combined with LC–DAD were compared with previously reported data, an identical value was obtained for quercetin [27], and lower values for hesperetin, quercetin, chrysin, myricetin and kaempferol than those obtained by Campone et al. [41], considering the higher injection volume and the reconstitution of the DLLME organic extract in a lower volume in the procedure presented here.

The slopes obtained by aqueous calibration using DLLME–LC–DAD–ESI–ToFMS were compared with those obtained in the absence of a preconcentration step, pointing to an increase in sensitivity of between 10 (for fisetin and myricetin) and 80-fold for chrysin.

3.4. Analysis of samples and validation of the method

The optimized procedure was applied to eight different honeys, three propolis samples and one royal jelly. Table 5 shows the results obtained using the DLLME combined with LC–ESI–ToFMS, which are similar to those obtained with DAD as detection system. Myricetin was not found in any of the samples above its detection limit (0.9 ng g⁻¹), whereas baicalein was found in four of the twelve samples analyzed at concentration levels ranging from 33 to 622 ng g⁻¹. Of note is the observation that the unique analyte found in lavender honey sample was chrysin. Of the different honeys analyzed, rosemary honey

showed the highest content for fisetin, naringenin, chrysin and kaempferol, while hesperetin was found at higher concentration in the orange blossom honey.

Recovery studies were carried out in order to verify the accuracy of the proposed method by fortifying three samples (heather honey, propolis 2 and royal jelly) in triplicate at two concentration levels in the range 15–1000 ng g⁻¹, depending on the compound. The results obtained appear in Table 6. Recovery values ranged between 80% and 111%, with an average recovery \pm standard deviation ($n=144$) of 97 ± 7 . There were no differences in the RSD values between the different samples, RSD ranging between 5% and 14%.

Table 6
Recovery studies.

Compound	Spiking level (ng g ⁻¹)	Concentration found ^a (ng g ⁻¹)		
		Heather honey	Propolis 2	Royal jelly
Baicalein	15	13 \pm 1	12 \pm 2	629 \pm 43
	150	155 \pm 17	141 \pm 12	754 \pm 67
Hesperetin	15	78 \pm 7	81 \pm 8	18 \pm 2
	150	205 \pm 15	199 \pm 21	165 \pm 15
Fisetin	100	203 \pm 26	127 \pm 16	263 \pm 31
	1000	986 \pm 81	936 \pm 84	1094 \pm 121
Naringenin	25	21 \pm 3	109 \pm 9	60 \pm 7
	250	267 \pm 24	308 \pm 27	316 \pm 28
Chrysin	15	606 \pm 58	271 \pm 14	69 \pm 7
	150	748 \pm 81	431 \pm 38	201 \pm 19
Myricetin	100	103 \pm 13	94 \pm 11	88 \pm 12
	1000	956 \pm 128	930 \pm 98	1056 \pm 129
Quercetin	50	70 \pm 8	160 \pm 12	241 \pm 25
	500	532 \pm 47	628 \pm 53	679 \pm 55
Kaempferol	25	153 \pm 14	355 \pm 37	298 \pm 27
	250	410 \pm 39	603 \pm 48	518 \pm 37

^a Mean \pm standard deviation ($n=3$).

Table 4
Slopes^a of standard additions calibration graphs by DLLME combined with LC–ToFMS (mL ng⁻¹).

Sample	Baicalein	Hesperetin	Fisetin	Naringenin	Chrysin	Myricetin	Quercetin	Kaempferol
Aqueous	38,900 \pm 1230	59,010 \pm 2410	6504 \pm 202	165,000 \pm 6300	395,000 \pm 11,100	5320 \pm 234	45,030 \pm 2200	132,700 \pm 6580
Eucalyptus honey	32,780 \pm 1860	59,460 \pm 5130	5260 \pm 412	50,220 \pm 4940	267,100 \pm 12800	4440 \pm 421	33,300 \pm 2860	104,300 \pm 7520
Heather honey	31,680 \pm 1790	63,000 \pm 4930	6100 \pm 566	51,160 \pm 5500	253,100 \pm 13200	4569 \pm 398	34,730 \pm 3020	107,200 \pm 8070
Thyme honey	30,340 \pm 2000	62,820 \pm 5260	5658 \pm 430	55,630 \pm 5900	283,700 \pm 17400	4381 \pm 459	30,210 \pm 2540	102,900 \pm 7070
Propolis 1	33,000 \pm 1650	62,540 \pm 4390	5246 \pm 460	49,880 \pm 4250	256,800 \pm 15400	4254 \pm 439	31,760 \pm 2920	108,400 \pm 9080
Royal jelly	31,060 \pm 1600	61,840 \pm 5910	5313 \pm 621	50,440 \pm 2660	270,500 \pm 19300	4621 \pm 489	35,020 \pm 3510	105,400 \pm 8780

^a Mean \pm standard deviation ($n=5$).

Table 5
Flavonoids content^a in the analyzed samples (ng g⁻¹).

Sample	Baicalein	Hesperetin	Fisetin	Naringenin	Chrysin	Quercetin	Kaempferol
Honey lavender	ND	ND	ND	ND	214 \pm 20	ND	ND
Orange blossom	ND	620 \pm 35	475 \pm 32	23 \pm 2	630 \pm 14	72 \pm 7	714 \pm 36
Rosemary	ND	82 \pm 6	1650 \pm 66	49 \pm 9	813 \pm 34	126 \pm 11	3806 \pm 100
Heather	ND	66 \pm 3	116 \pm 10	ND	619 \pm 25	13 \pm 1	143 \pm 6
Eucalyptus	ND	65 \pm 4	417 \pm 22	ND	425 \pm 31	1350 \pm 55	241 \pm 13
Chesnut	214 \pm 15	30 \pm 3	99 \pm 12	14 \pm 2	284 \pm 25	1108 \pm 60	455 \pm 22
Thyme	ND	32 \pm 3	73 \pm 10	16 \pm 1	205 \pm 11	206 \pm 10	101 \pm 11
Flowers	33 \pm 4	35 \pm 4	292 \pm 11	35 \pm 4	125 \pm 12	132 \pm 13	901 \pm 15
Royal jelly	622 \pm 48	2.0 \pm 0.3	149 \pm 15	41 \pm 3	65 \pm 5	205 \pm 14	294 \pm 15
Propolis 1	ND	466 \pm 23	867 \pm 70	25 \pm 3	846 \pm 58	1885 \pm 83	498 \pm 20
Propolis 2	ND	61 \pm 5	47 \pm 5	75 \pm 3	267 \pm 19	101 \pm 8	339 \pm 17
Propolis 3	266 \pm 23	207 \pm 15	714 \pm 36	12 \pm 1	63 \pm 4	474 \pm 29	60 \pm 3

ND means not detected.

^a Mean \pm standard deviation ($n=3$).

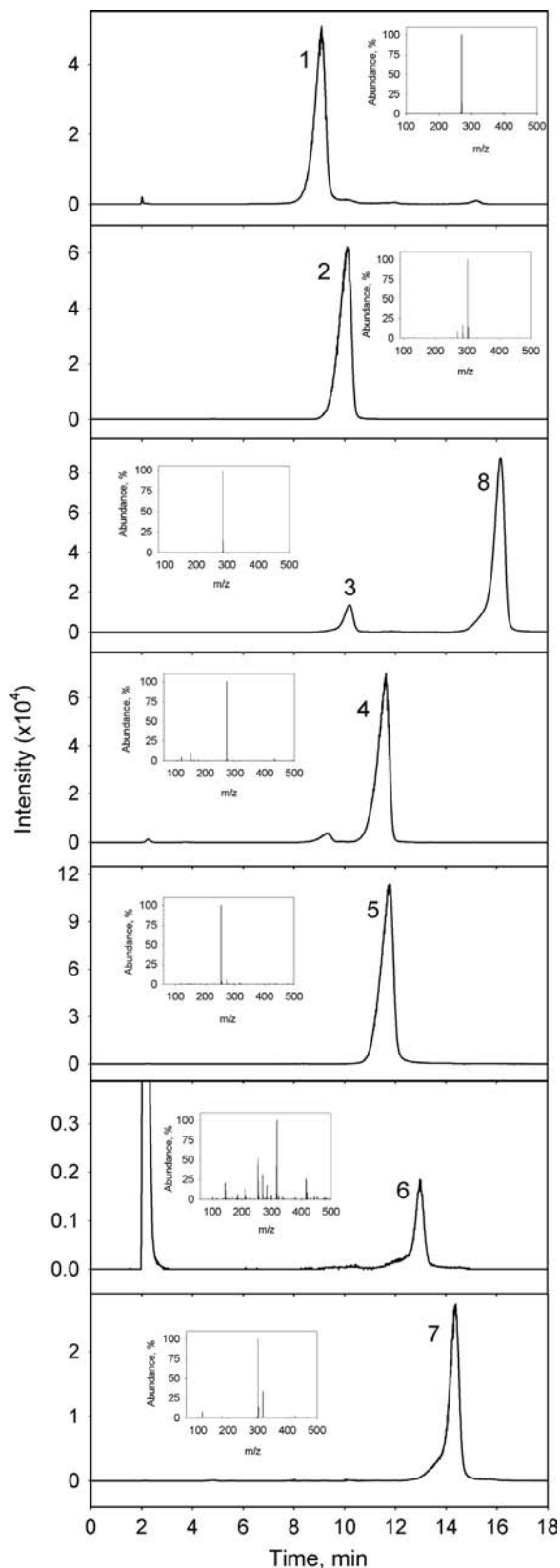


Fig. 3. Extracted ion chromatograms by DLLME combined with LC–ESI–ToFMS for flowers honey sample fortified at 200 ng g^{-1} for all compounds. (1) Baicalein, (2) hesperetin, (3) fisetin, (4) naringenin, (5) chrysin, (6) myricetin, (7) quercetin and (8) kaempferol.

The flavonoid compounds were identified according to their retention times, the UV spectra and molecular weights compared with commercial standards. Accurate masses were obtained for all

the standards, non-spiked and spiked samples analyzed. The mass error was calculated by using the theoretical mass values provided in Table 1 as reference, which were given by the ToF software. The errors obtained for all the standards and spiked and non-spiked samples were between -1.88 and 2.8 ppm. These values were, in all cases, lower than the accepted accuracy threshold of 5 ppm necessary to confirm elemental compositions.

Fig. 3 shows the DLLME combined with LC–ESI–ToFMS extracted ion chromatograms (EICs) obtained for the flowers honey sample fortified at 200 ng g^{-1} .

4. Conclusion

The simple extraction and preconcentration of the analytes from honey using a low volume of organic solvent and the environmentally friendly miniaturized technique DLLME allows quantification at low levels to be carried out. Eight flavonoid aglycones can be separated by LC, dual detection with DAD and ToFMS being appropriate for the final measurement. Accurate mass measurements, concordance in retention times and UV spectra provide unequivocal identification of the individual analytes.

Acknowledgments

The authors acknowledge to Comunidad Autónoma de la Región de Murcia (CARM, Fundación Séneca, Project 15217/PI/10) and the Spanish MEC (CTQ2012–34722) for financial support. G. Férrez-Melgarejo acknowledges a fellowship financed by CARM.

References

- [1] K. Brandt, L.P. Christensen, J. Hansen-Møller, S.L. Hansen, J. Haraldsdottir, L. Jespersen, S. Purup, A. Kharazmi, V. Barkholt, H. Frokiaer, M. Kobaek-Larsen, *Trends Food Sci. Technol.* 15 (2004) 384–393.
- [2] C. Sánchez-Moreno, L. Plaza, B. de Ancos, P. Cano, *J. Sci. Food Agric.* 83 (2003) 430–439.
- [3] M. Viuda-Martos, Y. Ruiz-Navajas, J. Fernández-López, J.A. Pérez-Álvarez, *J. Food Sci.* 73 (2008) R117–R124.
- [4] P. Viñas, N. Campillo, Gas chromatography–mass spectrometry analysis of polyphenols in foods, in: R.R. Watson, V.R. Preedy, S. Zibadi (Eds.), *Polyphenols Human Health and Disease*, Elsevier, London, 2014.
- [5] V. Kaskoniene, P.R. Venskutonis, *Comp. Rev. Food Sci. Food Saf.* 9 (2010) 620–634.
- [6] H.M. Merken, G.R. Beecher, *J. Agric. Food Chem.* 48 (2000) 577–599.
- [7] A.M. Gómez-Caravaca, M. Gómez-Romero, D. Arráez-Román, A. Segura-Carretero, A. Fernández-Gutiérrez, *J. Pharm. Biomed. Anal.* 41 (2006) 1220–1234.
- [8] K. Pyrzyńska, M. Biesaga, *Trends Anal. Chem.* 28 (2009) 893–902.
- [9] A. Uzel, K. Sorkun, O. Oncag, D. Cogulu, O. Gencay, B. Salihi, *Microbiol. Res.* 160 (2005) 189–195.
- [10] M. Campo Fernández, O. Cuesta-Rubio, A. Rosado Pérez, R. Montes De Oca Porto, I. Márquez Hernández, A. Lisa Piccinelli, L. Rastrelli, *J. Agric. Food Chem.* 56 (2008) 9927–9932.
- [11] V.A. Isidorov, A.G. Isidorova, L. Szczepaniak, U. Czyżewska, *Food Chem.* 115 (2009) 1056–1063.
- [12] N. Kalogeropoulos, S.J. Konteles, E. Troullidou, I. Mourtzinou, V.T. Karathanos, *Food Chem.* 116 (2009) 452–461.
- [13] W. Maciejewicz, M. Daniewski, K. Bal, W. Markowski, *Chromatographia* 53 (2001) 343–346.
- [14] D. Arráez-Román, A.M. Gómez-Caravaca, M. Gómez-Romero, A. Segura-Carretero, A. Fernández-Gutiérrez, *J. Pharm. Biomed. Anal.* 41 (2006) 1648–1656.
- [15] I. Martos, F. Ferreres, L.H. Yao, B. D’Arcy, N. Caffin, F.A. Tomás-Barberán, *J. Agric. Food Chem.* 48 (2000) 4744–4748.
- [16] L.H. Yao, Y.M. Jiang, B. D’Arcy, R.T. Singanusong, N. Datta, N. Caffin, K. Raymont, *J. Agric. Food Chem.* 52 (2004) 210–214.
- [17] L. Estevinho, A.P. Pereira, L. Moreira, L.G. Dias, E. Pereira, *Food Chem. Toxicol.* 46 (2008) 3774–3779.
- [18] M.O. Iurlina, A.I. Saiz, R. Fritz, G.D. Manrique, *Food Chem.* 115 (2009) 1141–1149.
- [19] E. Pichichero, L. Canuti, A. Canini, *J. Sci. Food Agric.* 89 (2009) 609–616.
- [20] M.R. Hadjmohammadi, S. Nazari, K. Kamel, *Chromatographia* 69 (2009) 1291–1297.

- [21] R. Socha, L. Juszcak, S. Pietrzyk, T. Fortuna, *Food Chem.* 113 (2009) 568–574.
- [22] I. Escriche, M. Kadar, M. Juan-Borras, E. Domenech, *Food Res. Int.* 44 (2011) 1504–1513.
- [23] M.I. Isla, A. Craig, R. Ordoñez, C. Zampini, J. Sayago, E. Bedascarrasbure, A. Álvarez, V. Salomon, L. Maldonado, *LWT—Food Sci. Technol.* 9 (2011) 1922–1930.
- [24] O. Escuredo, L.R. Silva, P. Valentao, M.C. Seijo, P.B. Andrade, *Food Chem.* 130 (2012) 671–678.
- [25] A. Cavazza, C. Corradini, M. Musci, P. Salvadeo, *J. Sci. Food Agric* 93 (2013) 1169–1175.
- [26] I. Escriche, M. Kadar, M. Juan-Borras, E. Domenech, *Food Chem.* 142 (2014) 135–143.
- [27] E. Ranjbari, P. Biparva, M.R. Hadjmohammadi, *Talanta* 89 (2012) 117–123.
- [28] A. Perna, I. Intaglietta, A. Simonetti, E. Gambacorta, *Int. Food Sci. Technol.* 48 (2013) 1899–1908.
- [29] Y. Liang, W. Cao, W.J. Chen, X.H. Xiao, J.B. Zheng, *Food Chem.* 114 (2009) 1537–1541.
- [30] M. Biesaga, K. Pyrzynska, *J. Chromatogr. A* 1216 (2009) 6620–6626.
- [31] A. Ciric, H. Prosen, M. Jelkic-Stankov, P. Durdevic, *Talanta* 99 (2012) 780–790.
- [32] S. Keckes, U. Gasic, T.C. Velickovic, D. Milojkovic-Opsenica, M. Natic, Z. Tesic, *Food Chem.* 138 (2013) 32–40.
- [33] I. Sergiel, P. Pohl, M. Biesaga, *Food Chem.* 145 (2014) 404–408.
- [34] N. Gheldof, X.H. Wang, N.J. Engeseth, *J. Agric. Food Chem.* 50 (2002) 5870–5877.
- [35] K. Petrus, H. Schwartz, G. Sontag, *Anal. Bioanal. Chem.* 400 (2011) 2555–2563.
- [36] A. Michalkiewicz, M. Biesaga, K. Pyrzynska, *J. Chromatogr. A* 1187 (2008) 18–24.
- [37] P. Truchado, E. Tourn, L.M. Gallez, D.A. Moreno, F. Ferreres, F.A. Tomás-Barberán, *J. Agric. Food Chem.* 58 (2010) 12678–12685.
- [38] J.M. Álvarez-Suárez, A.M. González-Paramas, C. Santos-Buelga, M. Battino, *J. Agric. Food Chem.* 58 (2010) 9817–9824.
- [39] J. Bertoncelj, T. Polak, U. Kropf, M. Korosec, T. Golob, *Food Chem.* 127 (2011) 296–302.
- [40] J.H. Zhou, L.H. Yao, Y. Li, L.Z. Chen, L.M. Wu, J. Zhao, *Food Chem.* 145 (2014) 941–949.
- [41] L. Campone, A.L. Piccinelli, I. Pagano, S. Carabetta, R. Di Sanzo, M. Russo, L. Rastrelli, *J. Chromatogr. A* 1334 (2014) 9–15.
- [42] F. Ferreres, F.A. Tomás-Barberán, C. Soler, C. García Viguera, A. Ortiz, F. Tomás Lorente, *Apidologie* 25 (1994) 21–30.
- [43] L. Ramos, *J. Chromatogr. A* 1221 (2012) 84–98.
- [44] P. Viñas, N. Campillo, I. López-García, M. Hernández-Córdoba, *Anal. Bioanal. Chem.* 406 (2014) 2067–2099.



A novel solid-state Ru(bpy)₃²⁺ electrochemiluminescence immunosensor based on poly(ethylenimine) and polyamidoamine dendrimers as co-reactants

Chengyi Xiong, Haijun Wang, Yali Yuan, Yaqin Chai*, Ruo Yuan*

Key Laboratory of Luminescent and Real-Time Analytical Chemistry (Southwest University), Ministry of Education, College of Chemistry and Chemical Engineering, Southwest University, Chongqing 400715, PR China

ARTICLE INFO

Article history:

Received 4 May 2014

Received in revised form

21 July 2014

Accepted 23 July 2014

Available online 1 August 2014

Keywords:

Electrochemiluminescence

Immunosensor

Ru(bpy)₃²⁺

Poly(ethylenimine)

Polyamidoamine dendrimers

Pt nanoparticles

Au nanoparticles

α-fetoprotein

ABSTRACT

In this study, a novel solid-state Ru(bpy)₃²⁺ electrochemiluminescence (ECL) sandwiched immunosensor for sensitive detection of α-fetoprotein (AFP) was constructed based on poly(ethylenimine) (PEI) functionalized reduced graphene oxide (PEI-rGO) and Au nanoparticles (AuNPs) decorated polyamidoamine (PAMAM) dendrimers. Both PEI and PAMAM are polymers with a lot of amino groups, which are able to serve as good co-reactant to remarkably enhance the ECL signal of Ru(bpy)₃²⁺. For improving the poor conductivity of PAMAM, the AuNPs were decorated on the amino groups of PAMAM. Through Au-N bonds, the formed AuNPs-PAMAM was decorated on the PEI-rGO. The obtained AuNPs-PAMAM/PEI-rGO was introduced to immobilize the detection antibody (Ab₂). Then, the Ab₂ labeled AuNPs-PAMAM/PEI-rGO was modified onto the glass carbon electrode surface via sandwiched immunoreactions. The ECL substrate was prepared by mixing nafion and the complex (Ru-PtNPs) of Pt nanoparticles (PtNPs) and Ru(bpy)₃²⁺, which could reduce the consumption of Ru complex, simplify the operation and enhance the ECL efficiency. The experimental results demonstrated that the proposed immunosensor had good response to AFP. The linear range was from 0.01 pg mL⁻¹ to 10 ng mL⁻¹ with a low detection limit of 3.3 fg mL⁻¹. Meanwhile, with satisfying stability, selectivity and reproducibility, the proposed sandwiched immunosensor was presented to possess good potential in clinical detection.

© 2014 Published by Elsevier B.V.

1. Introduction

Highly sensitive detection for tumor biomarker that is associated with a particular cancer is significant for early diagnosis and prognosis. Meanwhile, the demands for it are increasing rapidly [1]. Up to now, some methods have been developed for the detection of tumor biomarker, such as enzyme-linked immunoassay [2], fluorescent immunoassay [3], electrochemical immunoassay [4,5] and electrochemiluminescence immunoassay [6]. Among those methods, electrochemiluminescence (ECL), with high sensitivity, selectivity, low background signal and rapid response, has attracted much attention in recent years. And based on those distinct advantages, ECL will have wider application in immunoassay for tumor biomarkers [7–9]. In fact, commercial systems have started to use ECL in some important clinical detection (such as digoxin, thyrotropin, protein, steroidal hormones

and various antibodies) [10,11]. Luminol, quantum dots and Ru complex are most common ECL reagents that are often used to construct biosensors [12–14]. Among these ECL systems, tris(2,2'-bipyridyl) ruthenium(II) (Ru(bpy)₃²⁺) and its derivatives have special advantages such as high luminous efficiency, good stability in different pH and superior electrochemical reversibility [15,16]. However, the high price limits its application in clinical detection [12]. In order to solve the problem, Ru(bpy)₃²⁺ was modified on the electrode surface to construct a solid-state ECL immunosensor, which could reduce the consumption of Ru complex, improve ECL efficiency and enhance the ECL signal.

According to the mechanisms, the co-reactants are important intermediates for ECL signal amplification [10,17]. The co-reactant ECL has high ECL efficiency, strong ECL signal and superior stability. Based on these advantages, the use of the co-reactant ECL has been increasing [17,18]. The previous reports have pointed out that many kinds of amine compounds could act as co-reactant to the ECL of Ru(bpy)₃²⁺ [19]. Poly(ethylenimine) (PEI), with a lot of amino groups in its molecular structure, is a good co-reactant that can enhance the ECL

* Corresponding authors. Tel.: +86 23 68252277; fax: +86 23 68253172.

E-mail addresses: yqchai@swu.edu.cn (Y. Chai), yuanruo@swu.edu.cn (R. Yuan).

signal [20,21]. In order to increase their immobilized amount when constructing a ECL sensor, the co-reactants are often immobilized on some nanomaterial, such as carbon nanotube, graphene and some metal nanomaterial [22]. Graphene, an atomical layer of sp^2 carbon atoms in a densely packed honeycomb two-dimensional lattice, has been paid great attention by both the experimental and theoretical scientific communities [23–25]. Due to its large specific surface area, superior electric conductivity and satisfactory stability, it is often used to fabricate biosensors. In this assay, graphene oxide was applied to immobilizing PEI. The formed PEI functionalized reduced graphene oxide (PEI-rGO) can enhance the ECL signal of $Ru(bpy)_3^{2+}$, improve the ECL efficiency and remarkably improve the electric conductivity of the proposed sensor. Moreover, the PEI-rGO can act as co-reactant and immobilized platform in the same time, which simplified the preparation of the sensor.

Polyamidoamine (PAMAM) dendrimers are hyper-branched and three-dimensional macromolecules with hundreds of functional groups at the periphery. It is well-known in designing biosensors due to its unique properties [26–28]. Aminated-terminated polyamidoamine (PAMAM, G4) dendrimers have many amino groups in their molecular backbones, which makes them serve as a co-reactant to the ECL of $Ru(bpy)_3^{2+}$. Therefore, they are introduced to construct the proposed sensor for further signal amplification and high sensitivity. However, the conductivity of PAMAM is poor, which limits its application in biosensors. In order to solve the problem, Au nanoparticles (AuNPs) were decorated on the surface of the PAMAM via Au-N bonds. The formed AuNPs-PAMAM can effectively immobilize the antibody and enhance the ECL signal.

Inspired by all those perspectives, we constructed a new sensitive solid-state $Ru(bpy)_3^{2+}$ ECL sandwiched immunosensor with two co-reactants labeled detection antibody (Ab_2). The capture antibody (Ab_1) was assembled on the Nafion-Ru-PtNPs layer which was modified on the bare glass carbon electrode (GCE). Simultaneously, the AuNPs-PAMAM was decorated on the PEI-rGO to obtain AuNPs-PAMAM/PEI-rGO which was used to immobilize the Ab_2 . With two different co-reactants in the AuNPs-PAMAM/PEI-rGO, the ECL signal of the immunosensor was drastically amplified and the detection sensitivity was accordingly improved. Moreover, based on this method, the preparation of the sensor was significantly simplified and the proposed sensor showed a new promising platform to clinical immunoassay.

2. Experimental

2.1. Reagents and material

AFP antibody (Anti-AFP), antigen (AFP), antigen (CEA) and antigen (PSA) standard solutions were purchased from Biocell (Zhengzhou, China). Phosphate buffer solutions (PBS) with pH 7.4 were prepared by mixing standard stock solutions of 0.1 M K_2HPO_4 , 0.1 M NaH_2PO_4 , and 0.1 M KCl and adjusting the pH with 0.1 M HCl or NaOH, then diluting with double distilled water. Gold chloride ($HAuCl_4 \cdot 4H_2O$) and Albumin from bovine serum (BSA) (96–99%) were obtained from Shanghai fine chemical materials institute. Polyamidoamine (PAMAM) dendrimers were purchased from Weihai CY Dendrimer Technology Co., Ltd. Poly(ethylenimine) (PEI), 3-thiophenemalonic acid (TA), $Ru(bpy)_3Cl_2 \cdot 6H_2O$, Nafion (5%, V/V), $H_2PtCl_6 \cdot 6H_2O$, $H_2AuCl_6 \cdot 4H_2O$ and sodium citrate were purchased from Sigma Chemical Co. (St. Louis, MO, USA). Graphene Oxide was received from Nanjing Xianfeng Nano Go. (Nanjing, China). All chemicals were of analytical grade and used without further purification. All solutions were prepared with double distilled water and stored in the refrigerator (4 °C).

2.2. Apparatus

The ECL emission was monitored by a model MPI-A electrochemiluminescence analyzer (Xi'An Remax Electronic Science & Technology Co. Ltd., Xi'An, China). Electrochemical impedance spectroscopy (EIS) measurements were carried out with a CHI 610A electrochemistry workstation (Shanghai CH Instruments, China). A three-electrode electrochemical cell was composed of a modified glass carbon electrode (GCE, $\phi=4$ mm) as the working electrode, a platinum wire as the auxiliary electrode, and an Ag/AgCl (sat. KCl) as the reference electrode. GCE, platinum wire and AgCl electrode were purchased from Tianjin Aidahengsheng technology Co. Ltd., China. Centrifuge was purchased from Hunan Xiangyi Centrifuge Instrument Co. Ltd., China. The morphologies of different nanomaterial were characterized by scanning electron microscopy (SEM, S-4800, Hitachi, Tokyo, Japan) at an acceleration voltage of 20 kV and transmission electron microscope (TEM, TECNAI 10, Philips Fei Co., Hillsboro, OR).

2.3. Preparation of Nafion-Ru-PtNPs

Nafion-Ru-PtNPs were prepared by a simple method. Firstly, Ru-PtNPs were prepared by mixing the PtNPs solution with $Ru(bpy)_3^{2+}$ aqueous solution according to a previous literature with a little modification [29]. Briefly, 2 mL of 0.019 M H_2PtCl_6 aqueous solution was diluted to 50 mL with water, and then 0.5 mL of 0.3 M TA was added into the solution. The solution was heated at 100 °C for 20 min. When it turned to be a dark brown solution, Pt nanoparticles (PtNPs) were well formed. Then, 1 mL of 0.038 M $Ru(bpy)_3Cl_2$ aqueous solution was added into 50 mL of PtNPs solution with vigorous stirring. Several minutes later, Ru-PtNPs were formed. In order to improve the film forming ability of Ru-PtNPs, 1 mL Nafion solution (5%, wt/wt) was added into Ru-PtNPs under stirring and Nafion-Ru-PtNPs were prepared successfully.

2.4. Preparation of PEI-rGO

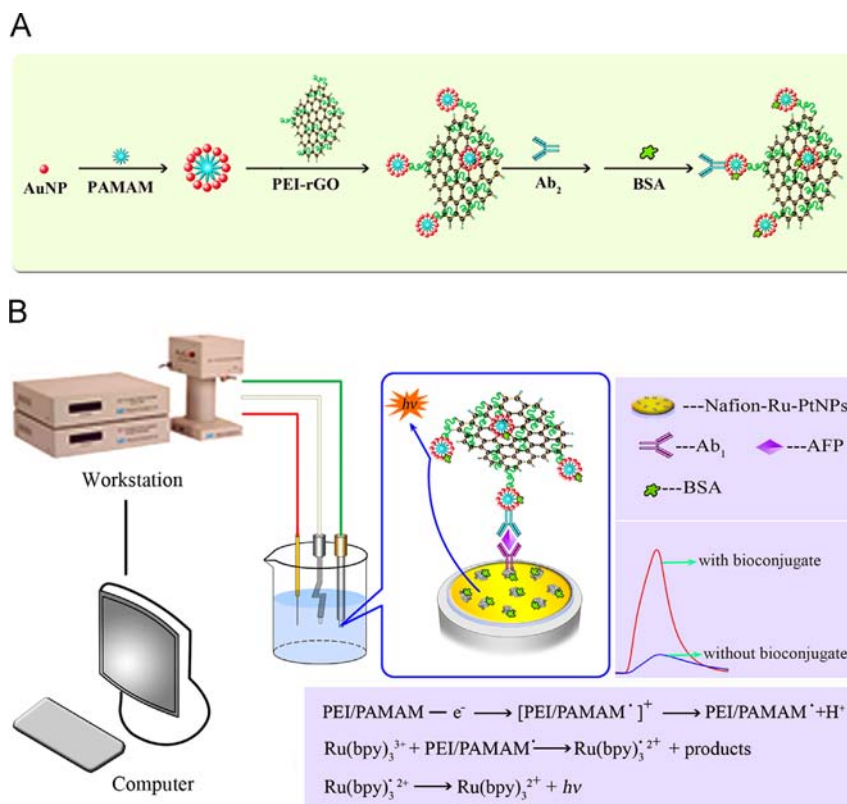
The PEI-rGO was prepared according to literature with a little modification [30]. A stable dispersion of exfoliated GO sheets (1 mg mL^{-1} , 10 mL) was mixed with PEI (3%, 1 mL) and heated under refluxing at 135 °C for about 3 h. The PEI here served as reductant to reduce graphene oxide sheets, which was immobilized on the graphene in the same time.

2.5. Preparation of Au nanoparticles

Au nanoparticles were prepared according to a previous literature with a little modification [31]. In brief, 2.5 mL of 1% sodium citrate was added into 100 mL of boiling 0.01% $HAuCl_4$ solution with vigorous stirring. When the color changed from yellow to red violet, the mixture was boiled continually for 10 min under stirring. Then, it was cooled in room temperature and Au nanoparticles were well formed.

2.6. Preparation of $Ab_2/AuNPs-PAMAM/PEI-rGO$ (Ab_2 bioconjugate)

The $Ab_2/AuNPs-PAMAM/PEI-rGO$ was synthesized by the following steps (Scheme 1A). Firstly, PAMAM (0.07 mM) was dissolved in 1 mL AuNPs solution which had been prepared before the step and stirred for 6 h in room temperature. Then, 1 mL PEI-rGO, which had been prepared before the step, was added into the mixture and stirred for another 6 h. Subsequently, the Ab_2 was added into the as-prepared AuNPs-PAMAM/PEI-rGO solution, and the mixture of them was slightly stirred for 12 h at 4 °C to conjugate Ab_2 to the complex. After that, 100 μL BSA solution (1%, wt/wt) was implemented to block the non-specific adsorption



Scheme 1. Illustration of (A) the preparation of Ab₂/AuNPs-PAMAM/PEI-rGO (B) the preparation and reaction mechanism of the ECL immunosensor.

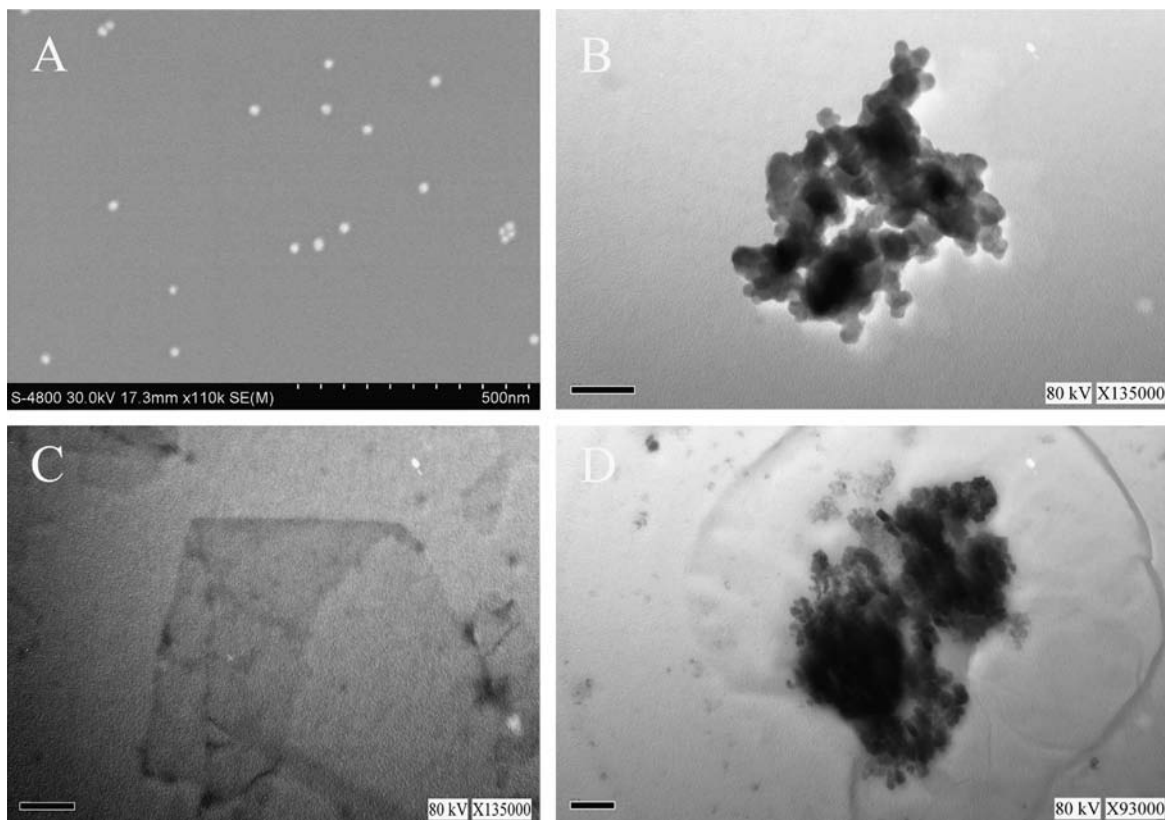


Fig. 1. SEM images of (A) AuNPs; TEM images of (B) AuNPs-PAMAM (C) PEI-rGO (D) AuNPs-PAMAM/PEI-rGO; the scale bar of TEM images is 100 nm.

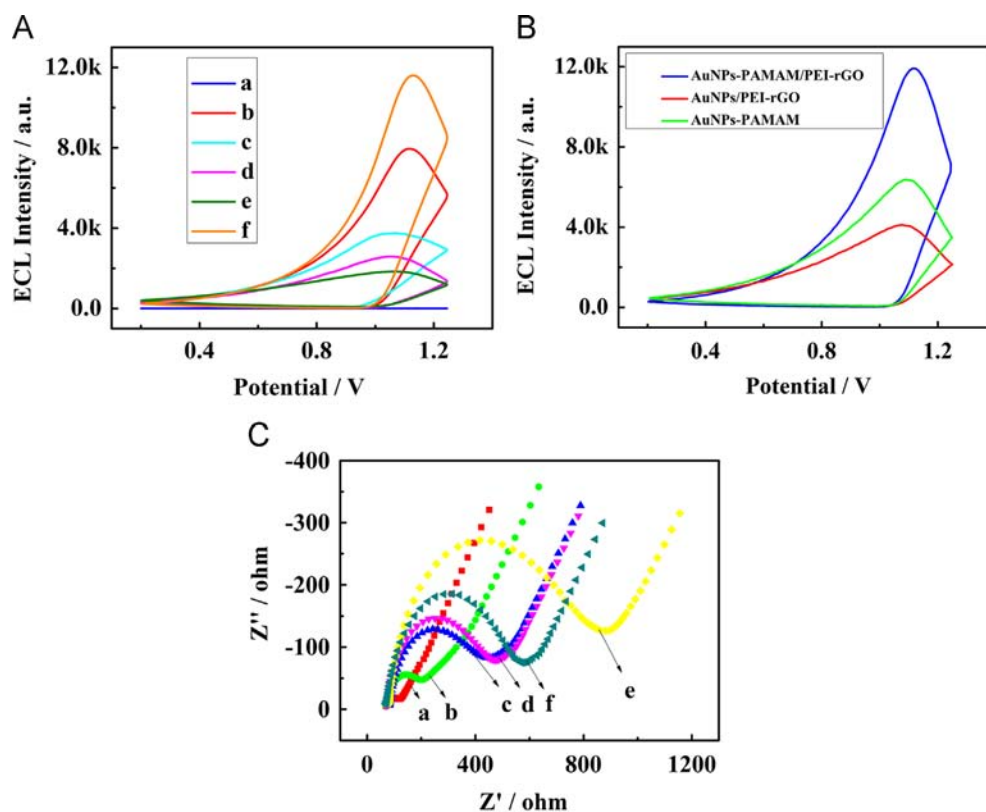


Fig. 2. (A) ECL-time profiles of (a) the bare GCE; (b) GCE/Nafion-Ru-PtNPs; (c) GCE/Nafion-Ru-PtNPs/Ab₁; (d) GCE/Nafion-Ru-PtNPs/Ab₁/BSA; (e) GCE/Nafion-Ru-PtNPs/Ab₁/BSA/AFP; (f) GCE/Nafion-Ru-PtNPs/Ab₁/BSA/AFP/Ab₂/AuNPs-PAMAM/PEI-rGO in 0.1 M PBS (pH 7.4) with a scanning potential from 0.2 to 1.25 V and at a scan rate of 100 mV s⁻¹. (B) ECL profiles of the proposed ECL immunosensor in 1 ng mL⁻¹ AFP incubated with different Ab₂ bioconjugates, AuNPs-PAMAM/PEI-rGO and AuNPs/PEI-rGO. (C) EIS image for (a) the bare GCE; (b) GCE/Nafion-Ru-PtNPs; (c) GCE/Nafion-Ru-PtNPs/Ab₁; (d) GCE/Nafion-Ru-PtNPs/Ab₁/BSA; (e) GCE/Nafion-Ru-PtNPs/Ab₁/BSA/AFP; (f) GCE/Nafion-Ru-PtNPs/Ab₁/BSA/AFP/Ab₂/AuNPs-PAMAM/PEI-rGO in 0.1 M KCl solution containing 5 mM (1:1) [Fe(CN)₆]^{3-/4-} with the range from 100 kHz to 10 MHz and an alternate voltage of 5 mV.

of the AuNPs surface with the reaction time of 20 min. The resulting complex was centrifuged (8000 rpm, 4 °C, 5 min) and washed three times with PBS (pH 7.4). The sandwiched Ab₂ bioconjugate, obtained after these steps, was redispersed in PBS (pH 7.4) and stored in 4 °C for further use.

2.7. Fabrication of the electrochemiluminescence immunosensor

The proposed sensor was fabricated by the following steps (Scheme 1B). Firstly, the GCE was polished with 0.3, 0.05 mm alumina powder sequentially to obtain a mirror like surface. Then, it was washed with doubly distilled water and successively sonicated in ethanol, distilled water, respectively. The cleaned electrode was coated with 5 μL as-prepared Nafion-Ru-PtNPs and air-dried at room temperature. Next, 18 μL Ab₁ was dropped on the electrode surface for 8 h in 4 °C. Subsequently, the electrode was incubated with 18 μL BSA solution (1%, wt/wt) to block the non-specific adsorption. Followed by these steps, 18 μL Ab₂ bioconjugate solution was incubated on the modified electrode for 30 min. Finally, the electrode was washed by doubly distilled water and PBS (pH 7.4) as above and prepared for ECL measurements.

3. Results and discussion

3.1. Characteristics of different nanomaterials

The size and morphologies of the synthesized nanocomposites were characterized by scanning electron microscope (SEM) and

transmission electron microscope (TEM). As shown in Fig. 1(A), the AuNPs were separated spherical particles with a diameter of 15 to 20 nm. In the presence of PAMAM, the AuNPs were gathered to clusters as observed from Fig. 1(B). As shown in Fig. 1(C), the PEI-rGO was presented to be a typical flake-like shape with slight wrinkles on the surfaces. Compared with Fig. 1(C), Fig. 1(D) showed that clusters of AuNPs were laid on the surface of PEI-rGO. All these proof indicated that the AuNPs-PAMAM/PEI-rGO was formed successfully.

3.2. Characteristics of the electrochemiluminescence immunosensor

The fabrication process of the ECL immunosensor was characterized by ECL in 3 mL 0.1 M PBS solution (pH 7.4). The voltage of the photo multiplier tube (PMT) was set at 800 V. And the applied potential was 0.2–1.25 V (vs. Ag/AgCl) with a scan rate of 100 mV s⁻¹ in the process of detection. The results of corresponding ECL signal were put in Fig. 2(A). First, there was almost no ECL signal observed on the bare GCE (curve a), which might be caused by the absence of luminescence reagent. When Nafion-Ru-PtNPs complex was placed on the surface of electrode, a quite high ECL signal was observed (curve b). Then, an obvious decreasing of the ECL signal was observed when the electrode was successfully immobilized by Ab₁ (curve c). That was because Ab₁ hindered the electron transport. When BSA was used to block non-specific adsorption, a further decreasing of ECL signal was obtained (curve d). The reason might be that BSA hindered the electron transport. Then the ECL signal declined after incubating with AFP (curve e), which could be attributed to the obstruction of antigen-antibody

immunocomplex. However, a large increase of ECL signal was obtained when the Ab_2 bioconjugate reacted with the antigen molecules on the electrode surface (curve f). The potential reason might be that PEI and PAMAM had strong enhancement to $\text{Ru}(\text{bpy})_3^{2+}$ ECL as expected and apparently improved the performance of sandwiched immunosensor. In order to further illustrate the enhancement of PAMAM, a contrast experiment was done and the results were presented in Fig. 2(B). The ECL signal of the immunosensor with AuNPs-PAMAM/PEI-rGO (blue curve) was obviously higher than that of AuNPs/PEI-rGO (red curve) and AuNPs-PAMAM (green curve). The potential reason was that PAMAM was an effective co-reactant which has strong enhancement to $\text{Ru}(\text{bpy})_3^{2+}$ ECL and gave the largest effect as co-reactant.

To further illustrate the fabrication process of the ECL immunosensor, the electrochemical impedance spectroscopy (EIS) was also performed at different modified electrodes in 5 mM $[\text{Fe}(\text{CN})_6]^{3-/4-}$. As shown in Fig. 2(C), the bare GCE showed a small semi-circle (curve a). While Nafion-Ru-PtNPs coated on the electrode, the R_{et} increased obviously (curve b), which was contributed to the inhibition effect of Nafion for electron transfer, indicating that Nafion-Ru-PtNPs complex was immobilized on the GCE surface successfully. Then, R_{et} increased when Ab_1 (curve c), BSA (curve d) and AFP (curve e) were successively adsorbed onto the electrode surface. The reason might be that a big molecular protein blocked the electron transport and hindered the diffusion of ferricyanide toward the electrode surface. Finally, when the Ab_2 bioconjugate was coupled with the AFP antigen on the electrode, an obvious decrease of the R_{et} could be observed (curve f), which was basically ascribed to the fact that AuNPs and graphene facilitated the electron transfer.

3.3. ECL detection of AFP with the proposed immunosensor

The quantitative range of the proposed ECL immunosensor was explored by incubating AFP with different concentrations. As shown in the Fig. 3, the intensity of the ECL increased linearly with the increasing concentration of AFP. The linear relationship between ECL intensity and the logarithm of AFP concentrations

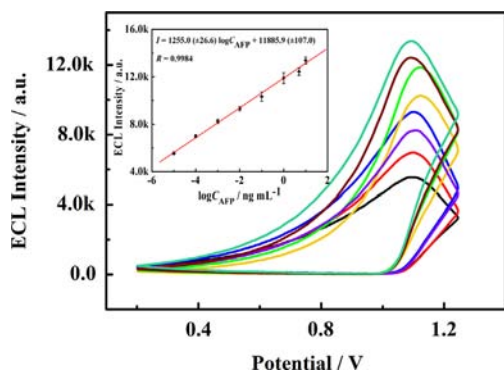


Fig. 3. ECL profiles of the proposed ECL immunosensor in different concentrations of AFP (ng mL^{-1}) (a) 0.00001, (b) 0.0001, (c) 0.001, (d) 0.01, (e) 0.1, (f) 1, (g) 5 and (h) 10. The inset is logarithmic calibration curve for AFP detection in 0.1 M PBS (pH 7.4).

Table 1
Comparison of our research with other methods for AFP detection.

Measurement protocol	Linear range / $\text{ng} \cdot \text{mL}^{-1}$	Detection limit / $\text{pg} \cdot \text{mL}^{-1}$	References
Electrochemical immunoassay	0.01–40	2.3	Parshetti et al., 2013
Chemiluminescence	0–1200	3000.0	Wang et al., 2008
Biosensor based on imaging ellipsometry	20.0–200.0	5000.0	Huang et al., 2011
Electrochemiluminescence	0.0001–80	0.03	Cao et al., 2011
Electrochemiluminescence	0.00001–10	0.0033	Present work

was ranged from 0.01 pg mL^{-1} to 10 ng mL^{-1} with a low detection limit of 3.3 fg mL^{-1} ($S/N=3$). The regression equation was $I = 1255.0 (\pm 26.6) \lg C_{\text{AFP}} + 11885.9 (\pm 107.0)$ with a correlation coefficient of 0.9984 (where I was the ECL intensity, and C_{AFP} was the concentration of AFP). Additionally, we made a comparative study between proposed methods with previous reported (Table 1) [6,32–34]. Obviously, it exhibited good sensitivity and low detection limit.

3.4. Stability, selectivity and reproducibility of the immunosensor

To investigate the stability, the immunosensor was studied under continuous cyclic potential scans for 10 cycles. As shown in Fig. 4(A), there were no obvious changes for ECL signal. The good stability may be caused by followed possible reasons. Firstly, Nafion-Ru-PtNPs has high chemical and thermal stability [29]. Secondly, the AuNPs has great biocompatibility and remarkably improve the poor conductivity of PAMAM. Thirdly, PEI and PAMAM immobilized the AuNPs-PAMAM/PEI-rGO were effective co-reactant which could improve the stability of $\text{Ru}(\text{bpy})_3^{2+}$ ECL.

To investigate the selectivity and specificity of the proposed immunosensor, carcinoembryonic antigen (CEA) and prostate specific antigen (PSA) were used as possible interfering substances. CEA and PSA were both considered as tumor biomarker in immunoassay detection, and they may have possible interference in the research of immunoassay [21,35,36]. The results were presented in the Fig. 4(B). The ECL signal of the immunosensor that was incubated with PSA or CEA had almost no difference compared with the blank solution. Simultaneously, the ECL signal of the immunosensor that was incubated with 0.1 ng mL^{-1} AFP containing different interfering substances had no obvious changes compared to the ECL response obtained in the pure 0.1 ng mL^{-1} AFP, which suggested that the proposed immunosensor had a good selectivity. The reproducibility of the proposed immunosensor was evaluated by the relative standard deviation (ECL response) of intra- and interassays. The relative standard deviation (RSD) of the intra-assay was 3.8%. The RSD of the inter-assay was 1.7%. Therefore, the reproducibility and repeatability of the proposed immunoassay was acceptable.

3.5. Preliminary analysis of real samples

In order to monitor the feasibility of the ECL immunosensor, recovery experiments were performed by standard addition methods in human serum. As shown in Table 2, the recovery (between 95.4% and 106.3%) was acceptable, which provided a promising tool for determining AFP in real biological samples.

4. Conclusions

In summary, a novel solid-state ECL immunosensor of $\text{Ru}(\text{bpy})_3^{2+}$ was constructed based on AuNPs-PAMAM and PEI-rGO. The ECL signal of $\text{Ru}(\text{bpy})_3^{2+}$ was remarkably enhanced by the following reasons: (1) PEI and PAMAM were two effective co-reactants to the ECL of $\text{Ru}(\text{bpy})_3^{2+}$; (2) Electron transfer was

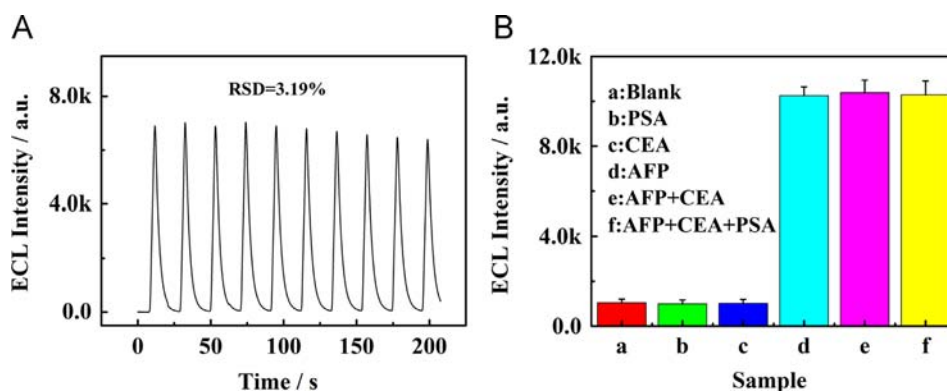


Fig. 4. (A) The stability of the proposed ECL immunosensor incubated with $0.0001 \text{ ng mL}^{-1}$ AFP under consecutive cyclic potential scans for 10 cycles. (B) The selectivity of the proposed ECL immunosensor. (a) Blank, (b) PSA (1 ng mL^{-1}), (c) CEA (1 ng mL^{-1}), (d) AFP (0.1 ng mL^{-1}), (e) a mixture containing AFP (0.1 ng mL^{-1}), CEA (1 ng mL^{-1}) and (f) a mixture containing AFP (0.1 ng mL^{-1}), CEA (1 ng mL^{-1}), PSA (1 ng mL^{-1}). Scanning from 0.2 to 1.25 V at a scan rate of 100 mV s^{-1} . (Error bars: SD, $n=3$).

Table 2

Preliminary analysis of real samples.

Sample number	Add / ng mL^{-1}	Found/ ng mL^{-1}	Recovery /%	RSD (%)
1	0.0001	0.000097	97.3	4.9
2	0.001	0.00106	106.3	2.0
3	0.1	0.095	95.4	3.8
4	1	1.004	100.4	3.9

significantly promoted by introducing rGO and AuNPs; (3) With good biocompatibility, the Ru-PtNPs was a superior solid-state ECL substrate which could enhance the ECL stability and improve ECL efficiency. The experimental results demonstrated that the proposed sandwiched immunosensor had high sensitivity, low limit detection, good stability, acceptable precision and accuracy. Therefore, the proposed immunosensor provided a new signal amplification strategy in ECL biosensor and extended the application of it in clinical diagnostics and research.

Acknowledgments

This work was financially supported by the NNSF of China (21075100, 21275119), State Key Laboratory of Electroanalytical Chemistry (SKLEAC2010009), Ministry of Education of China (Project 708073), Natural Science Foundation of Chongqing City (CSTC-2010BB4121, CSTC-2011BA7003), Specialized Research Fund for the Doctoral Program of Higher Education (20100182110015), China Postdoctoral Science Foundation (2014M550454) and the Fundamental Research Funds for the Central Universities (XDJK2013A008, XDJK2013A027, XDJK2014C138).

References

- [1] M. Shiwa, Y. Nishimura, R. Wakatabe, A. Fukawa, H. Arikuni, H. Ota, T. Yamori, *Biochem. Biophys. Res. Commun.* 309 (2003) 18–25.
- [2] J.J. Flanagan, A. Arjomandia, M.L. Delanoya, E. Du Paty, P. Galeab, D. Launeb, F. Rieunierb, R.P. Walkera, S.R. Bindera, *J. Immunol. Methods* 406 (2014) 34–42.
- [3] J.N. Tian, L.J. Zhou, Y.C. Zhao, Y. Wang, Y. Peng, S.L. Zhao, *Talanta* 92 (2012) 72–77.
- [4] Y.L. Wang, Y. Zhang, Y. Su, F. Li, H.M. Ma, H. Li, B. Du, Q. Wei, *Talanta* 124 (2014) 60–66.
- [5] Y.B. Lou, T.T. He, F. Jiang, J.J. Shi, J.J. Zhu, *Talanta* 122 (2014) 135–139.
- [6] Y.L. Cao, R. Yuan, Y.Q. Chai, L. Mao, H. Niu, H.J. Liu, Y. Zhuo, *Biosens. Bioelectron.* 31 (2012) 305–309.
- [7] L. Mao, R. Yuan, Y.Q. Chai, Y. Zhuo, Y. Xiang, *Biosens. Bioelectron.* 26 (2011) 4204–4208.
- [8] Y. Zhuo, G.F. Gui, Y.Q. Chai, N. Liao, K. Xiao, R. Yuan, *Biosens. Bioelectron.* 53 (2014) 459–464.
- [9] G.F. Blackburn, H.P. Shah, J.H. Kenten, J. Leland, R.A. Kamin, J. Link, D.B. Talley, *Clin. Chem.* 37 (1991) 1534–1539.
- [10] M.M. Richter, *Chem. Rev.* 104 (2004) 3003–3036.
- [11] W.J. Miao, J.P. Choi, A.J. Bard, *J. Am. Chem. Soc.* 124 (2002) 14478–14485.
- [12] H.J. Wang, R. Yuan, Y.Q. Chai, H. Niu, Y.L. Cao, H.J. Liu, *Biosens. Bioelectron.* 37 (2012) 6–10.
- [13] M.L. Yang, B.Y. Jiang, J.Q. Xie, Y. Xiang, R. Yuan, Y.Q. Chai, *Talanta* 125 (2014) 45–50.
- [14] L.J. Xiao, Y.Q. Chai, R. Yuan, Y.L. Cao, H.J. Wang, L.J. Bai, *Talanta* 115 (2013) 577–582.
- [15] W.Z. Zhang, J.M. Zhang, H.L. Zhang, L.Y. Cao, R. Zhang, Z.Q. Ye, L.J. Yuan, *Talanta* 116 (2013) 354–360.
- [16] X.Y. Yang, A.G. Wang, J.L. Liu, *Talanta* 114 (2013) 5–10.
- [17] R. Pyati, M.M. Richter, *Annu. Rep., Prog. Chem. Sect. C: Phys. Chem* 103 (2007) 12–78.
- [18] J.P. Choi, A.J. Bard, *Anal. Chim. Acta* 541 (2005) 141–148.
- [19] M.C. Daniel, D. Astruc, *Chem. Rev.* 104 (2004) 293–346.
- [20] N. Liao, Y. Zhuo, Y.Q. Chai, Y. Xiang, Y.L. Cao, R. Yuan, J. Han, *Chem. Commun.* 48 (2012) 7610–7612.
- [21] Y. Zhuo, N. Liao, Y.Q. Chai, G.F. Gui, M. Zhao, J. Han, R. Yuan, *Anal. Chem.* 86 (2013) 1053–1060.
- [22] X.Y. Jiang, Y.Q. Chai, R. Yuan, Y.L. Cao, Y.F. Chen, H.J. Wang, X.X. Gan, *Anal. Chim. Acta* 783 (2013) 49–55.
- [23] A.K. Geim, K.S. Novoselov, *Nat. Mater.* 6 (2007) 183–191.
- [24] D. Li, M.B. Müller, S. Gilje, R.B. Kaner, G.G. Wallace, *Nat. Nanotech.* 3 (2008) 101–105.
- [25] Y.L. Yuan, X.X. Gou, R. Yuan, Y.Q. Chai, Y. Zhuo, X.Y. Ye, X.X. Gan, *Biosens. Bioelectron.* 30 (2011) 123–127.
- [26] B. Kavosi, A. Salimi, R. Hallaj, K. Amani, *Biosens. Bioelectron.* 52 (2014) 20–28.
- [27] M. Štofik, Z. Štrýhal, J. Malý, *Biosens. Bioelectron.* 24 (2009) 1918–1923.
- [28] L.H. Tang, Y.H. Zhu, L.H. Xu, X.L. Yang, C.Z. Li, *Electroanalysis* 19 (2007) 1677–1682.
- [29] X.P. Sun, Y. Du, L.X. Zhang, S.J. Dong, E.K. Wang, *Anal. Chem.* 78 (2006) 6674–6677.
- [30] L.Y. Cao, Y.L. Liu, B.H. Zhang, L.H. Lu, *A.C.S. Appl., Mater. Interfaces* 2 (2010) 2339–2346.
- [31] L.L. Pang, J.S. Li, J.H. Jiang, G.L. Shen, R.Q. Yu, *Anal. Biochem.* 358 (2006) 99–103.
- [32] G.K. Parshetti, F.H. Lin, R.A. Doong, *Sens. Actuators, B* 186 (2013) 34–43.
- [33] C.H. Huang, Y.Y. Chan, C.X. Wang, W. Zhu, H.W. Ma, G. Jin, *Thin Solid Films* 519 (2011) 2763–2767.
- [34] X. Wang, Q.Y. Zhang, Z.J. Li, X.T. Ying, J.M. Lin, *Clin. Chim. Acta* 393 (2008) 90–94.
- [35] H.J. Wang, L.J. Bai, Y.Q. Chai, R. Yuan, *Small* 10 (2014) 1857–1865.
- [36] J. Ji, L. He, Y.Y. Shen, P.P. Hu, X.H. Li, L.P. Jiang, J.R. Zhang, L.L. Li, J.J. Zhu, *Anal. Chem.* 86 (2014) 3284–3290.



Determination of trace uranyl ion by thermoresponsive porphyrin-terminated polymeric sensor

Xiaowen Shu^{a,b,1}, Yingjie Wang^{a,b,1}, Shuang Zhang^{a,b}, Li Huang^{a,b}, Shuao Wang^a, Daoben Hua^{a,b,c,*}

^a Jiangsu Key Laboratory of Radiation Medicine and Protection, School for Radiological and Interdisciplinary Sciences (RAD-X), and School of Radiation Medicine and Protection, Medical College, Soochow University, Suzhou 215123, China

^b Department of Polymer Science and Engineering, College of Chemistry, Chemical Engineering and Materials Science, Soochow University, Suzhou 215123, China

^c Collaborative Innovation Center of Radiological Medicine of Jiangsu Higher Education Institutions, Suzhou 215123, China

ARTICLE INFO

Article history:

Received 4 April 2014

Received in revised form

25 July 2014

Accepted 30 July 2014

Available online 6 August 2014

Keywords:

Uranyl ion

Fluorescent sensor

Thermo-responsive

High sensitivity

ABSTRACT

Uranyl ion exists at trace levels in the environment and can cause severe adverse effects to human health. Therefore, it is desirable to develop analytical methods that can determine the trace uranyl ion in aqueous medium. We report here a new method using a thermo-responsive polymeric fluorescent sensor. Specifically, 5,10,15,20-tetrakis(4-carboxyphenyl)-porphyrin terminated poly(*N*-isopropylacrylamide) (TCPP-PNIPAM) was synthesized by controlled free radical polymerization for the detection of uranyl ion. The maximum fluorescence intensity at ~658 nm of TCPP-PNIPAM increases with molecular weights and is also closely related to the temperature. The polymeric sensor is sensitive to pH (1.0~5.0) with a fast responsive time (~3 min). Under optimized experimental conditions, the sensor exhibits a stable response for uranyl ion with high selectivity over a concentration range from 1.0×10^{-3} to 1.0×10^{-7} mol/L. For the trace uranyl ion (such as 1.0×10^{-8} or 10^{-9} mol/L), the determination could be successfully achieved after concentrating 100 times by centrifugation above 32 °C. The properties enable the polymeric sensor to have great potential for environmental application.

© 2014 Elsevier B.V. All rights reserved.

1. Introduction

Uranium is a radioactive element that exists naturally in the environment [1]. Nowadays human beings have a high chance of

Abbreviations: (UO_2^{2+}), Uranyl ion; (THF), tetrahydrofuran; (TCPP-PNIPAM), 5,10,15,20-tetrakis(4-carboxyphenyl)-porphyrin terminated poly(*N*-isopropylacrylamide); (EPA), Environmental Protection Agency; (PNIPAM), poly(*N*-isopropylacrylamide); (TCPP), 5,10,15,20-tetrakis(4-carboxyphenyl)porphyrin; (RAFT), reversible addition-fragmentation chain transfer; (DMF), *N,N*-dimethylformamide; (EG), ethylene glycol; (AIBN), 2, 2'-Azobisobutyronitrile; (DDACT), *S*-1-dodecyl-*S'*-(α,α' -dimethyl-*a*"-acetic acid) trithiocarbonate; (^1H NMR), ^1H nuclear magnetic resonance; (HPPS), high-performance particle sizer; (FT-IR), Fourier transform infrared; (GPC), gel permeation chromatographer; (DCC), *N,N'*-dicyclohexylcarbodiimide; (DMAP), dimethylaminopyridine; (PDI), polydispersity; (LCST), low critical solution temperature

* Corresponding author at: Jiangsu Key Laboratory of Radiation Medicine and Protection, School of Radiological and Interdisciplinary Sciences (RAD-X), and School of Radiation Medicine and Protection, Medical College, Soochow University, Suzhou 215123, China. Tel.: +86 512 65882050; fax: +86 512 65883261.

E-mail addresses: shuxiaowen1204@163.com (X. Shu), wangyingjie0707@126.com (Y. Wang), zhangshuang8922@gmail.com (S. Zhang), huanglizby@163.com (L. Huang), shuaoawang@suda.edu.cn (S. Wang), dbhua_lab@suda.edu.cn (D. Hua).

¹ These two authors contributed equally to this work.

<http://dx.doi.org/10.1016/j.talanta.2014.07.085>

0039-9140/© 2014 Elsevier B.V. All rights reserved.

being exposed to uranium that can cause severe adverse effects to human health [2,3], since uranium is one of the main sources in nuclear energy generation and enriched uranium is a major component in nuclear weapons. Uranium has many forms in aqueous solution, and the most soluble or bioavailable form is uranyl (UO_2^{2+}). The maximum contamination level of UO_2^{2+} in drinking water is defined as 1.30×10^{-7} mol/L by U.S. Environmental Protection Agency (EPA) [4]. Therefore, it is desirable to have simple and convenient analytical methods that can determine the uranyl present in the aqueous medium at trace level.

Many analytical techniques, such as inductively coupled plasma-mass spectrometry [5–7], atomic absorption spectrometry [8,9] require expensive and complicated instruments, making on-site real-time sensing difficult. Optical sensing approaches (e.g. laser fluorimetry [10,11], absorption [12,13], luminescence [14]) and electrochemical approaches [15,16] for the detection of environmental and biological uranium have been developed in the field of chemical sensors for several decades. Among the optical sensors, the fluorescence-based one is a very appealing technique for future practical applications due to its intrinsic sensitivity and high spatial resolution [17,18]. For example, Ganesh et al. reported the determination of uranium concentration in raffinate stream of Purex process during reprocessing of spent

nuclear fuel by using fluorescence enhancing reagent such as sodium pyrophosphate [19]; Angel et al. reported the detection of uranyl ion via fluorescence quenching and photochemical oxidation of calcein with the detection limit of 4.0×10^{-8} mol/L [20]; recently Liao et al. reported the separation and determination of trace uranium using a double-receptor sandwich supramolecule method based on immobilized salophen and fluorescence labeled oligonucleotide [21]. However, these methods always require additional chemicals (such as sodium pyrophosphate, calcein and oligonucleotide) or devices (such as ball lens [22]) to obtain high sensitivity and high selectivity.

Recently we noticed the fluorescence-signaling DNA aptamers and deoxyribozymes were used as novel biosensing moieties for heavy metal ions [23–25]. For example, Lu et al. reported a catalytic beacon sensor for UO_2^{2+} based on an in vitro-selected UO_2^{2+} -specific DNAzyme, and this method has a 45 pM detection limit and million-fold selectivity [26]. However, this kind of biosensors (such as the uranyl-specific DNAzyme) is costly due to the complication in vitro-selection. Therefore, it is still desirable to develop new simple and convenient methods with high sensitivity and high selectivity for the detection of trace uranium in the environment.

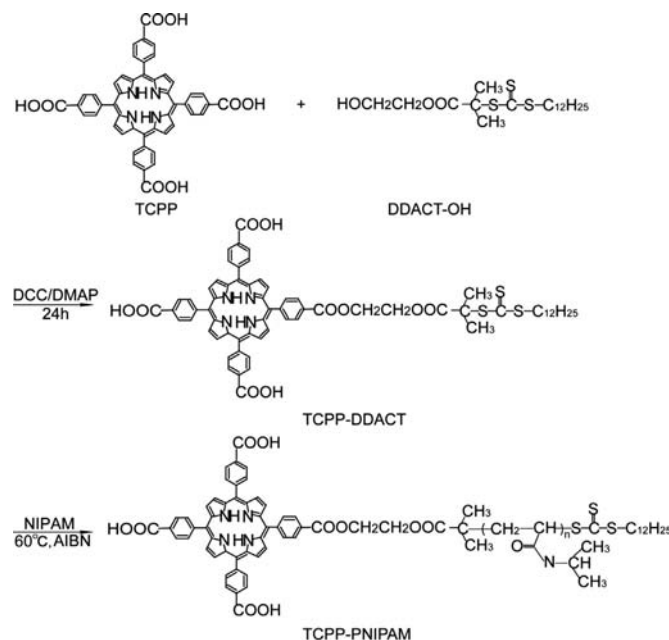
Porphyrin derivatives have been employed widely as fluorophores in probes owing to their excellent photophysical properties [27,28], but their applications were always limited by their poor solubility in water [29], which can lead to aggregation and function degradation. Recently Tian et al. [30] reported a random copolymer, poly(*N*-isopropylacrylamide-co-PtPorphyrin), consisting of *N*-isopropylacrylamide and platinum (II) phenylporphyrin units, behaving as an optical dual sensor for oxygen and temperature. However, the fluorescence intensity was low due to the aggregation quenching of the hydrophobic phenylporphyrins, and the molecular weights could not be controlled for the design of the sensor by this method.

We report here a new method using a thermo-responsive polymeric fluorescent sensor. Specifically, 5,10,15,20-tetrakis(4-carboxyphenyl) porphyrin (TCPP) terminated poly(*N*-isopropylacrylamide) (PNIPAM) was synthesized by controlled reversible addition-fragmentation chain transfer (RAFT) radical polymerization [31] (Scheme 1) for the detection of UO_2^{2+} . The carboxyl groups and the soluble PNIPAM polymer chain would improve the solubility of TCPP-PNIPAM in water, and the specific-coordination property of porphyrin with uranyl would endow the sensor a good selectivity. In general, porphyrin exhibits strong fluorescence in visible region owing to the conjugated double bond system and the high mobility of its π -electron [32], and the selective coordination with uranyl [33] would result in a decrease of porphyrin fluorescence. Furthermore, the thermo-responsive polymer PNIPAM has a hydrophilic coil-hydrophobic globule transition around 32 °C [34,35], which makes the aqueous solution be easily concentrated by the centrifugation above 32 °C for the effective detection of trace uranyl, thereby greatly extending the detection limit of this method. To the best of our knowledge, it is the first time to determine trace uranyl by thermo-responsive polymeric sensors.

2. Experimental section

2.1. Materials and reagents

N-isopropylacrylamide (NIPAM, 99%) was purchased from J&K Chemical Co. Ltd. and was purified by re-crystallization in benzene/*n*-hexane (3:1) before use. Tetrahydrofuran (THF, Sinopharm Chemical Reagent Co., Ltd., AR), *N,N*-dimethylformamide (DMF, Sinopharm Chemical Reagent Co., Ltd., AR) and ethylene glycol



PNIPAM: *N*-isopropylacrylamide

TCPP: 5,10,15,20-Tetrakis(4-carboxyphenyl)porphyrin

DDACT: S-1-dodecyl-S'-(α,α' -dimethyl- α' -acetic acid) trithiocarbonate

Scheme 1. The schematic for the synthesis of TCPP-PNIPAM.

(EG, Sinopharm Chemical Reagent Co., Ltd., AR) were dried by molecular sieves (4 Å). 2, 2'-Azobisobutyronitrile (AIBN, Sinopharm Chemical Reagent Co., Ltd., CP) was purified by re-crystallization in methanol and dried in a vacuum oven at room temperature. TCPP was synthesized according to the standard Adler method [36] (Fig. S1, see Supporting Information). S-1-dodecyl-S'-(α,α' -dimethyl- α' -acetic acid) trithiocarbonate (DDACT) and DDACT-OH were synthesized according to the modified literature method [37] (Figs. S2 and S3, see Supporting Information). All other chemical agents were used as received.

2.2. Characterization methods

^1H nuclear magnetic resonance (^1H NMR) spectra were obtained on a Varian INVOA-400 instrument working at 300 MHz. The Z average size and the polydispersity index of the particles were measured by a Malvern HPP5001 high-performance particle sizer (HPPS). Fourier transform infrared (FT-IR) spectra were recorded on a Varian-1000 spectrometer: the samples were ground with KBr crystals and the mixture was then pressed into a pellet for IR measurement. The molecular weights and polydispersities of the homopolymers were determined with a Waters 1515 gel permeation chromatographer (GPC) equipped with refractive index detector, using HR1, HR3, and HR4 column with molecular weight range 100–500,000 calibrated with PS standard samples, and THF as the eluent at a flow rate of 1.0 mL/min operated at 30 °C. All fluorescence measurements were conducted on a FLS920 fluorescence spectrometer with the excitation wavelength of 425 nm with an emission wavelength range from 500 to 800 nm.

2.3. Synthesis of TCPP-DDACT

TCPP (1.19 g, 1.5 mmol), *N,N'*-dicyclohexylcarbodiimide (DCC) (0.205 g, 1.0 mmol) and dimethylaminopyridine (DMAP) (0.015 g, 0.12 mmol) were dissolved in dry THF (20 mL), and then DDACT-OH (0.414 g, 1.0 mmol) was added dropwise to the mixture over 2 h

and stirred magnetically for 24 h at room temperature. The resulting mixture was poured into 10-fold petroleum ether, and the precipitate was collected on a filter and washed completely by petroleum ether, and finally dried to give a purple powder. Then the product was re-dissolved in THF, and was poured into 10-fold chloroform to remove un-reacted TCPP as the precipitate. The filtrate was condensed by evaporation under reduced pressure to give TCPP-DDACT as the purple powder, which was dried in vacuum oven at 40 °C (0.89 g, 75.3% yield). The yield was determined by gravimetric methods and calculated based on equation: Yield (%) = $(W_p / W_0) \times 100\%$, where W_p and W_0 stand for weight of crude product and theoretical weight of product, respectively.

2.4. Preparation of TCPP-PNIPAM

A mixture of TCPP-DDACT (0.2953 g, 0.25 mmol trithio groups) and dry THF (5 mL) was stirred magnetically under argon atmosphere. After dissolving completely, AIBN (0.0082 g, 0.050 mmol) and NIPAM (2.50 g, 0.016 mol) were added. The polymerization proceeded at 60 °C for 10, 20 and 30 hours for the preparation of polymers with different molecular weights, respectively. After the polymerization, the polymer was precipitated in 10-fold diethyl ether, and then filtered and dried in a vacuum oven at 40 °C until a constant weight was obtained gravimetrically. Conversions were determined by gravimetric method.

2.5. Effect of temperature and molecular weight on fluorescence property of TCPP-PNIPAM

The stock solution of TCPP-PNIPAM was prepared by dissolving an appropriate amount of TCPP-PNIPAM in water and adjusting the volume to 50 mL in a volumetric flask. Then the solution was stirred in the darkness to avoid decomposition for 48 h to ensure complete dissolution at room temperature.

The fluorescence emission spectra were recorded at the excitation wavelength of 425 nm according to the UV-vis absorption spectra (Fig. S4, see Supporting Information) and with an emission wavelength range from 500 to 800 nm. The fluorescence measurements were performed for the effect of temperature in the temperature range of 26–36 °C with TCPP-PNIPAM ($M_n = 15,500$ g/mol, polydispersity (PDI) = 1.42) at 1×10^{-5} mol/L, and for the effect of molecular weight of TCPP-PNIPAM with (a) $M_n = 8500$ g/mol, PDI = 1.29, (b) $M_n = 10,000$ g/mol, PDI = 1.27, and (c) $M_n = 15,500$ g/mol, PDI = 1.42, respectively.

2.6. Determination of trace uranyl ion with TCPP-PNIPAM

All the experiments were strictly carried out at 25 °C to eliminate the influence of environment temperature. Effect of pH on the detection of uranyl ion with TCPP-PNIPAM was first tested for uranyl determination. The fluorescence experiments were carried out at a pH range from 2.0 to 5.0 for complex solution of UO_2^{2+} (1×10^{-5} mol/L) / TCPP-PNIPAM (1×10^{-5} mol/L, $M_n = 15,500$ g/mol, PDI = 1.42). The pH values were adjusted by the addition of dilute NaOH or HCl solution. The selectivity of the sensor for uranyl was also investigated in the presence of Na^+ , Ca^{2+} , Mg^{2+} , Cl^- , HCO_3^- , Fe^{3+} , Cu^{2+} , Ni^{2+} , and Zn^{2+} , respectively. All stock solutions of these ions were prepared from analytical grade salts.

For the calibration curve, the complex solutions of UO_2^{2+} / TCPP-PNIPAM were prepared by adding 5.0 mL of the stock solution of TCPP-PNIPAM (2×10^{-5} mol/L) and 1.0 mL of the stock solution of UO_2^{2+} (1×10^{-2} – 1×10^{-8} mol/L) in a 10 mL volumetric flask. Then the mixture was diluted to 10 mL with dilute HCl solution. The fluorescence measurements were carried out in the complex solution of TCPP-PNIPAM (1×10^{-5} mol/L) / UO_2^{2+} (1×10^{-3} – 1×10^{-7} mol/L) at the optimal pH = 5. The calibration graph was obtained with the fluorescence intensity (Y) as a function of UO_2^{2+} concentration (X).

For the trace uranyl at 1×10^{-8} or 1×10^{-9} mol/L, the concentrated complex solution was obtained from 100 mL of UO_2^{2+} / TCPP-PNIPAM solution by the centrifugation (10,000 rpm, 30 min) at 38 °C. Then the concentrated solution was cooled to 25 °C and fluorescence measurements were performed.

To test the application of this method, simulated seawater with the different concentrations of UO_2^{2+} (10^{-5} mol/L and 10^{-8} mol/L) was prepared according to the related reference [38]. Briefly, solution A was obtained by dissolution of 17.3593 g NaCl, 2.9038 g Na_2SO_4 , 0.4906 g KCl, 0.1417 g $NaHCO_3$, 0.07164 g KBr, 0.01904 g H_3BO_3 and 0.00147 g NaF in 700 g H_2O ; solution B by mixing 59.1406 g 1 mol/L $MgCl_2$, 11.6204 g 1 mol/L $CaCl_2$ and 0.0912 g 0.1 mol/L $SrCl_2$ and adding water up to a total mass of 306.45 g. Then solution A and solution B were combined to solution C as matrix and air was passed through for 12 h, and the pH was adjusted to 5.0 by the addition of dilute HCl solution. UO_2^{2+} (0.0502 g, 0.1 mmol) was dissolved in solution C (1 L) as stock solution (10^{-4} mol/L UO_2^{2+}), and then the stock solution was diluted 10 and 10^4 times by solution C, respectively, to give the simulated seawater with the different concentrations of UO_2^{2+} (10^{-5} mol/L and 10^{-8} mol/L). The concentrations were detected by TCPP-PNIPAM at 25 °C and pH = 5.0.

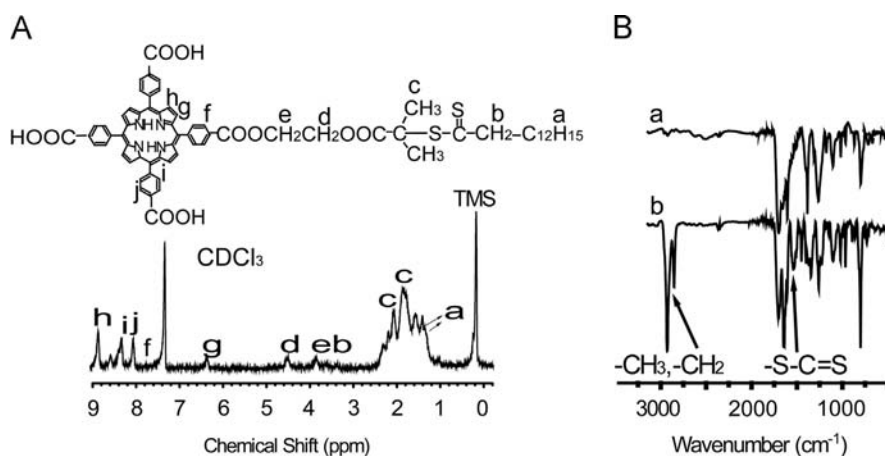


Fig. 1. (A) 1H NMR spectrum (400 M, $CDCl_3$) of TCPP-DDACT-RAFT. (B) FT-IR spectra of (a) TCPP and (b) TCPP-DDACT.

3. Results and discussion

In order to synthesize porphyrin-terminated polymeric sensor TCPP-PNIPAM, TCPP-DDACT was first synthesized by the reaction of TCPP with DDACT-OH (Scheme 1). The structure of TCPP-DDACT were confirmed by ^1H NMR spectra (Fig. 1A). Besides the characteristic peaks for TCPP ($\delta = 8.05\text{--}8.90$ ppm), the characteristic resonances of DDACT-OH were detected at $\delta = 1.01\text{--}2.20$ ppm, suggesting that DDACT-OH had been successfully grafted onto TCPP. The ratio of TCPP to DDACT is 1:1, which can be calculated according to the equation:

$$[\text{TCPP}]/[\text{DDACT}] = (I_{6.29}/2)/(I_{4.41}/2) = 1.02$$

where $I_{6.29}$ and $I_{4.41}$ are the integration values of the peaks at $\delta = 6.20\text{--}6.56$ ppm and $4.62\text{--}4.21$ ppm corresponding to the characteristic peaks of TCPP and DDACT, respectively (Fig. 1A). The structure of TCPP-DDACT can be further confirmed by FT-IR spectra (Fig. 1B). In comparison with TCPP (Fig. 1B, trace a), the characteristic peak ($-\text{S}-\text{C}=\text{S}$) occurred at 1520 cm^{-1} , and the characteristic peaks at $2800\text{--}3000\text{ cm}^{-1}$ for $-\text{CH}_3$ and $-\text{CH}_2$ were markedly enhanced (Fig. 1B, trace b). These results further demonstrate the successful synthesis of TCPP-DDACT.

The controlled polymerizations of NIPAM were performed with TCPP-DDACT as the RAFT reagent in DMF at 60°C . The structures of TCPP-PNIPAM were characterized by ^1H NMR spectra, and

a typical ^1H NMR spectrum is depicted in Fig. 2A. Besides the characteristic peaks for TCPP-DDACT, the characteristic resonances of NIPAM were detected at $\delta = 1.34\text{--}2.21$ and 4.11 ppm, suggesting that PNIPAM had been successfully grafted onto TCPP by the polymerization. Fig. 2B shows the typical GPC curves for PNIPAM homopolymers from the polymerization mixtures. The symmetric peaks and narrow molecular weight distributions indicate the proceeding of the controlled RAFT polymerization.

It was known that porphyrin derivatives had been employed widely as fluorophores in probes due to their excellent photo-physical properties [27,28], but their applications were hampered by the poor solubility and dispersion in water [29]. In this study, the soluble PNIPAM polymer chain and the carboxyl groups would improve the solubility of the polymeric sensor in water. The effect of molecular weight was investigated on the fluorescence property of TCPP-PNIPAM. The results showed that the fluorescence intensity of TCPP-PNIPAM increases with molecular weights of PNIPAM at the wavelength (~ 658 nm) of maximum fluorescence (Fig. 3A), which may be ascribed to the improved solubility and the better control over the porphyrin microenvironment by the polymer, since more polymer around the porphyrin moiety would better prevent self-quenching of the chromophore. Moreover, the wavelength of maximum fluorescence at $700\text{--}750$ nm for TCPP-PNIPAM ($M_n = 15,500$ g/mol, $\text{PDI} = 1.42$) was ~ 25 nm blue-shifted (Fig. 3A, trace c) in comparison with TCPP-PNIPAM

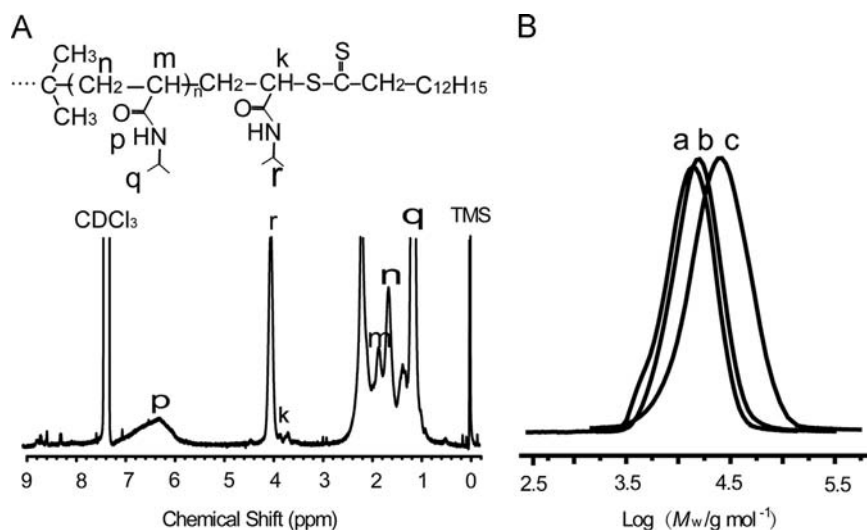


Fig. 2. (A) ^1H NMR spectrum (400 M, CDCl_3) of TCPP-PNIPAM ($M_n = 15,500$ g/mol, $\text{PDI} = 1.42$). (B) GPC curves of TCPP-PNIPAM: (a) $M_n = 8500$ g/mol, $\text{PDI} = 1.29$, Conversion = 67.4%; (b) $M_n = 10,000$ g/mol, $\text{PDI} = 1.27$, Conversion = 71.2%; and (c) $M_n = 15,500$ g/mol, $\text{PDI} = 1.42$, Conversion = 75.2%.

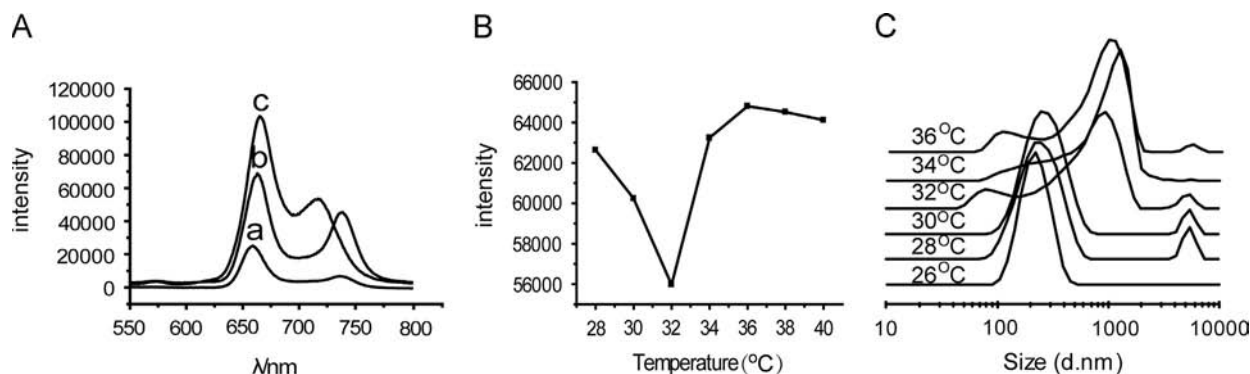


Fig. 3. (A) Fluorescence spectra of TCPP-PNIPAM (10^{-4} mol/L): (a) $M_n = 8500$ g/mol, $\text{PDI} = 1.29$; (b) $M_n = 10,000$ g/mol, $\text{PDI} = 1.27$; (c) $M_n = 15,500$ g/mol, $\text{PDI} = 1.42$. (B) Temperature-dependent fluorescence spectra of TCPP-PNIPAM (10^{-5} mol/L, $M_n = 15,500$ g/mol, $\text{PDI} = 1.42$) at 658 nm. (C) Temperature-dependent hydrodynamic diameters of TCPP-PNIPAM ($M_n = 15,500$ g/mol, $\text{PDI} = 1.42$) by dynamic laser scattering.

($M_n=10,000$ g/mol, PDI=1.27; Fig. 3A, trace b), possibly due to restricted inter-porphyrin interactions with more PNIPAM around the porphyrin moiety in water.

On the other hand, PNIPAM can undergo a volume transition in water upon heating above 32 °C, during which the extended hydrophilic coils collapse into hydrophobic globules [35]. Therefore, the effect of the temperature was also investigated on fluorescence property of TCPP–PNIPAM (Fig. 3B). Below 32 °C, the higher temperature resulted in lower fluorescence intensity ($\lambda=658$ nm), which may be associated with the thermal rotation of porphyrin and water interaction [39]: the faster molecular rotation and more efficient interaction at higher temperatures lead to more significant non-radiation energy loss and therefore a lower fluorescence intensity. The similar result was reported by Uchiyama et al. [40].

When the temperature was above 32 °C, the emission intensity became stronger at $\lambda=658$ nm, which may be associated with the aggregation-induced emission [41] of TCPP–PNIPAM: above the low critical solution temperature (LCST), the hydrophobic globules would aggregate to provide viscous microdomains to suppress the rotation of the fluorophores and alleviate the interaction with water, which results in fluorescence efficiency enhancement [30]. Therefore, the temperature significantly changed the porphyrin's photophysical property. HPPS was used to characterize the LCST stimulated micro-structures (Fig. 3C). At the temperature range of 26–30 °C, the single peak at $d\sim 258$ nm was observed; whereas, when the temperature is above 32 °C, new peaks appeared at ~ 1000 nm, suggesting TCPP–PNIPAM aggregation above LCST due to the transition of hydrophilic coils to hydrophobic globules. These results further demonstrated the point of aggregation-induced emission.

For uranyl sensing, the effect of pH on the detection of uranyl with TCPP–PNIPAM was first investigated. The hydrolysis of the uranyl ion in aqueous solutions results in the formation of insoluble uranyl hydroxide at $\text{pH} > 5.5$ [12], so the fluorescence experiments were carried out at a pH range from 2.0 to 5.0 for the complex solution of UO_2^{2+} (1×10^{-6} mol/L) / TCPP–PNIPAM (1×10^{-5} mol/L, $M_n = 15,500$ g/mol). The results showed that the fluorescence intensity was very high at $\text{pH}=2\sim 5$, and there was a significant decrease at $\text{pH}=1.0$ (Fig. 4A), which may be ascribed to the fluorescence quenching of H^+ reported by Yu et al. [42]. Therefore, $\text{pH}=5.0$ was selected for the uranyl determination.

A short response time is another important factor for a fluorescent sensor to monitor UO_2^{2+} in environmental samples in real applications. To study the response time of TCPP–PNIPAM to UO_2^{2+} , the fluorescence intensity ($\lambda=658$ nm) of TCPP–PNIPAM (10^{-5} mol/L; $M_n=15,500$ g/mol, PDI=1.42) upon UO_2^{2+} (10^{-6} mol/L) was recorded at 658 nm over a period of 5 min in $\text{pH}=5.0$ aqueous solution at 25 °C, and the result was shown in Fig. 4B. It can be seen that the stable reading could be obtained in less than 3 min, and the fluorescence intensity at 658 nm stays almost unchanged in the rest of the time. In general, the interaction of porphyrin with metal ion in aqueous solution at room temperature is a slow process. The fast response of the polymeric sensor toward UO_2^{2+} might be ascribed to the improved solubility of the TCPP–PNIPAM.

In certain environmental samples, such as seawater, the concentrations of some other ions (such as Na^+ , Ca^{2+} , Mg^{2+} , Cl^- , HCO_3^-) are significantly higher than that of UO_2^{2+} . Therefore, selective detection of UO_2^{2+} in the presence of these metal ions with high concentration is a challenge for most common probes. To test the practical applicability of our fluorescent sensor for UO_2^{2+} , competition experiments were also carried out under

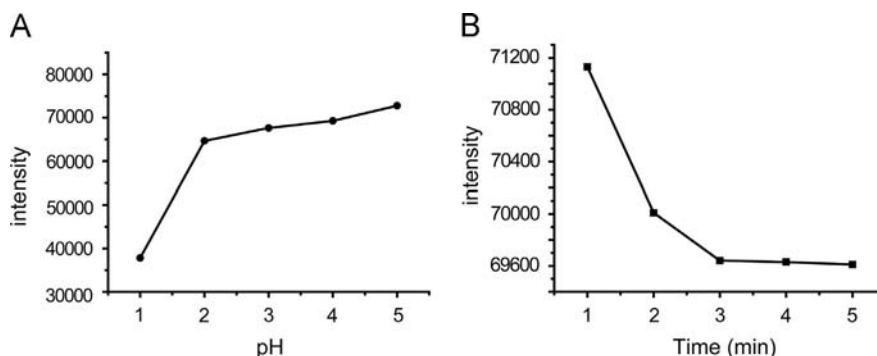


Fig. 4. (A) The effect of pH on the fluorescence intensity at 658 nm of TCPP–PNIPAM (10^{-5} mol/L, $M_n=15,500$ g/mol, PDI=1.42) in the presence of UO_2^{2+} (10^{-6} mol/L) at 25 °C in aqueous solution. (B) The response time curve of the TCPP–PNIPAM (10^{-5} mol/L, $M_n=15,500$ g/mol, PDI=1.42) to UO_2^{2+} (10^{-6} mol/L) at 658 nm in $\text{pH}=5.0$ aqueous solution at 25 °C.

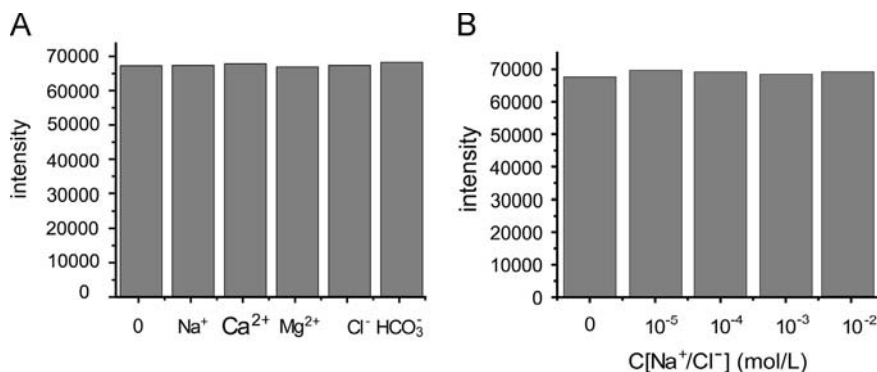


Fig. 5. The selectivity of TCPP–PNIPAM (10^{-5} mol/L) to UO_2^{2+} over competing metal ions at $\text{pH}=5.0$: (A) the fluorescence intensity of TCPP–PNIPAM with UO_2^{2+} (10^{-6} mol/L) in the presence of competing ions (10^{-4} mol/L for Na^+ , Ca^{2+} , Mg^{2+} , Cl^- , HCO_3^-); and (B) the fluorescence intensity of TCPP–PNIPAM with UO_2^{2+} (10^{-6} mol/L) in the presence of Na^+/Cl^- with different concentrations.

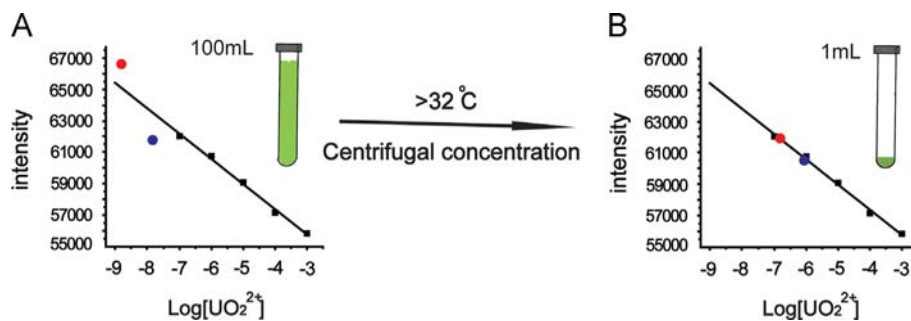


Fig. 6. The fluorescence intensity ($\lambda=658$ nm) for the trace uranyl (red and blue dots represent the concentrations of 1.0×10^{-9} mol/L and 1.0×10^{-8} mol/L, respectively) at 25 °C and $\text{pH}=5.0$: A) before concentration and B) after concentration of TCPP–PNIPAM (10^{-5} mol/L, $M_n=15,500$ g/mol, $\text{PDI}=1.42$) by the centrifugation (10,000 rpm, 30 min, 38 °C). (Color reproduction only on the Web) (For interpretation of the references to color in this figure legend, the reader is referred to the web version of this article.)

optimized experimental conditions (i.e. $\text{pH}=5.0$ and 25 °C). An excess amount of above-mentioned ions (10^{-4} mol/L for Na^+ , Ca^{2+} , Mg^{2+} , Cl^- , HCO_3^-) are added to UO_2^{2+} (10^{-6} mol/L) aqueous solution. The results showed there were similar responses of TCPP–PNIPAM to UO_2^{2+} after addition of Na^+ , Ca^{2+} , Mg^{2+} , Cl^- , and HCO_3^- , respectively (Fig. 5A). In addition, it is well-known that the seawater contains a large number of Na^+/Cl^- , so it is necessary to investigate the influence of Na^+/Cl^- concentration on the fluorescent sensor for UO_2^{2+} . The results are shown in Fig. 5B. Although the Na^+/Cl^- concentrations changed from 10^{-5} mol/L to 10^{-2} mol/L, the responses of the probe to UO_2^{2+} were unaffected by the increase of the Na^+/Cl^- concentration, even Na^+/Cl^- with a concentration 10^4 times higher than uranyl (Fig. 5B). For transition elements as interfering ions, Fe^{3+} , Cu^{2+} , Ni^{2+} and Zn^{2+} were selected for this study because their concentrations are higher than the other transition elements in seawater. The fluorescence intensity just decreased slightly in the presence of Fe^{3+} , Cu^{2+} , Ni^{2+} and Zn^{2+} at the concentrations of 10^{-9} mol/L and 10^{-7} mol/L; whereas, if the concentration was increased to 10^{-5} mol/L, there was a marked decrease of fluorescence intensity (Fig. S5, see Supporting Information). All these results indicated that the polymeric sensor is relatively selective to uranyl ion to some content and has a great potential for environmental application.

Under optimized experimental conditions, the calibration graph was obtained for uranyl determination with the fluorescence intensity (Y , $\lambda=658$ nm) as a function of UO_2^{2+} concentration (X , $1.0 \times 10^{-7} \sim 1.0 \times 10^{-3}$ mol/L): $Y=-1590X+51008$ (Fig. 6, black dots). However, when the concentration of UO_2^{2+} below 1.0×10^{-7} mol/L, the fluorescence intensity at 25 °C and $\text{pH}=5.0$ could not meet with the standard curve and there was a large deviation for the concentrations of 1.0×10^{-9} mol/L and 1.0×10^{-8} mol/L, respectively (Fig. 6A, red and blue dots). Before detecting the concentration of uranyl ion every time, the calibration graph should be calibrated under the experimental conditions, so the method should have a good reproducibility.

It is known that there is a transition of hydrophilic coils to hydrophobic globules for PNIPAM above 32 °C [35]. Therefore, the UO_2^{2+} aqueous solution could be concentrated for the uranyl determination by the centrifugation above the LCST. As can be seen from Fig. 6B, after concentrating 100 times by the centrifugation (10,000 rpm, 30 min) at 38 °C, the solutions were cooled to 25 °C for the measurements, the fluorescence intensity is consistent with the calibration curve for the uranyl concentrations of 1.0×10^{-9} mol/L and 1.0×10^{-8} mol/L (Fig. 6B, red and blue dots), respectively. Detection limit of the sensor which is defined as the concentration of the sample yielding a signal equal to the blank signal plus three times of its standard deviation was found to be 1.1×10^{-9} mol/L. The results showed that the determination of UO_2^{2+} at trace levels was successfully achieved by the centrifugal concentration, which is below the maximum contamination level

Table 1

Results of UO_2^{2+} detected by TCPP–PNIPAM in simulated seawater.

Sample	UO_2^{2+} spiked (log mol · L ⁻¹)	UO_2^{2+} recovered (log mol · L ⁻¹) ^a	Standard deviation (log mol · L ⁻¹)
Seawater-1	-5	-5.08	± 0.20
Seawater-2	-8	-8.22	± 0.13

^a Average of three determinations.

of 1.30×10^{-7} mol/L for UO_2^{2+} in drinking water defined by the U.S. EPA.

To test the application of this method, simulated seawater as matrix was prepared according to the reference [38]. The simulated solutions with the different uranyl concentrations (10^{-5} mol/L and 10^{-8} mol/L) were determined by TCPP–PNIPAM and the results are shown in Table 1. The concentrations were detected as $10^{-5.02}$ mol/L and $10^{-8.22}$ mol/L. In comparison with the spiked amount, there is only little matrix effect on the determination of uranyl ion (Table 1). The results suggested that TCPP–PNIPAM can effectively detect the magnitude of UO_2^{2+} concentration in simulated seawater.

4. Conclusion

In summary, we demonstrate here a thermo-responsive polymeric sensor TCPP–PNIPAM for the determination of trace uranyl with high sensitivity and selectivity. TCPP–PNIPAM was first successfully synthesized by the controlled RAFT polymerization. The fluorescence intensity of TCPP–PNIPAM increased with molecular weights of PNIPAM at the wavelength (~ 658 nm) of maximum fluorescence, and there was a ~ 25 nm blue-shift of the wavelength of maximum fluorescence at 700 – 750 nm for TCPP–PNIPAM ($M_n=15,500$ g/mol, $\text{PDI}=1.42$). The fluorescence property of TCPP–PNIPAM was also closely related to the temperature: below 32 °C, the higher temperature resulted in lower fluorescence intensity ($\lambda=658$ nm); and when the temperature is above 32 °C, the emission intensity becomes stronger due to aggregation-induced emission. The polymeric sensor with a fast responsive time (~ 3 min) is sensitive to pH at the range of 1 – 5 , and is highly selective to UO_2^{2+} over competing ions (such as Na^+ , Ca^{2+} , Mg^{2+} , Cl^- , HCO_3^- , Fe^{3+} , Cu^{2+} , Ni^{2+} and Zn^{2+}). Under optimized experimental conditions, the determination of UO_2^{2+} at trace levels (such as 1.0×10^{-8} mol/L, and 1.0×10^{-9} mol/L) could be successfully achieved after concentrating 100 times by the centrifugation (10,000 rpm, 30 min) above LCST. This method can effectively detect the magnitude of UO_2^{2+} concentration in simulated seawater. The properties enable the polymeric sensor to have

great potential for environmental applications. To the best of our knowledge, this is the first report to determine trace uranyl by thermo-responsive polymeric sensors.

Acknowledgment

We thank Natural Science Foundation of China (91326202, 21174100), A Project Funded by the Priority Academic Program Development of Jiangsu Higher Education Institutions (PAPD), the Qing-Lan Project of Jiangsu Province, and Program of Innovative Research Team of Soochow University for their financial support.

Appendix A. Supporting information

Supplementary data associated with this article can be found in the online version at <http://dx.doi.org/10.1016/j.talanta.2014.07.085>.

References

- [1] K.B. Gongalsky, *Environ. Monit. Assess.* 89 (2003) 197–219.
- [2] E. Schnug, B.G. Lottermoser, *Environ. Sci. Technol.* 47 (2013) 2433–2434.
- [3] N. Casacuberta, P. Masque, J. Garcia-Orellana, J.M. Bruach, M. Anguita, J. Gasa, M. Villa, S. Hurtado, R. Garcia-Tenorio, *J. Hazard. Mater.* 170 (2009) 814–823.
- [4] U.S. EPA, EPA Integrated Risk Information System (IRIS) Electronic Database. U.S., Environmental Protection Agency, Washington, DC, 1996.
- [5] K. Chandrasekaran, D. Karunasagar, J. Arunachalam, *Anal. Methods* 3 (2011) 2140–2147.
- [6] J.J. Gonzalez, D. Oropeza, X. Mao, R.E. Russo, *J. Anal. Atom. Spectrom.* 23 (2008) 229–234.
- [7] C. Moeser, R. Kautenburger, H. Philipp Beck, *Electrophoresis* 33 (2012) 1482–1487.
- [8] S.A. Abbasi, *Int. J. Environ. Anal. Chem.* 36 (1989) 163–172.
- [9] M. Mlakar, M. Branica, *Anal. Chim. Acta* 221 (1989) 279–287.
- [10] A.K. Brown, J. Liu, Y. He, Y. Lu, *Chembiochem* 10 (2009) 486–492.
- [11] R.S. Addleman, M. Carrott, C.M. Wai, T.E. Carleson, B.W. Wenclawiak, *Anal. Chem.* 73 (2001) 1112–1119.
- [12] A. Safavi, M. Bagheri, *Anal. Chim. Acta* 530 (2005) 55–60.
- [13] Y. Luo, Y. Zhang, L. Xu, L. Wang, G. Wen, A. Liang, Z. Jiang, *Analyst* 137 (2012) 1866–1871.
- [14] P.T. Varineau, R. Duesing, L.E. Wangen, *Appl. Spectrosc.* 45 (1991) 1652–1655.
- [15] A. Becker, H. Tobias, D. Mandler, *Anal. Chem.* 81 (2009) 8627–8631.
- [16] R.M.Z. Kakhki, G. Rounaghi, *Mat. Sci. Eng. C* 31 (2011) 1637–1642.
- [17] A.M. Powe, K.A. Fletcher, N.N. Luce St, M. Lowry, S. Neal, M.E. McCarroll, P.B. Oldham, L.B. McGown, I.M. Warner, *Anal. Chem.* 76 (2004) 4614–4634.
- [18] O.S. Wolfbeis, *Anal. Chem.* 76 (2004) 3269–3283.
- [19] S. Ganesh, F. Khan, M.K. Ahmed, P. Velavendan, N.K. Pandey, U.K. Mudali, S.K. Pandey, *J. Radioanal. Nucl. Chem.* 292 (2012) 331–334.
- [20] D.A. Nivens, Y.K. Zhang, S.M. Angel, *J. Photoch. Photobio. A* 152 (2002) 167–173.
- [21] M. Wu, L. Liao, M. Zhao, Y. Lin, X. Xiao, C. Nie, *Anal. Chim. Acta* 729 (2012) 80–84.
- [22] D. Pestov, C.-C. Chen, J.D. Nelson, J.E. Anderson, G. Tepper, *Sens. Actuators B* 138 (2009) 134–137.
- [23] J. Liu, Y. Lu, *Angew. Chem. Int. Edit* 46 (2007) 7587–7590.
- [24] J. Li, Y. Lu, *J. Am. Chem. Soc.* 122 (2000) 10466–10467.
- [25] N. Rupcich, W. Chiuman, R. Nutiu, S. Mei, K.K. Flora, Y.F. Li, J.D. Brennan, *J. Am. Chem. Soc.* 128 (2006) 780–790.
- [26] J. Liu, A.K. Brown, X. Meng, D.M. Crokek, J.D. Istok, D.B. Watson, Y. Lu, *Pro. Natl. Acad. Sci. USA* 104 (2007) 2056–2061.
- [27] C.-Y. Li, X.-B. Zhang, L. Qiao, Y. Zhao, C.-M. He, S.-Y. Huan, L.-M. Lu, L.-X. Jian, G.-L. Shen, R.-Q. Yu, *Anal. Chem.* 81 (2009) 9993–10001.
- [28] W. Lin, L. Yuan, L. Long, C. Guo, J. Feng, *Adv. Funct. Mater.* 18 (2008) 2366–2372.
- [29] M.O. Senge, M. Davis, *J. Porphy. Phthalocya.* 14 (2010) 557–567.
- [30] X. Zhou, F. Su, Y. Tian, R.H. Johnson, D.R. Meldrum, *Sens. Actuators B* 159 (2011) 135–141.
- [31] J. Chiefari, Y.K. Chong, F. Ercole, J. Krstina, J. Jeffery, T.P.T. Le, R.T.A. Mayadunne, G.F. Meijs, C.L. Moad, G. Moad, E. Rizzardo, S.H. Thang, *Macromolecules* 31 (1998) 5559–5562.
- [32] Y. Yang, J. Jiang, G. Shen, R. Yu, *Anal. Chim. Acta* 636 (2009) 83–88.
- [33] H. Dehghani, M.R. Mansournia, *Polyhedron* 27 (2008) 849–853.
- [34] K. Kubota, S. Fujishige, I. Ando, *J. Phys. Chem.* 94 (1990) 5154–5158.
- [35] C. Wu, S. Zhou, *Macromolecules* 28 (1995) 8381–8387.
- [36] A.D. Adler, F.R. Longo, J.d. Finarell, J. Goldmach, J. Assour, L. Korsakof, *J. Org. Chem.* 32 (1967) 476.
- [37] J.T. Lai, D. Filla, R. Shea, *Macromolecules* 35 (2002) 6754–6756.
- [38] H.J. Fischer, K.H. Lieser, *Fresen. J. Anal. Chem.* 346 (1993) 934–942.
- [39] D. Wang, R. Miyamoto, Y. Shiraiishi, T. Hirai, *Langmuir* 25 (2009) 13176–13182.
- [40] S. Uchiyama, Y. Matsumura, A.P. de Silva, K. Iwai, *Anal. Chem.* 75 (2003) 5926–5935.
- [41] J.D. Luo, Z.L. Xie, J.W.Y. Lam, L. Cheng, H.Y. Chen, C.F. Qiu, H.S. Kwok, X.W. Zhan, Y.Q. Liu, D.B. Zhu, B.Z. Tang, *Chem. Commun.* (2001) 1740–1741.
- [42] X.B. Zhang, C.C. Guo, Z.Z. Li, G.L. Shen, R.Q. Yu, *Anal. Chem.* 74 (2002) 821–825.



Simple SPE–HPLC determination of some common drugs and herbicides of environmental concern by pulsed amperometry



L. Rivoira^a, R.M. De Carlo^a, S. Cavalli^b, M.C. Bruzzoniti^{a,*}

^a Department of Chemistry, University of Torino, via P. Giuria 5, 10125 Turin, Italy

^b Istituto di Ricerca Sulle Acque, Consiglio Nazionale delle Ricerche (IRSA-CNR) Via del Mulino, 19, 20861 Brugherio, MB, Italy

ARTICLE INFO

Article history:

Received 26 May 2014

Received in revised form

17 July 2014

Accepted 21 July 2014

Available online 31 July 2014

Keywords:

Amperometric detection

Glassy carbon electrode

RP-HPLC

Emerging contaminants

Water

ABSTRACT

In this work the electrochemical behavior of substances of environmental concern [bentazone, atrazine, carbamazepine, phenytoin and its metabolite 5-(4-hydroxyphenyl)-5-phenylhydantoin, HPPH] on a glassy carbon working electrode (Ag/AgCl reference electrode) was studied with the aim to develop a HPLC method coupled with amperometric detection. Constant potential (DC), pulsed amperometric detection modes were studied. For the pulsed mode, several waveforms were set and investigated. Detection conditions were optimized as a function of eluent pH.

In order to reduce the limits of detection and to analyze natural water samples, a SPE protocol was optimized to be coupled to the developed procedure. For this aim, five sorbents of different physico-chemical characteristics were tested optimizing a recovery procedure for each of the cartridge evaluated.

At the optimized SPE conditions, recoveries were included in the range ($R=90.2\text{--}100.5\%$ for all the analytes, with excellent reproducibility ($<5\%$, $n=3$). The method detection limits obtained by pulsed amperometry after the SPE protocol (preconcentration factor 100) were 113 ng L^{-1} (0.47 nmol L^{-1}), 67 ng L^{-1} (0.25 nmol L^{-1}), 234 ng L^{-1} (1.1 nmol L^{-1}), for bentazone, HPPH and carbamazepine, respectively. Robustness of the method was assessed for each analyte at a concentration level corresponding to about three times the limit of detection, through the evaluation of intra-day ($n=13$) and inter-day tests (4 days, $n=52$). Finally the method was successfully applied for the analysis of a river sample (Po River, Turin, Italy).

© 2014 Elsevier B.V. All rights reserved.

1. Introduction

Contaminants of emerging concern in water sources have been of particular interest in the last decade and could pose a risk to human health as well as to the environment as a function of their presence, frequency and occurrence; their impact on aquatic wildlife populations has been demonstrated to occur at very low concentrations. Among them, herbicides and pharmaceutical compounds are among the most widely occurring pollutants [1] due to their extensive use.

Many herbicides are potentially dangerous not only to human health but also to other organisms in the environment. Among them, bentazone and atrazine are of environmental concern. Both herbicides inhibit, in chloroplast, the Hill reaction, necessary for the oxygen evolution in the photosynthetic process [2,3]. Health effects of atrazine as a human carcinogen still remain controversial [4].

The widespread contamination of drinking water by atrazine was associated with birth defects and hormonal disturbance effects [5,6]. Even though banned in the EU, atrazine is the most widely used herbicide in the US.

Bentazone belongs to the thiazidiazine group and is widely used as post-emergence herbicide. It exhibits little sorption in soil and due to its relatively high mobility [7], the potential risk of leaching and ground water contamination is very high. Bentazone is commonly detected in ground and surface waters [8]. Toxicologic studies show that bentazone has acute and chronic toxicity (inflammation of the mucous membranes, tachycardia, renal failure).

Pharmaceuticals, like antiepileptic drugs, are found regularly in surface waters, phenytoin and carbamazepine are anti-epileptic and anticonvulsant substances and just like many active drugs, if overdosed are toxic. Recent studies show their presence in finished drinking waters [9]. In addition it was proved that the presence of phenytoin and carbamazepine in wastewater decreases the efficiency of wastewater treatment plants [10,11].

The monitoring of these contaminants in the aquatic environment is progressively becoming a priority for government agencies, regulatory agencies and the general public.

* Corresponding author. Tel.: +39 0116705277; fax: +39 0116705242.

E-mail address: mariaconcetta.bruzzoniti@unito.it (M.C. Bruzzoniti).

With regard to the analytical determination, the mainly used techniques are based on chromatographic mechanisms (gas chromatographic and HPLC) coupled to specific mass spectrometric and spectrophotometric detectors. Although gas chromatographic methods can successfully be employed for the determination of some compounds like carbamazepine and bentazone at ng L^{-1} levels after solid-phase extraction, GC requires the choice of the correct derivatizing agent that avoids decomposition of the analytes. This in turn implies that the same derivatizing agent cannot be used for the simultaneous analysis of different classes of compounds of interest [12].

With regard to HPLC methods, this approach has been chosen for the determination of bentazone, atrazine, phenytoin, carbamazepine in environmental matrices like natural waters, soils, and in foodstuff like rice and cereals. Limits of detection (LODs) depend mainly upon the detection mode and the extraction technique used. For example, LODs ranging from 5–15 $\mu\text{g L}^{-1}$ for bentazone [13,14] have been obtained by SPE extraction-HPLC with UV detection after a 500-fold preconcentration. Lower detection limits have been achieved with higher preconcentration ratios (e.g. for carbamazepine: 50 ng L^{-1} [15]). Less satisfying LOD values have been obtained with liquid-liquid extraction techniques (e.g. about 100 $\mu\text{g L}^{-1}$ for carbamazepine with UV detection [16]). Techniques such as LC-MS and LC-MS/MS have been used to determine herbicides and pharmaceutical compounds in natural waters at generally lower detection limits [17–19], but with the main drawback of requiring expensive equipments with high maintenance costs and skilled technical staff.

Electroanalytical techniques have been shown to be useful in the study of toxic substances of environmental concerns such as pesticides [20] and they have been recently used in pulsed amperometric mode also on glassy carbon electrodes for the determination of chlorophenols [21]. When coupled to chromatography, the specificity of the electrochemistry techniques is increased significantly. In recent years, the number of published papers dealing with the use of chromatographic methods with amperometric detection is growing thanks to selectivity, sensitivity and low cost of the detection technique [22]. Amperometric detection proved to be successful for the determination of compounds of environmental concern [23–27].

According to the characteristics of the molecules to be determined, the amperometric detection can be considered for identification and quantification of target compounds.

The aim of this work was to study the chromatographic separation and the electrochemical behavior of bentazone, atrazine, phenytoin, and carbamazepine. Since phenytoin is metabolized by cytochrome P450 enzymes primarily to 5-(p-hydroxyphenyl)-5-phenylhydantoin (HPPH), and is mainly excreted as 5-(4'-hydroxyphenyl)-5-phenylhydantoin O-glucuronide in humans [28], HPPH was included in our study, too. Constant potential (DC) amperometry, pulsed amperometric detection were compared to assess the best electrochemical response for the analytes tested. The chromatographic method optimized was coupled to a solid-phase extraction step which provided reduced detection limits with a simultaneous clean-up of the matrix analyzed. The study performed allowed us to develop a sensitive, affordable analytical procedure based on pulsed amperometry which is of simple application.

This work is the first study devoted to the analysis of bentazone, atrazine, carbamazepine, phenytoin and HPPH by HPLC with amperometric detection.

2. Material and methods

2.1. Chemicals and standard solutions

All reagents used throughout this work were of analytical grade. Acetonitrile (99.9%), bentazone, HPPH, phenytoin, carbamazepine,

atrazine, nitric acid (65% w/w, $d=1.40 \text{ g/mL}$) and acetic acid (99.8% w/w, $d=1.052 \text{ g/mL}$) were from Sigma-Aldrich (Chemie, Steinheim, DE). Methanol and NaOH (purity >98%) were from Carlo Erba (Milano IT).

A Milli-Q Plus ultra-pure water system from Millipore (Milford, MA, USA) was used for standard and eluent preparation.

2.2. Instruments

For the chromatographic separations, a Dionex ICS-3000 chromatograph (Thermo Scientific, Sunnyvale, CA, USA), equipped with a reversed-phase C-18 pre-column and analytical column (LiChro-Cart PuroSphere RP-18, 125 mm \times 3.0 mm, 5 μm , Merck) was used. The mobile phases were sodium acetate or sodium formate buffers (50 mM) at different pH values. CH_3CN was used as organic modifier. The analysis were performed in isocratic mode (eluent flow rate 0.5 mL min^{-1}). A 10 μL -injection loop was used throughout this work. Pre-column and analytical column were periodically washed by isopropanol and reconditioned with eluent for 35 min.

Two detectors coupled in series were used, namely an AD25 Absorbance Detector ($\lambda=252 \text{ nm}$) and a AD40 Electrochemical Detector (both by Thermo Scientific, Dionex), with a Ag/AgCl reference electrode and a glassy carbon (GC) working electrode. The parameters of the electrochemical detector were optimized as described in Section 3.4. Chromatographic and amperometric data were collected and elaborated by the software Chromeleon 6.80 (Thermo Scientific, Dionex).

2.3. Solid phase extraction (SPE)

For the extraction of the analytes, the performance of five SPE supports of different compositions were compared. In detail, two C18 based adsorbents: Bond Elut C18 Jr (Agilent), ENVI 18 (Supelco), two polymeric sorbents: LiChroLut EN (Merck), Baker-Bond SDB (JT Baker) and one carbon based substrate: ENVI Carb (Supelco) cartridges were activated according to manufacturer's indications before use.

For each cartridge, aliquots of 5 mL containing 1 mg L^{-1} each of bentazone, atrazine, phenytoin, HPPH and carbamazepine were loaded at 2 mL min^{-1} flow rate. For each cartridge, the eluent solution was optimized according to the expected analyte-sorbent interactions. Before elution, each cartridge was washed with 2 mL H_2O to remove unretained compounds. In order to check the retention of the analytes in each step of the SPE protocol, the following three fractions were collected and injected in the HPLC system: (i) the solution after loading; (ii) the washing solution and (iii) the eluate.

Recoveries are expressed as average of three independent extractions. In parallel, a blank was processed for all the cartridges tested. For the optimization of the SPE protocol, the UV detection was used.

2.4. Real sample analysis

A river sample (Po river, Turin, Italy) was collected on 24/07/2013 between 104 km and 105 km, stored in a Pyrex bottle at 4 $^\circ\text{C}$, protected from light until analysis. Analysis was performed within 24 h from the sampling.

Analytes were SPE extracted and analyzed according to the procedure optimized throughout this work which is summarized in Fig. 1 of Supplementary Material section, where all the steps of the protocol are given in detail.

3. Results and discussion

The analytes considered in this study are shown in Fig. 2 of Supplementary Material section. Bentazone displays keto–enol tautomerism [29] whereas phenytoin displays tautomerism of the imine–imide type [30], as shown in the figure. A similar behavior should be expected even for the metabolite HPPH.

The experimental work consisted in a preliminary optimization of the chromatographic separation, followed by a voltammetric study before optimizing the experimental conditions for the electrochemical detection.

3.1. Chromatographic optimization

In order to optimize the separation of the analytes, four mobile phases (50 mM CH₃COOH/CH₃COONa, pH 5.0) with CH₃CN content ranging from 28–35% were tested (Fig. 3 of Supplementary Material section).

At all the eluent compositions investigated, bentazone is the species less retained by the column since according to its pK_a value bentazone is present in the ionized form (see equilibrium depicted in Fig. 2 of Supplementary Material section). The presence of the –OH group in the phenyl substituent dramatically reduce retention for HPPH in respect to phenytoin. It should be remarked that phenytoin is not ionized at the elution pH condition.

As shown in Fig. 3 of Supplementary Material section, capacity factors for all analytes except bentazone and HPPH are significantly affected by the CH₃CN content, due to the decreased hydrophobic interactions that in turn reduce the retention in the column.

Additionally, the effect of pH on separation was also investigated. The decrease of pH caused an increase in the retention of bentazone (see Fig. 4 of Supplementary Material section), since at this condition the undissociated form of bentazone is also present. The chromatographic behavior for both HPPH and carbamazepine is affected by pH, observing a decreased retention with more acidic pH values.

According to the results obtained, an eluent containing 28% CH₃CN buffered at pH 5 was chosen for the further step of optimization of electrochemical detection conditions.

3.2. Optimization of a SPE protocol

In order to extract the analytes from environmental water samples and to reduce the LOD values, a SPE step was optimized comparing the performance of five sorbents of different chemical composition (see Table 1).

According to the expected analyte–substrate interactions for the octadecyl-silanized silica phases (*Bond Elut* C18, *ENVI* 18), the analytes were eluted by 100% CH₃CN. Very satisfactory recoveries were obtained for the *Bond Elut* C18 phase for all the analytes, whereas a milky eluate was obtained with the *ENVI* 18 sorbent. The *LiChroLut EN* phase required sample acidification to pH 3 in

order to enhance the retention of bentazone in the sorbent. For this cartridge, several eluents were tested for the recovery of the analytes (100% CH₃CN, 80:20 CH₃CN:H₂O, 70:20:10 CH₃CN:H₂O:isopropanol). An increase of eluent polarity was beneficial to increase the recovery for all the analytes except for carbamazepine, whereas the recovery of this last species was favored by the presence of isopropanol. It should be mentioned that in order to avoid peak broadening caused by isopropanol, the eluate was evaporated and reconstituted with H₂O before injection. For this cartridge, the best recoveries (Table 1) were obtained with 70:20:10 CH₃CN:H₂O:isopropanol. Due to the physico-chemical similarity of the *BakerBond SDB* and *LiChroLut EN* phases, the same eluent solution was also used for *BakerBond SDB* cartridge (Table 1). With regard to the *ENVI Carb* phase, several elution mixtures at different polarities were tested: CH₃CN; 60:40 CH₃CN:CH₃OH; 50:50 CH₃CN:HNO₃ pH 2; CH₃COCH₃; 80:20 isopropanol:H₂O. Partial recovery (Table 1) was obtained only by the last eluent mixture.

To summarize, the SPE cartridges which provided the best recoveries were the *Bond Elut* Jr. C18, *LiChroLut EN* and *Bakerbond SDB*. For further method performance evaluation and real sample analysis, *Bond Elut* Jr. C18 was chosen for the faster and simpler procedure involved.

3.3. Preliminary characterization of electrochemical behavior of target compounds

In order to set proper electrochemical conditions for the detection of the analytes, cyclic voltammeteries (CV) were initially performed from –1.00 V to +2.00 V, back again to –1.00 V in 60 s (scan rate 0.1 V s^{–1}) directly inside the detection cell of the ICS-3000 system, under static conditions. Cyclic voltammeteries were performed on a blank (eluent solution: 72% of a 50 mM CH₃COOH/CH₃COONa, pH 5.0 solution and 28% CH₃CN), and on solutions of individual analytes prepared in the eluent. The CV profiles shown in Fig. 1 point out that some capacitive current is present in the system. As shown, both atrazine and HPPH do not present any current peak in the range of potentials investigated. The other three analytes show oxidation peaks (E_p^{ox}) at 1.30 V (bentazone), 1.55 V (carbamazepine) and 1.10 V (phenytoin) proving their electroactivity at the GC electrode. Their voltammograms show that they are oxidized in single irreversible processes. In order to better understand the electrochemical behavior of the molecules and in order to define an operative pH range for the following amperometric detection optimization, experiments were repeated at pH 8 (72% of a 50 mM NaH₂PO₄, pH 8.0 solution and 28% CH₃CN).

This value was chosen accordingly to the pK_a values of the tested analytes in order to explain the electrochemical behavior with the chemical form of the species.

For bentazone, the oxidation potential decreased of 0.18 V in agreement with the shift of approximately –60 mV pH^{–1}. Peak current values (i_p^{ox}) decreased from 0.225 μ A to 0.04 μ A, suggesting that the –OH group is unlikely to be involved in the oxidation process. The oxidation peak observed at 1.1 V at pH 5 suggests the fouling of the electrode and a restored electrode activity for the amount of species remained in solution. The fouling of the glassy carbon electrode in presence of bentazone was also evidenced by Garrido et al. [31] while studying the electrochemical oxidation of bentazone, who hypothesized a dimerization after the oxidation reaction (corresponding to an electron transfer) and the adsorption of the product on the electrode surface.

For phenytoin, voltammograms at pH 8 do not reveal oxidation peaks, confirming also for this molecule the fact that the hydroxyl group (see Fig. 2 of Supplementary Material section) should be probably not involved in the electrochemical process.

Table 1

Recovery yields optimized for each tested substrates. Concentration of analytes: 1 mg L^{–1} each; sample volume: 5 mL; elution volume: 5 mL. For activation and recovery procedures see text.

Sorbent	Recovery (%)				
	Bentazone	HPPH	Carbamazepine	Phenytoine	Atrazine
Bond Elut C18	90 ± 3	100 ± 2	98 ± 3	100 ± 2	90 ± 2
LiChroLut EN	82 ± 3	88 ± 8	85 ± 1	73 ± 9	85 ± 0
Bakerbond SDB	90 ± 1	103 ± 1	99 ± 3	85 ± 2	90 ± 6
ENVI Carb	2 ± 0	18 ± 0	43 ± 0	45 ± 1	47 ± 0

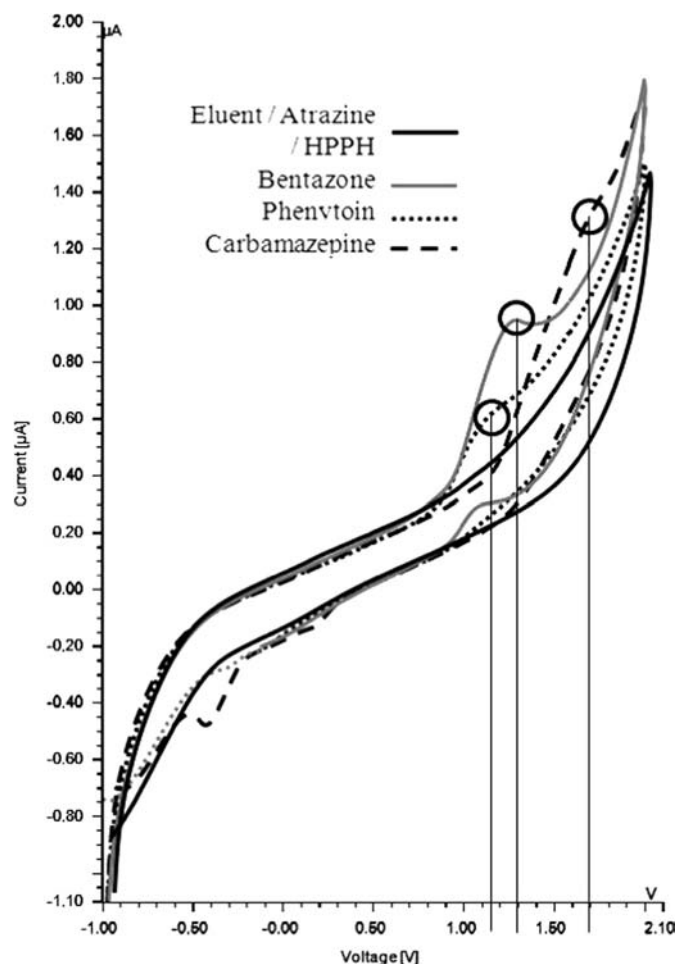


Fig. 1. Cyclic voltammograms for bentazone, HPPH, carbamazepine, phenytoin, atrazine individually prepared at 1 mgL^{-1} in eluent solution (72% of a $50 \text{ mM CH}_3\text{COOH/CH}_3\text{COONa}$, pH 5.0 solution and 28% CH_3CN) at a glassy carbon electrode, with a potential scan rate of 0.1 V s^{-1} . Cyclic voltammetry for the eluent is also shown. Oxidation potential peaks for each analyte are indicated by circles.

According to carbamazepine's pK_a values, dissociation for this species is not affected by pH variations. According to the voltammetry performed at pH 8, the oxidation potential decreases to 0.3 V. Peaks observed at 0.2 V and -0.4 V confirm the irreversibility of the oxidation process and suggest that the reduction of species different from the oxidation product of carbamazepine is occurring.

3.4. Optimization of amperometric detection

This part of the work was accomplished by coupling an amperometric detection, both in the DC and pulsed amperometry modes, to the chromatographic separation previously optimized. We tested the capabilities of DC detection at six potential values (1.0, 1.1, 1.2, 1.3, 1.4, 1.5 V) around the oxidation potentials observed in the CV study. As a consequence of the reversible fouling behavior observed for the electrode when performing the cyclic voltammeteries, in addition to DC mode, pulsed amperometry mode was also studied for the determination of the target analytes, comparing four waveforms and setting the oxidation potential at 1.2 V.

Four types of waveforms were studied (see Table 2); time of delay, time of integration, detection potential and cleaning potential were set through the software Chromeleon 6.80.

Waveforms 1 and 4 differ in the step for electrode cleaning: for waveform 1 a reduction/oxidation cycle is performed, whereas for

waveform 4 an oxidation/reduction cycle is set. It should be remarked that in waveform 4 it was not possible to set the same negative potential as for waveform 1 (-2.0 V), since the baseline was not stable. Therefore, the most negative potential value that still ensured baseline stability was chosen (-1.1 V).

Analytes were injected at a concentration of $4 \mu\text{mol L}^{-1}$. As a further optimization, in order to evaluate the response of analytes, three different pH values in the weak acidic range (pH 3–5) were evaluated. Since the pK_a for bentazone is included within the weak acidity pH range, it is reasonable to expect also a change in the chromatographic behavior for this compound, as shown in Fig. 4 of Supplementary Material section.

For each pH condition tested and for each analyte, the performance of the DC and pulsed amperometry detection modes was evaluated calculating both peak areas and the signal/noise (S/N) ratio. During this study, a UV detector (252 nm) was coupled before the electrochemical detector in order to univocally identify the compounds.

3.4.1. Eluent pH 5.0

First analyses were performed by the DC detection mode. Different from what expected by the previous CV studies, phenytoin which showed $E_p^{\text{ox}} = 1.1 \text{ V}$, could not be detected at any of the potential values investigated (see hydrodynamic voltammograms in Fig. 2), probably for the slow kinetics of the oxidation reaction, preventing detection under flow conditions. The opposite behavior was observed for phenytoin's metabolite (HPPH) for which a chromatographic peak in hydrodynamic conditions is observed. It can be hypothesized that during CV analysis, performed in static conditions, HPPH adsorption on the electrode hampered the electrochemical process. In agreement with CV results, atrazine was not detected even in hydrodynamic conditions. As expected by the CV studies, carbamazepine is not detectable for E values lower than 1.1 V. According to the data obtained, the highest S/N values were obtained at 1.2 V. This value was subsequently set as the oxidation potential in the pulsed amperometry waveforms (see Table 2).

As shown in Fig. 3, for pulsed amperometry, the best detection conditions can be achieved by waveform 1, where the highest S/N ratios (Fig. 3b) are obtained. It is interesting to note that the inversion of the order between oxidation and reduction processes in the electrode cleaning cycle (waveforms 1 and 4) greatly affects the sensitivity of the detection, especially for bentazone and HPPH. Typical chromatograms obtained by the waveforms investigated are shown in Fig. 3c. Owing to the low sensitivity exhibited by waveforms 2–4, they were not further included in the electrochemical study performed at pH 4 and 3 (see following sections).

The best results in terms of S/N values and peak area obtained at pH 5 (namely DC: 1.2 V and pulsed amperometry: waveform 1) which are compared in Fig. 5 of Supplementary Material Section, show that waveform 1 provided the best S/N ratio values for all the species, although the highest areas were obtained by the DC mode. This situation is clearly depicted in Fig. 4 where a far less noisy baseline is obtained for pulsed amperometry detection, resulting in a better S/N .

3.4.2. Eluent pH 4.0

The same study was repeated at pH 4. As regards the analysis by DC mode, $E = 1.2 \text{ V}$ still represents the compromise value for the highest S/N ratio for all the analytes. At this value, S/N ratios are lower than those obtained at pH 5 (carbamazepine: 42, bentazone: 62, HPPH: 92). For $E > 1.3 \text{ V}$, S/N for bentazone highly increases (120) at the expense of sensitivity for carbamazepine and HPPH whose S/N value is dramatically low (below 10). Pulsed amperometry mode provides S/N values included within 68–72 for the

Table 2
Waveforms set for pulsed amperometry.

Waveform no. 1			Waveform no. 2			Waveform no. 3			Waveform no. 4		
Time (s)	Potential (V)	Integration	Time (s)	Potential (V)	Integration	Time (s)	Potential (V)	Integration	Time (s)	Potential (V)	Integration
0.00	1.20		0.00	1.20		0.00	-0.20		0	1.20	
0.20	1.20	Begin	0.20	1.20	Begin	0.04	-0.20		0.20	1.20	Begin
0.40	1.20	End	0.40	1.20	End	0.05	0.00		0.40	1.20	End
0.41	-2.00		0.41	1.80		0.21	0.00	Begin	0.41	1.80	
0.42	-2.00		0.60	1.80		0.22	1.20		0.42	1.80	
0.43	1.80		0.61	-1.00		0.46	1.20		0.43	-1.10	
0.44	1.20		1.00	-1.00		0.47	0.00	End	0.44	1.20	
0.50	1.20					0.56	0.00		0.50	1.20	
						0.57	-1.00				
						0.58	-1.00				
						0.59	1.80				
						0.60	-0.20				

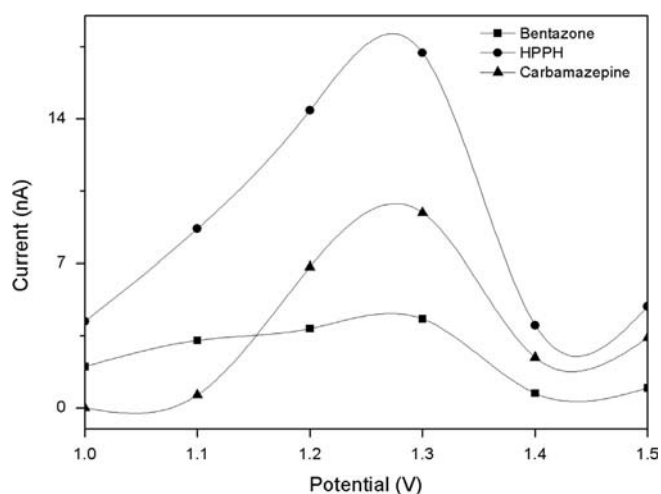


Fig. 2. Hydrodynamic voltammograms for the target analytes. HPLC separation and DC detection mode (glassy carbon electrode). Oxidation potential as shown. Column: LiChroCart PuroSphere RP-18, 125 mm × 3.0 mm, 5 μm. Mobile phase: 50 mM CH₃COOH/CH₃COONa, pH 5. Eluent flow rate: 0.5 mL min⁻¹. Analytes' concentration: 1 mg L⁻¹.

three analytes and hence it can be considered preferable in respect to the DC mode.

3.4.3. Eluent pH 3.0

According to the chromatographic behavior shown in Fig. 4 of the Supplementary Material section, in order to solve the coelution between carbamazepine and bentazone observed at pH 3, the eluent composition was slightly changed increasing CH₃CN content to 32%.

The data obtained for DC mode analysis indicate that for $E = 1.3$ V, S/N ratios close to those obtained at pH 5 can be obtained for bentazone (50) and carbamazepine (150) but not for HPPH (20). $E = 1.4$ V is the compromise potential for the S/N ratios for HPPH (102), bentazone and carbamazepine.

The pulsed amperometry mode was unsatisfactory for carbamazepine ($S/N = 5$).

The best detection conditions achieved for each pH value are summarized in Table 3. Despite carbamazepine has a better S/N ratio value at pH 3 with DC detection, the other two substances are poorly detectable at this pH value. The overall best S/N values are obtained at pH 5 by waveform 1, therefore the figures of merit of the method were evaluated at these experimental conditions.

3.5. Glassy carbon electrode activation

During this experimental work, a decreased electrode response and/or a non-reproducible response was noticed. This decreased reactivity could not even be restored by the polishing procedure with alumina, as recommended by the manufacturer.

It is now generally recognized [32–35] that the presence of carbonaceous material microstructures, the purity of the electrode surface and the presence of functional groups on the surface are crucial to determine the reactivity of the glassy carbon electrode. Reports involving the use of carbon electrodes often describe pretreatment procedures that were found necessary to observe reproducible and well-defined electrochemical behavior.

In order to overcome the lack of reproducibility observed, a pretreatment step of the electrode which consisted in a 24 h-storage of the electrode in the eluent solution 28%: CH₃CN, 72%: 50 mM CH₃COOH/CH₃COONa, pH 5, was adopted. The explanation for the restored electrode activity can be found in the presence of functional groups on the surface of glassy carbon (typically carboxylic and hydroxyl groups), which, depending on pH conditions, could increase the density of active sites at the electrode surface and improve the electron transfer of the reaction [36]. Electrostatic and/or hydrogen bonds between the electrode surface and analytes can also be established, promoting analytes' oxidation.

3.6. Figures of merit

Linearity of the method was verified over two order of magnitude (see Table 4). Limits of detection (LODs) and limits of quantification (LOQs) were evaluated as the concentration referred to a signal S_m defined as $S_m = S_b + 3s_b$ for LOD and $S_m = S_b + 10s_b$ for LOQ, where S_b and s_b are the average signal for blank and its standard deviation, respectively. LODs and LOQs were calculated performing subsequent analysis of the blank ($n = 14$; any "outlier" was highlighted by the Q test). The signal was integrated in the "elution window" of each species.

The LOD values obtained by pulsed amperometry and reported in Table 4 are significantly better than those obtained by UV detection [16,37], especially for HPPH for which LOD is about two order of magnitude lower [38].

Inter-day and intra-day reproducibility of the method (expressed as relative standard deviation, % RSD) were determined both for retention times and peak areas by repeatedly running a mixture of 125 μg L⁻¹ bentazone, 67 μg L⁻¹ HPPH, 240 μg L⁻¹ carbamazepine for 4 days ($n = 52$).

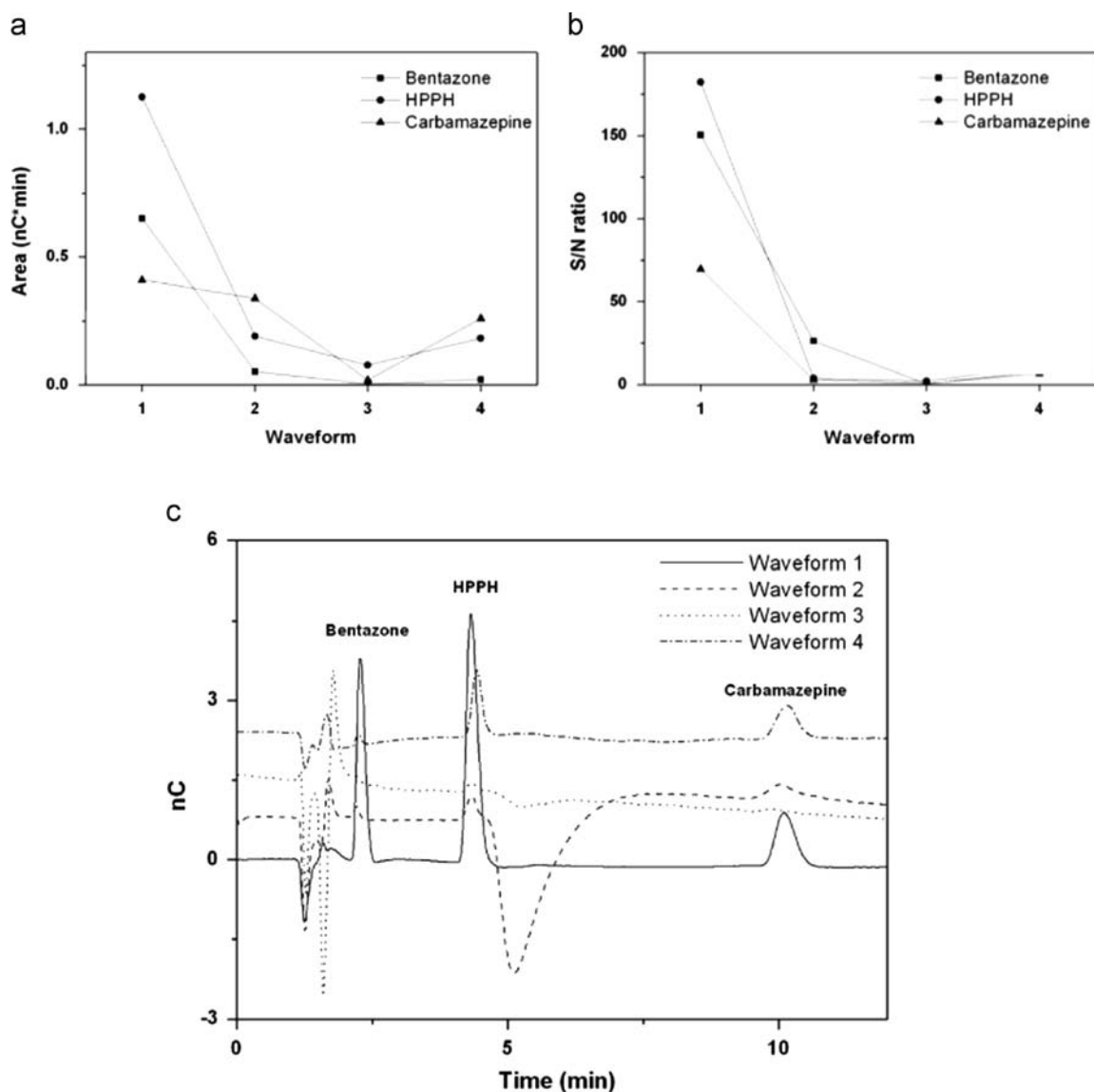


Fig. 3. HPLC separation coupled with pulsed amperometry (glassy carbon electrode). Details of waveforms are shown in Table 2. Column: LiChroCart PuroSphere RP-18, 125 mm × 3.0 mm, 5 μm. Mobile phase: 50 mM CH₃COOH/CH₃COONa, pH 5. Eluent flow rate: 0.5 mL min⁻¹. Analytes' concentration: 1 mg L⁻¹. For each analyte, peak areas (a), S/N ratios (b) and typical chromatograms obtained (c) are shown.

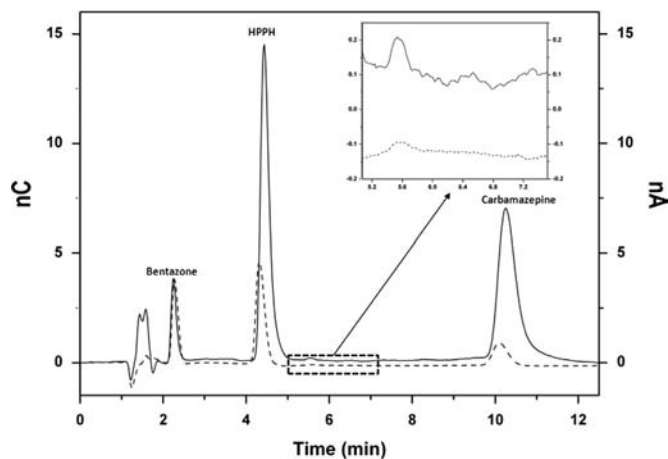


Fig. 4. Comparison of the separation obtained by DC (dashed line) and pulsed amperometry – waveform 1 (continuous line) modes at pH 5. The inset highlights the baseline for each mode. Chromatographic conditions as for Fig. 3.

Table 3

Comparison of the S/N ratios at the best detection conditions obtained for each pH value.

pH	S/N		
	Bentazone	HPPH	Carbamazepine
3 ^a	43	37	121
4 ^b	74	69	69
5 ^b	150	182	70

^a DC, $E = 1.4$ V.

^b Pulsed amperometry, waveform 1.

For intra-day (within day, $n = 13$) measurements, % RSD for retention times is included within 0.2% and 0.7% whereas for peak areas, % RSD was below 5.3% for bentazone, 4.1% for HPPH and 6.2% for carbamazepine, with the exception of day 3 (6.4% for bentazone, 11.3% for HPPH and 17.3% carbamazepine). For inter-day measurements, % RSD for retention times is lower than 1.0%

Table 4

Linearity, LOD and LOQ values for the optimized method. Chromatographic conditions: column: LiChroCart PuroSphere RP-18; eluent: 72% of a solution containing 50 mM CH₃COOH/CH₃COONa, pH 5.0 and 28% CH₃CN, eluent flow rate 0.5 mL min⁻¹. Injection volume: 10 μL. Detection: pulsed amperometry, waveform 1.

Analyte	Equation	Range (μg L ⁻¹)	R ²	LOD (μg L ⁻¹)	LOQ (μg L ⁻¹)
Bentazone	$y = 3.5 \times 10^{-4}x + 9.8 \times 10^{-3}$	15–1500	0.9993	12.5	41.7
HPPH	$y = 1.3 \times 10^{-3}x + 1.4 \times 10^{-2}$	10–1000	0.9989	6.6	22.2
Carbamazepine	$y = 2.22 \times 10^{-4}x + 1.31 \times 10^{-2}$	25–2500	0.9965	24.0	80.0

for all the analytes. The peak area % RSD was lower than 13.1%. The values obtained are satisfactory in respect to the concentration tested that are only slightly higher than LOQ values.

At the optimized chromatographic and SPE conditions (preconcentration factor 100), the method detection limits calculated for the amperometric detection of bentazone, HPPH and carbamazepine are 113 ± 3 ng L⁻¹, 67 ± 1 ng L⁻¹, 234 ± 1 ng L⁻¹ respectively, whereas the method quantitation limits were 377 ± 10 ng L⁻¹, 222 ± 4 ng L⁻¹, 782 ± 2 ng L⁻¹ respectively. These limits can be improved by increasing the preconcentration factor.

It is interesting to note that our method quantitation limits for bentazone and carbamazepine are in the same range of those reported by Loos et al. [39] and by Pedrouzo et al. [40] who applied a solid-phase extraction followed by triple–quadrupole liquid chromatography mass spectrometry (LC–MS(2)) and by ESI–MS respectively. To the best of our knowledge no reports on HPPH determination in environmental samples by HPLC–MS techniques are available for a comparison.

The optimized detection and extraction conditions (summarized in Fig. 1 of the Supplementary Material section) were used for the analysis of a river sample (Po river, Turin, Italy). According to the chromatograms obtained, bentazone was present in the sample analyzed. Bentazone was identified by the standard addition method, by injection of four aliquots of the sample spiked with known amounts of bentazone up to 40 μg L⁻¹ ($R^2 = 0.9970$). According to the data obtained, a final concentration of 0.216 μg L⁻¹ in the river sample was found.

4. Conclusions

This work presents the first report on the study and optimization of the amperometric detection on a glassy carbon electrode of compounds of current environmental concern belonging to different classes (herbicides, pharmaceutical compounds and metabolites).

After optimization of chemical and electrochemical parameters through the evaluation of *S/N* ratios, it was shown that pulsed amperometry showed better sensitivity than the DC mode. Satisfactory results were achieved for bentazone, HPPH and carbamazepine in terms of sensitivity and method robustness.

The coupling of a properly optimized SPE technique allowed to enhance sensitivity and the application of the method developed to a natural water sample.

The monitoring of the peculiar behavior of glassy carbon electrode, due to its surface structure, allowed us to provide a robust protocol to maintain the performance of the electrode.

The use of amperometric techniques can offer a valid, simple and not expensive analytical approach for the determination of compounds of current environmental concern.

Acknowledgments

The authors would like to thank Dr. Petr Jandik (Thermo Scientific, Dionex) for assistance and fruitful discussion during the experimental work. Financial support from Ministero

dell'Istruzione, dell'Università e della Ricerca (MIUR, Italy) is gratefully acknowledged.

Appendix A. Supplementary materials

Supplementary data associated with this article can be found in the online version at <http://dx.doi.org/10.1016/j.talanta.2014.07.070>.

References

- [1] J.A. Dougherty, P.W. Swarzenski, R.S. Dinicola, M. Reinhard, *J. Environ. Qual.* 39 (2010) 1173–1180.
- [2] R. Huber, S. Otto, *Rev. Environ. Contam. Toxicol.* 137 (1994) 111–134.
- [3] R.H. Shimabukuro, H.R. Swanson, *J. Agric. Food Chem.* 17 (1969) 199–205.
- [4] Bentazon: Emergency Medical Treatment, in *Hazardous Substances Data Bank*, <<http://toxnet.nlm.nih.gov/>>, last accessed July 2014.
- [5] Hazardous Substances Data Bank, in, 2013.
- [6] T.B. Hayes, A. Collins, M. Lee, M. Mendoza, N. Noriega, A.A. Stuart, A. Vonk, *Proc. Natl. Acad. Sci. USA* 99 (2002) 5476–5480.
- [7] K. Li, W. Liu, D. Xu, S. Lee, *J. Agric. Food Chem.* 51 (2003) 5362–5366.
- [8] R. Loos, G. Locoro, S. Comero, S. Contini, D. Schwesig, F. Werres, P. Balsaa, O. Gans, S. Weiss, L. Blaha, M. Bolchi, B.M. Gawlik, *Water Res.* 44 (2010) 4115–4126.
- [9] M. Huerta-Fontela, M.T. Galceran, F. Ventura, *Water Res.* 45 (2011) 1432–1442.
- [10] K. Stamatelidou, C. Frouda, M.S. Fountoulakis, P. Drillia, M. Kornaros, G. Lyberatos, *Water Sci. Technol.: Water Supply* 3 (2003) 131–137.
- [11] J.T. Yu, E.J. Bouwer, M. Coelhan, *Agric. Water Manag.* 86 (2006) 72–80.
- [12] K. Reddersen, T. Heberer, *J. Sep. Sci.* 26 (2003) 1443–1450.
- [13] R. Zanella, E.G. Primel, F.F. Goncalves, M.H.S. Kurz, C.M. Mistura, *J. Sep. Sci.* 26 (2003) 935–938.
- [14] G.M.F. Pinto, I.C.S.F. Jardim, *J. Chromatogr. A* 846 (1999) 369–374.
- [15] L. Patrolecco, N. Ademollo, P. Grenni, A. Tolomei, A. Barra Caracciolo, S. Capri, *Microchem. J.* 107 (2013) 165–171.
- [16] L. Budakova, H. Brozmanova, M. Grundmann, J. Fischer, *J. Sep. Sci.* 31 (2008) 1–8.
- [17] D.-D. Shi, B.-Y. Chang, B. Shi, Y. Tian, *Zhongguo Nongye Keji Daobao* 14 (2012) 145–152.
- [18] L. Pareja, V. Cesio, H. Heinzen, A.R. Fernández-Alba, *Talanta* 83 (2011) 1613–1622.
- [19] M.E. Abdel-Hamid, *Il Farmaco* 55 (2000) 136–145.
- [20] C.M.P. Vaz, P.R.V. Silva Jr., I. Prado, G. Castanho, F. Simões, S.A.S. Machado, *Quim. Nova* 31 (2008) 1310–1314.
- [21] A. Bebeslea, F. Manea, G. Burtica, L. Nagy, G. Nagy, *Talanta* 80 (2010) 1068–1072.
- [22] G. Limpert, *Am. Lab.* 43 (2011) 28–30.
- [23] G. Henze, A. Meyer, J. Hausen, *Fresenius' J. Anal. Chem.* 346 (1993) 761–765.
- [24] M. Maruyama, *Fresenius' J. Anal. Chem.* 343 (1992) 890–892.
- [25] A. Pachinger, E. Eisner, H. Begutter, H. Klus, *J. Chromatogr.* 558 (1991) 369–373.
- [26] H.-J. Kwon, S.-H. Choi, C.-S. Yoo, H.-Y. Choi, S.-E. Lee, Y.-D. Park, *J. Sep. Sci.* 36 (2013) 690–698.
- [27] N. Kishikawa, N. Kuroda, *J. Pharm. Biomed. Anal.* 87 (2014) 261–270.
- [28] H. Yamanaka, M. Nakajima, Y. Hara, M. Katoh, O. Tachibana, J. Yamashita, T. Yokoi, *Drug Metab. Pharmacokinet.* 20 (2005) 135–143.
- [29] C.O. Ania, F. Béguin, *Water Res.* 41 (2007) 3372–3380.
- [30] D. Cairns, *Essentials of Pharmaceutical Chemistry*, Pharmaceutical Press, 2012.
- [31] E. Manuela Garrido, J.L. Costa Lima, C.M. Delerue-Matos, A. Maria Oliveira Brett, *Talanta* 46 (1998) 1131–1135.
- [32] K. Kinoshita, *Carbon: Electrochemical and Physicochemical Properties*, Wiley, 1988.
- [33] S. Sarangapani, J.R. Akridge, B. Schumm, Eds., in: *Proceedings of the Workshop on the Electrochemistry of Carbon*, August 17–19, 1983, Case Center for Electrochemical Sciences, Case Institute of Technology, Case Western University, Cleveland, Ohio, The Electrochemical Society, Inc., 1984.
- [34] R.L. McCreery, K.K. Cline, C.A. McDermott, M.T. McDermott, *Colloids Surf. A* 93 (1994) 211–219.

- [35] P. Kissinger, W.R. Heineman, *Laboratory Techniques in Electroanalytical Chemistry*, second ed., CRC Press, 1996.
- [36] H. Alemu, L. Hlalele, *Bull. Chem. Soc. Ethiop.* (2007) 1–12.
- [37] A. Serralheiro, G. Alves, A. Fortuna, M. Rocha, A. Falcao, *J. Chromatogr. B: Anal. Technol. Biomed. Life Sci.* 925 (2013) 1–9.
- [38] A. Khedr, M. Moustafa, A.B. Abdel-Naim, A. Alahdal, H. Mosli, *Anal. Chem. Insights* 3 (2008) 61–67.
- [39] R. Loos, G. Locoro, S. Contini, *Water Res.* 44 (2010) 2325–2335.
- [40] M. Pedrouzo, S. Reverte, F. Borrull, E. Pocurull, R.M. Marce, *J. Sep. Sci.* 30 (2007) 297–303.



Restricted access carbon nanotubes for direct extraction of cadmium from human serum samples followed by atomic absorption spectrometry analysis



Adriano F. Barbosa^{a,b}, Valéria M.P. Barbosa^{a,b}, Jefferson Bettini^c, Pedro O. Luccas^b, Eduardo C. Figueiredo^{a,*}

^a Laboratory of Toxicant and Drug Analysis – LATF, Gabriel Monteiro da Silva St. 700, Federal University of Alfenas – Unifal-MG, 37130-000 Alfenas, MG, Brazil

^b Institute of Chemistry, Gabriel Monteiro da Silva St. 700, Federal University of Alfenas – Unifal-MG, 37130-000 Alfenas, MG, Brazil

^c Brazilian Nanotechnology National Laboratory, 13083-970 Campinas, SP, Brazil

ARTICLE INFO

Article history:

Received 29 April 2014

Received in revised form

17 July 2014

Accepted 20 July 2014

Available online 27 July 2014

Keywords:

Carbon nanotubes

Restricted access material

Restricted access carbon nanotubes

Cadmium

Serum

Atomic absorption spectrometry

ABSTRACT

In this paper, we propose a new sorbent that is able to extract metal ions directly from untreated biological fluids, simultaneously excluding all proteins from these samples. The sorbent was obtained through the modification of carbon nanotubes (CNTs) with an external bovine serum albumin (BSA) layer, resulting in restricted access carbon nanotubes (RACNTs). The BSA layer was fixed through the interconnection between the amine groups of the BSA using glutaraldehyde as cross-linker. When a protein sample is percolated through a cartridge containing RACNTs and the sample pH is higher than the isoelectric point of the proteins, both proteins from the sample and the BSA layer are negatively ionized. Thus, an electrostatic repulsion prevents the interaction between the proteins from the sample on the RACNTs surface. At the same time, metal ions are adsorbed in the CNTs (core) after their passage through the chains of proteins. The Cd²⁺ ion was selected for a proof-of-principle case to test the suitability of the RACNTs due to its toxicological relevance. RACNTs were able to extract Cd²⁺ and exclude almost 100% of the proteins from the human serum samples in an online solid-phase extraction system coupled with thermospray flame furnace atomic absorption spectrometry. The limits of detection and quantification were 0.24 and 0.80 µg L⁻¹, respectively. The sampling frequency was 8.6 h⁻¹, and the intra- and inter-day precisions at the 0.80, 15.0, and 30.0 µg L⁻¹ Cd²⁺ levels were all lower than 10.1% (RSD). The recoveries obtained for human blood serum samples fortified with Cd²⁺ ranged from 85.0% to 112.0%. The method was successfully applied to analyze Cd²⁺ directly from six human blood serum samples without any pretreatment, and the observed concentrations ranged from < LOQ to 2.52 µg L⁻¹.

© 2014 Elsevier B.V. All rights reserved.

1. Introduction

An adequate sample preparation is indispensable for metal analyses in complex samples using spectrometry techniques. The matrix effect can modify analytical responses and damage equipment, mainly when the samples are slimy and rich in proteins, for example, biological fluids (e.g., total blood, plasma, serum, milk). Thus, strategies based on organic matrix decomposition have been frequently employed as the combustion [1] and microwave-assisted techniques [2]. In both cases, mineralization processes are carried out in drastic conditions with high temperatures,

pressures in acidic and oxidant media, or both. To the best of our knowledge, matrix decomposition is the main sample preparation procedure for metal analyses in biological fluids, despite its slowness and potential danger when used.

Unlike metals, organic compounds are extracted from different samples employing soft techniques such as solvent extraction [3,4], solid phase extraction [5], and cloud point [6,7], among others. These techniques are able to extract molecules without damaging them because drastic conditions in terms of temperature and acidity are not employed. However, when these extractions are carried out in biological fluids, the proteins from the sample are not totally excluded, and several problems can occur during the analyses, such as the matrix effect and blockage of tubes. For such samples, an additional protein precipitation step is frequently employed as a cleanup process.

* Corresponding author. Tel.: +55 35 3299 1268; fax: +55 35 3299 1063.
E-mail address: eduardocfig@yahoo.com.br (E.C. Figueiredo).

An alternative for facilitating a gentle extraction of analytes from the biological fluids and total protein elimination is to do so through restricted access materials (RAMs) [8]. RAMs are sorbents that are able to retain organic compounds (with low molecular weight) from biological fluids, eliminating macromolecules as proteins. These sorbents limit the accessibility into sites within the pores only to small molecules (physical barrier), whereas macromolecules are excluded due to the presence of hydrophilic groups covering the sorbent surface (chemical barrier) [8]. Recently, some studies have been devoted to chemically modifying the surface of common sorbents as silica or organic polymers, converting them to sorbents that are able to exclude macromolecules. A very successful strategy is based on the formation of a bovine serum albumin (BSA) layer around silica [9–13] or molecularly imprinted polymers [14]. In these cases, when the sample is percolated through the sorbent in a pH larger than the isoelectric point of the proteins, both proteins from the sample and proteins from the sorbent layer (BSA) are negatively ionized, causing an electrostatic repulsion between both. Then, the proteins from the sample are excluded, and the analytes of low molecular weight pass through the BSA layer and are retained in the internal sorbent.

As far as we know, the RAMs have never been employed to extract metals from biological fluids, and their use has been exclusively devoted to the organic compound extractions. However, we believe that if a sorbent that is able to adsorb metals is covered with a BSA layer, the metals can be retained and the proteins excluded. This possibility is extremely promising for metal analyses from biological fluids because the slow and dangerous procedures of sample preparation based on matrix decomposition could be replaced by a simple solid phase extraction with RAM.

Carbon nanotubes (CNTs) are excellent sorbents for the preconcentration of metals due to their high surface area and inner volume, stability, and mechanical strength, as well as the possibility of establishing π - π interactions [5]. Several applications have been described in the literature using CNTs to concentrate metals from water [15–17], the environment [18–20], and food [21], among others. However, the use of CNTs in direct extractions of metals from protein fluids has not yet been successful because these sorbents can be blocked by proteins retained from the sample [22].

Based on the proven characteristics of CNTs to preconcentrate different metals, we propose, for the first time, the modification of these sorbents with an external BSA layer, resulting in restricted access carbon nanotubes (RACNTs) that are able to extract metals directly from untreated protein fluids, excluding all of the macromolecules. The RACNTs were synthesized, characterized, and used in an online solid-phase extraction of Cd^{2+} ions directly from human serum samples without any pretreatment. The analyses were carried out using the flow injection analysis (FIA) system with detection by thermospray flame furnace atomic absorption spectrometry (TS-FF-AAS). The Cd^{2+} ions were employed for a proof-of-principle case to appraise the suitability of the RACNTs due to its high toxicity in living organisms and its bioaccumulation potential because of the frequent occupational and environmental expositions of humans to this metal [23].

2. Materials and methods

2.1. Instrumentation

An atomic absorption spectrometer Shimadzu AA-6800 (Shimadzu[®], Tokyo, Japan) equipped with a hollow cathode lamp for cadmium and a deuterium lamp for background correction was

used in the analyses. Measurements were carried out at the peak height at 228.8 nm, and the lamp currents were set at 5 mA. The TS-FF-AAS was operated with acetylene and airflow rates of 3.0 L min^{-1} and 10.0 L min^{-1} , respectively. Moreover, the apparatus was composed of a nickel tube (Ni 200 Realum, UNS N 2200, São Paulo, Brazil) of 10-cm length and 2.5-cm i.d., containing six holes of 2.5-mm i.d. addressed to the burner, allowing for flame penetration inside the tube. A non-porous Al_2O_3 ceramic capillary (Friatec[®], Mannheim, Germany) (10-cm length, 0.5-mm i.d., and 2.0-mm o.d.) was used to conduct the sample towards the nickel tube. A JEOL LV-JSM 6360 microscope (Tokyo, Japan) was used to obtain the images of scanning electron microscopy (SEM) and the spectra of energy-dispersive spectroscopy (EDS). Transmission electron microscopy (TEM) images were carried out using a JEOL JEM 2100 microscope. A chromatograph from Shimadzu[®] equipped with a 20AD pump (Shimadzu[®]), an electronic six-port switching-valve model 11R-0016H (Valco[®] Instruments, Houston, USA), and a UV-detector model SPD-20A (Shimadzu[®]) was used in the protein elimination tests.

The FIA system consisted of a peristaltic pump (Ismatec[®] IPC-08, Glattzbrugg, Switzerland), furnished with Tygon[®] tubes to propel all sample and reagent solutions, while a homemade injector commutator (in acrylic) was used to select the preconcentration-washing and elution/sampling steps.

2.2. Reagents and solutions

All solutions were prepared using ultra-high purity water ($18.2 \text{ M}\Omega \text{ cm}$) from a Milli-Q system (Millipore[®], Bedford, MA, USA). All chemicals were of analytical grade and used without further purification.

The multi-walled CNTs with outer wall diameters from 6 nm to 9 nm and lengths of $5 \mu\text{m}$ were purchased from Sigma-Aldrich[®] (St. Louis, MO, USA). BSA, glutaraldehyde, and sodium borohydride (all from Sigma-Aldrich[®]) were used for the CNTs coating.

A standard stock solution of Cd^{2+} (1000 mg L^{-1}) was purchased from Sigma-Aldrich[®]. Nitric acid and phosphate buffer (all from Sigma-Aldrich[®]) were used in the FIA system in the elution and cleaning steps.

2.3. RACNTs preparation

Initially, 500 mg of CNTs were oxidized with 30 mL of HNO_3 (65%) according to the method described by Zhijie et al. [24]. The material was then extensively washed with water and coated with a BSA layer, following the procedure of Moraes et al. [14] on coating a molecularly imprinted polymer. A 20 mL 1% (m/v) BSA prepared in 50 mmol L^{-1} phosphate buffer (pH 6.0) was poured through a cartridge containing 500 mg of oxidized CNT at 1.0 mL min^{-1} . Next, 5 mL of 25% (m/v) glutaraldehyde aqueous solution was slowly percolated through the cartridge, and the system was maintained in standby during 5 h. Finally, 10 mL of 1% (m/v) sodium borohydride aqueous solution was poured through the material at 1 mL min^{-1} . The cartridge was extensively washed with water (pH approximately 7.0) to eliminate all residues from the synthesis. The new covered material was defined as restricted access carbon nanotubes (RACNTs).

2.4. RACNTs characterization

The presence of the BSA layer on the RACNT was investigated by SEM, EDS and TEM. For the SEM and EDS, the samples were previously covered with a thin layer of platinum. The electron acceleration voltage was 15.0 kV. For TEM, the samples were dropped on the copper grid with holey carbon film and analyzed using an acceleration voltage of 200 kV.

The CNTs and RACNTs were appraised as to their abilities to exclude proteins. Initially, 25 μL of 44 mg mL^{-1} BSA standard aqueous solution (approximately the same concentration found in the human plasma) was injected into an HPLC system without any column, with a UV detector at 280 nm and using deionized water as the mobile phase at 1 mL min^{-1} . The signal area represents 100% of BSA; in other words, all BSA arrived at the detector. Secondly, the column containing 30 mg of the material (CNTs or RACNTs) was coupled in the HPLC system, and the same BSA solution was injected in each case (with CNTs or RACNTs column). The peak areas obtained for each case (CNTs or RACNTs column) divided by the signal area of 100% BSA represent the percentage of eluted BSA.

The kinetic study was performed by adding 10 mg of the CNTs or RACNTs at 25 $^{\circ}\text{C}$ to each of the eight polypropylene tubes containing 5 mL of 50 mg L^{-1} of Cd^{2+} solution (prepared by nitrate of cadmium in pH 7.0). The tubes were vortexed at 10, 25, 40, 55, 70, and 90 min at 252g and immediately centrifuged at 699g for 10 min. The Cd^{2+} concentrations in the supernatants were analyzed by FAAS. For the adsorption studies, 10 mg of the CNTs or RACNTs were added into the polypropylene tube containing Cd^{2+} concentrations that ranged from 5 to 300 mg L^{-1} . The tubes were vortexed at 30 min at 252g and immediately centrifuged at 699g. The Cd^{2+} concentrations in the supernatants were analyzed by FAAS.

2.5. Flow injection system with online preconcentration

The FIA system with detection by TS-FF-AAS is shown in Fig. 1. In step 1 (Fig. 1a), the sample loop is filled with 2 mL, whereas the 0.1 mol L^{-1} HNO_3 solution elutes the analytes (of a previous extraction) through the TS-FF-AAS at 0.75 mL min^{-1} . In step 2, the injector is switched (Fig. 1b), and the sample is carried to the RACNTs column at 4.5 min by using a phosphate buffer solution (0.01 mmol L^{-1} , pH 7.0) as the carrier at 0.75 mL min^{-1} . The Cd^{2+} is retained in the RACNTs, and the proteins are excluded from the waste. Finally, the injector is switched again to the initial position (Fig. 1a), and the extracted Cd^{2+} is eluted and conducted to the TS-FF-AAS. A conditioning loop was used to eliminate the HNO_3 residues from the column immediately before the sample extraction.

2.6. Samples

The human blood sample handling was approved by the ethics committee of the Federal University of Alfenas (process CAEE: 11401412.0.0000.5142). After coagulation, the samples were centrifuged for 15 min at 1000g. The blood serum samples were

diluted in a phosphate buffer 0.01 mol L^{-1} and pH 7.0 at a proportion of 3:7 v/v (serum:buffer). The samples were analyzed directly in the system without any pretreatment.

2.7. Data treatment and method validation

The Cd^{2+} standards were prepared in a pool of human blood serum ($n=25$) by fortifying then with Cd^{2+} from 0.8 to 30.0 $\mu\text{g L}^{-1}$. The standards were diluted before the analyses with phosphate buffer 0.01 mol L^{-1} and pH 7.0 at a proportion of 3:7 - v:v (serum:buffer). The limits of detection (LOD) and quantification (LOQ) were defined according to IUPAC [25] as $3\sigma m^{-1}$ and $10\sigma m^{-1}$, respectively, where σ is the standard deviation of 10 blank readings and m is the slope of the analytical curve.

The preconcentration factor, consumptive index, and concentration efficiency parameters were calculated to evaluate the performance of the online preconcentration system. The preconcentration factor is defined with the enhancement of TS-FF-AAS sensitivity by inserting the step of preconcentration and is calculated as the ratio of the slope of the analytical curves obtained by the proposed method and the TS-FF-AAS system without preconcentration. The preconcentration factor operated at 1 min defines the concentration efficiency. The consumptive index is the volume of samples (mL) necessary to attain a unit of preconcentration factor.

The intra-day precision was assessed as the relative standard deviation (RSD) of five independent preconcentration cycles using a pool of blank human blood serum fortified with Cd^{2+} at 0.80, 15.0, and 30.0 $\mu\text{g L}^{-1}$ levels. Inter-day precision was evaluated by repeating the steps to the same standards of cadmium on three different days.

The developed extraction/preconcentration method was validated by the direct analysis of blood serum samples diluted in the buffer phosphate (pH 7.00, 0.01 mol L^{-1}) at the 3:7 - v:v ratio. The accuracy of the proposed method was evaluated through recovery tests by fortifying six different human blood serum samples with Cd^{2+} at 2.0, 5.0, 10.0, 14.0, 20.0, and 25 $\mu\text{g L}^{-1}$ levels.

3. Results and discussion

3.1. RACNTs synthesis and characterization

The BSA layer was fixed on the CNTs surface through the interconnection between the amine groups of the BSA by using glutaraldehyde as cross-linker. The resulting imines (very labile function) were reduced to amines by using sodium borohydride to give stability to the BSA layer [26]. The presence of the BSA was

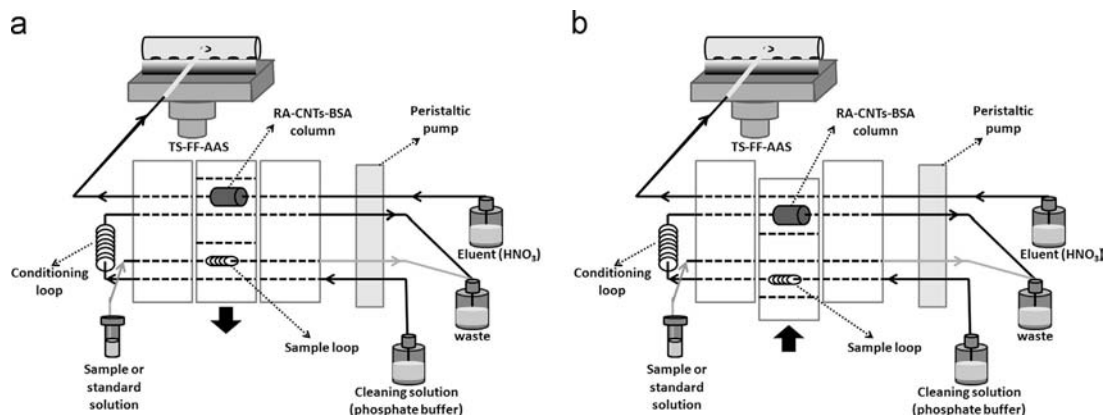


Fig. 1. Flow system manifold for the sampling/elution steps (a) and the preconcentration/cleaning steps (b). Eluent: HNO_3 0.1 mol L^{-1} , mass of RACNTs: 35 mg, sample loop: 2.0 mL, and conditioning loop: 300 μL .

confirmed by scanning electron micrographs and transmission electron micrographs of the CNTs and RACNTs, as shown in Fig. 2a–d. Fig. 2a shows the CNTs with a slight variation in size, which is in agreement with the commercial nanotube characteristics. Fig. 2b shows the RACNTs, and only a gross mass can be observed (CNTs are not visible). From these results, it is possible to attest to the presence of the BSA layer covering the CNTs. TEM images were obtained for the same samples to examine the details. Fig. 2c shows CNTs isolated and, again, with slight variation in size. In Fig. 2d, an amorphous layer with some nanotubes inside can be observed. As was supposed, the BSA layer (amorphous because of the treatment) is covering the CNTs and gluing them. The CNT surface was also analyzed by EDS resulting in a percentage larger than 99% of carbon. After the BSA covering (RACNT), the percentages were the following: 73.88% carbon, 14.46% nitrogen, 5.40% oxygen and 0.5% sulfur. These results confirm the presence of the BSA layer due to the decreasing of carbon percentages and the appearance of nitrogen, oxygen and sulfur, commonly present in the BSA.

The protein elimination abilities of CNTs and RACNTs can be accessed in Fig. 3. It shows that when the BSA solution (44 mg L^{-1}) was injected through the CNT column, approximately 99% of the proteins were retained. This result allows us to conclude that the direct extraction of any analyte from protein samples (e.g., plasma, serum, and milk, among others) is unviable in columns filled with commercial CNTs. Conversely, when the RACNTs column was used, the obtained peak area was practically equal to that obtained in the system without the column, attesting to the good performance of the RACNTs in excluding proteins (approximately 99%). The possible exclusion mechanism is based on the electrostatic repulsion between the BSA layer and the proteins from the sample when the pH of the medium is larger than the isoelectric point of the proteins. In this way, to obtain the best performance in terms of protein elimination, we recommend

a sample pH of at least 6.0 (or higher) once the BSA isoelectric point is 4.7–5.6 [27,28].

The kinetic studies of the Cd^{2+} adsorption in the CNTs and RACNTs were executed from 1 to 90 min. Both equilibria were reached in approximately 25 min. In this way, the adsorption isotherms for CNTs and RACNTs were carried out with 30 min of interaction between the Cd^{2+} and each sorbent to guarantee that equilibrium is reached. The isotherms are shown in Fig. 4, and a low adsorption capacity can be observed for the RACNTs in comparison with the CNTs. The protein layer probability makes the access of the Cd^{2+} ions to the sorbent difficult. However, this lower sensitivity was not a problem because obtained detectability was enough to analyze Cd^{2+} in concentrations lower than the reference values found in the human serum [29]. The

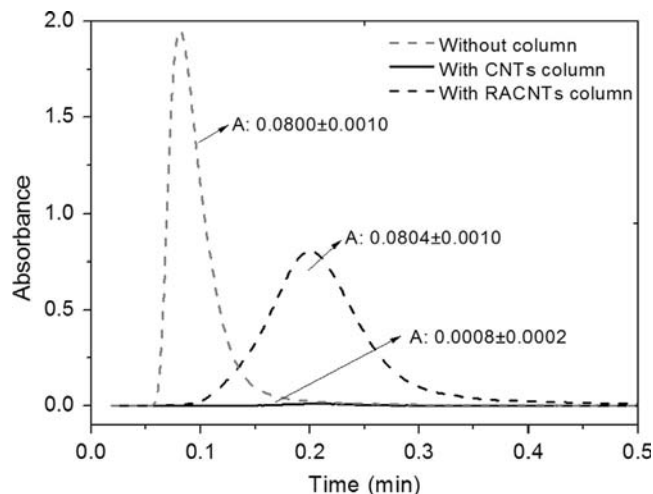


Fig. 3. The exclusion assay of proteins in columns packed with RACNTs and CNTs.

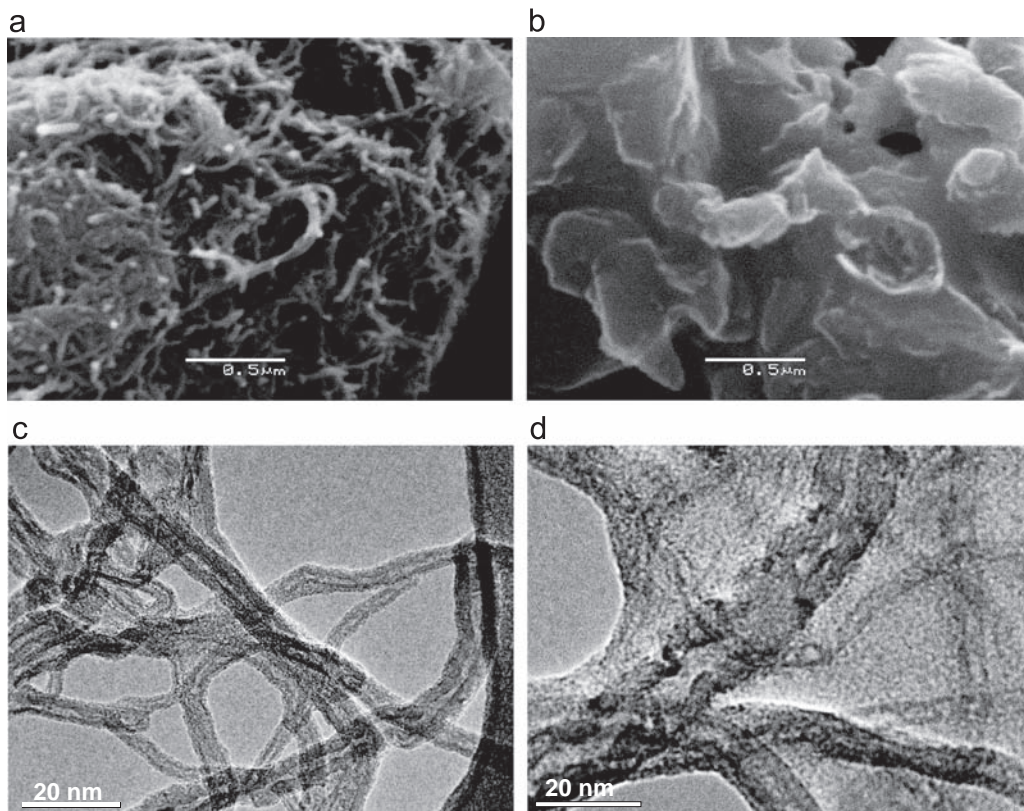


Fig. 2. Scanning electron micrographs (a and b) and transmission electron micrographs (c and d) of the CNTs (a and c) and RACNTs (b and d).

experimental data for the CNTs and RACNTs were applied to the Langmuir and Freundlich linear mathematical models, and for both materials, the best fits were obtained for the Langmuir model ($r > 0.99$ for both CNTs and RACNTs; see also Table 1). The results suggest that the adsorbent contains homogeneous sites distributed in a monolayer. Each site retains one Cd^{2+} ion and all sites are energetically and sterically independent of the adsorbed quantity [30,31].

3.2. Optimization of the online preconcentration system

All of the optimizations were carried out using a Cd^{2+} standard solution prepared in an aqueous medium containing 44 mg mL^{-1} of BSA (to simulate the human serum samples in terms of protein concentration).

The cleaning solution (please identify it in Fig. 1) flow rate was appraised from 0.5 to 1.0 mL min^{-1} . The analytical signals were equal for 0.5 and 0.75 mL min^{-1} flow rates and decrease for high flow rates, probably due to the fast and insufficient contact of the Cd^{2+} ions with the sorbent. Additionally, when higher flow rates were used, the system pressure increased with the blood serum samples percolation, causing leakage and imprecision. In this way, 0.75 mL min^{-1} flow rate was selected as a working condition to ensure the best detectability and analytical frequency.

During sequential analyses using a system without the conditioning loop (see conditioning loop in Fig. 1), when a sample volume was injected (Fig. 1a), it arrived quickly to the RACNTs column that was filled with the eluent from a previous elution step (Fig. 1b). In this case, the eluent residues impair the Cd^{2+} retention, decreasing the sensitivity. Thus, a $300\text{-}\mu\text{L}$ conditioning loop was inserted in the system between the RACNTs column and the sample loop, as shown in Fig. 1. During the elution/sampling step, the conditioning loop is filled with a phosphate buffer solution (7.0 , 0.01 mmol L^{-1}) that is percolated through the column to clean it before the passage of the sample (Fig. 1b).

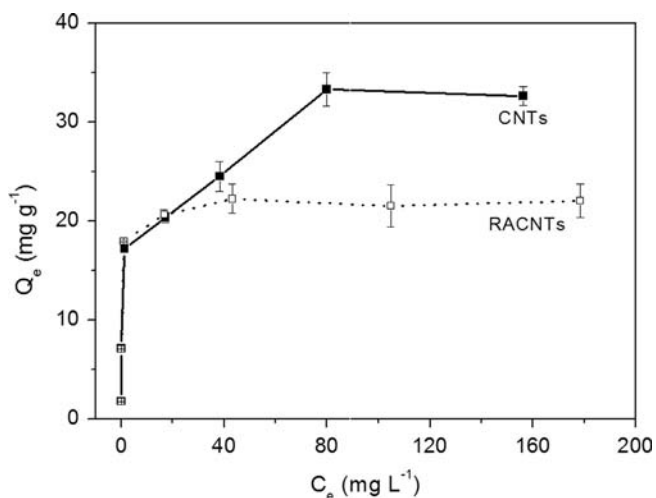


Fig. 4. The adsorption behavior of Cd^{2+} ions on CNT and RACNT sorbents.

Table 1
The Langmuir model parameters obtained for CNTs and RACNTs.

	R^2	Q_m (mg g^{-1})	K (L mg^{-1})
CNTs	0.9883	33.30	0.238
RACNTs	0.9998	21.98	1.967

Equation of Langmuir model: $Q_e = KQ_m C_e / (1 + K C_e)$; C_e = equilibrium concentration of ions; Q_m = maximum adsorption capacity (mg g^{-1}); K = parameter related to the affinity of adsorbate and adsorbent.

When Cd^{2+} is extracted from protein samples such as blood serum, a washing solution needs to be sequentially flowed through the RACNTs to remove all of the proteins. In this case, we used the carrier solution to conduct the sample and remove the proteins. Thus, if a high extraction time is fixed, the sample passes through the column, and a fraction of the carrier (cleaning solution) eliminates the proteins. Therefore, the extraction time was fixed at 4.5 min. At a carrier flow rate of 0.75 mL min^{-1} , this time was sufficient to flow 2.00 mL of sample through the column, as well as approximately 1.38 mL of cleaning solution. Extraction times less than 4.5 min were not sufficient to eliminate all of the proteins, impairing the thermospray formation.

In addition to its protein elimination ability, the washing solution needs to be appropriate to promote the effective adsorption of the Cd^{2+} ions in the RACNTs once it is also used as a conditioning solution (filling the conditioning loop), as previously noted. For this reason, the cleaning solution was studied at pH levels between 4.0 and 9.0 using 0.002 mol L^{-1} acetate ($4.0 \leq \text{pH} \leq 6.0$) or phosphate ($7.0 \leq \text{pH} \leq 9.0$) buffer solutions. The results, in terms of Cd^{2+} adsorption, are shown in Fig. 5, and the best results were obtained for $\text{pH} = 6.0$ or higher. This result attests to the presence of carboxylic groups on the CNT after acid treatment, once the optimum adsorption pH (6.0) is higher than the pK_a values for the carboxylic groups. Thus, these groups are negatively ionized, interacting with the Cd^{2+} ions through electrostatic forces [32]. It is important to note that in these pH proteins both the RACNTs layer and the sample are negatively ionized because the pH is larger than the BSA isoelectric point ($4.7 < \text{pI} < 5.6$) [27,28]. This ionization causes electrostatic repulsion between both, avoiding protein retention on the RACNTs surface. For pH 5.0 (pH of zero charge for BSA), there was a gradual increasing of pressure due to the blockage of the RACNT by proteins from the sample. This effect can be explained by the low protein exclusion capacity of the RACNT, once there is not electrostatic repulsion between proteins from both the sample and the BSA layer. Moreover, the low analytical signal for Cd^{2+} obtained with this pH can be attributed to the inefficient diffusion of the sample through the RACNT core. Thus, the pH 7.0 (phosphate buffer) was selected as the working condition due to the lower experimental error in comparison with the other pHs. The serum sample was also studied at pH levels between 4.0 and 9.0 by the sample dilution in 0.01 mol L^{-1} acetate ($4.0 \leq \text{pH} \leq 6.0$) or phosphate ($7.0 \leq \text{pH} \leq 9.0$) buffer solutions at the proportion of 3:7 (v/v). The results (Fig. 5) are very similar to those obtained

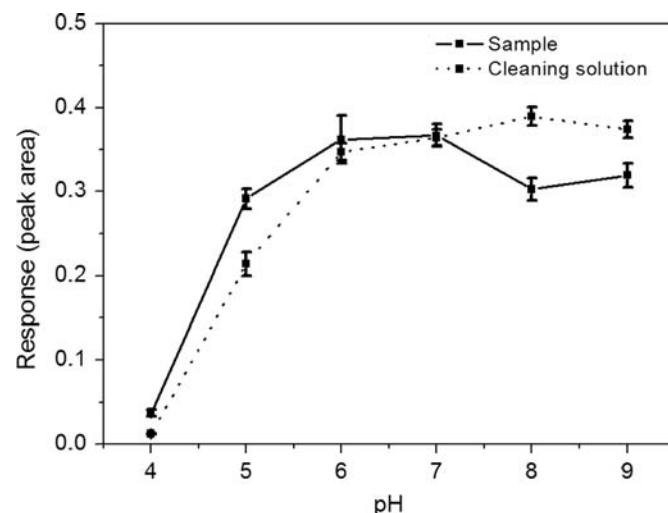


Fig. 5. Effect of the cleaning solution and sample pH values in the analytical response.

during the washing solution optimization, and the pH 7.0 (phosphate buffer) was also selected for further experiments.

The effect of the phosphate buffer concentration of the washing solution was also evaluated from 0.001 to 0.040 mol L⁻¹. The Cd²⁺ peak areas increased approximately 20% when the buffer concentration was increased from 0.001 to 0.010 mol L⁻¹, demonstrating a probable salting-out effect. However, when the buffer concentration was increased from 0.010 to 0.040 mol L⁻¹, the Cd²⁺ peak areas decreased approximately 25%, probably due to the high ionic strength that caused the Cd²⁺ elution. Then, 0.010 mol L⁻¹ was selected as the buffer concentration of the cleaning solution.

The peak area increased by approximately 28% when the sample volume was increased from 0.5 to 2.02 mL. This result demonstrates that the maximum adsorption capacity has not been reached yet. However, volumes larger than 2 mL were not appraised because of the limited sample volume that can be removed from patients using commercial tubes.

To evaluate the optimized system for the Cd²⁺ adsorption and the protein exclusion, a human serum sample fortified with 50 µg L⁻¹ of Cd²⁺ was injected into the flow system, and the molecular (proteins) and atomic (Cd) absorptions were simultaneously monitored. For the molecular absorption monitoring, a spectrometer (280 nm) was coupled in the end of the cleaning solution (see Fig. 5). As shown in Fig. 6, an extraction time of 4.5 min was sufficient to exclude all of the proteins present in the RACNTs column due to the end of the molecular absorption peak. After 4.5 min, the system switched, and the RACNTs column was put in TS-FF-AAS path, where Cd²⁺ is eluted and analyzed. The background was very low, indicating the absence of proteins in the RACNTs. Additionally, the thermospray profile was not modified with the column switching, unlike what is observed when the plasma is directly injected into the thermospray (the spray stops due to the high level of proteins and high viscosity).

3.3. Effect of interference

Based on our experience in previous work [32] and the work of other authors [33,34], the interference effect of coexisting ions in the Cd²⁺ adsorption on CNTs was not observed until there was high concentration of the coexisting ions. Thus, this study was not conducted in the present work. Moreover, the accuracy and precision results shown in the next section demonstrated that there are no interferences in the Cd²⁺ extraction from human serum samples.

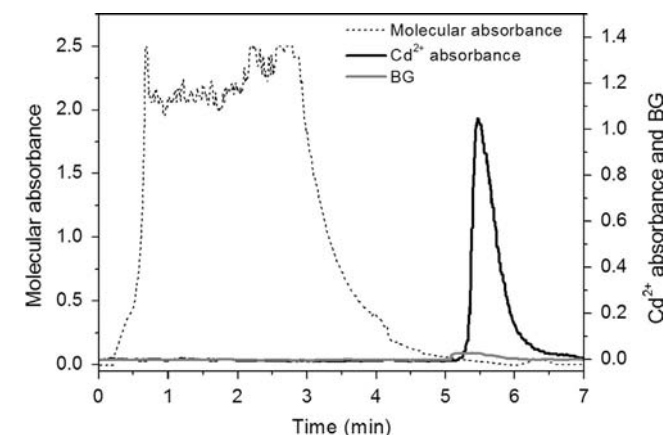


Fig. 6. Molecular and atomic absorption responses for the injection of a human serum sample fortified with 50 µg L⁻¹ of Cd²⁺ in the optimized system. To monitor the molecular absorption, a spectrometer (280 nm) was coupled to the end of cleaning solution channel (see Fig. 1).

3.4. Method validation and applications

The method was validated for Cd²⁺ analyses in human blood serum samples. The analytical calibration standards were prepared by fortifying a pool of human blood serum from individuals not exposed to cadmium (matrix-matching calibration). This strategy was necessary because the online solid-phase extraction was not exhaustive and the extraction recovery was lower than 100%, unlike what happens when the sample is mineralized and all of the analytes are injected into the system. It is important to emphasize that this strategy of using the matrix-matching calibration has been widely used for organic compound analyses after no exhaustive extractions [14,35–37]. Fig. 7 shows the analytical responses obtained by the analyses of this pool of human blood serum unfortified (blank) and fortified with Cd²⁺ at concentrations between 0.8 and 30 µg L⁻¹. The peaks observed for the blank analyses correspond to approximately 0.51 µg L⁻¹ of Cd²⁺ naturally present in the human serum samples. This obtained cadmium concentration is in accordance with the literature, which stipulates that the reference values for unexposed individuals are

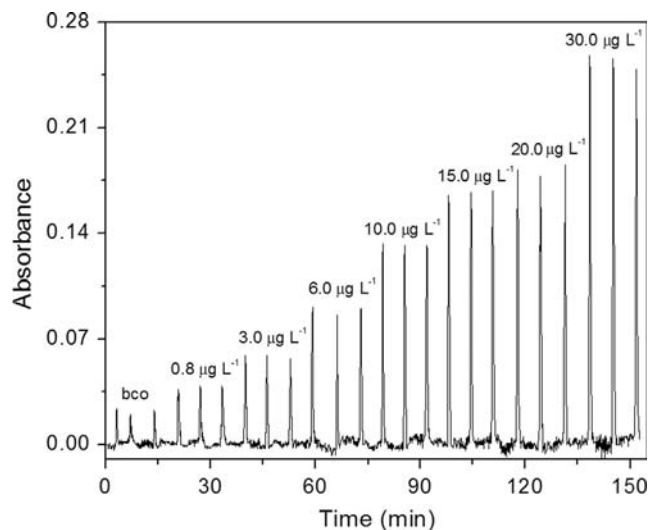


Fig. 7. Analytical responses obtained by the analyses of a pool of human blood serum unfortified (blank) and fortified with Cd²⁺ at concentrations from 0.8 to 30 µg L⁻¹.

Table 2

Analytical parameters for direct extraction and determination of Cd²⁺ from human blood serum sample using the proposed method.

Analytical range (µg L ⁻¹)	0.80–30.00	
Equation (n=3)	A=0.0368C+0.003	
Correlation coefficient	0.993	
Detection limit (µg L ⁻¹)	0.24	
Limit of quantification (µg L ⁻¹)	0.80	
Preconcentration factor	10.8	
Sampling frequency (h ⁻¹)	8.6	
Consumptive index (mL)	0.185	
Concentration efficiency (min ⁻¹)	4.04 ^a	
	Concentration (µg L ⁻¹)	RSD (%)
Intra-day precision (n=5)	0.8	7.8
	15.0	3.1
	30.0	4.0
Inter-day precision (n=3; 5)	0.8	10.1
	15.0	7.5
	30.0	5.3

^a Considering 2.67 and 2.23 min as the preconcentration and washing times, respectively.

Table 3

Cd²⁺ determination in human serum samples by the proposed method (without mineralization) and by conventional TS-FF-AAS method after mineralization, *n*=3.

Sample	Added ($\mu\text{g L}^{-1}$)	Proposed method ($\mu\text{g L}^{-1}$)	Recovery for the proposed method (%)	TS-FF-AAS ($\mu\text{g L}^{-1}$) ^a
1	0	1.11 ± 0.02	–	0.99 ± 0.02
	10.0	10.8 ± 0.1	97.2	–
2	0	1.4 ± 0.1	–	1.3 ± 0.1
	14.0	14.4 ± 0.1	93.5	–
3	0	2.1 ± 0.1	–	2.3 ± 0.2
	2.0	3.8 ± 0.2	92.7	–
4	0	2.5 ± 0.1	–	–
	25.0	30.5 ± 0.9	110.9	–
5	0	< LOD	–	–
	20.0	18.8 ± 0.3	94.0	–
6	0	< LOQ	–	–
	5.0	5.4 ± 0.2	108.0	–

^a The samples were analyzed by conventional TS-FF-AAS after their mineralizations.

Table 4

Comparison of different atomic absorption spectrometry methods to analyze Cd²⁺ from protein fluids.

Technique	Sample	Previous sample preparation step	Limit of detection ($\mu\text{g L}^{-1}$)	Reference
ETAAS	Whole blood	Protein precipitation	0.026	[23]
ETAAS	Whole blood	Without sample preparation	0.54	[39]
FAAS	Milk	Solid phase extraction	0.2	[40]
FAAS	Blood serum	Cloud point extraction	2.0	[41]
FAAS	Milk	Acid extraction	14.0	[42]
TS-FF-AAS	Blood serum	Without sample preparation	0.24	This work

approximately 0.6 $\mu\text{g L}^{-1}$ [29]. The validation parameters of the proposed method are presented in Table 2. The method was linear, and the limit of quantification was lower than the reference values [29], qualifying the method to be used to quantify Cd²⁺ in unexposed individuals. The intra-day and inter-day precisions were adequate, with RSD lower than 10.1%. The accuracy was evaluated by recovery tests, analyzing six human blood serum samples before and after fortification at different Cd²⁺ concentration levels. The obtained recoveries (Table 3) ranged from 92.7% to 110.4%, attesting to the method's efficiency and the absence of interferences for this type of samples. Cadmium concentration in the human blood serum samples ranged between < 0.24 and 2.52 $\mu\text{g L}^{-1}$. Additionally, samples 1–3 from Table 3 were mineralized by using HNO₃ and H₂O₂ in a hot plate, and the Cd²⁺ concentrations were determined by conventional TS-FF-AAS. The obtained results were statistically similar to that obtained by the proposed method, as shown in Table 3.

Finally, we would like to emphasize that the methods for Cd²⁺ determination in biological fluids are commonly carried out after a mineralization step to avoid the matrix effect. Conversely, our method is the first that proposes an online cleanup of the protein fluids, avoiding the need for complex mineralization steps. According to Table 4, the detectability of the present method was better than that obtained with electrothermal atomic absorption spectrometry (ETAAS) without sample preparation (direct injection). Moreover, the method can be used to analyze Cd²⁺ in human serum samples once the reference values for Cd²⁺ are approximately 0.6 $\mu\text{g L}^{-1}$ [29]. To the best of our knowledge, there are not published methods about Cd²⁺ determination in blood or milk samples by TS-FF-AAS. We believe that the main difficulty is perhaps due to the high protein concentration and high sample viscosity, that causes perturbation in the thermospray and imprecision.

Finally, we believe that the RACNTs can be used efficiently to extract several other ions from biological samples, which can also be simultaneously analyzed by multi-element techniques such as ICP-OES and ICP-MS, among others.

4. Conclusions

The new RACNTs capped with BSA showed a high ability to extract cadmium directly from biological matrices (e.g., human serum), avoiding the conventional and time-consuming sample preparation procedures such as those based on a microwave oven and combustion. The matrix proteins from the biological samples were quantitatively excluded, whereas cadmium was concentrated with high-enrichment factors. Each column presented the same performance during at least approximately 300 sequential extractions of human serum, without any sample preparation procedure, attesting to its long lifetime.

The proposed method was adequately validated for the online Cd²⁺ determination, which is advantageous due to the low limit of quantification, strong precision and accuracy, and the low reagent and sample consumption. Additionally, the analytical frequency (considering the sample preparation and analysis steps) was significantly lower compared to conventional procedures based on FAAS due to the needed external sample preparation steps (combustion and microwave oven, among others) for conventional procedures.

Finally, we believe that the RACNTs can be easily employed to extract different metals from protein fluids because the adsorption characteristics of the CNTs to retain different analytes are already well known in the literature [38].

Acknowledgments

We thank the “Fundação de Amparo à Pesquisa do Estado de Minas Gerais” (FAPEMIG, Belo Horizonte, Brazil), Project CDS-APQ-01612-10, and the “Conselho Nacional de Desenvolvimento Científico e Tecnológico” (CNPq, Brasília, Brazil), Project 483371/2012-2 for their financial support. We also thank Mariane Gonçalves Santos for assistance in the sample collections.

References

- [1] E.M.M. Flores, J.S. Barin, M.F. Mesko, G. Knapp, *Spectrochim. Acta B* 62 (2007) 1051–1064.

- [2] L.C. Trevisan, J.L. Donati, A.R. Araujo, Trends in Sample Preparation Nova Science Publishers, New York (2006) 29–52.
- [3] A. Parus, K. Wieszczycka, A. Olszanowski, Hydrometallurgy 105 (2011) 284–289.
- [4] M.K. Jha, V. Kumar, J. Jeong, J. Lee, Hydrometallurgy 111–112 (2012) 1–9.
- [5] C.H. Latorre, J.Á. Méndez, J.B. García, S.G. Martín, R.M.P. Crecente, Anal. Chim. Acta 749 (2012) 16–35.
- [6] K. Pytlakowska, V. Kozik, M. Dabioch, Talanta 110 (2013) 202–228.
- [7] A. Tang, D. Jiang, X. Yan, Anal. Chim. Acta 507 (2004) 199–204.
- [8] S. Souverain, S. Rudaz, J. Veuthey, J. Chromatogr. B 801 (2004) 141–156.
- [9] A.J. Santos-Neto, C. Fernandes, J.C. Rodrigues, C. Alves, F.M. Lanças, J. Sep. Sci. 31 (2008) 78–85.
- [10] J.C. Barreiro, K.L. Vanzolini, Q.B. Cass, J. Chromatogr. A 1218 (2011) 2865–2870.
- [11] A.J. Santos-Neto, J.C. Rodrigues, C. Fernandes, G.M. Titato, C. Alves, F.M. Lanças, J. Chromatogr. A 1105 (2006) 71–76.
- [12] N.M. Cassiano, V.V. Lima, R.V. Oliveira, A.C. de Pietro, Q.B. Cass, Anal. Bioanal. Chem. 384 (2006) 1462–1469.
- [13] R.F. Gomes, N.M. Cassiano, J. Pedrazzoli Jr., Q.B. Cass, Chirality 22 (2010) 35–41.
- [14] G.O.I. Moraes, L.M.R. Silva, A.J. Santos-Neto, F.H. Florenzano, E.C. Figueiredo, Anal. Bioanal. Chem. 405 (2013) 7687–7696.
- [15] D. Afzali, S. Ghaseminezhad, M.A. Taher, J. AOAC Int. 93 (2010) 1287–1292.
- [16] N. Aydemir, N. Tokman, A.T. Akarsubasi, A. Baysal, S. Akman, Microchim. Acta 175 (2011) 185–191.
- [17] A.H. El-Sheikh, J.A. Sweileh, Y.S. Al-Degs, Anal. Chim. Acta 604 (2007) 119–126.
- [18] P. Liang, Y. Liu, L. Guo, J. Zenga, H. Lua, J. Anal. At. Spectrom. 19 (2004) 1489–1492.
- [19] J.P. Xiao, Q.X. Zhou, H.H. Bai, J. Environ. Sci. 19 (2007) 1266–1271.
- [20] Y. Liu, Y. Li, X.P. Yang, Adv. Funct. Mater. 18 (2008) 1536–1543.
- [21] M. Tuzen, K.O. Saygia, C. Ustab, M. Soylak, Bioresour. Technol. 99 (2008) 1563–1570.
- [22] C. Zhou, Z. Du, G. Li, Y. Zhang, Z. Cai, Analyst 138 (2013) 5783–5790.
- [23] F. Kummrow, F.F. Silva, R. Kuno, A.L. Souza, P.V. Oliveira, Talanta 75 (2008) 246–252.
- [24] J. Zhijie, Z. Wang, J. Liang, B. Wei, D. Wu, Carbon 37 (1999) 903–906.
- [25] L.A. Currie, Anal. Chim. Acta 391 (1999) 127–134.
- [26] M.L. Menezes, G. Fèlix, J. Liq. Chromatogr. Relat. Technol. 21 (1998) 2863–2871.
- [27] T.E. Emerson, Crit. Care Med. 17 (1989) 690–694.
- [28] R.J. Goldberg, J. Am. Chem. Soc. 74 (1952) 5715–5725.
- [29] R. Kuno, M.H. Roquetti, K. Becker, M. Seiwert, N. Gouveia, Int. J. Hyg. Environ. Health 216 (2013) 243–249.
- [30] E.F. Covelo, F.A. Vega, M.L. Andrade, J. Hazard. Mater. 147 (2007) 852–861.
- [31] G. Limousin, J.-P. Gaudet, L. Charlet, S. Szenknect, V. Barthès, M. Krimissa, Appl. Geochem. 22 (2007) 249–275.
- [32] C.R.T. Tarley, A.F. Barbosa, M.G. Segatelli, E.C. Figueiredo, P.O. Luccas, J. Anal. At. Spectrom. 21 (2006) 1305–1313.
- [33] B. Parodi, L.D. Savio, R.A. Martinez, P.S. Gil, Microchim. J. 98 (2011) 225–230.
- [34] J. Wang, X. Ma, G. Fang, M. Pan, X. Ye, S. Wang, J. Hazard. Mater. 186 (2011) 1985–1992.
- [35] R. Papp, W.M. Mullett, E. Kwong, J. Pharm. Biomed. Anal. 36 (2004) 457–464.
- [36] W.R.G. Baeyens, G.V. der Weken, J. Haustraete, H.Y. Aboul-Enein, S. Corveleyn, J.P. Remon, A.M. García-Campaña, P. Deprez, J. Chromatogr. A 71 (2000) 153–161.
- [37] P. Sadílek, D. Šatinský, P. Solich, Trends Anal. Chem. 26 (2007) 375–384.
- [38] R. Sitko, B. Zawisza, E. Malicka, Trends Anal. Chem. 37 (2012) 21–31.
- [39] C.D. Palmer, M.E. Lewis Jr., C.M. Geraghty, F. Barbosa Jr., P.J. Parsons, Spectrochim. Acta B 61 (2006) 980–990.
- [40] G.Q. Xiang, Y. Huang, Y.F. Luo, Microchim. Acta 165 (2009) 237–242.
- [41] A. Shokrollahi, S. Joybar, H.E. Haghghi, K. Niknam, E. Niknam, Quim. Nova 36 (2013) 368–374.
- [42] S. Cancela, M.C. Yebra, J. AOAC Int. 89 (2006) 185–191.



Method validation using weighted linear regression models for quantification of UV filters in water samples

Claudia Pereira da Silva, Elissandro Soares Emídio, Mary Rosa Rodrigues de Marchi*

Analytical Chemistry Department, Institute of Chemistry, São Paulo State University (UNESP), Araraquara, SP 14801-970, Brazil

ARTICLE INFO

Article history:

Received 21 May 2014

Received in revised form

14 July 2014

Accepted 16 July 2014

Available online 30 July 2014

Keywords:

UV filters

Validation

Matrix effect

Heteroscedasticity

Weighted regression

ABSTRACT

This paper describes the validation of a method consisting of solid-phase extraction followed by gas chromatography–tandem mass spectrometry for the analysis of the ultraviolet (UV) filters benzophenone-3, ethylhexyl salicylate, ethylhexyl methoxycinnamate and octocrylene. The method validation criteria included evaluation of selectivity, analytical curve, trueness, precision, limits of detection and limits of quantification. The non-weighted linear regression model has traditionally been used for calibration, but it is not necessarily the optimal model in all cases. Because the assumption of homoscedasticity was not met for the analytical data in this work, a weighted least squares linear regression was used for the calibration method. The evaluated analytical parameters were satisfactory for the analytes and showed recoveries at four fortification levels between 62% and 107%, with relative standard deviations less than 14%. The detection limits ranged from 7.6 to 24.1 ng L⁻¹. The proposed method was used to determine the amount of UV filters in water samples from water treatment plants in Araraquara and Jau in São Paulo, Brazil.

© 2014 Elsevier B.V. All rights reserved.

1. Introduction

Ultraviolet (UV) filters are compounds designed to absorb ultraviolet (UVA and UVB) radiation, and they are commonly used in sunscreen products to attenuate the negative effects of solar radiation. Because of their effectiveness against the harmful effects of ultraviolet radiation, these compounds have begun to be added not only to sunscreen products but also to the formulations of many everyday products, such as cosmetics, skin creams, body lotions, shampoos, sprays and hair dyes, among many other personal care products (PCPs).

In addition to their considerable use in PCPs, UV filters also have other smaller applications in textiles, household products, plastics, optical products and agricultural products [1]. Because of their wide use, UV filters are introduced into the environment in significant amounts, both directly, due to recreational activities (diffuse sources) and industrial wastewater discharges (point sources), and indirectly, due to the discharge of wastewater effluents [2].

Because of these significant inputs, there has been growing interest in the study of UV filters in various environmental compartments and of their negative effects with regard to human

and animal life. Consequently, several methods have been developed and/or optimized for the detection and quantification of these compounds in environmental matrices. These methods have predominantly consisted of chromatographic techniques that typically require a clean-up step and/or concentration of analyte using, for example, SPE, SPME, DLMME or SBSE [3–7].

However, the use of an existing method or the development of a new method is not sufficient for proper quantification. To ensure that the method used for extraction and analysis provides reliable data with regard to quantification of the analytes, method validation is essential prior to its application [8].

Validation studies are an essential tool during the implementation and continuation of best practices in all analytical areas. Such studies are usually structured and contain reference guide documents. However, because several differences can exist between these documents, more than one document is typically used [9]. Despite the differences, it is necessary to have consensus that the method is validated for the intended purpose and that it meets all requirements for the intended analytical applications, thus ensuring the reliability of the results. To accomplish this goal, the analytical performance parameters must be verified [10].

One of the parameters that must be evaluated is the selection of the calibration curve to be used for quantification. Generally, linear regression by the method of ordinary least squares (OLS) is used. However, it is important to highlight that heteroscedasticity in the analytical curve should not be neglected, as it can lead to a significant loss of precision, especially at low concentrations of

* Corresponding author. Tel.: +55 16 33019610; fax: +55 16 33019692.

E-mail addresses: claudiaufs@yahoo.com.br (C.P. da Silva), elissandro_se@yahoo.com.br (E.S. Emídio), mssqam@iq.unesp.br, maryrmarchi@gmail.com (M.R.R. de Marchi).

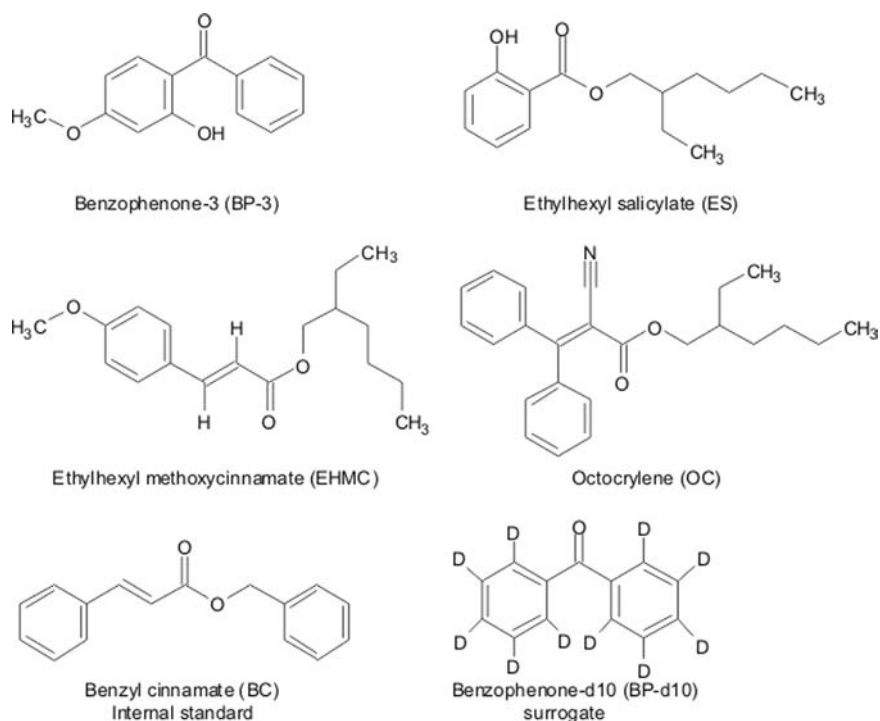


Fig. 1. Structures of UV filters.

the curve. It should be noted that UV filters are present at low concentrations in the environment; therefore, maintaining precision at the low end of the curve is especially important for UV filters. The wrong regression method can also contribute to systematic errors of measurement [11].

In this article, we validated a method for the determination of the UV filters benzophenone-3 (BP-3), ethylhexyl salicylate (ES), ethylhexyl methoxycinnamate (EHMC) and octocrylene (OC) (Fig. 1) in aqueous samples. The proposed method consisted of a solid-phase extraction (SPE) followed by gas chromatography coupled to tandem mass spectrometry (GC–MS/MS). Even, method validation be the subject of many discussions, there are still many inconsistencies between the guide documents, in some cases different terminology can be found throughout the same document. With this, much confusion is found in adequate definition of the criteria assessed in method validation. An example, error quite common in analytical chemistry, is the use of the correlation coefficient as a test for linearity and the negligence in the heteroscedasticity of the data in the analytical curve. There are few data in the literature addressing these criteria regression models. The validation method was performed to evaluate the following figures of merit: selectivity, analytical curve, precision, trueness, limit of detection and limit of quantification.

2. Experimental

2.1. Standards, solvents and sorbents

Benzophenone-3 98%, ethylhexyl salicylate 99%, ethylhexyl methoxycinnamate 98%, octocrylene 97%, benzophenone-d10 (surrogate), and the internal standard benzyl cinnamate (BC) 99%, were supplied by Sigma-Aldrich (St. Louis, MO, USA). Methanol (MeOH) and ethyl acetate (AcOEt) were HPLC grade and were obtained from Mallinckrodt Baker, Inc. (Paris, KY, USA). Hydrochloric acid (HCl, 37% m/v) was purchased from JT Baker Chemical Co. (Phillipsburg, NJ, USA) and was used to adjust the pH of the

sample. The solid-phase extraction (SPE) cartridges (200 mg/6 mL) were acquired from Phenomenex (Torrance, CA, USA).

Individual standard solutions of each UV filter (1000 mg L^{-1}) were prepared in ethyl acetate and then diluted to mixtures with concentration of 5 mg L^{-1} . These solutions were stored in the dark at $-20 \text{ }^\circ\text{C}$. Further dilutions to working standard solutions, which were used to prepare the spiked water samples employed during validation, were also prepared in ethyl acetate daily.

2.2. Sample collection and pre-treatment

Water samples were collected in October 2012 and March 2013 at the water treatment plants (WTPs) in Araraquara and Jau (São Paulo, Brazil). The water samples were collected in 4 L capacity amber Pyrex glass bottles with screw caps and were transported to the laboratory under refrigeration at $4 \text{ }^\circ\text{C}$ (ice packs) and stored in the dark. Prior to extraction, the samples were filtered through a glass fiber filter (Macherey-Nagel GF3) with a $0.6 \text{ }\mu\text{m}$ pore size.

Samples were extracted using SPE. The SPE cartridges were first conditioned with 5 mL of AcOEt, 5 mL of MeOH and 5 mL of deionized water. Sample volumes of 500 mL at pH 3 were passed through the cartridge at a flow rate of approximately 10 mL min^{-1} . Next, the cartridge was rinsed using 50 mL of a 5% MeOH/deionized water solution. The cartridge was then dried under total vacuum for 5 min and a total of 500 μL of MeOH was added to facilitate drying. The analytes were eluted with $3 \times 2 \text{ mL}$ of ethyl acetate. Then, 500 μL of the internal standard solution of $100 \text{ }\mu\text{g L}^{-1}$ benzyl cinnamate was added to the eluate. The volume of the eluate was reduced to 1 mL under a gentle flow of nitrogen gas prior to analysis by GC–MS/MS.

2.3. Instrumentation

The analytes were analyzed by GC–MS/MS using a Varian CP-3800 gas chromatograph that was equipped with a Saturn 2000 ion trap mass spectrometer. The chromatography was performed under the following conditions. Helium was used as the carrier gas at a constant flow rate of 1.2 mL min^{-1} . The temperature of the injector was

maintained at 300 °C in splitless injection mode with a sampling time of 1 min. A fused-silica ZB-5MSi capillary column (30 m length × 0.25 mm i.d. and 0.25 μm film thickness) (Phenomenex, Torrance, CA, USA) was used for the separation. The column temperature program was as follows: initial temperature 60 °C, maintained for 1 min, then ramped at 25 °C min⁻¹ to 160 °C, maintained for 1 min, ramped at 10 °C min⁻¹ to 300 °C and held at this temperature for 2 min. The total run time was 22.0 min. The transfer line, trap and manifold temperatures were maintained at 300, 50 and 220 °C, respectively.

2.4. Optimization of operating conditions for SPE and GC–MS/MS

The detailed procedure for the extraction of the UV filters and the details of the chromatographic method can be found in previous reports published from our laboratory [7].

2.5. Validation procedure

Validation studies were planned and executed using reference guide documents published nationally and internationally and articles published in recent years. We demonstrated that the method was validated for the intended purpose by evaluating the following performance parameters: selectivity, analytical curve, precision, trueness, limit of detection and limit of quantification.

3. Results and discussion

3.1. Method validation

The optimization of the extraction and analysis parameters is performed using a method that enables the efficient quantification of analytes. For this purpose, the performance of the method was evaluated under optimized extraction and analytical conditions, and the method was validated in terms of selectivity, analytical curve, precision, trueness, limit of detection and limit of quantification.

3.1.1. Selectivity

The selectivity of this method was ensured through the use of MS/MS following the chromatographic separation. The investigation of nonspecific selectivity (also known as matrix effects) was conducted by investigating the presence of matrix interferents that altered the performance measurements. Calibration curves were prepared in the solvent and in the matrix extract. These curves, shown in Fig. 2, were prepared at the same concentrations as in [8,12,13]. Through visual analysis of the curves, it appeared that only ES exhibited no pronounced matrix effects. The BP-10, EHMC and OC exhibited matrix-induced decreased responses, while BP-3 showed an increased chromatographic response in the matrix extract.

Mathematically, the calculation to assess the matrix effects can be achieved using Eq. (1) [12].

$$\% \text{ matrix effect} = \frac{X_2 - X_1}{X_2} \times 100 \quad (1)$$

where X_1 is the slope of the curve obtained by injection of the analytical solutions of each analyte prepared in the matrix, and X_2 is the slope of the curve obtained by injection of the analytical solutions of each analyte prepared in the solvent.

The matrix effect is not considered significant, i.e., it should not influence the quantitative analysis, at values < 20% or > -20% [12]. The calculated matrix effect values for BP-10, ES, BP-3, EHMC and OC were 62%, 5%, -280%, 44% and 52%, respectively. These values confirmed the visual analysis that indicated four of the five UV filters under study were influenced by the matrix. Significant matrix effect

values were observed for BP-3 (-280%), which was likely due to the high polarity of BP-3. The active sites of the chromatographic system were available to retain the more polar analytes in the pure solvent injection, and thus a smaller amount of BP-3 was detected. However, a competition existed between the matrix components and the more polar analytes for the active sites of the chromatographic system in the matrix extract, which led to an enhancement of the response [14].

For most analytes studied, the signals were influenced by the co-extracted substances. It was concluded that, to ensure the reliable quantification of analytes, it was necessary to prepare analytical curves from calibration standards in the matrix extract.

3.1.2. Analytical curve

The analytical curves were prepared in water samples prior to the SPE procedure from a minimum of six concentration levels from 20 to 4000 ng L⁻¹ for BP-10, ES and BP-3 and from 50 to 4000 ng L⁻¹ for EHMC and OC (curves shown in Table 1).

According to Table 1, all curves possessed correlation coefficients, “ r ”, greater than or equal to 0.99. However, the value of r or r^2 is inappropriate as a test model fit [15–17]. Therefore, it was necessary to evaluate the fit of the model using an alternative approach, namely, by assessing the homoscedasticity of data [18].

The study of the homoscedasticity of the data was performed using the F -test and the residual plot. In the F -test, the data are assumed to be uniformly distributed when the tabulated F -value (F_{tab}) is greater than the experimental F -value (F_{exp}) ($F_{tab} > F_{exp}$). The F_{tab} is obtained from a table of F distribution critical values with confidence levels of 99% for $(n-1)$ degrees of freedom, and the F_{exp} is obtained using Eq. (2) [19,20].

$$F_{exp} = \frac{S_2^2}{S_1^2} \quad (2)$$

where the experimental F -value is expressed as the ratio between the variances obtained at the lowest (S_1^2) and highest (S_2^2) concentration level of the working range.

In the F -test, the results obtained for BP-10, ES, BP-3, EHMC and OC were 20009, 1173, 24583, 1178 and 8274, respectively. All of these values were greater than $F_{tab}=99$ (tabulated F -value obtained with a confidence level of 99% and $(n-1)$ degrees of freedom equal to 2). It was evident that the data were heteroscedastic, as the condition of homoscedasticity ($F_{tab} > F_{exp}$) was not realized for any of the analytes.

In the evaluation of homoscedasticity by residual graphs, the residual (R) is calculated by Eq. 3, which establishes the difference between the measured values (S_{exp}) and the calculated values from the regression equation (S_{int}) [21].

$$R = S_{exp} - S_{int} \quad (3)$$

where the (S_{exp}) is the experimental signal, and (S_{int}) is the interpolated signal from the regression equation.

After the residual calculations are performed, the graphs are plotted as the residuals vs. concentration (Fig. 3). From the analysis of the residual graphs, the residues were not randomly distributed around the axis of concentrations. Additionally, the variance was more pronounced at higher concentrations, confirming the heterogeneity of the data that was previously revealed by the F -test.

The heterogeneity of the data was confirmed, and the choice of a new, more appropriate calibration model to define the relationship between concentration and response of the analytes was necessary [18]. Often, reduces calibration range to improve the model. However, the goal was not to work with a narrower calibration range, as UV filters have been found in the environment from ng L⁻¹ to low μg L⁻¹ levels. Thus, a large calibration range was ideal for quantification. Therefore, we used a weighted least squares linear regression model. Weighted models are commonly adopted to minimize the greater

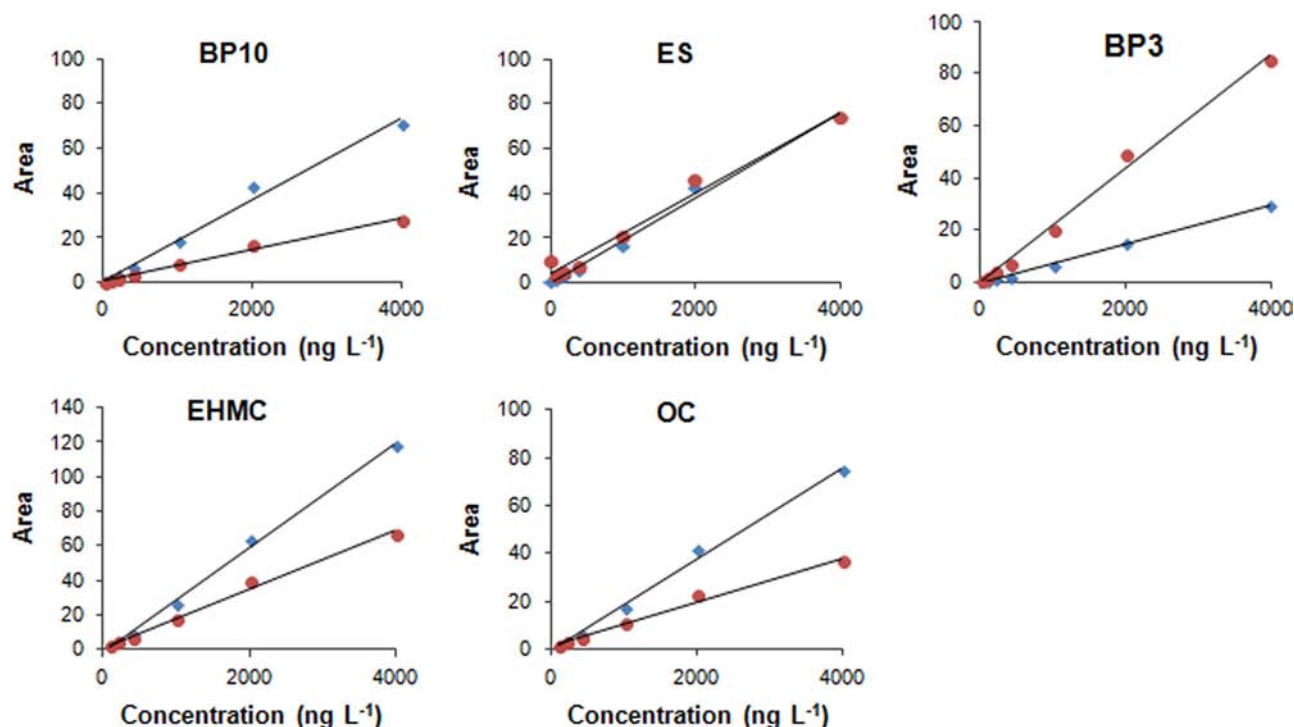


Fig. 2. Analytical curves (GC-MS/MS) in solvent (blue quadrangle) and in the matrix extract (red circle) for the studied UV filters. (For interpretation of the references to color in this figure legend, the reader is referred to the web version of this article.)

Table 1
Analytical curves (GC-MS/MS) for analytes in the matrix.

Analyte	Range (ng L ⁻¹)	Calibration equation ($y=ax+b$)	r
BP-10	20–4000	$y=0.0078x+0.7028$	0.994
ES	20–4000	$y=0.0144x+2.2911$	0.991
BP-3	20–4000	$y=0.0241x-0.2487$	0.998
EHMC	50–4000	$y=0.0111x+1.2692$	0.991
OC	50–4000	$y=0.0067x+1.2121$	0.987

influence of the higher concentrations of the regression [20]. The residual plots are shown in Fig. 3.

An ideal weighted model will balance the regression line to generate an error that is uniformly distributed throughout the calibration range [19]. The appropriate weighting factors, w_i , can be calculated from the inverse of the variance (S_i^{-2}) using Eq. (4) [18].

$$w_i = \frac{S_i^{-2}}{\sum_i \frac{S_i^{-2}}{n}} \quad (4)$$

However, this weighting factor is generally impractical, because it requires several determinations for each calibration point and because a fresh calibration line should be performed each time the method is used. Other empirical weights based on the variable x (concentration) or variable y (response) can provide a simple approximation of the variance. The empirical weights (w_i) most widely used are $1/y^{0.5}$, $1/y$, $1/y^2$, $1/x^{0.5}$, $1/x$, $1/x^2$ [20].

Each of these weights can be applied to the linear regression equation. The conversion of a linear regression equation without weighting to a weighted linear regression is performed using the term w_i in the calculations of the parameters “ a ” and “ b ”. The weighted coefficients “ a ” and “ b ” are calculated by Eqs. (5) and (6) [18].

$$a_w = \frac{\sum_i w_i x_i y_i - n \bar{X}_w \bar{Y}_w}{\sum_i w_i x_i^2 - n \bar{X}_w^2} \quad (5)$$

$$b_w = \bar{Y}_w - b \bar{X}_w \quad (6)$$

The weighted correlation coefficient (r_w) can be calculated by Eq. (7)

$$r = \frac{\sum w_i \sum w_i x_i y_i - \sum w_i x_i \sum w_i y_i}{\sqrt{\sum w_i \sum w_i x_i^2 - (\sum w_i x_i)^2} \sqrt{\sum w_i \sum w_i y_i^2 - (\sum w_i y_i)^2}} \quad (7)$$

The choice of the weighting model must consider models that possess a small sum of the relative errors calculated by Eq. (8) in combination with a random distribution around the axis of concentrations. As an example, Table 2 reports the regression parameters of the calibration curve generated for each of the eight weighting models for BP-10 and the sums of the relative errors for each of the eight models.

$$\% RE = \frac{C_{(exp)} - C_{(nom)}}{C_{(nom)}} \times 100 \quad (8)$$

where the experimental concentration $C_{(exp)}$ is obtained from the weighted equation, and $C_{(nom)}$ is the theoretical or nominal concentration.

The models 2, 4 and 8 presented the smallest sums of the relative errors. While models 2, 4 and 8 all had low values for the sums of %RE, as shown in plots of %RE vs. concentration in Fig. 4, model 2 exhibited the best distribution of %RE around the axis of concentrations. Therefore, model 2 was selected to best define the correlation between the concentration and the response of BP-10.

The same approach was followed to define the best weighting factor for the other analytes (data not shown). The models chosen for each analyte in the study are shown in Table 3. Therefore, these new curves (weighted values of a and b) were used for the quantification of the UV filters in the water samples.

3.1.3. Precision and trueness

To evaluate the trueness of this method, recovery experiments were performed in triplicate at four fortification levels: LOQ, 200, 1000 and 2000 ng L⁻¹. The precision was evaluated by testing the

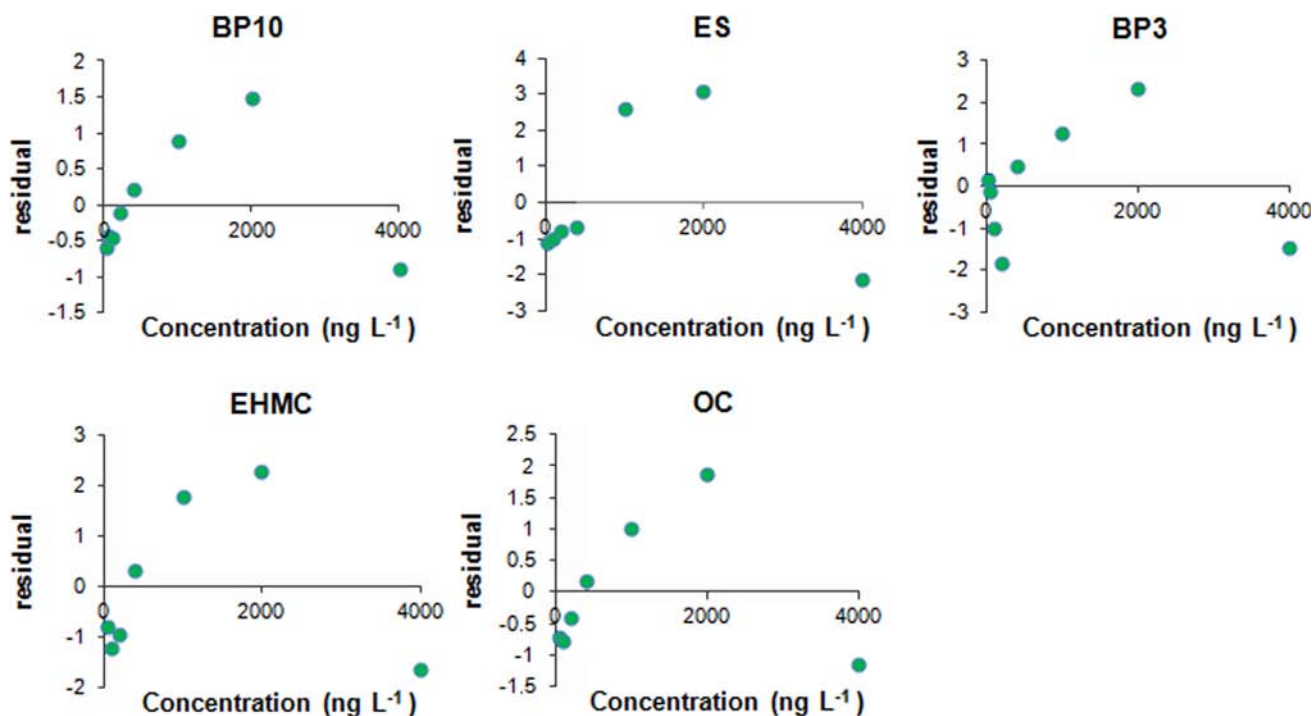


Fig. 3. Statistical residuals plotted against concentrations.

Table 2

Regression parameters of the analytical curve ($y=ax+b$) generated for each weight (w) and the respective sums of the relative errors ($\sum ER\%$) for BP-10.

BP-10 Model	w_i	a^b	b^c	r^d	$\sum ER\%$
1	1 ^a	0.0155	0.7028	0.9972	-538
2	$\frac{s_i^{-2}}{\sum s_i^{-2}/n}$ *	0.0184	0.0887	0.9941	16
3	$\frac{1}{y^{0.5}}$	0.0161	0.2592	0.9968	-53
4	$\frac{1}{y}$	0.0165	0.1834	0.9958	11
5	$\frac{1}{y^2}$	0.0140	0.3854	0.9922	-103
6	$\frac{1}{x^{0.5}}$	0.0163	0.0334	0.9967	181
7	$\frac{1}{x}$	0.0170	0.0038	0.9955	176
8	$\frac{1}{x^2}$	0.0208	0.0001	0.9912	0

^a Unweighted.

^b Slope.

^c y-Axis intercept.

^d Correlation coefficient

repeatability of the recovery through calculations of coefficients of variation (CV). The recoveries and the coefficients of variation obtained for the UV filters are shown in Table 4.

As shown in Table 4, the proposed method was demonstrated to be suitable and reliable for the determination of UV filters because the recoveries and coefficients of variation obtained at the four levels of fortification were within the acceptable limits recommended by [22,23].

3.1.4. Limit of detection and limit of quantification

The detection limits of the UV filters were calculated from the parameters of the analytical curves. Specific calibration curves were used in the range of LOD of 1–100 ng L⁻¹ for BP-10, ES and BP-3; 1–200 ng L⁻¹ for EHMC; and 10–200 ng L⁻¹ for OC. The corresponding LOD concentrations were calculated using both

Eq. (9) and also an equation that is statistically more defensible, published by ISO 11843-2:2000 [24] (Eq. (10)) [25].

$$LOD = \frac{3s_{y/x}}{a} \quad (9)$$

$$LOD = \frac{2t_{0.05, n-2} S_{y/x}}{a} \sqrt{\frac{1}{k} + \frac{1}{l \times j} + \frac{\bar{x}^2}{j \sum_i (x_i - \bar{x})^2}} \quad (10)$$

Unlike the LODs, the limits of quantification must exhibit acceptable precision and trueness. Some authors, such as those in [3,26], have used Eq. (11) to calculate LOQs. However, the proposal that the LOQs must be calculated using this equation has not found great benefit [25] because a higher concentration must be reported for the LOQ to ensure greater precision. Alternatively, if concentrations lower than the calculated LOQ exhibit acceptable precision and trueness, a lower concentration can be reported for the LOQ. In summary, the LOQ calculated by Eq. (11) is only a rough estimate, and a good rule to follow is assumed to be a compromise between precision and trueness.

$$LOQ = \frac{10 S_{y/x}}{a} \quad (11)$$

The values obtained for the LODs and LOQs of the method using Eqs. (9), (10) and (11) for the UV filters are shown in Table 5.

The LOD values obtained in this study were comparable to and sometimes better than those obtained in previous studies in which the extraction was performed by SPME [27–30], DLLME [3,26], SBSE [4,31] and SPE [32].

The recovery experiments performed with concentrations below the LOQs calculated by Eq. (11) (data shown in the second column of Table 4) showed acceptable precision and recovery. Therefore, the values of the method LOQs established as the first point of the calibration curve within the regression range (Table 4) were lower than the LOQs calculated by Eq. (11), except for ES. Therefore, according to the definition, the LOQs of the method were the lowest concentrations that were quantitatively determined with acceptable precision and trueness.

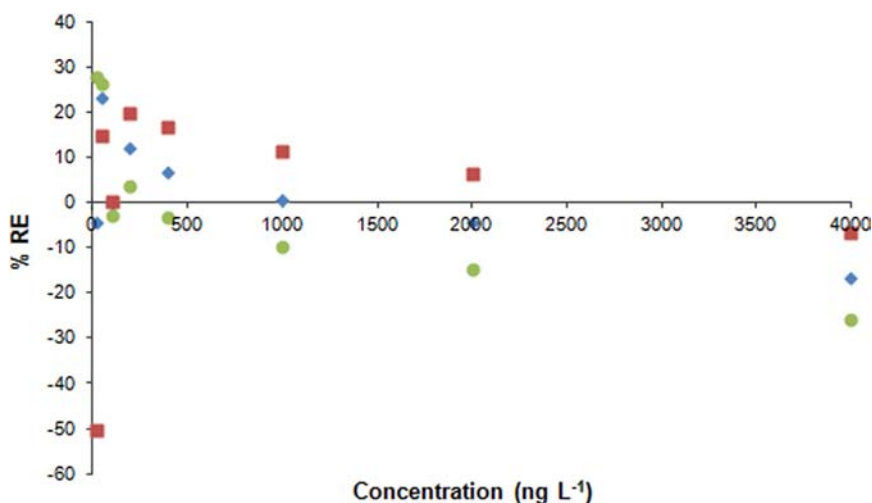


Fig. 4. Percentage of relative error (RE%) versus concentration, obtained for different regression models: model 2 (blue diamond), model 4 (red quadrat) and model 8 (green circle). (For interpretation of the references to color in this figure legend, the reader is referred to the web version of this article.)

Table 3

Regression parameters (optimized) of the analytical curve generated for each analyte and the respective sums of the relative errors ($\sum\%RE$).

Analyte	Model	w_i	a^a	b^b	r^c	$\sum\%RE$
BP-10	2	$\frac{s_i^{-2}}{\sum s_i^{-2}/n}$	0.0184	0.0887	0.9941	16
ES	2	$\frac{s_i^{-2}}{\sum s_i^{-2}/n}$	0.0321	1.0877	0.9977	20
BP-3	3	$\frac{1}{y_i^{0.5}}$	0.0484	-0.3162	0.9985	-13
EHMC	3	$\frac{1}{y_i^{0.5}}$	0.0233	0.2815	0.9949	51
OC	2	$\frac{s_i^{-2}}{\sum s_i^{-2}/n}$	0.0163	0.4134	0.9912	-13

^a Slope.

^b y-Axis intercept.

^c Correlation coefficient.

Table 4

Average recoveries and coefficients of variation (CV) for $n=3$.

Analyte	LOQ ^a ng L ⁻¹ (%CV)	200 ng L ⁻¹ (%CV)	1000 ng L ⁻¹ (%CV)	2000 ng L ⁻¹ (%CV)
BP-10	107 (11)	96 (3)	98 (3)	105 (10)
ES	77 (10)	72 (5)	72 (5)	69 (5)
BP-3	91 (12)	85 (3)	95 (4)	94 (4)
EHMC	85 (7)	76 (5)	74 (5)	65 (10)
OC	62 (13)	76 (5)	70 (5)	63 (14)

^a LOQ – limits of quantification obtained visually. Spiked at 10, 100, 10, 50 and 50 ng L⁻¹ for BP-10, ES, BP-3, EHMC and OC, respectively. The internal standard BC was spiked at 50 µg L⁻¹.

3.2. Application of the method to the analysis of water samples

The validated method was applied to the determination of UV filters in water samples. Water samples were collected (March 2013) at water treatment plants in Araraquara and Jau in São Paulo, Brazil. Three points of sampling were performed: at the entrance prior to treatment (river water), post-treatment without chlorination (treated water), and post-treatment with chlorination (chlorinated water). The samples were analyzed by SPE and GC–MS/MS, and the results of the measured concentrations of BP-3, ES, EHMC and OC are shown in Table 6. For BP-10, the use of the surrogate revealed the average recoveries and the coefficients of variation ($n=3$).

The low levels found did not indicate that these substances are not present in the environment because only water was analyzed.

Table 5

Limits of detection and quantification for the SPE and GC–MS/MS method.

Analyte	LOD ^a (ng L ⁻¹)	LOD ^b (ng L ⁻¹)	LOQ (ng L ⁻¹)
BP-10	9.3	10.0	30.9
ES	12.1	13.1	40.4
BP-3	7.1	7.6	23.5
EHMC	23.5	24.1	78.2
OC	19.3	20.8	64.4

^a From Eq. (9).

^b From Eq. (10).

Table 6

Concentrations of UV filters in natural, treated and chlorinated water (ng L⁻¹). BP-10 was used as a surrogate. Average recoveries and coefficients of variation (%CV) for $n=3$.

Analyte	Araraquara			Jau		
	Chlorinated water	Treated water	River water	Chlorinated water	Treated water	River water
BP-10 ^a	110 (10%)	100 (2%)	102 (5%)	105 (6%)	100 (3%)	96 (5%)
ES	< LOQ	< LOQ	< LOQ	< LOD	< LOD	< LOD
BP-3	< LOQ	< LOQ	< LOQ	n.d.	< LOQ	< LOQ
EHMC	< LOD	< LOQ	< LOD	< LOD	< LOD	< LOQ
OC	< LOQ	< LOQ	< LOD	< LOQ	< LOQ	< LOD

LOD and LOQ from Table 5.

n.d.: not detected.

^a BP-10 at 200 ng L⁻¹.

Furthermore, the analyses were performed at a time when there was likely minimal sunscreen usage.

From Table 6, the method performed very efficiently, as indicated by the recoveries and coefficients of variation of the surrogate. The results showed recoveries very close to 100% and coefficients of variation < 10%, indicating that the method demonstrated acceptable precision and trueness.

4. Conclusions

The analytical performance parameters evaluated were satisfactory in terms of selectivity, analytical curve, precision, trueness, limit of detection and limit of quantification. The specific selectivity was

verified through the use of detection by MS/MS. The nonspecific selectivity was confirmed from the observation of matrix effects (both overestimation and underestimation) for most analytes. Therefore, to minimize these effects, the analytical curves used for quantification were prepared in the matrix extract.

Due to the large concentration range of the analytical curve, homoscedasticity was not achieved. Therefore, weighted models were applied to obtain analytical curves with the best fits of the data and hence more reliable quantifications. Although these models were more complicated and laborious than linear regression by ordinary least squares, their implementation led to results with greater trueness, mainly because for large concentration ranges.

The potential of the method for the quantification of the UV filters BP-3, ES, EHMC and OC in water samples was further evidenced by the recoveries obtained, which confirmed the trueness and precision of the method. The recoveries for four fortification levels of the analytes ranged from 63% to 107%, with repeatability between 3% and 14%. The calculated limits of quantification ranged from 23.5 to 78.2 ng L⁻¹, with clear evidence that the lower values were quantified based on the lowest concentration of the calibration curve within the range of values validated with acceptable trueness and precision.

Acknowledgments

The authors are grateful for doctoral studentships from CAPES (Brazilian Coordination for the Improvement of Higher Education Personnel) and CNPq (Brazilian National Counsel of Technological and Scientific Development) for C.P. da Silva and E.S. Emídio, respectively. The research support provided by Foundation for Science, Technology and Education Support (FACTE; Grant no. 1018/2012) is also thanked.

References

- [1] K. Fent, P.Y. Kunzack, E. Gomez, *Chimia* 62 (2008) 368–375.
- [2] D.L. Giokas, A. Salvador, A. Chisvert, *Trends Anal. Chem.* 26 (2007) 360–374.
- [3] I. Tarazona, A. Chisvert, Z. León, A. Salvador, *J. Chromatogr. A* 1217 (2010) 4771–4778.
- [4] K.T.N. Nguyen, C. Scapolla, M. Di Carro, E. Magi, *Talanta* 85 (2011) 2375–2384.
- [5] M.S. Díaz-Cruz, P. Gago-Ferrero, M. Llorca, D. Barceló, *Anal. Bioanal. Chem.* 402 (2012) 2325–2333.
- [6] H. Zhang, H.K. Lee, *Anal. Chim. Acta* 742 (2012) 67–73.
- [7] C.P. da Silva, E.S. Emídio, M.R.R. de Marchi, *J. Braz. Chem. Soc.* 24 (2013) 1433–1441.
- [8] A.C.M. Bernardes, S.V.C. Souza, *Rev. Anal.* 51 (2011) 66–77.
- [9] E. Rozet, A. Ceccato, C. Hubert, E. Ziemons, R. Oprean, S. Rudaz, B. Boulanger, P. Hubert, *J. Chromatogr. A* 1158 (2007) 111–125.
- [10] M.H.W.W. Cardoso, A.W. Nóbrega, S. Abrantes, *Rev. Anal.* 34 (2008) 48–55.
- [11] R.S. Nascimento, R.E.S. Froes, N.O.C.E. Silva, R.L.P. Naveira, D.B.C. Mendes, W.B. Neto, J.B.B. Silva, *Talanta* 80 (2010) 1102–1109.
- [12] A. Economou, H. Botitsi, S. Antoniou, D. Tsiipi, *J. Chromatogr. A* 1216 (2009) 5856–5867.
- [13] M.B.R. Cerqueira, A.N. Dias, S.S. Caldas, F.B. Santana, M.G.M. D'oca, E.G. Primel, *Quim. Nova* 34 (2011) 156–159.
- [14] C.F. Poole, *J. Chromatogr. A* 1158 (2007) 241–250.
- [15] E. Rozet, R.D. Marini, E. Ziemons, B. Boulanger, P.H. Hubert, *J. Pharm. Biomed. Anal.* 55 (2011) 848–858.
- [16] M. Thompson, S.R.L. Ellison, R. Wood, *Pure Appl. Chem.* 74 (2002) 835–855.
- [17] N.M. Cassiano, J.C. Barreiro, L.R.R. Martins, R.V. Oliveira, Q.B. Cass, *Quim. Nova* 32 (2009) 1021–1030.
- [18] C. Mansilha, A. Melo, H. Rebelo, I.M.P.L.V.O. Ferreira, O. Pinho, V. Domingues, C. Pinho, P. Gameiro, *J. Chromatogr. A* 1217 (2009) 6681–6691.
- [19] T. Singtoroj, J. Tarning, A. Annerberg, M. Ashton, Y. Bergqvist, N.J. White, N. Lindegardh, N.P.J. Day, *J. Pharm. Biomed. Anal.* 41 (2006) 219–227.
- [20] A.M. Almeida, M.M. Castel-Branco, A.C. Falcão, *J. Chromatogr. B* 774 (2002) 215–222.
- [21] INMETRO – Instituto Nacional de Metrologia, Normalização e Qualidade Industrial. Orientação sobre validação de métodos de ensaios químicos. Revisão 02, DOQ-CGCRE-008, 2007.
- [22] Guidance for Industry: Bioanalytical Method Validation. US Department of Health and Human Services, US Food and Drug Administration (FDA), Center for Drug Evaluation and Research (CDER), Center for Biologics Evaluation and Research (CBER), Rockville, May 2001.
- [23] International Conference on Harmonization (ICH) of Technical Requirements for registration of Pharmaceuticals for Human Use, Topic Q2 (R1): Validation of Analytical Procedures: Text and Methodology, 2005.
- [24] Capability of Detection – Part 2: Methodology in the Linear Calibration Case, BS ISO 11843-2:2000, 2007.
- [25] D.B. Hibbert, J.J. Gooding, *Data Analysis for Chemistry: An Introductory Guide for Students and Laboratory Scientists*, Oxford University Press, New York, 2006.
- [26] J.L. Benedé, A. Chisvert, A. Salvador, D. Sánchez-Quiles, A. Tovar-Sánchez, *Anal. Chim. Acta* 812 (2014) 50–58.
- [27] N. Negreira, I. Rodríguez, M. Ramil, E. Rubí, R. Cela, *Anal. Chim. Acta* 638 (2009) 36–44.
- [28] G. Basaglia, L. Pasti, M.C. Pietrogrande, *Anal. Bioanal. Chem.* 399 (2011) 2257–2265.
- [29] G. Basaglia, M.C. Pietrogrande, *Chromatographia* 75 (2012) 361–370.
- [30] H. Liu, L. Liu, Y. Xiong, X. Yang, T. Luan, *J. Chromatogr. A* 1217 (2010) 6747–6753.
- [31] E. Magi, M. Di Carro, C. Scapolla, K.T.N. Nguyen, *Chromatographia* 75 (2012) 973–982.
- [32] P. Cuderman, E. Heath, *Anal. Bioanal. Chem.* 387 (2007) 1343–1350.



Nitrite/nitrate detection in serum based on dual-plate generator–collector currents in a microtrench

Andrew J. Gross^{a,*}, Stephanie Holmes^a, Sara E.C. Dale^a, Miranda J. Smallwood^c,
Stephen J. Green^{b,*}, C. Peter Winlove^b, Nigel Benjamin^c, Paul G. Winyard^c, Frank Marken^a

^a Department of Chemistry, University of Bath, Bath BA2 7AY, UK

^b Department of Physics, College of Engineering, Mathematics and Physical Sciences, University of Exeter, Stocker Road, Exeter EX4 4QL, UK

^c University of Exeter Medical School, University of Exeter, St Luke's Campus, Exeter EX1 2 LU, UK

ARTICLE INFO

Article history:

Received 30 May 2014

Received in revised form

23 July 2014

Accepted 27 July 2014

Available online 5 August 2014

Keywords:

Nitrate
Electrochemical sensor
Electroanalysis
Serum
Bipotentiostat
Microtrench

ABSTRACT

A dual-electrode sensor is developed for rapid detection of nitrite/nitrate at micromolar levels in phosphate buffer media and in dilute horse serum without additional sample pre-treatment. A generator–collector configuration is employed so that on one electrode nitrate is reduced to nitrite and on the second electrode nitrite is oxidised back to nitrate. The resulting redox cycle gives rise to a specific and enhanced current signal which is exploited for sensitive and reliable measurement of nitrite/nitrate in the presence of oxygen.

The electrode design is based on a dual-plate microtrench (approximately 15 μm inter-electrode gap) fabricated from gold-coated glass and with a nano-silver catalyst for the reduction of nitrate. Fine tuning of the phosphate buffer pH is crucial for maximising collector current signals whilst minimising unwanted gold surface oxidation. A limit of detection of 24 μM nitrate and a linear concentration range of 200–1400 μM is reported for the microtrench sensor in phosphate buffer and dilute horse serum. Relative standard deviations for repeat measurements were in the range 1.8–6.9% ($n=3$) indicating good repeatability in both aqueous and biological media. Preliminary method validation against the standard chemiluminescence method used in medical laboratories is reported for nitrate analysis in serum.

© 2014 Elsevier B.V. All rights reserved.

1. Introduction

The construction of an electrochemical nitrate sensor that functions in the presence of oxygen in biological fluids with high selectivity against common background interferents such as cells, proteins and electrolytes, is highly desired for clinical studies and opens up the possibility of point-of-care assays for use in hospitals and healthcare settings [1,2]. The use of electrochemical sensors is attractive as they are easily miniaturised, provide relatively quick results, are of good accuracy and are suitable for use in a wide range of solutions. These advantages can enable low level detection of analytes for clinical applications, as previously demonstrated by the success of electrochemical glucose biosensors [3].

Testing for the presence of nitrate in biological fluids such as serum has attracted increasing interest in recent years for clinical and sports science applications [4]. Nitrate levels produced endogenously represent the final product of nitric oxide (NO) and

nitrite oxidation pathways, therefore providing an indication of NO levels and activity [4]. In clinical studies, nitrate levels have been used as a biomarker for potential diagnosis and monitoring of human health conditions such as infective and inflammatory diseases [5], cardiovascular [6] and neurological conditions [7]. Dietary or environmental exposure to nitrate has long been considered to be harmful due to risks associated with gastric cancer [8] and methemoglobinemia [9]. More recently, dietary nitrate supplementation has been shown to reduce blood pressure and lower the oxygen cost of sub-maximal exercise through enhancement of NO bioavailability [10–12].

Numerous methods have been established for detection of nitrate in aqueous and biological solutions including the Griess colorimetric assay [13,14], fluorometric [15] and chemiluminescence [16,17] methods, and methods based on solid-phase separation such as high-performance liquid chromatography [18], gas chromatography–mass spectrometry [14], ion chromatography [19] and capillary electrophoresis [20]. Whilst ion-selective electrodes are established for sensitive detection of nitrate in aqueous solutions [21], these electrodes are not used for nitrate analysis in biological fluids due to the presence of ionic interferents. The two best established methods for determining nitrate in biological fluids involve the reduction of nitrate to NO using vanadium (III)

* Corresponding authors.

E-mail addresses: A.Gross@bath.ac.uk (A.J. Gross),
S.J.Green@exeter.ac.uk (S.J. Green).

chloride, followed by either a relatively complex chemical test, the Griess reaction, coupled with colorimetric detection, or gas-phase chemiluminescent detection [13,14,17]. In general, these techniques provide very accurate results but require the use of specialist equipment, tedious procedures and take extended periods of time to perform. Furthermore, vanadium chloride and alternative reducing agents based on cadmium reagents are highly toxic. Nitrate reductase is also used as a reducing agent but requires careful handling in a controlled environment. Despite the wide range of methods available for nitrate detection in blood there is currently no rapid and convenient means of doing so for point-of-care testing.

Several electrochemical sensors and biosensors have been developed for detection of nitrate ions in aqueous solutions [22]. However, the electrochemical response is hindered by slow charge transfer kinetics leading to poor sensitivity and irreproducible measurements [22]. A wide range of electrode materials have been sought to combat this restriction including electrodeposited and bulk reactive metals [23–26], chemically-modified electrodes with metal complexes [24], and composites based on silver graphite. Excellent limits of detection and good reproducibility have been reported in aqueous solutions but a lack of selectivity of bulk and chemically modified electrodes limits their applications in biological fluids [22]. Furthermore, the presence of dissolved oxygen impedes the reduction of nitrate and hence most electrochemical sensors to date require using degassed solutions. More sophisticated approaches have been developed based on the use of biological catalysts such as reductase enzymes which enable good sensitivity and impart a greater degree of selectivity [27–29]. However, these bio-sensor systems suffer from the limitations of costly biological reagents, increasing complexity, and fragility of the electrode.

Small gap sensor electrodes operating in generator–collector mode *via* bipotentiostatic control are emerging as excellent candidates for sensing redox-active analytes at low concentrations [30]. Of particular interest are nano-gap electrodes [31–34], and simple low-cost microtrench electrodes developed recently in our laboratory [35–37]. The small spacing of these electrodes combined with the ability to control both electrode potentials independently provides access to enhanced current signals. Advantages included the ability to obtain amplified currents for a given molecule by redox-cycling ions between the two electrodes, access to steady state current responses free of capacitive current, and the ability to separate desired signals from interferents by elimination of chemically irreversible processes or by size-exclusion effects. To date, electroanalytical applications of generator–collector electrodes have been demonstrated for analytes including, for example, quinones [35,37] and dopamine in the presence of known interferents [35].

In this work, we report the development of a silver-modified gold–gold microtrench electrode for nitrate detection which shows

good sensitivity in generator–collector mode within a physiologically relevant concentration range (200–1400 μM). The proposed sensing mechanism is shown in Fig. 1 (the redox system nitrite/nitrate is represented by Red/Ox). Within the microtrench, nitrate is converted by reduction to nitrite at one electrode (the “generator”), while nitrite is converted back to nitrate by oxidation at the other electrode (the “collector”). A repeating – and so signal-amplifying – redox cycle is achieved as these species interconvert and diffuse across the gap between the electrodes. After development of the electrode system in aqueous buffer, the analytical parameters of the electrode were investigated in horse serum diluted in phosphate buffer. The concentration of nitrate present in the samples was determined by the method of standard addition and compared against a standard gas-phase chemiluminescence method using a chemical analyser.

2. Experimental

2.1. Reagents

Potassium nitrate ($\text{KNO}_3 \geq 99\%$), potassium nitrite ($\text{KNO}_2 \geq 96\%$), silver nitrate ($\text{AgNO}_3 \geq 99\%$), sodium hydroxide (98%), potassium chloride ($\text{KCl} \geq 99.0\%$), monosodium phosphate monohydrate (98–102%), disodium hydrogen phosphate heptahydrate (98–102%), sulphuric acid (H_2SO_4 , 95–98%), hydrochloric acid (HCl, 37%), nitric acid (HNO_3 , 70%), hydrogen peroxide (H_2O_2 , 30 wt% in water) were all purchased from Sigma Aldrich, UK. Zinc sulphate, sodium nitrate (98+%) and sodium iodide (99+%) were purchased from Fisher. Vanadium (III) trichloride from Merck (99+%) and glacial acetic acid (100%) from VWR International. The serum was prepared from fresh horse blood obtained from a local abattoir and stored in the freezer. Aqueous solutions were made with ultrapure water at 20 °C (resistivity $\geq 18.2 \text{ M}\Omega\text{cm}$). Nitrogen (BOC) was employed for de-aerating solutions as required. Experiments were conducted at 20 ± 2 °C.

2.2. Instrumentation

Electrochemical measurements were obtained using either a CompactStat with bipotentiostat module (Ivium Technologies, Netherlands) with IviumSoft software 2.178 or a PGSTAT12 biopotentiostat system (Autolab, EcoChemie, Netherlands) with GPES 4.7 software. A conventional three or four-electrode cell was employed with a Pt wire counter electrode and saturated calomel electrode (SCE, Radiometer). The three electrode cell employed either a gold rod electrode ($\varnothing = 2 \text{ mm}$) or one of the two electrodes of the microtrench. The four-electrode cell set-up employed the two working electrodes of the microtrench electrode.

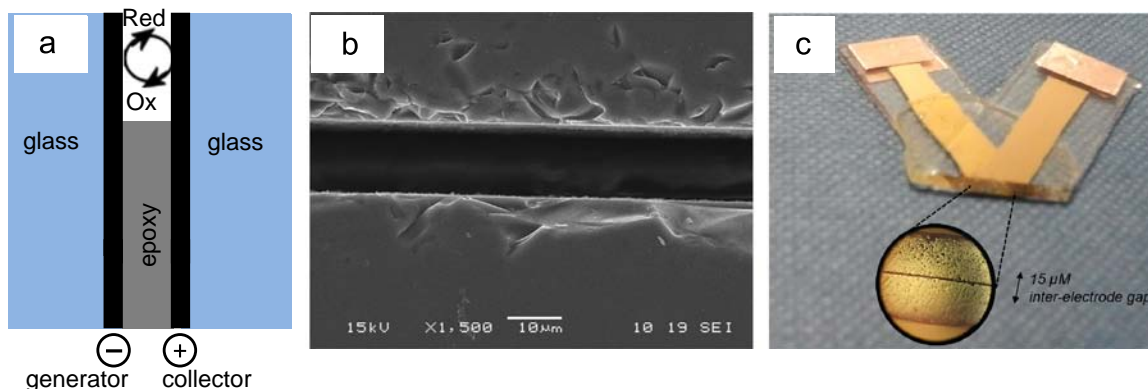


Fig. 1. (a) Schematic drawing of the nitrate sensing mechanism by coupled nitrate reduction and nitrite oxidation. (b) Scanning electron microscopy (SEM) micrograph of the microtrench. (c) Photograph of the microtrench electrode with optical image of the inter-electrode gap.

Scanning electron microscopy (SEM) micrographs were recorded using a JSM-6480LV (JEOL, Japan). A 5 nm layer of chromium was sputter-coated onto the substrate prior to SEM analysis to remove charging and increase contrast.

Gas-phase chemiluminescent measurement of nitrate was performed using a Sievers Nitric Oxide Analyser (Sievers NOA 280i, Analytix Ltd., Durham, UK) [10,38]. Prior to analysis, horse serum samples were thawed at room temperature then deproteinised using zinc sulphate precipitation. 200 μ L of serum was added to 400 μ L of 10% sodium hydroxide, followed by addition of 400 μ L of 10% (w/v) zinc sulphate. The samples were thoroughly mixed using a vortex then allowed to react for 15 min. The mixture was subsequently centrifuged and the supernatant analysed. The deproteinised samples were refluxed in 0.3 M sodium iodide and glacial acetic acid at 35 $^{\circ}$ C then analysed using the Nitric Oxide Analyser according to the methods described by Bateman and coworkers [38]. The nitrate concentrations of diluted serum samples were determined by the reduction to NO in a solution of 0.1 M vanadium (III) chloride in 1 M HCl at 95 $^{\circ}$ C. The gas-phase chemiluminescent reaction between NO and ozone was detected from the spectral emission of the electronically excited nitrogen dioxide product, using a thermoelectrically cooled, red-sensitive photomultiplier tube housed in the Sievers analyser. Calibration plots were obtained using standard sodium nitrate solutions.

2.3. Electrode fabrication

Silver–gold microtrench electrodes were prepared from gold–gold microtrench electrodes fabricated using a method described previously [37]. Deposition of silver particles by chronoamperometry onto gold was employed here because silver is known to enhance the reduction of nitrate compared to bulk gold electrodes [39]. Gold-coated (100 nm) glass slides with a titanium adhesion layer were cut into 10 mm \times 25 mm substrates then masked using Kapton tape (Farnell, UK) to give a masked strip in the centre of the electrode (\approx 5 mm \times 25 mm). The exposed gold was then etched using aqua regia (1:3 v/v HNO₃: HCl; **WARNING:** this solution is highly aggressive) for 3 min. After thorough rinsing of the samples in ultrapure water then drying with a stream of nitrogen, the Kapton tape was removed. The gold slides were heated at 500 $^{\circ}$ C for 30 min in the presence of air then cooled to room temperature. Two gold slides were placed on top of each other, with the gold surfaces face-to-face, and glued under pressure in a home-made press using epoxy (SP106 multi-purpose epoxy, SP Gurit). After curing for 90 min, the end of the glued gold–gold electrode was sliced off using a diamond cutter and the new exposed surface polished using SiC paper (P320,

Buehler). The epoxy layer between the gold–gold electrode was partially etched out by immersion in Piranha solution (1:5H₂O₂: H₂SO₄; **WARNING:** this solution is highly aggressive) for 3 min to yield the gold–gold microtrench electrode. It is noted that removal of the epoxy has no effect on the trench width. Silver was electrodeposited onto one of the gold electrodes by immersion of the polished end of the electrode into a solution of 1 mM AgNO₃ containing 0.1 M KNO₃. Using optimised chronoamperometry conditions, a fixed potential of -0.2 V vs. SCE was applied for 50 s on the first working electrode. These parameters were chosen to facilitate the deposition of several layers of silver particles whilst minimising the possibility of a short-circuit between the two working electrodes. After deposition, the silver–gold microtrench was thoroughly rinsed with ultrapure water then dried with a stream of nitrogen prior to analysis. A silver–gold microtrench electrode was examined using SEM imaging (see Fig. 1b) to confirm the gap size of approximately 15 μ m. The microtrench electrodes can be re-used and cleaned several times and were used for up to typically one week.

3. Results and discussion

3.1. Dual-plate microtrench electrode preparation and characterisation

The electrochemical responses of each of the gold electrode surfaces were first analysed in 0.1 M phosphate pH 5 to verify the successful fabrication of a clean gold–gold microtrench. Well-defined behaviour at positive potentials due to surface oxidation and subsequent reduction of the gold oxide was observed at both electrodes (Fig. 2a).

Deposition of the silver layer on the bare gold “generator” electrode was performed using chronoamperometry by applying a fixed potential of -0.2 V vs. SCE for 50 s in an unstirred 1 mM AgNO₃ solution with 0.1 M KNO₃ as supporting electrolyte. Supporting evidence confirming the presence of silver was obtained by cyclic voltammetry in phosphate buffer pH 5 (Fig. 2b). The peaks are consistent with the successful deposition of silver on one of the electrodes [40].

3.2. Voltammetric Responses for nitrite/nitrate and phosphate buffer at gold

The electrochemical oxidation of 10 mM KNO₂ in 0.1 M phosphate buffer solutions was initially examined using a gold electrode of the microtrench to observe the influence of solution pH on the electrochemical response of nitrite. The cyclic voltammograms obtained

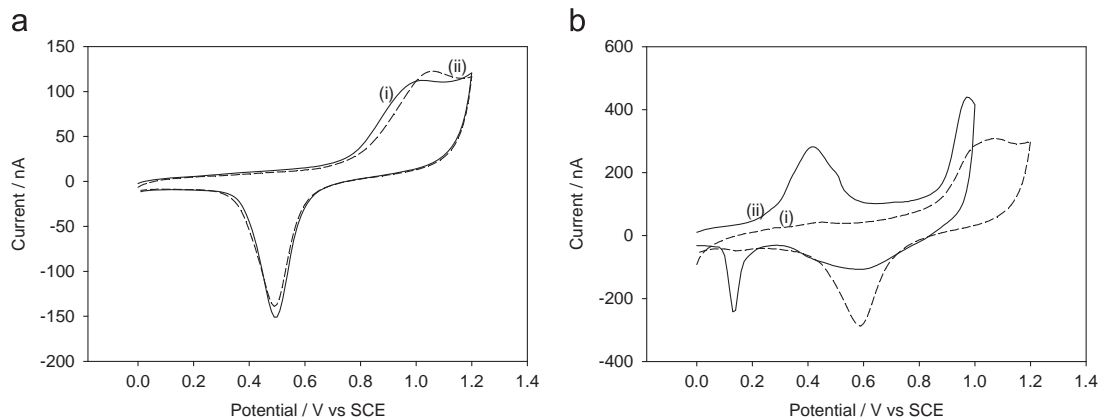


Fig. 2. (a) Cyclic voltammograms (CVs) obtained at a gold–gold microtrench (i) generator and (ii) collector in 0.1 M phosphate buffer pH 5. (b) CVs obtained at the microtrench (i) collector and (ii) generator electrodes after silver deposition. Scan rate = 20 mV/s.

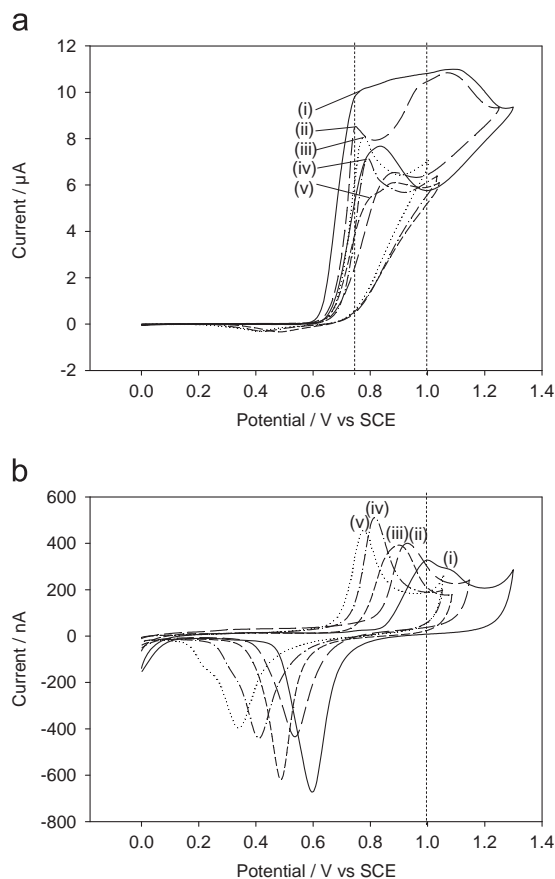


Fig. 3. (a and b) CVs of a gold microtrench working electrode in 0.1 M phosphate buffer (a) containing 10 mM KNO_2 and (b) with no KNO_2 added at (i) pH 5, (ii) pH 6, (iii) pH 7, (iv) pH 8, and (v) pH 9. Vertical dashed lines at 0.75 V and 1.0 V vs. SCE indicate the nitrite and gold surface oxidation peak positions at pH 5, respectively. Scan rate = 20 mV/s.

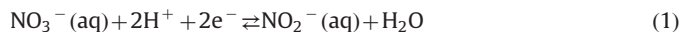
between pH 5 and pH 9 (Fig. 3a) show that the peak current corresponding to nitrite oxidation ($E_{pa}=0.7\text{--}1.0$ V vs. SCE) generally increases with decreasing pH whilst the peak potential shifts to less positive potentials with decreasing pH, consistent with previous studies [41]. As it has previously been observed that the oxide layer formed on gold electrodes hinders nitrite oxidation, experimental conditions were sought where oxide layer formation is minimised [42].

Fig. 3b shows CVs obtained on the gold electrode in 0.1 M phosphate buffer (pH 5–pH 9) solutions with no KNO_2 present. The well-known gold oxidation peak corresponding to surface oxide formation is observed on the forward sweeps in all cases and is found to shift to increasing potentials with increasing solution pH. Greater stability towards gold surface oxidation is therefore obtained at more acidic potentials (Fig. 3b, i). Based on the CVs recorded in Fig. 3, the optimal pH for nitrite oxidation on the gold surface in the microtrench is pH 5. At this pH the overpotential required for nitrite oxidation is such that the rate of reaction is maximised and the influence of gold oxidation is minimised.

3.3. Voltammetric responses for nitrite/nitrate at gold/silver microtrench electrodes: potential optimisation

The electrochemical reduction of nitrate ions is known to be a complex process in which nitrite, ammonia and nitrogen have been reported as bi-products depending on factors such as the electrode material, solution pH, and the electrode potential [23–25,43,44]. In neutral and acidic media (\geq pH 3), using metal-catalyst modified electrodes, it has been shown that reduction of

nitrate yields nitrite as the main product via a two-electron process [23,43]. Electrochemical oxidation of nitrite to nitrate via a multi-step two-electron process in neutral and acidic media ($>$ pH 4) has been demonstrated on gold electrodes. On the basis of these studies, the proposed redox system exploited here for detection of nitrate using the microtrench electrode is shown in Eq. (1).



Detection of nitrate using the generator–collector approach is employed here by using the first working electrode (“the generator”) to reduce nitrate to nitrite, and the second working electrode (“the collector”) to oxidise nitrite back to nitrate. Fig. 4a and b illustrates the electrochemical responses obtained using the silver–gold microtrench electrode in 0.1 M phosphate buffer pH 5 solution before (i) and after (ii) addition of 10 mM KNO_3 . In these experiments, the generator electrode was cycled between 0 V and -1.4 V vs. SCE, a potential range in which nitrate ions are known to be reduced, whilst the collector electrode was held at a fixed potential of 0.8 V vs. SCE, a potential sufficient to oxidise nitrite to nitrate (see Fig. 3a). At the generator electrode (Fig. 4a), the cyclic voltammograms reveal an increase in cathodic current in the potential range $-0.6\text{--}-1.4$ V vs. SCE following addition of KNO_3 , consistent with electrochemical reduction of nitrate ions. A weak reduction peak observed at -0.2 V vs. SCE occurs due to oxygen reduction, and a well-defined reduction peak at -1.1 V vs. SCE is attributed to reduction of the aqueous electrolyte solution (protons). At the collector electrode (Fig. 4b), the electrochemical response observed in phosphate buffer without nitrate shows two characteristic peaks on the forward scan at -0.25 V and -1.25 V vs. SCE. The weak peak observed at -0.25 V vs. SCE is attributed to the two-electron oxidation of H_2O_2 which was generated by reduction of oxygen at ~ -0.2 V vs. SCE on the generator electrode. The peak at -1.25 V vs. SCE is attributed to processes associated with the electrolyte solution. On the collector electrode, following addition of 10 mM KNO_3 (Fig. 4b, ii), a distinctly larger current signal which reaches a current plateau at -0.95 V vs. SCE is observed compared to the case with no nitrate present. The well-defined and expected limiting current plateau of the collector signal following addition of KNO_3 confirms the utility of the microtrench electrode to identify nitrate in a simple aqueous solution.

The interference of dissolved oxygen on the electrochemical reduction of nitrate is well-known, and as a result, electrochemical studies of nitrate reduction are typically performed in de-oxygenated solutions. Data obtained comparing the influence of oxygen on the generator and collector current responses in 0.1 M phosphate buffer pH 5 containing 10 mM KNO_3 are shown in Fig. 4c and d, respectively. The presence of oxygen was found to have little effect on the generator or collector response for nitrite/nitrate.

The effect of collector potential on the collector limiting currents was also investigated in phosphate buffer pH 5 containing 2 mM KNO_3 . In these experiments, generator–collector voltammograms were obtained at 100 mV/s with the generator cycled between 0 and -1.4 V vs. SCE and the collector varied between -0.1 V and $+0.9$ V vs. SCE. A plot of the feedback currents as a function of collector potential is shown in Fig. 5. The feedback currents were obtained by measuring the maximum current response at -0.95 V vs. SCE and subtracting these from the residual background current for each of the voltammograms recorded. As expected, the collector potential has a substantial effect on the observed feedback currents. At low potentials ($-0.1\text{--}+0.5$ V vs. SCE) no current amplification effects are observed due to absence of redox-cycling of the nitrite/nitrate system between the generator and collector electrodes. When the

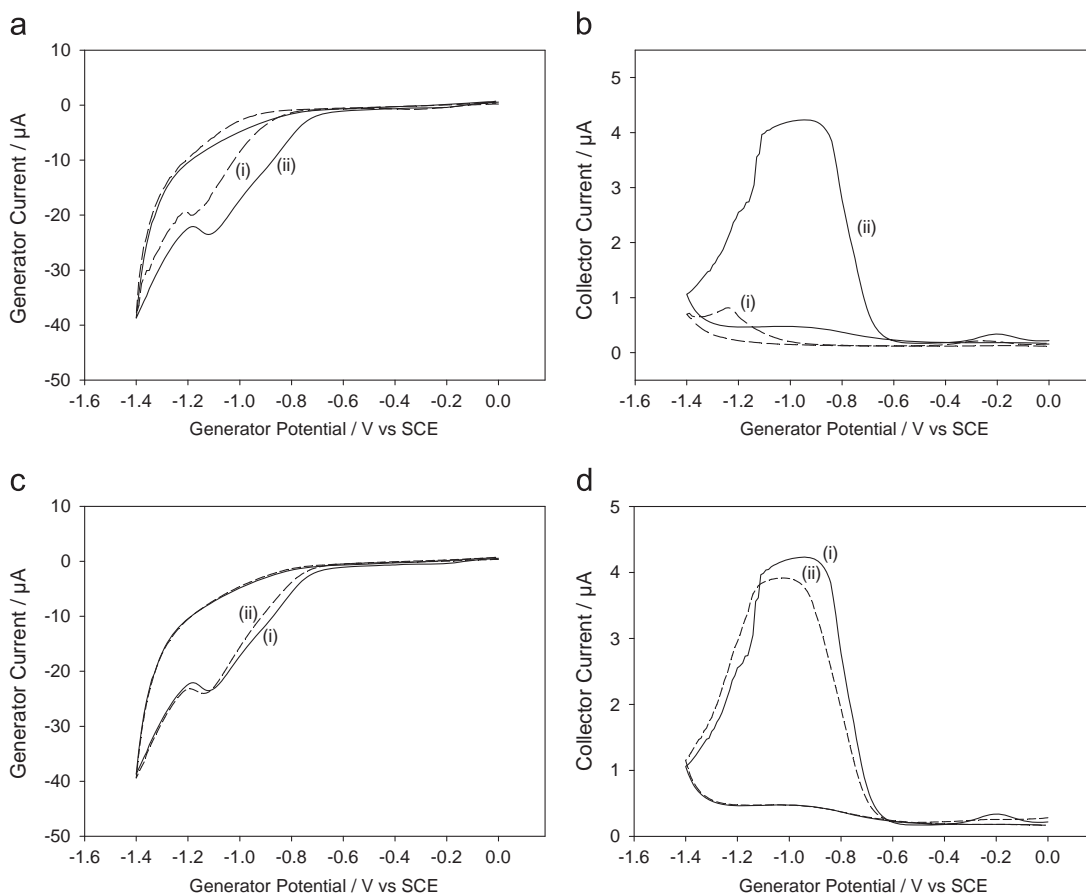


Fig. 4. (a) Generator and (b) collector voltammograms obtained at a silver–gold microtrench in 0.1 M phosphate buffer pH 5 (i) before and (ii) after addition of 10 mM KNO_3 . (c) Generator and (d) collector signals obtained at a silver–gold microtrench (i) before and (ii) after removal of oxygen by nitrogen degassing for 10 min. Scan rate = 25 mV/s. Collector potential = 0.8 V vs. SCE.

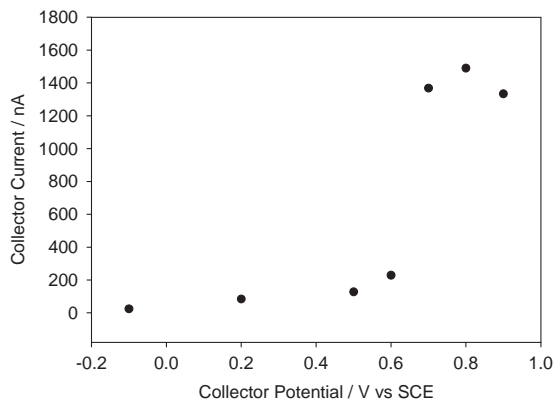


Fig. 5. Plot of the collector feedback currents as a function of collector potential in 0.1 M phosphate buffer pH 5 + 2 mM KNO_3 . Scan rate = 100 mV/s.

collector potential is held at 0.6 V vs. SCE, a slightly larger current is observed compared to that observed between -0.1 and $+0.5$ V vs. SCE but a limiting current was not reached. At 0.6 V vs. SCE partial oxidation of nitrite is apparent and consequently a small amount of redox cycling takes place. Significantly larger feedback currents are observed when the collector potential is held in the range 0.7–0.9 V vs. SCE, with the highest feedback current observed at 0.8 V vs. SCE. At these potentials, the collector is set at or close to the redox potential of nitrite oxidation on gold ($E_{\text{pa}} = 0.8$ V vs. SCE, see Fig. 3a) and hence nitrite ions are efficiently oxidised back to nitrate ions, resulting in large limiting feedback currents. The slight drop in collector current observed when

changing the collector potential from 0.8 V to 0.9 V vs. SCE is consistent with greater gold surface oxidation, which is known to hinder the nitrite oxidation process [42], therefore reducing redox-cycling efficiency. The scan rate in the range of 20–100 mV/s had no significant effect on the optimised collector potential.

3.4. Electrochemical determination of nitrite/nitrate at gold/silver microtrench electrodes: phosphate buffer experiments

Fig. 6a and b shows generator and collector voltammograms recorded at 25 mV/s for the reduction of nitrate in 0.1 M phosphate buffer pH 5 in the (i) absence and (ii–viii) presence of KNO_3 at increasing concentrations in the range 200–1400 μM . Importantly, at this stage in the development of the microtrench sensor, an electrode pre-treatment step was introduced to minimise possible gold surface oxidation effects. The pre-treatment involved performing a generator–collector cyclic voltammogram with the collector held at 0.5 V vs. SCE (to initially reduce the collector electrode surface to gold metal). The pre-treatment was applied before recording each analytical voltammogram with the collector held at 0.8 V vs. SCE. The solution was agitated prior to recording each analytical voltammogram. At the generator electrode, very similar current responses were observed before and after addition of nitrate at various concentrations (Fig. 6a). The generator current signal is therefore insensitive to nitrate addition. In contrast, at the collector electrode, a significant and systematic increase in current at ~ -0.95 V vs. SCE (limiting current plateau, see Fig. 6b) was observed with increasing nitrate concentration. Simple measurement of the limiting currents is possible due to the well-defined nature of both the current plateau and the residual background

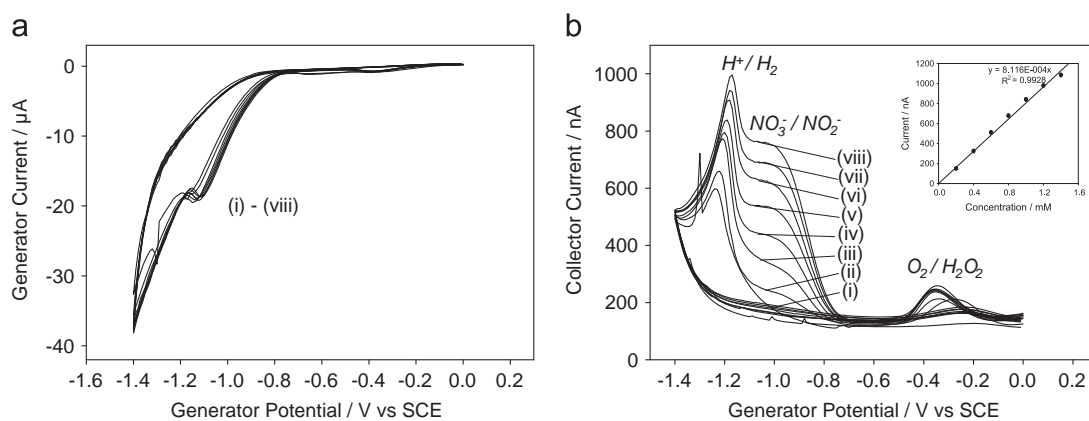


Fig. 6. (a) Generator and (b) collector voltammograms obtained at a silver–gold microtrench in 0.1 M phosphate buffer pH 5 (i) before and (ii–viii) after addition of KNO_3 : (ii) 200 μM , (iii) 400 μM , (iv) 600 μM , (v) 800 μM , (vi) 1000 μM , (vii) 1200 μM , (viii) 1400 μM . Scan rate = 25 mV/s. Collector potential = 0.8 V vs. SCE. Inset shows plot of the collector feedback limiting currents vs. KNO_3 concentration with background subtraction (line of best fit forced through zero, in accordance with the equation).

current. Additional peaks are observed at the collector electrode at -0.3 V and -1.2 V vs. SCE, tentatively assigned to the $\text{O}_2/\text{H}_2\text{O}_2$ and H^+/H_2 redox systems, respectively. These signals do not impact on measurement of the nitrate signal. The data in Fig. 6b (inset) show the blank subtracted calibration plot of collector feedback current as a function of KNO_3 concentration. A linear dependence of the collector current on concentration was observed over the concentration range tested with a coefficient of determination of 0.99, confirming that the microtrench sensor provides a suitable route for determination of nitrate concentration.

In order to test the method reproducibility several silver–gold microtrench electrodes was prepared and used for nitrate detection. Variability in collector current responses were observed due to variations in catalyst deposition and trench geometry. Typical analytical data are summarised in Table 1. Repeat measurements ($n=3$) using one electrode were obtained in background electrolyte and for each of the calibration standards to test repeatability of the sensor. For the concentration range 100–1500 μM , the relative standard deviation (RSD) for the blank and each of the calibration standards was $\leq 3.9\%$, demonstrating good within-run precision. Using the data in Table 1, the limit of detection (LOD), expressed as the analyte concentration corresponding to the blank mean value plus three standard deviations of the blank, was also determined. The estimated LOD using the method of standard addition in phosphate buffer is 5.3×10^{-7} A which corresponds to a standard concentration of 24 μM .

3.5. Voltammetric responses for nitrite/nitrate at gold/silver microtrench electrodes: serum experiments

The feasibility of using the silver–gold microtrench electrode for application in biological fluids was investigated using horse serum. Prior to analysis, horse serum samples were thawed to room temperature then minimally diluted (1:1) in phosphate buffer pH 5, thoroughly mixed, then allowed to settle for 5 min. Fig. 7 shows the generator and collector voltammograms obtained before and after addition of increasing amounts of potassium nitrate in the medically relevant concentration range 200–1400 μM . Concentrations between 4 and 45 μM are typical in human blood [45] but concentrations in patients with infectious medical conditions, for example, infective gastroenteritis, are known to increase to values in excess of 200 μM and as high as 1428 μM [5]. On the generator electrode, the current was found to increase but no systematic increase is discernible. On the collector electrode, surprisingly well-defined current responses were observed in serum before and after addition of nitrate (apart from a small shift in baseline), and importantly, were found to increase

Table 1

Repeatability testing data using a silver–gold microtrench electrode for nitrate detection in 0.1 M phosphate buffer pH 5 using the method of standard addition.

Phosphate buffer pH 5				
[KNO_3] (mM)	Mean current (A)	Standard deviation	Relative standard deviation (%)	Number of measurements
0.0	4.8×10^{-7}	1.7×10^{-8}	3.6	3
0.1	5.8×10^{-7}	1.7×10^{-8}	3.0	3
0.25	7.8×10^{-7}	1.3×10^{-8}	1.7	3
0.5	1.2×10^{-6}	2.3×10^{-8}	1.8	3
0.75	1.6×10^{-6}	4.6×10^{-8}	2.9	3
1.0	1.9×10^{-6}	3.8×10^{-8}	2.0	3
1.25	2.1×10^{-6}	8.4×10^{-8}	3.9	3
1.5	2.4×10^{-6}	6.3×10^{-8}	2.6	3

steadily with addition of aliquots of the same known concentration (200 μM). In comparison to the collector response obtained in phosphate buffer solution, a negative shift of 200 mV in the potential at which the limiting current is reached, is observed. The negative shift in potential observed in serum is, at least in part, attributed to adsorption of species such as proteins onto the silver electrocatalyst surface.

Fig. 7b (inset) shows a standard calibration plot of collector feedback current as a function of KNO_3 concentration in unspiked diluted serum. A linear dependence of the collector current on concentration with $r^2 \geq 0.997$ is observed for both unspiked serum and 500 μM spiked serum samples (where spiking of the sample from a stock solution of KNO_3 was undertaken prior to sample dilution).

Repeat measurements ($n=3$) were obtained in background electrolyte and for calibration standards in the range 200–1400 μM to assess method precision (see Table 2). The RSD for the blank and each of the calibration standards ranged between 1.1% and 6.9%, with greater precision being observed at the two highest concentrations. With the exception of the lowest calibration standard (200 μM), the relative standard deviations of $< 5\%$ obtained show that the method exhibits a good level of reliability.

The KNO_3 concentration of the unspiked and spiked horse serum samples were obtained by extrapolation from the linear plots and determined to be 240 ± 10 μM ($n=2$) and 781 μM , respectively (see Table 3). The spike recovery of 108% is within 10% of the expected spike value, providing evidence for good method accuracy. To assess the analytical performance of the method further, separate fractions of the same unspiked and spiked horse serum samples were analysed using a well-known routine chemical analyser method based on gas-phase

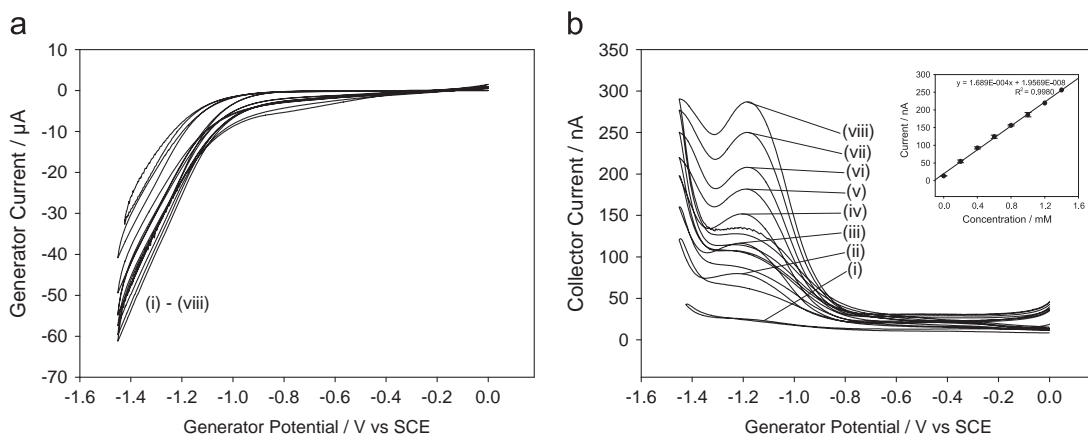


Fig. 7. (a) Generator and (b) collector voltammograms obtained at a silver–gold microtrench in horse serum diluted 1:1 in 0.1 M phosphate buffer pH 5 (i) before and (ii–viii) after addition of KNO_3 : (ii) 200 μM , (iii) 400 μM , (iv) 600 μM , (v) 800 μM , (vi) 1000 μM , (vii) 1200 μM , (viii) 1400 μM . Scan rate = 25 mV/s. Collector potential = 0.8 V vs. SCE. Inset shows plot of the collector feedback limiting currents vs. KNO_3 concentration. Error bars correspond to one standard deviation of the mean.

Table 2

Repeatability testing data using a silver–gold microtrench electrode for nitrate detection in horse serum samples diluted 1:1 in 0.1 M phosphate buffer pH 5 using the method of standard addition.

Horse serum diluted in phosphate buffer pH 5 (1:1)				
[KNO_3] (mM)	Mean current (A)	Standard deviation	Relative standard deviation (%)	Number of measurements
0.0	1.3×10^{-8}	5.8×10^{-10}	4.4	3
0.2	5.5×10^{-8}	3.8×10^{-9}	6.9	3
0.4	9.3×10^{-8}	3.3×10^{-9}	3.6	3
0.6	1.2×10^{-7}	4.6×10^{-9}	3.7	3
0.8	1.6×10^{-7}	1.9×10^{-9}	1.2	3
1.0	1.9×10^{-7}	6.2×10^{-9}	3.3	3
1.2	2.2×10^{-7}	n/a	n/a	1
1.4	2.6×10^{-7}	n/a	n/a	1

Table 3

Summary of estimated nitrate concentrations obtained by redox-cycling using microtrench electrodes and by chemical analysis using the chemical analyser method.

Estimated nitrate concentrations in horse serum samples			
Sample	Analysis method	Concentration (μM)	Number of measurements
Horse serum	Electrochem.	233, 247	2
Horse serum	Chem. analyser	50.7, 64.7	2
500 μM spiked horse serum	Electrochem.	781	1
500 μM spiked horse serum	Chem. analyser	539	1

chemiluminescence [38]. Unlike the electrochemical method which requires only minimal dilution of the serum, the chemical analyser method requires deproteinisation and five-fold dilution prior to analysis. Using the chemical analyser, the unspiked and spiked horse serum samples were determined to be $58 \pm 10 \mu\text{M}$ ($n=2$) and 539 μM , respectively (Table 3). These values are lower than those obtained using the electrochemical method and hence method bias arising from systematic error exists between the two methods. The discrepancy in concentrations between the two methods could potentially be reconciled by a simple offset. Further

study and improvement of the microtrench method will be required to resolve this problem.

4. Conclusions

It has been shown that generator–collector amplification for the nitrate-reduction/nitrite-oxidation redox cycle is possible with beneficial effects on the sensor current in a dual-plate gold/silver microtrench electrode system. Although sensitivity issues remain to be resolved, the major conclusions from this work are:

- Microtrench sensors can operate in the presence of dioxygen (no degassing required).
- Microtrench sensors function in serum-buffer media without further purification or separation.
- Microtrench sensors provide selectivity due to the use of two independently controlled electrodes set with different potentials (both generator and collector potential need to be correct to give the analytical response).
- Microtrench sensors can operate in the presence of low levels of interferences such as chloride or protein.

In future work, microtrench electrodes will be fabricated with a smaller inter-electrode gap using automated high-accuracy production techniques (e.g. photolithography) to significantly enhance sensitivity yet provide low-cost and reproducible sensor elements. Variation of the sensor catalyst and the type of electrode material should further widen the range of applications.

Acknowledgements

A.J.G. and F.M. gratefully acknowledge Higher Education Innovation Funding (HEIF) and the Engineering and Physical Sciences Research Council (EP/I028706/1) for financial support. S.J.G. acknowledges the University of Exeter for funding through the Higher Education Funding Council for England HEIF-5.

References

- [1] Y. Wang, H. Xu, J. Zhang, G. Li, *Sensors* 8 (2008) 2043–2081.
- [2] A.I. Mian, M. Aranke, N.S. Bryan, *Open Biochem. J.* 7 (2013) 24–32.
- [3] J. Wang, *Chem. Rev.* 108 (2008) 814–825.
- [4] G. Ellis, I. Adatia, M. Yazdanpanah, S.K. Makela, *Clin. Biochem.* 31 (1998) 195–220.

- [5] R.S. Dykhuizen, J. Masson, G. McKnight, A.N.G. Mowat, C.C. Smith, L.M. Smith, N. Benjamin, *Gut* 39 (1996) 393–395.
- [6] S.G. Ayub, T. Ayub, S.N. Khan, R. Dar, K.I. Andrabi, J. *Cardiovasc. Dis. Res.* 2 (2011) 172–176.
- [7] S. Milstien, N. Sakai, B.J. Brew, C. Krieger, J.H. Vickers, K. Saito, M.P. Heyes, *J. Neurochem.* 63 (1994) 1178–1180.
- [8] S.R. Tannenbaum, P. Correa, *Nature* 317 (1985) 675–676.
- [9] F.R. Greer, M. Shannon, *Pediatrics* 116 (2005) 784–786.
- [10] J. Kelly, J. Fulford, A. Vanhatalo, J.R. Blackwell, O. French, S.J. Bailey, M. Gilchrist, P.G. Winyard, A.M. Jones, *Am. J. Physiol. Regul. Integr. Comp. Physiol.* 304 (2013) R73–R83.
- [11] A.M. Jones, S.J. Bailey, A. Vanhatalo, *Med. Sport Sci.* 59 (2012) 29–35.
- [12] S.K. Ferguson, D.M. Hirai, S.W. Copp, C.T. Holdsworth, J.D. Allen, A.M. Jones, T. I. Musch, D.C. Poole, *J. Physiol.* 591 (2013) 547–557.
- [13] I. Guevara, J. Iwanejko, A. Dembińska-Kieć, J. Pankiewicz, A. Wanat, P. Anna, I. Gołębek, S. Bartus, M. Malczewska-Malec, A. Szczudlik, *Clin. Chim. Acta* 274 (1998) 177–188.
- [14] D. Tsikas, F.M. Gutzki, S. Rossa, H. Bauer, C. Neumann, K. Dockendorff, J. Sandmann, J.C. Frolich, *Anal. Biochem.* 244 (1997) 208–220.
- [15] A.K. Nussler, M. Glanemann, A. Schirmeier, L. Liu, N.C. Nussler, *Nat. Protoc.* 1 (2006) 2223–2226.
- [16] C.L. Walters, P.N. Gillatt, R.C. Palmer, P.L. Smith, *Food Addit. Contam.* 4 (1987) 133–140.
- [17] A. Vanhatalo, J. Fulford, S.J. Bailey, J.R. Blackwell, P.G. Winyard, A.M. Jones, *J. Physiol.* 589 (2011) 5517–5528.
- [18] W.S. Jobgen, S.C. Jobgen, H. Li, C.J. Meininger, G. Wu, *J. Chromatogr. B* 851 (2007) 71–82.
- [19] J.M. Monaghan, K. Cook, D. Gara, D. Crowther, *J. Chromatogr. A* 770 (1997) 143–149.
- [20] P.N. Bories, E. Scherman, L. Dziedzic, *Clin. Biochem.* 32 (1999) 9–14.
- [21] P.J. Milham, A.S. Awad, R.E. Paull, J.H. Bull, *Analyst* 95 (1970) 751–757.
- [22] M.J. Moorcroft, J. Davis, R.G. Compton, *Talanta* 54 (2001) 785–803.
- [23] X. Xing, D.A. Scherson, C. Mak, *J. Electrochem. Soc.* 137 (1990) 2166–2175.
- [24] H.L. Li, J.Q. Chambers, D.T. Hobbs, *J. Appl. Electrochem.* 18 (1988) 454–458.
- [25] G.E. Dima, A.C.A. De Vooy, M.T.M. Koper, *J. Electroanal. Chem.* 554–555 (2003) 15–23.
- [26] M.-C. Tsai, D.-X. Zhuang, P.-Y. Chen, *Electrochim. Acta* 55 (2010) 1019–1027.
- [27] T. Madasamy, M. Pandiaraj, A.K. Kanugula, S. Rajesh, K. Bhargava, N.K. Sethy, S. Kotamraju, C. Karunakaran, *Adv. Chem. Lett.* 1 (2013) 2–9.
- [28] T. Madasamy, M. Pandiaraj, M. Balamurugan, K. Bhargava, N.K. Sethy, C. Karunakaran, *Biosens. Bioelectron.* 52 (2014) 209–215.
- [29] D. Quan, J.H. Shim, J.D. Kim, H.S. Park, G.S. Cha, H. Nam, *Anal. Chem.* 77 (2005) 4467–4473.
- [30] S.E.C. Dale, F. Marken, *Electrochemistry within nanogaps*, in: J.D. Wadhawan, R.G. Compton (Eds.), *Electrochemistry: Nanoelectrochemistry*, RSC publishing, Cambridge, 2014, pp. 132–154.
- [31] S.G. Lemay, S. Kang, K. Mathwig, P.S. Singh, *Acc. Chem. Res.* 46 (2013) 369–377.
- [32] M.A.G. Zevenbergen, P.S. Singh, E.D. Goluch, B.L. Wolfrum, S.G. Lemay, *Nano Lett.* 11 (2011) 2881–2886.
- [33] S. Kang, A.F. Nieuwenhuis, K. Mathwig, D. Mampallil, S.G. Lemay, *ACS Nano* 7 (2013) 10931–10937.
- [34] A.T. Hubbard, D.G. Peters, *Crit. Rev. Anal. Chem.* 3 (1973) 201–242.
- [35] M.A. Hasnat, A.J. Gross, S.E.C. Dale, E.O. Barnes, R.G. Compton, F. Marken, *Analyst* 139 (2014) 569–575.
- [36] S.E.C. Dale, F. Marken, *Electrochim. Acta* 125 (2013) 94–100.
- [37] S.E.C. Dale, F. Marken, *Faraday Discuss.* 164 (2013) 349–359.
- [38] R.M. Bateman, C.G. Ellis, D.J. Freeman, *Clin. Chem.* 48 (2002) 570–573.
- [39] K. Fajerwerg, V. Ynam, B. Chaudret, V. Garçon, D. Thouron, M. Comtat, *Electrochem. Commun.* 12 (2010) 1439–1441.
- [40] B. Habibi, M. Jahanbakhshi, M. Pournaghi-Azar, *Microchim. Acta* 177 (2012) 185–193.
- [41] Y. Wang, E. Laborda, R.G. Compton, *J. Electroanal. Chem.* 670 (2012) 56–61.
- [42] B. Piela, P.K. Wrona, *J. Electrochem. Soc.* 149 (2002) E55–E63.
- [43] M.R. Majidi, K. Asadpour-Zeynali, B. Hafezi, *Int. J. Electrochem. Sci.* 6 (2011) 162–170.
- [44] O. Ghodbane, M. Sarrazin, L. Roué, D. Bélanger, *J. Electrochem. Soc.* 155 (2008) F117–F123.
- [45] H. Moshage, B. Kok, J.R. Huizenga, P.L. Jansen, *Clin. Chem.* 41 (1995) 892–896.



Chemometric optimization of the robustness of the near infrared spectroscopic method in wheat quality control

Milica Pojić^{a,*}, Dušan Rakić^b, Živorad Lazić^c

^a Institute of Food Technology, University of Novi Sad, Bulevar cara Lazara 1, 21000 Novi Sad, Serbia

^b Faculty of Technology, University of Novi Sad, Bulevar cara Lazara 1, 21000 Novi Sad, Serbia

^c BASF Catalysts LLC, Technical Center, 108 Briarcliff Rd. Gordon, GA 31031, USA

ARTICLE INFO

Article history:

Received 14 March 2014

Received in revised form

21 July 2014

Accepted 21 July 2014

Available online 30 July 2014

Keywords:

Near infrared spectroscopy

Screening design

Fractional factorial design

Optimization

Propagation of error

Wheat quality control

ABSTRACT

A chemometric approach was applied for the optimization of the robustness of the NIRS method for wheat quality control. Due to the high number of experimental ($n=6$) and response variables to be studied ($n=7$) the optimization experiment was divided into two stages: screening stage in order to evaluate which of the considered variables were significant, and optimization stage to optimize the identified factors in the previously selected experimental domain. The significant variables were identified by using fractional factorial experimental design, whilst Box-Wilson rotatable central composite design (CCRD) was run to obtain the optimal values for the significant variables. The measured responses included: moisture, protein and wet gluten content, Zeleny sedimentation value and deformation energy. In order to achieve the minimal variation in responses, the optimal factor settings were found by minimizing the propagation of error (POE). The simultaneous optimization of factors was conducted by desirability function. The highest desirability of 87.63% was accomplished by setting up experimental conditions as follows: 19.9 °C for sample temperature, 19.3 °C for ambient temperature and 240 V for instrument voltage.

© 2014 Elsevier B.V. All rights reserved.

1. Introduction

The optimization in analytical chemistry is performed in order to discover the operational conditions at which the observed procedure provides the most reliable response, and therefore to improve the performance of an analytical system [1]. In this regard, it is closely associated with the determination of method robustness. The traditional optimization techniques which included the monitoring of the influence of one factor at a time (OVAT) have been overcome by application of chemometrics techniques involving the design of experiments (DOE). DOE techniques imply the reduction of the number of experiments to be performed, the development of mathematical models enabling the assessment of the relevance of the factor effects being studied, their interactions and statistical significance [1–7]. Among them, the most frequently used technique for optimization of analytical methods and understanding of system performance is response surface methodology (RSM) [1,8,9]. The multivariable optimization of analytical methods has been widely performed especially for extraction methods, spectroanalytical methods, chromatographic

methods, capillary electrophoresis, electroanalytical methods and thermogravimetry [6].

The robustness of the near infrared spectroscopic method (NIRS) has not been extensively studied due to the fact that it is considered as a built-in method characteristic accomplished by employment of so-called repeatability file (REP file) during the development of the NIRS calibration model. REP file is commonly introduced during calibration model development so that it contains spectral information on the uncontrolled variations that may occur in routine operation which must be minimized and hence improve the model robustness (i.e., temperature variations, small differences between cups, different levels of cup wear, and differences between instruments). Adequately designed and structured REP file enables the minimization of the uncontrolled variations affecting NIRS analysis. However, the REP file concept is a special feature only available in WinISI calibration software – software by Infracore International, LLC [10–14]. However, the background of calibration development procedure is not commonly available to the average end-user of the NIRS method, who nevertheless must demonstrate its suitability for intended purpose. The robustness test of the NIRS method for its application in analyzing wheat samples examines the potential sources of variability in responses (analytical and spectral). To achieve this, a number of factors related to the operating procedure (operational factors) and ambient conditions (ambient factors) are

* Corresponding author. Tel.: +381 21 485 3782; fax: +381 21 450 730.

E-mail address: milica.pojic@fins.uns.ac.rs (M. Pojić).

examined in an experimental design, in an intervals that slightly exceed the variation that can be expected in a routine use of the method [7,15]. By examining the impact of various factors (operational and ambient) using screening Plackett–Burman factorial experimental design, Pojić et al. [16] identified the factors with the most influencing impact on analytical and spectral responses of the NIRS method as being applied for wheat moisture, protein and wet gluten content predictions. Starting from the importance of reliable results of wheat quality in trade, where, for example, the premiums of 1.30–1.50\$ are paid for increments of 0.1% in protein content per ton [17], as well as the growing importance of ensuring of confident measurement results, the objectives of the present study were defined: to (i) indicate the most important factors that might affect the variations in NIRS responses when determining the selected wheat quality parameters and to (ii) use the response surface methodology to find the optimal factor settings which exhibit the minimum variability in responses around the specified target values.

2. Materials and methods

The chosen experimental design was performed in two stages. The initial stage involved a *screening design* performed to select the most important factors that might affect variations in the NIRS responses. The subsequent stage involved the performance of response surface methodology with previously identified significant factors, to obtain the least square adequate model to test the robustness by the propagation of error (POE) method, hereinafter called *optimization design* [1,7,18]. The POE method was used to find the factor settings that minimize the variation in responses [19,20]. Both screening and optimization designs were setup and processed using software Design-Expert 9, trial version (StatEase, Inc., Minneapolis, USA).

2.1. Screening design

Two-level fractional factorial design (minimum run resolution V, $n=22$ runs) was set up in a way to vary six experimental factors: number of subsamples in the NIRS measurement (A), ambient temperature (B), sample temperature (C), ambient air humidity (D), instrument voltage (E) and lamp aging (F). Experimental factors and their levels in screening design are given in Table 1. The levels were selected on the basis of the NIR systems specification as well as variations that are most likely to happen when the method is transferred between different laboratories, different instruments or over time. All experiments were carried out in duplicate and averaged. The significant effects were identified by graphical interpretation of the estimated effects and analyzing half-normal probability plot, where the significant effects were identified as outliers from the straight line (the non-significant effects were lying on a straight line passing through zero) (these data not shown). Contribution of main effects and their interactions is calculated as ratio of sum of squares for observed effect and total sum of squares.

Table 1
Factors and their levels investigated during the screening design.

Factor	Low value (-1)	High value (+1)
Number of subsamples (A)	5	15
Sample temperature (B) (°C)	5	35
Ambient temperature (C) (°C)	10	30
Ambient humidity (D) (%)	40	80
Instrument voltage (E) (V)	200	240
Lamp aging (F)	New	Old

2.2. Optimization design

The next step was to determine the optimal factor settings to achieve the minimal variation in responses. For this purpose, the response surface methodology (RSM) using a Box–Wilson rotatable central composite design (CCRD) was adopted. The significant factors identified in the previous phase comprised: sample temperature (A), ambient temperature (B) and instrument voltage (C). A CCRD comprised of a two-level full factorial design (2^f experiments), a star design (2^f experiments) and six center points, thus requiring 20 experiments to examine the impact of f factors ($N=2^f+2f+6$). The points of the full factorial design were set at -1 and $+1$ factor levels, whilst those of star design were set at 0 , $-\alpha$ and $+\alpha$, where α level was 1.682 due to three factors selected [8]. The central points were set at the factors level 0. Experimental factors and their levels in optimization design are given in Table 2. The measurements of all responses were carried out in duplicate and averaged.

A second-degree polynomial (quadratic) model was used to describe the relation between the response(s) and the three factors under consideration:

$$Y = b + \sum_{i=1}^3 a_i X_i + \sum_{i=1}^3 a_{ii}^2 X_{ii}^2 + \sum_{i=1}^3 \sum_{j=i+1}^3 a_{ij} X_i X_j$$

Where: Y is the modeled response(s) for obtained response(s) (protein content, moisture content, wet gluten content, Zeleny sedimentation value and deformation energy), b_0 is an intercept; X_i is the factor and a_i is the corresponding coefficient; X_{ii} is the quadratic factor; a_{ii} is the quadratic coefficient; X_{ij} is the two-factor interaction; and a_{ij} is the two-factor interaction coefficient. The statistical significance of the terms in the regression equation was determined by analysis of variance (ANOVA) for each response.

The adequacy of the model was evaluated by coefficient of determination (R^2) and model p -value. A subsequent step in optimization design comprised the determination of the optimal factor settings derived from response surfaces built with the design results. The optimal factor settings were specified to achieve the minimal variation in responses, which was conducted by minimizing the propagation of error (POE). POE is defined as the amount of variation transmitted to the response and it was derived from variability originating from control factors and the normal process variation obtained from ANOVA [9,21]:

$$POE = \sqrt{\sigma_Y^2}$$

$$\sigma_Y = \sum_{i=1}^n \left(\frac{\partial f}{\partial X_i} \right)^2 \sigma_{X_i}^2 + \sigma_{resid}^2$$

The simultaneous optimization was conducted by desirability function.

2.3. Experimental conditions

The sample temperature was adjusted by using chamber convection thermostat (TMA Bodalec & Bodalec, Oborovo, Croatia), whilst the ambient temperature was adjusted by using air

Table 2
Experimental factors and their levels in optimization design.

Factor	Lowest value ($-\alpha$)	Low value (-1)	Central value (0)	High value (+1)	Highest value ($+\alpha$)
Sample temperature (A) (°C)	-5	5	20	35	45
Ambient temperature (B) (°C)	3	10	20	30	37
Instrument voltage (C) (V)	186	200	220	240	254

conditioner on the one hand and by placing the instrument in the ambient with the temperature of 10 °C. The relative ambient humidity was adjusted by using portable evaporative humidifier (De'Longhi, Treviso, Italy) and portable dehumidifier (De'Longhi, Treviso, Italy). The instrument voltage was adjusted by using variable transformer (IEV, Industrija za elektrozeve, Ljubljana, Yugoslavia). The experiments with an old lamp were carried out with the tungsten-halogen lamp that previously had been operated during 1560 h.

2.4. NIRS measurements

The NIRS measurement was conducted on whole-grain wheat samples with a scanning monochromator Infracore 1241 Grain Analyzer (Foss, Denmark) used in transmittance mode over the spectral range 850–1050 nm, using 100 wavelength points with

2 nm steps. Prediction models used were global ANN prediction models (Foss, Denmark). Sample was scanned in five replicates for each experimental setting defined by experimental design. Spectra were collected and managed using WinISI software, version 4.01 (Infrasoft International LLC, PA, USA).

3. Results and discussion

DOE is often divided into a screening phase and an optimization phase. The screening phase commonly involves the examination of all factors that potentially could affect the method performance in order to identify the most influential ones, which are subsequently optimized in the optimization phase in order to find the optimal experimental conditions [7].

3.1. Screening design and factor selection

The application of screening designs is suitable since it allows the examination of a relatively high number of factors in a rather small number of experiments [7]. Therefore, the selection of potentially influential factors included those that might have the effect on the output results – spectral and analytical response on the NIRS method: the number of subsamples (*A*), sample temperature (*B*), ambient temperature (*C*), ambient humidity (*D*), instrument voltage (*E*) and lamp aging (*F*) [16]. The results of the screening experiments are given in Table 3. The results were evaluated in order to identify the most important factors in the experiment.

Considering the contribution of the main effects on the analytical response of the NIRS method which is presented in Fig. 1a, sample temperature (*B*) had the dominant influence affecting all responses, followed by ambient temperature (*C*). Moreover, two-factor interactions were observed so that moisture content was affected by the interaction between sample and ambient temperature (*BC*), whilst wet gluten content was affected by the interaction between sample temperature and instrument voltage (*BE*) (Fig. 1b). The difficulty in keeping these variables constant during the routine application the NIRS method imposes the necessity of studying their influence on the NIR spectra and therefore the reliability of the obtained results [21]. Considering the previously reported consequences of temperature variations on the modification of NIR spectrum caused by the changes in vibration intensity of molecular bonds and the number of hydroxyl groups involved in hydrogen bonding the variations in the sample temperature must not be neglected [11,12,22,23]. The obtained results confirmed the previously reported findings of Pojić et al.

Table 3
Resolution V experimental design (screening design) and obtained responses.

Factors						Responses				
A	B	C	D	E	F	PC	MC	WGC	Z	W
5	35	30	40	200	New	12.54	9.84	30.64	41.0	295
15	5	10	80	240	New	12.73	10.14	31.43	42.9	317
15	5	10	40	240	Old	12.73	10.41	31.23	42.0	311
5	5	10	80	200	New	12.74	10.16	31.27	42.5	321
5	35	10	80	200	Old	12.54	10.12	30.84	41.3	287
15	5	30	40	200	New	12.74	10.42	31.30	42.8	308
5	35	10	80	240	New	12.49	10.04	30.69	41.0	291
5	5	30	80	240	New	12.79	10.36	31.45	43.7	313
15	35	30	40	200	Old	12.55	9.89	30.71	40.8	294
5	5	10	40	240	New	12.87	10.43	31.70	43.9	323
5	5	30	40	240	Old	12.79	10.38	31.46	42.8	316
15	35	10	40	200	New	12.62	10.10	31.03	41.8	292
5	35	30	80	240	Old	12.51	9.95	30.46	41.0	287
15	35	10	80	240	Old	12.58	9.94	30.80	41.7	290
5	5	10	40	200	Old	12.69	10.15	31.19	42.4	319
15	35	30	80	200	New	12.59	10.05	30.95	40.8	293
15	5	10	80	200	Old	12.73	10.15	31.21	43.2	319
15	5	30	80	240	Old	12.75	10.39	31.22	42.6	311
5	5	30	80	200	Old	12.65	10.38	31.19	42.1	301
15	35	30	40	200	New	12.57	9.88	30.71	40.9	294
5	35	10	40	240	New	12.58	10.06	30.82	41.0	293
15	35	30	40	240	New	12.49	9.97	30.49	40.6	287

A – number of subsamples in the NIRS measurement; *B* – sample temperature (°C); *C* – ambient temperature (°C); *D* – ambient air humidity (%); *E* – instrument voltage (V); and *F* – lamp aging.

PC – protein content (% d.m.); MC – moisture content (%); WGC – wet gluten content (%); Z – Zeleny sedimentation value; and W – alveograph deformation energy (10^{-4} J).

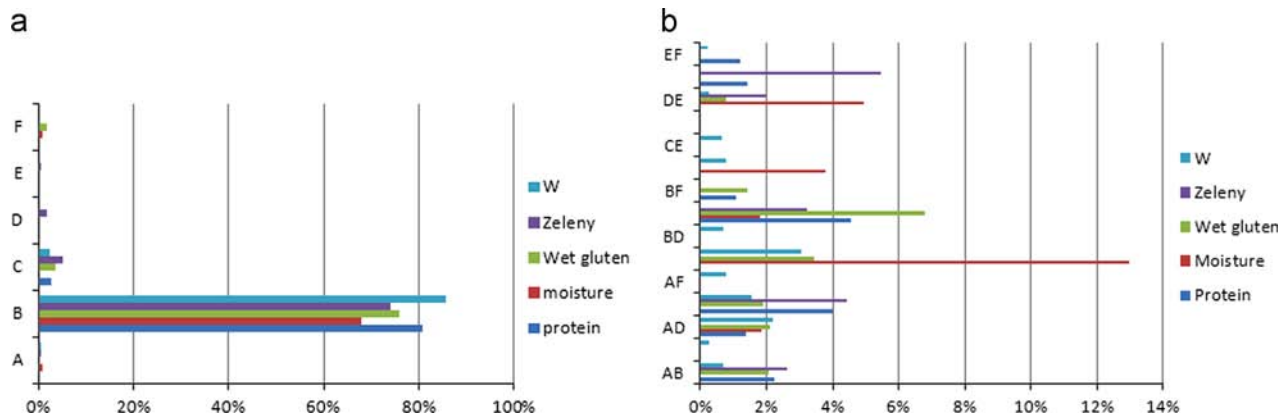


Fig. 1. Contribution of main effects (a) and interactions between main effects (b) in screening design on individual responses (*A* – number of subsamples in the NIRS measurement; *B* – sample temperature; *C* – ambient temperature; *D* – ambient air humidity; *E* – instrument voltage; *F* – lamp aging).

indicating the significant effects of the sample temperature on moisture content of wheat samples when applying either OVAT design or Plackett–Burman design [16].

Although the use of voltage stabilizers is generally recommended for providing constant voltage current to electric appliances and their protection from damage due to voltage fluctuations, this is often not the case. In the mains electricity supplies the voltage fluctuations are very common, and could be even more pronounced within the electrical network where huge power consumers are in use, such as those at large grain terminals. The importance of supply voltage of the NIRS device must not be ignored due to the fact that the energy emitted by a tungsten filament lamp, used as a source of visible light within the spectrometer, is proportional to the power of the operating voltage which means that stable energy output requires the stable lamp voltage as well. The variability in the voltage supply may be the cause of the malfunctioning of other parts of the NIRS instrument as well as the number of readings taken in unit of time thus deteriorating the reliability of the NIRS measurements [24]. The sample temperature is considered as one of the external factors that to a large extent affects the robustness of the NIRS method, but it is often overlooked in the routine application of the NIRS analysis [23,24].

Table 4
Central composite design (optimization design) and obtained responses.

Factors			Responses				
A	B	C	PC	MC	WGC	Z	W
20.00	20.00	253.64	12.79	10.84	32.37	43.4	284
35.00	30.00	200.00	12.81	10.60	32.06	45.0	278
20.00	20.00	220.00	12.83	10.89	32.51	44.3	284
35.00	10.00	240.00	12.73	10.60	31.81	44.0	273
5.00	30.00	200.00	12.97	10.93	33.02	45.9	293
20.00	36.82	220.00	12.86	10.67	32.43	43.8	290
–5.23	20.00	220.00	13.00	10.81	33.16	45.7	307
20.00	20.00	220.00	12.78	10.86	32.31	43.6	283
20.00	20.00	220.00	12.78	10.87	32.44	43.4	282
20.00	20.00	186.36	12.76	10.83	32.35	42.7	281
20.00	20.00	220.00	12.64	10.86	32.07	42.4	280
5.00	10.00	200.00	12.93	10.95	32.98	45.9	298
35.00	30.00	240.00	12.83	10.58	32.03	45.0	279
20.00	20.00	220.00	12.80	10.85	32.51	43.4	283
45.23	20.00	220.00	12.76	10.43	31.58	44.6	279
5.00	30.00	240.00	12.73	10.87	32.32	43.2	281
20.00	3.18	220.00	12.74	10.69	32.26	43.6	286
35.00	10.00	200.00	12.85	10.64	32.20	43.9	283
20.00	20.00	220.00	12.68	10.86	32.09	42.1	278
5.00	10.00	240.00	12.76	10.88	32.50	44.0	288

A – sample temperature (°C); B – ambient temperature (°C); and C – instrument voltage (V).
PC – protein content (% d.m.); MC – moisture content (%); WGC – wet gluten content (%); Z – Zeleny sedimentation value; and W – alveograph deformation energy (10⁻⁴ J).
Measurements in center points are given in bold.

Table 5
Analysis of variance (ANOVA) for the parameters of response surface methodology fitted to second-order polynomial equation.

Response	Residual			Model					
	DF	SS	MS	DF	SS	MS	F-value	p-value	R ²
PC	14	0.068	0.00487	5	0.086	0.017	3.52	0.0286	0.5570
MC	14	0.018	0.001303	5	0.37	0.074	56.72	< 0.0001	0.9530
WGC	15	0.47	0.031	4	2.38	0.59	18.94	< 0.0001	0.8347
Z	14	9.15	0.65	5	13.54	2.71	2.69	0.0693	0.7080
W	15	301.54	20.10	4	825.06	206.27	4.14	0.0161	0.5967

DF – degrees of freedom; SS – sum of squares; and MS – mean squares.
PC – protein content; MC – moisture content; WGC – wet gluten content; Z – Zeleny sedimentation value; and W – alveograph deformation energy.

3.2. Optimization design

According to the results obtained from the screening design, sample temperature (A), ambient temperature (B) and instrument voltage (C) were identified significant and included in a more complex experimental design (CCRD) to evaluate the influence of these factors on experimental responses. The CCRD layout, which included the combinations of all factors at different levels in randomized order, along with obtained responses is given in Table 4. In this respect, the sample temperature was identified the most influential factor, contributing to the determination of wet gluten content with 89%, deformation energy 78%, moisture content 66%, protein content 27% and Zeleny sedimentation value 5%. Instrument voltage contributed the most to protein content determination with 18%, wet gluten content 8%, Zeleny sedimentation value 6%, deformation energy 5%, whilst contribution to moisture content determination was negligible. Ambient temperature influenced the most protein content determination with 6%, whilst its effect on other responses was insignificant [25].

In order to determine the factor settings which will minimally affect the variation in responses arising from input factors, a propagation of error (POE) was applied [18,25]. POE reveals the regions in obtained response surface that will provide the most robust responses to variations in input factors. Therefore, a non-linear (quadratic) predictive model obtained by a response surface method (RSM) was determined beforehand (Tables 5–6) [18,25], along with anticipation of variability in all the variables (factor and responses) in the form of standard deviations, which was used for the calculation of POE (Table 7). The ANOVA results for selected responses are presented in Table 5 indicating that models for all

Table 6
Regression equation coefficients^a obtained for selected responses.

Effects	PC	MC	WGC	Z	W
Intercept	12.77136	10.86527	32.34976	43.46113	282.5573
Linear					
A	–0.041107	–0.135519	–0.393677	–0.213019	–6.881695
B	0.019166	–0.007997	0.016438	0.121441	–0.205555
C	–0.033919	–0.0114	–0.116102	–0.243808	–1.823683
Interaction					
AB					
AC	0.040487		0.094975	0.584012	
BC					
Quadratic					
A ²	0.044311	–0.075763		0.7908	3.002696
B ²		–0.053896			
C ²					

A – sample temperature; B – ambient temperature; C – instrument voltage; PC – protein content; MC – moisture content; WGC – wet gluten content; Z – Zeleny sedimentation value; and W – alveograph deformation energy.

^a Standardized coefficients.

responses were significant. The significance was determined by *F*-test and *p*-values. The larger the magnitude of the *F*-value and smaller the *p*-value the more significant the corresponding coefficient was. Regression equation coefficients obtained for selected responses in terms of coded variables are presented in Table 6.

Ultimately, a propagation of error (POE) was generated for all response to indicate how that error was transmitted to all the responses. Fig. 2 shows the main effects of the sample and ambient temperature and instrumental voltage to propagation of error in protein determination. Due to the fact that the lower POE indicates the more robust measurement system, it can be observed that the higher variability in protein content determination can be expected at a lower sample temperatures (Fig. 2a) and lower instrument voltage (Fig. 2c), whilst ambient temperature appeared to have no effect on the variation in protein determination (Fig. 2b). The same applies to the wet gluten (Supplementary material 1) and Zeleny sedimentation value determination (Supplementary material 2). One of the most important assumptions for the statistical analysis of data from experiments is that the data come from a normal distribution. The normality of the data can be checked by plotting a normal probability of the residuals. If the points on the plot fall fairly close to a straight line, then data are normally distributed [20]. The normal probability plot of the residual for protein is shown in Fig. 3. Higher variability in moisture content can be expected at higher sample temperatures and equally at higher and lower ambient temperatures, with no influence of instrument voltage (Supplementary material 3). Considering determination of deformation energy (*W*), higher variability can be expected at lower sample temperatures with no influence of ambient temperature and instrument voltage (Supplementary material 4). As POE basically represents the measurement uncertainty, it must be noted that POE for all

observed responses appeared to be lower than those of standard laboratory methods.

A multiple response method – desirability function was used to optimize the experimental settings of the NIRS system that would yield the minimal variability in all observed responses (protein, moisture and wet gluten content, Zeleny sedimentation value and deformation energy). The maximum desirability was achieved by setting instrument voltage, sample and ambient temperature to be within the range, and POE to be at minimal level (Table 8).

The results of optimization are shown in Table 9 by descending desirability. The highest desirability of 87.63% was accomplished by setting up experimental conditions as follows: 19.9 °C for

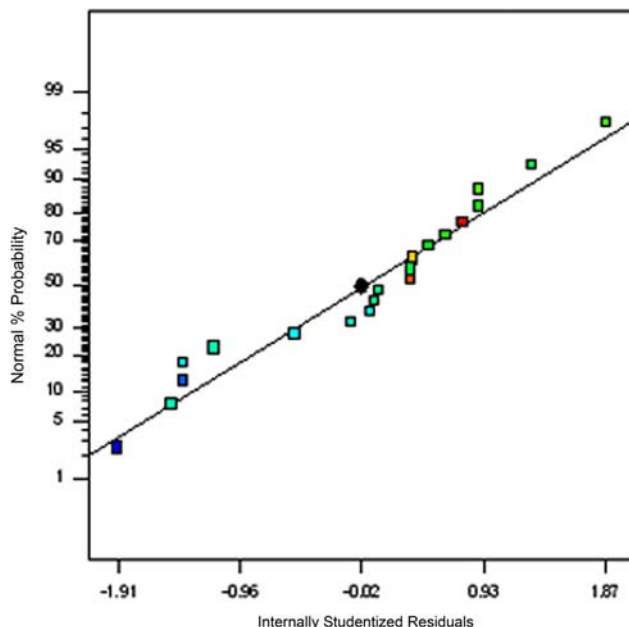


Fig. 3. Normal plot of residuals for POE in protein determination.

Table 7
Ranges and standard deviations of factors and responses.

Name	Type	σ	Low	High
A	Factor	12.39514	5	35
B	Factor	8.26343	10	30
C	Factor	16.52686	200	240
PC	Response	0.0783635	126.439	130.013
MC	Response	0.0419878	104.277	109.501
WGC	Response	0.184191	31.5769	33.1589
Z	Response	0.813982	42.1156	45.915
W	Response	520.725	272.993	306.896

σ – Standard deviation.

A – sample temperature (°C); B – ambient temperature (°C); C – instrument voltage (V); PC – protein content (% d.m.); MC – moisture content (%); WGC – wet gluten content (%); Z – Zeleny sedimentation value; and W – alveograph deformation energy (10^{-4} J).

Table 8
Optimization constrains.

Variable	Goal	Lower limit	Upper limit
POE (protein)	Minimize	0.080341	0.195471
POE (moisture)	Minimize	0.0939238	0.325617
POE (wet gluten)	Minimize	0.284115	0.502602
POE (Zeleny)	Minimize	0.862696	270.921
POE (W)	Minimize	547.183	150.494

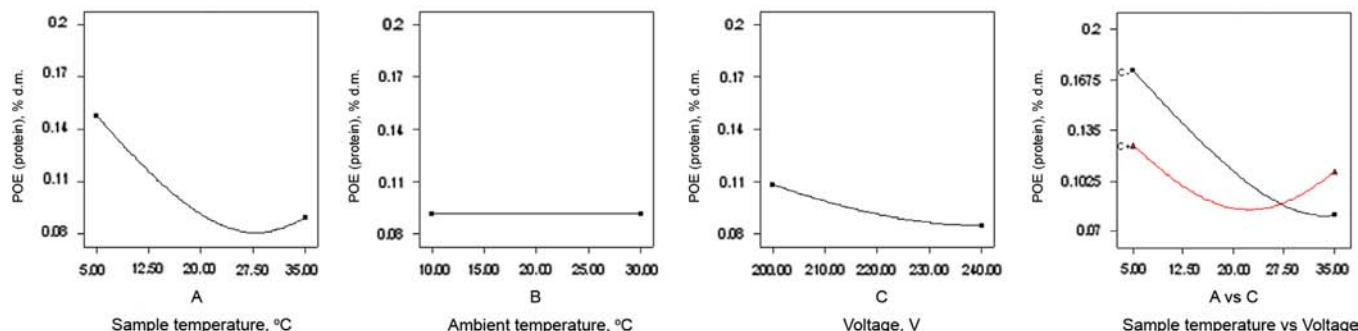


Fig. 2. Main effect plot for POE in protein determination for sample temperature, ambient temperature and voltage, and interaction effects plot for POE in protein determination between sample temperature and voltage.

Table 9
Optimization results.

A	B	C	POE (PC)	POE (MC)	POE (WGC)	POE (Z)	POE (W)	Desirability
19.88	19.26	240	0.084819	0.11904	0.323137	0.895757	7.88986	0.876305
19.96	19.10	240	0.084749	0.119738	0.322999	0.897688	7.868598	0.876291
19.84	19.60	240	0.084851	0.118776	0.323199	0.894928	7.899223	0.876269
20.06	19.48	240	0.084674	0.120508	0.322852	0.89989	7.845184	0.876253
19.93	18.76	240	0.084772	0.11958	0.323048	0.897025	7.875737	0.87623
20.01	17.84	240	0.084716	0.120722	0.322933	0.898642	7.858397	0.875725
20.33	20.98	240	0.084485	0.12355	0.322434	0.906436	7.781084	0.875258
19.24	21.07	240	0.085399	0.115243	0.324146	0.884038	8.043697	0.874912

A – sample temperature (°C); B – ambient temperature (°C); and C – instrument voltage (V).

PC – protein content (% d.m.); MC – moisture content (%); WGC – wet gluten content (%); Z – Zeleny sedimentation value; and W – alveograph deformation energy (10^{-4} J).

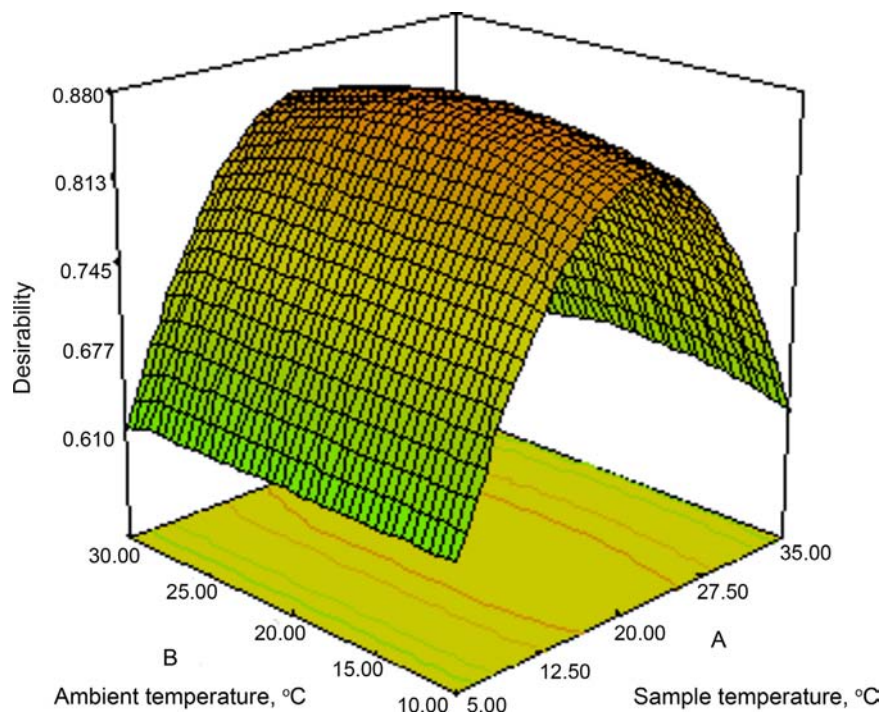


Fig. 4. Three-dimensional response surface plot of the POE in protein determination as a function of sample and ambient temperature at voltage of 240 V.

sample temperature, 19.3 °C for ambient temperature and 240 V for instrument voltage. Fig. 4 shows the graphical desirability for minimization of POE, related to ambient and sample temperature (instrument voltage is set on 240 V), generated from optimum points given in Table 9.

4. Conclusion

Instrument voltage, sample and ambient temperature were designated as significant variables affecting variability in output responses – moisture, protein and wet gluten content, Zeleny sedimentation value and deformation energy. Propagation of error (POE) in conjunction with response surface methodology (RSM) enables the finding of robust operating conditions of near infrared spectrometer whose setting provides the minimal variations of output responses. The minimal variation transmitted to the responses was achieved for sample temperature of 19.9 °C, ambient temperature of 19.3 °C and instrument voltage of 240 V. POE for all observed responses determined by near infrared spectroscopy appeared to be lower than those of standard laboratory methods.

Acknowledgments

This work was financially supported by the Ministry of Education, Science and Technological Development, Republic of Serbia (TR31007).

Appendix A. Supplementary materials

Supplementary data associated with this article can be found in the online version at <http://dx.doi.org/10.1016/j.talanta.2014.07.059>.

References

- [1] M.A. Bezerra, R.E. Santelli, E.P. Oliveira, L.S. Villar, L.A. Escaleira, *Talanta* 76 (2008) 965–977.
- [2] D.C. Montgomery, *Design and Analysis of Experiments*, fifth, John Wiley & Sons Inc., New York, 2001.
- [3] J. Antony, *Design of Experiments for Engineers and Scientists*, Butterworth-Heinemann, New York, 2003.
- [4] Ž.R. Lazić, *Design of Experiments in Chemical Engineering*, WILEY-VCH Verlag GmbH & Co. KGaA, Weinheim, 2004.
- [5] G.E.P. Box, J.S. Hunter, W.G. Hunter, *Statistics for Experimenters*, 2nd ed., John Wiley & Sons Inc., New York, 2005.

- [6] S.L.C. Ferreira, R.E. Bruns, H.S. Ferreira, G.D. Matos, J.M. David, G.C. Brandão, E. G.P. da Silva, L.A. Portugal, P.S. dos Reis, A.S. Souza, W.N.L. dos Santos, *Anal. Chim. Acta* 597 (2007) 179–186.
- [7] B. Dejaegher, Y. Vander Heyden, *J. Pharm. Biomed. Anal.* 56 (2011) 141–158.
- [8] D. Bas, I.H. Boyaci, *J. Food Eng.* 78 (2007) 836–845.
- [9] R.H. Myers, D.C. Montgomery, *Response Surface Methodology – Process and Product Optimization Using Designed Experiments*, 2nd ed., John Wiley & Sons Inc., Canada, 2008.
- [10] J.S. Shenk, J.J. Workman Jr., M.O. Westerhaus, *Application of NIR spectroscopy to agricultural products*, in: D.A. Burns, E.W. Ciurczak (Eds.), *Handbook of Near-Infrared Analysis*, CRC Press, Taylor & Francis Group, Boca Raton, 2008, pp. 347–386.
- [11] W.G. Hansen, S.C.C. Wiedemann, M. Snieder, V.A.L. Wortel, *J. Near Infrared Spectrosc.* 8 (2000) 125–132.
- [12] H. Swierenga, F. Wülfert, O.E. de Noord, A.P. de Weijer, A.K. Smilde, L.M.C. Buydens, *Anal. Chim. Acta* 411 (2000) 121–135.
- [13] J.A. Guthrie, *Robustness of NIR calibrations for assessing fruit quality*, (Ph.D. thesis) Faculty of Arts, Health and Sciences, Central Queensland University, Rockhampton, 2005.
- [14] D. Pérez-Marín, A. Garrido-Varo, E. De Pedro, J.E. Guerrero-Ginel, *Chemometr. Intell. Lab.* 87 (2007) 241–246.
- [15] Y. Vander Heyden, A. Nijhuis, J. Smeyers-Verbeke, B.G.M. Vandeginste, D.L. Massart, *J. Pharm. Biomed.* 24 (2001) 723–753.
- [16] M. Pojić, J. Mastilović, N. Majcen, *Food Chem.* 134 (2012) 1699–1705.
- [17] P. Williams, *Near-infrared spectroscopy of cereals*, in: J.M. Chalmers, P.R. Griffiths (Eds.), *Handbook of Vibrational Spectroscopy*, vol. 5, John Wiley, Chichester, 2002, pp. 3693–3719.
- [18] M.J. Anderson, P.J. Whitcomb, *Robust design – reducing transmitted variation*, *Proceedings from the 50th Annual Quality Congress*, American Society of Quality, Milwaukee (1996) 642–651.
- [19] H. Watzig, *Acceptance criteria and analytical variability*, in: J. Ermer, J.H. McB. Miller (Eds.), *Method Validation in Pharmaceutical Analysis. A Guide to Best Practice*, WILEY-VCH Verlag GmbH & Co. KGaA, Weinheim, 2005, pp. 265–280.
- [20] *Design-Expert, 8 User's Guide*, Stat-Ease, Inc., Minneapolis, 2010.
- [21] P. Whitcomb, *Robust Design, Propagation of Error and Tolerance Analysis*, Webinar, (<http://www.statease.com/training/webinar.html>) (accessed 13.03.14).
- [22] F. Wülfert, W.T. Kok, A.K. Smilde, *Anal. Chem.* 70 (1998) 1761–1767.
- [23] D. Cozzolino, L. Liua, W.U. Cynkar, R.G. Damberg, L. Janik, C.B. Colby, M. Gishen, *Anal. Chim. Acta* 588 (2007) 224–230.
- [24] P. Williams, *Sampling, sample preparation and sample selection*, in: D.A. Burns, E.W. Ciurczak (Eds.), *Handbook of Near-Infrared Analysis*, CRC Press, Taylor & Francis Group, Boca Raton, 2008, pp. 268–295.
- [25] M.J. Anderson, S.L. Kraber, *Cost-effective and information-efficient robust design for optimizing processes and accomplishing Six Sigma objectives*, *Annual Quality Congress Proceedings*, Denver (2003) 141–149.



Hydrogen peroxide biosensor based on microperoxidase-11 immobilized on flexible MWCNTs-BC nanocomposite film



Bingyan Zhang^a, Jianhai Zhou^b, Shaohui Li^a, Xiaofan Zhang^a, Dekang Huang^a, Yahui He^a, Mingkui Wang^a, Guang Yang^{b,*}, Yan Shen^{a,*}

^a Wuhan National Laboratory for Optoelectronics, School of Optoelectronic Science and Engineering, Huazhong University of Science and Technology, Wuhan 430074, P.R. China

^b National Engineering Research Center for Nano-Medicine, College of Life Science and Technology, Huazhong University of Science and Technology, Wuhan, 430074, P.R. China

ARTICLE INFO

Article history:

Received 20 March 2014
Received in revised form
8 July 2014
Accepted 10 July 2014
Available online 18 July 2014

Keywords:

Biosensor
Bacterial cellulose
Multi-walled carbon nanotubes
Microperoxidase-11
H₂O₂ detection

ABSTRACT

In the present work, we report on an experimental study of flexible nanocomposite film for electrochemical detection of hydrogen peroxide (H₂O₂) based on bacterial cellulose (BC) and multi-walled carbon nanotubes (MWCNTs) in combination with microperoxidase-11 (MP-11). MWCNTs are used to functionalize BC and provide a flexible conductive film. On the other hand, BC can improve MWCNTs' biocompatibility. The investigation shows that MP-11 immobilized on the flexible film of MWCNTs-BC can easily present a pair of well-defined and quasi-reversible redox peaks, revealing a direct electrochemistry of MP-11 on the nanocomposite film. The apparent heterogeneous electron-transfer rate constant k_s is estimated to be 11.5 s⁻¹. The resulting flexible electrode presents appreciated catalytic properties for electrochemical detection of H₂O₂, comparing to traditional electrodes (such as gold, glassy carbon electrode) modified with MP-11. The proposed biosensor exhibits a low detection limit of 0.1 μM (at a signal-to-noise ratio of 3) with a linear range of 0.1–257.6 μM, and acquires a satisfactory stability.

© 2014 Elsevier B.V. All rights reserved.

1. Introduction

The detection of hydrogen peroxide (H₂O₂) is of great importance in food and environmental analyses, diagnosis, industry, pharmaceutical laboratories and biological studies. H₂O₂ is harmful for biological systems and appears to be involved in the neuropathology of central nervous system diseases. It has been reported that H₂O₂ induces oxidative stress in CGNs, involving both apoptotic and necrotic death [1]. The increased production of H₂O₂ has been implicated in the pathogenesis of several neurodegenerative diseases, including Parkinson's and Alzheimer's diseases, as well as in the damage produced by ischemia and reperfusion [2]. In the past years, various methods have been developed for determination of H₂O₂, including oxidimetry [3], chemi-luminescence [4,5], surface plasmon resonance [6,7], fluorescence [8], and so on. Among these methods, the electrochemical method offers advantages including simplicity, high reliability, sensitivity, low cost and ease of use [9,10].

In recent years, great attention has been attracted to carbon nanotubes (CNTs) for biosensors application because of its unique

physical, electronic and chemical properties [9–11]. Several studies have demonstrated that CNTs have excellent electro-catalytic abilities and antifouling properties and have the ability to promote electron transfer reactions when they were used as electrode material in electrochemical reactions [12–15]. CNTs have been widely used to detect several biomolecules such as dopamine, H₂O₂ and glucose [16–19]. However, most of CNTs without modification have limitation of poor dispensability and biocompatibility. In order to solve these problems, surface modification with surfactant and chitosan and other methods were introduced [20,21]. Recently, bacterial cellulose (BC) has been received much attention due to its biocompatibility, ultrafine network, and biodegradability compared with plant cellulose [22,23]. BC can be produced with different microorganisms [24]. Biosensors based on nanostructured carbon materials and BC might benefit from their complementary advantage to enhance their biocompatibility. Yoon and Zhou reported that the insulating BC could become conductive by incorporation of CNTs (1.4 × 10⁻¹ S cm⁻¹) and graphite nanoplatelets (1.2 S cm⁻¹), respectively [25,26]. It was demonstrated that horseradish per-oxidase (HRP) immobilized on gold nanoparticles-bacteria cellulose nanofibers nanocomposite showed high performance of detecting H₂O₂ with a wide range of concentration from 0.3 μM to 1.00 mM, and a low detection limit of 0.1 μM based on S/N=3 [27]. Recently, flexible biosensors that can

* Corresponding authors.

E-mail addresses: yang_sunny@yahoo.com (G. Yang), ciac_sheny@mail.hust.edu.cn (Y. Shen).

accommodate dramatic shape changes have got a fast development for the minimally invasive implantable devices and compact diagnostic platforms. Kim et al. first reported a flexible and ultrathin BC–CNTs film as a candidate to the ubiquitously employed glucose oxidase electrodes for glucose detection [28], which demonstrated a successful application for BC as a flexible matrix electrode in bioelectrochemistry.

Several proteins can be used to construct H₂O₂ biosensors, such as microperoxidase-11 (MP-11), HRP, myoglobin and hemoglobin [29,30]. MP-11 is a widely used enzyme for the construction of H₂O₂ biosensors due to its high purity, sensitivity and low cost [31,32]. Herein, we communicate preliminary results on the application of MWCNTs to functionalize BC and provide a flexible conductive film. The resulting flexible MWCNTs–BC film can effectively immobilize the MP-11 and improve the stability of the biosensor compared to the bare MWCNTs, showing high performance for electrochemical detection of H₂O₂.

2. Experimental

2.1. Reagents and apparatus

MWCNTs (diameter 10–20 nm, length 2 μm, purity 97%) were purchased from Chengdu Organic Chemicals Co. Ltd. A fresh aqueous solution of H₂O₂ was prepared daily. All the reagents were of analytical grade and used without purification. The supporting electrolyte used for the electrochemical studies was 0.1 M phosphate buffered solutions (pH 7.0) which were prepared from stock solutions of 0.1 M NaH₂PO₄, 0.1 M Na₂HPO₄, 0.1 M NaCl. H₂O (18 Ω M) was obtained from a Millipore-Q water purification system.

The morphology of prepared materials was examined on a field emission scanning electron microscopy (FE-SEM) (Hitachi S-4800 electron microscope, Hitachi, Japan). The infrared spectra were carried out using a VERTEX 70 Fourier Transform Infrared spectrometer. Raman spectra was carried out using LabRAM HR800 Confocal Raman Spectroscopy, and UV–vis absorption spectroscopic measurements were carried out using a Hitachi U-3300 spectrophotometer.

The measurements of cyclic voltammetry (CV) and amperometric *I*–*t* curve (*I*–*t*) were carried out using a CHI 920C electrochemical analyzer (CHI). A conventional three electrode cell consisting of an Ag/AgCl (3 M KCl) reference electrode and a twisted platinum wire as an auxiliary electrode was employed. All experiments were performed at room temperature.

2.2. Preparation of MWCNTs–BC and MP-11/MWCNTs–BC film flexible electrode

Gluconacetobacter xylinum (ATCC53582) was used for the biosynthesis of BC [33]. The bacterium was cultured in a Hestrin and Schramm (HS) medium, which was composed of 2% (wt) glucose, 0.5% (wt) yeast extract, 0.5% (wt) peptone, 0.27% (wt) disodium phosphate, and 0.15% (wt) citric acid. After having been incubated statically at 26 °C for 14 days, the BC membranes were formed and then dipped in distilled water and NaOH solution, respectively. The pH was lowered to 7.0 by washing with distilled water. The purified cellulose pellicles were stored in distilled water at 4 °C to avoid drying. Then some pieces of the purified cellulose pellicles were put into the sulfuric acid solution (40%). Afterwards, the obtained BC whiskers were centrifuged and dialyzed in deionized water successively for further purified to get 0.3% BC whiskers aqueous solution. 5 mg mL⁻¹ MWCNTs aqueous suspension was added into BC whiskers aqueous solution to get a uniformly mixed solution and then put it filtered. Finally, the flexible conductive

MWCNTs–BC films were produced, and the mass ratio of BC and MWCNTs was 1:10. Then the film was cut into suitable shape. The obtained flexible film was immersed in the PBS solution containing 1 mg mL⁻¹ MP-11 (pH 7.0) for 16 h, and then the MP-11 molecular was immobilized onto the surface of MWCNTs–BC film. The final modified flexible film was washed with deionized water for several times.

2.3. Platelet adhesion studies

The platelet-rich plasma (PRP) was purchased from Pingrui Biotechnology Company (Beijing, China), and the experimental method has been reported by Meyerhof [23c]. Briefly, BC–MWCNTs was preincubated at 37 °C for 20 min. BC–MWCNTs film previously conditioned in phosphate-buffered saline (PBS, containing 10 mM phosphate, 138 mM sodium chloride, and 2.7 mM potassium chloride, pH 7.4) for 3 days were immersed in PRP for 2 h at 37 °C. It was then rinsed in PBS and fixed in a PBS solution containing 2.0% (w/v) glutaraldehyde for 2 h at room temperature. Samples were dehydrated by immersion in serial dilutions of ethanol (30, 50, 70, 90, and 95% v/v), two immersions in absolute ethanol.

3. Results and discussion

3.1. Characterization of the MWCNTs–BC and MP-11/MWCNTs–BC flexible film electrode

The surface morphology of MWCNTs, BC and MWCNTs–BC films were examined by field emission scanning electron microscopy (FE-SEM). The pure MWCNTs with a diameter of about 15–20 nm was evenly spread out, that result in a uniform sample as shown in Fig. 1(a). BC whisker film with ultra-fine network is shown in Fig. 1(b), which leads it to be a good candidate for flexible substrate. Fig. 1c presented the morphology of MWCNTs–BC composite film. It was observed that the diameter of MWCNTs was obviously bigger than BC, and MWCNTs were well-incorporated and distributed within the BC. The BC hydrogel itself works as a nano-sized filter. CNTs efficiently infiltrated into a network of BC when they were filtered through BC hydrogel by vacuum [28].

Fig. 1(d) shows the tensile property for the flexible film substrate tested by HY-0230 electronic universal material testing machine. The result demonstrated that the max stress was about 52.36 MPa for the flexible film with a stretch distance of 1.1 mm, although the thickness of the BC–MWCNTs film was only about 135.2 μm. It indicated that the flexible film performed a good mechanical property.

Fourier transform infrared (FTIR), Raman, and UV–visible spectrum measurements were performed to clearly characterize MWCNTs–BC film. As shown in Fig. 2a, the appearance of the peaks at 1305, 1418, 1625, 1717, 2886 and 3220 cm⁻¹ were assigned to C–O, –CH₂–, C=C, –COOH, C–H and O–H vibrations, respectively. MP-11 molecular has functional groups, including –COOH, O–H, and –NH₂. It is worthy noted that the carboxyl group from MWCNTs induced by concentrated nitric acid (HNO₃, 68%) treatment is beneficial to the adsorption of MP-11 onto MWCNTs surface, and the hydroxyl group from BC is beneficial to the combination to MWCNTs. Fig. 2b shows Raman spectra of MWCNTs–BC film, exhibiting two prominent peaks at 1363 and 1596 cm⁻¹, corresponding to the disorder (D band) and the crystalline (G band) graphite, respectively. This indicates the structure of MWCNTs is not affected by BC. The UV–visible spectrum revealed that MP-11/MWCNTs–BC film presents a Soret band at 408 nm. The corresponding Soret band of MP-11 in solution with 0.2 μM was found at 402 nm (Fig. 2c). The bathochromic

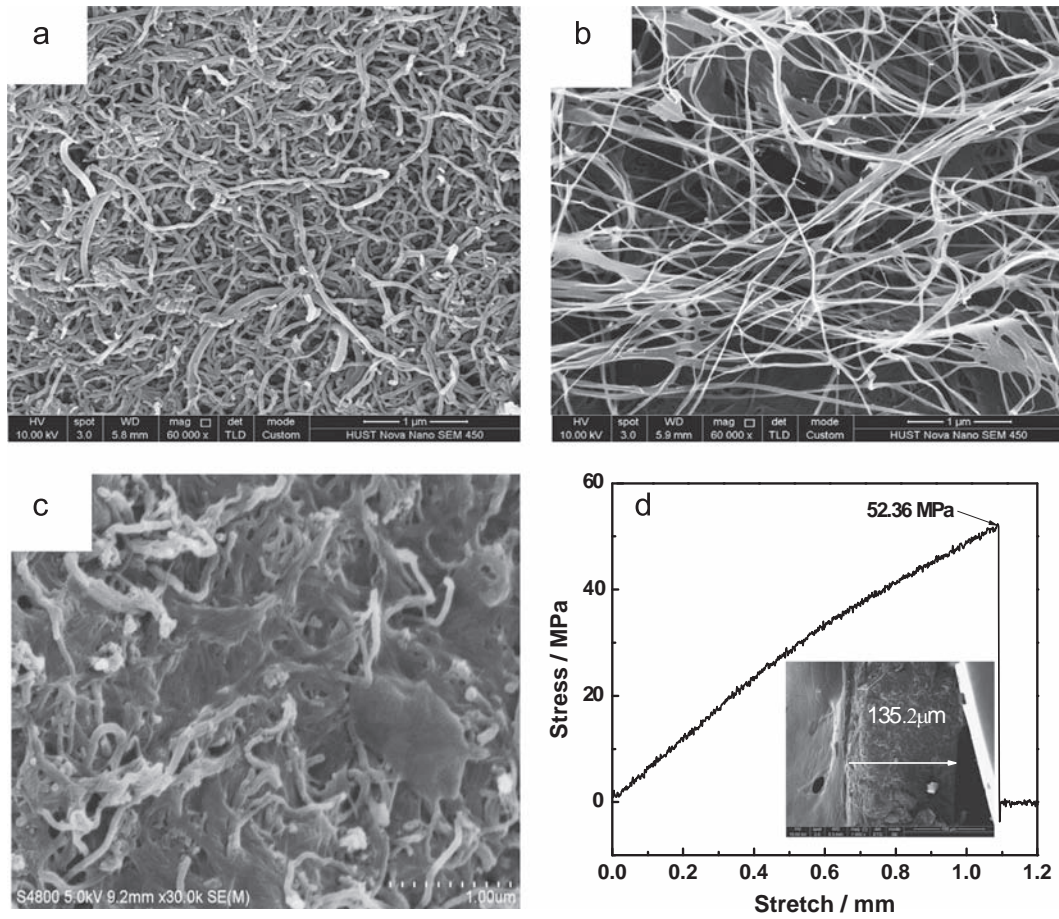


Fig. 1. Field-emission scanning electron micrographs: (a) MWCNTs, (b) pure BC, (c) MWCNTs-BC film, and (d) tensile properties test and the cross section of MWCNTs-BC film.

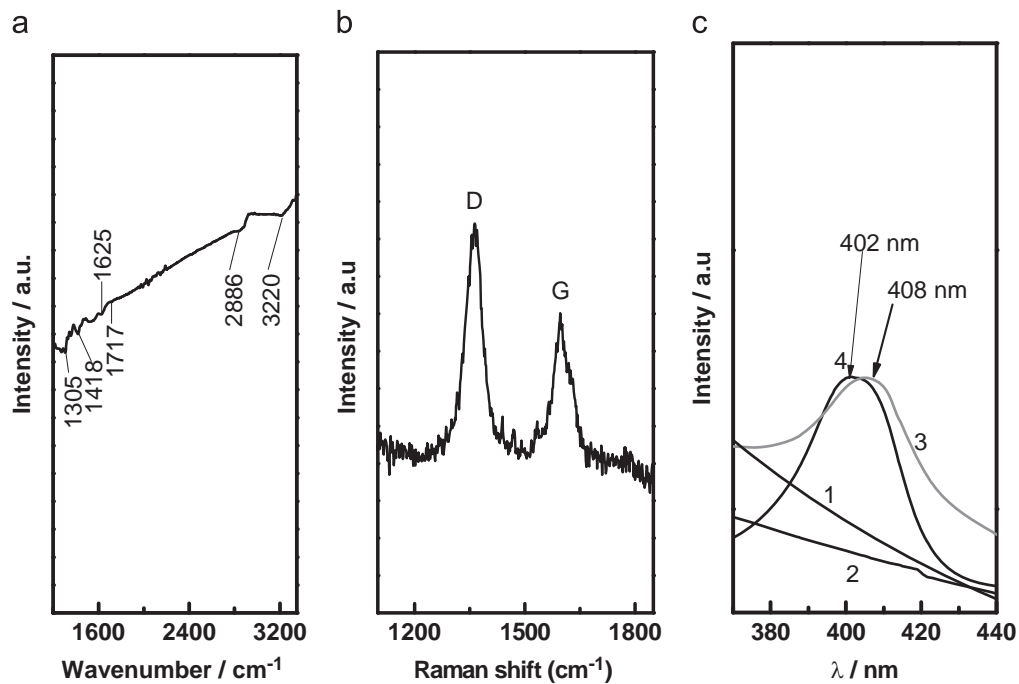


Fig. 2. Normalized intensity of (a) Fourier transform infrared spectra, (b) Raman spectra for BC-MWCNTs, and (c) UV-vis absorption spectra of 1-BC, 2-MWCNTs-BC, 3-MP-11/MWCNTs-BC and 4-MP-11 aqueous solution with 0.2 μM.

shift may be attributed to the aggregation of the adsorbed MP-11 molecules onto substrate [34,35]. The blank experiments on BC and MWCNTs-BC samples presented featureless adsorption in the wavelength range. This result indicated that the flexible composite electrode of MWCNTs-BC was an ideal substrate for adsorption of MP-11 molecules.

3.2. Electrochemical characterization of MP-11 on the flexible MWNTs-BC film electrode

Fig. 3a and b shows the cyclic voltammograms (CVs) obtained at the MWCNTs (dotted line), MP-11/MWCNTs film electrode (dashed line) and MP-11/MWCNTs-BC film electrode (solid line) in 0.1 M N₂-saturated PBS solution (pH 7.0) with and without 2 mM H₂O₂ at a scan rate of 50 mV s⁻¹. CV of MP-11/MWCNTs-BC electrode clearly illustrated a pair of redox peaks at a potential (E^0) of -0.33 V with a very low peak to peak separation (ΔE_p) of 50 mV. Under the similar condition, MP-11/MWCNTs presented a wider ΔE_p (Fig. 3a). Obviously, this redox couple corresponds to the direct electron transfer (DET) of MP-11 onto MWCNT-BC film electrode. Meanwhile, MP-11/MWCNTs-BC electrode showed a better catalytic performance to H₂O₂ compared to MP-11/MWCNTs and MWCNTs electrode (Fig. 3b). The effect of scan rate on the voltammetric response of MP-11 was examined in 0.1 M N₂-saturated PBS of pH 7.0. A good linear relationship between the peak currents versus scan rates (Fig. 3c, inset) indicates the

electron transfer of the flexible electrode being a surface-controlled process. The amount of electro-active enzyme on the electrode surface (Γ) can be evaluated from the slope of peak currents plotted versus scan rate by the following Eq. (1) [36]:

$$I_p = n^2 F^2 \nu A \Gamma / (4RT) \quad (1)$$

where ν is the scan rate, A is the active area of the working electrode, n is the number of electron per reactant molecule, respectively. F , R and T are the constants. In the present case, the calculated surface coverage for the electro-active species was 1.17×10^{-9} mol cm⁻², which is higher than MP-11/MWCNTs (8.4×10^{-10} mol cm⁻²) [31], MP-11/AuNPs/MWCNTs (5.93×10^{-10} mol cm⁻²) [32]. This result could be caused by the network structure of BC, which promotes the adsorption of MP-11 onto the MWCNTs with three-dimensional microstructure. As shown in Fig. 3c, both I_{pa} and I_{pc} increased linearly upon increasing the scan rates from 10 to 200 mV s⁻¹. For scan rates from 0.01 to 1.2 V s⁻¹, the electrochemical response of MP-11 shows a quasi-reversible process. With the increasing of the scan rate, the reduction peak shifted negatively and the oxidation peak shifted positively with ΔE less than 200 mV. According to the Laviron's equation for quasi-reversible thin-layer electrochemistry when the $n \times \Delta E < 200$ mV, the apparent heterogeneous electron transfer rate constant (k_s) could be calculated with the following equations [37]:

$$E_{pc} = E^0 - \frac{2.3RT}{\alpha nF} \log \nu \quad (2)$$

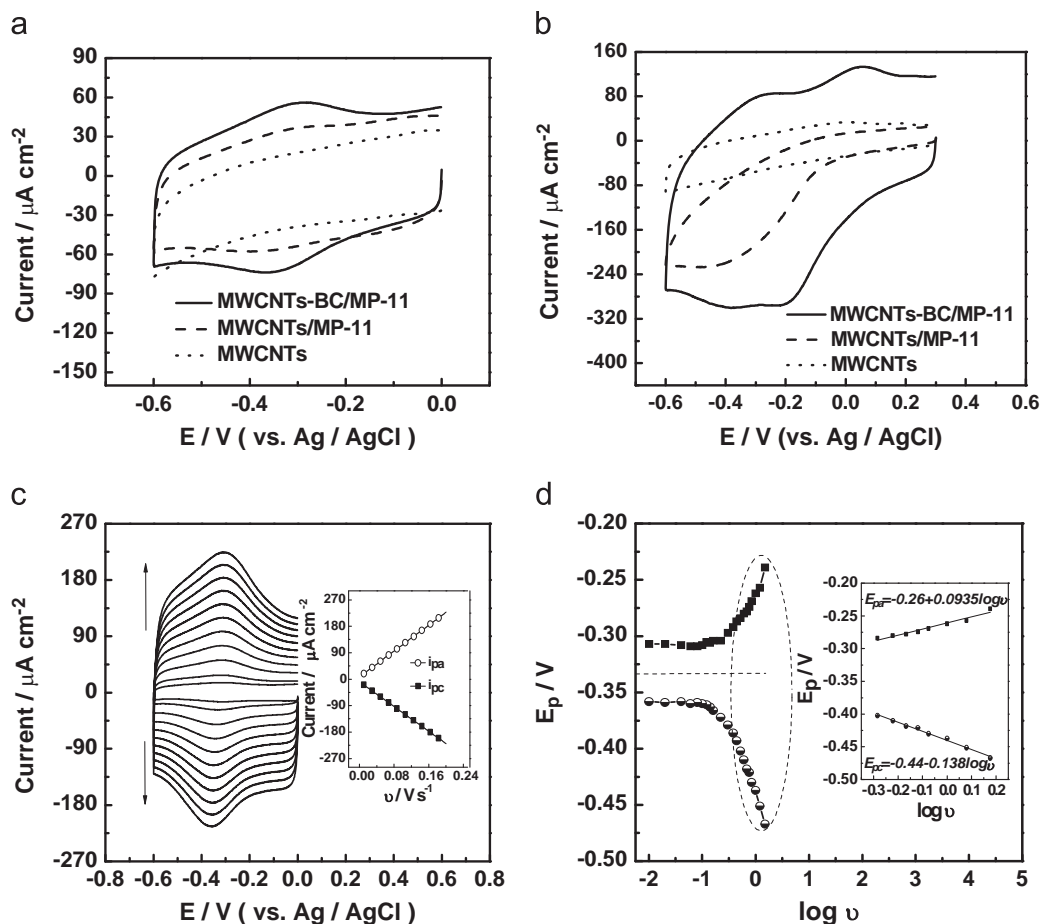


Fig. 3. Cyclic voltammetric responses at MWCNTs-BC film (dot line), MP-11/MWCNTs film electrode (dash line), and MP-11/MWCNTs-BC film electrode (solid line), in N₂-saturated solution (0.1 M PBS, pH 7.0), without H₂O₂ (a), and with 2 mmol L⁻¹ H₂O₂ (b), scan rate, 50 mV s⁻¹, (c) CVs of MP-11/MWCNTs-BC film in 0.1 M PBS (pH 7.0) at different scan rates (from inner to outer: 10, 20, 40, 60, 80, 100, 120, 140, 160, 180, 200 mV s⁻¹), in N₂-saturated solution (0.1 M PBS, pH 7.0). Inset is the plot of cathodic and anodic peak current vs. scan rate; (d) plots of anodic peak potential and cathodic peak potential against the logarithm of scan rate. Inset is linear dependence of E_{pa} and E_{pc} on $\log \nu$.

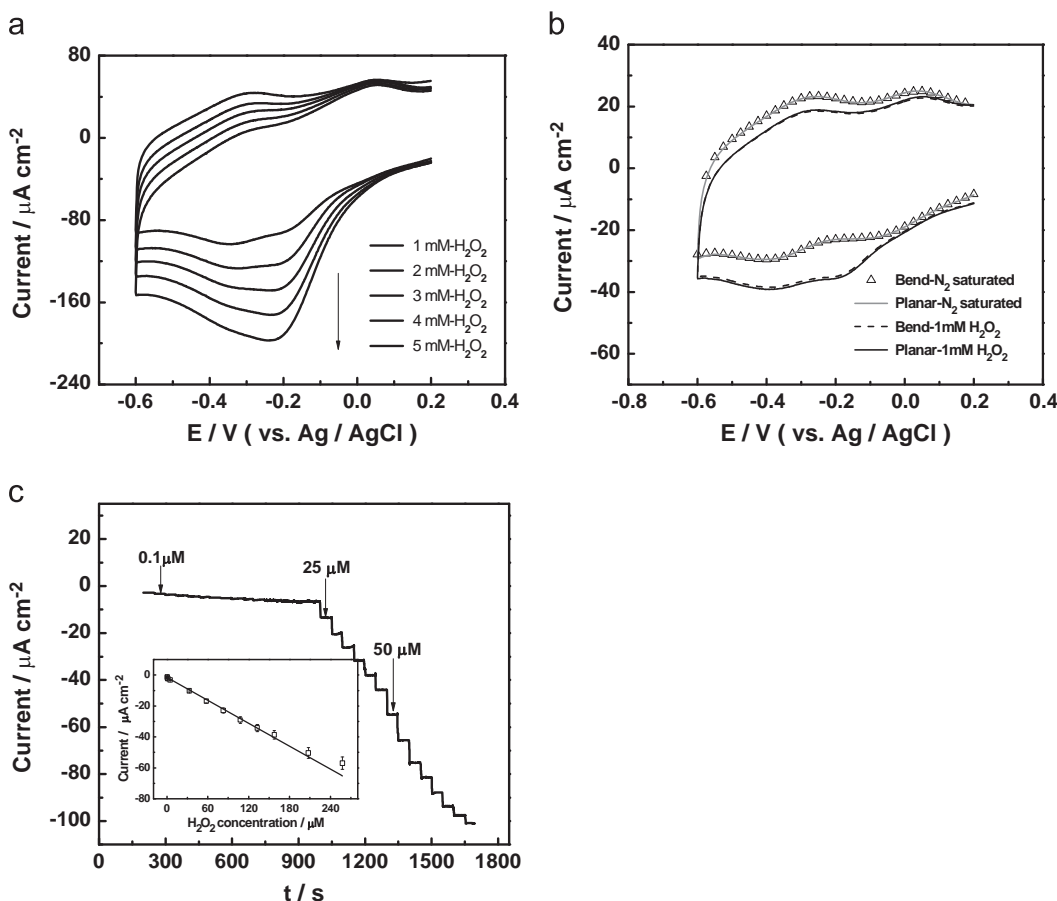


Fig. 4. Cyclic voltammograms of MP-11/MWCNTs-BC film electrode in N_2 -saturated PBS solution (0.1 M, pH 7.0), scan rate, 50 mV s^{-1} : (a) with different concentrations of 1 mmol, 2 mmol, 3 mmol, 4 mmol, 5 mmol H_2O_2 , and (b) with 1 mM H_2O_2 at two different shapes of bend and planar; (c) amperometric $I-t$ response of the hydrogen peroxide biosensor upon addition of H_2O_2 , applied potential of -0.3 V . Inset is the linear relationship between catalytic current and the concentration of H_2O_2 , in N_2 -saturated solution (0.1 M PBS, pH 7.0).

$$E_{pa} = E^{0'} - \frac{2.3RT}{(1-\alpha)nF} \log v \quad (3)$$

$$\log k_s = \alpha \log(1-\alpha) + (1-\alpha) \log \alpha - \log \frac{RT}{nFv} - \frac{nF\Delta E_{pa}(1-\alpha)}{2.3RT} \quad (4)$$

The relationship between ΔE_p and $\log v$ was calculated and shown in Fig. 3d. From the slope and the intercept, the values of n and α were evaluated to be 1.06 and 0.4, respectively, indicating a reversible one electron concerned electrochemical reaction. From the eq. (4), the value of k_s was calculated to be 11.5 s^{-1} . This is close to the best result among the previous reports [31,34]. The large rate constant informs a fast electron transfer between redox active sites of enzyme and the MWCNTs-BC flexible electrode surface. This result could be attributed to MP-11 remains highly redox activity due to the strong hydrophilic property of BC, which enhances the biocompatibility of BC-MWCNTs film. The assessment for the biocompatibility of the composite film has been performed using platelet adhesion study [23b,23c]. Fig. S1 shows the morphology of bare MWCNTs and MWCNTs-BC composite film before and after 2 h contact with platelet-rich plasma (FRP). We can clearly see that the morphology of MWCNTs-BC composite film has no any change after 2 h contact with platelet. However, the morphology of bare MWCNTs has a significant change. It means that more platelet adhered to the bare MWCNTs film, but no platelet adhered to MWCNTs-BC composite film. This confirmed that BC has big effect on the biocompatibility of the composite film.

3.3. Electrochemical detection of H_2O_2 on the flexible MP-11/MWCNTs-BC film electrode

Fig. 4a shows the electro-catalytic response of the prepared flexible electrode towards H_2O_2 in 0.1 M N_2 -saturated PBS. With a consecutive addition of H_2O_2 from 1 mM to 5 mM, the cathodic peak current increased. It is significant that there is nearly no difference in the cyclic voltammetric response for the flexible electrodes at a bended and planar shape in N_2 -saturated solution (0.1 M PBS, pH 7.0) with or without H_2O_2 (Fig. 4b). The first redox couple near 0 V (vs. Ag/AgCl) can be due to MWCNTs, the other one near at -0.3 V (vs. Ag/AgCl) being the quasi-reversible process of MP-11. And the peak at -0.2 V (vs. Ag/AgCl) is from the reduction of H_2O_2 . Fig. 4c displays the amperogram at a MP-11/MWCNT-BC film electrode with an applied electrode potential (E_{app}) of -0.3 V . H_2O_2 solution was injected sequentially into the continuously stirred PBS at regular intervals (50 s). Well-defined amperometric responses were observed for the each addition of H_2O_2 . The amperometric response current increased linearly with H_2O_2 concentration increasing in the ranges of 0.1–257.6 μM as shown in the calibration plot (Fig. 4c). The linear regression equation can be expressed as $I_p (\mu\text{A cm}^{-2}) = -1.53 - 0.247[H_2O_2] (\mu\text{M})$ ($R=0.998$). The limit of detection (LOD) and sensitivity were calculated to be 0.1 μM and $0.247 \text{ A mol}^{-1} \text{ cm}^{-2}$ based on a signal/noise ratio of 3, suggesting that H_2O_2 could be easily detected at a very low concentration using the flexible film electrode. The fabricated sensor exhibited a wide linear range of 0.1–257.6 μM for H_2O_2 detection compared with that of MP-11/

MWCNTs (3.3–38.4 μM) [31], HRP-PTBA@RTIL (5–175 μM) [38], Hb-AgNPs/CS (0.75–216 μM) [39] and HRP-SnO₂ nanorod array (0.8–35 μM) [40]. In addition, the flexible electrode possessed low detection limit of 0.1 μM , comparatively lower than that of MP-11/MWCNTs (0.7 μM) [31], MP-11-DMPG-G (0.72 μM) [35], HRP-Sb-doped SnO₂ (0.8 μM) [41], HRP-SnO₂ nanorod array (0.2 μM) [40].

The apparent Michaelis–Menton constant (K_M) as one of indication of the enzyme–substrate kinetics, can be estimated with the Lineweaver–Burk equation [42]

$$1/I_{ss} = 1/I_{max} + (K_M/I_{max})(1/C_{H_2O_2}) \quad (5)$$

where I_{ss} is the steady-state current after the addition of substrate, C is the bulk concentration of the substrate, I_{max} is the maximum current measured under saturated substrate condition, respectively. The K_M value for MP-11/MWCNTs–BC film electrode for H₂O₂ detection was calculated to be 0.419 mM. This result is lower than that of MP-11/MGN-CHI/Au (0.54 mM) [43]. The low value of K_M indicates that MP-11 molecules on the BC–MWCNTs thin films retain their bioactivity and have high affinity for H₂O₂.

3.4. Reproducibility and stability studies

The reproducibility of the biosensors was evaluated with five electrodes via comparing their amperometric current response to H₂O₂ independently. The result showed a good reproducibility with a relative standard deviation of 2.67% for the currents determined at a H₂O₂ concentration of 2.0 mM. In order to measure the stability of the system, the flexible MP-11/MWCNTs–BC film electrode was examined by monitoring the remained amount of current response for amperometric I – t response of the H₂O₂. It was found that the peak current for 25 μM H₂O₂ reduction retained 94% of its initial value after bending for 2 days, but only 82% for MP-11/MWCNTs electrode. This indicates that he adsorbed MP-11 on the surface of MWCNTs–BC film electrode is more stable compared with the pure MWCNTs film electrode.

4. Conclusion

In summary, the present study has demonstrated a flexible film electrode based on MP-11 and MWCNTs–BC nanocomposite film for electrochemical detection of H₂O₂. The obtained flexible film electrode, taking advantage of BC's unique three-dimensional structure and biocompatibility, provides a suitable microenvironment for immobilization of MP-11 and retaining its intrinsic structure and biological activity. The MP-11 immobilized on flexible MWCNTs–BC film electrode has realized its direct electrochemistry and shows a good stability and redox activity. The kinetic rate constants ($k_s = 11.5 \text{ s}^{-1}$, $\alpha n = 0.4$) and a detection limit as low as 0.1 μM are obtained. This facile, general and inexpensive approach for redox proteins immobilization is applied as a promising platform for the fabrication of biosensors and bioelectronic devices.

Acknowledgments

Financial support from the 973 Program of China (2013CB922104, 2014CB643506, 2011CBA00703), the NSFC (21103057, 21161160445, 21173091), the Fundamental Research Funds for the Central Universities (HUST: CXY12Q022), is gratefully acknowledged. The authors thank the Analytical and Testing Centre at the HUST for performing characterization of various samples. Y. Shen thanks

Oldenburg University for supporting visiting. Thanks Professor Jianhua Xiao, who has provided a lot of help for this work.

Appendix A. Supporting information

Supplementary data associated with this article can be found in the online version at <http://dx.doi.org/10.1016/j.talanta.2014.07.027>.

References

- [1] A.A. Fatokun, T.W. Stone, R.A. Smith, *Brain Res.* 1132 (2007) 193–202.
- [2] E.A. Mazzi, K.F. Soliman, *Neurochem. Res.* 28 (2003) 733–741.
- [3] E.C. Hurdiss, H. Romeyn, *J. Anal. Chem.* 26 (1954) 320–325.
- [4] G.L. Kok, T.P. Holler, M.B. Lopez, A.H. Nachtrieb, M. Yuan, *Environ. Sci. Technol.* 12 (1978) 1072–1076.
- [5] Y.B. Tsaplev, *Anal. Chem.* 67 (2012) 506–514.
- [6] Y. Mao, Y. Bao, W. Wang, Z. Li, F. Li, L. Niu, *Talanta* 85 (2011) 2106–2112.
- [7] P. Vasileva, B. Donkova, I. Karadjova, C. Dushkin, *Colloids Surf. A: Physicochem. Eng. Asp.* 382 (2011) 203–210.
- [8] Y. Gao, G. Wang, H. Huang, J. Hu, S.M. Shah, X. Su, *Talanta* 85 (2011) 1075–1080.
- [9] C. Hu, S. Hu, *J. Sens.* 2009 (2009) 1–40.
- [10] J. Qu, Y. Shen, X. Qu, S. Dong, *Chem. Commun.* (2004) 34–35.
- [11] X. Zhao, R. Liu, *Environ. Int.* 40 (2012) 244–255.
- [12] M.G. Zhang, A. Smith, W. Gorski, *Anal. Chem.* 76 (2004) 5045–5050.
- [13] F. Patolsky, Y. Weizmann, I. Willner, *Angew. Chem. Int. Ed.* 43 (2004) 2113–2117.
- [14] M. Wang, F. Zhao, Y. Liu, S. Dong, *Biosens. Bioelectron.* 21 (2005) 159–166.
- [15] S. Liu, C. Cai, *J. Electroanal. Chem.* 602 (2007) 103–114.
- [16] J. Wan, J. Bi, P. Du, S. Zhang, *Anal. Biochem.* 386 (2009) 256–261.
- [17] S. Deng, G. Jian, J. Lei, Z. Hu, H. Ju, *Biosens. Bioelectron.* 25 (2009) 373–377.
- [18] J.M. You, Y.N. Jeong, M.S. Ahmed, S.K. Kim, H.C. Choi, S. Jeon, *Biosens. Bioelectron.* 26 (2011) 2287–2291.
- [19] B. Zhang, D. Huang, X. Xu, G. Alemu, Y. Zhang, F. Zhan, Y. Shen, M. Wang, *Electrochim. Acta* 91 (2013) 261–266.
- [20] K. Wusiman, H. Jeong, K. Tulugan, H. Afrianto, H. Chung, *Int. Commun. Heat Mass Trans.* 41 (2013) 28–33.
- [21] R.M. Santos, M.S. Rodrigues, J. Laranjinha, R.M. Barbosa, *Biosens. Bioelectron.* 44 (2013) 152–159.
- [22] M. Iguchi, S. Yamanaka, A. Budhiono, *J. Mater. Sci.* 35 (2) (2000) 261–270.
- [23] (a) F.K. Andrade, N. Alexandre, I. Amorim, F. Gartner, A.C. Mauricio, A.L. Luis, M. Gama, *J. Bioact. Compat. Polym.* 28 (2012) 97–112;
- (b) M.J. Berrocal, I.H.A. Badr, D.Y. Gao, L.G. Bachas, *Anal. Chem.* 73 (2001) 5328–5333;
- (c) C.E. Tom, M.E. Meyerhoff, *Anal. Chem.* 67 (1995) 3108–3114.
- [24] D. Klemm, F. Kramer, S. Moritz, T. Lindstrom, M. Ankerfors, D. Gray, A. Dorris, *Angew. Chem. Int. Ed. Engl.* 50 (2011) 5438–5466.
- [25] S.H. Yoon, H.J. Jin, M.C. Kook, Y.R. Pyun, *Biomacromolecules* 7 (2006) 1280.
- [26] T. Zhou, *Express Polym. Lett.* 7 (2013) 756–766.
- [27] W. Wang, T.J. Zhang, D.W. Zhang, H.Y. Li, Y.R. Ma, L.M. Qi, Y.L. Zhou, X.X. Zhang, *Talanta* 84 (2011) 71–77.
- [28] Y.H. Kim, S. Park, K. Won, H.J. Kim, S.H. Lee, *J. Chem. Technol. Biotechnol.* 88 (2013) 1067–1070.
- [29] J. Yu, T. Zhao, F. Zhao, B. Zeng, *Electrochim. Acta* 53 (2008) 5760–5765.
- [30] C.J. Mao, X.B. Chen, H.L. Niu, J.M. Song, S.Y. Zhang, R.J. Cui, *Biosens. Bioelectron.* 31 (2012) 544–547.
- [31] M. Wang, Y. Shen, Y. Liu, T. Wang, F. Zhao, B. Liu, S. Dong, *J. Electroanal. Chem.* 578 (2005) 121–127.
- [32] Y. Liu, M. Wang, F. Zhao, Z. Guo, H. Chen, S. Dong, *J. Electroanal. Chem.* 581 (2005) 1–10.
- [33] Z. Shi, S. Zang, F. Jiang, L. Huang, D. Lu, Y. Ma, G. Yang, *RSC Adv.* 2 (2012) 1040.
- [34] C. Renault, C.P. Andrieux, R.T. Tucker, M.J. Brett, V. Balland, B. Limoges, *J. Am. Chem. Soc.* 134 (2012) 6834–6845.
- [35] J. Liu, L. Han, T. Wang, W. Hong, Y. Liu, E. Wang, *Chem. Asian J.* 7 (2012) 2824–2829.
- [36] A.J. Bard, L.R. Faulkner, *Electrochemical Methods*, 2nd ed., John Wiley & Sons, New York, 2001.
- [37] E. Laviron, *J. Electroanal. Chem.* 101 (1979) 19–22.
- [38] L. Cui, M. Xu, J. Zhu, S. Ai, *Synth. Met.* 161 (2011) 1686–1690.
- [39] C. Yu, X. Zhou, H. Gu, *Electrochim. Acta* 55 (2010) 8738–8743.
- [40] J. Liu, Y. Li, X. Huang, Z. Zhu, *Nanoscale Res. Lett.* 5 (2010) 1177–1181.
- [41] L. Li, J. Huang, T. Wang, H. Zhang, Y. Liu, J. Li, *Biosens. Bioelectron.* 25 (2010) 2436–2441.
- [42] R. Kamin, G. Wilson, *Anal. Chem.* 52 (1980) 1198–1205.
- [43] Y. Zhou, S. Liu, H. Jiang, H. Yang, H. Chen, *Electroanalysis* 22 (2010) 1323–1328.



Surface exploration of a room-temperature ionic liquid-chitin composite film decorated with electrochemically deposited PdFeNi trimetallic alloy nanoparticles by pattern recognition: An elegant approach to developing a novel biotin biosensor

Mohammad-Bagher Gholivand^{a,*}, Ali R. Jalalvand^{a,b}, Hector C. Goicoechea^b, Giti Paimard^a, Thomas Skov^c

^a Faculty of Chemistry, Razi University, Kermanshah 671496734, Iran

^b Laboratorio de Desarrollo Analítico y Quimiometría (LADAQ), Cátedra de Química Analítica I, Universidad Nacional del Litoral, Ciudad Universitaria, CC 242 (S3000ZAA) Santa Fe, Argentina

^c Quality & Technology, Department of Food Science, Faculty of Science, University of Copenhagen, Copenhagen, Denmark

ARTICLE INFO

Article history:

Received 27 March 2014

Received in revised form

12 July 2014

Accepted 15 July 2014

Available online 8 August 2014

Keywords:

Biotin

Chitin

Electrodeposition

Trimetallic alloy nanoparticles

Digital image processing

ABSTRACT

In this study, a novel biosensing system for the determination of biotin (BTN) based on electrodeposition of palladium-iron-nickel (PdFeNi) trimetallic alloy nanoparticles (NPs) onto a glassy carbon electrode (GCE) modified with a room-temperature ionic liquid (RTIL)-chitin (Ch) composite film (PdFeNi/ChRTIL/GCE) is established. NPs have a wide range of applications in science and technology and their sizes are often measured using transmission electron microscopy (TEM) or X-ray diffraction. Here, we used a pattern recognition method (digital image processing, DIP) for measuring particle size distributions (PSDs) from scanning electron microscopic (SEM) images in the presence of an uneven background. Different depositions were performed by varying the number of cyclic potential scans (N) during electroreduction step. It was observed that the physicochemical properties of the deposits were correlated to the performance of the PdFeNi/ChRTIL/GCE with respect to BTN assay. The best results were obtained for eight electrodeposition cyclic scans, where small-sized particles (19.54 ± 6.27 nm) with high density (682 particles μm^{-2}) were obtained. Under optimized conditions, a linear range from 2.0 to 44.0×10^{-9} mol L^{-1} and a limit of detection (LOD) of 0.6×10^{-9} mol L^{-1} were obtained. The PdFeNi/ChRTIL nanocomposite showed excellent compatibility, enhanced electron transfer kinetics, large electroactive surface area, and was highly sensitive, selective, and stable toward BTN determination. Finally, the PdFeNi/ChRTIL/GCE was satisfactorily applied to the determination of BTN in infant milk powder, liver, and egg yolk samples.

© 2014 Elsevier B.V. All rights reserved.

1. Introduction

Biotin (BTN, also called vitamin B6, B7 or H, Fig. 1) is a water-soluble vitamin and an essential co-factor for five BTN-dependent carboxylase enzymes. It is synthesized in a wide variety of bacteria and plants. However, several microorganisms as well as higher animals are notable to synthesize it and their needs in this vitamin are met by dietary intake [1]. Besides the typical clinical features, recent evidence indicates that the pregnant women develop BTN deficiency during normal pregnancy [2,3].

Although a maximum level of BTN in food is not specified, 1.5 mg in 100 kcal is recommended by the current regulation in infant formula in substitution of breast-milk to satisfy the nutritional requirements of infants during the first months of life [4]. Consequently, the diagnosis of BTN deficiency and the monitoring of its levels in patients receiving BTN treatment are important issues as well as its determination in foods and food supplement products. For this reason, analytical methods were developed in order to determine BTN in biological fluids as well as in food products and pharmaceutical preparations [5–10]. The analytical techniques for biotin determination can be divided into four main categories: (1) Microbiological methods, based on growth of microorganisms in presence of BTN, are very sensitive but they lack specificity and they are very time-consuming [11]. (2) Biological techniques are based on the animal development curve. These are used mainly for the determination of BTN in food [11]. (3) Binding

* Corresponding author. Tel.: +98 831 4274557; fax: +98 831 4274559.

E-mail addresses: mbgholivand2013@gmail.com, mbgholivand@yahoo.com (M.-B. Gholivand).

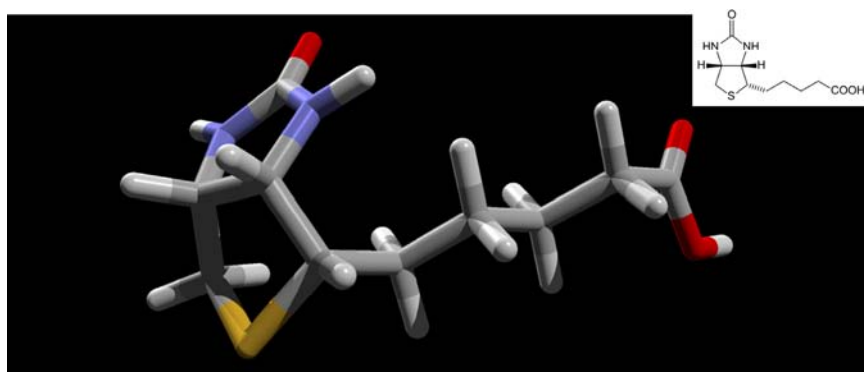


Fig. 1. Molecular structure of BTN.

assays make use of formation of a specific avidin (or streptavidin)–BTN complex [11]. (4) The last group of methods includes all physicochemical methods such as spectrophotometry, polarography, thin layer chromatography, gas chromatography, high performance liquid chromatography and capillary zone electrophoresis [11,12]. However, these methods suffer from some disadvantages such as high costs, long analysis times and requirement for sample pretreatment, and in some cases low sensitivity and selectivity that makes them unsuitable for routine analysis. To overcome these defects, electrochemical methods which are low costs are used extensively for the elegant and sensitive properties such as selectivity, simplicity, repeatability, and reproducibility [13–17].

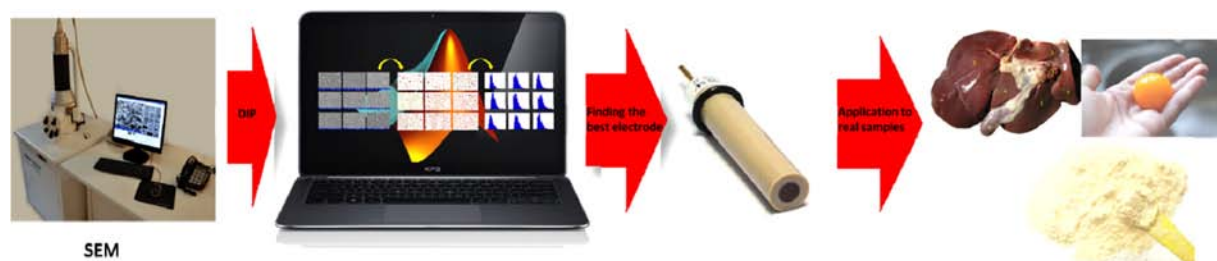
Chitin (Ch) is the second most abundant polysaccharide in biomass after cellulose with excellent film forming ability, biocompatibility, nontoxicity, good water permeability and high mechanical strength. Ch production was about 25,000 t in 2006 [18]. This polymer is a linear chain consisting of poly $\beta(1 \rightarrow 4)$ -N-acetyl-*D*-glucosamine. Ch is usually isolated from the exoskeletons of crustaceans and more particularly from shrimps and crabs where α -chitin isomorph is produced [19]. Ch is largely widespread in biomass [20], and its main application is in the production of its water-soluble derivative chitosan. Ch and chitosan have exactly the same chemical structure, corresponding to the series of linear copolymers of (1 \rightarrow 4)-2-amino-2-deoxy- β -*D*-glucan and (1 \rightarrow 4)-2-acetamido-2-deoxy- β -*D*-glucan. Ch can accumulate metal ions through various mechanisms, such as chelation, electrostatic attraction, and ion exchange, depending on the nature of the metal ion and pH of the solution.

Room-temperature ionic liquids (RTILs) are liquid (molten) salts that exist for certain salts in a liquid state at and above room-temperature because of the particular kinds of interactions between certain cations and anions. In recent years, the research and development of RTILs to achieve the functions of low-flammability, low volatility, low-viscosity, and high electrochemical stability have been actively promoted [21–24]. Against such a background, applications such as various electrochemical devices (lithium secondary batteries [25–28], fuel cells [28,29], electric double-layer capacitors [30], dye-sensitized solar cells [31], field-effect transistors [32,33] etc.), tribology solvents [34], synthetic solvents [35], and biomass solvents [36] as functional uses of RTILs have been developed.

Nanoparticles (NPs) have been used extensively in the fields of physical, chemical and material sciences in the past few years [37]. These materials having a high specific surface area, large pore size and unique features, such as surface plasmon absorption, improved magnetic property, high reactivity, and enhanced catalytic activity [38]. They are also expected to show advantages for use as electrocatalysts due to their large active surface areas, small catalyst loading and abilities to prevent aggregation between particles [39]. Among the nanoparticles, metal nanoparticles are objects of great interest in modern chemistry and materials research, where they

find application in such diverse fields as photochemistry, nanoelectronics, optics, catalysis and electrocatalysis [40]. Their sizes are commonly linked directly to their catalytic activity, with different crystal nucleation and growth processes giving rise to different particle size distributions (PSDs). PSDs are measured routinely in industrial environments, with the requirement that they should be statistically meaningful. The adsorption technique for the determination of metal particle size is based on the fact that over an appropriate temperature range certain gases such as ethylene, carbon monoxide, oxygen and hydrogen form a chemisorbed monolayer on the surface of transition metals. It is an easy and simple experimental technique. The surface of the metal area can be inferred from the amount of adsorbed gas in combination with the metal content of the supported catalyst, only if assumptions are made about the particle shape (normally assumed to be spherical or cubic) [41]. The two complementary techniques that are typically used are X-ray diffraction and transmission electron microscopy (TEM). X-ray diffraction can be used to provide averaged information from large numbers of particles, but the interpretation of the results can be difficult, especially if the particles are not single crystals. TEM measurements rely on the acquisition of images and subsequent digital processing from typically no more than a few hundreds of particles [42,43]. However, even using digital image processing (DIP) tools, the quantification of the sizes and distributions of nanoparticles using TEM is difficult task. First, for supported catalysts, the particle sizes of interest are in the range of nanometers. The detection and analysis of small aggregates that are supported on amorphous or crystalline substrates is difficult, especially when the particle size approaches that of phase contrast arising from the support [44,45]. Second, this difficulty is exacerbated by the fact that the clusters may be present at different heights, they may be embedded in the support, they may be overlapped by other particles and the support itself may be thick or rough. Although the visibility of metal nanoparticles can often be enhanced by recording bright-field images slightly away from Gaussian focus, it is not possible to perform accurate size measurements from such images because the image resolution is then poorer. Inferences from bright-field TEM images are also complicated by diffraction effects, particularly as small particles possess large reciprocal-space shape functions that can be intersected by the Ewald sphere at large tilts from zone axes [46]. In order to provide statistically meaningful size distributions from scanning electron microscopy (SEM) images, many particles should be analyzed. Manual segmentation of SEM images can be time-consuming because, in most cases, it is difficult to analyze an image locally to obtain only the desired information from the particles. In order to address these issues, we are going to use DIP that makes use of a locally varying threshold.

Alloy NPs are widely used in catalysis and sensing fields. Owing to the interaction among components in alloy NPs, they generally show many favorable properties in comparison with the



Scheme 1. Schematic representation of the methodology employed to BTN assay.

corresponding monometallic counterparts, which include high catalytic activity, catalytic selectivity, and better resistance to deactivation [47]. Electrodeposition is the most controllable and robust technique for synthesis of metal NPs, in which the size, density, composition of alloys and even the shape of NPs can be well-controlled by electrodeposition potential, time, concentration, and composition of metal precursor solutions [48,49].

This paper presents a study concerning electrodeposition of PdFeNi trimetallic alloy NPs by cyclic voltammetry (CV) onto a glassy carbon electrode (GCE) modified with a room-temperature ionic liquid (RTIL)-chitin (Ch) composite film (PdFeNi/ChRTIL/GCE) aiming at BTN trace detection using differential pulse voltammetry (DPV) which has been reported for the first time. Different deposits were obtained by varying the number of cyclic potential scans during electroreduction step and we used a computerized method (DIP) for measuring PSDs from SEM images in the presence of an uneven background. Finally the sensitivity of the best resulting PdFeNi/ChRTIL/GCE sensor toward BTN assay was evaluated (Scheme 1).

2. Experimental and theoretical backgrounds

2.1. Experimental details

2.1.1. Chemicals and solutions

1-Ethyl-3-methylimidazolium bis(trifluoromethylsulfonyl)imide (EMIMBTI), Ch, and BTN were purchased from Sigma-Aldrich. All other reagents were of analytical grade and used as received from Merck. A concentration of 0.05 mol L^{-1} phosphate buffered solution (PBS, prepared from NaH_2PO_4 , and Na_2HPO_4) was used to control the pH at 4.0. $[\text{Fe}(\text{CN})_6]^{3-/4-}$ solution (redox probe, $5.0 \times 10^{-3} \text{ mol L}^{-1}$) was prepared in PBS (0.05 mol L^{-1} , pH 4.0) and used for electrochemical impedance spectroscopic (EIS) measurements. A stock solution of BTN was prepared in PBS (0.05 mol L^{-1} , pH 4.0) with a concentration level of 0.01 mol L^{-1} , and was stored at dark in a refrigerator. Working solutions were prepared by appropriate dilution of the stock solution. A stock solution of 0.2% Ch was prepared in 1.0% (v/v) acetic acid by ultrasonication for 30.0 min. Doubly distilled water (ddH_2O) was used throughout the study.

2.1.2. Apparatus and softwares

Electrochemical experiments were performed using a μ -Auto-labIII/FRA2 controlled by the Nova software (Version 1.8). A conventional three-electrode cell was used with a saturated calomel electrode (SCE) as reference electrode, a Pt wire as counter electrode and a bare or modified GCE as working electrode. The EIS measurements were performed in the redox probe solution and plotted in the form of complex plane diagrams (Nyquist plots). The SEM experiments were performed by a KYKY-EM 3200 scanning electron microscope. A JENWAY-3345 pH-meter equipped with a combined glass electrode was used to pH measurements. Energy dispersive X-ray spectroscopy (EDS) was conducted by an EDS-integrated Hitachi S-4800 (Hitachi, Japan) for surface elemental

composition analysis. Digital image processing (DIP) was carried out using a MATLAB code and an adaptive thresholding algorithm for particles counting (density estimation) and average diameter measurement. The density and average size of PdFeNi NPs were evaluated from a $6.1 \mu\text{m}^2$ GCE surface analysis. The recorded experimental data was smoothed, when necessary, and converted to matrices by means of several homemade MATLAB files. All computations were performed on a DELL XPS laptop (L502X) with Intel Core i7-2630QM 2.0 GHz, 8 GB of RAM and Windows 7–64 as its operating system.

2.1.3. Preparation of the PdFeNi/ChRTIL/GCE

Prior to each modification, the GCE surface was polished successively by silicon carbide grinding paper (grit 1200.0) for 5.0 s, and by a 9.0, 5.0 and $1.0 \mu\text{m}$ alumina slurry (Presi) on a cloth polishing pad for 10.0, 5.0 and 3.0 min, respectively. Between each polishing step, the surface was cleaned in an ultrasonic ethanol bath (5.0 min) in order to remove any impurity. Finally, they were rinsed in an ultrasonic ddH_2O bath (5.0 min) and dried for 1.0 min using a N_2 stream. A distinct amount ($15.0 \mu\text{L}$) of EMIMBTI was added to the Ch solution (0.2%, $75.0 \mu\text{L}$) and with the aid of ultrasonic agitation a uniform solution (ChRTIL) was prepared. Then, $4.0 \mu\text{L}$ of ChRTIL solution was dropped on the cleaned GCE and the solvent was evaporated by passing slow rate of warm air for 10.0 min. The electrochemical deposition of PdFeNi trimetallic alloy NPs was performed using CV on ChRTIL/GCE in 0.2 mol L^{-1} KCl solution containing $0.5 \times 10^{-3} \text{ mol L}^{-1}$ PdCl_2 , $0.5 \times 10^{-3} \text{ mol L}^{-1}$ NiCl_2 , and $0.5 \times 10^{-3} \text{ mol L}^{-1}$ FeCl_3 by scanning potential from 0 to -1 V for a given number of scans (N).

2.1.4. Preparation of real samples

Three commercial infant formula milk powders (Aptamil, Similac and Bebelac), three pieces of Calf, Sheep and Chicken livers, and three Goose, Turkey and Chicken eggs were purchased from local markets. Before the experiments, the infant formula were mixed with 1.5% formic acid and then centrifuged for 10.0 min at 5000.0 rpm and the supernatant was collected for further sample assay [50]. Liver and egg yolk samples were incubated with 2.25 mol L^{-1} hydrochloric acid at $100.0 \text{ }^\circ\text{C}$ for 120.0 min. Then, the samples were centrifuged for 10.0 min at 5000.0 rpm and the supernatants were filtered through a $0.22 \mu\text{m}$ filter [51]. The filtrate was collected for further sample assay. The BTN concentration was ascertained from calibration curve and reported as μg BTN in 100.0 g sample.

2.2. Theoretical details

Image segmentation is an essential preliminary step in most automated pattern recognition and scene analysis problems [52]. Segmentation is used to subdivide an image into its constituent regions, and its accuracy determines the eventual success or failure of computerized analysis procedures. The detection of particles in a SEM image is usually performed by thresholding

the entire image at once using a single “global threshold” value. Individual pixels in the image are then marked as “object” pixels if their value is greater (or smaller) than a chosen threshold intensity and as “background” pixels otherwise. This approach works well if all of the particles have a sufficiently different intensity from that of the background. Once a binary (thresholded) image is obtained, an opening operator (erosion followed by dilation) can be used to smooth the boundaries by removing small protrusions, to break narrow isthmuses and to remove regions that are smaller than the size of a chosen

structuring element. Choosing the size of the kernel is possible to set a minimum size of particles to be detected. The image is then analyzed in order to measure and count the particles [53,54]. Unfortunately, in most cases of practical interest it is difficult to find a unique value for thresholding the entire picture correctly, and only a fraction of the particles in the image is outlined correctly in the binary image.

In order to address these issues, a method for improving the thresholding step before processing such images has been described [52]. The method is based on an “automatic local

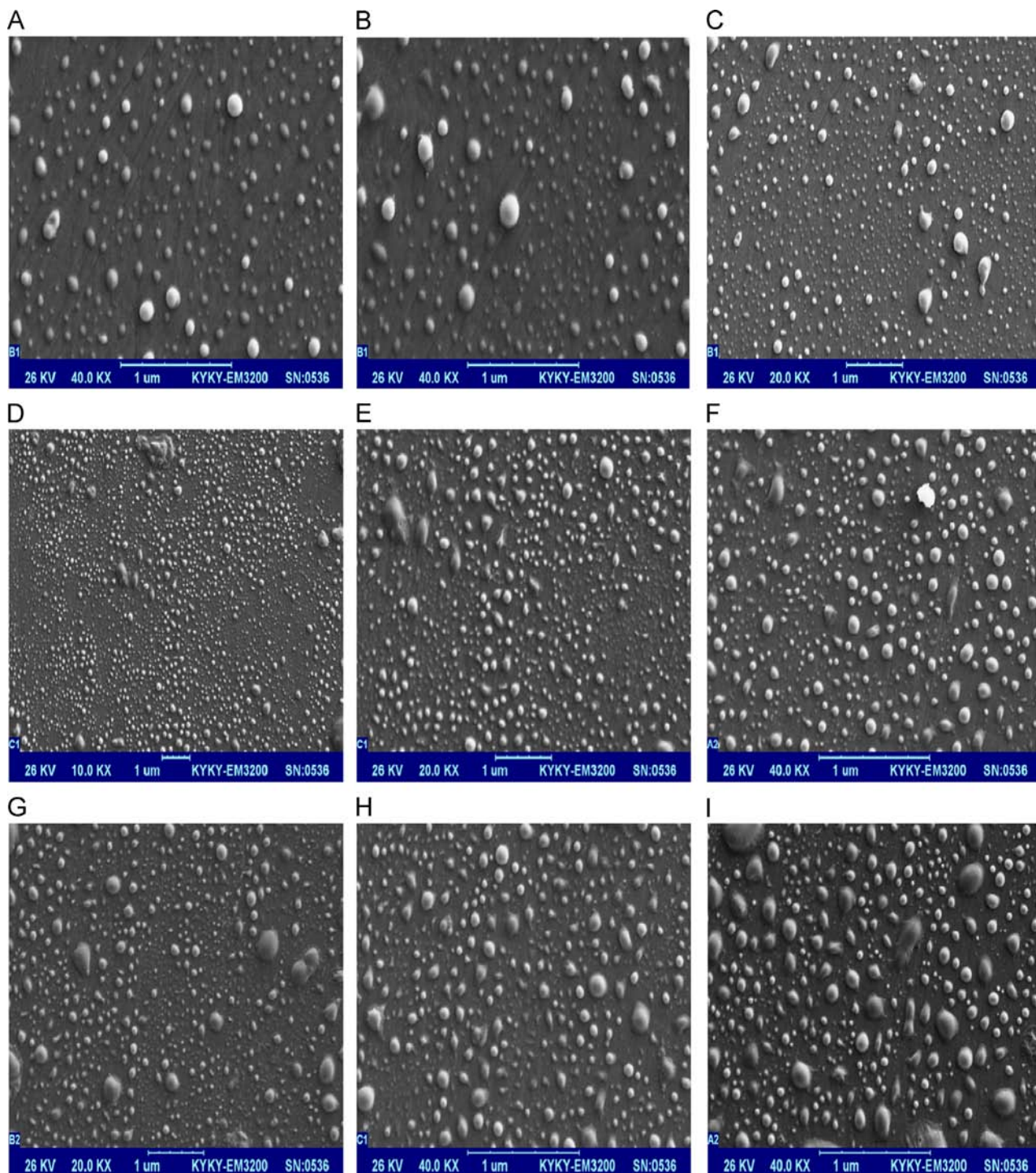


Fig. 2. SEM images of PdFeNi/ChRTIL/GCEs prepared by CV from a 0.2 mol L^{-1} KCl solution containing $0.5 \times 10^{-3} \text{ mol L}^{-1}$ PdCl_2 , $0.5 \times 10^{-3} \text{ mol L}^{-1}$ NiCl_2 and $0.5 \times 10^{-3} \text{ mol L}^{-1}$ FeCl_3 (see Section 2 for conditions). Number of cyclic scans (N): (A) 1, (B) 2, (C) 4, (D) 8, (E) 12, (F) 16, (G) 20, (H) 24, and (I) 28.

thresholding” algorithm, which is applied to sub-regions of the image sequentially. The individual steps in the program include: (1) Selection of how many sub-divisions to use. (2) Cutting of sub-images from the original. (3) Thresholding of each sub-image. The output from this procedure is a binary image. (4) Opening (dilation plus erosion) with a chosen kernel size. (5) Combination and analysis of the processed sub-images. The resulting binary image is processed, particles counted and the boundaries are overlapped onto the original image to

check the results. The algorithm assumes that each sub-image to be thresholded contains two classes of pixels (e.g., foreground and background) and determines the optimal threshold automatically, in one of the several ways. The simplest way consists of (1) scaling the intensities in each sub-image and (2) selecting a threshold value equal to the median intensity range in each sub-image. After initial segmentation (e.g., using the mid-point between the minimum and the maximum intensities), the average of the intensities in each group of pixels

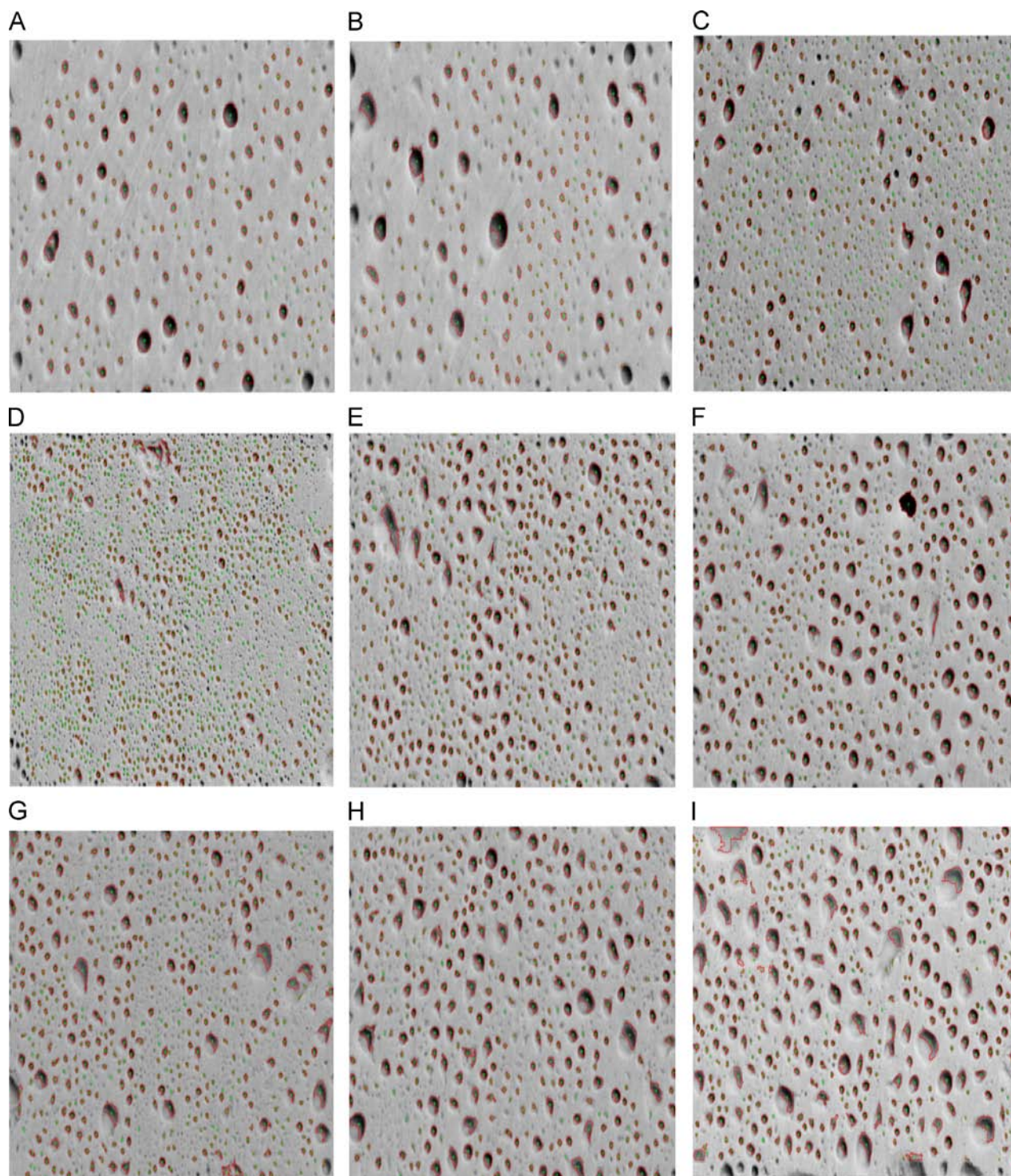


Fig. 3. The inversed images of the original SEM images presented in Fig. 1A–I processed by MATLAB image processing Toolbox.

is used to refine the threshold value. This procedure is repeated until the difference between successive threshold values is smaller than a pre-defined value. A more sophisticated approach, which is known as "Otsu's method" can be used to determine the optimal threshold separating two classes of pixels so that the combined spread (intra-class variance) of the foreground and background pixels is minimized [55].

Table 1

Characterization of PdFeNi NPs for different number of cyclic scans (N) during the electrodeposition step.

N	Number of NPs	NPs density (counts μm^{-1})	Mean diameter (nm)
1	1313	215	22.48 ± 10.42
2	1440	236	21.78 ± 9.42
4	1706	280	21.50 ± 9.57
8	4158	682	19.54 ± 6.27
12	2818	462	19.68 ± 7.88
16	2371	389	19.86 ± 6.69
20	2325	381	20.18 ± 8.24
24	1927	316	20.67 ± 5.43
28	1617	265	21.29 ± 5.20

3. Results and discussion

3.1. Electrodeposition of PdFeNi trimetallic alloy NPs onto ChRTIL/GCE

In this study, ChRTIL/GCE was chosen as a platform for electrodeposition of PdFeNi trimetallic alloy NPs. As suggested by other researchers, Ch can interact with the NPs, blocking the aggregation of NPs [56,57] and ILs have low interfacial tension and thus can enhance the nucleation rate, which is favorable to the formation of smaller NPs [58]. Nine ChRTIL/GCEs modified with PdFeNi trimetallic alloy NPs were elaborated using CV by scanning potential from 0 to -1 V upon varying number of cyclic scans (N) from 1.0 to 28.0.

3.2. Characterizations

In order to characterize the PdFeNi trimetallic alloy NPs, SEM analyzes were carried out for nine significant values of N (Fig. 2A–I). For analyzing the SEM images by adaptive thresholding it was necessary to have a bright background with gray objects therefore, the original SEM images were loaded in MATLAB Workspace and inverted (Fig. 3A–I). The inverted SEM images were then submitted for analyzing by adaptive thresholding. As can be seen in Fig. 3A–I,

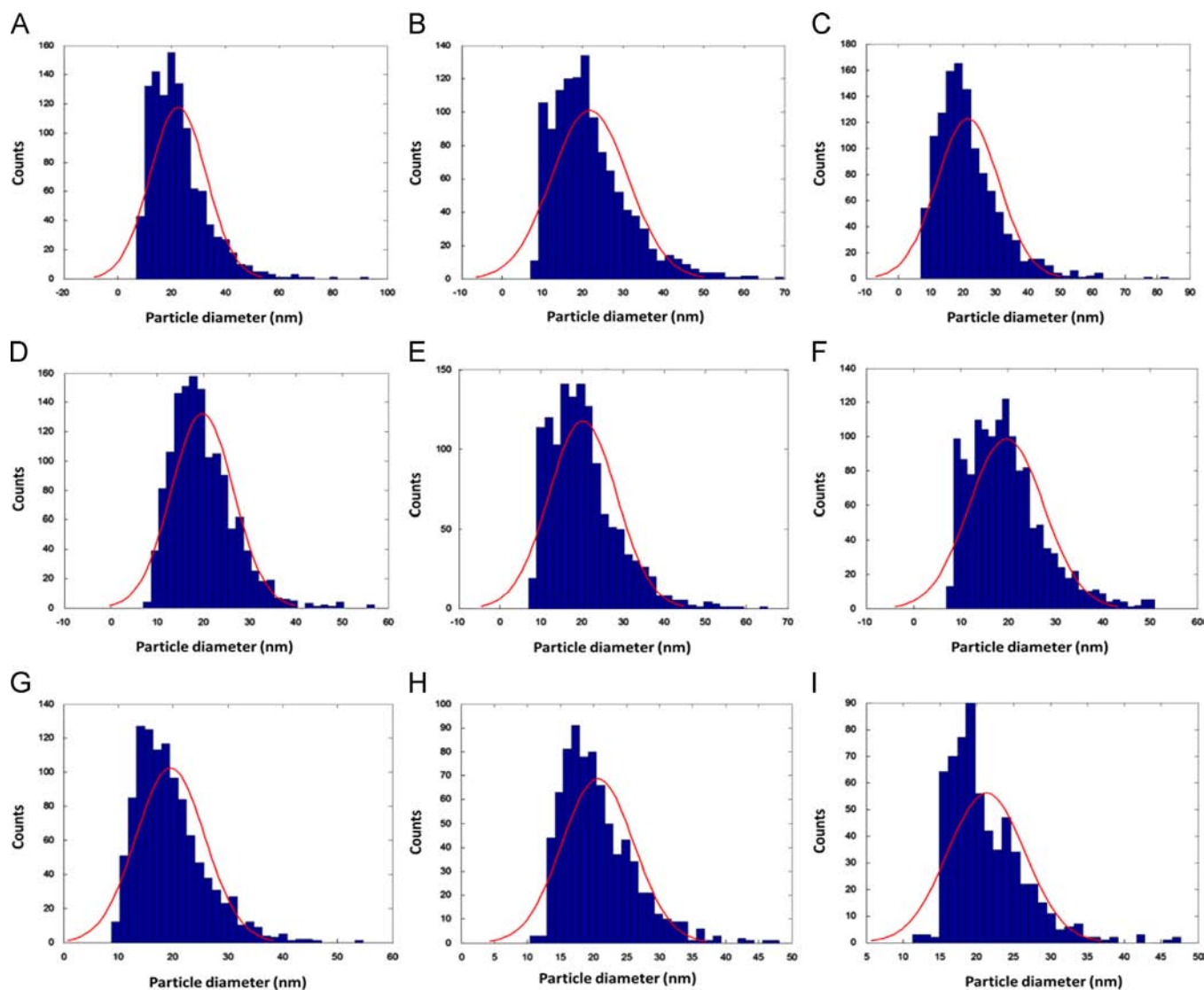


Fig. 4. Histograms of PSDs measured by DIP from the images presented in Fig. 2A–I.

the detected NPs were marked by pluses and surrounded by red circles. For the calculation of the particles size it was assumed the diameter of a circle with the same area as the particle. Table 1 summarizes the results obtained by DIP. Number of PdFeNi NPs, NPs densities, and mean diameters obtained by processing SEM images are reported in Table 1. Fig. 4A–I shows histograms of the measured PSDs for different applied N s and best-fitting curves. The electro-deposited PdFeNi NPs can be separated into two distinct populations: the first one is related to small and spherical-shaped NPs (Fig. 2A–F) and the second one to larger, aggregate-like NPs (Fig. 2G–I). An increase in the particles' densities as a function of N can be noticed up to eight potential scans, then the densities decreased (Table 1). By contrast, the average size of the particles decreased with respect to eight potential scans, then increased (Table 1). This evolution of both the density of PdFeNi NPs and the average size clearly illustrates a gradual coalescence phenomenon from $N=8$. However, while increasing N between 1 and 8 scans, small, and well spherical-shaped NPs formation is favored, and density reaches a maximum value at $N=8$ and then decreases and NPs begin to coalesce, leading to larger NPs. Therefore, $N=8$ was chosen as the best number of cyclic scans for the next measurements.

PdFeNi NPs were also characterized by energy dispersive X-ray spectroscopy (EDS) and signature peaks for Pd, Fe and Ni were observed (Fig. 5A). These peaks indicated that Pd, Fe and Ni can be electrochemically synthesized under the given conditions and contribute toward formation of trimetallic alloy NPs during the synthesis.

Electrochemical impedance spectroscopy (EIS) is an effective method for probing the features of surface of the modified electrodes. The Nyquist plot of impedance spectra includes a semicircle portion and a linear portion, with the former at higher frequencies corresponding to the electron transfer limited process and the latter at lower frequencies corresponding to the diffusion process. The electron transfer resistance (R_{ct}) at the electrode surface is equal to the semicircle diameter, which can be used to describe the interface properties of the electrode. Fig. 5B displays the Nyquist plots of different electrodes in PBS (0.05 mol L⁻¹, pH 4.0) containing 5.0×10^{-3} mol L⁻¹ [Fe(CN)₆]^{3-/4-}. It can be seen that the impedance curve of bare GCE (curve a) consists of a big semicircle, and the electron transfer resistance (R_{ct}) is estimated to be 22.75 k Ω , whereas the R_{ct} of Ch/GCE (29.08 k Ω , curve b) is larger than that of bare GCE, manifesting that the Ch has a blocking effect on the electron transfer of [Fe(CN)₆]^{3-/4-}. When compared with Ch/GCE, ChRTIL/GCE exhibits a smaller R_{ct} (15.67 k Ω , curve c). This can be attributed to the good ionic conductivity of RTIL. In addition, the electrostatic interaction

between ChRTIL and [Fe(CN)₆]^{3-/4-} may favor the electron transfer of [Fe(CN)₆]^{3-/4-}. When the ChRTIL/GCE is coated with Fe (curve d), Ni (curve e), Pd (curve f), PdNi (curve h), FeNi (curve i), PdFe (curve g), and PdFeNi (curve j) NPs, the R_{ct} decreases 14.08, 8.55, 6.18, 5.34, 4.2, 3.25, and 2.29 k Ω , respectively. These results reveal that PdFeNi trimetallic alloy NPs can provide the necessary conduction pathways which cause better electron-transfer interface between electrode surface and electrolyte solution compared to monometallic or bimetallic NPs and also imply that there is a synergistic action between Pd, Fe, and Ni in decreasing electron transfer resistance.

Fig. 6 shows the CV responses for electrochemical oxidation of 40.0×10^{-9} mol L⁻¹ BTN in PBS (0.05 mol L⁻¹, pH 4.0) at bare GCE (curve a), Ch/GCE (curve b), ChRTIL/GCE (curve c), Fe/ChRTIL/GCE (curve d), Ni/ChRTIL/GCE (curve e), Pd/ChRTIL/GCE (curve f), PdFe/ChRTIL/GCE (curve g), PdNi/ChRTIL/GCE (curve h), FeNi/ChRTIL/GCE (curve i) and PdFeNi/ChRTIL/GCE (curve j). As it can be seen, while the anodic peak potential for BTN oxidation at bare GCE, Ch/GCE, ChRTIL/GCE, are 1.21, 1.32, and 1.28 V, respectively, the corresponding potentials at Fe/ChRTIL/GCE, Ni/ChRTIL/GCE, Pd/ChRTIL/GCE, PdFe/ChRTIL/GCE, PdNi/ChRTIL/GCE, FeNi/ChRTIL/GCE, and PdFeNi/ChRTIL/GCE are 1.13, 1.18, 1.14, 1.08, 1.12, 1.18, and 1.07,

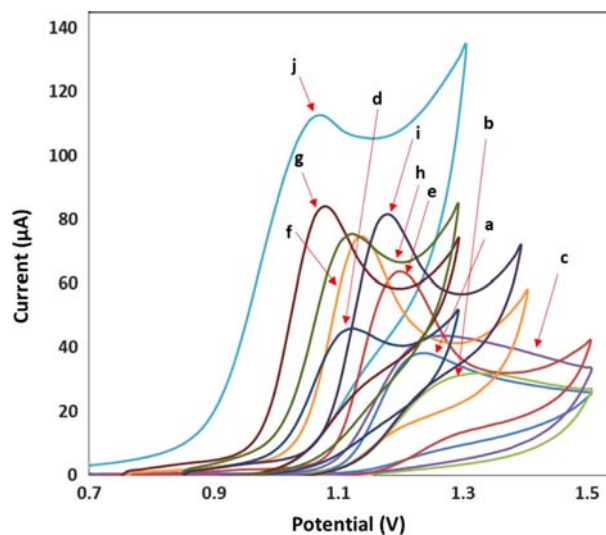


Fig. 6. CVs recorded at (a) bare GCE, (b) Ch/GCE, (c) ChRTIL/GCE, (d) Fe/ChRTIL/GCE, (e) Ni/ChRTIL/GCE, (f) Pd/ChRTIL/GCE (g) PdFe/ChRTIL/GCE, (h) PdNi/ChRTIL/GCE, (i) FeNi/ChRTIL/GCE and (j) PdFeNi/ChRTIL/GCE in the presence of 40.0 nM BTN in PBS (0.05 mol L⁻¹, pH 4.0). Scan rate: 50.0 mV s⁻¹.

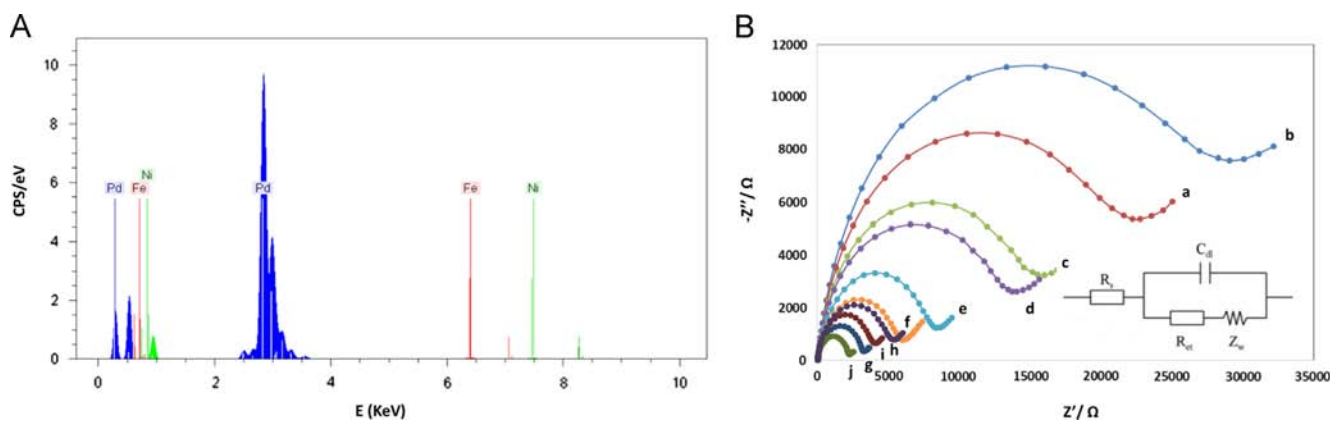


Fig. 5. (A) EDS spectra for confirming the presence of PdFeNi NPs on ChRTIL/GCE. (B) EIS spectra of (a) bare GCE, (b) Ch/GCE, (c) ChRTIL/GCE, (d) Fe/ChRTIL/GCE, (e) Ni/ChRTIL/GCE, (f) Pd/ChRTIL/GCE (g) PdFe/ChRTIL/GCE, (h) PdNi/ChRTIL/GCE, (i) FeNi/ChRTIL/GCE and (j) PdFeNi/ChRTIL/GCE in PBS (0.05 mol L⁻¹, pH 4.0) containing 5.0×10^{-3} mol L⁻¹ [Fe(CN)₆]^{3-/4-}. Inset shows the equivalent circuit used for fitting the EIS data: R_s , Z_w , R_{ct} and C_{dl} represent the solution resistance, the Warburg diffusion resistance, the electron-transfer resistance and the double layer capacitance, respectively.

respectively. These results indicate that the peak potential for BTN oxidation at PdFeNi/ChRTIL/GCE shifts by 140.0 mV toward less positive values compared to bare GCE. However, PdFeNi/ChRTIL/GCE shows much higher anodic peak current for the oxidation of BTN compared to bare GCE, indicating that the combination of PdFeNi and ChRTIL has significantly improved the performance of the electrode toward BTN oxidation.

3.3. The influences of scan rate and pH on electrochemical response of BTN at PdFeNi/ChRTIL/GCE biosensor

The effect of scan rate (ν) on the electrocatalytic oxidation of BTN at PdFeNi/ChRTIL/GCE was investigated by CV (not shown). Results showed, the oxidation peak potential shifted to more positive potentials with increasing scan rate, confirming the kinetic limitation in the electrochemical reaction. Also, a plot of peak height (I_p) vs. the square root of scan rate ($\nu^{1/2}$) was found to be linear in the range of 10–500 mV s^{-1} suggesting that the process is diffusion rather than surface controlled.

In general, pH is one of the variables, which commonly affects the current and shape of voltammograms. Taking into account that for analytical purposes both maximal and stable currents are necessary, the electrochemical behavior of BTN (0.05 mol L^{-1}) in PBS

(0.05 mol L^{-1}) with various pHs (2.0–10.0) at the surface of PdFeNi/ChRTIL/GCE was studied using cyclic voltammetry (Fig. 7). This study showed that both peak current and peak potential depended on the solution pH. It can be seen that the anodic peak current of BTN reaches a maximum value at pH 4.0 and then decreases gradually with increasing of pH (inset of Fig. 7). Therefore, pH 4.0 was taken as the optimum pH for the determination of BTN. Also, the anodic peak potential of BTN at the surface of PdFeNi/ChRTIL/GCE shifts to less positive values with increasing pH of the buffered solution.

3.4. Analytical characterizations

Fig. 8 displays the differential pulse voltammetric (DPV) response of PdFeNi/ChRTIL/GCE biosensor for the successive increase in BTN concentrations. The calibration curve for the biosensor under the optimized experimental conditions is shown in the inset of Fig. 8. The biosensor exhibited a wide linear range of response to BTN, in the concentration range of $2.0\text{--}44.0 \times 10^{-9} \text{ mol L}^{-1}$ with a correlation coefficient of 0.9973. The sensitivity of the biosensor was $2.34 \mu\text{A nM}^{-1}$ and the limit of detection (LOD) was $0.6 \times 10^{-9} \text{ mol L}^{-1}$.

Long-term stability of the biosensor was also evaluated by measuring its performance after every few days. The biosensor shows high stability for BTN detection, and retains about 92% of its original response to BTN after 30.0 days of storage. These results suggest that the PdFeNi/ChRTIL/GCE possesses the long term stability. To ascertain the repeatability of the proposed biosensor, 10.0 measurements of $10.0 \times 10^{-9} \text{ mol L}^{-1}$ BTN were carried out using the PdFeNi/ChRTIL/GCE at intervals of 1.0 h. The RSD was found to be 2.2%, indicating that the PdFeNi/ChRTIL/GCE has good repeatability. Six PdFeNi/ChRTIL/GCEs fabricated independently were used to determine $10.0 \times 10^{-9} \text{ mol L}^{-1}$ BTN, and the RSD was 2.5%, revealing excellent reproducibility of the electrode preparation procedure. PdFeNi/ChRTIL/GCE biosensor can be prepared within 15.0 min and by manual polishing with alumina slurry we can retain the original nature of the GCE very easily.

The obtained results by the proposed biosensor with some reported methods [59–69] for the determination of BTN were compared and given in Table 2. The proposed biosensor provides better results over the most of the reported methods.

3.5. Interference study

Under optimal experimental conditions, the interference from selected metal ions and organic compounds was evaluated. The tolerance limit for interfering species was considered as the maximum concentration that gave a relative error less than $\pm 5.0\%$

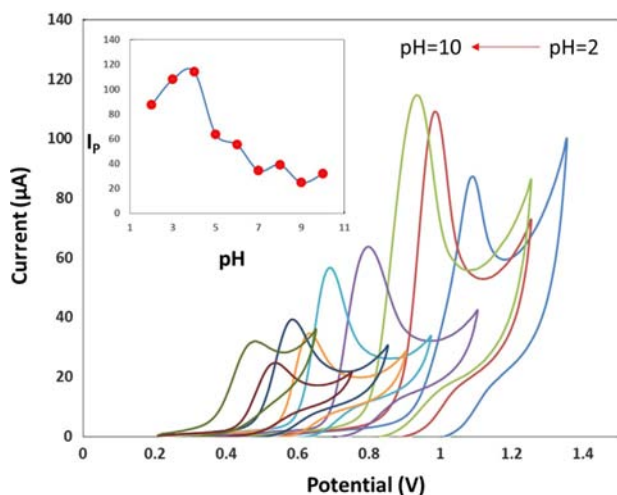


Fig. 7. Cyclic voltammograms for $40.0 \times 10^{-9} \text{ mol L}^{-1}$ BTN on PdFeNi/ChRTIL/GCE (prepared by applying 8.0 cycles) in PBS (0.05 mol L^{-1}) with pH values of 2.0–10.0.

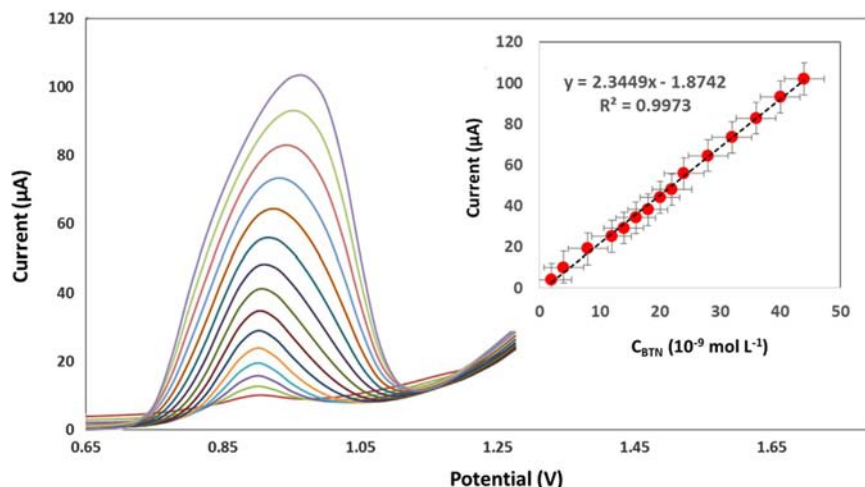


Fig. 8. Differential pulse voltammograms of PdFeNi/ChRTIL/GCE (prepared by applying 8.0 cycles) in PBS (0.05 mol L^{-1} , pH 4.0) containing $2.0\text{--}44.0 \times 10^{-9} \text{ mol L}^{-1}$ BTN from inside to outside. Inset shows linear dependence of peak currents on BTN concentrations as calibration curve.

Table 2
Electrochemical methods for BTN determination.

Technique	Method description	Linear range (mol L ⁻¹)	LOD (mol L ⁻¹)	Original applications	Ref.
HPLC- ^a SWV	Avidin-modified electrode	0–2 × 10 ⁻⁶	1.3 × 10 ⁻⁶	Pharmaceutical drug	[59]
^b QCM sensor	Avidin immobilized on the crystal surface	7 × 10 ⁻⁸ –7 × 10 ⁻⁶	7 × 10 ⁻⁸	Pharmaceutical drug	[60]
^c DPV	Competition between BTN and labeled BTN with daunomycin	3 × 10 ⁻⁹ –5 × 10 ⁻⁸	3 × 10 ⁻⁸	Pharmaceutical drug	[61]
DPV	Competition between BTN and labeled BTN with daunomycin	–	2 × 10 ⁻⁹	Pharmaceutical drug	[62]
DPV	Competition between BTN and labeled BTN with Nile Blue A	3 × 10 ⁻¹⁰ –5 × 10 ⁻⁸	1 × 10 ⁻⁹	Vitamin tablet	[63]
Amperometry	Competition between BTN and biotinylated glucose oxidase	2.86 × 10 ⁻⁷ – 8.19 × 10 ⁻⁶	2.86 × 10 ⁻⁷	Vitamin tablet	[64]
Amperometry	Anti-BTN antibody immobilized in electrode and BTN-HRP	4.09 × 10 ⁻⁸ – 1.23 × 10 ⁻⁵	4.09 × 10 ⁻⁸	Vitamin tablet	[65]
SWV	Anti-BTN antibody immobilized in screen printed electrode using K ₄ Fe(CN) ₆ as electroactive substance	10 ⁻⁶ –10 ⁻⁹	1.4 × 10 ⁻⁸	Vitamin tablet	[66]
SWV	Electrochemical magneto biosensor	0.94–2.4 × 10 ⁻⁷	8.4 × 10 ⁻⁸	Dietary supplement and milk powder	[67]
Chromatography	HPLC-MS/MS	2 × 10 ⁻⁹ –2 × 10 ⁻⁷	2 × 10 ⁻⁹	Vitamin tablet	[68]
Chromatography	Postcolumn derivatization with <i>o</i> -phthalaldehyde and 3-mercaptopropionic acid	4.1 × 10 ⁻⁶ –4.1 × 10 ⁻⁵	2 × 10 ⁻⁶	Pharmaceutical preparations	[69]
DPV	PdFeNi/ ^d ChRTIL/GCE	2.0–44.0 × 10 ⁻⁹	6 × 10 ⁻¹⁰	Milk powder, liver, and egg yolk	This work

^a SWV: Square wave voltammetry.

^b QCM: Quartz crystal microbalance.

^c DPV: Differential pulse voltammetry.

^d Chitin room temperature ionic liquid.

Table 3
Results of determination of BTN in real samples.

Sample	Found (μg 100 g ⁻¹)	Added (μg 100 g ⁻¹)	Found (μg 100 g ⁻¹)	Recovery (%)	RSD (% , n=3)
Milk powder (Aptamil) ^a	38.2	15.0	55.4	103.97	3.31
Milk powder (Similac) ^b	63.4	10.0	71.1	96.87	2.82
Milk powder (Bebelac) ^c	7.11	20.0	27.6	101.77	4.15
Calf liver	218.2	30.0	252.3	101.62	1.88
Sheep liver	231.9	25.0	258.5	100.61	2.43
Chicken liver	182.5	12.0	195.3	100.4	3.21
Goose egg yolk	18.6	6.0	24.2	98.38	3.666
Turkey egg yolk	28.4	14.0	41.6	98.12	2.71
Chicken egg yolk	31.3	15.0	47.2	101.90	2.55

^a Labeled 40 μg 100 g⁻¹.

^b Labeled 60 μg 100 g⁻¹.

^c Labeled 6.5 μg 100 g⁻¹.

at a concentration of 10.0 × 10⁻⁹ mol L⁻¹ of BTN. Phenol, ascorbic acid, caffeine, uric acid, glucose, citric acid, urea, cysteine, arginine, lysine, and aspartic acid were the most common constituents found with BTN. From the studies, an 80-fold excess of ascorbic acid had no effect on the *I*_p of BTN. Glucose, cysteine, arginine, lysine, aspartic acid, uric acid, citric acid and urea also did not interfere until a 100-fold excess was achieved. In addition, phenol, and caffeine showed no changes in *I*_p until a 70-fold excess was used. Even a 200-fold excess of K⁺, Ca²⁺, NO₃⁻, NH₄⁺, Cl⁻ or Mg²⁺ had no effect on the *I*_p of BTN. These results suggested that the determination of BTN at PdFeNi/ChRTIL/GCE biosensor was not significantly affected by the most common interfering species.

3.6. Real sample analysis

To evaluate the feasibility of the proposed biosensing system in real sample analysis, it was applied to the determination of BTN in infant milk powder, liver, and egg yolk samples, and the results are shown in Table 3. For the accuracy studies, a recovery study was carried out and the recovery values were between 96.87% and 103.97%. The RSD values were lower than 4.9% which confirmed

that acceptable values were also obtained for RSDs. Moreover, the differences between the results of this work for BTN determination in infant milk powders and the nominal values labeled by the manufacturer companies are small (see Table 3). These results suggested that the PdFeNi/ChRTIL/GCE biosensor was very reliable and sensitive enough for the determination of BTN in real samples.

4. Conclusions

For the first time we are reporting a simple method based on CV assisted by DIP for electrodeposition of PdFeNi trimetallic alloy NPs onto ChRTIL/GCE to fabricate a novel biosensor for efficient determination of BTN in real samples. Although not often used, CV proved to be an efficient method for spherical-like shaped NPs electrodeposition. The systematic characterization of the electrodes using CV and SEM for different values of *N* allowed a correlation to be made between both PdFeNi NPs density and size and the performances of the biosensor toward BTN detection. Measurement of PSDs from SEM images is difficult, especially on an uneven background. Therefore, this problem was tackled by

partitioning SEM micrographs into sub-images automatically and segmenting them using an adaptive threshold referred to as Otsu's method. Using this approach, images are analyzed with little human intervention and more accurately and objectively than when using a global threshold. PdFeNi/ChRTIL/GCE exhibits interesting performances with respect to BTN trace determination, and the best electrochemical responses were obtained for a high density (682 particles μm^{-2}) of small NPs (19.54 ± 6.27 nm). From those observations, both NPs density and diameter appeared to be key features with respect to analytical performances. The proposed biosensor was sensitive, selective, free of common interferences with the analyte of interest, and had a sub-nanomolar detection limit. This biosensor is recommended for the determination of BTN at trace levels in quality control laboratories.

Acknowledgements

The financial supports of this project by Razi University Research Council, UNL, CONICET and ANPCyT are gratefully acknowledged. We wish to express our sincere thanks and appreciation both to Mr. Abdolhamid Rezaee (SEM Operator) who provided the SEM images of our electrodes.

References

- [1] E. Livaniou, D. Costopoulou, I. Vassiliadou, L. Leondiadis, J.O. Nyalala, D.S. Ithakissios, G.P. Evangelatos, J. Chromatogr. A 881 (2000) 331–343.
- [2] C.G. Staggs, W.M. Sealey, B.J. McCabe, A.M. Teague, D.M. Mock, J. Food Compos. Anal. 17 (2004) 767–776.
- [3] R.J. Stratton, T.R. Smith, Best Pract. Res. Clin. Gastroenterol 20 (2006) 441–466.
- [4] Código Alimentario Argentino based on Codex Alimentarius Commission, 2007. Standards for Infant Formulas and Formulas for Special Medical Purposes Intended for Infants (Codex Stan 72-1981) (Revised 2007).
- [5] H. Martin, C. Murray, J. Christeller, T. McGhie, Anal. Biochem. 381 (2008) 107–112.
- [6] S. Tanaka, K. Yoshida, H. Kuramitz, K. Sugawara, H. Nakamura, Anal. Sci. 15 (1999) 863–866.
- [7] L. Thompson, D. Schmitz, S. Pan, J. AOAC Int. 89 (2006) 1515–1558.
- [8] R. Kizek, M. Masarik, K.J. Kramer, D. Potesil, M. Bailey, J.A. Howard, B. Klejdus, R. Mikelova, V. Adam, L. Trnkova, F. Jelen, Anal. Bioanal. Chem. 381 (2005) 1167–1178.
- [9] T. Deng, J. Li, S. Huan, H. Yang, H. Wang, G. Shen, R. Yu, Biosens. Bioelectron. 21 (2006) 1545–1552.
- [10] J.M. Fowler, D.K.Y. Wong, H.B. Halsall, W.R. Heineman, Recent developments in electrochemical immunoassays and immunosensors, in: X. Zhang, H. Ju, J. Wang (Eds.), Electrochemical Sensors, Biosensors and their Biomedical Applications, Elsevier Inc., Amsterdam, 2008, pp. 115–143.
- [11] E. Livaniou, D. Costopoulou, I. Vassiliadou, L. Leondiadis, J.O. Nyalala, D.S. Ithakissios, G.P. Evangelatos, J. Chromatogr. A 881 (2000) 331–343.
- [12] J. Schiewe, S. Gobel, M. Schwarz, R. Neubert, J. Pharm. Biomed. Anal. 14 (1996) 435–439.
- [13] Y. Ikariyama, M. Furuki, M. Aizawa, Anal. Chem. 57 (1985) 496–500.
- [14] F. Delgado Reyes, J.M. Fernandez Romero, M.D. Luque de Castro, Anal. Chim. Acta 436 (2001) 109–117.
- [15] Y. Gao, F. Guo, S. Gokavi, A. Chow, Q. Sheng, M. Guo, Food Chem. 110 (2008) 769–776.
- [16] R.M. Stuetz, Application of electronic nose technology for monitoring water and wastewater, in: S. Alegret (Ed.), Comprehensive Analytical Chemistry, Elsevier B.V., Amsterdam, 2003.
- [17] A. Lermo, S. Fabiano, S. Hernández, R. Galve, M.P. Marco, S. Alegret, M.I. Pividori, Biosens. Bioelectron. 24 (2009) 2057–2063.
- [18] M. Zhang, A. Smith, W. Gorski, Anal. Chem. 76 (2004) 5045–5050.
- [19] X. Lu, Z. Wen, J. Lin, Biomaterials 27 (2006) 5740–5747.
- [20] J. Lin, W. Qu, S. Zhang, Anal. Biochem. 360 (2007) 288–293.
- [21] M. Koel, Crit. Rev. Anal. Chem. 35 (2005) 177–192.
- [22] M. Rantwijk, R.A. Sheldon, Chem. Rev. 107 (2005) 2757–2785.
- [23] M. Haumann, A. Riisager, Chem. Rev. 108 (2008) 1474–1497.
- [24] M.A.P. Martins, C.P. Frizzo, D.N. Moreira, N. Zantta, H.G. Bonacorso, Chem. Rev. 108 (2008) 2015–2050.
- [25] H. Sakaebe, H. Matsumoto, Electrochem. Commun. 5 (2003) 594–598.
- [26] M. Ishikawa, T. Sugimoto, M. Kikuta, E. Ishiko, M. Kono, J. Power Sources 162 (2006) 658–662.
- [27] S. Seki, Y. Kobayashi, H. Miyashiro, Y. Ohno, Y. Mita, A. Usami, N. Terada, M. Watanabe, Electrochem. Solid-State Lett. 8 (2005) 577–578.
- [28] A. Noda, M.A.B.H. Susan, K. Kudo, S. Mitsuhashi, K. Hayamizu, M. Watanabe, J. Phys. Chem. B 107 (2003) 4024–4033.
- [29] R. Hagiwara, T. Nohira, K. Matsumoto, Y. Tamba, Electrochem. Solid-State Lett. 8 (2005) 231–233.
- [30] M. Ue, M. Takeda, T. Takahashi, M. Takehara, Electrochem. Solid-State Lett. 5 (2002) 119–121.
- [31] D. Kuang, P. Wang, S. Ito, S.M. Zakeeruddin, M. Gratzel, J. Am. Chem. Soc. 128 (2006) 7732–7733.
- [32] J. Lee, M.J. Panzer, Y. He, T.P. Lodge, C.D. Frisbie, J. Am. Chem. Soc. 129 (2007) 4532–4533.
- [33] S. Ono, S. Seki, R. Hirahara, Y. Tominari, J. Takeya, Appl. Phys. Lett. 92 (2008) 103313 (103313).
- [34] R.D. Rogers, K.R. Seddon, Science 302 (2003) 792–793.
- [35] P. Wasserscheid, W. Keim, Angew. Chem. Int. Ed. 39 (2000) 3772–3789.
- [36] Y. Fukaya, K. Hayashi, M. Wada, H. Ohno, Green Chem. 10 (2008) 44–46.
- [37] M. Dienerowitz, M. Mazilu, K. Dholakia, J. Nanophoton. 2 (2008) (art.no. 021875).
- [38] P.K. Jain, X. Huang, I.H. El-Sayed, M.A. El-Sayed, Plasmonics 2 (2007) 107–118.
- [39] F.W. Campbell, R.G. Compton, Anal. Bioanal. Chem. 396 (2010) 241–259.
- [40] K. Watanabe, D. Menzel, N. Nilius, H.J. Freund, Chem. Rev. 106 (2006) 4301–4320.
- [41] C.R. Adams, H.A. Benesi, R.M. Curtis, R.G. Meisenheimer, J. Catal. 1 (1962) 336–344.
- [42] M.T. Reetz, M. Maase, T. Schilling, B. Tesche, J. Phys. Chem. B 104 (2000) 8779–8781.
- [43] D.M. Rubin, J. Sediment Res. 74 (2004) 160–165.
- [44] K. Heinemann, F. Soria, Ultramicroscopy 20 (1986) 1–14.
- [45] M.J. Hytch, M. Gandais, Philos. Mag. A 72 (1995) 619–634.
- [46] M.M.J. Treacy, A. Howie, J. Catal. 63 (1980) 265–269.
- [47] A. Safavi, F. Farjami, Biosens. Bioelectron. 26 (2011) 2547–2552.
- [48] J.C. Claussen, A.D. Franklin, A. ul Haque, D.M. Porterfield, T.S. Fisher, ACS Nano 3 (2009) 37–44.
- [49] J. Yang, W.D. Zhang, S. Gunasekaran, Biosens. Bioelectron. 26 (2010) 279–284.
- [50] S.V. Kergaravat, G.A. Gomez, S.N. Fabiano, T.I.L. Chavez, M.I. Pividori, S.R. Hernandez, Talanta 97 (2012) 484–490.
- [51] V. Roman-Pizarro, J.M. Fernandez-Romero, A. Gomez-Hens, Talanta 99 (2012) 538–543.
- [52] L.C. Gontard, D. Ozkaya, R.E. Dunin-Borkowski, Ultramicroscopy 111 (2011) 101–106.
- [53] J.C. Russ, The Image Processing Handbook, CRC Press Inc., Boca Raton, FL, USA, 2002.
- [54] R.C. Gonzalez, R.E. Woods, Digital Image Processing, Prentice Hall, 2002.
- [55] N. Otsu, IEEE Trans. Syst. Man Cybern. 9 (1979) 62–66.
- [56] P. Sorlier, A. Denuziere, C. Viton, A. Domard, Biomacromolecules 2 (2001) 765–772.
- [57] H. Huang, Q. Yuan, X. Yang, Colloids Surf., B 39 (2004) 31–37.
- [58] F. Xiao, F. Zhao, Y. Zhang, G. Guo, B. Zeng, J. Phys. Chem. C 113 (2009) 849–855.
- [59] R. Kizek, M. Masarik, K.J. Kramer, D. Potesil, M. Bailey, J.A. Howard, B. Klejdus, R. Mikelova, V. Adam, L. Trnkova, F. Jelen, Anal. Bioanal. Chem. 381 (2005) 1167–1178.
- [60] T. Deng, J. Li, S. Huan, H. Yang, H. Wang, G. Shen, R. Yu, Biosens. Bioelectron. 21 (2006) 1545–1552.
- [61] K. Sugawara, S. Tanaka, H. Nakamura, Anal. Chem. 67 (1995) 299–302.
- [62] S. Tanaka, F. Yamamoto, K. Sugarwara, H. Nakamura, Talanta 44 (1997) 357–363.
- [63] K. Sugawara, Y. Yamauchia, S. Hoshi, K. Akatsuka, F. Yamamoto, S. Tanaka, H. Nakamura, Bioelectrochem. Bioenerg. 41 (1996) 167–172.
- [64] J. Wright, K. Rawson, Biosens. Bioelectron. 10 (1995) 495–500.
- [65] B. Lu, E.I. Iwuoha, M.R. Smyth, R. O'Kennedy, Anal. Chim. Acta 345 (1997) 59–66.
- [66] J. Ho, W. Hsu, W. Liao, J. Chiu, M. Chen, H. Chang, C. Li, Biosens. Bioelectron. 26 (2010) 1021–1027.
- [67] S.V. Kergaravat, G.A. Gómez, S.N. Fabiano, Tamara I. Laube Chávez, M.I. Pividori, S.R. Hernández, Talanta 97 (2012) 484–490.
- [68] U. Holler, F. Wächter, C. Wehrli, C. Fizez, J. Chromatogr. B 831 (2006) 8–16.
- [69] S. Nojiri, K. Kamata, M. Nishijima, J. Pharm. Biomed. 16 (1998) 1357–1362.



Preparation of a magnetofluorescent nano-thermometer and its targeted temperature sensing applications in living cells



Zhuyuan Wang, Xueqin Ma, Shenfei Zong, Yuzhong Wang, Hui Chen, Yiping Cui*

Advanced Photonics Center, School of Electronic Science and Engineering, Southeast University, Nanjing 210096, China

ARTICLE INFO

Article history:

Received 15 April 2014

Received in revised form

25 July 2014

Accepted 30 July 2014

Available online 6 August 2014

Keywords:

Magnetic

Thermoresponsive

Targeted temperature sensing

ABSTRACT

A magnetic fluorescent nano-thermometer is presented. To fabricate the nano-thermometer, magnetic nanoparticles (Fe_3O_4) were first encapsulated with a silica layer. Then a poly (*N*-isopropylacrylamide) (pNIPAM) copolymer shell with Rhodamine B isothiocyanate (RhBITC) embedded inside was further coated, which was denoted as the pNIPAM-co-RhBITC shell. Finally, gold nanoparticles were introduced onto the copolymer shell by *in-situ* growth method and the nano-thermometer (denoted as $\text{Fe}_3\text{O}_4@SiO_2@(pNIPAM-co-RhBITC)/Au$) was obtained. The nano-thermometer shows dual responses to both magnetism and temperature. Specifically, the fluorescence intensity of the nano-thermometer decreases as the temperature increases, which makes the nano-thermometer suitable for intracellular temperature sensing. Using this nano-thermometer, temperature changes in live HeLa cells can be successfully detected. Moreover, due to the Fe_3O_4 component, magnetic field guided targeting can be realized, thus targeted temperature sensing can be achieved for living cells. Cellular temperature changes can be easily detected using the proposed nano-thermometer in the range of 26 °C to 41 °C with a sensitivity of $-4.84\% \text{ } ^\circ\text{C}^{-1}$.

© 2014 Elsevier B.V. All rights reserved.

1. Introduction

Temperature is a fundamental thermodynamic variable, the measurement of which is crucial in countless scientific investigations and technological developments. As a result, thermometer occupies 75–80% of the sensor market throughout the world [1]. Today, the unusual thermal effects at microscopic scales, and the unprecedented possibilities provided by nanomaterials have opened up a new avenue toward the development of thermometry on a sub-micron scale with a high spatial resolution [2,3]. When the spatial resolution decreases to the submicron scale (e.g. in intracellular temperature fluctuations [4–11], temperature mapping of microcircuits [12–16] and microfluids [17–22]), the conventional thermometry cannot meet the requirements. Specifically, cellular biological processes are highly temperature dependent, since temperature determines the reactivity and dynamics of most biomolecules. Abnormality in cellular temperature is often an indicator of cellular dysfunction and more importantly occurrence of diseases. For example, temperature in cancerous cells is higher than normal cells due to the increased metabolism of cancer cells. Consequently, monitoring intracellular temperature can provide detailed information on therapeutics and diagnosis of human diseases. However, the microscale

and nanoscale intracellular environment makes ordinary temperature sensing techniques inapplicable, which brings an urgent need in the development and fabrication of nanoscale thermometer. Until now, various methods have been proposed for the nanoscale temperature measurement. Commonly used materials in the construction of nanoscale thermometers include quantum dots [23], copolymers [24,25], nanogels [26–28], nanoparticles [29], and biomaterials [30]. Among these, stimuli-responsive copolymer is an attractive candidate because it can be manipulated by external stimuli. Besides, these stimuli-responsive copolymers possess some unique features, for example, well defined structure, self-assembling behavior, plentiful and tunable reactive groups, which enable the labeling with bichromophoric fluorophores. As one of the stimuli-responsive copolymers, poly (*N*-isopropylacrylamide) (pNIPAM) is a very promising material, since pNIPAM can undergo a unique reversible temperature-induced phase transition at the lower critical solution temperature (LCST) in water. Therefore, it has been widely used for drug delivery [31], sensor [32], and on-off valve [33] etc.

In recent years, magnetic nanomaterials have become a worldwide research focus because they could provide exciting advantages for targeted drug delivery [34], magnetic resonance imaging [35], bioseparation [36], biosensor [37], and hyperthermia [38]. As one of the typical magnetic nanoparticles, superparamagnetic iron oxide nanoparticles (SPIONs) have gained enormous popularity. They can be guided to and maintained at the precise location with an external magnetic field. Coating magnetic nanoparticles with

* Corresponding author.

E-mail address: cyp@seu.edu.cn (Y. Cui).

pNIPAM can result in “smart” nanomaterials with dual responses to both magnetic field and temperature [39–41]. Consequently, by combining magnetic nanoparticles and temperature sensitive polymers, it is possible to construct a nanoscale thermometers.

Here, we present a magnetofluorescent nano-thermometer. To fabricate this nano-thermometer, first, SPIONs are encapsulated with a silica layer. Then a thermo-responsive shell of pNIPAM is deposited on the silica coated SPIONs by emulsion polymerization. Meanwhile, a fluorescent dye (RhBITC) is doped in the pNIPAM shell in this step. Finally, gold nanoparticles (Au NPs) are introduced onto the polymer shell through an *in-situ* growth method. Due to the temperature induced phase transition of pNIPAM, changes in surrounding temperature will eventually result in changes of the distance between the dye molecules and Au NPs. As a result, the fluorescence quenching efficiency will be different, which gives rise to a thermo-sensitive fluorescence emitting behavior. The experimental results showed that the fluorescence intensity had a linear relationship with temperature between 10 °C and 45 °C. In addition, live cell temperature sensing was realized using the nano-thermometer. Moreover, in the presence of an external magnetic field, targeted temperature sensing was achieved.

2. Experimental section

2.1. Materials

Iron(III) chloride hexahydrate (97%), iron(II) chloride tetrahydrate (98%), sodium borohydride, hydrogen tetrachloroaurate(III) trihydrate ($\text{HAuCl}_4 \cdot 3\text{H}_2\text{O}$), and tetraethoxysilane (98%) (TEOS) were purchased from Alfa Aesar. Ammonia water and cetyltrimethylammonium bromide (CTAB) were purchased from Shanghai Chemical Reagents Company (China). *N*-isopropylacrylamide (NIPAM), *N,N*-methylenebis (acrylamide) (BIS), *α,α*-azodiisobutyramidinedihydrochloride (97%) (AAPH), and methacryloxypropyl-trimethoxysilane (MPS) were obtained from Aladdin. Rhodamine B isothiocyanate (RhBITC) was obtained from Sigma. Trisodium citrate dehydrate and ascorbic acid (AA) were purchased from Sinopharm Chemical Reagent Co, Ltd. All of the above chemicals were used as received. Deionized water was used in all experiments.

2.2. Synthesis of superparamagnetic Fe_3O_4 nanoparticles

The Fe_3O_4 nanoparticles (NPs) were synthesized using a coprecipitation recipe reported previously [42]. A three-neck round-bottom flask containing 40 mL of H_2O was heated up to 80 °C under mechanical stirring and N_2 atmosphere. After that, 2.78 g of FeCl_3 and 1 g of FeCl_2 were added. The mixture was stirred for 20 min. Then, 8 mL of ammonia water was added into the above solution and stirred at 80 °C for 1 h. Next, 10 mL of H_2O containing 4 g trisodium citrate dehydrate was added dropwise. Then, the temperature was heated up to 90 °C. After stirring for 1 h, the mixture solution was allowed to cool to room temperature naturally. After that, the Fe_3O_4 NPs were separated with a magnet and washed several times with deionized water.

2.3. Synthesis of $\text{Fe}_3\text{O}_4@SiO_2$ -MPS nanoparticles

$\text{Fe}_3\text{O}_4@SiO_2$ core/shell NPs were prepared by a modified Stöber method [43]. Typically, 80 μL of Fe_3O_4 NPs was added into a mixture of 30 mL of ethanol and 5 mL of deionized water. The above solution was stirred at room temperature. Then 600 μL of TEOS was added dropwise, the mixture was stirred for 20 min. After that, 750 μL ammonia water was injected rapidly into the above solution. After stirring for 24 h, the $\text{Fe}_3\text{O}_4@SiO_2$ NPs were separated with a magnet

and washed repeatedly with ethanol. To functionalize the surface of $\text{Fe}_3\text{O}_4@SiO_2$ NPs with MPS, the $\text{Fe}_3\text{O}_4@SiO_2$ NPs were redispersed in 120 mL of ethanol, then 4 mL of MPS was added to the dispersion. After stirring for 24 h at 35 °C, the $\text{Fe}_3\text{O}_4@SiO_2$ -MPS NPs were washed with ethanol and water several times.

2.4. Synthesis of $\text{Fe}_3\text{O}_4@SiO_2@(pNIPAM-co-RhBITC)/Au$ nanoparticles (the nano-thermometer)

The $\text{Fe}_3\text{O}_4@SiO_2@(pNIPAM-co-RhBITC)$ composites were achieved by a conventional emulsion polymerization method [44] with some modification. Typically, 1 mL of $\text{Fe}_3\text{O}_4@SiO_2$ -MPS was dispersed in a solution containing 0.1 g of NIPAM, 0.01 g of BIS, 200 μL of RhBITC, and 60 mL of deionized water. The above solution was heated to 72 °C, under mechanical stirring and N_2 atmosphere. Then, 1 mL of 4 mg/mL AAPH solution was injected to initiate the polymerization. The polymerization proceeded for 4 h at 72 °C. The mixture solution was then cooled to room temperature. The $\text{Fe}_3\text{O}_4@SiO_2@(pNIPAM-co-RhBITC)$ composites were washed with water several times.

Next, the $\text{Fe}_3\text{O}_4@SiO_2@(pNIPAM-co-RhBITC)/Au$ NPs were prepared by the *in-situ* growth method. First, 0.5 mL of $\text{Fe}_3\text{O}_4@SiO_2@(pNIPAM-co-RhBITC)$ was added into a solution containing 0.182 g of CTAB, 12 μL of HAuCl_4 (5%), and 4 mL of deionized water. The mixture was stirred for 1 h at 25 °C. Then 0.6 mL of NaBH_4 (0.01 M) was added rapidly, which resulted in the formation of a brownish yellow solution. The seed solution was stirred vigorously for 2 min. Second, the growth solution was prepared by the follow procedures. 0.728 g CTAB was dispersed in 10 mL of H_2O and stirred at 25 °C. Then, 400 μL of AgNO_3 (4 mM) and 120 μL of HAuCl_4 (5%) were added. After that, the mixing solution was diluted into 20 mL. Then 10 mM of AA was added dropwise until the growth solution became colorless. After that, 3 mL of the seed solution was injected into the growth solution. The solution was stirred for 5 min and then stood for 30 min. The $\text{Fe}_3\text{O}_4@SiO_2@(pNIPAM-co-RhBITC)/Au$ NPs were washed with water three times and thus the nano-thermometer was obtained.

2.5. Culture of HeLa cells

HeLa cells were cultured in DMEM medium at 37 °C in air/ CO_2 (95:5) condition. Media were supplemented with 10% fetal bovine serum (Biochrom) and 1% penicillin-streptomycin (Nanjing Key-Gen Biotech. Co., Ltd.).

In the intracellular temperature sensing experiments, HeLa cells were seeded into the culture dishes and incubated for 24 h at 37 °C. Then the $\text{Fe}_3\text{O}_4@SiO_2@(pNIPAM-co-RhBITC)/Au$ NPs solution was added into the cell culture dishes (1:5, v/v). After incubation for 2 h, the culture media were discarded and the culture dishes were gently washed with PBS before fluorescence measurements. Four control experiments were performed to prove that targeted temperature sensing can be achieved for living cells.

2.6. Characterization

Extinction spectra were measured by a Shimadzu UV-3600 PC spectrophotometer with quartz cuvettes of 1 cm optical path length. Photoluminescence emission spectrum was measured by an Edinburgh FLS 920 spectrofluorimeter. Transmission electron microscope (TEM) images were obtained with an FEI Tecnai G²T20 electron microscope operating at 200 kV. Fluorescence images were recorded by a confocal laser scanning microscopy (FV 1000, Olympus) with a 10 × microscope objective and the excitation wavelength is 543 nm. The hydrodynamic diameter of the hybrid microspheres was measured by dynamic light scattering (DLS) using an autosizer Zen3690 (Malvern).

3. Results and discussion

3.1. Synthesis and characterization of the nano-thermometer

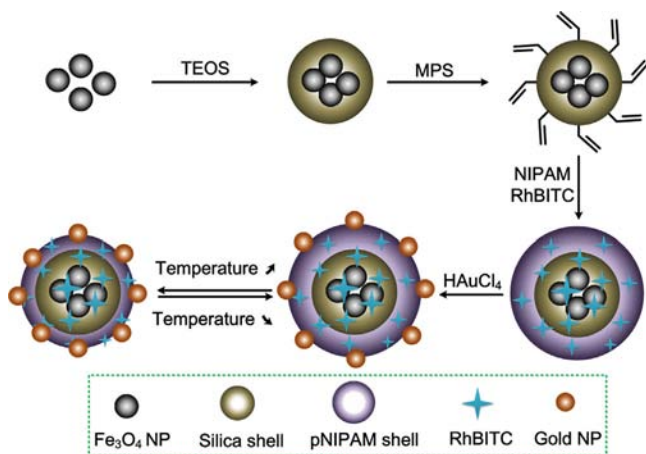
The synthesis procedures for the nano-thermometer ($\text{Fe}_3\text{O}_4@(\text{pNIPAM-co-RhBITC})/\text{Au}$) was presented in Scheme 1. First, the Fe_3O_4 NPs (SPIONs) were prepared by a facile coprecipitation method [42]. Then a sol-gel process was used to coat the as-prepared Fe_3O_4 NPs with a layer of silica. Then MPS was used as the silane coupling agent which contains carbon-carbon double bonds. The C=C bond modified surfaces of the silica-coated magnetic NPs can react with the monomer of a polymer in aqueous phase radical polymerization. This step is essential to realize the encapsulation of template cores via radical polymerization. Second, the polymerization of NIPAM, RhBITC, and BIS on the silica surface was carried out in deionized water, resulting in double-shell magnetic pNIPAM microspheres. Finally, Au NPs were grown onto the surface of the composite magnetic microspheres by an *in-situ* growth method.

Fig. 1 displays the TEM images of the core/shell structured NPs. As can be seen, the average diameter of the SPIONs synthesized by the coprecipitation process [42] is 10 nm (Fig. 1a). In the reaction, trisodium citrate dehydrate was used for biocompatible surface modification, which led to the formation of abundant carboxyl groups on the surfaces of the SPIONs. After being coated with a silica layer by a modified Stöber sol-gel method [43], $\text{Fe}_3\text{O}_4@(\text{pNIPAM-co-RhBITC})/\text{Au}$ NPs were obtained, which are uniform both in size and shape. The average diameter of the $\text{Fe}_3\text{O}_4@(\text{pNIPAM-co-RhBITC})/\text{Au}$ NPs is 150 nm (Fig. 1b). In such a structure, the silica coating plays an important role in two aspects. First, the silica coating can effectively screen the magnetic dipolar

attraction between magnetic NPs, which facilitates the dispersion of magnetic NPs in organic or inorganic solutions without swelling as well as protects them from leaching in an acidic environment. Second, this coating provides the SPIONs with a silica surface, which possesses a large amount of terminated silanol. This allows further modification with various groups or ligands through well-developed silane chemistry that are useful for practical applications [45]. To functionalize the magnetic silica NPs, various methods such as surface-initiation polymerization and precipitation polymerization can be used, resulting in a variety of functional polymeric shells [45]. Here, a thermoresponsive shell of pNIPAM anchored with Au NPs was deposited onto the surfaces of the core/shell magnetic NPs by precipitation polymerization [44], thus the $\text{Fe}_3\text{O}_4@(\text{pNIPAM-co-RhBITC})/\text{Au}$ particles were obtained (Fig. 1c). Due to the thermosensitive characteristics of the polymer layer, the distance between the dye molecules and Au NPs can be adjusted by changing the surrounding temperature, which eventually changes the fluorescence quenching effect between the Au NPs and dye molecules. In this way, a thermo-sensitive fluorescence emitting property was obtained. By monitoring the fluorescence intensity, information about the surrounding temperature can be acquired, realizing a fluorescence based nano-thermometer. Besides, by employing an external magnetic field, the $\text{Fe}_3\text{O}_4@(\text{pNIPAM-co-RhBITC})/\text{Au}$ NPs (*i.e.* the nano-thermometer) could also be used as targeted temperature sensor.

Fig. 2a shows the extinction spectra of the as-synthesized $\text{Fe}_3\text{O}_4@(\text{pNIPAM-co-RhBITC})/\text{Au}$ NPs, $\text{Fe}_3\text{O}_4@(\text{pNIPAM-co-RhBITC})$ NPs and $\text{Fe}_3\text{O}_4@(\text{pNIPAM-co-RhBITC})/\text{Au}$ NPs. It can be observed that the $\text{Fe}_3\text{O}_4@(\text{pNIPAM-co-RhBITC})$ NPs (curve a) have no obvious extinction peak in the visible region. The $\text{Fe}_3\text{O}_4@(\text{pNIPAM-co-RhBITC})$ NPs (curve b) have a similar spectral shape compared to the $\text{Fe}_3\text{O}_4@(\text{pNIPAM-co-RhBITC})$ NPs (curve a), but a small extinction peak at around 550 nm could be observed, which is attributed to RhBITC. After growing Au NPs on the surfaces of the $\text{Fe}_3\text{O}_4@(\text{pNIPAM-co-RhBITC})$ NPs, the composite NPs exhibit an obvious extinction peak at 525 nm, which confirms the successful deposition of Au NPs.

Dynamic light scattering (DLS) was used to investigate the swelling/shrinking behavior of $\text{Fe}_3\text{O}_4@(\text{pNIPAM-co-RhBITC})/\text{Au}$ NPs. Fig. 2b shows the dependence of hydrodynamic diameter as a function of temperature. As expected, the composite magnetic NPs exhibit continuous thermo-responsive volume phase-transition characteristics. This result confirms that NIPAM monomers have been successfully polymerized onto the surface of the NPs, which is consistent with the TEM observation. Comparing the diameter of the $\text{Fe}_3\text{O}_4@(\text{pNIPAM-co-RhBITC})$ NPs determined from TEM images and DLS measurements, it could be found that the diameter obtained in DLS measurement is larger. This is probably due to the fact that the DLS measurements were performed in aqueous solution, while the TEM measurements were performed



Scheme 1. Schematic illustration of the preparation process of the nano-thermometer (denoted as $\text{Fe}_3\text{O}_4@(\text{pNIPAM-co-RhBITC})/\text{Au}$).

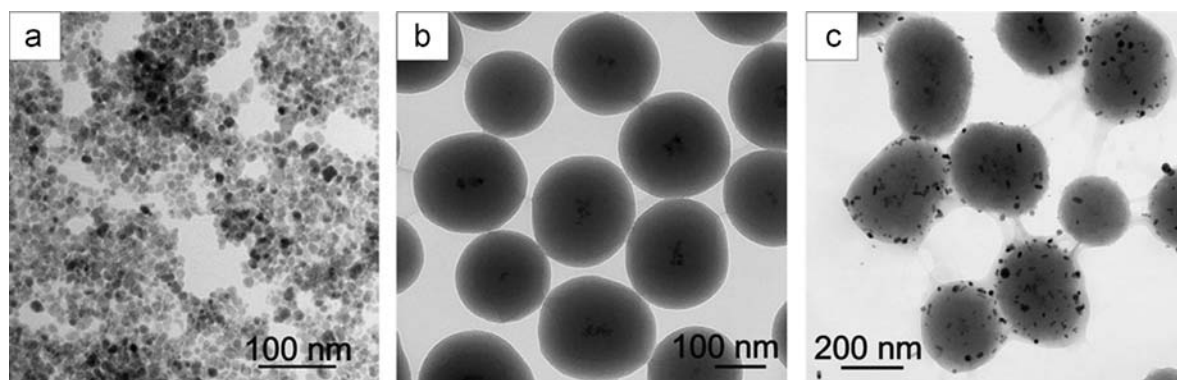


Fig. 1. TEM images of (a) the Fe_3O_4 NPs (SPIONs); (b) the $\text{Fe}_3\text{O}_4@(\text{pNIPAM-co-RhBITC})/\text{Au}$ NPs; (c) the nano-thermometer.

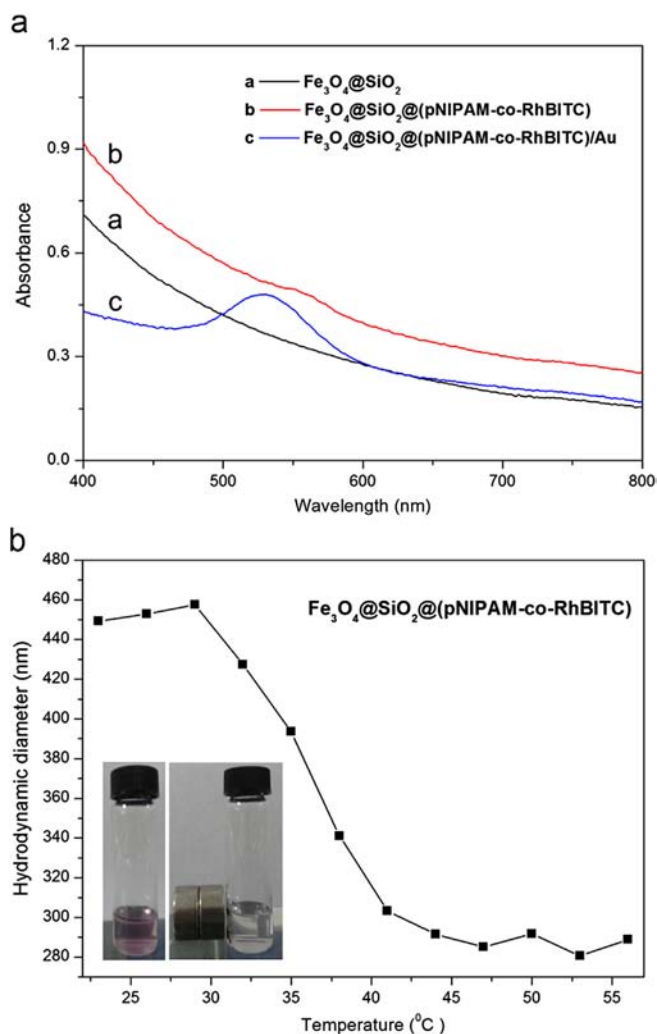


Fig. 2. (a) Extinction spectra of the aqueous dispersion of $\text{Fe}_3\text{O}_4@\text{SiO}_2$ NPs, $\text{Fe}_3\text{O}_4@\text{SiO}_2@(\text{pNIPAM-co-RhBtC})$ NPs, and $\text{Fe}_3\text{O}_4@\text{SiO}_2@(\text{pNIPAM-co-RhBtC})/\text{Au}$ NPs. (b) Dependence of the hydrodynamic diameter of $\text{Fe}_3\text{O}_4@\text{SiO}_2@(\text{pNIPAM-co-RhBtC})$ upon temperature. The inset shows the photograph of the nano-thermometer ($\text{Fe}_3\text{O}_4@\text{SiO}_2@(\text{pNIPAM-co-RhBtC})/\text{Au}$ NPs) suspension before and after magnetic separation by an external magnet.

in the dry state. The difference between these measurements are probably caused by the swelling of the pNIPAM shell [45]. As shown in Fig. 2b, the hydrodynamic diameter of the $\text{Fe}_3\text{O}_4@\text{SiO}_2@(\text{pNIPAM-co-RhBtC})$ NPs decreased with increased temperature. A much steeper decrease was observed from 35 $^{\circ}\text{C}$ to 38 $^{\circ}\text{C}$, where the diameter decreased from 393 to 341 nm, indicating that the phase transition temperature was about 36 $^{\circ}\text{C}$. The inset in Fig. 2b exhibits the separation and redispersion of the nano-thermometer ($\text{Fe}_3\text{O}_4@\text{SiO}_2@(\text{pNIPAM-co-RhBtC})/\text{Au}$ NPs) in deionized water. Upon the placement of an external magnet beside the vial, all the composite particles were accumulated on the side of the vial, leaving the solution transparent. When the magnet was removed, the particles were well-redispersed by shaking and ultrasonication. The above experimental results demonstrated that the nano-thermometer exhibited an excellent magnetic response.

3.2. Temperature dependent fluorescence emission of the nano-thermometer

It is well-known that thermo-responsive pNIPAM microgels exhibit thermo-induced swelling/collapse behavior in aqueous dispersion,

accompanied by considerable volume changes. In this composite structure, RhBtC molecules acted as the fluorophore, and Au NPs acted as the quencher. Owing to the temperature sensitive characteristics of the polymer layer, the distance between the dye molecules

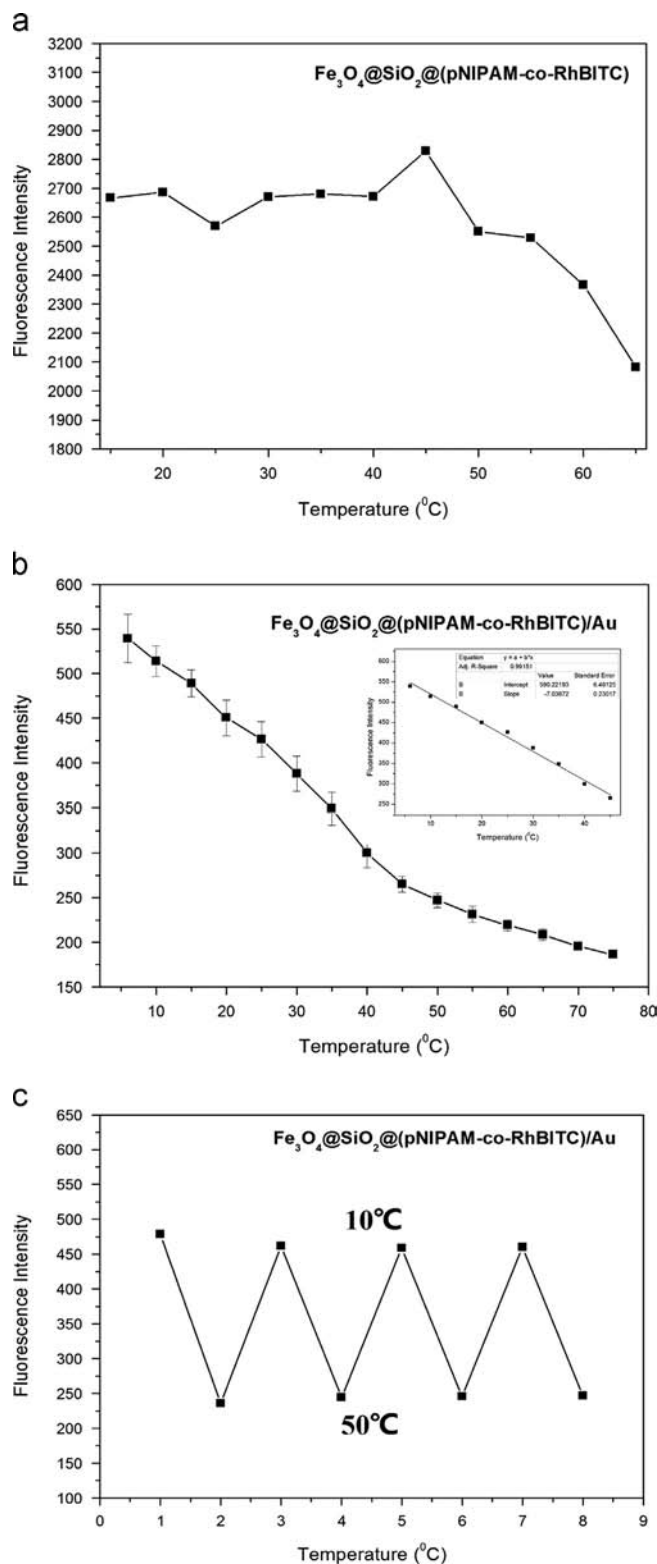


Fig. 3. Fluorescence emission spectra of (a) $\text{Fe}_3\text{O}_4@\text{SiO}_2@(\text{pNIPAM-co-RhBtC})$ NPs and (b) $\text{Fe}_3\text{O}_4@\text{SiO}_2@(\text{pNIPAM-co-RhBtC})/\text{Au}$ NPs at various temperatures. (c) Change in fluorescence emission intensity of $\text{Fe}_3\text{O}_4@\text{SiO}_2@(\text{pNIPAM-co-RhBtC})/\text{Au}$ NPs during repeated heating or cooling processes. All the emission spectra are obtained after irradiating the solution at 550 nm. The error bars represent the standard deviation of 5 measurements using different batches of nano-thermometer.

and Au NPs can be adjusted by the surrounding temperature. Under different temperatures, the distance between dyes and Au NPs will be different, resulting in different fluorescence quenching efficiency and different fluorescence intensity. Thus a temperature dependent fluorescence behavior can be obtained. When the temperature is lower than the LCST of pNIPAM, the pNIPAM layer is in a swollen state, so the Au NPs and RhBITC are apart from each other. As a result, Au NPs can hardly affect the fluorescence emitting from the dye molecules. On the other hand, when the temperature is higher than the LCST of pNIPAM, the pNIPAM layer shrinks, therefore the distance between Au NPs and RhBITC becomes short enough for Au NPs to effectively quench the fluorescent emission of the dye molecules.

Fig. 3 shows the emission spectra of $\text{Fe}_3\text{O}_4@SiO_2@(pNIPAM-co-RhBITC)$ and $\text{Fe}_3\text{O}_4@SiO_2@(pNIPAM-co-RhBITC)/Au$ NPs as a function of temperature. The emission spectra were obtained with an excitation wavelength of 550 nm, which was determined according to the absorption wavelength of RhBITC. Fig. 3a shows that the intensity of $\text{Fe}_3\text{O}_4@SiO_2@(pNIPAM-co-RhBITC)$ NPs did not change obviously as the temperature decreased from 65 °C to 15 °C. On the other hand, for $\text{Fe}_3\text{O}_4@SiO_2@(pNIPAM-co-RhBITC)/Au$ NPs (the nano-thermometer), as shown in Fig. 3b, when the temperature decreased from 75 °C to 45 °C, the fluorescence intensity did not change significantly. However, when the temperature continued to decrease, the intensity increased significantly and showed a linear relationship with temperature (shown in the inset of Fig. 3b). Moreover, the thermo-induced changing of the fluorescence intensity of the nano-thermometer is reversible. Upon heating from 10 °C to 50 °C, the fluorescence intensity of the nano-thermometer decreased back to the original intensity at 50 °C and this cycle can be repeated for at least 4 times without any apparent fatigue effects and hysteresis.

3.3. Intracellular temperature sensing

The nano-thermometer can also be used for cellular temperature sensing. To demonstrate magnetic field guided targeting and

temperature sensing capabilities of the nano-thermometer, we used the nano-thermometer ($\text{Fe}_3\text{O}_4@SiO_2@(pNIPAM-co-RhBITC)/Au$ NPs) for measuring intracellular temperature. Here, $\text{Fe}_3\text{O}_4@SiO_2@(pNIPAM-co-RhBITC)/Au$ NPs were taken up by live HeLa cells *via* endocytosis without any additional reagents. A magnet was put under one sample dish, while the control dish was not exposed to a magnet. After taking up the nano-thermometer, the cells were washed with PBS buffer to remove the excess $\text{Fe}_3\text{O}_4@SiO_2@(pNIPAM-co-RhBITC)/Au$ NPs that were suspended in the culture medium or adhered on the cell surfaces. Before fluorescence measurement, cells were placed at 4 °C or 25 °C for 20 min. Then fluorescence images were acquired as fast as possible. Fig. 4 shows the confocal microscopic images of HeLa cells incubated with $\text{Fe}_3\text{O}_4@SiO_2@(pNIPAM-co-RhBITC)/Au$ NPs. As shown in Fig. 4a and b, the cells incubated at 4 °C displayed stronger fluorescence than those incubated at 25 °C (Fig. 4c and d). Moreover, the superparamagnetism of the nano-thermometer could provide a strong contrast effect, as shown in the left and right panels. When a magnet was placed under the culture dish, the cells were relatively dense. These results demonstrated that the nano-thermometer could sense the intracellular temperature changes in living cells. In addition, with the aid of an external magnetic field, magnetic targeting are realized.

Next, to carefully investigate the intracellular sensing behavior of the proposed nano-thermometer, the fluorescence images of HeLa cells incorporated with the nano-thermometer were collected, under different temperatures. The temperature of the cells was controlled by placing the cell culture dish on a thermo-plate, which is capable of precisely control the surrounding temperature. As can be seen from the fluorescence images of HeLa cells shown in Fig. 5, when the temperature was relatively low, bright fluorescence was observed. When the temperature gradually increased from 4 °C to 25 °C, fluorescence intensity in these HeLa cells gradually decreased. When the temperature increased continuously, an abrupt decrease in fluorescence intensity was observed. This temperature dependent intracellular behavior of

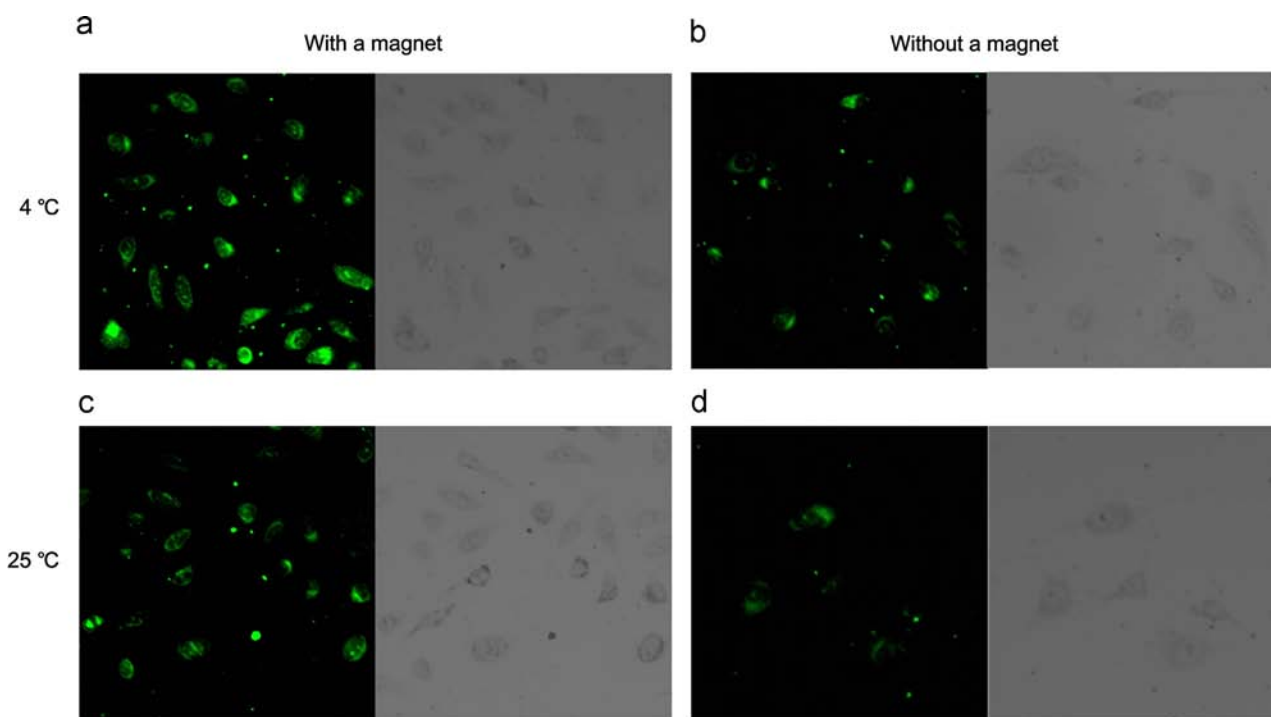


Fig. 4. Confocal microscopy images of HeLa cells treated with $\text{Fe}_3\text{O}_4@SiO_2@(pNIPAM-co-RhBITC)/Au$ NPs, (a, b) at 4 °C and (c, d) at 25 °C. Left panel: with a magnet placed under the culture dish, right panel: without a magnet placed under the culture dish. The excitation wavelength is 543 nm.

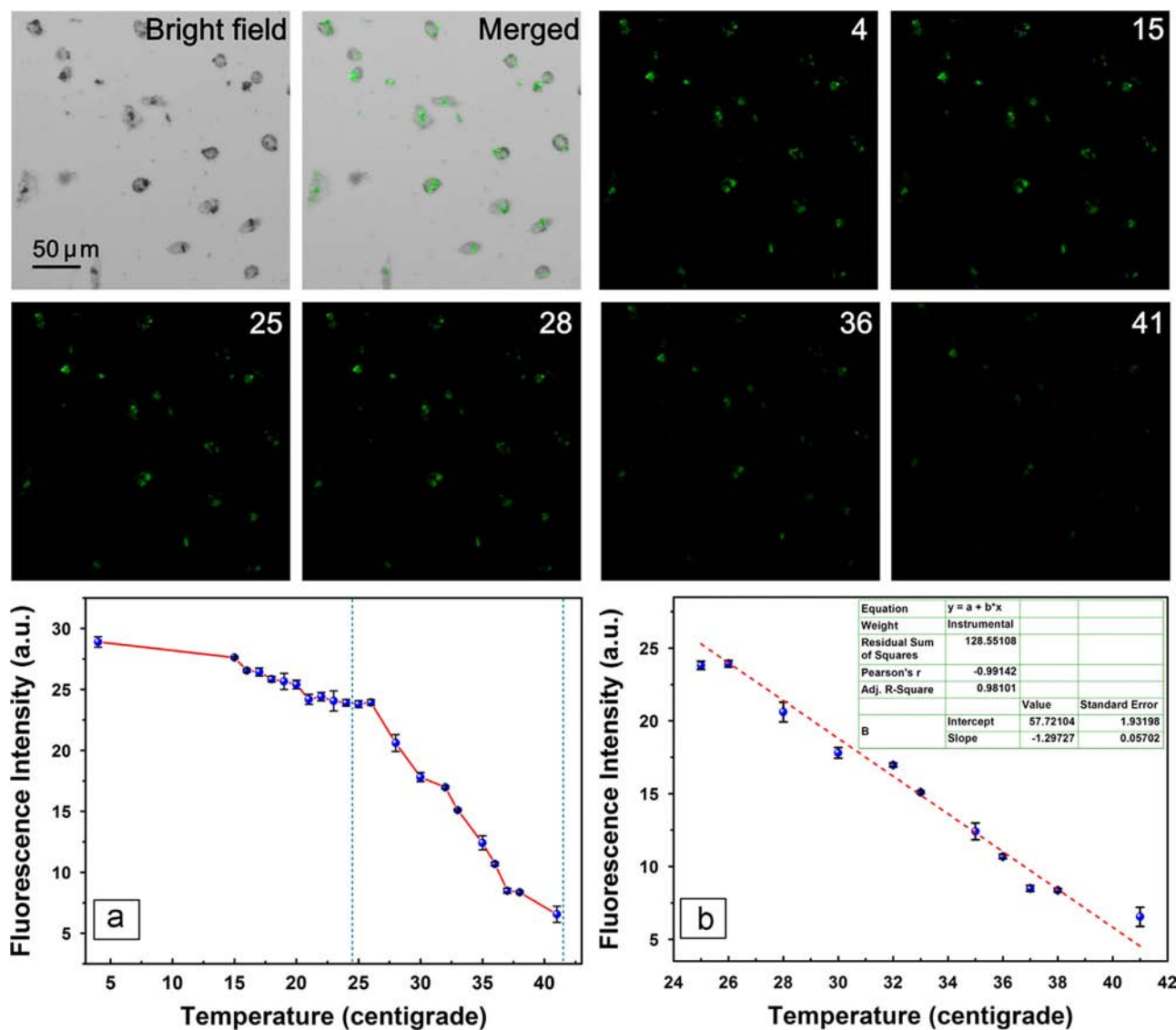


Fig. 5. Bright field and fluorescence images of HeLa cells incorporated with the nano-thermometer under different temperatures. (a) Temperature dependent fluorescence intensity, (b) the fluorescence intensity is linearly correlated with the cellular temperature in the range from 26 °C to 41 °C (Fig. 5b). Fluorescence intensities were analyzed by the Olympus Fluoview Software (Ver. 1.7c). The error bars represent standard deviation of three measurements using different batches of nano-thermometer.

the nano-thermometer was better demonstrated in the two curves in Fig. 5a and b. Interestingly, the fluorescence intensity acquired from these HeLa cells was linearly dependent on the cellular temperature in a quite large range (from 26 °C to 41 °C) (Fig. 5b). Since the temperature sensitivity is defined as $\Delta I / (I_{ref} \Delta T)$, where ΔI is the decrement of fluorescence intensity over the measured temperature range (ΔT), and I_{ref} is the initial (26 °C) fluorescence intensity, the temperature sensitivity of the presented nano-thermometer is estimated to be $-4.84\% \text{ } ^\circ\text{C}^{-1}$. The nano-thermometer also has a good reproducibility. In the intracellular experiments, three different batches of nano-thermometer were tested, and they all exhibited a similar temperature dependent fluorescence emission property as demonstrated in Fig. 5a and b. These experimental results well confirmed the intracellular thermo-sensing ability of the presented nano-thermometer.

It is worth mentioning that a major limitation of such nanomaterial based thermometers is that they have to be incorporated into cells before they can sense the cellular temperature. Cellular temperature before the nano-thermometer is taken up by cells cannot be measured. However, once the nano-thermometer is taken up by cells, *in-situ* measurements of intracellular temperatures can be realized using

our nano-thermometer, as demonstrated in the revised Fig. 5. Fluorescence of the same HeLa cells was measured under different temperatures. Besides, in the experiment, we did not observe any biological and morphological changes of the cells after taking up these nano-thermometers, which indicated that the nano-thermometer had little impact on the physiological function of the cells. As a result, despite of its limitation, the nano-thermometer is still a potential intracellular temperature sensor.

Although the sensitivity is not as high compared with previously published works [46–48], the major advantage of the nano-thermometer presented here is its ability to simultaneously realize magnetic field guided targeting and temperature sensing. For example, in *in vivo* applications, the nano-thermometer can be guided to the tumor site using an external magnetic field, and subsequently detect the temperature in tumor. Aside from the magnetic field guided temperature sensing ability, the magnetic component of the nano-thermometer also provides a possibility of realizing hyperthermia-based therapy [49]. This makes the proposed nano-thermometer a multifunctional sensing nanoplatform compared with other thermometers which were designed solely to accomplish temperature sensing [50,51].

4. Conclusions

In this work, a magnetic fluorescent nano-thermometer ($\text{Fe}_3\text{O}_4@-\text{SiO}_2@(\text{pNIPAM-co-RBITC})/\text{Au}$) was fabricated for intracellular temperature sensing as well as magnetic field guided targeting. The fluorescence intensity of the nano-thermometer decreased as the temperature increased, and it could be used to detect the temperature in the range from 10 °C to 45 °C. The nano-thermometer was also introduced into live HeLa cells via endocytosis for measuring intracellular temperatures. The results demonstrated that it could sense different temperatures in living cells. Cellular temperature changes can be easily detected using the proposed nano-thermometer in the range of 26 °C to 41 °C with a sensitivity of $-4.84\% \text{ } ^\circ\text{C}^{-1}$. Moreover, with the aid of an external magnetic field, the targeted temperature sensing can be achieved. With the ability to fulfill magnetic targeted intracellular temperature sensing, the proposed nano-thermometer holds a great potential in the analysis of cellular physical and biological environments, which can facilitate the detailed investigation of some complicated biological processes, such as metabolism of anticancer drugs or cellular damage responses.

Acknowledgements

This work was supported by the Natural Science Foundation of China (NSFC) (Nos. 61275182, 61177033, 21104009), Science Foundation for The Excellent Youth Scholars of Southeast University, the Scientific Research Foundation of Graduate School of Southeast University (YBJJ1125), the Scientific Innovation Research Foundation of College Graduate in Jiangsu Province (CXZZ12_0094) and the Fundamental Research Funds for the Central Universities.

References

- [1] P.R.N. Childs, J.R. Greenwood, C.A. Long, *Rev. Sci. Instrum.* 71 (2000) 2959.
- [2] J. Lee, N.A. Kotov, *Nano Today* 2 (2007) 48–51.
- [3] K.M. McCabe, M. Hernandez, *Pediatr. Res.* 67 (2010) 469–475.
- [4] C.F. Chapman, Y. Liu, G.J. Sonek, B.J. Tromberg, *Photochem. Photobiol.* 62 (1995) 416–425.
- [5] O. Zohar, M. Ikeda, H. Shinagawa, H. Inoue, H. Nakamura, D. Elbaum, D.L. Alkon, T. Yoshioka, *Biophys. J.* 74 (1998) 82–89.
- [6] M. Suzuki, V. Tseeb, K. Oyama, S. Ishiwata, *Biophys. J.* 92 (2007) L46–L48.
- [7] C. Gota, K. Okabe, T. Funatsu, Y. Harada, S. Uchiyama, *J. Am. Chem. Soc.* 131 (2009) 2766–2767.
- [8] H. Huang, S. Delikanli, H. Zeng, D.M. Ferkey, A. Pralle, *Nat. Nanotechnol.* 5 (2010) 602–606.
- [9] J.M. Yang, H. Yang, L.W. Lin, *ACS Nano* 5 (2011) 5067–5071.
- [10] K. Okabe, N. Inada, C. Gota, Y. Harada, T. Funatsu, S. Uchiyama, *Nat. Commun.* 3 (2012) 705.
- [11] C.L. Wang, R.Z. Xu, W.J. Tian, X.L. Jiang, Z.Y. Cui, M. Wang, H.M. Sun, K. Fang, N. Gu, *Cell Res.* 21 (2011) 1517–1519.
- [12] P. Kolodner, J.A. Tyson, *Appl. Phys. Lett.* 42 (1983) 117–119.
- [13] L. Aigouy, G. Tessier, M. Mortier, B. Charlot, *Appl. Phys. Lett.* 87 (2005) 184105.
- [14] G. Tessier, M. Bardoux, C. Boue, D. Fournier, *Appl. Phys. Lett.* 90 (2007) 171112.
- [15] W.J. Liu, B.Z. Yang, *Sens. Rev.* 27 (2007) 298–309.
- [16] W. Jung, Y.W. Kim, D. Yim, J.Y. Yoo, *Sens. Actuators, A* 171 (2011) 228–232.
- [17] H.B. Mao, T.L. Yang, P.S. Cremer, *J. Am. Chem. Soc.* 124 (2002) 4432–4435.
- [18] R. Samy, T. Glawdel, C.L. Ren, *Anal. Chem.* 80 (2008) 369–375.
- [19] C. Gosse, C. Bergaud, P. Lw, *Topics in Advanced Physics*, (Ed.), S. Volz. Springer-Verlag, Berlin, 2009, 118, 301–341.
- [20] T. Barilero, T. Le Saux, C. Gosse, L. Jullien, *Anal. Chem.* 81 (2009) 7988–8000.
- [21] E.M. Graham, K. Iwai, S. Uchiyama, A.P. deSilva, S.W. Magennis, A.C. Jones, *Lab Chip* 10 (2010) 1267–1273.
- [22] J. Feng, K.J. Tian, D.H. Hu, S.Q. Wang, S.Y. Li, Y. Zeng, Y. Li, G.Q. Yang, *Angew. Chem. Int. Ed.* 50 (2011) 8072–8076.
- [23] L.M. Maestro, E.M. Rodriguez, F.S. Rodriguez, M.C. IglesiasdelaCruz, A. Juarranz, R. Naccache, F. Vetrone, D. Jaque, J.A. Capobianco, J.G. Sole, *Nano Lett.* 10 (2010) 5109.
- [24] S. Uchiyama, N. Kawai, A.P. de Silva, K. Iwai, *J. Am. Chem. Soc.* 126 (2004) 3032.
- [25] Q. Yan, J.Y. Yuan, W.Z. Yuan, M. Zhou, Y.W. Yin, C.Y. Pan, *Chem. Commun.* 6 (2008) 188.
- [26] C. Gota, K. Okabe, T. Funatsu, Y. Harada, S. Uchiyama, *J. Am. Chem. Soc.* 131 (2009) 2766.
- [27] H.S. Peng, J.A. Stolwijk, L.N. Sun, J. Wegener, O.S. Wolfbeis, *Angew. Chem. Int. Ed.* 49 (2010) 4246.
- [28] C.Y. Chen, C.T. Chen, *Chem. Commun.* 47 (2011) 994.
- [29] F. Vetrone, R. Naccache, A. Zamarron, A.J. de la Fuente, F. Sanz-Rodriguez, L.M. Maestro, E.M. Rodriguez, D. Jaque, J.G. Sole, J.A. Capobianco, *ACS Nano* 4 (2010) 3254.
- [30] R. Tashiro, H. Sugiyama, *Angew. Chem. Int. Ed.* 42 (2003) 6018.
- [31] G.H. Hsiue, S.H. Hsu, C.C. Yang, *Biomaterials* 23 (2003) 457–462.
- [32] J.M. Weissman, H.B. Sunkara, A.S. Tse, S.A. Asher, *Science* 274 (1996) 959.
- [33] C.E. Reese, A.V. Mikhonin, S.A. Asher, *J. Am. Chem. Soc.* 126 (2004) 1493–1496.
- [34] J. Gautier, E. Munnier, A. Paillard, K. Hervé, L. Douziech-Eyrolles, M. Soucé, P. Dubois, I. Chourp, *Int. J. Pharm.* 423 (2011) 16–25.
- [35] C. Fan, W. Gao, Z. Chen, H. Fan, M. Li, F. Deng, Z. Chen, *Int. J. Pharm.* 404 (2011) 180–190.
- [36] Y. Zhuo, P.X. Yuan, R. Yuan, Y.Q. Chai, C.L. Hong, *Biomaterials* 30 (12) (2009) 2284–2290.
- [37] B.D. Wang, J. Hai, Z.C. Liu, Q. Wang, Z.Y. Yang, S.H. Sun, *Angew. Chem. Int. Ed.* 49 (2010) 4576–4579.
- [38] C.H. Hou, S.M. Hou, Y.S. Hsueh, J. Lin, H.C. Wu, F.H. Lin, *Biomaterials* 30 (2009) 3956–3960.
- [39] R.A. Frimpong, J.Z. Hilt, *Nanotechnology* 19 (2008) 175101–175107.
- [40] Y. Sun, X. Ding, Z. Zheng, X. Cheng, X. Hu, Y. Peng, *Chem. Commun.* (2006) 2765–2767.
- [41] J.L. Zhang, R.S. Srivastava, R.D.K. Misra, *Langmuir* 23 (2007) 6342–6351.
- [42] Y. Sahoo, A. Goodarzi, M.T. Swihart, et al., *J. Phys. Chem. B* 109 (9) (2005) 3879–3885.
- [43] W. Stöber, A. Fink, J. Colloid Interface Sci. 26 (1) (1968) 62–69.
- [44] R.H. Pelton, P. Chibante, *Colloids Surf* 20 (1986) 247–256.
- [45] B. Luo, X.J. Song, F. Zhang, A. Xia, W.L. Yang, J.H. Hu, C.C. Wang, *Langmuir* 26 (3) (2010) 1674–1679.
- [46] L. Yang, H.S. Peng, H. Ding, F.T. You, L.L. Hou, F. Teng, *Microchim. Acta* 181 (2014) 743–749.
- [47] H. Wang, F. Ke, A. Mararenko, Z. Wei, P. Banerjee, S. Zhou, *Nanoscale* 6 (2014) 7443–7452.
- [48] L. Shang, F. Stockmar, N. Azadfar, G. Nienhaus, *Angew. Chem. Int. Ed.* 52 (2013) 11154–11157.
- [49] C. Kumar, F. Mohammad, *Adv. Drug Deliv. Rev.* 63 (2011) 789–808.
- [50] G. Ke, C. Wang, Y. Ge, N. Zheng, Z. Zhu, C.J. Yang, *J. Am. Chem. Soc.* 134 (2012) 18908–18911.
- [51] J. Qiao, L. Qi, Y. Shen, L. Zhao, C. Qi, D. Shangquan, L. Mao, Y. Chen, *J. Mater. Chem.* 22 (2012) 11543–11549.



Simultaneous speciation analysis of inorganic arsenic, chromium and selenium in environmental waters by 3-(2-aminoethylamino) propyltrimethoxysilane modified multi-wall carbon nanotubes packed microcolumn solid phase extraction and ICP-MS

Hanyong Peng, Nan Zhang, Man He, Beibei Chen, Bin Hu*

Key Laboratory of Analytical Chemistry for Biology and Medicine (Ministry of Education), Department of Chemistry, Wuhan University, Wuhan 430072, PR China

ARTICLE INFO

Article history:

Received 4 April 2014

Received in revised form

17 July 2014

Accepted 21 July 2014

Available online 25 July 2014

Keywords:

AAPTS functionalized MWCNTs adsorbent

Simultaneous speciation of inorganic

arsenic, selenium and chromium

ICP-MS

Environmental waters

ABSTRACT

Speciation analysis of inorganic arsenic, chromium and selenium in environmental waters is of great significance for the monitoring of environmental pollution. In this work, 3-(2-aminoethylamino) propyltrimethoxysilane (AAPTS) functionalized multi-wall carbon nanotubes (MWCNTs) were synthesized and employed as the adsorbent for simultaneous speciation analysis of inorganic arsenic, chromium and selenium in environmental waters by microcolumn solid-phase extraction (SPE)-inductively coupled plasma mass spectrometry (ICP-MS). It was found that As(V), Cr(VI) and Se(VI) could be selectively adsorbed on the microcolumn packed with AAPTS-MWCNTs adsorbent at pH around 2.2, while As(III), Cr(III) and Se(IV) could not be retained at this pH and passed through the microcolumn directly. Total inorganic arsenic, chromium and selenium was determined after the oxidation of As(III), Cr(III) and Se(IV) to As(V), Cr(VI) and Se(VI) with $10.0 \mu\text{mol L}^{-1}$ KMnO_4 . The assay of As(III), Cr(III) and Se(IV) was based on subtracting As(V), Cr(VI) and Se(VI) from the total As, Cr and Se, respectively. Under the optimized conditions, the detection limits of 15, 38 and 16 ng L^{-1} with the relative standard deviations (RSDs) of 7.4, 2.4 and 6.2% ($c = 1 \mu\text{g L}^{-1}$, $n = 7$) were obtained for As(V), Cr(VI) and Se(VI), respectively. The developed method was validated by analyzing four Certified Reference Materials, rainwater, Yangtze River and East Lake waters.

© 2014 Elsevier B.V. All rights reserved.

1. Introduction

Recently, there has been increasing interest in the field of arsenic, selenium and chromium speciation due to their toxicological and biological properties [1–5]. Arsenic contamination in natural waters is a world-wide problem and the World Health Organization (WHO) guideline value for As in drinking water has been reduced from 50 to $10 \mu\text{g L}^{-1}$ (daily intake) [6]. The concentration range between selenium as an essential and toxic element is rather narrow, only in the range of $50\text{--}200 \mu\text{g d}^{-1}$, selenium is beneficial to human health [7], and the permissible limit of Se in drinking waters prescribed by WHO is $10 \mu\text{g L}^{-1}$. Chromium is widely used in various industries, such as plating, tanning, paint and pigment production and metallurgy, which could possibly

contaminate the environmental waters and enter human body through intake of water [8].

In most environmental matrices (such as river, lake and rain water), arsenic, selenium and chromium were usually present as their inorganic forms of As(III)/As(V), Se(IV)/Se(VI) and Cr(III)/Cr(VI) [9–11]. It is well known that the toxicological and biological properties of most elements depend upon their chemical forms. Because these elements could enter organisms from environmental waters through food chains, the information about the concentration of inorganic As, Se and Cr species in environment waters is important for environmental monitoring and water treatment. Therefore, it is particularly important to develop analytical methods for the simultaneous speciation analysis of inorganic arsenic, selenium and chromium in environmental water samples.

The speciation analysis of arsenic, selenium and chromium in environmental waters could be performed by combining high efficient separation techniques with elements specific detection techniques [1,12,13]. Of all element specific detection techniques,

* Corresponding author. Tel.: +86 27 68752162; fax: +86 27 68754067.

E-mail address: binhu@whu.edu.cn (B. Hu).

inductively coupled plasma mass spectrometry (ICP-MS) has been considered to be one of the most efficient and robust element-specific techniques due to its low detection limit, wide linear range, multielement and isotope capability [14]. The separation techniques for elemental speciation include chromatographic approaches such as high performance liquid chromatography (HPLC) [12], ion chromatography [15] as well as capillary electrophoresis [16], and non-chromatographic methods such as solvent extraction, coprecipitation, cloud point extraction (CPE) [17], solid phase extraction (SPE) [18] and liquid phase microextraction (LPME) [19]. For a simple elemental speciation, especially valence state of arsenic, chromium and selenium, non-chromatographic methods are more diffused than the chromatographic techniques. Among the above non-chromatographic methods, SPE is the most commonly used separation technique for a simple elemental speciation, due to the advantages such as absence of emulsion, high enrichment factors, flexibility and easy automation. Since the adsorption materials play a very important role in SPE, the current researches in SPE are mainly focused on the development of new adsorbents. More recently, some novel SPE adsorbents such as nanometer-sized materials [20,21], mesoporous materials [18], fullerene [22], and carbon nanotubes [23] have been explored for SPE.

Carbon nanotubes (CNTs) [24], which were first discovered by Iijima, have aroused greatest interest in many interdisciplinary investigations [25]. Although raw CNTs walls are not reactive, oxidation of CNTs (such as HNO₃, NaOCl, and KMnO₄ solutions) can lead to surface functionalization with oxygen-containing groups (e.g., carboxylic, carbonyl and hydroxyl) [25–28], allowing retention of cations. To improve the adsorption property of CNTs, the modification of CNTs by physical or chemical procedure is usually suggested [29]. The adsorption behaviors of metal ions (such as Cd²⁺, Cu²⁺, Ni²⁺, Pb²⁺, Zn²⁺, Co²⁺ and Mn²⁺) on CNTs or modified CNTs were studied in recent publications [30–33]. The use of multi wall CNTs (MWCNTs) as the SPE adsorbents for the speciation analysis of Cr [34] and V [35] has also been reported. These research works have demonstrated the great potentiality of CNTs as the SPE adsorbents for trace elements and their species analysis.

In recent years, the simultaneous speciation analysis of different elements has received extensive attention [17], and some studies on simultaneous multielemental speciation of As, Cr, Sb by combining non-chromatographic separation techniques with ICP-MS have been reported [36].

In this study, a new method of 3-(2-aminoethylamino) propyltrimethoxysilane (AAPTS) [37] modified MWCNTs packed microcolumn separation/preconcentration combined with ICP-MS was developed for the simultaneous speciation of inorganic arsenic, selenium and chromium in environmental waters. The AAPTS modified MWCNTs adsorbent was prepared in a simple step and the parameters affecting microcolumn separation/preconcentration of inorganic arsenic, selenium and chromium species were studied. The developed method was applied to the simultaneous speciation of inorganic arsenic, selenium and chromium in environmental water samples for accuracy verification.

2. Experimental

2.1. Instrumentations

For the determination of the target species, the experiment was performed by a quadrupole (Q) ICP-MS (Model Agilent 7500a, Hewlett-Packard, Yokogawa Analytical Systems, Tokyo, Japan) with a Babington nebulizer and the optimum operation conditions are summarized in Table 1. The pH values were controlled with a

Table 1
Operating parameters of ICP-MS with a Babington nebulizer.

ICP-MS	Parameters
RF power	1200 W
RF matching	1.6 V
Outer gas flow rate	15 L min ⁻¹
Intermediate gas flow rate	0.7 L min ⁻¹
Nebulizer gas flow rate	0.5 L min ⁻¹
Nebulizer pump	0.05 rps
Sampling depth	5.8 mm
Sampler/skimmer diameter orifice	Nickel 1.0 mm/0.4 mm
Time-resolved data acquisition	
Scanning mode	Peak-hopping
Dwell time	10–20 ms
Integration mode	Peak area
Points per spectral peak	1
Detected isotopes	⁷⁵ As ⁸⁰ Se ⁵⁰ Cr

Mettler Toledo 320-S pH meter (Mettler Toledo Instruments Co. Ltd., Shanghai, China) supplied with a combined electrode. Infrared spectra (4000–400 cm⁻¹) in KBr were recorded using a 170SX Fourier transform infrared spectrometer (FT-IR, NICOLET, USA). A HL-2 peristaltic pump (Shanghai Qingpu Huxi Instrument Factory, Shanghai, China) was used for the separation/preconcentration process. A self-made PTFE micro-column (20 mm × 2.0 mm i.d.) packed with AAPTS modified MWCNTs was used for the separation/preconcentration. PTFE tubing with 0.5 mm i.d. was used for all connections. These connections were kept as short as possible to minimize the dead volume.

2.2. Standard solutions and reagents

As(III)/As(V) (1.0 g L⁻¹ as As), Cr(III)/Cr(VI) (1.0 g L⁻¹ as Cr) and Se(IV)/Se(VI) (1.0 g L⁻¹ as Se) stock solutions were prepared from analytical grade of NaAsO₂, NaAsO₃, CrCl₃ · 6H₂O, K₂Cr₂O₇, Na₂SeO₃ and Na₂SeO₃, respectively, by dissolving their appropriate amounts in high-purity deionized water. These reagents were all purchased from Shanghai Reagent Factory, Shanghai, China. Working standard solutions were prepared daily by stepwise dilution of their stock solutions with high-purity deionized water. 3-(2-aminoethylamino) propyltrimethoxysilane (AAPTS) was obtained from Chemical Plant of Wuhan University, Wuhan, China. MWCNTs-OH was purchased from Chengdu Organic Chemicals Co., Ltd. (o.d. < 8 nm; -OH content: 5.58%; Length: 30 μm; purity > 95 wt%). Ultra pure grade of HNO₃ was further purified by sub-boiling distillation prior to use. All other chemicals were of analytical reagent grade. All stock standard solutions were stored in polyethylene bottles in refrigerator held at 4 °C. The pH of the solution was adjusted using nitric acid for pH=1–2, sodium acetate/nitric acid for pH=2–3, and sodium acetate/acetic acid for pH=4–8. The high purity deionized water (18.2 MΩ cm) obtained from a Labconco system (Kansas City, MO, USA) was used throughout this work.

2.3. Contamination control

All laboratory wares were made of polyethylene or polypropylene material and thoroughly cleaned by soaking in 10% (v/v) nitric acid for at least 24 h. Prior to use, all acid-washed wares were rinsed with high purity deionized water.

2.4. Synthesis of AAPTS modified MWCNTs adsorbent

2.0 g MWCNTs-OH was dispersed in 100 mL dried CHCl₃ with the aid of ultrasonication and 2 mL AAPTS was added dropwise.

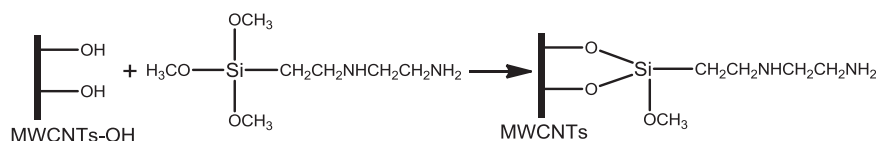


Fig. 1. Scheme for preparation of APTS modified MWCNTs.

The mixture was vigorously stirred in ice bath for 30 min and it was refluxed with stirring for 12 h in nitrogen atmosphere. The slurry was filtered and the product was washed with CHCl_3 for three times. The product was then dried and degassed at 80°C . The scheme of the reaction is shown in Fig. 1.

2.5. General procedure for preconcentration/separation

A total of 40 mg of APTS modified MWCNTs adsorbent was filled into the PTFE microcolumn plugged with a small portion of glass wool at both ends. Prior to use, ethanol and high purity deionized water were passed through the column in sequence in order to clean it. The column was then conditioned to the desired pH with buffer solution.

4 mL aqueous sample solution containing 1.0 ng mL^{-1} of each species was adjusted to $\text{pH}=2.2$ and passed through the column at a flow rate of 2.0 mL min^{-1} . After washing with water, the retained As(V), Cr(VI) and Se(VI) were eluted by 0.4 mL of $0.8\text{ mol L}^{-1}\text{ HNO}_3$ at 1.0 mL min^{-1} , and their concentrations were obtained by analyzing the eluent with ICP-MS.

By using $10.0\text{ }\mu\text{mol L}^{-1}\text{ KMnO}_4$ as oxidation reagent, As(III), Cr(III) and Se(IV) in solution could be transformed to their high valence of As(V), Cr(VI) and Se(VI) at $\text{pH} 7.5$, and the total amount of each species could be obtained by the same method as mentioned above, including pH adjusting, sampling, eluting and detecting of As, Cr and Se. The amount of As(III), Cr(III) and Se(IV) was calculated by subtracting As(V), Cr(VI) and Se(VI) from their total amount, respectively. The blank solution and the series of standard solution were prepared using the same procedure.

The recovery (expressed as a percentage) was evaluated based on the measured analyte concentrations divided by the spiked concentration of corresponding analyte ($C_{\text{measured}}/C_{\text{added}} \times 100\%$).

2.6. Sample preparation

Rainwater was sampled in a polyethylene bottle using a 30 cm diameter plastic funnel on the roof of the Chemistry building, Department of Chemistry, Wuhan University. Lake water and river water were collected from the central part of East Lake and Yangtze River, Wuhan, China. Immediately after sampling, all water samples were filtered through a $0.45\text{ }\mu\text{m}$ membrane (Tianjing Jinteng Instrument Factory, Tianjin, China) and stored in precleaned polypropylene bottles in a refrigerator at 4°C until the analysis was carried out.

The Environmental Water Reference Materials (ERMs) of GSBZ 50009-88 and GSBZ 50027-94 were provided by the Institute for Reference Materials of Sepa, Beijing, China. Prior to use, the ampoule was broken carefully at the neck, 10 mL of the sample was pipetted into 250 mL volumetric flask and diluted to the calibrate using high purity deionized water according to the instructions of the supplier. The sample was further diluted and adjusted to desired pH for analysis. Furthermore, two other Certified Reference Materials (CRMs) of BW3209 and BW3210 environmental water samples (National Research Center for CRMs, Beijing, China) were diluted with high purity deionized water and adjusted to the desired pH with $0.1\text{ mol L}^{-1}\text{ HCl}$ and $0.1\text{ mol L}^{-1}\text{ NH}_3 \cdot \text{H}_2\text{O}$ before analysis [38]. The blank samples were also prepared by the same procedure except that no analytes were added.

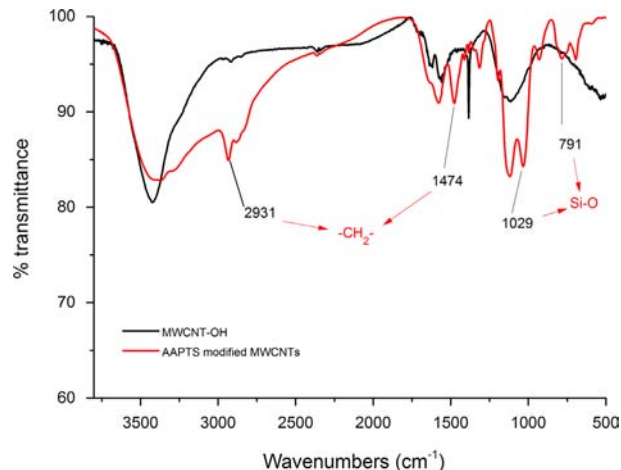


Fig. 2. Infrared spectra of MWCNTs and APTS modified MWCNTs obtained by FT-IR.

3. Results and discussion

3.1. Characterization of the prepared APTS modified MWCNTs by FT-IR

To ascertain whether APTS has been successfully grafted onto MWCNTs, FT-IR was employed to characterize MWCNTs and APTS modified MWCNTs. Fig. 2 is the FT-IR spectra for MWCNTs and APTS modified MWCNTs. The absorption around 1570 cm^{-1} is attributed to $\text{C}=\text{C}$ stretching vibrations of MWCNTs. Compared with the FT-IR spectra of MWCNTs, a series of characteristic peaks of APTS appeared in the spectra of APTS modified MWCNTs. Among them, absorption peaks at 1474 and 2931 cm^{-1} are attributed to bending and stretching vibrations of $-\text{CH}_2-$, while 1029 and 791 cm^{-1} could be attributed to $\text{Si}-\text{O}$ from APTS. These results showed that APTS had been successfully grafted onto MWCNTs although the relative weak ν_{NH_2} band which normally appeared around 1560 and 3400 cm^{-1} was possibly overlapped by strong stretching bond of $\text{C}=\text{C}$ and $-\text{OH}$. The modification of APTS was further proved in the pH test.

3.2. Effect of pH

The effect of pH on the retention of As(III)/As(V), Cr(III)/Cr(VI) and Se(IV)/Se(VI) on APTS modified MWCNTs packed microcolumn were investigated separately. For this purpose, 4 mL sample solutions containing 1.0 ng mL^{-1} each target species were prepared separately and pH values of the sample solutions were adjusted to a range of 1–8 with buffer solution. These sample solutions were passed through the microcolumn, and the effluents were determined by ICP-MS as described in the recommended procedure. Fig. 3 is the effect of pH on the adsorption percentage of As(III)/As(V) (Fig. 3a), Cr(III)/Cr(VI) (Fig. 3b) and Se(IV)/Se(VI) (Fig. 3c). As can be seen, when the pH value was above 2, As(V), Cr(VI) and Se(VI) were quantitatively retained ($>95\%$) on the microcolumn, while As(III), Cr(III) and Se(IV) exhibited a different extraction behaviors. There was hardly any adsorption in the

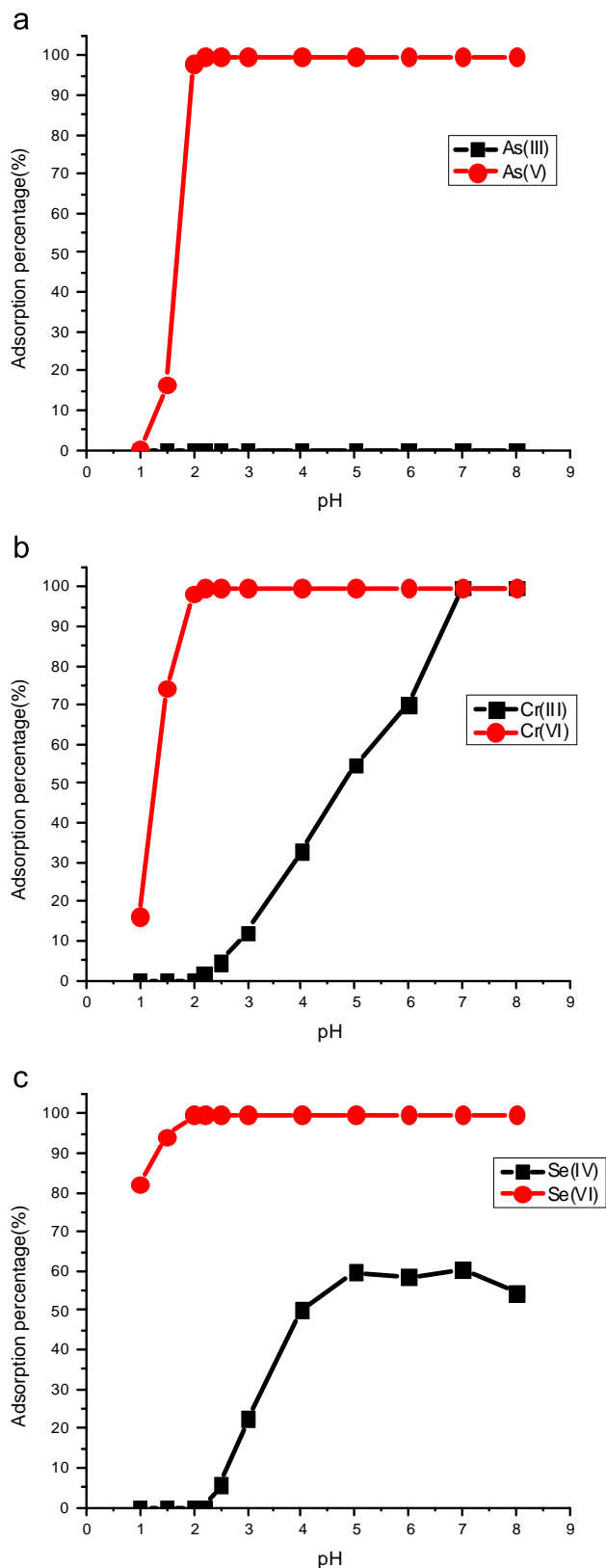


Fig. 3. Effect of pH on the adsorption percentage (%) of target species. (a) As(III) and As(V); (b) Cr(III) and Cr(VI); (c) Se(IV) and Se(VI). Sample volume: 4 mL; concentration for each species: 1.0 ng mL⁻¹; sample flow rate: 2.0 mL min⁻¹; eluent: 0.8 mol L⁻¹ HNO₃; elution flow rate: 1.0 mL min⁻¹.

whole tested pH range for As(III); while the adsorption percentage for Se(IV) was negligible in the pH range of 1–2.5, it was increased with the increase of pH from 2.5 to 5.0 and then kept at around

60% from 5.0 to 8.0; for Cr(III), the adsorption percentage was negligible in the pH range of 1–2.5, it was increased sharply with the increase of pH from 2.5 to 7.0 and then remained constant (> 95%) with further increase of pH to 8. The different pH trend of As(III)/As(V), Cr(III)/Cr(VI) and Se(IV)/Se(VI) made it possible to separate different species of each element at a relative narrow pH range of 2.2–2.5. In this work, pH of 2.2 was selected for separation of As(V), Cr(VI) and Se(VI) from As(III), Cr(III) and Se(IV).

The selective interaction of the APTS-modified MWCNT with target species could be explained by the theory of R.G. Pearson's HSAB (Hard and Soft Acids and Bases). Based on the theory of R.G. Pearson's HSAB, the $-\text{NH}_3^+$ and target analytes in anionic form were soft acid and soft bases, and the interaction between the target analytes and the APTS-modified MWCNT is stronger than that between the other anionic ions (such as Cl^- , SO_4^{2-} and NO_3^- , which are hard bases) and the APTS-modified MWCNT.

The different adsorption behaviors of As(III)/As(V), Cr(III)/Cr(VI) and Se(IV)/Se(VI) on APTS modified MWCNTs can be explained by their pKa values (Table 2) and different ionic characters. In the tested pH range of 1–8, the $-\text{NHCH}_2\text{CH}_2\text{NH}_2$ was abundant of positive charge (which was similar to weak-base anion-exchange resin), while As(V), Cr(VI) and Se(VI) existed mainly in anion form (such as $\text{H}_2\text{AsO}_4^{2-}$ and HAsO_4^{2-} for As(V), HCrO_4^- for Cr(VI), and HSeO_4^- and SeO_4^{2-} for Se(VI)), therefore, As(V), Cr(VI) and Se(VI) could be adsorbed by APTS modified MWCNTs adsorbent through electrostatic interaction. Whereas, As(III) existed mainly in the molecular form of H_3AsO_3 in the whole tested pH range, and no adsorption by the APTS modified MWCNTs adsorbent took place. At low pH values, Cr(III) existed as its kinetically inert aquacomplex $\text{Cr}(\text{H}_2\text{O})_3^{3+}$. As the pH increased, the coordinated water was displaced by the more reactive OH^- , rendering the former complex to a more labile form ($\text{Cr}(\text{H}_2\text{O})_2(\text{OH})^{2+}$ or $\text{Cr}(\text{H}_2\text{O})(\text{OH})^{2+}$), which allows for better reactivity with chelating group of $-\text{NHCH}_2\text{CH}_2\text{NH}_2$ on the surface of APTS modified MWCNTs. As for Se(IV), in the tested pH range, it existed in both form of H_2SeO_3 and HSeO_3^- and only anion species could be retained on the APTS modified MWCNTs packed microcolumn.

3.3. The optimization of oxidization conditions

According to Ref [19,39], As(III), Cr(III) and Se(IV) could be oxidized to As(V), Cr(VI) and Se(VI) by KMnO_4 at room temperature. In our experiment, KMnO_4 was selected to oxidize 1.0 ng mL⁻¹ of As(III), Cr(III) and Se(IV) in 4 mL sample solution to their high valence. It was found that at pH 7.5, 10 $\mu\text{mol L}^{-1}$ KMnO_4 was sufficient to quantitatively transform As(III), Cr(III) and Se(IV) to their higher valence of As(V), Cr(VI) and Se(VI), while the KMnO_4 concentration higher than 1 mmol L⁻¹ could oxidize functional group of $-\text{NHCH}_2\text{CH}_2\text{NH}_2$ and damage the adsorbent. Therefore, 10 $\mu\text{mol L}^{-1}$ KMnO_4 was employed to oxidize As(III), Cr(III) and Se(IV) to their higher valence. The reaction time was also investigated and the results showed that 1 min was enough for the reaction. Hence, in our experiment, 10 $\mu\text{mol L}^{-1}$ KMnO_4 was used to oxidize As(III), Cr(III) and Se(IV) to their high valence and the reaction time was 1 min.

Table 2
pKa values of different As, Cr and Se species.

Species	pKa ₁	pKa ₂	pKa ₃
H ₂ SeO ₃	2.46	7.3	11.6
H ₂ SeO ₄	Strong acid	1.92	–
H ₃ AsO ₃	9.2	12.1	–
H ₃ AsO ₄	2.4	6.8	11.6
H ₂ CrO ₄	0.7	6.5	–

3.4. The optimization of eluent concentration

From Fig. 3, it can be concluded that the adsorption of As(V), Cr(VI) and Se(VI) on the AAPTS modified MWCNTs was decreased with decreasing the pH value when the pH was lower than 2, therefore, 4 mL sample solutions containing 1.0 ng mL^{-1} each target species were treated with the SPE procedure, and acid was chosen to elute the retained species from the AAPTS modified MWCNTs packed microcolumn. HNO_3 is a recommended acid for ICP-MS detection and the functional group of $-\text{NHCH}_2\text{CH}_2\text{NH}_2$ is stable at least in $1 \text{ mol L}^{-1} \text{ HNO}_3$ [8]. For this reason, various concentrations of HNO_3 were studied independently for desorption of the adsorbed species. The experimental results indicated that $0.8 \text{ mol L}^{-1} \text{ HNO}_3$ was sufficient for complete elution of As(V), Cr(VI) and Se(VI) from the microcolumn. Furthermore, the prepared AAPTS modified MWCNTs adsorbent can withstand $2 \text{ mol L}^{-1} \text{ HNO}_3$ without lost its adsorption performance. Therefore, $0.8 \text{ mol L}^{-1} \text{ HNO}_3$ was chosen as eluent in subsequent experiments.

3.5. Elution volume and elution flow rate

The effect of elution volume on the elution of As(V), Cr(VI) and Se(VI) from the AAPTS modified MWCNTs packed microcolumn was investigated separately. It was found that 0.4 mL of elution solution containing $0.8 \text{ mol L}^{-1} \text{ HNO}_3$ was sufficient to recover all the species quantitatively.

The effect of elution flow rate on the recovery of As(V), Cr(VI) and Se(VI) was investigated by using 0.4 mL of $0.8 \text{ mol L}^{-1} \text{ HNO}_3$ as the eluent. The experimental results indicated that all target species could be recovered quantitatively (above 95%) at a flow rate range of $0.5\text{--}2.0 \text{ mL min}^{-1}$. Consequently, elution flow rate of 1.0 mL min^{-1} was selected in the subsequent experiments.

3.6. Sample flow rate and sample volume

The sample flow rate should be optimized to ensure quantitative retention along with minimization of the time required for sample processing. 4 mL sample solutions containing 1.0 ng mL^{-1} each target species were used for the optimization. It was found that the recoveries of As(V), Cr(VI) and Se(VI) were decreased slowly with the increase of sample flow rate from 0.5 to 2.5 mL min^{-1} , but still above 95%. In this work, the sample flow rate of 2.0 mL min^{-1} was selected.

In order to investigate the breakthrough volume, the sample solutions of 2, 4, 10, 20, 30 and 40 mL containing 40 ng of As(V), Cr(VI) and Se(VI) were prepared and then subjected to the general procedure. It was found that the target species could be quantitatively retained (above 90%) when sample volumes were less than 10 mL. To trade off the enrichment factor and analytical speed, a sample volume of 4 mL and an elution volume of 0.4 mL were used, so that an enrichment factor of 10 was obtained in this work.

3.7. Effect of coexisting ions

The effects of common coexisting ions on the preconcentration and determination of As(V), Cr(VI) and Se(VI) were examined under the optimal conditions as described above. For this purpose, solutions containing 1.0 ng mL^{-1} of As(V), Cr(VI) and Se(VI) and the added interfering ions were treated according to the general procedure as described previously. The tolerance of the coexisting ions, defined as the largest amount making the recovery of the studied species less than 90%, are given in Table 3. It can be seen that the presence of major cations and anions had no obvious influence on the determination of all species under the selected conditions, which shows that the AAPTS modified MWCNTs

adsorbent has a good selectivity for target species and is suitable for the analysis of environmental water samples.

3.8. Adsorption capacities for As(V), Cr(VI) and Se(VI) by AAPTS modified MWCNTs adsorbent

The adsorption capacity is an important factor to evaluate the adsorbent, because it determines how much adsorbent is required to quantitatively concentrate the target analytes from a given solution. The capacity study method used in this work was adapted from that recommended by Maquieira et al. [40]. The adsorption capacity of AAPTS-MWCNTs adsorbent was found to be 8.01 , 9.79 and 7.02 mg g^{-1} for As(V), Cr(VI) and Se(VI), respectively, which is comparable to that obtained by other materials reported in literatures (as listed in Table 4).

The regeneration is one of the key factors in evaluating the performance of the adsorbent. The column packed with prepared adsorbent can be reused for more than 100 times when $0.8 \text{ mol L}^{-1} \text{ HNO}_3$ was used as the eluents, indicating that the adsorbent has good stability under acidic conditions.

3.9. Analytical performance

According to the definition of IUPAC, the detection limit (3σ) of this method for As(V), Cr(VI) and Se(VI) were 15, 38 and 16 pg mL^{-1} , respectively. The linear range for As(V), Cr(VI) and Se(VI) were $0.05\text{--}100$, $0.1\text{--}100$, $0.05\text{--}100 \text{ ng mL}^{-1}$, respectively. The relative standard deviations (RSDs) for 7 replicate determinations of 1 ng mL^{-1} of As(V), Cr(VI) and Se(VI) were 7.4, 4.2 and 6.2%, respectively. Table 5 is the comparison of the detection limits of this work with other literature works on the speciation of the same elements in environmental water samples. As can be seen, the detection limits obtained by this work are the lowest for most of the species. It should be also mentioned that the detection limits of this work were obtained by simultaneous determination of As(V), Cr(VI) and Se(VI), while the detection limits reported in

Table 3
The tolerance limits of the common coexisting ions.

Coexisting ions	Tolerance limit of ions (mg L^{-1})
K^+ , Na^+	1000
Ca^{2+} , Mg^{2+}	400
Fe^{3+}	30
SO_4^{2-}	1000
Cl^-	1000
NO_3^-	2000
MnO_4^-	1500

Table 4
The comparison of adsorption capacity of Cr(VI), As(V) and Se(VI) by different materials.

Adsorbents	Adsorption capacities of different metal ions (mg g^{-1})			Reference
	Cr(VI)	As(V)	Se(VI)	
Magnetite–polyethylenimine–montmorillonite	8.80			[12]
Mesoporous NiO nanoparticles	4.73			[18]
MWCNTs	9.50			[34]
Akaganeite		30.75		[41]
Lepidocrocite		19.05		[1]
DMSA modified mesoporous TiO_2			3.8	[42]
AAPTS modified MWCNTs	9.79	8.01	7.02	This work

the most literatures were obtained for single element species. Therefore, this method is far more convenient and rapid for speciation analysis of inorganic As, Cr and Se in environmental water samples.

3.10. Accuracy verification and applications

In order to establish the validity of the developed procedure, the method has been applied to the determination of total Cr and

Cr(III) in Certified Reference Materials of environmental waters (total Cr in GSBZ 50009–88 and Cr(VI) in GSBZ 50027–94) and As (III)/As(V) in Certified Reference Materials of environmental waters (As(III) in GBW 3209 and As(V) in GBW 3210). The results are listed in Tables 6 and 7, respectively. As can be seen, a good agreement between determined values and the certified values were obtained. Furthermore, the developed method was applied to the speciation analysis of As, Cr and Se in rainwater, Yangtze River and East Lake waters, and the analytical results are given in Table 8.

Table 5

Comparison of detection limits reported in literatures for inorganic As, Cr and Se.

Analytical procedures	LOD (ng L ⁻¹)						Reference
	As(III)	As(V)	Cr(III)	Cr(VI)	Se(IV)	Se(VI)	
SPE-ICP-MS	–	15	–	38	–	16	This work
HPLC-ICP-MS	90	100	–	–	710	–	[3]
SPE-CE-UV	–	–	–	–	57	71	[16]
HPLC-ICP-MS	19	22	–	–	321	312	[43]
ICP-OES	–	–	80	150	–	–	[4]
HPLC-ICP-MS	–	–	30	30	–	N	[44]

Table 6

Analytical results of chromium in certified reference materials of GSBZ 50009–88 and GSBZ 50027–94 environmental waters (mean ± s.d., n=3).

Reference materials	Species	Certified (μg mL ⁻¹)	Determined (μg mL ⁻¹)
GSBZ 50009–88	Cr (total)	1.49 ± 0.06	1.45 ± 0.02
GSBZ 50027–94	Cr(VI)	0.12 ± 0.005	0.12 ± 0.003

Table 7

Analytical results of arsenic in certified reference materials of GBW 3209 and GBW 3210 environmental waters (mean ± s.d., n=3).

Reference materials	Species	Certified (μmol g ⁻¹)	Determined (μmol g ⁻¹)
GBW 3209	As(III)	1.01 ± 0.02	0.99 ± 0.04
GBW 3210	As(V)	0.233 ± 0.004	0.232 ± 0.007

Table 8

Analytical results of inorganic species of As, Cr and Se in rain water, Yangtze River and East Lake (ng mL⁻¹, mean ± s.d., n=3).

Samples	Rain water		Yangtze River		East Lake	
Cr(VI)						
Added	0	5	0	5	0	5
Found	1.17 ± 0.02	5.86 ± 0.08	1.39 ± 0.06	6.96 ± 0.19	3.88 ± 0.13	8.40 ± 0.18
Recovery (%)	–	94.0	–	111.4	–	90.4
Cr(III)						
Added	0	5	0	5	0	5
Found	0.90 ± 0.02	5.94 ± 0.07	0.79 ± 0.05	5.39 ± 0.14	1.68 ± 0.08	6.72 ± 0.21
Recovery (%)	–	100.8	–	92	–	100.8
As(V)						
Added	0	5	0	5	0	5
Found	0.64 ± 0.02	5.11 ± 0.07	2.32 ± 0.11	7.83 ± 0.19	2.12 ± 0.11	7.2 ± 0.21
Recovery (%)	–	89.4	–	110.2	–	101.6
As(III)						
Added	0	5	0	5	0	5
Found	0.22 ± 0.01	5.43 ± 0.13	0.43 ± 0.05	5.52 ± 0.14	0.4 ± 0.03	4.95 ± 0.17
Recovery (%)	–	104.2	–	101.8	–	90.1
Se(VI)						
Added	0	5	0	5	0	5
Found	0.22 ± 0.02	4.67 ± 0.18	1.19 ± 0.03	6.26 ± 0.21	1.78 ± 0.07	6.78 ± 0.2
Recovery (%)	–	88.9	–	101.4	–	102
Se(IV)						
Added	0	5	0	5	0	5
Found	0.30 ± 0.02	4.66 ± 0.10	1.02 ± 0.04	5.92 ± 0.27	1.07 ± 0.05	6.01 ± 0.26
Recovery (%)	–	87.2	–	98	–	98.8

4. Conclusions

In this work, a new SPE adsorbent of AAPTS modified MWCNTs was prepared for simultaneous selective extraction of As(V), Cr(VI) and Se(VI) at low pH value. Besides its good selectivity, the new adsorbent also has some other characteristics such as good stability under acidic conditions, fast adsorption and desorption kinetics, large adsorption capacity and good tolerance to coexisting ions, making it an ideal adsorbent for As(V), Cr(VI) and Se(VI). By combining AAPTS modified MWCNTs microcolumn SPE with ICP-MS, a new method was developed for the simultaneous speciation analysis of inorganic arsenic, selenium and chromium in environmental water samples. The developed method is characterized with simplicity (does not require separation by chromatography), selectivity (good anti-disturbance ability), safety (without organic solvent), low cost (cheap reagent) and rapidness (high sample throughput), and it could be adapted for rugged and routine use by the contract lab population and practitioners in water field who utilize such analyses.

Acknowledgments

This work is financially supported by the National Basic Research Program of China (973 Program, 2013CB933900), the National Nature Science Foundation of China (nos. 21175102, 21075095, 21205090), the Science Fund for Creative Research Groups of NSFC (nos. 20621502, 20921062), the Fundamental

Research Funds for the Central Universities (114009), Hubei Key Laboratory of Pollutant Analysis and Reuse Technique (Hubei Normal University, KL2013M11) and “Academic Award for Excellent Ph.D. Candidates Funded by Ministry of Education of China”.

References

- [1] J.F. Wan, S. Simon, V. Deluchat, M.C. Dictor, C. Dagot, J. Environ. Sci. Health Part A 48 (2013) 1272–1279.
- [2] Q.H. Zhang, G.P. Yang, J. Chromatogr. A 1325 (2014) 83–91.
- [3] F. Pan, J.F. Tyson, P.C. Uden, J. Anal. At. Spectrom. 22 (2007) 931–937.
- [4] T. Sumida, T. Ikenoue, K. Hamada, A. Sabarudin, M. Oshima, S. Motomizu, Talanta 68 (2005) 388–393.
- [5] R.-Y. Wang, Y.-L. Hsu, L.-F. Chang, S.-J. Jiang, Anal. Chim. Acta 590 (2007) 239–244.
- [6] E. Terlecka, Environ. Monit. Assess. 107 (2005) 259–284.
- [7] F.E. Huggins, C.L. Senior, P. Chu, K. Ladwig, G.P. Huffman, Environ. Sci. Technol 41 (2007) 3284–3289.
- [8] N. Zhang, J.S. Suleiman, M. He, B. Hu, Talanta 75 (2008) 536–543.
- [9] R.A. Gil, S. Cerutti, J.A. Gasquez, R.A. Olsina, L.D. Martinez, Talanta 68 (2006) 1065–1070.
- [10] J. Gailer, G.N. George, I.J. Pickering, R.C. Prince, S.C. Ringwald, J.E. Pemberton, R.S. Glass, H.S. Younis, D.W. DeYoung, H.V. Aposhian, J. Am. Chem. Soc. 122 (2000) 4637–4639.
- [11] A.L. Moxon, Science (New York, NY) 88 (1938) 81 (–81).
- [12] I. Larraza, M. Lopez-Gonzalez, T. Corrales, G. Marcelo, J. Colloid Interface Sci. 385 (2012) 24–33.
- [13] E. Birlik, A. Ersoz, E. Acikkalp, A. Denizli, R. Say, J. Hazard. Mater. 140 (2007) 110–116.
- [14] X.L. Pu, B. Hu, Z.C. Jiang, C.Z. Huang, Analyst 130 (2005) 1175–1181.
- [15] C.-Y. Kuo, S.-J. Jiang, J. Chromatogr. A 1181 (2008) 60–66.
- [16] J.K. Duan, B. Hu, M. He, Electrophoresis 33 (2012) 2953–2960.
- [17] Y.J. Li, B. Hu, M. He, G.Q. Xiang, Water Res. 42 (2008) 1195–1203.
- [18] H.M. Jiang, T. Yang, Y.H. Wang, H.Z. Lian, X. Hu, Talanta 116 (2013) 361–367.
- [19] F. Shemirani, M. Baghdadi, M. Ramezani, Talanta 65 (2005) 882–887.
- [20] X.L. Pu, Z.C. Jiang, B. Hu, H.B. Wang, J. Anal. At. Spectrom. 19 (2004) 984–989.
- [21] J. Yin, Z.C. Jiang, G. Chang, B. Hu, Anal. Chim. Acta 540 (2005) 333–339.
- [22] J.R. Baena, M. Gallego, M. Valcarcel, TrAC, Trends Anal. Chem. 21 (2002) 187–198.
- [23] M. Valcarcel, S. Cardenas, B.M. Simonet, Y. Moliner-Martinez, R. Lucena, TrAC, Trends Anal. Chem. 27 (2008) 34–43.
- [24] S. Iijima, Nature 354 (1991) 56–58.
- [25] M. Trojanowicz, TrAC, Trends Anal. Chem. 25 (2006) 480–489.
- [26] H. -H. Cho, K. Wepasnick, B.A. Smith, F.K. Bangash, D.H. Fairbrother, W.P. Ball, Langmuir 26 (2010) 967–981.
- [27] Y.H. Li, S.G. Wang, A.Y. Cao, D. Zhao, X.F. Zhang, C.L. Xu, Z.K. Luan, D.B. Ruan, J. Liang, D.H. Wu, B.Q. Wei, Chem. Phys. Lett. 350 (2001) 412–416.
- [28] C.H. Latorre, J.A. Mendez, J.B. Garcia, S.G. Martin, R.M.P. Crecente, Anal. Chim. Acta 749 (2012) 16–35.
- [29] R. Sitko, B. Zawisza, E. Malicka, TrAC, Trends Anal. Chem. 37 (2012) 22–31.
- [30] B.Y. Dai, M.R. Cao, G.Z. Fang, B. Liu, X. Dong, M.F. Pan, S. Wang, J. Hazard. Mater. 219 (2012) 103–110.
- [31] M. Ghaedi, K. Mortazavi, M. Jamshidi, M. Roosta, B. Karami, Toxicol. Environ. Chem. 94 (2012) 846–859.
- [32] A.H. El-Sheikh, J.A. Sweileh, Y.S. Al-Degs, Anal. Chim. Acta 604 (2007) 119–126.
- [33] Y.H. Li, J. Ding, Z.K. Luan, Z.C. Di, Y.F. Zhu, C.L. Xu, D.H. Wu, B.Q. Wei, Carbon 41 (2003) 2787–2792.
- [34] M. Tuzen, M. Soylak, J. Hazard. Mater. 147 (2007) 219–225.
- [35] R.A. Gil, S.N. Goyanes, G. Polla, P. Smichowski, R.A. Olsina, L.D. Martinez, J. Anal. At. Spectrom. 22 (2007) 1290–1295.
- [36] W.L. Hu, F. Zheng, B. Hu, J. Hazard. Mater. 151 (2008) 58–64.
- [37] D. Chen, C. Huang, M. He, B. Hu, J. Hazard. Mater. 164 (2009) 1146–1151.
- [38] H. Jiang, B. Hu, B. Chen, L. Xia, Anal. Chim. Acta 634 (2009) 15–21.
- [39] A. Tunceli, A.R. Turker, Talanta 57 (2002) 1199–1204.
- [40] A. Maquieira, H.A. Elmahadi, R. Puchades, Anal. Chem. 66 (1994) 1462–1467.
- [41] F. Kolbe, H. Weiss, P. Morgenstern, R. Wennrich, W. Lorenz, K. Schurk, H. Stanjek, B. Daus, J. Colloid Interface Sci. 357 (2011) 460–465.
- [42] C.Z. Huang, B. Hu, M. He, J. Duan, J. Mass Spectrom. 43 (2008) 336–345.
- [43] S. Afton, K. Kubachka, B. Catron, J.A. Caruso, J. Chromatogr. A 1208 (2008) 156–163.
- [44] H.J. Wang, X.M. Du, M. Wang, T.C. Wang, O.Y. Hong, B. Wang, M.T. Zhu, Y. Wang, G. Jia, W.Y. Feng, Talanta 81 (2010) 1856–1860.



The analytical calibration in (bio)imaging/mapping of the metallic elements in biological samples – Definitions, nomenclature and strategies: State of the art

Kamil Jurowski^{a,b}, Bogusław Buszewski^c, Wojciech Piekoszewski^{a,d,*}

^a Department of Analytical Chemistry, Faculty of Chemistry, Jagiellonian University in Kraków, R. Ingardena 3, 30-060 Krakow, Poland

^b Malopolska Centre for Translational Medicine, Faculty of Medicine, Medical College, Jagiellonian University in Kraków, Kraków, Poland

^c Department of Environmental Chemistry and Bioanalytics, Faculty of Chemistry, Nicolaus Copernicus University, Toruń, Poland

^d Laboratory of High Resolution Mass Spectrometry, Regional Laboratory of Physicochemical Analysis and Structural Research, Faculty of Chemistry, Jagiellonian University in Kraków, Krakow, Poland

ARTICLE INFO

Article history:

Received 24 May 2014

Received in revised form

26 July 2014

Accepted 30 July 2014

Available online 6 August 2014

Keywords:

Calibration strategy

Calibration nomenclature

Calibration methods

Calibration procedure

(Bio)imaging

Mapping

Distribution

ABSTRACT

Nowadays, studies related to the distribution of metallic elements in biological samples are one of the most important issues. There are many articles dedicated to specific analytical atomic spectrometry techniques used for mapping/(bio)imaging the metallic elements in various kinds of biological samples. However, in such literature, there is a lack of articles dedicated to reviewing calibration strategies, and their problems, nomenclature, definitions, ways and methods used to obtain quantitative distribution maps. The aim of this article was to characterize the analytical calibration in the (bio)imaging/mapping of the metallic elements in biological samples including (1) nomenclature; (2) definitions, and (3) selected and sophisticated, examples of calibration strategies with analytical calibration procedures applied in the different analytical methods currently used to study an element's distribution in biological samples/materials such as LA ICP-MS, SIMS, EDS, XRF and others. The main emphasis was placed on the procedures and methodology of the analytical calibration strategy. Additionally, the aim of this work is to systematize the nomenclature for the calibration terms: *analytical calibration*, *analytical calibration method*, *analytical calibration procedure* and *analytical calibration strategy*. The authors also want to popularize the division of calibration methods that are different than those hitherto used. This article is the first work in literature that refers to and emphasizes many different and complex aspects of analytical calibration problems in studies related to (bio)imaging/mapping metallic elements in different kinds of biological samples.

© 2014 Elsevier B.V. All rights reserved.

1. Introduction

1.1. Idea and definitions of analytical calibration

In quantitative analysis it is well known, that *calibration* is a very important step during an analytical procedure [1]. However, despite the extreme attention to the nomenclature in this chemistry discipline, a clear and established definition for *analytical calibration* terms remains insubstantial. On the one hand, it is surprising that there are no *universal* or *commonly used* definitions which would be recommended by the IUPAC in accordance to the definition described by, for example, the International Organization for Standardization (ISO), while, on the other hand, there are

misunderstandings and obscurities, which can cause improper or wrong analytical proceedings and can create didactic difficulties; themselves sometimes leading to an improper or wrong proceeding [2].

Moreover, the term '*calibration*' can be considered from both a metrological and an analytical viewpoint, where the requirements and aims are not necessarily similar. *Analytical calibration* is often understood by a chemist as a process which attempts to verify or state the relationship between a measurement signal and an analyte's (or analytes') quantity [3]. From a metrological point of view, analytical calibration is based on the analytical one, and is just related to a "measuring system" understood as a set of one or more measuring instruments and, often, other devices, including any reagent and supply, assembled and adapted to give measured quantity values within specified intervals for quantities of specified kinds [3,4].

As mentioned earlier, many definitions exist in literature concerning analytical calibration, which is not coherent. For

* Corresponding author at: Department of Analytical Chemistry, Faculty of Chemistry, Jagiellonian University in Kraków, R. Ingardena 3, 30-060 Krakow, Poland. Tel.: +48 12 663 56 00; fax: +48 12 663 56 01.

E-mail address: wojciech.piekoszewski@uj.edu.pl (W. Piekoszewski).

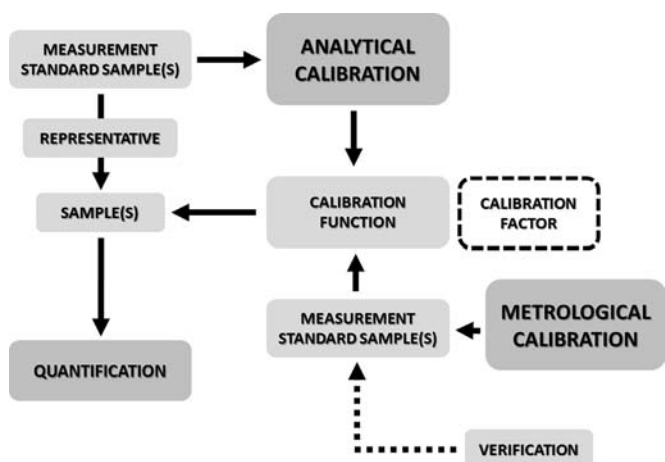


Fig. 1. A diagram showing the relationships between analytical calibration definitions, according to metrological calibration (ISO recommendation) and analytical quantification (IUPAC) – based on [3].

example, the IUPAC recommendation defines the calibration as the operation that determines the functional relationship between measured values (signal intensities), y -variable, and analytical quantities characterizing the types of analytes and their amount (content, concentration), x -variable [5]. In turn, the ISO standard defined the calibration as a complete set of operations which estimates under specified conditions the calibration function from observation of the response variable, y , obtained on reference states (described by the values of variable states, x) [6]. The interrelations between both definitions are presented in Fig. 1.

Due to these divergences, the authors of this article propose the practical approach to the analytic calibration as the process that takes into account the earlier mentioned factors. Hence, *analytical calibration* ought to be understood as denoting a process which consists of representing the actual (whether real or theoretical) dependence of the signal (potential, electric current, etc.) on the concentration of the analyte (which in this context is called a calibration function) in an empirical form (calibration plot/graph or, more precisely, the calibration function), and then using a plot to determine the concentration of the analyte of the examined sample (i.e. obtaining the analytical results) [1,2,7–9]. Due to this fact, the idea behind analytical calibration is to find an empiric relationship, known as a measurement function, which subsequently makes it possible to calculate the values of the amount (x -variable) of a substance in an analytical sample, from the measured values on it of an analytical signal (y -variable) [9,10]. The *calibration function* (calibration graph/plot) is constructed under specified and constant conditions (physicochemical and instrumental), with the use of up to several already established *standard samples*; i.e. solutions of known, precisely determined, concentrations of at least one component (usually an analyte) [1,7,11,12]. Furthermore, these calibration functions are characteristics only for the standard samples used and depend on the actual instrumental and operational conditions due to the presence of *influential quantities*. These quantities in a direct measurement do not affect the quantity that is actually measured, but affects the relationship between the signal intensity and the measurement results [3].

On the basis of the above information it transpires that analytical calibration consists of three steps: (1) the laboratory step – the preparation of the *standard samples*; (2) the measurement step – the construction of the calibration function; and (3) the mathematical step – the calculation of the analytical result [7]. The laboratory step includes preparing standard samples and adjusting the composition and physicochemical properties to the

composition and the physicochemical properties of the samples. Equally, the measuring step consists of taking measurements of the samples and standard samples in constant (well-defined) experimental conditions. The interpretation stage consists of assigning a value corresponding to the measured signals of the analyte concentrations in the standard samples (determination of the experimental data points). The final stage, or the mathematical stage, involves matching the appropriate function with the experimental data points.

It must be emphasized that, the detailed mode of performing particular stages (laboratory, measurement, interpretative and mathematical) of the analytical calibration is defined by term, *calibration procedure* [7,11]. It is very important that the calibration procedures should be performed strictly in accordance with the established rules, which define a more general way of the procedure, except in the leading to the main tasks of calibration where there are some additional analytical purposes [7].

1.2. Analytical calibration methods – nomenclature and classification

There are many kinds of well-known calibration methods in analytical chemistry. Unfortunately, they appear under different, often arbitrarily chosen names, which may cause numerous misunderstandings and errors. However, there is no suitable, clear and established classification and nomenclature system of those methods. This phenomenon probably arises from the fact that the names of calibration methods refer (in most situations), only to the laboratory stage of the calibration procedure.

The laboratory step includes preparing *standard samples* [1], and adjusting the composition and physicochemical properties to the composition and the physicochemical properties of the samples. Equally, the measuring step consists of taking measurements of the samples and standard samples in constant (well-defined) experimental conditions. The interpretation stage consists of assigning a value corresponding to the measured signals of the analyte concentrations in the standard samples (the determination of the experimental data points). The final stage (or the mathematical stage), involves matching the appropriate function with the experimental data points. Moreover, the calibration procedures should be performed strictly in accordance with the established rules, which define a more general way of the procedure, except in the leading to the main tasks of calibration where there are some additional analytical purposes.

The *calibration method* can be defined as the realization of the calibration procedure of certain specificity, leading to the achievement (apart from the main task of calibration) of preconceived, additional analytical purposes [7]. Due to the lack of classification and the nomenclature problem regarding the calibration method, it is important to establish and apply a unified way for the classification and nomenclature of calibration methods. The authors of this article propose that the computational and measurement aspects should be the fundamental criteria for the diversification of calibration methods, as opposed to the generally used laboratorial aspects [7]. The authors feel the well-established, clear and useful classifying calibration methods in analytical chemistry are based on (1) how the calibration dependence is reconstructed, and (2) how the measurement data are transformed. The new classification is then characterized in this [2]:

- *it is open* – it is possible to take into consideration the development of new calibration methods and introduce them to this classification;
- *inspires the development of new methods* – by means of coupling existing calibration approaches.

Table 1
General characterization of the calibration methods [1,2,7,8,17,18].

Calibration method	Reconstruction of the calibration dependence	Transformation of the measurement data
Interpolative	On the basis of measurement data obtained separately for a set of standard solution (rarely for a single standard solution) containing analyte and for the sample solution	With the aid of the calibration graph in the interpolative way
Extrapolative	On the basis of measurement data obtained for a set of standard solution (rarely for a single standard solution) containing analyte being added the sample solution	With the aid of the calibration graph in the extrapolative way
Indicative	On the basis of measurement data obtained as a result of chemical reaction occurring between an analyte contained in the sample solution and a component of a single standard solution being progressively coupled with the sample	With the aid of the calibration graph taking into account the location of a characteristic experimental point

Due to these facts, all the known calibration methods in analytical chemistry can be divided into three categories: (1) interpolation, (2) extrapolation, and (3) indicator.

In extrapolative methods, the analytical results are calculated after being based on the section which is beyond the field [13]. In turn, the interpolative methods are those where the analytical result is calculated from the part of the calibration graph that includes a field determined in an experimental way [14]. In both cases, the plot in the section used for calculating the analytical result does not contain an experimental point with mathematical properties that distinguish it from other points. Indicative methods are based on the result that is calculated from the location of the characteristic point on the calibration plot. This point takes different forms from the other points comprising the plot. All titration techniques constitute the indicative methods [15,16]. Table 1 summarizes the described calibration methods.

1.3. Calibration strategy – between the calibration procedure and the calibration method

As was mentioned earlier, there is a big difference between the calibration procedure and calibration method. What is a calibration strategy, though? Modern analytical chemistry has a lot of calibration methods, and the exact realization of the determination by a suitable calibration procedure makes it possible to obtain very good results characterized by the reliability and qualities. However, some calibration procedures used and some calibration methods should (or must) be changed regarding certain problems. These problems can be different, however it must be possible to (1) makes possible the realization of the determination; (2) causes the essential changes into the calibration procedure. Those essential changes which became original ways/solutions in the calibration step in the analytical procedure can be defined as a *calibration strategy*.

2. (Bio)imaging/mapping metallic elements in biological samples

2.1. Bio(imaging)/mapping studies and applied biological samples

In many fields of life science disciplines (medicine, toxicology, biology, biochemistry) information is needed about the concentrations of ultratrace and trace metals in different biological samples [19,20]. In such studies, the idea of analytical studies was based on the application of large amounts of homogenized tissue (organs, tissues), which is digested so that a total metal analysis can be performed. It is possible that in biomedical studies this was sufficient and that the analytical methods were very sensitive (e.g. parts per billion – AAS; parts per trillion (ICP-MS)), but all the spatial information was lost due to homogenization of the material prior to measurements [21]. Hence, nowadays it is often desirable to gain knowledge about the distribution of a trace

element in a soft tissue. In the case of biological materials, heterogeneity is the result of development processes responsible for the differentiation of tissues, cells and/or subcellular compartments [22].

Presently, there are many studies relating to research about the distribution of metallic elements in different biological samples. In connection with this, the metallic elements (as ions) perform many structural (cofactors for protein function) and functional roles in proteins and enzymes, and are responsible for metal ion homeostasis in biological function [23–26]. Moreover, elements at the trace level, play a considerable role in the physiology and pathology of biological systems [21]. For example, some trace metallic elements (e.g. Mo, Cu, Fe, Zn, Co) are known to be essential or beneficial (e.g. V, Cr, Ni) for human health, nutrition and plant growth [27]. Other metals (e.g. Cd, Hg, Pb – heavy metals) are potentially toxic and homeostatic mechanisms are required to regulate their intracellular levels [24,27]. As such, the (bio)imaging/mapping of metallic elements is an essential tool to gain insight into how metals behave in biological systems [21,28,29].

The distribution analysis of metallic elements plays a very important role in many disciplines [21,24,30,31]. Depending on the discipline, a suitable biological sample is needed. Without a doubt, biological samples and their preparation are playing a very important role in modern analytical chemistry studies [32,33]. Biological samples are very complex [34] and classification can be very different; e.g. biological samples used in medical studies can be divided into two groups: (1) *classical biological materials* – biological samples used for routine analyses (e.g. excrement, urine, blood and derivatives – serum, plasma); (2) *alternative (unconventional) biological materials* (e.g. hair, saliva, nails, meconium) – biological samples used for supplementary analyses. Currently, however, the most popular are alternative biological materials, and due to the fact that, for example, human tissues, animal models, and cell culture models are being used, (bio)imaging/mapping studies provide important, spatially-resolved information about how metals behave in situ [21,28]. However, it is also possible to use samples taken for routine analyses for some special investigations.

Huge progress over the years has caused large changes in both the interest and application of many different kinds of samples of biological origin. Table 2 presents examples of kinds of bio (imaging)/mapping studies and related examples of used biological samples.

2.2. Modern analytical methods used in bio(imaging)/mapping studies

In studies related to distribution of metallic elements, it is possible to use two terms: (bio)imaging and mapping. Unfortunately, those terms are commonly used interchangeably. However, the author feels that those terms are different and should be defined as

Table 2
Examples of types of bio(imaging)/mapping studies and related examples of used biological samples.

Discipline	Subdiscipline	Examples of bio(imaging)/mapping studies	Examples of biological samples	Source
Medicine	Pathophysiology	Distribution of toxic metals in organs	Brain, liver, heart	[19,23,35,36]
	Metabolic disorders	Distribution of essential metals in tissues	Brain, lens	[20,28,37]
	Toxicology	Distribution of toxic/heavy metals in organs	Epithelial cells, leukocytes, lung cells	[38–41]
	Pharmacology	Distribution of metallopharmaceutics in organs	Kidneys, brain, hair	[1,35,42,43]
Environment	Ecotoxicology	Distribution of toxic metals in plant tissues	Leaves	[44–47]
		Distribution of toxic metals in animals tissues	Snails	[30, 48–49]
Archeology	Paleontology	Distribution of metals in human	Bones, teeth	[50–52]
	Paleozoology	Distribution of metals in animals	Bones, teeth, fossils	[53–56]

Table 3
Characteristics of selected analytical techniques and methods applicable in (bio)imaging/imaging metallic elements in different biological materials [21,28,47,65,66].

Analytical techniques	Analytical method*	Spatial resolution [μm]	Detection limit [$\mu\text{g g}^{-1}$]	Selectivity
Mass spectrometry techniques	LA ICP-MS	5–150	0.01	Multielemental and isotopic
	SIMS (dynamic mode)	0.05	0.1	Multielemental and isotopic
X-ray micro-analytical techniques	PIXE	0.2**–2	1–10	Multielemental
	XRF/XFM	0.1–1	0.1–1	Multielemental ($Z \geq 10$)
	EDS/EPMA	0.03*** – 0.04	100–1000	Multielemental
	μ -XAS	0.1–1	100	($Z < 6$) multielemental Chemical species

Abbreviations: LA ICP MS: ablation inductively coupled plasma mass spectrometry; PIXE: particle induced X-ray emission; XFM: X-ray fluorescence microscopy; μ – XAS: micro-X-ray absorption spectroscopy; EDS: energy dispersive X-ray spectroscopy; EPMA: electron probe microanalysis; SIMS: secondary ion mass spectrometry.

* Depending on the analytical instrument character.

** For the latest generation of instruments.

*** For ultrathin samples.

- *imaging of elements* – a test result showing distribution of the analyte on the all-over surface of the sample using an analytical technique that allows for the measurement in its picture mode; especially – (*bio*)imaging: the imaging distribution of biochemical analytes (elements playing a biological role) [57];
- *mapping of elements* – a test result showing distribution of the analyte on the surface of the sample using an analytical technique that allows for distribution, point by point (mapping/raster mode) [57].

(Bio)imaging/mapping analytical techniques are presently of key interest in life science studies [58–63]. Much appreciable progress has been made to improve the sensitivity and spatial resolution of metallic elements in determination by (bio)imaging/mapping techniques [64]. Most of these techniques are characterized by micron to submicron spatial resolution and have a detection limit from 0.1 to 100 $\mu\text{g g}^{-1}$ [24,28]. Due to this fact, these techniques are appropriate for studies related to the distribution of metallic elements in biological samples. Table 3 summarizes the primary analytical (bio)imaging/mapping techniques for analysis of metallic elements and methods' parameters important in this kind of analysis.

3. Application of certified reference material (CRM) and standard reference material (SRM) in the techniques of (bio)imaging/mapping metallic elements in biological materials

Standards reference material (SRM) and certified reference material (CRM) are very important tools for maintaining a suitable quality of analytical measurement results [67,68].

In life science studies, the matrix (biological matrix) of standard samples and analyzed samples are very complex and never exactly equal [3,34]. However, due to the lack of suitable SRM and CRM to (bio)imaging/mapping studies, different calibration strategies are being developed; e.g., a matrix matched calibration

strategy (based on the conventional extrapolative method (CEM), or extrapolative method; known popularly as the “standard addition method [1,17]). Of course, there are commercially available SRMs or CRMs that can be used in (bio)imaging/mapping metallic elements' studies; e.g. CRM LGC 7112 – pig liver [36], NIST SRM 1577b – bovine liver [69], NIST SRM 1547 – for peach leaves [70,71] MICROMATTER™ XRF calibration standards – universal standards for XRF analysis, and SRM NIST 1515 – an apple's leaves [70]. However, application of these reference materials is limited to several chosen examples and is not practical, except when there are no other possibilities. Application of CRMs or SRMs are characterized by problems connected with the homogeneity of standard samples required for distribution analysis; e.g., the standard reference materials of biological materials where the certified values of elemental mass fractions are provided occur typically in lyophilized powder form. Therefore, they are not appropriate for microprobe analyses due to a large degree of heterogeneity [72].

4. The calibration strategies in (bio)imaging metallic elements by the different analytical techniques

4.1. The calibration procedure in (bio)imaging metallic elements by the LA ICP-MS method in biological samples

The laser ablation inductively coupled plasma mass spectrometry (LA ICP-MS) technique with multi-element capability and high spatial resolution is a modern and sensitive analytical tool for the mapping of metals in biological tissues [73–76]. Out of all of the inorganic mass spectrometric techniques, the LA ICP-MS method plays a suitable role as a sensitive microanalytical technique, enabling multi-element trace analysis and isotope ratio measurements at the trace and ultra-trace level in medical sciences [70]. This analytical method uses a focused laser beam to ionize a part of an analytical sample. The laser-ablated portion

Table 4
The calibration strategies elemental mapping in biological materials by the LA ICP-MS method.

Calibration strategy		Source
Kind of standard samples (physical state)	Idea of calibration strategy	
Solid	Pressed pellets of biological certified reference materials	[20,79]
	Sol-gel tissue pellets (sol-gel capsules)	[80–84]
	Gelatin (films) standard samples	[85,86]
	Agarose/agar gel standard samples	[87,88]
	Printed patterns on paper	[89–92]
	Metal spiked polymer films	[93,94]
	Metal spiked tissue homogenates (matrix-matched standard samples)	[1,11,37,42,74–77,98,100–103]
	Isotope dilution mass spectrometry (ID MS) combined to conventional nebulisation ICP-MS	[37,78,104]
Liquid (solutions)	On-line solution-based	[69,105,106]

of the sample is sent through an ICP torch, where the collected sample atomizes and ionizes the elements [77]. Then the ions are sent through a mass spectrometer and separated by their mass-to-charge ratio. Since the laser ablates only one area at a time, this technique is spatially resolved. Because the distribution map of elements is made by ablation gradually, the most appropriate term for it is mapping rather than (bio)imaging. The LA ICP-MS has a detection limit of approximately $0.01 \mu\text{g g}^{-1}$ [73].

As was mentioned earlier, the LA ICP-MS method is difficult to quantify due to a lack of sufficient standard reference materials for all of the different biological samples [31,74]. All calibration strategies in quantitative mapping by the LA ICP-MS method are based on the conventional extrapolative method (CEM) (popularly known as the “standard addition method”) [1,17]. Hence, several calibration strategies have been developed, which can be classified as calibration strategies, depending on whether the standard samples are solid standard samples or liquid standard samples (solutions) [78]. Table 4 presents an overview of the calibration strategies for elemental mapping in biological samples by the LA ICP-MS method.

4.1.1. Calibration strategies in LA ICP-MS mapping based on solid standard samples

When considering the solid standard samples, there are a few possible ways to make them, including (1) pressed pellets of biological certified reference materials; (2) sol-gel tissue pellets, (4) gelatin standards, (5) agarose gel standards, (6) printed patterns on paper, (7) metal spiked polymer films, and (8) metal spiked tissue homogenates (matrix-matched standard samples).

4.1.1.1. Pressed pellets of biological certified reference materials. The first kind of calibration strategy is the application of pressed pellets of biological certified reference materials. This quantification with the application of reference materials way was first described by Jackson et al. [20] for the mapping of metallic elements in rat brain tissue. This strategy is based on Lobster Hepatopancreas (TORT-2), Dogfish liver (DOLT-2) and Dogfish muscle (DORM-2) reference materials for trace metals analysis. The pressed pellets of the certified reference standards (TORT-2, DOLT-2, and DORM-2) are prepared using approximately 100 mg of the certified material by laboratory press (15×10^5 Pa for 5 min). The pellets are then affixed to a microscope slide. The potential disadvantage of this strategy is possible that air can be entrained into the calibration standard sample during the pressing of a pellet. This could then lead to a false positive signal caused by ArO^+ at m/z 56, which is connected with potential errors in Fe concentration [20]. This calibration strategy can be very useful when chemically and structurally matched calibration standards for elements (e.g. Hg, Ag and Cu) are not available. This situation may occur in the elemental mapping of bones and teeth [79].

However, in this approach the solid reference materials are not required. The major substance in tooth materials, – CaPO_4 – are not available with a the purity necessary for the preparation of standards. Hence, a series of standards can be prepared using CaSO_4 powder as the matrix material. Element standard solutions of Hg, Ag and Cu then are added, and the powder is dried, homogenized and pressed into pellets (8 bar, 5 min) [79]. The mass difference between CaSO_4 and CaPO_4 , as well as the content of organic material in dental material, must be taken into account. Due to the fact that, there is a growing interest in the use of metals (e.g. gold) in amalgam for dental restorations and that, additionally such elements may migrate into the human body and may have an effect on health, this calibration strategy has potential application in future studies.

4.1.1.2. Sol-gel tissue pellets (sol-gel capsules). Another kind of calibration strategy is based on sol-gel tissue pellets (sol-gel capsules).

The standard samples are prepared by a simple technique based on CEM, mixed with homogenized tissue (e.g. rat brain), into sol-gel matrix matched pellets (capsules). A sol-gel process can be defined as the preparation of ceramic materials using preparation of a sol, gelation of the sol, and the removal of the solvent [80]. These approaches applied the fact that certain SiO_2 -liquids may be made to set very rapidly and produce a stiff “gel”. The structure of a pure SiO_2 -gel consists of a 3D-network of Si–O linkage with a high porosity. The pores can be filled with the liquid used in the gel preparation, normally water and/or alcohol [80]. The first application of sol-gel capsules consisting of ground rat brains was described by Fitzpatrick et al. [81]. The sol-gel process for the production of a silica glass begins with hydrolysis of silica alkoxide and subsequent polymerization to particles (sols). The sols grow and aggregate to chains and 3D network structures that encase the fluids (gel). Acid can be used for the catalyst of the process can be used acid or base and silica linkage is increased with the addition of a simple alcohol. The net reaction using tetraethyl orthosilicate (TEOS) [82] can be written as $\text{C}_8\text{H}_{20}\text{OSiO}_4 + 2\text{H}_2\text{O} \rightarrow 4\text{C}_2\text{H}_5\text{OH} + \text{SiO}_2$. After one hour, an aliquot of water and one drop of concentrated HNO_3 (69–70%) is added and stirred for 15 min. Four drops of concentrated HF (40%) on is then added and 10 min stirring is required. After preparation of the sol-gel solution and the spiked tissue samples, approximately 0.1 g aliquot of the ground brain tissue is added to 1 mL of the TEOS-xerogel solution [82]. The resulting solution is then shaken gently by hand for 30 s and poured into molds. The obtained molds are then covered with perforated parafilm and placed in a fume hood at room temperature. The extent of perforation of the parafilm affects the evaporation rate. The filled molds are considered ready when the resulting xerogels achieve a constant mass ($< 0.5\%$ daily change in weight), typically after about one week [82]. The big

advantage of the production process is the manufacturing homogeneous and stable standard samples with a long shelf life. Moreover, the application of sol–gel as a matrix to produce stable standard samples is a developing area of research [83,84].

4.1.1.3. Gelatin (films) standard samples. This calibration strategy is based on application of gelatin to prepared standard samples. The main idea of this concept is that, a gelatin is organic, readily available, non-toxic, inexpensive, and can provide a soft matrix similar to biological tissues. The major advantages when preparing biological standard samples is homogeneity of the analyte distribution. This strategy was described e.g. by Gholap et al. [85] in the studies of distribution and bioavailability of an intraperitoneally administered Pt-containing chemotherapeutic drug. Moreover, this method was also applied by Izmer et al. [86] in studies about the distribution of a drug and its metabolites across the body compartments of rats. In both cases, the procedure is similar. A gelatin solution (10% w/v) is prepared by mixing gelatin powder with Milli-Q water and heating this mixture at 60 °C, until all the gelatin melts and the solution becomes clear and consistent. In a separate experiment, a stock solution containing analytes (e.g. Pt, Br) is prepared. Different volumes of the standard solutions are taken and diluted to with the gelatin solution, according to the required analytes concentration range. From each of these standard solutions the portion (e.g. 100 µL for Pt) is carefully withdrawn and placed on a flat glass support. Another portion (e.g. 100 µL for Pt) is then introduced into a glass vial. Both the glass vial and the glass support are allowed to stand at room temperature overnight. The hardened gelatin film on the glass support can be then applied for LA ICP-MS mapping. This approach offers a quick, inexpensive, and convenient way for preparing homogeneous standard samples.

4.1.1.4. Agarose/agar gel standard samples. Dried thin films of doped agarose gel were investigated as a novel calibration strategy for LA ICP-MS mapping and were first described by Stärk et al. [87]. In this approach agarose for electrophoresis is added to sodium acetate solution (1 M) and the multi-elemental standard samples required for the spikes. Deionized water is added to obtain the constant mass (approximately 10 g). Buffering is required because the gel will not set, due to the acid from the standard stock solutions. The mixture is then heated (80–90 °C) using a water bath and then is shaken to dissolve the agarose in the mixture homogeneously. A clean glass microscope slide is put on a laboratory balance previously aligned horizontally to guarantee uniform distribution of the gel. The hot agarose mixture (approximately 4 g) is then quickly pipetted on to the slide, to avoid significant evaporation. After cooling (for a few minutes), this large droplet sets to a semi-solid “pudding” which is then dried under clean conditions. After drying a thin film of agarose is formed that sticks to the glass slide surface. It seems that, these strategy is very promising, although studies by Li [88] related to the application of agar gel standard in LA ICP-MS mapping of Cu and Zn in rat liver tissues indicate that agar is not a good for preparing standard samples. However, future investigations are required in this field.

4.1.1.5. Printed patterns on paper. Another possible approach of a sophisticated calibration strategy is based on preparing thin layers with the use of modified inkjet printers. Preparation and the drying of small amounts of liquids in the microliter range is a subject for the optimization of total reflection X-ray fluorescence (TXRF) applications [89] due to the fact that homogeneous thin sample structures are of utmost importance for TXRF analysis. Additionally, nanoliter droplets of ink have been used as a

reference in mPIXE but without any additional characterization besides the PIXE analysis [90]. Fittschen et al. [91] described the characterization of dried residues of picoliter droplet as standards for LA ICP-MS mapping. Fittschen stated that elemental fractionation and laser ablation-related matrix effects can be excluded if the dried droplet is completely evaporated and the whole signal is integrated. On the other hand, Bellis et al. [92] described the application of inkjet-printed patterns of Cu which can be applied as model samples for evaluation of the lateral resolution capability of an LA ICP-sf-MS mapping.

4.1.1.6. Metal spiked polymer films. A new calibration strategy for metallic elements mapping by LA ICP-MS in biological soft tissue samples based on spin coated calibration standard samples was described by Austin et al. [93]. Spin coating can be defined as a process widely employed for the fabrication of thin film coatings with high structural uniformity [94]. The film standards fabricated by spin coating spiked solutions onto quartz slides is used to quantify copper and zinc in a homogenized soft tissue sample. The film standards fabricated by spin coating spiked solutions onto quartz slides is used to quantify Zn and Cu in a homogenized soft tissue sample. In the first step quartz slides (approximately 25 × 25 mm²) are washed successively in acetone, 5% nitric acid solution and distilled and deionized water. Glass vials used for the preparation and storage of spin solutions are acid washed overnight in 30%, then 5% nitric acid before rinsing with Milli-Q water and being baked dry. Standards samples are spin coated from solutions of PMMA (poly(methylmethacrylate)) (10%), xylene (40%), and chlorobenzene (50%), then spiked with organometallic Cu and Zn standards at required concentration range (e.g. 0.1–30 mg g⁻¹). In Austin et al. [93] ruthenium phthalocyanine dye and an organometallic yttrium standard were applied as internal standards. After the spin coated process, clean slides are placed on the vacuum chuck of a single wafer spin processor and 200 mL of the spin solution deposited on the slide using a micropipette. The solution is allowed to sit for 10 s before accelerating to 4000 rpm for 40 s. Substrates are then baked on a hot plate at 130 °C for 2 min. In this strategy, the tissue sample can be placed on top of a thin film containing the adequate IS, but the complete ablation of the sample, including the polymeric film, has to be performed to ensure reproducible analysis. Additionally, a time-consuming step is added to the sample preparation process.

4.1.1.7. Metal spiked tissue homogenates (matrix-matched standard samples). The last kind of calibration strategy is the application of matrix-matched standard samples (self-prepared standard samples). This idea is advantageous because it can be assumed that the ablation behavior of the standard and the sample is identical [78]; however matrix effects may occur and some other quantification strategies should be preferably used. This calibration strategy requires the sophisticated preparation procedure described by Becker et al. [74–77], and the similarly modified methodology by Jurowski et al. [1,11]. In this strategy, the first step is homogenization of biological material (e.g. brain tissue) and transfer of homogenate portions into several Eppendorf vials. The next step is preparation of multielement standard sample solutions by dissolving salts of the considered elements and mixing solutions. The obtained standard sample solutions (multistandard solutions) are then spiked in to biological material homogenates. Then, the homogenous spiked standards are immediately frozen in liquid nitrogen to save the homogeneity. After that, the solid standard samples are cryo-cut by a cryostat to thin sections on microscope slides. The obtained solid standard samples are stored until analysis at 20 °C.

For preparing matrix-matched standard samples it is also possible to apply CRM and SRM. For example, Kidness et al. [19] developed an

analytical procedure using LA ICP-MS with a cooled laser ablation chamber for the quantitative determination of two-dimensional element mapping of metal (such as Cu and Zn) in sections of sheep liver tissue. In these studies, a homogeneous certified reference material (CRM LGC 7112, pig liver) was applied to quantify the analytical data [36]. Another example can be in the application of apple leaves, SRM NIST 1515 [74], in distribution studies of essential elements in *Elsholtzia splendens* leaves. The calibration approach of essential metals' mapping in the fresh leaves of this plant's tissue proposed by Becker et al. [71] requires the certified standard reference material for apple leaves (SRM NIST 1515) for semi-quantitative measurements (for characterizing the material), whilst standard reference material, NIST SRM 1547, for peach leaves was used to validate the analytical procedure. The idea of the calibration strategy in this case is based on the preparation of a standard stock solution mixture, and then adding to the standard reference material at different concentration levels. After absorption for 48 h, the materials are dried, ground into fine powder and pressed under 8 atm. These standards are scanned first with five lines each, and then the leaf of *Elsholtzia splendens* are scanned in the line-by-line mode with a focused laser beam. To compensate for the possible inhomogeneity of the materials due to the preparation procedures, each measured of the values are corrected by the ion intensity of ^{13}C isotope (as an internal standard). Moreover, the concentrations of the analyzed elements in peach leaves were measured by the LA ICP-MS method and were then correlated with the certified values. In this research, fresh leaves were measured directly by the LA ICP-MS method without sample preparation. The quantitative distribution maps of the studied leaf veins can be clearly observed, indicating the importance of the vein in transporting macro-essential elements.

4.1.1.8. The internal standard(s) in mapping by LA ICP-MS. The internal standard (IS) can be a powerful tool in the calibration of LA ICP-MS. One of the primary factors limiting precision in LA ICP-MS measurements, however, is the instrument's fluctuation. To overcome this limitation it is possible to use a single internal standard. In internal standardization the mass ablated is monitored by measurement of one or more reference elements. Additionally, the IS(s) should be homogeneously distributed in the solid standard sample, is required in an analyzed sample in constant concentration (or can be spiked) and have similar behavior to analyte(s) in the ICP and an absence of potential interferences. However, it can be difficult to find elements suitable for use internal references. Using all the main elements together, a robust kind of internal standardization is achieved; which is known as the 100%-normalization technique. Nonetheless, in most cases (biological studies) to standardize the results, each analytical signal is divided usually by the value of the corresponding carbon isotope ^{13}C signal (or ^{12}C). This is possible due to the facts that (1) carbon is the main component of tissues, and its spatial concentration within a sample may therefore be assumed as constant; (2) due to its availability and (3) apparent homogeneity in biological tissues. Accordingly, the signal values for ^{13}C are closer to the values of analyte isotopes, and this isotope may be considered as an internal standard in tissue analysis [94]. In the case of (bio)imaging, the signal standardization allows for the distinguishing of the natural variability of signals related to the concentration of local analytes' concentration from its variability, which is caused both by different interaction of the laser with the surface of a sample and by local differences in tissue thickness (differently ablated sample masses) [1,11]. However, Frick and Günther [95] as well as other authors (e.g. Jackson [20]) described that application of ^{13}C or ^{12}C as an internal standard may lead to inaccurate results, due to the fact that the ablation of carbon-containing matrices demonstrating the formation of two individual phases, a gaseous carbon-containing species and a carbon-containing particle phase. This suggests that the ^{12}C signal

and ^{13}C signal are not a good indicator of how signal intensities of other analytes vary for these standards, even if a close matrix matching is performed. That means, it would not be an effective internal standard because its value remained relatively constant for all standards, while other analyte(s) signals varied significantly between the calibration dates. All the same, application of carbon as an internal standard may improve precision compared to raw counts. However further studies are required. For these reasons, in some cases calibration functions can be constructed without referencing analyte responses to an internal standard intensity (raw results) or other internal standard(s) should be preferably used. In this field it is possible to apply: multiple internal standards or elements characterized by with their rareness (low natural abundance), but with a presence in the investigated sample – e.g. ^{101}Ru with ^{89}Y (as mentioned in *Metal spiked polymer films*), ^{197}Au , ^{103}Rh , ^{115}In and ^{185}Re .

A novel approach for the internal standardization of LA ICP-MS mapping, based on multiple internal standards was first described by De Ridder et al. [96]. The novelty of this approach is that it (1) takes into account the measurement uncertainties; (2) allows one to check and dismiss the mass dependency of the standardization procedure; and (3) generates uncertainty bounds on the normalized measurements.

Another interesting standardization procedure described by Konzo et al. [97] is based on the deposition of a homogeneous thin gold film on the tissue surface and the use of the $^{197}\text{Au}^+$ signal as an internal standard. In these studies an eye section from a paraffin-embedded human eye of normal donors was used as the model tissue. To prepare suitable standard samples with IS, the thin sections (15 μm) of the sample (paraffin-embedded human eye tissues) are metallized for 40 s with gold. The total duration of the thin film deposition is below 5 min. This time-effective strategy offers the possibility for a more robust direct and simultaneous qualitative determination of metallic elements distribution in tissue structures having different compositions and morphology.

Application of ^{103}Rh as internal standards was described by O'Reilly et al. [98] in studies related to the mapping of Fe in mouse brains. This choice of internal standard was possible from among Ga, Ge, Rh, Sc and Y. The IS was investigated by determining the RSDs (%) of a Fe-to-internal standard ratio to rank the relative quality of each Fe-internal standard pair and their response to changing conditions. Due to the facts, that the best measurement precision on the tissue-matched calibration standard samples was obtained when using Rh and this element is distributed homogeneously across the matrix-matched standard samples, this element can be chosen as an IS in Fe mapping studies by LA ICP-MS.

^{115}In and ^{103}Re applied as internal standards for Ru and Pt mapping by LA ICP-MS, respectively, in samples originating from animal experiments was first described by Egger et al. [99]. However, data analysis employing the mentioned internal standards demonstrated that neither of them improved the precision significantly. Hence, standardization solely via raw counts and matrix-matched standards is feasible for mapping Ru and Pt.

4.1.2. Calibration strategies in LA ICP-MS mapping based on liquid standard samples

When considering solution standard samples there are two possible ways: (1) the isotope dilution mass spectrometry (ID MS) combined with conventional nebulisation ICP-MS; and (2) the solution-based calibration strategy.

4.1.2.1. The isotope dilution mass spectrometry (ID MS) combined with conventional nebulisation ICP-MS. The isotope dilution mass spectrometry (ID MS) combined with conventional nebulisation ICP-MS is a relatively simple and reliable procedure for the determination of trace

elements in powdered organic and inorganic samples [78]. The unique advantages of the isotope dilution technique are successfully transferred to the direct analysis of powdered samples. In this strategy, the analyzed sample with a known isotopic composition of the analyte element, yet unknown element content, are mixed with a known amount of spike. The spike consists of the analyte element in a different isotopic composition: ideally enriched in the most rare natural isotope [93]. After a complete mixing of the sample and spike, the so-called sample-spike blend or isotope-diluted sample gained a new isotope ratio between the isotope ratio of the sample and that of the spike. This blend of isotope ratio directly reflects the analyte concentration in the sample. In ICP-MS the isotope ratio measurements are in fact largely unaffected by the matrix due to the ionization conditions, as both isotopes will be affected in the same way [93]. Hence, LA ICP-IDMS is a very important component of the existing calibration procedures in LA ICP-MS.

4.1.2.2. The solution-based calibration strategy. Another calibration strategy that was solution-based was invented for the validation of analytical data obtained using the calibration procedure with matrix-matched synthetic laboratory standard samples. This strategy was introduced using an inserted micronebulizer in the cooled laser ablation chamber by Becker et al. [105]. During the laser ablation of thin sections of the biological sample, the defined standard sample (solution) with increasing concentration was nebulized. In this procedure, LA ICP-MS analysis can be performed with a single line scan mode over the sample surface. For example, in [105] the regression coefficients for calibration functions are better than 0.999. In these studies, the $^{232}\text{Th}^+ / ^{238}\text{U}^+$ intensity ratio by standard addition mode for different standard solutions used micronebulization in LA ICP-MS. For all the measured concentrations of the standard solution, the $^{232}\text{Th}^+ / ^{238}\text{U}^+$ intensity ratio was nearly constant. To obtain quantitative data in a solution-based calibration strategy, different element sensitivity in ICP-MS and LA ICP-MS must be considered. For the correction of different element sensitivities in ICP-MS and LA ICP-MS, the correction factor (concentration of internal standard element determined by solution-based calibration strategy in LA ICP-MS/true concentration of internal standard element in the analyzed sample) was determined by application of either uranium or thorium. Due to the fact that both elements have been found to be homogeneous and distributed within the human brain sample, this element was therefore applied as an internal standardization in the calibration procedure [85].

Another possibility for element quantification in, for example, brain tissue or single hair [105] analysis, is the SRM-free approach of solution-based calibration in LA ICP-MS that was developed recently in the BrainMet laboratory [106,107]. In these kinds of studies a dual argon flow of the carrier gas and nebulizer gas is applied. A dry aerosol produced by laser ablation of the biological sample and an aqueous aerosol generated by pneumatic nebulisation of standard solutions are carried by two different flows of argon as a carrier or nebulizer gas, respectively, and are introduced separately in the injector tube of a special ICP torch, through two separated apertures [95]. Both argon flows are mixed directly in the ICP torch. External calibration via defined standard solutions before distribution analysis of brain tissue or single hair was employed as the calibration strategy. A correction factor, calculated using hair with a known analyte concentration (measured by ICP-MS), is applied to correct the different elemental sensitivities of ICP-MS and LA-ICP-MS.

4.2. The calibration procedure in (bio)imaging metals by the SIMS method in different biological samples

The secondary ion mass spectrometric (bio)imaging (SIMS-MSI) is characterized by higher spatial resolution images directly from

biological materials [28,60,108]. SIMS can be applied to the analysis of many biological materials, such as tissues or cell types, enabling the acquisition of images of submicrometer spatial resolution with a minimum amount of sample preparation [39,60,109–115]. The SIMS (bio)imaging technique is becoming an increasingly valuable tool in many areas of medical studies due to its capabilities to analyze in situ elemental and molecular at subcellular scale resolution [111]. The most suitable for the studying of elements (isotopes) and isotopically labeled molecules are the SIMS technique with dynamic beams [60]. Imaging MS techniques of metals and metal-containing species by SIMS have been well-known in biological studies for many years. However, the elemental and metal cofactor analyses are also showing significant promise [116,117]. The live cells cannot be analyzed directly in the instrument due to the high vacuum requirements of SIMS [113,114]. Hence, the sample preparation of samples plays a critical role in preserving the original chemical composition for analysis [32,64,111]. Special preparation of a sample in SIMS (bio) imaging analysis is not required, but there are some optional methods that improve the (bio)imaging results [62,109,102,115–118]. However, if sample preparation for SIMS imaging is required, in most cases this is straightforward (for dry solid materials) [109].

When using metals such as silver or gold, small organic acids used as a coating agent can improve the ionization of intact molecules larger than 1000 Da [39]. (Bio)imaging by the SIMS method can be applied to a wide range of biological samples [59,98,106,107,113] including single cells [40,41,110,119–121], plants tissues [110,113], bones and teeth [51,53,54] hair [121], kidneys [33], aorta [58], liver [122] or whole brain sections [123,124]. This method can be used to obtain fine (bio)images at high spatial resolution of light metals such as sodium, potassium, magnesium and calcium in different organelles in cells [39,62].

The subject of the analytical calibration mapping of metals in various biological samples by the SIMS method is very rare in related literature; perhaps in view of one possible approach developed by Morrison et al. in 1975 [125]. In this approach, a calibration strategy in the SIMS method has been well established and is based on the illumination (I) of a dynamic SIMS ion microscopy image [126]. This physical quantity may be expressed by a simple equation [64]. In this equation [127,128], the illumination (I) is related to the concentration of the imaged element M , t means the practical ion yield of element M or the ratio of the number of M^+ ions collected to the number of M atoms removed from the sample, C_M is the atomic concentration of element M corrected for its isotopic abundance, S is the total sputtering yield or number of atoms of any kind removed from the sample per incoming primary ion, i_p means the primary beam current density, and a_0 is the analyzed area of the sample surface [60].

The variables' primary beam current density and analyzed area of the sample surface are controllable, but the practical ion yield of the analyzed element and total sputtering yield depend on many factors. The practical ion yield of an element depends on the chemical state of the element, the chemical and physical properties of the sample matrix, instrument transmission of ions, the sampling conditions, and is inversely proportional to the exponential of the element's first ionization potential [65].

Variations of the practical ion yield of the element and total sputtering yield within the imaged field have been considered as matrix effects, along with mass interferences due to the matrix, which can augment the measured intensities [60]. The basic requirements for any dynamic SIMS image quantification scheme are [61,129,130]: (1) the evaluation of the matrix effects must be made; (2) the sample preparation procedure must preserve the native elemental distribution of the analytical sample; (3) analytical calibration of the ion microscope's imaging system; and (4) the quantification standard sample should have the same matrix composition as the sample.

The method complying with the above assumptions consists of preparing homogenates generated from cultured cells that are used for the Ion Microscope's (IM) relative sensitivity factors (e.g. Ca, K, Mg, and Na), with respect to the matrix element that is determined by the correlation of IM and inductively coupled plasma atomic emission spectrometry analyses of the cellular homogenates [58].

After calibration of the IM imaging system, the relative sensitivity factors are used to determine local intracellular concentrations of calcium, potassium, magnesium, and sodium in analyzed samples. In the SIMS method, there is a possibility to also make 3-D (bio)imaging, which is ideal for studies of fractured freeze-dried cells where the subcellular structures of interest are hidden beneath the top surface layers [64].

4.3. The calibration procedure in (bio)imaging metals by the analytical method using X-rays in different biological samples

(Bio)imaging using X-ray is very important in research studying the role of essential elements in biological systems due to the possibility of studying them at the cellular level [131–133]. By analyzing the energies where the X-rays are emitted or absorbed, it is possible to identify an element and the chemical speciation of this element in an analyzed sample [28]. For (bio) imaging at a high spatial resolution, the beam must be focused on a small spot [134]. The X-ray analysis may have a better analytical sensitivity by using synchrotron radiation [65,135], which is a synchrotron radiation X-ray fluorescence (SR-XRF) method, or a particle-induced X-ray emission (PIXE) method. The X-ray absorption spectroscopy (XAS method) makes it possible to study chemical speciation. All of the methods are characterized by sensitivity, selectivity and spatial resolution [136]. Table 5 summarizes the commonly used analytical techniques using an X-ray described in the article and its application in (bio)imaging studies.

4.3.1. Synchrotron X-ray fluorescence microscopy/X-ray fluorescence

X-ray fluorescence (XRF) is a well-established multi-element analytical technique of high precision and accuracy for determining the elements in different kinds of samples. Recently, the XRF spectrometry has been widely used to study the elemental composition of a wide range of biomedical samples, such as soft tissues [147] and also bones and teeth [54]. As was shown in Table 5, this technique is particularly useful for applications in many fields of medicine, chemistry and biology studies; XRF analysis finds application in study samples of different body organs: liver, heart, brain, kidneys, breast or lung.

The (bio)imaging/mapping studies by X-ray fluorescence (XRF) analysis requires the conversion of measured intensities of the characteristic radiation to the concentrations of the elements to be determined (analytes). This process is based on the relationship between the measured characteristic X-rays and the excitation source intensity, concentration of the analyte, overall composition and absorption properties of the sample [148]. The principle of

XRF analysis is based on excitation of electrons by incident X-radiation [28]. Ejection of electrons from inner atomic shells creates vacancies that are filled by electrons falling back from the outer shells, whereby the surplus energy is emitted as a pulse of secondary X-radiation [133]. The emitted fluorescence energy and wavelength spectra are characteristic for atoms of specific elements and permit the estimation of their relative abundances [21]. The idea of XRF analysis is to identify an element in a sample to a high degree of certainty. When performing the analysis on an XRF spectrum, the main objective is to be able to detect any characteristic peaks present in the sample above the background.

XRF can be used also for quantitative mapping of metallic element distributions [64]. It means that by quantitative XRF analysis it is possible to obtain distribution maps based on measured XRF spectra to the actual chemical composition of the analyzed sample. It is worth pointing out that a sample's mass thickness is critical for quantitative XRF analysis [134]. X-ray microanalysis may have a better analytical sensitivity by using synchrotron radiation, which is a synchrotron radiation X-ray fluorescence (SR-XRF or SXRF) [136].

There are two possible calibration strategies regarding solid standard samples: (1) the matrix-matched standard samples strategy [136], and (2) matrix correction strategies.

XRF (bio)imaging studies using empirical calibration strategy requires a large number of reference standards with similar physical and chemical properties as the unknown samples. If matrix-matched standard samples are possible to make and are characterized by the same thickness, density and bulk composition, the standard samples can be analyzed. The fluorescence intensities can be obtained, and then a calibration function of intensity vs. concentration is generated. This way is the most accurate solution, but unfortunately it is also the most impractical. Spatially homogeneous matrix-matched standard samples at the μm scale are very rare to obtain. This calibration strategy is very similar to the described matrix-matched standard strategy for LA ICP-MS (see Section 4.1). The spectral data collected for each measurement point are normalized to the detector live time, as well as the beam flux before the sample. This normalization procedure is applied to all of the standard samples and tissue samples. The concentrations of elements in each sample point were determined according to a simple equation.

The second calibration strategy is based on the matrix correction strategies [150]. A matrix correction is applied after raw count data are smoothed and peak areas are calculated. This strategy can be categorized as two types [151]: (1) experimental (empirical) strategies and (2) fundamental parameter (FP) strategies (very similar to the method used in EDS imaging – see Section 4.3.3). In the experimental strategy, calibration functions are obtained to determine the concentration for elements in the sample from processed XRF energy count data. Two experimental strategies widely applied in commercially available XRF instruments are the Lucas-Tooth and Pyne [152] and Lucas-Tooth and Price [153] calibration algorithms. The difference between The Lucas-Tooth and Pyne algorithm vs. Lucas-Tooth and Price is that the first uses a

Table 5
Commonly use analytical techniques using an X-ray described in the article and its application in (bio)imaging studies.

X-ray microanalytical technique	(Bio)imaging studies	Source
XRF/XFM	Toxicology studies, distribution of metals in cells, metals distribution in bones, neurodegenerative disorders, subcellular topography	[21,131,137–139]
PIXE	Metals distribution in bones, organelles and cells studies, biomonitoring of metalopharmaceutics distribution, neuro-degenerative disorders, cancer studies, plant tissue imaging	[140–144]
EDS/EPMA	Distribution of metals in cells, neuro-degenerative disorders	[28,41,63,142,145]
μ -XAS	Tumor studies, environmental studies	[146, 149]

non-linear interpolation step to correct inter-element interactions, whereas the second uses linear interpolation.

The fundamental parameter (FP) strategy is very old, and first was introduced by Sherman in 1955 [154]. Another popular fundamental parameter-based calibration strategy was developed by Criss [155] and Rousseau [156] (see Section 4.3.3).

4.3.2. Particle induced X-ray emission (PIXE)

The particle induced X-ray emission (PIXE) method is based on the detection of characteristic X-rays emitted by the element in a sample when excited by an ion beam [157]. The particle beam encounters a metal atom that causes the ejection of an inner shell electron. An outer shell electron then relaxes and emits a photon which is then detected as an analytical signal. The energy of the emitted X-rays is characteristic of the excited element [28].

The emission energies of all the chemical elements can be tabulated, thus enabling the identification of the composition of the atoms constituting the sample [158]. The PIXE method offers good sensitivity for elements, and it is a multi-elemental technique for atoms with atomic numbers (Z): $20 < Z < 35$ and $75 < Z < 85$ [65,148]. All these possibilities are well suited to the detection of toxic heavy metals (Hg, Pb, Cd), essential trace elements (i.e. Zn, Se, Fe, Mn, Cu, etc.), or pharmacological compounds (like Pt). The detection limits depend on the nature of the sample, the considered element, analytical conditions, and the experimental set-up. The parts per million detection limit may make it possible to collect meaningful data from animals exposed to environmentally relevant metal concentrations [28,68].

To obtain quantitative elemental concentrations and to generate quantitative elemental maps, the X-ray spectra from the analysis at each pixel in a data set are analyzed to account for the presence of any continuum X-ray background to extract characteristic X-ray peak areas or yields for interesting elements [159]. For analyzing X-ray data, the computational iterative PIXE spectrum fitting code (PIXEF) can be used, where target matrix effects are calculated in absolute terms for the sample. With this spectrum fitting code, a wide range of tissues may be analyzed with a small suite of appropriately chosen thin film standard samples (as in the SR XRF calibration strategy) used to calibrate the detector efficiency. It is worth noting that the PIXE spectrum fitting code has a quantitative accuracy greater than 95% for biological samples [160]. Due to the fact that this technique is not very popular in (bio)imaging/mapping studies (in comparison to other X-ray techniques), there are not many calibration strategies. One of the interesting and well-known calibration strategies was described in 1989 by Lapatto et al. [127]. However, because this trace element analysis referred to human nails, a calibration strategy was necessary as no commercial nail standard samples were available. This calibration strategy is based on solid standard samples; pellets about the same density as the nail samples. Because keratin is the major constituent of nails, the calibration standard samples were prepared by making a mixture of keratin with suitable amounts of standard salt solutions containing the trace elements of interest, which were then added to the mixture. The different standard samples were used for each element and added concentration. After thorough mixing, the standard samples were dried at 30 °C and then pressed into pellets using a constant pressure of 6 MPa. The pressure used gave the pellets about the same density as the nail samples. It is important to note that the surfaces were thus also smooth in order to avoid errors owing to surface irregularities. This calibration strategy yielded a better homogeneity for the standard sample than the procedure based on ground nails with the addition of the element in powder form. In order to evaluate the possibility and accuracy of using a single multielement standard sample for nail analysis, different

biological samples (the standard materials of bovine liver, animal muscle and horse kidney) can be prepared as pellets for comparison purposes this same way [159].

4.3.3. Energy dispersive X-ray spectroscopy (EDS)/electron photon micro analysis (EPMA)

In EDS (EDX, EPMA) studies, a calibration strategy is available for [134]: (1) thin samples, (2) samples with intermediate thickness, and (3) thick samples.

A thick sample means its thickness is greater than a limiting value (called saturation thickness), above which practically no further increase in the intensity of the characteristic radiation can be observed, even when the sample thickness is increased [148]. For thin samples, the mass per unit area (concentration) of the analyte is a linear function of the intensity of its characteristic X-rays, due to the fact that the absorption and also enhancement effects can be neglected [148]. The calibration of an EDXRF spectrometer is straightforward and can be done either theoretically or experimentally based on the measurements of thin homogeneous (single or multielement) standard samples [161]. This simple strategy is not appropriate for the analysis of heterogeneous thin samples, so that an additional correction for the heterogeneous sample loading, combined with the distribution of the excitation detection factor, can be used as a solution. Thin samples are often applied in total reflection XRF. However, to correct the inhomogeneous excitation and geometric effects, an internal standard method is applied to the experimental calibration procedure [162].

Samples with a thickness range between the thin and thick are characteristic for the intermediate thickness samples. In some cases, this type of sample is preferable and provides an advantageous detection limit and accuracy as well as flexibility in the sample preparation [148]. The well-known correction method for the calibration strategy of the intermediate thickness samples is the emission-transmission method whereby the absorption properties of the sample are then determined experimentally using a multielement target before being applied to calculate the absorption correction factors [162]. However, some problems exist in the analysis of heterogeneous samples and samples containing minor and major elements. Other groups of correction methods are based on scattered primary radiation [163,164]. The scattered peaks of the primary radiation undergo matrix absorption and geometrical/instrumental variations similar to those of the fluorescent peaks, which can be treated as sort of fluorescent peaks from internal standard samples. An alternative way for the assessment of the enhancement effect is based on the enhancement factor for a thick sample and the thickness of the sample. This simple method appears to be very convenient to define the region of the sample thickness where the enhancement effect is negligible and/or to determine the minimum sample thickness for which the bulk enhancement correction can safely be used [165]. A more useful calibration strategy is based on a backscatter fundamental parameter (BFP) model which can also be applied for samples containing low- Z elements (dark matrix) that are not detected in characteristic X-rays [166]. In this case, two additional light elements are defined to represent the dark matrix of the analyzed sample and to perform a full correction for the matrix absorption and enhancement effects. To improve the quality of the analytical data, other modifications of the BFP method, such as applying differential mass scattering cross-sections integrated over the average scattering angle, instead of the total scattering cross-sections, experimentally determining effective incident and take-off angles (to take into account a broad geometry experimental set-up) and taking thin (or intermediate thickness) samples for calibration (to minimize the influence of the uncertainties of the fundamental parameters on the accuracy of the calibration factors) were proposed [148,166].

The thick samples are those that are characterized by a thickness greater than a limiting value (saturation thickness)

above which practically no further increase in the intensity of the characteristic radiation is observed even when the sample thickness is increased. In this case a simplified equation for the intensity of the characteristic radiation can be applied where dependence on the sample thickness disappears [163]. Since the majority of the samples analyzed by the EDXRF technique are thick, various calibration strategies were developed and are currently commercially used in XRF spectrometers. They include relatively simple calibration strategies based on [167]: (1) the fundamental parameter (FP) strategy, (2) the scattered radiation strategy (Compton alone or Compton combined with Rayleigh scattered radiation); and (3) the theoretical influence coefficient strategy.

The fundamental parameter (FP) strategy is fully theoretical. The idea is to calculate the theoretical intensities of the characteristic radiation of the analytes from a composite sample of known composition [168,169]. The analytical calibration step is based on the measurements of pure element samples to calculate the relative intensities for each analyte. During the application of iterative calculation in the analysis step, which involves the comparison of the theoretical results with the experimental data, concentrations of the elements are found. The main problems in applying this strategy are (1) the necessity to normalize the concentrations to 100% (which is obviously impossible when very light elements like C, N, O are present in a sample); and (2) evaluation of the first estimate of the composition [148]. To extend the applicability of these methods for the analysis of samples with low-Z elements (dark matrix), a backscatter fundamental parameter (BFP) strategy was developed [166].

The scattered radiation strategy is based on the ratio of intensities of the characteristic X-rays of the analyte element and the Compton scattered radiation. The intensities of the characteristic X-rays of the analyte element and the Compton scattered radiation depend in a similar way on the composition of the sample material, and their ratio becomes less sensitive to the variation in the composition of the analyzed material and can be used for the correction of the matrix absorption effects [170]. This strategy is similar to the 'fluorescent-to-Compton' correction strategy and can profitably applied if no significant absorption edges occur between the Compton line and the fluorescent line of the analyte, and the matrix variations are limited [170, 171]. Scattered primary radiation can also be applied for characterizing low-Z elements in the analyzed sample (dark matrix) in the backscatter fundamental parameter strategies [166].

The influence coefficient strategy is based on numerical coefficients that correct the effect of each matrix element on the element to be determined (analyte) in a given sample. The influence coefficients can be classified into two categories: (1) theoretical and (2) empirical [173]. Both categories can be calculated from binary or multielement standard samples [148]. The binary coefficient solution is based on the assumption that the total matrix effect on the analyte is equal to the sum of the effects of each element of the matrix calculated independently of each other [148]. In the multielement mode the empirical coefficients are calculated from linear multiple regression analysis using measured intensities and compositions of multielement CRM. Hence, the empirical coefficient methods are particularly suitable for the EDX (bio)imaging of nonhomogeneous samples and also when some elements present in the sample are not detected.

4.3.4. Micro-X-ray absorption spectroscopy (μ -XAS) and X-ray absorption near the edge of the structure spectroscopy (XANES)

An X-ray absorption spectroscopy (XAS) can often be performed using the same experimental set up as XRF. This technique scans the energy of the incident monochromatic X-ray beam

across the absorption edge of an element of interest. X-ray absorption near the edge of the structure (XANES) extends from a few electronvolts before the absorption edge to about 150 eV above the edge, and provides information about the oxidation state of the element [65,29]. The XANES technique, which provides information primarily about coordination geometry and oxidation states, is one of the most widely used techniques for investigating the local structural environment of metal ions, the active sites of metalloproteins including speciation, and ligand binding [172].

Most of the articles are limited to (bio)imaging aspects or semi-quantitative evaluation. An interesting example of this research is fully quantitative analysis, which allows for the determination of the masses per unit area of each chemical form of iron in tissue slices, as described by Szczerbowska-Boruchowska et al. [173]. In this strategy, the tissue sections used can each be considered a thin sample, and the external standard method for quantitative analysis is used. The full XANES spectra were collected at selected points for samples of the analyzed sample (brain gliomas), as well as for the powder samples of reference materials ($\text{FeSO}_4 \cdot 7\text{H}_2\text{O}$ and $\text{Fe}_2(\text{SO}_4)_3 \cdot n\text{H}_2\text{O}$). Each interesting fragment of the biological sample (a tumor taken for standard histopathological intraoperational examination) was cryocut into thin slices (20 μm) for XANES analysis. The slices destined for Fe speciation studies were mounted immediately onto ultralene foil of 4 μm thickness, suspended in a Plexiglas holder, and finally freeze-dried at -80°C . Based on the spectral data from each point of the scanned areas of the samples, the masses per unit area of the total Fe was determined according to the simple equation [173].

5. Conclusion

The calibration procedures are important not only as one of the most significant stages of the analytical calibration, but also because by a properly developed/modified calibration strategy it is possible to create a quantitative map of the distribution of biological samples. Each calibration procedure has advantages and disadvantages, but the most important parameter in evaluation is the reliability of the analytical results. It is clear that the use of the appropriate calibration procedure based on the assumptions of known and used calibration methods is much better than the use of such universal/general algorithms or standard samples attached to the analytical instrument (e.g. in XRD distribution analysis).

The development of an analytical calibration strategy appropriate for the analysis of the distribution of elements in the biological samples is not easy, but this is the key for obtaining quantitative distribution studies. The included overview calibration methods used in various techniques used to determine the distribution map shows the variety of solutions and approaches that enable quantitative studies of metal distribution in tissues.

There are a lot of analytical methods that can be applied to (bio)imaging/mapping studies, such as LA ICP-MS, SIMS, EDS, XRF and others. However, the most popular, advanced and in common use are LA ICP-MS, EDS and XRF, probably due to the analytic possibilities and well-developed analytic calibration procedures.

The authors would like the readers to pay attention to the fact that, in the literature, the subject matter concerning analytic calibration in experimental and also review articles is treated very marginally. However, we feel that this stage of the analytic procedure is the most important because without it, quantitative studies of the distribution of metals in biological samples are impossible. The application and development of well-known analytical calibration procedures and calibration strategies are a major key for (bio)imaging/mapping of metallic elements in different biological samples. These studies will help to better understand the biochemical basis of many physiological and

pathological processes. Moreover, these fields of studies have a lot of perspectives in interdisciplinary spheres such as pharmacology, toxicology and metallomics etc.

Acknowledgments

This article was made by the support of Kamil Jurowski scholarship by the Krakow Marian Smoluchowski Consortium “Matter-Energy-Future” (KNOW Grant).

The authors wish to draw attention to the very valuable project “Development and validation of new types of reference materials necessary to obtain accreditation by the Polish European laboratories for industrial analytics” – MODAS (www.pg.gda.pl/chem/modas/).

References

- [1] K. Jurowski, S. Walas, W. Piekoszewski, *Talanta* 115 (2013) 195–199.
- [2] P. Kościelniak, *BAŹ Fen Bilim. Enst.* 3 (2001) 65–90.
- [3] L. Cuadros-Rodríguez, M. Gracia Bagur-Gonzalez, M. Sanchez-Vinas, A. Gonzalez-Casado, A.M. Gomez-Saez, *J. Chromatogr. A* 1158 (2007) 33–46.
- [4] International Vocabulary of Metrology – Basic and General Concepts and Associated Terms (VIM), third ed., Final Draft, August 2006. Available from: [http://www.ncsli.org/vim/wg2docN318VIM3rdedition2006-08-01%20\(3\).pdf](http://www.ncsli.org/vim/wg2docN318VIM3rdedition2006-08-01%20(3).pdf).
- [5] K. Danzer, L. Currie, *Pure Appl. Chem.* 70 (1998) 993.
- [6] ISO 11843-1, Capability of Detection – Part 1: Terms and Definitions, I.O.F.S. (ISO), (Ed.), Geneva, 1997.
- [7] P. Kościelniak, in: W. Chrzanowski, J. Namiesnik (Eds.), *New Horizons and Challenges in Environmental Analysis and Monitoring*, CEEAM, Gdańsk, 2003, pp. 110–129.
- [8] P. Kościelniak, J. Kozak, *Crit. Rev. Anal. Chem.* 34 (2004) 25–37.
- [9] M. Meloun, J. Militký, K. Kupka, R.G. Brereton, *Talanta* 57 (2002) 721–740.
- [10] E. Besalú, *Talanta* 116 (2013) 45–49.
- [11] K. Jurowski, M. Szewczyk, W. Piekoszewski, M. Herman, B. Szewczyk, G. Nowak, S. Walas, N. Miliszewicz, A. Tobiasz, *J. Anal. At. Spectrom.* 26 (2014) 1425–1431.
- [12] G. Galbács, I. Gornushkin, J. Winefordner, *Talanta* 63 (2004) 351–357.
- [13] P. Kościelniak, M. Wiczorek, *Anal. Lett.* 43 (2010) 424–435.
- [14] P. Kościelniak, *Chemom. Intell. Lab. Syst.* 47 (1999) 275–287.
- [15] M. Wójtowicz, J. Kozak, P. Kościelniak, *Anal. Chim. Acta* 600 (2007) 78–83.
- [16] M. Wiczorek, J. Kozak, P. Kościelniak, P. Knihnicki, E. Pieprzyca, *Talanta* 66 (2012) 34–38.
- [17] P. Kościelniak, M. Wiczorek, J. Kozak, M. Herman, *Anal. Chim. Acta* 600 (2007) 6–13.
- [18] P. Kościelniak, *Anal. Lett.* 44 (2001) 398–410.
- [19] A. Kindness, *Clin. Chem.* 49 (2003) 1916–1923.
- [20] B. Jackson, S. Harper, L. Smith, J. Flinn, *Anal. Bioanal. Chem.* 384 (2006) 951–957.
- [21] M. Ralle, S. Lutsenko, *Biomaterials* 22 (2009) 197–205.
- [22] F. Adams, C. Barbante, *Talanta* 102 (2012) 16–25.
- [23] R. Hutchinson, A.G. Cox, C.W. McLeo, P.S. Marshall, A. Harper, E.L. Dawson, D. R. Howlett, *Anal. Biochem.* 346 (2005) 225–233.
- [24] Z. Qin, J.A. Caruso, B. Lai, A. Matusch, J. Sabine Becker, *Metallomics* 3 (2011) 28–37.
- [25] W. Blackstock, M. Weir, *Trends Biotechnol.* 17 (1999) 121–127.
- [26] A. Rosenzweig, *Chem. Biol.* 9 (2002) 673–677.
- [27] W. Mertz, *Science* 213 (1981) 1332–1338.
- [28] M.W. Bourassa, L.M. Miller, *Metallomics* 4 (2012) 721–738.
- [29] M. Setou, *Imaging Mass Spectrometry – Protocols for Mass Microscopy*, Springer, New York, 2010.
- [30] R. McRae, P. Bagchi, S. Sumalekshmy, C. Fahrni, *Chem. Rev.* 109 (2009) 4780–4827.
- [31] J.S. Becker, *J. Mass Spectrom.* 48 (2013) 255–268.
- [32] M.E. Kurczyk, P.D. Piehowski, S.A. Parry, M. Jiang, G. Chen, A.G. Ewing, N. Winograd, *Appl. Surf. Sci.* 255 (2008) 1298–1304.
- [33] H. Nygren, K. Börner, P. Malmberg, E. Tallarek, B. Hagenhoff, *Microsc. Res. Tech.* 68 (2005) 329–334.
- [34] M.A. Meyers, P. Chen, A. Yu-Min Lin, Y. Seki, *Prog. Mater. Sci.* 53 (2008) 1–206.
- [35] A. Matusch, J.S. Becker, *Biomed. Spectrosc. Imaging* 1 (2012) 57–65.
- [36] M. Pornwilard, R. Weiskirchen, N. Gassler, A.K. Bosserhoff, J. Sabine Becker, *PLoS One* 8 (2013) e587021–e5870212.
- [37] I. Konz, M.L. Fernández, R. Pereiro, H. González-Iglesias, M. Coca-Prados, A. Sandoval, *Anal. Bioanal. Chem.* 406 (2014) 2343–2348.
- [38] M. Carrière, B. Gougeta, J. Galliena, L. Avoscana, R. Gobinb, J. Verbavatzb, H. Khodjaa, *Nucl. Instrum. Methods Phys. Res. B* 231 (2005) 268–273.
- [39] S. Chandra, *Methods Mol. Biol.* 656 (2010) 113–130.
- [40] C. Petitbois, *Anal. Bioanal. Chem.* 397 (2010) 2051–2065.
- [41] C. Dillon, P.A. Lay, B.J. Kennedy, A.P. Stampfl, Z. Cai, P. Ilinski, W. Rodrigues, D.G. Legnini, B. Lai, J. Maser, *J. Biol. Inorg. Chem.* 7 (2002) 640–645.
- [42] M. Zoriy, A. Matusch, T. Spruss, J.S. Becker, *Int. J. Mass Spectrom.* 260 (2007) 102–106.
- [43] H.M. Chang, W.C. Liao, J.N. Sheu, C.C. Chang, C.T. Lan, F.D. Mai, *Microsc. Microanal.* 18 (2012) 425–435.
- [44] J.S. Becker, *Spectrochim. Acta B* 63 (2008) 1248–1252.
- [45] M.A. da Silva, M.A. Arruda, *Metallomics* 5 (2013) 62–67.
- [46] J. Koelmel, D. Amarasiwardena, *Environ. Pollut.* 168 (2012) 62–70.
- [47] R. Lobiński, C. Moulin, R. Ortega, *Biochimie* 88 (2006) 1591–1604.
- [48] M.C. Santos, M. Wagner, B. Wu, J. Scheider, J. Oehlmann, S. Cadore, J.S. Becker, *Talanta* 80 (2009) 428–433.
- [49] J.S. Becker, M. Zoriy, J. Susanne Becker, J. Dobrowolska, A. Matusch, *J. Anal. At. Spectrom.* 22 (2007) 736–744.
- [50] D. Wang, G. Poologasundarampillai, W. van den Bergh, R.J. Chater, T. Kasuga, J.R. Jones, D.S. McPhai, *Biomed. Mater.* 9 (2014) 015013.
- [51] M. Kępa, T. Kozłowski, K. Szostek, A. Drozd, S. Walas, H. Mrowiec, B. Stepańczak, H. Głab, M. Grupa, *J. Biol. Clin. Anthropol.* 69 (2012) 367–377.
- [52] C. Eriksson, P. Malmberg, H. Nygren, *Rapid Commun. Mass Spectrom.* 22 (2008) 943–949.
- [53] J.S. Robach, S.R. Stock, A. Veis, *J. Struct. Biol.* 155 (2006) 87–95.
- [54] R.S. Bockman, *Proc. Natl. Acad. Sci. USA* 87 (1990) 4149–4153.
- [55] D.J. Bellis, K.M. Hetter, J. Jones, D. Amarasiwardena, P.J. Parsons, *J. Anal. At. Spectrom.* 21 (2006) 948–954.
- [56] M.G. Vašinová, M.F. Nývltová, J. Kynický, L. Prokeš, H. Neff, A.Z. Mason, P. Gadas, J. Košler, V. Kanický, *Talanta* 105 (2013) 235–243.
- [57] K. Jurowski, B. Buszewski, W. Piekoszewski, *Bioanalytics in quantitative (bio) imaging/mapping of metallic elements in biological samples*, CRAC, 2015 (in press).
- [58] J.S. Becker, U. Breuer, H.F. Hsieh, T. Osterholt, U. Kumtabtım, B. Wu, A. Matusch, J.A. Caruso, Z. Qin, *Anal. Chem.* 82 (2010) 9528–9533.
- [59] A. Brunelle, D. Touboul, O. Laprevote, *J. Mass Spectrom.* 40 (2005) 985–999.
- [60] R. Heeren, L.A. McDonnell, E. Amstalden, S.L. Luxembourg, A.F.M. Altelaaar, S.R. Piersma, *Appl. Surf. Sci.* 252 (2006) 6827–6835.
- [61] A. Walker, *Anal. Chem.* 80 (2008) 8865–8870.
- [62] P. Williams, *J. Biol.* 5 (2006) 18.
- [63] J.S. Wu, A.M. Kim, R. Bleher, B.D. Myers, R.G. Marvin, H. Inada, K. Nakamura, X.F. Zhang, E. Roth, S.Y. Li, T.K. Woodruff, T.V. O'Halloran, V.P. Dravid, *Ultramicroscopy* 128 (2013) 24–31.
- [64] C.B. Lietz, E. Gemperline, L. Li, *Adv. Drug Deliv. Rev.* 68 (2013) 1074–1085.
- [65] R. Ortega, G. Deves, A. Carmona, J. R. Soc. Interface 6 (Suppl. 5) (2009) S649–S658.
- [66] R.D. Leapman, *J. Microsc.* 210 (2003) 5–15.
- [67] J. Namiesnik, P. Szefer, *Ecol. Chem. Eng. S* 15 (2008) 167–244.
- [68] E. Maier, *Trends Anal. Chem.* 10 (1991) 340–347.
- [69] D.J. Hare, J.L. George, R. Grimm, S. Wilkins, P.A. Adlard, R.A. Cherny, A.I. Bush, D.I. Finkelstein, P. Doble, *Metallomics* 2 (2010) 745–753.
- [70] J.S. Becker, M. Zoriy, A. Matusch, B. Wu, D. Salber, C. Palm, J.S. Becker, *Pure Appl. Chem.* 80 (2008) 2643–2655.
- [71] B. Wu, J.S. Becker, *Metallomics* 4 (2012) 403–416.
- [72] D.M. Drummer, J.D. Fassett, G.H. Morrison, *Anal. Chim. Acta* 100 (1978) 15–22.
- [73] J.S. Becker, *Inorganic Mass Spectrometry – Principles and Application*, WILEY, Weinheim, 2007.
- [74] J.S. Becker, M. Zoriy, V. Dressler, B. Wu, J.S. Becker, *Pure Appl. Chem.* 80 (2008) 2643–2655.
- [75] J.S. Becker, A. Matusch, C. Palm, D. Salber, K.A. Morton, J.S. Becker, *Metallomics* 2 (2010) 104–111.
- [76] J.S. Becker, J. Su, M.V. Becker, J. Zoriy, A. Dobrowolska, *J. Anal. At. Spectrom.* 23 (2008) 1275–1280.
- [77] J.S. Becker, M. Zoriy, M. Dehnhardt, C. Pickhardt, K. Zilles, *J. Anal. At. Spectrom.* 20 (2005) 912–917.
- [78] M. Tibi, K.G. Heumann, *J. Anal. At. Spectrom.* 18 (2003) 1076–1081.
- [79] E. Hoffmann, H. Stephanowitz, E. Ullrich, J. Skole, C. Lüdke, B. Hoffmann, *J. Anal. At. Spectrom.* 15 (2000) 663–667.
- [80] C.J. Brinker, G.W. Scherer, *Sol-gel Science: The Physics and Chemistry of Sol-gel Processing*, Academic Press, Toronto, 1990.
- [81] A.J. Fitzpatrick, T.K. Kyser, Don Chiplea, Diane Beaucheminb, *J. Anal. At. Spectrom.* 23 (2008) 244–248.
- [82] H. Sela, Z. Karpas, H. Cohen, Y. Zakon, Y. Zeiri, *Int. J. Mass Spectrom.* 307 (2011) 142–148.
- [83] K.W. Warnken, H. Zhang, W. Davison, *Anal. Chem.* 76 (2004) 6077–6084.
- [84] M. Gaboridi, M. Humayun, *J. Anal. At. Spectrom.* 24 (2009) 1188–1197.
- [85] D.S. Gholap, J. Verhulst, W. Celeen, F. Vanhaecke, *Anal. Bioanal. Chem.* 402 (2012) 2121–2129.
- [86] A. Izmer, D. Gholap, K. De Houwer, F. Cuyckens, F. Vanhaecke, *J. Anal. At. Spectrom.* 27 (2012) 413–418.
- [87] H.J. Stärk, R. Wennrich, *Anal. Bioanal. Chem.* 399 (2011) 2211–2217.
- [88] G. Li, Determination of trace elements levels in human plasma and radiated mice tongue by inductively coupled plasma-mass spectrometry (ICP-MS) (Doctoral dissertation) (<https://mospace.umsystem.edu/xmlui/bitstream/handle/10355/15081/research.pdf?sequence=2>).
- [89] S. Pahlke, L. Fabry, L. Kotz, C. Mantler, T. Ehmman, *Spectrochim. Acta B* 56 (2001) 2261–2274.
- [90] A. von Bohlen, A.S. Röhrs, J. Salomon, *Anal. Bioanal. Chem.* 387 (2007) 781–790.
- [91] U.E. Fittschen, N.H. Bings, S. Hauschild, S. Förster, A.F. Kiera, E.F. Karavani, A. Frömsdorf, J. Thiele, G. Falkenberg, *Anal. Chem.* 80 (2000) 1967–1977.

- [92] D.J. Bellis, R. Santamaria-Fernandez, *J. Anal. At. Spectrom.* 25 (2010) 957–963.
- [93] C. Austin, D. Hare, T. Rawling, A.M. McDonagh, P. Doble, *J. Anal. At. Spectrom.* 25 (2010) 722–725.
- [94] K. Norrman, A. Ghanbari-Siahkali, N.B. Larsen, *Annu. Rep. Prog. Chem. C* 101 (2005) 174–201.
- [95] D. Frick, D. Günther, *J. Anal. At. Spectrom.* 27 (2012) 1294–1303.
- [96] F. De Ridder, R. Pintelon, J. Schoukens, J. Navez, L. André, F. Dehairs, *J. Anal. At. Spectrom.* 17 (2002) 1461–1470.
- [97] I. Konz, B. Fernández, M.L. Fernández, R. Pereiro, H. González, L. Alvarez, M. Coca-Prados, A. Sanz-Medel, *Anal. Bioanal. Chem.* 405 (2013) 3091–3096.
- [98] J. O'Reilly, D. Douglas, J. Braybrook, P.W. So, E. Vergucht, J. Garrevoet, B. Vekemans, L. Vincze, H. Goenaga-Infante, *J. Anal. At. Spectrom.* 29 (2014) 1378–1384.
- [99] A.E. Egger, S. Theiner, C. Kornauth, P. Heffeter, W. Berger, B.K. Keppler, C.G. Hartinger, *Metallomics* (2014) <http://dx.doi.org/10.1039/C4MT00072B>, in press.
- [100] J.S. Becker, R. Lobiński, J.S. Becker, *Metallomics* 1 (2009) 312–316.
- [101] A. Matusch, C. Depboylu, C. Palm, B. Wu, U.H. Günter, M.K. Schäfer, J. Sabine Becker, *J. Am. Soc. Mass Spectrom.* 21 (2010) 161–171.
- [102] M.V. Zoriy, M. Dehnhardt, G. Reifensberger, K. Zilles, J.S. Becker, *Int. J. Mass Spectrom.* 257 (2006) 27–33.
- [103] C. Pickhardt, A.V. Izmera, M.V. Zoriya, D. Schaumlöffel, J. Sabine Becker, *Int. J. Mass Spectrom.* 248 (2006) 136–141.
- [104] J. Vogl, W. Pritzkow, *J. Metrol. Soc. India* 25 (2010) 135–164.
- [105] V.L. Dressler, D. Pozebon, M.F. Mesko, A. Matusch, U. Kumtabtim, B. Wu, B.J.S. Becker, *Talanta* 82 (2010) 1770–1777.
- [106] J.S. Becker, M.V. Zoriy, C. Pickhardt, N. Palomero-Gallagher, K. Zilles, *Anal. Chem.* 77 (2005) 3208–3216.
- [107] D. Pozebon, V.L. Dressler, M.F. Mesko, A. Matusch, J.S. Becker, *J. Anal. At. Spectrom.* 25 (2010) 1739–1744.
- [108] M. Kilburn, P. Clode, *Methods Mol. Biol.* 1117 (2014) 733–755.
- [109] S. Chandra, *Appl. Surf. Sci.* 255 (2008) 1273–1284.
- [110] S. Chandra, R.F. Barth, S.A. Haider, W. Yang, T. Huo, A.L. Shaikh, G.W. Kabalka, *PLoS One* 8 (2013) e753771–e753779.
- [111] S. Chandra, D.F. Smith, G. Morrison, *Anal. Chem.* 72 (2000) 104–114.
- [112] J. Pett-Ridge, P.K. Weber, *Methods Mol. Biol.* 881 (2012) 375–408.
- [113] M. Burns, *J. Microsc.* 127 (1982) 237–258.
- [114] C. Derue, *Microsc. Res. Tech.* 69 (2006) 53–63.
- [115] D.F. Smith, A. Kiss, F.E. Leach, E.W. Robinson, L. Paša-Tolić, R.M. Heeren, *Anal. Bioanal. Chem.* 405 (2013) 6069–6076.
- [116] S.S. Rubakhin, J.C. Jurchen, E.B. Monroe, J.V. Sweedler, *Drug Discov. Today* 10 (2005) 823–837.
- [117] P. Fragu, J. Clerc, C. Briançon, C. Fourré, J. Jeusset, S. Halpern, *Micron* 25 (1994) 361–370.
- [118] D. Locker, *Methods Mol. Biol.* 1117 (2014) 707–732.
- [119] H. Nygren, B. Hagenhoff, P. Malmberg, M. Nilsson, K. Richter, *Microsc. Res. Tech.* 70 (2007) 969–974.
- [120] K.L. Moore, E. Lombi, F.J. Zhao, C.R. Grovenor, *Anal. Bioanal. Chem.* 402 (2012) 3263–3273.
- [121] G.S. Gillen, S.M. Roberson, *Scanning* 21 (1999) 173–181.
- [122] F.D. Mai, B.J. Chen, L.C. Wu, F.Y. Li, W.K. Chen, *Appl. Surf. Sci.* 252 (2006) 6809–6812.
- [123] J.H. Kim, B.J. Ahn, J. Park, H.K. Shon, Y.S. Yu, D.W. Moon, T.G. Lee, K. Kim, *Biophys. J.* 94 (2008) 4095–4102.
- [124] L.A. McDonnell, S.R. Piersma, A.F. MaartenAltelaar, T.H. Mize, S.L. Luxembourg, P.D. Verhaert, J. van Minnen, R.M. Heeren, *J. Mass Spectrom.* 40 (2005) 160–168.
- [125] G.H. Morrison, G. Slodzian, *Anal. Chem.* 75 (1975) 932A–943A.
- [126] W.A. Ausserer, Y.C. Ling, S. Chandra, G.H. Morrison, *Anal. Chem.* 61 (1989) 2690–2695.
- [127] R. Lapatto, A. Hietamäki, J. Räisänen, *Biol. Trace Elem. Res.* 19 (1989) 161–170.
- [128] J.M. Chabala, K.K. Soni, J. Li, K.L. Gavrilov, R. Levi-Setti, *Int. J. Mass Spectrom. Ion Process.* 143 (1995) 191–212.
- [129] B. Hagenhoff, *Microchim. Acta* 132 (2000) 259–271.
- [130] J.L. Guerquin-Kern, T.D. Wu, C. Quintana, A. Croisy, *Biochim. Biophys. Acta* 1724 (2005) 228–238.
- [131] P. Bertsch, B. Hunter, Applications of synchrotron-based X-ray microprobes, *Chem. Rev.* 101 (2001) 1809–1842.
- [132] I. Snigireva, A. Snigirev, *J. Environ. Monit.* 8 (2005) 33–42.
- [133] B. Scruggs, M. Hascke, L. Herczeg, J. Nicolosi, *Adv. X-Ray Anal.* 42 (2000) 19–25.
- [134] M. Szczerbowska-Boruchowska, *X-Ray Spectrom.* 41 (2012) 328–337.
- [135] A. Snigirev, I. Snigireva, *Rev. Sci. Instrum.* 66 (1995) 5486–5492.
- [136] M. Szczerbowska-Boruchowska, A. Krygowska-Wajs, D. Adamek, *J. Phys. Condens. Matter* 24 (2012) 244104.
- [137] H. Harris, A. Levina, C.T. Dillon, I. Mulyani, B. Lai, B.Z. Cai, P.A. Lay, *J. Biol. Inorg. Chem.* 10 (2005) 105–118.
- [138] B. Pemmer, A. Roschge, A. Wastl, J.G. Hofstaetter, P. Wobruschek, R. Simon, H.W. Thaler, P. Roschger, K. Klaushofer, C. Strelti, *Bone* 57 (2013) 184–193.
- [139] M. Szczerbowska-Boruchowska, *X-Ray Spectrom.* 37 (2008) 21–31.
- [140] D.J. Bellis, D. Li, Z. Chen, W.M. Gibson, P.J. Parsons, *J. Anal. At. Spectrom.* 24 (2009) 622–626.
- [141] W. Kaabar, O. Gundogdu, A. Lakloul, O. Bunk, F. Pfeiffer, M.J. Farquharson, D.A. Bradley, *Appl. Radiat. Isot.* 68 (2010) 730–734.
- [142] R. Ortega, *Nucl. Instrum. Methods Phys. Res. Sect. B* 231 (2005) 218–223.
- [143] M. Ugarte, G.W. Grime, G. Lord, K. Geraki, J.F. Collingwood, M.E. Finnegan, H. Farnfield, M. Merchant, M.J. Bailey, N.I. Ward, P.J. Foster, P.N. Bishop, N.N. Osborne, *Metallomics* 4 (2012) 1245–1254.
- [144] H. Sakurai, M. Okamoto, M. Hasegawa, T. Satoh, M. Oikawa, T. Kamiya, K. Arakawa, T. Nakano, *Cancer Sci.* 99 (2008) 901–904.
- [145] S. Yumoto, S. Kakimi, A. Ohsaki, A. Ishikawa, *J. Inorg. Biochem.* 103 (2009) 1579–1584.
- [146] M.D. Hall, C.T. Dillon, M. Zhang, P. Beale, Z. Cai, B. Lai, A.P. Stampfl, T.W. Hamble, *J. Biol. Inorg. Chem.* 8 (2003) 726–732.
- [147] C.J. Fahrni, *Curr. Opin. Chem. Biol.* 11 (2007) 121–127.
- [148] A. Markowicz, *Pramana* 76 (2011) 321–329.
- [149] M. Szczerbowska-Boruchowska, M. Lankosz, N. Czyżycki, D. Adamek, *Anal. Chim. Acta* 699 (2011) 153–160.
- [150] R. Tertian, *X-Ray Spectrom.* 15 (1986) 177–190.
- [151] R. Sitko, B. Zawza, Quantification in X-ray fluorescence spectrometry, in: S. Sharma (Ed.), *X-Ray Spectroscopy 2012*.
- [152] H.J. Lucas-Tooth, C. Pyne, *Adv. X-ray Anal.* 7 (1963) 523–541.
- [153] H.J. Lucas-Tooth, B.J. Price, *Metallurgia* 164 (1961) 149–152.
- [154] J. Sherman, *Spectrochim. Acta* 7 (1955) 283–306.
- [155] J.R. Rhodes, C.S. Barret, D.E. Leyden, J.B. Newkirk, P.K. Predecki, C.O. Ruud, *Advances in X-ray Analysis*, Springer, Denver, 1980.
- [156] R.M. Rousseau, J.A. Boivin, *Rigaku J.* 15 (1998) 13–28.
- [157] J.L. Campbell, in: S.A. Johansson, J.L. Campbell, K.G. Malmqvist (Eds.), *Particle-Induced X-ray Emission Spectrometry*, Wiley, New York, 1995.
- [158] D.D. Cohen, *Particle Induced X-ray Emission*, Australian Nuclear Science and Technology Organisation (ANSTO), Sydney, 1991.
- [159] C.G. Ryan, *Int. J. Imag. Syst. Technol.* 11 (2001) 219–230.
- [160] K. Divine, J.L. Lewis, P.G. Grant, G. Bench, *Chem. Res. Toxicol.* 12 (1999) 575–581.
- [161] A. Markowicz, N. Haselberger, U. Whai Zin, *X-Ray Spectrom.* 22 (2005) 160–162.
- [162] R.E. Van Grieken, A.A. Markowicz, *Handbook of X-ray Spectrometry*, Marcel Dekker, New York, 2002.
- [163] A. Markowicz, A. Abdunnabi, *X-Ray Spectrom.* 20 (1991) 97–101.
- [164] A. Markowicz, N. Haselberger, *Int. J. Radiat. Appl. Instrum. A* 43 (1992) 777–779.
- [165] A. Markowicz, N. Haselberger, H.S. El Hassan, M.S.A. Sewando, *J. Radioanal. Nucl. Chem.* 158 (1992) 409–415.
- [166] D. Węgrzynek, A. Markowicz, C. Chinea-Cano, *X-Ray Spectrom.* 32 (2003) 119–128.
- [167] J.L. de Vries, B.A. Vrebois, in: R.E. Van Grieken, A. Markowicz (Eds.), *Handbook of X-ray Spectrometry*, Marcel Dekker, New York, 2002.
- [168] P.A. Pella, L. Feng, A. Small, *X-Ray Spectrom.* 14 (2005) 125–135.
- [169] N. Broll, R. Tertian, *X-Ray Spectrom.* 12 (2005) 30–37.
- [170] A. Markowicz, *X-Ray Spectrom.* 13 (1984) 166–169.
- [171] R.M. Rousseau, *Rikagu J.* 18 (2001) 33–47.
- [172] M. Szczerbowska-Boruchowska, Z. Stegowski, M. Lankosz, M. Szpaka, D. Adamek, *J. Anal. At. Spectrom.* 27 (2012) 239–247.
- [173] M. Szczerbowska-Boruchowska, M. Lankosz, D. Adamek, *J. Biol. Inorg. Chem.* 16 (2011) 1217–1226.



β -Cyclodextrin coated CdSe/ZnS quantum dots for vanillin sensing in food samples



Gema M. Durán^{a,b}, Ana M. Contento^a, Ángel Ríos^{a,*}

^a Department of Analytical Chemistry and Food Technology, University of Castilla-La Mancha, Ciudad Real, Spain

^b IIRICA (Regional Institute of Applied Scientific Research), Avenida Camilo José Cela, s/n. 13071 Ciudad Real, Spain

ARTICLE INFO

Article history:

Received 21 May 2014

Received in revised form

28 July 2014

Accepted 31 July 2014

Available online 8 August 2014

Keywords:

CdSe/ZnS quantum dots

β -Cyclodextrin

Functionalization

Fluorescence

Vanillin sensing

Food samples

ABSTRACT

An optical sensor for vanillin in food samples using CdSe/ZnS quantum dots (QDs) modified with β -cyclodextrin (β -CD) was developed. This vanillin-sensor is based on the selective host–guest interaction between vanillin and β -cyclodextrin. The procedure for the synthesis of β -cyclodextrin–CdSe/ZnS (β -CD–CdSe/ZnS-QDs) complex was optimized, and its fluorescent characteristics are reported. It was found that the interaction between vanillin and β -CD–CdSe/ZnS-QDs complex produced the quenching of the original fluorescence of β -CD–CdSe/ZnS-QDs according to the Stern–Volmer equation. The mechanism of the interaction is discussed. The analytical potential of this sensing system was demonstrated by the determination of vanillin in synthetic and food samples. The method was selective for vanillin, with a limit of detection of $0.99 \mu\text{g mL}^{-1}$, and a reproducibility of 4.1% in terms of relative standard deviation (1.2% under repeatability conditions). Recovery values were in the 90–105% range for food samples.

© 2014 Elsevier B.V. All rights reserved.

1. Introduction

The use of quantum dots (QDs) for the development of sensors is one of the most developing fields of nanotechnology so far. Their fluorescence efficiency is sensitive to different compounds on their surface. Therefore, molecular recognition at the surface of QDs can be utilized in the development of fluorescent-based sensors. For this purpose, several strategies for surface-modified QDs have been employed. Thiol ligands were used to modify quantum dots such as L-cysteine or D-cysteine for carnitine enantiomers determination [1], mercaptoacetic acid for L-cysteine detection [2], 3-mercaptopropionic acid for detection and quantification of parquat [3], among other applications. Other surface-modified quantum dots, such as ionic-liquid modified CdSe/ZnS QDs for trimethylamine fluorimetric determination [4], silica-coated CdSe/ZnS nanoparticles for Cu^{2+} detection [5], calix [8] arene coated CdSe/ZnS quantum dots as C_{60} -nanosensor [6], have also been used.

Cyclodextrins (CDs) are considered one of the best host molecules. β -Cyclodextrins are cyclic receptors consisting of seven glucose units linked one to another by 1–4 glycoside bonds. Their cavity-shaped cyclic phenol molecules are capable to forming host–guest complexes with a variety of organic molecules. The hydrophobic cavities of cyclodextrins were used to develop

different sensors [7,8] and separation matrices [9]. Thus, CDs have attracted great interest in supramolecular chemistry. Cyclodextrins coating ensures the high emission efficiency and the smaller size of QDs and provides selectivity. Therefore, several methods for the preparation of highly fluorescent and stable CdSe/ZnS quantum dots, using cyclodextrins as surface coating agents, have recently reported. Optical sensing and chiroselective sensing of different substrates were reported using β -CD functionalized CdSe/ZnS QDs based on a fluorescence resonance transfer (FRET) or an energy transfer mechanism [10]. β -CD-coated CdSe/ZnS QDs was also applied as enantioselective fluorescent sensors for amino acids, such as tyrosine and a significant fluorescence enhancement was observed [11], which can be used for the optical detection of phenol pollutants in water samples [12]. Other β -CD modified CdTe QDs were also used as a nanosensor for acetylsalicylic acid and its metabolites [13], as fluorescent probes for polycyclic aromatic hydrocarbons (PHAs) [14], and β -CD modified CdSe QDs as a recognition system for tyrosine enantiomers [15].

Vanillin is one of the most popular flavoring substances and it is widely used in food, beverages, perfumery and pharmaceutical industry. Natural vanillin is obtained from vanilla pods, through a long and expensive process. Furthermore, natural vanillin obtained in this way can supply less than 1% of the market demand. Therefore, most of the vanillin employed is synthesized through chemical processes from eugenol (4-allyl-2-methoxyphenol), guaiacol (2-methoxyphenol) or lignin. The chemical synthesis leads to a cheaper vanillin, but of lower quality with a wide variety of complex

* Corresponding author.

E-mail address: Angel.Rios@uclm.es (Á. Ríos).

matrices that need selective and sensitive clean-up procedures for its extraction and/or analysis [16]. The yield and purification of vanillin (a biomolecule relevant for several purposes) are still of major interest. Different methods for determination of vanillin in several samples have been developed. Many of these methods involve electrochemical detection with several types of electrodes [17–20]. Other methods include the use of supported liquid membranes with amperometric [21] or piezoelectric [22] detection. Spectrophotometric [23] detection, liquid chromatography with mass spectrometry detection [24], capillary electrophoresis [25] or gas chromatography [26] has also been used for determining vanillin. However, these techniques usually need complicated sample pre-treatment. Nowadays, as a useful analytical technique, fluorescent detection has been extensively employed with high sensitivity and selectivity. To our knowledge, the use of CDs functionalized QDs as selective probes for fluorescent determination of flavoring is almost unexplored. In this paper, it is reported the synthesis of water soluble and stable semiconductor CdSe/ZnS QDs using β -CD as surface coating agent by a very simple sonochemical method. Its potential application as a selective fluorescent sensor for vanillin in several samples has also been investigated, obtaining satisfactory results for its determination in food samples.

2. Experimental

2.1. Reagents

All chemical reagents were obtained from commercial sources of analytical grade and were used as received without further purification. Cadmium oxide (CdO, $\geq 99.99\%$ metal basis), trioctylphosphine oxide (TOPO, 99%), trioctylphosphine (TOP, 90.0%), selenium (Se powder, 100 mesh, 99.99% metals basis), diethyl-zinc solution (ZnEt_2 , 1 M in hexane), bis(trimethylsilyl) sulfide ($(\text{TMS})_2\text{S}$), anhydrous methanol, ethanol and acetonitrile were purchased from Sigma-Aldrich (Steinheim, Germany). Hexylphosphonic acid (HPA) was obtained from Alfa Aesar (Karlsruhe, Germany). These reagents were used to prepare CdSe(ZnS) QDs. 4-Hydroxy-3-methoxybenzaldehyde (Vanillin, $\geq 98\%$) and α cyclodextrin ($\geq 98\%$) were obtained from Fluka (Steinheim, Germany). β -Cyclodextrin was purchased from Sigma Aldrich (Steinheim, Germany) and γ -cyclodextrin ($> 98\%$) was purchased from Tokyo Chemical Industry America (Portland, USA).

Di-sodium hydrogen phosphate anhydrous buffer was purchased from Panreac (Barcelona, Spain). 4-Hydroxy-3-methoxybenzyl alcohol (Vanillin alcohol, 98%), 4-hydroxybenzaldehyde (98%) and 4-hydroxybenzyl alcohol (99%) were purchased from Sigma Aldrich (Steinheim, Germany).

Analytical standard stock solutions of vanillin at 1 mg mL^{-1} were prepared in water. The stock solutions were stored under refrigerator conditions (4°C) and protected from the light. The stock solution of Se/TOP was prepared using 0.051 g of Se in 3 mL of TOP. Buffer solutions was prepared using di-sodium hydrogen phosphate buffer fixing the pH to 8.

2.2. Apparatus

Fluorescence emission spectra were measured on a Photon Technology International (PTI) Inc. QuantaMaster 40 spectrofluorometer that was equipped with a 75-W continuous xenon arc lamp. An ASOC-10 USB interface FeliXGX software was used for fluorescence data acquisition and also controlled the hardware for all system configurations. The slits for excitation and emission widths were both 5 and 3 nm. All optical measurements were performed in a 10 mm quartz cell at room temperature under ambient conditions. UV–vis spectra were obtained on a SECOMAM

UVI Light XS 2 spectrophotometer equipped with a LabPower V3 50 for absorbance data acquisition using 10 mm quartz cuvettes. QDs were precipitated and purified using a centrifuge Centrifiger BL-II model 7001669, J.P. Selecta (Barcelona, Spain). The pH measurements were achieved in a Crison Basic 20 pH-meter with a combined glass electrode (Barcelona, Spain). An ultrasonic cleaning bath Ultrasons, J.P. Selecta (Barcelona, Spain) and a 254/365 nm UV lamp 230 V, E2107 model, Consort nv (Turnhout, Belgium) were also used.

2.3. Preparation of hydrophobic CdSe/Zn QDs

CdSe core nanocrystals were prepared via a modified process reported Peng et al. [27]. Typically, 0.06 g of CdO, 0.22 g HPA, and 7 g of TOPO were loaded in a 250 mL three-neck flask clamped in a heating mantle and air in the system was pumped off and replaced with N_2 . The mixture was stirred and heated at $300\text{--}310^\circ\text{C}$ for 15 min, and CdO was dissolved in HPA and TOPO. The solution was cooled down to 270°C and 2.5 mL of the solution of Se/TOP was swiftly injected. After the injection, the temperature was adjusted to 250°C for nucleus growth during 20 min and a change in the color of the solution to red was observed. To make ZnS shell on the CdSe, 3 mL of a solution of ZnS/TOP (0.58 g of ZnEt_2 , 0.087 mL of $(\text{TMS})_2\text{S}$ and 3.4 mL of TOP) was added dropwise to the mixture under vigorous stirring. The mixture was kept to 90°C for 4 h to improve the crystallinity of ZnS shell. After cooling the solution down to room temperature, QDs were diluted with 10 mL of anhydrous chloroform. Finally, the synthesized QDs were purified by adding 10 mL of methanol to 10 mL of the QD solution. Then, QDs were precipitated, collected by ultracentrifugation (at 13,000 rpm during 15 min), and washed with methanol four times. The purified QD nanocrystals were finally dispersed in 10 mL of anhydrous chloroform and stored in darkness.

2.4. Preparation of *n*-cyclodextrin capped CdSe/ZnS QDs

Different cyclodextrins were studied ($n = \alpha, \beta, \gamma$). The *n*-CD-CdSe/ZnS-QDs were prepared by using a modified procedure previously reported [28]. Thus, a 0.5 mL (200 mg L^{-1}) of TOPO-capped CdSe/ZnS QDs in chloroform (0.1 mg) were added into a 2 mL polypropylene vial and the chloroform was dried by nitrogen atmosphere. Then, *n*CD powder (3.1, 3.6 or 4.2 mg for α, β or γ -CD, respectively) was added to dried QDs and the mixture was dispersed in acetonitrile (2 mL). The mixture was placed in a high-intensity ultrasound bath for about 45 min at room temperature. When the reaction was finished, a rosy precipitate was obtained. The precipitate was separated by centrifuging at 13,500 rpm. The resulting supernatant was eliminated and the remained acetonitrile was evaporated. Finally, it was purified by further cycles of centrifugation in water. The resulting precipitate of the *n*-CD-CdSe/ZnS-QDs was dispersed in water (10 mL) and stored at room temperature in the dark for further investigations.

2.5. Preparation of samples and analytical procedure

Several commercial food samples, such as sugar, milk or custard, were purchased from a local market. These samples were prepared as follows:

Sugar samples were ground to a fine powder. Then, 0.5 g of this powder and 2 mL of absolute ethanol were placed into a tube and shaken by a laboratory shaker for 10 min. This mixture was centrifuged at 10,000 rpm. The clear part of the solution in the tube was used for analysis. Ethanol was evaporated and the resulting residue was dissolved in water.

Milk samples. 1 mL of milk sample and 2 mL of absolute ethanol were placed into a tube and shaken by a laboratory shaker

at 40 °C for 10 min. This mixture was centrifuged at 12,000 rpm for 15 min for precipitate the proteins. The supernatant was evaporated and the resulting sample residue was dissolved in water.

Custard samples. 0.05 g of custard powder and 2 mL of absolute ethanol were placed into a tube and shaken by a laboratory shaker at 40 °C for 10 min. This mixture was centrifuged at 6000 rpm for 15 min. The supernatant was used for analysis. The absolute ethanol was evaporated and the resulting sample residue was dissolved in water.

For vanillin determination, suitable amount of these samples and 0.4 mL of β -CD modified CdSe/ZnS fixed at pH 8 were transferred into a volumetric flask. The mixture was stirred at room temperature and stored at ambient light in the dark for 30 min for reaction. Then, this mixture was transferred into a 10 mm quartz cuvette and the emission fluorescent spectrum was measured, at an excitation wavelength of 450 nm, between 500 and 670 nm. I_0/I was used as analytical signal, where I_0 and I were the fluorescence intensity at 590 nm of the systems in the absence and presence of vanillin, respectively.

3. Results and discussion

Studies for QDs modification was carried out using different cyclodextrins ($n = \alpha, \beta$ or γ). The solubilization procedure of the QDs was conducted by ultrasonic irradiation of a mixture of TOPO-coated CdSe/ZnS QDs and n -CD. The assayed strategy for creating n CD-QDs was a chemical procedure based on the formation of a host-guest complex between the passivized ligand (TOPO) and n CD by hydrophobic interaction (Fig. 1A). In order to obtain the optimal conditions in the modification procedure, several parameters were studied.

3.1. Influence of experimental factors in the modification of n -CD-CdSe/ZnS-QDs

The effect of solvent reaction on the fluorescence intensity and stability of QDs was tested using absolute ethanol, anhydrous methanol and acetonitrile. It was found that fluorescence intensity

of n -CD-CdSe/ZnS-QDs when it was used acetonitrile as a reaction solvent was dramatically higher than when ethanol or methanol were used. Therefore, this solvent was used for further experiments. Fig. 2A shows the effect of these solvents using β -CD-CdSe/ZnS-QDs.

The concentration of n -CD was varied between 0.5 and 4.5 mM, maintaining constant the other parameters. It was observed that the complexation of TOPO with n -CD is essential to produce the solubilization of CdSe/ZnS QDs in an aqueous medium. When the concentration of n -CD is too low, only small portions of surface-bound TOPO molecules on the surfaces of CdSe/ZnS QDs form complexes with n -CD, which is not enough to give a hydrophilic property to the nanoparticles, and hence to produce their stabilization in the aqueous phase. At relatively high concentrations of n -CD, substantial amounts of TOPO molecules are able to form host-guest complexes with n -CD, which led to an increase in the stability of the QDs in the hydrophilic media. However, when the dosage of n -CD is very high, although phase transfer was efficiently achieved, the resulting complex was found to be unstable in water, and the n CD excess could mask the determination of the analyte. Therefore, 1.6 mM of n -CD was chosen for further experiments, as the maximum fluorescence intensity was obtained at this concentration. Finally, time-dependent experiments were performed by exposing the reaction of modification of QDs at several times between 15 and 180 min to ultrasonic irradiation. The best results were obtained when 45 min of ultrasonic irradiation was used.

The resulting n -CD-CdSe/ZnS-QDs thus obtained were highly fluorescent and stable. Fig. 2A shows the emission spectra of n -CD-CdSe/ZnS-QDs in water and TOPO-CdSe/ZnS-QDs in chloroform. As it can be seen the maximum emission band around 590 nm ($\lambda_{exc} = 450$ nm) were obtained in all cases. The line width of the fluorescence spectrum is relatively narrow (with the fullwidth at half-maximum of 44 nm), indicating that the n -CD-CdSe/ZnS-QDs nanoparticles have a narrow size distribution. Compared to TOPO-CdSe/ZnS QDs in chloroform, n -CD-CdSe/ZnS-QDs increased the fluorescence intensity. It was also observed no change in emission wavelength and the spectral width regarding to TOPO-CdSe/ZnS-QDs. The UV/Vis spectrum of TOPO-CdSe/ZnS-QDs, α -CD-CdSe/ZnS-QDs, β -CD-CdSe/ZnS-QDs and γ -CD-CdSe/ZnS-QDs are also illustrated in Fig. 2B. As it can be seen, absorption bands at ca. 255 and ca. 585 nm were obtained in all cases. Therefore, no significant differences were observed in the modification procedure of QDs. The stability of obtained for n -CD-CdSe/ZnS-QDs in water was estimated by measurements of the emission intensity at room temperature at several times. From the results obtained it was concluded that n -CD-CdSe/ZnS-QDs were stable at least for two weeks, with any significant changes in their fluorescence spectra.

3.2. Effect of vanillin on the luminescence response of modified QDs

In the n -cyclodextrin modified QDs, the hydrophobic pockets of the cyclodextrin molecules interact with the aliphatic chains of the TOPO present on the nanoparticle surface from the QDs synthesis (Fig. 1A). Nevertheless, the immobilized cyclodextrins retain their capability of engaging molecular recognition. In this way, it was studied the use of n -CD-CdSe/ZnS-QDs nanoparticles as a selective luminescence sensors of vanillin. First, preliminary studies were made in order to know the best recognition of vanillin when α, β or γ -CD-CdSe/ZnS-QDs were used. It was found that vanillin affects luminescence of β -CD-CdSe/ZnS-QDs in a more drastic way, producing a quenching effect on the QDs emission band, as it can be seen in Fig. 3. Therefore, β -CD-CdSe/ZnS-QDs was selected to develop the vanillin sensors.

The selective host-guest interaction between vanillin and β -cyclodextrin, through the vanillin binds to the receptor sites,

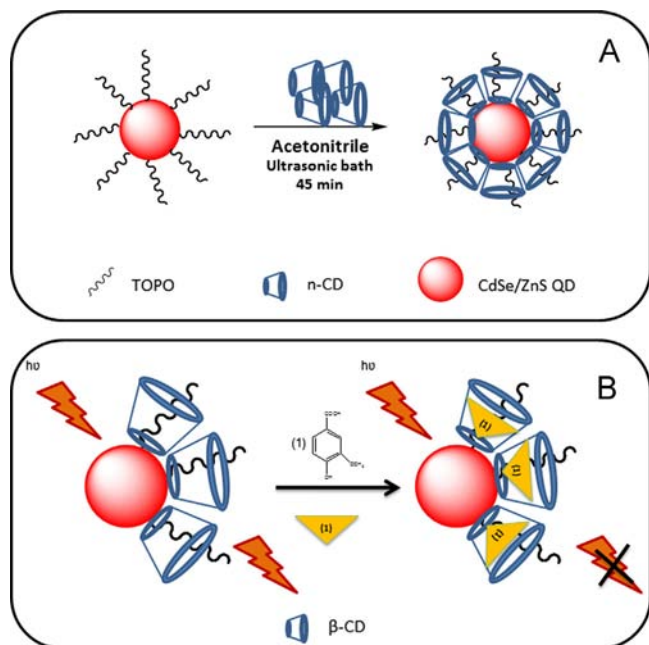


Fig. 1. Schematic illustration of surface modification of TOPO-CdSe/ZnS-QDs with n -cyclodextrins (A). Host-guest interaction between β -CD-CdSe/ZnS-QDs and vanillin (B).

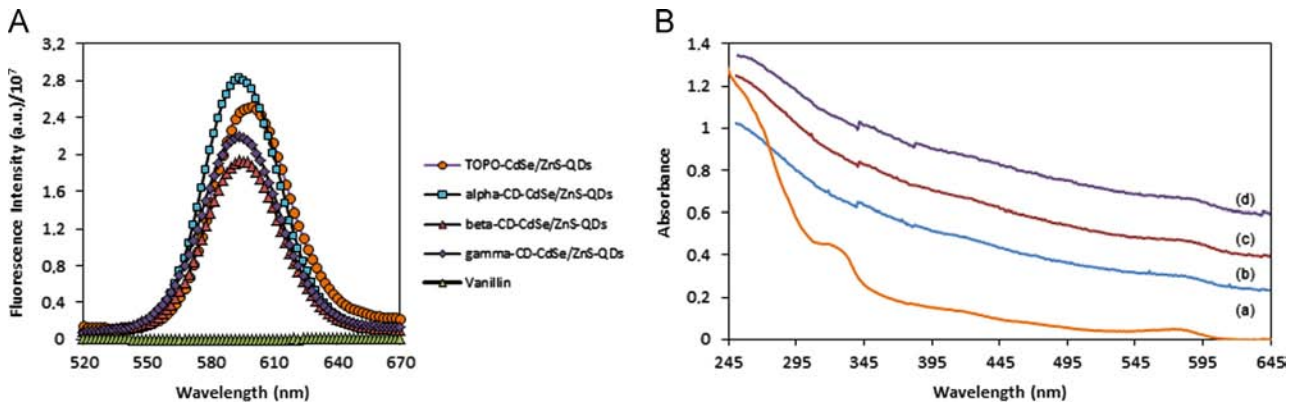


Fig. 2. Emission (A) and absorption (B) spectra of TOPO-CdSe/ZnS-QDs (a), α -CD-CdSe/ZnS-QDs (b), β -CD-CdSe/ZnS-QDs (c) and γ -CD-CdSe/ZnS-QDs (d).

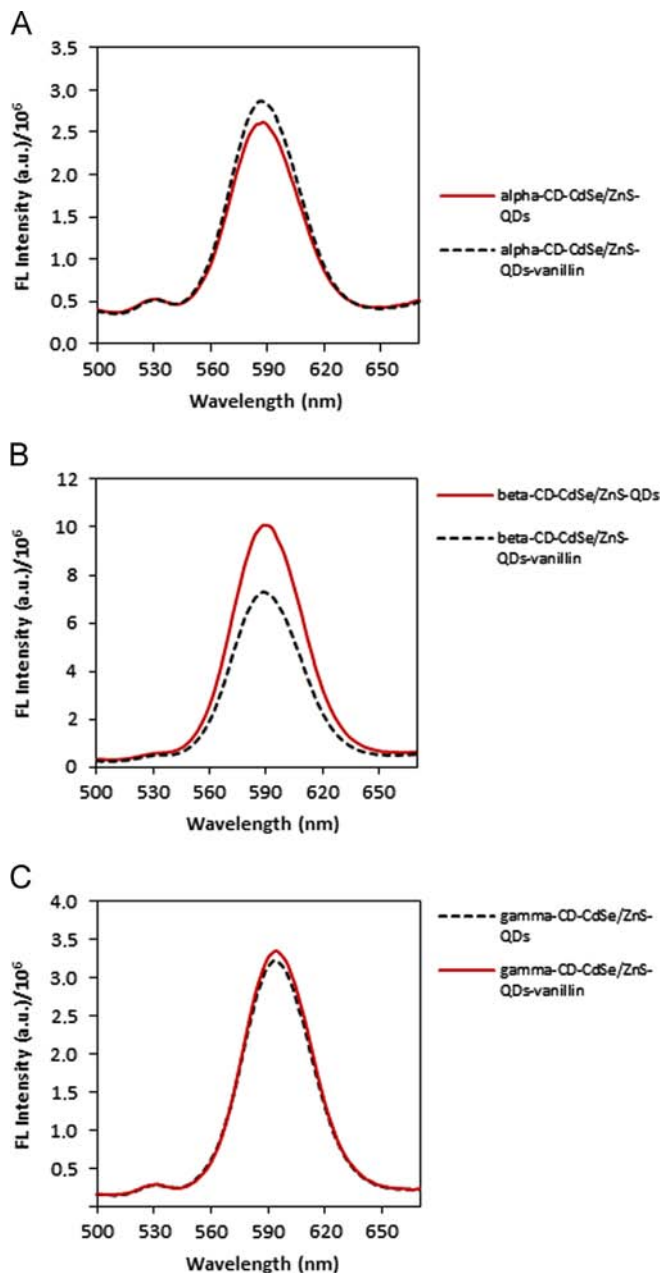


Fig. 3. Effect of 4.2 mg L⁻¹ vanillin concentration over luminescence of α -CD-CdSe/ZnS-QDs (A), β -CD-CdSe/ZnS-QDs (B) and γ -CD-CdSe/ZnS-QDs (C).

can act as an electron transfer quencher of luminescence of the particles (Fig. 1B). Under these conditions the association of the vanillin to the β -CD cavities concentrates the analyte on the semiconductor QDs surface. The time-dependent luminescence changes of the β -CD-QDs upon their interaction with 4.2 mg L⁻¹ of vanillin were investigated. From the results obtained, it can be concluded that luminescence of the β -CD-QDs in the presence of vanillin decreased until 30 min, and remained constant after this time value. The same behavior was also observed by recording of absorbance-time spectra of vanillin- β -CD-CdSe/ZnS-QDs complex.

The pH effect in the recognition of vanillin using β -CD-CdSe/ZnS-QDs nanoparticles was studied by measurements of fluorescence intensity of the β -CD-CdSe/ZnS-QDs without (I_0) and at given vanillin concentration (I). It was found that the pH significantly influenced the fluorescence intensity of the vanillin- β -CD-CdSe/ZnS-QDs system. The maximum value of I/I_0 was obtained when the pH was 8.0. Therefore, this value was chosen as optimum. As a second part of this study, the influence of the concentration of buffer solution, fixed with Na₂HPO₄ pH=8, was carried in order to evaluate the effect of this parameter in the fluorescence intensity of vanillin- β -CD-CdSe/ZnS-QDs system. The results showed that the maximum value I/I_0 was obtained when the buffer solution concentration was 1.2 mM. Therefore, this value was chosen in all experiments.

According to the literature [29], the surface of the n -CD-CdSe/ZnS-QDs affords a finite number of binding sites. Each of the binding sites could absorb one vanillin molecule from the solution. Therefore, according to Langmuir equation [28]:

$$\frac{C}{I} = \left(\frac{1}{BI_{\max}} \right) + \left(\frac{1}{I_{\max}} \right) C \quad (1)$$

where C is the concentration of vanillin and I the fluorescence intensity obtained for this concentration level. According to the literature, if the Langmuir description of the binding of vanillin on the surface of β -CD-CdSe/ZnS-QD is correct, a linear plot of c/I as a function of c must be obtained. In this case, a good linearity was observed throughout the entire range of vanillin concentration (2 to 20 mg L⁻¹). The binding constant B of β -CD-CdSe/ZnS-QDs with vanillin is found to be 0.99.

3.3. Analytical features for vanillin determination

In order to develop an analytical method to determine vanillin in foods, several analytical performance characteristics were evaluated under the optimized experimental conditions. The quenching effect of the vanillin can be described using the following

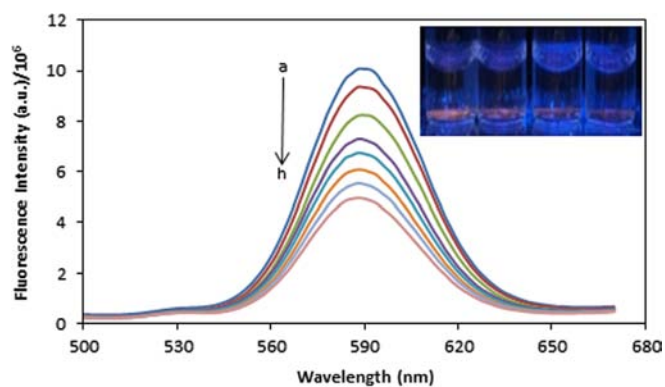


Fig. 4. Fluorescence spectra of β -CD-CdSe/ZnS-QDs with different concentrations of vanillin between 2 and 20 mg L^{-1} .

Stern–Volmer equation:

$$\frac{I_0}{I} = 1 + K_{sv}[Q] \quad (2)$$

where I_0 and I are the fluorescence intensity of β -CD-CdSe/ZnS-QDs in absence and presence of vanillin. A linear relationship between I_0/I and vanillin concentration in the range of 2–20 mg L^{-1} with a correlation coefficient of 0.9963 was obtained. Fig. 4 shows the fluorescence spectra of β -CD-CdSe/ZnS-QDs at different concentrations of vanillin between 2 and 20 mg L^{-1} . The calibration equation was:

$$\frac{I_0}{I} = 1.094 + 0.051[\text{vanillin}] \quad (3)$$

The precision of the methodology was evaluated in terms of repeatability and reproducibility. To determine the repeatability of the method, 10 analysis of samples containing 4.12 mg L^{-1} of vanillin were carried out and the obtained relative standard deviation (R.S.D.) was 1.2%. Then, the reproducibility was estimated for three replicates of 4.12 mg L^{-1} vanillin under inter-day conditions (for two consecutive days), obtaining a R.S.D. of 4.7%. A limit of detection (LOD) of 0.99 mg L^{-1} was obtained for vanillin determination, based on the IUPAC method (blank signal plus 3 times its standard deviation). 10 measurements were used to obtain the LOD. According to these results, it can be concluded that this approach opens the possibilities to develop an analytical method using β -CD-CdSe/ZnS-QDs for the determination of vanillin.

In order to apply the method to food samples a selectivity study was also carried out. For vanillin determination in food samples, the main interferences come from several colorant additives, such as curcumin or riboflavin. However, following the procedure reported in Section 2.5, the interferences of these compounds were eliminated. By contrast, glucose and lactose could be present in the sample as principal interfering compound. For this purpose, two different level of concentration were used in combination with vanillin. From the results obtained it can be concluded that when the concentration of interferences were increase, not difference were observed in the vanillin signal, given values of R.S.D of 3.9 and 4.5%, respectively. The coexisting compounds caused a relative error of less than $\pm 5\%$ in the fluorescence intensity of the vanillin- β -CD-CdSe/ZnS-QDs. Therefore it can be considered to have no interference with the detection of vanillin. The data revealed that the proposed method might be applied to the detection of vanillin in food samples.

On the other hand, sucrose and another related vanillin compounds, such as vanillin alcohol, 4-hydroxybenzaldehyde or 4-hydroxybenzyl alcohol were tested. For this purpose, three different levels of concentration were used in combination with

Table 1
Effect of coexisting foreign substances at three different concentration levels with respect to vanillin concentration.

Foreign substances	Foreign species ratio	Error in vanillin determination (%)
Sucrose	1:10	+1.9
	1:20	+2.5
	1:0.5	-0.1
Vanillin alcohol	1:1	+0.3
	1:2	+0.2
	1:0.5	-2.5
4-Hydroxybenzyl alcohol	1:1	+0.4
	1:2	+2.9
	1:0.5	-6.5
4-Hydroxyaldehyde	1:1	-8.2
	1:2	-9.7

Conditions: pH 8; [vanillin]=6.65 $\mu\text{g mL}^{-1}$.

Table 2
Determination of vanillin in several food samples ($n=5$).

Sample	Added (mg L^{-1})	Found (mg L^{-1})	Recovery (%)
Sugar 1	5	5.26 \pm 0.2	105 \pm 4
	10	9.96 \pm 0.5	100 \pm 5
	20	19.2 \pm 1	96 \pm 5
Sugar 2	5	4.9 \pm 0.2	99 \pm 3
	10	10.0 \pm 0.4	100 \pm 4
	20	20.0 \pm 0.3	99 \pm 1.5
Sugar 3	5	5.0 \pm 0.2	101 \pm 4
	10	9.6 \pm 0.4	96 \pm 4
	20	18.2 \pm 0.9	91 \pm 4.5
Milk 1	5	5.2 \pm 0.2	104 \pm 4
	10	9.0 \pm 0.4	90 \pm 4
	20	20.0 \pm 1.0	99 \pm 5
Milk 2	5	5.1 \pm 0.2	103 \pm 4
	10	9.0 \pm 0.5	90 \pm 5
	20	19.6 \pm 0.8	98 \pm 4

vanillin. From the results obtained it can be concluded that when the concentration of interference was increased, no difference was observed in the vanillin signal, with less of $\pm 5\%$ of R.S.D. when vanillin alcohol and 4-hydroxybenzyl alcohol were used. However, the results obtained in the presence of 4-hydroxybenzaldehyde indicated that this compound can produce interference in the vanillin determination. This fact demonstrated that the structure of the analyte and pH of solution system could play an important role in the selectivity of vanillin determination with β -CD-CdSe/ZnS-QDs. Table 1 shows the obtained change of fluorescence intensity (%) at the three concentration levels studied.

4. Application

To demonstrate the applicability of the proposed method, it was applied to determine vanillin in several commercial sugar and milk samples, purchased in different supermarkets. Each one of these samples was spiked with several concentrations of vanillin and were prepared according to the steps described in Section 2.5. The summary of these results are shown in Table 2. The obtained recoveries indicated an acceptable agreement between the amounts added and those found for all types of samples.

The proposed method was also used for the quantitation of vanillin in custard with vanilla flavor. These samples contained vanillin as flavor additive. This product was analyzed by triplicate, according the procedure described in Section 2.5. To evaluate the matrix effect, the standard addition method was also used for the

determination of vanillin in the studied product. The obtained results were 75.6 ± 0.6 and $76.3 \pm 0.9 \text{ mg L}^{-1}$ with and without standard addition, respectively, corresponding to the original sample (samples were diluted before analyses). The application of Student statistical test for a confidence level of 95% demonstrated the statistical coincidence between the concentration found with those found by the standard addition method ($n=6$, $t_{\text{crit}}=2.92 > t_{\text{exp}}=0.48$).

5. Conclusions

In this work, an optical sensor for vanillin determination based on the selective supramolecular recognition of vanillin with β -cyclodextrin modified CdSe/ZnS QDs was developed. The procedure for the synthesis of n -CD–CdSe/ZnS-QDs complex was simple and very effective. Different coating agents, such as α , β and γ -CD, were studied, and the effect of several experimental parameters was optimized. The proposed methodology presents some advantages. Thus, the solubilization of TOPO–CdSe/ZnS-QD, initially in organic media, was allowed in aqueous media. This fact allows its compatibility with biological samples, and aqueous media in general, and in addition the conservation in organic media over long periods of time. In this way, it is possible to modify only the necessary amount of QDs when required. On the other hand, the methodology demonstrated that the surface coating of QDs with different n -cyclodextrins keeps the emission intensity of the quantum dots and their diameter. In addition, the immobilized β -cyclodextrins on the surface of the QDs retain their capability of engaging molecular recognition. Therefore, the use of β -cyclodextrin for QDs surface modification showed selectivity in vanillin recognition to alpha and gamma cyclodextrins. Thus, the potential of the sensor for the analysis of food samples was demonstrated, opening other possible alternatives for the selective fluorimetric sensing of other compounds through the appropriated modification of quantum dots surface.

Acknowledgements

This research was supported by Project CTQ2013-48411-P (MINECO). Gema M. Durán thanks the Spanish Ministry of Economy and Competitiveness for a Predoctoral Grant.

References

- [1] C. Carrillo-Carrion, S. Cardenas, B.M. Simonet, M. Valcarcel, *Anal. Chem.* 81 (2009) 4730–4733.
- [2] S. Huang, Q. Xiao, R. Li, H.-L. Guan, J. Liu, X.-R. Liu, Z.-K. He, Y. Liu, *Anal. Chim. Acta* 645 (2009) 73–78.
- [3] G.M. Duran, A.M. Contento, A. Ríos, *Anal. Chim. Acta* 801 (2013) 84–90.
- [4] C. Carrillo-Carrion, B.M. Simonet, M. Valcarcel, *Analyst* 137 (2012) 1152–1159.
- [5] T.-W. Sung, Y.-L. Lo, *Sens. Actuators, B* 165 (2012) 119–125.
- [6] C. Carrillo-Carrion, B. Lendl, B.M. Simonet, M. Valcarcel, *Anal. Chem.* 83 (2011) 8093–8100.
- [7] P. Ncube, R.W. Krause, B.B. Mamba, *Sensors* 11 (2011) 4598–4608.
- [8] A.T. Ogoshi, A. Harada, *Chem. Sens. Based Cyclodextrin Derivatives Sens.* 8 (2008) 4961–4982.
- [9] M. Li, X. Liu, F.Y. Jiang, L.P. Guo, L. Yang, *J. Chromatogr. A* 1218 (2011) 3725–3729.
- [10] R. Freeman, T. Finder, L. Bahshi, I. Willner, *Nano Lett.* 9 (2009) 2073–2076.
- [11] C.P. Han, H.B. Li, *Small* 4 (2008) 1344–1350.
- [12] H.B. Li, C.P. Han, *Chem. Mater.* 20 (2008) 6053–6059.
- [13] M. Algarra, B.B. Campos, F.R. Aguiar, J.E. Rodriguez-Borges, J.C.G. Esteves da Silva, *Mater. Sci. Eng., C* 32 (2012) 799–803.
- [14] C.P. Han, H.B. Li, *Chin. Chem. Lett.* 19 (2008) 215–218.
- [15] Y. Cao, S. Wu, Y. Liang, Y. Yu, *J. Mol. Struct.* 1031 (2013) 9–13.
- [16] S. Ramachandra Rao, G.A. Ravishankar, *J. Sci. Food Agric* 80 (2000) 289–304.
- [17] Y. Yardim, M. Gülcan, Z. Şentürk, *Food Chem.* 141 (2013) 1821–1827.
- [18] D. Zheng, C. Hu, T. Gan, X. Dang, S. Hu, *Sens. Actuators, B* 148 (2010) 247–252.
- [19] F. Bettazzi, I. Palchetti, S. Sisalli, M. Mascini, *Anal. Chim. Acta* 555 (2006) 134–138.
- [20] J.L. Hardcastle, C.J. Paterson, R.G. Compton, *Electroanalysis* 13 (2001) 899–905.
- [21] M. Luque, E. Luque-Pérez, A. Ríos, M. Valcárcel, *Anal. Chim. Acta* 410 (2000) 127–134.
- [22] M. Avila, M. Zougagh, A. Escarpa, A. Rios, *Talanta* 72 (2007) 1362–1369.
- [23] Y. Ni, G. Zhang, S. Kokot, *Food Chem.* 89 (2005) 465–473.
- [24] U. Pyell, B. Pletsch-Viehmänn, U. Ramus, *J. Sep. Sci.* 25 (2002) 1035–1042.
- [25] M. Ohashi, H. Omae, M. Hashida, Y. Sowa, S. Imai, *J. Chromatogr., A* 1138 (2007) 262–267.
- [26] A. Perez-Silva, E. Odoux, P. Brat, F. Ribeyre, G. Rodriguez-Jimenes, V. Robles-Olvera, *Food Chem.* 99 (2006) 728–735.
- [27] Z.A. Peng, X. Peng, *J. Am. Chem. Soc.* 123 (2001) 183–184.
- [28] C. Han, H. Li, *Small* 4 (2008) 1344–1350.
- [29] Y. Chen, Z. Rosenzweig, *Anal. Chem.* 74 (2002) 5132–5138.



Review

Total indices as a tool to estimate sum content of similar analytes



Viacheslav I. Vershinin

Department of Analytical Chemistry, Omsk State University, Omsk 644077, Russia

ARTICLE INFO

Article history:

Received 28 May 2014

Received in revised form

28 July 2014

Accepted 31 July 2014

Available online 8 August 2014

Keywords:

Chemical analysis

Environmental analysis

Determination of organic substances

Sum content of similar analytes

Total indices

Standard substance

Uncertainty of results

ABSTRACT

The estimation of sum content of similar analytes without their separation often requires the use of total indices (TIs) expressed in terms of the standard substance concentration. Theoretic and metrological features of such indices are discussed in the review. The sum content of similar analytes is estimated by any TI with a certain systematic error. It can be minimized by selecting a standard substance and/or with the justification of sensitivity coefficients for individual analytes. The publications are pointed out in which new TIs are offered or new methods to measure known TIs are described. The corresponding studies are predominantly associated with two kinds of estimates: (a) total content of organic substances in waters and (b) the total antioxidant activity of foodstuffs.

© 2014 Elsevier B.V. All rights reserved.

Contents

1. Introduction.....	292
2. Methodology to determine the total content of similar analytes.....	293
2.1. Selection of the similar analytes.....	293
2.2. Determination of total content without recalculation to X_{st}	294
2.2.1. Direct determination of C_{Σ} by the measuring of generalized signal if it is equally sensitive to all compounds of the required group.....	294
2.2.2. Indirect methods based on the summation of individual analytes concentrations.....	294
2.2.3. Indirect methods based on the multivariate calibrations.....	294
2.3. Estimation of total content recalculated to X_{st} : terminology and metrological aspects.....	295
2.4. The selection of optimal standard substance.....	296
2.5. Total index as a function of similar analytes sum content.....	296
2.6. Justification (leveling) of sensitivity coefficients for individual analytes.....	297
2.7. New methods for total indices determination.....	298
3. Conclusions.....	299
Acknowledgments.....	299
References.....	300

1. Introduction

The problems which arise in the chemical analysis of unseparated mixtures, as well as the methods to solve these problems, do not depend so much on the mixture composition as on the task to be solved during the analysis. The general approach to the problem solution (with or without the components separation)

is important too. The quantitative analysis of technologic or natural mixtures on the molecular level includes four main objectives [1]: (a) the determination of a certain component (X) in the presence of other components; (b) simultaneous and separate determination of several components (X_1, X_2, X_3, \dots); (c) determination of the total content of a number of components (usually similar ones) which form a certain group (ΣX); and

(d) simultaneous and separate determination of several groups (ΣX , ΣY , ΣZ ...).

The problems of c-type are permanently solved in the analysis of waters, petroleum products, foodstuff and biological objects. The proportion of the relevant procedures in the general array of methods of chemical analysis is considered to constitute about 20% [2]. The rejection of separate determination of numerous similar substances accelerates, cheapens and simplifies the analysis of any object, and consumers still get the information they need. The ways to solve the problems of c-type and the allied but more complicated problems of d-type have been developed empirically since the 1930s. The corresponded techniques were often created not by professional analysts but by other specialists (engineers, hydrochemists, biochemists, etc.). In an analysts' opinion, the general theoretical problems arising from the evaluation of the total content (C_{Σ}) of similar substances without their separation are not studied enough [3–5]. The article of Valcarcel and Baena [2] had fundamental significance for the correct appreciation of these problems. After that the fruitful discussion of methods to estimate the sum content of similar analytes was started. Corresponding experiments were developed, especially in Russia [3]. Generalized approach [2] will be used in this review too, but it is worthwhile to limit the problem for discussion by quite narrow bounds. Namely, we are going to discuss the only kind of sum estimates- so-called *total indices* (TIs) expressed in terms of standard substance concentration. The examples can be the phenol index, hydrocarbon index, COD, antioxidant activity index, "total protein", "total organic carbon", etc. "Recalculated" TIs are usually determined by spectrometric methods (Fig. 1). Some titrimetric and electrochemical methods are used too.

TI-system has proved to be useful, but so far poorly substantiated in relation to metrology. The result of determination of TI (C^*) is often very different from C_{Σ} , sometimes several times as much [5]. Plausible reasons of corresponding errors and the ways to diminish them would be briefly examined in this review. We believe that the theoretical aspects of TI application are better considered in a general way, without singling out special groups of analytes or objects to analyze. The works in the field of analysis of natural and waste waters, petroleum products and foodstuff published since 2000 will be used as examples.

2. Methodology to determine the total content of similar analytes

2.1. Selection of the similar analytes

To determine any group of substances it is necessary to properly form the group content. It is recommended to use the following criteria for the selection of substances [2].

- 1) *Structural similarity of molecules*: proteins, alcohols, phenols, nucleic acids and others are singled out as certain groups of analytes. Such groups can be formed at different levels (hydrocarbons on the whole, aromatic hydrocarbons, polycyclic aromatic hydrocarbons, etc.). The group may include all the substances containing some element; their total content is recalculated to this element ("total carbon", "total nitrogen," etc.).
- 2) *Similar properties and similar application of the substances*: the compounds of different chemical nature may have similar properties (antioxidants, pesticides, etc.) which causes the need to evaluate their sum content. Sometimes groups of analytes are formed by taking into consideration both criteria simultaneously (polyphenol antioxidants, organophosphorous pesticides, cationic detergents).

Obviously, it is necessary to develop methods of sample preparation or signal measuring based on the desired composition of the group, and not vice versa. Unfortunately, groups of analytes are often formed, taking into account only the possibility of simultaneous extraction (adsorption, distillation, precipitation) or their simultaneous light absorption at a certain wavelength. This approach facilitates the elaboration of analytical methods, but the obtained results are difficult to interpret and apply. The data on group composition of objects of this type obtained by using different methods turn out to be incomparable! "Phenol index" (PI) widely applied in hydrochemical analysis can serve as a good example. PI characterizes the total content of volatile phenols which react with 4-aminoantipyrine in alkaline medium, recalculated to simplest phenol. However, certain substituted phenols (e.g. p-cresol) do not react with 4-aminoantipyrine and their content in a sample is not taken into account [6]. On the contrary, some non-phenolic components of the sample can react with 4-aminoantipyrine and make their contribution to the PI value. So the PI

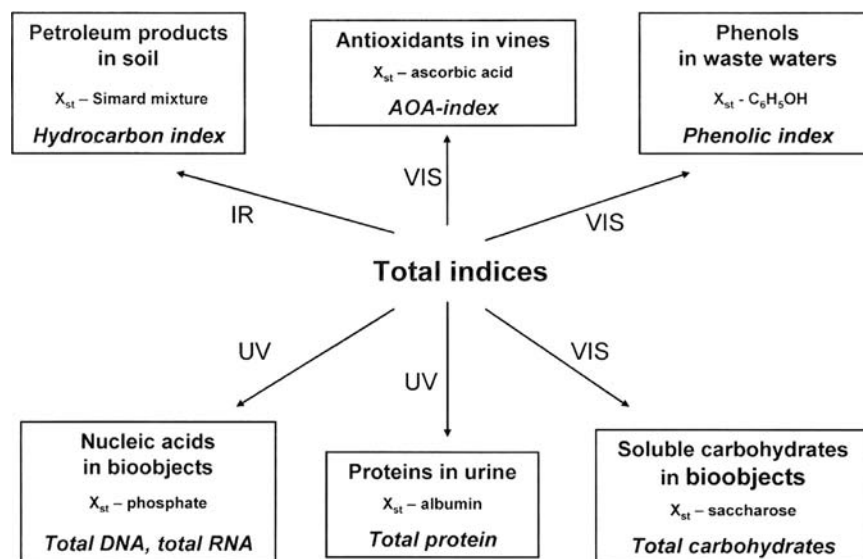


Fig. 1. The examples of total indices determined by UV, IR or visible (VIS) spectra.

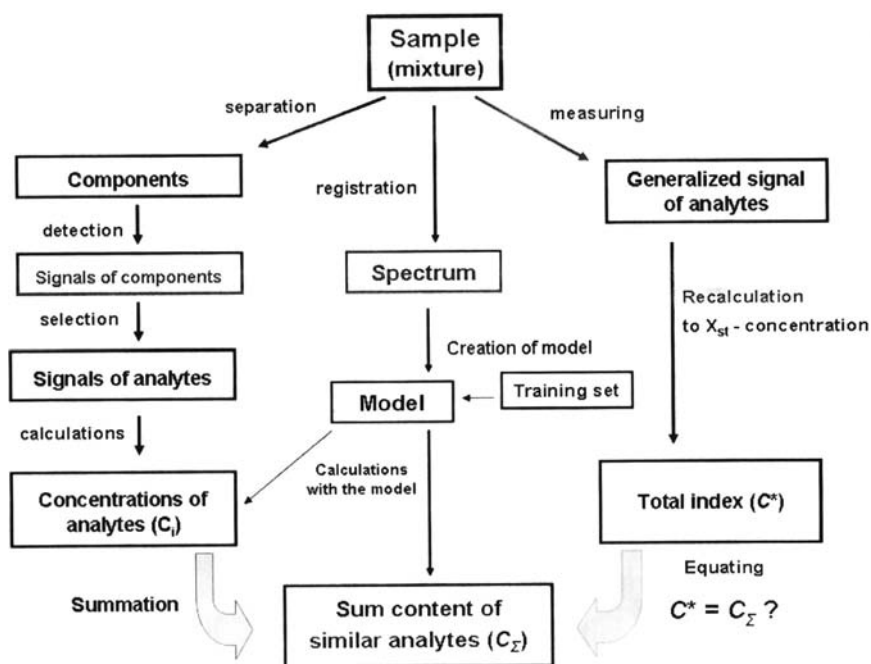


Fig. 2. The schemes to evaluate sum content of analytes: chromatographic analysis (left); application of multivariate calibrations (center); and recalculation to X_{st} (right).

value can be both less and more than the actual C_{Σ} value found by GLC or HPLC methods [5].

2.2. Determination of total content without recalculation to X_{st}

Nowadays the most popular way to determine C_{Σ} is chromatographic analysis. The sample is separated, its components are detected, the analytes of the required group are identified, and their individual concentrations (C_i) are calculated and summarized (Fig. 2, left).

The determination of the group composition of gasoline by the standard method [7] can serve as an example. Similar techniques are widely used in environmental monitoring, especially in the USA and EU countries. However, GC or HPLC methods are not applicable in certain cases, as chromatographic separation of some mixtures can lead to the destruction of components, shifting the equilibria and other undesirable consequences [8]. Moreover, the separation itself sometimes takes too long. False identifications are inevitable; especially when they interpret chromatographic peaks only with the retention times [9]. This effect distorts the group composition indices. False identifications are most dangerous in the GLC analysis of the environmental objects, since the qualitative composition of such objects is unpredictable. Chromatography should be used in solving analytical problems of b-type, and for problems of c- and d-type it is better to use alternative express methods that do not require the separation of mixtures, in particular, the methods of molecular spectroscopy [11].

C_{Σ} values can be determined with high precision without separating the analytes or recalculating the signal to a standard substance. The following methods are used.

2.2.1. Direct determination of C_{Σ} by the measuring of generalized signal if it is equally sensitive to all compounds of the required group

Extraneous compounds should not affect the generalized signal or they should be separated from the mixture of X_i in advance. The extraction-gravimetric determination of the sum of hydrocarbons (HC) derived from petroleum in highly polluted waste waters can serve as an example [10]. Specially selected extragents provide the same extraction degree of all HCs (close to 100%). Non-hydrocarbon

components of the extract are absorbed and the sum of remaining hydrocarbons is weighed. “The detector” (scales) is equally sensitive to any HC. Direct methods to determine C_{Σ} include the titrimetry too, if all X_i react with the non-selective reagent in accordance with the law of equivalents, the result is expressed in mol-eq/dm³, the same as when the water hardness is determined.

2.2.2. Indirect methods based on the summation of individual analytes concentrations

If the number of analytes in a mixture is small and their signals are free from overlap, the concentrations of all analytes (C_i) can be calculated from the spectrum of an unseparated mixture, using one-dimensional calibrations, and then C_i -values are summed. In this case different sensitivity of analytes detection does not matter. The example of such techniques can be NMR spectrometric determination of the total content of fatty acids [11]. Unfortunately, the accuracy with which the total content evaluated by summation is much to be desired.

2.2.3. Indirect methods based on the multivariate calibrations

In these techniques C_i -values are determined by the spectrum of an unseparated sample, and the sensitivity of the different X_i varies. However, unlike the previous case, the signals of different X_i overlap. To solve the problem, a multidimensional calibration (a mathematical model) is received in advance by designing the training set (spectra of mixtures with known composition) and processing it with the help of corresponding chemometric algorithm (e.g., PLS). The found C_i -values are summed (Fig. 2, center). It is possible to calculate C_{Σ} values using multivariate calibrations without intermediate calculation of C_i . For this purpose the spectra of a number of natural or man-made mixtures are included in the training sample. These mixtures are similar to test samples. The C_{Σ} values are found by a reliable and independent reference method (e.g. HPLC) for each mixture. Then the model is calculated. Using this model, the total content (C_{Σ} desired) can be found by the spectra of any test sample. The above mentioned approach is implemented in determining the content of phenolic compounds in green tea [12], the amount of tannins in red wines [13], the determination of group composition of

gasoline [14] and in other instances. It should be noted that the method [14] allows to determine the total contents of alkanes, cycloalkanes and arenes in gasoline with almost the same accuracy as the standard GLC method [7], but the analysis takes 20 times less time. Nowadays the methods based on the calculation of multivariate calibrations are used in pharmaceutical and oil refinery industrial laboratories.

Indirect methods to determine C_{Σ} listed in this section are not universally applicable. Their application is prevented by the necessity to know the qualitative composition of the samples in advance. It is required to build adequate calibrations (one-dimensional or multidimensional). There are other problems: non-additivity of the generalized signal and the absence of reliable reference methods. It is difficult to predict the impact of extraneous agents too. In such cases, the way out is the transition to the evaluation of total indices (TIs).

2.3. Estimation of total content recalculated to X_{st} : terminology and metrological aspects

The total content of similar analytes in an unseparated mixture can be estimated by recalculating the generalized analytic signal to the standard substance (Fig. 2, right). One and the same group of analytes can be characterized by various TIs which are different in the way of signal measuring and in the choice of standard substance (X_{st}); their numerical values for the only sample do not coincide either. Most often TIs are determined by measuring the light absorbance of the sample in the UV, IR or visible region at a fixed wavelength. Standard procedure to determine TPH (hydrocarbon index) by IR-spectrometry [15] can be the appropriate example. Sometimes refractometry, conductometry, fluorimetry and other instrumental methods are used. These methods have to provide an additivity of signals as well as the linearity of calibrations and the results reproducibility [16]. The C^* value is calculated by the generalized signal of the mixture (A_{Σ}) using the calibration graph obtained with model solutions of X_{st} .

The expediency of using TIs is obvious: to determine TI it is not necessary to separate the components or know the qualitative composition of the sample in advance. The relevant simple methods have a good repeatability. The results of the analysis (C^* values) allow to characterize the object of study, to compare the similar objects and to make express screening.

Analysts emphasize the importance of the correct interpretation of the obtained data and the inadmissibility of equating TI and the total content of the relevant analytes. Thus, the statement “the phenol index of a sample in terms of C_6H_5OH is 3 mg/l” only means that after processing by 4-aminoantipyrine the sample has the same optical density as the solution containing 3 mg of C_6H_5OH in 1 l. It is quite impossible to accurately determine the total content of phenols in this sample by the experimentally obtained value of PI, that is only the minimal estimate of C_{Σ} [17]. It is possible to diminish inevitable differences between C^* and C_{Σ} by the correct choice of X_{st} and/or by justification of sensitivities to determine individual analytes (see Sections 2.4 and 2.6).

The term “total index” is not quite familiar to the staff of analytical laboratories, even if somebody personally determines certain TI everyday. This term is rarely used in academic and regulatory literature. In scientific literature a variety of characteristics is referred to as “total” or “integral”, up to the smell and taste of samples. To avoid misunderstandings, the clear definition for “recalculated” TIs was proposed in [5].

Total index is the rough evaluation of the total content of the group of similar substances which are present in the object under study and forming a generalized analytical signal, expressed in terms of standard substance.

This definition is not the only possible or generally accepted. Several authors call any measurand characterizing the total content of a certain group of similar analytes as total indice. From our point of view, the drawback of this (too generalized!) approach is that it does not take into account the metrological specificity of measurands. *The use of TIs expressed in terms of X_{st} is a characteristic of one physical value in the units of another physical value*, which is inconsistent with the general rules governing the choice of units to measure physical values [18]. Metrologically incorrect C_{Σ} evaluations in terms of the standard substance depend on the choice of X_{st} and the conditions of measuring the signal, so they are not to be confused with the results of conventional measurements. These “method-dependent” evaluations should be isolated in a special group of composition indices and have their own generalizing name that distinguishes them from the results of conventional measurements.

Equating total contents and total indices leads to a relative error $\delta c = (C^* - C_{\Sigma})/C_{\Sigma}$, which can make up tens or even hundreds of percent. While taking repeated measurements δc are well reproduced. As usual, the uncertainty of C_{Σ} estimation is predominantly systematic. When total content of similar analytes and all other conditions being constant, the qualitative composition of the sample and components' ratio strongly affect the result of analysis. Let us take as an example the results of IR-spectrometric analysis of hydrocarbon mixtures. The increase in alkylarenes content here leads to the increase (in modulo) of a negative error or the decrease of a positive error (Table 1, taken from [19]). The revealed tendency is maintained regardless of what device was used to measure the generalized signal as alkylarenes in this range of spectrum have much lower coefficients of spectral absorption than alkanes or cycloalkanes. On the other hand, at a constant content of arenes, δc value increases as the content of cycloalkanes goes up, since they are determined by a slightly higher sensitivity than a standard substance-Simard mixture [20].

As pointed out by analysts and ecologists, “recalculated” TIs are quality indices, as well as many other sum characteristics of the objects under research [2,4]. Thus, natural waters are characterized not only by total indices but also by many other indicators of composition (individual and group ones), as well as by microbiological, organoleptic and other indicators. Directly measured values characterizing the properties of an object conditioned by the joint action of the components are called generalized indices by environmental monitoring specialists. Generalized indices of properties (GIs) are very close to TIs. For natural and waste waters GIs are pH, index of refraction, conductivity, etc. Measuring some

Table 1

Errors of IR-spectrometric estimations of total hydrocarbon content recalculated to Simard mixture for some model objects.

Object (mixture to analyze)	Ratio of components	Part of toluene (% rel.)	δc (%)	
			FT-801	IKN-025
Cyclohexane–toluene	3:1	25	77	11
	1:1	50	16	–6
	1:3	75	–35	–33
n-Hexane–toluene	3:1	25	–3	9
	1:1	50	–31	–39
n-Hexane–cyclohexane	1:3	75	–57	–61
	3:1	0	52	44
	1:1	0	76	48
n-Hexane–cyclohexane– toluene	1:3	0	100	60
	2:3:1	17	64	44
	1:1:1	33	26	8
	1:1:3	60	–23	–22

Note: HC signals were measured with an IR-Fourier spectrometer FT-801 or with IR-concentratometer IKN-025. In all cases $C_{\Sigma} \approx 100$ mg/dm³, solvent–CCl₄ and RSD < 5%.

GIs of water (especially luminescence) it is possible to control the security of water supply systems [21]. Some TIs are calculated by GI-values; in particular, the conductivity of seawater determines TI “salinity”. However, GIs themselves are not the evaluations of the total content of analytes; they should not be confused with TIs.

2.4. The selection of optimal standard substance

There have been repeated discussions about which X_{st} are better to be used in each particular case, for example, while estimating the total HC content [5] or the total content of antioxidants [22]. The problem has not been considered more generally. The strict algorithm of the standard substance selection that minimizes the systematic error of C_{Σ} estimate is designed only for the particular case when the sample with a known set and known relations of analytes is investigated [16]. The authors suggest that the δc error occurs only due to the mismatch of the absorption coefficients of all or some of the components of a sample (K_i) with an absorption coefficient of X_{st} under the same conditions (K_{st}). Simple calculations lead to the formula:

$$\delta c = \sum p_i R_i - 1 \quad (1)$$

where $p_i = K_i/K_{st}$ is the normalized value of the sensitivity coefficient of i -th analyte while using this measurement technique, and R_i is X_i share in the mixture of n analytes presenting in the sample. Eq. (1) was confirmed while determining different TIs with the use of different tool methods. The errors arising when evaluating the total content of the polyphenol type antioxidants can serve as an example (Table 2, taken from [16]).

To ensure equality $C^* = C_{\Sigma}$ it is recommended [23] to use as X_{st} the substance which meets condition (2) which is derived from (1)

$$K_{st} = \sum K_i R_i \quad (2)$$

If the concentration of all the analytes in the sample is approximately the same, it is recommended to be guided by the rule:

$$K_{st} = \frac{\sum K_i}{n} = \bar{K}_i \quad (3)$$

For other ratios of analytes the optimal value of K_{st} will differ from \bar{K}_i , but in any case it must belong to the interval (K_1, K_n), where K_1 and K_n are sensitivity coefficients for the analytes which are detected with minimum and maximum sensitivity. If it is impossible to find a single compound which is detected with the desired sensitivity, a mixture of different compounds has to be used as a X_{st} . These compounds have to be mixed in a ratio to obtain the desired K_{st} value. The standard Simard mixture to determine the hydrocarbon index of natural or waste waters can serve as an example. To a certain extent the composition of Simard mixture simulates the group composition of hydrocarbon mixtures presented in natural and waste waters.

Table 2

The errors (δc , %) of total content estimates for the same model mixture of antioxidants when using different standard substances.

X_{st}	Method 1		Method 2	
	Forecast	Experiment	Forecast	Experiment
Quercetin	-62	-62	-64	-69
Gallic acid	-43	-43	-61	-67
Ruthin	-12	-10	-12	-25
Protocatechic acid (PCA)	-11	-10	-25	-36
Ascorbic acid (AA)	-9	-8	+20	0
Ferulic acid (FA)	+59	+61	+20	+12

Note: the composition of the mixture is AA—1.5 mcM; PCA—1.0 mcM; and catechol—1.5 mcM.

It was theoretically proved that the smaller the systematic error of C_{Σ} estimation, the larger the X_{st} share in the test mixture [23]. This is consistent with the practice of analysis. Thus, while determining the phenol index of waste waters, the phenol itself is used as a X_{st} [17] since usually it is the main component of anthropogenic phenolic mixtures [24].

Results of analysis of only sample substantially differ to each other when different antioxidants (AOs) are used as X_{st} [25]. While determining the index of antioxidant activity by the FRAP method it is possible to obtain accurate C_{Σ} estimations if ascorbic acid is used as a X_{st} [26]. The sensitivity of detection of this compound is close to optimum calculated by Eq. (2), taking into account the sensitivity coefficients for different polyphenol AOs. Sometimes quercetin or gallic acid is used as X_{st} . Compounds deliberately absent in the samples are also used as X_{st} . Thus, the total content of antioxidants (AO) in foodstuff or in blood plasma is often expressed in terms of Trolox, a synthetic analog of certain natural AO (vitamin E).

Well-grounded X_{st} selection is possible even in the case when the qualitative composition of individual mixtures is unknown and only the sensitivity coefficients of all m analytes of this type are known, regardless of which of them and in what ratio are found in the investigated sample. Corresponding calculations and experimental data confirming this are given in [23]. In such cases authors recommend to use the substance which is defined under given conditions with a certain average sensitivity. Namely, optimal K_{st} value is

$$K_{st} = 0.5(K_1 + K_m) \quad (4)$$

The stability, availability and cost of X_{st} should also be taken into account [22].

2.5. Total index as a function of similar analytes sum content

Sometimes $C^* \neq C_{\Sigma}$ but the stable linear correlation between C^* and C_{Σ} exists at least for certain set of samples. It happens in the cases when all the samples have the same qualitative composition, the relative content of any X_i in all the samples is the same, and C^* values are obtained with the same procedure. Unfortunately, such favorable cases are quite rare. Nevertheless it is tempting to use the information about sample composition and to pass from founded C^* values to the real values of C_{Σ} . As shown in [16], if the main reason for the differences between C^* and C_{Σ} is different detection sensitivity of analytes and standard substance, δc does not depend on C_{Σ} . This follows Eq. (1). In such cases, recalculation to the standard substance leads to the *multiplicative* systematic error, which can be eliminated by introducing a correction factor calculated in advance:

$$C_{\Sigma} \approx C^* / \sum p_i R_i \quad (5)$$

The correction factor depends on the choice of X_{st} . Therefore the introduction of corrections should lead to C_{Σ} estimations theoretically independent of the choice of X_{st} . It was confirmed in experiments with model mixtures of antioxidants. The real examples also exist. Thus, the sum content of salts in seawater can be accurately determined using salinity indices measured with standard techniques. These figures are expressed in terms of chloride ions (argentometry) or recalculated to a standard mixture of salts (conductometry) [27]. Corresponding calculations or simple instrumental calibration with some standards are possible due to the constant salt composition of sea water, which does not depend on the total salt content. Undoubtedly, the possibility of introducing abovementioned corrections in each particular case requires the special preliminary research.

Eqs. (1) and (2–5) derived from it are not applicable to the objects with an unknown set or unknown ratio of similar analytes.

In these cases it is possible to predict only the limiting values of δc which do not depend on the composition of a single sample, but only on the detection sensitivity of each X_i under selected conditions [23]. This approach was developed for characterizing C_Σ in interval form, as $(C^* \pm \Delta C)$ [28].

Such estimates are not applicable entirely if C^* deviations from C_Σ do not arise due to the wrong choice of a standard substance or different detection sensitivities of different analytes, but for other reasons, for example, due to incomplete extraction of the desired analytes from the sample [29] or due to non-additivity of the analytical signals [1]. The change of the concentration conditions during the formation of a generalized analytic signal allowed to make it additive and the value of δc significantly decreased [26].

2.6. Justification (leveling) of sensitivity coefficients for individual analytes

It was proved that the uncertainty of C_Σ estimations is increasing with the widening of “fan of calibrations” which characterizes all analytes of the required group [23]. Independently of X_{st} selection the inequality (6) is fulfilled:

$$T^{-1} - 1 \leq \delta c \leq T - 1 \quad (6)$$

where nondimensional parameter T is the ratio of maximum and minimum coefficients characterizing the sensitivity of analytes detection by used method. At $T=2$ δc can reach 100% rel. in modulo, at $T=1.5$ it can reach up to 50%, etc. Obviously, the leveling of detection sensitivity of similar analytes is a good way to reduce the uncertainty of total contents estimation. T -value can serve as a parameter of optimization (Fig. 3, taken from [30]).

When using the “optimal” standard substance corresponding to the condition (4), the uncertainty of estimates is significantly reduced:

$$|\delta c| \leq (T - 1)/(T + 1). \quad (7)$$

Thus, when $T=2$, the relative error of the estimation of total content should not exceed 33%, at $T=1.5$ –20%, etc. The use of unmatched standards can lead to errors that exceed these limits. In such cases, the δc value has to be limited by more complex relations similar to Eq. (6). Derived formulas are valid for all mixtures of the specified type regardless of their qualitative and quantitative composition. This was confirmed in the analysis of 20 different phenolic compounds of different (known) compositions

by the same procedure [23]. Error values obtained in the experiment (while recalculating the signal to the same standard substance) lie within certain boundaries. They were compared with the theoretically calculated error interval. The composition of each mixture was not taken into account. The predicted interval of errors nearly coincided with the experiment (Table 3, taken from [23]).

It follows from Eq. (6) that at $T \neq 1$ it is impossible to entirely eliminate the error of the estimation of total content by picking up X_{st} . Leveling the detection sensitivity of different analytes is a more promising way to solve this problem. With the help of Eqs. (6) and (7) they can even calculate the critical values of T that provide the reduction of the limiting error to the desired level of δc (Table 4, taken from [28]).

The analysis of published data allows to understand what methods of leveling are really used in the estimation of the total content of analytes (Table 5). These methods are quite effective; especially the selection of the wavelength at which the analytical signal is measured. Thus, in spectrometric determination of phenols by the reaction with diazotized sulfanilic acid the change of wavelength, as well as the change in pH of the solution (see Fig. 3) reduced T parameter from 3.0 to 1.5 units. As a result,

Table 3

Predicted and actual intervals of errors (% rel.) in spectrometric determining of total phenol content recalculated to different standard substances.

X_{st}	Theoretical forecast	Experiment
Simplest phenol (C_6H_5OH)	From –63 till 0	From –66 till 0
Ortho-cresol	From –54 till +22	From –58 till +16
1-Naphtol	From 0 till +168	From –9 till +154

Table 4

Critical values of T parameter.

δc_{crit} , % rel.	Arbitrary X_{st} , calculation with (6)	Optimal X_{st} , calculation with (7)
1	1.01	1.02
5	1.05	1.10
10	1.1	1.22
20	1.2	1.50
30	1.3	1.85
50	1.5	3.0

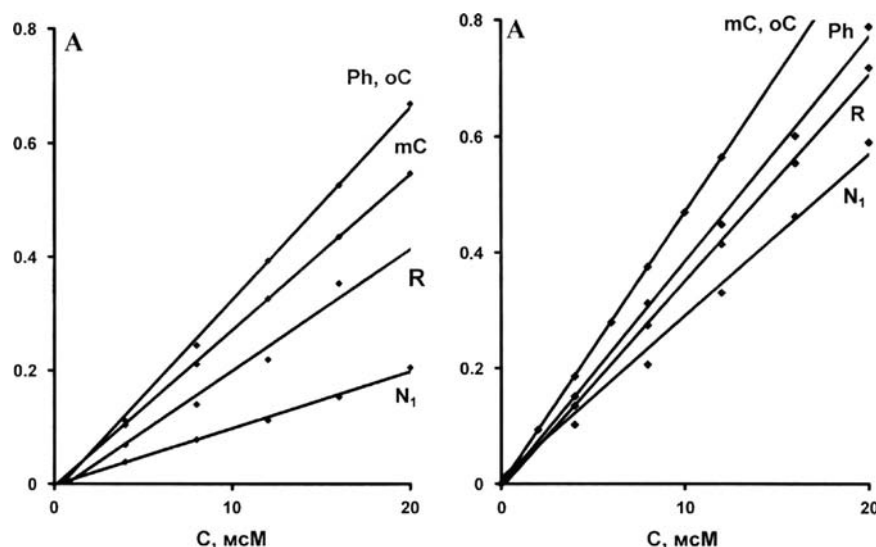


Fig. 3. Calibration fans in spectrometric determination of different phenols before (left) and after (right) the optimization of the analysis conditions. Left— $\lambda=450$ nm, pH 8.3; right— $\lambda=360$ nm, pH 7.3. Legend: Ph—phenol, oC—ortho-cresol, mC—meta-cresol, R—resorcinol, N_1 —1-naphthol.

Table 5
Methods of sensitivity leveling in the measurement of total indices.

Mixture to determine	Method of analysis	Method of sensitivity leveling	References
Phenols	UV-spectrometry, vis-spectrometry	Reagent selection, optimization of pH, optimization of the wavelength	[30]
Hydrocarbons	IR-spectrometry	Transition to another method of signal measuring	[19]
Antioxidants (polyphenols)	Vis-spectrometry	Transition to another way of expressing concentration (mol-eq/l)	[26]
Thiols	Stripping voltammetry	Introduction of an additional reagent	[31]
Proteins	UV-spectrometry, vis-spectrometry	Reagent selection, optimization of concentration conditions	[32]

the error of the total phenol content decreased from 50–80% rel. to 20–30% [30]. The results of waste water analysis obtained by the optimized procedure were confirmed by HPLC method.

2.7. New methods for total indices determination

Among a great number of publications devoted to particular methods of determining the TIs, it is rational to select those that propose new indices or recommend fundamentally new methods of measurement of known TIs. Progress was mainly connected with two areas of research, i.e. the evaluation of the total content of organic substances in waters and the evaluation of total content of antioxidants in foodstuff.

Zuev proposed the new index “thermal oxygen consumption” (ThOC), which is in many ways close to COD, but it does not require chemical agents. ThOC is determined by the oxythermographic method based on a programmed high temperature oxidation of organic substances by an oxygen-containing gas [33]. The amount of oxygen used for oxidation is measured by a solid electrolytic cell operating in the coulometric mode. The calibration of tools is done by the solutions of particular organic compounds. T -parameter is approximately 1, it ensures the independence of results from the qualitative composition of a sample. When ThOC value of waste water is determined, the water volume ranges from 1 to 10 mcl, the analysis time is 3–5 min, the relative standard deviation does not exceed 0.15. The limit of organic substances detection recalculated to O_2 makes up 5 mg/dm³. The influence of dissolved oxygen is eliminated; the oxygen discharge rate in the oxidation of inorganic substances is ignored. This factor can lead to positive errors when determining the amount of organic substances. The method is applied in the analysis of natural and waste waters [34], the determination of petroleum products in the form of thin layer on the water surface [35], the determination of humus in soil, and even for the objective assessment of oily skin.

To evaluate the content of organic substances in slightly polluted waters, TOC index (total organic carbon) is conventionally used, it is expressed in mg C/dm³. TOC determination is based on high-temperature oxidation of a sample followed by IR spectrometry or conductometric detection of produced CO_2 . In recent years, the method was significantly improved (see review [36]), which allowed to establish mass production of a variety of TOC analyzers. Tests showed that due to these analyzers almost all organic compounds are completely converted into CO_2 . Incomplete conversion is characteristic only for some of the compounds which are absent in natural and waste waters (caffeine), or present as minor components (m-cresol) [37].

Widespread automated TOC analyzers reduced the interest in such total indices as COD and BOD. Nevertheless, there have been articles that offer new methods of these indices measuring. The new methods of COD determination are based on the application of instrumental methods and are entirely automated. Interesting techniques were developed by Chinese researchers. A convenient photocatalytic method of COD determination with the use of nano-TiO₂-K₂Cr₂O₇ system was suggested. The technique involves the direct measurement of Cr^{3+} concentration [38]. The

technique that uses another photocatalytic system (nano-TiO₂-Ce(SO₄)₂) has a lower limit of determination of organic substances (~0.4 mg O₂/dm³) [39]. A simple and fast method of COD estimation in water has been patented. Namely, a sample (1 ml) is treated sequentially with mercury sulfate, potassium dichromate and silver sulfite in sulfuric acid and then the measurements of the optical density at wavelengths 586 and 635 nm are taken using a photometer. For calibration glucose solutions in water are used [40]. Sensitivity coefficients for different organic substances were not shown in this patent.

A much more complicated problem is the objective estimation of total content of AOs in foodstuff and biological samples. Many authors estimated it in vitro with variety of TIs (DPPH, ABTS, FRAP, ORAC, etc.) as a rule these indices are expressed in units of X_{st} concentration (see review [41]). The first type indices (so-called HT-indices) are focused on the estimation of the total content of substances that inhibit free radical processes. TIs of the second type (ET-indices) are to assess the total content of deoxidizing agents. Their numerical values can vary greatly for the same object and even be expressed in different units, but for a set of similar objects the values of similar TIs usually are correlated (see Section 2.5). ET-indices FRAP and ORAC, characterizing the antioxidant activity of different varieties of carrots in terms of Trolox concentration can serve an example [42]. There is no such correlation between ET and HT indices [43]. For many food products (wine, tea, juices, fruits) the proportionality of ET-indices of integral antioxidant activity (C^*) and total polyphenol content (C_{Σ}) has been revealed [44]. This feature of investigated objects allows to calculate C_{Σ} values using Eq. (7) or simple proportion, if we shall have adequate SRMs or reliable referent methods.

A number of new publications are devoted to the methods of measuring FRAP-index (ferric reducing antioxidant power) and interpretation of the results (Table 6, taken from [26]). In the papers by Tsytko the causes of differences of this index from the total content of polyphenol AOs are revealed. Apart from different sensitivity of individual polyphenol detecting, the other cause is non-additivity of the signal, which can be eliminated by changing the analysis conditions. It is important when they have to optimize corresponding analytical procedures. Comparing different foods as the sources of AO, Norwegian researchers analyzed over 3000 samples by FRAP assay [45].

Apak, Berker and their co-authors have proposed and applied new spectrometric method to measure antioxidant activity index based on the interaction of AOs (reducing agents) with Cu^{2+} ions in the presence of neocuproine (CUPRAC assay) [53]. While developing corresponding techniques, the authors did not seek the accurate estimation of the total content of antioxidants. The emphasis was put on the correspondence of the analysis conditions in vitro and the conditions in which the same antioxidants act in vivo (the choice of pH and so on). The correspondence of a set of substances determined together with the help of a new index in vitro and the list of substances that exhibit antioxidant activity in vivo is also very important (see Section 2.1). Reducing agents which are not AOs in vivo conditions (citric acid, carbohydrates) do not affect this TI value. The generalized analytic signal in the CUPRAC method is

Table 6
Application FRAP assay to evaluate the antioxidant activity of various objects.

Authors and reference	Year	Reagent	X _{st}	Objects to analyze	Notes
Benzie and Strain [46]	1996	TPTZ	Fe(II)	Blood plasma	Stoichiometry of the reaction and additivity are studied
Benzie and Szeto [47]	1999	TPTZ	Fe(II)	Tea	Different kinds of tea are compared with their integral antioxidant activity
Pulido et al. [25]	2000	TPTZ	Fe(II)	Model solutions	t=30 min. The influence of non-aqueous solvent is revealed
Kleszczewsky and Kleszczewska [48]	2002	DIP	AA	Blood, tissues	Method FIA. The effect of foreign substances is revealed
Firuzi et al. [49]	2004	TPTZ	Fe(II)	Model solutions	The sensitivity of detection of different analytes is studied
Katalinić et al. [50]	2004	TPTZ	CT	Variety of wines	Different methods for detection of the AOA of wines are compared
Berker et al. [51]	2007	DIP, TPTZ, Fe(CN) ₆ ³⁻ , etc	Fe(II)	Model solutions	6 Variants of the method are compared. In Fe(CN) ₆ ³⁻ case non-additivity of the signal is detected
Tsytko et al. [44]	2008	DIP, PHEN	AA	Dry wines	FRAP and other TIs are compared
Berker et al. [52]	2010	FZ	Fe(II)	Model mixtures	The limits of detection for different AOs are studied
Vershinin et al. [1]	2010	DIP, PHEN	AA	Model mixtures	Signal non-additivity with the lack of oxidant is revealed
Tsytko et al. [26]	2011	DIP, PHEN	AA	Model mixtures	t=10 min. Accuracy of estimations is raised

Notes: FIA—flow injection analysis, TPTZ—tripiridiltriazine, DIP—2,2'-dipyridil, PHEN—o-phenantroline, FZ—ferrozine, AA—ascorbic acid, CT—catechol, and t—exposure time, min.

recalculated to Trolox concentration. The advantages of the new TI in comparison with other TIs are discussed in [54].

New ET-index proposed by Ukrainian researchers can be a good alternative to FRAP and CUPRAC [55]. Generalized signal of reducing agents is generated upon its interaction with the copper(II) complex. The organic reagent tetrabenzotetranitrogenocyclohexadecine immobilized on silica gel is used. The signal is measured by solid-phase spectrometry, and recalculated to the concentration of quercetin. The method is used in the analysis of medical plants.

As a result of systematic study of electroreduction process of dissolved oxygen in the presence of different types of AOs [56], Korotkova et al. proposed a new TI which allows estimating the total AO content by a voltammetric method in terms of ascorbic acid [57]. In the range 0.1–1.0 mg/ml C_Σ relative error does not exceed 23%. The method is used for the analysis of food additives, pharmaceuticals, cosmetics, and also in clinical analysis. A simple and express potentiometric method to measure the total antioxidant activity is proposed by Brainina et al. [58]. It is based on the change of potential of Pt-electrode in the presence of mediator system Fe(III)/Fe(II) after the addition of a sample containing ET-antioxidant mixture. The analysis result is expressed in millimole eq./dm³, without recalculating the signal to a preselected standard substance. The techniques are metrologically verified and applied to study the composition of foodstuff and pharmaceuticals. C* and C_Σ values are not compared. A reliable linear correlation between the new index and other total indices of the same type is revealed.

Ending the review, some works related to the TPH determination should be mentioned. Special review [5] and [59] were devoted to this problem. The most interesting aspect is the application of multiwavelength spectrometry to measure generalized analytic signal of different hydrocarbons (HC). Thus, it is possible to measure the optical density of a sample at three different wavelengths in the infrared region of the spectrum and then calculate the average signal using a predetermined empirical formula. This method underlies some official standards for analysis of natural and waste waters [60,61]. The most elaborated suggestion is the work by Shagidullin in which to estimate the total HC content in water the author measured the area under the spectral curve as a generalized signal [62]. In all cases, the signal is recalculated to the certain X_{st}. Transition to multiple-wavelength spectrometry leads to leveling the sensitivity coefficients of individual hydrocarbons [19]. Therefore new methods provide more correct estimates of hydrocarbon total content than traditional ones.

3. Conclusions

The analysis of new publications on the total indices problem leads to some conclusions.

1. Total indices, resulting from the recalculation of the analytical signal to the standard substance concentration, allow estimating the sum content of similar analytes. Corresponding procedures are fast, easy and, in some cases, quite precise. These indices take a prominent place among the various indices of chemical composition of natural and technological objects. Their application should not be considered a consequence of the lack of suitable chromatographic methods of analysis of the real objects.
2. Applying the “recalculated” total indices, one should remember their peculiar metrological character. The data included in this review confirm theoretical theses proposed early by Valcarse and coauthors [2]. Namely, unlike the conventional indices of group composition, total indices predictably depend on the choice of the standard substance, and also on the method and conditions of signal measuring; TIs are subjective, “method-dependent” characteristics. Therefore the standards of chemical composition (MAC, etc.) in terms of TI values should not be introduced.
3. In recent years, the mathematic theory of total indices has been gradually developed, mainly by Russian analysts. Now it allows to predict the uncertainty in estimates of the total content and to optimize the techniques of TI determining. For this purpose, optimal standard substances are chosen, the sensitivity of detection of similar analytes is leveled, the factors causing deviations from the additivity of the signal are eliminated, etc.
4. In recent 15 years a number of new TIs were suggested, predominantly to estimate the total content of organic substances in waters and the total content of antioxidants in food products. A variety of new methods of measurement the known TIs have been developed too. However, majority of corresponding analytical procedures were proposed and developed still empirically. Undoubtedly, the TI system will continue to evolve and improve, especially with regard to the analysis of environment.

Acknowledgments

This investigation was supported by the Ministry of Education and Science of the Russian Federation (official assignment to the Omsk State University, 2014, Project 2436). The author thanks

Prof. V.P. Antonovich (Ukraine), Prof. Yu.M. Dedkov (Russia) and reviewers from "Talanta" for their valuable remarks and suggestions.

References

- [1] I.V. Vlasova, V.I. Vershinin, T.G. Tsytko, *J. Anal. Chem.* 66 (2011) 22.
- [2] J.R. Baena, M. Valcarcel, *Trends Anal. Chem.* 22 (2003) 641.
- [3] Ju.A. Zolotov, *J. Anal. Chem.* 59 (2004) 599.
- [4] W. Merz, *J. Anal. Chem.* 49 (1994) 557.
- [5] V.I. Vershinin, T.V. Antonova, M.A. Fedorova, *Ind. Lab. Diagn. Mater.* 79 (10) (2013) 3 (in Russian).
- [6] ASTM D1783-01, Standard test methods for phenolic compounds in water, Annual book of ASTM Standards, 2012.
- [7] ASTM D5134-98, Standard test method for detailed analysis of petroleum naphthas through n-nonane by capillary gas chromatography, Annual book of ASTM Standards, 1998.
- [8] V.J. Barwick, *J. Chromatography A* 849 (1999) 13.
- [9] V.I. Vershinin, *J. Accred. Qual. Assur.* 9 (2004) 415.
- [10] n-Hexane extractable material and silica gel treated n-hexane extractable material by extraction and gravimetry, EPA method 1664. Revision A. EPA-821-R-98-002, 1999, 28 p.
- [11] G. Knothe, J.A. Kenar, *Eur. J. Lipid Sci. Technol.* 106 (2004) 88.
- [12] C. Quansheng, Z. Jiewen, L. Muhua, *J. Pharm. Biomed. Anal.* 46 (2008) 568.
- [13] D. Cozzolino, M.J. Kwiatkowski, M. Parker, *Anal. Chim. Acta* 513 (2004) 73.
- [14] V.I. Vershinin, E.V. Kopteva, V.V. Troitsky, *Ind. Lab. Diagn. Mater.* 71 (11) (2005) 10 (in Russian).
- [15] ASTM D7678-11, Standard test method for total petroleum hydrocarbons in water and wastewater with solvent extraction using mid-IR laser spectroscopy.
- [16] V.I. Vershinin, N.S. Brilenok, T.G. Tsytko, *J. Anal. Chem.* 67 (2012) 649.
- [17] ASTM D1783-01, Standard test methods for phenolic compounds in water, 2007.
- [18] International vocabulary of metrology. Basic and general concepts and associated terms (VIM), 3rd ed. JCGM 200, 2008, p. 6.
- [19] M.A. Fedorova, S.V. Usova, *Anal. Control* 18 (2014) 91 (in Russian).
- [20] R.G. Simard, J. Hasegawa, W. Bandaruk, *Anal. Chem.* 23 (1951) 1384.
- [21] A.M. Worontsov, A.P. Patsovskii, M.N. Nikanorova, G.B. Krivtsova, *Russ. J. Appl. Chem.* 87 (2014) 444.
- [22] N. Nenadis, O. Lazaridou, M.Z. Tsimidou, *J. Agric. Food Chem.* 55 (2007) 5452.
- [23] V.I. Vershinin, M.P. Kuleshova, N.A. Isachenko, P.V. Shiligin, *J. Anal. Chem.* 68 (2013) 477.
- [24] R. Soniassy, P. Sandra, C. Schlett, *Water Anal.: Org. Micropollut. Hewlett-Packard* (1994) 1, 248.
- [25] R. Pulido, L. Bravo, F. Saura-Calixto, *J. Agric. Food Chem.* 48 (2000) 3396.
- [26] T.G. Tsytko, I.V. Petrakova, N.S. Brilenok, *Anal. Control* 15 (2011) 287 (in Russian).
- [27] P.A. Kalashnikov, I.Yu. Shkvoret, Yu.A. Egorov, *Phys. Oceanogr.* 9 (1) (1998) 71.
- [28] V.I. Vershinin, N.A. Isachenko, *Vestn. Omsk. Univ. [Omsk Univ. Her.]* 4 (2012) 96 (in Russian).
- [29] M.C. Santana, Z.S. Ferrera, M.E.T. Padron, J.J.S. Rodrigues, *Molecules* 14 (2009) 298.
- [30] T.V. Antonova, V.I. Vershinin, V.A. Ivanova, P.V. Shiligin, *Anal. Control* 16 (2012) 343 (in Russian).
- [31] I.E. Stas, E.A. Leites, B.P. Shipunov, M.I. Lykova, *Khimija rastitelnogo sir'ja [Chem. Plant Mater.]* 1 (1997) 35 (in Russian).
- [32] D.A.M. Zaia, F.R. Marques, C.T. Zaia, *Braz. Arch. Biol. Technol.* 48 (2005) 3.
- [33] B.K. Zuev, O.K. Timonina, V.D. Podrugina, *J. Anal. Chem.* 50 (1995) 603.
- [34] B.K. Zuev, A.A. Korotkov, V.G. Filonenko, A.N. Mashkovtsev, V.P. Zvolinskii, *J. Anal. Chem.* 59 (2004) 163.
- [35] B.K. Zuev, V.V. Kovalenko, E.V. Kul'bachevskaya, A.Y. Olenin, V.V. Yagov, *J. Anal. Chem.* 56 (2001) 481.
- [36] G. Spyres, M. Nimmo, P.J. Worsfold, *Trends Anal. Chem.* 19 (2000) 498.
- [37] D.A. Recklov, *Analysis of Total Organic Carbon*, University of Massachusetts, Amherst (2012) 32.
- [38] A. Shiyun, L. Jiaqing, Y. Yaea, *Anal. chim. acta.* 509 (2004) 237.
- [39] C. Yihao, D. Hongchun, *Zh. Zhonghai, Talanta* 68 (2006) 610.
- [40] V. Kalia, V. Sonakya, N. Raizada, A.P. Joahi, *Rapid Method For Estimation Of Chemical Oxygen Demand*. US Patent 6967104. Publ. 22.11.2005.
- [41] A. Karadag, B. Oselic, S. Saner, *Food Anal. Methods* 2 (2009) 41.
- [42] B. Ou, D. Huang, M. Hampsch-Woodell, J.A. Flanagan, E.K. Deemer, *J. Agric. Food Chem.* 50 (2002) 3122.
- [43] M.S. Fernandez-Pashon, D. Villano, M.S. Garcia-Parilla, *Anal. Chim. Acta* 513 (2004) 113.
- [44] T.G. Tsytko, Z.A. Temerdashev, O.B. Voronova, *Ind. Lab. Diagn. Mater.* 74 (6) (2008) 14 ([in Russian]).
- [45] M.H. Carlsen, B.L. Halvorsen, K. Holte, S.K. Bohn, *Nutr. J.* 9 (2010) 3.
- [46] I.F.F. Benzie, J.J. Strain, *Anal. Biochem.* 239 (1996) 70.
- [47] I.F.F. Benzie, Y.T. Szeto, *J. Agric. Food Chem.* 47 (1999) 633.
- [48] T. Kleszczewsky, E. Kleszczewska, *J. Pharm. Biomed. Anal.* 29 (2002) 755.
- [49] O. Firuzi, A. Lacanna, R. Petrucci, G. Marrosu, L. Saso, *Biochim. Biophys. Acta Gen. Subj.* 1721 (2005) 174.
- [50] V. Katalinić, M. Milos, D. Modun, I. Musić, M. Boban, *Food Chem.* 86 (2004) 593.
- [51] K.I. Berker, K. Guçlu, I. Tor, R. Apak, *Talanta* 72 (2007) 1157.
- [52] K.I. Berker, K. Guçlu, B. Demirata, R. Apak, *Food Anal. Methods* 2 (2010) 1770.
- [53] R. Apak, K. Guçlu, M. Ozyurek, S.E. Karademir, *J. Agric. Food Chem.* 52 (2004) 7970.
- [54] R. Apak, K. Güçlü, B. Demirata, *Molecules* 12 (2007) 1496.
- [55] O.A. Zaporozhets, O.A. Kryshinska, N.A. Lipkovska, V.N. Barvinchenko, *J. Agric. Food Chem.* 52 (1) (2004) 21.
- [56] E.I. Korotkova, Ju.A. Karbainov, *Voltammetric method to estimate antioxidant activity*, Russian Patent 2224997, Publ. 6.06.2002.
- [57] E.I. Korotkova, Yu.A. Karbainov, O.A. Avramchik, *Anal. Bioanal. Chem.* 375 (2003) 465.
- [58] Kh.Z. Brainina, A.V. Ivanova, E.N. Sharafutdinovaea, *Talanta* 71 (2007) 13.
- [59] Analysis of petroleum hydrocarbons in environmental media. (Ed.) W. Weisman, in: *Total Petroleum Hydrocarbon Criteria Working Group Series*, Amherst Scientific Publishers, Vol. 1, 1998.
- [60] DIN 38409-H18, Bestimmung von Kohlenwasserstoffen, Ausgabe 02-1981.
- [61] Nederlandse norm NEN 6675, Determination of mineral oil content by infrared spectrometry, October 1989.
- [62] R.R. Shagidullin, L.V. Avvakumova, G.M. Doroshkina, *J. Anal. Chem.* 57 (2002) 203.



Elucidation of molybdosilicate complexes in the molybdate yellow method by ESI-MS



Mariko Takahashi^a, Yoshihiro Abe^b, Miho Tanaka^{a,*}

^a Division of Marine Science, Graduate School of Marine Science and Technology, Tokyo University of Marine Science and Technology, Konan, Minato-ku, Tokyo 108-8477, Japan

^b Faculty of Pharmacy, Keio University, Shibakoen, Minato-ku, Tokyo 105-8512, Japan

ARTICLE INFO

Article history:

Received 21 April 2014

Received in revised form

25 July 2014

Accepted 26 July 2014

Available online 12 August 2014

Keywords:

Molybdosilicate

Molybdate yellow

Electrospray Ionization Mass Spectrometry

(ESI-MS)

Silicic acid

pH dependence

ABSTRACT

The formation of molybdosilicate in the molybdate yellow method is elucidated by ESI-MS. Polymeric silicic acids were hydrolyzed to monomers, and molybdosilicates with a Keggin structure were formed. Each step of the formation reaction of molybdosilicate from molybdic and silicic acids between pH 1 and 2 was clarified by ESI-MS at the molecular level. In a solution below pH 0.5, the polymers of the molybdic acids were decomposed because of the high concentration of sulfuric acid. Excess sulfuric acid prevented the formation of molybdosilicate. Thus, none of the silicic acids reacted to form molybdosilicate at this pH, despite the presence of silicic acid and sulfate ions in the solution. Above pH 2, the condensation of molybdic acids occurred to form α -molybdosilicate. ESI-MS provides information on the formation of molybdosilicate and the individual reaction species present in the reaction mixture.

© 2014 Elsevier B.V. All rights reserved.

1. Introduction

The concentration of silicic acid is one of the most important indicators of nutrients in seawater as well as other water. The molybdate yellow method is the standard recommended method for determining the concentration of silicic acid in natural waters between pH 7 and 10 *on site*. The method led to an extensive study of characterizing polyoxomolybdates. Strickland reported α - and β -molybdosilicates [1] and the pH dependence for the formation of molybdosilicate [2]. Similar studies by Truesdale and Smith [3,4] were applied to natural freshwater. With the advent of modern instruments, complexes of $[\text{SiMo}_{12}\text{O}_{40}]^{4-}$ have been studied by UV [1–4], Raman spectrometry [5–8], EXAFS [9,10], NMR [9,11–13], ESR and NMR [14], tandem ES-MS [15,16], ES-MS [17], vibrational spectrometry [18,19], and voltammetric studies [20,21]. However, the investigation and clarification of the intermediate complexes in solutions are challenging tasks, and studies on the formation of intermediate complexes at the molecular level are lacking. Raman Spectroscopy identified polynuclear molybdates in an aqueous solution, and $\text{Mo}_6\text{O}_{19}^{2-}$, $\text{Mo}_{12}\text{O}_{37}^{2-}$, $\text{Mo}_7\text{O}_{24}^{6-}$, and $\text{Mo}_8\text{O}_{24}^{6-}$ were found in an aqueous solution [7]. ESI-MS has also been used as a tool for the identification of polyoxoanions and isopolyoxomolybdates [15,17].

Dietzel reported the reaction rate of molybdosilicate and silica species, such as the monomers, dimers, trimers, and hexamers. [22].

In our previous studies [23,24] with fast atomic bombardment mass spectrometry (FAB-MS), it was not possible to determine all of the silicic acid species, such as the monomers, dimers and polymers. During the formation of molybdosilicates, the interaction process between molybdic acid and silicic acid has not been well elucidated.

In this paper, we perform a detailed study of the complex intermediates formed during the reaction. In electrospray ionization mass spectrometry (ESI-MS), the rapid measurement time enables the measurement of reaction changes, simultaneously ionizing most of the elements in the electrospray, thereby elucidating large ion clusters. ESI-MS has been used to examine the oxidation states of metal ions in various solutions [5,6,9,11,12,14,15,17]. The spray chamber in ESI-MS easily measures the ionic species of silicic and molybdic acids at very low concentrations that are present in natural waters. The ESI-MS spectrum of molybdic acid has been previously reported [25,26], but we report here an extensive study of various parameters related to the formation of molybdosilicates.

The poor solubility of silicic acid in pure water is a drawback for the purpose of these studies; to overcome this, we developed a new method of dissolving silicic acid in pure water, enabling the formation of molybdosilicate, for measurement by ESI-MS. In this study, we analyzed the intermediates formed in the reaction mixtures of silicic and molybdic acids during the formation of

* Corresponding author. Tel./fax: +81 3 5463 0457.

E-mail address: mihotnk@kaiyodai.ac.jp (M. Tanaka).

molybdosilicate, the role of sulfuric acid in the decomposition of silicic acid oligomers, and the condensation of molybdic acid. Finally, when phosphoric acid coexists in the silicic acid solution, oxalic acid is added to prevent the color formed by molybdophosphate [7]. We will discuss the complexes that are formed when oxalic acid is added to the reaction mixture.

2. Experimental

2.1. Preparation

Analytical-grade hexaammonium heptamolybdate tetrahydrate $[(\text{NH}_4)_6(\text{Mo}_7\text{O}_{24})]$ powder (ammonium molybdate) (Kanto Chemical Co. Ltd.), molybdosilicate $[\text{H}_4\text{Mo}_{12}\text{SiO}_{40}]$ (Wako Pure Chemical Industries Ltd), and molybdophosphate $[\text{H}_3\text{PMo}_{12}\text{SiO}_{40} \cdot n\text{H}_2\text{O}]$ (Kanto Chemical Co. Ltd.) were purchased. The other reagents were of analytical grade or ultrapure grade. All of the water used was of the ultrapure grade (18.2 M Ω).

Silica gel (Grade hydroxyl gel A type 5–10 mesh) was obtained from Fuji Silysia Chemical Ltd, Japan. This silica gel is used as a nutrient for the cultivation of rice. Forty grams of silica gel was added to 400 mL of ultrapure water, the mixture was stirred at 100 rpm at 25 °C for a week, and the supernatant liquid was used in all of the experiments.

The concentration of silicic acid as determined by Molybdate Yellow Method was 2 mM. This silicic acid solution is referred to as “silicic solution” hereafter.

2.2. Molybdate yellow method

We replaced hydrochloric acid with sulfuric acid in all of our studies.

Five grams of ammonium molybdate was dissolved in 50 mL of pure water (ammonium molybdate solution). To a 50 mL sample solution, 2 mL of 0.18 M sulfuric acid and 2 mL of ammonium molybdate solution was added. After 10 min, the absorption was measured at 385 nm. The total pH of the solution was varied with the appropriate amount of sulfuric acid: the concentration of sulfuric acid was 6.7 mM (pH 2.415), 67 mM (pH 1.142), 134 mM (pH 0.832) and 335 mM (pH 0.440). Hereafter, 67 mM H_2SO_4 is maintained as the standard procedure.

To study the effect of oxalic acid during the reaction, the following experiment was performed.

To a solution containing 0.2 mM silicic acid and 0.2 mM phosphoric acid, the molybdate yellow method was carried out. The molybdosilicate or molybdophosphate complexes were formed after 5 min. To these solutions, 0.3 mL of 10% oxalic acid was added, and after 1 min, the mass spectrum was obtained by ESI-MS.

2.3. Measurement

Impurities in silicic acid were detected by ICP-MS (Thermo Fisher Sci. Element XR).

A UV–vis spectrometer, UV-2450 (Shimadzu Co.) was used to monitor the absorbance in the molybdenum yellow method.

An ESI-MS LCMS-2010 A (Shimadzu Co.) was employed in all of the studies with no column. The conditions were optimized by tuning with PEG (polyethylene glycol) and raffinose. Ultrapure water was used as the mobile phase. Five microliters of sample solution was directly injected via a HAMILTON MICROLITERTM #710 syringe into the ESI probe through a RHEODYNE 8125 manual sample injector during flow injection analysis. A mass range of 10 to 2000 was maintained with a negative polarity and a –3.5 kV interface voltage [26–28]. As several isotopes of molybdenum, such

as ^{92}Mo (0.148), ^{94}Mo (0.093), ^{95}Mo (0.159), ^{96}Mo (0.167), ^{97}Mo (0.096), ^{98}Mo (0.241) and ^{100}Mo (0.096), are present in nature, several peaks were observed in the mass spectra. In this study, the peak identification was presented by ^{98}Mo , as its abundance is the highest.

Each of the following processes were monitored by obtaining the ESI-MS spectra of the solution at every stage.

- (1) The addition of sulfuric acid in ammonium molybdate solution when molybdates were formed. The concentration of sulfuric acid was varied and added to a solution containing 0.2 mM silicic acid, and the resultant colored solution of molybdic acid exhibited an absorption at 385 nm.
- (2) The role of sulfuric acid in the decomposition of silicic acid.
- (3) The reaction of molybdosilicate with sulfuric acid in the formation of molybdates.
- (4) The complexes formed at low pH in the molybdate yellow method.
- (5) The role of oxalic acid in silicic and phosphoric acids.

3. Results and discussion

3.1. Role of sulfuric acid in the reaction of molybdate yellow

The concentration of the prepared silicic acid was found to be 2.04 mM by the molybdate yellow method. This silicic acid contained Na 480 ppb, Sr 10.3 ppb, Ba 5.5 ppb, Mg 440 ppb, Ca 480 ppb, K 0.80 ppm as impurities, which were measured by ICP-MS.

Sulfuric or hydrochloric acid may be used in the molybdate yellow method; in particular, sulfuric acid is examined in this paper. The use of sulfuric acid was preferred to detect the peaks of intermediates derived during the formation and decomposition of silicic acids by ESI-MS. In the absence of metal ions, the concentration of silicic acid was sufficiently high to be observed in ESI-MS measurements.

We first examined the pH dependence of the reaction with the sample solution. The obtained absorption intensity plotted for different concentrations of sulfuric acid is shown in Fig. 1. The optimal concentration of sulfuric acid was 67 mM, and 10 min was required for the formation of β -molybdosilicate [3,4]. When the concentration of sulfuric acid was 6.7 mM, the absorption intensity decreased monotonically, indicating the formation of α -molybdosilicic acid [3]. At concentrations higher than 67 mM sulfuric acid, the time required for the formation of molybdosilicate was more than 120 min. Under these conditions, each step of the formation of α - and β -molybdosilicic acids were observed by ESI-MS.

3.2. Measurement of ammonium molybdate

A 3.1 mM ammonium molybdate solution at pH 4.9 and an aliquot of the same solution in which the pH was adjusted to 1.1 with sulfuric acid, with a sulfuric acid concentration of 67 mM, were examined by ESI-MS. The obtained spectra are shown in Fig. 2 (a) and (b). Here, the highest peak is assigned to the molybdic complexes, which are listed in Table 1. In Fig. 2 (a), the peak with the highest intensity was assigned to $[\text{HMoO}_4]^-$ (m/z 163) in the ammonium molybdate solution. Peaks of $[\text{Mo}_n\text{O}_{(3n+1)}]^{2-}$ ($n=2-4, 6, 7$), $[\text{HMo}_n\text{O}_{(3n+1)}]^-$ ($n=2-4, 6$), and other polymers of molybdic acid were also identified. When ammonium molybdate $[(\text{NH}_4)_6(\text{Mo}_7\text{O}_{24})]$ is dissolved in pure water, $[\text{Mo}_7\text{O}_{24}]^{6-}$ is considered to be the main negative ion. However, this was not detected in the experimental solution, whereas $[\text{HMoO}_4]^-$ and $[\text{Mo}_4\text{O}_{13}]^{2-}$ and/or $[\text{Mo}_8\text{O}_{26}]^{4-}$ were observed at relatively high concentrations.

When sulfuric acid was added to the solution, as shown in Fig. 2 (b), the peaks of monomers, such as $[\text{HMoO}_4]^-$ (m/z 163), decreased, and the peaks of sulfuric acid adducts were observed. However, the peaks of $[\text{Mo}_4\text{O}_{13}]^{2-}$ and/or $[\text{Mo}_8\text{O}_{26}]^{4-}$ were observed at similar m/z , and the peaks of polymers increased. Therefore, it can be concluded that molybdic acid underwent a condensation reaction to form polymers at low pH [25]. This led us

to further investigate the formation of molybdosilicate species in the molybdate yellow method.

3.3. Silicic acid solutions in low pH

A solution containing 1 mM silicic acid and a solution containing a mixture of 1 mM silicic acid and 67 mM sulfuric acid were

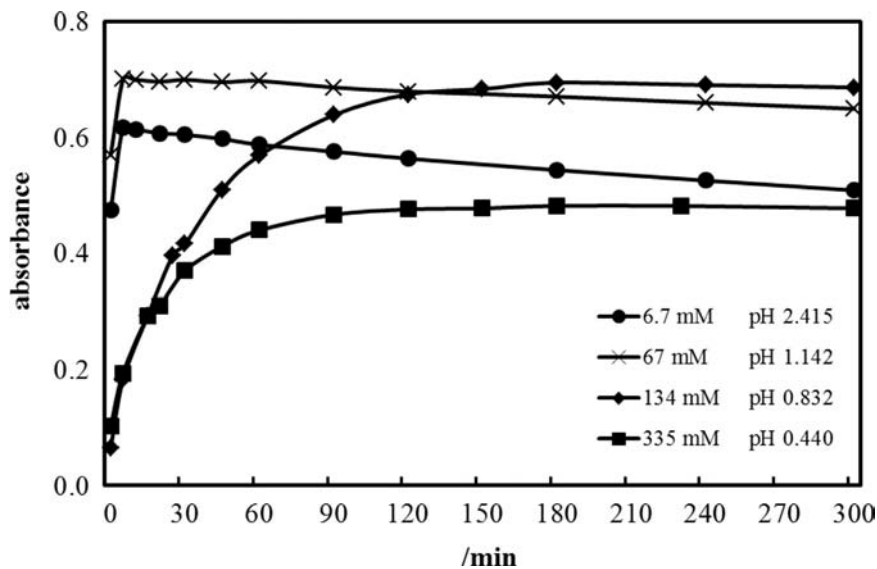


Fig. 1. Change in absorption with elapsed time for different concentrations of sulfuric acid.

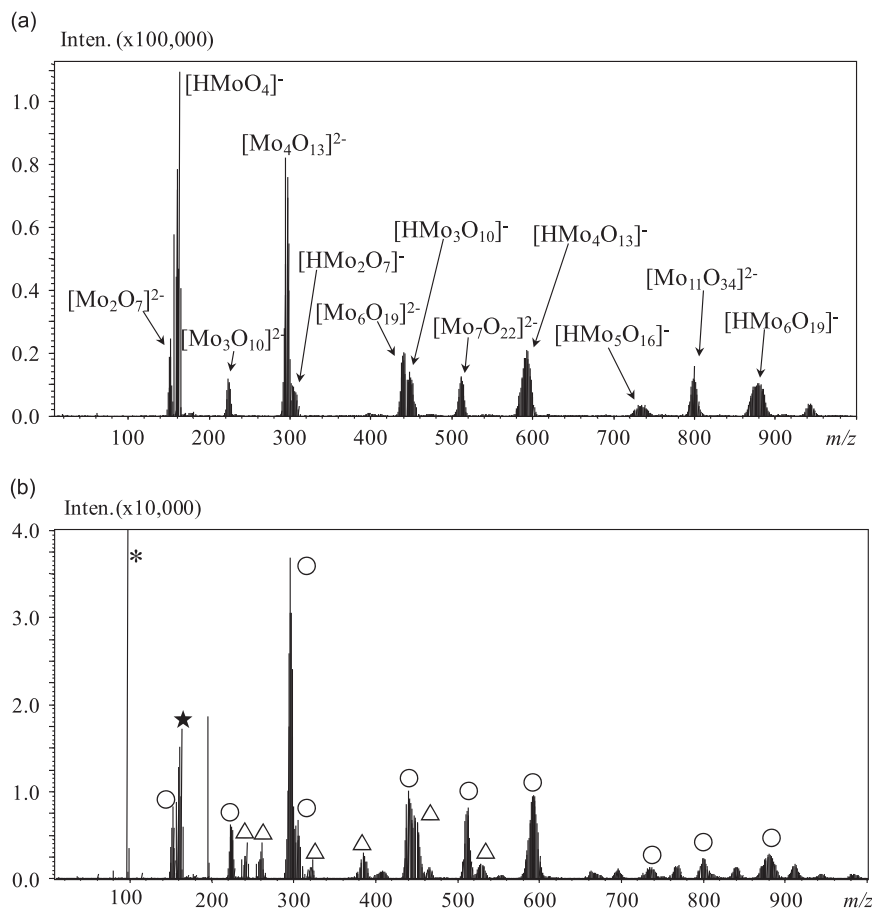


Fig. 2. ESI-MS spectra of a) 3.1 mM ammonium molybdate solution (pH 4.9) and b) 3.1 mM ammonium molybdate solution with 67 mM sulfuric acid. \star ; $[\text{HMoO}_4]^-$, \circ ; $[\text{Mo}_m\text{O}_{3m+1}]^{2-}$ or $[\text{HMo}_m\text{O}_{3m+1}]^-$ ($m \geq 2$), Δ ; molybdic acid + H_2SO_4 adducts, \ast ; $[\text{HSO}_4]^-$ and $[\text{HSO}_4 + \text{H}_2\text{SO}_4]^-$.

measured by ESI-MS, and the results are shown in Fig. 3(a) and (b), respectively, as well as in Table 2. Monomers and polymers of silicic acids were observed in these silicic solutions.

Analysis of the solution containing 1 mM silicic acid and 67 mM sulfuric acid (pH 1.1), shown in Fig. 3 (b), yielded a peak at m/z 255 assigned to $[\text{SiO}(\text{HSO}_4)_2\text{OH}]^-$ or $[\text{SiO}_2(\text{H}_2\text{SO}_4)(\text{HSO}_4)]^-$ (silicic acid with sulfate ion) and additional peaks assigned to $[\text{HSO}_4]^-$ and $[\text{H}_2\text{SO}_4(\text{HSO}_4)]^-$. The complex $[\text{SiO}(\text{HSO}_4)_2\text{OH}]^-$ or $[\text{SiO}_2(\text{H}_2\text{SO}_4)(\text{HSO}_4)]^-$ is not thought to form in a solution at pH 4.9; we therefore presume that it would be formed in the gas phase of the ESI-MS. However, we cannot deny that the 67 mM sulfuric acid solution (pH 1.1) contained such a high concentration

Table 1
Identified molybdc species.

	Ion identified	m/z
monomer	$[\text{HMoO}_4]^-$	163
dimers	$[\text{Mo}_2\text{O}_7]^{2-}$	152
	$[\text{HMo}_2\text{O}_7]^-$	305
trimers	$[\text{Mo}_3\text{O}_{10}]^{2-}$	224
	$[\text{HMo}_3\text{O}_{10}]^-$	449
tetramers	$[\text{Mo}_4\text{O}_{13}]^{2-}$	296
	$[\text{HMo}_4\text{O}_{13}]^-$	593
pentamer	$[\text{HMo}_5\text{O}_{16}]^-$	737
hexamers	$[\text{Mo}_6\text{O}_{19}]^{2-}$	440
	$[\text{HMo}_6\text{O}_{19}]^-$	881
heptamer	$[\text{Mo}_7\text{O}_{22}]^{2-}$	512

of sulfuric acid that sulfate ions may combine with silicic acid in solution. It is believed that monomers and polymers of silicic acid, present in a solution at pH 4.9, convert to unique monomers upon the addition of sulfate ions, which are inserted in the center of the molybdosilicate ions.

3.4. Molybdosilicate ions in solution

When a 0.1 mM molybdosilicate reagent was dissolved in ultra-pure water, three peaks were observed, as seen in Fig. 4(a): $[\text{SiMo}_{12}\text{O}_{40}]^{4-}$ (m/z 455), $[\text{HSiMo}_{12}\text{O}_{40}]^{3-}$ (m/z 607) and $[\text{SiMo}_{12}\text{O}_{40}]^{2-}$ (m/z 911). When 20 mM sulfuric acid was added to this reagent, additional peaks of sulfate ions and their derivatives were observed. This indicates that $[\text{SiMo}_{12}\text{O}_{40}]^{4-}$, $[\text{HSiMo}_{12}\text{O}_{40}]^{3-}$

Table 2
Identified silica species.

	Identified ions	m/z
monomer Si	$[\text{Si}(\text{OH})_3\text{O} \cdot 2\text{H}_2\text{O}]^-$	131
	$[\text{Si}_2(\text{OH})_5\text{O}_2]^-$	173
dimers Si_2	$[\text{Si}_2(\text{OH})_5\text{O}_2 \cdot 2\text{H}_2\text{O}]^-$	209
	$[\text{Si}_3(\text{OH})_5\text{O}_4]^-$	233
trimers Si_3	$[\text{Si}_3(\text{OH})_7\text{O}_3 \cdot 2\text{H}_2\text{O}]^-$	287
	$[\text{Si}_4(\text{OH})_5\text{O}_6]^-$	293
tetramers Si_4	$[\text{Si}_4(\text{OH})_7\text{O}_5]^-$	311
	$[\text{Si}_5(\text{OH})_7\text{O}_7]^-$	371
pentamer Si_5		

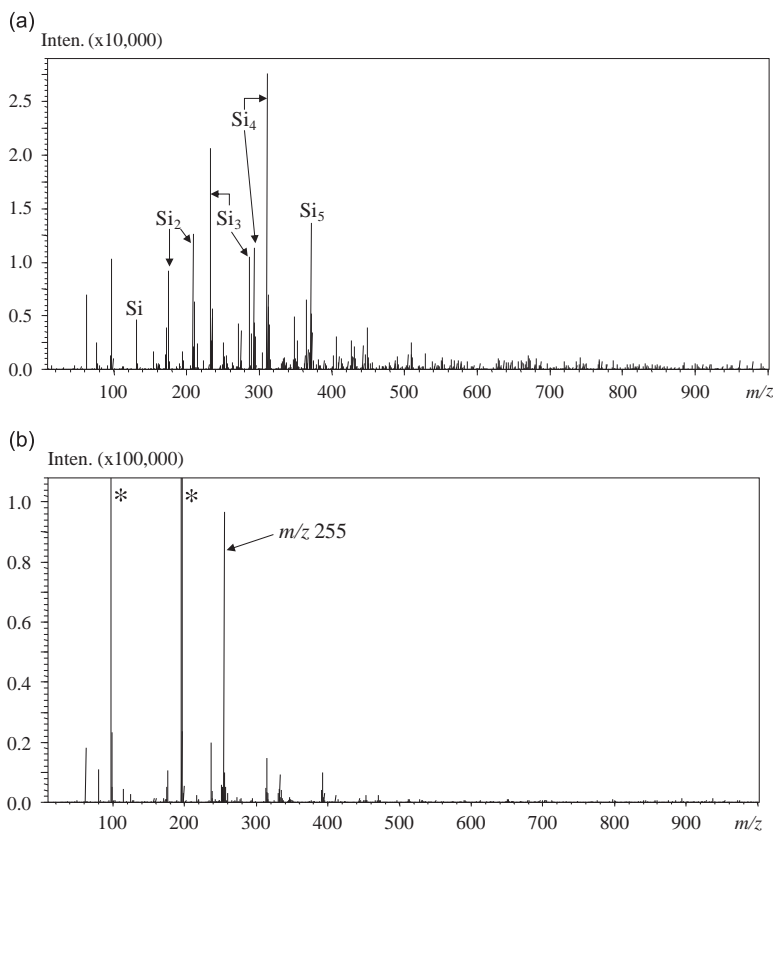


Fig. 3. ESI-MS spectra of (a) solution containing 1 mM silicic acid, (b) solution containing 1 mM silicic acid and 67 mM sulfuric acid. *: $[\text{HSO}_4]^-$ and $[\text{HSO}_4 + \text{H}_2\text{SO}_4]^-$ (c) Structure of silicic acid in Fig. 3 (a) and Table 2.

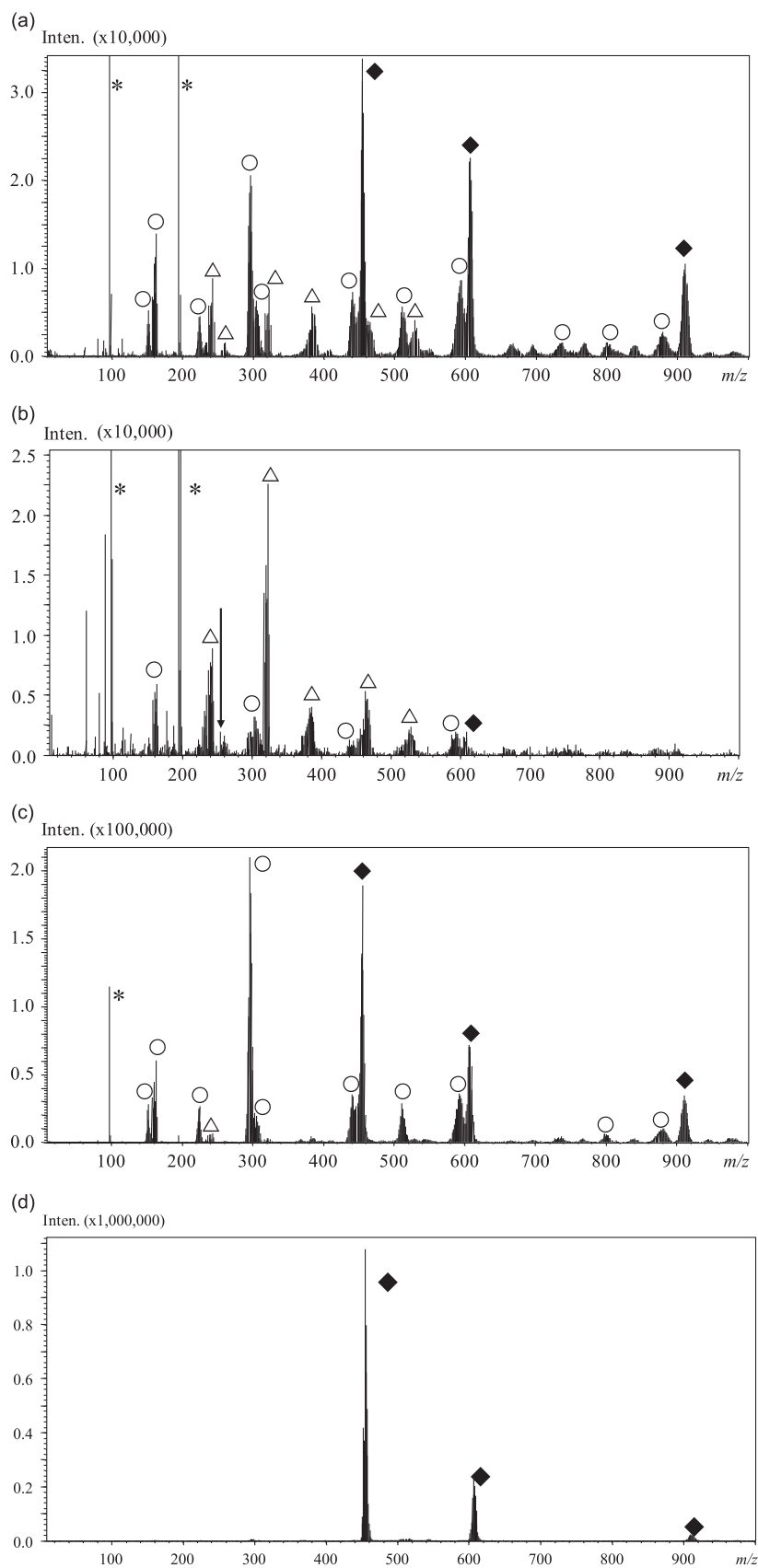


Fig. 4. ESI-MS mass spectra of (a) 0.2 mM molybdosilicate solution (pH 3.5); (b) solution with 0.2 mM silicic acid, 67 mM sulfuric acid, and 3.1 mM ammonium molybdate (pH 1.1) (ordinary condition); (c) solution with 0.2 mM silicic acid, 335 mM sulfuric acid, and 3.1 mM ammonium molybdate (pH 0.3); (d) solution with 0.2 mM silicic acid, 6.7 mM sulfuric acid, and 3.1 mM ammonium molybdate (pH 2.4) \blacklozenge ; molybdosilicate ions ($[\text{SiMo}_{12}\text{O}_{24}]^{4-}$, $[\text{SiMo}_{12}\text{O}_{24}]^{3-}$, $[\text{SiMo}_{12}\text{O}_{24}]^{2-}$) \circ ; $[\text{Mo}_m\text{O}_{3m+1}]^{2-}$ or $[\text{HMo}_m\text{O}_{3m+1}]^-$ ($m \geq 2$), Δ ; molybdic acid + H_2SO_4 adducts, $*$; $[\text{HSO}_4]^-$ and $[\text{HSO}_4 + \text{H}_2\text{SO}_4]^-$. In Figs. (b) and (d), a peak at m/z 255 was not observed. In (c), a peak at m/z 255 (shown by an arrow) was observed.

and $[\text{SiMo}_{12}\text{O}_{40}]^{2-}$ are stable upon the addition of sulfuric acid, despite silicic acid combining with sulfuric acid in ESI-MS. The complex undergoes a change, either protonation or decomposition, in the nebulizer of ESI-MS [27–32]. It is presumed that during the ionization process, the $[\text{SiMo}_{12}\text{O}_{40}]^{4-}$ ion in solution undergoes proton adduction, producing $[\text{HSiMo}_{12}\text{O}_{40}]^{3-}$. Additionally, as the interface voltage was -3.5 kV, reduction of $[\text{SiMo}_{12}\text{O}_{40}]^{4-}$ occurs, forming $[\text{SiMo}_{12}\text{O}_{40}]^{2-}$, just as Fe(III) was reduced to Fe(II) by an ionization process [33]. In the case of molybdosilicate complexes with a high negative charge, an expected series of hydrated complexes as not observed, thereby demonstrating that the number of oxygen atoms in the dissolved structure is considered equal to the number of oxygen atoms in the molybdosilicate. We thus presume that the species observed in the mass spectra were the same as the original and the proton-adducted species in solution [27].

As a result, the molecular formula of the molybdosilicate complexes can be uniquely determined, and they are considered to have distinct molecular structures (forms) in solution. Although a number of oxygen ligands in the identified molybdosilicate complexes are not exactly the same as those in the original structures in solution (for example, the molybdosilicate complexes are entirely dehydrated during the ionization process), the complexes in the gas phase preserve their original chemical states in the sample solution. To summarize, we understand that the negative molybdosilicate complexes, identified by ESI-MS, reflect the original structure of the complexes in solution after the ionization process in the mass spectrometer.

3.5. Formation of molybdosilicate in the molybdic yellow method

To elucidate the effect of the sulfuric acid concentration on molybdosilicate formation, we studied complex formation at three sulfuric acid concentrations. A solution consisting of 0.2 mM silicic acid, 67 mM sulfuric acid, and 3.1 mM ammonium molybdate was prepared (pH 1.1). The obtained spectrum is shown in Fig. 4(b). The mass spectrum includes peaks derived from molybdosilicate, molybdic acids, silicate, and sulfate ions, whereas no peaks derived from silicic acids combined with sulfuric acid (m/z 255) were observed. Peaks of $[\text{SiMo}_{12}\text{O}_{40}]^{4-}$ (m/z 455) and $[\text{HSiMo}_{12}\text{O}_{40}]^{3-}$ (m/z 607) were identified. In addition, the peak of $[\text{SiMo}_{12}\text{O}_{40}]^{2-}$ (m/z 911) was observed, similar to that in the molybdosilicate solution as shown in Fig. 4(d). Molybdosilicates of the form $[\text{SiH}_n\text{Mo}_{12}\text{O}_{40}]^{(4-n)-}$ ($n=0, 1, \text{ and } 2$) were also observed. In Fig. 4 (a), the peaks identified as $[\text{Mo}_n\text{O}_{(3n+1)}]^{2-}$ ($n=2-4, 6, 7$), $[\text{HMo}_n\text{O}_{(3n+1)}]^{-}$ ($n=2-4, 6$), and other polymers of molybdic acid overlapped with the peaks of the molybdosilicates $[\text{SiMo}_{12}\text{O}_{40}]^{4-}$ and $[\text{HSiMo}_{12}\text{O}_{40}]^{3-}$. This was attributed to the proton adduct in the gas phase reaction, as shown in ESI-MS [27–32]. In particular, the peak intensities of the molybdic acids $[\text{HMoO}_4]^{-}$ and $[\text{Mo}_4\text{O}_{13}]^{2-}$ and/or $[\text{Mo}_8\text{O}_{26}]^{4-}$ were high. We see that these molybdic acids were precursors in the formation of the complexes $[\text{SiMo}_{12}\text{O}_{40}]^{4-}$ and $[\text{HSiMo}_{12}\text{O}_{40}]^{3-}$. Especially at high sulfuric acid concentrations, $[\text{HSiMo}_{12}\text{O}_{40}]^{3-}$ and $[\text{H}_2\text{SiMo}_{12}\text{O}_{40}]^{2-}$ were easily formed.

A solution consisting of 0.2 mM silicic acid, 335 mM sulfuric acid, and 3.1 mM ammonium molybdate (pH 0.3) prepared by the same procedure was left to stand for 10 min, and its spectrum is shown in Fig. 4(c). In this case, there was no complete complex formation of silicic acid; thus, the formation of molybdic acid and its condensation may have occurred. Here, high intensity peaks representing complexes formed by the combination of molybdic acid with sulfuric acid were observed, but the peak intensities were lower than those in Fig. 4(b).

Although molybdic acid and molybdosilicates (m/z 455, 607, 911) were identified at a lower sulfuric acid concentration (6.7 mM, pH 2.4), peaks corresponding to molybdic acid with sulfuric acid adducts (m/z 243, 323, 403, 385, 465, 529) were hardly observed, as seen in Fig. 4(d). Thus, it is inferred that the addition of sulfuric acid causes the initial condensation of molybdic acids, followed by the formation of molybdosilicate species. As no peaks corresponding to complexes derived from silicates combined with sulfuric acid were observed, the complete formation of molybdosilicate species may be presumed.

At a sulfuric acid concentration of 335 mM, the peak intensities of molybdic acid with sulfuric acid adducts were higher than that of molybdic acid, and a peak corresponding to a silicic acid complex was also observed. A peak (shown by an arrow) derived from silicic acid can be observed in Fig. 4(c) but not in Fig. 4(b) and (d). Therefore, at a high sulfuric acid concentration, molybdic acid reacted with sulfuric acid, but molybdosilicates were not formed in the solution. Here, the incomplete reaction of silicic acids with molybdic acid results in a solution with a pale color. In the case of 6.7 mM sulfuric acid, the peak intensities of molybdosilicates were lower than those in the case of 67 mM sulfuric acid. As shown in Fig. 4(b) and (d), all of the silicic acids reacted with molybdosilicates, but the absorptions of molybdate yellow shown in Fig. 1 differed with decreases in the concentration of sulfuric acid. Moreover, silicic acid and its complexes with sulfuric acid were not observed. In this solution, not only β -molybdosilicates but also α -molybdosilicate are produced, and the total ϵ (the absorption coefficient) changed from that in 67 mM of sulfuric acid. On the basis of the above results, ESI-MS is shown to be a powerful tool for the detection of complex species in solution.

3.6. Effect of oxalic acid in the molybdate yellow method

Finally, the effect of oxalic acid in the molybdate yellow method is discussed. When both silicic and phosphoric acids were contained in solution, after 10 min of formation of the molybdosilicate complexes, 0.3 mL of 10% oxalic acid was added to avoid the formation of molybdophosphate complexes [7]. To clarify the effect of oxalic acid, two solutions, one containing silicic acid and the other containing phosphoric acid, were examined following the procedure of the molybdate yellow method.

First, as shown in Fig. 5(a), $[\text{PMo}_{12}\text{O}_{40}]^{3-}$ (m/z 608) and $[\text{HPMo}_{12}\text{O}_{40}]^{2-}$ (m/z 912) were observed in a 0.2 mM molybdophosphate solution (pH 3.4). In this spectrum, peaks derived from molybdic acid were observed with molybdophosphate, and $[\text{H}_2\text{PO}_4]^{-}$ (m/z 97) was identified. Here, it is observed that molybdophosphate decomposed, indicating that the complex is unstable. In addition, the 9-polyphosphate of $[\text{H}_6\text{PMo}_9\text{O}_{34}]^{3-}$ (m/z 482), $[\text{HPMo}_9\text{O}_{31}]^{2-}$ (m/z 697) was observed. These peaks are reported by ^{31}P NMR. [34,35].

The mass spectra of the silicic acid solution and phosphoric acid solution after the addition of oxalic acid are shown in Fig. 5 (b) and (c), respectively; the mass spectra of the solutions overlapped, as shown in the Figure and Table 3.

Peaks derived from the molybdosilicate complexes were identified, but peaks derived from the molybdophosphate complexes ($[\text{PMo}_{12}\text{O}_{40}]^{3-}$ (m/z 608) and $[\text{HPMo}_{12}\text{O}_{40}]^{2-}$ (m/z 912)) were not observed. The rate of the decomposition of the molybdophosphate complexes is much faster than that of the molybdosilicate complexes. Thus, it is important to measure the absorption after the addition of oxalic acid to maintain the molybdosilicate complexes and to prevent the decomposition of the molybdophosphate complexes.

4. Conclusion

The chemical complexes producing color in the molybdate yellow method were determined by ESI-MS, and the following results were obtained.

- (1) Silicic acid (including monomers and polymers) was decomposed by sulfuric acid to form monomers in a pH range between 1 and 2. Silicic acid combined with sulfate ions.
- (2) Molybdic acids were condensed by sulfuric acid to form polymer complexes. ESI-MS enabled the observation at each step in the formation of molybdosilicate at the molecular level.
- (3) At pH 1, the molybdic acids were decomposed because of the high concentration of sulfuric acid, and thus, the reaction with

silicic acid to form molybdosilicate was not observed. Silicic acid coexisted with sulfate ions in solution without reacting. However, monomers of silicic acid and polymers of molybdic acids formed molybdosilicates.

Table 3

Molybdate species adducted with oxalic acid identified in the negative ion mode (ESI-MS).

Species	Theoretical m/z
$[\text{MoO}_3(\text{COOH})(\text{COO})]^-$	235
$[\text{MoO}_2(\text{COOH})_3(\text{COO})]^-$	309
$[\text{Mo}_2\text{O}_6(\text{COOH})(\text{COO})]^-$	377
$[\text{Mo}_2\text{O}_5(\text{COOH})_3(\text{COO})]^-$	451

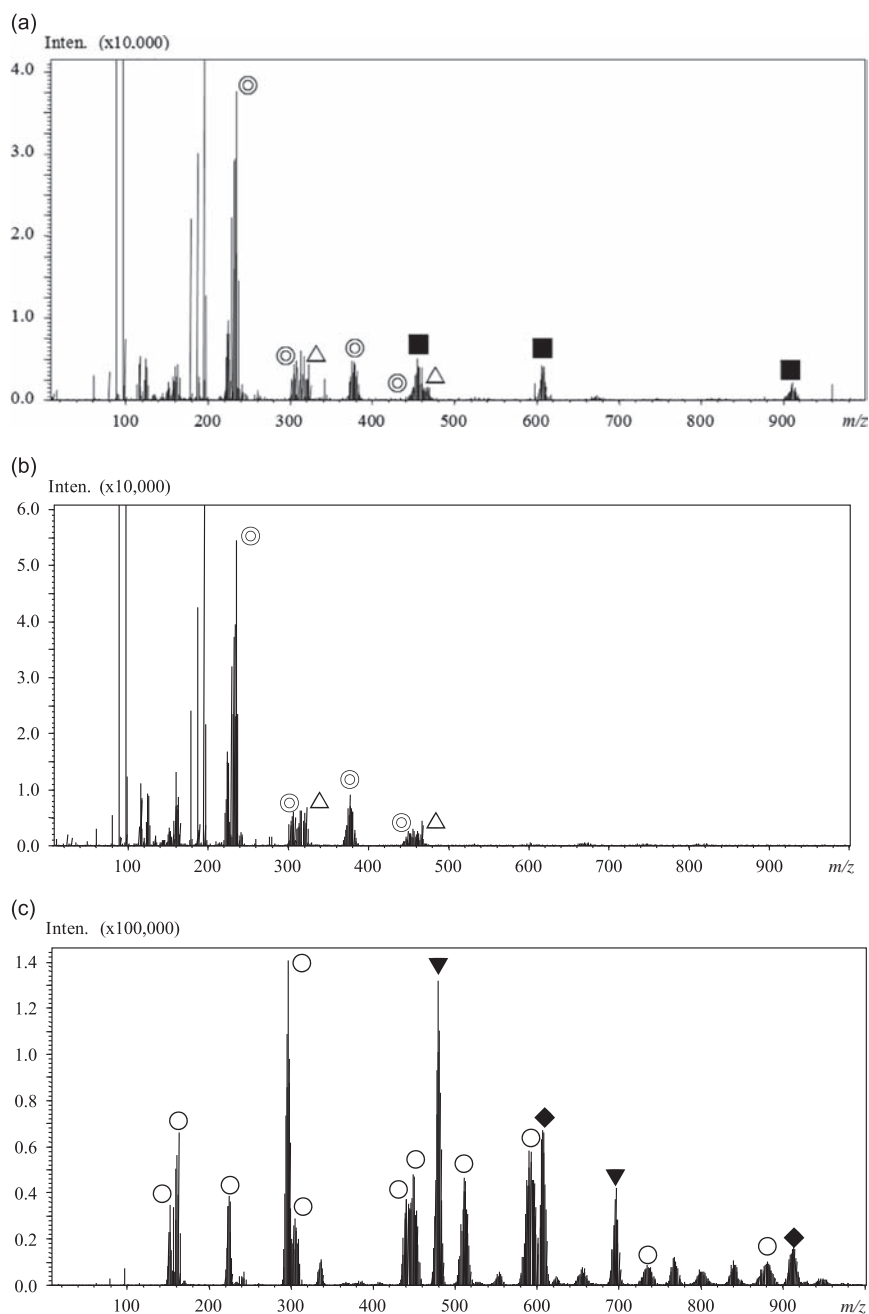


Fig. 5. (a) ESI-MS spectrum of a 0.2 mM molybdophosphate solution (pH 3.4). ○: Molybdate species, ◆: Molybdophosphate species (PMo_{12}), ▼: Species of molybdophosphate (PMo_9), *: H_2SO_4 derived species. (b) ESI-MS spectrum of solution containing 0.2 mM silicic acid and oxalic acid and colored with molybdate yellow method. ○: Molybdate species, △: Molybdate + H_2SO_4 species, ■: Molybdosilicate species (SiMo_{12}), ⊙: Molybdate + oxalic acid species (c) ESI-MS spectrum of solution containing 0.2 mM phosphoric acid and oxalic acid and colored with molybdate yellow. ○: Molybdate species, △: Molybdate + H_2SO_4 species, ⊙: Molybdate + oxalic acid species, *: H_2SO_4 derived species.

- (4) When the pH of the solution was above 2, the condensation of molybdic acids and the formation of molybdosilicate occurred. Unreacted silicic acid was present in the solution. However, the reaction of molybdic acids with sulfates could not be observed due to an insufficient number of protons to form molybdosilicates.
- (5) In this study, a pH between 1 and 2 was found to be suitable for the formation of molybdosilicates.
- (6) Upon addition of oxalic acid, the rate of the decomposition of the molybdophosphate complexes was much faster than that of the molybdosilicate complexes.

We have thus examined the role of sulfuric acid in the molybdate yellow method. The importance of realizing a suitable pH by the addition of an appropriate acid was ascertained. It was possible to investigate high-concentration silica solutions in the absence of metal ions by ESI-MS. On the basis of the above results, ESI-MS was shown to be a powerful tool for the detection of complexes dissolved in a solution at the molecular level.

Acknowledgments

We greatly appreciate Dr. Yu Vin Sahoo for her advice on this manuscript. The cost of this study was partly defrayed by a Grant-in-Aid from the Faculty of Marine Science, Tokyo University of Marine Science and Technology (the Research Foundation of a Hundred Foundation of Tokyo University of Fisheries in 2013). This study was partly supported by the Steel Industry Foundation for the Advancement of Environmental Promotion Technology (09, C-38), (10, C-31) and the Steel Foundation for Environmental Protection Technology (11, C-29) and by the Japan Boiler Association. This study was also supported by a Grant-in-Aid for Scientific Research (C)(2)(No. 21550073) and a Grant-in-Aid for Challenging Exploratory Research (No. 24651072) from the Japan Society for the Promotion of Science.

References

- [1] J.D. H. Strickland, *J. Am. Chem. Soc.* 74 (1951) 868–871.
- [2] J.D. H. Strickland, *J. Am. Chem. Soc.* 74 (1951) 872–875.
- [3] V.W. Truesdale, C.J. Smith, *Analyst* 100 (1975) 203–212.
- [4] V.W. Truesdale, C.J. Smith, *Analyst* 100 (1975) 797–805.
- [5] M.S. Kasprzak, S.R. Crouch, G.E. Leroi, *Appl. Spectrosc.* 32 (1978) 527–593.
- [6] K. Murata, S. Ikeda, *Spectrochim. Acta* 39A (1983) 787–794.
- [7] C.X. Galhardo, J.C. Masini, *Anal. Chim. Acta* 417 (2000) 191–200.
- [8] S. Himeno, H. Niya, T. Ueda, *Bull. Chem. Soc. Jpn.* 70 (1997) 631–637.
- [9] T. Miyana, T. Fujikawa, N. Matsubayashi, T. Fukumoto, K. Yokoi, I. Watanabe, S. Ikeda, *Bull. Chem. Soc. Jpn.* 62 (1989) 1791–1796.
- [10] T. Miyana, N. Matsubayashi, T. Fukumoto, K. Yokoi, I. Watanabe, K. Murata, *Chem. Lett.* 17 (1988) 487–490.
- [11] M. Filowitz, R.K. C. Ho, W.G. Klemperer, W. Shum, *Inorg. Chem.* 18 (1979) 93–103.
- [12] P. Sarrazin, B. Mouchel, S. Kasztelan, *J. Phys. Chem.* 93 (1989) 904–908.
- [13] O.W. Howarth, P. Kelly, *J. Chem. Soc. Dalton Trans.* (1990) 81–84.
- [14] B. Török, M. Török, M. Rózsa-Tarjani, I. Pálínkó, L.I. Horváth, I. Kiricsi, Á. Molnár, *Inorg. Chim. Acta* 298 (2000) 77–83.
- [15] T.-C. Lau, J. Wang, R. Guevremont, K.W. M. Siu, *J. Chem. Soc. Chem. Commun.* (1995) 877–878.
- [16] J.L. Q. Tuoi, E. Müller, *Rapid Commun. Mass Spectrom.* 8 (1994) 692–694.
- [17] D.K. Walanda, R.C. Burns, G.A. Lawrence, E.I. Nagy-Felsobuki, *J. Chem. Soc. Dalton Trans.* 28 (1999) 311–321.
- [18] A.J. Bridgeman, *Chem. Phys.* 287 (2003) 55–69.
- [19] A.J. Bridgeman, *Chem. Phys.* 287 (2003) 55–69.
- [20] J. Zhang, A.M. Bond, D.R. MacFarlane, S.A. Forsyth, J.M. Pringle, A.W. A. Mariotti, A.F. Glowinski, A.G. Wedd, *Inorg. Chem.* 44 (2005) 5123–5132.
- [21] S. Himeno, M. Takamoto, T. Ueda, *J. Electroanal. Chem.* 485 (2000) 49–54.
- [22] M. Dietzel, *Geochim. Cosmochim. Acta* 64 (2000) 3275–3281.
- [23] M. Tanaka, K. Takahashi, *Anal. Chim. Acta* 429 (2001) 117–123.
- [24] M. Tanaka, K. Takahashi, *J. Mass Spectrom.* 35 (2000) 853–859.
- [25] M.J. Deery, O.W. Howarth, K.R. Jennings, *J. Chem. Soc. Dalton Trans.* 26 (1997) 4783–4788.
- [26] M. Takahashi, M. Tanaka, *Bunsekikagaku* 61 (2012) 1049–1054.
- [27] T. Urabe, M. Tanaka, S. Kumakura, T. Tsugoshi, *J. Mass Spectrom.* 42 (2007) 591–597.
- [28] T. Oikawa, T. Urabe, S. Kawano, M. Tanaka, *J. Sol. Chem.* 40 (2011) 1094–1107.
- [29] L. Tang, P. Kebarle, *Anal. Chem.* 65 (1993) 3654–3668.
- [30] P. Kebarle, L. Tang, *Anal. Chem.* 65 (1993) 972A–986A.
- [31] C.G. Enke, *Anal. Chem.* 69 (1997) 4885–4893.
- [32] K. Tang, J.S. Page, R.D. Smith, *J. Am. Soc. Mass Spectrom.* 15 (2004) 1416–1423.
- [33] H. Hellman, R.S. Laitinen, L. Kaila, J. Jalonen, V. Hietapelto, J. Jokela, A. Sarpola, J. Rämö, *J. Mass Spectrom.* 41 (2006) 1421–1429.
- [34] S. Himeno, M. Hashimoto, T. Ueda, *Inorg. Chim. Acta* 284 (1999) 237–245.
- [35] L. Petterson, I. Anderson, L.-O. Öhman, *Inorg. Chem.* 25 (1986) 4726–4733.



Determination of seven pyrethroids biocides and their synergist in indoor air by thermal-desorption gas chromatography/mass spectrometry after sampling on Tenax TA[®] passive tubes



Caroline Raeppl^{a,b}, Brice M. Appenzeller^b, Maurice Millet^{a,*}

^a Institut de Chimie et Procédés pour l'Energie, l'Environnement et la Santé (ICPEES UMR 7515 CNRS – Université de Strasbourg) – 1 rue Blessig – F-67084 Strasbourg Cedex, France

^b Laboratory of Analytical Human Biomonitoring – CRP-Santé – Université du Luxembourg – 162 A Avenue de la Faiencerie – L-1511 Luxembourg, France

ARTICLE INFO

Article history:

Received 17 June 2014

Received in revised form

26 July 2014

Accepted 31 July 2014

Available online 8 August 2014

Keywords:

Pyrethroids biocides

TD–GC/MS

Tenax TA[®] passive sampling

Indoor air

ABSTRACT

A method coupling thermal desorption and gas chromatography/mass spectrometry (GC/MS) was developed for the simultaneous determination of 7 pyrethroids (allethrin, bifenthrin, cyphenothrin, imiprothrin, permethrin, prallethrin and tetramethrin) and piperonyl butoxide adsorbed on Tenax TA[®] passive samplers after exposure in indoor air. Thermal desorption was selected as it permits efficient and rapid extraction without solvent used together with a good sensitivity. Detection ($S/N > 3$) and quantification ($S/N > 10$) limits varied between 0.001 ng and 2.5 ng and between 0.005 and 10 ng respectively with a reproducibility varied between 14% (bifenthrin) and 39% (permethrin). The method was used for the comparison indoor air contamination after low-pressure spraying and fumigation application in a rubbish chute situated in the basement of a building.

© 2014 Elsevier B.V. All rights reserved.

1. Introduction

Biocidal products are defined in the European directive 98/8/CE from 16 February 1998 as “Active substances and preparations containing one or more active substances, put up in the form in which they are supplied to the user, intended to destroy, deter, render harmless, prevent the action of, or otherwise exert a controlling effect on any harmful organism by chemical or biological means”. They are classified in four main categories “Disinfectants and general biocidal products (i.e. human hygiene biocidal products, private area and public health area disinfectants and other biocidal products, etc.)”, “Preservatives (i.e. wood preservatives, in-can preservatives, etc.)”, “Pest control (i.e. rodenticides, acaricides, etc.)” and “Other biocidal products (i.e. preservatives for food or feedstocks, antifouling products, etc.)”.

Biocides are used by professional and non professional users in diverse activities like the textile and leather industry where biocides are used during manufacturing and storage to protect against moths, bacteria or algae development, or the wood industry against insects or fungus contamination.

Among biocides molecules, synthetic pyrethroids are widely used indoors to control households insects like mosquitoes, termites, etc. in place of more toxic insecticides such as organophosphorous and

organochlorine molecules. Indeed, they are much more effective against a wide spectrum of pests than the organochlorine, organophosphate, and carbamate insecticides. Consequently, they are used in many applications like surface sprays in common houses, airplanes, in active or passive evaporators, in incense products, or to make textiles insect resistant [1].

Among pyrethroids available, allethrin, phenothrin, tetramethrin and cyphenothrin are mainly used for household insects commercially combined with synergist compounds like piperonyl butoxide [2].

When applied in confined atmosphere, their release in air is the most important route of human exposure through inhalation. Their quantification in indoor atmosphere remains consequently important for exposure assessment.

Due to relatively low expected concentrations in air, sampling of airborne pyrethroids are made by pumping a large amount of air through filters and one of a combination of different adsorbents like Porapak C₁₈, Chromosorb 102, Tenax GC, Carbowax 20M or polyurethane foam [4]. Analytes adsorbed on traps were solvent extracted, cleaned and analysed by gas chromatography coupled to electron capture or mass spectrometer detectors [2–4].

These sampling systems are well efficient but are requiring excessive time and are expensive especially due to the many steps involved which, in addition, could enhance the risk of analytes losses. For the particular case of pyrethroids, a risk of photodecomposition has been reported [3] and a rapid and careful trapping-extraction process is recommended [2]. In addition,

* Corresponding author.

E-mail address: mmillet@unistra.fr (M. Millet).

when used in indoor environment, the noise and dimensions have to be considered. An alternative to these techniques is commonly called “passive sampling”, as opposed to “active sampling”. Using this approach, analytes migrate from the sampled medium to the sampler (collecting medium) through molecular diffusion. Indeed, any sampling technique can be described as “passive” when a non-forced flow of analytes is established between the sample and the collecting medium. This flow is induced by a potential difference between the air and the adsorbent. These techniques are commonly referred to as “diffusive sampling”, “passive sensors” or “integrative sampling techniques”. This flow continues until reaching equilibrium between the two environments [5] or until sampling is interrupted by the user. No pump and power are needed, limiting inconvenience at the sampling point (important for indoor use), and costs for samplers deployment. The equipment used for passive sampling is generally very simple and does not require any skilled workers. After sampling, extraction techniques and analysis methods are similar to those used for active sampling and consist generally to a solvent extraction with Soxhlet, Accelerated Solvent Extraction (ASE) or Microwave Accelerated Extraction (MAE), a purification step and an injection on GC [6–9].

Some other techniques using thermal desorption followed by direct injection into GC can be used for passive sampling. These techniques used Tenax[®] tubes and/or SPME. Thermal desorption can present some advantages since it substantially simplifies analyses (no concentration step after sampling is needed) and increases sensitivity (a large part of the pre-concentrated material may be recovered for determination), and detection limits and background noise are lower because of the disappearance of solvent components [10–14]. Moreover, this technique is easily automatable. Because of these aspects, it seems to be an interesting alternative to solvent extraction to assess atmospheric exposure to pesticides in indoor and outdoor atmosphere through passive sampling. Moreover, thermal desorption coupled to passive sampling requires one unique injection and consequently needs a multi-class analytical method.

The aim of this paper is the development of a thermal desorption coupled to GC–MS method for the simultaneous determination of 7 pyrethroids biocides (allethrin, bifenthrin, cyphenothrin, imiprothrin, permethrin, prallethrin and tetramethrin) and their synergist piperonyl butoxide. This method will be applied for the detection and quantification of these biocides adsorbed on Tenax[®] passive sampling tubes (PAS) after exposure on indoor environment when biocides are applied. The design of the PAS from Radiello[™] in a cylinder allows analytes to access the adsorbent material throughout the 360° surrounding diffusive barrier permitting a significant uptake rate. These samplers are reusable, permit sampling time ranges from 15 min to 30 days and thermal desorption use.

2. Materials and methods

2.1. Chemicals

Standards of individual pesticides (allethrin, bifenthrin, cyphenothrin, imiprothrin, permethrin, piperonyl butoxide, prallethrin and tetramethrin) of Pestanal[®] quality (> 99% purity) were obtained from Riedel de Haën (Sigma Aldrich, St. Quentin Fallavier, France).

Internal standards DDE d⁸, DDT d⁸ and Trans-cypermethrin d⁶ were supplied from Cluzeau Info Labo (St Croix la Grande, France).

For calibration and thermal desorption optimisation, a stock solution of each pesticide at 1 g L⁻¹ was prepared in acetonitrile. A working solution at 80 mg L⁻¹ was prepared for each compound

together with a mixture solution for full scan injection. For SIM injection and calibration, mixture solutions in acetonitrile between 1 mg L⁻¹ and 10 µg L⁻¹ were prepared from stock solution.

2.2. Passive sampling tubes preparation

Just before sampling, Radiello[®] Tenax-TA[®] passive sampling (PAS) tubes (100 mesh, 4.8 mm diam.), purchased from Sigma-Aldrich (L'Isle d'Abeau, France) were introduced into empty stainless steel tubes (89 mm × 5 mm i.d.), purchased from Perkin-Elmer Corp. (Norwalk, CT, USA), and were conditioned at 350 °C for 45 min, at a flow rate of 45 mL min⁻¹ of He (maximum impurities: 1 ppm). After that, Tenax-TA[®] tubes were stored in capped glass tubes and stored at room temperature in a close box. After exposure, passive sampling tubes were immediately capped, rounded with Teflon film and stored in the dark at -18 °C and desorbed no later than one month storage.

2.3. Field sampling

A sampling campaign has been done in two different rubbish chute situated in the basement of a building where pest control was performed by using two different techniques: low-pressure spraying directly on soils and wall surfaces and fumigation permitting the diffusion of fog droplets in all part of the room. Details are presented in Table 1. Collectors used during this study were similar to those designed and described by Wania et al. [15].

A sampler was installed out of the rubbish chute in order to evaluate the potential diffusion after application and closing of the access of the rubbish chute during treatment. For each application techniques, a Tenax TA[®] passive sampler (PAS) in a PVC shelter was installed in the centre of the rubbish chute at 1.70 m from ground before the starting of the application.

This sampler, adapted in dimensions from the system designed and described by Wania et al. [15] (Supplementary material S1), was removed after 24 h exposure and replaced by a new one each day for the first week of sampling (except week end) and each two days the second week. Details of the date and periods of sampling are presented in Table 2. As radial diffusion body provided by Radiello[™] was not calibrated for biocides compounds, the use of a shelter similar to the one designed by Wania et al. [15] was selected as it is important, in passive sampling, to limit the effect of wind which can impact the sampler performance. The deployment of the sampler inside a protective tool is then required [5].

2.4. ATD–GC/MS analysis of pesticides adsorbed on Tenax[®] passive samplers

Analyses were carried out by using an automatic thermal desorption unit (ATD 350, Perkin-Elmer Corp., Norwalk, CT, USA), connected to an Autosystem XL GC coupled to a Turbomass gold detector (Perkin-Elmer Corp., Norwalk, CT, USA). ATD 350 was coupled to GC–MS via a valve and a transfer line maintained at 300 °C and 280 °C respectively.

Table 1
Characteristics of the application techniques and substances made in the rubbish chute.

Application type	Active substance	Applied amount
Low-pressure spraying	Permethrin (16.74 g L ⁻¹) o-Tetramethrin (1.86 g L ⁻¹) Piperonyl butoxide (9.5 g L ⁻¹)	–
Fumigation	Cyphenothrin (72 g kg ⁻¹)	1.44 g

Table 2
Sampling procedure made for each rubber chute biocide application.

Sample no.	Sampling period	Duration of PAS exposition (h)
1	28–29 june	22.4
2	29–30 june	24.8
3	30 june–1 july	23.3
4	1–2 july	24.3
5	2–5 july	71.8
6	5–7 july	47.8
7	7–9 july	47.8

Table 3
Retention times and SIM ions (Q for quantification ion) for the seven pyrethroids, their synergist and internal standards (IE).

Biocides and *IE	t_R (min) of the different isomers	m/z SIM (Da)
Allethrin	21.27+21.32+21.47+21.52	123 (Q)-136–168
Prallethrin	22.01+22.07	123 (Q)-134–168–153
*DDE d ⁸	23.89	254 (Q)-256–326–184
*DDT d ⁸	25.83	243 (Q)-245–173
Imiprothrin	26.08+26.42	123 (Q)-151
Piperonyl butoxide	28.80	176 (Q)-177–149–338
Tetramethrin	29.95+30.40	164 (Q)-135–123
Bifenthrin	30.21	181 (Q)-165–166
Cyphenothrin	34.35+34.59+34.71	123 (Q)-181–152–375
Permethrin	35.49+35.89	183 (Q)-163–165
*Trans-cypermethrin d ⁶	38.38+38.69	169 (Q)-181–171

Pyrethroids and piperonyl butoxide were separated on a Macherey–Nagel OPTIMA 5MS ACCENT[®] capillary column (60 m × 0.25 mm I.D., 0.25 μm film thickness). Helium was used as carrier gas at an electronically regulated constant flow of 1.5 mL min⁻¹. The GC oven temperature was 50 °C hold 5 min, first rate 25 °C/min to 200 °C, second rate 3 °C/min to 300 °C hold 5 min, with a total acquisition programme of 49.3 min.

Spectra of pesticides were obtained by electron impact ionisation (EI) at 70 eV. Depending on the pesticide, some ions were selected from the spectrum of each pesticide in the selected ion monitoring mode (SIM). The ions selected for SIM analysis of the compounds are listed in Table 3.

Internal standards were selected to permit the quantification of biocides in three groups on the chromatogram; *p,p'*-DDE d⁸ for prallethrin and allethrin isomers, *p,p'*-DDT d⁸ for imiprothrin, piperonyl butoxide, tetramethrin and bifenthrin and, trans-cypermethrin d⁶ for cyphenothrin and permethrin isomers.

Before extraction, tubes were spiked with 10 μL of a mixture of internal standards (each 1 mg L⁻¹) deposited on the top of the tubes. They were recapped with Teflon caps and put in up-right position for few minutes permitting the internal standard to make contact with the adsorbent. After that, tubes were placed on the carousel of the ATD 350 in the inverse position.

For the ATD desorption, the sample tube is heated at 320 °C for 30 min under a stream of He (desorb flow: 50 mL min⁻¹) to extract biocides from the passive sampling tube by thermal desorption and sweep them onto a secondary trap without an inlet split. This second trap, containing no Tenax TA[®] adsorbent or wool, was maintained at -30 °C by the Peltier effect (Table 4).

The cold trap refocused all the components eluting from the sample tube. When primary desorption stage is complete, the cold trap is electrically heated at a rate of 20 °C s⁻¹ (trap fast) to 320 °C (maintained for 5 min) so as to elute all the retained components in a vapour band as narrow as possible. The outlet-split flow is

Table 4
Thermal-desorption conditions.

Parameter	Fixed values
Outlet split	10 mL min ⁻¹
Column flow rate	1.5 mL min ⁻¹
Valve temperature	250 °C
Transfer line temperature	280 °C
Tube purge duration before desorption	1 min
Primary desorb flow rate	50 mL min ⁻¹
Primary desorb duration	30 min
Primary desorb temperature	320 °C
Cold trap heating rate	20 °C s ⁻¹
Cold trap temperature duration	5 min at 320 °C

adjusted for high-resolution capillary column to 10 mL min⁻¹ leading to a fraction of 13% of the sample entering the column (see Briand et al. [13], for details).

Calibration curves were obtained by deposition on the top of tubes from 1 ng to 300 ng of each biocides and 20 ng (20 μL of a mixture at 1 mg L⁻¹ each) of internal standards (DDE d⁸, DDT d⁸ and trans-cypermethrin d⁶). Detection ($S/N > 3$) and quantification ($S/N > 10$) limits varied between 0.001 ng and 2.5 ng and between 0.005 and 10 ng respectively with a reproducibility varied between 14.5% (bifenthrin) and 38.9% (permethrin) (Table 5).

3. Results and discussion

3.1. Chromatographic separation and mass spectrometric determination

The separation of the eleven compounds, including the three internal standards was achieved by 49.3 min. The choice of the length of the column was conducted by the fact than other kind of pesticides requiring a 60 m length will also analysed by the same ATD-GC/MS [16]. In order to not remove frequently the column from the system, it was decided to adapt all separations with the same column. The chromatogram in full scan of the biocides and the internal standards are shown in Fig. 1.

The selection of ions for the Single Ion Monitoring mode (SIM) is presented together with the retention time of each compound and their isomers in Table 3.

3.2. Optimisation of ATD parameters

The optimisation of thermal desorption parameters were tested separately and in order to validate the better value. Three injections were realised for each tested parameter. For these experiments tubes were spiked with 100 ng and 20 ng of the biocides and of the internal standards mixtures respectively. The flow rate on the column and the outlet split were fixed to 1.5 mL min⁻¹ and 20 mL min⁻¹ respectively.

Firstly, primary desorb temperature was tested between 250 and 320 °C. It appears that the ratio of area between compound and its respective internal standard showed higher intensities as higher is the temperature. Indeed, at 250 °C, some compounds are not detected (imiprothrin, cyphenothrin). Then, 320 °C was selected. The flow rate of helium through the tube during heating can play an important role on the desorption efficiency, then different flows were experimented: 45, 50, 55 and 60 mL min⁻¹. Maximum areas were observed between 50 and 55 mL min⁻¹ except for permethrin where 60 mL min⁻¹ shows a slightly higher response. Since the difference between 50 mL min⁻¹ and 55 mL min⁻¹ is low, a flow rate of 50 mL min⁻¹ was selected. Indeed, a fast desorb flow induces a high flow of warm helium

Table 5

Linear correlation and variation coefficients, detection and quantification limits for the seven pyrethroids and their synergist.

Biocide	Linear correlation R^2	Repeatability (%)	Reproducibility (%)	Quantification limits (pg PAS ⁻¹)	Detection limits (pg PAS ⁻¹)
Allethrin	0.995	23	32	750	5
Prallethrin	0.995	39	37	7500	2500
Imiprothrin	0.975	25	28	10,000	7500
Piperonyl butoxide	0.989	22	21	100	5
Tetramethrin	0.988	23	31	1000	50
Bifenthrin	0.996	14	16	5	1
Cyphenothrin	0.972	43	39	750	50
Permethrin	0.975	32	35	750	5

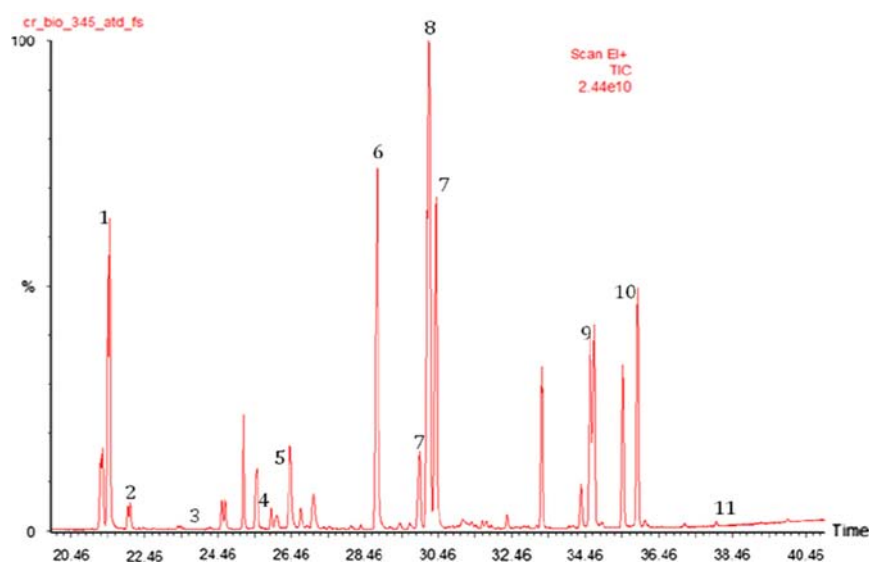


Fig. 1. Chromatogram of a mix (10 mg L⁻¹ each) of standards of the seven biocides, their synergist and internal standards (Full scan mode). 1. Isomers of allethrin, 2. isomers of prallethrin, 3. DDE d⁸, 4. DDT d⁸, 5. imiprothrin, 6. piperonyl butoxide, 7. isomers of tetramethrin, 8. bifenthrin, 9. isomers of cyphenothrin, 10. isomers of permethrin, and 11. trans-cypermethrin d⁶.

through the cold trap and consequently difficulties to maintain the temperature of the trap to $-30\text{ }^{\circ}\text{C}$. The duration of desorption is also an important parameter and its optimisation can improve the desorption efficiency and the sensitivity. Then, three desorption times were selected for testing: 15, 30 and 45 min. However, it was shown in a previous study, in particular for pesticides with the longest retention times, that a duration of desorption of 30 min increases areas of compounds for a factor from 2 to 4 while for 45 min, a strong decrease of areas was observed. This phenomenon can be explained by the low volatility of pyrethroids in addition to their thermal sensibility [16]. Then, duration of 30 min was confirmed as the better duration.

Secondly, parameters regarding second step desorption can be considered; the rate and duration of the heating of the cold trap. After accumulation of pesticides on the cold trap maintained at $-30\text{ }^{\circ}\text{C}$ during tube desorption, injection onto the column is performed by a rapid heating of the trap from $-30\text{ }^{\circ}\text{C}$ to $300\text{ }^{\circ}\text{C}$. Different velocities of trap heating are available ($5\text{ }^{\circ}\text{C s}^{-1}$, $20\text{ }^{\circ}\text{C s}^{-1}$ and $40\text{ }^{\circ}\text{C s}^{-1}$). Faster is the velocity of heating as faster the pesticides are transferred to the column and it can be expected a better resolution when the velocity is at maximum. From experiments on velocities, it appears clearly that the $20\text{ }^{\circ}\text{C s}^{-1}$ velocity was the better permitting the moving of pesticides from the trap to the column without any loss of resolution and sensitivity. It can be observed that many of the pesticides were not detected when the velocity of $40\text{ }^{\circ}\text{C s}^{-1}$ was employed. The only explanation which can be advanced is a thermal degradation of pyrethroids due to the fast strong increase of temperature. Experiments with different trap heating duration (5, 10 and

15 min) were also performed in order to evaluate the influence of this parameter on the analysis of pesticides desorbed from the tube. Results obtained are surprising since in theory, a longer duration of the trap temperature will permit a total desorption from the trap and consequently a better detection. This is not the case since 5 min duration shows the better response. As for the precedent sub-section, the influence of the exposure of pesticides to elevated temperature can explain this observation and this observation is corroborated by the loss of pyrethroids when the duration of heating goes from 5 to 15 min. Finally, optimal thermal desorption conditions are presented in Table 4.

The potential “memory effect” was checked by desorption of a spiked tube with 50 ng of pesticides and 20 ng of internal standards followed by the desorption of two clean non-spiked tubes. This experiment was realized two times. Only DDE d⁸ and bifenthrin were detected in the two non-spiked tube (1% and 0.5% of the amount of the spiked tube respectively). These values were extremely low and can be considered as negligible as they can be including into the uncertainty of the method.

3.3. ATD-GC/MS repeatability and calibration range

A calibration range (8 points) was performed three times between 1 and 300 ng, of each of the biocides, deposited on tubes together with 20 μL of a solution of internal standard at solution 1 mg L^{-1} . The linearity range varied with the quantification limit of each compound. However correlation coefficient which varied between 0.972 (cyphenothrin) and 0.996 (bifenthrin) are satisfactory (Table 5).

The reproducibility of the method was evaluated by the successive analysis of six spiked tubes with 50 ng of each compound per day during three successive days. From results obtained by a variance analysis at one factor, coefficients of variation of repeatability (CV_{repe}) and reproducibility (CV_{repro}) were calculated in order to determinate the repeatability and the intermediate fidelity. Calculated CV_{repe} varied between 14.5% (bifenthrin) and 42.7% (cyphenothrin) and are below 25% for five compounds. The highest CV_{repe} corresponds to prallethrin, cyphenothrin and permethrin eluting at the end of the temperature ramp. CV_{repro} are generally higher than CV_{repe} and varied 16% (bifenthrin) and 35% (permethrin).

Detection ($S/N > 3$) and quantification ($S/N > 10$) limits were determined by consecutive injections of decreasing amounts of biocides and by using Turbomass software. They varied between 1 pg PAS^{-1} and 7.5 ng PAS^{-1} for detection limits and between 5 pg PAS^{-1} and 10 ng PAS^{-1} quantification limits. Generally expressed in other studied in ng m^{-3} of air, the obtained values cannot be compared easily. However, obtained values can be compared with those obtained by Ion Mobility Spectrometry (IMS) [17]. Indeed, this method consists of a thermal desorption of pyrethroids adsorbed on a Teflon membrane and analysis by IMS of volatilised pesticides. Detection limits obtained by IMS for tetramethrin are in the same order of magnitude (3.2 ng vs 1 ng PAS^{-1} for this study) and slightly higher for permethrin (3.1 ng vs 0.75 ng PAS^{-1} for this study) and for bifenthrin (0.6 ng vs $0.001 \text{ ng PAS}^{-1}$ for this study). The thermal desorption and the direct analysis of pesticides permits, in comparison to classical methods, the decrease of detection limits.

3.4. Application to atmospheric samples

For each application technique (low pressure spraying and fumigation), concentrations expressed in ng PAS^{-1} are presented in Figs. 2 and 3.

Profiles obtained are equivalent in terms of evolution since higher concentration are measured in the first PAS, installed just before application (without direct application on the PAS), followed by a decrease of concentration on the days following the application.

In the case of low-pressure spraying, biocides and synergist have detected and quantified in the first sample with values between 1 and 5.6 ng PAS^{-1} . For next sampling, tetramethrin was not detected while bifenthrin was detected but below quantification limits. The synergist was not quantified on the next sampling due to problems on chromatogram. Indeed a strong tailing was observed for piperonyl butoxide which does not permit the quantification. This molecule was then detected but not

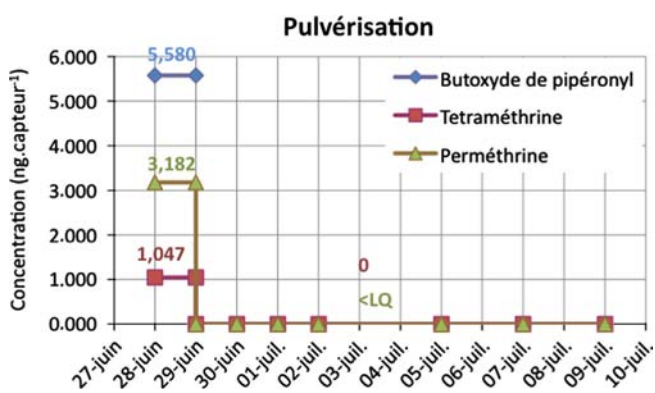


Fig. 2. Variation of biocide concentration for low-pressure spraying.

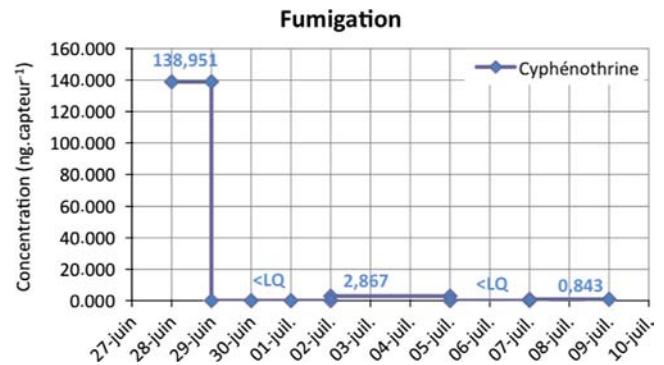


Fig. 3. Variation of biocide concentration for fumigation of cyphenothrine.

quantifiable. For this technique of application it seems that the air contamination is slow and decreases rapidly. This can be explained by the technique of application which consists on the deposit near surfaces (soil and walls) which is not in favour of a dispersion of active substances to the air.

Regarding concentration measured on PAS, it can be observed that the highest amount was not correlation with the concentration of the solution to be sprayed (Table 1) since the more concentrated substance in the commercial solution is bifenthrin and the more concentrated substance in PAS is piperonyl butoxide. This observation can be explained by a different behaviour of the substance in relation to their physical and chemical properties of by a different adsorption kinetic on Tenax.

For fumigation experiment, a strongly higher contamination has been observed on the first sampler (139 ng PAS^{-1}) but with a rapid decrease of concentration on the second day of sampling (Fig. 3). However air remains contaminated the days after application. This observation can be explained by the technique of application which generates a strong fog, permitting the rapid dispersion and deposition of cyphenothrin in all part of the room, and by volatilisation potential of this molecule where Henry's law constant and vapour pressure (respectively $1.85 \times 10^{-3} \text{ Pa m}^3 \text{ mol}^{-1}$ and $1.2 \times 10^{-1} \text{ mPa}$) are in favour of volatilisation.

4. Conclusions

Thermal desorption coupled to GC–MS can be used for the determination of pyrethroids biocides and piperonyl butoxide adsorbed on Tenax-TA[®] resin. This method is simple, solvent free and easily applicable to routine analysis of trace levels of biocides collected on Tenax-TA[®] resin. Detection and quantification limits are in the range for the application of thermal desorption for the evaluation of the temporal variation of indoor contamination after a biocidal application. In particular, this analytical method could be efficient for long term monitoring of indoor contamination by biocides by using passive sampling methodology. This method permits also the observation of difference of behaviour of biocides in relation with the application technique.

Passive sampling can be used as a substitute of conventional active sampling for studies needed many sampling experiments. Passive sampling coupled to thermal desorption simplifies strongly the laboratory working and permits the rapid obtention of results as analysis can be performed immediately after sampling without any treatment.

However, some further investigations are required for the determination of sampling rates for biocides in order to permit the determination of concentrations of biocides in indoor air.

Acknowledgements

The authors acknowledge the regional research programme “REseau Alsacien Laboratoires d'Ingénierie et Sciences de l'Environnement (RE.A.LI.SE)”, the “Région Alsace”, the “Hygiène Habitat” and the “Chambre Syndicale de la Désinfection, Dératisation and Désincetisation (CS3D)” for their help in this work. Caroline Reappel wants to particularly thank the ADEME for their support of a Ph.D grant.

Appendix A. Supplementary material

Supplementary data associated with this article can be found in the online version at <http://dx.doi.org/10.1016/j.talanta.2014.07.098>.

References

- [1] J. Pauluhn, *Toxicol. Lett.* 107 (1999) 193–199.
- [2] R. Barro, C. Garcia-Jares, M. Llompart, M.H. Bollain, R. Cela, J. Chromatogr. A 1111 (2006) 1–10.
- [3] L. Elflein, E. Berger-Preiss, K. Levsen, G. Wünsch, J. Chromatogr. A 985 (2003) 147–157.
- [4] T. Yoshida, J. Chromatogr. A 1216 (2009) 5069–5076.
- [5] M.E. Bartkow, K. Booij, K.E. Kennedy, J.F. Müller, D.W. Hawker, *Chemosphere* 60 (2005) 170–176.
- [6] A. Scheyer, S. Morville, Ph. Mirabel, M. Millet, *Atmos. Environ.* 41 (2007) (3604–368).
- [7] C. Schummer, L. Tuduri, O. Briand, B.M.R. Appenzeller, M. Millet, *Environ. Pollut.* 170 (2012) 88–94.
- [8] Cl. Coscollà, M. Castillo, A. Pastor, V. Yusà, *Anal. Chim. Acta* 693 (2011) 72–81.
- [9] F.A. Esteve-Turrillas, A. Pastor, M. de la Guardia, *Anal. Chim. Acta* 560 (2006) 118–127.
- [10] N. Van der Hoed, M.T.H. Halmans, *Am. Ind. Hyg. Assoc. J.* 48 (1987) 364–373.
- [11] C.A. McCaffrey, J. MacLachlan, B.I. Brookes, *Analyst* 119 (1994) 897–902.
- [12] M. Clément, S. Arzel, B. Le Bot, R. Seux, M. Millet, *Chemosphere* 40 (2000) 49–56.
- [13] O. Briand, M. Millet, F. Bertrand, M. Clément, R. Seux, *Anal. Bioanal. Chem.* 374 (2002) 848–857.
- [14] J.F. Pankow, T.J. Kristensen, L.M. Isabelle, *Anal. Chem.* 55 (1983) 2187–2192.
- [15] F. Wania, L. Shen, Y.D. Lei, C. Teixeira, D.C.G. Muir, *Environ. Sci. Technol.* 37 (2003) 1352–1359.
- [16] C. Raepfel, M. Nief, M. Fabritius, L. Racault, B.M.R. Appenzeller, M. Millet, *J. Chromatogr. A* 1218 (2011) 8123–8129.
- [17] S. Armenta, M. Blanco, *Anal. Bioanal. Chem.* 404 (2012) 635–648.



Exploring petroleum hydrocarbons in groundwater by double solid phase extraction coupled to gas chromatography–flame ionization detector



Oscar Pindado Jiménez^{a,*}, Rosa M^a Pérez Pastor^a, Olga Escolano Segovia^b, Susana del Reino Querencia^c

^a Division of Chemistry, Technology Department, CIEMAT. Av. Complutense 40, 28040 Madrid, Spain

^b Division of Soil and Environmental Geology, Environment Department, CIEMAT. Av. Complutense 40, 28040 Madrid, Spain

^c Environment and Hydrogeology, AITEMIN. C/Río Cabriel, 45007 Toledo, Spain

ARTICLE INFO

Article history:

Received 9 May 2014

Received in revised form

16 June 2014

Accepted 19 June 2014

Available online 17 July 2014

Keywords:

Groundwater

Hydrocarbons fractions

Petroleum hydrocarbons

Solid phase extraction

Uncertainty

Validation

ABSTRACT

This work proposes an analytical procedure for measuring aliphatic and aromatic hydrocarbons fractions present in groundwater. In this method, hydrocarbons are solid phase extracted (SPE) twice from the groundwater and the resulting fractions are analyzed by gas chromatography with flame ionization detection. The first SPE disposes the hydrocarbons present in groundwater in organic solvents and the second SPE divides them into aliphatic and aromatic hydrocarbons. The validation study is carried out and its uncertainties are discussed. Identifying the main sources of uncertainty is evaluated through applying the bottom-up approach. Limits of detection for hydrocarbons ranges are below $5 \mu\text{g L}^{-1}$, precision is not above of 30%, and acceptable recoveries are reached for aliphatic and aromatic fractions studied. The uncertainty due to volume of the sample, factor of calibration and recovery are the highest contributions. The expanded uncertainty range from 13% to 26% for the aliphatic hydrocarbons ranges and from 14% to 23% for the aromatic hydrocarbons ranges. As application, the proposed method is satisfactorily applied to a set of groundwater samples collected in a polluted area where there is evidence to present a high degree of hydrocarbons. The results have shown the range of aliphatic hydrocarbons $> \text{C}_{21}\text{--}\text{C}_{35}$ is the most abundant, with values ranging from $215 \mu\text{g L}^{-1}$ to $354 \mu\text{g L}^{-1}$, which it is associated to a contamination due to diesel.

© 2014 Elsevier B.V. All rights reserved.

1. Introduction

The Directive 2006/118/EC [1] of the European parliament and of the Council of the European Union on the protection of groundwater against pollution and deterioration, establishes groundwater quality standards for nitrates and pesticides. Moreover, threshold values for groundwater pollutants and indicators of pollution have been established. However, quality standards for petroleum hydrocarbons have not been established yet. Petroleum hydrocarbons are common environmental contaminants and comprise a wide range of hydrocarbons (aliphatic, aromatic and a minor amount of heterocyclic compounds) from light gases to heavy residues [2,3]. Nevertheless, as most petroleum hydrocarbons have negative effects on human health and the ecological system, their presence in soil, groundwater and surface waters is

considered to be problematic [4]. This is the reason why discharges of hydrocarbons in sewer system were already regulated by European legislation since 1975 by Directive 76/160/CEE [5] and most recently by Directive 2006/7/EC [6] with the aim of protecting public health and environment.

Despite that extensive regulation, it is well-known that large quantities of petroleum products are released into environment, either by exploration, production, transportation, refining or storage [4]. Moreover, these products undergo weathering processes with time. These processes include volatilization, biodegradation (chemical oxidation and microbial) and leaching. Leaching processes, introduce hydrocarbons into water phase by solubility and entrainment. Its persistence in environment is reflected by physical properties so it must take into account that these products are comprised by a wide range of hydrocarbons. Chemical structure and composition of hydrocarbons will determine water concentration of these compounds. This is why aromatics and especially BTEXs predispose to be the most water-soluble fraction of petroleum hydrocarbons, because they are the

* Corresponding author. Tel.: +34 913 466 523; fax: +34 913 466 121.

E-mail address: oscar.pindado@ciemat.es (O. Pindado Jiménez).

most polar compounds. However, relatively insoluble hydrocarbons can be entrained in water through adsorption into particles suspended in the water or by agglomeration of oil droplets [7].

In the literature, analytical procedures are available for the determination of petroleum hydrocarbons in water [8–16]. However, no single method gives a precise and accurate measurement of the total petroleum hydrocarbons. In fact, different analytical methods used for the determination of environmental concentration of Total Petroleum Hydrocarbon (TPH) will provide very different information [17]. TPH is a non-specific, method-defined parameter that is currently used for expressing the total concentration of nonpolar petroleum hydrocarbons. It is noteworthy that many of petroleum hydrocarbons have sufficiently similar intrinsic physicochemical properties so that they can be classed into fractions when considering fate and transport behavior as well as toxicity [3]. Thereby, TPH fractionation methods are commonly used. As stated by the *Total Petroleum Hydrocarbons Criteria Working Group* (TPHCWG), the equivalent carbon (EC) of any given hydrocarbon is based on the comparison of its boiling point with that of the reference compound *n*-hexane [18,19]. The variable EC is used to define hydrocarbon fractions.

The present work has the aim of developing a double solid phase extraction (SPE) procedure coupled to a gas chromatography with a flame ionization detector (GC–FID), for detection and quantification of TPH and the further fractions in contaminated groundwater by petroleum products. The SPE has been already satisfactorily applied to the analysis of polyaromatic hydrocarbons (PAHs) in seawater [20–22], but less so for the analysis of TPH and fractions of hydrocarbons. Before applying any analytical methodology to a routine analysis, its ability to provide reliable results must be demonstrated, and thus, a validation study must be performed. The main parameters to validate an analytical methodology encompass assays of precision, bias, trueness, linearity, detection limit, sensitivity and finally the uncertainty [23]. A proper estimate of expanded uncertainty should also be appended to whatever TPH results, because only then can the reliability of the results be guaranteed [24]. It is remarkable that validating the proposed method to analyze TPH and the further fractions in groundwater and assessing the uncertainty associated to the measurement are the goals of this work.

2. Experimental

2.1. Chemical and reagents

The analytical standard of aliphatic hydrocarbons (C_8 – C_{40} , phytane and pristane at $500 \mu\text{g mL}^{-1}$ in hexane) was purchased from AccuStandard (New Haven, USA). The analytical standard of polyaromatic hydrocarbons (acenaphthene, acenaphthylene, anthracene, benzo(a)anthracene, benzo(a)pyrene, benzo(b)fluoranthene, benzo(k)fluoranthene, benzo(g,h,i)perylene, chrysene, dibenzo(a,h)anthracene, fluoranthene, fluorine, indeno(1,2,3-cd)pyrene, naphthalene, phenanthrene and pyrene at $100 \mu\text{g mL}^{-1}$ in cyclohexane) was supplied by Dr. Ehrenstorfer GmbH (Augsburg, Germany). The analytical standard of TPH mix was acquired to Supelco (Bellefonte, USA). The above standards were used to verify chromatographic separation quality. Three certified reference materials; PE1800, PE1799 and PE1619 (TPH – water) were acquired from RT – Corp (Laramie, USA). These materials were used to determine the accuracy of the results provided by the proposed analytical procedure. Sep-pak tC_{18} (6 mL/1 g) extraction cartridges of Waters (Massachusetts, USA), Isolute sorbent EPH (25 mL/5 g) extraction cartridges of Biotage (Uppsala, Sweden) and a vacuum manifold Agilent (Santa Clara, USA) were used for sample extraction, fractionation and elution. GC grade acetone, dichloromethane, hexane and methanol were purchased

from Sigma Aldrich (St Louis, USA) and used as extraction solvents. Deionized water and chlorhydric acid from Merck (Darmstadt, Germany) were also employed.

2.2. Water test matrices

Deionized water was spiked with different amount of standards of petroleum hydrocarbons and was used in this study as test matrices to optimize analytical conditions.

2.3. Groundwater samples

The sampling site is located in San Fernando (Cádiz, Spain), in the area known as “La Clica”. The collection area was used as a petrol station during the 1970s, and shows a high degree of oil pollution.

Before taking groundwater samples, water from piezometer was pumped out until stable parameters were established. Monitoring wells were pumped prior to collecting a sample with a 12 V pump; due to an evacuation of a minimum of three volumes of water in the well casing is recommended for a representative sample [25,26] and taking into account Eq. (1):

$$V = \pi \times r \times 2h \quad (1)$$

where V is the static volume of water in well (in m^3), r is the inner radius of well casing (2.54 cm) and h is the length of water column (2 m). And thus, the total volume extracted for each well was 11.7 L.

Groundwater samples were collected in 250 mL amber glass bottles acidified with 5 mL of chlorhydric acid.

Ground-water sample collection should take place 24 h following well purging with bailers made of Teflon[®]. Sampling occurred in a progression from the least to most contaminated well. Likewise, measurements for temperature, pH, ORP, pH, conductivity and O_2 were made in the moment of the sampling.

2.4. Analytical method

Fig. 1 shows a scheme of the developed methodology. In this proposed method 100 mL of groundwater are employed to analyze petroleum hydrocarbons. Groundwater sample is acidified with chlorhydric acid up to pH 2–3 and 10 mL of acetone is poured to the sample in order to avoid adsorption of hydrocarbons on glass walls.

The Sep-pak tC_{18} cartridges are used for the SPE extraction. Firstly, cartridges were conditioned with 10 mL of methanol and then 10 mL of water/methanol 5%. Secondly, when cartridges are still wet, water sample is passed through it at a flow rate of 5 mL min^{-1} . Later, cartridges are dried for 20 min under a stream of nitrogen. Finally, extracts are eluted with 3 mL hexane and 2 mL dichloromethane at a rate of 1 mL min^{-1} . Then, 1 g of anhydrous sodium sulfate is added to take out humidity and extracts are concentrated with nitrogen to 1 mL and go toward the fractionation procedure.

Extracts are fractionated using Isolute EPH cartridges (25 mL/5 g). Cartridges were conditioned prior to sample loading with 30 mL of hexane without letting cartridges become dry. After loading the extract, elution is performed with 12 mL of hexane (aliphatic fraction) and then 20 mL of dichloromethane (aromatic fractions) at flow rate of 2–3 mL min^{-1} . The two fractions are evaporated under nitrogen to 1 mL and finally injected into a GC–FID.

Fractions are analyzed by gas chromatography using an Agilent 7820A equipped with a FID detector, an Agilent G4513A auto sampler with a HP5 capillary column (30 m \times 0.32 mm i.d.) with a nominal film thickness of 0.25 μm . Splitless injection method is

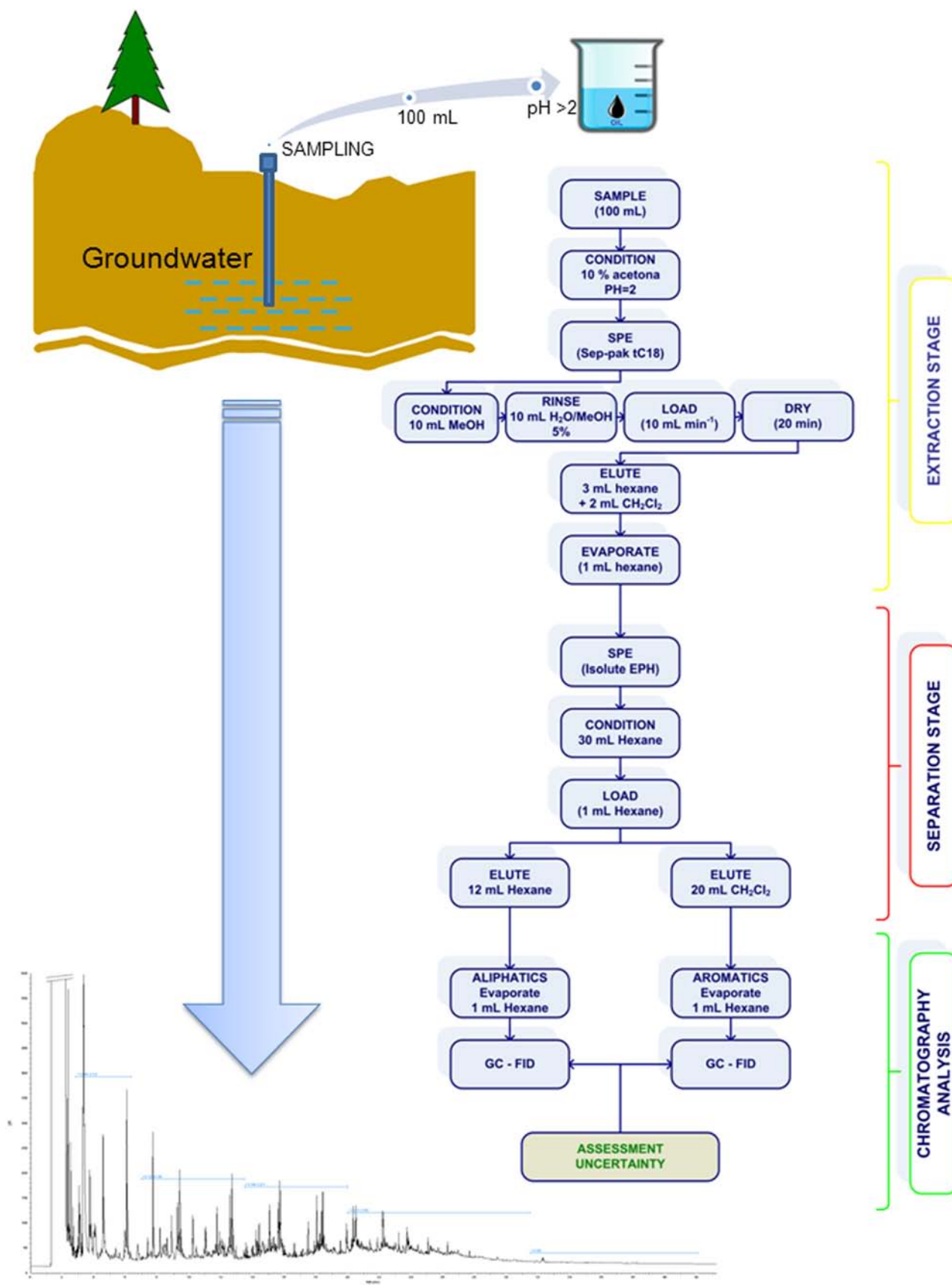


Fig. 1. Scheme of the proposed analytical method for measuring hydrocarbons in groundwater.

employed with a deactivated inlet liner (4 mm i.d.) with glass wood and single taper. Injection temperature was 250 °C, injection volume 3 µL and Helium as carrier gas (10.744 psi). Oven operating conditions are as follows: initial oven temperature 80 °C, increased at a rate of 7 °C min⁻¹ to 200 °C, then increased at rate of 11 °C min⁻¹ to 300 °C and held for 17 min. FID operated at 325 °C and 20 Hz.

2.5. Selection of hydrocarbons fractions

Fractions of aliphatic and aromatic hydrocarbons detected in this work are defined on the basis of their equivalent carbon numbers (EC) and were elsewhere published [27]. Moreover, details of the selection of hydrocarbons fractions can see in the electronic supplementary material (Tables S1–S26). Concretely, Table S1 shows the EC and Table S2 summarizes the ranges of aliphatic and aromatic hydrocarbons.

3. Results and discussion

3.1. Validation of the analytical methodology

The validation of the proposed method is undertaken according to International Union of Pure and Applied Chemistry (IUPAC) [28,29]. The following variables are therefore determined: linearity, sensitivity traceability, bias, accuracy, repeatability, intermediate precision, limit of detection (LOD) and limit of quantification (LOQ).

The use of calibration factors (CF) is the preferred approach to determine the relationship between detector response and range concentration. Six dissolutions at different concentration of hydrocarbons are injected by triplicate to determinate CF as ratio of the summation of the peak areas of all components in that fraction against total concentration injected (Eq. (2)).

$$\text{Range CF} = \frac{\text{Area summation of range components}}{\text{Total concentration injected}} \quad (2)$$

Total concentration injected of each aliphatic and aromatic hydrocarbon ranges are provided in the electronic supplementary material (Table S3). The lowest concentration therefore reflects the lower limit of the linear range, while the highest concentration defined the upper limit. Linearity within this range is proved by the s_r , which must be equal to or less than 25%. Table S4 shows the mean calibration factor values, the working range and s_r for each hydrocarbon fractions.

Sensitivity is studied in terms of magnitude of CF within working range. Results of sensitivity are acceptable for each studied range. It must be noted that sensitivity of >C₂₁–C₃₅ aliphatic range are four times lower than others aliphatic ranges and also sensitivity of >C₂₁–C₃₅ aromatic range are two time lower.

The traceability of the proposed method is demonstrated through recovery experiments, quantifying two certified reference material (CRM): PE-1619 and PE-1799. Each CRM is analyzed eight times. Table 1 summarizes these results.

Traceability is established at two levels of concentration. PE-1619 certifies several ranges of hydrocarbons in water at high concentration and PE-1799 certifies them at low concentration. Results for aliphatic ranges in both certified reference material have shown concentrations slightly lower than the certified value. In the same way, the concentrations measured for aromatic ranges are below the certified concentration, but it is remarkable that these values are within the acceptance limits established in both certified reference material. (Table S5). These results demonstrate

Table 1
Results of recovery test using two certified reference materials.

	Certified value (mg L ⁻¹)	Measure value (mg L ⁻¹)	Mean recovery (%)	s_r (%)	Bias (%)
PE-1619					
Aliphatics					
> C ₁₀ –C ₁₂	8 ± 1	5.3 ± 0.8	67	9	7
> C ₁₂ –C ₁₆	15 ± 3	12 ± 2	78	12	14
> C ₁₆ –C ₂₁	10 ± 2	8 ± 2	74	13	9
> C ₂₁ –C ₃₅	4.0 ± 0.5	3.4 ± 0.4	84	7	3
Aromatics					
> EC ₁₀ –EC ₁₂	8 ± 2	4 ± 1	45	31	54
> EC ₁₂ –EC ₁₆	15 ± 2	7 ± 2	49	22	51
> EC ₁₆ –EC ₂₁	10 ± 2	8 ± 2	81	18	18
> EC ₂₁ –EC ₃₅	6.7 ± 0.7	1.5 ± 0.1	20	3	77
PE-1799					
Aliphatics					
> C ₁₀ –C ₁₂	0.45 ± 0.04	0.50 ± 0.03	102	4	2
> C ₁₂ –C ₁₆	1.8 ± 0.1	1.5 ± 0.3	84	13	16
> C ₁₆ –C ₂₁	1.2 ± 0.1	1.5 ± 0.1	124	5	24
> C ₂₁ –C ₃₅	0.3 ± 0.1	0.7 ± 0.1	> 150	5	57
Aromatics					
> EC ₁₀ –EC ₁₂	0.58 ± 0.06	0.4 ± 0.3	56	56	43
> EC ₁₂ –EC ₁₆	1.8 ± 0.2	1.2 ± 0.2	64	37	35
> EC ₁₆ –EC ₂₁	0.92 ± 0.08	0.9 ± 0.5	97	10	2
> EC ₂₁ –EC ₃₅	0.250 ± 0.007	0.5 ± 0.1	> 150	8	50

that the proposed procedure is suitable to extract and fractionate the hydrocarbons present in groundwater.

The bias of the proposed analytical method is related to systematic errors and may be expressed as an analytical recovery. The recovery experiments allowed the closeness of agreement between the measured value and the true concentration to be examined. Table 1 shows the results obtained. It is found that recovery of the aliphatic ranges is higher than the aromatic ranges at both levels of concentration. Lower recoveries showed by aromatic ranges are attributed to losses during the second solid phase extraction, because part of these compounds could pass joined to the first fraction. Nevertheless, it is noticeable recoveries showed by the aliphatic ranges are higher than 70% and higher than 50% for the aromatic ranges, at two different levels of concentrations. The results of >C₂₁–C₃₅ aliphatic and aromatic ranges, at low concentration, show bigger bias, being the signal overestimated by the proposed procedure. Because these ranges are less abundant and show good accuracy (less of 8%), this may be due to these ranges are more susceptible to interference from the sample matrices, and thus a more thoroughly cleaning procedure must be accomplished. According to the standard deviation, results have shown analysis of the aliphatic ranges is more accurate than analysis of the aromatics ranges. Relative deviation standard for the aliphatic hydrocarbons has been up to 13%, and meanwhile for aromatic hydrocarbons has been generally higher than 20%.

Several precision measures are available for validating an analytical procedure. Precision is determined in terms of intra-day precision (repeatability) and inter-day test (intermediate precision). Repeatability is determined by repeating the whole procedure on the same day. It is calculated from the coefficient of variation for eight aliquots. Intermediate precision is calculated from the relative standard deviation of twelve aliquots carried out on different days. Table 2 shows the values of the precision parameters.

Repeatability and intermediate precision expressed as relative standard deviation (%) at two levels of concentration are satisfactory. As expected, intermediate precision shows higher values than repeatability for most of the aliphatic and aromatic ranges. No significant differences are found between the aliphatic and

aromatic ranges and between the two levels of concentration. With the exception of the repeatability of the $>C_{10}$ – C_{12} aromatics range, the rest of values lies below the relative standard deviation certificated, namely a s_r of 30% for low concentration and a s_r of 20% for high concentration. Thus, it is confirmed that analyzing aliphatics and aromatics ranges in water is precise at low and high level of concentration.

To confirm the sensitivity of the developed procedure, spiked blanks are used to calculate LODs and LOQs. Eight blanks, consisted by 100 mL of acidified water at pH 2, are spiked with hydrocarbons at a level of $0.1 \mu\text{g mL}^{-1}$. These blanks are analyzed according to the procedure. LOD is calculated as three times the standard deviation and LOQ is calculated as ten times the standard deviation. Table 3 summarized the results.

It must be highlighted that LOD and LOQ are mainly theory. According to the bias of $>C_{21}$ – C_{35} aliphatic and $>C_{21}$ – C_{35} aromatic ranges at low concentration, as can be seen in Table 1, LOD and LOQ must be higher than those showed in Table 3. Considering the bias, these results lead us to conclude that LOD and LOQ for these ranges should be lower than 0.5 mg L^{-1} .

3.2. Assessment of uncertainty associated with the proposed methodology

The term uncertainty is widely known, and related to the general concept of doubt, but not implies doubt about the validity of a measurement, in fact implies increased confidence in the validity of a measurement result [30]. There are several

Table 2
Repeatability and intermediate precision at two levels of concentration.

	Low concentration (PE-1799)		High concentration (PE-1619)	
	Repeatability ($n=4$) s_r (%)	Precision ($n=8$) s_r (%)	Repeatability ($n=8$) s_r (%)	Precision ($n=12$) s_r (%)
Aliphatics				
$>C_{10}$ – C_{12}	36	31	17	26
$>C_{12}$ – C_{16}	13	20	10	21
$>C_{16}$ – C_{21}	5	22	13	25
$>C_{21}$ – C_{35}	5	24	15	14
Aromatics				
$>EC_{10}$ – EC_{12}	56	59	15	23
$>EC_{12}$ – EC_{16}	37	29	11	18
$>EC_{16}$ – EC_{21}	10	12	9	24
$>EC_{21}$ – EC_{35}	8	14	8	18

Table 3
Limits of detection and quantification for the analysis of hydrocarbons in water.

	Limit of detection ($\mu\text{g L}^{-1}$)	Limit of quantification ($\mu\text{g L}^{-1}$)
Aliphatics		
$>C_{10}$ – C_{12}	2	5
$>C_{12}$ – C_{16}	1	3
$>C_{16}$ – C_{21}	3	9
$>C_{21}$ – C_{35}	5	18
$>C_{35}$	2	8
Aromatics		
$>EC_{10}$ – EC_{12}	0.3	1
$>EC_{12}$ – EC_{16}	1	2
$>EC_{16}$ – EC_{21}	1	4
$>EC_{21}$ – EC_{35}	1	5
$>EC_{35}$	2	6

approached to evaluate measurement uncertainty. The bottom-up approach enables estimating measurement uncertainty in four steps: first, specify the measurand, second, identify each uncertainty source, later quantify all components and finally calculate combined and expanded uncertainty.

In order to specify the measurand, the relationship between measurand and input quantities upon which it depends must be clearly defined. Thus, the hydrocarbons range concentration in groundwater, is obtained from Eq. (3):

$$[HC] = \frac{A \times V_f}{CF \times V_s \times R} \quad (3)$$

where $[HC]$ is the concentration of each range of hydrocarbons, A is the sum of the area of each range components; V_f is the final diluted volume before injection into gas chromatograph; CF is the calibration factor, V_s is the volume of groundwater analyzed and R is the recovery.

The second step is to identify each uncertainty source. All parameters in Eq. (3) have an uncertainty associated with their values and therefore are sources of uncertainty. Moreover, there are other parameters than are not explicit in Eq. (3) and could affect to concentration of hydrocarbons in water.

Uncertainty associated to the concentration of an analyte from a calibration curve is a combination of several uncertainties, being the most significant and thus the unique evaluated in this study the random variations in the peak area. Preparation of standard solutions to calculate CF involves preparation of calibration solutions from pure compounds, and therefore contribution of volume, purity and mass of each compound must be assessed. Influence of repeatability is calculated, where factors as instrument precision and interferences from matrix or reagents have been considered. Uncertainty associated to volume includes uncertainty of calibration, which is given by manufacturer of volumetric material, uncertainty due to variations in filling of volumetric material and also variations in temperature may be affecting to volume. Several factors contribute to uncertainty associated with the loss of hydrocarbons mass during the analytical procedure. This uncertainty has been evaluated as uncertainty derived from recovery. This recovery study take into account the influence of each stage of the analytical procedure as well as other sources of uncertainty associated to the sample preparation as being homogeneity of sample, dissolution of sample or the fractionation by SPE.

3.2.1. Uncertainty associated to area

The data acquisition system of the GC used returned the FID signal in picoamperes (pA), and the chromatographic peak area is therefore measured in pA s^{-1} . According to manufacturer, the data acquisition system has a resolution of 1 pA s^{-1} ; the uncertainty associated with the peak area is therefore calculated assuming a rectangular distribution according to Eq. (4).

$$u_r(A) = \frac{u(A)}{A} = \left(\frac{r/\sqrt{3}}{A} \right) \quad (4)$$

where A is the chromatographic area of the precision study and r the resolution. It is demonstrated that uncertainty derived for the area is negligible, due to hydrocarbons range areas measured are large. More details are summarized in the electronic supplementary material (Table S6).

3.2.2. Uncertainty from volume

Three uncertainty components are taken into account to calculate uncertainty associated with the volume: influence of temperature, tolerance of volumetric material and repeatability. The uncertainty associated with the variations in temperature is calculated via the coefficient of expansion of n -hexane (for

syringe) and water (for pipette) assuming a rectangular distribution for a temperature variation of 20 ± 5 °C. The volumetric accuracy of the volumetric material, syringe and pipette, is calculated assuming a triangular distribution for the smallest marked divisions of the volumetric material used. The uncertainty of repeatability is due to variations in filling the volumetric material to the mark and is calculated by the standard deviation obtained from eight weightings of the volumetric material full of solvent. Consequently, uncertainty due to volume is given in Eq. (5).

$$u_r(V) = \frac{u(V)}{V} = \sqrt{\left(\frac{V \times \Delta T \times C_e}{\sqrt{3}}\right)^2 + \left(\frac{v_m/\sqrt{6}}{V}\right)^2 + \left(\frac{s}{m}\right)^2} \quad (5)$$

The detailed estimation of the uncertainty associated with the volume of the syringe and the pipette are explained in the supplementary material: Table S7–S10 (uncertainty from the volume of the pipette) and Table S11–S14 (uncertainty from the volume of the syringe). Concretely, the $u_r(V_{\text{pipette}}) = 5.65 \times 10^{-3}$ and $u_r(V_{\text{syringe}}) = 60.2 \times 10^{-3}$.

3.2.3. Uncertainty derived from estimation of calibration factor

The expression to calculate CF for each hydrocarbon range is shown in Eq. (6), where A_r is the sum of the peak areas of all components and C_i is the total concentration injected in that fraction.

$$CF = \frac{1}{n} \sum_{i=1}^n \left(\frac{A_r}{C_i}\right) \quad (6)$$

Thus, the uncertainty associated with the estimation of the CF is a combination of two uncertainties: first, the contribution of the chromatographic area and second, the concentration of standard solutions (Eq. (7)). These sources are, in turn, combinations of several other uncertainties.

$$u_r(CF) = \sqrt{\left(\frac{u(A_{std})}{A_{std}}\right)^2 + \left(\frac{u(C_{std})}{C_{std}}\right)^2} \quad (7)$$

3.2.3.1. Uncertainty due to chromatography area of standard solutions. The uncertainty of chromatography area of the standard solutions has two components: the uncertainty associated with resolution of the data acquisition system (similar to that described in Section 4.2.1) and uncertainty due to the repeatability. A standard solution, at a concentration within the corresponding calibration range is injected eight times, and the uncertainty due to chromatography area is determined as follows in Eq. (8).

$$u_r(A_{std}) = \sqrt{\left(\frac{r/\sqrt{3}}{A_{std}}\right)^2 + \left(\frac{s}{A_{std}}\right)^2} \quad (8)$$

The results of this uncertainty can be seen in the electronic supplementary material (Fig. S1 and Table S15–S25).

3.2.3.2. Uncertainty derived from preparation of standard solutions. In order to estimate CF for each hydrocarbon fraction, six standard solutions at different concentrations (in triplicate) are prepared by dilution of the analytical standards according to Eq. (9):

$$C_{std} = C_0 \times \frac{V_0}{V_f} \quad (9)$$

where C_{std} is the concentration of the calibrate solution, C_0 is the concentration of the initial standard solution, V_0 is the volume of

standard solution and V_f is the final volume of calibrate solution. Concentrations of each calibration solution are summarized in the electronic supplementary material (Table S3). Therefore, the uncertainty derived from preparation of standard solutions is calculated according to Eq. (10):

$$u_r(C_{std}) = \sqrt{\left(\frac{u(C_0)}{C_0}\right)^2 + \left(\frac{u(V_f)}{V_f}\right)^2 + \left(\frac{u(V_0)}{V_0}\right)^2} \quad (10)$$

The uncertainty associated with concentration of the initial standard is provided by the manufacturer. The uncertainties associated with the volume were calculated according to Eq. (5). Specifically, two syringes of 50 and 100 μL were employed to prepare the calibration solutions. Table S24 summarizes uncertainty associated to each calibration solution. More details can be seen in the electronic supplementary material.

Thus, the uncertainty associated with the preparation of the standard solution for each range of hydrocarbons is the sum of the uncertainties associated with each calibration solution. This uncertainty can be determined according to Eq. (11):

$$u_r(C_{std})_{total} = \sqrt{\sum_{i=1}^n \left(\frac{u(C_{std})}{C_{std}}\right)^2} \quad (11)$$

After assessing the contributions to the uncertainty of the calibrate factor, Table S25 summarizes each uncertainty calculated according to Eq. (7).

3.2.4. Uncertainty from recovery

The recovery study is performed using the certified reference material PE-1619. Eight replicates are used and the percentage recovery is calculated as in Eq. (12):

$$R(\%) = \left(\frac{C_{found}}{C_{real}}\right) \quad (12)$$

The uncertainty associated with the recovery value covers among others the contribution from incomplete extraction by SPE, losses through evaporation, losses onto glassware material, incomplete fractionation by SPE and the stability of GC/FID instrument. This uncertainty can be calculated according to Eq. (13).

$$u_r(R) = \left(\frac{s/\sqrt{n}}{R}\right) \quad (13)$$

Table S26 provides the uncertainty associated with the recovery value for each hydrocarbon fraction.

3.2.5. Estimation of combined and expanded uncertainty

Once all individual contributions are calculated, combined uncertainty for the SPE/SPE/GC–FID method is evaluated. The uncertainty on the result may arise from many possible sources. For the purpose of choosing main uncertainty components, Figs. 2 and 3 displays the relative standard uncertainty of the five sources identified, $u(V_f)$, $u(A)$, $u(CF)$, $u(R)$, $u(V_s)$ for each aliphatic and aromatic hydrocarbon respectively.

Relative standard uncertainties displayed in Fig. 2 have confirmed that uncertainty associated with the chromatographic area can be dismissed. Main contributions to uncertainty are those due to volume of sample, determination of calibration factor and recovery. Thus, in order to decrease uncertainty associated to analysis of ranges of aliphatics compounds, these contributions should be reduced as much as possible. Uncertainty of the volume of the analysed groundwater is due to volumetric material employed while uncertainty associated with calibration factor is due to repeatability of GC–FID and to calibration standards. It would

therefore be very hard to make any practical improvement in these two uncertainties. Nevertheless, the use of new chromatography columns and more robust detectors will enable to reduce the uncertainty associated. However, the uncertainty related to recovery can be reduced somewhat. Some authors have associated this contribution to losses of volatile compounds during concentration under a gentle stream of N₂, and because of adsorption of hydrocarbons on glass walls. In addition, extraction of the sample might be optimized to reduce the losses of the most volatile compounds. The micro solid phase extraction (MSPE) is an adequate alternative to analyse the most volatile compounds but have to be optimized to evaluate the TPH in environmental matrices.

As can be seen in Fig. 3, relative standard uncertainties of aromatics hydrocarbons shows similar pattern to aliphatic hydrocarbons. It is noteworthy that the uncertainty associated to the calibration factor of the heaviest aromatic hydrocarbons is high. This contribution comes from dispersion of chromatographic peak areas of these compounds.

For a measurement result, the combined uncertainty denoted by $u_c(HC)$ is a estimated standard deviation equal to the positive square root of the total variance obtained by combining the five uncertainty components. Because the five individual contributions to uncertainty are not independent, combined uncertainty must be calculated including covariance between parameters according to

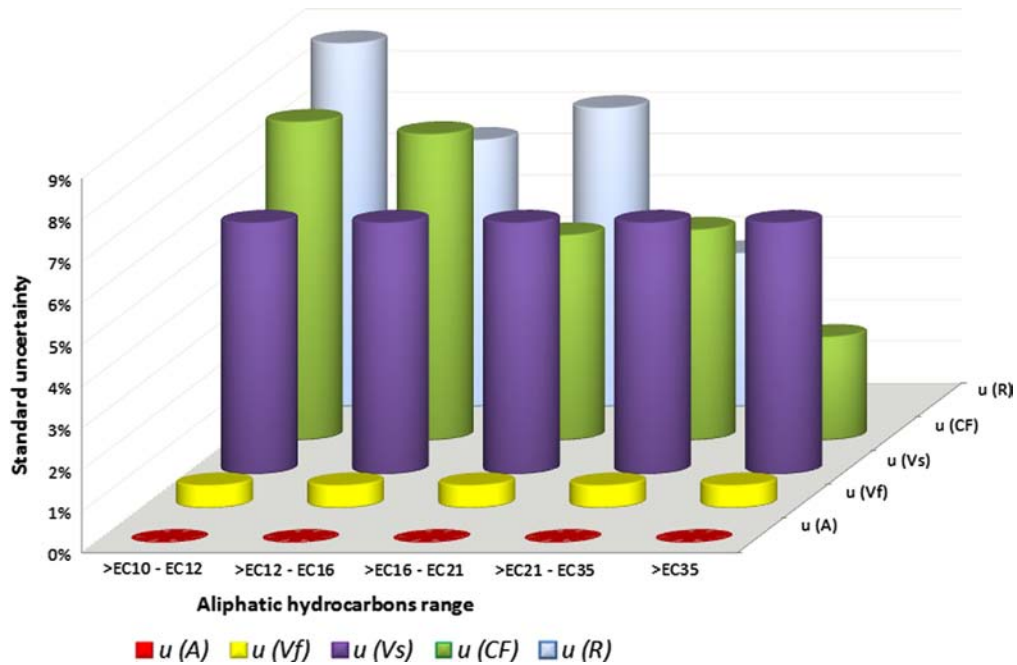


Fig. 2. Standard uncertainty for aliphatic hydrocarbons range.

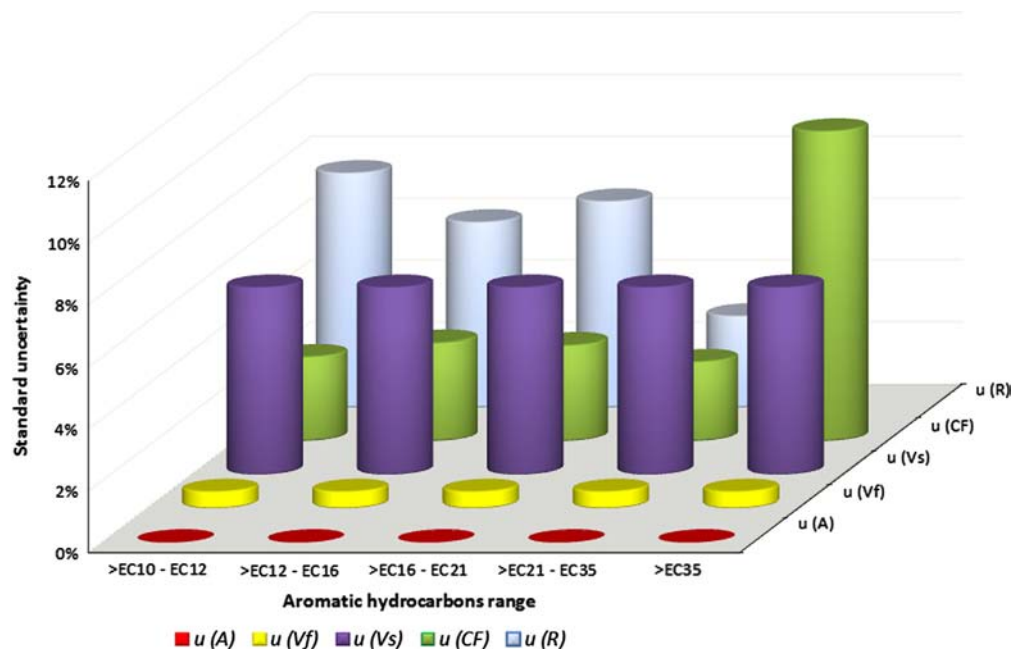


Fig. 3. Standard uncertainty for aromatic hydrocarbons range.

Eq. (14):

$$u_c(HC)^2 = u_r(A)^2 + u_r(V_f)^2 + u_r(CF)^2 + u_r(V_s)^2 + u_r(R)^2 + u_r(A)^2 u_r(V_f)^2 + u_r(A)^2 u_r(CF)^2 + u_r(A)^2 u_r(V_s)^2 + u_r(A)^2 u_r(R)^2 + u_r(V_f)^2 u_r(CF)^2 + u_r(V_f)^2 u_r(V_s)^2 + u_r(V_f)^2 u_r(R)^2 + u_r(CF)^2 u_r(V_s)^2 + u_r(CF)^2 u_r(R)^2 + u_r(V_s)^2 u_r(R)^2 \quad (14)$$

For most purposes in analytical chemistry, an expanded uncertainty, denoted by U_{exp} , should be used. This is the reason why the last step in determining the overall uncertainty is to calculate the expanded uncertainty by multiplying the combined standard uncertainty by a coverage factor, according to Eq. (15):

$$U_{exp}(HC) = u_c(HC) \times k \quad (15)$$

where k is set to 2, because the combined uncertainty is based on statistical observations with more than six degrees of freedom. The expanded uncertainty provides an interval which may be expected to encompass a large fraction of the distribution of values which could reasonably be attributed to measurand. Table 4 summarizes the combined and the expanded uncertainty.

Uncertainty of measurement does not imply doubt about the validity of a measurement; on the contrary, knowledge of the uncertainty implies increased confidence in the validity of a measurement result [30]. The values of the expanded uncertainty, range between 13 and 26% for the aliphatic hydrocarbons, and between 14 and 23% for the aromatics hydrocarbons, and thus there are not

Table 4
Combined and expanded uncertainty.

Aliphatic hydrocarbons	u_c (%)	U_{exp} (%)	Aromatic hydrocarbons	u_c (%)	U_{exp} (%)
> C ₁₀ –C ₁₂	13	26	> EC ₁₀ –EC ₁₂	10	20
> C ₁₂ –C ₁₆	12	23	> EC ₁₂ –EC ₁₆	9	18
> C ₁₆ –C ₂₁	11	21	> EC ₁₆ –EC ₂₁	10	19
> C ₂₁ –C ₃₅	9	18	> EC ₂₁ –EC ₃₅	7	14
> C ₃₅	7	13	> EC ₃₅	12	23

significant differences between the ranges studied in this work. Unfortunately, there are not published values of the uncertainty associated to the analysis of the aliphatic and the aromatic hydrocarbons by others procedures. Furthermore, these values are in concordance with others works that have evaluated the analysis of several organic compounds in complex environmental matrices [31–34]. Moreover, the certified reference materials of hydrocarbons in water matrix showed errors of 30%, so that the values of expanded uncertainty calculated in this work are below it.

3.3. Analysis of groundwater samples

To evaluate the efficiency of the proposed method in real samples, we successfully applied the method to assay aliphatic and aromatic hydrocarbon ranges in groundwater samples. For this purpose, nine groundwater samples collected in an area contaminated by hydrocarbons during a sampling campaign in the summer of 2013 are analyzed.

It is well known that the real life hydrocarbons mixtures in groundwater are complex and show a wide spectrum of GC–FID chromatograms, depending of the sources of hydrocarbons and the geologic environment in which they migrated and from which reservoir [35]. If hydrocarbons are generated from fresh light distillates, the chromatogram will be featured with dominance of light-end, resolved hydrocarbons and minimal unresolved complex mixture of hydrocarbons (UCM). However, if diesel fuels are the principal components, the chromatograms will be dominated by resolved peaks in the C₁₀–C₁₇ range and will show the UCM. On the other hand, if heavy fuels are majority, the chromatograms will show broad resolved alkanes in the C₁₄–C₃₆ range and a large UCM.

Overlapping the nine chromatograms of aliphatic hydrocarbons (Fig. 4) and of aromatic hydrocarbons (Fig. 5) analyzed in groundwater samples is presented.

As can be seen in Fig. 4, GC–FID chromatograms provide a similar fingerprint for all samples analyzed. The aliphatic hydrocarbons are demonstrated to be composed of two sources:

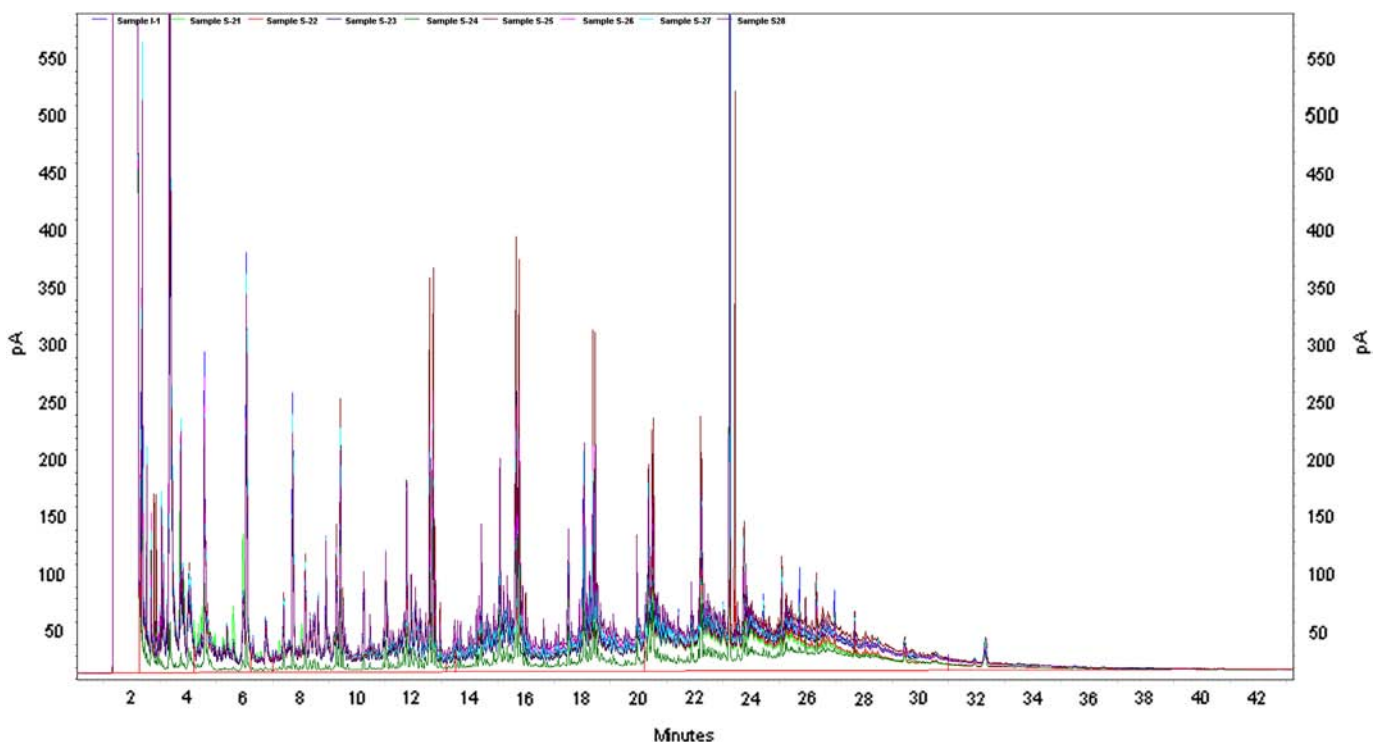


Fig. 4. Overlapping of nine chromatograms of aliphatic hydrocarbons measured in groundwater.

mid-range distillates attributed to a relative broad carbons range C₆–C₂₆ can be due to diesel fuels; and slightly higher-molecular-mass hydrocarbons could be attributed to heavy petroleum products. The resolved peaks in the C₁₀–C₁₇ range confirm diesel meanwhile the resolved peaks up to C₂₅ confirm heavy petroleum products.

As we can see in Fig. 5, these chromatograms showed low-molecular-mass hydrocarbons due to these compounds are the most soluble hydrocarbons in water. It is well known that light distillate gasoline has considerable amounts of aromatics compounds, so these compounds can be attributed to light petroleum products such as automotive gasoline.

Table 5 summarizes the concentration and uncertainty of the nine groundwater samples analysis, indicating that all of the samples are polluted by petroleum hydrocarbons. The selected area was used as petrol station during the 1970s. Thanks these results the authors could attribute this contamination to the stored fuels during the 1970s. These hydrocarbons have polluted the soils and also the groundwater, possibly due to losses in the connections or accidental spills. Nowadays this area has been selected to

identify the best strategy to attain a sensible reduction of contamination levels by different technologies related to restoration of soil contamination [36].

In general, concentrations of aliphatic and aromatics ranges, are relatively stable in the nine samples analyzed. Only, sample S-25 shows a different distribution pattern. This could be attributed to sampling issue. It is interesting to note that >C₁₆–C₂₁ and >C₂₁–C₃₅ aliphatic ranges show high abundance. This is because these hydrocarbons are common constituent of diesel. On the other hand, aromatic ranges of low-molecular-mass hydrocarbons are the most abundant, which can be attributed to automotive gasoline.

Results from groundwater samples confirmed that this area is contaminated by petroleum hydrocarbon, which may have harmful health and environmental effects.

4. Conclusion

This work describes a new analytical procedure for quantifying the fractions of aliphatic and aromatic hydrocarbons in groundwater.

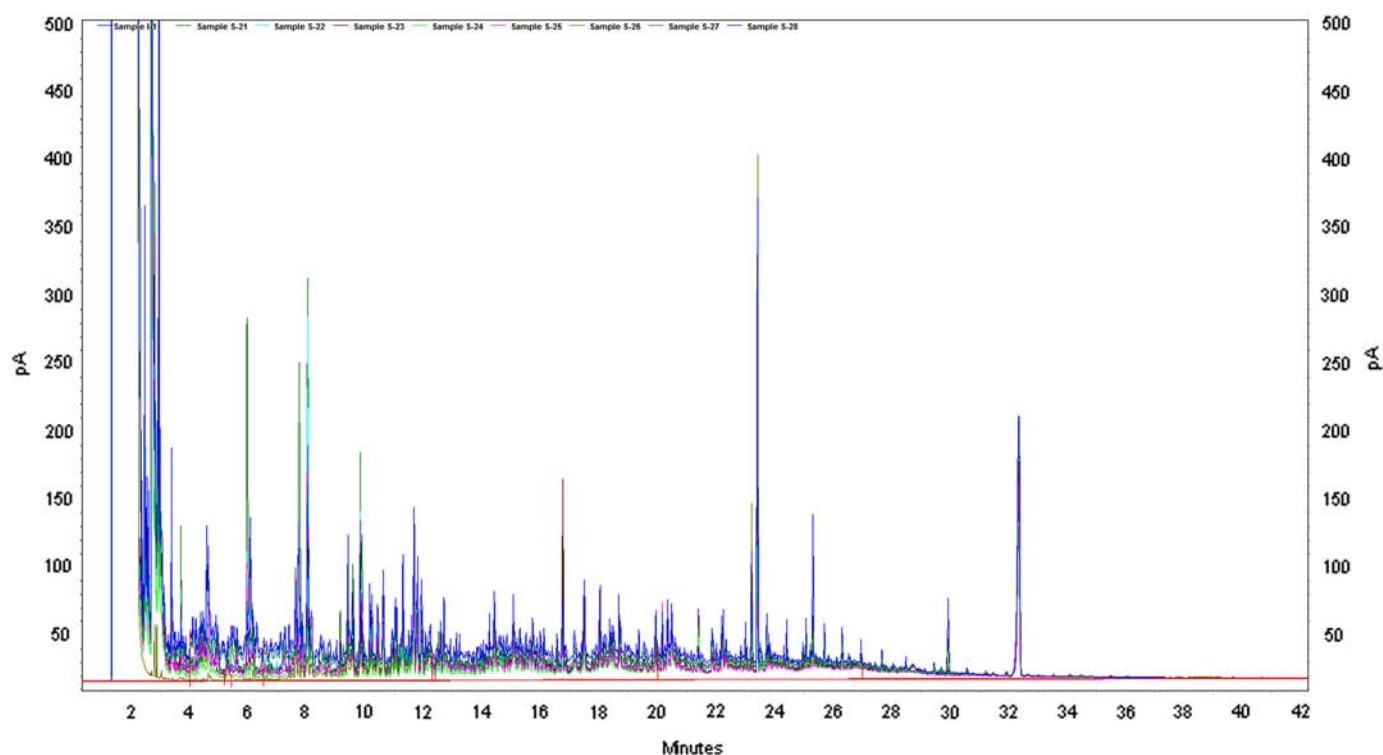


Fig. 5. Overlapping of nine chromatograms of aromatic hydrocarbons measured in groundwater.

Table 5

Concentration and uncertainty associated with the analysis of ranges of hydrocarbons in groundwater.

	Aliphatics ($\mu\text{g L}^{-1}$)					Aromatics ($\mu\text{g L}^{-1}$)				
	> C ₁₀ –C ₁₂	> C ₁₂ –C ₁₆	> C ₁₆ –C ₂₁	> C ₂₁ –C ₃₅	> C ₃₅	> C ₁₀ –C ₁₂	> C ₁₂ –C ₁₆	> C ₁₆ –C ₂₁	> C ₂₁ –C ₃₅	> C ₃₅
I-1	51 (10)	138 (30)	186 (40)	354 (60)	75 (10)	64 (13)	170 (30)	124 (20)	67 (9)	33 (8)
S-21	70 (20)	162 (40)	183 (40)	228 (40)	31 (4)	21 (4)	110 (20)	80 (10)	33 (5)	5 (1)
S-22	48 (10)	136 (30)	160 (30)	243 (40)	47 (6)	b.d.l	64 (10)	88 (20)	27 (4)	9 (2)
S-23	19 (5)	94 (20)	129 (30)	270 (50)	82 (10)	b.d.l	13 (2)	26 (5)	b.d.l	b.d.l
S-24	b.d.l	44 (10)	89 (20)	215 (40)	53 (7)	11 (2)	64 (10)	43 (8)	b.d.l	b.d.l
S-25	b.d.l	b.d.l	b.d.l	b.d.l	13 (2)	b.d.l	50 (9)	147 (30)	76 (10)	12 (3)
S-26	24 (6)	122 (30)	211 (40)	296 (50)	70 (9)	37 (7)	86 (10)	88 (20)	31 (4)	14 (3)
S-27	24 (6)	88 (20)	115 (20)	253 (50)	73 (9)	55 (11)	167 (30)	197 (40)	112 (16)	24 (6)
S-28	11 (3)	97 (20)	181 (40)	245 (40)	56 (7)	64 (13)	170 (30)	124 (20)	67 (9)	33 (8)

b.d.l.: Below detection limit.

The method involves a double solid phase extraction and then GC–FID analysis. By using the first solid phase extraction (reverse phase), the hydrocarbons are extracted from groundwater, meanwhile the second solid phase extraction (normal phase) is accomplished for fractionating hydrocarbons into aliphatics and aromatics. The method is more environmentally friendly than the conventional methods currently in use because less amount of sample is employed and thus less organic solvent is need.

The developed method shows adequate validation parameters such as linearity, sensitivity, bias, accuracy, traceability, repeatability, and intermediate precision, and has appropriate limits of detection and quantification. Moreover, an easy to follow guide for calculating the uncertainty associated to this procedure is described. In fact, five uncertainty sources are identified, a detailed analysis of each contributions is carried out and finally, the combined and expanded uncertainty is established. In terms of results, the expanded uncertainty range from 13% to 26% (Aliphatics hydrocarbons) and from 14% to 23% (aromatics hydrocarbons).

The proposed method provides a rapid, environmentally friendly and accurate method for identifying and quantifying the aliphatic and aromatic hydrocarbons contaminating the groundwater. It becomes, therefore, a good choice accurately determinate the ranges of hydrocarbons in groundwater by using the developed method. In order to confirm it, this work applies the developed methodology to analyze the ranges of aliphatic and aromatic hydrocarbons in the groundwater from “La Cllica”, an area with high degree of oil pollution because it was used as petrol station in the 70s. Our results clearly provide the viability of this methodology to be employed in real samples.

Acknowledgements

This work is part of the project “New approach on soil remediation by combination of biological and chemical oxidation processes” (BIOX-ISOIL). The authors thank the funding received from LIFE+2011 Environment policy and governance project application (LIFE11 ENV/ES/505).

Appendix A. Supporting information

Supplementary data associated with this article can be found in the online version at <http://dx.doi.org/10.1016/j.talanta.2014.06.042>.

References

- [1] EC 2006, Directive 2006/11/EC on the Protection of Groundwater Against Pollution and Deterioration.
- [2] E. Saari, P. Peramaki, J. Jalonen, *Microchem. J.* 87 (2) (2007) 113–118. <http://dx.doi.org/10.1016/j.microc.2007.06.002>.
- [3] F. Coulon, M.J. Whelan, G.I. Paton, K.T. Semple, R. Villa, S.J.T. Pollard, *Chemosphere* 81 (11) (2010) 1454–1462.
- [4] D. Mao, R. Lookman, H. Van de Weghe, R. Weltens, G. Vanermen, N. De Brucker, L. Diels, *Environ. Sci. Technol.* 43 (20) (2009) 7651–7657. <http://dx.doi.org/10.1021/es9015603>.
- [5] EC 1975, Directive 76/160/CEE on Quality of Bathing Water.
- [6] EC 2006, Directive 2006/7/CE on Quality of Bathing Water.
- [7] Analysis of Petroleum Hydrocarbons in Environmental Media 1998. Total Petroleum Hydrocarbons Criteria Working Group.
- [8] G. Moussavi, A. Bagheri, *Environ. Technol.* 33 (16) (2012) 1905–1912. <http://dx.doi.org/10.1080/09593330.2011.650223>.
- [9] J.M.E. Ahad, L. Burns, S. Mancini, G.F. Slater, *Environ. Sci. Technol.* 44 (13) (2010) 5092–5097. <http://dx.doi.org/10.1021/es100080c>.
- [10] I. Zrafi-Nouira, Z. Khedir-Ghenim, R. Bahri, I. Cheraeif, M. Rouabhia, D. Saidane-Mosbahi, *Water Air Soil Pollut.*, 202, 200919–31. <http://dx.doi.org/10.1007/s11270-008-9955-x>.
- [11] I.A. Ololade, L. Lajide, I.A. Amoo, *Cent. Eur. J. Chem.* 7 (1) (2009) 83–89. <http://dx.doi.org/10.2478/s11532-008-0086-4>.
- [12] H. Shim, W. Ma, A. Lin, K. Chan, *Environ. Sci.—China* 21 (6) (2009) 758–763. [http://dx.doi.org/10.1016/s1001-0742\(08\)62337-2](http://dx.doi.org/10.1016/s1001-0742(08)62337-2).
- [13] WHO 2008, Petroleum Products in Drinking-Water. Background Document for Development of WHO Guidelines for Drinking-water Quality. WHO/SDE/WSH/05.08/123.
- [14] G. Reeves, *Understanding and Monitoring Hydrocarbons in Water*, Arjay Engineering Ltd, Oakville, Ontario, Canada, 2000.
- [15] X. Zhu, A.D. Venosa, M.T. Suidan, EPA/600/R-04/075. Cincinnati, USEPA, 2004.
- [16] 9377-2:2000 DI 2000, Water quality—Part 2 Method Using Solvent Extraction and Gas Chromatography. International Organization for Standardisation, Geneva.
- [17] S. Drozdova, W. Ritter, B. Lendl, E. Rosenberg, *Fuel* 113 (2013) 527–536. <http://dx.doi.org/10.1016/j.fuel.2013.03.058>.
- [18] J.B. Gustafson, J.G. Tell, D. Orem (ed.), *Selection of Representative TPH Fractions Based on Fate and Transport Considerations*, vol. 3, Amherst Scientific Publishing, Amherst, MA, 1997.
- [19] W. Weisman (vol), *Petroleum Hydrocarbon Analysis of Soil and Water in the Environment*, vol. 1, Amherst Scientific Publishers, Amherst, MA, 1997.
- [20] X. Song, J. Li, S. Xu, R. Ying, J. Ma, C. Liao, D. Liu, J. Yu, L. Chen, *Talanta* 99 (0) (2012) 75–82.
- [21] S. Xingliang, L. Jinhua, L. Chunyang, C. Lingxin, *Chromatographia* 74 (1) (2011) 89–98.
- [22] J. Ma, R. Xiao, J. Li, J. Yu, Y. Zhang, L. Chen, *J. Chromatogr. A* 1217 (34) (2010) 5462–5469.
- [23] E. Rozet, R.D. Marini, E. Ziemons, B. Boulanger, P. Hubert, *J. Pharm. Biomed. Anal.* 55 (4) (2011) 848–858.
- [24] E. Saari, P. Perämäki, J. Jalonen, *Anal. Bioanal. Chem.* 392 (6) (2008) 1231–1240.
- [25] USEPA, RCRA Ground-water Monitoring Technical Enforcement Guidance Document, OSWER-9950.1 U.S. government Printing Office, Washington, 1986.
- [26] F.D. Wilde, D.B. Radtke, J. Gibs, R.T. Iwatsubo, National Field Manual for the Collection of Water-quality Data. U.S. Geological Survey Techniques of Water-resources Investigations, Book 9, Handbooks for Water-resources Investigations, Variousy Paginated, 1998.
- [27] O. Pindado Jiménez, R.M. Pérez Pastor, O. Escolano Segovia, *Validation and Assessment Uncertainty of the Determination of Petroleum Hydrocarbons Fractions in Soils*, *Accred Qual Assur.* 2013.
- [28] M. Thompson, S.L.R. Ellison, R. Wood, *Pure Appl. Chem.* 74 (5) (2002) 835–855.
- [29] EURACHEM 1996, The Fitness for Purpose of Analytical Methods. A Laboratory Guide to Method Validation and Related Topics.
- [30] EURACHEM 2000, CITAC Guide CG 4. Quantifying Uncertainty in Analytical Measurement. Second ed..
- [31] A. Díaz, L. Vázquez, F. Ventura, M.T. Galceran, *Anal. Chim. Acta* 506 (1) (2004) 71–80.
- [32] N. Ratola, L. Santos, P. Herbert, A. Alves, *Anal. Chim. Acta* 573–574 (2006) 202–208.
- [33] I. Ortiz González, R.M. Pérez Pastor, J.M. Sánchez Hervás, *Talanta* 87 (0) (2011) 60–66.
- [34] O.P. Jiménez, R.M.P. Pastor, *Aerosol Air Qual. Res.* (2014), <http://dx.doi.org/10.4209/aaqr.2013.07.0250>.
- [35] Z.D. Wang, K. Li, M. Fingas, L. Sigouin, L. Menard, *J. Chromatogr. A* 971 (1–2) (2002) 173–184. [http://dx.doi.org/10.1016/s0021-9673\(02\)01003-8](http://dx.doi.org/10.1016/s0021-9673(02)01003-8).
- [36] BIOXISOIL (LIFE+2011 Environment Policy and Governance Project Application) New Approach on Soil Remediation by Combination of Biological and Chemical Oxidation Processes. (<http://www.bioxisoil.eu/en/>).



Removal of copper and iron by polyurethane foam column in FIA system for the determination of nickel in pierced ring



Monnapat Vongboot*, Monrudee Suesoonthon

Department of Chemistry, Faculty of Science, King Mongkut's University of Technology Thonburi, 126 Pracha-utid Road, Bangmod, Bangkok 10140, Thailand

ARTICLE INFO

Article history:

Received 25 May 2014

Received in revised form

30 July 2014

Accepted 31 July 2014

Available online 7 August 2014

Keywords:

Nickel determination

Polyurethane foam column

FIA system

Pierced rings

ABSTRACT

Polyurethane foam (PUF) mini-column was used to eliminate copper and iron for the determination of nickel in pierced rings. The PUF mini-column was connected to FIA system for on-line sorption of copper and iron in complexes form of CuSCN^+ and FeSCN^{2+} . For this season, the acid solution containing a mixture of Ni(II), Fe(III), Cu(II) and SCN^- ions was firstly flew into the PUF column. Then, the percolated solution which Fe(III) and Cu(II) ions is separated from analysis was injected into FIA system to react with 4-(2-pyridylazo) resorcinol (PAR) reagent in basic condition which this method is called pH gradient technique. The Ni–PAR complexes obtained were measured their absorbance at 500 nm by UV visible spectrophotometer. In this study, it was found that Cu(II) and Fe(III) were completely to form complexes with 400 mmol/L KSCN and entirely to eliminate in acidic condition at pH 3.0. In the optimum condition of these experiments, the method provided the linear relationship between absorbance and the concentration of Ni(II) in the range from 5.00 to 30.00 mg/L. Linear equation is $y = 0.0134x + 0.0033$ ($R^2 = 0.9948$). Precision, assessed in the term of the relative standard deviation, RSD, and accuracy for multiple determinations obtained in values of 0.77–1.73% and 97.4%, respectively. The level of an average amount of Ni(II) in six piercing rings was evaluated to be 14.78 mg/g.

© 2014 Elsevier B.V. All rights reserved.

1. Introduction

At present, pierced earrings become increasingly popular methods to decorate the body [1]. Since nickel is one of common components of some pierced jewelries including ear piercing, it is likely cause of the allergic contact reaction occurred or other types of skin problem. Studies on the effect of ear piercing on sensitization to nickel and others metals showed that a significant number of patients who have ear piercing developed allergic sensitivity afterwards types of dermatitis and skin irritation, referred to as nickel allergies [2]. Some studies have stated that 10–15% of the female population and 6% of the male population are computed to be allergic to nickel. Nickel is the most frequency cause of the allergic contact dermatitis and is a factor in the production of dermatitis, especially eczema [3]. In fact, the allergy is not caused by nickel itself but by nickel salts which are produced under the effect of perspiration in contact with the jewelry piercings. In 2004, there were some reports that the regulation for all post assemblies which are inserted into pierced ears and other pierced parts of the human body unless the rate of nickel release from

such post-assemblies is less than $0.2 \mu\text{g}/\text{cm}^2/\text{week}$. The direct and prolonged contact with the skin, 12.8% of decorative parts and 17.1% of clasps exceeded the migration limit [4,5].

The 4-(2-pyridylazo)-resorcinol (PAR) has been widely used as a reagent to form complex with several metals. The PAR performs as a chelating agent in the determination of several heavy metals for example Mn(II), Co(II), Ni(II), and Zn(II) etc. and could produce colorful and stable metal chelates, which are soluble in aqueous solution. Some studies were displayed that the order of decreasing stability for PAR chelates are $\text{Ni(II)} > \text{Co(II)} > \text{Zn(II)} > \text{Mn(II)}$ [6]. It was found that Cu, Zn, Cd and Ni in water sample can be formed stable complexes with PAR in the aqueous solution at pH 5.0 and the complexes can be measured their absorbance by spectrophotometry [7]. Furthermore, the major interference in the determination of Ni(II) is in the presence of copper and Iron.

Polyurethane foam (PUF) is a good sorbent material in solid phase extraction. For the purpose of the determination of nickel in silicates and alloys by an on-line separation, a PUF mini-column was used to eliminate interference by several metal ions that formed complex with thiocyanate and sorbed them on the PUF [8,9]. Basically, nickel does not form complex with thiocyanate ion in the acidic condition at pH 3.0 and passes through the solid absorbent [10]. One study showed that on-line preconcentration and determination of Cu, Pb, and Cr(VI) at sub $\mu\text{g}/\text{L}$ levels in

* Corresponding author.

E-mail address: sumalee.tan@kmutt.ac.th (M. Vongboot).

natural water and biological sample was used ammonium pyrrolidinedithiocarbamate (APDC) as a reagent to form metal-ammonium pyrrolidine dithiocarbamate complexes which could be absorbed on the unloaded commercial PUF [11].

In 1991, one researcher group developed a general multivariate technique for the pH gradients determination in flow-injection analysis (FIA) systems in which an injected sample is combined with a non-linear pH gradient and the method was illustrated by the injection of acid and base in the range from 3.4 to 8.9 [12]. A FIA method for the simultaneous determination of iron and zinc in the human hair using a pH-gradient technique has been developed for simple, rapid and accurate method [13]. Designed to provide highly reproducible pH gradients in FIA system was used to discriminate between fluorescent metal chelates of zinc and cadmium [14].

The aim of this work is to describe the application of an on-line separation using a polyurethane foam mini-column in FIA system in order to remove copper and iron ions for the determination of nickel in piercing rings. Moreover, a critical work demonstrated the performance of pH-gradient technique is easier than buffer controlling technique while accuracy and precision were not decreased. Detection was rapid by using a UV-vis spectrophotometer.

2. Experimental

2.1. Apparatus

A SECOMAM 30319 spectrophotometer (Fabrique, France) and a Lab Power Junior Program were used to record the spectra of Ni-PAR complexes. A Rheodyne 7125 (Cotati, California, USA) pump and a Masterflex L/S peristaltic pump (Cole-Parmer, USA) were employed to propel all solutions. A homemade polyurethane foam column was applied for interferential removal step. A digital pH meter (AE240, Mettles, Switzerland) was used to measure the pH of all solutions.

2.2. Reagents and solutions

All chemicals used were analytical grade prepared with deionized water.

The concentrations of 10.00, 20.00, 40.00, 60.00, 80.00 and 100.00 mg/L Ni(II) solutions were prepared by adequate dilution of 1000 mg/L of nickel solution (Ajax Finechem) with a 1.0×10^{-3} mol/L of nitric acid solution.

The solutions of 0.05% of 4-(2-pyridylazo) resorcinol (PAR) at the pH of 9.0 and 10.0 were prepared by dissolution of 0.05 g of 4-(2-pyridylazo) resorcinol in 5 mL of 1 mol/L NaOH and diluted to 90 mL by deionized water. The pH was adjusted to 9.0 and 10.0 with 10 mol/L NaOH solution and volume was filled up to 100 mL. The other concentrations of PAR reagent were prepared in the same procedures.

1.0 mol/L of potassium thiocyanate solution was prepared by dissolution of 9.7 g of potassium thiocyanate in 80 mL of deionized water. The pH was adjusted to 3.0 with concentrated nitric acid and volume was filled up to 100 mL.

Polyurethane foam was formed by polymerization reaction of isocyanate (IRPC POLYOL) with polyol (IRPC POLYOL) in a ratio of 1:2. The polyurethane foam was broken to small pieces and size 250–500 μm was used to pack in column. An accurately weighed 3.0 g of polyurethane foam was contained in column and cleaned with deionized water.

2.3. Sample preparation

The proposed method: All ring samples (S1–S6) were cut to small pieces. An accurate weight, to the nearest 500 mg, of each ring sample was digested in an acidic mixture of 5 mL concentrated hydrochloric acid and 5 mL concentrated nitric acid in a fume hood for 30 min or complete dissolution. The concentrated sample solution obtained was diluted with deionized water and then adjusted to pH 3.0 with 10 mol/L NaOH. The total volume was made to 250 mL in volumetric flask. The sample solution was mixed with 1.0 mol/L KSCN solution before flowing into the PUF mini-column in FIA system.

The AAS method: ring samples (S1 and S3) were cut to small pieces. An accurate weight, to the nearest 200 mg, of ring samples was digested in an acidic mixture of 5 mL concentrated hydrochloric acid and 5 mL concentrated nitric acid in a fume hood for 30 min or complete dissolution. The concentrated sample solution obtained was diluted to 50 mL in volumetric flask.

2.4. Flow injection system

Fig. 1 illustrates a block diagram of the pH-gradient flow injection system. In this system, a PAR reagent and a sample solution were pumped at a flow rate of 1.0 ml/min. The sample solution containing a mixture of Ni(II), Cu(II), Fe(III) and potassium thiocyanate solution was passed into the PUF mini-column. The interfering ions, formed complexes with thiocyanate ion as thiocyanate complexes, were adsorbed on PUF mini-column. The next step, the pH gradient occurred by the percolated nickel sample solution (pH 3.0) was injected to 0.05%w/v PAR (pH 9.0) and reacted at mixing coil where construct the online pH-gradient at the optimum pH to occur Ni-PAR complexes which were measured absorbance at 500 nm.

Fig. 2 displays a block diagram of the FIA system as the same Fig. 1 but a line of buffer for a pH controlling system was subjoined.

3. Results and discussion

3.1. Optimization of PUF mini-column

Owing to the thiocyanate complexes formation of Cu(II) and Fe(III) is dependent upon the pH of solution and it has known that these complexes are completely well occur in acid condition solution, thence, the appropriated pH condition was investigated. At the outset, the effect of pH was observed in a range from 2.0 to 5.0. From the result showed in Fig. 3, both interference ions gave magnificent absorbance at pH 3.0, although the absorbance data of

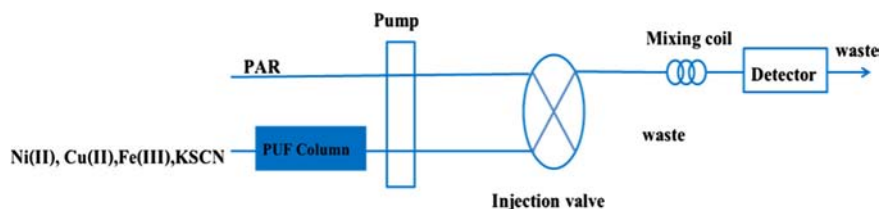


Fig. 1. A block diagram of the pH-gradient in FIA system.

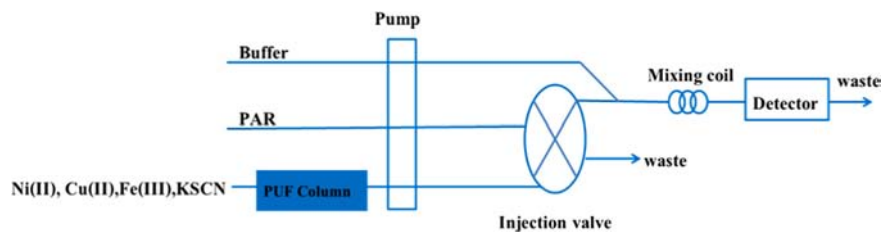


Fig. 2. A block diagram of the buffer using control pH in FIA system.

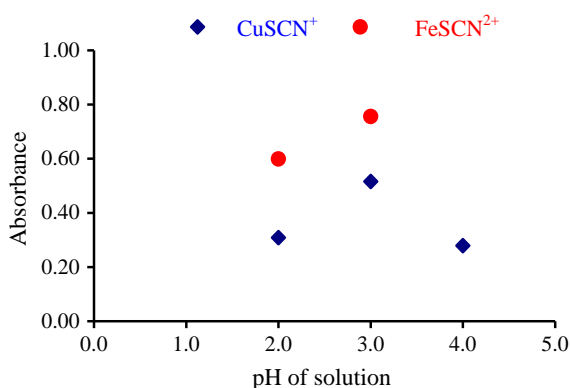


Fig. 3. pH of the solution for the complexes formation. The absorbance of CuSCN^+ and FeSCN^{2+} measure at the wavelength of 350 nm and 480 nm, respectively.

FeSCN^{2+} complexes at pH 4.0 was unavailable because they were precipitate. It could be decided that the solution at pH 3.0 would be appropriate to completely form the thiocyanate complexes and be employed as the optimal condition.

Potassium thiocyanate is a complexing agent for thiocyanate complex formations of Cu (II) and Fe (III). The concentration of the complexing agent is also an important contributor to the results. It was necessary to investigate a sufficient amount of KSCN that the concentration ranging from 50 mmol/L to 1000 mmol/L was considered. Firstly, experiments were monitored the concentration of KSCN in the range from 50 mmol/L to 400 mmol/L. It was found that the absorbance signals were logically increasing. On this useful experiment, it was revealed that an amount of thiocyanate was not adequate to form complexes with Cu(II) and Fe(III). On the other hand, the absorbance signals remained constant when the concentration of thiocyanate ranging from 400 mmol/L to 1000 mmol/L was used. This indicates that an excess of the complexing agent does not have any significant effect on the complex formation of Cu(II) and Fe(II), 400 mmol/L potassium thiocyanate was therefore used as the optimum concentration for further studies, as illustrated in Fig. 4.

3.2. Absorption spectrum of Ni-PAR complex

An acidic solution of pH 3.0 containing Ni(II) and 400 mmol/L KSCN was filtered through the PUF mini-column and afterwards, the percolated solution was injected continuously into the mixing coil to react with the PAR solution of pH 9.0 for the pH gradient generation. The formations of Ni-PAR complexes were produced at the optimum pH. The absorption spectrum of Ni-PAR complexes were recorded by using the SECONAM 30319 spectrophotometer. The absorption spectrum of Ni-PAR complexes shows the maximum absorbance at 500 nm. In all causes, measurements were made at 500 nm against similarly prepared reagent blank.

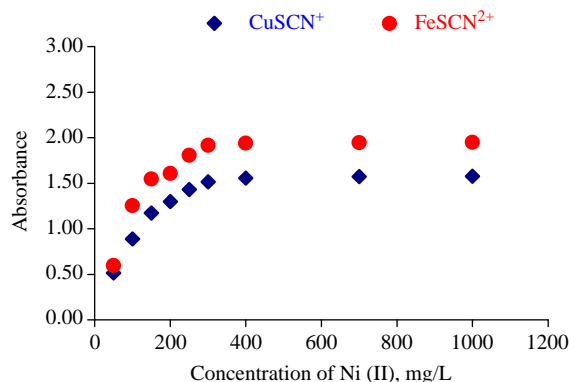


Fig. 4. Effect concentration of KSCN in the range of 50–1000 mmol/L. The absorbance of CuSCN^+ and FeSCN^{2+} measure at the wavelength of 350 and 480 nm, respectively.

3.3. Removal check of copper(II) and iron(III) by PUF mini-column

In a solution of a ring sample containing Cu(II), Fe(III) and Ni(II), these ions can react with the PAR reagent in the identical conditions to give metal-PAR complexes, thus a removal step to get rid of the interferences was necessary. On the basis of that Ni (II) does not chelate with thiocyanate ion, only Cu(II) and Fe(III) ions were reacted with thiocyanate ion to form thiocyanate complexes which were eliminated by sorption on a PUF mini-column. However, checking of this removal step is also important for confirmation that no interferences effect to the determination of Ni (II). There were two sets of observation that one experiment was carried on a mixture of a standard Ni(II) (12.00 mg/L) and an excess KSCN, another was carried out by adding a known amount of standard interfering ions and an excess KSCN to a standard Ni (II) solution of 12.00 mg/L. For the identical procedure, both mixing solutions were firstly passed into the PUF mini-column and for the determination check the concentration of Ni(II) was measured by using FIA and ICP-AES techniques. As shown in Table 1 the analytical data obtained from both techniques was no significant different. In both cases, amounts of Ni(II) recovered were considerably in agreement with that given in an initial sample (12.00 mg/L). Moreover, Cu(II) and Fe(III) were not found in set 2. From this result, it confirmed that the PUF mini-column is potential to be used to remove Cu(II) and Fe(III) in the determination of Ni(II).

3.4. Comparison of Ni-PAR formation between pH-gradient and buffer pH controlling techniques

The optimal condition of Ni-PAR formation in FIA system was used pH-gradient and buffer pH controlling technique. Both techniques were observed at the identical conditions such the same concentration of PAR reagent, concentration of Ni(II) solution and flow rate. In addition, the wavelength was set similarly at 500 nm. The pH of PAR reagent and Ni(II) solution were adjusted to

Table 1
Removal check of copper(II) and iron(III) by PUF mini-column.

Set	Elution from PUF column	FIA			ICP-AES		
		Ni(II) (mg/L)	Cu(II) (mg/L)	Fe(III) (mg/L)	Ni(II) (mg/L)	Cu(II) (mg/L)	Fe(III) (mg/L)
1	Std. Ni(II) 12.00 mg/L+excess KSCN	11.94	–	–	12.01	ND	ND
2	Std. Ni(II) 12.00 mg/L+ Std. Cu(II) 120 mg/L+ Std. Fe(III) 120 mg/L+excess KSCN	11.94	–	–	12.03	ND	ND

ND: Lower detection limit
(–): No determination

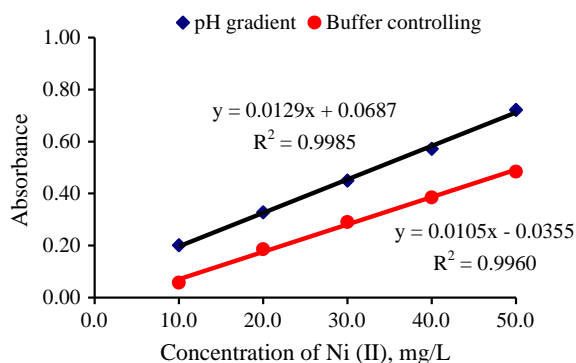


Fig. 5. Formation of Ni–PAR complexes by using pH-gradient and buffer controlling at flow rate 1.5 ml/min, concentration of PAR 0.05% w/v and wavelength 500 nm. pH of Ni(II) and PAR were 3.0 and 9.0 for pH-gradient technique. Buffer solution at pH 6.0 was used for buffer controlling technique.

9.0 and 3.0, respectively, for the pH-gradient technique. For the buffer pH controlling technique, a line of buffer at pH 6.0 was subjoined in the FIA system as presented in Fig. 2. The results were evaluated as the linear equation of which the pH-gradient and the buffer pH controlling techniques are $y=0.0129x+0.0687$ ($R^2=0.9985$) and $y=0.0105x-0.0355$ ($R^2=0.9960$), respectively. As shown in Fig. 5, the slope of the pH-gradient was higher than the buffer controlling technique. It means that the sensitivity of the technique was also high. Therefore, the pH-gradient technique is better than the buffer pH controlling technique.

3.5. Effect of pH-gradient range

pH-gradient was generated by injection of a Ni(II) solution into a PAR reagent, a range of pH depended on the initial pH of both solutions. Ni–PAR complexes are produced completely in basic region [15]. The initial pH of Ni(II) solution and the PAR reagent were observed in the pH range from 3.0 to 9.0 and from 3.0 to 10.0, respectively. The results were indicated that both of the pH ranges gave a good linear relationship between absorbance and the concentration of Ni(II), whereas the peak characteristic of pH range from 3.0 to 9.0 was absolutely better than another pH range as shown in Fig. 6. It means that the pH range from 3.0 to 9.0 was higher sensitivity as well, so this pH range was selected to use in further.

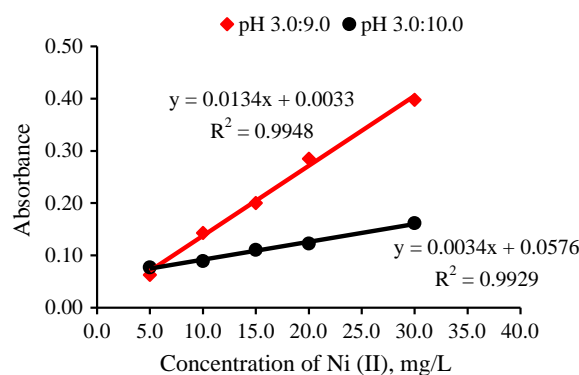


Fig. 6. Effect of the initial pH of the Ni(II) standard solution and the PAR solution. flow rate 1.0 ml/min, concentration of PAR 0.05% w/v, length of mixing coil 100 cm and wavelength 500 nm. (For interpretation of the references to color in this figure, the reader is referred to the web version of this article.)

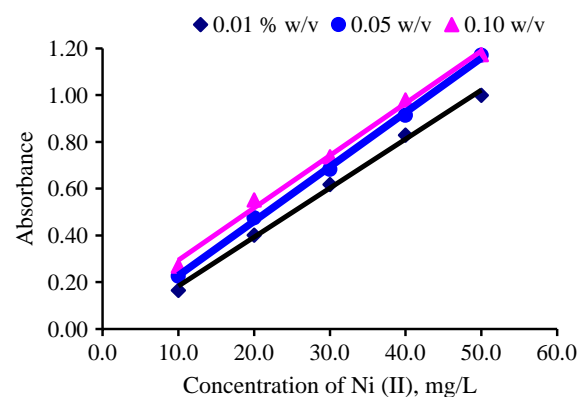


Fig. 7. Effect concentration of PAR solution. pH of Ni(II) and PAR: 3.0 and 9.0 flow rate 1.5 ml/min, length of mixing coil 100 cm and wavelength 500 nm.

3.6. Effect of reagent concentration

As found in 3.5 that the pH range of 3.0–9.0 is the optimum condition for generating the suitable pH-gradient. The concentrations of PAR reagent were also investigated which the concentration in a range of 0.01–0.1% w/v was considered and the injection volume of PAR reagent into Ni(II) solution was 0.10 mL. First, it was observed at 0.01% w/v, the absorbance spectrum obtained was the lowest. Next, we turned our attention to concentrations of 0.05% w/v and 0.1% w/v and it was found that absorbance obtained of both was high sensitive and no significant different as shown in Fig. 7. To save the reagent, 0.05% w/v PAR solution was altered as the optimal concentration.

3.7. Effect of flow rate

The flow rate of system is an important matter since it affects to dispersion of the gradient zone. Thereby, this study searched the flow rate in a varied range from 1.0 ml/min to 2.0 ml/min. From Fig. 8, it was found that the signal was the highest at the flow rate of 1.0 ml/min, but analytic time was too long. Whereas, the signal of flow rates of 1.5 ml/min and 2.0 ml/min occurred at nearby position and particularly, analytical time of both was appropriate. For retaining some reagents the flow rate of 1.5 ml/min was selected to be used as an optimum value for the further determinations of Ni(II).

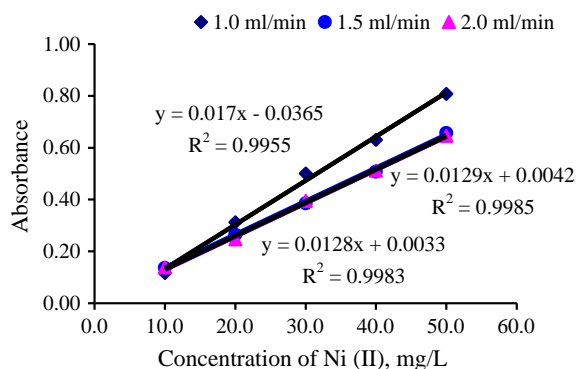


Fig. 8. Effect of flow rate of PAR solution. pH of Ni(II) and PAR: 3.0 and 9.0 Concentration of PAR 0.05% w/v, length of mixing coil 100 cm and wavelength 500 nm.

Table 2

Amount of Ni(II) in piercing ring samples.

Samples	Amount of Ni(II), mg/g		
	AAS	Proposed method	
	Mean ^a	Mean ^a	Average
S1	14.66 ± 0.09	14.54 ± 0.18	
S2	–	14.58 ± 0.12	
S3	14.76 ± 0.04	14.80 ± 0.16	14.78 ± 0.24
S4	–	14.69 ± 0.08	
S5	–	15.00 ± 0.11	
S6	–	15.09 ± 0.10	

(–): No determination.

^a Average of 3 determinations.

3.8. Analytical feature

To confirm the precision of the method, multiple replicate analyses of a standard Ni(II) solution were performed. The results are illustrated in Fig. 6 (red line) that the calibration graph for the determination of Ni(II) was obtained under this optimum condition. The proposed method provided the respected linear relationship between absorbance and concentrations of Ni(II) in the range from 5.00 mg/L to 30.00 mg/L. The linear equation was $y = 0.0134 + 0.0033x$ (correlation coefficient, $R^2 = 0.9948$) where y is the absorbance and x is the concentration of Ni(II) solution. The detection limit estimated from signal to noise in ratio of 3:1 ($S/N = 3$) was 0.70 mg/L Ni(II). The relative standard derivation, RSD ($n = 10$) was 0.77–1.73%, indicating that the method is highly precise and reproducible. The reliability of the proposed method was evaluated in term of the percent recovery of Ni(II). The results were found that the average percent recovery was 97.4%.

3.9. Determination of nickel (II) in piercing ring samples

Following the procedure for sample preparation in 2.3, six samples of piercing ring were cut to small pieces and digested with an acidic mixture of concentrated HCl and HNO₃ in fume hood.

The clear solution obtained was diluted and adjusted to pH 3.0. The sample preparation process was taken within 1 h and then each sample was divided in three sample portions for that the determination was repeated three times. The data from experiments was summarized in Table 2. It has seen that measurements of each sample have differed insignificant from each other. The quantity of nickel in six piercing ring samples was measured as milligram of Ni (II) per gram of piercing ring. The average of nickel contained in each piercing ring (S1–S6) was found 14.54, 14.58, 14.80, 14.69, 15.00 and 15.09, respectively, and the level of the amount of nickel in ring samples was 14.78 mg/g or 1.48% w/w. In addition, Atomic Absorption Spectroscopy (AAS) was used for the method validation of the nickel determination in piercing ring samples (S1 and S3). The analytical data obtained was compared to an amount of nickel of the proposed method. In Table 2, it shows that amounts of nickel in samples S1 and S3 were 14.66 mg/g and 14.76 mg/g, respectively, which they are in agreement of those obtained from the proposed method.

4. Conclusion

The determination of nickel in the presence of copper and iron interferences can be advantageously effected by the pH-gradient procedure in FIA system in which the PUF mini-column is applied for online removal step of these metal interferences. Outstandingly, nickel can be determined with great accuracy, high sensitivity and significant precision and furthermore, this optimum method can be applied for nickel determination in piercing jewelries such as brass, steel and bronze etc. It is interesting to report that the Ni(II) complexes formation was produced efficiently under the optimum condition of the pH-gradient technique without using the buffer pH controlling system. Especially, the nickel determination by pH gradient technique can be expediently performed and economized the amounts of chemical reagents and samples.

References

- [1] D. Bociaga, K. Mitura, *Diam. Relat. Mater.* 17 (2008) 1410–1415.
- [2] T. Nakada, M. Iuima, H. Nakayama, H.I. Maibach, *Contact Dermat.* 36 (1997) 233–236.
- [3] C. Liden, S. Johnsson, *Contact Dermat.* 44 (2001) 7–12.
- [4] Commission directive 2004/96/EC of 27 September 2004. Official Journal of European Union 2004, pp. 51–52.
- [5] A. Schnuch, J. Wolter, J. Geier, W. Uter, *Contact Dermat.* 64 (2011) 142–150.
- [6] A. Corsini, I.M. Yih, Q. Fernando, H. Freiser, *Anal. Chem.* 34 (1962) 1090–1093.
- [7] E.L. Silva, P.d.S. Roldan, M.F. Giné, *J. Hazard. Mater.* 171 (2009) 1133–1138.
- [8] V.A. Lemos, M.S. Santos, E.S. Santos, M.J.S. Santos, W.N.L. dos Santos, A. S. Souza, D.S. de Jesus, C.F. das Virgens, M.S. Carvalho, N. Oleszczuk, M.G. R. Vale, B. Welz, S.L.C. Ferreira, *Spectrochim. Acta Part B: Atom. Spectrosc.* 62 (2007) 4–12.
- [9] D.S. de Jesus, R.J. Cassella, S.L.C. Ferreira, A.C.S. Costa, M.S. de Carvalho, R. E. Santelli, *Anal. Chim. Acta* 366 (1998) 263–269.
- [10] S.L.C. Ferreira, D.S. Jesus, R.J. Cassella, A.C.S. Costa, M.S. Carvalho, R.E. Santelli, *Anal. Chim. Acta* 378 (1999) 287–292.
- [11] A.N. Anthemidis, G.A. Zachariadis, J.A. Stratis, *Talanta* 58 (2002) 831–840.
- [12] L. Nørgaard, *Anal. Chim. Acta* 255 (1991) 143–148.
- [13] S. Zhao, X. Xia, G. Yu, B. Yang, *Talanta* 46 (1998) 845–850.
- [14] N. Porter, B.T. Hart, R. Morrison, I.C. Hamilton, *Anal. Chim. Acta* 281 (1993) 229–242.
- [15] J. Ghasemi, A. Niazi, M. Maeder, *J. Braz. Chem. Soc.* 18 (2007) 267–272.



Combination of poly(diallyldimethylammonium chloride) and hydroxypropyl- γ -cyclodextrin for high-speed enantioseparation of phenothiazines by capillary electrophoresis

Po-Lin Yu, Yi-Yi Tu, Ming-Mu Hsieh*

Department of Chemistry, National Kaohsiung Normal University, Kaohsiung City, Taiwan, ROC

ARTICLE INFO

Article history:

Received 9 June 2014

Received in revised form

5 August 2014

Accepted 5 August 2014

Available online 13 August 2014

Keywords:

Capillary electrophoresis

Phenothiazines

Chiral separation

Poly(diallyldimethylammonium chloride)

Cyclodextrins

ABSTRACT

High-speed capillary electrophoresis (CE) enables the simple, rapid, and inexpensive analysis of large sets of chiral samples in the pharmaceutical industry. Hence, we developed a novel method for separating enantiomers of *D,L*-phenothiazines simply and rapidly, based on using poly(diallyldimethylammonium chloride) (PDDAC) as an additive and hydroxypropyl- γ -cyclodextrin (Hp- γ -CD) as a chiral selector in capillary electrophoresis. Adding 0.9% PDDAC to the background electrolyte generated a stable, high, and reversed electroosmotic flow (EOF). Hp- γ -CD not only worked as a complexing agent to increase the chiral resolution between *D,L*-phenothiazines but also decreased the effective electrophoretic mobility of these drugs. Combining PDDAC and Hp- γ -CD as buffer additives enabled CE to achieve a high-speed enantioseparation of five pairs of *D,L*-phenothiazines. A decrease in capillary length and an increase in the intensity of the electric field further shortened the separation time. When the background electrolyte contained 0.9% PDDAC, 5 mM Hp- γ -CD, and 75 mM formic acid (pH 3.0), enantioseparation of the *D,L*-phenothiazines was attained within 230 s by applying a capillary length of 32.5 cm and an electric field of 292 V cm⁻¹. The limit of detection (LOD) of the *D,L*-phenothiazines at a signal-to-noise ratio of 3 ranged from 2 to 8 μ M. We demonstrated the feasibility of this method by detecting the five pairs of *D,L*-phenothiazines in urine samples.

© 2014 Elsevier B.V. All rights reserved.

1. Introduction

Since the 1950s, phenothiazine drugs have become widely used in treating schizophrenia and other psychiatric disorders. Phenothiazines are also used as antipsychotic, antihistaminic, antiemetic, anesthetic and neuroleptic drugs. Phenothiazine overdoses may cause coma, miosis, and respiratory depression. It has been demonstrated that a dose of 15 mg of chlorpromethazine, 50 mg of thioridazine, and 75 mg of promethazine could be fatal. In Japan, these drugs usually caused fatal intoxication, because a patient may take several drugs in combination, resulting in fatal poisoning [1]. In addition, several phenothiazines, such as *DL*-thioridazine (*DL*-Thi), *DL*-methotrimeprazine (*DL*-Met), *DL*-ethopropazine (*DL*-Eth), *DL*-trimeprazine (*DL*-Tri), and *DL*-promethazine (*DL*-Pro), are enantiomeric drugs, and using a single enantiomer of a drug might lead to a substantial therapeutic improvement [2–5]. Thus, to help the physician evaluate the effectiveness and safety using phenothiazines for the patients who need medication, developing a simple

and efficient chiral separation method for simultaneously monitoring therapeutic drugs in urine and plasma is urgent.

Current available methods for separating and quantifying phenothiazines include high-performance liquid chromatography (HPLC) [6–8] and capillary electrophoresis (CE) [9,10]. Compared with HPLC, CE is highly appealing because of the small sample injection volumes required, low solvent consumption, short analysis time [11], and high separation efficiency [12,13]. Adding a chiral selector, such as macrocyclic antibiotics [14], proteins [15,16], or cyclodextrin (CD) derivatives [17,18], to the background electrolyte results in efficient separation of *D,L*-phenothiazines. For example, *DL*-Tri and *DL*-Pro were completely enantioseparated by partially filling a capillary with human serum albumin [13]. Lin et al. used tetradecyltrimethyl ammonium bromide to reverse the electroosmotic effect, and used mixed chiral selectors to separate three pairs of *D,L*-phenothiazines within 16 min [19]. However, two pairs of *DL*-Pro and *DL*-Met were not resolved under the same separation conditions. These CE methods for chiral separation of *D,L*-phenothiazines require a long migration time and demonstrate poor separation efficiency, and they have yet to be used to detect *D,L*-phenothiazines in human fluids.

Poly(diallyldimethylammonium chloride) (PDDAC) is composed of quaternary amines, and has been proved to function as

* Correspondence to: Department of Chemistry, National Kaohsiung Normal University, No. 62, Shengzhong Rd., Yanchao District, Kaohsiung City 82446, Taiwan, ROC. Tel.: +11 886 7 717 2930 7162; fax: +11 886 7 6051083.

E-mail address: t3644@nknuc.nknu.edu.tw (M.-M. Hsieh).

a buffer additive for enhancing the separation of positively charged analytes including high-pI proteins [20–22] aminothiols [23,24], biogenic amine neurotransmitters [25,26], melamine [27], and pseudomonas quinolones [28]. Because an uncoated capillary exhibits a highly negative charge, analytes of opposite charges are readily adsorbed onto the capillary surface. When an uncoated capillary is filled with an aqueous PDDAC solution, electrostatic attraction between PDDAC and the capillary surface creates a monolayer of positively charged PDDAC to suppress the adsorption of cationic analytes and improve their separation efficiency [20]. By contrast, modifying a capillary with PDDAC generates a stable reversed electroosmotic flow (EOF), altering the migration order and improving selectivity [24,25,28]. Therefore, we assumed that the combination of PDDAC and cyclodextrin (CD) derivatives as a buffer additive could enhance the chiral separation of positively charged phenothiazines in CE.

The aim of this study was to develop a rapid and highly efficient enantioseparation method for five pairs of *D,L*-phenothiazines by incorporating 0.9% PDDAC as a buffer additive, and using 5 mM Hp- γ -CD as a chiral selector in CE. The chemical structures of the *D,L*-phenothiazines and their physical properties are shown in (Table S1 Supplementary material). Filling the capillary with PDDAC produced a stable, fast, and reversed EOF, and suppressed analyte adsorption, whereas the presence of Hp- γ -CD in the background electrolyte enhanced the complexation and chiral selectivity toward analytes. The parameters, including the PDDAC concentration, CD content, electric field, and capillary length, were studied and optimized for rapid and efficient separation. The five pairs of *D,L*-phenothiazines were baseline-separated within 4 min by combining PDDAC and Hp- γ -CD. To demonstrate the practicality of this separation system, we applied it to detect the five pairs of *D,L*-phenothiazines in urine. To the best of our knowledge, this is first report for rapid analysis of five pairs of *D,L*-phenothiazines by CE.

2. Experimental

2.1. Chemicals

PDDAC (20 wt% in water; M.W. 400,000–500,000), mesityl oxide, sodium hydroxide, formic acid, tris(hydroxymethyl)amino-methane (Tris), *DL*-Thi, *DL*-Tri, *DL*-Eth, *DL*-Pro, *DL*-Met, tyramine (TA), 5-hydroxyindole-3-acetic acid (5-HIAA), homovanillic acid (HVA), vanillylmandelic acid (VMA) dopamine (DA), epinephrine (E), *L*-tryptophan (*L*-Trp), 3-Indoxyl sulfate (3-IXS), hydroxypropyl- α -cyclodextrin (Hp- α -CD), hydroxypropyl- β -cyclodextrin (Hp- β -CD), Hp- γ -CD, and γ -cyclodextrin (γ -CD) were obtained from Sigma-Aldrich Corporation (St. Louis, MO). The pH of formic acid was adjusted to 2.0–4.0 by adding 100 mM Tris. Water used in all experiments was doubly distilled and purified by a Milli-Q system (Millipore, Milford, MA).

2.2. CE

The detection wavelength of a commercial UV absorbance detector (ECOM, Germany) was set to 254 nm for phenothiazines and mesityl oxide (1 mM). Note that mesityl oxide is a neutral marker for the measurement of EOF. A high-voltage power supply (Bertan, Hicksville, NY, USA) was used to drive electrophoresis. A computer that was connected to the Peak-ABC chromatography data-handling system (Great Tide Instrument Company, Taipei, Taiwan) was used to record the electropherograms and for the quantitative measurements of the peak area. The fused-silica capillaries (Polymicro Technologies, Phoenix, AZ, USA) with 75 μ m I.D. and 365 μ m O.D. were used for separation of analytes.

Prior to analysis, capillaries were flushed with 0.5 M of NaOH for 10 min using a syringe pump (KD Scientific, New Hope, PA) at a flow rate of 5 μ L min⁻¹, followed by water flushing for 1 min. After that, the capillary was treated with a solution containing 2% PDDAC and 5 mM formic acid (pH 2.0–4.0) for 10 min, resulting in reversed EOF. Before conducting separation, the capillary was filled with a solution containing 0–1.2% PDDAC and 0–15 mM CD derivative using syringe pumping at a flow rate of 5 μ L min⁻¹. Phenothiazines were injected by hydrodynamic injection at a 20 cm height for 10 s. All separations were conducted at 250–300 V cm⁻¹. After each run, the capillary was flushed with 0.9% PDDAC for 10 min using syringe pumping at a flow rate of 5 μ L min⁻¹.

2.3. Quantification of 5 pairs of *D,L*-phenothiazines

The calibration curve was constructed by plotting the peak area against the analyte concentration (0, 0.01, 0.4, 0.8, 1, 2, and 3 mM). The limits of detection (LODs) of *D,L*-phenothiazines were estimated to be the analyte concentration that generates a peak height with a signal-to-noise (*S/N*) ratio of 3. The separation of 5 pairs of *D,L*-phenothiazines was repeated three times within the same day to obtain the repeatability (intraday precision) and three times over five consecutive days to obtain the intermediate precision (interday precision); the repeatability and intermediate precision were expressed as relative standard deviation (RSD%) values.

Human urine samples (24 h) collected from six volunteers were centrifuged at 3000 rpm for 10 min. The obtained supernatant (950 μ L) was spiked without and with standard solution of *D,L*-phenothiazines (50 μ L, 0–3.0 mM). The calibration curve was obtained by plotting the peak area against the spiked concentration of analyte.

3. Results and discussion

3.1. Role of PDDAC in high-speed separation

Previous studies have reported that the chiral separation of phenothiazines by using CE was time consuming; thus, we aimed to develop a method requiring a short separation time (Table S2, Supplementary material) [9,10,22,29–31]. The following equation is associated with the migration time (t_{mig}) of the analyte [32]:

$$t_{\text{mig}} = l/v = L/(\mu + \mu_{\text{EOF}}) \times V \quad (1)$$

where v is the velocity of the analyte, l is the effective capillary length, L is the total capillary length, V is the voltage applied to L , μ is the effective electrophoretic mobility of the analyte, and μ_{EOF} is the EOF. This equation indicates that the time required to separate the analytes can be reduced by shortening the capillary, increasing the EOF, or increasing the effective electrophoretic mobility of the analytes. In addition, the resolution between analytes can be expressed using the following equation [32]:

$$R_s = 0.177(\mu_1 - \mu_2)(V)/(D(\mu_{\text{avg}} + \mu_{\text{EOF}})^{1/2}) \quad (2)$$

where D is the diffusion coefficient of the analyte, μ_1 is the effective electrophoretic mobility of the analyte, μ_2 is the effective electrophoretic mobility of another analyte, and μ_{avg} is the average of μ_1 and μ_2 . This equation suggests that an increase in the EOF enhances the resolution if the EOF is in the opposite direction of the ion movement. Consequently, we assumed that fast separation of the five pairs of phenothiazines could be successfully achieved at a low pH in the presence of a reversed EOF. Under this separation condition, phenothiazines exhibit positive charges, and their effective electrophoretic mobility is in the opposite

direction of the EOF. To satisfy these conditions, PDDAC was used to reverse the EOF at a low pH, because PDDAC exhibits no interaction with phenothiazines or chiral selectors. To test our hypothesis, we initially investigated the effect of the PDDAC concentration on the separation of three pairs of *D,L*-phenothiazines in the presence of a reversed EOF. Note that reversed high EOF was generated when the capillary was modified with positively PDDAC (the capillary pretreated before experiment). The result (Fig. S1, Supplementary material) reveals that the migration time of the three pairs of *D,L*-phenothiazines progressively decreased with an increase in the PDDAC concentration, which enhanced the reversed EOF [21,22,25]. Monitoring the change in the migration time of mesityl oxide revealed that the reversed EOF increased from 3.9 to $5.5 \times 10^{-4} \text{ cm}^2 \text{ V}^{-1} \text{ s}^{-1}$ as the concentration of PDDAC increased from 0 to 1.2%. In the absence of PDDAC, the separation efficiencies of *DL*-Thi, *DL*-Tri, and *DL*-Pro were 16 000, 27 000 and 28 000 plates m^{-1} , and resolution of *DL*-Thi/*DL*-Tri and *DL*-Tri/*DL*-Pro were 4.2 and 1.9, respectively (Fig. S1A, Supplementary material). As indicated in (Fig. S1D Supplementary material), adjusting the PDDAC concentration to 0.9% boosted the separation efficiencies (58 000, 72 000, and 84 000 plates m^{-1} for *DL*-Thi, *DL*-Tri, and *DL*-Pro, and resolution of *DL*-Thi/*DL*-Tri and *DL*-Tri/*DL*-Pro were 7.1 and 2.27, respectively), suggesting that the high PDDAC concentration efficiently suppressed the adsorption of *D,L*-phenothiazines on the capillary surface. Another possibility is that a high EOF enabled the analyte to spend little time in the capillary, thereby decreasing the time for longitudinal diffusion broadening.

The current generated at 253 V cm^{-1} was $120 \mu\text{A}$ when 1.2% PDDAC was used as a buffer additive. Although high EOF will result in Joule heating, changes in the peak profiles and unstable baseline and peak broadening. Finally, we chose a 0.9% PDDAC concentration ($80 \mu\text{A}$) to obtain highly reproducible separation conditions.

3.2. Role of cyclodextrin derivatives in chiral separation of *D,L*-phenothiazines

Chiral compounds have been separated by adding CD to the background electrolyte [33–35]. Likewise, enantioseparation of *D,L*-phenothiazines has been attained using CD derivatives as chiral selectors (Table S2, Supporting information) [9,10,22,29–31]. Accordingly, a series of CD derivatives (Hp- α -CD, Hp- β -CD, Hp- γ -CD, and γ -CD) were tested to separate three pairs of *D,L*-phenothiazines in the presence of a reversed EOF. In comparison to other CD derivatives, only Hp- γ -CD provided enantioseparation of the three pairs of *D,L*-phenothiazines (Fig. 1). This could be attributed to the fact that Hp- γ -CD contains polar and nonpolar substituent groups and extra chiral centers [36–38], which in turn provide excellent selectivity for separation of *D,L*-phenothiazines. When the concentration of Hp- γ -CD was changed to 5 mM, the resolution between *D*- and *L*-phenothiazines reached maximum (Table 1). Moreover, the addition 5 mM Hp- γ -CD into the background electrolyte resulted in a substantial change in the migration time of the *D,L*-phenothiazines. This result demonstrated the formation of an inclusion complex between neutral Hp- γ -CD and *D,L*-phenothiazines, lowering the effective electrophoretic mobility of the *D,L*-phenothiazines. Consequently, the presence of Hp- γ -CD not only enabled the enantioseparation of *D,L*-phenothiazines but also shortened their separation time.

3.3. Effect of capillary length and electric field

According to Eq. (1), a decrease in capillary length can shorten the time of analysis when the electric field remains unchanged. The results (Fig. S2, Supplementary material) show the effect of capillary length (from 47.5 to 32.5 cm) on the enantioseparation of the three pairs of *D,L*-phenothiazines, performed under an electric field of 253 V cm^{-1} . The shortest allowable capillary length in our CE equipment was 32.5 cm. The enantioseparation speed of the *D,L*-phenothiazines progressively increased with a decrease in capillary length. Moreover, the resolution between *D*- and *L*-phenothiazines was still higher than 1.3, indicating that a decrease in capillary length did not induce poor separation efficiency. The successful rapid separation of the three pairs of *D,L*-phenothiazines motivated us to apply the proposed method to analyze other *D,L*-phenothiazines. By increasing the electric field from 253 to 292 V cm^{-1} , the high-speed enantioseparation of five pairs of *D,L*-phenothiazines was achieved completely within 230 s when the background electrolyte contained 0.9% PDDAC, 5 mM Hp- γ -CD, and 75 mM formic acid (pH 3.0) (Fig. 2). Under this separation

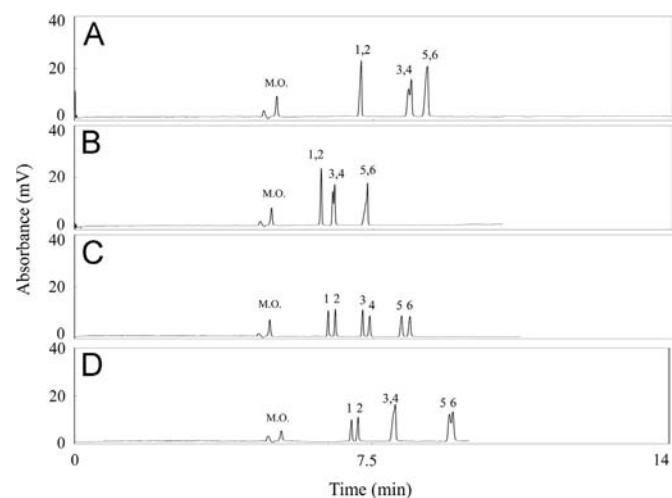


Fig. 1. Effect of the type of CD derivative on the CE enantioseparation of 3 pairs of *D,L*-phenothiazines: (A) 10 mM Hp- α -CD, (B) 5 mM Hp- β -CD; (C) 5 mM Hp- γ -CD; and (D) 5 mM γ -CD. Electrophoresis conditions: separation buffer, 75 mM formic acid (pH 3.0), 0.9% PDDAC, and CD derivative. applied voltage, -12 kV ; hydrodynamic injection at 20-cm height for 10 s; and direct UV detection at 254 nm. Peak identities (concentration): M.O. (1 mM); 1, *D*-Thi (0.25 mM); 2, *L*-Thi (0.25 mM); 3, *D*-Tri (0.25 mM); 4, *L*-Tri (0.25 mM) 5, *D*-Pro (0.30 mM); 6, *L*-Pro (0.30 mM).

Table 1

Effects of the concentration and type of CD derivatives on chiral separation of 3 pairs of *D,L*-phenothiazines.

Compounds	Resolution											
	HP- α -CD (mM)			HP- β -CD (mM)			HP- γ -CD (mM)			γ -CD (mM)		
	5	10	15	5	10	15	5	10	15	5	10	15
<i>D/L</i> Thi	0	0	0	0	0	0	2.66	1.68	1.07	2.11	1.18	0.85
<i>D/L</i> Tri	0.38	0.63	0.61	0.59	0	0	2.55	2.66	2.08	0	0	0
<i>D/L</i> Pro	0	0	0	0	0	0	1.97	1.95	2.41	0.65	0.92	0.81

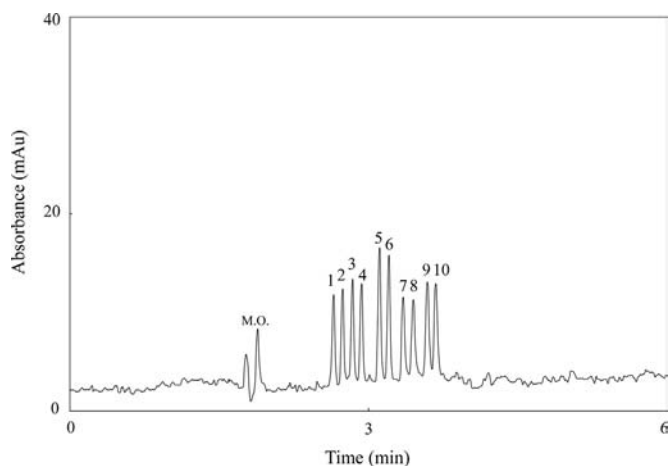


Fig. 2. High-speed CE enantioseparation of 5 pairs of *D,L*-phenothiazines. Electrophoresis conditions: 32.5-cm capillary (22.5-cm to detector); separation buffer, 75 mM formic acid (pH 3.0), 0.9% PDDAC, and 5 mM Hp- γ -CD; applied voltage, -9.5 kV; hydrodynamic injection at 20-cm height for 10 s; and direct UV detection at 254 nm. Peak identifies (concentration): M.O. (1 mM); IS (0.5 mM); 1, *D*-Thi (0.25 mM); 2, *L*-Thi (0.25 mM); 3, *D*-Met (0.25 mM); 4, *D*-Met (0.25 mM); 5, *D*-Tri (0.25 mM); 6, *L*-Tri (0.25 mM); 7, *D*-Eth (0.25 mM); 8, *L*-Eth (0.25 mM); 9, *D*-Pro (0.25 mM); 10, *L*-Pro (0.25 mM).

Table 2
Quantification and reproducibility of 5 pairs of *D,L*-phenothiazines.

Compounds	R^2	LOD (μ M)	RSD (%) of peak area ($n=3$)	
			Intraday	Interday
<i>D</i> -Thi	0.9982	2	2	4
<i>L</i> -Thi	0.9966	3	3	4
<i>D</i> -Tri	0.9954	2	2	5
<i>L</i> -Tri	0.9972	3	2	4
<i>D</i> -Eth	0.9986	3	2	4
<i>L</i> -Eth	0.9967	4	2	5
<i>D</i> -Pro	0.9908	3	2	4
<i>L</i> -Pro	0.9978	8	3	4
<i>D</i> -Met	0.9972	3	2	4
<i>L</i> -Met	0.9983	3	2	4

condition, the resolution between *D*- and *L*-phenothiazines was still acceptable for all analytes ($R_s > 1.3$). The relative standard deviation (RSD) of the migration time of each analyte was less than 2% ($n=5$). The peak areas varied linearly ($R^2 > 0.9900$) with an increase in the concentrations of the five pairs of *D,L*-phenothiazines (Table 2). The LODs of the five pairs of *D,L*-phenothiazines ranged from 2 to 8 μ M. The intraday and interday migration time precisions of the 10 analytes were in the ranges of 2–3% and 4–5%, respectively.

3.4. Analysis of *D*- and *L*-phenothiazines in urine

Because the detection wavelength of the UV detector was set at 254 nm, we tested whether other compounds, namely VMA, HVA, Trp, 5-HIAA, E, 3-IXS, DA, and TA, potentially interfered with detecting *D,L*-phenothiazines in urine. These compounds, which commonly exist in urine, exhibit a strong absorbance at 254 nm. This study did not test the effects of ascorbic acid, nonaromatic amino acids, carbohydrates, or salts on the detection of *D,L*-phenothiazines in urine because such compounds exhibit an extremely weak absorbance at 254 nm. The migration time of the tested compounds did not overlap that of the five pairs of *D,L*-phenothiazines (Fig. S3, Supplementary material), suggesting that

the proposed method could be applied for directly detecting the five pairs of *D,L*-phenothiazines in urine.

Encouraged by this result, we next validated the feasibility of the proposed method for detecting the five pairs of *D,L*-phenothiazines in urine. Because urine samples contain a high salt content, the electric field was decreased to 262 V cm^{-1} . When the proposed method was used to analyze urine directly, only one peak was observed at 2.6 min (Fig. 3A). Urine samples were spiked with the five pairs of *D,L*-phenothiazines, and analyzed by combining PDDAC and Hp- γ -CD in CE (Fig. 3B). Apparently, a baseline resolution between *D* and *L*-phenothiazines was still obtained. The slope of the calibration curve obtained using spiked samples was similar to that obtained using standard samples (Table 3). Moreover, the mean recoveries of the five pairs of *D,L*-phenothiazines at the three spiking levels (0.8, 1, and 2 mM) ranged from 89% to 109%. Subsequently, the applicability of this method for biological and clinical analyses was evaluated by analyzing urine samples obtained from six healthy adults. The mean recoveries of the five pairs of *D,L*-phenothiazines spiked into six urine samples were in the range between $92 \pm 4.1\%$ and $105 \pm 4.6\%$. These results clearly indicated that this separation method was largely free from the matrix effect of the urine sample.

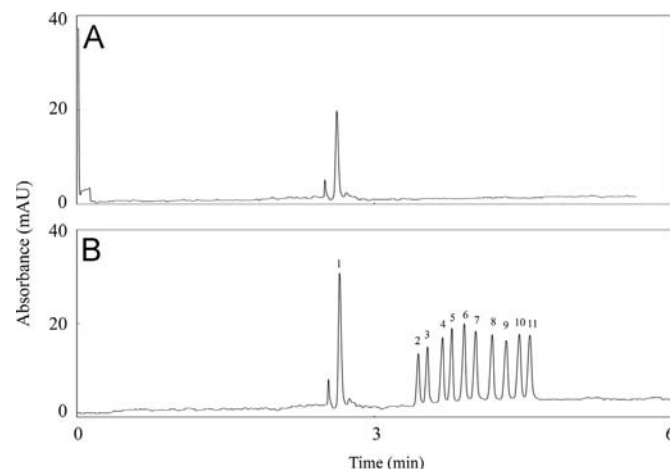


Fig. 3. High rapid enantioseparation of (A) a blank urine sample, (B) five pairs of *D,L*-phenothiazines spiked urine. applied voltage, -8.5 kV Other operating condition and peak identifies are the same as those in Fig. 2.

Table 3
Quantification of 5 pairs of *D,L*-phenothiazines in urine.

Compounds	Regression equation		Recovery (%) ^c
	Standard samples ^a	Spiked samples in urine ^b	
<i>D</i> -Thi	$y = 14800x + 0.268$	$y = 13200x + 0.499$	89
<i>L</i> -Thi	$y = 16300x + 0.129$	$y = 14600x + 0.737$	92
<i>D</i> -Tri	$y = 21300x + 0.574$	$y = 22900x + 1.420$	107
<i>L</i> -Tri	$y = 20100x + 0.296$	$y = 21300x + 0.705$	109
<i>D</i> -Eth	$y = 14600x + 0.825$	$y = 13600x + 0.685$	96
<i>L</i> -Eth	$y = 12910x + 1.114$	$y = 12300x + 0.185$	95
<i>D</i> -Pro	$y = 20390x + 1.386$	$y = 22660x + 2.135$	94
<i>L</i> -Pro	$y = 20800x + 0.783$	$y = 20620x + 2.091$	94
<i>D</i> -Met	$y = 19300x + 0.556$	$y = 18370x + 1.563$	96
<i>L</i> -Met	$y = 18480x + 1.085$	$y = 17820x + 2.091$	94

^a The equations were obtained by plotting the peak area (y) against the concentration (x) of analyte.

^b The equations were obtained by plotting the peak area (y) against the spiked concentration (x) of analyte in urine.

^c The recovery were determined in triplicate at the spiked concentrations phenothiazines of 0.8, 1 and 2 mM in urine.

4. Conclusion

This study investigated the effects of several parameters on the enantioseparation of five pairs of D,L-phenothiazines by using CE. The following steps enhanced the enantioseparation of these compounds: (1) Adding 0.9% PDDAC to the background electrolyte generated a stable, fast, and reversed EOF. (2) Adding 5 mM Hp- γ -CD to the background electrolyte slowed the effective electrophoretic mobility of the analyte. (3) Decreasing the capillary length shortened the migration time of the analyte, and (4) increasing the intensity of the electric field augmented the flow velocity. Moreover, Hp- γ -CD acted as a chiral selector for D,L-phenothiazines, whereas PDDAC suppressed the adsorption of D,L-phenothiazines on the capillary. The baseline chiral separation of the five pairs of D,L-phenothiazines was achieved within 230 s. Under optimal separation conditions, the LODs of the five pairs of D,L-phenothiazines were as low as 2–8 μ M. We demonstrated the proposed method to be not only simple and straightforward but also practical and convenient for monitoring the concentration of therapeutic drugs in human urine. Because of its advantages of simplicity, high speed, favorable reproducibility, the proposed method exhibits considerable potential for use in the pharmaceutical industry and clinical diagnosis without matrix effects.

Acknowledgment

This work was supported by the National Science Council of Taiwan under contracts NSC 101-2113-M-017-001-MY2.

Appendix A. Supporting information

Supplementary data associated with this article can be found in the online version at <http://dx.doi.org/10.1016/j.talanta.2014.08.015>.

References

- [1] E. Tanaka, T. Nakamura, M. Terada, T. Shinozuka, C. Hashimoto, K. Kurihara, K. Honda, *J. Chromatogr. B* 854 (2007) 116–120.
- [2] C.B. Eap, L. Koeb, K. Powell, P. Baumann, *J. Chromatogr. B* 669 (1995) 271–279.

- [3] F.J. Lara, A.M. Garcia-Campana, F. Ales-Barrero, J.M. Bosque-Sendra, *Electrophoresis* 26 (2005) 2418–2429.
- [4] S.A. Jortani, A. Poklis, *J. Anal. Toxicol.* 17 (1993) 374–377.
- [5] K. Pluta, B. Morak-Młodawska, M. Jeleń, *Eur. J. Med. Chem.* 46 (2011) 3179–3189.
- [6] R. Bhushan, D. Gupta, *J. Chromatogr. B* 837 (2006) 133–137.
- [7] E. Tesařová, Z. Bosáková, *J. Sep. Sci.* 26 (2003) 661–668.
- [8] F.G. Sánchez, A. Navas Díaz, E. Sánchez Torreño, A. Aguilar, I. Medina Lama, M. Algarra, *Biomed. Chromatogr.* 26 (2012) 1241–1246.
- [9] M.A. Martínez-Gomez, S. Sagrado, R.M. Villanueva-Camanas, M.J. Medina-Hernandez, *Anal. Chim. Acta* 582 (2007) 223–228.
- [10] W.S. Liao, C.H. Lin, C.Y. Chen, C.M. Kuo, Y.C. Liu, J.C. Wu, C.E. Lin, *Electrophoresis* 28 (2007) 3922–3929.
- [11] S. Souverain, L. Geiser, S. Rudaz, J.-L. Veuthey, *J. Pharm. Biomed. Anal.* 40 (2006) 235–241.
- [12] C.-C. Wang, J.-L. Chen, Y.-L. Chen, H.-L. Cheng, S.-M. Wu, *Anal. Chim. Acta* 744 (2012) 99–104.
- [13] C.E. Lin, W.S. Liao, K.H. Chen, W.Y. Lin, *Electrophoresis* 24 (2003) 3154–3159.
- [14] Z. Bosáková, I. Kloučková, E. Tesařová, *J. Chromatogr. B* 770 (2002) 63–69.
- [15] M.A. Martínez-Gomez, R.M. Villanueva-Camanas, S. Sagrado, M.J. Medina-Hernandez, *Electrophoresis* 27 (2006) 4364–4374.
- [16] M.A. Martínez-Gomez, R.M. Villanueva-Camanas, S. Sagrado, M.J. Medina-Hernandez, *Electrophoresis* 28 (2007) 3056–3063.
- [17] C.E. Lin, W.S. Liao, H.T. Cheng, C.M. Kuo, Y.C. Liu, *Electrophoresis* 26 (2005) 3869–3877.
- [18] C.E. Lin, T.C. Ko, C.M. Kuo, O. Trapp, W.Y. Lin, C.H. Lin, J.C. Wu, Y.C. Liu, *Electrophoresis* 30 (2009) 3071–3078.
- [19] C.E. Lin, K.H. Chen, Y.Y. Hsiao, W.S. Liao, C.C. Chen, *J. Chromatogr. A* 971 (2002) 261–266.
- [20] E. Córdova, J. Gao, G.M. Whitesides, *Anal. Chem.* 69 (1997) 1370–1379.
- [21] C.J. Yu, W.L. Tseng, *Electrophoresis* 27 (2006) 3569–3577.
- [22] R. Wang, X. Lu, M. Wu, *J. Sep. Sci.* 24 (2001) 658–662.
- [23] M.D. Li, T.L. Cheng, W.L. Tseng, *Electrophoresis* 30 (2009) 388–395.
- [24] C.W. Chang, W.L. Tseng, *Anal. Chem.* 82 (2010) 2696–2702.
- [25] W.L. Tseng, S.M. Chen, C.Y. Hsu, M.M. Hsieh, *Anal. Chim. Acta* 613 (2008) 108–115.
- [26] T.H. Lin, C.Y. Lu, W.L. Tseng, *Electrophoresis* 34 (2013) 297–303.
- [27] C.W. Chang, S.P. Chu, W.L. Tseng, *J. Chromatogr. A* 1217 (2010) 7800–7806.
- [28] L. Zhou, F.J. Reen, F. O’Gara, C.M. McSweeney, S.L. Clarke, J.D. Glennon, J.H. T. Luong, G.P. McGlacken, *J. Chromatogr. A* 1251 (2012) 169–175.
- [29] C. Masetto de Gaitani, A.S. Martinez, P.S. Bonato, *Chirality* 15 (2003) 479–485.
- [30] F.G. Sánchez, A. Navas Díaz, E. Sánchez Torreño, A. Aguilar, I. Medina Lama, M. Algarra, *Biomed. Chromatogr.* 26 (2012) 1241–1246.
- [31] S.C. Lin, C.W. Whang, *J. Sep. Sci.* 31 (2008) 3921–3929.
- [32] J.W. Jorgenson, K.D. Lukacs, *Anal. Chem.* 53 (1981) 1298–1302.
- [33] S. Fanali, *J. Chromatogr. A* 875 (2000) 89–122.
- [34] K. Otsuka, S. Terabe, *J. Chromatogr. A* 875 (2000) 163–178.
- [35] G. Gübitz, M.G. Schmid, *Electrophoresis* 21 (2000) 4112–4135.
- [36] M. Heuermann, G. Blaschke, *J. Chromatogr. A* 648 (1993) 267–274.
- [37] C.-E. Lin, K.-H. Chen, *J. Chromatogr. A* 930 (2001) 155–163.
- [38] I. Bechet, P. Paques, M. Fillet, P. Hubert, J. Crommen, *Electrophoresis* 15 (1994) 818–823.



Investigating the performance of *in situ* quantitative nuclear magnetic resonance analysis and applying the method to determine the distribution of saccharides in various parts of carrot roots (*Daucus carota* L.)



Elsa Bauchard^{a,b,c}, Hervé This^{a,b,*}

^a INRA, UMR 1145, Group of Molecular Gastronomy, 16 rue Claude Bernard, 75005 Paris, France

^b AgroParisTech, Laboratoire de chimie analytique, Group of Molecular Gastronomy, 16 rue Claude Bernard, 75005 Paris, France

^c AliXan Inc, France

ARTICLE INFO

Article history:

Received 1 April 2014

Received in revised form

28 July 2014

Accepted 31 July 2014

Available online 13 August 2014

Keywords:

Carrot

NMR

Saccharides

Glucose

Fructose

Sucrose

Root

Daucus carota L.

Is q NMR

ABSTRACT

In order to explore the performance of the analytical method called *in situ* quantitative nuclear magnetic resonance spectroscopy – *is q* NMR – the distribution of glucose, fructose and sucrose in various parts of a carrot root (*Daucus carota* L.) – primary xylem, secondary xylem, phloem, cortex; top part and lower part – was determined. The influence on the quality of spectra of drying samples before analysis was studied, as well as the influence of the length of strips of tissue used in analysis. Finally samples as small as 240 mm³ could be studied directly, with minimum prior treatment (only drying), along with deuterated water for locking and a sealed capillary tube containing a solution of 0.5% of the sodium salt of (trimethylsilyl)propionic-2,2,3,3-d₄ acid, used both as an internal reference and for quantification. With optimized parameters, the coefficients of variation for measurements were observed to have an average value of 0.038, with a standard deviation of 0.047.

© 2014 Elsevier B.V. All rights reserved.

1. Introduction

During food preparation (“cooking”) or food consumption, food ingredients such as plant or animal tissues exchange “bio-active” compounds – *i.e.* compounds with sensory or nutritional receptors for them existing in the human body, bc – with their environment [1]. In order to investigate the phenomena occurring during food preparation, it is useful not only to be able to determine quantitatively the bc content inside food ingredients before and after “culinary” (for example, thermal) treatments, but also to validate the observed changes with a determination of the quantity of bc released in the environment [2]. The latter determination is straightforward, but for the first one, most analytical methods involve extraction steps, which use important masses of samples [3], and this impedes comparisons. Changes in bioactivity during processes such as thermal treatment of plant tissues were studied, but with no validation of measurements

performed solely in the liquid phase, which means that only assumptions could be made about possible molecular modifications during processing.

Some authors investigated the compositional changes of plant tissues such as the roots of *Daucus carota* L. (“carrots”) or the bulbs of *Allium cepa* L. (onions), because such tissues are widely consumed by human populations, being important food ingredients both for home culinary production or in the food industry [4,5]. These plant tissues are storage systems having complex micro-structure. Their main bc are saccharides and amino acids [6–8]. In carrots for example, the main water soluble compounds are water, pectins, saccharides, amino acids and organic acids, some of these being in a liquid phase, such as inside the cytosol compartments of the parenchyma tissue [9]. Sucrose (Suc), glucose (Glc) and fructose (Fru) are considered to be the common saccharides of carrot roots. In fresh carrot roots, the total saccharide content ranges from 3.46 to 10.74% [10–12]. According to Rodríguez-Sevilla et al. [13], in raw carrots purchased at local market, Suc was the major saccharide and represented 56.9% of total saccharides, followed by Glc (24.6%) and Fru (18.5%).

* Corresponding author at: AgroParisTech, Laboratoire of Analytical Chemistry, Group of Molecular Gastronomy, 16 rue Claude Bernard, 75005 Paris, France.

E-mail address: herve.this@agroparistech.fr (H. This).

Moreover a number of investigations indicated that the concentrations in free saccharides vary considerably among carrot varieties and are influenced by environmental, farming, and storage conditions [14]. The time-course and spatial distribution of saccharides and ions in carrot roots was studied at cell resolution by Korolev et al. [15] by microfluorometric enzymatic assay [16,17], but with high standard deviation. Many chromatographic methods such as GC/MS, LC/UV and LC/MS have also been used recently for metabolomic studies [18–21], but they ask for a long preparation of samples.

Quantitative ^1H NMR (q ^1H NMR) spectroscopy can be useful for the fast quantification, in a single analysis, of the major saccharides [22,23,18], organic acids, amino acids and phenolic compounds, giving metabolic profiles of complex mixtures [24]. NMR methods have often less sensitivity than chromatographic ones [25–27], but q ^1H NMR allows the detection of most proton-containing metabolites above a minimum threshold level [28], detecting a broad range of metabolites in a non-targeted way. Such ^1H NMR chemical fingerprinting has been widely developed for biomedical applications [29–31] but also for food analysis and authentication [32,23,33], for the study of the biochemical mode of action of herbicides [34], or for the study of compositional changes during fruit ripening [25] among many applications. For example, in tomato, q ^1H NMR spectroscopy, coupled or not with liquid chromatography, was used for cultivar comparison [35], for the demonstration of substantial equivalence of transgenic plants [36] and for the detection of unintended effects following a genetic modification [37].

The preparation of extracts in view of analysis is a difficult question. In many former studies, bc compounds from plant tissues were extracted before analysis. For saccharides, an optimized method for the determination of the saccharide content of plant tissues was devised by Davis et al. [38] after O'Donoghue [3] and others [39]. In this “modified O'Donoghue” (MOD) method, plant tissues are lyophilised, heated under reflux in a mixture of methanol and water (62.5:37.5, w-w) for 15 min at 55 °C; after filtration, solvent evaporation and lyophilization, the resulting product is analyzed using various analytical techniques, among which q ^1H NMR [5,40].

However, analyses done by using this MOD method are long, destructive and they need hazardous manipulations with toxic solvent. Moreover This et al. [41] showed that the results obtained can be statistically different from results obtained by *in situ* quantitative ^1H NMR (*is q* NMR) methods, where plant tissues are directly analyzed by liquid high resolution NMR in the frequency domain [42]. Such methods are based on the fact that the water content of plant tissues is high. For carrot roots, it is about 88% of fresh weight [43]: in these tissues, as in most plant tissues, the cytoplasm of plant cells can be considered to be a jellified system [26], where metabolites and ions are in an aqueous, liquid environment that can be described by the DSF formula $D_0(W)/D_3(S)$ [1,31]. Indeed, in the cytoplasm, the cytoskeleton forms a network which includes an aqueous solution of metabolites (cytosol) where organelles are dispersed [44]. Moreover, some free aqueous solution makes up the sap which fills the vessels called xylem and phloem; saccharides are dissolved in the elaborated sap [9]. This observation was at the foundation of low magnetic field (time-domain NMR) NMR spectroscopy applied to whole plant tissues, and indeed carrot tissues were formerly studied by time domain NMR spectroscopy [45–47], but these studies intended to determine the hydration state of compounds rather than the concentration of metabolites.

On the other hand, gels such as silica gel were analyzed by high-field (frequency domain) NMR spectroscopy [48]. In previous studies, frequency-domain NMR analysis were performed in order to compare the quantity of saccharides extracted using the MOD

method and the quantity of saccharides as determined by the *in situ* method, where non-treated samples of plant tissues are simply analyzed after being introduced in a 5 mm glass NMR tube with enough D_2O for locking.

In other tests, the plant samples were put in the NMR tubes along with a sealed capillary tube containing enough D_2O for locking and a reference compound such as the sodium salt of (trimethylsilyl)propionic-2,2,3,3- d_4 acid (TSP), this tube being formerly calibrated using a precisely known solution of potassium phthalate; TSP dissolved in D_2O was used for chemical shift calibration and as a standard. In this way, the analysis of the content of plant tissues (for compounds in the liquid phase) is fast, as there is no preparation, except some drying of samples. Indeed the beneficial effect of this drying was observed but not determined quantitatively, and it was shown that the quantities of saccharides determined by the *is q* NMR methods are higher than with extraction. The study then revealed that the *is q* method is also useful because it is more environmentally friendly than previously used methods, as it does not require the use D_2O nor organic solvents.

One goal of this new work was to investigate the performance of the *is q* NMR method, while applying it to the analysis of the distribution of saccharides inside plant tissues. The aim was to determine the minimum quantity of plant tissue necessary for the quantitative determination of saccharides. It was considered a secondary goal to study the influence of the duration of drying of samples before NMR acquisition. Finally a question was to know whether the distribution of saccharides in a carrot root could be determined.

2. Material and methods

2.1. Chemicals

D_2O (99.9%) and 3-(trimethylsilyl)propionic-2,2,3,3- d_4 acid, sodium salt (TSP; 98%) were from Aldrich (Steinheim, Germany). $\text{D}(+)\text{-Glucose}$ was from Prolabo, Sucrose from Merck, $\text{D}(-)\text{-Fructose}$, minimum 99% from Sigma. The purity of all chemicals was checked by q ^1H NMR. All samples, hardware and solutions, at each step of the analytical process, were weighed three times, using a 0.1 mg precision balance (Mettler Toledo AG 153).

2.2. Sample preparation for the calibration curves

Because the main saccharides contained in carrot roots are Suc, Glc, Fru, calibration curves were made for each saccharide as all of them relax differently [49]. Calibrations curves were also made using a NMR analysis of a mixture of the three saccharides with different proportions in order to allow for possible interactions [50]. The solvent used to make those solutions was D_2O . For a better dissolution of the saccharides in D_2O , solutions were sonicated during 15 min without heating. Some of the solutions were made several times in order to validate the results. During this step, it was measured that a gradient of concentration exists in a saccharide solution [51] and that the viscosity can affect NMR spectra [52]. These two factors were taken into account for analysis of saccharides in carrot roots. The NMR uncertainties have been estimated differently for the various studied saccharides.

2.3. Sample preparation for the study of carrots

Carrots (variety “Nantaise améliorée”, produced in France and Spain, cat 1, season 2011) were obtained from a local supermarket on the day of each experiment. The samples were prepared as

followed [4]: after removal of 0.5-cm segments at both ends (to eliminate leaves and secondary roots), the carrot roots were peeled by hand (thickness of the dropped part less than 1 mm). Each root was then cut lengthwise into three sectors using a scalpel, as preliminary studies showed that the shape of blades has an influence on the chemical composition of plant tissues (to be published). Each part was then divided in two, in order to compare the bottom to the top of the carrot. Finally, in each of the six parts prepared in this way from roots, thin strips were cut in the different areas studied (primary xylem, secondary xylem, phloem and cortex). The strips were weighed and left to dry at room temperature.

2.4. Optimum size of the thin strips

A previous study showed that the optimum weight of liquid to be put in the NMR tube for a good NMR analysis is about 800 mg, which means about 6 cm height in the NMR tube [53]. In this part of the study, several strips were cut in the various parts of a carrot root, with various lengths, from 3.0 to 6.0 cm (for size measurement, a caliper rule was used, precision 0.02 mm). For each length tested, NMR spectra were recorded in the same conditions as for saccharide analysis. The preparation of strips of same width was difficult, but the analysis of NMR spectra showed that the exact quantity of saccharides in samples was not necessary for interpretations.

2.5. Study of the effect of drying of strips

In order to reduce the resonance of water protons (4.6 ppm) and consequently the possible interactions with other resonances, a strip of the same size as the sample studied for saccharide determination was left to dry in air during up to 1500 min, and weighed regularly during this time. It was analyzed by ^1H NMR at various times. Water suppression sequences were shown to be less efficient, as some resonances near the one of protons in water were modified in a way which impeded the interpretation of the area of resonances; as a consequence, it was decided not to apply these water suppression sequences, and to calculate the saccharide quantities directly from spectra acquired using simple NMR proton sequences.

2.6. ^1H NMR

For NMR analyses, a superconducting Ultrashield 300 MHz (7.05 T) 54 mm magnet NMR spectrometer BZH 30/300/70 E Bruker Biospin (Wissembourg, France) was used. All NMR spectra were recorded at 18 °C to avoid changes in the mutarotation equilibrium [54]. For each spectrum, 32 scans of 32 K data points were acquired with a spectral width of 6 Hz, an acquisition time of 5.3 s, and a recycle delay of 25 s per scan to allow complete relaxation and absolute quantification [49]; the pulse angle was 90°.

After the drying step, each thin strip was put in an NMR tube with about precisely 0.7 g of D_2O and a sealed capillary tube containing a well-known concentration of TSP (standard) in D_2O (about 5% of TSP; the content of the capillary tube was analyzed separately using a precisely prepared potassium phthalate solution in D_2O).

Three spectra were recorded for each sample. The analysis of each sample was performed using D_2O as an internal lock. Spectra were acquired under an automation procedure (automatic shimming and automatic sample loading). They were Fourier-transformed with 0.3 Hz line broadening, phase and baseline were corrected using XWIN NMR 3.5 software (Bruker Biospin, Rheinstetten, Germany). The resonances in all spectra were integrated and autocorrected three times using NMR Notebook 2.5 (NMR

Notebook 2.50, build 0.0, 2000–2008, Illkirch-Graffenstaden, France) software [40].

Then all calculation were done using the software Maple 14.01 (Maplesoft, Waterloo Maple Inc, Ontario, Canada).

2.7. Identification and quantification

The resonances of the major saccharides in carrot roots were identified using reference data of pure saccharide solutions and also results from analogous studies using the same plant material or from different plant tissues [29,55]. A confirmation for the identification of the different resonances was given by the addition of pure compounds in solutions being analyzed.

For interpretations, two protons were used to characterize each saccharide. Suc was determined using a doublet at 5.42 ppm (H1 (d)) and a doublet at 4.2 ppm (H2 (d)). Fru was characterized with two protons: H3 and H4 which have very close chemical shifts, the signal for those two protons was a doublet at 4.12 ppm. For Glc, the doublet of the H1 (dd) proton at 5.24 ppm and H2 α proton at 3.2 ppm were used.

For quantification, the area of the TSP resonance was used as a reference of area fixed equal to 1. Quantification was performed using calibration curves for each saccharide, as each compound relaxes differently. However, calibration curves of Glc, Fru, and Suc were established using NMR spectra obtained with solutions containing the three saccharides together, in order to take into account possible interactions [59]. The obtained mass of saccharides was put in relation with the mass of each fresh thin strips.

3. Results and discussion

3.1. Calibration curves

The regression coefficients for Glc (H1), Glc (H2), Suc (H1), Suc (H3'), Fru (H3) are respectively 0.9959, 0.9987, 0.9990, 0.9965, 0.9986.

3.2. Influence of the partial drying of samples

Previous studies [47] showed that drying the thin carrot strips was useful to obtain high quality spectra, with a straight baseline, and it was debated whether this drying process was useful to avoid any interaction between the resonance of water and the resonances of the different saccharides. Here the optimum time of drying of the different strips was investigated.

First the variation of the mass of strips was studied in function of time (Fig. 1). Two distinct slopes were observed. From 0 to 400 min, a linear mass decrease was determined (the mass m being measured equal to $-0.00125 \times t + 21.8$, where t is the time; coefficient of correlation 0.996); then, from 600 to 1500 min, a horizontal plateau was reached. The percentage of water released from the samples was then calculated (Fig. 2). The maximum percentage of released water (90.37%) was obtained after 600 min.

NMR spectra were acquired from the same thin strips at different times during drying. When the strips of carrot root are dried, the resonances obtained in the NMR spectra show a better resolution and separation than when the strips are not dried. Also, drying leads to a reduction of the resonance of water protons and therefore avoids its overlapping with other resonances, like the one at 4.8 ppm chemical shift.

The amount of water contained in a carrot was published to be 88% of the fresh weight [56,57]. As the mass of water theoretically in the carrot root (0.37118 g) and the mass of water lost experimentally (0.37276 g) are very similar, it could be assumed that almost all the water contained in the carrot root is evaporated after 600 min, but

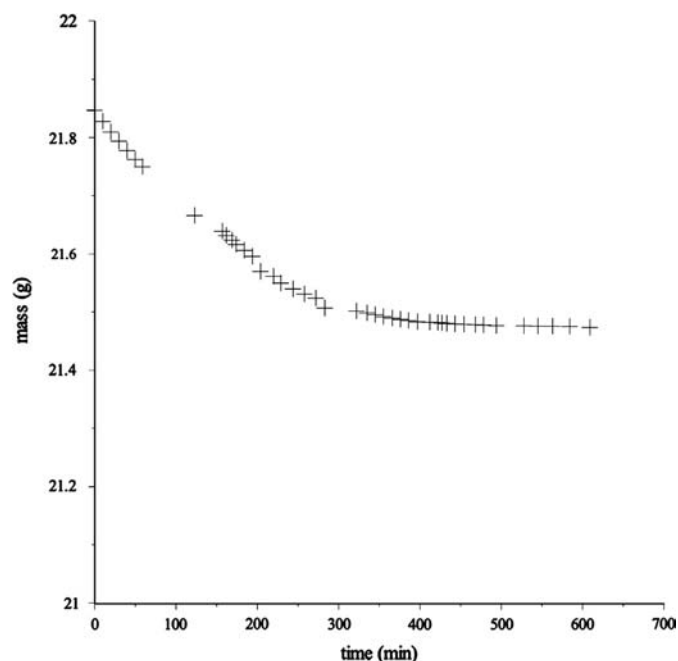


Fig. 1. The mass variation of plant strips with time was studied, in order to compare the mass with the quantity of water and metabolites as determined by *is q* NMR (in the particular curve given here, the temperature was fixed at 18 °C, with a relative humidity of 78%). The mass stabilization occurs apparently after about 600 min. This was a criterion for the selection of 800 min as the drying time used for all samples of this study.

NMR spectra of dried samples showed a large resonance for water protons, showing that a lot of liquid remains inside the tissues.

In order to get reproducible and accurate results, it was decided to dry all the different strips in the same way: for the application of the improved method to the determination of the distribution of Glc, Fru and Suc in the various parts of a carrot root, each stripe of plant tissue was dried for 800 min.

3.3. Determination of the optimum size of strips

For this study, spectra were acquired for different lengths of strips. For each sample, 3 NMR spectra were acquired (see Fig. 3). When the length of the strip is between 3.0 and 4.5 cm, the different resonances are not fully resolved and separated. The longer the strips, the better the resolution and the separation of the resonances. Spectra acquired with 6.0 cm long strips showed the better separation and resolution. This length was used for the determination of saccharides in carrot roots.

3.4. Study of the various saccharides in carrot roots

The quantity of Glc, Fru and Suc was determined in the various parts of carrots (Fig. 4) with an average coefficient of variation (CV) of 0.038 (standard deviation 0.047 for the CV) (Fig. 5). The total mass of saccharides in the various parts is between 4.84% and 15.37% of fresh carrot mass. The reducing saccharides represent between 17.49% and 54.08% of the total free saccharides in the carrot root, their quantity decreasing from the center of the roots toward the periphery, for both the upper and lower parts. On the contrary, the Suc quantity increases, from the center to the cortex. There is more Suc than Glc and Fru, for both top and bottom parts.

Goris investigated the distribution of saccharides in the carrot roots [7]. Because the quantity of the different saccharides was given only according to the dried mass of carrot roots and not the fresh mass as we have done in this work, the quantities cannot be compared. Only trends of the different quantities can be studied. According to Goris, Suc is the less abundant saccharide present in carrot roots. This result is not coherent with our results, and with others results [56,5]. The difference can be explained by the extraction method used in Goris et al. study: it consists in a hot ethanol treatment at 96 °C for 20 min before a drying step at 90 °C. The different steps including heating can be responsible for the difference of Suc quantity. Indeed, heating Suc can convert it in Glc and Fru [58,59]. This hypothesis can be confirmed by the important measured proportion of Fru and Glu in tissues where Suc concentration is the lowest. The proportion of saccharides was also investigated by Seljasen et al. [60]: for carrot roots collected during different harvests and in different years, it is comprised between 4.5% et 7.5% of fresh mass [61–63], which is in accordance with our results.

In the same work by Seljasen et al., it was published that the quantity of Suc is higher in the liberian parenchyma (cortex and phloem) than in vascular parenchyma (primary and secondary xylem), and our study shows a similar result. Also it was shown that *is q* NMR method gives significantly different results than methods involving extraction, in particular for Suc. Using the optimized *is q* NMR method, this difference could now be investigated.

If only more recent results are compared, it can be observed that the results shown here are in accordance with other previously published values, showing for example that the quantity of reducing sugars (Glc and Fru) represents 48.7% of the total free saccharides [12]. The measured quantity of reducing saccharides is also coherent with the ones found in literature.

Interestingly, whereas there is no consistent variation in the top part of carrot root, the Glc and Fru concentration decreases from the center to the cortex, and the Suc concentration increases, in the bottom part. Moreover, for this bottom part, the sum

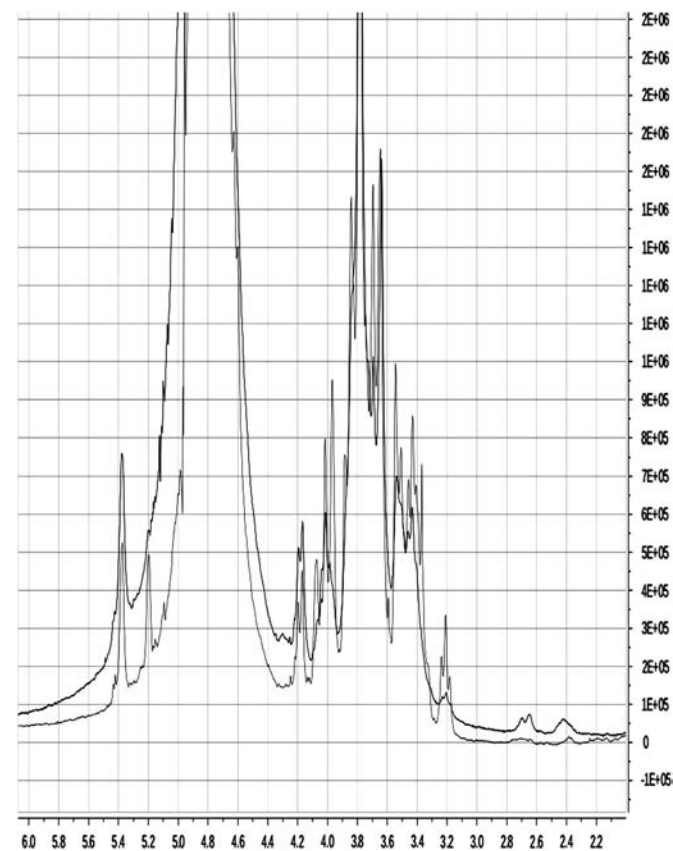


Fig. 2. The effect of the partial drying of samples on NMR spectra is shown. The lower spectrum was obtained for a strip of freshly-cut tissue, and the upper spectrum was obtained for the same strip, but after 1500 min of drying in air at room temperature.

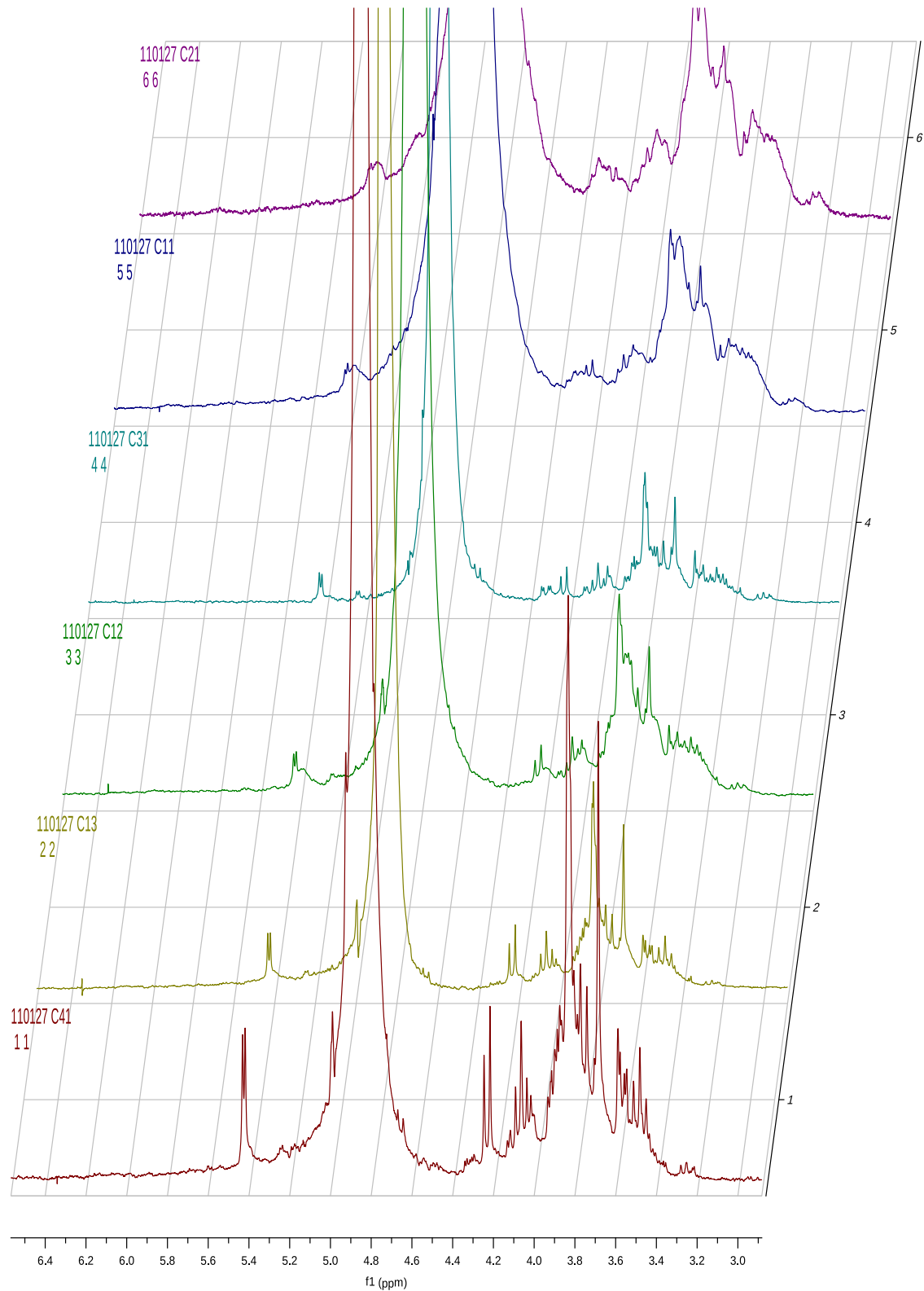


Fig. 3. The size of the strip of carrot put in the NMR tube has an influence on the resolution of the NMR recorded spectra. In order to have an optimum NMR spectrum (resonance resolution, baseline), different lengths of strips have been tested (in cm: 3, 4, 4.5, 5, 6). For each, three NMR spectra were obtained and the different spectra were superimposed. When the length of the strips varies between 3 and 5 cm, the different resonances obtained in the NMR spectra do not present a good resolution and a good separation. The longer the strips, the better the resolution and the separation of the peaks. Therefore, the length of the strips chosen for this study has been set to 6 cm because of the good separation and the good resolution obtained on the NMR spectrum. The width of the strips was set to 3 mm, which is the minimum width which can be cut properly. This small width allows studying only one zone of the carrot root.

Glc+ Fru+ Suc is equal respectively to 0.07, 0.07, 0.07, 0.08 in the various parts of the root (primary xylem, secondary xylem, phloem, cortex).

For the cortex, the quantity of all saccharides is significantly higher ($p=0.05$) at the top than at the bottom. For the primary xylem, Fru and Glc are more abundant at the bottom, while Suc is

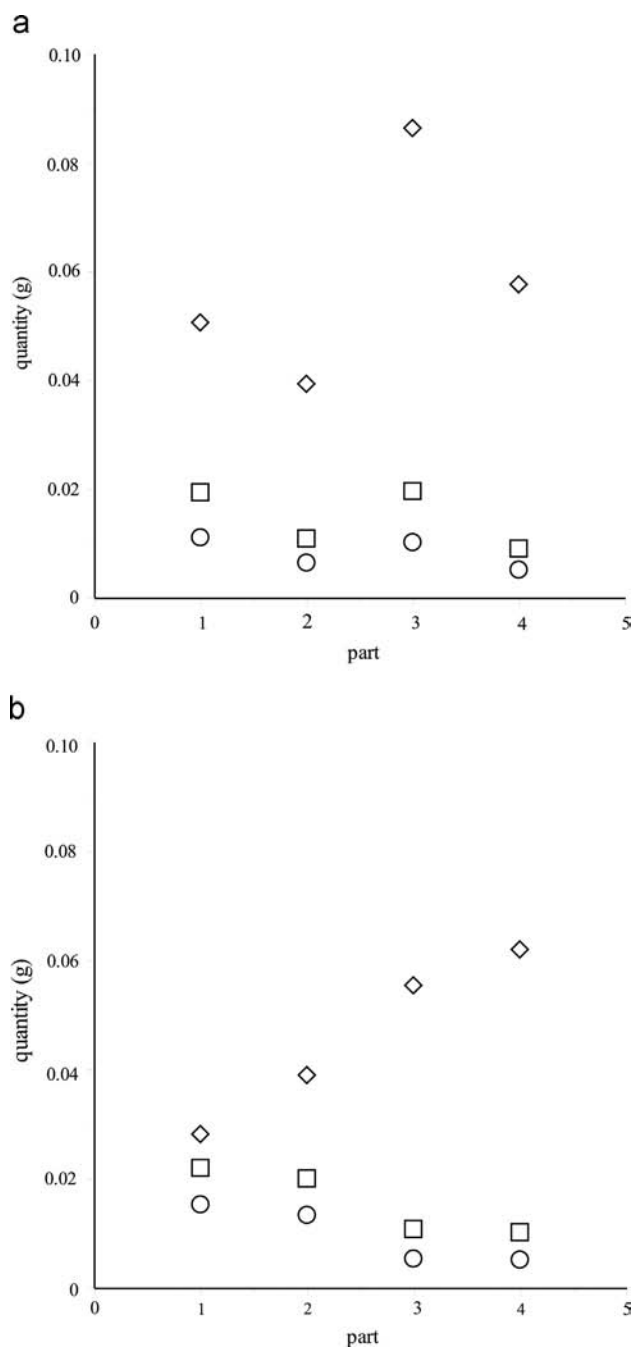


Fig. 4. In carrot tissues, Suc was determined using a doublet at 5.42 ppm (H1 (d)) and a doublet at 4.2 ppm (H2 (d)). Fru was characterized with the resonance of two protons: H3 and H4 which have very close chemical shifts, the signal for those two protons was a doublet at 4.12 ppm. For Glc, the doublet of the H1 (dd) proton at 5.24 ppm and H2 α proton at 3.2 ppm were used. Using such resonances, the mass of the three saccharides was studied for top (a) and bottom (b) part of a carrot root, at various distances from the axis of the root (primary xylem, secondary xylem, phloem, cortex).

prevalent at the top. For the secondary xylem, the three saccharides have a different distribution. The Suc quantity is not significantly different in the top and bottom part; Glc is more abundant at the bottom, and Fru is more abundant at the top. The inhomogeneity of xylem is high, as saccharide concentration is concerned. This can be explained by the fact that the xylem part includes a lot of conductive tissue [12], with dimensions of channels as large as 0.140 mm [2]. As this is only 10 times smaller than the diameter of strips, it could be assumed that some strips

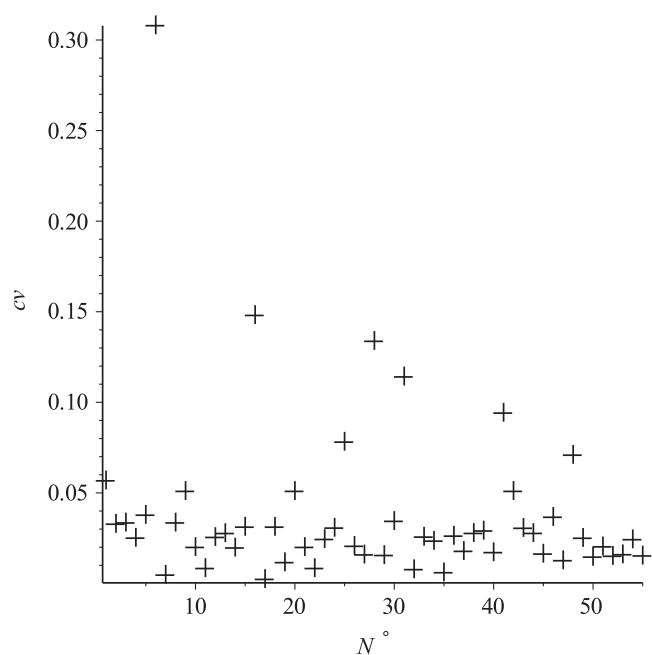


Fig. 5. Variation coefficients of saccharide determination for various analyses using *is q* NMR applied to strips of carrot roots.

included more of these channels than others, hence a larger coefficient of variation.

As the top of the roots is the youngest part of the organ, it should present more variability than the bottom of the carrot. Indeed, the results obtained showed that the distribution of saccharides at the top is more variable than at the bottom. According to the literature, the phloem area transport mostly Suc [64], which can explain the high quantity of this saccharide at the bottom as at the top of the carrot root.

Finally using *is q* NMR, the distribution of saccharides could be studied in carrot roots. This method gives access to precise results using a fast, sustainable method using no organic solvent and ensuring lesser risks of degradation to the compounds studied, because of the minimal treatment applied to each sample. Another advantage of this technique is that it is a non-destructive method; the different samples used can then be used again for complementary analysis. This technique can be applied to a lot of other applications such as the health field or the soil field. Also the method can be used to study most metabolites – such as amino acids – when abundant enough (more than 1 mg in the strips).

Novelty statement

The analytical method called *in situ* quantitative nuclear magnetic resonance spectroscopy has been explored in various conditions in the last years, but the effectiveness of the method was not known. As previous research has showed that extraction methods used for the determination of saccharides and amino acids give poor results, it was decided to test the new method in this particular case.

In this paper, it is shown that:

- the method yields very good results (coefficient of variation CV < 0.05)
- the method gives information which cannot be obtained using other methods (saccharide determination from small samples as small as ~ 250 mm³)

- the method makes it possible to give satisfactory answers to questions otherwise very difficult to answer.

Acknowledgements

The authors wish thank Yann Padellec and Stephane Besançon, Stephanie Debrie and Pascale Debeuver for their support.

References

- [1] H. This, *Pure Appl. Chem.* 5 (2012) 257.
- [2] A. Tardieu, A. Guerez, S. Phana, W. De Man, H. This, *Food Chem.* 74 (2009) 319–325.
- [3] E.M. O'Donoghue, S.D. Somerfield, M. Bendall, D. Hedderley, J. Eason, I. Sims, *J. Agric. Food Chem.* 52 (2004) 5383–5390.
- [4] B.W. Li, P.J. Schuhmann, *J. Food Sci.* 48 (1983) 633–635.
- [5] A. Cazor, C. Deborde, A. Moing, D. Rolin, H. This, *J. Agric. Food Chem.* 54 (2006) 4681–4686.
- [6] T. Suojala, *Sci. Hortic.* 85 (2000) 1–19.
- [7] A. Goris, *Qualitas Plantarum et Materiae Vegetabiles* 18 (1969) 283–306.
- [8] C.P.P. Ricardo, *F. Sovia, Planta* 118 (1974) 43–55.
- [9] N. Campbell, *Biologie, De Boeck-Wesmael*, 1995.
- [10] F.A. Lee, *The Chemistry and Technology of Food and Food Products*, second ed., Interscience, 1951.
- [11] B.K. Watt, A.L. Merrill, R.K. Pecot, C.F. Adams, M.L. Orr, D.F. Miller, *Composition of Foods, Raw, Processed, Prepared. Agriculture Handbook no. 8*, U.S. Government Printing Office, 1963.
- [12] D.M. Alabran, A.F. Mabrouck, *J. Agric. Food Chem.* 21 (1973) 205–208.
- [13] M.D. Rodríguez-Sevilla, M.J. Villanueva-Suárez, A. Redondo-Cuenca, *Food Chem.* 66 (1999) 81–85.
- [14] W.A. Sistrunk, G.A. Bradley, D. Smittle, *Proc. Am. Soc. Hortic. Sci.* 90 (1967) 239–251.
- [15] A.V. Korolev, A.D. Tomos, R. Bowtell, J.F. Farrar, *J. Exp. Bot.* 51 (1999) 567–577.
- [16] A.D. Tomos, P. Hinde, P. Richardson, J. Pritchard, W. Fricke, *Plant Cell Biology—A Practical Approach*, Oxford, 1994, pp. 297–314.
- [17] O.A. Koroleva, J.F. Farrar, A.D. Tomos, *C.J. Pollock, New Phytol.* 136 (1997) 97–104.
- [18] O. Fiehn, *Plant Mol. Biol.* 48 (2002) 155–171.
- [19] P.D. Fraser, M.E.S. Pinto, D.E. Holloway, P.M. Bramley, *Plant J.* 24 (2000) 551–558.
- [20] U. Roessner, A. Luedemann, D. Brust, O. Fiehn, T. Linke, L. Willmitzer, A.R. Fernie, *Plant Cell* 13 (2001) 11–29.
- [21] U. Roessner, L. Willmitzer, A.R. Fernie, *Plant Cell Rep.* 21 (2002) 189–196.
- [22] I.F. Duarte, A. Barros, P.S. Belton, R. Righelato, M. Spraul, E. Humpfer, A.M. Gil, *J. Agric. Food Chem.* 50 (2002) 2475–2481.
- [23] G. Le Gall, M. Puaud, I.J. Colquhoun, *J. Agric. Food Chem.* 49 (2001) 580–588.
- [24] A.M. Gil, I.F. Duarte, I. Delgadillo, I.J. Colquhoun, F. Casuscelli, E. Humpfer, M. Spraul, *J. Agric. Food Chem.* 48 (2000) 1524–1536.
- [25] P.S. Belton, I.J. Colquhoun, E.K. Kemsley, I. Delgadillo, P. Roma, M.J. Dennis, M. Sharman, E. Holmes, J.K. Nicholson, M. Spraul, *Food Chem.* 61 (1998) 207–213.
- [26] H.P. Noteborn, A. Lommen, R.C. Van der Jagt, J.M. Weseman, *J. Biotechnol.* 77 (2000) 103–114.
- [27] J.L. Ward, C. Harris, J. Lewis, M.H. Beale, *Phytochemistry* 62 (2003) 949–957.
- [28] T.W.M. Fan, *Prog. Nucl. Magn. Reson. Spectrosc.* 28 (1996) 161–219.
- [29] H. Antti, M.E. Bollard, T. Ebbels, H. Keun, J.C. Lindon, J.K. Nicholson, E. Holmes, *J. Chemom.* 16 (2002) 461–468.
- [30] J.T. Brindle, H. Antti, E. Holmes, G. Tranter, J.K. Nicholson, H.W.L. Bethell, S. Clarke, P.M. Schofield, E. McKilligin, D.E. Mosedale, D.J. Grainger, *Nat. Med.* 9 (2003) (477–477).
- [31] J.C. Lindon, E. Holmes, J.K. Nicholson, *Prog. Nucl. Magn. Reson. Spectrosc.* 39 (2001) 1–40.
- [32] I.J. Colquhoun, *Spectrosc. Eur.* 10 (1998) 8–18.
- [33] J.T. W.E. Vogels, L. Terwel, A.C. Tas, F. Van den Berg, F. Dukel, J. Van der Greef, *J. Agric. Food Chem.* 44 (1996) 175–180.
- [34] K.H. Ott, N. Aranibar, B.J. Singh, G.W. Stockton, *Phytochemistry* 62 (2003) 971–985.
- [35] A.P. Sobolev, A. Segre, R. Lamanna, *Magn. Reson. Chem.* 41 (2003) 237–245.
- [36] H.P. Noteborn, A. Lommen, R.C. Van der Jagt, M. Weseman, *J. Biotechnol.* 77 (2000) 103–114.
- [37] G. Le Gall, I.J. Colquhoun, A.L. Davies, G.J. Collins, M.E. Verhoeven, *J. Agric. Food Chem.* 51 (2003) 2447–2456.
- [38] F. Davis, L.A. Terry, G.A. Chope, C.F.J. Faul, *J. Agric. Food Chem.* 55 (2007) 4299–4306.
- [39] R. Viola, H.V. Davies, *Potato Res.* 35 (1992) 55–58.
- [40] A. Tardieu, H. This, *J. Food Sci.* (2009) C319–C325.
- [41] H. This, L. Weberskirch, M. Plassais, A. Luna, A. His, S. Skoglund, *L'Actualité Chimique* 337 (2010) 10–13.
- [42] L. Weberskirch, A. Luna, S. Skoglund, H. This, *Anal. Bioanal. Chem.* 399 (2011) 483–487.
- [43] L.G. Bartolome, J.E. Hoff, *J. Agric. Food Chem.* 20 (1972) 266–270.
- [44] N.D. Gershon, K.R. Porter, B.L. Trus, *Proc. Nat. Acad. Sci. U.S.A.* (1985) 5030–5034.
- [45] J.P. Monteiro-Marques, D.N. Rutledge, C.J. Ducauze, *Int. J. Food Sci. Technol.* (1991) 173–183.
- [46] J.P. Monteiro-Marques, D.N. Rutledge, C.J. Ducauze, *Lebensm. Wiss. Technol.* 17 (1991) 93–98.
- [47] J.P. Monteiro-Marques, D.N. Rutledge, C.J. Ducauze, *Sci. Aliments* (1992) 613–624.
- [48] D.W. Sindorf, G.E. Maciel, *J. Am. Chem. Soc.* (1983) 1487–1493.
- [49] A. Moing, M. Maucourt, C. Renaud, G. Gaudillère, R. Brouquisse, B. Lebouteiller, A. Goussot-Dupont, J. Vidal, D. Granot, B. Denoyes-Rothan, E. Lerceteau-Köhler, D. Rolin, *Funct. Plant Biol.* 31 (2004) 889–902.
- [50] S.L. Kaufman, F.D. Dorman, *Langmuir* 24 (2008) 9979–9982.
- [51] G. Raposo, H.W. Nijman, W. Stoorvogel, *J. Exp. Med.* 183 (1996) 1161.
- [52] S.P.E. Freedman, N. Heaton, S.P.E. Schlumberger, M. Flaum, G.J. Hirasaki, U. Rice, C. Flaum, M. Hürlimann, *SPE J.* (2003) 317–327.
- [53] V. Pinciroli, R. Biancardi, G. Visentin, V. Rizzo, *Org. Process Res. Dev.* 8 (2004) 381–384.
- [54] M. Cockman, D.G. Kubler, A.S. Oswald, L. Wilson, *J. Carbohydr. Chem.* 6 (1987) 181–201.
- [55] A. Cazor, C. Deborde, A. Moing, D. Rolin, H. This, *J. Agric. Food Chem.* 54 (2006) 4681–4686.
- [56] I.L. Nonnecke, *Vegetable Production*, Van Nostran Reinhold (1989) 75.
- [57] C. Alasalvar, J.M. Grigor, D. Zhang, P.C. Quantick, F. Shahidi, *J. Agric. Food Chem.* 49 (2001) 1410–1416.
- [58] H.R. Goldschmid, A.S. Perlin, *Can. J. Chem.* 38 (1960) 2178–2186.
- [59] W. Moody, G.N. Richards, *Carbohydr. Res.* 97 (1981) 247–255.
- [60] R. Seljasen, G. Bengtsson, H. Hoftun, G. Vogt, *J. Sci. Food Agric.* 81 (2001) 436–447.
- [61] G. Balvoll, J. Apeland, J. Auranaune, *Forsking og forsk i landbruket* 27 (1976) 327–337.
- [62] A.M. Evers, *J. Agr. Sci. Finland* 60 (1988) 135–152.
- [63] S. Hogstad, E. Risvik, K. Steinholt, *Soil Plant Sci.* 47 (1997) 253–264.
- [64] C. Alasalvar, J.M. Grigor, D. Zhang, P.C. Quantick, F. Shahidi, *J. Agric. Food Chem.* 9 (2001) 1410–1416.



A fluorescence method for detection of DNA and DNA methylation based on graphene oxide and restriction endonuclease HpaII



Wei Wei^a, Chunyan Gao^a, Yanxiang Xiong^a, Yuanjian Zhang^a, Songqin Liu^{a,*}, Yuepu Pu^{b,1}

^a Key Laboratory of Environmental Medicine Engineering, Ministry of Education, School of Chemistry and Chemical Engineering, Southeast University, Jiangning District, Nanjing 211189, PR China

^b Key Laboratory of Environmental Medicine Engineering, Ministry of Education, School of Public Health, Southeast University, Jiangning District, Nanjing 211189, PR China

ARTICLE INFO

Article history:

Received 22 June 2014

Received in revised form

25 July 2014

Accepted 30 July 2014

Available online 6 August 2014

Keywords:

DNA methylation

Restriction endonuclease

HpaII

Graphene oxide

Fluorescence

ABSTRACT

DNA methylation plays an important role in many biological events and is associated with various diseases. Most traditional methods for detection of DNA methylation are based on the complex and expensive bisulfite method. In this paper, we report a novel fluorescence method to detect DNA and DNA methylation based on graphene oxide (GO) and restriction endonuclease HpaII. The skillfully designed probe DNA labeled with 5-carboxyfluorescein (FAM) and optimized GO concentration keep the probe/target DNA still adsorbed on the GO. After the cleavage action of HpaII the labeled FAM is released from the GO surface and its fluorescence recovers, which could be used to detect DNA in the linear range of 50 pM–50 nM with a detection limit of 43 pM. DNA methylation induced by transmethyase (Mtase) or other chemical reagents prevents HpaII from recognizing and cleaving the specific site; as a result, fluorescence cannot recover. The fluorescence recovery efficiency is closely related to the DNA methylation level, which can be used to detect DNA methylation by comparing it with the fluorescence in the presence of intact target DNA. The method for detection of DNA and DNA methylation is simple, reliable and accurate.

© 2014 Elsevier B.V. All rights reserved.

1. Introduction

Genomic DNA methylation is one of the most important epigenetic modifications in eukaryotes, which serves a wide variety of biological functions. DNA transmethyase (Mtase) can catalyze the transfer of a methyl group to DNA and all the known DNA methyltransferases use S-adenosylmethionine (SAM) as the methyl donor. In animals, most of the methylations occur at the 5' position of the pyrimidine ring of the cytosine. The methylcytosine (mC) is mainly found in cytosine–guanine (CpG) dinucleotides. The presence of 5-mC in the promoter of specific genes alters the binding of transcriptional factors and other proteins to DNA and recruits methyl-DNA-binding proteins and histone deacetylases that compact the chromatin around the gene-transcription start site. Both mechanisms block transcription and cause gene silencing. Thus methylation of cytosine residues in genomic DNA plays a key role in the regulation of gene expression in many biological events and is closely associated with various diseases, especially

cancer [1–3]. So, it is significant to develop a simple and sensitive method for the detection of DNA methylation.

The traditional method for detection of DNA methylation is based on bisulfite. Bisulfite modification converts unmethylated cytosine to uracil, while methylated cytosine cannot react. After denaturation and bisulfite modification, double-strand DNA is obtained by primer extension and the fragment of interest is amplified by PCR. There is an extensive range of methods based on the sodium bisulfite treatment for quantifying the methylation status of cytosines located in specific DNA regions [4,5]. The bisulfite-based methods are currently considered gold standard assay techniques because they are reliable, accurate, and can help understand the methylation status of each CpG in target DNA, while complex and expensive clone and sequencing procedures are needed in this method. A lot of new methods, including gel electrophoresis [6], real-time quantitative polymerase chain reaction [7], high-performance liquid chromatography (HPLC) [8,9] and gas chromatography/mass spectrometry (GC/MS) [10], are also developed. They are also complicated to operate, time consuming and expensive. Recently, alternative approaches such as electrochemical [11–13], electrogenerated chemiluminescence strategy [14,15], colorimetric [16–19] and fluorescence methods [20–25]

* Corresponding author.

E-mail addresses: liusq@seu.edu.cn (S.Q. Liu), yppu@seu.edu.cn (Y.P. Pu).

¹ Tel.: +86 25 52090613; fax: +86 25 5209061.

have been developed to detect DNA methylation. Endonucleases can recognize and cleave specific short DNA sequences. Combined with methyltransferase they are usually used to detect DNA methylation [26–29]. GO has been reported as an excellent quenching material for the fluorescence dye due to fluorescence resonance energy transfer. The other superior property is that GO has a strong binding force with ssDNA strands due to π -stacking interaction between nucleobases and GO surface [30–33].

Herein, a graphene oxide (GO) based platform coupled with HpaII and Mtase M.SssI is studied to detect DNA methylation. First, GO was used to quench the probe DNA that was modified with 6-carboxyfluorescein (FAM) on its 5' end. The probe DNA are skillfully designed to have 10 bases longer than that of target DNA in order to make their hybridism still adsorbed on the GO surface (Scheme 1, a). After the cleavage of specific site 5'-CCGG-3' through HpaII, the labeled FAM is released to the solution and the fluorescence recovers (Scheme 1, b). The DNA detection limit of this method is 43 pM without signal amplification strategy. When the target DNA is methylated, the fluorescence cannot recover because HpaII digestion function is blocked by methylated cytosine base (Scheme 1, c). Therefore, the fluorescence intensity of FAM is closely related to the methylation level. Based on this, a sensitive fluorescence method for detection of DNA and DNA methylation is proposed. The method avoids bisulfite treatment of DNA and is simple, reliable and selective.

2. Experimental

2.1. Reagents and apparatus

The GO was synthesized by our group following the Hummers method [34]. Tris(hydroxymethyl)aminomethane (Tris) was purchased from Sigma-Aldrich. Hydrogen peroxide (30% in water) (H_2O_2) was purchased from Sinoreagent. S-adenosylmethionine (SAM), *Escherichia coli* CpG methyltransferase (M.SssI), and *E. coli* restriction endonuclease (HpaII) were obtained from New England BioLabs (NEB, UK). All these standard solutions were prepared and stored at under 4 °C. All other chemical reagents were of analytical reagent grade and used without further purification. Millipore Milli-Qwater (18 M Ω cm) was used throughout.

The DNA oligonucleotides were synthesized by Shanghai Sangon Biological Engineering Technology and Services Co., Ltd., China. 1 μ M DNA stock solution was prepared by using 33 mM Tris-acetate buffer solution (pH 7.4) containing 66 mM NaAc and 10 mM Mg(Ac)₂. The sequences of oligonucleotides used in this work are shown in Table 1.

The buffers employed in this work were as follows: DNA hybridization buffer was 33 mM Tris-acetate (pH 7.4) containing 66 mM NaAc and 10 mM Mg(Ac)₂. The buffer for MTase work was 10 mM Tris-HCl (pH 7.9) containing 50 mM NaCl, 10 mM MgCl, and 1 mM DTT. The buffer for endonuclease HpaII digestion experiment was 33 mM Tris-acetate (pH 7.9) containing 10 mM Mg(Ac)₂, 66 mM KAc and 0.1 mg/mL BSA.

Safety note: dimethyl sulfoxide (DMSO) and acetaldehyde (CH_3CHO) are suspected human carcinogens and somewhat volatile. Gloves were worn; manipulations were done under a closed hood. All reactions were done in closed vessels.

A fluoromax 4 spectrofluorometer (Horiba, Japan) was used in the experiment.

2.2. Endonuclease digestion of probe/target DNA on GO surface

FAM-labeled probe DNA was mixed with target DNA (10 bases longer than probe DNA) in 33 mM pH 7.4 Tris-acetate buffer solution containing 66 mM NaAc and 10 mM Mg(Ac)₂. Then, the solution was heated to 90 °C for 5 min followed by slow cooling to room temperature to ensure complete hybridization. Then, HpaII was incubated with probe/target DNA in 33 mM pH 7.9 Tris-acetate buffer solution containing 10 mM Mg(Ac)₂, 66 mM NaAc and 0.1 mg/mL BSA at 37 °C. Finally, 25 μ g/mL GO was added to the mixture and the fluorescence intensity of the FAM was monitored.

2.3. DNA cytosine methylation induced by M.SssI Mtase

The methylation was prepared by incubating M.SssI MTase with prepared double strands DNA in 1 \times MTase reaction buffer (10 mM pH 7.9 Tris-HCl containing 50 mM NaCl, 10 mM MgCl, 1 mM dithiothreitol and 160 μ M SAM) at 37 °C.

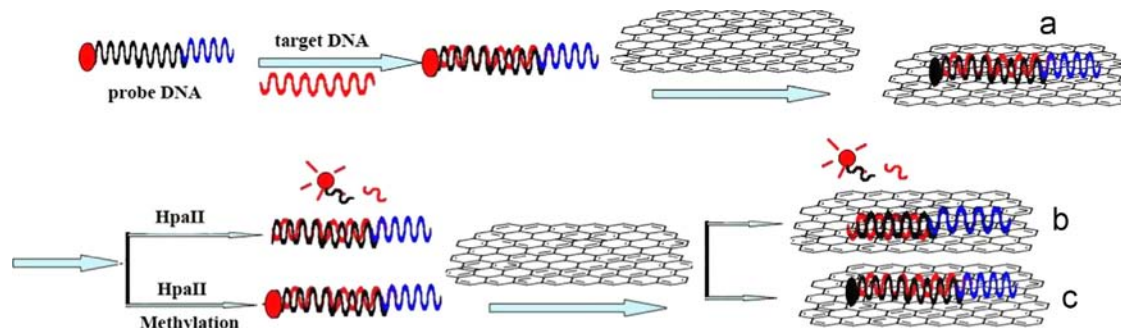
2.4. DNA methylation induced by chemical reagents

25 μ L of 1 μ M double strands DNA was mixed with 5.0 μ M FeSO₄, 20.0 μ M H₂O₂, 10.0 μ M L-ascorbic acid, 3.0 μ M ethylene diamine tetraacetic acid (EDTA)-2Na and 100 μ M DMSO or CH₃CHO. The solution reacted under N₂ atmosphere. After reaction, the mixture solution was centrifuged to separate chemical reagents from DNA. The followed detection procedure was the same as that for M.SssI methyltransferase.

Table 1
Sequence of used DNA.

Oligonucleotides	Sequences (5'–3')
Probe DNA	FAM-ACCCGGATAAGATGCTACTTACTCAC
Target DNA	AGCATCTTATCCGGGT
One base mismatched target DNA (T1)	AGCATCTTATCC <u>AG</u> GT
Non-complementary target DNA (T2)	GAACATCATAGCCGGAC

Mismatched base is underlined.



Scheme 1. Fluorescence detection of DNA and DNA methylation based on GO and endonuclease HpaII. .

3. Results and discussion

3.1. Strategy for detection of DNA and DNA methylation based on GO and endonuclease HpaII

As demonstrated in Scheme 1, first, probe DNA was hybridized with target DNA to form double strands and labeled FAM that emitted strong fluorescence (Fig. 1a). As previously reported the signal of FAM labeled on the single strand DNA was quenched efficiently in the presence of certain amount of GO, while the fluorescence was recovered when it was hybridized with the perfect matched DNA due to the separation of double strands DNA from GO surface [28,31]. In our assay, the probe DNA are designed to have 10 bases longer than that of target DNA, which can keep their hybrids still adsorbed on GO and the fluorescence is still quenched (Fig. 1b). After incubation with HpaII that can recognize the double strands sequence of “CCGG” and cleave it ($5' \dots \overset{\text{C}}{\text{C}} \overset{\text{C}}{\text{G}} \overset{\text{G}}{\text{G}} \dots 3'$), FAM is released from GO surface and the fluorescence is recovered (Fig. 1c). Thus, the target DNA can be detected based on the recovered fluorescence intensity. The cleavage action of HpaII is prevented by the presence of a 5-methyl group at the second C base of its recognition sequence of “CCGG” (i.e. “CCmGG”). As a result, the fluorescence cannot recover (Fig. 1d). So, DNA methylation

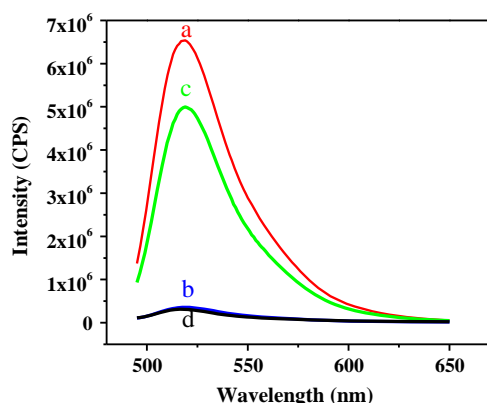


Fig. 1. The fluorescence spectra of hybrid of probe DNA and target DNA (a) without GO, (b) in the presence of GO, (c) in the presence of GO and HpaII, and (d) hybrid of methylated probe DNA and target DNA in the presence of GO and HpaII.

can be discriminated from the intact DNA by comparing their fluorescence recovery efficiencies.

3.2. Optimization of detection condition

GO concentration is one of the important factors for the DNA and DNA methylation detection. The fluorescence intensity of the probe DNA/target DNA varies considerably with the GO concentration. The quench efficiency increases with increasing amount of GO and begins to level off at 25 $\mu\text{g}/\text{mL}$ (Fig. 2A).

On the other hand, GO concentration has large impact on the fluorescence recovery efficiency induced by HpaII. Fig. 2B demonstrates that the most efficient fluorescence recovery is obtained at 25 $\mu\text{g}/\text{mL}$ of GO, while further increased amount of GO decreases the fluorescence recovery efficiency. High fluorescence quench efficiency induced by GO decreases the background signal, while high recovery efficiency induced by HpaII increases the detection sensitivity. Thus, 25 $\mu\text{g}/\text{mL}$ GO is chosen as the optimal condition. The cleavage time for HpaII was optimized.

The cleavage time for HpaII was optimized. Fig. 3 shows that the fluorescence cannot recover in the absence of HpaII, while it recovers in the presence of 0.02 U/ μL of HpaII and the recovery efficiency is dependent on the incubation time of HpaII and probe/target DNA. The fluorescence intensity increases with increasing incubation time and levels off at 1 h. In order to obtain the best recognition and cleavage function of HpaII, 2 h incubation is chosen in the experiments.

3.3. Detection of target DNA

Fig. 4A shows the fluorescence spectra of 50 nM probe DNA in the presence of different concentrations of target DNA from 0 to 100 nM, 25 $\mu\text{g}/\text{mL}$ of GO and 0.02 U/ μL of HpaII. The fluorescence recovery efficiency increased with increment of target DNA. Fig. 4B reveals that the increased fluorescence intensity is linear with the target DNA concentration in the range of 50 pM–50 nM. The calibration equation is $y=95,244x+48,847$, with correlation coefficient $R^2=0.998$. The detection limit was 43 pM obtained in terms of 3 times deviation of blank sample, which was much lower than that of reported result based on GO induced fluorescence quench [35].

One-base mismatched (T1) and non-complementary (T3) target DNA were used to evaluate the selectivity of the method. Compared with the complementary DNA (Fig. 5a) the fluorescence

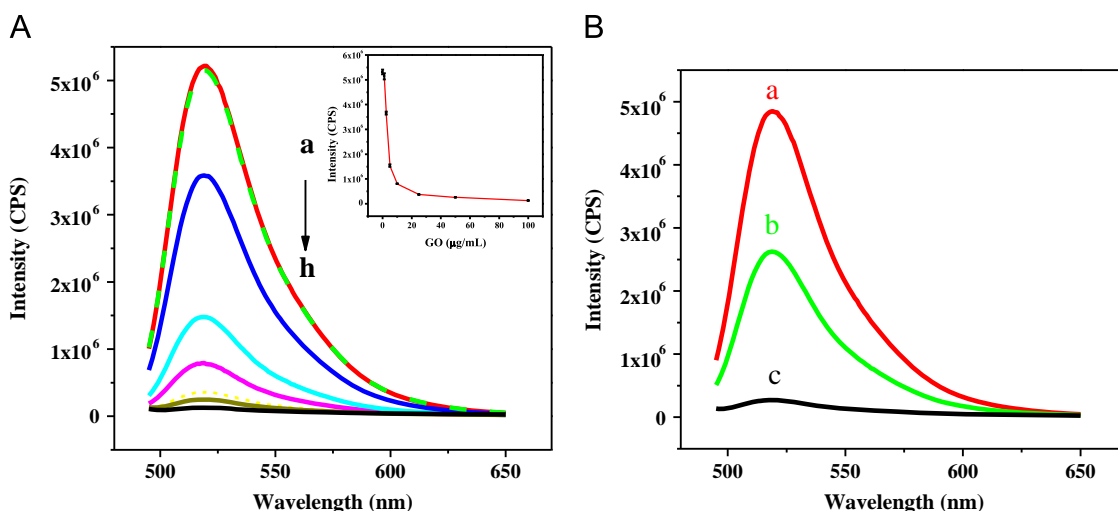


Fig. 2. (A) Fluorescence quench of probe/target DNA at 0, 1.25, 2.5, 5, 10, 25, 50, and 100 $\mu\text{g}/\text{mL}$ of GO (from a to h). The inset shows the plot of fluorescence intensity versus different GO concentrations. (B) Fluorescence recovery induced by HpaII at (a) 25, (b) 50, and (c) 100 $\mu\text{g}/\text{mL}$ of GO.

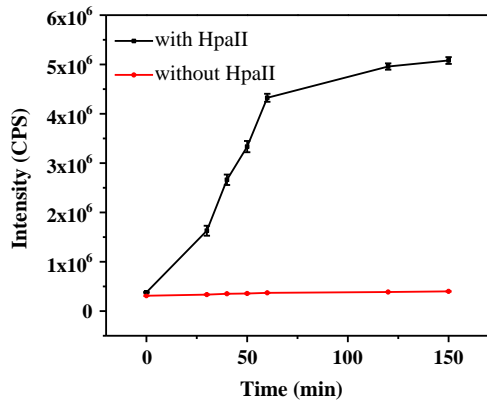


Fig. 3. Time-dependent fluorescence intensity of probe/target DNA in the presence of 0.02 U/μL HpaII and 25 μg/mL of GO.

intensity for T1 (b) and T3 (c) decreased 96%, only a little higher than that without target DNA (d). This demonstrated that HpaII and Exo III do not work on one-base mismatched or non-complementary target DNA, indicating that the proposed method has good selectivity. The method can make a distinction between one-base mismatched DNA and complementary target DNA, which possesses more advantages than those of previously reported methods.

3.4. Detection of DNA methylation induced by *M.SssI* MTase

Based on the good selectivity of the method, it is used to detect the DNA methylation induced by *M.SssI* in the presence of SAM. The synthetic methylated DNA containing 5'-CCmGG-3' sequence is used as standard methylated DNA for comparison. Experiments showed that no fluorescence was recovered in the presence of HpaII because it cannot recognize and cleave the methylated DNA.

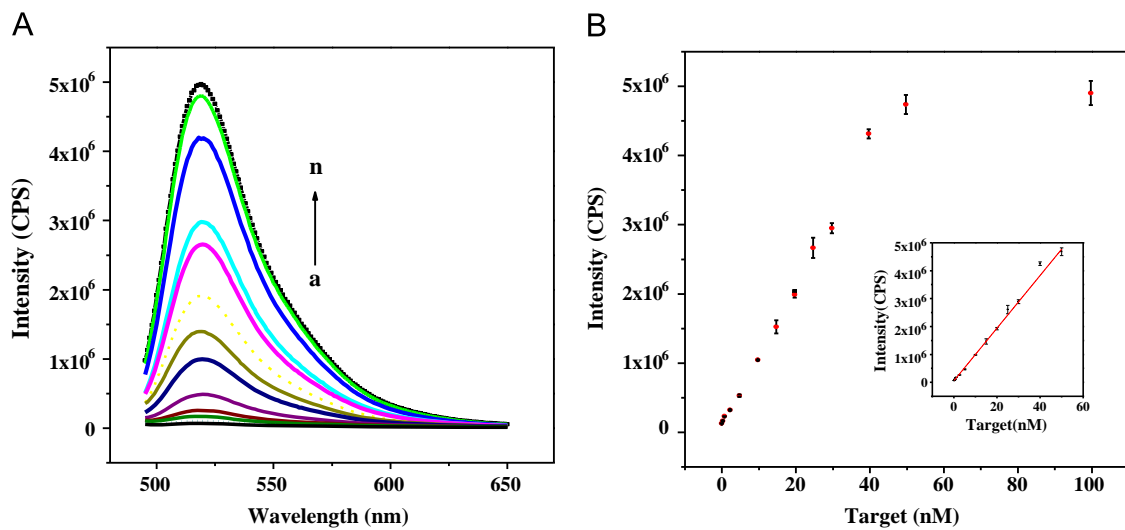


Fig. 4. (A) Fluorescence spectra of the hybrid of 50 nM probe DNA and various concentrations of target DNA (0, 0.2, 0.5, 1, 2.5, 5, 10, 15, 20, 25, 30, 40, 50, 100 nM from a to n in order). (B) Dependence of fluorescence intensity on different target DNA concentrations; the inset shows the plot of fluorescence intensity versus target DNA concentration from 0 to 50 nM. HpaII concentration: 0.02 U/μL, incubation time: 2 h.

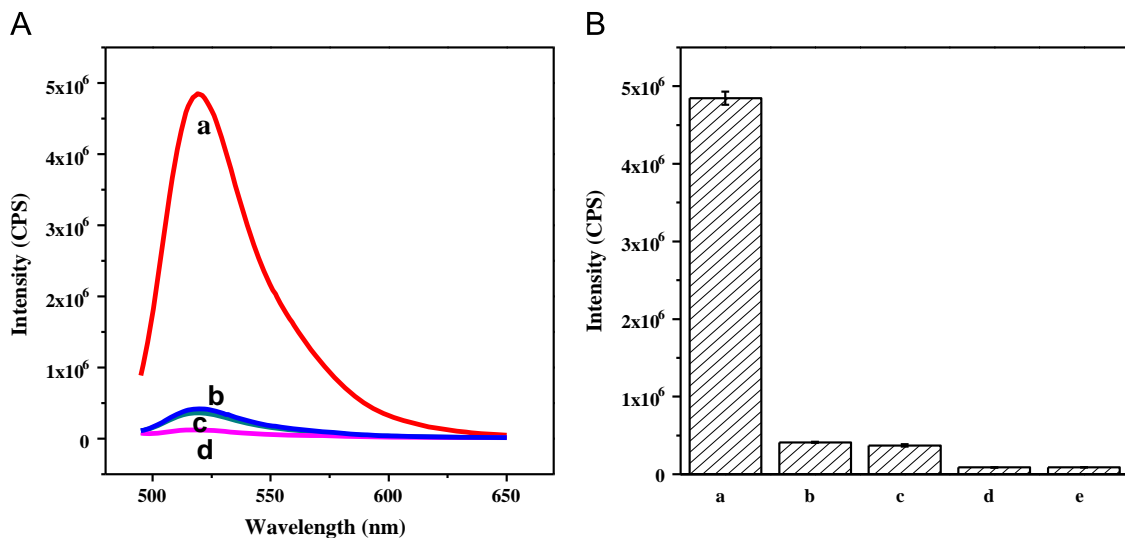


Fig. 5. Selectivity of the method. (A) Fluorescence spectra in the presence of (a) complementary target DNA, (b) one-base mismatched target DNA, (c) noncomplementary target DNA and (d) without DNA. (B) The histogram corresponds to the fluorescence spectra in (A). HpaII concentration: 0.02 U/μL, incubation time: 2 h.

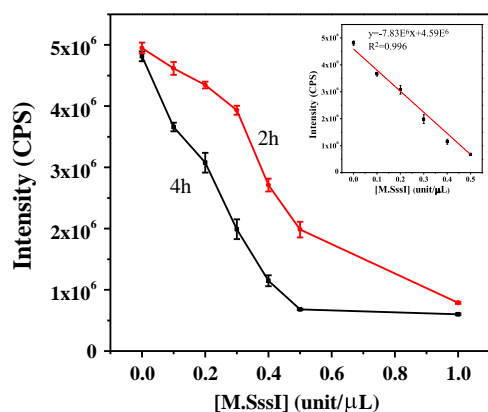


Fig. 6. HpaII concentration dependence and time dependence of fluorescence intensity of probe/target DNA treated with M.SssI.

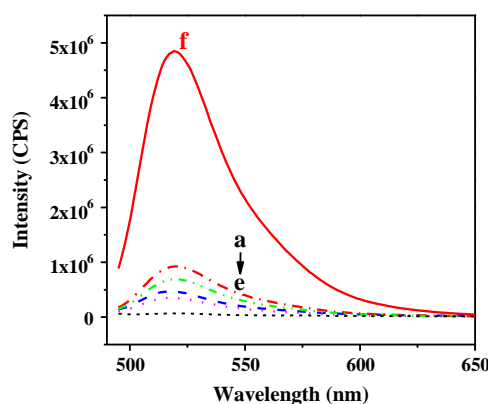


Fig. 7. Fluorescence intensity of probe/target DNA treated with (a) CH₃CHO in the presence of Fe²⁺ and H₂O₂; (b) DMSO in the presence of Fe²⁺ and H₂O₂; (c) M.SssI Mtase and SAM; (d) probe/standard methylated target DNA; (e) no target DNA; and (f) intact target DNA.

Probe/target DNA are treated with various concentrations of M.SssI and 160 μM SAM for 2 h and 4 h followed by detection of their fluorescence in the presence of GO and HpaII. Fig. 6 shows that the fluorescence intensity of treated probe/target DNA decreases with the increase of M.SssI concentration from 0 to 1.0 U/μL. Both higher concentration and longer incubation time of HpaII lead to lower fluorescence recovery efficiency, which indicates that a higher level of DNA methylation occurs. When the probe/target DNA are treated for 4 h, their fluorescence intensity decreases linearly with the HpaII concentration in the range of 0–0.5 U/μL; the calibration equation is $y = 7.83E^6 + 4.50E^6$ with correlation coefficient $R^2 = 0.996$. So, the method can not only be used to detect DNA methylation but also has the potential to be used to detect the activity of M.SssI.

3.5. Detection of DNA methylation induced by chemical reagents

DNA methylation induced by chemical reagents such as DMSO and CH₃CHO in the presence of the Fenton reagents (Fe²⁺, H₂O₂) is detected by the proposed method. The fluorescence spectra of the double strands DNA treated by different reagents are shown in Fig. 7. Fluorescence in the absence of target DNA is very low, while it is very strong in the presence of intact target DNA. All the fluorescence recoveries corresponding to standard methylated DNA and the target DNA treated with chemical reagents or M.SssI are recovered slightly; however, their recovery efficiencies are still different from each other. This indicates that all of these reagents

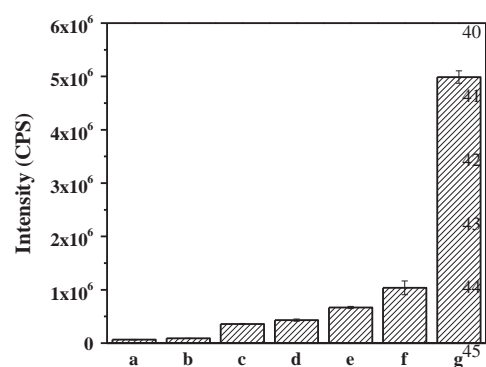


Fig. 8. Comparison of fluorescence intensity of hybrid of probe DNA and various target DNA: (a) no target, (b) non-complementary target DNA, (c) HpaII recognized sequence is methylated to 5'-CCmGG-3', (d) target DNA treated with 1.0 U/μL M.SssI and 160 μM SAM, (e) target DNA treated with Fe²⁺, H₂O₂ and DMSO, (f) target DNA treated with Fe²⁺, H₂O₂ and CH₃CHO, and (g) intact target DNA. Other conditions: 50 nM probe and target DNA, 0.02 U/μL HpaII. All target DNA were treated for 4 h at 37 °C, and the fluorescence was tested after adding 25 μg/mL GO.

induce DNA methylation and the different methylation levels between them could be discerned by this method. CH₃CHO (curve a) or DMSO (curve b) in the presence of Fenton reagents gives rise to DNA methylation because of the methyl radicals that are generated by the reaction of OH radicals with CH₃CHO or DMSO [36–38], while their DNA methylation level is lower than that induced by M.SssI Mtase (curve c). Also, the DNA methylation level induced by M.SssI is lower than that of the synthetic standard methylated DNA (curve d). So, it is reasonable to judge DNA methylation level from their fluorescence intensity. Fig. 8 shows comparison of fluorescence intensity in the presence of different types of target DNA. It shows that the fluorescence intensity for intact complementary DNA is different obviously from those of various methylated DNA and the non-complementary target DNA. Therefore, the developed method has good selectivity to detect intact target DNA and methylated DNA.

4. Conclusions

In summary, a platform based on GO and endonuclease HpaII is constructed for detection of DNA and DNA methylation. The assay is based on the fluorescence recovery of probe/target DNA on the GO surface after the recognition and cleavage action of endonuclease HpaII. The method avoids complex bisulfite treatment of DNA, PCR, and antibody, and is simple, reliable and of low-cost. On the other hand, the method has potential to be used to detect MTase activity and is expected to screen appropriate inhibitor drugs in DNA MTase and disease diagnosis related to DNA methylation.

Acknowledgments

The project is supported by National Natural Science Foundation of China (21205014), Natural Science Foundation of Jiangsu province (BK2012734), the Social Development Project of Jiangsu (BE2012731) and the Social Development Project of Suzhou (ZXY2012027).

References

- [1] J.Y. Zhang, B.L. Xing, J.Z. Song, F. Zhang, C.Y. Nie, L. Jiao, L.B. Liu, F.T. Lv, S. Wang, *Anal. Chem.* 86 (2014) 346–350.
- [2] R.K. Chodavarapu, S.H. Feng, Y.V. Bernatavichute, P.Y. Chen, H. Stroud, Y.C. Yu, J. A. Hetzel, F. Kuo, J. Kim, S.J. Cokus, D. Casero, M. Bernal, P. Huijser, A.T. Clark,

- U. Krämer, S.S. Merchant, X.Y. Zhang, S.E. Jacobsen, M. Pellegrini, *Nature* 466 (2010) 388–392.
- [3] J. Frigola, J. Song, C. Stirzaker, R.A. Hinshelwood, M.A. Peinado, S.J. Clark, *Nat. Genet.* 38 (2006) 540–549.
- [4] S.J. Docherty, O.S.P. Davis, C.M.A. Haworth, R. Plomin, J. Mill, *Methods* 52 (2010) 255–258.
- [5] E. Aichinger, C. Kohler, *Methods Mol. Biol.* 655 (2010) 433–443.
- [6] X.L. Wang, Y.L. Song, M.Y. Song, Z.X. Wang, T. Li, H.L. Wang, *Anal. Chem.* 81 (2009) 7885–7891.
- [7] J. Wang, Z.Q. Zhu, H.W. Ma, *Anal. Chem.* 85 (2013) 2096–2101.
- [8] A.L. Torres, E.Y. Barrientos, K. Wrobel, K. Wrobel, *Anal. Chem.* 83 (2011) 7999–8005.
- [9] X. Ming, B. Matter, M. Song, E. Veliath, R. Shanley, R. Jones, N. Tretyakova, *J. Am. Chem. Soc.* 136 (2014) 4223–4235.
- [10] Y. Tang, X.D. Gao, Y.S. Wang, B.F. Yuan, Y.Q. Feng, *Anal. Chem.* 84 (2012) 7249–7255.
- [11] H.W. Wu, S.C. Liu, J.H. Jiang, G.L. Shen, R.Q. Yu, *Chem. Commun.* 48 (2012) 6280–6282.
- [12] D. Kato, K. Goto, S.I. Fujii, A. Takatsu, S. Hirono, O. Niwa, *Anal. Chem.* 83 (2011) 7595–7599.
- [13] X.F. Wei, X.M. Ma, J.J. Sun, Z.Y. Lin, L.H. Guo, B. Qiu, G.N. Chen, *Anal. Chem.* 86 (2014) 3563–3567.
- [14] Y. Li, X.E. Luo, Z. Yan, J.B. Zheng, H.L. Qi, *Chem. Commun.* 49 (2013) 3869–3871.
- [15] H. Zhang, M.X. Li, M.X. Fan, J.X. Gu, P. Wu, C.X. Cai, *Chem. Commun.* 50 (2014) 2932–2934.
- [16] Y.Z. Lin, P.L. Chang, *A.C.S. Appl., Mater. Int.* 5 (2013) 12045–12051.
- [17] Y.J. Zhao, X.W. Zhao, B.C. Tang, W.Y. Xu, Z.Z. Gu, *Langmuir* 26 (2010) 6111–6114.
- [18] Y.X. Zhao, F. Chen, M.L. Lin, C.H. Fan, *Biosens. Bioelectron.* 54 (2014) 565–570.
- [19] X.Y. Jing, X.Q. Cao, L. Wang, T. Lan, Y.Y. Li, G.M. Xie, *Biosens. Bioelectron.* 58 (2014) 40–47.
- [20] F. Chen, Y.X. Zhao, *Analyst* 138 (2013) 284–289.
- [21] F.D. Feng, H.Z. Wang, L.L. Han, S. Wang, *J. Am. Chem. Soc.* 130 (2008) 11338–11343.
- [22] X.Y. Ouyang, J.H. Liu, J.S. Li, R.H. Yang, *Chem. Commun.* 48 (2012) 88–90.
- [23] Y. Tao, Y.H. Lin, Z.Z. Huang, J.S. Ren, X.G. Qu, *Analyst* 137 (2012) 2588–2592.
- [24] Y. Wang, J. Chen, Y. Chen, W.Y. Li, C. Yu, *Anal. Chem.* 86 (2014) 4371–4378.
- [25] Y. Huang, M. Shi, L.M. Zhao, S.L. Zhao, K. Hu, Z.F. Chen, J. Chen, H. Liang, *Biosens. Bioelectron.* 54 (2014) 285–291.
- [26] A. Sudina, E. Volkov, T. Oretskaya, N. Naryshkin, M. Ivanovskaya, E. Kubareva, *IUBMB Life* 56 (2004) 139–143.
- [27] F.D. Feng, Y.L. Tang, F. He, M.H. Yu, X.R. Duan, S. Wang, Y.L. Li, D.B. Zhu, *Adv. Mater.* 19 (2007) 3490–3495.
- [28] W. Li, P. Wu, H. Zhang, C.X. Cai, *Anal. Chem.* 84 (2012) 7583–7590.
- [29] M. Ronen, D. Avrahami, D. Gerber, *Lab Chip* 14 (2014) 2354–2362.
- [30] Z. Dai, X. Hu, H. Wu, X.Y. Zou, *Chem. Commun.* 48 (2012) 1769–1771.
- [31] S.R. Ryoo, J. Lee, J. Yeo, H.K. Na, Y.K. Kim, H. Jang, J.H. Lee, S.W. Han, Y. Lee, V. N. Kim, D.H. Min, *ACS Nano* 7 (2013) 5882–5891.
- [32] X.H. Zhao, Q.J. Ma, X.X. Wu, X. Zhu, *Anal. Chim. Acta* 727 (2012) 67–70.
- [33] L. Cui, Z.R. Chen, Z. Zhu, X.Y. Lin, X. Chen, C.J. Yang, *Anal. Chem.* 85 (2013) 2269–2275.
- [34] W.S. Hummers, R.E. Offeman, *J. Am. Chem. Soc.* 80 (1958) 1339–1339.
- [35] J. Zhou, Q. Lu, Y. Tong, W. Wei, S.Q. Liu, *Talanta* 99 (2012) 625–630.
- [36] K. Kawai, Y.S. Li, M.F. Song, H. Kasai, *Bioorg. Med. Chem. Lett.* 20 (2010) 260–265.
- [37] D.R. Lloyd, P.L. Carmichael, D.H. Phillips, *Chem. Res. Toxicol.* 11 (1998) 420–427.
- [38] Y.P. Wu, B.T. Zhang, L.H. Guo, *Anal. Chem.* 85 (2013) 6908–6914.



Short communication

Dispersive liquid–liquid microextraction for metals enrichment: A useful strategy for improving sensitivity of laser-induced breakdown spectroscopy in liquid samples analysis



M.A. Aguirre, E.J. Selva, M. Hidalgo*, A. Canals

Department of Analytical Chemistry and Food Science and University Institute of Materials, University of Alicante, P.O. Box 99-03080, Alicante, Spain

ARTICLE INFO

Article history:

Received 22 May 2014

Received in revised form

25 July 2014

Accepted 30 July 2014

Available online 11 August 2014

Keywords:

Dispersive liquid–liquid microextraction

LIBS analysis

Liquid samples

Trace metals determination

ABSTRACT

A rapid and efficient Dispersive Liquid–Liquid Microextraction (DLLME) followed by Laser-Induced Breakdown Spectroscopy detection (LIBS) was evaluated for simultaneous determination of Cr, Cu, Mn, Ni and Zn in water samples. Metals in the samples were extracted with tetrachloromethane as pyrrolidinedithiocarbamate (APDC) complexes, using vortex agitation to achieve dispersion of the extractant solvent. Several DLLME experimental factors affecting extraction efficiency were optimized with a multivariate approach. Under optimum DLLME conditions, DLLME-LIBS method was found to be of about 4.0–5.5 times more sensitive than LIBS, achieving limits of detection of about 3.7–5.6 times lower. To assess accuracy of the proposed DLLME-LIBS procedure, a certified reference material of estuarine water was analyzed.

© 2014 Elsevier B.V. All rights reserved.

1. Introduction

Modern trends in analytical chemistry are toward the development of new miniaturized and field-operable instrumentation allowing *in-situ* and on-line analysis, and on the use of hyphenated techniques having complementary capabilities, leading to analytical methodologies able to both separation and quantification of analytes in complex matrices. New trends also involve continuous advances for improving sensitivity and specificity, reducing sample size and toxic reagent consumption, and achieving lower time and costs per analysis [1,2].

Some of the potentials of Laser-Induced Breakdown Spectroscopy technique (LIBS) fulfill the trends of modern analytical chemistry [3,4]. LIBS allows fast multi-elemental analysis of very small quantities of sample. Moreover, due to the striking technological improvements in lasers and spectrometers during the last decades, a number of portable and easily automatable commercial LIBS instruments are currently available in market [5–7], which makes this technique especially suitable for field measurement. However, in spite of its numerous advantages, the low sensitivity of LIBS when compared with other well established atomic spectrometric techniques constitutes its most important limitation for (ultra) trace elemental analysis, in special for liquid samples analysis [8–11].

Several strategies, aimed to improve the analytical capabilities of LIBS when applied to liquid samples analysis, have been developed in recent years [12–16]. These strategies, however, even if greatly contribute to enhance LIBS sensitivity in liquid analysis, are still insufficient to make LIBS competitive with other atomic spectrometric techniques for (ultra) trace elemental determination.

One common way to increase sensitivity and decrease limits of detection in analytical chemistry is analyte separation and enrichment, thereby increasing the concentration of an analyte, or analytes, to a level compatible with an analytical technique. Conventional liquid–liquid extraction is the most popular in routine sample preparation, but it uses a great amount of solvent, it is tedious, time consuming and difficult to automate. Nowadays, there are novel microextraction techniques that are faster and more easily automatable than conventional extraction procedures and use negligible volume of extractant solvents, which are often hazardous and expensive [17]. As a consequence, traditional liquid–liquid extraction procedures are being increasingly replaced by Liquid Phase Microextraction (LPME) methodologies, which are now widely used for analyte separation and enrichment. In the field of elemental analysis, LPME has been extensively used in combination with atomic spectrometric techniques such as Electrothermal Atomic Absorption Spectrometry (ETAAS), Flame Atomic Absorption Spectrometry (FAAS), Inductively Coupled Plasma Optic Emission Spectrometry (ICP-OES), or X-ray Fluorescence spectrometry (XRF) for trace metal determination in a great variety of samples [18–20]. However, it was not till 2013 than

* Corresponding author. Tel.: +34 965903400; fax: +34 965903697.

E-mail address: montserrat.hidalgo@ua.es (M. Hidalgo).

Aguirre et al. introduced the idea of combining LPME with LIBS [21]. These authors suggested LPME-LIBS as being a synergistic association for overcoming the well known sensitivity limitation of LIBS for liquid samples analysis, proving LIBS technique to be able to afford the analysis of microamounts of liquids resulting from a microextraction procedure. Recently, the LPME-LIBS combination proposal was experimentally tested by the same authors, using Single Drop Microextraction (SDME) as LPME procedure for metals extraction prior to LIBS detection (SDME-LIBS) [22]. Preliminary results obtained from this research work showed that sensitivity of LIBS analysis of liquid samples improved due to the use of a previous SDME procedure, proving the viability of this association. Such results were considered by the authors as a starting point for future research aimed to improve the analytical capabilities of LPME-LIBS hyphenation, with the final goal focused on the future development of a fully automated system useful for *in-situ* trace elemental analysis of liquid samples.

A possible way for improving the analytical potential of this association is the use of alternative and more efficient LPME procedures. Dispersive Liquid-Liquid Microextraction (DLLME) is a microextraction methodology based on the dispersion of few microliters of an organic extractant solvent in the aqueous sample, which can be accomplished by several ways, such as the use of a disperser solvent or vortex agitation. After extraction, phase separation is achieved by centrifugation and analytes in the organic phase can be determined by the detection technique [23–25]. Since many fine droplets of organic solvent are dispersed throughout the aqueous solution, the very large interfacial area makes DLLME process to be very efficient and quick, being considered easier to handle and faster than SDME.

In this work, combination of LIBS with DLLME procedure for analyte enrichment was evaluated for the first time. Tetrachloromethane (CCl_4) was used as extractant solvent for DLLME of several metals as pyrrolidinedithiocarbamate (APDC) complexes, using vortex agitation to achieve dispersion of the extractant solvent. Multivariate analysis was employed for optimization of the experimental factors affecting metals extraction. Under optimum DLLME conditions, sensitivity of DLLME-LIBS methodology in the analysis of model aqueous samples was tested and compared with that achieved by LIBS. Accuracy of the proposed method was evaluated from the analysis of a Certified Reference Material (estuarine water).

2. Experimental

2.1. LIBS experimental setup

Technical details on the LIBS system used in this work have been previously reported [21]. As shown in Fig. 1, the system basically consists of a 10 Hz pulsed Nd-YAG laser (model HYL Handy-YAG, Q-switched, Quanta System S.P.A., Varese, Italy) for plasma creation, a 100 mm focal length plano-convex lens for laser focusing, a five channel spectrometer (model AvaSpec-2048-SPU, 200 nm–800 nm coverage, Avantes, Eerbeek, The Netherlands) coupled to a five-furcated optical fiber ($5 \times 400 \mu\text{m}$ fiber optic cable, model FC5-UV400-2, Avantes) for plasma emission detection and a delay system consisting of two pulse generators (a Digital delay/pulse generator, model DG 535, Stanford Research Systems Inc., Sunnyvale, USA and 1–50 MHz pulse/function generator, model 8116 A, Hewlett Packard/Agilent Technologies, Santa Clara, USA). In this work, the laser was operated in single pulse mode, emitting at its fundamental wavelength (*i.e.*, 1064 nm) with energy 130 mJ per pulse. Data were acquired 1.3 μs after the laser firing, using 1 ms acquisition time. CrI (357.869 nm), CuI (324.754 nm), MnII (259.373 nm), NiI (352.454 nm) and ZnII (202.548 nm) were the emission lines evaluated.

2.2. Sample preparation and analysis

Since the main aim of the work was to evaluate the possible sensitivity improvement of DLLME-LIBS hyphenation over LIBS in the analysis of liquid matrices, both LIBS and DLLME-LIBS methodologies were tested, in parallel, to the determination of different analytes in water samples. For LIBS analysis, the aqueous samples were converted into solid by drying on an aluminum substrate, as already described elsewhere [21]. In order to do this, 10 μL of standard (or sample) aqueous solution were transferred to an aluminum foil, where the solution was confined into a small circular cell (3.2 mm diameter) to avoid liquid spreading. After that, the aluminum foil, placed on a thicker (8 mm) aluminum plate, was heated by a hot plate (model 500 Darlab Egara S.L., Barcelona, Spain) to completely evaporate the water. The remaining solid residue was then analyzed by LIBS. In all cases, the result of LIBS analysis was the mean of three replicate measurements

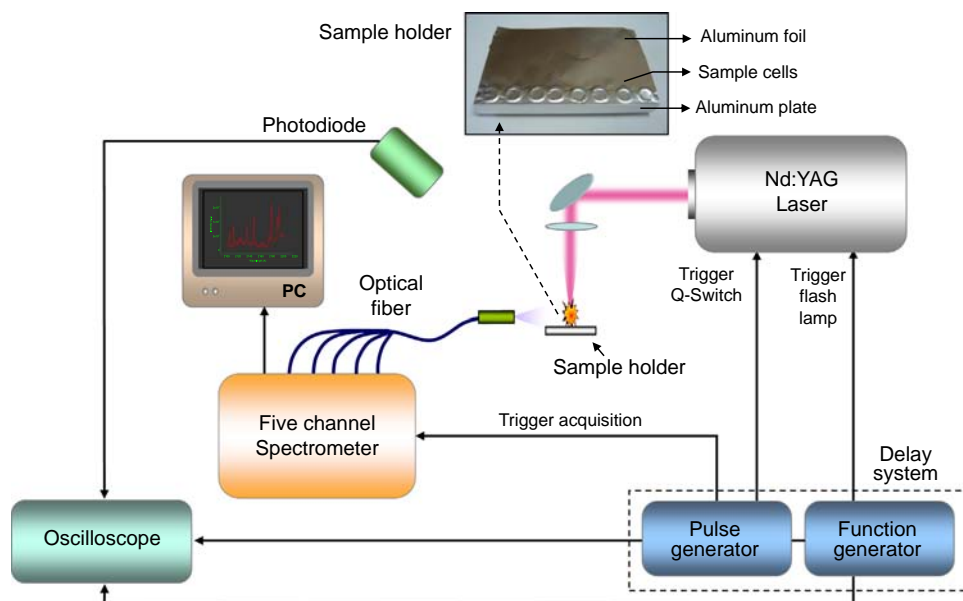


Fig. 1. LIBS experimental system used in the analysis of liquid samples.

(i.e., three single laser shots) made on different positions of the same solid residue.

On the other hand, for DLLME-LIBS analysis, analytes were firstly extracted from the aqueous samples and concentrated in a small volume of extractant solvent (i.e., tetrachloromethane) using the DLLME procedure. After that, 10 μL of the analyte-enriched extractant solvent (i.e., the same volume than that used for direct LIBS analysis of the aqueous samples) were transferred to the aluminum foil, heated by the hot plate to completely evaporate the tetrachloromethane and, as described above for direct LIBS analysis, irradiated by the laser for LIBS measurement.

For DLLME procedure, 9 g of aqueous sample was placed in a 12 mL conical centrifuge tube. An excess of chelating agent (solid ammonium pyrrolidinedithiocarbamate (APDC)) was added to the solution and pH was adjusted with diluted hydrochloric acid and ammonia solutions. pH measurements were carried out using a pH meter (model micropH 2000, Crison Instruments S. A., Barcelona, Spain). Additionally, sodium chloride was added to this mixture up to a concentration of 5% w w⁻¹ in order to evaluate the influence of the medium ionic strength on extraction (i.e., salting out phenomenon [23,25]. See Sections 2.4 and 3.1 below). The sample weight was then brought to 10 g with deionized water. The resulting metal-APDC complexes were extracted from the aqueous solution by injecting few μL of extractant solvent (tetrachloromethane), shaking vigorously the mixture with a vortex agitator in order to obtain a cloudy solution, and finally achieving phase separation by centrifugation (model 2690/5 centrifuge, Nahita). The analyte-enriched organic phase, settled at the bottom of the conical tube, was then retrieved with a microsyringe (model 1702, Hamilton, Bonaduz, Switzerland) for LIBS analysis.

2.3. Reagent and solutions

Aqueous calibration standards containing all analytes under study were prepared by appropriate dilution of 1000 mg L⁻¹ mono-element standard solutions of Cr, Cu, Mn, Ni and Zn (High-Purity mono-element standard solutions, Charleston, United Kingdom) in distilled deionized water (18 M Ω cm resistivity). Solid ammonium pyrrolidinedithiocarbamate (APDC) (Sigma-Aldrich Co., St. Louis, United States) was used as chelating agent. Diluted hydrochloric acid solution and diluted ammonia solution, used for pH adjustment, were prepared from Suprapur 30% (w w⁻¹) HCl solution (Merck, Darmstadt, Germany) and Reagent Grade 32% (w w⁻¹) (in NH₃) solution (Scharlau, Barcelona, Spain), respectively. Tetrachloromethane (Panreac, Barcelona, Spain) was used as extractant solvent in the microextraction procedure. Sodium chloride (Scharlau, Barcelona, Spain) was added to the samples for evaluation of salting out phenomenon. Estuarine water certified reference material (LGC6016, LGC Deselares S.L., Middlesex, United Kingdom) was used for evaluation of method accuracy.

2.4. Optimization of DLLME experimental parameters

DLLME procedure was optimized by using a multivariate analysis consisting of two steps: (i) a Plackett–Burman design to assess the significance of the experimental factors affecting DLLME (i.e., extraction time, pH, extractant volume, concentration of chelating agent and salt concentration) followed by (ii) a Circumscribed Central Composite Design (CCCD) to optimize those factors identified as significant in the step (i). Both the screening study using Plackett–Burman design and the optimization with CCCD involved 12 microextraction experiments each, (in CCCD, these 12 experiments included three replicate experiments in the central point for estimation of the experimental variance). In both studies, the experiments were randomly performed in order to minimize

the effect of uncontrolled variables. A standard solution containing 0.5 $\mu\text{g g}^{-1}$ of the analytes was used for all the extractions. LIBS emission signal obtained in the analysis of the organic solvent resulting from the microextraction procedures was always used as response variable. Data were evaluated with the NemrodW statistical software (NemrodW[®] version 2007, LPRAI, Marseille, France). Since optimum microextraction conditions is usually analyte-dependent, a separate data evaluation was performed for each analyte (i.e., for each emission line evaluated) in both screening and optimization studies.

3. Results and discussion

3.1. DLLME procedure: screening and optimization studies

Table 1 shows the experimental factors and levels considered in the Plackett–Burman design. The result obtained from this screening for DLLME of Zn is shown in Fig. 2a, represented as a main effects Pareto chart. Pareto charts obtained for all analytes under study can be seen in Fig S1 (Appendix A). In these Pareto charts, the bar lengths are proportional to the relative influence of that factor on the metal extraction, and the direction of the bar is related to the “sign” of the effect produced by that factor (i.e., bars to the right of the origin indicate positive effect in the response when increasing the value of the factor and bars to the left indicate negative effect). The charts also include two vertical reference lines corresponding to the 95% confidence level. A bar exceeding a reference line indicates the corresponding factor to be significant for the extraction.

As observed in Fig. 2a, pH and extractant volume can be considered significant factors and extraction time, concentration of chelating agent and salt concentration (i.e., salting out phenomenon) do not have significant impact on the microextraction. Similar results were obtained for most target analytes (Fig. S1). Therefore, extraction time and salt concentration were fixed at their lower level (i.e., extraction time: 1 min; NaCl concentration: 0%), concentration of chelating agent was fixed at its higher level (i.e., APDC concentration: 0.5%) and, under these conditions, pH and extractant volume were optimized by using a CCCD.

Table 2 shows the different level values chosen in the CCCD. An example of the results obtained in this study is given in Fig. 2b, corresponding to the extraction of Zn. In this figure, LIBS emission signal variation versus pH and extractant volume is represented as both a contour plot and a response surface. The same graphics are included in Figs. S2–S6 (Appendix A) for all analytes under study.

As observed from Fig. 2b, extractant solvent volume reaches an optimum value for extraction of Zn at 106 μL . Increasing the extractant volume in DLLME leads to an increase in the quantity of tiny droplets dispersed throughout the aqueous solution, therefore increasing the interfacial contact area for analyte diffusion and, consequently, the extraction efficiency. On the other hand, increasing the volume of extractant solvent also leads to an increase in the sedimented phase, and therefore to a decrease in

Table 1
Experimental factors and levels of the Plackett–Burman design.

Experimental factor	Level	
	Low (–1)	High (+1)
pH	4	10
Extraction time (min)	1	3
[NaCl] (% w w ⁻¹)	0	5
[APDC] (% w w ⁻¹)	0.25	0.50
Extractant volume (μL)	50	100

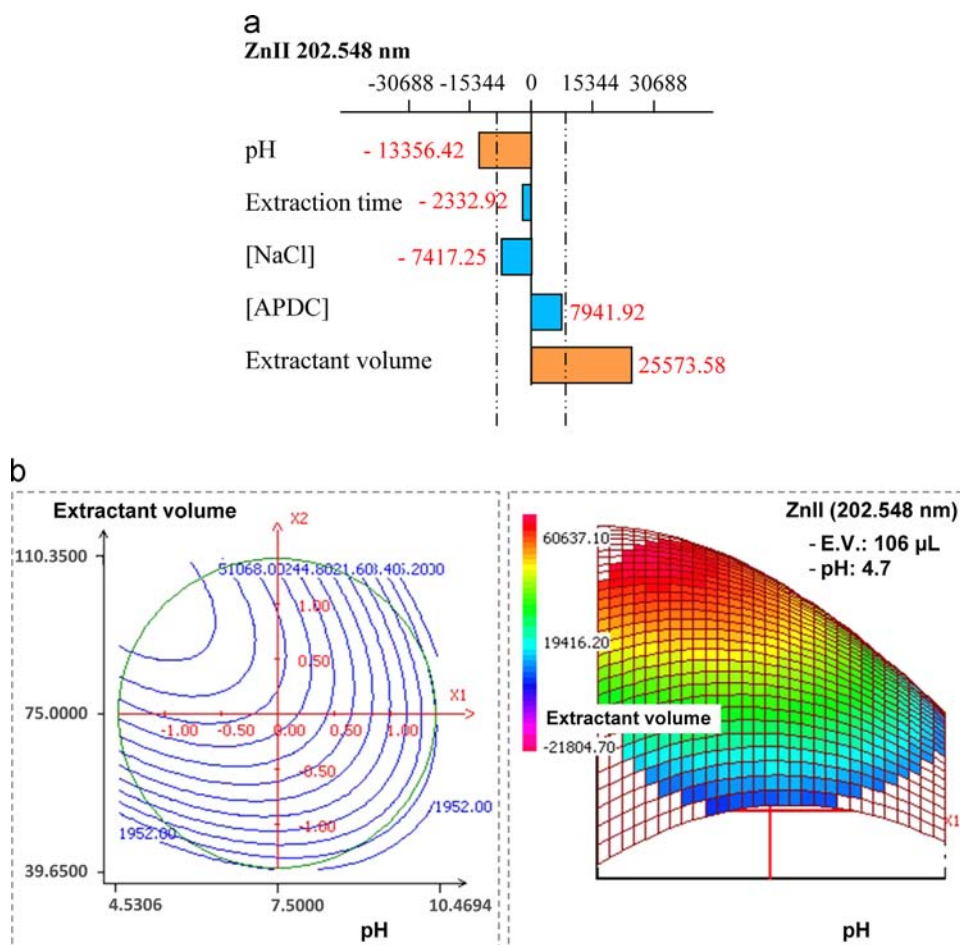


Fig. 2. Optimization of DLLME of zinc (ZnII (202.548 nm) emission line): (a) Pareto chart from Plackett–Burman design and (b) contour plot and response surface from circumscribed central composite design.

Table 2
Experimental factors and levels of the Circumscribed Central Composite Design (CCCD).

Experimental factor	Level			Star points ($\alpha=1.4142$)	
	Low (-1)	Central (0)	High (+1)	$-\alpha$	$+\alpha$
pH	5.6	7.5	9.4	4.5	10.5
Extractant volume (μL)	50	75	100	110	40

the analyte concentration in the organic phase [24,26]. The observed optimum value for extractant solvent volume could therefore be explained as a consequence of these two competitive effects.

The optimum pH value for extraction of Zn is obtained at 4.7 (Fig. 2b). Separation of metals ions by DLLME involves the previous formation of metal complexes with enough hydrophobicity to be extracted in the organic phase and, as already well known, pH plays an essential role in metal complexes formation. Increasing pH leads to an increase in the formation of uncharged metal complexes that are readily extracted into organic phase. However, further increase in solution pH can also lead to the formation of stable hydroxo complexes of the metal ions, thus decreasing extraction efficiency.

As can be seen from Figs. S2 to S6, no substantial differences were obtained for the different analytes studied, with optimum

extractant volumes ranging from 93 μL (Mn) to 106 μL (Zn) and optimum pH values ranging from 4.1 (Mn) to 6.2 (Cr). Therefore, average values were chosen as the common pH and extractant volume optimum condition for simultaneous extraction of all the analytes from the samples.

In summary, optimum experimental conditions for DLLME procedure were set at: extraction time, 1 min; pH, 5.5; extractant volume, 100 μL ; APDC concentration, 0.5% and salt concentration, 0%.

It is worth mentioning here that this optimization study was performed on model aqueous solutions prepared in deionized water. Therefore, possible matrix effects influencing DLLME procedure due, for instance, to competitive chelate formation with concomitant metals, or to preferential diffusion of such concomitant metals chelates into the organic phase, were not considered. However, in order to evaluate possible matrix effects, estuarine water certified reference material containing Ca, Mg, K and Na, among others, as majority elements [27], was successfully analyzed by using the proposed DLLME procedure (see Section 3.2. below). In any case, for application of the proposed DLLME procedure to more complicated aqueous samples matrices (e.g., residual water); an exhaustive matrix effect study should be carried out.

3.2. Comparison of LIBS with DLLME-LIBS methodologies for analysis of aqueous samples

In order to compare the analytical capabilities of both LIBS and DLLME-LIBS methodologies, six-point calibration curves were constructed in both cases. For LIBS analysis, aqueous calibration

Table 3
Analytical figures of merit obtained with LIBS and DLLME-LIBS analytical methodologies.

Emission line (nm)	LIBS		DLLME-LIBS		Enhancement factor ^b	LOD ratio ^c
	Sensitivity ^a (cts Kg μg^{-1})	LOD ($\mu\text{g Kg}^{-1}$)	Sensitivity ^a (cts Kg μg^{-1})	LOD ($\mu\text{g Kg}^{-1}$)		
CrI (357.869)	4.1 \pm 0.7	184	19 \pm 3	41	4.8	4.5
CuI (324.754)	12.8 \pm 1.4	84	52 \pm 2	23	4.0	3.7
MnII (259.373)	13.0 \pm 1.0	276	71 \pm 5	49	5.5	5.6
NiI (352.454)	1.5 \pm 0.3	475	7.1 \pm 0.8	107	4.7	4.4
ZnII (202.548)	13 \pm 2	90	71 \pm 6	18	5.5	5.0

^a Uncertainty expressed as standard deviation.

^b Calculated as the ratio of sensitivity values obtained with DLLME-LIBS and LIBS.

^c Calculated as the ratio of LOD values obtained with LIBS and DLLME-LIBS

standards with analyte concentration increasing up to 1 $\mu\text{g g}^{-1}$ were used. These standards were directly analyzed by LIBS as described in the experimental part of this work (Section 2.2). For DLLME-LIBS analysis, concentration of the standards was reduced to a half of the used for LIBS analysis, being 0.5 $\mu\text{g g}^{-1}$ the maximum concentration used. In this case, analytes were first extracted from the aqueous standards under optimum DLLME conditions. Afterward, the resulting analyte-enriched organics were analyzed by LIBS (Section 2.2). In both methodologies, LIBS signal corresponding to the different emission lines evaluated was found to be linear in the concentration range studied.

Sensitivity values obtained from these calibration graphs for the different analytes are shown in Table 3. In this Table, limit of detection (LOD) values, based on 3 times the standard deviation of 10 blank determinations (i.e., deionized water for LIBS and tetrachloromethane for DLLME-LIBS), are also included. As observed, DLLME-LIBS methodology improves sensitivity compared to LIBS. Sensitivity improvement was very similar for all analytes studies, as can be seen from the enhancement factors calculated (Table 3). From these data, it can be concluded that, on average, sensitivity of the DLLME-LIBS methodology was about 5-fold higher than that provided by LIBS. This fact led to a decrease of about 4.5-fold, on average, in the detection limits obtained with DLLME-LIBS.

As already mentioned in the introductory part of this work (Section 1), a different liquid phase microextraction procedure (i.e., Single Drop Microextraction (SDME)) was previously evaluated by the authors as a possible way to increase sensitivity of LIBS analysis of liquid samples [22]. Preliminary results obtained in that work shown that sensitivity of the tested SDME-LIBS methodology led to about 2.0–2.6 times improvement, depending on the analyte, compared with direct LIBS analysis of the samples. Consequently, LOD values were found to be 1.4–2.9 times lower in SDME-LIBS analysis. As can be seen from the results obtained in this work, the use of DLLME procedure leads to further improvements in sensitivity and detection limits compared with SDME method, proving that DLLME-LIBS is a more efficient combination than SDME-LIBS for enhancing the analytical capability of LIBS analysis of liquid samples.

Accuracy of the DLLME-LIBS method was evaluated from the analysis of a certified reference material (estuarine water). Table 4 shows the results obtained in this study. As can be seen, concentration values obtained with DLLME-LIBS match the certified concentration intervals for all the elements studied. Recovery values were in the range of 81–109%, with the lower and upper limits corresponding to recoveries obtained for Zn and Ni, respectively. For both elements, certified concentrations in the CRM were below their respective theoretical limits of quantification (i.e., 357 $\mu\text{g Kg}^{-1}$ for Ni and 60 $\mu\text{g Kg}^{-1}$ for Zn). Nevertheless, an acceptable recovery value was obtained for Ni. On the other hand, Zn was, by far, the analyte with the worst recovery. However, as stated in the certificate of measurement provided by the material

Table 4
Analysis of LGC6016 certified reference material (estuarine water) by DLLME-LIBS.

Emission line (nm)	Certified value ^a	DLLME-LIBS	
		Found value ^a	Recovery value (%)
CuI (324.754)	190 \pm 4	204 \pm 40	107 \pm 21
MnII (259.373)	976 \pm 31	906 \pm 157	93 \pm 16
NiI (352.454)	186 \pm 3	202 \pm 29	109 \pm 16
ZnII (202.548)	55 ^b	45 \pm 10	81 \pm 20

^a In $\mu\text{g L}^{-1}$ \pm confidence interval at 95%.

^b Indicative value. In $\mu\text{g L}^{-1}$.

supplier [27], concentration of Zn was not a certified value in this CRM, because the last stability test performed by the supplier pointed out that Zn concentration had decrease since the release of the material in July 2000. Therefore, Zn concentration in the recently distributed CRM is marked as indicative value rather than certified.

4. Conclusions

This work presents a new advance in the use of analytical methodologies based on LPME-LIBS combination for trace elemental analysis of liquid samples. In previous preliminary studies, hyphenation of LIBS with Single Drop Microextraction (SDME-LIBS) was shown to improve approximately 2.3 times both sensitivity and LOD of LIBS [22]. The work presented here demonstrates that further improvement can be achieved just by using a more efficient microextraction procedure. The use of DLLME-LIBS methodology leads to sensitivity and LOD enhancements of about 5.0 and 4.5-fold, respectively, that of LIBS, therefore proving DLLME to be approximately twice more efficient than SDME for LPME-LIBS hyphenation.

The results shown with DLLME reassert the viability of the LPME-LIBS hyphenation as a way to extend the applicability of LIBS to trace elemental analysis of liquid samples and, in addition, demonstrate the possibility of improvement of analytical methodologies based on this combination. However, these results should be only considered as a small step forward the pursued goal. That is, the development of a LPME-LIBS based analytical methodology useful for multielement determination at trace level, with on-line capabilities for liquid samples analysis. The use of different extracting solvents and chelating agents with this or others microextraction procedures, the improvement of LIBS measurement reproducibility and the development of possible strategies for automation of the whole analytical process are all possible ways for further improving the method performance, which are currently under study in our laboratory.

Acknowledgments

The authors are grateful to the Spanish Government (project no. CTQ2011-23968) and Regional Government of Valencia (Spain) (project no. ACOMP/2013/072) for the financial support.

Appendix A. Supporting information

Supplementary data associated with this article can be found in the online version at <http://dx.doi.org/10.1016/j.talanta.2014.07.090>.

References

- [1] A. Rios, A. Escarpa, B. Simonet, *Miniaturization of Analytical Systems: Principles, Designs and Applications*, first ed., John Wiley & Sons, Chichester (West Sussex), 2009.
- [2] M. de la Guardia, *J. Braz. Chem. Soc.* 10 (1999) 429–437.
- [3] D.A. Cremers, L.J. Radziemski, *Handbook of laser-induced breakdown spectroscopy*, first ed., John Wiley & Sons, Chichester (West Sussex), 2006.
- [4] D.A. Cremers, R.C. Chinni, *Appl. Spectrosc. Rev.* 44 (2009) 457–506.
- [5] StellarNet, Inc., Tampa (USA), Porta LIBS 2000, (http://www.stellarnet-inc.com/popularconfigurations_plasmasystems.htm) (Last access in May 2014).
- [6] Avantes. Solutions in spectroscopy, Apeldoorn (The Netherlands), AvaLiBS, (<http://www.avantes.com/products/systems-bundles/item/314-avalibs-modules-laser-induced-breakdown-spectroscopy>), (Last access in May 2014).
- [7] Ocean Optics, Inc., Dunedin (USA), LIBS2500plus system, (<http://www.oceanoptics.com/products/libs.asp>), (Last access in May 2014).
- [8] D.W. Hahn, N. Omenetto, *Appl. Spectrosc.* 64 (2010) 335A–366A.
- [9] D.W. Hahn, N. Omenetto, *Appl. Spectrosc.* 66 (2012) 347–419.
- [10] V.N. Raia, F.Y. Yuehb, J.P. Singh, *Laser-Induced Breakdown Spectroscopy of Liquid Samples*, in: J.P. Singh, S.N. Thakur (Eds.), *Laser Induced Breakdown Spectroscopy*, Elsevier, Amsterdam, 2007, pp. 223–252.
- [11] A. de Giacomo, M. dell'Aglio, O. de Pascale, *Appl. Phys. A* 79 (2004) 1035–1038.
- [12] V. Lazic, J.J. Laserna, S. Jovicevic, *Spectrochim. Acta Part B* 82 (2013) 42–49.
- [13] V. Lazic, J.J. Laserna, S. Jovicevic, *Spectrochim. Acta Part B* 82 (2013) 50–59.
- [14] K. Rifai, S. Laville, F. Vidal, M. Sabsabi, M. Chaker, *J. Anal. At. Spectrom.* 27 (2012) 276–283.
- [15] V. Lazic, S. Jovicevic, R. Fantoni, F. Colao, *Spectrochim. Acta Part B* 62 (2007) 1433–1442.
- [16] V. Lazic, F. Colao, R. Fantoni, V. Spizzicchino, *Spectrochim. Acta Part B* 60 (2005) 1002–1013.
- [17] J. Pawliszyn, S. Pedersen-Bjergaard, *J. Chromatogr. Sci.* 44 (2006) 291–307.
- [18] F. Pena-Pereira, I. Lavilla, C. Bendicho, *Spectrochim. Acta Part B* 64 (2009) 1–15.
- [19] B. Hu, M. He, B. Chen, L. Xia, *Spectrochim. Acta Part B* 86 (2013) 14–30.
- [20] R. Sitko, K. Kocot, B. Zawiska, B. Feist, K. Pytlakowska, *J. Anal. At. Spectrom.* 26 (2011) 1979–1985.
- [21] M.A. Aguirre, S. Legnaioli, F. Almodóvar, M. Hidalgo, V. Palleschi, A. Canals, *Spectrochim. Acta Part B* 79–80 (2013) 88–93.
- [22] M.A. Aguirre, H. Nikolova, M. Hidalgo, A. Canals, *Hyphenation of single-drop microextraction with laser-induced breakdown spectrometry for trace analysis in liquid samples: a viability study*. Unpublished results.
- [23] A.N. Anthemidis, K.I.G. Ioannou, *Talanta* 80 (2009) 413–421.
- [24] M. Rezaee, Y. Yamini, M. Faraji, *J. Chromatogr. A* 1217 (2010) 2342–2357.
- [25] M.S. El-Shahawi, H.M. Al-Saidi, *Trac Trends Anal. Chem.* 44 (2013) 12–24.
- [26] V. Andruch, I.S. Balogh, L. Kocúrová, J. Šandrejová, *J. Anal. At. Spectrom.* 28 (2013) 19–32.
- [27] LGC standards, Ltd., Middlesex (UK), Certificate of measurement of estuarine water certified reference material LGC6016, (<https://www.lgcstandards.com/WebRoot/Store/Shops/LGC/FilePathPartDocuments/ST-WB-CERT-1051271-1-1-1.PDF>), (Last access in May 2014).



Electrochemical sensor based on magnetic graphene oxide@gold nanoparticles-molecular imprinted polymers for determination of dibutyl phthalate



Xiangjun Li, Xiaojiao Wang, Leilei Li, Huimin Duan, Chuannan Luo*

Key Laboratory of Chemical Sensing & Analysis in Universities of Shandong (University of Jinan), School of Chemistry and Chemical Engineering, University of Jinan, Jinan 250022, PR China

ARTICLE INFO

Article history:

Received 4 March 2014

Received in revised form

3 July 2014

Accepted 10 July 2014

Available online 30 July 2014

Keywords:

Molecularly imprinted polymers

Magnetic graphene oxide

Gold nanoparticles

Electrochemical sensor

Dibutyl phthalate

ABSTRACT

A novel composite of magnetic graphene oxide @ gold nanoparticles-molecular imprinted polymers (MGO@AuNPs-MIPs) was synthesized and applied as a molecular recognition element to construct dibutyl phthalate (DBP) electrochemical sensor. The composite of MGO@AuNPs was first synthesized using coprecipitation and self-assembly technique. Then the template molecules (DBP) were absorbed at the MGO@AuNPs surface due to their excellent affinity, and subsequently, selective copolymerization of methacrylic acid and ethylene glycol dimethacrylate was further achieved at the MGO@AuNPs surface. Potential scanning was presented to extract DBP molecules from the imprinted polymers film rapidly and completely. As a consequence, an electrochemical sensor for highly sensitive and selective detection of DBP was successfully constructed as demonstration based on the synthesized MGO@AuNPs-MIPs composite. Under optimal experimental conditions, selective detection of DBP in a linear concentration range of 2.5×10^{-9} – 5.0×10^{-6} mol/L was obtained. The new DBP electrochemical sensor also exhibited excellent repeatability, which expressed as relative standard deviation (RSD) was about 2.50% for 30 repeated analyses of 2.0×10^{-6} mol/L DBP.

© 2014 Elsevier B.V. All rights reserved.

1. Introduction

Phthalate esters, such as dibutyl phthalate (DBP), are widely used as additives in the manufacturing of poly (vinyl chloride) plastics to make them flexible in industry [1]. Extensive use of these chemicals results in their presence in various environmental matrices such as personal care products (e.g., perfumes, lotions, and cosmetics) [2], paints [3], industrial plastics [4], certain medical devices [5] and pharmaceuticals [6], including drinking water [7] and other environmental samples [8]. Due to the wide spread use in industry, they are considered as ubiquitous environmental pollutants [9]. They have adverse effects on human health, regarding as endocrine disrupting compounds by means of their carcinogenic action [10,11]. According to the previous report, these methods used for determination of DBP such as solid-phase extraction [12], liquid chromatography [13,14] always lead to high cost and low limit detection due to complex matrices in sample preparation procedures. Therefore, it is practically necessary to

establish a new method with high selectivity and sensitivity to determine DBP in the complex samples.

Graphene has enjoyed widespread attention owing to its unique electronic [15], thermal [16], and mechanical properties [17] since Geim and coworkers first isolated single layer samples from graphite in 2004 [18]. In recent years, unique electronic properties, mechanical properties and extremely large surface area endow graphene with more applications. For instance, graphene nanosheets could serve as the reinforcing element in a polymer matrix in fabricating new advanced materials [19–21]. Specifically, in nanocomposite materials, controlling of interfacial interaction between the graphene and the polymer, as well as homogeneous dispersion into polymer matrices are essential to achieve the required performance of the resulting hybrids [22]. Correspondingly, this combination between graphene and polymer offers an attractive route to introduce some novel properties. Some groups have already functionalized graphene with various polymers to assemble the composites with desired properties. The efforts were mainly made on the effective dispersibility of the composites [23], and improvement of the electrical conductivity [24], thermal stability and mechanical strength of the composites [21,25]. Whereas, the reports involved the preparation of composite based on graphene and high cross-linked polymers were seldom referred as the molecularly recognized element [26,27].

* Corresponding author at: University of Jinan, Analytical Chemical No. 106, Jiwei Road Jinan, Shandong Province China. Tel.: +8615154168170.

E-mail address: Lixiangjun0713@163.com (C. Luo).

Molecular imprinting technology is a newly developed technology, which has become a powerful tool for the preparation of polymeric materials with special recognition capacity [28]. The inherent advantages of molecularly imprinted polymers (MIPs) compared to biochemical recognition systems include robustness, storage endurance and lower costs [29]. Although the bulk MIPs prepared by conventional method exhibit high selectivity, certain drawbacks are still suffered, such as time-consuming and complicated preparation process, low binding capacity, poor site accessibility, and slow binding kinetics, etc. [30]. The attempts to solve these problems are generally required to optimize the structure of imprinted materials with suitable forms, which means that controlling templates to be situated at the surface or in the proximity of materials surface. The surface binding sites hold great promise as a means to achieve the excellent performances, such as the complete removal of templates, good accessibility to the target species, and low mass-transfer resistance, etc. Because nanostructured imprinted materials have a small dimension with extremely high surface-to-volume ratio, most of template molecules are situated at or approximate to the materials surface. Eventually, the nanosized imprinted materials are expected to possess several remarkable advantages over normal imprinted materials (e.g. easier removal of template molecules, higher binding capacity, faster binding kinetics, easier installing onto the surface of nanodevices, etc.) [31]. Some researchers have reported a surface monomer directing strategy for highly dense imprinting of molecules at the surface of some nanosized substrates, such as monodispersed silica nanoparticles [32], polystyrene core colloids [33], and polymer nanowires/nanotubes [31]. Graphene, with unique mechanical properties and extremely large area, would therefore propose to be an excellent candidate as a supported material for preparing imprinted materials. The prepared MIPs would be in possession of large surface area in case the polymerization occurring at the surface of graphene. The binding sites in the outer layer of the MIPs composite would provide complete removal of templates, improve the accessibility to target species, and also reduce the binding time.

During these decades, metal nanoparticles have been applied to the fabrication of nanocomposites. They have many excellent properties such as good electrical properties, strong adsorption ability, high surface reaction activity, small particle size and good surface properties [34]. Recently, magnetite nanoparticles (Fe_3O_4) and gold nanoparticles (AuNPs) have been widely used in many applications [35,36]. Fe_3O_4 are coated on MIPs, and the resulting polymer material is magnetically susceptible and therefore easily separated by external magnetic fields after adsorption and recognition. Meanwhile, AuNPs have good conductivity and electrocatalysis. Therefore, in this work, magnetite nanoparticles were applied to make the preparative nanocomposites easy to be separated, AuNPs were used to fabricate electrochemical sensor to improve the electrical conductivity of the sensor.

Herein, a novel composite of MGO@AuNPs and MIPs was prepared by using DBP as a template molecule. The MGO@AuNPs was used as the supported material in the MIPs matrix to prepare MGO@AuNPs-MIPs hybrids with molecular recognition capacity, then drop their suspensions onto a gold electrode surface. An electrochemical sensor fabricated by modifying the MGO@AuNPs-MIPs composite was successfully employed to detect the concentration of DBP.

2. Experimental

2.1. Materials

Graphite was purchased from Red Rock Chemical Reagent Factory (Tianjin, China). Nitric acid (HNO_3), hydrochloric acid (HCl), sulfuric

acid (H_2SO_4) and acetic acid were purchased from Kant Chemical Co., LTD (Laiyang, China). Hydrogen peroxide (H_2O_2) and anhydrous alcohol were purchased from Fuyu Fine Chemical Co., LTD (Tianjin, China). Ferric chloride (FeCl_3), ferrous chloride (FeCl_2), chloroauric acid (HAuCl_4), trisodium citrate, methanol, toluene, ammonia and chitosan were obtained from the Chemical Reagent Third Company (Tianjin, China). Dibutyl phthalate (DBP), acetonitrile, 3-(trimethoxysilyl)propyl methacrylate (MPS), dimethylformamide (DMF), methacrylic acid (MAA) and ethylene glycol dimethacrylate (EGDMA) were obtained from Aladdin Reagent Co., LTD (China). MAA and EGDMA were distilled under reduced pressure to remove inhibitors. Azodiisobutyronitrile (AIBN) was purchased from Chemical Plant (Beijing, China) and employed after twice recrystallization. All chemicals were of analytical grade and used as received except for special statements. All aqueous solutions were prepared with ultrapure water.

2.2. Apparatus

Nanocomposites were examined on a scanning electron microscopy (SEM, S-2500, Hitachi High-tech International Trading Co., LTD, Shanghai, China), a transmission electron microscope (TEM, JEM-1011, Can Treasure Technology Co., LTD, Xiamen, China) and X-ray diffraction (XRD, Philips, Germany) using $\text{Cu K}\alpha$ radiation (0.154178 nm). Electrochemical measurements were carried out on CHI832B electrochemical workstation (CH1760D, ChenHua Instruments Co., LTD, Shanghai, China). A three-electrode system (Gaosunion Technology Co., LTD, Wuhan, China) was used in the experiment with the bare and the modified gold electrodes (3 mm in diameter) as the working electrodes, respectively. An Ag/AgCl electrode (saturated KCl) and a Pt wire electrode were used as reference and counter electrode, respectively.

2.3. Synthesis of silanization modification of MGO

GO was synthesized from natural graphite by Hummers' method with little modification [37]. Magnetic graphene oxide (MGO) was synthesized by the modified in situ chemical coprecipitation of Fe^{2+} and Fe^{3+} in an alkaline solution at the presence of GO. Briefly, It was prepared by suspending 50.0 mg GO in 50.0 mL of solution containing 50.0 mg FeCl_3 and 35.0 mg FeCl_2 under N_2 atmosphere. After the solution was sonicated for 30 min, ammonia was added dropwise to precipitate the iron oxides while the mixture solution was under constant mechanical stirring at 90°C . The pH of the final mixture should be 9.0 and the reaction was continued carrying out for about 60 min to promote the complete growth of the nanoparticle crystals. The obtained precipitate of MGO was isolated in the magnetic field, and the supernatant was separated from the precipitate by decantation. Then 100.0 mg of MGO were dispersed in 40.0 mL of toluene for 1.0 h with continuous stirring, and 3.0 mL of MPS was added. The solution was heated for 48 h under N_2 atmosphere and the resulting solid was washed with toluene for several times. Subsequently, the nanocomposite was dried under vacuum and finally silanization modification of MGO was obtained.

2.4. Synthesis of AuNPs and MGO@AuNPs

AuNPs were prepared by a trisodium citrate reduction method as reported before [38] with little modified. Briefly, 3.65 mL of 0.01 mol/L HAuCl_4 aqueous solutions was diluted with deionized water to 150.0 mL and then heated under vigorous stirring. While boiling, 3.0 mL of trisodium citrate aqueous solution (1 wt%) was added very quickly. When the solution turned to wine red, the heating was stopped but the stirring was kept until the solution was cooled to room temperature (RT). The final sol had good

colloid stability and a wine red color, indicating the formation of gold nanoparticles. The product was stored in a refrigerator at 4 °C. The mean size of the prepared Au colloids was about 20 nm.

Decoration of AuNPs onto silanization modification of MGO was achieved by forming S–Au bond as follows. The all above obtained nanocomposites and 15.0 mL above gold colloids were kept in a flask under vigorous stirring for 2.0 h until the solution turned to colourless. The solid was isolated in the magnetic field and dried under vacuum. Finally MGO@AuNPs was obtained.

2.5. Synthesis of MGO@AuNPs-MIPs

DBP molecules were used as the template. MAA, EGDMA and AIBN were used as the functional monomer, cross-linking agent and initiator of the imprinting polymerization, respectively. In brief, about 100 mg of MGO@AuNPs were added to 50 mL of acetonitrile and dimethylformamide (DMF) mixture (v/v, 3/1). The dried MGO@AuNPs nanocomposites were dispersed in the organic mixture solvent by ultrasonication for about 15 min. 0.2 mmol DBP molecules were dispersed in the mixture solvent by ultrasonication for another 15 min. Then, 0.8 mmol MAA, 4 mmol EGDMA, and 20 mg AIBN were added to the mixture and purged with N₂ under magnetic stirring. The temperature was increased to 60 °C, and the reaction was allowed to proceed for 24 h. The resulting product was collected in the magnetic field and washed thoroughly with methanol to discard the reagents. The procedure for MGO@AuNPs-MIPs preparation was described in Scheme 1.

For comparison, blank non-imprinted polymers (MGO@AuNPs-NIPs) were prepared by the same procedure, only without using the template molecules in the polymerization process.

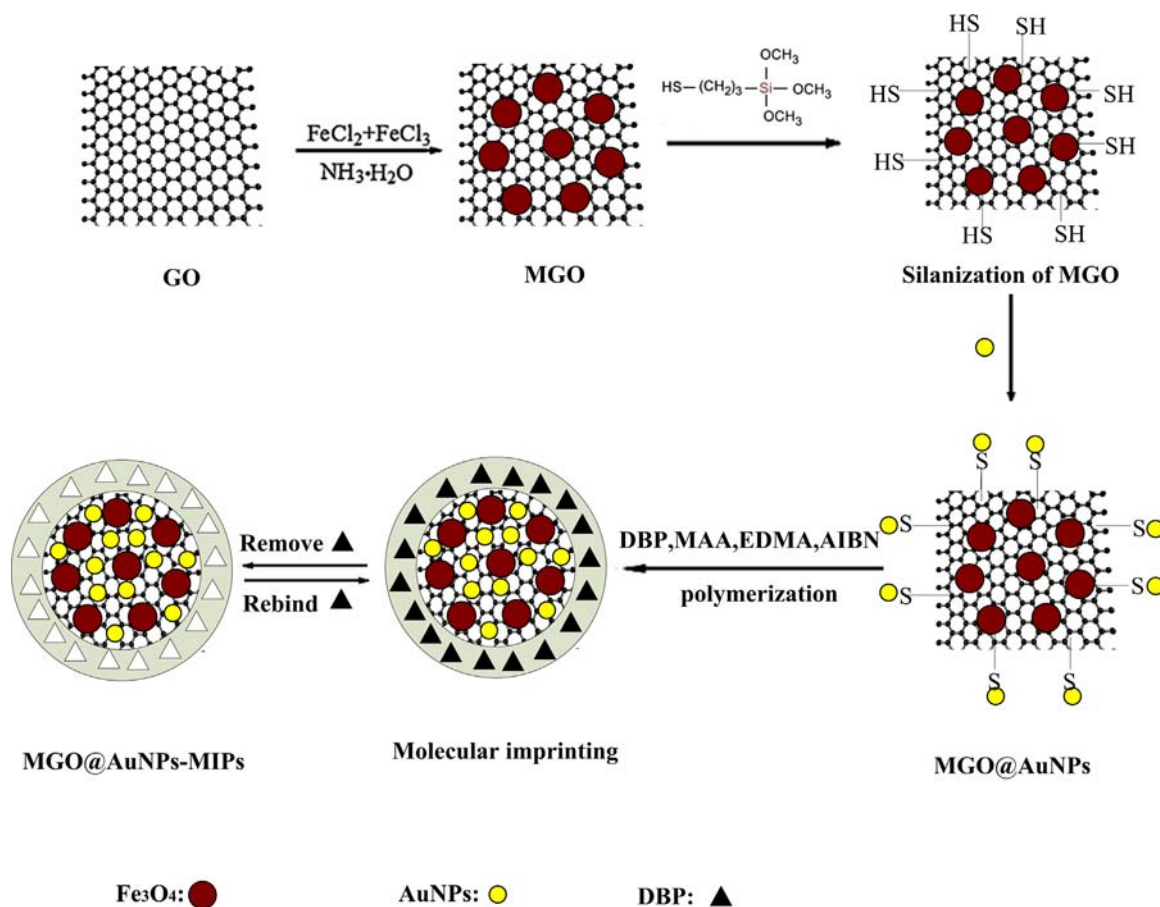
2.6. Electrochemical measurements

20 mg of MGO@AuNPs-MIPs were dispersed in 1 mL of 0.1 mol/L acetic acid containing 0.5% chitosan by ultrasonication for 20 min. The above suspensions were dropped on the clean gold electrode surface and dried at room temperature (RT) overnight. Removal of the template molecules was achieved by linear sweeping the modified electrodes in phosphate buffer solution (PBS). The linear sweep voltammetry was carried out by potential scanning repeatedly between –0.2 and 0.7 V till there was no signal of DBP. After extraction of the templates, the electrodes were rinsed thoroughly with double distilled water and then submitted to the experiments. The modified electrodes were examined by differential pulse voltammetry (DPV) in 2.0×10^{-6} mol/L DBP with PBS ranging from 0 to 0.8 V, potential step was 0.004 V, amplitude was 0.05 V, pulse width was 0.05 s, sampling width was 0.0167 s and pulse period was 0.2 s. After the measurements, the template-entrapped electrodes were submitted to potential scanning with the purpose of removing DBP molecules in the polymer films.

3. Results and discussion

3.1. Characterization of the GO, AuNPs and MGO@AuNPs-MIPs

The typical TEM images of AuNPs and MGO@AuNPs-MIPs, SEM images of the GO and MGO@AuNPs-MIPs were shown in Fig. 1. From Fig. 1A, GO presented the sheet-like structure with the smooth surface, large thickness, and some wrinkles. These wrinkles might be important for preventing aggregation of GO and maintaining high surface area. Fig. 1B showed that the mean size



Scheme 1. Illustrations of the fabrication procedure for the MGO@AuNPs-MIPs.

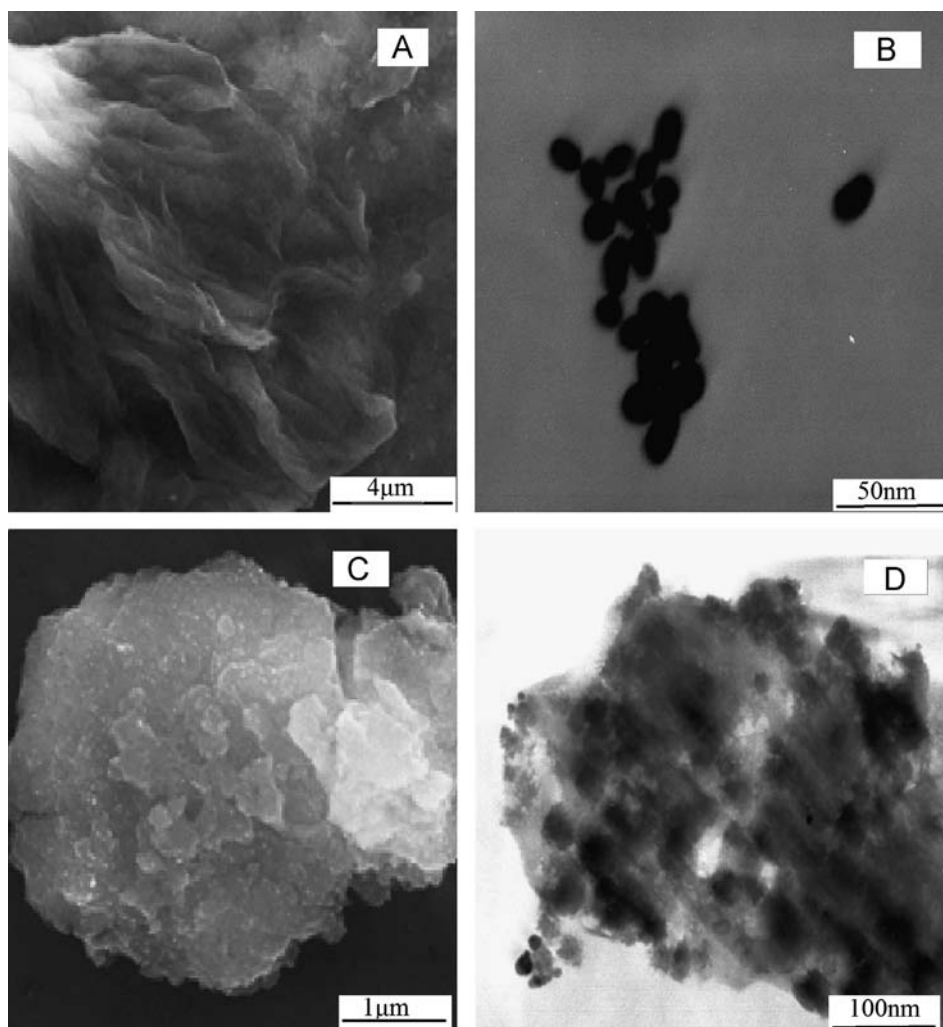


Fig. 1. (A) SEM image of GO. (B) TEM image of AuNPs. (C) SEM image of MGO@AuNPs-MIPs. (D) TEM image of MGO@AuNPs-MIPs.

of the prepared AuNPs was about 25 nm. What's more, as shown in Fig. 1C and D, the MGO@AuNPs-MIPs exhibited irregular shape in morphology, and no significant folding or overlapping was observed, so almost all MGO@AuNPs were decorated with the MIPs films, which indicated that the imprinted sites were generated in the MGO@AuNPs hybrids.

XRD patterns of GO, pure Fe_3O_4 and MGO were shown in Fig. 2. As shown, after oxidation, the characteristic graphite peak ($2\theta=26^\circ$) disappeared and was replaced by a well-defined peak at $2\theta=10.8^\circ$ with 0.8 nm d -spacing. The increased d -spacing of GO was due to the presence of abundant oxygen-containing functional groups on both sides of the graphene causing an atomic-scale roughness on the graphene. Six characteristic peaks for Fe_3O_4 ($2\theta=30.1, 35.5, 43.3, 53.4, 57.2$ and 62.5), marked by their indices ((2 2 0), (3 1 1), (4 0 0), (4 2 2), (5 1 1), and (4 4 0)), were observed, which was consistent with the standard XRD data for the cubic phase Fe_3O_4 with a face-centered cubic (fcc) structure. The broad diffraction peaks were indications of the nanoparticles with very small sizes.

3.2. Electrochemical characteristics of electrochemical sensor

Electrochemical impedance spectroscopy (EIS) could provide detailed information on the impedance changes of the electrode surface to characterize the stepwise construction process of the sensor [39]. The impedance spectra included a semicircle portion

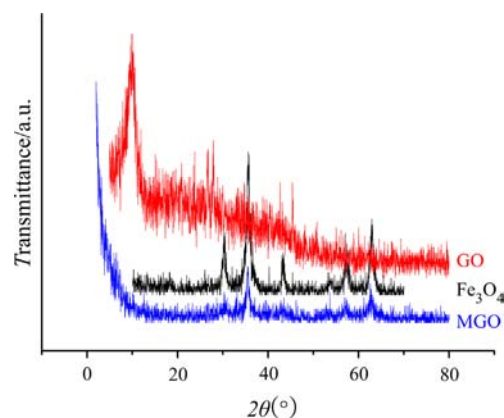


Fig. 2. XRD patterns of GO, pure Fe_3O_4 and MGO.

and a linear portion. The semicircle diameter at higher frequencies corresponds to the electron-transfer resistance (R_{et}), and the linear part at lower frequencies corresponds to the diffusion process. Fig. 3 illustrated the impedance spectra observed at each step in the presence of 2.0 mmol/L $\text{K}_3[\text{Fe}(\text{CN})_6]$ solution. It was observed that MGO (curve b) and MGO@AuNPs (curve c) displayed two almost straight lines in the Nyquist plot and the slope of lines increased dramatically, indicating that there was improved diffusion of

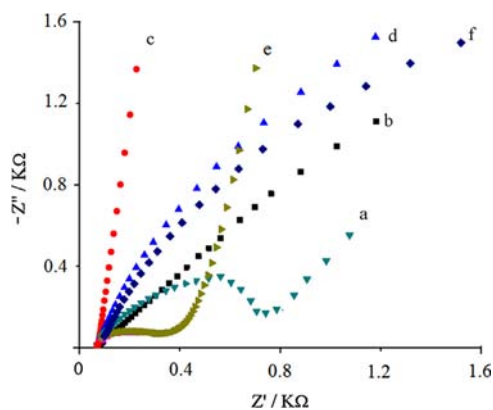


Fig. 3. EIS recorded in 2.0 mmol/L $K_3[Fe(CN)_6]$ solution. (a) bare. (b) MGO. (c) MGO@AuNPs. (d) MGO@AuNPs-MIPs before extracting DBP. (e) MGO@AuNPs-MIPs after extracting DBP. (f) MGO@AuNPs-NIPs modified electrodes.

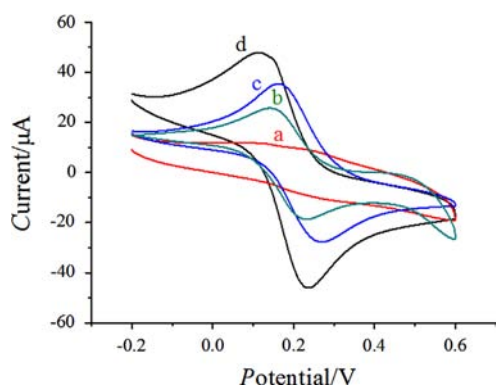


Fig. 4. Cyclic voltammetry in 2.0 mmol/L $K_3[Fe(CN)_6]$ solution, scan rate was 0.1 V/s and scan range was from -0.2 V to 0.6 V. (a) bare electrode, (b) GO, (c) MGO, (d) MGO@AuNPs modified electrodes.

ferricyanide toward the electrode surface [40]. The R_{et} of bare electrode (curve a) increased indicated that the MGO and MGO@AuNPs composites were excellent electric conducting materials, which can form high electron conduction pathways between the electrode and electrolyte to accelerate the electron transfer. After coating with the MGO@AuNPs-MIPs before removing of the template, the R_{et} increased (curve d), indicating that the MIPs was successfully composited on the surface. The MIPs formed an additional barrier on the surface of electrode to block the electron exchange between the solution and the electrode. After removing the template, the R_{et} decreased (curve e), indicating that the template was successfully removed and formed some cavities which facilitated the electron exchange between the redox. When composited with NIPs in the same method, the R_{et} was between MIPs before removing of the template and MIPs after removing of the template (curve f). The reason might be attributed to the fact that NIPs were composited on surface of electrode hindering the electron exchange but without the addition of DBP might increase the electron exchange.

The different electrochemical behaviors of various modified electrodes were investigated by cyclic voltammetry (CV) with $K_3Fe(CN)_6$ as the redox probe. As shown in Fig. 4, (a) bare electrode, (b) GO, (c) MGO, (d) MGO@AuNPs in 2.0 mmol/L $K_3[Fe(CN)_6]$ solution were depicted by typical cyclic voltammograms. Scan rate was 0.1 V/s and scan range was from -0.2 V to 0.6 V. Small anodic and cathodic peaks could be observed at bare electrode (curve a). After dropping GO, it was found that the current increased (curve b), indicating the dropped material can increase the conductivity and adsorbability of electrode and then increase the current. Upon dropping MGO in the electrode surface, the

cyclic voltammogram exhibited stable redox peaks and the current increased (curve c). The results indicated that conductivity of electrode was enhanced by modified Fe_3O_4 nanoparticles and specific surface area of the electrode was increased. Then the addition of AuNPs to the material results in the clear increasing of redox peaks (curve d) and the peak potentials moved about 0.05 V to the negative direction because of the electrocatalysis of AuNPs.

3.3. Optimization of the electrochemical sensor preparation and determination conditions

3.3.1. Optimization of the amount of MGO@AuNPs-MIPs suspensions

The relationship between the peak currents of DBP and the amount of MGO@AuNPs-MIPs suspensions on the gold electrode was investigated. The peak currents of 5.0×10^{-6} mol/L DBP enhanced to maximum when the amount of MGO@AuNPs-MIPs suspension (0.25 mg/mL) increased to 5.0 μ L. However, when the amount of suspension exceeded 5.0 μ L, the peak current decreased dramatically (Fig. 5A). The results may be attributed to the thicker film of MGO@AuNPs-MIPs, which blocked the electrical conductivity. Consequently, a MGO@AuNPs-MIPs suspension of 5.0 μ L was utilized to modify the electrode.

3.3.2. Optimization of the pH value

To achieve an optimal electrochemical signal, the pH value of PBS solution was an important factor to the current response. The PBS at different pH values was studied from 5.5 to 8.0 shown in Fig. 5B. The experimental result showed that the maximum current response occurred at 6.0, and high acidic or alkaline surroundings would damage the structure of the polymer to make the current response decrease. Therefore, PBS with pH 6.0 was used as the supporting electrolyte in all determinations.

3.3.3. Optimization of the incubation time

The sensitivity of the proposed method was undoubtedly improved by the incubation time. As shown in Fig. 5C, with the incubation time increased from 0 to 14 min, the peak currents of DBP increased linearly, owing to the increased amount of DBP on the MGO@AuNPs-MIPs. After that, no further increase was observed due to the surface saturation, therefore, 14 min was chosen as the optimal incubation time.

3.4. Calibration curve

Under optimal conditions, a linear relation (Fig. 5D) between current response and DBP concentration in the range of 2.5×10^{-9} – 5.0×10^{-6} mol/L with a correlation coefficient of 0.998 was obtained which was wider and lower than the common methods as shown in Table 1. The regression equation was $I (\mu A) = 1.06c + 1.61 \times 10^{-6}$ mol/L. The detection limit was estimated to be 8.0×10^{-10} mol/L at a signal-to-noise ratio of 3σ (where σ is the standard deviation of the blank, $n=6$).

3.5. Selectivity of the sensor

The selectivity experiments were carried out by using biphenol A, L-tryptophan, epinephrine and sulfamethoxazole as the similarities toward DBP detection during the binding process. The current responses of MGO@AuNPs-MIPs toward DBP were much higher than other analogues, indicating a better adsorption and binding capacity for the template molecules, because the oxidation peak current increased with increasing target molecule concentration. The high specificity was probably due to the shape of the cavities in the imprinted polymers matrix just fitting for the unique molecular structure of DBP, so they cannot bind other analogues tightly.

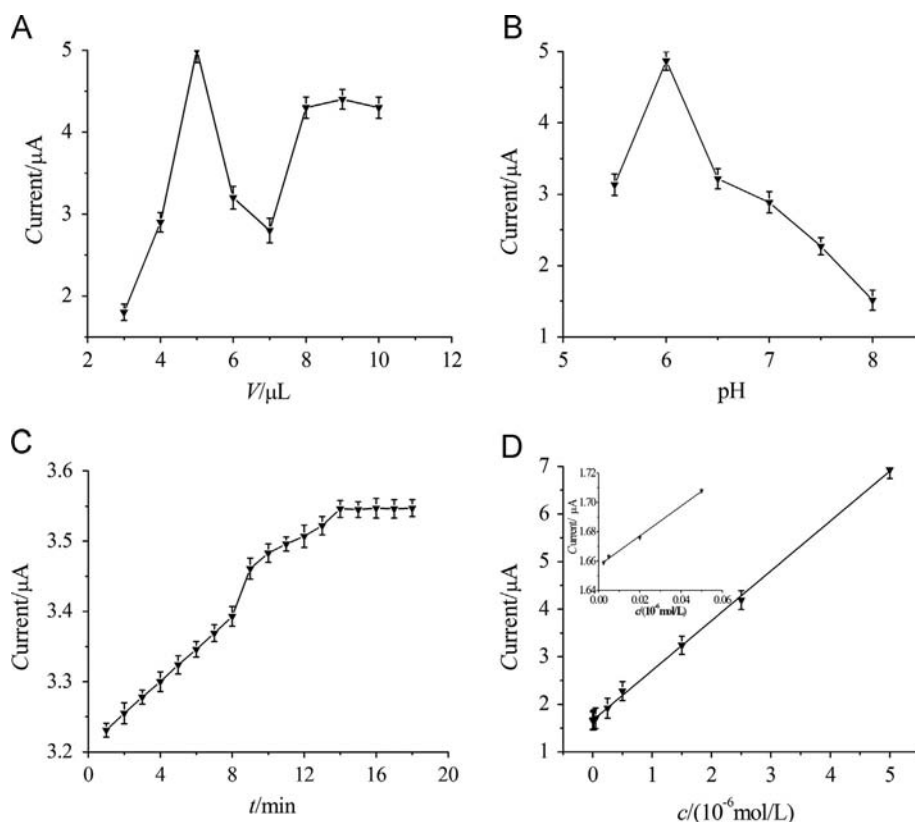


Fig. 5. (A) Effect of the amount of nanocomposites on the prepared electrode response. (B) Effect of different pH on the prepared electrode response. (C) Effect of the incubation time on the prepared electrode response. (D) The linear relationship between the peak current and the concentration of DBP in a range of 2.5×10^{-9} – 5.0×10^{-6} mol/L. The concentration of DBP were as follows: 2.5×10^{-9} , 5.0×10^{-9} , 2.0×10^{-8} , 5.0×10^{-8} , 2.5×10^{-7} , 5.0×10^{-7} , 1.5×10^{-6} , 2.5×10^{-6} and 5.0×10^{-6} mol/L, respectively.

Table 1
Analytical properties of different detection methods.

Method	Detection limit (mol/L)	Linear range (mol/L)	References
Microflow chemiluminescence sensor	2.09×10^{-9}	3.84×10^{-8} – 2.08×10^{-5}	[41]
Chromatographic	3.95×10^{-7}	1.26×10^{-7} – 1.08×10^{-5}	[42]
Gas chromatography–mass spectrometry	6.47×10^{-8}	6.47×10^{-8} – 1.80×10^{-5}	[43]
MCGO@AuNPs-MIPs/GCE	8.0×10^{-10}	2.5×10^{-9} – 5.0×10^{-6}	Present work

Thus, the above results suggested that MGO@AuNPs-MIPs show potential applications as molecular recognition element owing to its excellent selectivity against the analogues.

3.6. Repeatability, reproducibility and stability on the electrochemical sensor

By using DPV to characterized the repeatability, reproducibility and stability on the electrochemical sensor in 2.0×10^{-6} mol/L DBP with PBS ranging from 0 to 0.8 V, potential step was 0.004 V, amplitude was 0.05 V, pulse width was 0.05 s, sampling width was 0.0167 s and pulse period was 0.2 s, the MGO@AuNPs-MIPs modified electrodes were able to be reused for several times. The excellent repeatability of MGO@AuNPs-MIPs modified electrode was also examined by using the same electrode for 30 repeated analyses of 2.0×10^{-6} mol/L DBP, with a relative standard deviation (RSD) of 2.50%. Good reproducibility was also observed with a RSD of 3.56% for 6 parallel detections. Moreover, the sensor retained a response of 96.3% of the initial current after storage for 4 weeks in room temperature.

3.7. Determination of DBP in real samples

In order to test the applicability and reliability of the imprinted sensor, drink samples (10.0 mL) were obtained from a brand wine drinks. The samples were centrifuged at 6000 rpm for 30 min. The supernatant was transferred into a flask and diluted with ultrapure water for analysis. The percentage of recovery and relative standard deviation were determined and presented in Table 2. The good recoveries of the samples indicated that the proposed method can be successfully applied in the detection of DBP concentration in real samples.

4. Conclusion

A novel MGO@AuNPs composite with a MIPs outer layer for selective recognition of DBP was successfully synthesized. Owing to the unique mechanical properties and extremely large area of MGO@AuNPs, the resulting MGO@AuNPs-MIPs composite possesses high selectivity compared with other analogues, and good sensitivity toward template molecules. The MGO@AuNPs-MIPs

Table 2
The determination of DBP in real samples. ($n=6$).

Samples	C_{DBP} (10^{-6} mol/L)	Added (10^{-6} mol/L)	Found (10^{-6} mol/L)	Recovery (%)	RSD (%)
1	5.0	3.0	7.9	97	3.3
		5.0	9.9	98	3.1
2	3.1	5.0	8.3	104	3.0
		7.0	10.0	99	2.8

modified electrodes can specially recognize DBP, and determine DBP with a wide linear range from 2.5×10^{-9} to 5.0×10^{-6} mol/L. The imprinted film building on a substrate with large surface area should be promising as it provides more binding sites for template recognition, and most of the binding sites were situated at or approximate to the surface of the outer MIPs layer. This strategy can be further expected to be used to fabricate various molecular imprinting-based sensors for advanced applications. Furthermore, the molecular imprinting techniques discussed herein could also find applications in the fields of separation, trace detection, and environmental monitoring.

Acknowledgements

This work was supported by the National Natural Science Foundation of China (NSFC, Nos. 21345005 and 21205048), the Shandong Provincial Natural Science Foundation of China (No. ZR2012BM020) and the Scientific and technological development Plan Item of Jinan City in China (No. 201202088).

References

- [1] M.C. Zhang, Q.E. Wang, H.S. Zhuang, *Anal. Bioanal. Chem.* 386 (2006) 1401–1406.
- [2] D. Koniecki, R. Wang, R.P. Moody, J. Zhu, *Environ. Res.* 111 (2011) 329–336.
- [3] Y.L. Feng, J.P. Zhu, R. Sensenstein, *Anal. Chim. Acta* 538 (2005) 41–48.
- [4] R.L. Self, W.H. Wu, *Food Control* 25 (2012) 13–16.
- [5] S. Singh, S.S.L. Li, *Gene* 494 (2012) 85–91.
- [6] G.A. Loraine, M.E. Pettigrove, *Environ. Sci. Technol.* 40 (2006) 687–695.
- [7] C. Bach, X. Dauchy, M.C. Chagnon, S. Etienne, *Water Res.* 46 (2012) 571–583.
- [8] J. Li, Y. Cai, Y. Shi, S. Mou, G. Jiang, *Talanta* 74 (2008) 498–504.
- [9] G. Latini, M. Wittassek, A.D. Vecchio, G. Presta, C.D. Felice, J. Angerer, *Environ. Int.* 35 (2009) 236–239.
- [10] J. Naarala, A. Korpi, *Toxicol. Lett.* 188 (2009) 157–160.
- [11] O.O. Olujimi, O.S. Fatoki, J.P. Odendaal, A.P. Daso, *Microchem. J.* 101 (2012) 11–23.
- [12] J. He, R. Lv, J. Zhu, K. Lu, *Anal. Chim. Acta* 661 (2010) 215–221.
- [13] D.D. Orsi, L. Gagliardi, R. Porrà, S. Berri, P. Chimenti, A. Granese, I. Carpani, D. Tonelli, *Anal. Chim. Acta* 555 (2006) 238–241.
- [14] T. Takeuchi, Y. Jin, D. Ishii, *J. Chromatogr. A* 321 (1985) 159–164.
- [15] N. Tombros, C. Jozsa, M. Popinciuc, H.T. Jonkman, B.J. van Wees, *Nature* 448 (2007) 571–574.
- [16] A.A. Balandin, S. Ghosh, W. Bao, I. Calizo, D. Teweldebrhan, F. Miao, C.N. Lau, *Nano Lett.* 8 (2008) 902–907.
- [17] D.A. Dikin, S. Stankovich, E.J. Zimney, R.D. Piner, G.H.B. Dommett, G. Evmenenko, S.T. Nguyen, R.S. Ruoff, *Nature* 448 (2007) 457–460.
- [18] K.S. Novoselov, A.K. Geim, S.V. Morozov, D. Jiang, Y. Zhang, S.V. Dubonos, I.V. Grigorieva, A.A. Firsov, *Science* 306 (2004) 666–669.
- [19] S. Tajik, M.A. Taher, H. Beitollahi, *Electroanalysis* 26 (2014) 796–806.
- [20] H.T. Hu, X.B. Wang, J.C. Wang, L. Wan, F.M. Liu, H. Zheng, R. Chen, C.H. Xu, *Chem. Phys. Lett.* 484 (2010) 247–253.
- [21] S. Tajik, M.A. Taher, H. Beitollahi, *Ionics* (2014) 1–7.
- [22] G. Mayer, *Science* 310 (2005) 1144–1147.
- [23] Y. Deng, Y.J. Li, J. Dai, M.D. Lang, X.Y. Huang, *J. Polym. Sci. Part A: Polym. Chem.* 49 (2011) 1582–1590.
- [24] D. Vuluga, J.M. Thomassin, I. Molenberg, I. Huynen, B. Gilbert, C. Jerome, M. Alexandre, C. Detrembleur, *Chem. Commun.* 47 (2011) 2544–2546.
- [25] H.M. Etmimi, M.P. Tonge, R.D. Sanderson, *J. Polym. Sci. Part A: Polym. Chem.* 49 (2011) 1621–1632.
- [26] L.M. Chang, S. Wu, S.N. Chen, X. Li, *J. Mater. Sci.* 46 (2011) 2024–2029.
- [27] Y. Li, X. Li, C. Dong, J. Qi, X. Han, *Carbon* 48 (2010) 3427–3433.
- [28] K. Haupt, K. Mosbach, *Chem. Rev.* 100 (2000) 2495–2504.
- [29] J.O. Mahony, K. Nolan, M.R. Smyth, B. Mizaikoff, *Anal. Chim. Acta* 534 (2005) 31–39.
- [30] B.J. Gao, Q.Y. Niu, R.K. Du, *J. Sep. Sci.* 33 (2010) 1338–1348.
- [31] C. Xie, Z. Zhang, D. Wang, G. Guan, D. Gao, J. Liu, *Anal. Chem.* 78 (2006) 8339–8346.
- [32] D. Gao, Z. Zhang, M. Wu, C. Xie, G. Guan, D. Wang, *J. Am. Chem. Soc.* 129 (2007) 7859–7866.
- [33] S.R. Carter, S. Rimmer, *Adv. Funct. Mater.* 14 (2004) 553–561.
- [34] R. Singh, R. Verma, A. Kaushik, G. Sumana, S. Sood, R.K. Gupta, B.D. Malhotra, *Biosens. Bioelectron.* 26 (2011) 2967–2974.
- [35] S. Tajik, M.A. Taher, H. Beitollahi, *Sens. Actuators, B* 197 (2014) 228–236.
- [36] X.L. Luo, J.J. Xu, Q. Zhang, G.J. Yang, H.Y. Chen, *Biosens. Bioelectron.* 21 (2005) 190–196.
- [37] W.S. Hummers, R.E. Offeman, *J. Am. Chem. Soc.* 80 (1958) 1339–1339.
- [38] N.I. Kovtyukhova, P.J. Ollivier, B.R. Martin, T.E. Mallouk, S.A. Chizhik, E.V. Buzaneva, A.D. Gorchinskiy, *Chem. Mater.* 11 (1999) 771–778.
- [39] Y.H. Liao, R. Yuan, Y.Q. Chai, Y. Zhuo, X. Yang, *Anal. Biochem.* 402 (2010) 47–53.
- [40] A. Pietrzyk, S. Suriyanarayanan, W. Kutner, E. Maligaspe, M.E. Zandler, F. D'Souza, *Bioelectrochemistry* 80 (2010) 62–72.
- [41] H.M. Qiu, L.L. Fan, X.J. Li, L.L. Li, M. Sun, C.N. Luo, *J. Pharm. Biomed.* 75 (2013) 123–129.
- [42] H. Shaikh, N. Memon, H. Khan, M.I. Bhangar, S.M. Nizamani, *J. Chromatogr. A* 1247 (2012) 125–133.
- [43] M.D. Carlo, A. Pepe, G. Sacchetti, D. Compagnone, D. Mastrocola, A. Cichelli, *Food Chem.* 111 (2008) 771–777.



Separation–preconcentration of nickel and lead in food samples by a combination of solid–liquid–solid dispersive extraction using SiO₂ nanoparticles, ionic liquid-based dispersive liquid–liquid micro-extraction

Nusrat Jalbani^{a,b}, Mustafa Soylak^{a,*}

^a Erciyes University, Fen Faculty, Department of Chemistry, 38039 Kayseri, Turkey

^b PCSIR Laboratories, Karachi, Pakistan

ARTICLE INFO

Article history:

Received 13 May 2014

Received in revised form

28 July 2014

Accepted 31 July 2014

Available online 8 August 2014

Keywords:

Microextraction

Nickel

Lead

Ammonium pyrrolidine dithiocarbamate

Ionic liquid

SiO₂ nanoparticle

ABSTRACT

A microextraction method for the determination of nickel and lead using solid–liquid–solid dispersive extraction followed by ionic liquid-based dispersive liquid–liquid microextraction (SLSDE-ILDLLME) was presented. It was applied to the extraction of nickel and lead from food samples. Ammonium pyrrolidine dithiocarbamate (APDC) as complexing agent, [C₄MIM][PF₆] as ionic liquid, SiO₂ as nanoparticles and 2 mol L⁻¹ HNO₃ as eluent were used. Several important parameters such as amount of IL, extraction time, pH and volume of the complexing agent were investigated. The quantitative recoveries were obtained at pH 7.0 for analytes. Under the optimum conditions, the limits of detection (LODs) calculated using $3(Sd)_{blank}/m$ were 0.17 for Ni(II) and 0.79 μg L⁻¹ for Pb(II) for aqueous solutions with 125 enrichment factor (EF). The limit of detections of the analyte ions ($3(Sd)_{blank}/m$) for solid samples were 0.09 μg g⁻¹ (Ni) and 0.40 μg g⁻¹ (Pb). The accuracy of the proposed method was confirmed by the analysis of standard reference material (1577c bovine liver) and spiked recovery test. The proposed method was applied to determine nickel and lead levels in chicken, fish and meat samples.

© 2014 Elsevier B.V. All rights reserved.

1. Introduction

The pollution of the environment by heavy metals has received considerable attention over last few years. Among the heavy metals, lead is one of the most dangerous and toxic element as compared to other metals, but nickel is a moderate toxic element and can cause allergic reactions and certain nickel compounds may be carcinogenic [1–3]. However, both these elements are found in the environment through various pathways which could be released to the water resources [4]. However, elevated levels of these metals in natural environmental samples can cause serious problems on human health and the environment [5,6]. Consequently, it is of great significance to environmental science and chemical science to determine trace amount of nickel and lead in food, soil and water samples [7–9].

In general, the most widely used sample pre-treatment techniques are liquid-phase microextraction (LPME) [10], dispersive liquid–liquid microextraction (DLLME) [11], solid phase extraction

(SPE) and liquid–liquid extraction (LLE) [12,13]. Nevertheless, most of these techniques require an extensive and time-consuming sample pre-treatment as compared to our developed methodology.

Nanomaterials have attracted much more attention in analytical chemistry and other fields over last few years because of their unique chemical, physical properties and high adsorption capacity. SiO₂ nanoparticles have been used to prepare complex materials and catalyzer carriers. This nanoparticle is used as a solid-phase sorbent because of its large surface area and having excellent adsorption ability [14].

A number of analytical methods based on flame atomic absorption spectrometry (FAAS), electrothermal atomic absorption spectrometry (ETAAS), inductively coupled plasma-atomic emission spectrometry (ICP-AES) and inductively coupled plasma-mass spectrometry (ICP-MS) have been employed for the determination of metals in real samples. Meanwhile, FAAS exquisite sensitivity and a large efficiency of metal ion can be achieved using micro-injection system [15–19].

A new method for the determination of nickel and lead using solid–liquid–solid dispersive extraction, followed by ionic liquid-based dispersive liquid–liquid microextraction (SLSDE-ILDLLME) was established in the present work. The influences of some

* Corresponding author. Tel./fax: +90 352 4374933.

E-mail address: soylak@erciyes.edu.tr (M. Soylak).

experimental parameters were studied. The procedure proposed was applied for the determination of nickel and lead in food samples.

2. Experimental

2.1. Chemical and reagents

All the reagents and chemicals of Merck (Darmstadt, Germany) used in this study were of analytical grade. Distilled/deionized water (Millipore Milli-Q system $18 \text{ M}\Omega \text{ cm}^{-1}$ resistivity) was used throughout the present study. Concentrated nitric acid (65%) of spectroscopic grades E. Merck, (Darmstadt, Germany) was used. Stock standard solution (1000 mg L^{-1}) of Pb(II) and Ni(II) were prepared by accurate weighting and dissolving appropriate amounts of nitrate salts in 1% nitric acid. While working standards of corresponding metal ions were prepared freshly from the dilution of stock standard solution with distilled water. Phosphate buffer of pH 7.0 was prepared by adding appropriate amounts of sodium di-hydrogen phosphate and disodium hydrogen phosphate for pH adjustment.

1-butyl-3-methylimidazolium hexafluorophosphate ($[\text{C}_4\text{mim}][\text{PF}_6]$) was purchased from E. Merck (no: 4.90065.0025, Darmstadt, Germany). A 0.1% w/v of ammonium pyrrolidine dithiocarbamate (APDC) was prepared in ethanol/water on daily basis which was purchased from (E. Merck, Darmstadt, Germany). Standard reference material (SRM) bovine liver (1577c) was used for the validation of proposed method.

2.2. Instrumentation

A Perkin Elmer Model 3110 flame atomic absorption was used for the determination of nickel and lead with the mode of air/acetylene flame. The hollow cathode lamps of nickel and lead were used as radiation source and operated at recommended current. All measurements were carried out without background correction. The operating parameters for studied metals were set as recommended by the manufacturer. The calibration curve was established by using working standard solutions. Analyte concentrations were measured using microinjection equipment and all injections were made in the peak height mode. A $50 \mu\text{L}$ of solution was injected to a home-made Teflon[®] funnel with an Eppendorf[®] pipette that was directly connected to the nebulizer-burner system of FAAS with a capillary tubing [19]. A model Nel pH 900 (Ankara-Turkey) pH meter equipped with a combined glass electrode was used for the pH adjustment of sample solution.

2.3. Preparation of SiO_2 nanoparticle

10 mL of ultra pure water, 310 mL of NH_3 ($2.5 \text{ mol}/500 \text{ mL}$ ethanol) and ethanol (70 mL) were added in 500 mL of beaker. After addition of all solvents, mixture was sonicated at 70°C for 16 h . After that tetraethyl orthosilicate (18 mL) was added swiftly during sonication. It was allowed to react at ambient temperature 50°C for 3 h with continuous sonication in order to obtain the cloudy solution as silica particles were formed and again the mixture was sonicated for a total of 18 h [20]. The resulting SiO_2 nanoparticles were activated by the addition of hydrochloric acid after 4 h . Finally, the resulting product was washed with distilled water and was separated by centrifugation, and dried under vacuum at 60°C for 6 h . In this way the obtained dried solid can be used as sorbent nanomaterial for further experiments.

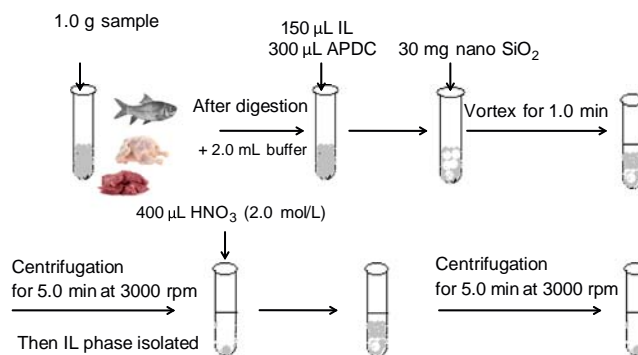


Fig. 1. Graphical representation of SLSDE-ILDLLME procedure.

2.4. Solid–liquid–solid dispersive extraction – followed by ionic liquid dispersive liquid–liquid microextraction (SLSDE-ILDLLME) procedure

A graphical diagram of the SLSDE-ILDLLME protocol is shown in Fig. 1. For the preconcentration of Ni(II) and Pb(II), an aliquot of 10 mL solution containing $100 \mu\text{g L}^{-1}$ of each analyte was transferred into 50 mL of conical bottom vials. The pH of this solution was adjusted to 7.0 with buffer solution. After adjusting pH, $300 \mu\text{L}$ (0.30 mg) of 0.1% APDC as complexing agent and $150 \mu\text{L}$ of IL ($[\text{C}_4\text{MIM}][\text{PF}_6]$) were added into the mixture of solution and the solution was left at room temperature for few minutes. After that, 30 mg of SiO_2 -NPs was added into the conical bottom vials. This solution was vortexed for 1.0 min . The mixture was accelerated for phase separation by centrifugation for 5 min at 3000 rpm . In this way the SiO_2 -NPs sorbent was collected at the bottom of vial. Then extract of IL phase was isolated carefully from nanoparticles by pipette. Finally $400 \mu\text{L}$ of $2 \text{ mol L}^{-1} \text{ HNO}_3$ was added to desorb the metal-APDC complex from NPs by 5 min centrifugation at 3000 rpm then the resulting solution was aspirated into FAAS nebulizer using microinjection system.

2.5. Pre-treatment of samples

The chicken, meat and fish samples were purchased from local market of Kayseri, Turkey. 1.0 g of food samples and SRM sample were accurately weighed in a 100 mL beaker, 10 mL of HNO_3 (65%) and 5.0 mL of H_2O_2 (35%) were added to each beaker and heated on electric hot plate at 100°C for about 2 h , till the clear solution was obtained. The digested samples were kept at room temperature for cooling. After cooling the samples were filtered through a $0.45 \mu\text{m}$ pore size membrane filter (Millipore Corporation, Bedford, MA, USA) into a 10 mL conical bottom flask and were diluted with distilled water. Thereafter, pH of the sample solutions was adjusted to pH 7.0 with the addition of 0.01 mol L^{-1} sodium hydroxide and buffered to pH 7.0 with buffer solution. This solution was treated under recommended procedure as described in Section 2.3 and then it was analyzed by FAAS for the determination of nickel and lead.

3. Result and discussion

3.1. Effect of pH

pH is the main parameter and plays a very important role on metal chelate formation and subsequent extraction [21–24]. The effect of pH on the chelate formation and determination of Ni(II) and Pb(II) from food samples was studied in the pH range of 2.0–9.0. As indicated from the results (Fig. 2), that at low and high pH

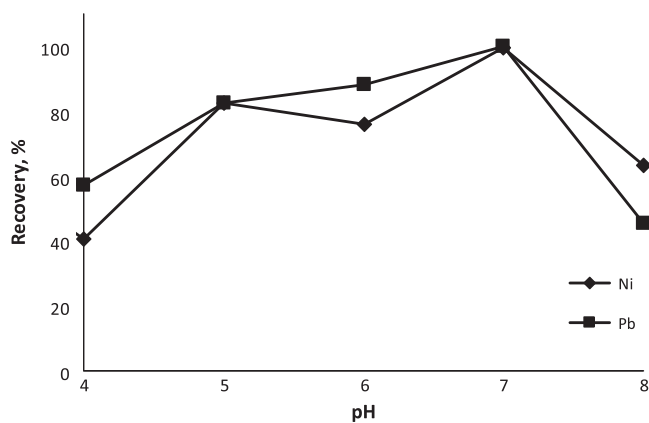


Fig. 2. Effect of the pH on the recoveries of Ni(II) and Pb(II) ($N=3$).

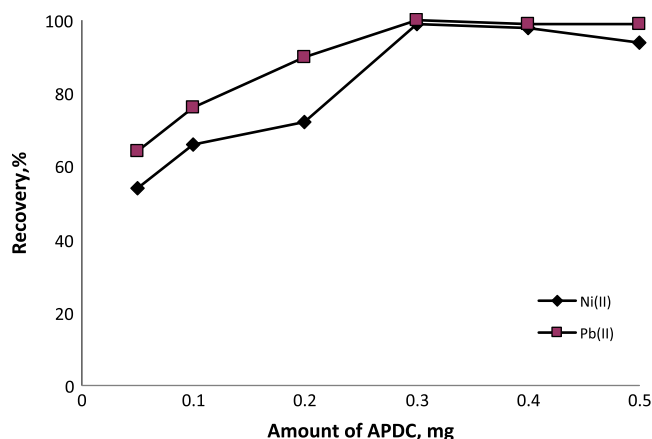


Fig. 3. Effect of amounts of APDC on the recoveries of Ni(II) and Pb(II) ($N=3$).

levels, the studied metal ions are less likely to be extracted. However from the results it was clearly seen that at pH 7.0 highest extraction efficiency of Ni(II) and Pb(II) was obtained thus pH 7.0 was chosen as an adequate pH value for further studies.

3.2. Effect of APDC amount

Since ammonium pyrrolidine dithiocarbamate (APDC) is a well-characterized reagent that reacts with over 30 metal ions to form very stable complexes [25], it was widely used in the separation–preconcentration studies as ligand. The influences of APDC amount on extraction efficiency were investigated in the range of 0.10–0.50 mg of ligand. The results are given in Fig. 3. As indicated in the results increasing the amount of ligand the recovery increases till 0.30 mg and after 0.30 mg extraction efficiency of metal ions remains constant and quantitative. Therefore the amount of 0.30 mg was chosen as optimum for further study.

3.3. Effect of IL volume

The effect of the IL volume on the extraction efficiency of Ni(II) and Pb(II) was examined in the range of 50–300 μL . The solutions containing different volumes of IL were subjected to developed procedures, while the other factors were constant. The maximum extraction efficiency of studied metal ions was obtained at 150 μL . The recoveries of analyte ions were increased to 150 μL and reached the quantitative value ($> 95\%$). The recoveries become

constant after 150 μL . Thus, 150 μL was chosen for further experiments.

3.4. Effect of sample volume

To acquire high enrichment factor, the effects of sample volume on the extraction efficiency of Ni(II) and Pb(II) were studied in the range of 10–100 mL model solutions that contain 100 $\mu\text{g L}^{-1}$ of each analyte. Both analytes were quantitatively recovered till 50 mL of sample volume. The enrichment factor for the present developed methodology is 125 and was calculated on the basis of 50 mL of initial and 0.4 mL of final volume.

3.5. Effect of the amount of SiO_2 -NPs

In this study, SiO_2 -NPs were employed as the sorbent for IL-based DLLME procedure. Different amounts (10–50 mg) of NPs were tested in the range of 0.0–50 mg in the SLSDE-ILDLLME procedure for the extraction and determination of Ni(II) and Pb(II). The results demonstrated that the extraction efficiency of metal ion was decreased after 30 mg of SiO_2 -NPs. This means that 30 mg was adequate for complete extraction. So 30 mg of NPs was used for further experiments.

3.6. Effect of the extraction time

Extraction time is one of the most imperative parameter in most of extraction procedures. Under constant experimental conditions, the effect of extraction time was studied in the range of 0.0–10.0 min. It was observed from the results that the extraction time has no noteworthy effect on the % recovery of analyte metal ions. Thus in this method, the centrifuging of sample solution was completed, about 5.0 min at 3000 rpm was chosen for further study. Based on these observations, an extraction time of 5.0 min was used for subsequent experiments.

3.7. Effect of foreign ions

Since matrix effects are well-known problem in the atomic absorption spectrometric determination of metals in real samples [26–30], the effects of foreign ions that may positively or negatively influence FAAS detection of metals were also studied. The results are given in Table 1. The tolerance limit is defined as the largest amount of interfering ions causing a relative error $\leq 5\%$ related to the preconcentration and determination of Ni(II) and Pb(II). Hence from the results it was confirmed that the applicability of our developed methodology has an excellent selectivity for the determination of Ni(II) and Pb(II) and is suitable for the analysis of samples with complicated matrix.

Table 1
Effects of foreign ions on the recoveries of analyte ions ($N=3$).

Foreign species	Added	Tolerance limit (mg L^{-1})	% Recovery	
			Ni(II)	Pb(II)
Ca^{2+}	CaCl_2	2000	95	98
Cu^{2+}	$\text{Cu}(\text{NO}_3)_2 \cdot 3\text{H}_2\text{O}$	20	99	98
F^-	NaF	20	99	95
Fe^{3+}	$\text{Fe}(\text{NO}_3)_3 \cdot 9\text{H}_2\text{O}$	2000	100	99
Mg^{2+}	$\text{Mg}(\text{NO}_3)_2$	1500	97	99
Na^+	NaCl	1500	96	97
Ni^{2+}	$\text{Ni}(\text{NO}_3)_2$	20	97	98
NO_3^-	KNO_3	1500	101	101
PO_4^{3-}	$\text{Na}_3\text{PO}_4 \cdot 12\text{H}_2\text{O}$	1500	100	100
SO_4^{2-}	Na_2SO_4	2000	98	100
Zn^{2+}	$\text{Zn}(\text{NO}_3)_2$	20	97	96

3.8. Analytical figures of merit

Under the optimum condition, the linear range obtained was 1.0–5.0 mg L⁻¹ for nickel and lead with a correlation coefficient of 0.999. The detection limits (LOD) of Ni(II) and Pb(II) ions ($N=11$, defined as $3(Sd)_{\text{blank}}/m$, where Sd is the standard deviation of the blank readings and m is the slope of the calibration curve) were 0.17 μg L⁻¹ and 0.79 μg L⁻¹, respectively. The limit of detections of the analyte ions ($3(Sd)_{\text{blank}}/m$) for solid samples were 0.09 μg g⁻¹ (Ni) and 0.40 μg g⁻¹ (Pb). The limit of quantification (LOQ) for nickel(II) and lead(II) are 0.28 μg g⁻¹ and 1.10 μg g⁻¹, respectively. The resultant repeatability expressed as relative standard

deviations (RSDs, $n=6$) were calculated as 2.3% and 2.5% for Ni and Pb, respectively.

3.9. Applications to real samples

The tests of addition/recovery in the experiments for analyte ions were performed for a chicken sample. Different amounts of analyte ions were spiked to estimate the accuracy of the procedure. The results are given in Table 2. Good agreement was obtained between the added and found analyte content using the recommended procedure.

The validation of the presented microextraction procedure is performed by the analysis of bovine liver (1577c) CRM for analytes. The certified and observed values for certified reference materials are given in Table 3. The results were in good agreement with the certified values of CRMs.

The proposed SLSDE-ILDLLME procedure was applied to determine nickel and lead from fish, meat and chicken samples. The samples were prepared according to Section 2.3. The results are presented in Table 4. The recoveries of obtained results were in a range of 99–100% which verified the accuracy and reliability of the approach. The results are also found within the permissible limits in all the studied food samples [31].

3.10. Comparison of SLSDE-ILDLLME with the other sample preparation techniques

A comparison of the developed methodology with the other reported preconcentration methods for determination of nickel and lead in food samples. The present method was combined with SLSDE-ILDLLME from matrix within a minimum time [32–39]. The present microextraction methodology shows high EF and low detection limit as represented in Table 5.

4. Conclusion

In the present study, to the best of our knowledge, the first time, SiO₂-NPs are used as an adsorbent for the efficient extraction and determination of nickel and lead in fish, chicken and meat and combined with IL-based DLLME procedure and employed by FAAS. The main advantages of the proposed methodology were minimum amount of IL, simplicity and enhancement of sensitivity. Moreover, SLSDE-ILDLLME was demonstrated to be a very efficient, easy, rapid extraction method and could be directly applied to the preconcentration and determination of nickel and lead in food samples.

Table 2

Determinations of nickel and lead in bovine liver Standard reference material (1577c) μg kg⁻¹ ($N=6$).

Analytes	Experimental value $\bar{x} \pm ts/\sqrt{n}$	Certified values $\bar{x} \pm ts/\sqrt{n}$	% Recovery ^a
Ni	43.8 ± 1.3	44.5 ± 9.2	98.4
Pb	6.25 ± 0.15	6.28 ± 1.0	99.5

^a % Recovery = [experimental value/certified value] × 100.

Table 3

Addition recovery/test procedure for a chicken sample (mg kg⁻¹).

Analytes	Added	Found	% Recovery
Ni	0.0	0.56 ± 0.02 ^a	–
	5.0	5.56 ± 0.17	100.0
	10	10.5 ± 0.31	99.4
Pb	0.0	< LOQ ^b	–
	5.0	5.44 ± 0.15	108.8
	10	10.4 ± 0.25	104.0

^a Mean ± standard deviation.

^b LOQ: limit of quantification.

Table 4

Analytical results for real samples (mg kg⁻¹), ($n=5$).

Samples	Ni	Pb
Chicken	0.56 ± 0.02 ^a	< LOQ ^b
Fish	0.48 ± 0.001	1.14 ± 0.05
Meat	0.66 ± 0.03	1.21 ± 0.06

^a Mean ± standard deviation.

^b LOQ: limit of quantification.

Table 5

Comparison of proposed method with other reported preconcentration techniques.

Metals	Methods	EF	LOD	Ref.
Co, Ni, Pb	Dispersive liquid–liquid microextraction based on solidification of floating organic drop (DLLME-SFO)	800	1.3 ^a	[32]
V, Cr, Cu, As, Pb	Schiff base-chitosan grafted Schiff base-chitosan grafted multiwalled carbon nanotubes (S-CS-MWCNTs)	52–128	1.3–3.8 ^a	[33]
Co, Ni	Dispersive liquid phase microextraction (DLPME)	101–200	21–33 ^b	[34]
Ni, Pb	Solid–liquid–solid dispersive extraction- followed by ionic liquid dispersive liquid–liquid microextraction (SLSDE-ILDLLME)	125	0.17–0.79 ^a	Present work

LOD: limit of detection; EF: enrichment factor.

^a μg L⁻¹.

^b pg mL⁻¹.

Acknowledgments

The authors wish to express their appreciation to the Scientific and Technological Research Council of Turkey (TUBITAK) under “2216 Research Fellowship Program for Foreign Citizens” for financial support.

References

- [1] Filiz Karadas, *Agric. Sci.* 5 (2014) 87–93.
- [2] D. Templeton, *Biological Monitoring of Chemical Exposure in the Workplace*, World Health Organization, Geneva, 1990.
- [3] L. Elci, M. Soylak, A. Uzun, E. Buyukpatir, M. Dogan, *Fresenius J. Anal. Chem.* 368 (2000) 358–361.
- [4] D. Mendil, T. Kiris, M. Tuzen, M. Soylak, *Int. J. Food Sci. Technol.* 48 (2013) 1201–1207.
- [5] H.G. Seiler, A. Sigel, H. Sigel, *Handbook on Toxicity of Inorganic Compounds*, Marcel-Dekker, New York, 1998.
- [6] L. Rassaei, M. Amiri, C.M. Cirtiu, M. Sillanpaa, F. Marken, M. Sillanpaa, *Trend Anal. Chem.* 30 (2011) 1704–1715.
- [7] M. Ghaedi, F. Marahel, A. Shokrollahi, M. Montazerzohori, M. Soylak, *Quim. Nova* 33 (2010) 404–410.
- [8] A. Rosell, C. Palet, M. Valiente, *Anal. Chim. Acta* 370 (1998) 141–147.
- [9] Z. Bahadir, D. Ozdes, V.N. Bulut, C. Duran, H. Elvan, H. Bektas, M. Soylak, *Toxicol. Environ. Chem.* 95 (2013) 737–746.
- [10] J.F. Huertas-Perez, A.M. Garcia-Campana, *Anal. Chim. Acta* 630 (2008) 194–204.
- [11] E. Yilmaz, M. Soylak, *Talanta* 116 (2013) 882–886.
- [12] V.A. Lemos, L.S.G. Teixeira, M.A. Bezerra, A.C.S. Costa, J.T. Castro, L.A.M., *Appl. Spectrosc. Rev.* 43 (2008) 303–334.
- [13] I. Narin, M. Soylak, K. Kayakirilmaz, L. Elci, M. Dogan, *Anal. Lett.* 36 (2003) 641–658.
- [14] Y. Cui, X. Chang, Y. Zhai, X. Zhu, H. Zheng, N. Lian, *Microchem. J.* 83 (2006) 35–41.
- [15] L. Elci, A.A. Kartal, M. Soylak, *J. Hazard. Mater.* 153 (2008) 454–461.
- [16] T.G. Kazi, N. Jalbani, J.A. Baig, G.A. Kandhro, H.I. Afridi, M.B. Arain, M.K. Jamali, A.Q. Shah, *Food Chem. Toxicol.* 47 (2009) 2163–2169.
- [17] M. Zougagh, A.G. de Torres, E.V. Alonso, J.M. Cano Pavon, *Talanta* 62 (2004) 503–510.
- [18] K. Ndungu, S. Hibdon, A.R. Flegel, *Talanta* 64 (2004) 258–263.
- [19] E. Sahmetlioglu, E. Yilmaz, E. Aktas, M. Soylak, *Talanta* 119 (2014) 447–451.
- [20] R.D. Badley, W.T. Ford, F.J. McEnroe, A. Assink, *Langmuir* 6 (1990) 792.
- [21] X.N. Chai, Q. Shuai, A.M. Lu, Q.Y. Yao, X.G. Liu, *Spectrosc. Spectral Anal.* 28 (2008) 1406–1409.
- [22] M. Shamsipur, N. Fattahi, Y. Assadi, M. Sadeghi, K. Sharafi, *Talanta* 130 (2014) 26–32.
- [23] M. Efecinar, N. Satiroglu, Hacet, *J. Biol. Chem.* 41 (2013) 321–330.
- [24] M. Soylak, *Anal. Lett.* 37 (2004) 1203–1217.
- [25] C.A. Watson, *Ammonium Pyrrhodine Ditiocarbamate*, Monograph, 74, Hopkin and Williams, Chadwellhearth, England, 1991.
- [26] D. Bakircioglu, N. Topraksever, Y.B. Kurtulus, *Food Chem.* 151 (2014) 219–224.
- [27] S. Saracoglu, M. Soylak, L. Elci, *Anal. Lett.* 35 (2002) 1519–1530.
- [28] S. Prevost, H. Coulombeau, K. Baczko, L. Berthon, N. Zorz, H. Desvaux, F. Testard, T. Zemb, C. Larpent, *Tenside Surfactants Deterg.* 46 (2009) 100–104.
- [29] U. Divrikli, M. Soylak, L. Elci, *Anal. Lett.* 36 (2003) 839–852.
- [30] E. Stanisz, A. Zgoła-Grzeskowiak, H. Matusiewicz, *Talanta* 129 (2014) 254–262.
- [31] G. Aragay, J. Pons, A. Merkoci, *Chem. Rev.* 111 (2011) 3433–3458.
- [32] M. Mirzaei, M. Behzadi, N.M. Abadi, A. Beizaei, *J. Hazard. Mater.* 186 (2011) 1739–1743.
- [33] B. Dai, M. Cao, G. Fang, B. Liu, X. Dong, M. Pan, S. Wang, *J. Hazard. Mater.* 219–220 (2012) 103–110.
- [34] H. Jiang, Y. Qin, B. Hu, *Talanta* 74 (2008) 1160–1165.
- [35] T.G. Kazi, F. Shah, H.R. Shaikh, H.I. Afridi, A. Shah, Naemullah, S.S. Arain, *Environ. Sci. Poll. Res.* 21 (2014) 3021–3030.
- [36] S. Su, B. Chen, M. He, B. Hu, *Talanta* 123 (2014) 1–9.
- [37] I. López-García, Y. Vicente-Martínez, M. Hernández-Córdoba, *Talanta* 124 (2014) 106–110.
- [38] M. Soylak, R.S. Cay, *J. Hazard. Mater.* 146 (2007) 142–147.
- [39] Q.G. Liao, Y.M. Zhou, L.G. Luo, L.B. Wang, X.H. Feng, *Microchim. Acta* 181 (2014) 163–169.



Capillary electrophoresis with laser-induced fluorescence detection for studying amino acid uptake by yeast during beer fermentation

Heidi Turkia^{a,b,*}, Heli Sirén^c, Merja Penttilä^a, Juha-Pekka Pitkänen^a

^a VTT Technical Research Centre of Finland, PO Box 1000, FIN-02044 VTT, Espoo, Finland

^b Lappeenranta University of Technology, PO Box 20, FIN-53580 Lappeenranta, Finland

^c University of Helsinki, Department of Chemistry, PO Box 55, University of Helsinki, FIN-00014 Helsinki, Finland

ARTICLE INFO

Article history:

Received 22 May 2014

Received in revised form

28 July 2014

Accepted 31 July 2014

Available online 13 August 2014

Keywords:

Bioprocess monitoring

Capillary electrophoresis

Amino acids

Laser-induced fluorescence detection

Beer fermentation

ABSTRACT

The amino acid composition of cultivation broth is known to affect the biomass accumulation, productivity, and vitality of yeast during cultivation. A separation method based on capillary electrophoresis with laser-induced fluorescence (LIF) detection was developed for the determination of amino acid consumption by *Saccharomyces cerevisiae* during beer fermentation. Intraday relative standard deviations were less than 2.1% for migration times and between 2.9% and 9.9% for peak areas. Interday relative standard deviations were less than 2.5% for migration times and between 4.4% and 18.9% for peak areas. The quantification limit was even as low as 62.5 pM which equals to below attomole level detection. The method was applied to study the rate of amino acid utilization during beer fermentation.

© 2014 Elsevier B.V. All rights reserved.

1. Introduction

Nitrogen is one of the main elements in macromolecules of all living organisms. It plays a central role in structure and function, and most organisms have detailed control mechanisms to maintain a constant supply of nitrogen. Yeast is able to use a wide variety of compounds as nitrogen sources, but it prefers ammonia, asparagine, glutamine or glutamate. In the absence of these primary nitrogen sources or if they are present in concentrations low enough to limit growth, other nitrogen sources such as nitrite, nitrate, amides, other amino acids and peptides are used [1].

Amino acid composition of cultivation broth is known to affect the biomass accumulation, productivity, and vitality of yeast during cultivation. In addition, it is known to affect the concentration of flavor-active higher alcohols, vicinal diketones, and esters in beer. The total concentration and composition of amino acids is also important because the use of sugar supplements in cultivation has the effect of reducing the nitrogen/carbon ratio, potentially limiting yeast growth and necessitating the addition of nitrogen supplements [2]. Thus, it is essential for the optimization of process parameters and cultivation performance to monitor amino acid uptake and consumption.

* Corresponding author at: Turku University Hospital, Turku, Finland. Tel.: +358 2 313 7931.

E-mail addresses: heidi.turkia@vtt.fi, heidi.turkia@tyks.fi (H. Turkia).

All-malt brewery wort contains a wide variety of natural nitrogen sources, of which amino acids are the most abundant. It contains all the physiologically active amino acids, but there can be differences in individual amino acid concentrations between wort types. However, the overall proportions of amino acids tend to be relatively constant. Amino acids are taken up sequentially, although the exact order of uptake is strain specific [2].

Capillary electrophoresis (CE) is an excellent analysis tool for bioprocess monitoring. It has high resolution, strong separation efficiency, fast analysis times and low consumption of sample and reagents [3]. CE has been used extensively for the analysis of amino acids in different matrices and with different detectors. Amino acids have been analyzed with indirect UV [4], mass spectrometric (MS) [5–8], conductivity [9] and laser-induced fluorescence (LIF) [10–15] detection.

Amino acid separation and identification by direct UV detection is very difficult, because they do not have a chromophore in their structure. It is possible to use indirect UV detection, in which chemicals containing chromophores are added to the background electrolyte (BGE) solution, but the sensitivity is even lower than with direct UV detection [13]. Laser-induced fluorescence (LIF) detection is used widely to improve the sensitivity of CE. It is the most sensitive detection method available with detection limits below 10^{-21} mol, which makes it almost 1000 times more sensitive than UV detection. Most of the analytes do not have native fluorescence and therefore the use of this detection method

involves attaching fluorescent probe molecules to the analyte. Most fluorescent probes can be designed to contain a reactive moiety capable of coupling to a specific functional group of a biomolecule. With this derivatization procedure it is possible to enhance the selectivity of the detection [16].

Oregon green™ 488 carboxylic acid, succinimidyl ester (OG-SE) is a fluorinated analogue of fluorescein. Conjugates of Oregon green fluorophores are more photostable than those of fluorescein and are less pH sensitive. The excitation and emission maxima of the label are at 496 nm and 524 nm, respectively, which are suitable for use with an argon-ion laser. Reaction of OG-SE with primary and secondary amines creates stable amide and imide linkages, respectively, and the reaction occurs rapidly in mild conditions.

In this study a derivatization technique coupled with capillary electrophoresis separation was developed for the simultaneous monitoring, identification and quantification of amino acids. This method was applied for monitoring the amino acid uptake of yeast during beer fermentation. The results were compared to the consumption of sugars present in the wort and to the production of ethanol during the bioprocess. This study provides a monitoring system with great importance for the optimization of process parameters and cultivation performance.

2. Experimental

2.1. Chemicals

Stock solutions of amino acid standards were prepared in 18 mΩ deionized water (Millipore, Bedford, MA, USA) at 10 mM concentration. Oregon green® 488 carboxylic acid, succinimidyl ester 6-isomer (Molecular Probes Inc., Eugene, OR, USA) was prepared in dimethylsulfoxide (DMSO, Sigma-Aldrich, Steinheim, Germany) as a 2 mM solution.

L-isoleucine (≥ 99.5%), L-serine (≥ 99%), L-leucine (≥ 99%), L-histidine (≥ 99.5%), L-threonine (≥ 99%), L-tryptophan (≥ 99%), L-lysine (≥ 98%), L-methionine (≥ 99%), L-arginine (≥ 99%), L-glutamic acid (≥ 99%), L-cysteine (≥ 99.5%), L-asparagine (≥ 99%), L-aspartic acid (≥ 99%), L-proline (≥ 99%), and L-glutamine (≥ 99%) were purchased from Fluka (Buchs, Switzerland). L-tyrosine (≥ 99%), L-phenylalanine (≥ 99%), L-alanine (≥ 99%) and glycine (≥ 99.7%) were from Merck (Darmstadt, Germany). DL-valine (≥ 97%) was from Sigma-Aldrich.

Background electrolyte (BGE) solutions were prepared from sodium tetraborate decahydrate (≥ 99.5%), sodium dodecyl sulfate (SDS) (≥ 99%), 18-crown-6-ether (99%), β-cyclodextrin (≥ 97%), and CHAPSO (≥ 98%), which were purchased from Sigma-Aldrich. A 0.1 M sodium hydroxide solution for the capillary conditioning was from FF-Chemicals Ab (Haukipudas, Finland).

2.2. Instrumentation

All the measurements were made with a P/ACE MDQ capillary electrophoresis system equipped with an LIF detector (Beckmann Coulter Inc., Fullerton, CA, USA). The LIF detector had an argon-ion laser with 488 nm excitation and 520 nm emission wavelengths. Bare fused-silica capillaries (Teknolab, Trollasen, Norway) with inner diameter 50 μm, outer diameter 360 μm, and total length 60 cm (50 cm to the detector) were used. The capillaries were conditioned before use with 0.1 M NaOH, milli-Q purified water, and BGE for 10 min each. Voltage (+30 kV) was then applied for 5 min. Between analyses, capillaries were rinsed with 0.1 M NaOH, 18 mΩ deionized water and with BGE for 2, 1 and 2 min, respectively. Data was collected and processed with 32Karat software (Beckmann Coulter Inc., Fullerton, CA, USA).

2.3. Analysis conditions

BGE was prepared with 50 mM sodium tetraborate, 30 mM SDS and 20 mM 18-crown-6-ether in milli-Q purified water. The pH of the solution was 9.0. Before analysis, the BGE was degassed by ultrasound and filtered through a 0.45 μm Acrodisc GHP syringe filter (Pall Life Science, Ann Arbor, MI, USA).

Standards and samples were injected by using 0.5 psi pressure for 10 s, giving rise to an injection volume of 8 nL. Separation was carried out at +30 kV at constant capillary temperature +15 °C. Sample cartridge temperature was set at +15 °C. The analytes were detected with the LIF detector using an excitation wavelength of 488 nm and emission wavelength of 520 nm. Concentrations of sugars and alcohols were analyzed by a Waters Alliance 2690 HPLC system (Milford, MA, USA) with Waters 2487 dual wavelength UV (210 nm) detector and Waters 2414 differential refractometer with an injection volume of 10 μL. The columns were an ICsep ION-310 Fast Analysis Column (150 mm × 6.5 mm, Transgenomic, Inc., Omaha, NE, USA) connected to an ICsep ICE-ORH-801 Column (300 mm × 6.5 mm, Transgenomic). The eluent was 5 mM H₂SO₄ (Titrisol, Merck), flow rate 0.5 mL/min and analysis temperature +55 °C. The optical density of the sample was measured by a Shimadzu UV-1201 spectrometer (Kyoto, Japan) at wavelength 600 nm (=OD₆₀₀). OD₆₀₀ is a measure of cell density. The cell dry weight (CDW) was determined by filtering 20 mL of sample through a measured filter paper, washing it with distilled water and drying it in an oven (105 °C) for at least 16 h. After that the cells were weighed with the filtration paper and the CDW was calculated.

2.4. Cultivation conditions and sampling

To obtain a pre-culture, *Saccharomyces cerevisiae* strain VTT A-6035 (VTT, Finland) was propagated as a 2 L culture in a Biostat

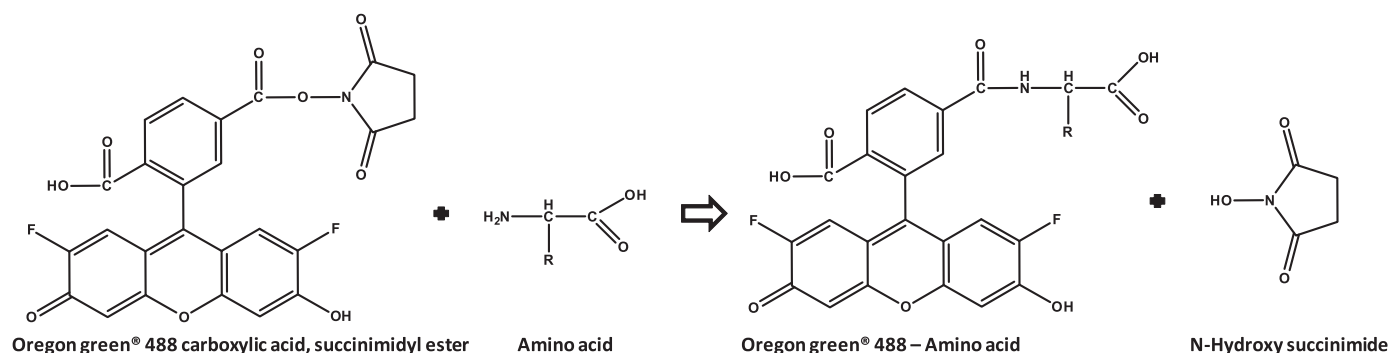


Fig. 1. Labeling reaction of Oregon green 488® succinimidyl ester (6-isomer) with an amino acid.

C-DCU bioreactor (B. Braun Biotech International, Germany) at temperature +24 °C, agitation 400 rpm, under aerobic conditions with 0.4 L/min air. The bioreactor was inoculated with cells grown for 16 h in YPD medium (10 g/L yeast extract, 20 g/L peptone and 20 g/L dextrose) at 28 °C and 200 rpm. Cultivation was performed in wort (Sinebrychoff, Finland) for 26 h. After this the yeast was allowed to sink to the bottom of the bioreactor without agitation for 22 h at 10 °C. Excess fermentation broth was removed and the cells were transferred to a 10 L Biostat C-DCU bioreactor (B. Braun Biotech International, Germany). The cultivation was maintained in wort at temperature +20 °C, agitation 200 rpm and nitrogen flow rate 0.4 L/min for 210 h. Samples were collected automatically from the bioreactor with a Jipster sampling carousel (Medicel, Espoo, Finland) every hour and stored at –30 °C. During

sampling the samples were filtered through 0.22 µm GV filtration paper (Millipore) with an automated A-SEP cross flow filtration module (Applikon, Delft, the Netherlands).

2.5. Sample preparation

The OG-SE derivatization procedure was performed by adding 10 µL of 2 mM OG-SE solution, 5 µL of sample and 35 µL of 30 mM tetraborate buffer (pH 9.0) to an Eppendorf tube. The reaction mixture was vortexed for 10 s and microcentrifuged for 20 s to bring possible droplets to the bottom of the tube before leaving it at room temperature for the reaction to proceed. After 15 min, the sample was diluted by adding 5 µL of labeled sample with 395 µL of 30 mM tetraborate buffer (pH 9.0) and analyzed with the optimized analysis method.

For calibration, six concentration levels of standard mixtures were prepared for the studied amino acids present in the cultivation samples. For proline and glycine the concentration varied between 62.5 nM and 1.25 µM, for arginine between 125 nM and 2.5 µM, for lysine and leucine between 250 nM and 5 µM, for histidine, glutamine, valine, phenylalanine, alanine, asparagine, glutamic acid and aspartic acid between 625 nM and 12.5 µM, and for threonine between 2.5 and 50 µM. Before analyses, cultivation samples were centrifuged at 10 000 rpm for 5 min and diluted 100-fold with milli-Q purified water.

3. Results and discussion

3.1. Fluorescence labeling chemistry

Succinimidyl esters react with nucleophiles, releasing *N*-hydroxysuccinimide (Fig. 1). Reaction with primary and secondary amines creates stable amide and imide linkages, respectively. In the case of succinimidyl esters, the hydrolysis and amine reactivity both increase with increasing pH [17]. For our purpose, it was important that the derivatization reaction should occur in mild

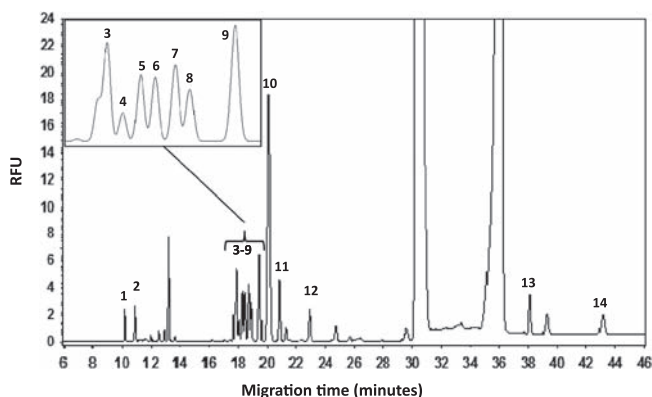


Fig. 2. Electrophoretic separation of the studied amino acids. BGE: 50 mM tetraborate, 30 mM SDS and 20 mM 18C6, pH 9.0. Other analysis conditions: voltage +30 kV, temperature 15 °C, capillary length 60 cm (50 cm to the detector), injection 0.5 psi 10 s and LIF excitation 488 nm and emission 520 nm. The current during analysis is ~62 µA. Peak assignments: (1) arginine, (2) lysine, (3) leucine/isoleucine, (4) tyramine, (5) histidine, (6) glutamine, (7) valine, (8) phenylalanine, (9) threonine/asparagine, (10) proline, (11) serine, (12) glycine, (13) glutamic acid, and (14) aspartic acid.

Table 1
Performance of the method under optimized conditions.

	Arginine	Lysine	Leucine/isoleucine	Tyramine	Histidine
RSD% of migration time (intraday) ^a	0.2	0.2	0.1	0.2	0.2
RSD% of migration time (interday) ^b	0.9	0.8	1.4	1.4	1.4
RSD% of peak area (intraday) ^a	4.4	3.8	2.9	9.9	3.5
RSD% of peak area (interday) ^b	6.2	7.0	5.7	18.9	6.2
Calibration correlation coefficient	0.9990	0.9997	0.9974	0.9946	0.9982
Concentration range (nM) ^c	0.25–12.5	0.125–12.5	0.875–87.5	0.625–62.5	0.625–62.5
Quantification limit (nM)	0.25	0.125	0.875	0.625	0.625
	Glutamine	Valine	Phenylalanine	Threonine/asparagine	Proline
RSD% of migration time (intraday) ^a	0.1	0.1	0.1	0.1	0.1
RSD% of migration time (interday) ^b	1.4	1.5	1.5	1.5	1.5
RSD% of peak area (intraday) ^a	3.8	4.2	3.7	3.8	3.7
RSD% of peak area (interday) ^b	5.7	4.4	7.3	4.4	5.7
Calibration correlation coefficient	0.9980	0.9977	0.9985	0.9983	0.9994
Concentration range (nM) ^c	0.625–62.5	0.625–62.5	0.625–62.5	2.5–250	0.625–62.5
Quantification limit (nM)	0.625	0.625	0.625	2.5	0.625
	Serine	Glycine	Glutamic acid	Aspartic acid	
RSD% of migration time (intraday) ^a	0.2	0.3	1.8	2.1	
RSD% of migration time (interday) ^b	1.6	1.6	2.2	2.5	
RSD% of peak area (intraday) ^a	3.8	3.7	5.9	8.8	
RSD% of peak area (interday) ^b	6.8	6.8	6.0	12.9	
Calibration correlation coefficient	0.9979	0.9960	0.9944	0.9995	
Concentration range (nM) ^c	0.375–37.5	0.0625–6.25	6.25–62.5	6.25–62.5	
Quantification limit (nM)	0.375	0.0625	6.25	6.25	

^a Percentage of relative standard deviation, *n* = 8.

^b Percentage of relative standard deviation, *n* = 4.

^c Concentration range for calibration correlation coefficient.

conditions and relatively fast. In this study, the reaction was tested at room temperature in tetraborate buffer concentrations between 10 and 150 mM, and pH values between 2 and 12. Derivatization reaction time was tested between 5 and 60 min. The optimal reaction occurred in 30 mM tetraborate buffer at pH 9.0, and the derivatization reached completion in approximately 15 min. The resulting reaction products were stable at room temperature for at least a week.

3.2. Method development

For the analysis of amino acids, an extensive study was made to determine the best BGE composition. The tested electrolyte chemicals were tetraborate [10,12–14,18], phosphate [15], tetraborate–phosphate, lithium carbonate [19], ammonium acetate [9] and ammonium formate [5–8] which are common electrolytes in

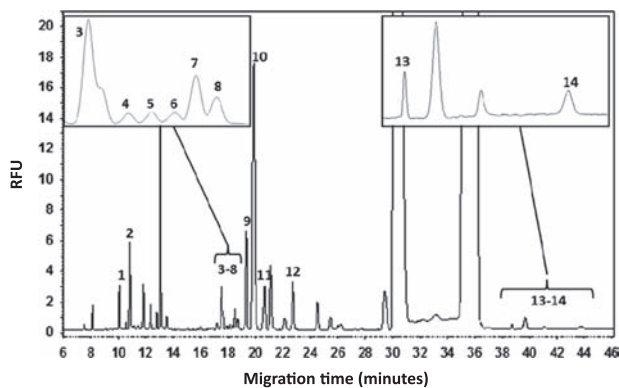


Fig. 3. Electrophoretic separation of a cultivation sample. Analysis conditions as in Fig. 2. Peak assignments: (1) arginine, (2) lysine, (3) leucine/isoleucine, (4) tyramine, (5) histidine, (6) glutamine, (7) valine, (8) phenylalanine, (9) threonine/asparagine, (10) proline, (11) serine, (12) glycine, (13) glutamic acid, and (14) aspartic acid.

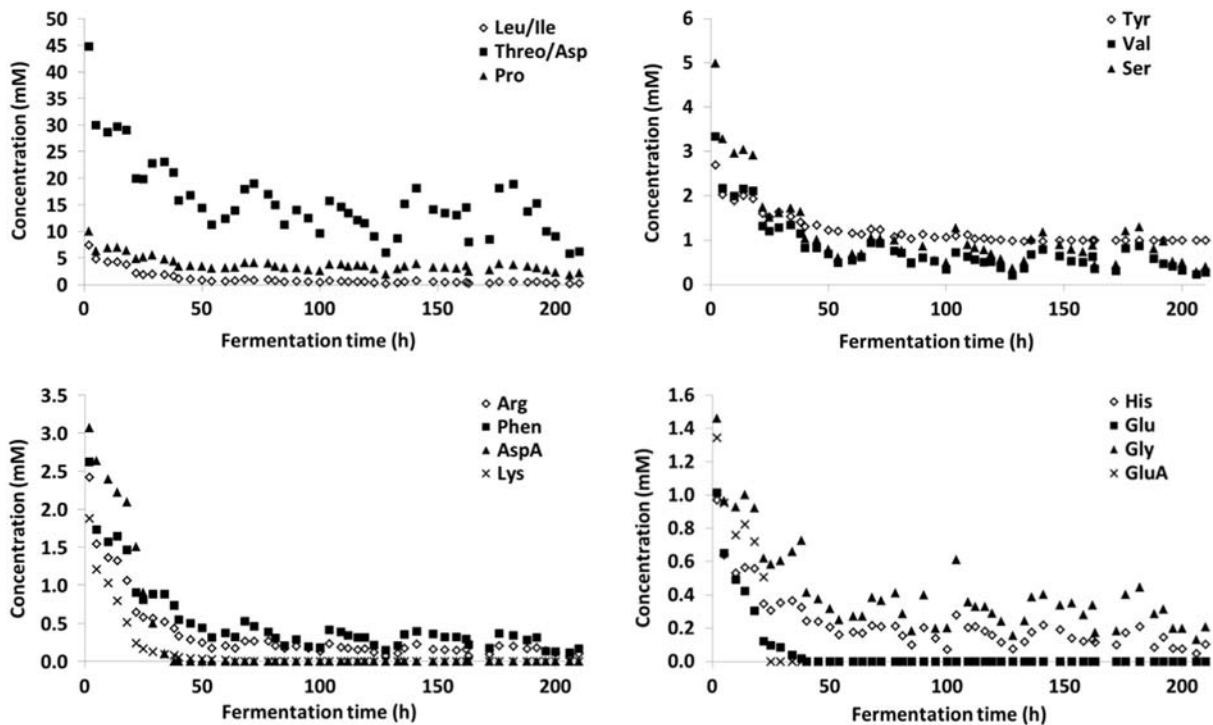


Fig. 4. The consumption of amino acids by *Saccharomyces cerevisiae* during beer fermentation.

amino acid analyses. The pH values of BGE solutions varied between 5 and 10. Tetraborate was found to be the most suitable electrolyte chemical for the method. Because the relative difference of molecular weights between labeled amino acids is small, the separation is not as straightforward as without labeling. To enhance the separation between amino acids, sodium dodecyl sulphate (SDS) [3,10,16,18], 3-[3-Cholamidopropyl]-dimethylammonio]-2-hydroxy-1-propanesulphonate (CHAPSO) [19], 18-crown-6-ether (18C6) [20] and β -cyclodextrin [10,13,21] were tested. It was noted that the addition of CHAPSO in 10 mM concentration gave the best separation efficiency of all the BGE solutions tested, but there were precipitation problems with the BGE that could not be resolved. The separation efficiency was not as good with SDS compared to CHAPSO, and therefore further modification was needed. β -Cyclodextrin and 18C6 were added to the BGE consisting of tetraborate and SDS. 18C6 is classified as a class I organic modifier in SDS-mediated MEKC and it is used to tune selectivity and resolution. Class I modifiers have an effect on the pseudostationary phase through direct interaction with the micelles [20]. The optimum pH of the optimized BGE was tested at values between 8 and 10.

Different analytical conditions were also examined. Voltage, analysis temperature, and capillary length were optimized in the ranges of 20–30 kV, 15–30 °C, and 60–80 cm (total length), respectively.

In the optimized method 50 mM sodium tetraborate decahydrate with 30 mM SDS and 20 mM 18-crown-6-ether, pH 9 was used for the analysis. Voltage was set to +30 kV, capillary temperature +15 °C and total capillary length was 60 cm. The sample was injected to the capillary with 0.5 psi pressure for 10 s. An electropherogram of standard solution containing amino acids of this study is presented in Fig. 2.

3.3. Method performance

Intraday relative standard deviations (RSD%, $n=8$) for migration times varied between 0.1% and 2.1% and those for peak areas

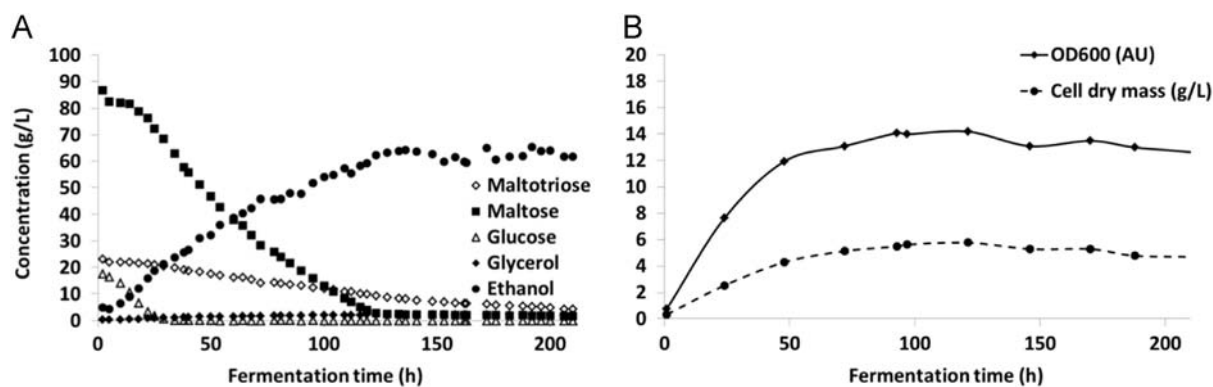


Fig. 5. (A) HPLC and (B) biomass results of the beer fermentation.

between 2.9% and 9.9%. Interday RSD% for migration times of the studied compounds were less than 2.5% and those for peak areas were between 4.4% and 18.9%. The concentrations of amino acids for the method performance studies were 25 nM for arginine, 12.5 nM for lysine and glycine, 75 nM for serine, 175 nM for leucine, 125 nM for tyramine, histidine, glutamine, valine, phenylalanine, proline, glutamic acid and aspartic acid, and 500 nM for threonine. The quantification limits ($S/N > 10$) for the amino acid standards were between 62.5 pM and 6.25 nM. Correlation coefficients for the calibration curves varied between 0.9944 and 0.9997 which indicate very good linearity in concentration ranges presented in Table 1 where the method performance parameters are summarized.

3.4. Analysis of cultivation samples

The optimized method was applied to the analysis of amino acids in beer fermentation broth samples. The purpose of this study was to monitor amino acid consumption of yeast during cultivation. An electropherogram of a cultivation sample is presented in Fig. 3.

Results of the cultivation are presented in Fig. 4, from which it may be noted that the most rapid amino acid consumption occurred during the first 30 h of cultivation when glucose was present in the cultivation broth as depicted in Fig. 5A. After glucose was consumed, the rate of amino acid consumption decreased significantly. Thus, the glucose and amino acids are used for growth of the yeast, which is also supported by the optical data and cell dry mass measurements presented in Fig. 5B. Aspartic acid, glutamine and glutamic acid were consumed most efficiently to a concentration below the quantification limit in less than 40 h which indicate them to be the most essential amino acids for the yeast growth. In addition, lysine, leucine and isoleucine were also utilized, although at a lower rate. The concentrations of proline and tyramine decreased only slightly. Other amino acids were utilized to some extent. The production of ethanol from other carbohydrate sources halted at the same time as maltose was consumed. The increase in some amino acid concentrations might have been caused by stress experienced by the yeast cells during the fermentation. When yeast cells are stressed they may release proteolytic enzymes, in particular protease A, which has the effect of liberating free amino acids from peptides or proteins.

4. Conclusions

An analysis method for the measurement of amino acids was developed for capillary electrophoresis. This method was used in

the monitoring of amino acid consumption of *Saccharomyces cerevisiae* during beer fermentation. The yeast utilized all amino acids to some extent, and was able to produce ethanol from maltose and maltotriose in addition to glucose. It was noted that the amino acid consumption halted at the same time as glucose was consumed from the fermentation media. This analysis method can be used for optimization of cultivation conditions and for the indication of cell stress during fermentation. The use of LIF as detection method enabled the analysis of amino acids even below the attomole level. The results correlated well with the results that can be found from the literature.

Acknowledgements

This work was carried out within the Finnish Centre of Excellence in White Biotechnology—Green Chemistry Research granted by the Academy of Finland (grant number 118573). Heidi Turkia was also supported by Graduate School for Chemical Sensors and Microanalytical Systems (CHEMSEM). Cultivations were performed within the project Biocontrol (project number 1050/31/07), which received funding from the National Technology Agency of Finland (TEKES) (grant number 1050/31/07). We also thank Toni Paasikallio for performing the cultivations, and Dr. Brian Gibson and Dr. John Londesborough for brewing discussions. We are very grateful to Sinebrychoff for providing the wort for the experiments.

References

- [1] S.H. da Cruz, E.M. Cilli, J.R. Ernandes, *J. Inst. Brew.* 108 (2002) 54.
- [2] B.R. Gibson, C.A. Boulton, W.G. Box, N.S. Graham, S.J. Lawrence, R.S.T. Linforth, K.A. Smart, *J. Am. Soc. Brew. Chem.* 67 (2009) 157.
- [3] N. Zhang, H. Wang, Z.-X. Zhang, Y.-H. Deng, H.-S. Zhang, *Talanta* 76 (2008) 791.
- [4] T. Soga, M. Imaizumi, *Electrophoresis* 22 (2001) 3418.
- [5] M. Wakayama, N. Aoki, H. Sasaki, R. Ohsugi, *Anal. Chem.* 82 (2010) 9967.
- [6] A.V.C. Simionato, E.P. Moraes, E. Carrilho, M.F.M. Tavares, E. Kenndler, *Electrophoresis* 29 (2008) 2051.
- [7] T. Atherton, R. Croxton, M. Baron, J. Gonzalez-Rodriguez, L. Gámiz-Gracia, A.M. García-Campaña, *J. Sep. Sci.* 35 (2012) 2994.
- [8] S. Sato, T. Soga, T. Nishioka, M. Tomita, *Plant J.* 40 (2004) 151.
- [9] P. Kubáň, P. Boček, *J. Chromatogr. A* 1234 (2012) 2.
- [10] M. Herrero, E. Ibáñez, S. Fanali, A. Cifuentes, *Electrophoresis* 28 (2007) 2701.
- [11] L. Qi, M. Liu, Z. Guo, M. Xie, C. Qiu, Y. Chen, *Electrophoresis* 28 (2007) 4150.
- [12] Z. Wagner, T. Tábi, T. Jakó, G. Zachar, A. Csillag, É. Szökő, *Anal. Bioanal. Chem.* 404 (2012) 2363.
- [13] M.P. Lorenzo, A. Navarrete, C. Balderas, A. Garcia, *J. Pharm. Biomed. Anal.* 73 (2013) 116.
- [14] H.-L. Chen, X.-J. Zhang, S.-D. Qi, H.X. Xu, J.J.Y. Sung, Z.-X. Bian, *J. Chromatogr. B* 877 (2009) 3248.
- [15] A.B. Martínez-Girón, C. García-Ruiz, A.L. Crego, M.L. Marina, *Electrophoresis* 30 (2009) 696.
- [16] L. Cruz, S.A. Shippy, J.V. Sweedler, *Capillary electrophoretic detectors based on light*, in: M.G. Khaledi (Ed.), *High Performance Capillary Electrophoresis*,

- Chemical Analysis Series, vol. 146, John Wiley & Sons, Inc., New York, USA, 1998.
- [17] G.T. Hermanson, *Bioconjugate Techniques*, second ed., Elsevier, San Diego, USA, 2008.
- [18] S. Anouti, O. Vandenabeele-Trambouze, D. Koval, H. Cottet, *Anal. Chem.* 80 (2008) 1730.
- [19] T.N. Chiesl, W.K. Chu, A.M. Stockton, X. Amashukeli, F. Grunthaner, R.A. Mathies, *Anal. Chem.* 81 (2009) 2537.
- [20] R.M. Burks, D.S. Hage, *Electrophoresis* 30 (2009) 657.
- [21] I. Fradi, A.-C. Servais, C. Lamalle, M. Kallel, M. Abidi, J. Crommen, M. Fillet, *J. Chromatogr. A* 1267 (2012) 121.



Metals in boat paint fragments from slipways, repair facilities and abandoned vessels: An evaluation using field portable XRF



Andrew Turner^{*}, Sean Comber, Aldous B. Rees, Dimitrios Gkiokas, Kevin Solman

School of Geography, Earth and Environmental Sciences, Plymouth University, Drake Circus, Plymouth PL4 8AA, UK

ARTICLE INFO

Article history:

Received 21 May 2014

Received in revised form

1 August 2014

Accepted 5 August 2014

Available online 13 August 2014

Keywords:

Boat paints

FP-XRF

ICP-MS

Metals

Contamination

Antifouling

ABSTRACT

Paint flaking off abandoned vessels or generated during boat repair is hazardous to human health and wildlife. In this study, a means of screening paint fragments using a field portable-X-ray fluorescence (FP-XRF) spectrometer is described. The technique is capable of delivering rapid, surficial measurements of Ba, Cu, Pb and Zn down to concentrations less than $150 \mu\text{g g}^{-1}$, and Sn and Cr to concentrations of a few hundred $\mu\text{g g}^{-1}$. Application of the technique to fragments collected from slipways, yards, hardstandings, abandoned boats and ships undergoing maintenance throughout the EU reveal highly variable concentrations of metals among samples from the same environment or from the same region of a given boat; in many cases, variability is also evident in different areas or on different surfaces of the same fragment. Of particular concern are elevated concentrations of substances that have been restricted or banned (e.g. Sn, an indicator of organotin, and up to concentrations of $40,000 \mu\text{g g}^{-1}$, and Pb up to concentrations of $200,000 \mu\text{g g}^{-1}$). Although FP-XRF can rapidly screen samples whose composition and origin are unknown and can assist in instantaneous decision making, a full risk assessment will rely on additional analyses of the precise species (including organo-forms) of the metals present.

© 2014 Elsevier B.V. All rights reserved.

1. Introduction

Because of the harsh and aggressive conditions that boats and ships are exposed to, many specialist paints are required with high corrosion protection [1]. Such paints include those that provide protection to steel hulls, boat-toppings and topsides, those that inhibit biofouling of the hull, and blast primers and tie-coats. More conventional primers, undercoats and enamels are also used internally and for the topsides of smaller boats.

The various functions and colours of boat paints are engendered by the addition of a variety of different chemical components with particular properties. Given that many of these components, like pigments, biocides, dryers and extenders, may be metal-based, boat paints pose a threat to human health and to wildlife if not managed properly. The greatest hazard arises when paint layers are removed during boat maintenance, repair or repainting because of the generation of fragments and dusts from sanding, blasting, scraping and chipping [2]. In commercial and military shipyards, paint waste is usually contained and disposed of safely [3,4]. The maintenance of smaller craft in boatyards or on slipways and hardstandings is unregulated, however, and despite

boaters being asked to comply with voluntary codes of practice, and in particular those related to the disposal of antifouling formulations [5,6], accumulations of paint waste are commonly observed at these facilities. Paint particles are readily transported to (or even swept in to) surrounding soils and sediments where metal contamination is often reported [7,8].

Another means by which paint particles may be introduced in to the environment is through the weathering and erosion of paint layers on abandoned boats and ships. Abandoned vessels of various ages and states of dereliction are commonplace on the shores of rivers, estuaries and coasts, but appear to be exempt from any kind of direct or enforceable environmental regulation [9]. With respect to the potential for local metal contamination, older boats are of particular concern because flaking paint may contain substances that have been restricted or banned since their original application.

Given the environmental risks and health hazards associated with high quantities of metals in boat paints there is a need for rapid and accurate chemical characterisation of flaking or discarded paint fragments. To date, the determination of metals has largely relied on analysis following sample decomposition in strong acid [8,10–12]. This approach is rather time consuming and decomposition is often incomplete because of the poor solubility of some paint matrices under acidic conditions. Field portable X-ray fluorescence (FP-XRF) is a non-destructive, multi-element technique

^{*} Corresponding author. Tel.: +44 1752 584570; fax: +44 1752 584710.

E-mail address: aturner@plymouth.ac.uk (A. Turner).

that has been applied to paints layers in situ in the domestic, commercial and industrial settings and for the study of cultural heritage objects [13–16]. Its application to boat paints, however, appears to be limited to a single, feasibility study in which it was proposed that ship hulls were screened for tin prior to discrimination and quantification of organotin compounds by GC–MS [17]. To this end, therefore, we describe how FP–XRF can be used to rapidly ascertain the surficial concentrations and distributions of a range of metals in fragments of spent boat paints collected from slipways, harbours, yards and abandoned boats. The XRF results are compared with those obtained using a more conventional approach (aqua regia digestion and analysis by inductively coupled plasma–mass spectrometry; ICP–MS) and are discussed in terms of the likely sources and types of historical and contemporary paints.

2. Materials and methods

2.1. Sampling and sample locations

Paint fragments were either collected directly from boatyards, shipyards, slipways and from boats abandoned on foreshores specifically for the purposes of this study, or were obtained from samples that had been archived (and stored in the dark in an airtight polyethylene box and in individual zip-lock bags) from previous research programmes [12,18]. Sampling locations are described below and details of the number and nature of samples analysed and their dates of collection and coding are given in Table 1.

Windermere is the largest freshwater lake in England (18 km in length). It is a popular venue for leisure craft and one of only six designated inland bathing areas in England. Boats are maintained and repaired on the slipways and hardstandings of a number of designated yards and marinas. The Gannel in north Cornwall, south west England, is a small (3.7 km in length), macrotidal, ria-type estuary that became silted due to mine waste. Abandoned moorings, derelict boats and the remains of old yards attest to the historical significance of boating and shipping in the estuary. The Taw-Torridge estuaries in north Devon form a twin, macrotidal, bar-built estuarine system (with a combined length of 22 km). As well as a number of marinas and small boatyards, the system supports a fish dock, large shipyard and two Royal Marine bases, and is also a Site of Special Scientific Interest (SSSI). The River Blackwater estuary (21 km in length) is a macrotidal, coastal plain complex in East Anglia, eastern England. It is home to several marinas and boatyards and is an internationally recognised conservation area for wading birds. Pin Mill is a hamlet on the southern shore of the River Orwell estuary (20 km in length), a mesotidal, coastal plain complex in East Anglia, and was once a busy landing point for ship-borne cargo and a centre for the repair of Thames sailing barges. The local mudflats are home to a variety of disused boats, including barges, in various states of decay. Malta is a small island in the central Mediterranean and an important

transshipment hub. Here, commercial boats and ships are maintained and repaired in regulated yards but small recreational vessels and fishing craft are often maintained along the shore, on roads and slipways and on makeshift hardstandings. Ampelakia is a small coastal town on the Greek island of Salamis. As in Malta, small boats are often maintained at unregulated sites along the coastal zone but the maintenance and repair of a variety of ships takes place in two regulated yards.

Samples of discarded paint from boat facilities, shipyards and slipways and samples of flaking paint from abandoned, derelict boats lying on the foreshore were collected using plastic tweezers and stored in individual zip-lock bags. Paint flakes from abandoned boats were collected from the hull region and, where accessible, from other parts of the vessel (e.g. deck, cabin, transom, winch, railings, nameboard). Where several, distinct layers of paint were exposed on the hull, multiple samples were retrieved accordingly. In the laboratory, samples were manually cleared of any significant, visible extraneous material (algae, shell debris, grit) and stored in clean zip-lock bags in a series of polyethylene boxes at room temperature and in the dark pending analysis.

2.2. FP–XRF analysis

In X-ray fluorescence, a sample (liquid, powder, solid or film) is irradiated with X-rays that cause electrons from an inner energy orbital (K or L level) to be ejected. Electrons from higher energy levels then fill the vacancies and excess energy is emitted in the form of X-ray photons whose wavelengths are characteristic of the elements present. Emissions are classified as K or L and as α or β depending on whether transitions from higher energy levels span one or two orbitals, respectively.

In the present study, paint fragments were analysed simultaneously for Ba, Cr, Cu, Pb, Sn and Zn by energy dispersive XRF spectrometry using a battery-powered Thermo Scientific Niton FP- (hand-held-) XRF analyser (model XL3t 950 He GOLDD+). The instrument is fitted with an X-ray tube with Ag anode target excitation source, operating at voltages up to 50 kV and at beam currents up to 200 μ A, and a geometrically optimised large area drift detector. A CCD camera stores sample images and data are transferred via USB, Bluetooth or an RS-232 serial communicator using Thermo Scientific Niton data transfer (NDT) PC software. In the present study, the instrument was placed in a bench top accessory stand for operation in the laboratory. Individual paint fragments were carefully placed in the centre of a 6 μ m polypropylene film slide using tweezers, and the slide was then placed over a 3 mm small-spot collimator above the detector. Overall measurement time was between 120 and 150 seconds and spectra up to 40 keV were quantified using a factory-installed algorithm (fundamental parameters calibration) for “plastics” mode, yielding elemental concentrations in parts per million (μ g g⁻¹) with an error of 2 σ or 95% confidence. Spectra were also inspected visually in order to ascertain the significance of any interferences arising from energy peak overlaps.

Table 1
Location and origin of the paint fragments collected for the study.

Location	Date	Origin	Sample code (no. samples)	No. XRF analyses
Lake Windermere	4/08	Boatyard slipways to lake	W1–W12 (12)	28
Gannel estuary	6/12	Abandoned boats on sandy foreshore	G1–G18 (18)	18
		Public slipway to foreshore	G19–G35 (16)	16
Taw-Torridge estuary	6/12	Abandoned boats on sandy foreshore	T1–T13 (13)	13
Blackwater	2/13	Abandoned boats on intertidal mudflats	B1–B13 (13)	37
Pin Mill, Orwell	2/13	Abandoned boats on intertidal mudflats	O1–O5 (5)	16
Malta	4/09	Boatyards and slipways	M1–M11 (11)	19
Ampelakia	12/12	Shipyards	A1–A11 (11)	46

By default, the centre of what appeared to be the outer (upper) face of each paint fragment was analysed. Additionally, where the face of a fragment was variable in appearance and sufficiently large, the spatial distribution of metals was mapped, and where two or more distinct layers were evident, both the outer and inner faces were analysed. For an evaluation of precision, selected fragments were analysed, fixed in position with respect to the collimator, five times.

The instrument detection limits, supplied by the manufacturer and in $\mu\text{g g}^{-1}$ for a SiO_2 matrix analysed using the optimum (“mining”) mode and for a period of 60 s, are as follows: Ba=50; Cr=25; Cu=12; Pb=4; Sn=16; Zn=6. Triplicate measurements of a reference material that was certified for concentrations of Cr and Pb (Niton PN 180-554, polyethylene impregnated with metals; Cr=995 $\mu\text{g g}^{-1}$; Pb=1002 $\mu\text{g g}^{-1}$) returned mean ($\pm 1\sigma$) concentrations of 1022 (± 51) $\mu\text{g g}^{-1}$ and 922 (± 3.3) $\mu\text{g g}^{-1}$, respectively. [Note that there is currently just one series of XRF paint standards that is certified on a mass basis (NIST 2569), and that certified values are restricted to relatively low concentrations (up to 300 $\mu\text{g g}^{-1}$) of Pb [19]].

2.3. Digestion and ICP analysis

For comparative purposes, the total concentrations of metals in selected paint fragments (from the Blackwater and Orwell estuaries and from a shipyard in Ampelakia) were also measured by inductively coupled plasma–mass spectrometry (ICP–MS) after acid digestion. Thus, whole fragments of up to 0.1 g were accurately weighed into individual 25 mL Pyrex beakers to which 5 mL of aqua regia (3:1 HCl:HNO₃; both Fisher Scientific TraceMetal grade) were added. The contents of each beaker were gently boiled under watch glasses for about an hour before being allowed to cool for 2 h. Digests were then transferred to individual 100 mL volumetric flasks and diluted to mark with Millipore Milli-Q water ($> 18 \text{ M}\Omega \text{ cm}$). Procedural controls were performed in triplicate likewise but in the absence of paint fragments.

Digests and, where necessary, dilutions thereof, were analysed for ¹³⁶Ba, ⁵²Cr, ⁶⁵Cu, ²⁰⁸Pb, ¹¹⁸Sn, ⁶⁶Zn and a range of other metals by collision cell-inductively coupled plasma–mass spectrometry (ICP–MS) using a Thermo X-series II (ThermoElemental, Winsford UK) with a concentric glass nebuliser and conical spray chamber. The instrument was calibrated externally using five mixed, matrix-matched standards in the range 10 to 200 $\mu\text{g L}^{-1}$ for each metal, and three matrix-matched blanks, and internally by the addition of 50 $\mu\text{g L}^{-1}$ of ¹¹⁵In and ¹⁹³Ir to all standards, samples, controls and blanks. RF power was set at 1400 W and coolant, auxiliary, nebuliser and collision cell gas flows rates were 13 L Ar min⁻¹, 0.70 L Ar min⁻¹, 0.75 L Ar min⁻¹ and 3.5 mL 7% H₂ in He min⁻¹, respectively. Data were acquired over a dwell period of 10 ms, with 50 sweeps per reading and three replicates. Metal concentrations

in the digests were corrected for any contamination measured in the controls and then converted to a dry wt/wt basis.

3. Results and discussion

3.1. Analytical figures of merit for the FP-XRF and potential spectral interferences

In total, 99 paint fragments were analysed by FP-XRF in the present study and, including replicate or multiple measurements of the same sample, about 200 analyses were performed. Analytical precision, based on measures of 95% confidence or 2σ , was generally better than 15% for all metals, but often declined towards about 30% as concentrations approached the lowest values that were detectable. An alternative measure of precision was derived from multiple analyses of the same paint fragments whose positions were fixed relative to the collimator. Results revealed relative standard deviations (1σ relative to the mean) of 15% for Ba and less than 10% for Cr, Cu, Pb, Sn and Zn for a fragment sampled from an the hull of an abandoned boat on the Gannel estuary (G8) and less than 10% for Cu, Pb, Sn and Zn in a fragment collected from a slipway in Lake Windermere (W10; Ba and Cr were not detected in this sample).

Although analysis of a reference material returned concentrations of Cr and Pb that were within 8% of certified values, it is important to assess the significance of any spectral interferences arising from a more heterogeneous, multi-element paint matrix and, therefore, limitations on the data delivered by the FP-XRF. (Note that while elements are associated with distinct fluorescence lines, the detector has resolution limitations and energy peaks have typical widths of 0.2 to 0.3 keV; [20].) To this end, we examined individual spectra arising from the analysis of 30 spent paint fragments where three or more metals were detectable. Spectra for two contrasting samples (a slipway sample from Windermere, W5, and a hull fragment from a boat abandoned on the Gannel, G7) are shown in Fig. 1 to exemplify the principal fluorescence peaks of the metals of interest and some of the interferences. Thus, where Cu was detected there was always a distinct, interference-free peak at 8.05 keV (corresponding to the Cu-K_α fluorescence line) but a secondary peak at 8.90 keV (Cu-K_β) was often present on the shoulder of a Zn peak at 8.64 keV (Zn-K_α). When Zn was detected, distinct peaks were present at 8.64 keV and 9.57 keV (Zn-K_β) while for Ba there was a distinct peak at 32.19 keV (Ba-K_α) but a secondary peak at 4.47 keV (Ba-L_α) overlapped with Ti-K_α at 4.51 keV. Regarding Pb, a distinct peak occurred at 12.61 keV (Pb-L_β) when the metal was detected, with a smaller secondary L peak at 14.76 keV (Pb-L_γ); a peak also occurred at 10.55 keV (L_α) and, although it exhibited some overlap with As-K_α at 10.54 keV, there was no evidence for the presence of

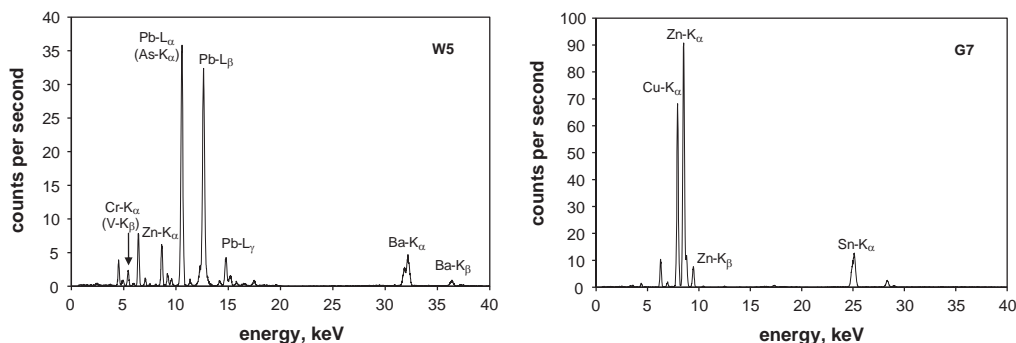


Fig. 1. XRF spectra for samples W5 and G7, illustrating the principal peaks of interest and, in parentheses, some of the potentially interfering peaks.

significant quantities of the metalloid in our samples from analysis of other As lines. Chromium exhibited a peak at 5.42 keV (Cr- K_{α}) that was close to V- K_{β} at 5.43 keV while a second peak at 5.95 keV (Cr- K_{β}) displayed some overlap with Mn- K_{α} at 5.90 keV. The Sn line at 3.65 keV (Sn- L_{α}) was generally obscured by a Ca peak at 3.69 keV (Ca- K_{α}) but a smaller, distinct peak at 25 keV (Sn- K_{α}) was observed when sufficient quantities of the metal were present. Subsequent analysis of paint fragment digests by ICP (see below) confirmed that Ca, Mn and Ti were present in many samples at concentrations in excess of 1000 $\mu\text{g g}^{-1}$, but that As and V were either undetectable ($< 1 \mu\text{g g}^{-1}$) or below concentrations of 10 $\mu\text{g g}^{-1}$.

In most cases, the factory-installed fundamental parameters calibration is able to confirm positive detection of an element from a single, distinct fluorescence peak, with or without corrections for other, less clear peaks. With respect to fragments of boat paints, we conclude that spectral interferences are unlikely to have a significant impact on the concentrations of Ba, Cu, Pb and Zn, but that false positives may be returned for Cr if V is present in appreciable quantities, and Sn when a secondary, higher energy peak is absent and Ca is present.

Table 2 shows the overall range of detectable concentrations encountered in the paint fragments and arising from all FP-XRF analyses. This represents an approximate working range for each metal that spans at least three orders of magnitude, although concentrations of Cr and Sn towards the lower end may be subject to some uncertainty as discussed above. Since all metals were undetectable in a number of cases, the lower limits reported in Table 2, with the exception of Cr and Sn, may be regarded as approximate indicators of the working detection

limits under the analytical conditions employed and for the matrix under investigation.

3.2. Inter-fragment variation of metal concentrations and source apportionment

Fig. 2 shows the concentrations of Ba, Cr, Cu, Pb, Sn and Zn measured by FP-XRF at the centre of the outer face of each paint fragment ($n=99$); also annotated on each panel is a statistical summary of the results. Concentrations are highly variable, both overall and for a given sampling campaign. This is perhaps not surprising since paints used on boats serve a variety of functions (e.g. priming, decoration, anticorrosion, antifouling), are a multitude of colours, and are derived from a diversity of contemporary and historical manufacturers. In general, however, the distribution and concentrations of metals measured by FP-XRF are consistent with known uses of metals in boat paints and as discussed briefly below.

The highest concentrations of Cu (in excess of 500,000 $\mu\text{g g}^{-1}$ on a dry wt/wt basis in some cases) and Sn (up to concentrations of about 40,000 $\mu\text{g g}^{-1}$) were found on the lower hulls of boats or in fragments of paint retrieved from yards and slipways where hull maintenance had been taking place, reflecting the use of Cu(I)- and organotin-based biocides in contemporary and historical antifouling formulations. The more diverse distributions of Ba, Pb and Zn are consistent with the more general application or range of applications of these metals in modern and historical paints. Specifically, Ba is used as a filler and whitener as BaSO_4 , while Zn compounds are used as booster biocides (e.g. Zn pyrithione), stabilisers and absorbers of uv radiation; Zn-based compounds are also used in

Table 2

Minimum and maximum concentrations of metals determined by FP-XRF analysis of the paint fragments (193 analyses of 99 samples). Also shown is the number of cases in which elements were detected.

	Ba	Cr	Cu	Pb	Sn	Zn
Minimum, $\mu\text{g g}^{-1}$ (sample code)	135 (A8)	32 (B8)	137 (B8)	39 (A10)	37 (A1)	83 (A8)
Maximum, $\mu\text{g g}^{-1}$ (sample code)	66,600 (P1)	31,700 (W5)	619,000 (P1)	196,000 (M4)	40,300 (G8)	271,000 (P1)
Number detected	124	50	167	137	99	193

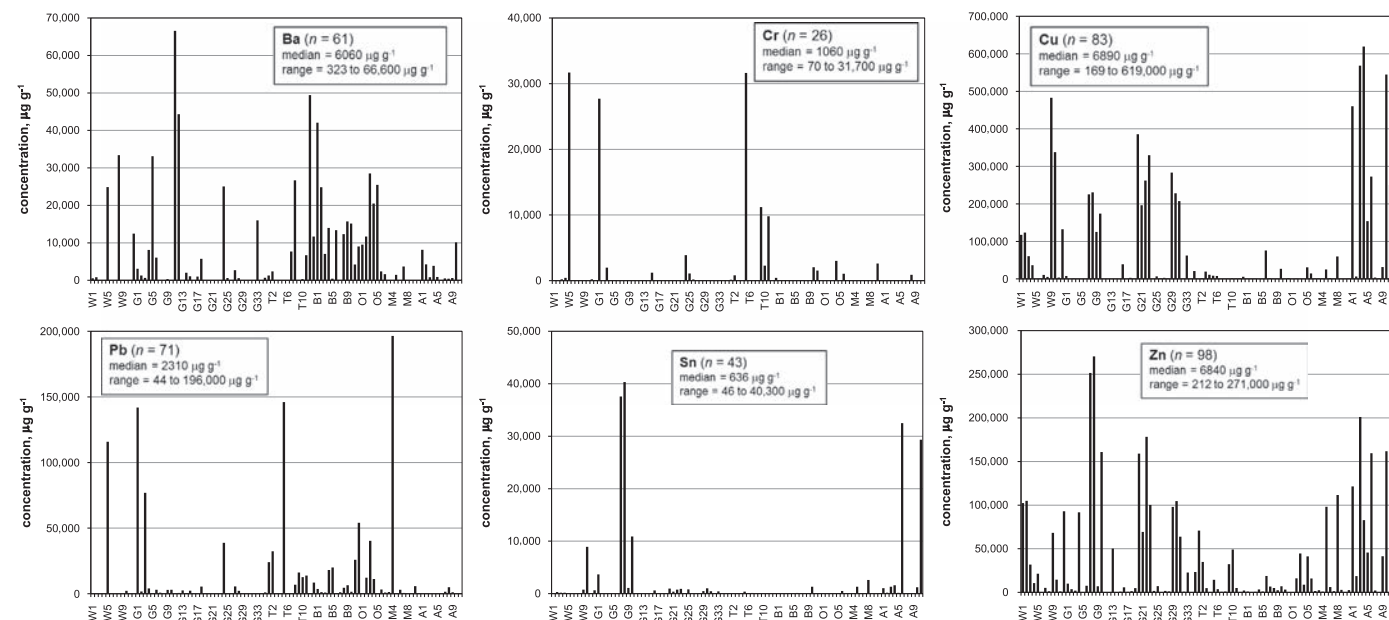


Fig. 2. “Default” concentrations of metals in the paint fragments, as measured in the centre of the upper face of each sample ($n=99$).

undercoats, blast primers and formulations that afford galvanic protection to steel hulls. Lead, although now restricted in use because of health concerns but measured at concentrations up to $200,000 \mu\text{g g}^{-1}$, has been used in primers (e.g. red lead: Pb_3O_4), in interior and exterior paints to enhance drying, provide corrosion resistance or pigment for colour or opacity, in tie-coats (e.g. PbSO_4) and in antifouling formulations as various organo-lead compounds [21]. Significantly, some products containing high concentrations of Pb still appear to be available to consumers (a primer scraped from the exterior of a recently discarded paint can from Ampelakia contained $350,000 \mu\text{g g}^{-1}$ of Pb). Chromium was detected in the lowest number of cases ($n=26$) but the highest concentrations (in excess of $20,000 \mu\text{g g}^{-1}$) were associated with yellow or red fragments containing high concentrations of Pb and in an atomic ratio with this metal consistent with the composition of the pigment, lead chromate (PbCrO_4).

3.3. Intra-fragment variability of metal concentrations

The results above have highlighted the range in absolute and relative concentrations of different metals in contemporary and historical boat paints. Also apparent from the results is that fragments arising from the same boat, or even the same region of a given boat, may be highly heterogeneous, especially if the vessel is abandoned and in a state of disrepair. This heterogeneity arises from different types of paint shedding from different parts of the boat or from multiple layers of paint that are variably exposed on the same section. The latter effect is exemplified in Fig. 3 from the FP-XRF analysis of fragments of differently coloured paints on the hull of an abandoned boat on the Taw-Torrige

estuary; thus, within less than a square metre, surficial concentrations of Cr, Cu and Pb range from not detected to $31,600 \mu\text{g g}^{-1}$, 449 to $19,500 \mu\text{g g}^{-1}$ and 166 to $146,000 \mu\text{g g}^{-1}$, respectively.

Because of the successive applications of paint, undertaken during a single repair or over a period of time, metals in the same fragment may also exhibit very different concentrations when the two faces are considered or even when the same face is mapped spatially. Spatial variability on an outer face may arise because the paint does not erode or weather homogeneously, thereby exposing different quantities of the layer beneath, while variations on an inner face may reflect inconsistencies in cleaning and preparation prior to the application of a new coat of paint. With respect to the hull, for example, typical methods of cleaning, such as hand sanding, high pressure water hosing or sand blasting, tend to remove variable quantities of old paint per unit area from the substrate.

In Table 3, results of analyses of different regions of the same fragments are exemplified for samples collected from the hulls of two steel ships undergoing repair (A1 and A6) and hull paint from an abandoned wooden houseboat and winch paint from an abandoned wooden barge (B4 and B12, respectively). Regional analysis of the same face reveals variability that, in many cases, is close to or marginally greater than our precision measurements; in other cases, however (e.g. Pb and Zn in the upper faces of B4 and B12), variability is considerably greater. The former observation suggests a rather uniform paint surface while the latter is more indicative of differential erosion and weathering of the surface. With the exception of Sn and Zn in fragment A6, and where metals were detected on both faces, there was a significant difference ($p < 0.05$ according to a series of two-sample *t*-tests) between mean concentrations of the upper and lower face. In some fragments (e.g. A6), mean metal concentrations in the two faces differed by less than 30%, suggesting the layering of different formulations of the same type of paint or the differential leaching of metals from the surface and back face of the same application. In other fragments (e.g. A1), mean concentrations of some metals differed by an order of magnitude, suggesting that layers are composed of different types of paint (for example, undercoats or primers versus top coats or antifoulants).

3.4. A comparison of results from FP-XRF and ICP-MS

Selected paint fragments sampled from abandoned boats in the Blackwater and Orwell estuaries and ships undergoing repair in Ampelakia were also analysed by ICP-MS after acid digestion. A comparison of the metal concentrations in the fragments derived by FP-XRF and ICP is shown in Fig. 4; note that single, total concentrations are obtained by ICP, while multiple concentrations are gained from spatial mapping by XRF (see above). Results of correlation analysis of each data set reveals relationships for Ba, Cu, Pb, Sn and Zn that are statistically significant ($p < 0.05$) and a relationship for Cr that is marginally significant ($p < 0.1$). For Cu, Pb and Zn there are approximately equal numbers of data points positioned either side of unit slope, while for Ba, Cr and Sn, more data points lie above unit slope than below.

Neither the strength of the relationship nor the closeness of the data to unit slope is necessarily indicative of the extent of agreement between the two analytical methods. Rather, the closest correlations (Pb and Zn) appear to reflect the relatively low heterogeneity within fragments that were analysed at multiple locations by XRF. Conversely, greater scatter in the relationships exhibited by the remaining metals appears to reflect, at least partly, greater dispersion of these elements within fragments that is ascertained by FP-XRF. In the few cases where multiple measurements returned by XRF were always greater than single measurements obtained by ICP (for example, Ba, Pb and Sn in one or more fragments from Ampelakia),

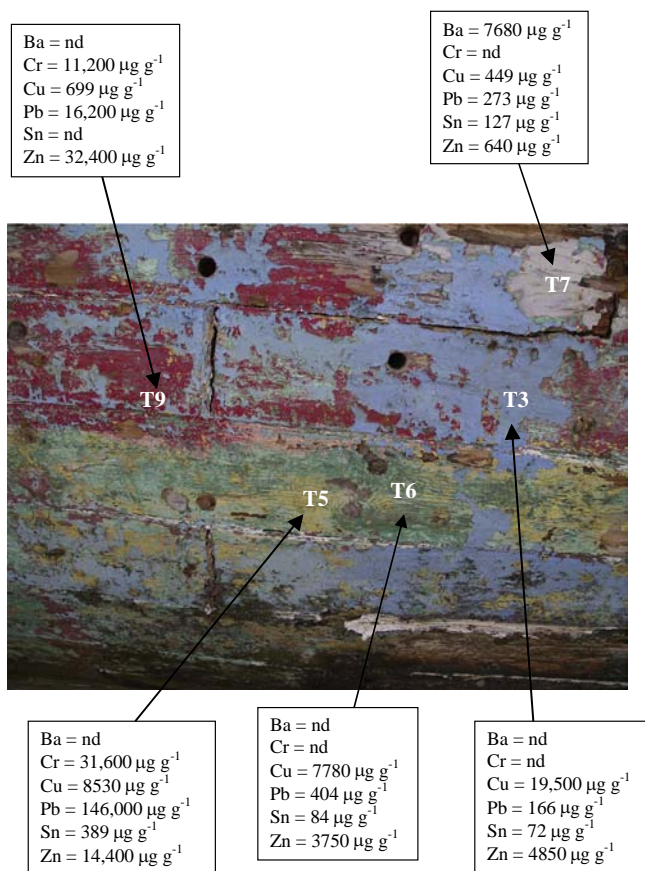


Fig. 3. Distribution of metals in paint fragments collected from a section of hull of an abandoned wooden boat lying on the sandy foreshore of the Taw-Torrige estuary. (For interpretation of the references to color in this figure legend, the reader is referred to the web version of this article.)

Table 3

Concentrations of metals in the upper and lower faces of the same paint fragments collected from abandoned boats or vessels undergoing repair (the mean and standard deviation arising from three spatial measurements of each face is given; nd=not detected in at least one of the measurements).

Sample	Ba	Cr	Cu	Pb	Sn	Zn
A1, hull paint (steel ferry undergoing repair)						
Upper face	8140 ± 1060	nd	460,000 ± 16,600	nd	1050 ± 146	121,000 ± 8070
Lower face	4790 ± 703	nd	5330 ± 1340	nd	222 ± 36	17,300 ± 1790
A6, hull paint (steel ship undergoing repair)						
Upper face	nd	nd	250,000 ± 25,000	nd	29,300 ± 3820	136,000 ± 24,400
Lower face	nd	nd	329,000 ± 15,300	nd	24,600 ± 1430	110,000 ± 16,500
B4, hull paint (abandoned wooden houseboat)						
Upper face	14,600 ± 818	nd	nd	14,100 ± 5650	nd	3640 ± 456
Lower face	5770 ± 491	nd	nd	4490 ± 244	nd	4940 ± 81
B12, winch paint (abandoned wooden barge)						
Upper face	9360 ± 452	nd	2170 ± 132	67,300 ± 18,700	nd	321 ± 138
Lower face	15,700 ± 4600	1940 ± 267	1560 ± 96	141,000 ± 23,200	nd	688 ± 50

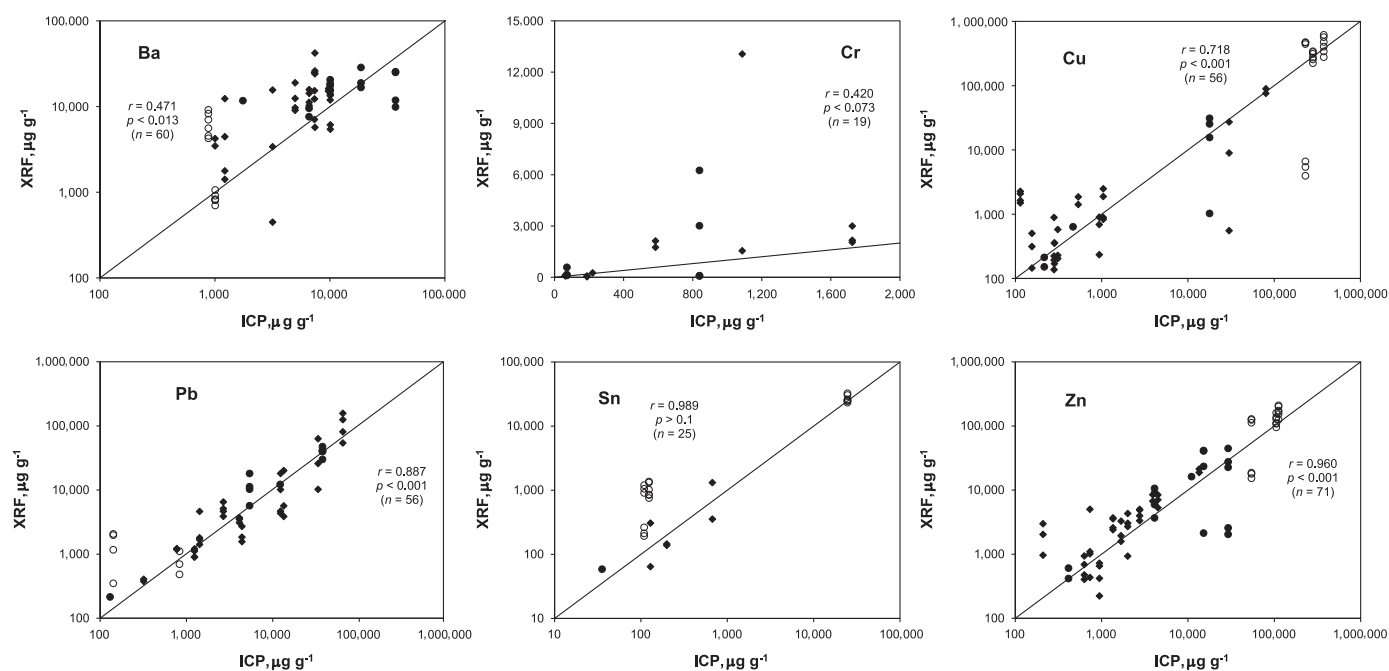


Fig. 4. A comparison of the concentrations of metals in paint fragments derived from FP-XRF analysis and ICP analysis following acid digestion (♦, Blackwater; ●, Orwell; ○, Ampelakia). The solid lines represent unit slope and statistical summaries are for correlation analyses of each dataset.

it is suspected that aqua regia digestion of the paint polymers may not have been complete. Visual inspection of the digests suggested that the degree of paint dissolution varied among the samples, and the results presented here suggest that partial digestion may affect metals differently depending on the nature of their binding or incorporation into the matrix. With respect to Sn, specifically, data above unit slope may reflect organotin bound to the polymer by an ester link which would be difficult to digest in acid, although interferences in the XRF analyses arising from the presence of Ca cannot be ruled out at concentrations below a few hundred $\mu\text{g g}^{-1}$.

3.5. Applications and advantages of FP-XRF

Fragments of boat paint represent a significant, heterogeneous source of contaminants in boatyards and on slipways where craft are maintained and repaired and in the vicinity of derelict vessels. Since finer particle of paint are highly mobile and many toxic metallic components contained therein are readily bioaccessible, paint waste is hazardous to human health and to wildlife [22,23]. Paint fragments also pose a threat to local sediment quality and, through their gradual dissolution, to both overlying and interstitial

waters [2]. ICP-MS affords a sensitive means of determining the bulk metallic content of individual paint fragments following acid digestion. However, a rapid means of inspecting and screening boat paint is critical for instantaneous decision-making and an initial evaluation of the risks posed by boats in a poor state of repair or by accumulations of waste whose sources are not clear. With developments in miniaturisation of X-ray excitation sources and improved detection systems, FP-XRF has become more commercially available and more affordable over the past decade and is an attractive proposition in this respect (the capital cost of FP-XRF is typically around five times lower than that of ICP-MS; 20). The technique requires minimal or no sample preparation and yet attains high sample throughputs (up to 30 per hour) and immediate, definitive identification of many metals without complex interpretation. Although we restricted our preliminary analyses to the laboratory, the instrument may be readily deployed in the field provided that irradiated and secondary X-rays are adequately shielded. Discrete paint fragments would be subject to the same process and limitations described herein, while for direct, in situ analyses of painted surfaces, potential spectral and matrix interferences arising from the underlying substrate may have to be considered.

FP-XRF has particular potential in rapidly identifying metals in boat paints that have been restricted or banned and/or that are classified as priority hazardous substances under the Water Framework Directive [24]. Thus, the technique is able to detect Pb at concentrations well below a 0.5% level recommended for human safety [25] and even towards a newer standard for lead in paints for consumer products of $90 \mu\text{g g}^{-1}$ [26]; concentrations of Sn in hull paints as low as a few hundred $\mu\text{g g}^{-1}$ are detectable provided that the analysis delivers a peak at the higher energy level (25 keV; Sn- K_{α}) (lower concentrations are detectable if significant quantities of Ca are not present). Following an initial evaluation using FP-XRF, further analyses involving sample preparatory work may be necessary for a full risk assessment. For Sn and, possibly Pb and Zn, discrimination and quantification of the precise organo-forms present by, for example, coupling gas chromatography and ICP-MS, would be desirable.

Acknowledgements

Dr Andy Fisher, UoP, is thanked for assistance with the ICP analysis. This study was funded by a Plymouth University Marine Institute grant.

References

- [1] R. Lambourne, The painting of ships, in: R. Lambourne, T.A. Strivens (Eds.), *Paint and Surface Coatings—Theory and Practice*, Woodhead Publishing, Cambridge, England, 1999, pp. 529–549.
- [2] A. Turner, *Mar. Pollut. Bull.* 60 (2010) 159–171.
- [3] K.V. Thomas, M. McHugh, M. Hilton, M. Waldoock, *Environ. Pollut.* 123 (2003) 153–161.
- [4] Y.C. Song, J.H. Woo, S.H. Park, I.S. Kim, *Mar. Pollut. Bull.* 51 (2005) 1048–1053.
- [5] British Marine Federation. *Environmental Code of Practice: Practical Advice for Marine Businesses, Sailing Clubs and Training Centres*. Egham, Surrey 2005.
- [6] DAFF, *Anti-fouling and In-water Cleaning Guidelines*, Department of Agriculture, Fisheries and Forestry 2012, Canberra, 26 pp.
- [7] N. Singh, A. Turner, *Mar. Pollut. Bull.* 58 (2009) 559–564.
- [8] A. Turner, *J. Soils Sediments* 13 (2013) 1052–1056.
- [9] C. Lord-Boring, I.J. Zelo, Z.J. Nixon, *Mar. Technol. Soc. J.* 38 (2004) 26–35.
- [10] L.E. Booher, *Am. Ind. Hyg. Assoc. J.* 49 (1988) 121–127.
- [11] H.C. Zedd, Y.P. Walker, J.E. Hernandez, R.J. Thomas, *Am. Ind. Hyg. Assoc. J.* 54 (1993) 392–396.
- [12] R. Parks, M. Donnier-Marechal, P.E. Frickers, A. Turner, J.W. Readman, *Mar. Pollut. Bull.* 60 (2010) 1226–1230.
- [13] K. Ashley, M. Hunter, L.H. Tait, J. Dozier, J.L. Seaman, P.F. Berry, P.F., *Field Anal. Chem. Technol.* 2 (1998) 39–50.
- [14] D.J. Kalnicky, R. Singhvi, *J. Hazard. Mater.* 83 (2001) 93–122.
- [15] X. Hou, Y. He, B.T. Jones, *Appl. Spectrosc. Rev.* 39 (2004) 1–25.
- [16] I. Sianoudis, E. Drakaki, A. Hein, *Eur. J. Phys.* 31 (2010) 419–431.
- [17] T. Senda, O. Miyata, T. Kihara, Y. Yamada, *Biofouling* 19 (2003) 231–237.
- [18] A. Turner A., N. Singh N, J.P. Richards, *Environ. Pollut.* 157 (2009) 1526–1532.
- [19] J.L. Molloy, J.R. Sieber, K.E. Murphy, S.E. Long, S.D. Leigh, *X-Ray Spectrom.* 41 (2012) 374–383.
- [20] P.T. Palmer, R. Jacobs, P.E. Baker, K. Ferguson, S. Webber, *J. Agric. Food Chem.* 57 (2009) 2605–2613.
- [21] I. Omae, *Appl. Organomet. Chem.* 17 (2003) 81–105.
- [22] I. Links, K.E. van der Jagt, Y. Christopher, M. Lurvink, J. Schinkel, E. Tielemans, J.J. van Hemmen, *Ann. Occup. Hyg.* 51 (2007) 207–218.
- [23] A. Turner, J. Hambling, *Water Air Soil Pollut.* 223 (2012) 2503–2509.
- [24] EU Directive, 2013/39/EU of the European Parliament and of the Council Amending Directives 2000/60/EC and 2008/105/EC as Regards Priority Substances in the Field of Water Policy 2013, 12.8.2013. 2011/0429 (COD).
- [25] J.M. Horner, *J. R. Soc. Health* 114 (1994) 245–247.
- [26] D. Cobb, D., *Study on the Effectiveness, Precision, and Reliability of X-ray Fluorescence Spectrometry and Other Alternative Methods for Measuring Lead in Paints*, Consumer Product Safety Commission, Gaithersburg MD (2009) 30.



Electrochemiluminescence immunosensor for highly sensitive detection of 8-hydroxy-2'-deoxyguanosine based on carbon quantum dot coated Au/SiO₂ core-shell nanoparticles



Ting-Ting Zhang, Hui-Min Zhao*, Xin-Fei Fan, Shuo Chen, Xie Quan

Key Laboratory of Industrial Ecology and Environmental Engineering, Ministry of Education, School of Environmental Science and Technology, Dalian University of Technology, Dalian 116024, China

ARTICLE INFO

Article history:

Received 30 May 2014

Received in revised form

1 August 2014

Accepted 6 August 2014

Available online 19 August 2014

Keywords:

Core-shell nanoparticle

8-hydroxy-2'-deoxyguanosine

Electrochemiluminescence immunosensor

Carbon quantum dot

ABSTRACT

An electrochemiluminescence (ECL) immunosensor using Pt electrode modified with carbon quantum dot (CQDs) coated Au/SiO₂ core-shell nanoparticles was proposed for sensitive detection of 8-hydroxy-2'-deoxyguanosine (8-OHdG) in this work. Rabbit anti-8-OHdG antibody was covalently bound to CQDs on the surface of Au/SiO₂ core-shell nanoparticles. Through signal amplification of Au/SiO₂ core-shell nanoparticles, 8-fold enhancement of the ECL signals was achieved. Under optimal conditions, a good linear range from 0.2 to 200 ng mL⁻¹ with a low detection limit of 0.085 ng mL⁻¹ (S/N=3) for 8-OHdG detection was obtained. Interfering substances tests showed that the corresponding ECL intensity (Δ ECL) of 8-OHdG is 8–18 times higher than that of guanine, uric acid (UA) and ascorbic acid, demonstrating its good selectivity for 8-OHdG detection. The ECL immunosensor exhibits long-term stability with a relative standard deviation (RSD) of 8.5% even after 16 cycles of continuous potential scans. The result of analytical detection of 8-OHdG in real samples was satisfactory. The proposed ECL immunosensor shows good performance with high sensitivity, specificity, repeatability, stability and provided a powerful tool for 8-OHdG monitoring in clinical samples.

© 2014 Elsevier B.V. All rights reserved.

1. Introduction

Reactive oxygen species, such as superoxide radical, singlet oxygen, hydroxyl radicals, superoxide anion and peroxy, are considered as harmful species due to their effect on oxidative DNA damage [1,2]. 8-hydroxy-2'-deoxyguanosine (8-OHdG, also known as 8-oxo-7, 8-dihydroguanine and 8-oxo-dGuo) (Scheme 1), one of the main products of oxidative DNA damage, can mispair with adenine, leading to G:C→T:A transverse mutation [3]. Many researches show that 8-OHdG has a much closer relationship with some disease, such as cancer, diabetes and neurological disorders [4–6]. Therefore, 8-OHdG is concerned as the most investigated biomarker of oxidative DNA damage [7].

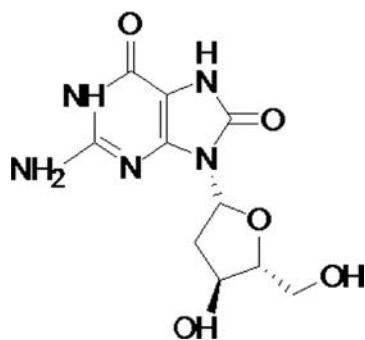
Traditional methods for 8-OHdG determination, such as high performance liquid chromatography with electrochemical detection [8], liquid chromatography combined with electrospray ionization tandem mass spectrometry multiple reaction monitoring [9], high performance liquid chromatography/positive electrospray ionization tandem mass spectrometry [10], enzyme-linked immunosorbent assay [11] and ³²P-labeling [12], are pretreatment

complex, specialized skills required and unavailable for in-situ detection. Electrochemistry sensors are widely applied in detecting various pollutants due to its rapid and high sensitivity [13,14]. It also been developed for 8-OHdG detection. For example, electrochemical method based on poly(3-methylthiophene) (P3MT) and polyethylenimine dispersed carbon nanotubes modified glassy carbon electrode (GCE) used as working electrode allowed the sensitive determination of 8-OHdG. But the results of electrochemistry methods above were likely to be affected by other biomolecules or matrix effects [15,16]. Fluorescent sensor is the another method for 8-OHdG detection which developed in recent years. Zhang et al. [2] reported a DNA aptamer fluorescent sensor for 8-OHdG determination using two triple-stranded DNAs as the scaffolds, which shows inherently insufficient binding constants between aptamers and 8-OHdG due to the small molecule of 8-OHdG.

Electrochemiluminescence (ECL) is a special kind of chemiluminescence (CL) with its light emission preceded by electrochemical reactions [17]. The ECL method presents widespread prospect due to its high sensitivity and good controllability compared to the conventional electrochemical and CL technique [18]. Its performance mainly depends on the favorable luminescent characterization of ECL materials. Recently, as a new group of ECL luminophores, quantum dots (QDs) attracted more and more

* Corresponding author.

E-mail address: zhaohuim@dlut.edu.cn (H.-M. Zhao).



Scheme 1. Chemical structure of 8-OHdG.

attention [19–21], since they not only exhibit excellent ECL activities but also have the merit of easy labeling. However, reports on QD-based ECL assay for 8-OHdG detection are relatively scarce since the inherently toxicity and low ECL intensity due to the poor stability of conventional QDs used in ECL at high electrochemical potentials [22]. Therefore, nontoxicity and reproducibility are urgently needed for the development of QD-based ECL sensors in 8-OHdG monitoring.

Carbon quantum dots (CQDs), a newly emerging ECL lumino-phores, have several significant advantages over the previously reported QDs, such as high stability, low toxicity, easy labeling and good biocompatibility [23–25]. To the best of our knowledge, the research report of CQD-based ECL 8-OHdG is hampered by the low ECL intensity of CQDs and the difficulty in reuse of CQDs in an aqueous system [26,27]. Thus, how to effectively amplify ECL signal and solve the reusability simultaneously is the key point in designing a CQDs-based ECL for 8-OHdG detection.

A structure of “core–shell” based on concentric multilayer semiconductor nanoparticles has recently attracted great attention in sensor field due to its large surface-to-volume ratio for modifying QDs. Liu et al. [28] reported a well-defined hybrid structures that comprised a gold core coated with a silica shell (Au/SiO₂), followed by the modification of CdSe-QDs (Au/SiO₂/CdSe-QD). The research on the photoluminescence intensities of CdSe-QD and the Au/SiO₂/CdSe-QD nanoparticles prove that the Au/SiO₂ core–shell nanoparticles exhibit excellent ability of signal amplification on photoluminescence. Moreover, due to its robust chemical stability, uniformity and biocompatibility of the SiO₂ shell coating, and ease of surface functionalization, we consider Au/SiO₂ core–shell can be used as suitable platform for CQDs immobilization to improve its ECL signal and reusability.

Here in, an advanced ECL immunosensor based on the hybrid of CQDs and Au/SiO₂ was fabricated for the supersensitive, rapid, and selective detection of 8-OHdG upon the amplification of CQD ECL signal by Au/SiO₂ core–shell. In the sensor Au/SiO₂ core–shell nanoparticles serve as the platform for CQDs immobilization, which can not only enhance the detection sensitivity but also achieve good recycle of the sensor through avoiding the loss of CQDs. Meanwhile the rabbit anti-8-OHdG antibody serves as the immunosorbent of antigen 8-OHdG. Compared to the previously reported methods, this approach provides a promising tool for the routine detection of 8-OHdG.

2. Experimental

2.1. Reagents and chemicals

8-OHdG (CAS: 88847-89-6), ethyl-3-(dimethyl aminopropyl) carbodiimide (EDC) and N-hydroxysuccinimide (NHS) were purchased from Sigma (America). Rabbit anti-8-OHdG (Ab) was obtained from

Beijing Biosynthesis Biotechnology Co., Ltd. (Beijing, China). HAuCl₄·3H₂O (99%), tetraethoxysilane (TEOS), poly(vinylpyrrolidone) (PVP) and trisodium citrate (99%) were bought from Xilong Chemical Co., Ltd. (Guangdong, China). NH₄OH was purchased from Tianjin Fuyu Fine Chemical Co., Ltd. (Tianjin, China). Uric acid (UA) was purchased from Tokyo Chemical Industry Co., Ltd. (Japan). Guanine and (3-Aminopropyl) trimethoxysilane (APS) were supplied by J&K Scientific Ltd. (Beijing, China). Bovine serum albumin (BSA) was purchased from Beijing Aoboxing Bio-tech Co., Ltd. (Beijing, China). Ascorbic acid, K₂S₂O₈ (potassium persulfate) and KCl were bought from Tianjin Bodi Chemical Co., Ltd. (Tianjin, China). Phosphate buffer solution (PBS, 0.1 mol L⁻¹, pH=7.4) was prepared by mixing the stock solutions of Na₂HPO₄ (0.1 mol L⁻¹) and NaH₂PO₄ (0.1 mol L⁻¹). Tris–EDTA (TE) buffer was used as dilution solvent of 8-OHdG. Ultrapure water purified by a Millipore water system (resistivity > 18.0 MΩ cm⁻¹, Laikie Instrument Co., Ltd., Shanghai, China) was used throughout the experiments.

2.2. Apparatus

The ECL emission was detected by a MPI-B multi-parameter chemiluminescence analysis test system (Xi'an Remax Analysis Instrument Co., Ltd., Xi'an, China) with a three electrode system consisting of a bare or modified Pt electrode (1 mm-diameter) as the working electrode, the standard calomel electrode (SCE, saturated KCl) and a Pt wire were used as the reference electrode and the auxiliary electrode, respectively. Electrochemical impedance spectroscopy (EIS) was performed on a CHI 660 electrochemical analyzer (Shanghai Chenhua Instrument, Shanghai, China). Unless noted, the photomultiplier tube (PMT) was 600 V. The morphology of the samples was observed by transmission electron microscopy (TEM) (FEI Tecnai G2 20, America) and scanning electron microscopy (SEM) (Hitachi S-4800) equipped with an X-ray energy dispersive spectroscopy (EDS) (Japan). Photoluminescence (PL) spectra were obtained on a Hitachi F-4500 fluorescence spectrometer (Japan). UV–visible spectra were carried out on a Jasco V-550 spectrometer (Japan). Sonications were carried out on a KQ5200B-type ultrasonic cleaner with the cleaning slot size 300*240*150 mm³ (Kun Shan Ultrasonic Instruments Co., Ltd., Jiangsu, China).

2.3. Synthesis of Au/SiO₂/CQDs core–shell nanoparticles

Preparation of CQDs: ascorbic acid was used as carbon source of CQDs. The mixed liquor of ascorbic acid and ethanol was heated at 180 °C for 4 h in a Teflon®-lined stainless steel autoclave and then cooled to room temperature. The dark brown solution was obtained, followed by extracting with dichloromethane. Then a yellow aqueous solution containing CQDs was obtained. The specific processes refer to previous literature [29].

Preparation of Au nanoparticles (AuNPs): The AuNPs core was synthesized through the seeded growth synthesis process according to literature [30]. Briefly, 2.2 mmol L⁻¹ sodium citrate solution (150 mL) was added into a 250 mL round-bottomed flask. The solution was heated reflux under vigorous stirring. When the solution start boiling, 1 mL of HAuCl₄ (25 mmol L⁻¹) was injected and kept boiling for 10 min. Then cooled the mixtures to 90 °C. 1 mL of sodium citrate (60 mmol L⁻¹) and 1 mL of HAuCl₄ solution (25 mmol L⁻¹) were sequentially injected, then kept reacting for 30 min at 90 °C. After repeating this process steps (sequential addition of 25 mmol L⁻¹) HAuCl₄ (1 mL) and 60 mmol L⁻¹ sodium citrate (1 mL) 5 times, a vinicolor aqueous solution containing AuNPs was finally obtained.

Preparation of Au/SiO₂ core–shell nanoparticles: The Au/SiO₂ core–shell nanoparticles were synthesized by Stöber processin accordance to literature [31]. An aqueous solution of poly

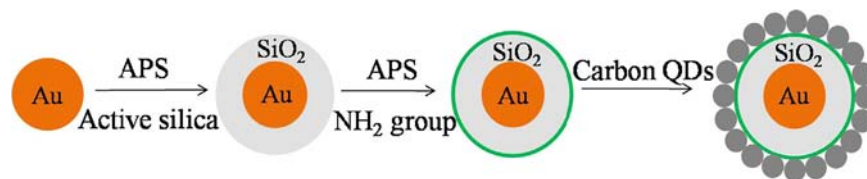
(vinylpyrrolidone) (PVP, 1 mL, 12.6 mg mL⁻¹) was added to the 180 mL aqueous solution of as-prepared AuNPs. Subsequently, the mixture stood for 48 h under magnetic stirring at room temperature, assuring the attachment of PVP molecules on the surfaces of AuNPs. The PVP attached AuNPs were then separated from solution by centrifuging at 12,000 rpm for 30 min and re-dispersed in 15 mL of ultrapure water. Thereafter, transfer 5.0 mL of PVP-modified AuNPs into a beaker containing a total volume of 15 mL mixture of ammonia (0.4 mL) and ethanol (14.6 mL) under magnetic stirring. The mixture composed of TEOS (0.1 mL) and ethanol (9.9 mL) were injected into the beaker within a period of 6 h. Then stirring reaction was kept for 12 h. The synthesized Au/SiO₂ core-shell nanoparticles were washed and centrifuged for two times by ethanol and ultrapure water in turn.

Formation of Au/SiO₂/CQDs core-shell nanoparticles: the synthesis process (shown in Scheme 2) was carried out according to previous literature [28]. The as-prepared Au/SiO₂ nanoparticles were dispersed in ethanol (20.0 mL). 2 μL of APS was added to the solution to modify the silica surface with amine groups. After that the mixture was magnetic stirred for 24 h at room temperature. The amine-functionalized Au/SiO₂ core-shell nanoparticles were collected by centrifugation and washed twice with ethanol. The as-prepared nanoparticles were re-dispersed in 20.0 mL of ethanol. Before immobilized on the amine-functionalized Au/SiO₂ nanoparticles, the hydroxyl groups on the surface of CQDs were covering into carboxyl by adding 0.005 g of NaOH and 0.01 g of

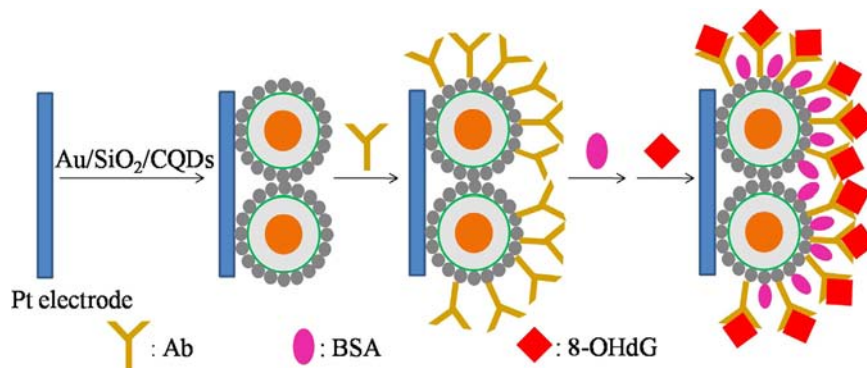
ClCH₂COOH (chloroacetic acid) into 2 mL of CQDs solution and bath sonicating for 3 h (frequency: 40 KHZ, power: 200 W) [32]. Then the mixture was added into ethanol solution of amine-functionalized Au/SiO₂ core-shell nanoparticles, and kept magnetic stirring for 12 h at room temperature. CQDs were self-assembled onto Au/SiO₂ nanoparticle surface due to the strong binding interaction between the -NH₂ and the -COOH of the CQDs. Finally, the hybrid Au/SiO₂/CQDs nanoparticles were collected by centrifugation and washed twice with ethanol and ultrapure water in turn.

2.4. Preparation of the ECL immunosensor

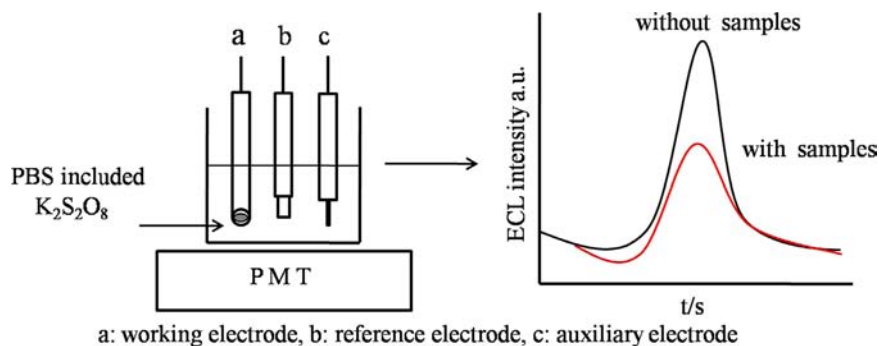
Prior to modification, the Pt electrode (1 mm-diameter) was mildly polished with 0.5 μm and 50 nm alumina slurry and then washed ultrasonically in ultrapure water and ethanol for a few minutes, respectively. 2 μL of the Au/SiO₂/CQDs nanoparticles suspension was dropped on the pretreated Pt electrode (noted as Pt/Au/SiO₂/CQDs) and then naturally dried at room temperature. The Pt/Au/SiO₂/CQDs electrode was carefully immersed in a solution containing 0.01 mol L⁻¹ EDC and 0.025 mol L⁻¹ NHS at least 12 h for activation. 2 μL of 10 μg mL⁻¹ Ab was dropped on the electrode surface and kept for at least 12 h at 4 °C (noted as Pt/Au/SiO₂/CQDs/Ab). Then, 2 μL of 1% BSA was dropped on the electrode surface and kept for 3 h to block the nonspecific sites (noted as Pt/Au/SiO₂/CQDs/Ab/BSA). Finally, the ECL immunosensor was



Scheme 2. Schematic illustration of the preparation procedure of Au/SiO₂/CQDs core-shell nanoparticles.



Scheme 3. Schematic illustration of the preparation processes of the ECL electrode modified by Au/SiO₂/CQDs core-shell nanoparticles and antibody.



Scheme 4. Schematic illustration of the detection procedures of the ECL immunosensor.

obtained (the whole procedure was presented in Scheme 3). Notably, after every step, the electrode was rinsed with 0.01 mol L^{-1} PBS (pH 7.4).

2.5. Immunoassay of 8-OHdG

The detection procedures of 8-OHdG are presented in Scheme 4. In summary, the modified electrode was immersed in the incubation solution containing various concentration of 8-OHdG for 10 h and this process was performed at 37°C isothermally in the incubator. After that the modified electrode was rinsed with 0.01 mol L^{-1} PBS (pH 7.4) thoroughly. The modified electrode above was scanned in 0.1 mol L^{-1} PBS (pH 7.4) containing 0.1 mol L^{-1} KCl and 0.05 mol L^{-1} $\text{K}_2\text{S}_2\text{O}_8$. The voltage of PMT was maintained at 600 V and the potential range was from -0.2 V to -1.0 V with a scan rate of 0.01 V s^{-1} .

3. Results and discussions

3.1. Characterization of CQDs

To evaluate the photoluminescence properties of CQDs the photoluminescence spectra and UV/vis absorption were obtained on the fluorescence spectrometer and the spectrometer (Fig. 1). The photoluminescence intensities of CQDs were obvious under the excitation with different wavelength (a: 300 nm–g: 420 nm). The photoluminescence spectra were shifted to longer wavelengths with the increase of excitation wavelength. An optical absorption was obtained in UV region. These results are almost consistent with the data reported in previous literature [33]. It indicates that the photoluminescence intensity of CQDs was satisfied for the ECL immunosensor.

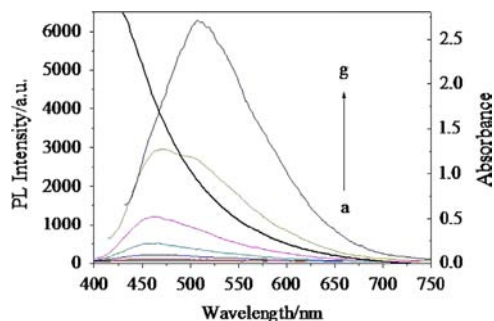


Fig. 1. Photoluminescence emission spectra (the left coordinates) and UV/vis absorption spectra (Abs) (the right coordinates) of the CQDs, excitation wavelength: (a) 300 nm, (b) 320 nm, (c) 340 nm, (d) 360 nm, (e) 380 nm, (f) 400 nm, and (g) 420 nm.

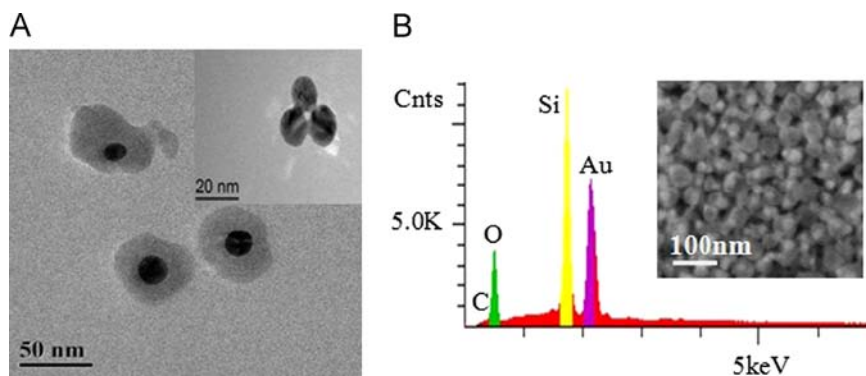


Fig. 2. (A) TEM images of Au/SiO₂/CQDs core-shell nanoparticles (inset: AuNPs). (B) EDS of Au/SiO₂/CQDs core-shell nanoparticles (inset: SEM images).

3.2. Characterization of Au/SiO₂/CQDs core-shell nanoparticles

TEM was used to investigate the morphologies of Au/SiO₂/CQDs core-shell nanoparticles. Fig. 2A shows TEM image of Au/SiO₂/CQDs core-shell nanoparticles. The diameters of AuNPs were found in the range of 20 nm to 30 nm, and the silica-shell thicknesses were between 25 nm and 30 nm. The AuNPs and the Au/SiO₂/CQDs core-shell nanoparticles were nearly spherical and apparently well-dispersed. To further verify the successful synthesis of Au/SiO₂/CQDs core-shell nanoparticles, EDS was used to investigate the elementary composition of Au/SiO₂/CQDs core-shell nanoparticles. It was clearly that Au, Si, O, and C were the elementary components of Au/SiO₂/CQDs core-shell nanoparticles (Fig. 2B), and the atomic ratios of them were 15.33%, 27.79%, 25.41% and 15.33%, respectively (table 1). The EDS results from different regions were similar, which confirmed that the composition of the obtained materials were uniform.

3.3. ECL behaviors of the ECL immunosensor

The ECL behaviors of the immunosensor were recorded in 0.1 mol L^{-1} PBS (pH 7.4) containing 0.1 mol L^{-1} KCl and 0.05 mol L^{-1} $\text{K}_2\text{S}_2\text{O}_8$, and ECL electrodes were scanned from -0.2 to -1.0 V (Fig. 3). The ECL signal of Pt electrode was very weak (curve a). After the modification with CQDs, the ECL intensity increased. It was noted that the ECL intensity of Au/SiO₂/CQDs nanoparticles modified electrode (curve f) was about 8 times as high as that of the CQDs modified electrode (curve b), which illustrates that the Au/SiO₂ nanoparticles have an excellent ability of signal amplification. A smaller ECL intensity (curve c) than that of in curve f was observed for Pt/Au/SiO₂/CQDs/Ab, indicating that Ab has been immobilized on the surface of electrode. After the electrode was encapsulated with BSA (curve d), the successive decline of ECL intensity was detected. Mainly depending on antibody and BSA as proteins were electron inert and they could partially hinder the electron transfer on the surface of working electrode [34]. The ECL intensity further decreased after the electrode was incubated with 8-OHdG sample (100 ng mL^{-1}) (curve e). It indicates that 8-OHdG was specifically bound to antibody, in the meantime the electron transfer on the surface of working electrode

Table 1

The atomic ratios of Au/SiO₂/CQDs core-shell nanoparticles.

Element	Intensity (c/s)	Wt%
C	24.46	15.333
O	75.52	25.461
Si	281.10	27.795
Au	213.85	31.412

was hindered by 8-OHdG. Therefore the electrode modified by Au/SiO₂/CQDs/Ab/BSA could be used for the detection of 8-OHdG.

3.4. Optimization parameters

Highly acidic or alkaline surroundings could reduce the biological activity of the protein [35] and further affect the ECL signal of ECL immunosensor. To achieve an optimal ECL signal, pH value of electrolyte solution 8-OHdG was investigated. As shown in Fig. 4A, a maximum value of the ECL intensity achieved when the pH value of electrolyte solution was adjusted to pH 7.4. Hence neutral surroundings at pH 7.4 was selected and used for test throughout this study. The incubation time was another effect factor of the ECL

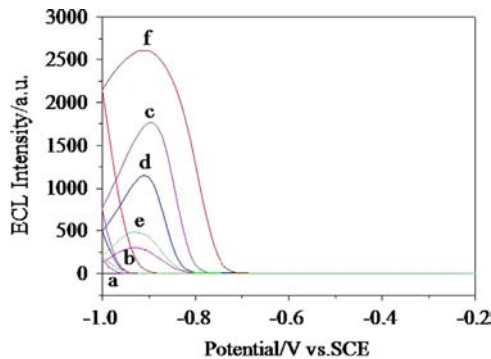


Fig. 3. The ECL signals of (a) bare Pt electrode, (b) Pt/CQDs, (c) Pt/Au/SiO₂/CQDs/Ab, (d) Pt/Au/SiO₂/CQDs/Ab/BSA, (e) Pt/Au/SiO₂/CQDs/Ab/BSA/8-OHdG, (f) Pt/Au/SiO₂/CQDs in 0.1 mol L⁻¹ PBS solution (pH 7.4) containing 0.1 mol L⁻¹ KCl and 0.05 mol L⁻¹ K₂S₂O₈. Scan rate, 0.01 V s⁻¹. The voltage of PMT was 600 V.

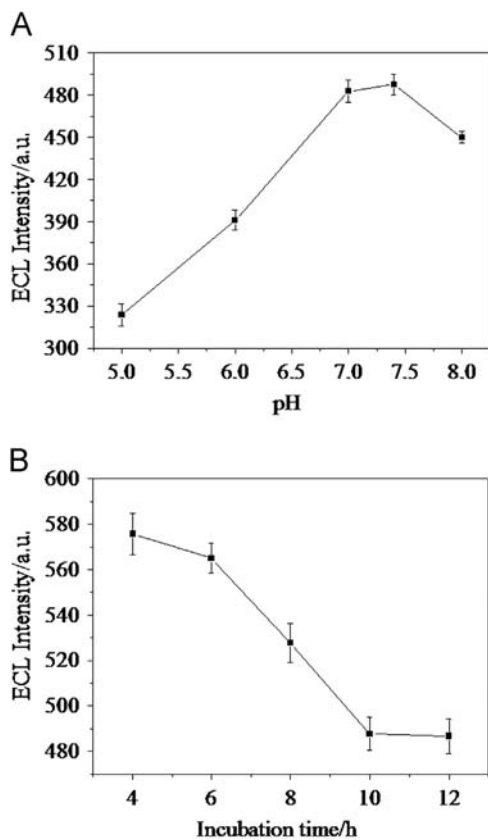


Fig. 4. (A) Effects of pH value of PBS solution and (B) incubation time of 8-OHdG on the response of ECL immunosensor for the detection of 100 ng mL⁻¹ 8-OHdG ($n=3$).

signal, thus different incubation times of 8-OHdG were studied in this part. Fig. 4B shows the effect of incubation time of 8-OHdG on ECL emission. The ECL emission was decreased with incubation time from 4 to 10 h, and a relatively stable value was obtained when the incubation time of 8-OHdG up to 10 h. Therefore, 10 h of the incubation time was chosen for subsequent experiments.

3.5. ECL detection of 8-OHdG

Under the optimal conditions, the linear response range and the detection limit of the 8-OHdG sensing system were measured as follows. The working electrode after incubating with a group of 8-OHdG concentrations (0, 0.2, 0.5, 1, 5, 10, 25, 50, 100, 150 and 200 ng mL⁻¹) were investigated to evaluate the sensitivity of the ECL immunosensor. With the increase of concentration, the ECL response was reduced (Fig. 5A). The ECL intensity reduced linearly with the concentration of 8-OHdG in the range of 0.2–200 ng mL⁻¹ (Fig. 5B). The regression equation is $\Delta\text{ECL} = 171.688 + 249.011x$, with a correlation coefficient (R^2) of 0.937. The limit of detection (LOD) was 0.085 ng mL⁻¹ ($S/N=3$). The low LOD might be attributed to the excellent ability of signal amplification with the Au/SiO₂ core-shell nanoparticles, and it is satisfactory to detect the concentration of 8-OHdG in some human biomatrices (the concentration of 8-OHdG in human urine, seminal plasma and breast milk were 2.3–9.3, 0.444–1.047 and 0.178–0.339 ng mL⁻¹, respectively, these data were mentioned in previous literature [36]). Although the LOD of the ECL immunosensor might not satisfy the ranges of all the biological samples, it has a relatively large linear range and a low detection limit compared to previous methods (Table 2).

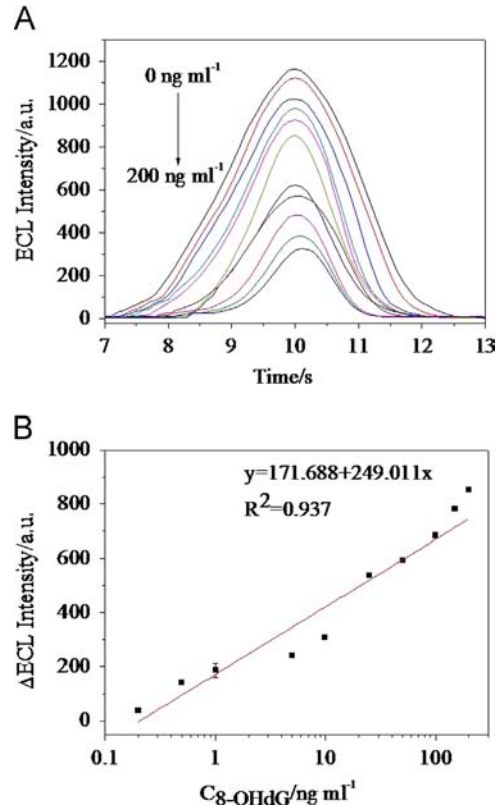


Fig. 5. (A) ECL responses of the proposed ECL immunosensor to different concentrations of 8-OHdG (0, 0.2, 0.5, 1, 5, 10, 25, 50, 100, 150 and 200 ng mL⁻¹) in 0.1 mol L⁻¹ PBS solution (pH 7.4) containing 0.1 mol L⁻¹ KCl and 0.05 mol L⁻¹ K₂S₂O₈. Scan rate, 0.01 V s⁻¹. The voltage of PMT was 600 V. (B) The calibration curve for 8-OHdG assay ($n=3$).

3.6. Specificity, reproducibility, stability and feasibility

For many 8-OHdG detection methods, false positive or errors caused by interferents which co-exist with 8-OHdG in human body or excretion inhibited the accurate detection of 8-OHdG. To examine the specificity of the fabricated immunosensor, interferences study was performed using guanine, UA, and ascorbic acid, which were co-exist with 8-OHdG. Here, the interfering substances mentioned above with three concentration levels (100 ng mL^{-1} , 1000 ng mL^{-1} and $10,000 \text{ ng mL}^{-1}$) were detected. By comparison the response signals of the interferents with 8-OHdG in 100 ng mL^{-1} , the ΔECL of the interferents is only 5.5–12.5% of that of 8-OHdG (Fig. 6). The result indicated that these interfering substances have little impact on the detection of 8-OHdG, even their concentrations were 100 times higher than that of 8-OHdG.

The reproducibility and operational stability were the major concerns for practical application of immunosensors. The reproducibility of the ECL immunosensor was investigated by prepared five electrodes for the detection 100 ng mL^{-1} of 8-OHdG. The relative standard deviation (RSD) of this measurement was 6.8%. The experimental results demonstrated acceptable reproducibility of the ECL immunosensor. Fig. 7 displays the ECL emission of the ECL immunosensor under 16 cycles of continuous potential scans between -0.2 and -1.0 V (vs SCE) in 0.1 mol L^{-1} PBS (pH7.4) at 0.01 V s^{-1} for the detection of 100 ng mL^{-1} of 8-OHdG. A stable ECL signal was observed with the RSD of 8.5%. The life time of the immunosensor was also investigated in 30-day period. The modified electrode was stored in the refrigerator at $4 \text{ }^\circ\text{C}$ and measured every 10 days. During the first 10 days, the response current decreased by 1.3% of its initial response. In the next 10 days and

Table 2
Comparison between the described ECL immune method and referenced methods for 8-OHdG detection.

Detection method	Linear range (ng mL^{-1})	Detection limit (ng mL^{-1})	References
DNA aptamer sensor	0.849–283	–	[2]
HPLC–ECD	–	0.34	[8]
Electrochemical	198.1–9905 9905–19,800	28.3	[13]
Electrochemical	141.5–8490	28.3	[14]
ECL immune method	0.2–200	0.085	This paper

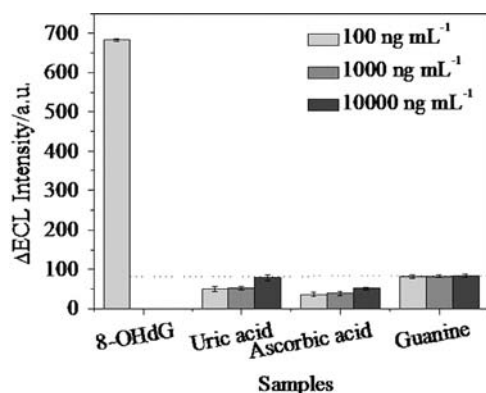


Fig. 6. ECL responses of the proposed ECL immunosensor of 8-OHdG, uric acid, ascorbic acid, and guanine at concentration of 100 ng mL^{-1} , respectively ($n=3$). All measurements were performed in 0.1 mol L^{-1} PBS solution (pH 7.4) containing 0.1 mol L^{-1} KCl and 0.05 mol L^{-1} $\text{K}_2\text{S}_2\text{O}_8$. Scan rate, 0.01 V s^{-1} . The voltage of PMT was 600 V .

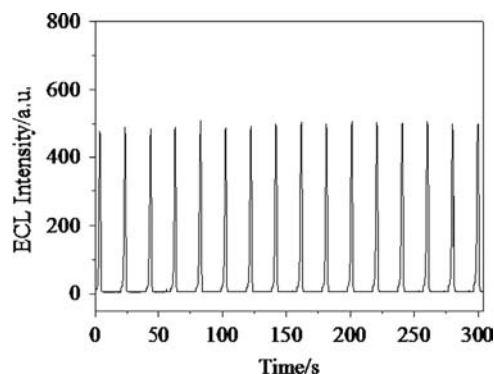


Fig. 7. The ECL intensities of sixteen consecutive cycles of the proposed ECL immunosensor incubated with 100 ng mL^{-1} 8-OHdG in 0.1 mol L^{-1} PBS solution (pH 7.4) containing 0.1 mol L^{-1} KCl and 0.05 mol L^{-1} $\text{K}_2\text{S}_2\text{O}_8$. Scan rate, 0.01 V s^{-1} . The voltage of PMT was 600 V .

Table 3
Determination of 8-OHdG in milk and recoveries of the samples with different concentrations of 8-OHdG.

Sample number	Added (ng mL^{-1})	Measured \pm SD (ng mL^{-1})	Recovery (%)	RSD (%), $n=3$
1	0.5	0.51 ± 0.02	102.0	5.2
2	1	1.11 ± 0.08	110.0	7.6
3	10	10.68 ± 0.82	107.0	7.7
4	50	51.60 ± 2.52	103.2	4.9
5	100	103.10 ± 5.99	103.1	5.8

the last 10 days it decreased by 3.7% and 6.5%, respectively, and maintained more than 93.5% of the initial response after storing for 30 days. It shows that the stability of the immunosensor was excellent and the life time of the immunosensor could be reach 30 days.

To monitor the feasibility of the developed ECL immunosensor in real samples analyses, the immunosensor was further applied in analyzing the concentrations of 8-OHdG in milk. Recovery experiments were carried out by the standard addition method. The results showed that the recovery ranges from 102.0% to 110.0%, and that the corresponding RSD ranges from 4.9% to 7.7% (Table 3). Therefore, the ECL immunosensor could be satisfactorily applied to the detection of 8-OHdG in real samples.

4. Conclusions

In this work, we developed an ECL immunosensor based on Au/SiO₂/CQDs core-shell nanoparticles for detection of 8-OHdG. ECL emission signal of CQDs increased greatly by using Au/SiO₂ core-shell nanoparticles as the substrate material. With the amplification of ECL signal, the ECL immunosensor displayed a highly sensitive ECL detection with specific immunoreactions. Under optimal conditions, the proposed immunosensor for 8-OHdG exhibited a low detection limit (0.085 ng mL^{-1}) and a wide linear range ($0.2\text{--}200 \text{ ng mL}^{-1}$). Moreover, this method was successfully applied to the detection of 8-OHdG in real samples. Given the excellent selectivity of the ECL immunosensor coupled with acceptable repeatability and stability, this ECL immunosensor could be promising for clinical detection of 8-OHdG. It is expected that to improve the application of CQDs in biological detection by synthesizing CQDs coated Au/SiO₂ core-shell nanoparticles.

Acknowledgments

This work was supported by the Research Project of Chinese Ministry of Education (No. 113017A) and National Natural Science Foundation of China (NSFC-JST 21261140334). Thanks Program for Changjiang Scholars and Innovative Research Team in University (IRT_13R05).

References

- [1] I.F.F. Benzie, *Eur. J. Nutr.* 39 (2000) 53–61.
- [2] Q. Zhang, Y.Q. Wang, X.Y. Meng, R. Dhar, H.D. Huang, *Anal. Chem.* 85 (2013) 201–207.
- [3] K.C. Cheng, D.S. Cahill, H. Kasai, S. Nishimura, L.A. Loebl, *J. Biol. Chem.* 267 (1992) 166–172.
- [4] L.L. Wu, C.C. Chiou, P.Y. Chang, J.T. Wu, *Clin. Chim. Acta* 339 (2004) 1–9.
- [5] M. Kakimoto, T. Inoguchi, T. Sonta, M. Imamura, T. Etoh, T. Hashimoto, H. Nawata, *Diabetes* 51 (2002) 1588–1595.
- [6] A. Kikuchi, A. Takeda, H. Onodera, T. Kimpara, K. Hisanaga, N. Sato, A. Nunomura, R.J. Castellani, G. Perry, M.A. Smith, Y. Itoyama, *Neurobiol. Disord.* 9 (2002) 244–248.
- [7] M. Erhola, S. Toyokuni, K. Okada, T. Tanaka, H. Hiai, H. Ochi, K. Uchida, T. Osawa, M.M. Nieminen, H. Alho, P.K. Lehtinen, *FEBS Lett.* 409 (1997) 287–291.
- [8] A. Gutiérrez, S. Osegueda, S.G. Granados, A. Alatorre, M.G. García, L.A. Godínez, *Electroanalysis* 20 (2008) 2294–2300.
- [9] M.I. Churchwell, F.A. Beland, D.R. Doerge, *Chem. Res. Toxicol.* 15 (2002) 1295–1301.
- [10] J.J. Hu, W.B. Zhang, H.M. Ma, Y.M. Cai, G.Y. Sheng, J.M. Fu, *J. Chromatogr. B* 878 (2010) 2765–2769.
- [11] B. Yin, R.M. Whyatt, F.P. Perera, M.C. Randall, T.B. Cooper, R.M. Santella, *Free Radic. Biol. Med.* 18 (1995) 1023–1032.
- [12] R.C. Gupta, J.M. Arif, *Chem. Res. Toxicol.* 14 (2001) 951–957.
- [13] S.K. Srivastava, V.K. Gupta, S. Jain, *Anal. Chem.* 68 (1996) 1272–1275.
- [14] R.N. Goyal, V.K. Gupta, S. Chatterjee, *Talanta* 76 (2008) 66–668.
- [15] T.H. Li, W.L. Jia, H.S. Wang, R.M. Liu, *Biosens. Bioelectron.* 22 (2007) 1245–1250.
- [16] A. Gutiérrez, S. Gutiérrez, G. García, L. Galicia, G.A. Rivasc, *Electroanalysis* 23 (2011) 1221–1228.
- [17] Y. Dong, H. Cui, Y. Xu, *Langmuir* 23 (2007) 523–529.
- [18] S. Xu, Y. Liu, T. Wang, J. Li, *Anal. Chem.* 82 (2010) 9566–9572.
- [19] L.J. Hua, J.J. Zhou, H.Y. Han, *Electrochim. Acta* 55 (2010) 1265–1271.
- [20] L. Li, X.F. Hu, Y.M. Sun, X.L. Zhang, W.R. Jin, *Electrochem. Commun.* 13 (2011) 1174–1177.
- [21] G.F. Jien, Y.B. Zhao, S.Y. Niu, *Biosens. Bioelectron.* 50 (2013) 368–372.
- [22] N. Gaponik, D.V. Talapin, A.L. Rogach, K. Hoppe, E.V. Shevchenko, A. Kornowski, A. Eychmüller, H. Weller, *J. Phys. Chem. B* 106 (2002) 7177–7185.
- [23] Y.P. Sun, B. Zhou, Y. Lin, W. Wang, K.A. Shiral Fernando, P. Pathaket, M.J. Mezziani, B.A. Harruff, X. Wang, H.F. Wang, P.G. Luo, H. Yang, M.E. Kose, B. Chen, L.M. Veca, S.Y. Xie, *J. Am. Chem. Soc.* 128 (2006) 7756–7757.
- [24] Q.L. Zhao, Z.L. Zhang, B.H. Huang, J. Peng, M. Zhang, D.W. Pang, *Chem. Commun.* 41 (2008) 5116–5118.
- [25] X.J. Mao, H.Z. Zheng, Y.J. Long, J. Du, J.Y. Hao, L.L. Wang, D.B. Zhou, *Spectrochim. Acta A Mol. Biomol. Spectrosc.* 75 (2010) 553–557.
- [26] H.T. Li, Z.H. Kang, Y. Liu, S.T. Lee, *J. Mater. Chem.* 22 (2012) 24230–24253.
- [27] Y.P. Sun, X. Wang, F.S. Lu, L. Cao, M.J. Mezziani, P.J.G. Luo, L.R. Gu, L.M. Veca, *J. Phys. Chem. C* 112 (2008) 18295–18298.
- [28] N.G. Liu, B.S. Prall, V.I. Klimov, *J. Am. Chem. Soc.* 128 (2006) 15362–15363.
- [29] B. Zhang, C.Y. Liu, Y. Liu, *Eur. J. Inorg. Chem.* 28 (2010) 4411–4414.
- [30] N.G. Bastús, J. Comenge, V. Puentes, *Langmuir* 27 (2011) 11098–11105.
- [31] Y.F. Huang, K.H. Ma, K.B. Kang, M. Zhao, Z.L. Zhang, Y.X. Liu, T. Wen, Q. Wang, W.Y. Qiu, D. Qiu, *Colloids Surf. A: Physicochem. Eng. Asp.* 421 (2013) 101–108.
- [32] K. Yang, S. Zhang, G. Zhang, X. Sun, S.T. Lee, Z. Liu, *Nano Lett.* 10 (2010) 3318–3323.
- [33] R.L. Liu, D.Q. Wu, S.H. Liu, K. Koynov, W. Knoll, Q. Li, *Angew. Chem. Int. Ed.* 48 (2009) 4598–4601.
- [34] Y.F. Cheng, R. Yuan, Y.Q. Chai, H. Niu, Y.L. Cao, H.J. Liu, L.J. Bai, Y.L. Yuan, *Anal. Chim. Acta* 745 (2012) 137–142.
- [35] R. Yuan, D.P. Tang, Y.Q. Chai, X. Zhong, Y. Liu, J.Y. Dai, *Langmuir* 20 (2004) 7240–7245.
- [36] P.M.W. Lam, V. Mistry, T.H. Marczylo, J.C. Konje, M.D. Evans, M.S. Cooke, *Free Radic. Biol. Med.* 52 (2012) 2057–2063.



An analytical method coupling accelerated solvent extraction and HPLC-fluorescence for the quantification of particle-bound PAHs in indoor air sampled with a 3-stages cascade impactor



Céline Liaud^a, Maurice Millet^a, Stéphane Le Calvé^{a,b,*}

^a Institut de Chimie pour les Procédés, l'Energie, l'Environnement et la Santé (ICPEES, UMR 7515 CNRS/Université de Strasbourg), 1 rue Blessig, 67084 Strasbourg Cedex, France

^b In'Air Solutions, 1 rue Blessig, 67000 Strasbourg, France

ARTICLE INFO

Article history:

Received 3 February 2014

Received in revised form

15 May 2014

Accepted 18 May 2014

Available online 4 June 2014

Keywords:

PAHs

Cascade impactor

Particles

Indoor air

ABSTRACT

Most of Polycyclic Aromatic Hydrocarbons (PAHs) are associated to airborne particles and their health impact depends on the particle size where they are bound. This work aims to develop a high sensitive analytical technique to quantify particulate PAHs sampled with a 3-stages cascade impactor in order to derive simultaneously their individual concentration in PM₁, PM_{2.5} and PM₁₀.

Three key steps of the method were evaluated separately in order to avoid any PAHs loss during the global sample preparation procedure: (1) the accelerated solvent extraction of PAHs from the filter; (2) the primary concentration of the extract until 1 mL by means of a rotary evaporator at 45 °C and 220 mbar and (3) the final concentration of the pre-concentrated extract to about 100–150 µL under a gentle nitrogen stream. Each recovery experiment was realized in triplicates. All these steps evaluated independently show that the overall PAHs loss, even for those with a low molecular weight, should not exceed more than a few percent. Extracts were then analyzed by using a HPLC coupled to fluorescence and Diode Array Detectors with the external standard method.

The resulting calibration curves containing between 9 and 12 points were plotted in the concentration range of 0.05–45 µg L⁻¹ for most of the 16 US-EPA priority PAHs and were fully linear ($R^2 > 0.999$). Limits Of Quantification were in the range 0.05–0.47 µg L⁻¹ corresponding to 0.75–7.05 pg m⁻³ for 20 m³ of pumped air.

Finally, taking into account the average PAHs concentrations previously reported in typical European indoor environments, and considering the use of a 3-stages cascade impactor to collect simultaneously PM > 10 µm, 2.5 µm < PM < 10 µm, 1 µm < PM < 2.5 µm and PM < 1 (and then to derive PM₁, PM_{2.5} and PM₁₀) for particle-bound PAHs quantification, the sampling duration was estimated to 20–40 h for a sampling flow fixed to 0.5 m³ h⁻¹.

© 2014 Elsevier B.V. All rights reserved.

1. Introduction

Polycyclic Aromatic Hydrocarbons (PAHs) are widespread environmental contaminants mostly formed during incomplete combustion or pyrolysis of organic material but they can also be of biogenic origin [1]. Their chemical structures contain 2 or more fused benzene rings arranged in linear, angular or in cluster structures. PAHs are ubiquitous in our environment and their emission sources are numerous: industrial processes; vehicle exhausts and domestic heating are among the major sources [2]. More than 100 of them are nowadays referenced but the American

* Corresponding author at: Institut de Chimie pour les Procédés, l'Energie, l'Environnement et la Santé (ICPEES, UMR 7515 CNRS/Université de Strasbourg), 1 rue Blessig, 67084 Strasbourg Cedex, France. Fax: +33 3 68 85 04 02.

E-mail address: slecalve@unistra.fr (S. Le Calvé).

Environmental Protection Agency (US-EPA) has listed 16 among the most hazardous. One of the most famous is the Benzo[a]Pyrene (B[a]P) due to its carcinogenic properties. Besides, the European ambient air legislation (directive no. 2004/107/CE) targets this PAH and recommends an annual maximum guideline value of 1 ng m⁻³. Because the PAHs structures are thermally stable, most of these compounds possess high boiling point and low vapor pressure favoring their association to particulate phase in the atmosphere. The lighter PAHs (MW ≤ 202 g mol⁻¹) are preferentially in the gas phase whereas the heavier ones (MW ≥ 202 g mol⁻¹) are associated to particles [3–5].

Since their atmospheric concentration is relatively low (in the range of pg m⁻³ to ng m⁻³), and especially in indoor air [6,7], the collection of airborne PAHs in vapor and particulate phases requires quite large volume of air to concentrate pollutants either on a sorbent material or on a filter. Pandey et al. reviewed sampling flow rate, for

high volume samplers, in the range 2–75 m³ h⁻¹ with sampling duration long enough to ensure a sufficient sampled volume of 150–900 m³ [8]. The most common sampling device is a high or low volume sampler composed of an adsorbent (XAD-2 or polyurethane foam) and a pre-filter for trapping the PAHs in the particulate phase by filtration of large air volume [9–11]. However, in the case mentioned above, the particles size is not limited. In fact, particles cause adverse respiratory health effects related to their ability to enter the lungs and potentially carrying numerous toxic compounds with them. Particle size, especially fine and ultrafine particles, is strongly related to the bad effects on human health. That is why it is of interest to focus on particle aerodynamic diameter and particle number concentrations [12,13]. The use of particulate matter (PM) sampling heads upstream the filter gives access to several cut off sizes and allow to sample particles with aerodynamic diameter (D_{ae}) usually below 10 μm, 2.5 μm or 1 μm [9,14–16]. Other sampling systems are inertial samplers and consist to remove particles from an air stream by impaction of the particles depending on their inertia [5,17]. Particles samples collected from cascade impactors give access to more data because this device separates particles depending on their D_{ae} . Thus, physical and chemical data related to the particle sizes can be simultaneously determined to assess health effects. If further details are desired, chemical analyses may be achieved on the filters obtained in each size range. Nevertheless, despite the power of cascade impactors, to our knowledge only a few studies were conducted in indoor air with this metrology tool to quantify particle-bound PAHs [5,17]. These latter were performed using a 11-stages or 3-stages cascade impactors with D_{ae} in the range 0.05–18 μm and 2.5–10 μm, respectively, which did not permit to easily compare the results on particles to those reported in the literature mentioning PM₁, PM_{2.5} and PM₁₀.

A third way to monitor particle-bound PAHs are photoelectric aerosol sensors (PAS) which are analyzers using ionization principle to detect PAHs in air [18–20]. However, PAS provides a measure of the total particle-bound PAHs concentration with no distinction between individual compounds.

Several studies performed in European Environments reported particle-bound PAHs concentrations values in the range of pg m⁻³ to ng m⁻³. Slezakova et al. [21] and Castro et al. [14] reported comparative values of PAHs concentrations bound to PM₁₀ and PM_{2.5} in a smoking and a non-smoking site in Porto (Portugal). Castro et al. found B[a]P average levels of 1.33 ng m⁻³ (0.45–2.18 ng m⁻³) in the smoking place and 0.573 ng m⁻³ (0.131–1.510 ng m⁻³) in the non-smoking apartments used as reference. The same tendency was observed in Spain by Pey et al. who studied differences in PAHs concentrations in PM₁₀ before and after a smoking ban in a cafeteria [22]. Fromme et al. in Germany, also studied differences in particle-bound PAHs concentration in street-side living-rooms and found median values of 0.65 ng m⁻³ for B[a]P in smoker's living while median value was 0.25 ng m⁻³ in non-smoker place [2]. Besides, Krugly et al. studied particulate phase PAHs in 5 schools located in urban, suburban and rural sites in Kaunas, Lithuania, and found total PAHs mean values in the range 20.3–131.1 ng m⁻³ [4]. Sangiorgi et al. also compared levels of PAHs in PM₁ and PM_{2.5} in 4 Italian offices in Milan between the cold and the warm season [23]. Again, particle-bound B[a]P sampled with Harvard impactors in homes in Amsterdam, The Netherlands, were in the range 0.49 ng m⁻³ (0.15–1.12 ng m⁻³) and 0.17 ng m⁻³ (0.03–0.39 ng m⁻³) for high-traffic and low-traffic density, respectively [7]. A last example of reported values in indoor air is the comparison of PAHs level in England where B[a]P values ranged between 0.09 ng m⁻³ (n.d.–2.40 ng m⁻³), 0.09 ng m⁻³ (n.d.–1.25 ng m⁻³) and 0.16 ng m⁻³ (0.04–0.79 ng m⁻³) in 81 homes, 30 offices and 7 restaurants, respectively [6].

As demonstrated with literature values, the sampling and analysis of PAHs indoors require a high sensitive analytical method

because of such low concentrations. In this study, we propose to evaluate the feasibility of using a cascade impactor to quantify particle-bound PAHs on PM > 10 μm, 2.5 μm < PM < 10 μm, 1 μm < PM < 2.5 μm and PM < 1 considering PAHs concentrations reported in literature for European studies in indoor environments. This methodology requires a classical high sensitive analytical technique with concentrations step before analysis to assess low indoor PAHs level with a limited sampling volume and could be applied to simultaneously determine PAHs in PM₁, PM_{2.5} and PM₁₀, 3 normalized particles sizes usually reported in the literature.

2. Materials and methods

2.1. Chemicals and materials

The overall analytical procedure, including calibration curves, was performed by using a certified standard solution obtained from LGC Standards (Molsheim, France) containing the 16 US-EPA priority PAHs (naphthalene NAP, acenaphthylene ACY, acenaphthene ACE, fluorene FLU, phenanthrene PHE, anthracene ANT, fluoranthene FLN, pyrene PYR, benzo[a]anthracene B[a]A, chrysene CHR, benzo[b]fluoranthene B[b]F, benzo[k]fluoranthene B[k]F, benzo[a]pyrene B[a]P, dibenzo[a,h]anthracene DB[a,h]A, benzo[g,h,i]perylene B[g,h,i]P, indeno[1,2,3-cd]pyrene IND). The initial concentration of the standard solution was 100 mg L⁻¹ with 0.6% uncertainty. Solvent used was acetonitrile (Chromasolv, HPLC grade, 99.9% purity, Sigma-Aldrich) and ultrapure water was obtained from a Milli-Q water system (Millipore, St. Quentin en Yvelines, France). For recovery experiments, filters were 25 mm Glass Fiber Filter (GFF) from Pall Life Sciences (Pall Corporation, France) and Fontainebleau sand was used to reduce dead volume in extraction cells. Besides, nitrogen (99.999%), used for concentration step and ASE purge cycle was obtained from Messer (Puteaux, France).

2.2. Cascade impactor theory

The impaction theory is based on the separation of particles from the air stream by the inertial forces. A cascade impactor is the result of the assembly of several impactors arranged in series in order to collect particles of decreasing size (Fig. 1a). They generally operates to remove particles of a given size range from the sample flow, either collecting them for later analysis or removing them to avoid problems of instrument contamination [24]. Different impactor designs exist such as round or rectangular impactors [25,26] and this part summarizes theoretical considerations for the round impactor.

Each impactor stage is constituted of an orifice or nozzle which leads a high velocity air jet (U_0), containing particles, towards a collection plate (Fig. 1b) which causes the airstream to change direction abruptly following a sharp bend [25,27]. Fig. 1b shows the air streamlines that are deflected to a sharp bend because of the collection plate. Particles which are small enough follow the streamlines and remain suspended, while those that have too much inertia impact on the plate.

The operating principle of an impactor is derived from the dimensionless Stokes number (Stk) defined as the ratio between the stopping distance of a particle and the characteristic dimension of the nozzle. Thus, considering an air flow perpendicular to a cylinder with a radius R (case of a circular jet impactor), the Stokes number is

$$\text{Stk} = \frac{\tau U_0}{R} \quad (1)$$

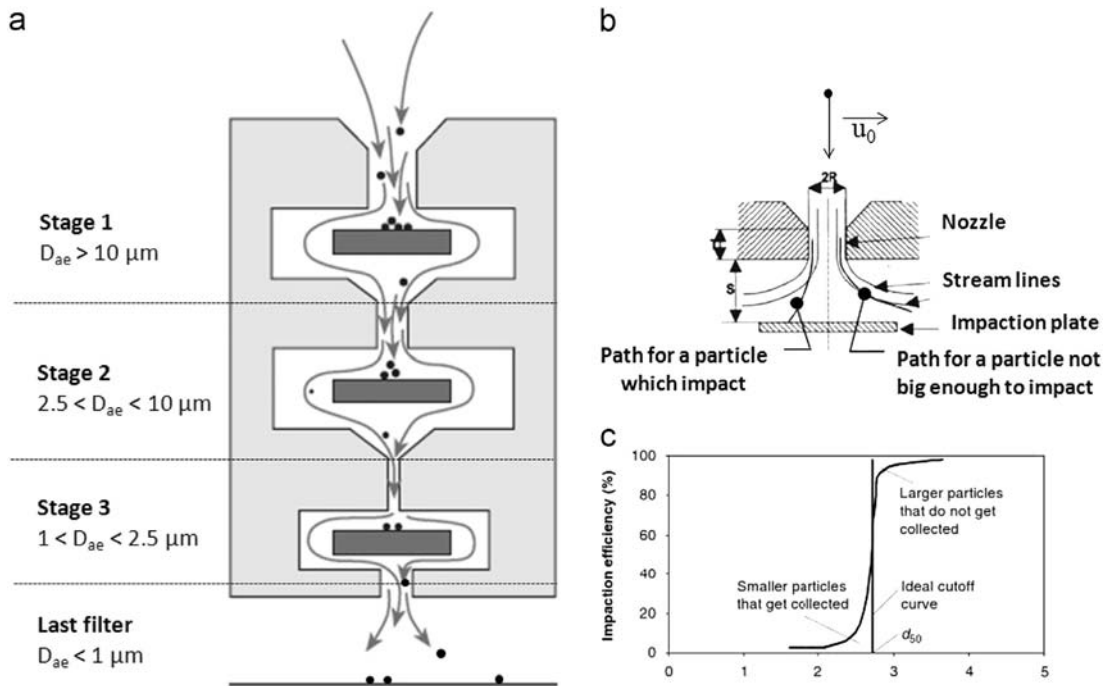


Fig. 1. Description of the sampling device: (a) cascade impactor scheme; (b) path of particles inside the cascade impactor (adapted from Marple and Willeke, 1976 [27]); (c) Scheme of an ideal and experimental cut sizes for one stage of an impactor (adapted from Zhang, 2005 [24]). D_{ae} : aerodynamic diameter, U_0 : air jet velocity, R : radius of the nozzle, S : jet-to-collection plate distance and T : throat length.

where U_0 is the air velocity (cm s^{-1}), R is the nozzle characteristic dimension, i.e. the radius (cm) and τ is the aerosol relaxation time (s) which is time until the aerosol direction is changing because of the Brownian motion effect.

However, relaxation time τ is the product between the particle mass m and its mobility B

$$\tau = m \cdot B = \left(\rho \cdot \frac{\pi}{6} \cdot d_p^3 \right) \cdot \frac{C_c}{3 \cdot \pi \cdot \mu \cdot d_p} = \frac{\rho \cdot C_c \cdot d_p^2}{18 \cdot \mu} \quad (2)$$

where d_p is the particles' diameter, C_c is the slip correction factor which correct differences between coarse and little particles' behavior, μ is the viscosity ($\text{g cm}^{-1} \text{s}^{-1}$) and ρ is the particles' density (g cm^{-3}).

The slip correction factor, C_c can be calculated from the mean free path of air λ , and the particle diameter [28]

$$C_c(d_p) = 1 + \left(\frac{\lambda}{d_p} \right) (2.514 + 0.800e^{-0.55(d_p/\lambda)}) \quad (3)$$

Therefore, the Stokes number, for a nozzle diameter $W=R/2$ is derived from (1) and (2)

$$\text{Stk} = \frac{\rho C_c U_0 d_p^2}{9 \mu W} \quad (4)$$

The Stokes number allows the characterization of the collection efficiency defined as the percentage of particles of a given size that are removed from the air flow by impaction. For a fixed impactor's geometry and flow condition, the Stokes number only depends on the particle properties and Eq. (4) shows that particle diameter is directly proportional to the square root of Stk . $\sqrt{\text{Stk}_{50}}$ is often used to determine the cut size of each impactor stage which represents the particle size with a collection efficiency of 50%. For most of the circular jet impactors, the number Stk_{50} , which corresponds to a collection efficiency of 50%, takes values in the range 0.22–0.25 [29,30]. Therefore, to collect particles with aerodynamic diameter even smaller it is necessary to increase U_0 or decrease W , i.e. R .

This is achieved by varying number and/or opening diameters from one stage to the other (see Fig. 1a).

As shown in Fig. 1c, the collection efficiency can be described with efficiency curves. And the collection efficiency increases for particles larger than the cut off size and decreases for smaller particles. In addition, the nondimensional Reynolds number (Re) which describe how turbulent or laminar is the flow has an impact on the collection efficiency. Marple and Liu show that high Reynolds numbers (until 3000) favor the development of sharp cut size impactor whereas for low values (below 300) the sharpness of cut size is less effective [26,31].

The Reynolds number for an impactor with round nozzles is defined as

$$\text{Re} = \frac{\rho U_0 W}{\mu} \quad (5)$$

Even if the most important advantage of impaction technique is that aerosol parameters, size and composition, can be simultaneously established, one of the main problems stays the particle bounce effect which can occur when particles larger than the cut off diameter impact on the collection plate and then bounce and re-enter in the airstream [26]. This problem in cascade impactors is an interference because particles which have bounced can be collected on later stages and potentially contaminating the analysis. Some techniques used to reduce this effect include the use of sticky substrates [32] such as oil or porous substrates or by changing the sampling method by using a virtual impactor [24].

In our study whose results are detailed elsewhere [33], Glass Fiber Filter systems were chosen because they are not suffering from problems of particle bounce [26]. We decided to work with a 3-stage cascade impactor operating at $0.5 \text{ m}^3 \text{ h}^{-1}$. Collected fractions corresponded to particles with aerodynamic diameter (D_{ae}) in the ranges $D_{ae} > 10 \mu\text{m}$, $10 \mu\text{m} < D_{ae} < 2.5 \mu\text{m}$, $2.5 \mu\text{m} < D_{ae} < 1 \mu\text{m}$ and a final filter which permitted to collect particles with $D_{ae} < 1 \mu\text{m}$.

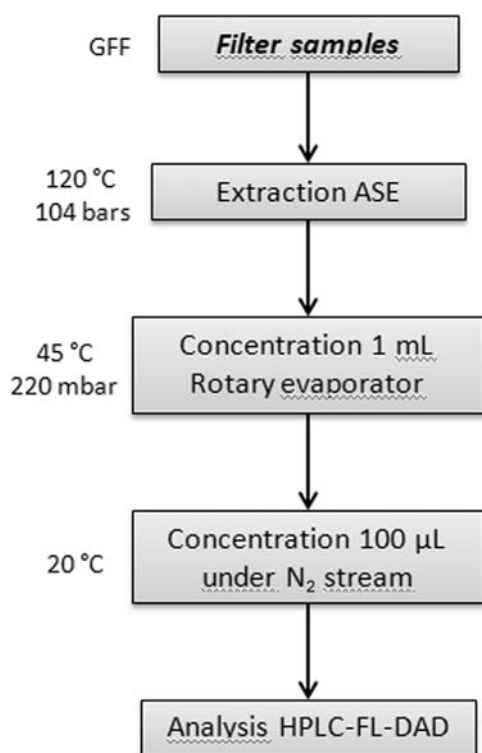


Fig. 2. Scheme of the analytical procedure for PAHs extraction and concentration procedure then followed by analysis.

2.3. Analytical procedure for sample treatment

The objective of our method is to use a cascade impactor as sampler which required to concentrate a lot the sample because this sampler, which separate particle size fractions, does not permit us to collect a lot of particles, especially in indoor air. As a consequence low LOD for the overall analytical procedure are needed. This latter consisted in a first step of extraction by means of an Accelerated Solvent Extractor (ASE 300, Dionex), a second step of concentration with a rotary evaporator and a final concentration step under a gentle nitrogen stream as described in Fig. 2. All of the 3 steps were considered separately in order to evaluate the effect on PAHs losses of each step.

The overall analytical procedure was previously validated by recovery experiments using certified standard solutions of the 16 US-EPA PAHs as discussed later.

2.3.1. ASE extraction

Glass Fiber Filters (GFF) were placed in 34 mL stainless steel cells provided by Dionex (ASE 300). Fontainebleau sand was added in the cell to reduce dead space and spare solvent. In our study, the extraction temperature was selected based on other studies in the literature, i.e. temperature in the range 100–150 °C [34–36]. One ASE cycle consisted in a heating step of 6 min to a set point value of 120 °C and ASE pressure was fixed to 1500 psi (104 bars) for all extractions. At the end of a cycle, a nitrogen purge of 120 s was realized to dry all the tubing. The choice of solvent for extraction and the number of static extraction were optimized in this study as mentioned below. If necessary, the extracts were then carefully filtered through a PVDF filter (0.45 µm, Restek, France).

Before use, both GFF and Fontainebleau sand were pre-cleaned with acetonitrile to remove any residual PAHs. They were stored in aluminum foil until use. Analytical blank composed of blank filters

and pre-cleaned sand were also analyzed and were taken into account for quantification of samples.

2.3.2. Concentration steps

After extraction, the extracts (approx. 70 mL) were then reduced to 1 mL using a rotary evaporator (Büchi) at 45 °C and 220 mbar. When necessary, a gentle stream of nitrogen was finally used to concentrate the extracts to approximately 100–150 µL.

2.3.3. Sample analysis

For the analysis of particle samples, the HPLC-Fluorescence technique which is a classical analytical method to quantify PAHs in environmental matrixes [37], was chosen.

Extracts were analyzed using a High Performance Liquid Chromatography system (Thermo Electron Corporation, Spectra System) equipped with a Diode Array Detector (DAD, Thermo Finnigan, Spectra System UV6000LP) and a fluorescence detector (Thermo Scientific, Finnigan Surveyor FL Plus) using the external standard method. The analytical column was a C₁₈ Pinnacle II PAH (Restek) 150 mm × 3.0 mm ID × 4 µm (particle size). Temperature oven was set to 30 °C. Acetonitrile and water was used as mobile phase with a flow rate of 1 mL min⁻¹. The elution gradient began with 50:50 (ACN:H₂O), then went to 60:40 (ACN:H₂O) in 7 min, then 70:30 (ACN:H₂O) until 9 min, and linear gradient to 100% of ACN was programmed until 20 min, with a final hold of 5 min. Initial conditions were reached in 1 min and maintained 5 min before next run. The overall run time was thus 30 min. Before HPLC analysis, the sample was diluted in Milli-Q water so that the sample was in the initial gradient conditions (50:50/ACN:H₂O) allowing sharper peaks.

Each compound (or group of PAHs compounds) was detected at its optimum emission/excitation wavelength: 270/330 nm (NAP, ACE, FLU), 250/370 nm (PHE), 250/400 nm (ANT), 270/440 nm (FLN), 270/400 nm (PYR), 270/390 nm (B[a]A, CHR), 290/430 nm (B[b]F, B[k]F, B[a]P, DB[a,h]A, B[g,h,i]P) and 305/500 nm (IND). ACY which is not fluorescent was quantified with the DAD at his optimum absorbance wavelength $\lambda = 229$ nm.

3. Results and discussion

3.1. Sample preparation

As shown in Table 2, many literature studies related to PAHs measurements mention an extraction step (solvent volume between 2 and 100 mL) then followed by a preliminary concentration step with rotary evaporator, then sometimes followed by a filtration and/or a purification step and finally a last concentration step (final volume in the range 10–4000 mL) to enhance PAHs detection. Since our samples may contain small amounts of PAHs, it is essential to reduce the number of sample treatments. In addition, it is of interest to avoid large solvent volumes because they require long concentration step, which hence increase the risk of PAHs loss by evaporation during concentration step.

Three key steps of our method were evaluated separately in order to avoid any PAHs loss during the global sample preparation procedure described in Fig. 2: (1) the accelerated solvent extraction of PAHs from the filter; (2) the primary concentration of the extract until 1 mL by means of a rotary evaporator at 45 °C and 220 mbar; and (3) the final concentration of the pre-concentrated extract to about 100–150 µL under a gentle nitrogen stream. Each recovery experiment was realized in triplicates and the error bars reported in Fig. 3a–c are the relative standard deviations.

Recovery experiments were first evaluated for the second step by adding 20 µL of a solution containing 16 PAHs at 1 mg L⁻¹, i.e. 20 ng for each PAH, in a typical volume of 70 mL of acetonitrile

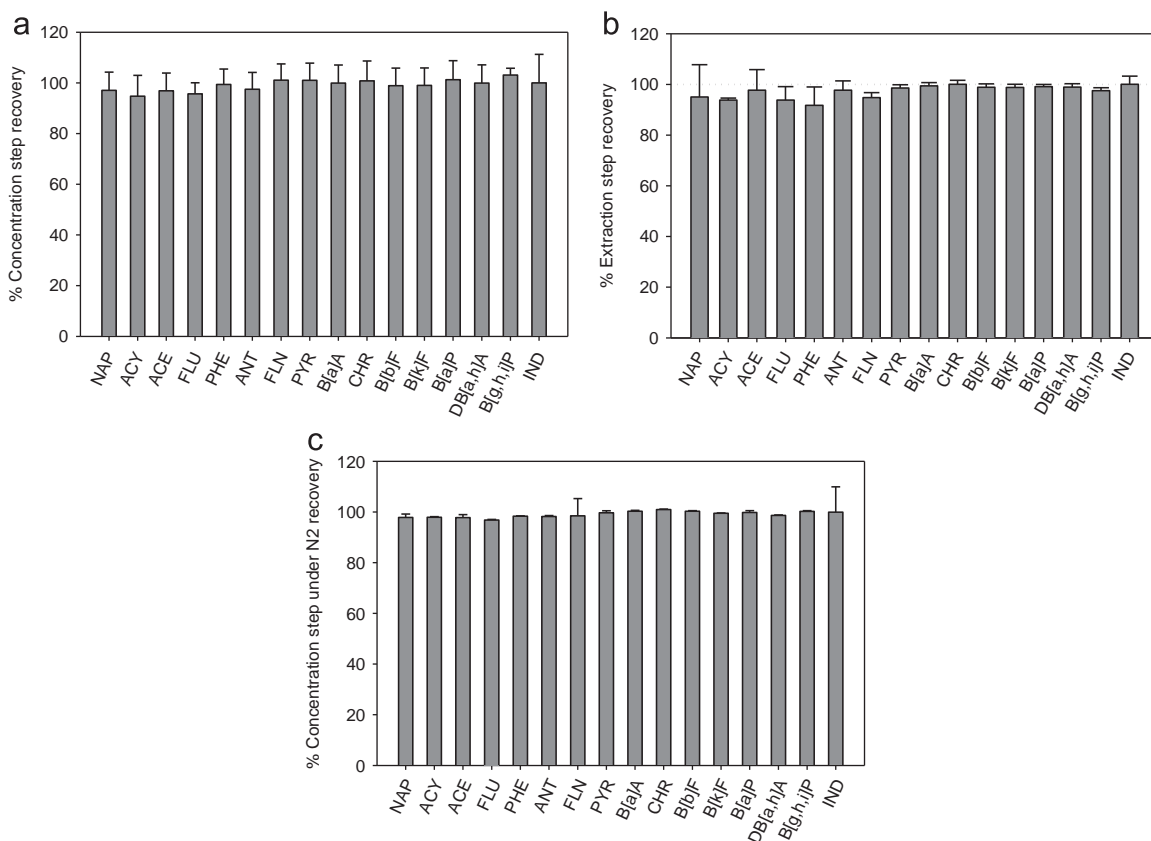


Fig. 3. Recoveries of the ASE extraction and concentration step based on 3 replicates: (a) concentration with rotary evaporator at $T=45\text{ }^{\circ}\text{C}$ and $P=220\text{ mbar}$; (b) ASE extraction; (c) concentration step to $100\text{ }\mu\text{L}$ under gentle nitrogen stream. The dotted line represents a recovery of 100%.

which is an estimated volume obtained after a 3-static ASE extraction with 34 mL cells. The solution was then concentrated to about 1 mL by using a rotary evaporator at $45\text{ }^{\circ}\text{C}$ and 220 mbar , in order to obtain PAHs concentrations of $\sim 20\text{ }\mu\text{g L}^{-1}$. The extract was then diluted by a factor 2 with milli-Q water and the resulting PAHs solution of $\sim 10\text{ }\mu\text{g L}^{-1}$ was analyzed by HPLC. Fig. 3a shows no significant PAHs loss within the experimental uncertainties during the primary concentration of the extracted solution by using a rotary evaporator.

Once this step of concentration by a rotary evaporator validated, the potential PAHs losses induced by the ASE extraction were also quantified. For this, as previously performed in other study [38], filters were spiked with $20\text{ }\mu\text{L}$ of a solution containing 16 PAHs at 1 mg L^{-1} , i.e. with 20 ng of each PAH, before extraction under different ASE conditions. The extraction of blank filters spiked with certified standards was preferred instead of extracting reference materials [2,39] for the same reasons cited by Delgado-Saborit et al. [38] which mentioned, first that the matrix is different between certified reference materials (powder) and particle collected onto filters and then, that a certified material is more expensive than a PAHs standard solution. Consequently, the use of a standard solution has been chosen regarding the number of tests performed to optimize the method. In order to evaluate the efficiency of extraction and finally choose optimum conditions, solvent and static time parameters were tested. Two solvents were tested, dichloromethane and acetonitrile (AcN). Static durations tested were 5 and 10 min. The evaluation of the number of static necessary to achieve a quantitative extraction of the 16 PAHs was realized by extracting 3 consecutive times the same spiked filter, $3 \times 5\text{ min}$ and $3 \times 10\text{ min}$, respectively. Our results show that extraction is almost quantitative after the first extraction, whatever its duration. The second static allows the

collection of the rest of PAHs. The extraction yield reached about 100% whatever the ASE extraction time so that 5 min was finally chosen. Consequently, the final ASE method chosen is based on 3 static steps of 5 min. Both solvents gave the same extraction efficiency for PAHs. However, dichloromethane contained many impurities and its use for extraction implied solvent exchange before HPLC analysis [5,11,40], so that acetonitrile was finally chosen. The extract of about 70 mL was then concentrated to 1 mL using the rotary evaporator before dilution with water and HPLC analysis. Only these latter results are presented in Fig. 3b.

The final sample concentration step was evaluated with 1 mL of a solution containing 16 PAHs at $10\text{ }\mu\text{g L}^{-1}$ introduced in a vial and evaporated under a gentle nitrogen stream to approximately $100\text{--}150\text{ }\mu\text{L}$. The final volume was determined by weighing. This solution was diluted 10 times in a $50:50\text{ v/v H}_2\text{O:AcN}$ mixture to obtain a final solution of about $10\text{ }\mu\text{g L}^{-1}$ which was analyzed by HPLC. The results reported in Fig. 3c highlight no significant PAHs loss during the third step.

Consequently, Fig. 3 shows no significant loss within the experimental uncertainties for the 3 steps investigated. However, small losses were observed for low molecular weight PAHs, i.e. PAHs containing 2 or 3 aromatic cycles such as NAP, ACY, ACE, FLU, PHE and ANT. For these PAHs, the losses reached 2–8% for the ASE extraction and varied in the range 1–5% for the primary concentration step with rotary evaporator although they were almost nonexistent during the final concentration step using a nitrogen stream varying in the range 2–3%. All these steps evaluated independently show that the overall PAHs loss, even for those with a low molecular weight, should not exceed more than a few percent. The overall recovery experiments of 92–99% obtained in this study are slightly better than most of those found in the literature: 77.6–90.3% for NAP and DB[a,h]A with 2 ASE cycles,

respectively [34], 73–88% for NAP and IND using ultrasonic extraction [40], 78.8–96.5% for NAP and PHE using ultrasonic extraction [5], 90.1–102.4% for 1-methylanthracene and B[a]P using also ultrasonic extraction [11], and up to 102% for DB[a,h]A with Soxhlet extraction [41]. Consequently, our sample preparation including both sample extraction and its concentration before HPLC analysis are validated and can be potentially applied to air particulate samples.

3.2. Calibrations

For the 16 studied PAHs, calibration curves were obtained by injecting 3 times the same concentrations, each calibration curves containing between 9 and 12 points. The calibration curves (see Supplementary data) were plotted in the concentrations ranges of 0.05–45 $\mu\text{g L}^{-1}$ for the most part of PAHs or alternatively in the range of 0.1(0.5)–92 $\mu\text{g L}^{-1}$ for PAHs exhibiting a less intense response such as NAP, ACY, DB[a,h]A and IND. Calibration curves up to 27 $\mu\text{g L}^{-1}$ for PAHs exhibiting a high responses such as B[k]F were achieved while calibration curve for ANT was in the range 0.01–18 $\mu\text{g L}^{-1}$ because the response reached the saturation detector for upper concentrations. As shown in Table 1, the calibrations were fully and remarkably linear ($R^2 > 0.999$) over the entire concentrations ranges investigated for all PAHs. Linearity was here determined by plotting the linear regression of the 9–12 calibration points repeated 3 times. This good linearity ($R^2 \geq 0.99$) was also observed within the uncertainties for concentrations lower than 2.5 $\mu\text{g L}^{-1}$.

3.3. Repeatability, reproducibility and Limits Of Detection and Quantification

For each PAH and for each concentration, repeatability defined as the intra-day variation (VC_{intra}) and reproducibility defined as the inter-day variation (VC_{inter}) for a given concentration were expressed using the variation coefficient (VC). VC_{inter} was determined by injecting the same concentration every week during 1 month. VC

is derived by the response's standard deviation to average value ratio, converted to a percentage. VC_{inter} , for an injected concentration of 1 $\mu\text{g L}^{-1}$, varied between 0.8% for CHR, PHE and B[a]P and 7.3% for ACY (UV detection). The accuracy was evaluated on 3 points; each one was injected 3 times. The method is considered accurate if the recalculated concentration is between 90% and 110% of the real concentration. We just accept an accuracy of 20% for B[g,h,i]P and IND because of their less intense response due to larger peaks.

Limits of Quantification (LOQ) were derived from the Food and Drug Administration (FDA) definition [42] which define the LOQ of an individual analytical procedure as the lowest amount of analyte in a sample which can be quantitatively determined with suitable precision ($VC \leq 20\%$) and accuracy (between 80% and 120% of the real concentration value). The Limit of Detection (LOD) is defined as the first point for which one of these 2 criteria is not respected. Every value was evaluated on the basis of three injections. The resulting LOQ reported in Table 1 have been converted in mass term by multiplying the injection volume (injection loop of 20 μL) to concentrations ($\mu\text{g L}^{-1}$), which correspond to injected quantity between 1 and 9.4 pg. As expected, ACY which was detected by UV at 229 nm exhibited the worst sensitivity with 7 other PAHs measured by fluorescence, namely NAP, ACE, FLN, PYR, DB[a,h]A, B[g,h,i]P and IND. Conversely, ANT, B[k]F and B[a]P showed more intense fluorescence response and then the best sensitivity. The LOD in mass term were approximately 5 times lower than the LOQ and were in the range 0.2–2 pg corresponding to 0.01–0.10 $\mu\text{g L}^{-1}$ (see Table 1). Again, our values are similar to those found in literature with LOD between 0.076 and 15.6 pg [11], 0.53 and 29.1 pg [43] or LOQ between 0.09 and 10 $\mu\text{g L}^{-1}$ for B[a]A and ACY, respectively [14]. LOD and LOQ corresponding to airborne concentrations with a sampling volume of 20 m^3 have been also derived and reported in Table 1. The comparison of these airborne concentrations with other values reported in the literature (Table 2) highlights the analytical method developed in this work presents lower LOD (in units of $\mu\text{g m}^{-3}$) if we consider all PAHs monitored. In addition, other methods that may be almost as sensitive for PAHs quantification were related to the global particulate phase or only one size fraction [11,15,44–47].

Table 1

Calibration parameters for the PAHs quantification with LOD and LOQ for the analytical instrument (LC for liquid chromatography) in $\mu\text{g L}^{-1}$, converted in injected mass (pg) and considering airborne concentrations (AC) in (pg m^{-3}).

PAH compounds	Linear regression	Determination coefficient R^2	Accuracy (%)	LOD_{LC} ($\mu\text{g L}^{-1}$)	LOQ_{LC} ($\mu\text{g L}^{-1}$)	LOD_{LC}^a (pg)	LOQ_{LC}^a (pg)	LOD_{AC}^b (pg m^{-3})	LOQ_{AC}^b (pg m^{-3})	VC_{intra}^c (%)	VC_{inter}^c (%)
Naphtalene	$y = 164,401x$	0.9995	10	0.10	0.47	2.0	9.4	1.50	7.05	3.1	2.4
Acenaphthylene (UV – 229 nm)	$y = 2,241x$	0.9998	10	0.10	0.47	2.0	9.4	1.50	7.05	7.9	7.3
Acenaphthene	$y = 350,901x$	0.9993	10	0.10	0.47	2.0	9.4	1.50	7.05	1.3	1.3
Fluorene	$y = 1,254,167x$	0.9997	10	0.05	0.10	1.0	2.0	0.75	1.50	0.3	0.4
Phénanthrene	$y = 582,417x$	0.9997	10	0.05	0.10	1.0	2.0	0.75	1.50	1.1	0.8
Anthracene	$y = 3,080,115x$	0.9989	10	0.01	0.05	0.2	1.0	0.15	0.75	0.3	0.9
Fluoranthene	$y = 128,572x$	0.9991	10	0.10	0.47	2.0	9.4	1.50	7.05	7.7	6.0
Pyrene	$y = 296,637x$	0.9994	10	0.10	0.47	2.0	9.4	1.50	7.05	3.6	3.4
Benzo[a]anthracene	$y = 971,500x$	0.9993	10	0.05	0.10	1.0	2.0	0.75	1.50	1.0	1.9
Chrysene	$y = 851,409x$	0.9995	10	0.05	0.10	1.0	2.0	0.75	1.50	1.1	0.8
Benzo[b]fluoranthene	$y = 359,208x$	0.9991	10	0.05	0.10	1.0	2.0	0.75	1.50	1.6	1.1
Benzo[k]fluoranthene	$y = 1,796,491x$	0.9994	10	0.01	0.05	0.2	1.0	0.15	0.75	2.2	1.6
Benzo[a]pyrene	$y = 1,014,880x$	0.9995	10	0.01	0.05	0.2	1.0	0.15	0.75	0.3	0.8
Dibenzo[a,h]anthracene	$y = 407,514x$	0.9997	10	0.10	0.47	2.0	9.4	1.50	7.05	0.8	1.8
Benzo[g,h,i]perylene	$y = 289,902x$	0.9993	20	0.10	0.47	2.0	9.4	1.50	7.05	0.1	3.5
Indeno[1,2,3-cd]pyrene	$y = 89,879x$	0.9990	20	0.10	0.47	2.0	9.4	1.50	7.05	1.7	6.1

^a The resulting LOD and LOQ have been converted in mass term by multiplying the LOD/ LOQ_{LC} by the injection volume (injection loop of 20 μL).

^b LOD and LOQ considering airborne concentration (AC) obtained by multiplying LOD_{LC} and LOQ_{LC} (in units of $\mu\text{g L}^{-1}$) by the final concentration volume of 300 μL and divided by a sampling volume of 20 m^3 .

^c Variation coefficient intra-day (VC_{intra}) and inter-day (VC_{inter}) calculated on the basis of RSD on 3 different concentrations. Results presented have been obtained with concentration of 1 $\mu\text{g/L}$.

Table 2
Comparison of our study with other methods present in literature data (non-exhaustive list).

Sampling device	Size fraction	Sampled volume (m ³)	PAH extraction	Number of targeted PAHs	Extraction volume (mL)	Final concentration volume (μL)	Analytical method	Sample LOD (pg m ⁻³)	Reference
3-Stages cascade impactor	$D_{ae} > 10 \mu\text{m}$ $2.5 < D_{ae} < 10 \mu\text{m}$ $1 < D_{ae} < 2.5 \mu\text{m}$ $D_{ae} < 1 \mu\text{m}$	10–20	ASE	16 US-EPA	70	150–200	HPLC-FL-DAD	0.15–1.50	This study
Personal environmental monitor sampler	PM 2.5	4.8	Ultrasonic	15 PAHs	30	≈ 100	GC-MS (Full-scan)	Not precised	[4]
11-Stages cascade impactor	$10 > D_{ae} > 1 \mu\text{m}$ $0.1 < D_{ae} < 1 \mu\text{m}$ $D_{ae} < 0.1 \mu\text{m}$	27	Ultrasonic	16 US-EPA	10	200	HRGC/HRMS	Not precised	[17]
High volume sampler	PM 10	90	Ultrasonic	7 PAHs	60	≈ 50	GC-MS (Full-scan)	Not precised	[22]
Low volume sampler	PM 2.5/PM 1	55.2	Ultrasonic	10 PAHs	2	2000	HPLC-FL	Not precised	[23]
Low volume sampler	Particulate phase	0.96	Ultrasonic	12 PAHs	60	600	HPLC-FL	8.8–1200 ^a	[40]
Micro-environment sampler	Particulate phase	1.44–4.32	Shaker	16 US-EPA	15	50	GC-MS (SIM)	4.4–255.9	[6,49]
Low volume sampler	PM 2.5/PM 10	27.6	MAE ^b	16 US-EPA	45	1000	HPLC-FL-DAD	1.6–181	[14]
Low volume sampler	Particulate phase	2.88	Shaker	23 PAHs	2	2000	GC-MS (SIM)	13,700–125,000 ^a	[10]
Low volume sampler	PM 2.5	30.1	Soxhlet	10 PAHs	–	1000	GC-MS (SIM)	30–150	[16]
Cascade impactor	$D_{ae} > 10 \mu\text{m}$ $2.5 < D_{ae} < 10 \mu\text{m}$ $D_{ae} < 2.5 \mu\text{m}$	1.8	Ultrasonic	16 US-EPA	30	1000	HPLC-FL-DAD	40–4650	[5]
Low volume sampler	PM 2.5/PM 10	27.6	MAE ^b	16 US-EPA	30	1000–4000	HPLC-FL-DAD	1.6–27	[21]
Air Chek HV30 pump	Particulate phase	28.8	Soxhlet	16 US-EPA	–	2000	GC-MS (SIM)	3–145	[9]
GRAVIKON PM 4 sampler	PM 7, 1 μm	28–32	Ultrasonic	12 PAHs	100	Not precised	HPLC-FL-DAD	40	[2]
Sampler with a pump	Particulate phase	1.44	Ultrasonic	39 PAHs	10	1000	HPLC-FL	0.1–10.8 ^c	[11]
Low noise small sampler	Particulate phase	0.72	Ultrasonic	12 PAHs	20	1000	HPLC-FL	0.7–40.5 ^c	[43]
Harvard impactor	PM 2.5	29	Ultrasonic	30 PAHs	50	10	GC-MS (SIM)	0.3–48 ^d	[45,46]
Low noise small sampler	Particulate phase	0.72	Ultrasonic	12 PAHs	10	1000	HPLC-FL	0.7–40 ^c	[44]
Sampler with a pump	Particulate phase	28.8	Ultrasonic	15 PAHs	Not precised	500	HPLC-FL	2–31 ^c	[47]
Sampler with a pump	PM 10	36	Ultrasonic	12 PAHs	100	Not precised	HPLC-FL	40	[15]

^a LOQ.

^b Microwave accelerated extraction.

^c Recalculated from LOD (in pg) given in literature divided by the sampling volume.

^d Method detection limit recalculated from LOD (in pg) given in literature divided by the sampling volume.

3.4. Minimum air sampling volumes for PAHs collection using a 3-stages cascade impactor

The goal of this work was to determine what is the minimum sampling volume needed to detect PAHs in indoor air at each collection plate of our cascade impactor.

The analytical LOQ (Table 1) of individual PAHs were then used to evaluate the sampling volume of air required to quantify particulate PAHs. Even if detection limit is a key criterion to assess the sensitivity of an analytical instrument, different approaches to evaluate this value are available and show differences. Kim and Kim [48] evaluated for several Volatile Organic Compounds both LOD (determined from three times the standard deviation of background noise ($n=7$)) and the method detection limit (MDL) (calculated following relevant US EPA Guidelines ($n=7$)) and show that MDL are always higher than LOD, both values being below the LOQ value. Finally, the LOQ was used instead of LOD because the objective of our study is to determine the minimum sampling volume needed to quantify PAHs in indoor air at each collection plate of the cascade impactor.

The detectable masses of PAHs were first calculated from the LOQ (in $\mu\text{g L}^{-1}$) and the final volume in the HPLC vial of 300 μL (taken into account the water dilution) after the concentration steps of the sample concentration. These detectable masses (in units of ng) were then divided by the concentrations of individual

PAHs (in units of ng m^{-3}) found in European indoor environments in order to calculate the minimum sampling air volume (in units of m^3) required to quantify PAHs with an acceptable accuracy. Several studies in Europe measured concentrations of particulate PAHs in indoor air [2,4,6,7,14,15,21–23]. Among the latter, one conducted by Delgado-Saborit et al. had a significant quantitative sample with 81 homes and 30 offices [6]. Considering the different PAHs, the geometric mean values ranged between 0.03 ng m^{-3} for DB[a,h]A and 0.36 ng m^3 for FLN in homes (see Table 3). In addition, these values were also representative of those found elsewhere in Europe. For instance, the concentrations of B[a]P in non-smoking area were as follows (in units of ng m^{-3}): 0.09 (n.d.–2.40) in homes and 0.09 (n.d.–1.25) in offices [6], 0.1 in a cafeteria after a smoking ban [22], 0.573 (0.131–1.510) [14], 0.612 (0.107–1.02) [21], between 0.09 and 0.25 ng m^{-3} in a street-side non-smoker living room [2], 0.17 ng m^{-3} (0.03–0.39) and 0.49 ng m^{-3} (0.15–1.12) in homes close to low and high-traffic density, respectively [7].

Based on these calculations and assumptions, the minimum sampling air volume in homes reported in Table 3 varies between 0.09 and 1.57 m^3 except for DB[a,h]A where the value reach 4.70 m^3 . Similarly, these calculated values are in the range 0.13–1.76 m^3 for the offices, when DB[a,h]A is still excluded. These estimated sampling volume are the same order of magnitude that those used by Delgado-Saborit et al. in their study, i.e. 1.44–4.32 m^3 [6,49]. The calculated sampling air volume depends on the PAH and its LOQ but

Table 3

Theoretical sampling volumes required to detect individual PAHs concentrations with the analytical method developed in this study. PAHs values reported by a representative European study.

PAH compounds	Injected quantity ^a (ng) (This study)	Measured values ^b (ng m ⁻³) (Delgado-Saborit et al. [6])		Theoretical sampling volume (m ³)	
	LOQ (ng)	81 Homes	30 Offices/workplace	81 Homes	30 Offices/workplace
Naphtalene	0.141	–	–	–	–
Acenaphthylene (UV – 229 nm)	0.141	0.12 (n.d.–1.33)	0.08 (n.d.–0.49)	1.18	1.76
Acenaphthene	0.141	0.09 (n.d.–12.4)	0.25 (n.d.–1.98)	1.57	0.56
Fluorene	0.030	0.13 (0.01–1.98)	0.04 (0.01–0.09)	0.23	0.75
Phénanthrene	0.030	0.34 (0.01–6.42)	0.22 (0.01–1.96)	0.09	0.14
Anthracene	0.015	0.05 (n.d.–0.58)	0.06 (n.d.–0.51)	0.30	0.25
Fluoranthene	0.141	0.36 (n.d.–5.94)	0.42 (n.d.–2.55)	0.39	0.34
Pyrene	0.141	0.29 (n.d.–24.1)	0.27 (n.d.–2.39)	0.49	0.52
Benzo[a]anthracene	0.030	0.06 (n.d.–2.71)	0.06 (n.d.–1.13)	0.50	0.50
Chrysene	0.030	0.14 (0.01–3.32)	0.16 (n.d.–1.59)	0.21	0.19
Benzo[b]fluoranthene	0.030	0.18 (n.d.–4.76)	0.2 (n.d.–3.75)	0.17	0.15
Benzo[k]fluoranthene	0.015	0.11 (0.01–3.40)	0.12 (n.d.–1.58)	0.14	0.13
Benzo[a]pyrene	0.015	0.09 (n.d.–2.40)	0.09 (n.d.–1.25)	0.17	0.17
Dibenzo[a,h]anthracene	0.141	0.03 (n.d.–0.38)	0.03 (n.d.–0.27)	4.70	4.70
Benzo[g,h,i]perylene	0.141	0.15 (0.01–2.06)	0.15 (n.d.–0.83)	0.94	0.94
Indeno[1,2,3-cd]pyrene	0.141	0.11 (n.d.–1.87)	0.1 (0.01–0.77)	1.28	1.41

^a Calculated on the basis of a total volume of 300 μL .

^b Geometric mean+range.

also on its average abundance in air. Note that these values could be 6 (1 mL:0.15 mL) times higher if the sample is maintained to 1 mL prior dilution and injection. The final concentration of the pre-concentrated extract down to 150 μL under a gentle nitrogen stream is therefore an essential step which allows the reduction of the sampling volume.

Considering the use of a 3-stages cascade impactor to collect simultaneously $\text{PM} > 10 \mu\text{m}$, $2.5 \mu\text{m} < \text{PM} < 10 \mu\text{m}$, $1 \mu\text{m} < \text{PM} < 2.5 \mu\text{m}$ and $\text{PM} < 1$ (and then to derive PM_{10} , $\text{PM}_{2.5}$ and PM_{10}) for particulate individual PAHs quantification, it appears that the reasonable air sampling volume is one order magnitude higher than those calculated above. Consequently, 10 or 20 m^3 should be enough to determine with a good accuracy the concentrations of the 16 investigated PAHs in this study. At a flow rate of $0.5 \text{ m}^3 \text{ h}^{-1}$, the duration of air sampling should be in the range 20–40 h. This sampling air volume range is between 7.5 and 90 times lower than those of 150–900 m^3 recommended by Pandey et al. for PAHs sampling in outdoor air.

4. Conclusion

This study proposes a sensitive and efficient method for quantification of particulate PAHs in ambient air, by coupling the particulate matter collection using a 3-stages cascade impactor and the classic analysis by HPLC-fluorescence (or UV in the case of Acenaphthylene). The development of this analytical method, and above all the sample treatment including its concentration to 100–150 μL followed by HPLC analysis, allows to quantify the 16 US-EPA PAHs related to the size particles ($\text{PM} > 10 \mu\text{m}$, $2.5 \mu\text{m} < \text{PM} < 10 \mu\text{m}$, $1 \mu\text{m} < \text{PM} < 2.5 \mu\text{m}$ and $\text{PM} < 1$) with a sampling duration occurring for only 24 or 48 h in relatively standard indoor environments such as homes and offices. This experimental approach allows to derive the individual PAHs concentrations in PM_{10} , $\text{PM}_{2.5}$ and PM_{10} .

LOD and LOQ corresponding to the potential airborne concentrations (in units of $\mu\text{g m}^{-3}$) with a sampling volume of 20 m^3 have been determined. These values compared to the literature ones highlight our analytical method coupling sampling, sample treatment and analysis, exhibit lower LOD.

This new sampling and analytical method has been implemented in different indoor environments and the results are detailed in another publication [33].

Acknowledgments

Financial support for this work has been provided by the French Ministry of Environment and ADEME through the PRIMEQUAL 2 program (Project MERMAID). This work was also supported by the region of Alsace and the REseau Alsace de Laboratoires en Ingénierie et Sciences pour l'Environnement (REALISE).

Appendix A. Supplementary information

Supplementary data associated with this article can be found in the online version at <http://dx.doi.org/10.1016/j.talanta.2014.05.027>.

References

- [1] S. Orecchio, S. Cannata, L. Culotta, J. Hazard. Mater. 181 (2010) 647–658, <http://dx.doi.org/10.1016/j.jhazmat.2010.05.061>.
- [2] H. Fromme, T. Lahrz, M. Piloty, H. Gebhardt, A. Oddoy, H. Rüdén, Sci. Total Environ. 326 (2004) 143–149, <http://dx.doi.org/10.1016/j.scitotenv.2004.02.002>.
- [3] L. Kliucininkas, D. Martuzevicius, E. Krugly, T. Prasauskas, V. Kauneliene, P. Molnar, et al., J. Environ. Monit. 13 (2011) 182–191, <http://dx.doi.org/10.1039/c0em00260g>.
- [4] E. Krugly, D. Martuzevicius, R. Sidaraviciute, D. Ciuzas, T. Prasauskas, V. Kauneliene, et al., Atmos. Environ. 82 (2014) 298–306, <http://dx.doi.org/10.1016/j.atmosenv.2013.10.042>.
- [5] L. Zhu, H. Lu, S. Chen, T. Amagai, J. Hazard. Mater. 162 (2009) 1165–1170, <http://dx.doi.org/10.1016/j.jhazmat.2008.05.150>.
- [6] J.M. Delgado-Saborit, C. Stark, R.M. Harrison, Environ. Int. 37 (2011) 383–392, <http://dx.doi.org/10.1016/j.envint.2010.10.011>.
- [7] P.H. Fischer, G. Hoek, H. van Reeuwijk, D.J. Briggs, E. Lebret, J.H. van Wijnen, et al., Atmos. Environ. 34 (2000) 3713–3722, [http://dx.doi.org/10.1016/S1352-2310\(00\)00067-4](http://dx.doi.org/10.1016/S1352-2310(00)00067-4).
- [8] S.K. Pandey, K.-H. Kim, R.J.C. Brown, TrAC: Trends Anal. Chem. 30 (2011) 1716–1739, <http://dx.doi.org/10.1016/j.trac.2011.06.017>.
- [9] A. Li, T.M. Schoonover, Q. Zou, F. Norlock, L.M. Conroy, P.A. Scheff, et al., Atmos. Environ. 39 (2005) 3491–3501, <http://dx.doi.org/10.1016/j.atmosenv.2005.02.029>.
- [10] J. Masih, A. Masih, A. Kulshrestha, R. Singhvi, A. Taneja, J. Hazard. Mater. 177 (2010) 190–198, <http://dx.doi.org/10.1016/j.jhazmat.2009.12.017>.
- [11] T. Ohura, T. Amagai, M. Fusaya, H. Matsushita, Environ. Sci. Technol. 38 (2004) 77–83, <http://dx.doi.org/10.1021/es030512o>.
- [12] G. Buonanno, G.B. Marks, L. Morawska, Environ. Pollut. 180 (2013) 246–250, <http://dx.doi.org/10.1016/j.envpol.2013.05.039>.
- [13] A. Zanobetti, M. Franklin, P. Koutrakis, J. Schwartz, Environ. Health 8 (2009) 58, <http://dx.doi.org/10.1186/1476-069X-8-58>.
- [14] D. Castro, K. Slezakova, C. Delerue-Matos, M.C. Alvim-Ferraz, S. Morais, M. C. Pereira, Atmos. Environ. 45 (2011) 1799–1808, <http://dx.doi.org/10.1016/j.atmosenv.2011.01.018>.

- [15] H. Fromme, A. Oddoy, M. Piloty, M. Krause, T. Lahrz, *Sci. Total Environ.* 217 (1998) 165–173, [http://dx.doi.org/10.1016/S0048-9697\(98\)00189-2](http://dx.doi.org/10.1016/S0048-9697(98)00189-2).
- [16] K.H. Jung, M.M. Patel, K. Moors, P.L. Kinney, S.N. Chillrud, R. Whyatt, et al., *Atmos. Environ.* 44 (2010) 4545–4552, <http://dx.doi.org/10.1016/j.atmosenv.2010.08.024>.
- [17] L.-Y. Lin, I.-J. Liu, H.-C. Chuang, H.-Y. Lin, K.-J. Chuang, *Atmos. Environ.* 77 (2013) 490–495, <http://dx.doi.org/10.1016/j.atmosenv.2013.05.045>.
- [18] M. Junker, C. Monn, *J. Aerosol Sci.* 29 (Supplement 1) (1998) S289–S290, [http://dx.doi.org/10.1016/S0021-8502\(98\)00433-9](http://dx.doi.org/10.1016/S0021-8502(98)00433-9).
- [19] M. Junker, T. Koller, C. Monn, *Sci. Total Environ.* 246 (2000) 139–152, [http://dx.doi.org/10.1016/S0048-9697\(99\)00452-0](http://dx.doi.org/10.1016/S0048-9697(99)00452-0).
- [20] L. Wallace, *Appl. Occup. Environ. Hyg.* 15 (2000) 39–47, <http://dx.doi.org/10.1080/104732200301836>.
- [21] K. Slezakova, D. Castro, M.C. Pereira, S. Morais, C. Delerue-Matos, M.C. Alvim-Ferraz, *Atmos. Environ.* 43 (2009) 6376–6382, <http://dx.doi.org/10.1016/j.atmosenv.2009.09.015>.
- [22] J. Pey, B.L. van Drooge, A. Ripoll, T. Moreno, J.O. Grimalt, X. Querol, et al., *Particuology* 11 (2013) 527–532, <http://dx.doi.org/10.1016/j.partic.2013.02.007>.
- [23] G. Sangiorgi, L. Ferrero, B.S. Ferrini, C. Lo Porto, M.G. Perrone, R. Zangrando, et al., *Atmos. Environ.* 65 (2013) 205–214, <http://dx.doi.org/10.1016/j.atmosenv.2012.10.050>.
- [24] Y. Zhang, *Indoor Air Quality Engineering*, CRC Press Inc., 2005, ISBN: 1566706742, 9781566706742.
- [25] V.A. Marple, B.Y.H. Liu, K.T. Whitby, *J. Aerosol Sci.* 5 (1974) 1–16, [http://dx.doi.org/10.1016/0021-8502\(74\)90002-0](http://dx.doi.org/10.1016/0021-8502(74)90002-0).
- [26] K. Willeke, J.J. Mcfeters, *J. Colloid Interface Sci.* 53 (1975) 121–127, [http://dx.doi.org/10.1016/0021-9797\(75\)90042-9](http://dx.doi.org/10.1016/0021-9797(75)90042-9).
- [27] V.A. Marple, K. Willeke, *Atmos. Environ.* 1967 (10) (1976) 891–896, [http://dx.doi.org/10.1016/0004-6981\(76\)90144-X](http://dx.doi.org/10.1016/0004-6981(76)90144-X).
- [28] M. Marjamäki, J. Keskinen, D.-R. Chen, D.Y.H. Pui, *J. Aerosol Sci.* 31 (2000) 249–261, [http://dx.doi.org/10.1016/S0021-8502\(99\)00052-X](http://dx.doi.org/10.1016/S0021-8502(99)00052-X).
- [29] D. Boulaud, P. Gerasimo, G. Martin, L. Martinot, A. Nourreddine, J.C. Sens, *Radio-protection* 38 (2003) 493–508, <http://dx.doi.org/10.1051/radiopro:2003015>.
- [30] A.H. de Boer, D. Gjaltema, P. Hagedoorn, H.W. Frijlink, *Int. J. Pharm.* 249 (2002) 219–231, [http://dx.doi.org/10.1016/S0378-5173\(02\)00526-4](http://dx.doi.org/10.1016/S0378-5173(02)00526-4).
- [31] V.A. Marple, B.Y.H. Liu, *J. Colloid Interface Sci.* 53 (1975) 31–34, [http://dx.doi.org/10.1016/0021-9797\(75\)90031-4](http://dx.doi.org/10.1016/0021-9797(75)90031-4).
- [32] A. Robache, F. Mathé, J.C. Galloo, R. Guillermo, *Analyst* 125 (2000) 1855–1859, <http://dx.doi.org/10.1039/B003048L>.
- [33] C. Liaud, M. Millet, V. Tschamber, G. Trouvé, S. Le Calvé Development of a 3-stages cascade impactor sampling method to measure particle-bound PAHs in indoor air: Application to different indoor environments, in: Proceedings from 13th International Conference on Indoor Air Quality and Climate, July 7–12, 2014, Hong-Kong.
- [34] J. He, R. Balasubramanian, *Anal. Lett.* 42 (2009) 1603–1619, <http://dx.doi.org/10.1080/00032710902993886>.
- [35] S. Percot, V. Ruban, P. Roupsard, D. Maro, M. Millet, *Atmos. Environ.* 74 (2013) 338–345, <http://dx.doi.org/10.1016/j.atmosenv.2013.03.056>.
- [36] P. Popp, P. Keil, M. Möder, A. Paschke, U. Thuss, *J. Chromatogr. A* 774 (1997) 203–211, [http://dx.doi.org/10.1016/S0021-9673\(97\)00337-3](http://dx.doi.org/10.1016/S0021-9673(97)00337-3).
- [37] L.D. Gratz, S.T. Bagley, D.G. Leddy, J.H. Johnson, C. Chiu, P. Stommel, *J. Hazard. Mater.* 74 (2000) 37–46.
- [38] J.M. Delgado-Saborit, N. Aquilina, S. Baker, S. Harrad, C. Meddings, R. M. Harrison, *Anal. Methods* 2 (2010) 231–242, <http://dx.doi.org/10.1039/B9AY00157C>.
- [39] S. Masala, T. Ahmed, C. Bergvall, R. Westerholm, *Anal. Bioanal. Chem.* 401 (2011) 3305–3315, <http://dx.doi.org/10.1007/s00216-011-5446-9>.
- [40] J. Cristale, F.S. Silva, G.J. Zocolo, M.R.R. Marchi, *Environ. Pollut.* 169 (2012) 210–216, <http://dx.doi.org/10.1016/j.envpol.2012.03.045>.
- [41] Morville, O. Delhomme, M. Millet, *Atmos. Pollut. Res.* 2 (2011) 366–373.
- [42] U.S. Department of Health and Human Services, Food and Drug Administration, Guidance for Industry Bioanalytical Method Validation, 2001.
- [43] L. Zhu, J. Wang, *Chemosphere* 50 (2003) 611–618, [http://dx.doi.org/10.1016/S0045-6535\(02\)00668-9](http://dx.doi.org/10.1016/S0045-6535(02)00668-9).
- [44] Y. Liu, L. Zhu, X. Shen, *Environ. Sci. Technol.* 35 (2001) 840–844, <http://dx.doi.org/10.1021/es001354t>.
- [45] Y.Y. Naumova, J.H. Offenberg, S.J. Eisenreich, Q. Meng, A. Polidori, B.J. Turpin, et al., *Atmos. Environ.* 37 (2003) 703–719, [http://dx.doi.org/10.1016/S1352-2310\(02\)00820-8](http://dx.doi.org/10.1016/S1352-2310(02)00820-8).
- [46] Y.Y. Naumova, S.J. Eisenreich, B.J. Turpin, C.P. Weisel, M.T. Morandi, S. D. Colome, et al., *Environ. Sci. Technol.* 36 (2002) 2552–2559, <http://dx.doi.org/10.1021/es015727h>.
- [47] C.-S. Li, Y.-S. Ro, *Atmos. Environ.* 34 (2000) 611–620, [http://dx.doi.org/10.1016/S1352-2310\(99\)00171-5](http://dx.doi.org/10.1016/S1352-2310(99)00171-5).
- [48] Y.-H. Kim, K.-H. Kim, *Anal. Chem.* 84 (2012) 8284–8293, <http://dx.doi.org/10.1021/ac301792x>.
- [49] J.M. Delgado-Saborit, N.J. Aquilina, C. Meddings, S. Baker, S. Vardoulakis, R. M. Harrison, *Environ. Sci. Technol.* 43 (2009) 4582–4588, <http://dx.doi.org/10.1021/es900504z>.



Application of neural networks with novel independent component analysis methodologies to a Prussian blue modified glassy carbon electrode array



Liang Wang^{a,b,*}, Die Yang^{a,b}, Cheng Fang^{a,b}, Zuliang Chen^{a,b}, Peter J. Lesniewski^c, Megharaj Mallavarapu^{a,b}, Ravendra Naidu^{a,b}

^a Centre for Environmental Risk Assessment and Remediation, University of South Australia, Mawson Lakes, SA 5095, Australia

^b CRC for Contamination Assessment and Remediation of Environment, Mawson Lakes Boulevard, Mawson Lakes, SA 5095, Australia

^c School of EIE (Applied Physics), University of South Australia, Mawson Lakes, SA 5095, Australia

ARTICLE INFO

Article history:

Received 6 May 2014

Received in revised form

4 August 2014

Accepted 5 August 2014

Available online 13 August 2014

Keywords:

Ion selective electrode (ISE) array

Prussian blue modified glassy carbon electrode (PB-GCE)

Genetic algorithm (GA)

Independent component analysis (ICA)

Back-propagation neural network (BPNN)

Orthogonal experimental design (OED)

ABSTRACT

Sodium potassium absorption ratio (SPAR) is an important measure of agricultural water quality, wherein four exchangeable cations (K^+ , Na^+ , Ca^{2+} and Mg^{2+}) should be simultaneously determined. An ISE-array is suitable for this application because its simplicity, rapid response characteristics and lower cost. However, cross-interferences caused by the poor selectivity of ISEs need to be overcome using multivariate chemometric methods. In this paper, a solid contact ISE array, based on a Prussian blue modified glassy carbon electrode (PB-GCE), was applied with a novel chemometric strategy. One of the most popular independent component analysis (ICA) methods, the fast fixed-point algorithm for ICA (*fastICA*), was implemented by the genetic algorithm (*geneticICA*) to avoid the local maxima problem commonly observed with *fastICA*. This *geneticICA* can be implemented as a data preprocessing method to improve the prediction accuracy of the Back-propagation neural network (BPNN). The ISE array system was validated using 20 real irrigation water samples from South Australia, and acceptable prediction accuracies were obtained.

© 2014 Elsevier B.V. All rights reserved.

1. Introduction

A major problem concerning the quality of irrigation water is the level of monovalent cations (Na^+ and K^+) present in water, because it influences the structural stability of clay minerals and potential for dispersion, erosion and drainage [1–6]. It can be indicated by the sodium potassium adsorption ratio (SPAR), in terms of the relative proportion of monovalent cations, compared to the bivalent cations (Ca^{2+} and Mg^{2+}) in solution [1,2]. The SPAR is calculated as (1):

$$SPAR = \frac{([Na^+] + [K^+])}{\sqrt{([Ca^{2+}] + [Mg^{2+}])}} / 2 \quad (1)$$

where: Na^+ , $[K^+]$, $[Ca^{2+}]$ and $[Mg^{2+}]$ are concentrations of the individual ions expressed in milliequivalents L^{-1} .

If the bivalent cations are dominant in the solution rather than the monovalent cations, the danger is minimal and vice versa [2]. To calculate the SPAR, four individual exchangeable cations must

be determined: Ca^{2+} , K^+ , Mg^{2+} and Na^+ . Since the SPAR value is calculated based on the proportions of these four exchangeable cations, even if the 4 cations' concentrations differ from the samples, the SPAR value may actually remain the same. Here we focus on determining these four exchangeable cations and using their predicted concentrations to calculate the SPAR. Normally, these cations are measured using inductively coupled plasma mass spectrometry (ICP/MS) or Optical Emission Spectrometry (OES) which are lab-based instruments. However, this approach is not suitable for online in situ monitoring because samples have to be preserved and sent to an analytical chemistry laboratory – where ICP/MS or OES is located – and measured by technicians.

Use of ISE's is a commonly used technique for online in situ monitoring of water quality [7,8]. They provide an electrical response suitable for digital manipulation and interfacing with control software that is proportional to the concentration of the particular ion the electrode is selected for. Compared to other analytical techniques, ISEs have the advantage of being relatively inexpensive, simple to use and exhibiting rapid responses, which are all essential for in situ monitoring of ions in environmental samples [7,8]. In the past ten years, solid contact ISE with ionophore-based membranes has been widely studied through electrochemistry [9–21]. Compared to classical ISE with internal

* Corresponding author at: Centre for Environmental Risk Assessment and Remediation, University of South Australia, Mawson Lakes, SA 5095, Australia
E-mail address: Liang.Wang@unisa.edu.au (L. Wang).

solution, solid contact ISE has the advantages of longer periodical service and size minimization [9,10]. As for the solid contact ISE [9], a conductor interface exists between the ionophore-based membrane (outer layer making contact with the testing solution) and the substrate (metal, carbon material, etc.). An oxidation/reduction equilibrium media should be added to this conductor interface to transit from ionic conductivity in solutions and in the membrane to electronic conductivity in the circuit [9]. The common conductors include silver/silver chloride, polypyrrole, etc. [9]. However, the cost of the former and stability of the latter have been queried. In the last decade, Prussian blue (PB), which is one of the most widely used electrochemical mediators for analytical application, has been fully investigated [10–14]. This stable conductor film can be easily and in-situ electro-deposited on the electrode surface. In this study, an ISE array based on the PB-GCE with ionophore-based PVC membranes was analyzed.

No matter whether solid contact ISEs or classical ISEs are being considered, they are both normally based on ionophores, designed for complexing, interacting, and holding the analyte in a molecular cavity. However, these interactions are actually non-specific so that interference from other undesired analytes of a similar size and charge commonly appear [9,10]. Since ISEs may be only partially or poorly selective for their target analyte, one alternative way to solve this cross-interference problem is to apply an ISE array in combination with multivariate calibration methods, such as BPNNs [15–21]. Recently, Mueller and Hemond, did a comprehensive study using BPNNs as a sensor post-processing method. Their aim was to simultaneously determine the major ions in environmental samples [15]. Furthermore, del Valle and colleagues did much research in this area [16–21]. Table 1 details some of their applications, including the ISE arrays and methodologies. In some of their studies, Fast Fourier Transfer (FFT) served as a data preprocessing method for improving the prediction accuracy of BPNNs [20,21]. ICA is the main method used in Blind Signal Separation, extracting independent components by searching the maximized non-Gaussian properties from observation data [22,23].

ICA can be realized using a fixed-point algorithm (*fastICA*) which has the advantage of fast convergence [23]. However, this method is based on a gradient algorithm that starts from one random matrix and is therefore a single point in the Probability Density Function (PDF) of the model [24]. In a scenario where the model involves many highly non-linear inputs, the *fastICA* will encounter the local maxima problem, which means the algorithm would just search in a much smaller sub-set of the multi-dimensional parameter space rather than in the whole parameter space [24]. In our study, *geneticICA*, was employed to implement ICA using the genetic algorithm (GA), to avoid the local maxima problem by starting with a number of random matrices as multi-points in the model's PDF. It has been noted in our previous studies that *geneticICA* constituted one of the most efficient data preprocessing methods for improving the prediction accuracy of BPNN [25,26].

For training the BPNN system, orthogonal experimental design (OED) is one of the most effective and time-saving methods, and it is employed for minimizing the amount of training samples without losing any quality characteristics for the specific ions [27]. As a hypothesis, assume each individual ion had simply four different levels of concentrations, the total amount of these four desired ion mixtures would be $4^4=256$; it is time-consuming to collect the combination of all concentration levels for each ion. Therefore, grouping the calibration dataset with the minimum number of samples required and maximum information is a key issue for building the neural network determination system. In this study, by using OED, the system calibration samples were minimized to 16. Validated with 20 real irrigation water samples from winery and urban locations in South Australia, using these small calibration samples enabled our ISE array system to

simultaneously determine the four exchangeable ions with acceptable prediction accuracies.

2. Experimental

2.1. Apparatus and ISE array

The homemade GCEs utilized 3.0 mm diameter glassy carbon rods (Aldrich), covered by 100–1000 μL pipet tips (Sigma) and sealed with epoxy (Araldite). Prior to surface modification, the GCE electrodes were polished, washed and dried according to the literature [14]. The PB electrodeposition was done on a CHI660B electrochemical workstation (CH Instruments Inc., USA) with a conventional three-electrode cell. This three-electrode cell contains an Ag/AgCl [sat. KCl] reference electrode, a platinum wire counter electrode and a modified glassy carbon working electrode. As shown in Fig. 1, the GCEs were treated with cyclic scanning in the potential range of -0.2 to 1.2 V at 100 mV/s for 20 cycles in a mixture solution containing 2 mM of $\text{K}_3[\text{Fe}(\text{CN})_6]$ + 2 mM of FeCl_3 + 0.1 M of KCl, + 0.1 M of HCl, as described in [13]. The PB-GCEs were then washed with deionized water and dried for 1 h at 80 °C. The ISE array contained an Ag/AgCl reference electrode and 4 PB-GCE working electrodes. The ion-sensitive membranes were prepared by adding a solution drop-wise and the formulation included: the ionophore (Fluka), an ionic additive ($\text{K}_+ \text{TpClPB}^-$, Fluka), the plasticizer and PVC in tetrahydrofuran (THF, from Fluka) [28–32]. These membranes' details are illustrated in Table 2.

The potentiometric system consisted of 4 pH amplifiers (ADInstruments Co.) applied as signal amplifiers while the PowerLab (ADInstruments Co.) served to interface the computer with the amplifiers. Chart5 for Windows software (ADInstruments Co.) was used for the data acquisition and filtering. Finally, data processing and analysis was undertaken in Matlab R2012b using the Statistical Analysis and neural network toolboxes. SPSS 15.0 for Windows was employed for generating the orthogonal experimental design and Pearson correlation coefficients for interference analysis. The electrodes were connected to electronic amps, sharing the same measuring conditions that included: the reference electrode and grounded earth. Noise due to signal granularity generated by electrodes was eliminated by a 10 Hz low-pass digital filter.

2.2. Orthogonal experimental design (OED)

To deal with multifactor experiments, theory suggests that firstly an orthogonal design table (ODT), with reasonable and representative levels of all factors should be determined [27]. The ODT for this study as $L_{16}(4^4)$ is detailed in Table 3. For the four chemicals having four levels of concentrations (i.e. 1, 10, 75 and 150 mg/L for Ca and Mg), the number of combination groups fell to 16. These 16 synthetic samples were diluted and combined from 1.0 g/L of chlorides (CaCl_2 , KCl, MgCl_2 and NaCl) using deionized water (milli Q plus System, with 18.2 M Ω /cm resistivity). 1000 mg/L tetramethylammonium chloride and hydrochloric acid solution was used as the support electrolyte, pH value was around 5.5 (measured by the Orion's pH electrode). Furthermore, to optimize the calibration model another set of 15 synthetic samples with random concentration mixtures was prepared in the same scenario and served as testing sample set. All measurements were carried out at the same temperature (25 °C) in triplicate and the average values were reported for processing. The final electrode potential was recorded only when the system was stabilized, i.e. a potential variation less than ± 0.05 mV, over 1 min. Hourly single point calibrations with standard solutions (100 mg/L CaCl_2 , KCl, MgCl_2 and NaCl) were performed. All the concentrations were measured and confirmed utilizing ICP-OES.

Table 1
BPNN applications in quantitative analysis.

Analytes	Sensor details	Variable reduction	BPNN structure	Calibration	Validation	Prediction range	Prediction accuracy (external)		Refs.
NH_4^+ , Na^+ , Cl^- , NO_3^- , K^+	10 Working electrodes; Body: epoxy graphite; 5 ISEs: NH_4^+ , Na^+ , Cl^- , NO_3^- , K^+ ; 2 Generic electrodes; Reference electrode: Ag/AgCl	No	Input: 10 Ns; Hidden: 1 Ns, Transfer: Tansig; Output: 5 Ns, Transfer: Purelin Training function: BR	27 Solutions (FFD) at range: 0.8–21 mM	7 Synthetic 9 Real samples	NH_4^+ : 0.8–6.2 mM Na^+ : 2–12 mM Cl^- : 2–12 mM NO_3^- : 5.3–21 mM K^+ : 4.3–20 mM	MRE(%) NH_4^+ : 5.9 Na^+ : 8.9 Cl^- : 10	NO_3^- : 7.7 K^+ : 7.2	[17]
NH_4^+ , Na^+ and K^+	5 Working electrodes; Body: epoxy graphite; 3 ISEs: NH_4^+ , Na^+ , K^+ ; 2 Generic electrodes; Reference electrode: Ag/AgCl	No	Input: 5 Ns; Hidden: 4 Ns, Transfer: Logsig; Output: 3 Ns, Transfer: Purelin; Training function: LM	32 Solutions Randomly at range 0.002–0.05 M	14 Synthetic 5 Real Samples	NH_4^+ : 2–50 mM Na^+ : 2–50 mM K^+ : 2–50 mM	Student's <i>t</i> -test NH_4^+ : 2.59 Na^+ : 6.84	K^+ : 0.39	[18]
NH_4^+ , Na^+ , Urea and K^+	12 Working electrodes; Body: epoxy graphite; 4 Urea biosensors; 7 ISEs: 2 NH_4^+ , 2 Na^+ , 2 K^+ , 1 H^+ ; 1 Generic electrode; Reference electrode: Ag/AgCl	No	Input: 12 Ns; Hidden: 1 Ns, Transfer: Tansig; Output: 4 Ns, Transfer: Purelin; Training function: BR	27 Solutions (FFD) at range: 0.04–10 mM	10 Synthetic 21 Real Samples	Urea: 0.1–10 mM NH_4^+ : 0.005–0.5 mM Na^+ : 0.05–5 mM K^+ : 0.05–5 mM	Corr Urea: 0.82 NH_4^+ : 0.98	Na^+ : 0.99 K^+ : 0.99	[19]
Ca^{2+} , Na^+ and K^+	5 Working electrodes; Body: epoxy graphite; 4 ISEs: 2 Ca^{2+} , Na^+ , K^+ ; 1 Generic electrode; Reference electrode: Ag/AgCl	FFT	Input: 5 Ns; Hidden: 6 Ns, Transfer: Tansig; Output: 4 Ns, Transfer: Tansig; Training function: BR	48 Solutions randomly at range: 0.05–10 mM	20 Synthetic 8 Real Samples	Ca^{2+} : 0.2–5 mM Na^+ : 0.05–1 mM K^+ : 0.02–0.5 mM	Corr Ca^{2+} : 0.97 Na^+ : 0.92	K^+ : 0.95	[20]
Ca^{2+} , Mg^{2+} , Na^+ and K^+	8 Working electrodes; Body: epoxy graphite; 6 ISEs: 2 Ca^{2+} , 2 Na^+ , K^+ , Mg^{2+} 2 Generic electrode; Reference electrode: Ag/AgCl	FFT	Input: 3 Ns; Hidden: 11 Ns, Transfer: Logsig; Output: 4 Ns, Transfer: Purelin; Training function: BR	67 Random solutions Range: 0–5 mM	25 Synthetic	Ca^{2+} : 0–5 mM Na^+ : 0–2 mM K^+ : 0–2 mM Mg^{2+} : 0–2 mM	Corr Ca^{2+} : 0.97 Na^+ : 0.91	K^+ : 0.95 Mg^{2+} : 0.88	[21]

RMSE—root mean square of errors; MRE—mean of relative errors; LM—Levenberg–Marquardt back-propagation; BR—Bayesian regulation back-propagation; Corr—Pearson correlation to the real concentrations; FFT—fractional factorial design.

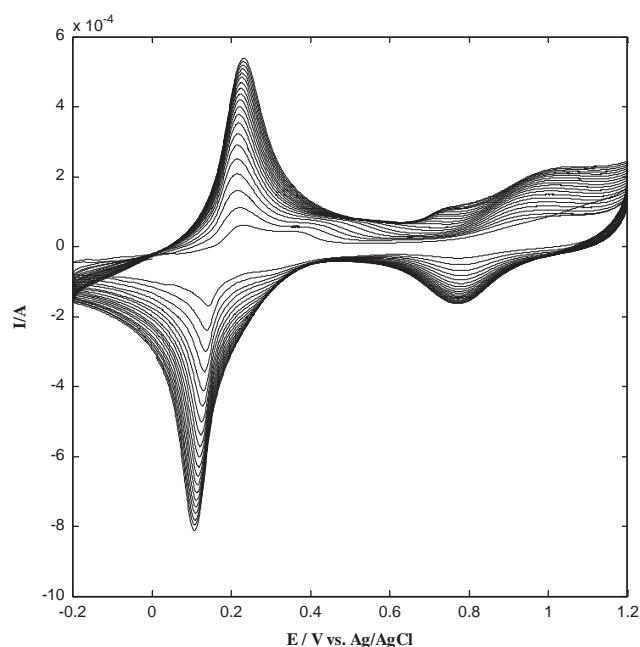


Fig. 1. Cyclic voltammograms of PB modified carbon electrode.

Table 2
PVC membranes for four exchangeable ions.

ISE	Ionophore (wt%)	Additive (wt%)	Plasticizer (wt%)	PVC (wt%)	Refs.
Na ⁺	ETH175 (1.0)	K ₊ TpCIPB ⁻ (0.1)	DOS (65.9)	33.0	[28]
K ⁺	Valinomycin (1.0)	K ₊ TpCIPB ⁻ (0.5)	DOS (65.5)	33.0	[28,29]
Ca ²⁺	ETH5234 (1.0)	K ₊ TpCIPB ⁻ (0.3)	oNPOE (66.0)	32.9	[30,31]
Mg ²⁺	ETH5506 (1.0)	K ₊ TpCIPB ⁻ (0.7)	oNPOE (66.3)	32.0	[32]

Table 3
Synthetic samples for calibration and validation (Unit: mg/L).

No.	Ca ²⁺	Mg ²⁺	K ⁺	Na ⁺	No.	Ca ²⁺	Mg ²⁺	K ⁺	Na ⁺
C1	1	1	1	5	V1	25	25	50	350
C2	75	75	1	100	V2	5	75	25	100
C3	150	150	1	500	V3	10	75	40	250
C4	10	10	1	50	V4	25	50	100	150
C5	10	150	50	5	V5	50	25	5	50
C6	150	75	10	5	V6	75	10	10	75
C7	75	10	125	5	V7	50	100	50	75
C8	1	150	125	100	V8	25	25	50	25
C9	150	1	125	50	V9	10	100	50	200
C10	1	75	50	50	V10	1	25	1	300
C11	10	75	125	500	V11	75	75	25	400
C12	10	1	10	100	V12	100	50	25	75
C13	75	1	50	500	V13	100	5	15	400
C14	75	150	10	50	V14	10	1	25	200
C15	150	10	50	100	V15	25	50	5	100
C16	1	10	10	500					

Cx: Calibration samples; Vx: validation samples.

3. Results and discussion

3.1. Electrode characteristics

A detection limit and linear detection range for each ISE was estimated using single ion standard solutions (CaCl₂, KCl, MgCl₂ and NaCl). As other calibration samples, these single ion standard

Table 4
The characters for the ISEs.

ISE	Sensitivity ^a	Stability ^b	Repeatability ^c	Reproducibility ^c	PRR ^d
Na ⁺	50.7	8.5	0.14	2.09	14.95
K ⁺	51.8	6.3	0.07	2.19	15.06
Ca ²⁺	24.3	9.1	0.18	3.38	18.86
Mg ²⁺	23.1	8.9	0.17	3.53	19.26

^a Unit: mV/dec.

^b % Of the decrease of sensitivity.

^c % Of Variance based on ANOVA Gauge R&R analysis.

^d % Of Gauge R&R of total variations.

solutions also employed the 1000 mg/L tetramethylammonium chloride and hydrochloric acid solution as the support electrolyte, pH value was around 5.5 at 22 °C. These concentrations ranged from 0.1 mg/L to 1000 mg/L, which was confirmed by ICP-OES. Each solution was measured in triplicate. The detection limits and linear detection ranges are listed in Table 4. For sodium and potassium, which are monovalent ions, the calibration curves' slopes were 50.7 and 51.8, respectively. For divalent ions the slopes were 24.3 and 23.1 for calcium and magnesium, respectively. The detection limit and linear response range were calculated according to the IUPAC recommendations [8]. Except for sodium, whose detection limit was around 0.5 mg/L and linear response ranged from 10 to 10⁴ mg/L, the remaining ions could be detected under 0.1 mg/L and linear response ranged from 1 to 10³ mg/L. In order to evaluate the influences of the cross-interferences, the ISE array was calibrated using all the single ion standard solutions, with 4-tenfold levels: 0.1 to 100 mg/L for ISEs of Ca, Mg and K; and 1 to 1000 mg/L for Na ISEs. The cross-interference phenomena for these four exchangeable cations and their ISEs are illustrated in Fig. 2. These phenomena existed in all ISEs that we employed, and the most severe interference occurred when the K ions influenced the Na ISE. The Na ISE utilized, gave a 7.8 mV/dec response to K ions.

With reference to temporal stability measurements, the ISE array was stored in a mixture solution – containing 100 mg/L CaCl₂, 100 mg/L KCl, 100 mg/L MgCl₂ and 100 mg/L NaCl with the same background as mentioned before – for 4 weeks. The sensitivity and selectivity of each ISE was measured in each one week period using the same 4 ten-fold calibration standard solutions. Over time both the sensitivity and selectivity of each ISE were gradually impaired, reflected in the decreasing calibration slopes (Table 4) and became more vulnerable to their interfering ions. Furthermore the potential values of all these ISEs gradually drifted lower. The most stable ISE was Ca with 7 mV drifting while the worst drifting belonged to Na ISE with 16 mV. Using the same data applied to temporal stability measurements, the repeatability and reproducibility (R&R) for the ISEs were estimated by ANOVA Gauge R&R analysis [33]. In this analysis, the response results of ISEs for each standard solution were considered as 'parts', and the data consisted of four parts. The measurements in each week were defined as different 'operators' and there were five operators: initial and week #1–4. The number of 'trials' was set at three since every solution was measured in triplicate. The R&R results – represented with % variations – are also shown in Table 4 with the relative variances. According to the results obtained, the best repeatability belonged to K ISE, while Na ISE had the best reproducibility. Percentage of Gauge R&R of total variations (PRR) provided a summary of these candidates and of these it emerged that Na ISE had the most stable characters, based on the results of measurements over four weeks.

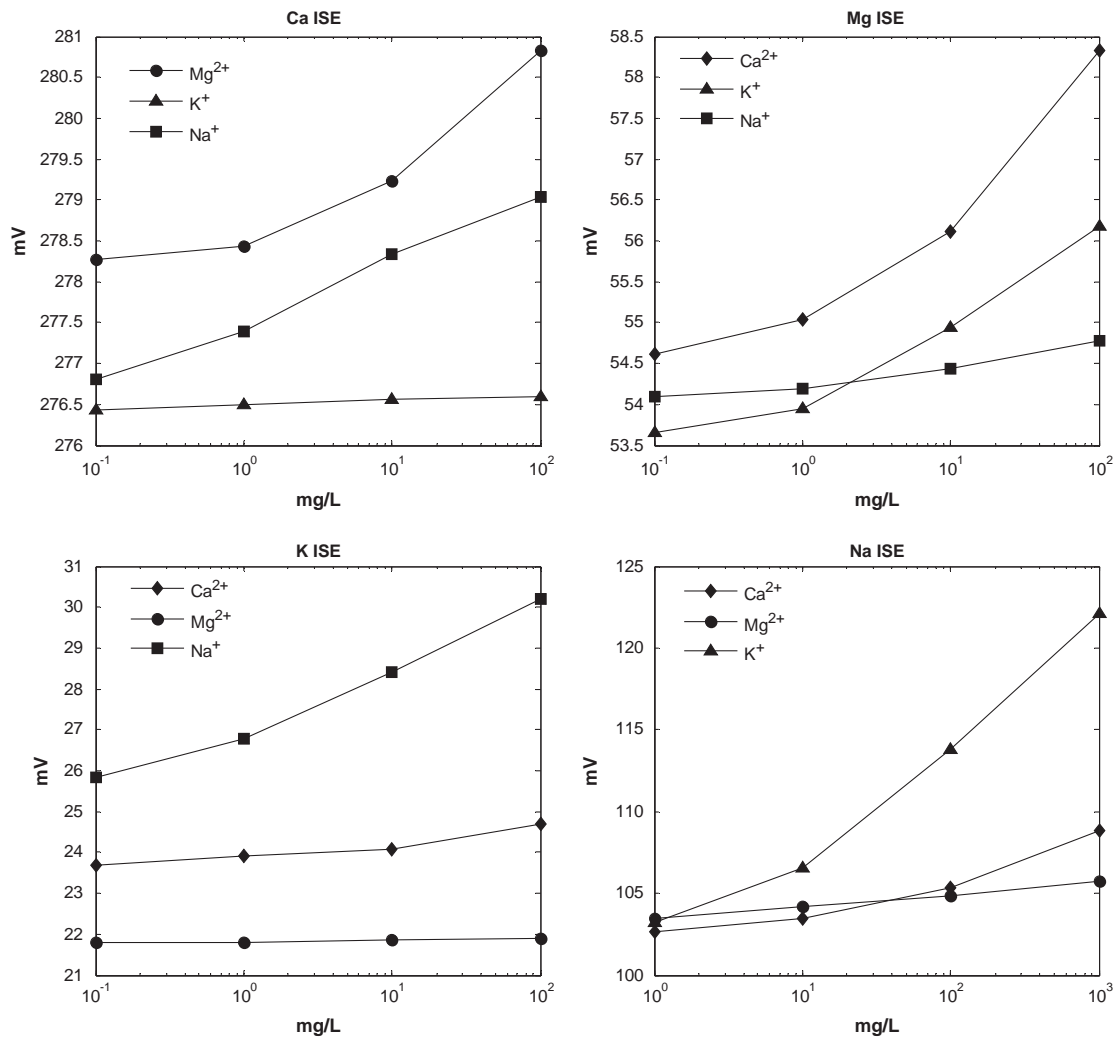


Fig. 2. Interference characteristics of the ISEs.

3.2. Implementation of geneticICA

As mentioned in our previous studies [25,26], we denoted the row input data matrix as $X = \{x_1, x_2, \dots, x_{15}, x_{16}\}$, where each x_i was an input vector containing the four components, the responding values from the four working ISEs for each training sample (16 samples). The multivariate calibration procedure is indicated in Fig. 3. Before the ICA can be applied, the input data should be centered and whitened [24]. Firstly, the input data X was centered as $E\{X\}$ by subtracting the mean of each component. Secondly, PCA was employed as a signal whitening method to linearly transform the data into new uncorrelated components [24]. This can be done using eigenvalue decomposition of the covariance matrix of the input $E\{X\}$. The new component with the highest eigenvalue indicated the most important principal component of the training data set, and the four new components captured 54%, 23%, 15% and 8% of the data variance, respectively.

Following PCA, ICA was implemented to produce independent components (ICs) by maximizing the statistical independence of the estimated components. We denoted the independent component matrix as $S = W^T Z$, where matrix S is a mixture of independent components, W is the weight matrix for the whitened signal and Z is the whitened data matrix. When the number of independent components is settled, *fastICA* will start by randomizing

the weight matrix W , then simply iteratively replace every weight vector w in W with (2) and orthogonalize the matrix symmetrically until they converge:

$$w_{new} = E\{zg(w^T z)\} - E\{g'(w^T z)\}w \quad (2)$$

where is the $g(w^T z) = (w^T z)^3$, based on kurtosis-based algorithms [24].

In *geneticICA*, the genetic algorithm was employed to fix the local maxima problem of *fastICA* by starting with a number of random matrices as multi-points in the model's PDF. Considering the computational ability of a personal computer, the genetic algorithm was set at 40 chromosomes in one generation (population=40). To create chromosomes, 40 numbers of the separating matrices W with unit norm random values were initialized and orthogonalized. These 40 matrices were encoded into 40 chromosomes, where there is one matrix for each chromosome. In chromosome encoding, each chromosome represented one possible weight matrix W . The weight matrix $W = \{w_1, w_2, \dots, w_{15}, w_{16}\}$ will be transformed into a vector chr , where $chr = (w_1, w_2, \dots, w_{15}, w_{16})$. During *fastICA* with the Gradient Algorithm, for each iterative step, a new matrix W_{new} was calculated by applying function (1). The iteration ceased when W_{new}^T reached identity I , with an absolute error of 10^{-6} . Following this property, instead of using the gradient function

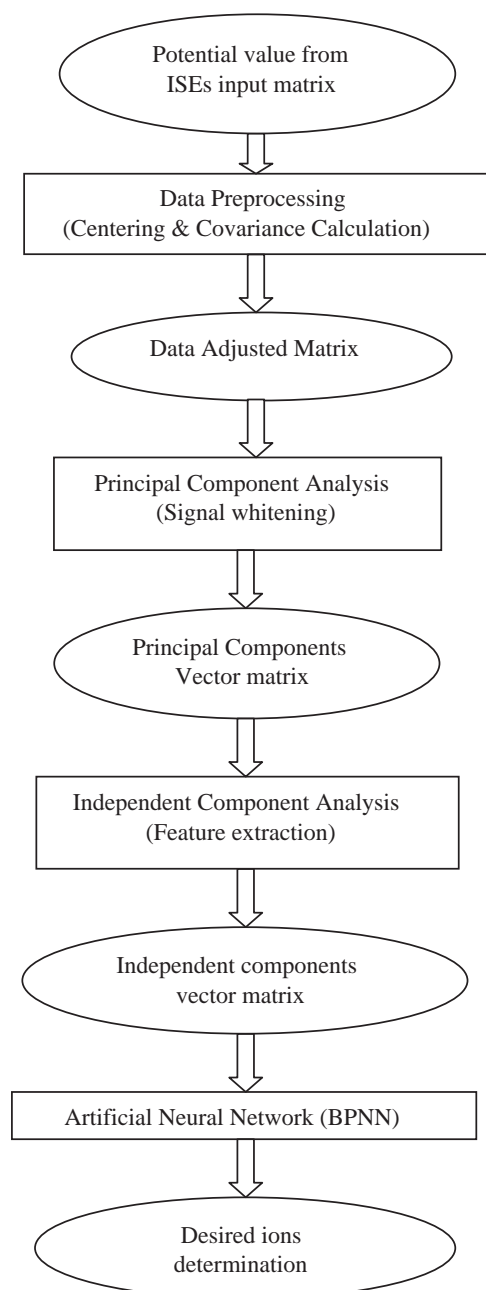


Fig. 3. A flow diagram identifying the multivariate calibration methods.

(1) iteratively, for each weight matrix W encoded in a chromosome, the *geneticICA* calculates the relative W_{new} with function (1) exactly once. Thus, the fitness value of each chromosome was estimated by how WW_{new}^T was close to identity I . The chromosome whose WW_{new}^T is closer to identity I would be regarded as having better fitness.

In every GA generation, the fitness value of each chromosome was calculated and checked. The GA continued until a proper chromosome was found, whose fitness value satisfied the accuracy (WW_{new}^T reached identity I , with an absolute error of 10^{-6}). If no acceptable chromosome was found then the algorithm was terminated when the maximum number of generations (set at 500) was reached. For offspring, the parents were selected using Stochastic Universal Sampling, recombined by multi-point crossover and mutating each element with an initial probability ($p=0.7$). By using this selection method, the chromosomes with better fitness values are more likely to be selected as the parents and breed the

offspring for the subsequent generations. Following *geneticICA*, four Independent Components (ICs) were obtained. The linear relationships between PCs, especially between PC 1 and PC 2, which can be observed from the scatter matrix of PCs (Fig. 4), were eliminated by the *geneticICA*. As revealed in Fig. 4, there is no linear correlation between the resultant ICs, since the ICs are mutually orthogonal. Although the ICs are considered to be latent variables, i.e. they are not able to be directly observed, they can be used as feature information for determining neural networks.

3.3. Artificial neural network

As ISEs have a logarithmic linear response to metal ion concentrations the BPNN system was trained in a logarithmic way, and the prediction results were expressed logarithmically. The architecture of the BPNN model for determination was $4 \times N \times 4$: one input layer with four neurons (one IC each); one hidden layer whereby the number of hidden neurons was determined by optimization; and one output layer with four output neurons, corresponding to the four predicted concentrations of Na^+ , K^+ , Ca^{2+} and Mg^{2+} , respectively. To optimize the performance of the BPNN, the training parameters were set to a maximum of 300 epochs, with a fixed error goal for the training subset of 0.001 of the Root Mean Square Error (RMSE). The robustness and appropriateness of the approach was assessed using the mean of the Relative Error (MRE) of the testing set (15 synthetic samples), between the predicted and the known concentrations. All neuron numbers of the hidden layer from 2 to 23 were parallel trained, and their performance was compared.

While there are several potential training algorithms which use the BPNN model in Matlab, no one algorithm is best suited to all applications [34,35]. Therefore, the performances of three transfer functions: linear, tangent sigmoid and log sigmoid; and five training functions: Bayesian regulation back-propagation, conjugate gradient back-propagation, gradient descent back-propagation, Levenberg–Marquardt back-propagation and scaled conjugate gradient back-propagation, were also compared [35]. After optimization, the architecture of the BPNN model was set at $4 \times 18 \times 4$ to simultaneously determine the four exchangeable ions. The tangent sigmoid transfer function was used for the hidden layer. The linear transfer function was employed as the output function for the output layer. The weights and biases of the BPNN were randomly initialized before applying the Bayesian regulation back-propagation training function. The mean of relative errors between predicted results and known values for the four exchangeable cations were all under 10%.

3.4. Real sample validation (case study)

To validate the system, twenty real irrigation water samples, including underground water, surface water and reserve water, were collected from five different areas in South Australia: Barossa Valley, Mawson Lakes, McLaren Vale, Woodside and Berri. The samples were collected using standard water sampling procedures, and these solutions were delivered to the laboratory and analyzed in 24 h [36]. During their transfer to the laboratory, these samples were covered with ice and kept in a sealed container. The prediction results by ISE array were compared to inductively coupled plasma optical emission spectrometry (ICP-OES). Each sample was measured in triplicate by ISE array and duplicate by the ICP-OES and the average values were recorded. The prediction results compared to ICP-OES for the four exchangeable cations are shown in Fig. 5. Compared to the 1:1 line, which is represented as one continuous line, it is clearly evident that Na and K were closer to 1:1 rather than Ca and Mg, which were underneath.

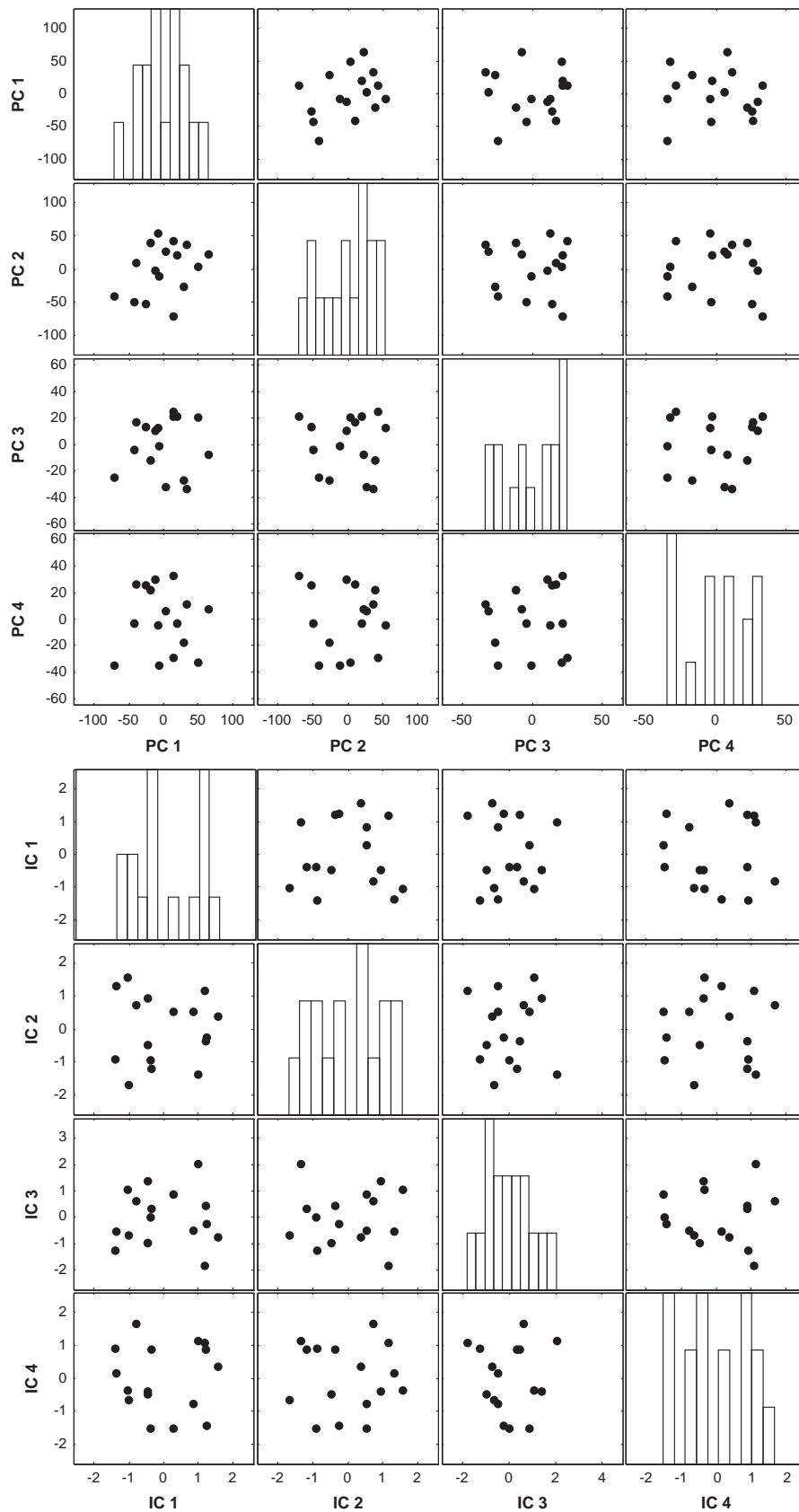


Fig. 4. Scatter matrices of principal components (PCs) and independent components (ICs) for training data set.

The reason is that ICP-OES calculates the total ion concentrations including free ions and their complex species, but ISEs are responsive to ion activities relative to free ions only. There will be

many complexities for Ca and Mg, since these samples' pH values were in the neutral range. For comparison, the prediction accuracies of *geneticICA_BPNN*, *fastICA_BPNN* and BPNN without the data

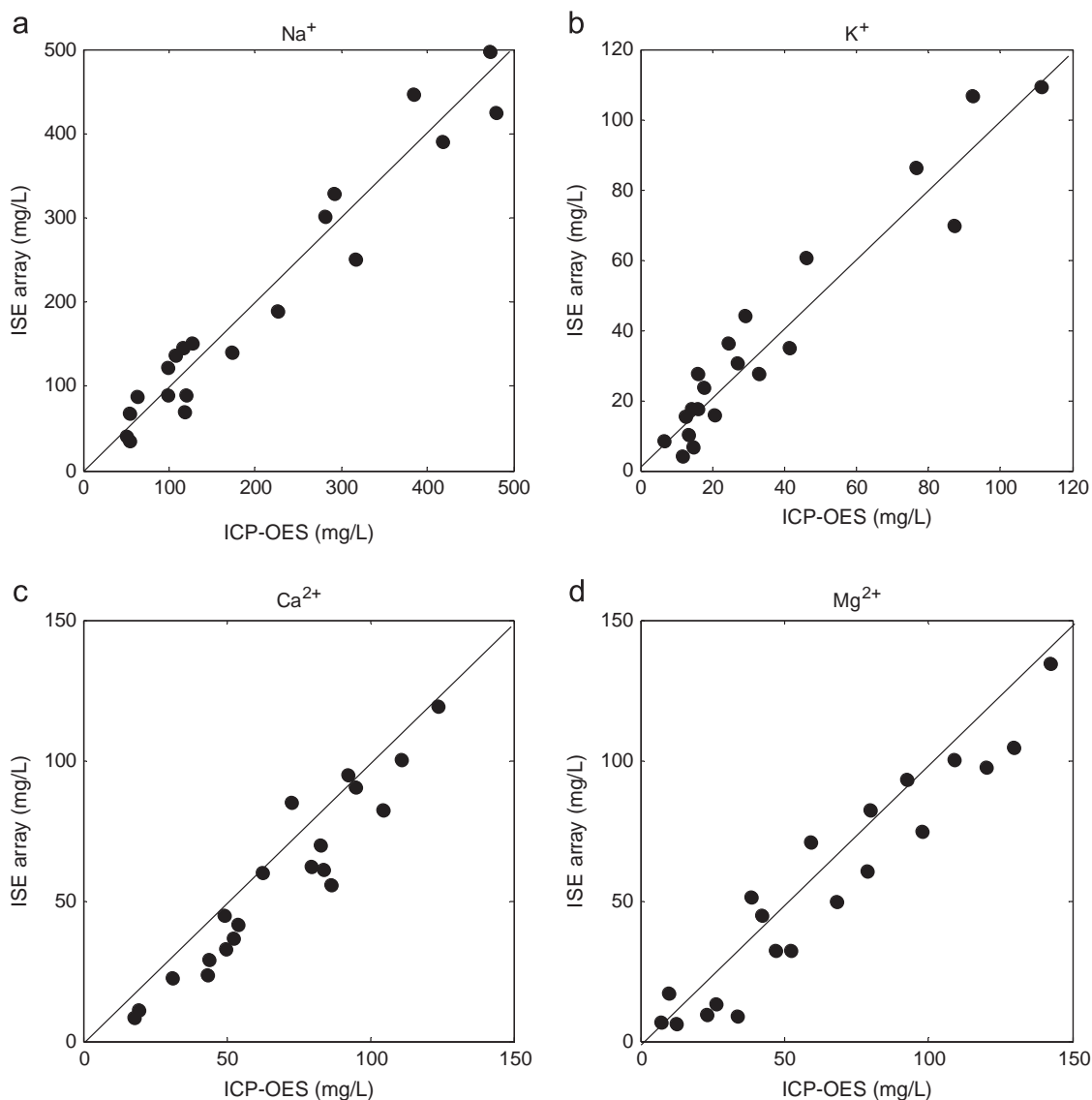


Fig. 5. Predicted results vs. ICP-OES for 20 real water samples (1:1: continuous line).

Table 5

Variation of accuracy with processing methods (mass concentrations, triplicated and average values were taken, unit: %).

Methods	Real irrigation water samples validation							
	Na ⁺		K ⁺		Ca ²⁺		Mg ²⁺	
	MRE	CL	MRE	CL	MRE	CL	MRE	CL
NONE	23.4	49.0	21.8	38.3	28.2	57.0	32.8	77.3
<i>fastICA</i>	21.8	44.4	21.5	37.6	27.3	51.8	31.4	73.2
<i>geneticICA</i>	20.2	38.2	21.6	36.2	22.9	45.7	28.8	57.7

None: artificial neural network implemented without data preprocessing methods; *fastICA*: independent component analysis implemented with Fix-point algorithm; *geneticICA*: independent component analysis implemented with genetic algorithm; MRE: mean of relative errors; CL: One-sided 95% confidence interval.

preprocessing method are summarized in Table 5. All the BPNN models adopted had the same structures.

Two parameters were applied for comparison: Mean Relative Errors (MRE), one side 95% confidence levels (CLs), and the findings are displayed in Table 5. There was a slight or no difference for

predicting potassium in our samples among the three candidates, since the potassium-selective electrode had little cross-interference impact. Moreover, by comparing *fastICA* and *geneticICA*, there was a mediocre improvement for predicting sodium and magnesium when using the genetic algorithm. Nonetheless it can be concluded that the prediction accuracies of BPNN can be enhanced by applying ICA methods (both *fastICA* and *geneticICA*). Furthermore, the *geneticICA* can further improve the prediction accuracies better than *fastICA*, especially for predicting calcium, where improvement was clearly evident.

The SPAR values were calculated and compared using the concentrations from ICP-OES and predicting results from *geneticICA*_BPNN (Fig. 6). Since most of the prediction results for Ca and Mg were lower than ICP-OES, it was expected some of the predicted SPAR values would be higher than ICP-OES. It can be seen in Fig. 6 that most of the water samples have no or moderate sodium hazard according to [37]. Two samples were located in the severe hazard cluster. These two samples are recycled water and therefore amendments should be applied for irrigation before they can be used. Only one recycled water sample collected from an artificial lake was not suitable for irrigation based on its SPAR value. The MRE between BPNN prediction and ICP-OES was 23.8% and 95% CL was 32.2%.

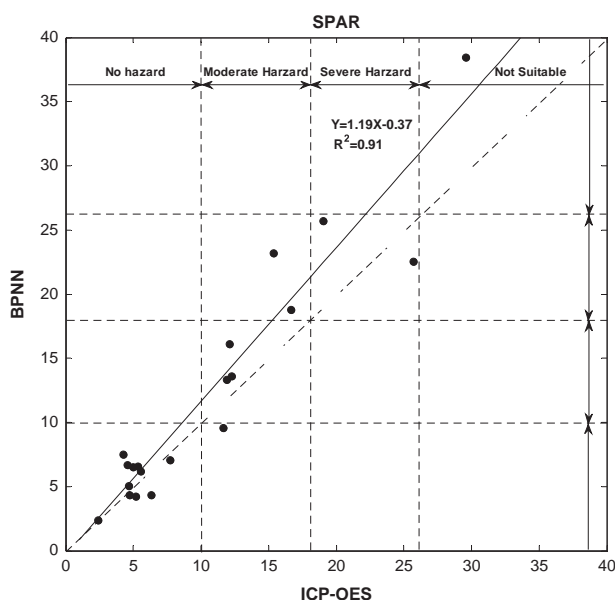


Fig. 6. Predicted results vs. ICP-OES for SPAR (1:1: dash line, regression: continuous line).

4. Conclusion

After being validated with 20 real irrigation water samples derived from South Australian winery and urban areas, it can be concluded that by using only a small number of calibration samples, this ET system was still able to simultaneously determine the four exchangeable ions with acceptable prediction accuracies. The concentration ranges for the training samples should be able to adjust according to the irrigation water conditions. The narrower the training range, then the more accurate will be predicting the SPAR value. Since the main irrigation source in South Australia is underground water (bore water), the water conditions vary from bore to bore, based on the depth and location. Giving a wider concentration training range is more practical for South Australia. Furthermore, since KNO_3 , $\text{Ca}(\text{NO}_3)_2$ and $\text{Mg}(\text{NO}_3)_2$ are popular fertilizers, this system can also be used to monitor K^+ , Ca^{2+} and Mg^{2+} nutrients in some fertilizer applications.

However, this study employed only relatively short-term measurements, and the decreasing influence of the sensitivity and selectivity that may occur over longer periods was not considered. It is still difficult to use 16 solutions and operate the software so that end users can calibrate the system. Based on our ISE temporal stability experiment, both the sensitivity and selectivity of ISEs became gradually impaired over time. In this situation re-calibration will be complicated, since the cross-interfering characters must also be considered. Future studies should concentrate on how to robustly re-calibrate the ISE array system with variable sensitivities for long-term and successful on-line monitoring. Finally, in this study, these desired cations were simultaneously determined in an ideal environmental scenario, where pH, ion strength, temperature and other forms of interference (from unknown ions) were all relatively constant. For field testing all these factors should be incorporated into the calibration process as variables.

Acknowledgements

The authors would like to thank the Cooperative Research Centre for Contamination Assessment and Remediation of the

Environment and the University of South Australia for making this research possible. This research was funded by CRC CARE Pty Ltd. and is the subject of a patent, patent number WO2012083371. The research was conducted in the laboratories of the Centre for Environmental Risk Assessment and Remediation (CERAR) at the University of South Australia.

Appendix A. Supporting information

Supplementary data associated with this article can be found in the online version at <http://dx.doi.org/10.1016/j.talanta.2014.08.010>.

References

- [1] D.L. Rowell, *Soil Science Methods and Applications*, Longman Scientific & Technical, UK, 1994.
- [2] P. Sarah, *J. Arid. Environ.* 59 (2004) 731–741.
- [3] N.F. Gray, *Drinking Water Quality*, Cambridge University Press, UK, 2008.
- [4] M. Liu, J. Yang, X. Li, M. Yu, J. Wang, *J. Integr. Agric.* 11 (2012) 502–511.
- [5] R.N. Carrow, R.R. Duncan, M.T. Huck, *Turfgrass and Landscape Irrigation Water Quality*, CRC Press, U.S., 2008.
- [6] M. Burnier, *Sodium in Health and Disease*, Informa Healthcare USA, Inc., U.S., 2008.
- [7] W.E. Morf, *The Principles of Ion-selective Electrodes*, Elsevier, U.S., 1981.
- [8] R.P. Buck, E. Lindner, *Pure Appl. Chem.* 66 (1994) 2527–2536.
- [9] N.M. Ivanova, M.B. Levin, K.N. Mikhelson, *Russ. Chem. Bull.* 61 (2012) 926–936.
- [10] E. Lindner, R.E. Gyurcsányi, *J. Solid State Electrochem.* 13 (2009) 51–68.
- [11] F. Ricci, G. Palleschi, *Biosens. Bioelectron.* 21 (2005) 389–407.
- [12] C. Gabrielli, P. Hémerly, P. Liatsi, M. Masure, H. Perrot, *J. Electrochem. Soc.* 152 (2005) 219–224.
- [13] R.C. Cretu, D.M. Gligor, L. Muresan, I.C. Popescu, L.M. Muresan, *J. Appl. Electrochem.* 36 (2006) 1327–1332.
- [14] D. Moscone, D. D'Ottavi, D. Compagnone, G. Palleschi, A. Amine, *Anal. Chem.* 73 (2001) 2529–2535.
- [15] A.V. Mueller, H.F. Hemond, *Talanta* 117 (2013) 112–118.
- [16] L. Nuñez, X. Cetó, M.I. Pividori, M.V.B. Zanon, M. del Valle, *Microchem. J.* 110 (2013) 273–279.
- [17] M. Gutiérrez, S. Alegret, R. Cáceres, J. Casadesús, O. Marfà, M. del Valle, *Comput. Electron. Agric.* 57 (2007) 12–22.
- [18] M. Cortina, A. Gutiérrez, S. Alegret, M. del Valle, *Talanta* 66 (2005) 1197–1206.
- [19] M. Gutierrez, S. Alegret, M. del Valle, *Biosens. Bioelectron.* 22 (2007) 2171–2178.
- [20] D. Calvo, A. Durán, M. del Valle, *Anal. Chim. Acta* 600 (2007) 97–104.
- [21] D. Calvo, A. Durán, M. del Valle, *Sens. Actuators, B* 131 (2008) 77–84.
- [22] A. Hyvärinen, E. Oja, *Finland Neural Networks* 13 (2000) 411–430.
- [23] T. Adali, C. Jutten, J.M.T. Romano, A.K. Barros, *Independent Component Analysis and Signal Separation*, in: Eighth International Conference, ICA 2009, Paraty, Brazil, Springer-Verlag, Berlin, Heidelberg, 2009.
- [24] T.W. Lee, *Independent Component Analysis*, Springer, U.S., 1998.
- [25] R. Naidu, L. Wang, Z. Chen, M. Megharaj, *Analyte Ion Detection Method and Device*, Patent: WO2012083371, 28 June 2012.
- [26] L. Wang, D. Yang, Z. Chen, P.J. Lesniewski, R. Naidu, *J. Chemom.* (2014) (<http://dx.doi.org/10.1002/cem.2599>).
- [27] L. Ji, Y. Si, H. Liu, X. Song, W. Zhu, A. Zhu, *Microporous Mesoporous Mater.* 184 (2014) 122–126.
- [28] M. Kessler, D.K. Harrison, J. Höper, *Ion Measurements in Physiology and Medicine*, Springer-Verlag, Berlin, Heidelberg, 1985.
- [29] D.M. Band, J. Kratochvil, P.A. Poole Wilson, T. Treasure, *Analyst* 103 (1978) 246–251.
- [30] U. Schefer, D. Ammann, E. Pretsch, U. Oesch, W. Simon, *Anal. Chem.* 58 (1986) 2282–2285.
- [31] I. Bedlechowicz-Sliwakowska, P. Lingenfelter, T. Sokalski, A. Lewenstam, M. Maj-Zurawska, *Anal. Bioanal. Chem.* 385 (2006) 1477–1482.
- [32] W. Zhang, L. Jenny, U.E. Spichiger, *Anal. Sci.* 16 (2000) 11–18.
- [33] R.K. Burdick, C.M. Borrer, D.C. Montgomery, *Am. Stat. Assoc. Soc. Ind. Appl. Math. U.S.* (2005).
- [34] J.N. Miller, J.C. Miller, *Statistics and Chemometrics for Analytical Chemistry*, Prentice Hall, U.S., 2005.
- [35] H. Tang, K.C. Tan, Z. Yi, *Neural Networks Computational Models and Applications*, Springer-Verlag, Berlin, Heidelberg, 2007.
- [36] N. Wilson, *Soil Water and Ground Water Sampling*, CRC Press, U.S., 1995.
- [37] D.S. Loch, R.E. Poulter, M.B. Roche, C.J. Carson, T.W. Lees, L. O'Brien, C.R. Durant, *Amenity Grasses for Salt-Affected Parks in Coastal Australia*, Horticulture Australia, Australia (2006).



Selective ionic liquid ferrofluid based dispersive–solid phase extraction for simultaneous preconcentration/separation of lead and cadmium in milk and biological samples



Negin Fasih Ramandi, Farzaneh Shemirani*

Department of Analytical Chemistry, University College of Science, University of Tehran, P.O. Box 14155-6455, Tehran, Iran

ARTICLE INFO

Article history:

Received 23 June 2014

Received in revised form

2 August 2014

Accepted 4 August 2014

Available online 12 August 2014

Keywords:

Selective Ionic liquid-Ferrofluid
TiO₂ coated magnetic nanoparticles
modified by 1-(2-pyridylazo)-2-naphtol
Ionic liquid-ferrofluid based
dispersive–solid phase extraction
Magnetic nanoparticles
Box–Behnken design.

ABSTRACT

For the first time, a selective ionic liquid ferrofluid has been used in dispersive solid phase extraction (IL-FF-D-SPE) for simultaneous preconcentration and separation of lead and cadmium in milk and biological samples combined with flame atomic absorption spectrometry. To improve the selectivity of the ionic liquid ferrofluid, the surface of TiO₂ nanoparticles with a magnetic core as sorbent was modified by loading 1-(2-pyridylazo)-2-naphtol. Due to the rapid injection of an appropriate amount of ionic liquid ferrofluid into the aqueous sample by a syringe, extraction can be achieved within a few seconds. In addition, based on the attraction of the ionic liquid ferrofluid to a magnet, no centrifugation step is needed for phase separation. The experimental parameters of IL-FF-D-SPE were optimized using a Box–Behnken design (BBD) after a Plackett–Burman screening design. Under the optimum conditions, the relative standard deviations of 2.2% and 2.4% were obtained for lead and cadmium, respectively ($n=7$). The limit of detections were 1.21 $\mu\text{g L}^{-1}$ for Pb(II) and 0.21 $\mu\text{g L}^{-1}$ for Cd(II). The preconcentration factors were 250 for lead and 200 for cadmium and the maximum adsorption capacities of the sorbent were 11.18 and 9.34 mg g^{-1} for lead and cadmium, respectively.

© 2014 Elsevier B.V. All rights reserved.

1. Introduction

Ferrofluids are stable magnetic nanoparticle suspensions in a carrier liquid. Basically, in ferrofluids, the single domain magnetic nanoparticles should be coated by a suitable material, to prevent particles from agglomerating [1]. The stability of the ferrofluid is due to the balance between repulsive (Brownian motions, steric and electrostatic forces) and attractive interactions (Van der Waals and dipolar attractive forces) [2]. Although the amount of magnetic nanoparticles in ferrofluids is about 3–10%, and many properties of ferrofluids, such as vapor pressure and density, are the same as the base fluid, these materials possess magnetic properties and fluidity simultaneously [3]. Therefore, the coating material and the carrier liquid have a crucial role in the field of ferrofluids. By choosing different carrier liquids and coating materials, wide applications of ferrofluids have been reported in different research areas such as biomedical [4], microelectronics [5], biological microelectromechanical systems [6] and also analytical chemistry [7–9]. As a result, research in this field has been focused on coating agent materials and carrier liquids.

For selecting an appropriate coating material, several criteria should be met. For instance, it should be non-toxic, low cost, chemically stable, and also compatible with carrier liquid. It has been proven that some chemical or physical surface modifications of coating material have improved its selectivity and/or affinity toward special species [10,11]. Due to its non-toxicity, low cost, long-term chemical stability, and easy surface modification, TiO₂ has been proven to be an excellent choice of coating material [12]. Also, chelating agents are the most common modifiers which consist of donor atoms such as oxygen, nitrogen, and phosphorus. Due to the presence of these donor atoms, selective binding with certain species on the surface of coating material will occur [13]. In some publications, ferrofluids were used in field of analytical chemistry, but in all of them magnetic nanoparticles were coated by silica [7–9]. Also, the selectivity of the ferrofluid was not the purpose of these studies. In spite of the wonderful properties of TiO₂ as an excellent coating agent, there is no report on using TiO₂, and also modified TiO₂, in the field of ferrofluids, although it can improve the selectivity of ferrofluids greatly. However, to provide a stable ferrofluid, in the next step, a unique structure and properties of carrier fluid are critical.

Ionic liquids (ILs) have been emerging in recent years as novel, stable, and environmentally friendly compounds with amazing properties such as negligible vapor pressure, low flammability, and

* Corresponding author. Tel.: +98 21 6111 2481; fax: +98 21 6640 5141.

E-mail address: shemiran@khayam.ut.ac.ir (F. Shemirani).

liquid state in a broad temperature range [14]. Additionally, due to the presence of electrostatic, hydrogen bonding, and Van der Waals interactions, ILs possess unique structure, which provides a protective shell around magnetic nanoparticles and improves the ferrofluids' stability greatly [15–17]. Therefore, by choosing ionic liquid as a carrier fluid, very stable ferrofluids can be prepared, which is suitable to use in sample preparation methods [18].

Determination of heavy metals in biological and in food samples has become a key interest because of their toxic effects on living beings [19,20]. Heavy metals such as Cd(II) and Pb(II) cause irreparable effects on the urinary tract, liver, blood chemistry and the cardiovascular system [21]. Several studies have been reported for preconcentration-separation of Cd(II) and Pb(II) such as solid phase extraction [22–25] liquid-liquid extraction [26] cloud point extraction [27,28] and dispersive liquid-liquid extraction [29,30]. In spite of some benefits, these methods suffer from many drawbacks. Therefore, improvements are necessary. In this study, we want to report a very simple, fast, efficient, and selective preconcentration-separation method which is assisted by ionic liquid ferrofluid for cadmium and lead.

The purpose of this work was to use TiO₂ as an excellent coating material for magnetic nanoparticles and also improve its selectivity by loading 1-(2-pyridylazo)-2-naphthol on its surface. Additionally, to provide a stable ferrofluid, 1-Hexyl-3-methylimidazolium tetrafluoroborate was chosen as the carrier liquid. Therefore, selective ionic liquid ferrofluid based dispersive solid phase extraction (IL-FF-D-SPE) was used for preconcentration-separation of cadmium and lead in milk, human urine, and blood plasma samples combined with flame atomic absorption spectrometry (FAAS), which is a very fast, easy, cheap, and selective determination technique in comparison with other methods such as ICP-MS. Additionally, different parameters which effected the extraction recovery of Pb(II) and Cd(II) were investigated with the help of chemometrics method.

2. Experimental

2.1. Instruments

The determination of Pb(II) and Cd(II) was carried out using a Varian Spectra AA-400 atomic absorption spectrometer (Santa Clara, USA, www.varianinc.com), equipped with a deuterium background correction and an air-acetylene burner. The lamp currents were set at 5 and 4 mA for Pb(II) and Cd(II), respectively. All measurements were carried out in the peak height mode at 217.0 and 228.8 nm, using a spectral band width of 1.0 nm and 0.5 nm for Pb(II) and Cd(II), respectively. A pH meter Model 692 from Metrohm (Herisau, Switzerland, www.metrohm-ag.com) equipped with a glass combination electrode was used for the pH measurements. Additionally, for magnetic separations, a strong neodymium-iron-boron (Nd₂Fe₁₂B) magnet (1.31 T) was used. A Field emission scanning electron microscope (FESEM), model S-4160 (www.hitachi.com/procurement/network/japan) was used for preparation of SEM images. Fourier transform infrared spectra (FT-IR) were recorded from a KBr disk using an Equinox 55 Bruker (Billerica MA, USA, www.bruker.com) with the ATR method over the wavelength range of 400–4000 cm⁻¹. For separation of human blood plasma from a blood sample, a refrigerated centrifuge (Hettich, Universal 320R, www.hettichcentrifuge.co.uk, Buckinghamshire, England) equipped with an angle rotor (6 place, 9000 rpm, cat no 1620 A) was used.

2.2. Reagents

All chemicals used were of analytical reagent grade unless otherwise stated. All aqueous solutions were prepared using

ultra-pure water. Water was purified using Milli-Q purification system. The stock standard solutions of Cd(II) and Pb(II) (1000 mgL⁻¹) were prepared from appropriate amounts of their nitrate salts (Merck, Darmstadt, Germany, www.merck.de) in ultra-pure water and working standard solutions were prepared by appropriate stepwise dilution of the stock standard solutions. 1-Hexyl-3-methylimidazolium tetrafluoroborate [Hmim]BF₄ 98%, 1-Hexyl-3-methylimidazolium hexafluorophosphate [Hmim]PF₆, 1-Hexyl-3-methylimidazolium bis(trifluoromethylsulfonyl) imide [Hmim][Tf₂N], 1-(2-pyridylazo)-2-naphthol, tetra-*n*-butyl orthotitanate (TBOT), NH₃, ethanol, and sodium dodecyl sulfate were purchased from Merck (Darmstadt, Germany). Nano-Fe₃O₄ was purchased from Sigma-Aldrich (St. Louis, MO, USA, www.sigmaaldrich.com, Fe₃O₄ spheres powder, < 40 nm, purity > 98%). Buffer solution (pH=6.7, 1 molL⁻¹) was prepared by dissolving appropriate amounts of potassium dihydrogen phosphate (1 molL⁻¹) and sodium hydroxide (1 molL⁻¹). High purity HNO₃, H₂O₂, HClO₄ and HCl were purchased from Merck (Darmstadt, Germany), which were used for the digestion of milk, urine, and blood plasma samples throughout this project. The pipettes and vessels were cleaned before use by soaking in 10% nitric acid solution for at least 24 hours and then rinsed thoroughly with distilled water.

2.3. Synthesis of titana-coated magnetite nanoparticles (Fe₃O₄/TiO₂)

First, 10 mL of tetra-*n*-butyl orthotitanate was dissolved in 70 mL ethanol to form a clear solution. Then, 0.2 g Fe₃O₄ nanoparticles were dispersed in this solution under sonication for approximately 5 min. While the suspension was stirred vigorously over a period of 15 min, a 1:5 (v/v) mixture of water and ethanol was added slowly with a dropper into this mixture. Then, the mixture was stirred further for 1 hour. Finally, after separating and washing the residue with ethanol, the obtained powder was oven-dried and calcinated at 200 °C for 6 h [31] (Fig. 1.).

2.4. Preparation of 1-(2-pyridylazo)-2-naphthol modified Fe₃O₄/TiO₂

In the present work, 1-(2-pyridylazo)-2-naphthol has been immobilized on sodium dodecyl sulfate-coated Fe₃O₄/TiO₂. The surface modification was done based on a previous report using some modifications [32]. In a 250 mL beaker, 1.0 g of Fe₃O₄/TiO₂ nanoparticles were dispersed in 20 mL of 0.001 molL⁻¹ HCl, under sonication. During sonication of this mixture, to avoid any changes in ionic strength, 0.3 mL of 1 molL⁻¹ NaNO₃ was added using a dropper. The pH of the solution was adjusted to 5. Then, 3 mL of 1 molL⁻¹ sodium dodecyl sulfate was added and solution was stirred for 1 h. After that 0.2 g 1-(2-pyridylazo)-2-naphthol was added and the solution was stirred for further 1 h at 60 °C in a water bath. Finally, the resulted suspension was filtered and dried under a vacuum.

2.5. Sample preparation

2.5.1. Human blood plasma sample

A fresh blood sample was obtained from a healthy volunteer a few minutes prior to this test. To obtain the blood plasma sample,

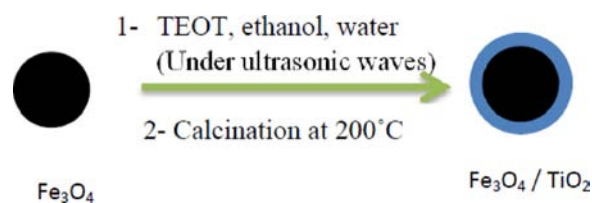


Fig. 1. Illustration for the formation process of Fe₃O₄/TiO₂.

the blood sample was centrifuged for 10 min at 4500 rpm. Then, 3 mL of the plasma sample was transferred to a clean polyethylene tube and 3 mL of nitric acid and 2 mL hydrogen peroxide were added to the sample. The tube was tightly capped and centrifuged for 10 minutes at 4400 rpm. Then, the sample was placed in a hot water bath at 95 °C for 90 min. Finally, the digested sample was diluted with 30 mL of distilled water.

2.5.2. Human urine sample

A fresh urine sample was obtained from a healthy volunteer a few minutes prior to this test. First, 10 mL of the urine sample was transferred to a 50 mL beaker. Next, 10 mL of a mixture of 2:1 concentrated HNO₃ and HClO₄ was added to urine sample. The beaker was covered with a watch glass and heated on a hot plate (100 °C 15 min, 150 °C 10 min). Then, the watch glass was removed and the acid evaporated to dryness at 150 °C. During the next step, by adding 3 mL HClO₄ to the resulting white residue, the mixture was heated at 160 °C until it was completely dried. Finally, 5 mL of 1 mol L⁻¹ H₂SO₄ was added and the mixture was heated at 150 °C for 1 min. After cooling the mixture, the volume was made up to the mark in a 50 mL volumetric flask.

2.5.3. Milk sample

A milk sample was purchased from local supermarket in Tehran. One milliliter of milk was transferred to a PTFE digestion vessel. Afterwards, 5 mL of concentrated HNO₃ and 2 mL H₂O₂ were added and the vessel was heated on a hot plate at a fairly low temperature, to avoid violent spurting. At the end of the digestion process, the vessel was cooled and reached room temperature. In the next step, the residue was dissolved in 1 mL 0.1 mol L⁻¹ HNO₃ and 10 mL of distilled water and filtered through a filter paper and transferred into a 50 mL volumetric flask and the volume was reached 50 mL by adding distilled water.

2.6. Preparation of ferrofluid

For the preparation of the ferrofluid, the adsorption of the stabilizing agent on sorbent is necessary; therefore, 10 mg of modified titana-coated magnetic nanoparticles with 1-(2-pyridylazo)-2-naphtol and 100 mL acetic acid, as a stabilizing agent, were mixed in a vial. The mixture was stirred and heated at 90 °C for approximately 45 min. Next, the resulted powder was dispersed in 0.1 g [Hmim]BF₄. After 30 min of sonication of this mixture, stable suspension of magnetic nanoparticles (ionic liquid-ferrofluid) was

obtained. The resulting suspension had a sorbent fraction of 9.1% and ionic liquid fraction of 90.9%.

2.7. Extraction procedure

The sample or standard solution contains 40 µg L⁻¹ Pb(II) and 30 µg L⁻¹ Cd(II), NaNO₃ (0% w/v), at pH 6.7, which were poured into a 50 mL tube. Then, by using a 1.0 mL syringe, the ionic liquid-ferrofluid, containing 0.03 g sorbent and 0.3 g ionic liquid, was injected into the sample solution to form a dark cloudy suspension (the volume of suspension was 0.28 mL). Due to the rapid injection of the ferrofluid into the aqueous sample, extraction was achieved within a few seconds. By using a strong magnet at the bottom of tube, the ferrofluid was settled and the solution became clear. After removing the supernatant by decanting, 1 mL nitric acid (1.59 mol L⁻¹) was added to the vial to desorb the Pb(II) and Cd(II) through 8 min sonication. Subsequently, a strong magnet was placed at the bottom of tube and immediately the solution became limpid. By using a syringe this clear solution was transferred to a vial for analyzing with FAAS.

3. Result and discussion

3.1. Characterization of adsorbent

Fig. 2 shows the SEM image of Fe₃O₄-coated nanoparticles with TiO₂. As it can be concluded from SEM image, the Fe₃O₄ nanoparticles were coated successfully with TiO₂ since the size of these nanoparticles has been changed from below 40 nm (before coating with TiO₂) to the range of 60–70 nm after coating.

Fig. 3 gives the FT-IR spectra pattern of Fe₃O₄ nanoparticles (a), Fe₃O₄/TiO₂ (b) and 1-(2-pyridylazo)-2-naphtol modified on Fe₃O₄/TiO₂ surface (c) in the range of 4000–400 cm⁻¹. Compared with the peaks of Fe₃O₄ in Fig. 3(a), many new peaks appeared in Fig. 3 (b and c). In Fig. 3(a–c), the presence of Fe-O band vibration at 534 cm⁻¹ is obviously observed. As seen in Fig. 3(b and c), the absorption peak at 550 cm⁻¹ assigned with stretching vibration of Ti-O band. Also, the absorption peak at 1041 cm⁻¹ is ascribed to Ti-O-H bond stretching. Peaks in region of 2864.4–2968.1 cm⁻¹ correspond to O-H stretch bond [33,12]. Due to presence of the band at 1640 cm⁻¹ which belong to pyridine ring of 1-(2-pyridylazo)-2-naphtol and 1436 cm⁻¹ which is attributed to N=N bond (Fig. 3(c)), the nanometer Fe₃O₄/TiO₂ is successfully modified by 1-(2-pyridylazo)-2-naphtol. [34].

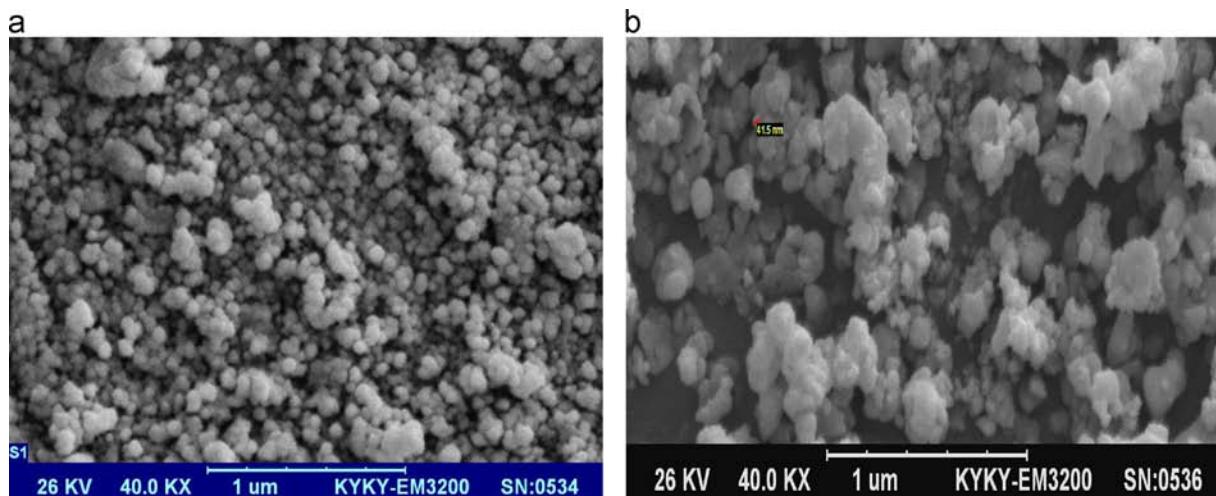


Fig. 2. The SEM images of (a) Fe₃O₄ NPs and (b) TiO₂-coated Fe₃O₄ NPs.

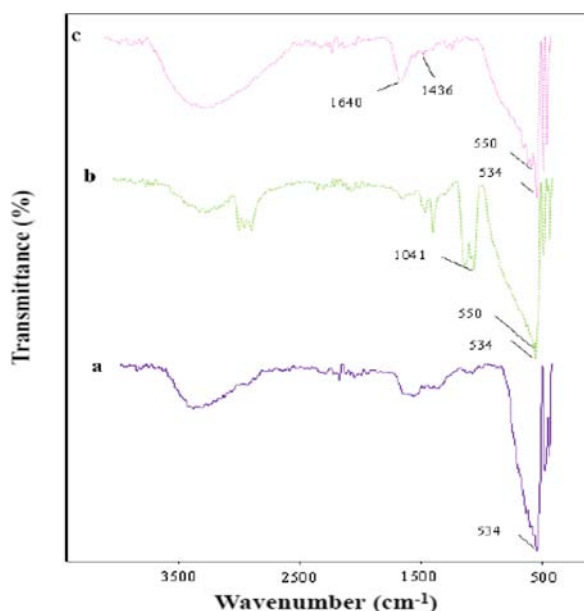


Fig. 3. FT-IR spectrums of Fe_3O_4 nanoparticles (a), $\text{Fe}_3\text{O}_4/\text{TiO}_2$ (b), and 1-(2-pyridylazo)-2-naphthol modified $\text{Fe}_3\text{O}_4/\text{TiO}_2$ (c).

3.2. Selection of ionic liquid for preparation of the ferrofluid

For selecting the best carrier fluid, apart from providing a stable ferrofluid, several criteria such as immiscibility with an aqueous solution, non-toxicity, having low vapor pressure to avoid any loss during extraction, and compatibility with coating material should be met. For this purpose, some ionic liquids such as 1-Hexyl-3-methylimidazolium tetrafluoroborate [Hmim] BF_4 , 1-Hexyl-3-methylimidazolium hexafluorophosphate [Hmim] PF_6 , and 1-Hexyl-3-methylimidazolium bis(trifluoromethylsulfonyl)imide [Hmim] Tf_2N were selected and, by the qualitative observation of sedimentation of each ferrofluid, the stability of the suspensions was checked. Finally, 1-Hexyl-3-methylimidazolium tetrafluoroborate [Hmim] BF_4 was chosen.

3.3. Selection of eluent

Based on the desorption of Pb(II) and Cd(II) from modified nanoparticles in the acidic medium, this medium would be preferred in desorption step. To avoid any losses of sorbent, chloric acid was not chosen because this acid can dissolve Fe_3O_4 nanoparticles. In addition, based on the possibility of formation of precipitate of lead in presence of sulfate ions, sulfuric acid was not chosen too. Therefore, the possibility of desorption of lead and cadmium ions in acidic medium was examined by using nitric acid [35]. Also, some organic solvent such as ethanol, ethanol (1% HNO_3) and acetone were selected to examine the possibility of desorption of these ions in organic medium. Based on the obtained result, nitric acid was chosen as the best eluent. The results are shown in Fig. 4.

3.4. Screening and optimization design

In this study, Plackett–Burman screening design was used to select the variables that mainly effect the extraction recovery of Pb (II) and Cd(II). Based on the preliminary experiments, the effects of seven factors, at two levels were investigated. Since pH would have significant effect on extraction recovery, to find the best pH value, both acidic and basic medium should be studied [36]. However in selecting of the two levels of pH, several criteria should be met. For instance, there was the possibility of

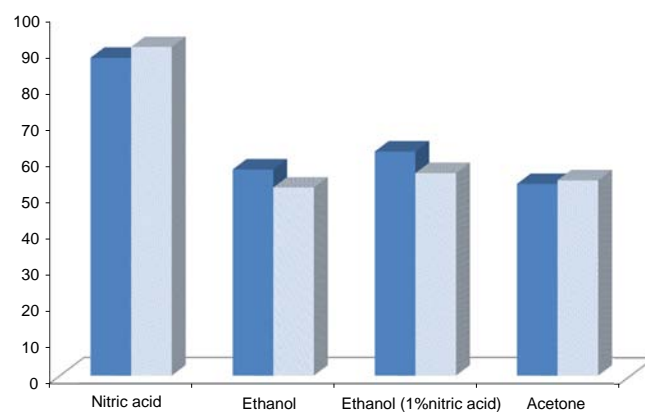


Fig. 4. Effect of type of eluent on the extraction recovery of Pb(II) (solid columns) and Cd(II) (downward diagonal columns).

protonation of 1-(2-pyridylazo)-2-naphthol at lower pH and also precipitation of metal ions at higher pH values. Therefore, pH 4 and 8 were selected. In addition, sorbent amount (0.01 and 0.03 g), ionic liquid amount (0.3 and 0.5 g), ionic strength (0 and 10% (w/v) NaNO_3), eluent volume (1 and 2 mL), eluent concentration (0.5 and 2 mol L^{-1}), and desorption time (5 and 10 min) were the other variables of interest in this experiment. The total design matrix showed 15 runs (12+3 center points) to be carried out randomly in order to eliminate the effects of extraneous or nuisance variables. The evaluation of the main effects was done based on ANOVA results and Pareto charts.

The normalized results of the experimental design were evaluated ($P=95\%$), and the standard effect is estimated for computing a t -statistic for each effect. A parameter is considered as significant when its value is higher than $\pm t$. All other variables are not significant factors in the studied range. As it can be concluded from Fig. 5(a and b), pH has significant positive effect on extraction recovery of Pb(II) and Cd(II). Also the results illustrated in Fig. 5(a and b) confirm that eluent concentration and desorption time have significant positive effects on extraction recovery of Pb(II) and Cd(II), respectively. And other parameters show no significant effect on the extraction recovery of both elements.

Therefore, the Box–Behnken design (BBD) was performed to evaluate the optimum condition of performance of IL-FF-D-SPE of Pb(II) and Cd(II) for the three significant parameters: pH, eluent concentration, and desorption time. The 3D response surface plots for the extraction recovery (%) of both elements were shown in Fig. 6. As seen in Fig. 6, an optimization showed that the best pH is 6.7, eluent concentration of 1.59 mol L^{-1} , and desorption time of 8 min.

The Box–Behnken design is suitable for exploration of the quadratic response surface and construction of a second order polynomial model which can be expressed as the following equations:

$$Y(\text{Cd}) = \alpha_0 + \alpha_1 A + \alpha_2 F + \alpha_3 G - \alpha_4 A^2 - \alpha_5 AF + \alpha_6 AG - \alpha_7 F^2 - \alpha_8 FG - \alpha_9 G^2$$

$$Y(\text{Pb}) = \beta_0 + \beta_1 A + \beta_2 F + \beta_3 G - \beta_4 A^2 + \beta_5 AF - \beta_6 AG - \beta_7 F^2 - \beta_8 FG - \beta_9 G^2$$

where α_0 and β_0 are intercepts, and α_1 – α_9 and also β_1 – β_9 are the regression coefficient, also $Y_{(\text{Pb})}$ and $Y_{(\text{Cd})}$ are response functions (extraction recovery) of lead and cadmium, respectively. In addition, A, F and G are pH, eluent concentration and desorption time, respectively. The quality of the fit of polynomial model equation was expressed by the coefficient of determination R^2 . However, to show more tangible how much obtained results are fitted to polynomial equations, the percentages of R^2 ($R^2\%$) are reported here. These equations have $R^2\%$ of 98.51% and 98.76% for lead and cadmium,

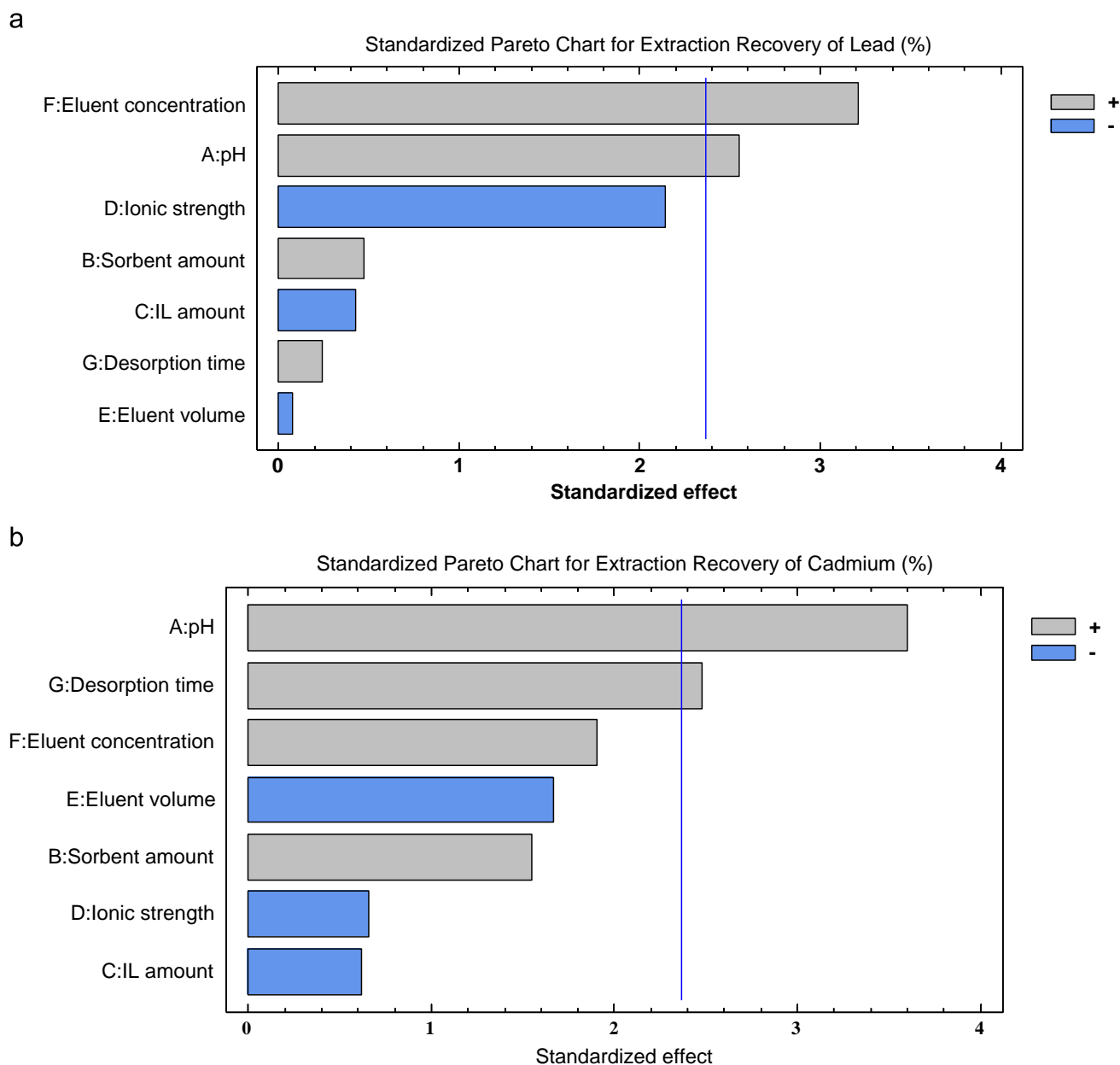


Fig. 5. Standardized ($P=0.05$) Pareto chart, representing the estimated effects of parameters obtained from the Plackett–Burman screening design for lead (a) and cadmium (b).

respectively. These results indicate that only 1.49% and 1.24% of the total variations were not explained by the model for lead and cadmium, respectively. At the optimum condition the highest extraction recovery of 99.3 and 99.8% were obtained for lead and cadmium, respectively.

3.5. Breakthrough volume

Due to the low concentration of trace metals in real samples, to achieve the higher preconcentration factor, the preconcentration step is inevitable. Therefore, after preconcentration step, samples with large volume should be taken into smaller volume. For this purpose, maximum applicable sample volume was determined by increasing the dilution of metal ions solution in range of 25–350 mL, while using the same amount of suspension (0.28 mL) for each sample and keeping the total amount of Pb(II) and Cd(II) fixed at 2.0 and 1.5 μg , respectively. The quantitative recoveries for Pb(II) and Cd(II) were found to be stable until 250 and 200 mL for Pb (II) and

Cd(II), respectively, and the adsorbed Pb(II) and Cd(II) could be eluted with 1 mL of eluent. Therefore, the concentration factor (CF) of 250 and 200 can be achieved for lead and cadmium ions, respectively.

3.6. Effect of potentially interfering ions

In order to assess the applications of the recommended procedure, the effect of potentially interfering ion on the extraction recoveries of Pb(II) and Cd(II) were also examined. For this purpose, by spiking appropriate amounts of potentially interfering ions in the range of 50–15000 $\mu\text{g mL}^{-1}$ to 50.0 mL of solution containing 40 $\mu\text{g L}^{-1}$ of Pb(II) and 30 $\mu\text{g L}^{-1}$ of Cd(II) evaluation was done. The obtained results are summarized in Table 1.

3.7. Adsorption isotherms

The interactive behavior of solution and the adsorbent can be predicted by equilibrium adsorption isotherm model which is

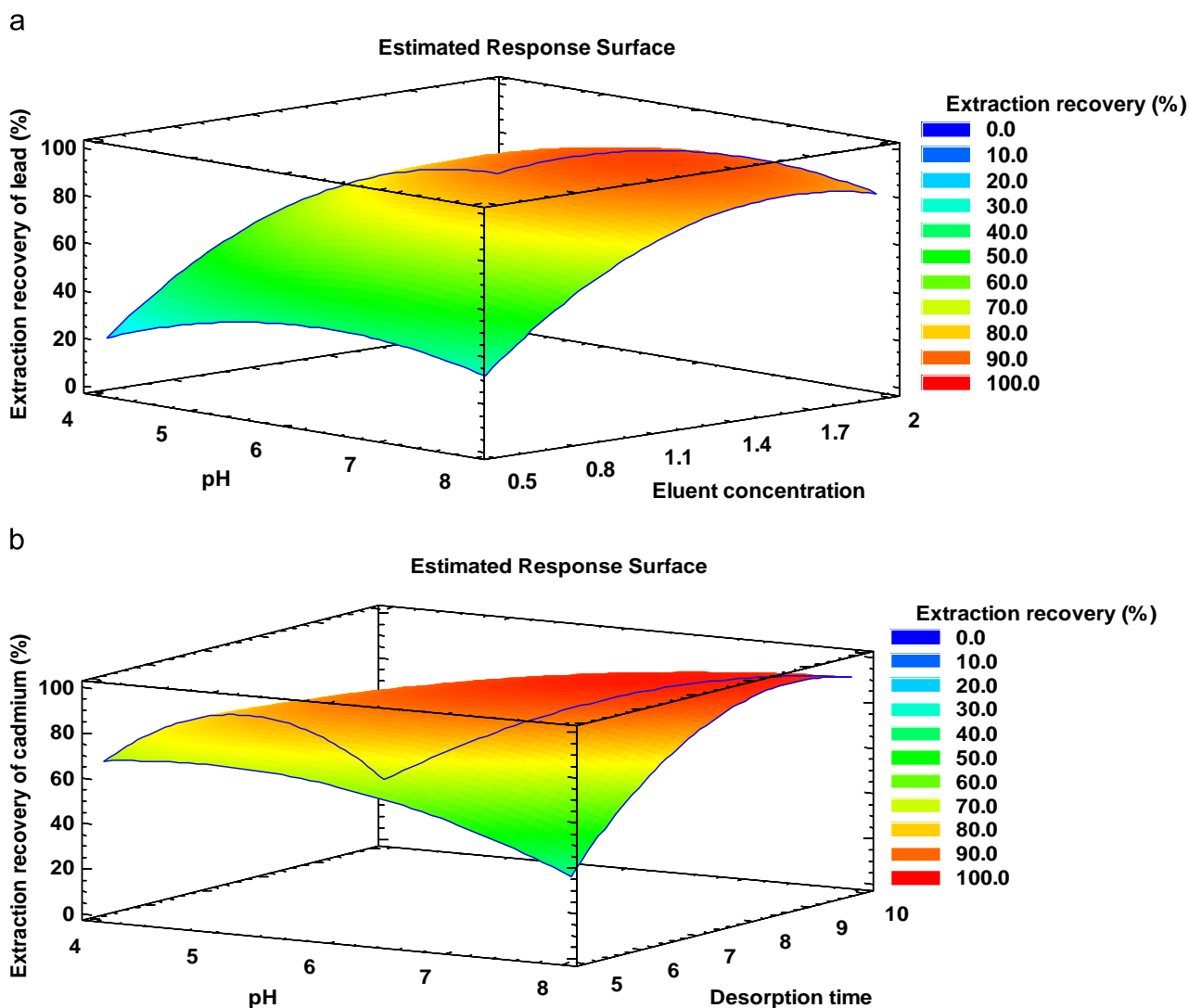


Fig. 6. Estimated response surface by plotting extraction recovery (%) versus pH and eluent concentration (a), pH and desorption time (b).

Table 1

Effect of coexisting ions on recovery of $40 \mu\text{g L}^{-1}$ of Pb(II) and $30 \mu\text{g L}^{-1}$ of Cd(II) ($n=3$).

Ions	Concentration ($\mu\text{g mL}^{-1}$)	Extraction recovery (%)	
		Pb(II)	Cd(II)
Na ⁺	15000	101.2 ± 2.4	98.8 ± 2.5
K ⁺	10000	97.8 ± 2.2	99.1 ± 2.5
Pd ²⁺	1000	96.9 ± 2.5	100.5 ± 2.6
Cu ²⁺	50	101.6 ± 2.4	101.3 ± 2.7
Ni ²⁺	100	98.4 ± 2.6	97.6 ± 2.4
Ag ⁺	50	98.9 ± 2.5	100.7 ± 2.6
Zn ²⁺	50	97.4 ± 2.3	96.9 ± 2.5
Mg ²⁺	500	99.2 ± 2.2	96.5 ± 2.4
Cl ⁻	10000	96.5 ± 2.3	97.2 ± 2.6
NO ₃ ⁻	15000	100.7 ± 2.4	98.4 ± 2.6

important for evaluating the sorption capacity of sorbent and designing an adsorption system.

In the present study for achieving this purpose, the mg of Pb(II) and Cd(II) adsorbed per gram of sorbent, q_e , versus equilibrium concentration (C_e) were investigated at a different initial concentration of Pb(II) ($0.25\text{--}20 \text{ mg L}^{-1}$) and Cd(II) ($0.25\text{--}2.5 \text{ mg L}^{-1}$). Then, by plotting C_e/q_e versus C_e the following equations (Eqs. (1) and (2)) were obtained for Pb(II) and Cd(II), respectively, which

showed that the adsorption models were in agreement with Langmuir isotherm.

$$C_e/q_e = 0.0894C_e + 0.3402 \quad (R^2 = 0.9966) \quad (1)$$

$$C_e/q_e = 0.1071C_e + 0.0267 \quad (R^2 = 0.9997) \quad (2)$$

where C_e is equilibrium concentration of Pb(II) and Cd(II) in the solution (mg L^{-1}), q_e is amount of Pb(II) and Cd(II) adsorbed per unit mass of adsorbent (mg g^{-1}). By comparing the obtained results with Langmuir isotherm model, the maximum sorption capacity can easily be calculated. Therefore, the maximum sorption capacity of lead and cadmium on 1-(2-pyridylazo)-2-naphthol modified $\text{Fe}_3\text{O}_4/\text{TiO}_2$ was 11.18 and 9.34 mg g^{-1} , respectively.

3.8. Figures of merit

Under the optimal experimental conditions, calibration curves were obtained for each metal ion by simultaneous preconcentrating of 50 mL of the sample solution. Table 2 features the analytical characteristics of the optimized method for each element, including linear range, correlation coefficient, limit of detection (LOD) and reproducibility expressed as a relative standard deviation (RSD). A concentration factor (CF) of about 250 (for lead) and 200 (for cadmium) were obtained as a ratio between the volume

Table 2

Limit of detection (LOD) ($\mu\text{g L}^{-1}$), correlation coefficient (r), linear range ($\mu\text{g L}^{-1}$), and relative standard deviation (RSD) for the proposed method.

Analyte	LOD ($\mu\text{g L}^{-1}$)	RSD (%)	Linear range ($\mu\text{g L}^{-1}$)	Correlation coefficient (r)
Lead	1.21	2.2	4–470	0.9988
Cadmium	0.21	2.4	1–110	0.9997

Table 3

Determination of Cd (II) and Pb(II) in real samples.

Sample	Pb(II)			Cd(II)		
	Spiked ($\mu\text{g L}^{-1}$)	Found ($\mu\text{g L}^{-1}$)	Recovery (%)	Spiked ($\mu\text{g L}^{-1}$)	Found ($\mu\text{g L}^{-1}$)	Recovery (%)
Milk ^a	0	ND ^b	–	0	ND	–
	10	10.2 ± 0.3	102.0	5	5.2 ± 0.2	104.0
	20	19.8 ± 0.5	99.0	15	14.6 ± 0.4	97.3
Urine	0	ND	–	0	ND	–
	10	10.4 ± 0.3	104.0	5	4.8 ± 0.2	96.0
	20	21.1 ± 0.6	105.5	15	15.3 ± 0.4	102.0
Blood Plasma plasma	0	ND	–	0	ND	–
	10	9.8 ± 0.3	98.0	5	5.2 ± 0.2	104.0
	20	20.9 ± 0.6	104.5	15	15.1 ± 0.5	100.6

^a Pegah milk, Tehran, Iran.

^b Not detected.

Table 4

Comparison of the proposed method with other SPE method used for preconcentration and FAAS determination of lead and cadmium ions.

Sorbent	PF/EF ^a		LOD ^b		RSD ^c (%)		Linear range ^d		Sorption capacity ^e		Ref.
	Pb ²⁺	Cd ²⁺	Pb ²⁺	Cd ²⁺	Pb ²⁺	Cd ²⁺	Pb ²⁺	Cd ²⁺	Pb ²⁺	Cd ²⁺	
Amberlite XAD-2 /PAN	50	50	23.2	0.8	4.1	2.9	0–3000	0–1000	1.35	2.56	[22]
Surfactant mediated Fe ₃ O ₄	25	25	0.74	0.15	3.82	3.15	1000–10000	100–1000	–	–	[23]
Chromosorb 101/ <i>Bacillus thuringiensis var.israelensis</i>	31	31	2.85	0.37	2.7	2.5	500–10000	20–2000	7.50	8.90	[24]
MWCN/tartrazine	40	40	6.6	0.8	–	–	500–8000	20–3000	–	–	[25]
Fe ₃ O ₄ /TiO ₂ /PAN	250	200	1.21	0.21	2.2	2.4	4–470	1–110	11.18	9.34	This study

^a Preconcentration factor or enrichment factor.

^b Limit of detection ($\mu\text{g L}^{-1}$).

^c Relative standard deviation.

^d ($\mu\text{g L}^{-1}$).

^e (mg g^{-1}).

of the sample solution and the final volume obtained after the elution step (1 mL).

3.9. Accuracy of the method

The validation of the presented procedure was performed by analyzing a certified reference material of water sample (NIST-1640A). It was found that the obtained results ($12.23 \pm 0.3 \mu\text{gkg}^{-1}$ Pb²⁺ and $3.7 \pm 0.1 \mu\text{gkg}^{-1}$ Cd²⁺) were in good agreement with the certified values ($12.005 \pm 0.040 \mu\text{gkg}^{-1}$ Pb²⁺ and $3.961 \pm 0.072 \mu\text{gkg}^{-1}$ Cd²⁺), and no significant differences have been observed (t -test, $P=0.05$).

3.10. Analysis of real samples

The recommended methodology was applied for simultaneous extraction and FAAS determination of investigated toxic metal ions in milk, human urine, and blood plasma samples. Fresh urine and blood plasma samples were obtained from healthy volunteers a few minutes prior to testing. The results obtained are summarized in Table 3.

3.11. Comparison of analytical performance data with literatures

Comparison of this method with other SPE extraction methods used for preconcentration and FAAS determination of lead and cadmium ions from various real samples signifies that the presented method has some improvements compared with the earlier reported methods with significant merits (Table 4). In addition to selectivity of ionic liquid ferrofluid, the presented IL-FF-D-SPE method has lower limit of detection ($1.21 \mu\text{g L}^{-1}$ for lead and $0.21 \mu\text{g L}^{-1}$ for cadmium), higher preconcentration factor (250 and 200 for lead and cadmium respectively), good repeatability (RSD%) and sorption capacity. All these results indicate that using 1-(2-pyridylazo)-2-naphthol modified Fe₃O₄/TiO₂ in IL-FF-D-SPE combined with FAAS is a very simple and sensitive and selective method for the preconcentration and determination of lead and cadmium ions.

4. Conclusion

In the present study, the determination of trace amounts of Pb(II) and Cd(II) in milk, human urine and blood plasma were investigated by a selective IL-FF-D-SPE. To improve chemical stability of magnetic nanoparticles, TiO₂ was used as coating

material. Additionally, selectivity and/or affinity of sorbent toward ions were done simply by surface modification with 1-(2-pyridylazo)-2-naphthol. Also, to provide stable ferrofluid, 1-Hexyl-3-methylimidazolium tetrafluoroborate was used as carrier solvent. Therefore, for the first time a selective ionic liquid ferrofluid was used in dispersive solid phase extraction. Due to dispersion of sorbent in the aqueous phase, this method is much faster in comparison with solid phase extraction which is a time-consuming column passing. Moreover, the magnetic separation greatly improved the separation rate. Therefore, no centrifugation is need for phase separation and sorbent is achieved from the aqueous bulk without using conical bottom glass tubes, which can be easily damaged and difficult to clean. Also in comparison with other literatures (Table 4), this sorbent and method have shown good advantages. In order to simplicity and low cost of this method, selective IL-FF-D-SPE is suitable for batch operations, which could greatly shorten the sample preparation time. Although this sorbent and IL-FF-D-SPE were applied for preconcentration of lead and cadmium from milk, human urine and blood plasma samples, we believe that this method has a wider scope and is capable for other samples with complicated matrices after a simple digestion step.

Acknowledgments

We gratefully acknowledge financial support of this investigation by The Research Council of University of Tehran through Grant. We are grateful to Ms. Shana Ramandi for her kindly help in editing the manuscript.

References

- [1] W. Huang, X. Wang, *Colloid Polym. Sci.* 290 (2012) 1695–1702.
- [2] C. Vollmer, C. Janiak, *Coord. Chem. Rev.* 255 (2011) 2039–2057.
- [3] R.E. Rosensweig, R. Kaiser, G. Miskolczy, *J. Colloid Interf. Sci.* 29 (1969) 680–686.
- [4] D. Shi, L. Sun, G. Mi, L. Sheikh, S. Bhattacharya, S. Nayar, T.J. Webster, *Nanotechnology* (2014), <http://dx.doi.org/10.1088/0957-4484/25/7/075101>.
- [5] V.K. Jain, R.P. Pant, V. Kumar, *Magneto hydrodynamics* 4 (2008) 417–424.
- [6] H. Chen, A. Abolmatty, M. Faghri, *Microfluid. Nanofluid.* 10 (2011) 593–605.
- [7] M. Davudabadi Farahani, F. Shemirani, *J. Colloid Interf. Sci.* 407 (2013) 250–254.
- [8] M.D. Farahani, F. Shemirani, M. Gharehbaghi, *Talanta* 109 (2013) 121–127.
- [9] Z.G. Shi, Y. Zhang, H.K. Lee, *J. Chromatogr. A* 1217 (2010) 7311–7315.
- [10] M. Brzozowska, P. Kryszinski, *Electrochim. Acta* 54 (2009) 5065–5070.
- [11] R.Y. Hong, B. Feng, G. Liu, S. Wang, H.Z. Li, J.M. Ding, Y. Zheng, D.G. Wei, *J. Alloy Compd.* 476 (2009) 612–618.
- [12] T. Xin, M. Ma, H. Zhang, J. Gu, S. Wang, M. Liu, Q. Zhang, *Appl. Surf. Sci.* 288 (2014) 51–59.
- [13] Y. Liu, M. Chen, H. Yongmei, *Chem. Eng. J.* 218 (2013) 46–54.
- [14] M. Soylak, E. Yilmaz, *Atom. Spectrosc.* 34 (2013) 15–19.
- [15] N. Jain, X. Zhang, B.S. Hawkett, G.G. Warr, *ACS Appl. Mater. Interf.* 3 (2011) 662–667.
- [16] F.C.C. Oliveira, L.M. Rossi, R.F. Jardim, J.C. Rubim, *J. Phys. Chem. C* 113 (2009) 8566–8572.
- [17] L. Rodríguez-Arco, M.T. López-López, J.D.G. Durán, A. Zubarev, D. Chirikov, *J. Phys. Condens. Matter.* 23 (2011) 455101–455116.
- [18] N. Fasih Ramandi, F. Shemirani, M. Davudabadi Farahani, *Microchim. Acta X* (2014), <http://dx.doi.org/10.1007/s00604-014-1254-1>.
- [19] F. Shah, T.G. Kazi, H.I. Afridi, M.B. Naeemullah, J.A. Arain, *Cloud Baig, J. Hazard. Mater.* 192 (2011) 1132–1139.
- [20] G. Xiang, S. Wen, X. Wu, X. Jiang, L. He, Y. Liu, *Food Chem.* 132 (2012) 532–536.
- [21] A. Ataro, R.I. McCrindle, B.M. Botha, C.M.E. McCrindle, P.P. Ndibewu, *Food Chem.* 111 (2008) 243–248.
- [22] P. Bermejo-Barrera, N. Martínez Alfonso, C. Díaz López, A. Bermejo Barrera, *Mikrochim. Acta* 142 (2003) 101–108.
- [23] N. Jalbani, M. Soylak, *Ecotox. Environ. Safe* 102 (2014) 174–178.
- [24] D. Mendil, M. Tuzen, C. Usta, M. Soylak, *J. Hazard. Mater.* 150 (2008) 357–363.
- [25] M. Soylak, Z. Topalak, *J. Ind. Eng. Chem.* 20 (2014) 581–585.
- [26] S. Kinaree, S. Chanthai, *Chem. Pap.* 68 (2014) 342–351.
- [27] E.L. Silva, P.d.S. Roldan, *J. Hazard. Mater.* 161 (2009) 142–147.
- [28] L. Zhao, S. Zhong, K. Fang, Z. Qian, J. Chen, *J. Hazard. Mater.* 239–240 (2012) 206–212.
- [29] A.N. Anthemidis, K.I.G. Ioannou, *Anal. Chim. Acta* 668 (2010) 35–40.
- [30] E.S. dos Silva, L.O. Correia, L.O. dos Santos, E.V.S. dos Vieira, V.A. Lemos, *Microchim. Acta* 178 (2012) 269–275.
- [31] L. Tong, J. Shi, X. Ren, Q. Li, H. Ding, H. Yang, *J. Nanopart. Res.* 15 (2013) 1626–1638.
- [32] N. Lian, X. Chang, H. Zheng, S. Wang, Y. Cui, Y. Zhai, *Microchim. Acta* 151 (2005) 81–88.
- [33] T. Bezrodna, G. Puchkovska, V. Shymanovska, J. Baran, H. Ratajczak, *J. Mol. Struct.* 700 (2004) 175–181.
- [34] L. Szabó, K. Herman, N.E. Mircescu, A. Fălămaș, L.F. Leopold, N. Leopold, C. Buzumurgă, V. Chiș, *Spectrochim. Acta A* 93 (2012) 266–273.
- [35] M. Tuzen, K. Parlar, M. Soylak, *J. Hazard. Mater.* 121 (2005) 79–87.
- [36] I. Narin, M. Soylak, L. Elc, M. Dogan, *Anal. Lett.* 34 (2001) 1935–1947.



Comparative study on the use of anthocyanin profile, color image analysis and near-infrared hyperspectral imaging as tools to discriminate between four autochthonous red grape cultivars from La Rioja (Spain)



Julio Nogales-Bueno, Francisco José Rodríguez-Pulido, Francisco José Heredia, José Miguel Hernández-Hierro*

Food Colour & Quality Laboratory, Department of Nutrition & Food Science, Universidad de Sevilla, Facultad de Farmacia, 41012 Sevilla, Spain

ARTICLE INFO

Article history:

Received 16 May 2014

Received in revised form

24 July 2014

Accepted 30 July 2014

Available online 6 August 2014

Keywords:

Anthocyanin profile

Color image analysis

Near infrared hyperspectral imaging

Stepwise linear discriminant analysis

Grapes

Chemometrics

ABSTRACT

Three independent methodologies were investigated to achieve the differentiation of red grapes from different grape varieties (Garnacha, Graciano, Mazuelo and Tempranillo) collected from five vineyards located in the D.O.Ca. Rioja. Anthocyanin chromatographic analysis, color image analysis and near infrared hyperspectral imaging were carried out for the grapes. Then, a Stepwise Linear Discriminant Analysis (SLDA) was developed for each data set in order to discriminate grapes according to their grape variety. As a result, using anthocyanin profile, color image analysis and near infrared hyperspectral imaging respectively, 88%, 54% and 100% of the samples were correctly classified in the internal validation process and 86%, 52% and 86% were correctly classified in the leave-one-out cross-validation process.

© 2014 Elsevier B.V. All rights reserved.

1. Introduction

The major factors impacting on wine quality are related to winemaking process and cultivar features. Grape composition – which depends on climate, soil where grapevines are grown and grape varieties – mainly influences wine composition and therefore wine sensory parameters such as aroma, color and flavor. Consumers value the quality characteristics of wine produced from high-quality grapes enough to pay higher prices, so for each harvest, grape price are closely linked to grape quality [1].

In a cellar it is really important to know the characteristics of grapes that are taken by the vine growers. Grape variety, maturity or sugar content are typically analyzed in order to determine grape quality, set grape price and classify grapes for the various wines produced. The grape maturity and sugar content are usually determined using analytical methods recommended by the O.I.V. [2], which are simple and reliable methods. However, in cellars, grape variety is typically determined by means of visual methods based on the staff experience and knowledge. Furthermore, in situ

vine analyses, such as ampelometry are also used. However, it is not possible to have a panel to classify the berries according to their variety, essentially because this is expensive, there are many samples to be classified, and there is insufficient time to carry out the abovementioned task at harvest time. It would be appropriate to have rapid and inexpensive analytical methods to classify grapes according to their variety.

There are several studies that try to classify grape and wine samples according to their grape variety. A number of them use polyphenol content or polyphenol profiles to classify or authenticate samples [3–7]. In addition, some studies only use anthocyanin profile to carry out these classifications [8–10]. These studies generally achieve very accurate results although they are destructive and time consuming analyses that also require the use of chemical reagents. Other authors have classified wine and grape samples using spectroscopic tools in the ultraviolet–visible and near-infrared regions in order to discriminate samples according to their grape variety and origin [11–13]. Urbano et al. [11] use ultraviolet–visible spectroscopy in order to discriminate wine samples according to their origin, grape variety and ageing process. The classification rates obtained by these authors were 90%, 75% and 75%, respectively. Ferrer-Gallego et al. [12] classify grape samples using NIR spectroscopy according to their origin

* Corresponding author. Tel.: +34 9545 56761; fax: +34 9545 57017.

E-mail address: jmhierro@us.es (J.M. Hernández-Hierro).

obtaining a prediction rate of entire grapes correctly classified of about 93%. Using MIR/NIR traditional spectroscopy, up to seven different grape variety wines are discriminated and over 95% of the samples were correctly classified [14]. Spectroscopy achieves good results in a fast and reasonably inexpensive way. Furthermore, the use of appropriate chemometric tools is needed to classify grape and wine samples according to their grape variety [14].

The area where the present study was conducted involving the wine-producing region of D.O.Ca. Rioja, in Northern Spain, which has vineyards extending over 63,593 ha. *Vitis vinifera* L. cv Tempranillo is the most widely grown red grape variety in Spain and it is cultivated in 75% of the D.O.Ca. Rioja. This variety is capable of producing wines with a good balance of alcohol content, color and acidity, and a fruity mouthfeel that turns velvety as it ages. Graciano, which is an autochthonous cultivar to the aforesaid region, is less known, but it is used as an integral component of many Rioja wines because it is considered to contribute significantly to the quality of the wine. It offers wines with a marked acidity and polyphenolic content, ideal for ageing, with a unique aroma. Furthermore, cultivars such as Garnacha and Mazuelo are also grown in this area. Garnacha is a high-yielding grape that produces vigorous wines of great texture, body and color. Finally, although short on flavors, Mazuelo produces wines with abundant tannins, high acidity and stable color [15,16].

Taking into account the importance of these grape varieties in the D.O.Ca. Rioja and the differences between wines produced from these varieties, it would be very useful to have a fast and inexpensive method to discriminate between these four autochthonous red grape cultivars from La Rioja.

As state above, hyperspectral imaging and digital imaging may provide fast, non destructive and green chemistry determinations compared with traditional methods. Furthermore, the number of samples that might be evaluated using these methods is higher than using the traditional ones and also the determination could be automated. Moreover the use of hyperspectral imaging over conventional spectroscopy in samples having small size, such as individual berries, provides the individual spectrum of each berry using the whole grape without any contact. This may be an advantage in order to use this device at line or in line at winery belts. Nevertheless, the availability of these new devices in conventional laboratories at that time due to their high cost could be a drawback. Digital imaging is a surrogate to human inspection in order to provide an objective analysis. Moreover, the digital image device is cheaper than the hyperspectral device and should be tested in order to find the cheapest way to perform the analysis.

The main aim of this work is to compare the use of anthocyanin profile, color image analysis and near infrared hyperspectral imaging as tools to discriminate between Tempranillo, Graciano, Garnacha and Mazuelo grapes in order to select the more useful and accurate tool. In a second strand, a second level data fusion has also been tried in order to improve the results. To our knowledge, this is the first time that near infrared hyperspectral imaging has been applied to red grapes to discriminate between cultivars. Furthermore, this is also the first time that a comparative study on the use of the three aforesaid analytical tools has been performed.

2. Material and methods

2.1. Samples

Vitis vinifera L. cv. Tempranillo (two different vineyards), Graciano, Garnacha and Mazuelo were collected from five vineyards located in the D.O.Ca. Rioja. Red grapes were collected at two

different developmental stages during berry maturity in the 2012 vintage: harvest time and over-ripening. Harvest time and over-ripening dates were selected in agreement with the cellar staff. Individual grapes were randomly separated from the top, middle and bottom of the cluster. Five berries were taken into account for each cultivar and developmental stage with the exception of Tempranillo. In the case of Tempranillo, 20 berries were used since two different vineyards were taken into account (i.e. 5 berries \times 2 vineyards \times 2 developmental stages). A total of 50 samples were used. Berries were immediately frozen and stored at $-20\text{ }^{\circ}\text{C}$ until analyses were performed.

2.2. Image analysis

An individual image for each grape was taken. For acquiring images, the DigiEye[®] system based upon a calibrated digital camera was used [17]. This system includes an illumination box specially designed by VeriVide Ltd. (Leicester, UK) to illuminate the samples consistently and a digital camera connected to a computer. The digital camera used for image acquisition was a 10.2-MP Nikon[®] D80 with Nikkor[®] 35 mm f/2D objective. In order to calibrate the digital camera, a color chart (DigiTizer, VeriVide Ltd., Leicester, UK) is used to characterize its response by relating its RGB signals to CIE specifications. The cabinet is equipped with two fluorescent tubes that emulate the CIE standard illuminant D65 and offer stable lighting conditions. They were switched on at least 10 min before being used, according to manufacturer indications, to stabilize them.

Image processing was carried out using MATLAB (The Mathworks, 2009). For obtaining CIELAB coordinates from RGB color space, the software DigiFood[®] [18] was used. The obtained CIELAB coordinates were used in the subsequent analyses.

2.3. Near-infrared hyperspectral imaging

Hyperspectral imaging device (Infaimon S.L., Barcelona, Spain) comprised a Xenics[®] XEVA-USB InGaAs camera (320 \times 256 pixel; Xenics Infrared Solutions, Inc., Leuven, Belgium), a spectrograph (Specim ImSpector N17E Enhanced; Spectral Imaging Ltd., Oulu, Finland) covering the spectral range between 900 and 1700 nm (spectral resolution of 3.25 nm). The images were recorded using the abovementioned mirror scanner pushbroom device, a 50 Hz frame rate, an exposure time of 9 ms and the instrument acquisition software SpectralDAQ v. 3.62 (Spectral Imaging Ltd., Oulu, Finland). The samples were thawed and tempered at room temperature and individual hyperspectral image of each grape was recorded. Equipment and procedure used to image recording are described in detail elsewhere in Hernández-Hierro et al. [19].

After calibration and segmentation processes, the average spectral profile for each individual grape was saved. Noisy wavebands at both extremes of the spectra range were removed and only spectral data in the resulting effective wavelength 950–1650 nm regions were used in data analysis due to reduced efficiency outside this range in the used device. Principal component analysis (PCA) was applied to reduce the dimension of the aforementioned spectral matrix. The software used for PCA analysis was Win ISI[®] (v1.50) (Infrasoft International, LLC, Port. Matilda, PA, USA). Overall, the spectral variability explained was 99.9% using 8 principal components. The obtained scores were used in the subsequent analyses.

2.4. Anthocyanins extraction and chromatographic analysis

After image acquisition process, grape skins were separated manually from the whole grapes. Individual grape skins were macerated twice at $4\text{ }^{\circ}\text{C}$ in 10 mL of methanol containing 0.1% of

12 M HCl until colorless of skins. In order to assist the extraction, the methanolic mixtures were sonicated (JP Selecta, Barcelona, Spain) for 30 min prior to the 24 h maceration step. Methanolic phases were centrifuged (3000 rpm, 10 min), successively pooled and finally made up to 25 mL with the extraction solvent. One aliquot of 1 mL was taken and a few microliters of 0.1 M HCl was added and the extract was concentrated under vacuum at 30 °C (Eppendorf Concentrator Plus, Germany) until methanol was removed and finally made up to 1 mL with 0.1 M HCl. The aqueous extract was filtered through 0.45 μm pore-size filters and directly injected into the chromatographic system to determine the anthocyanins. Anthocyanin chromatographic analysis was carried out following a modification of García-Marino et al. [20] as described elsewhere in Hernández-Hierro et al. [19]. All analyses were performed in duplicate. Results were expressed as normalized chromatographic areas. Up to 11 anthocyanins were identified and their sum was expressed as total anthocyanins, which was used to normalize the anthocyanins areas. Moreover, taking into account their basic structures anthocyanins were grouped as acylated or non-acylated anthocyanins. Individual, acylated and non-acylated anthocyanin normalized areas were used in the subsequent analyses.

2.5. Supervised pattern recognition analysis

Supervised pattern recognition methods usually indicate whether samples fall into pre-defined groups, how well, and what causes this separation. The supervised pattern recognition method used in the present study was linear discriminant analysis (LDA). Stepwise feature selection was used to select the most significant variables for the discrimination between classes using *F*-statistic to test the significance of the change in Wilks' Lambda by adding or removing a variable. Prior probabilities of classification were used in this analysis taking into account each group size. The prediction ability was estimated considering the percentage of samples correctly classified by the rules developed with the training set using a leave-one-out cross-validation procedure. This approach has the advantage of being utilized when the number of total samples is low. The variables used were anthocyanin normalized areas, colorimetric parameters and the scores from the PCA performed on the hyperspectral data set. Moreover, a second level data fusion has also been tried in order to improve the results.

All discriminant analyses were carried out via SPSS 22.0 for Windows software package (SPSS, Inc., Chicago, IL, USA).

3. Results and discussion

3.1. Chromatographic data

Fig. 1a shows the average normalized area for each grape variety of the eleven chromatographic peaks. The first five peaks are nonacylated anthocyanins. This group accounts for almost 80% of total anthocyanins in red grape skins. Taking into account these pseudo chromatograms, some differences can be found between the studied varieties. Nevertheless, the use of appropriate chemometric tools is needed in order to classify grape samples according to their grape cultivar.

In order to discriminate between these four red grape cultivars, a stepwise linear discriminant analysis (SLDA) was performed as a supervised pattern recognition method using individual, acylated and non-acylated anthocyanin normalized areas to allocate the grape samples to their grape variety group. Three variables were retained that allowed 88% of the samples were correctly classified in the internal validation process and 86% were correctly classified in the leave-one-out cross-validation process. The three normalized

areas retained correspond to peaks 2, 6 and 8 (cyanidin-3-*O*-glucoside, malvidin-3-*O*-(6''-acetyl) glucoside and petunidin-3-*O*-(6''-*p*-coumaroyl) glucoside (*trans*) respectively). Fig. 1b compares normalized areas for these peaks and it is possible to observe some differences between the four varieties in this figure. Similar differences have been reported by other authors between Garnacha, Graciano and Tempranillo varieties [21,22]. However, no comparative study has been found for the minority variety Mazuelo.

Table 1 includes the results obtained for the discrimination of La Rioja grape varieties according to its chromatographic profile. The results are expected, since it is well known the relationship between grape varieties and their chromatographic profiles [23].

3.2. Color data

Fig. 2 shows the CIELAB coordinates for all grape samples (L^* , a^* and b^*), polar coordinates (C^*_{ab} and h_{ab}) are also readily available from this figure. Majority of Garnacha, Mazuelo and Tempranillo samples present positive values of a^* coordinate, and Graciano samples present the fewest values of chroma. Moreover, all samples present very low values for a^* and b^* coordinates and the four varieties are overlapped in the CIELAB diagram.

In order to achieve the classification goal using discriminate variables more easily obtained, a new SLDA model was developed using the aforesaid color data.

After develop the stepwise discriminant analysis only C^*_{ab} and h_{ab} were retained and this allowed 54% of the samples were correctly classified in the internal validation process and 52% were correctly classified in the leave-one-out cross-validation process. Consequently, image analysis, although is a rapid and inexpensive tool, has lower discriminant power in red grape samples than chromatographic analysis. This can be due to the sample nature with low values of a^* and b^* coordinates which lead to low signal to noise ratio.

3.3. Near-infrared hyperspectral data

Fig. 3 shows the scores of the first and second principal components, the four varieties are completely overlapped in this space. The same discriminant procedure (i.e. a new SLDA model) was applied to the dataset using the scores of the 8 first principal components obtained from near infrared hyperspectral data. In this case all variables were retained and 100% of the samples were correctly classified in the internal validation process and 86% were correctly classified in the leave-one-out cross-validation process. These results are better in the internal validation and similar in the leave-one-out cross-validation than the results obtained from the chromatographic data. In addition, hyperspectral imaging is a non-destructive and faster than the chromatographic technique, which highlights the importance of these results. Fig. 4 represents the grape samples in the space defined by the three obtained discriminant functions. In this space, grape variety groups are almost completely separated.

3.4. Data fusion

In order to improve the results obtained using the hyperspectral data set a second level data fusion was carried out. The aim of second level data fusion includes performing high-level inferences and identifying significant activities and events (patterns in general) [24]. Color and hyperspectral data were fused; they are non-destructive and fast tools. Hyperspectral data have shown potential classifying these grape varieties and color data could be linked with visible spectra and could add some discriminant information.

A SLDA was performed with this new data set. Only near infrared hyperspectral image variables were retained and, as a

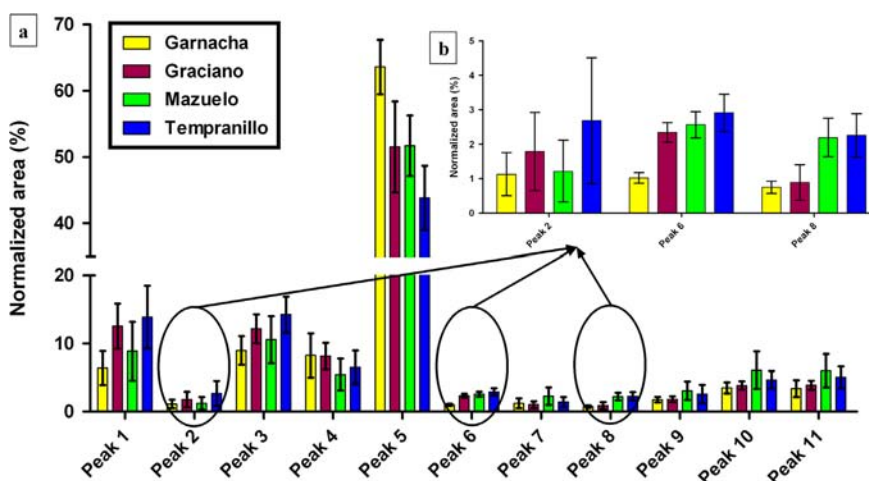


Fig. 1. (a) Average normalized areas for the 11 anthocyanins detected for Garnacha, Graciano, Mazuelo and Tempranillo grape varieties. In order of elution: delphinidin-3-*O*-glucoside, cyanidin-3-*O*-glucoside, petunidin-3-*O*-glucoside, peonidin-3-*O*-glucoside, malvidin-3-*O*-glucoside, malvidin-3-*O*-(6'-acetyl) glucoside, cyanidin-3-*O*-(6'-*p*-coumaroyl) glucoside (*trans*), petunidin-3-*O*-(6'-*p*-coumaroyl) glucoside (*trans*), malvidin-3-*O*-(6'-*p*-coumaroyl) glucoside (*cis*), peonidin-3-*O*-(6'-*p*-coumaroyl) glucoside (*trans*) and malvidin-3-*O*-(6'-*p*-coumaroyl) glucoside (*trans*). (b) Average normalized areas for the three anthocyanins selected by the stepwise linear discriminant analysis: cyanidin-3-*O*-glucoside, malvidin-3-*O*-(6'-acetyl) glucoside and petunidin-3-*O*-(6'-*p*-coumaroyl) glucoside (*trans*).

Table 1

Results of the different stepwise linear discriminant analyses developed to classify Garnacha, Graciano, Mazuelo and Tempranillo grapes.

Data set	Retained variables	Internal validation		Leave-one-out cross-validation	
		Samples correctly classified	% of Samples correctly classified	Samples correctly classified	% of Samples correctly classified
Chromatographic data ^a	Cyg ^b , Mvac ^c , Ptcp ^d	44/50	88	43/50	86
Color data ^e	C _{ab} [*] , h _{ab} [*]	27/50	54	26/50	52
NIR Hyperspectral data ^f	NIR Hyperspectral data ^f	50/50	100	43/50	86
Data fusion (NIR+ color)	NIR Hyperspectral data ^f	50/50	100	43/50	86

^a Chromatographic data: individual, acylated and non-acylated anthocyanin normalized areas.

^b Cyg: average normalized area of cyanidin-3-*O*-glucoside.

^c Mvac: average normalized area of malvidin-3-*O*-(6'-acetyl) glucoside.

^d Ptcp: average normalized area of petunidin-3-*O*-(6'-*p*-coumaroyl) glucoside (*trans*).

^e Color data: CIELAB coordinates (*L**, *a** and *b**) and polar coordinates (*C_{ab}^{*}* and *h_{ab}^{*}*) for all grape samples.

^f NIR Hyperspectral data: scores of the eight first principal components obtained from the near infrared hyperspectral data.

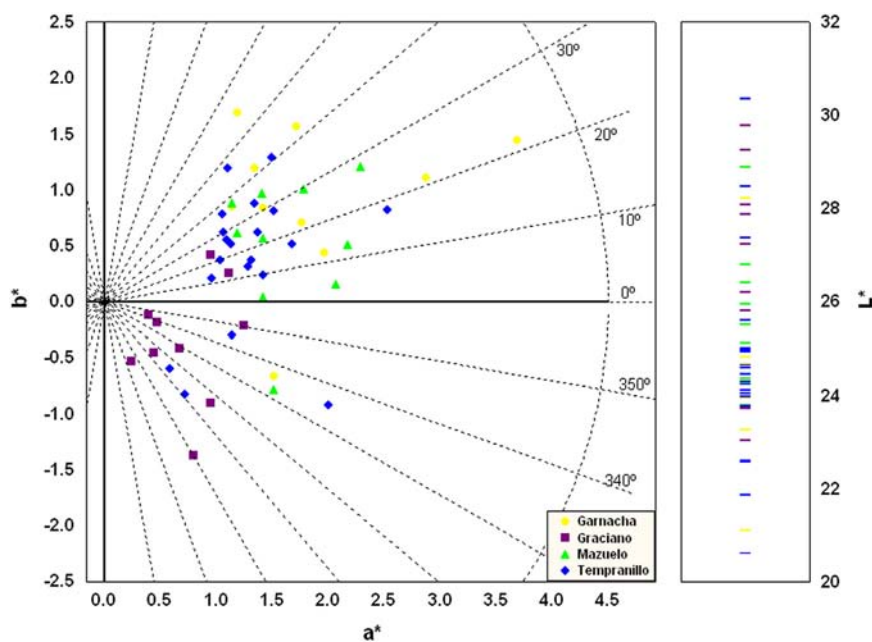


Fig. 2. CIELAB coordinates for Garnacha, Graciano, Mazuelo and Tempranillo grape samples.

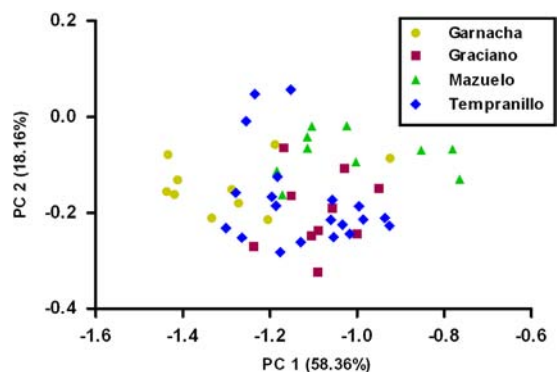


Fig. 3. Score plot of grape samples in the space defined by the first and second principal component codified according to grape variety.

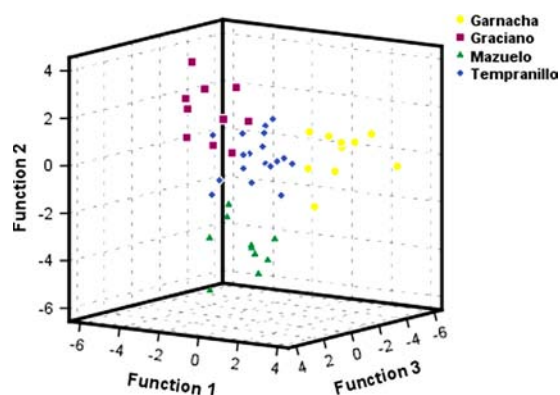


Fig. 4. Representation of the grape samples in the space defined by the first, second and third discriminant functions obtained from the hyperspectral data.

result, the same discriminant functions were obtained with the same discriminant power. Taking that into account, color data do not improve the results obtained from near infrared hyperspectral image. Table 1 resumes data fusion results and the results obtained in the previous stepwise linear discriminant analyses.

4. Conclusions

Chromatographic analysis is a widespread and reliable tool to classify red grapes according to grape variety and the results obtained in this study confirm it. Color image analysis is a rapid and inexpensive tool that has lower discriminant power for red grape samples than chromatographic analysis. Near-infrared hyperspectral analysis is a non-destructive and fast technique that shows better or similar results than the chromatographic technique. A second level data fusion between color data and near infrared hyperspectral data does not improve the results obtained from near infrared hyperspectral image. Nonetheless, a comprehensive study

should be made in order to evaluate several abiotic factors, including vintage, watering, sun exposure, wine age, soil, ripening etc in the complete development of these models.

Acknowledgements

The Spanish MINECO is thanked for J. Nogales-Bueno FPI grant (BES-2012-060192), J.M. Hernández-Hierro Juan de la Cierva contract (JCI-2011-09201) and project AGL2011-30254-C02. Junta de Andalucía is also thanked for financial support (project P10-AGR6331). The authors also thank Bodegas RODA (La Rioja, Spain) for supplying the grape samples and to technical staff of Biology Service (SGI, Universidad de Sevilla) for the technical assistance.

References

- [1] A. Golan, H. Shalit, *J. Agric. Econ.* 44 (1993) 311–321.
- [2] OIV. Recueil de methods internationaux d'Analyse des vins. Caracteristiques chromatiques, 1990. Paris, OIV.
- [3] A. Hosu, V.M. Cristea, C. Cimpoi, *Food Chem.* 150 (2014) 113–118.
- [4] A. de Villiers, P. Majek, F. Lynen, A. Crouch, H. Lauer, P. Sandra, *Eur. Food Res. Technol.* 221 (2005) 520–528.
- [5] F. Galgano, M. Caruso, G. Perretti, F. Favati, *Eur. Food Res. Technol.* 232 (2011) 889–897.
- [6] I. Hermosin-Gutierrez, N. Castillo-Munoz, S. Gomez-Alonso, E. Garcia-Romero, *Abstr. Pap. Am. Chem. Soc.* 239 (2010).
- [7] L. Jaitz, K. Siegl, R. Eder, G. Rak, L. Abranko, G. Koellensperger, S. Hann, *Food Chem.* 122 (2010) 366–372.
- [8] D. von Baer, M. Rentzsch, M.A. Hitschfeld, C. Mardones, C. Vergara, P. Winterhalter, *Anal. Chim. Acta* 621 (2008) 52–56.
- [9] A. de Villiers, G. Vanhoenacker, P. Majek, P. Sandra, *J. Chromatogr. A* 1054 (2004) 195–204.
- [10] M.L. Gonzalez San Jose, C. Diez, *Agrochimica* 37 (1993) 86–92.
- [11] M. Urbano, M.D. Luque de Castro, P.M. Perez, J. Garcia-Olmo, M.A. Gomez-Nieto, *Food Chem.* 97 (2006) 166–175.
- [12] R. Ferrer-Gallego, J.M. Hernández-Hierro, J.C. Rivas-Gonzalo, M.T. Escribano-Bailón, *J. Sci. Food Agric.* 93 (2013) 967–972.
- [13] C.J. Bevin, R.G. Damberg, A.J. Fergusson, D. Cozzolino, *Anal. Chim. Acta* 621 (2008) 19–23.
- [14] A. Versari, V. Laurie, A. Ricci, L. Laghi, G.P. Parpinello, *Food Res. Int.* 60 (2014) 2–18.
- [15] Denominación de Origen Calificada Rioja. Denominación de Origen Calificada Rioja, 2014. URL: (<http://es.riojawine.com/en/5-learn-about-rioja.html>), Accessed 23.04.13.
- [16] ICEX España Exportación e Inversiones. Vinos de España. 2014. URL: (<http://www.winesfromspain.com/>) Accessed 23.04.13.
- [17] M.R. Luo, G.H. Cui, L. C. British Patent entitled apparatus and method for measuring colour (DigiEye System), Derby University Enterprises Limited. [0124683.4], 4-10-2001.
- [18] F.J. Heredia, M.L. González-Miret, C. Álvarez, A. Ramírez. DigiFood, [Registration No. Se-01298], 2006.
- [19] J.M. Hernández-Hierro, J. Nogales-Bueno, F.J. Rodríguez-Pulido, F.J. Heredia, *J. Agric. Food Chem.* 61 (2013) 9804–9809.
- [20] M. García-Marino, J.M. Hernández-Hierro, J.C. Rivas-Gonzalo, M.T. Escribano-Bailón, *Anal. Chim. Acta* 660 (2010).
- [21] E. Revilla, E. García-Beneytez, F. Cabello, G. Martín-Ortega, J.M. Ryan, *J. Chromatogr. A* 915 (2001) 53–60.
- [22] I. Arozarena, B. Ayestarán, M. Cantalejo, M. Navararro, M. Vera, I. Abril, A. Casp, *Eur. Food Res. Technol.* 214 (2002) 303–309.
- [23] A.L. Waterhouse, *Wine Phenolics*, New York Acad Sciences, New York, 2002.
- [24] F. Castanedo, *Sci. World J.* 10 (2013) 1–19.



A glucose biosensor based on the synergistic action of nanometer-sized TiO₂ and polyaniline



Wenwei Tang^{a,*}, Lei Li^b, Xiping Zeng^{b,*}

^a Department of Chemistry, Tongji University, Shanghai 200092, China

^b School of Life Science and Technology, Tongji University, Shanghai 200092, China

ARTICLE INFO

Article history:

Received 25 April 2014

Received in revised form

6 August 2014

Accepted 7 August 2014

Available online 19 August 2014

Keywords:

Amperometric glucose sensor

Polyaniline

n-TiO₂

Direct electron transfer

Linear range

Detection limit

ABSTRACT

Polyaniline/active carbon (PANI) and nanometer-sized TiO₂ (n-TiO₂) were prepared by oxidation and sol-gel methods, respectively, and were then used as a zymophore to modify a glassy carbon electrode (GCE) and a GOx/n-TiO₂/PANI/GCE sensor with a synergistic effect was established. A series of performance evaluations for the modified material and sensor was studied in detail through cyclic voltammetry (CV) and a chronoamperometry (CA) method. The results showed that the sensor had a good response to glucose and that the electron of the GOx molecule was transferred directly onto the sensor, and a linear relationship between the GOx redox peak current and the sweep speed was found. The apparent transmission speed constant, *k*, for dissimilar electrode charges was 1.35 s⁻¹, 95% of the maximum steady current for the GOx/n-TiO₂/PANI/GCE sensor could be reached in 10 s, the linear range of the detected glucose concentration was from 0.02 mM to 6.0 mM, the sensitivity was 6.31 μA mM⁻¹ cm⁻², and the limit of detection was 18 μM. The sensor had good selectivity and stability and could be maintained at 82% of the initial activity for 30 days.

© 2014 Elsevier B.V. All rights reserved.

1. Introduction

Diabetes mellitus is a serious disease that is harmful to human health, and currently, the effective way to treat it is to severely restrict the diet and control the blood sugar. The blood sugar content is the objective indicator for diabetes mellitus, and it is therefore of great significance to establish a quick, efficient, and inexpensive detection method for glucose. The development of a glucose sensor meets this developmental requirement. Conductive polymer and nanometer-sized materials have received much attention due to their good electrical conductivity, large specific surface area, and small size. Both of these materials have broad application in biosensors.

Nanometer-sized TiO₂ (n-TiO₂), a new inorganic material with a special crystal structure, has been used to affix to biomacromolecules such as enzymes to achieve good biocompatibility and electron transfer ability. n-TiO₂ therefore has a good prospective application in the area of bioelectrochemistry. Li et al. accomplished the fixation and the direct electron transfer process of myohemoglobin, hemoglobin, and cytochrome C to a nanometer-level TiO₂ membrane [1,2]. Zhang et al. prepared a glucose sensor

with a detection limit of 0.1 μM by using a multi-walled carbon nanotube/n-TiO₂/gold nanoparticle to modify a GCE [3]. Li et al. made a direct electron transfer of GOx happen on the electrode surface by using mesoporous n-TiO₂/multi-walled carbon nanotube material [4].

Polyaniline, when used as a typical conducting polymer to establish an enzyme-type sensor, has been a topic of intense research interest over the past few years. Due to the conjugated structure that exists in the polyaniline molecule, the electron has a high degree of transferability. In polyaniline, “mixing” could change its electronic structure, magnetic properties, optical properties, electrical conductivity, and structural features remarkably [5]. Lee et al. modified the GOx with functionalized polyaniline and a multiwalled carbon nanotube and accomplished the direct electrochemistry of an enzyme sensor [6]. Dhand et al. found that the GOx showed good electrochemical activity after being wrapped by nanoscale electro-deposited polyaniline, which indicated that the polyaniline has good biocompatibility [7]. Zhai et al. prepared a highly sensitive glucose enzyme sensor based on Pt nanoparticles–polyaniline hydrogel heterostructures, which exhibited unprecedented sensitivity, as high as 96.1 μA mM⁻¹ cm⁻², with a linear range of 0.01–8 mM, and a low detection limit of 0.7 μM [8].

Polyaniline/active carbon (PANI) and n-TiO₂ were prepared by oxidation and sol-gel methods, respectively, and they were then used to co-modify the electrode surface. By utilizing the good electrical conductivity and the effects of the small sizes of the two

* Corresponding authors.

E-mail addresses: tangww@tongji.edu.cn (W. Tang), zengxp@tongji.edu.cn (X. Zeng).

types of materials, an amperometric glucose sensor with a synergistic effect was established, and the detection limit, response time, linear detection range, stability, and anti-jamming capability were studied systematically.

2. Experimental

2.1. Main instruments and reagents

The working electrode was a glassy carbon electrode (GCE, GC130, $\varnothing 3$ mm) from Tianjin Aidahengsheng Technology Co., Ltd. The aniline, chitosan, and tetra-*n*-butyl titanate were of analytical purity from the Sinopham Chemical Reagent Co., Ltd., and the GOx, uric acid (UA), L-cysteine, and ascorbic acid (AA) were of biochemical purity from Sigma.

2.2. Preparation of *n*-TiO₂

Five milliliters (mL) of isopropanol was added into 10 mL of tetra-*n*-butyl titanate, and component A was obtained by stirring for 30 min. Component B consisted of 2 mL of distilled water, 2.5 mL of isopropanol, and a small amount of glacial acetic acid. Component C was obtained by adding the appropriate amount of Polyethylene glycol into 2.5 mL of isopropanol. During the stirring process, component B was dropped into solution C first, and component A was then added dropwise to the BC solution. The duration of the reaction was 0.5 h. The solution that was obtained was aged for 1 day, and then a yellow and transparent sol was obtained. Afterwards, the sol was put into a dryer at 80 °C for 10 h. A xerogel was obtained and was then calcined in the muffle furnace at 500 °C for 2 h, resulting in the TiO₂ powder.

2.3. Preparation of the PANI composite material

Aniline monomer (0.9 mL) and the activated carbon powder (0.84 g) were dispersed in 30 mL of a 1 mol L⁻¹ hydrochloric acid solution, and N₂ was blown into the solution to deoxidize it for 30 min. After stirring the solution at a constant speed for 1 h, the aniline monomer was uniformly adsorbed onto the AC surface. An appropriate amount of ammonium peroxydisulfate (APS) was added to 20 mL of the 1 mol L⁻¹ hydrochloric acid solution. Then, N₂ was blown into the solution, and the APS was dissolved after stirring. The prepared APS hydrochloric acid solution was dropped into the aniline hydrochloric acid solution gradually over 1 h, the reaction temperature was maintained at 0 °C, and the reaction lasted for 5 h with stirring. After the reaction, the product was washed and filtered repetitively with hydrochloric acid, alcohol, and distilled water to eliminate any oligomer that had not reacted or had not reacted completely. After 24 h of drying in a vacuum oven at 60 °C, the PANI composite material with an atrovirens color was obtained. The optimum molar ratio of AC:ANI:APS for the PANI material was 7:1:1.

2.4. Preparation of the GOx/*n*-TiO₂/PANI/GCE

Electrode Pre-treatment: Alumina powder with particle diameters of 0.3 μ m, 0.1 μ m, and 0.05 μ m was put on a polishing cloth and soaked in distilled water. The form of the GCE in the alumina powder turbid liquid was the “8” type. The electrode was then polished, and the polished electrode was placed in nitric acid aqueous solution with a volume ratio of 1:1 for 20 min. The electrode was washed with distilled water and alcohol, and the electrode underwent distilled water ultrasonic cleaning. The treated electrode was scanned by cyclic voltammetry (CV) in a solution of 0.1 M KCl and 5 mM K₃[Fe(CN)₆], as $\Delta E_p < 80$ mV, and

the electrode was taken out, re-washed with the distilled water, and preserved.

Dispersion of the modified material: PANI or *n*-TiO₂ powder (1 mg) was put into a 0.5% chitosan solution respectively, and then dispersed uniformly in the chitosan solution after being treated with ultrasound.

Preparation of the GOx solution: Two milligrams of GOx and 15 mg of BSA was placed in 200 μ L of standard phosphate buffer, which was then vibrated until the GOx was well distributed and placed in a refrigerator.

PANI/GCE or *n*-TiO₂/GCE: PANI dispersion (6 μ L) or *n*-TiO₂ dispersion (6 μ L) was coated onto the GCE surface respectively, and dried with infrared irradiation.

***n*-TiO₂/PANI/GCE:** 6 μ L of the *n*-TiO₂ dispersion liquid was dropped and coated onto the PANI/GCE surface and dried with infrared irradiation.

GOx/*n*-TiO₂/PANI/GCE: An appropriate amount of GOx solution and 2.5% glutaraldehyde were rapidly mixed by the glutaraldehyde crosslinking method. The mixture above (6 μ L) was quickly placed onto the *n*-TiO₂/PANI/GCE, dried in the air, and put in the refrigerator at 4 °C for 1 h to complete the GOx and glutaraldehyde crosslinking. The modified electrode was taken out, dried in the air, and preserved in the refrigerator at 4 °C.

2.5. Characterization and detection method

The *n*-TiO₂ and PANI materials were characterized using SEM, XRD, and electrochemical methods. The preparation method for SEM was that PANI dispersion (6 μ L) or *n*-TiO₂ dispersion (6 μ L) was coated onto the GCE surface respectively, and dried with infrared irradiation. The modified electrode was tested in a glucosidic or non-glucosidic situation with CV, electrochemical impedance spectroscopy (EIS), and chronoamperometry (CA). The reproducibility and stability of the sensor were also determined.

3. Results and discussion

3.1. Properties of *n*-TiO₂

3.1.1. SEM characterization

Fig. 1 shows that the prepared TiO₂ reached sizes on the scale of nanometers, which was directly related to the formation of the sol particles and TiO₂ anatase. Thus, the TiO₂ prepared with the sol-gel method could have good electrical conductivity and the metal ion nanometer effect, and could easily be imbedded into the active center of the enzyme molecule.

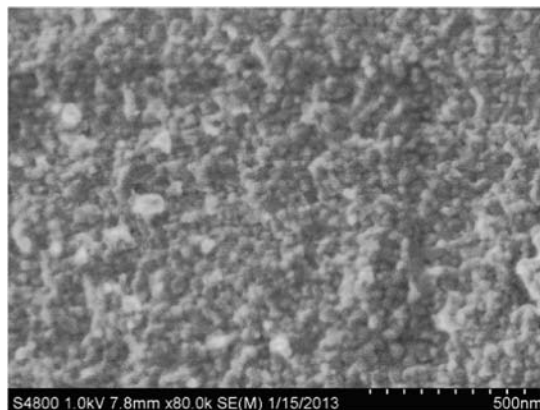


Fig. 1. SEM image of nano-titanium dioxide (80,000 \times).

3.1.2. XRD characterization

The XRD instrument used was a FOCUS D8 X-ray diffractometer from the Bruker Company in Germany, the maximum tube pressure was 40 kV, and the tube current was 40 mA. In the test, the scanning speed was set at $10^\circ/\text{min}$, and the scanning angle was $10\text{--}70^\circ$.

An XRD image (Fig. 2) shows that diffraction peaks occurred at $2\theta=25.34^\circ, 37.84^\circ, 48.06^\circ, 53.72^\circ, 54.98^\circ,$ and 62.68° , consistent with the specific diffraction peak of the anatase crystalline-type TiO_2 and indicating that the powder was anatase-phase TiO_2 . The size of a crystal in the powder was calculated according to the Scherrer formula

$$D = \frac{K\lambda}{B \cos \theta} \quad (1)$$

where D is the crystal size, K is the Scherrer constant (0.89°), λ is the X-ray wavelength (0.154056 nm), B is the half-height width of the diffraction peak, and θ is the diffraction angle.

According to the crystal face parameters of the characteristic peak (101), the crystal size calculated with Formula (1) was 17 nm .

3.2. Properties of PANI

3.2.1. SEM characterization

An SEM image of PANI (Fig. 3(A) and (B)) shows that the active carbon particle was on the micron scale and that the PANI particles adsorbed onto it had diameters of dozens of nanometers, which meant that this composite material could provide more active adsorption sites for the enzyme molecules and could greatly increase the loading capacity of GOx. The electron transfer

capability and the bioelectrical activity of the sensor could be improved by combining the good electrical conductivity and biocompatibility of the PANI particle itself.

3.2.2. FTIR characterization

In Fig. 4, the peak at 3448 cm^{-1} corresponds to the stretching vibration absorption peak of N–H, the peak at 1635 cm^{-1} is the deformation vibration absorption peak of N–H, the peak at 1568 cm^{-1} is the vibration absorption peak of C=C in a quinone-type ring, the peak at 1504 cm^{-1} is the vibration absorption peak of C=C in a benzene-type ring, the peak at 1170 cm^{-1} is the vibration absorption peak of $-\text{H}+\text{N}=\text{C}$ related to a quinone-type ring, and the peak at 1068 cm^{-1} is the stretching vibration absorption peak of C–N. The positions of these peaks met the characteristic peak ranges of an amine substance: the stretching vibration absorption peak of N–H was in the range of $3500\text{--}3100 \text{ cm}^{-1}$, and the stretching vibration absorption and the deformation vibration peaks of C–N were in the ranges of $1350\text{--}1000 \text{ cm}^{-1}$ and $1640\text{--}1560 \text{ cm}^{-1}$, respectively. These ranges are close to the peak positions in the spectrum of PANI [9], and these results indicated that the polymerization of the aniline molecule occurred during the mixing process.

3.3. Conductivity of n-TiO₂ and PANI

3.3.1. CV during the electrode assembly process

A pair of redox peaks from $[\text{Fe}(\text{CN})_6]^{3-/4-}$ via a complete and reversible process were observed on the surface of the bare electrode, as shown in Fig. 5. The redox peak currents of the

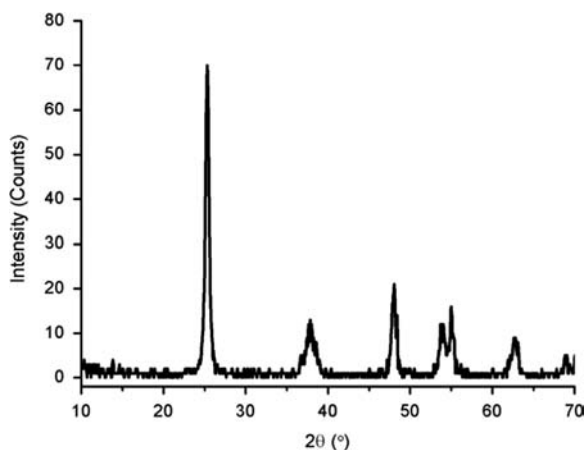


Fig. 2. XRD image of nano-titanium dioxide.

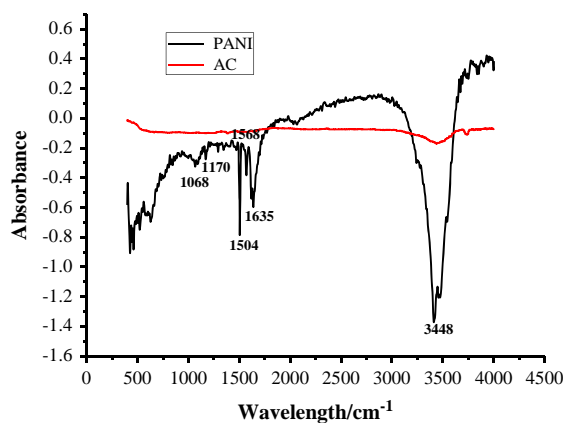


Fig. 4. FTIR spectrum of AC and PANI.

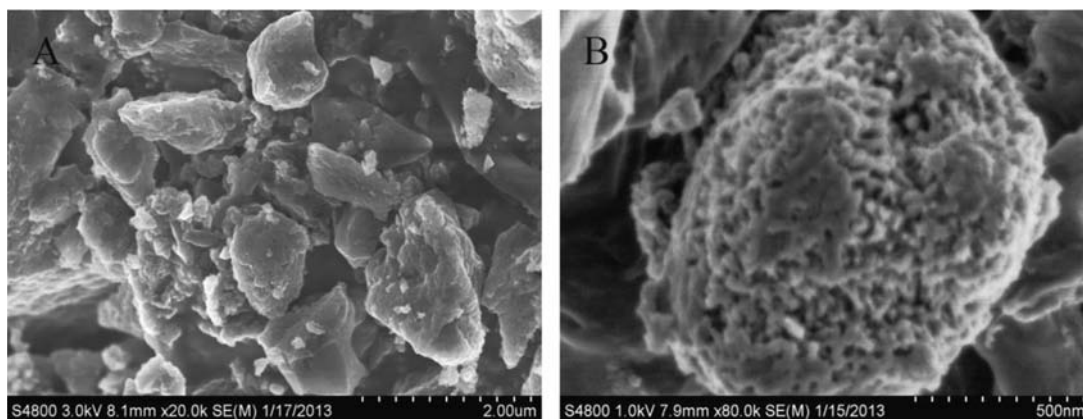


Fig. 3. SEM image of AC and PANI (A: AC, B: PANI).

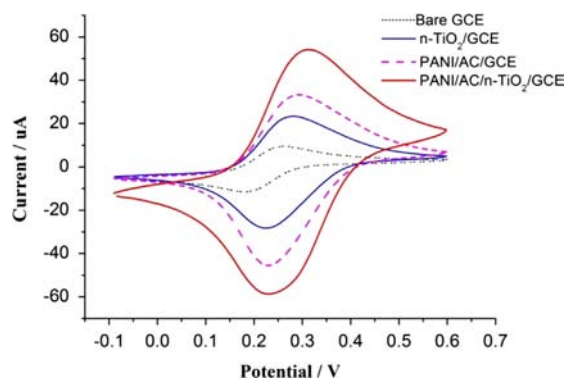


Fig. 5. CV of bare GCE, n-TiO₂/GCE, PANI/GCE, and n-TiO₂/PANI/GCE electrodes in a 1.0 mM K₃Fe(CN)₆ solution.

electrodes modified by n-TiO₂ and PANI obviously increased to values that were 2 and 3 times the values of the bare electrode, which indicated that the PANI had a better conductivity than the n-TiO₂. For the electrode that was modified by a composite of both the n-TiO₂ and PANI, the redox peak current of [Fe(CN)₆]^{3-/-4-} increased to almost six-fold over the bare electrode, which was larger than the sum of the peak currents of the electrodes modified by the two separately. These results indicated that a good synergistic effect occurred when the n-TiO₂ and PANI were combined, and in combination, they could greatly improve the electron transfer ability of the sensor interface.

3.3.2. EIS of the electrode assembly process

The surface resistances of the electrodes modified by different materials were different (see Fig. 6); the impedance atlas diameter and the resistance value with the n-TiO₂ and n-TiO₂/PANI modifications were comparatively smaller, which meant that the prepared n-TiO₂ had a good conductivity and that the synergistic effect occurred when it was combined with PANI. The synergistic effect could greatly improve the interfacial electron transfer ability and the redox reaction of the probe on the electrode surface. When the GOx was introduced into the modification, the impedance atlas diameter of the sensor increased greatly again, the main reason being that the fixed GOx is a biomacromolecule with a large resistance value, which demonstrated that the enzyme was successfully assembled on the electrode surface layer-by-layer.

3.4. Direct electrochemistry of GOx/n-TiO₂/PANI

Fig. 7 shows that, compared with the bare electrode (a), the current response of the electrode modified by the PANI and n-TiO₂ (b) increased significantly. A pair of unobvious redox peaks of the GOx/n-TiO₂/GCE (c) and the GOx/PANI/GCE (d) electrodes appeared at -0.45 V, which meant that only weak direct electron transfer of the enzyme could occur if the electrode was modified by PANI or n-TiO₂. The electrode that was modified by the composite of PANI and n-TiO₂, and loaded with the enzyme had a pair of very obvious GOx redox peaks ($E_{pa} = -0.415$ V, $E_{pc} = -0.451$ V) near -0.45 V, which meant that the GOx had already been successfully modified on the electrode surface and that an obvious direct electron transfer occurred. The reason behind this phenomenon might be that modification with the PANI and n-TiO₂ composite not only provided a large specific surface area, good biocompatibility, and more active center sites for GOx but also helped to decrease the steric hindrance of the enzyme active centers and the electrode surface and made the direct electron transfer of the enzyme occur. Meanwhile, for the sample with the enzyme as the bioactive molecule, its large resistance resulted in a low current response compared with the

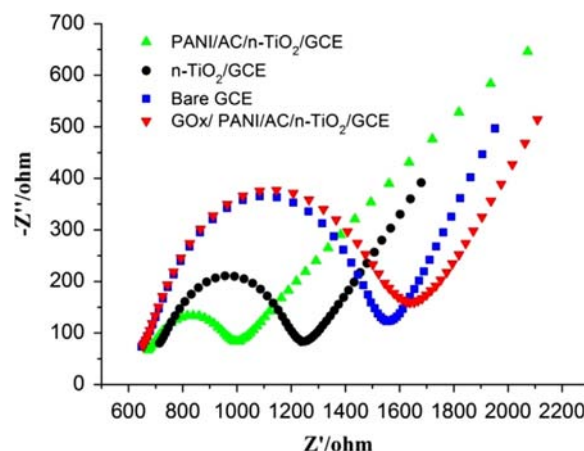


Fig. 6. Electrochemical impedance spectra of bare GCE, n-TiO₂/GCE, n-TiO₂/PANI/GCE, and GOx/n-TiO₂/PANI/GCE electrodes. Supporting electrolyte: 5.0 mM solution of [Fe(CN)₆]^{3-/-4-}.

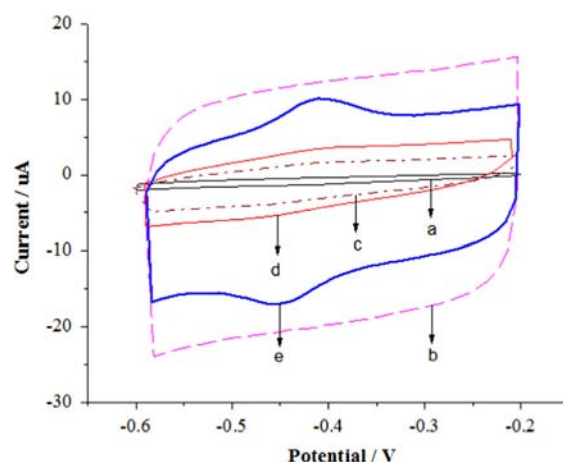


Fig. 7. CV of bare GCE (a), n-TiO₂/PANI/GCE (b), GOx/n-TiO₂/GCE (c), GOx/PANI/GCE (d), and GOx/n-TiO₂/PANI/GCE (e) electrodes in 0.1 M nitrogen-saturated PBS.

sample without modification by the enzyme, which also agreed with the conclusion from the EIS and CV.

The electroactivity density (Γ , mol cm⁻²) of GOx on the electrode surface was calculated by Formula (2)

$$Q = nFA\Gamma \quad (2)$$

where Q is the total charge quantity (c) through the electrode surface, n is the electron transfer amount, F is Faraday's constant, and A is the electrode surface area (cm⁻²).

The reduction peak of GOx/n-TiO₂/PANI/GCE under a scanning speed of 100 mV/s was integrated (Fig. 8) according to Formula (2). The degree that the electroactive oxidase covered the electrode surface, Γ , was 2.79×10^{-10} mol cm⁻², which was much larger than the theoretical value (2.97×10^{-12} mol cm⁻²) of the monolayer enzyme on the bare electrode surface (assuming that the long axis of the GOx molecule ($5.5 \times 7.0 \times 8.0$ nm³) [10] was parallel to the electrode surface). The fact that the actual value was much larger than the theoretical value meant that the GOx on the electrode surface modified the electrode with multiple layers and that direct electron transfer occurred. At the same time, the value was also larger than the coverage density of a fixed enzyme modified by a porous material, such as TiO₂ (2.57×10^{-10} mol cm⁻²) [11], AuNPs/MWCNTs/PVA (2.56×10^{-10} mol cm⁻²) [12], SWCNT/chitosan (1.3×10^{-10} mol cm⁻²) [13], PEDOT-NiO NS (1.56×10^{-10} mol cm⁻²) [14], CdS (1.54×10^{-11} mol cm⁻²) [15],

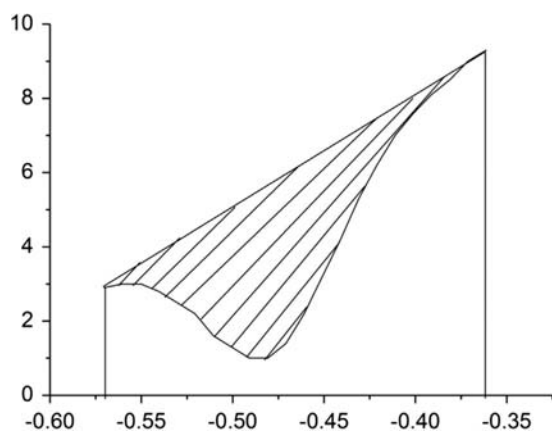


Fig. 8. Integration of the reduction peak at 100 mV s^{-1} .

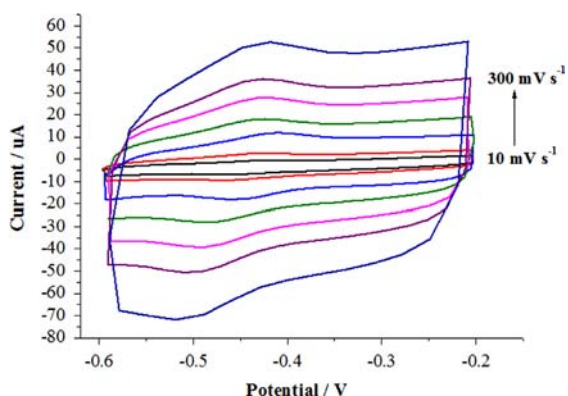


Fig. 9. CV of the GOx/n-TiO₂/PANI/GCE modified electrode in 0.1 M nitrogen-saturated PBS at scan rates of 10, 20, 50, 100, 150, 200, and 300 mV s^{-1} from inner to external.

and AuNPs ($9.8 \times 10^{-12} \text{ mol cm}^{-2}$) [16], indicating that the n-TiO₂ and PANI composite had good biocompatibility and could maintain the microstructure and the bioelectrical activity of the GOx.

3.5. CVs of GOx/n-TiO₂/PANI/GCE under different scanning speeds

Fig. 9 shows that the redox peak current value of GOx increased as the scanning speed increased from 10 mV s^{-1} to 300 mV s^{-1} , and a good linear relationship is demonstrated (Fig. 10). The peak redox current value had a linear relationship with the scanning speed, V , and the R^2 of the reduction peak value reached 0.999, which meant that the process was controlled by the adsorption reaction of the redox material on the electrode surface and not by the diffusion process [17,18]. The GOx was also demonstrated to be well-modified on the electrode surface and formed a CV graph that was similar to the adsorption reactant.

The data in Fig. 11 are from Fig. 9 and show the redox peak potential change of GOx at different scanning speeds. This electrochemical process at the surface can also be described by the Laviron Equation [19,20]

$$E_{pc} = E^{\circ} - \frac{2.3RT}{\alpha nF} \left\{ \log \frac{\alpha F n}{RT} + \log [v] - \log [k] \right\} \quad (3)$$

$$E_{pa} = E^{\circ} - \frac{2.3RT}{(1-\alpha)nF} \left\{ \log \frac{(1-\alpha)F n}{RT} + \log [v] - \log [k] \right\} \quad (4)$$

$$\log k = \alpha \log (1-\alpha) + (1-\alpha) \log \alpha - \log \left(\frac{RT}{nFv} \right) - \frac{\alpha(1-\alpha)nF\Delta E_p}{2.3RT} \quad (5)$$

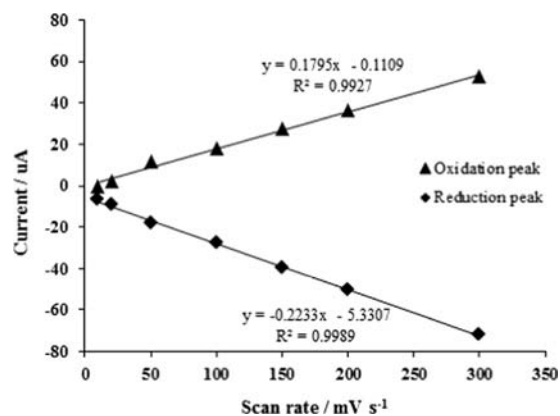


Fig. 10. Values of the enzyme peak current as it changed with the scanning speed.

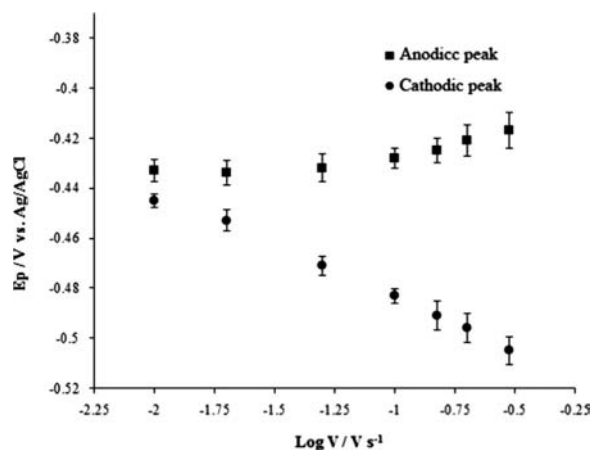


Fig. 11. Plots of the anodic and cathodic peak potentials (E_p vs. $\log v$).

where E_{pa} and E_{pc} represent the positive electrode and the reduction peak potentials, respectively, $\Delta E_p = E_{pa} - E_{pc}$, α is the negative electrode transfer coefficient, v is the scanning speed (V s^{-1}), k is the apparent dissimilar charge transfer speed constant (s^{-1}), n is the electron transfer number, R is the ideal gas constant, and T is the reaction temperature.

According to the locus change slope of the redox peak in Fig. 11 (the linear equation was $y = -0.040x - 0.524$, $R^2 = 0.9917$) and Formula (3), α was deduced to be 0.365. According to the ΔE_p and $\log v$ curves from Formula (5) in Fig. 12, the apparent dissimilar charge transfer speed constant, k , was deduced to be 1.35 s^{-1} ($n=4$), which was smaller than that for the electrode modified by the CNT/GOx (1.6 s^{-1}) [21] but larger than that for GC/CNT/Au/PDDA-GOD (1.01 s^{-1}) [22], this finding indicated that the composite modification with PANI and n-TiO₂ had a good charge transfer ability.

3.6. Current response of GOx/n-TiO₂/PANI/GCE to glucose

3.6.1. Voltamperometric response

Without the addition of glucose, the reduction peak of the enzyme could be observed at -0.47 V , as shown in Fig. 13, and the peak current decreased with an increase in the glucose concentration. As the glucose concentration increased, the glucose entered the enzyme active center competitively and accelerated the transformation of GOx (FAD) to GOx (FADH₂), directly resulting in a decrease in the reduction current in the system.

The change in the sensor reduction peak value with the glucose concentration is described in Fig. 14, which shows that the cathode current decreased greatly over the glucose concentration range of

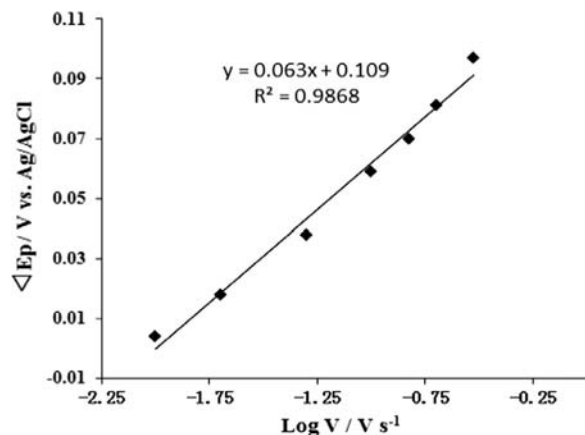


Fig. 12. Plots of the anodic and cathodic peak potentials (E_p vs. $\log v$).

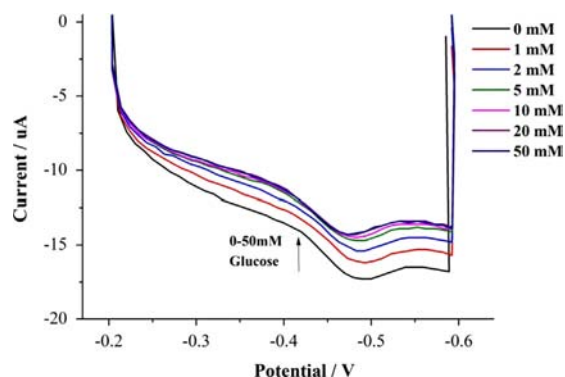


Fig. 13. Reduction current curve of the GOx/n-TiO₂/PANI/GCE biosensor in a 0.1 M solution of nitrogen-saturated PBS (pH=7.0) with different glucose concentrations.

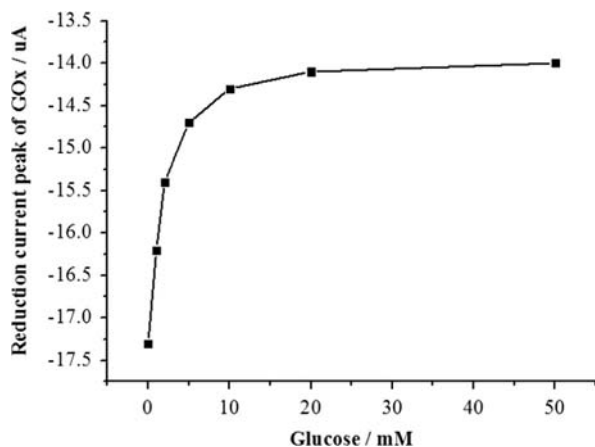


Fig. 14. Plot of the reduction current peak of GOx vs. the glucose concentration.

0–10 mM. As the glucose concentration continued to increase, the FAD and FADH₂ transformation of the active centers gradually tended to be saturated, and the current decrease tended to smooth out. This finding is similar to the results reported by Si et al. [23], which meant that the GOx participated in the direct electron transfer on the electrode surface and the glucose molecule directly reacted catalytically. Thus, the sensor can be classified as of the third generation.

3.6.2. Amperometric response

Figs. 15 and 16 show that the current could reach 95% of the maximum stable current in 10 s, indicating that the response of

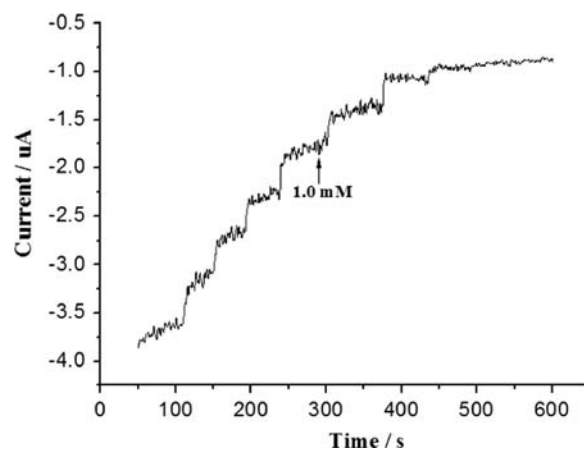


Fig. 15. Amperometric response of the GOx/n-TiO₂/PANI/GCE-modified electrode in a stirred 0.1 M PBS solution (pH=7.0) for successive additions of 1.0 mM glucose at -0.45 V.

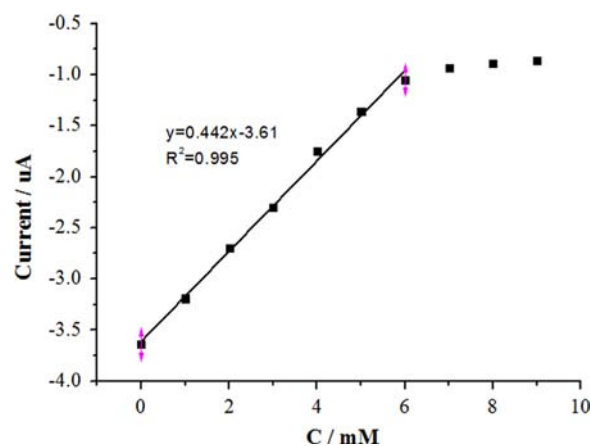


Fig. 16. Calibration curve (current vs. glucose concentration) obtained from the amperometric response.

the sensor was fast and that the GOx modified on the surface could effectively catalyze the glucose molecule reduction reaction. The linear range of the detected glucose concentration was from 0.02 mM to 6.0 mM, the linear equation was $I = 0.442x - 3.61$, and the correlation coefficient was 0.995. A 1.0 mM increase in glucose resulted in an approximately 442 nA decrease in the cathode current, and the cathode current reached a minimum current value of $-1.05 \mu\text{A}$. The sensitivity of the sensor was approximately $6.31 \mu\text{A mM}^{-1} \text{cm}^{-2}$, and the detection limit of the sensor estimated by the triple SNR formula ($s = 2.4 \times 10^{-9}$) was $18 \mu\text{M}$.

3.7. Anti-interference, repeatability, reproducibility and stability of GOx/n-TiO₂/PANI/GCE

The current changes following the addition of 2.0 mM UA, L-cysteine, and AA are shown in Fig. 17, and the changes are negligible compared with the current change brought about by the addition of a glucose solution of the same concentration. The GOx/n-TiO₂/PANI/GCE electrode had better selectivity and anti-jamming capability than other electrodes because the sensor measured the glucose with a reduction method at a low working voltage (-0.45 V) and could avoid the interference by the high voltage oxidation of an interfering substance.

We put eight sensors in PBS solution, which had a glucose concentration of 2.0 mM, to perform current tests. The relative standard deviation (RSD) of the biosensor was 2.66%, which has been shown to be an acceptable reproducibility. After the

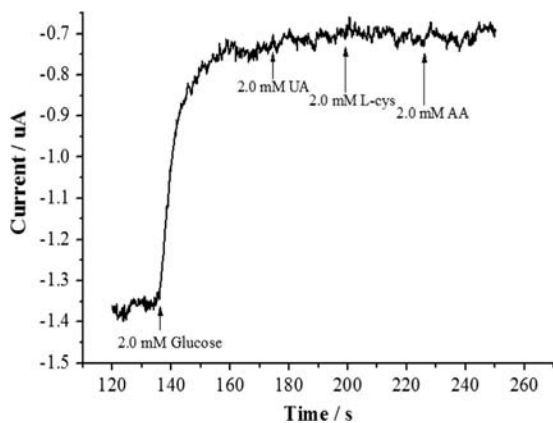


Fig. 17. Effect of possible interferences in the biosensor. The arrows show the moment at the injection of each of the interfering compounds: 2.0 mM glucose, 2.0 mM UA, 2.0 mM L-cysteine, and 2.0 mM AA in a stirred solution of 0.1 M PBS (pH=7.0) at -0.45 V.

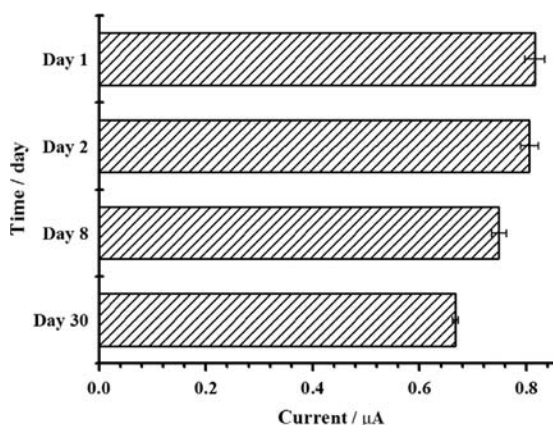


Fig. 18. Stability of the modified biosensors over a storage period of four weeks.

experiment, the sensor was preserved at 4 °C and detected at different times. As shown in Fig. 18, the electrode response did not obviously change in the beginning after 2 days. After the electrode was preserved for 1 week, the electrode current response reached 91.8% of the original, and after 30 days, the response reached 81.7% of the original. In Fig. 18, RSD for five successive measurements was small and the repeatability was good, all which meant that the GOx/n-TiO₂/PANI/GCE electrode had good stability. The main reasons for this outcome are as follows: first, the chitosan could wrap and fix the PANI and n-TiO₂ onto the electrode surface well, and the particle combination could improve the electrode conductivity and increase the solid loading of the enzyme. Second, the glutaraldehyde crosslinking method is a classic covalence enzyme connection method, which can effectively prevent enzyme loss. In addition, the average life expectancy of the working electrode is 70 days.

4. Conclusions

PANI and n-TiO₂ were prepared by oxidation and sol-gel methods, respectively. The CV and EIS both showed that the two

were good conductive materials. The synergistic effect occurred when the electrode was modified by the composite of the two, and the electron transfer ability was greatly improved. An amperometric glucose sensor was established with the PANI composite and n-TiO₂ as the GOx carrier. This sensor had a good response to the glucose, the electron of the GOx molecule was transferred directly onto the sensor, and a linear relationship between the GOx redox peak current and the sweep speed was found. The apparent transmission speed constant, k , for the dissimilar electrode charges was 1.35 s⁻¹, 95% of the maximum steady current for the GOx/n-TiO₂/PANI/GCE sensor could be reached in 10 s, the linear range of the detected glucose concentration was from 0.02 mM to 6.0 mM, the linear equation was $I=0.442x-3.61$, and the correlation coefficient was 0.995. The sensitivity was 6.31 μ A mM⁻¹ cm⁻², and the limit of detection was 18 μ M. The sensor had good selectivity and stability, and it could be maintained at 82% of the initial activity for 30 days.

Acknowledgments

This work was supported by the National Natural Science Foundation of China (No. 21277098), the Natural Science Foundation of Shanghai (No. 10ZR1432500), and the Shanghai Municipal Commission of Economy and Informatization (No. 12CH-12).

Reference

- [1] Y. Zhang, R.L. He, N.E. Hu, *Electrochim. Acta* 49 (2004) 1981–1988.
- [2] M. Addamo, V. Augugliaro, A.D. Paola, E. García-López, V. Loddo, G. Marci, R. Molinari, L. Palmisano, M. Schiavello, *J. Phys. Chem. B* 108 (2004) 3303–3310.
- [3] M.H. Zhang, R. Yuan, Y.Q. Chai, W.J. Li, H. Zhong, C. Wang, *Bioprocess Biosys. Eng.* 34 (2011) 1143–1150.
- [4] J.H. Li, D.Z. Kuang, Y.L. Feng, F.X. Zhang, M.Q. Liu, *Microchim. Acta* 176 (2012) 73–80.
- [5] A.G. Macdiarmid, A.J. Epstein, *Synth. Met.* 69 (1995) 85–92.
- [6] K.P. Lee, S. Komathi, N.J. Nam, A.I. Gopalan, *Microchem. J.* 95 (2010) 74–79.
- [7] C. Dhand, G. Sumana, M. Datta, B.D. Malhotra, *Thin Solid Films* 519 (2010) 1145–1150.
- [8] D.Y. Zhai, B.R. Liu, Y. Shi, L.J. Pan, Y.Q. Wang, W.B. Li, R. Zhang, G.H. Yu, *ACS Nano* 7 (2013) 3540–3546.
- [9] W. Qiu, Master Degree thesis, Chongqing University, China, 2008.
- [10] M. Hartmann, *Chem. Mater.* 17 (2005) 4577–4593.
- [11] S.J. Bao, C.M. Li, J.F. Zang, X.Q. Cui, Y. Qiao, J. Guo, *Adv. Funct. Mater.* 18 (2008) 591–599.
- [12] H.F. Zhang, Z.C. Meng, Q. Wang, J. Zheng, *Sens. Actuators B Chem.* 158 (2011) 23–27.
- [13] Y. Zhou, H. Yang, H.Y. Chen, *Talanta* 76 (2008) 419–423.
- [14] C.X. Guo, C.M. Li, *Phys. Chem. Chem. Phys.* 12 (2010) 12153–12159.
- [15] Y.X. Huang, W.J. Zhang, H. Xiao, G.X. Li, *Biosens. Bioelectron.* 21 (2005) 817–821.
- [16] S.Q. Liu, H.X. Ju, *Biosens. Bioelectron.* 19 (2003) 177–183.
- [17] A.J. Bard, L.R. Faulkner, *Electrochemical methods: Fundamentals and applications*, John Wiley & Sons, New York, 2001.
- [18] Y.H. Wu, S.S. Hu, *Bioelectrochemistry* 70 (2007) 335–341.
- [19] R.W. Murray, A.J. Bard, *Electroanalytical Chemistry*, Marcel Dekker, New York, 1984.
- [20] E. Laviron, *J. Electroanal. Chem.* 101 (1979) 19–28.
- [21] Y.D. Zhao, W.D. Zhang, H. Chen, Q.M. Luo, *Anal. Sci.* 18 (2002) 939–941.
- [22] Y.L. Yao, K.K. Shiu, *Electroanalysis* 20 (2008) 1542–1548.
- [23] P. Si, S. Ding, J. Yuan, X.W. Lou, D.H. Kim, *ACS Nano* 5 (2011) 7617–7626.



Review

Synthesis and utilisation of graphene for fabrication of electrochemical sensors



Abdulazeez T. Lawal*

Department of Chemical and Geological Science. Al-Hikmah University Ilorin, Nigeria

ARTICLE INFO

Article history:

Received 24 April 2014

Received in revised form

4 July 2014

Accepted 7 July 2014

Available online 12 August 2014

Keywords:

Enzymes

DNA biosensor

Immunosensor

Enzyme biosensor

Graphene electrode

Glucose

Ascorbic acid

ABSTRACT

This review summarises the most recent contributions in the fabrication of graphene-based electrochemical biosensors in recent years. It discusses the synthesis and application of graphene to the fabrication of graphene-based electrochemical sensors, its analytical performance and future prospects. An increasing number of reviews and publications involving graphene sensors have been reported ever since the first design of graphene electrochemical biosensor. The large surface area and good electrical conductivity of graphene allow it to act as an “electron wire” between the redox centres of an enzyme or protein and an electrode’s surface, which make it a very excellent material for the design of electrochemical biosensors. Graphene promotes the different rapid electron transfers that facilitate accurate and selective detection of cytochrome-*c*, β -nicotinamide adenine dinucleotide, haemoglobin, biomolecules such as glucose, cholesterol, ascorbic acid, uric acid, dopamine and hydrogen peroxide.

© 2014 Elsevier B.V. All rights reserved.

Contents

1. Introduction	425
2. Synthesis of graphene	425
2.1. Chemical vapour deposition (CVD) method	425
2.2. Graphene sheet (Gs)	426
2.3. Other methods	427
3. Review studies	427
3.1. Review of graphene synthesis and production	427
3.2. Graphene electrochemical reviews	427
4. Graphene nanocomposites (GN)	428
5. Electrochemical sensing	429
5.1. Graphene electrochemical sensing	429
5.2. Graphene-based electrochemical enzymatic biosensors	430
6. Use of electrodes based on graphene for sensing different analytes	430
6.1. Glucose oxidase biosensor	430
6.2. Haemoglobin (Hb) biosensor	432
6.3. Hydrogen peroxide biosensor (H ₂ O ₂)	432
6.4. β -Nicotinamide adenine dinucleotide (NADH)	434
6.5. Cholesterol biosensor	434
6.6. Electrochemical immunosensing	436
6.7. DNA sensors	437
6.8. Ascorbic acid (AA), uric acid (UA) and dopamine (DA)	438
6.9. Cytochrome <i>c</i> (Cyt- <i>c</i>)/cysteine	439
7. Conclusions	440

* Tel.: +23 481 7432 8856.

E-mail address: abdul.lawal@yahoo.com

8. Future work	440
References	440

1. Introduction

Recently, great attention has been focused on graphene and its derivatives and they are being studied in nearly every field of science [1], medicine [2,3] and engineering [4]. Graphene-based materials can have a profound impact on electronic and optoelectronic devices [5], chemical sensors [6,7], nanocomposites [8–14], optical biosensor [15] and energy storage [16,17]. New applications of graphene nanomaterials in electrochemical sensors and biosensors are now on the rise with the advent of nanotechnology [4,18–21]. Various graphene nanomaterials [20–28], including graphene metal nanoparticle (NP) [29–36], nanocomposite [14,37–41], metal alloy NP, magnetic NP [42], nanowires [22,43–45], nanofibers [46], nanorod [47], CNT [21,48–57], and CNF [58], have been used as electrical connectors between the electrodes and the redox centres of the biomolecules [57–62]. The use of graphene as a nanomaterial can avoid the problems associated with metal alloy NP and CNT. The properties of graphene, such as fast electron transportation, high thermal conductivity, excellent mechanical flexibility and good biocompatibility, make it a potential candidate in the fabrication of sensitive electrochemical biosensor [63–67]. Graphene was discovered in 2004 by scientists [68], and since the 2010 Nobel Prize in Physics “for groundbreaking experiments regarding the two-dimensional material graphene” graphenes have been the goal of numerous researchers due to their unique structural, electronic and mechanical properties that make them a very

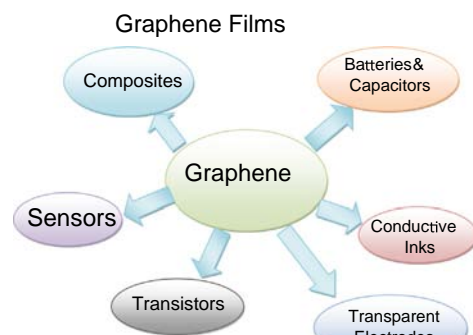


Fig. 1. Applications of graphene [166].

Table 1
Applications of graphene and related materials.

S/N	Application	Reference
1	Energy storage	[16,17]
2	Batteries	[63,84–87]
3	Gas sensor	[74,96–99]
4	Capacitors	[75–78]
5	Chemical and biosensors	[7,91–95]
6	Fuel cell	[79–83]
7	Photocatalysis	[17,63]
8	Photovoltaics	[25,90]
9	Solar cell	[17,75,102]
10	Light emitting diode	[103,104]
11	Laser	[105]
12	Optoelectronics	[100,106]
13	Photocatalyst	[107,108]
14	Thin-film transistor	[103,109]
15	FET	[110–113]

attractive material for a wide range of applications [4,54,69–71] (Fig. 1. Table 1).

Graphene is the basic structure of all graphitic materials and is a one-atom-thick planar sheet of sp² bonded carbon atoms in a honeycomb crystal lattice [66]. Its remarkable electronic, optical, mechanical, thermal, and electrochemical properties have made it a suitable electronic material for electrochemical sensing, as graphene has a very good electronically low-noise [5,72]. Many groups all over the world are carrying out exciting work using graphene and its hybrids in applications such as super capacitors [73–77], fuel cells [78–82], batteries [63,83–86], photocatalysis [17,63,87,88], photovoltaics [25,89], chemical and biosensors [7,90–94], gas sensors [73,95–98], photonics [99,100], solar cell [17,74,101], light-emitting diodes (LEDs) [102,103], laser [104], optoelectronics [99,105], photocatalyst [106,107], thin-film transistors [102,108] and field effect transistor (FET) [109–112] (Table 1).

2. Synthesis of graphene

A number of different routes to synthesise graphene have been demonstrated over recent years. There are two ways to synthesise graphene: mechanical method and chemical method. The chemical method is through oxidation, usually the Standenmaier method [113], the Brodie method [114] and the Hummers method [115]. The mechanical method, ‘Scotch tape technique’, was used in 2005, to fabricate graphene where multiple layers of graphene are peeled from a slab of highly ordered pyrolytic graphite using adhesive tape and transferred onto an appropriate substrate [116]. Majority of other fabrication methods of graphene are produced and supplied in solution, such that graphene has to be immobilised onto the desired surface [117,118]. Graphene and related materials, such as graphene oxide (GO) [119] and reduced graphene oxide (rGO) [120,121], have come to the forefront of research in electrochemical sensors during recent years. Ratinac et al. [122] synthesised GO following a modified Hummer’s method, which has been subsequently reduced by electrochemical procedures. This reduction strategy precludes the employment of toxic solvents, leading to a product, electrochemically reduced graphene (ERG), free of contaminants. There are other several reported methods for the synthesis of graphene [84,89,123,124], including exfoliation, cleavage of natural graphite, micromechanical exfoliation of graphite, epitaxial growth on electrically insulating surfaces, such as SiC, opening CNT and the solution-based reduction of GO [89,125–127].

2.1. Chemical vapour deposition (CVD) method

CVD, a fabrication process where graphene is grown upon a substrate, has emerged as an important method for the preparation and production of graphene for various applications since the method was first reported in 2008/2009 [102,128–130] Fig. 2. Recently, Zhang et al. [131] reviewed graphene CVD on various metal substrates with emphasis on Ni and Cu. In addition, they discussed important and representative applications of graphene formed by CVD, which includes flexible transparent conductors for organic photovoltaic cells as well as field effect transistors. Growth on polycrystalline Ni films leads to both monolayer and few-layer graphene with multiple layers because of the grain boundaries on Ni films. They were able to increase the percentage of monolayer graphene by using single-crystalline Ni (111) substrates, which

have a smooth surface and no grain boundaries. Due to the extremely low solubility of carbon in Cu, Cu has emerged as an even better catalyst for the growth of monolayer graphene with a high percentage of single layers. Zhang et al. [131] also described a method for transferring graphene sheets from the metal using polymethyl methacrylate (PMMA). Paniagua et al. [132] produced heavily n- and p-doped CVD graphene with solution-processed redox-active metal-organic species.

CVD can produce large areas of single layer graphene [133]. Ambrosi et al. [65] investigated the electrochemical properties of a multilayer graphene film grown by CVD and transferred to an insulating flexible poly (ethylene terephthalate) (PET) sheet. They carefully characterised PET with optical microscopy, Raman spectroscopy, and X-ray photoelectron spectroscopy of the transferred graphene film. They tested its heterogeneous electron transfer properties with $\text{Fe}(\text{CN})_6^{3+/4+}$ and $\text{Ru}(\text{NH}_3)_6^{2+/3+}$ redox mediators and its sensing capability toward dopamine (DA), ascorbic acid (AA), and the reduced form of nicotinamide adenine dinucleotide (NADH) as biological relevant molecules. The CVD grown multilayer graphene film transferred to a PET substrate showed an electrochemical behaviour that resembles that of basal plane graphite with a low density of edge-plane defects sites. Li et al. [112] and Reina et al. [133] synthesised graphene by CVD using centimeter-scale copper substrates. Recently, Zhang et al. [134] synthesised graphene by CVD from solid PMMA deposited on a Cu substrate. CVD graphene has electronic properties that are potentially valuable in a number of applications. Zhang et al. [135] found that few-layer graphene grown on Ni can function as flexible transparent conductive electrodes for organic photovoltaic cells. In addition, they synthesised large-grain graphene on Cu foil; such large-grain graphene has electronic properties suitable for use in field effect transistors. CVD of graphene on Cu and Ni substrates

are the most promising procedures to synthesize large-area and good-quality graphene films [136]. Ambrose et al. [137] investigated the electrochemical properties of a multilayer graphene film grown by CVD and transferred to an insulating flexible poly (ethylene terephthalate) (PET) sheet Fig. 2. Wu et al. [129] reported wafer-scale synthesis of graphene by CVD and its application in hydrogen sensing. Kim et al. [138,139] synthesised graphene films on Ni substrates for stretchable transparent electrodes.

2.2. Graphene sheet (Gs)

The characterization of the synthesized nanomaterials by a combination of techniques confirms that the synthesis methodology affords the production of GO nanosheets, which present a typical lateral dimension of several hundreds of nanometers and a thickness value of 1.3 ± 0.1 nm, and the production of graphene nanosheets free of oxygen functionalities with an average lateral dimension of at least 1 micrometer and a thickness value of 2.8 ± 0.2 nm [140].

Alwarrapan et al. [141,142] chemically synthesised graphene nanosheets as electrode materials and their electrochemical properties were systematically characterised. The surface morphologies of graphene nanosheets were evaluated using Raman spectroscopy and transmission electron microscopy (TEM) as shown in Fig. 3. They also reported electrochemical properties of graphene nanosheets for biosensing applications. Rattana et al., Park, Rauf, Fowler et al. and Wu et al. [143–146] produced GO nanosheets by a chemical exfoliation technique.

Recent studies by Stankovich et al. and other researchers [41,147–149] have shown that Gs can be prepared in large quantity through chemical conversion from graphite, which can be used in the fabrication of graphene-based electronic devices [136,150–152] and chemical conversion also made it possible to create new bulk materials comprising graphene sheets for a broader range of applications [153,154]. It has been recently demonstrated that chemically modified Gs can be dispersed throughout a polymeric [147,148] or inorganic matrix [154] to make electrically conducting composites with a percolation threshold as low as 0.1 vol%. Studies by Chen et al. [136] also showed one novel step of the exfoliated accompanying carboxylated graphene sheet from pristine, which is achieved via Friedel-Crafts acylation. By electrophilic aromatic substitution, the succinic anhydride ring is opened and it attaches covalently to the Gs to form exfoliated graphene with grafted 1-one-butyric acid (Gs-BA). The grafting chain converts anions in aqueous solution to maintain Gs-BA in a stable dispersion and noticeably decreases the π - π stacking of the exfoliated Gs during

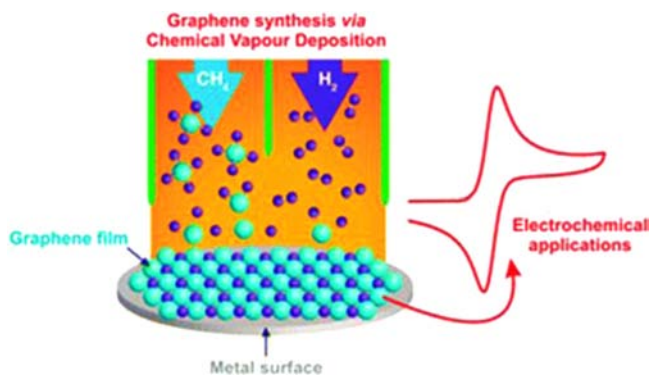


Fig. 2. CVD processes [165].

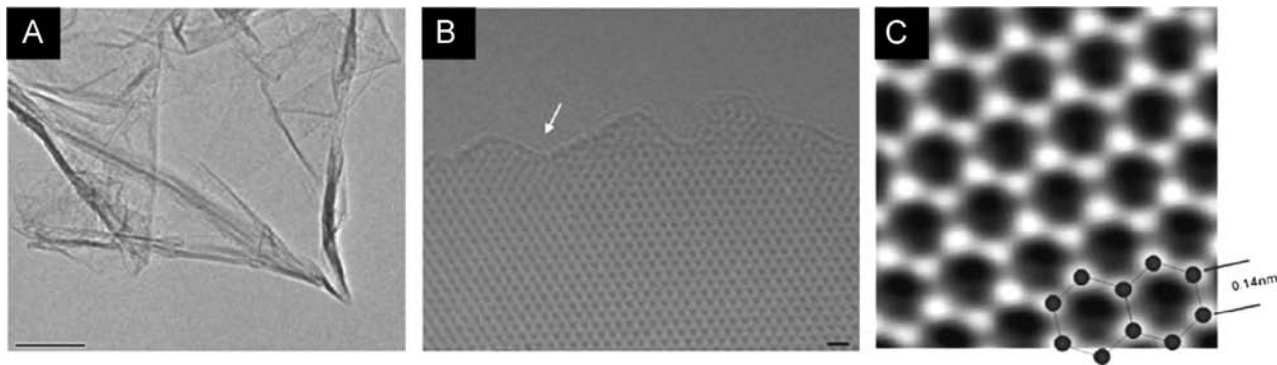


Fig. 3. (A) A typical low-magnification TEM image of the graphene sheets; the scale bar is 100 nm. (B) A high-resolution TEM image, where the white arrow indicates the edge of the graphene sheet; the scale bar is 4 Å. (C) An atomic-resolution image (TEAM 0.5) of a clean and structurally perfect synthesised graphene sheet. Individual carbon atoms appear white in the image. The image was obtained through the reconstruction of the electron exit wave function from 15 lattice images using MacTempas software [356].

the drying process. Gs-BA retains the Gs electrical properties favourable for developing electrochemical sensors [155].

2.3. Other methods

Dong et al. [156] prepared monolayers of graphene from natural flake graphite using 1, 3, 6, 8-pyrenetetrasulfonic acid and D₂O. Graphene can also be produced via a substrate-free gas-phase synthesis method. This involves sending an aerosol consisting of liquid ethanol droplets and argon gas directly into a microwave-generated argon plasma (at atmospheric-pressure), where over a time scale in the order of 10⁻¹ s, ethanol droplets evaporate and dissociate in the plasma forming solid matter. It was confirmed to be true graphene through characterisation by transmission electron microscopy (TEM) and Raman spectroscopy. Graphene can also be prepared on H₂-etched surfaces of 6H-SiC when heated to 1250–1450 °C for a short time (1–20 min) [144]. Another mass production method involves the chemical or thermal reduction of GO [157] and to date is the most common and economical method. Graphene synthesized by chemical oxidation–reduction has been reported to possess many structural defects, which are advantageous for electrochemical applications [59]. Chakrabati et al. [158] reported on progress made in the electrochemical modification of graphene-based materials and their applications. Kumar [159] recently reported laser flash synthesis of graphene and its inorganic analogues. This was an innovative breakthrough with immense promise. Jelili et al. [160] worked on graphene oxide dispersion. They showed that GO dispersions exhibit unique viscoelastic properties which show them as a new class of soft materials. The fundamental insights accrued from here provide the basis for the development of fabrication protocols for the two-dimensional soft materials produced in a diverse array of processing techniques.

3. Review studies

Because of the excellent properties of graphene, such as large surface-to-volume ratio, high conductivity and electron mobility at room temperature, as well as low energy dynamics of electrons with atomic thickness, robust mechanical and flexibility, it is at the centre of an ever-growing research. These unique properties have made many researchers review the synthesis of graphene and its applications in recent years. Graphene, a single-layered atom, emerging as a true two-dimensional nanomaterial, has tremendous potential for electrochemical catalysis, biosensing and as a novel electrode material.

3.1. Review of graphene synthesis and production

There are many reviews on graphene and its applications to various devices. However, few of the review articles connect the intrinsic properties of graphene with its energy [161]. Wei et al. [62] stated in their review that a number of scientific results on graphene published to date actually deal with multi-layer groupings or reduced graphenes from insulating GO, which contains defects and contaminants from the reactions and do not possess any of the intrinsic physical properties of pristine graphene. Bonaccorso et al. [162] reviewed the state of the art of graphene preparation, production, placement and handling. Geim [163] reviewed graphene's status and prospects and Wee [164] reviewed prospects and applications of graphene. Zhang et al. [131] reviewed graphene CVD on various metal substrates with an emphasis on Ni and Cu. In addition, they discussed important and representative applications of graphene formed by CVD, including as flexible transparent conductors for organic photovoltaic cells and in field effect

transistors. Brownson et al. [165] also reviewed recent developments in the fabrication of CVD graphene and explored its utilisation in electrochemistry, considering its fundamental understanding to applications in sensing and energy-related devices.

Edwards et al. [166] reviewed and highlighted the different methods available for the synthesis of graphene and discusses the viability and practicalities of using the materials produced via these methods for different graphene-based applications. Allen et al. [66] called graphene a honey comb carbon in their review of graphene. Choi et al. [89], also in their review presented an overview of the advancement of research in graphene in the area of synthesis, properties and applications, such as field emission, sensors, electronics, and energy. They enumerated and highlighted future research directions. Chen et al. [125] in their critical review described recent advances in the development of graphene-based materials from the standpoint of electrochemistry. They discussed electron transfer properties of graphene involving its unusual electronic structure, extraordinary electronic properties and fascinating electron transport. Walcarius et al. [24], in their review, discussed the interest of both nano-objects (metal nanoparticles and quantum dots, carbon nanotubes and graphene) and nano-engineered and or nanostructured materials (template-based materials, advanced organic polymers) for the rational design of bio-functionalized electrodes and related biosensing systems. The attractiveness of such nanomaterials relies not only on their ability to act as effective immobilization matrices, which are likely to enhance the long-term stability of bioelectrochemical devices, but also on their intrinsic and unique features. Kumar et al. [159] presented an overview of the progress made into laser-based synthesis of graphene and its inorganic analogue. Singh et al.'s [167] review provided a comprehensive scientific progress of graphene to date and evaluated its future perspective. Various synthesis processes of single-layer graphene, graphene nanoribbons, chemically derived graphene, and graphene-based polymer and nanoparticle composites are reviewed. Their structural, thermal, optical and electrical properties were also discussed, along with their potential applications. The article concluded with a brief discussion of the impact of graphene and related materials on the environment, its toxicological effects and its future prospects in this rapidly emerging field. Wang et al. [168] reviewed nitrogen-doped graphene, including various synthesis methods to introduce N-doping and various characterization techniques for the examination of various N-bonding configurations. Potential applications of N-graphene were also reviewed on the basis of experimental and theoretical studies.

3.2. Graphene electrochemical reviews

Fang and Wang [169] provided an overview of electrochemical biosensing with graphene related materials and discussed the role of graphene in different sensing protocols. Artiles et al. [110] comprehensively reviewed the most recent trends in graphene-based biosensors and attempted to identify the future directions in which the field is likely to thrive. Brownson et al. [63,124] reviewed the potential application of graphene and looked into recent understanding of graphene-modified electrodes, highlighting prominent applications reported in the current literature. Chakrabarti et al. [158] reviewed the electrochemical modification of graphene. They discussed different composite materials that have been prepared with reduced graphene and enumerated six different methods of electrochemical modification of graphene to prepare composite materials. These include cathodic reduction of GO, electrochemical deposition, electro-deposition techniques, electrospinning, electrochemical doping, and electrochemical polymerisation.

Over the past few years, much work has been done in the design and preparation of novel graphene-based materials for a wide range of applications in photoelectron chemistry, ranging from photo electrochemical solar cells, photo catalytic decomposition of organic pollutants, photo catalytic splitting of H_2O , and photo catalytic conversion to fuels. Chen et al. [17,21,125] summarised the state of research on graphene-based materials from the standpoint of photoelectron chemistry and electrochemistry. The prospects and further developments in this exciting field of graphene-based materials were also discussed. They also presented the current advances in the field of graphene electroanalytical chemistry, including the modern methods of graphene production and graphene functionalisation. Gan and Hu [170] gave a general view of recent advances in electrochemical sensors based on graphene. They emphasised the important applications of graphene and graphene nanocomposites, and the assayed strategies in electrochemical sensors for DNA, proteins, neurotransmitters, phytohormones, pollutants, metal ions, gases, hydrogen peroxide and in medical, enzymatic and immunosensors. Kuila et al. [123] reviewed and discussed the application of graphene for the detection of glucose, Cyt-c, NADH, Hb, cholesterol, AA, UA, DA, GO and H_2O_2 RGO that had been used for the fabrication of heavy metal ion sensors, gas sensors and DNA sensors. Graphene-based FETs were also discussed in details. Putzbach and Ronkainen [20] reviewed immobilisation techniques in the fabrication of graphene nanomaterial-based electrochemical biosensors.

4. Graphene nanocomposites (GN)

Graphene-inorganic nanocomposites have opened up an exciting new field in the science and technology of GN. GN-metal nanoparticles have excellent conductivity and catalytic properties, which make them suitable for acting as 'electronic wires' to enhance the electron transfer between the redox centres in proteins and electrode surfaces, and as catalysts to increase electrochemical reaction rates [36]. The conductivity of nanoparticles enhances electron transfer between the active centers of enzymes and electrodes so that the particles act as electron transfer conduits or mediators [171]. Bai et al. [172] presented an overview of the synthesis and application of GN-inorganic nanocomposites. They also discussed challenges and perspectives of these emerging nanocomposites. Li et al. [173] presented an overview of the latest design of structures, synthetic methods and applications of graphene-based inorganic nanocomposites. The challenges and perspectives of these emerging hybrid heterostructures were also discussed.

Graphene has been incorporated into nanocomposites in order to couple its unique properties with the properties of other nanomaterials. Lui et al. [174] recently produced graphene nanoplatelet-titanate nanotube composite and its advantages over the two single components as biosensor immobilization materials. Feng et al. [175] synthesised graphene-Au nanocomposites through the hydrothermal route. TEM images gave direct evidence of the thin and transparent sheet structure of graphene. X-ray photoelectron spectroscopic (XPS) and X-ray diffraction (XRD) results also showed the presence of Au and the reduction of GO. The graphene-Au nanocomposites provide a novel matrix for protein immobilization and the construction of biosensors via the direct electron transfer of protein. Gao et al. [176] developed a novel electrochemiluminescence (ECL) ethanol biosensor based on Ru (bpy) $_3^{2+}$ and alcohol dehydrogenase (ADH) immobilized by graphene/bovine serum albumin composite film. The graphene film was directly formed on a glassy carbon electrode surface via an in situ reduction of GO, and (bpy) $_3^{2+}$ was immobilized during its formation. The graphene film acted as both a decorating agent for

immobilization of Ru (bpy) $_3^{2+}$ and a matrix to immobilize bovine serum albumin (BSA). Meanwhile, BSA not only acted as reductants to reduce GO, but also provided a friendly environment for ADH immobilization. Furthermore, ADH was separated from Ru (bpy) $_3^{2+}$ by the electron-conductive graphene/BSA composite film to retain its enzymatic activity.

Huang et al. [177] synthesised layered MoS $_2$ -graphene composites by a modified l-cysteine-assisted solution-phase method, and they were characterised by XRD, field emission SEM, and high-resolution TEM. The electrochemical properties of the nanocomposite film were investigated by electrochemical impedance spectroscopy (EIS) and cyclic voltammetry (CV). Acetaminophen as model molecular was employed to study its electrochemical responses at the MoS $_2$ -graphene modified electrode, which shows more favourable electron transfer kinetics than graphene-modified glassy carbon and bare glassy carbon electrodes. This novel electrochemical sensor exhibits excellent analytical performance for acetaminophen detection, with a detection limit of $2.0 \times 10^{-8} \text{ mol L}^{-1}$ ($S/N=3$) and a linear range of $0.1\text{--}100 \mu \text{ mol L}^{-1}$.

Yue et al. [178] developed a sensing platform composed of single-layer graphene nanoplatelet and hemeprotein. They found that single-layer graphene nanoplatelet provided a biocompatible microenvironment for protein immobilisation, with suitable electron transfer characteristics. The resulting composite film was characterised and used for the indirect determination of nitrite. Using a polyol process, Zhang et al. [179] prepared a Cu $_2$ O-graphene nanocomposite, which was then deposited on a GC electrode. The modified electrode was then used to selectively determine the concentration of dopamine with a detection limit of 10 n mol L^{-1} . Fan et al. [180] prepared a TiO $_2$ -graphene nanocomposite, using hydrolysis and in situ hydrothermal treatment. The composite was then used to modify a GC electrode, which showed significant improvement in the electro catalytic activity towards adenine and guanine. Du et al. [181] prepared a ZrO $_2$ -graphene nanocomposite, using an electrochemical deposition method. Due to the strong affinity of the composite for phosphoric moieties, it can be used as a capturing agent or as a sensing material for organophosphorous agents. The use of metal NP with graphene has been reported to form exceptionally stable and cost-effective biosensors [182,183]. Shan et al. [184] reported a graphene/AuNPs/chitosan composites film-based biosensor which exhibited good electrocatalytic activity toward H_2O_2 and O_2 . Hong et al. [185] also reported the preparation of gold nanoparticle/graphene composites with controlled weight contents and their application in biosensor. The composite structure is as shown in Fig. 4. Zhang et al. [186] prepared sensitive electrogenerated chemiluminescence (ECL). Cholesterol biosensor was prepared based on cerium oxide-graphene (CeO $_2$ -graphene) composites as an efficient matrix. CeO $_2$ -graphene composites were prepared by depositing CeO $_2$ onto graphene and were characterized by scanning electron microscopy. The experimental results demonstrated that CeO $_2$ -graphene could catalyze the ECL of a luminol- H_2O_2 system to amplify the luminol ECL signal greatly. In addition, the use of CeO $_2$ -graphene provided a better biocompatible microenvironment for the immobilised enzyme, resulting in excellent stability and a long lifetime of the ECL biosensor. The surface assembly process, ECL behaviours, and electrochemistry of the biosensor were investigated in detail. The quantity of cholesterol was in the linear range from $12 \mu \text{ mol L}^{-1}$ to 7.2 m mol L^{-1} , with a detection limit of $4.0 \mu \text{ mol L}^{-1}$ (signal/noise=3). In addition, the biosensor exhibited outstanding reproducibility, long-term stability and selectivity. Yang et al. [187] electrodeposited a composite film consisting of GO, chitosan and glucose oxidase directly on a glassy carbon electrode (GCE) through electrochemical reduction of a solution of the 3 components under controlled direct electrical

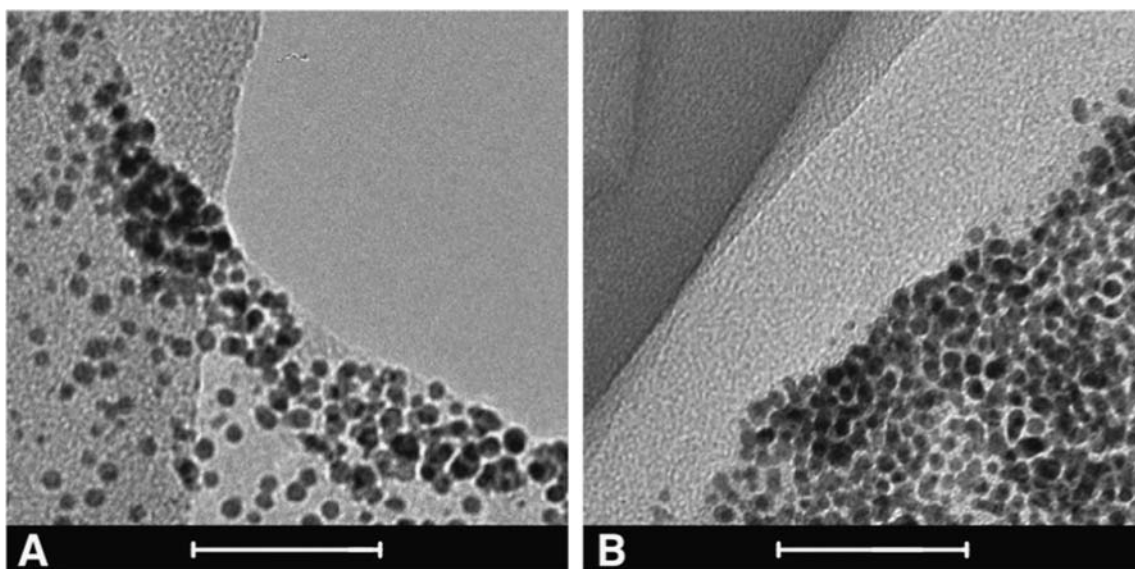


Fig. 4. TEM images of gold nanoparticle-pyrolytic functionalised graphene composites with a gold to graphene weight ratio of (A) 10:1 and (B) 300:1. Scale bar: 50 nm [185,357].

potential. The procedure took only several minutes, and the thickness of the resulting film is uniform and controllable. The GOx has uncompromised bioactivity and exhibits reversible 2-proton and 2-electron transfer in the presence of glucose. It therefore can be used as amperometric sensing of glucose. The biosensor has a fast response (< 3 s), a detection limit of $0.4 \mu\text{mol L}^{-1}$ (which is 50-fold lower compared to the biosensor prepared by drop-casting solutions of the same materials onto a GCE), and a linear response in the $0.4 \mu\text{mol L}^{-1}$ – 2m mol L^{-1} concentration range (which again is much better than that of the biosensor prepared by the drop-casting method). Other features include high reproducibility, long-time storage stability, and satisfactory selectivity. They presumed that the direct single-step electrodeposition of this nanocomposite offers a promising approach towards novel types of highly sensitive and stable electrochemical biosensors. Cao et al. [14] used the TiO_2 -graphene-Pt-Pd hybrid nanocomposites (TGPHs) as an enhanced element of the integrated sensing platform for increasing the surface area as well as improving the electronic transmission rate. Subsequently, Au nanoparticles (AuNPs) and cholesterol oxidase (ChOx) were successively self-assembled to TGPHs, with high load amount and superior biological activity. The morphology of TGPHs and stepwise fabrication processes were characterized with CV, AFM, X-ray photoelectron spectroscopy (XPS) and SEM. Based on the efficient catalytic ability of TGPHs and AuNPs, the fabricated biosensor exhibited wide linear ranges of responses to cholesterol in the concentration ranges of 5.0×10^{-8} – $5.9 \times 10^{-4} \text{mol L}^{-1}$, while the limit of detection was $0.017 \mu\text{mol L}^{-1}$ ($S/N=3$). Cao et al. [188] also developed cholesterol biosensor for the detection of cholesterol by using platinum-palladium-chitosan-graphene hybrid nanocomposites (PtPd-CS-GS) functionalized glassy carbon electrode (GCE). An electro-deposition method was applied to form PtPd nanoparticle-doped chitosan-graphene hybrid nanocomposites (PtPd-CS-GS), which were characterised by SEM and electrochemical methods. The presence of the PtPd-CS-GS nanocomposites not only accelerated direct electron transfer from the redox enzyme to the electrode surface, but also enhanced the immobilized amount of cholesterol oxidase (ChOx). Under optimal conditions, the fabricated biosensor exhibited wide linear ranges of responses to cholesterol in the concentration ranges of 2.2×10^{-6} – $5.2 \times 10^{-4} \text{mol L}^{-1}$. The limit of detection was

$0.75 \mu\text{mol L}^{-1}$ ($S/N=3$). Gan and Hu [170] highlighted important applications of graphene, graphene nanocomposites, and assayed strategies in electrochemical sensors for DNA, proteins, neurotransmitters, phytohormones, pollutants, metal ions, gases, H_2O_2 , enzymatic and immunosensors.

5. Electrochemical sensing

5.1. Graphene electrochemical sensing

Electrochemical detection is highly sensitive to electroactive molecules and also offers detection selectivity, as different molecules can be oxidised/reduced at different potentials. Carbon materials (graphene, graphite, fullerene and CNT) are often used for electrochemistry due to their low residual current, readily renewable surface and wide potential window. The large overpotential for O_2 reduction and H_2 density of edge-plane defect sites on it provides multiple active sites for electron transfer to biospecies [7]. Graphene is an excellent conductor of electrical charge and heterogeneous electron transfer occurs at the edges of the graphene or at defects in the basal plane [189]. The high surface area of graphene facilitates large amounts of defects and a large number of electroactive sites [23]. Electrodes made from graphene have more uniform distribution of electrochemically active sites than do those made from graphite [11]. Its entire volume is exposed to the surroundings due to its 2D structure, making it very good in detecting adsorbed molecules on the electrode [89].

Efficient electrochemistry takes place when metals nanoparticles (NP) decrease the distance between the redox site of a protein and the electrode surface, as the rate of the electron transfer (ET) is inversely proportional to the exponential distance between them [190]. The direct wiring of enzymes to an electrode surface is essential to amplify the electrochemical signal of the biochemical reaction [191,192]. Graphene supports efficient electrical wiring of the redox centers of several metalloproteins containing heme (cytochrome c, myoglobin, and horseradish peroxidase) to the electrode as shown in Fig. 5. Nanowiring of redox enzyme can also take place by metal NP [192]. Direct electron transfer (DET) between redoxenzymes and the electrode surfaces can be used

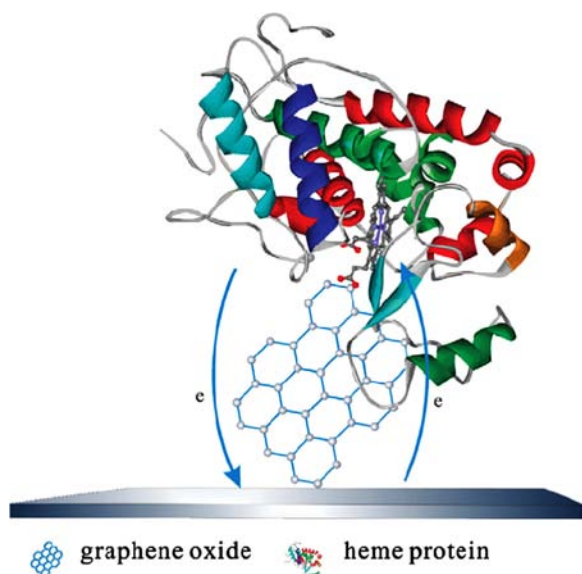


Fig. 5. Wiring of proteins by graphene for electrochemistry. Graphene-oxide (GO)-supported heme proteins at the surface of glassy-carbon electrodes [225].

for the study of enzyme kinetics and thermodynamics of redox transformation of enzymic molecules involving redox transformations. It can also be used to investigate enzyme catalyzed reactions in biological systems [56,193]. Direct electrochemistry of enzymes involves direct ET between the electrode and the active centre of the enzymes without the participation of mediators or other reagents [184,194,195]. New mediator-free (or reagentless) biosensors [196–199], enzymatic bioreactor, and biomedical devices employ DET by immobilizing enzymes on conducting substrates. The redox centers of the biomolecules are usually embedded deep in their large three-dimensional structures. Recent research has shown that graphene can enhance DET between enzymes and electrodes. The electron transfer between graphene and redox active species occurs at the edges of the graphene sheet and/or at defects in the basal plane [200]. The high surface area of graphene typically provides a large number of electroactive sites [155,201] that enhance ET and promote potential applications in electrochemical sensing.

5.2. Graphene-based electrochemical enzymatic biosensors

Clark and Lyons [202] proposed the first enzymatic electrode and since then, electrochemical biosensors based on the use of enzymes have received great attention, because of the advantages of the association of the biocatalytic activity of enzymes with the high sensitivity and versatility of the electrochemical transduction. The immobilisation of enzyme is critical, since the enzyme has to remain active to perform an efficient biorecognition of the substrate. The transducer where the enzyme is immobilized has to allow a fast charge transfer to ensure a rapid and sensitive response for a good biosensor as shown in Fig. 6. Several strategies for immobilizing redox enzymes and other proteins on graphene modified electrodes have been explored [203,204]. Proper conjugation between biological molecules such as enzymes, ssDNA, RNA, Ab, receptors and aptamers needs to be developed for graphene-based electrochemical sensing electrodes. Appropriate functionalisation of graphene and the immobilisation of biomaterials on it are important, as functional groups can create defects on graphene surfaces [59]. Table 2 shows the different types of enzymatic graphene-based biosensor with their limit of detection and RSD.

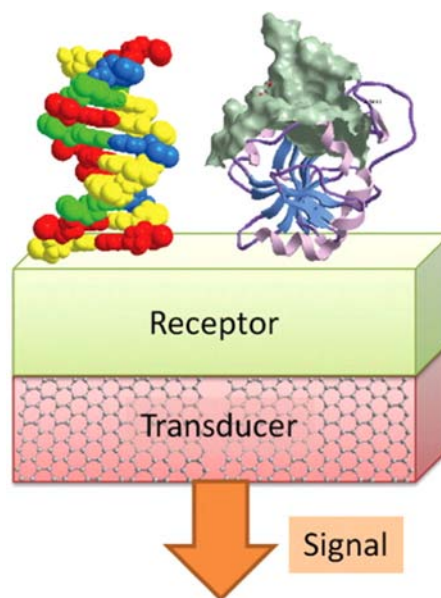


Fig. 6. Scheme of a biosensor. The biosensor consists of a receptor layer, which consists of a biomolecule (e.g., DNA or protein), and a transducer, which is a graphene-based material [107]. Reproduced by permission of American Chemical Society, USA.

6. Use of electrodes based on graphene for sensing different analytes

6.1. Glucose oxidase biosensor

The metabolic disorder of diabetes mellitus results in the deficiency of insulin and hyperglycemia and is reflected by blood glucose concentration higher or lower than the normal range of 80–120 mg dL⁻¹ (4.4–6.6 mmol L⁻¹). The disease is a leading cause of death and disability [205]. This is reflected by the multibillion USD glucosensing markets [206]. Therefore, the diagnosis and management require close monitoring of blood glucose levels. The application of graphene in highly sensitive and cost-effective biosensors can aid the monitoring of diabetic diseases [19]. Graphene has been employed in many schemes for sensing glucose [138,187,207–221]. The glucose oxidase oxidises glucose to gluconic acid and shuffles electrons into oxygen, which is dissolved in the solution, and then reduced to hydrogen peroxide. Hydrogen peroxide is detected electrochemically. The direct electrochemistry of GOx based on redox-active centers was confirmed by CV experiments in the potential range of 0.8–0 V [187,222]. Direct electron transfer from the enzyme is possible, making this an analytically valuable signal [206]. Cui et al. [223] reported direct electrochemistry of glucose oxidase (GOD) on three-dimensional (3D) interpenetrating porous graphene electrodes, which have been fabricated by one-step electrochemical reduction of GO from its aqueous suspension. Hui et al. [224] studied direct electrochemistry of GOD based on Nafion–Graphene–GOD-modified gold disk electrode (GE). Immobilised GOD on graphene protected by nafion film exhibited good bioactivity, stability and apparent electron transfer rate constant (k_s) 1.96 s⁻¹. DET from GOD has been reported by several authors. Fu et al. [225] immobilised glucose oxidase enzyme on a Nafion polymer film with graphene nanoplatelets, which demonstrated that such simple non-covalent bonding enhances the redox current of a ferrocyanide solution and leads to a lowering of the overpotential of hydrogen peroxide. Other direct electron transfer was observed in graphene/ionic liquid/glucose oxidase systems [226] and in graphene CdS nanocrystal [227]. Wang et al. [19,227] and Shan et al. [184,226] used

Table 2
Various types of enzymatic electrodes made from graphene and GO [123].

Type of biosensor	Sensor materials	RSD (%)	Detection limit	References
Glucose	Graphene-PPy	–	$3 \pm 0.5 \mu\text{mol L}^{-1}$	[257]
	Metal decorated graphene	–	$1 \mu\text{mol L}^{-1}$	[260]
	Graphene/Nafion	4.21	$1.0 \times 10^{-6} \text{mol L}^{-1}$	[125]
	CVD grown graphene	–	0.1m mol L^{-1}	[58]
	CS-GR	5.3	0.02n mol L^{-1}	[221]
	GO	5.8	–	[251]
	PVDF-protected graphene	3.2	$2\text{--}14 \text{m mol L}^{-1}$	[226]
	CS-GR-AuNP	4.7	$180 \mu\text{mol L}^{-1}$	[59]
	GO	–	–	[19]
	Graphene-CdS	5.3	0.7m mol L^{-1}	[227]
	CS-GR-AuNP	6.0	0.6mol L^{-1}	[144]
	Graphene	2.5	$10 \pm 2 \mu\text{mol L}^{-1}$	[247]
	CMG	–	$0.376 \text{m mol L}^{-1}$	[254]
	Graphene	–	$0.168 \text{m mol L}^{-1}$	[250]
	CR-GO	4.3	$2.0 \mu\text{mol L}^{-1}$	[120]
	NADH	Graphene	3.2	$5 \mu\text{mol L}^{-1}$
IL functionalized graphene		4.2	$5 \mu\text{mol L}^{-1}$	[184]
Hb	Graphene	3.5	–	[355]
	Fe ₃ O ₄ -graphene	1.6	$0.5 \mu\text{mol L}^{-1}$	[269]
HRP	Graphene	–	$5.1 \times 10^{-7} \text{mol L}^{-1}$	[15]
	Graphene	4.48	$1.05 \times 10^{-7} \text{mol L}^{-1}$	[327]
	SDBS-graphene	–	$1.0 \times 10^{-7} \text{mol L}^{-1}$	[250]
	AuNP-graphene	3.6	$1.0 \times 10^{-6} \text{mol L}^{-1}$	[138]
Cholesterol	CS-GR/Fe ₃ O ₄ /HRP	–	$6.0 \times 10^{-7} \text{mol L}^{-1}$	[67]
	PtNP-graphene	–	0.5n mol L^{-1}	[289,290]

a polyvinylpyrrolidone-protected graphene/polyethylenimine-functionalised IL/GOx electrochemical biosensor to study the DET of GOx. CV measurements revealed characteristic reversible ET of the redox active centre.

Shan et al. [184] reported another method for enzymatic detection of glucose, using Au NPs/graphene/chitosan composites. Zhang et al. [228] recently explored and investigated the effect of the structure of enzyme electrodes with glucose oxidase (GOD) that were modified by reduced graphene oxide (rGO) sheets. The rGO sheets, with different defect density, layers, and oxygen concentrations, were chosen to modify the enzyme electrode, and all the modified enzyme electrodes exhibited excellent electrocatalytic activities and performances towards glucose. The abundant defects in rGO induce easy absorption of GOD. Yu et al. [229] also reported direct electron transfer of GOD and biosensing for glucose based on PDDA-capped gold nanoparticle-modified graphene/multi-walled carbon nanotubes electrode. Luo et al. [230] synthesised highly dispersed titanium dioxide nanocluster (TDN) on rGO in a toluene–water system under microwave irradiation. The prepared rGO-TDN hybrids were used to modify glassy carbon electrode for loading GOD. The fabricated glucose biosensor exhibits excellent performance for glucose sensing, including low work potential (-0.7V), high sensitivity ($35.8 \mu\text{A m mol L}^{-1} \text{cm}^{-2}$), low detection limit ($4.8 \mu\text{mol L}^{-1}$), wide linear range from 0.032 to 1.67m mol L^{-1} , small Michaelis–Menten constant (K_m) (0.81m) and short response time (10s).

Yuan et al. [231] developed a bimetallic PdCu nanoparticle (NP)-decorated three-dimensional graphene hydrogel (PdCu/GE) by a simple one-step hydrothermal method. The PdCu/GE hybrids exhibited an interconnected microporous framework with PdCu NPs dispersed and encapsulated within the GE layers. The PdCu/GE hybrids showed significant electrocatalytic activity toward glucose oxidation. Lu et al. [232] used graphene platelets as a transducing material for the biosensing of glucose.

Various groups have shown that graphene-based glucose biosensors exhibit good sensitivity, selectivity and reproducibility [184,219,224,232–246]. Wang et al. [153] used electrochemically reduced single layers of graphene to detect glucose. The presence of CdS nanocrystal with graphene showed a very low detection

limit of 0.7m mol L^{-1} . Kang et al. [221,245,247] fabricated CS-GR/GOx modified electrodes for direct electrochemical glucose sensing. The excellent performance of the biosensors was attributed to the large surface area to volume ratio and high conductivity of graphene and the good biocompatibility of chitosan with GOx. CS-GR/PtNP nanocomposite film has also been used for the detection of glucose. Introduction of PtNP increased the sensor's sensitivity, allowing a detection limit of $0.6 \mu\text{mol L}^{-1}$ glucose. The biosensor possessed good reproducibility and long-term stability with negligible interference signals from AA and UA. Guets et al. [248] also developed a glucose biosensor that reduced the interference from AA and UA. Shan et al. [184,226] designed CS-GR/AuNP nanocomposite films for glucose sensing, which exhibited good amperometric responses to glucose with a linear range of $2\text{--}10 \text{m mol L}^{-1}$ ($R=0.999$) at -0.2V and $2\text{--}14 \text{m mol L}^{-1}$ ($R=0.999$) at 0.5V . This was attributed to the synergy effect of graphene and the AuNP. Zhou et al. [138,203] investigated glucose sensitivity of Nafion-GR/AuNP biocomposite films. The linear range of the sensor was $15\text{--}5.8 \text{m mol L}^{-1}$, with a detection limit of 5m mol L^{-1} ($S/N=3$). Andreescu and Luck [182] used studies of the binding and signalling of surface-immobilized periplasmic glucose receptors on gold nanoparticles for glucose biosensor application. Zeng et al. [249,250] used organically modified graphene for enzyme-based glucose and maltose biosensing. The CV response of the modified electrode increased with increasing concentration of glucose in buffer solution. The detection limit and sensitivity were $0.168 \text{m mol L}^{-1}$ ($S/N=3$) and $0.261 \mu\text{A m mol L}^{-1} \text{cm}^{-2}$, respectively. GO has often been used for the detection of glucose [251–253]. Its biocompatibility with GOx led to a stable glucose biosensor with a sensitivity of $8.045 \text{mA cm}^{-2} \text{mol L}^{-1}$. Yang et al. [254] developed a glucose biosensor, using CMG and IL. Chen et al. [125] prepared Nafion-GR/GOx film-modified electrodes for the detection of glucose. The sensor showed good stability, with an RSD of 4.21% ($n=5$). Huang et al. [255,256] used CVD-grown graphene to develop real-time glucose biosensors. Alwarappan et al. [257] employed PPy-GR/GOx-based enzymatic biosensors for invitro electrochemical glucose detection. Nafion-GR/PtNP or AuNP-modified electrodes exhibited best sensing performances, with a linear response

up to 30 m mol L^{-1} and an excellent detection limit of $1 \mu \text{ mol L}^{-1}$. Alwarappan et al. [258] also used enzyme-doped graphene nano-sheets for enhanced glucose biosensing. Wang et al. [168,259] showed that N-doped graphene provides significantly enhanced oxidation currents for the enzymatic detection of glucose compared to ordinary graphene materials. Baby et al. [260] and Wang et al. [153] also investigated the effect of nitrogen doping on the biosensing performances of graphene electrode. N-doped graphene exhibited excellent electrocatalytic activity for the reduction of H_2O_2 , fast ET kinetics, high sensitivity and selectivity for glucose biosensing. Ruan et al. [261] fabricated a glucose biosensor based on polydopamine-graphene hybrid film modified glucose oxidase enzyme electrode. Dopamine, GO and GOD were mixed and casted on Au electrode. After electrochemical processing, polydopamine, glucose oxidase and graphene modified electrode were obtained. The as-synthesized enzyme electrodes were characterized by scanning electron microscopy, transmission electron microscopy, Fourier transform infrared and X-ray diffraction spectra. The biosensor showed excellent amperometric biosensing performances, e.g., a high period (4 s) and a low Michaelis-Menten constant ($6.77 \text{ m mol L}^{-1}$). Vinu Moham et al. [262] developed amperometric detection of glucose using Prussian blue-graphene oxide-modified platinum electrode. Gupta et al. [263] developed a novel glucose biosensor platform based on AgAuNPs modified graphene oxide nanocomposite and SERS application. The linearity range of glucose was obtained as 2–6. m mol L^{-1} with a detection limit of $0.33 \text{ m mol L}^{-1}$. The developed biosensor was also applied successfully for the determination of glucose in blood samples. The concentration value of glucose in blood samples was calculated to be $1.97 \pm 0.002 \text{ m mol L}^{-1}$ from measurements repeated for six times.

Zou et al. [264] fabricated Amperometric glucose biosensor prepared with self-compatible material and carbon nanotube by layer-by-layer self-assembly technique. Lui et al. [30] fabricated a bionanocomposite film of glucose oxidase/Pt nanoparticles/graphene-chitosan (GOD/PtNPs/GR-Chit) for glucose sensing. The hybrid bionanocomposite-modified GCE was characterised by SEM, CV, and an amperometric *i-t* curve. Cai et al. [265] reported the utilisation of graphene-chitosan-ZrO₂ (ER-GO/CS/ZrO₂) composite as an immobilisation matrix for GOD. In comparison with electrodes modified with the component materials individually, the ER-GO/CS/ZrO₂-modified electrode exhibited excellent electron transfer properties for GOD with a rate constant of 3.12 s^{-1} . The obtained glucose biosensor displayed satisfactory performance over an acceptable linear range from 0.2 m mol L^{-1} to 1.6 m mol L^{-1} , with a detection limit of $45.6 \mu \text{ mol L}^{-1}$ at -0.4 V and a sensitivity of $7.6 \mu \text{A m mol L}^{-1}/\text{cm}^2$. Chen et al. [266] reported electrochemiluminescence biosensor for glucose, based on Graphene/Nafion/GOD film-modified glassy carbon electrode. Ge et al. [267] fabricated a glucose biosensor based on immobilization of glucose oxidase on polyaniline/graphene composite membrane-modified glassy carbon electrode. CV demonstrated that modified electrodes had good electrochemical activity, superior sensitivity and high stability. The good electrocatalytic activity toward H_2O_2 and O_2 might be attributed to the synergistic effect of graphene and polyaniline. The results showed that the electrochemical biosensor had a wide linear response from 0.1 to 10 m mol L^{-1} . Jang et al. [237] synthesised graphene-based noble metal composites such as Pt- Graphene and Au-Graphene for sensitive glucose biosensors. Aerosol spray pyrolysis (ASP) was employed to synthesize the noble metal nanoparticles-Graphene composites, using a colloidal mixture of GO and noble metal precursor ($\text{H}_2\text{PtCl}_6 \cdot 6\text{H}_2\text{O}$ and $\text{AuCl}_4 \cdot 3\text{H}_2\text{O}$). The amperometric response of the glucose biosensor, based on the Pt-crumpled graphene composite, indicated the highest sensitivity as $62 \mu\text{A}/\text{m mol L}^{-1} \text{ cm}^2$. Lee et al. [268] fabricated graphene and Nafion

polymer composite not only for enhancing processability, but also for maintaining properties. The easily fabricated glucose biosensor shows good performances with fast electron transfer rate, high selectivity, and low concentration range of detection with linear response.

6.2. Haemoglobin (Hb) biosensor

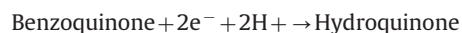
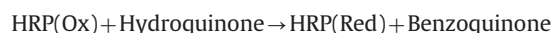
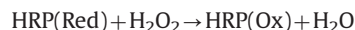
Hb is the most important part of blood and is responsible for transporting O_2 throughout the circulatory system. Change of Hb concentration in blood can cause several diseases such as anaemia and even death. Therefore, accurate determination of Hb content in blood is medically very essential.

Xu et al. [15] used a CS-Graphene-modified electrode for the electroanalysis of Hb. The cyclic voltammogram of Hb at the CS-Graphene/GC electrode showed a well-resolved redox peak compared with a CS/GC electrode. The current response of Hb at the CS-Graphene/GC electrode increased linearly with a scan rate from 30 to 150 mV s^{-1} , indicating a surface-controlled electrochemical process. He et al. [269] studied the effect of magnetite-graphene NP on Hb detection. The biosensor exhibited fast response time ($< 3 \text{ s}$), broad linear response to H_2O_2 in the range of $1.50\text{--}585 \mu \text{ mol L}^{-1} \text{ L}^{-1}$ and a relatively low detection limit of $0.5 \mu \text{ mol L}^{-1}$ ($S/N=3$). Wang et al. [153] designed CS-Graphene/Hb/GR/IL/GC electrode for the detection of nitromethane. The designed biosensor achieved a detection limit down to $6.0 \times 10^{-10} \text{ mol L}^{-1}$ for quantitative nitromethane analysis. He et al. [269] used magnetite-graphene for the direct electrochemistry of haemoglobin and its biosensing application. Sun et al. [270–272] prepared a graphene and Mg_2Al layered double hydroxide (LDH) composite, which was used for the immobilisation of haemoglobin (Hb) on a carbon ionic liquid electrode (CILE) to obtain an electrochemical biosensor. The presence of Graphene-LDH composite could facilitate the electron transfer rate between CILE and the electroactive centre of Hb. The immobilized Hb in Graphene-LDH modified electrode exhibited excellent electrocatalytic reduction to trichloroacetic acid in the concentration range from 1.6 to $25.0 \text{ m mol L}^{-1}$, with the detection limit as $0.534 \text{ m mol L}^{-1}$. The CV spectra indicated the successful preparation of a third-generation electrochemical biosensor.

6.3. Hydrogen peroxide biosensor (H_2O_2)

Hydrogen peroxide (H_2O_2) is a general enzymatic product of oxidases and a substrate of peroxidases, which is important in biological processes and biosensor development [273,274]. H_2O_2 is an important analyte in chemistry, biology, biochemical and food industry, clinical control and environmental protection. Thus the rapid and accurate analysis of H_2O_2 is of great importance [59]. The high level of H_2O_2 is closely associated with cancer and progressive neurodegenerative diseases, such as Parkinson's disease. High level of oxidative stress is involved in the formation of incipient tumour and carcinomatous cells. Recent studies have shown that graphene-based H_2O_2 biosensors exhibit good sensitivity, selectivity and reproducibility [175,259,275–281] Chang et al. [282] explored a facile strategy to assess the oxidative stress elicited by H_2O_2 in cells with amperometric current-time technique in vitro. An electrochemical biosensor exhibiting high sensitivity and selectivity to H_2O_2 is fabricated by integration. Bai et al. [283] developed a novel CuS nanoparticle-decorated reduced graphene oxide-based electrochemical biosensor for the reliable detection of H_2O_2 . The new electrocatalyst, CuS/RGO composites were successfully prepared by heating the mixture of CuCl_2 and Na_2S aqueous solutions in the presence of PVP-protected graphene oxide at $180 \text{ }^\circ\text{C}$. The application of CuS/RGO composite-modified electrode as a biosensor to monitor H_2O_2 was investigated.

The steady-state current response increases linearly with H_2O_2 concentration from 5 to $1500 \mu\text{mol L}^{-1}$, with a fast response time of less than 2 s. The detection limit (3σ) for determination of H_2O_2 was estimated to be $0.27 \mu\text{mol L}^{-1}$, which was lower than certain enzymes and noble metal nanomaterial-based biosensors. Electrochemical methods are more convenient for this than other conventional methods. Zeng et al. [250] developed an SDBS-Graphene/HRP-modified electrode for the detection of H_2O_2 . It displayed high electrocatalytic activity to H_2O_2 with high sensitivity, wide linear range, low detection limit and fast amperometric response. The current signal was proportional to the concentration of H_2O_2 and closely related to the activity of HRP. The reaction mechanism of the catalytic process can be summarised as follows:



The HRP/Graphene electrode remained stable after 30 measurements without significant loss of sensitivity ($> 90\%$). Lu et al. [284,285] developed another biosensor for the detection of H_2O_2 , using horseradish peroxidase or haemoglobin. The modified electrode (Graphene/HRP) could reach 95% of the steady state current within 1 s, indicating very fast electrocatalytic response. Liu et al. [251] developed a sensor for the detection of glucose and hydrogen peroxide on the basis of Cu_2O nanocubes wrapped by graphenenanosheets ($\text{Cu}_2\text{O}/\text{GNs}$) as electrocatalysts. Cubic Cu_2O nanocrystals/graphene hybrid has been successfully fabricated by a chemical reduction method at low temperature. Qing et al. [274] developed a novel electrochemical sensing system for direct electrochemistry-based hydrogen peroxide biosensor single-layer graphene nanoplatelet (SLGNP). The composite film demonstrated excellent electrochemical responses for the electrocatalytic reduction of H_2O_2 , thus suggesting its great potential applications in direct electrochemistry-based biosensors. Lu et al. [286] reported self-assembly of cyclodextrin (CD) functionalized graphene and adamantane-modified horseradish peroxidase (HRP-ADA) by host-guest supramolecular interaction into novel nanostructures in aqueous solution. The proposed biosensor showed good reproducibility and high sensitivity to H_2O_2 with the detection limit of $0.1 \mu\text{mol L}^{-1}$. In the range of $0.7\text{--}35 \mu\text{mol L}^{-1}$, the catalytic reduction current of H_2O_2 was proportional to H_2O_2 concentration.

Another novel H_2O_2 biosensor was designed by Zhou et al. [138] based on CS-GR/AuNP/HRP biocomposites. The linear response range to H_2O_2 was $5 \times 10^{-6}\text{--}5.13 \times 10^{-3} \text{mol L}^{-1}$, with a detection limit of $1.7 \times 10^{-6} \text{mol L}^{-1}$ ($S/N=3$). Zhou et al. [8,287] prepared CS-GR/ Fe_3O_4 /HRP composite biosensor for the detection of H_2O_2 . The resultant biosensor exhibited high sensitivity, low detection limit, wide linear range, and long-term stability. Song et al. [288] researched and developed hemin-graphenenanosheets (H-GNs)/gold nano-particles (AuNPs) electrochemical biosensor for the detection of H_2O_2 . It was constructed by consecutive, selective modification of the GCE electrode. Performance of the H-GNs/AuNPs/GCE was investigated by chronoamperometry and AFM measurements suggested that the graphene flakes thickness was $\sim 1.3 \text{nm}$ and that of H-GNs was $\sim 1.8 \text{nm}$, which ultimately indicated that each hemin layer was $\sim 0.25 \text{nm}$. This biosensor exhibited significantly better electrocatalytic activity for the reduction of H_2O_2 in comparison with the simpler AuNPs/GCE and H-GNs/GCE. It also displayed a linear response for the reduction of H_2O_2 in the range of $0.3 \mu\text{mol L}^{-1}\text{--}1.8 \text{mmol L}^{-1}$, with a detection limit of $0.11 \mu\text{mol L}^{-1}$ ($SN=1=3$), high sensitivity of $2774.8 \mu\text{Amol L}^{-1} \text{cm}^{-2}$ and a rapid response, which

reached 95% of the steady state condition within 5 s. In addition, the biosensor was unaffected by any interfering substances and was stable over time. The biosensor was potentially suitable for H_2O_2 analysis in many types of sample. Dey and Raj [289,290] developed a highly sensitive amperometric biosensor based on a hybrid material derived from PtNP and graphene for the detection of H_2O_2 . You et al. [278] used GO with aminothiophenol (ATP) and covalently bonded to the palladium (Pd) NPs via sulfur atom. The GO-ATP-Pd was electrochemically reduced to graphene oxide (ERGO) at a potential range of $0\text{--}-1.5 \text{V}$ and was used in electrochemical biosensing for H_2O_2 . The ERGO-ATP-Pd-modified electrode showed the advantages of excellent electrocatalytic activity toward H_2O_2 in PBS solution. The ERGO-ATP-Pd was characterized by transmission electron microscopy (TEM), X-ray photoelectron spectroscopy (XPS), energy dispersive X-ray spectroscopy (EDS) and electrochemical impedance spectroscopy (EIS). CV and chronoamperometry (CA) were used to characterize the performance of the biosensor. The proposed H_2O_2 biosensor exhibited a wide linear range from $0.1 \mu\text{mol L}^{-1}$ to 10mmol L^{-1} , and a low detection limit of $0.016 \mu\text{mol L}^{-1}$ ($S/N=3$), with a fast response time of less than 10 s. The biosensor, therefore, demonstrated excellent capability for the analysis of H_2O_2 . Recently, Kung et al. [275] used 3D Graphene foam (GF), incorporating it with platinum-ruthenium (PtRu) bimetallic nanoparticles as an electrochemical nanocatalyst for the detection of H_2O_2 . PtRu/3D GF nanocatalyst exhibited a remarkable performance toward electrochemical oxidation of H_2O_2 without any additional mediator, showing a high sensitivity ($1023.1 \mu\text{A m mol L}^{-1} \text{cm}^{-2}$) and a low detection limit ($0.04 \mu\text{mol L}^{-1}$) for H_2O_2 . Amperometric results demonstrated that GF provided a promising platform for the development of electrochemical sensors in biosensing and PtRu/3D GF nanocatalyst possessed excellent catalytic activity toward the H_2O_2 detection. Huang et al. [291] performed electrochemical sensing using conductive carbon composite films containing rGO and single-walled carbon nanotubes (SWCNTs) as electrode modifiers on glassy carbon electrodes (GCEs). Raman spectroscopy, transmission electron microscopy, atomic force microscopy and scanning electron microscopy, all suggested that the rGO acted as a surfactant, covering and smoothing out the surface and that the SWCNTs acted as a conducting bridge to connect the isolated rGO sheets, thereby minimising the barrier for charge transfer between the rGO sheets and increasing the conductivity of the film. They used the rGO/SWCNT-modified GCE as a sensor to analyze H_2O_2 and B-nicotinamide adenine dinucleotide (NADH), obtaining substantial improvements in electrochemical reactivity and detection limits relative to those obtained from rGO- and SWCNT-modified electrodes. The electrocatalysis response was measured by cyclic voltammetry and amperometric current-time ($i\text{--}t$) curve techniques. The linear concentration range of H_2O_2 and NADH detection at rGO/SWCNT-modified electrode is $0.5\text{--}5 \text{M}$ and $20\text{--}400 \mu\text{M}$. The sensitivity for H_2O_2 and NADH detection is 2732.4 and $204 \mu\text{A mM}^{-1} \text{cm}^{-2}$, and the limit of detection is 1.3 and $0.078 \mu\text{M}$, respectively.

Bai et al. [283] used copper sulphide-decorated reduced graphene oxide composites for enhanced detection of H_2O_2 in cancer/tumour growth. The sensor was applied to determine the H_2O_2 levels in human serum and urine samples and H_2O_2 released from human cervical cancer cells, with satisfactory results. Chang et al. [282] used layer-by-layer assembly of graphene, Au and poly (toluidine blue O) films sensor for evaluation of oxidative stress of tumour cells elicited by H_2O_2 . The efflux of H_2O_2 from several representative tumour cells and normal cells on exposure to ascorbic acid could be detected by using the graphene-based nanocomposite films. The results indicated that tumour cells release much more H_2O_2 than do the normal cells. The novel sensor raises the possibility for clinical diagnostic application to

evaluate the higher level of intracellular oxidative stress of tumour cells in comparison with normal cells.

Chen et al. [155] used highly conjugated water-dispersible graphene-butyrac acid for the enhancement of electron transfer within polyamic acid-benzoxazole for high-performance H_2O_2 sensing. Cheng et al. [10] developed a biosensor based on carboxymethyl cellulose functionalised reduced graphene oxide and haemoglobin hybrid nanocomposite film that exhibited excellent catalytic activity toward H_2O_2 over a wide linear range of $0.083\text{--}13.94 \mu\text{mol L}^{-1}$ with a detection limit of $0.08 \mu\text{mol L}^{-1}$ at 3σ . Li et al. [292] synthesised 1,3-Di(4-amino-1-pyridinium) propane tetrafluoroborate (DAPPT) ionic liquid, which was used as a modifier to functionalize graphene nanosheets through covalent binding of amino groups and epoxy groups in an alkaline solution. The as-prepared graphene-DAPPT nanosheets (Gr-DAPPT) were confirmed with TEM, X-ray diffraction XRD, X-ray photoelectron spectroscopy (XPS), UV/vis and FTIR spectroscopy. This was used for biosensing H_2O_2 . Zhong et al. [287] reported a double pulse electrochemical method to controllably prepare silver nanocrystals (AgNCs) on graphene thin film electrode for fabricating a high-performance H_2O_2 biosensor. The approach relies on two potential pulses that can independently control the nucleation and subsequent growth processes of AgNCs on graphene substrate. This method also allows the observation of AgNCs growing from a particle shape to a nanoplate form by increasing the growth time with the maximum lateral scale up to micrometer scale range. A proposed mechanism for this silver nanoplates (AgNPLs) formation was the oriented growth of small AgNCs and two-dimensional graphene template inducing effect. Such obtained graphene-AgNPLs hybrid thin films exhibit remarkable electrocatalytic activity toward H_2O_2 electrochemical reduction. The fabricated nonenzymatic H_2O_2 biosensor displays a fast amperometric response time of less than 2 s and a good linear range from $2 \times 10^{-5} \text{ mol L}^{-1}$ to $1 \times 10^{-2} \text{ mol L}^{-1}$, with an estimated detection limit of $3 \times 10^{-6} \text{ mol L}^{-1}$. This biosensor also exhibits good stability (RSD, 1.3%) and high sensitivity of $183.5 \mu\text{A cm}^{-2} \text{ mol L}^{-1}$, as well as high selectivity. Kung et al. [275] produced graphene foam (GF), a three-dimensional (3D) porous architecture, consisting of extremely large surface and high conductive pathways. In their study, 3D GF was used, incorporating platinum-ruthenium (PtRu) bimetallic nanoparticles as an electrochemical nanocatalyst for the detection of H_2O_2 . PtRu/3D GF nanocatalyst exhibited a remarkable performance toward electrochemical oxidation of H_2O_2 without any additional mediator, showing a high sensitivity ($1023.1 \mu\text{A m mol L}^{-1} \text{ cm}^{-2}$) and a low detection limit ($0.04 \mu\text{mol L}^{-1}$) for H_2O_2 . Amperometric results demonstrated that GF provided a promising platform for the development of electrochemical sensors in biosensing and PtRu/3D GF nanocatalyst possessed excellent catalytic activity toward H_2O_2 detection. A small particle size and a high degree of the dispersion in obtaining a large active surface area were important for the nanocatalyst for the best H_2O_2 detection in biosensing and interference by ascorbic acid and uric acid appeared to be negligible. Deng et al. [293] prepared a nanoscale hybrid of chemically reduced graphene oxide (CRGO) with ferrocene (Fc), through π - π stacking interaction between Fc and CRGO. FT-IR, Raman spectroscopy, SEM and CV were utilised to characterize the nanohybrid of Fc with CRGO (Fc-CRGO). Fc-CRGO exhibited good stability and greatly improved electron-transfer behaviour. Fc-CRGO and HRP were casted on the surfaces of glass carbon electrode (GCE) with the aid of chitosan for the determination of H_2O_2 .

Ma et al. [294] reported the layer-by-layer assembly of polyelectrolyte functionalized graphene sheets. The electrode exhibited electrocatalytic activity for the reduction of H_2O_2 .

6.4. β -Nicotinamide adenine dinucleotide (NADH)

The electrochemical detection of NADH is one of the most studied areas of bioelectroanalysis because of the importance of NAD(P)H-based enzymatic reactions in nature [295–297]. Radoi

et al. [295] used pristine graphene platelets and GO as electrode modifiers, aiming at investigating their electrochemical efficacy towards NADH. l-lactic dehydrogenase (l-LDH) was successfully immobilised in a 1% Nafion[®] membrane. The developed biosensor, working at +250 mV versus Ag/AgCl reference electrode, was used to assess l-lactic acid in four different types of yogurts, revealing l-lactic acid concentration ranging between 0.3% and 0.6%. Shan et al. [298] reported that low-potential NADH detection and biosensing for ethanol are achieved at an ionic liquid-functionalised graphene (IL-graphene) modified electrode. A substantial decrease (440 mV) in the overvoltage of the NADH oxidation was observed using IL-graphene/chitosan coating, with oxidation starting at 0.0 V (vs. Ag/AgCl). The NADH amperometric response at such a modified electrode is more stable (95.4% and 90% of the initial activity remaining after 10 min and 30 min at 1 mM NADH solution) than that at bare electrode (68% and 46%). Furthermore, the IL-graphene/chitosan-modified electrode exhibited a good linearity from 0.25 to 2 m mol L⁻¹ and high sensitivity of $37.43 \mu\text{A m mol L}^{-1} \text{ cm}^{-2}$. The ability of IL-graphene to promote the electron transfer between NADH and the electrode exhibited a novel and promising biocompatible platform for the development of dehydrogenase-based amperometric biosensors.

Li et al. [299] prepared a nanocomposite film by cyclic voltammetric deposition of electroreduced graphene oxide (ERGO) and polythionine (PTH) on a glassy carbon (GC) electrode. The electrochemical quartz crystal microbalance (EQCM) method for more in-depth understanding of the process. The ERGO-PTH nanocomposite film is applied as a transducer for facilitated electrocatalytic oxidation of NADH and for the construction of dehydrogenase-based amperometric biosensor. Under optimum conditions, the amperometric detection of NADH provides a wide linear detection range ($0.01\text{--}3.9 \text{ m mol L}^{-1}$), a high sensitivity ($143 \mu\text{A m mol L}^{-1} \text{ cm}^{-2}$) and a low limit of detection (LOD = $0.1 \mu\text{mol L}^{-1}$, $S/N=3$). Lin et al. [115] used graphene-modified basal and edge plane pyrolytic graphite electrodes for electrocatalytic oxidation of H_2O_2 and NADH.

Ambrose et al. [137] used a multilayer graphene film grown by CVD and transferred to an insulating flexible poly(ethylene terephthalate) (PET) sheet to sense dopamine (DA), ascorbic acid (AA), and the reduced form of NADH as biological relevant molecules. Huang et al. [291] performed electrochemical sensing using conductive carbon composite films containing rGO and single-walled carbon nanotubes (SWCNTs) as electrode modifiers on glassy carbon electrodes (GCEs) for electrochemical sensing. They used the rGO/SWCNT-modified GCE as a sensor to analyze H_2O_2 and NADH. The electrocatalysis response was measured by CV and amperometric current-time (i-t) curve techniques. The linear concentration range of H_2O_2 and NADH detection at rGO/SWCNT-modified electrode were $0.5\text{--}5 \text{ mol L}^{-1}$ and $20\text{--}400 \mu\text{mol L}^{-1}$. The sensitivity for H_2O_2 and NADH detection is 2732.4 and $204 \mu\text{A m mol L}^{-1} \text{ cm}^{-2}$, and the limit of detection is 1.3 and $0.078 \mu\text{mol L}^{-1}$, respectively. Furthermore, interference tests indicated that the carbon composite film exhibited high selectivity toward H_2O_2 and NADH. Li et al. [300] reported the fabrication of a sensitive NADH and ethanol biosensor based on graphene-Au nanorods nanocomposite. The hybrid nanosheets exhibited excellent performance toward NADH oxidation, with a low detection limit of $6 \mu\text{mol L}^{-1}$.

Zang et al. [301] reported electrocatalytic oxidation of NADH on graphene oxide and rGO modified screen-printed electrode.

6.5. Cholesterol biosensor

Increases in cholesterol levels can cause life-threatening coronary heart diseases, cerebral thromboses and arteriosclerosis [289]. Therefore, accurate detection of cholesterol level is

medically very important. In recent years, most researchers have shown that graphene-based cholesterol biosensor exhibits good sensitivity, selectivity and reproducibility [186].

Dey et al. [290] developed graphene-platinum-nanoparticle (GR/PtNP) cholesterol biosensor by immobilizing cholesterol oxidase and cholesterol esterase on the surface of the GR/PtNP hybrid material. The sensitivity and detection limit of the electrode towards cholesterol ester were $2.07 \pm 0.1 \mu\text{A} \mu\text{mol L}^{-1} \text{cm}^{-2}$ and $0.2 \mu\text{mol L}^{-1}$, respectively. The high sensitivity and low detection limit were due to the synergistic effect of the synergy between graphene and PtNP. The sensitivity is as shown in amperometric results in Fig. 7. Cao et al. [188] developed a new electrochemical biosensor with enhanced sensitivity for the detection of cholesterol by using platinum-palladium-chitosan-graphene hybrid nanocomposites (PtPd-CS-GS) functionalized glassy carbon electrode (GCE). An electrodeposition method was applied to form PtPd nanoparticles-doped chitosan-graphene hybrid nanocomposites (PtPd-CS-GS), which were characterized by SEM and electrochemical methods. The presence of the PtPd-CS-GS nanocomposites not only accelerated direct electron transfer from the redox enzyme to the electrode surface, but also enhanced the immobilised amount of cholesterol oxidase (ChOx). Under optimal conditions, the fabricated biosensor exhibited wide linear ranges of responses to cholesterol in the concentration ranges of 2.2×10^{-6} – $5.2 \times 10^{-4} \text{mol L}^{-1}$. The limit of detection was

$0.75 \mu\text{mol L}^{-1}$ ($S/N=3$). The response time was less than 7 s and the Michaelis–Menten constant (K_m app) was found to be 0.11m mol L^{-1} . In addition, the biosensor also exhibited excellent reproducibility and stability. Along with these attractive features, the biosensor also displayed very high specificity to cholesterol with complete elimination of interference from UA, AA and glucose. Cao et al. [14] also used the TiO_2 -graphene-Pt-Pd hybrid nanocomposites (TGPHs) as an enhanced element of the integrated sensing platform for increasing the surface area as well as improving the electronic transmission rate. Au nanoparticles (AuNPs) and cholesterol oxidase (ChOx) were successively self-assembled to TGPHs with high load amount and superior biological activity. The morphology of TGPHs and stepwise fabrication processes were characterized with CV, AFM, X-ray photoelectron spectroscopy (XPS) and scanning electron microscopy (SEM). Based on the efficient catalytic ability of TGPHs and AuNPs, the fabricated biosensor exhibited wide linear ranges of responses to cholesterol in the concentration ranges of 5.0×10^{-8} – $5.9 \times 10^{-4} \text{mol L}^{-1}$. The limit of detection was $0.017 \mu\text{mol L}^{-1}$ ($S/N=3$). Manjunathar et al. [302] covalently-immobilised Cholesterol oxidase (ChOx) and cholesterol esterase (ChEt) onto functionalised graphene (FG)-modified graphite electrode. Enzymes modified electrodes were characterized using cyclic voltammetry (CV) and electrochemical impedance spectroscopy (EIS). FG accelerates the electron transfer from electrode surface to the immobilised ChOx, achieving the direct electrochemistry of ChOx. A well-defined redox peak was observed, corresponding to the direct electron transfer of the FAD/FADH₂ of ChOx. The electron transfer coefficient (α) and electron transfer rate constant (K_s) were calculated and their values are found to be 0.31 and 0.78s^{-1} , respectively. For the free cholesterol determination, ChOx-FG/Gr electrode exhibits a sensitive response from 50 to $350 \mu\text{mol L}^{-1}$ ($R=-0.9972$) with a detection limit of $5 \mu\text{mol L}^{-1}$. For total cholesterol determination, co-immobilisation of ChEt and ChOx on modified electrode, i.e. (ChEt/ChOx)-FG/Gr electrode, showed a linear range from 50 to $300 \mu\text{mol L}^{-1}$ ($R=-0.9982$) with a detection limit of $15 \mu\text{mol L}^{-1}$. Some common interferents like glucose, ascorbic acid and uric acid did not cause any interference, due to the use of a low operating potential. Ruecha et al. [303] recently prepared a nanocomposite of graphene (G), polyvinylpyrrolidone (PVP) and polyaniline (PANI) and used it for the modification of paper-based biosensors via electrospraying. The droplet-like nanostructures of G/PVP/PANI-modified electrodes are obtained with an average size of $160 \pm 1.02 \text{nm}$. Interestingly, the presence of small amounts of PVP (2mg mL^{-1}) in the nanocomposites can substantially improve the dispersibility of graphene and increase the electrochemical conductivity of electrodes, leading to the enhanced sensitivity of the biosensor. The well-defined cyclic voltammogram of standard ferri/ferrocyanide is achieved on a G/PVP/PANI-modified electrode, with a 3-fold increase in the current signal compared to an unmodified electrode. Cholesterol oxidase (ChOx) is attached to G/PVP/PANI-modified electrode for the amperometric determination of cholesterol. Under optimum conditions, a linear range of $50 \mu\text{mol L}^{-1}$ – 10m mol L^{-1} is achieved and the limit of detection is found to be $1 \mu\text{mol L}^{-1}$ for cholesterol. The proposed system can be applied for the determination of cholesterol in a complex biological fluid (i.e. human serum).

Zhang et al. [186] developed a simple and sensitive electro-generated chemiluminescence (ECL) cholesterol biosensor based on cerium oxide-graphene (CeO_2 -graphene) composites as an efficient matrix. CeO_2 -graphene composites were prepared by depositing CeO_2 onto graphene and were characterized by SEM. The experimental results demonstrated that CeO_2 -graphene could catalyze the ECL of a luminol- H_2O_2 system to amplify the luminol ECL signal greatly. In addition, the use of CeO_2 -graphene provided

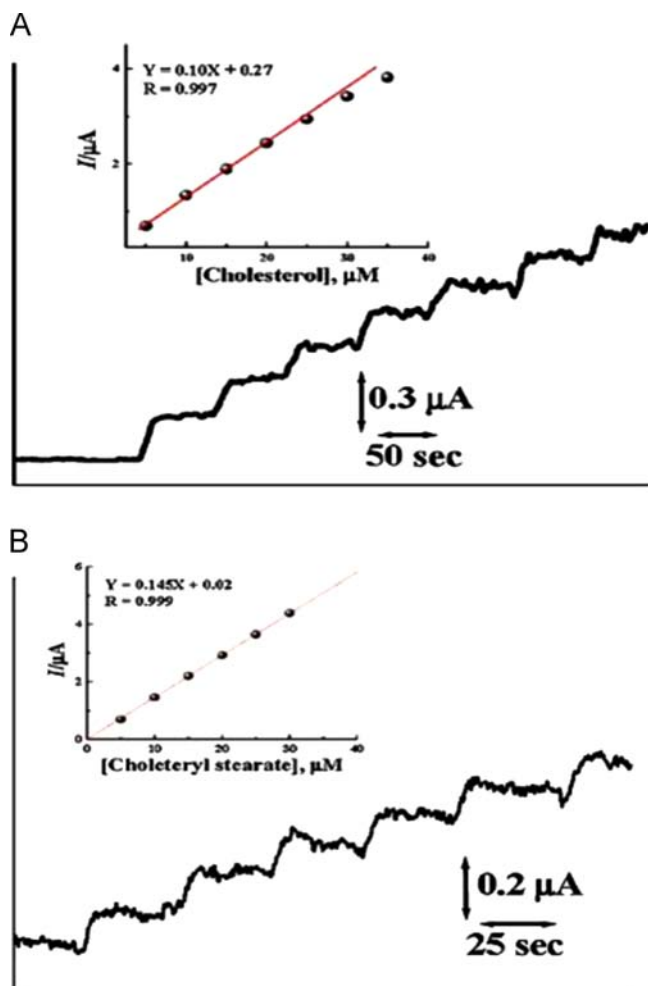


Fig. 7. Amperometric responses of cholesterol (A) and cholesterol ester (B) biosensors. Cholesterol ($5 \mu\text{M}$) and cholesteryl stearate ($5 \mu\text{M}$) were injected at regular intervals [290].

a better biocompatible microenvironment for the immobilised enzyme, resulting in excellent stability and a long lifetime of the ECL biosensor. The surface assembly process, ECL behaviours, and electrochemistry of the biosensor were investigated in detail. The quantity of cholesterol was in the linear range of $12 \mu\text{mol L}^{-1}$ – 7.2m mol L^{-1} , with a detection limit of $4.0 \mu\text{mol L}^{-1}$ (signal/noise=3). In addition, the biosensor exhibited outstanding reproducibility, long-term stability and selectivity.

6.6. Electrochemical immunosensing

Immunosensors are based on the high affinity reactions antigen/antibody. Several strategies can be used to immobilise the recognition element, either the antibody or the antigen, depending on the selected scheme. The detection of the recognition event uses the same principle as the enzymatic immunoassay. In general, an enzyme is coupled to the recognition layer (the antigen or antibody) and the enzymatic reaction is developed once the antigen/antibody interaction occurs and after the addition of the substrate and electrochemical detection of the product [304].

Graphene has been used for electrochemical immunosensing, the direct electrochemical detection of antibody antigen recognition is usually not possible and electrochemically active labels must typically be used. There are two strategies in which graphene can be used. First, graphene can be used as an electrode surface for sensitive detection of a label [305]. This case was employed for the graphene-enhanced detection of α -fetoprotein, which is a cancer biomarker. Graphene sheets were modified with antibodies, then the α -fetoprotein was added and consequently, secondary antibodies loaded with microspheres bearing horseradish peroxidase enzyme as a sensitive label. The second approach employs graphene as a label-bearing nanocarrier [306]. A gold nanoparticle electrode was modified with a probe antibody, to which phosphorylated protein was entrapped. The secondary antibody was conjugated with GO and horseradish peroxidase to generate large amounts of electroactive molecules and thus a larger signal [305]. Huang et al. [307] developed a simple label-free amperometric immunosensor for protein detection based on TiO_2 -graphene (TiO_2 -Gr), chitosan and gold nanoparticles (AuNPs) composite film-modified glassy carbon electrode (GCE). The negatively charged AuNPs can be adsorbed on the positively charged chitosan/ TiO_2 -graphene composite film by electrostatic adsorption, and then used to immobilise α -fetoprotein antibody for the assay of α -fetoprotein (AFP).

Recently, Lui et al. [308] fabricated an Au-ionic liquid functionalized reduced graphene oxide nanocomposite (IL-rGO-Au) via the self-assembly of ionic liquid functionalized reduced graphene oxide (IL-rGO) and gold nanoparticles (AuNPs) by electrostatic interaction. The IL-rGO can be synthesized and stabilized by introducing the cations of the amine-terminated ionic liquids (IL- NH_2) into the graphene oxide (GO). With the assistance of IL- NH_2 , AuNPs were uniformly and densely adsorbed on the surfaces of the IL-rGO. The proposed IL-rGO-Au nanocomposite can be used as an immunosensing platform because it can not only facilitate the electrons transfer of the electrode surface, but also provide a large accessible surface area for the immobilisation of abundant antibody.

Feng et al. [199] prepared azearalenone (ZEN) biosensor by immobilising nitrogen-doped graphene sheets (N-GS) captured primary antibody (Ab1) on GCE. The analytes were then bound to Ab1 for further capture of antibodies, labelled by the nanoporous bimetallic alloy, nanoporous PtCo alloy (NP-PtCo). NP-PtCo, with three-dimensional bicontinuous spongy structures and various hollow channels, was prepared by corrosion of PtCoAl alloy and it exhibited remarkably improved electrocatalytic activity toward

H_2O_2 . Within the ZEN concentration range (0.005 – 25ng mL^{-1}), the biosensor exhibited a highly sensitive response to ZEN with a detection limit of 2.1pg mL^{-1} . Zhang et al. [309] developed novel surface plasmon resonance (SPR) biosensors based on Au-graphene (Au-Gra) nanohybrids and Ag-graphene (Ag-Gra) nanohybrids for the detection of mouse IgG. The biosensors proposed are label-free, and have high sensitivity and selectivity for biosensing. Au-Gra and Ag-Gra nanohybrids were synthesised in a simple, effective and rapid way. It was further characterized by X-ray photoelectron spectroscopy (XPS), transmission electron microscopy (TEM) and UV-vis absorption spectroscopy. These nanohybrids were assembled on the Au film through 1,6-hexanedithiol by covalent attachment. The antibody was bounded to the nanohybrids through 3-mercaptopropionic acid. Some experimental conditions were determined and optimised. In the optimal conditions, the biosensors based on Au-Gra nanohybrids and Ag-Gra nanohybrids showed a good response to mouse IgG in the concentration range of 0.30 – $40.00 \mu\text{g mL}^{-1}$ and 0.15 – $40.00 \mu\text{g mL}^{-1}$, respectively. Xu et al. [15] developed a graphene-based signal-amplification nanoprobe by combining anti-immunoglobulin G (anti-IgG) and horseradish peroxidase (HRP) with graphene oxide (GO). The structure and function of HRP in the nano-interface of GO were firstly investigated, which demonstrated that the enzyme retained 78% of its native activity and 77% of its native α -helix content. HRP and anti-IgG were then co-adsorbed onto GO to form bifunctional nanoprobe. The nanoprobe provide both improved binding ability and signal-amplification ability. Compared with conventional bioconjugates such as enzyme-linked antibody, co-adsorption could avoid chemical conjugation between biomolecules, keeping their bioactivity well. As an example of their application, the nanoprobe were used to obtain amplified signals in a sandwich-type immunoassay for cancer marker, instead of conventional colorimetric conjugates. This approach provided a detection limit of 10Pg/mL alpha-fetoprotein (AFP), which was much more sensitive than conventional enzyme-linked immunosorbent assay (ELISA) methods. Jung et al. [310] developed a novel GO-based immuno-biosensor that could quickly detect viruses with high sensitivity and selectivity. The fluorescence quenching efficiency of GO arrays was affected by several factors, such as the concentration of immobilised Ab, their surface area and the number of AuNP quenchers. Su [311] used Graphene modified basal and edge plane pyrolytic graphite electrodes for electrocatalytic oxidation of hydrogen peroxide and β -nicotinamide adenine dinucleotide. Zhu et al. [312] designed a novel immunoassay protocol for simultaneous electrochemical determination of alpha-fetoprotein (AFP), carcinoembryonic (CEA) and streptococcus suis serotype 2 (SS2). As standard sandwich-type immunoassay format, three primary antibodies (Ab1), anti-CEA and anti-AFP and anti-SS2, were immobilised via protein A (PA) adsorbed by Nafion-modified electrodes, and functionalized graphene sheets (GS) containing abundant gold nanoparticles (AuNPs) and carboxyl group were used to immobilise secondary antibody redox-probe so as to act as a tracer. Concentration of each analyte was quantitatively related to the reduction peak current of the corresponding redox-probe in differential pulse voltammetry (DPV) scan. The resulting immunosensor exhibited high selectivity and sensitivity in simultaneous determination of three analytes. The linear range was from 0.016 to 50ng/mL for AFP, with a detection limit of 5.4pg/mL , 0.010 – 50ng/mL for CEA, with a detection limit of 2.8pg/mL and 0.012 – 50ng/mL for SS2, with a detection limit of 4.2pg/mL ($S/N=3$).

Du et al. [305] also described a novel electrochemical immunosensor for sensitive detection of cancer biomarker α -fetoprotein (AFP) that uses a graphene sheet sensor platform and functionalised carbon nanospheres (CNSs) labelled with horseradish peroxidase-secondary antibodies (HRP-Ab2). Greatly enhanced

sensitivity for the cancer biomarker is based on a dual signal amplification strategy: first, the synthesised CNSs yielded a homogeneous and narrow-size distribution, which allowed several binding events of HRP-Ab2 on each nanosphere.

6.7. DNA sensors

Electrochemical DNA sensors offer high sensitivity, high selectivity and low cost for the detection of selected DNA sequences or mutated genes associated with human disease and promise to provide a simple, accurate and inexpensive platform of patient diagnosis. Various research groups have demonstrated that graphene-based DNA biosensors exhibit good sensitivity, selectivity and reproducibility [6,313–317].

Gupta et al. [318] developed a highly sensitive method for the detection of DNA hybridization. This method was based on the modification of glassy carbon electrode with gold nanoparticles (AuNPs) involving p-aminothiophenol (ATP) functionalised GO. This GO was used as a platform for impedimetric genosensing, using 5′-TA GGG CCA CTT GGA CCT-(CH₂)₃-SH-3′ single-stranded probe (ss-DNA), 5′-AGG TCC AAG TGG CCC TA-3′ (target DNA), 5′-SH-C6-TAG GGC CA-3′ (non-complementary-1) and 5′-SH-C6-TGC CCG TTA CG-3′ (non-complementary-2) oligonucleotide sequences. The film exhibited excellent properties for immobilising DNA probes and sensing DNA hybridization. The DNA immobilisation and hybridization on the film were studied by CV, and electrochemical impedance spectroscopy (EIS), and it was found that the charge transfer resistance (*R*_{ct}) of the electrode increased with the concentration of the target DNA hybridized with the ss-DNA. The linear detection range was from 1.0×10^{-13} mol L⁻¹ to 1.0×10^{-7} mol L⁻¹ and the detection limit was 1.10×10^{-14} mol L⁻¹ (*n*=6). Chen et al. [128] used graphene-based field-effect transistors based on large-area monolayer graphene produced by chemical vapour deposition for label-free electrical detection of DNA hybridisation. The gate materials, buffer concentration and surface condition of graphene have been optimized to achieve a DNA detection sensitivity as low as 1 pmol L⁻¹ (10^{-12} mol L⁻¹), which is more sensitive than the existing report based on few-layered graphene.

Cho et al. [128] developed chemiluminescence (CL) detection of DNA, using ssDNA aptamer-conjugated 6-FAM fluorescein (DAF), GO bound with magnetic nanoparticle (GMN), and 3, 4,5-trimethoxyphenylglyoxal (TMPG). When thrombin was incubated in TE buffer (pH 7.5) containing 200 n mol L⁻¹ DAF for 10 min, thrombin binds strongly to DAF.

Fojta et al. [128] detected DNA directly, using the oxidative signals of DNA bases or by using electroactive labels [319]. Direct detection has an advantage because it is label free, but offers poorer sensitivity than label-based DNA assays. Adenine (A) and guanine (G) bases give analytically useful signals while cytosine (C) and thymine (T) do not provide well-resolved signals. Huang et al. fabricated a novel electrochemical sensor based on functionalized graphene for the simultaneous determination of adenine and guanine in DNA [320].

Shou et al.'s [120] biosensor revealed that chemically reduced graphene oxide provides well-resolved signals of all four A, G, C, and T bases with higher sensitivity than with graphite. This is attributed to the high defect density of the CRGO, and thus has superior electrochemical performance when compared to graphite. Lim et al. [113] compared the electrochemistry of DNA bases on epitaxially grown graphene. Electrochemical oxidation of pristine epitaxially grown graphene led to the creation of defects on its surface and also leads to a significantly higher response. It was suggested that electrochemically oxidised graphene or graphene with large amounts of defects

could be used for highly sensitive electrochemical sensing. Zhu et al. [321] applied electrochemically oxidized graphene to discriminate between ssDNA and hybridised DNA. Liu et al. [322] used adsorption of a fluorophore-labeled DNA probe by GO to produce a sensor that gives fluorescence enhancement in the presence of its complementary DNA (cDNA). Ambrose et al. [46] showed that large amounts of defects are beneficial for the electrochemical detection of DNA, using stacked graphene platelet nanofibers. These nanofibers are the direct opposites of carbon nanotubes, because they consist of perpendicularly stacked graphene sheets along the *c*-axis, exhibiting exclusively electrochemically active edges (with the exception of terminal basal planes). Such nanofibers also provide significantly enhanced signals for all four DNA bases when compared to graphite, glassy carbon or pure carbon nanotubes. Lui et al. [323] fabricated a novel electrochemical DNA biosensor based on graphene-three-dimensional nanostructure gold nanocomposite modified glassy carbon electrode (G-3D Au/GCE) for the detection of surviving gene which was correlated with osteosarcoma. The G-3D Au film was prepared with one-step electrochemical coreduction with graphite oxide and HAuCl₄ at cathodic potentials. The active surface area of G-3D Au/GCE was 2.629 cm², which was about 3.8 times compared to that of an Au-coated GCE under the same experimental conditions, and 8.8 times compared to a planar gold electrode with a similar geometric area.

Recently, Li et al. and Lu et al. [112,324–326] reported that graphene and ssDNA assemblies can be used for the homogeneous detection of biomolecules. The electrochemical detection of four free bases (G, A, T and C) has been considered in the discussion of DNA sensors. Lu et al. [112] and Lui et al. [252,322] studied fluorescence quenching properties of GO in DNA biosensing. GO sheets were employed as a novel DNA biosensor by applying the GO in an array to recognize specific DNA–DNA hybridization. Lu et al. [327–329] used MB with GO as a “nanoquencher” to construct a highly sensitive, selective and economic sensor of biomolecules. Zhou et al. prepared CR-GO electrodes for label-free electrochemical detection of four DNA bases in ssDNA/dsDNA. DPV of G, A, T and C were studied at GC, graphite/GC and CR-GO/GC electrodes at pH 7. Shou et al. [120] characterised and applied a chemically rGO modified glassy carbon (CR-GO/GC) electrode, a novel electrode system, for the preparation of electrochemical sensing and biosensing platform. Different kinds of important inorganic and organic electroactive compounds (i.e., probe molecule (potassium ferricyanide), free bases of DNA (G, A, T, and C), oxidase/dehydrogenase-related molecules H₂O₂/β-nicotinamide adenine dinucleotide (NADH), neurotransmitters DA, and other biological molecules AA, UA, and acetaminophen (APAP)) were employed to study their electrochemical responses at the CR-GO/GC electrode, which shows more favourable electron transfer kinetics than graphite-modified glassy carbon (graphite/GC) and glassy carbon (GC) electrodes. Zhao et al. [67] designed a simple but smart platform in this work to fabricate electrochemical biosensors by using graphene quantum dots-modified pyrolytic graphite electrode, coupled with specific sequence ssDNA molecules, as probes. Due to the excellent conductivity of graphene material, the modified electrode can exhibit very fine electrochemical response. Nevertheless, the probe ssDNA will inhibit the electron transfer between the electrochemical active species [Fe(CN)₆]^{3-/4-} and the electrode, after the probe molecules are strongly bound to the surface of the modified electrode via their interaction with graphene. However, when the target molecules, such as target ssDNA and target protein, also exist in the test solution, the probe ssDNA will bind with the target instead of graphene if the sequence of the probe ssDNA is designed as complementary to the target DNA or as the aptamer of the target protein. As a result, the obtained peak currents of [Fe(CN)₆]^{3-/4-} will increase with the target molecules; thus

various electrochemical biosensors can be easily developed with this proposed platform.

Bo et al. [91,92] reported the fabrication of a DNA biosensor, based on graphene paste electrode modified with Prussian blue and chitosan and a novel electrochemical DNA biosensor, based on graphene and polyaniline nanowires.

Nui et al. [330] constructed a novel and sensitive electrochemical DNA biosensor based on the gold electrode, modified by graphene and gold nanoparticles (AuNPs), whose sensitivity was improved by using 1,10-phenanthroline cobalt ($[\text{Co}(\text{phen})_2(\text{Cl})(\text{H}_2\text{O})]^+$) as an electroactive indicator. The gold electrode was firstly modified with sulfurgraphene (GR-SH) and then covalently grafted with AuNPs via sulfur-gold affinity. The target DNA from *Escherichia coli* (*E. coli*) could be detected in a linear range from 2.50×10^{-11} to 1.25×10^{-9} mol L⁻¹ ($R=0.9981$) with a detection limit of 8.33×10^{-12} mol L⁻¹ (3σ , $n=11$). Du et al. [331] described the fabrication of a novel electrochemical deoxyribonucleic acid (DNA) biosensor based on electrochemical-reduced graphene oxide (ERGO) and peptide nucleic acid (PNA)-DNA hybridisation. Primarily, the ERGO-modified electrode was achieved by one-step electrodeposition technique on the glassy carbon electrode (GCE) through CV reduction of a graphene oxide colloidal solution. Subsequently, PNA was immobilised onto the surface of the ERGO through a linker (1-pyrenebutanoic acid succinimidyl ester-PASE), and then the PNA-functionalised electrochemical biosensor was used to detect DNA via PNA-DNA hybridisation. Differential pulse voltammetry (DPV) was employed to monitor the hybridisation event by using methylene blue (MB) as the electrochemical indicator. It was found that the peak currents of MB were linear with the logarithm of the complementary target DNA concentrations, and the dynamic detection range for the target DNA was from 1.0×10^{-7} to 1.0×10^{-12} mol L⁻¹, with a detection limit of 5.45×10^{-13} mol L⁻¹ ($3\sigma/S$). Furthermore, the fabricated biosensor could successfully discriminate the one-base mismatched and non-complementary DNA sequences from the complementary DNA sequence.

Chen et al. [128] used high transconductance and low noise of graphene-based field-effect transistors based on large-area monolayer graphene produced by CVD for label-free electrical detection of DNA hybridization. The gate materials, buffer concentration and surface condition of graphene have been optimised to achieve the DNA detection sensitivity as low as 1 pmol L⁻¹ (10^{-12} mol L⁻¹), which is more sensitive than the existing report based on few-layer graphene. The graphene films obtained using conventional PMMA-assisted transfer technique exhibit PMMA residues, which degrade the sensing performance of graphene. Li et al. [332] used GO as an electrode material on which double-stranded DNA was effectively immobilised. The electrochemical experimental results indicated that the electrochemical response of DNA on the electrode was dramatically increased by GO, which facilitates the electron transfer between DNA and electrode. While hydroquinone, a typical environmental pollutant, was present in the electrolytic solution, the electrochemical response of DNA on the GO electrode was decreased, owing to the interaction of hydroquinone with DNA. Accordingly, the DNA-immobilised GO electrode was developed as the electrochemical biosensor for the monitoring of hydroquinone. Under optimal condition, the as-prepared electrochemical biosensor showed a linear response to hydroquinone in the concentration range from 1.0×10^{-7} to 1.0×10^{-4} mol L⁻¹. Lui et al. [322] observed that adsorption of a fluorophore-labeled DNA probe by GO produces a sensor that gives fluorescence enhancement in the presence of its complementary DNA (cDNA). Lui et al. [334] prepared a new nanocomposite, which was composed of ionic liquid functionalised graphene sheet (IL-GS)-loaded gold nanoparticles (AuNPs). The IL-GS was directly synthesized by the electrochemical exfoliation of graphite in ionic liquid (IL). Due to the modification of the IL, IL-GS cannot only be dispersed easily in aqueous

solution to form a homogeneous colloidal suspension of individual sheet, but also exhibits an improved conductivity. Meanwhile, the loaded AuNPs on the nanocomposites can increase the specific surface area to capture a large amount of antibodies as well as improve the capability of electron transfer. The IL-GS-Au nanocomposites were successfully employed for the fabrication of a facile and sensitive electrochemical immunosensor. Carcinoembryonic antigen (CEA) was used as a model protein. The immunosensor exhibited a wide linear detection range (LDR) from 1 fg mL⁻¹ to 100 ng mL⁻¹, and an ultralow limit of detection (LOD) of 0.1 fg mL⁻¹ ($S/N=3$). Lui et al. [333] also designed graphene/DNA-based label-free colorimetric biosensors.

6.8. Ascorbic acid (AA), uric acid (UA) and dopamine (DA)

Determination of AA is a problem in analytical neuro-chemistry and biochemistry [120]. Recently, graphene-based electrodes have been used for simultaneous detection of AA, DA and UA. Shang et al. [335] used MGNF for the selective determination of DA, AA and UA in 50 m mol L⁻¹ PBS solution containing 1 m mol L⁻¹ AA, 0.1 m mol L⁻¹ DA, 0.1 m mol L⁻¹ UA, and their ternary mixture at a scanrate of 100 mV s⁻¹. The MGNF demonstrated good ET kinetics and allowed well-resolved simultaneous discrimination of AA, DA and UA at a detection limit of 0.17 m mol L⁻¹.

Zhou et al. [120] investigated the biosensing efficiency of CR-GO. The electroanalytical performances towards the detection of AA, DA and UA were much better, compared to bare GC or graphite/GC electrode. Wang et al. [56] employed a graphene-modified electrode for the selective detection of DA. The CV curve of 1 m mol L⁻¹ DA on CS-GR/GC, CS/GC, and GC electrodes showed well-defined and resolved voltammetric peaks for the direct oxidation of DA on CS-GR/GC as compared with CS/GC or GC. Tan et al. [336] developed a CD/GR nanocomposite platform for the detection of DA in the presence of AA. Hou et al. [337] modified the surface graphene with N-trimethoxysilylpropyl-EDTA-silane for the sensitive and selective detection of DA. EDTA-silane linked to the graphene surface and provided a favourable environment for the oxidation of DA with a negative oxidation peak potential. Li et al. [338] fabricated PtNP/IL/GR nanocomposites for the simultaneous determination of AA and DA. The difference between the two oxidation peak potentials is > 200 mV, sufficient for the distinction between AA and DA. Three independent oxidation peaks have been detected at PtNP/IL/GR-modified electrodes in human urine samples containing AA and DA. Such electrodes displayed satisfying life times and reproducibility. Therefore, IL functionalised graphene can play an important role in the clinical analysis of AA and DA.

Alwarappan et al. [141] fabricated a novel biosensor for DA sensing in which chemically synthesized graphene nanosheets were used as electrode materials and their electrochemical properties were systematically characterized. The surface morphologies of graphene nanosheets were evaluated using Raman spectroscopy and transmission electron microscopy. They found that graphene electrodes exhibited a superior biosensing performance than SWCNTs toward dopamine detection in the presence of common interfering agents such as ascorbic acid and serotonin. Gao et al. [339] prepared a graphene oxide-modified glassy carbon electrode (GCE), namely GO/GCE, by covalent coupling method which was characterised by AFM, CV and electrochemical impedance spectra (EIS). On this modified electrode, it was found that the electrochemistry of DA is greatly enhanced, while that of AA is totally impressed, showing that the modified layer of GO has completely different impacts on the electrochemical response of DA and AA. Pakapongpan et al. [340] successfully fabricated electrochemical sensor based on graphene/ copper phthalocyanine (CuPc)/ polyaniline (PANI) nanocomposite-modified screen printed electrode

(SPE) for the detection of AA. Copper phthalocyanine was immobilised on graphene by using PANI as a matrix. The nanocomposites were characterized by electrochemical techniques such as CV. The sensor exhibited a linear range from 100 μM to 3.6 m mol L^{-1} (a correlation coefficient of 0.9967). The sensitivity of the sensor was found to be 22.92 $\text{mA mol L}^{-1}/\text{cm}^{-2}$ and the limit of detection was 8.3 $\mu\text{mol L}^{-1}$ ($S/N=3$). This sensor exhibited good electrocatalytic properties and lowered the potential for the oxidation of AA, which makes it a suitable sensor for the detection of AA. Lu et al. [341] synthesized graphene-poly (3, 4-ethylenedioxythiophene) (graphene-PEDOT) nanocomposite film based on simultaneous electrodeposition of PEDOT and electrochemical reduction of GO on a GC electrode. Data from SEM, UV-vis spectroscopy (UV-vis) and EIS demonstrated that the graphene/PEDOT nanocomposite film was successfully synthesised. The obtained graphene-PEDOT nanocomposite film showed large specific area, high conductivity, good biocompatibility, fast redox properties and had encapsulated structures, which make it a promising novel material for biological applications. As an enzyme model, ascorbate oxidase (AO) was entrapped onto the film-modified electrode and used to construct an electrochemical AA biosensor. The modified-electrode showed good electrocatalytic performance towards AA with high selectivity, wide linear range and good stability.

Mishra et al. [342] reported a new chemical method for the synthesis of graphene with good yield. Graphene obtained by this chemical route was subjected to electrochemical characterisation, using two different redox materials for their suitability in electrochemical biosensing applications. The synthesised graphene was used for the detection of neurotransmitters like DA and serotonin. The electrodes exhibited $20\% \pm 5\%$ ($N=5$) decrease in their signal after forty-five days storage in the laboratory atmosphere. Zeng et al. [343] prepared a composite of SiO_2 -coated GO and molecularly imprinted polymers (GO/ SiO_2 -MIPs). The GO/ SiO_2 -MIPs sensor had a wide linear range over DA concentration from 5.0×10^{-8} to 1.6×10^{-4} mol L^{-1} , with a detection limit of 3.0×10^{-8} mol L^{-1} ($S/N=3$). The sensor based on this novel imprinted composite was applied for the determination of DA in injections and human urine samples with satisfactory results. Yu et al. [344] fabricated a facile electrochemical sensor based on poly(diallyldimethylammonium chloride) (PDDA)-functionalised graphene (PDDA-G) and graphite. The composite electrode exhibited excellent selectivity and sensitivity towards UA, owing to the electrocatalytic effect of graphene nanosheets and the electrostatic attractions between PDDA-G and UA. The anodic peak current of UA obtained by CV increased over 10-fold, compared with bare carbon paste electrode (CPE). The reversibility of the oxidation process was improved significantly. Differential pulse voltammetry (DPV) was used to determine UA in the presence of AA and DA. It was found that all of the oxidation peaks of the three species could be well resolved and the peak current of UA was much stronger than the other two components. More importantly, considerable amount of AA and DA showed negligible interference to UA assay. The calibration curve for UA ranged from 0.5 to 20 $\mu\text{mol L}^{-1}$, with a correlation coefficient of 0.9934. The constructed sensor has been employed to quantitatively determine UA in urine samples. Li et al. [345] prepared a biosensor using water-soluble sulfonated graphene with the aim of achieving the selective and sensitive determination of DA in the presence of AA and uric acid UA. The aromatic π - π stacking and electrostatic attraction between positively charged DA and negatively charged sulfonated graphene can accelerate the electron transfer, though weakening AA and UA oxidation on the sulfonated graphene-modified electrode. The proposed method was used to detect DA in real hydrochloride injection sample, human urine and serum samples with satisfactory recovery results.

Kaur et al. [346] reported the synthesis of silver nanoparticle-decorated reduced GO composite (AgNPs/rGO) by heating the mixture

of GO and silver nitrate aqueous solution in the presence of sodium hydroxide. The analytical performance of this material as a chemical sensor was demonstrated for the determination of ascorbic acid and dopamine in commercial pharmaceutical samples, such as vitamin C tablets and dopamine injections, respectively. The applicability of this sensor was also extended in the determination of uric acid in human urine samples.

Sheng et al. [347] prepared nitrogen-doped graphene (NG) by thermally annealing graphite oxide and melamine mixture, the electrochemical sensor based on NG was constructed to simultaneously determine small biomolecules such as AA, DA and UA. The sensor shows a wide linear response for AA, DA and UA in the concentration range of 5.0×10^{-6} – 1.3×10^{-3} mol L^{-1} , 5.0×10^{-7} – 1.7×10^{-4} mol L^{-1} and 1.0×10^{-7} – 2.0×10^{-5} mol L^{-1} , with a detection limit of 2.2×10^{-6} mol L^{-1} , 2.5×10^{-7} mol L^{-1} and 4.5×10^{-8} mol L^{-1} at $S/N=3$, respectively. Wang et al. [348] reported the application of graphene-modified electrode for selective detection of DA.

6.9. Cytochrome c (Cyt-c)/cysteine

Song et al. [349] developed a novel biosensor by entrapping Cyt-c in thin films of room temperature ionic liquid (RTIL) containing nanocomposites of poly(diallyldimethylammonium chloride)-graphenenanosheets-goldnanoparticles (PDDA-Gp-AuNPs) at an 11-mercaptoundecanoic acid-6-mercapto-1-hexanol modified gold electrode. The synthesised PDDA-Gp-AuNPs hybrid nanocomposites were characterized by UV-vis spectroscopy, Raman spectroscopy, SEM and AFM. The PDDA-Gp-AuNPs nanocomposites could increase the effective surface of the electrode, enhance the fixed amount of Cyt-c on the electrode surface, promote the electron transfer and facilitate the catalytic activity of Cyt-c.

Chen et al. [350] prepared nanocomposite of polymerised ionic liquid (PIL), poly (1-vinyl-3-ethyl imidazolium) bromide, and modified graphene nanosheet (PIL-Gr). The PIL-Gr nanosheet composite was evaluated using scanning electron microscopy, transmission electron microscopy and Fourier transform infrared spectroscopy. Direct electrochemistry and electrocatalysis of immobilised Cyt-c were investigated in detail. The CV results indicated that the PIL-Gr nanocomposite film showed an obvious promotion for the direct electron transfer between Cyt-c and the underlying electrode. The immobilised Cyt-c exhibited an excellent electrocatalytic activity towards the reduction of nitric oxide (NO). Wu et al. [351] prepared graphene nanoflakes that were successfully immobilised on glassy carbon electrode to construct a graphene modified electrode. Cytochrome c was adsorbed tightly on the surface of the modified electrode and the direct electron transfer of Cytochrome c was achieved. Cytochrome c on the surface of electrode maintains its bioactivity and shows an enzyme-like activity for the reduction of nitric oxide, displaying a potential application for the fabrication of novel biosensors to sense nitric oxide. Xiang et al. [352] reported the direct electron transfer of cytochrome c and its biosensor, based on gold nanoparticles/room temperature ionic liquid/carbon nanotubes composite film.

Recently, Hosseine [353] synthesised Graphene oxide-cobalt phthalocyanine (GO-PcCo) hybrid material as a new electrocatalyst and was used successfully for the fabrication of new biosensor for the electrooxidation of L-cysteine (CSH) in aqueous media. Fourier transform infrared spectroscopy (FT-IR), X-ray photoelectron spectroscopy (XPS), thermogravimetric analysis (TGA) and transmission electron microscopy (TEM) images revealed that cobalt phthalocyanine is covalently attached on graphene oxide sheets as single layers GO-PcCo. CV studies

showed that the GO–PcCo/glassy carbon electrode (GO–PcCo/GCE) improves electrochemical behaviour of CSH oxidation, as compared to the GO and PcCo. Li et al. [354] demonstrated on the basis of cytochrome c-induced self-assembled graphene quantum dots, a novel fluorescent biosensor for trypsin, with remarkable fluorescence enhancement, as well as high selectivity and sensitivity.

Zhang et al. [9] developed a novel electrochemical biosensor for highly sensitive and selective detection of cysteine. Based on in-situ synthesis of gold nanoparticles (AuNPs)/reduced graphene oxide (RGO), nanocomposites were developed. GO was reduced by DA, and then in situ synthesis of AuNPs by the phenolic hydroxyl groups of DA on the RGO surface. The sulphhydryl group of cysteine could bind not only with AuNPs through AuS bond, but also with polydopamine on the RGO surface through Michael addition reaction. Combination of cysteine with the AuNPs/RGO leads to the decrease in the peak currents of electrochemical probe $[\text{Ru}(\text{NH}_3)_6]^{3+}$, which could be used for indirect electrochemical sensing of cysteine. The change of the peak currents value of $[\text{Ru}(\text{NH}_3)_6]^{3+}$ was linear with the concentration of cysteine in the range from 1.0×10^{-9} to 3.0×10^{-8} mol L⁻¹, with a linear coefficient of 0.991. The detection limit was 1.0×10^{-10} mol L⁻¹ ($S/N=3$). The proposed electrochemical biosensor is rapid, convenient and cost-effective for the effective sensing of cysteine.

7. Conclusions

This review presents recent synthesis and applications of graphene for electrochemical biosensing. A rapid growth in the use of graphene-based electrodes for electrochemical sensing and biosensing has been witnessed. These biosensors have exhibited excellent sensitivity and selectivity towards the detection of glucose, cholesterol, Hb, H₂O₂, UA, AA, DA and DNA. Studies of graphene-based materials will enhance research in the field of biosensor, because graphenes are excellent materials for the development of electrochemical sensors. Graphene immobilised within composites offers the advantages of an easy preparation and the dispersion of graphene in polyelectrolytes is another excellent platform for the further design of different sensors or biosensors once immobilised on an electrode.

Future development of sensors and biosensors will address future sensing and biosensing challenges in clinical diagnostics, environmental monitoring and security control. This will depend on the unique properties of graphene, with the powerful recognition properties of biomolecules and the known advantages of the electrochemical techniques.

8. Future work

The future of graphene and some of the graphene-like materials produced in the pursuit of graphene in many applications will emerge because of high surface area of graphene prepared by CVD and chemical exfoliation. Many different strategies will be explored for the construction of novel biosensors that employ graphene or graphene-like materials as sensing elements, to detect small biomolecules, i.e. DNA. Heteroatom-doped graphene can be used to form novel biosensor and more research will be carried out on graphene/conducting polymer/nanocomposites and graphene/carbon paste electrode. Biocompatibility of graphene in different sensing applications will need to be addressed further in future works, while mass production of single-layer graphene is a major challenge that needs to be overcome in the future.

References

- [1] J. Yao, Y. Sun, M. Yang, Y. Duan, *J. Mater. Chem.* 22 (2012) 14313–14329.
- [2] H. Zhang, G. Gruner, Y. Zhao, *J. Mater. Chem. B* 1 (2013) 2542–2567.
- [3] Y. Ni, F. Zhang, S. Kokot, *Anal. Chim. Acta* 769 (2013) 40–48.
- [4] M.L. Cohen, *Mater. Sci. Eng. C* 15 (2001) 1–11.
- [5] C. Berger, *J. Phys. Chem. B* 108 (2004) 19912–19916.
- [6] F.P. Ouyang, H. Zou, X. Ni, S.L. Peng, J. Ouyang, Y. Chen, *Wuli Huaxue Xuebao/Acta Physico-Chim. Sin.* 29 (2013) 250–254.
- [7] Y. Shao, J. Wang, H. Wu, J. Liu, I. Aksay, Y. Lin, *Electroanalysis* 21 (2010) 139–152.
- [8] K. Zhou, Y. Zhu, X. Yang, C. Li, *Electroanalysis* 23 (2011) 862–869.
- [9] Y. Zhang, A. Yang, X. Zhang, H. Zhao, X. Li, Z. Yuan, *Colloids and Surf. A: Physicochem. Eng. Asp.* 436 (2013) 815–822.
- [10] Y. Cheng, B. Feng, X. Yang, P. Yang, Y. Ding, Y. Chen, J. Fei, *Sens. Actuators, B: Chem.* 182 (2013) 288–293.
- [11] X.S. Du, M. Xiao, Y.Z. Meng, A.S. Hay, *Synth. Met.* 143 (2004) 129–132.
- [12] S. Wu, F. Huang, X. Lan, X. Wang, J. Wang, C. Meng, *Sens. Actuators B: Chem.* 177 (2013) 724–729.
- [13] K. Radhapyari, P. Kotoky, M.R. Das, R. Khan, *Talanta* 111 (2013) 47–53.
- [14] S. Cao, L. Zhang, Y. Chai, R. Yuan, *Biosens. Bioelectron.* 42 (2013) 532–538.
- [15] H. Xu, D. Wang, S. He, J. Li, B. Feng, P. Ma, P. Xu, S. Gao, S. Zhang, Q. Liu, J. Lu, S. Song, C. Fan, *Biosens. Bioelectron.* 50 (2013) 251–255.
- [16] C. Xu, B. Xu, Y. Gu, Z. Xiong, J. Sun, X.S. Zhao, *Energy Environ. Sci.* 6 (2013) 1388–1414.
- [17] D. Chen, H. Zhang, Y. Liu, J. Li, *Energy Environ. Sci.* 6 (2013) 1362–1387.
- [18] U. Yogeswaran, S.M. Chen, *Sensors* 8 (2008) 290–313.
- [19] Q. Wang, X. Cui, J. Chen, X. Zheng, C. Liu, T. Xue, H. Wang, Z. Jin, L. Qiao, W. Zheng, *RSC Adv.* 2 (2012) 6245–6249.
- [20] W. Putzbach, N.J. Ronkainen, *Sensors (Switzerland)* 13 (2013) 4811–4840.
- [21] X.-m. Chen, G.-h. Wu, Y.-q. Jiang, Y.-r. Wang, X. Chen, *Analyst* 136 (2011) 4631–4640.
- [22] C.I.L. Justino, T.A.P. Rocha-Santos, S. Cardoso, A.C. Duarte, T.A.P. Rocha-Santos, S. Cardoso, *TrAC – Trends Anal. Chem.* 47 (2013) 27–36.
- [23] M. Pumera, *Chem. Soc. Rev.* 39 (2010) 4146–4157.
- [24] A. Walcarius, S.D. Minter, J. Wang, Y. Lin, A. Merkoçi, *J. Mater. Chem. B* 1 (2013) 4878–4908.
- [25] D. Jariwala, V.K. Sangwan, L.J. Lauhon, T.J. Marks, M.C. Hersam, *Chem. Soc. Rev.* 42 (2013) 2824–2860.
- [26] Q. Tang, Z. Zhou, Z. Chen, *Nanoscale* 5 (2013) 4541–4583.
- [27] J. Li, X. Yang, *Prog. Chem* 25 (2013) 380–396.
- [28] G. Zhao, T. Wen, C. Chen, X. Wang, *RSC Adv.* 2 (2012) 9286–9303.
- [29] S. Cho, L. Park, R. Chong, J.H. Lee, Background free biosensor using the combination of graphene oxide and Fe₃O₄ nanoparticles, Washington, DC, 2013, pp. 711–712.
- [30] H.P. Liu, G.Y. Zhan, Q.Z. Dong, Y.A. Lv, J.F. Wang, C.A. Tao, Z.H. Hu, Glucose biosensor based on Pt nanoparticles/graphene–chitosan bionanocomposites, Hong Kong, 2013, pp. 695–699.
- [31] S. Zhu, J. Guo, J. Dong, Z. Cui, T. Lu, C. Zhu, D. Zhang, J. Ma, *Ultrason. Sonochem.* 20 (2013) 872–880.
- [32] J. Jiang, W. Fan, X. Du, *Biosens. Bioelectron.* 51 (2014) 343–348.
- [33] P.T. Yin, T.-H. Kim, J.-W. Choi, K.-B. Lee, *Phys. Chem. Chem. Physics* 15 (2013) 12785–12799.
- [34] X. Zan, Z. Fang, J. Wu, F. Xiao, F. Huo, H. Duan, *Biosens. Bioelectron.* 49 (2013) 71–78.
- [35] Y. Xu, E. Wang, *Electrochim. Acta* 84 (2012) 62–73.
- [36] X. Luo, A. Morrin, A. Killard, M. Smyth, *Electroanalysis* 18 (2006) 319–326.
- [37] J. Li, D. Kuang, Y. Feng, F. Zhang, Z. Xu, M. Liu, D. Wang, *Biosens. Bioelectron.* 42 (2013) 198–206.
- [38] Z.M. Liu, Y.F. Jing, Z.L. Wang, H.J. Zhan, Q. Shen, *Nanocompos. Sens. Lett.* 11 (2013) 531–538.
- [39] J. Zheng, X. Ma, X. He, M. Gao, G. Li, *Proc. Eng.* 27 (2012) 1478–1487.
- [40] L. Zhang, A. Zhang, D. Du, Y. Lin, *Nanoscale* 4 (2012) 4674–4679.
- [41] S. Stankovich, D.A. Dikin, G.H.B. Dommett, K.M. Kohlhaas, E.J. Zimney, E.A. Stach, R.D. Piner, S.T. Nguyen, R.S. Ruoff, *Nature* 442 (2006) 282–286.
- [42] H. Teymourian, A. Salimi, S. Khezrian, *Biosens. Bioelectron.* 49 (2013) 1–8.
- [43] J. Kong, N.R. Franklin, C. Zhou, M.G. Chapline, S. Peng, K. Cho, H. Dai, *Science* 287 (2000) 622–625.
- [44] Z. Fan, B. Liu, X. Liu, Z. Li, H. Wang, S. Yang, J. Wang, *Electrochim. Acta* 109 (2013) 602–608.
- [45] Q. Li, J.Y. Zheng, Y. Yan, Y.S. Zhao, J. Yao, *Adv. Mater.* 24 (2012) 4745–4749.
- [46] A. Ambrosi, M. Pumera, *Phys. Chem. Chem. Phys.* 12 (2010) 8943–8947.
- [47] N.C. Khe, L. Van Giat, M.N.T. Anh, B.T.T. Thao, B.Q. Thuan, H.D. Truong, B. Van Nam, H. Dinh, Graphene alloy with nano carbon: novel nano material for biosensor? Ho Chi Minh City, 2013, pp. 298–300.
- [48] L. Huang, B. Wu, G. Yu, Y. Liu, *J. Mater. Chem.* 21 (2011) 919–929.
- [49] K. Balasubramanian, M. Burghard, *Anal. Bioanal. Chem.* 385 (2006) 452–468.
- [50] N. Grossiord, J. Loos, C.E. Koning, *J. Mater. Chem.* 15 (2005) 2349–2352.
- [51] J. Li, Y. Lu, Q. Ye, M. Cinke, J. Han, M. Meyyappan, *Nano Lett.* 3 (2003) 929–933.
- [52] H. Cai, X. Cao, Y. Jiang, P. He, Y. Fang, *Anal. Bioanal. Chem.* 375 (2003) 287–293.
- [53] S. Kruss, A.J. Hilmer, J. Zhang, N.F. Reuel, B. Mu, M.S. Strano, *Adv. Drug Deliv. Rev.* 65 (2013) 1933–1950.
- [54] G.A. Rivas, M.D. Ruianes, M.C. Rodríguez, N.F. Ferreyra, G.L. Luque, M. L. Pedano, S.A. Miscoria, C. Parrado, *Talanta* 74 (2007) 291–307.

- [55] S.N. Kim, J.F. Rusling, F. Papadimitrakopoulos, *Adv. Mater.* 19 (2007) 3214–3228.
- [56] J. Wang, S. Yang, D. Guo, P. Yu, D. Li, J. Ye, L. Mao, *Electrochem. Commun.* 11 (2009) 1892–1895.
- [57] Y. Yun, Z. Dong, V. Shanov, W.R. Heineman, H.B. Halsall, A. Bhattacharya, L. Conforti, R.K. Narayan, W.S. Ball, M.J. Schulz, *Nano Today* 2 (2007) 30–37.
- [58] J. Huang, Y. Liu, T. You, *Anal. Methods* 2 (2010) 202–211.
- [59] Y. Shao, J. Wang, H. Wu, J. Liu, I.A. Aksay, Y. Lin, *Electroanalysis* 22 (2010) 1027–1036.
- [60] Y. Sun, H. Buck, T.E. Mallouk, *Anal. Chem.* 73 (2001) 1599–1604.
- [61] B. Huang, Z. Li, Z. Liu, G. Zhou, S. Hao, J. Wu, B.L. Gu, W. Duan, *J. Phys. Chem. C* 112 (2008) 13442–13446.
- [62] J.B. Haun, T.J. Yoon, H. Lee, R. Weissleder, *Wiley Interdiscip. Rev.: Nanomed. Nanobiotechnol.* 2 (2010) 291–304.
- [63] D.A.C. Brownson, C.E. Banks, *Analyst* 135 (2010) 2768–2778.
- [64] M. Pumera, *Chem. Record* 9 (2009) 211–223.
- [65] M. Pumera, A. Ambrosi, A. Bonanni, E.L.K. Chng, H.L. Poh, *TrAC Trends Anal. Chem.* 29 (2010) 954–965.
- [66] M.J. Allen, V.C. Tung, R.B. Kaner, *Chem. Rev.* 110 (2010) 132–145.
- [67] J. Zhao, G. Chen, L. Zhu, G. Li, *Electrochem. Commun.* 13 (2011) 31–33.
- [68] K.S. Novoselov, *Science* 306 (2004) 666–669.
- [69] J. Slater, *Physics* 81 (1951) 385.
- [70] E. Wigner, *Phys. Rev.* 46 (1934) 1002–1011.
- [71] M.L. Cohen, M. Schlüter, J.R. Chelikowsky, S.G. Louie, *Phys. Rev. B* 12 (1975) 5575–5579.
- [72] C. Berger, *Science* 312 (2006) 1191–1196.
- [73] R. Arsat, M. Breedon, M. Shafiei, P.G. Spizziri, S. Gilje, R.B. Kaner, K. Kalantar-zadeh, W. Wlodarski, *Chem. Phys. Lett.* 467 (2009) 344–347.
- [74] T. Kuila, S. Bose, A.K. Mishra, P. Khanra, N.H. Kim, J.H. Lee, *Prog. Mater. Sci.* 57 (2012) 1061–1105.
- [75] Y.B. Tan, J.-M. Lee, *J. Mater. Chem. A* 1 (2013) 14814–14843.
- [76] M.D. Stoller, S. Park, Z. Yanwu, J. An, R.S. Ruoff, *Nano Lett.* 8 (2008) 3498–3502.
- [77] Q. Wu, *ACS Nano* 4 (2010) 1963–1970.
- [78] J. Hou, Y. Shao, M.W. Ellis, R.B. Moore, B. Yi, *Phys. Chem. Chem. Phys.* 13 (2011) 15384–15402.
- [79] X. Feng, R. Li, X. Yang, W. Hou, *Prog. Chem.* 24 (2012) 2158–2166.
- [80] Y. Sun, Q. Wu, G. Shi, *Energy Environ. Sci.* 4 (2011) 1113–1132.
- [81] Y. Wang, H. Chang, H. Wu, H. Liu, *J. Mater. Chem. B* 1 (2013) 3521–3534.
- [82] I. Willner, Y.M. Yan, B. Willner, R. Tel-Vered, *Fuel Cells* 9 (2009) 7–24.
- [83] M. Yang, Y. Hou, N.A. Kotov, *Nano Today* 7 (2012) 430–447.
- [84] X. Huang, X. Qi, F. Boey, H. Zhang, *Chem. Soc. Rev.* 41 (2012) 666–686.
- [85] Z.-S. Wu, *ACS Nano* 4 (2010) 3187–3194.
- [86] P. Martin, *Chem. Record* 9 (2009) 211–223.
- [87] O. Akhavan, E. Ghaderi, *J. Phys. Chem. C* 113 (2009) 20214–20220.
- [88] B.F. Machado, P. Serp, *Catal. Sci. Technol.* 2 (2012) 54–75.
- [89] W. Choi, I. Lahiri, R. Seelaboyina, Y.S. Kang, *Crit. Rev. Solid State Mater. Sci.* 35 (2010) 52–71.
- [90] X. Bai, G. Chen, K.K. Shiu, *Electrochim. Acta* 89 (2013) 454–460.
- [91] Y. Bo, W. Wang, J. Qi, S. Huang, *Analyst* 136 (2011) 1946–1951.
- [92] Y. Bo, H. Yang, Y. Hu, T. Yao, S. Huang, *Electrochim. Acta* 56 (2011) 2676–2681.
- [93] Y. Liu, X. Dong, P. Chen, *Chem. Soc. Rev.* 41 (2012) 2283–2307.
- [94] S. Kochmann, T. Hirschi, O.S. Wolfbeis, *TrAC - Trends Anal. Chem.* 39 (2012) 87–113.
- [95] F. Schedin, *Nat. Mater.* 6 (2007) 652–655.
- [96] Y.H. Zhang, Y.B. Chen, K.G. Zhou, C.H. Liu, J. Zeng, H.L. Zhang, Y. Peng, *Nanotechnology* 20 (2009) 20–25.
- [97] R. Moradian, Y. Mohammadi, N. Ghobadi, *J. Phys. Condens. Matter* 20 (2008) 91–95.
- [98] F. Schedin, A.K. Geim, S.V. Morozov, E.W. Hill, P. Blake, M.I. Katsnelson, K.S. Novoselov, *Nat. Mater.* 6 (2007) 652–655.
- [99] Q. Bao, *ACS Nano* 6 (2012) 3677–3694.
- [100] X. Huang, Z. Yin, S. Wu, X. Qi, Q. He, Q. Zhang, Q. Yan, F. Boey, H. Zhang, *Small* 7 (2011) 1876–1902.
- [101] N. Yang, *ACS Nano* 4 (2010) 887–894.
- [102] J. Kang, D. Shin, S. Bae, B.H. Hong, *Nanoscale* 4 (2012) 5527–5537.
- [103] X. Huang, Z. Zeng, Z. Fan, J. Liu, H. Zhang, *Adv. Mater.* 24 (2012) 5979–6004.
- [104] Z. Sun, *ACS Nano* 4 (2010) 803–810.
- [105] S. Nardecchia, D. Carriazo, M.L. Ferrer, M.C. Gutierrez, F. del Monte, *Chem. Soc. Rev.* 42 (2013) 794–830.
- [106] N. Zhang, Y. Zhang, Y.-J. Xu, *Nanoscale* 4 (2012) 5792–5813.
- [107] L. Han, P. Wang, S. Dong, *Nanoscale* 4 (2012) 5814–5825.
- [108] N. Mohanty, V. Berry, *Nano Lett.* 8 (2008) 4469–4476.
- [109] Y. Ohno, K. Maehashi, K. Matsumoto, *J. Am. Chem. Soc.* 132 (2010) 18012–18013.
- [110] M.S. Artiles, C.S. Rout, T.S. Fisher, *Adv. Drug Deliv. Rev.* 63 (2011) 1352–1360.
- [111] Y. Ohno, K. Maehashi, K. Matsumoto, *Biosens. Bioelectron.* 26 (2010) 1727–1730.
- [112] X. Li, W. Cai, J. An, S. Kim, J. Nah, D. Yang, R. Piner, A. Velamakanni, I. Jung, E. Tutuc, S.K. Banerjee, L. Colombo, R.S. Ruoff, *Science* 324 (2009) 1312–1314.
- [113] C.X. Lim, H.Y. Hoh, P.K. Ang, K.P. Loh, *Anal. Chem.* 82 (2010) 7387–7393.
- [114] X. Li, G. Zhang, X. Bai, X. Sun, X. Wang, E. Wang, H. Dai, *Nat. Nanotechnol.* 3 (2008) 538–542.
- [115] W.J. Lin, C.S. Liao, J.H. Jhang, Y.C. Tsai, *Electrochem. Commun.* 11 (2009) 2153–2156.
- [116] K.S. Novoselov, *Proc. Natl. Acad. Sci. USA* 102 (2005) 10451–10453.
- [117] A.B. Bourlinos, V. Georgakilas, R. Zboril, T.A. Sterioti, A.K. Stubos, *Small* 5 (2009) 1841–1845.
- [118] Y. Hernandez, V. Nicolosi, M. Lotya, F.M. Blighe, Z. Sun, S. De, I.T. McGovern, B. Holland, M. Byrne, Y.K. Gun'ko, J.J. Boland, P. Niraj, G. Duesberg, S. Krishnamurthy, R. Goodhue, J. Hutchison, V. Scardaci, A.C. Ferrari, J.N. Coleman, *Nat. Nanotechnol.* 3 (2008) 563–568.
- [119] D.R. Dreyer, S. Park, C.W. Bielawski, R.S. Ruoff, *Chem. Soc. Rev.* 39 (2010) 228–240.
- [120] M. Zhou, Y. Zhai, S. Dong, *Anal. Chem.* 81 (2009) 5603–5613.
- [121] J.T. Robinson, F.K. Perkins, E.S. Snow, Z. Wei, P.E. Sheehan, *Nano Lett.* 8 (2008) 3137–3140.
- [122] K.R. Ratinac, W. Yang, J.J. Gooding, P. Thordarson, F. Braet, *Electroanalysis* 23 (2011) 803–826.
- [123] T. Kuila, S. Bose, P. Khanra, A.K. Mishra, N.H. Kim, J.H. Lee, *Biosens. Bioelectron.* 26 (2011) 4637–4648.
- [124] D.A.C. Brownson, D.K. Kampouris, C.E. Banks, *Chem. Soc. Rev.* 41 (2012) 6944–6976.
- [125] D. Chen, L. Tang, J. Li, *Chem. Soc. Rev.* 39 (2010) 3157–3180.
- [126] V.C. Tung, M.J. Allen, Y. Yang, R.B. Kaner, *Nat. Nanotechnol.* 4 (2009) 25–29.
- [127] M. Lotya, Y. Hernandez, P.J. King, R.J. Smith, S.K. Mohapatra, L.S. Karlsson, F. M. Blighe, S. De, W. Zhiming, I.T. McGovern, G.S. Duesberg, J.N. Coleman, *J. Am. Chem. Soc.* 131 (2009) 3611–3620.
- [128] T.Y. Chen, P.T.K. Loan, C.L. Hsu, Y.H. Lee, J. Tse-Wei Wang, K.H. Wei, C.T. Lin, L. J. Li, *Biosens. Bioelectron.* 41 (2013) 103–109.
- [129] W. Wu, Z. Liu, L.A. Jauregui, Q. Yu, R. Pillai, H. Cao, J. Bao, Y.P. Chen, S.S. Pei, *Sens. Actuators B: Chem.* 150 (2010) 296–300.
- [130] A.N. Obraztsov, *Nat. Nanotechnol.* 4 (2009) 212–213.
- [131] Y. Zhang, L. Zhang, C. Zhou, *Acc. Chem. Res.* 46 (2013) 2329–2339.
- [132] S.A. Paniagua, J. Baltazar, H. Sojoudi, S.K. Mohapatra, S. Zhang, C. L. Henderson, S. Graham, S. Barlow, S.R. Marder, *Mater. Horiz.* 1 (2014) 111–115.
- [133] A. Reina, X. Jia, J. Ho, D. Nezich, H. Son, V. Bulovic, M.S. Dresselhaus, K. Jing, *Nano Lett.* 9 (2009) 30–35.
- [134] M.S. Dresselhaus, *ACS Nano* 4 (2010) 6297–6302.
- [135] N.S. Kim, J.F. Rusling, F. Papadimitrakopoulos, *Adv. Mater.* 19 (2007) 3214–3228.
- [136] H. Chen, M.B. Müller, K.J. Gilmore, G.G. Wallace, D. Li, *Adv. Mater.* 20 (2008) 3557–3561.
- [137] A. Ambrosi, M. Pumera, *J. Phys. Chem. C* 117 (2013) 2053–2058.
- [138] K. Zhou, Y. Zhu, X. Yang, C. Li, *Electroanalysis* 22 (2010) 259–264.
- [139] K.S. Kim, Y. Zhao, H. Jang, S.Y. Lee, J.M. Kim, J.H. Ahn, P. Kim, J.Y. Choi, B. H. Hong, *Nature* 457 (2009) 706–710.
- [140] E. Casero, C. Alonso, L. Vázquez, M.D. Petit-Domínguez, A.M. Parra-Alfambra, M. delaFuente, P. Merino, S. Álvarez-García, A. deAndrés, F. Pariente, E. Lorenzo, *Electroanalysis* 25 (2013) 154–165.
- [141] S. Alwarappan, A. Erdem, C. Liu, C.-Z. Li, *J. Phys. Chem. C* 113 (2009) 8853–8857.
- [142] S. Alwarappan, A. Erdem, C. Liu, C.Z. Li, *J. Phys. Chem. C* 113 (2009) 8853–8857.
- [143] Rattana, S. Chaiyakun, N. Witit-anun, N. Nuntawong, P. Chindaudom, S. Oaew, C. Kedkeaw, P. Limsuwan, *Proc. Eng.* 32 (2012) 759–764.
- [144] Z.-S. Wu, W. Ren, L. Gao, B. Liu, C. Jiang, H.-M. Cheng, *Carbon* 47 (2009) 493–499.
- [145] S. Park, R.S. Ruoff, *Nat. Nanotechnol.* 4 (2009) 217–224.
- [146] J.D. Fowler, M.J. Allen, V.C. Tung, Y. Yang, R.B. Kaner, B.H. Weiller, *ACS Nano* 3 (2009) 301–306.
- [147] S. Stankovich, *Nature* 442 (2006) 282–286.
- [148] S. Stankovich, *J. Mater. Chem.* 16 (2006) 155–158.
- [149] S. Stankovich, D.A. Dikin, R.D. Piner, K.A. Kohlhaas, A. Kleinhammes, Y. Jia, Y. Wu, S.T. Nguyen, R.S. Ruoff, *Carbon* 45 (2007) 1558–1565.
- [150] S. Gilje, S. Han, M. Wang, K.L. Wang, R.B. Kaner, *Nano Lett.* 7 (2007) 3394.
- [151] C. Gomez-Navarro, R.T. Weitz, A.M. Bittner, M. colari, A. Mews, M. Burghard, K. Kern, *Nano Lett.* 7 (2007) 3499.
- [152] L. Brey, H.A. Fertig, *Phys. Rev. B* 73 (2006) 235411.
- [153] Y. Wang, Y. Shao, D.W. Matson, J. Li, Y. Lin, *ACS Nano* 4 (2010) 1790–1798.
- [154] S. Watcharotone, D.A. Dikin, S. Stankovich, R. Piner, I.G.H. Jung, B. Dommett, G. Evmenenko, S.E. Wu, S.F. Chen, C.P. Liu, S.T. Nguyen, R.S. Ruoff, *Nano Lett.* 7 (2007) 1888.
- [155] H.C. Chen, Y.H. Chen, S.L. Chen, Y.T. Chern, R.Y. Tsai, M.Y. Hua, *Biosens. Bioelectron.* 46 (2013) 84–90.
- [156] X. Dong, Y. Shi, Y. Zhao, Y. Chen, J. Ye, Y. Yao, F. Gao, Z. Ni, T. Yu, Z. Shen, Y. Huang, P. Chen, L.J. Li, *Phys. Rev. Lett.* 102 (2009) 135501–135504.
- [157] H.C. Schniepp, J.L. Li, M.J. McAllister, H. Sai, M. Herrera-Alonson, D. H. Adamson, R.K. Prud'homme, R. Car, D.A. Seville, I.A. Aksay, *J. Phys. Chem. B* 110 (2006) 8535–8539.
- [158] M.H. Chakrabarti, C.T.J. Low, N.P. Brandon, V. Yufi, M.A. hashim, M.F. Irfan, J. Akhtar, E. Ruitz-Trejo, M.A. Hussain, *Electrochim. Acta* 107 (2013) 425–440.
- [159] P. Kumar, *RSC Adv.* 3 (2013) 11987–12002.
- [160] R. Jilili, S.H. Aboutalebi, D. Esralzadeh, K. Konstantinov, S.E. Moulton, J. M. Razal, G.G. Wallace, *ACS Nano* 7 (2013) 3981–3990.
- [161] D. Wei, J. Kivioja, *Nanoscale* 5 (2013) 10108–10126.
- [162] F. Bonaccorso, A. Lombardo, T. Hasan, Z. Sun, L. Colombo, A.C. Ferrari, *Mater. Today* 15 (2012) 564–589.
- [163] A.K. Geim, *Science* 324 (2009) 1530–1534.
- [164] A.T.S. Wee, *ACS Nano* 6 (2012) 5739–5741.
- [165] D.A.C. Brownson, C.E. Banks, *Phys. Chem. Chem. Phys.* 14 (2012) 8264–8281.

- [166] R.S. Edwards, K.S. Coleman, *Nanoscale* 5 (2013) 38–51.
- [167] V. Singh, D. Joung, L. Zhai, S. Das, S.I. Khondaker, S. Seal, *Prog. Mater. Sci.* 56 (2011) 1178–1271.
- [168] H. Wang, T. Maiyalagan, X. Wang, *ACS Catal.* 2 (2012) 781–794.
- [169] Y. Fang, E. Wang, *Chem. Commun.* 49 (2013) 9526–9539.
- [170] T. Gan, S. Hu, *Microchim. Acta* 175 (2011) 1–19.
- [171] T. Liu, J. Zhong, X. Gan, C. Fan, G. Li, N. Matsuda, *Chemphyschem* 4 (2003) 1364–1366.
- [172] S. Bai, X. Shen, *RSC Adv.* 2 (2012) 64–98.
- [173] N. Li, M. Cao, C. Hu, *Nanoscale* 4 (2012) 6205–6218.
- [174] X. Liu, J. Zhang, R. Yan, Q. Zhang, X. Liu, *Biosens. Bioelectron.* 51 (2014) 76–81.
- [175] X.M. Feng, Z. Yan, *Chin. J. Inorg. Chem.* 29 (2013) 1051–1056.
- [176] W. Gao, Y. Chen, J. Xi, S. Lin, Y. Chen, Y. Lin, Z. Chen, *Biosens. Bioelectron.* 41 (2013) 776–782.
- [177] K.-J. Huang, L. Wang, J. Li, Y.-M. Liu, *Sens. Actuators B: Chem.* 178 (2013) 671–677.
- [178] R. Yue, Q. Lu, Y. Zhou, *Biosens. Bioelectron.* 26 (2011) 4436–4441.
- [179] F. Zhang, Li Y, Gu Y, Z. Wang, C. Wang, *Microchim. Acta* 173 (2011) 103–109.
- [180] Y. Fan, K.-J. Huang, D.-J. Niu, C.-P. Yang, *Electrochim. Acta* 56 (2011) 4685–4690.
- [181] D. Du, J. Liu, X. Zhang, X.L. Cui, Y.H. Lin, *J. Mater. Chem.* 21 (2011) 8032–8037.
- [182] S. Andreescu, L.A. Luck, *Anal. Biochem.* 375 (2008) 282–290.
- [183] Z. Zheng, Y. Du, Z. Wang, Q. Feng, C. Wang, *Analyst* 138 (2013) 693–701.
- [184] C. Shan, H. Yang, D. Han, Q. Zhang, A. Ivaska, L. Niu, *Biosens. Bioelectron.* 25 (2010) 1070–1074.
- [185] W. Hong, H. Bai, Y. Xu, Y. Yao, Z. Gu, G. Shi, *J. Phys. Chem. C* 114 (2010) 1822–1826.
- [186] M. Zhang, R. Yuan, Y. Chai, C. Wang, X. Wu, *Anal. Biochem.* 436 (2013) 69–74.
- [187] S. Yang, Z. Lu, S. Luo, C. Liu, Y. Tang, *Microchim. Acta* 180 (2013) 127–135.
- [188] S. Cao, L. Zhang, Y. Chai, R. Yuan, *Talanta* 109 (2013) 167–172.
- [189] P.M. Ostrovsky, I.V. Gornyi, A.D. Mirlin, *Phys. Rev. B* 74 (2006) 235443.
- [190] R.A. Marcus, *Angew. Chem. Int. Ed. Engl.* 32 (1993) 1111–1121.
- [191] J.F. Rusling, *Acc. Chem. Res.* 31 (1998) 363–369.
- [192] Y. Xiao, F. Patolsky, E. Katz, J.F. Hainfeld, I. Willner, *Science* 299 (2003) 1877–1881.
- [193] X. Zhao, Z. Mai, X. Kang, X. Zou, *Biosens. Bioelectron.* 23 (2008) 1032–1038.
- [194] C. Leger, P. Bertrand, *Chem. Rev.* 108 (2008) 2379–2438.
- [195] Y.L. Yao, K.K. Shiu, *Electroanalysis* 20 (2008) 1532–1548.
- [196] W. Schuhmann, C. Kranz, J. Huber, H. Wohlschläger, *Synth. Met.* 61 (1993) 31–35.
- [197] H.L. Schmidt, W. Schuhmann, *Biosens. Bioelectron.* 11 (1996) 127–135.
- [198] A. Chaubey, B.D. Malhotra, *Biosens. Bioelectron.* 17 (2002) 441–456.
- [199] R. Feng, Y. Zhang, H. Ma, D. Wu, H. Fan, H. Wang, H. Li, B. Du, Q. Wei, *Electrochim. Acta* 97 (2013) 105–111.
- [200] M. Pumera, *Mater. Today* 14 (2011) 308–315.
- [201] V.M. Apalkov, T. Chakraborty, *Phys. Rev. Lett.* 97 (2006) 126801.
- [202] M. Clark, C. Lyons, *Ann. N. Y. Acad. Sci.* 102 (1962) 29.
- [203] L. Zhou, Y. Jiang, J. Gao, X. Zhao, L. Ma, Q. Zhou, *Biochem. Eng. J.* 69 (2012) 28–31.
- [204] C. Léger, P. Bertrand, *Chem. Rev.* 108 (2008) 2379–2438.
- [205] J. Wang, *Chem. Rev.* 108 (2008) 814–825.
- [206] G.S. Wilson, Y. Hu, *Chem. Rev.* 100 (2000) 2693–2704.
- [207] J.W. Evans, P.A. Thiel, M.C. Bartelt, *Sur. Sci. Rep.* 61 (2006) 1–128.
- [208] D. Wang, F. Wang, J. Yan, Y. Gao, H. Li, J. Nanopart. Res. 15 (2013) 1762–1767.
- [209] A. Wisitsoraat, S. Pakapongpan, C. Sriprachuabwong, D. Phokharatkul, P. Sritongkham, T. Lomas, A. Tuantranont, *J. Electroanal. Chem.* 704 (2013) 208–213.
- [210] Y. Wang, H. Zhang, D. Yao, J. Pu, Y. Zhang, X. Gao, Y. Sun, *J. Solid State Electrochem.* 17 (2013) 881–887.
- [211] Y. Qin, Y. Kong, Y. Xu, F. Chu, Y. Tao, S. Li, *J. Mater. Chem.* 22 (2012) 24821–24826.
- [212] T. Kavitha, A.I. Gopalan, K.P. Lee, S.Y. Park, *Carbon* 50 (2012) 2994–3000.
- [213] J.-D. Qiu, J. Huang, R.-P. Liang, *Sens. Actuators B: Chem.* 160 (2011) 287–294.
- [214] L.-M. Lu, H.-B. Li, F. Qu, X.-B. Zhang, G.-L. Shen, R.-Q. Yu, *Biosens. Bioelectron.* 26 (2011) 3500–3504.
- [215] B.G. Choi, J. Im, H.S. Kim, H. Park, *Electrochim. Acta* 56 (2011) 9721–9726.
- [216] G. Zeng, Y. Xing, J. Gao, Z. Wang, X. Zhang, *Langmuir* 26 (2010) 15022–15026.
- [217] P. Wu, Q. Shao, Y. Hu, J. Jin, Y. Yin, H. Zhang, C. Cai, *Electrochim. Acta* 55 (2010) 8606–8614.
- [218] Y. Song, K. Qu, C. Zhao, J. Ren, X. Qu, *Adv. Mater.* 22 (2010) 2206–2210.
- [219] D. Zheng, S.K. Vashist, M.M. Dykas, S. Saha, K. Al-Rubeaan, E. Lam, J.H. T. Luong, F.S. Sheu, *Mater* 6 (2013) 1011–1027.
- [220] T.T. Baby, S.S.J. Aravind, T. Arockiadoss, R.B. Rakhi, S. Ramaprabhu, *Sens. Actuators, B: Chem.* 145 (2010) 71–77.
- [221] X. Kang, J. Wang, H. Wu, I.A. Aksay, J. Liu, Y. Lin, *Biosens. Bioelectron.* 25 (2009) 901–905.
- [222] M.H. Yang, B.G. Choi, H. Park, W.H. Hong, S.Y. Lee, T.J. Park, *Electroanalysis* 22 (2010) 1223–1228.
- [223] M. Cui, B. Xu, C. Hu, H.B. Shao, L. Qu, *Electrochim. Acta* 98 (2013) 48–53.
- [224] J. Hui, J. Cui, G. Xu, S.B. Adeloju, Y. Wu, *Mater. Lett.* 108 (2013) 88–91.
- [225] C. Fu, *Electrochem. Commun.* 11 (2009) 997.
- [226] C. Shan, H. Yang, J. Song, D. Han, A. Ivaska, L. Niu, *Anal. Chem.* 81 (2009) 2378–2382.
- [227] K. Wang, Q. Liu, Q.M. Guan, J. Wu, H.N. Li, J.J. Yan, *Biosens. Bioelectron.* 26 (2011) 2252–2257.
- [228] X. Zhang, Q. Liao, M. Chu, S. Liu, Y. Zhang, *Biosens. Bioelectron.* 52 (2014) 281–287.
- [229] Y. Yu, Z. Chen, S. He, B. Zhang, X. Li, M. Yao, *Biosens. Bioelectron.* 52 (2014) 147–152.
- [230] Z. Luo, X. Ma, D. Yang, L. Yuwen, X. Zhu, L. Weng, L. Wang, *Carbon* 57 (2013) 470–476.
- [231] M. Yuan, A. Liu, M. Zhao, W. Dong, T. Zhao, J. Wang, W. Tang, *Sens. Actuators B: Chem.* 190 (2014) 707–714.
- [232] J. Lu, I. Do, L.T. Drzal, R.M. Worden, I. Lee, *ACS Nano* 2 (2008) 1825–1832.
- [233] X. Zhu, L. Sun, Y. Chen, Z. Ye, Z. Shen, G. Li, *Biosens. Bioelectron.* 47 (2013) 32–37.
- [234] Y.Q. Zhang, Y.J. Fan, L. Cheng, L.L. Fan, Z.Y. Wang, J.P. Zhong, L.N. Wu, X.C. Shen, Z.J. Shi, *Electrochim. Acta* 104 (2013) 178–184.
- [235] B. Unnikrishnan, S. Palanisamy, S.-M. Chen, *Biosens. Bioelectron.* 39 (2013) 70–75.
- [236] V. Mani, B. Devadas, S.M. Chen, *Biosens. Bioelectron.* 41 (2013) 309–315.
- [237] H.D. Jang, S.K. Kim, H. Chang, J.W. Choi, J. Huang, *Mater. Lett.* 106 (2013) 277–280.
- [238] C.X. Xu, K.J. Huang, X.M. Chen, X.Q. Xiong, *J. Solid State Electrochem.* 16 (2012) 3747–3752.
- [239] Y.H. Kwak, D.S. Choi, Y.N. Kim, H. Kim, D.H. Yoon, S.S. Ahn, J.W. Yang, W. S. Yang, S. Seo, *Biosens. Bioelectron.* 37 (2012) 82–87.
- [240] H.D. Jang, S.K. Kim, H. Chang, K.M. Roh, J.W. Choi, J. Huang, *Biosens. Bioelectron.* 38 (2012) 184–188.
- [241] Y.-W. Hsu, T.-K. Hsu, C.-L. Sun, Y.-T. Nien, N.-W. Pu, M.-D. Ger, *Electrochim. Acta* 82 (2012) 152–157.
- [242] Q. Zhang, S. Wu, L. Zhang, J. Lu, F. Verproot, Y. Liu, Z. Xing, J. Li, X.-M. Song, *Biosens. Bioelectron.* 26 (2011) 2632–2637.
- [243] Q. Zeng, J.-S. Cheng, X.-F. Liu, H.-T. Bai, J.-H. Jiang, *Biosens. Bioelectron.* 26 (2011) 3456–3463.
- [244] H. Yin, Y. Zhou, X. Meng, K. Shang, S. Ai, *Biosens. Bioelectron.* 30 (2011) 112–117.
- [245] H. Wu, J. Wang, X. Kang, C. Wang, D. Wang, J. Liu, I.A. Aksay, Y. Lin, *Talanta* 80 (2009) 403–406.
- [246] Z. Wang, X. Zhou, J. Zhang, F. Boey, H. Zhang, *J. Phys. Chem. C* 113 (2009) 14071–14075.
- [247] J.F. Wu, M.Q. Xu, G.C. Zhao, *Electrochem. Commun.* 12 (2010) 175–177.
- [248] A. Gutiérrez, C. Carraro, R. Maboudian, *Biosens. Bioelectron.* 33 (2012) 56–59.
- [249] D. Zheng, S.K. Vashist, K. Al-Rubeaan, J.H.T. Luong, F.S. Sheu, *Talanta* 99 (2012) 22–28.
- [250] Q. Zeng, J. Cheng, L. Tang, X. Liu, Y. Liu, J. Li, J. Jiang, *Adv. Funct. Mater.* 20 (2010) 3366–3372.
- [251] M. Liu, R. Liu, W. Chen, *Biosens. Bioelectron.* 45 (2013) 206–212.
- [252] K. Liu, J. Zhang, G. Yang, C. Wang, J.-J. Zhu, *Electrochem. Commun.* 12 (2010) 402–405.
- [253] W. Song, D.W. Li, Y.T. Li, Y. Li, Y.T. Long, *Biosens. Bioelectron.* 26 (2010) 3181–3186.
- [254] N.L. Yang, J. Zhai, D. Wang, Y.S. Chen, L. Jiang, *ACS Nano* 4 (2010) 887.
- [255] J. Huang, L. Zhang, R.P. Liang, J.D. Qiu, *Biosens. Bioelectron.* 41 (2013) 430–435.
- [256] K.J. Huang, L. Wang, J. Li, T. Gan, Y.M. Liu, *Measurement* 46 (2013) 378–383.
- [257] S. Alwarappan, C. Liu, A. Kumar, C.-Z. Li, *J. Phys. Chem. C* 114 (2010) 12920–12924.
- [258] S. Alwarappan, C. Liu, A. Kumar, C.Z. Li, *J. Phys. Chem. C* 114 (2010) 12920–12924.
- [259] L. Fan, Y. Fan, S. Wang, T. Lai, L. Wu, X. Shen, *Chin. J. Sens. Actuators* 26 (2013) 446–451.
- [260] T.T. Baby, S.S.J. Aravind, T. Arockiadoss, R.B. Rakhi, S. Ramaprabhu, *Sens. Actuators B: Chem.* 145 (2010) 71–77.
- [261] C. Ruan, W. Shi, H. Jiang, Y. Sun, X. Zhang, Z. Sun, L. Dai, D. Ge, *Sens. Actuators, B: Chem.* 177 (2013) 826–832.
- [262] A.M. Vinu Mohan, K.K. Aswini, A. Maria Starvin, V.M. Biju, *Anal. Methods* 5 (2013) 1764–1770.
- [263] V.K. Gupta, N. Atar, M.L. Yola, M. Eryilmaz, H. Torul, U. Tamer, T.H. Boyaci, Z. Üstündağ, *J. Colloid Interf. Sci.* 406 (2013) 231–237.
- [264] Y. Zou, C. Xiang, L. Sun, F. Xu, *Electrochim. Acta* 53 (2008) 4089–4095.
- [265] C.J. Cai, M.W. Xu, S.J. Bao, C. Lei, D.Z. Jia, *RSC Adv.* 2 (2012) 8172–8178.
- [266] X. Chen, H. Ye, W. Wang, B. Qiu, Z. Lin, G. Chen, *Electroanalysis* 22 (2010) 2347–2352.
- [267] Y. Ge, Z. Chen, Q. Jin, H. Mao, J. Liu, J. Zhao, *Asian J. Chem.* 25 (2013) 5036–5038.
- [268] S.U. Lee, B.G. Choi, W.H. Hong, Simple fabrication of exfoliated graphene/ nafion hybrid as glucose bio-sensor electrodes, Ho Chi Minh City, 2013, pp. 54–56.
- [269] Y. He, Q. Sheng, J. Zheng, M. Wang, B. Liu, *Electrochim. Acta* 56 (2011) 2471–2476.
- [270] W. Sun, Y. Guo, Y. Lu, A. Hu, F. Shi, T. Li, Z. Sun, *Electrochim. Acta* 91 (2013) 130–136.
- [271] W. Sun, Y. Guo, X. Ju, Y. Zhang, X. Wang, Z. Sun, *Biosens. Bioelectron.* 42 (2013) 207–213.
- [272] W. Sun, Y. Zhang, X. Wang, X. Ju, D. Wang, J. Wu, Z. Sun, *Electroanalysis* 24 (2012) 1973–1979.
- [273] M. Li, S. Xu, M. Tang, L. Liu, F. Gao, Y. Wang, *Electrochim. Acta* 56 (2011) 1144–1149.
- [274] L. Qing, D. Xiaochen, L. Lain-Jong, H. Xiao, *Talanta* 82 (2010) 1344–1348.
- [275] C.-C. Kung, P.-Y. Lin, F.J. Buse, Y. Xue, X. Yu, L. Dai, C.-C. Liu, *Biosens. Bioelectron.* 52 (2014) 1–7.

- [276] L. Zheng, D. Ye, L. Xiong, J. Xu, K. Tao, Z. Zou, D. Huang, X. Kang, S. Yang, J. Xia, *Anal. Chim. Acta* 768 (2013) 69–75.
- [277] Y. Zhang, Y. Liu, J. He, P. Pang, Y. Gao, Q. Hu, *Electrochim. Acta* 90 (2013) 550–555.
- [278] J.M. You, D. Kim, S.K. Kim, M.S. Kim, H.S. Han, S. Jeon, *Sens. Actuators, B: Chem.* 178 (2013) 450–457.
- [279] D. Ye, H. Li, G. Liang, J. Luo, X. Zhang, S. Zhang, H. Chen, J. Kong, *Electrochim. Acta* 109 (2013) 195–200.
- [280] Y. Xin, X. Fu-Bing, L. Hong-Wei, W. Feng, C. Di-Zhao, W. Zhao-Yang, *Electrochim. Acta* 109 (2013) 750–755.
- [281] S. Nandini, S. Nalini, R. Manjunatha, S. Shanmugam, J.S. Melo, G.S. Suresh, *J. Electroanal. Chem.* 689 (2013) 233–242.
- [282] H. Chang, X. Wang, K.K. Shiu, Y. Zhu, J. Wang, Q. Li, B. Chen, H. Jjiang, *Biosens. Bioelectron.* 41 (2013) 789–794.
- [283] J. Bai, X. Jjiang, *Anal. Chem.* 85 (2013) 8095–8101.
- [284] Q. Lu, X. Dong, L.J. Li, X. Hu, *Talanta* 82 (2010) 1344–1348.
- [285] H. Xu, H. Dai, G. Chen, *Talanta* 81 (2010) 334–338.
- [286] L.M. Lu, X.L. Qiu, X.B. Zhang, G.L. Shen, W. Tan, R.Q. Yu, *Biosens. Bioelectron.* 45 (2013) 102–107.
- [287] L. Zhong, S. Gan, X. Fu, F. Li, D. Han, L. Guo, L. Niu, *Electrochim. Acta* 89 (2013) 222–228.
- [288] H. Song, Y. Ni, S. Kokot, *Anal. Chim. Acta* 788 (2013) 24–31.
- [289] R.S. Dey, C.R. Raj, *ACS Appl. Mater. Interf.* 5 (2013) 4791–4798.
- [290] R.S. Dey, C.R. Raj, *J. Phys. Chem. C* 114 (2010) 21427–21433.
- [291] T.Y. Huang, J.H. Huang, H.Y. Wei, K.C. Ho, C.W. Chu, *Biosens. Bioelectron.* 43 (2013) 173–179.
- [292] R. Li, C. Liu, M. Ma, Z. Wang, G. Zhan, B. Li, X. Wang, H. Fang, H. Zhang, C. Li, *Electrochim. Acta* 95 (2013) 71–79.
- [293] K. Deng, J. Zhou, X. Li, *Electrochim. Acta* 95 (2013) 18–23.
- [294] J. Ma, P. Cai, W. Qi, D. Kong, H. Wang, *Colloids Surf. A: Physicochem. Eng. Asp.* 426 (2013) 6–11.
- [295] A. Radoi, A.C. Obreja, S.A.V. Eremia, A. Bragaru, A. Dinescu, G.L. Radu, *J. Appl. Electrochem.* 43 (2013) 985–994.
- [296] C. Retna Raj, T. Ohsaka, *Electrochem. Commun.* 3 (2001) 633–638.
- [297] M. Musameh, J. Wang, A. Merkoci, Y. Lin, *Electrochem. Commun.* 4 (2002) 743–746.
- [298] C. Shan, H. Yang, D. Han, Q. Zhang, A. Ivaska, L. Niu, *Biosens. Bioelectron.* 25 (2010) 1504–1508.
- [299] Z. Li, Y. Huang, L. Chen, X. Qin, Z. Huang, Y. Zhou, Y. Meng, J. Li, S. Huang, Y. Liu, W. Wang, Q. Xie, S. Yao, *Sens. Actuators, B: Chem.* 181 (2013) 280–287.
- [300] L. Li, H. Lu, L. Deng, *Talanta* 113 (2013) 1–6.
- [301] L. Zhang, Y. Li, D.W. Li, D. Karpuzov, Y.T. Long, *Int. J. Electrochem. Sci.* 6 (2011) 819–829.
- [302] R. Manjunatha, G. Shivappa Suresh, J. Savio Melo, S.F. D'Souza, T. Venkatarangaiah Venkatesha, *Talanta* 99 (2012) 302–309.
- [303] N. Ruecha, R. Rangkupan, N. Rodthongkum, O. Chailapakul, *Biosens. Bioelectron.* 52 (2014) 13–19.
- [304] J. Wang, in: J. Wang (Ed.), *Analytical Electrochemistry*, Wiley-VCH, New York, 2000.
- [305] D. Du, Z. Zou, Y. Shin, J. Wang, H. Wu, M.H. Engelhard, J. Liu, L.A. Aksay, Y. Lin, *Anal. Chem.* 82 (2010) 2989–2995.
- [306] O. Akhavan, E. Ghaderi, A. Esfandiari, *J. Phys. Chem. B* 115 (2011) 6279–6288.
- [307] K.J. Huang, J. Li, Y.Y. Wu, Y.M. Liu, *Bioelectrochemistry* 90 (2012) 18–23.
- [308] N. Liu, Z. Ma, *Biosens. Bioelectron.* 51 (2014) 184–190.
- [309] H. Zhang, D. Song, S. Gao, J. Zhang, H. Zhang, Y. Sun, *Sens. Actuators B: Chem.* 188 (2013) 548–554.
- [310] J.H. Jung, D.S. Cheon, F. Liu, K.B. Lee, T.S. Seo, *Angew. Chem. – Int. Ed.* 49 (2010) 5708–5711.
- [311] B. Su, J. Tang, H. Yang, G. Chen, J. Huang, D. Tang, *Electroanalysis* 23 (2011) 832–841.
- [312] Q. Zhu, Y. Chai, R. Yuan, Y. Zhuo, J. Han, Y. Li, N. Liao, *Biosens. Bioelectron.* 43 (2013) 440–445.
- [313] Y. Tao, Y. Lin, J. Ren, X. Qu, *Biomaterials* 34 (2013) 4810–4817.
- [314] A. Singh, G. Sinsinbar, M. Choudhary, V. Kumar, R. Pasricha, H.N. Verma, S. P. Singh, K. Arora, *Sens. Actuators B: Chem.* 185 (2013) 675–684.
- [315] T.-Y. Chen, P.T.K. Loan, C.-L. Hsu, Y.-H. Lee, J. Tse-Wei Wang, K.-H. Wei, C.-T. Lin, L.-J. Li, *Biosens. Bioelectron.* 41 (2013) 103–109.
- [316] F.A.H. Karimi, M.T. Ahmadi, M. Rahmani, E. Akbari, M.J. Kiani, M. Khalid, *Sci. Adv. Mater.* 4 (2012) 1142–1147.
- [317] Y. Hu, S. Hua, F. Li, Y. Jjiang, X. Bai, D. Li, L. Niu, *Biosens. Bioelectron.* 26 (2011) 4355–4361.
- [318] V.K. Gupta, M.L. Yola, M.S. Qureshi, A.O. Solak, N. Atar, Z. Üstündağ, *Sens. Actuators, B: Chem.* 188 (2013) 1201–1211.
- [319] M. Fojta, E. Paleček, *Anal. Chem.* 73 (2001) 74A.
- [320] K.J. Huang, D.J. Niu, J.Y. Sun, C.H. Han, Z.W. Wu, Y.L. Li, X.Q. Xiong, *Colloids Surf. B: Biointerf.* 82 (2011) 543–549.
- [321] L. Zhu, L. Luo, Z. Wang, *Biosens. Bioelectron.* 35 (2012) 507–511.
- [322] B. Liu, Z. Sun, X. Zhang, J. Liu, *Anal. Chem.* 85 (2013) 7987–7993.
- [323] A.L. Liu, G.X. Zhong, J.Y. Chen, S.H. Weng, H.N. Huang, W. Chen, L.Q. Lin, Y. Lei, F.H. Fu, Z.L. Sun, X.H. Lin, J.H. Lin, S.Y. Yang, *Anal. Chim. Acta* 767 (2013) 50–58.
- [324] C.H. Lu, H.H. Yang, C.L. Zhu, X. Chen, G.N. Chen, *Angew. Chem. – Int. Ed.* 48 (2009) 4785–4787.
- [325] G. Lu, L.E. Ocola, J. Chen, *Appl. Phys. Lett.* 94 (2009) 08311.
- [326] G. Lu, L.E. Ocola, J. Chen, *Nanotechnology* 20 (2009) 445–502.
- [327] C.H. Lu, J. Li, J.J. Liu, H.H. Yang, X. Chen, G.N. Chen, *Chem. Eur. J.* 16 (2010) 4889–4894.
- [328] C.H. Lu, H.H. Yang, C.L. Zhu, X. Chen, G.H. Chen, *Angew. Chem.* 48 (2009) 4785–4787.
- [329] G. Lu, L.E. Ocola, J. Chen, *Nanotechnology* 20 (2009) 445502.
- [330] S. Niu, J. Sun, C. Nan, J. Lin, *Sens. Actuators, B: Chem.* 176 (2013) 58–63.
- [331] D. Du, S. Guo, L. Tang, Y. Ning, Q. Yao, G.J. Zhang, *Sens. Actuators, B: Chem.* 186 (2013) 563–570.
- [332] D. Li, H. Tong, X. Li, Z. An, W. Li, W. Liu, X. Zhang, Q. Wang, Application of graphene oxide to the construction of electrochemical biosensor for environmental monitoring, San Antonio, TX, 2013, pp. 25–32.
- [333] N. Liu, X. Chen, Z. Ma, *Biosens. Bioelectron.* 48 (2013) 33–38.
- [334] M. Liu, H. Zhao, S. Chen, H. Yu, X. Quan, *ACS Nano* 6 (2012) 3142–3151.
- [335] N.G. Shang, P. Papakonstantinou, M. McMullan, M. Chu, A. Stamboulis, A. Potenza, S.S. Dhesi, H. Marchetto, *Adv. Func. Mater.* 18 (2008) 3506–3514.
- [336] L. Tan, K.G. Zhou, Y.H. Zhang, H.X. Wang, X.D. Wang, Y.F. Guo, H.L. Zhang, *Electrochem. Commun.* 12 (2010) 557–560.
- [337] S. Hou, M.L. Kasner, S. Su, K. Patel, R. Cuellari, *J. Phys. Chem. C* 114 (2010) 14915–14921.
- [338] F. Li, J. Chai, H. Yang, D. Han, L. Niu, *Talanta* 81 (2010) 1063–1068.
- [339] F. Gao, X. Cai, X. Wang, C. Gao, S. Liu, F. Gao, Q. Wang, *Sens. Actuators, B: Chem.* 186 (2013) 380–387.
- [340] S. Pakapongpan, J.P. Mensing, T. Lomas, A. Tuantranont, Electrochemical sensor for ascorbic acid based on graphene/CuPc/PANI nanocomposites, Bangkok, 2012.
- [341] L. Lu, O. Zhang, J. Xu, Y. Wen, X. Duan, H. Yu, L. Wu, T. Nie, *Sens. Actuators, B: Chem.* 181 (2013) 567–574.
- [342] M. Mishra, S. Alwarappan, R.K. Joshi, T. Mohanty, *J. Nanosci. Nanotechnol.* 13 (2013) 4040–4044.
- [343] Y. Zeng, Y. Zhou, L. Kong, T. Zhou, G. Shi, *Biosens. Bioelectron.* 45 (2013) 25–33.
- [344] Y. Yu, Z. Chen, B. Zhang, X. Li, J. Pan, *Talanta* 112 (2013) 31–36.
- [345] S.-J. Li, J.-Z. He, M.-J. Zhang, R.-X. Zhang, X.-L. Lv, S.-H. Li, H. Pang, *Electrochim. Acta* 102 (2013) 58–65.
- [346] B. Kaur, T. Pandiyan, B. Satpati, R. Srivastava, *Colloids Surf. B: Biointerfaces* 111 (2013) 97–106.
- [347] Z.-H. Sheng, X.-Q. Zheng, J.-Y. Xu, W.-J. Bao, F.-B. Wang, X.-H. Xia, *Biosens. Bioelectron.* 34 (2012) 125–131.
- [348] Y. Wang, Y. Li, L. Tang, J. Lu, J. Li, *Electrochem. Commun.* 11 (2009) 889–892.
- [349] Y. Song, H. Liu, L. Wan, Y. Wang, H. Hou, L. Wang, *Electroanalysis* 25 (2013) 1400–1409.
- [350] H. Chen, G. Zhao, *J. Solid State Electrochem.* 16 (2012) 3289–3297.
- [351] J.-F. Wu, M.-Q. Xu, G.-C. Zhao, *Electrochem. Commun.* 12 (2010) 175–177.
- [352] C. Xiang, Y. Zou, L.X. Sun, F. Xu, *Electrochem. Commun.* 10 (2008) 38–41.
- [353] H. Hosseini, M. Mahyari, A. Bagheri, A. Shaabani, *Biosens. Bioelectron.* 52 (2014) 136–142.
- [354] X. Li, S. Zhu, B. Xu, K. Ma, J. Zhang, B. Yang, W. Tian, *Nanoscale* 5 (2013) 7776–7779.
- [355] L. Tang, Y. Wang, Y. Li, H. Feng, J. Lu, J. Li, *Adv. Funct. Mater.* 19 (2009) 2782–2789.
- [356] A. Dato, Z. Lee, K.J. Jeon, R. Erni, V. Radmilovic, T.J. Richardson, M. Frenklach, *Chem. Commun.* (2009) 6095.
- [357] W. Hong, H. Bai, Y. Xu, Z. Yao, Z. Gu, G. Shi, *J. Phys. Chem. C* 114 (2010) 1822–1826.



HS–GC–MS method for the analysis of fragrance allergens in complex cosmetic matrices



B. Desmedt^{a,b}, M. Canfyn^a, M. Pype^a, S. Baudewyns^a, V. Hanot^c, P. Courselle^a,
J.O. De Beer^b, V. Rogiers^b, K. De Paepe^{b,1}, E. Deconinck^{a,*,1}

^a Division of Food, Medicines and Consumer Safety, Section Medicinal Products, Scientific Institute of Public Health (IPH), Juliette Wytsmanstraat 14, 1050 Brussels, Belgium

^b Department of Toxicology, Dermato-Cosmetology and Pharmacognosy, Centre for Pharmaceutical Research (CePhar), Vrije Universiteit Brussel (VUB), Laarbeeklaan 103, 1090 Brussels, Belgium

^c Division of Food, Medicines and Consumer Safety, Section Pesticides, Scientific Institute of Public Health (IPH), Juliette Wytsmanstraat 14, 1050 Brussels, Belgium

ARTICLE INFO

Article history:

Received 26 May 2014

Received in revised form

29 July 2014

Accepted 1 August 2014

Available online 11 August 2014

Keywords:

Headspace

Perfume

GC–MS

Illegal cosmetics

Method validation

Full evaporation

ABSTRACT

Potential allergenic fragrances are part of the Cosmetic Regulation with labelling and concentration restrictions. This means that they have to be declared on the ingredients list, when their concentration exceeds the labelling limit of 10 ppm or 100 ppm for leave-on or rinse-off cosmetics, respectively. Labelling is important regarding consumer safety. In this way, sensitised people towards fragrances might select their products based on the ingredients list to prevent elicitation of an allergic reaction. It is therefore important to quantify potential allergenic ingredients in cosmetic products.

An easy to perform liquid extraction was developed, combined with a new headspace GC–MS method. The latter was capable of analysing 24 volatile allergenic fragrances in complex cosmetic formulations, such as hydrophilic (O/W) and lipophilic (W/O) creams, lotions and gels. This method was successfully validated using the total error approach. The trueness deviations for all components were smaller than 8%, and the expectation tolerance limits did not exceed the acceptance limits of $\pm 20\%$ at the labelling limit.

The current methodology was used to analyse 18 cosmetic samples that were already identified as being illegal on the EU market for containing forbidden skin whitening substances. Our results showed that these cosmetic products also contained undeclared fragrances above the limit value for labelling, which imposes an additional health risk for the consumer.

© 2014 Elsevier B.V. All rights reserved.

1. Introduction

Many people use cosmetic products. This can be done for various reasons, including cleaning, perfuming, protecting, keeping in good condition and correcting body odours. Regarding consumer safety, article 3 of the Cosmetic Regulation states that “A cosmetic product made available on the market shall be safe for human health when used under normal or reasonably foreseeable conditions of use, taking account, in particular, of the following: (i) presentation including conformity with Directive 87/357/EEC; (ii) labelling; (iii) instructions for use and disposal; and (iv) any

other indication or information provided by the responsible person defined in Article 4”[1].

To ensure that cosmetic products are safe, guidance for the safety of ingredients for which concern exists (e.g. annex substances) for human health are provided by the Scientific Committee on Consumer Safety (SCCS). For Fragrance ingredients, the International Fragrance Association (IFRA) provides a risk management system for their safe use through the so-called IFRA standards, which are part of the IFRA code of practice. Safe use is ensured by prohibiting or restricting the usage of selected fragrance materials [2]. In general, fragrances can be seen as a commercial aid for selling products, or mask unpleasant odours from raw materials used in cosmetics [3].

Twenty-six often used fragrance ingredients, are a well-recognised cause of sensitisation and consequent allergic response reactions. Indeed, when in contact with the skin in sufficient amounts, these low molecular weight substances can cause a type

* Corresponding author. Tel.: +32 2 642 51 36; fax: +32 2 642 53 27.

E-mail address: Eric.Deconinck@wiv-isp.be (E. Deconinck).

¹ Equally contributing project leaders.

IV immunologic reaction, i.e. allergic contact dermatitis (ACD) in already sensitised persons [3]. This is why they are enlisted in the Cosmetic Regulation on a negative ingredient list (Annex III), with labelling and concentration restrictions [1]. The regulation allows that fragrances, perfumes and their raw materials are referred in the ingredients list as “parfum” or “flavor”, except when their thresholds, as mentioned in annex III, are exceeded. At that point, fragrance ingredients have to be mentioned individually with their INCI name (International Nomenclature of Cosmetic Ingredients) in the ingredients list. Until today, these thresholds are set at 0.01% (100 ppm) and 0.001% (10 ppm) for rinse-off and leave-on cosmetics, respectively.

Labelling is important with respect to consumer's safety. In this way, patients who know the cause of their allergy towards fragrances are able to avoid cosmetics that could cause allergic reactions. In addition, if a person develops an allergy, it allows medical doctors to diagnose more easily allergies to fragrance ingredients. Together with appropriate diagnostic techniques, adequate labelling is the cornerstone of fragrance allergy prevention [3].

To control for possible infringements on the Code of Practice or the Cosmetic Regulation, a GC–MS method, well documented by IFRA, can be used [4–6]. This method is developed to only analyse fine fragrances, which are analysed directly after dilution. This methodology, however, cannot be applied for complex matrices such as creams and lotions, because these formulas contain non-volatile components, which will result in contamination problems [7].

There is a rising interest to analyse allergenic fragrance ingredients in more complex matrices, because these are equally important as a source of ACD as shown by Heisterberg et al. [8]. One way to overcome the interference provoked by the matrix, is a separation based on molecular weight. This was done by Niederer et al. [9] who developed a method to quantify 24 allergenic fragrance ingredients in cosmetic samples by size exclusion chromatography combined with GC–MS. Lamas et al. [10] applied a solid-phase dispersion-pressurized liquid extraction, and Sanchez-Prado et al. [11] used matrix solid phase dispersion for the sample clean-up. A method developed by Devos et al. [12] used dynamic full evaporation 2D-GC–MS and David et al. made use of a Programmed Temperature Vaporisation (PTV) injection with an automated liner exchange [13]. The majority of these methods are based upon extensive and/or expensive extraction and clean-up procedures. Therefore, a newly developed head-space GC–MS method is described here, capable of analysing 24 allergenic fragrances in complex cosmetic formulations such as, water/oil and oil/water creams, lotions and gels. In accordance with literature, the remaining two fragrances (tree- and oak-moss) were not analysed by GC–MS because they are not volatile [4,7].

To the best of our knowledge, a simple liquid extraction was applied for the first time to analyse suspected allergenic fragrances in different complex cosmetic matrices by HS–GC–MS. After validation of this methodology, 18 cosmetic products of different formulation types, including creams, lotions and gels were analysed for the presence of undeclared allergenic fragrance ingredients. These cosmetic products were already classified as being illegal. Indeed, they contained in the EU banned skin whitening ingredients, as previously described by our research group [14,15].

2. Materials and method

2.1. Standards and reagents

The reference standards **amyl cinnamal** (batch MKBF7610V, purity $\geq 97\%$), **cinnamal** (batch MKBJ0027V, purity $\geq 93\%$), **citral**

(batch STBC5273V, purity $\geq 95\%$), **hydroxycitronellal** (batch BCBH2848V, purity $\geq 95\%$), **α -hexylcinnamaldehyde** (batch BCBH2848V, purity $\geq 95\%$), **lyral** (batch 211061327-01, purity $\geq 99\%$), **benzyl alcohol** (batch SHBB3628V, purity $\geq 99\%$), **eugenol** (batch BCBG6867V, purity $\geq 99\%$), **anisyl alcohol** (batch STBC0995V, purity $\geq 98\%$), **benzyl benzoate** (batch MKBG9990V, purity $\geq 99\%$), **benzyl cinnamate** (batch MKBK4160V, purity $\geq 99\%$), **benzyl salicylate** (batch 1413141V, purity $\geq 99\%$), **coumarin** (batch SLBB9006V, purity $\geq 99\%$), **limonene** (batch MKBH774V, purity $\geq 99\%$), **α -isomethyl ionone** (batch 1381297V, $\geq 99\%$), and **methyl 2-octynoate** (batch MKBJ9021V, purity $\geq 99\%$), were purchased from Sigma-Aldrich (St. Louis, USA). **Lilial** (batch YZE31-CQ, $\geq 95\%$) was bought from TCI (Tokyo, Japan) and **amyl cinnamyl alcohol** (batch 210051082-01, purity $\geq 99\%$) from Accustandard (new haven, USA). **Cinnamyl alcohol** (batch 10171038, purity $\geq 98\%$), **citronellol** (batch 10145005, purity $\geq 95\%$), **geraniol** (batch 10164702, purity $\geq 97\%$), **isoeugenol** (batch 10166245, purity $\geq 98\%$), **linalool** (batch 10158737, purity $\geq 97\%$), and **1-fluoronaphthalene** (batch 10113574, purity $\geq 98\%$), were obtained from Alfa Aesar, (Karlsruhe, Germany). **Farnesol** (batch S27103232, purity $\geq 97\%$), **methyl decanoate** (batch C24VV137337, purity $\geq 99.5\%$), **methyl laurate** (batch 620K102493, purity $\geq 99.5\%$), and **methyl pentadecanoate** (batch VV253941, purity $\geq 99.5\%$) were purchased from merck KGaA (Darmstadt, Germany).

The extraction solvent n-hexane was bought from Biosolve (purity $\geq 99\%$, Valkenswaard, the Netherlands). Blank cosmetic formulations, used during method development and validation, were purchased from Fagron (Waregem, Belgium).

2.2. Illegal cosmetic samples

The samples, analysed for their content on illegal skin bleaching agents, were taken by inspectors affiliated with the Belgian federal public service “Animal, Plant and Food Directorate-General” (DG4) and the Belgium Federal Agency for Medicinal and Health Products (FAMHP) and were also used here for this study.

2.3. Standard solutions and validation formulations

Standard fragrance ingredients were divided into three groups based upon their chemical structure. Stock solutions of 10 mg/ml were prepared in hexane in order to ensure the stability of the 24 fragrance ingredients [16]. Out of these, fragrance mix solutions of 10, 20, 30 and 100 $\mu\text{g/ml}$ in hexane were made. To further improve stability and to limit solvent evaporation, All solutions were prepared in amber glass and stored at $-20\text{ }^{\circ}\text{C}$ [4,10].

In addition a mix of four internal standards, consisting of 100 $\mu\text{g/ml}$ of 1-fluoronaphthalene, methyl decanoate, methyl laurate and methyl pentadecanoate, was prepared in hexane.

As, the purpose was to analyse allergenic fragrance ingredients in complex cosmetic matrices, different cosmetic formulations were used to develop and validate the method. Cosmetic formulations and corresponding ingredients are given in Table 1. For preparing the validation samples, 0.5 g of a blank cosmetic formulation was spiked with an aliquot of the fragrance mix solution in a glass vial of 20 ml. To obtain formulations containing 8, 10 or 15 ppm of the fragrance ingredients, 40, 50 or 75 μl of the 100 $\mu\text{g/ml}$ fragrance mix solution was added, respectively. In line with the cosmetic validation protocol, a lag time of 10 min was respected before the start of the extraction procedure, in order to complete incorporation of the fragrances into the matrix [17].

Table 1
Cosmetic formulations used during method development and validation.

#	Cosmetic formulation	Ingredients	% (m/m)
1	Cream (hydrophilic) O/W	Cetostearyl alcohol	15.0
		Glycerol	5.0
		Sodium lauryl sulphate	1.5
		Water	78.5
2	Cream (hydrophilic) O/W	Cetostearyl alcohol	7.2
		Cetomacrogol 1000	1.8
		White petrolatum	15.0
		Liquid paraffin	6.0
		Water	70.0
3	Cream (lipophilic) W/O	White petrolatum	54.0
		Sorbitan sesquioleate	6.0
		Sorbic acid	0.15
		Water	39.85
4	Lotion	Cetostearyl alcohol	2.5
		Glycerol	2.5
		Sodium lauryl sulphate	0.5
		Water	94.5
5	Gel	Propylene glycol	10.0
		Carbopol 980	1.0
		Trometamol	1.0
		Edetate disodium	0.1
		Water	87.9

2.4. Extraction procedure

For each sample extraction, 0.5 g of the cosmetic formulation was weighted in a glass vial of 20 ml and covered with a Teflon seal. To these, 50 μ l of the internal standard mix, 0.5 g of NaCl, and 10 ml hexane were added. During the first extraction step, vials were vortexed for 10 s and then sonicated for 3 min at 50 °C. Afterwards, vials were transferred to a cooling bath of –78 °C (dry ice dissolved in acetone) for 2 min, followed by centrifugation of 1 min at 860 g. Three quarters of the supernatants was transferred in a glass vial. These extraction steps were repeated after adding 5 ml of hexane.

After extraction, four times 1 ml of the combined supernatants was transferred in a glass vial of 3 ml and to obtain a standard addition curve 100 μ l of 0, 10, 20 and 30 μ g/ml of fragrance mix was added, respectively. After mixing for 5 s, 300 μ l of each solution was transferred to a headspace vial of 10 ml.

2.5. GC–MS conditions

Samples were injected on a GC–MS system using a G188A headspace sampler (Agilent Technologies, Palo Alto, USA). The GC–MS analyses were performed on an Agilent 6890 N gas chromatograph coupled to an Agilent 5973N single quad mass selective detector. After incubation of the sample at 135 °C for 10 min, during which it was shaken, 1 ml of the vapour phase was injected into the GC/MS system in split injection mode (split ration 6.8:1). Temperatures of the headspace loop, the transfer line, and the EPC volatiles interface, were 145, 155 and 160 °C, respectively. A VF-5 ms column (Factor four, Agilent, California, VS) of 40 m (\varnothing 0.25 mm and film thickness of 0.25 μ m) with 10 m inactive phase was used. Helium was delivered as carrier gas at a constant pressure of 14.65 psi with an initial flow of 1.3 ml/min.

The temperature gradient started at 50 °C (held for 1 min) and raised with 7 °C/min to reach 162 °C. The temperature gradient continued at 30 °C/min, until 320 °C, which was held for 1 min. The total run time was 23.27 min. Temperatures of the injection

port, the ion source, the quadrupole, and the interface, were set at 160, 230, 150 and 280 °C, respectively. For the identification of the fragrance ingredients, present in the samples, the mass spectrometer was operated in full scan mode. For quantification and validation, the mass spectrometer was operated in selective ion monitoring (SIM) mode (100 ms dwell times). Table 2 presents the specific m/z ratios, the retention times, and the group start times, for each fragrance ingredient and internal standard monitored. For quantification, the first ion was used. The fragrances farnesol, lylal and citral were each detected as 2 separate single peaks.

2.6. Method validation

Method validation was according to ISO-17025, applying accuracy profiles, which are based upon the total error approach [18]. This estimates the total error by combining the systemic error and the random error, to know the difference between the observed result and the true value. Based upon the concentrations that were needed to be able to perform the analyses, and the difficulties experienced with the different matrices, the acceptance limits were set at $\pm 20\%$ and β -per cent at 90%. In practice, the anionic hydrophilic cream (formulation 1) was used to validate the method. The validation samples were analysed in triplicate for four consecutive days, and the corresponding concentrations, corrected for the recovery, were back-calculated using standard addition calibration curves. To ensure that this method was capable of analysing different types of cosmetics, a recovery study for four additional formulations was performed.

Table 2

Specific m/z ratios and retention times for fragrance ingredients and internal standards.

#	Standard	Specific m/z ratios	Group start times (min)	Retention times (min)
1	Limonene	68.10, 93.1	7.50	9.27
2	Benzyl alcohol	79.10, 108.10	7.50	9.38
3	Linalool	71.10, 93.10	10.00	10.75
4	1-Fluoronaphthalene	146.00	12.00	12.88
5	Methyl 2-octynoate	95.10, 123.10	12.00	12.96
6	Citronellol	69.10, 156.10	13.20	13.53
7	Citral 1	94.10, 109.00	13.70	13.87
8	Geraniol	93.10, 123.10	13.94	14.06
9	Citral 2	69.10, 84.10	14.26	14.49
10	Cinnamal	131.10, 132.00	14.60	14.74
11	Anisyl alcohol	138.10, 109.10	14.60	14.86
12	Hydroxycitronellal	59.10, 43.10	14.60	14.89
13	Cinnamyl alcohol	134.10, 115.10	15.20	15.40
14	Methyl decanoate	74.00	15.20	15.55
15	Eugenol	164.10, 149.10	16.00	16.32
16	Coumarin	118.00, 146.00	17.00	18.00
17	Isoeugenol	164.10	17.00	18.01
18	α -Isomethyl ionone	135.10, 150.10	18.19	18.33
19	Methyl laurate	74.00	18.50	18.79
20	Lilial	189.10, 204.20	18.50	18.95
21	Amyl cinnamal	115.10, 202.10	19.50	20.03
22	Lylal 1	91.10, 104.10	19.50	20.11
23	Lylal 2	136.10, 192.20	19.50	20.20
24	Amyl cinnamyl alcohol	115.00	20.25	20.31
25	Farnesol 1	81.10, 137.00	20.25	20.31
26	Farnesol 2	81.10, 137.00	20.25	20.48
27	Hexyl cinnamal	216.20	20.60	20.74
28	Benzyl benzoate	105.00, 212.10	20.82	20.94
29	Methyl pentadecanoate	74.00	20.82	21.10
30	Benzyl salicylate	91.10	21.30	21.55
31	Benzyl cinnamate	91.10, 192.10	22.00	22.59

The fragrances numbered as 1–13, 15–18, 20–28 and 30–31, (Table 2), were corrected for quantification with the internal standard 1-fluoronaphthalene, methyl decanoate, methyl laurate and methyl pentadecanoate, respectively.

3. Results and discussion

3.1. Method development and optimisation

IFRA has published a guidance document to analyse allergenic fragrance ingredients present in perfumes and fine fragrances [5]. These formulations do not require sample treatment and can be injected after dilution with an appropriate solvent. This IFRA document together with a published method by Agilent were used as a starting point to develop the GC–MS conditions [5,19].

Different extraction procedures to isolate the fragrance ingredients from their matrix were tested including distillation, vacuum distillation, vacuum transfer and liquid extraction. Liquid extraction was tested using several solvents, such as ethyl acetate, methyl-tert-butyl ether, butanol, ethanol, dichloromethane and hexane. The latter gave the best overall recovery.

A problem encountered with hexane extraction, was that the extraction yield of alcoholic fragrance ingredients was below 60%. This was resolved by repeating the extraction process. Due to this, additional matrix components were co-extracted and this resulted in a lower sensitivity for the fragrances with a high boiling point such as benzyl salicylate (320 °C). Therefore, it was tried to perform a clean-up step using a freeze-out. Different temperatures (–20, –40 and –80 °C) and durations (1 and 4 h), were tested. These results led to the conclusion that a cooler solution contained less matrix components and a duration of 1 h was sufficient. To shorten this clean-up, a flash cooling technique was tested with a cooling bath at –78 °C of dry ice dissolved in acetone. Using this bath for 2 min eliminates the greasy components of the formulations without resulting in lower recoveries.

When the method was used for pure standards dissolved in hexane, it was shown that the repeatability deteriorated after several injections. This so-called memory effect has also been described by IFRA and they suggested to cut the column, change the liner and clean the MS source and injector after 40 injections, or when the R^2 of the calibration lines dropped below 0.995 [5,6]. The problem observed could also be attributed to the low volatile matrix components present in several formulations [5–7,10,11,20]. To overcome this issue, headspace was considered, which improved the life span of the column and reduced the total number of cuts. Additionally, it was also decided to use a deactivated pre-column to be sure that the column build-up did not affect the analytical column. This made it possible to cut a piece of the pre-column without changes occurred at the level of the integration and SIM windows.

The incubation temperature of the headspace vial and the volume added to the vial were individually assessed. Different incubation temperatures between 80 and 145 °C were tested. All chromatograms were visually inspected. It was found that a temperature of 135 °C was necessary to transfer the fragrances with a high boiling point from the headspace vial onto the column. Further, volumes between 50 and 400 μ l were tested and it could be shown that a volume of 300 μ l did not introduce any change in injection repeatability or deviation of the vial septum. This headspace technique has been applied before and is known as full evaporation static headspace [21].

The method used to analyse complex formulations, requires to cut the column less frequently. Up to 250 injections have been performed without the need to cut a piece of the column, although this depended on the type of formulation extracted. To decide

when the column had to be cut, a fragrance mix of 10 ppm was regularly injected and the overall performance of the HS–GC–MS system was looked at (repeatability, peak intensity and peak shape).

Quantification problems were observed when calibration lines were prepared in hexane. To verify whether this was due to a matrix effect, full standard addition was also performed. When the calibration lines obtained with both techniques were compared, it was clearly observed that the slopes of both calibration lines were significantly different (P -value < 0.05; data not shown). This means that there was a clear proportional matrix effect. As proposed by several authors, analysing complex matrices, and by the cosmetic validation ISO-norm, standard addition was used for further quantitation [7,17,22]. A well-known drawback of conventional standard addition is the increased workload. Therefore, standard addition after the sample extraction was tested. This is described in Section 2.4. The latter did not correct for recovery-related problems, but because the sample only needed to be extracted once, the amount of matrix used for each standard addition curve was always the same. With this technique, the matrix-related quantification problems were resolved, and sufficient recoveries of at least 80% were found for all fragrance ingredients. Another drawback of conventional standard addition is the use of an extrapolation. Consequently, the results could be heavily influenced by even a minor drift of the calibration points. To avoid this, interpolation was used to minimise the bias in the prediction and variance associated with the result, as described by Andrade et al. [23].

3.2. Method validation

Validation samples of formulation 1, (Table 1), containing 8, 10 and 15 ppm of the fragrance mix, were made in triplicate and analysed for four consecutive days. This method was developed in such a way that a high degree of certainty was given at the labelling limit of 10 ppm. The validation was limited to the range of 8–15 ppm because quantification above the labelling limit is from a legal point of view not necessary.

3.2.1. Selectivity and specificity

Selectivity and specificity were ensured by monitoring specific ions of the fragrance ingredients in SIM mode. A chromatogram, obtained in SIM mode for the validation matrix of formulation 1 at 10 ppm, is shown in Fig. 1A. Co-elution, seen in the chromatogram for some compounds, could be separated in individual peaks using their extracted ion.

3.2.2. Linearity of the standard addition curves

To evaluate the relationship between the area under the curve and the concentration, standard addition curves, obtained from three samples containing 10 ppm, were evaluated. This was done by R^2 values and quality coefficients [24]. Results are summarised in Table 3. It could be concluded that the standard addition curves were linear for all allergenic fragrance ingredients.

3.2.3. Linearity trueness, precision, accuracy and uncertainty assessment

Method validation was according to ISO-17025, by applying accuracy profiles. The theoretical background and a more in-detail application of these accuracy profiles, have been well described [14,25–27]. Concentrations of the validation samples were calculated with the standard addition curves and corrected for the recovery to determine the linearity of the results, the trueness, the precision (repeatability and intermediate precision) and accuracy. The results are given in Table 4 and Fig. 2.

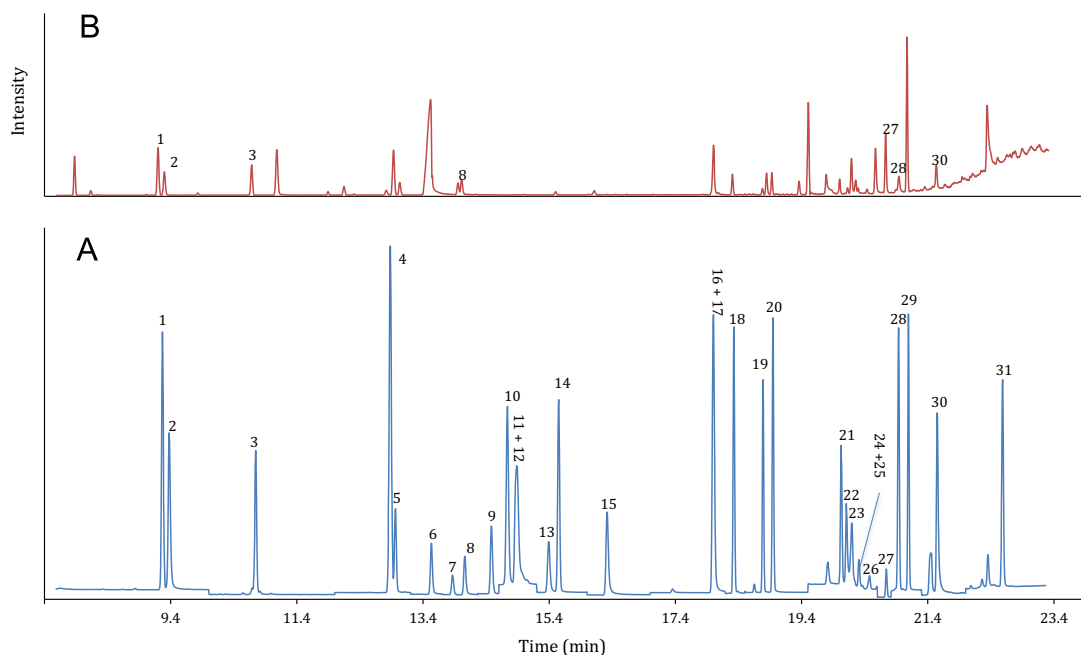


Fig. 1. (A) Chromatogram of formulation 1 containing all investigated allergenic fragrance ingredients at 10 ppm. The chromatogram was recorded in SIM mode. (B) Chromatogram recorded in full scan mode of a cosmetic sample containing seven fragrance ingredients above labelling limit.

Table 3
 R^2 and QC values from the standard addition curves.

Standard	QC (%)	R^2
Limonene	0.59	0.9999
Benzyl alcohol	1.21	0.9998
Linalool	1.14	0.9998
Methyl 2-octynoate	0.53	1.0000
Citronellol	0.86	0.9999
Citral 1	0.64	1.0000
Geraniol	1.50	0.9997
Citral 2	0.74	0.9999
Cinnamal	0.93	0.9999
Anisyl alcohol	0.60	0.9999
Hydroxycitronellal	1.42	0.9998
Cinnamyl alcohol	1.05	0.9999
Eugenol	1.98	0.9996
Coumarin	0.64	0.9999
Isoeugenol	1.72	0.9997
α -Isomethyl ionone	1.23	0.9998
Lilial	0.66	0.9999
Amyl cinnamal	2.23	0.9993
Lylal 1	4.53	0.9976
Lylal 2	4.94	0.9963
Amyl cinnamyl alcohol	4.65	0.9973
Farnesol 1	4.38	0.9975
Farnesol 2	3.38	0.9985
Hexyl cinnamal	4.17	0.9978
Benzyl benzoate	2.68	0.9985
Benzyl salicylate	2.62	0.9993
Benzyl cinnamate	3.94	0.9983

The linearity of the result is the ability of an analytical procedure to provide a linear relationship between the measured and theoretical concentration. These were acceptable with R^2 -values from 0.999 to 1.000 (data not shown).

According to ISO, **the trueness** of an analytical procedure expresses the closeness of agreement between the average value obtained from repeated measurements and a conventional true value. This is a measure for the systemic errors of the method, and is expressed in terms of relative bias. The results from Table 4

show that the relative bias for all fragrance ingredients was acceptable, since the highest value was 8% for farnesol 1.

Also according to ISO, **the precision** of an analytical method expresses the closeness of agreement between the values obtained from repeated measurements. This is expressed as relative standard deviations from repeatability and intermediate precisions. Out of Table 4, the highest relative standard deviation (RSD) was seen for α -isomethyl ionone with a repeatability and intermediate precision of 13.7%, which was considered acceptable.

Accuracy takes the total error of the results in account, and is represented by the β -expectation tolerance limits. Based upon the concentrations needed to analyse, and the difficulties experienced with the matrices the acceptance limits were set at $\pm 20\%$.

As shown in Table 4 and Fig. 2 the expectation tolerance intervals did not exceed the acceptance limits, except for α -isomethyl ionone, lylal 2, farnesol 1 and benzyl cinnamate only at the lowest concentration. This was not seen as a problem, since the labelling limit is 10 ppm. This means that future measurements of unknown samples will be included in the tolerance limits.

The measurement uncertainty is a parameter associated with the result of a measurement and characterises the dispersion of the values that could reasonably be attributed to the analyte. The expanded uncertainty represents an interval around the results where the unknown true value can be observed with a confidence level of 90%. The relative expanded uncertainties are obtained by dividing the corresponding expanded uncertainties by the corresponding concentration. These results are shown in Table 4.

3.3. Recovery

Validation has been based upon a simple anionic hydrophilic cream as this is the most common cosmetic formulation. Recoveries for an additional non-ionic hydrophilic cream, a lipophilic cream, gel and lotion were also investigated. Those four formulations were analysed in triple at a concentration of 10 ppm and the results are shown in Table 5. The obtained recoveries were all between 80% and 120%, which was considered sufficient for this

Table 4

Trueness, precision, accuracy and uncertainty of the chromatographic method for all investigated fragrance ingredients (RSD: relative standard deviation).

Compounds	Trueness			Precision						Accuracy			Uncertainty		
	Relative bias (%)			Repeatability (RSD %)			Intermediate precision (RSD%)			β -Expectation limit (%)			Relative expanded uncertainty (%)		
	8	10	15	8	10	15	8	10	15	8	10	15	8	10	15
Limonene	-2.30	0.74	1.56	3.34	2.37	2.02	6.97	5.27	5.93	[-14.02; 9.41]	[-8.18; 9.67]	[-8.86; 11.98]	15.35	11.62	13.16
Benzyl alcohol	-0.29	0.66	-0.637	7.38	3.77	3.63	7.75	6.68	7.80	[-11.42; 10.83]	[-10.23; 11.56]	[-13.53; 12.79]	16.24	14.61	17.20
Linalool	-2.04	2.26	-0.07	2.88	2.12	1.76	10.04	4.08	5.24	[-19.92; 15.83]	[-4.51; 9.03]	[-9.29; 9.14]	22.33	8.96	11.62
Methyl 2-octynoate	-0.51	0.29	0.22	4.04	1.03	1.77	6.12	6.03	6.09	[-10.17; 9.15]	[-10.65; 11.24]	[-10.62; 11.05]	13.28	13.47	13.55
Citronellol	1.75	-0.83	-0.92	1.93	1.81	1.97	6.19	3.98	4.63	[-9.22; 12.71]	[-7.56; 5.90]	[-8.83; 7.00]	13.76	8.77	10.22
Citral 1	-0.45	0.61	-0.17	10.14	3.92	2.62	12.75	10.21	8.12	[-19.63; 18.74]	[-17.09; 18.32]	[-14.50; 14.16]	27.29	22.60	18.03
Geraniol	0.55	-1.10	0.55	10.86	7.23	4.40	12.07	8.94	10.31	[-17.04; 18.14]	[-14.48; 12.28]	[-17.07; 18.17]	25.50	19.09	22.76
Citral 2	0.37	0.54	-0.91	5.92	2.07	1.85	5.92	3.75	4.47	[-8.04; 8.78]	[-5.61; 6.69]	[-8.58; 6.76]	12.32	8.21	9.87
Cinnamal	-2.03	0.62	1.41	6.46	2.04	1.89	6.46	5.64	5.76	[-11.21; 7.15]	[-9.23; 10.47]	[-8.74; 11.56]	13.45	12.50	12.78
Anisyl alcohol	2.88	-0.49	-2.39	4.56	3.94	3.62	8.98	4.86	8.77	[-12.07; 17.83]	[-7.75; 6.78]	[-17.46; 12.69]	19.73	10.37	19.39
Hydroxycitronellal	-3.98	0.96	3.02	7.26	2.27	4.06	7.41	6.72	8.87	[-14.56; 6.61]	[-10.86; 12.78]	[-11.96; 17.99]	15.48	14.92	19.55
Cinnamyl alcohol	3.84	-1.71	-2.13	4.68	2.10	2.48	9.76	4.65	5.11	[-12.56; 20.24]	[-9.58; 6.16]	[-10.70; 6.44]	21.50	10.25	11.25
Eugenol	3.07	0.24	-3.45	7.42	8.36	3.79	11.05	9.54	6.67	[-14.28; 20.42]	[-13.74; 14.23]	[-14.32; 7.43]	23.95	20.20	14.59
Coumarin	-0.87	-0.42	1.29	12.45	5.36	3.10	12.45	9.13	3.83	[-18.56; 16.83]	[-15.20; 14.36]	[-4.45; 7.03]	25.92	19.95	8.19
Isoeugenol	0.13	-0.17	0.04	9.58	4.17	3.11	12.09	7.69	6.77	[-18.08; 18.34]	[-12.84; 12.50]	[-11.39; 11.47]	25.89	16.86	14.93
α -Isomethyl ionone	-3.23	0.96	2.28	13.67	7.73	2.55	13.67	9.49	2.96	[-22.65; 16.19]	[-13.23; 15.15]	[-2.08; 6.63]	28.45	20.27	6.28
Lilial	0.93	-0.51	-0.42	5.04	2.39	2.45	5.13	3.39	4.09	[-6.38; 8.24]	[-5.77; 4.75]	[-7.01; 6.17]	10.70	7.32	8.93
Amyl cinnamal	-0.66	-0.34	1.00	6.75	5.85	4.31	6.75	5.85	5.67	[-10.26; 8.94]	[-8.66; 7.98]	[-7.63; 9.63]	14.06	12.18	12.18
Lylal 1	2.29	-1.20	-1.10	10.77	11.27	5.75	10.77	11.36	5.77	[-13.01; 17.60]	[-17.36; 14.97]	[-9.30; 7.10]	22.42	23.68	12.01
Lylal 2	4.85	-4.26	-0.59	10.99	9.12	5.62	12.17	9.12	10.15	[-12.86; 22.55]	[-17.21; 8.70]	[-17.22; 16.05]	25.68	18.98	22.22
Amyl cinnamyl alcohol	2.80	-0.03	-2.38	10.47	10.51	6.93	10.47	10.51	6.93	[-12.08; 17.67]	[-14.97; 14.90]	[-12.23; 7.47]	21.80	21.88	14.43
Farnesol 1	8.10	-3.75	-1.14	10.00	9.63	7.08	12.81	10.17	7.08	[-11.27; 27.47]	[-18.38; 10.88]	[-11.20; 8.93]	27.46	21.34	14.74
Farnesol 2	2.66	-6.93	1.51	8.12	7.11	6.59	10.34	8.48	10.13	[-12.95; 18.27]	[-19.52; 5.66]	[-14.52; 17.54]	22.15	18.06	22.00
Hexyl cinnamal	2.10	-2.43	0.33	10.42	8.25	5.25	10.42	8.25	5.66	[-12.71; 16.90]	[-14.15; 9.29]	[-7.85; 8.52]	21.69	17.17	11.92
Benzyl benzoate	1.36	-1.80	0.45	8.87	7.32	3.73	8.87	7.93	4.26	[-11.25; 13.96]	[-13.29; 9.68]	[-5.80; 6.69]	18.47	16.71	9.02
Benzyl salicylate	0.46	1.50	-1.96	7.87	4.55	11.29	10.36	8.81	11.29	[-15.31; 16.23]	[-13.14; 16.13]	[-17.99; 14.08]	22.26	19.35	23.50
Benzyl cinnamate	3.19	-2.11	-1.33	11.82	11.81	10.05	12.35	12.06	10.05	[-14.53; 20.92]	[-19.31; 15.10]	[-15.62; 12.95]	25.88	25.17	20.93

type of concentrations and matrices [7,9–12,28–30]. For the lipophilic cream and lotion the recoveries of citral 1 and farnesol 2 were lower than 80%. For the gel formulation the detection of citral 1 and lylal 1 was no possible due to co-eluting matrix components that were not separated in SIM mode. Because they all showed a second peak that could be used for quantification, this was not considered as a limitation.

3.4. Cosmetic samples

After validation, the method was used to analyse 18 skin whitening cosmetics. These cosmetic products were already analysed before and categorised as illegal because they all contained an illegal whitening agent [15].

The samples to be analysed consisted of 9 creams, 7 lotions and 2 gels. Because of the complex nature of the cosmetics involved, samples are first analysed in full scan mode to ensure interfering matrix components are not identified as the targeted fragrances [6,10,31,32]. Afterwards quantification was done using SIM mode as described in this paper. A library spectral match quality of 85% was considered as a positive identification of the fragrance ingredients. Although, in none of these samples chromatographic resolution problems were seen, it could be a potential problem as described by Debonneville et al. [33]. A chromatogram obtained in full scan, from a sample positive for limonene, benzyl alcohol, linalool, geraniol, hexyl cinnamal, benzyl benzoate and benzyl salicylate is shown in Fig. 1B.

The analyses revealed that all 18 samples contained at least one allergenic fragrance ingredient that exceeded the labelling limit, while none of these samples declared these on their package. In total, more than 16 samples contained at least one fragrance ingredient that exceeded the labelling limit by a 10-fold.

The most often found fragrance ingredients above the labelling limit, were linalool, limonene and benzyl alcohol, which could be

detected in 17, 16 and 13 samples, respectively. The fragrances methyl 2-octynoate, citral, cinnamal, anisylalcohol, cinnamyl alcohol, isoeugenol, lylal, amyl cinnamyl alcohol, farnesol, benzyl cinnamate, could not be detected in the samples, the results obtained are very comparable to data previously published [7,10,11].

This means that the investigated cosmetic samples did not only contain illegal substances for skin lightening, but also allergenic fragrance ingredients that were not labelled. This could be an additional health risk for consumers using this type of cosmetic products.

Three legal samples purchased in a local supermarket were also analysed. All the fragrances declared on the ingredient list were found at a concentration higher than 10 ppm and allergenic fragrances that were detected but not declared had always a concentration lower than 10 ppm meaning that these samples always complied with the Cosmetic Regulation.

4. Conclusion

The current Cosmetic Regulation 1223/2009/EC contains a list of 26 allergenic fragrance ingredients that need to be individually labelled on the package when they exceed a fixed concentration limit. In order to be able to control this regulation, the necessity exists for analytical methods that are capable to detect and quantify these allergenic fragrance ingredients. Adequate methodology is already available for analysis of simple cosmetic matrices, such as fine fragrances. However, because of contamination problems with low-volatile high molecular weight matrix components that are present in more complex formulations such as creams and lotions, these methods cannot be applied to the latter formulations.

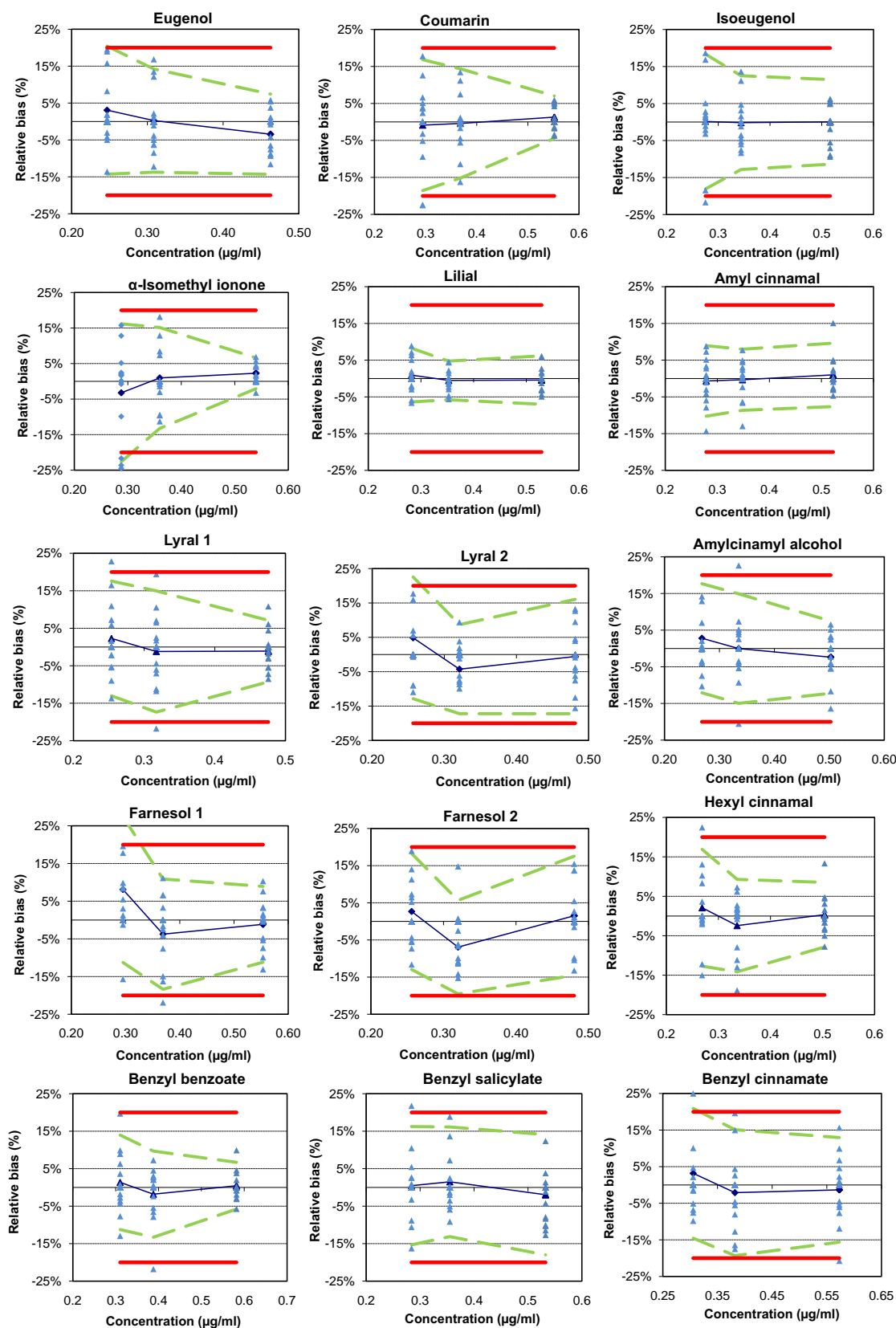


Fig. 2. Accuracy profiles of all investigated allergenic fragrance ingredients with β set at 90%. Relative bias (—), β -expectation tolerance limits (---), acceptance limits (—), relative back-calculated concentrations (\blacktriangle).

The newly developed method presented here, uses static headspace combined with an easy liquid extraction and was validated for several cosmetic formulations. The validation

results were considered to be satisfactory as the high determination variability problems of up to 20% described by several authors for benzyl salicylate, farnesol and amyl cinnamal,

Table 5

Recovery (mean % ± standard deviation) for five different cosmetic formulations analysed at 10 ppm (n=3).

Compounds	Recovery (%)					
	Formulation	1	2	3	4	5
Limonene		113.76 ± 2.32	122.09 ± 3.33	106.15 ± 2.59	110.93 ± 6.34	103.45 ± 1.82
Benzyl alcohol		101.64 ± 0.59	103.51 ± 3.83	85.76 ± 6.67	98.39 ± 4.41	92.33 ± 7.80
Linalool		110.98 ± 2.47	112.74 ± 1.85	106.30 ± 5.40	90.77 ± 4.30	81.79 ± 4.13
Methyl 2-octynoate		104.99 ± 0.47	114.75 ± 11.86	107.48 ± 1.60	97.00 ± 2.82	91.91 ± 4.39
Citronellol		93.83 ± 1.42	96.54 ± 6.35	103.93 ± 2.42	90.58 ± 2.20	90.99 ± 6.62
Citral 1		100.55 ± 0.55	97.50 ± 14.62	< 80	< 80	–
Geraniol		96.93 ± 0.92	106.49 ± 8.05	112.07 ± 1.05	115.00 ± 8.43	89.71 ± 8.28
Citral 2		100.72 ± 0.80	114.55 ± 9.86	115.78 ± 5.08	93.49 ± 3.33	86.62 ± 4.39
Cinnamal		99.05 ± 1.78	106.41 ± 11.48	97.45 ± 2.87	94.37 ± 1.55	96.94 ± 3.81
Anisyl alcohol		84.07 ± 2.24	81.13 ± 3.78	81.24 ± 2.70	80.51 ± 6.38	78.19 ± 5.33
Hydroxycitronellal		82.26 ± 2.96	94.40 ± 6.32	82.79 ± 4.64	96.65 ± 10.79	80.49 ± 3.96
Cinnamyl alcohol		87.38 ± 2.91	81.25 ± 4.21	86.55 ± 4.45	83.75 ± 0.75	84.61 ± 6.46
Eugenol		91.75 ± 3.06	89.71 ± 5.08	90.78 ± 2.08	86.78 ± 1.18	82.51 ± 3.42
Coumarin		109.97 ± 1.25	116.91 ± 5.49	97.78 ± 5.66	107.30 ± 2.43	103.43 ± 3.93
Isoeugenol		102.05 ± 0.16	85.59 ± 2.54	89.84 ± 10.92	93.82 ± 0.69	96.16 ± 3.84
α-Isomethyl ionone		106.23 ± 3.05	116.81 ± 3.30	96.32 ± 4.43	101.56 ± 0.96	101.88 ± 5.27
Lilial		105.48 ± 0.85	112.33 ± 6.78	101.49 ± 1.38	99.87 ± 2.02	92.38 ± 3.26
Amyl cinnamal		100.42 ± 0.89	114.72 ± 5.83	95.73 ± 3.46	95.62 ± 1.03	92.11 ± 4.39
Lylal 1		95.15 ± 1.89	100.09 ± 2.45	95.37 ± 8.53	84.25 ± 2.71	82.86 ± 4.59
Lylal 2		96.29 ± 4.41	97.41 ± 6.82	88.83 ± 5.06	103.80 ± 1.06	–
Amyl cinnamyl alcohol		100.52 ± 2.63	106.26 ± 5.31	108.72 ± 7.89	99.18 ± 5.35	84.49 ± 5.72
Farnesol 1		109.50 ± 4.85	105.06 ± 8.76	121.45 ± 5.46	86.09 ± 2.24	80.55 ± 7.48
Farnesol 2		94.99 ± 5.82	104.39 ± 7.82	< 80	< 80	85.79 ± 8.60
Hexyl cinnamal		100.53 ± 2.29	111.35 ± 3.25	90.24 ± 4.61	92.10 ± 4.07	88.20 ± 9.10
Benzyl benzoate		114.29 ± 1.86	119.95 ± 0.05	107.12 ± 7.36	105.61 ± 2.25	95.59 ± 5.39
Benzyl salicylate		106.27 ± 1.88	107.57 ± 11.60	108.62 ± 12.00	93.83 ± 2.93	84.38 ± 2.65
Benzyl cinnamate		114.12 ± 3.17	117.70 ± 5.89	109.89 ± 10.20	85.26 ± 1.91	84.82 ± 4.72

were not seen with our method at the 10 ppm threshold [4,7,20].

After validation, the method was used to analyse 18 cosmetic samples already shown before to contain illegal whitening substances. Study results revealed that these cosmetic products contained fragrance ingredients that were not present in the ingredients list. Concentrations measured were above the labelling limit. For several samples, it was shown that a number of undeclared fragrance ingredients were present in tenfold too high concentrations which imposes an additional health risk for the consumers.

References

- [1] Regulation 1223/2009, Official Journal L 342/59, 2009. Available online: <http://eur-lex.europa.eu/LexUriServ/LexUriServ.do?uri=OJ:L:2009:342:0059:0209:en:PDF> (accessed March 2014).
- [2] IFRA, Code of Practice. Available from: <http://www.ifraorg.org/en-us/code-of-practice>.
- [3] SCCS 2011: SCCS/1459/11, Opinion on Fragrance Allergens in Cosmetic Products, Adopted during the 13th Plenary Meeting, 2011. Available online: http://ec.europa.eu/health/scientific_committees/consumer_safety/docs/sccs_o_073.pdf (accessed March 2014).
- [4] A. Chaintreau, D. Joulain, C. Marin, C.O. Schmidt, M. Vey, J. Agric. Food Chem. 51 (2003) 6398–6403.
- [5] IFRA, Analytical Procedure: GC/MS Quantitation of Potential Fragrance Allergens in Fragrance Compounds, 2013. Available from: www.ifraorg.org/view_document.aspx?docId=22183.
- [6] IFRA, GC/MS Analysis of Allergens Usual Pitfalls, 2013. Available from: www.ifraorg.org/view_document_annex.aspx?annexId=21417.
- [7] M. Nogal Sánchez, J.L. Pérez-Pavón, B. Moreno Cordero, Anal. Bioanal. Chem. 397 (2010) 2579–2591.
- [8] M.V. Heisterberg, T. Menné, J.D. Johansen, Contact allergy to the 26 specific fragrance ingredients to be declared on cosmetic products in accordance with the EU cosmetics directive, Contact Dermat. 65 (2011) 266–275.
- [9] M. Niederer, R. Bollhalder, C. Hohl, J. Chromatogr. A 1132 (2006) 109–116.
- [10] J.P. Lamas, L. Sanchez-Prado, C. Garcia-Jares, M. Lores, M. Llompard, J. Chromatogr. A 1217 (2010) 8087–8094.
- [11] L. Sanchez-Prado, J.P. Lamas, G. Alvarez-Rivera, M. Lores, C. Garcia-Jares, M. Llompard, J. Chromatogr. A 1218 (2011) 5055–5062.
- [12] C. Devos, N. Ochiai, K. Sasamoto, P. Sandra, F. David, J. Chromatogr. A 1255 (2012) 207–215.
- [13] F. David, C. Devos, D. Joulain, A. Chaintreau, P. Sandra, J. Sep. Sci. 29 (2006) 1587–1594.
- [14] B. Desmedt, V. Rogiers, P. Courselle, J. De Beer, K. De Paep, E. Deconinck, J. Pharm. Biomed. Anal. 83 (2013) 82–88.
- [15] B. Desmedt, E. Van Hoeck, V. Rogiers, P. Courselle, J. De Beer, K. De Paep, E. Deconinck, J. Pharm. Biomed. Anal. 90 (2014) 85–91.
- [16] Restek, Fragrance Allergen Standards Kit, <http://www.restek.com/catalog/view/32561>, March 2014.
- [17] ISO, ISO 12787:2011, Cosmetics Analytical Methods Validation Criteria for Analytical Results Using Chromatographic Techniques, 2011, 1 pp.
- [18] A. Gustavo Gonzalez, M. Angeles Herrador, Trends Anal. Chem. 26 (2007) 227.
- [19] Agilent, Application Note: GC/MS Identification of Flavour and Fragrance Allergens in Some Common Snack Foods Using an Agilent J&W DB-17ms Capillary GC Column, 2009, 19809 pp.
- [20] A. Chisvert, A. Salvador, A. Chaintreau, R. Negri, in: A. Salvador, A. Chisvert (Eds.), Analysis of Cosmetic Products, Elsevier Science, The Netherlands, (243 pp).
- [21] M. Markelov, Anal. Chim. Acta 276 (1993) 235–245.
- [22] A. Garrido Frenich, J.L. Martínez Vidal, J.L. Fernández Moreno, R. Romero-González, J. Chromatogr. A 1216 (2009) 4798–4808.
- [23] J. Andrade, J. Terán-Baamonde, R. Soto-Ferreiro, A. Carlosena, Anal. Chim. Acta 780 (2013) 13–19.
- [24] J.O. De Beer, T.R. De Beer, L. Goeyens, Anal. Chim. Acta 584 (2007) 57–65.
- [25] M. Feinberg, J. Chromatogr. A 1158 (2007) 174–183.
- [26] P. Hubert, J.J. Nguyen-Huu, B. Boulanger, E. Chapuzet, N. Cohen, P. A. Compagnon, W. Dewé, M. Feinberg, M. Laurentie, N. Mercier, G. Muzard, L. Valat, E. Rozet, J. Pharm. Biomed. Anal. 45 (2007) 82–96.
- [27] Arlenda Home Page, Validation Training, 2013. Available from: <http://www.arlenda.com/en/training.html>.
- [28] APVMA, Guidelines for the Validation of Analytical Methods for Active Constituent, Agricultural and Veterinary Chemical Products, 2004, 1 pp.
- [29] AOAC, Guidelines for Single Laboratory Validation of Chemical Methods for Dietary Supplements and Botanicals, 2002, 2002 pp.
- [30] SANCO/10684/2009, Method Validation and Quality Control Procedures for Pesticide Residues Analysis in Food and Feed, 2010, 1133 pp.
- [31] H. Leijts, J. Broekmans, L. van Pelt, C. Mussinan, J. Agric. Food Chem. 53 (2005) 5487–5491.
- [32] L. Mondello, D. Sciarrone, A. Casilli, P.Q. Tranchida, P. Dugo, G. Dugo, J. Sep. Sci. 30 (2007) 1905–1911.
- [33] C. Debonneville, M.A. Thomé, A. Chaintreau, J. Chromatogr. Sci. 42 (2004) 450–455.



CYN determination in tissues from freshwater fish by LC–MS/MS: Validation and application in tissues from subchronically exposed tilapia (*Oreochromis niloticus*)

Remedios Guzmán-Guillén^{a,*}, I. Moreno^a, Ana I. Prieto Ortega^a, M. Eugenia Soria-Díaz^b, Vitor Vasconcelos^{c,d}, Ana M. Cameán^a

^a Area of Toxicology, Faculty of Pharmacy, University of Sevilla, Sevilla, Spain

^b Mass Spectrometry Facility, Centro de Investigación Tecnológica e Investigación (CITIUS), University of Sevilla, Sevilla, Spain

^c Biology Department, Faculty of Sciences, University of Porto, Rua do Campo Alegre, Porto 4169-007, Portugal

^d Marine and Environmental Research Center (CIIMAR/CIMAR), University of Porto, Rua dos Bragas, m289, 4050-123 Porto, Portugal

ARTICLE INFO

Article history:

Received 19 May 2014

Received in revised form

26 July 2014

Accepted 30 July 2014

Available online 12 August 2014

Keywords:

Cylindrospermopsin

Fish tissues

Method validation

LC–MS/MS

ABSTRACT

Harmful cyanobacterial blooms are occurring in eutrophic freshwater lakes and reservoirs throughout the world and, because of the production of toxins such as cylindrospermopsin (CYN), they can present a public safety hazard through contamination of seafood and fish for human consumption. Therefore it is important to develop methods to determine CYN at trace levels in those organisms. A new method for unconjugated CYN determination in tissues (liver and muscle) of tilapia (*Oreochromis niloticus*) is herein described and discussed; it is based on solvent extraction and purification with C18 and graphitized carbon cartridges, and quantification by liquid chromatography coupled with tandem mass spectrometry (LC–MS/MS). The method was optimized and suitably validated, with a linear range from 0.125–12.5 µg CYN/g dry weight (dw) in the case of the liver, and 0.02–1 µg CYN/g dw for the muscle. Limits of detection and quantitation were 0.07 and 0.12 µg/g dw for the liver, and 0.002 and 0.007 µg/g dw for the muscle, respectively. Mean recoveries ranged 80–110% in liver, and 94–104% in muscle, and intermediate precision values from 6 to 11%. The method is robust against the three factors considered for purification (batch of the graphitized carbon cartridges, time for the sample to pass through the cartridge, and final dissolving water volume). Furthermore, it has been successfully applied to the extraction and quantification of CYN in tissue samples from tilapia subchronically exposed to CYN in the laboratory. This represents a sensitive, reproducible, accurate, and robust method for extraction and determination of unconjugated CYN in tissues of fish exposed to the toxin. This procedure can be used for confirmatory routine monitoring of CYN in fish samples in environmental studies.

© 2014 Elsevier B.V. All rights reserved.

1. Introduction

Cyanobacteria are prokaryotic organisms growing in eutrophic freshwaters and lakes, and they are able to produce toxic secondary metabolites called cyanotoxins. Cylindrospermopsin (CYN) is an emerging toxin known to be produced by eleven species of cyanobacteria [1], *Aphanizomenon ovalisporum* among them. It is a polyketide-derived alkaloid with a central functional guanidine moiety combined with hydroxymethyluracil attached to its tricyclic carbon skeleton. CYN has a relatively low molecular weight of 415 Da and is highly

soluble in water [2], so CYN concentration dissolved in the fraction of water could be more than 99% of total toxin available [3].

CYN is a potent inhibitor of proteins [4] and glutathione (GSH) synthesis [5,6]. It is known that oxidative stress *in vitro* and *in vivo* [7–9] are involved in CYN mechanism of toxicity. Moreover, CYN may play a potential role as endocrine disruptor [10] and genotoxic [11]. Histopathological lesions have been found in the liver, kidney, intestine, lungs, and thymus of different experimental models exposed to CYN [4,12–14].

A derivation of a guideline value for CYN is in progress by the WHO [15]. A guideline safety value of 1 µg/L in drinking water and a no-observed-adverse-effect level value of 30 µg/kg body weight/day were reported for CYN by Humpage and Falconer [16], who also proposed a tolerable daily intake (TDI) of 0.03 µg/kg body weight/day for human exposure.

* Correspondence to: Area of Toxicology, Faculty of Pharmacy, University of Sevilla, Profesor García González n° 2, 41012 Sevilla, Spain. Tel.: +34 954 556762; fax: +34 954 233765.

E-mail address: rguzman1@us.es (R. Guzmán-Guillén).

Many aquatic animals are capable of living under the presence of cyanotoxins, and able to accumulate them in their tissues, becoming toxin reservoirs for animals higher up the trophic chain, including humans. The extent to which the concentrations found in these aquatic animals present a risk to humans after consumption has been discussed and reviewed by some authors [17–19]. Because CYN shows high stability and slow degradation in many water bodies [20], this toxin can bioaccumulate in different aquatic organisms even if they are exposed to trace quantities of the toxin. Moreover, taking into account that many incidents of human poisonings involving CYN may be unnoticed because of complicated toxin detection procedures [1], the development of highly sensitive, quantitative validated methods for its determination in animal tissues is essential for food safety and risk assessment.

Many methods for CYN analysis in different matrices are reported in the literature: from enzyme-linked immunosorbent assay (ELISA) for fast screening [21,22] and capillary electrophoresis [23,24], to confirmation tests by liquid chromatography (LC) with diode-array detection (DAD) [25,26], with single quadrupole LC/MS [27,28], or triple quadrupole LC/MS/MS [29–34]. LC–MS/MS is the ideal method for small amounts of toxin in water samples [29,32] and for complicated sample types (fish muscle) [35], as well as the addition of a clean-up step by solid phase extraction (SPE) helps to obtain a clean background from animal tissue extracts. Although CYN has been extracted and detected in different aquatic organisms [35–38] validation studies and robustness assays are scarce and have not been widely developed. Gallo et al. [35] developed a method for CYN determination in freshwaters and fish muscle by LC/ESI–MS/MS, but the method was not applied to those muscle samples, as has been carried out in the present work.

Analytical method validation strategies used to compare a performance measure with a reference value, not reflecting the consumer's needs, and they rarely consider the robustness study, which is essential for the "method transfer", following harmonization purposes [39]. Besides, the assessment of intra-laboratory accuracy is a fundamental stage in method validation [40]. Following all these considerations, we have previously validated two methods in our laboratory for determining CYN in waters [33] and in cyanobacterial cultures [34] by LC–MS/MS, which were applied to samples from aquaria of an in vivo experiment and to lyophilized cultures of *A. ovalisporum* to evaluate CYN content.

In the present study, we aimed to develop an analytical procedure based on solvent extraction and purification with C18 and graphitized carbon cartridges, followed by LC–MS/MS for CYN detection and quantification in fish tissue samples (liver and muscle). Optimization and validation of the proposed method was carried out according to the holistic approach [39,40]. The present procedure has been intended for routine determination in fish samples (*Oreochromis niloticus*) for human consumption with risk assessment purposes.

2. Materials and methods

2.1. Chemicals and reagents

Cylindrospermopsin (CYN) standards (purity > 95%) were supplied by Alexis Corporation (Lausen, Switzerland). Standard solutions of CYN were prepared in Milli-Q water (100 µg/mL) and diluted as required for their use as working solutions (5–500 µg/L). All chemicals and reagents used in this study were analytical grade materials. HPLC-grade methanol, dichloromethane, acetonitrile, and trifluoroacetic acid (TFA) were purchased from Merck (Darmstadt, Germany). Deionized water (> 18 MΩ/cm resistivity) was obtained from a Milli-Q water purification system (Millipore, Bedford, USA).

Bakerbond[®] C18 cartridges (500 mg, 6 mL) and BOND ELUT[®] Carbon cartridges (PGC column) (500 mg, 6 mL) were supplied by Dicsa (Andalucía, Spain) and Agilent Technologies (The Netherlands, Europe), respectively.

2.2. Extraction and clean up procedures

In order to study the efficiency of the extraction and purification procedures, control lyophilized fish liver (0.04 g) and muscle (0.5 g) samples were spiked with CYN standard solutions at three concentration levels: 20, 200 and 400 µg/L, equivalent to 0.5, 5.0 and 10.0 µg CYN/g dry liver, or 0.04, 0.4 and 0.8 µg CYN/g dry muscle. Afterward, the toxin was extracted from the samples using a modified version of Gallo et al.'s method [35] intended for CYN determination in freshwaters and fish muscle, by increasing the proportion of TFA contained in the extraction solvents and introducing 15 min of sonication for tissue disruption. The liquid-liquid partitioning with *n*-hexane in the original method was eliminated. Briefly, the liver was extracted with 10 mL Milli-Q water/acetonitrile (30:70, v/v), containing 0.5% TFA (v/v); after ultraturrax homogenization for 2 min, the sample was sonicated for 15 min. The resulting mixture was centrifuged at 20,000 rpm for 10 min. This procedure was repeated one more time. In the case of the muscle, 20 mL of the same extraction solvent was used, following the above-mentioned procedure. Regarding sample preparation prior SPE, Foss and Auel [41] presented a methodology for the extraction of CYN from human serum and urine by ELISA and LC/MS/MS. For the first matrix, they explored different extraction techniques: sonication (probe and bath) and protein precipitation with four different solutions (100% methanol, 100% acetone, 1% formic acid in methanol, and 1% formic acid in acetonitrile). Finally, they suggested sample homogenization (water bath sonication), followed by protein precipitation with 100% methanol and centrifugation, and SPE with graphitized carbon cartridges. In the case of the urine analysis, pH manipulation was used (pH > 10) as a means to precipitate salts and other interfering agents before SPE.

Once the extracts of each sample had been obtained (liver and muscle), a purification step was applied. These extracts (≈ 20 mL from liver or ≈ 40 mL from muscle extracts) were passed through a combined SPE system consisting of a C18 column and a PGC column, following the method of Liu and Scott [42] for algal food supplements optimizing it in our laboratory for biological samples (liver and muscle). The C18 columns were preconditioned with 10 mL of methanol containing 0.1% TFA (v/v), followed by 10 mL of water. The extracts were passed through the columns and washed with 10 mL of Milli-Q water; both fractions were collected together and concentrated to ≈ 10 mL for further purification with the second cartridge, the PGC column. This column was activated with 10 mL of methanol containing 0.1% TFA (v/v) and rinsed with 10 mL of Milli-Q water. Subsequently, the sample was passed through the cartridge, washed with 10 mL of Milli-Q water and eluted with 16 mL of methanol containing 0.1% TFA (v/v). The extracts were evaporated to dryness and redissolved in 1 mL of Milli-Q water. Then, they were transferred to a microcentrifuge tube and centrifuged (10 min, 13200 rpm). The supernatant was centrifuged again using ultrafree-MC PVDF (0.45 µm Millipore Corporation, Bedford, MA) (10 min, 11400 rpm). Finally, the extract was passed through a syringe filter (0.22 µm) before injection into the Liquid chromatography coupled with tandem mass spectrometry (LC–MS/MS) system.

2.3. Chromatographic conditions

Chromatographic separation was performed using a Perkin Elmer Series 200 HPLC system (Wellesley, USA) coupled to an Applied Biosystems QTRAP LC/MS/MS system (Foster City, USA)

consisting of an hybrid triple quadrupole linear ion trap (QqQlit) mass spectrometer equipped with an electrospray ion source. LC analyses were performed on a 150×2.1 mm Zorbax Sb–Aq column. The flow rate was 0.2 mL/min.

Chromatographic separation was performed using a binary gradient consisting of (A) water, and (B) methanol. Both components contained 0.05% TFA (v/v). The injection volume was 20 μ L. The elution profile was: 0% B (1 min), linear gradient to 90% B (10 min), 90% B (5 min) and finally 0% B (5 min). Multiple Reaction Monitoring (MRM) experiment was applied where the parent ions and fragments ions were monitored at Q1 and Q3, respectively. The transitions for the detection of CYN are: 416.2/194.0, 416.2/274.0, 416.2/336.0 and 416.2/175.9. The transition 416.2/194.0 was chosen for quantification of CYN. For LC/ESI–MS/MS analyses, the mass spectrometer was set to the following optimised tune parameters: curtain gas 35 psi, 185 source gas 60 psi, ion spray voltage 5500 V, and the Turboprobe temperature was maintained at 350 °C.

2.4. Evaluation of CYN in fish tissues

2.4.1. Experimental set up and fish acclimation

In order to apply the validated method to real samples, six groups of fish ($n=8$) were used to perform the present study. Fish (Male *O. niloticus*, Nile tilapia, Perciformes: Cichlidae) were obtained from a fish hatchery “Aquaculture Valencia” and maintained at the laboratory to reach the average weight of 25 ± 7 g and 8 ± 2 cm length. Fish were held in aquaria with 96 L of fresh water, minimizing exposure to chlorine by filling the tanks at least 3 days before the fish were introduced. The aquaria were also set up with a continuous system of water filtration and aeration (Eheim Liberty and Bio-Espumador cartridges (Bio-Espumador)). The temperature was kept constant (21 ± 2 °C). Dissolved oxygen values were maintained between 6.5 and 7.5 mg/L. Mean values for additional parameters of water quality were: pH 7.6 ± 0.3 , conductivity 287 μ S/cm, Ca^{2+} 0.60 mM/L and Mg^{2+} 0.3 mM/L. Fish were fed only with 0.3 g/d of commercial fish food (ciprinidos, 2 mm, Dibaq, Segovia, Spain) being left to acclimatize for 15 days before the beginning of the experiment.

2.4.2. Experimental exposure and application of the validated method

The *A. ovalisporum* (LEGE X-001) cyanobacterial CYN–producing strain (CYN+) was isolated from Lake Kinneret, Israel [43] and kindly supplied by Dr. Vitor Vasconcelos (Marine Research Centre, Porto, Portugal). Once cultivated in our laboratory, the biomass obtained was frozen at -80 °C, for lyophilization (Cryodos-80, Telstar, Tarrasa, Spain), and CYN extraction from the lyophilized cells of *A. ovalisporum* (CYN+) was performed according to the method of Guzmán-Guillén et al. [34]. Extracts were injected into the LC–MS/MS system, detecting CYN at a retention time of 9.55 min, and with a concentration of 2.14 μ g CYN mg^{-1} of lyophilized cells.

After the acclimation period, three groups of fish were exposed to CYN by a manually-crushed mixture of fish food and lyophilized cyanobacterial cells (to obtain 30 μ g CYN/fish), resulting in small, sticky pellets that were placed in the aquaria and allowed to drift to the bottom, ensuring the fish ate them within an hour. This procedure was repeated every 2 days along the exposure periods of 7, 14 or 21 d, adding to the aquaria the same quantity of lyophilized cells every time. Other three aquaria were used as the control groups (without CYN), being only fed with the commercial fish food for the whole experiment and sacrificed after their respective exposure times (7, 14 or 21 d).

At the end of the experiment, fish muscle of each specimen was portioned and lyophilized, together with the entire fish liver (Cryodos-80, Telstar, Tarrasa, Spain), for unconjugated, free CYN extraction. Samples were weighed and the median water losses were 78–80% for fish muscle and $\approx 87\%$ for fish liver. In addition, CYN levels in the aquaria were analyzed every 48 h throughout the exposure periods by LC–MS/MS [33].

2.5. Statistical criteria for method validation

Once the method had been developed, it must be validated, in order to verify that it satisfies the requirements of the application domain. Thus, the proposed method was validated taking into account the ICH Guidelines for linearity, sensitivity, precision and recovery [44].

Three validation standards covering the optimal working range were used, which were measured in triplicate for three different days. One mL of three different concentrations (20, 200, and 400 μ g CYN/L) was added to the matrices to obtain 0.5, 5.0 and 10.0 μ g CYN/g dry liver, or 0.04, 0.4 and 0.8 μ g CYN/g dry muscle. By applying a one-factor analysis of variance (ANOVA), as explained in the *Results and Discussion* section, both the precision and the recovery are obtained, and then they are compared with tabulated reference values.

Besides, a robustness study was performed by spiking the matrices with an intermediate validation standard of 200 μ g CYN/L (equivalent to 5 μ g CYN/g dry liver or 0.4 μ g CYN/g dry muscle), according to the Youden procedure [45]. The influential factors (batch of the graphitized carbon cartridges, time for the sample to pass through the cartridge, and final dissolving water volume) were tested with Student's *t* test as indicated below.

3. Results and discussion

Before starting the analysis of CYN extraction efficiency, the LC–MS/MS method needed to be set up for this use. In order to do that, commercially available standard solutions of CYN were assayed, acquiring mass spectra and adjusting mobile phase strength, as previously developed in our laboratory [33,34].

3.1. Method validation

The responses as a function of concentration were calculated from CYN standards prepared in extracts from lyophilized liver and muscle, and were measured by a 6-point calibration curve with a linear range within 5–500 μ g/L, equivalent to 0.125–12.5 μ g CYN/g dry tissue in the case of the liver, and by a 5-point calibration curve with a linear range of 10–500 μ g/L, equivalent to 0.02–1 μ g CYN/g dry tissue for the muscle. The regression equations obtained were $y=88.36x - 43.97$ ($r^2=0.999$) and $y=23.67x + 9.656$ ($r^2=0.995$), for the liver and the muscle, respectively.

3.1.1. Linearity and goodness of the fit

The linearity of an analytical method represents the range of analyte concentrations over which the method gives test results proportional to the concentration of the analyte [46]. Six and five different concentrations of CYN were spiked to blank extracts of fish liver (0.125–12.5 μ g CYN/g dw) and muscle (0.02–1 μ g CYN/g dw), respectively, submitting them to the proposed method. The calibration plot (signal response/analyte concentration against their concentrations) was established according to Huber [47] by replicate analysis ($n=3$) at all concentration levels (Fig. 1). The target line has zero slopes, representing the median of the response factors obtained. Then, two parallel horizontal lines are

drawn in the graph at 0.95 and 1.05 times the median value. As can be observed, no intersections with the lines were found in neither of the matrices, thus the linear ranges of the methods apply to the full ranges studied.

With the same signal responses, we carried out the corresponding ANOVA of the regression lines, indicating a lack-of-fit F ratio of 0.72 for the liver and 7.79 for the muscle, compared to a tabulated F value of 19.4. As the calculated ratios are below the reference value, there is no lack of fit and the calibration functions can be considered as linear.

3.1.2. Sensitivity

For validation purposes it is normally sufficient to provide an indication of the level at which detection becomes problematic and quantitation is acceptable in terms of repeatability precision

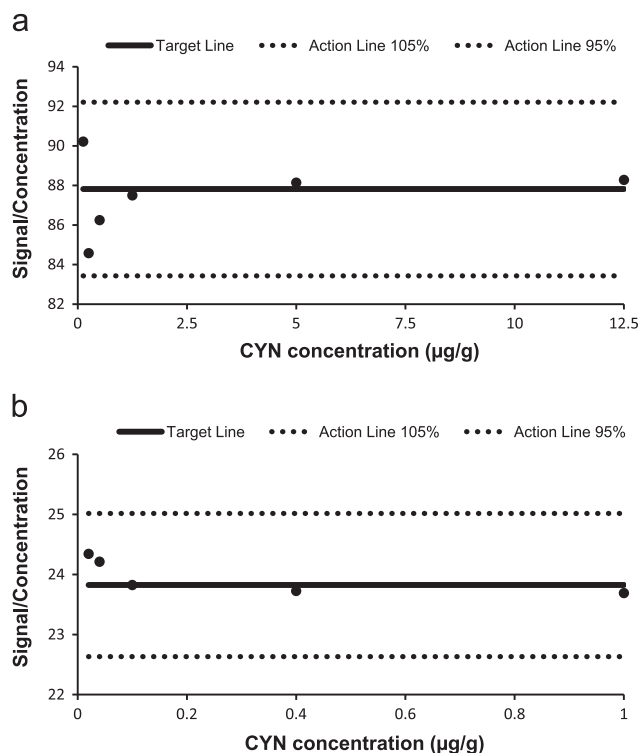


Fig. 1. Huber plot for assessing the linear range in (a) liver and (b) muscle of tilapia.

Table 1

Estimations of within-condition repeatability (S_w), between-condition repeatability (S_B), intermediate precision (intra-laboratory reproducibility, S_{IP}) and its relative standard deviations (%RSD $_{IP}$), and recoveries of CYN assayed in liver and muscle of fish, at three concentration levels, in three different days. Reference RSD values and recovery percentages by AOAC. Limits of detection (LOD) and quantitation (LOQ) for both matrices.

	CYN concentration level (validation standards)					
	20 µg/L		200 µg/L		400 µg/L	
	Liver (0.5 µg/g)	Muscle (0.04 µg/g)	Liver (5.0 µg/g)	Muscle (0.4 µg/g)	Liver (10.0 µg/g)	Muscle (0.8 µg/g)
S_w	2.42	1.88	2.92	8.64	13.94	26.81
S_B	1.33	3.72	15.02	27.52	25.21	22.10
S_{IP}	2.12	2.64	8.99	17.38	18.47	25.34
RSD $_{IP}$ (%)	9.60	11.00	6.00	8.10	6.00	6.77
Recoveries (%)	110	104	80	103	81	94
1/2 RSD $_{AOAC}$ (%)	8–11		6–8		6–8	
Acceptable Recovery Range (%)	80–110					
	Liver			Muscle		
LOD	0.07 µg/g dw ^a			0.002 µg/g dw ^a		
LOQ	0.12 µg/g dw ^a			0.007 µg/g dw ^a		

^a dw: Dry weight.

and trueness. For this purpose, the limits of detection (LOD) and quantitation (LOQ) were determined based on the standard deviation of the blank, by measuring 10 independent sample blanks once each, and were estimated according to the equation $Y_{LOD \text{ or } LOQ} = Y_{blank} + nS_{blank}$, where Y_{blank} and S_{blank} are the average value of the blank signals and its corresponding standard deviation, and n is a constant (3 for LOD and 10 for LOQ). These values are then converted into concentration by using the calibration functions obtained before. The LOD and LOQ obtained are 0.07 µg/g dw and 4.66 µg/g dw for the liver, and 0.002 µg/g dw and 0.007 µg/g dw for the muscle, respectively, and are recorded in Table 1. Other authors obtained values of 0.6 and 1.0 ng/g for LOD and LOQ, respectively, for CYN determination in fish muscle by LC coupled to electrospray ion trap mass spectrometry (LC/ESI-MS/MS), but they did not show any values of CYN detected in those tissue samples [35]. Our values were lower or of the same order than those obtained by Ríos et al. [48] for MCs determination in tench (*Tinca tinca*).

3.1.3. Precision

Precision refers to the closeness of agreement between independent test results obtained under stipulated conditions and, according to the International Conference on Harmonisation Guidelines [44], the measure of precision is usually expressed in terms of three concepts: repeatability, intermediate precision and reproducibility. The first one represents the closeness of the agreement between the results of successive measurements of the same measurand carried out in the same conditions, and it is called “within run” [49]. On the other hand, intermediate precision, also termed “between run”, “inter-assay precision” or “intra-laboratory reproducibility”, expresses within-laboratories variation: different days, different analysts, different equipment, etc. [44].

To assess the precision study, we spiked blank extracts from lyophilized liver or muscle at three concentrations of CYN standard (20, 200 and 400 µg/L, equivalent to 0.5, 5 and 10 µg CYN/g dry liver, or 0.04, 0.4 and 0.8 µg CYN/g dry muscle), in triplicate ($n=3$) within the same day, as recommended by the ICH guidelines, and over a period of three days; afterward, they were subjected to the proposed method and results were obtained. Considering three different days as the main source of variation, an analysis of variance (ANOVA) was performed for each validation standard and, operating with those results according to González and Herrador [39] and González et al. [40], the estimations of within-day repeatability (S_w), between-day repeatability (S_B) and intermediate precision (intra-laboratory reproducibility, S_{IP}) are obtained. From this last parameter and the mean

concentration values obtained for the validation standard, the corresponding relative standard deviation (RSD_{IP}) is computed and checked with the expected value issued by the AOAC Peer Verified Methods Program [40,47]. The RSD_{IP} are compared with one-half the corresponding RSD_{AOAC} tabulated values, and they should be lower or of the same order than 8–11% for 20 $\mu\text{g/L}$, and lower or by 6–8% for 200 and 400 $\mu\text{g/L}$. In our case, this requirement is fulfilled at the three concentration levels assayed, exhibiting suitable values, so the proposed method can be considered as precise. The results for all these parameters are summarized in Table 1.

3.1.4. Trueness and recovery

The trueness of an analytical assay expresses the closeness of agreement between the average value obtained from a series of measurements and an accepted reference value. It can be obtained from the same ANOVA results previously described for the intermediate precision, and it is normally expressed in terms of bias or recovery obtained for each validation standard considered [46]. These recoveries are defined as the ratio between the mean concentration of analyte measured in the fortified sample and the concentration of analyte added ("true" reference value, not determined by method) in the fortified sample, expressed as a percentage. The recoveries obtained for the three validation standards are shown in Table 1.

Once recovery is computed, it can be checked for suitability by comparison with the published acceptable recovery percentages as a function of the analyte concentration by the AOAC Peer Verified Methods Program. As observed in Table 1, very satisfactory mean recoveries were calculated: 110%, 80% and 81% (liver), and 104%, 103% and 94% (muscle) for the three concentrations assayed, respectively. For our analyte concentrations, the acceptable recovery range (%) could oscillate between 80 and 110%; accordingly, the collected results indicate that the method can be considered as bias-free and reliable in terms of recoveries. These values are higher

than the recoveries obtained by Gallo et al. [35] in fish muscle by LC/ESI-MS/MS (63.6%).

Taking into account these considerations, the analytical procedure developed in this work can be considered suitably validated.

3.1.5. Robustness

This concept represents the capacity of an analytical procedure to remain unaffected by small, but deliberate variations in method parameters and provides an indication of its reliability during normal usage [44]. The assay is based on the procedure suggested by Youden [45], according to the practical guide of González and Herrador [39]. Youden robustness test can be performed either during the optimization of the separation technique or during the optimization of sample preparation, investigating potential factors important for the analytical procedure; for the SPE, these factors may be the sorbent type or manufacturer, the wash or elution solvent or the evaporation temperature, for example [50]. In this work, we identified three influential factors in the SPE clean-up procedure to consider for the robustness study: the batch of the graphitized carbon cartridges employed (X_1); time for the sample to pass through the cartridge (X_2); and the final dissolving water volume after the SPE (X_3). By combination of those parameters, we obtained 8 different possibilities that were all tested. The levels were coded according to the rule represented in Table 2. The effect of every factor is calculated by the difference between the mean result obtained at the level +1 and that obtained at the level -1. Once the effects have been estimated, to determine whether variations have a significant impact on the results, a significance t test is applied [39], and the t values obtained (X_k) are compared with the 95% confidence level two-tailed tabulated value (t_{tab}) corresponding to the degrees of freedom from the precision study for the concentration assayed.

In our study, the experiments were carried out using tissue samples fortified with a medium validation standard of 200 μg CYN/L, and the amount of CYN added was 5 $\mu\text{g/g}$ dry liver and 0.4 $\mu\text{g/g}$ dry muscle. Each factor was analyzed in triplicate on three different days, thus obtaining 8 degrees of freedom (df). The tabulated t value (t_{tab}) for an experiment with 8 df is 2.306 and, as can be observed in Table 2, $t(X_k) < t_{tab}$ in all cases, so then the procedure can be considered as robust against the three factors considered for both matrices (at the levels fixed in the study).

3.2. CYN determination in tissues from freshwater fish by the proposed validated method

The developed and validated method was applied to detect and quantify the unconjugated CYN fraction in tissues of fish submitted

Table 2

Coding rules for combination of the parameters in the robustness study. X_1 : batch of the graphitized carbon cartridges employed; X_2 : time for the sample to pass through the cartridge; and X_3 : the final dissolving water volume after the SPE. t values obtained for each parameter after the significance t test applied.

Condition	X_1	X_2	X_3
High (+)	Batch 1	1 min	1000 μL
Low (-)	Batch 2	1.5 min	950 μL

t Values	Liver	Muscle	Liver	Muscle	Liver	Muscle
	1.07	2.13	0.36	0.76	0.80	0.19

Table 3

CYN (μg) detected in water samples from aquaria (96 L) after 7, 14 or 21 days of exposure to lyophilized cells of *Aphanizomenon ovalisporum*. CYN concentrations ($\mu\text{g/kg}$ dry weight) detected in liver and muscle of fish exposed to lyophilized cyanobacterial cells of *Aphanizomenon ovalisporum* (LEGE X-001) for 7, 14 and 21 days under laboratory conditions, showing the yield (%) in each case, compared to the total CYN (μg) added to aquaria after exposure periods.

CYN exposure periods (days)	Waters from aquaria (average \pm SD ^a)		Tissue (average \pm SD ^a)	
	Theoretical CYN (μg) added to aquaria after exposure periods	Detected CYN (μg) in aquaria (Yield %) ^b	μg CYN/kg dw ^c (Yield %) ^b	
			Liver	Muscle
7	3840	3456 (90 \pm 5.0) ^b	83 \pm 4.0 (2.2 \pm 0.1) ^b	9 \pm 5.0 ^d (0.23 \pm 0.1) ^b
14	6720	5568 (83 \pm 1.4) ^b	240 \pm 103.0 ^d (3.6 \pm 1.5) ^b	n.d. ^e
21	9600	8928 (93 \pm 0.4) ^b	703 \pm 548.0 ^d (7.3 \pm 5.7) ^b	4 \pm 0.4 (0.04 \pm 0.0) ^b

^a SD: standard deviation.

^b Yield: in relation to theoretical CYN added to aquaria.

^c dw: Dry weight.

^d Above Limit of Quantitation (LOQ).

^e n.d.: Not detected.

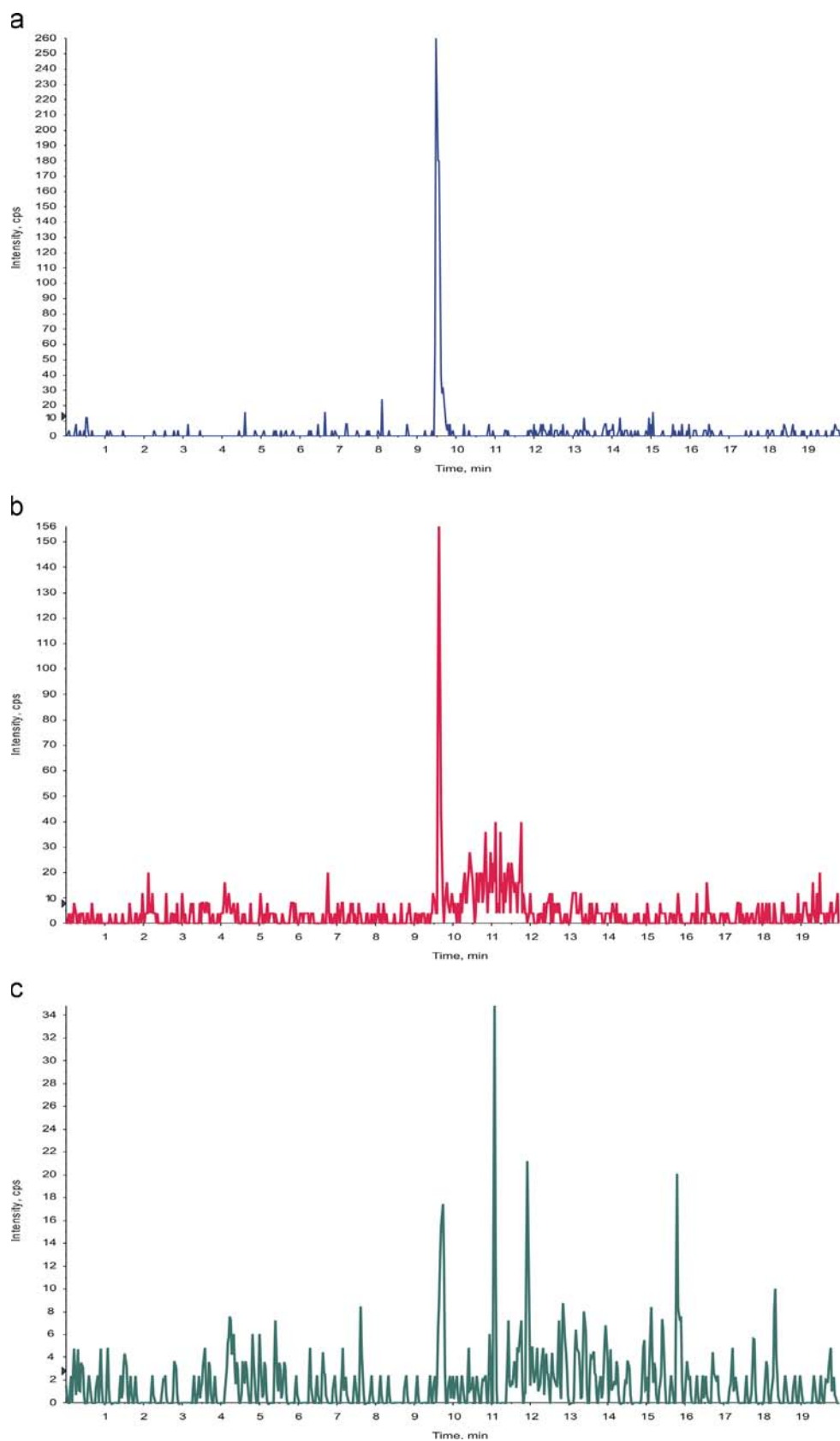


Fig. 2. LC-MS/MS chromatograms of a CYN standard (10 µg/L) (A), and CYN from extracts from a liver sample (B) and a muscle sample (C).

to the experimental conditions previously described (see [Section 2.4.2](#)) and [Table 3](#) shows these results. The LC-MS/MS chromatograms for a CYN standard (10 µg/L), a liver sample and a muscle

sample from tilapia intoxicated with the toxin in the laboratory are displayed in [Fig. 2](#). No free CYN was detected in control tissue samples. In the case of the liver, it was possible to quantify the toxin

above the LOD after 7 days of exposure to the lyophilized cyanobacterial cells, whereas we were able to determine CYN above the LOQ after 14 or 21 days. On the other hand, CYN quantification was possible above the LOQ even after a short-term exposure (7 d) in the case of the muscle. Muscle presented much lower CYN values in comparison with the liver, which is an important consideration taking into account human consumption of possibly contaminated fish, as the muscle is usually the edible portion. These results are in accordance with previous studies reporting that concentrations of cyanotoxins accumulated in muscle are usually lower than in other tissues, being mainly high in the less edible parts [51].

A few experimental studies have been made on cyanotoxins accumulation in aquatic organisms such as bivalves, crustaceans, snails and amphibian [36,52–55] under laboratory conditions. However, laboratory and field studies on presence and accumulation of CYN in these aquatic organisms are scarce, especially in the case of fish. Gallo et al. [35] developed a method for determination of CYN both in fish muscle and in freshwaters by LC/ESI–MS/MS, but they only successfully applied it to freshwater samples, not to tissues.

On the other hand, some field studies demonstrated presence and accumulation of CYN not only in fish, but also in other aquatic species [19,37,56,57]. In fish, Messineo et al. [38] demonstrated for the first time that CYN was present in trouts from a deep natural lake during an *A. ovalisporum* bloom (2.7 µg/kg dw in liver and 0.8 µg/kg dw in muscle). More recently, Berry et al. [58] performed a study on CYN accumulation in fish muscle, showing CYN values between 0.09 and 1.26 µg/kg of wet weight (ww) in different fish species. However, in both cases, CYN concentration was determined by ELISA. Although previous studies have shown that ELISA correlates with other analytical methods, it is known the fact that it possibly overestimates concentrations relative to other techniques such as HPLC–PDA and LC/MS [28,59] for CYN determination in water reservoirs, and LC/MS for measurement of MCs in strains of *Microcystis aeruginosa* [60]. Indeed, tissue concentration values given by the above-mentioned authors may be overestimated, indicating the need for using more sensitive techniques, such as LC–MS/MS. In our study, CYN concentrations found were of the same order or higher than the reported by those authors, especially in the case of the liver, where we detected a much higher amount of the toxin (83.1–703.4 µg CYN/kg dry liver and 3.7–9.2 µg CYN/kg dry muscle). Although relatively little data exists for CYN safety limits in tissues, a maximum allowable intake of 18 µg CYN/day can be calculated based on a TDI of 0.03 µg/kg/d proposed by Humpage and Falconer [16]. Besides, taking into account a fish consumption of 1600 g over a fortnight period obtained from surveys [61], a derived health alert level in fish flesh of approximately 158 µg/kg ww is obtained [36]. Based on these guidelines, none of the concentrations of CYN found in fish tissue in our study would exceed the maximum allowable values indicated, thus suggesting there would be no potential human risk. What is important for human consumption of potential contaminated fish is the muscle (edible fraction), nevertheless, it is noteworthy to mention that the higher accumulation of CYN in the fish liver contributes additionally to the total toxin intake. That would not represent a higher risk in the case of fish, as viscera are removed, but it would be of particular interest with other seafood which is eaten whole. Moreover, according to Ibelings and Chorus [17], although consumption of aquatic animals is often restricted to muscle tissue, especially with fish, this is not always the case everywhere.

3.3. CYN determination in water samples from aquaria

In our study, we also applied a LC–MS/MS method previously validated in our laboratory [33] to analyze CYN levels in waters from the aquaria every 48 h throughout the exposure periods of 7, 14 or 21 d, and the actual CYN concentrations found are recorded

in Table 3. CYN was not detected in waters from control aquaria, and the total amount of toxin found in waters plus liver and muscle, after the respective exposure periods, tends to correspond to the total theoretical CYN concentrations added to the aquaria.

4. Conclusions

In this study, a LC–MS/MS method was developed and validated for the determination of unconjugated, not cell-bound CYN in fish tissues (liver and muscle), proving to be sensitive, reproducible, accurate and robust. Its recoveries (80–110% in liver and 94–104% in muscle) and intermediate precisions obtained (6.0–9.6% in liver and 6.8–11.0% in muscle) permit its validation. Moreover, it has been possible to apply the present method for detection and quantification of CYN in liver and muscle of fish exposed to the toxin under laboratory conditions, showing that CYN can also accumulate in the edible portion of fish which may be consumed by humans. Hence, these results emphasize the need for monitoring CYN in fish tissues so that the associated potential health risks can be reduced or prevented, and the proposed method would be of usefulness for that purpose.

Acknowledgements

This work was supported by the Ministerio de Ciencia e Innovación of Spain (AGL2009–10026) and the Junta de Andalucía (P09–AGR–4672). The authors would like to acknowledge the European Cooperation in Science and Technology, COST Action ES 1105 “CYANOCOST–Cyanobacterial blooms and toxins in water resources: Occurrence, impacts and management” for adding value to this study through networking and knowledge sharing with European experts and researchers in the field. Remedios Guzmán Guillén also gratefully acknowledges the Spanish Ministerio de Educación for her grant “Formación del Profesorado Universitario (FPU)”.

References

- [1] B. Poniedziałek, P. Rzymiski, M. Kokociński, *Environ. Toxicol. Pharmacol.* 34 (2012) 651–660. <http://dx.doi.org/10.1016/j.etap.2012.08.005>.
- [2] K. Sivonen, G. Jones, *Cyanobacterial toxins*, in: I. Chorus, M.J. Bartram (Eds.), *Toxic Cyanobacteria in Water: A Guide to Their Public Health Consequences, Monitoring and Management*, E & FN Spon, London, 1999, pp. 41–111.
- [3] J. Rücker, A. Stüken, B. Nixdorf, J. Fastner, I. Chorus, C. Wiedner, *Toxicol. Environ. Chem.* 50 (2007) 800–809.
- [4] K. Terao, S. Ohmori, K. Igarashi, I. Ohtani, M.F. Watanabe, K.I. Harada, E. Ito, M. Watanabe, *Toxicol. Environ. Chem.* 32 (1994) 833–843.
- [5] M.T. Runnegar, S.M. Kong, Y.Z. Zhong, J.L. Ge, S.C. Lu, *Biochem. Biophys. Res. Commun.* 201 (1994) 235–241.
- [6] M.T. Runnegar, C. Xie, B.B. Snider, G.A. Wallace, S.M. Weinreb, J. Kuhlkamp, *Toxicol. Environ. Chem.* 67 (2002) 81–87.
- [7] D. Gutiérrez-Praena, S. Pichardo, Á. Jos, A. María Cameán, *Ecotoxicol. Environ. Saf.* 74 (2011) 1567–1572.
- [8] D. Gutiérrez-Praena, A. Jos, S. Pichardo, A.M. Cameán, *Aquat. Toxicol.* 105 (2011) 100–106.
- [9] R. Guzmán-Guillén, A.I. Prieto, V.M. Vasconcelos, A.M. Cameán, *Chemosphere* 90 (2013) 1184–1194.
- [10] F.M. Young, J. Micklem, A.R. Humpage, *Reprod. Toxicol.* 25 (2008) 374–380.
- [11] B. Zegura, A. Straser, M. Filipic, *Mutat. Res.* 727 (2011) 16–41.
- [12] D. Gutiérrez-Praena, A. Jos, S. Pichardo, R. Moyano, A. Blanco, J.G. Monterde, A.M. Cameán, *Ecotoxicol. Environ. Saf.* 76 (2012) 102–113.
- [13] M. Puerto, A. Jos, S. Pichardo, R. Moyano, A. Blanco, A.M. Cameán, *Environ. Toxicol. Environ. Chem.* 29 (2014) 371–385.
- [14] R. Guzmán-Guillén, A.I. Prieto, I. Moreno, V.M. Vasconcelos, R. Moyano, A. Blanco, A.M. Cameán, *Environ. Toxicol.* (2013), <http://dx.doi.org/10.1002/tox.21904>.
- [15] M. Welker, G. Christiansen, H. von Döhren, *Arch. Microbiol.* 182 (2004) 288–298.
- [16] A.R. Humpage, I.R. Falconer, *Environ. Toxicol.* 18 (2003) 94–103.
- [17] B.W. Ibelings, I. Chorus, *Environ. Pollut.* 150 (2007) 177–192.
- [18] T. Papadimitriou, I. Kagalou, C. Stalikas, G. Pilidis, I.D. Leonardos, *Ecotoxicology* 21 (2012) 1155–1166.

- [19] D. Gutiérrez-Praena, A. Jos, S. Pichardo, I.M. Moreno, A.M. Cameán, *Food Chem. Toxicol.* 53 (2013) 139–152.
- [20] R.K. Chiswell, G.R. Shaw, G. Eaglesham, M.J. Smith, R.L. Norris, A.A. Seawright, M.R. Moore, *Environ. Toxicol.* 14 (1999) 155–161.
- [21] Masten, S., Carson, B., *Cylindrospermopsin-Review of Toxicological Literature. Toxicological Summary for Cylindrospermopsin. CASRN 143545-90-8; National Institute of Environmental Health Sciences: Research Triangle Park, NC, USA, 2000.*
- [22] A.I. Prieto, A. Campos, A.M. Cameán, V.M. Vasconcelos, *Ecotoxicol. Environ. Saf.* 74 (2011) 1973–1980.
- [23] G. Vasas, A. Gáspár, G. Surányi, G. Batta, G. Gyémant, M. Hamvas, C. Máthé, E. Molnár, G. Borbély, *Anal. Biochem.* 302 (2002) 95–103.
- [24] G. Vasas, A. Gáspár, C. Páger, G. Surányi, C. Máthé, M.M. Hamvas, G. Borbély, *Electrophoresis* 25 (2004) 108–115.
- [25] M. Welker, H. Bickel, J. Fastner, *Water Res.* 36 (2002) 4659–4663.
- [26] J. Meriluoto, G.A. Codd (Eds.), *Toxic Cyanobacterial Monitoring and Cyanotoxin Analysis*, Abo Akademi University Press, Abo, Finland, 2005, p. 149.
- [27] S. Kikuchi, T. Kubo, K. Kaya, *Anal. Chim. Acta* 583 (2007) 124–127.
- [28] L. Bláhová, M. Oravec, B. Marsalek, L. Sejnohova, Z. Simek, L. Blaha, *Toxicol* 53 (2009) 519–524.
- [29] G. Eaglesham, K.R. Norris, G.R. Shaw, M.J. Smith, R.K. Chiswell, B.C. Davis, G. R. Neville, A.A. Seawright, B.S. Moore, *Environ. Toxicol.* 14 (1999) 151–155.
- [30] D.J. Stirling, M.A. Quilliam, *Toxicol* 39 (2001) 1219–1222.
- [31] C. Dell'Aversano, G.K. Eaglesham, M.A. Quilliam, *J. Chromatogr. A* 1028 (2004) 155–164.
- [32] S. Bogialli, M. Bruno, R. Curini, A.D. Corcia, C. Fanali, A. Laganà, *Environ. Sci. Technol.* 40 (2006) 2917–2923.
- [33] R. Guzmán-Guillén, A.I. Prieto, A.G. González, M.E. Soria-Díaz, A.M. Cameán, *Environ. Toxicol. Chem.* 31 (2012) 2233–2238.
- [34] R. Guzmán-Guillén, A.I. Prieto Ortega, I. Moreno, A.G. González, M.E. Soria-Díaz, V. Vasconcelos, A.M. Cameán, *Talanta* 100 (2012) 356–363.
- [35] P. Gallo, S. Fabbrocino, M.G. Cerulo, P. Ferranti, M. Bruno, L. Serpe, *Rapid Commun. Mass Spectrom.* 23 (2009) 3279–3284.
- [36] M.L. Saker, J.S. Metcalf, G.A. Codd, V.M. Vasconcelos, *Toxicol* 43 (2004) 185–194.
- [37] J.P. Berry, O. Lind, *Toxicol* 55 (2010) 930–938.
- [38] V. Messineo, S. Melchiorre, A. Di Corcia, P. Gallo, M. Bruno, *Environ. Toxicol.* 25 (2010) 18–27.
- [39] A.G. González, M.A. Herrador, *Trends Anal. Chem.* 26 (2007) 227–238.
- [40] A.G. González, M.A. Herrador, A.G. Asuero, *Talanta* 82 (2010) 1995–1998.
- [41] A.J. Foss, M.T. Aubel, *Toxicol* 70 (2013) 54–61. <http://dx.doi.org/10.1016/j.toxicol.2013.04.007>.
- [42] H. Liu, P.M. Scott, *Food Addit. Contam.* 28 (2011) 786–790.
- [43] R. Banker, S. Carmeli, O. Hadas, B. Teltsch, R. Porat, A. Sukenik, *J. Phys.* 33 (1997) 613–616.
- [44] ICH Harmonised Tripartite Guideline, Validation of Analytical Procedures: Text and Methodology, ICH Working Group, November 2005. (http://www.ich.org/fileadmin/Public_Web_Site/ICH_Products/Guidelines/Quality/Q2_R1/Step4/Q2_R1_Guideline.pdf).
- [45] W.Y. Youden, *Statistical Techniques for Collaborative Tests*, AOAC Inter, Washington DC, USA, 1967.
- [46] Association of Official Analytical Chemists. Peer Verified Methods Program, Manual on Policies and Procedures, AOAC, Arlington, VA, USA, 1998.
- [47] L. Huber, *Validation and Qualification in Analytical Laboratories*, Interpharm, East Englewood, CO, USA, 1998.
- [48] V. Ríos, I. Moreno, A.I. Prieto, M. Puerto, D. Gutiérrez-Praena, M.E. Soria-Díaz, A.M. Cameán, *Food Chem. Toxicol.* 57 (2013) 170–178.
- [49] IUPAC Analytical Chemistry Division, *Compendium of Analytical Nomenclature (The IUPAC 'Orange Book')*, Prepared for Publication by Inczédy, in: J. Lengyel, T. Ure, A.M. (Eds.), third ed. Blackwell Science, Ltd., Oxford, UK, 1998.
- [50] E. Karageorgou, V. Samanidou, *J. Chromatogr. A* (2014), <http://dx.doi.org/10.1016/j.chroma.2014.01.050> (in press).
- [51] J.C. Martins, V.M. Vasconcelos, *J. Toxicol. Environ. Health B: Crit. Rev.* 12 (2009) 65–82.
- [52] V.M. Vasconcelos, *Aquat. Toxicol.* 32 (1995) 227–237.
- [53] V. Vasconcelos, S. Oliveira, F.O. Teles, *Toxicol* 39 (2001) 1461–1470.
- [54] S.H. White, L.J. Duivenvoorden, L.D. Fabbro, G.K. Eaglesham, *Toxicol* 47 (2006) 497–509.
- [55] S.H. White, L.J. Duivenvoorden, L.D. Fabbro, G.K. Eaglesham, *Environ. Pollut.* 147 (2007) 158–167.
- [56] S. Kinnear, *Mar. Drugs* 8 (2010) 542–564.
- [57] C. Moreira, J. Azevedo, A. Antunes, V. Vasconcelos, *J. Appl. Microbiol.* 114 (3) (2013) 605–620.
- [58] J.P. Berry, A. Jaja-Chimedza, L. Dávalos-Ling, O. Lind, *Food Addit. Contam. Part A: Chem. Anal. Control. Exp. Risk Assess.* 29 (2012) 314–321.
- [59] M. Yilmaz, E.D. Phillips, N.J. Szabo, S. Badylak, *Toxicol* 51 (2008) 130–139.
- [60] V. Ríos, I. Moreno, A.I. Prieto, M.E. Soria-Díaz, J.E. Frías, A.M. Cameán, *J. Water Health* 12 (1) (2014) 69–80.
- [61] P.G. Van Buynder, T. Oughtred, B. Kirby, S. Phillips, G. Eaglesham, K. Thomas, M. Burch, *Environ. Toxicol.* 16 (2001) 468–471.



A novel morphine electrochemical biosensor based on intercalative and electrostatic interaction of morphine with double strand DNA immobilized onto a modified Au electrode

Rasoul Pourtaghavi Talemi, Mohammad Hossein Mashhadizadeh*

Faculty of Chemistry, Kharazmi University, Tehran, Iran

ARTICLE INFO

Article history:

Received 5 June 2014

Received in revised form

3 August 2014

Accepted 4 August 2014

Available online 11 August 2014

Keywords:

Morphine

DNA biosensor

Au electrode

Differential Pulse Voltammetry

Mercaptobenzaldehyde

ABSTRACT

The intercalative and electrostatic interaction of morphine with double-stranded DNA (ds-DNA), which was immobilized onto mercapto-benzaldehyde-modified Au electrode, was employed for designing a sensitive biosensor. The interaction of morphine with the immobilized ds-DNA onto the electrode surface has been studied by differential pulse voltammetry (DPV). Under the optimum conditions, a linear dependence for the morphine concentration in the range of $0.05\text{--}500\ \mu\text{mol L}^{-1}$ and its oxidation signal were observed and a detection limit of $0.01\ \mu\text{mol L}^{-1}$ for the morphine was obtained. The reproducibility and applicability of the analysis to real samples were also investigated and results demonstrated that this DNA biosensor could be utilized for the sensitive, rapid, simple, and cost effective determination of morphine in urine and blood plasma samples.

© 2014 Elsevier B.V. All rights reserved.

1. Introduction

Intercalation and groove binding are the two most common modes by which small molecules bind directly and selectively to DNA [1]. Intercalation, which is an enthalpically driven process, results from the insertion of a planar aromatic ring system between DNA base pairs with concomitant unwinding and lengthening of the DNA helix [2]. In contrast, groove binding, which is predominantly entropically driven, involves covalent or non-covalent (electrostatic) interactions that do not perturb the duplex structure to any great extent [3]. Groove-binders are typically crescent-shaped, and fit snugly into the minor groove with little distortion of the DNA structure. It has been suggested that some DNA-binding drugs, especially those classified as minor groove-binders, such as morphine, may exhibit mixed binding modes [4–7].

Morphine is the most abundant alkaloid found in opium. Morphine is used to treat moderate to serious pain. Short-acting formulations are taken as needed for pain. To date, many analytical methods have been developed to determine of morphine concentrations, including high performance liquid chromatography [8–10], gas chromatography–mass spectroscopy [11,12], fluorimetry [13,14], chemiluminescence [15–17], surface plasma resonance (SPR) [18], and electrochemical methods [19–25].

* Corresponding author. Tel.: +98 21 88848949; fax: +98 21 88820993.

E-mail addresses: mashhadizadeh@khu.ac.ir, mashhadizadeh@yahoo.com (M.H. Mashhadizadeh).

Electrochemical methods are generally fast and economical in trace analysis. Compared with other analytical techniques, electrochemical analysis has the advantages of simplicity and high sensitivity, and simultaneously and can give out some mechanism information of medical and biological molecules.

Recently, various modified electrodes have been reported for the electrochemical detection of morphine as cobalt hexacyanoferrate-modified glassy carbon electrode (GCE) [19], Prussian blue-modified indium tin oxide (ITO) electrode [26], molecularly imprinted polymer films to fabricate a microfluidic system for amperometric detection of morphine [27], chemically modified-palladized aluminum electrode [28], Au microelectrode [29,30] in a flow injection system and multiwalled carbon nanotubes modified preheated glassy carbon electrode have also been used for the morphine detection [31], PEDOT modified Pt-electrode [32], and gold nanoparticles-modified carbon paste electrode [33].

Electrochemical investigation of DNA-drug interactions can provide a rapid, sensitive, selective, and cheaper method for the determination of drugs. The electrochemical DNA biosensors are assayed more easily and rapidly compared to the conventional DNA biosensors.

In recent years we used some nano-compounds modified electrodes as sensors or biosensors for determination of some metal ions [34–38]. In this work, we presented a novel sensitive morphine biosensor based on intercalative and electrostatic interaction between morphine and ds-DNA modified Au electrode. For this purpose, firstly Au electrode was self-assembled with mercapto-benzaldehyde as an

arm linker through well-known Au-S bond. Then the residual aldehyde group on the other end of MB was reacted with the modified amino on the ss-DNA and ss-DNA was covalently immobilized to the sensing surface. The ds-DNA was prepared with simple hybridization of ss-DNA with complementary target DNA. Finally, ds-DNA-modified Au electrode was used as an analytical tool to evaluate the interaction of morphine with the ds-DNA. The new biosensor was used for the voltammetric determination of morphine in urine and blood plasma samples.

2. Experimental

2.1. Materials

Morphine was prepared from the Pharma Shimi Pharmaceutical Company (Tehran, Iran). Potassium monohydrogen phosphate, potassium dihydrogen phosphate, $K_3Fe(CN)_6$, and $K_4Fe(CN)_6$ were obtained from the Merck Company. Mercaptohexanol (MCH) and Mercapto-benzaldehyde (MB) were obtained from the Sigma-Aldrich Company. Probe and complementary DNA used in this study were acquired from the Amisan Company (Iran) with the following sequence:

Probe ss-DNA (S_1): 5'-NH₂- GAGGAGTTGGGGGAGCACATT-3'

Complementary ss-DNA (S_2): 5'-AATGTGCTCCCCAACTCCTC -3'

All oligonucleotides were dissolved in 0.1 mol L⁻¹ phosphate buffer solutions (prepared using KH₂PO₄ and K₂HPO₄, PBS, pH 5.0) and were kept in refrigerator at 4 °C. All other chemicals were of analytical reagent grade and double distilled water (DDW) was used throughout.

2.2. Apparatus and instrumentations

CVs and DPVs were performed with an EN50081-2 electrochemical workstation (Declaration of the company, Netherlands). A three-electrode system was employed with Pt wire as auxiliary electrode, Ag/AgCl (saturated KCl) as reference electrode, and Au or modified-Au electrode as the working electrodes (Azar electrode-Iran). Electrochemical impedance spectroscopy (EIS) measurements were performed on an Autolab 302 electrochemical workstation.

2.3. Biosensor fabrication

Initially, the Au electrode was polished to a mirror-like surface with 10–50 μm alumina slurry and was washed with ethanol and water. Then, Au electrode thoroughly was rinsed with Piranha solution (7:3 mixtures of concentrated sulfuric acid and 30% hydrogen peroxide). Then, the Au electrode was electrochemically cleaned using several potential cycling between -0.2–1.6 V versus Ag/AgCl in 0.5 mol L⁻¹ H₂SO₄. For assembly of MB, the cleaned Au electrode was immersed into 1 mmol L⁻¹ MB solution for 12 h at room temperature, where the assembly of MB monolayer was performed via sulfur–Au reaction. Then, the obtained electrode was completely cleaned with DDW to remove unassembled thiol component and was denoted as (Au/MB). Following MB self-assembling, the sensor surface was washed with DDW and was subsequently back-filled by spotting 50 μL of a 0.01 mol L⁻¹ aqueous solution of MCH onto the electrode surface and let to incubate for 30 min. This step was performed in order to improve the organization of the sensing surface by reorienting the MB for optimal and efficient operation by removing those non-specifically physisorbed onto the electrode surface. The sensor was then thoroughly washed by DDW, leaving an organized mixed SAM of chemisorbed MB and MCH. Then the Au/MB electrode was incubated at 10⁻⁷ mol L⁻¹ S_1 for another 2 h to covalently immobilize the 5'-NH₂ modified ss-DNA (S_1), and thus the ss-DNA

modified electrode was obtained after washing with PBS, was denoted as Au/MB/ S_1 . For constructing of the Au/MB/ds-DNA, Au/MB/ S_1 was immersed in 0.1 mol L⁻¹ PBS (pH 5.0) containing 10⁻⁷ mol L⁻¹ of target S_2 with shaking for 30 min at 37 °C. After hybridization, the obtained electrode was washed with the same PBS solution and DDW to remove nonspecifically bounded DNA and the resulted biosensor was denoted as Au/MB/ds-DNA. For comparative purpose, Au/ds-DNA was prepared immersing the cleaned Au electrode in 10⁻⁷ mol L⁻¹ S_1 followed by hybridization with 10⁻⁷ mol L⁻¹ S_2 .

2.4. Preparation of real samples

Urine samples were stored in refrigerator immediately after collection. Ten milliliters of the sample was centrifuged for 30 min at 2000 rpm. The supernatant was filtered out using a 0.45 μm filter and then was diluted five times with the PBS (pH 5.0). The solution was transferred into the voltammetric cell to be analyzed without any further pretreatment. The standard addition method was used for the determination of morphine in urine real sample.

In order to precipitate proteins in the plasma samples, 1.0 mL of the sample was treated with 20 mL perchloric acid (HClO₄, 20% v/v). Then, the mixture was vortexed for a further 30 s and then was centrifuged at 1000 rpm for 20 min. The solution was diluted five times with the PBS (pH 5.0) and was transferred into a voltammetric cell. Once more, the standard addition method was applied for the determination of morphine contents.

2.5. Electrochemical measurements

Twenty milliliters of 0.1 mol L⁻¹ PBS buffer solution (pH 5.0) containing a specific amount of standard solution of morphine was added to an electrochemical cell. CV measurements were recorded in the potential range of 0.0–0.8 V at a scan rate of 100 mV/S. DPV was employed with the following parameters: $E_{initial}$ = 0.2 V, E_{final} = 0.7 V, scan rate = 50 mV/S, pulse amplitude = 50 mV, and pulse width 50 ms. The EIS measurements were performed in 5.0 mmol L⁻¹ [Fe(CN)₆]^{3-/4-} containing 0.10 mol L⁻¹ KNO₃ with the frequency range from 10⁵ to 0.1 Hz at the formal potential of the system, E^0 = 0.182 V.

3. Result and discussion

3.1. Optimization of DNA biosensor conditions

The effect of ds-DNA concentration based on morphine oxidation signal was explored in different ds-DNA concentrations from 10⁻⁹ to 10⁻⁵ mol L⁻¹ (Fig. 1A) by DPV in 0.1 mol L⁻¹ phosphate buffer solution (pH 5.0) containing 50 μmol L⁻¹ of morphine at the scan rate of 50 mV/S. The morphine oxidation signal increased up with increasing in the DNA concentration to 10⁻⁷ mol L⁻¹. After this concentration value, the magnitude of the morphine signal leveled off. Thus, the optimum immobilization concentration for ds-DNA was chosen as 10⁻⁷ mol L⁻¹ in order to obtain the full surface coverage of MB-modified Au electrode.

Proton is always involved in the electrochemical reaction of organic compounds and exerts significant impact on the reaction speed. Therefore, the effect of varying pH (3.0–8.0) on the electrochemical responses of Au/MB/ds-DNA to determine morphine was studied by DPV in a solution containing 50 μmol L⁻¹ of morphine at the scan rate of 50 mV/s (Fig. 1B). The maximum anodic peak current for morphine was found at pH 5.0 (Fig. 1B). Decrease in Morphine oxidation signal at lower and higher pHs can be related to the devaluation of electrostatic interaction

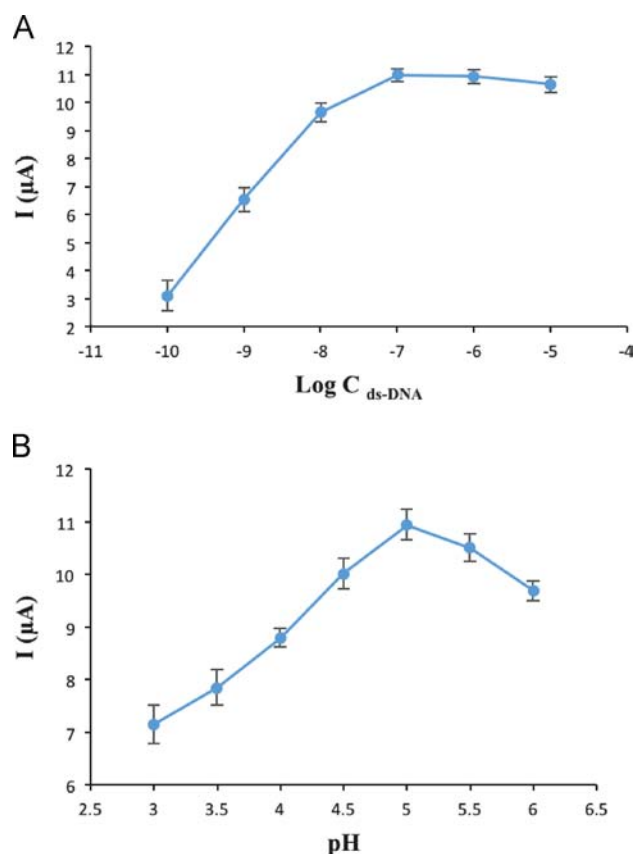


Fig. 1. DPVs of $50 \mu\text{mol L}^{-1}$ morphine oxidation signals ($n=3$) measured using (A) various concentration of ds-DNA immobilized onto the surface of MB-modified Au electrode. (B) Au/MB/ds-DNA at different pHs (3.0, 3.5, 4.0, 4.5, 5.0, 5.5, 6.0) at a scan rate of 50 mV/S.

between ds-DNA and morphine, because protonation of phosphate groups of DNA in lower pHs or diminish the positive charge of morphine at higher pHs. Therefore, pH 5.0 was chosen for the determination of morphine in this work.

Melting temperature is also a characteristic of a DNA duplex and a function of the duplex length [39]. The melting temperature of a DNA duplex can be defined as temperature at which, under a given set of conditions, 50% of the double-stranded DNA (ds-DNA) is denatured to single-stranded DNA (ss-DNA). The melting temperature for the Au/MB/S₁ that was hybridized with the complementary DNA was studied using previously reported procedure [40]. The melting temperature (T_m) for the fully complementary duplex was obtained 42 °C, which indicated good stability of the biosensor at room temperature.

3.2. Electrochemical characterization of modified electrode

The biosensor fabrication process could be monitored based on the electron transfer of ferricyanide through the modified electrodes. Fig. 2A shows the cyclic voltammograms obtained for differently modified electrodes in $1 \text{ mmol L}^{-1} \text{Fe}(\text{CN})_6^{3-/4-}$ of 0.1 mol L^{-1} PBS solution (pH 5.0, $0.1 \text{ mol L}^{-1} \text{KNO}_3$) at the scan rate of 50 mV/S [41]. A pair of well defined redox peaks can be observed at the bare gold electrode (curve a). These peaks could be definitely attributed to the redox behaviors of $[\text{Fe}(\text{CN})_6]^{3-/4-}$. On the cyclic voltammogram of the Au/MB (curve b), the redox peak current decreased with the increase of the peak-to-peak separation, indicated a quasi-reversible electrochemical redox reactions on the Au/MB and illustrated the MB film has successfully self-assembled on Au electrode. The immobilization of ds-DNA on

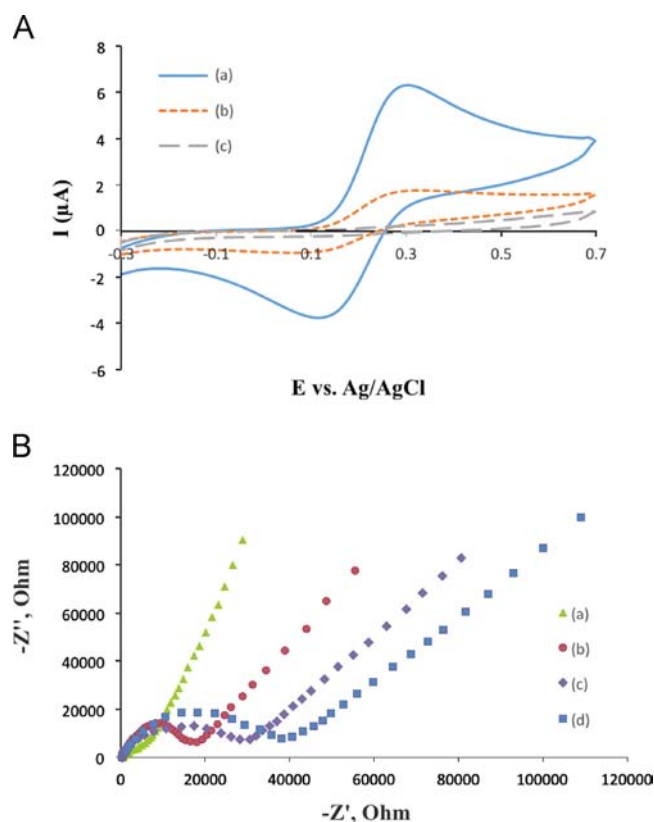


Fig. 2. (A) Cyclic voltammograms of the bare Au (a), Au/MB (b), and Au/MB/ds-DNA (c) in $1 \text{ mmol L}^{-1} [\text{Fe}(\text{CN})_6]^{3-/4-}$ and $0.1 \text{ mol L}^{-1} \text{KNO}_3$ at the scan rate of 50 mV/S. (B) Electrochemical impedance spectrograms of the bare Au (a), Au/MB (b), Au/MB/ds-DNA (c), and Au/MB/ds-DNA/morphine (d) in $5 \text{ mmol L}^{-1} [\text{Fe}(\text{CN})_6]^{3-/4-}$ and $0.1 \text{ mol L}^{-1} \text{KNO}_3$ with the frequency varied from 0.1 Hz to 10^5 Hz.

electrode surface induced a big decrease of the peak current and an increase of the peak to peak potential separation (curve c), indicated that the ds-DNA has been successfully immobilized on the electrode surface and the peak current decrease could be well assigned to the repulsion of $[\text{Fe}(\text{CN})_6]^{3-/4-}$ by the negatively charged phosphate backbone of DNA.

Electrochemical impedance spectroscopy (EIS) can reflect the impedance changes of the electrode surface during the modification process. Fig. 2B shows the Nyquist plot of the differently modified electrodes in $5 \text{ mmol L}^{-1} [\text{Fe}(\text{CN})_6]^{3-/4-}$ and $0.1 \text{ mol L}^{-1} \text{KNO}_3$ with the frequency was varied from 0.1 Hz to 10^5 Hz. The bare Au electrode exhibited a relatively low impedance value and almost a straight line (curve a). The R_{et} increased to be about 17820 Ω after Au electrode modification with MB (curve b). Impedance value continued to increase to 30500 Ω after ds-DNA immobilization (curve c). It may be attributed to the limited diffusion of $[\text{Fe}(\text{CN})_6]^{3-/4-}$ toward electrode surface by the negative charged phosphate backbone of ss and ds-DNA. After incubating with $50 \mu\text{mol L}^{-1}$ morphine, the R_{et} value further increased to be about 37840 Ω (curve d), which could be well ascribed to the repulsion of redox probe from approaching electrode surface by the specific combination of morphine and ds-DNA.

3.3. Voltammetric behavior of morphine on the surface of the modified electrode

To elucidate the electrode reaction of morphine, cyclic voltammetric technique was used. The cyclic voltammograms were recorded in 0.1 mol L^{-1} PBS solution with pH 5.0 as supporting electrolyte in the absence and presence of $50 \mu\text{mol L}^{-1}$ of morphine at modified electrodes and were shown in Fig. 3. In our

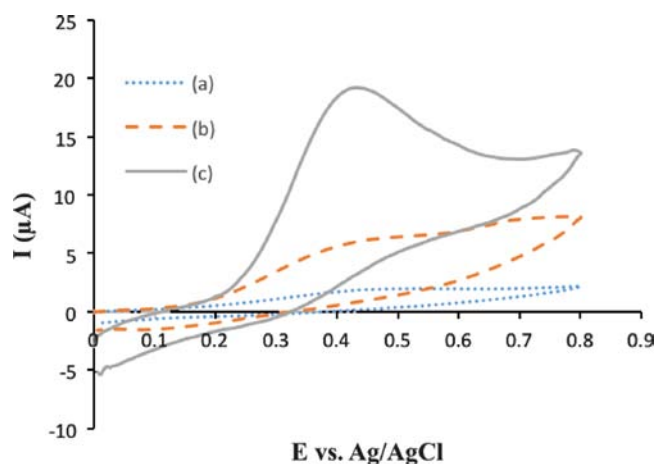


Fig. 3. Electrochemical responses of bare and MB/ds-DNA modified Au electrodes at absence of morphine (a), Au at presence of $50 \mu\text{mol L}^{-1}$ morphine (b), and Au/MB/ds-DNA at presence of $50 \mu\text{mol L}^{-1}$ morphine (c) in 0.1 mol L^{-1} PBS solution, scan rate 100 mV/S .

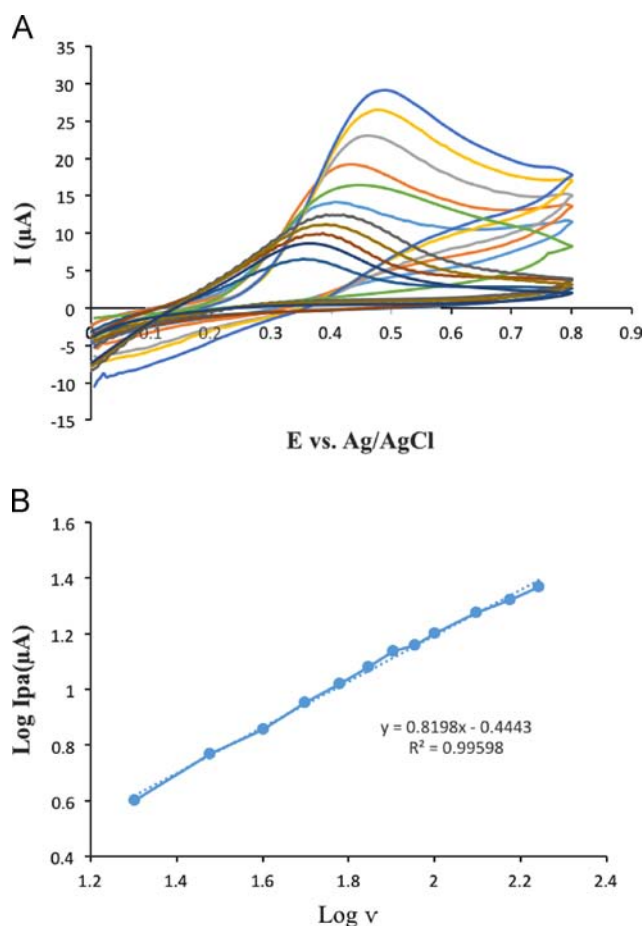


Fig. 4. (A) Cyclic voltammograms of $50 \mu\text{mol L}^{-1}$ Morphine in 0.1 mol L^{-1} PBS (pH 5.0) at Au/MB/ds-DNA at various scan rates: 20, 30, 40, 50, 60, 70, 80, 90, 100, 125, 150, and 175 mV/s from inner to outer, respectively. (B) Plot of $\log I_p$ vs. $\log v$.

experiments, no redox peak was observed in the absence of morphine at the surface of both modified and unmodified electrodes (Fig. 3a). A weak and broad anodic peak (Fig. 3b) at Au electrode in the presence of $50 \mu\text{mol L}^{-1}$ morphine indicated that morphine was electroactive at the Au electrode in this electrolyte solution, but this oxidation peak has less sensitivity for drug monitoring, while the Au/MB/ds DNA electrode, exhibited a

dramatic increase of current (Fig. 3c). This behavior can be attributed to the presence of ds-DNA that interacted greatly with morphine and hence more morphine can be introduced onto modified electrode surface and its oxidation peak can be observed.

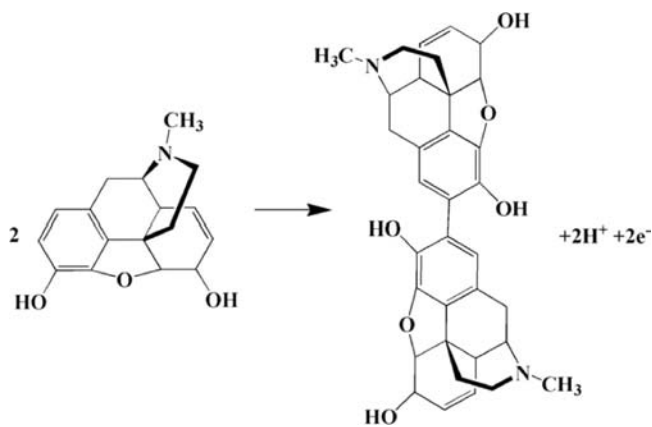
On the other hand, as shown in Fig. 4A, the peak currents (i_p) at the Au/MB/ds-DNA electrode in $50 \mu\text{mol L}^{-1}$ morphine solution (pH 5.0) varied with change of scan rate (v). In the range of 20–175 mV/s , the relations obey the following equation ($R^2=0.996$, where v is in mV/s and I_p is in μA),

$$\log i_p = -0.444 + 0.820 \log v$$

These results indicated that the electrode process was controlled simultaneously by both diffusion and adsorption [42].

Cyclic voltammetry was also carried out to characterize the effects of solution pH on oxidation peak potential of morphine at the Au/MB/ds-DNA. The oxidation peak potential of morphine shifted negatively with the increase of solution pH indicated that protons take part in the electrode reaction process. The anodic peak potential of morphine was proportional with the solution pH in the range of 4.5–7.5.

A good linear relationship between the peak potential (E) and the solution pH was also established (data not shown). The linear regression equation was gotten as $E \text{ (mV)} = -62.6 \text{ pH} + k$ ($n=4$, $R^2=0.998$). According to the Nernstian slope ($-59.0x/n$), where x is the hydrogen ion participating the electrode reaction and n is the number of electron transferred ≈ -62.6 , the loss of electrons



Scheme 1. The mechanism for electrooxidation of morphine at a surface of modified electrode.

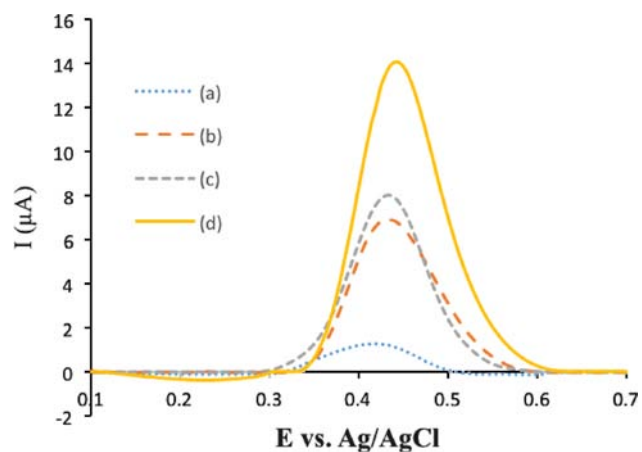


Fig. 5. DPV for the bare Au (a), Au/ds-DNA (b), Au/MB/ss-DNA (c), and Au/MB/ds-DNA (d) in PBS (pH 5.0) with $50 \mu\text{mol L}^{-1}$ morphine. The concentration of all DNAs immobilized onto electrodes surface was $10^{-7} \text{ mol L}^{-1}$.

was accompanied by the loss of an equal amount of protons and $x=n=1$ [43].

According to the electron-transfer number n obtained in literature [44], one can conclude that the electrode reaction of morphine on Au/MB/ds-DNA is a two-electron and two-proton process. The proposed reaction mechanism is as scheme 1:

3.4. Effect of DNA

DPVs of $100 \mu\text{mol L}^{-1}$ morphine (Fig. 5) at the bare Au, Au/ds-DNA, Au/MB/ss-DNA, and Au/MB/ds-DNA were displayed. As can be seen, a weak peak was found for morphine at bare Au electrode (Fig. 5a). A dramatic increase in the peak currents with a little positive shift in potential for morphine oxidation signal was observed for Au/MB/ss-DNA (Fig. 5c) and Au/MB/ds-DNA

(Fig. 5d), respectively. These results indicated formation of a new association interaction between DNA and morphine. According to the previous research [45] intercalative binding of small molecules with DNA shifted potential to more positive value, while electrostatic binding displaced potential to negative potential value. Ensafi et al. [46] reported the intercalative interaction between DNA and morphine with positive shift in DPV current at pH 7.0. In our study, all morphine and DNA solutions were prepared in pH 5.0. In this pH, all morphine molecules were in their cationic form and could interact with negative charge of DNA backbone electrostatically. Therefore, both intercalative and electrostatic interaction could be possible between Morphine and DNA. A little positive shift in peak potential of Morphine oxidation in DPV responses indicated that the intercalative interaction between morphine and ds-DNA overcame the electrostatic interaction. Furthermore, the oxidation peak current of morphine, obtained with the Au/MB/ds-DNA (Fig. 5d) was higher than Au/MB/ss-DNA (Fig. 5c) that can be assigned to more intercalative and electrostatic interaction of ds-DNA with morphine.

Compared with the signal obtained with the Au/ds-DNA (Fig. 5b), the Au/MB/ds-DNA (Fig. 5d) produced an obvious increase in signal. This may be due to mercaptobenzaldehyde effect in increasing the immobilization of DNA onto electrode surface because of covalent interaction between MB and ds-DNA that increases the signal of morphine biosensor.

3.5. Differential pulse voltammetry detection of morphine at Au/MB/Ds-DNA

The calibration curve for morphine was characterized by differential pulse voltammetry. The differential pulse voltammograms obtained for a series of morphine solutions with various concentrations were illustrated in Fig. 6A. The calibration graph of the peak current versus concentration was constructed using data from these measurements and the least squares were evaluated using the linear regression method. The results of the measurements were summarized in Fig. 6B. As can be seen from Fig. 6B, there is a linear relationship in the plot of I versus concentration between 0.05 and $500 \mu\text{mol L}^{-1}$. That relationship can be described with the following linear regression equation in the mentioned concentration range:

$$I(\mu\text{A}) = 0.059C + 7.750,$$

where C is concentration of morphine in $\mu\text{mol L}^{-1}$, with a correlation coefficient of 0.998. The calculated limit of the detection value, $\text{LOD} = 0.01 \mu\text{mol L}^{-1}$ with $\text{RSD} = 3.1\%$ was obtained with the $S/N = 3$. The comparison of proposed method with other electrochemical methods for morphine determination was listed in Table 1 [44,45,47–50]. It can be seen that this method provided

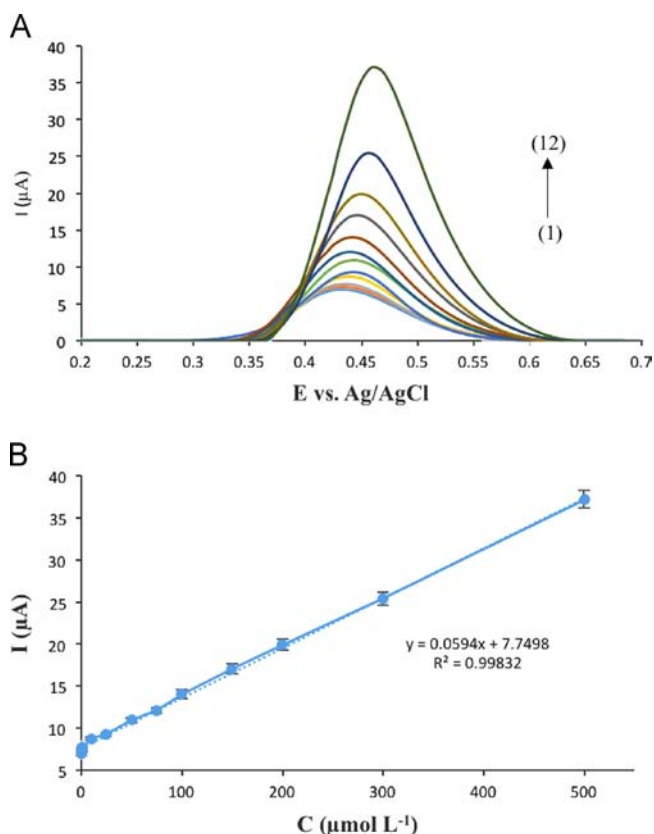


Fig. 6. (A) Differential pulse voltammograms for morphine at a Au/MB/ds-DNA electrode in the presence of various concentrations of morphine. The numbers 1–12 correspond to 0.05, 0.5, 1, 10, 25, 50, 75, 100, 150, 200, 300, and $500 \mu\text{mol L}^{-1}$ of the morphine. (B) Calibration curve for morphine at an Au/MB/ds-DNA electrode.

Table 1

Comparison of the analytical parameters with some previously reported morphine sensors.

Ref no	Modification method	Detection method	Linear range ($\mu\text{mol L}^{-1}$)	Detection limit ($\mu\text{mol L}^{-1}$)
47	Prussian blue film modified–palladized aluminum electrode	Hydrodynamic amperometry	2–50	0.8
44	ZnO/CNT nanocomposite room temperature ionic liquid modified carbon paste electrode	Square wave voltammetry	0.1–700	0.06
45	NiO/CNTs ionic liquid carbon paste electrode	Square wave voltammetry	0.05–520	0.01
48	Gold nanoparticles–ferrocene– modified carbon paste electrode	Differential pulse voltammetry	1–1800	0.003
49	Multiwall carbon nanotubes paste electrode	Square wave voltammetry	0.2–250	0.09
50	N-hexyl-3-methylimidazolium hexafluoro phosphate/multiwall carbon nanotubes paste electrode	Differential pulse voltammetry	0.6–600	0.02
This work	Mercaptobenzaldehyde and ds-DNA modified Au electrode	Differential pulse voltammetry	0.05–500	0.01

a broader linear range and lower detection limit for morphine detection than most of methods listed in Table 1. So the Au/MB/ds-DNA electrode was proved to be an efficient platform for the electrochemical sensor.

3.6. Selectivity of the biosensor

In order to evaluate the selectivity of the proposed biosensor for the determination of morphine, under optimized experimental conditions described above, the effects of some foreign species on the determination of morphine at $50 \mu\text{mol L}^{-1}$ were evaluated in detail. Usually there are a number of inorganic ions in urine samples, such as Na^+ , Mg^{2+} , Ca^{2+} , Cl^- , and SO_4^{2-} , so these inorganic ions and some other potentially interference compounds were tested to check their levels of interference in the determination of morphine. For this purpose, the tolerance limit was taken as the maximum concentration of the foreign substances, which caused an approximately $\pm 5\%$ relative error in the determination. After the experiments, the results revealed that neither 500-fold of glucose, sucrose, lactose, and fructose, nor 300-fold of Na^+ , Li^+ , Ca^{2+} , Mg^{2+} , Al^{3+} , NH_4^+ , SO_4^{2-} , Cl^- , and ClO_4^- , nor fivefold of cysteine, codeine, acetaminophen, and diclofenac interfered with the determination of morphine. These results confirmed the suitable selectivity of the proposed biosensor for determination of morphine.

3.7. Stability, reproducibility, and repeatability of Au/MB/Ds-DNA

Stability of the Au/MB/ds-DNA was tested by keeping the electrode in phosphate buffer solution (pH 5.0) for 10 days and then recording the DPVs for $100 \mu\text{mol L}^{-1}$ of morphine and comparing them with the DPVs obtained in the same solution before immersion. The results indicated that peak current decreased only slightly for the Au/MB/ds-DNA, indicated that the Au/MB/ds-DNA had good stability (data not shown). Five Au/MB/ds-DNA examples fabricated independently were used to determine $100 \mu\text{mol L}^{-1}$ of morphine, and the RSD was 4.1%, revealed good reproducibility of the electrode. To ascertain the repeatability of the electrode, 10 measurements of morphine were carried out using the Au/MB/ds-DNA at intervals of 1 h. The RSD was found to be 3.6%, indicated that the Au/MB/ds-DNA had also excellent repeatability.

3.8. Analytical application

In order to investigate the accuracy of the method, urine and blood plasma samples were analyzed to determine their morphine contents. In this regard, the samples were prepared as described in the sample preparation section. For blood plasma and urine samples, the concentrations of morphine in the samples were determined. Then, known concentrations of morphine were added into the same sample volume before their being centrifuged. After sample preparation, the morphine in the spiked samples was

Table 2
Analytical results of spiked morphine to urine and blood plasma samples.^a

Sample	Added ($\mu\text{mol L}^{-1}$)	Found ($\mu\text{mol L}^{-1}$)	Recovery (%)
Urine	–	–	–
	50.0	48.5 (± 0.1)	97.0
	100.0	104.9 (± 0.2)	104.9
Blood plasma	–	–	–
	50.0	51.6 (± 0.2)	103.2
	100.0	104.8 (± 0.2)	105.8

^a Values in parentheses are RSDs based on three replicates.

measured simultaneously. The data obtained with the proposed biosensor for spiked morphine in urine and blood plasma samples were presented in Table 2. The results showed that the determination of morphine was satisfactorily accurate.

4. Conclusions

CV and DPV techniques studied the electrochemical behavior of morphine at the surface of Au/MB/ds-DNA. The results revealed that the morphine interacted with ds-DNA with both electrostatic and intercalation modes in (pH 5.0). Under the optimized conditions, the anodic peak currents were linear to morphine concentrations in the range of $0.05\text{--}500 \mu\text{mol L}^{-1}$, and a detection limit about $0.01 \mu\text{mol L}^{-1}$ was obtained. This electrode presents advantages of easy fabrication, excellent stability, and sensitivity. The results obtained are promising and demonstrate the utility of the developed method for the determination of morphine content in urine and blood plasma samples without additional steps of extraction, clean-up, and derivatization.

References

- [1] U. Pindur, M. Jansen, T. Lemster, *Curr. Med. Chem.* 12 (2005) 2805–2847.
- [2] J.B.A. Chaires, *Arch. Biochem. Biophys.* 453 (2006) 26–31.
- [3] M.J. Waring, *Annu. Rev. Biochem.* 50 (1981) 159–192.
- [4] R.D. Wells, J.E. Larson, *J. Mol. Biol.* 49 (1970) 319–342.
- [5] J.K. Barton, J.M. Goldberg, C.V. Kumar, N.J. Turro, *J. Am. Chem. Soc.* 108 (1986) 2081–2088.
- [6] N. Zhou, T.L. James, R.H. Shafer, *Biochemistry* 28 (1989) 5231–5239.
- [7] F.A. Tanius, J.M. Veal, H. Buczak, L.S. Ratmeyer, W.D. Wilson, *Biochemistry* 31 (1992) 3103–3112.
- [8] M.E. Soares, V. Seabra, M.D.A. Bastos, *J. Liq. Chromatogr.* 15 (1992) 1533–1541.
- [9] P. Glare, T. Walsh, C. Pippenger, *Thera. Drug Monit.* 13 (1991) 226–232.
- [10] S. Hara, S. Mochinaga, M. Fukuzawa, O.N.T. Kuroda, *Anal. Chim. Acta* 387 (1999) 121–134.
- [11] A.M. Bermejo, I. Ramos, P. Fernandez, M. Lopezrivadulla, A. Cruz, M. Chirotti, N. Fucci, R. Marsilli, *J. Anal. Toxicol.* 16 (1992) 372–374.
- [12] J.C. Guillot, M. Lefebvre, J.P. Weber, *J. Anal. Toxicol.* 21 (1997) 127–133.
- [13] X.X. Zhang, J. Li, J. Gao, L. Sun, W.B. Chang, *J. Chromatogr. A* 895 (2000) 1–7.
- [14] R. Dams, T. Benijts, W.E. Lambert, A.P. De Leenheer, *J. Chromatogr. B* 773 (2002) 53–61.
- [15] N.W. Barnett, S.W. Lewis, D.J. Tucker, *J. Anal. Chem.* 355 (1996) 591–595.
- [16] N.W. Barnett, C.E. Lenehan, S.W. Lewis, D.J. Tucker, K.M. Essery, *Analyst* 123 (1998) 601–605.
- [17] S.W. Lewis, P.S. Francis, K.F. Lim, G.E. Jenkins, X.D. Wang, *Analyst* 125 (2000) 1869–1874.
- [18] G. Sakai, K. Ogata, T. Uda, N. Miura, N. Yamazoe, *Sens. Actuatur. B* 49 (1998) 5–12.
- [19] F. Xu, M. Gao, L. Wang, T. Zhou, L. Jin, J. Jin, *Talanta* 58 (2002) 427–432.
- [20] A. Salimi, R. Hallaj, G.R. Khayatian, *Electroanalysis* 17 (2005) 873–879.
- [21] A.A. Ensafi, B. Rezaei, H. Krimi-Maleh, *Ionics* 17 (2011) 659–668.
- [22] A.A. Ensafi, M. Izadi, B. Rezaei, H. Karimi-Maleh, *J. Mol. Liq.* 174 (2012) 42–47.
- [23] F. Li, J. Song, D. Gao, Q. Zhang, L. Niu, *Talanta* 79 (2009) 845–850.
- [24] B. Nigovic, M. Sadikovic, M. Sertic, *Talanta* 122 (2014) 187–194.
- [25] M.H. Pournaghi-Azar, A. Saadatirad, *J. Electroanal. Chem.* 624 (2008) 293–298.
- [26] K.C. Ho, C.Y. Chen, H.C. Hsu, L.C. Chen, S.C. Shiesh, X.Z. Lin, *Biosens. Bioelectron.* 20 (2004) 3–8.
- [27] C.H. Weng, W.M. Yeh, K.C. Ho, G.B. Lee, *Sens. Actuatur. B* 121 (2007) 576–582.
- [28] H.M. Pournaghi-Azar, A. Saadatirad, *J. Electroanal. Chem.* 624 (2008) 293–298.
- [29] A. Niazi, A. Yazdanipour, *Chin. Chem. Lett.* 19 (2008) 465–468.
- [30] A. Niazi, J.B. Ghasemi, M. Zendeheh, *Talanta* 74 (2007) 247–254.
- [31] A. Salimi, R. Hallaj, G.R. Khayatian, *Electroanalysis* 17 (2005) 873–879.
- [32] N.F. Atta, A. Gala1, R.A. Ahmed, *Electroanalysis* 23 (2011) 737–746.
- [33] N.F. Atta, A. Galal, S.M. Azab, *J. Electrochem. Sci.* 6 (2011) 5066–5081.
- [34] M.H. Mashhadizadeh, H. Khani, *Anal. Methods* 2 (2010) 24–31.
- [35] M.H. Mashhadizadeh, R.P. Talemi, *Anal. Chim. Acta* 692 (2011) 109–115.
- [36] M.H. Mashhadizadeh, H. Khani, A. Foroumadi, P. Sagharichi, *Anal. Chim. Acta* 665 (2010) 208–214.
- [37] M.H. Mashhadizadeh, R.P. Talemi, *Spectrochim. Acta A* 132 (2014) 403–409.
- [38] M. Kalate Bojdi, M.H. Mashhadizadeh, M. Behbahani, A. Farahani, S.S. Hosseini Davarani, A. Bagheri, *Electrochim. Acta* 136 (2014) 59–65.
- [39] S. Annette-Enrica, F. Gerd-Uwe, *Electroanalysis* 21 (2009) 1119–1123.
- [40] R. Meunier-Prest, S. Raveau, E. Finot, G. Legay, M. Cherkaoui-Malki, N. Latruffe, *Nucl. Acids Res.* 31 (2003) 150–156.
- [41] H.S. Wang, A.M. Zhang, H. Cui, D.J. Liu, R.M. Liu, *Microchem. J.* 64 (2000) 67–71.
- [42] M.H. Mashhadizadeh, R.P. Talemi, *Talanta* 103 (2013) 344–348.

- [43] E. Afsharmanesh, H. Karimi-Maleh, A. Pahlavan, J. Vahedi, *J. Mol. Liq.* 181 (2013) 8–13.
- [44] A.L. Sanati, H. Karimi-Maleh, A. Badiei, P. Biparva, A.A. Ensafi, *Mat. Sci. Eng. C* 35 (2014) 379–385.
- [45] M.T. Carter, M. Rodriguez, A.J. Bard, *J. Am. Chem. Soc.* 111 (1989) 8901–8911.
- [46] A.A. Ensafi, E. Heydari-Bafrooei, B. Rezaei, *Biosens. Bioelectron.* 41 (2013) 627–633.
- [47] M.H. Pournaghi-Azar, A. Saadatirad, *J. Electroanal. Chem.* 624 (2008) 293–298.
- [48] N.F. Atta, A. Galal, A.A. Wassel, A.H. Ibrahim, *Int. J. Electrochem. Sci.* 7 (2012) 10501–10518.
- [49] A. Mokhtari, H. Karimi-Maleh, A.A. Ensafi, H. Beitollahi, *Sens. Actuat. B* 169 (2012) 96–105.
- [50] A.A. Ensafi, B. Maedeh Izadi, H. Rezaei, *J. Mol. Liquids* 174 (2012) 42–47.



A vapor response mechanism study of surface-modified single-walled carbon nanotubes coated chemiresistors and quartz crystal microbalance sensor arrays

Hung-Ling Lu^a, Chia-Jung Lu^{a,*}, Wei-Cheng Tian^b, Horn-Jiunn Sheen^c

^a Department of Chemistry, National Taiwan Normal University, Taipei, Taiwan

^b Department of Electrical Engineering, National Taiwan University, Taipei, Taiwan

^c Institute of Applied Mechanics, National Taiwan University, Taipei, Taiwan

ARTICLE INFO

Article history:

Received 25 April 2014

Received in revised form

8 August 2014

Accepted 9 August 2014

Available online 19 August 2014

Keywords:

Carbon nano-tubes

Gas sensor

Volatile organic compounds

Chemiresistor

Quartz crystal microbalance

ABSTRACT

This paper compares the selectivity and discusses the response mechanisms of various surface-modified, single-walled carbon nanotube (SWCNT)-coated sensor arrays for the detection of volatile organic compounds (VOCs). Two types of sensor platforms, chemiresistor and quartz crystal microbalance (QCM), were used to probe the resistance changes and absorption masses during vapor sensing. Four sensing materials were used in this comparison study: pristine, acidified, esterified, and surfactant (sodium dodecyl sulfate, SDS)-coated SWCNTs. SWCNT-coated QCMs reached the response equilibrium faster than the chemiresistors did, which revealed a delay diffusion behavior at the inter-tube junction. In addition, the calibration lines for QCMs were all linear, but the chemiresistors showed curvature calibration lines which indicated less effectiveness of swelling at high concentrations. While the sorption of vapor molecules caused an increase in the resistance for most SWCNTs due to the swelling, the acidified SWCNTs showed no responses to nonpolar vapors and a negative response to hydrogen bond acceptors. This discovery provided insight into the inter-tube interlocks and conductivity modulation of acidified SWCNTs via a hydrogen bond. The results in this study provide a stepping-stone for further understanding of the mechanisms behind the vapor selectivity of surface-modified SWCNT sensor arrays.

© 2014 Elsevier B.V. All rights reserved.

1. Introduction

Volatile organic compounds (VOCs) represent a special category of hazardous substances that pose adverse effects to both the environment and human health [1]. Due to the diversity in chemical structures, the analyses of VOCs are usually performed using field sampling methods (i.e., canisters or adsorbent tubes) followed by in-lab analysis using a gas chromatograph–mass spectrometer (GC–MS) [2]. Although these analytical methods provide accurate assessments of VOC concentrations, they are often too expensive for continuous use and/or real-time analyses. On the other hand, chemical sensor arrays with cross sensitivity to VOCs can provide sufficient selectivity and detection limits for applications where immediate attention or continuous monitoring is called for [3].

Over the past few decades, several types of chemical sensors have been developed for the purpose of volatile compound or scent detection [4]. These sensor applications include metal oxide sensors [4], acoustic wave sensors (i.e., QCM and SAW) [5,6], optical sensors [7–9], and chemiresistors [10–12]. Recent research effort has been focused on improving the performance of these sensors by either employing nano structures to conventional materials such as metal oxide [13], or by applying newly developed nano materials such as metal nanoparticles [8–12] and nano carbon materials [14–16].

Among these newly developed nano materials for chemical sensing applications, carbon nanotubes have drawn much attention due to their highly adsorptive surfaces and their susceptible conductivity to environmental changes. Both single-walled carbon nanotubes (SWCNTs) and multi-walled carbon nanotubes (MWCNTs) have been demonstrated as highly sensitive materials for gas and vapor detection [14,17]. The earliest gas sensor employing SWCNTs was a field effect transistor device that measured the conductivity changes of a single carbon nano-tube [18]. Several recent studies have shown that measuring the film of randomly stacked CNTs on an interdigit electrode can also achieve a highly sensitive chemiresistor

* Correspondence to: No. 88, Sec. 4, Ting-Chou Rd., Taipei City, ROC, 11677, Taiwan. Tel.: +886 2 77346132; fax: +886 2 29324249.

E-mail address: cjlu@ntnu.edu.tw (C.-J. Lu).

[17,19]. Aside from measuring the conductivity changes, CNTs have also been tested on QCM, SAW and optical fiber sensor platforms [20–24]. The efficacy of using CNT-based sensors for VOCs in the environment, for detecting explosives, and for breath analysis has been recently reviewed [25–27].

In addition to the application of pristine CNTs as a sensing material, both covalent and non-covalent surface modifications of CNTs have been attempted in order to create a diversified selectivity for CNT-based sensors [28]. Non-covalent modifications can be achieved via either a polymer composite [24,28–31] or surface adsorption with π - π stacking attractions [32]. The swelling mechanism that is particularly important for polymer-coated CNT sensors was explored by Feller et al. [33]. Covalent modification requires a few more steps in the chemical synthesis. Functional groups that provide specific chemical forces can be grown on the surface of CNTs [34]. Several recent studies have demonstrated surface modifications using porphyrin or other metal complexes on CNTs for highly selective detection [21,35–38].

In the present study, we investigated a series of surface-modified SWCNTs coated on both chemiresistors and QCMs. Both covalent and non-covalent modified SWCNTs were tested. By simultaneously observing both sorption mass and conductivity changes, we were able to investigate the mechanism behind selectivity changes as well as the progression of surface modifications. Different response behaviors for both sensor platforms were used to interpret how surface-modified SWCNTs react to incoming vapors as well as the role of the interactions among nanotubes in a film. The experiment design in this work enabled the observation of different aspects of surface-modified SWCNTs during vapor sensing.

2. Experimental

2.1. Materials

High purity (>90%) single walled carbon nanotubes were purchased from Sigma-Aldrich and used as obtained. Chemicals for surface modification synthesis such as nitric acid, thionyl chloride, octanol and sodium dodecyl sulfate (SDS) were purchased from J. T. Baker. Organic solvents for both the synthesis process and test vapor generation were obtained from either Fluka (Japan) or Alfa Aesar (UK) with a purity of 98% or higher.

2.2. Surface modification of SWCNTs

Four different SWCNTs were tested in this study: pristine, acidic surface, ether surface, and SDS-coated (Fig. 1a). The non-covalent modification of SDS surface adsorption was prepared by suspending SWCNTs in a SDS/toluene solution. The molar ratio of SDS to the carbon atoms of SWCNTs was 1:10. The mixture solution was stirred and then ultrasonically resonated for 30 min. The SWCNT in the SDS solution was then filtered, rinsed with excess amount of toluene and dried in an oven for later use. The covalent modification of SWCNTs started with acidification to form a carboxylic acid group at the surface. SWCNTs were suspended in a mixed-acid solution containing H_2SO_4 : HNO_3 =3:1. The suspended solution was stirred and ultrasonically resonated and then refluxed for 3 h. The acidified SWCNTs (i.e., SWCNT-COOH) were filtered, washed with an excess amount of deionized water and then dried in an oven.

Esterification was carried out by mixing 0.2 g of dried SWCNT-COOH with excess thionyl chloride (SOCl_2) in dimethylformamide (DMF) with refluxing under nitrogen at 70 °C for 24 h. The SWCNT-COOHs were converted to SWCNT-COCl in this step. After allowed to cool to room temperature, the SWCNT-COCl were

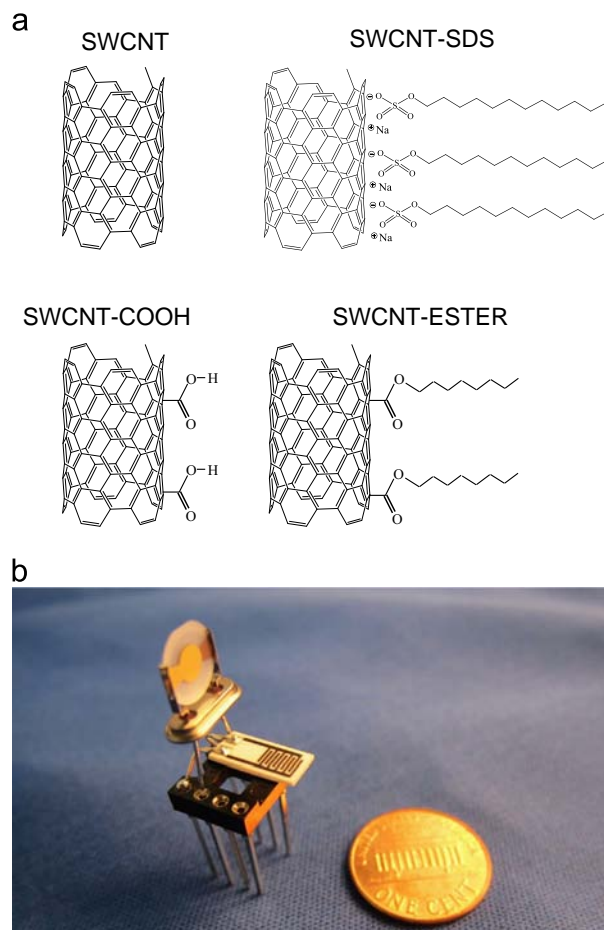


Fig. 1. (a) Chemical structures of surface modified SWCNTs (b) Photo of QCM and chemiresistor sensor platforms.

rinsed with a large amount of dehydrated tetrahydrofuran (THF) and dried in a vacuum oven. Dried SWCNT-COCl was then mixed with 1 mL pyridine and 80 mL octanol and then refluxed at 117 °C for 4 days. After reflux, the solution was cooled to room temperature. The excess octanol was removed by a filtering of the solid SWCNT-COOC₈H₁₇ (i.e., labeled as SWCNT-ESTER for later discussions) and the final product was washed repeatedly with ethanol and THF. In terms of interacting with analytes, the polar attraction was more important than the weak dispersion from the interaction with an aliphatic chain in this SWCNT-ESTER structure.

2.3. Sensor devices

10-MHz, AT-cut, gold-electrode QCM devices were purchased from Taitein electronics, CO., Taiwan. The 10-MHz driving circuitry was constructed in-house. A screen-printed interdigit electrode (IDE) was obtained from Ghitrion Technology Co., Ltd (Taiwan). There were 5 pairs of carbon electrodes with lengths of 4 mm and widths of 0.25 mm that were spaced 0.15 mm apart. The SWCNTs were dissolved in THF and spray-coated on both QCM and IDE. The spray-coat procedure was performed using a small airbrush with regulated-pressure nitrogen gas from a cylinder. The electrodes were buried under the SWCNT film. The resistance of the chemiresistor was measured through a bridge circuit. The thickness of the films was examined by cross-section SEM images (i.e., see Supporting information). The thickness of the SWCNTs on IDE was ~17 μm . The thickness of the SWCNTs on QCM was ~33 μm . We intentionally added more mass to the QCM to enhance the sensitivity for this device. Fig. 1b shows the photos of both sensors as one unit. The

frequency shift and voltage signal was recorded via a data acquisition interface card (DAQ-Pad 6015, National Instruments, USA). The software for continuous acquisition of frequency and voltage changes was written in-house using LabVIEW.

2.4. Instruments and apparatus

The infrared spectra of SWCNTs during the synthetic process were measured by FTIR (Spectrum RX-1, Perkin Elmer). A field emission scanning electron microscope (FE-SEM, S4800, Hitachi, Japan) was used to observe the image of the SWCNT film. A frequency counter (HP-5313A, Agilent, USA) and a resistance meter (model 6487, Keithley, USA) were used to monitor the oscillating frequency of QCM and resistance changes of chemiresistor during the spray coating of SWCNTs.

2.5. Vapor testing system

Test vapor was generated by a dynamic dilution system consisting of three mass flow controllers, stainless steel or Teflon manifolds, adsorbent traps, and a solvent evaporator. Clean background air was generated by passing compressed air through the tandem traps of a molecular sieve, charcoal, and a highly efficient particle filter (HEPA) to remove moisture, VOCs, and fine particles, respectively. The temperature was maintained at 25 ± 1 °C and relative humidity was kept below the lowest readable level ($< 1\%$) for a humidity meter (DO9861T-R1, Delta Ohm, Padua, Italy). The organic vapor concentration was generated by passing the background air through a bubbler to produce a saturated vapor concentration, and was diluted with different ratios of background air, and both were controlled using mass flow controllers (5850i, Brooks Instrument, PA). Two solenoid 3-way valves were connected to the front of the test cell and vent that allowed computer-controlled switching between the background air and the test vapor concentration. The generated vapor concentration was confirmed by GC-FID (HP5890, Agilent). The test cell that was used to house both the sensor arrays had an internal volume of ~ 250 mL. The volumetric flow rates were maintained at 5 L/min to ensure that the switching between test atmosphere and background air could be achieved in a few seconds.

3. Results and discussion

3.1. Characterization of surface modified SWCNTs

Fig. 2 shows the FTIR spectrums of pristine SWCNT, SWCNT-COOH, SWCNT-ESTER, and SWCNT-SDS. The pristine SWCNTs showed two small absorbance bands located at 1570 cm^{-1} that represented C=C stretching. Another small absorbance at 3410 cm^{-1} indicated a small fraction of oxidization on the surface of “as-purchased” SWCNT. After the acidification to SWCNT-COOH, narrower and sharper bands appeared at $1580\text{--}1750\text{ cm}^{-1}$ which indicated the absorbance of the C=O and COO⁻ functional groups. Another huge and broad absorbance band at $3000\text{--}3600\text{ cm}^{-1}$ was the contribution of -OH on the carboxylic acid group. When the SWCNT-COOH was further converted to a SWCNT-ESTER, the broad absorbance band at $3000\text{--}3600\text{ cm}^{-1}$ disappeared. Instead, a group of sharp absorbance peaks was seen at $2800\text{--}3000\text{ cm}^{-1}$, which indicated the replacement of -OH by the long alkane chain (-CH₂-, sp³) of an ester group (i.e., from -COOH to -COOR). The FTIR spectrum of the SWCNT-SDS showed both the similar signature of sp³ band from the long alkane chain of SDS and the absorbance signals of pristine SWCNT. These FTIR spectrums confirmed the changes in chemical structure as we progressively modified the SWCNT.

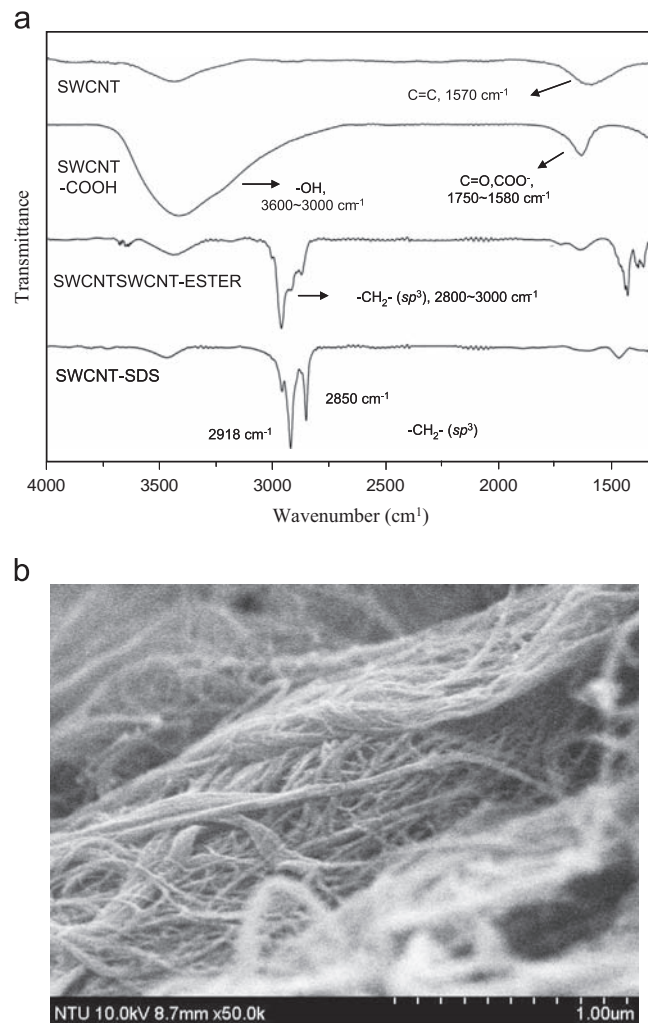


Fig. 2. (a) Infrared spectra of SWCNTs with and without surface modifications (b) SEM image of spray-coated SWCNT film.

Fig. 2b shows an example SEM image of a spray-coated SWCNT-ESTER film. The morphologies of all four SWCNT sensing films were very similar regardless of surface modification. The randomly stacked nanotubes created a naturally porous film. The pores among these randomly stacked nanotubes were ranged from submicron to several microns and were beneficial for rapid gas diffusion into the film. The gas response times of such a porous sensing film were expected to be short. A different study demonstrated by Feller et al. using polymer-coated CNTs as sensing film showed a faster rate of response equilibrium while significantly reducing the film thickness [33]. This showed how the diffusion through the polymer matrix contributed significantly to the response time. Unlike the film created by dense polymer coatings where gas diffusion time through sensing film contributes significantly to sensor response time, the small difference in the thickness of SWCNT film was expected to have a minor effect on the response time due to its porous structure.

3.2. Response time differences between QCMs and chemiresistors

Fig. 3 shows examples for the response signals of a chemiresistor (CR) and that of a QCM sensor. The chemiresistor circuitry was configured in such a way that the increases in resistance caused the increases in output voltage. The frequency shift of the QCM during vapor adsorption was always negative. The response signals of the QCM were reversed and overlapped with the chemiresistor signal in

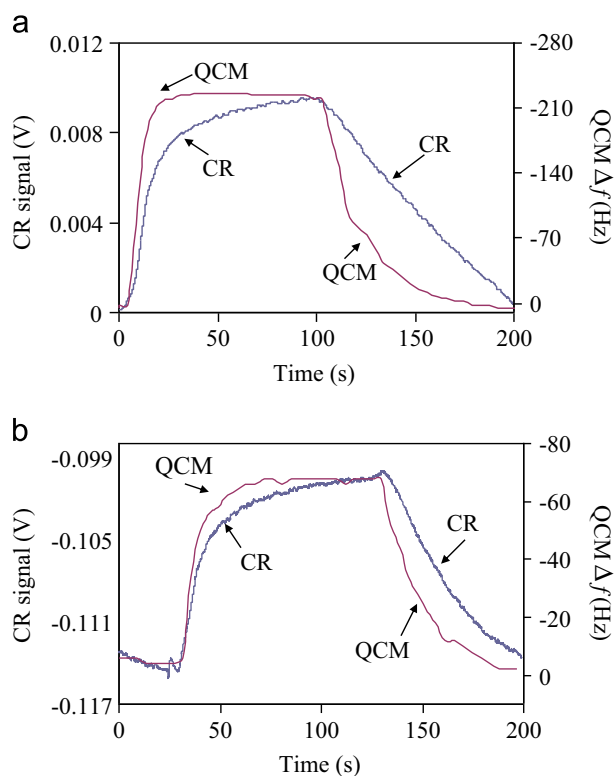


Fig. 3. Examples for overlapped response signals of QCM and chemiresistor (CR) (a) SWCNT-SDS sensors and the response to 3000 ppm butanol. (b) SWCNT-ESTER sensors and the response to 3500 ppm butyl acetate. (note: 2nd y-axis is in reversed order).

order to compare the times required for reaching equilibrium for both sensors. Fig. 3a shows the response signals of SWCNT-SDS-coated QCM and CR to 3000 ppm butanol. Fig. 3b shows the signals of SWCNT-ESTER-coated QCM and CR to 3500 ppm butyl acetate. In both cases, the responses of the QCM reached equilibrium faster than the chemiresistor did. Similar results were observed in all cases of pristine SWCNT, SWCNT-SDS and SWCNT-ESTER. This was particularly noteworthy because both sensors were coated with the same material at a similar thickness. As shown in the SEM image (Fig. 2b), the porous nature of randomly stacked SWCNT films was expected to enable a fast equilibrium between the gas phase and the surface adsorption. However, the increases in resistance require vapor molecules to intercalate between the junctions of two nanotubes. A proposed response mechanism is illustrated in Fig. 4. With the onset of vapor concentration, the vapor molecules diffused rapidly into the porous SWCNT films and were readily adsorbed onto the non-overlapped surfaces of SWCNTs. This was the adsorption-mass-increase stage, and a frequency shift of the QCM occurred. The remaining kinetic energy of adsorbed vapor molecules allowed the molecules to move into the overlapped regions between the nanotubes. The overlapped regions provided van der Waal attraction from both sides of the nanotube wall, which was better stabilized by the adsorbates. Thus, the adsorbed molecules had a greater tendency to stay within the overlapped regions. The swelling between carbon nanotubes needed to overcome the attractions between nanotube surfaces and a slight displacement of these nanotubes. Therefore, even though it was thermodynamically favorable for adsorbed molecules to partition into the overlapped regions between SWCNTs, a certain amount of reaction time was still required to complete the displacement of SWCNTs during the swelling. The response behavior of SWCNT-COOHs differed from that of the other three sensing materials, which will be addressed in the following sections.

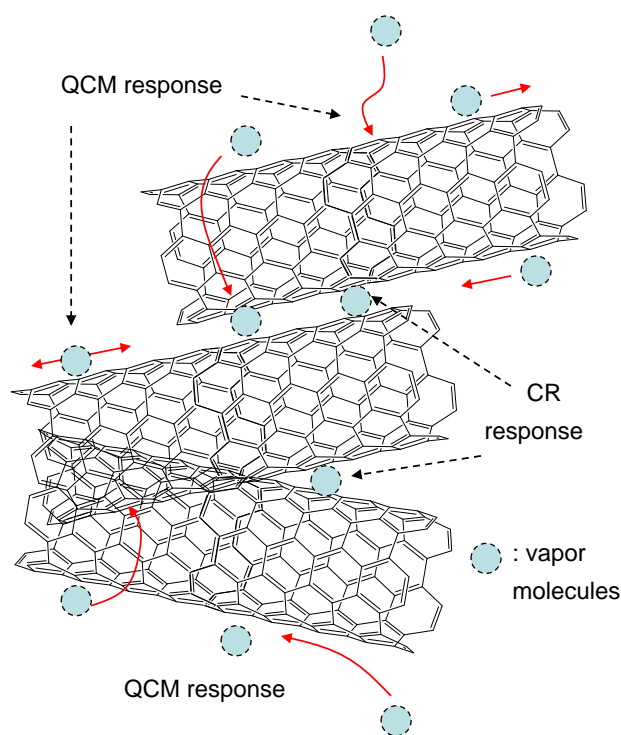


Fig. 4. Scheme for the response mechanism of pristine SWCNT-coated QCMs and chemiresistors.

3.3. Response signals of surface modified SWCNTs

Fig. 5 shows examples of the response signals for both a non-polar vapor (i.e., octane) and a highly polar vapor (i.e., butanol) for the four SWCNTs coated on both CR and QCM. As both Fig. 5a and b show, the coating of SDS on SWCNTs can significantly enhance the response for QCM sensors, which means an increase in vapor partition. When SDS was coated on the SWCNTs, the static charge of the $-\text{SO}_3^- \text{Na}^+$ terminal was attracted to the surface of the SWCNTs due to the highly polarizable conjugating electrons on the surface of the SWCNTs. After we had rinsed the SWCNT-SDS with toluene, the excessive SDS was eliminated leaving only the strongly adsorbed SDS that bind to the surface via a static charge-induced dipole attraction. The long alkane chain of the SDS layer provided an additional “stationary phase” for the partition of hydrophobic compounds. Hydrophilic compounds are more likely to be attracted by the $-\text{SO}_3^- \text{Na}^+$ group of SDS. When octane was absorbed by SWCNT-SDS, octane could partition into the overlapped alkane chain “spacer” and caused swelling between the nanotubes. As a result, the increased absorption of octane on SWCNT-SDS QCM showed an equivalent increase in the responses on the SWCNT-SDS chemiresistor. In the case of butanol, the SWCNT-SDS chemiresistor did not show sensitivity enhancement that matched the increase in absorption mass. This was because the overlapped regions of SWCNT-SDSs were spaced by non-polar alkane chains. Butanol was greatly attracted to the $-\text{SO}_3^- \text{Na}^+$ site near the SWCNT surface. An increase in mass adsorption can be seen in the QCM responses (Fig. 4b). The effectiveness of increasing the distances between SWCNT-SDS nanotubes by butanol adsorption was reduced because it did not contribute to the swelling of the non-polar end of the SDS shell. Also, the static charge of the $-\text{SO}_3^- \text{Na}^+$ site hindered the hydrogen bond formation of *n*-butanol directly to the surface of the SWCNTs. The possibility of reducing conductivity by scattering points [39,40] created from *n*-butanol adsorption was reduced; therefore, the resistance change exerted by *n*-butanol adsorption was less sensitive.

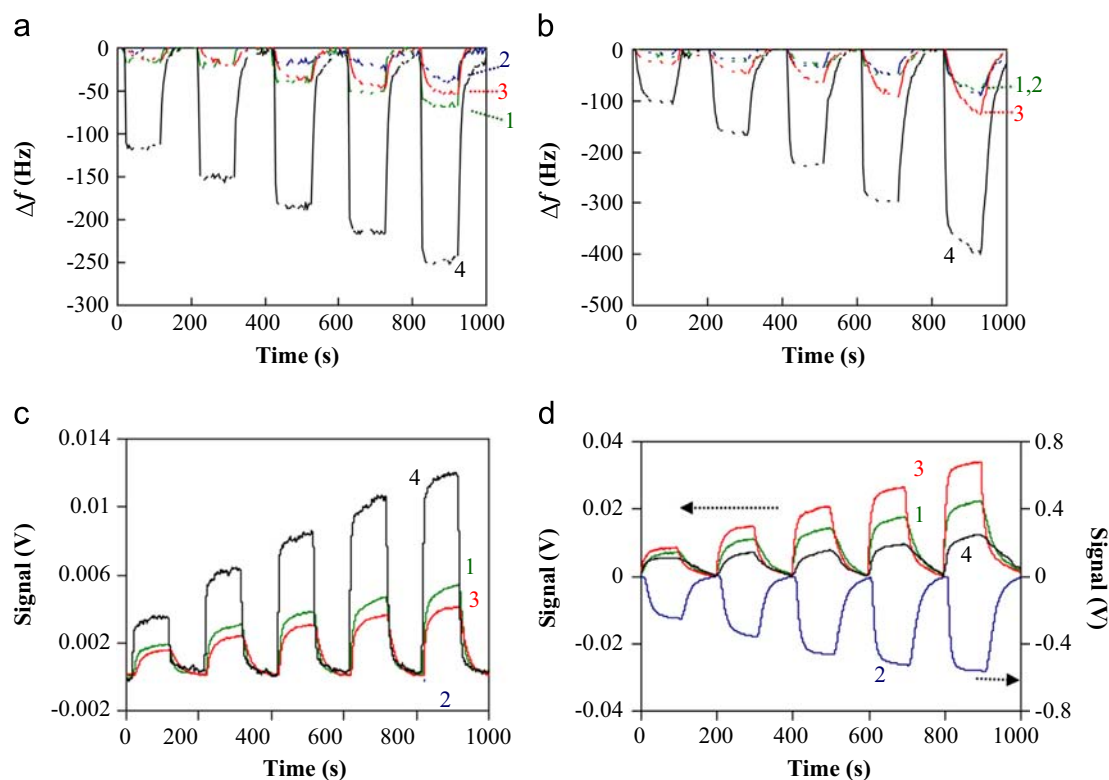


Fig. 5. Vapor responses of various SWCNT-coated QCMs and chemiresistors. Test concentrations: octane: 1916–9580 ppm; butanol: 981–4866 ppm. (a) QCM vs. octane (b) QCM vs. butanol (c) chemiresistor vs. octane (d) chemiresistor vs. butanol.

SWCNT-COOHs showed a sensing behavior that was more distinct than that of the other three materials. Judging from the response of the SWCNT-COOH-coated QCM, there was only a relatively small but detectable amount of octane adsorption on the SWCNT-COOH. However, the SWCNT-COOH-coated chemiresistor showed absolutely no response to octane even at very high concentrations. On the other hand, SWCNT-COOHs showed a higher adsorption mass for butanol than that of either pristine SWCNTs or SWCNT-ESTERS, but lower than that of SWCNT-SDSs. Surprisingly, a huge reverse response (i.e., resistance decrease) was seen with the SWCNT-COOH chemiresistor (Fig. 5d). It should be noted that the scale of the second y-axis on the right of Fig. 5d for SWCNT-COOH is 20 times larger than the scale of the first y-axis for the other three chemiresistors.

Unlike the NH_3 or NO_2 that were used as target gases for SWCNT sensors in earlier studies [25,41], nonpolar VOCs, such as octane, lack the ability to change the electron density of SWCNT. Therefore, the chemiresistor responses of octane on SWCNT, SWCNT-ESTER and SWCNT-SDS are mainly due to the swelling between the carbon nanotubes that increases the resistance of electron-hopping at the junctions of nanotubes. SWCNT-COOH has very strong hydrogen bonding terminals. The massive hydrogen bonds at the junction regions held SWCNT-COOH nanotubes tightly together. The adsorbed octane on the surface was not capable of breaking the hydrogen bond “interlocks” between the SWCNT-COOH nanotubes (Fig. 6). Therefore, SWCNT-COOH-coated chemiresistors showed no response to octane.

Butanol is neither a strong electron donor nor an acceptor by comparison with either NH_3 or NO_2 . The increases in resistance indicate that the swelling remains to be the dominant mechanism for pristine SWCNT, SWCNT-SDS and SWCNT-ESTER chemiresistors. However, a huge decrease in resistance was observed when butanol was adsorbed onto SWCNT-COOH. Although the hydroxyl group ($-\text{OH}$) of butanol can act as a hydrogen bond donor or acceptor, its acidity is much lower than that of the carboxyl group

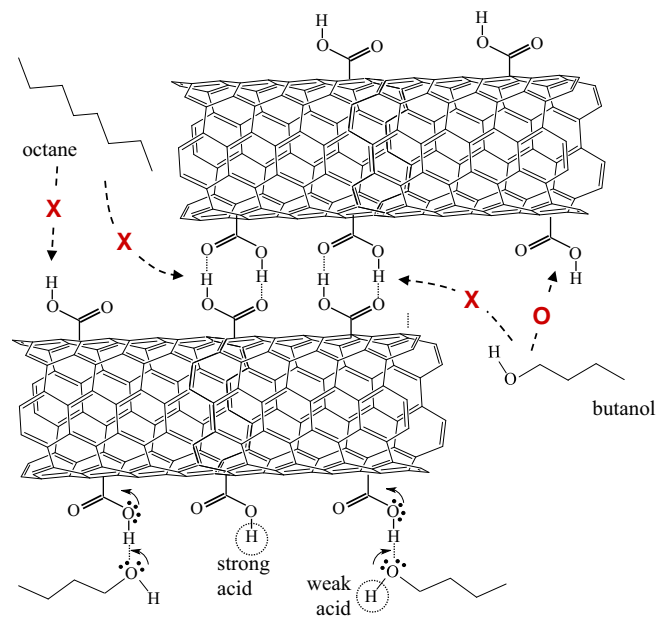


Fig. 6. Scheme for the response mechanisms of SWCNT-COOH-coated chemiresistors.

($-\text{COOH}$). Therefore, we believe that hydroxyl groups accept protons from carboxyl groups when hydrogen bonds are formed, which allows the conjugating electrons of carboxylic groups to increase the electron density on carbon nanotubes and the conductivity of SWCNT-COOH film to increase. This reverse response is also known as Negative Vapour Coefficient (NVC) and is sometimes observed with Poly aniline (PANI) or other Intrinsically Conducting Polymers (ICP) [42,43].

3.4. Calibration lines of SWCNTs coated QCMs and chemiresistors

Fig. 7 shows the calibration lines of toluene for both QCM and chemiresistor arrays. The y-axis units for the QCM arrays were $\Delta f/\Delta f_s$, which stands for the vapor response frequency shift (Δf) normalized to the frequency shift induced by the coating thickness (Δf_s) of SWCNT film. The output signal of the chemiresistor was voltage, which was converted to the change in resistance (ΔR) using Ohm's law. The y-axis units for the chemiresistor calibrations were expressed as $\Delta R/R_0$, which represented a change in the resistance normalized to the film resistance (R_0) in clean air. The units on the y-axis of Fig. 7a and b are changes in parts per million (ppm). The calibration lines of QCM for all SWCNTs (Fig. 7a) were linear over a wide range of vapor concentrations. On the contrary, the calibration lines of chemiresistors were all curved for pristine SWCNTs, SWCNT-ESTERS, and SWCNT-SDSs. There was no calibration data for toluene from the SWCNT-COOH-coated chemiresistor, because it did not respond to toluene. Due to the high signal-to-noise ratios of chemiresistors, the responses of this array can be measured at lower concentrations. The inset of Fig. 7b shows the calibration lines of a chemiresistor array at a lower concentration range. The chemiresistor responses appeared to be closer to linear at low concentrations and gradually leveled off at high concentrations.

The linear calibrations of the QCM sensors indicated that the partition coefficients for surface adsorption over the tested concentration range were constant. The surface adsorption mass was

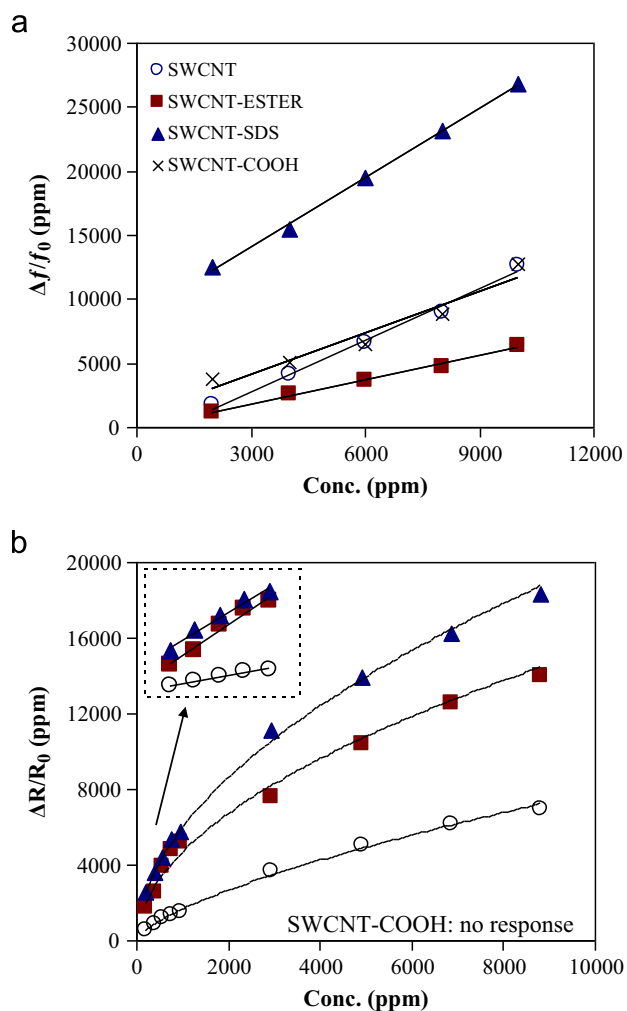


Fig. 7. Examples of toluene calibration curves for SWCNT-coated (a) QCMs and (b) chemiresistors. The inset in (b) shows the blow-up of low concentration responses for chemiresistors.

always in a linear proportion to the concentration in the test atmosphere. However, increases in adsorbed molecules at high concentrations did not seem to swell the nanotube films as effectively as they had at lower concentrations. As illustrated in Fig. 4, vapor molecules were first adsorbed onto the non-overlapped surface of SWCNTs. Some kinetic energy remained on the adsorbed molecules, which allowed them to move along the SWCNT surface, and some of them were stabilized at the junction point of the nanotubes. In general, the overlapped regions provided better stabilization by offering the conjugating π -electrons for dispersion attractions from both sides of two adjacent SWCNT walls. A partition equilibrium exists between the non-overlapped surface and the overlapped regions. The concentration inside the overlapped region could be higher than that on the non-overlapped surface due to stabilization. At low concentration, adsorbed molecules were rapidly diffused into the overlapped region and effectively increased the resistance at the junction point. When vapor concentrations were high, these small overlapped regions approached saturation. When a second or third layer of adsorption occurred inside the overlapped region, the stability from both SWCNT walls was reduced due to the increased separation between SWCNT walls. The partition into the overlapped region became less favorable than it was at low concentration. Therefore, the calibration lines of swelling-dependent SWCNT chemiresistors appeared to be nonlinear over a large concentration range. This adsorption/diffusion behavior was previously fitted to an LHC (i.e., Langmuir Henry Clustering) model. Details regarding the use of this model can be found elsewhere [33,44].

In addition to the discrepancy in the linearity between the QCM and chemiresistor calibrations, the relative sensitivities of these SWCNTs were also different on two platforms. The sensitivity trend for toluene on the QCM array was SWCNT-SDS > SWCNT=SWCNT-COOH > SWCNT-ESTER. The sensitivity order of toluene on the chemiresistor array was SWCNT-SDS > SWCNT-ESTER > SWCNT \gg SWCNT-COOH (i.e., no response). As indicated earlier, the responses of the QCM revealed the partition coefficients between the air and the SWCNT film. The responses of the chemiresistors were affected by at least three factors: the partition between the air and the SWCNT surfaces, the partition between non-overlapped and overlapped surfaces, and the effectiveness of the swelling. The effectiveness of the swelling is mainly determined two factors: the free volume associated with the adsorbed organic molecules, and the attractions between the nanotubes. Both factors could be affected by the surface modification of the SWCNTs. For example, the strong hydrogen bonds between the

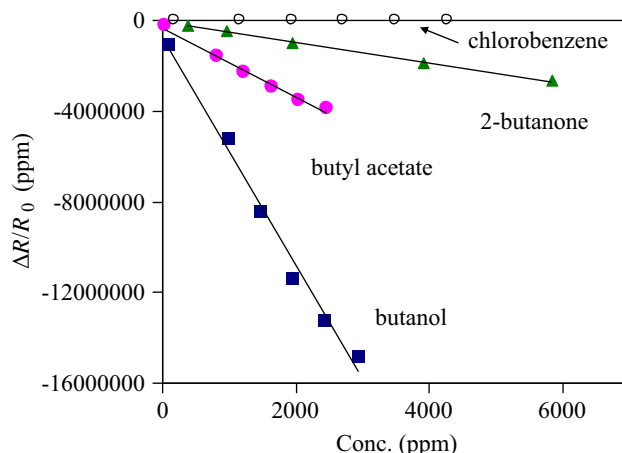


Fig. 8. Calibration curves of four polar compounds tested with a SWCNT-COOH coated chemiresistor.

carboxylic acid groups on adjacent SWCNT-COOHs inhibited the swelling completely and resulted in the lack of a response to nonpolar compounds in chemiresistor (Fig. 6).

Fig. 8 shows the calibration curves of several polar organic vapors that were tested using a SWCNT-COOH chemiresistor. Similar to toluene or octane, chlorobenzene showed only a barely detectable response on a SWCNT-COOH chemiresistor. The remaining compounds in Fig. 8 were able to either accept or partially stabilize the positive charge (i.e., proton) from carboxylic terminals. The responses of these compounds were all “negative,” which equated to a reduction in film resistance. In addition, unlike the other three swelling-

dependent chemiresistors, the negative calibration curves of SWCNT-COOH were all linear, which indicated clear differences in the response mechanism. Salehi-Khojin et al. recently proved that modulation of the conductivity of carbon nanotubes itself plays an important role in highly defected SWCNTs [45]. In the present study, the reactions of covalent modifications (i.e., acidification) created a highly defective SWCNT. All these polar organics in Fig. 8 were basic related to carboxylic acid. With the mechanism that we proposed in Fig. 6, these molecules attracted protons via hydrogen bonds accepting and releasing some of the electron density back to the carbon nanotubes, thus, the conductivity of the chemiresistor was increased. We have

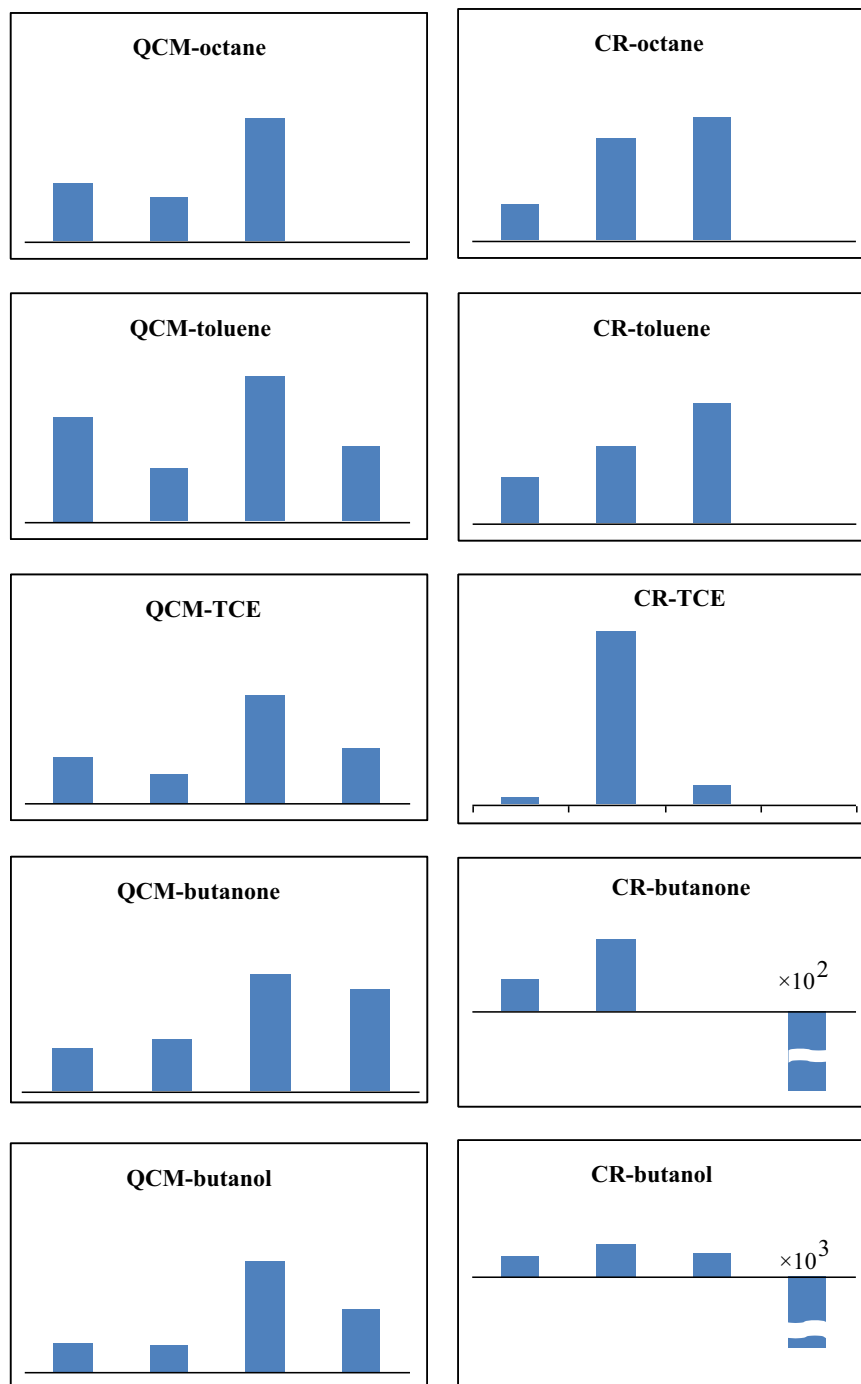


Fig. 9. Response patterns of five VOCs obtained from SWCNT-coated QCM and chemiresistor arrays. Coatings (from left to right): SWCNT, SWCNT-ESTER, SWCNT-SDS, SWCNT-COOH.

also tested several nonpolar organic vapors such as xylene and trichloroethylene, and none of these compounds showed measurable responses on the SWCNT-COOH chemiresistor.

3.5. QCM and chemiresistor response patterns

Response patterns are usually plotted as either a bar chart or a radar chart that shows the relative sensitivity of a sensor array to a target analyte. The most common approach is to normalize the sensitivity (i.e., calibration slope) with respect to the highest sensitivity in the sensor array. In the present study we plotted the response pattern of a QCM array in a conventional manner for five tested vapors, as shown in Fig. 9a–e. The extraction of response patterns from chemiresistor calibrations is somewhat difficult because the calibrations of swelling-dependent chemiresistors are nonlinear over the tested concentration range. We used the first portion of a calibration curve at low concentration range that could be approximated as a straight line, and then used the slope of this section to draw the response patterns (Fig. 9f–j).

The response patterns of the QCM arrays indicated that the surface modifications with SDS coating significantly increased the amount of absorption mass for most compounds. The covalent modification of a SWCNT into a COOH or ester group can alter the preferences to different functional groups to some degree. The response patterns of the chemiresistors were dramatically different from those of the QCM arrays. Despite the unique sensing behavior of the SWCNT-COOH chemiresistor, the relative sensitivities of the other three chemiresistors were also highly distinguishable. The additional mechanisms that were involved in the resistive changes led to the differences between chemiresistor and QCM patterns. It is noteworthy that the same set of SWCNTs can express different response patterns on two different sensor platforms. The versatile properties of sensing materials and the choice of proper sensing platforms are essential for constructing a hybrid array [46]. This discrepancy between QCMs and chemiresistors can be used to create a hybrid array that can potentially improve the recognition rate for vapors.

In the present study, the covalent surface modification started with converting a pristine SWCNT to a SWCNT-COOH. Dramatic changes in chemiresistor selectivity were observed: insensitive to nonpolar compounds and an increase in conductivity versus polar compounds. When the carboxyl acid groups further reacted to esters, these characteristics disappeared and the behavior of SWCNT-ESTER chemiresistors returned to swelling-dependent. This result indicated that the proton of a carboxyl acid plays an essential role in the unique response selectivity of a SWCNT-COOH chemiresistor.

4. Conclusion

In the present study, QCM and chemiresistor platforms were used to investigate the selectivity mechanisms of one pristine and three surface-modified SWCNTs. The results of the QCM provided a direct indication of the VOC partition selectivity of SWCNT surfaces. The chemiresistors responded to either swelling or charge modulation depending on the type of SWCNT. Surface-acidified SWCNT-COOHs showed a unique H-bond interlock that prohibited the swelling mechanism. However, the resistance of SWCNT-COOHs could be modulated via H-bond formation. The response time, linearity and relative sensitivities were all different between QCM and chemiresistor arrays coated with the same set of SWCNTs. The signal transduction mechanisms behind SWCNT-coated QCMs and chemiresistors were quite different, which implies that the diversified properties of surface-modified SWCNTs can be used to create a highly selective hybrid array.

Acknowledgements

The funding for this work was supported by the National Science Council of Taiwan under the project number NSC-100-2113-M-003-001-MY2.

Appendix A. Supporting information

Supplementary data associated with this article can be found in the online version at <http://dx.doi.org/10.1016/j.talanta.2014.08.027>.

References

- [1] L. Mølhave, *Indoor Air* 1 (1991) 357–376.
- [2] B. Tolnai, J. Hlavay, D. Möller, H.-J. Prümke, H. Becker, M. Dostler, *Microchem. J.* 67 (2000) 163–169.
- [3] J. Gutiérrez, M.C. Horrillo, *Talanta* 124 (2014) 95–105.
- [4] D.L. García-González, N. Tena, R. Aparicio-Ruiz, R. Aparicio, *Talanta* 120 (2014) 342–348.
- [5] C.L. Li, C.J. Lu, *Talanta* 79 (2009) 851–855.
- [6] S.J. Patrash, E.T. Zellers, *Anal. Chem.* 65 (1993) 2055–2066.
- [7] J.C. Echeverría, P. Vicente, J. Estella, J.J. Garrido, *Talanta* 99 (2012) 433–440.
- [8] Y.Q. Chen, C.J. Lu, *Sens. Actuators, B* 135 (2009) 492–498.
- [9] K.J. Chen, C.J. Lu, *Talanta* 73 (2007) 358–365.
- [10] W.H. Steinecker, M.P. Rowe, E.T. Zellers, *Anal. Chem.* 79 (2007) 4977–4986.
- [11] C.Y. Yang, C.L. Li, C.J. Lu, *Anal. Chim. Acta* 565 (2006) 17–26.
- [12] R.S. Jian, R.X. Huang, C.J. Lu, *Talanta* 88 (2012) 160–167.
- [13] M.A. Andio, P.N. Browning, P.A. Morris, S.A. Akbar, *Sens. Actuators, B* 165 (2012) 13–18.
- [14] E.S. Snow, F.K. Perkins, J.A. Robinson, *Chem. Soc. Rev.* 35 (2006) 790–798.
- [15] S. Basu, P. Bhattacharyya, *Sens. Actuators, B* 173 (2012) 1–21.
- [16] T.T. Tung, M. Castro, T.Y. Kim, K.S. Suh, J.F. Feller, *J. Mater. Chem.* 2 (2012) 21754–21766.
- [17] I. Sayago, H. Santos, M.C. Horrillo, M. Aleixandre, M.J. Fernández, E. Terrado, I. Tacchini, R. Aroz, W.K. Maser, A.M. Benito, M.T. Martínez, J. Gutiérrez, E. Muñoz, *Talanta* 77 (2008) 758–764.
- [18] J. Kong, N.R. Franklin, C. Zhou, M.G. Chapline, S. Peng, K. Cho, H. Dai, *Science* 287 (2000) 622–625.
- [19] J. Li, Y. Lu, Q. Ye, M. Cinke, J. Han, M. Meyyappan, *Nano Lett.* 3 (2003) 929–933.
- [20] M. Consales, S. Campopiano, A. Cutolo, M. Penza, P. Aversa, G. Cassano, M. Giordano, A. Cusano, *Sens. Actuators, B* 118 (2006) 232–242.
- [21] L. Lvova, M. Mastroianni, G. Pomarico, M. Santonico, G. Pennazza, C. Di Natale, R. Paolesse, A. D'Amico, *Sens. Actuators, B* 170 (2012) 163–171.
- [22] C. Viespe, C. Grigoriu, *Sens. Actuators, B* 147 (2010) 43–47.
- [23] I. Sayago, M.J. Fernández, J.L. Fontecha, M.C. Horrillo, C. Vera, I. Obieta, I. Bustero, *Sens. Actuators, B* 156 (2011) 1–5.
- [24] S. Manivannan, A.M. Saranya, B. Renganathan, D. Sastikumar, G. Gobi, *Kyu Chang Park, Sens. Actuators, B* 171–172 (2012) 634–638.
- [25] D.R. Kauffman, A. Star, *Angew. Chem. Int. Ed.* 47 (2008) 6550–6570.
- [26] U. Tisch, H. Haick, *J. Breath Res* 8 (2014) 1–8.
- [27] C. Di Natale, R. Paolesse, E. Martinelli, R. Capuano, *Anal. Chim. Acta* 824 (2014) 1–17.
- [28] S. Liu, Q. Shen, Y. Cao, L. Gan, Z. Wang, M.L. Steigerwald, X. Guo, *Coord. Chem. Rev.* 254 (2010) 1101–1116.
- [29] J. Lu, J.F. Feller, B. Kumar, M. Castro, Y.S. Kim, Y.T. Park, J.C. Grunlan, *Sens. Actuators, B* 155 (2011) 28–36.
- [30] S. Badhulika, N.V. Myung, A. Mulchandani, *Talanta* 123 (2014) 109–114.
- [31] B. Kumar, M. Castro, J.F. Feller, *Sens. Actuators, B* 161 (2012) 621–628.
- [32] Y.L. Zhao, J.F. Stoddart, *Acc. Chem. Res.* 42 (2008) 1161–1171.
- [33] B. Kumar, M. Castro, J.F. Feller, *Chem. Senses* 3 (2013) 1–7.
- [34] K. Balasubramanian, M. Burghard, *Small* 1 (2005) 180–192.
- [35] F. Wang, T.M. Swager, *J. Am. Chem. Soc.* 133 (2011) 11181–11193.
- [36] M. Penza, R. Rossi, M. Alvisi, M.A. Signore, E. Serra, R. Paolesse, A. D'Amico, C. Di Natale, *Sens. Actuators, B* 144 (2010) 387–394.
- [37] M.D. Shirsat, T. Sarkar, J. Kakoullis Jr., N.V. Myung, B. Konnanath, A. Spanias, A. Mulchandani, *J. Phys. Chem. C* 116 (2012) 3845–3850.
- [38] B. Esser, J.M. Schnorr, T.M. Swager, *Angew. Chem. Int. Ed.* 51 (2012) 5752–5756.
- [39] A. Star, T.-R. Han, V. Joshi, J.P. Gabriel, G. Gruner, *Adv. Mater.* 16 (2004) 2049–2052.
- [40] A. Star, J.P. Gabriel, K. Brasley, G. Gruner, *Nano Lett.* 3 (2003) 459–463.
- [41] N. Peng, Q. Zhang, C.L. Chow, O.K. Tan, N. Marzari, *Nano Lett.* 9 (2009) 1626–1630.
- [42] J. Lu, B. Kumar, M. Castro, J.F. Feller, *Sens. Actuators, B* 140 (2009) 451–460.
- [43] A. Bouvree, J.F. Feller, M. Castro, Y. Grohens, M. Rinaudo, *Sens. Actuators, B* 138 (2009) 138–147.
- [44] B. Kumar, J.F. Feller, M. Castro, *J. Lu, Talanta* 81 (2010) 908–915.
- [45] A. Salehi-Khojin, F. Khalili-Araghi, M.A. Kuroda, K.Y. Lin, J.-P. Leburton, R. I. Masel, *ACS Nano* 5 (2011) 153–158.
- [46] C.L. Li, Y.F. Chen, M.H. Liu, C.J. Lu, *Sens. Actuators, B* 169 (2012) 349–359.



A highly sensitive resonance light scattering probe for Alzheimer's amyloid- β peptide based on $\text{Fe}_3\text{O}_4@Au$ composites



Ling Yu^a, Yintang Zhang^b, Ran Chen^c, Danhua Zhang^c, Xiuhua Wei^b, Fang Chen^b, Jianxiu Wang^a, Maotian Xu^{a,b,*}

^a College of Chemistry and Chemical Engineering, Central South University, Changsha 410083, PR China

^b College of Chemistry and Chemical Engineering, Shangqiu Normal University, Shangqiu 476000, PR China

^c College of Chemistry and Molecular Engineering, Zhengzhou University, Zhengzhou 450052, PR China

ARTICLE INFO

Article history:

Received 11 April 2014

Received in revised form

17 July 2014

Accepted 21 July 2014

Available online 11 August 2014

Keywords:

Amyloid- β peptide

$\text{Fe}_3\text{O}_4@Au$ composites

Core/shell

Resonance light scattering

ABSTRACT

The fabrication of $\text{Fe}_3\text{O}_4@Au$ composites as a novel resonance light scattering (RLS) probe for the sensitive detection of Alzheimer's amyloid- β peptide ($A\beta$) was demonstrated. Amino groups coated magnetic Fe_3O_4 nanoparticles were covered with gold shell by the classical Frens method. The resultant colloids were characterized with X-ray diffraction (XRD), transmission electron microscopy (TEM), X-ray photoelectron spectroscopy (XPS), dynamic light scattering (DLS) and UV–visible spectra. The results indicated that the composite particles with core/shell structure and an average diameter of ~ 320 nm were stable and biocompatible. The RLS intensity of $\text{Fe}_3\text{O}_4@Au$ composites was significantly enhanced by interacting with $A\beta$. Under optimal conditions, good linear relationship between the ratio of RLS intensity I/I_0 at 463.0 nm and the logarithmic value of $A\beta$ concentration in the range of 5.0×10^{-15} – 5.56×10^{-9} M was found. The limit of detection (LOD) was 1.2×10^{-15} M. The proposed method is simple, sensitive and cost-effective and complementary to other existing methods for protein analysis.

© 2014 Elsevier B.V. All rights reserved.

1. Introduction

Alzheimer's disease (AD), the most common type of dementia in the elderly, is a progressive and devastating neurodegenerative disease causing memory loss, impaired thinking and other symptoms [1]. The hallmarks of AD pathology are extracellular amyloid- β peptide ($A\beta$) plaques and intracellular neurofibrillary tangles (NFT). $A\beta$ is an ~ 4 kDa peptide consisting of 39–43 amino acid residues and derived from amyloid precursor protein (APP) [2]. In recent studies, $A\beta$ indicates a biomarker for AD in cerebrospinal fluid (CSF), blood, plasma and serum [3–5]. Therefore, it is important to determine the $A\beta$ concentration for early diagnosis and treatment of AD.

Many techniques have been developed for $A\beta$ quantification, which include, but are not limited to, molecular spectroscopy (e.g., congo red staining [6], Fourier spectral analysis [7]), immunoassay (e.g., capillary isoelectric focusing immunoassay [8], enzyme-linked immunosorbent assay (ELISA) [9], immunoprecipitation [10], dot-blot [11] and western blot analysis [12]), molecular

imaging (e.g., positron emission tomography (PET) [13] and fluorescence microscopy [14]), probe (e.g., small probe molecules [15] and quantum-dot nanoprobe [16]), electrochemical techniques [17,18], mass spectrometry (e.g., TOF-MS [19], MALDI-MS [20]), chromatographic method (e.g., high performance liquid chromatography coupled with mass spectrometry (LC–MS) [21], capillary electrophoresis [22] and immobilized metal affinity chromatography [23]) and synthetic analysis method (e.g., meta-analysis [24]). However, each of these techniques has one or several undesirable limitations, such as expensive instrument, low sensitivity, and not environmental-friendly or instability of some reagents. Thus, it is important to develop alternative techniques which can be complementary to the existing techniques for specific applications.

Resonance light scattering (RLS) has emerged as a powerful optical technique based on elastic light-scattering [25]. Due to the advantages of high sensitivity, rapidness, simplicity and convenience (using a common spectrofluorometer), RLS has attracted much more attention from analytical chemists and physicists. Recently, RLS has been applied to determine inorganic ions [26,27], nanoparticles [28], proteins [29–31], nucleic acids [32,33], and so on.

Colloidal gold nanoparticles including different surface coatings have been investigated extensively to quantify protein concentrations. Enhanced RLS signal is often observed when the interaction between gold nanoparticles and protein molecules occurs as

* Corresponding author at: College of Chemistry and Chemical Engineering, Shangqiu Normal University, Shangqiu 476000, PR China. Tel.: +86 370 2594306.

E-mail addresses: xumaotian@163.com, xumaotian@sqnc.edu.cn (M. Xu).

a result of the formation of aggregation or network structure of gold nanoparticles [34]. Detection of A β by spectroscopic techniques based on gold nanoparticles has been reported recently [35–38]. Wang and coworkers were the first to use gold nanoparticles as RLS probes to realize A β determination at level of ng/mL [36]. The blood A β levels in healthy and AD individuals are in the order of pg/mL [39]. Therefore, it is necessary to improve the RLS sensitivity based gold nanoparticles. To best of our knowledge, the RLS study of Fe₃O₄@Au composites has not been reported in the literature. The Fe₃O₄@Au composite particles possess the advantages of both colloidal gold and magnetic particles, indicating that Fe₃O₄@Au composites can be a new approach to spectral RLS assay, and have numerous successful applications in the fields of biology and medicine [40–44].

In the present work, we report a highly sensitive probe based on Fe₃O₄@Au composites combined with RLS technique to determine the content of Alzheimer's β -amyloid peptide. Firstly, magnetic Fe₃O₄ nanoparticles are prepared. After amino groups coating, Fe₃O₄ nanoparticles are covered with gold shell by the classical Frens method. The resultant Fe₃O₄@Au composites are stable and biocompatible. The ratio of RLS intensity I/I_0 at 463.0 nm is taken to provide a distinguished sensitivity and satisfactory linear range for A β detection. Our approach is simple, sensitive and cost-effective in protein analysis.

2. Materials and methods

2.1. Materials and reagents

A β 1–42 peptide (hereinafter to be referred as A β) was obtained from ChinaPeptides Co., Ltd. (Shanghai, China). Tetrachloroauric acid tetrahydrate (HAuCl₄·4H₂O), iron (III) chloride hexahydrate (FeCl₃·6H₂O), Sodium acetate anhydrous, ethylene glycol and ethanol were obtained from Sinopharm Chemical Reagent Co., Ltd. (Shanghai, China). Sodium citrate trihydrate (Na₃C₆H₅O₇·3H₂O) was obtained from Amersco (USA). (3-Aminopropyl) triethoxysilane (APTES) was purchased from Sigma (USA). Hydrochloric acid (HCl) was purchased from Fangjing Chemical Reagent Co., Ltd. (Kaifeng, China). 1,1,1,3,3,3-Hexafluoro-2-propanol (HFIP) was obtained from Nanjing viochem Co., Ltd. (Nanjing, China). All chemicals were A.R. grade and used as received without any further purification. Millipore water (18.2 M Ω cm at 25 °C) was used throughout all experiments.

2.2. Preparation of amyloid- β peptide

A β was prepared as described previously [45]. Briefly, the lyophilized A β peptide was treated with HFIP at room temperature for 1 h in a sealed vial to dissolve potential aggregates. After that, HFIP was removed under a gentle stream of nitrogen and the peptide film was dissolved in DMSO to a concentration of 2 mM. Thus the peptide stock solutions were prepared.

2.3. Synthesis of Fe₃O₄ nanoparticles

Fe₃O₄ nanoparticles were prepared by hydrothermal treatment of FeCl₃·6H₂O and CH₃COONa in ethylene glycol solution. In a typical procedure, 0.2425 g FeCl₃·6H₂O was dissolved in 15 mL of ethylene glycol to form a clear solution, followed by the addition of 0.3751 g anhydrous CH₃COONa. The mixture was vigorously mixed by ultrasonication to give a homogeneous solution. Then the solution was transferred into a stainless steel autoclave (30 mL capacity) followed by hydrothermal treatment at 200 °C for 4.5 h. After the autoclave was cooled down to room temperature, the products were magnetically separated and washed several times

with water and ethanol alternately to eliminate organic and inorganic impurities. After that, the products were dispersed in ethanol for further experiments.

2.4. Synthesis of Fe₃O₄@Au composites

To modify the surface of the magnetic nanoparticles with amino groups, Fe₃O₄ suspension (10 mg/mL, 2 mL) was added into 50 mL ethanol in a flask followed by the addition of 1 mL of APTES under stirring. The mixture was refluxed at 80 °C for 4 h. The APTES-coated Fe₃O₄ NPs were then magnetically separated, washed several times under sonication with water and ethanol and dispersed in ethanol.

Next, gold coating was implemented by the classical Frens method [46]. Briefly, 0.5 mL of APTES-coated Fe₃O₄ NPs (0.5 mg/mL) was added into 200 mL of 7.76 mM sodium citrate solution when the temperature was raised to 99 °C, followed by the dropwise addition of 10 mL of HAuCl₄ solution (10 mM) under a nitrogen atmosphere while stirring. The heating mantle was removed 30 min later. The solution was kept stirring for another 15 min and was cooled to room temperature.

The resulting dark particles were separated with a NdFeB magnet and washed with water several times. Uncoated Fe₃O₄ material was dissolved by a rinse with 30% HCl for more than 20 h, leaving largely pure Fe₃O₄@Au composites in the system [47].

2.5. Characterization of nanoparticle and composites

The phase structure was examined by powder X-ray diffraction (XRD), using X'Pert Pro MRD instrument (PANalytical B.V., Netherlands), with Cu K α radiation at a scan rate of 0.033° 2 θ s⁻¹. Transmission electron microscopy (TEM) was obtained with Hitachi-800 instrument (Hitachi, Japan), operated at 120 kV. X-ray photoelectron spectroscopy (XPS) was measured on a K-Alpha 1063 Instrument (Thermo Fisher Scientific, UK). The size distribution of the microspheres was determined by Zetasizer Nano ZS (Malvern Instruments, UK). Ultraviolet–visible spectra were recorded using a Cary 60 spectrophotometer (Agilent technologies, USA) between 200 and 800 nm using a 1-cm path length quartz cuvette.

2.6. Resonance light scattering measurements

A certain amount of Fe₃O₄@Au dispersion was pipetted into a 1-cm path length quartz cuvette and diluted to 1 mL with H₂O, while the final concentration of A β varied from 5.0 \times 10⁻¹⁵ to 5.56 \times 10⁻⁹ M by successive addition of appropriate volume of A β (2.5 or 5 μ L). The mixture was incubated for 10 min. Then RLS measurements were carried out using a Cary Eclipse fluorospectrophotometer (Agilent technologies, USA). The RLS intensities were recorded by synchronously scanning the excitation and emission monochromators ($\Delta\lambda=0$ nm) between 200 and 800 nm. The excitation and emission slit width were both set to 5 nm. All the experiments were carried out at room temperature and repeated at least three times. The intensity was measured at 463.0 nm. The enhanced RLS intensity of Fe₃O₄@Au composites was termed as I/I_0 (I and I_0 were the RLS intensities of the systems with and without A β). In order to eliminate the effect of instrumental factors on the light scattering measurement, the scattering intensities were corrected by using the reported correction methods [48]. Briefly, corrected RLS intensities were calculated by division of the signal intensity at the wavelength by the corresponding source intensity. Meanwhile, the scattering intensities were also corrected for dilution effect.

3. Results and discussion

3.1. Characterization of Fe₃O₄@Au composites

Fig. 1 shows the XRD patterns of the prepared Fe₃O₄ NPs and Fe₃O₄@Au composites. In curve (a) for Fe₃O₄, the diffraction peaks can be assigned to the cubic structure of Fe₃O₄ crystal according to JCPDS card no. 19-0629. In curve (b) for Fe₃O₄@Au, the shape peaks are consistent with that of Au nanocrystal (JCPDS card no. 04-0784). No peak was found for Fe₃O₄ due to the heavy atom effect of Au indicating complete coverage of the Fe₃O₄ core by Au shell [49], which is consistent with previous reports [50].

The morphology of the as-synthesized particles was investigated by TEM. Fig. S1 (Supporting information, SI) shows the typical TEM images of Fe₃O₄ NPs (A) with a diameter of ~156 nm and Fe₃O₄@Au composites (B) with a diameter of ~320 nm. It can be seen from Fig. S1A that the Fe₃O₄ NPs are of well spherical structure with relatively smooth surfaces. After coating with amine groups, gold was then deposited onto the surface of amine-coated Fe₃O₄ NPs. The diameter of Fe₃O₄@Au composites increases, as shown in Fig. S1B, which is twice as large as that of Fe₃O₄ NPs. However, the thickness of gold shells on the surface of Fe₃O₄ NPs was determined to be only approximate 9 nm, suggesting that Fe₃O₄ clusters may exist inside a single Fe₃O₄@Au composite [50].

The size distribution of Fe₃O₄@Au composites was determined by dynamic light scattering (DLS). Fig. S2 shows that the average hydrodynamic diameter of Fe₃O₄@Au composites is 337 nm, in good agreement with the TEM results.

XPS results of Fe₃O₄@Au composites are shown in Fig. 2. Two characteristic peaks of Au 4f_{5/2} and Au 4f_{7/2}, positioned at 83.3 eV and 87.0 eV, respectively, are clearly observed in Fig. 2B, while no Auger peaks of Fe are found (Fig. 2A), indicating that the Fe₃O₄@Au composite surface is mainly composed of gold with a thickness of more than 5 nm [51].

UV–vis spectrum of Fe₃O₄@Au composites is shown in Fig. 3A. The absorption peak of Fe₃O₄@Au composites was red-shifted to 546 nm compared with that of colloid gold at 529 nm. The reason for this might be that the composite diameter is much larger than that of colloid gold [47]. When the Fe₃O₄@Au dispersion was exposed to the external magnetic field for 2 min, no obvious colloid gold were detected in the supernatant, indicating that not pure gold nanoparticles but magnetic Fe₃O₄ particles existed in the as-prepared Fe₃O₄@Au composites. Furthermore, as can be seen in

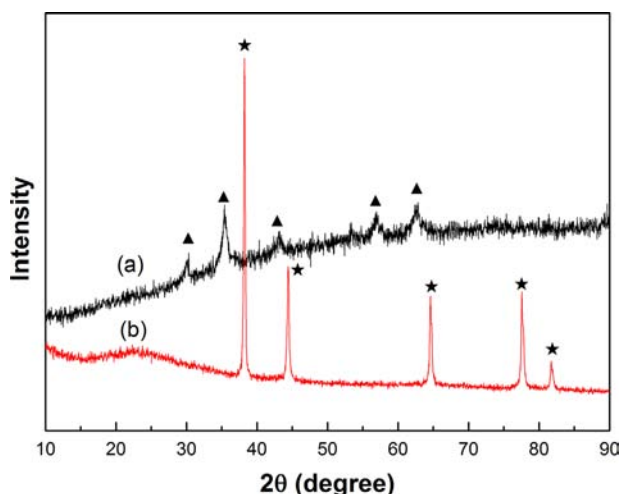


Fig. 1. XRD patterns of (a) Fe₃O₄ NPs and (b) Fe₃O₄@Au hybrid composites. ▲ shows the diffraction peaks of Fe₃O₄ and ★ shows the diffraction peaks of gold.

Fig. 3B, Fe₃O₄@Au composites have scattering characteristic peaks of both Fe₃O₄ and colloid gold. These results are a further proof of core/shell structure of the Fe₃O₄@Au composites.

3.2. Spectral characteristics

The RLS spectra of Aβ (1), water (2), Fe₃O₄@Au composite (3) and Aβ-Fe₃O₄@Au composite (4) are shown in Fig. S3. It can be seen that both Aβ and Fe₃O₄@Au composite have weak scattering signal. When Aβ is mixed with Fe₃O₄@Au composite, the RLS signal is remarkably enhanced with two obvious peaks at 408.0 nm and 463.0 nm. The RLS intensity of the system reaches its maximum at 463.0 nm. Hence, 463.0 nm was selected as the determination wavelength.

3.3. Possible reasons for RLS enhancement

According to the RLS theory [25], the RLS intensity is proportional to r^6 where r is the radius of the particle. However, too larger particle size is not recommended due to its instability. The average diameter of Fe₃O₄@Au composites is ~320 nm, which is much greater than 1/20 of the wavelength of incident light. Therefore, the light scattering of Fe₃O₄@Au composites can be considered as the Mie scattering rather than the Rayleigh scattering. According to the Mie scattering theory, the RLS properties have close relationship with the molecular volume and morphology of the particles [52]. The bigger the molecular volume, the higher the RLS intensity can be obtained.

Once the Fe₃O₄@Au composites are exposed to Aβ molecules, Aβ is believed to bind to the surface of gold shell via both the apolar and the N-donors containing side-chains of amino acids [53]. The formation of conjugates of Fe₃O₄@Au-Aβ results in increasing the size of scatters. Therefore, the RLS intensity of the system is enhanced.

It should be noted that the Mie scattering can be affected by small magnetic spheres magnetism, called as the Magnetic Mie scattering, and the magnetization of small clusters of radius larger than 10 nm is size dependent [54]. However, the mechanism of the effect of magnetic Fe₃O₄ core on the RLS remains unclear.

3.4. Effect of pH and buffer

The surrounding matrix may greatly affect the scattering spectrum of particles. The effects of pH and type of buffer were investigated. As can be seen in Fig. S4(1A) and (1B), the maximum RLS peak wavelengths varies with pH values. When pH value decreases, negatively charged Au particles covered with citrate have the tendency to form aggregation because the electrostatic repellency among Au particles becomes weak. As a result, the maximum RLS peak redshift happens. When pH is in the range of 6.80–7.96, the RLS intensities at the maximum RLS peak wavelengths were much smaller than with other pH values indicating lower background determination. However, the RLS signals were not so stable along with the time. Thus, the effects of different buffer with similar pH values including HEPES buffer, Tris-HCl buffer (Tris) and Britton–Robinson buffer (BR) together with H₂O were investigated. It can be seen from Fig. S4(2B) that the RLS intensity in H₂O keeps very stable and is also small. The results indicated that high ionic strength was the possible reason for RLS instability [55]. Therefore, H₂O is chosen for further research.

3.5. The incubation time and stability

The effect of time of the RLS intensity of the composite-Aβ system was studied. The results showed that the reaction between Fe₃O₄@Au composite and Aβ occurred rapidly at room temperature

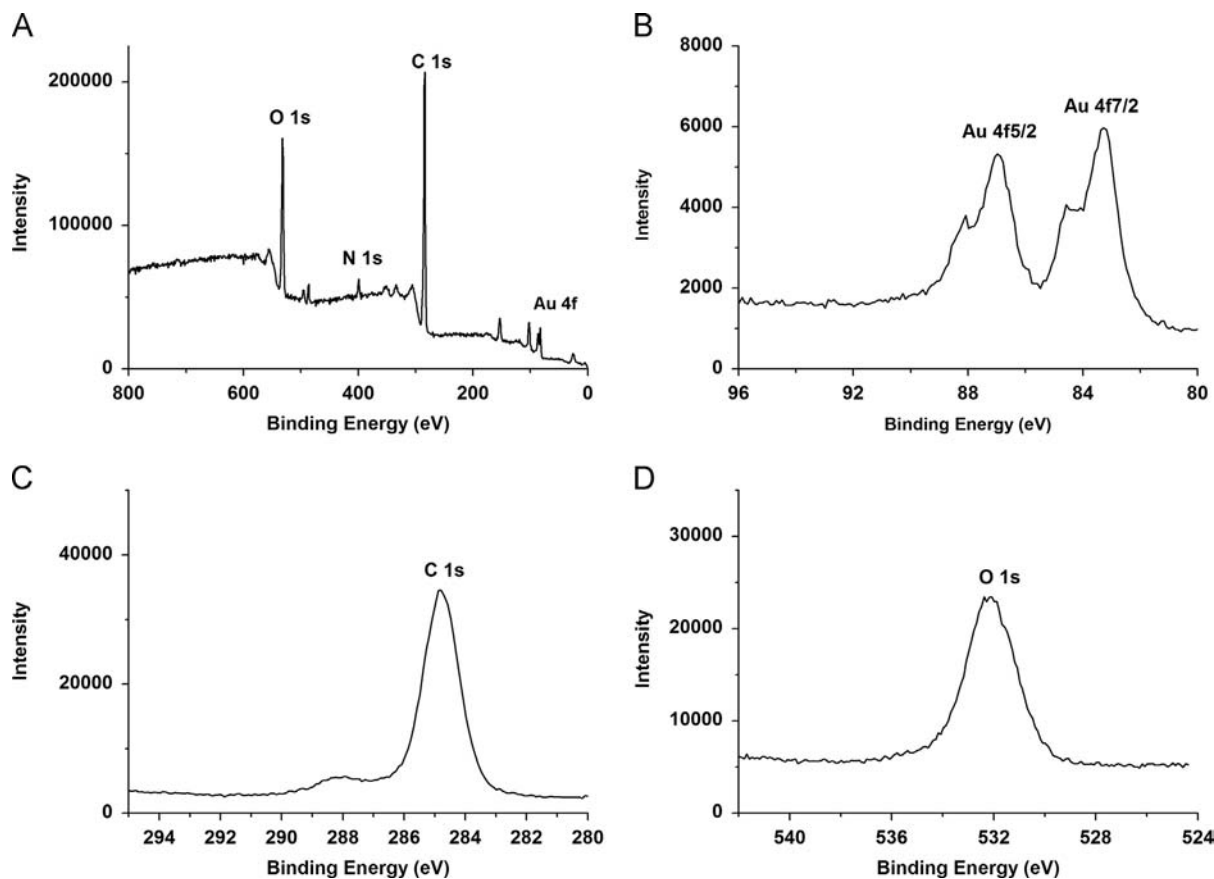


Fig. 2. XPS spectra of Fe_3O_4 @Au composites.

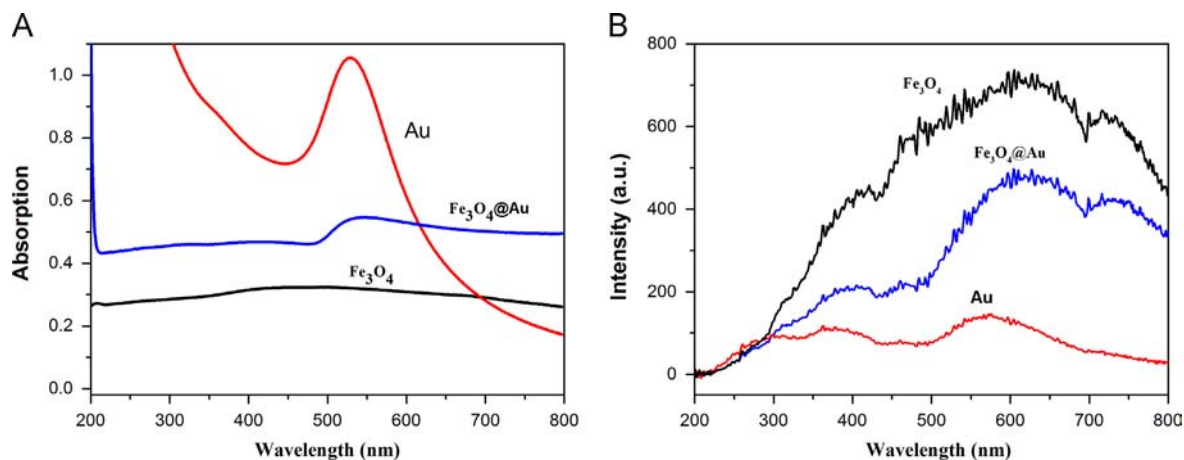


Fig. 3. UV-vis (A) and RLS (B) spectra of Fe_3O_4 , colloidal gold and Fe_3O_4 @Au composites.

(< 10 min). The scattering intensity is stable for at least 60 min. Thus, 10 min of incubation time was considered. The assay exhibits good stability and can be used for practical determination of A β .

3.6. Analytical performance

Under the optimal conditions, the dependence of the RLS intensity on the concentration of A β was determined. As shown in Fig. 4, the RLS intensity increases with the increase of A β concentration. There is a good linear relationship between the ratio of RLS intensity I/I_0 and the logarithmic value of A β

concentration in the range of 5.0×10^{-15} – 5.56×10^{-9} M (the inset in Fig. 4), and the linear regression equation is $I/I_0 = 24.77 + 1.65 \log C$ (M) with the correlation coefficient $R^2 = 0.986$. The limit of detection (LOD) is calculated to be 1.2×10^{-15} M. Each concentration was repeated at least three times and the relative standard deviations (RSD) are between 2.2% and 13.8%. The proposed RLS approach exhibits sufficient low detection level and significant wide linear range, and compares well with other A β assays [36–38]. Meanwhile, the detection limit is far lower than that of the present commercial A β_{1-42} ELISA kit (in the order of a few to a few hundred pg/mL or pM).

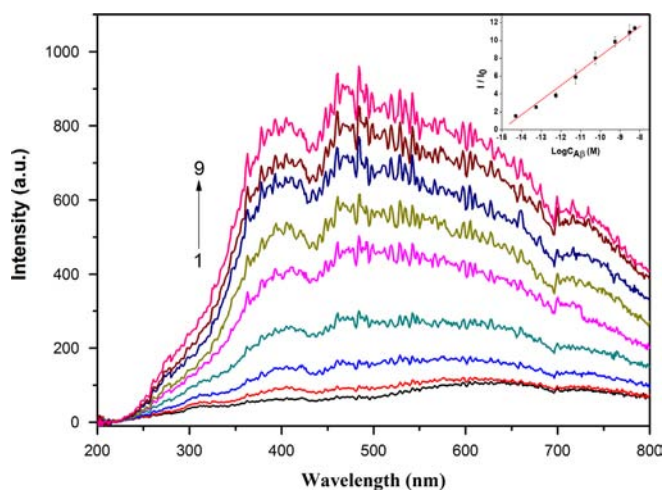


Fig. 4. The RLS spectra of $\text{Fe}_3\text{O}_4@Au$ composites in the presence of different concentration of $A\beta$. $c(\text{Fe}_3\text{O}_4@Au \text{ composite})=0.2 \text{ mg/mL}$; $C(A\beta)/(10^{-12} \text{ M})$, 1–9: 0, 0.005, 0.055, 0.56, 5.56, 55.6, 556, 3056 and 5556. Inset: the linear relationship corresponding to the ratio of RLS intensity I/I_0 at 463.0 nm vs. logarithmic value of $A\beta$ concentration. Each concentration was repeated at least three times.

4. Conclusions

We have demonstrated the fabrication of $\text{Fe}_3\text{O}_4@Au$ composites as a RLS probe for the sensitive detection of Alzheimer's $A\beta$. The resultant composite has an average diameter of $\sim 320 \text{ nm}$. The Fe_3O_4 core was completely covered by Au shell with a thickness of $\sim 9 \text{ nm}$. The RLS signal intensity of $\text{Fe}_3\text{O}_4@Au$ was enhanced by interacting with $A\beta$. Under optimal conditions, the ratio of RLS intensity I/I_0 at 463.0 nm is proportional to the logarithmic value of $A\beta$ concentration in the range of 5.0×10^{-15} – $5.56 \times 10^{-9} \text{ M}$. The detection limit is as low as $1.2 \times 10^{-15} \text{ M}$. The discrimination for the structural diversity of $A\beta$, e.g. monomers, oligomers, and even fibrils, is still under study. Our approach has proved to be simple, sensitive, label-free and cost-effective. The proposed method is complementary to other existing methods for protein analysis.

Acknowledgments

We gratefully acknowledge partial support of this work by the National Natural Science Foundation of China (Nos. 20905045, 21175091), the Program for Innovative Research Team (in Science and Technology) in University of Henan Province (No. 2012IRT-STHNO18), the Innovation Scientists and Technicians Troop Construction Projects of Henan Province, the Science and Technique Foundation of Henan province (Nos. 102102310385, 1121023-10217) and the Foundation for University Young Key Teacher Program of Henan Province (No. 2012GGJS-168).

Appendix A. Supporting information

Supplementary data associated with this article can be found in the online version at <http://dx.doi.org/10.1016/j.talanta.2014.07.067>.

References

- [1] M.R. Boyd, Alzheimer's Disease Diagnosis and Treatments, Nova Science, Hauppauge, N.Y., 2011.
- [2] Q.M. Wang, N. Shah, J. Zhao, C.S. Wang, C. Zhao, L.Y. Liu, L.Y. Li, F.M. Zhou, J. Zheng, Phys. Chem. Chem. Phys. 13 (2011) 15200–15210.
- [3] N.S.M. Schoonenboom, Y.A.L. Pijnenburg, C. Mulder, S.M. Rosso, E.J. Van Elk, G.J. Van Kamp, J.C. Van Swieten, P. Scheltens, Neurology 62 (2004) 1580–1584.
- [4] P.D. Mehta, Curr. Alzheimer Res. 4 (2007) 359–363.
- [5] H. Hampel, Y. Shen, D.M. Walsh, P. Aisen, L.M. Shaw, H. Zetterberg, J.Q. Trojanowski, K. Blennow, Exp. Neurol. 223 (2010) 334–346.
- [6] W.E. Klunk, R.F. Jacob, R.P. Mason, Anal. Biochem. 266 (1999) 66–76.
- [7] R.A. Armstrong, N.J. Cairns, Neuropathol. Appl. Neurobiol. 36 (2010) 248–257.
- [8] U. Haussmann, O. Jahn, P. Linning, C. Janssen, T. Liepold, E. Portelius, H. Zetterberg, C. Bauer, J. Schuchhardt, H.J. Knolker, H. Klafki, J. Wiltfang, Anal. Chem. 85 (2013) 8142–8149.
- [9] M. Jensen, T. Hartmann, B. Engvall, R. Wang, S.N. Uljon, K. Sennvik, J. Naslund, F. Muehlhauser, C. Nordstedt, K. Beyreuther, L. Lannfelt, Mol. Med. 6 (2000) 291–302.
- [10] E. Portelius, A. Westman-Brinkmalm, H. Zetterberg, K. Blennow, J. Proteome Res. 5 (2006) 1010–1016.
- [11] C.K. Wang, D.J. Liu, Z.X. Wang, Chem. Commun. 48 (2012) 8392–8394.
- [12] A. Potempska, K. Mack, P. Mehta, K.S. Kim, D.L. Miller, Amyloid–Int. J. Exp. Clin. Investig. 6 (1999) 14–21.
- [13] C. Hommet, K. Mondon, V. Camus, M.J. Ribeiro, E. Beaufils, N. Arlicot, P. Corcia, M. Paccalin, F. Minier, T. Gosselin, G. Page, D. Guilloteau, S. Chalou, Dement. Geriatr. Cogn. 37 (2014) 1–18.
- [14] P.T. Chang, Y. Su, Brain Res. Protoc. 6 (2000) 6–12.
- [15] H.B. Hong, I.H. Nam, S.W. Sohn, K.B. Song, J. Biomed. Nanotechnol. 9 (2013) 1088–1091.
- [16] K. Tokuraku, M. Marquardt, T. Ikezu, PLoS One 4 (2009) 11.
- [17] L. Liu, F. Zhao, F.J. Ma, L.P. Zhang, S.L. Yang, N. Xia, Biosens. Bioelectron. 49 (2013) 231–235.
- [18] J.V. Rushworth, A. Ahmed, H.H. Griffiths, N.M. Pollock, N.M. Hooper, P.A. Millner, Biosens. Bioelectron. 56 (2014) 83–90.
- [19] A. Matsumoto, R. Matsumoto, K. Kadoyama, T. Nishimoto, S. Matsuyama, O. Midorikawa, Int. J. Pept. Res. Ther. 15 (2009) 205–210.
- [20] S. Trimpin, M.L. Deinzer, J. Am. Soc. Mass Spectrom. 18 (2007) 1533–1543.
- [21] K. Matsumiya, J. Kamiie, S. Ohtsuki, T. Terasaki, Drug Metab. Rev. 39 (2007) 59–60.
- [22] R. Verpillot, H. Esselmann, M.R. Mohamadi, H. Klafki, F. Poirier, S. Lehnert, M. Otto, J. Wiltfang, J.L. Viovy, M. Taverna, Anal. Chem. 83 (2011) 1696–1703.
- [23] A.H. Simonsen, S.F. Hansson, U. Ruetschi, J. McGuire, V.N. Podust, H.A. Davies, P. Mehta, G. Waldemar, H. Zetterberg, N. Andreasen, A. Wallin, K. Blennow, Dement. Geriatr. Cogn. 23 (2007) 246–250.
- [24] F. Song, A. Poljak, M. Valenzuela, R. Mayeux, G.A. Smythe, P.S. Sachdev, J. Alzheimers Dis. 26 (2011) 365–375.
- [25] R.F. Pasternack, C. Bustamante, P.J. Collings, A. Giannetto, E.J. Gibbs, J. Am. Chem. Soc. 115 (1993) 5393–5399.
- [26] H. Cao, M. Wei, Z. Chen, Y. Huang, Analyst 138 (2013) 2420–2426.
- [27] Y. Wang, K. Tan, R. Yuan, Acta Chim. Sin. 70 (2012) 643–648.
- [28] J. Zhu, Y.C. Wang, L.Q. Huang, Y.M. Lu, Phys. Lett. A 323 (2004) 455–459.
- [29] Z. Chen, J. Liu, Y. Han, Talanta 71 (2007) 1246–1251.
- [30] B. Gu, H. Zhong, X.M. Li, Y.Z. Wang, B.C. Ding, Z.P. Cheng, L.L. Zhang, S.P. Li, C. Yao, J. Appl. Spectrosc. 80 (2013) 486–491.
- [31] Q.E. Cao, Z.T. Ding, R.B. Fang, X. Zhao, Analyst 126 (2001) 1444–1448.
- [32] W.J. Zhang, H.P. Xu, S.Q. Wu, X.G. Chen, Z.D. Hu, Analyst 126 (2001) 513–517.
- [33] Q. Zou, Q. Yan, G. Song, S. Zhang, L. Wu, Biosens. Bioelectron. 22 (2007) 1461–1465.
- [34] G. Weng, J. Li, J. Zhu, J. Zhao, Colloids Surf. A 369 (2010) 253–259.
- [35] C.K. Wang, J.E. Wang, D.J. Liu, Z.X. Wang, Talanta 80 (2010) 1626–1631.
- [36] C. Wang, D. Liu, Z. Wang, Chem. Commun. 47 (2011) 9339–9341.
- [37] W.A. El-Said, T.H. Kim, C.H. Yea, H. Kim, J.W. Choi, J. Nanosci. Nanotechnol. 11 (2011) 768–772.
- [38] M. Sakono, T. Zako, M. Maeda, Anal. Sci. 28 (2012) 73–76.
- [39] A. Ruiz, P. Pesini, A. Espinosa, V. Pérez-Grijalba, S. Valero, O. Sotolongo-Grau, M. Alegret, I. Monleón, A. Lafuente, M. Buendía, M. Ibarria, S. Ruiz, I. Hernández, I. San José, L. Tárraga, M. Boada, M. Sarasa, PLoS One 8 (2013) e81334.
- [40] H. Yin, C. Wang, H. Zhu, S.H. Overbury, S. Sun, S. Dai, Chem. Commun. (2008) 4357–4359.
- [41] C. Yang, J. Wu, Y. Hou, Chem. Commun. 47 (2011) 5130–5141.
- [42] G.K. Kouassi, Curr. Nanosci. 7 (2011) 510–523.
- [43] K.C.F. Leung, S. Xuan, X. Zhu, D. Wang, C.P. Chak, S.F. Lee, W.K.W. Ho, B.C. T. Chung, Chem. Soc. Rev. 41 (2012) 1911–1928.
- [44] Y.H. Bai, J.Y. Li, J.J. Xu, H.Y. Chen, Analyst 135 (2010) 1672–1679.
- [45] D. Brambilla, R. Verpillot, M. Taverna, L. De Kimpe, B. Le Droumaguet, J. Nicolas, M. Canovi, M. Gobbi, F. Mantegazza, M. Salmona, V. Nicolas, W. Scheper, P. Couvreur, K. Andrieux, Anal. Chem. 82 (2010) 10083–10089.
- [46] G. Frens, Nat. Phys. Sci. 241 (1973) 20–22.
- [47] Y.L. Cui, W.L. Hui, J. Su, Y.N. Wang, C. Chen, Sci. China Ser. B 48 (2005) 273–278.
- [48] P. McPhie, Anal. Biochem. 348 (2006) 157–159.
- [49] Z. Xu, Y. Hou, S. Sun, J. Am. Chem. Soc. 129 (2007) 8698–8699.
- [50] X. Zhou, W. Xu, Y. Wang, Q. Kuang, Y. Shi, L. Zhong, Q. Zhang, J. Phys. Chem. C 114 (2010) 19607–19613.
- [51] K. Siegbahn, Philos. Trans. R. Soc. Lond., Ser. A 268 (1970) 33–57.
- [52] W. Hergert, T. Wriedt, The Mie Theory: Basics and Applications, Springer, Berlin, 2012.
- [53] A. Majzik, L. Fülöp, E. Csapó, F. Bogár, T. Martinek, B. Penke, G. Bíró, I. Dékány, Colloids Surf. B 81 (2010) 235–241.
- [54] R.J. Tarento, K.H. Bennemann, P. Joyes, J. Van de Walle, Phys. Rev. E 69 (2004) 5.
- [55] J.K. Lim, S.A. Majetich, R.D. Tilton, Langmuir 25 (2009) 13384–13393.



Application of a novel metabolomic approach based on atmospheric pressure photoionization mass spectrometry using flow injection analysis for the study of Alzheimer's disease



Raúl González-Domínguez^{a,b,c}, Tamara García-Barrera^{a,b,c,*}, José Luis Gómez-Ariza^{a,b,c,**}

^a Department of Chemistry and CC.MM, Faculty of Experimental Science, University of Huelva, Campus de El Carmen, 21007 Huelva, Spain

^b Campus of Excellence International ceiA3, University of Huelva, Spain

^c Research Center of Health and Environment (CYSMA), University of Huelva, Campus de El Carmen, 21007 Huelva, Spain

ARTICLE INFO

Article history:

Received 22 May 2014

Received in revised form

21 July 2014

Accepted 25 July 2014

Available online 21 August 2014

Keywords:

Alzheimer's disease

Metabolomics

Atmospheric pressure photoionization

Flow injection

ABSTRACT

The use of atmospheric pressure photoionization is not widespread in metabolomics, despite its considerable potential for the simultaneous analysis of compounds with diverse polarities. This work considers the development of a novel analytical approach based on flow injection analysis and atmospheric pressure photoionization mass spectrometry for rapid metabolic screening of serum samples. Several experimental parameters were optimized, such as type of dopant, flow injection solvent, and their flows, given that a careful selection of these variables is mandatory for a comprehensive analysis of metabolites. Toluene and methanol were the most suitable dopant and flow injection solvent, respectively. Moreover, analysis in negative mode required higher solvent and dopant flows (100 $\mu\text{l min}^{-1}$ and 40 $\mu\text{l min}^{-1}$, respectively) compared to positive mode (50 $\mu\text{l min}^{-1}$ and 20 $\mu\text{l min}^{-1}$). Then, the optimized approach was used to elucidate metabolic alterations associated with Alzheimer's disease. Thereby, results confirm the increase of diacylglycerols, ceramides, ceramide-1-phosphate and free fatty acids, indicating membrane destabilization processes, and reduction of fatty acid amides and several neurotransmitters related to impairments in neuronal transmission, among others. Therefore, it could be concluded that this metabolomic tool presents a great potential for analysis of biological samples, considering its high-throughput screening capability, fast analysis and comprehensive metabolite coverage.

© 2014 Elsevier B.V. All rights reserved.

1. Introduction

The main challenge in metabolomics is to obtain comprehensive and unbiased metabolic fingerprints of samples due to the huge heterogeneity and dynamism of metabolome [1]. In this context, mass spectrometry represents a very interesting analytical platform, since complexity of metabolome may be overcome through the use of complementary atmospheric pressure ionization methods [2]. Electrospray (ESI) is the most common ionization source employed

<http://dx.doi.org/10.1016/j.talanta.2014.07.075>
0039-9140/© 2014 Elsevier B.V. All rights reserved.

in metabolomic studies because it is able to ionize compounds in a wide range of masses and polarities, and it may be coupled to liquid chromatography [3,4], capillary electrophoresis [5,6] or used by direct infusion mass spectrometry [7]. A second alternative is atmospheric pressure chemical ionization (APCI), more suitable for less polar compounds [8,9]. Finally, atmospheric pressure photoionization (APPI) complements ESI and APCI for the analysis of little polar or non-polar compounds, but it has been considerably less used in metabolomics. Atmospheric pressure photoionization is the most recent soft ionization technique for mass spectrometry, introduced simultaneously by Bruins and Syage in 2000 [10,11], extending the range of ionizable compounds to less polar ones, which are not readily ionized by ESI and APCI. Nevertheless, APPI is capable of ionizing both polar and non-polar compounds through proton transfer and charge exchange reactions respectively, so it could be considered a universal ionization source [12]. The APPI interface uses a photoionization lamp and a dopant flow to form dopant radical ions, which can directly ionize non-polar analytes through charge exchange reactions. On the other hand, for polar

* Corresponding author at: Department of Chemistry and CC.MM, Faculty of Experimental Science, University of Huelva, Campus de El Carmen, 21007 Huelva, Spain. Tel.: +34 959 219962; fax: +34 959 219942.

** Corresponding author at: Department of Chemistry and CC.MM, Faculty of Experimental Science, University of Huelva, Campus de El Carmen, 21007 Huelva, Spain. Tel.: +34 959 219968; fax: +34 959 219942.

E-mail addresses: raul.gonzalez@dqcm.uhu.es (R. González-Domínguez), tamara.garcia@dqcm.uhu.es, tamara@dqcm.uhu.es (T. García-Barrera), ariza@dqcm.uhu.es, ariza@uhu.es (J.L. Gómez-Ariza).

compounds dopant photoions can produce intermediate reactive species by reactions with solvent or oxygen molecules, in positive and negative ionization modes respectively, followed by a proton transfer reaction to the analyte [12]. Thereby, for the simultaneous analysis of both polar and non-polar compounds, the two reaction pathways must be accessible, which requires a careful selection of solvent, dopant, and their flows. Firstly, the carrier solvent employed can lead to a preferential mechanism, being favored charge exchange for low proton affinity solvents, whereas the addition of methanol or acetonitrile initiates proton transfer [13]. In the case of dopant, the most common reagent is toluene, but it may be not suitable for the ionization of non-polar compounds in high proton affinity solvents since it tends to transfer its proton to the solvent [14]. Alternatively, other dopants less reactive with the solvent have been proposed, such as anisole [15] or substituted benzenes [16]. Finally, the flow-rate of both solvent and dopant also play important roles in the photoionization process. In the case of solvent, ionization efficiency decreases when the flow increases, due to the formation of large unreactive protonated-solvent cluster ions, while signal increases with the dopant flow, until reach 5–10% of solvent flow [17]. Moreover, it has been reported that toluene can provide high ionization efficiency simultaneously to both polar and non-polar compounds delivered in reversed-phase solvents, simply limiting the solvent flow rate in order to avoid that reactions between toluene photoions and solvent were driven to completion [18].

In this way, APPI might present a considerable potential in metabolomics, not only because of its universality in terms of ionization capability, but also because is less susceptible to matrix effects and presents a linear dynamic range generally higher than that for ESI [19,20]. In addition, it requires less heat for desolvation than APCI allowing the analysis of thermally labile compounds [21]. APPI has been used for the analysis of many classes of compounds, including pharmaceutical drugs and metabolites [22], steroids [21], aldehydes and ketones [23] or pesticides [24]. However, only a few non targeted approaches include APPI as an alternative in metabolomics. Thereby, metabolomics based on liquid chromatography mass spectrometry and the integration of multiple ionization modes (ESI, APCI and APPI) has been previously proposed for the study of urine [25] and plasma samples [26], or to perform a more comprehensive analysis of lipidome [27–28]. Although APPI is normally coupled to liquid chromatography [29] or capillary electrophoresis [30], several reports confirm the ability of flow injection analysis for the determination of fullerenes and perfluorinated compounds [31], characterization of wine [32], olive oil [33] or Iberian ham [34], or the study of drugs [35] and petroleum [36]. This high-throughput approach exhibits several advantages in metabolomics such as fast and reproducible analysis, comprehensive metabolite coverage and simple data pre-processing [7], but it also presents important drawbacks associated with the lack of resolution for the differentiation of isobars and difficulty of quantification due to ion suppression. In order to overcome problems associated with isobaric interferences, the use of high resolution systems has become the main workhorse for accurate MS-fingerprinting, including time-of-flight (TOF), Fourier transform ion cyclotron resonance (FTICR), and especially the hybrid system Q-TOF, which allows more accurate mass measurement than single TOF instruments and structural elucidation by MS/MS experiments [37]. On the other hand, although ion suppression is a potential problem in any MS-based metabolomic platform, there is no evidence that it presents a more detrimental effect on flow infusion fingerprinting than in hyphenated approaches [7]. In fact, the large amount of different compounds in biological samples helps to regulate matrix effects, so that ion suppression becomes a constant factor imposed uniformly in all samples derived from

similar types of tissues [38]. Thereby, MS-fingerprinting has proved to be an excellent tool for high-throughput metabolomic characterization of complex samples, usually using electrospray ionization, as recently reviewed by Draper et al. [7]. However, to date, the use of FIA-APPI-MS has not been considered in metabolomic analysis.

This work explores for the first time the potential of flow injection analysis and high resolution tandem mass spectrometry with atmospheric pressure photoionization source (FIA-APPI-QTOFMS) in metabolomics. Several critical parameters were optimized for the simultaneous analysis of both polar and non-polar compounds in positive and negative ionization modes, such as type of dopant, flow injection solvent and their working flows. For this purpose, a test mixture of representative metabolites from human serum was used. Then, the optimized approach was applied to blood serum samples in order to investigate metabolic abnormalities associated with Alzheimer's disease (AD). This neurodegenerative disorder is poorly understood, and its etiology is still unknown, although it is likely to be a conglomeration of different pathological entities. There is currently no cure for Alzheimer's disease, but early diagnosis could help monitor disease progression and target therapies earlier in the course of the disease, so identification of reliable biomarkers is becoming increasingly important. Multivariate statistics demonstrated the ability of this high-throughput metabolomic tool for discriminating between AD patients and healthy controls, and allowed the identification of different metabolic failures underlying to pathological features of this health disorder.

2. Material And methods

2.1. Chemicals and samples

The solvents (HPLC-grade) methanol, ethanol, chloroform, dichloromethane, acetonitrile and isopropanol were purchased from Fisher Scientific (Leicestershire, UK), while dopants toluene, anisole and chlorobenzene were supplied by Aldrich (Steinheim, Germany). Water was purified with a Milli-Q Gradient system (Millipore, Watford, UK). Standards of L-glutamine, L-valine, L-cysteine, L-aspartic acid, L-arginine, L-histidine, L-glutamic acid, L-phenylalanine, D-glucose, creatine, creatinine, cholesterol, di-oleoyl-phosphocholine and triolein were from Sigma Aldrich. Blood samples were collected in the morning by puncture of the antecubital vein and collected in BD Vacutainer SST II tubes with gel separator and Advance vacuum system. The samples were immediately cooled and protected from light for 30 min, and after centrifugation (3500 rpm for 10 min) serum was aliquoted and frozen at -80°C until analysis. Alzheimer's disease patients (AD, $N=30$, age 80.3 ± 5.0 , male/female 12/18) were newly diagnosed of sporadic Alzheimer's disease by the Neurologic Service of Hospital Juan Ramón Jiménez (Huelva, Spain), according to the criteria of the NINCDS-ADRDA [39], and only subjects that had not yet received any type of medication were included in the study. Healthy controls (HC, $N=30$, age 73.5 ± 5.9 , male/female 10/20), who had not more than two reported cases of Alzheimer's disease in their families, were studied by neurologists to confirm the absence of neurological disorders. Demographic characteristics of groups considered in the study are listed in the [Supporting information](#), including age, gender, co-morbidities, medication and family history of AD. It is noteworthy that most subjects suffered other co-morbidities and were under different medical treatments, but there were not significant differences among the groups considered. The study was performed in accordance with the principles contained in the Declaration of Helsinki and approved by the Ethical Committee of University of Huelva.

2.2. Preparation of samples

Optimization of experimental conditions was performed with a solution containing standards of representative metabolites from blood serum in methanol:water (1:1, v/v), including different low molecular weight compounds from different chemical classes and lipids, ranging diverse acid–base properties and polarities. The composition of this mixture was selected according to their usual concentrations in human serum described in the Human Metabolome Database (HMDB), as shown in Table 1. This metabolomic approach was further tested in real serum, for which samples were treated in a two-stage sequential procedure described elsewhere for comprehensive serum metabolomics [40]. For the extraction of metabolites, 100 μL of serum are mixed with 400 μL of methanol/ethanol 1:1 and stirred for 5 min, followed by centrifugation at 4000 rpm for 10 min at 4 °C. The supernatant is transferred to another tube, and the precipitate is kept for further treatment. Then, supernatant is dried under nitrogen stream and the resulting residue reconstituted with 80 μL of methanol and 20 μL of water (polar extract). On the other hand, the precipitate isolated in the first step is extracted with 400 μL of chloroform:methanol 1:1 by stirring during 5 min, followed by centrifugation at 10,000 rpm for 10 min at 4 °C. Finally, the resulting supernatant is dried under nitrogen stream and reconstituted with 100 μL of 60:40 dichloromethane:methanol (lipophilic extract).

2.3. Instrumentation

Mass spectrometry experiments were performed on a QSTAR XL Hybrid system (Applied Biosystems, Foster City, CA, USA) equipped with an atmospheric pressure photoionization (APPI) source. Samples were introduced by flow injection using an Accela LC system (Thermo Fisher Scientific) equipped with autosampler and quaternary pump. In addition, a model KDS 100 syringe pump from KD scientific (New Hope, PA, USA) was employed to deliver the dopant for photospray ionization. For accurate mass measurement, the TOF analyzer is calibrated before analyzing each batch of samples using renin as standard. Data were obtained both in positive and negative ion modes, injecting 10 μL of sample, and acquiring full scan spectra in the m/z range 50–1100 with 1.005 s of scan time. Acquisition time was selected according to the LC flow employed to consider the dispersion of the plug of sample into the solvent stream, and employing some delay time between injection and analysis to allow enough time for the sample to reach the mass spectrometer (settings shown in Table 2). The ion spray voltage (IS) was set at 1500 V and –2300 V in positive and negative modes respectively, with declustering potential (DP) of ± 50 V and focusing potential (FP) of ± 250 V. The source

Table 1
Composition of the standard test mixture.

Compound	Concentration (μM)
Creatinine (Crn)	60
Valine (Val)	230
Cysteine (Cys)	200
Creatine (Cr)	50
Aspartic acid (Asp)	20
Glutamine (Gln)	600
Glutamic acid (Glu)	50
Histidine (His)	90
Phenylalanine (Phe)	70
Arginine (Arg)	100
Glucose (Glc)	5000
Cholesterol (Chol)	5000
Di-oleoyl-phosphocholine (PC)	5
Triolein (TG)	30

Table 2
Acquisition time parameters according to the LC flow.

LC flow ($\mu\text{L min}^{-1}$)	Delay time (s)	Acquisition time (min)
50	20	0.7
100	12	0.5
200	5	0.4
300	3	0.3
500	0	0.2

temperature was maintained at 400 °C, and the gas flows (high-purity nitrogen) were fixed at 1.13 L min^{-1} for curtain gas, 1.50 L min^{-1} for nebulizer gas, 3.0 L min^{-1} for heater gas, and 1 L min^{-1} for lamp gas. To acquire MS/MS spectra, nitrogen was used as collision gas and the collision energy was ranged between 10 and 60 V. The optimization of FIA conditions was performed in four steps: type of dopant, type of carrier solvent, solvent flow and, finally, dopant flow. For the analysis of serum samples, the optimal dopant was toluene delivered at 20/40 $\mu\text{L min}^{-1}$, in positive and negative ion mode respectively. Furthermore, methanol was used as flow injection solvent at 50/100 $\mu\text{L min}^{-1}$, in both ionization modes.

2.4. Statistical analysis

Metabolomic data were submitted to peak detection by MarkerView™ software (Applied Biosystems) in order to filter the mass spectrometry results, and to carry out the reduction into a two-dimensional data matrix of spectral peaks and their intensities. For this, the peak search was done with a mass tolerance of 0.1 Da, and a minimum response of 10 counts was considered for filtering. Finally, data were normalized according to the total area sum. Then, data was processed in SIMCA-P™ software (version 11.5, published by UMetrics AB, Umeå, Sweden) in order to find differences between the groups of study (AD patients and healthy controls). Partial least squares discriminant analysis (PLS-DA) was performed to build predictive models that provide class separation and allow the further study of discriminant metabolites. Quality of the models was assessed by the R^2 and Q^2 values, which provide information about the class separation and predictive power of the model, respectively. These parameters are ranged between 0 and 1, and they indicate the variance explained by the model for all the data analyzed (R^2) and this variance in a test set by cross-validation (Q^2). In addition, these models were validated using permutation tests (Y-scrambling) of the Y-predicted values. In Y-scrambling, class labels are randomly permuted for refitting a new model with the same number of components as the original one, and then these new models are compared with the original models to test the possibility that the original model arose by chance. Thus, an overfitted model will have similar R^2 and Q^2 to that of the randomly permuted data, while well fitted and meaningful models will have R^2 and Q^2 values higher than that of the permuted data. Finally, discriminant compounds were selected according to the Variable Importance in the Projection, or VIP (a weighted sum of squares of the PLS weight, which indicates the importance of the variable in the model), considering only variables with VIP values higher than 2.0, indicative of significant differences among groups. Furthermore, these potential biomarkers were subjected to receiver operating characteristic (ROC) analysis to assess their diagnostic ability. The ROC curve analysis was performed using the GraphPad Prism software (version 6.04, Intuitive Software for Science, San Diego, CA), and the area under the curve (AUC) was used as a metric of sensitivity and specificity of these biomarkers. Thereby, a marker is excellent when AUC ranges from 0.9 to 1, good if AUC is 0.8 to 0.9, moderate if AUC is 0.8 to 0.7 and poor below 0.7 [41].

2.5. Identification of metabolites

Discriminant metabolites were identified matching the experimental accurate mass and tandem mass spectra (MS/MS) with those available in metabolomic databases (HMDB, METLIN, LIPID-MAPS), using a mass accuracy of 50 ppm. Then, different classes of lipids were confirmed based on characteristic fragmentation patterns previously described. It is noteworthy that signals from APPI mass spectra can be mainly attributed to protonated or deprotonated adducts (in positive and negative modes, respectively), but the possibility to produce dehydrated molecular ions has been also previously demonstrated [42–44]. Ceramides presented characteristic product ions in positive ionization mode at m/z 264 and 282 due to the fragmentation in the sphingosine moiety [45]. On the other hand, fragmentation of glycerolipids (diacylglycerols) occurs through the release of fatty acids generating different types of ions (named A, B, C and D), which show characteristic m/z values according to the fatty acid attached to the glycerol backbone [34]. Finally, fatty acid amides were confirmed with characteristic fragments described in the literature [46].

3. Results and discussion

3.1. Selection of experimental conditions

The effect of experimental conditions on the photoionization efficiency was evaluated by flow injection analysis of a mixture solution of representative metabolites (Table 1), acquiring in both positive and negative ion modes. Firstly, for the selection of dopant the other parameters were adjusted according to previous studies for

the simultaneous determination of both polar and non-polar compounds [18], employing a mixture of methanol:water (1:1, v/v) as solvent at a flow rate of $100 \mu\text{l min}^{-1}$. Dopant flow was fixed at a 10% of solvent flow ($10 \mu\text{l min}^{-1}$), since a plateau in ionization efficiency is reached in this source as more dopant is added [17]. The most common dopants described in literature were tested in this study (i.e. toluene, chlorobenzene and anisole), and the ionization efficiencies were compared in function of peak intensities (Fig. 1). In positive ionization mode (Fig. 1a) the best sensitivity was obtained with toluene for most of the standards, followed by chlorobenzene (it should be noted that the great increase in intensity observed for histidine with chlorobenzene is attributable to the presence of an impurity in this solvent with the same mass, which was checked using a blank test). However, for lipid compounds the peak intensity is slightly increased with anisole and chlorobenzene, although none of these dopants allowed the ionization of di-oleoyl-phosphocholine. On the other hand, intensities of low molecular weight metabolites were very similar in negative mode using the three dopants, although generally lower than that in positive mode, while lipids were not detected. The enhanced ionization observed with toluene and chlorobenzene compared to anisole could be due to their higher ionization energy (IE) values (8.83, 9.07, and 8.20 eV, respectively), given that for an effective photoionization the IE of the dopant must be higher than that of the analytes. Moreover, the better sensitivity of toluene compared to chlorobenzene for polar metabolites in positive mode, despite its lower IE, may be due to the impossibility of chlorobenzene to perform photoionization by proton transfer [16]. Conversely, this low reactivity of chlorobenzene and anisole with the solvent is also responsible for the increased signal of non-polar analytes such as cholesterol and triolein using these dopants, although good results were also obtained with toluene. Therefore,

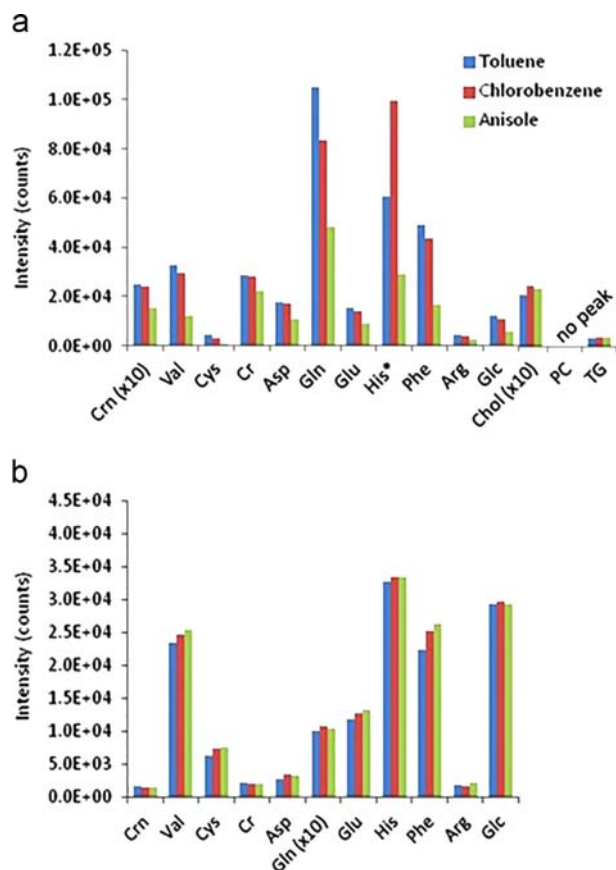


Fig. 1. Average peak intensities ($n=3$) of metabolites in positive ion mode (a) and negative ion mode (b) using different dopants.

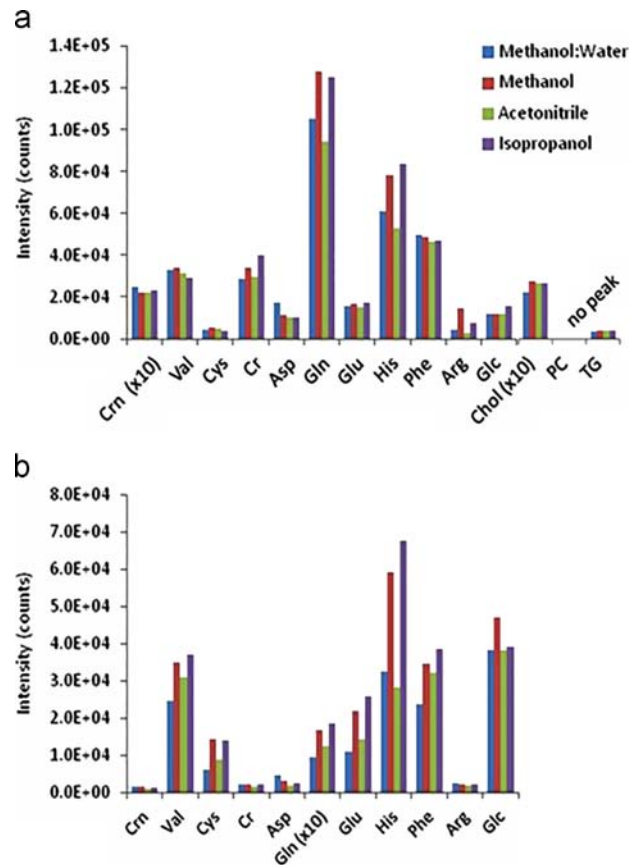


Fig. 2. Average peak intensities ($n=3$) of metabolites in positive ion mode (a) and negative ion mode (b) using different solvents.

toluene was selected as dopant for further experiences, since it provides acceptable results with most of metabolites with the highest mean sensitivity. In a second step, different solvents were evaluated for the analysis of metabolites by FIA-APPI-MS (Fig. 2). Besides the mixture methanol:water 1:1, other solvents usually employed in liquid chromatography mass spectrometry such as methanol and acetonitrile were tested, as well as isopropanol, a photoionizable solvent that may initiates ionization of analytes [27,42]. The solvent was delivered at a flow rate of $100 \mu\text{l min}^{-1}$, and mixed with toluene at $10 \mu\text{l min}^{-1}$. Compared with methanol:water, the use of pure methanol slightly increased sensitivity, according to previous works in which a reduction of the water content produced a general increase of sensitivity [47]. However, acetonitrile reduced the photoionization efficiency respect to methanol, probably due to more effective nebulization and vaporization processes provided by methanol [22] and the higher proton affinity (PA) of acetonitrile [24]. Finally, isopropanol produced comparable results to methanol, so it could be concluded that is not necessary to use photoionizable solvents if experimental conditions are well selected. The solvent flow is other important factor to be considered when the APPI source is employed, as it has been previously revised [17,48,49]. Using methanol as solvent and toluene as dopant, solvent flow was ranged between 50 and $500 \mu\text{l min}^{-1}$ maintaining the dopant flow at a 10%. The monitoring of the intensity for three representative standards depending on the flow is represented in Fig. 3, which shows a different tendency when results from positive and negative ionization modes are compared. In positive mode, the maximum intensity was reached at low flow rates (about $50 \mu\text{l min}^{-1}$), decreasing progressively when solvent flow increases.

The loss of sensitivity at higher solvent flow rates can be attributed to different processes, such as the growth of ion–solvent clusters, because larger clusters may be unreactive and stimulate the loss of ions by recombination processes [17]. Furthermore, charge exchange is reduced due to the loss of dopant radical cations by reaction with the solvent molecules [48]. On the other hand, the highest ionization efficiency in negative mode is achieved with a solvent flow of $100 \mu\text{l min}^{-1}$ (Fig. 3b). Negative ionization is much less used in APPI, and the effect of solvent flow in photoionization has not been previously considered. However, negative ionization takes place through different mechanisms, such as electron capture, charge exchange, proton transfer, or substitution reactions [50,51], so it is not rare to find a different behavior according to the flow of solvent compared with positive mode. Finally, dopant flow was tested around 10–50% of the solvent flow previously selected. Thus, in positive ionization mode the dopant flow was ranged between 5 and $25 \mu\text{l min}^{-1}$, but higher values were employed in negative mode, in the range of 10– $50 \mu\text{l min}^{-1}$ (Fig. 4). Results show that ionization efficiency reaches a plateau at high dopant flows (around 30–40% of solvent flow) in both analysis modes. This finding is consistent with data presented by other authors for low flow applications, as is the case of the present study. Thereby, although under conventional LC conditions ionization efficiency quickly remains constant as more dopant is added, at about 5–10% of the solvent flow [17], it has been observed that this may result in a low rate of reagent ion production when solvent flow is reduced, so that the addition of more dopant may be advantageous [12]. Therefore, optimal dopant flows were set at 20 and $40 \mu\text{l min}^{-1}$ for positive and negative modes of analysis, respectively.

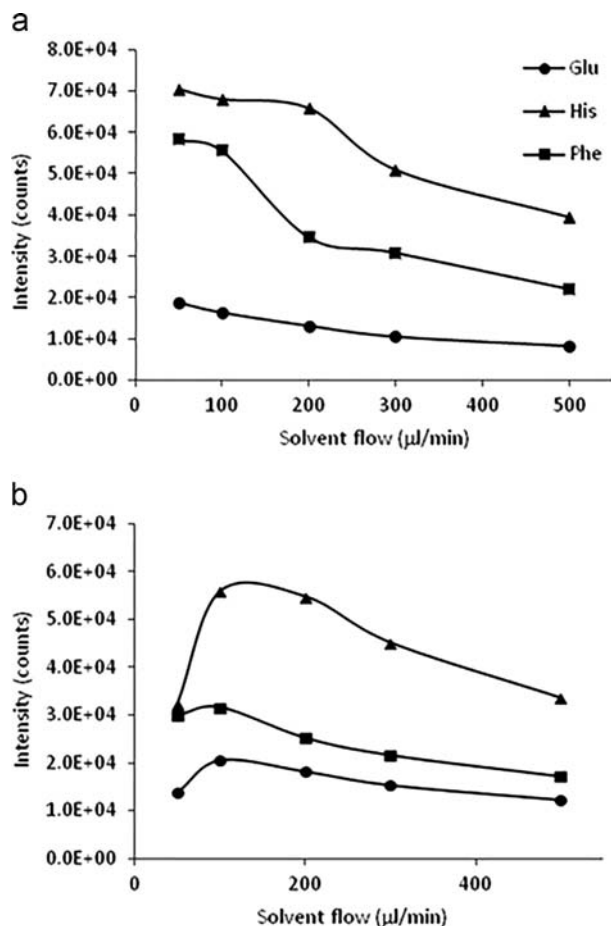


Fig. 3. Average peak intensities ($n=3$) of metabolites in positive ion mode (a) and negative ion mode (b) using different solvent flows.

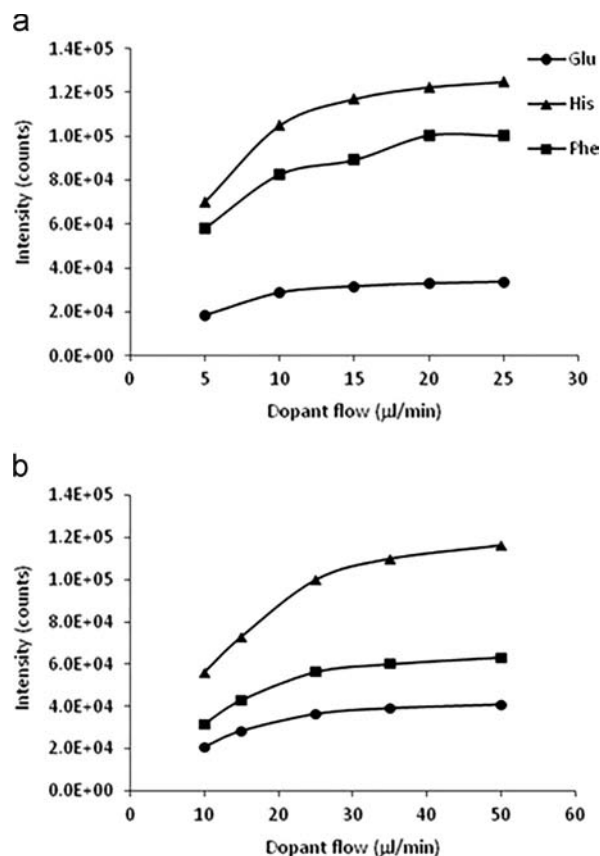


Fig. 4. Average peak intensities ($n=3$) of metabolites in positive ion mode (a) and negative ion mode (b) using different dopant flows.

3.2. Application of FIA-APPI-MS to a metabolomic study of Alzheimer's disease

The suitability of the optimized APPI approach for the analysis of blood serum samples was confirmed in a metabolomic investigation of Alzheimer's disease. The potential of a two-steps methodology for serum extraction, complemented by the use of positive and negative ionization modes has been previously demonstrated for comprehensive metabolomic fingerprinting of serum samples by direct infusion electrospray mass spectrometry [40]. Similarly, analysis by FIA-APPI-MS of these serum extracts generated mass spectra with a high diversity of signals, as shown in Fig. 5. It is noteworthy that for polar extracts the most prominent signals are observed at low m/z values, below 500 amu (Fig. 5a1 and a2), while in lipophilic extracts several clusters of peaks are obtained in the m/z range 500–1000 (Fig. 5b1 and b2), allowing a comprehensive assessment of serum metabolites. Then, results were submitted to partial least squares discriminant analysis (PLS-DA) in order to discriminate between AD patients and healthy controls. Fig. 6 shows the scores plots of all the models, for APPI(+)-MS and APPI(-)-MS data from polar and lipophilic extracts, which provides a good classification of samples. The parameters R^2 and Q^2 , listed in Table 3, were used to evaluate the performance of these models. As can be observed, satisfactory values for the quality parameters R^2 and Q^2 were obtained, with a variance explained around 100% and variance predicted above 80%, demonstrating the potential of flow injection analysis with APPI-MS for serum metabolomics. In addition, the validation plots from the permutation tests (not shown) demonstrated the validity of this discrimination given that Q^2 regression showed a negative intercept and R^2 values of permuted models were lower than the R^2 value of the original one, indicating that the models were not overfitted. Finally, metabolites responsible for discrimination were selected according to the Variable Importance in the Projection parameter ($VIP > 2$). These discriminant metabolites are listed in Table 4, including several low molecular weight metabolites and

different lipid classes. The reproducibility of the method was excellent, with coefficients of variation (CV) below 10% for all the metabolites identified (CV values were calculated from a sample analyzed in triplicate). Furthermore, it should be noted that all these compounds presented AUC values higher (or close) than 0.7, indicative of good diagnostic power.

3.3. Metabolic alterations in serum from Alzheimer's disease

Metabolic fingerprints have shown important differences in serum from AD patients respect to healthy controls, considering up- or down-regulation of metabolites belonging to diverse classes, from lipids such as fatty acids or ceramides to amino acids and neurotransmitters. After the identification of altered metabolites, it is important to decipher disturbed cellular pathways in order to understand the biochemical processes underlying to disease. Thus, a tentative biochemical interpretation of results is presented in the next paragraphs.

3.3.1. Fatty acid amides and the endocannabinoid system

Primary fatty acid amides (PFAM) are bioactive lipids found in several tissues and biological fluids of mammals, including humans [46,52]. These compounds are important endogenous signaling molecules in the mammalian nervous system, binding to many receptors and demonstrating control over a variety of biological processes such as sleep regulation, modulation of monoaminergic systems, locomotion, inhibition of phospholipase A₂ (PLA₂) and epoxide hydrolase (EH), and many other processes [53,54]. Moreover, although these lipids do not interact with cannabinoid receptors, they are catabolically related to endocannabinoids and might regulate biological activities in mammals in a similar fashion [55]. Furthermore, PFAMs are also degraded by fatty acid amide hydrolase (FAAH) [56], the principal catabolic enzyme of the endocannabinoid system. In the context of Alzheimer's disease, there is growing evidence for the involvement of

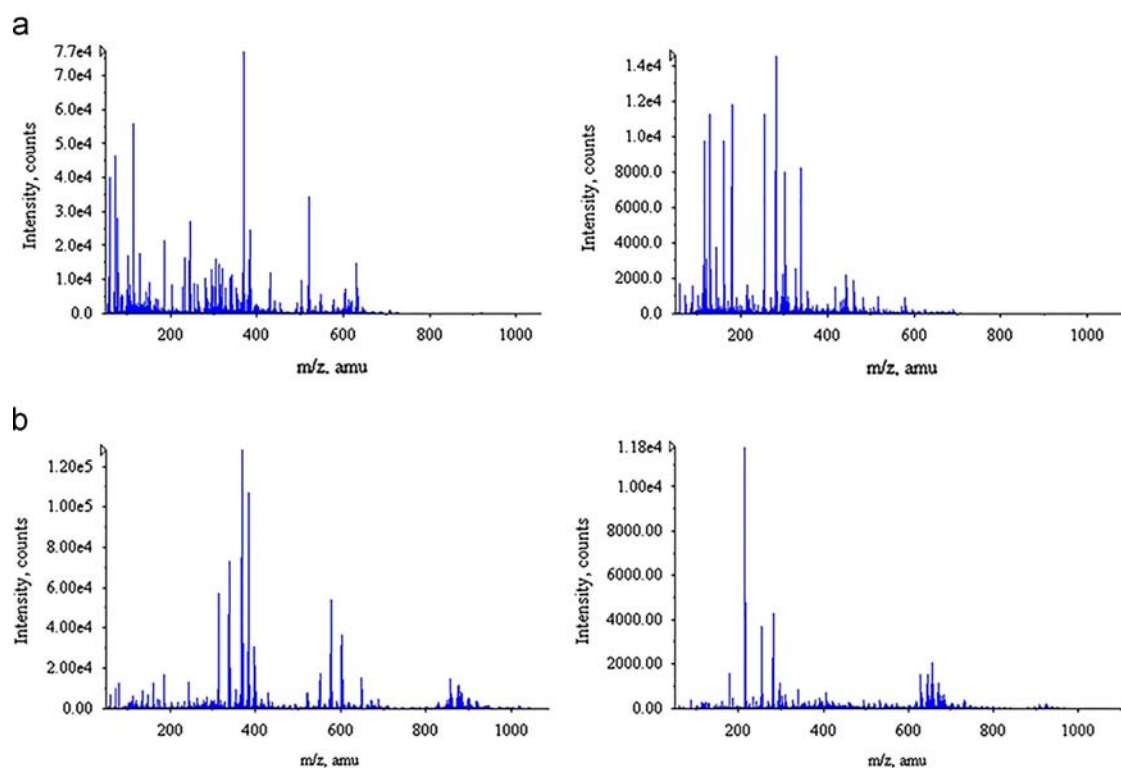


Fig. 5. Mass spectra from serum samples for APPI+ (1) and APPI- (2), with polar (a) and lipophilic (b) extracts.

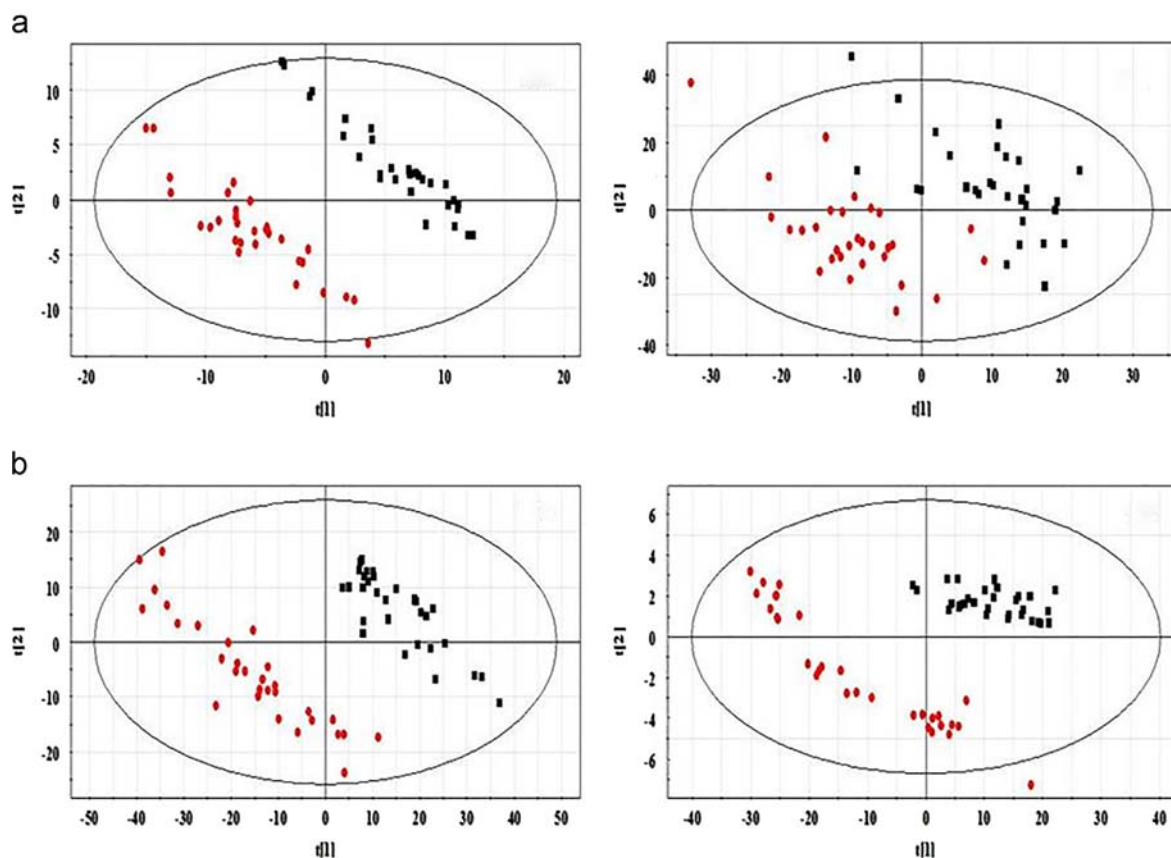


Fig. 6. Scores plots of the PLS-DA for APPI+ (1) and APPI– (2), with polar (a) and lipophilic (b) extracts. Black squares: Alzheimer's disease patients; red circles: healthy controls (For interpretation of the references to color in this figure legend, the reader is referred to the web version of this article).

Table 3
Statistical parameters of the PLS-DA models.

Ion mode	Extract	R^2	Q^2
APPI+	polar	0.998	0.849
	lipophilic	0.997	0.859
APPI–	polar	0.999	0.873
	lipophilic	1	0.883

the endocannabinoid system in the development of neurodegeneration [57]. Thereby, the expression levels of cannabinoid receptors (CB) have been found altered in AD brains, including a decrease of CB1 receptors and up-regulation of CB2 receptors in the hippocampus [58]. In addition, a considerable over-expression of FAAH activity has been also associated with AD [59]. Therefore, the decrease of different fatty acid amides observed in this work (palmitoleamide, palmitamide, linolenamide, linoleamide, oleamide and stearamide) could be considered as an indirect marker of endocannabinoid dysregulation in Alzheimer's disease, as previously reported for serum oleamide [60].

3.3.2. Alterations in sphingolipid metabolism: increase of ceramides

The increase of serum ceramides (CER) and ceramide-1-phosphate (C1P) shown in Table 4 is consistent with impaired sphingolipid metabolism, whose involvement in AD has been extensively discussed [61]. The proper balance of sphingolipids is essential for neuronal function, given that sphingomyelins (SM) are critical components of lipid membrane rafts, and their catabolites are bioactive compounds and second messengers in cellular signaling and apoptosis. The sphingolipid pathway is altered at the gene expression level in AD, with up-regulated activities of

enzymes controlling ceramide synthesis [62] and acid sphingomyelinase [63], suggesting a shift in metabolism towards the accumulation of ceramides. Moreover, the contribution of ceramides to AD pathogenesis has been proposed on the basis of their activity as second messengers, being directly involved in apoptotic signaling, controlling secretion of APP and $A\beta$, or stimulating PLA₂ [64]. Thereby, high levels of total ceramides have been previously associated with AD, mainly in post-mortem studies of brain tissue [62,63,65], but also in cerebrospinal fluid [66] and once in plasma [67], in agreement with our metabolomic findings.

3.3.3. Diacylglycerols and fatty acids: the role of phospholipases

The accumulation of diacylglycerols (DAGs) and free fatty acids (FFAs) in serum from AD patients (Table 4) has been previously associated with cellular membrane breakdown due to over-activation of phospholipases [60]. Abnormalities in membrane phospholipids in AD are principally related to altered expression of phospholipase A₂ (PLA₂) function [68], but there is also evidence for the role of phospholipases C and D, although they have been much less studied [69,70]. Furthermore, it is known the inter-connections between the metabolism of phospholipids and sphingomyelins [71]. Ceramides and ceramide-1-phosphate induce overactivation of PLA₂, as stated in the previous section, while arachidonic acid (one of the most abundant fatty acids contained in neural phospholipids) released from the hydrolysis of these phospholipids by the action PLA₂ causes the overexpression of sphingomyelinase (SMase). Therefore, it could be concluded that membrane breakdown processes in Alzheimer's disease are finally reflected in multiple inter-related metabolites that are altered in serum samples, as schematized in Fig. 7.

Table 4
Discriminant metabolites identified in serum from Alzheimer's disease patients.

Compound	MS/MS fragments		Fold change	% CV	p value	AUC
	APPI+	APPI–				
Fatty acid amides (PFAM)						
Palmitoleamide	254.22 [M+H] ⁺ , 237.24, 219.23, 57.07	–	0.84	1.3	8.6 × 10 ^{−5}	0.78
Palmitamide	256.24 [M+H] ⁺ , 102.09, 88.08, 57.07	–	0.84	4.6	4.5 × 10 ^{−5}	0.80
Linolenamide	278.22 [M+H] ⁺ , 261.22, 243.21, 57.07	–	0.82	7.4	2.0 × 10 ^{−5}	0.82
Linoleamide	280.25 [M+H] ⁺ , 263.24, 245.22, 57.07	–	0.76	6.6	5.5 × 10 ^{−5}	0.82
Oleamide	282.26 [M+H] ⁺ , 265.26, 247.25, 57.07	–	0.72	8.8	1.0 × 10 ^{−6}	0.90
Stearamide	284.27 [M+H] ⁺ , 102.09, 88.08, 57.07	–	0.75	6.5	3.6 × 10 ^{−5}	0.79
Ceramides (CER)						
CER(d18:1/16:1)	518.48 [M+H−H ₂ O] ⁺ , 500.50, 282.27, 264.25	516.48 [M−H−H ₂ O] [−] , 253.22	1.24	7.7	1.7 × 10 ^{−3}	0.89
CER(d18:1/16:0)	520.50 [M+H−H ₂ O] ⁺ , 502.50, 282.27, 264.25	518.49 [M−H−H ₂ O] [−] , 255.22	1.28	3.5	4.4 × 10 ^{−4}	0.90
CER(d18:1/18:1)	546.49 [M+H−H ₂ O] ⁺ , 528.46, 282.27, 264.25	–	1.16	6.8	2.0 × 10 ^{−6}	0.86
CER(d18:1/18:0)	–	546.46 [M−H−H ₂ O] [−] , 283.26	1.56	2.3	5.4 × 10 ^{−3}	0.70
CER(d18:1/18:0)–1P	628.57 [M+H−H ₂ O] ⁺ , 610.56, 282.27, 264.25	626.56 [M−H−H ₂ O] [−] , 283.26, 96.97	1.33	6.9	7.5 × 10 ^{−3}	0.95
CER(d18:1/24:1)	630.60 [M+H−H ₂ O] ⁺ , 612.56, 282.27, 264.25	–	1.39	6.2	1.0 × 10 ^{−6}	0.92
Diacylglycerols (DAG)						
DAG(14:1/16:0)	539.42 [M+H] ⁺ , 313.26, 283.25	–	1.21	7.7	1.0 × 10 ^{−6}	0.85
DAG(16:0/18:3)	591.48 [M+H] ⁺ , 335.26, 313.26, 261.20	–	1.38	6.8	1.0 × 10 ^{−6}	0.85
DAG(16:0/18:1)	595.48 [M+H] ⁺ , 339.29, 313.27, 265.22, 239.22	–	1.17	6.1	3.0 × 10 ^{−6}	0.84
DAG(18:3/18:3)	613.50 [M+H] ⁺ , 335.24	–	1.20	2.3	3.0 × 10 ^{−6}	0.82
DAG(18:3/18:2)	615.48 [M+H] ⁺ , 337.27, 335.24, 263.20, 261.20	–	1.22	7.9	2.5 × 10 ^{−4}	0.75
DAG(16:0/20:4)	617.50 [M+H] ⁺ , 361.33, 313.27, 287.21	–	1.25	5.3	1.5 × 10 ^{−4}	0.76
DAG(18:2/18:1)	619.51 [M+H] ⁺ , 339.29, 337.24	–	1.26	3.2	1.2 × 10 ^{−4}	0.75
Free fatty acids (FFA)						
Palmitoleic acid	–	253.22 [M−H] [−]	1.49	5.1	7.2 × 10 ^{−4}	0.81
Palmitic acid	–	255.22 [M−H] [−]	1.36	10.6	1.3 × 10 ^{−3}	0.78
Oleic acid	–	281.24 [M−H] [−]	1.44	6.7	5.4 × 10 ^{−4}	0.80
Low molecular weight metabolites						
Urea	61.04 [M+H] ⁺ , 44.02	–	0.76	4.1	9.9 × 10 ^{−3}	0.68
Alanine	90.06 [M+H] ⁺ , 44.04	–	1.43	2.9	1.0 × 10 ^{−6}	0.92
Taurine	–	124.00 [M−H] [−] , 79.97	0.88	11.6	2.7 × 10 ^{−3}	0.73
Picolinic acid	124.05 [M+H] ⁺ , 106.02, 78.03	–	1.15	4.1	4.1 × 10 ^{−5}	0.80
Creatine	–	130.06 [M−H] [−] , 88.05	0.87	0.9	4.9 × 10 ^{−3}	0.69
Malic acid	–	133.02 [M−H] [−] , 115.03, 71.02	0.88	3.6	9.7 × 10 ^{−4}	0.84
Dopamine	136.07 [M+H−H ₂ O] ⁺ , 119.05, 91.04	–	0.77	3.3	1.0 × 10 ^{−6}	0.93
Serotonin	177.09 [M−H] [−] , 160.07, 115.05	–	0.90	3.3	1.2 × 10 ^{−2}	0.89

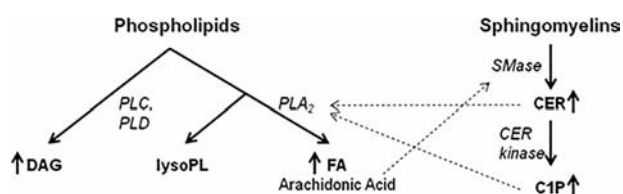


Fig. 7. Membrane degradation and interconnections between metabolism of phospholipids and sphingolipids. ↑: compounds up-regulated, ↓: compounds down-regulated, and dashed arrows: enzymatic stimulation.

3.3.4. Involvement of low molecular weight metabolites

The involvement of low molecular weight metabolites in central pathways of metabolism makes them important targets in the study of pathological alterations underlying to diseases. In this study, the most important changes could be related to disturbances in neurotransmitter systems, given that decreased serum levels of serotonin, dopamine and taurine were found (Table 4). Serotonin and dopamine are two important monoaminergic neurotransmitters, whose altered synthesis has been previously associated with synaptic failure leading to neurodegeneration in Alzheimer's disease [72]. On the other hand, taurine presents several roles in neurotransmission, neuromodulation, osmoregulation, control of calcium influx and cell excitability, whose implication in neurodegeneration and AD has been previously demonstrated [73]. Hypometabolism is also documented in AD, with depleted neuronal energy production by decreased rate of carbohydrate catabolism [74] and oxidative deficiency characterized by mitochondrial dysfunction [75]. This

energetic deficiency is in accordance with the altered levels of alanine, creatine and malate observed in metabolomic profiles (Table 4), given that these compounds participate in overall cellular bioenergetics. Picolinic acid is a tryptophan metabolite from the kynurenine pathway, which is up-regulated in AD by over-expression of indole-2,4-dioxygenase. Thereby, altered synthesis of related neuroactive compounds and the accumulation of different derivatives have been previously reported in AD [76], in agreement with the increased levels of picolinic acid observed in this study. Finally, the reduction of urea levels points to a perturbation of the urea cycle, responsible for controlling ammonia concentrations in the organism. The alteration of this pathway in AD has been previously demonstrated on the basis of altered levels of expression in different enzymes and the corresponding genes [77], which finally results in altered content of related metabolites as found in our metabolomic study.

4. Conclusions

A high throughput approach based on flow injection analysis and high resolution tandem mass spectrometry with atmospheric pressure photoionization source (FIA-APPI-QTOFMS) has been developed for metabolomic analysis of serum samples. Several experimental parameters affected considerably the ionization efficiency, such as dopant, carrier solvent or the flow rate of both. Toluene and methanol were selected as optimal dopant and flow injection solvent respectively, providing the highest sensitivity for

the analysis of most of the metabolites. Considering the delivery speed of solvent and dopant, different behavior was observed for positive and negative analysis modes. In negative mode, the ionization was favored at higher solvent and dopant flows (100 $\mu\text{l min}^{-1}$ and 40 $\mu\text{l min}^{-1}$), while in positive mode lower flows are recommended (50 $\mu\text{l min}^{-1}$ and 20 $\mu\text{l min}^{-1}$). Then, the suitability of this APPI-MS technique was demonstrated in a metabolomic investigation of Alzheimer's disease. Eight low molecular weight metabolites and numerous lipids belonging to four different classes were detected as potential markers of disease, with good diagnostic power (AUC > 0.7). Altered levels of primary fatty acid amides and major neurotransmitters such as serotonin or dopamine could be related to severe failures in neurotransmission. Moreover, important impairments associated with cellular membrane destabilization were also found, considering increased serum levels of ceramides, diacylglycerols and free fatty acids. Furthermore, other metabolic changes may be related to hypometabolism, hyperammonemia or up-regulation of the kynurenine pathway associated with this disease. Although previous studies have suggested that blood biochemistry could reflect biochemical changes in the central nervous system, these findings should be confirmed in a next step in cerebrospinal fluid and/or post-mortem brain samples. Furthermore, as future plan, it would be interesting to extend this study to other types of dementia in order to assess the specificity of these potential markers against other neurodegenerative disorders.

Novelty statement

This work describes for the first time the use of a metabolomic platform based on flow injection analysis and atmospheric pressure photoionization mass spectrometry for the investigation of metabolic alterations associated with Alzheimer's disease.

Acknowledgments

This work was supported by the projects CTM2012-38720-C03-01 from the Ministerio de Ciencia e Innovación and P012-FQM-0442 and P009-FQM-4659 from the Consejería de Innovación, Ciencia y Empresa (Junta de Andalucía). Raúl González Domínguez thanks the Ministerio de Educación (Grant no. AP2010-4278) for a predoctoral scholarship.

Appendix A. Supporting information

Supplementary data associated with this article can be found in the online version at <http://dx.doi.org/10.1016/j.talanta.2014.07.075>.

References

- [1] C.W.W. Beecher, in: G.G. Harrigan, R. Goodacre (Eds.), *Metabolic Profiling: Its Role in Biomarker Discovery and Gene Function Analysis*, Springer, New York, 2003, pp. 311–320.
- [2] W.B. Dunn, *Phys. Biol.* 5 (2008) 011001. <http://dx.doi.org/10.1088/1478-3975/5/1/011001>.
- [3] S. Cubbon, T. Bradbury, J. Wilson, J. Thomas-Oates, *Anal. Chem.* 79 (2007) 8911–8918. <http://dx.doi.org/10.1021/ac071008v>.
- [4] A.M. Evans, C.D. De Haven, T. Barrett, M. Mitchell, E. Milgram, *Anal. Chem.* 81 (2009) 6656–6667. <http://dx.doi.org/10.1021/ac901536h>.
- [5] M.R.N. Monton, T. Soga, *J. Chromatogr. A* 1168 (2007) 237–246. <http://dx.doi.org/10.1016/j.chroma.2007.02.065>.
- [6] T. Lapainis, S.S. Rubakhin, J.V. Sweedler, *Anal. Chem.* 81 (2009) 5858–5864. <http://dx.doi.org/10.1021/ac900936g>.
- [7] J. Draper, A.J. Lloyd, R. Goodacre, M. Beckmann, *Metabolomics* 9 (2013) S4–S29. <http://dx.doi.org/10.1007/s11306-012-0449-x>.
- [8] Y. Sato, I. Suzuki, T. Nakamura, F. Bernier, K. Aoshima, Y. Oda, *J. Lipid Res.* 53 (2012) 567–576. <http://dx.doi.org/10.1194/jlr.M022376>.

- [9] J. Williams, L. Pandarinathan, J.A. Wood, P. Vouros, A. Makriyannis, *AAPS J.* 8 (2006) E655–E660. <http://dx.doi.org/10.1208/aaps080474>.
- [10] D.B. Robb, T.R. Covey, A.P. Bruins, *Anal. Chem.* 72 (2000) 3653–3659. <http://dx.doi.org/10.1021/ac0001636>.
- [11] J.A. Syage, M.D. Evans, K.A. Hanold, *Am. Lab.* 32 (2000) 24–29.
- [12] D.B. Robb, M.W. Blades, *Anal. Chim. Acta* 627 (2008) 34–49. <http://dx.doi.org/10.1016/j.aca.2008.05.077>.
- [13] T.J. Kauppila, T. Kuuranne, E.C. Meurer, M.N. Eberlin, T. Kotiaho, R. Kostiainen, *Anal. Chem.* 74 (2002) 5470–5479. <http://dx.doi.org/10.1021/ac025659x>.
- [14] G. Koster, A.P. Bruins, Mechanisms for ion formation in LC/MS by atmospheric pressure photo-ionization, in: Proceedings of the 49th ASMS Conference on Mass Spectrometry and Allied Topics, Chicago, IL, May 27–31, 2001.
- [15] T.J. Kauppila, R. Kostiainen, A.P. Bruins, *Rapid Commun. Mass Spectrom.* 18 (2004) 808–815. <http://dx.doi.org/10.1002/rcm.1408>.
- [16] D.B. Robb, D.R. Smith, M.W. Blades, *J. Am. Soc. Mass Spectrom.* 19 (2008) 955–963. <http://dx.doi.org/10.1016/j.jasms.2008.03.013>.
- [17] D.B. Robb, M.W. Blades, *J. Am. Soc. Mass Spectrom.* 16 (2005) 1275–1290. <http://dx.doi.org/10.1016/j.jasms.2005.03.017>.
- [18] D.B. Robb, M.W. Blades, *Anal. Chem.* 78 (2006) 8162–8164. <http://dx.doi.org/10.1021/ac061276d>.
- [19] C. Cavaliere, P. Foglia, E. Pastorini, R. Samperi, A. Lagana, *J. Chromatogr. A* 1101 (2006) 69–78. <http://dx.doi.org/10.1016/j.chroma.2005.09.060>.
- [20] H.B. Theron, M.J. van der Merwe, K.J. Swart, J.H. van der Westhuizen, *Rapid Commun. Mass Spectrom.* 21 (2007) 1680–1686. <http://dx.doi.org/10.1002/rcm.3006>.
- [21] M.J. Greig, B. Bolaños, T. Quenzer, J.M.R. Bylund, *Rapid Commun. Mass Spectrom.* 17 (2003) 2763–2768. <http://dx.doi.org/10.1002/rcm.1257>.
- [22] Y. Hsieh, K. Merkle, G. Wang, J.M. Brisson, W.A. Korfmacher, *Anal. Chem.* 75 (2003) 3122–3127. <http://dx.doi.org/10.1021/ac0300082>.
- [23] S.M. Van Leeuwen, L. Hendriksen, U. Karst, *J. Chromatogr. A* 1058 (2004) 107–112. <http://dx.doi.org/10.1016/j.chroma.2004.08.149>.
- [24] M. Takino, K. Yamaguchi, T. Nakahara, *J. Agric. Food Chem.* 52 (2004) 727–735. <http://dx.doi.org/10.1021/jf0343377>.
- [25] Z. An, Y. Chen, R. Zhang, Y. Song, J. Sun, J. He, J. Bai, L. Dong, Q. Zhan, Z. Abliz, *J. Proteome Res.* 9 (2010) 4071–4081. <http://dx.doi.org/10.1021/pr100265g>.
- [26] H. Tian, J. Bai, Z. An, Y. Chen, R. Zhang, J. He, X. Bi, Y. Song, Z. Abliz, *Rapid Commun. Mass Spectrom.* 27 (2013) 2071–2080. <http://dx.doi.org/10.1002/rcm.6666>.
- [27] S.S. Cai, J.A. Syage, *Anal. Chem.* 78 (2006) 1191–1199. <http://dx.doi.org/10.1021/ac0515834>.
- [28] L. Imbert, M. Gaudin, D. Libong, D. Touboul, S. Abreu, P.M. Loiseau, O. Laprévotte, O. Chaminate, *J. Chromatogr. A* 1242 (2012) 75–83. <http://dx.doi.org/10.1016/j.chroma.2012.04.035>.
- [29] K.A. Hanold, S.M. Fischer, P.H. Cormia, C.E. Miller, J.A. Syage, *Anal. Chem.* 76 (2004) 2842–2851. <http://dx.doi.org/10.1021/ac035442i>.
- [30] R. Mol, G.J. de Jong, G.W. Somsen, *Electrophoresis* 26 (2005) 146–154. <http://dx.doi.org/10.1002/elps.200406101>.
- [31] L. Song, A.D. Wellman, H. Yao, J. Adcock, *Rapid Commun. Mass Spectrom.* 21 (2007) 1343–1351. <http://dx.doi.org/10.1002/rcm.2963>.
- [32] J.L. Gómez-Ariza, T. García-Barrera, F. Lorenzo, *Anal. Chim. Acta* 570 (2006) 101–108. <http://dx.doi.org/10.1016/j.aca.2006.04.004>.
- [33] J.L. Gomez-Ariza, A. Arias-Borrego, T. Garcia-Barrera, R. Beltran, *Talanta* 70 (2006) 859–869. <http://dx.doi.org/10.1016/j.talanta.2006.02.019>.
- [34] R. González-Domínguez, T. García-Barrera, J.L. Gómez-Ariza, *Rapid Commun. Mass Spectrom.* 26 (2012) 835–844. <http://dx.doi.org/10.1002/rcm.6155>.
- [35] Y. Cai, O. McConnell, A.C. Bach, *Rapid Commun. Mass Spectrom.* 23 (2009) 2283–2291. <http://dx.doi.org/10.1002/rcm.4146>.
- [36] Y. Kim, S. Kim, *J. Am. Soc. Mass Spectrom.* 21 (2010) 386–392. <http://dx.doi.org/10.1016/j.jasms.2009.11.001>.
- [37] P.J. Weaver, A.M.F. Laures, J.C. Wolff, *Rapid Commun. Mass Spectrom.* 21 (2007) 2415–2421. <http://dx.doi.org/10.1002/rcm.3052>.
- [38] K.O. Boernsen, S. Gatzek, G. Imbert, *Anal. Chem.* 77 (2005) 7255–7264. <http://dx.doi.org/10.1021/ac0508604>.
- [39] G. McKahn, D. Drachman, M. Folstein, R. Katzman, D. Price, E.M. Stadlan, *Neurology* 34 (1984) 939–944. <http://dx.doi.org/10.1212/WNL.34.7.939>.
- [40] R. Gonzalez-Dominguez, T. Garcia-Barrera, J.L. Gomez-Ariza, *J. Proteomics* 104 (2014) 37–47. <http://dx.doi.org/10.1016/j.jprot.2014.01.014>.
- [41] J. Xia, D.I. Broadhurst, M. Wilson, D.S. Wishart, *Metabolomics* 9 (2013) 280–299. <http://dx.doi.org/10.1007/s11306-012-0482-9>.
- [42] S.S. Cai, J.A. Syage, *J. Chromatogr. A* 1110 (2006) 15–26. <http://dx.doi.org/10.1016/j.chroma.2006.01.050>.
- [43] T.J. Kauppila, T. Nikkola, R.A. Ketola, R. Kostiainen, *J. Mass Spectrom.* 41 (2006) 781–789. <http://dx.doi.org/10.1002/jms.1034>.
- [44] A. Muñoz-García, J. Roa, J.C. Brown, J.B. Williams, *J. Chromatogr. A* 1133 (2006) 58–68. <http://dx.doi.org/10.1016/j.chroma.2006.06.067>.
- [45] M. Gu, J.L. Kerwin, J.D. Watts, R. Aebersold, *Anal. Biochem.* 244 (1997) 347–356. <http://dx.doi.org/10.1006/abio.1996.9915>.
- [46] K.K. Nichols, B.M. Ham, J.J. Nichols, C. Ziegler, K.B. Green-Church, *Investig. Ophthalmol. Vis. Sci.* 48 (2007) 34–39. <http://dx.doi.org/10.1167/jovs.06-0753>.
- [47] C. Yang, J. Henion, *J. Chromatogr. A* 970 (2002) 155–165. [http://dx.doi.org/10.1016/S0021-9673\(02\)00882-8](http://dx.doi.org/10.1016/S0021-9673(02)00882-8).
- [48] T.J. Kauppila, A.P. Bruins, R. Kostiainen, *J. Am. Soc. Mass Spectrom.* 16 (2005) 1399–1407. <http://dx.doi.org/10.1016/j.jasms.2005.03.051>.
- [49] D.B. Robb, M.W. Blades, *J. Am. Soc. Mass Spectrom.* 17 (2006) 130–138. <http://dx.doi.org/10.1016/j.jasms.2005.09.013>.

- [50] T.J. Kauppila, T. Kotiaho, R. Kostiainen, A.P. Bruins, *J. Am. Soc. Mass Spectrom.* 15 (2004) 203–211. <http://dx.doi.org/10.1016/j.jasms.2003.10.012>.
- [51] L. Song, A.D. Wellman, H. Yao, J.E. Bartmess, *J. Am. Soc. Mass Spectrom.* 18 (2007) 1789–1798. <http://dx.doi.org/10.1016/j.jasms.2007.07.015>.
- [52] E.S. Arafat, J.W. Trimble, R.N. Andersen, C. Dass, D.M. Desiderio, *Life Sci.* 45 (1989) 1679–1687. [http://dx.doi.org/10.1016/0024-3205\(89\)90278-6](http://dx.doi.org/10.1016/0024-3205(89)90278-6).
- [53] C. Ezzili, K. Otrubova, D.L. Boger, *Bioorg. Med. Chem. Lett.* 20 (2010) 5959–5968. <http://dx.doi.org/10.1016/j.bmcl.2010.08.048>.
- [54] E.K. Farrell, D.J. Merkler, *Drug Discov. Today* 13 (2008) 558–568. <http://dx.doi.org/10.1016/j.drudis.2008.02.006>.
- [55] H.H.O. Schmid, E.V. Berdyshev, *Prostaglandins Leukot. Essent. Fat. Acids* 66 (2002) 363–376. <http://dx.doi.org/10.1054/plf.2001.0348>.
- [56] B.F. Cravatt, A.H. Lichtman, *Chem. Phys. Lipids* 121 (2002) 135–148. [http://dx.doi.org/10.1016/S0009-3084\(02\)00147-0](http://dx.doi.org/10.1016/S0009-3084(02)00147-0).
- [57] C. Benito, E. Núñez, M.R. Pazos, R.M. Tolón, J. Romero, *Mol. Neurobiol.* 36 (2007) 75–81. <http://dx.doi.org/10.1007/s12035-007-8006-8>.
- [58] B.G. Ramirez, C. Blazquez, T. Gomez del Pulgar, M. Guzman, M.L. de Ceballos, *J. Neurosci.* 25 (2005) 1904–1913. <http://dx.doi.org/10.1523/JNEUROSCI.4540-04.2005>.
- [59] C. Benito, E. Nuñez, R.M. Tolon, E.J. Carrier, A. Rabano, C.J. Hillard, J. Romero, *J. Neurosci.* 23 (2003) 11136–11141.
- [60] R. González-Domínguez, T. García-Barrera, J.L. Gómez-Ariza, *J. Pharm. Biomed. Anal.* 98 (2014) 321–326. <http://dx.doi.org/10.1016/j.jpba.2014.05.023>.
- [61] M.M. Mielke, C.G. Lyketsos, *NeuroMol. Med.* 12 (2010) 331–340. <http://dx.doi.org/10.1007/s12017-010-8121-y>.
- [62] P. Katsel, C. Li, V. Haroutunian, *Neurochem. Res.* 32 (2007) 845–856. <http://dx.doi.org/10.1007/s11064-007-9297-x>.
- [63] X. He, Y. Huang, B. Li, C.X. Gong, E.H. Schuchman, *Neurobiol. Aging* 31 (2010) 398–408. <http://dx.doi.org/10.1016/j.neurobiolaging.2008.05.010>.
- [64] A.A. Farooqui, W.Y. Ong, T. Farooqui, *Biochim. Biophys. Acta* 2010 (1801) 906–916. <http://dx.doi.org/10.1016/j.bbali.2010.02.002>.
- [65] X. Han, D. Holtzman, D.W. McKeel Jr., J. Kelley, J.C. Morris, *J. Neurochem.* 82 (2002) 809–818. <http://dx.doi.org/10.1046/j.1471-4159.2002.00997.x>.
- [66] H. Sato, H. Tomimoto, R. Ohtani, T. Kitano, T. Kondo, M. Watanabe, N. Oka, I. Akiguchi, S. Furuya, Y. Hirabayashi, T. Okazaki, *Neuroscience* 130 (2005) 657–666. <http://dx.doi.org/10.1016/j.neuroscience.2004.08.056>.
- [67] X. Han, S. Rozen, S.H. Boyle, C. Hellegers, H. Cheng, J.R. Burke, K.A. Welsh-Bohmer, P.M. Doraiswamy, R. Kaddurah-Daouk, *PLoS ONE* 6 (2011) e21643. <http://dx.doi.org/10.1371/journal.pone.0021643>.
- [68] A.A. Farooqui, H.C. Yang, L. Horrocks, *Neurochem. Int.* 30 (1997) 517–522. [http://dx.doi.org/10.1016/S0197-0186\(96\)00122-2](http://dx.doi.org/10.1016/S0197-0186(96)00122-2).
- [69] J.K. Jin, N.H. Kim, Y.J. Lee, Y.S. Kim, E.K. Choi, P.B. Kozlowski, M.H. Park, H.S. Kim, D.S. Min, *Neurosci. Lett.* 407 (2006) 263–267. <http://dx.doi.org/10.1016/j.neulet.2006.08.062>.
- [70] S. Shimohama, Y. Sasaki, S. Fujimoto, S. Kamiya, T. Taniguchi, T. Takenawa, J. Kimura, *Neuroscience* 82 (1998) 999–1007. [http://dx.doi.org/10.1016/S0306-4522\(97\)00342-4](http://dx.doi.org/10.1016/S0306-4522(97)00342-4).
- [71] A.A. Farooqui, L.A. Horrocks, T. Farooqui, *J. Neurosci. Res.* 85 (2007) 1834–1850. <http://dx.doi.org/10.1002/jnr.21268>.
- [72] D. Storga, K. Vrecko, J.G.D. Birkmayer, G. Reibnegger, *Neurosci. Lett.* 203 (1996) 29–32. [http://dx.doi.org/10.1016/0304-3940\(95\)12256-7](http://dx.doi.org/10.1016/0304-3940(95)12256-7).
- [73] P.R. Louzada, A.C.P. Lima, D.L. Mendoça-Silva, F. Noël, F.G. de Mello, S.T. Ferreira, *FASEB J.* 18 (2004) 511–518. <http://dx.doi.org/10.1096/fj.03-0739com>.
- [74] L. Mosconi, R. Mistur, R. Switalski, W.H. Tsui, L. Glodzik, Y. Li, E. Pirraglia, S. De Santi, B. Reisberg, T. Wisniewski, M.J. de Leon, *Eur. J. Nucl. Med. Mol. Imaging* 36 (2009) 811–822. <http://dx.doi.org/10.1007/s00259-008-1039-z>.
- [75] A. Maruszak, C. Zekanowski, *Prog. Neuropsychopharmacol. Biol. Psychiatry* 35 (2011) 320–330. <http://dx.doi.org/10.1016/j.pnpbp.2010.07.004>.
- [76] S. Duleu, A. Mangas, F. Sevin, B. Veyret, A. Bessede, M. Geffar, *Int. J. Alzheimer's Dis.* 2010 (2010) 501541. <http://dx.doi.org/10.4061/2010/501541>.
- [77] F. Hansmannel, A. Sillaire, M.I. Kamboh, C. Lendon, F. Pasquier, D. Hannequin, G. Laumet, A. Mounier, A.M. Ayral, S.T. DeKosky, J.J. Hauw, C. Berr, D. Mann, P. Amouyel, D. Campion, J.C. Lambert, *J. Alzheimer's Dis.* 21 (2010) 1013–1021. <http://dx.doi.org/10.3233/JAD-2010-100630>.



Well-crystalline porous ZnO–SnO₂ nanosheets: An effective visible-light driven photocatalyst and highly sensitive smart sensor material

Randeep Lamba^a, Ahmad Umar^{b,c,*}, S.K. Mehta^a, Sushil Kumar Kansal^{d,**}

^a Department of Chemistry, Panjab University, Chandigarh 160014, India

^b Department of Chemistry, College of Science and Arts, Najran University, P.O. Box-1988, Najran 11001, Kingdom of Saudi Arabia

^c Promising Centre for Sensors and Electronic Devices (PCSED), Najran University, P.O. Box-1988, Najran 11001, Kingdom of Saudi Arabia

^d Dr. S.S. Bhatnagar University Institute of Chemical Engineering & Technology, Panjab University, Chandigarh 160014, India

ARTICLE INFO

Article history:

Received 3 June 2014

Received in revised form

29 July 2014

Accepted 31 July 2014

Available online 6 August 2014

Keywords:

Porous ZnO–SnO₂ nanosheets

Visible-light driven

Photo-degradation

Direct blue-15

Chemical sensor

4-Nitrophenol

ABSTRACT

This work demonstrates the synthesis and characterization of porous ZnO–SnO₂ nanosheets prepared by the simple and facile hydrothermal method at low-temperature. The prepared nanosheets were characterized by several techniques which revealed the well-crystallinity, porous and well-defined nanosheet morphology for the prepared material. The synthesized porous ZnO–SnO₂ nanosheets were used as an efficient photocatalyst for the photocatalytic degradation of highly hazardous dye, i.e., direct blue 15 (DB 15), under visible-light irradiation. The excellent photocatalytic degradation of prepared material towards DB 15 dye could be ascribed to the formation of ZnO–SnO₂ heterojunction which effectively separates the photogenerated electron-hole pairs and possess high surface area. Further, the prepared porous ZnO–SnO₂ nanosheets were utilized to fabricate a robust chemical sensor to detect 4-nitrophenol in aqueous medium. The fabricated sensor exhibited extremely high sensitivity of $\sim 1285.76 \mu\text{A}/\text{mmol L}^{-1} \text{ cm}^{-2}$ and an experimental detection limit of $0.078 \text{ mmol L}^{-1}$ with a linear dynamic range of $0.078\text{--}1.25 \text{ mmol L}^{-1}$. The obtained results confirmed that the prepared porous ZnO–SnO₂ nanosheets are potential material for the removal of organic pollutants under visible light irradiation and efficient chemical sensing applications.

© 2014 Elsevier B.V. All rights reserved.

1. Introduction

The environmental pollution has reached at an alarming level with the revolution of scientific and technological disciplines, research areas and industries [1–8]. The release of organic pollutants, such as dyes, drugs, saturated hydrocarbons, aromatic compounds, polymers, insecticides, pesticides, etc., in the water resources are posing a great nuisance to the surroundings due to their carcinogenic, mutagenic and toxic effects. Particularly, the discharge of synthetic dyes and pigments by many industries are prime source of water pollution which disturbed the ecosystem and create eutrophication and perturbation to marine life [8]. In addition, due to the particular chemical structure and stability of these organic dyes and pigments, they are resistant to aerobic digestion and hence it is necessary to treat the industrial effluents [9–14].

* Corresponding author at: Department of Chemistry, College of Science and Arts, Najran University, P.O. Box-1988, Najran 11001, Kingdom of Saudi Arabia.

** Corresponding author.

E-mail addresses: ahmadumar786@gmail.com (A. Umar), sushilkk1@yahoo.co.in, sushilkk1@pu.ac.in (S. Kumar Kansal).

Heterogeneous photocatalysis is known as environment friendly, benign, cost effective and green process for efficient degradation of various harmful wastewater organic dyes and pigments [15–19]. For this, various semiconductor photocatalysts such as TiO₂, ZnO, Fe₂O₃, CdS, ZnS, SnO₂, Bi₂O₃, V₂O₅, and so on, have been explored which lead the total mineralization of organic pollutants and produce biodegradable and less toxic substances at relatively lower costs [15–19]. Nevertheless, the extensive practical applications of such photocatalysts are highly impeded due to certain limitations such as e⁻/h⁺ recombinations which decrease the photocatalytic degradation efficiencies [20]. Such photocatalysts drawbacks can be conquered to some extent by coupling the semiconductors which increases the charge separation and hence increasing the photocatalytic efficiencies. Several coupled semiconductor photocatalysts, mainly based on ZnO and TiO₂, were explored for the photocatalytic degradation of organic dyes and pigments under different light irradiations. These coupled semiconductor photocatalysts demonstrated improved photocatalytic efficiencies by lowering the e⁻/h⁺ recombinations [21–25].

Nitrophenols (NPs) are toxic and hazardous organic compounds which are commonly found in wastewater. These compounds are released from the pharmaceuticals, explosives, rubber,

pesticides, fungicides, petrochemical plants, etc. [26]. According to the US environmental protection agency (EPA), the 2-nitrophenol (2-NP), 4-nitrophenol (4-NP), and 2,4-dinitrophenol (2,4-NP) are the priority pollutants [27–29]. In particular, 4-nitrophenol (4-NP) is carcinogenic, mutagenic and has cyto- and embryonic toxicity [30] and hence its exposure may cause headaches, drowsiness, nausea and cyanosis through acute inhalation or ingestion [31]. Thus, it is highly needed to monitor the release of 4-NP in the environment. Several methods have been employed to determine 4-NP, such as, high performance liquid chromatography [32,33], gas chromatography [34], flow injection analysis [35], spectrophotometry [36], capillary electrophoresis [37], fluorescence analysis [38], electro-analytical methods [39,40], etc. Among various methods, the electro-analytical method has attracted a considerable attention as it provides an effective platform for efficient, robust, inexpensive and fast detection of hazardous chemicals at room-temperature. Recently, α -Fe₂O₃ hexagonal nanoparticles based chemical sensor was fabricated for the detection of 4-NP which exhibited an experimental detection limit of 1.56 mmol and sensitivity of $\sim 367.6 \mu\text{A} (\text{mol L}^{-1})^{-1} \text{cm}^{-2}$ [39]. Further, Lima et al. have used chitosan-stabilized silver nanoparticles/GCE electrode for fabrication of 4-NP sensor which exhibited good repeatability, stability and shows a detection limit of 70 nmol L⁻¹ [40].

In the present study, porous ZnO–SnO₂ nanosheets have been synthesized by the facile hydrothermal method and characterized in detail in terms of their morphological, structural, compositional and optical properties. The synthesized nanosheets were used as an efficient photocatalyst for the photocatalytic degradation of hazardous organic dye; i.e., direct blue 15 (DB 15) under visible light irradiation. Further, the prepared nanosheets were also used as efficient electron mediators for the fabrication of 4-NP chemical sensor in aqueous phase.

2. Experimental details

2.1. Materials

All the chemicals, zinc nitrate hexahydrate [Zn(NO₃)₂ · 6H₂O], tin chloride [SnCl₄ · 5H₂O], ammonium carbonate, ethanol, direct blue 15 dye, and 4-nitrophenol were obtained from Sigma-Aldrich and used as received without further purification. All the solutions were prepared in de-ionized (DI) water.

2.2. Synthesis of porous ZnO–SnO₂ nanosheets

For the synthesis of porous ZnO–SnO₂ nanosheets, in a typical reaction process, appropriate amount of Zn(NO₃)₂ · 6H₂O and SnCl₄ · 5H₂O (molar ratio=1:1) were dissolved in 50 mL DI water under continuous stirring to form a transparent solution. Consequently, an appropriate amount of ammonium carbonate was dissolved in 50 mL DI water and drop-wise poured into previous solution under continuous stirring. Finally, the obtained solution was transferred to 150 mL teflon-lined stainless steel autoclave which was heated to 120 °C for 24 h. After terminating the reaction, the autoclave was cooled to room-temperature and finally grayish-white precipitate was obtained which was decanted and washed with distilled water and ethanol sequentially. The obtained powder was then dried in an oven at 60 °C and calcined at 500 °C for 4 h.

2.3. Characterization of porous ZnO–SnO₂ nanosheets

The prepared porous ZnO–SnO₂ nanosheets were characterized in detail using several characterization techniques. The crystallinity of the prepared porous nanosheets was examined by X-ray diffraction (XRD) patterns, measured with Panalytical Model

X'Pert PRO diffractometer using Cu-K α radiation ($k=1.54056 \text{ \AA}$) at 45 kV and 40 mA. The morphological properties were investigated by field emission scanning electron microscopy (FESEM; JEOL-JSM-7600F) and transmission electron microscopy (TEM; JEOL-JEM-2100F) equipped with high-resolution TEM. The elemental and chemical compositions of prepared porous ZnO–SnO₂ nanosheets were investigated by energy dispersive spectroscopy (EDS) attached with FESEM and Fourier transform infrared (FTIR) spectroscopy, respectively. The FTIR analysis was done at room-temperature in the range 400–4000 cm⁻¹ using KBr as a reference. The UV–vis absorption spectra were recorded with UV–vis spectrophotometer (Systronics-2202) in the range of 200–800 nm. Brunauer–Emmett–Teller (BET) surface area was determined using Quantachrome Nova 2000e BET analyzer. The sample was degassed at 150 °C prior to BET measurements.

2.4. Photocatalytic decomposition of direct blue 15 using synthesized porous ZnO–SnO₂ nanosheets

The photocatalytic degradation of direct blue 15 (DB-15) dye was carried out in a doubled walled 500 mL reaction vessel with circulating water using porous ZnO–SnO₂ nanosheets as photocatalyst under visible light illumination. For the photocatalytic degradation of DB-15, 0.05 g of prepared porous ZnO–SnO₂ nanosheets catalyst was added to 100 mL aqueous solution of dye under continuous stirring. After achieving the equilibrium, the dye solution was exposed to visible light for about 90 min. The photocatalytic degradation was estimated by measuring the absorbance of dye solution in the presence of photocatalyst exposed at different time intervals. The absorbance was measured by UV–vis spectrophotometer. For this, a small amount of sample was withdrawn after definite time interval and filtered using 0.45 μm Millipore syringe filter. Absorption spectra of the dye solution were recorded and degradation efficiency was calculated using following equation:

$$\text{Degradation efficiency} = (1 - C/C_0)100\% \quad (1)$$

where C_0 is the initial dye concentration and C is the concentration of dye solution after irradiation under visible light.

2.5. Fabrication and characterization of 4-nitrophenol chemical sensor using current–voltage (*I*–*V*) technique

To fabricate 4-nitrophenol chemical sensor, slurry of porous ZnO–SnO₂ nanosheets was made by adding the appropriate amount of prepared nanomaterial and binder (butyl carbital acetate). The prepared slurry was then casted on the active area of the glassy carbon electrode (GCE; surface area=0.0316 cm²). Before coating, the electrode surface was polished with alumina and thoroughly rinsed with DI water. After coating, the electrode was dried in an oven at $\sim 60 \text{ }^\circ\text{C}$ for 4–6 h to get uniform layer. The sensing performance was evaluated using two electrodes system in which the porous ZnO–SnO₂ nanosheets modified GCE was used as a working electrode and the Pt wire as a counter electrode. The current response was measured from 0.0 to +1.5 V. The concentration and volume of phosphate buffer solution (PBS) were kept constant to 0.1 mol L⁻¹ and 10.0 mL, respectively. A wide concentration range of 4-nitrophenol (from 0.078 mmol L⁻¹ to 2.5 mmol L⁻¹) was used to check the sensing performance.

3. Results and discussion

3.1. Structural, morphological, and compositional properties of porous ZnO–SnO₂ nanosheets

The crystal structure and phase composition of prepared porous ZnO–SnO₂ nanosheets were analyzed by XRD. Fig. 1 shows

the typical XRD pattern of prepared ZnO–SnO₂ nanosheets which exhibited various well-defined diffraction reflections. The appearance of diffraction reflections at $2\theta=31.8^\circ$, 34.6° , 36.3° , 47.5° , 56.7° , 63.0° , 68.1° and 69.2° are related with the wurtzite hexagonal phase of ZnO and can be assigned as (100), (002), (101), (102), (110), (103), (112) and (201), respectively. The observed diffraction reflections are well matched with the reported literature and JCPDS card no. 36-1451 for wurtzite hexagonal phase of ZnO. In addition, other well-defined diffraction reflections appeared at $2\theta=26.6^\circ$, 37.9° , 51.7° , 54.6° , 57.9° , 62.0° , 64.8° , 65.9° , 71.3° and 78.8° are related with the tetragonal rutile phase of pure SnO₂ and can be assigned as (110), (111), (211), (220), (002), (310), (112), (301), (202) and (321), respectively. The observed diffraction reflections are well-matched with the reported JCPDS card no.

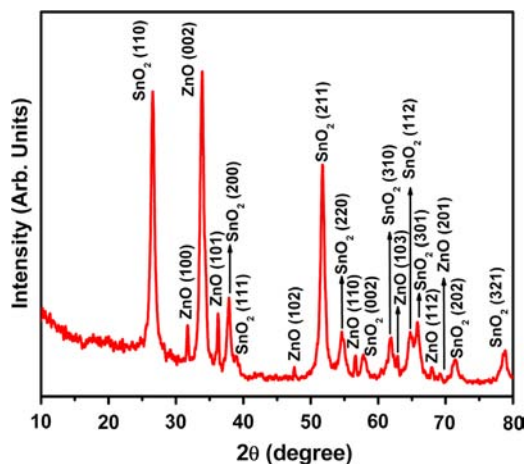


Fig. 1. Typical XRD pattern of synthesized porous ZnO–SnO₂ nanosheets.

41–1445 for tetragonal rutile phase of SnO₂. Further, the appearance of sharp and strong diffraction reflections in the XRD pattern confirmed that the prepared nanosheets are well-crystalline. No characteristic reflection related with the impurities such as ZnSnO₃ and Zn₂SnO₄ were observed in the pattern, up to the detection limit of XRD machine which further suggest that the prepared nanosheets are made of ZnO and SnO₂. The average crystallite sizes of the prepared nanosheets were calculated by Debye–Scherrer formula as mentioned below:

$$D = K\lambda/\beta \cos \theta \quad (2)$$

where D is the crystallite size, K is the constant, λ is the X-ray wavelength, β is the FWHM (full width half maximum) and θ is the diffraction angle. According to the mentioned above equation, the average crystallite sizes of ZnO and SnO₂ in ZnO–SnO₂ nanosheets were found to be 12 nm and 15 nm, respectively.

The general morphologies of prepared ZnO–SnO₂ material was characterized by FESEM and results are shown in Fig. 2. Fig. 2 (a) and (b) exhibits the typical low-magnification FESEM images which revealed that the prepared material possess sheet-shaped morphologies which are grown in high density. Due to high growth, the nanosheets are intermingled in each other and form network like morphologies (Fig. 2(a)). It is also observed that the sample consists of 2D sheet-like morphology having lateral size distribution of nanometer to micrometer range. Fig. 2(c) and (d) shows the high-resolution FESEM images which confirmed that the nanosheets are made by the accumulation of hundreds of nanoparticles. The typical thicknesses of the nanosheets are $\sim 35 \pm 10$ nm while sizes are in several micrometers. Further detailed morphological and structural characterizations of prepared nanosheets were done by TEM and HRTEM. Fig. 3(a) exhibits the typical TEM image of prepared nanosheet which exhibits full consistency with the observed FESEM results in terms of

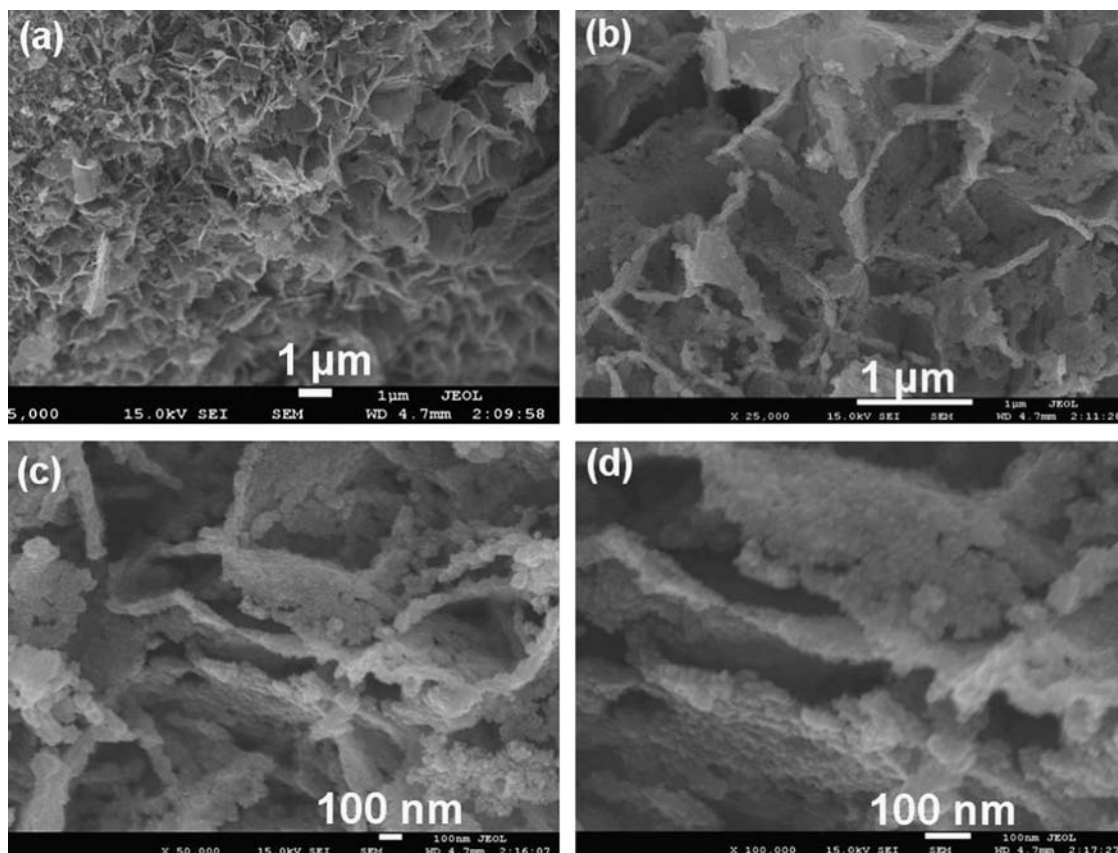


Fig. 2. Typical (a) and (b) low-magnification and (c) and (d) high-resolution FESEM images of synthesized porous ZnO–SnO₂ nanosheets.

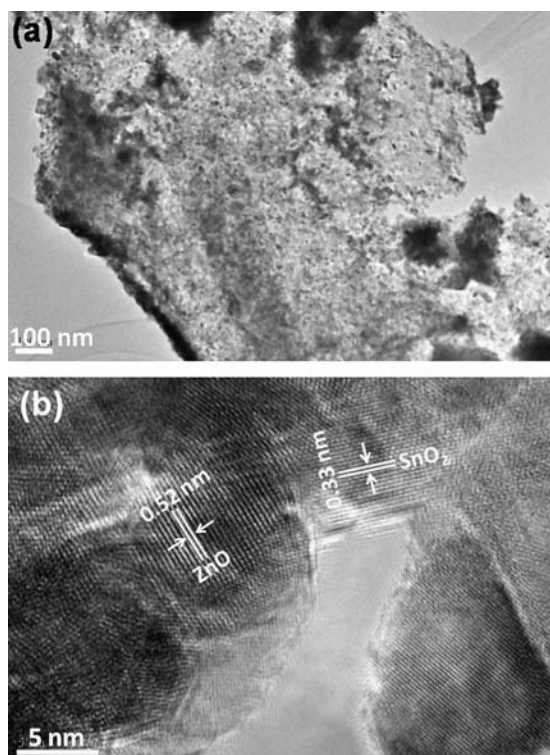


Fig. 3. Typical (a) TEM and (b) HRTEM images of synthesized porous ZnO-SnO₂ nanosheets.

morphology and dimensionality. It is clear from TEM image that the nanosheets possess porous morphologies. Fig. 3(b) depicts the high-resolution TEM image of prepared nanosheets. It is clear from the HRTEM image that the nanosheets are made of ZnO-SnO₂ crystallites. As can be seen different lattice planes are seen in the prepared nanosheets. It is clear that the observed interplanar distance of 0.33 nm is close to the *d*-spacing of the (110) plane of the tetragonal rutile SnO₂ [41,42]. Interestingly, the other adjacent crystal exhibits different interplanar distance of ~0.52 nm which is well agreed with the lattice spacing of the (002) planes of the wurtzite hexagonal phase of ZnO. The observed results clearly confirmed that the prepared porous nanosheets are made of ZnO and SnO₂ [41,42].

The elemental and chemical compositions of prepared porous ZnO-SnO₂ nanosheets were investigated by EDS attached with FESEM and FTIR spectroscopy. Fig. 4(a) exhibits typical EDS spectrum which revealed that the prepared porous ZnO-SnO₂ nanosheets are made of Zn, Sn and O. Except Zn, Sn and O, no peak related with other element is seen in the spectrum which further confirms the purity of prepared nanosheets. Fig. 4(b) depicts the typical FTIR spectrum of prepared porous ZnO-SnO₂ nanosheets. Several well-defined peaks appearing at 539, 1023, 1381, 1627 and 3427 cm⁻¹ are seen in the observed FTIR spectrum. The appearance of broad peak at ~3427 cm⁻¹ is attributed to stretching frequency of the hydroxyl group [43]. Two short peaks located at ~1627 cm⁻¹ and 1023 cm⁻¹ are due to stretching vibration of C=O group and C-O bond, respectively. The appearance of sharp peak at 539 cm⁻¹ is due to stretching vibration of metal-oxygen (M-O) bond.

Fig. 5 depicts the N₂ adsorption-desorption isotherm and pore size distribution curve (inset) for the prepared porous ZnO-SnO₂ nanosheets. It shows a large uptake of nitrogen due to capillary condensation at relative pressure (*P/P*₀) in the range of 0.6–0.99 indicating multifiform pore distribution. The isotherm is type IV with a hysteresis loop at relative pressure of > 0.8 which is typical

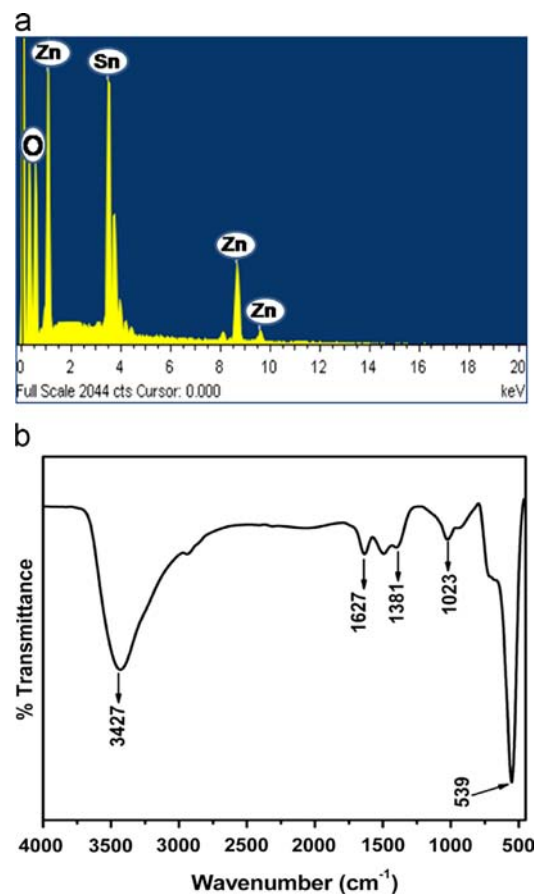


Fig. 4. Typical (a) EDS spectrum and (b) FTIR spectrum of synthesized porous ZnO-SnO₂ nanosheets.

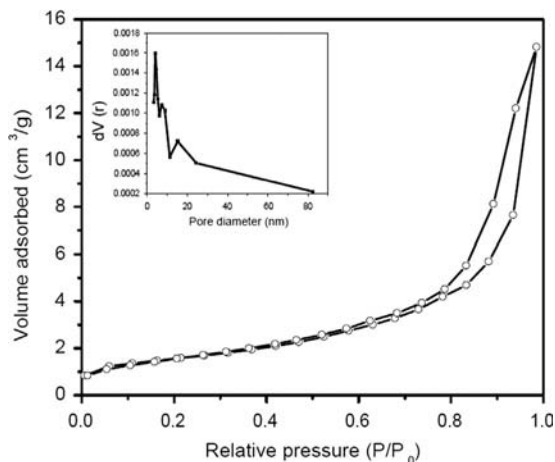


Fig. 5. N₂ adsorption-desorption isotherm for porous ZnO-SnO₂ nanosheets (inset pore size distribution curve from BJH adsorption curve).

for mesoporous solids. The pore size distribution curve was obtained from the adsorption branch of the isotherm and shown in inset of Fig. 5. The Brunauer-Emmett-Teller (BET) surface area and pore volume of the prepared porous ZnO-SnO₂ nanosheets were found to be ~51.603 m²/g and 0.2157 cm³/g, respectively. The pore diameter of the sample, calculated by the different method, was found to be 4.032 nm (BJH method), 13.992 nm (DFT method) and 4.032 nm (DH method), respectively. It was observed that the porous structure with large surface area and

high pore volume could play a significant role in the photocatalytic activities of the prepared porous ZnO–SnO₂ nanosheets.

3.2. Photocatalytic degradation of direct blue 15 using porous ZnO–SnO₂ nanosheets under visible light irradiation

To evaluate the photocatalytic activity of the prepared porous ZnO–SnO₂ nanosheets under visible light irradiation, direct blue 15 (DB 15) dye was taken as a model dye. Inset of Fig. 6 exhibits the typical chemical structure of DB-15 dye. Fig. 6 demonstrates the typical UV–vis spectrum of DB-15 dye. It is clear from the

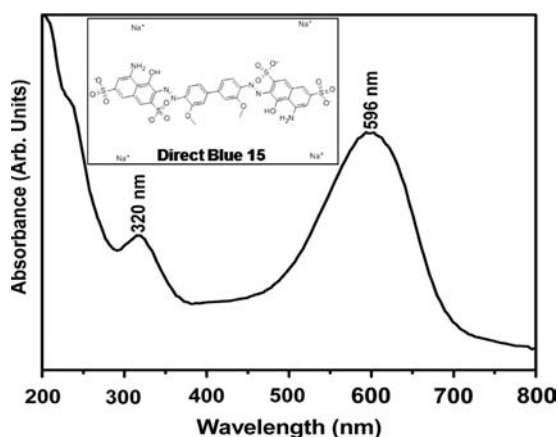


Fig. 6. Typical UV–vis absorption spectrum for Direct Blue 15 dye. Inset shows the chemical structure of Direct Blue 15 dye.

observed UV–vis spectrum that the dye exhibited two absorption characteristic peaks at ~ 320 nm and 596 nm. The degradation of DB 15 dye over porous ZnO–SnO₂ nanosheets was evaluated from UV–vis absorption spectra of dye solution as shown in Fig. 7(a). It was observed that the intensity of absorption peaks at 596 nm was continuously decreasing with increasing the irradiation time which revealed the photo-degradation of DB 15 dye over porous ZnO–SnO₂ nanosheets. The plot of degradation rate versus irradiation time is shown in Fig. 7(b). The results depict the gradual increase in the degradation rate of DB 15 dye under visible light. Similarly, decrease in the relative concentration (C_0/C) of DB 15 dye with respect to irradiation time also confirmed the degradation of DB 15 dye under visible light (Fig. 7(c)). Fig. 7(d) shows the bar diagram for the % degradation of DB 15 dye in the presence of various photocatalysts. It is clear from the bar diagram that $\sim 87\%$ degradation of DB 15 was achieved in 90 min in the presence of porous ZnO–SnO₂ nanosheets. However, in the absence of any photocatalyst, only 3% degradation was observed. The photocatalytic efficiency of the prepared ZnO–SnO₂ nanosheets was also compared with other commercially available photocatalysts and presented in Fig. 7(d). The synthesized ZnO–SnO₂ nanosheets showed a better photocatalytic performance compared to commercially available ZnO (48%), SnO₂ (19%) and TiO₂–PC50 (54%) (Fig. 7(d)). It is well-known that the photocatalytic activities are strongly depend on the surface area of the photocatalysts as the reactant molecules are adsorbed on their surfaces [44]. Thus, large surface area photocatalysts provide higher photocatalytic efficiencies. As the prepared ZnO–SnO₂ nanosheets shows high surface area hence it exhibited higher photocatalytic efficiencies. The large surface area and large pore volume of prepared ZnO–SnO₂

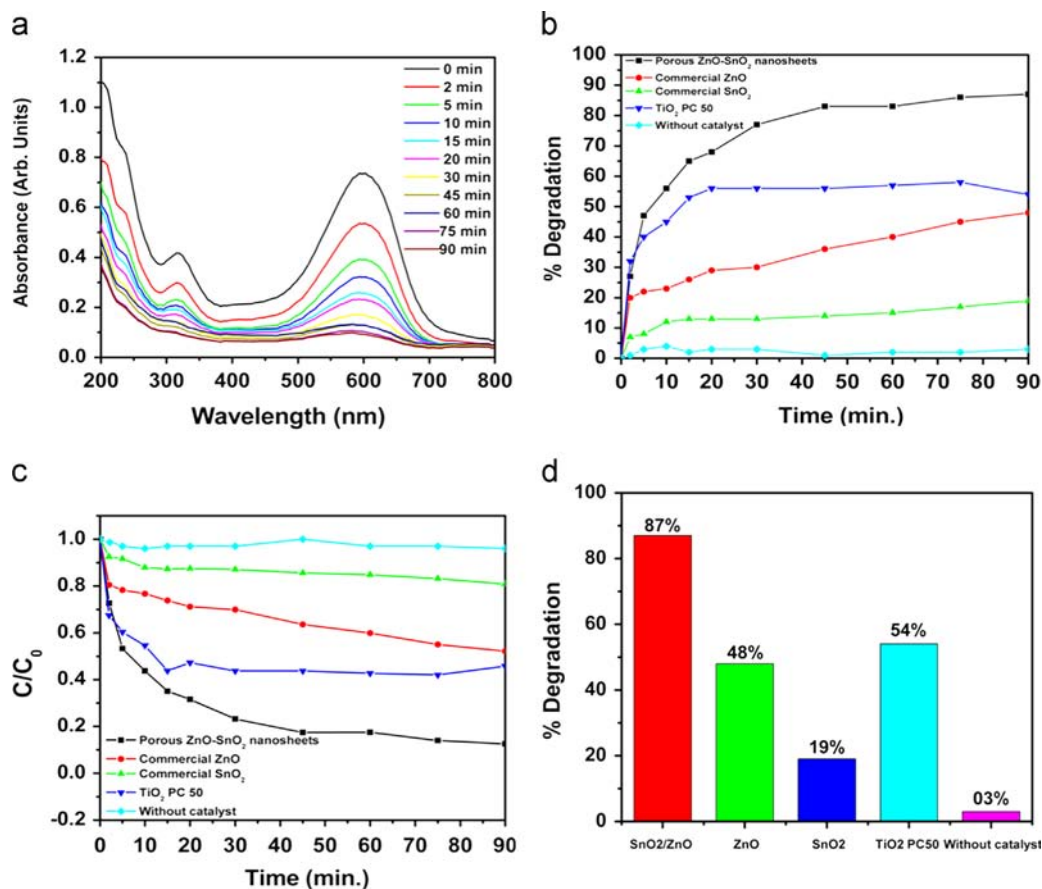


Fig. 7. (a) Time-dependent UV–vis absorption spectra for Direct Blue 15 dye in the presence of porous ZnO–SnO₂ nanosheets (Dye conc. = 25 mg/L, catalyst dose = 0.50 g/L, pH = natural); (b) % degradation in the presence of different photocatalysts; (c) C/C_0 vs time plot for various photocatalysts, and (d) bar diagram for the % degradation of Direct Blue 15 dye in the presence of various photocatalysts.

nanosheets provide more active sites for the photocatalytic reactions. In addition, porous morphologies help to promote the fast diffusion of reactant molecules thereby increasing the quantum efficiency of photocatalytic reaction [45].

The kinetic study of the photocatalytic degradation of DB 15 dye was also done using kinetic model proposed by Langmuir-Hinshelwood [46,47] according to mentioned below equation:

$$C_0/C = kt \quad (3)$$

Where C_0 is the initial concentration of DB 15 dye and C is the concentration of DB 15 dye at time t . According to the equation, it was observed that the photo-degradation of DB 15 dye obeys pseudo first order reaction kinetics as the linear relationship was observed between $\ln(C_0/C)$ and irradiation time. Fig. 8(a) shows the plot of $\ln(C_0/C)$ vs irradiation time for porous ZnO–SnO₂ nanosheets, commercial ZnO and commercial SnO₂. The kinetics data is also summarized in Table 1.

To check the stability of the prepared porous ZnO–SnO₂ nanosheets, recyclability experiments were performed under

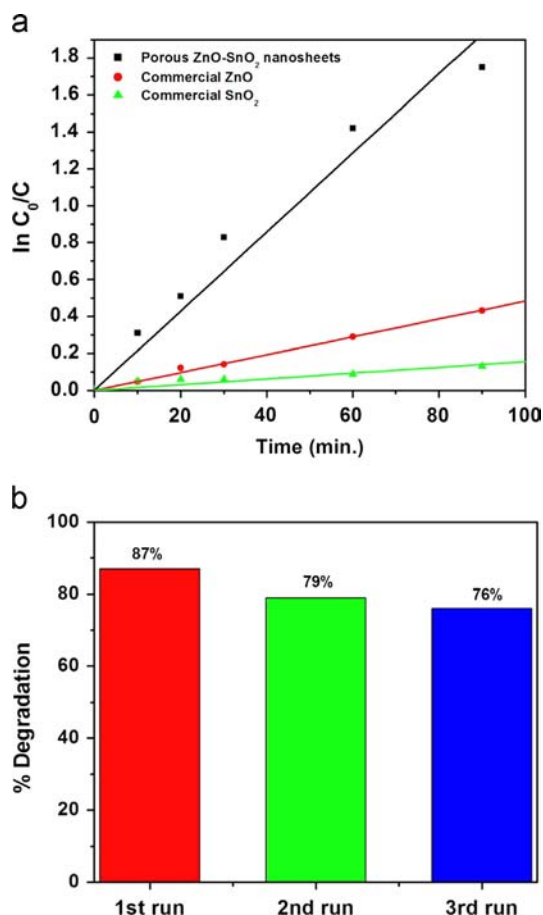


Fig. 8. (a) Pseudo-first order kinetics for Direct Blue 15 dye in presence of various photocatalysts, and (b) reusability of porous ZnO–SnO₂ nanosheets for the degradation of DB 15 dye for three consecutive cycles.

Table 1
Kinetics data of DB 15 photodegradation in the presence of different photocatalysts.

Photocatalyst	R ²	k (min ⁻¹)
Porous ZnO-SnO ₂ nanosheets	0.986	0.0214
Commercial ZnO	0.998	0.0048
Commercial SnO ₂	0.944	0.0016

similar conditions. The photodegradation experiments were repeated 3 times with the same catalyst under visible light irradiation. For reusability experiments, the catalyst was filtered, thoroughly washed and dried after each experiment. The results from recycling runs are shown in Fig. 8(b). The degradation efficiencies for three consecutive cycles were ~87%, 79% and 76%, respectively. There was a slight decrease in photodegradation efficiency after each run. However, the porous ZnO–SnO₂ nanosheets exhibited 76% activity after three successive cycles under visible light. Hence, it may be inferred that the prepared catalyst is effective and reusable under visible light.

The schematic representation of photocatalytic degradation of DB 15 dye using porous ZnO–SnO₂ nanosheets is presented in Fig. 9. When the light falls on the ZnO–SnO₂ heterojunction assembly, electron and holes are generated in the conduction band (CB) and valence band (VB) of ZnO and SnO₂. The conduction band (CB) of ZnO lies above the conduction band (CB) of SnO₂ and the valence band (VB) of ZnO lies below the valence band (VB) of SnO₂ [48]. The photogenerated electrons (e⁻) are then transferred from the CB of ZnO to the CB of SnO₂ and photogenerated holes (h⁺) from the VB of SnO₂ to the VB of ZnO. The electrons in the CB of SnO₂ reacted with the O₂ adsorbed on the surface of photocatalyst and form a highly reactive species, a radical anion (O₂⁻). This radical anion undergoes further reactions to form [•]OH which degrades the organic pollutant into the smaller compounds. On the other hand, the holes in the VB of ZnO also contribute to the generation of [•]OH by reacting with ⁻OH. Hence, e⁻/h⁺ recombination is hindered which improves the photocatalytic efficiency under visible light. The reactions occurring on the surface of photocatalyst can be summarized as mentioned below [49]:



Based on above equations, the high surface area of porous ZnO–SnO₂ nanosheets sufficiently provides more active sites for the reactant molecule to adsorb and generate the active oxygen species (O₂⁻, [•]OOH and [•]OH). These active species are responsible for the degradation of DB 15 dye to smaller molecules.

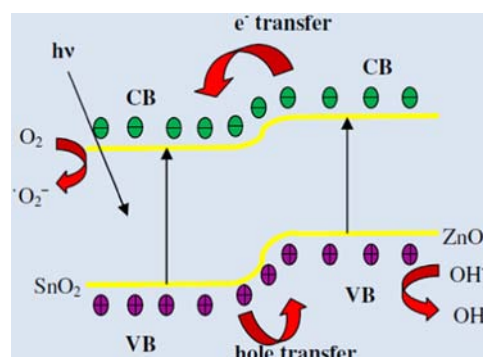


Fig. 9. Schematic representation of photocatalytic degradation of Direct Blue-15 dye using nanoporous ZnO–SnO₂ nanosheets.

3.3. 4-Nitrophenol chemical sensor application of porous ZnO–SnO₂ nanosheets

To evaluate the sensing properties such as sensitivity, detection limit and correlation coefficient, 4-nitrophenol chemical sensor was fabricated and the current (*I*)–voltage (*V*) measurements were performed. The 4-nitrophenol chemical sensor was fabricated using porous ZnO–SnO₂ nanosheets as a working electrode and Pt wire as a counter electrode in 0.1 mol L⁻¹ phosphate buffer solution (PBS). Fig. 10 shows *I*–*V* response of ZnO–SnO₂ nanosheets modified GCE with and without 4-nitrophenol. It can clearly be seen that there is a large increment in the current after the addition of 4-nitrophenol (0.078 mmol L⁻¹) in phosphate buffer solution. However, a low current was observed in the absence of 4-nitrophenol which indicates the high activity of porous ZnO–SnO₂ nanosheets towards 4-nitrophenol.

Fig. 11 illustrates the mechanism of the fabricated 4-nitrophenol sensor with porous ZnO–SnO₂ nanosheets modified electrode. For the sensing, the oxygenated species get adsorbed on the surface of porous ZnO–SnO₂ nanosheets and these oxygenated species after gaining electron from the CB of porous ZnO–SnO₂ nanosheets generate O₂⁻ and O⁻ species according to the following reactions [50].

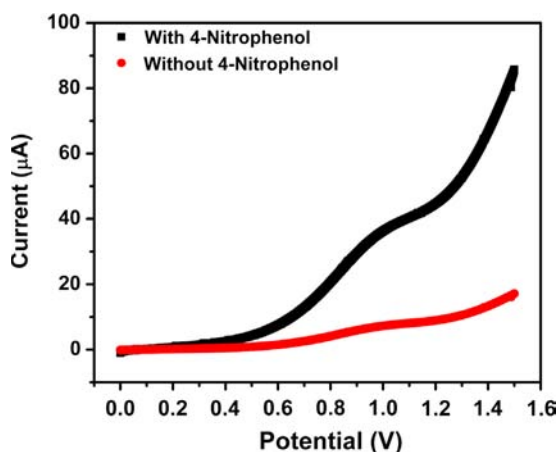


Fig. 10. Typical *I*–*V* responses of porous ZnO–SnO₂ nanosheets modified GCE in 10 ml, 0.1 mol L⁻¹ PBS solution, (■) with 4-nitrophenol (0.078 mmol L⁻¹) and (●) without 4-nitrophenol.

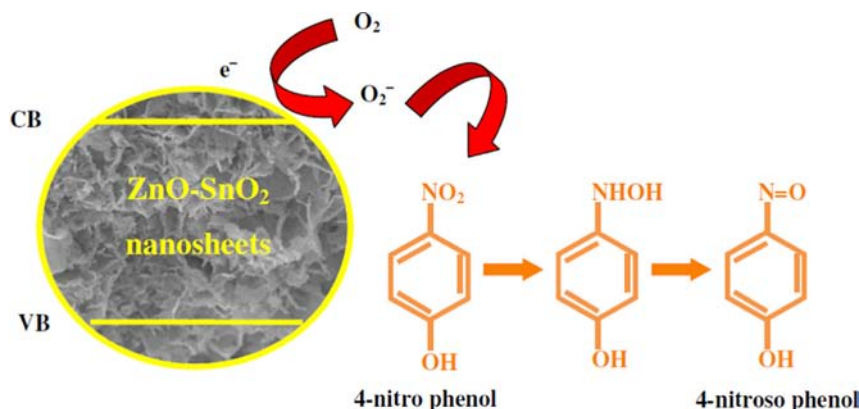


Fig. 11. Schematic representation of the fabricated 4-nitrophenol chemical sensor fabricated based on *I*–*V* technique using porous ZnO–SnO₂ nanosheets modified GC electrode as working electrode.



These ionic species first converts 4-nitrophenol to p-hydroxylaminophenol which then converts to 4-nitrosophenol. The electrons thus generated revert back to CB of the ZnO–SnO₂ nanosheets. Further, different 4-NP chemical sensors with porous ZnO–SnO₂ nanosheets based electrode have been fabricated having different concentration of 4-NP (from 0.078 mmol L⁻¹ to 2.5 mmol L⁻¹). Fig. 12(a) exhibits a series of the *I*–*V* curves of the fabricated 4-NP chemical sensor fabricated based on porous ZnO–SnO₂ nanosheets. Different concentration experiments for

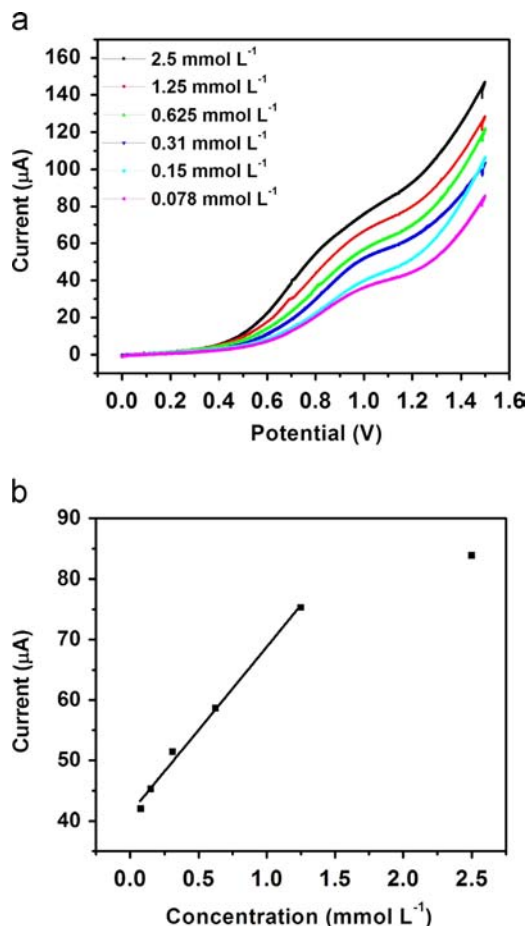


Fig. 12. (a) *I*–*V* response for various concentrations of 4-nitrophenol (from 0.078 mmol L⁻¹ to 2.5 mmol L⁻¹) and (b) calibration curve.

Table 2

The comparison summary of the performances of 4-NP chemical sensors fabricated based on the utilization of various nanomaterials as electron mediators.

Material	Limit of detection	Linearity	Sensitivity	Reference
CuO nano hybrids	0.67 nmol L ⁻¹	1.0 nmol L ⁻¹ –1.0 mmol L ⁻¹	4.50 μA/mmol L ⁻¹ cm ⁻²	[51]
Mn₂O₃/ZnO NPs/AgE	0.83 nmol L ⁻¹	0.1 nmol L ⁻¹ –50.0 μmol L ⁻¹	4.6667 μA/mmol L ⁻¹ cm ⁻²	[43]
Pt/PEDOT-PB	8.23 μmol L ⁻¹	2–100 μmol L ⁻¹	0.116 μA/μmol L ⁻¹	[52]
Ag₂O NPs/AuE	0.19 μmol L ⁻¹	1.0 μmol L ⁻¹ –0.5 mmol L ⁻¹	4.740 μA/mmol L ⁻¹ cm ⁻²	[53]
Porous ZnO–SnO₂ nanosheets	0.078 mmol L ⁻¹	0.078–1.25 mmol L ⁻¹	1285.76 μA/mmol L ⁻¹ cm ⁻²	This work

the fabricated chemical sensor were done to investigate the detail sensing behavior and parameters. The fabricated 4-NP chemical sensor presents a continuous increase in current upon the incremental addition of 4NP with the concentrations range from ~0.078 mmol L⁻¹ to 2.5 mmol L⁻¹. The continuous increase in the current may be attributed to the generation of large number of ions and increase in the ionic strength with the addition of 4-NP [39]. In order to estimate the sensitivity of the fabricated 4-NP chemical sensor, the current was calibrated and the plot of calibrated current versus 4-NP concentrations is shown in Fig. 12 (b). It can be seen that the calibrated current is linearly increasing with enhancing the concentrations of 4-NP. The fabricated 4-NP chemical sensors with porous ZnO–SnO₂ nanosheets based electrode showed a good linearity in the range of 0.078–1.25 mmol L⁻¹ and showed a high sensitivity of ~1285.76 μA/mmol L⁻¹ cm⁻² with an experimental detection limit of 0.078 mmol L⁻¹. The high sensitivity of fabricated 4-NP chemical sensor may be attributed to the high surface area of the porous ZnO–SnO₂ nanosheets electrode. Further, it can also be seen from the *I*–*V* and calibration curves that the fabricated sensors are re-useable and do not require any treatment for recovery. Table 2 shows the comparison of performances of 4-NP chemical sensors fabricated using various nanomaterials as electron mediators. It is clear from Table 1 that the fabricated 4-NP chemical sensor based on porous ZnO–SnO₂ nanosheets exhibited better sensitivity compared to other reported 4-NP chemical sensors [43,51–53]. Thus the fabricated chemical sensor based on porous ZnO–SnO₂ nanosheets is presenting itself as promising candidate for the effective detection of 4-NP in liquid medium.

4. Conclusion

In summary, well-crystalline porous ZnO–SnO₂ nanosheets were synthesized by the facile and simple hydrothermal method at low-temperature and characterized in detail using various techniques. The detail characterizations revealed that the prepared nanosheets are well-crystalline ZnO–SnO₂ heterojunctions, possessing porous morphologies and grown in high density. The prepared porous ZnO–SnO₂ nanosheets were applied for the photocatalytic degradation of DB 15 dye under visible light and for the detection of toxic 4-NP in liquid phase. By using porous ZnO–SnO₂ nanosheets as an efficient photocatalyst, ~87% degradation of DB-15 dye was achieved in 90 min under visible light irradiation. Interestingly, the prepared porous ZnO–SnO₂ nanosheets exhibited better photocatalytic performance compared to commercially available ZnO (48%), SnO₂ (19%) and TiO₂–PC50 (54%). Further, the fabricated porous ZnO–SnO₂ nanosheets based 4-NP chemical sensor showed very high and reproducible sensitivity of ~1285.76 μA/mmol L⁻¹ cm⁻², experimental detection limit of 0.078 mmol L⁻¹ and linear dynamic range from 0.078 to 1.25 mmol L⁻¹. Thus, the presented work demonstrates that the prepared ZnO–SnO₂ nanosheets can be used as an efficient visible-light driven photocatalyst and effective electrode materials for the

fabrication of highly sensitive sensor for the detection of hazardous and toxic chemicals.

Acknowledgments

The authors greatly acknowledge the financial support obtained under the AICTE (RPS), Government of India through a project Grant 8023/RID/RPS-16/(POLICY-IV)(GOVT)/2011-12 and TEQIP-II Grant of Dr. S.S. Bhatnagar UICET, Panjab University, Chandigarh for financial support. Ahmad Umar would like to acknowledge the Ministry of Higher Education, Kingdom of Saudi Arabia for the research Grant (PCSED-001-11) under the Promising Centre for Sensors and Electronic Devices (PCSED) at Najran University.

References

- [1] S. Wang, T. Wang, Y. Ding, Q. Su, Y. Xu, Z. Xu, G. Jiang, W. Chen, *Sci. Adv. Mater.* 5 (2013) 1006–1012.
- [2] G. Ciobanu, S. Ilisei, M. Harja, C. Luca, *Sci. Adv. Mater.* 5 (2013) 1090–1096.
- [3] N.M. Mahmoodi, M. Arami, *J. Photochem. Photobiol. B* 94 (2009) 20–24.
- [4] Y. Koriche, M. Darder, P. Aranda, S. Semsari, E.R. Hitzky, *Sci. Adv. Mater.* 5 (2013) 994–1005.
- [5] S.K. Mehta, S. Chaudhary, B. Bharti, M. Gradzielski, *Sci. Adv. Mater.* 4 (2012) 78–92.
- [6] C.L. Wong, Y.N. Tan, A.R. Mohamed, *J. Environ. Manag.* 92 (2011) 1669–1680.
- [7] S. Senthilkumaar, P.R. Varadarajan, K. Porkodi, C.V. Subbhuraam, *J. Colloid Interface Sci.* 284 (2005) 78–82.
- [8] A. Khan, Niyaz A. Mir, M.M. Haque, M. Muneer, C. Boxall, *Sci. Adv. Mater.* 5 (2013) 160–165.
- [9] R.O. Cristovao, A.P.M. Tavares, A.I. Brigida, J.M. Loureiro, R.A.R. Boaventura, E.A. Macedo, M.A.Z. Coelho, *J. Mol. Catal. B: Enzym.* 72 (2011) 6–12.
- [10] G.R. Chaudhary, P. Saharan, Ahmad Umar, S.K. Mehta, S. Mor, *Sci. Adv. Mater.* 5 (2013) 1886–1894.
- [11] Q. Sun, L. Yang, *Water Res.* 37 (2003) 1535–1544.
- [12] C.K.S. Goh, Y. Wang, J. Hong, R. Xu, *Sci. Adv. Mater.* 5 (2013) 1658–1666.
- [13] J. Wang, F. Qu, X. Wu, *Sci. Adv. Mater.* 5 (2013) 1364–1371.
- [14] B. Li, Y.L. Feng, J.Z. Guo, L.Q. Bai, J. Chen, L. Liu, L.J. Zhang, *Sci. Adv. Mater.* 5 (2013) 341–345.
- [15] S.K. Kansal, A.H. Ali, S. Kapoor, D.W. Bahnemann, *Sci. Adv. Mater.* 5 (2013) 630–636.
- [16] S.K. Kansal, R. Lamba, S.K. Mehta, A. Umar, *Mater. Lett.* 106 (2013) 385–389.
- [17] S.K. Kansal, S. Sood, A. Umar, S.K. Mehta, *J. Alloys Compd.* 581 (2013) 392–397.
- [18] M. Farbod, N.M. Ghaffari, I. Kazeminezhad, *Ceram. Int.* 40 (2014) 517–521.
- [19] X. Cheng, J. Jiang, C. Jin, C. Lin, Y. Zeng, Q. Zhang, *Chem. Eng. J.* 236 (2014) 139–148.
- [20] M.R. Hoffmann, S.T. Martin, W.Y. Choi, D.W. Bahnemann, *Chem. Rev.* 95 (1995) 69–96.
- [21] P. Shah, K.S. Siddhapara, D.V. Shah, J. Pandya, *Carbon: Sci. Technol.* 5 (2013) 265–268.
- [22] H. Tang, D. Zhang, G. Tang, X. Ji, W. Li, C. Li, X. Yang, *Ceram. Int.* 39 (2013) 8633–8640.
- [23] Y. Xia, L. Yin, *Phys. Chem. Chem. Phys.* 15 (2013) 18627–18634.
- [24] R. Saravanan, S. Karthikeyan, V.K. Gupta, G. Sekaran, V. Narayanan, A. Stephen, *Mater. Sci. Eng. C* 33 (2013) 91–98.
- [25] X. Luo, F. Liu, X. Li, H. Gao, G. Liu, *Mater. Sci. Semicond. Process.* 16 (2013) 1613–1618.
- [26] W. Frenzel, J.O. Frenzel, J. Moeler, *Anal. Chim. Acta* 261 (2006) 253–259.
- [27] J. Zeyer, H.P. Kocher, K.N. Timmis, *Appl. Environ. Microbiol.* 52 (1986) 334–339.
- [28] R.A. Kristanti, T. Toyama, T. Hadibarata, Y. Tanaka, K. Mori, *RSC Adv.* 4 (2014) 1616–1621.
- [29] S.S. Li, D. Du, J. Huang, H.Y. Tu, Y.Q. Yang, A.D. Zhang, *Analyst* 138 (2013) 2761–2768.
- [30] K.B. Narayanan, N. Sakthivel, *Bioresour. Technol.* 102 (2011) 10737–10740.
- [31] Y. Zhou, Z. Qu, Y. Zeng, T. Zhou, G. Shi, *Biosens. Bioelectron.* 52 (2014) 317–323.

- [32] F. Ni, L. Thomas, T.M. Cotton, *Anal. Chem.* 61 (1989) 888–894.
- [33] G.D. Teresa, G.C. Agustina, M.D. Nielen, P.V. Piedad, S.L. Francisco, *J. Agric. Food Chem.* 48 (2000) 4508–4513.
- [34] E. Tesarova, D. Sykora, Z. Voznakova, *Fresenius Environ. Bull.* 4 (1995) 609–616.
- [35] C.H. Fischer, J.G. Rabe, *Anal. Chim. Acta* 284 (1993) 257–263.
- [36] A. Uzer, E. Ercag, R. Apak, *Anal. Chim. Acta* 505 (2004) 83–93.
- [37] X. Guo, Z. Wang, S. Zhou, *Talanta* 64 (2004) 135–139.
- [38] W. Seaman, A.R. Norton, O.E. Sundberg, *Ind. Eng. Chem. Anal. Ed.* 12 (1940) 403–405.
- [39] A. Umar, M.S. Akhtar, G.N. Dar, S. Baskoutas, *Talanta* 116 (2013) 1060–1066.
- [40] C.A. de Lima, P.S. da Silva, A. Spinelli, *Sens. Actuator B* 196 (2014) 39–45.
- [41] G.W. Ho, A.S.W. Wong, *Appl. Phys. A* 86 (2007) 457–462.
- [42] X. Xue, Z. Chen, C. Ma, L. Xing, Y. Chen, Y. Wang, T. Wang, *J. Phys. Chem. C* 114 (2010) 3968–3972.
- [43] M.M. Rahman, G. Gruner, M.S. Al-Ghamdi, M.A. Daous, S. Khan, A.M. Asiri, *Chem. Cent. J.* 7 (2013) 60–72.
- [44] J. Tang, Z. Zou, Y. Jinhua, *Chem. Mater.* 16 (2004) 1644–1649.
- [45] Z. Bian, J. Zhu, S. Wang, Y. Cao, X. Qian, H. Li, *J. Phys. Chem. C* 112 (2008) 6258–6262.
- [46] C.C. Lin, Y.J. Chiang, *Chem. Eng. J.* 181–182 (2012) 196–205.
- [47] S.K. Kansal, G. Kaur, S. Singh, *React. Kinet. Catal. Lett.* 98 (2009) 177–186.
- [48] Z. Zhang, C. Shao, X. Li, L. Zhang, H. Xue, C. Wang, Y. Liu, *J. Phys. Chem. C* 144 (2010) 7920–7925.
- [49] R. Liu, Y. Huang, A. Xiao, H. Liu, *J. Alloys Compd.* 503 (2010) 103–110.
- [50] P.P. Sahay, S. Tewari, S. Jha, M.J. Shamsuddin, *Mater. Sci.* 40 (2005) 4791–4793.
- [51] S.M.M. Rahman, K. Akhtar, A.M. Asiri, K.A. Alamry, J. Seo, H. Han, *Int. J. Electrochem. Sci.* 7 (2012) 10965–10975.
- [52] S. Lupua, C. Lete, M. Marin, N. Totir, P.C. Balaure, *Electrochim. Acta* 54 (2009) 1932–1938.
- [53] M.M. Rahman, A.M. Asiri, A.G. Al-Sehemi, *Electrochim. Acta* 112 (2013) 422–430.



Desorption corona beam ionisation (DCBI) mass spectrometry for in-situ analysis of adsorbed phenol in cigarette acetate fiber filter

Wen Du^{a,b}, Li-Juan Tang^b, Jian-Hui Wen^{a,*}, Ke-Jun Zhong^a, Jian-Hui Jiang^b, Hua Wang^{c,*}, Bo Chen^c, Ru-Qin Yu^b

^a Technology Center of China Tobacco Hunan Industrial Co., Ltd., Changsha 410007, PR China

^b State Key Laboratory for Chemo/Biosensing and Chemometrics, College of Chemistry and Chemical Engineering, Hunan University, Changsha 410082, PR China

^c Key Laboratory of Phytochemical R&D of Hunan Province, Hunan Normal University, Changsha 410081, PR China

ARTICLE INFO

Article history:

Received 26 April 2014

Received in revised form

4 August 2014

Accepted 6 August 2014

Available online 20 August 2014

Keywords:

Absorbent material

Spatial distribution characteristic

In-situ analysis

Desorption corona beam ionization

Mass spectrometry

Ambient ionization

ABSTRACT

The study of spatial distribution characteristics of the adsorbed compounds for absorbent materials has significant importance in understanding the behaviors of aerosols while they migrating in the absorbent materials. Herein, for the first time, desorption corona beam ionization–mass spectrometry (DCBI–MS) has proposed for direct in-situ analysis of adsorbed aerosol for absorbent materials. DCBI is a novel atmospheric pressure chemical ionization (APCI)-related technique developed by our group in recent years. It can facilitate accurately localizing sampling by forming a visible thin corona beam and avoid the risk of sample contamination and matrix interference compared with other similar techniques. The advantages of DCBI–MS allow rapid screening of the spatial distribution characteristics of the adsorbed compounds for absorbent materials. The distribution characteristic of phenol in cigarette filter tip filled with cellulose acetate fiber was studied as a model case for demonstrating the feasibility of the developed method. As a comparison, conventional HPLC was also used for the study of the distribution characteristic of phenol. The results revealed DCBI–MS had highly improved assay simplicity in spatial distribution characteristic analysis of phenol for the acetate fiber tip, therefore, exhibiting a great potential for convenient, rapid and cost-efficient analysis of the spatial distribution characteristic investigation of adsorbed compounds for adsorbent materials.

© 2014 Elsevier B.V. All rights reserved.

1. Introduction

Aerosol adsorption and retention has widely applications in many fundamental industries including chemical, food, medicine and so on [1–3]. Especially, it is becoming a unique technology in solving environmental pollution recent years, and has attracted great interest in the development of various absorbent materials [4,5]. Beyond developing novel absorbent materials, the study of the distribution characteristics of the adsorbed compounds for the absorbent materials is also an important task in such research area [6,7].

Analysis of the adsorbed aerosol for an absorbent material has been carried out by diverse analytical techniques, such as UV absorption spectroscopy [8], infrared spectroscopy [9], and gas or high performance liquid chromatography–mass spectrometry

(GC or HPLC–MS) [10,11]. However, no matter using what kind of the techniques, most of them are requiring multiple-step pre-treatment and time-consuming separation. Moreover, it is hard for almost all the methods to get the spatial distribution information about the adsorbed compound for the adsorbent material [10–13]. Nevertheless, the spatial distribution characteristics of the adsorbed compounds may provide more useful information for understanding the behaviors of aerosols while they migrating in the absorbent materials. In the context, the development of convenient techniques with desirable operational attributes for rapid spatial distribution analysis of the adsorbed compounds should be a topic of intensive interest for the study of adsorbent materials.

In the last decade, ambient ionization–mass spectrometry (API–MS) techniques, including desorption electrospray ionization (DESI) [14], electrospray laser desorption/ionization (ELDI) [15], direct analysis in real time (DART) [16], dielectric discharge barrier ionization (DBDI) [17], atmosphere solid analysis probe (ASAP) [18], plasma assisted laser desorption ionization mass spectrometry (PALDI) [19] and so forth, have attracted considerable

* Corresponding authors. Tel.: +86 731 85516888 22132.

E-mail addresses: jhwen_hnu@aliyun.com (J.-H. Wen), wanghnnu@qq.com (H. Wang).

attention in different fields of biomedicine, food security, anti-terrorism, environmental emergencies and forensic analysis due to their unique sample desorption/ionization and injection mechanisms [20–25]. The greatest advantage of them is little or no need for sample pre-treatment even in complex matrix. For example, Jana Hajslova and coworkers used DART ionization coupled to high resolution mass spectrometry to analyze multiple mycotoxins in wheat and maize [26]. Katerina Riddellova and coworkers reported an approach, coupling DART to a medium high-resolution/accurate mass time-of-flight mass spectrometer (TOFMS), for rapid examination of the fish muscle extracts [27]. A novel desorption corona beam ionization (DCBI) technique for direct analysis of samples from surface in mass spectrometry under ambient condition was reported [28,29]. Compared with the current ionization and sampling methods, such DCBI–MS can form a visible thin corona beam for sampling by using a hollow needle/ring electrode, which greatly facilitates localizing sampling areas and performing imaging/profiling experiments. To be an atmospheric pressure chemical ionization (APCI)-related technique, it is also no need for spray solutions, thus overcoming some common drawbacks of electrospray ionization (ESI)-related ones, such as sample contamination and matrix interference. DCBI is also capable of performing progressive temperature scans from room temperature to 450 °C during sample desorbing to achieve a rough separation of the individual components in complex matrices [28]. Successful applications of DCBI–MS have been made for a broad range of compounds, such as pesticides, illegal additives, drugs and explosive materials [30,31].

Considering the advantages of the DCBI–MS in direct in-situ analysis, herein we developed this technique for rapid screening of the spatial distribution characteristics of the adsorbed compounds for absorbent materials. To demonstrate the feasibility of the developed method, cigarette filter tip filled with cellulose acetate fiber [32] which was treated using a certain amount of tobacco smoke was studied as a model case. As far as we know, the retention distribution of the compounds in cigarette filter released during smoking is an issue that has never been reported. Among the thousands of compounds existing in tobacco smoke, we focused on the spatial distribution characteristic of phenol [33]. Besides DCBI–MS, conventional HPLC was also used as a comparison.

2. Experimental section

2.1. Materials and reagents

Ethyl alcohol and ethanoic acid were purchased from Fuyu Fine Chemical Co., Ltd. (Tianjin, China). Acetonitrile (Fisher, Hampton, NH, USA) was of HPLC grade. Standard (> 97%) of phenol was purchased from the National Institutes for the Control of Pharmaceutical and Biological Products (NICPBP, Beijing, China). Acetate fiber filter tips adsorbed certain amount of tobacco smoke were provided by China Tobacco Hunan Industrial Co., Ltd. All solutions were prepared and diluted using ultra-pure water produced by a Millipore Milli Q system.

2.2. Sample preparation

2.2.1. Sample preparation for DCBI–MS analysis

For in-situ analysis of the trapped phenol in acetate fiber tips using DCBI–MS, the tobacco smoke-treated acetate fiber tips (21 mm in length and 7.6 mm in diameter) were carefully cut into seven equal parts along an axial direction as illustrated in Fig. 1a by using a sharp blade. The resulted seven pieces were 3 mm in thickness and 7.6 mm in diameter, which were directly used for

the investigation of the axial, radial and 2-dimensional (2D) distribution characteristic of phenol using DCBI–MS without any treatment.

2.2.2. Sample preparation for HPLC analysis

For comparison, the distribution characteristic of phenol for acetate fiber tip was also analyzed using HPLC. The tip was cut into seven pieces along an axial direction and the obtained pieces of the tip were used for investigating the axial distribution characteristic of phenol. For radial distribution investigation, limited by the shape and size, the acetate fiber tip was cut for two times along the radial direction as illustrated in Fig. 1b using a precision laser cutting machine (ILS-IIINM, Taiwan). Such a cutting mode

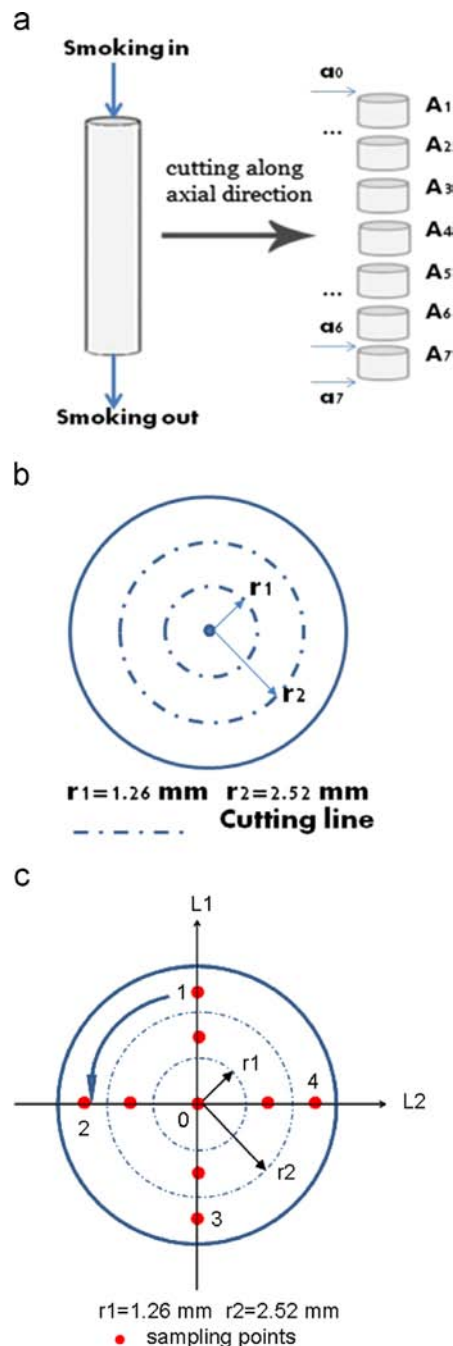


Fig. 1. Illustration of the cutting modes of the acetate fiber tip for the investigation of phenol distribution characteristics: (a) along axial direction; (b) along radial direction; (c) DCBI–MS sampling points on the surface of the acetate fiber tip piece.

resulted three parts of the tip, one cylinder with a radius of 1.26 mm, one hollow cylinder with an inner radius of 1.26 mm and an outer radius of 2.52 mm, and one hollow cylinder with an inner radius of 2.52 mm and an outer radius of 3.8 mm. For 2D space distribution investigation, the acetate fiber tip was first cut into three equal parts along a axial direction and the obtained each piece was then further cut into three parts using the cutting mode illustrated in Fig. 1b using a precision laser cutting machine (ILS-IIIINM, Taiwan). Finally, nine pieces were obtained. Such a cutting mode was considered to guarantee the reliability of the space distribution information about phenol, at the same time, to minimize the loss of the target chemicals during laser cutting of the acetate fiber tip.

The resulted small pieces of the acetate fiber tips were separately treated for HPLC analysis by separately added into 20 mL 1% ethanoic acid and incubated overnight under dark followed by 20 min of ultrasonic treatment. After that, the solutions were stood for 5 min and filtered using 0.45 μm membrane filters for HPLC analysis.

2.3. Instrumentation

2.3.1. DCBI-MS

The in-situ analysis of phenol adsorbed by acetate fiber tip was implemented using DCBI-MS. The DCBI source was provided by Shimadzu Research Laboratory (Shanghai) Co., Ltd. (Shanghai, China), and was coupled to a Finnigan LCQ Advantage Max ion trap mass spectrometer (Thermo Finnigan, San Jose, CA, USA) by replacing the ESI source of LCQ. The DCBI source is perpendicular to the axis of the mass spectrometer inlet. During working, the DCBI source initiates the corona discharge between a hollow needle and a ring counter-electrode under a direct current (DC) high voltage, as illustrated in Fig. 2. While heated helium gas is delivered through the hollow needle, a visible plasma beam forms at the needle tip and protrudes through the ring counter-electrode to ablate the sample surface. The DCBI was controlled by a mating controller and xcalibur workstation software (Thermo Electron Corporation) was used for data recording and analysis. In the present study, a positive-ion mode was applied with a discharge current sustained at 20 mA. Helium was employed to work as both discharge and heat transfer medium with gas flow of 0.6 L/min, and the temperature acted on the sample surface was maintained at $\sim 190^\circ\text{C}$. The capillary voltage of LCQ was set to 5 V, and the tube lens voltage was 15 V. The automatic gain mode for a maximum ion trap injection time was set to 100 ms and two

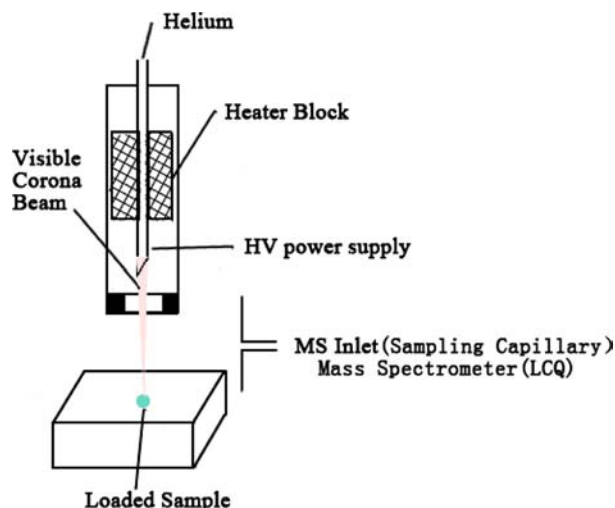


Fig. 2. Schematic diagram of the DCBI-MS and experimental construction.

microscans per spectrum. Sampling was performed on the surface of each obtained piece of the acetate fiber tip as illustrated in Fig. 1c, and for the last piece, both sides were used for sampling. All the sampling points were aligned with the DCBI when the interrogation began, and the interrogation strictly lasted 10 s for each sampling to avoid any possible cross-contaminant and to ensure the reproducibility of the method. During the sampling process, the cigarette filter was not wholly kept in the DCBI source but just a sampling point interested. In addition, the spatial resolution of the distribution image relies on the number of sampling points and the upper limit is determined by the diameter of the corona beam which can be controlled via adjusting the flow rate of helium. In the present study, the diameter of the corona beam was controlled to be less than 0.3 mm. Therefore, the upper spatial resolution of the image can reach to 0.3 mm in theory.

2.3.2. HPLC

The analysis of phenol adsorbed by acetate fiber tip was performed using HPLC (Agilent Technologies 1100, Palo Alto, CA) equipped with Agilent G1321A fluorescence detector (FLD). The analytical column used was a phenomenex luna C18 column (150 \times 4.6 mm, 5.0 μm). The operating conditions were as follows: column temperature, 30 $^\circ\text{C}$; column flow rate, 1.00 mL/min; injection volume, 10 μL ; mobile phase A: 1% acetic acid solution, mobile phase B: acetic acid + methyl cyanide + water (1:30:69), elution gradient: 0 min: flow phase A 80%, flow phase B 20%; 15 min: flow phase A 40%, flow phase B 60%; 23 min: flow phase A 0%, flow phase B 100%; 40 min: flow phase A 80%, flow phase B 20%; 5 min post run after 40 min, flow phase A 80% and flow phase B 20%. The total run time for a sample prepared using one small piece of the acetate fiber tip was ~ 45 min.

All the curves in the figures were fitted using a cubic smoothing spline algorithm which was written in Matlab 5.3 and run on a personal computer (Intel(R) Core(TM)2 Duo CPU T9550 @ 2.66 GHz, 2.67 GHz, 4 GB RAM).

3. Results and discussion

3.1. Investigation of phenol distribution characteristic for acetate fiber tip using HPLC

The distribution characteristic of phenol was first investigated using HPLC along an axial direction, along a radial direction and in a 2D space of the acetate fiber tip. Fig. 3a shows a typical HPLC fluorescence data of phenol in filter tip pieces. For the axial distribution analysis, HPLC was utilized to separately measure the phenol amount in seven pieces of the acetate fiber tip which were obtained by cutting the tip along an axial direction. Then, a curve was fitted using a cubic smoothing spline algorithm based on the obtained phenol amount in each piece to represent the axial distribution characteristic of phenol. As shown in Fig. 3b, the amount of phenol in each piece was first quickly decreasing along the axial direction and then became almost leveled off at ~ 10 mm. Such a result implied that during the tobacco smoke getting through the acetate fiber tip, most phenol in the smoke was retained at the first half part of the tip where the tobacco smoke entered, indicating that the acetate fiber tip has strong retention effect to phenol. With the decreasing of phenol in the tobacco smoke, less phenol might be retained by the following acetate fiber. Therefore, the highest concentration of phenol was observed in the first piece of the acetate fiber tip. For the radial distribution characteristic investigation, the two times cutting resulted in three parts of the acetate fiber tip. In Fig. 3c, it can be seen that the highest concentration of phenol occurred at the center of the acetate fiber tip, and the phenol concentration decreased obviously

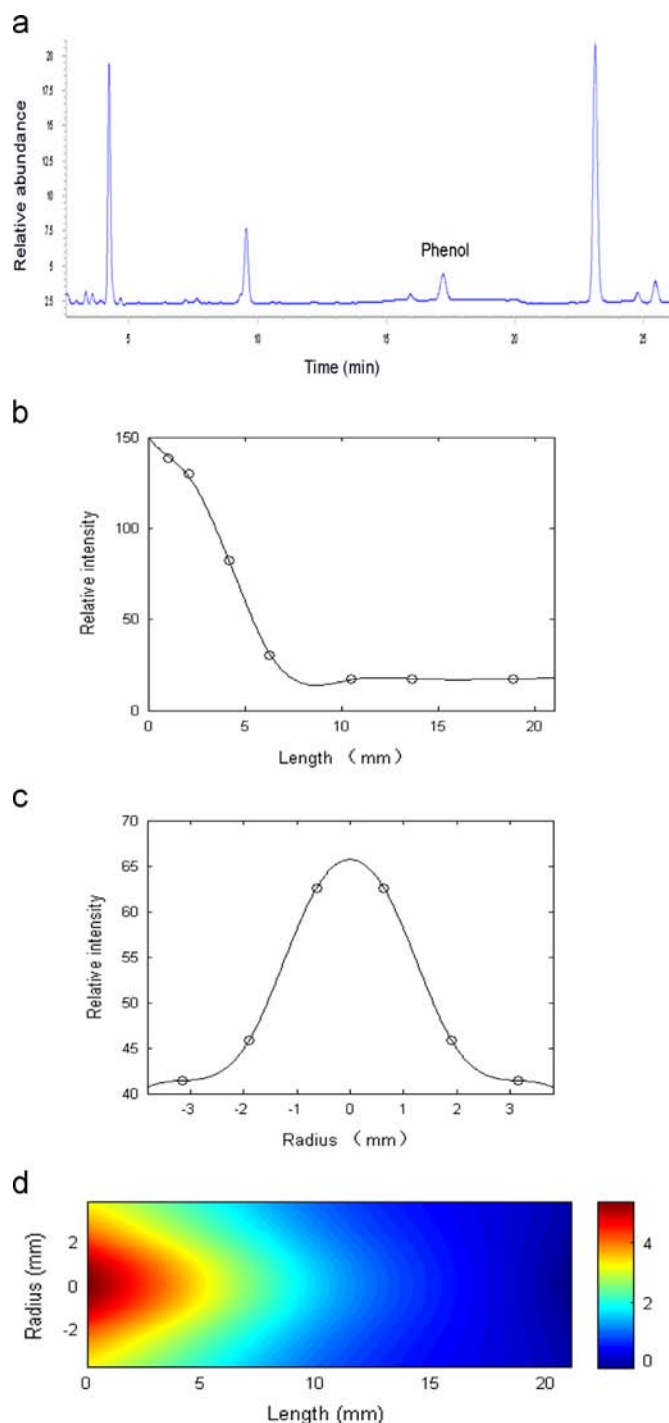


Fig. 3. Typical HPLC fluorescence of phenol in filter tip pieces: (a) distribution characteristics of phenol for the acetate fiber tip obtained using HPLC; (b) axial; (c) radial; (d) 2D space.

along the radial direction. To acquire the space distribution information of phenol, the acetate fiber tip was cut into nine pieces as illustrated in Fig. 1c, and their phenol amounts were measured using HPLC (Table 1). Fig. 3d displayed the space distribution of phenol in a 2D plot which was represented by the calculated phenol amount at each point of the acetate fiber tip using a cubic smoothing spline algorithm. It can be found that from the tip side where the smoke stream entered, the amount of the trapped phenol was decreasing with the extending both along the axial and radial directions, which agreed with the patterns of the axial and radial distribution characteristics shown in Fig. 3b and c.

3.2. Investigation of phenol distribution characteristic for acetate fiber tip using DCBI-MS

For DCBI-MS analysis, the acetate fiber tip was cut into seven equal parts along an axial direction as illustrated in Fig. 1a, and the obtained pieces were directly used for the in-situ analysis of phenol without any other treatment. Compared with conventional HPLC that can only reported the total amount of phenol in each piece of the acetate fiber tip because of their intrinsic limitations, DCBI-MS using a visible thin corona beam allows the alignment of sampling at any point on the surface of each piece. It meant for each piece, there was more than one data could be used to depict the distribution characteristic of phenol. In the present study, on each piece of the acetate fiber tip, nine sampling points (Fig. 1c) corresponding to nine different axes were selected for phenol analysis. So that, nine sets of data were obtained to depict the axial distribution characteristic of phenol for the acetate fiber tip (Table 2). In situ quantitation of phenol was based on the most intensification of molecular ion (peak height in extracted ion chromatogram). Typical mass spectrum of phenol interrogating with DCBI was shown as inset in Fig. 4a. Wherein, the peak m/z 94.10 was assigned to be the molecular ion of phenol. Attributing to the relative high discharge energy of DCBI, in which the energy of excited (triplet) state of a helium atom is 19.8 eV, the phenol can be analyzed in positive mode directly. The peak m/z 163.07 was assigned to be the protonated nicotine ion. Fig. 4b displayed the axial distribution characteristic of phenol along different axes.

Overall, the amount of phenol was decreasing with the extending length along the axial directions, which agreed with the tendency investigated using HPLC. However, DCBI-MS provided more information about the distribution characteristic in different axes than HPLC. It could be found that, along different axes, the decreasing tendencies were varying. The one at the center sampling point had an abrupt decreasing tendency, and the ones sampling around the outer circles were flatter than the other ones. It was hard for a HPLC method to get so rich information in such a direct way. In addition, based on the data in Table 2, the radial

Table 1

Relative concentration of phenol in each piece of the acetate fiber tip obtained using HPLC.

Radial direction (mm)	Axial direction		
	A1	A2	A3
$r = 1.26$	136.49	97.79	88.40
$r_{\text{inner}} = 1.26$	34.12	25.64	22.80
$r_{\text{outer}} = 2.52$			
$r_{\text{inner}} = 2.52$	17.16	14.24	13.07
$r_{\text{outer}} = 3.80$			

Table 2

Relative concentration of phenol at each sampling point on the surface of the piece of the acetate fiber tip obtained using DCBI-MS.

No.	Cutting position (mm)	Center				Inner round ($r = 1.9$ mm)				Outer round ($r = 3.17$ mm)			
		R00	R11	R12	R13	R14	R21	R22	R23	R24			
a0	0	25.30	13.60	13.40	12.90	13.60	7.20	6.78	6.77	6.80			
a1	3	21.40	10.90	10.60	10.70	10.80	6.17	6.12	6.12	6.10			
a2	6	16.10	8.32	8.22	8.17	8.25	5.27	5.26	5.18	5.19			
a3	9	11.50	6.43	6.36	6.32	6.40	3.69	3.60	3.59	3.65			
a4	12	8.07	5.26	5.18	5.17	5.19	3.05	2.79	2.79	2.87			
a5	15	7.89	5.19	5.18	5.16	5.17	2.77	2.73	2.68	2.76			
a6	18	7.51	4.70	4.68	4.62	4.68	2.10	1.93	1.83	2.09			
a7	21	6.78	4.49	4.47	4.40	4.42	1.93	1.79	1.62	1.83			

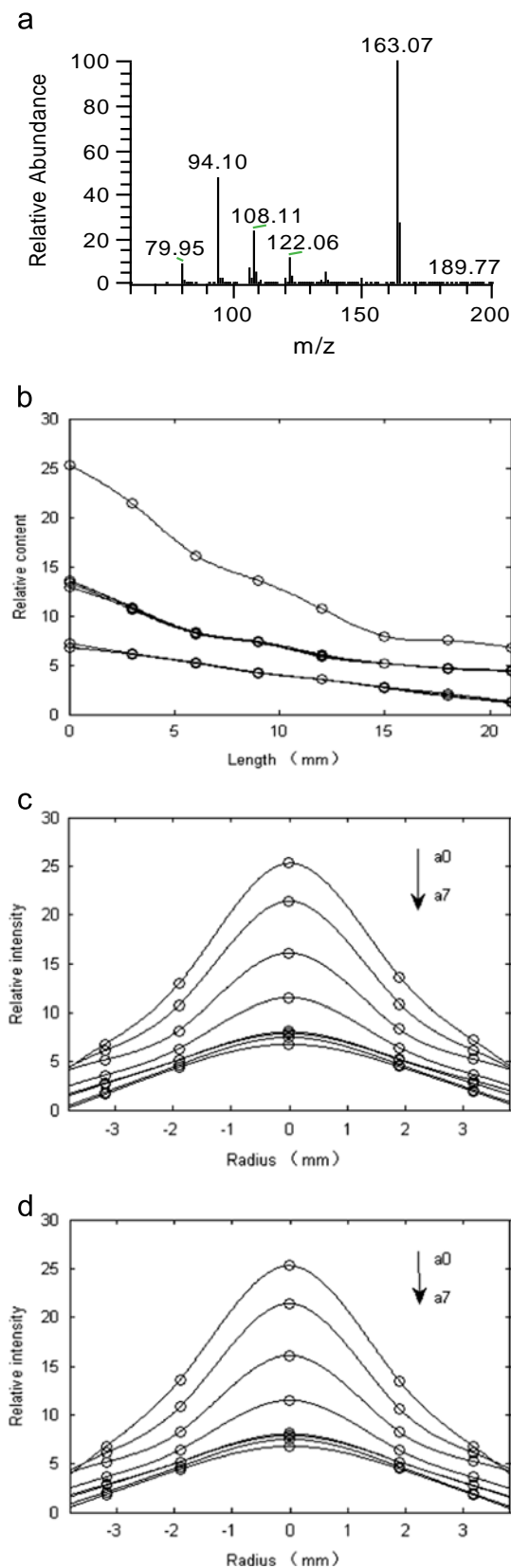


Fig. 4. Typical mass spectrum of phenol interrogating with DCBI: (a). distribution characteristics of phenol for the acetate fiber tip obtained using DCBI-MS; (b) axial; (c) radial along L1; (d) radial along L2.

distribution characteristic was directly exhibited in Fig. 4c and d. Radial distribution pattern of phenol was displayed for each piece of the acetate fiber tip, and for every piece the amount of the

trapped phenol was gradually decreased with the increasing in radius. The data in Table 2 also allowed the observation of the distribution patterns in a 2D space for two profiles along L1 and L2 directions respectively as shown in Fig. 5. The distribution patterns of phenol in these two profiles were similar to each other, but were different from the pattern obtained using HPLC (Fig. 3c). For the analysis using HPLC, it measured the amount of phenol in each piece of the tip. So, we can only roughly assignment the estimated concentration value of phenol to calculated positions along the radial direction. Such a manipulation may lead to bias. In contrast, the use of DCBI-MS directly provided the concentration values of phenol at a certain position. The distribution characteristics of phenol in 2D spaces exhibited using DCBI-MS were more consistent with the behavior of the tobacco smoke while it migrated in the acetate fiber tip. Because the tip was uniformly filled using acetate fiber, from the center of the tip, the smoke stream was on the decline while spreading around. Under a stable mode of gas pumping, the distribution of the trapped phenol should be consistent with the distribution pattern of the smoke stream. Indeed, more profiles could be readily achieved by sampling along different radial directions. However, it can be hardly realized by using HPLC.

3.3. Comparisons between HPLC and DCBI-MS

Generally, despite of the semi quantitative ability, DCBI-MS has more desirable operational attributes than HPLC. First, for sample pretreatment, DCBI-MS uses a direct and in-situ sampling format on the surface of an adsorbent material, while for HPLC the target compounds have to be extracted from the adsorbent material in advance. Second, because it uses a direct in-situ sampling format, DCBI-MS has little limitation on the shape and size of the adsorbent material and can easily sample almost at any point of an adsorbent material. In contrast, the sampling of HPLC relies on special cutting mode of the adsorbent material, thus requiring special cutting machine. Moreover, because the cutting time is limited, it means only limited information can be obtained. It is also hard to avoid the loss of the target chemical under a complex cutting mode. Third, DCBI-MS is more rapid and cost-efficient. For one time sampling and analysis, DCBI-MS needs less than 30 s, while such operation of HPLC costs more than 45 min, and

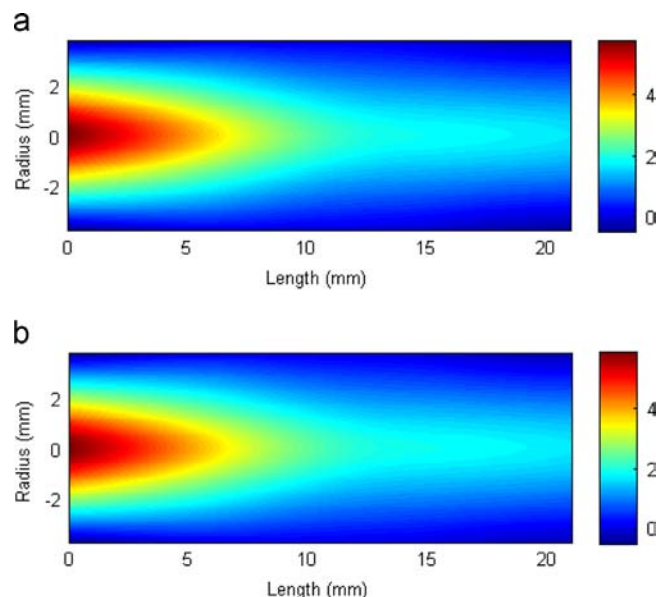


Fig. 5. 2D distribution characteristics of phenol for the acetate fiber tip obtained using DCBI-MS: (a) along R1R3; (c) along R2R4.

DCBI–MS needs only a small amount of helium gas during an analysis process. Taking together, the use of DCBI–MS should provide a convenient method with desirable operational attributes for rapid and cost efficient analysis of the distribution characteristics of the adsorbed chemicals for adsorbent materials.

4. Conclusion

An in-situ analysis technique using DCBI–MS was proposed for the distribution characteristic investigation of adsorbed chemicals for adsorbent materials. The use of DCBI allowed direct analysis of samples from surface in mass spectrometry under ambient conditions. The distribution characteristic analysis of an adsorbed chemical could be very easily achieved by simply splitting the adsorbent material into several pieces and sampling on them. Moreover, DCBI–MS furnished easy alignment of sampling area, thus affording convenient and rapid spatial distribution analysis of the targets. The spatial distribution characteristic of phenol was studied for the acetate fiber tip both using DCBI–MS and HPLC. DCBI–MS was demonstrated to have highly improved assay simplicity in rapid and cost-efficient analysis of the spatial distribution characteristic of phenol for the acetate fiber tip, thus exhibiting a great potential for spatial distribution characteristic investigation of adsorbed compounds for adsorbent materials.

Acknowledgements

This work was supported by NSFC (21205034, 21035001, 21190041, 91317312), Doctoral Fund of Ministry of Education of China (New Teachers, 20120161120032), Hunan Provincial NSFC (13JJ4031).

References

- [1] G. Srinivas, J. Burrell, T. Yildirim, *Energy Environ. Sci* 5 (2012) 6453–6459.
- [2] V. Redondas, X. Gómez, S. García, C. Pevida, F. Rubiera, A. Morán, J.J. Pis, *Waste Manage* 32 (2012) 60–66.
- [3] J.-S. Qin, D.-Y. Du, W.-L. Li, J.-P. Zhang, S.-L. Li, Z.-M. Su, X.-L. Wang, Q. Xu, K.-Z. Shao, Y.-Q. Lan, *Chem. Sci* 3 (2012) 2114–2118.
- [4] K.C. Kemp, H. Seema, M. Saleh, N.H. Le, K. Mahesh, V. Chandra, K.S. Kim, *Nanoscale* 5 (2013) 3149–3171.
- [5] R. Zou, Z. Zhang, L. Yu, Q. Tian, J. Wu, Y. Sun, Z. Chen, J. Hu, *Chemistry* 16 (2010) 14307–14312.
- [6] R. Pacciani, J. Torres, P. Solsona, C. Coe, R. Quinn, J. Hufton, T. Golden, L.F. Vega, *Environ. Sci. Technol.* 45 (2011) 7083–7088.
- [7] L. Verdolotti, A. Salerno, R. Lamanna, A. Nunziata, P. Netti, S. Iannace, *Microporous Mesoporous Mater* 151 (2012) 79–87.
- [8] J. Arango, M.I. Rubino, R. Auras, A.A. Rachford, Z. Bai, A.L. Grzesiak, T. Kijchavengkul, *J. Food Eng.* 131 (2014) 75–81.
- [9] H. Leclerc, A. Vimont, J.-C. Lavalley, M. Daturi, A.D. Wiersum, P.L. Llewellyn, P. Horcajada, G. Férey, C. Serre, *Phys. Chem. Chem. Phys.* 13 (2011) 11748–11756.
- [10] Z.-Y. Gu, J.-Q. Jiang, X.-P. Yan, *Anal. Chem.* 83 (2011) 5093–5100.
- [11] W. Guan, C. Li, X. Liu, S. Zhou, Y. Ma, *Food Addit. Contam. A* 31 (2014) 250–261.
- [12] R. Jain, P. Sharma, S. Sikarwar, *Environ. Sci. Pollut. Res. Int* 20 (2013) 1493–1502.
- [13] A.D. Wiersum, C. Giovannangeli, D. Vincent, E. Bloch, H. Reinsch, N. Stock, J.S. Lee, J.-S. Chang, P.L. Llewellyn, *ACS Comb. Sci* 15 (2013) 111–119.
- [14] Z. Takáts, J.M. Wiseman, B. Gologan, R.G. Cooks, *Science* 306 (2004) 471–473.
- [15] H. Chen, A. Venter, R.G. Cooks, *Chem. Commun.* (2006) 2042–2044.
- [16] R.B. Cody, J.A. Laramée, H.D. Durst, *Anal. Chem.* 77 (2005) 2297–2302.
- [17] N. Na, M. Zhao, S. Zhang, C. Yang, X. Zhang, *J. Am. Soc. Mass Spectrom* 18 (2007) 1859–1862.
- [18] C.N. McEwen, R.G. McKay, B.S. Larsen, *Anal. Chem.* 77 (2005) 7826–7831.
- [19] C. Chang, X. Li, Y. Bai, G. Xu, B. Feng, Y. Liao, H. Liu, *Talanta* 114 (2013) 54–59.
- [20] W.Z. Shou, H.-Z. Bu, T. Addison, X. Jiang, W. Naidong, *J. Pharm. Biomed. Anal.* 29 (2002) 83–94.
- [21] B.M. Kolakowski, P.A. D'Agostino, C. Chenier, Z. Mester, *Anal. Chem.* 79 (2007) 8257–8265.
- [22] A.M. Llamas, C.B. Ojeda, F.S. Rojas, *Appl. Spectrosc. Rev.* 42 (2007) 345–367.
- [23] L.G. Apollonio, D.J. Pianca, I.R. Whittall, W.A. Maher, J.M. Kyd, *J. Chromatogr. B Anal. Technol. Biomed. Life. Sci.* 836 (2006) 111–115.
- [24] M.E. Monge, G.A. Harris, P. Dwivedi, F.M. Fernández, *Chem. Rev.* 113 (2013) 2269–2308.
- [25] M.-Z. Huang, S.-C. Cheng, Y.-T. Cho, J. Shiea, *Anal. Chim. Acta* 702 (2011) 1–15.
- [26] L. Vaclavik, M. Zachariasova, V. Hrbek, J. Hajslova, *Talanta* 82 (2010) 1950–1957.
- [27] T. Cajka, H. Danhelova, A. Vavrecka, K. Riddellova, V. Kocourek, F. Vacha, J. Hajslova, *Talanta* 115 (2013) 263–270.
- [28] H. Wang, W. Sun, J. Zhang, X. Yang, T. Lin, L. Ding, *Analyst* 135 (2010) 688–695.
- [29] H. Wang, Y. Wu, B. Guo, W. Sun, L. Ding, B. Chen, *Analyst* 137 (2012) 3982–3988.
- [30] H. Wang, Y. Wu, Y. Zhao, W. Sun, L. Ding, B. Guo, B. Chen, *Food Addit. Contam. A* 29 (2012) 1194–1201.
- [31] X. Li, H. Wang, W. Sun, L. Ding, *Anal. Chem.* 82 (2010) 9188–9193.
- [32] P.S. Thayer, C.J. Kensler, *Science* 146 (1964) 642–644.
- [33] R.L. Stedman, *Chem. Rev.* 68 (1968) 153–207.



Determination of traces of As, B, Bi, Ga, Ge, P, Pb, Sb, Se, Si and Te in high-purity nickel using inductively coupled plasma-optical emission spectrometry (ICP-OES)



S. Thangavel, K. Dash, S.M. Dhavile, A.C. Sahayam*

National Centre for Compositional Characterization of Materials, Bhabha Atomic Research Centre, ECIL-Post, Hyderabad-500062, India

ARTICLE INFO

Article history:

Received 22 May 2014

Received in revised form

7 August 2014

Accepted 8 August 2014

Available online 19 August 2014

Keywords:

Nickel

Impurities

Nickel perchlorate

Nickel alloys

ABSTRACT

A method has been developed for the determination of traces of arsenic, boron, bismuth, gallium, germanium, phosphorus, lead, antimony, selenium, silicon and tellurium in nickel matrix. The sample was dissolved in HClO_4 ($\sim 150^\circ\text{C}$) and nickel was settled as crystalline nickelperchlorate $[\text{Ni}(\text{ClO}_4)_2]$ on cooling. The mixture was ultrasonicated and after the separation of $\text{Ni}(\text{ClO}_4)_2$, analytes of interest were determined in the supernatant using ICP-OES. Similarly, it was also found that, after the dissolution of nickel in perchloric acid, when the solution temperature was maintained at $\sim 100^\circ\text{C}$, long needle like crystals of nickel perchlorate were formed. The crystals were separated from the mixture and trace elements in the supernatant were determined using ICP-OES. In both methods the matrix removal was $> 99\%$ and the recoveries of analytes were in the range 92–97%. The limits of detection for As, B, Bi, Ga, Ge, P, Pb, Sb, Se, Si and Te were found to be 0.18, 0.21, 0.07, 0.06, 0.25, 0.11, 0.09, 0.10, 0.17, 0.20 and $0.07 \mu\text{g g}^{-1}$ respectively. The procedure was applied for the analysis of a standard reference material nickel oxide (SRM 761, Nickel Oxide No.1, NBS, USA) and the values obtained are in close agreement with the certified values.

© 2014 Elsevier B.V. All rights reserved.

1. Introduction

Nickel base super alloys, by virtue of their excellent high temperature properties coupled with corrosion resistance, have been widely used in jet engine, gas turbine engine components where high strength at high temperature is needed [1,2]. The quality of nickel-base alloys is highly dependent on the amounts of trace elements present as the presence of trace elements has serious effects on the mechanical and physical properties of these high temperature alloys [3,4]. Among the impurities in nickel base alloys, low melting elements such as As, Se, Te, Pb etc. are detrimental to the strength of high temperature alloys even when present at very low concentrations [5]. Therefore it is essential to determine traces of these low melting elements (As, Se, Te and Pb) in nickel matrix.

Hydride generation atomic absorption spectrometry (HG-FAAS) and Hydride generation Inductively Coupled Plasma Optical Emission Spectrometry (HG-ICP-OES) are among the most sensitive techniques for the determination of traces of As, Se and Te [6,7]. However, due to the strong interference of nickel in hydride generation process, it is difficult to analyze nickel matrices for

low melting elements mentioned above by hydride generation [8,9]. In these techniques, the interference caused by nickel is minimized by masking the interferents [6,10] or by rapid hydride generation followed by fast separation of hydride from the liquid phase [11]. Inductively Coupled Plasma Mass Spectrometry (ICP-MS) is a powerful technique for the trace multi-element analysis. The determination of traces of Te in alloys by ICP-MS suffers from severe non-spectroscopic interference when conventional pneumatic nebulizer was used for sample introduction. This problem was overcome by applying the vapor generation of Te and its introduction to ICP-MS [12]. Graphite Furnace Atomic Absorption Spectrometry (GFAAS) methods were developed for the determination of selenium, tellurium in nickel after the matrix separation by reductive co-precipitation with palladium using ascorbic acid [13,14]. As per our knowledge, no single method has been reported to date for trace level determination of these impurities (As, Sb, Bi, B, Ga, Ge, Pb, P, Se, Si and Te) in nickel matrix.

Herein, a new method has been described for the determination of traces of As, Sb, Bi, B, Ga, Ge, Pb, P, Se, Si and Te in nickel matrix. The sample was dissolved in con. HClO_4 at hot condition and after cooling, the matrix (nickel) was separated from the sample solution either as crystalline precipitate or needle like crystals of $\text{Ni}(\text{ClO}_4)_2$. The crystalline precipitate was ultrasonicated

* Corresponding author. Tel.: +91 40 27121365.

E-mail address: sahayamac@gmail.com (A.C. Sahayam).

to leach out the impurities from crystals and the concentration of trace impurities in the supernatant was measured using ICP-OES. In the second procedure, needle like crystalline $\text{Ni}(\text{ClO}_4)_2$ was prepared by maintaining the sample solution at $\sim 100^\circ\text{C}$ and the supernatant was analyzed for trace impurities by ICP-OES.

2. Experimental

2.1. Apparatus

A Horiba scientific model of ULTIMA-2 Inductively Coupled Plasma-Optical Emission Spectrometer (ICP-OES) was used. The instrumental specifications are given in Table 1. A Bandelin model of SONOREX DIGITEC 35 kHz ultrasonic bath with heater ($20\text{--}80^\circ\text{C}$) was used.

2.2. Reagent and standard solutions

Suprapur grade HClO_4 (70%,w/v) from Merck, Germany was used. Standard stock solutions of all the elements (1000 mg L^{-1}) were obtained from Merck, Germany. Working standard solutions were freshly prepared from these stock solutions as required.

2.3. Procedure

2.3.1. Matrix separation after precipitation of $\text{Ni}(\text{ClO}_4)_2$ followed by ultrasonication

Around 0.5 g of nickel sample was taken in a flat bottom quartz test tube of 25 mL capacity, 10 mL suprapur grade HClO_4 (70%,w/v) was added, the tube was covered with watch glass and heated over a hot plate at $\sim 150^\circ\text{C}$ (solution temperature) for 30 min. After the complete dissolution of the sample, the sample solution was allowed to cool to $\sim 60^\circ\text{C}$. Then the sample solution was sonicated at 50°C (35 kHz) for ~ 40 min. After ultrasonication, the sample solution was taken out from the ultrasonic bath and cooled to room temperature and was centrifuged between 1000 and 1500 rpm and the supernatant was separated using a micropipette. Then the supernatant (~ 3 mL) was diluted to 25 mL and impurities present were measured using ICP-OES. If the concentration of impurities is not detectable, pre-concentration of impurities can be carried out by evaporating the supernatant on a hot plate (surface temperature of $\sim 130^\circ\text{C}$) in a fume hood till no more dense fumes came out from the sample solution. Then after cooling it was diluted to 10 mL using mill-Q water and the analytes were measured using ICP-OES.

2.3.2. Matrix separation after the formation of needle like crystals of $\text{Ni}(\text{ClO}_4)_2$

Around 0.5 g of nickel sample was dissolved in perchloric acid as described above. After complete dissolution of sample, the test tube was removed from the hot plate and temperature of the solution was maintained at 100°C using Infra Red (IR) lamp (IR lamp was kept by the side with respect to sample solution). After the

appearance of needle like crystals, the sample solution was kept at this temperature for around 30 min. Then the IR lamp was switched off and allowed the solution to cool to room temperature ($\sim 25^\circ\text{C}$). The sample solution was carefully transferred into a clean 25 mL quartz beaker using a micropipette. Then the separated sample solution (~ 3 mL) was diluted to 25 mL and measured for the impurities using ICP-OES. To reduce the dilution factor, the separated sample solution could be diluted to 10 mL after the evaporation of excess HClO_4 as described in the above procedure.

3. Result and discussion

3.1. Role of HClO_4 on dissolution and separation of nickel

Nickel/nickel oxide reacts with con. HClO_4 (70%,w/v) at $\sim 150^\circ\text{C}$ (solution temperature) forming intense green color $\text{Ni}(\text{ClO}_4)_2$ solution. When this solution is allowed to cool $> 99\%$ of nickel is settled as crystalline form of $\text{Ni}(\text{ClO}_4)_2$. This unique property of $\text{Ni}(\text{ClO}_4)_2$ is utilized to separate the matrix for its trace element analysis. Due to high solubility of $\text{Ni}(\text{ClO}_4)_2$ in water, after the crystallization, any dilution of HClO_4 with water leads to redissolution of the matrix and decrease in matrix separation. Therefore, sample dissolution and matrix separation were carried out using concentrated HClO_4 . The effective matrix separation was not affected when the concentration of HClO_4 is maintained $> 95\%$ (v/v). Any increased dilution of HClO_4 drastically increases the dissolution of $\text{Ni}(\text{ClO}_4)_2$ and leads to complete dissolution when the concentration of HClO_4 is $< 50\%$ (v/v). However, the matrix separation ($\sim 99\%$) was independent of the amount of HClO_4 (70%, w/v) used for the sample dissolution.

3.2. Ultrasonic extraction of analytes

Preliminary experiments were carried out for the separation of Ni as $\text{Ni}(\text{ClO}_4)_2$ precipitate and the recovery of analytes in the supernatant was found to be only 20–30%. Lower recovery of analytes could be due to the occlusion of the analytes during the formation of bulky molecule of $\text{Ni}(\text{ClO}_4)_2$ (~ 5 times the weight of nickel) precipitate. Therefore, after the precipitation of crystalline form of $\text{Ni}(\text{ClO}_4)_2$, ultrasonication was carried out to leach out the analytes from $\text{Ni}(\text{ClO}_4)_2$ precipitate. Even after the ultrasonication, the recovery of analytes was in the range of $\sim 80\%$. Increase in the temperature of the sample solution and ultrasonication bath lead to further improvement in recovery of analytes. However, it also leads to increase in the dissolution of $\text{Ni}(\text{ClO}_4)_2$ which resulted in poor matrix separation. Therefore these two parameters are required to be optimized. After the separation of nickel, a high concentration of HClO_4 remains in the sample solution requiring large dilution prior to the determination of impurities using ICP-OES which lead to poor limit of detection (LOD). Hence, to obviate large dilution, excess HClO_4 from sample solution needed to be evaporated. Due to hazardous nature of HClO_4 , it is very essential to optimize its amount to as minimum as possible.

3.3. Optimization of ultrasonic extraction of analytes

Based on the recovery of arsenic, ultrasonic extraction was optimized for each parameter, i.e., amount of HClO_4 , temperature of the sample solution/ sonication bath and time duration of ultrasonication. To study the effect of amount of HClO_4 on matrix removal and analyte recovery, after the dissolution of sample, ultrasonication was carried out at a solution temperature of $\sim 60^\circ\text{C}$ and ultrasonic bath temperature of $\sim 50^\circ\text{C}$ for 30 min. The amount of HClO_4 was increased from 5 mL onwards (minimum 5 mL of HClO_4 is required for the dissolution of 0.5 g of nickel) in steps of 2 mL and when it was

Table 1
Operating conditions of ICP-OES.

Power	1.1 kW
Wavelengths (nm)	Se (196.090), As (197.198), Sb (206.833), Ge (209.426), P (213.618), Te (214.281), Pb (220.353), Bi (223.061), B (249.772), Si (251.611) and Ga (294.364)
Plasma gas flow rate	12.1 l min^{-1}
Nebulizer gas flow rate	0.83 l min^{-1} , concentric nebulizer
Auxiliary gas flow rate	0.52 l min^{-1}
Solution uptake rate	2.0 mL min^{-1}

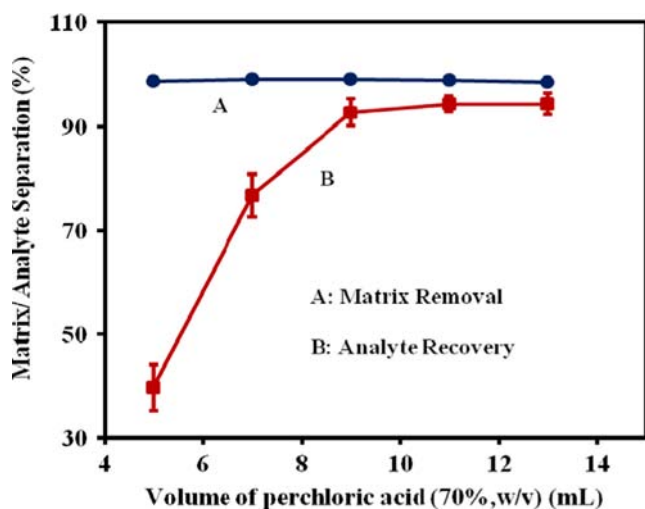


Fig. 1. Effect of amount of con.HClO₄ on 0.5 g of sample on matrix (A)/analyte (B) separation (No. of replicates (n)=3).

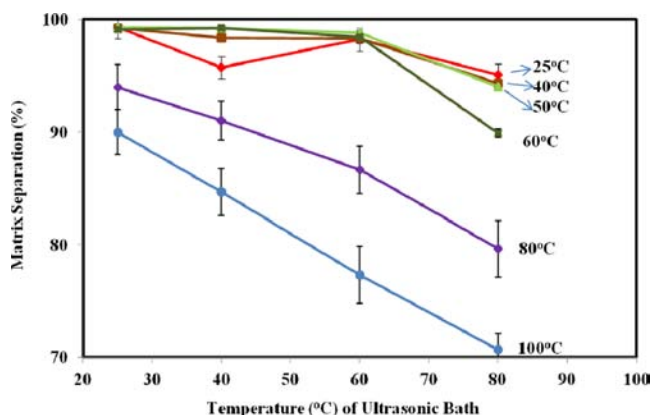


Fig. 2. Effect of temperature of ultrasonication bath/sample solution on separation of matrix (n=3).

10 mL or higher the recovery of analyte (As) was more than 92% (Fig. 1). From this figure, it can be seen that no significant increase in the separation of matrix was observed by further increasing the amount of acid. Hence, 10 mL of acid was used for further studies. The effect of temperature of the sample solution and the temperature of the ultrasonication bath on matrix separation and recovery of analytes are given in Figs. 2 and 3 respectively. For these studies, after the dissolution (0.5 g of sample in 10 mL of HClO₄) the sample solution was cooled to various temperatures (100–25 °C) and kept inside the ultrasonication bath maintained at a temperature between 25 and 80 °C. When the temperature of ultrasonic bath and sample solution were between 25 and 60 °C matrix separation was ~99%. However, when these temperatures were between 50 and 60 °C, the recovery of analytes was found to be more than 93%. Therefore optimized temperature of between 50 and 60 °C was employed in subsequent studies. At optimized temperatures, the required time duration of ultrasonic bath was also studied and the results are shown in Fig. 4. It can be seen from this figure that optimized time duration was ~40 min to achieve near quantitative recovery of all the analytes.

3.4. Preparation of needle like crystals of Ni(ClO₄)₂

In our preliminary experiments after the dissolution of nickel, when the sample solution was allowed to cool, during transition of temperature formation of needle like crystals was observed occasionally. When these crystals were formed, the recovery of

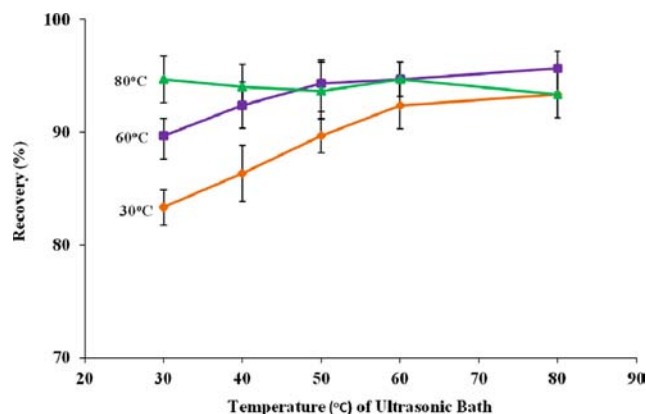


Fig. 3. Effect of temperature of ultrasonication bath/sample solution on recovery of analyte (n=3).

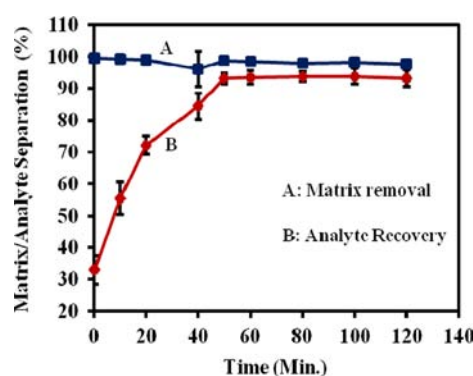


Fig. 4. Effect of time duration of ultrasonic bath (50 °C) on matrix/analyte separation. A-matrix separation; B-analyte recovery (n=3).

analytes was in the range of 92–96%, thus obviating the need for ultrasonic extraction. However, it was very difficult to achieve reproducible preparation of long needle like crystals. From repeated experiments, it has been observed that the following parameters namely heating apparatus, the crystallization temperature and dimension of the container (where crystallization is carried out) were crucial for the formation of long needle like crystals. As in the case of ultrasonic extraction, even in this matrix separation method, no significant variation in the separation of matrix (>99%) was observed with the amount of HClO₄ used for the dissolution sample.

3.5. Optimization of crystallization

Preliminary experiments were carried out for the formation of needle like crystals by maintaining the temperature of the sample solution using a hot plate. On hot plate it is very difficult to maintain the temperature of solution and hence it was found to be very intricate to produce needle like crystals. After the dissolution of sample at ~150 °C, when the temperature of the hot plate was decreased nickel perchlorate was precipitated in crystalline form and is completely dissolved when the temperature was increased. Therefore, crystallization was attempted by maintaining the temperature of the sample solution using IR lamp. In this case also, it was stringent to develop needle like crystals when IR lamp was kept above or below the sample solution. When the IR lamp was kept in horizontal position (by the side) with respect to sample solution, long needle like crystals were formed that were not settled down as precipitate (Fig. 5). The distance between IR lamp and test tube was also optimized. In our laboratory atmosphere the optimized distance was found to be ~10 cm. When the

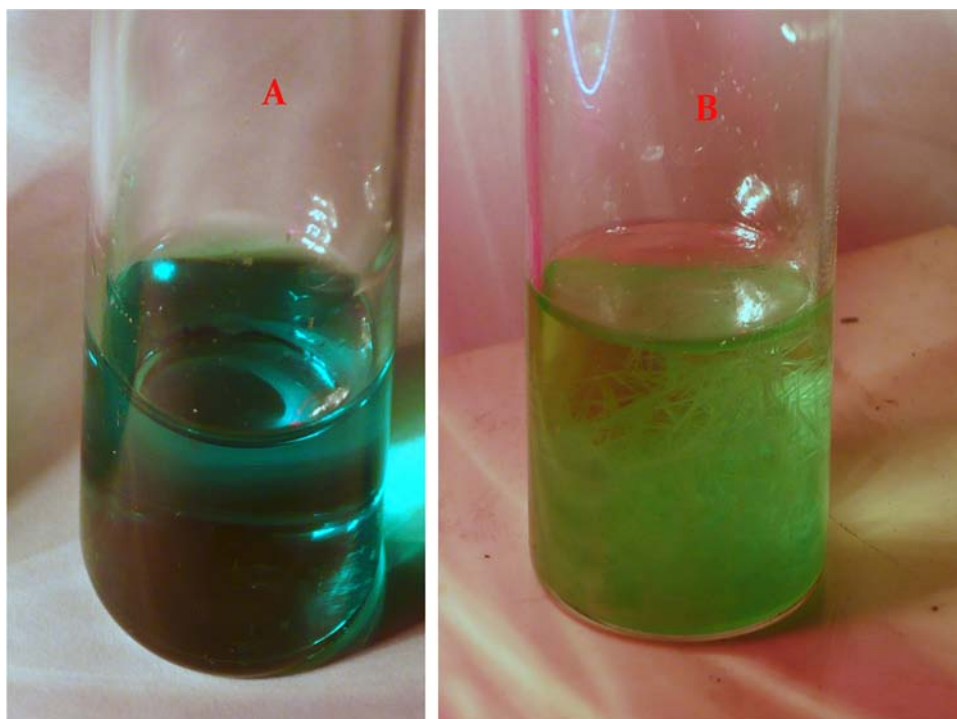


Fig. 5. $\text{Ni}(\text{ClO}_4)_2$ in solution form (A) and needle like crystalline form (B).

Table 2
Recovery study and limit of detection.

Element	After evaporation of HClO_4		Without evaporation of HClO_4		Limit of Detection ($\mu\text{g g}^{-1}$)
	After crystallization	After ultrasonication	After crystallization	After ultrasonication	
As	95	94	94	96	0.18
B	46	28	42	93	0.21
Bi	94	96	97	95	0.07
Ga	45	95	42	99	0.06
Ge	45	22	46	92	0.25
P	95	97	96	99	0.11
Pb	42	94	48	97	0.09
Se	94	95	93	94	0.17
Sb	38	36	95	96	0.10
Si	32	40	32	96	0.20
Te	94	94	97	96	0.07

temperature of the sample solution was $> 120^\circ\text{C}$, $\text{Ni}(\text{ClO}_4)_2$ remained in the solution form. As soon as the temperature was decreased below 115°C , needle like crystals started to form and did not settle down as precipitate till the temperature of the sample solution remained above 90°C . As described earlier, settling down of crystals as precipitate leads to poor recovery of analytes. Therefore, to keep the $\text{Ni}(\text{ClO}_4)_2$ as needle like crystals, optimized temperature of the solution was found to be $100 \pm 10^\circ\text{C}$. If this temperature was maintained for 30 min, $> 99\%$ of 0.5 g of nickel was formed as long needle crystals of $\text{Ni}(\text{ClO}_4)_2$. The IR lamp was switched off to bring the solution to room temperature. After reaching room temperature, the sample solution needs to be separated from the crystals within one hour. Otherwise, the needle like crystals starts to settle as precipitate, which leads to lower recovery of analytes.

It was observed that the dimensions of container also play an important role in the formation of needle like crystals. Since the volume of HClO_4 optimized is 10 mL for the dissolution of 0.5 g of sample, diameter of the tube should be as low as possible. Therefore flat bottom quartz test tubes with different diameters

were taken for crystal formation. If the vessel is very narrow the crystals started to form from the wall of the vessel in horizontal direction and hence complete crystal growth could not taken place. The crystals formed on the wall of the tube fell down and settled as precipitate. The optimized diameter of the tube was found to be between 2 and 3 cm.

3.6. Recovery of other elements

In both matrix separation methods (crystallization and ultrasonication), since most of the transition elements such as Fe, Al, Cu, Mn etc. form perchlorates, these elements will co-precipitate with $\text{Ni}(\text{ClO}_4)_2$ resulting in poor recovery ($< 30\%$). However, after the matrix separation in the form of needle like crystals, poorer recovery of B, Ga, Ge, Pb and Si was observed (Table 2). It could be due to the adsorption of perchlorates of B, Ga, Ge and Pb on $\text{Ni}(\text{ClO}_4)_2$ resulting in poorer recovery for these analytes. Silicon is prone to hydrolysis on treatment with concentrated acids (except HF). In this method since crystallization was carried out in concentrated HClO_4 medium, silicon might be hydrolyzed and

Table 3
Analysis of nickel oxide (SRM 761, Nickel Oxide No.1, NBS, USA).

Element	SRM value ($\mu\text{g g}^{-1}$)	Present method value ($\mu\text{g g}^{-1} \pm \sigma$) $n=4$
Pb	16 \pm 2	15 \pm 2
Se	2.0 \pm 0.3	1.9 \pm 0.4
As	59 ^a , 45 ^b	56 \pm 4
Te	< 0.2	< 0.2

^a Average of atomic absorption methods.

^b Average of extraction-photometric and distillation-photometric procedures.

adsorbed on $\text{Ni}(\text{ClO}_4)_2$. However, matrix separation followed by ultrasonication, improved recoveries of these analytes to > 92%. It could be due to the fact that ultrasonication was carried out at 50 °C and at this condition these analytes are quantitatively leached out from $\text{Ni}(\text{ClO}_4)_2$ precipitate. After the separation of matrix, when excess HClO_4 is evaporated on hot plate, poor recovery was found out for B, Ge and Sb. It could be due to the loss of these analytes on evaporation of HClO_4 .

3.7. Sample analysis, limit of detection (LOD) and recovery

To validate the developed method, this procedure was applied to a standard reference material of Nickel oxide (Standard Sample 671, Nickel Oxide, No.1, National Bureau of Standards, Washington) and the results are in close agreement with certified values (Table 3). The limit of detection (LOD), given as three times the variation on repeated measurements of blank ($n=6$) for all the analytes in solid sample is given in Table 2 and it was calculated based on the dilution factor of 0.5 g of sample made upto 10 mL whereas for B, Ge and Sb it was calculated based on the dilution

factor of 0.5 g made upto 25 mL as loss of these analytes was observed on evaporation of HClO_4 .

4. Conclusion

This new sample digestion and matrix separation approach is simple and all the critical elements in nickel matrix could be determined. HClO_4 is the only reagent used for the dissolution of sample as well as for the separation of matrix and is available in very pure grade (suprapur grade), which results in very less process blank. The proposed method can also be used for crystal growth of $\text{Ni}(\text{ClO}_4)_2$ for the preparation of high-pure $\text{Ni}(\text{ClO}_4)_2$.

References

- [1] D.R. Wood, R.M. Cook, *Metallurgia* 67 (1963) 109–117.
- [2] B. Geddes, H. Leon, X. Huang, *Super Alloys: Alloying and Performance*, ASM International, Ohio (2010) 15.
- [3] D.G. Andrews, J.B. Headridge, *Analyst* 102 (1977) 436–445.
- [4] S. Backman, R.W. Karlsson, *Analyst* 104 (1979) 1017–1029.
- [5] R.J. Henricks, M.L. Gel, *Trace Element Effects in Cast Nickel-Base Superalloys, III*, ASM Materials Engineering Congress, Chicago, 1973 (October 3).
- [6] I. Wickstrøm, W. Lund, R. Bye, *Analyst* 120 (1995) 2695–2698.
- [7] H. Wiltzsche, I.B. Brenner, K. Prattes, G. Knapp, *J. Anal. At. Spectrom.* 23 (2008) 1253–1262.
- [8] C. Rigby, I.D. Brindle, *J. Anal. At. Spectrom.* 14 (1999) 253–258.
- [9] B. Weltz, M. Melcher, *Spectrochim. Acta B* 36 (1981) 439–462.
- [10] I. Wickstrøm, W. Lund, R. Bye, *J. Anal. At. Spectrom.* 10 (1995) 803–808.
- [11] W.W. Ding, R.E. Sturgeon, *Anal. Chem.* 69 (1997) 527–531.
- [12] Y.L. Chen, S.J. Jiang, *J. Anal. At. Spectrom.* 15 (2000) 1578–1582.
- [13] T. Ashino, K. Takada, *Anal. Chim. Acta* 312 (1995) 157–163.
- [14] Hui-Ming Liu, Shi-Yang Chen, Pin-Hsuan Chang, Suh-Jen Jane Tsai, *Anal. Chim. Acta* 459 (2002) 161–168.



Development and analytical comparison of microflow and nanoflow liquid chromatography/mass spectrometry procedures for quantification of cardiac troponin T in mouse hearts

Mariola Olkowicz^{a,b,*}, Iwona Rybakowska^c, Stefan Chlopicki^{d,e}, Ryszard T. Smolenski^a

^a Department of Biochemistry, Medical University of Gdansk, Debinki 1, 80-211 Gdansk, Poland

^b Department of Biotechnology and Food Microbiology, Poznan University of Life Sciences, Wojska Polskiego 48, 60-627 Poznan, Poland

^c Department of Biochemistry and Clinical Physiology, Medical University of Gdansk, Debinki 1, 80-211 Gdansk, Poland

^d Department of Experimental Pharmacology, Jagiellonian University Medical College, Grzegorzewska 16, 31-531 Krakow, Poland

^e Jagiellonian Centre for Experimental Therapeutics, Jagiellonian University, Bobrzyńskiego 14, 30-348 Krakow, Poland

ARTICLE INFO

Article history:

Received 16 May 2014

Received in revised form

5 August 2014

Accepted 11 August 2014

Available online 19 August 2014

Keywords:

Heart

Troponin T

Nanoflow liquid chromatography

Multiple reaction monitoring

Quantitative proteomics

Atherosclerotic mice

ABSTRACT

Three procedures for the quantification of cardiac troponin T (cTnT) based on liquid chromatography/mass spectrometry (LC/MS) were developed, validated and compared. The procedures were applied to estimate the cTnT content in the hearts of wild type mice C57BL/6J (WT) and double knock-outs for apolipoprotein E and receptor for LDL (AL KO).

Three variants of the procedure proposed include microflow, direct injection nanoflow and preconcentration nanoflow LC/MS. Troponin T tryptic peptide YEINVLK and its analog (internal standard) were monitored in a multiple reaction monitoring mode using triple quadrupole mass detector with electrospray (ESI) ion sources.

The preconcentration nanoflow LC/MS method offered the best sensitivity with a lower limit of quantification (LLOQ) of 0.25 fg μL^{-1} and a minimal matrix effect. The LLOQ value was 8 times better, compared with that in direct injection nanoflow LC/MS and 200 times better than in microflow LC/MS. The accuracy or precision for all three methods were not different. Separation time in the direct injection nanoflow (8 min) was equivalent to the microflow method (6 min). The cTnT contents in the mice hearts measured by the methods developed by the present authors were not different between the WT and AL KO.

We conclude that nanoflow LC/MS based quantitative proteomics offers fundamentally better sensitivities while maintaining analytical quality and separation times equivalent to microflow procedures.

© 2014 Elsevier B.V. All rights reserved.

1. Introduction

The troponin complex is bound to the thin filament in the striated muscle and is involved in the regulation of the skeletal and cardiac muscle contraction [1,2]. This protein complex consists

Abbreviations: AL KO, double knock-out for ApoE and receptor for LDL; ApoE, apolipoprotein E; AST, aspartate transaminase; CK, creatine kinase; cTnT, cardiac troponin T; TnC, troponin C; TnI, troponin I; HESI, heated electrospray; ICAT, isotope-coded affinity tags; iTRAQ, isobaric tags for relative and accurate quantification; KO, knock-out (mouse); LDH, lactate dehydrogenase; LDL, low-density lipoprotein; LDLr, receptor for low-density lipoprotein; WT, wild type (mouse)

* Corresponding author at: Department of Biochemistry, Medical University of Gdansk, Debinki 1, 80-211 Gdansk, Poland. Tel.: +48 58 349 1464; fax: +48 58 349 1460.

E-mail address: m.olkowicz@gumed.edu.pl (M. Olkowicz).

<http://dx.doi.org/10.1016/j.talanta.2014.08.029>

0039-9140/© 2014 Elsevier B.V. All rights reserved.

of several subunits that include troponin C (TnC), troponin I (TnI), and troponin T (TnT). At the onset of systole, calcium ions bind to TnC, initiating a conformational change that activates the myofibrillar thin filament. Activation of the thin filament facilitates crossbridge cycling, myofibrillar activation, and contraction. There are specific patterns of development, physiological-state and disease associated changes in the expression of troponins that are particularly important in the cardiac muscle [2,3]. Troponins have isoforms specific to the cardiac and skeletal muscle that are considerably different in their structure. This has important practical implications as it facilitates their use as a biomarker of tissue-specific injuries [1,2]. Following incidents such as cardiac infarction, the troponin complex is gradually released into the blood, where it degrades into two predominant forms in circulation: the binary IC complex and the free troponin T. Troponins (especially troponin T) are regarded as optimal biomarkers for

detecting myocardial damage with a better specificity and timing of release, compared with cardiac isoforms of aspartate transaminase (AST), creatine kinase (CK), and lactate dehydrogenase (LDH) [2].

The analytical aspect is vital for progress in studies on troponin function and diagnostic applications. Currently, the troponin content is usually determined by immunoenzymatic methods both in cardiac tissue and serum [1,4–7]. These procedures, however, suffer from limitations such as narrow range, suboptimal accuracy and poor reproducibility. Accurate quantification of troponins is particularly important in the tissue, as even minor changes may have implications for their use as a biomarker. Mass spectrometry-based quantitative proteomics may offer an optimal tool for the purpose [8–15]. The resolving power of liquid chromatography combined with selectivity and sensitivity of tandem mass spectrometry could bring identification and quantification of peptides and proteins in complex biological samples onto a new level. Various quantitative approaches have been developed in the field of mass spectrometry proteomics; mostly, they rely on relative strategies that use labels or isotopic tags: isotope-coded affinity tags (ICAT) and isobaric tags for relative and accurate quantification (iTRAQ) [16]. Although labeling methodologies provide excellent results, the time-consuming and expensive step of sample preparation represents a significant drawback. Therefore, recent efforts have focused on the development of label-free procedures [17]. While several alternatives are available, the mass spectrometry detection step in most of the above procedures is based on selected reaction monitoring in triple quadrupole mass spectrometer that currently offers the best sensitivity [18–24].

The aim of this study was a comparison of three analytical solutions based on label-free LC/MS for the absolute quantification of cTnT in the mouse heart with a particular focus on the suitability of nanoflow LC/MS for a routine quantification of protein. Three proposed analytical solutions: the microflow, direct injection nanoflow and preconcentration nanoflow LC/MS methods were tested for analytical quality and employed to quantify cTnT in the heart of wild type and atherosclerotic mice.

2. Materials and methods

2.1. Materials

All reagents used for protein extraction and preparation for LC/MS analysis were of analytical grade. 1 M 4-(2-hydroxyethyl)-1-piperazineethanesulfonic acid (HEPES) solution (pH=7.0–7.6), protease inhibitor cocktail for mammalian tissue, ethylenediaminetetraacetic acid (EDTA), sodium vanadate (Na_3VO_4), sodium fluoride (NaF), Tris(2-carboxyethyl)phosphine hydrochloride (TCEP), trifluoroacetic acid (TFA), 1,4-dithiothreitol (DTT), iodoacetamide (IAM), and trypsin from porcine pancreas were purchased from Sigma-Aldrich (Steinheim, Germany). Tris(hydroxymethyl)amino-methane (TRIS) and urea were obtained from Bio-Rad (München, Germany). The BCA protein assay kit used for determination of protein concentration was purchased from Merck (Darmstadt, Germany).

All HPLC-grade organic solvents (methanol, acetonitrile, formic acid) were purchased from Sigma-Aldrich (Steinheim, Germany). Ultrapure water was produced from distilled water by an appropriate Mili-Q system. C18 silica bonded SPE cartridges (100 mg/1 mL) were obtained from Waters, Sep-Pak type (Milford, USA) and Sigma-Aldrich, Discovery®DSC-18 type (Steinheim, Germany). Filter membranes Vivaspin®2 (membrane 10,000 MWCO, CTA) were supplied by Sartorius (Göttingen, Germany). Cellulose triacetate (CTA) syringe filters (0.45 µm pore size, 4 mm diameter) were obtained from Labhut (Gloucester, UK). All the solutions containing proteins or

peptides were kept in Eppendorf®Protein LoBind microcentrifuge tubes (Hamburg, Germany).

Synthetic peptide standards: YEINVLK and YEIQVLR were obtained from Lipopharm (Poland). Their purity and masses were verified with the use of an accurate mass LC/MS system (Ultimate 3000, Dionex, Thermo Scientific, Waltham, MA; MicrOTOF-QII, Bruker Daltonik GmbH, Bremen, Germany).

2.2. Animal preparation

Six-month-old male ApoE/LDLr KO mice ($n=6$) and wild type C57BL/6 J mice ($n=6$) were used in this study. Both the ApoE/LDLr KO and the wild type mice were fed a standard laboratory diet. At the time of the experiment, the mice were sacrificed, their hearts were excised, perfused with saline and the left ventricular free walls were dissected. Next, the samples were snap-frozen in liquid nitrogen and stored at -80°C until used. The study was approved by the Ethics Committee on Animal Experimentation at the Medical University of Gdansk.

2.3. Sampling procedures

2.3.1. Protein extraction

Protein extraction was carried out according to the 'in sequence' extraction procedure, described by Kane et al. [25], with slight modifications. The mouse heart left ventricle was dissected and homogenized twice on ice for 1 min in a neutral buffer (pH=7.4), containing 25 mM HEPES, 50 mM NaF, 0.25 mM Na_3VO_4 , 2.5 mM EDTA, and 1% (v/v) protease inhibitor mixture. The tissue–buffer ratio was maintained at 1:5 (w/v). The homogenate was centrifuged at 4°C for 15 min at 15,000g and the supernatant was discarded. In the next step, the remaining pellet was homogenized twice on ice for 1 min in an acidic buffer (pH=2.2), containing 1 mM TCEP and 0.1% (v/v) aqueous solution of TFA. The sample–buffer ratio was the same as above. The homogenate was centrifuged at 4°C for 15 min at 15,000g and the supernatant was retained as a myofibrillar protein-enriched extract. The obtained fraction was filtered through a cellulose triacetate (CTA) syringe filter, lyophilized and stored at -80°C until used. The protein concentration was determined with a BCA Protein Assay Kit.

2.3.2. In-solution enzymatic digestion

In-solution digestion was carried out according to the protocol described by Kinter et al. [26]. The lyophilized fraction was resuspended in 200 µL of buffer (pH=7.8) consisting of 100 mM Tris-base and 6 M urea. Denatured proteins were reduced with 10 mM dithiothreitol (60 min at room temperature) and alkylated with 40 mM iodoacetamide (60 min in the dark). An excess of the reagents was removed by buffer exchange with 100 mM Tris-base (pH=7.8) buffer using a 10 kDa cut-off spin filter. The samples were digested with a proteomics-grade trypsin for 18 h at 37°C and then the digestion was stopped by adding of 10% (v/v) formic acid. At the end of this step, IS peptide solution (0.1 µg) was added to the tryptic digest (in order to estimate the recovery of the solid phase extraction procedure).

2.3.3. Peptide desalting

The peptides obtained in the previous step were desalted and cleaned up using C18 silica cartridges. In this study, two types of sorbents with different degrees of filling by aliphatic groups were tested: the first one was as Sep-Pak supplied by Waters with 18% C loading, and the second one was Discovery®DSC-18Lt (Supelco) with 11% C loading. Moreover, different types of elution solvents were examined to improve the total peptide recovery during the extraction process.

Briefly, the solid phase extraction procedure consisted of the following steps: (a) conditioning with 3 mL of H₂O/AcN solution (20:80, v/v); (b) equilibration with 3 mL of 0.1% (v/v) aqueous solution of FA/TFA; (c) sample loading; (d) sequentially washing out the contaminants with the use, in appropriate order, of: 1.5 mL of 0.1% (v/v) aqueous solution of FA/TFA; 1.5 mL of H₂O/AcN (95:5, v/v) solution with 0.1% (v/v) FA/TFA; and (e) elution of the retained peptides. The peptide recovery was evaluated using three different elution phases: H₂O/AcN (50:50, v/v) with 0.1% (v/v) TFA; H₂O/AcN (20:80, v/v) with 0.1% (v/v) FA; H₂O/AcN (20:80, v/v) with 0.1% (v/v) TFA.

The eluate was concentrated on a vacuum centrifuge, lyophilized and finally reconstituted with 500 μL of H₂O/AcN (80:20, v/v) solution acidified with 0.1% (v/v) FA. This solution was considered as a sample stock solution and, depending on the system set-up used, appropriately diluted for the LC/MS analysis (microflow mode: 100 times; direct injection nanoflow mode: 1000 times; preconcentration nanoflow mode: 5000 times, respectively).

2.4. Quantitative LC–MS/MS analysis

The LC–MRM–MS assays were performed in three LC/MS setups: (1) microflow HPLC–MS/MS; (2) nanoflow UHPLC–MS/MS with direct injection of sample; (3) nanoflow UHPLC–MS/MS with the step of sample preconcentration.

Setup 1: The analyses performed in the LC microflow mode were carried out on a Surveyor HPLC system (Thermo Scientific, Waltham, MA) coupled with a TSQ Vantage triple quadrupole mass spectrometer (Thermo Scientific) equipped with HESI-II Heated Electrospray interface. The chromatography apparatus consisted of a quaternary low-pressure gradient pump, an autosampler with 20 μL loop and thermostated column compartment. Separations were performed on a reversed-phase (RP) chromatographic column, Hypersil BDS C18 (100 × 1 mm I.D., 3 μm particle size, 130 Å pore size, Thermo Scientific), connected with a security guard C18 (4 × 2 mm) supplied by Phenomenex (Torrance, CA, USA). The LC/MS system, data acquisition and processing were managed by the Xcalibur software (version 2.1, Thermo Scientific).

The mobile phases used for chromatographic elution consisted of two solvents: A – formic acid (0.1%, v/v) in water, B – formic acid (0.1%, v/v) in acetonitrile. The gradient elution program was performed as follows: 25% B, 0–1 min; 25–95% B, 1–6 min; 95% B, 6–7 min; 95–25% B, 7–8 min; 25% B, 8–13 min. The flow rate was set at 400 μL min⁻¹ with the liquid stream division before

entering the column, giving the resultant flow rate of 80 μL min⁻¹. The temperature of the column packing was 35 °C and the injection volume was 2.5 μL.

Mass spectrometric conditions were optimized for two synthetic peptides by infusing, at a flow rate of 5 μL min⁻¹, their standard solution (50 pg μL⁻¹) prepared in a water/acetonitrile (25:75, v/v) mixture acidified with formic acid (0.1%, v/v). Doubly charged molecules were selected as a target for fragmentation. Three transitions per each peptide were monitored (see Table 1 for details) in a scheduled SRM mode. SRM transitions were acquired in Q1 and Q3 operated at a unit resolution (0.7 FWHM) while the collision gas pressure in the Q2 cell was set to 1.5 mTorr. To optimize the ions transmission, appropriate tuned S-lens values were also used. The HESI interface was operated in the positive ionization mode by applying a voltage of 3 kV to the capillary. Nitrogen was used as a nebulizing and desolvation gas, whereas argon was the collision gas. The appropriate collision energies were optimized for each ion. Specific parameters of the LC/MS analysis are shown in Table 1.

Setup 2: All LC experiments in the nanoflow mode were carried out using the Dionex Ultimate 3000 nanoRSLC system (Thermo Scientific, Waltham, MA) coupled to the TSQ Vantage mass spectrometer.

PicoChip system was used for separation and as ion source (New Objective, Woburn, USA). Injections were made in a partial loop mode (0.5 μL). The LC/MS system was controlled by the Xcalibur software (v. 2.1, Thermo Scientific). PicoChip consisted of a fused silica column (10 cm long, 75 μm I.D.) packed with ProteoPep™ II, C18 resin 5 μm/300 Å (New Objective). The elution solvent A consisted of H₂O and solvent B consisted of AcN/H₂O (80:20, v/v), each containing 0.1% FA. The nano LC gradient for separation was linear from 15% to 80% B in 8 min, followed by 80% B for 2 min and returning to 15% B in 1 min. Subsequently, the column was re-equilibrated with 15% B for 5 min, resulting in a total run time of 16 min. The compounds of interest were eluted from the column at a flow rate of 600 nL min⁻¹.

The MS parameters were optimized during the repeated chromatographic separation, not in the infusion mode. As previously, detection was performed in a positive ionization mode and quantification was executed in a multiple reaction monitoring mode. The compound-specific parameters (precursor and product ions, collision energy, S-lens values) were independent of the flow-rate and were constant compared with the method with higher flow-rate. Detailed MS/MS assay conditions are summarized in Table 1.

Table 1
MS/MS parameters of the microflow, direct injection nanoflow and pre-concentration nanoflow LC–MS/MS for the quantification of cTnT YEINVLRL peptide.

	YEINVLRL microflow	Nanoflow LC/MS	YEIQVLR microflow	Nanoflow LC/MS
Precursor ion (<i>m/z</i>)	[M+2H] ²⁺ /2	[M+2H] ²⁺ /2	[M+2H] ²⁺ /2	[M+2H] ²⁺ /2
MRM transitions ^a (<i>m/z</i>)	453.75 → 136.1 453.75 → 293.0 453.75 → 614.7	453.75 → 136.1 453.75 → 293.0 453.75 → 614.7	460.75 → 136.1 460.75 → 292.9 460.75 → 628.7	460.75 → 136.1 460.75 → 292.9 460.75 → 628.7
Collision energy (eV)	27 14 16	27 14 16	27 14 16	27 14 16
ESI source	Standard	Nano	Standard	Nano
Capillary voltage (kV)	3.0	1.8	3.0	1.8
ESI capillary I.D./tip (μm)	100/100	75/15	100/100	75/15
Nebulizing gas flow (a.u.)	15	–	15	–
Source temperature (°C)	320	220	320	220
Desolvation temperature (°C)	100	–	100	–
Desolvation gas pressure (psi)	5	–	5	–

^a All three transitions for each peptide were monitored. LOD and LOQ values (presented in Table 3) as well as transition used for the quantification of cTnT-specific peptide in biological matrix refer to the transition in bold.

Setup 3: Preconcentration LC/MS assays were carried out using the same Ultimate/TSQ Vantage system that was used for direct injection mode, with the additional application of high-pressure 10-port switching valves, a UV detector and an auto-sampler equipped with a 20 μL sample loop. UV detection was proven useful during system performance testing and was also helpful for detection of problems with the chromatographic system. The samples were injected in 2.5 μL aliquots onto a trapping column (Acclaim PepMap100 C18, 2 cm \times 75 μm , 3 μm , 100 \AA , Thermo), employing a mobile phase AcN/H₂O 2/98 (v/v) containing 0.1% (v/v) FA delivered by a loading pump at a flow rate of 5 $\mu\text{L min}^{-1}$. Next, the trapping column was switched in-line with the separation column and the peptides were eluted with an increasing percentage of the organic solvent at a flow rate of 300 nL min^{-1} . The peptides separations were carried out at 40 $^{\circ}\text{C}$ using a 75 μm I.D. \times 15 cm C18 column (Acclaim PepMap100 RSLC C18, 2 μm , 100 \AA , Thermo). Phase A was H₂O and phase B was H₂O/AcN (20:80, v/v), both with 0.1% (v/v) FA. The analytes were separated and eluted using the following gradient: 4–25% B in 10 min, 25–95% B in 22.5 min. After that time, 95% B was held constant for 3 min to rinse the column. Finally, the content of B was lowered to 4% over 2.5 min and the column was re-equilibrated for the next 22 min. The MS/MS parameters were the same as for the previous setting (direct injection nanoLC/MS).

2.5. Evaluation of methods performance

2.5.1. Preparation of stock solutions, calibration standards and quality control samples

Standard stock solutions of YEINVLRL peptide and its analog (1 mg mL^{-1}) were prepared by dissolving a required amount in 0.1% (v/v) aqueous formic acid. Their working solutions for spiking were prepared by suitable dilution of stocks with acidified water (0.1% formic acid). All the above solutions were stored at -20°C . Calibration standards and quality control (QC) samples were prepared by spiking the processed heart tissue with the working solutions.

2.5.2. System suitability experiments, system performance and carry-over effect

The system suitability experiment was performed by injecting four consecutive injections of an aqueous standard mixture of a cTnT-specific peptide and IS at the start of each batch, whereas the system performance was studied by injecting one extracted LLOQ sample with internal standard at the beginning of each analytical run. Carry over was checked by observing the peaks in subsequent runs. The design of the study comprised of the following sequence of injections, i.e., mobile phase solution [H₂O/AcN (50:50, v/v) with 0.1% FA (v/v)] \rightarrow LLOQ sample \rightarrow mobile phase solution \rightarrow ULOQ sample \rightarrow mobile phase solution \rightarrow ULOQ sample \rightarrow mobile phase solution. Otherwise for routine carry over experiments, the mobile phase injection was inserted between the injections of QC samples. It is related to the endogenous non-zero analyte level, which may exist even in the blank sample.

2.5.3. Calibration curves, linearity and method sensitivity

The linearity of each method was determined by the analysis of five calibration curves containing seven non-zero concentrations, covering the total ranges: 0.05–20 $\text{pg } \mu\text{L}^{-1}$ (I setup), 0.01–2 $\text{pg } \mu\text{L}^{-1}$ (II setup), 0.00025–0.4 $\text{pg } \mu\text{L}^{-1}$ (III setup), including the LLOQ point. Three samples of each concentration were measured and the curves were fitted by a linear weighted ($1/x^2$) least square regression method by the measurement of the peak area ratio of the analyte to

IS. A correlation coefficient (r^2) value > 0.99 was desirable for all the calibration curves. The lowest concentration point on the calibration curve was accepted as the lower limit of quantification (LLOQ), if the analyte response was at least ten times more than that of analyte free matrix.

Appropriate calibration curves were prepared by the standard addition method, as the analyzed matrix contained some amount of the endogenous analyte. The endogenous level of the analyte was assessed by using the linear part of the concentration curve. The 99% confidence interval of the regression line intercept was determined using bootstrap estimation [5,27]. If the lower limit of the confidence interval is positive, then it is assumed that the analyte has an endogenous level equal to the regression intercept. If the lower 99% confidence interval is zero or negative, then no endogenous concentration is expected for that compound.

2.5.4. Accuracy and precision

For determining the intra-batch accuracy and precision, a replicate analysis of matrix samples of cTnT-specific peptide was performed on the same day. The run consisted of a calibration curve and five replicates of LLOQ QC, LQC, MQC, HQC samples. The inter-batch accuracy and precision were assessed by analyzing three precision and accuracy batches on three consecutive validation days.

2.5.5. Relative recovery, absolute matrix effect and process efficiency

The relative recovery, absolute matrix effect and process efficiency were assessed as recommended by Matuszewski et al. [28,29]. All three parameters were evaluated at the LQC, MQC and HQC levels in five replicates. Relative recovery (RE) was calculated by comparing the mean area response of the extracted samples (spiked before extraction) to that of unextracted samples (spiked after extraction) at each QC level. The recovery of IS was estimated in a comparable manner. The absolute matrix effect (ME) was assessed by comparing the mean area response of the unextracted samples (spiked after extraction) with the mean area of neat standard solutions (prepared in a mobile phase). The above-mentioned matrix effect was calculated by using pooled tissue matrices coming from six different sources, whereas, the overall 'process efficiency' (% PE) was calculated as $(\text{ME} \times \text{RE})/100$.

2.6. Data analysis

Data analysis was performed using the Xcalibur software version 2.1. Quantification was based on the corresponding specific peptide and its analog peak area ratios established by automatic software routines. All the data were manually inspected to confirm the correct peak detection. Concentrations of cTnT in the heart were compared using Student's *t*-test to indicate any statistically significant difference between the values obtained for the examined groups ($P < 0.05$, was regarded as significant).

3. Results and discussion

This study developed and compared three analytical procedures for the absolute quantification of troponin T in mouse hearts. All three procedures: microbore, direct injection nano- and preconcentration nanoLC–MS/MS provided excellent linearity, precision and accuracy. A switch from micro- to nanoflow offered better sensitivity without loss of accuracy or reproducibility. Application of the step of sample preconcentration provided further gain in sensitivity at the expense of longer separation time.

3.1. Selection of cTnT-specific peptide and internal standard

The quantitative approach presented in this paper required the application of a peptide which is specific for the target protein, cTnT, and its analog, not found in any cardiac or blood protein to be used as internal standard. Based on previous reports [6,7] and databases, such as Peptide Atlas, gpmDB, SRM Atlas sequence: YEINVLR was selected as the cTnT-specific peptide, corresponding to the amino acids 272–278 in sequence of mouse cTnT, with a monoisotopic mass of 905.50 Da. This peptide (formed during the proteolytic digestion with trypsin) generates a strong ion current during MS analysis, has no potential sites for post-translational modifications and has a unique amino acid sequence for cardiac TnT. YEIQVLR peptide with a monoisotopic mass of 919.50 Da that is different from the cTnT-specific peptide by one amino acid residue (glutamine instead of asparagine) was chosen as the internal standard. The peptide was comparable to YEINVLR in terms of its chromatographic and ionization behavior.

3.2. Optimization of sample preparation

The protein extraction procedure was based on a protocol established for the heart tissue fractionation which enables separation of the myofilament proteins in a manner that is compatible with one- or two-dimensional electrophoresis and high-performance liquid chromatography [25]. The method, termed 'in sequence' extraction, relies on protein solubility at various pH levels, generates three fractions: (1) cytoplasmic-enriched extract (neutral pH), (2) sarcomeric-enriched extract (acidic pH), and (3) membrane protein-enriched pellet.

Previous data indicated that myofilament proteins are hard to dissolve, readily aggregate and, therefore, they require high salt and often high detergent concentrations [30–33]. Such conditions are not compatible with most separation technologies. Moreover, these extraction protocols are often time-consuming processes, potentially triggering artificial posttranslational modifications within the proteome. The extraction protocol proposed by Kane et al. [25] not only is robust and reproducible but, more importantly, it enables preservation of the original proteome during isolation process.

Isolated proteins were subjected to complete tryptic digestion to provide cleavage peptides that can quantitatively represent the parent protein. For these purposes, optimal enzymatic hydrolysis conditions, including the substrate-to-enzyme ratio, were maintained. The resulted peptide mixture was desalted and cleaned up with 100 mg C18 cartridges. As described in Section 2, in order to obtain maximum recovery, different types of sorbents and elution solvents were tested. In particular, the recovery degree of tryptic digest fortified with 2 $\mu\text{g } \mu\text{L}^{-1}$ of the cTnT-specific peptide was evaluated using two kinds of sorbents (Sep-Pak, Discovery) and three different elution phases (see details in Section 2.3.3).

The data presented in Table 2 indicate that the best cTnT-peptide recovery was obtained with use of the Sep-Pack sorbent

Table 2

Recoveries and precisions for different C18 SPE cartridges and eluting phases. Analyses performed with the use of microflow LC/MS device. Values represent means ($n=5$).

Sorbent/eluent phase	Recovery (%)	RSD (%)
Sep-Pak-tC18 ^a /80% AcN (v/v)+0.1% FA	89.9	0.3
Discovery® DSC-18Lt ^b /50% AcN (v/v)+0.1% TFA	78.2	3.6
Discovery® DSC-18Lt/80% AcN (v/v)+0.1% TFA	85.0	5.1
Discovery® DSC-18Lt/80% AcN (v/v)+0.1% FA	75.1	2.8

^a Endcapped, particle size: 37–55 μm , 125 Å pore size, 18% C loading.

^b Endcapped, particle size: 50 μm , 75 Å pore size, 11% C loading.

and by eluting with H₂O/AcN (20/80, v/v) solution acidified with 0.1% (v/v) formic acid. A slightly lower recovery was observed for the Discovery sorbent when the same eluting phase was used, only by replacing the ion-pairing reagent type. As the residues of trifluoroacetic acid can interfere with the ionization process (during MS detection), the mixture of H₂O/AcN with a trace amount of formic acid was used as an eluting solution. The studies described by the present authors confirm the importance of silica coverage by aliphatic groups for peptide recovery from biological samples. A higher degree of C-chain filling worked better for the recovery of the compounds considered in this paper. The data presented in it are in good agreement with the results published previously [6,7].

3.3. Assay development and analytical parameters

The MS assay parameters were optimized by direct infusion with HESI-II source used for microflow LC–MS/MS. The most intense, doubly charged precursor ion was chosen for each peptide, consistent with the previous reports [6,7], where monoprotonated molecules for both of the analyzed peptides (m/z 906.50 and 920.50, respectively) were observed only at specific MS conditions. Moreover, selection of the single charge molecule as a precursor ion in SRM acquisition mode led to a substantial variability in the relative abundances of transitions pair signal observed in the spectrum.

Doubly charged molecules (m/z 453.75 and 460.75, respectively) were subjected to fragmentation (at the optimal instrument conditions) resulting in product ions as presented in Figs. 1 and 2. The three most intense fragment ions of the YEINVLR peptide (m/z 136.1; 293.0; 614.7) were chosen for MRM experiments. The internal standard peptide (YEIQVLR) is characterized by a very similar fragmentation profile, and, also in this case, the three most intense ions were selected for further analysis. The detailed MS/MS parameters of the microflow, direct injection and preconcentration nanoflow LC/MS methods are summarized in Table 1.

In this study, three types of chromatographic configurations were compared to estimate whether gain in detection sensitivity in nanoflow methods is possible while retaining accuracy and precision of the method. In all three cases, relatively similar chromatographic parameters (i.e., type of sorbent, type of mobile phase, elution profile) were maintained to eliminate its effects on the results obtained. Fig. 3 presents LC–MRM–MS chromatograms (as a sum of the selected transitions) of the cTnT-specific peptide from the mouse heart extract obtained with (a) microflow, (b) direct injection nanoflow, and (c) preconcentration nanoflow LC–MS/MS.

With reference to retention time for the cTnT-specific peptide, the best reproducibility was obtained for the microflow (RSD < 0.2%) and preconcentration nanoflow LC/MS (RSD < 0.1%) methods; however, the RSD's of the retention times of the analyzed compound were comparable for three different methods (< 0.5%), indicating that delivery of the gradient of the mobile phase at the different flow-rates was robust. Also the microflow mode resulted in the best repeatability of injection (RSD < 1%) of all the methods used. Similar findings were reported by Lanckmans et al. [34], who noticed that downscaling from microbore to capillary and nano-dimensions resulted in a slight decrease in this aspect of system performance.

3.4. Evaluation of methods performance

3.4.1. Linearity and sensitivity of the methods

The results of linearity (i.e., linear range, slope, Y-intercept) and the detection sensitivity (LOQ and LOD) for the microflow, direct injection nanoflow, and preconcentration nanoflow LC–MS/MS

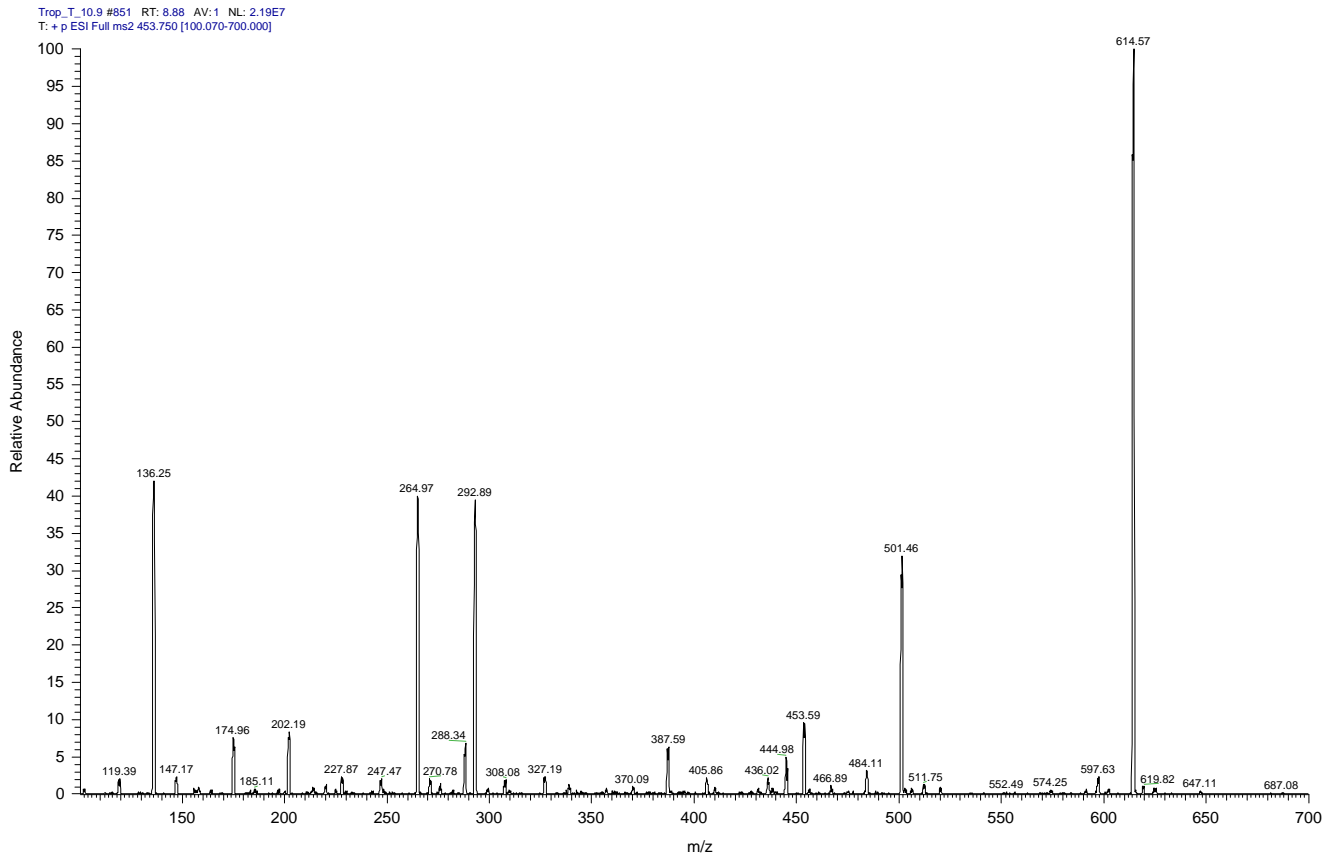


Fig. 1. Product ion spectrum of diprotonated cTnT YEINVLK peptide obtained during infusion of $50 \text{ pg } \mu\text{L}^{-1}$ standard solution (18 eV collision energy was used).

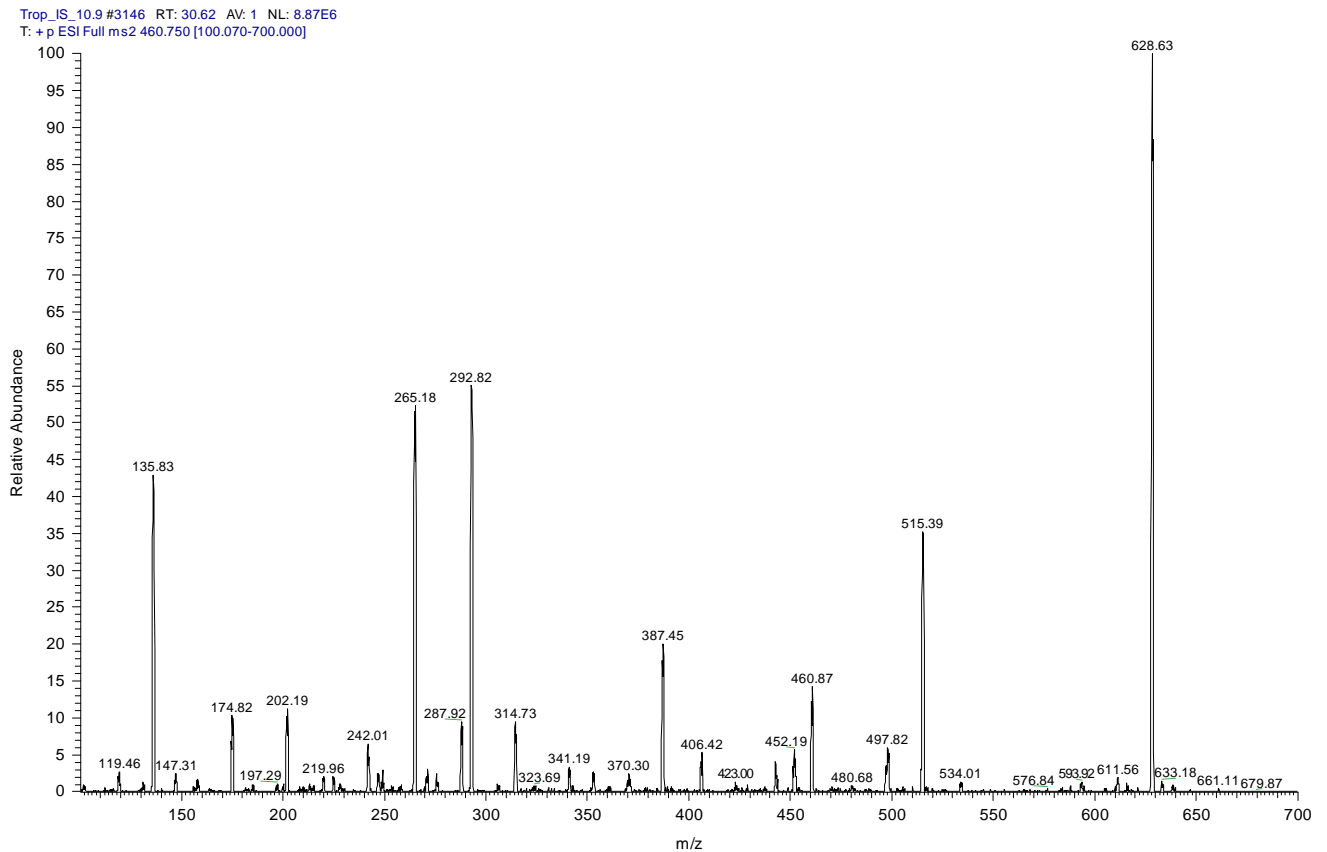


Fig. 2. Product ion spectrum of diprotonated internal standard YEIQVLR peptide obtained during infusion of $50 \text{ pg } \mu\text{L}^{-1}$ standard solution (18 eV collision energy was used).

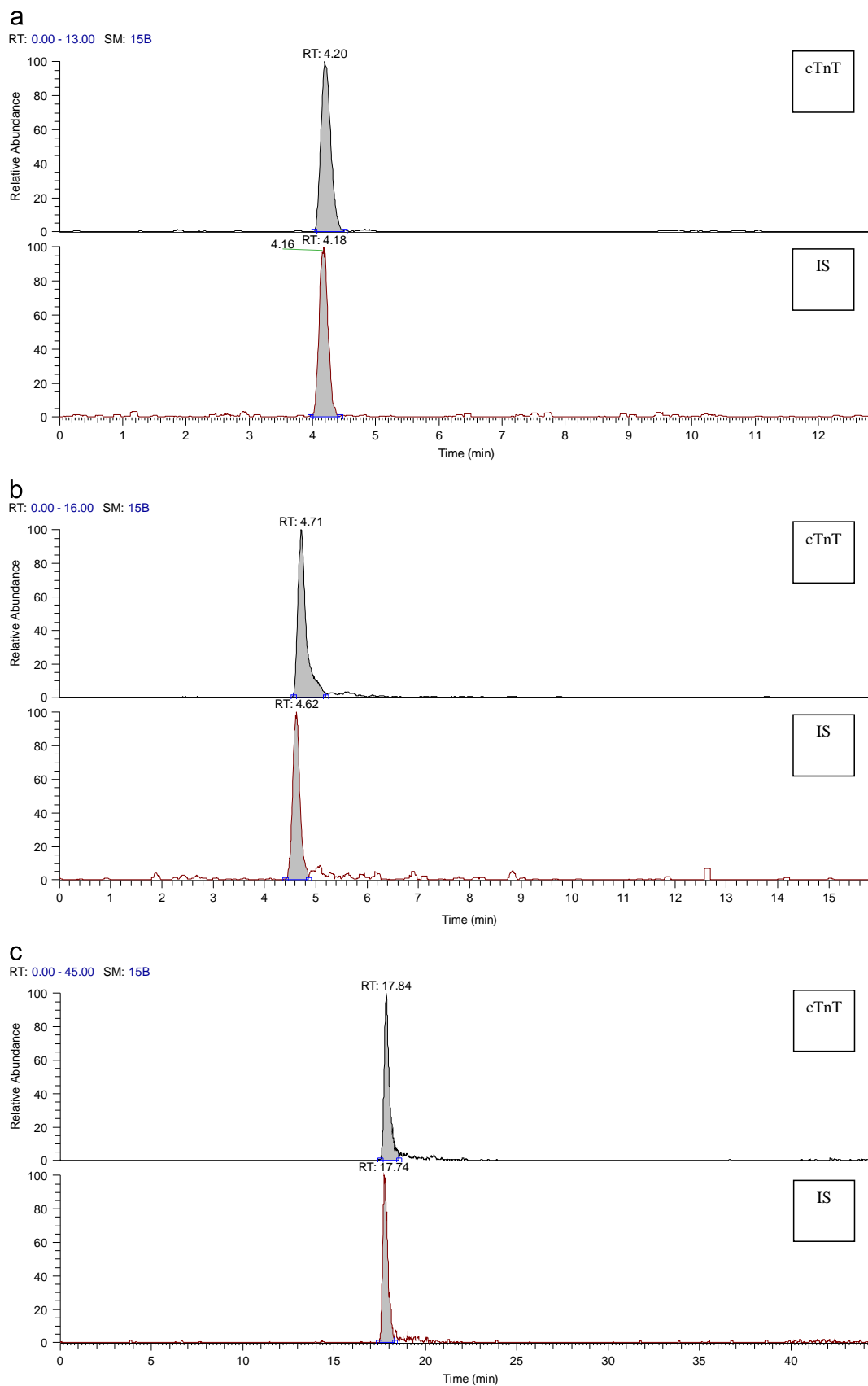


Fig. 3. Representative LC-MRM-MS chromatograms of cTnT-specific peptide ($m/z=453.75$) and internal standard ($m/z=460.75$) obtained by analysis of a selected unspiked sample using (a) microflow, (b) direct injection nanoflow, (c) preconcentration nanoflow LC-MS/MS. The sample was obtained from the trypsin digested myofilament protein extract from mouse heart as described in Section 2.

Table 3

Comparison between the microflow, direct injection nano-, preconcentration nanoflow LC–MS/MS method in terms of linear range, slopes and Y-intercepts of the weighted calibration curves. Values are mean \pm SD, $n=5$.

	Microflow	Direct injection nanoflow	Preconcentration nanoflow
Linear range [$\text{pg } \mu\text{L}^{-1}$]	0.05–20	0.01–2	0.00025–0.4
Slope	0.86 ± 0.05	8.8 ± 0.5	31 ± 2
Y-intercept	0.39 ± 0.02	0.37 ± 0.02	0.27 ± 0.02
LOD [$\text{pg } \mu\text{L}^{-1}$]	0.02	0.003	0.0001
LOQ [$\text{pg } \mu\text{L}^{-1}$]	0.05	0.01	0.00025

methods are summarized in Table 3. The linear ranges of the microflow and nanoflow LC/MS methods covered about two to three orders of magnitude, as is desired during ESI–MS detection. The linear range of the nanoflow techniques included lower concentrations: 0.00025–0.4 $\text{pg } \mu\text{L}^{-1}$ (preconcentration), 0.01–2 $\text{pg } \mu\text{L}^{-1}$ (direct injection) compared with 0.05–20 $\text{pg } \mu\text{L}^{-1}$ for the microflow mode, since the nanosource is saturated at lower concentrations, compared with the standard ESI source. The established scopes of linearity were much broader than the ranges examined in this paper, selected on the basis of the expected endogenous signal response.

For the characterization of the assay linearity, appropriate calibration curves were generated with regression coefficients better than 0.99. The observed slopes of calibration curves reflect the sensitivity of each method (Table 3). These slopes of calibration curves for the cTnT-specific peptide increased about 10 and 36 times, respectively, when downscaling from microbore LC/MS dimension to nano direct injection and preconcentration. Additionally, the LOQ value was employed as a parameter to investigate whether miniaturization enhances assay sensitivity. The LOQ values of the peptide of interest were as follows: 0.05 $\text{pg } \mu\text{L}^{-1}$ (0.125 pg on column), 0.01 $\text{pg } \mu\text{L}^{-1}$ (0.005 pg on column) and 0.00025 $\text{pg } \mu\text{L}^{-1}$ (0.000625 pg =0.625 fg on column) for the microbore, direct injection nano, preconcentration nanoLC/MS systems, respectively. The observed gain in sensitivity is assigned to the combination of the enhanced mass sensitivity of the miniaturized chromatographic system and the increased concentration sensitivity of the miniaturized ESI source device. Lanckmans et al. [34] and Meiring et al. [35] have shown, that, theoretically, the gain in sensitivity by miniaturization of a 1 mm I.D. column to a 75 μm I.D. column should be about 180. They also suggested, that, practically, the obtained gain is usually lower due to the variable column parameters (e.g., flow-rate, column length, porosity) and different absolute amount of the analyte introduced into both systems. Kranendijk et al. [36] and Abian et al. [37] also noticed, that the method sensitivity does not reach the theoretical expected value after miniaturization of the LC/MS system.

3.4.2. Accuracy and precision of the methods

The microflow LC/MS method exhibited the best recoveries (the intra-batch precision, (% CV) ranged from 2 to 5 and the accuracy was within 97.5–104%). Slightly worse results were obtained for the preconcentration nanoflow LC/MS method (accuracy: 95–104%, precision: 4–6%). However, the recovery percentages of the micro- and nanoflow LC/MS methods all met bioanalytical acceptance criteria (80–120%). The detailed results for intra- and inter-assay accuracy and precision for the three analyzed methods are provided in Table 4. The weakest accuracy observed in the nano direct injection mode is probably related to some variations in spray performance of the nano ESI device. However, the result obtained by the authors is not as significant as previously noted [34,38–40]; this has been attributed to

Table 4

Intra-batch and inter-batch accuracy and precision for cTnT-specific peptide.

QC ID	Nominal conc. [$\text{pg } \mu\text{L}^{-1}$]	Intra-batch				Inter-batch			
		<i>n</i>	Mean conc. ^a found [$\text{pg } \mu\text{L}^{-1}$]	Accuracy (%)	CV (%)	<i>n</i>	Mean conc. ^b found [$\text{pg } \mu\text{L}^{-1}$]	Accuracy (%)	CV (%)
<i>Microflow</i>									
LLOQ QC	0.05	5	0.052	104	3	15	0.047	94	8
LQC	0.2	5	0.21	104	5	15	0.19	95	7
MQC	5	5	4.90	98	2	15	4.90	98	4
ULOQ QC	20	5	19.50	97.5	2	15	19.25	96	5
<i>Direct injection nanoflow</i>									
LLOQ QC	0.01	5	0.009	90	9	15	0.008	80	11
LQC	0.02	5	0.018	90	7	15	0.018	90	9
MQC	0.5	5	0.47	94	5	15	0.475	95	5
ULOQ QC	2	5	1.85	92.5	5	15	1.90	95	4
<i>Preconcentration nanoflow</i>									
LLOQ QC	0.00025	5	0.00026	104	6	15	0.00024	96	7
LQC	0.004	5	0.0041	102.5	5	15	0.00395	98.7	5
MQC	0.1	5	0.095	95	4	15	0.096	96	3
ULOQ QC	0.4	5	0.39	97.5	4	15	0.39	97.5	4

n – total number of observations;

CV – coefficient of variation.

^a Mean of five replicates at each concentration.

^b Mean of 15 replicates for three precision and accuracy batches.

the difficulty in obtaining a stable spray in nano-dimensions methods. In the present case, the differences in the method accuracy, during the quantification process, were not significant. Additionally, a negligible (less than 5% of LLOQ area) carryover effect (observed in double blank matrix run after ULOQ) did not affect the accuracy and precision of the proposed methods.

3.4.3. Relative recovery, absolute matrix effect and process efficiency

The RE, ME and PE data at different QC levels for different methods are presented in Table 5. The relative recovery of the analyte is the ‘true recovery’ (unaffected by the matrix) and is calculated by comparing the area ratio response (analyte/IS) of the extracted samples (spiked before extraction) and the unextracted ones (spiked after extraction). The mean relative recovery obtained for the cTnT-specific peptide was approximately 90% for all the methods used (i.e., 87–93% for the microflow mode, 88–96% for the direct injection nanoflow mode, and 85–89% for the preconcentration nanoflow mode). The determined recovery refers to the efficiency of the solid phase extraction process as the recovery assessment of the whole procedure was not performed. Previous data [6,7] have shown that spiking the mouse heart tissue before the extraction of proteins with a standard of cTnT protein may be useless, since it leads to the formation of complexes with other proteins (cTnI, cTnT, myosin, etc.). We have only verified that the extraction under neutral conditions (pH=7.4) contributes to less than 1% loss of protein from the total recovery.

One of the key parameters established during the development and validation of the bioanalytical method is the matrix effect, that occurs due to the sample constituents co-eluting with the compounds of interest. This affects the ionization of the target analytes, resulting either in ion suppression, or in ion enhancement. Several papers

Table 5
Absolute matrix effect, relative recovery and process efficiency for cTnT-specific peptide analysis.

	Absolute matrix effect, % ME, (B/A) × 100	Relative recovery, % RE, (C/B) × 100	Process efficiency, % PE, (C/A) × 100
<i>Microflow</i>			
LQC [0.2 pg μL ⁻¹]	117.1 (5.6) ^a	87.0 (4.5) ^a	103.2
MQC [5 pg μL ⁻¹]	115.3 (3.9) ^a	90.6 (2.3) ^a	104.7
HQC [20 pg μL ⁻¹]	104.0 (2.1) ^a	92.9 (4.1) ^a	95.8
<i>Direct injection nanoflow</i>			
LQC [0.02 pg μL ⁻¹]	80.6 (7.6) ^a	88.1 (5.0) ^a	68.7
MQC [0.5 pg μL ⁻¹]	88.7 (5.8) ^a	96.1 (7.5) ^a	85.2
HQC [2 pg μL ⁻¹]	87.6 (4.3) ^a	92.3 (3.4) ^a	80.8
<i>Preconcentration nanoflow</i>			
LQC [0.004 pg μL ⁻¹]	91.5 (4.2) ^a	84.6 (6.1) ^a	75.8
MQC [0.1 pg μL ⁻¹]	94.8 (4.1) ^a	89.3 (3.6) ^a	84.7
HQC [0.4 pg μL ⁻¹]	92.1 (2.7) ^a	88.7 (2.6) ^a	81.8

A – mean area response of five replicate samples for cTnT-specific peptide prepared in mobile phase;

B – mean area response of five replicate samples prepared by spiking in extracted matrix;

C – mean area response of five replicate samples prepared by spiking before extraction;

^a RSD (%).

which focused on the evaluation of matrix effects have been published [28,29,41–47], proposing different strategies to assess and eliminate its impact. There are two common approaches to assess the matrix effects: the post-column infusion method and the post-extraction spike method (used in this work). The first method provides a qualitative assessment of the matrix effects (identifying the chromatographic regions which are most exposed to the influence of the matrix), while the latter provides quantitative information. The data in Table 5 present the matrix effects for the analyte at different concentrations for all the methods used. Values lower than 100% indicate ion suppression, while values higher than 100% indicate ion enhancement by the matrix components.

In the case of the microflow LC/MS method, we can observe the ion enhancement phenomenon (4–17%), which is particularly noticeable at low concentrations. Interestingly enough, the opposite effect was observed for the nanoflow LC/MS methods (i.e., ion suppression). This regularity was also observed by other authors [42,45], who noticed that the severity and nature of suppression or enhancement may be associated with the concentration of the co-eluting matrix components. As biological samples analyzed by the micro- or nanoflow LC/MS method were differently diluted, this can have a direct impact on the quality of the analytical signal. In addition, a significant matrix effect observed at the lowest concentration in the microbore system may be related to the relatively high flow-rate. Indeed, several previous studies [34,41,42,44,45] have shown, that miniaturized ESI methods are proven to be more tolerant towards contamination of the analyte solution. A lower flow-rate reduces the size of the charged droplets, thus less competition between the charged ions is observed and less solvent evaporation is required for ion release in the gas phase. Consequently, this leads to reduction in the contaminant concentration. Accordingly, the method based on nanochromatography, using a column-switching device (with sample preconcentration), seems to give the best results in terms of accuracy and precision, as it is characterized by a minimal matrix effect (5–8% ion suppression). Slightly worse results obtained for the direct injection nano mode confirm the usefulness of the sample preconcentration stage, enabling the removal of the matrix interferents.

Many strategies that enable the reduction or elimination of the matrix effects have been described [41–43,46,47]. The most

important ones are: optimization of sample preparation and/or chromatographic parameters, the use of an internal standard (often a stable isotope labeled (SIL) analog of analyte) to compensate for the alteration in signal, injection of smaller volumes or dilution of the samples (useful as long as instrumental sensitivity remains adequate), the use of lower flow-rates, flow splitting and the use of alternative ionization source (which is less sensitive to the matrix effects), such as APCI. The protocols used in this work adopted several approaches discussed above that enabled the present authors to obtain adequate quantitative results.

3.4.4. Comparison with published methods

Several methods have been reported for the analysis of cardiac troponins in biological matrices by LC/MS, either the cardiac troponin T alone [6,7] or in combination with other forms of troponin [4,5]. The methods presented in this work had the highest sensitivity compared with the other procedures [5–7] with a maximum loading at LLOQ per injection – 0.6 fg for the preconcentration nanoflow mode. The significantly lower on-column loading of the compound at LLOQ enabled the column efficiency to be maintained for many more injections. Moreover, in two procedures developed by the present authors, the total time of chromatographic analysis was shorter than in the existing methods. A detailed comparison of the selected procedures with the methods developed by the authors for cTnT determination in biological matrices is presented in Table 6. An important aspect in any LC/MS based procedure is its long term performance and ease of use. Despite complexity of the nanoflow system, its day to day use was not much more complicated than microflow system. In fact, once flow calibration procedures were completed and column connected in nanoflow system, routine analytical procedures were similar to microflow. Nanoflow column life allowed for several hundred of analyses in both direct injection and preconcentration modes. Samples for nanoflow systems could be more diluted and therefore are less challenging for the columns. Overall, microflow LC/MS could be the recommended when analyzing relative high concentrations of analytes mainly because of shorter analysis time. Nanoflow LC/MS, however, could be successfully used for routine analysis even of large sample pools when high sensitivity is desired.

3.5. cTnT quantification in heart tissue

The standard addition calibration curves (constructed as reported in Section 2) were used for the cTnT-specific peptide quantification. The molar concentration of the peptide corresponds to the molar concentration of the protein. The cTnT concentration in the mouse heart was assessed in six wild type C57BL/6J and six ApoE/LDLr KO mice. Since, the ApoE/LDLr KO mice are frequently used as a model for the disease associated with cardiac ischemia with troponin T used as an indicator of cardiac damage, it is important to estimate the change in the cardiac troponin T level between the two groups. The cTnT amounts obtained with the three different LC/MS methods were consistent although a trend for higher values was noticed in the nanoflow methods, as compared to the microflow procedure (Table 7). The results obtained by the present authors are in good agreement with previous data. Cavaliere et al. estimated the cTnT amount to be 4.3 μg mg⁻¹ of sarcomeric protein in an analogous LC/MS setup [7]. Based on MALDI-TOF detection, Bizzari et al. assessed the cTnT content in murine hearts and found it to be about 2.2 μg mg⁻¹ of the total sarcomeric protein [6]. Consistent with previous studies conducted with the use of ELISA kits, no difference was observed in the cTnT content in the heart muscle between C57BL/6J and ApoE/LDLr KO mice [48].

Table 6
Comparison of selected analytical methods developed for cTnT determination in biological matrices.

Sr. no/Ref.	Sample preparation procedure; internal standard	Column; elution process; mobile phase; flow rate; injection volume, maximum loading at LLOQ per injection	Detection technique; analytical run time; retention time; linear dynamic range; application	Validation parameters set
1/[6]	Protein chromatographic isolation; peptides clean-up on homemade C18 silica SPE cartridges; synthetic analog	1 μ L, 0.45 pg	MS/MS (MALDI-TOF); 0.01–0.1 mg L ⁻¹ (10–100 pg μ L ⁻¹); absolute quantification of troponin T in cardiac tissue of mice	Linearity; LOD; LOQ; matrix effect; recovery
2/[7]	Protein chromatographic isolation; peptides clean-up on homemade C18 silica SPE cartridges; synthetic analog	ReproSil-Pur 300 ODS-3 (150 mm \times 1 mm I.D., 5 μ m, 300 Å); gradient; ACN/MeOH 60:40 (v/v) (A) and H ₂ O (B), both containing 25 mmol L ⁻¹ FA; 70 μ L min ⁻¹ ; 3 μ L; 1.5 pg	LC-ESI-MS/MS; 13 min; 7.7 min; 0–100 pg μ L ⁻¹ ; absolute quantification of troponin T in cardiac tissue of mice	Linearity; LOD; LOQ; recovery
3/[5]	Protein depletion on a IgY-12 high capacity LC column; peptides desalting on Oasis HLB reversed phase cartridges; fractionation with SCX chromatography; stable isotope-labeled peptide	ReproSil-Pur C18-AQ, packed in house with 11–12 cm resin (75 μ m I.D., 3 μ m, 120 Å); gradient; A (0.1% FA) and B (90% AcN in 0.1% FA); 300 nL min ⁻¹ ; 1 μ L; 0.16 fmol (0.14 pg)	LC-ESI-MS/MS; 41 min; 0–10 fmol; quantification of cardiovascular biomarkers in plasma	Linearity; LOD; LOQ;
4/PM	Protein pre-fractionation; peptides desalting on Sep-Pak reversed phase cartridges; synthetic analog	Microflow: 2.5 μ L; 0.125 pg ^a Direct injection nanoflow: 0.5 μ L; 5 fg ^a Preconcentration nanoflow: 2.5 μ L; 0.625 fg ^a	LC-ESI-MS/MS; microflow: 6 min; 4.2 min; 0.05–20 pg μ L ⁻¹ Direct injection nanoflow: 8 min; 4.7 min; 0.01–2 pg μ L ⁻¹ Preconcentration nanoflow: 32.5 min; 17.7 min; 0.00025–0.4 pg μ L ⁻¹ (0.25–400 fg μ L ⁻¹); quantification of troponin T in cardiac tissue of mice	System performance; linearity; LOD; LOQ; intra- and inter-batch accuracy and precision; matrix effect; recovery; process efficiency

PM – present methods.

^a Chromatographic conditions in Section 2.

Table 7
cTnT quantification in mouse heart from C57BL/6J (WT) and ApoE/LDLr knock-out (AL KO). Values are expressed as mean \pm SD, n=6.

	Name of sample	Concentration of cTnT-specific peptide [pg μ L ⁻¹] (determined from the calibration curve)	cTnT protein [μ g mg ⁻¹ of total sarcomeric protein extract]	cTnT protein [μ g mg ⁻¹ tissue]
Microflow	WT	5.4 \pm 1.1	4.9 \pm 0.9	0.21 \pm 0.02
	AL KO	4.5 \pm 1.9	4.5 \pm 1.4	0.22 \pm 0.02
Direct injection nanoflow	WT	0.65 \pm 0.10	6.0 \pm 1.0	0.24 \pm 0.01
	AL KO	0.53 \pm 0.20	5.3 \pm 1.4	0.25 \pm 0.03
Preconcentration nanoflow	WT	0.14 \pm 0.03	6.5 \pm 1.4	0.28 \pm 0.02
	AL KO	0.12 \pm 0.04	6.1 \pm 1.7	0.30 \pm 0.03

4. Conclusions

This work established an optimal methodology for the extraction, isolation and absolute quantification of cardiac troponin T in the mouse heart. The developed procedures were successfully used to estimate the cTnT content in the heart of C57BL/6J WT and ApoE/LDLr KO mice. All the methods tested (microflow, direct injection nano- and preconcentration nanoflow LC/MS) offered adequate analytical quality, providing specific advantages of selectivity, sensitivity and quantification reliability, compared with published procedures/methodologies. Downscaling the microflow LC-MS/MS method to nanoflow resulted in a significant gain in

sensitivity while maintaining the accuracy and precision of the method. Nanochromatography with preconcentration offered further gain in sensitivity with complete elimination of matrix effect, but at the expense of longer separation time. The proposed methodology for absolute quantification of cTnT could be a good template when designing procedures for other targets in quantitative proteomics.

Acknowledgments

This study was supported by the European Union from the resources of the European Regional Development Fund under the Innovative Economy Program (a grant coordinated by JCET-UJ, No. POIG.01.01.02-00-069/09) and TEAM program of the Foundation for Polish Science (TEAM/2011-8/7).

References

- [1] D.A. Morrow, Cardiovascular Biomarkers: Pathophysiology and Disease Management, Humana Press, New Jersey, 2006.
- [2] K. Lewandrowski, A. Chen, J. Januzzi, Am. J. Clin. Pathol. 118 (Suppl.) (2002) S93–S99.
- [3] A.G. Katrukha, A.V. Bereznikova, T.V. Esakova, K. Pettersson, T. Lovgren, M.E. Severina, K. Pulkki, L.M. Vuopio-Pulkki, N.B. Gusev, Clin. Chem. 43 (1997) 1379–1385.
- [4] R. Labugger, J.A. Simpson, M. Quick, H.A. Brown, C.E. Collier, I. Neverova, J.E. Van Eyk, Clin. Chem. 49 (2003) 873–879.
- [5] H. Keshishian, T. Addona, M. Burgess, D.R. Mani, X. Shi, E. Kuhn, M.S. Sabatine, R.E. Gerszten, S.A. Carr, Mol. Cell. Proteomics 8 (2009) 2339–2349.

- [6] M. Bizzarri, C. Cavaliere, P. Foglia, C. Guarino, R. Samperi, A. Lagana, *Anal. Bioanal. Chem.* 391 (2008) 1969–1976.
- [7] C. Cavaliere, F. Cucci, C. Guarino, R. Gubbiotti, R. Samperi, A. Lagana, *Rapid Commun. Mass Spectrom.* 22 (2008) 1159–1167.
- [8] A.V. Edwards, M.Y. White, S.J. Cordwell, *Mol. Cell. Proteomics* 7 (2008) 1824–1837.
- [9] C. Napoli, A. Zullo, A. Picascia, T. Infante, F.P. Mancini, *J. Cell. Biochem.* 114 (2013) 7–20.
- [10] P. Sharma, J. Cosme, A.O. Gramolini, *J. Proteomics* 81 (2013) 3–14.
- [11] G. Liu, Q.C. Ji, R. Dodge, H. Sun, D. Shuster, Q. Zhao, M. Arnold, *J. Chromatogr. A* 1284 (2013) 155–162.
- [12] S. Gallien, E. Duriez, K. Demeure, B. Domon, *J. Proteomics* 81 (2013) 148–158.
- [13] M. Rauh, *J. Chromatogr. B* 883–884 (2012) 59–67.
- [14] O. Núñez, H. Gallart-Ayala, C.P.B. Martins, P. Lucci, R. Busquets, *J. Chromatogr. B* 927 (2013) 3–21.
- [15] L. Nováková, H. Vlčková, *Anal. Chim. Acta* 656 (2009) 8–35.
- [16] M. Bantscheff, S. Lemeer, M.M. Savitski, B. Kuster, *Anal. Bioanal. Chem.* 404 (2012) 939–965.
- [17] D.S. Kirkpatrick, S.A. Gerber, S.P. Gygi, *Methods* 35 (2005) 265–273.
- [18] D.C. Liebler, L.J. Zimmerman, *Biochemistry* 52 (2013) 3797–3806.
- [19] D. Domanski, A.J. Percy, J. Yang, A.G. Chambers, J.S. Hill, G.V. Freue, C.H. Borchers, *Proteomics* 12 (2012) 1222–1243.
- [20] E. Kuhn, T. Addona, H. Keshishian, M. Burgess, D.R. Mani, R.T. Lee, M.S. Sabatine, R.E. Gerszten, S.A. Carr, *Clin. Chem.* 55 (2009) 1108–1117.
- [21] M. Rezeli, A. Vegvari, F. Donnarumma, O. Gidlof, J.G. Smith, D. Erlinge, G. Marko-Varga, *J. Proteomics* 87 (2013) 16–25.
- [22] S.A. Agger, L.C. Marney, A.N. Hoofnagle, *Clin. Chem.* 56 (2010) 1804–1813.
- [23] N.R. Kitteringham, R.E. Jenkins, C.S. Lane, V.L. Elliott, B.K. Park, *J. Chromatogr. B* 877 (2009) 1229–1239.
- [24] I. van den Broek, W.M. Niessen, W.D. van Dongen, *J. Chromatogr. B Anal. Technol. Biomed. Life Sci.* 929 (2013) 161–179.
- [25] L.A. Kane, I. Neverova, J.E. Van Eyk, *Methods Mol. Biol.* 357 (2007) 87–90.
- [26] M. Kinter, N.E. Sherman, *The Preparation of Protein Digests for Mass Spectrometric Sequencing Experiments, Protein Sequencing and Identification Using Tandem Mass Spectrometry*, John Wiley & Sons, Inc., Hoboken, NJ, USA (2005) 147–165.
- [27] A.C. Davison, D.V. Hinkley, G.A. Young, *Stat. Sci.* 18 (2003) 141–157.
- [28] B.K. Matuszewski, M.L. Constanzer, C.M. Chavez-Eng, *Anal. Chem.* 75 (2003) 3019–3030.
- [29] B.K. Matuszewski, *J. Chromatogr. B Anal. Technol. Biomed. Life Sci.* 830 (2006) 293–300.
- [30] I. Neverova, J.E. Van Eyk, *Proteomics* 2 (2002) 22–31.
- [31] B.A. Stanley, I. Neverova, H.A. Brown, J.E. Van Eyk, *Proteomics* 3 (2003) 815–820.
- [32] R. Labugger, J.L. McDonough, I. Neverova, J.E. Van Eyk, *Proteomics* 2 (2002) 673–678.
- [33] A.M. Bland, L.R. D'Eugenio, M.A. Dugan, M.G. Janech, J.S. Almeida, M.R. Zile, J.M. Arthur, *J. Biomol. Tech.* 17 (2006) 195–199.
- [34] K. Lanckmans, A. Van Eeckhaut, S. Sarre, I. Smolders, Y. Michotte, *J. Chromatogr. A* 1131 (2006) 166–175.
- [35] H.D. Meiring, E. van der Heeft, G.J. ten Hove, A.P.J.M. de Jong, *J. Sep. Sci.* 25 (2002) 557–568.
- [36] M. Kranendijk, J.C. Waterval, G.W. Somsen, G.J. de Jong, *J. Sep. Sci.* 28 (2005) 1796–1802.
- [37] J. Abian, A.J. Oosterkamp, E. Gelpi, *J. Mass Spectrom.* 34 (1999) 244–254.
- [38] A. Schmidt, M. Karas, T. Dulcks, *J. Am. Soc. Mass Spectrom.* 14 (2003) 492–500.
- [39] M. Wilm, *Principles of electrospray ionization*, *Mol. Cell. Proteomics* 10 (2011) (M111.009407).
- [40] D. Tao, L. Zhang, Y. Shan, Z. Liang, Y. Zhang, *Anal. Bioanal. Chem.* 399 (2011) 229–241.
- [41] P.J. Taylor, *Clin. Biochem.* 38 (2005) 328–334.
- [42] E. Chambers, D.M. Wagrowski-Diehl, Z. Lu, J.R. Mazzeo, *J. Chromatogr. B Anal. Technol. Biomed. Life Sci.* 852 (2007) 22–34.
- [43] C. Cote, A. Bergeron, J.N. Mess, M. Furtado, F. Garofolo, *Bioanalysis* 1 (2009) 1243–1257.
- [44] A. Van Eeckhaut, K. Lanckmans, S. Sarre, I. Smolders, Y. Michotte, *J. Chromatogr. B Anal. Technol. Biomed. Life Sci.* 877 (2009) 2198–2207.
- [45] F. Gosetti, E. Mazzucco, D. Zampieri, M.C. Gennaro, *J. Chromatogr. A* 1217 (2010) 3929–3937.
- [46] A.K. Hewavitharana, *J. Chromatogr. A* 1218 (2011) 359–361.
- [47] M. Yadav, V. Trivedi, V. Upadhyay, G. Shah, G.A. Baxi, S. Goswami, P.S. Shrivastav, *J. Chromatogr. B Anal. Technol. Biomed. Life Sci.* 885–886 (2012) 138–149.
- [48] C. Lowbeer, A.M. Forsberg, S. Tokuno, A.L. Hemdahl, S.A. Gustafsson, G. Valen, *Clin. Chim. Acta* 344 (2004) 73–78.



Enzymatic amplification detection of peanut allergen Ara h1 using a stem-loop DNA biosensor modified with a chitosan-mutiwalled carbon nanotube nanocomposite and spongy gold film



Xiulan Sun^{a,*}, Min Jia^a, Jian Ji^a, Lu Guan^a, Yinzhi Zhang^a, Lili Tang^a, Zaijun Li^b

^a State Key Laboratory of Food Science and Technology, School of Food Science of Jiangnan University, Synergetic Innovation Center of Food Safety, Wuxi 214122, Jiangsu, China

^b School of Chemical and Material Engineering of Jiangnan University, Wuxi 214122, Jiangsu, China

ARTICLE INFO

Article history:

Received 14 April 2014

Received in revised form

24 July 2014

Accepted 26 July 2014

Available online 14 August 2014

Keywords:

Electrochemical biosensor

Stem-loop probe

Chitosan-mutiwalled carbon nanotube

nanocomposite

Spongy gold film

Peanut allergen

Arachis hypogaea allergen 1 (Ara h1)

ABSTRACT

In this paper, a highly sensitive biosensor was constructed for peanut allergen Ara h1 detection. The biosensor was constructed by coating a glassy carbon electrode with a chitosan-mutiwalled carbon nanotube nanocomposite and then adding a spongy gold film via electro-deposition to increase the effective area. The probe switched from an “on” to an “off” state in the presence of target DNA, which detached biotin from the electrode surface. This also detached streptavidin–horseradish peroxidase (HRP-SA), which was bound to the electrode via specific interaction with biotin. The HRP-SA catalyzed chemical oxidation of hydroquinone by H₂O₂ to form benzoquinone, and when it was detached, electrochemical reduction of the signal of benzoquinone could be used to monitor DNA hybridization via chronoamperometry. Under optimum conditions, a wide dynamic detection range (3.91×10^{-17} – 1.25×10^{-15} mol L⁻¹) and a low detection limit (1.3×10^{-17} mol L⁻¹) were achieved for the complementary sequence. Furthermore, the DNA biosensor exhibited an excellent ability to discriminate between a complementary target and a one-base mismatch or non-complementary sequence. The sensor was successfully applied to Ara h1 analysis in peanuts.

© 2014 Elsevier B.V. All rights reserved.

1. Introduction

Electrochemical DNA biosensors have been widely used for specific gene sequences detection because of their unique advantages such as low-cost, rapid response, simplicity, good selectivity and high sensitivity [1,2]. Currently, the electrochemical DNA biosensor has played a major role in food safety [3], genetic disorders [4], biological research [5] and environmental monitoring [6]. Various sensing strategies have been proposed for detection of specific DNA sequences, with the aim of improving the sensitivity and selectivity of the biosensor.

The construction of an electrochemical DNA biosensor usually involves two critical steps: immobilization of probe DNA on the transducer and electrochemical signal amplification. To date, different kinds of strategies have been exploited to enhance the immobilization amount of probe DNA [7–9]. Including which, nano-materials have received increasing attention in electrode surface modification for DNA biosensor, owing to their unique physical and chemical properties of high surface area, favorable

electronic properties, electrocatalytic activity and good biocompatibility [10–14]. The construction of nanostructure-modified electrode for DNA detection with high sensitivity is highly desirable. A new era in the field of nanotechnology has begun with the discovery of carbon nanotubes (CNTs) by Iijima [15]. As one kind of CNTs, multi-wall carbon nanotubes (MWCNTs) show ultrahigh electrocatalysis capacity and surface area effects in biosensing analysis [16]. MWCNTs can be employed to bind with DNA through covalent bond or electrostatic attraction [17]. However, lack of stability and uniformity of MWCNTs directly immobilized onto the electrode surface without other reagents is the major challenge to their use as modifiers in the fabrication of biosensors. Then, chitosan which possesses distinct chemical and biological properties was employed to disperse MWCNTs [18,19]. The advantages of using MWCNTs for electrode surface modification in the development of new designs of electrochemical sensors have been recently highlighted by many authors. Wang et al. [20] reported an electrochemical DNA (E-DNA) biosensor based on a CNT and polypyridyl copper complex for the detection of the PAT gene. Chung et al. [21] developed an E-DNA sensor modified with ionic liquid-multiwalled CNTs (IL-MWNTs) for ultrasensitive DNA sequence-specific detection of *Salmonella typhi*. Recently, gold nanoparticles have been widely applied in the fabrication of

* Corresponding author. Tel./fax: +86 510 85328726.

E-mail address: xlzjzz@jiangnan.edu.cn (X. Sun).

biosensors because these sensors are simple to prepare, relatively inexpensive, and provide huge interfaces for biomolecule detection. To date, simple electro-deposition has been widely used for preparation of gold nanoparticles [22]. Different morphologies of the gold nanostructures have been obtained by electro-deposition, including spherical [23], flower-like [24] and dendritic [25]. In DNA sequence detection, the MWCNTs and gold nanoparticles were introduced in this work can act as the immobilizing carrier to increase the immobilization amount of the DNA probe, and as the signal particle to magnify the detection signal and lower the detection limit.

From the previous reports, enzyme amplification technology in electrochemical methods plays an important role in the sensitive determination of DNA [26–28]. Horseradish peroxidase (HRP), as an enzymatic label, is generally immobilized using streptavidin–biotin in a stem-loop probesystem [29–31]. To enhance the sensitivity, improve the selectivity, and reduce the detection limit and cost, electrochemical biosensors based on enzymatic signal amplification have been investigated to detect DNA. For example, Meng et al. [32] built an enzyme-based E-DNA sensor for sensitive detection of DNA with a low detection limit of 6.0 pmol L^{-1} ($S/N=3$). Yin et al. [23] constructed a highly sensitive biosensor for sequence specific miRNA-21 detection based on dendritic gold nanostructure, graphene nano-sheets and a HRP labeling amplification strategy. The biosensor showed excellent selectivity and high sensitivity with a low detection limit of 0.06 pmol L^{-1} . Additionally, it has been reported that stem-loop DNA can amplify the electrochemical signal. Several biosensors based on stem-loop DNA have been developed with good performance, such as for *Pseudomonas aeruginosa* 16S rRNA detection in compost [33], sensitive and portable detection of RNA mutations [34], and adenosine-5'-triphosphate detection in *Escherichia coli* O157:H7 in water samples [35]. Significantly, stem-loop probes inherently possess high specificity because of their conformational constraints, and thus are superior to linear probes for DNA detection [36,37].

In this work, a promising enzyme-based DNA biosensor was developed for detection of the peanut allergen Ara h1. To improve the sensitivity of the biosensors, chitosan (CS)–MWCNT nanocomposite (CS–MWCNT) and spongy gold film were used as the probe immobilization platform. The CS–MWCNT was coated on an electrode, followed by spongy gold film via simple electro-deposition to increase the effective area. A stem-loop probe dually labeled with 3'-thiol and 5'-biotin was assembled on the spongy gold film/CS–MWCNT/GCE via a thiol–Au interaction. The results showed that the CS–MWCNT nanocomposite and spongy gold film could effectively immobilize the captured DNA probe and promote electron transfer kinetics of the foreign molecules. Next, HRP was immobilized through conjugation between biotin of the stem-loop probe and streptavidin for enzyme amplification. When the target DNA was captured by the probe, conformation of the stem-loop structure changed to trigger a specific interaction between biotin and streptavidin HRP on the electrode surface. Thus, the target was quantified via electrochemical detection of the enzymatic product in the presence of substrate. The electrochemical DNA biosensor based on gold film/CS–MWCNT/GCE could be used for recognition of target DNA using the stem-loop DNA as the capture probe for hybridization with Ara h1 in food.

2. Experimental

2.1. Materials and chemicals

All synthetic oligonucleotides were purchased from Sangon Biotech Co., Ltd. (Shanghai, China). The sequences of the oligonucleotides used

in this work are given in Table S1. The stem-loop probes, dually labeled with 3'-thiol and 5'-biotin, contained a stem of complementary 6 bp segments and a loop recognition sequence complementary to a 24 bp segment of Ara h1. Gold chloride tetrahydrate ($\text{HAuCl}_4 \cdot 4\text{H}_2\text{O}$) and 6-mercaptophexanol (MCH) were obtained from Sigma-Aldrich Inc. (St. Louis, MO). Mutiwalled carbon nanotubes were provided by XFANO Co., Ltd. (Nanjing, China). BSA and streptavidin–horseradish peroxidase (HRP-SA) were obtained from BOYAO Biotech Co., Ltd. (Shanghai, China). Chitosan (CS) and other chemicals were obtained from Sinopharm Chemical Reagent Co., Ltd. (Beijing, China). The solutions used in the experiments were prepared with ultrapure water (Milli-Q 18.2 $\text{M}\Omega \text{ cm}$, Millipore Co., Billerica, MA).

2.2. Apparatus

Electrochemical measurements were performed at room temperature using a CHI760C electrochemical workstation (Shanghai Chenhua Instrument Co., Ltd., Yangpu, China). A conventional three-electrode cell was employed, and included a glassy carbon working electrode ($\phi 2 \text{ mm}$), a platinum wire counter electrode, and a saturated Ag/AgCl reference electrode. Potentials were determined with respect to the reference electrode. All spectra were measured in phosphate buffer (0.1 mol L^{-1} phosphate, pH 7.0) containing 0.1 mol L^{-1} KCl and 2.5 mmol L^{-1} $\text{Fe}(\text{CN})_6^{3-/4-}$ as a redox couple. All experiments were performed at least three times to ensure the consistency of the response. A S4800 type scanning electron microscope (Hitachi, Japan) and a C1000 thermal PCR cyler (Bio-Rad, America) were used.

2.3. Preparation of the electrode

Before use, the working GCE was etched with piranha solution ($\text{H}_2\text{SO}_4/\text{H}_2\text{O}_2$, 7/3 v/v) for 15 min and rinsed with ultrapure water. Next, the bare GCE was sequentially polished with 0.3 and 0.05 μm alumina powder on a microfiber cloth to obtain a mirror-like surface, and then by ultrasonic cleaning with ethanol and ultrapure water for 3 min. Subsequently, the electrode was dried thoroughly under a N_2 stream.

2.4. Construction of the E-DNA sensor

It is well known that carbon nanotubes are not easy to dissolve, which limits their application in biosensors. As a polysaccharide biopolymer, CS is widely used in sensors because of its numerous advantages, including excellent film forming ability, high permeability, and good dispersion of carbon nanotubes [38,39]. To enhance the electrical conductive properties and specific surface area of the biosensor, chitosan were doped into the MWNT to form a CS–MWNT nanocomposite. Purified MWCNTs (5 mg) was put into 5 mL of 2% acetic acid containing 5 mg of CS, and the mixture was treated with ultrasonication for 2 h. Then, 4 mL of the CS–MWNT dispersion was dropped onto a prepared GCE and dried under an infrared lamp. Afterwards, the electrode was washed with PBS buffer and dried thoroughly under a N_2 stream. This produced a CS–MWCNT modified GCE (CS–MWCNT/GCE). Spongy gold film was electrodeposited on the CS–MWCNT/GCE surface via amperometry (-0.25 V for 600 s) in a 3 mmol L^{-1} HAuCl_4 solution containing 0.1 mol L^{-1} KNO_3 . The obtained electrode was named a spongy gold film/CS–MWCNT/GCE.

Immobilization of the stem-loop probe was accomplished by dropping $4 \mu\text{L}$ of $1 \mu\text{mol L}^{-1}$ stem-loop probe solution onto the surface of the spongy gold film/CS–MWCNT/GCE and incubating at $4 \text{ }^\circ\text{C}$ for 12 h. The modified electrode was then thoroughly rinsed with PBS to remove any excess probe. Then, $10 \mu\text{L}$ of PBS buffer containing 10 mmol L^{-1} MCH was dropped onto the electrode surface for 30 min to block any remaining bare regions. Finally, the

electrode was washed with PBS to remove residual MCH. The electrode was stored at 4 °C until use. The preparation of the electrochemical DNA biosensor is illustrated in Scheme 1.

2.5. Hybridization and detection

Hybridization experiments were performed by dropping 4 μL of different concentrations of complementary target DNA onto the probe/spongy gold film/CS–MWCNT/GCE. This was followed by incubation at 37 °C for 30 min to yield complementary target DNA–probe/spongy gold film/CS–MWCNT/GCE. Unhybridized target DNA on the electrode was removed by rinsing the electrode with PBS buffer (pH 7.4). Subsequently, the electrode was immersed in 1% BSA solution for 30 min to cover the active site. The electrode was then washed and dried under a stream of N_2 . After that, 8 μL of 10 $\mu\text{g mL}^{-1}$ streptavidin–HRP was added to the modified electrode and incubated at room temperature for 30 min. Before using the electrode, unspecific immobilized streptavidin–HRP was washed with PBS. Hybridization of the probe/spongy gold film/CS–MWCNT/GCE with single-base mismatch and non-complementary sequences followed the same protocol as above.

All the electrochemical measurements were performed at room temperature using a CHI760C electrochemical work station. Cyclic voltammetry (CV) was performed in PB buffer (pH 7.0) containing 0.1 mol L^{-1} KCl and 2.5 mmol L^{-1} $\text{Fe}(\text{CN})_6^{3-/4-}$. The CV experimental parameters were as follows: scan rate, 0.1 V s^{-1} ; initial potential, 0.6 V; high potential, 0.6 V; and low potential, -0.2 V. CV and chronoamperometry were performed in a working solution of 0.1 mol L^{-1} PBS (pH 7.4) containing 1.0 mmol L^{-1} H_2O_2 and 0.2 mmol L^{-1} hydroquinone with an applied potential of -0.2 V for chronoamperometry and a scan rate of 0.1 V s^{-1} in the potential range from -0.5 to 0.6 V.

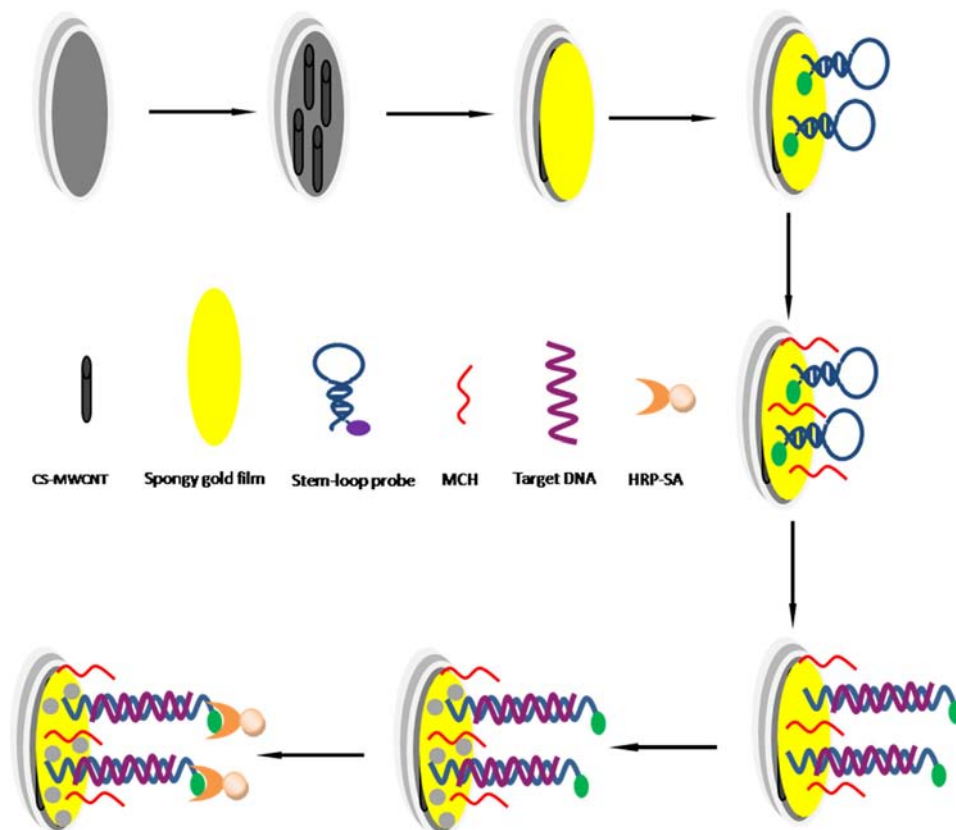
2.6. Detection of the peanut allergen Ara h1 gene in peanuts

The E-DNA sensor was tested in application to detect the Ara h1 gene in peanuts purchased from a local supermarket. The CTAB-based method was used for extracting DNA from the peanut [40]. After the DNA was extracted, PCR amplification was used to amplify the extracted DNA. A 7.5% PAGE was used to identify the Ara h1 gene in the PCR products. A 125 bp region in the Ara h1 gene (GenBank no. AF432231) was the target segment for PCR amplification. The loop sequence of the probe (Oligo 1) used in this study was the conserved sequence of the 125 bp region. The sequences of the upstream primer and the downstream primer are shown in Table S1 (Supporting information). The amplification protocol was as follows: 10 min at 95 °C, followed by 30 cycles at 95 °C for 30 s, 60 °C for 40 s, and 72 °C for 60 s. The reaction system was further incubated for 10 min at 72 °C to completely extend any incomplete products. After confirming the Ara h1 gene was extracted from the peanuts, the biosensor was used to extract genome DNA. Fluorescence real-time quantitative PCR was used to authenticate the test results from the DNA biosensor. Then the extracted genome DNA was also detected using this fluorescence real-time quantitative PCR system.

3. Results and discussion

3.1. Fabrication of the sensor

The stem-loop probe specific to the Ara h1 gene had six complementary bases at its 5' and 3' ends (five of them are G–C pairs), and the DNA strand was closed by thermostable G–C pairs to form a stem-loop. The stepwise fabrication process of the DNA



Scheme 1. The schematic diagram of fabricating the stem-loop DNA biosensor of amplifying signal by enzyme catalysis.

biosensor is shown in Scheme 1. The sensor was constructed by immobilizing CS–MWCNT on the GCE surface, and then the spongy gold film was electrodeposited on the CS–MWCNT surface. Through facile gold–thiol affinity, the probe labeled with 5′-SH was assembled on the surface of the spongy gold film/CS–MWCNT/GCE. Then, the electrode surface was blocked using MCH to decrease any non-specific adsorption of undesirable material to the modified electrode surface. In the absence of the target, the immobilized stem-loop probe was in the “closed” state, locating the biotin unit at the 3′ end in proximity to the electrode surface. Then, the added target hybridized with the stem-loop probe, bringing about a conformational change of the probe. This put the stem-loop probe in the “open” state, and favored formation of the more thermodynamically stable rigid target–probe duplex. Then, biotin was detached from the electrode surface. The BSA was added to block protein non-specific adsorption sites on the modified electrode surface. Because of the affinity interaction between biotin and streptavidin, the HRP–SA bonded with the detached biotin. Because of HRP catalysis, the redox signal of H_2O_2 can be measured from changes in the current and potential signal.

3.2. Characterization of the CS–MWCNT and spongy gold film

Transmission electron microscopy of the CS–MWCNTs (Fig. 1A) showed the MWCNTs were consistent in length and thickness, and were uniformly dispersed in the chitosan solution. These properties

would facilitate electron transfer. Scanning electron microscopy of the spongy gold film (Fig. 1B) showed the gold nanoparticles had a dense structure like a porous sponge. The gold nanoparticles were distributed uniformly and orderly on the electrode surface, and provided fixed sites for the stem-loop probe.

3.3. Electrochemical behavior of the modified electrodes

The modified electrode was characterized in $\text{Fe}(\text{CN})_6^{3-/4-}$ buffer. As shown in Fig. 2A, compared with the bare GCE (curve a), the peak current of the CS–MWCNT/GCE (curve b) and spongy gold film/CS–MWCNT/GCE (curve c) increased gradually, while the peak-to-peak separation decreased. These results indicate that because of the high electron transfer rate of the MWCNT for catalysis of the redox reaction, when the GCE was modified by CS–MWCNT, the peak current increased. When highly conductive gold nanoparticles were distributed densely on the surface of CS–MWCNT/GCE as a spongy gold film, the conductivity and electrocatalytic activity of the modified electrode improved. Consequently, the peak current increased further. After the stem-loop probes were assembled on the spongy gold film/CS–MWCNT/GCE, the peak current decreased (curve d), which indicates that the probes were successfully immobilized on the modified electrode surface. Because the stem-loop probe occupied a large area on the modified electrode surface, the electrode could not efficiently exchange electrons with the solution, and this reduced the electron-transfer efficiency of the electrode. After immobilization of MCH, the

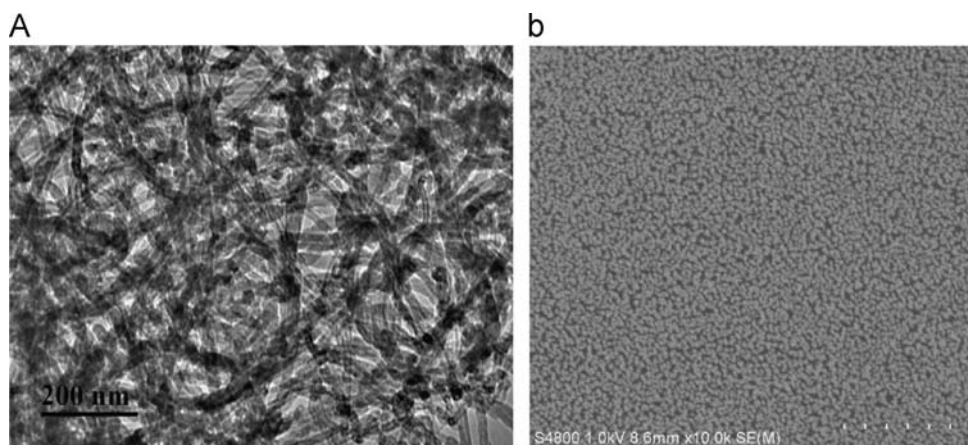


Fig. 1. The TEM photo of CS–MWCNT (A) and SEM photo of spongy gold film (B).

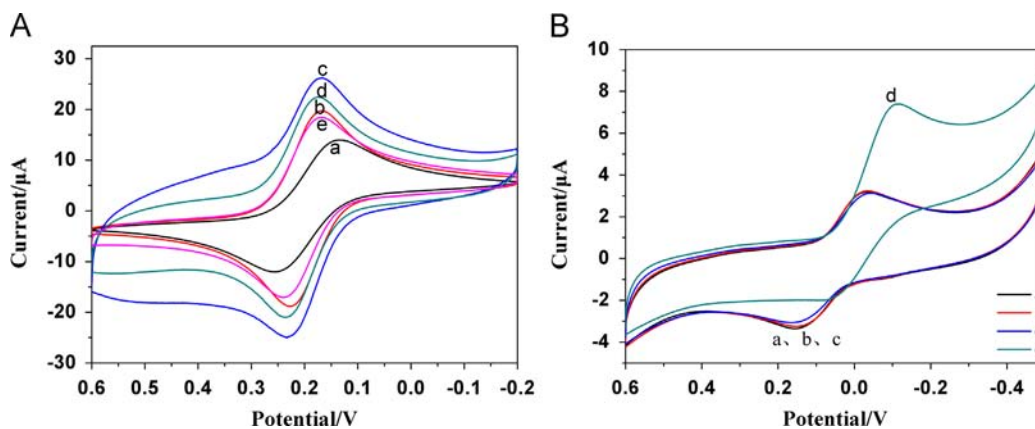


Fig. 2. The characterization of CV in the progress of electrode's modification in the $\text{Fe}(\text{CN})_6^{3-/4-}$ buffer (A) and characterization of CV in the progress of hybridization in the buffer containing H_2O_2 and hydroquinone (B). In figure (A), a: GCE, b: CS–MWCNT/GCE, c: spongy gold film/CS–MWCNT/GCE, d: probe/spongy gold film/CS–MWCNT/GCE, e: MCH/probe/spongy gold film/CS–MWCNT/GCE. In figure (B), a: MCH/probe/spongy gold film/CS–MWCNT/GCE, b: target DNA/MCH/probe/spongy gold film/CS–MWCNT/GCE, c: BSA/target DNA/MCH/probe/spongy gold film/CS–MWCNT/GCE, d: HRP–SA/BSA/target DNA/MCH/probe/spongy gold film/CS–MWCNT/GCE.

effective area of the modified electrode reduced and the peak current decreased further (curve e).

The hybridization was characterized in buffer containing H_2O_2 and hydroquinone. As shown in Fig. 2B, the CVs of the MCH/stem-loop probe/spongy gold film/CS-MWCNT/GCE (curve a), target DNA/MCH/stem-loop probe/spongy gold film/CS-MWCNT/GCE (curve b), and BSA/target DNA/MCH/stem-loop probe/spongy gold film/CS-MWCNT/GCE (curve c) were almost the same, and the redox peak positions and peak currents showed no remarkable differences. However, when HRP-SA was attached to the surface of BSA/target DNA/MCH/stem-loop probe/spongy gold film/CS-MWCNT/GCE, the reductive peak current increased sharply, and redox peak-to-peak separation decreased. This indicated that the benzoquinone were produced by oxidation of hydroquinone by H_2O_2 via the catalytic action of HRP, and the benzoquinone was reduced back to hydroquinone which greatly increased the reduction peak current of the benzoquinone.

3.4. Quantification of target DNA

In this study, chronoamperometry was used to examine the sensitivity of the prepared electrochemical DNA biosensor. The chronoamperometry current was measured in 0.1 mol L^{-1} PB (pH 7.0) containing 1 mmol L^{-1} H_2O_2 and 0.2 mmol L^{-1} hydroquinone. As shown in Fig. 3, the current increased gradually as the target DNA concentration increased from 3.91×10^{-17} to $1.25 \times 10^{-15} \text{ mol L}^{-1}$. The inset of Fig. 3 shows the change in the measured current (I) as a function of the target concentration (C). There was a linear relationship between the current and the logarithm of target concentration, with a regression equation of

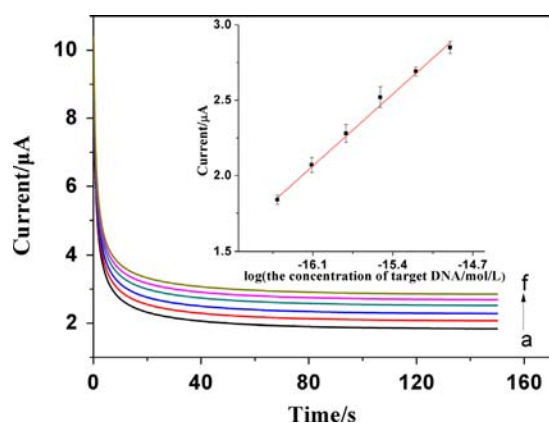


Fig. 3. The chronoamperometry curve and standard curve of hybridization of DNA biosensor with target DNA with different concentrations (a–f: 3.91×10^{-17} , 7.81×10^{-17} , 1.56×10^{-16} , 3.13×10^{-16} , 6.25×10^{-16} , $1.25 \times 10^{-15} \text{ mol L}^{-1}$).

$I = 0.6756 \log C + 12.953$ and a correlation factor of 0.9943. The detection limit calculated using three times the standard deviation of the background signal was $1.3 \times 10^{-17} \text{ mol L}^{-1}$. The performance of this biosensor was compared with that published in similar work (Table 1). The present DNA sensor had good analytical performance for DNA detection with the target sequences.

3.5. Selectivity of the DNA biosensor

The selectivity of the DNA biosensor was investigated, and the results are shown in Fig. 4. The prepared sensor was hybridized with various DNA sequences (complementary oligonucleotides, one base mismatch oligonucleotides and non-complementary oligonucleotides), and then the chronoamperometry current was measured. As Fig. 4 shows, compared with the current of MCH/stem-loop probe/spongy gold film/CS-MWCNT/GCE (curve a), the current obtained following hybridization with the non-complementary oligonucleotides (curve b) was almost the same. The current obtained following hybridization with the one-base mismatch oligonucleotides (curve c) was slightly higher. After hybridization with the complementary oligonucleotides (curve d), the current increased obviously. This result indicates that the immobilized stem-loop probes react only slightly with the one base mismatch and non-complementary oligonucleotides, and complete hybridization does not occur because of the base mismatch. In other words, the prepared DNA biosensor has excellent selectivity for detection of target DNA sequences, which means the ability of the DNA biosensor to discriminate between non-complementary or single-base mismatch oligonucleotides and complementary oligonucleotides are remarkable.

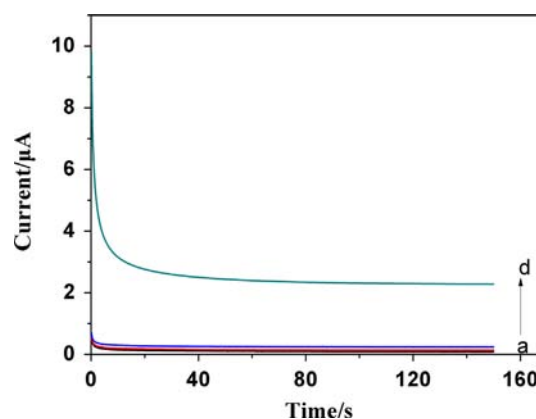


Fig. 4. The chronoamperometry curve of MCH/stem-loop probe/spongy gold film/CS-MWCNT/GCE (a) hybridization with non-complementary sequence (b), single mismatched sequence (c) and complementary target sequence (d), then reaction with SA-HRP.

Table 1
Comparison of linear ranges and detection limits of several electrochemical DNA sensors.

Layers for DNA immobilization	Detection limit (nmol L^{-1})	Linear range (mol L^{-1})	Reference
AuNPs/pThion/graphene/GCE ^a	0.035	1.0×10^{-8} – 1.0×10^{-13}	[41]
PANI/AuNPs/GSPE ^b	0.1	1.0×10^{-8} – 2.0×10^{-8}	[42]
AuNPs/PANI/CS-GS/GCE ^c	2.11×10^{-3}	1.0×10^{-9} – 1.0×10^{-11}	[43]
PANIw/graphene/GCE ^d	3.25×10^{-8}	2.12×10^{-6} – 2.12×10^{-12}	[44]
Spongygoldfilm/CS-MWCNT/GCE ^e	4.1×10^{-8}	3.91×10^{-17} – 1.25×10^{-15}	This work

^a AuNPs/pThion/graphene/GCE: GCE modified with gold nanoparticles, polythionine, and graphene.

^b PANI/AuNPs/GSPE: graphite screen-printed electrode modified with polyaniline film and gold nanoparticles.

^c AuNPs/PANI/CS-GS/GCE: gold nanoparticles, PANI layer (polymerization of aniline), chitosan-graphenemodified GCE.

^d PANIw/graphene/GCE: graphene and polyaniline nanowires modified GCE.

^e Spongygoldfilm/CS-MWCNT/GCE: chitosan-multiwalled carbon nanotubes nanocomposite and spongy gold film modified GCE.

3.6. Optimization of experimental conditions

Analytical performance by this new electrode was optimized by investigating the effects of some important detection parameters, including deposition time of gold nanoparticles, probe concentration during immobilization and hybridization time and temperature. In order to improve determination sensitivity for Ara h1 the effect of deposition time on peak current were investigated by the differential pulse voltammogram (DPV). It was observed that the peak current increased obviously as deposition time increases from 200 to 600 s (Fig. S1). When the time increased to 800 and 1000 s the current value increased slightly or not at all. Thus, we chose 600 s as the optimal deposition time for this work.

The effect of probe concentration, hybridization time and temperature was estimated by chronoamperometry. The reduction peak current of benzoquinone was investigated. It showed that the signal increased as the probe concentration increased from 10^{-9} to 10^{-5} M, with the maximum value at 10^{-6} M (Fig. S2). As the DNA probe concentration increased, more probe material was immobilized on the electrode until saturation adsorption. Many studies have shown that hybridization temperature is related to the T_m of the probe and the optimal hybridization temperature considered being at 25 °C lower than the T_m . In the present study, the DNA probe T_m was 74.61 °C and the theoretical optimal hybridization temperature thus under 50 °C. Therefore, the temperature was analyzed at three levels (27, 37, 47 °C). Fig. S3 shows the effects of hybridization time and temperature on the reduction current of benzoquinone. It was observed the hybridization of DNA reached to the highest within 20 min at 47 °C, with time extending the current signal increasingly only slightly or not at all. It may be explained higher temperatures significantly affect the hairpin dynamics, which is reflected in increased sensor sensitivity. When hybridization temperature were 27 and 37 °C, the current value increased to the highest at 30 min. Then the current changed slightly during longer times. Moreover, compared to 27 °C the reduction current is higher at 37 °C. Thus, we choose 37 °C, 30 min as the optimal hybridization conditions for the following experiment.

3.7. Stability of the DNA biosensor

Because of the activity of streptavidin and HRP, the stability of the DNA biosensor was evaluated over a 10 day period. The HRP-SA/BSA/target DNA/MCH/stem-loop probe/spongy gold film/CS-MWCNT/GCE were stored in 10 mmol L^{-1} PBS buffer (pH 7.4) at 4 °C for 10 days. After this time, the chronoamperometry current of the sensor decreased to 80.62% of its initial response. This indicated that the stability of the developed DNA biosensor would be greatly affected by the activity of streptavidin and HRP.

3.8. Detection of the peanut allergen Ara h1 in peanuts

With the high sensitivity and selectivity, the biosensor could detect Ara h1 residues directly in foods. In this study, a PCR study confirmed the successful extraction of the Ara h1 gene from peanuts. After the extracted genome DNA from the peanuts was amplified by PCR, the products were detected by gel electrophoresis with 7.5% PAGE. In Fig. S4, the bands in the rightmost lane were markers, and the bands in the left three lanes were amplified DNA. The 125 bp band was the amplified target strip.

After the extracted genome DNA was incubated in a 95 °C water bath for 10 min, it was diluted to different concentrations for hybridization with the MCH/stem-loop probe/spongy gold film/CS-MWCNT/GCE. Then after the hybridized electrode was blocked with BSA, and bonded to HRP-SA, the chronoamperometry current was measured. The concentration of Ara h1 gene in the peanuts was calculated as $(2.74 \pm 0.11) \times 10^{-11} \text{ mol L}^{-1}$.

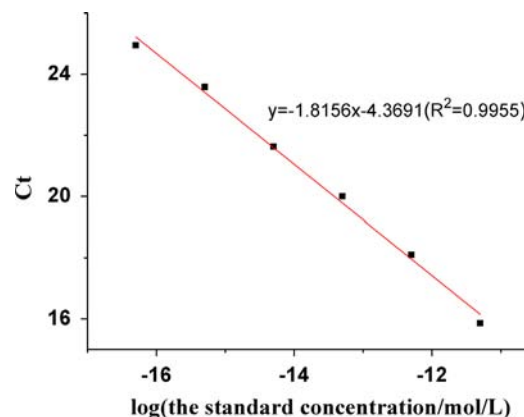


Fig. 5. The standard curve of real-time quantitative PCR.

We also used a fluorescence real-time quantitative PCR method to authenticate the test results obtained with the DNA biosensor. As Fig. 5 shows, a linear relationship existed between the Ct value and the logarithm of the standard concentration from 5×10^{-17} to $5 \times 10^{-12} \text{ mol L}^{-1}$ with a regression equation of $Ct = -1.8156 \log C - 4.3691$ and a correlation factor of 0.9955. Then the extracted genome DNA was also detected using this fluorescence real-time quantitative PCR system. The concentration of Ara h1 gene in the peanuts was $(2.88 \pm 0.05) \times 10^{-11} \text{ mol L}^{-1}$. The two results were consistent, which indicates that the developed DNA biosensor is reliable for sample detection. However, the relative standard deviation shows the electrochemical sensing method is less stable than fluorescence quantitative PCR method.

4. Conclusions

We developed a novel electrochemical DNA biosensor using CS-MWNTs, spongy gold film, and an immobilized stem-loop probe that was dually labeled with 5'-SH and 3'-biotin. The DNA biosensor showed high sensitivity, with a detection limit of $0.013 \text{ fmol L}^{-1}$. The DNA biosensor had excellent selectivity for the detection of target DNA sequences. In addition, the proposed DNA biosensor was also beneficial for the analysis of peanut DNA extracts. The concentration of the Ara h1 gene in the peanuts tested was $(2.74 \pm 0.11) \times 10^{-11} \text{ mol L}^{-1}$, which is consistent with fluorescence real-time quantitative PCR results. It is expected that the proposed electrochemical assay using the newly developed electrochemical DNA biosensor will be widely applied in the clinical diagnosis of peanut allergens and in food safety.

Acknowledgments

This work has been supported by National research program (no. 2011BAK10B03), "973" National Basic Research Program of China (no. 2012CB720804), Commonwealth project of the Ministry of Agriculture (no. 201203069-1), synergetic Innovation Center Of Food Safety and quality control, the project of QingLan, and Priority Academic Program Development of Jiangsu Higher Education Institutions.

Appendix A. Supporting information

Supplementary data associated with this article can be found in the online version at <http://dx.doi.org/10.1016/j.talanta.2014.07.078>.

References

- [1] P. Du, H. Li, Z. Mei, S. Liu, *Bioelectrochemistry* 75 (2009) 37–43.
- [2] J.O. Katherine, J.J. Gooding, *Analyst* 132 (2007) 603–610.
- [3] L. Wang, Q. Wei, C. Wu, Z. Hu, J. Ji, P. Wang, *Chin. Sci. Bull.* 53 (2008) 1175–1184.
- [4] L. Alfonta, A. Bardea, O. Khersonsky, E. Katz, I. Willner, *Biosens. Bioelectron.* 16 (2001) 675–687.
- [5] C. LÜ, T.-F. Kang, L.-P. Lu, Y. Xiong, *Chin. J. Anal. Chem.* 40 (2012) 1822–1826.
- [6] W. Hui, L. Bingling, L. Jing, D. Shaojun, W. Erkang, *Nanotechnology* 19 (2008) 095501.
- [7] S.-f. Liu, Y.-f. Li, J.-r. Li, L. Jiang, *Biosens. Bioelectron.* 21 (2005) 789–795.
- [8] D. Brassard, L. Clime, K. Li, M. Geissler, C. Miville-Godin, E. Roy, T. Veres, *Lab Chip* 11 (2011) 4099–4107.
- [9] H.O. Ham, Z. Liu, K. Lau, H. Lee, P.B. Messersmith, *Angew. Chem.* 123 (2011) 758–762.
- [10] S. He, B. Song, D. Li, C. Zhu, W. Qi, Y. Wen, L. Wang, S. Song, H. Fang, C. Fan, *Adv. Funct. Mater.* 20 (2010) 453–459.
- [11] L. Lin, Y. Liu, L. Tang, J. Li, *Analyst* 136 (2011) 4732–4737.
- [12] A. Bonanni, M. Del Valle, *Anal. Chim. Acta* 678 (2010) 7–17.
- [13] A. Chen, S. Chatterjee, *Chem. Soc. Rev.* 42 (2013) 5425–5438.
- [14] G.-j. Li, L.-h. Liu, X.-w. Qi, Y.-q. Guo, W. Sun, X.-l. Li, *Electrochim. Acta* 63 (2012) 312–317.
- [15] S. Iijima, *Nature* 354 (1991) 56–58.
- [16] M.E. Ghica, R. Pauliukaite, O. Fatibello-Filho, C.M.A. Brett, *Sens. Actuators, B* 142 (2009) 308–315.
- [17] J. Li, Q. Liu, Y.J. Liu, S.C. Liu, S.Z. Yao, *Anal. Biochem.* 346 (2005) 107–114.
- [18] Q. Zhang, X. Chen, F. Tu, C. Yao, *Biosens. Bioelectron.* 59 (2014) 377–383.
- [19] V.K. Rana, S. Akhtar, S. Chatterjee, S. Mishra, R.P. Singh, C.S. Ha, J. Nanosci. *Nanotechnol.* 14 (2014) 2425–2435.
- [20] Q. Wang, J. Shi, J. Ni, F. Gao, F. Gao, W. Weng, K. Jiao, *Electrochim. Acta* 56 (2011) 3829–3834.
- [21] D.-J. Chung, A.K. Whittaker, S.-H. Choi, *J. Appl. Polym. Sci.* 126 (2012) E28–E33.
- [22] S. Liu, J. Liu, L. Wang, F. Zhao, *Bioelectrochemistry* 79 (2010) 37–42.
- [23] L. Lin, A. Liu, C. Zhao, S. Weng, Y. Lei, Q. Liu, X. Lin, Y. Chen, *Biosens. Bioelectron.* 42 (2013) 409–414.
- [24] Y. Zheng, Z. Huang, C. Zhao, S. Weng, W. Zheng, X. Lin, *Microchim. Acta* 180 (2013) 537–544.
- [25] H. Yin, Y. Zhou, H. Zhang, X. Meng, S. Ai, *Biosens. Bioelectron.* 33 (2012) 247–253.
- [26] S. Niu, Y. Jiang, S. Zhang, *Chem. Commun.* 46 (2010) 3089–3091.
- [27] Y. Zhang, Z. Tang, J. Wang, H. Wu, A. Maham, Y. Lin, *Anal. Chem.* 82 (2010) 6440–6446.
- [28] W. Gao, H. Dong, J. Lei, H. Ji, H. Ju, *Chem. Commun.* 47 (2011) 5220–5222.
- [29] A. Upadhyay, T.-W. Ting, S.-M. Chen, *Talanta* 79 (2009) 38–45.
- [30] R. Akter, M.A. Rahman, C.K. Rhee, *Anal. Chem.* 84 (2012) 6407–6415.
- [31] X. Mao, J. Jiang, X. Xu, X. Chu, Y. Luo, G. Shen, R. Yu, *Biosens. Bioelectron.* 23 (2008) 1555–1561.
- [32] X. Meng, M. Xu, J. Zhu, H. Yin, S. Ai, *Electrochim. Acta* 71 (2012) 233–238.
- [33] B. Bockisch, T. Grunwald, E. Spillner, R. Bredehorst, *Nucleic Acids Res.* 33 (2005) e101 (e101).
- [34] Y.-J. Zheng, Z.-J. Huang, J. Chen, K. Wang, A.-L. Liu, X.-H. Lin, W. Zheng, *Sens. Actuators, B* 181 (2013) 227–233.
- [35] Y. Wang, X. He, K. Wang, X. Ni, *Biosens. Bioelectron.* 25 (2010) 2101–2106.
- [36] R.Y. Lai, B. Walker, K. Stormberg, A.J. Zaitouna, W. Yang, *Methods* 64 (2013) 267–275.
- [37] G. Chatelain, M. Ripert, C. Farre, S. Ansanay-Alex, C. Chaix, *Electrochim. Acta* 59 (2012) 57–63.
- [38] D. Feng, F. Wang, Z. Chen, *Sens. Actuators, B* 138 (2009) 539–544.
- [39] D. Du, X. Huang, J. Cai, A. Zhang, J. Ding, S. Chen, *Anal. Bioanal. Chem.* 387 (2007) 1059–1065.
- [40] C. Niu, H. Kebede, D.L. Auld, J.E. Woodward, G. Burow, R.J. Wright, *Afr. J. Biotechnol.* 7 (2008).
- [41] Y. Zhang, L. Huang, *Microchim. Acta* 176 (2012) 463–470.
- [42] R.S. Saberi, S. Shahrokhian, G. Marrazza, *Electroanalysis* 25 (2013) 1373–1380.
- [43] L. Wang, E. Hua, M. Liang, C. Ma, Z. Liu, S. Sheng, M. Liu, G. Xie, W. Feng, *Biosens. Bioelectron.* 51 (2014) 201–207.
- [44] Y. Bo, H. Yang, Y. Hu, T. Yao, S. Huang, *Electrochim. Acta* 56 (2011) 2676–2681.



Evaluation of sequential injection chromatography for reversed phase separation of triazine herbicides exploiting monolithic and core–shell columns



Ricardo de Prá Urio, Jorge C. Masini*

Instituto de Química, Universidade de São Paulo, C.P. 26077, 05513-970 São Paulo, SP, Brazil

ARTICLE INFO

Article history:

Received 1 May 2014

Received in revised form

5 August 2014

Accepted 6 August 2014

Available online 19 August 2014

Keywords:

Atrazine

Simazine

Metabolites

Soil

Sequential injection

ABSTRACT

This paper describes the development of reversed phase sequential injection chromatography (SIC) methods for separation of simazine (SIM) and atrazine (AT), as well as their metabolites deethylatrazine (DEA), deisopropylatrazine (DIA) and hydroxyatrazine (HAT) exploiting silica based monolithic (50×4.6 mm) and core–shell (30×4.6 mm, $2.7 \mu\text{m}$ particles) columns. The separation was made by stepwise elution with two mobile phases: MP_1 composed of 15:85 (v/v) acetonitrile: 2.5 mmol L^{-1} acetic acid/ammonium acetate buffer (pH 4.2), and MP_2 , composed of 35:65 (v/v) acetonitrile: 2.5 mmol L^{-1} acetic acid/ammonium acetate buffer (pH 4.2). The less hydrophobic compounds (DIA, HAT and DEA) eluted with MP_1 , whereas SIM and AT eluted with MP_2 . The method using core–shell column exhibited better chromatographic efficiency compared with monolithic column for separation of SIM and AT, but failed to provide base line separation of DIA and HAT. The proposed composition of mobile phases enabled the monolithic column to separate all the studied compounds with resolution > 2.3 at flow rate of $35 \mu\text{L s}^{-1}$ and sampling throughput of 8 analyses per hour, whereas in the core–shell the maximum flow rate allowed in the SIC system was $8 \mu\text{L s}^{-1}$ (sampling throughput of 3 analyses per hour). The limits of detection were between $24 \mu\text{g L}^{-1}$ (AT) and $40 \mu\text{g L}^{-1}$ (DEA) using the monolithic column, and between $20 \mu\text{g L}^{-1}$ (SIM) and $38 \mu\text{g L}^{-1}$ (DEA) with the core–shell. Ultrasound-assisted extraction (80:20 v/v acetonitrile:water) of a soil sample enriched with the five triazines (250, 500 and $1000 \mu\text{g kg}^{-1}$) resulted recoveries between 51% and 121% of the spiked concentrations.

© 2014 Elsevier B.V. All rights reserved.

1. Introduction

Sequential injection chromatography (SIC) [1] evolved from sequential injection analysis (SIA) [2], conferring to this versatile technique the capability to perform high performance separations. The sequential injection systems used in the early SIC applications were prone to leaking of mobile phase, but mechanical reconfigurations with high- and medium-pressure components of high performance liquid chromatographs enabled the construction of equipments suitable to handle pressures up to 1000 psi [3,4]. This medium-pressure configuration enhanced the separation capabilities of SIC, enabling the use of modern short columns packed with core–shell particles, as well as narrow-bore monolithic columns [5]. For instance, Chocholous et al. [5] described the separation of four estrogens and the internal standard using core–shell packed particle (30×4.6 mm, $2.7 \mu\text{m}$ particle diameters) and narrow bore (100×3 mm) RP-18 monolithic columns. The improved robustness of medium-pressure SIC systems enabled exploitation of

diverse separation mechanisms provided by commercially available core–shell packed columns. The separation of seven phenolic compounds in core–shell particle columns with different surface chemistries (C_{18} , amide and phenyl-hexyl) was demonstrated by Chocholous et al. [6].

The morphology of monolithic and core–shell columns enhances the mass transfer (lower C term of the Van Deemter equation) in comparison with columns packed with totally porous particles. Whereas in monolithic column the mass transport is governed by convective rather than slow diffusive processes [7], in the core–shell particles the mass transfer is enhanced because the particle is constituted by a fused impenetrable silica nucleus (typically from 1.3 to $5.0 \mu\text{m}$) recovered by a 0.23 – $0.5 \mu\text{m}$ thick layer of porous silica gel [8], that is, the diffusive paths are much shorter than those of totally porous particles. Both monolithic (especially the narrow bore ones) and core–shell columns provide faster separations and reduced consumption of mobile phase in comparison with columns packed with totally porous particles, attending the demand for cleaner analytical methods [9].

Sequential injection chromatography has been mostly applied to pharmaceutical and biological samples [10,11], although some few

* Corresponding author. Tel.: +55 11 30911469; fax: +55 11 3815 5579.

E-mail address: jcmasini@iq.usp.br (J.C. Masini).

works have demonstrated its applicability to environmental analysis [12–15]. Atrazine (AT) and simazine (SIM) are herbicides widely used to stop pre- and post-emergence of broadleaf and grassy weeds in major crops such as sugar cane, maize, soybean and citrus fruits [16]. Atrazine and SIM were banned from European Community since 2004, but they are still used in large areas of Brazil and United States [17,18]. Microbial mediated oxidation of one or both of the side chains of triazines produces deethylatrazine (DEA) or deisopropylatrazine (DIA), compounds that are less hydrophobic than the parent herbicide and which toxicities are not so well known [19]. Deethylatrazine is the more frequently detected metabolite because the ethyl group of AT or SIM is more easily metabolized than the isopropyl group (present only in AT) by soil microorganisms [20,21]. Structures and physicochemical properties of the studied triazines is given in Table 1S [22,23].

The present paper describes the development of SIC methods for separation and quantification of AT and SIM, as well as the metabolites DEA, DIA and hydroxyatrazine (HAT) using a 50×4.6 mm monolithic column and a 30×4.6 mm core-shell (2.7 μ m particle diameter, 0.5 μ m thick shell) by stepwise elution [24] with acetonitrile: acetic acid/ammonium acetate mobile phases.

2. Experimental

2.1. Apparatus and reagents

A SICrom™ – accelerated liquid chromatograph was provided by FIALab® Instruments (Bellevue, WA, USA). The FIALab 5.1 software synchronized the movements of the syringe pump and the selection valve (Fig. 1), as well as data acquisition from the UV detector. Details on the instrumental configuration and mode of operation were described elsewhere [4]. Spectrophotometric measurements were carried out with a 4-cm optical path SMA-Z-40 μ vol PEEK flow-through cell (10 μ L of internal volume) from FIALab Instruments. Detection was made at 223 and 238 nm using a 200–850 nm USB 4000 spectrometer (Ocean Optics, Dunedin, FL, USA) with a grating of 600 lines mm^{-1} , resolution of 1.5 nm and slit width of 25 μ m (height of 1000 μ m). An integration time of 50 ms was used. A DH 2000 Deuterium Tungsten Halogen lamp (Mikropack GmbH, Germany) was used as light source. Two 600 μ m diameter UV/vis optical fibers

(20 in. long) were used to transmit radiation from the source to the flow cell and to the spectrometer.

Separations were made in a 50×4.6 mm i.d. Onyx™ C₁₈ monolithic column coupled to 5×4.6 mm C₁₈ monolithic guard column from Phenomenex® (Torrance, CA, USA). Separations were also made in a 30×4.6 mm i.d. Ascentis Express C18 column packed with 2.7 μ m core-shell particles, coupled to a 5×4.6 mm i.d. guard column packed with the same material, both acquired from Supelco Analytical (Bellfonte, PA, USA).

The analytical standards (Pestanal® grade) of DEA (6-chloro-*N*-(propan-2-yl)-1,3,5-triazine-2,4-diamine), DIA (6-chloro-*N*-ethyl-1,3,5-triazine-2,4-diamine), HAT (4-(ethylamino)-6-(isopropylamino)-1,3,5-triazin-2-ol), SIM (6-chloro-*N,N'*-diethyl-1,3,5-triazine-2,4-diamine) and AT (6-chloro-*N*-ethyl-*N'*-(propan-2-yl)-1,3,5-triazine-2,4-diamine) were purchased from Sigma-Aldrich (Sigma-Aldrich Brazil, São Paulo, SP). Stock solutions of these compounds were prepared at concentration of 500.0 mg L^{-1} in methanol. These standards, solids or solutions, were stored in freezer at -18 °C. Methanol (MeOH) and acetonitrile (ACN) of HPLC grade was supplied by J.T. Baker (Phillipsburg, NJ, USA). Ammonium acetate (NH₄Ac) and acetic acid (HAc) were purchased from Merck (Rio de Janeiro, RJ, Brazil). Water used in all experiments was distilled in an all-glass equipment and deionized using the Simplicity 185 system from Millipore (Billerica, MA, USA) coupled to an UV lamp. All other reagents used in this work were of analytical grade from Merck, Sigma or Aldrich.

Chromatographic separations on monolithic column employed two mobile phases (MP): MP₁=(15:85, v/v) ACN: 2.5 mM HAc/NH₄Ac buffer at pH 4.2, and MP₂=(35:65, v/v) ACN:HAc/NH₄Ac buffer (2.5 mM, pH 4.2). In most of experiments with the core-shell column the composition of MP₁ was (13:87, v/v) ACN: 2.5 mM HAc/NH₄Ac buffer at pH 4.2. All mobile phases were filtered through 0.45 μ m regenerated cellulose acetate membranes, sonicated for 30 min and purged with high purity He for 20 min prior to use.

2.2. SIC procedure

The SICrom™ system was modified to use a stainless steel high pressure selection valve (5000 psi) which configuration and mode of operation was described elsewhere [4]. The procedure is described in Tables 1 and 2 for the monolithic and core-shell column, respectively, based on the instrumental scheme shown in Fig. 1. In steps 1–3 (Tables 1 and 2) the system fills the syringe pump with the mobile phase and the sampling line with the sample solution to be analyzed. In the step 4 the sample solution is aspirated inside the holding coil (200 μ L for the monolithic column and 80 μ L for the core-shell column). The flow is reversed toward the detector flow cell passing through the separation column (step 5) while the spectrophotometer register the peaks corresponding to DIA, HAT and DEA. After that the system is programmed to fill the holding coil and part of the syringe with 4000 μ L of MP₂ (step 6; 2500 μ L in the case of core-shell column). The flow is reversed toward the column at 35 $\mu\text{L s}^{-1}$ for the separation of SIM and AT (step 7). Finally the syringe pump is refilled with MP₁ (step 8) and the flow is reversed toward the column and flow cell, conditioning the system for the next analysis (step 9). To assure reproducible elution from sample-to-sample these reconditioning steps were repeated in steps 10 and 11. The major steps are similar for both procedures used for separation in the monolithic and in the core-shell columns, with differences in the sample volumes, mobile phase volumes and flow rates (Tables 1 and 2). Retention times, peak areas and peak heights were computed using the signal processing feature of the Origin 8.5.1 software.

2.3. Soil sample and soil extraction

The soil sample was collected at the experimental farm of the Escola Superior de Agricultura Luiz de Queiroz da Universidade de São

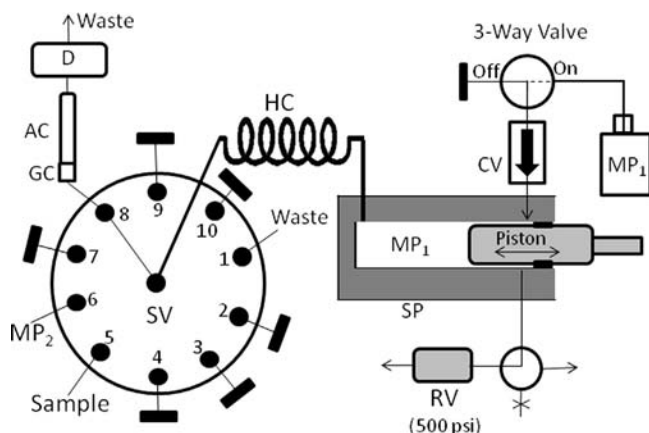


Fig. 1. Sequential injection chromatograph used for separation of triazines and metabolites. SP=Syringe pump; RV=Relief valve; CV=Check valve; HC=Holding coil (4 m \times 0.8 mm i.d.); SV=selection valve; GC=guard column; AC=Analytical Column (50 \times 4.6 mm C₁₈ Phenomenex monolithic column or 30 \times 4.6 mm Ascentis Express 2.7 μ m C₁₈ core-shell column); D=UV detector (223, 238 and 300 nm) with a 4-cm light pathlength 10- μ L flow cell; MP₁=mobile phase 1: 13% or 15% (v/v) ACN: 2.5 mmol L⁻¹ HAc/NH₄Ac (pH 4.2); MP₂=mobile phase 2: 35% (v/v) ACN: 2.5 mmol L⁻¹ HAc/NH₄Ac (pH 4.2).

Table 1
SIC Procedure for the monolithic column.

Step	SV port	SP command	Comment
1	9	Aspirate 3900 μL at $100 \mu\text{L s}^{-1}$	Filling the pump with MP_1
2	5	Aspirate 100 μL at $100 \mu\text{L s}^{-1}$	Filling the sampling line
3	1	Dispense 200 μL at $100 \mu\text{L s}^{-1}$	Discarding the excess of sample that entered HC
4	5	Aspirate 200 μL at $100 \mu\text{L s}^{-1}$	Aspirating sample for analysis
5	8	Empty at $35 \mu\text{L s}^{-1}$	Separating compounds with MP_1
6	6	Aspirate 4000 μL at $100 \mu\text{L s}^{-1}$	Filling HC and pump with MP_2
7	8	Empty at $35 \mu\text{L s}^{-1}$	Separating compounds with MP_2
8	9	Aspirate 3000 μL at $100 \mu\text{L s}^{-1}$	Filling the pump with MP_1
9	8	Empty at $35 \mu\text{L s}^{-1}$	Reconditioning the system with MP_1
10	9	Aspirate 2000 μL at $100 \mu\text{L s}^{-1}$	Filling the pump with MP_1
11	8	Empty at $35 \mu\text{L s}^{-1}$	Reconditioning the system with MP_1

SV=selection valve; SP=syringe pump; HC=holding coil.

Table 2
SIC procedure for the core-shell column.

Step	SV port	SP command	Comment
1	9	Aspirate 3920 ^a μL at $100 \mu\text{L s}^{-1}$	Filling the pump with MP_1
2	5	Aspirate 80 μL at $100 \mu\text{L s}^{-1}$	Filling the sampling line
3	1	Dispense 160 μL at $100 \mu\text{L s}^{-1}$	Discarding the excess of sample that entered HC
4	5	Aspirate 80 μL at $100 \mu\text{L s}^{-1}$	Aspirating sample for analysis
5	8	Empty at $8 \mu\text{L s}^{-1}$	Separating compounds with MP_1
6	6	Aspirate 2500 μL at $100 \mu\text{L s}^{-1}$	Filling HC and pump with MP_2
7	8	Empty at $8 \mu\text{L s}^{-1}$	Separating compounds with MP_2
8	9	Aspirate 2500 μL at $100 \mu\text{L s}^{-1}$	Filling the pump with MP_1
9	8	Empty at $8 \mu\text{L s}^{-1}$	Reconditioning the system with MP_1
10	9	Aspirate 1000 μL at $100 \mu\text{L s}^{-1}$	Filling the pump with MP_1
11	8	Empty at $8 \mu\text{L s}^{-1}$	Reconditioning the system with MP_1

SV=selection valve; SP=syringe pump; HC=holding coil.

^a 3420 μL if the composition of MP_1 is 15:85 (v/v) ACN:HAc/ NH_4Ac buffer.

Paulo (ESALQ-USP) in the Piracicaba municipality, São Paulo state, Brazil, in an area with no history of application of herbicides. This is a clay rich soil (53% clay, 18% silt and 29% sand) with a total organic carbon content of 1.58% (m/m) [12]. For recovery studies the samples were spiked with a mixture of triazines to generate soil contents of 250, 500 and 1000 $\mu\text{g kg}^{-1}$. These concentrations are consistent with a previous study by Konda and Pasztor [25] who verified a decay in the atrazine concentration from 670 to 250 $\mu\text{g kg}^{-1}$ in a time interval of 30 days after the application of herbicide. After an incubation time of 24 h, extractions of 2.0 g (± 0.01 mg) of soil were made with 3.0 mL of 80% (v/v) ACN: water inside 15 mL centrifuge tubes [26]. Ultrasonic-assisted extractions were made for 30 min at 42 kHz using a Branson 2510 (Branson Ultrasonics, Danbury, CT, USA) ultrasonic bath. After extractions the suspensions were centrifuged at 5000 r.p.m for 10 min and the supernatant was transferred to a desiccator and kept under vacuum to evaporate the ACN. The resulting solution was diluted to 3.0 mL with deionized water, filtered through 0.2 μm cellulose acetate syringe filters and analyzed by the proposed SIC methodologies. Experiments were made in triplicate and included non spiked sample. To verify if ultrasound radiation or adsorption on the centrifuge tubes have influence on the concentrations of the triazines, a set of similar experiments was made under identical conditions, but in absence of soil. These solutions were analyzed and the peak heights and areas were compared with those of the chromatograms used for construction of the calibration curve.

3. Results and discussion

3.1. Method development

Previous works on separation of triazine herbicides and metabolites in monolithic columns by SIC used phosphate buffers for

pH control and methanol as organic modifier [12,27]. In the present paper the methodology was modified, using ACN as organic modifier and HAc/ NH_4Ac as aqueous buffer, aiming to facilitate further hyphenation of SIC with electron spray ionization-mass spectrometry detection. Mobile phases composed of 1.25 mmol L^{-1} HAc/ NH_4Ac buffer (pH 4.7) and ACN contents varying (discrete variations) from 10% to 80% (v/v) were studied. A 15% (v/v) ACN solution enabled reasonable separation of DIA, DEA and HAT in both core-shell and monolithic columns, whereas SIM and AT did not elute from the column even with additional refilling of the syringe pump. Elution and separation of SIM and HAT was achieved using 35% (v/v) ACN. Thus, as a consequence of the significant difference in polarities between the metabolites and the parent herbicides, their separation required the use of two elution steps with solvents of different elution strengths (MP_1 and MP_2), followed by reconditioning with MP_1 (Fig. 1S).

To avoid pump refilling during the elution of SIM and AT, a volume of MP_2 larger than that of the internal volume of the holding coil was used (Tables 1 and 2). This approach would cause irreproducible mixture of MP_1 and MP_2 inside the syringe pump because the syringe has an internal diameter much larger than that of the holding coil. Even so, the relative standard deviations (RSD) of retention times did not exceed 2%. This low RSD can be explained by the fact that SIM was eluted just after reversing the flow of MP_2 from the holding coil toward the column, that is, SIM was eluted with the portion of MP_2 adjacent to the rotary selection valve (Fig. 1) which had neglectable dispersion with MP_1 . Elution of AT might be affected by the dispersion of MP_1 in MP_2 , but even so, as shown in Fig. 1S, AT was eluted with a mobile phase composed predominantly of MP_2 . The lack of reproducible conditions of mixture would affect the retention of compounds less polar than AT. After the elution of AT, the syringe was emptied and the refilling with MP_1 was made from the rear port of the pump so that the solution inside the holding coil (irreproducible mix of MP_1

and MP₂) was not likely to go inside the syringe again. This last step was repeated twice (Tables 1 and 2) assuring reproducible elution conditions (Fig. 2S).

A serious limitation using the stepwise elution in SIC methodologies with spectrophotometric detection is the gradient of refractive index which appears in the interpenetration zone of two mobile phases with different concentrations of ACN (MP₁ and MP₂). The distortion of signal makes difficult the definition of base line and the computation of peak areas and peak heights. As this signal distortion is independent of the wavelength, we monitored the absorbance at 300 nm, at which the triazines do not absorb. The subtraction of the chromatograms obtained at 223 or 238 nm from that at 300 nm reduced the distortion of the signal (Fig. 3S).

After defining the number of elution steps and composition of the mobile phases, the influence of pH of the mobile phase was investigated in the range between 3.5 and 4.7 using the 1.25 mmol L⁻¹ HAC/NH₄Ac buffer. Critical separation pairs were DIA and HAT (pH 3.5), and HAT and DEA (pH 4.7), but base line separation among the three compounds was achieved at pH 4.2 for the monolithic column (Fig. 2). Base line separation of DIA and HAT in the core-shell column was not possible with the MP₁ composed 15% (v/v) ACN:1.25 mmol L⁻¹ HAC/NH₄Ac, pH 4.2 (resolution=0.72). A small decrease in the ACN content to 13% (v/v) improved the resolution between DIA and HAT to 1.3, but required an increase of 500 μL of MP₁ to complete the elution of DEA (Table 2). Separation of SIM and AT was not affected by the pH of the mobile phase. Concentration of the buffer (at pH 4.2) was studied between 1.25 and 10 mmol L⁻¹ with no significant effect in retention times and resolution. A 2.5 mmol L⁻¹ concentration was used in the sequence of studies to assure better buffering capacity compared with the previously used buffer (1.25 mmol L⁻¹).

The sample volumes used in the present work were planned to increase the sensitivity without compromising resolution. According to Snyder et al. [28] if the ratio $V_s/V_c < 0.1$ (where V_s is the sample volume and V_c is the peak volume estimated at the base line) there is no effect of sample volume on peak width or separation. If $V_s/V_c < 0.4$ the increase of peak width and loss in resolution is lower than 10%, that is considered as acceptable. In our experiments the ratio V_s/V_c never exceeded 0.35 for the monolithic column and 0.16 for the core-shell column. The sample volume used in the monolithic column was 200 μL, as described in previous works [12]. Injection of a large sample volume in a solvent of elution power weaker than that of mobile phase (water in the present work) is a strategy that has been exploited to increase the sensitivity in trace analysis [28]. Sample volumes as large as 500 μL have been injected in a similar 50 × 4.6 mm i.d. C₁₈ monolithic column for quantification of triazines in environmental waters using conventional HPLC instrumentation [29]. For the core-shell column the variation of peak heights with the sample volumes up to 80 μL may be fitted by linear equations ($r^2 > 0.97$), but with a tendency for leveling-off at larger volumes (Fig. 4S). Thus, the 80 μL was used in the continuation of the studies with the core-shell column.

The maximum flow rate (elution steps) was set to not exceed the limit of 500 psi, defined by the back pressure regulator fitted to the syringe pump (Fig. 1). These flow rates were 35 μL s⁻¹ (2.1 mL min⁻¹) for the monolithic column, and 8 μL s⁻¹ (0.48 mL min⁻¹) for the core-shell column. As a consequence, the chromatographic runs last about 7.2 and 20 min in the monolithic and core-shell columns, respectively (Fig. 2).

3.2. Analytical features

The linearity of the peak area as a function of triazine concentrations were studied in the concentration range between 25 and 1000 μg L⁻¹. From 100 or 250 to 1000 μg L⁻¹ the peak areas and

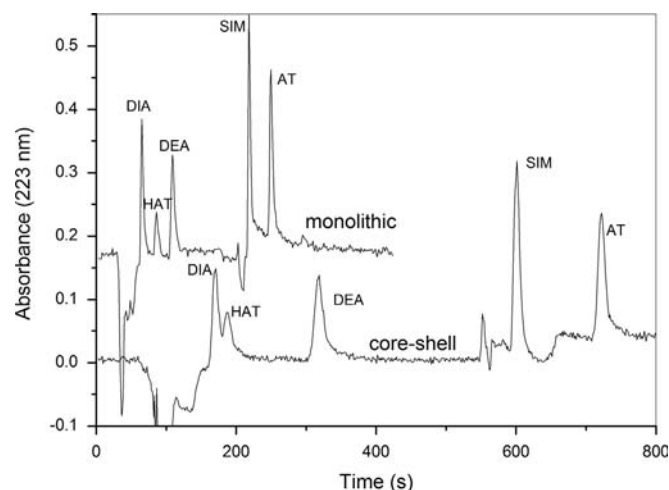


Fig. 2. Comparison of chromatograms obtained in monolithic and core-shell column for a mixture of triazines with concentration of 500 μg L⁻¹. For monolithic column the sample volume was 200 μL and flow rate was 35 μL s⁻¹ in the elution steps, whereas for the core-shell column the sample volume was 80 μL and the flow rate 8 μL s⁻¹. MP₁ = 13% (v/v) ACN: 2.5 mmol L⁻¹ HAC/NH₄Ac (pH 4.2) in the core-shell and 15% (v/v) ACN: buffer for the monolithic column; MP₂ = 35% (v/v) ACN: 2.5 mmol L⁻¹ HAC/NH₄Ac (pH 4.2) for both monolithic and core-shell columns.

peak heights were linear with the concentration for both monolithic and core-shell columns (Table 3). The limits of detection (LOD) and quantification (LOQ) were computed as $LOD = 3S_d/m$ and $LOQ = 10S_d/m$ where m is the slope of the calibration curves (peak heights) and S_d is the standard deviation of the noise in the base line measured around the retention time (t_R). The LOD values varied between 20 μg L⁻¹ for SIM (core-shell column) and 40 μg L⁻¹ for DEA (monolithic column). Although these values are too high for monitoring residual concentrations in environmental waters, they enable the determination in soil extracts of several samples, as well as monitoring of triazine concentrations in adsorption and degradation studies [12,25,26]. The core-shell column provided 2.5 times higher sensitivity compared with the monolithic column. This statement is based on the fact the LOD and LOQ in both monolithic and core shell columns were quite similar despite of using a sample volume 2.5 times greater in the monolithic column.

The intraday relative standard deviation of the retention times did not exceed 1.2% and 0.3% (triplicates) in the separations made with the monolithic and core-shell columns, respectively. Interday variations in retention times increased, but the relative standard deviations were less than 5% (three different days). Interday and intraday relative standard deviation of peak areas varied from 9% to 20% for the mixture of all compounds at concentration of 100 μg L⁻¹. For the 1000 μg L⁻¹ mixture, the relative standard deviations varied from 1% to 9%. The larger deviations were observed for SIM because of the distortion of base line near the retention time. As pointed out before, this distortion occurred as a consequence of the gradient of refraction index, which influence was reduced by subtracting the data at 300 nm (Fig. 2S), but without being completely eliminated. Modern and conventional HPLC instruments can provide better precision, but at much higher price of instrumentation, so that the proposed methodologies with both monolithic and core-shell columns may find applicability in trial studies.

Separation of the studied compounds under the described conditions consumed 1709 and 2585 μL of ACN in the core-shell and in the monolithic columns, respectively. This finding is related to the larger sample volume used and the longer length of the monolithic column, but it may also be related to the short diffusion paths of the core-shell column. On the other hand, the greater permeability of the monolithic column enabled the use flow rates

Table 3
Retention times, calibration curve parameter and limits of detection and quantification obtained for monolithic and core-shell columns sample volumes of 80 and 200 μL for the core-shell and monolithic columns, respectively.

Compound	Monolithic						Core-shell					
	t_R (min)	Slope $\times 10^4$ ($\text{L } \mu\text{g}^{-1}$)	Intercept	r	LOD ($\mu\text{g L}^{-1}$)	LOQ ($\mu\text{g L}^{-1}$)	t_R (min)	Slope $\times 10^4$ ($\text{L } \mu\text{g}^{-1}$)	Intercept	r	LOD ($\mu\text{g L}^{-1}$)	LOQ ($\mu\text{g L}^{-1}$)
DIA	1.15 \pm 0.01 ^b	18 \pm 1	-0.01 \pm 0.01	0.999	30	99	3.11 \pm 0.01	21 \pm 1	0.08 \pm 0.04	0.999	32	106 ^c
HAT ^a	1.55 \pm 0.01	12 \pm 1	-0.02 \pm 0.01	0.998	38	129 ^c	3.75 \pm 0.01	31 \pm 1	-0.06 \pm 0.03	0.994	34	113 ^c
DEA	1.83 \pm 0.01	16 \pm 1	-0.02 \pm 0.01	0.998	40	132 ^c	6.17 \pm 0.01	35 \pm 1	0.02 \pm 0.08	0.999	38	126 ^c
SIM	3.06 \pm 0.02 ^d	30 \pm 4	-0.12 \pm 0.08	0.999	30	99	10.66 \pm 0.03 ^d	62 \pm 2	-0.11 \pm 0.10	0.999	20	57
AT	3.60 \pm 0.05 ^d	23 \pm 2	0.01 \pm 0.03	0.998	24	79	12.80 \pm 0.02 ^d	49 \pm 3	-0.11 \pm 0.13	0.998	25	74

^a Monitored at 238 nm.

^b Mean and standard deviation of triplicates.

^c For these cases the slope was determined for concentrations between 250 and 1000 $\mu\text{g L}^{-1}$. For all the other cases the concentration range was between 100 and 1000 $\mu\text{g L}^{-1}$.

^d Computed by discounting 43 and 28 s (monolithic and core-shell, respectively) from the total retention time to consider the time for pump refilling with MP_2 .

Table 4
Chromatographic parameters from the triazine peaks obtained from injections of 1000 $\mu\text{g L}^{-1}$ mixture of the five compounds computed under the optimized conditions of each column (sample volume=200 μL , flow rate=35 $\mu\text{L s}^{-1}$ for the monolithic column; sample volume=80 μL , flow rate=8 $\mu\text{L s}^{-1}$ for the core-shell column).

Compound	Monolithic					Core-shell				
	k	Resolution	Asymmetry	Plates (m^{-1}) ^b	HETP (μm)	k	Resolution	Asymmetry	Plates (m^{-1}) ^b	HETP (μm)
DIA	1.1		2.4	6030	166	1.3		1.6	8489	117
HAT	1.7	2.3	2.2	7043	142	1.7	1.3	2.3	7390	135
DEA ^a	2.5	2.4	2.3	17371	57.5	2.7	3.0	2.2	25616	39
SIM ^a	3.9	7.7	2.2	-	-	5.5	6.0	2.3	-	-
AT	4.7	4.7	2.3	-	-	6.8	5.0	2.4	-	-

^a Resolution was computed as $(2(t_2 - t_1))/(1.7(w_{1/2,1} + w_{1/2,2}))$. Resolution between DEA and SIM was computed discounting the time spent for syringe refilling (43 and 28 s), for the monolithic and core-shell columns, respectively.

^b Number of plates per meter was computed as $N = (5.55t_R^2)/(w_{1/2}^2)$ considering 36.7 and 89.2 s as the mobile phase holdup time (t_M) for the monolithic and core-shell columns, respectively. Column lengths were 50 mm (monolithic) and 30 mm (core-shell).

as high as 35 $\mu\text{L s}^{-1}$, providing a sampling throughput of 8 analysis per hour (including reconditioning of the column), whereas in the core-shell column (8 $\mu\text{L s}^{-1}$) the maximum sampling throughput was 3 analysis per hour.

3.3. Chromatographic parameters

Retention factor (k), resolution and asymmetry factor were computed for separation of all the five triazines (Table 4). Plate number and height equivalent to theoretical plate (HETP) were computed only for DIA, HAT and DEA that were eluted isocratically with MP_1 (Table 4). Base line separation (resolution > 2.3) was achieved in the methodology using the monolithic column for all triazines. Assuming the limit of resolution for baseline separation as 1.5, the separation between DIA and HAT was a critical issue in the core-shell column (resolution of 1.3), decreasing to 0.7 if MP_1 is composed of 15% (v/v) ACN: 2.5 mmol L^{-1} HAc/ NH_4Ac (pH 4.2). Despite of the poor resolution between DIA and HAT, the short diffusion path of the core-shell column lead to larger number of plates per meter and shorter HETP in comparison with the monolithic column. These parameters suggest that the SIC methodology exploiting the core-shell column has potentially better efficiency for the separation of DEA, SIM and AT.

3.4. Selectivity

Other herbicides that can be present in soils and are retained in reversed phase chromatography were studied as potential

interferences by monitoring the absorbance at 223 and 238 nm. Among other triazines, metribuzin and ametryn were not potential interferences because they were much more strongly retained in the columns (Fig. 3). Previous works [14] verified that propazine is more strongly retained in C_{18} columns than AT, so that propazine is not an interference under the studied conditions. To minimize cross contamination, a column cleanup step with a solvent of high elution strength (80:20 v/v ACN: water, for instance) should be included in the procedure at the end of each analysis. Among the herbicides of the class of ureas, linuron and tebuthiuron did not exhibit any chromatographic peak within the studied gradient, suggesting strong retention by the columns (Fig. 3). Diuron showed a peak overlapping with the tail of the peak of atrazine in the monolithic column (Fig. 3a). At 223 nm this peak height corresponded to about 25% of peak height for atrazine (both compounds at concentration of 1 mg L^{-1}). Diuron was well resolved from atrazine in the core-shell column (Fig. 3b) as a consequence of the high efficiency of this column providing sharp chromatographic peaks. Bromacil, an urea herbicide, eluted together SIM in both columns, exhibiting a height < 10% of that for SIM (both compounds at concentration of 1 mg L^{-1}), being a potential interference in the quantification of this herbicide in real samples.

3.5. Application to soil samples

As expected, no residues of the studied herbicides were found in the studied soil sample. Comparison of chromatograms

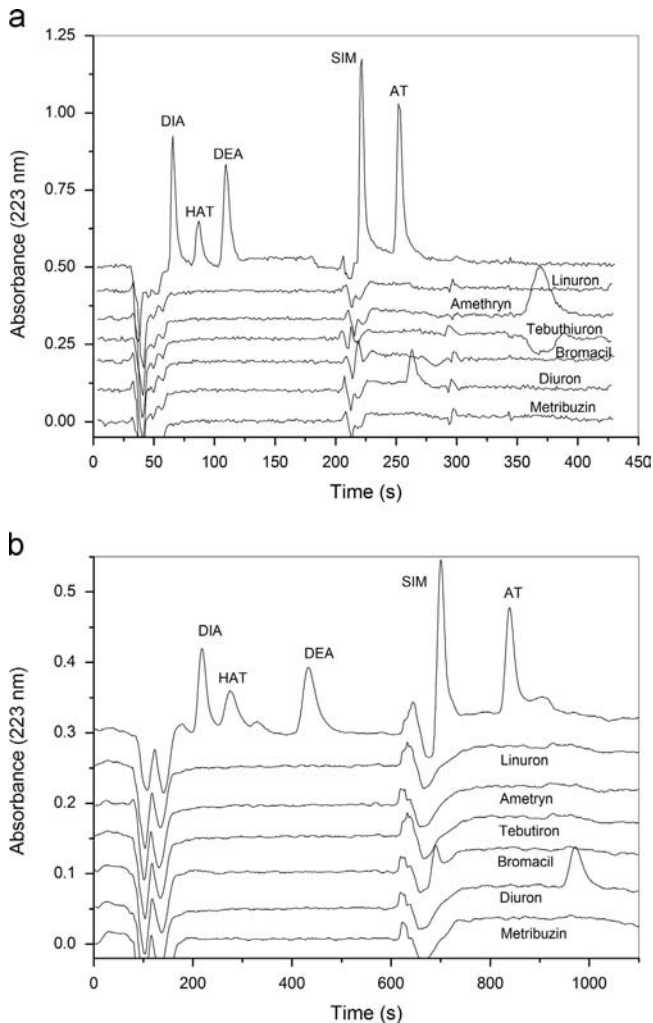


Fig. 3. Comparison of the chromatogram of the mix of the studied mix of triazines ($1000 \mu\text{g L}^{-1}$) with chromatograms of other herbicides (also at concentration of $1000 \mu\text{g L}^{-1}$) in (a) monolithic column and (b) core-shell column. Composition of mobile phases, sample volumes and flow rates were as described in the caption of Fig. 2.

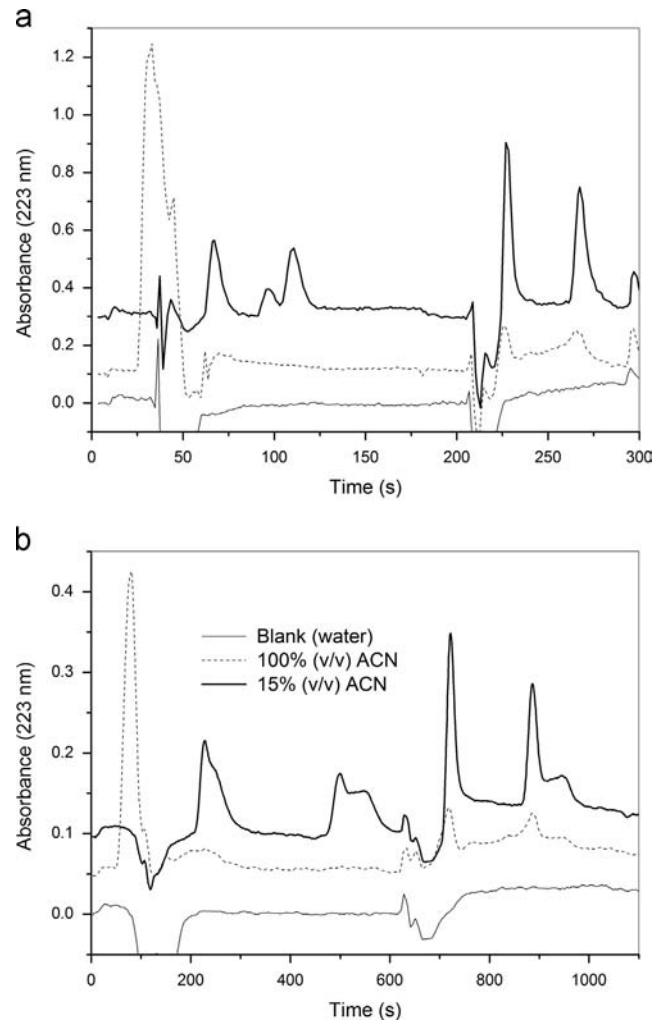


Fig. 4. Effect of the sample solvent on the elution of triazines ($1000 \mu\text{g L}^{-1}$) in the (a) monolithic and (b) core-shell columns. Composition of mobile phases, sample volumes and flow rates were as described in the caption of Fig. 2.

obtained from the solution exposed or not to the sonication in the centrifuge tubes were undistinguishable, indicating that neither adsorption of herbicides in the centrifuge tubes nor chemical degradation occurred at significant levels. The retention of the triazines was strongly affected by the composition of the extract (Fig. 4). For instance, the metabolites in extracts containing high contents of ACN were not retained in both the monolithic and core-shell columns (Fig. 4). The monolithic column performed better than the core-shell in 15% (v/v) ACN (Fig. 4), which is an interesting feature because less sample treatment is necessary (the total evaporation of ACN can be avoided). The poor retention of the solutes in high contents of ACN is a consequence of the large sample volume injected, and the better performance of the monolithic column in 15% (v/v) ACN may be explained by its longer length. Dilution of the extract in water could overcome the problem of poor retention at the cost of loss of sensitivity.

Major potential interference peaks in soil extracts, probably soluble components of natural organic matter (humic substances, organic acids, amino acids, etc.), eluted in the dead volume of both columns (Fig. 5). A chromatographic peak was observed just before the peak corresponding to SIM, worsening the precision and accuracy of the quantification of this herbicide. This interference could be minimized by increasing the retention of SIM by

decreasing the ACN content in MP₂. This approach, however, would decrease the sampling throughput. Even with the described limitations, the recoveries for the three levels of enrichment (250 , 500 and $1000 \mu\text{g kg}^{-1}$) were mostly within the range of 70–120% (Table 5) which is considered acceptable for the analysis of herbicides in soil samples [30].

4. Conclusion

The use of core-shell columns in SIC is possible, as pointed out by Chocholous et al. [5], and can be exploited for environmental analysis, as a consequence of the enhanced chromatographic efficiency in comparison with the silica-based monolithic column, as showed in the present paper. However, with the pressure limitations of the current SIC instrumentation, the core-shell columns cannot be explored to their full potential for fast separations. The present work showed that for determination of triazines in soil extracts the gain in chromatographic efficiency of the core-shell column was not compensated by the mandatory reduction in flow rate, so that, for the studied problem, the use of monolithic column was advantageous in the SIC system.

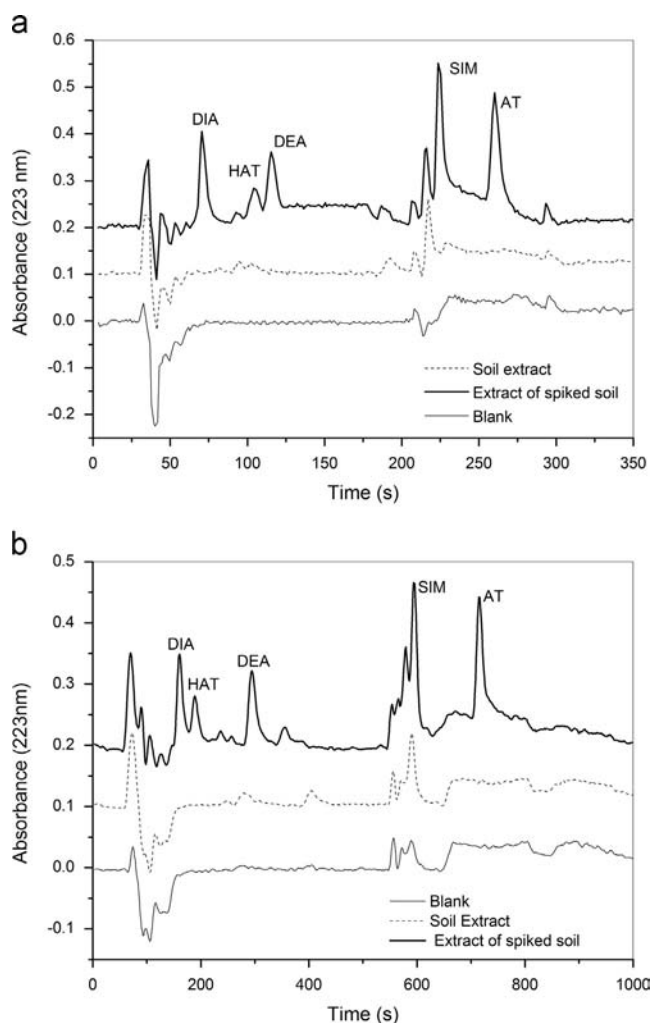


Fig. 5. Comparison of chromatograms of blank solutions (deionized water) with extracts of soil free of the studied triazines and the extract obtained from the soil spiked with $1000 \mu\text{g kg}^{-1}$ of herbicides and metabolites in (a) monolithic and (b) core-shell columns. For the monolithic column the chromatographic conditions are the same as described in the caption of Fig. 2. For both the monolithic and core-shell column the MP₁ was composed of 15% (v/v) ACN; 2.5 mmol L⁻¹ HAc/NH₄Ac buffer (pH 4.2).

Table 5
Recovery results for ultrasonic-assisted extraction of spiked soil samples.

Compound	Spike ($\mu\text{g kg}^{-1}$)	Recoveries (%)	
		Monolithic	Core-shell
DIA	250	77 ± 7	108 ± 8
	500	81 ± 5	100 ± 5
	1000	89 ± 9	121 ± 10
HAT	250	78 ± 7	101 ± 5
	500	71 ± 8	79 ± 3
	1000	70 ± 8	88 ± 9
DEA	250	93 ± 5	99 ± 7
	500	82 ± 7	75 ± 5
	1000	101 ± 10	106 ± 8
SIM	250	51 ± 5	108 ± 8
	500	81 ± 10	75 ± 5
	1000	118 ± 8	107 ± 9
AT	250	101 ± 3	90 ± 7
	500	91 ± 5	87 ± 8
	1000	99 ± 7	100 ± 2

Acknowledgment

This work was funded by Grants 475554/2009-4 and 304178/2009-8 from the Conselho Nacional de Desenvolvimento Científico e Tecnológico (CNPq) and Grant 2009/09771-4 from the São Paulo Research Foundation (FAPESP). A fellowship from FAPESP to Ricardo de Prá Urio (Contract 2011/08309-5) is acknowledged.

Appendix A. Supporting information

Supplementary data associated with this article can be found in the online version at <http://dx.doi.org/10.1016/j.talanta.2014.08.020>.

References

- [1] D. Satinsky, P. Solich, P. Chocholous, R. Karlicek, *Anal. Chim. Acta* 499 (2003) 205–214.
- [2] J. Ruzicka, G.D. Marshall, *Anal. Chim. Acta* 237 (1990) 329–343.
- [3] S.K. Hartwell, A. Kehling, S. Lapanantnoppakhun, K. Grudpan, *Anal. Lett.* 46 (2013) 1640–1671.
- [4] M. Rigobello-Masini, J.C. Masini, *Phytochem. Anal.* 24 (2013) 224–229.
- [5] P. Chocholous, L. Kosarova, D. Satinsky, H. Sklenarova, P. Solich, *Talanta* 85 (2011) 1129–1134.
- [6] P. Chocholous, J. Vackova, I. Sramkova, D. Satinsky, P. Solich, *Talanta* 103 (2013) 221–227.
- [7] F. Svec, C.G. Huber, *Anal. Chem.* 78 (2006) 2100–2107.
- [8] J.J. Kirkland, T.J. Langlois, J.J. DeStefano, *Am. Lab.* 39 (2007) 18.
- [9] W.R. Melchert, B.F. Reis, F.R.P. Rocha, *Anal. Chim. Acta* 714 (2012) 8–19.
- [10] A.M. Idris, R.E.E. Elgorashe, *J. AOAC Int.* 96 (2013) 282–289.
- [11] P. Chocholous, P. Solich, D. Satinsky, *Anal. Chim. Acta* 600 (2007) 129–135.
- [12] R.D. Urio, C.M.C. Infante, J.C. Masini, *J. Agric. Food Chem.* 61 (2013) 7909–7915.
- [13] C.M.C. Infante, R.D. Urio, J.C. Masini, *Anal. Lett.* 44 (2011) 503–513.
- [14] L.B.O. dos Santos, C.M.C. Infante, J.C. Masini, *J. Sep. Sci.* 32 (2009) 494–500.
- [15] E. Bjorklund, F. Maya, S.A. Bak, M. Hansen, J.M. Estela, V. Cerda, *Microchem. J.* 98 (2011) 190–199.
- [16] M. Graymore, F. Stagnitti, G. Allinson, *Environ. Int.* 26 (2001) 483–495.
- [17] J.B. Sass, A. Colangelo, *Int. J. Occup. Environ. Health* 12 (2006) 260–267.
- [18] E.N. Nogueira, E. Dores, A.A. Pinto, R.S.S. Amorim, M.L. Ribeiro, C. Lourencetti, *J. Braz. Chem. Soc.* 23 (2012) 1476–1487.
- [19] K. Ralston-Hooper, J. Hardy, L. Hahn, H. Ochoa-Acuna, L.S. Lee, R. Mollenhauer, M.S. Sepulveda, *Ecotoxicology* 18 (2009) 899–905.
- [20] E.L. Kruger, L. Somasundaram, R.S. Kanwar, J.R. Coats, *Environ. Toxicol. Chem.* 12 (1993) 1959–1967.
- [21] G.V. Steele, H.M. Johnson, M.W. Sandstrom, P.D. Capel, J.E. Barbash, *J. Environ. Qual.* 37 (2008) 1116–1132.
- [22] N.M.J. Vermeulen, Z. Apostolides, D.J.J. Potgieter, P.C. Nel, N.S.H. Smit, *J. Chromatogr.* 240 (1982) 247–253.
- [23] J.R. Dean, G. Wade, I.J. Barnabas, *J. Chromatogr. A* 733 (1996) 295–335.
- [24] M. Rigobello-Masini, J.C.P. Penteado, C.W. Liria, M.T.M. Miranda, J.C. Masini, *Anal. Chim. Acta* 628 (2008) 123–132.
- [25] L.N. Konda, Z. Pasztor, *J. Agric. Food Chem.* 49 (2001) 3859–3863.
- [26] M.F. Amadori, G.A. Cordeiro, C.C. Rebouças, P.G. Peralta-Zamora, M.T. Grassi, G. Abate, *J. Braz. Chem. Soc.* 24 (2013) 483–491.
- [27] L. Zarpon, G. Abate, L.B.O. dos Santos, J.C. Masini, *Anal. Chim. Acta* 579 (2006) 81–87.
- [28] L.R. Snyder, J.J. Kirkland, J.L. Glajch, *Practical HPLC Method Development*, 2nd ed., Wiley, New York, 1997.
- [29] D.J. Beale, S.L. Kaserzon, N.A. Porter, F.A. Roddick, P.D. Carpenter, *Talanta* 82 (2010) 668–674.
- [30] M. Ribani, C.B.G. Bottoli, C.H. Collins, I. Jardim, L.F.C. Melo, *Quim. Nova* 27 (2004) 771–780.



Determination of tamoxifen and its main metabolites in plasma samples from breast cancer patients by micellar liquid chromatography



Juan Peris-Vicente^{a,*}, Enrique Ochoa-Aranda^{b,1}, Devasish Bose^{c,1},
Josep Esteve-Romero^{a,1}

^a Química Bioanalítica, QFA, ESTCE, Campus Riu Sec, Universitat Jaume I, 12071 Castelló, Spain

^b Biopatología Molecular, Hospital Provincial, Dr. Clara, 12003 Castelló, Spain

^c Department of Criminology and Forensic Sciences, Dr. H. S. Gour University, 470003 Sagar, India

ARTICLE INFO

Article history:

Received 3 June 2014

Received in revised form

24 July 2014

Accepted 30 July 2014

Available online 20 August 2014

Keywords:

Genotype

Metabolization

Micellar liquid chromatography

Plasma

Tamoxifen

ABSTRACT

A method was developed for the analysis of tamoxifen and its main derivatives (4-hydroxytamoxifen, N-desmethyl-tamoxifen, tamoxifen-N-oxide and endoxifen) in human plasma, using micellar liquid chromatography coupled with fluorescence detection. Analytes were off-line derivatized by sample UV-irradiation for 20 min to form the photocycled fluorescent derivatives. Then samples were diluted, filtered and directly injected, thus avoiding extraction steps. The analytes were resolved using a mobile phase containing 0.08 M SDS–4.5% butanol at pH 3 running at 1.5 mL/min through a C18 column at 40 °C, without interferences from endogenous compounds in plasma. Excitation and emission wavelengths were 260 and 380 nm, respectively. The chromatographic analysis time was less than 40 min. The analytical methodology was validated following the International Conference on Harmonization of Technical Requirements for Registration of Pharmaceuticals for Human Use (ICH) guidelines in terms of: selectivity, linear range (0.3–15 µg/mL), linearity ($r^2 > 0.999$), sensitivity (LOD, 65–80 ng/mL; LOQ, 165–200 ng/mL), intra- and interday accuracy (–12.2–11.5%) and precision (< 9.2%) and robustness (< 6.3%). The method was used to quantify the tamoxifen and tamoxifen derivatives in several breast cancer patients from a local hospital, in order to study the correlation between the genotype of the patient and the ability to metabolize tamoxifen.

© 2014 Elsevier B.V. All rights reserved.

1. Introduction

Tamoxifen (TAMO; MW=371 g/mol; Fig. 1) is an endocrine therapeutic drug widely prescribed as chemopreventive in women to prevent and to treat all stages of breast cancer [1,2]. However, the clinical response to tamoxifen is variable and 30–50% of the patients, which initially respond to the therapy, relapse and finally die [3]. Moreover, this drug can provoke undesirable side effects depending on the patient [4]. This variability is related to the metabolism of the drug, as the antitumor activity and side effects are caused by tamoxifen and its biological derivatives [1,2,5].

Tamoxifen is a prodrug, *in vivo* metabolized by the enzyme cytochrome P450 2D6 (CYP2D6) [6]. The metabolic pathway begins with the biotransformation of tamoxifen in its two primary metabolites, 4-hydroxy-tamoxifen (4-OH-TAMO) and N-desmethyl-tamoxifen (N-desCH₃-TAMO) and finally leads to the formation of 22 metabolites, such as tamoxifen-N-oxide

(TAMO-N-O), α -hydroxytamoxifen (α -OH-TAMO), α -hydroxy-tamoxifen-N-oxide, N-didesmethyltamoxifen (N-didesCH₃-TAMO), 3,4-epoxytamoxifen, 3,4-epoxytamoxifen N-oxide, 4-hydroxytamoxifen-N-oxide, 3,4-dihydroxytamoxifen, α -hydroxy-N-desmethyltamoxifen and 4-hydroxy-N-desmethyltamoxifen (endoxifen, ENDO). Some of them are more active than TAMO itself, as 4-OH-TAMO and ENDO. As the plasmatic level of endoxifen is 5–10 times higher than 4-OH-TAMO, endoxifen is considered as the main active metabolite of tamoxifen [2,7].

Several clinical studies have proposed that the diminishing of the CYP2D6 function, by genetic polymorphism [8] or drugs inhibiting the enzyme [9], provokes minor clinic results of tamoxifen therapy [10], due to the minor plasmatic concentrations of ENDO and 4-OH-TAMO [2,8]. A high number of genetic variations of CYP2D6, associated with different degree of enzymatic activities (from inactive to strong) are known. Therefore, the ability of cytochrome P450 to synthesize ENDO and 4-OH-TAMO from tamoxifen can strongly vary depending on the patient [10]. This would be one of the most important factors which are involved in the variability of the response to tamoxifen treatment. Patients with low-active CYP450 enzyme variant slowly metabolize tamoxifen and then show elevated amount of the prodrug and low

* Corresponding author. Tel.: +34 964728093.

E-mail address: vicentej@uji.es (J. Peris-Vicente).

¹ All the authors participate equally.

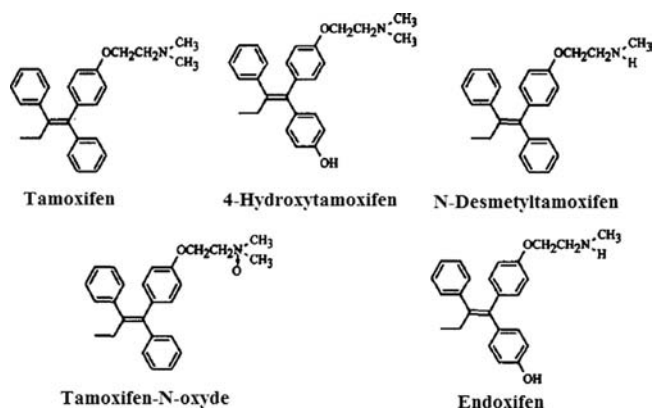


Fig. 1. Structure of tamoxifen and its main derivatives.

concentrations of the metabolites. These patients would have a higher risk of primary failure to TAMO treatment at normal doses [6].

The activity of CYP2D6, and then the effectiveness of TAMO treatment, can be envisaged by measuring the concentration of tamoxifen, the intermediate metabolites N-desCH₃-TAMO and TAMO-N-O, as well as 4-OH-TAMO and ENDO in blood (Fig. 1). This allows the personalization of the treatment and improves the survival ratio of the patient [2]. The development of an analytical methodology to adequately quantify tamoxifen and the main metabolites is needed to perform this study.

Several hydroorganic HPLC-based methods have been developed to simultaneously quantify tamoxifen and its main derivatives in plasma. A recent paper reports the use of HPLC-MS [8], but mass spectrometry has a high cost and requires an expensive maintenance. Other authors have proposed analytical methods using liquid chromatography coupled with spectrophotometric detectors, as HPLC-DAD [11,12] (with low sensitivity) and HPLC-FLD [13–16], previous derivatization by UV-irradiation. However, due to the high number of analytes to separate, the hydroorganic mobile phases are usually programmed as gradient. Thus, large volumes of pollutant organic solvents are used in the analysis of a large amount of samples. Prior to injection into the chromatographic system, a purification procedure, as liquid/liquid [13] or liquid/solid [15] extraction, or deproteinization with acetonitrile [14,16], is needed. However, these clean-up steps are complex, time-consuming, tedious and source of experimental mistakes, reducing the reliability of the methods. Moreover, a large amount of organic solvents is needed, improving the cost and the environmental impact of the method.

A micellar liquid chromatographic (MLC) methodology was developed to quantify tamoxifen and endoxifen in plasma of breast cancer patients [1,5]. Samples were irradiated at 254 nm to induce photocyclation, forming products with an intense fluorescence. This photoreaction also occurs in compounds with tamoxifen-base structure, then it is applicable to the main metabolites (4-OH-TAMO, N-desCH₃-TAMO, TAMO-N-O and endoxifen) [5,14]. The composition of the mobile phase was an aqueous solution of SDS (as surfactant) and butanol as organic modifier. The benefits of MLC over hydroorganic HPLC in plasma analysis have been widely discussed [17,18]. One of the more interesting advantage is the high reproducibility of the chromatographic behavior of the analytes. Therefore, a chemometric approach provides retention time and shape of the analytes in a wide range of SDS and organic modifier concentration values, from the data obtained using few mobile phases following an experimental design [19]. Thus, the composition of the mobile phase providing the maximum resolution-minimum analysis time, is selected as optimal. This would be especially useful when a large number of similar compounds have to be resolved [20].

The aim of the work was to develop a MLC-based methodology to quantify tamoxifen and its main metabolites (4-OH-TAMO, N-desCH₃-TAMO, TAMO-N-O and ENDO) in plasma of breast cancer patients. The analytes must be separated from other compounds of the matrix with high sensitivity in a short time, to be useful for routine analysis in hospital laboratories. The proposed procedure incorporates the main advantages of the use of micellar media, such as reduced cost, fast and easy preparation and the use of a smaller amount of pollutant compounds. This analytical method has been validated following the International Conference on Harmonization of Technical Requirements for Registration of Pharmaceuticals for Human Use (ICH) guidelines [21,22] in terms of linearity, limits of detection (LOD) and quantification (LOQ), intra- and inter-day precisions, selectivity, recovery and robustness.

2. Experimental

2.1. Reagent and solutions

Tamoxifen, 4-OH-TAMO, N-desCH₃-TAMO, TAMO-N-O and ENDO and endoxifen standards (purity > 99.99%) were supplied by Sigma (St. Louis, MO, USA). The other reagents used were sodium dodecyl sulfate (Merck, Darmstadt, Germany), sodium dihydrogenphosphate monohydrate, HCl (purity > 99%, Panreac, Barcelona, Spain), NaOH (Scharlab, Barcelona). Methanol (J.T. Baker, Holland) and butanol (Scharlab) were HPLC grade. Ultrapure water (Millipore S.A.S., Molsheim, France) was used to prepare all the aqueous solutions and mobile phases.

Analyte standard solutions were prepared by solubilizing the appropriate amount in ultrapure water, and the mixture was ultrasonicated for 2 min. These solutions were prepared in amber flasks to avoid the extensive photochemical degradation of the drug. Fresh solutions were prepared weekly. Blood samples were collected as indicated in [1,5].

2.2. Apparatus, experimental procedure and chromatographic conditions

The instrumentation and experimental procedure were as indicated in [1,5]. The separation and quantification of the analytes were performed using a mobile phase containing 0.08 mol/L SDS and 4.5% (v/v) butanol buffered at pH 3, running under isocratic mode at a constant flow of 1.5 mL/min. Injection volume was 20 µL. The buffer was made adding 0.01 mol/L sodium dihydrogenphosphate monohydrate and adjusting the pH by using suitable volumes of 0.1 mol/L HCl. The mobile phase was filtered through 0.45 µm nylon membranes (Micron Separations, Westboro, MA, USA). The column temperature was kept constant at 40 ± 0.5 °C. The excitation and emission wavelengths were set at 260 and 380 nm, respectively.

3. Results and discussion

The irradiation conditions, the pH of the mobile phase and optimal wavelength detection were taken from [1,5], because the tamoxifen metabolites share the core structure with tamoxifen and have similar spectrophotometric properties [16].

3.1. Mobile phase selection

Tamoxifen, 4-OH-TAMO, N-desCH₃-TAMO, TAMO-N-O and ENDO and its metabolites are quite hydrophobic according to their high log Po/w (6.64; 5.80; 6.42; 5.93; 6.01) [23], and then a strong retention is expected using micellar liquid chromatography [1,5],

indicating that a short-chain alcohol must be added to the mobile phase [1,5]. Pentanol was tested as organic modifier, but the analytes elute close to the dead time. On the other hand, propanol provides too high retention times. Therefore, butanol was finally selected as organic modifier.

Using SDS/butanol mobile phases, a blank plasma sample shows no peaks, apart from the protein band between 1.0 and 4.0 min, therefore only the analytes were considered in the optimization of the mobile phase [1,5]. Consequently, the mobile phase was optimized to elute tamoxifen, 4-OH-TAMO, N-desCH₃-TAMO, TAMO-N-O and ENDO without overlapping between them (maximal resolution), in a minimal analysis time, at retention times > 4.0 min, avoiding the interference of the protein band.

In order to select the more adequate SDS/butanol concentration to detect the analytes, an interpretative strategy was applied. The values of retention time (t_R), retention factor (k), efficiency (N) and asymmetry (B/A) of the peaks to resolve were taken at several mobile phase compositions of SDS (M)/butanol (%): 0.05/2; 0.05/7; 0.10/4; 0.15/2 and 0.15/7. From these results, the Michrom software allows to predict the chromatographic behavior of the studied compounds at intermediate SDS/butanol concentration values (0.05–0.15 M and 2–7%, respectively). With these data, the program simulates the corresponding chromatogram and evaluates the resolution, using the overlapping fractions-criterion [24]. The equation used to model the retention time was [20]

$$k = \frac{K'_{AS}/(1+K_{AD}\phi)}{1+[M](K_{AM}(1+K_{MD}\phi)/(1+K_{AD}\phi))}$$

$[M]$ and ϕ are the surfactant and modifier concentrations, respectively. K_{AS} and K_{AM} correspond to the equilibrium constants between the solute in pure water and the stationary phase or micelle, respectively. K_{AD} and K_{MD} measure the relative variation in the solute concentration in pure water and micelles due to the presence of butanol, as compared to a pure micellar solution. The errors in the prediction of the retention times were < 3%.

Using the maximum resolution-minimum analysis time criteria, the optimal mobile phase composition was 0.08 M SDS; 4.5% butanol at pH 3. Under these conditions, the five analytes were resolved without overlapping among them or with the protein band in less than 40 min. The chromatographic parameters are shown in Table 1. The global resolution of the chromatogram was $R=0.99998$. Fig. 2B shows the chromatogram obtained from the analysis of a blank plasma sample spiked with a mixture of 5 $\mu\text{g}/\text{mL}$ of each analyte, under the optimized conditions. As previously indicated, no peaks from the matrix were detected, except the protein-band between 1.0 and 4.0 min (Fig. 2A).

3.2. Method validation

The validation was performed following the requirements of the ICH Tripartite Guideline [21,22] in matrix, using blank plasma samples spiked. The considered validation parameters were: selectivity, linear range, linearity, sensitivity (LOD and LOQ), intra- and inter-day precision and accuracy and robustness.

Table 1
Chromatographic parameters of the analytes studied under the optimized conditions.

Compound	Retention time (min)	Efficiency (N)	Asymmetry (B/A)
4-OH-TAMO	10.25 \pm 0.01	3230	1.36
TAMO-N-oxide	14.52 \pm 0.03	2985	1.18
ENDO	21.04 \pm 0.02	3125	1.24
N-desCH ₃ -TAMO	28.10 \pm 0.03	3350	1.15
TAMO	35.75 \pm 0.04	3458	1.42

$n=3$.

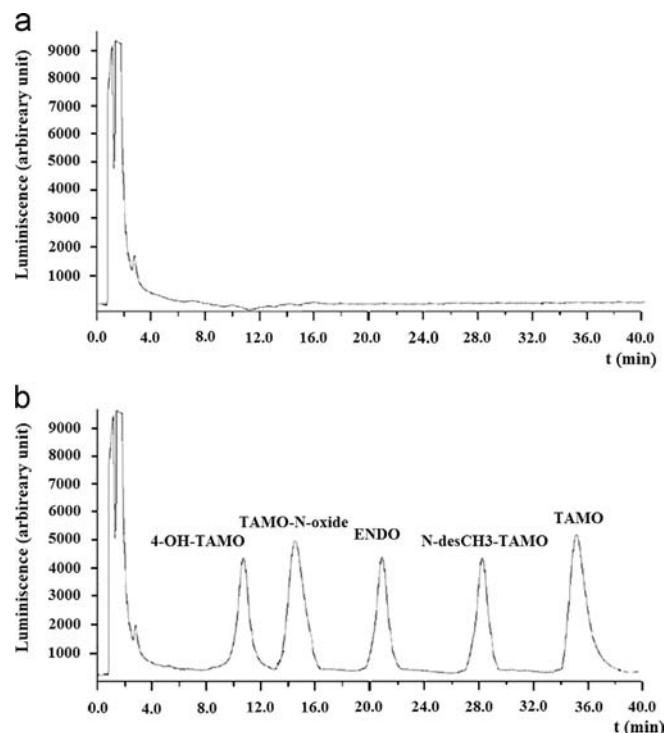


Fig. 2. Chromatograms obtained in the analysis of a blank plasma sample: (A) free of analytes; (B) spiked with 5 $\mu\text{g}/\text{mL}$ of tamoxifen and each tamoxifen derivative.

3.2.1. Specificity

In order to check the absence of endogenous compounds in plasma, which could interfere with the analytes, ten samples of plasma were analyzed under the optimized conditions (Fig. 2A). The protein band appears between the dead time and 4.0 min, and no peak was detected near the elution time of any of the analytes. A plasma sample spiked with 5 $\mu\text{g}/\text{mL}$ of tamoxifen and tamoxifen derivatives was studied. As can be seen in Fig. 2B; each analyte was eluted far enough from the other, avoiding overlapping.

3.2.2. Carry over effect

The carry over effect was studied by analyzing a plasma sample spiked with 15 $\mu\text{g}/\text{mL}$ of TAMO and the studied metabolites. Immediately after, a blank plasma sample free of analytes was analyzed.

No peak of the studied compounds was detected in the chromatogram corresponding to the blank plasma samples. Consequently, no residue of the analytes remains in the needle, in the studied concentration range, and affects the next injection.

3.2.3. Linearity and sensitivity

In order to determine the linear correlation between fluorescence signal and concentration, a blank sample of plasma free of analyte was spiked at nine concentration levels of tamoxifen, 4-OH-TAMO, N-desCH₃-TAMO, TAMO-N-O and ENDO in the range 0.3–15 $\mu\text{g}/\text{mL}$. Slope, intercept and determination coefficient (r^2) were calculated by least square linear regression, plotting the areas of the chromatographic peaks for each analyte vs. concentration ($n=3$). The calibration was repeated five times at separate days (preparing the standard sample on each occasion), over a 2-months period, to consider the interday variation. The regression curves, taken as average of this five calibration curves, are shown in Table 2.

Limit of detection and quantification were calculated as three and ten times, respectively, the standard deviation of the blank

Table 2

Linearity and sensitivity obtained for the analysis of tamoxifen and tamoxifen derivatives analyzed under the optimized conditions (average of 5 intraday calibration curves).

Compound	Slope (for µg/mL)	Intercept	r^2	LOD (ng/mL)	LOQ (ng/mL)
4-OH-TAMO	1380 ± 20	-50 ± 60	0.993	75	200
TAMO-N-oxide	1590 ± 40	50 ± 20	0.998	55	165
ENDO	1420 ± 140	-110 ± 200	0.995	80	220
N-desCH ₃ -TAMO	1450 ± 110	-10 ± 40	0.9998	70	190
TAMO	1750 ± 40	-280 ± 30	0.9992	65	170

Concentration levels=9; replicates (each level)=3.

Table 3

Intra-day ($n=6$) and inter-day ($n=5$) precision and accuracy obtained in the quantification of the analytes.

Compound	Spiked concentration (µg/mL)	Intraday		Interday	
		Accuracy (ϵ_R , %)	Precision (RSD, %)	Accuracy (ϵ_R , %)	Precision (RSD, %)
4-OH-TAMO	0.3	-7.4	6.5	-7.5	9.2
	2	+4.2	5.0	3.5	5.5
	5	-1.0	0.8	-1.5	2.5
TAMO-N-oxide	0.3	+6.5	4.8	+4.2	7.2
	2	+3.8	3.9	+2.5	6.1
	5	-1.2	0.7	-3.5	4.8
ENDO	0.3	-12.2%	6.5%	-8.2	7.2
	2	-4.8	5.0%	-3.2	3.8
	5	+1.8	2.8	+0.5	2.0
N-desCH ₃ -TAMO	0.3	+9.0	5.0	+6.5	6.5
	2	-4.2	3.5	-3.5	5.2
	5	+1.0	0.9	+1.5	2.5
TAMO	0.3	+11.5	6.8	+7.5	8.0
	2	-3.8	4.5	-1.7	3.2
	5	0.9	1.5	2.7	5.0

($n=10$) divided by the slope of the calibration curve [21,22]. The results are shown in Table 2.

The high sensitivity and the linear range cover the concentration levels that can be found in plasma from breast cancer patients treated with tamoxifen formulations.

3.2.4. Accuracy and precision

Blank samples of plasma were spiked with the analytes at three concentrations (0.3; 2.5; 5.0 µg/mL). The intraday accuracy was measured by injecting aliquots of these standards ($n=6$). Accuracy was calculated as the error (%) of the calculated concentration compared to the added concentration. Precision was calculated as the relative standard deviation of the obtained areas (RSD, %). The intraday values were calculated as the average of five measurements of the intraday values taken over a 2-months period. The data show high accuracy (-12.2% to 11.5%) and adequate precision (<9.2%) for all the analytes (Table 3). These results are under the maximal tolerated values by ICH (<15%), indicating that the methodology is useful for routine analysis.

3.2.5. Robustness

The robustness of the method was examined by analyzing a standard solution of tamoxifen and tamoxifen derivatives at 5 µg/mL ($n=3$), by making slight changes to the main chromatographic

conditions (SDS concentration, butanol amount, pH and flow-rate). The variation of sensitivity (peak area) and retention time was calculated for each analyte (Table 4). The low variability of sensitivity (<4.4%) and retention time (<6.3%) indicate that these parameters remain nearly unaffected by low variation of the main chromatographic conditions, indicating the high reliability in the identification and the quantification of the analytes.

3.2.6. Stability

The stability of tamoxifen and its main metabolites in storage conditions was evaluated. A blank plasma sample was spiked with 5 µg/mL of each analyte, analyzed and kept in a fridge (at -20 °C in darkness.). The following day, the sample was thawed, analyzed and replaced in the fridge. This procedure was repeated each day during a 2-months period. No significant diminution in peak area was observed for any of the analytes. Therefore, tamoxifen and the studied metabolites are quite stable during this period.

As the normal storage time of plasma samples extracted from patients is ten days, the method does not show significant degradation problems.

3.3. Analysis of tamoxifen and tamoxifen derivatives in real samples

The method was applied to the analysis of plasma from breast cancer patients, after the oral administration of a single dose of 10 mg of tamoxifen. Samples were taken over a 24-h period and analyses were made by triplicate. For confidentiality reasons, no information about the patients can be provided. The results are shown in Table 5. Fig. 3 shows the chromatogram obtained by analyzing the sample from patient T-2. The analytes were clearly quantified without interferences. A standard sample of plasma containing 1 µg/mL was used as quality control and analyzed at the beginning, each ten samples and at the end, to evaluate the accuracy of the method during sample analysis. As the results were near the true value, the analysis run was considered correct.

The obtained values were: tamoxifen 6.4–16.6 µg/mL; 4-OH-TAMO 0.22–0.40 µg/mL (mainly near LOQ); N-desCH₃-TAMO 3.21–6.0 µg/mL; TAMO-N-oxide 0.75–9.10 µg/mL and endoxifen 0.32–0.9 µg/mL. The presence of significant concentrations of tamoxifen and the detection of lower amounts of endoxifen indicates that the time elapsed between the intake of the tamoxifen formulation and the extraction of the blood for the analysis (24 h) was not enough to find the maximal rate for metabolization of the prodrug. The amount of 4-OH-TAMO remains quite low, indicating that this metabolite is formed at similar rate as it is transformed. However, the intermediate N-desCH₃-TAMO shows higher concentration, indicating that its formation is more fast than its transformation. The variability of tamoxifen, endoxifen and TAMO-N-oxide concentration in plasma indicate that the rate of tamoxifen metabolization is different for each patient. For instance, the patients T-4, T-10 and T-13, show high concentrations of tamoxifen compared with endoxifen, indicating that the patient has a slow tamoxifen metabolism. However, in T-1, T-2 and T-15 and plasma, the amount of endoxifen compared to tamoxifen is higher, indicating the biosynthesis of endoxifen is fast.

The metabolization of tamoxifen depends on the CYP2D6 genotype, but also on other factors (weight, other genes, global metabolism of nutrients, taken food, frame of mind...) then more studies must be made before relating CYP2D6 genotype and the ability to metabolize tamoxifen.

Table 4
Evaluation of the robustness of the MLC method.

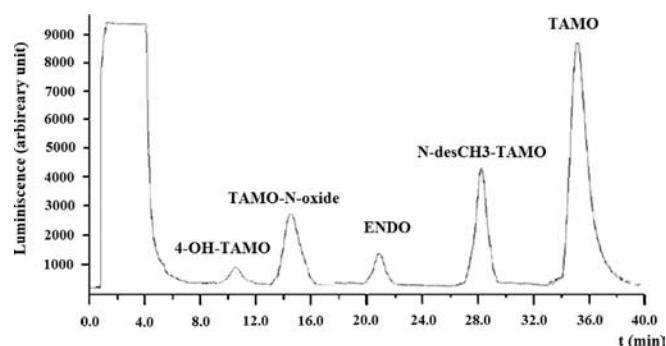
Parameter (levels)	Compound	Retention time (min) (RSD, %)	Peak area (arbitrary unit) (RSD, %)
SDS concentration (0.075–0.085 M)	4-OH-TAMO	10.3 ± 0.4 (3.9)	6880 ± 240 (3.5)
	TAMO-N-oxide	14.6 ± 0.6 (4.1)	7940 ± 350 (4.4)
	ENDO	20.9 ± 0.3 (1.4)	7020 ± 170 (2.3)
	N-desCH ₃ -TAMO	28.1 ± 1.1 (3.9)	7310 ± 190 (2.6)
	TAMO	35.9 ± 0.9 (2.5)	8510 ± 260 (3.1)
Butanol amount (4.4–4.6%)	4-OH-TAMO	9.9 ± 0.5 (5.1)	7010 ± 160 (2.3)
	TAMO-N-oxide	14.2 ± 0.7 (4.9)	7950 ± 190 (2.4)
	ENDO	21.0 ± 0.8 (3.8)	6940 ± 210 (3.0)
	N-desCH ₃ -TAMO	28.5 ± 1.3 (4.6)	7370 ± 110 (1.5)
	TAMO	36.2 ± 2.0 (5.5)	8610 ± 230 (2.7)
pH (2.9–3.1)	4-OH-TAMO	10.6 ± 0.4 (3.8)	6980 ± 90 (1.3)
	TAMO-N-oxide	14.5 ± 0.5 (3.5)	8040 ± 100 (1.5)
	ENDO	21.5 ± 1.0 (4.7)	6890 ± 210 (3.0)
	N-desCH ₃ -TAMO	28.8 ± 1.2 (4.1)	7450 ± 180 (2.4)
	TAMO	35.8 ± 1.8 (5.0)	8680 ± 190 (2.2)
Flow-rate (0.95–1.05 mL/min)	4-OH-TAMO	10.3 ± 0.6 (5.8)	6890 ± 110 (1.6)
	TAMO-N-oxide	13.8 ± 0.7 (5.1)	7950 ± 140 (1.8)
	ENDO	22.0 ± 1.0 (4.5)	6940 ± 190 (2.7)
	N-desCH ₃ -TAMO	27.9 ± 1.6 (5.7)	7620 ± 170 (2.2)
	TAMO	34.9 ± 2.2 (6.3)	8540 ± 200 (2.3)

n=3.

Table 5
Concentration (µg/mL) of the analytes in plasma of breast cancer patients, 24 h after intake of tamoxifen pharmaceutical (n=3).

Patient	4-OH-TAMO	TAMO-N-oxide	ENDO	N-desCH ₃ -TAMO	TAMO
QC1*	0.98	1.04	0.95	1.02	1.1
T-1	0.32 ± 0.04	0.75 ± 0.03	0.65 ± 0.03	3.21 ± 0.09	8.0 ± 0.3
T-2	0.40 ± 0.04	2.11 ± 0.07	0.90 ± 0.05	4.07 ± 0.14	11.3 ± 0.4
T-3	0.29 ± 0.03	4.85 ± 0.18	0.68 ± 0.04	6.0 ± 0.2	14.0 ± 0.5
T-4	0.27 ± 0.04	3.53 ± 0.09	0.32 ± 0.04	4.32 ± 0.18	10.6 ± 0.4
T-5	0.36 ± 0.03	6.0 ± 0.2	0.58 ± 0.03	5.4 ± 0.2	10.7 ± 0.5
T-6	0.36 ± 0.03	9.1 ± 0.4	0.75 ± 0.04	5.13 ± 0.19	15.6 ± 0.7
T-7	0.26 ± 0.04	2.28 ± 0.09	0.41 ± 0.03	4.7 ± 0.2	9.1 ± 0.4
T-8	0.27 ± 0.03	3.71 ± 0.17	0.40 ± 0.03	5.23 ± 0.13	7.6 ± 0.3
T-9	0.22 ± 0.03	0.78 ± 0.03	0.27 ± 0.04	4.39 ± 0.15	6.4 ± 0.3
T-10	0.34 ± 0.04	1.30 ± 0.04	0.48 ± 0.03	5.8 ± 0.2	16.6 ± 0.6
QC2*	0.94	1.05	1.04	0.92	0.94
T-11	0.35 ± 0.04	1.02 ± 0.03	0.41 ± 0.03	4.22 ± 0.17	9.6 ± 0.3
T-12	0.40 ± 0.03	1.09 ± 0.04	0.69 ± 0.04	5.6 ± 0.2	14.0 ± 0.5
T-13	0.32 ± 0.03	1.17 ± 0.06	0.30 ± 0.03	5.42 ± 0.19	12.1 ± 0.4
T-14	0.23 ± 0.02	0.76 ± 0.04	0.40 ± 0.04	4.6 ± 0.2	7.0 ± 0.3
T-15	0.31 ± 0.04	2.17 ± 0.08	0.77 ± 0.05	4.36 ± 0.18	11.9 ± 0.5
QC3*	0.97	0.95	1.02	0.94	0.95

QC=quality control, a plasma sample spiked with 1µg/mL of each analyte; *No replicates.

**Fig. 3.** Chromatogram obtained in the analysis of plasma from a breast cancer patient (T-2).

4. Conclusion

Micellar liquid chromatography has proved a suitable and reliable technique to analyze tamoxifen and its main derivatives (4-OH-TAMO, N-desCH₃-TAMO, TAMO-N-O and ENDO) in human plasma. Diluted samples were directly injected into the chromatographic system, thus avoiding long and tedious extractions. The use of an interpretative strategy and the application of chemometrical statistics allow the determination of the optimal SDS/butanol concentration by testing only five different mobile phases. After sample irradiation to improve sensitivity, the analytes were satisfactorily resolved in a total analysis time under 40 min. Validation was performed according to the ICH guidelines with satisfactory results in terms of linearity, selectivity, precision, accuracy and robustness. The sensitivity and the linear range were sufficient to detect the concentration of tamoxifen and tamoxifen derivatives that could be found in plasma from breast cancer patients taking tamoxifen treatment. Moreover, this method is environmentally friendly, as uses smaller amount of toxic organic solvents and pollutant inorganic salts, and relatively inexpensive, thus making it highly interesting. The analytical method is rapid and useful for routine analysis of these kinds of samples in hospital laboratories. The results were further used to evaluate their ability to metabolize tamoxifen.

Conflict of interest

The authors state that there are not commercial/financial conflict of interest.

Acknowledgments

This study has been supported by the projectP1.1B2012.36, funded by the University Jaume I.

References

- [1] J. Esteve-Romero, E. Ochoa-Aranda, D. Bose, M. Rambla-Alegre, J. Peris-Vicente, A. Martinavarro-Domínguez, *Anal. Bioanal. Chem.* 397 (2010) 1557–1561.
- [2] V.C. Jordan, *Steroids* 72 (2007) 829–842.
- [3] Early Breast Cancer Trialists' Collaborative Group, *Lancet* 365 (2005) 1687–1717.

- [4] S. Aebi, O. Pagani, *Drugs* 67 (2007) 1393–1401.
- [5] E. Ochoa Aranda, J. Esteve-Romero, M. Rambla-Alegre, J. Peris-Vicente, D. Bose, *Talanta* 84 (2011) 314–318.
- [6] S. Borges, Z. Desta, L. Li, T.C. Skaar, B.A. Ward, A. Nguyen, Y. Jin, A.M. Storniolo, D.M. Nikoloff, L. Wu, G. Hillman, D.F. Hayes, V. Stearns, D.A. Flockhart, *Clin. Pharmacol. Ther.* 80 (2006) 61–74.
- [7] Y.C. Lim, Z. Desta, D.A. Flockhart, T.C. Skaar, *Cancer Chemoth. Pharm.* 55 (2005) 471–478.
- [8] M. Zafrá-Ceres, T. de Haro, E. Farez-Vidal, I. Blancas, F. Bandres, E.M. de Dueñas, E. Ochoa-Aranda, J.A. Gomez-Capilla, C. Gomez-Llorente, *Int. J. Med. Sci.* 10 (2013) 932–937.
- [9] V. Stearns, M.D. Johnson, J. Rae, A. Morocho, A. Novielli, P. Bhargava, D.F. Hayes, Z. Desta, D.A. Flockhart, *J. Natl. Cancer Inst.* 95 (2003) 1758–1764.
- [10] M.P. Goetz, S.K. Knox, V.J. Suman, J.M. Rae, S.L. Safgren, M.M. Ames, D.W. Visscher, C. Reynolds, F.J. Couch, W.L. Lingle, R.M. Weinshilboum, E.G. B. Fritcher, A.M. Nibbe, Z. Desta, A. Nguyen, D.A. Flockhart, E.A. Perez, J.N. Ingle, *Breast Cancer. Res. Treat.* 101 (2007) 113–121.
- [11] M.V. Antunes, D.D. Rosa, T.D.S. Viana, H. Andreolla, T.O. Fontanive, R. Linden, *J. Pharm. Biomed. Anal.* 76 (2013) (2013) 13–20.
- [12] J.G. Hiremath, V. Kusum Devi, D. Kshama, K.R. Amarnath, *Indian Drugs* 44 (2007) 103–107.
- [13] Y.B. Zhu, Q. Zhang, C.X. Yu, J.J. Zou, T. Lu, D.W. Xiao, *Chin. Pharm. J.* 44 (2009) 1658–1661.
- [14] E.R. Kisanga, L.L. Haugan Moi, J. Gjerde, G. Mellgren, E.A. Lien, *J. Steroid Biochem* 94 (2005) 489–498.
- [15] C.M. Camaggi, E. Strocchi, N. Canova, F. Pannuti, *J. Chromatogr. B* 275 (1983) 436–442.
- [16] E.A. Lien, P.M. Ueland, E. Solheim, S. Kvinnsland, *Clin. Chem.* 33 (1987) 1608–1614.
- [17] I. Casas-Breva, J. Peris-Vicente, M. Rambla-Alegre, S. Carda-Broch, J. Esteve-Romero, *Analyst* 137 (2012) 4327–4334.
- [18] S. Marco-Peiró, B. Beltrán-Martinavarró, M. Rambla-Alegre, J. Peris-Vicente, J. Esteve-Romero, *Talanta* 88 (2012) 617–622.
- [19] M.L. Chin-Chen, S. Carda-Broch, J. Peris-Vicente, M. Rambla-Alegre, J. Esteve-Romero, S. Marco-Peiró, *J. Food Compos. Anal.* 29 (2013) 32–36.
- [20] M. Rambla-Alegre, J. Peris-Vicente, J. Esteve-Romero, S. Carda-Broch, *Food Chem.* 123 (2010) 1294–1302.
- [21] ICH Harmonized Tripartite Guideline, Validation of Analytical procedures, text and methodologies Q2(R1), Geneva, Switzerland, 2005. Available at: (http://www.ich.org/fileadmin/Public_Web_Site/ICH_Products/Guidelines/Quality/Q2_R1/Step4/Q2_R1__Guideline.pdf), 2013 (accessed: 01.06.13).
- [22] J. Peris-Vicente, S. Carda-Broch, J. Esteve-Romero, M. Rambla-Alegre, D. Bose, B. Beltrán-Martinavarró, S. Marco-Peiró, A. Martinavarró-Domínguez, E. Ochoa-Aranda, M.L. Chin-Chen, *Bioanalysis* 5 (2013) 484–491.
- [23] V. Law, C. Knox, Y. Djoumbou, T. Jewison, A.C. Guo, Y. Liu, A. Maciejewski, D. Arndt, M. Wilson, V. Neveu, A. Tang, G. Gabriel, C. Ly, S. Adamjee, Z.T. Dame, B. Han, Y. Zhou, D.S. Wishart, *Nucleic Acids Res.* 42 D1091–D1097. Available at: (<http://www.drugbank.ca/>), 2014 (accessed: 01.06.14)
- [24] J.R. Torres-Lapasió, *Michrom software*, Marcel Dekker, New York, 2000.



Influence of Pluronic F127 on the distribution and functionality of inkjet-printed biomolecules in porous nitrocellulose substrates

Liyakat Hamid Mujawar^{a,b,*}, Aart van Amerongen^{a,**}, Willem Norde^{b,c}

^a Food and Biobased Research, Biomolecular Sensing and Diagnostics, Wageningen University and Research Centre, Bornse Weilanden 9, 6708 AA Wageningen, The Netherlands

^b Laboratory of Physical Chemistry and Colloid Science, Wageningen University, Dreijenplein 6, 6703 HB Wageningen, The Netherlands

^c University Medical Center Groningen, University of Groningen, A. Deusinglaan 1, 9713 AV Groningen, The Netherlands

ARTICLE INFO

Article history:

Received 29 April 2014

Received in revised form

30 July 2014

Accepted 2 August 2014

Available online 12 August 2014

Keywords:

Inkjet printing

Pluronic

Spot morphology

Nitrocellulose

Orientation

ABSTRACT

The distribution of inkjet-printed biomolecules in porous nitrocellulose substrates often results in a non-homogeneous spot morphology commonly referred to as ‘doughnut-shaped’ spots. We have studied the influence of Pluronic F127 (an amphiphilic surfactant) on the functionality of inkjet-printed primary antibody molecules and on the final assay result by performing a one-step antibody binding assay in the nitrocellulose substrate. The primary antibody was printed with and without Pluronic, followed by the addition of double-labelled amplicons as antigen molecules and a fluorophore-labelled streptavidin as detection conjugate. The distribution of the fluorescence intensity down into the nitrocellulose substrate was investigated by confocal laser scanning microscopy in ‘Z’ stacking mode. Each horizontal slice was further analysed by applying a concentric ring format and the fluorescence intensity in each slice was represented in a colour-coded way. The mean and total fluorescence intensity of the antibody binding assay (fluorescent streptavidin) showed a peak at 0.2% (w/v) Pluronic F127. In addition, an improved spot morphology was observed also peaking at the same Pluronic concentration. Subsequently, we investigated the direct influence of Pluronic F127 on the location of the primary antibody molecules by labelling these molecules with the fluorophore Alexa-488. Our results show that upon increasing the concentration of Pluronic F127 in the printing buffer, the spot diameter increased and the number of primary antibody molecules bound in the spot area gradually decreased. This was confirmed by analysing the distribution of fluorescently labelled primary antibody molecules down into the membrane layers.

We conclude that a particular ratio between primary antibody and Pluronic F127 molecules in combination with available substrate binding capacity results in an optimal orientation, that is *Fab*-UP, of the primary antibody molecules. Consequently, an increased number of antigen molecules (in our case the labelled amplicons) and of the fluorescent detection conjugate (streptavidin) will give an optimal signal. Moreover, distribution of the primary antibody molecules was more homogeneous at the optimal Pluronic F127 concentration, contributing to the better spot morphology observed.

© 2014 Elsevier B.V. All rights reserved.

1. Introduction

Non-contact arraying is a modern tool for printing biomolecules [1] on a range of porous and non-porous substrates. Researchers have shown that high-quality microarrays are produced on porous substrates like nitrocellulose [2,3], porous silicon

[4], alumina [5–7] and hydrogels [8] as compared the non-porous substrates like glass [9] and polystyrene [10]. On porous substrates, a lower limit of detection can be obtained as compared to non-porous substrates [11]. The 3-D matrix of the porous substrates [12] enables more molecules to bind as projected per unit surface area and this results in a better signal-to-noise (S/N) ratio [13]. Of all the available porous substrates, the nitrocellulose membrane has been used extensively in diagnostic applications [2,14–16] and for producing biochips [3,17].

It has been commonly observed that, upon printing, biomolecules often distribute non-homogeneously which results in ‘doughnut-shaped’ spots, also referred to as the ‘coffee-stain’ effect [18–20]. Researchers have successfully demonstrated that

* Corresponding author. Present address: Center of Excellence in Environmental Studies, King Abdulaziz, University, P.O. Box 80216, Jeddah 21589, Saudi Arabia.

** Corresponding author. Tel.: +31 317 480 164; fax: +31 317 483 011.

E-mail addresses: Liyakat.mujawar@gmail.com (L. Hamid Mujawar), Aart.vanamerongen@wur.nl (A. van Amerongen), Willem.Norde@wur.nl (W. Norde).

for DNA microarrays, incorporation of various additives like DMSO [21], polyvinyl alcohol [22], betaine [23] and Triton-X 100 [24] can result in a more homogeneous spot morphology. However, the chemical aspects of DNA microarrays cannot be easily translated to the production of protein microarrays due to the fundamental biophysical and biochemical differences between these two classes of biological substances.

Recently, Norde and Lyklema have shown that Pluronic molecules enhance the functionality of deposited antibodies by forcing them to adsorb at the substrate surface with their antigen binding sites oriented towards the solution [25]. They have also reported that in the presence of Pluronic (P75), the adsorbed IgG molecules showed both improved stability and biological activity. Pluronics are tri-block copolymers with repeating polyoxyethylene-polyoxypropylene-polyoxyethylene (PEO-PPO-PEO) units where the central part (PPO) is hydrophobic and the ends (PEO) are hydrophilic in nature. For our study, we have used Pluronic F-127 which belongs to a class of polymers called as poloxamers [26].

However, Pluronic P75 is very different from Pluronic F127 used by us. Earlier studies performed by Alexandridis *et al.* [27] have shown significant difference in the properties of the two classes of tri-block polymers. More specifically, the molar mass of F127 is 12600 Da whereas that of P75 is 4150 Da and the percentage of PEO in F127 is 70% whereas in P75 it is only 50%. This corresponds to $(\text{PEO})_{100}-(\text{PPO})_{65}-(\text{PEO})_{100}$ for F127 and $(\text{PEO})_{24}-(\text{PPO})_{36}-(\text{PEO})_{24}$ for P75, the subscripts indicating the average number of monomers in the polymer blocks. Thus the two Pluronics differ strongly in length of the respective PPO and PEO blocks. The larger PPO block in F127 allows this Pluronic to attach more strongly to the substratum surface and, more importantly, the longer PEO moieties in F127 allows for a much stronger influence on the orientation of IgG molecules on the substratum surface (see Sections 3.1 and 3.3). On the other hand, Pluronic F127 has been used for inkjet printing applications [28,29] of protein microarrays. Wolter *et al.* have successfully demonstrated that the application of Pluronic F127 improves the signal as well as the limit of detection on a 2-D substrate surface [30]. Therefore, we have selected Pluronic F127 for studying its influence on the functionality of inkjet-printed primary antibody molecules, the final assay result, spot morphology as well as the distribution of biomolecules in nitrocellulose membrane pads.

We have assessed the influence of various concentrations of Pluronic F127 (0 to 1% (w/v)) on the spot morphology and functionality of the primary antibody (anti-FITC). Using a non-contact inkjet printer, primary anti-FITC antibodies were printed on nitrocellulose membrane slides, and the functionality of the primary antibodies was investigated by performing a one-step diagnostic antibody assay based on the binding of a double-labelled amplicon (FITC- and biotin-labelled), as was reported for the nucleic acid microarray immunoassay (NAMIA) [2,9,10]. The distribution as well as the functionality of the primary antibody was judged from the distribution of the fluorescence signal of the final assay (i.e. fluorescent streptavidin). Using confocal laser scanning microscopy, the NAMIA spots were sliced horizontally ('Z' stack method) and the signal distribution profile in each slice was calculated using a concentric ring format. The results are presented in a colour-coded format. Additionally, we also investigated the direct influence of the amphiphilic surfactant (Pluronic F127) on the distribution of the primary antibody molecules that had been labelled with Alexa-488.

2. Material and methods

2.1. Reagents

Pluronic F127 was purchased from Sigma Aldrich (St. Louis, MO, USA), and a 1% (w/v) stock solution was prepared in 150 mM

phosphate buffered saline (PBS, pH 7.4). Running buffer (100 mM borate buffer containing 1% BSA and 0.05% Tween-20) was used as a diluent for the conjugates/labels and also during the intermediate washing steps.

2.2. Biomolecules

Anti-fluoroisothiocyanate (FITC) was purchased from Bioconnect (Huissen, The Netherlands). The DNA templates for *Corynebacterium bovis* were provided by the Animal Health Service, Deventer, The Netherlands. Streptavidin-Alexa-633 for labelling biotinylated amplicons was from Invitrogen (Bleiswijk, The Netherlands).

2.3. Substrates for printing biomolecules

Nexterion nitrocellulose membrane coated slides in 16-pad format were purchased from Schott AG (Mainz, Germany). The dimension of each pad was 6 × 6 mm, whereas the thickness was ~ 11 μm.

2.4. Labelling of the primary anti-FITC antibody

The primary anti-FITC antibody molecules were labelled with Alexa-488 fluorophore using an Alexa-Fluor 488 antibody labelling kit (Invitrogen, Oregon, USA). The labelling procedure was carried out as described by Invitrogen, and the concentration of the fluorophore-conjugated antibody (anti-FITC-Alexa-488) was measured using a Nanodrop-1000-v3.6 spectrophotometer (Wilmington, DE, USA).

2.5. Printing of antibodies on NC membrane slides

Anti-FITC and Alexa-488 conjugated anti-FITC antibodies were diluted ($200 \mu\text{g mL}^{-1}$) in various Pluronic F127 concentrations (0%, 0.01%, 0.05%, 0.1%, 0.2%, 0.4, 0.8% 1.0% w/v) and loaded into the wells of a Genetix microplate (384 wells). The diluted antibodies were printed on the nitrocellulose membrane pads using a non-contact inkjet printer, sciFLEXARRAYER S3 (Scienion AG, Berlin, Germany). The printer was placed in a hood to maintain constant temperature and humidity. Spotting of the biomolecules was performed at room temperature and $70 \pm 1\%$ humidity. The voltage and pulse of the piezo-dispensing capillary (PDC) were optimized to print a droplet of ~250 pL throughout the experiment. The slides were stored overnight in a sealed Al pouch.

2.6. PCR reaction

DNA template from *Corynebacterium bovis* was amplified using primers Cb-F2 and Cb-R3 according to a published protocol [10]. The PCR protocol was optimized to 30 minutes using Phire Hot Start polymerase (Finnzymes) and the Piko thermal cycler (Finnzymes). The forward primer was labelled with a FAM tag and the reverse primer with biotin. The amplification resulted in a double stranded amplicon with at each end a tag, FAM or biotin. Gel electrophoresis confirmed that the amplicon obtained after PCR had the correct band length [31].

2.7. Nucleic acid microarray immunoassay (NAMIA)

To investigate the influence of Pluronic F127 in the printing buffer of the primary anti-FITC antibody a one-step diagnostic assay was performed on the NC membrane slides based on the principle of the Nucleic Acid Microarray Immuno Assay, NAMIA [2,9,10]. Anti-FITC antibodies (specific for the FAM tag) were diluted in various concentrations of Pluronic F127 and printed onto the NC membrane slides. Prior to performing NAMIA, the NC

membrane pads were incubated with running buffer (1 h) as a blocking step. The test was performed as a short incubation (60 min) of the PCR amplicon containing the FAM and the biotin labels and streptavidin-Alexa-633 (see Fig. 1). The final washing was performed with running buffer (two times) followed by rinsing with MQ water. The fluorescence intensity of the signal was related to the functionality of the primary anti-FITC antibody molecules with respect to the Pluronic F127 concentration in the printing buffer.

2.8. Confocal laser scanning microscopy (CLSM)

The spot morphology and the distribution of the biomolecules in the porous NC membranes were analysed by confocal laser scanning microscopy (CLSM; Carl Zeiss Axiovert 200 microscope, Zeiss, Jena, Germany), equipped with a LSM 5 Exciter. The fluorophore-labelled spots were first scanned at a 10x magnification (overall surface fluorescence), where the configuration of the objective was LD Plan-Neofluar 10x/0.30 Korr M27. For Alexa-633 conjugated NAMIA spots, the He-Ne laser set at 633 nm was used, whereas for the Alexa-488 conjugated anti-FITC antibodies, an Ar laser set at 488 nm was used. The size of the pinhole was 182 μm and the transmission was 11%. The dimension of the scanner was X: 1270 μm and Y: 1270 μm . The detector gain values for Alexa-633 and Alexa-488 were 850 and 700, respectively. The gain values were chosen such that no background was obtained for the scanned spot. Using LSM software, the mean intensity, that is the mean intensity per pixel, was calculated per spot. The average of the mean intensities of four NAMIA spots was determined, and data plots were represented along with the standard deviation. For other purposes, the total fluorescence intensity (product of mean intensity and spot pixel area) was used.

The distribution of the fluorescence intensity down into the NC membrane was studied by 'Z' stacking using an oil-immersion lens

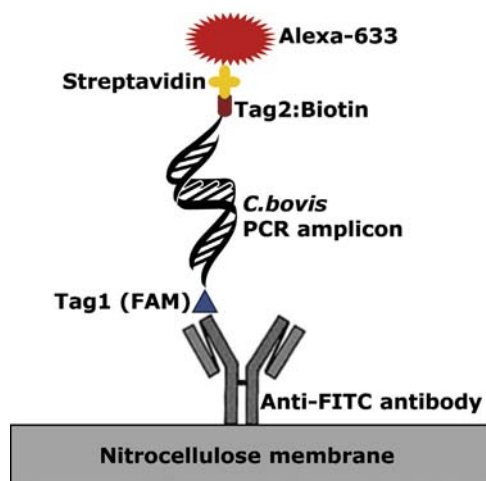


Fig. 1. Schematic representation for detection principle of NAMIA.

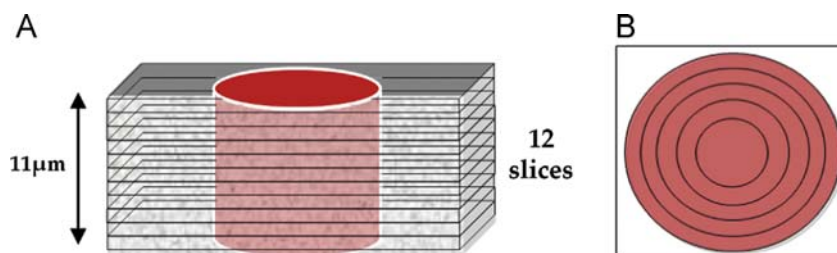


Fig. 2. (A) Schematic representation of the 'Z' stacking method. (B) Schematic view of the five concentric ring model to calculate the distribution of the mean intensity of the concentric rings in each slice of the spot.

(100x magnification). The transmission of He-Ne laser (633 nm) was 24%. The configuration of the objective was LD Plan-Neofluar 100x/0.6 Korr Ph2 M27 and the dimensions of the scanner were X: 127.0 μm , Y: 127.0 μm , Z: 11.03 μm respectively. The pinhole diameter was adjusted to 1.02 μm such that each spot of biomolecule on NC membranes was sliced horizontally into 12 slices with a thickness of 1 μm per slice (Fig. 2-A). Such slicing technique has been already used in the past to investigate the penetration of colloidal ink in paper substrates [32] and to study the distribution of antibodies in NC membrane slides [33,34]. Furthermore, each slice was divided in five concentric-rings (the thickness of each ring was constant and was equal to the radius of the inner ring). The mean intensity of each ring was determined to assess the (in-)homogeneity of the spots (Fig. 2-B). Earlier, Mujawar *et al.* have demonstrated that the interpretation of 'Z' stack data in a colour-coded format gave a clear overview of the distribution of the biomolecules in 3-D substrates [34].

3. Results and discussion

3.1. Influence of Pluronic F127 in the printing buffer of the primary anti-FITC antibody molecules on the final diagnostic assay signal

In order to investigate the influence of Pluronic F127 on the functionality of the primary anti-FITC antibody, a diagnostic antibody assay was performed based on the principle of NAMIA (see Fig. 1) [9,10]. The final assay signal was scored on the basis of the fluorescence of the bound secondary conjugate, streptavidin. With increasing concentration of Pluronic in the printing buffer, the spot radii of the NAMIA spots also increased from 58 to 83 μm (see Fig. 3, panel I-A). The property of a surfactant to enhance the spreading and uniform distribution of a droplet on a substrate surface has also been reported by Dugas *et al.* [35]. They showed that during evaporation of a droplet in the presence of surfactant, the hydrodynamic flow causes the accumulation of the surface-active agents at the periphery of the droplet. This increased concentration lowers the evaporation on the edge of the droplet, thus assisting in a uniform spot deposition throughout the droplet area.

The fluorescence intensity of the assay spots was influenced by the concentration of Pluronic. In the absence of Pluronic (i.e. only PBS in the printing buffer of the primary antibody), the fluorescence signal intensity was low and the spot morphology was doughnut-like (see Fig. 3, panel I-B,C). However, in the presence of Pluronic in the printing buffer, the mean and total fluorescence intensity increased and the doughnut spot morphology was substantially suppressed when the Pluronic concentration was increased to 0.2%. A further increase in the concentration of Pluronic up to 0.4% resulted in a similar spot morphology, but the mean and total fluorescence intensity of the spot was less than that observed for the 0.2% spot. At 1% Pluronic, the fluorescence intensity of the spot was almost vanished (see Fig. 3, panel I-B,C). Wolter *et al.* [30] also observed a similar enhancement in the signal due to incorporation of Pluronic

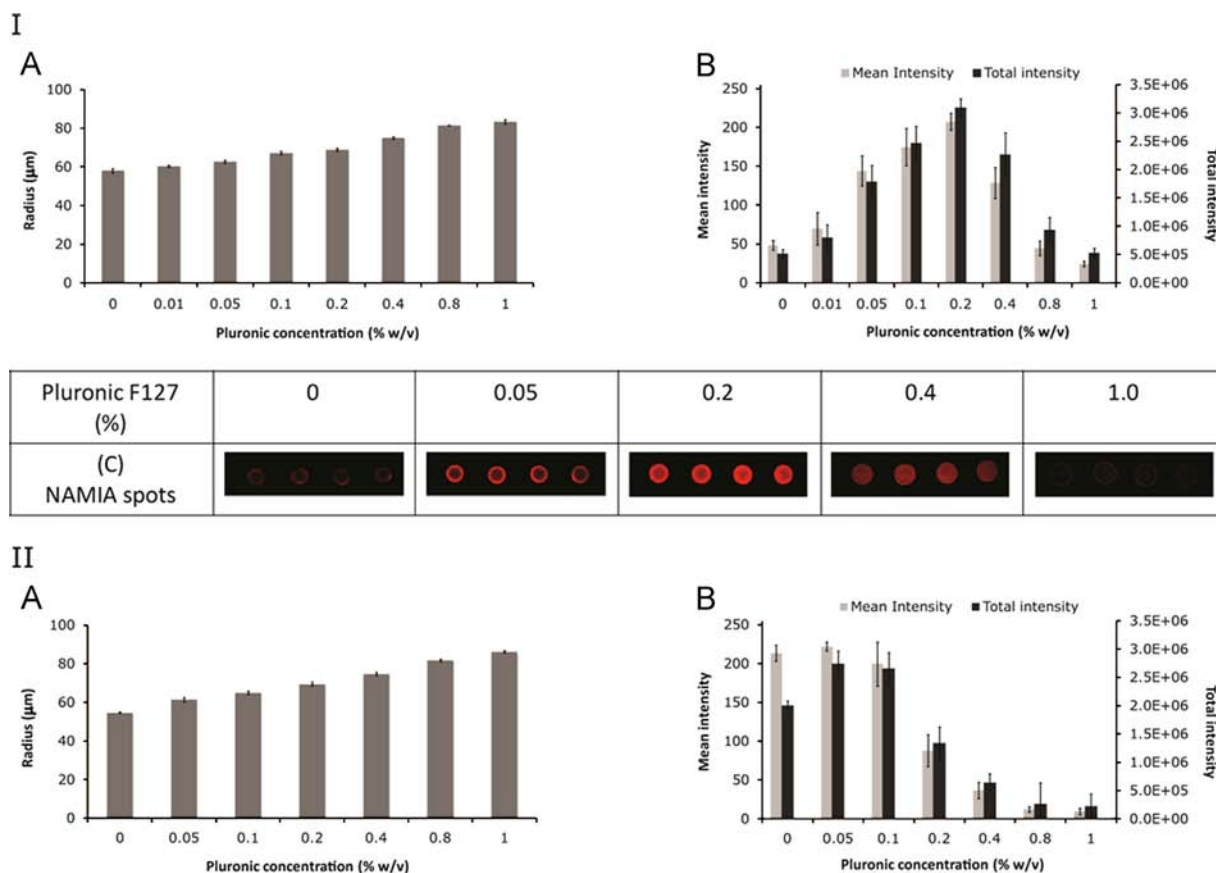


Fig. 3. Panel I shows the influence of Pluronic F127 on the final spot radius upon printing the primary anti-FITC antibody with Pluronic F127 (A) and on the mean and total fluorescence signal intensity, Strep-Alexa-633 (B) of the diagnostic assay. In C, CLSM (10x) images of the assay spots are shown. Panel II shows the spot radius (A) and the mean and total fluorescence (B) of the fluorescently-labelled primary antibody molecules (Alexa-488).

F127. The signal enhancement on a non-porous substrate was mainly due to improved stabilization of protein molecules in the presence of Pluronic F127. However, they noticed excessive spreading of the spots on non-porous substrates, which was further improved by addition of trehalose. We have used a similar approach for improvement of the signal on porous substrate but in addition to this we also studied the distribution of the diagnostic assay signal into the three dimensional matrix of the nitrocellulose substrate and the possible mechanism for signal improvement.

3.2. Influence of Pluronic F127 on the fluorescence signal distribution in a porous substrate and the final signal of the antibody assay ('Z' stack analysis)

Based on the fluorescent dye attached, we also demonstrated the distribution of the primary anti-FITC antibody molecules down into the NC membrane using a 'Z' stacking mode (slicing of the spots) of the CLSM (100x magnification). This kind of slicing technique to study the distribution of the inkjet-printed antibodies down into the NC substrate has been used in the past by Lieshout *et al.* and Mujawar *et al.* [33,34]. In addition, we applied a concentric ring model to measure the fluorescence in rings across the spot in order to assess its morphology, as demonstrated by Mujawar *et al.* [34].

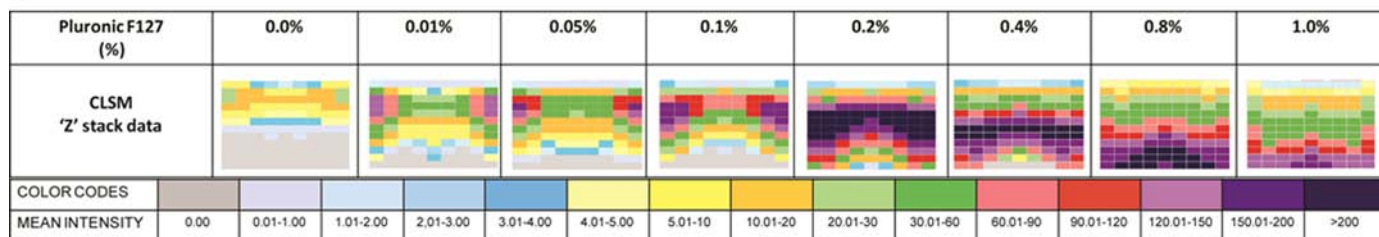
In the absence of Pluronic F127, the distribution of the fluorescence intensity (i.e. assay signal) of the spot in the subsequent slices was non-homogeneous, thus resembling a doughnut-shape distribution, that is higher intensity at the edges than in the centre. As indirectly judged from the final spot fluorescence, it was also observed that in the absence of the amphiphilic surfactant,

the biomolecule penetrates only up to 6 μm deep in the NC membrane (see Fig. 4, panel I). This shows that upon inkjet printing, most of the NC volume beneath the spot was still unoccupied by any biomolecule. Similar observations were reported by Mujawar *et al.* who showed that the substrate properties of NC membrane slides (hydrophobicity/hydrophilicity, wettability) play an important role in the distribution and penetration depth of antibody molecules and also influence the functionality of these inkjet-printed biomolecules [34]. The low fluorescence signals in the absence of Pluronic in the slices just below the surface could be well explained by unfavourable orientations of the antibody molecules that restrict the accessibility of the antigen-binding sites by the antigen [36].

Incorporation of Pluronic (0.01%) in the printing buffer resulted in an increase of the fluorescence intensity of the final assay spot in each slice, along with deeper penetration of the antibody molecules into the membrane. With a further increase in the Pluronic concentration (0.05% and 0.1%), the fluorescence intensity in the horizontal slices not only increased, but was also found to be more homogeneously distributed. The best homogeneously distributed fluorescence intensity distribution was observed throughout all the slices of the assay spots when the anti-FITC antibody was printed with 0.2% Pluronic. Based on the NAMIA spot images and 'Z' stack data, it can be concluded that the distribution of biomolecules in the spots was less homogeneous in the absence of Pluronic F127 as compared to the spots of primary antibodies printed with 0.2% Pluronic (see Fig. 3, panel I-C and Fig. 4, panel I).

A further increase in the Pluronic concentration resulted in spots with a diameter larger than the dimensions of the CLSM scanner, frustrating 'Z' stacking analysis at 100x magnification for

I



II

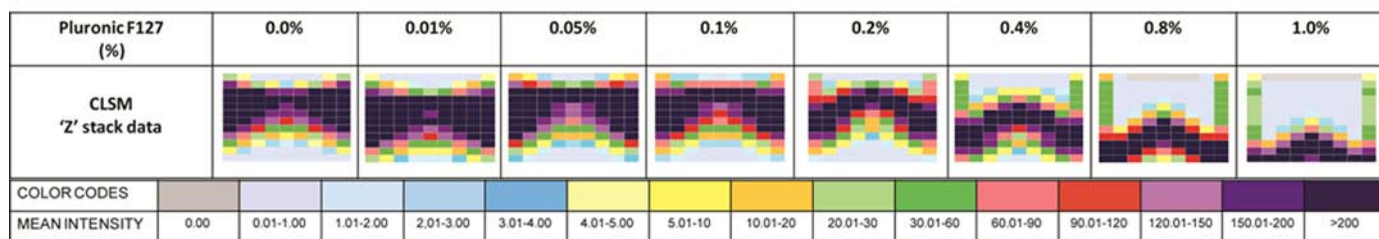


Fig. 4. Influence of Pluronic F127 on the distribution and functionality of primary antibody molecules. Panel I shows the CLSM (100x) 'Z' stack data in colour-coded format of the distribution of the fluorescent signal (Strep-Alexa-633) of the diagnostic assay in 1 μm layers. Panel II shows the CLSM (100x) 'Z' stack data of the distribution of the fluorescently-labelled primary antibody molecules (Alexa-488).

the spots printed with higher Pluronic concentration (i.e. above 0.2%). Even then, we have provided the 'Z' stacks data for the spots printed with 0.4%, 0.8% and 1.0% Pluronic, but limited to the same dimensions as those used for the spots printed with 0.2% Pluronic and lower. As the concentration increases, the biomolecules present in the liquid droplet not only spread horizontally (X-Y) on the NC substrate (see Fig. 3, panel I-A), but also penetrates deeper in the vertical (Z) direction (Fig. 4, panel I). The spreading of liquid droplets in a porous substrate is three-dimensional as compared to a non-porous substrate, onto which it is only two-dimensional. In the presence of surfactant the biomolecules in the liquid droplet spread more homogeneously on non-porous substrates, which is a well-studied phenomenon [35,37].

We also observed that in the absence of Pluronic (i.e. 0% (w/v)) the printed biomolecules were confined to the upper layers of the membrane, indicating a very rapid binding of antibody molecules to the upper nitrocellulose fibres. However, on these porous NC substrates and with increasing Pluronic concentration, the biomolecules penetrated deeper into the NC matrix, that is into layers beneath and outside the visible spot area. The 'Z' stack colour-coded data shows that at higher Pluronic concentration (> 0.2%) less fluorescence (i.e. the fluorescence in the 1 μm NC slices) was observed, whereas the higher fluorescent signals showed up in deeper layers of the membrane. Since the thickness of the NC membrane is only 11 μm and at higher concentrations of the tri-block copolymer molecules binding to the nitrocellulose fibres, the primary antibody molecules most probably were forced to deeper layers of the membrane and to regions outside the spot area as analysed by the Z-stack method. Since the fluorescence signal at deeper layers of the membrane will be weaker as recorded from above the membrane (10x magnification), the final assay signal will be lower at higher Pluronic F127 concentrations, which is indeed the case as shown in Fig. 3, panel I-B and in line with the distribution of the fluorescent signal in the membrane layers as shown in Fig. 4, panel I.

3.3. Influence of Pluronic F127 on the distribution and functionality of the primary antibody molecules

In order to investigate whether the explanation of a lower final fluorescent assay signal upon Pluronic F127 concentrations above 0.2%, the effect of Pluronic 127 on the binding of the primary

antibody molecules was determined. We printed Alexa-488 conjugated primary anti-FITC antibody molecules in various Pluronic concentrations. The NC membrane pads were rinsed twice with running buffer and finally with MQ water. After air drying, the spots of IgG-Alexa-488 on NC pads were scanned (10x) to analyse the total spot fluorescence at various Pluronic concentrations. With increasing concentration of Pluronic, the spot radii of the Alexa-488 conjugated primary anti-FITC antibody molecules also increased (see Fig. 3, panel II-A) as was observed for the final assay spots (compare with Fig. 3, panel I-A). However, the fluorescence intensity of the Alexa-488 conjugated primary antibody molecules was highest in the absence of Pluronic and continued to decrease with increasing Pluronic concentration; an inverse relationship was observed between Pluronic concentration and the mean fluorescence intensity (see Fig. 3, panel II-B). However, the total fluorescence intensity slightly increased when the Pluronic concentration was raised from 0% to 0.05%, but beyond 0.05% the trend for the total fluorescence intensity was similar to that observed for the mean intensity. When the concentration of Pluronic was 0% and 0.05%, the mean intensity was highest whereas for higher Pluronic concentration (up to 1%), the fluorescence intensity was very low. The decrease in the mean and total intensity with increasing Pluronic concentration (Fig. 3, panel II-B), strongly implies that Pluronic F127 molecules itself do not increase (or enhance) the fluorescence intensity of a fluorophore. Pluronics are known to form layers at solid-liquid interfaces where the PPO part have strong affinity to the surface [38]. A recent study by Mohanty *et al.* showed that Pluronic F127 does not result in fluorescence quenching [39]. Increasing the Pluronic concentration up to 20% did not quench the fluorescence signal of the fluorophore (8-anilino-1-naphthalene-sulfonic acid (ANS)). Moreover, the application of the amphiphilic surfactant in pharmacokinetic studies showed a higher fluorescence by the increased uptake of drug molecules upon increasing the concentration of Pluronic molecules [40,41]. From these studies, it can be concluded that the results we observed were not due to the influence of Pluronic F127 molecules on fluorescent signals.

To further investigate the influence of Pluronic molecules, we decided to determine the distribution of the primary Alexa-488 labelled antibodies using the 'Z' stacking mode (slicing of the spots) of the CLSM (100x magnification). In Fig. 4, panel II, it can be

Pluronic F127 (%)	0	0.05	0.2	0.4	1.0
(A) NAMIA spots					
(B) Schematic representation					
Legends					
	Antibody	DNA (PCR) amplicon	Fluorophore	NC membrane	Pluronic F127

Fig. 5. A schematic illustration to explain the optimal diagnostic assay performance at 0.2% Pluronic F127.

seen that the fluorescence distribution is quite similar for the primary antibodies printed with 0 up to 0.1% Pluronic F127. However, at 0.2% the distribution started to differ, especially at the edges of the spots where the higher fluorescent signals was observed in lower layers. A further increase in the Pluronic concentration shifted the higher fluorescent signals even deeper down in the membranes. This observation coincides with the gradual decrease of the total fluorescence as resulting from printed fluorescently-labelled primary antibody molecules (see Fig. 3, panel II-B).

Comparison of data in Fig. 3, panel I-B and II-B and Fig. 4, panel I and II shows that at 0.2% the printed primary antibody molecules are less in number in the spot area (as judged from the total spot fluorescence) but are obviously highly functional. From our results, we have to conclude that the presence of Pluronic in the printing buffer has an effect on the functionality of the primary antibody molecules. Apparently, a particular ratio between primary antibody and Pluronic F127 molecules in combination with available substrate binding capacity in the spot area triggers an optimal orientation of the primary antibody molecules. Consequently, an increased number of antigen molecules (in our case the labelled amplicons) and, hence, of the fluorescent detection conjugate (streptavidin-Alexa-633) will bind, resulting in the highest total signal. Moreover, the distribution of the primary antibody molecules was more homogeneous at the optimal Pluronic F127 concentration, contributing to the better spot morphology observed.

In any immunoassay, the correct orientation of the antibody molecule is crucial as it plays a role in defining the final assay signal. The primary antibodies upon printing on NC membranes may adopt 'Side-ON', 'Flat-ON', 'Fab-UP' and 'Fab-DOWN' orientations [25,42]. When the antibody molecule deposits in a Side-ON or Flat-ON orientation and, even more so, in a 'Fab-DOWN' orientation, fewer 'Fab' binding sites are available for binding antigen molecules. However, in the 'Fab-UP' orientation maximum accessibility of the antigen binding sites is ensured [36]. Thus, in the absence of Pluronic, the printed anti-FITC antibody molecules may orient themselves more or less randomly at the NC surface, that is in any of the before mentioned orientations. In the presence of Pluronic, this polymer competes with the antibody molecules for binding to the substrate surface. Consequently, the density of the antibody molecules at and under the spot is lowered, which would result in a reduced fluorescence intensity of the anti-FITC assay. However, because the Pluronic molecules tend to bind to the surface through their central apolar PPO part, leaving their two terminal polar PEO parts dangling in the solution, antibody molecules most likely dock in the interstitial spaces between the adsorbed Pluronic molecules. At a particular Pluronic concentration, these interstitial spaces are confined such that they prohibit Side-ON, Flat-ON and 'Fab-DOWN' orientations of the antibodies, but

allow accommodation of the less bulky part of the antibody molecule, its Fc part, resulting in a 'Fab-UP' orientation [25]. Docking of the Fc part of the IgG molecule into the PEO layer will more easily occur when the thickness of the brush (~5.5 nm for Pluronic F127) [43] does not exceed the length of Fc part (7.7 nm) [44]. Thus, the adsorbed Pluronic molecules may act as a sieve to force the antibody molecules to adsorb via their Fc part and with their binding sites away from the surface, leaving the 'Fab' binding sites available for binding the antigen molecules. The interaction of the protein molecules with the PEO brushes has been discussed in detail by Norde *et al.* [25,45]. This sieving effect and, hence, the fluorescence intensity of the assay is enhanced with increasing coverage of the NC surface by Pluronic up to a certain degree (i.e. 0.2%) beyond which the Pluronic molecules are too densely packed to allow for sufficient antibody molecules to be incorporated (i.e. 0.4% and higher). As a result, a lower fluorescence intensity of the assay spots was observed when the Pluronic concentration was 0.4% and higher.

The proposed role of Pluronic in assisting IgG molecules has been schematically illustrated in Fig. 5, which most probably explains the differences observed in the fluorescence signals between spots of which the primary anti-FITC antibody was printed with different concentrations of Pluronic F127.

4. Conclusions

Incorporation of the amphiphilic surfactant, Pluronic F127, at a particular concentration in the printing buffer improves the functionality and also the distribution of primary antibodies in porous NC substrates. CLSM data (10x) confirmed that in the presence of Pluronic F127, a more homogeneous morphology was obtained and that the biomolecules distributed more uniformly down into the NC membrane (confirmed by 'Z' stack analysis). A diagnostic assay on top of these primary antibodies with antigen and fluorophore-labelled streptavidin showed that the mean fluorescence intensity was best at a concentration of 0.2% Pluronic F127 in the printing buffer. It is concluded that at this optimal concentration, Pluronic F127 molecules induced the preferred orientation of the primary antibody molecules, that is 'Fab-UP', resulting in an improved final assay signal.

Acknowledgements

This research is supported by the Dutch Technology Foundation STW, Applied-Science Division of NWO (Dutch Organisation for Scientific Research) and the Technology Program of the Ministry of Economic Affairs of The Netherlands

References

- [1] J.B. Delehanty, F.S. Ligler, *Anal. Chem.* 74 (2002) 5681–5687.
- [2] P.S. Noguera, G.A. Posthuma-Trumpie, M. van Tuil, F.J. van der Wal, A.d. Boer, A. P.H.A. Moers, A. van Amerongen, *Anal. Chem.* 83 (2011) 8531–8536.
- [3] L.H. Mujawar, A. Moers, W. Norde, A. Van Amerongen, *Anal. Bioanal. Chem.* 405 (2013) 7469–7476.
- [4] A. Ressine, G.r. Marko-Varga, T. Laurell, M.R. El-Gewely, Porous silicon protein microarray technology and ultra-/superhydrophobic states for improved bioanalytical readout, in: *Biotechnology Annual Review, Elsevier* (2007) 149–200.
- [5] S.Y. Kim, J. Yu, S.J. Son, J. Min, *Ultramicroscopy* 110 (2010) 659–665.
- [6] Y. Wu, P. de Kievit, L. Vahlkamp, D. Pijnenburg, M. Smit, M. Dankers, D. Melchers, M. Stax, P.J. Boender, C. Ingham, N. Bastiaensen, R. de Wijn, D. van Alewijk, H. van Damme, A.K. Raap, A.B. Chan, R. van Beuningen, *Nucleic Acids Res* 32 (2004) e123.
- [7] R. Hilhorst, L. Houkes, A. van den Berg, R. Ruijtenbeek, *Anal. Biochem.* 387 (2009) 150–161.
- [8] J.C. Miller, H. Zhou, J. Kwekel, R. Cavallo, J. Burke, E.B. Butler, B.S. Teh, B.B. Haab, *Proteomics* 3 (2003) 56–63.
- [9] L.H. Mujawar, W. Norde, A. van Amerongen, *Analyst* 138 (2013) 518–524.
- [10] L.H. Mujawar, A. van Amerongen, W. Norde, *Talanta* 98 (2012) 1–6.
- [11] M. Reck, F. Stahl, J.G. Walter, M. Hollas, D. Melzner, T. Scheper, *Biotechnol. Progr* 23 (2007) 1498–1505.
- [12] M. Dufva, *Biomol. Eng* 22 (2005) 173–184.
- [13] J.-G. Walter, F. Stahl, M. Reck, I. Praulich, Y. Nataf, M. Hollas, K. Pflanz, D. Melzner, Y. Shoham, T. Scheper, *Eng. Life Sci.* 10 (2010) 103–108.
- [14] J. Petrik, *Transfusion Med* 16 (2006) 233–247.
- [15] T. Kukar, S. Eckenrode, Y. Gu, W. Lian, M. Megginson, J.-X. She, D. Wu, *Anal. Biochem.* 306 (2002) 50–54.
- [16] L. Mujawar, A. Moers, W. Norde, A. Amerongen, *Anal. Bioanal. Chem.* 405 (2013) 7469–7476.
- [17] B.A. Stillman, J.L. Tonkinson, *BioTechniques* (2000) 630–635.
- [18] R.D. Deegan, *Phys. Rev. E* 61 (2000) 475.
- [19] R.D. Deegan, O. Bakajin, T.F. Dupont, G. Huber, S.R. Nagel, T.A. Witten, *Nature* 389 (1997) 827–829.
- [20] R.D. Deegan, O. Bakajin, T.F. Dupont, G. Huber, S.R. Nagel, T.A. Witten, *Phys. Rev. E* 62 (2000) 756.
- [21] M.K. McQuain, K. Seale, J. Peek, S. Levy, F.R. Haselton, *Anal. Biochem.* 320 (2003) 281–291.
- [22] P. Wu, D.W. Grainger, *J. Proteome Res* 5 (2006) 2956–2965.
- [23] F. Diehl, S. Grahmann, M. Beier, J.D. Hoheisel, *Nucleic Acids Res* 29 (2001).
- [24] Y. Deng, X.Y. Zhu, T. Kienlen, A. Guo, *J. Am. Chem. Soc.* 128 (2006) 2768–2769.
- [25] W. Norde, J. Lyklema, *Adv. Colloid Interfac.* 179–182 (2012) 5–13.
- [26] M. Bohorquez, C. Koch, T. Trygstad, N. Pandit, *J. Colloid Interfac.* 216 (1999) 34–40.
- [27] P. Alexandridis, T. Alan Hatton, *Colloid Surface A* 96 (1995) 1–46.
- [28] B. Fousseret, M. Mougenot, F. Rossignol, J.-F. Baumard, B. Soulestin, C. Boissière, F. Ribot, D. Jalabert, C. Carrion, C. Sanchez, M. Lejeune, *Chem. Mater* 22 (2010) 3875–3883.
- [29] A. Kosmala, Q. Zhang, R. Wright, P. Kirby, *Mater. Chem. Phys.* 132 (2012) 788–795.
- [30] A. Wolter, R. Niessner, M. Seidel, *Anal. Chem.* 79 (2007) 4529–4537.
- [31] K.-H. Lee, J.-W. Lee, S.-W. Wang, L.-Y. Liu, M.-F. Lee, S.-T. Chuang, Y.-M. Shy, C.-L. Chang, M.-C. Wu, C.-H. Chi, *J. Vet. Diagn. Invest.* 20 (2008) 463–471.
- [32] A. Isogai, M. Naito, Y. Ozaki, H. Nagashima, T. Enomae, *J. Imaging Sci* 55 (2011) (20201–20201–20201–20208).
- [33] R.M.L. van Lieshout, T. van Domburg, M. Saalmink, R. Verbeek, R. Wimberger-Friedl, M.P. van Diejen-Visser, C. Punyadeera, *Anal. Chem.* 81 (2009) 5165–5171.
- [34] L.H. Mujawar, A.A. Maan, M.K.I. Khan, W. Norde, A. van Amerongen, *Anal. Chem.* 85 (2013) 3723–3729.
- [35] V. Dugas, J. Broutin, E. Souteyrand, *Langmuir* 21 (2005) 9130–9136.
- [36] A.K. Trilling, J. Beekwilder, H. Zuilhof, *Analyst* 138 (2013) 1619–1627.
- [37] A. Mohammad Karim, H.P. Kavehpour, *J. Coat. Technol. Res.* (2013) 1–6.
- [38] V.N. Luk, G.C.H. Mo, A.R. Wheeler, *Langmuir* 24 (2008) 6382–6389.
- [39] M.E. Mohanty, V.J. Rao, A.K. Mishra, *Spectrochim. Acta A* 121 (2014) 330–338.
- [40] A. Al-Nahain, S.Y. Lee, I. In, K.D. Lee, S.Y. Park, *Int. J. Pharm.* 450 (2013) 208–217.
- [41] Y. Zhao, D.Y. Alakhova, J.O. Kim, T.K. Bronich, A.V. Kabanov, *J. Control. Release* 168 (2013) 61–69.
- [42] M.E. Wiseman, C.W. Frank, *Langmuir* 28 (2012) 1765–1774.
- [43] M.R. Nejadnik, A.L.J. Olsson, P.K. Sharma, H.C. van der Mei, W. Norde, H. J. Busscher, *Langmuir* 25 (2009) 6245–6249.
- [44] L.F. Pease, J.T. Elliott, D.-H. Tsai, M.R. Zachariah, M.J. Tarlov, *Biotechnol. Bioeng.* 101 (2008) 1214–1222.
- [45] W. Norde, D. Gage, *Langmuir* 20 (2004) 4162–4167.



New nano-composite potentiometric sensor composed of graphene nanosheets/thionine/molecular wire for nanomolar detection of silver ion in various real samples

Abbas Afkhami^{a,*}, Ali Shirzadmehr^a, Tayyebeh Madrakian^a, Hasan Bagheri^b

^a Faculty of Chemistry, Bu-Ali Sina University, Hamedan, Iran

^b Chemical Injuries Research Center, Baqiyatallah University of Medical Sciences, Tehran, Iran

ARTICLE INFO

Article history:

Received 12 May 2014

Received in revised form
20 July 2014

Accepted 2 August 2014

Available online 20 August 2014

Keywords:

Potentiometric sensor

Graphene

Carbon paste electrode

Silver(I)

Molecular wire

ABSTRACT

A novel nanographene carbon composite potentiometric sensor for the determination of trace amounts of silver(I) ion was fabricated. Its sensing layer was prepared with the addition of graphene nanosheets into the matrix consisting of graphite powder, diphenylacetylene “a typically molecular wire (MW) as the conductive binder” and thionine as an efficient ionophore. For investigation of the ion-to-electron transducing ability of graphene nanosheets and molecular wire on the electrode surface, the electrochemical impedance spectroscopy measurements were done and the morphology and properties of the electrode surfaces were characterized by scanning electron microscopy. Under the optimized experimental conditions, the suggested potentiometric silver(I) sensor exhibited an excellent Nernstian slope of 59.70 mV decade⁻¹ with a rapid response to silver(I) ion within ~6 s. The response was linear in the range 8.00 × 10⁻⁹ to 1.00 × 10⁻² mol L⁻¹ and calculated detection limit was 4.17 × 10⁻⁹ mol L⁻¹. The suggested sensor was successfully applied to the determination of silver in radiological film, environmental and drug samples with satisfactory results.

© 2014 Elsevier B.V. All rights reserved.

1. Introduction

Due to strict environmental legislations and to protect natural resources, it is now necessary to develop a new techno-economical process for recycling treatment of industrial effluents [1,2]. The presence of soluble silver species in waste waters is one of the problems shared by many industrial processes. Silver is an important element that is mainly used in electroplating, photographic and imaging industries, graphic arts, dental and medical products, electrical and electronic equipments [3–5]. Also, it is an important ion in some drugs like silver sulfadiazine cream that has been a standard treatment for burns over the past decades and silver deposition has been found in the skin, gingival, cornea, liver, and kidney of patients [6]. In addition, silver is the most ancient metal and finds numerous applications in other fields like jewelry, coins, mirrors, anti-corrosive alloys and in the production of light sensitive devices [7]. It is reported that the concentration of silver in water sources higher than 1.6 nmol L⁻¹ is toxic for fish and microorganisms. It has also been found that silver is toxic for humans at a concentration higher than 0.9 μmol L⁻¹ in drinking water [8–10].

With attention to these cases, determination of trace amount of silver ions in environmental and industrial samples has great importance. Various instrumental techniques have been employed for the determination of silver species in different real samples, including atomic absorption spectroscopy (AAS) [11,12], inductively coupled plasma-mass spectrometry (ICP-MS) [13,14], inductively coupled plasma optical emission spectrometry (ICP-OES) [15] and flow injection analysis [16]. However, these techniques are too expensive that are not applicable for in-situ analysis. So, the development of convenient and direct methods for the assay of silver in different real samples is an urgent need. Electrochemical sensors have been widely used to determine various species due to their high sensitivity and desirable selectivity in their responses [17–30]. Among these sensors, potentiometric carbon paste electrodes (CPEs), due to the ease of their construction, easy renewability of the surface, inexpensive techniques, chemical inertness, robustness, stability of response, low ohmic resistance, no need of internal solution and compatibility with various types of modifiers have been widely used as simple tools for detecting various analytes. Further, their modification can improve the surface state of the electrode, which may lead to increase target signals significantly [18–26]. The ion-sensing properties of potentiometric CPEs largely depend on the nature of the employed sensing materials. In recent years, research activities are related to the optimization and rational design of both ionophores

* Corresponding author.

E-mail address: afkhami@basu.ac.ir (A. Afkhami).

and matrices targeted to particular applications [21–26]. At the same time, the search for novel matrices became the subject of increasing interest. Graphene has attracted in electrochemical sensing field in recent years [31] due to its unique physicochemical properties such as high specific surface area, chemical stability and electrical conductivity [32], excellent thermal conductivity [33] and strong mechanical strength [34]. Furthermore, in comparison to carbon nanotubes (CNTs), graphene compounds provide the advantages of low production cost and low metallic contamination levels [35]. For the potential application of a certain kind of carbon materials in electrochemical studies, their basic electrochemical behaviors should be first studied to determine several important parameters of sensors [36,37], e.g., electrochemical potential window, heterogeneous electron transfer rate, etc. For these reasons, graphene has begun to be exploited as an alternative choice for electrical sensors, especially during the fabrication of electrochemical sensing devices [38]. Herein, we report application of a novel sensing composite that act as a matrix and ionophore for improving response of the sensor. It is based on graphene nanosheets (GNS), diphenylacetylene (DPA), and thionine and was fabricated for the determination of Ag(I). Thionine (TH) showed good behaviour as an efficient ionophore due to the excellent interactions with silver(I) ion [39]. The results showed that the sensor response was enhanced by replacing paraffin oil with a conductive binder agent (DPA). Also, combination of GNS and Th into the paste could amplify the signal significantly. Moreover, the sensor could also be renewed easily by mechanical polishing whenever needed.

2. Experimental

2.1. Apparatus

The constructed Ag(I) selective CPE, as the working electrode, and a double junction Ag/AgCl (Azar electrode, Iran) as the reference electrode, were placed in a glass cell and used for the potentiometric measurements. Both the electrodes were connected to a digital milli-voltmeter (HIOKI 3256.50). Electrochemical impedance spectroscopy (EIS) was performed using an Autolab PGSTAT 302 N potentiostat/galvanostat. A Metrohm pH-meter with a combined glass electrode was used for pH controlling, and a Heidolph type of (MR 2000) stirrer was used for stirring the solutions. Scanning electron microscopy (SEM) was performed to survey the electrode surface (SEM-EDX, XL30, Philips Netherland). Inductively coupled plasma-atomic emission spectroscopy (ICP-AES) was used as its manual. An Agilent 8453 diode array UV–vis spectrophotometer (Agilent, USA) equipped with a 1.0 cm path length quartz cell was used to obtain absorbance spectra and absorbance curves.

2.2. Reagents and materials

Natural graphite powder (98%, 50 mesh, and 2–5 mm in lateral size) was obtained from Hyundai Coma Ind. Co., Korea. DPA (Merck), and high-purity paraffin oil (Aldrich) were used for the preparation of carbon pastes. Chloride and nitrate salts of the cations were purchased from Merck and TH was purchased from Sigma-Aldrich. Distilled deionized water was used throughout all experiments.

2.3. Preparation of graphene nanosheets

For synthesis of graphene nanosheets first, the graphene oxide (GO) was prepared with a modified Hummer's method [40]. GNS was prepared by the reduction of GO according to the literature [41] as follow: about 100 mg of GO was loaded in a 250 mL round

bottom flask and then 100 mL of water was added, yielding an inhomogeneous yellow–brown dispersion. This dispersion was sonicated until it became clear with no visible particulate matter. Then 1.00 mL, 32.1 mmol, hydrazine hydrate was added and the solution was heated in an oil bath at 100 °C under a water-cooled condenser for 24 h over which the reduced GO gradually precipitated out as a black solid. This product was filtrated and isolated, washed copiously with appropriate volume of water and methanol, and dried on the funnel under a continuous air flow through the solid product cake.

2.4. Preparation of working electrodes

The unmodified CPE (Table 1, No. 1) was prepared by hand-mixing of graphite powder with paraffin oil at a ratio of 70:30 (w/w) in an agate mortar and grounded homogeneously for about 25 min. For fabrication of CPEs modified with ionophore, the pastes were prepared by hand-mixing of graphite powder with paraffin oil and different ratio of TH (Table 1, No. 2–4). The GNS modified pastes (Table 1, No. 5, 6) were prepared by hand-mixing of the graphite powder, GNS, TH and paraffin oil with an appropriate ratio in an agate mortar to form a homogeneous paste. Eventually, the (GNS/TH/MW)-CPEs (Table 1, No. 7, 8) were prepared by mixing the appropriate amounts of graphite powder, TH, GNS and DPA together in an agate mortar. The mixture should be heated in an oven at 65 °C for 3 min, which is higher than the melting point of DPA (m.p.=62.5 °C). It was then left to cool to room temperature [42]. By this procedure graphite powder and graphene nanosheets could be totally mixed with DPA to get a stable modified carbon paste.

The resulting mixtures (prepared by the above-mentioned method) were transferred into an insulin syringe with an internal diameter of 2.5 mm and a height of 3 cm as an electrode body. After the homogenization of each mixture, a portion of the prepared paste was carefully packed into the tube tip to avoid possible air gaps, which often enhance the electrode resistance. A copper wire was inserted into the opposite end of the CPE to establish electrical contact. Prior to use, the external surface of the carbon paste was smoothed with a soft paper. A new surface was produced by scraping out the old surface and replacing the new carbon paste.

Finally, the electrodes were conditioned for 24 h by soaking in a 1.00×10^{-3} mol L⁻¹ silver(I) nitrate solution. The pH of the solution was adjusted at 5.5.

Table 1
Optimization of the carbon paste compositions.

Electrode no	Binder	Ionophore (TH) (%)	Graphite powder (%)	GNS (%)	Slope (mV decade ⁻¹)
1	30%-Paraffin	0.0	70	0.0	9.87 ± 0.14
2	30%-Paraffin	5.0	65	0.0	36.72 ± 0.13
3	30%-Paraffin	7.0	63	0.0	41.32 ± 0.22
4	30%-Paraffin	.0	62	0.0	40.91 ± 0.31
5	30%-Paraffin	7.0	58	5.0	48.71 ± 0.31
6	30%-Paraffin	7.0	53	10.0	54.89 ± 0.31
7	30%-MW (DPA)	7.0	53	10.0	59.70 ± 0.10
8	30%-MW (DPA)	7.0	48	15.0	59.23 ± 0.11

2.5. Preparation of real samples

In order to demonstrate the applicability and reliability of the suggested silver sensitive sensor, for five real samples including mineral water, river water and industrial manufactory waste water samples, silver sulphadiazine burning cream and radiological film were prepared and analyzed by the method.

The river water sample was collected in polyethylene bottle and acidified with nitric acid. This sample was filtered to remove any solid particles before the analysis. Standard Ag(I) solution was spiked into appropriate of the mineral water. The pH of the water samples was adjusted at pH 5.5.

Industrial manufactory waste water sample was taken from Hamedan industrial zone. This water sample was acidified with $1.0 \text{ mol L}^{-1} \text{ HNO}_3$ and heated for 1 h until its volume reach to one tenth. Then, the pH of the water sample was adjusted at pH 5.5 via dilute NaOH.

For the preparation of cream sample, about 2 g of silver sulphadiazine cream was weighed and dissolved in $\text{HNO}_3/\text{HClO}_4/\text{H}_2\text{O}_2$ as described in the literature [43].

The radiological film sample was prepared as follows [44]: radiology films (2 g) were dry ashed in a muffle furnace at 450°C for 90 min. The residue was dissolved in nitric acid, boiled for 3 h and evaporated to dryness at low heating rate. The residue was dissolved in 80 mL of distilled water and filtered. The filtrate was adjusted to pH 5.5 using NaOH solution and then quantitatively diluted with appropriate double distilled water.

2.6. Spectrophotometric studies

TH with a sulfur atom and two amine groups donating ligand is insoluble in water. Consequently, we investigated the complexation of silver ion in ethanol solution. A typical spectrum was depicted in Fig. S1 (Supplementary data). As it can be observed, significant apparent changes in the peaks intensity and appearance of a new peak for Th after adding of analyte ions indicate that, the ligand has strong interaction with Ag(I) ions. Therefore, it may be used as an efficient ionophore for detecting of Ag(I). Further analyzing the absorbance at maximum absorbance wavelength, using a nonlinear least-squares curve-fitting program (Kinfit program), provided the stoichiometry and stability constant of Th complex with the Ag(I) [27]. From the results observed for analyte at a mole ratio of 0.5, it can be immediately concluded that a 2:1 complex of $[\text{ML}_2]$ with the stability constant of $\log K_f = 6.10$ is formed in the ethanol solution. Furthermore, we decided to use TH as a suitable ionophore for the selective determination of silver ion using potentiometric carbon paste electrode because of its excellent metal-binding properties and water insolubility.

3. Results and discussion

The obtained results from some experimental works revealed that the performance of the suggested Ag(I) potentiometric carbon paste sensor based on nanographene composite can be highly improved by adding GNS and TH into paste and application of DPA instead of paraffin oil. For this purpose, the potentiometric responses of the unmodified CPE and modified CPE with the new nano-composite towards Ag(I) ions were studied in terms of linear range, detection limit, selectivity coefficients, response time, lifetime and response stability, which are important characteristics of every ion selective CPEs, and compared with some previously reported Ag(I) potentiometric sensors based on different compositions [45–50].

3.1. Electrode composition and modification

It is well known that the sensitivity, linear dynamic range and selectivity obtained for an ion selective electrode (ISE) depend significantly on the composition of the electrode [17–26]. Thus, it is necessary to investigate the influence of the paste composition on the potential responses of the modified CPEs. For this purpose, several electrodes with different compositions were investigated in this study. Unmodified CPE was prepared by mixing 70% of graphite powder with 30% of paraffin oil in a mortar and pestle. Modified pastes were prepared in a similar fashion, except that the graphite powder was mixed with a desired weight of TH, GNS and DPA to get different compositions as given in Table 1. As can be seen, the electrode without the ionophore (sensor No. 1) showed poor sensitivity to silver cation. Also, an increase at the TH level in the CPE (sensor No. 2, 3) caused a slope increase of the calibration curve, whereas, in the presence of the ionophore, the electrode showed remarkable selectivity for Ag(I). It is possible that the presence of S and N atoms in TH generate a great affinity between the ionophore and the Ag(I) ion. This indicated that ionophore is the most important component in the proposed carbon paste electrodes for sensing silver ion. Further addition of the ionophore (sensor No. 4), however, resulted in a little decrease in the response of the electrode. This phenomenon can arise from the decrease of graphite powder/TH ratio, thereupon decreases of paste homogeneities and conductivity [51].

According to Table 1, the electrode composed of 30% DPA, 7% TH, 53% graphite powder, 10% GNS, (No. 7) has optimum composition for sensing Ag(I). This new composition was selected for further examinations.

Recent years MWs have aroused great attention due to their specific characteristics such as good chemical and thermal stability, high conductivity and wide electrochemical windows [52–54]. They are molecular scale compounds that have been exhibited excellent electrical conductivity. DPA is the smallest conjugated oligomer and can be used as a conducting binder in CPEs. Safavi et al. fabricated a DPA based MW modified carbon paste electrode (MW-CPE) and investigated its electrochemical behavior, which exhibited better performances than the prepared CPE using paraffin oil [42]. In this study we used DPA as the conductive binder instead of paraffin oil in the carbon paste, provides higher sensitivity in the determination of Ag(I). Due to the effects of conjugated system of DPA and its π - π interaction with graphene and graphite powder, with their combination, a stable modified carbon paste electrode and a higher sensitivity for the target analyte detection was achieved (Table 1) [55–57].

Also, for improving the electrochemical performance of the sensor, the GNS can be used as an excellent candidate of conventional modifier for the modification of CPE owing to its superior electrical conducting ability and high specific surface area [32]. So, we used GNS into the carbon paste that increased the available surface area and improved the conductivity property of the electrode surface and, therefore, conversion of the chemical signal to an electrical one.

3.2. Effect of the GNS/graphite ratio on the performance of the suggested modified CPE

As an electrical conducting modifier, the amount of GNS mixed in the carbon paste would influence the performance of the suggested modified electrode. The redox couple of $[\text{Fe}(\text{CN})_6]^{3-/4-}$ was chosen to characterize the electron transfer properties of different amount of GNS added into the carbon pastes. According to the literature [58] the electron transfer property of the redox couple is strongly dependent on the surface chemistry and microstructure as well as the density of electronic states of electrode

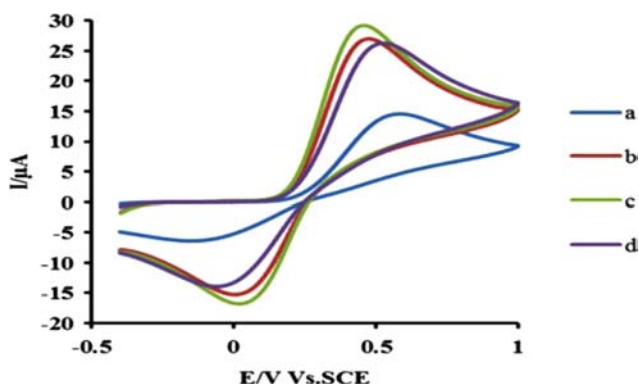


Fig. 1. CVs of 1.0 mmol L^{-1} $[\text{Fe}(\text{CN})_6]^{4-}$ at the unmodified CPE (a) and different GNS mixed CPEs with GNS/graphite ratios of 5/58% (b), 10/53% (c), 15/48% (d), respectively. Scan rate: 100 mV s^{-1} .

materials near the Fermi level. Fig. 1 shows CVs of $[\text{Fe}(\text{CN})_6]^{3-/4-}$ at the unmodified CPE and CPE modified with different amounts of GNS. It was evident that $[\text{Fe}(\text{CN})_6]^{3-/4-}$ exhibited a poor electrochemical behavior on unmodified CPE (curve a), with a larger peak-to-peak potential separation (ΔE_p) than others, and relatively broadened wave shape. However, by increasing the GNS ratio up to about 10% into the pastes the electrochemical response of $[\text{Fe}(\text{CN})_6]^{3-/4-}$ was improved. With increasing the GNS/graphite ratio (from curve a to curve c), both cathodic and anodic peak current increased, and the ΔE_p values for the suggested modified CPEs (curves b to d) were 425, 402 and 518 mV, respectively. It is obvious that the GNS mixed CPE at the weight ratio of 10/53% exhibited the relatively smallest ΔE_p and highest peak currents (curve c). The excellent conducting property of GNS could contribute to the improved electrochemical response of the modified CPEs toward $[\text{Fe}(\text{CN})_6]^{3-/4-}$. However, increasing the amount of the GNS higher than 10% in the composition of the paste may lead to undesirable mechanical properties of the suggested CPE, which correspondingly decreased the electron transfer rate of $[\text{Fe}(\text{CN})_6]^{3-/4-}$ (curve d). Accordingly, an optimized GNS/graphite ratio for the preparation of suggested CPE was selected as 10/53% (c).

3.3. Electrochemical behavior of Ag(I) at the surface of various electrodes

The CVs were obtained for the unmodified CPE, TH-CPE, (GNS/TH)-CPE and (GNS/TH/MW)-CPE in the absence and presence of analyte in KNO_3 0.1 mol L^{-1} solution. The results are summarized in Fig. S2. There is no observable peaks for an unmodified CPE in the absence of Ag(I) (curve a). Curves b, c, d and e show CVs of unmodified CPE, TH-CPE, (GNS/TH)-CPE and (GNS/TH/MW)-CPE in the presence of $1.00 \times 10^{-3} \text{ mol L}^{-1}$ Ag(I), respectively. Concerning Ag reversible wave with oxidation peak on the forward scan at about 0.38 V vs. SCE and cathodic peak on the reverse scan at 0.22 V vs. SCE. A comparison of oxidation and reduction peak currents for Ag at the unmodified CPE, TH-CPE, (GNS/TH)-CPE and (GNS/TH/MW)-CPE indicate an enhancement with each step of modifications, which are due to the increase in the surfaces area and functionality of (GNS/TH/MW)-CPE, as compared with unmodified CPE. Therefore, as expected for a modified process, GNS/TH/MW composite caused an increase in the sensitivity of the sensor.

3.4. EIS studies

EIS is a powerful technique to study the conductivity properties of the modified sensor surface. The curve of the EIS includes a semicircular part and a linear part. The semicircular part at higher frequencies corresponds to the electron-transfer limited process

and its diameter is equal to the electron transfer resistance, which controls the electron transfer kinetics of the redox probe at the electrode interface [28]. For investigation of the effects of GNS and DPA on the conductivity property of the prepared potentiometric sensors surface, EIS measurements were done. Nyquist diagrams of $[\text{Fe}(\text{CN})_6]^{3-/4-}$ solution containing 0.1 mol L^{-1} KNO_3 at different electrodes (unmodified CPE and modified CPEs) are shown in Fig. 2. To obtain the detailed information of the EIS, a simple equivalent circuit model was used to fit the results. In this circuit, R_s , C and R_{et} represent solution resistance, a capacitance for the double-layer and electron transfer resistance, respectively. W is a finite-length Warburg short-circuit term coupled to R_{et} , which accounts for the Nernstian diffusion. R_{et} at the electrode surface is equal to the semicircle diameter, which can be used to describe the interface properties of the electrode. Fig. 2, curve a represents impedance spectrum at unmodified CPE. Curves b and c show impedance spectra at CPE modified with GNS and with GNS and DPA, respectively. As can be seen from this figure, the semicircle diameter decreases from curves a to c. So, semicircle diameter comparison of these curves clearly shows that charge transfer resistance decreased by adding 10% GNS into the paste and also by using DPA as conducting binder instead of paraffin oil. By increasing the conductivity, the dynamic working range, sensitivity and response time of the sensor improve. If the transduction property of the sensor increases, the potential response of the sensor improves to Nernstian values.

3.5. The surface morphology of the prepared CPEs

The surface morphology of the prepared electrodes plays a key role in the selective and sensitive detection of the analytes. So, the SEM measurements were carried out to investigate the surface morphologies of two electrodes (unmodified CPE and new suggested nano-composite modified CPE), as shown in Fig. 3. The unmodified CPE (Fig. 3A) is characterized by a surface formed by irregularly shaped of graphite powder that were isolated with each other and a closer look of the film reveals a broken surface. After the modification of the carbon paste with GNS and DPA, it can be seen that materials were distributed on the surface of electrode with relatively uniform which shows the good adherence of DPA to graphite and GNS (Fig. 3B). Significant improvement in the available high specific surface area of the suggested composite CPE is observed.

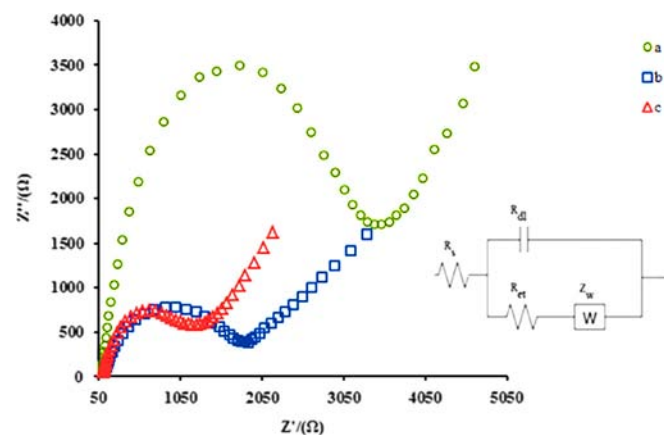


Fig. 2. Impedance plots for different electrodes in $[\text{Fe}(\text{CN})_6]^{3-/4-}$ -containing 0.1 mol L^{-1} KNO_3 : (a) unmodified CPE (b) modified CPE with GNS (c) modified CPE with GNS and DPA.

3.6. Emf measurements

All emf measurements were carried out with the following cell assembly:

Ag/AgCl(sat'd)/KNO₃(1 mol L⁻¹)|sample solution|working electrode

All of the emf observations were made relative to a double junction Ag/AgCl electrode with a digital milli-voltmeter. Calibration graph was drawn by plotting the potential, *E*, versus the logarithm of the Ag(I) ion concentration. All measurements were carried out at 25 °C.

3.7. Response of the electrode to various cations

In preliminary experiments, the suggested modified Ag(I) carbon paste sensor was examined for the wide variety of metal ions. The potential obtained for the most sensitive ion selective electrode based on the new nano-composite (Table 1, No. 7) are shown in Fig. 4A. As can be seen, the proposed modified CPE exhibited a Nernstian behavior and the most sensitive response toward Ag(I) among different tested cations over a wide concentration range.

3.8. Measuring range and detection limit

Measuring range and detection limit (DL) of the optimal modified Ag(I) carbon paste sensor (Table 1, No. 7) was evaluated using linear curve fitting based on IUPAC recommendations. The suggested Ag(I) selective electrode exhibited linear response to the logarithm of the concentration of Ag(I) ions with the calibration

equation of $y=59.70x+785.49$ and correlation coefficient of $r=0.998$ within the concentration range of 8.00×10^{-9} to 1.00×10^{-2} mol L⁻¹ of silver(I) nitrate with Nernstian slope of 59.70 ± 0.10 mV decade⁻¹ at 25 ± 1 °C. The DL for the determination of Ag(I) by the suggested sensor was 4.17×10^{-9} mol L⁻¹, which was calculated by the extrapolating of the two segments of the calibration curve in Fig. 4B.

3.9. Effect of pH on the sensor response

The most important factor on the performance of the most ISEs is the pH value of the test solution. The pH influence of the solution on the response of the suggested modified electrode was studied on 1.00×10^{-5} mol L⁻¹ silver(I) ion having different pH values. The pH varied from 2 to 12 by the addition of dilute solutions of HNO₃ or NaOH. The potential variation as a function of pH is plotted in Fig. 5A. The composition of the electrode was kept constant during all experiments. The results obtained indicated that the working range of the suggested modified electrode to be between pH 3.5 and 10.5. The increase in the potential below the pH value of 3.5 could be attributed to the partial protonation of the employed ionophore. Moreover, above pH 10.5 the measured potential decreased, due to the generation of silver hydroxides.

3.10. Response time and reversibility of the proposed Ag(I) CPE

The response time is a significant factor for any sensor in analytical applications. The practical response time (the time required to achieve a 90% of final steady potential value of the electrodes after successive immersion of Ag(I) ion solutions, each having a 10-fold difference in

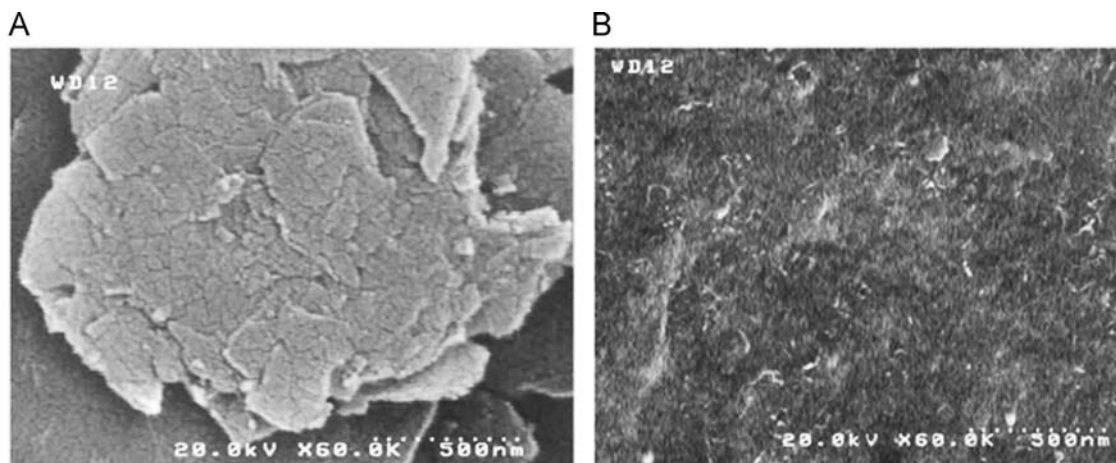


Fig. 3. SEM images of unmodified CPE (A) and suggested modified CPE with GNS and DPA (B).

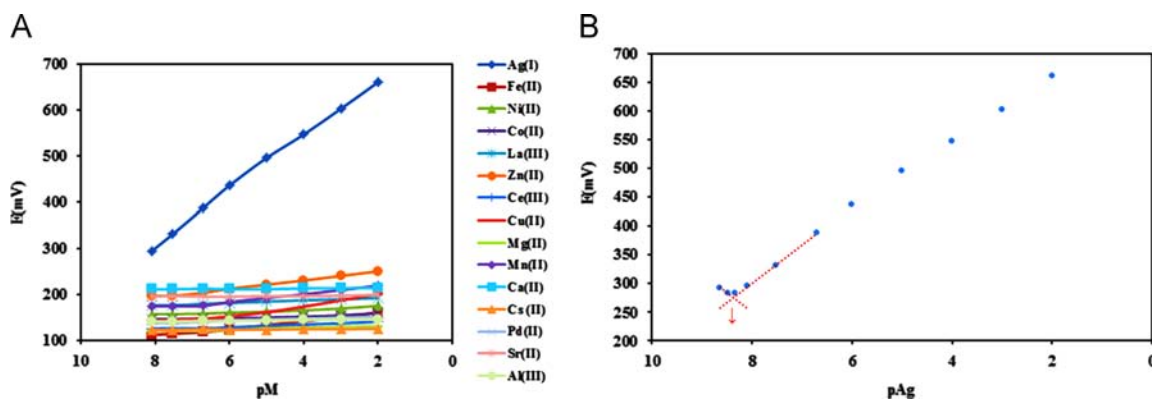


Fig. 4. (A) Schematic diagram of the electrode (Table 1, No. 7) response to various cations. (B) Calibration curve of the Ag(I) modified CPE (Table 1, No. 7).

concentration) has been recorded at different Ag(I) concentrations. In this study, the practical response time (for sensor No. 7) was recorded by changing the Ag(I) ion concentration in the range 1.00×10^{-6} to 1.00×10^{-3} mol L⁻¹ (Fig. 5B). As it is seen, the electrode reached the equilibrium response in a very short time of about 6 s. To evaluate the reversibility of the electrode a similar procedure in the opposite direction was adopted. The measurements were performed in the sequence of high-to-low (1.00×10^{-3} to 1.00×10^{-6} mol L⁻¹) concentrations as shown in Fig. 5B. The results showed that the response of the electrode was reversible; although the time needed to reach equilibrium values (about 18 s) was longer than that for low-to-high sample concentrations (about 6 s), because residual silver will still be adsorbed on the surface of the CPEs, and cause to occupy the site of surface of the indicator electrode significantly, therefore the proposed electrodes don't can sense the silver ions that exist in the bulk of the solution promptly, which will lead to less response time [59,60].

3.11. Selectivity of the electrode

An important characteristic of any ISE is its response to the primary ion in the presence of other ions in the solution, which is expressed in terms of the potentiometric selectivity coefficient.

The potentiometric selectivity coefficients of the suggested modified Ag(I) sensor were evaluated by the matched potential method (MPM) [61]. According to this method, the potentiometric selectivity coefficient is defined as the activity (concentration) ratio of primary (A) and interfering (B) ions that give the same potential change under identical conditions. At first, a known activity of the primary ion (a'_A) solution is added into a reference solution that contains a fixed activity (a_A) of primary ion, and the corresponding potential change (ΔE) is recorded. Next, a solution of an interfering ion (B) is added to the reference solution until the same potential change (ΔE) is recorded. The change in potential produced at the constant background of the primary ion must be the same in both cases. The selectivity coefficient (K) is given by the expression:

$$K_{A,B}^{pot} = \frac{a'_A - a_A}{a_B}$$

The resulting values of the selectivity coefficients are given in Table 2. According to this table, all the investigated cations would not affect the response of the suggested sensor, and had very small value of selectivity coefficients. Table 2 also shows that the obtained selectivity coefficients for the proposed sensor for most of the investigated cations are smaller than those for the previously

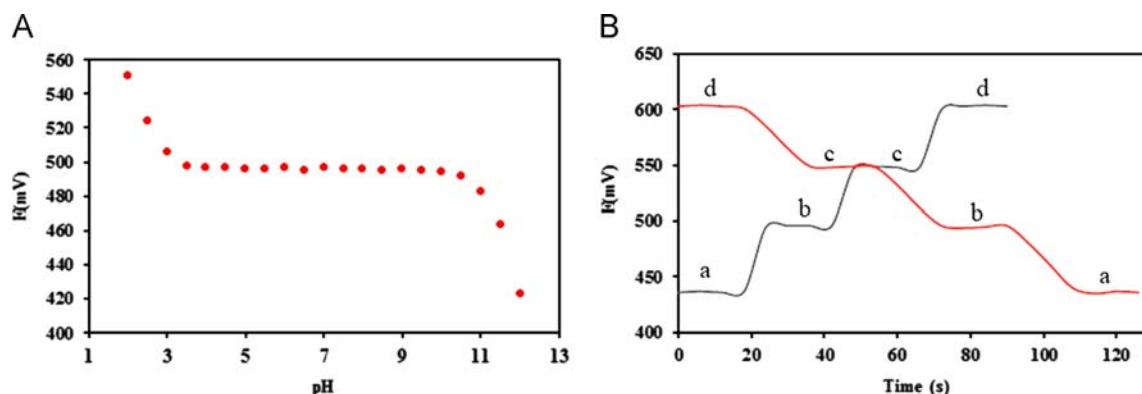


Fig. 5. (A) Effect of pH on the potential response of the proposed Ag(I) modified CPE (No. 7). (B) Dynamic response of the proposed Ag(I) modified CPE for step changes in Ag(I) concentration (from low to high and vice versa): (a) 1.00×10^{-6} (mol L⁻¹), (b) 1.00×10^{-5} (mol L⁻¹), (c) 1.00×10^{-4} (mol L⁻¹), (d) 1.00×10^{-3} (mol L⁻¹).

Table 2
Selectivity coefficient ($K_{i,j}$) for various interfering cations for Ag(I) selective carbon paste electrode.

Interference (j)	$K_{Ag,j}$						
	[45]	[46]	[47]	[48]	[49]	[50]	This work (MPM)
Pb ²⁺	3.98×10^{-5}	1.48×10^{-5}	2.45×10^{-5}	4.70×10^{-3}	1.50×10^{-4}	6.10×10^{-3}	2.81×10^{-3}
Mg ²⁺	7.94×10^{-6}	1.66×10^{-5}	6.76×10^{-6}	3.90×10^{-6}	2.00×10^{-4}	1.70×10^{-4}	1.23×10^{-6}
Fe ²⁺	–	–	–	–	–	–	3.49×10^{-4}
Mn ²⁺	–	2.14×10^{-5}	5.37×10^{-6}	–	–	–	3.86×10^{-6}
Al ³⁺	1.26×10^{-5}	5.50×10^{-3}	2.14×10^{-4}	2.20×10^{-5}	1.60×10^{-3}	7.80×10^{-6}	9.81×10^{-6}
Sr ²⁺	6.31×10^{-6}	1.58×10^{-5}	8.13×10^{-6}	–	–	–	4.76×10^{-6}
Cr ³⁺	–	7.94×10^{-4}	7.56×10^{-5}	–	–	1.40×10^{-5}	5.17×10^{-5}
Cu ²⁺	6.31×10^{-6}	7.76×10^{-4}	4.90×10^{-5}	2.16×10^{-2}	2.50×10^{-3}	8.10×10^{-4}	4.37×10^{-6}
Ni ²⁺	1.00×10^{-5}	1.05×10^{-5}	1.23×10^{-5}	–	1.50×10^{-4}	4.10×10^{-4}	1.13×10^{-5}
Ca ²⁺	6.31×10^{-6}	1.23×10^{-5}	6.03×10^{-6}	1.80×10^{-5}	–	2.40×10^{-6}	5.92×10^{-6}
Ba ²⁺	1.00×10^{-5}	1.32×10^{-5}	7.76×10^{-6}	1.80×10^{-6}	–	–	1.63×10^{-6}
Hg ²⁺	3.98×10^{-4}	–	–	2.10×10^{-2}	2.50×10^{-2}	2.20×10^{-4}	2.41×10^{-3}
Zn ²⁺	1.00×10^{-5}	1.23×10^{-5}	7.41×10^{-6}	3.20×10^{-5}	1.10×10^{-3}	4.30×10^{-4}	9.86×10^{-4}
Na ⁺	2.00×10^{-4}	2.82×10^{-6}	8.13×10^{-7}	8.80×10^{-3}	1.10×10^{-4}	4.30×10^{-4}	2.27×10^{-6}
Cs ⁺	1.58×10^{-4}	–	–	–	–	–	9.41×10^{-5}
K ⁺	6.31×10^{-5}	2.19×10^{-6}	3.31×10^{-7}	2.30×10^{-4}	–	–	1.11×10^{-6}
Cd ²⁺	1.00×10^{-5}	1.78×10^{-5}	1.23×10^{-5}	6.30×10^{-6}	4.00×10^{-3}	2.10×10^{-5}	8.94×10^{-4}
Co ²⁺	6.31×10^{-6}	4.37×10^{-6}	8.13×10^{-6}	3.10×10^{-6}	1.20×10^{-4}	4.30×10^{-3}	2.84×10^{-6}
Fe ³⁺	1.00×10^{-4}	–	–	–	1.00×10^{-3}	3.60×10^{-5}	6.71×10^{-5}
Tl ⁺	5.01×10^{-4}	–	–	–	–	–	9.26×10^{-5}
La ³⁺	–	4.47×10^{-5}	1.91×10^{-5}	–	–	–	8.76×10^{-6}
NH ₄ ⁺	2.51×10^{-5}	3.31×10^{-6}	3.72×10^{-7}	5.20×10^{-3}	3.10×10^{-4}	3.30×10^{-5}	4.71×10^{-7}

Table 3
Comparison of the proposed Ag(I) selective electrode with the some previously reported electrodes.

DL (mol L ⁻¹)	Linear range (mol L ⁻¹)	Slope (mV decade ⁻¹)	Life time (Weeks)	Response time (s)	Ref.
4.17 × 10 ⁻⁹	8.00 × 10 ⁻⁹ –1.00 × 10 ⁻²	59.70	19	~6	Proposed electrode
4.00 × 10 ⁻⁷	1.00 × 10 ⁻⁶ –1.00 × 10 ⁻¹	56.40	4	30	[45]
9.50 × 10 ⁻⁷	1.00 × 10 ⁻⁶ –1.00 × 10 ⁻¹	60.40	12	50	[46]
8.00 × 10 ⁻⁸	8.60 × 10 ⁻⁸ –1.00 × 10 ⁻¹	60.80	4	~20	[47]
7.00 × 10 ⁻⁸	1.10 × 10 ⁻⁷ –1.00 × 10 ⁻³	61.20	N. R. ^a	~3	[48]
6.30 × 10 ⁻⁸	8.20 × 10 ⁻⁸ –1.50 × 10 ⁻²	58.60	N. R.	8	[49]
5.00 × 10 ⁻⁸	2.20 × 10 ⁻⁷ –2.20 × 10 ⁻²	59.54	~8	< 10	[50]

^a N. R.: Not reported.

Table 4
Determination of Ag(I) recovery by the suggested electrode in the different real samples.

Samples	Ag(I) added	Ag(I) found ^a	Recovery (%)	Ag(I) found ^a by ICP-OES	t _{exp} ^b	F _{exp} ^b
Mineral water (mg L ⁻¹)	–	N.D. ^c	–	N.D.	–	–
	5.00	4.88 ± 0.41	97.6	5.02 ± 0.24	0.71	2.92
	20.00	19.78 ± 0.29	98.9	19.95 ± 0.11	1.33	6.95
River water (mg L ⁻¹)	–	< LOD	–	3.14 × 10 ⁻⁴ ± 0.24	–	–
	5.00	4.91 ± 0.31	98.2	5.09 ± 0.26	1.07	1.42
	20.00	20.21 ± 0.28	101.1	20.32 ± 0.19	0.79	2.17
Industrial manufactory waste water (mg L ⁻¹)	–	0.14 ± 0.42	–	0.31 ± 0.27	0.84	2.42
	5.00	5.08 ± 0.24	98.8	5.19 ± 0.16	0.95	2.25
	20.00	20.58 ± 0.22	102.2	20.72 ± 0.13	1.34	2.86
Silver sulphadiazine burning cream (mg g ⁻¹)	–	0.076 ± 0.018	–	0.093 ± 0.010	1.95	3.24
	1.50	1.62 ± 0.13	102.7	1.65 ± 0.10	0.47	1.69
Radiology film (mg g ⁻¹)	–	2.12 ± 0.33	–	2.18 ± 0.21	0.37	2.47
	1.50	3.64 ± 0.20	101.3	3.77 ± 0.17	1.25	1.38

^a Average of six replicate measurements ± standard deviation.

^c N.D. not detected.

^b The critical value of F_{5,5}=7.146 and the critical value of t₁₀=2.23 for P=0.05

reported sensors for silver(I) determination [45–50]. This sensor displays significantly high selectivity for Ag(I) ion.

3.12. Stability and lifetime of the electrode

The long terms stability and lifetime of the suggested silver sensor were investigated by periodically recalibrating in standard solution and calculating the slope of the optimized sensor over a period of 25 weeks in working concentration range of 8.00 × 10⁻⁹ to 1.00 × 10⁻² mol L⁻¹ silver nitrate solutions. During this period, the sensor was used weekly. The proposed sensor was gently washed with distilled water, dried and stored at room temperature when not in use. The results exhibited that the slope of the electrode responses before 19 weeks was reproducible and no significant drift and also no significant change in the performance of the sensor was observed for this period of time. After this time, there was a slight gradual decrease in the slopes from 59.70 to 58.89 mV decade⁻¹. This shows that the lifetime of the proposed silver selective sensor was about 5 months.

3.13. Comparison study

In Table 3, some important characteristics of the proposed electrode are compared with the corresponding values for some previously reported Ag(I)-selective electrodes based on different composites [45–50]. It is evident from this table that in most cases, the performance of the proposed electrode show superior behavior in comparison with some previously reported Ag(I) sensors.

3.14. Analytical applications

The suggested (GNS/TH/MW)–CPE was applied to the determination of trace amounts of silver ions in a wide variety of real

samples. Mineral water, river water and industrial manufactory waste water samples, silver sulphadiazine burning cream and radiological film were analyzed. The analysis was performed by the standard addition method. As Table 4 shows, the results were comparable with those obtained by ICP-OES [62]. Thus the sensor provides a good alternative for the determination of Ag(I) in different real samples.

The suggested electrode was also successfully applied as an indicator electrode for the titration of 9.0 mL of 1.00 × 10⁻³ mol L⁻¹ Ag(NO₃) with a 1.00 × 10⁻³ mol L⁻¹ NaCl solution. Typical results of titration of Ag(I) is shown in Fig. S3. The results show that the amount of silver ions in the solution can be accurately determined with the proposed electrode.

3.15. Statistical treatment of results

For comparing the results of the suggested method with those obtained by ICP-OES, the *F*-test and *t*-test were applied. *F*-test was used for comparing the precisions of the two methods and *t*-test was used for comparing the accuracy. It can be concluded from Table 4 that there is no significant difference between the results obtained by the two methods for P=0.05. The results confirm applicability of the suggested method for precise and accurate determination of the Ag(I) ions in the different real samples with different complex matrices.

4. Conclusions

A novel nano-composite potentiometric sensor for the determination trace amounts of Ag(I) ion based on (GNS/TH/MW)–CPE was fabricated successfully. The performance of modified (GNS/TH/MW)–CPE in comparison to the unmodified CPE was dramatically

improved due to the excellent electrical conductivity of both MW and GNS and also large specific surface area of GNS. This study indicated that after the modification of the carbon paste with GNS and DPA, the electrode surface was relatively uniform which shows the good adherence of DPA to graphite and GNS. High sensitivity, reproducibility and selectivity, and very low detection limit with the ease of preparation and surface regeneration make the proposed modified electrode as a very useful sensor for accurate determination of target analyte in various real samples in nanomolar levels.

Acknowledgments

The authors acknowledge The Bu-Ali Sina University Research Council and Center of Excellence in Development of Environmentally Friendly Methods for Chemical Synthesis (CEDEFMCS) for providing support to this work.

Appendix A. Supporting information

Supplementary data associated with this article can be found in the online version at <http://dx.doi.org/10.1016/j.talanta.2014.08.004>.

References

- [1] P. Stasch, Pollution Prevention and Treatment Alternatives for Silver Bearing Effluents with Special Emphasis on Photo Processing, Olympia, Washington, 1997.
- [2] Environment Protection Agency, Ambient Water Quality Criteria for Silver, EPA 4405-80-071, Office of Water Regulations, Washington, DC, 1980.
- [3] Silver: Occurrence, Distribution and Effects of Silver in the Environment, Report 4664, Swedish EPA, Stockholm, Sweden, 1996.
- [4] D.E. Kimbrough, P.W. Wong, J.K. Biscoe, J. Solid Waste Technol. Manage 23 (1996) 197–207.
- [5] M.J. Eckelman, T.E. Graedel, Environ. Sci. Technol. 41 (2007) 6283–6289.
- [6] M. Kazuyuki, H. Nobuo, K. Takatoshi, K. Yuriko, H. Osamu, I. Yashihisa, S. Kiyoko, Clin. Chem. 47 (2001) 763–766.
- [7] P.N.J. Dennis, Photodetectors, Plenum Press, New York, 1986.
- [8] C.-Z. Lai, M.A. Fierke, R.C. Costa, J.A. Gladysz, A. Stein, P. Buhlmann, Anal. Chem. 82 (2010) 7634–7640.
- [9] K. Wygladacz, A. Radu, C. Xu, Y. Qin, E. Bakker, Anal. Chem. 77 (2005) 4706–4712.
- [10] EPA (Environmental Protection Agency), EPA 7440-7422-7444, Office of Water Regulations, Washington, DC, 1989.
- [11] G. Chakrapani, P.L. Mahanta, D.S.R. Murty, B. Gomathy, Talanta 53 (2001) 1139–1147.
- [12] S. Dadfarnia, A.M. Haji Shabani, M. Gohari, Talanta 64 (2004) 682–687.
- [13] P. Jitaru, K. Tirez, N.D. Brucker, At. Spectrosc. 24 (2003) 1–36.
- [14] M. Krachler, C. Mohl, H. Emons, W. Shotyk, Spectrochim. Acta, Part B 57 (2002) 1277–1289.
- [15] X.J. Yang, R. Foley, G.K.C. Low, Analyst 127 (2002) 315–318.
- [16] W.S. Han, M.Y. Park, K.C. Chung, D.H. Cho, T.K. Hong, Electroanalysis 13 (2001) 955–959.
- [17] V.K. Gupta, A.K. Singh, B. Gupta, Anal. Chim. Acta 583 (2007) 340–348.
- [18] I. Svancara, K. Vytras, K. Kalcher, A. Walcarius, J. Wang, Electroanalysis 21 (2009) 7–28.
- [19] H. Abbastabar-Ahangar, A. Shirzadmeh, K. Marjani, H. Khoshsafar, M. Chaloosi, L. Mohammadi, J. Inclusion Phenom. Macrocyclic Chem. 63 (2009) 287–293.
- [20] M.R. Ganjali, H. Khoshsafar, A. Shirzadmeh, M. Javanbakht, F. Faridbod, Int. J. Electrochem. Sci. 4 (2009) 435–443.
- [21] A. Afkhami, T. Madrakian, A. Shirzadmeh, M. Tabatabaee, H. Bagheri, Sens. Actuators, B 174 (2012) 237–244.
- [22] A. Afkhami, T. Madrakian, A. Shirzadmeh, H. Bagheri, M. Tabatabaee, Ionics 18 (2012) 881–889.
- [23] A. Afkhami, H. Bagheri, A. Shirzadmeh, H. Khoshsafar, P. Hashemi, Electroanalysis 24 (2012) 2176–2185.
- [24] M.H. Mashhadizadeh, S. Ramezani, S. Ebrahimi, Sens. Actuators, B 169 (2012) 305–311.
- [25] H. Bagheri, A. Afkhami, A. Shirzadmeh, H. Khoshsafar, J. Mol. Liq. 197 (2014) 52–57.
- [26] A. Afkhami, A. Shirzadmeh, T. Madrakian, Ionics 20 (2014) 1145–1154.
- [27] A. Afkhami, H. Bagheri, H. Khoshsafar, M. Saber-Tehrani, M. Tabatabaee, A. Shirzadmeh, Anal. Chim. Acta 746 (2012) 98–106.
- [28] H. Bagheri, A. Afkhami, H. Khoshsafar, M. Rezaei, A. Shirzadmeh, Sens. Actuators, B 186 (2013) 451–460.
- [29] A. Afkhami, H. Ghaedi, T. Madrakian, D. Nematollahi, B. Mokhtari, Talanta 121 (2014) 1–8.
- [30] A. Afkhami, F. Soltani-Felehgari, T. Madrakian, Talanta 128 (2014) 203–210.
- [31] Y. Shao, J. Wang, H. Wu, J. Liu, I.A. Aksay, Y. Lin, Electroanalysis 22 (2010) 1027–1036.
- [32] A.K. Geim, K.S. Novoselov, Nat. Mater. 6 (2007) 183–191.
- [33] A.A. Balandin, S. Ghosh, W.Z. Bao, I. Calizo, D. Teweldebrhan, F. Miao, C.N. Lau, Nano Lett. 8 (2008) 902–907.
- [34] C. Lee, X.D. Wei, J.W. Kysar, J. Hone, Science 321 (2008) 385–388.
- [35] K.S. Kim, S.-J. Park, Electrochim. Acta 56 (2011) 6547–6553.
- [36] J.B. Jia, D. Kato, R. Kurita, Y. Sato, K. Maruyama, K. Suzuki, S. Hirono, T. Ando, O. Niwa, Anal. Chem. 79 (2007) 98–105.
- [37] O. Niwa, J. Jia, Y. Sato, D. Kato, R. Kurita, K. Maruyama, K. Suzuki, S. Hirono, J. Am. Chem. Soc. 128 (2006) 7144–7145.
- [38] W. Li, C. Tan, M.A. Lowe, H.C.D. Abruna, D.C. Ralph, ACS Nano 5 (2011) 2264–2270.
- [39] M. Tabatabaee, M.R. Nateghi, S.J. Mosavi, Anal. Sci. 22 (2006) 1601–1603.
- [40] W.S. Hummers, R.E. Offeman, J. Am. Chem. Soc. 80 (1985) 1339 (1339).
- [41] S. Stankovich, D.A. Dikin, R.D. Piner, K.A. Kohlhaas, A. Kleinhammes, Y. Jia, Y. Wu, S.T. Nguyen, R.S. Ruoff, Carbon 45 (2007) 1558–1565.
- [42] A. Safavi, N. Maleki, F. Honarasa, F. Tajabadi, Electrochem. Commun. 11 (2009) 1113–1115.
- [43] A. Abbaspour, A. Izadyar, H. Sharghi, Anal. Chim. Acta 525 (2004) 91–96.
- [44] M.H. Mashhadizadeh, A. Mostafavi, H.A. Abadi, I. Sheikhsheoi, Sens. Actuators, B 113 (2006) 930–936.
- [45] M.E.M. Hassouna, S.A.A. Elsuccary, J.P. Graham, Sens. Actuators, B 146 (2010) 79–90.
- [46] T. Zhang, Y. Chai, R. Yuan, J. Guo, Mater. Sci. Eng., C 32 (2012) 1179–1183.
- [47] Q. Zhao, Y. Chai, R. Yuan, T. Zhang, C. Yang, Mater. Sci. Eng., C 32 (2012) 1352–1357.
- [48] H.M. Abu-Shawish, S.M. Saadeh, H.M. Dalloul, B. Najri, H. Al Athamna, Sens. Actuators, B 182 (2013) 374–381.
- [49] M.H. Mashhadizadeh, R.P. Talemi, A. Shockravi, M. Kamali, Anal. Methods 4 (2012) 742–747.
- [50] A. Dadkhah, M.K. Rofouei, M.H. Mashhadizadeh, Sens. Actuators, B 202 (2014) 410–416.
- [51] M. Arvand, S.A. Asadollahzadeh, Talanta 75 (2008) 1046–1054.
- [52] A. Nitzan, M.A. Ratner, Science 300 (2003) 1384–1389.
- [53] X.J. Tian, J.F. Song, X.J. Luan, Y.Y. Wang, Q.Z. Shi, Anal. Bioanal. Chem. 386 (2006) 2081–2086.
- [54] G. Liu, M.N. Paddon-Row, J.J. Gooding, Electrochem. Commun. 9 (2007) 2218–2223.
- [55] Y. Li, J. Zhao, X. Yin, H. Liu, G. Yin, Phys. Chem. Chem. Phys. 9 (2007) 1186–1193.
- [56] C. Ruan, L. Xu, X. Wang, J. Lou, W. Gao, W. Sun, Electroanalysis 24 (2012) 286–292.
- [57] W. Sun, L. Xu, T. Li, X. Wang, G. Li, Z. Sun, J. Chin. Chem. Soc. 59 (2012) 1571–1577.
- [58] N.G. Shang, P. Papakonstantinou, M. McMullan, M. Chu, A. Stamboulis, A. Potenza, S.S. Dhessi, H. Marchetto, Adv. Funct. Mater. 18 (2008) 3506–3514.
- [59] M.H. Mashhadizadeh, H. Khani, A. Foroumadi, P. Saghari, Anal. Chim. Acta 665 (2010) 208–214.
- [60] M.H. Mashhadizadeh, S. Ramezani, A. Shockravi, M. Kamali (In Press), J. Inclusion Phenom. Macrocyclic Chem. 76 (2013) 283–291. <http://dx.doi.org/10.1007/s10847-012-0197-6>.
- [61] Y. Umezawa, P. Buhlmann, K. Umezawa, K. Tohda, S. Amemiya, Pure Appl. Chem. 72 (2000) 1851–2082.
- [62] A.A. Argekar, M.J. Kulkarni, J.N. Mathur, A.G. Page, R.H. Lyer, Talanta 42 (1995) 1937–1942.



Determination of urine ionic composition with potentiometric multisensor system



Irina Yaroshenko^{a,b,c}, Dmitry Kirsanov^{a,c,*}, Lyudmila Kartsova^a, Alla Sidorova^b,
Irina Borisova^b, Andrey Legin^{a,c}

^a Chemistry Department, St. Petersburg State University, Universitetskaya nab. 7/9, Mendeleev Center, 199034 St. Petersburg, Russia

^b Bioanalytical Laboratory CSU "Analytical Spectrometry", St. Petersburg State Polytechnical University, Box 27, Gzhatskaya Street 27, 198220 St. Petersburg, Russia

^c ITMO University, Kronverkskiy pr., 49, 197101 St. Petersburg, Russia

ARTICLE INFO

Article history:

Received 22 April 2014

Received in revised form

6 August 2014

Accepted 11 August 2014

Available online 20 August 2014

Keywords:

Urine ionic composition

Biochemical analysis of urine

Potentiometric multisensor system

Electronic tongue

Chemometrics

ABSTRACT

The ionic composition of urine is a good indicator of patient's general condition and allows for diagnostics of certain medical problems such as e.g., urolithiasis. Due to environmental factors and malnutrition the number of registered urinary tract cases continuously increases. Most of the methods currently used for urine analysis are expensive, quite laborious and require skilled personnel. The present work deals with feasibility study of potentiometric multisensor system of 18 ion-selective and cross-sensitive sensors as an analytical tool for determination of urine ionic composition. In total 136 samples from patients of Urolithiasis Laboratory and healthy people were analyzed by the multisensor system as well as by capillary electrophoresis as a reference method. Various chemometric approaches were implemented to relate the data from electrochemical measurements with the reference data. Logistic regression (LR) was applied for classification of samples into healthy and unhealthy producing reasonable misclassification rates. Projection on Latent Structures (PLS) regression was applied for quantitative analysis of ionic composition from potentiometric data. Mean relative errors of simultaneous prediction of sodium, potassium, ammonium, calcium, magnesium, chloride, sulfate, phosphate, urate and creatinine from multisensor system response were in the range 3–13% for independent test sets. This shows a good promise for development of a fast and inexpensive alternative method for urine analysis.

© 2014 Elsevier B.V. All rights reserved.

1. Introduction

Chemical analysis of biological liquids (blood, saliva, urine, etc.) plays a very significant role in medical diagnostics. Analysis of urine is one of the most informative for medical doctor since it reveals general condition of organism and nutrition character. Urine is an aqueous solution of various substances in different concentrations. It is a convenient object for analysis, components being easily extracted or analyzed right after plain dilution step. Any serious deviation from the normal composition of urine indicates certain metabolic disorder. One of the most widespread metabolic disorders is urolithiasis characterized by the formation of stones in the kidneys and urinary organs [1].

The stone formation begins if equilibrium between urine components is disturbed. The main markers of urolithiasis are separated

* Corresponding author at: Chemistry Department, St. Petersburg State University, Universitetskaya nab. 7/9, Mendeleev Center, 199034 St. Petersburg, Russia
E-mail address: d.kirsanov@gmail.com (D. Kirsanov).

into promoters and inhibitors. Increased concentrations of promoters (calcium, ammonium, oxalate, phosphate, urate) indicate a risk of possible stone formation. The presence of inhibitors (magnesium, citrate) reduces a possible stone formation since these components enter into competing interaction. The history of urolithiasis markers study is very long [2] and the interest to this issue is growing. The main problem of urolithiasis is that at early stages this disease proceeds asymptotically. The patient becomes aware of his illness only when the stone is already formed and starts obstructing normal organism activities [3]. Early diagnostics is a half of successful treatment, thus biochemical analysis of urine ionic composition is very important to fight against the urolithiasis. The adequate medical conclusion can be given in laboratory on the basis of biochemical analysis consisted of 14 parameters: contents of sodium, potassium, ammonium, calcium, magnesium, chloride, sulfate, phosphate, oxalate, citrate, urate, creatinine, pH level and density. Also a registration of sex, age and diuresis is required. The analysis of combination of these parameters can indicate a possible stone formation [4].

Various analytical methods are employed on routine basis for determination of urine composition in medical laboratories.

Capillary electrophoresis (CE) is considered to be one of the most accurate analytical techniques for urine analysis, offering a number of simple techniques for quantification of inorganic and organic cations and anions in urine. Direct and indirect UV-detection is used most often in CE [4–10]. Spectrophotometric techniques are applied for calcium, magnesium, phosphate, uric acid and creatinine quantification. In this case a preliminary derivatization reaction with specific agent is required to yield colored substance which can be analyzed [11]. Ion-selective electrodes are employed for determination of sodium, potassium and chloride [12].

There are also a number of approaches for urine analysis which were suggested in literature but were not massively introduced into a common laboratory practice so far. A very interesting diagnostic technology is so called “Lithos-system” [13]. The main principle of this system is in observation of crystals of the dried urine sample. The shape and arrangement of crystals is further compared with certain standard figures and this methodology allows to judge on the risk of stone formation [13].

Determination of urine components can be carried out using ion chromatography with piezoelectric or conductivity detectors [14,15]. Classical chromatography (liquid and gas) can be successfully applied for analysis of nonionic substances [16–18]. Creatinine and urate as uric acid can be quantified with liquid chromatography–tandem mass spectrometry in urine samples [16,17]. The derivatization with 2,3,4,5,6-pentafluorobenzyl bromide is used for creatinine determination in urine sample by gas chromatography–tandem mass spectrometry [18].

The application of electrochemical methods for urine components analysis is usually hindered by the presence of interfering signals. For example, limited selectivity towards different ions of PVC-plasticized potentiometric sensors in the presence of ammonium lead to attempts to create more selective electrodes for sodium [19] and calcium [20]. An important issue is adsorption of organic urine components on a membrane surface, which leads to reduced reproducibility and lifetime of the sensors. The authors of [21] proposed to use solvent–solvent extraction, membrane-immobilized solvent extraction and solid phase extraction to remove lipophilic compounds from urine samples. However, such kind of sample preparation significantly reduces the benefits of sensors ensuring fast and simple analysis.

There are many reports on application of different biosensors for urine analysis. The analytical signal of these devices is typically based on reactions of target analyte with a biomolecule immobilized on the surface of chemically modified electrode [22]. The content of urate or oxalate in urine can be determined by biosensors based on uricase [23] or oxidase [24] respectively. The main advantage of biosensors is their high selectivity due to specificity of biological reactions. However, it is often hard to obtain reproducible microstructure of a substrate layer to warrant good batch reproducibility.

The idea to use the sensor arrays (“electronic tongues”) for simultaneous determination of numerous chemical parameters seems to be quite obvious for urine analysis and there were several attempts reported in literature [25–27]. The authors of [25] have proposed the sensor array consisting of urea biosensor and ion-selective electrodes for ammonium, potassium, sodium, hydrogen and one sensor with generic response towards alkaline ions. The response of the array in 37 model solutions was processed with artificial neural network (ANN) and partial least squares (PLS) to construct regression models for simultaneous quantification of urea, ammonium, potassium and sodium. Validation was done with 21 samples (three real urine samples and 18 spiked samples were prepared by addition of different quantities of urea, ammonium, potassium and sodium). It was possible to quantify individual components with relative errors around 8% for ANN-models

and 13% for PLS-models. Later the same authors extended this sensor array with a creatinine biosensor [26]. TRIS buffer (tris (hydroxymethyl)aminomethane) pH=7.5 was used as a solvent since biosensors require this acidity level to support the catalytic activity of the enzymes. The training of this system was performed on 27 model solutions consisting of five analytes in various concentrations. Independent test-set (13 model solutions) was applied for validation and after that 11 samples (three real urine samples and eight spiked samples were prepared by addition of different quantities of urea, creatinine, ammonium, potassium and sodium) were analyzed. The maximum relative error was 9% in the determination of creatinine [26].

Another report [27] dealt with the sensor array of eight 8 metallic electrodes (Co, two component alloys – Sn/Pb, Cu/P, Cu/Zn, four alloys of silver – Ag/Cu/Zn/Cd, Ag/Cu/Sn, Ag/Cu/Zn/Sn – in two different ratios) and five polymeric membrane sensors. The purpose of the study was to detect urinary system dysfunctions and to analyze creatinine levels. 51 urine samples were classified in four classes according to the creatinine content by PLS-Discriminant Analysis (PLS-DA) and neural net. It was shown that this sensor system is able to distinguish between urine samples from healthy patients and those with malignant and non-malignant tumor diagnosis of bladder.

The idea of the present study was to construct the sensor array which would be capable of exhaustive analysis of urine ionic composition. These data are of ultimate importance for early medical diagnosis of several disorders, such as e.g., urolithiasis. Furthermore the intention was to validate this approach with sufficient number of real urine samples employed in independent test sets. The issue of proper validation of promising methods is, unfortunately, ignored in literature pretty often and far-reaching conclusions are being done just with cross-validation on model samples or only a small number of real ones. This is not enough for proper evaluation of such systems for urine analysis.

2. Materials and methods

2.1. Urine samples preparation

136 urine samples were collected for this study. 117 samples from patients were provided by Urolithiasis Laboratory (Medical Center of Laboratory Diagnostics, St. Petersburg). 19 samples from healthy people were collected from persons who did not express complaints. The accumulation of sufficient number of samples took about six months since only three to six urine samples per week are available from the Urolithiasis Laboratory. All urine samples (50 ml of each) were frozen in a biomedical fridge at -25°C . The literature suggests that ionic composition of urine varies by less than 5 percent on freezing-thawing during 5 years [28].

The urine samples were prepared for analysis with potentiometric multisensor system by unfreezing on a water bath at room temperature (25°C) and then by thorough mixing. 10 ml of urine were diluted with 90 ml of distilled water and the resulted solution was employed for direct potentiometric measurements. Each sample was measured in 4 physically different replicas. Replicated measurements were randomized between the samples.

2.2. Potentiometric multisensor systems

The potentiometric multisensor system consisted of 19 chemical sensors. Ten ion-selective electrodes for Na^+ , K^+ , NH_4^+ , Ca^{2+} , Mg^{2+} , $\text{Ca}^{2+} + \text{Mg}^{2+}$, NO_3^- , Cl^- , CO_3^{2-} , SO_4^{2-} were prepared based on standard Fluka® ionophores following the producer recommendations. Five poly (vinylchloride) (PVC)-plasticized anion-sensitive sensors were based on various anion-exchangers, three were PVC-plasticized cation-sensitive

sensitive sensors based on different tetraphenyl borate derivatives and finally one standard glass pH-electrode. Besides that the system contained the standard Ag/AgCl reference electrode. All sensors were connected with shielded wires to the 32-channel high input impedance digital mV-meter (Sensor Systems, LLC, St. Petersburg, Russia). Potential readings were recorded with 0.1 mV precision in a custom made software installed on a Windows PC. Measurement time in each urine sample was 3 min. After that the sensors were washed with three portions of distilled water for 1 min each. All samples were measured four times. This was done with physically different portions of the same sample. Normally four or five urine samples were defrosted per day and all their replicates were measured in a random order. The results were averaged over the replicas for further processing, the resulted data matrix from the sensor system was 136 samples \times 19 sensors.

2.3. Reference data on urine samples

All urine samples were analyzed by capillary electrophoresis as a reference method in Bioanalytical Laboratory CSU “Analytical Spectrometry” (St. Petersburg, Russia) according to the procedure described in [4]. Capillary electrophoresis system “Capel 105 M” (Lumex, Russia) with spectrophotometric detector with a wavelength range 190–400 nm was used for analysis of inorganic cations (calcium, magnesium, sodium, potassium, ammonium) and anions (chloride, sulfate, phosphate) in urine samples diluted in 400–800 times. The content of organic components (oxalate, citrate, urate, creatinine) in 5–20 times diluted urine sample was determined by capillary electrophoresis system Agilent 1100 CE (Agilent, USA) with diode array detector (190–600 nm). pH-level of urine samples was analyzed by pH-sensor InLab Expert Pro (Mettler Toledo, Switzerland). Urine density was evaluated by refractometer IRF-454 B2M (Kazan Optical and Mechanical Plant, Russia).

The data matrix from reference methods was 136 samples \times 14 concentrations.

To yield the medical conclusion on the results diuresis (urine amount excreted per day) has to be considered. For this purpose concentration of particular component in [mmol/l] is multiplied by diuresis in [l/day] to yield the concentration in [mmol/day]. This value is compared with the norm for medical conclusion.

2.4. Data processing

Principal Component Analysis (PCA) was employed for exploratory data analysis. PCA is widely in use in modern analytical chemistry and detailed description can be found elsewhere [29]. PCA models were computed with The Unscrambler® 9.7 (CAMO Software AS, Norway).

Logistic Regression (LR) is a type of probabilistic statistical classification model. It is used for prediction of a categorical dependent variable (i.e. a class label) based on predictor variables (features). In binary Logistic Regression, the outcome is usually encoded as “0” or “1” as this leads to the most straightforward interpretation. In this study class labels were “unhealthy” or “healthy” and the features were the reference data or the data from the multisensor system. All patients of Urolithiasis Laboratory were considered to be unhealthy. The probability $p(X)$ of a class label is calculated as follows:

$$p(X) = \frac{e^{\beta_0 + \beta_1 X_1 + \dots + \beta_n X_n}}{1 + e^{\beta_0 + \beta_1 X_1 + \dots + \beta_n X_n}} \quad (1)$$

where $\beta_0, \beta_1 \dots \beta_n$ are coefficients of the model, $X_1 \dots X_n$ – predictors (sensor responses or reference data on ionic composition from capillary electrophoresis), and n – number of a predictor.

In assessing statistical medical data it is recommended to consider a prevalence rate for particular location [30]. For this

purpose β_0 is transformed in β_0^*

$$\beta_0^* = \beta_0 + \ln \frac{\pi}{1-\pi} - \ln \frac{\pi^*}{1-\pi^*} \quad (2)$$

where π is a morbidity for a certain location (in case of urolithiasis it is up to 15% ($\pi=0.15$) [1]);

π^* – a number of the incidence of the disease in the particular study (in our case we have 117 cases seeking medical attention among 136 samples ($\pi^*=0.86$)).

LR models were computed with RStudio (Version 0.98.501) and R (Version 3.0.2) [31].

The quantification of urine components with multisensor system was the main objective of this work. PLS regression was applied for this purpose. Detailed description of PLS regression technique can be found in [29]. The data on ionic composition of urine samples obtained from capillary electrophoresis were employed as reference in modeling. PLS models were computed with The Unscrambler® 9.7 (CAMO Software AS, Norway).

3. Results and discussion

3.1. Selecting the optimal sample dilution

The range of ionic composition of urine in the sample set is known from the reference data. On the other hand, we know the working concentration range of the ion-selective sensors in the array. The comparison shows that for analysis with a multisensor system all the samples can be diluted 5–20 times. It is also noteworthy that dilution can help fighting against the adsorption of organic molecules on polymeric sensor membranes. The series of experiments was performed to select the most appropriate dilution rate. For this purpose urine content in the water was varied over three levels: 5, 10 and 20%. Urine portions from the same patient were measured five times consequentially at each dilution with multisensor system and sensor readings in these replicas were recorded. Moreover, sensor readings in final washing water between the measurements were also registered. The stability of sensor responses in the water indicates the stability of the sensor array (an imaginary instrument’s “baseline”).

For each sensor the standard deviation value in five replicated measurements in the urine sample and in five corresponding washing water were calculated. Table 1 shows resulted sums of standard deviations for all of the sensors of the array for three dilution levels.

These results show that with increasing content of the urine the reproducibility of sensor response increases while that in water gets worse. Probably this is associated with higher interference due to more pronounced interaction of organic matter with polymeric sensor membranes at lower dilution rates, which leads to poorer washing. As a compromise between these trends tenfold dilution was chosen for all further experiments.

3.2. Stability testing of sensors

All 136 urine samples were analyzed by the multisensor system. It is known [21] that organic components of urine can adsorb on a

Table 1

The sum of standard deviations of sensor response in replicate measurements at different dilutions levels (mV).

	Sample dilution		
	5%	10%	20%
Sample	194	109	79
Water	112	121	154

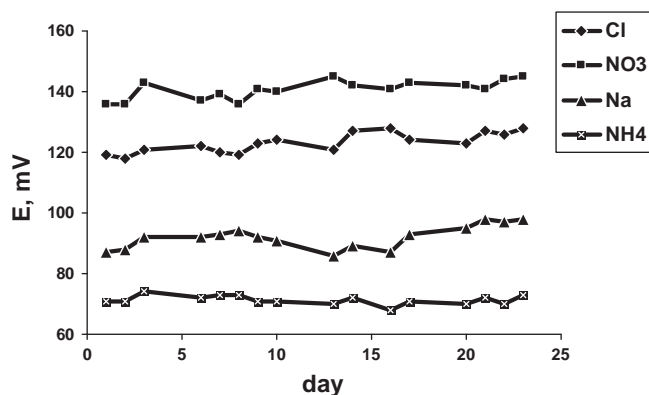


Fig. 1. The responses of four sensors during the experiment.

surface plasticized polymeric membranes causing drift in response values. It was necessary to clarify the impact of this process on the measurements. For this purpose one particular urine sample was split into several portions which were analyzed each day thrice during the whole experiment. The results of these measurements are represented in Fig. 1.

As an example Fig. 1 shows the responses stability of four sensors through 23 days of measurements. For all 19 sensors the standard deviation values of potentials were within 2–10 mV, which is probably due to rather high dilution level and extensive washing procedure. This stability was considered to be reasonable for multisensor measurements.

3.3. Exploratory data analysis

PCA was applied to get the initial insight into the data. PCA score plots obtained from capillary electrophoresis and multisensor system data (Fig. 2) did not demonstrate the separation between the classes of patients and healthy people. Neither some clustering was visualized in higher PCs. The plots are different and the variance structure is also different for these two methods. The percentage of the explained variance in the first ten PCs was as follows: 39, 33, 12, 6, 3, 2, 2, 1, 1, 1% – for multisensor system data and 43, 14, 7, 7, 6, 6, 5, 5, 4, 3% – for data from capillary electrophoresis. The low percentage of the explained variance in the first PCs can be attributed to the fact that there are numerous sources of variance in the data. Thus, the main variability in the data is not associated with a person's status with respect to urolithiasis. This is quite obvious since the urine ionic composition depends on a gender, age, diet and habits. Medical doctors use a complex combination of several parameters for diagnostics. These factors are not highlighted in an overall variance structure and consequently in PCA score plots.

3.4. Classification of samples

Logistic Regression models were calculated for two data sets obtained from capillary electrophoresis and potentiometric multisensor system measurements. All samples were split into calibration (101 samples) and validation (35 samples) sets. Probability of class label (unhealthy (1) or healthy (0)) was calculated taking into consideration the incidence of urolithiasis. Prevalence of urolithiasis is up to 15% ($\pi=0.15$) [1] while in our data set which was employed for LR calibration there were 87 cases seeking medical attention among 101 samples ($\pi^*=0.86$). The corresponding β_0 values were corrected as described in the experimental section.

The LR models were validated by an independent test-set which contained the data on 30 unhealthy and 5 healthy persons. The results of this analysis are prediction errors in class label

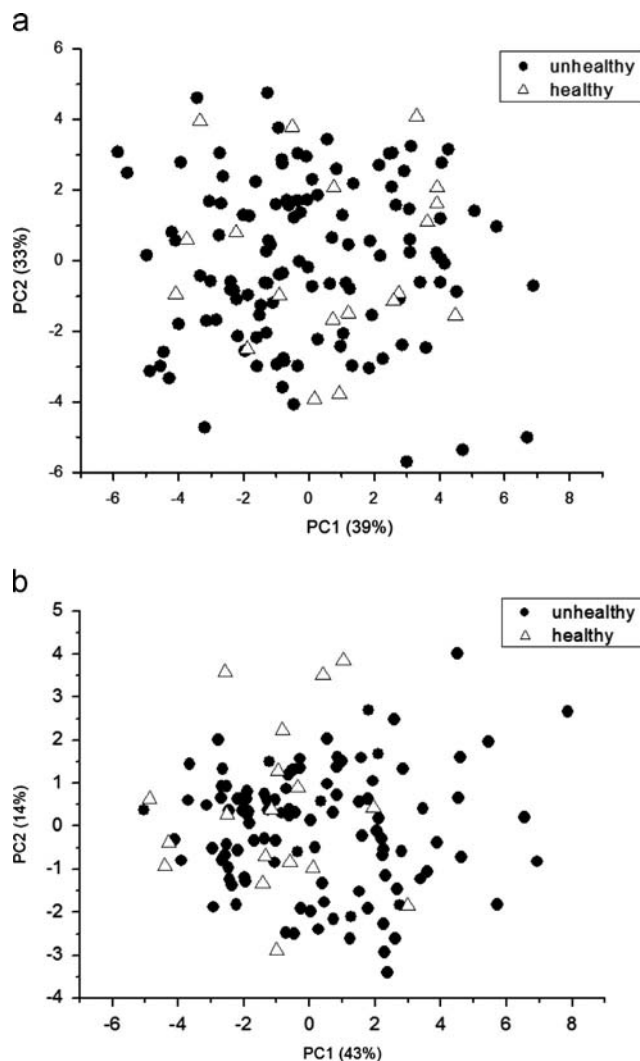


Fig. 2. PCA score plot for multisensor system data (a) and for capillary electrophoresis data (b).

(unhealthy or healthy) from the two data sets. A “0” value was assigned to healthy people and “1” characterizes the patients of Urolithiasis Laboratory. LR models predict the class label for each sample. The probability $p(X)$ of a class label for each sample has the value between “0” and “1”. $p(X)$ values which are close to “1” assume that there is a high probability of being unhealthy for particular patient.

It is important to establish reliable decision boundary for LR classifier. This boundary determines which particular value of $p(X)$ is used to distinguish between two classes. We have $p(X)$ values of a class label for each sample. Then we choose some particular level $p(X)$ and calculate a number of errors (unhealthy as healthy and healthy as unhealthy) in %. Then we choose new level $p(X)$ and calculate a number of errors in this case. This operation is repeated with all $p(X)$ values between “0” and “1”. The way to choose this boundary is to determine $p(X)$, which allows for minimal sum of errors in determination of classes for all samples (Fig. 3). These operations were performed for calibration set only.

Fig. 3 demonstrates minimal sum of errors at decision boundary 0.2 – for capillary electrophoresis data and 0.04 – for multisensor system data.

At these values of decisions boundary the confusion matrix was calculated (Table 2).

It can be seen that LR in case of capillary electrophoresis (CE) allows for 100% precise classification of the samples, which is not

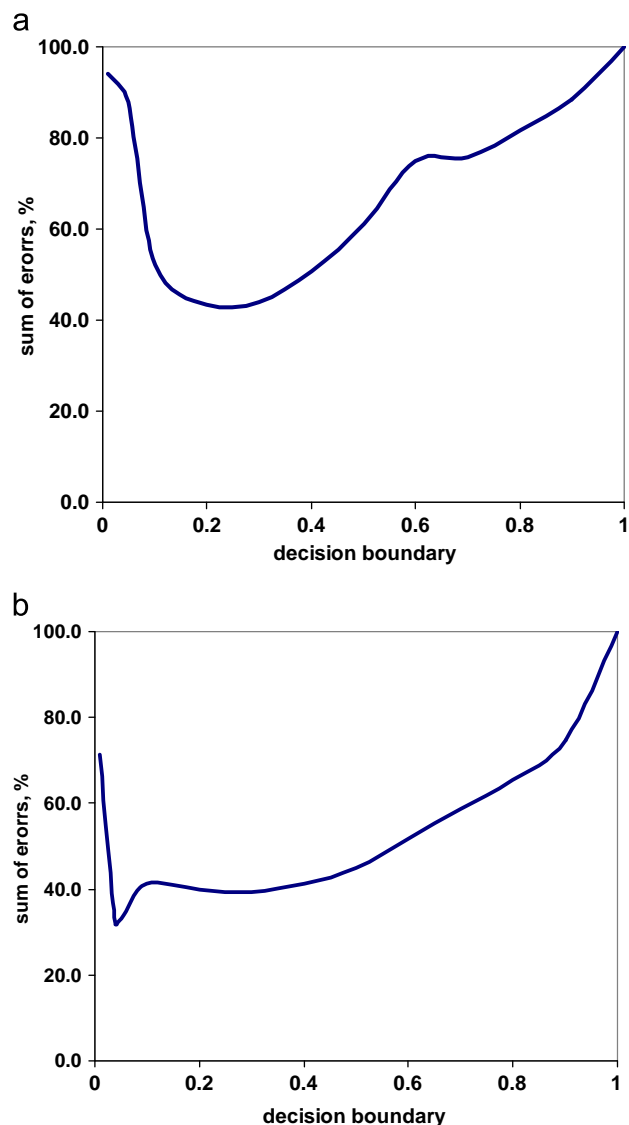


Fig. 3. The choice of decision boundary: (a) – capillary electrophoresis data, and (b) – multisensor system data.

Table 2

Confusion matrix obtained for validation of LR models with independent test set of 35 persons.

	Unhealthy as healthy	Healthy as unhealthy
Capillary electrophoresis data	0/30	0/5
Multisensor system data	4/30	3/5

surprising since these CE data are employed by medical doctors for deriving their conclusions, thus LR in this case just emulates the performance of a medical specialist. Classification precision was somewhat lower when LR models were constructed with potentiometric data, in total 7 out of 35 patients were misclassified.

3.5. Quantitative analysis

The quantification of urine components with multisensor system was the main objective of this work. PLS regression models were constructed with reference data from biochemical laboratory. In case of potentiometric sensors there is a linear dependence between sensor response in mV and logarithm of ion concentration (activity).

Table 3

The mean relative errors in determination of urine compounds (from independent test sets of 40 samples).

	Calibration range (mmol/l)	MRE (%)
Sodium	3.8–255.5	2.7
Potassium	4.2–100.0	8.6
Ammonium	4.0–81.8	7.2
Calcium	0.6–10.7	11.6
Magnesium	0.7–8.7	12.3
Chloride	11.1–222.3	3.1
Sulfate	1.5–25.9	10.9
Phosphate	3.1–48.4	8.2
Oxalate	0.1–0.4	17.0
Citrate	0.2–5.5	21.5
Urate	0.5–7.0	11.5
Creatinine	2.1–26.7	11.6

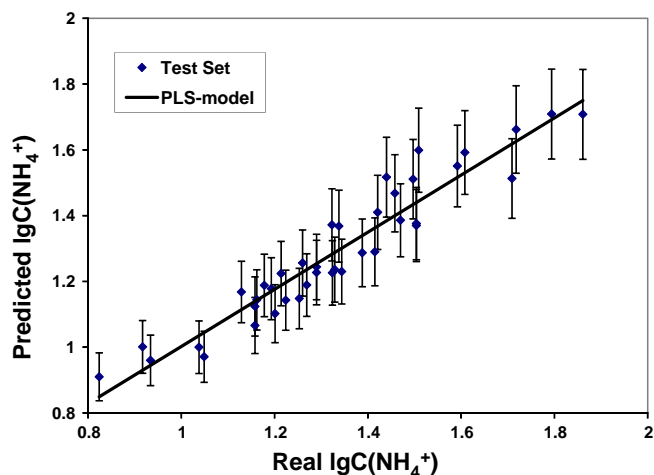


Fig. 4. Measured vs. predicted plot for ammonium.

Thus before modeling the reference data on ion content from capillary electrophoresis were translated into logarithmic scale. Two parameters (pH level and density in g/l) were used as is.

40 randomly selected samples were employed as independent test set, while the rest of the samples were employed for building cross-validated PLS1 regression models for each of the 12 parameters. The number of components in PLS models was selected according to traditional criteria – the minimum at the “RMSEP” vs. “number of PLS components” curve. The number of components was typically three (four components were optimal only for ammonium and oxalate). Table 3 represents the results of prediction of these 12 parameters in 40 independent test set samples. Fig. 4 shows typical view of the “measured vs. predicted” plot for ammonium to give an impression on precision of the model at low and high concentrations of analyte.

It was found that potentiometric multisensor system can determine concentrations of certain urine components with mean relative errors in the range 3–13%. The precision in determination of some analytes (oxalate and citrate) was comparatively low. This may be due to the fact that the calibration range for these two ions was quite narrow. Another reason is that significant background concentration of chloride hinders simultaneous determination of small amounts of other ions due to selectivity reasons. Surprising correlation with phosphate content (which is hardly available from potentiometric measurements with polymeric membranes due to its high hydrophilicity) can be partially explained by the fact that this value has reasonably high intercorrelation with all other parameters. For

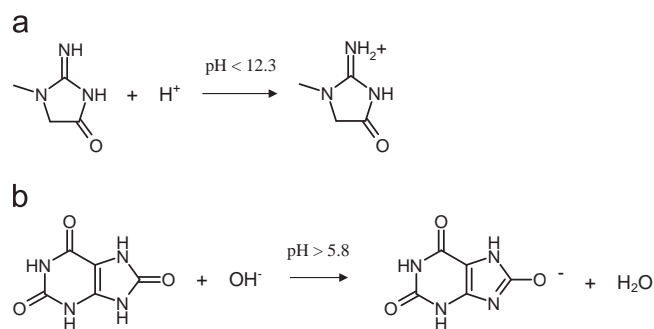


Fig. 5. The forms of creatinine (a) and uric acid (b) in real urine samples.

example PLS1 regression built with CE data on all ions for prediction of phosphate has R^2 values around 0.75 in validation.

A high correlation of sensor responses with creatinine and urate contents deserves separate discussion. Creatinine is one of the end products of protein metabolism in human body, its content being important for medical doctors to judge on condition of kidneys and human muscular system. Creatinine is a convenient substance for potentiometric determination because at pH below 12.3 it exists in a cationic form ($pK_a=12.3$), which can be determined by cation-sensitive sensors. The authors of [27] did manage to achieve RMSEP values for creatinine determination of 0.0019 mol/l in model urine samples.

Uric acid and its salts – urates are the end products of purines metabolism. Increased concentrations of urate indicate a possible stone formation. It is dibasic acid ($pK_{a1}=5.8$, $pK_{a2}=10.3$). In urine it forms an anion, which can be analyzed by potentiometric sensors. pH level of urine is normally in the range 5.5–7.0 [1]. The forms of these analytes in real urine samples are shown in Fig. 5. It is assumed that the observed sensitivity of the sensor array towards creatinine and urate levels is associated with these ionic forms; however this issue requires further detailed studies.

In certain cases multisensor system is able to evaluate not only chemical parameters, but also physical. It was possible to determine the density of urine during the analysis. Certainly, the urine density depends on chemical composition. It was established that reference data and multisensor system can help determining density with mean relative errors about 5% and 8%, respectively, by means of corresponding PLS models with independent test set validation.

4. Conclusions

Potentiometric multisensor system can be employed as convenient tool for rapid assessment of 10 ionic substances in human urine (sodium, potassium, ammonium, calcium, magnesium, chloride, sulfate, phosphate, urate, creatinine). The validation of the PLS regression models for quantitative determination of particular constituents with large independent test sets allows for mean relative errors below 10% for major urine components

(sodium, ammonium, chloride) and below 15% for the rest. The lack of potentiometric selectivity can be effectively compensated in the framework of multisensor approach and chemometric data processing. The further development of this approach into clinical practice looks promising since it is much cheaper and faster than e.g., capillary electrophoretic measurements.

Acknowledgment

This work was partially financially supported by Government of Russian Federation (Grant 074-U01).

References

- [1] M. Resnick, A. Novick, *Urology Secrets*, third ed., Hanley and Belfus, Inc., USA, 2003.
- [2] G. Gambaro, J.M. Reis-Santos, N. Rao, *Eur. Urol.* 45 (2004) 547–556.
- [2] C. Barbas, A. Garcia, L. Saavedra, M. Muros, *J. Chromatogr. B* 781 (2002) 433–455.
- [4] A.A. Sidorova, A.V. Grigoriev, *J. Anal. Chem.* 67 (5) (2012) 478–485.
- [5] Q. Wan, P. Kuban, J. Tanyanyiwa, A. Rainelli, P. Hauser, *Anal. Chim. Acta* 525 (2004) 11–16.
- [6] W. Guo, K. Lau, Y. Fung, *Electrophoresis* 31 (2010) 3044–3052.
- [7] V. Galli, A. Garcia, L. Saavedra, C. Barbas, *Electrophoresis* 24 (2003) 1951–1981.
- [8] J. Munoz, M. Lopez-Mesas, M. Valiente, *Talanta* 81 (2010) 392–397.
- [9] A. Garcia, M. Muros, C. Barbas, *J. Chromatogr. B* 755 (2001) 287–295.
- [10] Z. Jarolimova, P. Lubal, V. Kanicky, *Talanta* 98 (2012) 49–53.
- [11] F.T. Fischbach, M.B. Dunning, *A Manual of Laboratory and Diagnostic Tests*, eighth ed., Lippincott Williams and Wilkins, Philadelphia, 2009.
- [12] C.C. Chernecky, B.J. Berger, *Laboratory Tests and Diagnostic Procedures*, fifth ed., Saunders Elsevier, St. Louis, Missouri, USA, 2008.
- [13] V.N. Shabalin, S.N. Shatokhina, *Morphology of human biological fluids (Morfologia biologicheskikh zhidkostey cheloveka)*, Chrysostom, Moscow, 2001 (in Russian).
- [14] B. Yu, Q. Yuan, L. Nie, S. Yao, *J. Pharm. Biomed. Anal.* 25 (2001) 1027–1032.
- [15] F. Zhao, Z. Wang, H. Wang, R. Zhao, M. Ding, *Chin. Chem. Lett.* 22 (2011) 342–345.
- [16] W. Kwon, J. Kim, S. Suh, M. Kyo M., *Forensic Sci. Int.* 221 (2012) 57–64.
- [17] Y. Zuo, Y. Yang, Z. Zhu, W. Hea, Z. Aydin, *Talanta* 83 (2011) 1707–1710.
- [18] D. Tsikas, A. Wolf, A. Mitschke, F. Gutzki, W. Will, M. Bader, *J. Chromatogr. B* 878 (2010) 2582–2592.
- [19] W. Machini, C. Martin, M. Martinez, S. Teixeira, H. Gomes, M. Teixeira, *Sens. Actuators B* 181 (2013) 674–680.
- [20] S. Beging, D. Mlynek, S. Hataihimakul, A. Poghosian, G. Baldsiefen, H. Busch, N. Laube, L. Kleinen, M. Schoning, *Sens. Actuators B*, 144 (2010) 374–379.
- [21] F. Phillips, K. Kaczor, N. Gandhi, B. Pendley, R. Danish, M. Neuman, B. Toth, V. Horvath, E. Lindner, *Talanta* 74 (2007) 255–264.
- [22] C. Pundir, S. Yadav, A. Kumar, *Trends Anal. Chem.* 50 (2013) 42–52.
- [23] P. Kanyong, R. Pemberton, S. Jackson, J. Hart, *Anal. Biochem.* 428 (2012) 39–43.
- [24] N. Chauhan, J. Narang, A. Shweta, C. Pundir, *Clin. Biochem.* 45 (2012) 253–258.
- [25] M. Gutierrez, S. Alegret, M. Valle, *Biosens. Bioelectron.* 22 (2007) 2171–2178.
- [26] M. Gutierrez, S. Alegret, M. Valle, *Biosens. Bioelectron.* 23 (2008) 795–802.
- [27] L. Lvova, E. Martinelli, F. Dini, A. Bergamini, R. Paolesse, C. Natale, A. Amico, *Talanta* 77 (2009) 1097–1104.
- [28] T. Fenton, M. Eliasziw, A. Lyon, S. Tough, J. Brown, A. David, D. Hanley, *Nutr. Res.* 29 (2009) 320–326.
- [29] K.H. Esbensen, *Multivariate Data Analysis – in Practice*, CAMO Software, Oslo, 2002.
- [30] G. James, D. Witten, T. Hastie, R. Tibshirani, *An Introduction to Statistical Learning with Applications in R*, Springer Science+Business, Media, New York, 2013.
- [31] R Development Core Team. R: A Language and Environment for Statistical Computing, R Foundation for Statistical Computing, Vienna, Austria, 2010 (<http://www.R-project.org>).



A direct competitive assay-based aptasensor for sensitive determination of tetracycline residue in Honey

Sai Wang^a, Jiahui Liu^a, Wei Yong^b, Qilong Chen^a, Liya Zhang^a, Yiyang Dong^{a,*}, Haijia Su^a, Tianwei Tan^a

^a Beijing Key Laboratory of Bioprocess, College of Life Science and Technology, Beijing University of Chemical Technology, Beijing 100029, P.R. China

^b Institute of Food Safety, Chinese Academy of Inspection and Quarantine, Beijing 100123, P.R. China

ARTICLE INFO

Article history:

Received 25 June 2014

Received in revised form

7 August 2014

Accepted 9 August 2014

Available online 19 August 2014

Keywords:

Aptasensor

Tetracycline

Direct competitive enzyme-linked

aptamer assay

Honey

ABSTRACT

Tetracycline (TC) is a common antibacterial agent used for prevention and control of animal diseases. The increasing concern about TC residue in food demands high-performing analytical techniques for food quality assessment. Biosensors represent a promising tool for food safety analysis as they can fulfill some demand that the conventional methods do not attain. In this study, a novel colorimetric aptasensor was developed for sensitive detection of TC in honey. The aptasensor was based on a modified direct competitive enzyme-linked aptamer assay (dc-ELAA) scheme utilizing a 76mer single-stranded DNA (ssDNA) aptamer selected by Systematic Evolution of Ligands by Exponential Enrichment (SELEX). The optimized aptasensor showed a good limit of detection (LOD of 0.0978 ng/mL), a wide linear range (0.1–1000 ng/mL) toward TC in honey, with good recoveries (92.09–109.7%) in TC-spiked honey, and was compared with an indirect competitive assay-based aptasensor and validated with a standard ELISA. The biosensor based on dc-ELAA with good limit of detection and simplicity can be applied for high-throughput detection of TC in food.

© 2014 Elsevier B.V. All rights reserved.

1. Introduction

Biosensors, which have experienced dramatic evolution since 1962 with the first introducing of enzyme electrodes [1], are a sub group of chemical sensors composed of a biological recognition element coupled to a chemical or physical transducer. Biosensors can be grouped into categories in agreement to the type of biological component or the mode of signal transduction or both of them, such as microbial biosensors, affinity-based biosensors, electrochemical biosensors, optical biosensors, etc [2]. Different biosensors have been developed for clinic, environment, agriculture and biotechnology in the past few years [3–9], and these biosensors demonstrate prominent advantages as alternatives to traditional methods in terms of specificity, simplicity, sensitivity, relative low cost, and potential for portable equipment construction [10].

Aptamers, first reported in 1990 [11,12], are artificial short single-stranded oligonucleotides of DNA or RNA selected by Systematic Evolution of Ligands by Exponential Enrichment (SELEX). Aptamers appear to be superior alternatives to antibodies or other biological recognition elements with the advantages of high affinity, high specificity, stable selecting process with uniform

reactivity and not involved with immunogenicity [13–16], adaptive folding and structural modulation upon the target molecules [17,18], and easy modification [19].

Aptasensors, a kind of affinity-based biosensors with aptamer as recognition element and commonly designed with different signal transducers, such as colorimetric [20,21], optical [22–24], and electrochemical [25,26], have emerged as a powerful tool in the domains of diagnostics and therapeutics, environmental monitoring, and food safety analysis.

Tetracycline (TC), which is a member of the most common broad-spectrum tetracycline group of antibiotics (tetracyclines, TCs), is extensively used as veterinary drug and feed additive, thus tends to accumulate in finished food products, posing serious risk to customers' health. During the production of honey, TC is often used for the treatment of bacterial brood diseases in apiculture, such as American foulbrood (*Bacillus larvae*) and European foulbrood (*Streptococcus pluton*) [27]. To ensure the security of consumers, some countries have set maximum residue limit (MRL) for TC in honey, and others ban use of TCs with bees at any level. In China, the MRL for TC in honey was formerly set [28] and updated by new regulation [29] at 0.05 mg/kg. Traditional chromatographic w/wo mass spectrometric methods have been reported for the quantification and verification of TC with precise results [30–32]. On the other hand, antibody-based methods for rapid screening of TC in food samples have also been developed

* Corresponding author. Tel.: +86 10 64446260; fax: +86 10 64445535.
E-mail address: yydong@mail.buct.edu.cn (Y. Dong).

with simplicity and high-throughput capability, such as enzyme-linked immunosorbent assay (ELISA) or gold immuno-chromatographic assay (GICA). However, the former chromatographic methods are expensive, require tedious sample-preparation and extended analysis time, and the latter screening techniques have some drawbacks in terms of antibody production, preservation, ethical problems with the use of animals, etc [33]. Thus there is an imperative need to develop efficient determination methods for detection of TC in honey.

In this study, we developed an optimized aptasensor as a sensitive and selective biosensor for the determination of TC in honey based on a simple direct competitive enzyme-linked aptamer assay (*dc*-ELAA) scheme. We improved the protocol with direct competitive format and successfully obtained an excellent limit of detection data. The present aptasensor involving no complicated sample extraction steps is more suitable for practical screening of TC residue in honey with a broad linear range. Additionally, confirmatory comparison of *ic*-ELAA (indirect competitive ELAA) and *dc*-ELAA with standard ELISA test for tetracycline detection in honey was made for the first time to demonstrate the merits of the two competitive assay formats and to provide two aptasensors for TC detection in honey matrix.

2. Materials and methods

2.1. Reagents

Streptavidin (SA), Bovine serum albumin (BSA) and 3, 3', 5, 5'-tetramethylbenzidine dihydrochloride (TMB) were purchased from KPL (Gaithersburg, MD, USA). Tetracycline standard (TC) and Hammerstein bovine casein (Casein) were purchased from Sigma-Aldrich (St. Louis, Mo, USA). The aptamer-3'-biotin (Mw. (23747.43), mp (83.77 °C)) was synthesized by Sangon Biotech Co., Ltd. (Shanghai, China), and the 76-oligomer sequence is (Fig. 1): 5'-CGTACGGAATTCGCTAGCCCCCGGCAGGCCACGGCTTGGGTTGGTCCCACTGCGCGTGGATCCCGAGTCCACGTG-3'. Two kinds of horseradish peroxidase labeled tetracycline (TC-HRP and TC-BSA-HRP) and a tetracycline ELISA kit were purchased from Shandong LvDu

Bio-sciences & Technology Co., Ltd (Shandong, China). All chemicals were of analytical grade and buffers were prepared with ultrapure water and filtered using 0.22 μm membrane filter before use.

2.2. Buffers

Coating buffer: bicarbonate buffer (0.05 M CB, pH 9.6). Dilution buffer for blocking agent: phosphate buffer saline (10 mM PBS, pH 7.4). Washing buffer: Tris-T buffer (10 mM Tris, 0.05% Tween 20, pH 7.6). Binding buffer for aptamer and TC (Binding Buffer, 100 mM NaCl, 20 mM Tris-HCl (pH 7.6), 2 mM MgCl₂, 1 mM CaCl₂, 5 mM KCl, 0.02% Tween-20 [34]); McIlvaine-Na₂EDTA buffer (0.1 M M-E, 12.93 g of citric acid, 37.33 g of Na₂EDTA, 22.38 g Na₂HPO₄ · 12 H₂O in 1 L of ultrapure water, pH 4.0).

2.3. Instrumentation

ELAA was performed in 8 well Flat-Bottom Immuno Plates (Nunc, Denmark). The plates were incubated in a *SPX-70* biochemical incubator (National Science Instrument and Technology Co., Ltd., Beijing, China), shaking with a *MX-M 96*-well plate mixer (Dragon Laboratory Instruments, Ltd., Beijing, China). Absorbance was measured using *ELx800* absorbance microplate reader (BioTek Instruments, Inc., Winooki, Vermont, USA) at both 450 nm and 630 nm. The plates were washed using *ELx50* microplate strip washer (BioTek Instruments, Inc., Winooki, Vermont, USA). The protein content of honey was measured by Nanodrop 2000C (Thermo Fisher Scientific Nanodrop 2000C, Wilmington, Delaware USA) at 280 nm. The ultrapure water was prepared by Thermo Scientific Barnstead GenPure Water Purification System (Thermo Electron LED GmbH, Stockland 3, D-56412 Niedereibert). Centrifugation was performed in Sigma refrigerated centrifuge 3K15 (Sigma Laborzentrifugen GmbH, An der Unteren Söse 50, D-37520 Osterode, German).

2.4. Optimization of assay conditions before competition

At the beginning of the optimization, a checkerboard study was performed to evaluate the concentration of SA and blocking agents, two critical factors respectively influencing on the specific and nonspecific immobilization of biotinylated aptamer on microtiter plates. The satisfactory concentration of SA was 1 μg/mL, and the superior condition of 1% (w/v) Casein or 2% (w/v) BSA was selected as blocking agent (data not shown). Based on this, concentrations of binder (aptamer) and competitor (TC-HRP or TC-BSA-HRP) were further analyzed. The labeled aptamer was prepared in concentrations of 1–50 nM and the TC-HRP conjugates was diluted to 1:800, 1:1600, 1:3200 and 1:6400. In addition, the specific binding ability of aptamer with TC in this aptasensor system was analyzed w/o thermal treatment. The thermal treatment means heating the aptamer at 95 °C for 10 min and then cooling rapidly in ice for 10 min before the immobilization of the biotinylated ssDNA.

2.5. Direct competitive enzyme-linked aptamer assay (*dc*-ELAA) for TC

The direct competitive assay was performed as shown in Fig. 2. SA was diluted to 1 μg/mL in CB coating buffer and 100 μL/well of SA was coated on the microtiter plates at 4 °C for 16 h. To remove unbound SA, wells were washed with 300 μL/well of Tris-T washing buffer for three times. The plates were then blocked with 200 μL/well of 1% Casein or 2% BSA in 10 mM PBS for 90 min at 37 °C with mild shaking, and the unbound protein was removed. Subsequently, 100 μL/well biotinylated aptamer in Binding Buffer

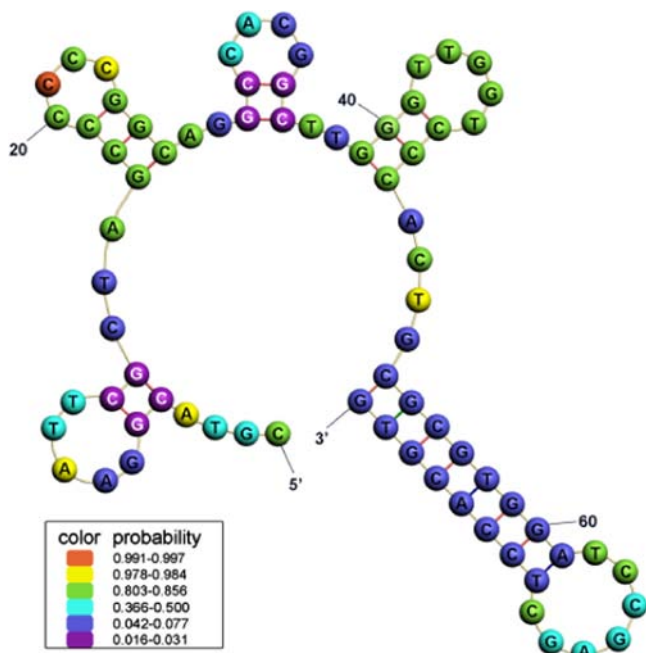


Fig. 1. Secondary structure of the 76mer ssDNA aptamer predicted by m-fold according to free energy minimization algorithm [36]. Color annotation means the probability.

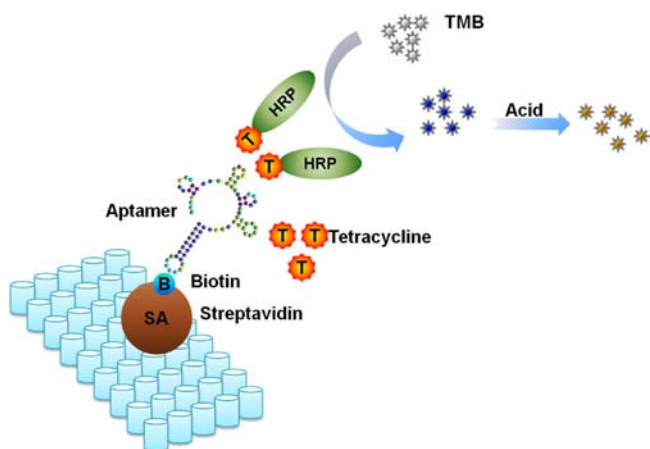


Fig. 2. Schematic illustration of *dc*-ELAA. Competition between TC–HRP and free TC in buffer or honey for the immobilized biotin labeled aptamer, and subsequent enzyme tracer detection.

and 50 μL /well various concentrations of TC solutions from 1×10^{-3} to 1×10^4 ng/mL were added and incubated for 45 min with mild shaking at 25 $^{\circ}\text{C}$. After washing, 100 μL /well HRP labeled TC diluted in Binding Buffer was added to the plates, and was allowed to bind with the immobilized aptamer for 30 min at 25 $^{\circ}\text{C}$. After removing the TC–HRP, 100 μL /well TMB solution was added and incubated for 20 min at 37 $^{\circ}\text{C}$. The color of the solution changed from colorless to blue and turned to yellow when adding 50 μL of 2 M H_2SO_4 to stop the color reaction. The absorbance was measured immediately at 450 nm with 630 nm as the reference wavelength. Each step was protected from light with silver paper. The corresponding test inhibition values were computed according to section 2.7.

2.6. Pretreatment for the analysis in Honey samples

Honey samples were purchased from local supermarket and stored at RT before use. The metal ions such as calcium, iron, magnesium, zinc [35] and protein (observed by Nanodrop 2000C) in honey will have negative influence on the combination of TC and aptamer. For removal of matrix effect, honey samples (5 g) were mixed with 20 mL of 0.1 M M-E buffer and 2 mL 0.5% trichloroacetic acid (TCA) for 5 min using a vortex mixer, then homogenized by ultrasonic for 5 min, and centrifuged at 4 $^{\circ}\text{C}$ for 20 min at 4000 rpm. Then 4 M NaOH was added dropwise to the supernatant to adjust the pH to 7.6. Finally, samples were stored at 4 $^{\circ}\text{C}$ in the dark and diluted with Binding Buffer (sample: buffer=1:5) before use. The detection of TC in honey was validated by *dc*-ELAA as described in section 2.5. TC standard was dissolved and diluted into concentrations from 1×10^{-3} to 1×10^4 ng/mL using honey solutions.

2.7. Data processing

2.7.1. Significance analysis

Significance analysis between different conditions was characterized by *P* value using two-tailed T-tests and marked using different colors in Fig. 2.

2.7.2. Inhibition values A/A_0

The absorbance was measured immediately at 450 nm with 630 nm as the reference wavelength. The optical density of each well, denoted by *B*, was consistent with the result of absorbance at 450 nm minus absorbance at 630 nm. B_0 means the optical density

value of the non-competitive control (with no TC). B_{blank} means the optical density value of the blank control (with no aptamer or TC). To reflect the actual competitive effect and improve the sensitivity, the absorbance of the competitive system is defined by *A*, namely *B* minus B_{blank} . The final absorbance values were converted into their corresponding test inhibition values A/A_0 .

2.7.3. LOD

The LOD was defined as the concentration corresponding to 3 standard deviations below the mean absorbance from non-competitive control.

3. Results and discussions

3.1. Optimization of assay conditions

Prior to the competition assay, detailed assay conditions were investigated for the optimized method. The immobilized SA was exposed to various concentrations (1–50 nM) of biotinylated aptamer. The absorbance increased with the growing concentration of aptamer until 20 nM (Fig. 3(A)). As 1 nM aptamer led to a relatively lower absorbance, which was not considered as a better choice for a wider linear range, 2–20 nM aptamer was applied for the subsequent optimization. As shown in Fig. 3(B), the satisfactory dilution ratio of TC–HRP was 1:1600 to obtain an absorbance around 1.0 in order to get dose-curves with desired sensitivity [36]. Several studies reported that TC can form chelate compounds with BSA [37–39]. Thus some ELISA kits manufacturers try another novel kind of horseradish peroxidase labeled tetracycline (TC–BSA–HRP) to improve the sensitivity of the detection system and make more binding sites of TC exposed for antibody. However, TC–BSA–HRP did not perform well in the present biosensor employing aptamer as the recognition element (Fig. 3(C)), thus TC–HRP was selected as the enzyme tracer. The pretreatment of heating ssDNA at 95 $^{\circ}\text{C}$ for 10 min and then cooling rapidly in ice for 10 min was performed in order to denature and block the aptamer in its unfolded structure [40]. Single DNA or RNA tends to be more ordered and comes into adaptive folding from uncertain conformation to energy-efficient three-dimension structures when meeting with their targets in solution [17,41]. Moreover, the denaturation can also make the biotin label available for the interaction with streptavidin. Thus comparison was made between the aptamer w/wo a thermal treatment before immobilization. Although the result showed no significant difference between the two kinds of usage mode (Fig. 3(D)), the absorbance of no treatment control was slightly smaller. To the authors' experience, it is better to apply the thermal treatment to aptamer before it binds with TC, especially after a prolonged preservation period.

3.2. Dose-response curves in buffer

The *dc*-ELAA in this study was not merely an analytical method with similar protocol to ELISA, changing the recognition element from antibody to aptamer. The detailed implementation scheme should be modified in light of the adaptive folding capability of aptamer. Thus comparison between two different operation schemes when adding aptamer and TC to wells was made as shown in Fig. 4(A). One dose-curve was obtained by adding 100 μL /well biotinylated aptamer and 50 μL /well various concentrations of TC solutions simultaneously and incubated for 45 min with mild shaking at 25 $^{\circ}\text{C}$, then TC–HRP for 30 min. The other curve was gained by adding 100 μL /well biotinylated aptamer incubating with SA for 45 min, and then 50 μL /well various concentrations of TC for 30 min with mild shaking at 25 $^{\circ}\text{C}$, then TC–HRP for 30 min. The former performed higher sensitivity

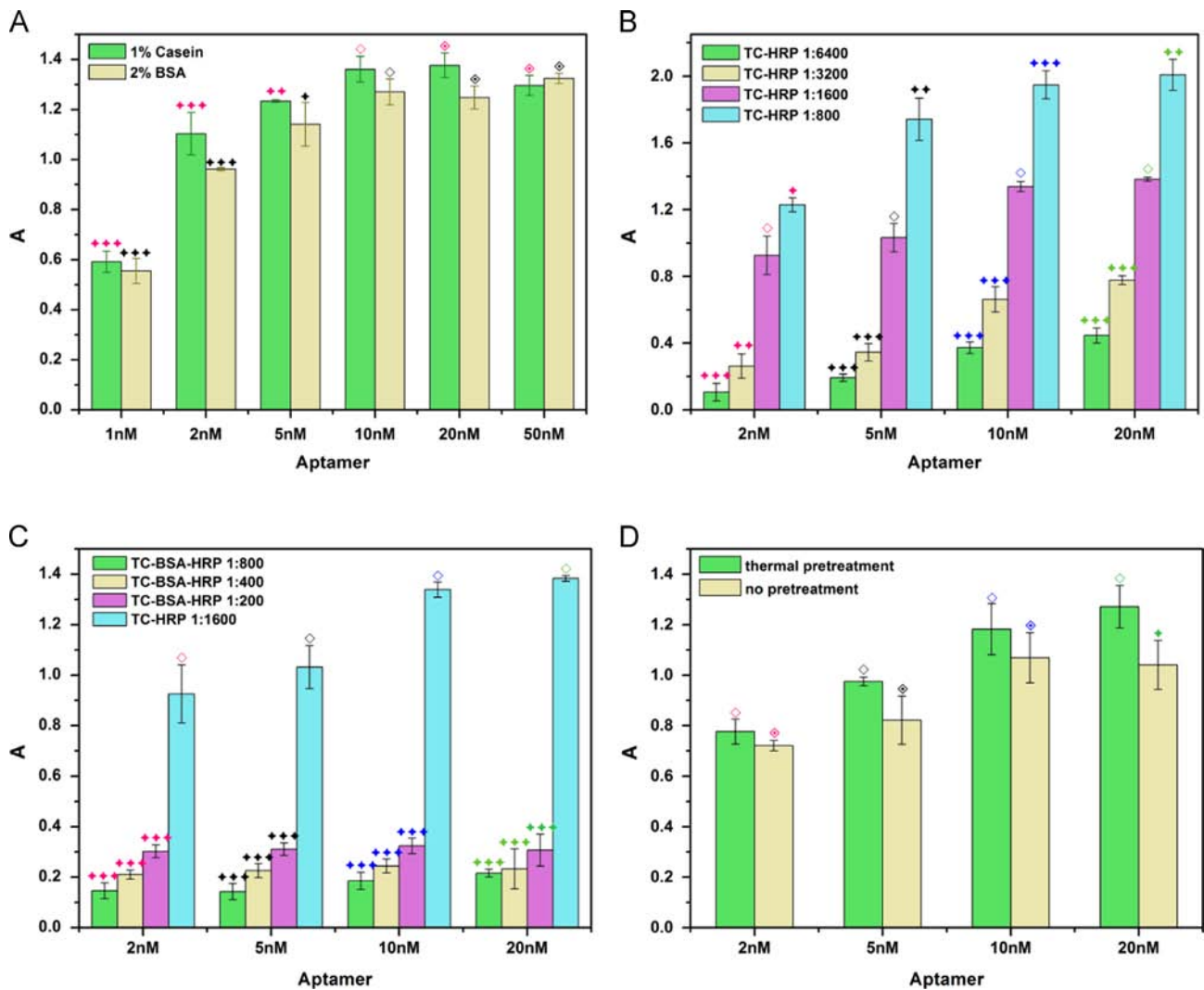


Fig. 3. Optimization of dc-ELAA assay conditions. Detailed working conditions were evaluated with $1\mu\text{g/mL}$ of SA. (A) Absorbance of 1–50 nM aptamer using 1% Casein or 2% BSA as blocking agent. (B) Absorbance of 2, 5, 10, 20 nM aptamer with different dilution ratio of TC-HRP. (C) Absorbance of 2, 5, 10, 20 nM aptamer under the condition of different enzyme tracers. (D) Absorbance of 2, 5, 10, 20 nM aptamer with thermal treatment or not. Significance analysis was characterized according section 2.7 and marked using different colors. The symbol \diamond denotes control group, \circ denotes $P > 0.05$, \blacklozenge denotes $P < 0.05$, $\blacklozenge\blacklozenge$ denotes $P < 0.01$, $\blacklozenge\blacklozenge\blacklozenge$ denotes $P < 0.001$.

owing to aptamer's advantage of adaptive folding. Aptamer can fold and bind upon the targets [17–18] and can be structurally modulated upon the target molecules [33]. In the present study, thermal-cooling treatment blocked the aptamer in unfolded state, and aptamer folded into specific secondary structure for TC with the presence of TC. Jeong and Rhee Paeng [40] developed an aptasensor for the determination of TC in bovine milk using the second scheme in Fig. 4(A), however, the LOD (15.7 ng/mL) was higher than the LOD (0.0978 ng/mL) in the present study and their dynamic range (88.8 ng/mL – $44.4\text{ }\mu\text{g/mL}$) was relatively narrower than that of this study (0.1 – 1000 ng/mL). Hence TC solutions had better be added with aptamer at the same step to induce an adaptive folding, and moreover the pre-incubation between TC and aptamer could contribute to obtain a more sensitive competitive curve.

The sensitivity of the competition assay depends on the immobilized aptamer concentration on the solid surface and the suitable concentration of competitor, TC-HRP conjugates. Concentrations of aptamer and TC-HRP were controlled, and dose-response curves were performed. Three concentrations of aptamer (2, 5, 10 nM) were used to investigate the sensitivity for TC detection. The 5 nM concentration of aptamer was found to provide optimum sensitivity and sufficient absorbance values for an easily detectable signal. The results in Fig. 4(B) demonstrated that sensitivity increased as lower

concentrations of aptamer were utilized. However, 2 nM aptamer showed a relatively narrower linear range than 5 nM because the lower concentration of aptamer provided less binding sites for TC and is easier to be fully occupied, while the higher concentration of 10 nM aptamer gave rise to low sensitivity in competition. As shown in Fig. 4(C), the selected dose-curve was compared with other two condition-changed curves, one with 2% BSA as blocking agent and the other with 1:3200 of TC-HRP as competitor. The dose-curve utilizing 2% BSA provided similar working range with the selected dose-curve, but had a lower sensitivity. This can be explained by the combination of TC and BSA [37–39]. The other dose-curve was obtained using a lower concentration of TC-HRP to optimize the assay performance. However, the inhibition difference between the high and low doses of TC was too small to be valuable. In light of the sensitivity and working linear range of the dose-curve, 5 nM aptamer, 1:1600 TC-HRP and 1% Casein were chosen as suitable conditions in the aptasensor and to be used for TC detection in honey samples.

3.3. Detection of TC in Honey using direct competitive ELAA

Matrix effects may influence the aptamer-analyte interaction and reduce the detection sensitivity. McIlvaine- Na_2EDTA buffer

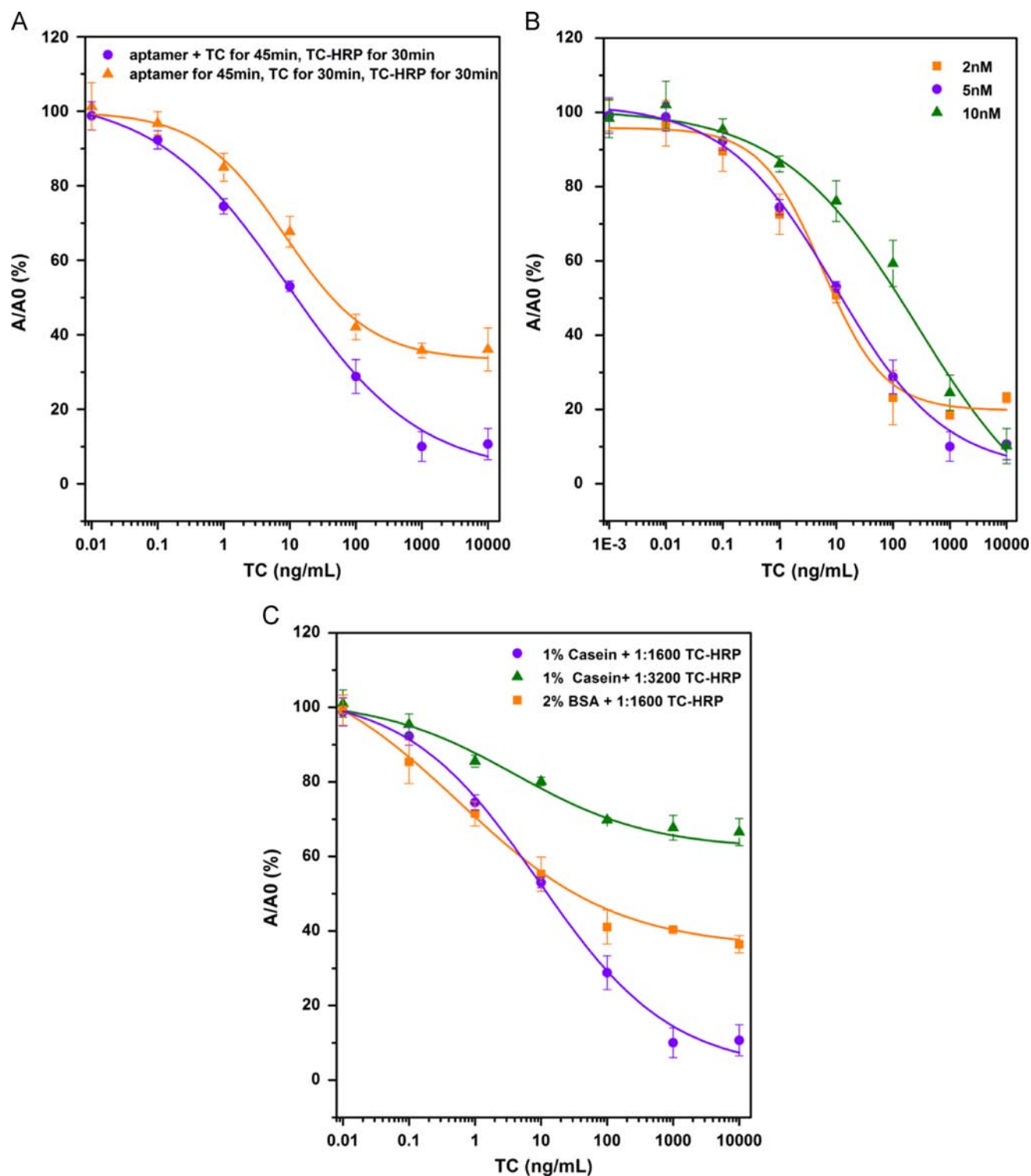


Fig. 4. Direct competitive ELAA in buffer. (A) Inhibition curves for TC by *dc*-ELAA using different operation procedure, with 5 nM aptamer and 1:1600 TC-HRP. (B) Inhibition curves for TC by *dc*-ELAA using various concentrations of biotinylated aptamer (2, 5, 10 nM). (C) Inhibition curves for TC by *dc*-ELAA using various concentrations of TC-HRP or different blocking agent. Data points are the average plus \pm one standard deviation ($n=3$).

was utilized to remove ions metals as Na_2EDTA has a greater affinity for cations than TC [42], and TCA was employed as acidic deproteination agent. Moreover, honey solutions were kept in the dark to keep TC stable in honey for subsequent detection, since TC is light-sensitive.

The resulting matrix-matched standard TC in honey solutions was used in this study. The dose-response curves were explored in

accordance with the selected dose-response curve in buffer (with 5 nM aptamer in Fig. 4(B)), using 1 $\mu\text{g}/\text{mL}$ SA, 5 nM aptamer, and 1:1600 TC-HRP. The competition in honey showed satisfactory inhibition curve (Fig. 5(A)). The dose-response curves in buffer and honey were calculated as following: (1) A/A_0 (%) of TC in buffer = $-20.71 \times \text{Log} [\text{TC}] + 73.31$, $R^2 = 0.9957$ (Fig. 5(B)); (2) A/A_0 (%) of TC in honey = $-21.83 \times \text{Log} [\text{TC}] + 80.75$, $R^2 = 0.9880$ (Fig. 5(B)).

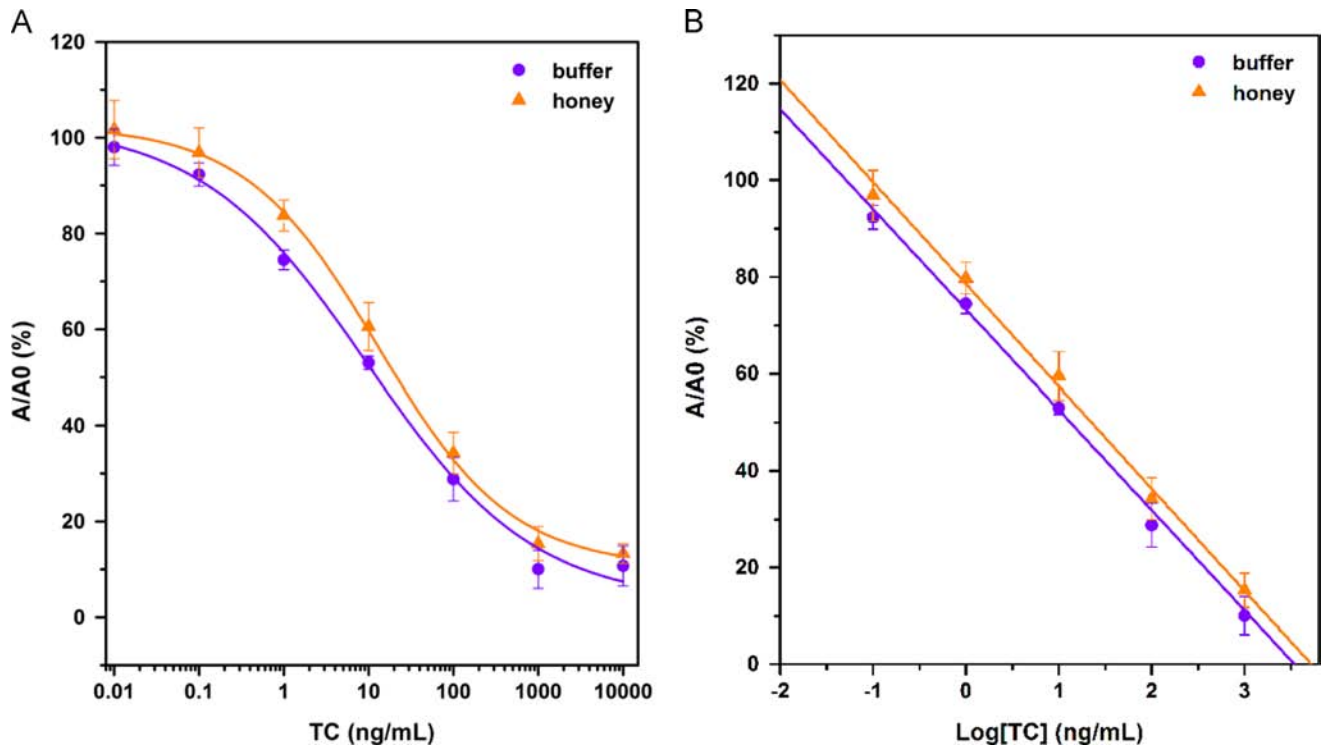


Fig. 5. Dose-response curves and calibration curves for TC. (A) Inhibition curves using 1 $\mu\text{g/mL}$ of SA, 5 nM aptamer and 1:1600 TC–HRP in buffer and honey. (B) Calibration curve for TC in buffer and honey. Data points are the average plus \pm one standard deviation ($n=3$).

Table 1

Comparison of methods reported for detection of TC in honey.

Analytical methods	LOD	Converted (ng/mL) ^a	Linearity ($y=ax+b$, a, b, r^2)	Linear range	Converted (ng/mL) ^a	References
dc-ELAA	9.78×10^{-2} ng/mL	0.0978	$y = -21.83x + 80.75$, $r^2 = 0.9880$	0.1–1000 ng/mL	0.1–1000	
ELISA	3.98×10^{-10} M	0.17	$y = -0.446x - 2.60$, $r^2 = 0.980$	$3.16\text{--}316 \times 10^{-9}$ M	1.4–140.4	[50]
ECL	2.0×10^{-12} g/mL	0.002	N/A	$4\text{--}400 \times 10^{-11}$ g/mL	0.04–4	[49]
FI-ECL	4.0×10^{-9} g/mL	4.0	$y = 0.3140x + 4.0997$, $r^2 = 0.9974$	$2\text{--}1000 \times 10^{-8}$ g/mL	20–10000	[51]
Dipsticks	7 $\mu\text{g/kg}$	7	N/A	N/A	N/A	[52]
CL	2.2×10^{-8} mol/L	9.78	$y = 8.586 \times 10^{10}x + 1.966 \times 10^4$, $r^2 = 0.9991$	$5.0\text{--}600 \times 10^{-8}$ mol/L	22.2–2666	[53]
HPLC	5.8 $\mu\text{g/kg}$	5.8	$y = 0.25x + 0.56$, $r^2 = 0.9998$	20.1–301.2 $\mu\text{g/kg}$	20.1–301.2	[54]
HPLC	0.12 ng/g	0.12	$y = 474.2x + 204.7$, $r^2 = 0.997$	1.0–125 ng/g	1.0–12	[55]
Fluorescence	0.3 $\mu\text{g/g}$	300	N/A	N/A	N/A	[56]
HPLC	8.3 $\mu\text{g/kg}$	8.3	N/A	N/A	N/A	[57]
TFC-UHPLC-Orbitrap- MS	5 $\mu\text{g/kg}$	5	N/A	5–250 $\mu\text{g/kg}$	N/A	[58]

N/A, not available/applicable

^a Converted for easy comparison

A LOD of 0.0659 ng/mL and a linear range of 0.1–1000 ng/mL were achieved in buffer. Additionally, the LOD and the linear range were 0.0978 ng/mL and 0.1–1000 ng/mL respectively in honey. The results indicate that the dc-ELAA method in this assay yields similar LOD values in buffer and honey without obvious matrix effect.

Several studies have reported to select specific DNA or RNA aptamer for TC [34,43,44] and developed aptasensors to detect TC in food. Most of the aptasensors are electrochemical aptamer-based biosensors to detect TC residue in milk [45–48], and few studies are performed on microtiter plate platform which can achieve high-throughput detection [36,40]. In recent years, some other novel analytical methods were reported for the quantification of tetracycline residue in honey (Table 1). The dc-ELAA in the present study demonstrated remarkable advantages in terms of detection limit, linear range compared with the other reported rapid analytical methods.

3.4. Recovery and cross-reactivity study

The specificity of the 76mer aptamer employed in the aptasensor was evaluated for cross-reactivity against several common members of TCs (oxytetracycline, tetracycline, doxycycline) when selected by SELEX [34]. The reported results showed the 76mer ssDNA aptamer yield a measurable specific binding to TC than its structural similarities. What's more, the specificity and high affinity of the aptamer-analyte interaction significantly simplified sample pretreatment.

Accuracy of the aptasensor detecting TC in honey samples was evaluated by recovery rate (%) and data reproducibility (% relative standard deviation, RSD). Free TC (0.1 ng/mL, 1 ng/mL, 10 ng/mL, 100 ng/mL and 1000 ng/mL) were spiked in honey solution and mean percentage recoveries were analyzed to be 92.09–109.7%, the RSD was lower than 7% in honey (Table 2). To validate the dc-

Table 2
Recovery study of *dc*-ELAA and ELISA.

Methods	Spiked concentration (ng/mL)	Measured concentration (ng/mL, mean \pm SD)	Recovery (% mean)	RSD (%)
<i>dc</i> -ELAA	0.1	0.1097 \pm 0.004993	109.7	4.550
	1	0.9209 \pm 0.05963	92.09	6.475
	10	9.331 \pm 0.5334	93.31	5.716
	100	97.48 \pm 3.944	97.48	3.944
	1000	987.5 \pm 25.13	98.75	2.544
ELISA	0.1	0.1118 \pm 0.006785	111.8	6.066
	1	0.8656 \pm 0.02987	86.56	3.451
	10	11.20 \pm 0.4946	112.0	4.416
	100	95.25 \pm 4.389	95.25	4.608
	1000	1021 \pm 26.66	102.1	2.610

SD: standard deviation ($n=7$).

RSD: relative standard deviation.

Table 3
Detection by *dc*-ELAA, *ic*-ELAA, and ELISA.

Honeys	Measured concentration (ng/mL, mean \pm SD)		
	<i>dc</i> -ELAA	<i>ic</i> -ELAA	ELISA
Acacia Honey	0.1782 \pm 0.001604	0.1067 \pm 0.07422	0.1239 \pm 0.01808
Pipa Honey	1.594 \pm 0.07190	1.583 \pm 0.1416	1.931 \pm 0.04943
Jujube Honey	1.157 \pm 0.07660	1.683 \pm 0.1445	1.629 \pm 0.1448
Polyfloral Honey	1.745 \pm 0.1063	1.65 \pm 0.02065	2.119 \pm 0.1576

SD: standard deviation ($n=7$).

ELAA, a standard ELISA was performed in the recovery study with the same spiked concentration of tetracycline in honey. As shown in Table 2, the results of the two methods demonstrate satisfactory consistency. The results enabled the use of *dc*-ELAA as satisfactory screening method.

3.5. Comparison of direct-competitive ELAA (*dc*-ELAA), indirect-competitive ELAA (*ic*-ELAA), and ELISA

As sandwich assay scheme is not available with TC detection owing to its small size (Mw 444.4), detection approaches based on competitive formats are preferred, performed directly or indirectly. An aptasensor based on *ic*-ELAA (indirect competitive enzyme-linked aptamer assay) scheme was developed in our previous study [36]. Analysis time of the two competitive methods was similar. The *dc*-ELAA in this study with a wider linear range can be used to detect higher concentration of TC in honey, thus applicable for countries with MRL more than 100 ng/mL, and is more practical for on-site detection. The *ic*-ELAA provided slightly higher sensitivity than the *dc*-ELAA in terms of LOD (0.0096 ng/mL in *ic*-ELAA) partly owing to the signal amplification of the indirect competition based on the highly specific biotin-streptavidin combination. In the indirect competitive aptasensor, SA-HRP (horse-radish peroxidase labeled streptavidin) was introduced to amplify the signal after the competition of TC, TC-BSA for aptamer-biotin. And in the present study, SA-B was used to immobilize the aptamer on the microtiter plates, TC-HRP was employed as competitor and enzyme tracer, while there is no other amplification of competition. In short, the direct and indirect competitive aptasensors have their own merits, and they can both be employed to detect TC in honey.

In addition, the *dc*-ELAA was applied to quantify the TC residue in several collected honey samples (from white to dark, monofloral and polyfloral), as well as the *ic*-ELAA and a standard ELISA (A/A_0 (%) = $-39.45 \times \log [TC] + 53.58$, $R^2 = 0.9905$). The results showed good proximity of the three methods (Table 3).

4. Conclusions

In conclusion, an improved direct competitive assay-based aptasensor for detection of tetracycline in honey was developed. In this study, detailed operating optimization was carried out and dose-response behavior was investigated both in buffer and honey samples. The optimized *dc*-ELAA showed a good limit of detection (LOD of 0.0978 ng/mL), a wide linear range (0.1–1000 ng/mL) and high recovery rates (92.09%–109.7% in TC spiked honey samples). The proposed method is promising to provide a simple and sensitive screening scheme for on-site quality surveillance of TC in honey and related ad hoc food safety issues.

Acknowledgments

Special thanks are given to Prof. Man Bock Gu from Korea University in South Korea for the valuable discussion and suggestions for the study.

References

- [1] L.C. Clark, C. Lyons, *Ann. NY Acad. Sci.* 102 (1962) 29–45.
- [2] L.D. Mello, L.T. Kubota, *Food Chem.* 77 (2002) 237–256.
- [3] A.J. Haes, R.P. Van Duyne, *J. Am. Chem. Soc.* 124 (2002) 10596–10604.
- [4] J.A. Hansen, J. Wang, A.N. Kawde, Y. Xiang, K.V. Gothelf, G. Collins, *J. Am. Chem. Soc.* 128 (2006) 2228–2229.
- [5] M. Li, X. Zhou, X. Ding, S. Guo, N. Wu, *Biosens. Bioelectron.* 41 (2013) 889–893.
- [6] J. Liu, Y. Lu, *J. Am. Chem. Soc.* 125 (2003) 6642–6643.
- [7] K. Maehashi, T. Katsura, K. Kerman, Y. Takamura, K. Matsumoto, E. Tamiya, *Anal. Chem.* 79 (2007) 782–787.
- [8] S. Myung, A. Solanki, C. Kim, J. Park, K.S. Kim, K.B. Lee, *Adv. Mater.* 23 (2011) 2221–2225.
- [9] B. Unnikrishnan, S. Palanisamy, S.M. Chen, *Biosens. Bioelectron.* 39 (2013) 70–75.
- [10] J.H.T. Luong, C.A. Groom, K.B. Male, *Biosens. Bioelectron.* 6 (1991) 547–554.
- [11] A.D. Ellington, J.W. Szostak, *Nature* 346 (1990) 818–822.
- [12] C. Tuerk, L. Gold, *Science* 249 (1990) 505–510.
- [13] S.D. Jayasena, *Clin. Chem.* 45 (1999) 1628–1650.
- [14] C.H. Kim, L.P. Lee, J.R. Min, M.W. Lim, S.H. Jeong, *Biosens. Bioelectron.* 51 (2014) 426–430.
- [15] S.M. Nimjee, C.P. Rusconi, B.A. Sullenger, *Annu. Rev. Med.* 56 (2005) 555–583.
- [16] S. Tombelli, M. Minunni, M. Mascini, *Biosens. Bioelectron.* 20 (2005) 2423–2434.
- [17] T. Hermann, D.J. Patel, *Science* 287 (2000) 820–825.
- [18] S.P. Song, L.H. Wang, J. Li, J.L. Zhao, C.H. Fan, *Trends Anal. Chem.* 27 (2008) 108–117.
- [19] J. Pultar, U. Sauer, P. Domnanich, C. Preininger, *Biosens. Bioelectron.* 24 (2009) 1456–1461.
- [20] J.W. Liu, Y. Lu, *Angew. Chem.* 45 (2006) 90–94.
- [21] M.N. Stojanovic, D.W. Landry, *J. Am. Chem. Soc.* 124 (2002) 9678–9679.
- [22] M. Lee, D.R. Walt, *Anal. Biochem.* 282 (2000) 142–146.
- [23] N. Li, C.M. Ho, *J. Am. Chem. Soc.* 130 (2008) 2380–2381.
- [24] T.G. McCauley, N. Hamaguchi, M. Stanton, *Anal. Biochem.* 319 (2003) 244–250.
- [25] Y.S. Kim, S.J. Lee, M.B. Gu, *BioChip J.* 2 (2008) 175–182.
- [26] I. Willner, M. Zayats, *Angew. Chem.* 46 (2007) 6408–6418.
- [27] A.C. Martel, S. Zeggane, P. Drajnudel, J.P. Faucon, M. Aubert, *Food Addit. Contam.* 23 (2006) 265–273.
- [28] National Standard of the People's Republic of China, Hygienic standard for honey, GB 14963–2003.
- [29] National Standard of the People's Republic of China, Hygienic standard for honey, GB 14963–2011.
- [30] S.P. Khong, Y.A. Hammel, P.A. Guy, *Rapid Commun. Mass Spectrom.* 19 (2005) 493–502.
- [31] G. Pagliuca, T. Gazzotti, G. Serra, A.G. Sabatini, *Apidologie* 33 (2002) 583–584.
- [32] V.F. Samanidou, K.I. Nikolaidou, I.N. Papadoyannis, *J. Sep. Sci.* 28 (2005) 2247–2258.
- [33] Y.Y. Dong, Y. Xu, W. Yong, X.G. Chu, D.N. Wang, *Crit. Rev. Food Sci. Nutr.* 54 (2013) 1548–1561.
- [34] J.H. Niazi, S.J. Lee, M.B. Gu, *Bioorg. Med. Chem.* 16 (2008) 7245–7253.
- [35] S. Huq, M. Garriques, K.M.R. Kallury, *J. Chromatogr. A* 1135 (2006) 12–18.
- [36] S. Wang, W. Yong, J.H. Liu, L.Y. Zhang, Q.L. Chen, Y.Y. Dong, *Biosens. Bioelectron.* 57 (2014) 192–198.
- [37] S. Bi, D. Song, Y. Tian, X. Zhou, Z. Liu, H. Zhang, *Acta Part A* 61 (2005) 629–636.
- [38] N. Keswani, S. Choudhary, N. Kishore, *J. Chem. Thermodyn.* 58 (2013) 196–205.
- [39] M.A. Khan, S. Muzammil, J. Musarrat, *Int. J. Biol. Macromol.* 30 (2002) 243–249.
- [40] S. Jeong, I. Rhee Paeng, *World J.* (2012), <http://dx.doi.org/10.1100/2012/159456>.

- [41] G.R. Bishop, J.S. Ren, B.C. Polander, B.D. Jeanfreau, *Biophys. Chem.* 126 (2007) 165–175.
- [42] C.R. Anderson, H.S. Rupp, W.H. Wu, *J. Chromatogr. A* 1075 (2005) 23–32.
- [43] C. Berens, A. Thain, R. Schroeder, *Bioorg. Med. Chem.* 9 (2001) 2549–2556.
- [44] M. Müller, J.E. Weigand, O. Weichenrieder, B. Suess, *Nucleic Acids Res.* 34 (2006) 2607–2617.
- [45] D. Chen, D. Yao, C. Xie, D. Liu, *Food Control* 42 (2014) 109–115.
- [46] Y.J. Kim, Y.S. Kim, J.H. Niazi, *Bioprocess. Biosyst. Eng.* 33 (2010) 31–37.
- [47] J. Zhang, B. Zhang, Y. Wu, S. Jia, T. Fan, Z. Zhang, C. Zhang, *Analyst* 135 (2010) 2706–2710.
- [48] L. Zhou, D.J. Li, L. Gai, J.P. Wang, Y.B. Li, *Sens. Actuators B: Chem* 162 (2012) 201–208.
- [49] Z. Guo, P. Gai, *Anal. Chim. Acta* 688 (2011) 197–202.
- [50] M. Jeon, I. RheePaeng, *Anal. Chim. Acta* 626 (2008) 180–185.
- [51] Y.Q. Pang, H. Cui, H.S. Zheng, G.H. Wan, L.J. Liu, X.F. Yu, *J. Lumin.* 20 (2005) 8–15.
- [52] W. Reybroeck, S. Ooghe, H.D. Brabander, E. Daeseleire, *J. Agric. Food Chem.* 55 (2007) 8359–8366.
- [53] I.N. Amin, H.S. Mohammad, A. Mohammad, N. Abdolhossein, *J. Lumin.* 151 (2014) 57–65.
- [54] X. Yang, S.H. Zhang, W. Yu, Z.L. Liu, L. Lei, N. Li, H.Q. Zhang, Y. Yu, *Talanta* 124 (2014) 1–6.
- [55] J.H. Kong, Y.Z. Wang, C. Nie, D. Ran, X.P. Jia, *Anal. Methods* 4 (2012) 1005–1011.
- [56] A. Yamamoto, S. Yoshii, C. Suematsu, M. Tatematsu, H. Shoji, Y. Kato, M. Saito, Y. Inoue, *Anal. Methods* 5 (2013) 773–777.
- [57] Y.K. Lv, J.Q. Zhang, Y.D. He, J. Zhang, H.W. Sun, *New J. Chem.* 38 (2014) 802–808.
- [58] M.M. Aguilera-Luiz, R. Romero-González, P. Plaza-Bolaños, J.L.M. Vidal, A. G. Frenich, *J. Agric. Food Chem.* 61 (2013) 829–839.



Resonance Rayleigh scattering method for determination of ethion using silver nanoparticles as probe

Hooshang Parham*, Sedighe Saeed

Chemistry Department, Faculty of Sciences, Shahid Chamran University, 6135714168 Ahvaz, Iran

ARTICLE INFO

Article history:

Received 19 June 2014

Received in revised form

31 July 2014

Accepted 1 August 2014

Available online 11 August 2014

Keywords:

Resonance Rayleigh scattering

Ethion

Silver nanoparticles

ABSTRACT

A simple, novel and sensitive method was developed to determine ethion insecticide in water samples. This method was based on the interaction of ethion with silver nanoparticles (AgNPs) and quenching of the resonance Rayleigh scattering (RRS) intensity. The change in RRS intensity (ΔI_{RRS}) was linearly correlated to the concentration of ethion over the range of 10.0–900.0 $\mu\text{g L}^{-1}$. Ethion can be measured in a short time (3 min) without any complicated or time-consuming sample pretreatment process. Parameters that affect the RRS intensities such as pH, concentration of AgNPs, standing time, electrolyte concentration, and coexisting substances were systematically investigated and optimized. Interference tests showed that the developed method has a very good selectivity and could be used conveniently for determination of ethion. The limit of detection (LOD) and limit of quantification (LOQ) were 3.7 and 11.0 $\mu\text{g L}^{-1}$, respectively. Relative standard deviations (RSD) for 15.0 and 60.0 $\mu\text{g L}^{-1}$ of ethion were 4.1 and 0.2, respectively. Possible mechanisms for the quenching of RRS of AgNPs were discussed and the method was successfully applied for the analysis of spiked real water samples.

© 2014 Elsevier B.V. All rights reserved.

1. Introduction

Pesticides and insecticides are used to protect agricultural crop against damaging caused by insects. However, ecological compartments such as lakes and rivers may be contaminated by these chemicals through rains and wind, affecting many other organisms far from the first target. Organothiophosphates (OTPs) with a thiophosphoryl (P=S) functional group constitute a broad class of widely used organophosphates (OPs) insecticides. Organophosphates insecticides include very lethal nerve agents and chemical warfare agents, such as, VX, Soman, and Sarin. OTP compounds are used frequently in agricultural lands worldwide and has resulted highly toxic residuals in crops, livestock, and poultry products which has further led to their migration into underground aquifers [1–3]. These compounds are highly toxic to human health and are powerful inhibitors of acetylcholinesterase (AChE) enzyme, causing accumulation of acetylcholine at nerve endings in the peripheral or central nervous system [4].

Current detection methods for OPs and OTPs include chromatography [5–13], a variety of other analytical approaches including enzymatic assays [14], potentiometry [15], UV–visible spectrophotometry [16], and ion mobility spectrometry [17]. From a practical agricultural viewpoint, many of the above-mentioned

approaches have limitations such as lack of instrument portability, limited selectivity, difficulties in real-time monitoring, operational complexity, and in some cases low sensitivity. Therefore, for the sake of human health and environmental pollution control, it is vital to develop fast, sensitive, convenient and effective methods for the analysis of OP pesticides in environmental samples.

Resonance Rayleigh scattering (RRS) has drawn much more attention in recent years and made important contributions in many scientific areas. When a particle is exposed to an electromagnetic radiation, the electrons in the particle oscillate at the same frequency as the incident wave. Resonance Rayleigh scattering takes place when the wavelength of Rayleigh scattering is located at or close to the molecular absorption band. The properties of scattered light depend on the size, composition, shape, homogeneity of the nanoparticles, and refractive index of the medium [18,19].

In recent years, Resonance Rayleigh scattering (RRS) or resonance light-scattering (RLS) technique has been widely applied to the determination of different analytes [20–23]. This method showed its high potential for the determination of metal ions [24], non-metallic inorganic substances [25,26], surfactants [27], biomacromolecules [28], and pharmaceuticals [29]. The method is characterized by high sensitivity, convenience in performance and simplicity in apparatus (usually common spectrofluorophotometer).

Both silver nanoparticles (AgNPs) and gold nanoparticles (AuNPs) possess novel physical and chemical properties and have received considerable interests in recent years for their unique

* Corresponding author. Tel.: +98 611 3360018; fax: +98 611 3337009.

E-mail address: hparham@yahoo.com (H. Parham).

optical and electrical properties. These metal nanoparticles have been investigated extensively for sensing [30–32], exhibit their signals in the visible spectral region under appropriate conditions and give corresponding localized surface plasmon resonance light scattering (LSPR-LS) band of the NPs [33,34].

Some of these noble metal nanoparticles show special optical properties such as strong resonance light scattering in the orders of magnitude higher than light emission from strongly fluorescent dye molecules [35]. Such a character makes them ideal optical probes for chemical, biological and clinical applications [36–38]. Silver nanoparticles (AgNPs) exhibit certain advantages such as higher extinction coefficients, sharper extinction bands and higher ratio of scattering to extinction. More recently, AgNPs are rapidly gaining popularity as a consequence, and some research groups have been developing several strategies for optical sensors and imaging techniques using AgNPs as building blocks and labeling probes [39–41]. In comparison, AgNPs are superior to AuNPs of the same size on the LSPR-LS for its high light scattering power [42]. It has recently been reported that AgNPs is a promising alternative to AuNPs in many applications in the fields of medicine, microbiology, and analytical chemistry [34].

Herein, we present a novel highly sensitive RRS method for the detection of ethion insecticide (Fig. 1) on the basis of the formation of ethion–AgNPs aggregates (Scheme 1) and quenching of the RRS intensity [43–45]. The detection sensitivity can be significantly improved to $\mu\text{g L}^{-1}$ level by monitoring of signal quenching of high sensitivity RRS by AgNPs.

2. Experimental

2.1. Materials and reagents

All chemicals used in the experiments were of analytical grade or higher without further purification. Ethion was purchased from Sigma-Aldrich (America) and a working solution of 10.0 mg L^{-1} was prepared for use in the experiment. Sodium citrate and silver nitrate were purchased from Merck (Darmstadt, Germany). Buffer solutions were prepared by adjusting the pH of 0.1 mol L^{-1} citric acid and phosphoric acid solutions to 6 using NaOH solution (0.1 mol L^{-1}). All solutions were prepared in high-purity water.

2.2. Apparatus

A Shimadzu RF-5301PC spectrofluorophotometer (Japan) was used for recording and measuring the RRS spectra. A pH-meter (827 pH lab, Metrohm1, Herisau, Switzerland) was used for pH adjustment. Transmission electron microscopy (906E, LEO, Germany) and scanning electron microscopy (SEM) (XL-30 electron microscope, Philips, Eindhoven, The Netherlands) were used to study the morphology of AgNPs and ethion–AgNPs.

2.3. Preparation of AgNPs

AgNPs were synthesized by citrate reduction of AgNO_3 [46]. Silver nanoparticles stock solution ($2.0 \times 10^{-1} \mu\text{g mL}^{-1}$) was prepared by dissolving 0.0158 g of AgNO_3 in 40 mL of ultrapure water and slow addition of 2 mL sodium citrate (1%) to the AgNO_3

solution by heating at 80°C with stirring for 30 min. The color of this solution changed gradually from colorless to yellow and it was finally diluted to 50 mL. Above solution was stored at 4°C .

2.4. Measurement of the RRS intensity of AgNPs–ethion system

Appropriate amounts of the AgNPs solution (2 mL of $2.0 \times 10^{-1} \mu\text{g mL}^{-1}$), 1 mL of citrate buffer (pH 6), 1.0 mL of the 0.01 mol L^{-1} of KCl electrolyte, and certain volumes of ethion standard solutions were added into a 10.0-mL flask. The resulting solution was diluted to 10 mL and was vortex-shaken to mix thoroughly and kept for 3 min. The RRS spectra of the solutions were recorded with synchronous scanning at $\lambda_{\text{ex}} = \lambda_{\text{sc}} = 281 \text{ nm}$ (i.e., $\Delta\lambda = 0 \text{ nm}$), slit widths were kept at 1.5 nm, and RRS intensity of AgNP solutions in the absence (I_0) and the presence of ethion (I_{RRS}) was recorded. Fig. 2 shows the recorded RRS spectra of the blank solution and the test solution and the difference in RRS intensity values ($\Delta I_{\text{RRS}} = I_0 - I_{\text{RRS}}$) in the wavelength range of 200–800 nm. As it is seen in Fig. 2, two peaks are obtained at $\lambda_{\text{ex}} = \lambda_{\text{sc}} = 281$ and $\lambda_{\text{sc}} = 2\lambda_{\text{ex}} = 562 \text{ nm}$ and 281 nm was selected as optimum RRS wavelength for further works. Fig. 3 shows the absorption spectrum (black, wavelength range 260–500 nm) and RRS spectrum (red, $\lambda_{\text{ex}} = 281 \text{ nm}$, scattering wavelength range 260–500 nm) of AgNPs solution (blank). It must be mentioned that AuNPs were also examined for detection of ethion and the results were compared with those obtained by AgNPs. The results showed that AuNPs can detect the target analyte (ethion), but they show longer response time (more than 7 min in comparison to 3 min for AgNPs) and lower sensitivity (smaller ΔI_{RRS}) with respect to AgNPs at the same conditions.

3. Results and discussion

3.1. Shape and size of AgNPs and AgNPs–ethion

The structural characteristics such as shape and size of AgNPs and AgNPs–ethion were investigated by TEM and SEM (Fig. 4). It can be seen from these TEM and SEM images that the average diameters of the as synthesized AgNPs were about 20.0 nm and also particles were comparatively homogenous, well dispersed, and almost spherically shaped without any obvious aggregation (Fig. 4A and C). It is well known that thiols will self-assemble into strictly arranged monolayers (SAMs) onto the surface of the metals, especially gold, silver, and copper [47]. These SAMs have been intensely studied and are of great interest due to unique properties of the resulting surfaces [47]. These properties include stabilization and passivation to other reactions. Silver metal has high affinity for reaction with thio groups and a new product is formed through the combination of ethion (containing 4 sulfur atoms). The shape of the new particles is different from that of the AgNPs and they are no longer spherically shaped, but aggregated together and form an inhomogeneous cluster which is obviously bigger than the original AgNPs (Fig. 4B and D). Overall, the combination of ethion with the AgNPs not only increased the size of the nanoparticles, but also changed their apparent shape. The AgNPs–ethion complex has a bigger size and contains an inhomogeneous aggregate in which the spherical shaped AgNPs were wrapped around by ethion molecules and covered the active optical surface of silver nanoparticles and sedimentation of complex that led to the quenching of RRS intensity of silver nanoparticles. It must be mentioned that prepared AgNPs are stable for 2 months (stored at refrigerator, 4°C) and the recorded RRS intensity of nanoparticles was changed from 940 (first day) to 910 after 50 days (changing about 3%).

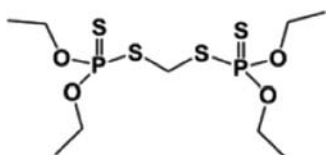
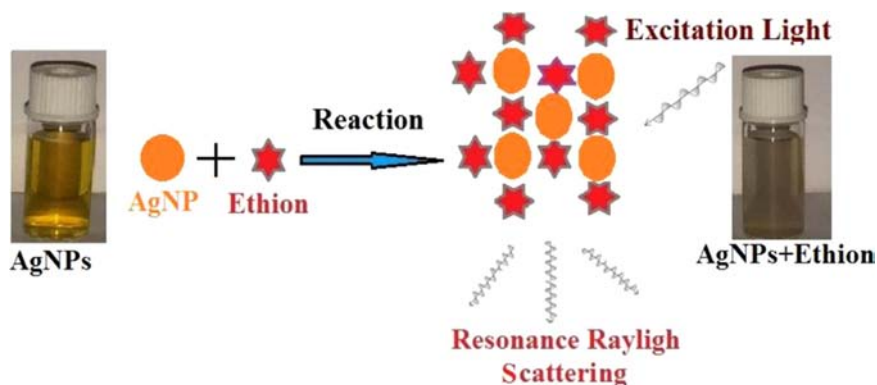


Fig. 1. Chemical structure of ethion insecticide.



Scheme 1. Schematic of reaction of AgNPs with ethion insecticide which produces AgNP–ethion cluster at pH 6.

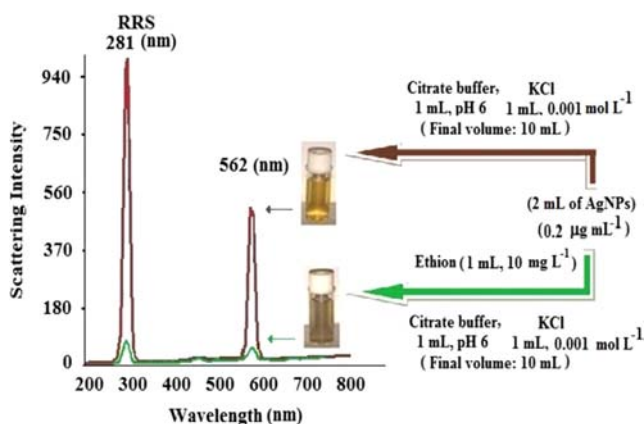


Fig. 2. RRS spectra of AgNPs in the absence (brown) and presence of ethion (green). (For interpretation of the references to color in this figure legend, the reader is referred to the web version of this article.)

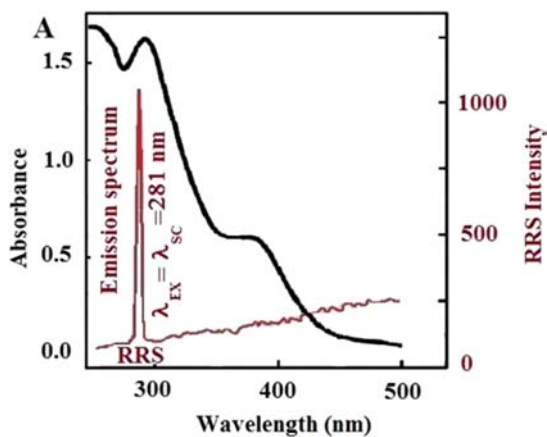


Fig. 3. (A) Absorption (black) and RRS (red) spectra of AgNPs solution. Conditions: $[AgNPs]=0.4 \mu g mL^{-1}$; $\lambda_{ex}=281 \text{ nm}$; scattering spectrum was scanned in the wavelength range of 260–500 nm and maximum RRS occurred at $\lambda_{sc}=281 \text{ nm}$; slit of excitation, 1.5 nm; slit of emission, 1.5 nm. (For interpretation of the references to color in this figure legend, the reader is referred to the web version of this article.)

3.2. Spectral characteristics

As well known, RRS is a process produced by the resonance of scattering and absorption of light when the wavelength of RRS is located at or close to its molecular absorption band. In such a case, the frequency of the exciting electromagnetic wave is equal to that of scattering light. In the present study, different wavelengths from 260 to 320 nm were examined and RRS spectra of AgNPs,

AgNPs–ethion complex and ethion solutions were compared. AgNPs showed intense scattering of light in the wavelength region of 270–300 nm and in presence of ethion insecticide, the RRS intensity is decreased significantly. The RRS spectra of AgNPs, AgNPs–ethion and ethion solutions were examined at excitation wavelengths of 260, 270, 280, 290, 300, 310 and 320 nm and the maximum ΔI is located at 281 nm for $\lambda_{ex}=\lambda_{sc}=281 \text{ nm}$. The RRS spectra of the AgNPs, AgNPs–ethion complex and ethion were overlaid (seven spectra for each solution) and the results showed that (1) the RRS intensity of the ethion solution is very weak and nearly zero; (2) the AgNPs shows somewhat strong RRS intensity, and the maximum RRS wavelength is located at around 290 nm; (3) the RRS intensity of the AgNPs greatly decreases after the addition of ethion, but the maximum difference between scattering signals from AgNPs and AgNPs–ethion (ΔI_{RRS}) occurs at 281 nm. This observation led to the development of a sensitive methodology using silver nanoparticles as optical sensor for ethion determination.

3.3. Optimization of the experimental conditions

3.3.1. Effects of pH, type and volume of buffer solution on RRS intensities

It is well known that pH value can readily affect the reaction between AgNPs and ethion molecules and influence the RRS signals of detection system. Therefore, the influence of pH on the RRS intensity of the system was studied over a pH range of 4–11, and the results are shown in Fig. 5. The pH of the working solutions was adjusted by dilute (0.01 mol L^{-1}) HCl and NaOH solutions. As can be seen from the figure, the ΔI_{RRS} of the system depends greatly on the pH value. It increased sharply when the pH increased from 4 to 6, whereas it decreased greatly with the continuous increase of pH above 6. At low pHs, thio groups of ethion interact with H_3O^+ ions (protonation of thio groups of ethion) which can compete with AgNPs and ΔI_{RRS} decreases. However, at pH values higher than 6, hydroxide ions seems to compete with ethion in terms of adsorption onto the surface of silver nanoparticles leading to inhibition of interaction between AgNPs and ethion which increases the I_{RRS} and consequently decreasing the ΔI_{RRS} ($\Delta I_{RRS}=I_0-I_{RRS}$).

Two buffer solutions were examined and citrate (0.1 mol L^{-1}) produced better results with respect to phosphate (0.1 mol L^{-1}). Into a 10 mL volumetric flask were added 2 mL of $2.0 \times 10^{-1} \mu g mL^{-1}$ of AgNPs solution, 1 mL of buffer (pH 6) and appropriate amounts of ethion solution, respectively. The solution was finally diluted to 10 mL, mixed thoroughly and kept for 10 min.

The effect of citrate buffer volume was also studied and the results showed that 1.0 mL can provide maximum ΔI_{RRS} . Therefore, 1.0 mL of the citrate buffer with pH 6 was selected as the optimum experimental medium.

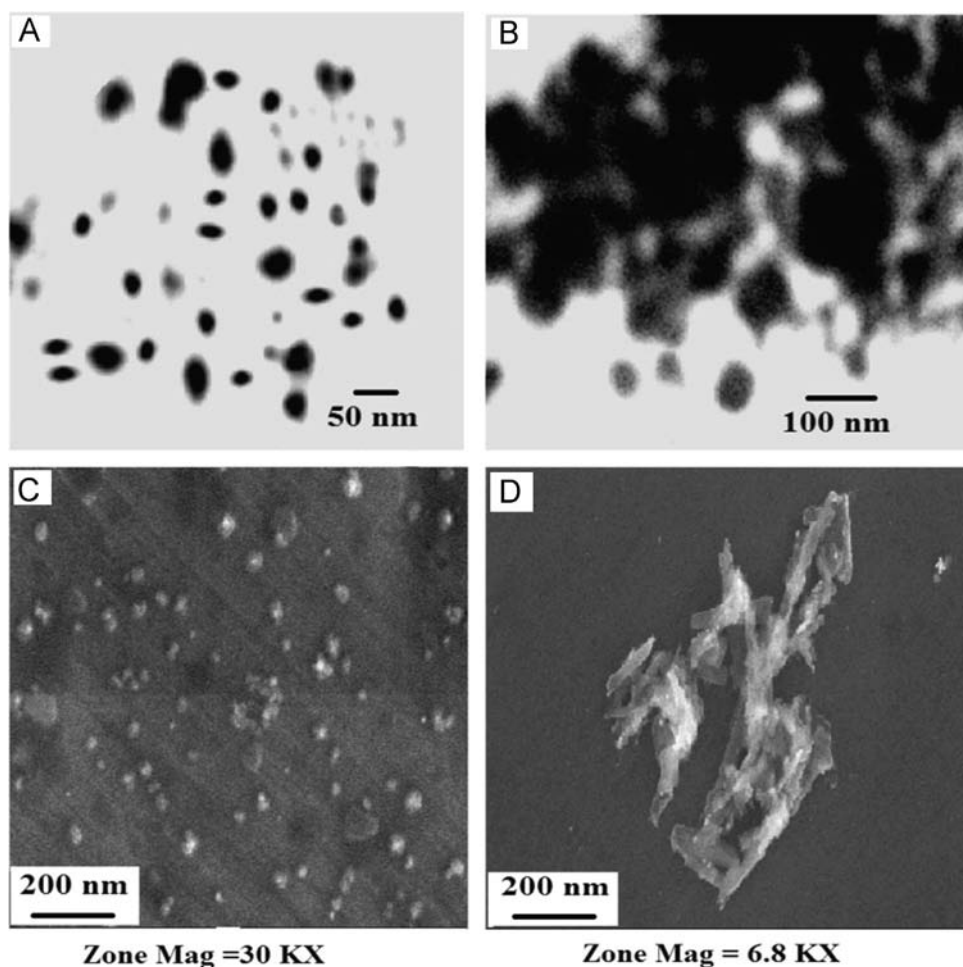


Fig. 4. TEM and SEM images of AgNPs before and after addition of ethion: (A) TEM of AgNPs, (B) TEM of AgNPs–ethion, (C) SEM of AgNPs and (D) SEM of AgNPs–ethion.

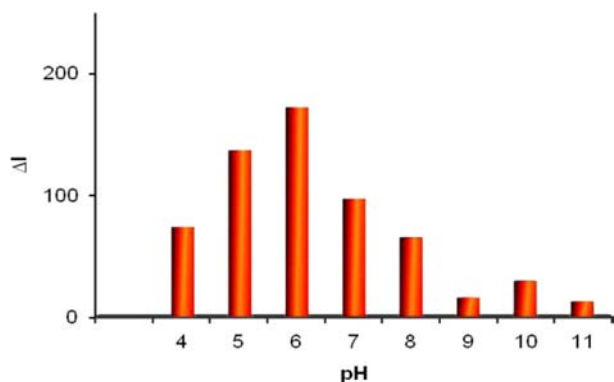


Fig. 5. Influence of pH on ΔI_{RRS} of AgNPs in presence of $0.4 \mu\text{g mL}^{-1}$ of ethion; the pH of test solution was adjusted with dilute NaOH or HCl.

3.3.2. Effect of AgNPs concentration

By increasing the amount of AgNPs in the experimental solution, the intensity of RRS of this system increased. Due to the limitations of spectrofluorophotometer which could not read intensities higher than 1000, a concentration of $0.08 \mu\text{g mL}^{-1}$ of AgNPs in the final solution was used as optimum. Considering the high RRS intensity of the system reagent blank, $0.08 \mu\text{g mL}^{-1}$ AgNPs, and low RRS intensity of AgNPs–ethion mixture, high ΔI_{RRS} was obtained and used for determination of trace concentrations of ethion in water samples.

3.3.3. Effect of surfactants

The effects of different surfactants on the system were studied. The results showed that the presence of cationic surfactants, such as cetyltrimethyl ammonium bromide (CTAB), can increase the RRS intensity of both AgNPs and AgNPs–ethion solutions. The RRS intensity of AgNPs–ethion solution (I_{RRS}) increases more than the RRS intensity of AgNPs (I_0) and so ΔI_{RRS} decreases in presence of such cationic surfactant. Sodium dodecyl sulfate (SDS) as an anionic surfactant was also tested on the system and RRS intensity of both solutions decreased dramatically. Based on the above results, it could be seen that the biggest ΔI_{RRS} and higher sensitivity was obtained in the absence of common surfactants.

3.3.4. Effect of ionic strength

The effect of ionic strength on RRS processes was examined using different salts such as KCl, KNO_3 and NaCl as electrolyte and KCl gave better results. Results show that ΔI_{RRS} is increased by increasing the salt concentration up to 0.001 mol L^{-1} of KCl. But, I_0 of the blank is decreased in more concentrated (up to 0.01 mol L^{-1}) solutions due to the aggregation of nanoparticles and ΔI_{RRS} decreases as a result. The decrease in RRS intensity of AgNPs (I_0) in the presence of KCl or NaCl should be related to the surface-state of nanoparticles rather than the size of nanoparticle aggregates. The RRS intensity should be sensitively dependent on the surface-state of nanoparticles as well as the aggregate size. Therefore, it is possible that KCl or NaCl could change the surface-state of AgNP in addition to driving the aggregation of AgNPs [48].

Therefore, 1.0 mL of the 0.01 mol L⁻¹ of KCl was used as the optimum electrolyte amount in the test solution medium.

3.3.5. The order of addition and standing time

Effect of the adding order of different reagents was investigated. The results indicated that the order of AgNPs–buffer–electrolyte–ethion is the best. Under the optimum condition, the effect of time on the stability of RRS intensity was studied. The results showed that the ΔI_{RRS} reached a maximum at 3 min after all reagents were added, and it remained stable for over 2.0 h. Therefore, this system exhibits good stability.

3.3.6. Effect of interfering substances

Under the optimal conditions, various coexisting substances such as Mg²⁺, Cl⁻, Na⁺, K⁺, NH₄⁺, Ca²⁺, Ac⁻, NO₃⁻, Fe³⁺, SO₄²⁻, parathion, simazine and atrazine were examined for the interference effect on determination of 0.5 $\mu\text{g mL}^{-1}$ of ethion. The permitted relative deviation from the ΔI_{RRS} value was $\pm 5\%$. The results indicated that most of the interfering substances tested could be tolerated at relatively higher levels (100 $\mu\text{g mL}^{-1}$). Parathion can be tolerated up to 50 $\mu\text{g mL}^{-1}$. Atrazine and simazine do interfere at 5 $\mu\text{g mL}^{-1}$.

3.3.7. Stern–Volmer constant

The experimental results of decreasing RRS intensity of AgNPs by ethion insecticide showed a good fit to Stern–Volmer plots, giving linear relationship with quencher concentration. In order to determine the quenching type mechanism, a study of the K_{sv} (Stern–Volmer constant) from the modified Stern–Volmer equation (Eq. (1)) was carried out at different experimental temperature conditions submerging the systems in thermostatic bath.

Stern–Volmer equation for RRS intensity quenching is as follows:

$$I_0/I = 1 + K_{sv}C_q \quad (1)$$

where I_0 and I are intensities of the resonance Rayleigh scattering of nanoparticles in the absence and presence of the quencher respectively; K_{sv} is the Stern–Volmer constant; and C_q is the concentration of the quencher.

The obtained K_{sv} values for each studied temperature are listed in Table 1. The linearity of the Stern–Volmer plot, as the value of K_{sv} which enhanced with increasing temperature (Fig. 6), indicate that the quenching mechanism of AgNPs (decrease in I_0) by presence of ethion is a single dynamic quenching [48].

4. Analytical applications

4.1. Calibration graphs and detection limits

Under the optimal experimental conditions, calibration curve for the determination of ethion by RRS was obtained. By increasing the concentration of ethion to the test solution RRS intensity by AgNPs decreases and the results show a good linear relationship

Table 1
 K_{sv} values^a for different experimental temperatures.

Temperature (K)	K_{sv} value (L mg ⁻¹)
298	1.0102
308	1.0573
318	1.0795

^a AgNPs were prepared and RRS intensity was measured as described in general procedure; [ethion]: 0.0, 0.05, 0.1, 0.2, 0.3, 0.4 and 0.5 mg L⁻¹.

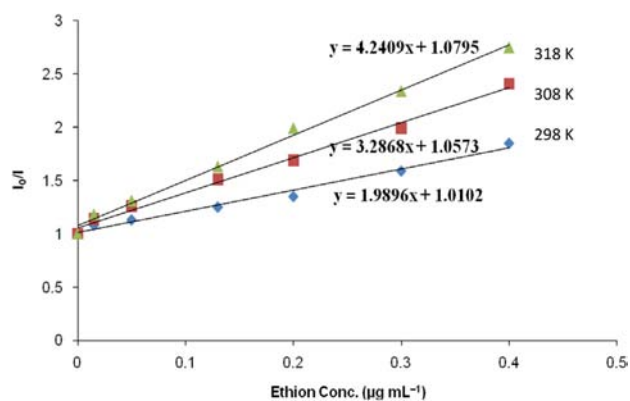


Fig. 6. Influence of temperature on AgNPs RRS signals in presence of ethion. [ethion]: 0.0, 0.05, 0.1, 0.2, 0.3, 0.4 and 0.5 $\mu\text{g mL}^{-1}$. Instrument conditions: $\lambda_{ex}=\lambda_{sc}=281$ nm; slit of excitation, 1.5 nm; slit of emission, 1.5 nm.

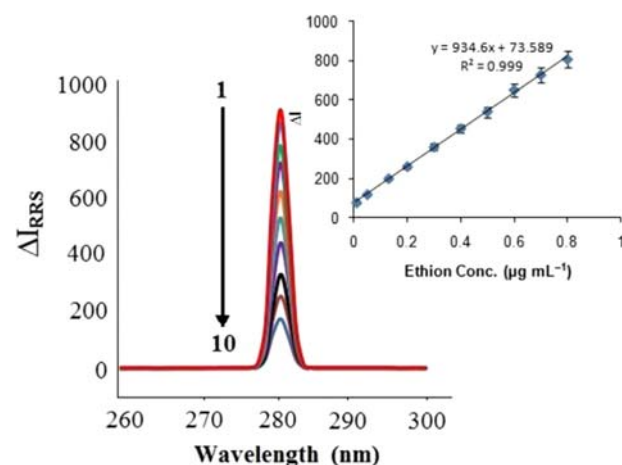


Fig. 7. Overlaid RRS spectra of AgNPs–ethion (1–10) and calibration graph for determination of ethion. [ethion]: 0.0, 0.01, 0.05, 0.15, 0.2, 0.3, 0.4, 0.5, 0.6, 0.7 and 0.8 $\mu\text{g mL}^{-1}$. Instrument conditions: $\lambda_{ex}=\lambda_{sc}=281$ nm; slit of excitation, 1.5 nm; slit of emission, 1.5 nm.

over the range 10.0–900.0 $\mu\text{g L}^{-1}$. The overlaid RRS spectra and calibration graph are presented in Fig. 7. The linear regression equation was $\Delta I_{RRS} = 934.6 C (\mu\text{g L}^{-1}) + 73.539$ with regression coefficient $r = 0.999$. The limit of detection (LOD) and quantification (LOQ) were calculated in accordance to the official compendia methods by $k(S_b)/m$, where $k = 3$ for LOD and $k = 10$ for LOQ, S_b is the standard deviation from 9 replicate blank measurements ($S_b = 1.16$) and m ($m = 937$) is the slope of the calibration curve. The LOD and LOQ estimated were 3.7 and 11.0 $\mu\text{g L}^{-1}$, respectively.

Intra- and inter-day precision and accuracy data (showing reproducibility and repeatability terms) for RRS detection of ethion in quality controlled (QC) water samples are summarized in Table 2. The precision and accuracy of the present method conform to the criteria for the analysis of water samples according to the guidance of US-FDA where the RSD determined at each concentration level is required not to exceed 15% (20% for LOQ) and R.E. within $\pm 15\%$ ($\pm 20\%$ for LOQ) of the actual value [49].

The recovery values from QC water sample solutions containing low, middle and high concentrations of ethion (50, 100 and 600 $\mu\text{g L}^{-1}$) were $98.0 \pm 2.3\%$, $107 \pm 4.9\%$ and $96.0 \pm 2.8\%$, respectively.

4.2. Determination of ethion in water samples

In order to test the validity of the method, the developed procedure was applied for determination of ethion in water

Table 2

Precision and accuracy data for detection of ethion in water sample using quenching of RRS of AgNPs (intra-day: $n=6$; inter-day: $n=6$ runs per day, 5 days).

Ethion conc. ($\mu\text{g L}^{-1}$)		RSD (%)		Relative error (%)
Added	Found (mean \pm S.D.)	Intra-day	Inter-day	
50	49 \pm 0.007	4.0	5.3	-2.0
100	103 \pm 0.011	3.3	4.1	+3.0
600	576 \pm 0.043	2.7	3.7	-4.0

Table 3

Analytical results of the determination of ethion content and recovery test of ethion in Dez dam and Karron river water samples with the proposed method ($n=6$). [Conditions: 5 mL of water sample; 2 mL of $2.0 \times 10^{-1} \mu\text{g mL}^{-1}$ AgNPs solution; 1 mL of citrate buffer pH 6; standing time: 3 min; excitation wavelength: 281 nm; scattering wavelength: 281 nm; slit width: 1.5 nm].

Sample	Ethion added ($\mu\text{g L}^{-1}$)	Ethion found ($\mu\text{g L}^{-1}$)	Recovery (%)
Dez dam water ^a	-	ND ^b	-
	25.0	23.1 \pm 0.003	92.8
	50.0	53.1 \pm 0.009	106.2
	100.0	96.7 \pm 0.012	96.7
Karron river water ^c	25.0	26.0 \pm 0.005	104.0
	50.0	48.0 \pm 0.011	92.0
	100.0	101.3 \pm 0.016	101.3

^a Dez dam water main components: $\text{Ca}^{2+}=52$; $\text{Mg}^{2+}=29$; $\text{Na}^+=37$; $\text{CO}_3^{2-}=61$; $\text{Cl}^-=24$; $\text{SO}_4^{2-}=25$; $\text{NO}_3^- = 9 \mu\text{g mL}^{-1}$; pH 7.3; EC=853.

^b Not detected.

^c Karron River water main components: $\text{Ca}^{2+}=82$; $\text{Mg}^{2+}=49$; $\text{Na}^+=68$; $\text{CO}_3^{2-}=91$; $\text{Cl}^-=44$; $\text{SO}_4^{2-}=35$; $\text{NO}_3^- = 9 \mu\text{g mL}^{-1}$; pH 7.1; TDS=387; EC=1340.

samples. Recovery tests were used to examine the reliability and accuracy of the method, different amounts of ethion were spiked into the dam (100 mL) and river (100 mL) water samples and ethion content of each sample was determined at optimum conditions. The ethion content of different water samples and recoveries of added analyte were evaluated and the results showed that it is possible to determine the ethion concentration in real sample solutions using the proposed method outlined in this investigation (Table 3). Water samples were taken from the Karoon River and Dez dam. After standing for 24 h in refrigerator, the samples were filtered by a piece of filter paper. Known amounts of ethion were added (20, 50 and $100 \mu\text{g L}^{-1}$) and were determined by the aforementioned procedure.

5. Conclusions

A novel and innovative methodology was developed for ultra-trace ethion quantification and successfully applied for its determination in water solutions. The developed methodology in this study is simple, fast, sensitive and cheap, especially when more sophisticated techniques such as chromatography are not available. In this paper, a new resonance Rayleigh scattering method was used based on quenching of scattered light from the silver nanoparticles (AgNPs) after ethion addition. TEM and SEM images showed the formation of huge clusters of AgNPs-ethion and sedimentation of complex. The quenching of AgNPs RRS and decreasing the intensity of scattered light in the presence of trace amounts of ethion was studied and quenching mechanism was proposed for RRS phenomenon. The proposed method is simple,

Table 4

The comparison of the proposed method (RRS) with some of other reported methods of ethion determination.

Method	LDR ^a ($\mu\text{g L}^{-1}$)	LOD ($\mu\text{g L}^{-1}$)	RSD	Ref.
GC-FPD ^b	40–1280	5–20	5.4	[5]
SDME/GC-MS ^c	0.5–25	0.36	7.7–15.4	[6]
MEPS-GC-MS ^d	0.5–500	0.05	7.6	[10]
GC-MS	0.023–70	0.023	10	[12]
Pot. Sensor	0–330	22	3.5–4.8	[13]
UV-vis	400–4000	-	-	[14]
IMS ^e	0.1–5.0	0.05	15	[17]
RRS	10–900	3.7	0.2–4.0	Present work

^a Linear dynamic range.

^b Gas chromatography with flame photometric detector.

^c Single-drop microextraction-gas chromatography coupled to mass spectrometry.

^d Microextraction in packed syringe-gas chromatography coupled to mass spectrometry.

^e Ion mobility spectrometry.

fast, sensitive and needs a simple spectrofluorophotometer. The main advantage of the proposed method is the possibility of direct ethion determination with very good accuracy, sensitivity and tolerance. The method needs no time consuming pretreatment processes such as solid phase extraction and micro-extractions for samples used. The LDR, LOD and LOQ of the method are good and better than most of the reported methods except gas chromatography and ion mobility spectrometry techniques (Table 4). The method needs no pretreatment processes like clean up of the sample and pre-concentration step which are mostly used in chromatographic procedures. The RSD of the method is better than all reported methods. The obtained results showed that the AgNPs can be applied as sensor for ethion determination in real water samples.

Acknowledgment

The authors wish to thank Shahid Chamran University Research Council and Environment Protection Agency (EPA) of Khosestan Province, Iran, for the financial support of this work (Grant 1392).

References

- [1] H. Zhang, S. Wang, Z. Zhou, C. Pan, J. Zhang, W. Niu, Phosphorus Sulfur 183 (2008) 280–290.
- [2] J.H. Salas, M.M. Gonzalez, M. Noa, N.A. Perez, G. Diaz, R. Gutierrez, H. Zazueta, I. Osuna, J. Agric. Food Chem. 51 (2003) 4468–4471.
- [3] R.J. Gilliom, Environ. Sci. Technol. 41 (2007) 3408–3414.
- [4] B.J. Walker, Organophosphorus Chemistry, London, Penguin Library of Physical Sciences: Chemistry, 1972.
- [5] H. Liu, W. Kong, Y. Qi, B. Gong, Q. Miao, J. Wei, M. Yang, Chemosphere 95 (2014) 33–40.
- [6] J.P. dos Anjos, J.B. de Andrade, Microchem. J. 112 (2014) 119–126.
- [7] T.M. Gutiérrez Valencia, M.P. García de Llasera, J. Chromatogr. A 1218 (2011) 6869–6877.
- [8] G.F. Pang, Y.Z. Cao, J.J. Zhang, C.H.L. Fan, Y.M. Liu, X.M. Li, G.Q. Jia, Z.Y. Li, Y.Q. Shi, Y.P. Wu, T.T. Guo, J. Chromatogr. A 1125 (2006) 1–30.
- [9] A. Garrido-Frenich, P. Plaza-Bolaños, J.L. Martínez-Vidal, J. Chromatogr. A 1153 (2007) 194–202.
- [10] H. Bagheri, Z. Ayazi, A. Es'haghi, A. Aghakhani, J. Chromatogr. A 1222 (2012) 13–21.
- [11] H. Bagheri, N. Alipour, Z. Ayazi, Anal. Chim. Acta 740 (2012) 43–49.
- [12] M. Schellin, B. Hauser, P. Popp, J. Chromatogr. A 1040 (2004) 251–258.
- [13] D.A. Lambropoulou, T.A. Albanis, J. Chromatogr. A 922 (2001) 243–255.
- [14] A.J. Russell, J.A. Berberich, G.E. Drevon, R.R. Koepsel, Annu. Rev. Biomed. Eng. 5 (2003) 1–27.
- [15] E. Khaled, M.S. Kamel, H.N.A. Hassan, H. Abdel-Gawad, H.Y. Aboul-Enein, Talanta 119 (2014) 467–472.
- [16] C. De, T.A. Samuels, T.L. Haywood, G.A. Anderson, K. Campbell, K. Fletcher, D.H. Murray, S.O. Obare, Tetrahedron Lett. 51 (2010) 1754–1757.
- [17] M.T. Jafari, Talanta 69 (2006) 1054–1058.

- [18] J. Ling, C.Z. Huang, Y.F. Li, L. Zhang, L.Q. Chen, S.J. Zhen, *Trends Anal. Chem.* 28 (2009) 447–453.
- [19] A. Liang, Q. Liu, G. Wen, Z. Jiang, *Trends Anal. Chem.* 37 (2012) 32–47.
- [20] H.Y. Wang, Y.F. Li, C.Z. Huang, *Talanta* 72 (2007) 1698–1703.
- [21] H. Guo, K. Xue, L. Yan, *Sens. Actuators B* 171–172 (2012) 1038–1045.
- [22] J.X. Dong, W. Wen, N.B. Li, H.Q. Luo, *Spectrochim. Acta A* 86 (2012) 527–532.
- [23] R. Sun, Y. Wang, Y. Ni, S. Kokot, *Talanta* 125 (2014) 341–346.
- [24] M. Chen, H.H. Cai, F. Yang, D. Lin, P. Yang, J. Cai, *Spectrochim. Acta A* 118 (2014) 776–781.
- [25] G. Wen, D. Yang, Z. Jiang, *Spectrochim. Acta A* 117 (2014) 170–174.
- [26] Z. Jiang, L. Zhou, A. Liang, *Chem. Commun.* 47 (2011) 3162–3164.
- [27] L. Kong, Z.F. Liu, X.L. Hu, S.P. Liu, *Sci. China Chem* 53 (2010) 2363–2372.
- [28] S. Bi, Y. Wang, B. Pang, L. Yan, T. Wang, *Spectrochim. Acta A* 90 (2012) 158–164.
- [29] Y.Q. Wang, S.P. Liu, Z.F. Liu, J.D. Yang, X.L. Hu, *Spectrochim. Acta A* 105 (2013) 612–617.
- [30] W.J. Qi, D. Wu, J. Ling, C.Z. Huang, *Chem. Commun.* 46 (2010) 4893–4895.
- [31] J. Ling, Y.F. Li, C.Z. Huang, *Anal. Chem.* 81 (2009) 1707–1714.
- [32] M. Fan, M. Thompson, M.L. Andrade, A.G. Brolo, *Anal. Chem.* 82 (2010) 6350–6352.
- [33] H. Wang, D. Chen, Y. Wei, L. Yu, P. Zhang, J. Zhao, *Spectrochim. Acta A* 79 (2011) 2012–2016.
- [34] S.L. Smitha, K.M. Nissamudeen, D. Philip, K.G. Gopchandran, *Spectrochim. Acta A* 71 (2008) 186–190.
- [35] X. Liu, Q. Dai, L. Austin, J. Coutts, G. Knowles, J. Zou, H. Chen, Q. Huo, *J. Am. Chem. Soc.* 130 (2008) 2780–2782.
- [36] B. Kong, A.W. Zhu, Y.P. Luo, Y. Tian, Y.Y. Yu, G.Y. Shi, *Angew. Chem. Int. Ed.* 50 (2011) 1837–1840.
- [37] X. Huang, I.H. El-sayed, W. Qian, M.A. El-sayed, *J. Am. Chem. Soc.* 128 (2006) 2115–2120.
- [38] Y. Jiang, H. Zhao, N. Zhu, Y. Lin, P. Yu, L. Mao, *Angew. Chem. Int. Ed.* 47 (2008) 8601–8604.
- [39] X. Han, H. Wang, X. Ou, X. Zhang, *J. Mater. Chem.* 22 (2012) 14127–14132.
- [40] M. Larginho, P.V. Baptista, *J. Proteomics* 75 (2012) 2811–2823.
- [41] T. Lan, C. Dong, X. Huang, J. Ren, *Talanta* 116 (2013) 501–507.
- [42] J. Yguerabide, E.E. Yguerabide, *Anal. Biochem.* 262 (1998) 157–176.
- [43] L. Ying, Y. Guangwei, M. Chen, G. Meiyang, Y. Chunxin, J. Nianqin, *Anal. Lett.* 44 (4) (2011) 709–716.
- [44] Z. Chen, G. Zhang, X. Chen, J. Chen, S. Qian, Q. Li, *Analyst* 137 (2012) 722–728.
- [45] C.C. Wang, M.O. Luconi, A.N. Masib, L.P. Fernández, *Talanta* 77 (2009) 1238–1243.
- [46] J. Zheng, X. Wu, M. Wang, D. Ran, W. Xu, J. Yang, *Talanta* 74 (2008) 526–532.
- [47] M.M. Sung, K. Sung, C.G. Kim, S.S. Lee, Y. Kim, *J. Phys. Chem. B* 104 (2000) 2273–2277.
- [48] J.H. Kim, J.S. Park, M.G. Kim, *Chem. Phys. Lett.* 600 (2014) 15–20.
- [49] J.C. Miller, J.N. Miller, *Statistics for Analytical Chemistry*, third ed., Ellis Harwood, New York, 1984 (hide affiliations).



Coulometric differential FFT admittance voltammetry determination of Amlodipine in pharmaceutical formulation by nano-composite electrode

Parviz Norouzi^{a,*}, Vinod Kumar Gupta^{b,*}, Bagher Larijani^c, Solmaz Rasoolipour^d, Farnoush Faridbod^{a,e}, Mohammad R. Ganjali^{a,e}

^a Center of Excellence in Electrochemistry, University of Tehran, Tehran, Iran

^b Department of Chemistry, Indian Institute of Technology Roorkee, Roorkee 247667, India

^c Diabetes Research Center, Endocrinology and Metabolism Clinical Sciences Institute, Tehran University of Medical Sciences, Tehran, Iran

^d Research Institute of Petroleum Industry (RIPI), Tehran, Iran

^e Biosensor Research Center, Endocrinology and Metabolism Molecular-Cellular Sciences Institute, Tehran University of Medical Sciences, Tehran, Iran

ARTICLE INFO

Article history:

Received 19 May 2014

Received in revised form

9 July 2014

Accepted 10 July 2014

Available online 13 August 2014

Keywords:

Fast Fourier transformation coulometric admittance voltammetry

Ionic liquid

Au nano-particles

Amlodipine

Multiwall carbon nanotube

ABSTRACT

An electrochemical detection technique based on combination of was coulometric differential fast Fourier transformation admittance voltammetry (CDFFTAV) and nano-composite film modified glassy carbon electrode was successfully applied for sensitive determination of Amlodipine. The nano-composite film was made by a mixture of ionic liquid, 1-ethyl-3-methylimidazolium tetrafluoroborate (EMIMBF₄), multiwall carbon nanotube and Au nanoparticles as electrochemical mediators. Studies reveal that the irreversible oxidation of Amlodipine was highly facile on the electrode surface. The electrochemical response was established on calculation of the charge under the admittance peak, which was obtained by discrete integration of the admittance response in a selected potential range, obtained in a flow injection analysis. Once established the best operative optimum conditions, the resulting nano-composite film electrode showed a catalytic effect on the oxidation of the analyte. The response is linear in the Amlodipine concentration range of 1.0×10^{-9} to 2.0×10^{-7} M with a detection limit of 1.25×10^{-10} M. Moreover, the proposed technique exhibited high sensitivity, fast response time (less than 6 s) and long-term stability and reproducibility around 96%, and it was successfully used to the determination of Amlodipine content in the pharmaceutical formulation.

© 2014 Elsevier B.V. All rights reserved.

1. Introduction

Amlodipine (S-2[(2-aminoethoxy) methyl]-4-(2-chlorophenyl)-3-ethoxycarbonyl-5-methoxycarbonyl-6-methyl-1,4-dihydropyridine) (Fig. 1), is a potent calcium channel blocker used for the treatment of hypertension and angina [1]. It is a third-generation dihydropyridine calcium antagonist which is used alone or in combination with other medications for treating high blood pressure, certain types of vasospastic angina, cardiac arrhythmias, coronary heart failure, and hypertension [2–4].

Various methods including high-performance liquid chromatography (HPLC) with amperometric detection [5], HPLC with UV detection [6], HPLC with fluorescence detection [7], liquid

chromatography mass spectrometry (LC/MS) [8], capillary gas chromatography (GC) with electron capture detection [9], GC with electron-impact mass spectrometry (EI-MS) [10] and offline solid-phase extraction (SPE) [11] have been used for the determination of Amlodipine.

Recently, nanostructures play interesting roles in various fields of analytical chemistry [12–14]. Multiwall carbon nanotube (MWCNT) has attracted extensive attention for their high electrical conductivity, good chemical stability, and extreme mechanical strength [15–18]. The improvement of electrocatalytic activity of redox couples at carbon nanotube-based electrodes can be attributed to the presence of edge-plane like sites located at the end and in the defect areas. In fact, the insolubility of carbon nanotubes in many solvents hinders the fabrication of carbon nanotubes modified electrodes. The unique properties of gold nanoparticles (AuNPs) such as providing a suitable microenvironment for enzymes to immobilize but keep their biological activity, and facilitating electron transfer between the species and electrode

* Corresponding authors. Tel.: +98 21 61112294/+911332285801; fax: +98 21 66495291.

E-mail addresses: norouzi@khayam.ut.ac.ir (P. Norouzi), vinodfcy@gmail.com (V.K. Gupta).

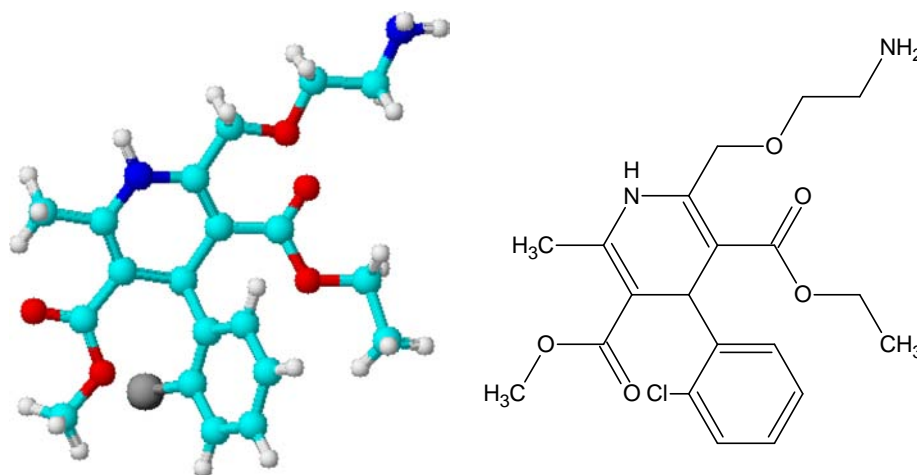


Fig. 1. Chemical 2D and 3D structures of Amlodipine.

surfaces, have led to a wide use of this nanomaterial in construction of electrochemical sensors [19–22]. Moreover, AuNPs play a crucial role in the electrode transduction enhancement of the affinity reaction as well as in the efficiency of MWCNT immobilization in a stable form.

The detection method, fast Fourier transform square wave voltammetry (FFTSWV), which is introduced here, is very sensitive, inexpensive and fast. The square wave voltammetry (SWV) has recently been shown to be advantageous for environmental detection of several compounds [23–27]. This paper describes a fundamentally different approach to SWV measurement, in which the detection limits are improved, while preserving the information content of the SW voltammogram. In fact, the analyte signal is calculated based on admittance changes related to the changes in electrical double layer.

Using fast Fourier transform (FFT) method was found very sensitive system in combination by electrochemical method for trace detection of compounds [28–39]. In particular, when the magnitude of current is in the range of nano and pico ampere, electrochemical response suffers from existence of environmental noises. This separation allows, digitally filtering some of the noises and decreasing the bandwidth of the measurement. Further improvement in the signal was gained by two-dimensional integration of the electrode response over a selected potential range and time window of the signal.

In the present paper, a new composite film was prepared by using Au NPs and MWCNT and 1-ethyl-3-methylimidazolium tetrafluoroborate (EMIMBF₄) as binder and modifier. Where, the electrode response was obtained by a special square wave electrochemical method called coulometric differential FFT admittance voltammetry (CDFFTAV), in flow injection system. For determination of Amlodipine, at first, the admittance of the electrode was measured during the potential ramp and then, the response of the electrode was calculated in form of coulomb.

2. Materials and methods

2.1. Reagents

Amlodipine was purchased from Sigma. The multiwall carbon nanotubes (MWCNTs) with 10–40 nm diameters, 1–25 μm length, SBET: 40–600 m^2/g , with 95% purity were purchased from a local company (Iran). Phosphate buffer solutions (PBS, 0.1 M) with various pH values were prepared by mixing stock standard

solutions of K_2HPO_4 and KH_2PO_4 and adjusting the pH with H_3PO_4 or NaOH . The room temperature IL, 1-ethyl-3-methylimidazolium tetrafluoroborate (EMIMBF₄) was purchased from Aladdin-Reagent Company (China). All other chemicals were of analytical grade and were used without further purification. All solutions were made up with doubly distilled water. The solution of 2 mM $\text{Fe}(\text{CN})_6^{4-}/^{3-}$ in 0.02 M PBS was prepared. All other chemicals and solvents used were of analytical grade and used as received without further purification. Double distilled water was used throughout the experiments.

2.2. The electrode preparation

A glassy carbon electrode, GCE (3 mm in diameter) were polished well with 1.0, 0.3 and 0.05 μm alumina slurry and then it was washed thoroughly with doubly distilled water. The electrodes were successively sonicated in 1:1 nitric acid, acetone and doubly distilled water, and then allowed to dry at room temperature.

0.1–0.8 mg of MWCNTs and EMIMBF₄ (20 μl) were dispersed in 2 ml *N,N*-dimethylformamide (DMF) with the aid of ultrasonic agitation to achieve a well-dispersed suspension. Then, 5 μl of the suspension was dropped on a cleaned GC electrode and let the solvent was evaporated in air. Hence, a uniform film of MWCNTs coats the surface of GC electrode. The electrochemical deposition of Au NPs was performed in 0.2 M Na_2SO_4 aqueous solution of HAuCl_4 (1.0 mM). The deposition time was about 20–110 s and the potential was -0.2 V. After that, the surface of the modified electrode was carefully washed with distilled water and dried at room temperature. Finally, the modified electrode was activated by several successive potential scans from 0.4 to 1.0 V with a scan rate of 50 mV/s in phosphate buffer solution (pH 6.0) until a steady voltammogram was obtained. The mean size of the prepared Au NPs was about 30–90 nm, estimated by transmission electron microscopy. The schematic diagram of construction steps and of the view of modified electrode was shown in Fig. 2A. The flow injection analysis, used for measurements, has an eight roller peristaltic pump, a four way injection valve (UltradeckLabs Co., Iran) with 300 μl sample injection loop and four ways cell. The cell was a three-electrode configuration was employed in all experiments, with potentials referring to an Ag/AgCl reference electrode and an auxiliary electrode (2.0 mm in diameter) in the flow cell. Fig. 2B and C shows the diagram of the flow injection analysis system and the electrochemical cell.

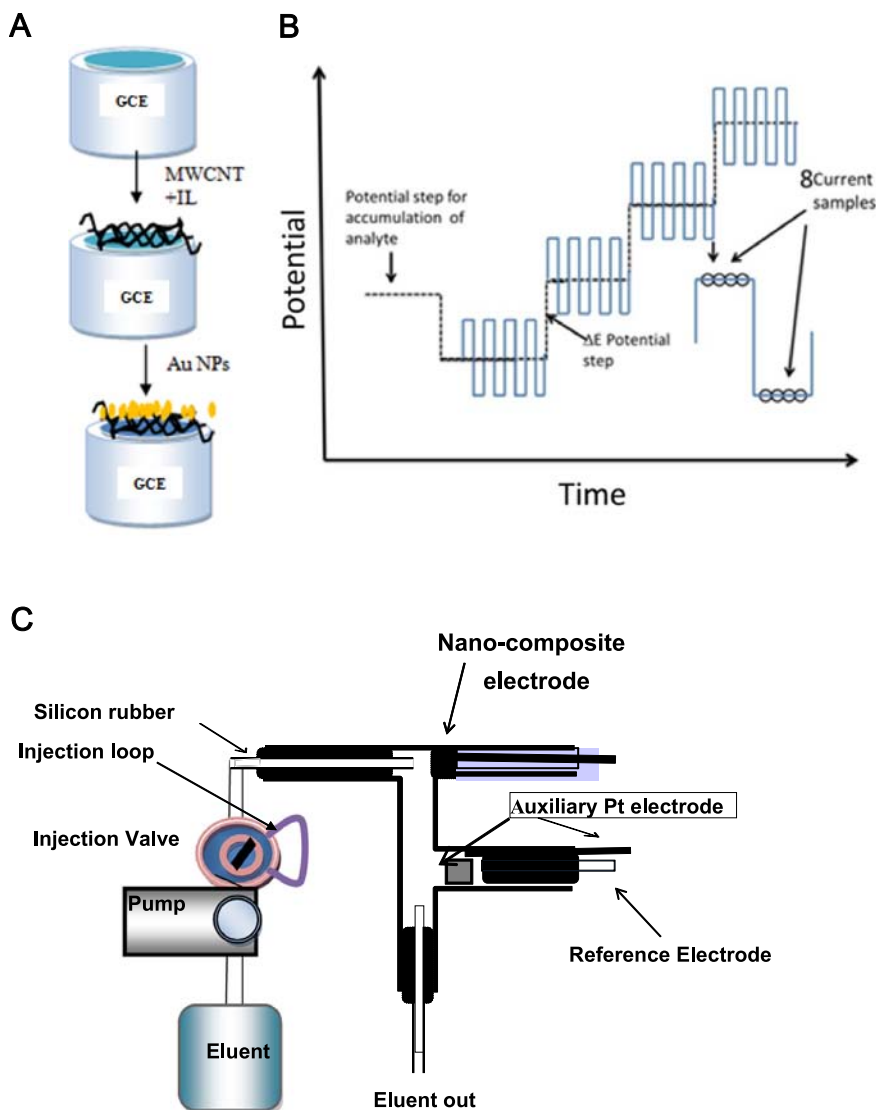


Fig. 2. (A) Schematic diagram of constructed electrode, and (B) the diagram of the potential ramp vs. time and (C) the diagram of electrochemical cell used in flow injection analysis.

2.3. Electrochemical instrumentation

The electrochemical CDFFTAV measurements carried out with a homemade potentiostat. For controlling, it was connected to a PC equipped by an analog to digital data acquisition board (PCL-818H, Advantech Co.). The measurements were carried out by CDFFTAV. In this technique to improve sensitivity of the analytes response, the appalled SW potential waveform, current sampling and data processing was modified. The modified potential waveform is shown in Fig. 2B. As shown, the measurement part of the waveform contains multiple SW pulses with amplitude of E_{sw} and frequency of f_o , were superimposed on a staircase potential function, which was changed by a small potential step of ΔE (10 mV). The potential of accumulation was 100 mV for 0.5 s. The value of SW potential pulse was in the range of 5–45 mV. In potential ramp, the currents were sampled eight times per each SW polarization cycle. During the measurements, the memory requirements of the computer were ordered or controlled by the electrochemical software that was developed in our lab. For the experiments, the current data was acquired, and stored by the software. The electrochemical program was employed to generate an analog waveform and acquire admittance readings. It, also, processed and plotted the data in real time.

3. Results and discussion

3.1. Surface characterization of modified electrode

The surface morphology of the GCE and AuNP/MWCNT-IL/GCE was characterized by SEM technique. A clear difference in terms of the surface roughness is observed among prepared electrodes. Compared to the unmodified GCE (Fig. 3A), it could be observed from Fig. 2B that a relatively dense MWCNT-IL film was formed, and completely covered the surface of the GC. Also, a network-like structure of MWCNT-IL with minimum aggregation was observed on the electrode surface, which indicated that the MWCNTs were well immobilized on the GCE surface. Moreover, Fig. 3C shows that the AuNPs are homogeneously distributed on the MWCNTs and are uniform in size, and that each Au NPs has an average diameter of 50 nm.

EIS is considered as an efficient tool for examining the interface properties of surface electrode, where the electron-transfer resistance (R_{ct}), of the formal potential of $\text{Fe}(\text{CN})_6^{4-3-}$ at the electrode surface is used to describe the interface properties of the modified electrode. Fig. 3D illustrates the results of EIS on GCE, MWCNT-IL/GCE and AuNP/MWCNT-IL/GCE in the presence of 3 mM $\text{Fe}(\text{CN})_6^{4-3-}$ and 0.1 M KCl Fast Fourier transformation coulometric admittance

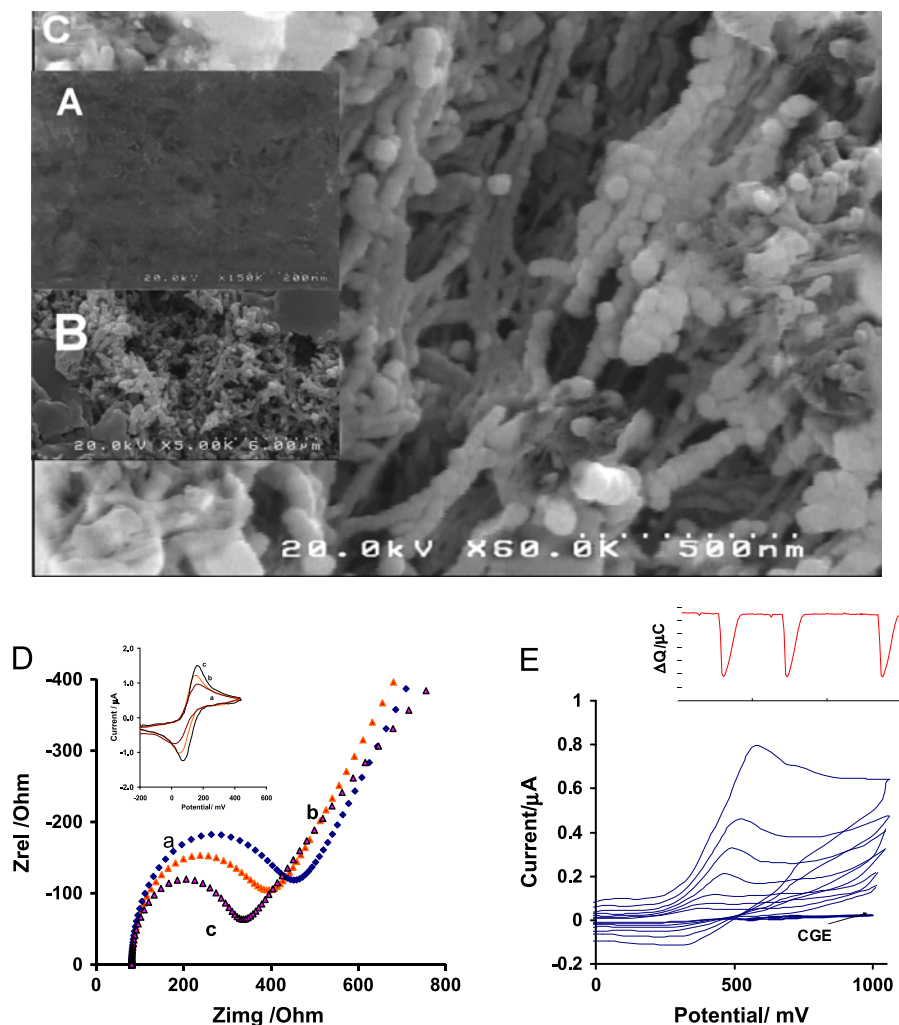
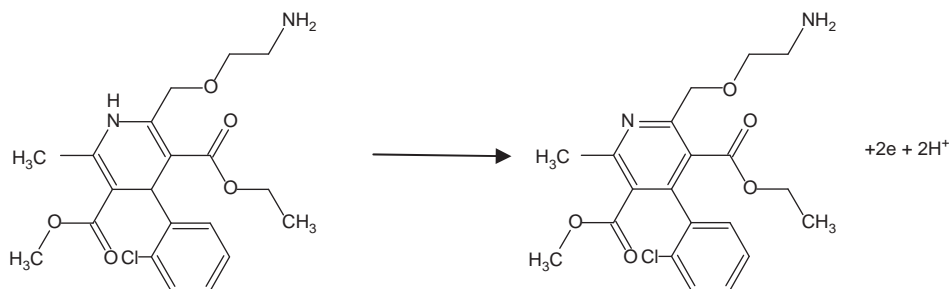


Fig. 3. SEM images of (A) GCE, (B) MWCNT-IL/GCE, (C) AuNP/MWCNT-IL/GCE; (D) EIS of GCE (a), MWCNT-IL/GCE (b), AuNP/MWCNT-IL/GCE (c), in 3 mM $\text{Fe}(\text{CN})_6^{4-3-}$ and 0.1 M KCl, (the inset recorded cyclic voltammograms at the same condition for 3 mM $\text{Fe}(\text{CN})_6^{4-3-}$ on, GCE (a), MWCNT-IL/GCE (b), AuNP/MWCNT-IL/GCE (c)) (E) Cyclic voltammograms of 2.0×10^{-5} M Amlodipine in buffer pH 11.0, on the modified AuNP/MWCNT-IL/GCE, scan rate 5–400 mV/s.

voltammetry; ionic liquid, Au NPs, Amlodipine, MWCNT. By fitting the data, R_{ct} was estimated to be 450Ω at the bare GCE (curve a). The diameter of the high frequency semicircle was obviously decreased to 385Ω by the surface modification of the MWCNT-IL layer (curve b), suggesting that due to a increase in conductivity of the surface, a sensible decline R_{ct} of the $\text{Fe}(\text{CN})_6^{4-3-}$ redox reaction. For the AuNP/MWCNT-IL/GCE, the R_{ct} decreased to 350Ω (curve c), revealing the much lower electron-transfer resistance on the AuNPs/compared with that on the MWCNT-IL/, which may be attributed to enhancement in conductivity of the surface deposited materials. While, the results were consistent with the obtained CV under the same condition (see the inset curves in Fig. 3D).

Fig. 3E demonstrates the electrochemical oxidation behavior of 2.0×10^{-5} M of Amlodipine at AuNP/MWCNT-IL/GCE, which was investigated in pH 11.0 BS by cyclic voltammetry. It was seen that there is no redox peak at GCE in the blank buffer solution, which indicating that the composite film is non-electroactive in the selected potential region. But, in present of Amlodipine, an irreversible peak appeared at potential of 480 mV, due to the electrochemical oxidation of Amlodipine. The increased peak current with root of scan rate (5–400 mV/s) suggested that the electrode processes is diffusion controlled. The mechanism of the oxidation at the surface of the electrode can be written based on formation pyridine derivative and releasing two electrons and protons.



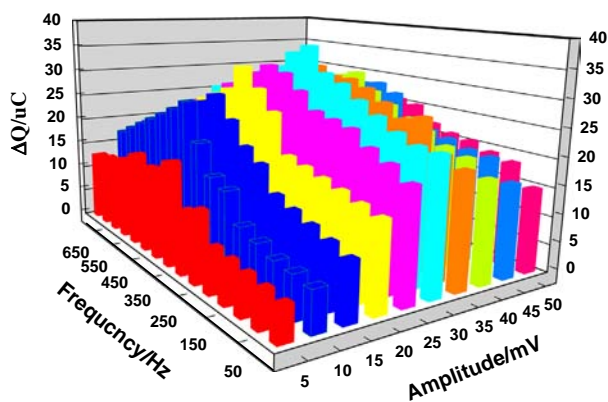


Fig. 4. (A) CDFFTA voltammograms of AuNP/MWCNT-IL/GCE in absent and with addition of 4.0×10^{-7} M Amlodipine in the buffer solution at pH 11.0. The square wave frequency was 400 Hz at amplitude 30 mV. Integration potential range for the admittance is 200 to 850 mV. (B) Illustrates a typical of sensor response, on standard solution of Amlodipine from 5 nM in PBS, pH 11.0.

As mentioned for the case $\text{Fe}(\text{CN})_6^{4-/3-}$ redox reaction, the results point out that the existence MWCNT and AuNPs in the composite could catalytically develop a facilitated the oxidation reaction of Amlodipine. One important reason for such current enhancement could be establishment of large specific surface area on the electrode surface, which was produced by MWCNT and Au NPs. Such surface area may support condition for more accumulation of the analyte on the surface of the electrode. Moreover, this property combines with synergistically improved conductivity in the mixture of MWCNT and IL, could facilitate the transfer of electrons at the electrode surface, and amplify the peak current.

As discussed above, in CDFFTAV technique, a special SW potential waveform was continually applied to the electrodes [16–19]. The current were sampled eight times per SW cyclic, and also four SW cycles in each potential step were applied and averaged. Fig. 4 shows CDFFTAV and the changes in voltammetric of the modified electrode in the potential range of 0 to 1000 mV. The time axis represents the time passing of the experiment. The figure shows that at the begging of the experiment there is not a significance signal in the voltammograms, but after addition of 1.0×10^{-7} M Amlodipine in the buffer solution at pH 11.0 a peak appears at potential 450 mV.

The coulometric response was calculated by integrating of the net admittance changes is over the selected potential range 200 to 850 mV. In this technique, ΔQ is calculated based on the admittance changes at the voltammograms in the integration potential range. The sensor response was calculated as ΔQ ;

$$\Delta Q_n = \int_{E_1}^{E_2} \Delta i_{(n,E)} dE - \text{ave} \left[\int_{E_1}^{E_2} \Delta i_{(m,E)} dE \right] \quad (1)$$

$$\Delta Q_n = Q_n - Q_{ave} \quad (2)$$

where Q_{ave} is the calculated average charges that obtained by integration of admittance voltammetric curve between 200 to 850 mV (E_1 to E_2), from m voltammograms, and Q_n the calculated charge at the same potential range from subsequent n^{th} voltammogram in absent of analyte, respectively. To calculate the sensor response in form of ΔQ based on Eq. (1) in selected potential range of integration. The unit for value of the sensor response for Amlodipine is in coulomb (μC). Fig. 4 inset, illustrates a typical of sensor response, on standard solution of Amlodipine from 5 nM in PBS, pH 11.0. The results shown in this figure represent the integrated admittance in potential range of 200 to 850 mV. Dependence of the electrode response on the experimental conditions needs to be investigated to obtain the best performance of the electrode, which the most important are, pH, the nano

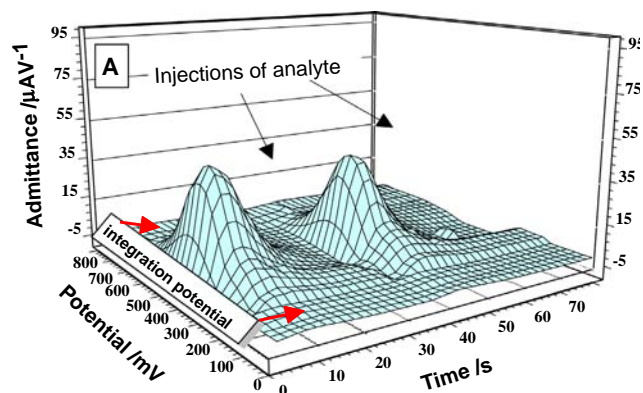


Fig. 5. The effect of frequency and amplitude on the response of sensor to addition of 1.0×10^{-7} M Amlodipine in the buffer solution at pH 11.0, Integration potential range for the admittance is 200 to 850 mV.

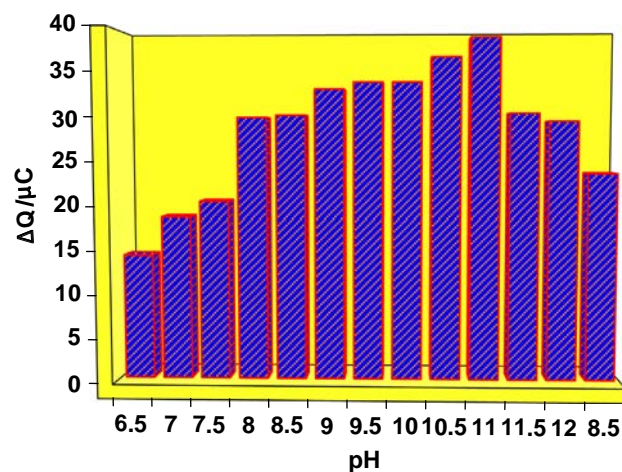


Fig. 6. The effect of pH, on the response of the sensor to addition of 1.0×10^{-7} M Amlodipine in the buffer solution. The square wave frequency was 400 Hz at amplitude 30 mV. Integration potential range for the admittance is 200 to 850 mV.

composite film composition and the parameters for square-wave voltammetry.

3.2. Optimization of the method

Due to this fact that, in CDFFTAV technique, the voltammetric admittance response of the sensor depends on the applied conditions on excitation waveform, it was needed the influence of the square wave frequency and amplitude to be examined. In this direction, the SW amplitude were studied in range of 5 to 50 mV, and the effect of frequency was studied in the range of 50–750 Hz. In Fig. 5 the results of change in the response at various values of the square wave frequency and amplitude is demonstrated for injection of solution of 1.0×10^{-7} M of Amlodipine at pH 11.0. As shown in the figure, the best analytical signal obtained was at 400 Hz, and the value of 30 mV was for the amplitude. These experimental conditions were selected for subsequent experiments. The enhancement of the signal with increasing frequency and amplitude value may due to improvement speed of excitation potential, which is similar to the enlargement of current in cyclic voltammetry with potential scan rate. However, after the optimal value the sensor response decline. This may due to kinetic limitation in electron transfer rate of the electrochemical process. Furthermore, the background noise and peak shape of Amlodipine are depends on the factors in the applied potential waveform.

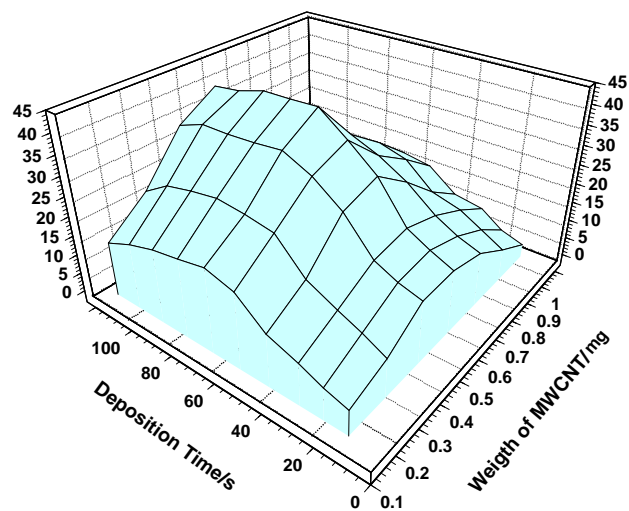


Fig. 7. The effect of weight of NPs on the response of AuNP/MWCNT-IL/GCE to addition of 1.0×10^{-7} M Amlodipine in the buffer solution at pH 11.0. The square wave frequency was 400 Hz at amplitude 30 mV. Integration potential range for the admittance is 200 to 850 mV.

3.3. Optimization of pH and the electrode composition

Fig. 6 shows the change in response of the sensor for injection of 1.0×10^{-7} M Amlodipine in the buffer solution at pHs 6 to 12. The following measurements were recorded at frequency 400 Hz and amplitude 30 mV. The results showed that when pH of the buffer solution was increased up to 11.0, oxidation admittance peak improved and oxidation potential shift to less positive potential. This is an induction of facilitated electron transfer at the sensor surface at pHs lower than 11. Conversely, at pHs higher than 11 the magnitude of the response decreased, which may be due to increasing noise level of the signal (it was seen that in absence of analyte the background signal increase with pH and solution is less clear at those pHs). Therefore, pH 11.0 was selected as the optimal pH for detection in the following experiments.

The composition of the electrode contains time of deposition of Au NPs, in range of 10–120 s, and various weights of MWCNT NPs, in range of 0.1–1 mg. **Fig. 7** shows the change in response of Au NP/MWCNT-IL/GCE for injection of 1.0×10^{-7} M Amlodipine in the buffer solution at pHs 11.0. These data indicate that the optimum deposition time is Au NPs 80 s, and the optimum weight of MWCNT is 0.7 mg. It can be suggested that up to the maximum deposition time of NPs, the oxidation process of the analyte advanced. However, after the optimum value, the excess weight of MWCNT may reduce the surface area for the reaction of Amlodipine with the electrode by filling the existing space in the composite. Also, it may be due to development of the distances between the analyte and the other MWCNT. Consequently, the sensor response reduces after the maximum value.

In case of Au NPs, at first, it could be seen that there is an increase in the response with increasing of deposition time up to 80 s, while after the optimum value, the sensor response declines. It means that Au NPs can help the sensitivity via increasing surface contact with Amlodipine.

3.4. Calibration curve and analytical characterization

Fig. 8 illustrates a typical ΔQ response of AuNP/MWCNT-IL/GCE for addition of standard solutions of Amlodipine, where the experimental parameters were set at optimum values of factors, in order to obtain the best detection limits for the detection technique. As mentioned above, the response could be expressed

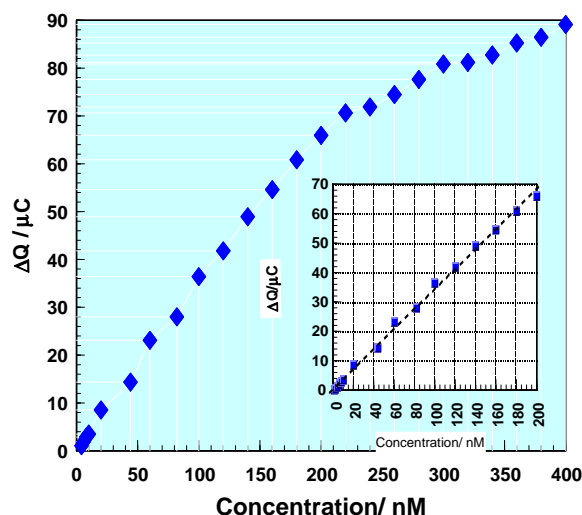


Fig. 8. The calibration curve for Amlodipine standard solutions in pH 11.0 inset response of the electrode upon the following addition of 8 nM of Amlodipine solutions. The inset, the linear part of calibration curve for Amlodipine standard solutions. Results shown in this figure represent the integrated signal for 3 consecutive additions of the Amlodipine standard solution.

Table 1

Determination of Amlodipine in pharmaceutical tablets by standard addition method (concentration in nM).

Samples	Detected	Added	Recovery (%)	%RSD
1	6.1	6.0	99.3	0.81
2	10.5	20.0	102.3	0.67
3	44.5	40.0	99.1	0.54
4	43.7	40.0	101.1	0.38

in integrated admittance in form of peak heights ($\Delta Q/\mu\text{C}$), which was dependent on the choice of the potential integration range. As can be seen in **Fig. 8** the ΔQ of Amlodipine solutions (from 1.0 to 400.0 nM in PBS (pH 11.0)) increased with increments of the concentration of the analyte and lastly leveled off to a more or less with a smaller slope.

To find detection limit of the technique for Amlodipine, at first, a stock solution of 5 mM Amlodipine was freshly prepared, and then for making the other standard solutions, an aliquot was diluted to the appropriate concentration. Before each measurement, the three-electrode system was installed in a blank solution, and the admittance voltammetry scan from 0 to 1000 mV. **Fig. 8** inset graph, shows the linear section of the curve (at low concentrations from 1.0×10^{-9} to 200.0×10^{-7} M), and the calibration equation of the best-fitted line was $y (\mu\text{C}) = 0.0048 \times (\text{nM}) + 0.0063$ with a correlation coefficient of 0.998 ($n=5$, $SD=0.0069$). A detection limit of 1.25×10^{-10} M, three times the standard deviation of the blank solution, was estimated.

In these measurements, the obtained recoveries for the spike tablet samples were ranged from 99.5% to 102.1% and the contents of Amlodipine found are in good agreement with that specified by the manufacturers. The results are shown in **Table 1**. These results indicate that the CDFFTAV technique has acceptable precision and accuracy for rapid and sensitive determination of Amlodipine in pharmaceutical tablets.

The proposed method was also compared with previous reported electrochemical methods used in determination of Amlodipine [40–55]. **Table 2** shows the results of this comparison.

Table 2

Comparison of the proposed method with some previous reported ones in determination of Amlodipine.

Electrode	Method	Detection limit	Linear range	[Refs.]
CNT/Pyrolytic graphite	Cyclic and square wave voltammetries	5.0×10^{-9} M	5.0×10^{-9} – 1.0×10^{-6} M	[40]
Carbon paste	Adsorptive square-wave anodic stripping voltammetry	2.0×10^{-10} M	9.9×10^{-9} – 1.4×10^{-7} M	[41]
GCE	Ratio voltammetric method	DPV: 8.01×10^{-7} M SWV: 8.53×10^{-7} M	4.0×10^{-6} – 1.0×10^{-4} M	[42]
MWCNTs:graphite paste	Cyclic and differential pulse voltammetric	1 μ g/ml	100–2.5 μ g/ml	[43]
GCE under stationary and rotating conditions	Differential-pulse voltammetry	Rotating:0.004 mg/ml Stationary:0.0072 mg/ml	Not reported	[44]
AuNP/MWCNT-IL/GCE	Coulometric differential fast Fourier transformation admittance voltammetry	1.25×10^{-10} M	1.0×10^{-9} – 2.0×10^{-7} M	This work

Interference study was also done. Since uric acid, and ascorbic acid are the major metabolites present in human urine which may interfere in the determination of Amlodipine due to their redox activities, therefore, the possible interferences of these compounds on the oxidation peak of amlodipine have been evaluated to examine the selectivity of the proposed method. The results show that up to 1000-fold excess of uric acid, and ascorbic acid, they have no interference on the determination of 1×10^{-7} M Amlodipine. The interference of major metabolite of Amlodipine, 2-([4-(2-chlorophenyl)-3-ethoxycarbonyl-5-methoxycarbonyl-6-methyl-2-pyridyl] methoxy) acetic acid [40] has also been examined. It was found that it does not interfere in the determination of Amlodipine up to 100-fold excess. The metabolite is not oxidizable hence, does not give any oxidation peak. Also, results in Table 1 shows that the proposed method is free from the interferences of the excipients used in the formulations and is sufficiently accurate and precise to be applied for pharmaceutical formulation analysis.

3.5. Stability and reproducibility of the electrode

The nano-composite electrode was evaluated by examining the analyte response, using CDFFTAV technique over a long time period. The electrode storage stability was investigated for 60 days at room temperature when not in use. The results showed that the sensitivity reduce only $4.6 \pm 0.2\%$ up that time, which gradually decreases afterwards might be due to the adsorption of impurities. This indicates that nano-composite electrode was fairly stable and good reproducibility.

4. Conclusion

We presented, a new determination technique has been developed for the detection of Amlodipine in real samples based on the electrochemical admittance or CDFFTAV response and nano-composite modified GCE. The nano-composite was made by mixing ionic liquid, AuNP and MWCNT as electrochemical mediators. Under optimal conditions, the designed nanocomposite electrode exhibited a wide linear response to Amlodipine concentration, good sensitivity, a fast response time, repeatability and long term stability in response. Also, the assay provides a much improved sensitivity for the detection of Amlodipine. Future experiments will be required to study the various factors in detail so as to lessen the influence of the environment, and investigate its application to CDFFTAV detection.

Acknowledgement

The authors are grateful to the Research Council of University of Tehran for the financial support of this work under (Grant no. 6102027).

References

- [1] J.E. Arrowsmith, S.F. Campbell, P.E. Cross, J.K. Stubbs, R.A. Burges, D.G. Gardiner, K.L. Blackburn, *J. Med. Chem.* 29 (1986) 1696–1702.
- [2] S. De Portu, E. Menditto, L. Scalone, S. Bustacchini, C. Cricelli, L.G. Mantovani, *Pharmacol. Res.* 54 (2006) 158–163.
- [3] K. Kario, *Am. J. Hypertens.* 10 (1997) 261–268.
- [4] B. Cindy Levine, R. Kyle Fahrback, D. Frame, E. Janet Connelly, P. Rhonda Estok, R. Linda Stone, V. Ludensky, *Clin. Ther.* 25 (2003) 35–57.
- [5] K. Shimooka, Y. Sawada, H. Tatematsu, *J. Pharm. Biomed. Anal.* 7 (1989) 1267–1272.
- [6] A. Zarghi, S. Foroutan, A. Shafaati, A. Khoddam, *Farmaco* 60 (2005) 789–792.
- [7] S. Tatar, S. Atmaca, *J. Chromatogr. B* 758 (2001) 305–310.
- [8] Y. Feng, L. Zhang, Z. Shen, F. Pan, Z. Zhang, *J. Chromatogr. Sci.* 40 (2002) 49–53.
- [9] A. Beresford, D. McGibney, M. Humphrey, P. Macrae, D. Stopher, *Xenobiotica* 18 (1988) 245–254.
- [10] H. Maurer, J. Arlt, *J. Anal. Toxicol.* 23 (1999) 73–80.
- [11] X. Wei, L. Qi, Y. Chen, *Talanta* 77 (2009) 1197–1202.
- [12] B.J. Sanghavi, W. Varhue, J.L. Chávez, C. Chou, N.S. Swami, *Anal. Chem.* 86 (2014) 4120–4125.
- [13] B.J. Sanghavi, S.M. Mobin, P. Mathur, G.K. Lahiri, A.K. Srivastava, *Biosens. Bioelectron.* 39 (2013) 124–132.
- [14] B.J. Sanghavi, S. Sitaula, M.H. Griep, S.P. Karna, M.F. Ali, N.S. Swami, *Anal. Chem.* 85 (2013) 8158–8165.
- [15] Bankim J. Sanghavi, Ashwini K. Srivastava, *Electrochim. Acta* 55 (2010) 8638–8648.
- [16] Y.C. Tsai, C.C. Chiu, M.C. Tsai, J.Y. Wu, T.F. Tseng, T.M. Wu, S.F. Hsu, *Carbon* 45 (2007) 2823–2827.
- [17] F. Faridbod, M.R. Ganjali, M. Pirali-Hamedani, P. Norouzi, *Int. J. Electrochem. Sci.* 5 (2010) 1103–1112.
- [18] M.R. Ganjali, H. Khoshafar, A. Shirzadmehr, M. Javanbakht, F. Faridbod, *Int. J. Electrochem. Sci.* 4 (2009) 435–443.
- [19] J.M. Pingarron, Y.S. Paloma, G.C. Araceli, *Electrochim. Acta* 53 (2008) 5848–5866.
- [20] P. Norouzi, V.K. Gupta, F. Faridbod, M. Pirali-Hamedani, B. Larijani, M.R. Ganjali, *Anal. Chem.* 83 (2011) 1564–1570.
- [21] P. Norouzi, B. Larijani, M.R. Ganjali, F. Faridbod, *Int. J. Electrochem. Sci.* 7 (2012) 10414–10426.
- [22] B.J. Sanghavi, P.K. Kalambate, S.P. Karna, A.K. Srivastava, *Talanta* 120 (2014) 1–9.
- [23] P. Norouzi, T.M. Garakani, H. Rashedi, H.A. Zamani, M.R. Ganjali, *Int. J. Electrochem. Sci.* 5 (2010) 639–652.
- [24] P. Norouzi, M.R. Ganjali, R. Dinarvand, M.H. Eshraghi, H.A. Zamani, *Russ. J. Electrochem* 46 (2010) 999–1006.
- [25] P. Norouzi, H. Rashedi, T. Mirzaei Garakani, R. Mirshafian, M.R. Ganjali, *Int. J. Electrochem. Sci.* 5 (2010) 377–391.
- [26] P. Norouzi, M.R. Ganjali, B. Larijani, A. Mirabi-Semnakoilii, F.S. Mirnaghi, A. Mohammadi, *Pharmazie* 63 (2008) 633–637.
- [27] P. Norouzi, M.R. Ganjali, S. Shirvani-Arani, A. Mohammadi, *J. Pharm. Sci.* 95 (2007) 893–904.
- [28] M.R. Pourjavid, P. Norouzi, M.R. Ganjali, *Int. J. Electrochem. Sci.* 4 (2009) 923–942.
- [29] P. Norouzi, M.R. Ganjali, M. Zare, A. Mohammadi, *J. Pharm. Sci.* 96 (2007) 2009–2017.
- [30] P. Norouzi, M. Qomi, A. Nemat, M.R. Ganjali, *Int. J. Electrochem. Sci.* 4 (2009) 1248–1261.

- [31] P. Norouzi, B. Larijani, M. Ezoddin, M.R. Ganjali, *Mater. Sci. Eng., C* 28 (2008) 87–93.
- [32] M.R. Ganjali, P. Norouzi, R. Dinarvand, R. Farrokhi, A.A. Moosavi-Movahedi, *Mater. Sci. Eng., C* 28 (2008) 1311–1320.
- [33] P. Norouzi, M.R. Ganjali, L. Hajiaghbabaei, *Anal. Lett.* 39 (2006) 1941–1953.
- [34] P. Norouzi, G.R. Nabi Bidhendi, M.R. Ganjali, A. Sepehri, M. Ghorbani, *Microchim. Acta* 152 (2005) 123–129.
- [35] P. Norouzi, M.R. Ganjali, T. Alizadeh, P. Daneshgar, *Electroanalysis* 18 (2006) 947–954.
- [36] M.R. Ganjali, P. Norouzi, M. Ghorbani, A. Sepehri, *Talanta* 66 (2005) 1225–1233.
- [37] P. Norouzi, H. Ganjali, B. Larijani, F. Faridod, M.R. Ganjali, H.A. Zamani, *Int. J. Electrochem. Sci.* 6 (2011) 5189–5199.
- [38] P. Norouzi, B. Larijani, F. Faridod, M.R. Ganjali, *Int. J. Electrochem. Sci.* 5 (2010) 1550–1562.
- [39] P. Norouzi, M.R. Ganjali, M. Qomi, A.N. Kharat, H.A. Zamani, *Chin. J. Chem.* 28 (2010) 1133–1139.
- [40] R.N. Goyal, V.K. Gupta, S. Chatterjee, *Electrochim. Acta* 53 (2008) 5354–5360.
- [41] M. Kazemipour, M. Ansari, A. Mohammadi, H. Beitollahi, R. Ahmadi, *J. Anal. Chem* 64 (2009) 65–70.
- [42] B. Dogan-Topal, B. Bozal, B.T. Demircigil, B. Uslu, S.A. Ozkan, *Electroanalysis* 21 (2009) 2427–2439.
- [43] A. Mohammadi, A.B. Moghaddam, K. Eilkanizadeh, E. Alikhani, S. Mozaffari, T. Yavari, *Micro Nano Lett.* 8 (2013) 413–417.
- [44] G. Altiokka, D. Dogrukol-Ak, M. Tuncel, H.Y. Aboul-Enein, *Pharm. Med. Chem.* 2 (2002) 104–108.
- [45] V.K. Gupta, A.K. Jain, G. Maheshwari, *Talanta* 72 (4) (2007) 1469–1473.
- [46] V.K. Gupta, M.R. Ganjali, P. Norouzi, H. Khani, A. Nayak, Shilpi Agarwal, *Critical Reviews in Analytical Chemistry* 41 (2011) 282–313.
- [47] R.N. Goyal, V.K. Gupta, S. Chatterjee, *Sens. Actuators B. Chemical* 149 (2010) 252–258.
- [48] V.K. Gupta, A.K. Jain, Shiva Agarwal, G. Maheshwari, *Talanta* 71 (2007) 1964–1968.
- [49] R. Jain, V.K. Gupta, N. Jadon, K. Radhapyari, *Analytical Biochemistry* 407 (2010) 79–88.
- [50] V.K. Gupta, A.K. Singh, S. Mehtab, B. Gupta, *Anal. Chim. Acta* 566 (2006) 5–10.
- [51] R.N. Goyal, V.K. Gupta, S. Chatterjee, *Electrochim. Acta* 53 (2008) 5354–5360.
- [52] V.K. Gupta, A.K. Singh, M. AlKhayat, Barkha Gupta, *Anal.Chim. Acta* 590 (2007) 81–90.
- [53] V.K. Gupta, R. Prasad, R. Mangla, P. Kumar, *Anal. Chim. Acta* 420 (2000) 19–27.
- [54] R.N. Goal, V.K. Gupta, S. Chatterjee, *Talanta* 76 (2008) 662–668.
- [55] V.K. Gupta, Imran Ali, Tawfik A. Saleh, Arunima Nayak, Shilpi Agarwal, *RSC Advances* 2 (2012) 6380–6388.



Determination of trace elements in medicinal activated charcoal using slurry sampling electrothermal vaporization inductively coupled plasma mass spectrometry with low vaporization temperature



Chien-Chou Chen^a, Shih-Jen Jiang^{a,b,*}, A.C. Sahayam^c

^a Department of Chemistry, National Sun Yat-sen University, Kaohsiung 80424, Taiwan

^b Department of Medical Laboratory Science and Biotechnology, Kaohsiung Medical University, Kaohsiung 80708, Taiwan

^c National Centre for Compositional Characterisation of Materials (CCCM), Hyderabad, India

ARTICLE INFO

Article history:

Received 7 June 2014

Received in revised form

10 August 2014

Accepted 12 August 2014

Available online 22 August 2014

Keywords:

Inductively coupled plasma mass spectrometry

Ultrasonic slurry sampling

Electrothermal vaporization

Medicinal activated charcoal

Multielement determination

ABSTRACT

The determination of Cd, Sb, Te, Hg, Tl and Pb in medicinal activated charcoal by ultrasonic slurry sampling electrothermal vaporization inductively coupled plasma mass spectrometry (USS-ETV-ICP-MS) was described. EDTA was used as the modifier to enhance the volatility of elements studied. The influences of instrument operating conditions and slurry preparation on the ion signals were studied. A relatively low vaporization temperature of 1000 °C was used, which separated the analyte from the major matrix components that improved ion signals. The method has been applied to determine Cd, Sb, Te, Hg, Tl and Pb in an NIST SRM 1633b Coal Fly Ash reference material and three brands of medicinal activated charcoal capsules using isotope dilution and standard addition calibration methods. The concentrations that are in ng g⁻¹ levels were in good agreement between different calibration methods. The precision between sample replicates was better than 7% with USS-ETV-ICP-MS technique. The method detection limit estimated from standard addition curves was 0.4, 0.3, 0.3, 0.3, 0.04 and 0.9 ng g⁻¹ for Cd, Sb, Te, Hg, Tl and Pb, respectively, in original medicinal activated charcoal.

© 2014 Elsevier B.V. All rights reserved.

1. Introduction

Inductively coupled plasma mass spectrometry (ICP-MS) is a powerful technique for trace multielement and isotopic analysis. It has been applied to a wide range of samples. The majority of analyses by ICP-MS are carried out on solutions using a conventional pneumatic nebulizer. Hence, solid samples need sample preparation prior to analysis.

The activated charcoal is a difficult to dissolve sample. The medicinal activated charcoal is used as medicine for many purposes, for instance to release toxic effects of organic and inorganic pollutants [1,2]. However, environmental pollution and the contamination during processing can cause the activated charcoal to contain toxic elements which on consumption will produce detrimental effects on human health. Thus, the determination of trace elements in medicinal activated charcoal is essential in order to know the level of toxicity. ICP-MS has been successfully applied to the determination of trace and minor elements in carbon samples

[3,4]. Most of the analyses need tedious sample dissolution and pretreatment steps [3]. Furthermore some of the volatile species might be lost during sample pretreatment. However, direct solid analysis is a simpler alternative for the graphite powder analysis. Solid sampling graphite furnace atomic absorption spectrometry has been successfully applied for the determination of trace elements in graphite samples [5,6]. ETV method has been used for the sample introduction of difficult to dissolve samples such as ceramic alumina, silicon nitride etc. [7,8]. The ETV-ICP-MS method has the advantages of multielemental capability and better detection power over the GFAAS method. Ultrasonic slurry sampling electrothermal vaporization is one of the methods for solid sample introduction in ICP-MS, which has been successfully applied to determine trace elements in various powder samples [9–13]. Compared to traditional sample preparation methods such as acid digestion and dry ashing, slurry sampling offers several benefits including reduced sample preparation time, less possibility of sample contamination and decreased possibility of analyte loss prior to analysis. Moreover, ETV sample introduction method has been employed to eliminate most of the oxide and hydroxide ion interferences in ICP-MS analysis [14,15]. In ETV-ICP-MS analysis, in order to alleviate non-spectroscopic interference, a relatively low vaporization temperature could be used that separates volatile

* Corresponding author at: Department of Chemistry, National Sun Yat-sen University, Kaohsiung 80424, Taiwan. Fax: +886 7 5253908.

E-mail address: sjjiang@faculty.nsysu.edu.tw (S.-J. Jiang).

analytes from major matrix components. This strategy has been applied to the determination of various trace elements in several previous studies [15,16]. Addition of certain organic compounds promote atomization of the analyte prior to vaporization of the bulk matrix, thus facilitating temporal separation of the analyte and the matrix and leading to less interference effects of sample matrix. For example, EDTA was used as the chemical modifier to improve the signals of Cd, Hg and Pb in previous ETV-ICP-MS application [15].

In the present work, ultrasonic slurry sampling electrothermal vaporization inductively coupled plasma mass spectrometry (USS-ETV-ICP-MS) is proposed as an alternative technique for the simultaneous determination of Cd, Sb, Te, Hg, Tl and Pb in medicinal activated charcoal samples. The optimization of the USS-ETV-ICP-MS technique and its analytical figures of merit, as well as its applications for the determination of Cd, Sb, Te, Hg, Tl and Pb in medicinal activated charcoal capsules, are described in this paper.

2. Experimental

2.1. Apparatus and conditions

A Perkin-Elmer SCIEX (Concord, Ontario, Canada) ELAN 6100 DRCII ICP-MS equipped with HGA-600MS electrothermal vaporizer was used for studies and analysis. Pyrolytic coated graphite tubes with same material platforms were used throughout. The transfer line consisted of 90-cm-long, 6-mm-i.d. PTFE tubing. The sample introduction system included a Model AS-60 autosampler equipped with an USS-100 ultrasonic slurry sampler. Teflon auto-sampler cups were used throughout. The USS-100 was set at 10 W, and a 5-s mix time was used to mix slurries before injection of 20- μ L sample aliquots for analysis.

The ICP conditions were selected to maximize Mg, In and U ion signals while a solution containing 1 ng mL⁻¹ of these elements in 1% HNO₃ was continuously introduced with an ARIDUS membrane desolvation sample introduction system (Cetac, Omaha, NB, USA) to produce dry aerosol. The ICP-MS and ETV operating conditions used throughout this work are summarized in Tables 1 and 2, respectively. Integrated analyte signals (peak area) were measured throughout at transient peak hopping mode.

2.2. Reagents

The reagents and standard solutions were procured from following sources. Suprapur HNO₃ was from Merck (Darmstadt, Germany);

Table 1
Equipment and operating conditions.

ICP-MS instrument	Perkin-Elmer Elan 6100 DRCII
Plasma conditions	
RF power (W)	1300
Outer argon flow rate (L min ⁻¹)	15
Auxiliary argon flow rate (L min ⁻¹)	1.13
Carrier argon flow rate (L min ⁻¹)	0.95
Data acquisition	
Dwell time (ms)	10
Scan mode	Peak-hopping
Sweeps/reading	2
Reading/replicate	130
Signal measurement	Integrated
Isotopes monitored	¹¹¹ Cd, ¹¹³ Cd, ¹²¹ Sb, ¹²³ Sb, ¹²⁵ Te, ¹²⁶ Te, ²⁰¹ Hg, ²⁰² Hg, ²⁰³ Tl, ²⁰⁵ Tl, ²⁰⁶ Pb, ²⁰⁸ Pb

Table 2
HGA-600MS temperature programming^a.

Step	Temperature (°C)	Ramp time (s)	Hold time (s)	Gas flow rate (mL min ⁻¹)	Read
Dry1	80	5	10	300	-
Dry2	100	5	10	300	-
Pyrolysis	150	10	10	300	-
Cooling	20	1	5	300	-
Vaporization	1000	0	4	0	On
Cooling	20	5	5	300	-
Condition	2500	1	5	300	-
Cooling	20	5	10	300	-

^a Slurry volume: 20 μ L.

Triton-X 100 and ammonium pyrrolidinecarbodithioate (APDC) were from Fluka (Buchs, Switzerland); 8-Hydroxyquinoline (8-HQ) was from JANSSEN CHIMICA (Geel, Belgium); Disodium ethylenediamine tetra-acetic acid (EDTA) was from Fisher (Fair Lawn, NJ, USA); Cd, Te and Hg element standard solutions were from Merck; Sb and Mo element standard solutions were from Fisher; Tl and Pb element standard solutions were from Accustandard (New Haven, USA); W element standard solution was from Spex (Edison, NJ, USA). Enriched isotopes were procured from the following sources, ¹¹¹Cd (96.4%) was from the Oak Ridge National Laboratory (Oak Ridge, TN, USA), ¹²³Sb (97.1%), ¹²⁵Te (92.6%), ²⁰¹Hg (80.5%) and ²⁰³Tl₂O (98.4%) were from Cambridge Isotope Laboratories (Andover, MA, USA) and ²⁰⁶Pb(NO₃)₂ (99.7%) was from Merck (Darmstadt, Germany). Activated charcoal was from Sigma-Aldrich (St. Louis, Mo, USA).

2.3. Slurries preparation

The applicability of the method to real samples was demonstrated by the analysis of Cd, Sb, Te, Hg, Tl and Pb in three brands of medicinal activated charcoal capsules and an NIST SRM 1633b Coal Fly Ash reference material (National Institute of Standards and Technology, USA).

The analytes in various medicinal activated charcoal samples were determined by the isotope dilution method and standard addition method. The slurries were prepared using the following procedure. A 1-g portion of the powder material was transferred into a 10 mL flask and diluted to mark with pure water. 1-mL aliquot of the stock slurry solution was transferred to 10 mL flasks. Suitable amount of EDTA was added to make the final solution containing 1% m/v charcoal powder and 1% m/v EDTA. Since the concentrations of Pb and several other elements in SRM 1633b Coal Fly Ash were quite high, to determine the elements studied simultaneously, an 0.01% m/v coal fly ash slurry was prepared for the analysis. After addition of suitable amount of enriched isotope or various amounts of Cd, Sb, Te, Hg, Tl and Pb element standard solutions (0, 0.5, 1, 2, 4 and 8 ng mL⁻¹ in the final solutions); these slurries were made up to the mark with pure water. To correct any analyte contamination in the reagent used, a blank solution containing 1% m/v EDTA was also prepared. There was no significant amount of the analyte in the blank. The concentrations of analytes in the samples were calculated by the equation described in a previous paper [17] and/or from the standard addition calibration curves. To study the effects of ETV conditions and slurry preparations on the ion signals, a Sigma-Aldrich activated charcoal slurry sample prepared using the procedure described above and spiked with 0.5 ng mL⁻¹ of Cd and Te was used for studies. Spiking of other analytes of interest was not carried out as they are present above detectable levels in the sample.

3. Results and discussion

3.1. Selection of modifier

Chemical modifiers play a critical role in eliminating interfering components, such as water, acids and matrix elements, without losing the analyte of interest. In addition, the vapors of the modifier formed upon atomization can act as a physical carrier for more efficient transport of the analyte vapor to plasma [18]. The use of modifier would change the chemical or physical characteristics of the sample and/or the atomizer surface in order to improve quantification. Various organic modifiers have been used as modifiers to increase the volatility of the elements studied which made the separation of analytes and the major matrix component possible [19]. In this study, several common organic modifiers, including EDTA, APDC and 8-HQ, were tested to obtain best signals of the elements of interest [15,20–22]. The pyrolysis and vaporization temperatures were set at 150 °C and 1000 °C, respectively, in this experiment. From the experiments it was found that except Hg, the ion signals of elements studied increased when 1% m/v EDTA was used as the modifier. Furthermore the signals of Sb and Te were insignificant due to their low volatility when no EDTA was added. Hence, data without EDTA has not been obtained for Sb and Te. After preliminary evaluation, EDTA was selected as the modifier. Fig. 1 shows the effect of the amount of EDTA on the ion signals. As shown the signals of Sb, Tl and Pb increased significantly with EDTA concentration when the concentration was less than 1% m/v, while the signals of the other elements increased slightly with the increase of EDTA concentration. 1% m/v EDTA concentration was selected in the following ETV-ICP-MS analysis.

Mixed modifiers were used in many previous ETV-ICP-MS applications for the multielement determination simultaneously [15,21,22]. It is of interest to see the effect of the addition of other additives on the ion signals. The kind and concentration of mineral acid in the slurry solution could play an important role in ETV-ICP-MS applications [23,24]. Effect of the addition of HNO₃ into the slurry solution on the ion signals was studied. We found that the signal of elements studied

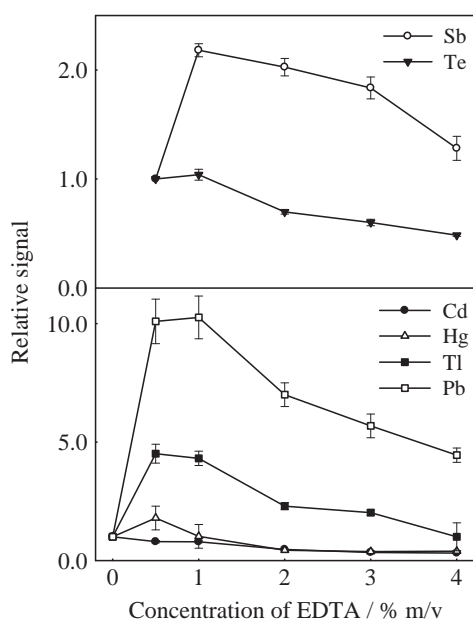


Fig. 1. Effect of EDTA concentration on ion signals. Slurry solution contained 0.5% m/v activated charcoal powders, 0.5 $\mu\text{g L}^{-1}$ Cd and Te, and spiked with various amounts of EDTA. Pyrolysis temperature was set at 150 °C; vaporization temperature was set at 1000 °C. Each data point represents the mean of five measurements. All data were relative to the first point.

decreased significantly when a small amount of HNO₃ (0.2% v/v–0.5% v/v) was added. Possibly analytes could not form volatile species with EDTA in presence of HNO₃, that volatilize at 1000 °C. Effect of the addition of Triton X-100, to the sample slurry, on the ion signals was also studied. From the experiments it was found that the addition of a small amount of surfactant (0.25% m/v) could improve the signals of Sb and Hg slightly. However, the signal of Cd, Tl, Te and Pb decreased when surfactant was added. In order to simplify slurry preparation and to reduce the reagent blank, no other reagents were added in the slurry preparation.

Effects of other parameters of the slurry preparation on the ion signals were also investigated. An important factor in the slurry technique is the slurry concentration i.e., dilution factor. Effect of the dilution factor on ion signals was studied at different dilution factors such as 400 (0.25% m/v), 200 (0.5% m/v), 100 (1% m/v) and 50 (2% m/v). From the experiments it was found that the sensitivity (peak area counts/mass of charcoal in slurry) of the elements studied decreased with the increase of slurry concentration. The variation of the sensitivities at different dilution factors could be due to the difference in the non spectral interferences that affect analyte transport efficiency. In order to balance sample homogeneity, analyte signals and the complete vaporization of introduced sample, a dilution factor of 100 (1% m/v) was selected in this study.

3.2. Selection of pyrolysis and vaporization temperatures

The effect of pyrolysis temperature on ion signals is shown in Fig. 2. As shown, the signal of Hg decreased rapidly when the pyrolysis temperature was greater than 150 °C. This means that a considerable amount of Hg volatilized before the vaporization stage. To retain the analytes, a pyrolysis temperature of 150 °C was set. The effect of vaporization temperature on the ion signals of the analytes of interest was also studied. As shown in Fig. S1 (Supplementary data), the signals of elements studied decreased with the increase in vaporization temperature. The decrease of the ion signals could be due to the non-spectral interference caused by

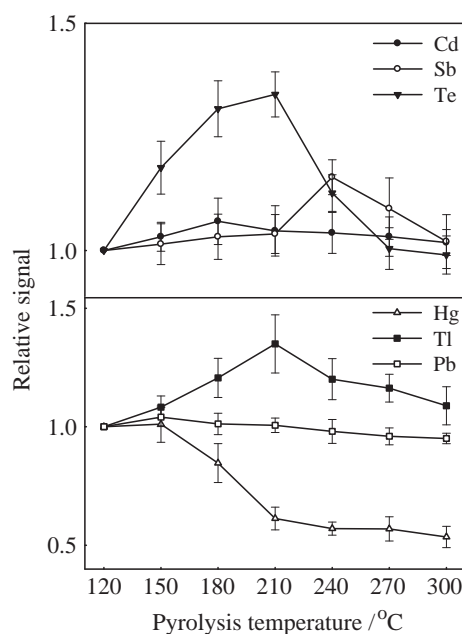


Fig. 2. Effect of pyrolysis temperature on ion signals. Slurry solution contained 1.0% m/v activated charcoal powders, 1.0% m/v EDTA and spiked with 0.5 $\mu\text{g L}^{-1}$ of Cd and Te. Vaporization temperature was set at 1000 °C. All data were relative to the first point.

the matrix element carbon when temperature was increased. The decrease in analyte signal in carbon rich matrices was reported by Fonseca and Miller-Ihli [25]. However, as shown in Fig. 3, the peak shape of Tl and Pb was improved and the peak width was reduced when the vaporization temperature was increased from 900 °C to 1000 °C. For better precision, in the following experiments, a vaporization temperature of 1000 °C was selected. The summary of the ETV operating conditions is listed in Table 2.

3.3. Spectral interferences study

For ICP-MS analysis, the components of the sample could produce several polyatomic ions which interfere in the determination of analytes of interest. The determination of Cd and Hg was interfered by various background ions. For instance, the isotopes of cadmium are interfered by molybdenum oxide ions and the isotopes of mercury are interfered by tungsten oxide ions. In order to evaluate the significance of interferences caused by Mo and W, the following experiments were performed. A 1% m/v activated charcoal slurry was prepared as the method described previously. And then the prepared slurry was spiked with 0, 0.5, 1.0 $\mu\text{g mL}^{-1}$ of Mo and 0, 0.5 $\mu\text{g mL}^{-1}$ of W. These slurries were injected for the determination of the isotope ratios $^{111}\text{Cd}/^{113}\text{Cd}$ and $^{201}\text{Hg}/^{202}\text{Hg}$ using ETV-ICP-MS. The isotope ratio was calculated from the peak areas of each injection peak. The spiked concentrations were higher than the concentration of matrix elements in the prepared slurry solution. From the experiments it was found that the isotope ratios of $^{111}\text{Cd}/^{113}\text{Cd}$ and $^{201}\text{Hg}/^{202}\text{Hg}$ were not affected by Mo and W at these concentrations for a confidence level of 95% in accordance with Student's *t*-test. The alleviation of the interferences could be due to the introduction of much more dry aerosol with ETV sample introduction device [15,26,27]. These experiments demonstrated that the concentrations of Cd and Hg in the activated charcoal samples can be determined directly by ETV-ICP-MS without significant interferences.

3.4. Determination of Cd, Sb, Te, Hg, Tl and Pb in medicinal activated charcoal

To apply the developed USS-ETV-ICP-MS technique, the concentrations of Cd, Sb, Te, Hg, Tl and Pb were determined in three medicinal activated charcoal samples. The accuracy of the procedure was verified by analyzing a certified reference material NIST SRM 1633b Coal Fly Ash. In order to evaluate the possibility of using external calibration method for the determination of trace elements in activated charcoal by USS-ETV-ICP-MS, calibration curves obtained by standard addition method of 1% m/v activated charcoal slurry and external calibration of aqueous standard were compared. From the experiments it was found

that the slopes obtained by external calibration method and standard addition method were 28,000 counts ng^{-1} mL and 278,000 counts ng^{-1} mL respectively for Cd; 503,000 counts ng^{-1} mL and 176,000 counts ng^{-1} mL respectively for Sb; 165,000 counts ng^{-1} mL and 133,000 counts ng^{-1} mL respectively for Te; 194,000 counts ng^{-1} mL and 511,000 counts ng^{-1} mL respectively for Hg; 6,840,000 counts ng^{-1} mL and 5,020,000 counts ng^{-1} mL respectively for Tl; 6,750,000 counts ng^{-1} mL and 5,150,000 counts ng^{-1} mL respectively for Pb. The calibration curves obtained by standard addition method of 1% m/v activated charcoal slurry and external calibration of aqueous standard were different significantly. Except Hg, there was signal suppression of all the other elements in the presence of sample compared to aqueous standards that were used for external calibration. However, as shown in Table S1 (Supplementary data), except for antimony, the slopes of the elements studied were quite similar between the Sigma-Aldrich activated charcoal slurry and the Brand 1 medicinal activated charcoal slurry. In order to obtain accurate results, the isotope dilution method and standard addition method were used for the determination of the elements studied in these samples. Typical element-selective ETV signal (ICP-MS detection) for a solution containing 1% m/v Brand 2 medicinal activated charcoal, 1% m/v EDTA and spiked with 0.5 ng mL^{-1} each of Cd, Sb, Te, Hg, Tl and Pb is shown in Fig. 4. Analysis results are shown in Table 3. As shown, the concentrations of Cd, Sb, Te, Hg, Tl and Pb determined in the Coal Fly Ash reference sample were in good agreement with the certified values according to the Student *t*-test for a confidence level of 95%. Moreover as shown in Table 3, the isotope dilution results were in good agreement with those obtained by standard addition calibration method for which no certified values were available. The precision between sample replicates was better than 7% for all determinations. This experiment indicated that Cd, Sb, Te, Hg, Tl and Pb in medicinal activated charcoal could be readily quantified by the proposed USS-ETV-ICP-MS technique.

Detection limits of Cd, Sb, Te, Hg, Tl and Pb in the medicinal activated charcoal samples were determined from the standard addition curves based on the usual definition as the concentration of the analyte yielding a signal equivalent to three times the standard deviation of the reagent blank signal ($n=7$). Detection limit estimated from standard addition curves was 0.4, 0.3, 0.3, 0.3, 0.04 and 0.9 ng g^{-1} for Cd, Sb, Te, Hg, Tl and Pb, respectively, in the original activated charcoal samples.

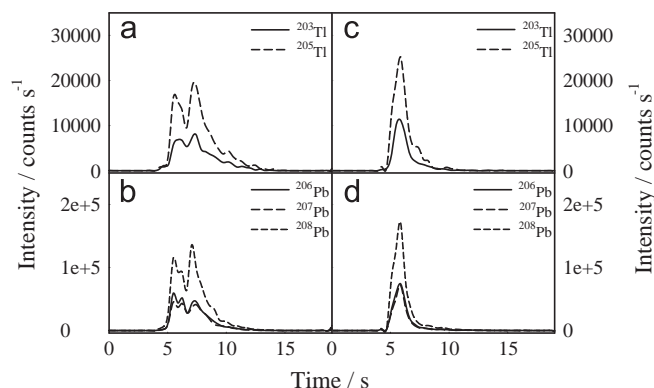


Fig. 3. Effect of vaporization temperature on ion signals of Tl and Pb. (a) and (b) 900 °C; (c) and (d) 1000 °C. Slurry solution contained 1.0% m/v activated charcoal powders and 1.0% m/v EDTA. Pyrolysis temperature was set at 150 °C.

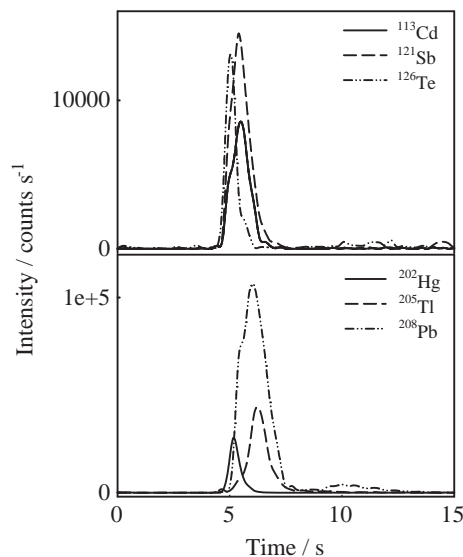


Fig. 4. ETV-ICP-MS signals of Cd, Sb, Te, Hg, Tl and Pb. Slurry solution contained 1% m/v Brand 2 medicinal activated charcoal, 1% m/v EDTA and spiked with 0.5 $\mu\text{g L}^{-1}$ each of Cd, Sb, Te, Hg, Tl and Pb. Pyrolysis temperature and vaporization temperature was set at 150 °C and 1000 °C, respectively.

Table 3
Determination of in Cd, Sb, Te, Hg, Tl and Pb in coal fly ash and medicinal activated charcoal by USS-ETV-ICP-MS^a (n=3).

Sample	Method ^b	Concentration (ng g ⁻¹)					
		Cd	Sb	Te	Hg	Tl	Pb
SRM1633b Coal Fly Ash	Method 1	790 ± 7	5870 ± 150	< 10	146 ± 9	5560 ± 180	68100 ± 2400
	Method 2	788 ± 8	5890 ± 180		147 ± 8	5610 ± 200	68100 ± 2700
	Certified	784 ± 6	(6000) ^b		141 ± 19	(5900) ^b	68200 ± 1100
Brand 1	Method 1	< 0.2	41.8 ± 2.2	< 0.1	19.5 ± 1.1	5.88 ± 0.24	80.8 ± 4.1
	Method 2		42.5 ± 1.5		19.4 ± 1.0	5.85 ± 0.19	82.1 ± 4.0
	MDL	0.2	0.1	0.1	0.1	0.02	0.6
Brand 2	Method 1	< 0.4	44.4 ± 2.4	< 0.3	18.2 ± 1.2	20.9 ± 1.4	151 ± 8
	Method 2		43.7 ± 2.5		18.3 ± 1.0	20.8 ± 1.3	154 ± 11
	MDL	0.4	0.3	0.3	0.3	0.03	0.9
Brand 3	Method 1	5.7 ± 0.4	21.8 ± 1.1	< 0.1	4.4 ± 0.2	4.2 ± 0.1	194 ± 11
	Method 2	5.4 ± 0.3	21.4 ± 1.3		4.2 ± 0.2	4.3 ± 0.2	200 ± 10
	MDL	0.2	0.3	0.1	0.2	0.04	0.9

^a Values are means of three measurements ± standard deviation.

^b Method 1: USS-ETV-ICP-MS standard addition method. Method 2: USS-ETV-ICP-MS isotope dilution method. Certified: NIST certified values. Values in parentheses are for information only. MDL: Method detection limit.

4. Conclusion

The determination of Cd, Sb, Te, Hg, Tl and Pb in medicinal activated charcoal samples has been carried out using USS-ETV-ICP-MS. A relatively low vaporization temperature of 1000 °C was used, which separated the analyte from the major matrix components that improved ion signals. Dry aerosol generated using ETV alleviated metal oxide based interferences due to Mo and W for the interference free measurements by ICP-MS. The method reported is simple compared to methods based on solution nebulization and can be adopted for routine quality check of medicinal activated charcoal for the industrial purpose.

Acknowledgment

This research was supported by a Grant from the Ministry of Science and Technology of the Republic of China (MOST) under Contract 100-2113-M-110-002-MY3 and 100-2627-M-110-003.

Appendix A. Supporting information

Supplementary data associated with this article can be found in the online version at <http://dx.doi.org/10.1016/j.talanta.2014.08.034>.

References

- [1] P. Gaudreault, Clin. Pediatr. Emerg. Med. 6 (2005) 76–80.

- [2] R.B. Raffa, C. Wu, D.J. Stone, M.R. Borenstein, E.E. Codd, T.P. Coogan J. Pharmacol. Toxicol. Methods 43 (2000) 205–210.
- [3] K.X. Yang, M.E. Kitto, J.P. Orsini, K. Swami, S.E. Beach, J. Anal. At. Spectrom. 25 (2010) 1290–1297.
- [4] C. Ge, F. Lao, W. Li, Y. Li, C. Chen, Y. Qiu, X. Mao, B. Li, Z. Chai, Y. Zhao, Anal. Chem. 80 (2008) 9426–9434.
- [5] A. Zacharia, S. Gucer, B. Izgi, A. Chebotarev, H. Karaaslan, Talanta 72 (2007) 825–830.
- [6] F.G. Lepri, D.L.G. Borges, R.G.O. Araujo, B. Welz, F. Wendler, M. Krieg, H. Becker-Ross, Talanta 81 (2010) 980–987.
- [7] M.C. Wende, J.A.C. Broekaert, Fresenius' J. Anal. Chem. 370 (2001) 513–520.
- [8] P. Barth, S. Hauptkorn, V. Krivan, J. Anal. At. Spectrom. 12 (1997) 1359–1365.
- [9] B.U. Peschel, F. Andrade, W.C. Wetzel, G.D. Schilling, G.M. Hieftje, J.A. C. Broekaert, R. Sperline, M.B. Denton, C.J. Baninaga, D.W. Koppelaar, Spectrochim. Acta Part B 61 (2006) 42–49.
- [10] S.M. Maia, M.G.R. Vale, B. Welz, A.J. Curtius, Spectrochim. Acta Part B 56 (2001) 1263–1275.
- [11] M. He, B. Hu, Z.C. Jiang, Anal. Chim. Acta 530 (2005) 105–112.
- [12] Y.F. Zhang, Z.C. Jiang, M. He, B. Hu, Environ. Pollut. 148 (2007) 459–467.
- [13] L.F. Dias, G.R. Miranda, T.D. Saint'Pierre, S.M. Maia, V.L.A. Frescura, A.J. Curtius, Spectrochim. Acta Part B 60 (2005) 117–124.
- [14] Y.-J. Tseng, Y.-D. Tsai, S.-J. Jiang, Anal. Bioanal. Chem. 387 (2007) 2849–2855.
- [15] H.-C. Liao, S.-J. Jiang, J. Anal. At. Spectrom. 14 (1999) 1583–1588.
- [16] J.W.H. Lam, R.E. Sturgeon, J.W. McLaren, Spectrochim. Acta Part B 54 (1999) 443–453.
- [17] K.-H. Lee, S.-J. Jiang, H.-W. Liu, J. Anal. At. Spectrom. 13 (1998) 1227–1231.
- [18] R.W. Fonseca, N.J. Miller-Ihli, Appl. Spectrosc. 49 (1995) 1403–1410.
- [19] H.-H. Lu, S.-J. Jiang, Anal. Chim. Acta 429 (2001) 247–255.
- [20] P.-H. Liao, S.-J. Jiang, A.C. Sahayam, J. Anal. At. Spectrom. 27 (2012) 1518–1524.
- [21] W.-H. Hsu, S.-J. Jiang, A.C. Sahayam, Anal. Chim. Acta 794 (2013) 15–19.
- [22] M.-L. Lin, S.-J. Jiang, Food Chem. 141 (2013) 2158–2162.
- [23] B. Fairman, T. Catterick, J. Anal. At. Spectrom. 12 (1997) 863–868.
- [24] D.C. Gregoire, D.M. Goltz, M.M. Lamoureux, C.L. Chakrabarti, J. Anal. At. Spectrom. 9 (1994) 919–926.
- [25] R.W. Fonseca, N.J. Miller-Ihli, Spectrochim. Acta B 51 (1996) 1591–1599.
- [26] S.-F. Chen, S.-J. Jiang, J. Anal. At. Spectrom. 13 (1998) 673–677.
- [27] M.-J. Liaw, S.-J. Jiang, J. Anal. At. Spectrom. 11 (1996) 555–560.



Sequential hollow-fiber liquid phase microextraction for the determination of rosiglitazone and metformin hydrochloride (anti-diabetic drugs) in biological fluids

Gazala Mohamed Ben-Hander, Ahmad Makahleh*, Bahruddin Saad**,
Muhammad Idris Saleh, Kek Wan Cheng

School of Chemical Sciences, Universiti Sains Malaysia, 11800 Minden, Penang, Malaysia

ARTICLE INFO

Article history:

Received 1 July 2014

Received in revised form

9 August 2014

Accepted 12 August 2014

Available online 20 August 2014

Keywords:

Sequential HF-LPME

HPLC–UV

Metformin hydrochloride

Rosiglitazone

Biological fluids

ABSTRACT

A new analytical method for the simultaneous determination of the antidiabetic drugs rosiglitazone (ROS) and metformin hydrochloride (MH) with marked differences in their affinity towards organic solvents ($\log P$ of 2.4 and -1.43 , respectively) was developed. Prior to the HPLC separation, the drugs were subjected to a sequential hollow fiber liquid phase microextraction (HF-LPME) procedure. Two sequential HF-LPME approaches were considered, the preferred one involves the use of two vials containing solution mixtures for the extraction of ROS (vial 1) and MH (vial 2), respectively, but using the same fiber and acceptor phase. Important parameters that affect the extraction efficiency such as extracting solvent, donor phase conditions, HCl concentration, agitation, extraction time, addition of salt, etc. were studied. Under the optimum conditions, good enrichment factors (EF, 471 and 86.6 for ROS and MH, respectively) were achieved. Calibration curves were linear over the range 1–500 ($r^2=0.998$) and 5–2500 ng mL^{-1} ($r^2=0.999$) for ROS and MH, respectively. The relative standard deviation values (RSD%) for six replicates were below 8.4%. Detection and quantitation limits based on S/N ratio of 3 and 10 were 0.12, 1.0 and 0.36, 3.0 ng mL^{-1} for ROS and MH, respectively. The proposed method is simple, sensitive and opens up new opportunities for the microextraction of analytes with contrasting properties.

© 2014 Elsevier B.V. All rights reserved.

1. Introduction

Treatment of diabetes mellitus using monotherapy with an oral anti-diabetic agent is insufficient to reach the target glycaemic goals in many patients, thus multi-drugs are necessary to achieve adequate control and satisfactory blood glucose levels. The combination of biguanides and thiazolidinedione derivatives is commonly used in clinical practice [1]. Metformin hydrochloride (MH) (biguanide class, Fig. 1), chemically [1,1-dimethylbiguanidehydrochloride], is an oral biguanide antihyperglycemic drug which is used to improve the insulin sensitivity, inhibits hepatic gluconeogenesis and reduces hepatic glucose production in patients that suffer from type 2 diabetes mellitus (T2DM) [2,3]. Rosiglitazone (ROS), (thiazolidinedione class, Fig. 1), chemically [(±)-5-[4-[2-[N-methyl-N (2-pyridyl) amino] ethoxy] benzyl]-2,4-dione thiazolidine], is a drug for the treatment of T2DM which works by

increasing the insulin sensitivity in the target tissues, as well as decreasing hepatic gluconeogenesis [4,5]. A combination of MH and ROS was found to be better in the treatment of T2DM compared to single-agent therapy alone due to its high effect on lowering blood glucose [6,7] and improving beta-cell function [8]. Furthermore, the combination tablet formulation is advantageous in terms of its convenience and patient compliance [9].

Several methods for the determination of ROS and MH either individually or simultaneously have been reported. High performance liquid chromatography with ultraviolet detection (HPLC–UV) [6–17] is the most commonly used method for the analysis of ROS and MH. However, high limit of quantitation ($\text{LOQ} \geq 20 \text{ ng mL}^{-1}$) was observed when UV detection was used [8,10,11,17]. Alternatively, HPLC with fluorescence detection (FL) [18,19] or tandem mass spectrometry (MS/MS) [2–4,20–27] was used. Although FL gives better sensitivity compared to UV detection, but the separation was rather long ($\geq 15 \text{ min}$) [18,19]. LC–MS/MS is an efficient analysis tool providing low quantitation limits ($\geq 1 \text{ ng mL}^{-1}$) [20–23], short run time, improved sensitivity and selectivity, but it is costly and the equipment is not always available in clinical laboratories. The use of gas chromatography

* Corresponding author. Tel.: +60 4 653 6018; fax: +60 4 657 4857.

** Corresponding author. Tel.: +60 4 653 2544; fax: +60 4 656 9869.

E-mail addresses: makahleha@yahoo.com (A. Makahleh),
bahrud@usm.my (B. Saad).

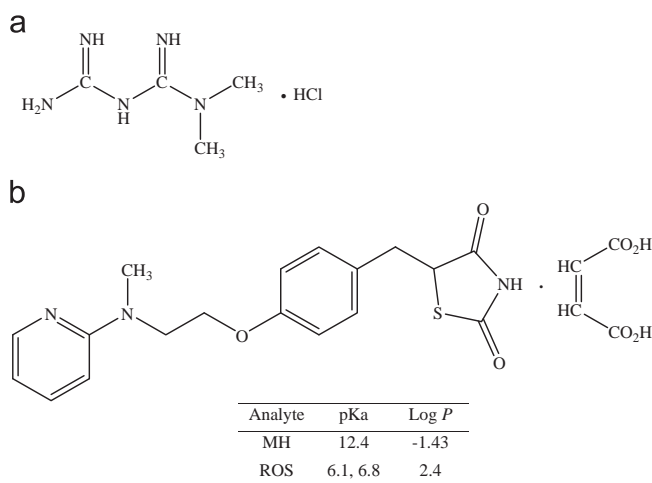


Fig. 1. Chemical structures, pKa and log *P* values of (a) metformin hydrochloride (MH) and (b) rosiglitazone (ROS).

coupled with nitrogen [28], flame ionization [29] or mass spectrometry (MS) detectors [30] for the analysis of MH was described. Capillary zone electrophoresis (CE) with UV detection [1,31–33] and MS [34] have also been reported.

Liquid–liquid extraction (LLE) [6,10,19,20,27], solid-phase extraction (SPE) [2,4,9,13,14,18,33] and protein precipitation [3,17,21,22,24–26,34] are the most widely used sample preparation technique for the analysis of ROS and MH in biological fluids. However, these techniques have many disadvantages as they usually require large volumes of high-purity solvents, multi-step and long extraction time which lead to analyte losses. To overcome these problems, microextraction techniques such as hollow fiber liquid phase microextraction (HF-LPME) has been used for the individual analysis of ROS [11,12] or MH [16] in biological fluids. The main advantages of the HF-LPME technique are fast, simple, inexpensive, low consumption of organic toxic solvents (only microliter volumes), no carry over due to the single use of the fiber and high enrichment factor. Also, the clean-up and pre-concentration of the analytes are done in a single step due to the small pore size of the hollow fiber membrane which act as a microfilter that eliminates interfering macromolecules and produce clean extracts that are suitable for direct instrumental analyses.

The simultaneous microextraction of ROS and MH is analytically challenging, if not impossible, due to the marked differences in their physical properties. Pertaining to extraction are the pKa and log *P* values of these drugs. MH is readily soluble in water, highly polar (log *P* = −1.43) and is strongly basic (pKa = 12.4) while log *P* and pKa of ROS are 2.4 and 6.1, 6.8, respectively. Furthermore, MH is non-chromophoric. It is rationalized that in the absence of a simultaneous method for the microextraction, a sequential microextraction approach that extracts one drug, followed by the next one would also be worth considering. Since these two drugs had been individually extracted using the HF-LPME technique, the present studies is aimed at modifying and integrating these work for the sequential approach, that will eventually lead to the simultaneous HPLC determination.

2. Experimental

2.1. Chemicals and reagents

Metformin HCl (MH) and rosiglitazone maleate (ROS) reference standards were kindly donated by Hikma Pharmaceuticals (Amman,

Jordan). Acetonitrile (HPLC-grade; 99.99%) was purchased from Fisher Scientific (Milwaukee, WI, USA). Methanol (HPLC-grade; ≥99.96%), hydrochloric acid (37%, w/w) were purchased from Merck (Darmstadt, Germany). *n*-Decane (99.0%) and *n*-tridecane (99.0%) were obtained from Acros Organics (Geel, Belgium). Pentafluorobenzoyl chloride (99.0%), Sodium hydroxide (≥98.0%), dihexyl ether (97.0%), *n*-heptane (99.0%), *n*-hexadecane (99.0%) and nitrobenzene (≥99.0) were purchased from Sigma-Aldrich (St. Louis, MO, USA). 1-Heptanol (≥99.9%) and 1-octanol (≥99.5%) were purchased from Fluka (Buchs, Switzerland). Phosphoric acid (85%) was purchased from Univar (Ingleburn, Australia). Ultrapure water (resistivity, 18.2 MΩ cm^{−1}) was produced by a Milli-Q system (Millipore, MA, USA). Blank plasma sample was kindly donated by Centre for Drug Research, Universiti Sains Malaysia, Penang. Human urine sample was obtained from a healthy student volunteer. Derivatizing solution was prepared by dilution 10 mg of Pentafluorobenzoyl chloride (PFBC) in 1 mL acetonitrile and stored at 4 °C until used.

2.2. Instrumentation

Chromatographic analyses were performed using a Hitachi LC-6200 intelligent pump (Tokyo, Japan) equipped with a Hewlett-Packard 1050 UV detector (Waldbronn, Germany). Sample injection was performed via a Rheodyne 7125 injection valve (Cotati, CA, USA) with a 5 μL loop. A PowerChrom data acquisition was obtained from eDAQ (Denistone East, Australia) and performed with PowerChrom software (version 2.7.2) to record and analyze the chromatographic data. The separation was obtained using a ODS Hypersil C18 column (250 × 4.6 mm, 5 μm). The mobile phase composition was a mixture of acetonitrile and 10 mM sodium phosphate buffer (pH 4.0) (60:40, v/v). The elution was performed under isocratic mode at a flow rate of 1.0 mL min^{−1}. The UV detection wavelength was set at 230 nm. Prior to the analysis, the mobile phase was filtered through nylon membrane filter (0.45 μm) from Agilent Technologies (Waldbronn, Germany) and degassed by ultrasonic bath for 15 min. For UV-scanning purpose, a Lambda 35 UV/vis system from Perkin Elmer (Waltham, MA, USA) was used. The extraction was performed using a 25 μL micro-syringe with a blunt needle tip (model 702SNR) and it was purchased from Hamilton (Reno, NV, USA). A multi-hotplate stirrer from DAIHAN scientific (Seoul, South Korea) was used for the stirring through the extraction process.

2.3. Preparation of stock standard solutions

ROS stock solution (1000 μg mL^{−1}) was prepared by dissolving the desired amount in acetonitrile, while MH stock solution (2000 μg mL^{−1}) was prepared in water. A mixture solution of ROS and MH (200 and 1000 μg mL^{−1}, respectively) was prepared by a proper dilution of the stock solutions in water and stored at 4 °C until use. Working standard solution was prepared daily by diluting the standard mixture in water as described in Section 2.5.

2.4. Minimizing the matrix effect of plasma and urine

In order to reduce the matrix effect of plasma sample, the following pretreatment steps have been conducted. 200 μL HCl (0.05 M) was added to the plasma sample (2 mL) spiked with standard mixture at the desired concentration. The sample mixture was vortex-mixed thoroughly for 30 s. The protein precipitation was accomplished by addition of acetonitrile (3 mL) and then the mixture was centrifuged at (1900 rpm) for 15 min. An aliquot of supernatant was collected and evaporated to dryness at 40 °C under gentle nitrogen stream. The dried residue was reconstituted with water as described in Section 2.5 for sequential HF-LPME analysis. In order to reduce the matrix effects (e.g., albumins,

sugars, urea, etc.) in the urine samples, urine sample spiked with standard mixture was diluted 1:1 with water.

2.5. Sequential HF-LPME procedure

Two sequential HF-LPME procedures were considered. In the first procedure (Fig. 2(a)), two different vials but sharing the same HF segment (4 cm) and acceptor phase (10 μL of 0.1 M HCl) were used. Each vial (12 mL) contains 10 mL of working standard or sample solutions. The first vial was dedicated for the extraction of ROS, it contained samples that had been diluted to 10 mL with water (pH adjusted to 9.0 using 0.05 M NaOH solution), while the second vial for the extraction of MH also contained samples that had been mixed with 600 μL NaOH (4.0 M) and 100 μL derivatizing solution (10 mg mL^{-1}) and diluted to 10 mL using water. A magnetic stirring bar (15 \times 5 mm^2) was placed in each vial. Acceptor phase (10 μL) was withdrawn using a micro-syringe and the syringe needle was inserted into the HF segment. The HF was bent to a U-shape and the assembly was immersed 10 s in dihexyl ether (as organic solvent) to impregnate the solvent into the porous wall of the fiber. It was next soaked in water for 5 s in order to wash the extra organic solvent. Subsequently, the HF was

placed immediately in the first vial. The acceptor phase (AP) was completely injected into the lumen of the HF and the sample solution was agitated at 300 rpm at room temperature. After 30 min, the fiber was placed in the second vial that was heated at 70 $^{\circ}\text{C}$ and agitated at the same speed as that for the first vial (300 rpm) for 30 min. At the end of the extraction time, the extract (5 μL) was carefully withdrawn into the syringe and the HF was discarded. Finally, the extract was directly injected into the HPLC system.

In the second procedure (Fig. 2(b)), a vial that contained a mixtures of ROS and MH (10 mL) was used. The pH of the solution mixture (donor phase) was adjusted to 9.0 and the HF-LPME extraction for ROS was performed as the first approach. After 30 min, PFCB and NaOH (4.0 M) were added to the same vial and the mixture was heated at 70 $^{\circ}\text{C}$ for 30 min. Finally, the acceptor phase was withdrawn from the lumen of the HF and injected into the HPLC unit.

3. Results and discussion

Initial chromatographic conditions used were adopted from our previous work [16], i.e., hypersil ODS column with mobile phase

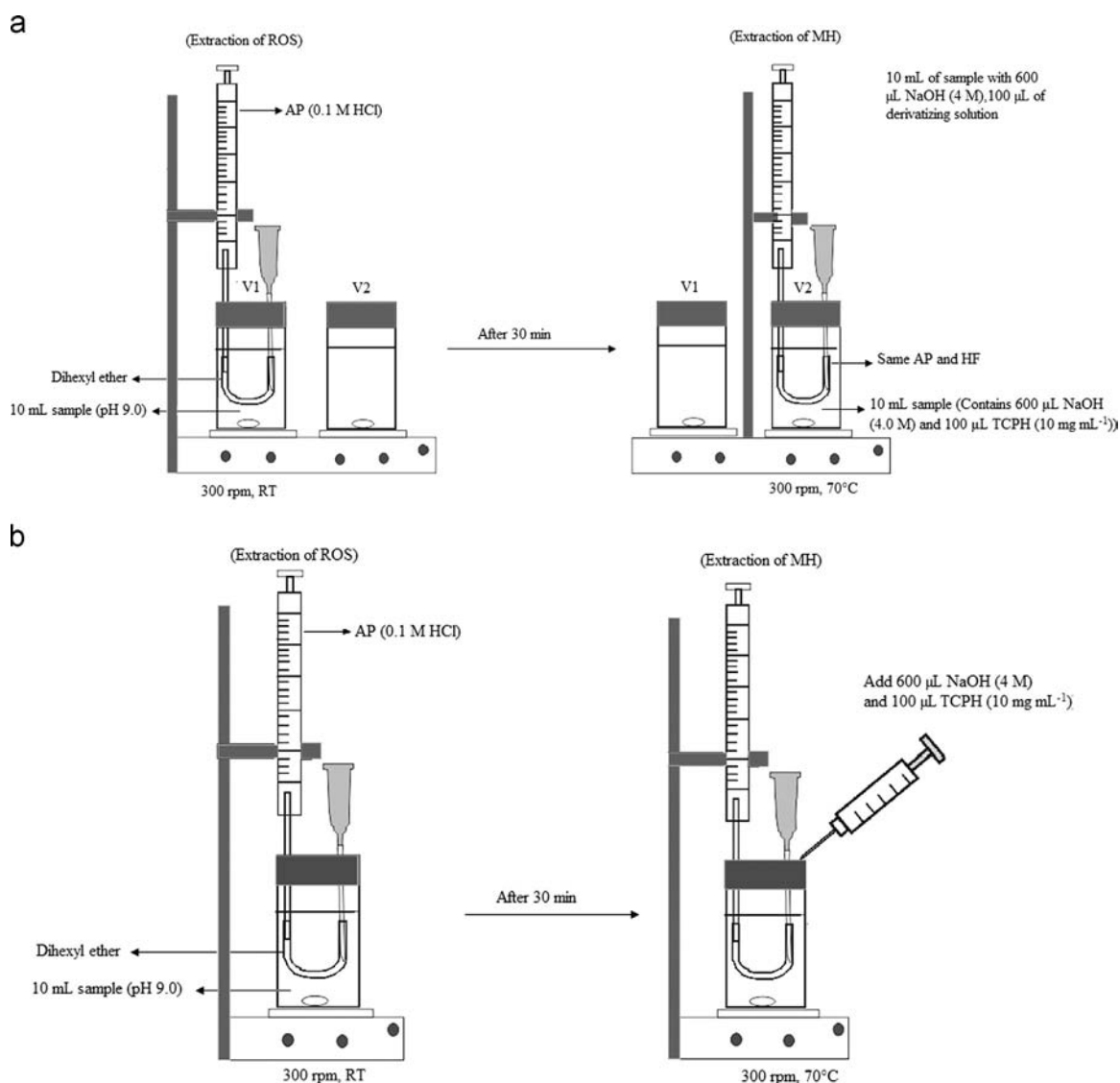


Fig. 2. First (a) and second (b) procedure of sequential HF-LPME. Where: AP, acceptor phase; HF, hollow fiber; V, vial; and RT, room temperature.

composition of acetonitrile: 10 mM phosphate buffer (pH 4.0) (60:40; v/v) at flow rate of 1 mL min^{-1} . Under these conditions, peak broadening of ROS was observed. Different compositions of mobile phase were investigated by varying the acetonitrile ratio (55–65%). An improvement in the ROS peak shape was observed as the ratio of acetonitrile was decreased. As a compromise between peak shape, resolution and run time, 60% acetonitrile was chosen. The effect of buffer pH (3.5–5.0) was also explored. Although low pH enhanced the peak shapes but a decrease in resolution between the peaks was observed. The best peak shape and resolution was observed at pH 4.0. Therefore, a mixture of 40% of 10 mM sodium phosphate buffer (pH 4.0) and 60% acetonitrile at flow rate 1.0 mL min^{-1} was selected as the optimum mobile phase composition.

3.1. Optimization of sequential HF-LPME parameters

ROS and MH are basic compounds with pKa values 6.8 and 12.1, respectively. However, their affinity towards the organic solvents is markedly different ($\log P$, 2.4 and -1.43 , respectively) [12,16]. In order to enhance the extraction of MH towards organic solvents, derivatization is required. We have previously reported an in-situ HF-LPME method for the extraction of MH in biological fluids where MH was derivatized using PFBC in the presence of high concentration of NaOH (4.0 M) [16]. However, the use of too concentrated base in the present work may hinder the extraction of ROS [12]. Thus, preliminary studies were conducted using UV-vis spectroscopy to study the stability of ROS in concentrated bases. Thus ROS in different concentrations of NaOH and KOH (3.0–5.0 M) was prepared, and their spectrum was recorded (Fig. 3). A big shift in the maximum wavelength of ROS that was prepared in concentrated NaOH or KOH was found. This is probably due to the decomposition of the diimide group under strongly basic conditions [35,12]. Further confirmation was carried out by mixing the standard mixture with PFBC and NaOH (4.0 M), then subjected to the previously reported in-situ HF-LPME conditions [16]. Only MH peak was observed.

Sequential HF-LPME involving first the extraction of ROS for 30 min, followed by the addition of PFBC and NaOH (4.0 M) to the sample for the extraction of MH in another 30 min was performed. It was observed that the two analytes were extracted when relatively large volumes of NaOH ($\geq 2 \text{ mL}$) were used. Good extraction for ROS was observed but not for MH (EF, 7.6), probably due to the dilution effect of the donor phase. As an alternative, sequential HF-LPME procedure was performed using the same HF and acceptor phase to extract ROS and MH in two different vials, i.e., first vial with pH adjusted to 9.0 for extraction of ROS, while the second contains PFBC and NaOH (4.0 M) for the extraction of MH. This procedure was preferred as better extraction was found (EF, 86.6 and 100 for MH and ROS, respectively) (Fig. 4). Thus,

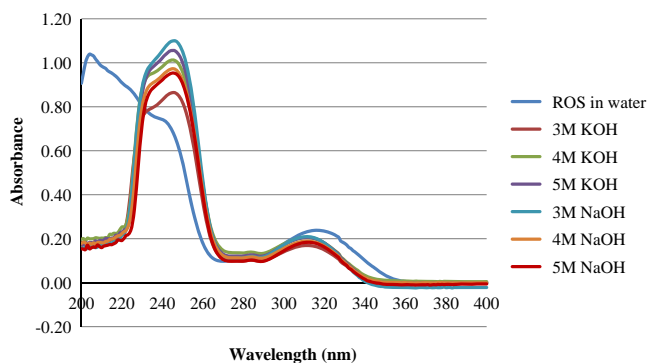


Fig. 3. UV scans of ROS prepared in different concentrations of NaOH and KOH.

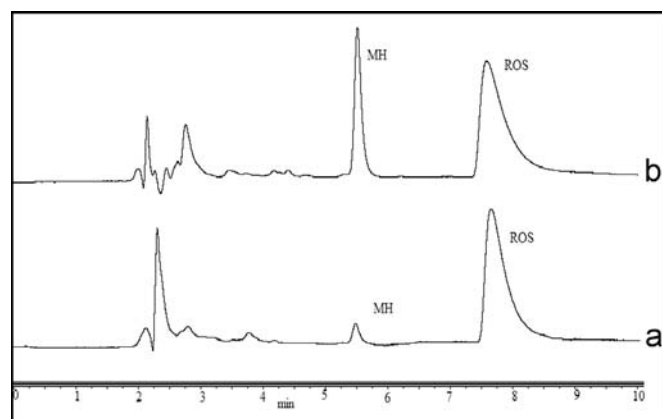


Fig. 4. Typical chromatograms of MH and ROS after subjected to sequential HF-LPME using (a) approach 1, and (b) approach 2. Please refer to text for experimental details.

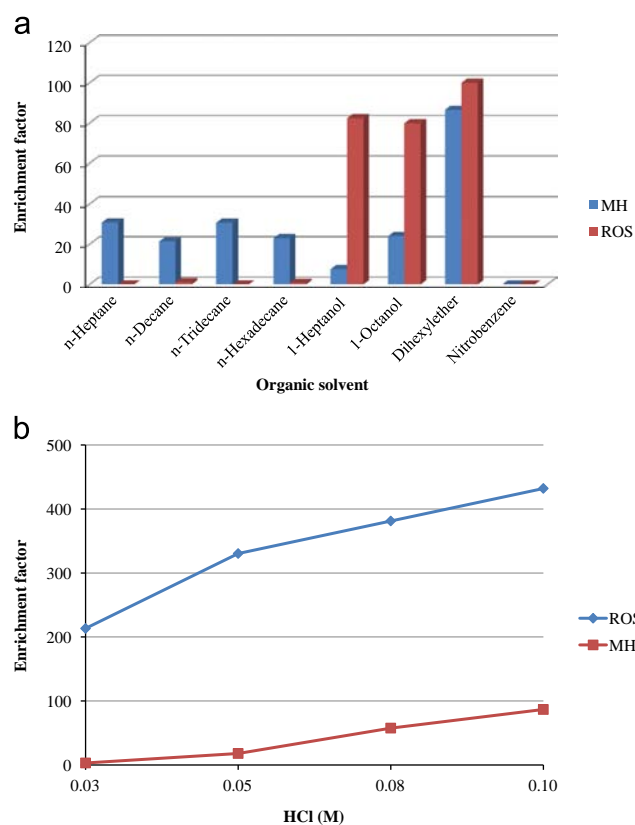


Fig. 5. Effect of organic solvent (A), concentration of acceptor phase (HCl) (B) on the enrichment factors ($n=3$).

several extraction parameters that influence the extraction efficiency (i.e., selection of organic solvent, donor phase conditions, acceptor phase (HCl) concentration, stirring speed, temperature, time and salt addition) of this procedure were investigated and optimized.

The selection of extraction organic solvent is important in HF-LPME technique [36]. The organic solvent should be insoluble in water, have good affinity for the fiber and analytes, and have low volatility to prevent solvent losses during the extraction process [37,38]. In view of these factors, eight organic solvents, i.e., dihexyl ether, nitrobenzene, 1-heptanol, 1-octanol, *n*-heptane, *n*-decane, *n*-tridecane and *n*-hexadecane were tested. Dihexyl ether produced the highest extraction for both ROS and MH (Fig. 5(A)). The selected organic solvent was in agreement with

our previous reports for the HF-LPME extraction of ROS and MH [12,16]. Thus, it was selected for subsequent studies.

The effect of the donor phase conditions (e.g., pH (for vial 1) and NaOH, PFBC volume and concentration (for vial 2)) on the extraction efficiency were investigated. The influence of pH (8.0–10.0) on the extraction of ROS (first vial) was found to increase as the pH is increased from 8.0 to 9.0, but drops abruptly thereafter. The significant drop in enrichment factor as pH is increased is probably due to deprotonation, decomposition and/or precipitation of ROS at high pH [12]. The optimum volume and concentration of NaOH and PFBC for the extraction of MH (vial 2) were 4.0 M NaOH (600 μL) and 10 mg mL^{-1} PFBC (100 μL) and these were in agreement with our previous report [16].

Due to the basic properties for both analytes, acidic acceptor phase is required to ionize them to enhance their solubilities and prevent their back-extraction to the organic phase [12,16]. The effect of HCl concentration (0.025–0.100 M) on the extraction efficiency for ROS and MH was studied. It was observed that the enrichment factor increased as the concentration of HCl increased (Fig. 5(B)). Higher concentration of HCl was avoided in order to prevent the possible corrosion of the injector and other HPLC parts [12]. Therefore, 0.1 M HCl was selected as the optimum acceptor phase for the subsequent experiments.

Table 1
Optimum conditions of the sequential HF-LPME method.

Extraction parameters	ROS (vial 1)	MH (vial 2)
Organic solvent	Dihexyl ether	
Acceptor phase	0.1 M HCl (10 μL)	
Donor phase	pH 9.00	600 μL NaOH (4 M) 100 μL PFBC (10 mg mL^{-1})
Stirring speed	300 rpm	
Extraction temperature	Ambient	70 $^{\circ}\text{C}$
Extraction time (min)	30	30
Salt addition	—	
Enrichment factor	471	86.6

Table 2
Repeatability (%RSD) for ROS and MH after subjected to the sequential HF-LPME-HPLC-UV method ($n=6$).

	%RSD		
	Spiked level (ng mL^{-1})		
	50	500	1000
ROS	4.1	7.3	8.1
MH	7.7	8.4	7.5

Table 3
Recoveries obtained by spiking plasma and urine samples with standard mixture and subjected to sequential HF-LPME-HPLC-UV method ($n=6$).

	ROS			MH		
	C_{added} (ng mL^{-1})	C_{found} (ng mL^{-1})	Recovery (% \pm SD)	C_{added} (ng mL^{-1})	C_{found} (ng mL^{-1})	Recovery (% \pm SD)
Plasma	200	200	100 \pm 4.3	1000	978	97.8 \pm 11
	100	98.1	98.1 \pm 8.5	500	481	96.2 \pm 13
	10	9.96	99.6 \pm 7.5	50	48.5	97.0 \pm 4.5
Urine	200	202	101 \pm 11	1000	941	94.1 \pm 5.0
	100	108	108 \pm 8.3	500	491	98.2 \pm 10
	10	9.91	99.1 \pm 7.3	50	49.1	98.2 \pm 3.5

Agitation of the sample solution increases the mass transfer of the target compounds and reduces the extraction time required to reach thermodynamic equilibrium [36,39]. Therefore, the extraction can be accelerated by stirring the sample solution. Different stirring speeds (200–700 rpm) were tested to determine the optimum stirring speed for the extractions of ROS and MH. The highest enrichment factors (EF) were obtained at stirring speeds of 600 and 300 rpm for ROS and MH, respectively. Further increasing of stirring speed may limit the mass transfer due to the dissolution of the membrane liquid and formation of air bubbles in the donor phase that is attached to the fiber surface, especially when heating is used [40–42]. As there is no significant difference in the EF of ROS over the range 300–600 rpm, 300 rpm was selected.

In order to balance the extraction efficiency of both analytes, the influence of extraction time was examined. The extraction time of each vial was varied from 20 to 35 min, thus total extraction time ranged from 50 to 65 min. It was observed that the extraction efficiency increased as the extraction time increased. Total extraction time of 60 min provided the highest extraction efficiency for both analytes. Longer extraction time was avoided in order to prevent the loss of organic solvent. The extraction of ROS was found to increase as the extraction time increased. 35 min resulted in the highest extraction. However, the longest extraction time for ROS gave the lowest extraction efficiency of MH. Thus, 30 min extraction time was chosen. Similarly, the EF for MH (vial 2) was found to increase as the extraction time was increased up to 30 min, and decreased thereafter. This is probably due to the possible formation of air bubbles on the fiber and evaporation of the organic solvent especially under heating conditions [16]. Therefore, 30 min was used for both analytes.

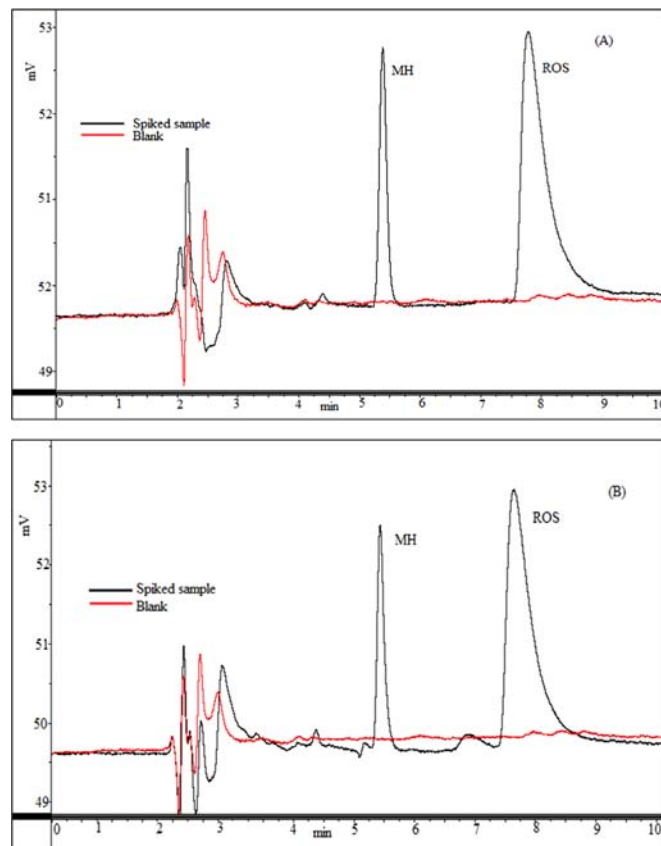


Fig. 6. Typical chromatograms of plasma (A) and urine (B) samples after subjected to the sequential HF-LPME procedure. Spiked concentration; 100 and 500 ng mL^{-1} for ROS and MH, respectively.

It has been reported that the addition of salt to the sample solution will increase the ionic strength of the DP and decrease the solubility of the organic analytes in the aqueous solution [43,44]. In order to investigate the influence of ionic strength on the extraction, experiments were performed by adding different amounts of NaCl (0–15%, w/v) into the sample solutions. As the concentration of NaCl decreased, the extraction efficiencies of the analytes decreased. This is probably due to the increase of the viscosity of the DP solutions which reduce the diffusion rate of the target analytes from DP solutions to the extraction solvent [12]. Therefore, no NaCl was used in this study.

The optimum conditions of the selected sequential HF-LPME procedure for the extraction of ROS and MH are summarized in Table 1. Under these conditions, EFs of 471 and 86.6 were obtained for ROS and MH, respectively. The EF for ROS was higher than those previously reported [11,12] but it was lower for MH.

3.2. Validation of the method

Under the optimized conditions, linearity of the proposed sequential HF-LPME method was investigated over the range 1–500 and 5–2500 ng mL⁻¹ for ROS and MH, respectively. The method was found to be linear over the studied range with regression equations and correlation coefficients (r^2) of $y=1.4772x$ ($r^2=0.998$) and $y=0.029x$ ($r^2=0.999$) for ROS and MH, respectively. The limits of detection (LODs) and quantitation (LOQs) were calculated based on the signal-to-noise ratio (S/N) of 3 and 10, respectively. The LOD was

0.12 and 1.0 ng mL⁻¹, while the LOQ was 0.36 and 3.0 ng mL⁻¹ for ROS and MH, respectively. The obtained LODs and LOQs results were better than the reported methods using LLE with LC-MS/MS, HPLC-FL or HPLC-UV [6,19,27], SPE with LC-MS/MS, HPLC-UV or HPLC-FL [2,14,18], protein precipitation (PP) followed by HPLC-UV, LC-MS/MS or CE-UV [17,24,31], solid-liquid extraction (SLE) with LC-MS/MS [23] and HF-LPME with HPLC-UV or CE-UV [11,12]. However, the results were comparable with the reported method using SPE with LC-MS/MS [4] but higher than the reported in situ HF-LPME with HPLC-UV [16]. The relative standard deviation (%RSD) values for six replicate extractions at three different concentration levels (10, 100, 200 ng mL⁻¹ for ROS and 50, 500, 1000 ng mL⁻¹ for MH) were below 8.4% (Table 2), indicating the good precision of the method.

3.3. Recovery in biological fluid samples

The recovery of the developed method was studied by the determination of ROS and MH in plasma and urine samples that were spiked at three different concentration levels (10, 100, 200 and 50, 500, 1000 ng mL⁻¹ for ROS and MH, respectively). Prior to the sequential HF-LPME step, the spiked samples were subjected to a pre-treatment procedure (Section 2.4) in order to minimize the protein binding of ROS and reduce possible matrix effect [12]. Good recoveries (94.1–108%) were obtained for both analytes (ROS and MH) in plasma and urine samples (Table 3). These results were better than the previous reported recoveries using PP with LC-MS/MS [22,24] CE with ESI-MS [34] or CE-UV [31], SPE

Table 4

Comparison between the proposed sequential HF-LPME-HPLC-UV method with previously reported methods.

Analyte	Instrumentation	Detection	Sample preparation	Type of sample	Linearity (ng mL ⁻¹)	LOD (ng mL ⁻¹)	LOQ (ng mL ⁻¹)	Recovery (%)	Reference
ROS	LC ^a	MS/MS ^b	SPE ^c	Urine	0.1–2000	0.1	0.3	91.2–99.3	4
ROS	HPLC ^d	UV ^e	LLE ^f	Plasma	5–1250	–	5.0	76.0–81.0	6
ROS	HPLC	UV	HF-LPME ^g	Rat liver	50–6000	–	49	63.2–81.3	11
ROS	HPLC	UV	HF-LPME	Urine	1–500	0.18	0.56	83.0–98.0	12
ROS	CE ^h	UV	HF-LPME	Plasma	5–500	2.8	5.0	87.0–105	12
ROS	HPLC	FL ⁱ	SPE	Plasma	1–1000	0.25	1.0	81.0–101	12
ROS	HPLC	FL	LLE	Sheep plasma	2.5–250	–	2.5	84.0–102	18
ROS	LC	MS/MS	SLE ^j	Amniotic fluid	2.5–250	–	2.5	86.6–92.4	19
ROS	LC	MS/MS	SPE	Plasma	1–500	–	1.0	85.4–105	23
MH	LC	MS/MS	PP ^k	Plasma	20–2500	–	20	78.6–80.7	24
MH	LC	MS/MS	SPE	Plasma	10–1000	–	10	69.3–71.2	2
MH	HPLC	UV	SPE	Plasma	50–2000	3.0	5.0	67.0	2
MH	HPLC	UV	In situ HF-LPME	Plasma	1–1000	0.56	1.7	97.9–101	14
MH	HPLC	UV	In situ HF-LPME	Urine	1–1000	0.56	1.7	82.7–99.0	16
MH	LC	MS/MS	LLE	Plasma	10–1500	–	10	97.0–105	16
MH	CE	UV	PP	Plasma	250–3500	100	250	≥91.0	27
ROS	HPLC	UV	PP	Plasma	100–2500	50	100	58.9–80.2	31
MH	HPLC	UV	PP	Plasma	250–2500	100	250	98.2–101	17
ROS	LC	MS/MS	PP	Plasma	1.05–263.5	–	1.1	91.4–97.6	17
MH	LC	MS/MS	PP	Plasma	4.04–5050	–	4.0	80.5–97.9	22
ROS	CE	ESI-MS	PP	Plasma	4–800	4.4	14.6	87.0–93.6	22
MH	CE	ESI-MS	PP	Serum	2–400	2.1	7.1	93.0	34
ROS	HPLC	UV	Sequential HF-LPME	Plasma	1–500	0.12	0.36	85.5	34
MH	HPLC	UV	Sequential HF-LPME	Urine	1–500	0.12	0.36	98.1–100	Present work
MH	HPLC	UV	Sequential HF-LPME	Plasma	5–2500	1.0	3.0	99.1–108	Present work
MH	HPLC	UV	Sequential HF-LPME	Urine	5–2500	1.0	3.0	96.2–97.8	Present work
MH	HPLC	UV	Sequential HF-LPME	Urine	5–2500	1.0	3.0	94.1–98.2	Present work

^a Liquid chromatography.

^b Tandem mass spectrometry.

^c Solid-phase extraction.

^d High performance Liquid Chromatography.

^e Ultraviolet detection.

^f Liquid-liquid extraction.

^g Hollow-fiber liquid phase microextraction.

^h Capillary electrophoresis.

ⁱ Fluorescence detection.

^j Supported liquid extraction.

^k Protein precipitation.

with LC–MS/MS [2], LLE with HPLC–UV or HPLC–FL [6,19] and HF-LPME with LC–UV [11,12,16] or CE–UV [12] but lower or comparable with the reported methods using SPE with LC–MS/MS, HPLC–FL or HPLC–UV [4,14,18]. The data obtained suggest that the proposed sequential HF-LPME procedure could be applied for therapeutic drug monitoring of ROS and MH. Typical chromatograms of the blank samples do not show any interfering peak at the retention time of ROS and MH (Fig. 6(A, B)). A comparison between the proposed sequential HF-LPME with the previously reported method is shown in Table 4.

4. Conclusions

For the first time, a sequential HF-LPME of two drugs with contrasting log *P* values is demonstrated using MH and ROS as model compounds. Microextracts of plasma and urine samples were finally simultaneously determined using HPLC–UV. The developed method has various benefits such as simple, sensitive, low consumption of organic solvents, cost-effective, and exhibit excellent repeatability. In addition, good enrichment factors of 86.6 and 471 for MH and ROS, respectively, were achieved. The method was validated, can be used in therapeutic drug monitoring of patients undergoing treatment using a combination therapy of ROS and MH. The sequential HF-LPME approach can be extended for the extraction of analytes with different properties that require contrasting extraction conditions.

Acknowledgments

Financial support of the work by Universiti Sains Malaysia via Research University Grant (1001/PKIMIA/811201) and postdoctoral fellowship scheme to Ahmad Makahleh are gratefully acknowledged. One of us (Gazala Ben-Hander) thanked the Government of Libya for providing a postgraduate scholarship.

References

- [1] C. Yardimci, N. Özaltın, *Anal. Chim. Acta* 549 (2005) 88–95.
- [2] N. Koseki, H. Kawashita, M. Niina, Y. Nagae, N. Masuda, *J. Pharm. Biomed. Anal.* 36 (2005) 1063–1072.
- [3] M.A.S. Marques, A.D.S. Soares, O.W. Pinto, P.T.W. Barroso, D.P. Pinto, M. Ferreira-Filho, E. Werneck-Barroso, *J. Chromatogr. B* 852 (2007) 308–316.
- [4] C.-C. Chou, M.-R. Lee, F.-C. Cheng, D.-Y. Yang, *J. Chromatogr. A* 1097 (2005) 74–83.
- [5] P. Gomes, J. Sippel, A. Jablonski, M. Steppe, *J. Pharm. Biomed. Anal.* 36 (2004) 909–913.
- [6] B.L. Kolte, B.B. Raut, A.A. Deo, M.A. Bagoool, D.B. Shinde, *J. Chromatogr. B* 788 (2003) 37–44.
- [7] A.-M. Muxlow, S. Fowles, P. Russell, *J. Chromatogr. B* 752 (2001) 77–84.
- [8] C. Yardimci, N. Özaltın, *Chromatographia* 66 (2007) 589–593.
- [9] S. Aburuz, J. Millership, J. McInay, *J. Chromatogr. B* 817 (2005) 277–286.
- [10] J.N. Jingar, S.J. Rajput, B. Dasandi, S. Rathnam, *Chromatographia* 67 (2008) 951–955.
- [11] L.A. Calixto, P.S. Bonato, *J. Sep. Sci.* 33 (2010) 2872–2880.
- [12] K.M. Al Azzam, A. Makahleh, B. Saad, S.M. Mansor, *J. Chromatogr. A* 1217 (2010) 3654–3659.
- [13] K. Tahara, A. Yonemoto, Y. Yoshiyama, T. Nakamura, M. Aizawa, Y. Fujita, T. Nishikawa, *Biomed. Chromatogr.* 20 (2006) 1200–1205.
- [14] S. Aburuz, J. Millership, J. McInay, *J. Chromatogr. B* 798 (2003) 203–209.
- [15] B.L. Kolte, B.B. Raut, A.A. Deo, M.A. Bagoool, D.B. Shinde, *J. Chromatogr. Sci.* 42 (2004) 70–73.
- [16] G.M. Ben-Hander, A. Makahleh, B. Saad, M.I. Saleh, *J. Chromatogr. B* 941 (2013) 123–130.
- [17] C. Yardimci, N. Özaltın, A. Gürlek, *Talanta* 72 (2007) 1416–1422.
- [18] R.S. Pedersen, K. Brøsen, F. Nielsen, *Chromatographia* 62 (2005) 197–201.
- [19] M. Bazargan, A.K. Davey, B.S. Muhlhauser, J.L. Morrison, I.C. Mcmillen, D.J. R. Foster, *J. Pharm. Biomed. Anal.* 55 (2011) 360–365.
- [20] J. He, Y.F. Hu, L.F. Duan, Z.R. Tan, L.S. Wang, D. Wang, W. Zhang, Z. Li, J. Liu, J. H. Tu, Y.M. Yao, H.-H. Zhou, *J. Pharm. Biomed. Anal.* 43 (2007) 580–585.
- [21] L. Zhang, Y. Tian, Z. Zhang, Y. Chen, *J. Chromatogr. B* 854 (2007) 91–98.
- [22] L. Chen, Z. Zhou, M. Shen, A. Ma, *J. Chromatogr. Sci.* 49 (2011) 94–100.
- [23] G. O'maille, S.M. Pai, X. Tao, G.T. Douglas Jr., R.G. Jenkins, *J. Pharm. Biomed. Anal.* 48 (2008) 934–939.
- [24] H.N. Mistri, A.G. Jangid, P.S. Shrivastav, *J. Pharm. Biomed. Anal.* 45 (2007) 97–106.
- [25] W. Zhang, F. Han, H. Zhao, Z.J. Lin, Q.M. Huang, N. Weng, *Biomed. Chromatogr.* 26 (2012) 1163–1169.
- [26] C.-G. Ding, Z. Zhou, Q.-H. Ge, X.-J. Zhi, L.-L. Ma, *Biomed. Chromatogr.* 21 (2007) 132–138.
- [27] P. Sengupta, U. Bhaumik, A. Ghosh, A.K. Sarkar, B. Chatterjee, A. Bose, T.K. Pal, *Chromatographia* 69 (2009) 1243–1250.
- [28] J. Brohon, M. Noël, *J. Chromatogr.* 146 (1978) 148–151.
- [29] S.A. Majidano, M.Y. Khuhawar, *Chromatographia* 75 (2012) 1311–1317.
- [30] E. Uçaktürk, *Anal. Methods* 5 (2013) 4723–4730.
- [31] J.-Z. Song, H.-F. Chen, S.-J. Tian, Z.-P. Sun, *J. Chromatogr. B* 708 (1998) 277–283.
- [32] I.I. Hamdan, A.K.B. Jaber, A.M. Abushoffa, *J. Pharm. Biomed. Anal.* 53 (2010) 1254–1257.
- [33] E.P.C. Lai, S.Y. Feng, *J. Chromatogr. B* 843 (2006) 94–99.
- [34] J. Znalezniona, V. Maier, V. Ranc, J. Ševčík, *J. Sep. Sci.* 34 (2011) 1167–1173.
- [35] J. McMurry, *Organic Chemistry*, 6th ed., Thomson Learning Academic Resource Center, United States, 2004.
- [36] M. Mirzaei, H. Dinpanah, *J. Chromatogr. B* 879 (2011) 1870–1874.
- [37] J. Wang, Z. Du, W. Yu, S. Qu, *J. Chromatogr. A* 1247 (2012) 10–17.
- [38] H. Zhang, Z. Du, Y. Ji, M. Mei, *Talanta* 109 (2013) 177–184.
- [39] J. Zhou, P. Zeng, J.B. Sun, F.Q. Wang, Q. Zhang, *J. Pharm. Biomed. Anal.* 81–82 (2013) 27–33.
- [40] M. Hyder, J.A. Jönsson, *J. Chromatogr. A* 1249 (2012) 48–53.
- [41] L. Chimuka, T.A.M. Msagati, E. Cukrowska, H. Tutu, *J. Chromatogr. A* 1217 (2010) 2318–2325.
- [42] W. Liu, L. Zhang, L. Fan, Z. Lin, Y. Cai, Z. Wei, G. Chen, *J. Chromatogr. A* 1233 (2012) 1–7.
- [43] I.S. Román, M.L. Alonso, L. Bartolomé, R.M. Alonso, *Talanta* 100 (2012) 246–253.
- [44] S.-P. Huang, S.-D. Huang, *J. Chromatogr. A* 1135 (2006) 6–11.



Ratiometric fluorescence detection of fluoride ion by indole-based receptor



Xiu-Ming Liu, Ya-Ping Li, Ying-Hui Zhang, Qiang Zhao, Wei-Chao Song, Jian Xu^{1,*}, Xian-He Bu

Department of Chemistry and TKL of Metal- and Molecule-Based Material Chemistry, Key Laboratory of Advanced Energy Materials Chemistry (Ministry of Education) and Collaborative Innovation Center of Chemical Science and Engineering (Tianjin), Nankai University, Tianjin 300071, China

ARTICLE INFO

Article history:

Received 17 April 2014
Received in revised form
31 July 2014
Accepted 6 August 2014
Available online 19 August 2014

Keywords:

Anions
Cations
Fluoride recognition
Ratiometric fluorescence
Colorimetric sensing

ABSTRACT

A novel artificial receptor **1** containing the indolocarbazole-NH moieties as the recognition sites exhibited high selectivity and sensitivity toward F^- over other typical anionic species in DMSO solution. Upon addition of F^- into the solution, receptor **1** showed a remarkable ratiometric shift of the fluorescence maximum from 535 to 590 nm, and also a prominent color change from light yellow to orange, which was observable by the naked eye. The recognition properties of receptor **1** were investigated by 1H NMR, UV-vis, and fluorescence titration experiments, with the results suggesting a two-step strategy of binding with F^- . In addition, the theoretical calculations were carried out to reveal the role of intramolecular charge transfer in the ratiometric fluorescence recognition process.

© 2014 Elsevier B.V. All rights reserved.

1. Introduction

Selective recognition and sensing of anionic species via artificial receptors have recently emerged as an important multidisciplinary research field across biology, chemistry, and environment science [1–6], considering the vital roles of anions in our daily life. Among various anions, fluoride ion (F^-), one of the most important nucleophilic anions, is of particular interest owing to its extensive application in dental health and clinical treatment for osteoporosis [7–11]. On the other hand, excess intake of F^- may cause many diseases due to its toxicity, such like gastric and kidney disorders, dental and skeletal fluorosis, urolithiasis, or even death [12–15]. Therefore, there is a significant requirement to develop novel artificial receptors with high selectivity and sensitivity toward fluoride anions.

To date, a diverse array of artificial receptors for detecting F^- have been reported [16–22], and most of them operate based on the measurement of fluorescence at a single wavelength, which is closely related to the photoinduced electron transfer (PET) in the complexation of receptors with anionic guests [23,24]. With the guest-induced “off-on” or “on-off” fluorescence indicating,

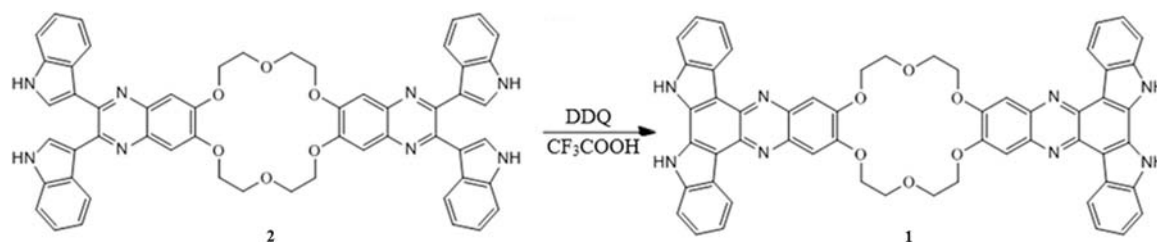
(i.e., the detectable fluorescence enhancement or quenching), such PET signaling systems demonstrate the natural “all or none” switch ability in the recognition of anion guests. However, the PET process can be of either intra- or intermolecular origin and inevitably suffers from the environmental influence, leading to some difficulty in signal rationing. On the other hand, the selective and sensitive sensing of anions could be alternatively achieved in a ratiometric manner by monitoring the changes in the ratio of the fluorescence intensities at two different wavelengths, thus providing a built-in correction for environmental effects and increasing the dynamic range of emission measurements [25–27]. Moreover, the ratiometric fluorescence measurement of analyte concentration can be rationalized by the intramolecular charge transfer (ICT) mechanism [28–30]. In view of aforementioned advantages, the development in the design and synthesis of the ratiometric fluorescent receptors with high affinity and selectivity for F^- has been actively pursued by chemists in recent years.

Herein, we report a new colorimetric and ratiometric fluorescent receptor **1** containing the indolocarbazole-NH moieties as the recognition sites, in line with our previously reported strategy [31]. Following a two-step anion binding strategy, receptor **1** exhibits a high sensing selectivity and sensitivity for F^- over other common anions, highlighted by a large ratiometric emission shift by about 55 nm and also a prominent color change visible to the naked eye. To further investigate the recognition properties of receptor **1**, the 1H NMR, UV-vis, and fluorescence titration studies

* Corresponding author. Fax: +86 22 23502458.

E-mail address: jxu@nankai.edu.cn (J. Xu).

¹ Present address: Nankai University, Tianjin 300071, China.



Scheme 1. The procedure for the synthesis of **1**.

are carried out, together with relevant theoretical calculations to reveal the role of ICT in spectroscopic recognition of fluoride anions (Scheme 1).

2. Experimental

2.1. Apparatus and reagents

All the starting materials for synthesis were purchased from Alfa Aesar and used as received. The solvents used for titration measurements were purified by standard procedures. In the titration experiments, all the anions were added in the form of tetrabutylammonium (TBA) salts, which were purchased from Alfa Aesar and Aladdin, stored in a vacuum desiccator containing self-indicating silica and dried fully before using. DMSO was dried with CaH₂ and then distilled in reduced pressure. Structural characterizations of [D₆]DMSO at 25 °C were carried out with Varian Unity Plus 400 MHz NMR spectrometer (Varian, USA). High resolution mass spectra (HRMS) were determined on an IonSpec 7.0T FT-ICR mass spectrometer (IonSpec, USA). UV–vis absorption spectra were measured with a Hitachi U-3010 UV–vis spectrophotometer (Hitachi, Japan). Fluorescence spectra were recorded at room temperature on a Varian Cary Eclipse fluorescence spectrometer (Varian, USA).

2.2. Synthesis of receptor **1**

The receptor **1** was prepared by the condensation of 2,3,15,16-tetra(1*H*-indol-3-yl)-7,8,10,11,20,21,23,24 -octahydro-[1,4,7,10,13,16]hexaoxacyclooctadecino[2,3-*g*:11,12-*g'*]diquinoxaline (**2**) [32] (100 mg, 0.11 mmol) and DDQ (96 mg, 0.35 mmol), which were dissolved in neat trifluoroacetic acid (12 mL) and heated under reflux for 4 h. Then, the trifluoroacetic acid was removed by vacuum distillation, followed by repeated wash with saturated aqueous NaHCO₃ and dried in vacuo to afford pure **1** as black solid (91 mg, about 90%) that is air stable and soluble in DMSO.

Receptor **1**

Black solid (90%). IR (KBr) ν 3160, 2367, 2171, 1621, 1491, 1470, 1435, 1331, 1281 cm⁻¹. ¹H NMR (DMSO-*d*₆, TMS, 400MHz) δ 4.10 (s, 4H), 4.52 (s, 4H), 7.54 – 7.37 (m, 4H), 7.74 (s, 4H), 7.88 (d, *J* = 8.2 Hz, 4H), 9.14 (d, *J* = 6.9 Hz, 4H), 11.88 (s, 4H). ESI-MS *m/z*(%): 921.6 [M+H]⁺, 943.7 [M+Na]⁺. HRMS: (ESI) *m/z*(%) for C₅₆H₄₀N₈O₆; calcd 920.3671; found 943.2968 [M+Na]⁺.

3. Results and discussion

3.1. Anion sensing

The selective recognition properties of receptor **1** were first investigated by monitoring the naked-eye visible color changes, induced by the addition of 20 equiv of different anions

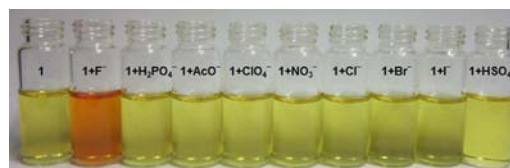


Fig. 1. Color changes induced by the addition of respective anions (20 equiv) to a DMSO solution of **1**. [**1**] = 5×10^{-5} M. (For interpretation of the references to color in this figure legend, the reader is referred to the web version of this article.)

(F⁻, H₂PO₄⁻, AcO⁻, ClO₄⁻, NO₃⁻, Cl⁻, Br⁻, I⁻ and HSO₄⁻) to the DMSO solution of **1**. As Fig. 1 demonstrates, only the addition of F⁻ caused a prominent color change from light yellow to orange, indicating the colorimetric selectivity of receptor **1** toward F⁻ over other anions.

Further investigations on the interaction of receptor **1** with anions were performed by using UV–vis absorption and fluorescence emission spectroscopy. As illustrated by Fig. 2a, a considerable UV–vis red shift appeared at 500 nm after addition of 50 equiv of F⁻ to the DMSO solution of **1**. For comparison, the addition of either H₂PO₄⁻ or AcO⁻ resulted in only a very minor shift toward lower energy in the absorption spectrum, while that of the other anions (i.e., ClO₄⁻, NO₃⁻, Cl⁻, Br⁻, I⁻ and HSO₄⁻) seemed to cause no change at all. A very similar situation also occurred in the emission spectra of receptor **1**. As illustrated by Fig. 2b, the addition of F⁻ caused a more significant fluorescence red shift (~55 nm) as compared to that induced by the presence of H₂PO₄⁻ or AcO⁻ (~20 nm), while the emission spectrum upon the addition of other anions almost remained unchanged. These results suggest that receptor **1** has an excellent ratiometric sensing selectivity to F⁻, which may arise from the fact that F⁻ is of stronger basicity than H₂PO₄⁻ and AcO⁻, and the latter two are insufficient to induce the complete deprotonation of receptor **1**.

3.1.1. UV–vis and fluorescence titration studies of **1** with F⁻

To assess the ratiometric fluorescence sensing ability of receptor **1** toward F⁻, we further studied the spectral changes upon the addition of F⁻ with increasing concentrations, ranging from 0 to 68 equiv. As depicted in Fig. 3a, the concentration increase of F⁻ led to a dramatic decrease in the intensity of absorption band at 433 nm, while in opposite, the intensity of the band centered at 344 nm moderately increased upon titration of F⁻, along with the appearance of a new band at around 500 nm. The presence of two sharp isosbestic points at 375 and 455 nm implies that only two chemical species coexist at the equilibrium throughout the titration process, in accompany with an obvious color change from light yellow to orange.

Upon excitation at 430 nm, the emission spectrum of receptor **1** exhibited the remarkable changes in response to the variation in the concentration of F⁻, illustrated by a large ratiometric shift of the fluorescence maximum from 535 to 590 nm, as shown in Fig. 3b. While the characteristic fluorescence at 535 nm was significantly

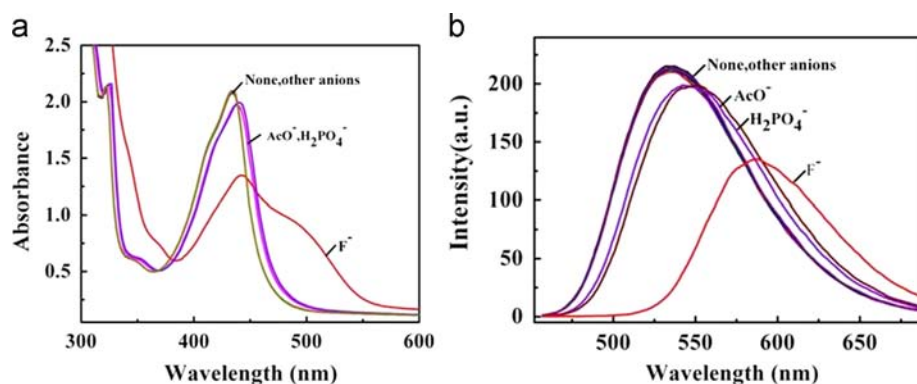


Fig. 2. (a) The changes in UV–vis spectra of receptor **1** measured in DMSO upon addition of 50 equiv of respective anions (as a $n\text{-bu}_4\text{N}^+$ salt). Other anions are H_2PO_4^- , AcO^- , ClO_4^- , NO_3^- , Cl^- , Br^- , I^- and HSO_4^- . $[\mathbf{1}] = 3 \times 10^{-5}$ M. (b) Changes in fluorescence ($\lambda_{\text{ex}} = 430$ nm) spectra of **1** measured in DMSO upon addition of 50 equiv of respective anions (as a $n\text{-bu}_4\text{N}^+$ salt). Other anions are ClO_4^- , NO_3^- , Cl^- , Br^- , I^- and HSO_4^- . $[\mathbf{1}] = 5 \times 10^{-5}$ M.

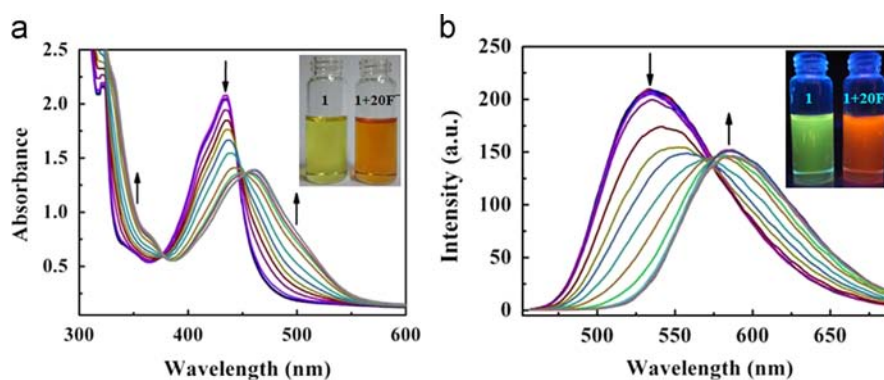


Fig. 3. (a) The changes in UV–vis spectra of receptor **1** after addition of F^- (as a $n\text{-bu}_4\text{N}^+$ salt) in DMSO (equiv. F^- from 0 to 68). $[\mathbf{1}] = 3 \times 10^{-5}$ M. Inset: color changes of the receptor **1** solution on the addition of F^- . (b) Fluorescence ($\lambda_{\text{ex}} = 430$ nm) titration of **1** with F^- (as a $n\text{-bu}_4\text{N}^+$ salt) in DMSO (equiv. F^- from 0 to 68). Inset: fluorescence emission color changes of the receptor **1** solution on the addition of F^- . $[\mathbf{1}] = 5 \times 10^{-5}$ M. (For interpretation of the references to color in this figure legend, the reader is referred to the web version of this article.)

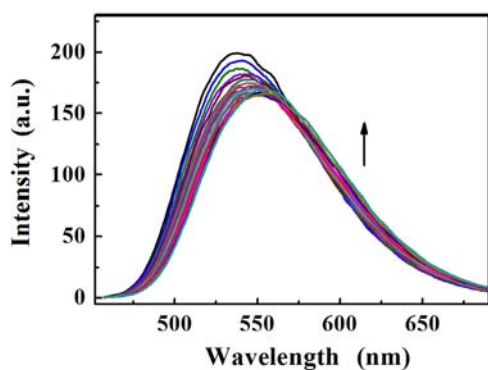


Fig. 4. Fluorescence ($\lambda_{\text{ex}} = 430$ nm) titration of **1** with F^- (as a $n\text{-bu}_4\text{N}^+$ salt, from 0 to 360 equiv F^-) in DMSO/ H_2O (95:5). $[\mathbf{1}] = 5 \times 10^{-5}$ M.

reduced upon titration of F^- , a new emission band gradually appeared at 590 nm, thus giving rise to a clear iso-emission point at 575 nm. Such ratiometric fluorescence shift reached a saturation level after the addition of 68 equiv of F^- . From the experimental data, we suggest that the spectral changes upon titration of F^- are probably due to the deprotonation of NH-indole and formation of FHF^- ion. Thereby, increasing the negative charge density at indole nitrogen would significantly enhance the extent of ICT from indole to phenyl rings, as reported in previous research [33,34].

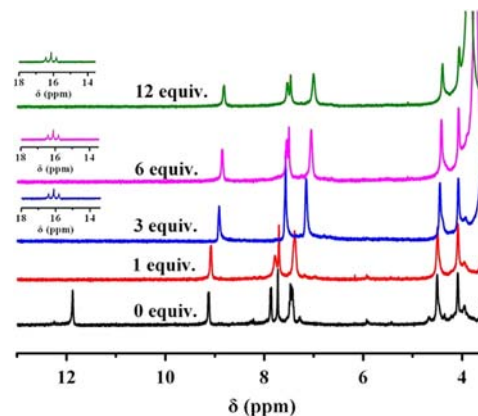


Fig. 5. ^1H NMR (400 MHz) spectra of receptor **1** (5.0×10^{-3} M) in $[\text{D}_6]\text{DMSO}$ with addition of TBAF.

Besides, we also concerned about the fluoride recognition characteristic and sensing sensitivity of receptor **1** in aqueous medium. To this end, we further examined the fluoride binding properties of receptor **1** in the reaction system containing up to 5% (v/v) water. Fig. 4 shows the ratiometric fluorescence changes upon the addition of 360 equiv of fluoride to the solution of receptor **1**. This result indicates that receptor **1** cannot exhibit sensitive fluorescent recognition of F^- in such aqueous medium, which might be due to the fact

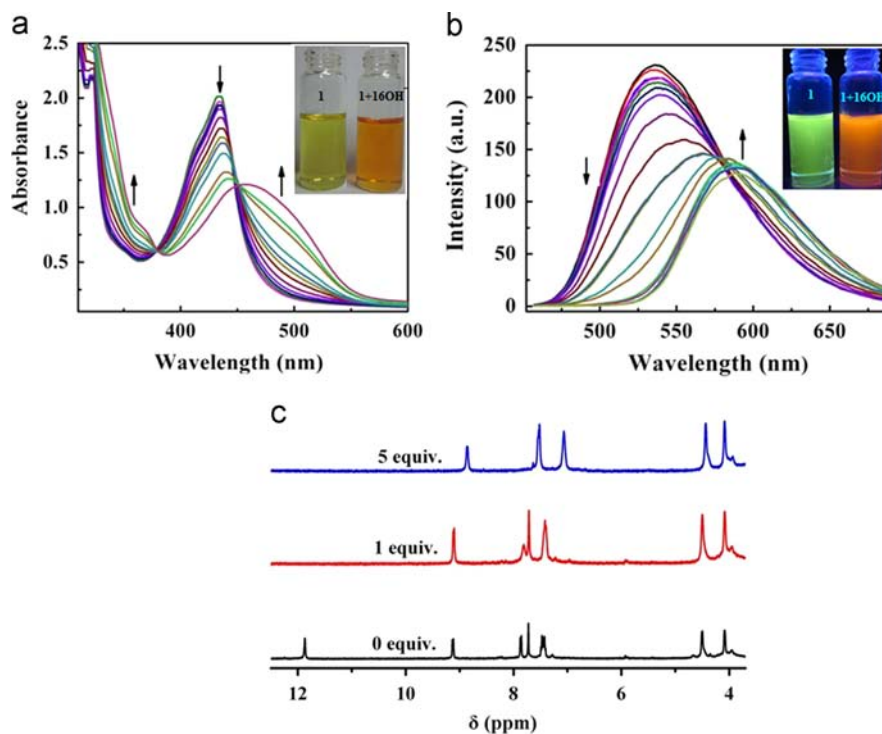


Fig. 6. (a) The changes in UV-vis spectra of receptor **1** after addition of OH^- (as a $n\text{-bu}_4\text{N}^+$ salt) in DMSO (equiv. OH^- from 0 to 46). $[\mathbf{1}] = 3 \times 10^{-5}$ M. Inset: color changes of the receptor **1** solution on the addition of OH^- (equiv. OH^- from 0 to 68). (b) Fluorescence ($\lambda_{\text{ex}} = 430$ nm) titration of **1** with OH^- (as an $n\text{-bu}_4\text{N}^+$ salt) in DMSO (equiv. OH^- from 0 to 68). Inset: fluorescence emission color changes of the receptor **1** solution on the addition of OH^- (equiv. OH^- from 0 to 16). $[\mathbf{1}] = 5 \times 10^{-5}$ M. (c) ^1H NMR (400 MHz) spectra of receptor **1** (5.0×10^{-3} M) in $[\text{D}_6]\text{DMSO}$ with addition of TBAOH. (For interpretation of the references to color in this figure legend, the reader is referred to the web version of this article.)

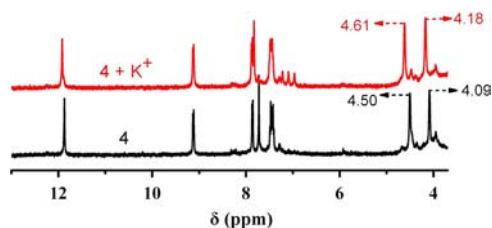


Fig. 7. ^1H NMR (400 MHz) spectra of receptor **1** (5.0×10^{-3} M) in $[\text{D}_6]\text{DMSO}$ with addition of KClO_4 .

that the presence of water or other protic solvents could influence the hydrogen bond between fluoride and the indole NH subunits of receptor **1**.

3.1.2. ^1H NMR titration studies of **1** with F^-

In order to identify the binding mode of receptor **1** to F^- , ^1H NMR titration studies were carried out with progressive addition of F^- to the DMSO solution of **1** at 25°C . As shown in Fig. 5, the NMR resonance at chemical shift of $\delta = 11.88$ ppm assigned to the indole-NH proton disappeared in the presence of 1 equiv of F^- , while that belonging to the FHF^- ion first appeared at $\delta = 16.11$ ppm when 3 equiv of F^- was titrated into the solution. This finding indicates that the deprotonation of NH fragment would increase the electron density around the phenyl rings primarily via a through-bond mechanism. Proceeding with further addition of F^- , both the indole $\alpha\text{-C-H}$ and Ar-H protons then underwent the significant downfield shifts. Therefore, it is reasonable to suggest that the combination of F^- with receptor **1** follows a two-step strategy: (1) the formation of a hydrogen bond

between ...F and the indole NH subunits of **1**; (2) the deprotonation of NH fragment. To confirm that, we also performed the analogous NMR titration experiments with strong bases (TBAOH), and the resulting titration curves, shown in Fig. 6, largely resembled those from the titration of F^- (see Fig. 5).

3.2. Cation sensing

The cation binding properties of receptor **1** were also studied by using both ^1H NMR and fluorescence spectroscopic titration methods in $[\text{D}_6]\text{DMSO}$ solution. Fig. 7 shows that the addition of 15 equiv of K^+ caused small downfield shifts of protons on the bis-benzocrown, suggesting the K^+ cation is bound to the crown ether moiety. Furthermore, the fluorescence spectroscopic titration study for the interaction of **1** with K^+ or Na^+ suggests 1:1 complex stoichiometry, inferred by the nonlinear regression of the resulting titration curves given in Fig. 8. For reference, the experimental stability constants are listed in Table 1.

3.3. Theoretical calculations

According to the experimental results, the crown ether subunit of **1** acts only as a linker through the whole recognition process. Therefore, theoretical evaluation on the effects of hydrogen bonds may be carried out with two reduced structures for **1** and $\mathbf{1}^{2-}$, respectively, as we depicted in Fig. 9. Our density functional theory calculations were implemented using B3LYP/6-31G(d) method [35] in Gaussian 09 program package [36]. From the calculated frontier orbital levels (see Table 2), the HOMO-LUMO energy gap (Δ) significantly decreases from **1** (0.12120) to $\mathbf{1}^{2-}$ (0.10137), which can be well reflected by the simulated UV-vis spectrum in Fig. 10. In a sense it can be considered as a qualitative indication

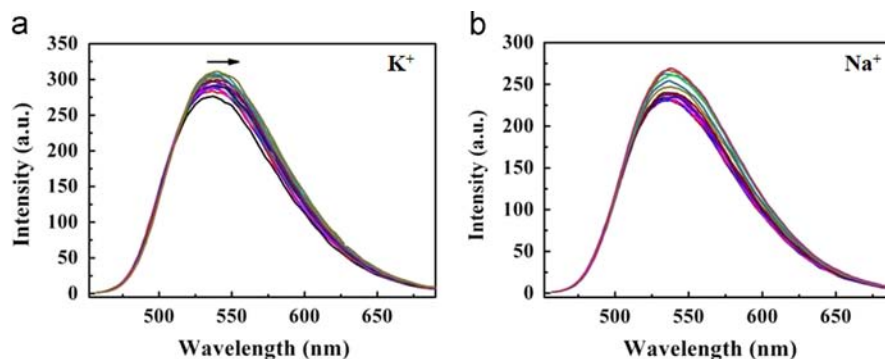


Fig. 8. (a) Fluorescence ($\lambda_{\text{ex}}=430$ nm) titration of **1** with K^+ in DMSO (equiv. K^+ from 0 to 750). (b) Fluorescence ($\lambda_{\text{ex}}=430$ nm) titration of **1** with Na^+ in DMSO (equiv. Na^+ from 0 to 750) [**1**] $=5 \times 10^{-5}$ M.

Table 1
Binding constants of receptor **1** with K^+ and Na^+ in DMSO mixture^a.

Receptor	log K_x with cations	
	K^+	Na^+
1	3.03	3.22

^a Determined in Dry DMSO at 25 °C by the fluorescent titration at 535 nm, errors estimated to be < 10%. Cations were added as their KClO_4 , NaClO_4 .

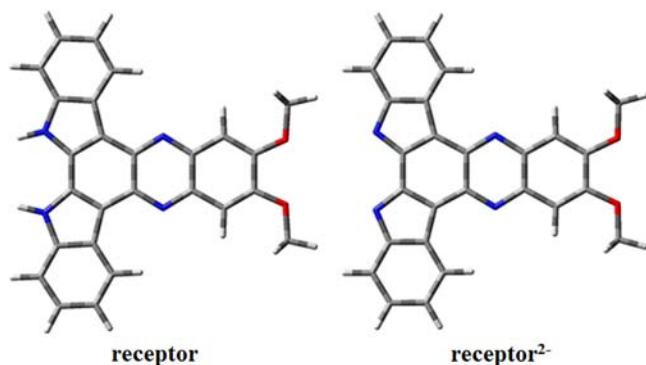


Fig. 9. The optimized structures in the simulation of electronic absorption spectrum.

Table 2
The frontier orbit levels of receptor and receptor²⁻ complexes (in Hartree).

Complex	HOMO-1	HOMO	LUMO	LUMO+1	$\Delta=LUMO-HOMO$
Receptor	-0.19163	-0.18480	-0.06360	-0.01967	0.12120
Receptor ²⁻	0.05719	0.06350	0.16487	0.21136	0.10137

of the spectral red shift observed in experimental fluorescence spectrum. In light of the aforementioned, our theoretical calculation results then strongly support the proposed ICT in the ratiometric recognition of fluoride anions.

4. Conclusion

We have successfully synthesized a novel artificial receptor **1**, which contains the indolocarbazole-NH moieties as the recognition sites and exhibits highly sensitive colorimetric and ratiometric

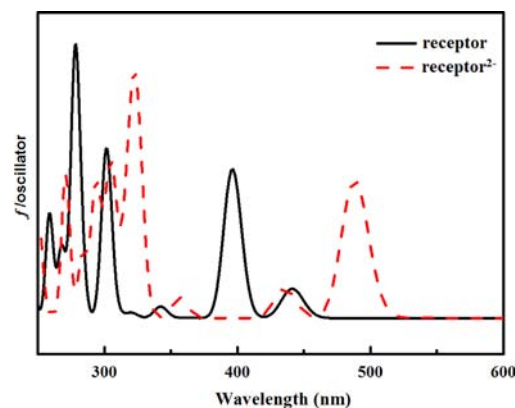


Fig. 10. UV-vis spectra of receptor (black curves) and receptor²⁻ (red curves) calculated by using B3LYP functional in Gaussian 09 program package. (For interpretation of the references to color in this figure legend, the reader is referred to the web version of this article.)

fluorescence response to F^- selectively over other common anions in DMSO solution. In addition to the spectroscopic titration studies for the interactions of receptor **1** with different anions and cations, the theoretical investigation based on density functional theory has been also performed to explore the ratiometric fluorescence recognition process in terms of the ICT mechanism.

Acknowledgements

We thank the financial supports from the National Science Foundation of China (21031002, 21403116, and 51073079) and the China Postdoctoral Science Foundation (2012M520570).

References

- [1] S. Hussain, P.R. Brotherhood, L.W. Judd, A.P. Davis, *J. Am. Chem. Soc.* 133 (2011) 614–1617.
- [2] S.-I. Kondo, Y. Bie, M. Yamamura, *Org. Lett.* 15 (2013) 520–523.
- [3] S.O. Kang, J.M. Llinares, V.W. Day, K. Bowman-James, *Chem. Soc. Rev.* 39 (2010) 3980–4003.
- [4] Z.H. Lin, S.J. Ou, C.Y. Duan, B.G. Zhang, Z.P. Bai, *Chem. Commun.* (2006) 624–626.
- [5] H.Y. Li, R.A. Lalancette, F. Jäkle, *Chem. Commun.* (2011) 9378–9380.
- [6] N.R. Chereddy, S. Thennarasu, A.B. Mandal, *Analyst* 138 (2013) 1334–1337.
- [7] H. Miyaji, W. Sato, J.L. Sessler, *Angew. Chem. Int. Ed.* 39 (2000) 1777–1780.
- [8] P.A. Gale, S.E. García-Garrido, J. Garric, *Chem. Soc. Rev.* 37 (2008) 151–190.
- [9] S.K. Kim, J.L. Sessler, *Chem. Soc. Rev.* 39 (2010) 3784–3809.
- [10] T.W. Hudnall, F.P. Gabbaï, *J. Am. Chem. Soc.* 129 (2007) 11978–11986.
- [11] J. Aaseth, M. Shimshi, J.L. Gabrilove, G.S. Birketvedt, *Trace Elem. Exp. Med* 17 (2004) 83–92.
- [12] S. Jagtap, M.K. Yenkie, N. Labhsetwar, S. Rayalu, *Chem. Rev.* 112 (2012) 2454–2466.
- [13] J. Ren, Z. Wu, Y. Zhou, Y. Li, Z.X. Xu, *Dyes Pigm.* 91 (2011) 442–445.

- [14] J.M. You, H. Jeong, H. Seo, S. Jeon, *Sens. Actuators, B* 146 (2010) 160–164.
- [15] K.L. Kirk, *Biochemistry of the Halogens and Inorganic Halides*, Plenum Press, New York, NY (1991) 58.
- [16] Y. Wang, H.R. Li, Y. Feng, H.J. Zhang, G. Calzaferri, T.Z. Ren, *Angew. Chem. Int. Ed.* 49 (2010) 1434–1438.
- [17] L.N. Wang, W.W. Qin, X.L. Tang, W. Dou, W.S. Liu, *J. Phys. Chem. A* 115 (2011) 1609–1616.
- [18] S. Avoob, A.K. Gupta, *Crit. Rev. Environ. Sci. Technol.* 36 (2006) 433–487.
- [19] A. Millick, T. Katayama, Y. Ishibasi, M. Yasuda, H. Miyasaka, *Analyst* 136 (2011) 275–277.
- [20] B.C. Zhu, F. Yuan, R.X. Li, Y.M. Li, Q. Wei, Z.M. Ma, B. Du, X.L. Zhang, *Chem. Commun.* 47 (2011) 7098–7100.
- [21] N. Kumari, S. Jha, S. Bhattacharya, *J. Org. Chem.* 76 (2011) 8215–8222.
- [22] M. Dong, Y. Peng, Y.M. Dong, N. Tang, Y.W. Wang, *Org. Lett.* 14 (2012) 130–133.
- [23] V. Thiagarajan, P. Ramamurthy, D. Thirumalai, V.T. Ramakrishnan, *Org. Lett.* 7 (2005) 657–660.
- [24] H.X. Wang, D.L. Wang, Q. Wang, X.Y. Li, C.A. Schalley, *Org. Biomol. Chem.* 8 (2010) 1017–1026.
- [25] J.L. Fan, P. Zhan, M.M. Hu, W. Sun, J.Z. Tang, J.Y. Wang, S.G. Sun, F.L. Song, X.J. Peng, *Org. Lett.* 15 (2013) 492–495.
- [26] G.P. Li, D.J. Zhu, Q. Liu, L. Xue, H. Jiang, *Org. Lett.* 15 (2013) 924–927.
- [27] L.Z. Gai, H.C. Chen, B. Zou, H. LU, G.Q. Lai, Z.F. Li, Z. Shen, *Chem. Commun.* 48 (2012) 10721–10723.
- [28] X.H. Zhang, Q. Zhao, X.M. Liu, T.L. Hu, J. Han, W.J. Ruan, X.H. Bu, *Talanta* 108 (2013) 150–156.
- [29] Q. Zhao, R.F. Li, S.K. Xing, X.M. Liu, T.L. Hu, X.H. Bu, *Inorg. Chem.* 50 (2011) 10041–10046.
- [30] Y.P. Li, H.R. Yang, Q. Zhao, W.C. Song, J. Han, X.H. Bu, *Inorg. Chem.* 51 (2012) 9642–9648.
- [31] X.M. Liu, Q. Zhao, W.C. Song, X.H. Bu, *Chem. Eur. J* 18 (2012) 2806–2811.
- [32] X.M. Liu, Y.P. Li, W.C. Song, Q. Zhao, X.H. Bu, *Talanta* 97 (2012) 111–117.
- [33] Z.M. Hudson, X.Y. Liu, S. Wang, *Org. Lett.* 13 (2011) 300–303.
- [34] F. Han, Y.H. Bao, Z.G. Yang, T.M. Fyles, J.Z. Zhao, X.J. Peng, J.L. Fan, Y.K. Wu, S.G. Sun, *Chem. Eur. J* 13 (2007) 2880–2892.
- [35] A.D. Becke, *J. Chem. Phys.* 98 (1993) 5648–5652.
- [36] (Gaussian 09, Revision D.01) M.J. Frisch, G.W. Trucks, H. B... J.V. Ortiz, J. Cioslowski, D.J. Fox, Gaussian, Inc., Wallingford CT, 2009.



Dispersive solvent-free ultrasound-assisted ionic liquid dispersive liquid–liquid microextraction coupled with HPLC for determination of ulipristal acetate



Aiqin Gong^{a,b}, Xiashi Zhu^{a,*}

^a College of Chemistry & Chemical Engineering, Yangzhou University, Yangzhou 225002, China

^b Yangzhou Polytechnic Institute, Yangzhou 225127, China

ARTICLE INFO

Article history:

Received 20 June 2014

Received in revised form

30 July 2014

Accepted 6 August 2014

Available online 23 August 2014

Keywords:

Ulipristal acetate

Ionic liquid

Liquid–liquid microextraction

HPLC

ABSTRACT

In this paper, a simple and efficient ultrasound-assisted ionic liquid dispersive liquid–liquid microextraction (UA IL-DLLME) coupled with high-performance liquid chromatography for the analysis of ulipristal acetate (UPA) was developed. UPA could be easily migrated into 1-octyl-3-methylimidazolium hexafluorophosphate [C_8mimPF_6] IL phase without dispersive solvent. The research of extraction mechanism showed that hydrophobic interaction force played a key role in the IL-DLLME. Several important parameters affecting the extraction recovery were optimized. Under the optimized conditions, 25-fold enrichment factor was obtained and the limit of detection (LOD) was 6.8 ng mL^{-1} (tablet) or 9.3 ng mL^{-1} (serum) at a signal-to-noise ratio of 3. The calibration curve was linear over the range of $0.03\text{--}6.0 \text{ } \mu\text{g mL}^{-1}$. The proposed method was successfully applied to the UPA tablets and the real mice serum samples.

© 2014 Elsevier B.V. All rights reserved.

1. Introduction

Ulipristal acetate [17α -acetoxy- 11β -(4-*N,N*-dimethyl amino-phenyl)-19-norpregna-4,9-diene-3,20-dione] (UPA), a selective progesterone receptor modulator (Fig. 1), can prevent unintended pregnancy by delaying ovulation for up to five days after contraceptive failure. In August 2010, UPA had gained the FDA's approval for use as an oral emergency contraception tablet in the U.S. with trade name Ella. Until now it is found that Ella may cause serious side effects including abdominal pain, menstrual disorder, headache, nausea and so on [1]. In addition, the study for UPA to treat contraceptive gynecological indications (fibroma uteri, adenomyosis) and Cushing's syndrome is in progress [2]. In view of safe medication and investigating pharmaceutical dynamics of drugs, a simple, sensitive analytical procedure is needed to determine UPA in pharmaceutical formulation and in biological fluids. HPLC has been used to determine UPA in bulk [3]. But to the best of our knowledge, there were few literatures to analyze UPA in biological samples.

An appropriate preconcentration/separation method should be developed due to matrix interference and low concentration of analytes in real biological samples before analysis [4]. In recent years, many preconcentration/separation steps have been oriented

toward the fast development of simplification and miniaturization. In particular, the use of alternative non-contaminant and non-toxic solvents instead of high quantities of organic solvents is preferred during preconcentration/separation. Solid phase microextraction (SPME) and liquid phase microextraction (LPME) have been extensively used to preconcentration/separation analytes in complex matrix with their high ability of sample clean up and analyte preconcentration, and low consumption of solvents. SPME would require a specific device loaded with certain adsorption material as well as a high-pressure delivery system that would be relatively expensive [4]. Moreover the operation of LPME is simpler and faster than that of SPME (which includes adsorption progress and desorption progress). Dispersive liquid–liquid microextraction (DLLME), developed by Assadi and co-workers in 2006 [5], is a miniaturized form of liquid phase extraction that employs microliter volumes of extraction solvent. Compared with other microextraction techniques, the advantages of DLLME are simplicity of operation, rapidness, accuracy, and it has been extensively applied in drugs analysis [4,6–8].

Extraction solvents (such as tetrachloroethylene [9], chlorobenzene [10] and carbon tetrachloride [11]) and dispersive solvents (such as methanol [12,13], acetone [9,10] and acetonitrile [11,14]) are usually used in DLLME. Because of the relatively high toxicity of these conventional chlorinated extraction solvents, developing environment-friendly “green” extraction solvents has inspired the great interest of examiners. Ionic liquids (IL) has been more and more used as extraction solvent in DLLME (IL-DLLME)

* Corresponding author. Tel./fax: +86 514 7975244.

E-mail addresses: xs Zhu@yzu.edu.cn, zhuxiashi@sina.com (X. Zhu).

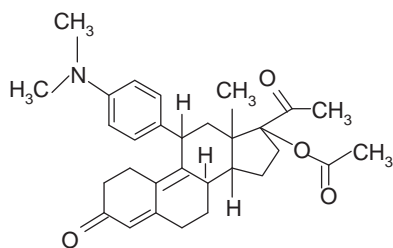


Fig. 1. The structure of ulipristal acetate.

because of its low volatility and low toxicity [4]. Recently ultrasound-assisted (UA) and temperature-controlled (TC) techniques are the most preferred modifications in IL-DLLME [15,16]. However, the technique of dispersive solvent-free UA IL-DLLME has seldom been applied for extraction of drugs in biological samples.

In this paper, hydrophobic IL 1-octyl-3-methylimidazolium hexafluorophosphate [C_8mimPF_6] as extraction solvent of dispersive liquid–liquid microextraction was first time used, which could be completely dispersed into the aqueous sample solution by sonication at 313 K without dispersive solvents, and UPA was easily migrated. The discussion of extraction mechanism showed that hydrophobic interaction force was the main driving force for UPA transfer from water into IL. The proposed method was successfully applied to the real mice serum samples and UPA tablets.

2. Experimental

2.1. Reagents and standards

UPA standard (with purity 99%), UPA tablet (30 mg tablet^{-1}) and blank tablet were kindly provided by Jiangsu Lianhuan Pharmaceutical Co., Ltd (Jiangsu, China). Methanol, ethanol, acetonitrile, acetone, ammonia, ammonium chloride, 1-bromobutane, 1-bromohexane, 1-bromooctane and triethylamine were purchased from Sinopharm Chemical Reagent Co., Ltd. (Shanghai, China). 1-methylimidazole was obtained from Shanghai Darui Specialty Chemicals Co., Ltd (Shanghai, China) and ammonium hexafluorophosphate from Shanghai Bangcheng Chemical Co., Ltd (Shanghai, China). Methanol and acetonitrile were chromatographic grade, 1-methylimidazole was chemical pure, and all other materials were analytical reagent grade and water was distilled, deionised.

UPA stock solution of 2.0 mg mL^{-1} was prepared by dissolving 0.20 g of UPA in 100.0 mL of anhydrous ethanol and kept in coolness and darkness. The stock solution was further diluted with anhydrous ethanol to obtain a standard working solution of 0.10 mg mL^{-1} before using.

2.0 mol L^{-1} NH_3-NH_4Cl buffer solution (pH 8.0) was prepared by dissolving appropriate amounts of ammonium chloride and ammonia.

2.2. Apparatus

The analysis of UPA was carried by a 1200 series liquid chromatography (Agilent Technologies Inc., USA) equipped with photodiode-array detector (PDA). All absorption spectral recordings and absorbance measurements were performed on a UV 2501 spectrophotometer (Shimadzu, Japan). The pH measurements were done by a pH S-25 pH meter (Shanghai, China). A DK-S22 thermostatic water-bath (Shanghai Jinghong Laboratory Instrument Co., Ltd., China) was used to control temperature. A centrifuge Model 80-2 (Shanghai Pudong Physical Optics Instrument

Factory, China) was used to accelerate the phase-separation process. The microextraction was assisted by a 40 kHz, 100 W ultrasonic generator (KQ 50E Kunshan Ultrasonic Instrument Co. Ltd., Kunshan, China).

2.3. Analytical method

2.3.1. Sample preparation

For UPA tablet, five tablets of UPA was weighed and crushed, and then sample powder of about one tablet was accurately weighed and placed in a 50 mL of beaker and dissolved with anhydrous ethanol. Insoluble excipient was removed by filtration through a $0.45\text{ }\mu\text{m}$ membrane filter. The filtered solution was diluted to 100.0 mL with anhydrous ethanol and kept in coolness and darkness before analysis.

For mice serum, abdominal artery blood samples from mice at different time points were collected into heparinized plastic tubes, upon oral administration of 0, 5, 10, 30 mg UPA of 1 kg healthy mice. After placing them at 310 K water bath for 1 h, mice serum samples were obtained after centrifuging the blood samples. According to the method of Chen et al. [17], to eliminate protein, 1.0 mL of serum samples was placed in a 10 mL glass tube and 4.0 mL of acetonitrile was added. The mixture was shaken for 30 s and centrifuged for 10 min at 3000 rpm. Finally the supernatant was determined for UPA.

2.3.2. Synthesis of IL

$[C_4mimPF_6]$, $[C_6mimPF_6]$ and $[C_8mimPF_6]$ were synthesized according to Ref. [18], using such materials as 1-bromobutane, 1-bromohexane, 1-bromooctane, 1-methylimidazole and ammonium hexafluorophosphate.

2.3.3. Extraction procedure

To a 10.0 mL centrifuge tube, $50.0\text{ }\mu\text{L}$ of $[C_8mimPF_6]$, 1.0 mL of buffer solution (pH=8.0) and adequate UPA standard or sample solutions were added; the solution was diluted to 10.0 mL with distilled water. After shaken, the mixture was ultrasonically extracted for 10 min at 313 K. Then a cloudy mixture was formed. After cooled at 278 K for 15 min, the cloudy solution was centrifuged for 5 min at 2500 rpm and the IL phase was deposited at the bottom of the tube. Then the upper aqueous phase was removed with a syringe. The IL phase was diluted with ethanol to 0.4 mL . The resulting analytical solution was homogenized ultrasonically and filtered with $0.45\text{ }\mu\text{m}$ filter membrane before HPLC analysis.

2.3.4. HPLC measurements

Chromatographic separation of UPA was performed on an Apollon C_{18} column ($150 \times 4.60\text{ mm}$, $5\text{ }\mu\text{m}$) (Evans Trade Co., Ltd, Shanghai, China). The mobile phase was a mixture of methanol and 0.05% triethylamine (90:10, v/v) at a flow rate of 1.0 mL min^{-1} . The injection volume was $10.0\text{ }\mu\text{L}$ and column temperature was kept at 303 K. The monitoring wavelength was 305 nm and reference wavelength and bandwidth were 350 nm and 4 nm, respectively.

2.3.5. Determination of partition ratio

The partition ratio of UPA in ILs (i.e. $[C_4mimPF_6]$, $[C_6mimPF_6]$, $[C_8mimPF_6]$) and water were determined. The partition ratio $D_{IL/W}$ was calculated according Eq. (1) [19]:

$$D_{IL/W} = \frac{C_i - C_f}{C_f} \times \frac{V_{eq}}{V_{IL}} \quad (1)$$

where C_i and C_f are the concentration of UPA in water phase before and after extraction, V_{eq} is the volume of water phase, and V_{IL} is the volume of IL phase.

3. Results and discussion

3.1. Optimization of extraction conditions

Single factor experimental scheme due to its simplicity was used to optimize extraction parameters in this paper (such as types and amount of extraction solvent, solution pH, extraction time and temperature, cooling time and centrifugation time) [20]. All experiments were performed in triplicates ($n=3$). The extraction recovery (ER) was calculated based on Eq. (2):

$$ER\% = \frac{C_{ex} \times V_{ex}}{C_0 \times V_0} \times 100 \quad (2)$$

The C_{ex} and C_0 are the concentration of analyte in the extraction phase and the initial analyte concentration in the sample solution, respectively. V_{ex} and V_0 are the volumes of extraction phase and sample solution, respectively.

3.1.1. Selection of extraction solvent

Characteristics of ILs, such as solubility in water, the viscosity and extraction capacity, play a key role in influencing the extraction recovery. When fixing the anion of IL, these characteristics are affected by the cationic part. In this work three hydrophobic ILs, including $[C_4mimPF_6]$, $[C_6mimPF_6]$ and $[C_8mimPF_6]$, were investigated. According to their solubility, 140.0 μL $[C_4mimPF_6]$, 70.0 μL $[C_6mimPF_6]$, and 40.0 μL $[C_8mimPF_6]$ were selected as extraction solvents in the absence of dispersion solvent [7]. Fig. 2 showed that the extraction recoveries (ER) were all over 90.0% in three ILs and a higher ER was obtained in $[C_8mimPF_6]$. Furthermore, adsorption capacities of three ILs for UPA were 1.99 mg g^{-1} ($[C_4mimPF_6]$), 9.33 mg g^{-1} ($[C_6mimPF_6]$) and 18.8 mg g^{-1} ($[C_8mimPF_6]$) (Fig. 2), respectively. With its higher adsorption capacity and ER, $[C_8mimPF_6]$ was chosen for following examination.

The effect of volume of $[C_8mimPF_6]$ on ER was shown in Fig. 3. The highest ER was achieved when 40.0–70.0 μL of $[C_8mimPF_6]$ was employed. Therefore 50.0 μL of $[C_8mimPF_6]$ was selected in the work.

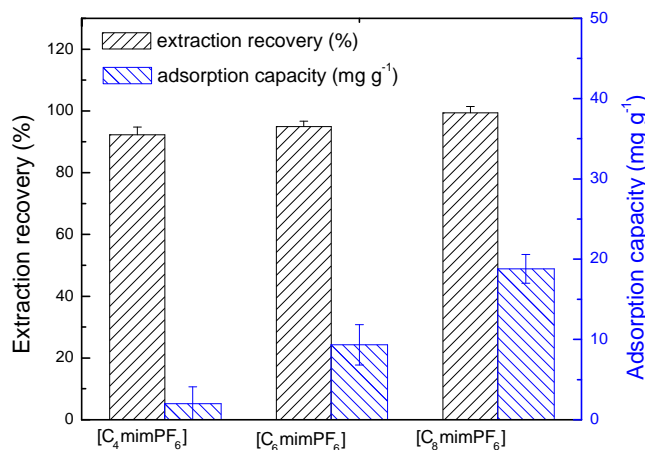


Fig. 2. Effect of the kind of extraction solvents on ER of UPA and adsorption capacity. Extraction conditions: sample volume, 10.0 mL; sample amount, 10.0 μg ; pH, 8.0; ultrasonic temperature, 313 K; ultrasonic time, 10 min; cooling temperature, 278 K; cooling time, 15 min; centrifugation time, 5 min. The error bars were standard deviation.

3.1.2. Dispersion solvent free

The dispersion degree of extraction solvents plays a crucial role in DLLME. The smaller fine droplet of extraction solvent forms, the higher extraction recovery achieves. Ultrasound energy or high temperature combined with dispersive solvents was usually used in DLLME to improve extraction effect [7,8]. In this paper, the results showed that the ER would be over 95.0% without any dispersive solvents. So in this work, dispersive solvent was free.

3.1.3. Effect of pH

In general, pH value of sample solution determines the existential state of analytes, thus affecting extraction recovery. In this paper the effect of sample solution pH value in the range of 2.0–12.0 on the extraction recovery was examined. Fig. 4 showed that the ER of UPA increased with pH from 2.0 to 7.0, and reached the maximum at pH 7.0 (ER > 95.0%), after that almost unchanged with further increasing pH. The log Dow (Dow, octanol–water

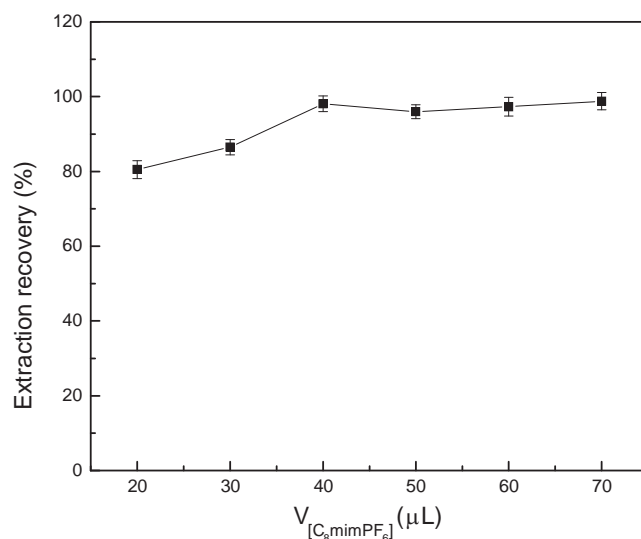


Fig. 3. Effect of $[C_8mimPF_6]$ volume on ER of UPA. Extraction conditions: sample volume, 10.0 mL; sample amount, 10.0 μg ; IL, $[C_8mimPF_6]$; pH, 8.0; ultrasonic temperature, 313 K; ultrasonic time, 10 min; cooling temperature, 278 K; cooling time, 15 min; centrifugation time, 5 min. The error bars were standard deviation.

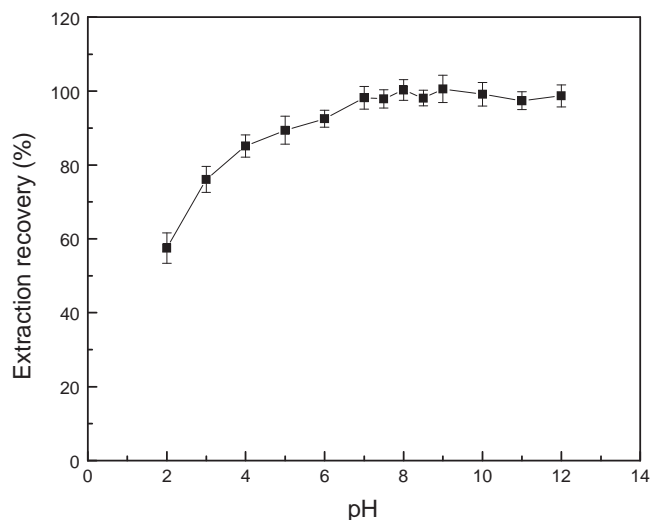


Fig. 4. Effect of pH on ER of UPA. Extraction conditions: sample volume, 10.0 mL; sample amount, 10.0 μg ; $[C_8mimPF_6]$ volume, 50.0 μL ; ultrasonic temperature, 313 K; ultrasonic time, 10 min; cooling temperature, 278 K; cooling time, 15 min; centrifugation time, 5 min. The error bars were standard deviation.

partition coefficient) values of UPA are higher than 4.0 (log Dow is 4.18 at pH 5.5 or 4.47 at pH 7.4), which means UPA is easily soluble in lipids and hardly miscible with water, and the lipophilic property of UPA is stronger at pH 7.4 than at pH 5.5 [21]. UPA would more easily distribute into the hydrophobic IL in alkaline medium. So a pH of 8.0 was used for all extraction experiments.

The effect of ionic strength was tested by adding KCl to UPA solutions. The results showed that ER was significantly decreased when the concentration of KCl was over 0.8 mol L^{-1} . In this study, 1.0 mL of $\text{NH}_3\text{-NH}_4\text{Cl}$ buffer solution (2.0 mol L^{-1}) added into 10.0 mL sample solution could satisfy the requirement of ionic strength.

3.1.4. Effect of temperature

Temperature has a significant effect on IL solubility in water. The solubility and dispersion degree of IL will be improved with increasing temperature that will accelerate the transfer of UPA from water to IL. In this work, the effects of extraction temperature were evaluated in the range of 288–343 K with an ultrasound time of 10 min. The ER was observed to increase with temperature from 288 to 308 K, and then remain constant up to 343 K. Therefore the extraction temperature of 313 K was selected in this study.

3.1.5. Effect of ultrasonic time

Dispersion is the key step whether extraction is successfully carried out or not. As a key procedure in IL-USA-DLLME, ultrasound can accelerate the formation of fine dispersive mixtures, and result in higher recoveries [22]. In this work, the sonication time was evaluated in the range of 2 min to 20 min. The experimental results indicated that the maximum ER (95.0%) could be attained within 5 min and longer extraction time would not affect the ER. In examination it was also found that when the ultrasound

irradiation was not applied and the sample solution was intensely shaken for 2 min, the ER could also achieved 95.0%. In order to alleviate manual operation, ultrasound time of 10 min was chosen.

3.1.6. Effect of cooling and centrifugation time

Phase separation can be improved with an additional cooling stage due to the decreased solubility of ILs in water [23]. In this work, the effect of the cooling time on the ER was assayed in the range of 5–30 min when fixing cooling temperature 278 K. The results showed a cooling time of 15 min was sufficient to achieve the maximum ER. In the study cooling time of 15 min was chosen.

For evaluating the effect of centrifugation on phase separation, the centrifugation time was studied in the range of 1–10 min at a constant rate of 2500 rpm after cooling. 5 min was found to be enough to achieve complete phase separation.

3.1.7. Effect of solution volume

The effect of solution volume on ER was examined from 5.0 mL to 30.0 mL when fixing the amount of UPA at 10.0 μg . The results showed that the ER would be less than 85.0% when the dilution volume of sample solution was over 15.0 mL. It is because the dissolved amount of $[\text{C}_8\text{mimPF}_6]$ will increase with enhancing solution volume thus affecting its extraction ability. In this work, the sample volume of 10.0 mL was adopted. The IL phase was diluted to 0.4 mL with ethanol after extraction for HPLC determination, and the preconcentration factor (defined as the volume ratio of dilution sample solution and IL phase, i.e. 10.0/0.4) was 25.

3.2. Analytical performance

As shown in Fig. 5(C) (chromatogram of UPA standard solution), the retention time of UPA was about at 2.70 min. Comparing with Fig. 5(C) UPA was undetectable and there were no interference peaks in blank tablet (Fig. 5(A)) and blank serum (Fig. 5(B)), therefore blank tablet and blank serum were used for the method validation.

3.2.1. Linearity and limits of detection

For evaluating matrix effect, a statistical comparison between the standard curve and working curve was made. The working curves were got with spiking the standard directly into blank tablet and blank serum and extracting under the same conditions. The results were listed in Table 1. The Student's test was applied and the statistical analysis indicated that the difference between the slope of working curve of blank tablet and standard curve was not obvious, but the difference between the slope of working curve of blank serum and standard curve was significant ($P=0.95$). So working curve was used to determine UPA in UPA tablet and mice serum. As shown in Table 1, the calibration graphs were linear over the concentration ranges of $0.03\text{--}6.0 \mu\text{g mL}^{-1}$, and the limits of detection (LOD) (the lowest concentration yielding a signal-to-noise ratio of 3) were 6.8 ng mL^{-1} (blank tablet) and 9.3 ng mL^{-1} (blank serum). When administered by mouth at a dose of 30 mg, ulipristal acetate is rapidly absorbed. The maximum mean serum concentration (C_{max}) \pm the standard deviation (SD) of $176 \pm 89 \text{ ng mL}^{-1}$ was observed at approximately 1 h [24], which

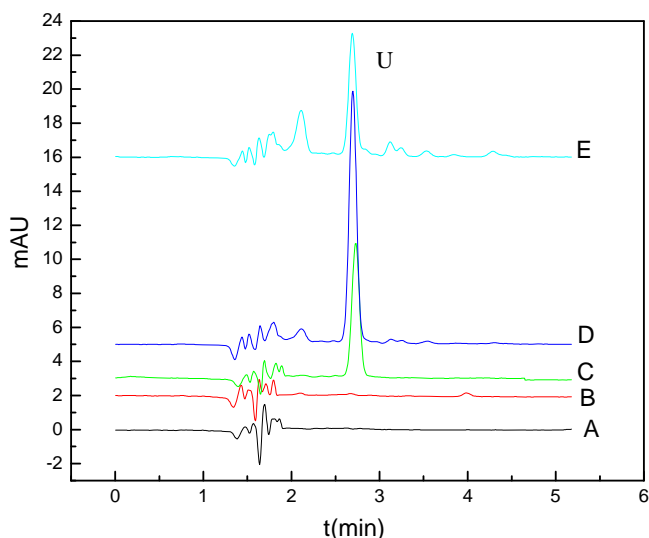


Fig. 5. Chromatograms of blank tablet (A), blank serum (B), standard solution (C), UPA tablet (D) and mouse serum sample (E) (collected at 1 h after oral administration of 10 mg UPA of 1 kg healthy mice). The concentration of standard solution: $0.10 \mu\text{g mL}^{-1}$. U: UPA.

Table 1
Linearity parameters and LOD of the proposed method in different matrices.

Sample	Linear range ($\mu\text{g mL}^{-1}$)	Slope \pm SD ($n=3$)	Intercept \pm SD ($n=3$)	Correlation coefficient	LOD (ng mL^{-1})
Standard solution	0.02–6.0	482.1 ± 4.2	8.92 ± 0.35	0.9985	5.7
Blank tablet	0.03–6.0	483.9 ± 6.1	12.9 ± 0.58	0.9963	6.8
Blank serum	0.03–6.0	495.0 ± 5.0	37.7 ± 1.6	0.9989	9.3

means the method can satisfy the determination requirement of UPA in serum.

3.2.2. Precision and repeatability

To evaluate intraday and interday precisions, analysis of UPA at three concentration levels (0.50, 1.0, 2.0 $\mu\text{g mL}^{-1}$) was carried out by performing five experiments on the same day using the same analyte solution and over five consecutive days using different solutions. The intraday and interday RSD values ranged from 2.5% to 3.6% and from 3.9% to 5.1% for blank tablet, and from 1.9% to 3.8% and from 3.6% to 5.5% for blank serum, respectively, reflecting the usefulness of the method in routine use.

3.2.3. Trueness

The trueness of the proposed method was evaluated by determining different UPA tablets and mice serum (through standard addition technique). The BIAS% was calculated according to the following equation: (detected content-stated content)/stated content $\times 100$. The data were illustrated in Table 2. Obtained values of BIAS% ranged from +3.00% to +5.30%, from +3.50% to +6.33% for UPA tablet and mice serum, respectively, suggesting the analytical utility of the UA IL-DLLME for UPA determination.

The stability of UPA in serum was investigated by extracting and analyzing the serum samples collected at 1 h after oral administration of 10 mg UPA of 1 kg healthy mice. The results indicated that UPA in serum samples was stable for at least 7 days.

3.2.4. Sample determination

Comparing the chromatograms of UPA tablet (Fig. 5(D)) and mice serum (Fig. 5(E)) with UPA standard solution (Fig. 5(C)), the reproducibility of the retention time can satisfy analysis requirement. Table 3 showed analytical results for UPA tablet and mice serum using the proposed methodologies. The result of UPA tablet obtained by the proposed method was in good agreement with the label value. The statistical *t*-test ($P=0.95$) was used to compare the results, which showed that there was no significant difference between them. From Table 3 it was also known that the UPA concentration in mice serum would rise with increasing intragastric administration dose and the maximum serum concentration was obtained at 1 h, which was consistent with that of the literature [24].

3.3. Discussion of extraction mechanism

The extraction effect of UPA by ILs depends on the dissolution degree of UPA in IL. The hydrophobic UPA is more likely to be dissolved by hydrophobic ILs than by water based on the hydrophobic interaction. In this work hydrophobic interaction force between UPA and ILs was verified by partition ratio and some

Table 2
The trueness evaluation of the proposed method.

Sample	Stated content ($\mu\text{g mL}^{-1}$)	Detected content ($\mu\text{g mL}^{-1}$) ^a	BIAS (%)
UPA tablet-1	0.10	0.104	+4.0
UPA tablet-2	0.20	0.206	+3.0
UPA tablet-3	0.30	0.316	+5.3
Serum-1 ^b	0.10	0.105	+5.0
Serum-2 ^b	0.20	0.207	+3.5
Serum-3 ^b	0.30	0.319	+6.3

^a Mean for three independent determinations.

^b Collected at 1 h after oral administration of 10 mg UPA of 1 kg healthy mice.

thermodynamic parameters depending on temperature such as enthalpy change, Gibbs energy and entropy change for elaborating extraction mechanism.

3.3.1. Partition ratio $D_{IL/W}$

The partition ratio $D_{IL/W}$ is the concentration ratio of UPA in two immiscible phases at partition equilibrium, and reflects differential solubility of UPA between two phases (ILs-H₂O). The $D_{IL/W}$ and ER of UPA in three ILs at 313 K were shown in Table 4. It could be seen from Table 4 that (1) the $D_{IL/W}$ was all over 10^3 in three ILs, i.e. the concentration ratio of UPA in ILs and in water was $> 10^3$, indicating there was stronger interaction between UPA and ILs than that of UPA and water, and UPA was more easily distributed in ILs; (2) the $D_{IL/W}$ of UPA in the ILs followed the order: [C₈mimPF₆] > [C₆mimPF₆] > [C₄mimPF₆] and the order $D_{IL/W}$ of was consistent with the order of ER. It is because the hydrophobicity of ILs will enhance with increasing the length of alkyl chains in imidazole ring. The $D_{IL/W}$ and ER were increased from [C₄mimPF₆] to [C₈mimPF₆], indicating hydrophobic interaction force played a key role on the partition of UPA between ILs and water.

3.3.2. Extraction thermodynamic parameters

From a thermodynamic perspective, the partition of UPA can be regarded as a transfer process of the UPA molecules from water phase to the IL phase. At a given temperature, the changes in Gibbs energy (ΔG_T^0), enthalpy (ΔH_T^0) and entropy (ΔS_T^0) of such a transfer process can be calculated from the partition data through following equations:

$$\ln D_{IL/W} = C + (-\Delta H_T^0/RT) \quad (3)$$

[25]

$$\Delta G_T^0 = -RT[\ln D_{IL/W} + \ln(V_{m,IL}/V_{m,w})] \quad (4)$$

[19]

$$T\Delta S_T^0 = \Delta H_T^0 - \Delta G_T^0 \quad (5)$$

Among them *C* is constant, *R* is molar gas constant (8.314 J mol⁻¹ K⁻¹), *T* is absolute temperature, and *V_{m,IL}* and *V_{m,w}* are molar volumes of ILs and water.

Table 3
Analytical results of UPA in real sample.^a

Sample	Label value	Intragastric dose	Collected time (h)	Found \pm SD ^a
Tablet	30 mg tablet ⁻¹	/	/	29.7 \pm 0.98 mg tablet ⁻¹
			0.5	0.65 \pm 0.04 $\mu\text{g mL}^{-1}$
			1	4.61 \pm 0.31 $\mu\text{g mL}^{-1}$
			2	1.46 \pm 0.04 $\mu\text{g mL}^{-1}$
			0.5	1.32 \pm 0.10 $\mu\text{g mL}^{-1}$
			0.5	1.32 \pm 0.10 $\mu\text{g mL}^{-1}$
Mice serum	/	10 mg kg ⁻¹	1	8.12 \pm 0.59 $\mu\text{g mL}^{-1}$
			2	3.10 \pm 0.13 $\mu\text{g mL}^{-1}$
			0.5	2.92 \pm 0.17 $\mu\text{g mL}^{-1}$
			0.5	22.8 \pm 0.99 $\mu\text{g mL}^{-1}$
			1	22.8 \pm 0.99 $\mu\text{g mL}^{-1}$
			2	6.03 \pm 0.15 $\mu\text{g mL}^{-1}$

^a Mean for three independent determinations.

Table 4
The $D_{IL/W}$ and ER of UPA in different IL.

IL	[C ₄ mimPF ₆]	[C ₆ mimPF ₆]	[C ₈ mimPF ₆]
$D_{IL/W} \times 10^3$	3.01	6.77	11.5
ER (%)	92.3	94.9	99.4

Table 5
M volumes of ILs and water, $\ln D_{IL/W}$ and thermodynamic parameters of UPA extracted by different IL under different temperature.

Parameters	T (K)			
	298.15	308.15	318.15	328.15
$\ln D_{IL/W}$	[C ₄ mimPF ₆]	7.75	7.96	8.22
	[C ₆ mimPF ₆]	8.18	8.54	9.04
	[C ₈ mimPF ₆]	8.54	9.06	9.70
Molar volumes (cm ³ mol ⁻¹) ^a	[C ₄ mimPF ₆]	207.6	209.4	211.2
	[C ₆ mimPF ₆]	241.6	243.1	244.6
	[C ₈ mimPF ₆]	275.7	277.4	279.1
	H ₂ O	18.05	18.11	18.18
ΔH_T^0 (kJ mol ⁻¹)	[C ₄ mimPF ₆]	21.8		
	[C ₆ mimPF ₆]	35.9		
	[C ₈ mimPF ₆]	48.9		
ΔG_T^0 (kJ mol ⁻¹)	[C ₄ mimPF ₆]	-25.3	-26.7	-28.2
	[C ₆ mimPF ₆]	-26.7	-28.5	-30.8
	[C ₈ mimPF ₆]	-27.9	-30.2	-32.9
$T\Delta S_T^0$ (kJ mol ⁻¹)	[C ₄ mimPF ₆]	47.1	48.5	50.0
	[C ₆ mimPF ₆]	62.6	64.4	66.7
	[C ₈ mimPF ₆]	76.8	79.1	81.8

^a Ref. [19].

It is clear that values of ΔH_T^0 can be directly obtained from the slope of the linear equation between $\ln D_{IL/W}$ and $1/T$ shown in Eq. (3). Molar volumes of ILs and water (got by Ref. [19]), $\ln D_{IL/W}$, ΔH_T^0 , and ΔG_T^0 and $T\Delta S_T^0$ calculated with Eqs. (4) and (5) under different temperature were shown in Table 5. From Table 5, the following conclusions were drawn that (1) $\Delta H_T^0 > 0$ and partition ratios in three ILs were increased with raising temperature, illustrating that extraction process was an endothermic process and higher temperature was beneficial to extraction; (2) $\Delta G_T^0 < 0$, pointing out extraction was spontaneous; (3) $\Delta S_T^0 > 0$ and $|\Delta H_T^0| < |T\Delta S_T^0|$, indicating that the transfer process of UPA from water to IL was driven by entropy change. It is generally recognized that hydrophobic interaction force is main feature of entropy control [26]. Based on these results, it could be deduced that hydrophobic interaction might be the main driving force for the transfer of UPA molecules from water to the IL phases.

4. Conclusion

In this paper a new and environmental friendly ultrasound-assisted ionic liquid dispersive liquid–liquid microextraction coupled with HPLC-PDA was developed for the determination of UPA in dosage form and biological sample. Without any dispersive solvent the ER could be over 95.0% under ultrasonication. The developed method can provide analytical technical support for UPA pharmacokinetics examination. Mechanism discussion of extraction indicated that hydrophobic interaction might be the main driving force for UPA extracted in IL phase.

Acknowledgements

The authors acknowledge the financial support from the National Natural Science Foundation of China (21375117, 21155001) and a project funded by the Priority Academic Program Development of

Jiangsu Higher Education Institutions and the Foundation of the Excellence Science and Technology Invention Team in Yangzhou University and the Graduate Innovation Project Foundation of Jiangsu province (CXLX13_895).

References

- [1] B.Q. Ma, Shanghai Med. Pharm. J 31 (2010) 315–316.
- [2] G.F. Yao, Chin. J. Med. Chem. 21 (2011) 78–80.
- [3] WO 2004/078709.
- [4] J.N. Sun, Y.P. Shi, J. Chen, J. Chromatogr. B 879 (2011) 3429–3433.
- [5] Y.F. Zhang, H.K. Lee, Anal. Chim. Acta 750 (2012) 120–126.
- [6] C. Noelia, P.P. Francisco, I. de la Calle, B. Carlos, L. Isela, Microchem. J. 99 (2011) 246–251.
- [7] S.Q. Gao, X. Yang, W. Yu, Z.L. Liu, H.Q. Zhang, Talanta 99 (2012) 875–882.
- [8] A.J. Toraj, F. Nazir, S. Mojtaba, P. Meghdad, J. Pharm. Biomed. Anal. 85 (2013) 14–20.
- [9] R. Mohammad, A. Yaghoub, M.H. Mohammad-Reza, A. Elham, A. Fardin, B. Sana, J. Chromatogr. A 1116 (2006) 1–9.
- [10] D. Nagaraju, S.D. Huang, J. Chromatogr. A 1161 (2007) 89–97.
- [11] M.A. Farajzadeh, M. Bahram, J. Jönsson, Anal. Chim. Acta 591 (2007) 69–79.
- [12] M. Hatami, Elham Karimnia, Khalil Farhadi, J. Pharm. Biomed. Anal. 85 (2013) 283–287.
- [13] J.M. Padro, M.E. Marso, G.E. Mastrantonio, J. Altchek, F. Garcia-Bournissen, M. Reta, Talanta 107 (2013) 95–102.
- [14] X. Liu, R. Fu, M. Li, L.P. Guo, L. Yang, Chin. J. Anal. Chem. 41 (2013) 1919–1922.
- [15] J.H. Zhang, H.X. Gao, B. Peng, S.Q. Li, Z.Q. Zhou, J. Chromatogr. A 1218 (2011) 6621–6627.
- [16] M.J. Trujillo-Rodríguez, P. Rocío-Bautista, V. Pino, A.M. Afonso, Trends Anal. Chem. 51 (2013) 87–106.
- [17] W.Y. Chen, H. Li, W.H. Luo, Chin. J. Mod. Med. 17 (2007) 1665–1673.
- [18] F.Y. Zhao, J.Y. Wang, H.J. Liu, R.J. Liu, Chem. Reagents 29 (2007) 229–231.
- [19] Y.C. Pei, Doctoral Dissertation of Lanzhou University (2008).
- [20] P. Arbeláez, F. Borrull, R.M. Marcé, E. Pocurull, Talanta 125 (2014) 65–71.
- [21] (<http://www.chemspider.com/Chemical-Structure.115762.html>).
- [22] S.Y. Dong, Q. Hu, Z. Yang, R. Liu, G.Q. Huang, T.L. Huang, Microchem. J. 110 (2013) 221–226.
- [23] R. Liu, J. Liu, Y. Yin, X. Hu, G. Jiang, Anal. Bioanal. Chem. 393 (2009) 871–883.
- [24] (<http://tec.k8008.com/html/124/124073.html>).
- [25] X.M. Fu, S.G. Dai, Y. Zhang, Chin. J. Anal. Chem. 34 (2006) 598–602.
- [26] H. Bianco-Peled, S. Gryc, Langmuir 20 (2004) 169–174.



On the feasibility of near infrared spectroscopy to detect contaminants in water using single salt solutions as model systems



A.A. Gowen^{a,b,*}, F. Marini^c, Y. Tsuchisaka^b, S. De Luca^c, M. Bevilacqua^c, C. O'Donnell^a, G. Downey^{a,d}, R. Tsenkova^b

^a School of Biosystems Engineering, University College Dublin, Dublin, Ireland

^b Biomeasurement Laboratory, Kobe University, Kobe, Japan

^c Department of Chemistry, University of Rome "La Sapienza", Rome, Italy

^d Teagasc Food Research Centre, Ashtown, Dublin, Ireland

ARTICLE INFO

Article history:

Received 8 May 2014

Received in revised form

13 August 2014

Accepted 18 August 2014

Available online 26 August 2014

Keywords:

Near infrared

NIR

Water

Salt

Contaminant

ABSTRACT

This research work evaluates the feasibility of NIRS to detect contaminants in water using single salt solutions as model systems. Previous research has indicated the potential of near infrared spectroscopy (NIRS) for detecting solutes in water; however, a comprehensive investigation of the limit of detection of this technique has not been carried out. Near infrared transmittance spectra of aqueous salt solutions in the concentration range 0.002–0.1 mol L⁻¹ (equivalent to 117–13,334 ppm or 0.0001–0.01% mass/mass) were investigated. The first overtone region of the near infrared spectrum (1300–1600 nm) was found to be the most effective wavelength range for prediction of salt concentration in aqueous solutions. Calibration models built using this wavelength range and employing the extended multiplicative scatter spectral pre-treatment resulted in root mean squared error of prediction values ranging from 0.004 to 0.01 mol L⁻¹. The limit of detection (LOD) was estimated to be of the order of 0.1% (mass/mass) or 1000 ppm. Within the framework of Aquaphotomics, it was possible to examine the effect of different salts on the NIR spectra of water in the first overtone range. Our results were confirmed through test experiments at various geographical locations employing dispersive and Fourier transform type NIRS instruments.

© 2014 Elsevier B.V. All rights reserved.

1. Introduction

Water quality monitoring is a complex multi-spatial and multi-temporal problem, extending from safety monitoring of drinking water to operational monitoring of waste waters. Standard methods for water quality analysis involve intensive sampling regimes and multi-step sample preparation, requiring manual inputs which prohibit their integration into continuous monitoring systems. Consequently, there is currently a need for the development of low-cost, robust, reliable monitoring techniques that can be easily integrated into water flow systems [1]. Vibrational spectroscopic techniques, including near infrared (NIR) and mid infrared (MIR) spectroscopy, have been proposed as potential tools to improve the speed and reduce the cost of water quality testing [2]. Such techniques have become standard quality analysis tools in the food and pharmaceutical industries, in which they are

commonly implemented as process analytical technologies for continuous quality monitoring.

Fundamental frequencies for molecular vibrations (e.g. stretching, bending) occur in the MIR region while their overtones and combinations appear in the NIR spectral range. Absorption bands tend to overlap in the NIR, resulting in a broad spectral response; consequently, the NIR range contains less accessible molecule-specific information than does the MIR. Analysis of aqueous samples in the MIR is challenging, due to the strong absorbance of MIR light by water, leading to a low signal to noise ratio. To overcome this problem, innovative sample presentation techniques, such as attenuated total reflectance (ATR), have been developed; however volume of sample that can be measured at any instant is inherently limited by this approach. The weaker absorption of NIR light by water facilitates the direct measurement of greater volumes of aqueous samples. For this reason, NIRS is an appealing technique.

The so-called water absorbance peaks of the NIR wavelength range are broad peaks located around 1300–1600 and 1900–2200 nm. These represent overlapped overtone and combination vibrations of fundamental stretching, bending and libration vibrations of intramolecular

* Corresponding author. Tel.: +353 1 7167675.

E-mail address: aoife.gowen@ucd.ie (A.A. Gowen).

OH bonds, and are also sensitive to changes in the intermolecular hydrogen bonds. They represent the most prominent features in the NIR spectrum of aqueous samples and they can dominate other, more subtle, absorbance features arising from other molecules in the solution. Although solutes such as metals and salts do not absorb NIR light, their presence can be detected via perturbation of water's hydrogen-bonded network. When solutes are added to water, intermolecular hydrogen bonds rearrange their orientation, resulting in changes in the shape and peak position of the water peaks in the NIR spectrum. The extent of these changes depends upon the properties of the solute, such as size and ionic strength [3]. It has previously been demonstrated that this effect could be used for the prediction of solute concentration in water [4,5]. However, the limit of detection of the technique was not investigated in those studies. More recently, Sakudo and co-workers [6] investigated the NIR spectra of metals (Copper, Magnesium, Zinc and Iron) in 0.1 M Nitric Acid solutions, using a range of concentrations from 0 to 10 mg L⁻¹ and estimated the limit of detection of their technique to be 1–4 mg L⁻¹.

Aquaphotomics has recently emerged as a framework to examine the behavior of water in various systems (e.g. biological systems such as plants and animals) through analysis of their NIR spectra [7]. It has been proposed that Aquaphotomics has potential for contaminant detection in aqueous systems. However, no studies have yet investigated this comprehensively [8]. In this study, we investigate the potential of NIRS for detection of low concentrations of contaminants in water, using salts as model contaminants. Salts were used for the following reasons: they represent relatively simple systems, exhibit no NIR absorption spectrum (therefore the resulting observed effects are solely due to changes in the water absorbance peaks), have relevance to salinity measurements and are comparable to previous studies. Although previous studies have investigated the effects of salts on water using NIRS, this is the first work employing low concentrations, which resemble those expected for major contaminants (0.002–0.1 mol L⁻¹, which corresponds to 0.01–1.3% w/w, or 117–13,334 ppm).

The main objectives of the work were to:

1. Evaluate the performance of NIR spectroscopy combined with chemometric modelling for prediction of salt concentration in water.
2. Evaluate the robustness of the results obtained using multiple geographical locations for testing.
3. Investigate the effects of low concentrations of salts on water structure using NIR spectroscopy.

2. Materials and methods

NIR transmittance spectra were measured over the wavelength region of 1000–2500 nm using quartz cuvette cells with 1 mm optical path length. Each experiment was repeated on three different days using independently prepared samples on each day (where “experiment” refers to the acquisition of NIR spectra for one salt solution at all concentrations). Aqueous solutions of 4 salts (NaCl, KCl, MgCl₂, AlCl₃) were prepared using Millipore water (Millipore, Molsheim, France, resistance ~20 mΩ). These salts were selected to create a set of solutions with different ionic strengths while keeping the anion constant. Ten concentrations (0.002, 0.004, 0.006, 0.008, 0.01, 0.02, 0.04, 0.06, 0.08, 0.1 mol L⁻¹) were prepared for each salt. NIR transmittance spectra of these samples were collected in an order randomised with respect to concentration. In order to monitor interfering signals (e.g. shifts in water absorbance bands temperature variations), control measurements of Millipore water were taken at the beginning, middle and end of each experiment. Ambient temperature over the three locations ranged from 21 to 26 °C.

In order to investigate the robustness of the results obtained, the experiment described below was carried out by three different researchers (1st, 2nd and 3rd authors) using different spectrometers, in three different geographical locations (Dublin (Ireland), Kobe (Japan) and Rome (Italy) respectively). NIR spectra in locations Ireland and Japan were obtained using NIR System 6500 spectrophotometers (Foss NIR-System, Laurel, USA), while those in Rome were obtained using a Nicolet 6700 FT-NIR instrument (Thermo Scientific Inc., Madison, WI).

2.1. Data analysis

Calibration models were built to predict salt concentration using PLS regression (PLSR), employing various spectral pre-treatments (standard normal variate (SNV), SNV+Savitsky Golay 1st and 2nd derivative smoothing (using 15 point smoothing window and 3rd order polynomial) and SNV+extended multiplicative scatter correction (EMSC, using 1st principal component loading of control (Millipore water) spectra as an interferent spectrum).

PLSR models were developed on various wavelength regions of the NIR spectrum (1000–2500 nm, 1000–1300 nm, 1300–1600 nm, 1600–1900 nm, 1900–2200 nm, 2200–2500 nm). In addition, two variable selection methods were applied to the data to evaluate their usefulness in terms of predictive model performance, as follows:

2.1.1. Genetic algorithm—Backward interval PLS (GA-biPLS)

Genetic algorithms are well known as powerful variable selection techniques. However, one of the main problems when dealing with GA is the risk of overfitting, i.e. to select, as meaningful, variables which are only by chance correlated with the responses. As the probability of chance correlation increases with the number of variables, one way to overcome this problem is to use a limited number of variables as an input to the GA selection. For this purpose, we chose a modified version of backward interval PLS (biPLS) [9]. The general concept of biPLS is to identify the spectral regions less meaningful for prediction and iteratively remove them from the data set in a backwards fashion. In its “normal” implementation, the number of intervals is defined only once (e.g. 50 intervals) and the procedure is stopped when a minimum in cross-validation error is reached. When used for pre-selection of spectral intervals prior to GA, backward elimination is performed up to the point when a ‘maximum number of variables retained’ criterion is met. In our case, a maximum of 300 variables was selected. GA was carried out using the PLS-Genetic Algorithm toolbox for Matlab [10] and biPLS was applied using functions in the iToolbox for Matlab [11].

2.1.2. Ensemble Monte Carlo variable selection (EMCVS)

This procedure selects the most informative variables in a dataset based on PLS regression coefficients. Compared to other state of the art variable selection methods, EMCVS increases consistency of variable selection and reduces processing time. This method is described in more detail elsewhere [12].

All models were constructed by sequentially leaving one experimental day out as a test set and using the remaining two experimental days as a calibration set. The number of latent variables for inclusion in each PLSR model was estimated by performing 2-fold cross validation on the calibration set, where the cancellation groups coincided with the different measurement days. Accordingly, to build the model, every second spectrum was left out of the calibration set, and then the model was applied to the remaining spectra. The rank corresponding to the minimum of the root mean squared error of cross validation was then selected as the optimal number of latent variables for each model. This method was selected as a fair means of comparison between competing models.

After selecting the optimal number of latent variables for inclusion, a root mean squared error of prediction (RMSEP) was calculated based on the predictive performance of the model on the test set. Initially, data from each test location was analysed separately.

2.2. Limit of detection

In order to estimate the limit of detection of the technique, data from the different test locations were combined. To facilitate this, spline interpolation was used to re-sample the spectra from the FTIR instrument at the wavelengths of the dispersive instrument. The limit of blank (LoB) and limit of detection (LoD) were calculated according to the equations below [16]:

$$\text{LoB} = \text{mean}_{\text{blank}} + 1.645 \times \text{SD}_{\text{blank}}$$

$$\text{LoD} = \text{LoB} + 1.645 \times \text{SD}_{\text{low}}$$

where the subscript “blank” refers to a sample not containing solute and “low” refers to a sample containing a low concentration of salt. In this study, the spectra of water were used as “blank” samples, while spectra of salt solutions of concentrations 0.002 mol L^{-1} were used as “low” samples. Models were built on data from experimental days 1–2 and spectra representing blank and low concentration samples obtained on day 3 were used to calculate the LoB and LoD.

2.3. Water absorbance pattern

Aquaphotomics aims to gain new knowledge on the structure-related functions of water in biological and aqueous systems using NIR spectroscopy [8]. Within aquaphotomics, the term “water absorbance pattern” is defined as changes in the NIR spectrum due to perturbation of the water peaks. A number of chemometric methods have been proposed for identification of water absorbance bands (i.e. wavelengths relating to water structure) from NIR spectra in order to characterise the so-called ‘water absorbance pattern’ (WAP). Examples include principal component analysis (PCA) loadings and partial least squares (PLS) regression vectors. Interpretation of PLS regression vectors is contentious for a number of reasons: first, the profile of a PLS regression vector is sensitive to model parameters (e.g. number of latent variables selected, which is subjective); second, due to the overlapping nature of vibrational overtone and combination bands in the NIR wavelength range, peaks in regression vectors cannot be directly related to absorbance peaks [13], and third, interfering factors, such as the strong influence of ambient temperature of NIR spectra on water, may confound the elucidation of spectral responses related to the perturbation of interest.

A more appealing method is PCA since it is an unsupervised technique in which the major variations in a spectral dataset are compressed into the first few principal components, which are orthogonal to each other. PCA loadings can be useful for interpretation, especially where the perturbation in question is well characterised. One well-known example involves aqueous systems in which the only perturbation is temperature [14]. However, in cases where multiple simultaneous (typically unknown) perturbations are present, it may be difficult to interpret the resultant PC loadings. An example of this kind of situation is the data obtained in this research. The perturbation we were most interested in characterising was the effect of low concentrations of salts on water structure. However, we were aware that unavoidable, though minor, fluctuations in ambient laboratory conditions (mainly temperature) would also have an influence on the hydrogen bond strength in water, chiefly manifest as a shift in the peak position of the OH first overtone peak (located at around 1450 nm). In order to diminish these effects, we measured spectra

of control samples of pure water during the course of each experiment. The principal variations in these spectra were obtained by applying PCA and extracting the 1st PC loading as an “interferent spectrum”. Extended multiplicative scatter correction (EMSC) could then be applied to the spectra of salt solutions, to correct the data for this interferent spectrum [15]. This would diminish the influence of ambient conditions on the spectra of salt solutions. Consequently, when applying PCA to the EMSC-corrected data, the 1st PCA loading could be related to the perturbation of interest (i.e. addition of salt), and would thus present us with a reasonable estimate of the WAP.

WAPs were constructed using data from each test location as follows. First, for each salt, spectra for each concentration studied and each experimental day were pooled, spectral data in the 1300–1600 nm wavelength region (the so-called ‘first overtone region’) were extracted and subjected to SNV pre-treatment. EMSC was applied to this data, using the 1st principal component loading of the control (Millipore water) spectra (obtained from the calibration set) as an interferent spectrum. Finally, principal component analysis was applied to the EMSC pre-treated data, and the 1st principal component loading was extracted. In order to avoid sign and scale ambiguities, this loading was squared and scaled to the range [0,1]. The resultant scaled loading was employed as a WAP for each salt/location.

3. Results and discussion

3.1. Initial comparison of NIR spectra obtained from different locations

Near infrared spectra (1000–2500 nm) of pure water, obtained using the three different spectrometers tested, are shown in Fig. 1. The optical arrangement of the Foss (Dublin and Kobe) and Nicolet (Rome) systems are completely different (i.e. dispersive v’s interferogram based). However, the NIR spectra of water obtained by each system in the 1300–1600 nm region are qualitatively similar in size and shape. It can be seen that beyond 1900 nm, major spectral variations among the three systems are evident. This can mainly be attributed to the nonlinearity of the detectors beyond absorbance values greater than 2.

3.2. Predictive model performance

The combination of spectral pre-treatment, wavelength range, salt and test day resulted in a large number of competing models ($n=121$) for each test location (see Table A1 in Appendix A).

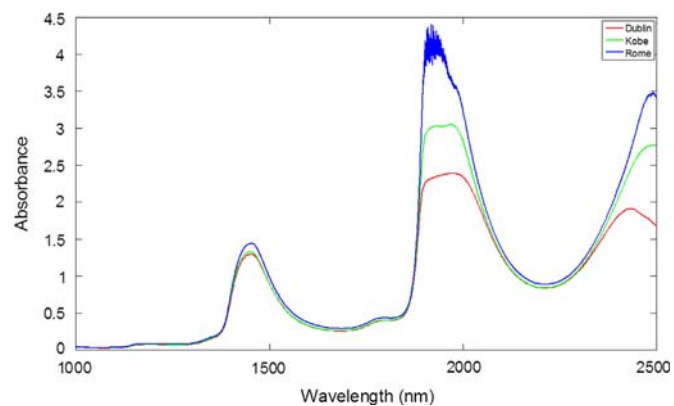


Fig. 1. Near infrared spectra (without any spectral pretreatments) for pure water samples. Red, green, blue represent different experimental locations (Red=Dublin, Green=Kobe, Blue=Rome). (For interpretation of the references to color in this figure legend, the reader is referred to the web version of this article.)

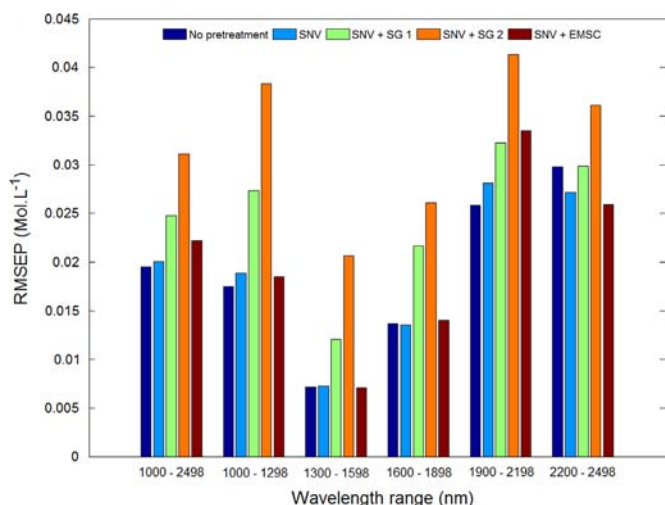


Fig. 2. Root mean squared error of prediction (RMSEP) averaged over test locations, salt and permuted experimental test day, plotted as a function of pre-treatment and wavelength range studied (SNV=standard normal variate, EMSC=extended multiplicative signal correction).

Therefore, in order to compare the effects of spectral pre-treatments and wavelength ranges on model performance, the RMSEP values corresponding to models for each salt, location and permutation of test set were averaged. These are plotted as a function of wavelength range and spectral pre-treatment in Fig. 2. It is evident from this figure that in all cases the 1300–1600 nm wavelength range resulted in the lowest prediction error. Previous studies have also demonstrated the importance of the OH first overtone region (1300–1600 nm) for prediction of solutes in aqueous solution [17]. This is due to the fact that the OH first overtone absorbance band changes according to perturbations in the water matrix [8]. Beyond 1900 nm, the RMSEP was approximately twice that obtained in the 1300–1600 nm region. Although water has absorption peaks in this region, the signal to noise ratio was lower in our study than for the H first overtone region (see also Fig. 1).

Within the 1300–1600 nm wavelength range, the most effective spectral pre-treatment, in terms of prediction error, was EMSC (see Fig. 2). When RMSEP values from the individual test locations were evaluated separately, similar findings were generally obtained (Table A1, Appendix A). Calibration models built in the 1300–1600 nm wavelength range and employing the EMSC pre-treatment resulted in RMSEP values ranging from 0.003 to 0.015 mol L⁻¹. Interestingly, both non-pretreated and SNV-only pretreated data also resulted in low prediction errors in the 1300–1600 nm wavelength range. However, this was generally at the cost of greater model complexity (i.e. higher number of latent variables). This can be understood as follows: the influence of interfering factors (mainly small changes in the temperature) is diminished when EMSC is applied to the data – when this pretreatment is not applied, extra latent variables are needed in the model to account for this confounding factor.

Variable selection techniques (GA-biPLS and EMCVS) were applied to spectral data from the full wavelength range (1000–2500 nm) both with and without application of the SNV+EMSC pretreatment, and also to the 1300–1600 range with SNV+EMSC pretreatment. The associated prediction errors (averaged over test location, salt and prediction day) are displayed in Table 1. The prediction error for SNV+EMSC pretreated data in the 1300–1600 nm region without variable selection is included for comparison. In general, the GA-biPLS procedure resulted in models with a higher prediction error (in terms of RMSEP) when compared to those built on the full 1300–1600 nm range (without further

Table 1

Predictive model performance in terms of root mean squared error of prediction (RMSEP) in mmol L⁻¹ for different pre-treatment and variable selection techniques (nlv=number of latent variables in PLS model). For comparative purposes, RMSEP and nlv were averaged over test day permutation, salt and, experimental location.

Range (nm)	Pretreatment	Variable selection	RMSEP (nlv)
1300–1600	SNV+EMSC	None	7 (5)
1000–2498	None	GA-biPLS	11 (8)
1000–2498	SNV+EMSC	GA-biPLS	10 (6)
1300–1600	SNV+EMSC	GA-biPLS	18 (5)
1000–2498	None	EMCVS	9 (7)
1000–2498	SNV+EMSC	EMCVS	10 (7)
1300–1600	SNV+EMSC	EMCVS	6 (6)

variable selection). EMCVS resulted in a slight improvement in model performance when applied to the 1300–1600 nm wavelength range. However, the variables selected by the techniques employed were not consistent over test locations. An example of this is shown in Fig. 3, in which the variables selected for the EMCVS procedure applied to SNV+EMSC pretreated spectral data in the 1300–1600 nm wavelength range are plotted (the common variables selected by each permutation of the test day are represented by a black bar). It is clear that the variables selected by the EMCVS procedure varied significantly over permutation of test location. Similar results were found for the GA-biPLS technique. This lack of consistency indicates models on the full 1300–1600 nm range (i.e. without further variable selection) would be more stable than a variable selection procedure.

3.3. Limit of blank and detection estimation

After combining the datasets from the different locations, limits of blank and detection (LOB and LOD) were calculated for prediction models based on SNV+EMSC pretreated data in 1300–1600 nm wavelength range location (Table 2). The linearity of the technique, estimated as the coefficient of determination (R^2) for the model for each salt applied to an independent test set of data, was greater than 0.9 in all models, indicating reasonable linearity. The obtained estimates of LoB ranged from 2 to 8 mmol L⁻¹, while LoDs in the range 8–16 mmol L⁻¹ were obtained. The relatively large LoDs estimated in our study indicate that although the linearity of the method is acceptable ($R^2 > 0.9$), the variation in predicted salt concentration was considerable. The LoD corresponds to approximately 0.1% salt concentration on a weight by weight basis. In previous research, NIR transmission spectra of seawater samples in the concentration range 1–35% were obtained (using a cuvette with pathlength of 2 mm) and calibration models were developed in the 1100–1900 nm wavelength range using principal component regression. The authors reported a standard error of prediction of 0.22%, however, the validation data set was not independent in that study (three spectra were measured for each sample: one of these was randomly selected to include in the validation set, which the remainder were used in the model calibration set) [4]. In another paper, researchers investigated prediction of sodium hydroxide, sodium carbonate and NaCl in aqueous solutions using NIR spectroscopy within the range 0–15%, reporting standard errors of prediction of 0.52% for NaCl [5]. Our research goes further than these by investigating the lower limit of detection obtainable by this method and adding the extra variation of multiple systems and testing locations.

3.4. Interpretation of water absorbance pattern

In order to investigate the effects of addition of low concentration of salts on water structure, further examination of the OH first overtone region (1300–1600 nm) is required. Let us first consider

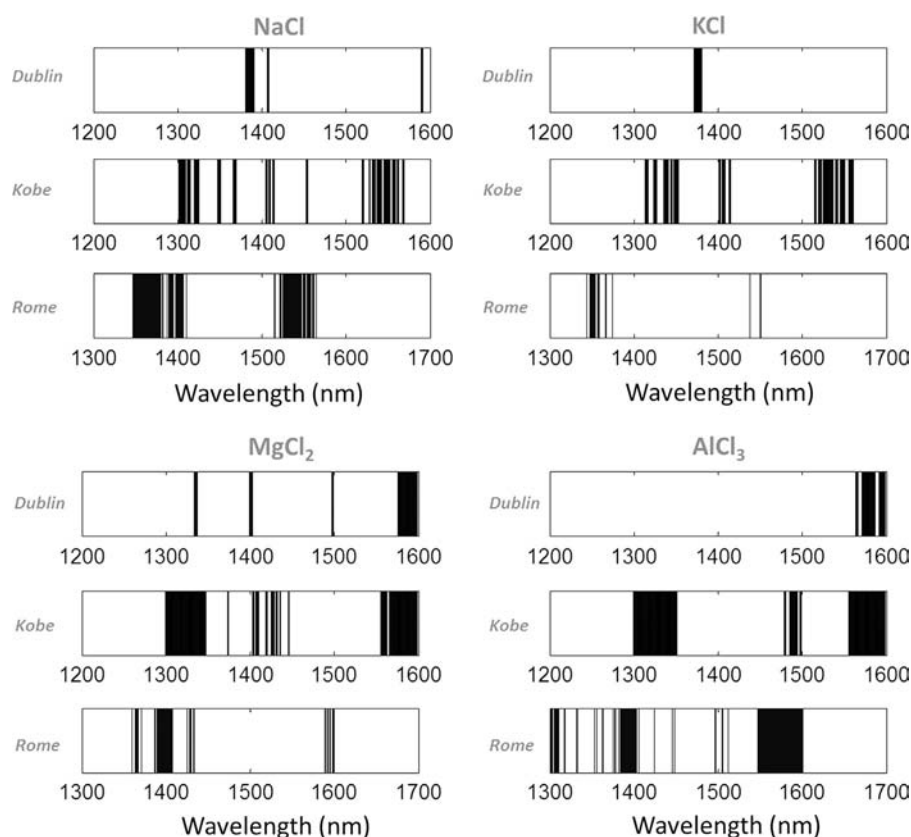


Fig. 3. Variables selected for EMCVS procedure applied to SNV+EMSC pretreated spectral data in the 1300–1600 nm wavelength range for the different salts and locations studied. For each bar chart shown (representing a given combination of salt and location), the common variables selected by each permutation of the test day are represented by a black bar.

Table 2

Limit of detection for prediction models based on SNV+EMSC pretreated data in 1300–1600 nm wavelength range for each salt studied in mmol L^{-1} and % (mass/mass).

Salt	R^2 (nlv)	LoB (mol L^{-1})	LoD (mol L^{-1})
NaCl	0.92 (6)	0.002	0.009
KCl	0.91 (8)	0.007	0.016
MgCl_2	0.96 (8)	0.007	0.012
AlCl_3	0.99 (7)	0.003	0.008

the spectra of pure water samples, obtained as control samples during each experiment. Applying PCA to these spectra allows us to inspect the major spectral variations that occurred during the course of each experiment. These can be largely attributed to small temperature variations in the environment, which in turn change the strength of hydrogen bond vibrations in water. Although efforts were made to control these effects, variation in sample temperature in the range of $\pm 1^\circ\text{C}$ during each experimental run were typically unavoidable. The 1st principal component (PC1) loading for pure water samples (obtained after SNV pretreatment) represented more than 98% total variance in each dataset, and the loadings were identical in shape for each test location (Fig. 4). These loadings are characterised by two peaks, located at 1414 and 1493–1502 nm. It should be noted that, by squaring the PC1 values, we lose information as to the relative sign of each peak. This was carried out to make it easier to compare loadings from different test locations (i.e. to overcome the sign ambiguities inherent in PCA loadings). However, the two peaks shown in Fig. 4 were opposite in sign. Due to the similar profile obtained in PC 1 of the water samples in our study and that obtained in previous investigations of NIR spectra of water at a wider range of

temperatures [14], we consider the PC 1 profile obtained in Fig. 4 to be characteristic of variations in hydrogen bond vibrations in water arising from small changes in temperature over the course of each experiment. As such, these PC1 loadings represent the water absorbance pattern related to a change in temperature.

PCA was also applied to the datasets with varying salt concentration, for each salt and test location, and the resultant PC1 loadings are shown in Fig. 5. These loadings, representing > 96% variation in each dataset, appear almost identical to both each other and to the PC1 loadings of pure water (with the exception of AlCl_3). This is most likely because variations in sample temperature encountered during the course of each experiment had a greater influence on the spectrum than did variations caused by the addition of salts at low concentrations. In other words, the main spectral variation captured in PC1 of the raw data was most likely due to temperature.

The 2nd PC (PC2) loadings for the salt solutions, which represent < 3% of the variation in the salt solutions' spectra shown in Fig. 5, represent the variation orthogonal to the 1st PC. It is difficult to ascribe physical meaning to them since it is possible that these loadings also contain latent information from mixed sources (i.e. due to the combined effects of temperature and salt addition). As a result, there are rather significant differences in the loadings for different test locations.

By applying EMSC to the data, the effects of temperature changes are diminished from the data, leaving the influence of salt on the water spectrum. Examination of the 1st PC of the EMSC pretreated data should then enable investigation of the effects of the different salts tested on the water spectra.

After applying PCA to the EMSC pretreated salt datasets, the resultant PC1 represented > 85% of the variability in the data set (as plotted in Fig. 7). The similarity among WAPs obtained by

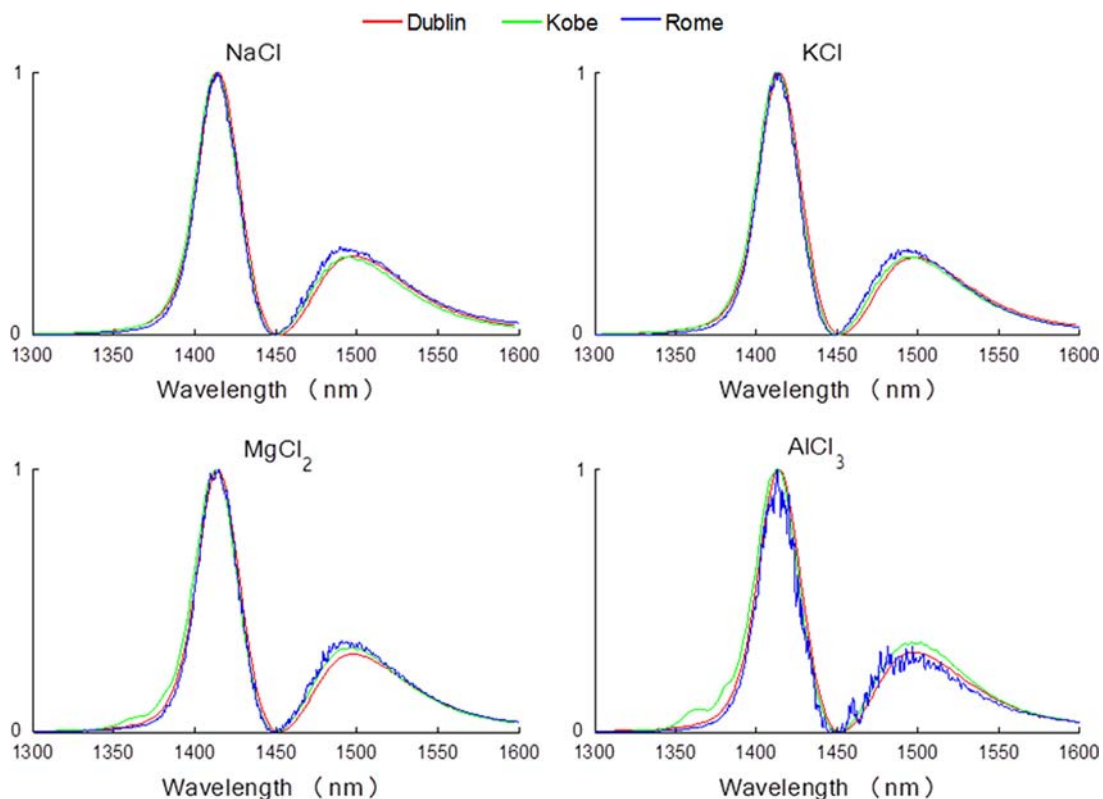


Fig. 4. First principal component loading for pure water samples (after SNV pretreatment) measured during the course of each experiment for each salt (representing > 98% total variance in each dataset). Red, green, blue represent different experimental locations (Red=Dublin, Green=Kobe, Blue=Rome). The principal spectral variations (corresponding to peaks at 1414 and 1493–1502 nm) are mainly due to changes in the hydrogen bond strength in water arising from small changes in temperature over the course of each experiment. (For interpretation of the references to color in this figure legend, the reader is referred to the web version of this article.)

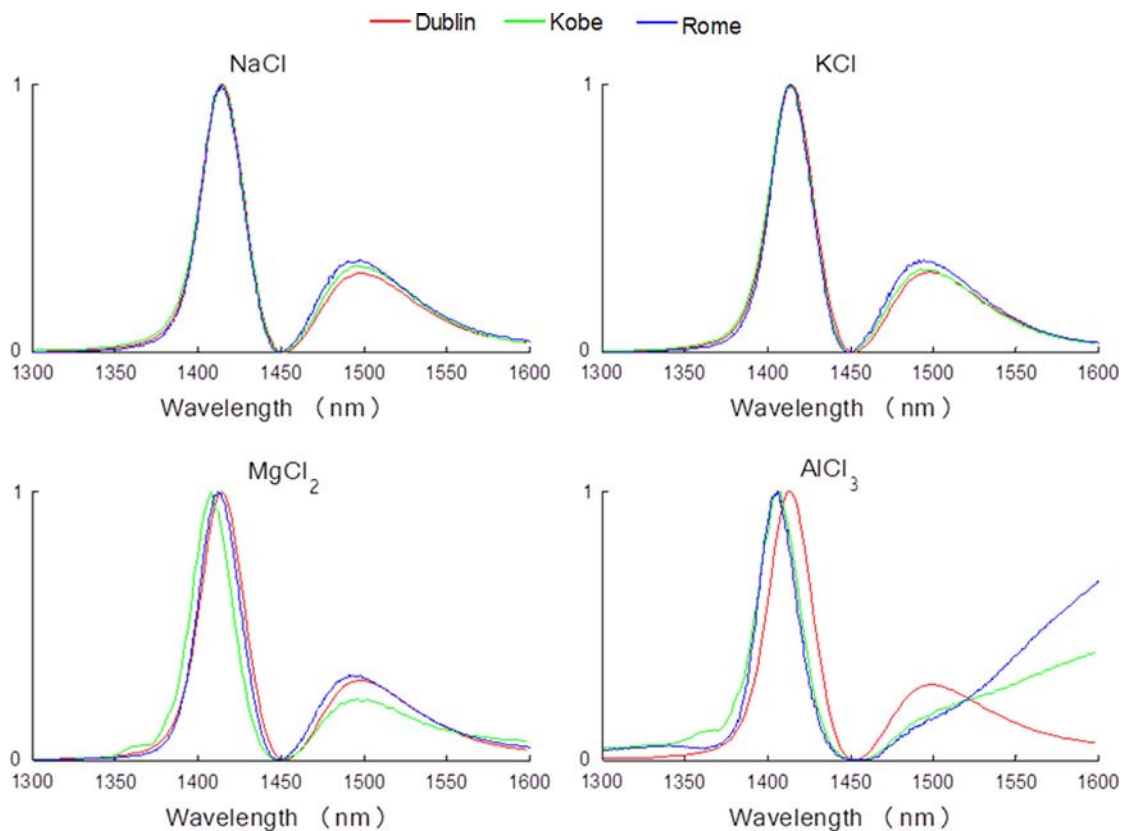


Fig. 5. First principal component loading for salt solutions (after SNV pretreatment). Red, green, blue represent different experimental locations (Red=Dublin, Green=Kobe, Blue=Rome). The principal spectral variations (peaks at 1414 and 1493–1502 nm) in the datasets (representing > 96% total variance in each dataset) are mainly due to changes in the hydrogen bond strength in water arising from small changes in temperature over the course of each experiment. (For interpretation of the references to color in this figure legend, the reader is referred to the web version of this article.)

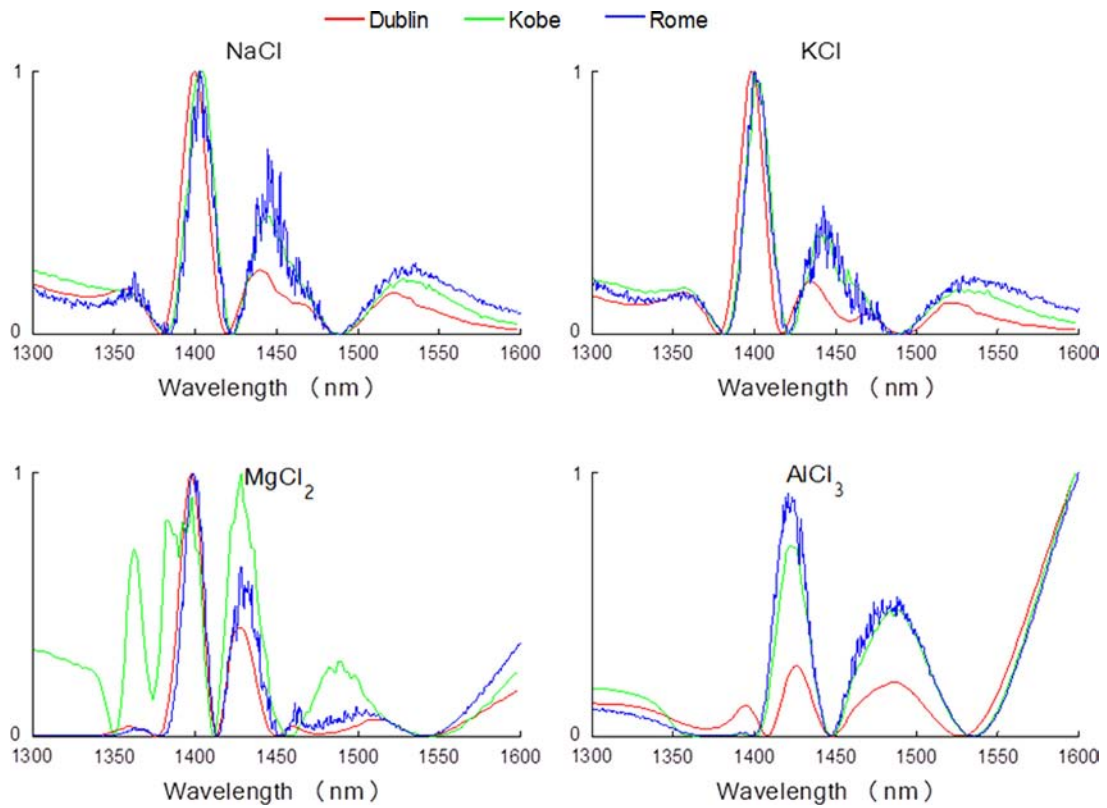


Fig. 6. Second principal component loading for salt solutions (after SNV pretreatment). Red, green, blue represent different experimental locations (Red=Dublin, Green=Kobe, Blue=Rome). The variations seen here (representing < 3% total variance in each dataset) can be related to changes in hydrogen bonding induced by the addition of salts. (For interpretation of the references to color in this figure legend, the reader is referred to the web version of this article.)

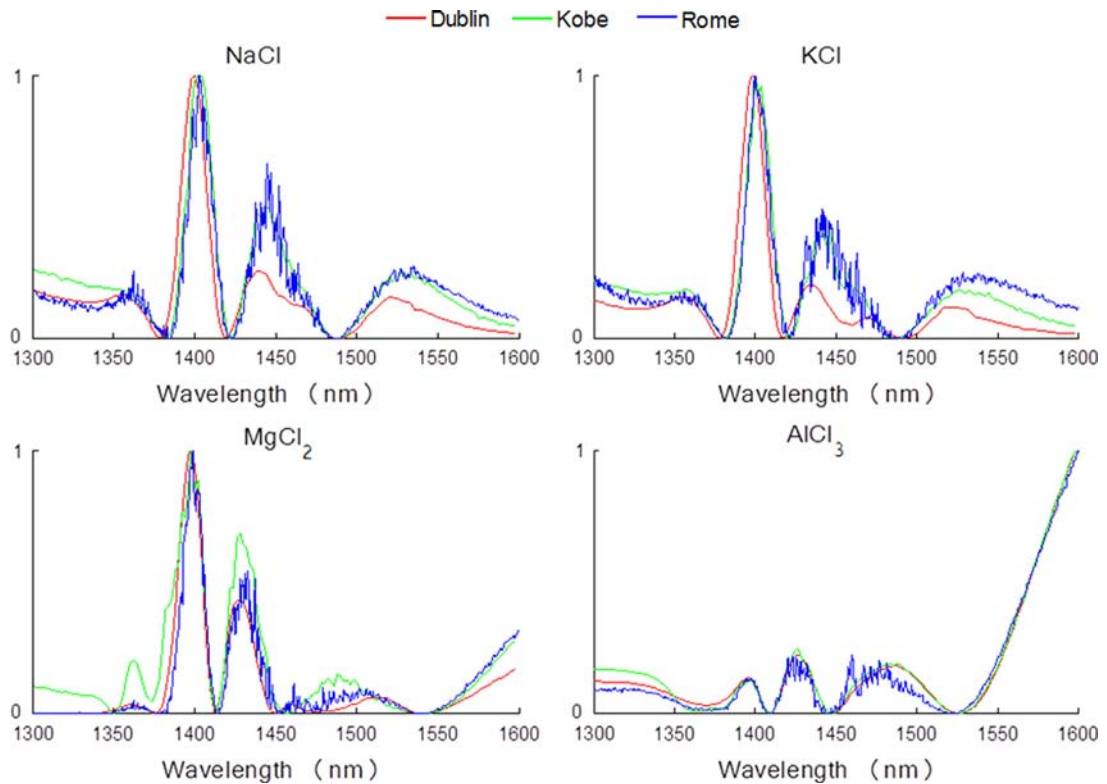


Fig. 7. First principal component loading for salt solutions (after SNV and EMSC pretreatment). Red, green, blue represent different experimental locations (Red=Dublin, Green=Kobe, Blue=Rome). The variations seen here (representing > 85% total variance in each dataset) are related to changes in hydrogen bonding induced by the addition of salts. (For interpretation of the references to color in this figure legend, the reader is referred to the web version of this article.)

Table 3
Peak locations for water absorbance patterns (WAPs) of for different salts (see also Fig. 7), relative sign refers to whether the turning point in the original PC1 loading was a peak (+) or a trough (–).

Pure water	NaCl	KCl	MgCl ₂	AlCl ₃
1414 (+)	1355–1362 (–)	1356–1357 (–)	1361–1362 (–)	1395 (+)
1493–1502 (–)	1400–1404 (+)	1398–1404 (+)	1398–9 (+)	1426–8 (–)
	1440–1445 (–)	1435–1444 (–)	1428–1432 (–)	1477–1488 (+)
	1522–1531 (+)	1522–1531 (+)	1488–1513 (+)	

different researchers operating in independent locations is remarkable. These profiles are somewhat similar to the PC2 loadings obtained on the non-pretreated data (see Fig. 6), but by correcting for the influence of sample temperature, the loadings for each location became very similar to each other, both in terms of PC1 profile and in peak locations. The profiles obtained with the dispersive grating systems (Dublin and Kobe) were smoother and more well defined than those obtained with the FTIR instrument (Rome), due to the higher signal to noise ratio inherent in the dispersive systems for the first overtone region (1300–1600 nm). Each of the salts' WAPs exhibited peaks around 1400, 1430–50 and 1500–20 nm. The peak locations in the WAPs for NaCl and KCl were similar to each other, while those for MgCl₂ and AlCl₃ were shifted (Table 3). Interestingly, the shapes of the profiles varied markedly with the number of chloride ions present. For instance, the WAPs for NaCl and KCl were similar, while those for MgCl₂ and AlCl₃ exhibited an increasing trend with wavelength from 1500 nm. Similar findings have been reported; for example, Frost and Molt [3] indicated that NaCl and KCl impose similar structural effects on water absorbance bands, making it impossible to measure concentration of both simultaneously in an aqueous mixture using NIRS.

4. Conclusions

In this research, we demonstrated that it is possible to predict the concentration of salts in water using NIRS and PLSR, attaining RMSEPs in the order of 4–10 mmol L⁻¹ (equivalent to 500–800 ppm) indicating the potential for this method to detect

contaminants in this concentration range. Limit of detection estimates indicated that NIR spectroscopy is capable of detecting contaminants in water at the 1000 ppm level, which is lower than expected, based on previous studies. The optimal wavelength range for prediction of salt concentration was found to be common to all test locations, i.e. the first overtone region of the NIR spectrum (1300–1600 nm). However, more advanced variable selection techniques (i.e. EMCVS and GA-biPLS) did not select common variables over the different testing locations. In order to evaluate the effects of addition of low concentrations of salts on water structure, it was necessary to correct for ambient environmental conditions (e.g. temperature), which are known to perturb hydrogen bond strength in aqueous solutions and thus impact on the WAP profile. The EMSC pre-treatment enabled suppression of these effects, resulting in lower prediction errors and replicable WAPs over three independent testing locations and different NIR spectrometers.

Acknowledgements

The first author acknowledges funding from the EU FP7 (AquaSense – EU FP7 237819, Biowater – EU FP7 335508) under the Marie Curie Outgoing International Fellowship and ERC starting grant.

Appendix A

See Table A1.

Table A1

Predictive model performance for different wavelength ranges and spectral pre-treatments for salt solutions studied: RMSEP=root mean squared error of prediction, nlv=number of latent variables for prediction model and D, K, R refer to the experiment location (Dublin, Kobe and Rome, respectively).

Salt	Range (nm)	Pretreatment	RMSEP (mmol L ⁻¹)			nlv		
			Dublin	Kobe	Rome	Dublin	Kobe	Rome
NaCl	1000–2498	None	38	10	45	6	15	4
NaCl	1000–2498	SNV	39	9	64	6	15	6
NaCl	1000–2498	SNV+1st der	43	12	33	9	18	2
NaCl	1000–2498	SNV+2nd der	59	19	35	9	14	2
NaCl	1000–2498	SNV+EMSC	38	9	78	7	12	9
NaCl	1000–1298	None	16	14	30	9	12	7
NaCl	1000–1298	SNV	14	27	24	7	13	6
NaCl	1000–1298	SNV+1st der	39	25	32	6	12	3
NaCl	1000–1298	SNV+2nd der	104	13	33	9	12	3
NaCl	1000–1298	SNV+EMSC	13	27	22	7	12	9
NaCl	1300–1598	None	8	3	9	9	6	7
NaCl	1300–1598	SNV	11	3	9	7	7	4
NaCl	1300–1598	SNV+1st der	19	2	17	7	9	5
NaCl	1300–1598	SNV+2nd der	24	3	36	6	17	2
NaCl	1300–1598	SNV+EMSC	9	3	7	7	5	7
NaCl	1600–1898	None	34	2	10	9	17	13
NaCl	1600–1898	SNV	31	2	8	9	17	14
NaCl	1600–1898	SNV+1st der	42	2	37	8	14	4
NaCl	1600–1898	SNV+2nd der	52	2	39	9	16	3
NaCl	1600–1898	SNV+EMSC	42	2	8	9	17	12
NaCl	1900–2198	None	22	19	55	5	7	5
NaCl	1900–2198	SNV	24	19	48	5	7	4

Table A1 (continued)

Salt	Range (nm)	Pretreatment	RMSEP (mmol L ⁻¹)			nlv		
			Dublin	Kobe	Rome	Dublin	Kobe	Rome
NaCl	1900–2198	SNV+1st der	40	22	36	9	12	1
NaCl	1900–2198	SNV+2nd der	31	32	43	7	2	3
NaCl	1900–2198	SNV+EMSC	29	19	77	8	5	10
NaCl	2200–2498	None	54	29	42	5	6	3
NaCl	2200–2498	SNV	25	27	39	5	6	2
NaCl	2200–2498	SNV+1st der	32	33	37	8	3	2
NaCl	2200–2498	SNV+2nd der	33	35	37	1	4	2
NaCl	2200–2498	SNV+EMSC	22	27	41	4	6	2
KCl	1000–2498	None	29	9	47	9	11	4
KCl	1000–2498	SNV	31	7	34	8	11	3
KCl	1000–2498	SNV+1st der	45	11	36	8	14	3
KCl	1000–2498	SNV+2nd der	58	15	36	6	17	3
KCl	1000–2498	SNV+EMSC	32	6	47	9	13	4
KCl	1000–1298	None	15	5	25	6	14	8
KCl	1000–1298	SNV	22	15	20	7	9	8
KCl	1000–1298	SNV+1st der	45	8	33	7	11	2
KCl	1000–1298	SNV+2nd der	94	12	34	6	15	2
KCl	1000–1298	SNV+EMSC	25	13	19	7	12	7
KCl	1300–1598	None	18	2	11	8	5	6
KCl	1300–1598	SNV	22	2	9	7	5	5
KCl	1300–1598	SNV+1st der	43	1	17	6	12	10
KCl	1300–1598	SNV+2nd der	43	3	34	6	8	3
KCl	1300–1598	SNV+EMSC	15	2	14	7	4	4
KCl	1600–1898	None	24	3	27	8	14	11
KCl	1600–1898	SNV	28	2	21	8	14	10
KCl	1600–1898	SNV+1st der	32	2	55	8	12	9
KCl	1600–1898	SNV+2nd der	45	2	48	8	16	4
KCl	1600–1898	SNV+EMSC	30	2	22	7	10	12
KCl	1900–2198	None	38	23	34	6	6	2
KCl	1900–2198	SNV	35	25	33	5	6	3
KCl	1900–2198	SNV+1st der	46	20	38	6	13	3
KCl	1900–2198	SNV+2nd der	56	33	45	5	4	5
KCl	1900–2198	SNV+EMSC	39	21	50	5	6	4
KCl	2200–2498	None	56	35	41	5	11	2
KCl	2200–2498	SNV	23	25	42	4	7	2
KCl	2200–2498	SNV+1st der	57	31	38	6	8	2
KCl	2200–2498	SNV+2nd der	41	32	38	2	2	2
KCl	2200–2498	SNV+EMSC	25	22	34	3	7	1
MgCl ₂	1000–2498	None	10	6	32	12	14	6
MgCl ₂	1000–2498	SNV	10	5	34	11	13	6
MgCl ₂	1000–2498	SNV+1st der	27	7	32	8	18	4
MgCl ₂	1000–2498	SNV+2nd der	45	9	33	9	18	3
MgCl ₂	1000–2498	SNV+EMSC	10	5	34	8	17	5
MgCl ₂	1000–1298	None	33	10	30	9	12	7
MgCl ₂	1000–1298	SNV	37	7	27	9	8	6
MgCl ₂	1000–1298	SNV+1st der	40	7	35	9	10	3
MgCl ₂	1000–1298	SNV+2nd der	49	6	34	8	8	3
MgCl ₂	1000–1298	SNV+EMSC	35	8	26	8	9	6
MgCl ₂	1300–1598	None	11	4	8	7	10	6
MgCl ₂	1300–1598	SNV	12	3	8	6	8	5
MgCl ₂	1300–1598	SNV+1st der	19	5	8	6	9	10
MgCl ₂	1300–1598	SNV+2nd der	20	6	33	7	8	3
MgCl ₂	1300–1598	SNV+EMSC	11	3	8	5	7	4
MgCl ₂	1600–1898	None	30	6	17	9	12	12
MgCl ₂	1600–1898	SNV	37	6	15	9	13	12
MgCl ₂	1600–1898	SNV+1st der	26	6	43	11	12	5
MgCl ₂	1600–1898	SNV+2nd der	27	7	51	6	16	4
MgCl ₂	1600–1898	SNV+EMSC	28	6	14	11	12	11
MgCl ₂	1900–2198	None	38	20	35	7	7	3
MgCl ₂	1900–2198	SNV	27	23	34	8	7	4
MgCl ₂	1900–2198	SNV+1st der	44	20	44	8	11	8
MgCl ₂	1900–2198	SNV+2nd der	74	29	48	7	6	6
MgCl ₂	1900–2198	SNV+EMSC	34	24	37	8	6	4
MgCl ₂	2200–2498	None	34	14	40	7	19	5
MgCl ₂	2200–2498	SNV	18	23	40	6	12	5
MgCl ₂	2200–2498	SNV+1st der	23	12	34	8	20	1
MgCl ₂	2200–2498	SNV+2nd der	38	25	39	8	14	2
MgCl ₂	2200–2498	SNV+EMSC	18	17	42	5	17	5
AlCl₃	1000–2498	None	3	1	5	5	10	6
AlCl₃	1000–2498	SNV	2	1	5	5	10	6
AlCl ₃	1000–2498	SNV+1st der	6	3	42	8	18	4
AlCl ₃	1000–2498	SNV+2nd der	16	5	43	11	17	4

Table A1 (continued)

Salt	Range (nm)	Pretreatment	RMSEP (mmol L ⁻¹)			nlv		
			Dublin	Kobe	Rome	Dublin	Kobe	Rome
AlCl₃	1000–2498	SNV+EMSC	2	1	5	6	13	6
AlCl ₃	1000–1298	None	18	4	11	10	11	7
AlCl ₃	1000–1298	SNV	17	4	11	8	14	7
AlCl ₃	1000–1298	SNV+1st der	21	3	38	6	13	3
AlCl ₃	1000–1298	SNV+2nd der	27	6	46	8	12	4
AlCl ₃	1000–1298	SNV+EMSC	17	4	12	7	6	6
AlCl₃	1300–1598	None	7	1	3	4	6	9
AlCl₃	1300–1598	SNV	5	1	3	5	6	5
AlCl ₃	1300–1598	SNV+1st der	10	1	5	6	11	7
AlCl ₃	1300–1598	SNV+2nd der	14	3	29	4	10	5
AlCl₃	1300–1598	SNV+EMSC	8	1	3	3	5	7
AlCl₃	1600–1898	None	5	1	5	6	16	8
AlCl ₃	1600–1898	SNV	8	1	4	6	7	8
AlCl ₃	1600–1898	SNV+1st der	7	1	6	8	14	11
AlCl ₃	1600–1898	SNV+2nd der	16	3	22	9	19	9
AlCl ₃	1600–1898	SNV+EMSC	8	1	5	6	5	6
AlCl ₃	1900–2198	None	6	5	15	7	3	8
AlCl ₃	1900–2198	SNV	11	10	48	8	13	7
AlCl ₃	1900–2198	SNV+1st der	22	9	45	6	20	6
AlCl ₃	1900–2198	SNV+2nd der	34	26	45	3	6	4
AlCl ₃	1900–2198	SNV+EMSC	12	10	49	8	11	6
AlCl ₃	2200–2498	None	5	1	6	5	6	10
AlCl ₃	2200–2498	SNV	14	27	22	7	14	2
AlCl ₃	2200–2498	SNV+1st der	14	18	28	10	18	3
AlCl ₃	2200–2498	SNV+2nd der	49	27	39	8	14	4
AlCl ₃	2200–2498	SNV+EMSC	10	27	26	7	13	3

References

- [1] European Commission. "Introduction to the new EU Water Framework Directive". (<http://ec.europa.eu/environment/water/water-framework/>). Accessed 16/01/2014.
- [2] A. Gowen, R. Tsenkova, M. Bruen, C. O'Donnell, *Crit. Rev. Environ. Sci. Technol* 42 (2012) 2546–2573.
- [3] V.J. Frost, K. Molt, *J. Mol. Struct.* 410 (1997) 573–579.
- [4] J. Lin, C.W. Brown, *Environ. Sci. Technol.* 27 (1993) 1611–1615.
- [5] A. Grant, A.M.C. Davies, T. Bilverstone, *Analyst* 114 (1989) 819–822.
- [6] A. Sakudo, R. Tsenkova, K. Tei, T. Onozuka, K. Ikuta, E. Yoshimura, T. Onodera, *Biosci. Biotechnol., Biochem.* 70 (2006) 1578–1583.
- [7] K. Kinoshita, H. Morita, M. Miyazaki, N. Hama, H. Kanemitsu, H. Kawakami, P. Wang, O. Ishikawa, H. Kusunokia, R. Tsenkova, *Anal. Methods* 2 (2010) 1671–1675.
- [8] R. Tsenkova, *J. Near Infrared Spectrosc.* 17 (2009) 303–313.
- [9] R. Leardi, L. Nørgaard, *J. Chemom* 18 (2004) 486–497.
- [10] R. Leardi, *J. Chemom* 14 (2000) 643–655.
- [11] L. Nørgaard, A. Saudland, J. Wagner, J.P. Nielsen, L. Munck, S.B. Engelsen, *Appl. Spectrosc.* 54 (2000) 413–419.
- [12] C. Esquerre, A. Gowen, C. O'Donnell, G. Downey, *J. Near Infrared Spectrosc.* 19 (2011) 443–450.
- [13] M.B. Seasholtz, B.R. Kowalski, *Appl. Spectrosc.* 44 (1990) 1247–1243.
- [14] V.H. Segtnan, S. Sasic, T. Isaksson, Y. Ozaki, *Anal. Chem.* 73 (2001) 3153–3161.
- [15] A. Gowen, E. Stark, Y. Tsuchisaka, R. Tsenkova, *NIR News* 22 (2011) 9–11.
- [16] D. Armbruster, T. Pry, *Clin. Biochem. Rev.* 29 (2008) S49–52.
- [17] A.A. Gowen, Y. Tsuchisaka, C. O'Donnell, R. Tsenkova, *Anal. Chem.* 8 (2011) 53–62.



Electrocatalytic determination of chloramphenicol based on molybdenum disulfide nanosheets and self-doped polyaniline

Ruirui Yang, Jinlong Zhao, Meijing Chen, Tao Yang*, Shizhong Luo, Kui Jiao

State Key Laboratory Base of Eco-chemical Engineering, College of Chemistry and Molecular Engineering, Qingdao University of Science and Technology, Qingdao 266042, China

ARTICLE INFO

Article history:

Received 1 July 2014

Received in revised form

8 August 2014

Accepted 12 August 2014

Available online 19 August 2014

Keywords:

Molybdenum disulfide nanosheet

Self-doped polyaniline

Liquid exfoliation

Differential pulse voltammetry

Chloramphenicol

Ultrasonication

ABSTRACT

In this paper, a novel molybdenum disulfide (MoS_2) intercalated by self-doped polyaniline (SPAN) via ultrasonic exfoliating method was prepared to show outstanding conductivity and synergistic electrocatalytic activity using chloramphenicol (CAP) as a case. In the ultrasonic process, due to the strong π - π^* stacking interaction and electrostatic repulsion, the negatively charged SPAN served as an intercalator to result in few-layers MoS_2 nanosheets, which were exfoliated from bulk MoS_2 . This nanocomposite was characterized by scanning electron microscopy, transmission electron microscopy and differential pulse voltammetry. The obtained nanocomposite owns large conjugated structure and rich negative charge, which can improve the adsorption of conjugate structured CAP with the detection range from 0.1 to $1000 \mu\text{mol L}^{-1}$. The results also showed that the electrocatalytic responses were further affected by the mass ratio of SPAN- MoS_2 and the ultrasonication time. Our electrocatalytic platform could be further applied in the adsorption and detection of other positively charged biomolecules or aromatic molecules.

© 2014 Elsevier B.V. All rights reserved.

1. Introduction

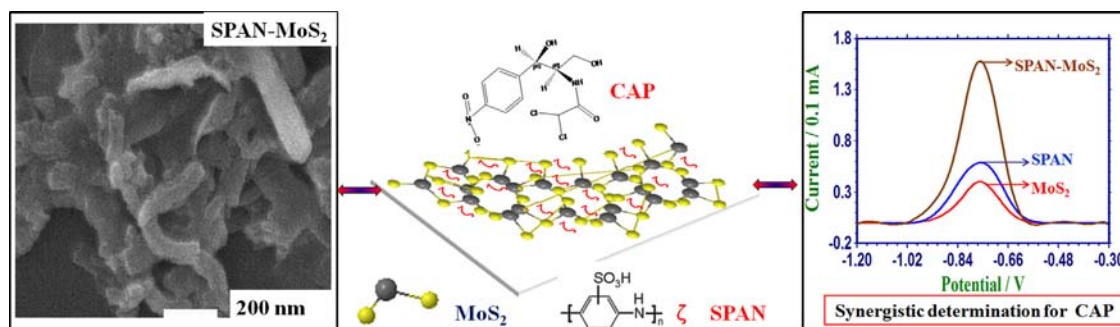
Molybdenum disulfide (MoS_2) nanosheet is a two-dimensional layered material similar to graphene [1]. Owing to its inherent properties, which overcome the shortcomings of the zero band gap of graphene [2,3], it has attracted extensive attention in electrochemical field. For example, the individual MoS_2 modified electrode has been employed for the reduction of H_2O_2 with a low detection limit of 2.5 nmol L^{-1} [4]. Moreover, the electrochemical reduced MoS_2 has been widely used for the determination of dopamine (DA) and ascorbic acid (AA) [5]. Besides, MoS_2 has been integrated with other functional materials, such as polyaniline (PANI), to construct novel nanocomposites showing obviously synergistic effect. MoS_2/PANI nanowires could greatly improve Li^+ -storage properties owing to the hierarchical structure of MoS_2/PANI . The optimal ratio of mixture (MoS_2 66.7%: PANI 33.1%) exhibited an excellent charge capacity [6]. Huang et al. prepared PANI/ MoS_2 nanocomposite with a larger contact surface area, which provided a direct and fast electron path and presented synergistic effect for improving electrochemical performance [7]. Additionally, this PANI/ MoS_2 nanocomposite could be further integrated with gold nanoparticles (AuNPs) to show a synergistic electrocatalytic oxidation to DA in the linear range from 1 to $500 \mu\text{mol L}^{-1}$ with the low detection limit of $0.1 \mu\text{mol L}^{-1}$ ($S/N=3$) [8].

Chloramphenicol (CAP) is a broad-spectrum antibiotic [9]. So far, the methods for determination of CAP mainly include high performance liquid chromatography method [10–12], chemiluminescence method [13], gas chromatography-mass spectrometry [14], surface plasmon resonance biosensor [15], and so on. However, these methods usually required expensive equipments and time-consuming extraction. In contrast, electrochemical method offers the advantages of low cost, simplicity, and relatively short analysis time, which was widely applied for the determination of CAP [16–18]. For example, Xiao et al. investigated the sensitive voltammetric determination of CAP based on single-wall carbon nanotube-gold nanoparticle-ionic liquid composite film modified glassy carbon electrodes [19]. Molecularly imprinted polymer also showed very high CAP recognition ability via differential pulse voltammetry (DPV) [20]. More recently, nitrogen-doped graphene nanosheets (N-G) decorated with AuNPs (Au/N-G) has been used for the electrochemical detection of CAP via the synergistic effect of two nanomaterials [21]. However, MoS_2 nanosheets have not been developed for the electrocatalytic detection of CAP so far.

As a confirmed effective preparation method of two-dimensional nanosheets, liquid exfoliation has been widely adopted with the help of some surfactants and polymers through ultrasonication [1,22,23]. Herein, for the first time, self-doped polyaniline (SPAN) was intercalated into bulk MoS_2 through a simple and low-cost method via ultrasonication to realize liquid exfoliation of bulk MoS_2 . The nanocomposite owns the benzene ring structure and the negative charge, which endow it could easily adsorb some conjugate structured or positively charged biomolecules or molecules [24], here,

* Corresponding author. Tel.: +86 532 84022858; fax: +86 532 84023927.

E-mail address: taoyang@qust.edu.cn (T. Yang).



Scheme 1. MoS₂ nanosheets enhanced by SPAN for synergistic determination of CAP.

CAP as a case. To our best knowledge, MoS₂ was first adopted for the electrochemical determination of CAP, which showed outstanding conductivity and synergistic electrocatalytic activity (Scheme 1).

2. Experimental

2.1. Apparatus and reagents

Electrochemical measurements were carried out with a CHI 660C (Shanghai CH Instrument Company, China). A platinum wire was used as auxiliary electrode, a saturated calomel electrode (SCE) was used as the reference electrode, and a carbon paste electrode (CPE) or modified electrode was used as the working electrode. The ultrasonic process was carried out by KQ-500B sonifier (500 W, Kunshan ultrasonic instruments Co., Ltd.), and the pH values were measured via a model PHS-25 digital acidometer (Shanghai Leici Factory, China). Scanning electron microscopy (SEM) and transmission electron microscopy (TEM) measurements were carried out on a JSM-6700F scanning electron microscope (Japan Electron Company) and JEM 2100 transmission electron microscope, respectively.

Bulk molybdenum disulfide (MoS₂, ≥ 99.0%, Tianjin BASF Chemical Co., Ltd.). Aniline (Tianjin Da Mao Chemical Factory). *m*-Aminobenzenesulfonic acid (ABSA, purity > 98.0%, Fluka, USA). Cetyltrimethyl ammonium bromide (CTAB, Tianjin Bodi Chemical Co., Ltd.). Chloramphenicol (C₁₁H₁₂N₂Cl₂O₅, Shanghai Bioengineering Co., Ltd., China). The chloramphenicol (CAP) reserving solution was prepared by dissolving it into a certain amount of ethanol solution. All the other chemicals were analytical grade and all aqueous solutions were prepared with Aquapro ultrapure water (resistivity: 18 MΩ, Aquaplast AWL-1002-P, Ever Young Enterprises Development Co., Ltd., China).

2.2. The fabrication of CPE and the modified electrodes

The CPE was fabricated by mixing graphite powder with solid paraffin at a ratio of 3/1 (w/w) in a mortar. Then it was heated at 72 °C, agitated and grounded using pestle for 5–6 times. Following, the homogeneous paste was packed firmly into one end of a glass tube (the diameter was about 4 mm), simultaneously inserting a copper wire to the paste in the inner hole of the tube as electrical contact [25,26]. SPAN was synthesized according to Ref. [27]. Detailed process is described as follows: First, a certain quality of aniline, ABSA, and CTAB were dissolved in 40 mL, 0.15 mol L⁻¹ HCl, then 20 mL, 0.06 mol L⁻¹ ammonium persulfate solution (APS) was added. In succession, it was put in refrigerator at 5 °C for 24 h. Finally, a puce flocculent precipitate was obtained and filtered, and then dried in the air naturally. Thus, SPAN was obtained. Later, 0.01 g SPAN and 0.01 g MoS₂ were mixed, dispersed in ultrapure water, followed by ultrasonication for a certain time, and then a

homogenous mixture of SPAN–MoS₂ was formed. For comparison, the MoS₂ nanosheets were obtained by mixing with ultrapure water with a concentration of 1.0 g L⁻¹ just without SPAN existing, and then ultrasonicated for a given time to form the dispersion solution. Changing the mass ratio between SPAN and MoS₂ or the ultrasonication time, a series of SPAN–MoS₂ hybrid materials can be acquired. 20 μL of the mixed liquor was dripped on the bare CPE surface and dried in the air naturally. The obtained electrode was named as SPAN–MoS₂/CPE. Similarly, MoS₂/CPE and SPAN/CPE were prepared. A refresh electrode surface was rapidly generated through extruding a small plug of the paste with a stainless steel rod and then polishing the obtained surface on a white paper [25] ready for next-step modification.

2.3. Electrochemical measurements

Cyclic voltammetry (CV) measurements were carried out in 1.0 mmol L⁻¹ [Fe(CN)₆]^{3-/4-} (1:1) containing 0.1 mol L⁻¹ KCl with the potential scanning range from 0.6 V to -0.3 V at a scan rate of 0.1 V s⁻¹.

DPV: The pulse amplitude, pulse width, and pulse period were set as 0.05 V, 0.06 s, and 0.2 s. Scan range from -0.3 V to -1.2 V. Unless especially noted, all the supporting electrolyte all experiments were PBS (pH 7.0) containing a certain amount of CAP.

In this assay, the reported result for every electrode was the mean value of three parallel measurements.

3. Result and discussion

3.1. Characterization of the SPAN–MoS₂ hybrid

The representative SEM and TEM images of MoS₂, SPAN, and SPAN–MoS₂ are displayed in Fig. 1. The SEM image of MoS₂ (Fig. 1A) displays an obviously layered structure, which can be further proved by the typical TEM image, showing multilayer nanosheets (Fig. 1B). From Fig. 1C, the SPAN nanofibres are interconnected together to form almost uniform netlike nanostructures with 65–85 nm in diameter. The TEM image of SPAN (Fig. 1D) further clearly displays the net-like nanostructure of SPAN nanofibres. Compared with the sole MoS₂ (Fig. 1A and B) or SPAN (Fig. 1C and D), fibrous and layered structure can be simultaneously observed for SPAN–MoS₂ in Fig. 1E, showing that the fibrous SPAN has successfully integrated with the layered MoS₂. Moreover, the intercalation of SPAN and MoS₂ can also be confirmed by the TEM image (Fig. 1F), where the SPAN nanofibers are coated by transparent MoS₂. In the process of intercalation, MoS₂ can serve as backbone to maintain the nanowired network structure. The π–π* interaction between SPAN and MoS₂ promotes the intercalation without damage their original properties.

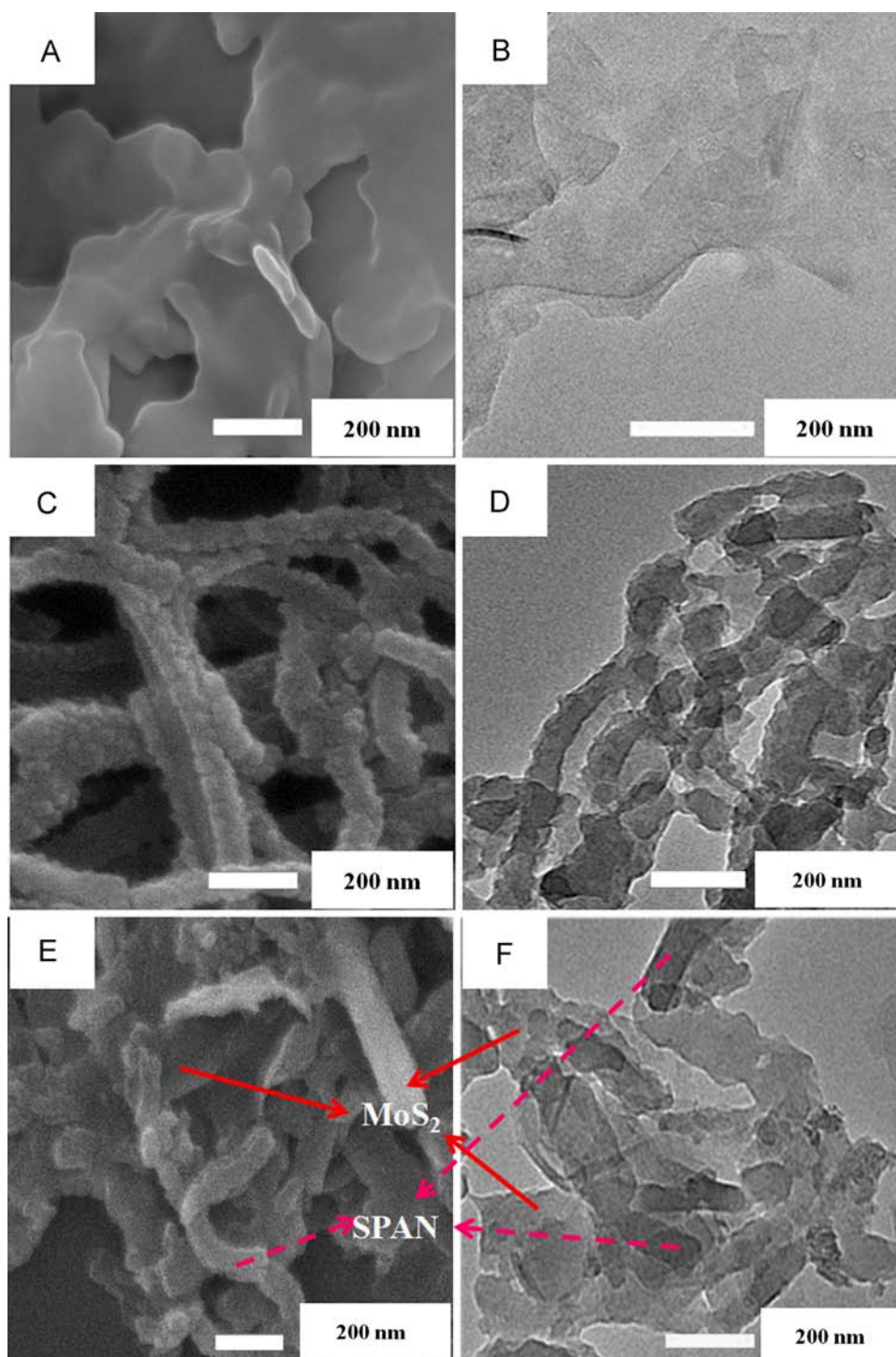


Fig. 1. SEM and TEM images of MoS₂ (A) and (B); SPAN (C) and (D); and SPAN–MoS₂ (E) and (F).

3.2. Electrochemical reduction behavior of CAP

The electrochemical behaviors of $1.0 \times 10^{-3} \text{ mol L}^{-1}$ CAP at different modified electrodes were investigated in phosphate buffer solution (PBS, pH 7.0), which are displayed in Fig. 2A. Compared with MoS₂/CPE (curve a) and SPAN/CPE (curve b), SPAN–MoS₂/CPE (curve c) displays the largest reduction peak current. This implied that SPAN–MoS₂ could promote the electron exchange between the electrode surface and the CAP, which is ascribed to the special benzene ring structure of SPAN–MoS₂ could

easily adsorb conjugate structured CAP (Scheme 1) and show the synergistic effect. The reduction mechanism is that CAP is irreversibly reduced from nitro group (Ph–NO₂) to hydroxylamine (Ph–NHOH) [28–30].

Furthermore, the mass ratio of the mixture can affect electrochemical behavior of CAP. Fig. 2B shows the reduction peak current of CAP being influenced by the hybrid materials with different mass ratio. Through the results, we discovered that the current response of CAP at SPAN–MoS₂ (1:3)/CPE (curve c) is larger than the other modified electrodes. That can be attributed to the

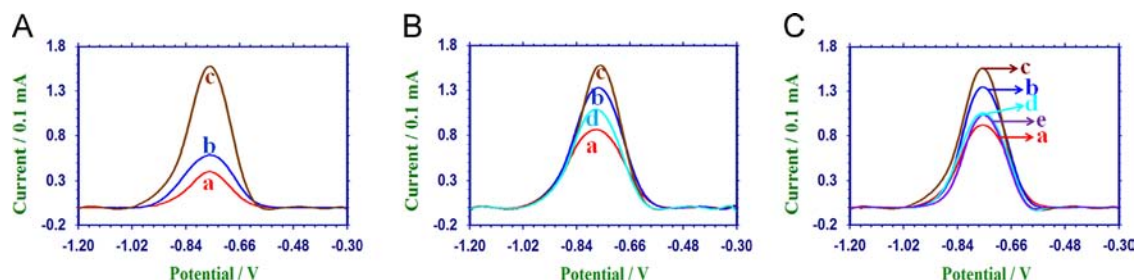


Fig. 2. (A) Representative DPVs of 1.0×10^{-3} mol L⁻¹ CAP at (a) MoS₂/CPE; (b) SPAN/CPE; (c) SPAN–MoS₂(1:3)/CPE; (B) Representative DPVs of CAP at different mass ratio of SPAN/MoS₂: (a) 1:1 (b) 1:2; (c) 1:3; (d) 1:4; (C) DPVs of CAP at SPAN–MoS₂(1:3)/CPE obtained from different ultrasonication time: (a) 3 h, (b) 4 h, (c) 5 h, (d) 6 h, (e) 7 h. DPV parameters: pulse amplitude: 0.05 V, pulse width: 0.06 s, pulse period: 0.2 s, scan range from –0.3 V to –1.2 V.

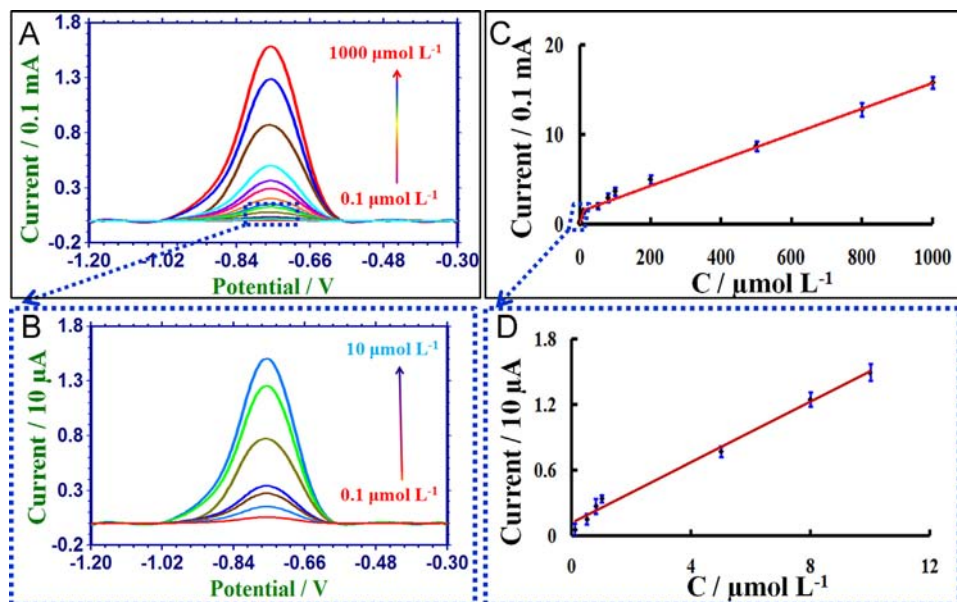


Fig. 3. (A) Representative DPV for the determination of CAP in PBS at SPAN–MoS₂(1:3)/CPE with CAP concentrations ranging from 0.1 to 1000 μmol L⁻¹ (0.1, 0.5, 0.8, 1, 5, 8, 10, 50, 80, 100, 200, 500, 800, 1000 μmol L⁻¹); and the concentrations of 0.1, 0.5, 0.8, 1, 5, 8, 10 μmol L⁻¹ (B); (C) and (D) calibration plots of the reduced peak current versus different concentrations of CAP. Note: DPV conditions are as same as Fig. 2. Error bars are the standard deviation of three replicates.

larger electroactive surface area (the details please see Table S1). Therefore, the mass ratio of the hybrid of 1:3 was selected as the optimum mass ratio for the subsequent experiments.

The effect of the ultrasonication time on the electroreduction responses of CAP are revealed in Fig. 2C. It can be seen that the intensity of the current peaks significantly increased by increasing the ultrasonication time, but after the hybrids being ultrasonicated for 5 h, it comes to the maximum (curve c) and then decreased. And, it can simultaneously be demonstrated from the variations in the active surface area (shown in Table S1). So, 5 h was selected.

Furthermore, the effect of the pH value of PBS on the electroreduction of 1.0×10^{-3} mol L⁻¹ CAP at SPAN–MoS₂/CPE modified electrode was also investigated with the pH value in the range of 4.0 to 8.0. As can be seen from Fig. S1, the reduction peak current was significantly affected by the pH value of buffer solution. When the pH value varies from 4.0 to 7.0 (curve a to curve d), the reduction peak current increased. When the pH reached 7.0, the peak current achieved the maximum. However, after further increasing the pH, the peak currents decreased (curve e). It indicated that alkaline environment is not benefit to the electron transfer during the reduction process. Therefore, pH 7.0 was chosen.

For comparison, to further show the function of SPAN–MoS₂, the DPVs results of 1.0×10^{-3} mol L⁻¹ CAP in different pH values of PBS at bare CPE is shown in Fig. S2A and B. As we can see, the peak potential and the change trends recorded at bare CPE were

similar to those recorded at SPAN–MoS₂/CPE, only accompanied with obviously decreased peak currents. Moreover, the DPV results of PBS with different pH values without CAP existing at bare CPE (Fig. S2C) and SPAN–MoS₂/CPE (Fig. S2D) were recorded. As can be seen, no peak appears in potential windows. It demonstrated that the effect of pH was according to the change in redox of CAP, and the formed nanocomposite can promote the adsorption of CAP without interference.

3.3. Detection of CAP with different concentrations

Based on the optimum results above, the response of CAP with different concentrations was detected. Fig. 3 shows the determination of a series of concentrations of CAP with the range of 0.1–1000 μmol L⁻¹. When the concentrations of CAP increased, the peaks current increased (Fig. 3A). To show low concentration range, the DPV results with concentrations of 0.1–10 μmol L⁻¹ are magnified in Fig. 3B. As shown in Fig. 3C and D, the linear relationships between the reduction peak current values (I_p) and the concentrations of CAP are displayed in two segments. In the high concentrations range (10–1000 μmol L⁻¹), the linear equation is $I_p = 0.014C + 1.7421$ ($R^2 = 0.9961$) (Fig. 3C), while at the range of the low concentrations (0.1–10 μmol L⁻¹), the linear equation is $I_p = 0.1388C + 0.1161$ ($R^2 = 0.9906$) (Fig. 3D) [31]. The limit of detection ($S/N=3$) is 6.5×10^{-8} mol L⁻¹. Our assay was also compared with previous reports (Please see Supplementary materials). Table S2 shows our

work possessed the wider linear range and lower detection limit as compared with other earlier reports.

3.4. Stability, repeatability and reproducibility of the modified electrode

In order to confirm the electrochemical sensor with long-term stability, the modified electrode was stored for 10 days at room temperature. During this period, the modified electrode was used to detect 1×10^{-3} mol L⁻¹ CAP. The analytical performances of the modified electrode were not significantly decreased (relative standard deviation (RSD) \leq 5%), indicating that the modified electrodes possessed good electrochemical stability [24].

To test the repeatability of SPAN–MoS₂/CPE, 1.0×10^{-3} mol L⁻¹ CAP solution was measured for ten times with a same modified electrode regenerated after every determination. The RSD for the peak current is 2.04%. Moreover, ten modified electrodes were prepared by the same procedure for studying the reproducibility. It is verified that the modified electrodes own good reproducibility, with the RSD of 3.48% for the reduction peak current of CAP [19].

3.5. Sample analysis

Finally, the proposed method was applied to real sample application by testing CAP in eye drops (purchased from a local pharmacy) via the standard addition method. The concentrations of the standard CAP added were 0, 5, 10, 20 and 30 μ mol L⁻¹, respectively [30]. DPVs were recorded via scanning range from -0.3 to -1.2 V, and then the calibration graph was obtained by plotting the peak current against CAP concentrations. The recoveries of the CAP standards added are 98.2–101.3% with RSD values at 1.2–4.4%. These results indicated that the recoveries and reproducibility of CAP in eye drops sample were very satisfactory.

4. Conclusion

In short, through ultrasonication of the mixed dispersion of bulk MoS₂ with SPAN co-existing, the negatively charged SPAN ceaselessly diffused and intercalated into the MoS₂ layers to form a homogenous and three-dimensional interconnected structure. Compared with the sole MoS₂ or SPAN, SPAN–MoS₂ interface with the mass ratio of 1:3 (SPAN/MoS₂) and ultrasonication time of 5 h have the highest peak currents, displaying remarkable synergistic effect for the reduction of CAP. The developed sensing platform displayed acceptable reproducibility, long-term stability, high sensitivity, and low detection limit, which can develop a great space for further application in biosensor and medicine fields.

Acknowledgments

This work was supported by the National Natural Science Foundation of China (nos. 21275084, 41476083), Doctoral Foundation of the Ministry of Education of China (no. 20113719130001), Outstanding Adult-Young Scientific Research Encouraging Foundation of Shandong Province (no. BS2012CL013), and Scientific and Technical Development Project of Qingdao (no. 12-1-4-3-(23)-jch).

Appendix A. Supporting information

Supplementary data associated with this article can be found in the online version at <http://dx.doi.org/10.1016/j.talanta.2014.08.035>.

References

- [1] J.N. Coleman, M. Lotya, A. O'Neill, S.D. Bergin, P.J. King, U. Khan, K. Young, A. Gaucher, S. De, R.J. Smith, I.V. Shvets, S.K. Arora, G. Stanton, H.Y. Kim, K. Lee, G.T. Kim, G.S. Duesberg, T. Hallam, J.J. Boland, J.J. Wang, J.F. Donegan, J. C. Grunlan, G. Moriarty, A. Shmeliov, R.J. Nicholls, J.M. Perkins, E. M. Grievson, K. Theuwissen, D.W. McComb, P.D. Nellist, V. Nicolosi, *Science* 331 (2011) 568–571.
- [2] H. Matte, A. Gomathi, A.K. Manna, D.J. Late, R. Datta, S.K. Pati, C.N.R. Rao, *Angew. Chem. Int. Ed.* 49 (2010) 4059–4062.
- [3] D.J. Late, Y.K. Huang, B. Liu, J. Acharya, S.N. Shirodkar, J.J. Luo, A. Yan, D. Charles, U.V. Waghmare, V.P. Dravid, C.N.R. Rao, *ACS Nano* 7 (2013) 4879–4891.
- [4] T.Y. Wang, H.C. Zhu, J.Q. Zhuo, Z.W. Zhu, P. Papakonstantinou, G. Lubarsky, J. Lin, M.X. Li, *Anal. Chem.* 85 (2013) 10289–10295.
- [5] S.X. Wu, Z.Y. Zeng, Q.Y. He, Z.J. Wang, S.J. Wang, Y.P. Du, Z.Y. Yin, X.P. Sun, W. Chen, H. Zhang, *Small* 8 (2012) 2264–2270.
- [6] L.C. Yang, S.N. Wang, J.J. Mao, J.W. Deng, Q.S. Ga, Y. Tang, O.G. Schmidt, *Adv. Mater.* 25 (2013) 1180–1184.
- [7] K.J. Huang, L. Wang, Y.J. Liu, H.B. Wang, Y.M. Liu, L.L. Wang, *Electrochim. Acta* 109 (2013) 587–594.
- [8] K.J. Huang, J.Z. Zhang, Y.J. Liu, L.L. Wang, *Sens. Actuators B: Chem.* 194 (2014) 303–310.
- [9] S. Moritz, T.S. Woodward, C. Cuttler, J.C. Whitman, J.M. Watson, *Neuropsychology* 18 (2004) 276–283.
- [10] A.M. Di Pietra, V. Piazza, V. Andrisano, V. Cavrini, J. Lip. *Chromatogr.* 18 (1995) 3529–3543.
- [11] R. Hirsch, T.A. Ternes, K. Haberer, A. Mehlich, F. Ballwanz, K.L. Kratz, *J. Chromatogr. A* 815 (1998) 213–223.
- [12] C. Hummert, B. Luckas, H. Siebenlist, *J. Chromatogr. B* 668 (1995) 53–58.
- [13] C.A. Lindino, L.O.S. Bulhoes, J. Braz, *Chem. Soc.* 15 (2004) 178–182.
- [14] P. Li, Y.M. Qiu, H.X. Cai, Y. Kong, Y.Z. Tang, D.N. Wang, M.M. Xie, *Chin. J. Chromatogr.* 24 (2006) 14–18.
- [15] V. Dumonta, A.C. Huet, I. Traynor, C. Elliott, P. Delahaut, *Anal. Chim. Acta* 567 (2006) 179–183.
- [16] J. Duda, U. Kucharska, *Anal. Lett.* 32 (1999) 1049–1064.
- [17] L. Yan, C.H. Luo, W. Cheng, W. Mao, D.C. Zhang, S.J. Ding, *J. Electroanal. Chem.* 687 (2012) 89–94.
- [18] S. Pilehvar, F. Dardenne, R. Blust, K. De Wael, *Int. J. Electrochem. Sci.* 7 (2012) 5000–5011.
- [19] F. Xiao, F.Q. Zhao, J.W. Li, R. Yan, J.J. Yu, B.Z. Zeng, *Anal. Chim. Acta* 596 (2007) 79–85.
- [20] T. Alizadeh, M.R. Ganjali, M. Zare, P. Norouzi, *Food Chem.* 130 (2012) 1108–1114.
- [21] J. Borowiec, R. Wang, L.H. Zhu, J.D. Zhang, *Electrochim. Acta* 99 (2013) 138–144.
- [22] K.G. Zhou, N.N. Mao, H.X. Wang, Y. Peng, H.L. Zhang, *Angew. Chem. Int. Ed.* 50 (2011) 10839–10842.
- [23] R.J. Smith, P.J. King, M. Lotya, M. Lotya, C. Wirtz, U. Khan, S. De, A. O'Neill, G. S. Duesberg, J.C. Grunlan, G. Moriarty, J. Chen, J.Z. Wang, A.I. Minett, V. Nicolosi, J.N. Coleman, *Adv. Mater.* 23 (2011) 3944–3948.
- [24] T. Yang, Q. Guan, Q.H. Li, L. Meng, L.L. Wang, C.X. Liu, K. Jiao, *J. Mater. Chem. B* 1 (2013) 2926–2933.
- [25] C. Jiang, T. Yang, K. Jiao, H.W. Gao, *Electrochim. Acta* 53 (2008) 2917–2924.
- [26] T. Yang, Q. Guan, X.H. Guo, L. Meng, M. Du, K. Jiao, *Anal. Chem.* 85 (2013) 1358–1366.
- [27] C.Q. Zhang, G.C. Li, H.R. Peng, *Mater. Lett.* 63 (2009) 592–594.
- [28] C.Y. Liao, C.C. Chang, C. Ay, J.M. Zen, *Electroanalysis* 19 (2007) 65–70.
- [29] H. Alemu, L. Hlalele, *Bull. Chem. Soc. Ethiop* 21 (2007) 1–12.
- [30] S. Chuanuwatanakul, O. Chailapakul, S. Motomizu, *Anal. Sci.* 24 (2008) 493–498.
- [31] F. Yang, K.J. Huang, D.J. Niu, C.P. Yang, Q.S. Jing, *Electrochim. Acta* 56 (2011) 4685–4690.



Sensitive analysis of amino acids and vitamin B₃ in functional drinks via field-amplified stacking with reversed-field stacking in microchip electrophoresis

Minglei Wu^a, Fan Gao^a, Yi Zhang^a, Qingjiang Wang^{a,*}, Hui Li^{b,**}

^a Department of Chemistry, East China Normal University, 500 Dongchuan Road, Shanghai 200241, PR China

^b College of Chemistry and Chemical Engineering, Shanghai Jiaotong University, 800 Dongchuan Road, Shanghai 200240, PR China

ARTICLE INFO

Article history:

Received 27 June 2014

Received in revised form

16 August 2014

Accepted 18 August 2014

Available online 23 August 2014

Keywords:

Field-amplified stacking

Reversed-field stacking

Amino acids

Vitamin B₃

Functional drinks

ABSTRACT

An on-line preconcentration strategy combining field-amplified stacking and reversed-field stacking was developed for efficient and sensitive analysis of amino acids and vitamin B₃ including lysine (Lys), taurine (Tau), and niacinamide (NA) by microchip electrophoresis with LIF detection. In this technique, the addition of a reversed-polarity step termed reversed-field stacking could enhance the preconcentration effect of field-amplified stacking and push most of the sample matrix out of the separation channel, thus greatly improving the sensitivity enhancement by 1–2 orders of magnitude over the classical MCE–LIF methods. The related mechanism as well as important parameters governing preconcentration and separation have been investigated in order to obtain strongest sensitivity amplification and maximum resolution. Under optimal conditions, all analytes were successfully focused and completely separated within 4 min. The limits of detection for Lys, Tau, and NA were 0.25, 0.50, and 0.20 nM (*S/N*=3), respectively, and enhancement factors of 165-, 285-, and 236-fold were obtained for Lys, Tau, and NA as compared to using the no concentration step. Other validation parameters such as linearity and precision were considered as satisfactory. The proposed method also gave accurate and reliable results in the analysis of these functional ingredients in eight functional drink samples.

© 2014 Elsevier B.V. All rights reserved.

1. Introduction

Functional drinks are non-alcoholic drinks fortified with functional ingredients, which are promoted with benefits such as heart health, improved immunity and digestion, joint health, satiety, and energy boosting [1,2]. Nowadays, the consumers' demand for functional drinks is clearly rising [2] and the fortification of functional drinks with vitamins and amino acids is very common in the modern food industry. Niacinamide (vitamin B₃), which exists in various kinds of functional drinks, is an important endogenous metabolite and dietary component. Niacinamide (NA) plays an important role in the cellular energy metabolism and influences oxidative stress. In deficiency states, inadequate NA leads to fatigue, loss of appetite, pigmented rashes of the skin, and oral ulcerations [3]. More severe states of deficiency cause the

development of pellagra [3,4]. Lys is a building block for proteins and an essential amino acid that cannot be synthesized by the human body, making it necessary to be supplied by external sources. For children, Lys is essential for healthy growth and development especially for proper growth of bones. In addition, it helps the body absorb calcium, maintain the proper nitrogen balance, and ensure lean body mass [5,6]. As a member of the family of sulfur-containing amino acids, Tau is naturally present in abundant concentrations in mammalian tissues [7,8]. This compound has been used as an additive in functional drinks because of its many important physiological functions, including the formation of bile salts, modulation of calcium flux, and neuronal excitability, osmoregulation, and immune function [9]. Some therapeutic effects have also been proposed for Tau supplementation such as treatment for diabetes [10], high blood pressure [11], heart failure [12], retinal degeneration [13], and skeletal muscle disorders [14].

The need for simultaneous reliable and sensitive analytical methods for the health promoting compounds in functional drinks is obvious. HPLC is the most common technique for separating micronutrients or amino acids in food products, which has been used for separating vitamins in functional drinks [15] and amino

Abbreviations: Cy5, sulfoindocyanine succinimidyl ester; FASS, field-amplified stacking; Lys, lysine; MCE, microchip electrophoresis; NA, niacinamide; Tau, taurine

* Corresponding author. Tel.: +86 21 54340015.

** Corresponding author. Tel.: +86 21 54743271.

E-mail addresses: qjwang@chem.ecnu.edu.cn (Q. Wang), chemlihui@sjtu.ecnu.edu.cn (H. Li).

<http://dx.doi.org/10.1016/j.talanta.2014.08.051>

0039-9140/© 2014 Elsevier B.V. All rights reserved.

acids in food, beverages and feedstuff [16,17]. However, this method usually requires larger sample volume with much more solvent consumption. In recent decades, CE has been accepted as a powerful analytical technique in analyzing nutritious compounds due to its lower consumption of sample and better separation efficiency compared to HPLC [18]. Szymom et al. presented a CE-based method for separation and sensitive analysis of vitamins B [19]. Additionally, Zhao et al. demonstrated separation and determination of vitamins B and essential amino acids in health drinks using CE [20].

In recent years, the development of micro-fluidic devices, also called “lab-on-a-chip”, has witnessed an explosive growth since their introduction. Microchip electrophoresis (MCE), which is one of the most important applications of micro-fluidics, is increasingly being viewed as a new trend in food analysis [21]. Microchips typically consume picoliters of samples [22], which is much less than the sample consumption of CE (at the nanoliter level) and HPLC (at the microliter level). In addition, MCE offers significant benefits such as miniaturization, reduced reagent consumption, and fast operation. Regarding the detection system, LIF has proved to be a potent detection method in terms of its high sensitivity and high selectivity in real sample analysis. However, the sensitivity of MCE–LIF is sometimes not sufficient because of the characteristically low sample volume and short optical pathlength of the microchannels [23]. Therefore, various on-line preconcentration methods have been developed and implemented to enhance the sensitivity of MCE [24,25], including field-amplified stacking (FASS) [26], transient isotachopheresis [27], isoelectric focusing [28], transient trapping [29], sweeping [30], reversed-field stacking [31], and so on. Such techniques can be performed individually or in combination, affording ten- to almost one million-fold improvements in detection sensitivity. Qiong et al. reported a highly effective on-chip preconcentration method combining FASI and bovine serum albumin sweeping for ultrasensitive detection of green fluorescent protein on a simple cross-channel microchip device, which yielded a concentration factor of 3570 [30]. Our group recently reported a multiple-concentration method combining chitosan sweeping, reversed-field stacking, and FAAS for ultrasensitive detection of bacteria by MCE–LIF, which achieved nearly 6000-fold signal enhancement [31].

The applications of FAAS to CE have been well described to provide high sensitivity enhancement in a number of studies [32,33]. However, microchip-based separation systems have short separation distances that are 10–100 times shorter than those of standard capillary-based systems, limiting the concentration enhancement of FAAS. In addition, the preconcentration effect of FAAS is detrimental to the separation efficiency of MCE, leading to

the decline in resolution. In this case, the addition of a reversed-polarity step called reversed-field stacking could lengthen the effective separation distance and provide a longer time for FAAS by pushing back the sample plug, thus enhancing the enrichment effect of FAAS and improving the resolution of all analytes. Simultaneously, most of the low-conductivity sample matrix was pumped out of the separation channel by using reversed-field stacking, thus further improving the concentration enhancement.

Herein, we applied an on-line preconcentration approach combining FAAS and reversed-field stacking to the MCE–LIF analysis of three health promoting compounds, including Lys, Tau, and NA (Fig. 1). To the best of our knowledge, this is the first report of combination of the FAAS-reversed-field stacking technique for the simultaneous determination of varied compounds in food samples by MCE. The sensitivity obtained by this strategy was improved by one to two orders of magnitude as compared to those of previously reported MCE–LIF methods [34,35]. Under optimal conditions, the two amino acids and vitamin B₃ were successfully focused and well separated within 4 min, and the detection sensitivities were improved 165-, 285-, and 236-fold for Lys, Tau, and NA using this concentration technique as compared to using a no concentration method. The proposed method allows fast and sensitive analysis of these amino acids as well as vitamin B₃ and it was successfully applied to the determination of the three functional ingredients in eight functional drinks. Therefore, it is self-evident that this approach could potentially be used for the simultaneous analysis of low-abundance beneficial compounds in food products.

2. Materials and methods

2.1. Apparatus and chemicals

All MCE experiments were conducted using a homemade MCE system coupled with a laser-induced fluorescence (LIF) detection device that was created by Shanghai Spectrum Ltd. Co., Zhejiang University and our research group [36]. Briefly, a diode laser (5 mW) was used to generate an excitation beam at 635 nm. The fluorescence signal was spectrally isolated using an edge filter and was subsequently collimated with an achromatic lens before being focused onto the photomultiplier tube (PMT). The high voltage power unit variable in the range 0 ± 6 kV was used for on-chip sample injection and zone electrophoretic separation. The amplified current was transferred directly through a 10 k Ω resistor to a 24 bit A/D interface at 10 Hz (Borwin, JMBS Developments, Le Fontanil, France) and stored in a personal computer.

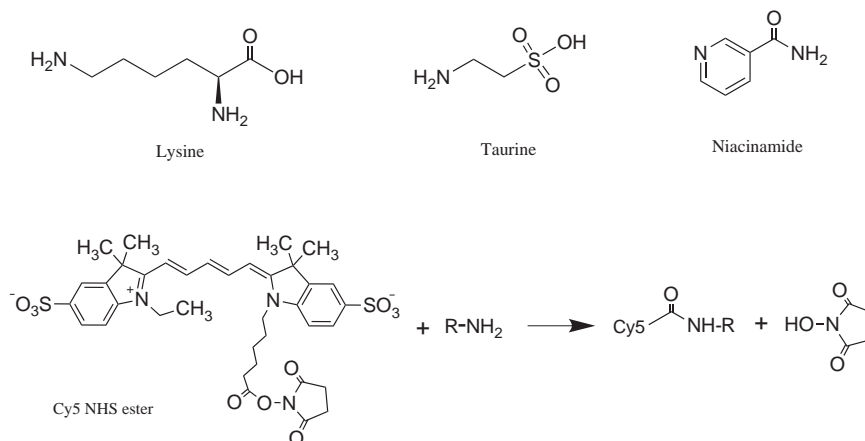


Fig. 1. Chemical structures of the analytes assayed and scheme of the labeling reaction with Cy5.

Analytical-grade chemicals were used unless otherwise stated. Lysine (Lys), taurine (Tau), and niacinamide (NA) were purchased from Sigma (St. Louis, MO, USA). Sodium tetraborate ($\text{Na}_2\text{B}_4\text{O}_7$), sodium hydroxide (NaOH), hydrochloric acid, and acetonitrile were from Sinopharm Chemical Reagent Co. Ltd. (Shanghai, China). Sulfoindocyanine succinimidyl ester (Cy5) was obtained from GE Healthcare Company (Shanghai, China). All solutions were prepared by ultrapure water supplied by Milli-Q water purification system (Millipore, Bedford, MA, USA).

2.2. Solutions

A running buffer solution was prepared by dilution of the appropriate amount of $\text{Na}_2\text{B}_4\text{O}_7$ in ultrapure water to a concentration of 100 mM, whereas sample buffer and derivatization buffer solutions were made by dissolving $\text{Na}_2\text{B}_4\text{O}_7$ with water to 10 mM and 20 mM, respectively. Desired pH values of these buffer solutions were obtained with 1 M NaOH or 0.5 M hydrochloric acid. Standard solutions of individual Lys, Tau, and NA were prepared with a concentration of 100 mM in ultrapure water and diluted to 100 μM with derivatization buffer. The stock solution Cy5 (100 μM) was made by dissolving in anhydrous acetonitrile. The above solutions were sealed and stored at 4 °C in a refrigerator.

2.3. Procedures of derivatization

Standard solutions of 100 mM Lys, Tau, and NA were diluted to 100 μM with derivatization buffer (20 mM borate solution at pH 8.60). Derivatization of individual compounds was performed by mixing diluted solution with 100 μM Cy5 solution 1:1 (v:v) in a 1.5 mL centrifuge tube. The three mixtures reacted in darkness for 4 h at room temperature, and then diluted to required concentrations with sample buffer (10 mM borate solution at pH 9.88) before using.

2.4. Preparation of drink sample

Eight functional drink samples purchased from supermarkets in Shanghai were named F1, F2, F3, F4, F5, F6, F7, and F8, respectively. The functional drink samples were diluted two-fold with 40 mM borate solution and adjusted to pH 8.60 with 1 M NaOH. Finally, the diluted sample solutions were derivatized as stated in Section 2.3, and then diluted to a certain concentration with sample buffer (10 mM borate solution at pH 9.88) before analysis.

2.5. MCE conditions

The glass microchip design used in these experiments consisted of a simple cross-channel. The separation channel was 60 mm in length and 45 mm from the injection intersection to the detection point. All other channels had a length of 10 mm measured from the channel intersection. Microchannels were etched to a depth of 25 μm and a width of 70 μm . Platinum electrodes were inserted into the reservoirs, providing electrical contact from the power supply to the electrolyte solutions. All experiments were running in full filling mode.

Before a new microchip was used for the first time, it was washed with 98% H_2SO_4 and ultrapure water for 10 min. Subsequently, the channels were flushed with 1 M NaOH for 20 min, ultrapure water for 10 min, and the MCE running buffer for 10 min. Before each injection, the microchannels were washed for 2 min with 1 M NaOH, for 1 min with ultrapure water and for 2 min with MCE running buffer.

2.6. Procedure of on-line pre-concentration method

For FASS, the samples were prepared with an appropriate sample buffer (10 mM borate solution) with a much lower conductivity compared with running buffer (100 mM borate solution). The reversed-field stacking step was maintained similar to the sample loading time, so that the sample plug could move to the injection cross within an appropriate distance. A four-step MCE procedure with the voltage configuration of each step was designed as shown in Fig. 2, which was responsible for the pre-concentration effect in the MCE method.

3. Results and discussion

3.1. Field-amplified stacking-reversed-field stacking mechanism

In order to realize the highly efficient detection of three beneficial compounds, an on-line multiple-pre-concentration method combining FASS and reversed-field stacking was employed. The schematic mechanism of this method is shown in Fig. 2. At the beginning, the voltages of each of the reservoirs were adjusted to ensure that the low-conductivity sample solution flowed from the sample reservoir to the sample waste reservoir through the injection cross and the running buffer solution flowed from the buffer reservoir to both waste reservoirs (Fig. 2A). The voltage configuration was then changed to the

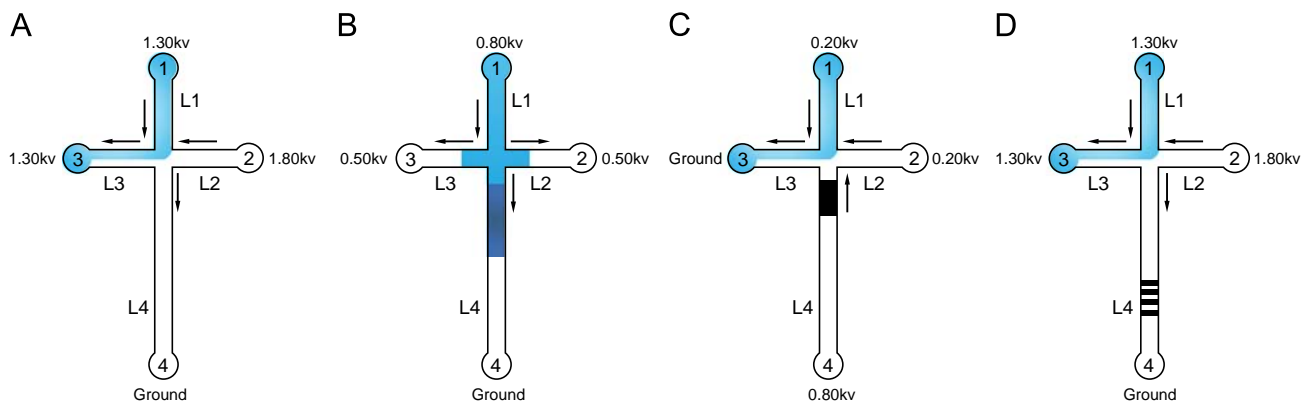


Fig. 2. Schematic diagram of the sample loading, on-line pre-concentration, and separation of nutritive compounds: (A) preloading, (B) FASS, (C) reversed-field stacking, and (D) separation. The dark blue zone represents the concentrated sample by FASS before using reversed-field stacking technique, the black zone represents the area of the concentrated sample after reversed-field stacking, the light blue zone represents the sample matrix, and the clear zone represents the running buffer. 1 = sample reservoir; 2 = buffer reservoir; 3 = sample waste reservoir; 4 = buffer waste reservoir. L 1–4 represent four channels of microchips. Arrows indicate bulk flow directions. The voltages (kV) applied to the reservoirs at each step are indicated. (For interpretation of the references to color in this figure legend, the reader is referred to the web version of this article.)

loading step. During the loading step, as shown in Fig. 2B, a gated injection method was selected to introduce the sample plug into the separation channel. Meanwhile, FASS occurred in the separation channel (the dark blue zone in Fig. 2B). In the process of FASS, the samples were prepared in a medium of lower conductivity than the running buffer. Charged analytes move more quickly in the low-conductivity sample zone and are immediately retarded at the interface between the two buffers with different ionic strengths and electric fields. However, the micro-fluidic devices have short separation distances, limiting the concentration enhancement of FASS. In addition, the enrichment effect of FASS is detrimental to the separation efficiency of MCE, leading to the decline in separation resolution of the analytes. To solve these problems, an additional step which was termed reversed-field stacking was performed by switching the polarity (Fig. 2C). Under the reversed-field stacking conditions, the concentrated sample zone in L4 was pushed back to the injection cross within an appropriate distance, which could give analytes a longer time for boundary enrichment and lengthen the effective separation distance, thus enhancing the enrichment effect of FASS and improving separation efficiency. Simultaneously, most of the long and vacant sample matrix was pumped from the separation channel (L4) into L3 in the process of reversed-field stacking, thus avoiding the reduction of effective separation length and leading to further concentration enhancement.

These two steps of the on-line concentration method were crucial in order to obtain the highest concentration enhancement. Fig. 3 displays the electrophoretic profiles for the different concentration steps. The standard electropherograms shown in Fig. 3B and C were obtained by 10-fold dilution of the sample used in Fig. 3A. The electropherogram of the typical gated injection method without any concentration is shown in Fig. 3A. For FASS (Fig. 3B), all analytes were enriched and the signal intensities increased. However, the decline in separation resolution can be observed in the magnifications attached to Fig. 3A and B. For the combined FASS and reversed-field stacking (Fig. 3C), signals of all analytes were greatly enhanced and baseline separation was realized for all analytes. These observations demonstrated the high efficiency of this multiple-concentration method.

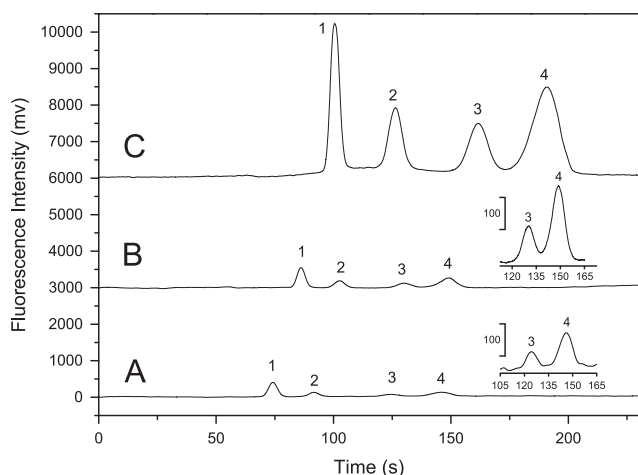


Fig. 3. Signal enhancement of the multiple concentration: (A) signal intensity without concentration. The running buffer was 100 mM borate solution at pH 9.88 and the sample was diluted with the running buffer solution. The sample injection time was 2 s. (B) Signal intensity with FASS. The sample was prepared in a 10-fold-diluted running buffer, and the sample injection time was 2 s. (C) Signal intensity with a combination of FASS and reversed-field stacking. The sample injection time was 10 s, and the reversed-polarity time was 8 s. The concentrations of Lys, Tau, and NA in (A) were 0.6, 0.9, and 0.6 μ M, respectively. The sample concentrations in (B) and (C) were 1/10 of that in (A). Peak identification: 1, the excess of Cy5; 2, Lys; 3, Tau; and 4, NA.

3.2. Optimization of derivatization conditions

As the analytes have no native fluorescence, they were derivatized with sulfoindocyanine succinimidyl ester (Cy5). The scheme of the labeling reaction with Cy5 can be seen in Fig. 1. The derivatization reaction was optimized with respect to the derivatization borate buffer, time, and temperature to enhance the detection sensitivity. The composition of the derivatization borate buffer was optimized by varying the pH and the concentration of borate solution over the range of 7.5–9.5 and 10–50 mM. It was found that the derivatization efficiency increased with increasing pH values up to 8.6 and then decreased up to a pH value of 9.5, which can be attributed to the hydrolytic degradation of the Cy5 [37]. Therefore, pH 8.6 was selected as optimum. From the experiments, 20 mM derivatization borate buffer was found to achieve maximum reaction efficiency in the labeling reaction. Further increases in the concentration of derivatization buffer provided a decrease in the reaction yield. Time and temperature played significant roles in the labeling process. It was found that the maximum yield was obtained at room temperature by applying 4 h of reaction time. These conditions were used for all subsequent experiments.

3.3. Optimization of MCE separation conditions

3.3.1. Effect of running buffer concentration

A series of running buffer consisting of 25, 50, 75, 100 mM borate solution (pH 9.26) was prepared to study the effect of running buffer concentration on the separation of Lys, Tau, and NA. Higher concentrations of running buffer were not considered because higher concentration buffer resulted in higher current, which generated the high Joule heat causing the instability of baseline. As shown in Fig. S1 (see Supplementary material), resolution was improved with the increase in buffer concentration. The peaks of Lys and the excess of Cy5 were separated with the higher concentrations and the best resolution of Tau and NA was achieved when the buffer concentration was increased to 100 mM (Fig. S1D). As a result, 100 mM borate solution was selected as optimum and used for the following experiments.

3.3.2. Effect of running buffer pH value

In MCE, the pH value of running buffer is an important parameter to be optimized as it affects both the charge of the analytes and EOF, which in turn plays a critical role in electrophoretic mobility and the separation of analytes. For the separation of Lys, Tau, NA, and the excess of Cy5, the effect of buffer pH values ranging from 9.26 to 10.85 was studied. It can be seen from Fig. 4 that the baseline separation of all analytes was achieved using 100 mM borate buffer at pH 9.88 (Fig. 4D). At pH lower than 9.8, the labeled Tau and NA co-migrated and overlapped, while at pH equal to or higher than 10, the baseline was unstable and the resolution was poor because of the high Joule heating. It was obvious that the perfect separation was obtained at pH 9.88, which was determined to be the best pH for MCE separation.

3.4. Optimization of on-line preconcentration conditions

3.4.1. Effect of sample buffer concentration

Theoretically, the concentration enhancement depends on the concentration ratio of running buffer to sample buffer, and higher ratios result in stronger fluorescent signals of analytes in FASS [38]. However, in a realistic system, the increase in concentration ratio of running buffer to sample buffer should be balanced against the negative effect of dispersion and advection on stacking efficiency caused by the mismatch of electroosmotic velocity [39]. Therefore,

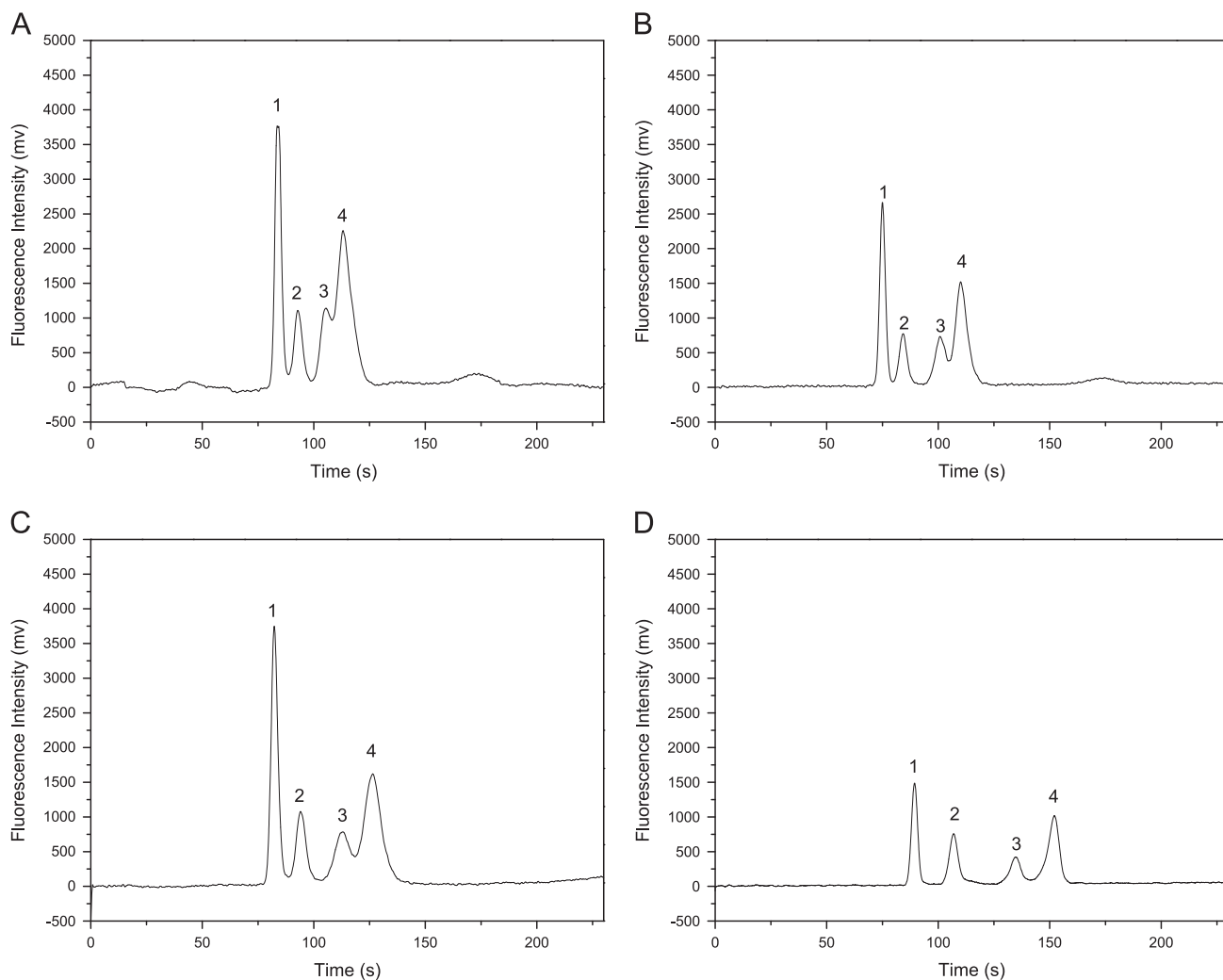


Fig. 4. Effect of pH of the running buffer on the separation of three Cy5-labeled nutritious compounds. The pH values of running buffer solution: (A) 9.26, (B) 9.42, (C) 9.65, and (D) 9.88. Buffer concentration: 100 mM. Concentration of Lys, Tau, and NA were 0.03, 0.03, and 0.025 μM , respectively. The samples were prepared in a 10-fold-diluted running buffer. Other conditions are the same as those in Fig. 3C.

under the optimized separation conditions (100 mM borate solution at pH 9.88 in running buffer), sample buffer concentration has been studied. Different concentrations of $\text{Na}_2\text{B}_4\text{O}_7$ (ranging from 10 to 75 mM) in sample buffer were investigated by testing the fluorescent signal intensity of NA. From Fig. 5A–D, it can be observed that the peak height increased with the decrease in sample buffer concentration and the best result for signal amplification was obtained with 10 mM borate solution as the sample buffer (Fig. 5D). Further decreases in sample buffer concentration did not serve to improve the enrichment effect in our experiments. Thus, the optimal sample buffer was chosen as 10 mM borate solution (pH 9.88).

3.4.2. Effect of injection time and reversed-polarity time

Injection time and reversed-polarity time have great influence on signal amplification (Fig. 6). As mentioned previously, both the injection step and reversed polarity step were accompanied by FASS, and the reversed polarity step using reversed-field stacking technique could provide stronger signal amplification by enhancing the enrichment effect of FASS and pushing most of the sample matrix out of the separation channel. However, with a longer reversed-polarity time, the analytes would potentially be pumped from the separation

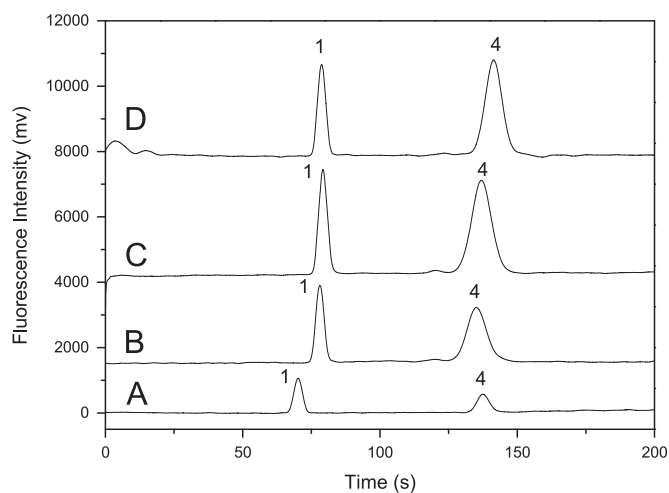


Fig. 5. Effect of the sample buffer concentration on signal enhancement. The concentration of borate buffer solution in sample buffer: (A) 75 mM, (B) 50 mM, (C) 20 mM, (D) 10 mM. Concentration of NA was 0.07 μM . The samples were diluted with the sample buffer solution and all buffer pH values were 9.88. Other conditions are the same as those in Fig. 3C.

channel with the sample matrix, leading to the reduction of all peak heights. After comprehensively considering every factor, the selected reversed-polarity time was 2 s shorter than the injection time, which made the sample plug move to the injection cross within an appropriate distance to avoid pushing out the concentrated sample. As shown in Fig. 6, the increase in injection time and reversed-polarity time could strengthen the signal intensities of all analytes. Considering the decrease in separation efficiency due to band

broadening of signals with a longer injection time, the optimal injection time and reversed-polarity time were selected to be 10 s and 8 s, respectively (Fig. 6C).

3.5. Method validation

The performance and reliability of the proposed method were assessed by determining linearity, limit of detection (LOD), precision (RSD) for amino acids and vitamin B₃. Table 1 gives the equations for the calibration curves obtained by plotting the peak height against analyte concentration in the linear range, the LODs calculated as the minimum analyte concentration providing signals 3 times the background noise, the intraday precision obtained by repeating the analysis three times, and the sensitivity enhancement factors of all analytes using the multiple-concentration method (Fig. 3C) compared to, when no concentration was performed (Fig. 3A). Under optimized conditions, the method proposed allowed the determination of these compounds at very low levels (LODs ranged from 0.20 to 0.50 nM) and the linearity was satisfactorily studied with correlation coefficients from 0.9958 to 0.9988. The RSDs of the migration time and peak height were in the range of 1.2–3.4% and 1.3–2.7%, respectively, indicating good reproducibility and high precision. The sensitivity enhancement factors in peak heights for Lys, Tau, and NA using this concentration method were 165, 285, and 236, respectively.

3.6. Method application for the analysis of functional drink samples

To demonstrate how the proposed MCE-LIF method can be applied for the analysis of the real sample, the method was further investigated by the analysis of functional ingredients in eight functional drink samples. The samples were prepared according

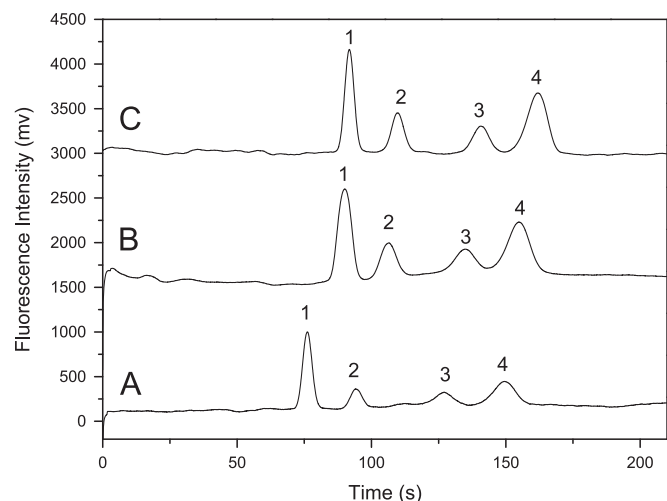


Fig. 6. Effect of injection time and reversed-polarity time on peak intensity. Injection time and reversed-polarity time: (A) 4 s, 2 s; (B) 8 s, 6 s; and (C) 10 s, 8 s. Concentration of Lys, Tau, and NA were 0.015, 0.025, and 0.015 μM , respectively. Other conditions are the same as those in Fig. 3C.

Table 1

Analytical performance and enrichment factor results of the multiple-concentration MCE method.

Compound	Linearity range (μM)	Linear regression ^a ($n=10$)	Correlation coefficients (R^2)	LOD (nM)	RSD% ($n=3$) ^b	MT/peak height	Enrichment factor
Lys	0.003–0.10	$y=28307x-8.4514$	0.9958	0.25	3.4/1.3		165
Tau	0.004–0.15	$y=14678x-33.3098$	0.9988	0.50	2.0/0.8		285
NA	0.003–0.10	$y=40174x+5.0533$	0.9982	0.20	1.2/2.7		236

^a In the regression equation, the x value was the concentration of analytes (μM), the y value was the peak height (mv).

^b MT, migration time. Concentrations of Lys, Tau, and NA were 0.013, 0.020, and 0.013 μM , respectively. Other conditions were the same as those in Fig. 3C.

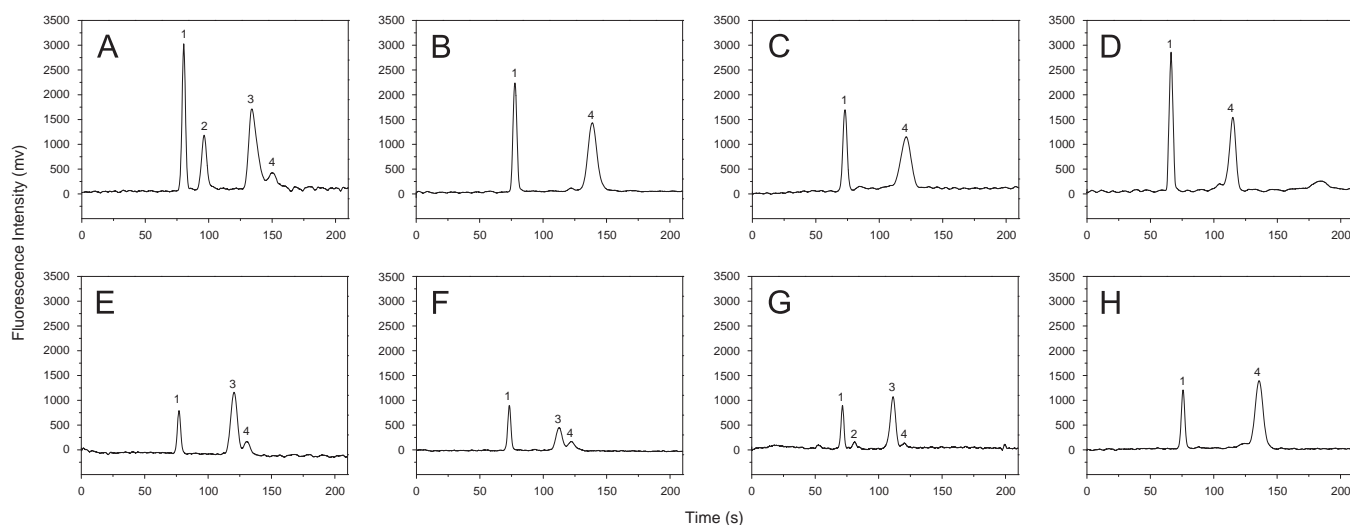


Fig. 7. Electropherograms of eight Cy5-labeled functional drink samples after dilution. (A) F1, (B) F2, (C) F3, (D) F4, (E) F5, (F) F6, (G) F7, and (H) F8. Dilution folds of eight drink samples are listed in Table 2. Other experiment conditions are the same as those in Fig. 3C.

Table 2
Quantitative determination of beneficial compounds in eight functional drinks.

Sample	Functional ingredient detected after dilution	Concentration ^a (μM)	Amount added (μM)	Amount found (μM)	Recovery (%)
F1	Lys	0.0424	0.0550	0.0978	100.7
	Tau	0.1201	0.0250	0.1454	101.2
	NA	0.0105	0.0095	0.0198	97.9
F2	NA	0.0350	0.0350	0.0713	103.7
F3	NA	0.0285	0.0200	0.0479	97.0
F4	NA	0.0380	0.0250	0.0642	104.8
F5	Tau	0.0819	0.0400	0.1249	107.5
	NA	0.0039	0.0125	0.0161	97.6
F6	Tau	0.0335	0.0300	0.0645	103.3
	NA	0.0046	0.0100	0.0145	99.0
F7	Lys	0.0056	0.0100	0.0159	103.0
	Tau	0.0758	0.0500	0.1252	98.8
	NA	0.0030	0.0025	0.0056	104.0
F8	NA	0.0343	0.0200	0.0558	107.5

^a The concentrations of the functional ingredients in eight functional drink samples were determined after dilution. Dilution fold: F1, 32000; F2, 1600; F3, 2000; F4, 2000; F5, 32000; F6, 64000; F7, 320000; and F8, 2000.

to procedures in Section 2.4 and analyzed by using the multiple-concentration method under optimized conditions. All drink samples were diluted before analysis in order to avoid instability of baseline and interference with resolution caused by impurities in real samples. Fig. 7 shows the electropherograms obtained from analysis of the eight functional drinks. Because the migration time of the analytes varied in the real sample analysis, the peaks were verified by a standard addition method. For F1 and F7, all three functional ingredients (Lys, Tau, and NA) were detected. Both Tau and NA were determined in F5 and F6, while only NA was detected in sample F2, F3, F4, and F8. The components detected in eight drink samples were consistent with the components listed in the labels of nutrition fact.

Concentrations of three beneficial compounds in eight functional drink samples and recoveries are summarized in Table 2. Satisfactory recoveries (97.0–107.5%) were obtained in real drink samples, indicating that real sample matrices had virtually no effect on the performance of the method proposed. Besides, the concentrations of functional ingredients detected by the proposed method met the standard of the values claimed in nutrition facts of all drink samples except for F6. In F6, the Tau content detected was about half of the labeled value. The concentrations of each functional ingredient in the drink samples were determined with the calibration equations elaborated in Section 3.5 (Table 1). Since little has been reported on the simultaneous separation and determination of these beneficial compounds in functional drinks, the proposed MCE method was compared with HPLC and CE by comparing the analysis of NA found in the same segment of functional beverages like energy drinks [20,40]. The NA content detected by the method developed was similar to the assay results found by HPLC and CE, and the analysis time of NA assayed in real drink samples using the proposed MCE method was within 3 min, which was less than that using HPLC (about 4 min) and CE (about 22 min) [20,40]. In summary, these results testify to the good performance of the proposed method in the determination of health promoting compounds in this type of sample.

4. Conclusions

We presented an on-line preconcentration MCE method combining FASS and reversed-field stacking for the simultaneous analysis of

two amino acids and vitamin B₃ in functional drinks. Using this method, three functional ingredients could be simultaneously focused on and separated within 4 min. Under optimal conditions, the strategy allowed for the determination of these beneficial compounds at very low concentrations (0.20–0.50 nM) and afforded approximately 150- to 300-fold improvements in peak height. Moreover, the method was successfully applied to functional drink samples with a satisfactory recovery. Compared with normal detection methods for beneficial compounds in food analysis, this multiple-concentration MCE method has many merits, including miniaturization, rapid operation, low sample consumption, and high sensitivity.

Acknowledgments

This work was financially supported by the Program New Century Excellent Talents in University (Grant NCET-08-0191) and the National Program on Development of Scientific Instruments and Equipment (Grant 2011YQ150072).

Appendix A. Supplementary materials

Supplementary data associated with this article can be found in the online version at <http://dx.doi.org/10.1016/j.talanta.2014.08.051>.

References

- [1] I. Siro, E. Kopolna, B. Kopolna, A. Lugasi, *Appetite* 51 (2008) 456–467.
- [2] J. Wan, *Food Ferment. Ind.* 33 (2007) 101–106.
- [3] K. Maiese, Z.Z. Chong, J. Hou, Y.C. Shang, *Molecules* 14 (2009) 3446–3485.
- [4] L.F. Sallum, F.L. Felipe Soares, J.A. Ardila, R.L. Carneiro, *Talanta* 118 (2014) 353–358.
- [5] S. Harakeh, M. Diab-Assaf, K. Abu-El-ardat, A. Niedzwiecki, M. Rath, *Chem. Biol. Interact.* 164 (2006) 102–114.
- [6] M. Kumar, M. Ali Khan, Z.A. Othman, *J. Chem. Technol. Biotechnol.* 88 (2013) 910–918.
- [7] M. Hohmann, C. Felbinger, N. Christoph, H. Wachter, J. Wiest, U. Holzgrabe, *J. Pharm. Biomed. Anal.* 93 (2014) 156–160.
- [8] T.R.I. Cataldi, G. Telesca, G. Bianco, D. Nardiello, *Talanta* 64 (2004) 626–630.
- [9] Y.-R. Yu, X.-C. Liu, J.-S. Zhang, C.-Y. Ji, Y.-F. Qi, *Parasitol. Res.* 112 (2013) 3457–3463.
- [10] S.J. Kim, C. Ramesh, H. Gupta, W. Lee, *J. Biol. Reg. Homeos. Ag.* 21 (2007) 63–77.
- [11] A. El Idrissi, E. Okeke, X. Yan, F. Sidime, L.S. Neuwirth, *Adv. Exp. Med. Biol.* 775 (2013) 407–425.
- [12] M.R. Beyranvand, M.K. Khalafi, V.D. Roshan, S. Choobineh, S.A. Parsa, M. A. Piranfar, *J. Cardiol.* 57 (2011) 333–337.
- [13] N. Froger, L. Cadetti, H. Lorach, J. Martins, A.-P. Bemelmans, E. Dubus, J. Degardin, D. Pain, V. Forster, L. Chicaud, I. Ivkovic, M. Simonutti, S. Fouquet, F. Jammoul, T. Leveillard, R. Benosman, J.-A. Sahel, S. Picaud, *Plos One* 7 (2012).
- [14] D.C. Camerino, D. Tricarico, S. Pierno, J.F. Desaphy, A. Liantonio, M. Pusch, R. Burdi, C. Camerino, B. Fraysse, A. De Luca, *Neurochem. Res.* 29 (2004) 135–142.
- [15] J.A. Mendiola, F.R. Marin, F.J. Senorans, G. Reglero, P.J. Martin, A. Cifuentes, E. Ibanez, *J. Chromatogr. A* 1188 (2008) 234–241.
- [16] D. Heems, G. Luck, C. Fraudeau, E. Verette, *J. Chromatogr. A* 798 (1998) 9–17.
- [17] E. Barrado, J.A. Rodriguez, Y. Castrillejo, *Talanta* 78 (2009) 672–675.
- [18] M. Castro-Puyana, A.L. Crego, M.L. Marina, C. Garcia-Ruiz, *Electrophoresis* 28 (2007) 4031–4045.
- [19] S. Dziomba, P. Kowalski, T. Baczek, *J. Chromatogr. A* 1267 (2012) 224–230.
- [20] D. Zhao, M. Lu, Z. Cai, *Electrophoresis* 33 (2012) 2424–2432.
- [21] A. Escarpa, M.C. Gonzalez, A.G. Crevillen, A.J. Blasco, *Electrophoresis* 28 (2007) 1002–1011.
- [22] V. Dolnik, S. Liu, S. Jovanovich, *Electrophoresis* 21 (2000) 41–54.
- [23] K. Sueyoshi, F. Kitagawa, K. Otsuka, *Anal. Sci.* 29 (2013) 133–138.
- [24] K. Sueyoshi, F. Kitagawa, K. Otsuka, *J. Sep. Sci.* 31 (2008) 2650–2666.
- [25] F. Kitagawa, T. Kawai, K. Sueyoshi, K. Otsuka, *Anal. Sci.* 28 (2012) 85–93.
- [26] B. Jung, R. Bharadwaj, J.G. Santiago, *Electrophoresis* 24 (2003) 3476–3483.
- [27] Z. Mala, P. Gebauer, P. Bocek, *Electrophoresis* 34 (2013) 19–28.
- [28] M. Kinoshita, Y. Nakatsujii, S. Suzuki, T. Hayakawa, K. Kakehi, *J. Chromatogr. A* 1309 (2013) 76–83.
- [29] K. Sueyoshi, F. Kitagawa, K. Otsuka, *Anal. Chem.* 80 (2008) 1255–1262.
- [30] Q. Pan, M. Zhao, S. Liu, *Anal. Chem.* 81 (2009) 5333–5341.
- [31] Z.-F. Wang, S. Cheng, S.-L. Ge, H. Wang, Q.-J. Wang, P.-G. He, Y.-Z. Fang, *Anal. Chem.* 84 (2012) 1687–1694.
- [32] X. Zheng, M. Lu, L. Zhang, Y. Chi, L. Zheng, G. Chen, *Talanta* 76 (2008) 15–20.

- [33] Y. He, X. Li, P. Tong, M. Lu, L. Zhang, G. Chen, *Talanta* 104 (2013) 97–102.
- [34] Y. Huang, M. Shi, S. Zhao, H. Liang, *J. Chromatogr. B* 879 (2011) 3203–3207.
- [35] M. Wu, S. Cheng, G. Li, Z. Wang, Q. Wang, P. He, Y. Fang, *Chin. J. Chem.* 30 (2012) 2517–2521.
- [36] G. Li, S. Ge, X. Ni, S. Dong, Q. Wang, P. He, Y. Fang, *Chin. J. Chem.* 27 (2009) 2207–2211.
- [37] E. Orejuela, M. Silva, *Electrophoresis* 26 (2005) 4478–4485.
- [38] D.S. Burgi, R.L. Chien, *Anal. Chem.* 63 (1991) 2042–2047.
- [39] R. Bharadwaj, J.G. Santiago, *J. Fluid. Mech.* 543 (2005) 57–92.
- [40] A. Gliszczyńska-Świgło, I. Rybicka, *Food Anal. Methods* (2014), <http://dx.doi.org/10.1007/s12161-014-9880-0> (Published online: 8 May 2014).



High-performance liquid chromatography coupled with mass spectrometry for analysis of ultrasmall palladium nanoparticles

Lei Zhang^{a,b,1}, Zhongping Li^a, Yan Zhang^{a,2}, Man Chin Paau^c, Qin Hu^c, Xiaojuan Gong^{a,1}, Shaomin Shuang^a, Chuan Dong^{a,*}, Xiaoguang Peng^b, Martin M.F. Choi^{c,**}

^a Institute of Environmental Science, and School of Chemistry and Chemical Engineering, Shanxi University, 92 Wucheng Road, Taiyuan 030006, China

^b Biology Institute of Shanxi, 50 Shifan Street, Taiyuan 030006, China

^c Partner State Key Laboratory of Environmental and Biological Analysis, and Department of Chemistry, Hong Kong Baptist University, 224 Waterloo Road, Kowloon Tong, Hong Kong SAR, China

ARTICLE INFO

Article history:

Received 19 May 2014

Received in revised form

9 August 2014

Accepted 12 August 2014

Available online 21 August 2014

Keywords:

Metal nanoparticles

Analytical separation

Chemical composition

ABSTRACT

Metal nanoparticles (NPs) have recently attracted considerable attention in many areas of research including bioscience, chemistry and material science. Regrettably, most current and past work usually focuses on studies of multi-component NPs mixture where there is a plethora of NPs species co-existing. This work highlights the merits of reverse-phase high-performance liquid chromatography (RP-HPLC) for disclosing the genuine properties of individual palladium nanoparticles (PdNPs) species present in an as-synthesized *N,N'*-dimethylformamide-stabilized PdNPs product (DMF-PdNPs) which might have been previously hidden or misinterpreted. DMF-PdNPs is successfully separated by RP-HPLC that smaller DMF-PdNPs are approximately eluted first and then follow by the large ones on a C18 column. The separation fractions are further collected and determined their chemical compositions by matrix-assisted laser desorption/ionization time-of-flight mass spectrometry. The results unambiguously reveal that the as-synthesized DMF-PdNPs product is indeed a complex mixture of ultrasmall Pd_xNPs (*x* = 10–20) stabilized with different numbers of DMF ligands. It is anticipated that the separated fractions afforded by RP-HPLC will offer more accurate determinations of the catalytic, electronic, optical and toxicological properties of metal NPs which might have been previously misinterpreted.

© 2014 Elsevier B.V. All rights reserved.

1. Introduction

Noble metal nanoparticles (NPs) with core sizes in the range of 1–100 nm have attracted considerable attention in many areas of research attributing to their unique catalytic, electrochemical and optical properties. Their promising applications have been found in the fields of catalysis [1–3], sensors [4,5], nanoelectronics [6,7], and bioscience [8]. Metal NPs are prone to the loss of reactivity because they precipitate or aggregate as bulk metals unless various stabilizers such as functionalized polymers [9], ligands [10,11], dendrimers [12] are used. The outstanding behavior of different kinds of particles arises from their distinctive electronic properties, which are intimately related to their size and the chemical nature of their core and surface species.

Palladium plays an important role in many industrial applications [13,14]. It is well-known that palladium nanoparticles (PdNPs) lies in

their as catalysts for low temperature reduction of automobile pollutants and for organic reactions such as Suzuki–Miyaura [15], Heck [16,17], Stille couplings [14]. They also possess remarkable performance in hydrogenation/dehydrogenation [17,18], and sensing [19]. In general, catalytic properties of PdNPs could be enhanced by controlling particle size. Hence, it is of particular importance to understand how the particle size affects its catalytic property. To date, sonochemical reduction [20], chemical liquid deposition [21], refluxing alcohol reduction [22], decomposition of organometallic precursors [23], hydrogen reduction [24] and electrochemical deposition [25] have been introduced to prepare PdNPs. The particles are commonly formed by reduction of metal ions in the presence of some stabilizers. They are promising techniques to synthesize various metal NPs due to its simplicity, reproducibility, ambient environment conditions and no additional chemical contamination during the process. Recently, Liu et al. [26], Kawasaki et al. [27,28] and Hyotanishi et al. [3] have also developed a novel route to prepare surfactant-free fluorescent gold nanoparticles (AuNPs), platinum nanoparticles (PtNPs) and PdNPs in *N,N'*-dimethylformamide (DMF). In these reactions no further stabilizing surfactant is needed as DMF is a mild reducing agent and a stabilizing ligand. The as-synthesized AuNPs, PtNPs and PdNPs are highly stable in organic, aqueous or salt solutions. However, the

* Corresponding author. Tel.: +86 351 7018842; fax: +86 351 7018613.

** Corresponding author. Tel.: +852 34117839; fax: +852 34117348.

E-mail addresses: dc@sxu.edu.cn (C. Dong), mfchoi@hkbu.edu.hk (M.M.F. Choi).

¹ Exchange student on visit to Hong Kong Baptist University.

² Postdoctoral research fellow on visit to Hong Kong Baptist University.

as-synthesized DMF-protected AuNPs product is found to be a mixture of various core sizes containing less than 20 Au atoms [27]. It is thus anticipated that other DMF-protected metal NPs products would contain various metal core sizes and/or, of same core size but with different numbers of stabilizing ligands. Unfortunately, the separation of DMF-protected PdNPs has not been investigated.

In reality, an as-synthesized PdNPs product should be a complex mixture which only represents the total or average properties and chemistries of all the individual PdNPs species present. As such, it is necessary to apply effective separation techniques in order to better understand the chemical composition of an as-synthesized PdNPs sample. Separation techniques like capillary electrophoresis [29,30], gel electrophoresis [31,32], size exclusion chromatography/gel permeation chromatography [33,34], ion-exchange chromatography [35], density gradient centrifugation [36], molecular imprinting [37], field-flow fractionation [38], diafiltration [39], size-selective precipitation [10], analytical ultracentrifugation [40], and reverse-phase high-performance liquid chromatography (RP-HPLC) [41–43] have been developed to fractionate various metal NPs. Among these NPs separation techniques, HPLC can be considered as an effective approach to isolate different metal NPs species [44].

To our knowledge, RP-HPLC has not previously been reported for separation of small-sized PdNPs. Herein, we have successfully applied our developed RP-HPLC methodology for fractionating various DMF-PdNPs species in an as-prepared DMF-PdNPs product. The spectral properties of each separated PdNPs fractions are *in situ* captured by a diode array detector (DAD). It is found that an as-synthesized DMF-PdNPs sample comprises more than 13 PdNPs entities. More importantly, matrix-assisted laser desorption/ionization time-of-flight mass spectrometry (MALDI-TOF MS) was used to characterize the separated PdNPs fractions. Our MS data unambiguously reveal that the as-synthesized DMF-PdNPs product is indeed a complex mixture of Pd_xNPs ($x = 10\text{--}20$) stabilized with different numbers of DMF ligands. It is our wish that the proposed RP-HPLC technique could offer the opportunity to fathom the catalytic, electronic, optical and toxicological properties of individual PdNPs species.

2. Experimental

2.1. Chemicals and reagents

Ammonium hexachloropalladate(IV) [(NH₄)₂PdCl₆] was purchased from Aladdin (Shanghai, China). AR-grade DMF and HPLC-grade methanol (MeOH) was purchased from Labscan (Bangkok, Thailand). 2,5-Dihydroxybenzoic acid (DHB, 98%) was from Sigma (St Louis, MO, USA). Water (H₂O) was purified through a Milli-Q-RO4 water purification system (Millipore, Bedford, MA, USA) with a resistivity higher than 18 MΩ cm.

2.2. Synthesis of DMF-PdNPs sample

The as-synthesized DMF-PdNPs product was prepared according to the literature method with slight modifications [3]. In brief, a solution of 150 μL of 0.10 M aqueous (NH₄)₂PdCl₆ was added to 15 mL DMF that had been preheated to 140 °C. The DMF mixture was refluxed for 6 h under vigorous stirring. After evaporating the excess solvent under vacuum (< 10 mg Hg) at 80 °C for an hour, the residue was further dried by a stream of nitrogen (N₂) and kept in a desiccator until analysis.

2.3. High-performance liquid chromatography

Chromatographic separation was conducted on a Waters Alliance 2690 HPLC comprising a 2695 separation module capable of gradient

elution and a 2996 DAD (Milford, MA, USA). The absorption spectra of the eluted peaks were taken over 200–400 nm by the DAD (1.2 nm resolution). All HPLC separations were performed on an Agilent Zorbax Eclipse Plus-C18 column (250 × 4.6 mm i.d. stainless steel) packed with 5 μm C18 bonded silica with 95 Å pore size (Santa Clara, CA, USA).

DMF-PdNPs sample solutions (3.0 mg/mL) were prepared in H₂O and then pre-filtered through Alltech 0.45-μm cellulose acetate membrane syringe filters (Deerfield, IL, USA) before injections. The mobile phases were prepared with solvent mixtures of MeOH and H₂O. The injection volume was 20 μL and the column was maintained at 22 ± 1 °C. To study the effect of MeOH on elution of DMF-PdNPs, isocratic elutions at 0.80 mL/min were initially performed under various MeOH% in the mobile phase of MeOH/H₂O. Afterwards, a gradient elution program at a flow rate of 0.80 mL/min was applied to analyze the 3.0 mg/mL DMF-PdNPs sample solution. The elution program was set up as: 3.0% v/v MeOH for 5.0 min, linearly increased to 5.0% v/v MeOH from 5.0 to 10 min, maintained at 5.0% v/v MeOH from 10 to 20 min, linearly increased to 7.0% v/v MeOH from 20 to 25 min, and kept at 7.0% v/v MeOH from 25 to 35 min, linearly increased to 12.0% v/v MeOH from 35 to 40 min, and kept at 12.0% v/v MeOH from 40 to 50 min, linearly increased to 15.0% v/v MeOH from 50 to 55 min, and finally kept at 15.0% v/v MeOH from 55 to 60 min. The chromatograms were monitored at 300 nm and the selected HPLC fractions were collected manually based on the appropriate UV signal threshold for further photoluminescence (PL) and MS studies.

2.4. UV-vis absorption, photoluminescence, infrared spectroscopy and thermogravimetric analysis

The UV-vis spectra of (NH₄)₂PdCl₆ and the as-synthesized DMF-PdNPs product were acquired on a Varian Cary 300 scan UV-vis absorption spectrophotometer (Palo Alto, CA, USA) at 200–550 nm. The PL properties of the HPLC fractions were recorded on a Photon Technology International QM4 spectrofluorometer (Birmingham, NJ, USA). The Fourier transform infrared (FTIR) spectra of the as-prepared DMF-PdNPs and the DMF ligand were obtained from a Thermo Scientific Nicolet Magna 550 FTIR spectrometer (West Palm Beach, FL, USA). Thermogravimetric analysis (TGA) was performed on a Perkin-Elmer TGA 6 thermogravimetric analyzer (Waltham, MA, USA).

2.5. Matrix-assisted laser desorption/ionization time-of-flight mass spectrometry

The collected PdNPs fractions were dried by a stream of N₂ and redissolved in 10 μL of water. Then 2.0 μL of each fraction was mixed (1:1 v-v) with a 1.0 M solution of DHB in MeOH/H₂O (1:1 v/v). 4.0 μL of each of these solutions was deposited on a MALDI target plate, air-dried and analyzed by a Bruker Autoflex MALDI-TOF mass spectrometer (Bremen, Germany). The sample was inserted into the instrument and irradiated by a pulsed N₂ laser at 337 nm. In general, 200 laser shots were averaged for each spectrum.

3. Results and discussion

3.1. Characterization of as-synthesized DMF-PdNPs

Fig. 1 displays the UV-vis absorption spectra of aqueous solutions of (NH₄)₂PdCl₆ and as-synthesized DMF-PdNPs sample. All samples were prepared in H₂O. Since H₂O has a cutoff wavelength of 190 nm, it will not cause any interference at the scan range 200–550 nm. (NH₄)₂PdCl₆ possesses a small peak at 217 nm and a shoulder band at 237 nm corresponding to the ligand-to-metal charge transfer of the complex [45,46]. By contrast, the as-synthesized DMF-PdNPs product displays a monotonic decrease in absorption with the increase in

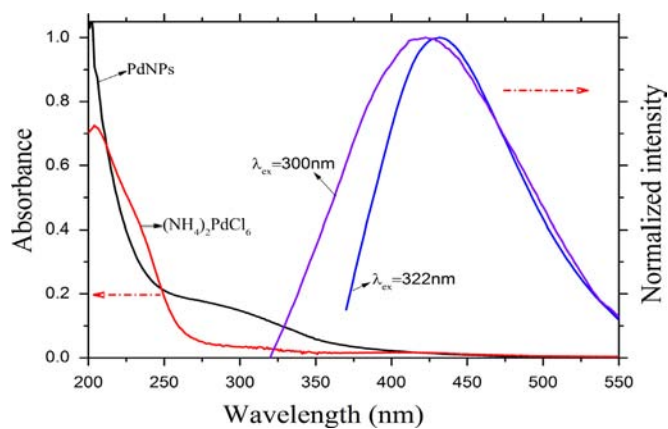


Fig. 1. UV-vis absorption spectra of $(\text{NH}_4)_2\text{PdCl}_6$ and as-synthesized DMF-PdNPs sample in aqueous solutions. Photoluminescence (PL) spectra of DMF-PdNPs in aqueous solution at excitation wavelengths (λ_{ex}) of 300 and 322 nm. The PL spectra are normalized at their emission peaks for ease of comparison.

scanning wavelength [47]. A broad absorption band at 250–400 nm is observed, possibly attributing to the metal-to-ligand charge transfer [10], *i.e.*, from the Pd core to the surface-attached DMF ligand. This band is more prominent in some of the separated PdNPs species (*vide infra*). No surface plasmon resonance (SPR) band is found as expected for PdNPs [48,49]. It is obvious that the UV-vis absorption feature of DMF-PdNPs is different from that of the $[\text{PdCl}_6]^{2-}$ complex. Fig. 1 also depicts the PL spectra of DMF-PdNPs at excitation wavelengths (λ_{ex}) of 300 nm and 322 nm, respectively. The strongest emission peak (λ_{em}) at 422 nm is obtained at λ_{ex} of 300 nm. The quantum yield of the as-prepared DMF-PdNPs sample is 2.3%. The PL of PdNPs is probably attributed to transitions between filled $4d^{10}$ band and vacant $5sp$ conduction band of the Pd atom which is similar to that of the fluorescent gold nanoclusters. The emission spectrum is red-shifted with the increase in λ_{ex} because of the presence of multiple transition bands [27]. No emission is found for $(\text{NH}_4)_2\text{PdCl}_6$.

Fig. 2 depicts the IR spectra of DMF and DMF-PdNPs. Broad bands at *ca.* 3500 cm^{-1} corresponding to the residual H_2O are found for both DMF and DMF-PdNPs. The band assignments for DMF have already been reported in the literature [50–52]. For the DMF-PdNPs sample, the CH_3 symmetric stretching at 2930 cm^{-1} , C–H stretching at 2857 cm^{-1} , C=O stretching at 1676 cm^{-1} , HCO–N bending at 1388 cm^{-1} , C–N asymmetric stretching at 1257 cm^{-1} , and HCO–N symmetric stretching at 659 cm^{-1} are observed. Most of these bands are slightly shifted and broader than that of DMF, owing to the electronic effect from the surface Pd atoms. The IR spectra again confirm that DMF molecules are attached to the surface of PdNPs.

3.2. Gradient elution of DMF-PdNPs

It is well-known that the MeOH content in mobile phase affects the chromatographic separation in a RP-HPLC system. As such, the effect of MeOH on the chromatographic behavior of the as-synthesized PdNPs product was investigated in detail. Fig. S1 depicts the effect of MeOH content (3.0–20.0% v/v) in the mobile phase on the retention of the DMF-PdNPs solutes. The chromatogram obtained at 3.0% v/v MeOH is tenfold enlarged for ease of comparison. The separation of DMF-PdNPs is unsatisfactory with the highest MeOH content (20.0% v/v) as only two major peaks are observed. The earlier eluted peak is broad and probably comprises numerous co-eluted PdNPs species. When the MeOH content is decreased, more PdNPs peaks are emerged and eluted at later times, indicating that the as-synthesized DMF-PdNPs product should contain different PdNPs species. The retention of PdNPs on the C18 column follows the typical RP-HPLC behavior which is

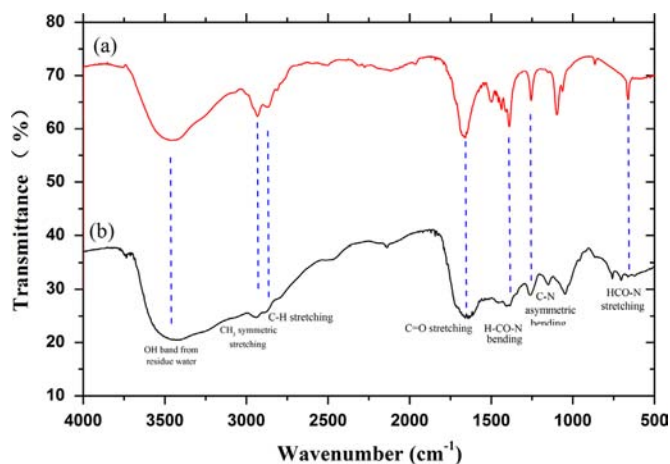


Fig. 2. Infrared spectra of (a) DMF and (b) DMF-PdNPs. The spectra are offset for ease of comparison.

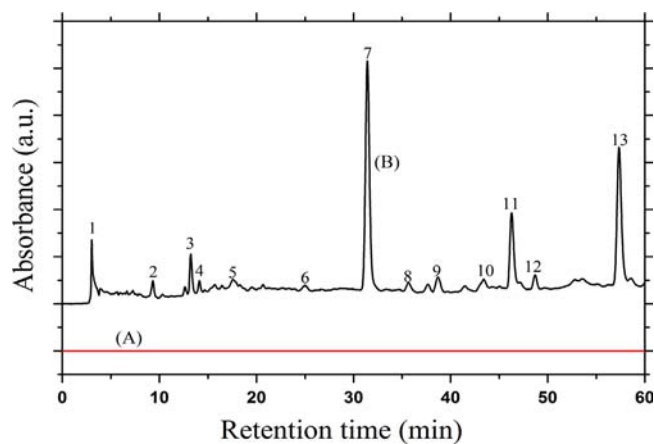


Fig. 3. Gradient elution of an aqueous solution of DMF-PdNPs sample (3.0 mg/mL). Chromatograms (A) H_2O and (B) DMF-PdNPs samples monitored at 300 nm.

governed by the surface-attached ligand (in here, DMF) and core size of PdNPs. The retention mechanism is illustrated in Fig. S2. When the MeOH content is too low (3.0% v/v), the later eluting peaks are strongly retained on the column and cannot be totally eluted. In summary, the earlier eluted peaks tend to be better separated with the lower MeOH content while the latter ones are better eluted with higher MeOH content in order to avoid their strong retention on the C18 column. As a result, a solvent program progressing with a low to high MeOH content in the mobile phase has to be applied to totally elute all of the PdNPs solutes in the sample (*vide infra*).

The as-synthesized DMF-PdNPs sample was efficiently separated by a gradient solvent program as shown in Fig. 3. A chromatogram of a pure H_2O sample (curve A) is displayed for comparison. No chromatographic peak is found in the H_2O injection. Under the optimal solvent program, many separated peaks are evolved in the chromatogram as compared to that of the chromatogram obtained from isocratic elution (Fig. S1). At least 13 separated peaks are observed within 60 min. Since these peaks are readily distinguished from the baseline, they are labeled as 1–13, respectively for characterization. These peaks are arbitrarily selected as they are satisfactorily separated from each other and are evenly distributed in the chromatogram from earlier to intermediate and then to later eluting PdNPs species. In addition, their absorption and PL spectra are unique and distinguishable from each other, representing each type of PdNPs compounds. Thus, all these fractions are collected for further UV, PL and MALDI TOF MS analyses (*vide infra*).

Fig. 4A and B depicts the UV–vis absorption spectra of the peaks in the chromatogram in Fig. 3, possessing more distinctive spectral features than that of the as-synthesized DMF-PdNPs sample. Peaks 11 and 13 are two times expanded for ease of comparison. Most peaks show stronger absorption below 250 nm and no obvious absorption bands are observed at longer wavelengths (> 360 nm). Some (Fractions 1–4, 6, 7, 11, and 13) even display more distinctive spectral features. For instances, Fractions 7, 11 and 13 possess clear absorption peaks at ca. 310, 290 and 300 nm, respectively which are hidden in the as-prepared PdNPs sample. In fact, these peaks are responsible for the broad band at 250–400 nm of the as-synthesized PdNPs sample in Fig. 1. All the peaks do not show distinct SPR band, suggesting that the separated DMF-PdNPs species have core size diameters smaller than ca. 3 nm [53]. Our results demonstrate that the as-synthesized PdNPs sample is indeed a complex mixture of PdNPs and its absorption spectrum only represent the summation of all the individual separated PdNPs species in the DMF-PdNPs.

Fig. 5 displays the PL spectra of the collected HPLC fractions. When the λ_{ex} is 300 nm, all the peaks display emissions at 350–500 nm, attributing to the radiative recombination of the $4d$ band and $5sp$ conduction band (interband transition) of the Pd atom [42]. This observation is consistent with the PL spectrum of the as-synthesized DMF-PdNPs sample at $\lambda_{\text{ex}}/\lambda_{\text{em}}$ of 300/422 nm. The fractions reveal their own characteristic emission bands which are not available from an as-prepared DMF-PdNPs sample. In essence, chromatographic

separation in conjunction with absorption and PL spectroscopy provides an important and powerful tool to evaluate the spectral features of the separated PdNPs species. Furthermore, the collected PdNPs fractions can also be characterized and studied by other techniques.

3.3. Mass spectrometric analysis of DMF-PdNPs fractions

It is a challenge to determine the exact mass of metal NPs including the numbers of Pd atoms and surface protecting ligands. In the past two decades, Whetten et al. [54] found that MS is a more reliable technique to measure the molecular mass of small-sized NPs and they were the pioneers to use laser desorption/ionization TOF MS to analyze AuNPs. Since then, MS has been widely adopted in almost all the structural analysis of metal NPs. So far various MS techniques such as MALDI-TOF MS [28,43,44,55,56], ESI-MS [57,58], LDI-MS [59], ion mobility MS [60,61] and fast atom bombardment MS [62] have been applied to explore the metal core mass of all kinds of metal NPs. Among them, MALDI-TOF MS is the most popular MS technique in determining the number of metal atom of NP fractions. Herein, MALDI-TOF MS is for the first time used to identify the chemical compositions of all the separated PdNPs species. In addition, this method is much faster and requires less sample size than NMR which is commonly used to characterize only the surface-attached

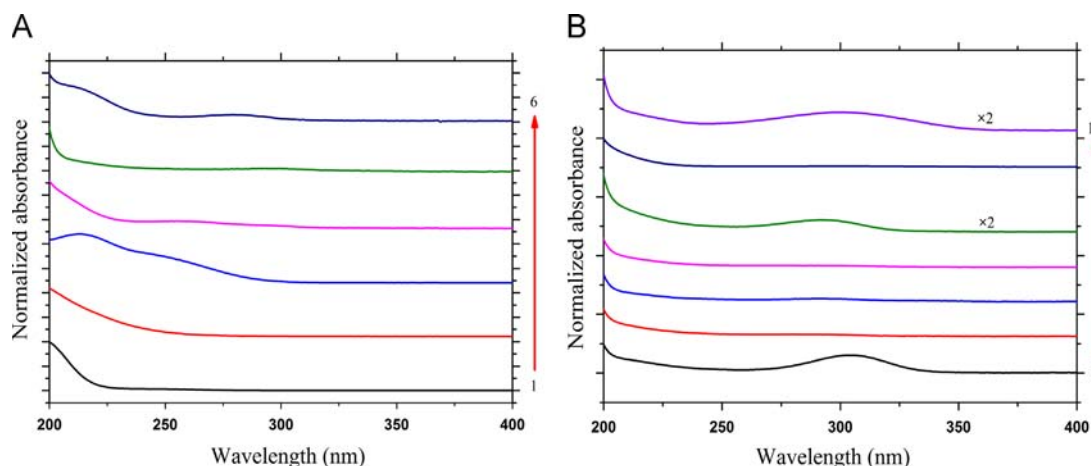


Fig. 4. Absorption spectra of Fractions (A) 1–6 and (B) 7–13. All the spectra are normalized at 200 nm and offset for clarity.

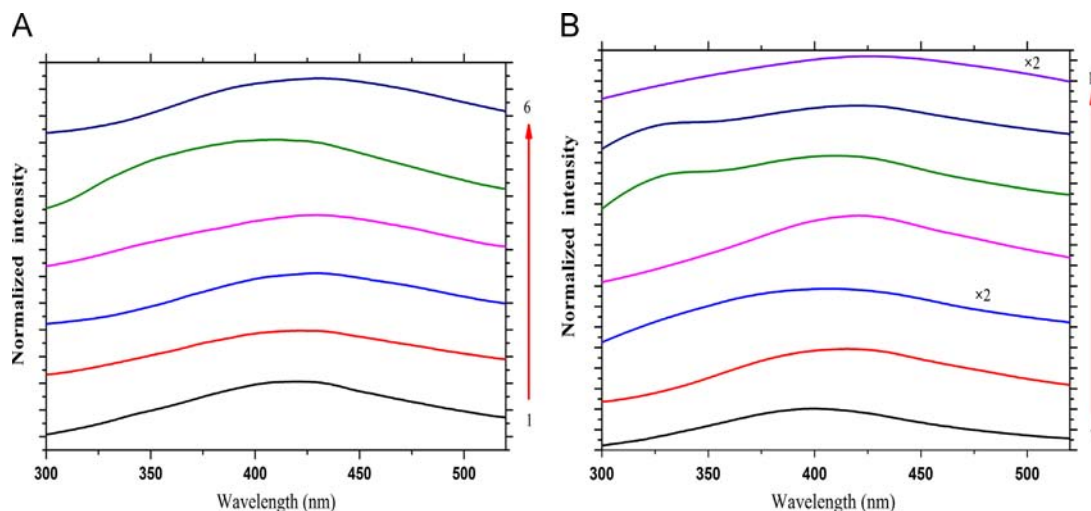


Fig. 5. Photoluminescence spectra of Fractions (A) 1–6 and (B) 7–13 at λ_{ex} of 300 nm. All the spectra are normalized at their emission peaks and offset for clarity.

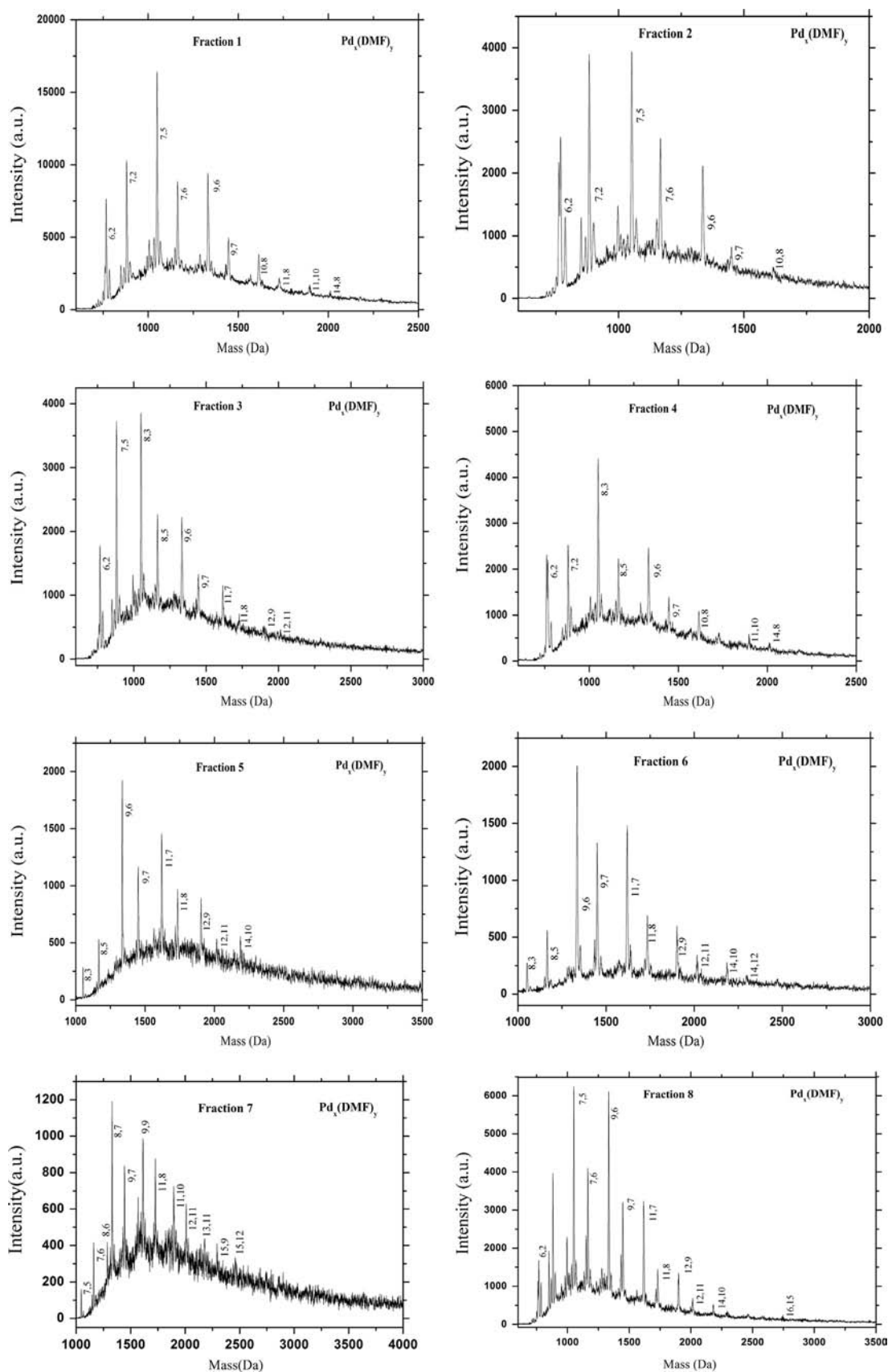


Fig. 6. MALDI-TOF mass spectra of Fractions 1–13. The mass peaks are assigned to Pd_x(DMF)_y, where x and y denote the numbers of Pd atom and intact DMF ligand, respectively. The numbers next to the peaks are assigned to the corresponding x and y values.

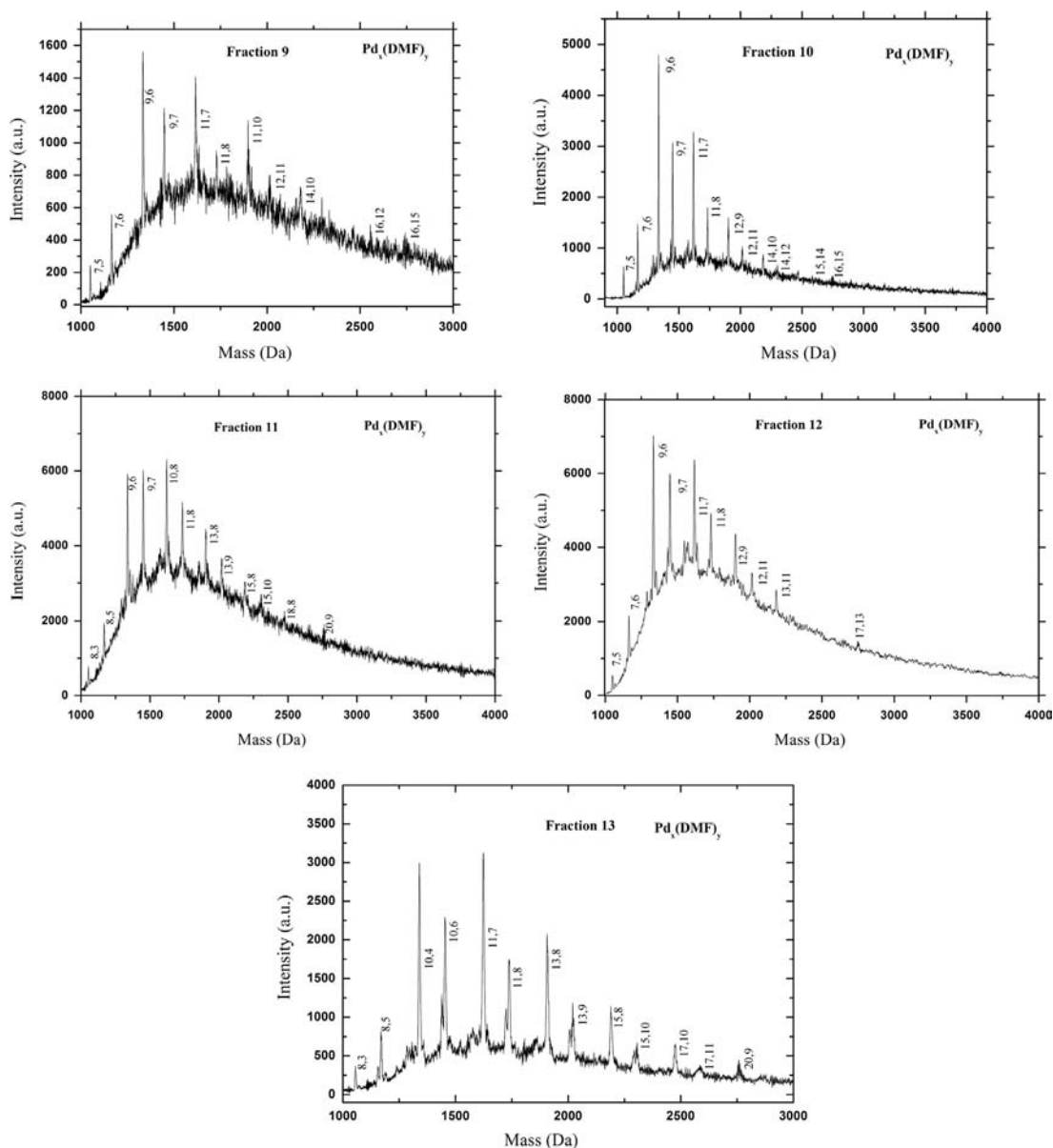


Fig. 6. (continued)

ligand. Fig. 6 displays the MS of PdNPs obtained from the HPLC fractions. These PdNPs fractions are prone to fragmentation, allowing clear assignment of the mass peaks of PdNPs species. Fragmentation of PdNPs species is unavoidable even though we have minimized the laser power of MALDI. When the laser power is too low, no mass peaks are observed. All the m/z peaks are below 3000 Da and all the peak assignments are within the m/z accuracy ($\pm 1-2$ m/z units) of the MALDI-TOF MS. Each fraction displays a series of major mass spacings, indicating the fragmented PdNPs ions. These mass peaks can be assigned to $\text{Pd}_x(\text{DMF})_y$, where x and y denote the numbers of Pd atom and intact DMF ligand, respectively. The numbers next to the peaks are the corresponding x and y values. There are also some minor mass spacings between the major mass peaks which will be discussed in the following.

Since most fractions display similar fragmentation patterns, Fraction 1 is chosen as an example to illustrate the mass patterns. The three selected groups of fragment peaks of Fraction 1 in Fig. 6 are anatomized in Fig. 7. It depicts a series of major m/z spacing in every three adjacent peaks ($285 \pm (1-2)$ mass units), corresponding to one DMF ligand (73 mass unit), and two Pd atoms

($106 \times 2 = 212$ mass unit), respectively. Some minor m/z spacings are also found in each group of fragments. The spacing mass within the peaks of each fragment was determined as 15, 17 or 18, 30, 44, and 58 corresponding to a methyl (CH_3), a hydroxyl (OH) or a H_2O molecule, two methyl (2CH_3)/protonated carbonyl ($\text{HC}=\text{O}^+\text{H}$), dimethylamino ($\text{N}(\text{CH}_3)_2$), and two formyl (2CHO) moieties, respectively. These fragment ions are commonly observed from the MS of DMF (not shown).

The highest mass ions of Fractions 1–13 in Fig. 6 approximately indicate their chemical composition as $\text{Pd}_{14}(\text{DMF})_8$, $\text{Pd}_{10}(\text{DMF})_8$, $\text{Pd}_{12}(\text{DMF})_{11}$, $\text{Pd}_{14}(\text{DMF})_8$, $\text{Pd}_{14}(\text{DMF})_{10}$, $\text{Pd}_{14}(\text{DMF})_{12}$, $\text{Pd}_{15}(\text{DMF})_{12}$, $\text{Pd}_{16}(\text{DMF})_{15}$, $\text{Pd}_{16}(\text{DMF})_{15}$, $\text{Pd}_{16}(\text{DMF})_{15}$, $\text{Pd}_{20}(\text{DMF})_9$, $\text{Pd}_{17}(\text{DMF})_{13}$, and $\text{Pd}_{20}(\text{DMF})_9$, respectively. The assignment of these highest mass peaks is based on the signal-to-noise ratio ≥ 3 . Fig. S3 displays the TGA of the as-synthesized DMF-PdNPs sample. The total weight (wt) loss is about 57%, arising from the dissociation and evaporation of the DMF ligand from the surface of PdNPs. The binding of DMF molecules to the PdNPs can be envisioned as two layers: the outer loose layer accounts for 20% wt loss and the surface-attached protecting layer on the Pd metal core corresponds to 37% wt loss. As a result, the average

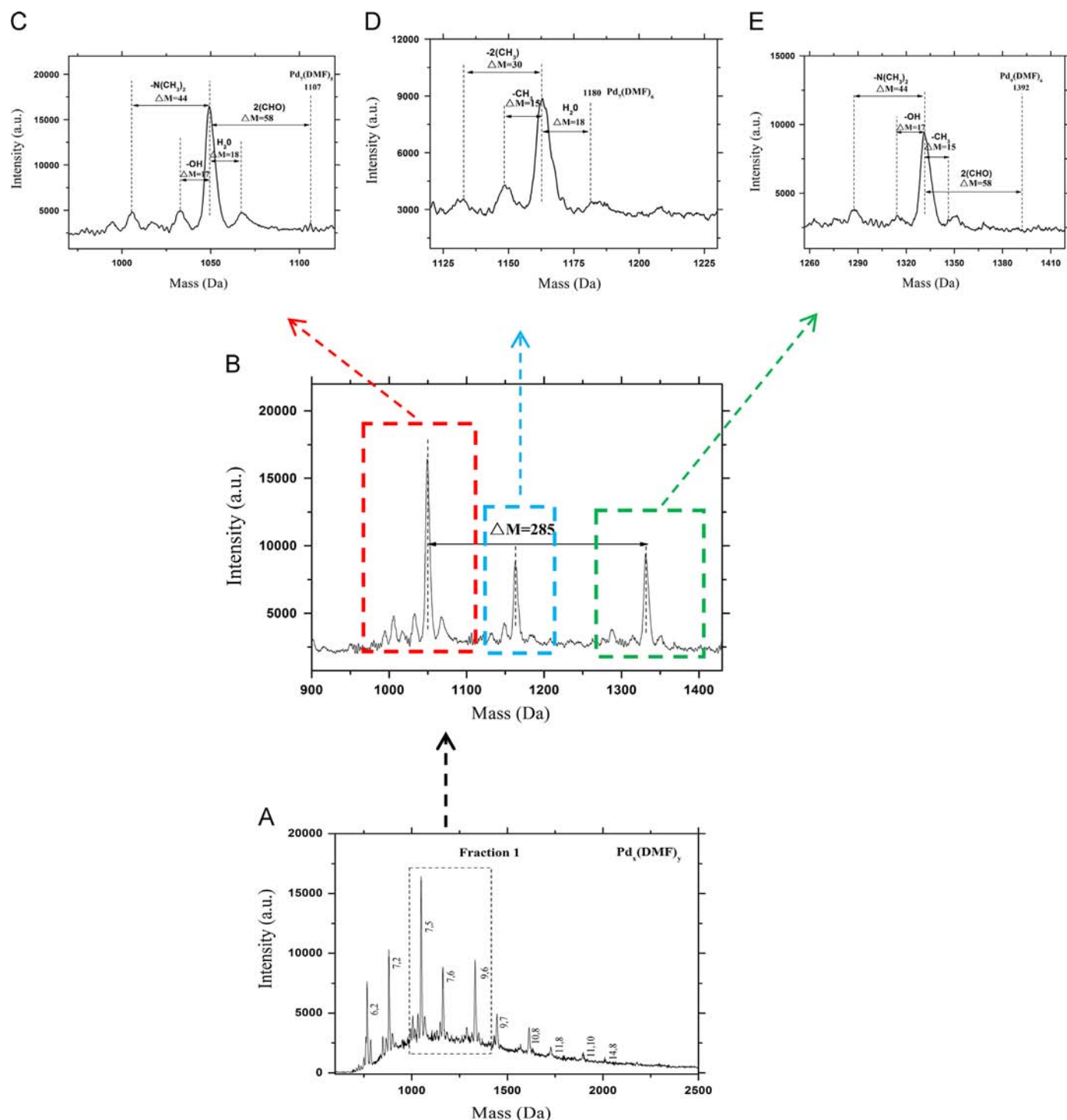


Fig. 7. (A) MALDI-TOF mass spectrum of Fraction 1. (B) The expanded mass spectrum of the dash rectangle in (A). (C), (D) and (E) The expanded mass spectra of the dash rectangles in (B) at various mass ranges.

composition of the as-synthesized DMF-PdNPs sample is roughly $\text{Pd}_{15}(\text{DMF})_{13}$ which is consistent with the chemical compositions of the separated fractions. The assignment of the mass peaks of the separated DMF-PdNPs fractions is summarized in Table S1. Interestingly, Fractions 8–10 possess the same molecular formula of $\text{Pd}_{16}(\text{DMF})_{15}$ and Fractions 11 and 13 have the formula of $\text{Pd}_{20}(\text{DMF})_9$ but their retentions are different on the C18 column. The differences in retention of the DMF-PdNPs species with the same molecular formula are possibly attributed to the differences in coordination of DMF ligands to the PdNPs, *i.e.*, coordination isomers [63]. On

the other words, different structures of PdNPs with the same molecular formula will elute differently. The shape of PdNPs could determine their retention on a C18 column in addition to molecular mass. In general, the elution order of these fractions seems to follow the numbers of Pd atom and ligand from the smallest to the largest with few exceptions. In summary, each PdNPs species with its own well-defined shape, mass and the protecting ligands might determine their retention on a C18 column. While the reasons how both the shape and size governing the interaction between PdNPs and C18 are intriguing, the investigation of this phenomenon requires more

experimental and theoretical studies. Further work could be directed to elucidate the retention of these DMF-PdNPs species under RP-HPLC conditions.

4. Conclusion

The as-synthesized DMF-PdNPs sample possesses spectral features or chemical and physical properties that only represent the total or average properties of its individual PdNPs. To our knowledge, RP-HPLC was for the first time shown to separate and analyze water-soluble DMF-PdNPs product. The elution order approximately follows with the total number of Pd atoms and DMF ligands to a certain extent from the smallest to the largest. The NPs chemical compositions of the fractions were confirmed by MALDI-TOF MS. The mass data show that the as-synthesized DMF-PdNPs sample comprises Pd₁₀, Pd₁₂, Pd₁₄, Pd₁₅, Pd₁₆, Pd₁₇, and Pd₂₀ NPs stabilized with various numbers of DMF ligands. However, the highest molecular mass does not permit to univocally distinguish some fractions as they have the same masses, inferring that the molecular mass is a property not sufficient to identify univocally each PdNPs species. Herein, HPLC is demonstrated to be a useful technique to separate different PdNPs species of the same masses. It should also take note that there is no guarantee the separated fractions are 100% pure. Thus, other characterization methods can be helpful to elucidate the exact structures of these PdNPs compounds.

In addition, it is anticipated that the developed RP-HPLC and MS technique can be applied to study the growth mechanism of PdNPs. Our proposed HPLC methodology opens new avenues to isolate individual NPs for their characterization and studies of physical and chemical properties. The isolated PdNPs species with well-defined structures might find their uses in catalysis, hydrogen storage, photodynamic therapy, and bioimaging.

Acknowledgments

Financial supports from the Hundred Talent Programme of Shanxi Province, HKBU Faculty Research Grant (FRG1/13–14/039), National Science Foundation of China (21175086 and 21305082), and Youth Foundation of Shanxi Province (2011021005-1) are gratefully acknowledged. We would express our sincere thanks to Ms Silva T. Mo of the Department of Chemistry, Hong Kong Baptist University for acquiring the MALDI-TOF MS.

Appendix A. Supporting information

Supplementary data associated with this paper can be found in the online version at <http://dx.doi.org/10.1016/j.talanta.2014.08.032>.

References

- [1] Q.-Y. Bi, X.-L. Du, Y.-M. Liu, Y. Cao, H.-Y. He, K.-N. Fan, *J. Am. Chem. Soc.* 134 (2012) 8926–8933.
- [2] M. Moreno, L.N. Kissell, J.B. Jasinski, F.P. Zamborini, *ACS Catal.* 2 (2012) 2602–2613.
- [3] M. Hyotanishi, Y. Isomura, H. Yamamoto, H. Kawasaki, Y. Obora, *Chem. Commun.* 47 (2011) 5750.
- [4] S.S. Kumar, K. Kwak, D. Lee, *Anal. Chem.* 83 (2011) 3244.
- [5] M. Moreno, F.J. Ibañez, J.B. Jasinski, F.P. Zamborini, *J. Am. Chem. Soc.* 133 (2011) 4389.
- [6] B.D. Gates, Q. Xu, M. Stewart, D. Ryan, C.G. Willson, G.M. Whitesides, *Chem. Rev.* 105 (2005) 1171.
- [7] R.J. Tseng, J. Huang, J. Ouyang, R.B. Kaner, *Nano Lett.* 5 (2005) 1077.
- [8] D. Drescher, J. Kneipp, *Chem. Soc. Rev.* 41 (2012) 5780.
- [9] H. Oyamada, R. Akiyama, H. Hagio, T. Naito, S. Kobayashi, *Chem. Commun.* 0 (2006) 4297.
- [10] S. Sharma, B. Kim, D. Lee, *Langmuir* 28 (2012) 15958.
- [11] N. Sakai, T. Tatsuma, *J. Mater. Chem. A* (2013).
- [12] Y. Jiang, Q. Gao, *J. Am. Chem. Soc.* 128 (2005) 716.
- [13] J. Choi, H.Y. Yang, H.J. Kim, S.U. Son, *Angew. Chem.* 122 (2010) 7884.
- [14] S.U. Son, Y. Jang, J. Park, H.B. Na, H.M. Park, H.J. Yun, J. Lee, T. Hyeon, *J. Am. Chem. Soc.* 126 (2004) 5026.
- [15] G. Wei, W. Zhang, F. Wen, Y. Wang, M. Zhang, *J. Phys. Chem. C* 112 (2008) 10827.
- [16] P. Zhou, H. Wang, J. Yang, J. Tang, D. Sun, W. Tang, *Ind. Eng. Chem. Res.* 51 (2012) 5743.
- [17] R. Xing, Y. Liu, H. Wu, X. Li, M. He, P. Wu, *Chem. Commun.* 0 (2008) 6297.
- [18] J. Broggi, V. Jurčík, O. Songis, A. Poater, L. Cavallo, A.M.Z. Slawin, C.S.J. Cazin, *J. Am. Chem. Soc.* 135 (2013) 4588.
- [19] F. Favier, E.C. Walter, M.P. Zach, T. Benter, R.M. Penner, *Science* 293 (2001) 2227.
- [20] Y. Mizukoshi, K. Okitsu, Y. Maeda, T.A. Yamamoto, R. Oshima, Y. Nagata, *J. Phys. Chem. B* 101 (1997) 7033.
- [21] S. Chen, K. Huang, J.A. Stearns, *Chem. Mater.* 12 (2000) 540.
- [22] T. Teranishi, M. Miyake, *Chem. Mater.* 10 (1998) 594.
- [23] S. Giorgio, C. Chapon, C.R. Henry, *Langmuir* 13 (1997) 2279.
- [24] G. Schmid, M. Harms, J.O. Malm, J.O. Bovin, J. Van Ruitenbeck, H. W. Zandbergen, W.T. Fu, *J. Am. Chem. Soc.* 115 (1993) 2046.
- [25] J.-C. Bradley, Z. Ma, *Angew. Chem. Int. Ed.* 38 (1999) 1663.
- [26] X. Liu, C. Li, J. Xu, J. Lv, M. Zhu, Y. Guo, S. Cui, H. Liu, S. Wang, Y. Li, *J. Phys. Chem. C* 112 (2008) 10778.
- [27] H. Kawasaki, H. Yamamoto, H. Fujimori, R. Arakawa, Y. Iwasaki, M. Inada, *Langmuir* 26 (2009) 5926.
- [28] H. Kawasaki, H. Yamamoto, H. Fujimori, R. Arakawa, M. Inada, Y. Iwasaki, *Chem. Commun.* 46 (2010) 3759.
- [29] C.K. Lo, M.C. Paa, D. Xiao, M.M.F. Choi, *Anal. Chem.* 80 (2008) 2439.
- [30] N. Urgau, P.L. Urban, *J. Sep. Sci. J. Sep. Sci.* 32 (2009) 1889.
- [31] M. Hanauer, S. Pierrat, I. Zins, A. Lotz, C. Sönnichsen, *Nano Lett.* 7 (2007) 2881.
- [32] K. Kimura, N. Sugimoto, S. Sato, H. Yao, Y. Negishi, T. Tsukuda, *J. Phys. Chem C* 113 (2009) 14076.
- [33] H. Tsunoyama, Y. Negishi, T. Tsukuda, *J. Am. Chem. Soc.* 128 (2006) 6036.
- [34] S. Knoppe, J. Boudon, I. Dolamic, A. Dass, T. Bürgi, *Anal. Chem.* 83 (2011) 5056.
- [35] W. Bos, J.J. Steggerda, S. Yan, J.A. Casaluovo, A.M. Muetting, L.H. Pignolet, *Inorg. Chem.* 27 (1988) 948.
- [36] D. Steinigeweg, M. Schütz, M. Salehi, S. Schlücker, *Small* 7 (2011) 2443.
- [37] Y. Ogasawara, S. Kato, *J. Am. Chem. Soc.* 132 (2010) 4608.
- [38] L. Calzolari, D. Gilliland, C.P. Garcia, F. Rossi, *J. Chromatogr. A* 1218 (2011) 4234.
- [39] S.F. Sweeney, G.H. Woehrle, J.E. Hutchison, *J. Am. Chem. Soc.* 128 (2006) 3190.
- [40] J.M. Zook, V. Rastogi, R.I. MacCuspie, A.M. Keene, J. Fagan, *ACS Nano* 5 (2011) 8070.
- [41] S. Xie, M.C. Paa, Y. Zhang, S. Shuang, W. Chan, M.M.F. Choi, *Nanoscale* 4 (2012) 5325.
- [42] Y. Zhang, S. Shuang, C. Dong, C.K. Lo, M.C. Paa, M.M.F. Choi, *Anal. Chem.* 81 (2009) 1676.
- [43] M.M.F. Choi, A.D. Douglas, R.W. Murray, *Anal. Chem.* 78 (2006) 2779.
- [44] Y. Niihori, M. Matsuzaki, C. Uchida, Y. Negishi, *Nanoscale* 6 (2014) 7889.
- [45] T. Harada, S. Ikeda, M. Miyazaki, T. Sakata, H. Mori, M. Matsumura, *J. Mol. Catal. A: Chem.* 268 (2007) 59.
- [46] S. Nath, S. Praharaj, S. Panigrahi, S.K. Ghosh, S. Kundu, S. Basu, T. Pal, *Langmuir* 21 (2005) 10405.
- [47] J.A. Creighton, D.G. Eadon, *J. Chem. Soc. Faraday Trans.* 87 (1991) 3881.
- [48] Z. Li, J. Gao, X. Xing, S. Wu, S. Shuang, C. Dong, M.C. Paa, M.M.F. Choi, *J. Phys. Chem. C* 114 (2009) 723.
- [49] X. Huang, S. Tang, X. Mu, Y. Dai, G. Chen, Z. Zhou, F. Ruan, Z. Yang, N. Zheng, *Nat. Nanotechnol.* 6 (2011) 28.
- [50] Z. Wang, B. Huang, Z. Lu, S. Wang, R. Xue, L. Chen, *Solid State Ion.* 92 (1996) 265.
- [51] A.S. Quist, J.B. Bates, G.E. Boyed, *J. Chem. Phys.* 54 (1971) 4896.
- [52] C.M.V. Stalhandske, J. Mink, M. Sandstrom, I. Papai, P. Johnsson, *Vib. Spectrosc.* 14 (1997) 207.
- [53] Y. Xiong, Y. Xia, *Adv. Mater.* 19 (2007) 3385.
- [54] R.L. Whetten, J.T. Khoury, M.M. Alvarez, S. Murthy, I. Vezmar, Z.L. Wang, P. W. Stephens, C.L. Cleveland, W.D. Luedtke, U. Landman, *Adv. Mater.* 8 (1996) 428.
- [55] H. Kouchi, H. Kawasaki, R. Arakawa, *Anal. Methods* 4 (2012) 3600.
- [56] C.A. Fields-Zinna, M.C. Crowe, A. Dass, J.E.F. Weaver, R.W. Murray, *Langmuir* 25 (2009) 7704.
- [57] G.E. Johnson, C. Wang, T. Priest, J. Laskin, *Anal. Chem.* 83 (2011) 8069.
- [58] X. Yang, M. Shi, R. Zhou, X. Chen, H. Chen, *Nanoscale* 3 (2011) 2596.
- [59] B. Yan, Z.-J. Zhu, O. Miranda, A. Chomposor, V. Rotello, R. Vachet, *Anal. Bioanal. Chem.* 396 (2010) 1025.
- [60] L.A. Angel, L.T. Majors, A.C. Dharmaratne, A. Dass, *ACS Nano* 4 (2010) 4691.
- [61] K.M. Harkness, B.C. Hixson, L.S. Fenn, B.N. Turner, A.C. Rape, C.A. Simpson, B. J. Huffman, T.C. Okoli, J.A. McLean, D.E. Cliffler, *Anal. Chem.* 82 (2010) 9268.
- [62] A. Dass, G.R. Dubay, C.A. Fields-Zinna, R.W. Murray, *Anal. Chem.* 80 (2008) 6845.
- [63] Y. Niihori, M. Matsuzaki, T. Pradeep, Y. Negishi, *J. Am. Chem. Soc.* 135 (2013) 4946–4949.



Peptidomics study of anthocyanin-rich juice of elderberry



Hanzhi Wu^{a,b,c}, Mitch C. Johnson^{b,c}, Chi-Hua Lu^{c,d}, Kevin L. Fritsche^{c,d},
Andrew L. Thomas^{c,e}, Yongquan Lai^a, Zongwei Cai^{a,*}, C. Michael Greenlief^{b,c,**}

^a Department of Chemistry, Hong Kong Baptist University, Kowloon Tong, Hong Kong SAR, PR of China

^b Department of Chemistry, University of Missouri, Columbia, MO, USA

^c Center for Botanical Interaction Studies, University of Missouri, Columbia, MO, USA

^d Division of Animal Sciences, University of Missouri, Columbia, MO, USA

^e Southwest Research Center, University of Missouri, Columbia, MO, USA

ARTICLE INFO

Article history:

Received 13 June 2014

Received in revised form

3 August 2014

Accepted 6 August 2014

Available online 27 August 2014

Keywords:

Elderberry

Peptidomics

Solid phase extraction

Orbitrap-MS/MS

Anthocyanin *sambucus*

ABSTRACT

Biologically active peptides play a role in plant signaling and defense. Elderberry juice is known to contain a variety of anthocyanin compounds, a sub-set of polyphenols, which are responsible for the deep purple color of the juice. In this paper, we describe a method utilizing solid phase extraction (SPE) to remove anthocyanins from peptides. Liquid chromatography coupled with tandem mass spectrometry was used to separate and identify the peptides. The results showed that the use of SPE was an effective method to separate peptides from anthocyanins and other background compounds including high polyphenol content in the juice samples. More than 1000 peptides present in elderberry juice were successfully identified.

© 2014 Elsevier B.V. All rights reserved.

1. Introduction

Thousands of peptides have been isolated and purified from microorganisms, animals, and plants. Plant peptides are often key players in cell-to-cell communication governing plant development. They also play a role in communication between plants and other organisms. Plants are an enormously rich source of peptides, with the potential to be developed as nutrients, medicines and biomarkers [1,2]. Some secreted peptides are recognized as important hormones that coordinate and specify cellular functions in plants. Peptides are of interest as they possess several advantages including low molecular weight, relatively simple structure, ease of absorption, and lower antigenicity [3–5]. The first functional plant peptide to be identified was tomato systemin, an 18 amino acid polypeptide, which acts in the rapid expression of defense-responsive genes via cellular communication [6]. In the 1990s, a disulfated pentapeptide was isolated by Matsubayashi and Sakagami, and named as phyto-sulfokine. It is a potent mitogenic factor from conditioned medium derived from cultures of asparagus mesophyll cells [7]. Studies over

the past decade have highlighted the diverse nature of peptides and explored their possible uses.

Peptidomics is a fast, efficient method that can detect low and transient concentrations of peptides and identify their post-translational modifications. It is a branch of proteomics that has been developing over several years. There are several approaches to peptide separation and identification [8]. Two-dimensional gel electrophoresis can be extended to detect smaller peptides (1 kDa and larger) by the use of tris-tricine in the second dimension. After extraction from the gel, the isolated peptides can be measured by MALDI-TOF-MS. The combination of high performance liquid chromatography (HPLC) coupled with MS/MS can help to overcome complex peptide mixtures and aid in the identification of less abundant peptides. The use of nano-liquid chromatography can increase the signal-to-noise ratio and sensitivity of MS for the detection of peptides in complex mixtures or those present in low concentrations [9–12].

Peptidomics studies the role of peptides and bridges the space between proteomics and metabolomics [13]. The full spectrum of peptide functions in plants is unknown. Peptide hormone signaling in plants is an emerging area of research and peptides have been shown to affect cell division, development, reproduction, nodulation and defense. The major difference between proteomics and peptidomics, regardless of peptide size, is that peptidomics identifies native peptides. Thus, it can be referred to as a version of top-down proteomics which considers only the peptidome (peptides).

* Correspondence to: University of Missouri, 125 Chemistry Bldg. Columbia, MO 65211, USA.

** Corresponding author at: Hong Kong Baptist University, Department of Chemistry, Kowloon Tong, Hong Kong SAR, PR of China.

E-mail addresses: greenliefm@missouri.edu (Z. Cai), zwcai@hkbu.edu.hk (C.M. Greenlief).

Elderberry (*Sambucus* spp) has been used as a traditional medicine and its use can be traced back to the Roman times. The juice is known to be rich in anthocyanin compounds and can contain peptides. Elderberry juices have been to vary with cultivar and growing regions and conditions [14,15]. Till date, no peptide profiling of elderberry has been reported [16–20]. In this paper, we describe a method to remove the anthocyanin from the peptides in elderberry juice by solid phase extraction and use LC-MS/MS to profile and *de novo* sequence the peptides. Analysis of the peptide sequences was then used to identify possible proteins present in the juice samples.

2. Materials and methods

2.1. Materials and instruments

Methanol, formic acid, ammonium hydroxide and other chemicals were purchased from Fisher Scientific (Fair Lawn, NJ, USA). American elderberry juice (*Sambucus nigra* L. subsp. *canadensis* (L.) Bolli; syn. *S. canadensis* L.) was prepared from fruit grown in a commercial orchard in central Missouri, USA. Berries from cultivar 'Wyldeewood' were harvested at peak ripeness in early September 2011, destemmed, pressed, and the juice frozen. The juice was later thawed and aliquoted (pH 4.51) and then filtered through a 0.45 μ m nylon filter to remove any suspended solids. The color of the juice was dark-violet. Solid phase extraction (SPE) cartridges (Oasis MCX (3cc, 60 mg) and C₁₈ Certified Sep-Pak Vac (3cc, 500 mg)), were purchased from Waters Corp. (Milford, MA). MALDI spectra were acquired on an Applied Biosystems 4700. LC-MS/MS spectra were acquired on a LTQ Orbitrap XL mass spectrometer (Thermo Scientific) with an interfaced nano-LC (Proxeon Easy nLC-1000).

2.2. Peptide separation and purification

The Oasis MCX stationary phase contains two types of materials: a strong cation-exchange phase with a C₁₈-reversed phase. Two cartridge volumes of elderberry juice in aqueous solution (12 mL) were applied to an MCX SPE cartridge (6 mL, 1 g sorbent; Waters Corp., Milford, MA). After washing with 12 mL of water (0.1% FA), the peptide fraction was collected by elution with 12 mL of methanol (0.1% FA) retaining the anthocyanins on the column. The anthocyanin fraction was then eluted with 6 mL of methanol and 6 mL of water:methanol (40:60, v/v), both containing 1% NH₄OH. The combined alkaline eluate was immediately mixed with an aliquot (250 μ L) of formic acid (99%) to lower the pH to less than 2 to prevent degradation of the anthocyanin fraction.

The peptide fraction was briefly evaporated in a rotovaporator at 90 °C for 10 min to remove the organic solvent, redissolved in water (0.1% FA), filtered through 0.45 μ m polypropylene filter, and then separated into two groups for analysis. One group was analyzed by MS directly (Group A) and the other group was further purified using a C₁₈ SPE cartridge (Group B) following the protocol provided by the manufacturer. Fig. 1 is an overall flow chart of the procedure used for the separation of the peptides from the elderberry juice.

2.3. MALDI-TOF MS/MS detection

Elderberry juice samples were tested by MALDI-TOF MS/MS. Each of the samples was combined 1:1 (v/v) with α -cyano-4-hydroxycinnamic acid (CHCA), 2,5-dihydroxybenzoic acid (DHB), or sinapinic acid (SA) matrix for application to the target for MALDI-TOF MS analysis. MS spectra were acquired in the positive ion reflector delayed-extraction mode with external calibration.

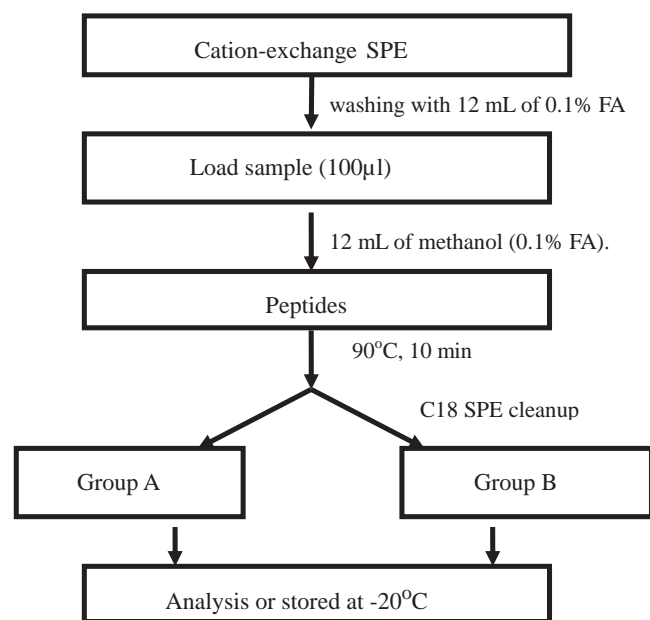


Fig. 1. Experimental scheme for the purification and isolation of peptides in elderberry juice.

2.4. Peptide identification

Data was acquired on an LTQ Orbitrap XL with an interfaced nano-HPLC system. Nano-liquid chromatography conditions are described below. Mobile phase A: 0.1% formic acid in water, mobile phase B: 0.1% formic acid in acetonitrile, flow rate 20 μ L/min, sample loading volume 30 μ L (flow rate 25 μ L/min), max pressure 200.00 bar. The gradient program is shown as Supplementary Table S1 with a total of 120 min running time. The following LC-MS parameters were applied. Scan event 1: analyzer FTMS, mass range normal, resolution 30,000, full-scan, polarity positive, data type profile; scan event 2: analyzer ion trap, mass range normal, scan rate normal, data type centroid.

The peptide mixture was loaded onto a trap column (C₁₈, 75 μ m \times 100 mm) and separated on a MonoSpray C₁₈ tip using a 120 min gradient from 10 to 50% acetonitrile in 0.5% formic acid at a flow rate of 200 nL/min. The protonated ion of polycyclodimethylsiloxane (445.120025 Da) was used for internal calibration throughout. The mass spectrometer alternated between a full FTMS scan (300–1500 Da) and subsequent MS/MS scans. Cations were isolated with an isolation window of 5 Da and provided a dynamic exclusion list for 2400 s after selected for at least two MS/MS scans. Singly charged precursors were excluded. Monoisotopic selection was disabled with an exclusion window setting of 1 Da. The four most intense ions were chosen for CID fragmentation. Automatic gain control was used to accumulate sufficient fragment ions (MS/MS target value 2E5; maximum injection time, 1000 ms) [9]. A sample blank was run before the analytical sample. The blank solution included 5% ACN and 1% FA. Peptide *de novo* sequencing was performed using the proteomics software PEAKS. A trial version of PEAKS 6 was downloaded from the bioinformatics solutions website (<http://www.bioinform.com>).

2.5. Protein sequence similarity searches

BLAST protein sequence searches were performed using the measured peptide sequences (<http://www.uniprot.org/blast>). The parameter settings were as follows:

Program blastp (BLASTP 2.2.28+), Database: uniprotkb_viridiplantae (Protein) generated for BLAST, Sequences: 1,711,995 sequences consisting of 584,837,709 letters, Matrix: blosum62, Threshold: 0.1, Filtering: none, Gapped: yes.

3. Results and discussion

3.1. MALDI-TOF MS analysis of elderberry juice

The original elderberry juice and its diluted solution were analyzed by MALDI-TOF MS using CHCA as a matrix (Fig. 2). Table S2 presented the MS/MS results from subsequent TOF/TOF MS analysis of the major peaks in Fig. 2. The presence of the fragment ion at 287.03 Da corresponded to cyanidins (expected 287.05 Da, monoisotopic) that belong to anthocyanins, which indicated that many of the precursor ions from were various modified forms of cyanidins or anthocyanins. Fragmentation patterns did not match those expected for peptides. Instead, the fragmentation patterns observed corresponded to the loss of hexose ($\Delta = 162.053$ Da, monoisotopic), deoxyhexose (146.058 Da), pentose (132.042 Da), deoxypentose (116.047 Da) and the disaccharide rutinose (308.111 Da). Based on these results, it appeared that the simple dilution of the elderberry juice was not sufficient to permit the

analysis of peptides and proteins directly because of the significant background interference. The interfering problem may be caused by the high concentration of anthocyanins compared to peptides in the juice. Another possibility for not-detected peptides might be that the peptide signal was suppressed by the presence of anthocyanins.

Table 1
Elderberry juice peptide sequences with ALC scores greater than 60 for Group A.

No.	M/Z	Charge	DENOVO	ALC
1	372.1201	2	EEMTCM	60.03
2	394.1062	2	CCCCAGPM	65.34
3	400.0883	2	CCCHGACC	62.05
4	490.1198	2	CMCGWACCC	61.73
5	386.1172	2	DSSDAACC	60.11
6	352.6239	2	YMEMM	61.47
7	408.1661	2	YCCGAGNK	60.79
8	320.1586	2	YPTMK	67.92

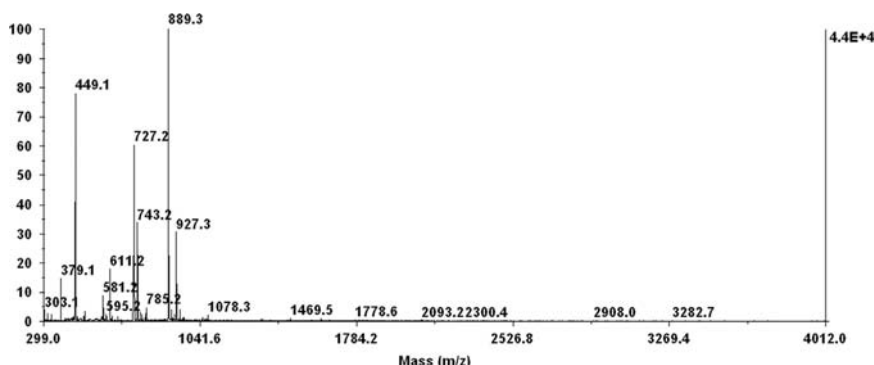


Fig. 2. MALDI-TOF MS spectrum of elderberry juice when using CHCA as a matrix.

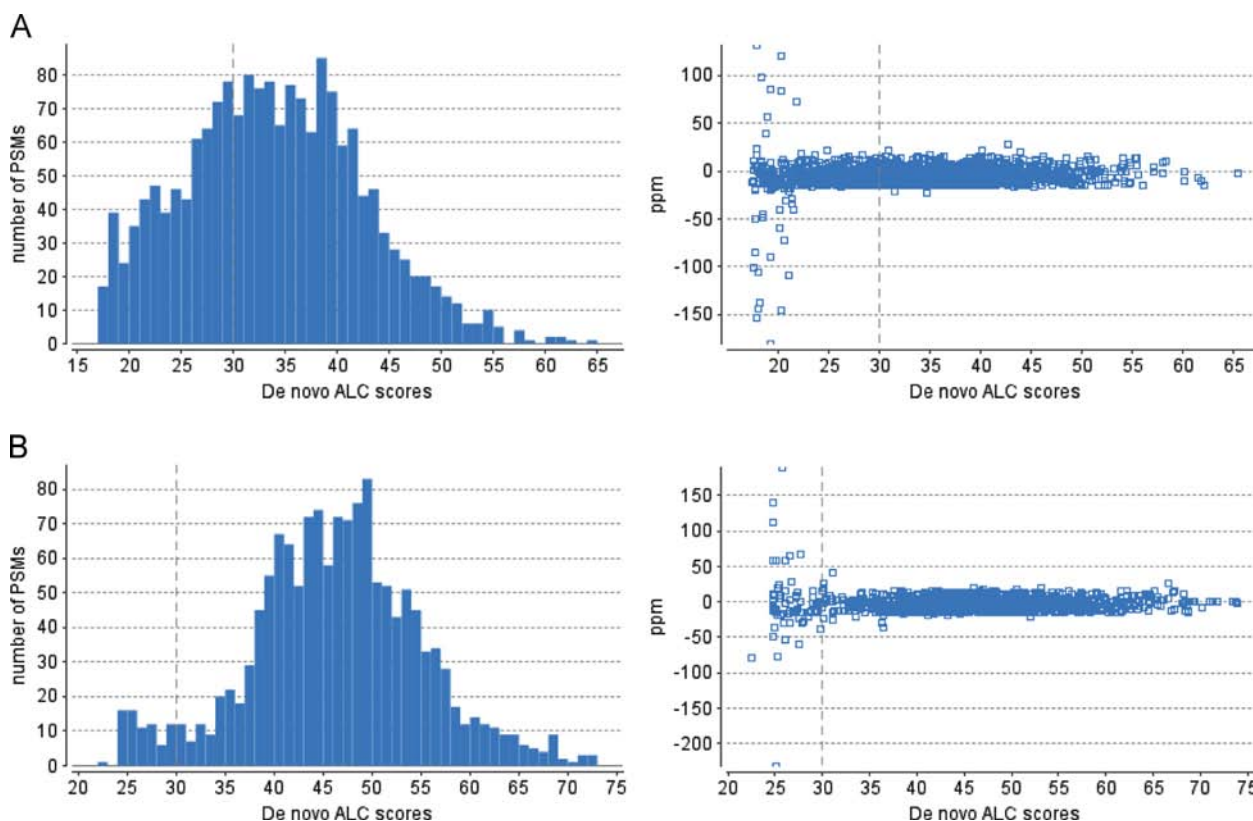


Fig. 3. A. De novo ALC scores of Group A: 2530MS/MS and 1789 detected peptides after filter. B. De novo ALC scores of Group B: 1833MS/MS scans and 1233 detected peptides after filter.

Table 2
Elderberry juice peptide sequences with ALC scores greater than 60 for Group B.

No.	M/Z	Charge	DENOVO	ALC
1	336.1234	2	EDHACP	70.2
2	357.6659	2	MAHAGLD	71.81
3	428.1912	2	SSGPAGGHW	71.25
4	472.2460	2	ATGSGNVQLP	73.37
5	472.2461	2	DGSGGNVKPL	73.76
6	678.8597	2	PSTSDGLPVTGLRG	71.03
7	332.5206	3	RGTSPKGVGH	62.73
8	497.7386	2	DGGGLDPHAR	61.3
9	368.6776	2	ESGTNKT	63.56
10	323.5389	3	TTPKKVVPV	66.92
11	497.7383	2	KVHNMPDGP	60.67
12	328.1086	2	ATGGCCGS	60.95
13	405.0637	2	CCCDGCCC	73.84
14	478.1087	2	YDCDMCCC	60.01
15	357.6664	2	MAHAGLD	65.71
16	457.2598	2	LVEAAPGLSG	67.26
17	629.3033	2	HSNKTVPAMWS	62.44
18	357.6658	2	MAGQNPP	68.99
19	357.6656	2	MAYSSR	68.90
20	471.2622	2	LNGNGTLPR	64.63
21	472.2463	2	NMAGGRQLP	62.24
22	472.2459	2	TASGGNVQLP	64.53
23	522.7886	2	RTPADGSVNK	66.67
24	522.7887	2	RTGNLATALQ	64.05
25	472.2461	2	DGSGGNVKPL	69.18
26	472.2466	2	DGSGGNVKPL	66.17
27	428.1910	2	SSGPANHW	69.41
28	546.1499	2	PTCGCCAGACCC	63.40
29	310.0999	2	ECHGCA	62.19
30	381.1158	2	YDCCCGSG	65.37
31	529.1376	2	YDCCCSASCC	64.10
32	689.3488	2	YYRKPAAADHW	62.21
33	381.0850	2	CDACCCSG	61.81
34	543.1358	2	DEECCHCCSG	60.66
35	398.0957	2	YSCCCCN	62.48
36	513.7769	2	GRLTHTDKA	67.09
37	303.1001	2	SHSGDC	61.06
38	455.1508	2	MDCSVDHC	61.64
39	454.1415	2	MMMCNYD	68.50
40	414.1455	2	MGVDSSCE	60.51
41	399.0947	2	CHDGGCCC	61.65
42	504.1649	2	YMYCCHMG	60.06
43	365.1260	2	AMCCASGS	68.16
44	536.2009	2	PTMTEMDCGS	61.54
45	618.2335	2	MGGPNTSSHCGGM	60.36
46	455.1838	2	MMSSCLTH	60.05
47	361.2049	2	LKKVMC	67.29
48	589.7829	2	CELPVLEQTF	61.51
49	304.0888	2	HAACCC	64.55
50	500.1712	2	YMCCEFF	63.46
51	557.1770	2	APCGCCCVDGV	61.12
52	365.6508	2	YNDVYG	68.38
53	379.1231	2	GMCMGDGS	63.09
54	570.2802	2	WVGVAANEF	63.80
55	540.1861	2	SHWGCMEDD	64.47
56	527.2130	2	EEPCEAGRY	63.29
57	315.1779	2	MLKTH	65.44
58	438.2373	2	RATKAAGSN	61.16
59	409.1599	2	MTPPGDPC	62.05
60	319.1409	2	DSKSGGS	60.89
61	362.1406	2	NQAGSCSG	61.07
62	517.2629	2	YGRRTYF	61.48
63	362.1413	2	TSTGGGED	62.44
64	363.2208	2	KKDVHV	66.63
65	416.1786	2	QCHGGSVGS	64.63
66	456.2362	2	KKHSGGGPSG	65.52
67	333.1389	2	YMGASH	62.52
68	328.1347	2	NGCAGPH	60.44
69	309.0813	2	MTGCC	61.47
70	301.0926	2	FDGGCC	66.66
71	430.2498	2	FKATAPPK	68.72
72	315.2166	2	LLAVTL	60.02
73	376.1566	2	TCCSAPGL	62.17
74	302.1472	2	YGVGAH	68.29
75	376.1566	2	SCCTAAVP	65.83

Table 2 (continued)

No.	M/Z	Charge	DENOVO	ALC
76	345.1477	2	FHPSPDS	64.60
77	345.1473	2	FHPSPDS	67.98
78	541.1912	2	MMDGHAGCPY	68.68

Therefore, solid phase extraction (SPE) cleanup procedure was developed to remove interference and enhance the peptide analysis.

3.2. Solid phase extraction for sample cleanup

Cation-exchange MCX SPE was used to remove anthocyanins present in the elderberry juice. Anthocyanins may be adsorbed to the MCX sorbent, allowing for easy separation. The anthocyanin molecules acquire a positive charge to become flavylium cations at acidic pH while at basic pH, they convert to negatively charged quinonoidal bases. Peptides were then easily eluted by the SPE method by lowering pH in the juice sample. After the removal of anthocyanins from the juice, peptides were extracted with organic solvent and dried at 90 °C. Under the conditions, the activities of endogenous proteases are decreased to their lowest levels. Sample collected after the cation-exchange SPE (Group A) was either analyzed by LC-MS or subject to further cleanup using C₁₈ SPE to produce Group B sample for the LC-MS analysis. The use of C₁₈ SPE helped remove highly polar interference and ionic compounds.

3.3. Peptide identification

It is relatively easy to get a peptide profile from the analysis of MALDI-TOF MS, but this method may fail to detect trace peptides. The combination of nano-LC with the Orbitrap MS acquires peptide information with better sensitivity and higher quality. A base peak ion chromatogram obtained from the data dependent LC-MS and MS/MS analysis of samples purified by SPE is shown in Fig. S1. After analyzing the Group A sample on the Orbitrap instrument, a total of 2530MS/MS spectra were obtained. These spectra were then analyzed by using the PEAKS program. A total of 1789 peptides were detected from the *de novo* sequencing testing in the program. The *de novo* sequencing rate was 69.84%. In the analysis of Group B sample, 1833MS/MS spectra were acquired and a total of 1233 peptides were found. The *de novo* sequencing rate for Group B was 78.94%. The average local confidence (ALC) score for the *de novo* sequencing of the peptides in Group A and B are shown as Fig. 3A and B, respectively. The ALC value considers each individual amino acid score and is divided by the number of amino acids. The ALC value is simply reporting the number of correctly identified sequenced peptides, whether there are 3 or 30 amino acids. There is good confidence in peptides with an ALC score > 30%. The manufacturer of the PEAKS program states that ALC scores > 55% have the highest confidence. This does not mean that the whole sequence is the correct sequence, as the beginning and end of the MS/MS spectrum are more difficult to interpret when it comes to *de novo* sequencing due to decreased signal-to-noise. The peptide sequences with ALC scores greater than 60% are showed in Tables 1 and 2. The obtained results indicated that the additional C₁₈ SPE step resulted in a significantly higher number of peptides identified in Group B with ALC scores > 60%.

Although the number of peptides detected in Group B was less than Group A, the *de novo* sequencing rate and the number of high confidence-level peptides (ALC > 30%) in Group B is larger than Group A. The C₁₈ cleanup resulted in fewer measured peptides, but raised the corresponding MS signal, and led to larger number of high confidence-level peptide sequences. The total number of

peptides detected was more than one thousand and is a larger number than animal or human tissue peptidome results reported in previous studies. Thus, the combination of cation-exchange MCX and C₁₈ SPE cleanup was proved to be an effective way to separate peptides from anthocyanins abundant in the elderberry juice, especially when compared to the MALDI-TOF MS results. The use of a relatively high temperature (90 °C) to denature the enzymes from sample might result in the loss of some peptides due to protein self-degradation or enzyme digestion. However, this step was found necessary to maintain a reasonable drying time [21].

3.4. Protein sequence similarity searches

A BLAST search using the peptide information (ALC > 60) found 56 proteins from Group A and 114 proteins from Group B. The protein information is included in the supplementary files (named protein-Group A and protein-Group B). Proteins with high confidence levels are matched to proteins from several kinds of plants. Since the proteome of elderberry is not well-established, we did not try to filter the results of the BLAST search. The number of proteins found is considerable and is larger than that reported from others by using peptidomics [22]. The function of the proteins and peptides needs further characterization and is beyond the scope of the present study.

Acknowledgments

The authors would like to thank for the financial supports from National Natural Science Foundation of China (NSFC21275020) and Grant P50AT006273 from the National Center for Complementary and Alternative Medicines (NCCAM), the Office of Dietary Supplements (ODS), and the National Cancer Institute (NCI). The contents in this publication are solely the responsibility of the authors and

do not necessarily represent the official views of the NCCAM, ODS, NCI, or the National Institutes of Health.

Appendix A. Supporting information

Supplementary data associated with this article can be found in the online version at <http://dx.doi.org/10.1016/j.talanta.2014.08.022>.

References

- [1] X.D. Maa, C.F. Wu, W. Wang, X.B. Li, *Asian J. Tradit. Med.* 2 (2006) 85–90.
- [2] D.H. Geho, L.A. Liotta, E.F. Petricoin, W. Zhao, R.P. Araujo, *Curr. Opin. Chem. Biol.* 10 (2006) 50–55.
- [3] N. Farrokhi, J.P. Whitelegge, J.A. Brusslan, *Plant Biotechnol. J.* 6 (2008) 105–134.
- [4] G. Menschaert, T.T. Vandekerckhove, G. Baggerman, L. Schoofs, W. Luyten, W. Van Criekinge, *J. Proteome Res.* 9 (2010) 2051–2061.
- [5] H. Fukuda, T. Higashiyama, *Plant Cell. Physiol.* 52 (2011) 1–4.
- [6] G. Pearce, D. Strydom, S. Johnson, C.A. Ryan, *Science* 253 (1991) 895–897.
- [7] Y. Matsubayashi, Y. Sakagami, *Proc. Natl. Acad. Sci.* 93 (1996) 7623–7627.
- [8] M.C. Baracat-Pereira, M. d Oliveira Barbosa, M.J. Magalhães Jr, L.C. Carrijo, P.D. Games, H.O. Almeida, J.F. Sena Netto, M.R. Pereira, E.G. de Barros, *Genet. Mol. Biol.* 35 (2012) 283–291.
- [9] K. Sasaki, T. Osaki, N. Minamino, *Mol. Cell Proteomics* 12 (2013) 700–709.
- [10] Y.G. Kim, A.M. Lone, W.M. Nolte, A. Saghatelian, *Proc. Natl. Acad. Sci.* 109 (2012) 8523–8527.
- [11] Y.G. Kim, A.M. Lone, A. Saghatelian, *Nat. Protoc.* 8 (2013) 1730–1742.
- [12] A. Panchoaud, M. Affolter, M. Kussmann, *J. Proteomics* 75 (2012) 3546–3559.
- [13] M. Soloviev, P. Finch, *Proteomics* 6 (2006) 744–747.
- [14] A.L. Thomas, P. Perkins-Veazie, P.L. Byers, C.E. Finn, J. Lee, *J. Berry Res.* 3 (2013) 159–168.
- [15] C.E. Finn, A.L. Thomas, P.L. Byers, S. Serçe, *Hort. Sci.* 43 (2008) 1385–1391.
- [16] D. Bagchi, S. Roy, V. Patel, et al., *Mol. Cell Biochem.* 281 (2006) 197–209.
- [17] D. Ghosh, T. Konishi, *Asia Pac. J. Clin. Nutr.* 16 (2007) 200–208.
- [18] M. Netzel, G. Strass, M. Herbst, et al., *Food Res. Int.* 38 (2005) 905–910.
- [19] R. Veberic, J. Jakopic, F. Stampar, et al., *Food Chem.* 114 (2009) 511–515.
- [20] J. He, M.M. Giusti, *J. Chromatogr. A* 1218 (2011) 7914–7922.
- [21] Y.H. Wang, C. Gehring, H.R. Irving, *Plant Cell Physiol.* 52 (2011) 837–850.
- [22] J. Wan, X.W. Cui, J. Zhang, Z.Y. Fu, X.R. Guo, L.Z. Sun, C.B. Ji, *Biochem. Biophys. Res. Commun.* 438 (2013) 236–241.



Use of switchable solvents in the microextraction context



Guillermo Lasarte-Aragonés, Rafael Lucena, Soledad Cárdenas, Miguel Valcárcel*

Department of Analytical Chemistry, Institute of Fine Chemistry and Nanochemistry, Marie Curie Building (Annex), Campus de Rabanales, University of Córdoba, 14071 Córdoba, Spain

ARTICLE INFO

Article history:

Received 26 May 2014

Received in revised form

7 August 2014

Accepted 11 August 2014

Available online 20 August 2014

Keywords:

Liquid phase microextraction

Green chemistry

Switchable hydrophilicity solvents

Polycyclic aromatic hydrocarbons

ABSTRACT

In this article, a new homogeneous liquid-liquid microextraction alternative, based on the use of switchable hydrophilicity solvents (SHS), is presented for the first time. The extraction technique makes use of a water-immiscible solvent (N,N-Dimethylcyclohexylamine) that can be solubilised in 1:1 ratio using CO₂ as reagent. After the extraction, phases' separation is induced by the addition of sodium hydroxide, which produces a change on the ionisation state of the amine, centrifugation not being necessary. The extraction technique has been optimised and characterised using the determination of benz[a]anthracene by fluorimetric measurements in water samples as model analytical problem. Although the native fluorescence of the compound is quenched in the organic phase, this attenuation is reduced by diluting the extractant (1:1) in acetic acid. The fluorescence intensity is 35% higher in the SHS-acetic acid mixture than that obtained in pure methanol. The proposed method allows the determination of the target analyte with limit of detection of 0.08 µg/L and good precision (relative standard deviation of 6.7% at the limit of quantification level). The recoveries were in the range of 72–100% fulfilling the Environmental Protection Agency criterion. Finally, the potential use of this microextraction technique in combination with gas chromatography is shown for several polycyclic aromatic hydrocarbons.

© 2014 Elsevier B.V. All rights reserved.

1. Introduction

Dispersive liquid-liquid microextraction (DLLME), introduced by Rezaee et al. in 2006 [1], consists of the introduction of an extractant/disperser mixture in the aqueous sample to form a cloudy solution where the extractant is divided into small droplets increasing its surface to volume ratio. This fact positively affects the extraction kinetics, which directly depends on the contact surface between the extractant phase and the sample. After the extraction, the cloudy state must be broken, usually by centrifugation, in order to isolate the extractant phase prior to its analysis. DLLME presents a great variety of advantages (easy operation, expeditiousness, low consumption of solvent and samples, etc.) that makes them a suitable sample treatment technique in many applications fields.

Homogeneous liquid-liquid extraction (HLL) involves the complete solubilisation of the extractant in the aqueous sample making the contact surface between phases infinitely large [2–4]. The solubilisation of the organic solvent is performed exploiting its chemical properties or using an external energy source like heat or

ultrasounds. The phases' separation, when the real extraction takes place, is chemically or physically induced. Among the chemical alternatives, the salting out effect [5–7], pH changes [8,9] and ion pairing [10] are the usual ones while the reduction of the temperature in the extraction vessel can be highlighted among the latter. Although HLL presents excellent characteristics, the extraction becomes tedious when heating/cooling cycles are employed. Moreover, special reagents are required when ion pairing is performed.

Microextraction techniques, which can be considered under the Green Chemistry [11,12] realm since they reduce the consumption of extractant materials, have evolved in the last years. The development of new sorbent/solvent has been a key research line in this context. Jessop et al. firstly investigated the behaviour of the so-called switchable hydrophilicity solvents (SHS) [13,14] for industrial applications [15]. They found solvents that exhibit a complete solubilisation in water under the presence of carbon dioxide, while the solvents become immiscible when the gas is purged from the solution [16]. The non-toxic nature of carbon dioxide as well as its low cost makes it an ideal phase transition trigger in extraction techniques. In addition, the use of SHS allows the extraction of the analytes in a homogeneous phase and it permits the easy phases' separation without additional apparatus. This process can be developed in industrial procedures due to their

* Corresponding author. Tel./fax: +34 957 218 616.
E-mail address: qa1vacam@uco.es (M. Valcárcel).

macroscale nature but its transference to the analytical context, especially to the microextraction field, has not been yet considered. On the one hand, the production of stable mixtures of the SHS and aqueous phases in the microscale would require special devices like extraction vessels with an exhaustive control of the CO₂ pressure. On the other hand, the purge of the CO₂ may produce extractant losses by projection (solvent dragged by the purge gas) or evaporation. The latter effect is especially important when volatile SHS are employed, although non-volatile SHS are available [17]. Extractant losses are not acceptable when low solvent volumes are employed in the microextraction context.

In the present work, the adaptation of the SHS to the microextraction context is proposed. The solubilisation of the solvent into the aqueous phase is performed prior to the extraction using dry ice as reagent, which provides a stable homogeneous SHS/water mixture. The final separation is achieved using a common reagent like sodium hydroxide. A polycyclic aromatic hydrocarbon (PAH), benz[a]anthracene, is employed as model analyte, its native fluorescence being exploited for the determination. The use of the SHS in combination with acetic acid enhances the fluorescence of the target analyte compared with a conventional medium such as methanol.

2. Experimental

2.1. Chemicals

All reagents were of analytical grade or better. Benz[a]anthracene, acetic acid (HOAc) and N,N-dimethylcyclohexylamine (DMCA) were purchased from Sigma-Aldrich (Madrid, Spain). Stock standard solution of the analyte was prepared in methanol (Panreac, Barcelona, Spain) at 500 mg/L and stored at 4°C. Working

solutions were prepared by the appropriate dilution of the stock in Milli-Q water (Millipore Corp., Madrid, Spain), methanol, DMCA or DMCA/HOAc mixtures, as required.

Dry ice, in the form of pellets of 3 mm, purchased from Cordogas (Cordoba, Spain) was employed for the solubilisation of the DMCA in water. NaOH from Sigma-Aldrich was employed to induce phase's separation. A 20 M NaOH solution was daily prepared and employed in the extraction procedure.

Tap and river water (Genil river, Córdoba, Spain) samples were collected in amber glass bottles without headspace and stored at 4°C until analysis. The samples were not filtered prior their analysis. Bottled water samples were purchased from a local market.

2.2. Apparatus

Fluorescence analyses were carried out on a fluorescence spectrophotometer model F-2500 (Hitachi Ltd., Tokyo, Japan) equipped with a Xenon lamp. The excitation and emission wavelengths were set at 289 nm and 388 nm, respectively, using 10 nm selector slits in both cases. The photomultiplier tube voltage was set at 400 V. Data acquisition was performed using FL solutions[®] software from Hitachi Ltd.

2.3. Amine aqueous-phase preparation

The procedure is presented in Fig. 1. First, 100 mL of Milli-Q water and 100 mL of DMCA are placed in a 1 L glass bottle with screw cap, forming a two phases system (Fig. 1A). Then, 10 g of dry ice are added and the glass bottle is tightly closed. The high volume of the bottle employed in this synthesis allows the use of this amount of dry ice without a risky increase of the internal pressure. Undissolved CO₂ remains at the top of the bottle and the

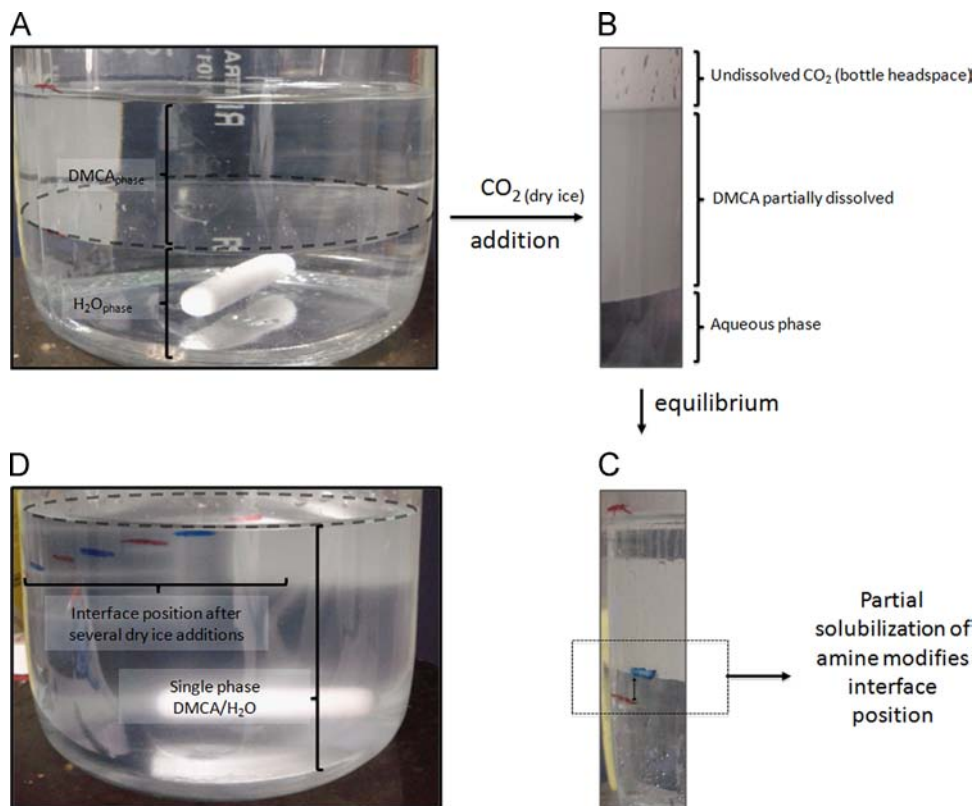


Fig. 1. Steps of the DMCA dissolution in water. (A) Initial state where the two immiscible phases are observed; (B) Detail of the bottle after the addition of 10 g of dry ice where three phases (two liquid and one gaseous) are observed; (C) Detail of the bottle after the solubilisation of the CO₂. The change in the interface position is shown; (D) Final state after the several dry ice additions showing a unique liquid phase.

amine phase became cloudy (Fig. 1B). The mixture is stirred for 5 min in order to favour the solubilisation of the carbon dioxide. After this time the biphasic system remains but the volume phases ratio varies due to the partial solubilisation of DMCA in water (Fig. 1C). This stage is repeated ten times until a single phase is observed, which corresponds to a 1:1 (v:v) water/ DMCA solution (Fig. 1D). The solution loses its turbidity 1 h later after the last dry ice addition.

Two hundred millilitre of the 1:1 (v:v) water/ DMCA solution can be easily prepared and this volume allows the development of more than 200 extractions since each one requires only 750 μL of the mixture.

2.4. Extraction procedure

The extraction, schematised in Fig. 2, consists of various well-defined steps. First of all, 750 μL of aqueous amine are added to 10 mL of aqueous standard or water sample previously located in a glass test tube. The mixture is agitated in a vortex for 15 s, until a homogeneous phase is observed. After this, 1 mL of a 20 M NaOH solution is added and cloudy solution appears. The solution is shaken again in the vortex for 15 s, and the test tube is left to stand for 5 min to achieve phase separation. Three hundred microlitre of DMCA are recovered and transferred to a glass vial for analysis.

For fluorescence analysis, a previous 1:1 (v/v) dilution in acetic acid is required to enhance sensitivity.

3. Results and discussion

In its neutral form, DMCA can be considered as a moderate non-polar solvent, taking into consideration that the logarithm of the octanol/water partition coefficient ($\log K_{ow}$) is equal to 1.95 [18]. Thanks to its nature, DMCA can be employed for the extraction of hydrophobic analytes from aqueous samples and therefore benz[a]anthracene has been selected as model analyte. As a polycyclic aromatic hydrocarbon, benz[a]anthracene presents a native fluorescence that allows its sensitive determination.

Some preliminary assays were performed in order to evaluate the potential of fluorescence measurements for the determination of the target analyte. Qualitative information (pictures) was obtained under UV radiation of the solutions using a commercial

lamp and quantitative measurements performed in a fluorescence spectrophotometer. For interpretation purposes, it is necessary to highlight that the pictures were obtained with an excitation wavelength of 365 nm while the quantitative measurements were obtained at the optimum excitation and emission wavelengths of benz[a]anthracene (289 nm and 388 nm, respectively).

The fluorescence of the analyte in pure DMCA was firstly evaluated at a concentration of 1 mg/L and it was compared with that obtained in methanol. As it can be observed in Fig. 3, the fluorescence of the analyte is quenched in the presence of DMCA. This quenching can be avoided if acetic acid is added to the DMCA phase. Moreover, the fluorescence in the DMCA /HOAc mixture is a 35% higher than that obtained in methanol.

To improve the sensitivity of the determination, the influence of the DMCA /HOAc ratio on the fluorescence of benz[a]anthracene was evaluated. The results, which are shown in Fig. 4 point out a fluorescence enhancement in DMCA /HOAc mixtures compared to the pure solvents. The spectra obtained are similar in shape in the different media as it can be observed in Fig. S1 (supplementary content), although the S/N ratio is higher for intermediate DMCA /HOAc ratio. According to the results, a 1:1 ratio was selected as optimum value which involves a 1:1 (v:v) dilution of the DMCA in acetic acid before the fluorimetric analysis of the sample extracts.

3.1. Solvent solubility switching

The aqueous solubility of DMCA can be switched controlling the CO_2 concentration in the extraction unit. In industrial applications, this concentration can be controlled playing with the CO_2 pressure, special vessels being necessary. In the microextraction context, this alternative is not feasible at all due to the high sample to extractant ratio required if a good preconcentration factor is intended to be obtained.

The solubilisation of the DMCA can be achieved using dry ice as CO_2 source (see experimental section) and conventional glassware. The water/DMCA mixture resulted to be stable at least for 7 months.

Once the extractant phase is added to an aqueous sample, the phases separation should be induced to recover the extractant with the isolated analyte. Several alternatives, including physical and chemical methods, were evaluated for this purpose. These methods are schematically presented in Fig. 5 and they are described in the

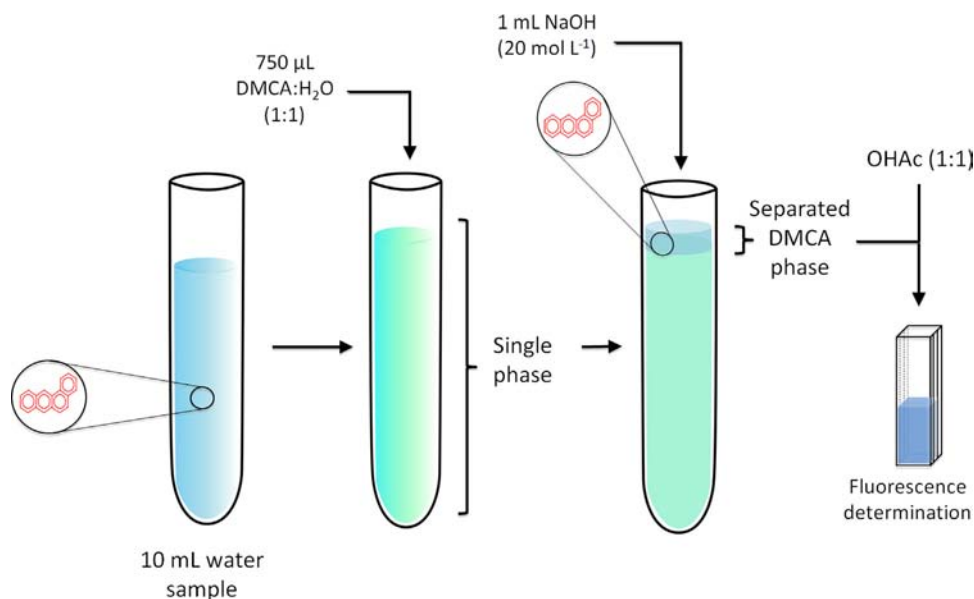


Fig. 2. Schematised extraction procedure.

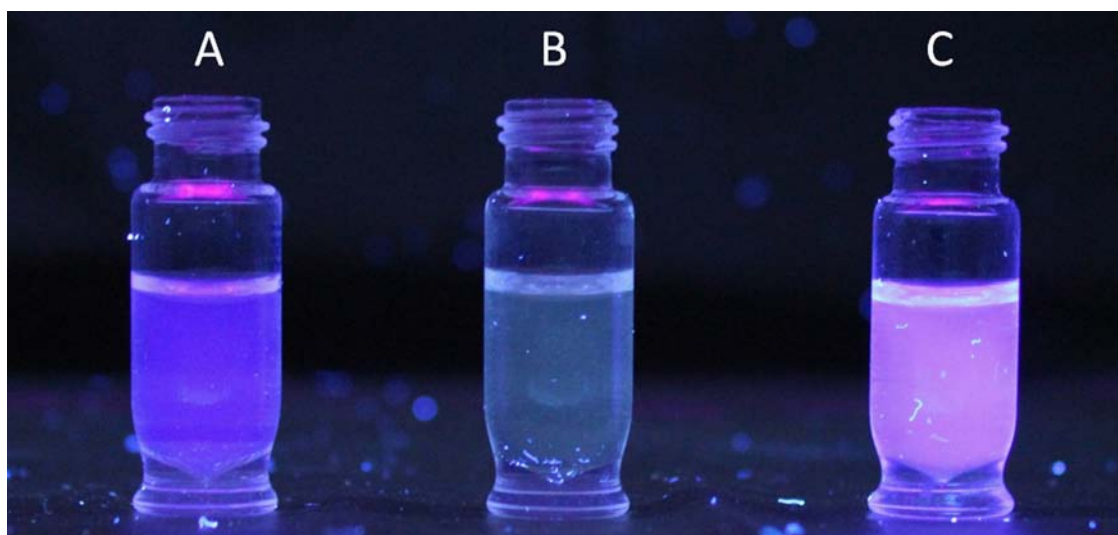


Fig. 3. Vials containing standard solutions of benzo[a]anthracene at the concentration of 1 mg/L prepared in different solvents, namely, (A) methanol, (B) DMCA and (C) DMCA/HOAc 1:1 (v:v). The picture has been obtained under UV irradiation at 365 nm.

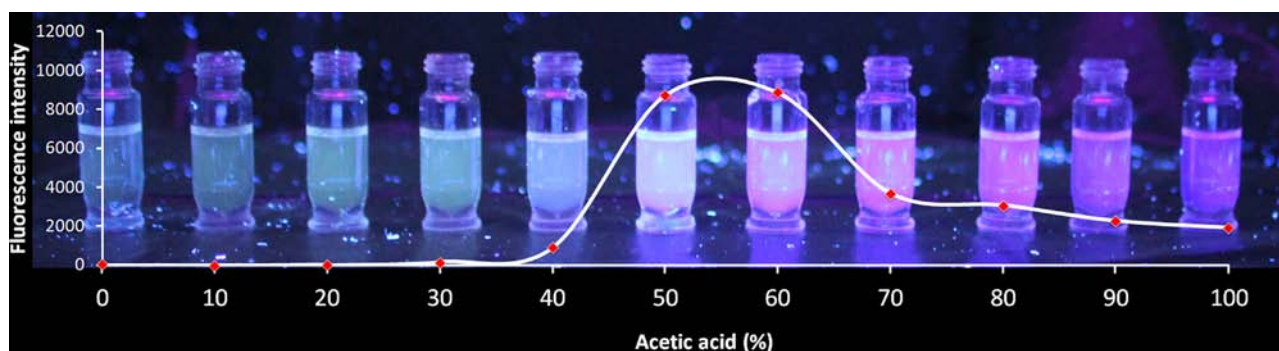


Fig. 4. Study of the DMCA/HOAc ratio on the fluorescence of benzo[a]anthracene. The fluorescence intensity values for different standards containing the analyte at the same concentration level but in different media are presented. The picture shows the vials emission under UV radiation at 365 nm.

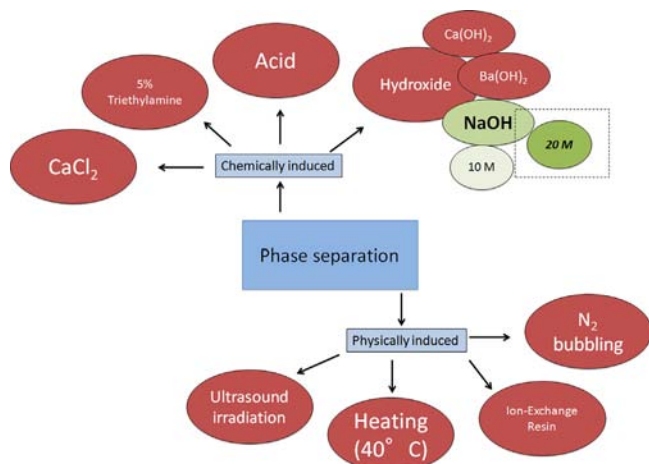


Fig. 5. Different alternatives evaluated to induce phases separation. For further details, read the supplementary content.

supplementary content. Among all the procedures, the addition of a 20 M sodium hydroxide solution provided the best results due to its efficiency (viz. quantitative recovery of DMCA), rapidity (5 min were enough to observe phase separation) and simplicity (no centrifugation was required).

3.2. Extractant volume

For simplicity, the aqueous sample volume was fixed to 10 mL, which allowed the use of conventional test tubes. The effect of the volume of DMCA aqueous phase on the extraction of the analyte was studied in depth. Three different volumes, namely, 1000 μ L, 750 μ L and 500 μ L, were evaluated in triplicate. Lower volumes were non-practical since the recovery of the solvent was unfeasible while larger volumes induced an excessive dilution of the analyte. Each volume was evaluated in triplicate using fluorescent measurements. As it can be observed in Fig. S2 (supplementary content), the higher signals are obtained when 500 μ L of the extractant are employed. However, 750 μ L is selected as the optimum value as a compromise between sensitivity and precision.

3.3. Analytical figures of merit

The optimised procedure was applied to the determination of benz[a]anthracene in water samples. A calibration graph was constructed for the analyte by extracting in triplicate five working aqueous standards within the concentration interval from 0.1 to 5 μ g/L. The limit of detection, which was calculated as the method detection limit (MDL) [19], is 0.08 μ g/L. The MDL value was obtained in an iterative process (starting with a spiked concentration of 0.5 μ g/L) and using seven independent replicates ($n=7$). The repeatability of the method, which was evaluated at a concentration level of 0.5 μ g/L, resulted to be

Table 1
Relative recovery study performed on real samples spiked with benz[a]anthracene at a concentration of 1 µg/L.

Analyte	Water sample (R% ^a ± SD ^b)		
	River	Tap	Bottled
Benz[a]anthracene	100 ± 9	72 ± 10	87 ± 10

^a R%. Extraction Recovery

^b SD, Standard Deviation (*n* = 3)

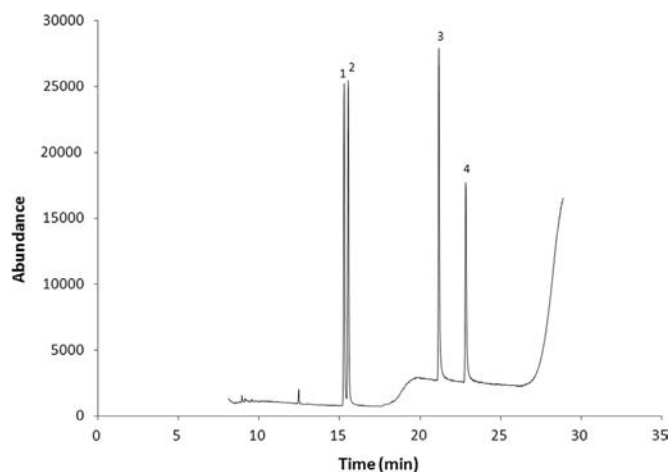


Fig. 6. Chromatogram obtained for the extraction of a water sample spiked with four PAHs (benzo[a]anthracene, benzo[a]pyrene, benzo[b]fluoranthene and chrysene) at 5 µg/L and direct injection of the separated DMCA phase (2 µL injection volume).

6.7% (expressed as relative standard deviation). In order to evaluate the applicability of the proposed method for the determination of benz[a]anthracene in waters, three different water samples (river, tap, and bottled) were analysed. As no positive results were obtained, a recovery study was performed at a concentration level of 1 µg/L. The results, which are listed in Table 1, fulfilled the 70–130% recovery criterion recommended by US-EPA, except in the case of tap water. This sample has a relatively high chlorine content, which is a well-known quencher agent and can reduce the fluorescence intensity [20].

We realise that its direct combination with fluorescence spectroscopy presents a limited selectivity since it would not be capable to discriminate among different PAHs. The potential of the technique can be clearly demonstrated if it is combined with a chromatographic technique allowing the multi-determination of compounds. Although it was not the main objective of this article, Fig. 6 shows the chromatogram (chromatographic conditions are described in the supplementary content) obtained for a water sample spiked with four PAHs (namely: benzo[a]anthracene, benzo[a]pyrene, benzo[b]fluoranthene and chrysene) at 5 µg/L after their extraction by the proposed method. As it can be observed, all the analytes are effectively extracted under the optimised conditions for benz[a]anthracene. For GC/MS analysis, it is not necessary the dilution of the DMCA with acetic acid.

4. Conclusions

In this article, the use of the so-called switchable hydrophilicity solvents in homogeneous liquid-liquid microextraction is presented for the first time. The proposal uses a low volume (375 µL) of pure

DMCA as extractant. The native amine, which is immiscible in water, is solubilised using dry ice as reagent yielding a stable (at least for 10 months) solution. This solubilisation can be reverted, inducing the phases' separation, by means of sodium hydroxide, which is a common and relatively cheap reagent. Additional centrifugation is not required.

Benz[a]anthracene has been selected as model analyte due to its polarity and native fluorescence. The target compound can be easily extracted to the DMCA phase, although its direct fluorimetric determination in this medium is not feasible due to a quenching process. This quenching has been successfully avoided using acetic acid; the fluorescence being actually 35% higher than that obtained in a conventional solvent such as methanol. The developed methodology permits the determination of the analytes with a low limit of detection (0.08 µg/L), good precision (RSD better than 6.7%) and accuracy.

According to the results, the proposed technique presents high extraction efficiency, it is simple and fast and it does not require complex or special labware for phases' separation.

Acknowledgements

Financial support from the Spanish Ministry of Science and Innovation (grant CTQ2011-23790) is gratefully acknowledged. G. Lasarte-Aragonés would like to express his gratitude for the pre-doctoral grant (ref. AP2009-2850) from the Spanish Ministry of Education.

Appendix A. Supporting information

Supplementary data associated with this article can be found in the online version at <http://dx.doi.org/10.1016/j.talanta.2014.08.031>.

References

- [1] M. Rezaee, Y. Assadi, M.R. Milani-Hosseini, E. Aghaee, F. Ahmadi, S. Berijani, *J. Chromatogr. A* 1116 (2006) 1–9.
- [2] K. Murata, S. Ikeda, *Bunseki Kagaku* 18 (1969) 1137.
- [3] J.D. Lamb, R.T. Peterson, *Sep. Sci. Technol.* 30 (1995) 3237–3244.
- [4] A. Schaadt, H.J. Bart, *Chem. Eng. Technol.* 26 (2003) 469–472.
- [5] R.S. Razmara, A. Daneshfar, R. Sahrai, *J. Ind. Eng. Chem.* 17 (2011) 533–536.
- [6] X. Wang, X. Zhao, X. Liu, Y. Li, L. Fu, J. Hu, C. Huanga, *Anal. Chim. Acta* 620 (2008) 162–169.
- [7] L. Tavakoli, Y. Yamini, H. Ebrahimzadeh, S. Shariati, *J. Chromatogr. A* 1196 (2008) 133–138.
- [8] M.A. Farajzadeh, M. Bahram, S. Zorita, S. GhorbaniMehri, *J. Hazard. Mater.* 161 (2009) 1535–1543.
- [9] S. Igarashi, T. Yotsuyanagi, *Mikrochim. Acta* 106 (1992) 37–44.
- [10] T. Sudo, S. Igarashi, *Talanta* 46 (1996) 233–237.
- [11] A. Spietelun, Ł. Marcinkowski, M. de la Guardia, J. Namiesnik, *Talanta* 119 (2014) 34–45.
- [12] A. Spietelun, Ł. Marcinkowski, M. de la Guardia, J. Namiesnik, *J. Chromatogr. A* 1321 (2013) 1–13.
- [13] P.G. Jessop, L. Phan, A. Carrier, S. Robinson, C.J. Dürr, J.R. Harjani, *Green Chem.* 12 (2010) 809–814.
- [14] P.G. Jessop, L. Kozyc, Z.G. Rahami, D. Schoenmakers, A.R. Boyd, D. Weschler, A.M. Holland, *Green Chem.* 13 (2011) 619–623.
- [15] A.R. Boyd, P. Champagne, P.J. McGinn, K.M. MacDougall, J.E. Melanson, P. G. Jessop, *Bioresour. Technol.* 118 (2012) 628–632.
- [16] P.G. Jessop, S.M. Mercer, D.J. Heldebrant, *Energ. Environ. Sci.* 5 (2012) 7240–7253.
- [17] J.R. Vanderveen, J. Durelle, P.G. Jessop, *Green Chem.* 16 (2014) 1187–1197.
- [18] Chemspider, Royal Society of Chemistry. (<http://www.chemspider.com/>).
- [19] US Environmental Protection Agency (EPA), Guidance on Evaluation, Resolution and Documentation of Analytical Problems Associated with Compliance Monitoring, US Environmental Protection Agency (EPA), Washington, DC, 1993.
- [20] S.A. Momin, R. Narayanaswamy, *Analyst* 117 (1992) 83–85.



Investigation of nonylphenol and nonylphenol ethoxylates in sewage sludge samples from a metropolitan wastewater treatment plant in Turkey



Seçil Ömeroğlu^a, Fadime Kara Murdoch^b, F. Dilek Sanin^{a,*}

^a Department of Environmental Engineering, Middle East Technical University, 06800 Ankara, Turkey

^b Department of Biotechnology, Middle East Technical University, 06800 Ankara, Turkey

ARTICLE INFO

Article history:

Received 1 April 2014

Received in revised form
31 July 2014

Accepted 5 August 2014

Available online 19 August 2014

Keywords:

Nonylphenol

Nonylphenol monoethoxylate

Nonylphenol diethoxylate

Gas chromatography–mass spectrometry

Sewage sludge

ABSTRACT

Nonylphenol ethoxylates (NPEOs) have drawn significant attention within the last decade for both scientific and legislative reasons. In Turkey, the *Regulation Regarding the Use of Domestic and Urban Sludges on Land* states a limit value for the sum of nonylphenol (NP), nonylphenol monoethoxylate (NP1EO) and nonylphenol diethoxylate (NP2EO) as NPE (NPE=NP+NP1EO+NP2EO). Unfortunately a standard method for the determination of these chemicals has not been yet set by the authorities and no data exists about the concentrations of NP and NPEOs in sewage sludge in Turkey. The aim of this study is to propose simple and easily applicable extraction and measurement techniques for 4-*n*-nonylphenol (4-*n*-NP), NP, NP1EO and NP2EO in sewage sludge samples and investigate the year round concentrations in a Metropolitan Wastewater Treatment Plant (WWTP) in Turkey.

Different extraction techniques and GC/MS methods for sewage sludge were tested. The best extraction method for these compounds was found to be ultrasonication (5 min) using acetone as the solvent with acceptable recovery of analytes suggested by USEPA and other studies. The optimized extraction method showed good repeatability with relative standard deviations (RSDs) less than 6%. The recovery of analytes were within acceptable limits suggested by USEPA and other studies. The limits of detection (LODs) were 6 µg kg⁻¹ for NP and NP1EO, 12 µg kg⁻¹ for NP2EO and 0.03 µg kg⁻¹ for 4-*n*-NP. The developed method was applied to sewage sludge samples obtained from the Central WWTP in Ankara, Turkey. The sum NPE (NP+NP1EO+NP2EO) was found to be in between 5.5 µg kg⁻¹ and 19.5 µg kg⁻¹, values which are in compliance with Turkish and European regulations.

© 2014 Elsevier B.V. All rights reserved.

1. Introduction

Alkylphenols are synthetic organic chemicals with wide industrial and domestic uses. Nonylphenol ethoxylates (NPEOs) represent approximately 80% of all alkylphenols produced [1]. Due to their surface active properties, NPEOs have extensive industrial (especially in pulp and paper and textile), commercial and domestic uses (as surface cleaners, lubricants, shampoos, detergents, and other products) [2]. Following use and disposal, they often reach wastewater treatment systems and consequently the receiving environments [3]. The nonyl group (C₉H₁₉) attached to the phenol ring is mostly branched. Due to this property the chemical can be formulated in a number of different isomeric forms. Industrial and

household chemicals include a mixture of branched NP isomers, rather than the linear molecule. For this reason, the chemicals observed in wastewaters and sewage sludge are mainly composed of these isomeric mixtures.

Biodegradation of NPEOs is possible and occurs by the elimination of ethoxy chains. Biodegradation of NPEOs in aerobic environments leads mainly to the formation of nonylphenol polyethoxy carboxylates (NPECs) and carboxyalkylphenol ethoxy carboxylates (CAPECs), whereas in anaerobic environments, the final metabolite is nonylphenol (NP) following degradation of nonylphenol diethoxylate (NP2EO) and nonylphenol monoethoxylate (NP1EO) [2,4].

The fate and behavior of NP and NPEO compounds in different environmental systems such as sediment, soil, surface waters and biota depend on their physico-chemical properties [5–7] and their molecular structure (Fig. 1(i)–(iii)). NP and NPEOs are known to be toxic to most organisms and carcinogenic to humans [8,9]. As illustrated in Fig. 2, the branched carbon chains on the NP molecule are similar to the 17-β-estradiol structurally [10,11].

* Corresponding author. Tel.: +90 312 210 26 42.

E-mail addresses: omeroglu@metu.edu.tr (S. Ömeroğlu), fkara@metu.edu.tr (F. Kara Murdoch), dsanin@metu.edu.tr (F. Dilek Sanin).

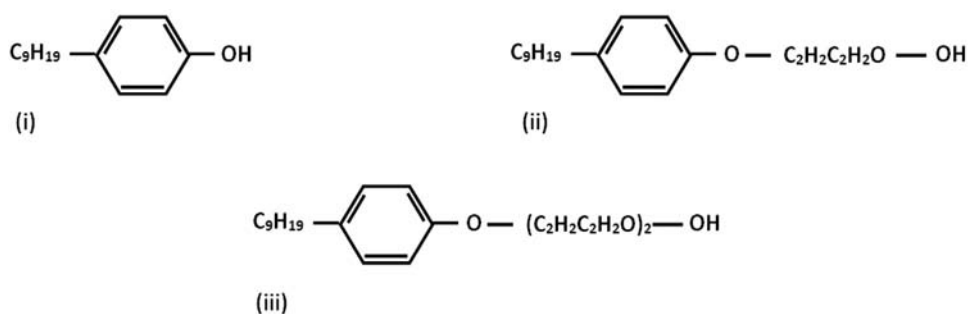


Fig. 1. Molecular structures of (i) NP (ii) NP1EO and (iii) NP2EO.

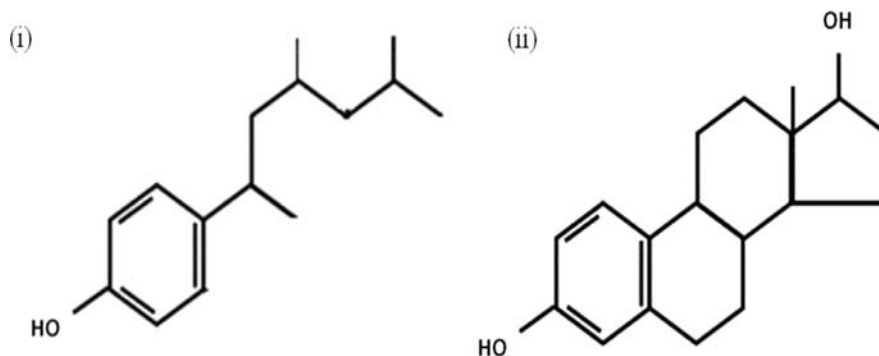


Fig. 2. Structural similarity between (i) NP and (ii) 17-β-estradiol.

Due to this structural similarity, NP is able to mimic estrogen hormone through a direct interaction with the estrogen receptor, blocking the action of the original hormone which can result in reproductive diseases. For this reason NP and some NPEOs are listed as endocrine disrupting chemicals (EDCs) and priority pollutants in the Water Framework Directive [12–14]. Also, due to their high K_{ow} values, NP and NPEO compounds tend to stay on surfaces like soil, sediment and sewage sludge. Persistence of these compounds in sewage sludge is an important issue since among other sludge handling methods, land application is the most favorable due to its low cost and beneficial recycle of nutrients. Since sewage sludge does not only contain nutrients but also contaminants such as NP and NPEO compounds; they must be monitored properly to judge about their suitability for land application [15]. Once sewage sludge containing NP and NPEOs are used for agricultural purposes, these compounds can build up along the food chain and accumulate in the fatty tissues of living organisms [3,9].

The increasing concerns on health and environmental effects of NP and NPEO compounds, it has become critical to determine the levels of these compounds in sewage sludge prior to disposal. Several methods have been suggested in the literature for the quantification of these compounds [16,17]. But, there is no consistency between methods in terms of extraction process (solvent, method and period), or analytical procedure (different instruments like GC/MS, GC/MS/MS, LC/MS/MS etc). The methods differ from each other even if the determination was carried out with the same type of instrument. For example, for solid samples like soil, sediment and sewage sludge, sonication-assisted extraction [18–20] combination of sonication and mechanical shaking assisted extraction [15,19], enhanced solvent extraction [21] and Soxhlet extraction [22] have been used for the analysis of NP, 4-*n*-NP, NP1EO and NP2EO. Among these methods, NP and NPEO compounds were analyzed using GC/MS [18,19] or LC/ESI/MS [23]. When extraction solvent is taken into consideration, dichloromethane:methanol (7:3) [19] acetone:methanol (1:1) [20] and hexane [24] have been used for sonication-assisted extraction from sewage sludge. In addition,

some of these methods aimed at measuring only one NP or NPEO compound [23,25], whereas others more than one compound simultaneously [15,18].

As stated earlier, these compounds tend to accumulate on sewage sludge solids and can be carried along the food chain threatening human health and environment. Therefore, to test the suitability of sewage sludge for land application, limit values have been suggested by countries worldwide. For this reason, in agricultural use of sewage sludge, European Union suggested a limit value for the sum of NP, NP1EO and NP2EO (called as NPE) as 50 mg kg⁻¹ dry mass (dm) in Working Document on Sludge, 3rd Draft [26].

In the EU accession period of Turkey, the limit value for NPE in sewage sludge was set as 50 mg kg⁻¹-dm in Regulation on the Land Use of Domestic and Urban Sludges [27]. However, a practical method for the qualitative and quantitative determination of NP and NPEO compounds has not been suggested for routine analysis in sewage sludge samples. With the need of a practicable and validated method for simultaneous quantification of all NP (NP+NPEO) compounds, this study aimed to come up with such a method and monitor NP, NP1EO and NP2EO concentrations in sewage sludge samples. The sludge samples obtained from Ankara Central WWTP were analyzed with the proposed sonication assisted-extraction method and the qualitative and quantitative determination of the chemicals were made using GC/MS.

2. Materials and methods

2.1. Chemicals and standards

Standard solutions of NP, NP1EO and NP2EO (analytical standard, 5 μg mL⁻¹ in acetone) were supplied by Fluka, Sigma Aldrich, USA (Product# 32889, 32895, 32899, respectively). The standard solution of 4-*n*-NP (10 ng μL⁻¹ in cyclohexane) (Product# L15630000CY) was purchased from Dr. Ehrenstorfer GmbH, Germany. Sodium sulfate, fine powder copper and GC/MS grade acetone (AC),

methanol (ME), hexane (HX) and dichloromethane (DCM) were supplied from Merck KGaA, Germany. Derivatizing agents MSTFA (*N*-methyl-*N*-(trimethylsilyl)trifluoroacetamide, Product# 69479) and BSTFA (*N,O*-bis(trimethylsilyl)trifluoroacetamide, Product# 15222) were purchased from Sigma Aldrich, USA. The catalysts pyridine and TMCS (trimethylchlorosilane) were supplied by Fluka, Sigma Aldrich, USA (Product# 270970 and 89595, respectively). The BSTFA+TMCS (99:1 Sylon BFT Kit) was obtained from Supelco Analytical, Sigma Aldrich, USA.

All working standard solutions were prepared freshly every analysis day using 1000 mg L⁻¹ stock solutions in acetone. Standard solutions and working solutions were kept at -18 °C in the dark.

2.2. Instrumentation

All experiments were carried out using Agilent Technologies GC (7890 series) coupled with Agilent Technologies 5975C inert MSD with triple axis detector. The column used was Agilent 19091S-433E HP-5MS 5% phenyl methyl siloxane (30 m × 0.25 mm × 0.25 μm) with helium as carrier gas (constant flow 1.0 mL min⁻¹). The volume of the sample injected into GC/MS was 1 μL (splitless mode) at 280 °C. The final selected oven program used was as follows: 100 °C for 5 min, 25 °C min⁻¹ to 160 °C, 10 °C min⁻¹ to 260 °C, 260 °C for 5 min, 35 °C min⁻¹ to 285 °C and 285 °C for 7 min. The temperatures of MS interphase, source and quadrupole (EI mode) were 280 °C, 230 °C and 150 °C, respectively.

For all compounds selective ion monitoring (SIM) mode was used. The *m/z* values for the derivatized compounds were: for 4-*n*-NP 179 and 292; for NP 179, 193, 207 and 235; for NP1EO 251, 265, 279 and 307; for NP2EO 295, 309 and 323. NP, NP1EO and NP2EO exist as a number of isomers due to variability in the branched nonyl moiety and thus appear as a cluster of peaks on the chromatogram. For this reason, the analytical parameter was the sum of integrated peak areas. On the other hand, 4-*n*-NP appears as a single peak due to its linear nonyl group. For each peak, the target and quantification ions were determined together with their retention times and quantification was carried out with respect to sum of the peak areas.

2.3. Collection and storage of sewage sludge samples

Sewage sludge samples were collected from the dewatering line of Central WWTP in Ankara, Turkey. This WWTP is the second largest municipal wastewater treatment plant in Turkey, receiving 765,000 m³ d⁻¹ of domestic and industrial influent. The WWTP is operated by classical activated sludge system with primary and secondary clarifiers. Combined sludge is anaerobically digested and dewatered by centrifuges before being disposed into the landfill of the city.

Sampling was carried out monthly between February 2012 and December 2012. Following the transfer of sludge samples to the laboratory, the samples were freeze-dried to remove moisture, immediately. Then they were grinded using a mortar and pestle and sieved through 1 mm sieve to obtain homogeneity. The samples were stored in dark at -18 °C until analysis.

2.4. Extraction from sewage sludge solids

Sonication and mechanical shaking extraction methods were chosen to evaluate the extraction efficiencies of NP and NPEO compounds from sewage sludge samples. Prior to recovery studies, 50–100 μg L⁻¹ (0.1–0.2 ng mg⁻¹) of each compound was spiked onto cleaned sewage sludge samples to compare both methods in terms of their efficiency. In both methods, spiked and unspiked sewage sludge samples (0.5 g) were placed in 12 mL amber teflon

capped bottles into which copper granules were added to remove sulfur. After 10 mL of extraction solvent was added, the vials were placed either into ultrasonic bath or mechanical shaker. Solid and liquid (solvent) phases were separated by centrifugation at 3000 rpm for 5 min. The liquid fraction was passed through anhydrous sodium sulfate to remove residual moisture and derivatized prior to GC injection. The tested experimental variables were the extraction time and the solvent used in both methods. Hexane, acetone, methanol and a mixture of acetone and methanol were the solvents tested. Time periods of 3 min, 5 min, 8 min, 10 min, 20 min and 30 min were compared for sonication-assisted extraction, whereas durations of 16 h, 24 h and 48 h were tested for mechanical shaking.

Following the selection of sonication-assisted extraction method, 0.5 g of freeze-dried sewage sludge sample from Ankara WWTP was placed in 12 mL amber teflon capped bottles. Copper granules and 10 mL acetone were added into bottles and then were placed into the ultrasonic bath and sonicated for 5 min. The vials were then centrifuged at 3000 rpm for 5 min and the resulting liquid was passed through anhydrous sodium sulfate column to remove moisture. The obtained eluate in acetone was used for further analysis.

2.5. Recovery studies

A 0.5 g of the sewage sludge sample was spiked with 50 μg L⁻¹ (0.1 ng mg⁻¹) of 4-*n*-NP, NP, NP1EO and NP2EO each. To determine the background effect, another 0.5 g of the same sewage sludge sample was used as blank without spiking.

In each recovery test triplicate extraction of the same sewage sludge sample spiked with 50 μg L⁻¹ (0.1 ng mg⁻¹) of each chemical was performed and triplicate injection to GC/MS was carried out from each extraction to characterize the repeatability of the method. During extraction tests, 4-*n*-NP was used as a surrogate and percent recoveries and relative standard deviations (RSDs) were calculated as given in EPA Method 8000C [28].

2.6. Derivatization

Due to polar and semi-volatile nature of NP compounds, derivatization was deemed necessary to convert these compounds into derivatives (with higher volatility and thermal stability) prior to GC/MS injection for quantification. For all compounds of interest, silylation was the most commonly applied technique in the literature [19,23,29]. Therefore, in this study, commonly used silylation agents MSTFA and BSTFA and the catalysts pyridine and TMCS were tested. After a series of trials, the final derivatization procedure developed was as follows: After extraction, 1 mL of eluate in acetone was dried completely under N₂ gas and 100 μL BSTFA+TMCS (99:1) was added. The vials were mixed for 1 min using vortex stirrer and then incubated at 70 °C for 30 min, cooled down to room temperature and vortexed for 1 min. Finally the mixture was transferred into silylated amber GC vials to be injected into GC/MS.

2.7. Quality assurance/quality control (QA/QC)

Instrument calibration for each compound was made between 10 μg L⁻¹ to 1000 μg L⁻¹ (8 concentrations) with three replicates (six GC/MS measurements) for each concentration. The targeted and achieved minimum coefficient of determination, *R*², was 0.99. The calibration curve was frequently checked with the injection of known concentration of NP and NPEO compounds and repeated when necessary.

In order to determine limits of detection (LOD) and limits of quantification (LOQ), signal-to-noise (*S/N*) ratio method was

employed. The minimum concentrations at which S/N ratio are “3” and “10” are accepted as the LOD and LOQ, respectively [30]. The LOD and LOQ values respectively for: 4-*n*-NP were 0.03 $\mu\text{g kg}^{-1}$ and 0.1 $\mu\text{g kg}^{-1}$; NP and NP1EO were 6 $\mu\text{g kg}^{-1}$ and 20 $\mu\text{g kg}^{-1}$ and NP2EO were 12 $\mu\text{g kg}^{-1}$ and 40 $\mu\text{g kg}^{-1}$.

Finally, to understand the effect of time elapsed, extraction tests were repeated for spiked samples kept in a desiccator for 10 days. The recovery percentages were all within the ranges suggested by USEPA (70–130%) [28] and Arditoglou and Voutsas (90–140%) [18], indicating that samples could be kept for at least 10 days without major loss.

3. Results and discussions

3.1. Optimization of the derivatization method for 4-*n*-NP, NP, NP1EO and NP2EO

Following a number of unsuccessful attempts to observe peaks for the selected analytes, derivatization was applied. Examining the literature data summarized in Supporting information Table S1, BSTFA and MSTFA were subjected to initial testing, in which BSTFA resulted in better peaks with higher abundances compared to MSTFA. Therefore BSTFA was chosen for derivatization of all target compounds. The use of BSTFA as a single derivatization agent led to incomplete derivatization, while the use of pyridine with BSTFA as a catalyst resulted in the increase of background interferences. So pyridine was eliminated due to concerns of possible background effects. Different combinations of times (30 min, 60 min, 90 min, 120 min, 5 h), temperatures (65 °C, 70 °C, 75 °C and 90 °C) and derivatization agents were tested in order to optimize the method. Temperature and time of derivatization was found to be best as 70 °C and 30 min, respectively, since increasing reaction times resulted in a negative effect on the efficiency of derivatization (data not shown).

Instead of pyridine, TMCS was further tested as a catalyst. Different volumetric ratios of TMCS were used with different volumes of BSTFA. The volumetric ratios of TMCS in the mix were 1%, 10% and 33.3% (v/v). Increasing ratio of TMCS in the mixture caused the peak areas to decrease. However, the results obtained for BSTFA + 1%TMCS and BSTFA + 10%TMCS were very close to each other; so BSTFA + 1%TMCS mix was chosen for further use. The mixture of BSTFA + TMCS was applied at different volumes (50 μL , 100 μL and 200 μL); 100 μL was found to be the most effective. As can be seen in Fig. S1, increasing the volume of BSTFA + TMCS mixture did not improve the effectiveness of derivatization but rather decreased the signal obtained. Both in terms of measured abundances and homogenous dissolution of NP compounds, 100 μL was chosen as the volume of BSTFA + TMCS mixture to be used.

3.2. Optimization of the GC/MS method for 4-*n*-NP, NP, NP1EO and NP2EO

Among the high number of tested GC/MS oven programs, the methods given by Field and Reed [31], Isobe et al. [32] and ISO 18857-2 [33] were applied but the peak quality and resolution were not promising, so these methods were not used for further studies (data not shown). This could be resulted from many reasons like laboratory conditions, difference in GC/MS type/brand, or personal errors. Derivatization is also an important parameter to determine the efficiency of methods applied. Some of the tested methods including Gatidou et al. [29] (BSTFA + pyridine), Barber et al. [34] (BSTFA + TMCS), Lian et al. [19] (BSTFA + TMCS), and Diaz et al. [35] (dimethyl sulfate) used derivatization for the measurement of the NP compounds,

whereas methods of Gibson et al. [36], Lu et al. [37] and Richter et al. [38] used no derivatization. Comparison of these methods is given in Supporting information Fig. S2 for NP. Methods by Gatidou et al. [29] and Diaz et al. [35] yielded the two highest results in terms of resolution and abundance for all chemicals considered. With the goal of improving peak quality and resolution, these two methods were used as starting points for development of an improved method. Four different in-house programs with different GC oven temperature ramps and EM volts were tested (Table S2). Among these tested programs, program 4 yielded the best results in terms of peak resolution and abundance and was selected as the final GC/MS method. Fig. 3 shows the final chromatograms obtained with the selected program for sewage sludge samples.

3.3. Optimization of extraction method for 4-*n*-NP, NP, NP1EO and NP2EO from sewage sludge

Among the number of extraction methods for NP and NPEO compounds from sewage sludge found in literature, Soxhlet and enhanced solvent extraction methods were eliminated due to the use of excessive amount of solvent. The remaining two widely applied methods; sonication and mechanical shaking were studied and compared. In both methods, extraction solvent is considered as a key parameter. Since hexane, acetone, methanol or a mixture of acetone and methanol were highly used in literature, these solvents/mixtures were selected to compare their extraction efficiencies. Dichloromethane was another commonly used solvent but due to its high toxicity, it was not preferred in this study. During the initial screening with sonication, it was observed that hexane yielded low extraction efficiency as judged by NP peak abundance (Fig. S3). Acetone resulted in higher abundance and better peak quality compared to the mixture of acetone:methanol (1:1). Therefore acetone was selected as extraction solvent for further analysis.

Following the selection of acetone as a solvent, the next parameter studied was the different time ranges for sonication and mechanical shaking extraction methods. The results of the extraction tests are given in Fig. 4.

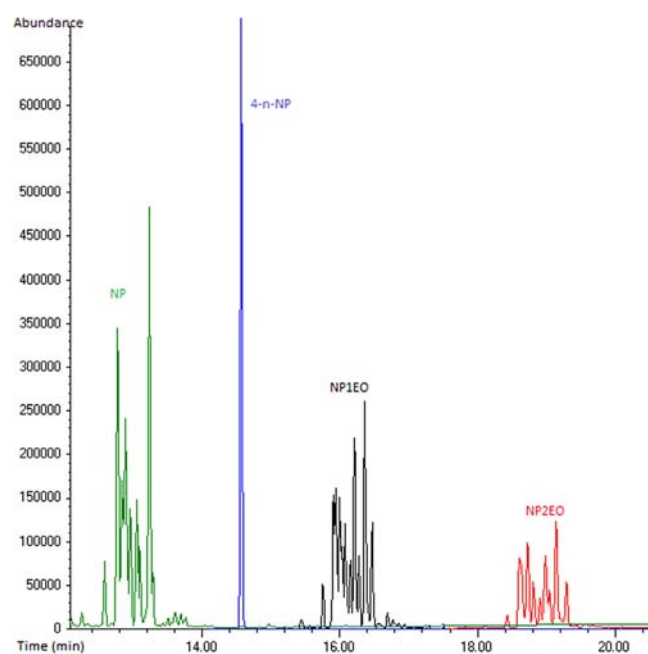


Fig. 3. Total ion chromatogram of silyl-derivatized NP, 4-*n*-NP, NP1EO and NP2EO in sewage sludge.

Fig. 4 shows the average percent recovery of analytes obtained in repeated extraction tests using sewage sludge samples. %RSD values were calculated based on concentrations as given in Method 8000C [28]. Since sonication employs a vigorous force, time becomes critical in order to maintain the integrity of the compounds as the extraction proceeds. Results showed that as time increased, NP2EO disappeared, and NP1EO and NP become higher. This created a concern about the degradation of NP2EO into NP1EO and NP during sonication. Fig. 4 shows that when sonication was applied for 30 min, NP2EO was not detected in the sample and NP1EO recoveries decreased from 114.9% (20 min) to 63.6%. This indicated that long sonication times possibly resulted in the loss of ethoxylate units, leading to lower extraction efficiency. Short sonication times such as 3, 5 and 8 min seemed more reasonable for the extraction of NP and NPEO compounds. As can be seen in Fig. 4, the recoveries obtained for mechanical shaking-assisted extraction were poorly repeatable (based on the %RSDs and standard deviations) and therefore considered to be unreliable. Additionally, the recovery values of all these compounds for each time-period tested for mechanical shaking do not satisfy the range suggested by USEPA as 70–130% at the same time [28].

According to the recovery of analytes obtained for all sonication times, 5 min sonication with acetone yielded the most repeatable results among the others (Fig. 4). Recovery of analytes for 8 min sonication in acetone for all three chemicals were closer to EPA guidelines; however, the repeatability was not reasonable based on standard deviations and the recovery for NP yielded the lowest value among the others. It is seen that 3 min and 5 min sonication tests gave similar results, except for NP2EO recovery which was 174.1 ± 3.8 . It is much higher than the ranges suggested in the literature. With all these considerations, 5 min sonication using acetone was chosen as the method to extract these compounds from sewage sludge solids. The percent extraction efficiencies calculated were 93.5 ± 2.9 for NP, 101.6 ± 2.7 for 4-*n*-NP, 134.1 ± 4.7 for NP1EO and 137.8 ± 4.5 for NP2EO after triplicate extractions. Even though the extraction efficiency for NP2EO was a bit higher compared to the USEPA's suggested upper limit [28], it is possible to find other ranges suggested in literature such as the 90–140% value given by Arditoglou and Voutsas [18].

3.4. Concentrations in a sewage sludge sample obtained from Ankara Central WWTP

One of the motivations of this study was to come up with an easily applicable and repeatable method so that the routine analysis of dewatered sewage sludge samples can be carried out. As stated above, a number of European countries require the total of NP, NP1EO and NP2EO to be less than $50 \text{ mg kg}^{-1}\text{-dm}$ for land

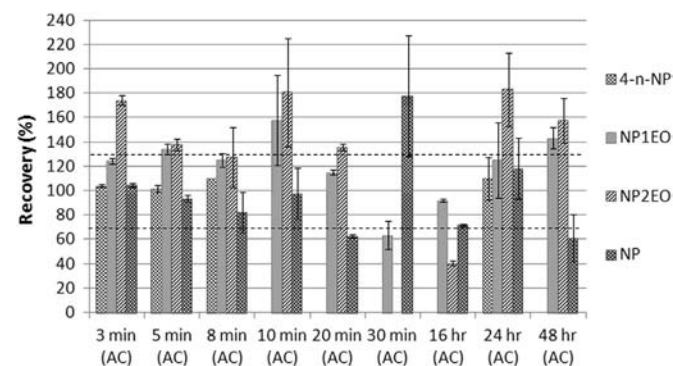


Fig. 4. Mean recovery values of 4-*n*-NP, NP, NP1EO and NP2EO for sonication and mechanical shaking (the dashed lines show the 70–130% recovery range given by USEPA [28]).

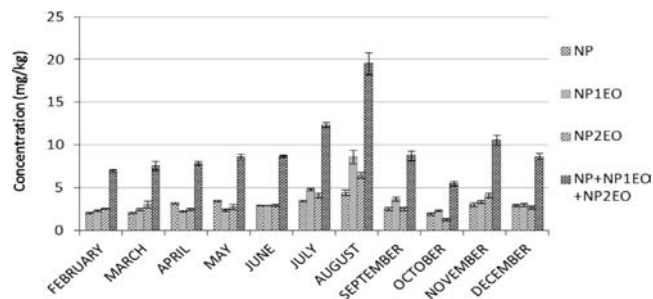


Fig. 5. Concentrations of NP, NP1EO and NP2EO measured in dewatered sludge of Ankara WWTP.

application of sewage sludge. In Turkey, this limit is the same with European Union, which is $50 \text{ mg kg}^{-1}\text{-dm}$. To show the applicability of the proposed quantification method, NP, NP1EO and NP2EO concentrations were analyzed in dewatered sludge samples collected from the Central WWTP in Ankara. The sludge samples were collected monthly (except for January) during the year of 2012. The methods for analysis were successfully applied judging from the fact that the highest RSD value was 12.8% (triplicate extraction with duplicate GC/MS analyses) which proved the repeatability of the method once again.

Fig. 5 shows the results obtained from Ankara Central WWTP during the year-round measurements. The sampling season had an effect on the concentrations, especially between winter and summer. In warmer months, the sum NPE started to increase and reached its highest values in July ($12.36 \pm 0.31 \text{ mg kg}^{-1}$) and August ($19.53 \pm 1.33 \text{ mg kg}^{-1}$), whereas in colder months (February, March, April, October) the concentrations remained lower. Similar pattern was reported by Li et al. [39]. The reason of the increase in summer months can be explained by an increase in microbial activity, dry weather conditions and/or an increase in bathing and laundry frequency. These activities lead to rise in detergent use and introduction of more NP and NPEO compounds to sewerage system. In winter and spring time, the decrease in these compounds could be attributed to snow and heavy rain regime. The total concentrations measured were all below $50 \text{ mg kg}^{-1}\text{-dm}$ limit required by European and Turkish regulations regardless of the season.

4. Conclusions

It is critical to determine NP and NPEO compounds in sewage sludge samples prior to land application due to human health and environmental concerns. The analysis of these chemicals is challenging due to the complicated matrix of sewage sludge. Therefore, there is a need for a reliable method for the quantification of NP and NPEO compounds. Unfortunately, in Turkey, there is a lack of a proposed method for the measurement of these compounds in sewage sludge although a limit value was set by the government. In this study, a practical method for the analysis of 4-*n*-NP, NP, NP1EO and NP2EO in sewage sludge samples is proposed and applied on sludge samples taken from a metropolitan WWTP in Turkey successfully.

To quantify NP, NP1EO and NP2EO compounds in sewage sludge, derivatization was deemed necessary, since without derivatization the target chemicals could not be determined. Among different agents tested, BSTFA+TMCS mixture at 70°C with 30 min reaction time gave a satisfactory result for the derivatization of these compounds. The derivatized forms were analyzed using GC/MS.

For sewage sludge samples, sonication and mechanical shaking were tested using different time intervals and solvents. It was revealed that 5 min sonication using acetone as solvent was a

better method for the extraction of these compounds in terms of extraction recovery and reproducibility.

Finally, the proposed method was tested on the sewage sludge samples taken from a WWTP in Ankara, Turkey. While a remarkable difference in sum of NPE was observed between winter and summer seasons, values were consistently below the 50 mg kg⁻¹-dm limit stated in European Union and Turkish regulations.

Acknowledgements

This research was a part of the project (Project no: 109Y018) funded by the Scientific and Technological Research Council of Turkey (TUBITAK). The authors would like to thank Muneer Ahmad and Hande Bozkurt for their support and contribution. They would also like to thank Dr. Robert W. Murdoch for his editorial comments on the manuscript.

Appendix A. Supporting information

Supplementary data associated with this article can be found in the online version at <http://dx.doi.org/10.1016/j.talanta.2014.08.014>.

References

- [1] A.M. Warhurst, An Environmental Assessment of Alkylphenol Ethoxylates and Alkylphenols, Published jointly by Friends of the Earth, Scotland and Friends of the Earth, England, Wales and Northern Ireland, 1995.
- [2] CEPA—Canada Environmental Protection Act, Priority Substances List Assessment Report—Nonylphenol and Its Ethoxylates, Environment Canada, Health Canada, 1999.
- [3] A. Soares, B. Guieysse, B. Jefferson, E. Cartmell, J.N. Lester, *Environ. Int.* 34 (2008) 1033–1049.
- [4] G.G. Ying, B. Williams, R. Kookana, *Environ. Int.* 28 (2002) 215–226.
- [5] M. Ahel, W. Giger, *Chemosphere* 26 (1993) 1461–1470.
- [6] M. Ahel, W. Giger, *Chemosphere* 26 (1993) 1471–1478.
- [7] M. Hesselsoe, D. Jensen, K. Skals, T. Olesen, P. Moldrup, P. Roslev G.K. Mortensen, K. Henriksen, *Environ. Sci. Technol.* 35 (2001) 3695–3700.
- [8] A.M. Soto, J. Honorato, J.W. Wray, C. Sonnenschein, *Environ. Health Perspect.* 92 (1991) 167–173.
- [9] C. Cox, *J. Pestic. Ref. Spring* 16 (1996) 15–20.
- [10] A.J. Porter, N.J. Hayden, Nonylphenol in the Environment: A Critical Review, (2002) See (<http://www.emba.uvm.edu/wnhayden/npreview.pdf>).
- [11] B. Thiele, K. Gunther, M.J. Schwuger, *Chem. Rev.* 97 (1997) 3247–3272.
- [12] J.W. Birkett, J.N. Lester, *Endocrine Disruptors in Wastewater and Sludge Treatment Processes*, Lewis Publishers, USA, 2003.
- [13] Directorate-General (DG) Environment, Water Framework Directive, Directive 2000/60/EC, European Union, 2000.
- [14] D. Barceló, *Emerging Organic Pollutants in Waste Waters and Sludge (The Handbook of Environmental Chemistry/Water Pollution)*, Springer, 2005.
- [15] I. Aparicio, J.L. Santos, E. Alonso, *Anal. Chim. Acta* 584 (2007) 455–461.
- [16] E. Olkowska, Z. Polkowska, J. Namiesnik, *Talanta* 88 (2012) 1–13.
- [17] M. Petrovic, D. Barceló, *Chromatographia* 56 (2002) 535–544.
- [18] A. Arditoglou, D. Voutsas, *Environ. Sci. Pollut. Res. Int.* 15 (2008) 228–236.
- [19] J. Lian, J.X. Liu, Y.S. Wei, *Sci. Total Environ.* 407 (2009) 4261–4268.
- [20] P. Pothitou, D. Voutsas, *Chemosphere* 73 (2008) 1716–1723.
- [21] M.J. LaGuardia, R.C. Hale, E. Harvey, T.M. Major, *Environ. Sci. Technol.* 35 (2001) 4798–4804.
- [22] S. Bennie, C.A. Sullivan, H.B. Lee, T.E. Peart, R.J. Maguire, *Sci. Total Environ.* 193 (1997) 263–275.
- [23] R. Jeannot, H. Sabik, E. Sauvard, T. Dagnac, K. Dohrendorf, *J. Chromatogr. A* 974 (2002) 143–159.
- [24] J.L. Santos, M. Del Mar Gonzalez, I. Aparicio, E. Alonso, *Int. J. Environ. Anal. Chem.* 87 (2007) 1033–1042.
- [25] S.W. Pryor, A.G. Hay, L.P. Walker, *Environ. Sci. Technol.* 36 (2002) 3678–3682.
- [26] Directorate-General (DG) Environment, Working Document on Sludge-3rd Draft, European Union, 2000.
- [27] Ministry of Environment and Urbanization, Regulation on the Land Use of Domestic and Urban Sludges Official Gazette No: 27661, Ankara, Turkey, 2010.
- [28] USEPA, Method 8000C—Determinative Chromatographic Separations, US Environmental Protection Agency 8000 Series Methods, Washington, DC, 2003.
- [29] G. Gatidou, N.S. Thomaidis, A.S. Stasinakis, T.D. Lekkas, *J. Chromatogr. A* 1138 (2007) 32–41.
- [30] International Conference on Harmonisation (ICH) Working Group, ICH Harmonised Tripartite Guideline—Validation of Analytical Procedure: Text and Methodology Q2(R1), ICH, 1996.
- [31] J.A. Field, R.L. Reed, *Environ. Sci. Technol.* 30 (1996) 3544–3550.
- [32] T. Isobe, H. Nishiyama, A. Nakashima, H. Takada, *Environ. Sci. Technol.* 35 (2001) 1041–1049.
- [33] ISO 18857, Water Quality—Determination of Selected Alkylphenols—Part 2: Gas Chromatographic—Mass Spectrometric Determination of Alkylphenols, their Ethoxylates and Bisphenol A in Non-filtered Samples Following Solid-phase Extraction and Derivatisation, first ed., International Standard, 2009.
- [34] L.B. Barber, G.K. Brown, S.D. Zaugg, *Potential Endocrine Disrupting Organic Chemicals in Treated Municipal Wastewater and River Water (Chapter 7)*, American Chemical Society (2000) 97–123.
- [35] A. Diaz, F. Ventura, M. Galceran, *Anal. Chem.* 74 (2002) 3869–3876.
- [36] R. Gibson, M.J. Wang, E. Padgett, A.J. Beck, *Chemosphere* 61 (2005) 1336–1344.
- [37] J. Lu, Q. Jin, Y. He, J. Wu, W. Zhang, J. Zhao, *Water Res.* 42 (2008) 1075–1082.
- [38] P. Richter, C. Leiva, C. Choque, A. Giordano, B. Sepulveda, *J. Chromatogr. A* 1216 (2009) 8598–8602.
- [39] D. Li, M. Kim, W.J. Shim, U.-H. Yim, J.R. Oh, Y.-J. Kwon, *Chemosphere* 56 (2004) 1–6.



Development of a LC–MS/MS methodology for the monitoring of the antichagasic drug benznidazole in human urine



Noelia Martínez^a, María Elena Marson^b, Guido Enrique Mastrantonio^b, Julio Raba^a, Soledad Cerutti^{a,*}

^a Instituto de Química de San Luis, Consejo Nacional de Investigaciones Científicas y Técnicas-Universidad Nacional de San Luis, Facultad de Química, Bioquímica y Farmacia, Bloque III, Avenida Ejército de los Andes 950, San Luis CP 5700, Argentina

^b Área de Toxicología, Departamento de Ciencias Biológicas, Facultad de Ciencias Exactas, Universidad Nacional de La Plata, Calle 47 y 115, La Plata, Provincia de Buenos Aires CP 1900, Argentina

ARTICLE INFO

Article history:

Received 16 March 2014

Received in revised form

12 August 2014

Accepted 14 August 2014

Available online 23 August 2014

Keywords:

Chagas disease

Benznidazole

Human urine

Liquid chromatography

Tandem mass spectrometry

ABSTRACT

Monitoring the drug benznidazole in biological fluids is a powerful tool for clinical diagnostic and pharmacological studies in chagasic patients. However, research in this concern needs to be done. The accurate quantitation of this drug in complex matrices represents a highly challenging task complicated by the absence of sensitive analytical methods. It follows that sample processing strategies, preparation/cleanup procedures, and chromatographic/ionization/detection parameters, were evaluated for method optimization. The summation of this work generated a rapid, selective, sensitive methodology based on reversed-phase chromatography–tandem mass spectrometry for the analysis of benznidazole in urine samples. To the best of our knowledge, this is a first report of a LC–MS/MS platform employed for this application. Matrix effect was determined; a 90% of signal suppression was observed. The limits of detection and quantification were 0.75 and 4.85 $\mu\text{g L}^{-1}$; respectively. The latter allowed the method's application to the detection of benznidazole in clinical studies and pharmacological monitoring analysis.

© 2014 Elsevier B.V. All rights reserved.

1. Introduction

Chagas disease (or American trypanosomiasis) is a deadly potentially disease caused by the *Trypanosoma cruzi* protozoan parasite. The geographical distribution of this disease is extensive, including mainly America, with endemic characteristics in South America [1]. At present, the number of people infected with Chagas disease worldwide is estimated to be about 10–12 million, causing 10,000 deaths per year due to complications [2]. The process of urbanization in Latin America and migratory population movements from endemic countries have led to the disease being diagnosed in non-endemic areas [3,4].

T. cruzi is a single-celled parasite transmitted primarily by blood-sucking insects, popularly called “kissing bugs”. *T. cruzi* enters the digestive tract of the insect when it bites a person or an infected mammal. The parasite is actively divided inside the insect and is transmitted through its feces which are deposited on the skin host. This transmission path, known as vectorial, was considered the most common in the American region.

On the other hand, the non-vector transfer pathways are related to (a) transplacental transmission (congenital), (b) blood transfusion, (c) organ transplant, (d) oral, by food intake with parasites, and (e) laboratory accidents [5].

In recent years the advances in the control of vectorial and transfusional transmission have converted the congenital transmission in the main source of transfer, especially in urban areas [1,6,7].

Nowadays, the only drugs existing for Chagas treatment are benznidazole (BNZ) and nifurtimox [8–10]. The first (N-benzyl-2-(2-nitroimidazole-1-yl) acetamide), $\text{C}_{12}\text{H}_{12}\text{N}_4\text{O}_3$, MW: 260.25 g mol^{-1} (Fig. 1); was obtained for veterinary purposes by Roche in 1974 and the second was developed by Bayer in 1960. Both commercially available pharmacotherapies are inadequate due to issues involving safety, efficacy, resistance, toxicity, difficulty of administration in impoverished conditions, and cost. Response to treatment depends greatly on the disease phase [11–14]; so early detection is not only important but critical for public health.

BNZ is the first pharmacotherapeutic option in Americas, its oral ingestion for acute stage treatment varies from 5 to 8 $\text{mg kg}^{-1} \text{day}^{-1}$ p.o. for 60 days [5]. However, information related to its pharmacokinetic distribution in special populations, such as lactating, children, elderly, and pregnant women, is poor or nonexistent. In addition, the chemotherapy with BZN requires prolonged administration

* Corresponding author. Tel.: +54 266 4520300x1311.

E-mail address: ecerutti@gmail.com (S. Cerutti).

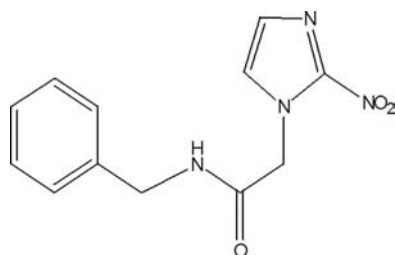


Fig. 1. Benznidazole structure.

(30–60 days) and has significant toxicity, especially in adults [15–17]. Moreover, the adverse drug reactions (ADRs) are the most important factor in therapeutic failure [18–20]. It follows the need for evaluation and monitoring of BNZ in biological fluids.

To date, the majority of studies focus on its therapeutic efficacy [21], pharmaceutical technology [22,23], preclinical pharmacokinetics evaluation [24] and metabolism study in animals [25,26]. There are only a few studies concerning to the quantification of this antichagasic drug by techniques such as electrochemistry [27,28], polarography [29], spectrophotometry [30,31] and liquid chromatography (LC) associated to UV detection [32–34]. However, it has been well documented the limitations of some of these analytical approaches to detect interferences and overcome some serious problems related to sample complexity. Moreover, only a few authors have developed LC–UV-based methodologies to quantify BNZ in plasma and animal urine for further implementation in human pharmacokinetic and health–safety studies [34–37]. A recent report, the unique one to the best of our knowledge, has been developed for applications in urine samples for studies in humans [37], with limited descriptions of analytical method performance.

Liquid chromatography coupled to mass spectrometric detection, in its various forms (LC–MS and LC–MS/MS), is an excellent alternative of analysis. The Ultra High Performance Liquid Chromatography (UHPLC) approach offers very important advantages associated finally with the time required for analysis. In many cases, it is necessary to use a cleaning/extraction/preconcentration procedure of the analytes in order to obtain the optimum conditions for the determination of them or to overcome the effects generated by the biological sample matrix. Following an exhaustive search in the scientific literature, it has been determined that a gold standard method employing a chromatographic approach coupled to mass spectrometry for the quantitative analysis of BNZ in biological samples has not been reported to date and it would be beneficial to the analytical community. Moreover, no studies applied to human samples with focus on clinical or therapeutic drug monitoring (TDM) have been reported. The analyte's determination in urine samples is important in order to obtain valuable information that could help to elucidate its pharmacokinetic behavior. Additionally, urine is a non-invasive sample, which is a valuable condition for TDM. In this study the optimization of a methodology for the extraction/chromatographic separation and mass spectrometric determination of BNZ in human urine samples is proposed. The optimized method provided a selective, sensitive, fast, and reliable strategy for the accurate detection of the antichagasic drug and, at the same time, it could be potentially used as a tool to generate relevant information for rational development of disease pharmacological therapy, today still scarce.

2. Experimental

2.1. Chemicals and reagents

BNZ analytical grade was donated by Hoffmann-La Roche Ltd. (Buenos Aires, Argentina). Water, methanol and acetonitrile Optima[®]

LC–MS grade, were purchased from Fisher Scientific (Fair Lawn, NJ, USA). Dichloromethane and trichloroacetic acid pro-analysis were purchased from Biopack (Buenos Aires, Argentina). Formic acid, 98%, was obtained from Fisher Scientific (Loughborough, UK). Ultrapure water (18 M Ω cm) was obtained from EASY pure (RF Barnstead, IA, USA). Organic standard solutions of BNZ were daily prepared by appropriate dilutions of a 100 mg L⁻¹ aqueous stock solution. Quantification was achieved by preparing spiked urine samples with proper amounts of the analyte. The solutions were maintained at 4 °C protected from light. For sample pre-treatment and filtering prior to LC–MS/MS analysis, 13 mm nylon hydrophilic membranes of 0.8 and 0.22 μ m diameter pore (Osmonics INC, USA) were used, respectively.

2.2. Instrumentation and conditions

Rotary evaporator Heidolph Laborota 4010 configured with ROTAVAP valve control equipment was used.

An Acquity[™] Ultra High Performance LC system (Waters, Milford) equipped with autosampler injection and pump systems (Waters, Milford) was used. The autosampler vial tray was maintained at 15 °C. The needle was washed with proper mixtures of acetonitrile and water. The separation was performed by injecting a 10 μ L sample onto an ACQUITY UPLC[®] BEH C₁₈ (Waters, Milford, USA) analytical column with 2.1 mm internal diameter, 50 mm length, and 1.7 μ m particle size. The binary mobile phases consisted of water with 0.1% (v/v) of formic acid (A) and acetonitrile with 0.1% (v/v) of formic acid (B) at a flow rate of 0.15 mL min⁻¹. The gradient was started at an initial composition of 90% A and 10% B, then 3-min linear gradient to 0% A, held for 0.3 min. A return to the initial conditions was accomplished by a 0.2-min gradient to 90% A, where it was held for 1.5 min. Thus, the total chromatographic run time was 5.0 min. The column was held at a temperature of 30 °C. Under these conditions, no sample contamination or sample to sample carryover was observed.

Mass spectrometry analyses were performed on a Quattro Premier[™] XE Micromass MS Technologies triple quadrupole mass spectrometer with a ZSpray[™] electrospray ionization source (Waters, Milford, USA). The source was operated in the positive (ESI⁺) mode at 350 °C with N₂ as the nebulizer and the source temperature was kept at 150 °C. The capillary voltage was maintained at 3.5 kV and the extractor voltage was set at 3.0 kV. Ultrapure nitrogen was used as desolvation gas with a flow of 200 L h⁻¹. Argon was used as the collision gas at a flow of 0.10 mL min⁻¹. Detection was performed in multiple reaction monitoring (MRM) mode of selected ions at the first (Q₁) and third quadrupole (Q₃). To choose the fragmentation patterns of m/z (Q₁) \rightarrow m/z (Q₃) for the analyte in MRM mode, direct infusion (via syringe pump) into the MS of BNZ standard solution in methanol was performed and the product ion scan mass spectra were recorded. Quantification of BNZ was done by measuring the area under the peak using MassLynx Mass Spectrometry Software (Waters, Milford, USA).

2.3. Sample collection and preparation

Urine samples were collected in sterile specimen collection bottles during 24 h from a pediatric chagasic patient and an adult volunteer, both after a 5 mg kg⁻¹ day⁻¹ p.o. BNZ doses. The whole procedure was made anonymous and the patients were enrolled in a clinical study approved by both ethical and research review committees of Children's Hospital Ricardo Gutierrez, Buenos Aires city, Argentina. All patients were informed about the purposes and scope of the study, and signed appropriate consent forms. Data assessment was complete for all patients.

2.3.1. Sample treatment

After collection, samples were divided into three aliquots and stored at $-21\text{ }^{\circ}\text{C}$ until analysis. Thaw was performed prior the three fractions underwent the following treatments.

2.3.1.1. Filtering. A measured volume of urine was centrifuged for 10 min at 12,000 rpm. A 500 μL aliquot of the supernatant was diluted with water:acetonitrile up to 1 mL final volume, filtered through a 0.22 μm syringe filter and stored in amber vials suitable for LC–MS/MS analysis.

2.3.1.2. Dryness. 2.5 mL urine volume was mixed with 5.0 mL acetonitrile volume, stirred and centrifuged. Supernatant was removed and brought to dryness in a rotary evaporator. Then it was reconstituted in water:acetonitrile, filtered through a 0.22 μm syringe filter and stored in an amber vial suitable for analysis.

2.3.1.3. Liquid–liquid extraction. Two consecutive extractions with 1.25 mL of dichloromethane each was performed on a 2.5 mL urine volume. The organic phase was separated and brought to dryness in a rotary evaporator. Then it was reconstituted with water:acetonitrile and filtered prior LC–MS/MS analysis.

2.4. Evaluation of matrix effect

As it is known, one downside of ESI–MS/MS ionization/detection is that the ionization process is susceptible to matrix signal suppression or enhancement [38–40]. The liquid chromatography–mass spectrometry response obtained from a standard can differ significantly from matrix samples. In this work, after optimizing the compound selective parameters, the effect of the urine matrix was assessed by comparing the signal of BNZ in pure solvent to the signal in the diluted and non-diluted sample matrix. Calibration curves for BNZ in the spiked biological fluid and in the pure solvent were created. The percentage of the quotient of the slopes (b) in the spiked and solvent samples was used as an indicator of the extent of the matrix effect, which was calculated as $100 - (b_{\text{spiked}}/b_{\text{solvent}} \times 100)$.

2.5. Assay performance

The calibration plots were measured under the optimal experimental conditions. Six levels of the calibration curve were determined (five technical replicates at each concentration level). The calibration equations were calculated by the least-squares linear regression method. Thus, linearity was evaluated from values closer to the limit of detection up to approximately $50,000\text{ }\mu\text{g L}^{-1}$.

Intra-day repeatability, and inter-day reproducibility, spiked urine samples were analyzed. Thus, 6 blank samples, 5 replicate measurements at 0, 10, 100, 500, 1000, 5000, 10,000, 25,000, and $50,000\text{ }\mu\text{g L}^{-1}$ BNZ concentrations were prepared.

3. Results and discussion

3.1. Sample preparation optimization

Although the technology related to chromatographic separations and mass spectrometry techniques advances, sample clean-up is still one of the most important bottlenecks of the analytical process. Effective sample preparation is essential for achieving good analytical results because matrix related compounds may also co-extract and interfere in the analysis.

The selection of the sample clean-up conditions in the analysis of BNZ in biological material is a difficult task taking into account the nature of the analyte. Consequently, optimization of the

clean-up steps paying special attention to the analytes recovery was carried out. The accuracy of the proposed method was evaluated by recovery experiments with spiking diluted sample solutions. Several approaches were considered, including filtering, dryness, and liquid–liquid extraction. The latter procedure demonstrated to be more proper in terms of the analyte's recovery, which resulted to be higher than 95%. Although, for clinical applications, recoveries equal or less than 70% with sufficient reproducibility may be appropriate. On the other hand, recoveries for sample filtering and dryness approaches ranged between 20% and 40%.

There has been little effort devoted to the study of drugs for the treatment of Chagas, a so-called “neglected disease”. It has been described that BNZ have hepatic metabolism with $< 20\%$ of the drug excreted unchanged by the kidney. However, there are virtually no studies on the metabolism of BNZ in humans, and very little information is available from animal studies [24,41–43]. Furthermore, there are no complete data on drug excretion through the urine, partially because of the lack of available techniques, as the one developed in this work. Although the samples used in this experience for validation and application of the proposed technique might not be enough to obtain general conclusions regarding this aspect, the higher BNZ value obtained in the pediatric urine is compatible with the reported for lower plasma dosage and higher plasmatic clearance from children below seven years old under a pharmacotherapeutic treatment [44].

3.2. Optimization of MS parameters and MRM transitions

Preliminary experiments were conducted with the purpose of finding the best instrumental conditions that would allow identification of BNZ in urine samples at trace levels. BNZ standard solution (1 mg L^{-1}) in methanol was introduced into the MS system at a flow rate of $20\text{ }\mu\text{L min}^{-1}$ via a syringe pump. The ion–full scan in positive mode (mass spectra from m/z 50 to 300 were recorded) of BNZ indicated the presence of its pseudomolecular ion $[\text{M}+\text{H}]^+$ as the predominant specie, with m/z value of 261.1. Multiple reaction monitoring mode of the precursor–product ion transitions was optimized. For quantitative mass spectrometric detection, it is generally accepted that a minimum of three identification points are required to meet the identification performance criteria. In this work, monitoring of one precursor ion and three daughter ions “earned” 5.5 identification points (1 for the parent ion and 1.5 for each daughter ion) and, therefore, fulfilled the mentioned criteria giving the necessary specificity to identify a substance correctly. Specific charged fragments for the studied analyte are listed in Table 1. The optimization of the ions production and fragmentation conditions permitted the analyte's sensitive and selective detection. As a result, the area under the most sensitive transition: $261.1 > 107.3$ was measured for quantification purposes.

3.3. Chromatographic procedure

To improve BNZ chromatographic retention, a reversed phase column was used and several mobile phases such as methanol, acetonitrile, and water were investigated. The results indicated

Table 1
Mass spectrometric conditions for the generation and fragmentation of BNZ.

Transitions (m/z)	Dwell (s)	Cone (V)	Collision (V)
261.1 > 148.2			
261.1 > 107.3 ^a	0.08	25	18
261.1 > 91.1			

^a Transition used for quantification.

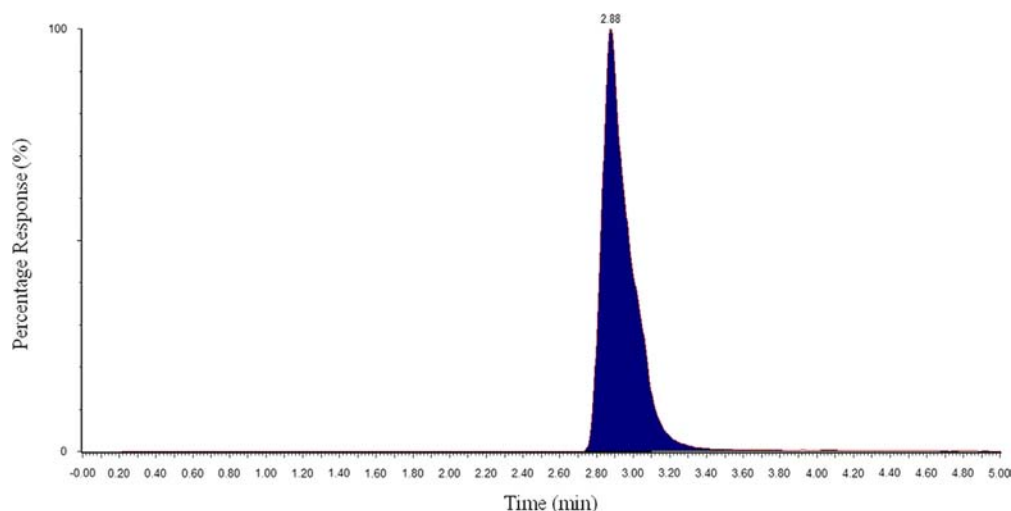


Fig. 2. Representative chromatogram of BNZ in spiked urine samples. Ionization and mass spectrometric conditions: electrospray ionization in positive mode associated to mass spectrometric detection in multiple reaction monitoring mode (experimental parameters as described in Section 2.2). Chromatographic approach: C₁₈ column; mobile phase H₂O:ACN gradient mode containing 0.1% (v/v) formic acid; mobile phase flow rate: 0.15 mL min⁻¹; temperature: 30 °C; BNZ standard concentration: 100 µg L⁻¹; sample injection volume: 10 µL.

that a mixture of water/acetonitrile as gradient solvents were optimal to allow formation of a fine spray of small droplets in the ESI interface. To enhance the signal response, mobile phase additives such as acetic acid and formic acid were also studied. The type (acetic or formic acid) and concentration (from 0.05% to 4.0% (v/v)) of additive were evaluated. The use of formic acid led to improved peak shape and retention time compared to acetic acid. The use of either one gave improved retention time, peak shape, and sensitivity compared to no additive. As a result, a 0.1% (v/v) formic acid concentration provided the maximum response for the generation of the protonated [M+H]⁺ BNZ ion, which was used for further MRM experiments. The effect of the mobile phase flow rate on the separation/retention of BNZ was evaluated using van Deemter plots. Ten microliters of the standard sample was injected onto the reversed phase system at varying flow rates, from 0.1 to 1.0 mL min⁻¹ with isocratic separation. Thus, a flow rate of 0.15 mL min⁻¹ gave the best results in terms of chromatographic conditions and ESI efficiency. Under the optimal mentioned conditions, the analyte was eluted at 2.88 min (Fig. 2) from the column within a 5.0 min total run cycle, which were shorter than the ones recently reported by other authors [33,34,36].

3.4. Evaluation of matrix effect

As mentioned in Section 2.4, after selecting the proper chromatographic conditions, the effect of the biological matrix under study (urine) was evaluated by comparing the signal of BNZ in pure solvent to the signal in the diluted and non-diluted sample matrix. Thus, calibration curves from spiked matrix and spiked pure solvent samples were created. Although analyte's liquid-liquid extraction was performed, BNZ response reduction of approximately 90% in both, diluted and non-diluted matrices, due to the urine interference was observed. As a consequence, its quantification was carried out following the standard addition method.

3.5. Analytical performance

A Certified Reference Material of the studied matrices with an informed value for BNZ does not exist. As a consequence, recovery of additions of known amounts of the analyte to a blank matrix was used. Thus, spiked urine samples were analyzed and recovery values better than 95.5% were achieved.

Table 2

Intra and inter-day variability for the LC–MS/MS analysis of benznidazole.

Concentration level (µg L ⁻¹)	Intra-day RSD (%) ^a	Inter-day RSD (%) ^a
10.0	3.9	7.0
100.0	3.7	5.8
500.0	3.2	6.5
1000.0	2.4	6.3
5000.0	2.8	6.2
10,000.0	2.1	6.2
25,000.0	2.0	6.3
50,000.0	2.1	6.0

^a RSD (%)=Relative Standard Deviation.

As mentioned in Section 2.5, repeatability (intraday precision) and reproducibility (interday precision) were evaluated. The obtained results are summarized in Table 2. In summary and taking into account the matrix complexity, the reported values for the method assessment parameters could be considered highly satisfactory.

The limit of detection (LoD) and limit of quantification (LoQ) were calculated as the signal equivalent to respectively 3 times and 10 times the background chromatography noise under working conditions. Thus, the obtained LoD and LoQ concentration values were 0.75 ± 0.03 and 4.85 ± 0.05 µg L⁻¹ respectively.

3.6. Sample analysis

Once the optimal conditions were established, the developed methodology was applied to the analysis of real urine samples. The mean BNZ concentration were 29.4 µg mL⁻¹ and 22.6 µg mL⁻¹ for the pediatric and the adult samples respectively.

4. Conclusions

A sensitive and selective analytical method for the chromatographic separation and determination of BNZ in urine samples based on the use of a reversed-phase liquid chromatography coupled to tandem mass spectrometry was developed and proposed for first time. The rapidness, selectivity, and sensitivity characteristics of the proposed methodology in the complex

matrix under study were demonstrated. Our studies showed that matrix effects should be carefully assessed when biological fluids are involved. Finally, methodology developed could be of great interest for monitoring BNZ variations in clinical and pharmacological studies.

Acknowledgments

The authors would like to gratefully acknowledge the financial support received from Consejo Nacional de Investigaciones Científicas y Técnicas (CONICET), Agencia Nacional de Promoción Científica y Tecnológica, Universidad Nacional de San Luis (INQUI-SAL). We also thank Drs. Jaime Altcheh and Facundo García-Bournissen (Servicio de Parasitología y Chagas, Hospital Gutierrez, Buenos Aires) for providing the real patient specimens used in this work, and Dr. Frank Kero for his assistance and comments.

References

- [1] WHO Expert Committee on the Control of Chagas Disease & World Health Organization. Report of the WHO Expert Committee on the Control of Chagas Disease, World Health Organization, Geneva, 2005.
- [2] J. Gascón, P. Albajar, E. Cañas, M. Flores, J. Gómez i Prat, R.N. Herrera, C. A. Lafuente, H.L. Luciarci, A. Moncayo, L. Molina, J. Muñoz, S. Puente, G. Sanz, B. Treviño, X.S. Salles, *Rev. Esp. Cardiol.* 60 (2007) 285–293.
- [3] Z.E. Yadon, G.A. Schmunis, *Am. J. Trop. Med. Hyg.* 81 (2009) 927–933.
- [4] G.A. Schmunis, Z.E. Yadon, *Acta Trop.* 115 (2010) 14–21.
- [5] Síntesis de la guía de diagnóstico y tratamiento de pacientes con enfermedad de Chagas, Programa Nacional de Chagas, Ministerio de Salud de la Nación, Argentina, 2012.
- [6] J. Altcheh, M. Biancardi, A. Lapena, G. Ballering, H. Freilij, *Rev. Soc. Bras. Med. Trop.* 38 (2005) 41–45.
- [7] J.A. Urbina, R. Docampo, *Trends Parasitol.* 19 (2003) 495–501.
- [8] F. García-Bournissen, J. Altcheh, N. Giglio, G. Mastrantonio, C. Omar Della Vedova, G. Koren, *Pediatr. Drugs* 11 (2009) 33–37.
- [9] J. Jannin, L. Villa, *Mem. Inst. Oswaldo Cruz* 102 (2007) 95–97.
- [10] F.S. Machado, H.B. Tanowitz, M.M. Teixeira, *Br. J. Pharmacol.* 160 (2010) 258–259.
- [11] J.C. Villar, J.A. Marín-Neto, S. Ebrahim, S. Yusuf, *Cochrane Database Syst Rev.* 1 (2002) CD003463.
- [12] World Health Organization, WHO Reporte sobre la enfermedad de Chagas, Updated in 2007, Buenos Aires (Argentina). Available at: (<http://www.who.int/tdr/publications/tdr-research-publications/reporte-enfermedad-chagas/en/index.html>) (accessed March 2014).
- [13] J. Rodrigues Coura, S.L. de Castro, *Mem. Inst. Oswaldo Cruz* 97 (2002) 3–24.
- [14] J.A. Pérez-Molina, A. Pérez-Ayala, S. Moreno, M.C. Fernández-González, J. Zamora, R. López-Vélez, *J. Antimicrob. Chemother.* 64 (2009) 1139–1147.
- [15] A.L. de Andrade, F. Zicker, R.M. de Oliveira, S. Almeida Silva, A. Luquetti, L. R. Travassos, I.C. Almeida, S.S. de Andrade, J.G. de Andrade, C.M. Martelli, *Lancet* 348 (1996) 1407–1413.
- [16] A.G. Schijman, J. Altcheh, J.M. Burgos, M. Biancardi, M. Bisio, M.J. Levi, H. Freilij, *J. Antimicrob. Chemother.* 52 (2003) 441–449.
- [17] S. Sosa-Estani, E.L. Segura, A.M. Ruiz, E. Velazquez, B.M. Porcel, C. Yampotis, *Am. J. Trop. Med. Hyg.* 59 (1998) 526–529.
- [18] J.A. Marin Neto, A. Rassi Jr., C.A. Morillo, A. Avezum, S.J. Connolly, S. Sosa-Estani, F. Rosas, S. Yusuf, *Am. Heart J.* 156 (2008) 37–43.
- [19] J.A. Marin Neto Jr., A. Rassi Jr., A. Avezum, A.C. Mattos, A. Rassi, *Mem. Inst. Oswaldo Cruz* 104 (2009) 319–324.
- [20] Apt B. Werner, I.A. Zulantay, *Rev. Med. Chile* 139 (2011) 247–257.
- [21] F. Pires Maximiano, L. Maria de Paula, V. Paulino Figueiredo, I. Mayer de Andrade, A. Talvani, L.C. Sá-Barreto, M.T. Bahia, M.S. Cunha-Filho, *Eur. J. Pharm. Biopharm.* 78 (2011) 377–384.
- [22] M.C. Lamas, L. Villaggi, I. Nocito, G. Bassani, D. Leonardi, F. Pascutti, E. Serra, C. Salomón, *Int. J. Pharm.* 307 (2006) 239–243.
- [23] A.A. Lima, J.L. Soares-Sobrinho, J.L. Silva, R.A. Correa, M.A. Lyra, F.L. Santos, B. G. Oliveira, M.Z. Hernandez, L.A. Rolim, P.J. Rolim-Neto, *J. Pharm. Sci.* 100 (2010) 2443–2451.
- [24] P. Workman, R.A. White, M.I. Walton, L.N. Owen, P.R. Twentyman, *Br. J. Cancer* 50 (1984) 291–303.
- [25] F.Y. Lee, P. Workman, K.H. Cheeseman, *Biochem. Pharmacol.* 36 (1987) 1349–1355.
- [26] S.N. Moreno, *Comp. Biochem. Phys. C* 91 (1988) 321–325.
- [27] A.N. Pappas, M.F. Delaney, *Anal. Lett.* 15 (1982) 739–745.
- [28] A.Z. Abu Zuhri, S.I. Al-Khalil, M.S. Suleiman, *Anal. Lett.* 19 (1986) 453–459.
- [29] P.J. Barbeira, G.M. Silva, M.D. Beatriz, N.R. Stradiotto, *J. Pharm. Biomed. Anal.* 20 (1999) 723–726.
- [30] R.F. Bullfer, J.A. Castro, S.L. Fanelli, *Acta Bioquím. Clín. Latinoam.* 45 (2011) 463–470.
- [31] M.S. Nothenberg, G.K. Takeda, R. Najjar, *J. Inorg. Biochem.* 42 (1991) 217–229.
- [32] M.I. Walton, P. Workman, *J. Chromatogr.* 375 (1986) 190–196.
- [33] J.M. Padró, M.E. Marsón, G.E. Mastrantonio, J. Altcheh, F. García-Bournissen, *M. Reta, Talanta* 107 (2013) 95–102.
- [34] L. Guerrero, M.J. Pinazo, E. Posada, J. Gascón, J. Ribas, D. Soy, *Clin. Chem. Lab. Med.* 49 (2011) 77–82.
- [35] R. Moreira da Silva, L.T. Oliveira, N.M. Silva Barcellos, J. de Souza, M. de Lana, *Antimicrob. Agents Chemother.* 56 (2012) 3344–3348.
- [36] Á.A. De Lima, J.L. Sobrinho, J.L. Da Silva Jr., R.A. Corrêa, M.A. Lyra, P.J. Neto, *Quim. Nova* 32 (2009) 2196–2199.
- [37] M.E. Marson, D. Dana, F. García Bournissen, J. Altcheh, G. Mastrantonio, *J. Clin. Lab. Anal.* 27 (2013) 384–390.
- [38] T.L. Constantopoulos, G.S. Jacksson, C.G. Enke, *J. Am. Soc. Mass Spectrom.* 10 (1999) 625–634.
- [39] A. Apffel, S. Fischer, G. Goldberg, F.E. Kuhlmann, *J. Chromatogr. A* 712 (1995) 177–190.
- [40] R.J. Steen, P.E. Leonards, U.A. Brinkman, D. Barceló, J. Tronczynski, T.A. Albanis, W.P. Cofino, *Environ. Toxicol. Chem.* 18 (1999) 1574–1581.
- [41] M.I. Walton, P. Workman, *Biochem. Pharmacol.* 36 (1987) 887–896.
- [42] R.W. Riehle, J. Raaflaub, *Acta Trop.* 37 (1980) 257–261.
- [43] P. Workman, M.I. Walton, F.Y. Lee, *Biochem. Pharmacol.* 35 (1986) 117–119.
- [44] J. Altcheh, G. Moscatelli, S. Moroni, N. Giglio, G. Koren, M.E. Marson, G. Mastrantonio, F. García Bournissen, Proceedings of the 30th Annual Meeting of the European Society for Paediatric Infectious Diseases, Thessaloniki, Greece, 2012.



Characterization of Fe₃O₄/SiO₂/Gd₂O(CO₃)₂ core/shell/shell nanoparticles as T1 and T2 dual mode MRI contrast agent

Meicheng Yang^{a,b,1}, Lipeng Gao^{c,1}, Kai Liu^c, Chunhua Luo^{c,*}, Yiting Wang^c, Lei Yu^c, Hui Peng^{c,d,e}, Wen Zhang^a

^a Chemistry Department, East China Normal University, Shanghai 200241, PR China

^b Antibiotics Department, Shanghai Institute for Food and Drug Control, Shanghai 201203, PR China

^c Key Laboratory of Polar Materials and Devices, Ministry of Education, East China Normal University, Shanghai 200241, PR China

^d Polymer Electronic Research Centre, The University of Auckland, Private Bag 92019, Auckland, New Zealand

^e State Key Laboratory of Chemo/Biosensing and Chemometrics, Hunan University, Changsha 410082, PR China

ARTICLE INFO

Article history:

Received 9 July 2014

Received in revised form

13 August 2014

Accepted 15 August 2014

Available online 26 August 2014

Keywords:

Fe₃O₄/SiO₂/Gd₂O(CO₃)₂

Nanoparticles

Magnetic resonance imaging

Contrast agents

ABSTRACT

Core/shell/shell structured Fe₃O₄/SiO₂/Gd₂O(CO₃)₂ nanoparticles were successfully synthesized. Their properties as a new type of T1–T2 dual mode contrast agent for magnetic resonance imaging were investigated. Due to the introduction of a separating SiO₂ layer, the magnetic coupling between Gd₂O(CO₃)₂ and Fe₃O₄ could be modulated by the thickness of SiO₂ layer and produce appropriate T1 and T2 signal. Additionally, the existence of Gd³⁺ enhances the transverse relaxivity of Fe₃O₄ possibly because of the magnetic coupling between Gd³⁺ and Fe₃O₄. The Fe₃O₄/SiO₂/Gd₂O(CO₃)₂ nanoparticles exhibit good biocompatibility, showing great potential for biomedical applications.

© 2014 Elsevier B.V. All rights reserved.

1. Introduction

Magnetic resonance imaging (MRI), one of noninvasive clinical diagnosis techniques with a high spatial resolution, is widely used for anatomical imaging of soft body tissues [1]. However, since normal tissues and lesions often show only small differences in relaxation time, the obtained images are not clear enough to make an accurate diagnosis. In order to improve the image contrast between normal and disease tissues, contrast agents are generally employed to change proton relaxation rates. Now, the most of available MRI contrast agents are paramagnetic complexes, such as gadolinium complexes [2,3], which facilitate the spin-lattice relaxation of protons and result in a positive MR image (T1-weighted images).

The tremendous advances in nanotechnology have led to the development of new types of contrast agents based on inorganic nanoparticles (NPs), such as superparamagnetic iron oxide NPs which cause protons in their vicinity to undergo spin–spin relaxation and result in a negative MR image (T2-weighted images) [2,4,5]. Compared to conventional molecular contrast agents, inorganic NPs show the advantages of tunable size and

shape, as well as surface modification, which allow different biodistribution. Among inorganic nanoparticles, iron oxide NPs have been intensively investigated as a T2 contrast agent in cell migration, apoptosis and cancer detection due to their relatively good biocompatibility [6–10]. However, the signal enhancement caused by conventional iron oxide NPs is still unsatisfactory compared to other imaging modalities such as fluorescence and PET [11], due to their less saturation magnetization (M_s) resulting in a limited effect on r_2 relaxivity. In order to enhance the saturation magnetization, magnetism-engineered iron oxide (MEIO) NPs have been reported with high MRI sensitivity for the detection of cancer markers [12]. Zn²⁺ doped Mn–Fe–O ferrite NPs with a high M_s value have also been developed [13]. Huang et al. synthesized Gd³⁺-chelated Fe₃O₄@SiO₂ magnetic nanoparticle with a M_s value of $\sim 94 \text{ emu g}^{-1}$ [14]. Due to the existence of Gd³⁺, the transverse relaxivity of the prepared NPs reached $681 \text{ (mmol/L)}^{-1} \text{ s}^{-1}$ [14].

Although the development of iron oxide NPs as T2 contrast agents has gained great successes, such single mode contrast agents are increasingly facing challenges arising from accurate imaging of small biological targets because of the negative contrast effect and magnetic susceptibility artifacts [11,15]. The obtained dark areas in MR images due to their negative contrast are often confused with a low-level MR signal arising from adjacent tissues such as bone or vasculature [11,16]. Therefore, the development of T1–T2 dual mode contrast agents is highly

* Corresponding author. Tel.: +86 21 54342726; fax: +86 21 54345119.

E-mail addresses: chunhua_luo@hotmail.com (C. Luo),

h.peng@auckland.ac.nz (H. Peng).

¹ These authors contributed equally.

attractive because two different T1 and T2 imaging modes can be selectively utilized to visualize different tissues and potentially give more accurate information [17,18]. For this aim, Bae et al. synthesized gadolinium-labeled Fe_3O_4 NPs and demonstrated the capability of these NPs as dual contrast agents for T1 and T2-weighted magnetic resonance imaging [18]. Seo et al. reported that FeCo/graphitic-shell nanocrystals exhibit high T1 and T2 contrast effects [19].

In the present work, we report the synthesis of $\text{Fe}_3\text{O}_4/\text{SiO}_2/\text{Gd}_2\text{O}(\text{CO}_3)_2$ core/shell/shell structured NPs (NPs) and their potential as a T1–T2 dual model contrast agent. In the designed structure of $\text{Fe}_3\text{O}_4/\text{SiO}_2/\text{Gd}_2\text{O}(\text{CO}_3)_2$ NPs, the SiO_2 layer acts as a separating layer to modulate the magnetic coupling between T1 contrast material ($\text{Gd}_2\text{O}(\text{CO}_3)_2$) and T2 contrast material (Fe_3O_4). The experimental results illustrates that the thickness of SiO_2 layer has a significant effect on the values of r_1 (longitudinal relaxivity) and r_2 (transverse relaxivity).

2. Experimental

2.1. Materials

Anhydrous iron chloride ($\geq 98\%$), sodium oleate ($\geq 95\%$, capillary GC), tetraethyl orthosilicate (TEOS, 98%) and $\text{Gd}(\text{NO}_3)_3$ (99%) were purchased from Sigma-Aldrich Ltd. Oleic acid (90%, technical grade), 1-octadecene (90%, technical grade) and Igepal CO-520 (containing 50 mol% hydrophilic group) were obtained from Alfa-Aesar Ltd. Other chemicals were purchased from the China National Medicine Company (Shanghai, China) and were analytical grade or better. All chemicals were used without further purification. HL-7702 (Hepatic cells), Bel-7404 and SMMC-7721 (Hepatocarcinoma cells) were purchased from Shanghai Cellular Institute of China Scientific Academy. These cells were cultured in PRMI-1640 medium (GIBCO, USA), supplemented with 10% FBS (BioInd, Israel), 100 units mL^{-1} penicillin G, and 100 $\mu\text{g mL}^{-1}$ streptomycin (GIBCO, USA). In all experiments, the cells were maintained in 100-mm culture dishes (Corning, USA) at 37 °C in a humidified atmosphere of 5% CO_2 and 95% air (FORMA Series 2 Water Jacket, Thermo Scientific, USA).

2.2. Synthesis of $\text{Fe}_3\text{O}_4/\text{SiO}_2/\text{Gd}_2\text{O}(\text{CO}_3)_2$ core/shell/shell NPs

Fe_3O_4 NPs were first synthesized according to Ref. [20]. In brief, 2.78 g (3 mmol) of iron-oleate which was treated at 30 °C in a vacuum oven for 24 h before use and 0.48 mL of oleic acid (1.5 mmol) were dissolved in 10 mL of 1-octadecene. The reaction mixture was heated to 320 °C at a constant heating rate of 3.3 °C min^{-1} , then kept at that temperature for 60 min. After the reaction, the solution was cooled to room temperature and a mixture of 10 mL of hexane and 40 mL of acetone were added to precipitate Fe_3O_4 NPs.

Coating Fe_3O_4 NPs with a SiO_2 shell was done by using a known method [21] with a slight modification. Polyoxyethylene(5)nonylphenyl ether (Igepal CO-520, 1.68 mmol) and Fe_3O_4 NPs (1.2 mg) were dispersed in cyclohexane and vortexed. Then, ammonium hydroxide (30%, 105 μL) was added to form a brown reverse microemulsion, followed by the addition of tetraethyl orthosilicate

(92 μL , TEOS). The reaction was kept for 72 h at room temperature. The formed $\text{Fe}_3\text{O}_4/\text{SiO}_2$ NPs were precipitated by the addition of methanol and collected by centrifugation. To control the SiO_2 thicknesses from 8 to 20 nm, the amount of TEOS were changed from 24 to 149 μL , respectively.

The growth of $\text{Gd}_2\text{O}(\text{CO}_3)_2$ shell followed the previous reported procedure [22]. The obtained $\text{Fe}_3\text{O}_4/\text{SiO}_2$ NPs were dispersed in a diethylglycol solution containing 38.0 mmol L^{-1} $\text{Gd}(\text{NO}_3)_3$ and 2.0 mol L^{-1} $(\text{NH}_2)_2\text{CO}$. The reaction mixture was heated to 80 °C under N_2 atmosphere with continuous stirring. After the reaction was finished, the NPs were precipitated by adding acetone and collected by centrifugation.

2.3. Characterization

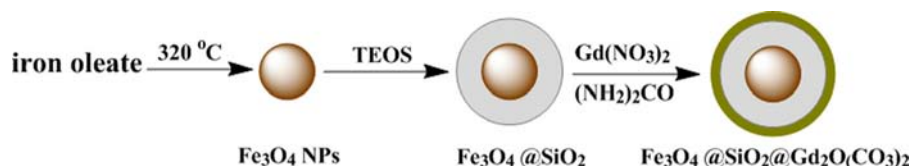
The micrographs of NPs were taken by using transmission electron microscope (TEM, JEM-2100F, JEOL, Japan). X-ray diffraction (XRD) spectra were collected from 10° to 70° (2θ), with a step of 0.02° by using a Ni filtered $\text{Cu K}\alpha$ ($\lambda=1.5418 \text{ \AA}$) radiation source (D/Max-2550V, Rigaku Co.). The JCPDS PDF database was utilized for phase identification. Magnetic measurements were performed on a superconducting Quantum Interference Device (SQUID, PPMS-9, Quantum Design Inc., USA). The samples were filled in a small container made of polyvinyl chloride, whose diamagnetic moment was subtracted from the measured magnetization values. The magnetic hysteresis loops were recorded at room temperature in a field sweep from –5000 Oe to 5000 Oe at a rate of 50 Oe s^{-1} .

2.4. MRI measurements

MR imaging of $\text{Fe}_3\text{O}_4/\text{SiO}_2/\text{Gd}_2\text{O}(\text{CO}_3)_2$ solutions were performed by using a 3T MRI (SIEMENS MAGNETOM Trio I-class, Germany). T1 images were measured with a slice thickness of 2 mm, the acquisition number of 1, 60 × 60 mm field of view (FOV), 256 × 256 matrices and an echo time (TE) of 12 ms. The T2 images were obtained by using in a fast spin-echo sequence (TR=4000 ms, TE=75 ms, FOV=60 mm, matrix=256 × 256, slice thickness=2 mm, acquisition number=1). r_1 was measured by using various TI in an inverse recovery (IR) pulse sequence (TI=24, 100, 200, 400, 600, 900, 1200, 2000, 3000, and 5000 ms, TR=7000 ms, TE=13 ms, FOV=89 × 179 mm, matrix=350 × 704 mm, slice thickness=5 mm, average=1). r_2 was measured by using Spin Echo (SE) pulse sequence (TR=3000 ms, TE=14.3 ms, FOV=87 × 280 mm, matrix=240 × 768 mm, slice thickness=5 mm, average=1).

2.5. MTT assay

The cytotoxicity of $\text{Fe}_3\text{O}_4/\text{SiO}_2/\text{Gd}_2\text{O}(\text{CO}_3)_2$ NPs was evaluated by MTT viability assay. HL-7702, Bel-7404 and SMMC-7721 cells were cultured at 1×10^5 cells on 96-well plates for 24 h, and then incubated with the different concentrations of NPs for 24, 48 and 72 h, respectively. After that, the cells were cultured with MTT reagents for 4 h. The products were dissolved with DMSO on the plate, and the absorbance at 490 nm was measured with a microplate reader (Multiskan MK3, Thermo Scientific, USA).



Scheme 1. The schematic synthesis of the $\text{Fe}_3\text{O}_4/\text{SiO}_2/\text{Gd}_2\text{O}(\text{CO}_3)_2$ NPs.

3. Results and discussion

The synthesis procedure of $\text{Fe}_3\text{O}_4/\text{SiO}_2/\text{Gd}_2\text{O}(\text{CO}_3)_2$ NPs is represented in Scheme 1 and described in detail in the experimental section. Fig. 1a shows a typical TEM image of prepared $\text{Fe}_3\text{O}_4/\text{SiO}_2/\text{Gd}_2\text{O}(\text{CO}_3)_2$ core/shell/shell structured NPs. The diameter of Fe_3O_4 core is about 12 nm. The thicknesses of SiO_2 shell and $\text{Gd}_2\text{O}(\text{CO}_3)_2$ shell are about 16 nm and 1.5 nm, respectively. To confirm the crystal structure of prepared $\text{Fe}_3\text{O}_4/\text{SiO}_2/\text{Gd}_2\text{O}(\text{CO}_3)_2$ NPs, X-ray diffraction (XRD) was employed to analyze the samples obtained in each synthetic step. The results are given in Fig. 2. Curve I in Fig. 2 is the XRD spectrum of prepared Fe_3O_4 NPs. There are six characteristic peaks at 30.50° (2 2 0), 35.84° (3 1 1), 43.46° (4 0 0), 53.90° (4 2 2), 57.38° (5 1 1) and 62.90° (4 4 0), which are in good agreement with the standard XRD data of Fe_3O_4 (JCPDS No. 19-06290). After coating with SiO_2 , the characteristic peaks of Fe_3O_4 NPs can still be seen (Fig. 2, curve II), although the intensities of the diffraction peaks were greatly weakened. This result illustrates that the coating of SiO_2 did not change the crystal structure of Fe_3O_4 NPs. The hump centered at $2\theta \approx 22^\circ$ is a typical feature of amorphous SiO_2 . While, after the growth of very thin $\text{Gd}_2\text{O}(\text{CO}_3)_2$ layer (~ 1.5 nm), the XRD signals of $\text{Gd}_2\text{O}(\text{CO}_3)_2$ are very weak because of very thin layer of $\text{Gd}_2\text{O}(\text{CO}_3)_2$. So the $\text{Gd}_2\text{O}(\text{CO}_3)_2$ shell was over grown and the measured XRD spectrum is shown in Fig. 2 (curve III) which is matched well with the literature values of $\text{Gd}_2\text{O}(\text{CO}_3)_2$ (JCPDS #: 430604).

The magnetic properties of prepared NPs were characterized at 300 K and are shown in Fig. 3. It can be seen from Fig. 3a that the sample of Fe_3O_4 NPs has a saturation magnetization (M_{sat}) value of 56 emu g^{-1} . This value is lower than that of bulk Fe_3O_4 (about

$85\text{--}100 \text{ emu g}^{-1}$) [23], because the magnetization of samples decreases with decreasing particle size. The magnetic hysteresis loop of Fe_3O_4 NPs also illustrates that the Fe_3O_4 NPs exhibit superparamagnetism at room temperature, since no hysteresis is observed and both remanence and coercivity are approximately zero [24]. After the growth of the separating SiO_2 layer, the M_{sat} value dramatically decreases to 1.4 emu g^{-1} (Fig. 3b, curve II) mainly due to a decrease of the content of Fe_3O_4 in one gram of the sample. However, the M_{sat} value increases to 2.0 emu g^{-1} after the further growth of $\text{Gd}_2\text{O}(\text{CO}_3)_2$ shell. This could be explained by the fact that $\text{Gd}_2\text{O}(\text{CO}_3)_2$ is paramagnetic and shows magnetization in the presence of an externally applied magnetic field.

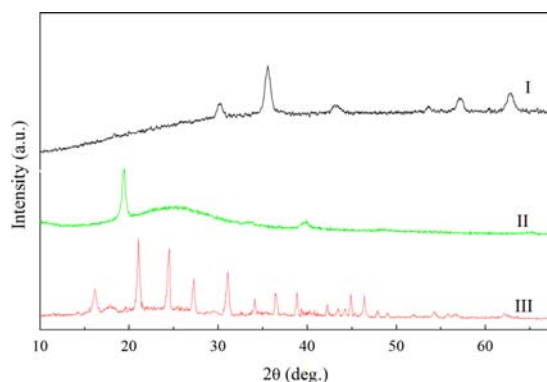


Fig. 2. X-ray diffraction patterns of (I) Fe_3O_4 NPs, (II) $\text{Fe}_3\text{O}_4/\text{SiO}_2$ and (III) $\text{Fe}_3\text{O}_4/\text{SiO}_2/\text{Gd}_2\text{O}(\text{CO}_3)_2$ NPs.

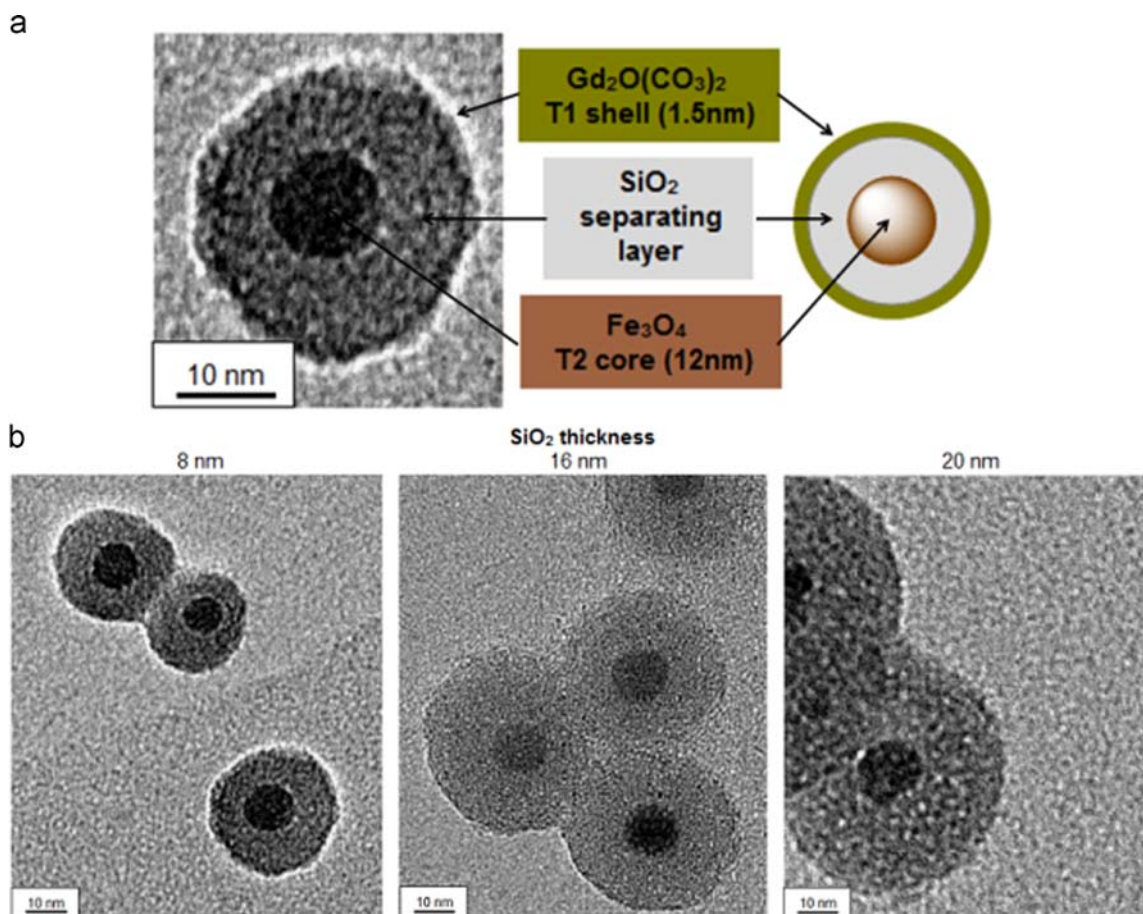


Fig. 1. (a) Schematic and TEM image of core-shell type $\text{Fe}_3\text{O}_4/\text{SiO}_2/\text{Gd}_2\text{O}(\text{CO}_3)_2$. (b) TEM images of $\text{Fe}_3\text{O}_4/\text{SiO}_2/\text{Gd}_2\text{O}(\text{CO}_3)_2$ with variable separating layer thickness (8, 16 and 20 nm), having a fixed Fe_3O_4 core (12 nm in diameter) and a $\text{Gd}_2\text{O}(\text{CO}_3)_2$ shell (1.5 nm).

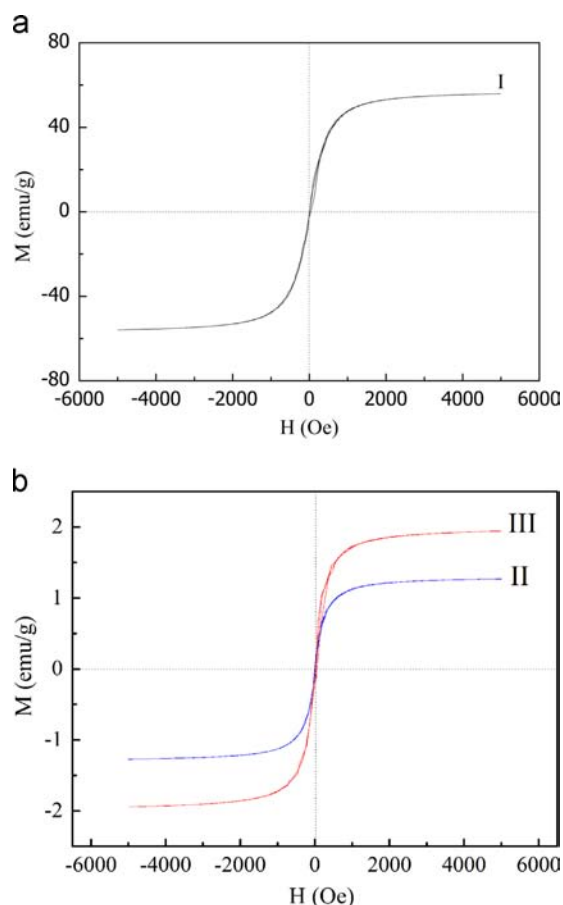


Fig. 3. The magnetic hysteresis loops of (I) Fe_3O_4 , (II) $\text{Fe}_3\text{O}_4@\text{SiO}_2$ and (III) $\text{Fe}_3\text{O}_4@\text{SiO}_2@\text{Gd}_2\text{O}(\text{CO}_3)_2$ NPs.

In the designed structure of $\text{Fe}_3\text{O}_4/\text{SiO}_2/\text{Gd}_2\text{O}(\text{CO}_3)_2$ NPs, SiO_2 acts as a separating layer to modulate the magnetic coupling between T1 contrast material ($\text{Gd}_2\text{O}(\text{CO}_3)_2$) and T2 contrast material (Fe_3O_4). So another two NPs samples were prepared with a SiO_2 layer of 8 nm and 20 nm. Their TEM images are shown in Fig. 1b. The performances of $\text{Fe}_3\text{O}_4/\text{SiO}_2/\text{Gd}_2\text{O}(\text{CO}_3)_2$ NPs with different SiO_2 layer thickness as T1–T2 dual model contrast agent were investigated and the results are shown in Fig. 4. From the images produced by T1-weighted MR sequences (Fig. 4a), it can be seen that the T1 contrast effect is dramatically changed with the thickness of the separating SiO_2 layer. When the SiO_2 layer was 8 nm thick, T1 contrast effect is very weak (Fig. 4a, left) due to the closely located T1 and T2 contrast agents. The magnetic field generated by the superparamagnetic Fe_3O_4 NPs perturbs the dipolar interactions between electron spins of gadolinium and nuclear spins of water, resulting in the quenching of T1 signal. Increasing the thickness of the SiO_2 layer to 16 nm and 20 nm causes the change of T1 contrast from dark grey to bright, which illustrates greatly improved T1 contrast effect. Such change can also be clearly seen in the color coded MR image (Fig. 4a, bottom). This result indicates that the perturbation to T1 signals caused by the Fe_3O_4 NPs could be tuned by the separating SiO_2 layer. The relaxivity coefficient r_1 , which is the value of MR contrast effects, changes in the order 3.7, 32.9, and 32.2 $(\text{mmol/L})^{-1} \text{s}^{-1}$ as the thickness of the SiO_2 layer increases in the respective order 8, 16, and 20 nm. The T2 contrast gradually changed from dark to dark grey with the increase of SiO_2 thickness, as shown in Fig. 4b. The T2 relaxivity coefficient (r_2) of the $\text{Fe}_3\text{O}_4/\text{SiO}_2/\text{Gd}_2\text{O}(\text{CO}_3)_2$ changes in the order 312, 269, and 208 $(\text{mmol/L})^{-1} \text{s}^{-1}$ as the SiO_2 thickness increases in the respective order 8, 16, and 20 nm

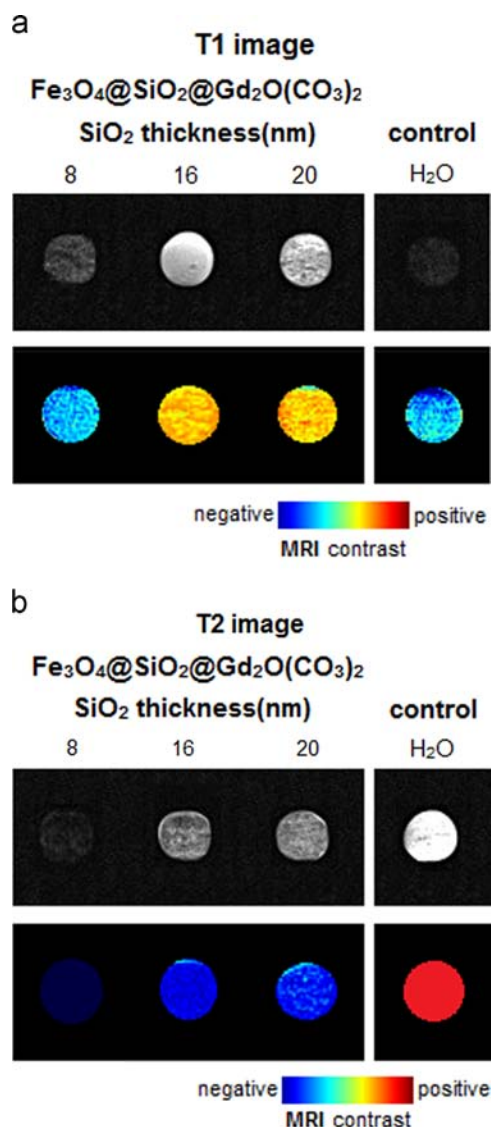


Fig. 4. (a) T1- and (b) T2-weighted MR images and their color coded images of $\text{Fe}_3\text{O}_4/\text{SiO}_2/\text{Gd}_2\text{O}(\text{CO}_3)_2$ with varying SiO_2 thickness by using 3T MRI. Contrast agents: 200 μM (Gd) for T1 image, 100 μM (Fe) for T2 images. The image of H_2O was taken together for the purpose of comparison. In the color coded image, positive and negative contrasts were indicated by the red and blue color, respectively. (For interpretation of the references to color in this figure legend, the reader is referred to the web version of this article.)

Table 1

r_1 and r_2 of $\text{Fe}_3\text{O}_4/\text{SiO}_2/\text{Gd}_2\text{O}(\text{CO}_3)_2$ NPs with different thickness of SiO_2 layer.

SiO_2 thickness	8 nm	16 nm	20 nm
$r_1 ((\text{mmol/L})^{-1} \text{s}^{-1})$	3.7	32.9	32.2
$r_2 ((\text{mmol/L})^{-1} \text{s}^{-1})$	312.0	269.4	208.0

(shown in Table 1). It is known that the local magnetic field generated by the Fe_3O_4 core prompts the transverse T2 relaxation rate of water nuclear spins in the vicinity [25]. However, this magnetic field is distance-dependent with $1/d^3$ (d is the distance from the T2 agent) [23]. So the increase of the thickness of SiO_2 layer reduces this magnetic field to the surrounding water molecules, resulting in reduced T2 contrast effects. Even so, the r_2 value of 208 $(\text{mmol/L})^{-1} \text{s}^{-1}$ in the case of 20 nm of SiO_2 layer is still higher than that of commercial MR imaging contrast agents (Ferumoxide: 190.5 $(\text{mmol/L})^{-1} \text{s}^{-1}$) [26]. The enhanced r_2 value

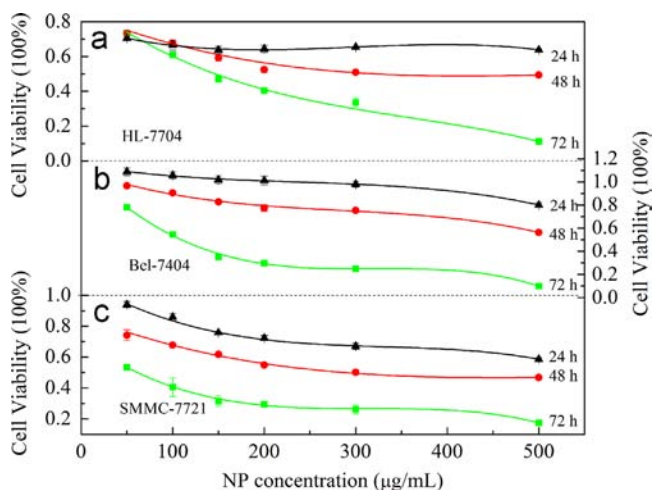


Fig. 5. Biocompatibility of $\text{Fe}_3\text{O}_4/\text{SiO}_2/\text{Gd}_2\text{O}(\text{CO}_3)_2$ NPs on (a) HL-7702, (b) Bel-7404 and (c) SMMC-7721 cell lines by MTT viability assay relative to untreated controls.

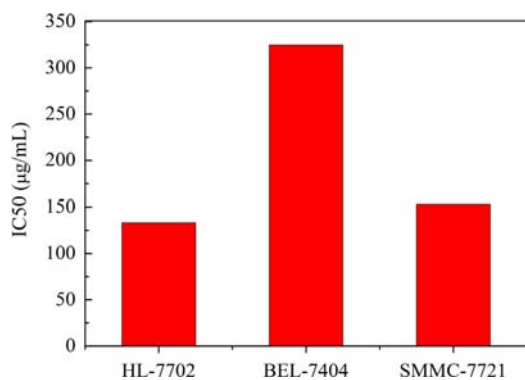


Fig. 6. Comparison of the IC_{50} values of $\text{Fe}_3\text{O}_4/\text{SiO}_2/\text{Gd}_2\text{O}(\text{CO}_3)_2$ NPs on HL-7702, Bel-7404 and SMMC-7721 cell lines after the incubation of 48 h.

is possibly due to the magnetic coupling between Gd^{3+} and Fe_3O_4 . The similar phenomenon has also been found in Gd^{3+} -chelated $\text{Fe}_3\text{O}_4@/\text{SiO}_2$ magnetic nanoparticle [14].

Due to the aim of biomedical application, it is necessary to evaluate the biocompatibility of $\text{Fe}_3\text{O}_4/\text{SiO}_2/\text{Gd}_2\text{O}(\text{CO}_3)_2$ NPs. The 3-(4,5-dimethyl-2-thiazolyl)-2,5-diphenyl-2H-tetrazolium bromide (MTT) viability assay was employed to measure the cytotoxicity of the NPs on hepatic cell line (HL-7702) and hepatocarcinoma cell lines (Bel-7404 and SMMC-7721). Fig. 5 shows the viability of each cell line exposed to $\text{Fe}_3\text{O}_4/\text{SiO}_2/\text{Gd}_2\text{O}(\text{CO}_3)_2$ NPs in a range of concentration from $50 \mu\text{g mL}^{-1}$ to $500 \mu\text{g mL}^{-1}$ for 24 h, 48 h and 72 h, respectively. As to the viability at 24 h, only 5% of cell viability loss has been seen for HL-7702 and Bel-7404 up to a concentration of $300 \mu\text{g mL}^{-1}$ (Fig. 5a and b). Though exposed up to $500 \mu\text{g mL}^{-1}$ $\text{Fe}_3\text{O}_4/\text{SiO}_2/\text{Gd}_2\text{O}(\text{CO}_3)_2$ NPs for 24 h, the cytotoxicity was under 30% on all three cells. There is no obvious dose-effect relationship on HL-7702 and Bel-7404 cells observed. After 48 h incubation, the cytotoxicity on HL-7702 and SMMC-7721 cells was still under 50% when the NPs concentration was under $100 \mu\text{g mL}^{-1}$. The cytotoxicity of the $\text{Fe}_3\text{O}_4/\text{SiO}_2/\text{Gd}_2\text{O}(\text{CO}_3)_2$ NPs was obviously higher after 72 h incubation on all three cell lines. Interestingly, at the concentration of 50 and $100 \mu\text{g mL}^{-1}$, the cytotoxicity on HL-7702 is almost the same at three designed time points. From these results, we could conclude that the cytotoxicity of $\text{Fe}_3\text{O}_4/\text{SiO}_2/\text{Gd}_2\text{O}(\text{CO}_3)_2$ NPs is nearly the same between hepatic and

hepatocarcinoma cells after 24 h incubation. Fig. 6 give the half maximal inhibitory concentrations (IC_{50}) of $\text{Fe}_3\text{O}_4/\text{SiO}_2/\text{Gd}_2\text{O}(\text{CO}_3)_2$ NPs to these three cell lines. It is obvious that $\text{Fe}_3\text{O}_4/\text{SiO}_2/\text{Gd}_2\text{O}(\text{CO}_3)_2$ NPs show the highest biocompatibility to Bel-7404 cell lines.

4. Conclusions

We have successfully synthesized a new type of magnetic NPs with a core/shell/shell structure. The SiO_2 layer was used as a separating layer to modulate the magnetic coupling between T1 contrast material ($\text{Gd}_2\text{O}(\text{CO}_3)_2$) and T2 contrast material (Fe_3O_4). T1- and T2-weighted MR images illustrate that the prepared $\text{Fe}_3\text{O}_4/\text{SiO}_2/\text{Gd}_2\text{O}(\text{CO}_3)_2$ NPs could be used as T1 and T2 dual model contrast agent. The r_2 value of $\text{Fe}_3\text{O}_4/\text{SiO}_2/\text{Gd}_2\text{O}(\text{CO}_3)_2$ NPs with 20 nm of SiO_2 layer is $208 (\text{mmol/L})^{-1} \text{ s}^{-1}$. The enhanced r_2 value is possibly due to the magnetic coupling between Gd^{3+} and Fe_3O_4 . The cytotoxicity studies show that the prepared NPs exhibit good biocompatibility to the tested cell lines.

Acknowledgements

We appreciate the financial support of Innovation Program of Shanghai Municipal Education Commission (12ZZ041), NSFC (61177011), Shanghai Municipal Commission for Science and Technology (11JC1403800), PCSIRT and NCET.

References

- [1] E. Van Reeth, I.W.K. Tham, C.H. Tan, C.L. Poh, *Concepts Magn. Reson. Part A* 40 (2012) 306–325.
- [2] H.B. Na, I.C. Song, T. Hyeon, *Adv. Mater.* 21 (2009) 2133–2148.
- [3] R.B. Lauffer, *Chem. Rev.* 87 (1987) 901–927.
- [4] A.S. Arbab, W. Liu, J.A. Frank, *Expert Rev. Med. Devices* 3 (2006) 427–439.
- [5] Y.w. Jun, J.H. Lee, J. Cheon, *Angew. Chem. Int. Ed.* 47 (2008) 5122–5135.
- [6] Y.-X.J. Wang, *Quant. Imaging Med. Surg.* 1 (2011) 35–40.
- [7] C. Ruemenapp, B. Gleich, A. Haase, *Pharm. Res.* 29 (2012) 1165–1179.
- [8] Y.-w. Jun, Y.-M. Huh, J.-s. Choi, J.-H. Lee, H.-T. Song, KimKim, S. Yoon, K.-S. Kim, J.-S. Shin, J.-S. Suh, J. Cheon, *J. Am. Chem. Soc.* 127 (2005) 5732–5733.
- [9] J.W.M. Bulte, T. Douglas, B. Witwer, S.-C. Zhang, E. Strable, B.K. Lewis, H. Zywickie, B. Miller, P. van Gelderen, B.M. Moskowitz, I.D. Duncan, J. A. Frank, *Nat. Biotechnol.* 19 (2001) 1141–1147.
- [10] H.W. Kang, L. Josephson, A. Petrovsky, R. Weissleder, A. Bogdanov, *Bioconjug. Chem.* 13 (2001) 122–127.
- [11] J.W.M. Bulte, D.L. Kraitchman, *NMR Biomed.* 17 (2004) 484–499.
- [12] J.-H. Lee, Y.-M. Huh, Y.-w. Jun, J.-w. Seo, J.-t. Jang, H.-T. Song, S. Kim, E.-J. Cho, H.-G. Yoon, J.-S. Suh, J. Cheon, *Nat. Med.* 13 (2007) 95–99.
- [13] J.-t. Jang, H. Nah, J.-H. Lee, S.H. Moon, M.G. Kim, J. Cheon, *Angew. Chem. Int. Ed.* 121 (2009) 1260–1264.
- [14] C.-C. Huang, C.-Y. Tsai, H.-S. Sheu, K.-Y. Chuang, C.-H. Su, U.-S. Jeng, F.-Y. Cheng, C.-H. Su, H.-Y. Lei, C.-S. Yeh, *ACS Nano* 5 (2011) 3905–3916.
- [15] J. Zhuo, R.P. Gullapalli, *Radiographics* 26 (2006) 275–297.
- [16] Y.B. Kim, K.H. Bae, S.-S. Yoo, T.G. Park, H. Park, *Magn. Reson. Imaging* 27 (2009) 601–610.
- [17] J.-s. Choi, J.-H. Lee, T.-H. Shin, H.-T. Song, E.Y. Kim, J. Cheon, *J. Am. Chem. Soc.* 132 (2010) 11015–11017.
- [18] K.H. Bae, Y.B. Kim, Y. Lee, J. Hwang, H. Park, T.G. Park, *Bioconjug. Chem.* 21 (2010) 505–512.
- [19] W.S. Seo, J.H. Lee, X. Sun, Y. Suzuki, D. Mann, Z. Liu, M. Terashima, P.C. Yang, M.V. McConnell, D.G. Nishimura, H. Dai, *Nat. Mater.* 5 (2006) 971–976.
- [20] J. Park, K. An, Y. Hwang, J.-G. Park, H.-J. Noh, J.-Y. Kim, J.-H. Park, N.-M. Hwang, T. Hyeon, *Nat. Mater.* 3 (2004) 891–895.
- [21] D.K. Yi, S.S. Lee, G.C. Papaefthymiou, J.Y. Ying, *Chem. Mater.* 18 (2006) 614–619.
- [22] G. Liu, G. Hong, D. Sun, *J. Colloid Interface Sci.* 278 (2004) 133–138.
- [23] J.C. Rife, M.M. Miller, P.E. Sheehan, C.R. Tamana, M. Tondra, L.J. Whitman, *Sens. Actuators, A* 107 (2003) 209–218.
- [24] W. Jiang, Y. Wu, B. He, X. Zeng, K. Lai, Z. Gu, *J. Colloid Interface Sci.* 347 (2010) 1–7.
- [25] S.H. Koenig, K.E. Kellar, *Magn. Reson. Med.* 34 (1995) 227–233.
- [26] E.-K. Lim, J. Yang, J.-S. Suh, Y.-M. Huh, S. Haam, *J. Mater. Chem.* 19 (2009) 8958–8963.



A profluorescent ratiometric probe for intracellular pH imaging



Qingqing Zhang^{a,b,d}, Ming Zhou^{a,c,*}

^a Division of Nanobiomedicine, Suzhou Institute of Nano-Tech and Nano-Bionics, Chinese Academy of Sciences, 398 Ruoshui Road, Suzhou Industrial Park, Suzhou, Jiangsu 215123, PR China

^b University of Chinese Academy of Sciences, 19A Yuquan Road, Beijing 100049, PR China

^c SunaTech Inc., bioBAY, Suzhou Industrial Park, Suzhou, Jiangsu 215125, PR China

^d Institute of Chemistry, Chinese Academy of Sciences, 2 Zhongguancun North First Street, Beijing 100190, PR China

ARTICLE INFO

Article history:

Received 10 May 2014

Received in revised form

11 August 2014

Accepted 15 August 2014

Available online 23 August 2014

Keywords:

Intracellular pH

Iridium(III) complex

Near-infrared

Ratiometric

Fluorescein

Profluorescent

ABSTRACT

A ratiometric pH probe composed of a fluorescein moiety and an ionic near-infrared-emitting phosphorescent cyclometalated iridium(III) complex bis(6-(benzo[b]thien-2-yl)phenanthridinato)(4-(3-carboxypropyl)-4'-methyl-2,2'-bipyridine)iridium(III) was synthesized. With good cell permeability, the probe demonstrated a linear ratiometric response to the pH variation in the physiological range in HeLa cell assay.

© 2014 Elsevier B.V. All rights reserved.

1. Introduction

Intracellular pH (pHi) has strong impact on cellular proliferation, endocytosis, modulation, and apoptosis [1–3]. Abnormality of pHi is associated with several diseases such as carcinoma. Hypoxia surrounding rapidly proliferating and metabolic cancer cells accompanies pH change inside and outside cancer cells [4–8]. On the other hand, different compartments and organelles in normal cell varied in pH values [9], for instance, endosomes [10] and lysosomes [11] have an acidic intracompartamental pH value 4–6. Thus the precise measurement of intracellular pH and its spatial-temporal distribution is of great importance to advance our knowledge of cell behavior and function as well as to understand disease mechanism and to develop diagnostic methods. Efforts in designing and developing new pHi probes [12–15] and sensors [16–18] have been made to achieve this goal.

With subtle molecular designs, ratiometric fluorescent probing [19–22] is promising because its signal detection modality avoids unfavorable influence of concentration variation and fluorescence fluctuation in different targets and time range. The ratiometric fluorescent probing is thus receiving increasing attention in acquiring quantitative information of intracellular pH.

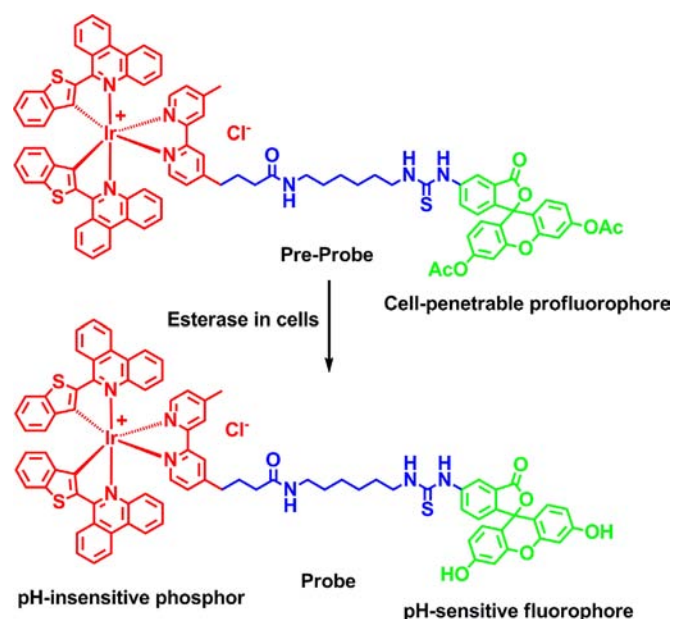
* Corresponding author at: Division of Nanobiomedicine, Suzhou Institute of Nano-Tech and Nano-Bionics, Chinese Academy of Sciences, 398 Ruoshui Road, Suzhou Industrial Park, Suzhou, Jiangsu 215123, PR China. Tel.: +86 512 62872558; fax: +86 512 62872181.

E-mail address: mzhou2007@sinano.ac.cn (M. Zhou).

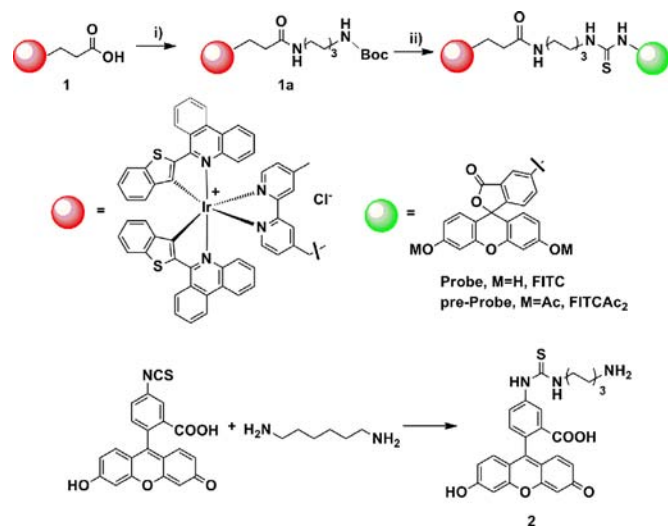
Fluorescein derivatives [23] are the most common in vitro and in vivo pH indicators. Their fluorescent intensity changes with the pH value of surrounding environment due to the pH-dependent dissociation equilibria wherein only monoanion and dianion emit fluorescence [24,25]. Fluorescein derivatives have been conjugated with other partnering luminescent substances (small molecules, nanoparticles and fluorescent proteins) to form ratiometric probes with dual emissions. These luminescent substances as fluorescein's partners have been extensively discussed in a recent review [20]. An unaddressed group of luminescent molecules is metal complexes, e.g., phosphorescent cyclometalated iridium(III) complexes, which, however, were thoroughly reviewed as promising bioimaging reagents in a more recent review paper [26]. Meanwhile, the anticancer activity of iridium(III) complexes [27–29] attracts increasing attention as their potential of inducing apoptosis [30,31] and antiangiogenesis [32]. The general chemical stability and wide tunability of photophysical properties of iridium(III) complexes offers possibility of designing ratiometric probes with unlimited combinations of luminophores meeting the requirements [14,20] for the pH probes. When choosing fluorescein as the pH-sensitive moiety, which emits light at 520–530 nm, an ideal pH-insensitive phosphorescent moiety as fluorescein's partners would be the one that, under the same excitation wavelength, emits phosphorescence with wavelength well separated from that of fluorescein.

The NIR emissive iridium(III) complexes (BTPH and its acid form BTPHSA) reported by Zhang et al. [33] were chosen by us to be our first demonstration of such fluorescein/iridium(III) complex

couple. The phosphorescent moiety demonstrated in Scheme 1 is a variation of BTPHSA with a 2,2'-bipyridine derivative, instead of acetylacetonato, as the ancillary ligand. It was synthesized as an acid form (**1** in Scheme 2) capable of coupling to the fluorescein moiety to yield the dual-emitting probe under a single wavelength excitation. Complex **1** possesses a larger Stokes' shift and thus is able to discriminate itself from fluorescein moiety in emission spectroscopy. The good separation of the emission wavelengths from these two luminophores also prevents the interference of each other in the confocal microscopy. It is well known that fluorescein refuses to enter the cell because of its negative charge under the physiological conditions [34]. Although the positive charge of iridium(III) moiety favors the cell penetration [26], it was found that the **Probe** was unable to penetrate into cells. As usual,



Scheme 1. Molecular design of the ratiometric pH probe based on a pH-sensitive fluorescein moiety and a pH-insensitive phosphorescent iridium(III) complex.



Scheme 2. The structures and syntheses of **1**, **Probe** and **pre-Probe**. (i) HDABoc, DCC/HOBt/DMF, 24 h; (ii) 20% TFA/CH₂Cl₂, 1 h; **Probe**, M=H, FITC, 1% TEA/CH₂Cl₂; **pre-Probe**, M=Ac, FITCAc₂, 1% TEA/CH₂Cl₂. Red and green balls indicate near-infrared phosphorescent iridium(III) complex and green-emitting fluorescein emitter, respectively. (For interpretation of the references to color in this scheme legend, the reader is referred to the web version of this article.)

we synthesized a **pre-Probe** with the iridium(III) moiety coupled to the fluorescein diacetate moiety, which is non-fluorescent, but turns into fluorescent fluorescein through esterase hydrolysis in the cell [35].

2. Materials and methods

2.1. Chemicals and instruments

Bis(6-(benzo[b]thien-2-yl)phenanthridinato)(4-(3-carboxypropyl)-4'-methyl-2,2'-bipyridine)iridium(III) chloride (**1**) was synthesized in our lab. FITC isomer I, di-tert-butyl dicarbonate (Boc₂O) and 1,6-hexylenediamine were purchased from Aladdin, N,N'-dicyclohexyl carbodiimide (DCC) from Sigma-Aldrich, and hydroxybenzotriazole (HOBt) from GL Biochem. Nigericin and 3-(4,5-dimethylthiazol-2-yl)-2,5-diphenyltetrazolium bromide (MTT) were purchased from Sigma-Aldrich. Other chemicals and solvents were commercially available in analytical grade and used without further purification except otherwise specified.

GC-MS was determined on the Agilent 7890A GC system equipped with 5975C inert triple-axel MS detector. ESI-TOF-MS was measured on the Agilent 1200/6200 TOF-MS system. ¹H and ¹³C NMR spectra were acquired from Varian 400 MHz NMR spectrometer. UV-visible absorption and excitation/emission spectra were measured on a Lambda 25 UV/Vis spectrometer (PerkinElmer) and F4600 fluorescence spectrophotometer (Hitachi), respectively. Deionized water (18 MΩ cm, Milli-Q prepared) and UPLC grade organic solvents were used for spectroscopic measurements. The pH values were determined with a PB-10 pH meter (Sartorius), calibrated with a triple-point method before use.

2.2. Cell culture

HeLa cells (American Type Culture Collection) were cultured in Dulbecco's modified Eagle medium (DMEM, Sigma-Aldrich) supplemented with 10% fetal bovine serum (FBS, Sigma-Aldrich) and 1% penicillin-streptomycin (Sigma-Aldrich) and grew to exponential phase prior to use. HeLa cells were grown at 37 °C under 5% CO₂ atmosphere.

2.3. Synthesis and characterization

2.3.1. Bis(6-(benzo[b]thien-2-yl)phenanthridinato)(4-(3-carboxypropyl)-4'-methyl-2,2'-bipyridine)iridium(III) chloride (**1**)

ESI-TOF-MS: m/z ([M-Cl]⁺) calcd 1069.2222, found 1069.2227. ¹H NMR (400 MHz, CDCl₃) δ 9.37 (t, *J*=8.6 Hz, 2H), 8.56 (s, 2H), 8.35–8.22 (m, 5H), 8.18 (s, 1H), 7.94 (s, 4H), 7.84–7.78 (m, 2H), 7.30–7.04 (m, 8H), 6.80–6.56 (m, 6H), 2.62 (s, 2H), 2.34 (s, 3H), 2.23 (d, *J*=6.0 Hz, 2H), 1.75 (s, 2H). ¹³C NMR (101 MHz, CDCl₃) δ 175.18, 167.88, 167.80, 159.45, 159.24, 156.29, 155.11, 155.01, 152.78, 145.61, 145.58, 143.72, 143.59, 143.54, 138.55, 138.42, 133.71, 133.56, 133.32, 128.86, 128.70, 128.41, 128.10, 127.92, 127.86, 127.77, 127.29, 127.00, 126.89, 126.74, 125.48, 125.40, 124.77, 124.73, 124.04, 124.02, 122.85, 122.79, 122.76, 122.70, 122.66, 122.55, 122.05, 122.00, 34.14, 34.00, 25.54, 21.11.

2.3.2. tert-Butyl 6-aminohexylcarbamate (HDABoc)

HDABoc was synthesized according to Dardonville et al. [36]. To CH₂Cl₂ solution of 1,6-hexylenediamine (20.06 g, 172.6 mmol) was added dropwise di-tert-butyl dicarbonate (7.6 g, 34.8 mmol) dissolved in CH₂Cl₂. After 20 h of stirring at room temperature, the mixture was filtered. The filtrate was concentrated and re-dissolved in ethyl acetate, washed with water. Removal of solvent yielded a milky liquid (5.36 g, 71.2%). GC-MS: m/z ([M-But]⁺)

calcd 159.11, found 159.1. ^1H NMR (400 MHz, CDCl_3): δ 4.66 (s, 1H), 3.10 (d, $J=6.3$ Hz, 2H), 2.68 (t, $J=6.9$ Hz, 2H), 1.44 (s, 9H), 1.52–1.22 (m, 10H).

2.3.3. Complex **1a**

A mixture of complex **1** (360.0 mg, 325.9 μmol), DCC (289.1 mg, 1.40 mmol) and HOBt (53.2 mg, 393.7 μmol) dissolved in dichloromethane was stirred in ice–water bath for 1 h, then added dropwise compound HDABoc (91.0 mg, 420.7 μmol) and reacted overnight. After removal of solvent, the residue was separated with silica gel chromatography using $\text{CH}_2\text{Cl}_2/\text{C}_2\text{H}_5\text{OH}$ (20:1, v/v) as eluent to afford a dark red powder (342.0 mg, 80.5%). ESI-TOF-MS: m/z ($[\text{M}-\text{Cl}]^+$) calcd 1267.3954, found 1267.3967. ^1H NMR (400 MHz, CDCl_3): δ 9.40 (d, $J=7.6$ Hz, 2H), 8.65–8.58 (m, 2H), 8.46 (s, 1H), 8.29 (dt, $J=9.6$, 4.9 Hz, 5H), 7.98 (td, $J=6.4$, 4.2 Hz, 4H), 7.88 (d, $J=8.1$ Hz, 2H), 7.75 (d, $J=8.3$ Hz, 1H), 7.68 (d, $J=8.3$ Hz, 1H), 7.35–7.25 (m, 2H), 7.25–7.11 (m, 3H), 7.04 (d, $J=5.8$ Hz, 1H), 6.79–6.61 (m, 6H), 3.00 (s, 4H), 2.64 (s, 2H), 2.37 (s, 3H), 2.22 (s, 2H), 1.78 (d, $J=39.9$ Hz, 2H), 1.52–1.27 (m, 17H).

2.3.4. Probe

Complex **1a** (164.8 mg, 126.5 μmol) was deprotected with TFA/ CH_2Cl_2 (20 vol%) for 2 h, then washed with water. After removal of solvent, to the crude immediate was added a TEA/ CH_3OH (1 vol%) solution of FITC isomer I (63.5 mg, 146.8 μmol) and stirred at ambient condition overnight. The resultant precipitate was collected by filtration, then purified by successive washing with water, methanol and dichloromethane. The final product was red powder (66.0 mg, 32.8%). ^1H NMR (400 MHz, $\text{CD}_3\text{OD}/\text{CDCl}_3$): δ 9.44–9.35 (m, 2H), 8.61 (s, 2H), 8.41 (dd, $J=13.8$, 5.8 Hz, 2H), 8.32 (d, $J=8.5$ Hz, 2H), 8.02–7.96 (m, 5H), 7.90–7.84 (m, 2H), 7.79 (d, $J=5.0$ Hz, 2H), 7.72 (s, 1H), 7.31–7.10 (m, 8H), 7.07 (d, $J=8.2$ Hz, 1H), 6.87 (d, $J=8.7$ Hz, 1H), 6.74–6.46 (m, 11H), 3.58 (s, 2H), 3.09 (t, $J=6.8$ Hz, 4H), 2.60–2.48 (m, 2H), 2.28 (s, 3H), 2.07 (t, $J=7.3$ Hz, 2H), 1.64 (d, $J=27.3$ Hz, 4H), 1.52–1.15 (m, 6H). ^{13}C NMR (101 MHz, DMSO- d_6) δ 171.43, 168.03, 159.64, 159.56, 156.50, 154.76, 154.52, 152.73, 147.27, 145.69, 143.60, 138.90, 134.41, 133.54, 129.84, 129.44, 129.15, 128.89, 128.51, 127.97, 127.35, 126.49, 125.53, 125.32, 123.87, 123.75, 123.04, 122.70, 102.68, 55.35, 42.19, 41.96, 41.78, 41.57, 34.71, 34.03, 29.45, 26.38, 25.96, 20.89.

2.3.5. Pre-Probe

The **pre-Probe** was synthesized in a similar way to the **Probe**, except FITC Ac_2 replaced FITC. FITC Ac_2 was prepared by direct acetylation of FITC (39.5 mg, 101.4 μmol) with fresh acetic anhydride (50 μL , 490.8 μmol). After acetylation for 30 min in ambient temperature, extra acetic anhydride was removed in vacuo, and the acquired FITC Ac_2 was used in reaction with deprotected **1a** (132.2 mg, 110.0 mg) without further purification. After purification by simple washing with methanol, the product (96.7 mg, 57.1%) was acquired as dark red powder. ^1H NMR (400 MHz, DMSO- d_6) δ 9.38 (dd, $J=5.8$, 3.1 Hz, 2H), 8.90 (t, $J=7.8$ Hz, 2H), 8.63–8.55 (m, 3H), 8.47 (dd, $J=12.4$, 6.4 Hz, 2H), 8.20–8.09 (m, 7H), 8.06 (d, $J=8.0$ Hz, 2H), 7.76 (s, 1H), 7.46 (d, $J=5.9$ Hz, 3H), 7.37 (dd, $J=15.6$, 7.7 Hz, 3H), 7.30–7.15 (m, 5H), 6.93–6.83 (m, 3H), 6.78–6.69 (m, 3H), 6.69–6.61 (m, 3H), 2.95 (d, $J=5.5$ Hz, 2H), 2.62–2.48 (m, 2H), 2.28 (s, 6H), 1.92 (m, 5H), 1.71–1.49 (m, 4H), 1.40–1.16 (m, 8H). ^{13}C NMR (101 MHz, DMSO- d_6) δ 171.41, 169.40, 169.29, 169.11, 168.05, 167.36, 159.89, 159.65, 159.58, 156.49, 154.77, 154.51, 152.73, 152.31, 147.42, 147.31, 147.02, 145.71, 143.62, 141.31, 138.91, 134.42, 133.54, 132.13, 132.01, 129.90, 129.50, 129.12, 128.88, 128.53, 127.98, 127.33, 126.58, 125.56, 125.42, 125.35, 124.81, 123.88, 123.80, 123.06, 122.71, 113.65, 112.99, 110.14, 110.02, 109.86, 102.62, 83.46, 71.58, 55.36, 38.82, 34.71, 31.72, 29.53, 29.14, 27.65, 26.54, 25.96, 24.51, 23.04, 22.53, 19.32.

2.3.6. Fluorescein thiocarbonyl hexamethylenediamine (**2**)

Compound **2** as a reference in vitro was synthesized according to Caulum et al. [37]. FITC isomer I (69.2 mg, 178.2 μmol) and 1,6-hexylenediamine (164.7 mg, 1.42 mmol) was reacted in 16 ml TEA/ CH_3OH (1 vol%) overnight under the protection from light at room temperature. After removal of solvents, the residue was separated on a silica gel chromatographic column with eluent ethyl acetate/methanol (3:1,v/v) to give an orange microcrystal (71.2 mg, 79.0%). ESI-TOF-MS: m/z (M^+) calcd 506.1744, found 506.1768. ^1H NMR (400 MHz, D_2O): δ 7.69 (d, $J=2.1$ Hz, 1H), 7.49 (s, 1H), 7.15 (dd, $J=28.9$, 8.5 Hz, 3H), 6.64 (dd, $J=9.2$, 2.2 Hz, 2H), 6.60 (d, $J=2.2$ Hz, 2H), 3.56 (s, 2H), 2.96 (dd, $J=14.7$, 7.2 Hz, 2H), 1.64 (d, $J=7.4$ Hz, 4H), 1.39 (dt, $J=13.3$, 7.1 Hz, 4H).

2.4. UV/visible and photoluminescence spectroscopy

UV/visible absorption, excitation and emission spectroscopy of **1**, **2**, the equimolar mixture of **1** and **2** (**1+2**) and **Probe** were collected in DMSO under ambient conditions. Quantum yields of **1**, **2**, and **Probe** in deaerated and air-saturated DMSO were calculated using the following equation with Ru(bpy) $_3\text{Cl}_2$ in N_2 -saturated CH_3CN ($\Phi=0.062$ [38]) as a reference

$$\Phi_{\text{sam}} = \Phi_{\text{ref}} \times \frac{I_{\text{sam}}}{I_{\text{ref}}} \times \frac{A_{\text{ref}}}{A_{\text{sam}}} \times \frac{n_{\text{sam}}^2}{n_{\text{ref}}^2}$$

where, Φ , I , A , and n are quantum yield, integral emission intensity, absorbance and refractive index of the solvents in which the sample or reference dissolved, respectively. The pH dependence of the emission spectra of **Probe** and the equimolar mixture of **1** and **2** was measured in a series of pH-variable $\text{NaH}_2\text{PO}_4/\text{Na}_2\text{HPO}_4$ buffer solution (0.01 M). In each measurement, 1 mM of DMSO solution of **Probe** or **1+2** was dispersed in 100-fold volume of 0.01 M phosphate buffer solution. The error originated from three independent measurements and calculation.

Luminescence ratio reversibility of the **Probe** (1 vol% DMSO/ H_2O) was determined in 0.01 M NaCl solution, the pH value (pH 5 and 9) was adjusted with 1 M NaOH or HCl solution and measured with a PB-10 pH meter.

2.5. Cytotoxicity

Cytotoxicity of complex **pre-Probe** was evaluated by MTT assay with HeLa cells. HeLa cells (ca. 1×10^4 cells/well) was seeded on a 96-well plate (Corning) and incubated for 24 h before treatment. The culture medium was then substituted with fresh medium containing **pre-Probe** (100–3.13 μM). After incubation for 24 h, 20 μl of aqueous MTT solution (5 mg/ml) was added to each well, and the cells were incubated continuously for another 4 h. After removal of MTT and medium, 150 μl of DMSO was added to each well and incubated at 37 $^\circ\text{C}$ for 10 min. The absorbance of samples at 490 nm were measured using a Victor X4 microplate reader (Perkin-Elmer). The assay was performed three times independently and IC_{50} values were calculated in SPSS 18 and presented as mean \pm standard deviation.

2.6. Cell staining

HeLa cells were seeded in 35 mm cell culture dish (Corning) at the densities of $5-8 \times 10^4$ cells/dish. After incubation for 24 h, cells were stained with **pre-Probe** (20 μM) for 30 min. After removal of culture medium and washing with fresh medium three times, the cells were cultured for another 15 min in a series of high K^+ buffer solutions with different pH values (30 mM NaCl, 120 mM KCl, 1 mM CaCl_2 , 0.5 mM MgSO_4 , 1 mM NaH_2PO_4 , 5 mM glucose, 10 mM HEPES, 10 mM PIPES) containing 10 μM nigericin [39].

3. Results and discussion

3.1. Syntheses and spectroscopy of the *pre-Probe* and *Probe*

The *pre-Probe* and *Probe* were both synthesized from the carboxy form of iridium(III) complex and the amino-reactive fluorescein isothiocyanate (FITC) through 1, 6-hexylenediamine linker (Scheme 2). The structures of both products were confirmed by ^1H and ^{13}C NMR. It was interesting that, while complex **1** and fluorescein moiety were readily soluble in dichloromethane and

methanol, respectively, both the *Probe* and *pre-Probe* were insoluble in both solvents and water. However, they are very soluble in DMSO.

Absorption and emission spectra of iridium(III) complex **1**, inactive fluorescein derivative fluorescein thiocarbonyl hexamethylenediamine **2**, the 1:1 mixture of **1** and **2** as well as the *Probe* in DMSO were shown in Fig. 1 a. As expected, the *Probe* has absorption and emission spectra similar to those of the **1**+**2** mixture and both are the overlay of **1** and **2**, within the experimental error (Table 1).

3.2. pH titration and O_2 -sensitivity of the *Probe* in phosphate buffer solution

Before performing the cell imaging, the *Probe* was subjected to the pH-responsive titration. The emission spectra (Fig. 1 b) of the *Probe* were measured in 0.01 M $\text{NaH}_2\text{PO}_4/\text{Na}_2\text{HPO}_4$ buffer solution under an excitation at 495 nm. As expected, the emission intensity of fluorescein moiety decreased sharply with elevated acidity while the near-infrared emission from iridium(III) moiety remains relatively stable with the change of pH. The emission bands from fluorescein moiety (500–650 nm) and iridium(III) complex (650–800 nm) are well separated from each other, favoring the observation in different confocal microscopic channels under a single-wavelength excitation. For ratiometric measurement, fluorescence intensities at maximum emission wavelengths of each moiety, i.e., 520 nm for fluorescein (I_{520}) and 710 nm for iridium(III) complex (I_{710}), were chosen to compare. The result revealed a logistic relationship between emission intensity ratio I_{520}/I_{710} and pH value in the range between 4.0 and 9.0, wherein a linear correlation ($R^2=0.9948$) exists in the pH 5.25–7.75 range, in which falls the physiological pH value appropriately [40]. In comparison, pH response of **1**+**2** mixture showed poor linearity in that pH range ($R^2=0.9699$). These indicate that the rationally designed ratiometric pH probe is applicable to monitoring physiological pH fluctuation, especially in the range of pH 5.25–7.75.

As phosphorescent iridium(III) complexes are known to be sensitive to molecular oxygen, the influence of O_2 concentration upon the *Probe* was measured in deaerated and air-saturated DMSO. The result (Fig. 2a) indicated that emission intensity of fluorescein moiety was stable while that of iridium(III) complex moiety diminished about 27% in aerated DMSO compared to that in deaerated DMSO. Considering that O_2 concentration change varies very little in most cell culture, the ratio error caused by the O_2 sensitivity of iridium(III) complex moiety is actually negligible. Meanwhile, the *Probe* exhibited a fine reversibility of luminescence ratio between pH 9 and pH 5 in aqueous solution (Fig. 2b).

3.3. Cytotoxicity, cell permeability and intracellular localization of the *pre-Probe*

MTT assay showed that the *pre-Probe* had medium toxicity to HeLa cells, with IC_{50} $48.0 \pm 2.2 \mu\text{M}$. To investigate the permeability and intracellular localization of the *Probe* into the cell, HeLa cells

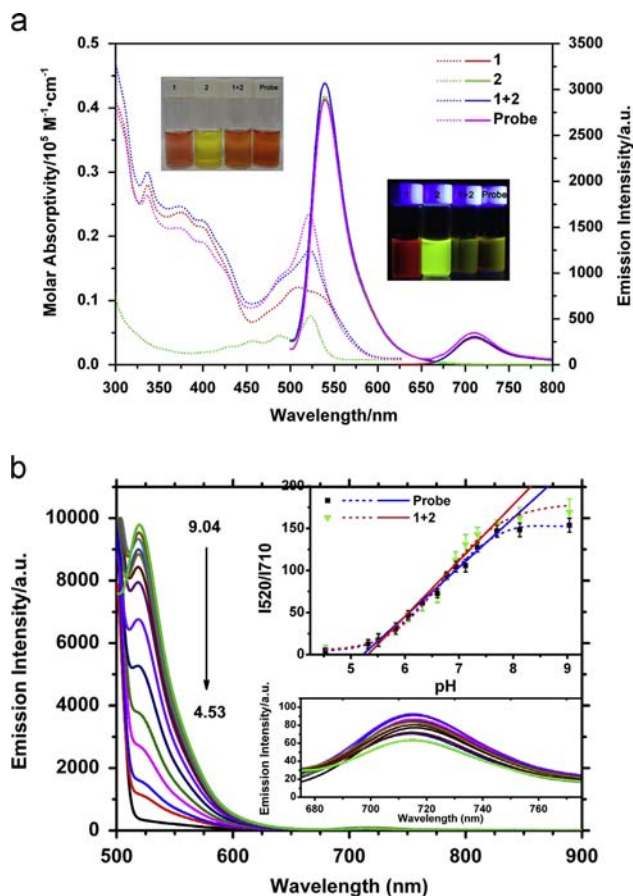


Fig. 1. Spectroscopic properties and ratiometric pH titration of the *Probe*. (a) Absorption (dot) and emission (solid, ex 495 nm) spectra of **1**, **2**, **1**+**2**, and the *Probe* in Ar-saturated DMSO, measured under an ambient condition. The inset photographs of **1**, **2**, **1**+**2**, and the *Probe* in DMSO were taken under natural light (left) and ultra-violet exposure (365 nm, right). (b) Emission spectra of the *Probe* in buffer solutions with different pH show a rapid intensity decrease of fluorescein moiety (left) and a stability of iridium(III) complex moiety (bottom inset) with pH variation from basic to acidic. The top inset gives a relationship of luminescent ratio (I_{520}/I_{710}) vs. pH of the *Probe* and **1**+**2**. The blue solid fitting curve suggests a good linear response ($R^2=0.9948$) of the *Probe* to pH change from pH 5.25–7.75. (For interpretation of the references to color in this figure legend, the reader is referred to the web version of this article.)

Table 1
Photophysical data of compounds in DMSO at room temperature^a.

Compound	$\lambda_{\text{abs}}/\text{nm}$ ($\epsilon/10^3 \text{ M}^{-1} \text{ cm}^{-1}$)	$\lambda_{\text{em}}/\text{nm}$	$\phi_{\text{em}}^{\text{b}}$
1	337 (28.0), 375sh (23.7), 396sh (21.5), 509 (12.0)	710	0.081 ^c , 0.047 ^d
2	433sh (2.8), 469 (3.4), 523 (7.6)	539	0.86 ^d
Probe	236 (26.4), 370sh (21.3), 396sh (21.5), 521(23.4)	539, 710	0.63 ^c , 0.55 ^d

^a Absorption and emission spectra were recorded in air-saturated DMSO.

^b Photoluminescent quantum yield (ϕ_{em}) was determined using $\text{Ru}(\text{bpy})_3^{2+}$ ($\phi_{\text{em}}=0.062$) as a reference.

^c In deaerated DMSO.

^d In air-saturated DMSO.

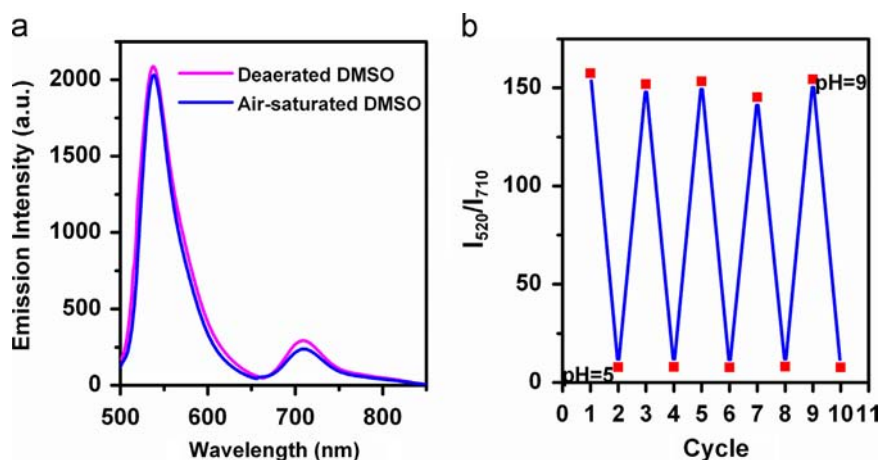


Fig. 2. (a) O_2 -sensitive emission spectra of the **Probe** in deaerated and air-saturated DMSO. (b) Luminescence ratio reversibility of the **Probe** in pH 5 and pH 9 aqueous solution. Ex 495 nm.

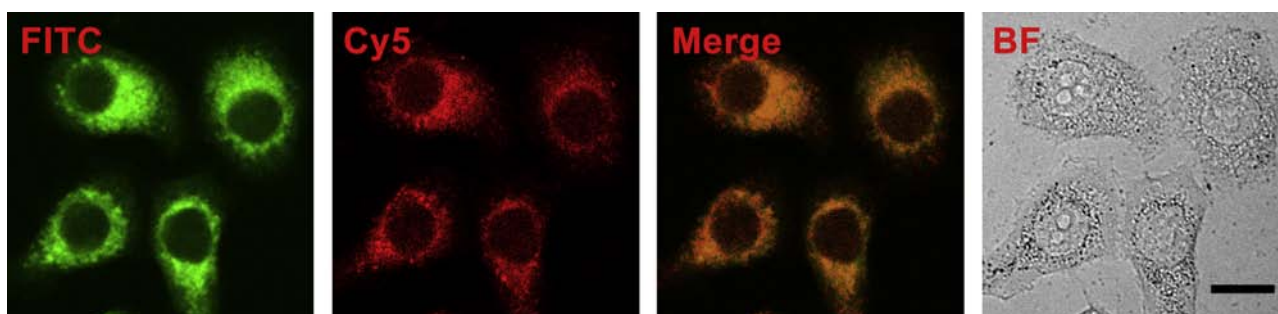


Fig. 3. Confocal microscopy imaging of **pre-Probe**-stained HeLa cells shows permeability and localization of **pre-Probe** into in living cells. Ex 488 nm. Scale bar: 20 μ m.

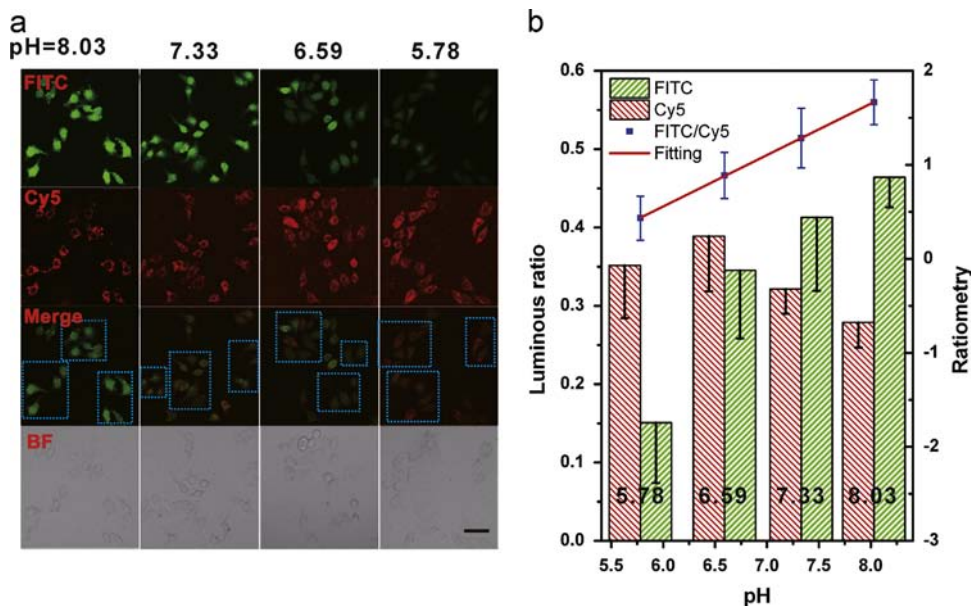


Fig. 4. (a) Confocal imaging of **pre-Probe**-stained HeLa cells in buffer solutions with different pH. HeLa cells was pre-stained with **pre-Probe** (20 μ M) in DMEM/FBS medium for 30 min, then incubated for another 15 min in high K^+ buffer containing 10 μ M nigericin. Ex 488 nm. Scale bar: 50 μ m. Dashed boxes indicate statistical ratiometric area. (b) Luminescent intensity ratiometry of **pre-Probe** in different intracellular pH. Histograms show luminous ratio in statistical area calculated in ImageJ2x software. The data is expressed in mean value minus standard deviation. Luminous ratio is defined as a ratio of luminance-weighted area of luminescent region after background correction versus total area of the chosen region. The fitting curve reveals a fine linear correlation between FITC vs. Cy5 channel luminescent ratiometry and intracellular pH values ($R^2=0.9978$).

were stained with the **pre-Probe** (20 μ M) in DMEM supplemented with 10% FBS (DMEM/FBS) culture medium for 30 min. Confocal microscopy imaging (excitation at 488 nm, Fig. 3) disclosed that the **pre-Probe** was able to enter into and retain in the cells, and

upon nonspecific esterase hydrolysis (to turn into the **Probe**), yielded bright images which can be observed by using the FITC and Cy5 channels of the imaging system. There was no sign indicating that the **Probe** targeted any specific organelle but

dispersed in the cytoplasm, which differed from other ratiometric pH probes [41–43] or nanosensors [44–46]. Moreover, the fact that, the images from FITC and Cy5 channels merged fairly well, implies a good robustness or stability of the **Probe** in the cell.

3.4. Ratiometric pH imaging of the **pre-Probe** in living cells

The ratiometric measurement of the intracellular pH was carried out by using the **pre-Probe**-stained HeLa cells for confocal imaging. The intracellular pH value was equilibrated with that of culture medium using H^+/K^+ ionophore nigericin to [39,47]. HeLa cells were stained with the **pre-Probe** (20 μ M) in DMEM/FBS for 30 min, followed by further 15 min in a high K^+ buffer containing 10 μ M nigericin with different pH values (8.03, 7.33, 6.59, 5.78).

As shown in Fig. 4, fluorescence intensity from FITC channel quenched significantly with decreasing intracellular pH, while the phosphorescence observed in Cy5 channel fluctuated slightly in a random manner due to the difference in imaging sampling (see the marked cell-inclusive squares in Fig. 4). Statistical fluorescence intensity from three stochastically chosen cell-inclusive regions using ImageJ2x software showed a linear correlation between the intensity ratio of fluorescence (FITC channel) to phosphorescence (Cy5 channel) and intracellular pH, indicating that the ratiometry based on the **Probe** is highly successful for quantitatively monitoring the intracellular pH change or localizing hydrogen ion distribution of the cells in the physiological range.

4. Conclusions

In summary, a ratiometric luminescent probe consisting intramolecularly a pH-responsive fluorescein moiety and a pH-insensitive near-infrared phosphorescent iridium(III) complex was rationally designed and readily synthesized. Its ester form has a good permeability into cells and distributes uniformly in cells. The dual-emission upon a single excitation combines with the cell permeability enable us to develop ratiometric assays in vitro and ex vivo. Practical applications to intracellular pH monitoring based on further improvement on molecular designs can be envisioned.

Acknowledgments

This work was supported by National Natural Science Foundation of China (Grant nos. 21005084 and 21072218) and “Hundred Talents Program” of the Chinese Academy of Sciences. We thank Dr. Yang Liu for his inspiring suggestion, and Ning Li and Rui Cao for their warm help in cell culture, MTT assay and confocal imaging.

References

- [1] M. Chesler, *Physiol. Rev.* 83 (2003) 1183–1221.
- [2] R.A. Gottlieb, J. Nordberg, E. Skowronski, B.M. Babior, *Proc. Natl. Acad. Sci. USA* 93 (1996) 654–658.
- [3] A. Roos, W.F. Boron, *Physiol. Rev.* 61 (1981) 296–434.
- [4] R.A. Gatenby, R.J. Gillies, *Nat. Rev. Cancer* 4 (2004) 891–899.
- [5] R.A. Gatenby, R.J. Gillies, *Nat. Rev. Cancer* 8 (2008) 56–61.
- [6] L.E. Gerweck, K. Seetharaman, *Cancer Res.* 56 (1996) 1194–1198.
- [7] I.F. Tannock, D. Rotin, *Cancer Res.* 49 (1989) 4373–4384.
- [8] P. Vaupel, F. Kallinowski, P. Okunieff, *Cancer Res.* 49 (1989) 6449–6465.
- [9] R.G. Anderson, L. Orci, *J. Cell Biol.* 106 (1988) 539–543.
- [10] R.G. Anderson, J.R. Falck, J.L. Goldstein, M.S. Brown, *Proc. Natl. Acad. Sci. USA* 81 (1984) 4838–4842.
- [11] S. Ohkuma, B. Poole, *Proc. Natl. Acad. Sci. USA* 75 (1978) 3327–3331.
- [12] J. Han, A. Loudet, R. Barhoumi, R.C. Burghardt, K. Burgess, *J. Am. Chem. Soc.* 131 (2009) 1642–1643.
- [13] Z. Li, S. Wu, J. Han, L. Yang, S. Han, *Talanta* 114 (2013) 254–260.
- [14] R. Pal, D. Parker, *Chem. Commun.* (2007) 474–476.
- [15] B. Tang, X. Liu, K. Xu, H. Huang, G. Yang, L. An, *Chem. Commun.* (2007) 3726–3728.
- [16] T. Jin, A. Sasaki, M. Kinjo, J. Miyazaki, *Chem. Commun.* 46 (2010) 2408–2410.
- [17] P.T. Snee, R.C. Somers, G. Nair, J.P. Zimmer, M.G. Bawendi, D.G. Nocera, *J. Am. Chem. Soc.* 128 (2006) 13320–13321.
- [18] X.-D. Wang, J.A. Stolwijk, T. Lang, M. Sperber, R.J. Meier, J. Wegener, O.S. Wolfbeis, *J. Am. Chem. Soc.* 134 (2012) 17011–17014.
- [19] S. Chen, Y. Hong, Y. Liu, J. Liu, C.W.T. Leung, M. Li, R.T.K. Kwok, E. Zhao, J.W.Y. Lam, Y. Yu, B.Z. Tang, *J. Am. Chem. Soc.* 135 (2013) 4926–4929.
- [20] J. Han, K. Burgess, *Chem. Rev.* 110 (2009) 2709–2728.
- [21] S.A. Hilderbrand, K.A. Kelly, M. Niedre, R. Weissleder, *Bioconjugate Chem.* 19 (2008) 1635–1639.
- [22] T. Myochin, K. Kiyose, K. Hanaoka, H. Kojima, T. Terai, T. Nagano, *J. Am. Chem. Soc.* 133 (2011) 3401–3409.
- [23] (a) (For example) BCPCF, T.J. Rink, R.Y. Tsien, T. Pozzan, *J. Cell Biol.* 95 (1982) 189–196;
(b) SNARF[®], SNAFL[®], J.E. Whitaker, R.P. Haugland, F.G. Prendergast, *Anal. Biochem.* 194 (1991) 330–344;
(c) FITC, E. Lanz, M. Gregor, J. Slavik, A. Kotyk, *J. Fluoresc.* 7 (1997) 317–319 (For more information, please search Sigma-Aldrich and Life Technologies websites).
- [24] L.D. Lavis, T.J. Rutkoski, R.T. Raines, *Anal. Chem.* 79 (2007) 6775–6782.
- [25] R. Sjöback, J. Nygren, M. Kubista, *Spectrochim. Acta, Part A* 51 (1995) L7–L21.
- [26] Q. Zhao, C. Huang, F. Li, *Chem. Soc. Rev.* 40 (2011) 2508–2524.
- [27] X. Song, Y. Qian, R. Ben, X. Lu, H.-L. Zhu, H. Chao, J. Zhao, *J. Med. Chem.* 56 (2013) 6531–6535.
- [28] G. Ludwig, S. Mijatović, I. Randelović, M. Bulatović, D. Miljković, D. Maksimović-Ivanić, M. Korb, H. Lang, D. Steinborn, G.N. Kaluderović, *Eur. J. Med. Chem.* 69 (2013) 216–222.
- [29] Q. Yang, J. Chang, J. Song, M.-T. Qian, J.-M. Yu, X. Sun, *Bioorgan. Med. Chem. Lett.* 23 (2013) 4602–4607.
- [30] C.-H. Leung, H.-J. Zhong, D.S.-H. Chan, D.-L. Ma, *Coord. Chem. Rev.* 257 (2013) 1764–1776.
- [31] V. Novohradsky, Z. Liu, M. Vojtiskova, P.J. Sadler, V. Brabec, J. Kasparkova, *Metalomics* 6 (2014) 682–690.
- [32] A. Wilbuer, D.H. Vlecken, D.J. Schmitz, K. Kräling, K. Harms, C.P. Bagowski, E. Meggers, *Angew. Chem. Int. Ed.* 49 (2010) 3839–3842.
- [33] S. Zhang, M. Hosaka, T. Yoshihara, K. Negishi, Y. Iida, S. Tobita, T. Takeuchi, *Cancer Res.* 70 (2010) 4490–4498.
- [34] I. Johnson, M. Spence, *The Molecular Probes[®] Handbook: A Guide to Fluorescent Probes and Labeling Technologies* (2010) (11th ed.).
- [35] M.M. Wu, J. Llopis, S. Adams, J.M. McCaffery, M.S. Kulomaa, T.E. Machen, H.-P. H. Moore, R.Y. Tsien, *Chem. Biol.* 7 (2000) 197–209.
- [36] C. Dardonville, C. Fernandez-Fernandez, S.-L. Gibbons, G.J. Ryan, N. Jagerovic, A.M. Gabilondo, J.J. Meana, L.F. Callado, *Bioorg. Med. Chem.* 14 (2006) 6570–6580.
- [37] M.M. Caulum, B.M. Murphy, L.M. Ramsay, C.S. Henry, *Anal. Chem.* 79 (2007) 5249–5256.
- [38] J.V. Caspar, T.J. Meyer, *J. Am. Chem. Soc.* 105 (1983) 5583–5590.
- [39] M. Tafani, J.A. Cohn, N.O. Karpnich, R.J. Rothman, M.A. Russo, J.L. Farber, *J. Biol. Chem.* 277 (2002) 49569–49576.
- [40] G.J. Tortora, B.H. Derrickson, *Principles of Anatomy and Physiology*, 13th ed., John Wiley & Sons, Inc., Hoboken, NJ, 2012.
- [41] J. Lei, L. Wang, J. Zhang, *Chem. Commun.* 46 (2010) 8445–8447.
- [42] B. Tang, F. Yu, P. Li, L. Tong, X. Duan, T. Xie, X. Wang, *J. Am. Chem. Soc.* 131 (2009) 3016–3023.
- [43] L. Wang, X. Zhu, C. Xie, N. Ding, X. Weng, W. Lu, X. Wei, C. Li, *Chem. Commun.* 48 (2012) 11677–11679.
- [44] R.V. Benjaminsen, H. Sun, J.R. Henriksen, N.M. Christensen, K. Almdal, T. L. Andresen, *ACS Nano* 5 (2011) 5864–5873.
- [45] A. Burns, P. Sengupta, T. Zedayko, B. Baird, U. Wiesner, *Small* 2 (2006) 723–726.
- [46] K.P. McNamara, T. Nguyen, G. Dumitrascu, J. Ji, N. Rosenzweig, Z. Rosenzweig, *Anal. Chem.* 73 (2001) 3240–3246.
- [47] W. Shi, X. Li, H. Ma, *Angew. Chem. Int. Ed.* 51 (2012) 6432–6435.



Determination of free tryptophan in serum with aptamer—Comparison of two aptasensors



Xiaojuan Yang^{a,b}, Qingxin Han^{a,b}, Yange Zhang^{a,b}, Jiang Wu^{a,b}, Xiaoliang Tang^{a,b}, Chunxu Dong^{a,b}, Weisheng Liu^{a,b,*}

^a Key Laboratory of Nonferrous Metals Chemistry and Resources Utilization of Gansu Province, Lanzhou University, Lanzhou 730000, China

^b State Key Laboratory of Applied Organic Chemistry, College of Chemistry and Chemical Engineering, Lanzhou University, Lanzhou 730000, China

ARTICLE INFO

Article history:

Received 4 June 2014

Received in revised form

31 July 2014

Accepted 6 August 2014

Available online 19 August 2014

Keywords:

Graphene oxide

L-tryptophan

Aptamer

Beacon

Complex sample

ABSTRACT

Two aptasensors based on graphene oxide (GO) and molecular beacon were designed for the detection of L-tryptophan (L-Trp) using L-Trp aptamer (Trp3a-1). The fluorescein (FAM) labeled Trp3a-1 was absorbed by GO, which resulted in the fluorescence quenching, and exhibiting minimal background fluorescence. Upon the addition of L-Trp, Trp3a-1 was not absorbed quickly. This effect allows for a quantitative assay of L-Trp over the concentration range of 10–500 μM and with a detection limit of 6.84 μM . However, due to the unspecific adsorption of GO, the GO based aptasensor can't be applied in complex matrixes. In respect of molecular beacon based aptasensor, FRET between Trp3a-1 labeled with FAM and CS-Trp3a-1 labeled with BHQ-1 (black hole quencher-1) which is partially complementary with the aptamer was used to detect L-Trp. L-Trp binding could induce the disassociation of CS-Trp3a-1, resulted in the enhancement of fluorescence in solution. With an excellent linear relationship in 10–500 μM and a detection limit of 6.97 μM in 25% serum, the aptasensor is expected to be improved for the detection of free L-Trp in other complex samples.

© 2014 Elsevier B.V. All rights reserved.

1. Introduction

Selective fluorescent sensing of free amino acids is a very important task in biochemistry and molecular biology, since the concentration of free amino acids is closely related to the metabolism of peptides and proteins in life and various physiological processes. L-Trp is an essential amino acid for many animals and human body. It also serves as a precursor for serotonin and melatonin [1,2] which is related to schizophrenia [3], hallucinations and delusions [4]. The concentration of free tryptophan in blood plasma of the liver cancer patients [5], autistic patients [6], depressive patients [7], patients with Kawasaki disease [8], colorectal cancer patients [9] and patients suffering from chronic uremia [10] is significantly different from the normal control. Besides, free tryptophan could also be taken as the nutritional value of yoghurt [11] and an index of soy sauce adulteration [12].

Several protocols have been proposed to determine L-Trp in biological fluids, such as spectrophotometric measurement after chemical derivation [13] and the HPLC with fluorescence detection

method without derivation [14–16]. In addition to the poor sensitivity, the spectrophotometric measurement cannot distinguish the free tryptophan from protein tryptophan either. So, HPLC-based analyses are the commonly used methods. However, the high cost, complicated operation procedure, the multi-step sample pretreatment and the time consuming approach about getting optimal chromatographic conditions prevented the practical application of HPLC-based analyses of L-Trp. Therefore, the development of simple, sensitive and low-cost molecular ligand to L-Trp is of great significance and would be helpful for the determination of L-Trp and the study of L-Trp associated molecular pathway.

Aptamers are artificial DNA or RNA molecules evolved by an *in vitro* selection technique named SELEX (systematic evolution of ligands by exponential enrichment) [17]. As the nucleic acid equivalent of antibodies, not only the binding affinity and specificity of aptamers can rival that of antibodies [18], but also aptamers possess a number of competitive advantages over antibodies for sensing application. Firstly, aptamers can be selected to bind essentially any target of choice by folding into well-defined tertiary structures [19]. Secondly, unlike antibodies, aptamers possess higher stability, low molecular weight, fast tissue penetration, and low immunogenesis. Furthermore, aptamers can be synthesized chemically with low cost and labeled easily with various modifications at any position of choice [20,21]. Finally,

* Corresponding author at: Key Laboratory of Nonferrous Metals Chemistry and Resources Utilization of Gansu Province, College of Chemistry and Chemical Engineering, Lanzhou University, Lanzhou, 730000, China. Tel.: +86 931 8915151; fax: +86 931 8912582.

E-mail address: liuws@lzu.edu.cn (W. Liu).

the predictable and tailored structure of aptamers would facilitate the design of signal transduction. Due to these advantages, various aptasensors have been advanced for transducing aptamer-target interaction into electrochemical, colorimetric and fluorescent signals [22]. Among these various optical signal transduction methods, fluorescence has been extensively used due to its high signal to noise ratio. In addition, fluorescence can be easily detected with simple instrument. Moreover, the availability of a great number of fluorophores and quenchers makes it a popular choice. However, most of aptasensors based on fluorescence focused on only a few well-characterized aptamers such as the aptamers against thrombin, ATP and cocaine. Additionally, a large proportion of aptasensors were not applied in the biological fluids.

In this study, based on GO and aptamer beacon, two fluorescence aptasensors for L-Trp were constructed to detect L-Trp in serum. The advantages and limitations of each aptasensor were also discussed, which would be helpful for practical application of aptamer.

2. Materials and methods

2.1. Chemicals and equipments

All oligonucleotides were synthesized by Shanghai Sangon Biotechnology Co., Ltd (Shanghai, China). L-Trp, L-Tyr, L-Phe were purchased from Aladdin Reagent Co., Ltd (Shanghai, China). D-Trp was obtained from Shanghai Sangon Biotechnology Co., Ltd (Shanghai, China), indole acetic(IAA), indole and L-Gly were obtained from sinopharm Chemical Reagent Co., Ltd. Fetal bovine serum (FBS) were purchased from Rong Ye biotechnology Co., Ltd (Lanzhou, China). The Tris-HCl buffer (20 mM, pH 7.4) used in the experiments consisted of 100 mM NaCl, 5 mM MgCl₂. All of the chemicals were of at least analytical grade. The GO was synthesized from natural graphite powder based on modified Hummers method [23]. Fluorescent emission spectra were obtained with an F-7000 Fluorescence Spectrophotometer, Hitachi High-Technology

Co., Ltd. The emission spectra were recorded in the wavelength of 495–630 nm upon excitation at 485 nm with slit widths of 5 nm. Varian Cary 100 UV/vis spectrophotometer was used to quantify the oligonucleotides

2.2. Determination of L-Trp based on GO in clean buffer and FBS

In a typical L-Trp detection assay, 50 nM FAM labeled Trp3a-1 (5'-FAM-AGCACGTTGGTTAGGTCAGGTTGGGTTTCGTGC-3') dissolved in 700 μ l Tris-HCl solution were denatured at 95 °C for 5 min, rapidly cooled on ice and kept at room temperature for 5 min prior to use, then incubated with a series concentration of L-Trp at 10–15 °C for 1 h. Then 14 μ l of graphene oxide (0.5 mg/ml) was added, the final concentration of GO is 10 μ g/ml. The fluorescence spectra were recorded after 30 s or 1 min in a 1 cm path-length quartz cell. For specificity assay, Trp3a-1 was incubated with 200 μ M other amino acids and indole analogs in Tris-HCl buffer at 10–15 °C for 1 h. Then 10 μ g/ml GO was added. The fluorescence spectra were recorded after 15 s in a 1 cm path-length quartz cell. The titration experiments in 10% FBS were same with that in clean buffer. In order to exclude the unspecific binding between GO and ssDNA, a DNA library containing 34 nucleotides of random sequence was used as control. The concentration of control sequence is same with Trp3a-1 in every protocol.

2.3. Determination of L-Trp by aptamer beacon in clean buffer and 25% FBS

For titration experiment of L-Trp by aptamer beacon, 0.3 μ M Trp3a-1 and 0.7 μ M CS-Trp3a-1(5'-CAACGTGCT-3') in 300 μ l Tris-HCl buffer were denatured at 95 °C for 5 min, rapidly cooled on ice for 15 min, then were incubated for 1 hour and different concentration of L-Trp was added. After 2 h incubation at 10–15 °C, the fluorescence spectra were collected in a 1 cm path-length quartz cell. For specificity assay, 200 μ M other amino acids and indole analogs were used. Other assay procedures were identical to the L-Trp titration experiment. The L-Trp detection and specificity assay protocol by aptamer beacon in 25%

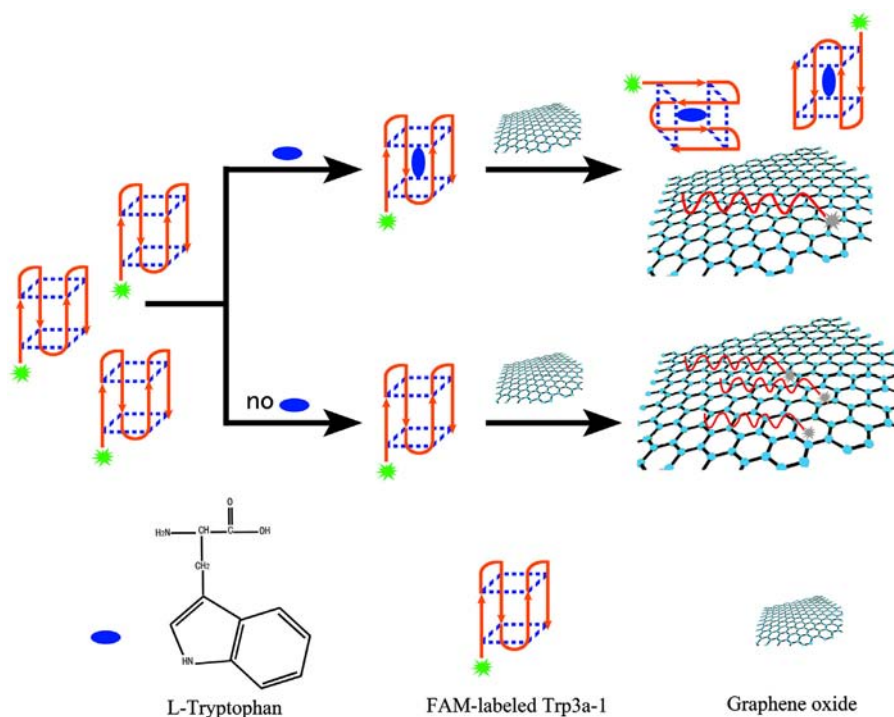


Fig. 1. Illustration of the principle of GO-based aptasensor.

FBS were same with that in clean buffer. To exclude the unspecific binding between L-Trp and the aptasensor, Trp3a-2 (5'-FAM-AGCACGTTGGTTAGGTCAGGTTTGTGTTTCGTGC-3') which can't bind L-Trp was used as control [24]. Trp3a-2 is only one base variant from Trp3a-1, and the mutation base was underlined.

3. Results and discussion

3.1. GO-based sensor for L-Trp sensing

Due to the great affinity for single-stranded DNA, GO has attracted extensive attention for biosensor application. Moreover, it was documented that sp^2 domain of the GO behaves as an efficient quencher for fluorescence resonance energy transfer. With this universal quenching and adsorbing property, various target detections based on quenching property of GO have been reported by using a dye-labeled aptamer [21,25]. We have reported that Trp3a-1 was an effective ligand for the chiral separation of D/L-tryptophan [24]. In this work, GO-based fluorescent bioassay for L-Trp was also carried out to investigate the analytical potential of the aptamer. The principle of the fluorescence response of this aptasensor was depicted in Fig. 1. In the absence of L-Trp, the FAM labeled Trp3a-1 is adsorbed on GO, and the fluorescence is almost quenched quickly. While in the

presence of L-Trp, the binding between L-Trp and Trp3a-1 will decrease the adsorbed rate of aptamer onto surface of GO, which resulted in the fluorescence intensity enhancement of the reaction system in a very short time.

As shown in Fig. 2A, when the fluorescence intensity was measured in 30 s, the fluorescence intensity of Trp3a-1 was quenched to about 20. Nevertheless, when the GO is absent, the fluorescence intensity of 50 nM Trp3a-1 is 1863 (Fig. 3A). So the fluorescence quenching efficiency is approximately 99%, suggesting that the quenching kinetics were fairly fast. As the Fig. 2A showed, with the increase of L-Trp concentration, the fluorescence intensity of Trp3a-1 was intensified. When L-Trp was increased to 2 mM, fluorescence intensity was recovered to about 750, suggesting the binding between Trp3a-1 and L-Trp could lower the adsorption rate of Trp3a-1 by GO. However, the fluorescence intensity of control group was also enhanced with the increase of L-Trp concentration, and the increasing rate of control sequence is just a bit slower than that of Trp3a-1 (Fig. 2A). Our previous research confirmed that the DNA library with 34 bases didn't bind with L-Trp [24]. So if the control experiments were not carried out, it is most likely to get false-positive results. This results demonstrated that GO could not only adsorb aptamer, but could also adsorb the free L-Trp in the solution, which resulted in the reduction of interaction area on the surface of GO and the enhancement of free aptamer in the solution [26]. Consequently, it is absolutely necessary to exclude the influence resulted from the unspecific binding between

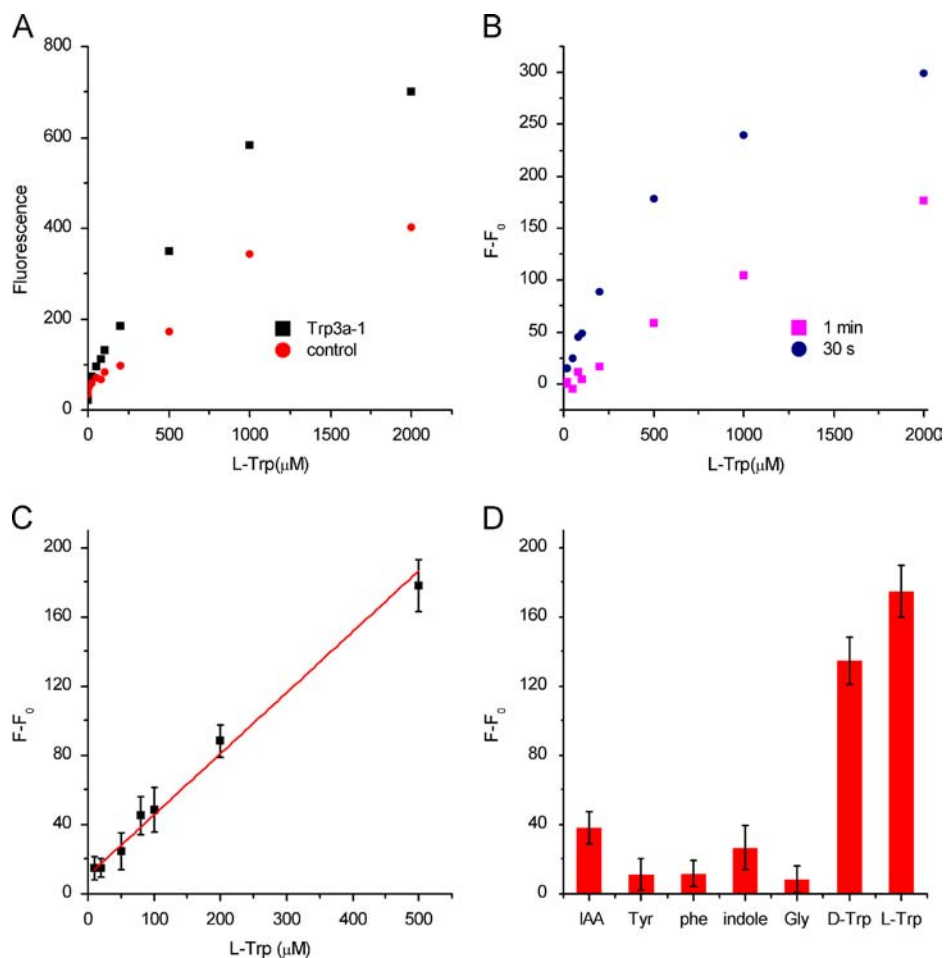


Fig. 2. (A) Comparison of fluorescence response between Trp3a-1 and control sequence with different concentration of L-Trp in 30 s. (B) The fluorescence intensity difference of Trp3a-1 and control group when the fluorescence were recorded in 30 s and 1 min, F and F_0 represented the fluorescence response of Trp 3a-1 and control group respectively. (C) Calibration curve for L-Trp detection in 30 s, F and F_0 represented the fluorescence response of Trp 3a-1 and control group respectively. Each data point represents an average \pm the standard deviation of three replicates. (D) the variation of $F - F_0$ in the presence of different analogs (200 μ M) in 15 s, F and F_0 represented the fluorescence intensity of Trp3a-1 and control sequence respectively, each data point represents an average \pm the standard deviation of three replicates.

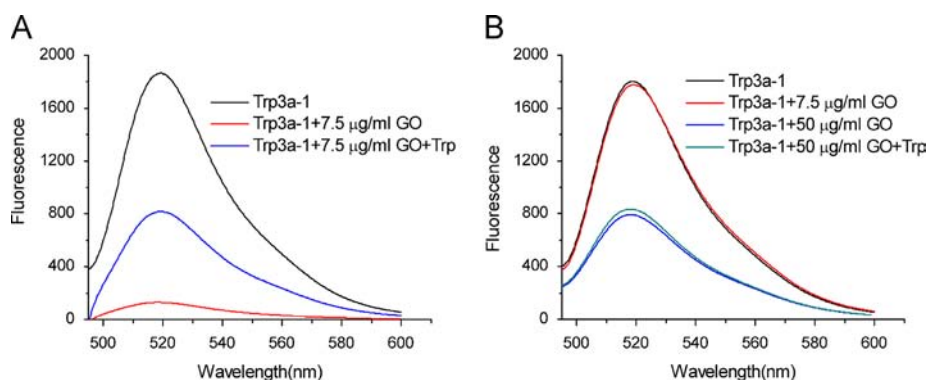


Fig. 3. (A) The effect of GO and L-Trp on the fluorescence intensity of Trp3a-1 in clean buffer, [Trp3a-1]=50 nM, [L-Trp]=500 μ M. (B) The effect of GO and L-Trp on the fluorescence intensity of Trp3a-1 in 10% fetal bovine serum, [Trp3a-1]=50 nM, [L-Trp]=500 μ M.

L-Trp and GO. So it is reasonable to take fluorescence intensity difference between Trp3a-1 and control sequence ($F-F_0$) at 520 nm as the output signal.

Fig. 2B exhibited the effect of incubation time after the introduction of GO on $F-F_0$. It can be seen that $F-F_0$ recorded after 1 min was lower than that of 30 s. With regard to the mechanism of GO-based aptasensor, researchers proposed that either the structure transformation induced by target binding or the low affinity between aptamer-ligand complex and GO contributed to the achievement of target detection [25,27]. It was well known that π - π interactions dominate the binding between GO and ssRNA. For Trp3a-1, our CD spectra showed that it remained an antiparallel G-quadruplex conformation no matter whether L-Trp was present or not. Moreover, the π - π stacking interaction played an important role for the binding of L-Trp and Trp3a-1 [24]. So it is irrational to take the structure switch induced by L-Trp as the leading cause for the principle of GO-based aptasensor. Limited studies demonstrate that the interactions between double-stranded DNA (and G-quadruplex) and GO were rather weak [28,29]. This is because nucleobases were effectively shielded within the densely negatively charged phosphate backbone of dsDNA/G-quadruplex. As for the reason for the lower affinity between target-aptamer and GO, the answer is still not completely clear. Based on our data illustrated in Fig. 2, we preferred to attribute the driving force to the competition between GO/aptamer adsorption and aptamer/target binding. As a small molecular, the binding between L-Trp and Trp3a-1 would not rival over the adsorption by GO unless with excessive L-Trp in solution and detecting within a very short time. With time prolonging, the aptamers in the solution would eventually be adsorbed by GO if the surface was not saturated, which resulted in less notable difference within 1 min than that in 30 s (Fig. 2B).

With a linear range of 10–500 μ M, a calibration curve with $R^2=0.9861$ was obtained when the fluorescence intensity was recorded within 30 s (Fig. 2C). The limit of detection (LOD) was 6.84 μ M as calculated from the $3\sigma/S$ calculation. (σ is the standard deviation for the blank solution, $n=11$, and S is the slope of the calibration curve). And the limit of the quantification (LOQ) was determined to be 22.80 μ M by $10\sigma/S$ standard. The relative standard deviations for determinations of 50 μ M L-Trp and 100 μ M L-Trp were 12.0% ($n=7$) and 10.8% ($n=7$) respectively.

To test the selectivity of this strategy, L-Gly, two aromatic amino acids (L-Tyr and L-Phe) as well as two structurally similar indole derivations and D-Trp were tested as parallel with standard steps. The reason for the selection of IAA, D-Trp and indole is indole derivatives can bind with Trp3a-1 partially [24]. Besides, the excitation and emission spectra of L-Phe, L-Tyr and L-Trp can overlap, usually they cannot be separately measured by

fluorescent method without derivation and separation unless chemistry metrology is also employed [30]. Thus L-Tyr and L-Phe were also introduced in the specificity experiments even though it has been reported Trp3a-1 don't bind with them [24]. As shown in Fig. 2D, $F-F_0$ for L/D-Trp, IAA and indole were higher than other substance, which was in agreement with our previous reports. Based on the results, it can be inferred the presence of D-Trp may considerably cause the overestimate of the concentration of tryptophan in a very complex matrix such as serum, while the existence of aromatic amino acid and other indole analogs would not remarkably influence the determination of L-Trp.

In order to demonstrate the feasibility of this analytical method in complex matrixes, it was then applied into FBS with the addition of trace amount of L-Trp. When 7.5 μ g/ml GO was added in 10% serum, the fluorescence quenching efficiency was almost undistinguished (Fig. 3B), which is markedly different from the quenching efficiency in clean buffer (Fig. 3A). When GO was increased to 50 μ g/ml, the fluorescence intensity was quenched just by 50%. This can be attributed to the adsorption of some other biomolecules in serum by GO, which reduced the interaction area between ssDNA and GO. The degree of fluorescence change was indistinctive even in the presence of 500 μ M L-Trp in the 10% serum as illustrated in Fig. 3B. We cannot get a satisfied linear relationship between the L-Trp concentration and the fluorescence intensity even with the optimization of the detection protocol. Thus, although this GO-based aptasensor provides a much better signal-to-noise ratio, it is not workable in the serum due to the unspecific adsorption of GO sheet.

3.2. Aptamer beacon for L-Trp sensing in clean buffer

To circumvent the limit of GO-based aptasensor, an aptamer beacon was designed as schematically shown in Fig. 4. The principle of the beacon to monitor L-Trp is as follows: Firstly, Trp3a-1 labeled with FAM at 5' terminal was hybridized with a 9-nt complementary sequence labeled with BHQ-1 at 3' terminal (CS-Trp3a-1), which led to quenched emission at 520 nm via efficient energy transfer due to the direct contact between FAM and BHQ-1. When L-Trp was present, the hybridized beacon undergoes a conformation change due to the interaction of L-Trp and Trp3a-1. Trp3a-1 would bind to L-Trp and form an antiparallel G-quadruplex structure, which resulted in the separation of the FAM and BHQ-1 and an enhanced fluorescence signal.

The fluorescence responses of this aptamer beacon to L-Trp in Tris-HCl buffer were shown in Fig. 5A. It can be seen that fluorescence intensity was enhanced with the increasing of concentration of L-Trp. To calculate the quenching efficiency, F_0 which is the fluorescence intensity of the aptamer beacon in the absence

of L-Trp and F_b which is the fluorescence intensity of Trp3a-1 in the absence of both L-Trp and CS-Trp3a-1 were introduced. $(F_b - F_a)/F_b$ was defined as the quenching efficiency. In this case, F_a is 4017 (data not shown). F_b is estimated to be 10,800 by internal standard method. So the quenching efficiency of aptamer beacon was close to 63%. However, the quenching efficiency of control sequence (Trp3a-2) which can not bind L-Trp is 96%. With only one G base variant which is likely to participate in the formation of G-quadruplex, Trp3a-2 showed no fluorescence response to L-Trp (Fig. S1). Thus it can be concluded that the weak Watson–Crick base pair of Trp3a-1 and CS-Trp3a-1 cannot effectively disrupt the Hoogsteen hydrogen binding of G-quadruplex in the buffer, which contribute the lower quenching efficiency of Trp3a-1. With a linear range of 40–400 μM , a calibration curve with $R^2=0.9826$ was obtained as showed in Fig. 5A. The limit of detection (LOD) was 17.08 μM as calculated from the $3\sigma/S$ calculation. (σ is the standard deviation for the blank solution, $n=11$, and S is the slope of the calibration curve). And the limit of the quantification (LOQ) was determined to be 56.94 μM by $10\sigma/S$ standard. The relative standard deviations for repetitive determinations of 100 μM L-Trp and 200 μM were 1.0% ($n=10$) and 0.8% ($n=10$) respectively.

Since without the false positive event, the selectivity of this aptamer beacon was carried out without control group. Fig. 5B illustrated the specificity of aptamer beacon, a significant difference was observed between L/D-Trp and other analogs. This suggested the indole ring, amino group and carboxyl group synergistically interact with Trp 3a-1. Based on the results, it can be inferred that only the presence of D-Trp may cause the overestimate of the concentration of tryptophan in a very complex matrix such as serum, while the existence of other aromatic amino acid would not influence the determination of L-Trp by the beacon aptasensor

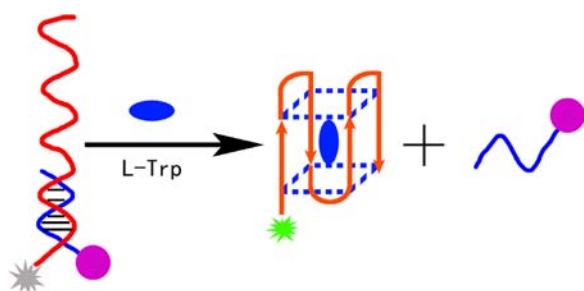


Fig. 4. Illustration of principle of aptamer beacon.

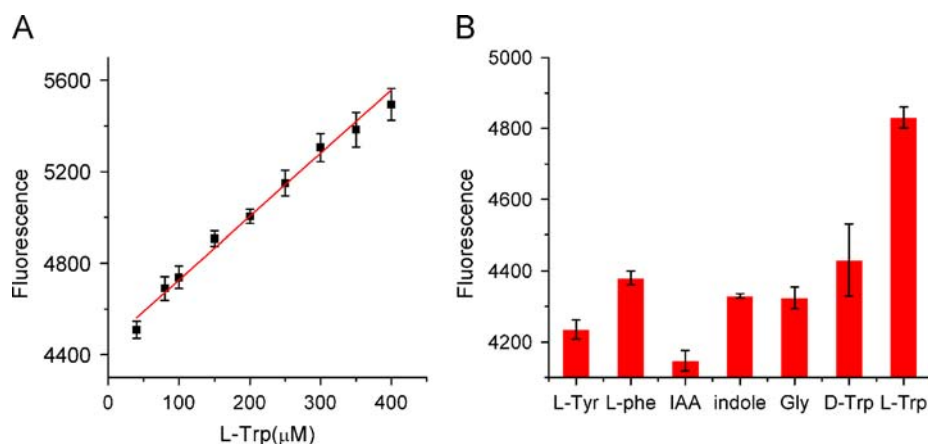


Fig. 5. (A) Calibration curve for L-Trp detection in clean buffer, each data point represents an average \pm the standard deviation of three replicates. (B) The variation of fluorescence intensity at 520 nm in the presence of different analogs (200 μM) in clean buffer, each data point represents an average \pm the standard deviation of three replicates.

3.3. Aptamer beacon for L-Trp sensing in 25% FBS

In the same way, to demonstrate the suitability of the aptamer beacon for complex samples, analyses of L-Trp in FBS were implemented. Spike sample analysis is used to test the method at varying concentrations of L-Trp. Fig. 6A showed that the quenching efficiency of the aptamer beacon in 25% serum was 90% which is higher than that in buffer (63%). Maybe it is the combined outcome of electrostatic repulsion [31], molecular crowding [32], protonation [31,33], DNA sequence, and the hydration [34], further studies were needed to elucidate the mechanism.

In light of the efficient quenching, the aptamer beacon showed an excellent linear relationship in the range of 10–500 μM with $R^2=0.9945$. The detection limit of the method, estimated from the $3\sigma/S$ standard (σ is the standard deviation for the blank solution with $n=11$, and S is the slope of the calibration curve) was 6.97 μM . And the limit of the quantification was determined to be 23.23 μM by $10\sigma/S$ standard. The relative standard deviations for repetitive determinations of 10 μM L-Trp and 50 μM L-Trp were 1.8% ($n=15$), 1.0% ($n=20$). The classical HPLC detection showed the concentration of L-Trp in FBS sample is about 9 μM . And in the case of human serum, it is about 43 μM [35]. Herein, despite the detection limit of this aptasensor is not comparable with that of the classic HPLC method, this aptamer beacon can be extended further to sense L-Trp in human serum if there is an internal standard or standard curve. Thus the 25% FBS samples were spiked with the low (10 μM), intermediate (60 μM) and high levels (150 μM) of L-Trp to examine recoveries with sample number of 3. The recovery ranges at low, intermediate and high spiked levels were 98.9–105.2%, 97.8–103.7%, 97.9–98.3%, respectively. The recovery levels were acceptable. Also, as would be expected, the specificity of aptamer beacon was not affected by the addition of FBS (Fig. 6B). The result demonstrated that the present off-on fluorescence probe is promising to detect L-Trp in some complex matrices

In a word, on contrary with the GO-based aptasensor, aptamer beacon aptasensor can be utilized in the FBS even with a higher background. Consequently, with the optimization of detection condition in the future, this aptamer beacon sensor can be used to detect free L-Trp in complex sample.

4. Conclusion

In conclusion, we have developed two novel L-Trp detection biosensors based on the aptamer of L-Trp. The GO-based

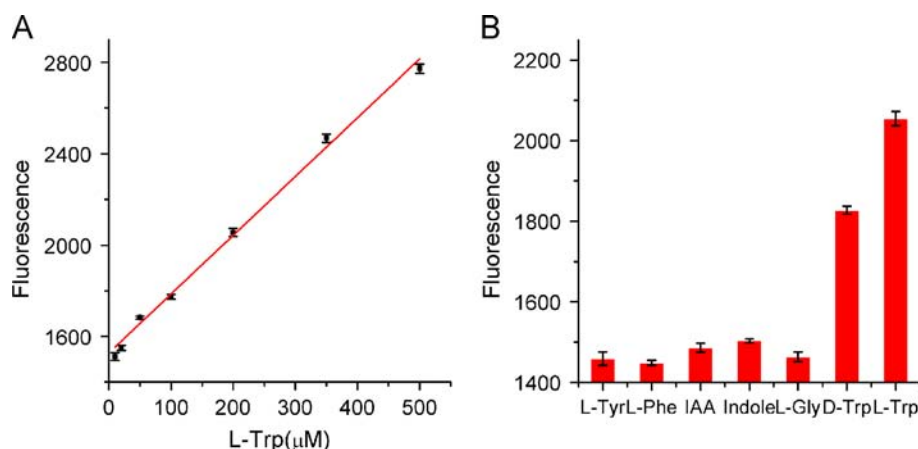


Fig. 6. (A) Calibration curve for L-Trp detection in 25% serum, each data point represents an average \pm the standard deviation of three replicates. (B) The variation of fluorescence intensity at 520 nm in the presence of different analogs (200 μ M) in 25% FBS, each data point represents an average \pm the standard deviation of three replicates.

aptasensor can provide a low background, but it cannot be applied in the complex sample due to the unspecific adsorption of GO sheet. In clean buffer, with a detection limit of 6.84 μ M, the GO-based aptasensor showed a linear relationship in the range of 10–500 μ M. In the case of aptamer beacon, the detection limit of L-Trp was found to be 6.97 μ M, and the calibration plots were linear in 25% FBS. Also, the aptamer beacon can be applied to detect L-Trp in clean buffer even with a higher background. Finally, this study has not only demonstrated the practical application of aptamer, but also compared the pros and cons of the two aptasensors for L-Trp. This is very useful for the application of different aptasensor.

Acknowledgments

We gratefully acknowledged the National Natural Science Foundation of China (Grant nos. 91122007 and 21201091), the Specialized Research Fund for the Doctoral Program of Higher Education (Grant no. 20110211130002), and the financial support from Fundamental Research Funds for the Central Universities (lzujbky-2013-193, lzujbky-2013-59 and lzujbky-2013-61).

Appendix A. Supporting information

Supplementary data associated with this article can be found in the online version at <http://dx.doi.org/10.1016/j.talanta.2014.08.023>.

References

- [1] P.J. Knott, G. Curzon, *Nature* 23 (1972) 452–453.
- [2] J.D. Fernstrom, R.J. Wurtman, *Science* 173 (1971) 149–152.
- [3] S. Striano, D. Grossi, S. Guardascione, *Electroencephal. Clin. Neurophysiol.* 50 (1980) 17–18.
- [4] C.L. Miller, I.C. Llenos, J.R. Dulay, M.M. Barillo, R.H. Yolken, S. Weis, *Neurobiol. Dis.* 15 (2004) 618–629.
- [5] A. Cozzi, A.L. Zignego, R. Carpendo, T. Biagiotti, A. Aldinucci, M. Monti, C. Giannini, M. Rosselli, G. Laffi, F. Moroni, *J. Viral Hepatitis.* 13 (2006) 402–408.
- [6] C.J. McDougle, S.T. Naylor, D.J. Cohen, G.K. Aghajanian, G.R. Heninger, L.H. Price, *Arch. Gen. Psychiatry* 53 (1996) 993–1000.
- [7] L. Capuron, A. Ravaut, P.J. Neveu, A.H. Miller, M. Maes, R. Dantzer, *Mol. Psychiatry* 7 (2002) 468–473.
- [8] X. Zhang, Y. He, M. Ding, *J. Chromatogr. B.* 877 (2009) 1678–1682.
- [9] A. Huang, D. Fuchs, B. Widner, C. Glover, D.C. Henderson, T.G. Allen-Mersh, *Br. J. Cancer* 86 (2002) 1691–1696.
- [10] S. Manabe, M. Suzuki, E. Kusano, O. Wada, Y. Asano, *Clin. Nephrol.* 37 (1992) 28–33.
- [11] M. Biasiolo, A. Bertazzo, C.B. Costa, G. Allegri, *Food. Chem.* 52 (1994) 87–92.
- [12] M. Horvatic, M. Gruner, *Nahrung-Food* 37 (1993) 147–152.
- [13] T.E. Barman, D.E. Koshland, *J. Biol. Chem.* 242 (1967) 5771–5776.
- [14] J. Zhang, X. Xue, J. Zhou, F. Chen, L. Wu, Y. Li, J. Zhao, *Biomed. Chromatogr.* 23 (2009) 994–998.
- [15] D.I. Sanchez-Machado, B. Chavira-Willys, J. Lopez-Cervantes, *J. Chromatogr. B.* 863 (2008) 88–93.
- [16] A.M. Krstulovic, P.R. Brown, D.M. Rosie, P.B. Champlin, *Clin. Chem.* 23 (1977) 1984–1988.
- [17] A.D. Ellington, J.W. Szostak, *Nature* 346 (1990) 818–822.
- [18] D. Shangguan, Y. Li, Z. Tang, Z.C. Cao, H.W. Chen, P. Mallikaratchy, K. Sefah, C.J. Yang, W. Tan, *Proc. Natl. Acad. Sci. USA* 103 (2006) 11838–11843.
- [19] H. Mei, T. Bing, X. Yang, C. Qi, T. Chang, X. Liu, Z. Cao, D. Shangguan, *Anal. Chem.* 84 (2012) 7323–7329.
- [20] T. Bing, T. Chang, X. Yang, H. Mei, X. Liu, D. Shangguan, *Bioorg. Med. Chem.* 19 (2011) 4211–4219.
- [21] C. Qi, T. Bing, H. Mei, X. Yang, X. Liu, D. Shangguan, *Biosens. Bioelectron.* 41 (2013) 157–162.
- [22] J. Liu, Z. Cao, Y. Lu, *Chem. Rev.* 109 (2009) 1948–1998.
- [23] M. Wu, R. Kempaiah, P.J. Huang, V. Maheshwari, J. Liu, *Langmuir* 27 (2011) 2731–2738.
- [24] X. Yang, T. Bing, H. Mei, C. Fang, Z. Cao, D. Shangguan, *Analyst* 136 (2011) 577–585.
- [25] Y. He, Z.G. Wang, H.W. Tang, D.W. Pang, *Biosens. Bioelectron.* 29 (2011) 76–81.
- [26] X.J. Xing, X.G. Liu, H. Yue, Q.Y. Luo, H.W. Tang, D.W. Pang, *Biosens. Bioelectron.* 37 (2012) 61–67.
- [27] J. Liang, R. Wei, S. He, Y. Liu, L. Guo, L. Li, *Analyst* 138 (2013) 1726–1732.
- [28] J. Liu, *Phys. Chem. Chem. Phys.* 14 (2012) 10485–10496.
- [29] C. Lu, H. Yang, C. Zhu, X. Chen, G. Chen, *Angew. Chem. Int. Ed.* 48 (2009) 4785–4787.
- [30] C. Gao, S. Fan, *Anal. Lett.* 47 (2014) 178–179.
- [31] N. Sugimoto, P. Wu, H. Hara, Y. Kawamoto, *Biochemistry* 40 (2001) 9396–9405.
- [32] Z. Kan, Y. Yao, P. Wang, X. Li, Y. Hao, Z. Tan, *Angew. Chem. Int. Ed.* 45 (2006) 1629–1632.
- [33] H. Tateishi-Karimata, M. Nakano, N. Sugimoto, *Sci. Rep.* 4 (2014) 1–5.
- [34] J. Zhou, C. Wei, G. Jia, X. Wang, Z. Feng, C. Li, *Chem. Commun.* 46 (2010) 1700–1702.
- [35] C. He, J. Wang, P. Wu, L. Jia, Y. Bai, Z. Zhang, C. Duan, *Chem. Commun.* 48 (2012) 11880–11882.



Conjugated polyelectrolyte-stabilized silver nanoparticles coupled with pyrene derivative for ultrasensitive fluorescent detection of iodide

Yi Xiao^a, Ye Zhang^a, Hongmei Huang^{a,*}, Youyu Zhang^a, Beilei Du^a, Fang Chen^a, Qiao Zheng^a, Xiaoxiao He^b, Kemin Wang^{b,**}

^a Key Laboratory of Chemical Biology and Traditional Chinese Medicine Research (Ministry of Education), College of Chemistry and Chemical Engineering, Hunan Normal University, Changsha 410081, PR China

^b State Key Laboratory of Chemo/Biosensing and Chemometrics, College of Chemistry and Chemical Engineering, College of Biology, Hunan University, Changsha 410082, PR China

ARTICLE INFO

Article history:

Received 10 May 2014

Received in revised form

4 August 2014

Accepted 6 August 2014

Available online 19 August 2014

Keywords:

Silver nanoparticles

Conjugated polyelectrolyte

Pyrene derivative

Iodide

Fluorescence

ABSTRACT

A new sensing system is developed for selective and ultrasensitive detection of iodide based on the inner filter effect (IFE) between conjugated polyelectrolyte-stabilized silver nanoparticles (P1–AgNPs) and 4-oxo-4-(pyren-1-ylmethoxy) butanoic acid (**probe 1**). P1–AgNPs are designed to be capable of functioning as a composite light-absorber. Meanwhile, **probe 1** is selected as an ideal fluorophore because its emission spectrum can perfectly overlap with the absorption band of P1–AgNPs. The intense fluorescence of **probe 1** quenched by P1–AgNPs can be efficiently recovered after adding H₂O₂ and I[−] via the oxidation-etching and regeneration of P1–AgNPs. Under the optimum conditions, this facile IFE-based approach allows the sensitive and selective determination of I[−] in tap water, iodized salt and urine with the detection limit as low as 0.3 nM (*S/N* = 3). Interestingly, the regenerated AgNPs is in smaller size and well-dispersed perhaps due to the particular role of P1 as a polymer localizer containing pyridinyl and sulfonate groups.

© 2014 Elsevier B.V. All rights reserved.

1. Introduction

In recent years, substantial efforts have been devoted to the design and synthesis of sensors capable of binding and sensing anions because of their pivotal roles in biological, chemical, and environmental processes [1–9]. Among these anions, iodide (I[−]) is extremely crucial for controlling many metabolic pathways and activities since thyroid hormones, triiodothyronine (T3) and thyroxine (T4) released by the thyroid gland are closely related to the concentrations of I[−]. Iodide deficiency or excess can result in human diseases and disorders [10]. To date, various methods, e.g., kinetic determination of iodide using the Sandell–Kolthoff reaction [11], optical emission spectrometry (OES) [12], ion chromatography [13], size-exclusion chromatography (SEC) coupled with ICP MS [14], capillary electrophoresis [15], and indirect atomic absorption spectrometry (IAAS) [16], have been used for the determination of iodide in foods, pharmaceutical products and biosamples. Nevertheless, the development of new, ultrasensitive

analytical approaches for I[−] (e.g., detection limit < 1 nM) without complex pretreatment is highly desirable.

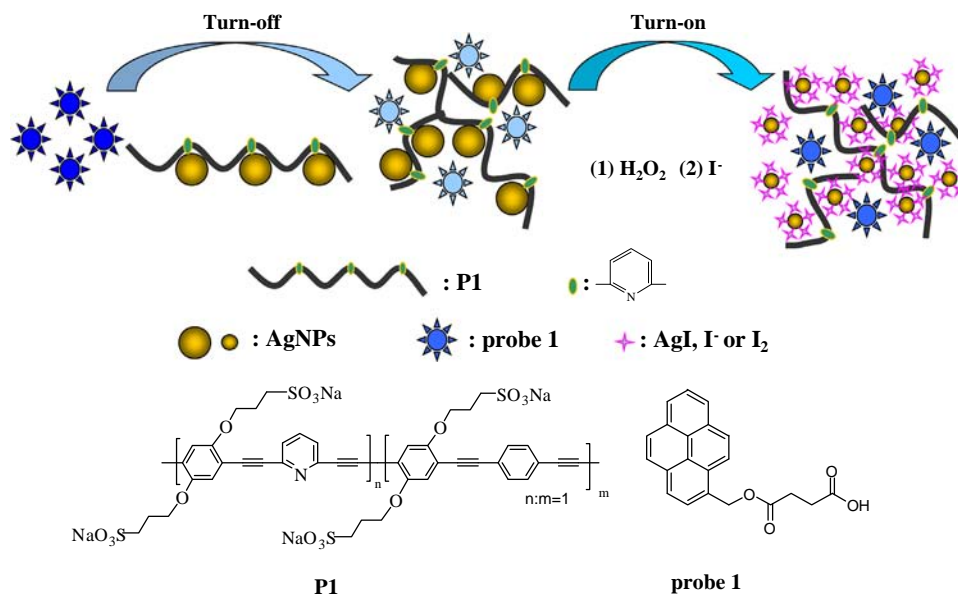
Noble metal nanoparticles (e.g., Ag and Au NPs) have emerged as attractive platforms for developing new sensors mainly due to their intrinsic properties such as high extinction coefficient, size-dependent optical properties, and convenient surface modification [17–19]. Compared to conventional analytical methods, the NPs-based sensing techniques can provide enhanced probing sensitivity [20,21]. In addition, fluorescence technique is a powerful tool for the detection of analytes owing to its simplicity, high sensitivity and selectivity, and facile imaging in vivo [22–26]. More recently, Tseng et al. reported fluorescein-5-isothiocyanate-modified gold nanoparticles (FITC–AuNPs) for selective turn-on fluorescence detection of I[−] [27]. It was also demonstrated by Huang and co-workers that FITC-labeled bovine serum albumin self-adsorbed on fluorescent gold nanoparticles (FITC–BSA–AuNPs) could be employed for the selective sensing of I[−] [28]. Accordingly, improved sensitivity (limits of detection 10 and 50 nM, respectively) was obtained by the aforementioned NPs-based I[−] sensors compared with other I[−] fluorescence sensors reported in literature [25].

Conjugated polyelectrolytes (CPEs) featuring a π -delocalized backbone and ionic pendant groups are among the most important tools for fluorescence detection of small ions, biomolecules

* Corresponding author. Tel.: +86 731 88872576; fax: +86 731 88872531.

** Corresponding author.

E-mail addresses: huanghongmei@hunnun.edu.cn (H. Huang), kmwang@hnu.edu.cn (K. Wang).



Scheme 1. Schematic illustration of the fluorescent iodide detection based on the inner filter effect between P1-AgNPs and **probe 1**.

and cells [29,30]. However, despite the pioneer work on the determination of DNA and cancerous cells, CPES-based metal NPs used for the highly sensitive analysis of iodide anion remain relatively unexplored [31,32]. On the other hand, pyrene has been used for the development of fluorescent probe with ultrasensitivity (e.g., detection limit for DNA in the fM range) due to its spatial sensitivity and long fluorescence lifetime [33]. Herein, we firstly design a fluorescence sensor for turn-on iodide detection based on the inner filter effect (IFE) between pyrene derivative and conjugated polyelectrolyte-stabilized silver nanoparticles (P1-AgNPs). The IFE-based approach is considerably more flexible, simple and sensitive when the absorption band of the absorbent dye possesses a perfect spectral overlap with the excitation and/or emission bands of the fluorophore [34,35]. The principle of our method is illustrated in Scheme 1. The fluorescence of **probe 1** can be quenched in the presence of P1-AgNPs. When H₂O₂ and I⁻ are added to the mixed solution of **probe 1** and P1-AgNPs, the fluorescence of **probe 1** can be restored. This facile IFE-based approach has the following advantages during the determination of I⁻ in real samples: (1) ultrasensitivity with the detection limit as low as 0.3 nM compared to conventional fluorescence-based techniques; (2) requiring no complex pretreatment of sample; (3) good recovery; (4) utilization of relatively inexpensive AgNPs [36]. Furthermore, the regenerated AgNPs is obviously in smaller size, which could be potentially generalized to design well-dispersed and highly stable nanoparticles.

2. Experimental

2.1. Materials

P1 was synthesized according to our previous report [37]. **Probe 1** was obtained according to literature procedures [38]. The chemical structures of P1 and **probe 1** were shown in Scheme 1. AgNO₃ and other reagents were purchased from Sinopharm Chemical Reagent Co., Ltd (Shanghai, China) and used as received without further purification. Citric acid–disodium hydrogen phosphate buffer solutions (H₃Cit–Na₂HPO₄ pH 3.0–8.0) were prepared with 0.2 M Na₂HPO₄ and 0.1 M citric acid. The aqueous buffer solutions (pH 9.0 and 10.0) were prepared with 0.1 M sodium carbonate and 0.1 M sodium bicarbonate. The concentrations of the stock solutions of P1 (in deionized water)

and **probe 1** (in methanol) are 2.4×10^{-4} M and 2.0×10^{-4} M, respectively. Tap water and iodized salt were collected from Hunan Normal University and Hunan Xiangli Salt Chemical Co., Ltd. (Jinshi, China), respectively. Urine samples obtained from three healthy volunteers were filtered through a 0.22 μm membrane and stored at 4 °C.

P1-stabilized AgNPs were prepared by a modified method reported in the literature [39]. Briefly, 0.6 mL of 0.02 M AgNO₃ and 0.2 mL of 0.24 mM P1 were added into 50 mL of water under stirring, then 0.48 mL of freshly prepared 0.25 M NaBH₄ was added rapidly under vigorous stirring. The resulting yellow colloidal silver solution was stirred for 30 min and stored at 4 °C overnight. The size and morphology of the silver nanoparticles were investigated by transmission electron microscopy (TEM). The concentration of as-prepared P1-AgNPs was calculated to be 2.4×10^{-4} M assuming that all silver in the AgNO₃ was reduced.

2.2. Apparatus

Fluorescence spectra were obtained on an F-4500 fluorometer (Hitachi Co., Japan). UV–visible absorption spectra were taken on a UV-2450 spectrophotometer (Shimadzu Co., Japan). All pH values were measured using a PHS-3C (Shanghai Pengshun Scientific Instrument Co., China) pH meter with a combined glass–calomel electrode. TEM was performed on a JEM-2010 (JEOL, Japan) operated at 200 kV. Each sample for TEM characterization was prepared by delivering a drop of colloidal solution on carbon-coated copper grid and drying at room temperature. The zeta potential of the AgNPs was measured using a Zetasizer 3000HS analyzer (Malvern, UK).

2.3. Detection of iodide

A freshly prepared solution containing P1-AgNPs, buffer solution, **probe 1** and H₂O₂ was placed in a quartz cell (10.0 mm width). This mixture was incubated for 1 h before recording the fluorescence spectra at room temperature. After the introduction of KI, this solution was incubated for another 5 min before recording the fluorescence spectra. The concentrations of stock solutions containing I⁻ or other anions are 0.01 M unless otherwise stated.

3. Results and discussion

3.1. The inner filter effect of P1–AgNPs on **probe 1**

P1, a novel conjugated polyelectrolyte with specific coordinating pyridyl segments, was chosen as the protective agent for AgNPs. As good electron donors, pyridine moieties in P1 spontaneously coordinate with AgNPs to form a stable complex P1–AgNPs, similar to the previous case of 4,4-bipyridine-stabilized silver nanoparticles [40]. As a new composite nanomaterial, P1–AgNPs presented remarkable stability in aqueous solution for months under ambient conditions. Pyrene derivative can act as a sensitive fluorescent probe [33,41]. Fig. 1 shows the fluorescence emission and excitation spectra of **probe 1** and the absorption spectrum of P1–AgNPs. **Probe 1** exhibits a maximum emission at 398 nm (Fig. 1b) and aqueous P1–AgNPs (no fluorescence is observed) display an intense absorption at 395 nm (Fig. 1c). It is obvious that the emission spectrum of **probe 1** perfectly overlaps with the absorption band of P1–AgNPs, which is critical for the IFE-based fluorescent assay [34,35,42]. Thus the emission light of **probe 1** should be easily absorbed by P1–AgNPs, leading to the fluorescence quenching of **probe 1** when the two components coexist. It can be seen from Fig. 2 that a gradual decrease in the fluorescence of **probe 1** appeared when increasing the concentration of P1–AgNPs. The fluorescence of **probe 1** was almost completely quenched as 2.4×10^{-4} M P1–AgNPs was added. Since both **probe 1** and P1–AgNPs (the zeta potential of P1–AgNPs is -22.1 mV) possess negative charges, it may indicate that there is neither complex formation nor energy transfer between them. All these results suggest that the decrease in **probe 1** fluorescence intensity could be mainly attributed to the IFE between P1–AgNPs and **probe 1**.

3.2. Influence of the detection conditions

The detection conditions such as pH, concentrations of P1–AgNPs and H_2O_2 were then optimized for the IFE-based fluorescent assay (see Figs. S1–S3). Waite et al. reported that the interaction between citrate-coated AgNPs and H_2O_2 is pH-dependent [43]. Wang and co-workers also demonstrated that pH is an important parameter influencing the detection of I^- when using colorimetric sensing system [18]. In our sensing system, H_2O_2 may decompose under alkaline environments and pyridyl moieties of P1 tend to protonate in a strongly acidic environment. As shown in Fig. S1, slightly acidic environments (pH=4.0–6.0) is favorable for I^- sensing. The fluorescence restoration reached a maximum at pH 6.0 after the addition

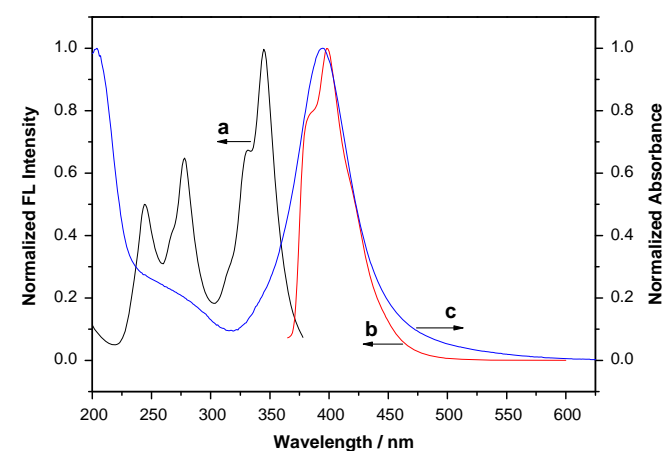


Fig. 1. Fluorescence excitation (a) and emission (b) spectra of **probe 1** and absorption spectrum (c) of P1–AgNPs. [**probe 1**] $=5.0 \times 10^{-7}$ M, [P1–AgNPs] $=2.4 \times 10^{-4}$ M, [P1] $=9.6 \times 10^{-7}$ M.

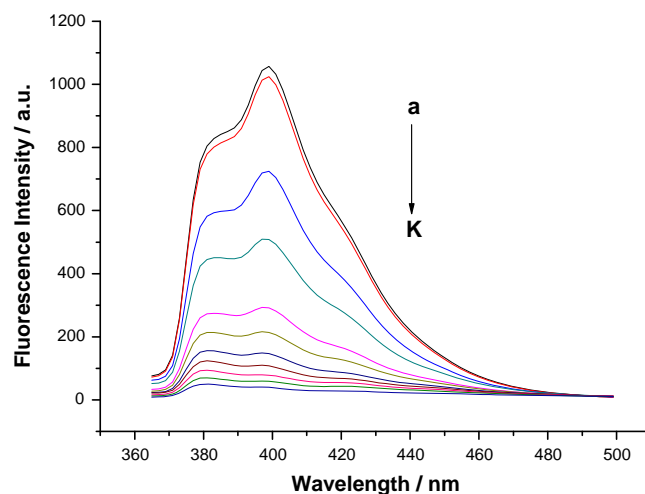


Fig. 2. Fluorescence emission spectra ($\lambda_{\text{ex}}=345$ nm) of 5.0×10^{-7} M **probe 1** in the presence of various concentrations of P1–AgNPs. Curves a to k: 0 , 2.4×10^{-6} , 2.4×10^{-5} , 4.8×10^{-5} , 7.2×10^{-5} , 9.6×10^{-5} , 1.2×10^{-4} , 1.44×10^{-4} , 1.68×10^{-4} , 1.92×10^{-4} and 2.4×10^{-4} M in $\text{H}_3\text{Cit-Na}_2\text{HPO}_4$ buffer solution (pH 6.0).

of I^- . The pH used in the following experiments was therefore set at 6.0. The relative amount of P1–AgNPs in the detection system also affected the fluorescence response toward I^- . As shown in Fig. S2, 2.28×10^{-4} M P1–AgNPs gave the best response when the sensitivity and linear range were taken into account. As shown in Fig. S3, the higher concentration of H_2O_2 would make the oxidation-etching of P1–AgNPs more efficient, which could be important for the fluorescence restoration of **probe 1**. Thus, the concentration of H_2O_2 used in the following experiments was 5.0×10^{-5} M.

3.3. Fluorescence restoration of **probe 1** by I^-

Under the above optimum conditions of pH=6.0, [P1–AgNPs] $=2.28 \times 10^{-4}$ M and [H_2O_2] $=5.0 \times 10^{-5}$ M, the fluorescence detection of I^- was carried out. As shown in Fig. 3, the fluorescence intensity of **probe 1** increases obviously at low concentration of I^- , and it increases steadily at high I^- concentration. Two linear curves were obtained when measured in the range of 5.0×10^{-10} – 1.0×10^{-5} M ($I_r/I_q=1.863+0.082 \log [\text{I}^-]$, correlation coefficient $R=0.991$) and 2.0×10^{-5} – 9.0×10^{-5} M ($I_r/I_q=6.265+1.029 \log [\text{I}^-]$, correlation coefficient $R=0.979$). I_r and I_q represent the fluorescence intensity of P1–AgNPs/**probe 1** system in the presence and absence of I^- at 398 nm, respectively. The full curve in Fig. 3B displays a sigmoidal progression, thereby indicating that multiple equilibria are involved in the process [44]. Since Ag^+ can be produced from the oxidation of AgNPs in the presence of H_2O_2 , the former equilibrium presumably involves the formation of AgI due to its low K_{sp} (8.5×10^{-17}) [45] and the latter equilibrium may involve the AgI-promoted formation of I_2 [18]. Notably, the limit of detection (LOD) of the above IFE-based approach is obtained as low as 0.3 nM at $S/N=3$. These results show that this method has excellent sensitivity, high correlation and a broad range for the quantitative analysis of I^- . Representative iodide measurement methods, including widely practiced Sandell–Kolthoff reaction and novel Ag or AuNPs-based fluorescence sensing, are summarized in Table 1.

3.4. Selectivity of the sensing system

To evaluate the selectivity of the P1–AgNPs/**probe 1**-based IFE system for I^- sensing, different aqueous anions such as Br^- , Cl^- , F^- , IO_3^- , HPO_4^{2-} , H_2PO_4^- , PO_4^{3-} , SO_3^{2-} , CO_3^{2-} , EDTA^{2-} ,

$\text{C}_2\text{O}_4^{2-}$ and NO_3^- were also investigated. As exhibited in Fig. 4, the addition of $2.5 \times 10^{-5} \text{ M I}^-$ to the P1-AgNPs/probe 1 sensing system resulted in a dramatic increase in fluorescence intensity. In comparison, when $2.5 \times 10^{-5} \text{ M}$ of each anion mentioned above was added,

only a slight change in the fluorescence intensity of probe 1 could be observed, thereby indicating that the IFE system provides good selectivity for I^- over various other anions.

3.5. Analysis of I^- in real sample

The good selectivity and ultrasensitivity of the P1-AgNPs/probe 1-based IFE system suggest that the novel method might be directly applied to determine I^- in real samples. Iodide levels in tap water, iodized salt and urine samples were measured according to the experimental procedure. Particularly, the determination of urinary I^- concentration is significant for the diagnosis of iodine deficiency since $\sim 90\%$ of total iodine in urine is present as iodide [46]. The results are shown in Table 2, which exhibits excellent recovery of $\sim 98\%$ (average value). The recovery values were between 91% and 108% in the presence of interfering species (e.g., 50- and 100-fold Cl^-), indicating that the proposed method can be simple and practical for the sensing of iodide.

3.6. Working mechanism for I^- sensing

P1-AgNPs functioning as a novel composite absorber can be readily tuned after the addition of H_2O_2 and I^- due to the fact that H_2O_2 and I^- may lead to the P1-AgNPs oxidation-etching and regeneration, respectively. Thus the optical property of P1-AgNPs will be significantly changed and the IFE between P1-AgNPs and probe 1 will be disrupted. UV-vis spectroscopic measurements and TEM analysis were performed to obtain insights into the

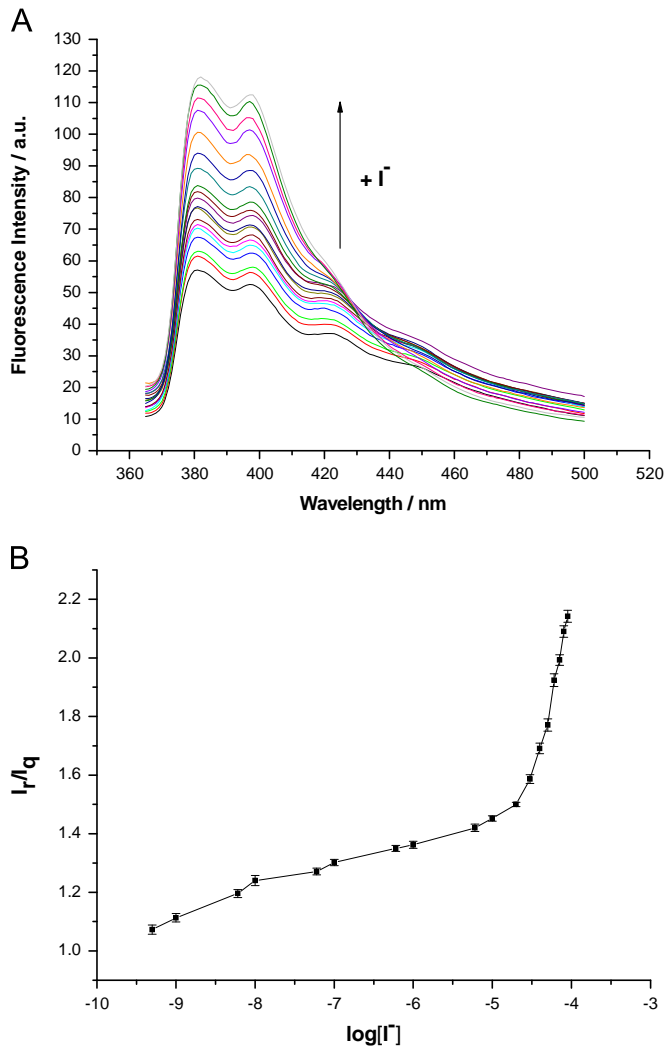


Fig. 3. (A) Fluorescence emission spectra of the P1-AgNPs/probe 1 system with different concentrations of I^- . Down to up: 0 , 5.0×10^{-10} , 1.0×10^{-9} , 6.0×10^{-9} , 1.0×10^{-8} , 6.0×10^{-8} , 1.0×10^{-7} , 6.0×10^{-7} , 1.0×10^{-6} , 6.0×10^{-6} , 1.0×10^{-5} , 2.0×10^{-5} , 3.0×10^{-5} , 4.0×10^{-5} , 5.0×10^{-5} , 6.0×10^{-5} , 7.0×10^{-5} , 8.0×10^{-5} and $9.0 \times 10^{-5} \text{ M}$. (B) Fluorescence recovery of P1-AgNPs/probe 1 system with various concentrations of I^- . I_r and I_q are the fluorescence intensity with and without I^- . $[\text{probe 1}] = 5.0 \times 10^{-7} \text{ M}$, $[\text{P1-AgNPs}] = 2.28 \times 10^{-4} \text{ M}$, $[\text{H}_2\text{O}_2] = 5.0 \times 10^{-5} \text{ M}$, $\text{pH} = 6.0$. Excitation and emission wavelengths of probe 1 were 345 nm and 398 nm, respectively.

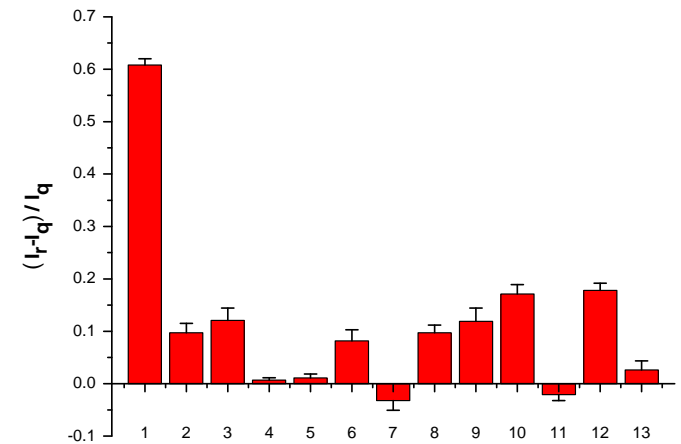


Fig. 4. The Fluorescence response of the P1-AgNPs/probe 1 system containing $5.0 \times 10^{-7} \text{ M}$ probe 1, $5.0 \times 10^{-5} \text{ M}$ H_2O_2 and $2.28 \times 10^{-4} \text{ M}$ P1-AgNPs in the presence of $2.5 \times 10^{-5} \text{ M I}^-$ or other anions at $\text{pH} 6.0$: (1) I^- , (2) Br^- , (3) Cl^- , (4) F^- , (5) IO_3^- , (6) HPO_4^{2-} , (7) H_2PO_4^- , (8) PO_4^{3-} , (9) SO_3^{2-} , (10) CO_3^{2-} , (11) EDTA^{2-} , (12) $\text{C}_2\text{O}_4^{2-}$, and (13) NO_3^- .

Table 1
Comparison of different iodide measurement methods.

Ref.	Detection method	System	Linear range (nM)	LOD (nM)
[11]	Sandell-Kolthoff reaction	CHIP-MSFIA	37–591	37
[12]	Optical emission spectrometry (OES)	DBD-OES	788– 7.88×10^4	236
[13]	Ion chromatography	Concentrator column	1.6–788	0.8
[14]	ICP MS	SEC-ICP MS	–	7.9
[15]	Capillary electrophoresis (CE)	tITP-CE	0–315	1.6
[16]	IAAS	AgI-CN ⁻	0–78.8	9.5
[20]	Raman spectroscopy	Rh6G-adsorbed AuNPs	0.2–47.3	0.2
[25]	Fluorescence sensor	Oligopyrrole derivative	100– 6.0×10^3	90
[28]	Fluorescence nanosensor	FITC-BSA-AuNPs	1– 1.0×10^3	50
[27]	Fluorescence detection	FITC-AuNPs	10.0–600.0	10.0
This work	Fluorescence detection	P1-AgNPs	0.5– 1.0×10^4	0.3

Table 2

Detection of iodide in real sample. All measurements were performed in 2.0 mL PBS, [probe 1] = 5.0×10^{-7} M, [P1-AgNPs] = 2.28×10^{-4} M, pH = 6.0. 20.0 μ L of urine or water sample was added into PBS, [I⁻] of iodized salt sample in 2.0 mL PBS was 1.0×10^{-6} M.

Sample	Spiked (nM)	Detected (nM)	Recovery (%)
Tap water	0	not detected	–
	10	9.8	98
	20	20.2	101
Iodized salt	0	not detected	–
	10	10.0	100
	20	19.2	96
Urine (child)	0	6.7	–
	10	17.5	108
	20	26.1	97
Urine (man)	0	9.1	–
	10	18.3	92
	20	29.5	102
Urine (woman)	0	11.8	–
	10	21.3	95
	20	30.0	91

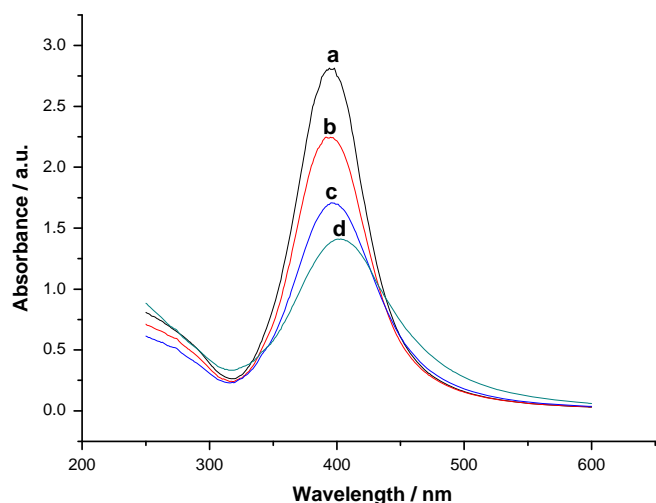


Fig. 5. Absorption spectra of P1-AgNPs in the presence of **probe 1** (a); P1-AgNPs in the presence of H₂O₂ (5.0×10^{-5} M) and **probe 1** (b); P1-AgNP in the presence of H₂O₂ (5.0×10^{-5} M), **probe 1** and I⁻ (5.0×10^{-5} M) (c); P1-AgNP in the presence of H₂O₂ (5.0×10^{-5} M), **probe 1** and I⁻ (5.0×10^{-4} M) (d). [probe 1] = 5.0×10^{-7} M, [P1-AgNPs] = 2.28×10^{-4} M, pH = 6.0.

mechanism of the P1-AgNPs-based I⁻ sensor. As presented in Fig. 5, the absorbance of P1-AgNPs is found to significantly decrease with increasing concentration of I⁻ and an obvious red shift (~ 12 nm, $b \rightarrow d$) in the spectra can be observed, which could be ascribed to the AgI, I⁻ or I₂ adsorbed on the surface of P1-AgNPs in the presence of iodide [18,47]. As a result, the IFE between P1-AgNPs and **probe 1** will be damaged. In addition, Fig. 6 reveals the typical process involving P1-AgNPs oxidation-etching and regeneration. As judged from about 150 individual particles for each sample, the mean diameters of AgNPs were ~ 17 nm (Fig. 6A), 7 nm (Fig. 6B) and 4 nm (Fig. 6C), respectively. Importantly, the AgNPs can be regenerated with a smaller diameter (Fig. 6A and C) after the addition of H₂O₂ and I⁻ via the P1-AgNPs oxidation-etching (Fig. 6B), which could be attributed to the particular role of P1 as a polymer localizer for AgNPs, similar to the previous case of poly(*o*-methoxyaniline) in stabilizing silver nanoparticles by coordination through the nitrogen atoms to AgNPs [48]. In the case of citrate-stabilized AgNPs, however, AgNPs aggregated after interacting with iodide in the presence of

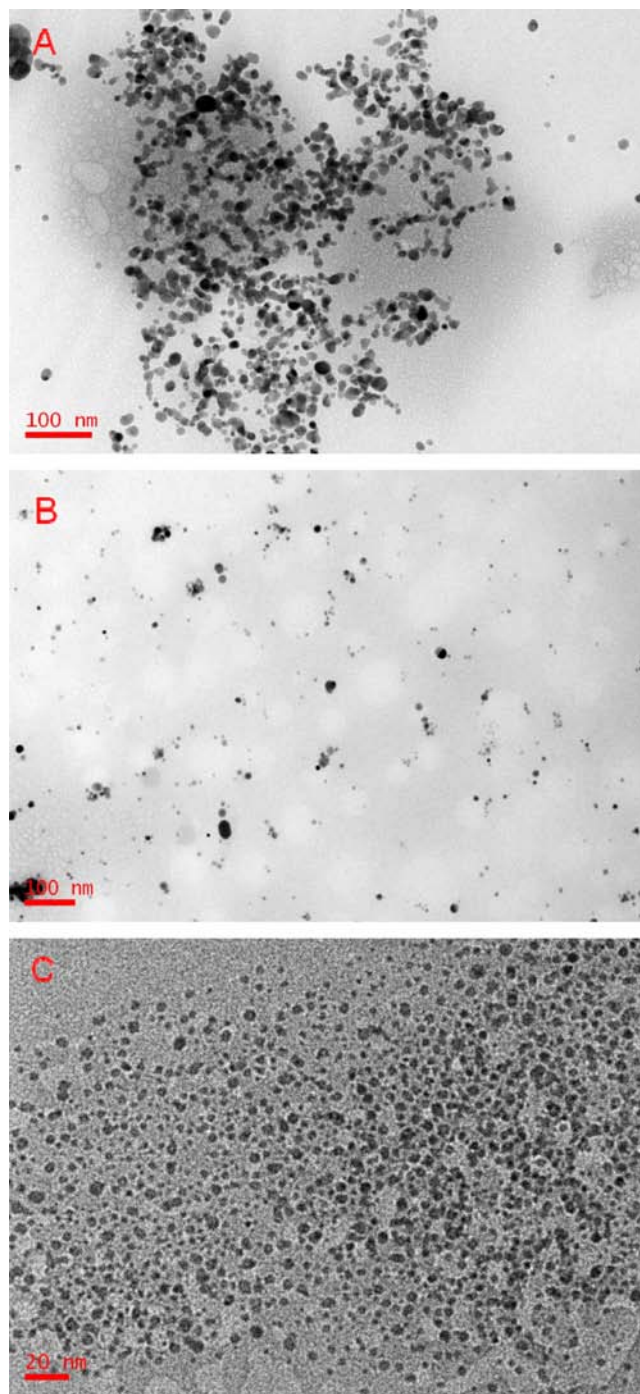


Fig. 6. TEM images of P1-AgNPs (A) and P1-AgNPs before (B) and after (C) adding I⁻ (5.0×10^{-5} M) in the presence of **probe 1** and H₂O₂ (5.0×10^{-5} M) at pH = 6.0.

H₂O₂ since the absorption of AgI could neutralize the negative charges of citrate on the surface of AgNPs (Fig. S4) [18]. Thus, as a new conjugated polyelectrolyte containing pyridinyl and sulfonate groups, P1 demonstrated the novel role of CPE in the design of well-dispersed and highly stable nanoparticles.

4. Conclusions

In summary, we have demonstrated a new and facile method for sensitive and selective detection of iodide anion based on the inner filter effect between P1-AgNPs and **probe 1** due to their

perfectly spectral overlap. The fluorescence of **probe 1** quenched by P1–AgNPs can be efficiently recovered after the addition of H₂O₂ and I[−]. The oxidation-etching and regeneration of P1–AgNPs can be verified by UV–vis and TEM analysis, which providing not only a promising method for the design of well-dispersed and highly stable nanoparticles but also an insight into the new role of conjugated polyelectrolyte. In addition, new CPE could endow novel sensory system with superior performance (i.e., regeneration of nanoparticles), which implies repeated sensing of iodide might be achieved. Under the proper concentration of H₂O₂ and P1–AgNPs at pH 6.0, the detection limit for I[−] is as low as 0.3 nM.

Acknowledgments

Financial support for this research from the National Natural Science Foundation of China (20805014), Natural Science Foundation of Hunan Province (09JJ3018), the Scientific Research Fund of Hunan Provincial Education Department (11C0809 and 12B077) and Program for Science and Technology Innovative Research Team in Higher Educational Institutions of Hunan Province, is gratefully acknowledged.

Appendix A. Supporting information

Supplementary data associated with this article can be found in the online version at <http://dx.doi.org/10.1016/j.talanta.2014.08.025>.

References

- [1] V. Amendola, L. Fabbri, M. Licchelli, A. Taglietti, in: K. Bowman-James, A. Bianchi, E. García-España (Eds.), *Anion Coordination Chemistry*, Wiley-VCH, Weinheim, 2012, pp. 521–552.
- [2] V.K. Gupta, A.K. Singh, P. Singh, A. Upadhyay, *Sens. Actuators B Chem.* 199 (2014) 201–209.
- [3] V.K. Gupta, A.K. Singh, S. Bhardwaj, K.R. Bandi, *Sens. Actuators B Chem.* 197 (2014) 264–273.
- [4] M.R. Ganjali, V.K. Gupta, M. Hosseini, Z. Rafiei-Sarmazdeh, F. Faridbod, H. Goldooz, A.R. Badii, P. Norouzi, *Talanta* 88 (2012) 684–688.
- [5] V.K. Gupta, A.K. Jain, M.K. Pal, A.K. Bharti, *Electrochim. Acta* 80 (2012) 316–325.
- [6] M. Hosseini, V.K. Gupta, M.R. Ganjali, Z. Rafiei-Sarmazdeh, F. Faridbod, H. Goldooz, A.R. Badii, P. Norouzi, *Anal. Chem. Acta* 715 (2012) 80–85.
- [7] V.K. Gupta, L.P. Singh, S. Chandra, S. Kumar, R. Singh, B. Sethi, *Talanta* 85 (2011) 970–974.
- [8] A.K. Jain, V.K. Gupta, L.P. Singh, P. Srivastava, J.R. Rasoni, *Talanta* 65 (2005) 716–721.
- [9] R. Prasad, V.K. Gupta, A. Kumar, *Anal. Chem. Acta* 508 (2004) 61–70.
- [10] P. Pienpinijtham, X.X. Han, S. Ekgasit, Y. Ozaki, *Anal. Chem.* 83 (2011) 3655–3662.
- [11] F.Z. Abouhiat, C. Henríquez, B. Horstkotte, F.E. Yousfi, V. Cerdà, *Talanta* 108 (2013) 92–102.
- [12] Y.L. Yu, S. Dou, M.L. Chen, J.H. Wang, *Analyst* 138 (2013) 1719–1725.
- [13] Y. Bichsel, U. von Gunten, *Anal. Chem.* 71 (1999) 34–38.
- [14] L.F. Sanchez, J. Szpunar, *J. Anal. At. Spectrom.* 14 (1999) 1697–1702.
- [15] K. Ito, T. Ichihara, H. Zhuo, K. Kumamoto, A.R. Timerbaev, T. Hirokawa, *Anal. Chim. Acta* 497 (2003) 67–74.
- [16] P. Bermejo-Barrera, L.M. Fernández-Sánchez, M. Aboal-Somoza, R.M. Anllo-Sendín, A. Bermejo-Barrera, *Microchem. J.* 69 (2001) 205–211.
- [17] J. Ai, Y. Xu, B. Lou, D. Li, E. Wang, *Talanta* 118 (2014) 54–60.
- [18] G.L. Wang, X.Y. Zhu, Y.M. Dong, H.J. Jiao, X.M. Wu, Z.J. Li, *Talanta* 107 (2013) 146–153.
- [19] B. Yang, X.B. Zhang, W.N. Liu, R. Hu, W. Tan, G.L. Shen, R.Q. Yu, *Biosens. Bioelectron.* 48 (2013) 1–5.
- [20] S.S.R. Dasary, P.C. Ray, A.K. Singh, T. Arbneshi, H. Yu, D. Senapati, *Analyst* 138 (2013) 1195–1203.
- [21] P.K. Jain, X.H. Huang, I.H. EL-Sayed, M.A. EL-Sayed, *Acc. Chem. Res.* 41 (2008) 1578–1586.
- [22] K. Wang, X. He, X. Yang, H. Shi, *Acc. Chem. Res.* 46 (2013) 1367–1376.
- [23] P. Zhu, S. Huang, M. Li, N. Ding, B. Peng, L. Kong, Y. Bo, J. Fluoresc. 21 (2011) 179–186.
- [24] S. Lin, M.T. Morris, P.C. Ackroyd, J.C. Morris, K.A. Christensen, *Biochemistry* 52 (2013) 3629–3637.
- [25] S. Nabavi, N. Alizadeh, *Sens. Actuators B Chem.* 200 (2014) 76–82.
- [26] J.N. Zhao, J.H. Deng, Y.H. Yi, H.T. Li, Y.Y. Zhang, S.Z. Yao, *Talanta* 125 (2014) 372–377.
- [27] Y.M. Chen, T.L. Cheng, W.L. Tseng, *Analyst* 134 (2009) 2106–2112.
- [28] S.C. Wei, P.H. Hsu, Y.F. Lee, Y.W. Lin, C.C. Huang, *ACS Appl. Mater. Interfaces* 4 (2012) 2652–2658.
- [29] S.W. Thomas III, G.D. Joly, T.M. Swager, *Chem. Rev.* 107 (2007) 1339–1386.
- [30] B. Liu, G.C. Bazan (Eds.), *Conjugated Polyelectrolytes: Fundamentals and Applications*, Wiley-VCH, Weinheim, 2013.
- [31] Y. Wang, B. Liu, A. Mikhailovsky, G.C. Bazan, *Adv. Mater.* 22 (2010) 656–659.
- [32] A. Bajaj, O.R. Miranda, I.B. Kim, R.L. Phillips, D.J. Jerry, U.H.F. Bunz, V.M. Rotello, *Proc. Natl. Acad. Sci. U. S. A.* 106 (2009) 10912–10916.
- [33] J. Huang, Y. Wu, Y. Chen, Z. Zhu, X. Yang, C.J. Yang, K. Wang, W. Tan, *Angew. Chem. Int. Ed.* 50 (2011) 401–404.
- [34] L. Shang, S.J. Dong, *Anal. Chem.* 81 (2009) 1465–1470.
- [35] L. Xu, B.X. Li, Y. Jin, *Talanta* 84 (2011) 558–564.
- [36] A. Desireddy, B.E. Conn, J.S. Guo, B. Yoon, R.N. Barnett, B.M. Monahan, K. Kirschbaum, W.P. Griffith, R.L. Whetten, U. Landman, T.P. Bigioni, *Nature* 501 (2013) 399–402.
- [37] Y.Q. Hu, Y. Xiao, H.M. Huang, D.L. Yin, X.M. Xiao, W.H. Tan, *Chem. Asian J.* 6 (2011) 1500–1504.
- [38] Y.J. Li, H. Li, Y.L. Li, H.B. Liu, S. Wang, X.R. He, N. Wang, D.B. Zhu, *Org. Lett.* 7 (2005) 4835–4838.
- [39] L. Shang, C.J. Qin, T. Wang, M. Wang, L.X. Wang, S.J. Dong, *J. Phys. Chem. C* 111 (2007) 13414–13417.
- [40] H.B. Li, F.Y. Li, C.P. Han, Z.M. Cui, G.Y. Xie, A.Q. Zhang, *Sens. Actuators B Chem.* 145 (2010) 194–199.
- [41] S. Nagatoishi, T. Nojima, B. Juskowiak, S. Takenaka, *Angew. Chem. Int. Ed.* 44 (2005) 5067–5070.
- [42] Y.L. Tang, Y. Liu, A. Cao, *Anal. Chem.* 85 (2013) 825–830.
- [43] D. He, S. Garg, T.D. Waite, *Langmuir* 28 (2012) 10266–10275.
- [44] D. Aldakov, M.A. Palacios, P. Anzenbacher Jr., *Chem. Mater.* 17 (2005) 5238–5241.
- [45] M. Luo, X. Hou, C. He, Q. Liu, Y. Fan, *Anal. Chem.* 85 (2013) 3715–3722.
- [46] Y.J. Li, Y.T. Tseng, B. Unnikrishnan, C.C. Huang, *ACS Appl. Mater. Interfaces* 5 (2013) 9161–9166.
- [47] P. Mulvaney, *Langmuir* 12 (1996) 788–800.
- [48] A. Dawn, P. Mukherjee, A.K. Nandi, *Langmuir* 23 (2007) 5231–5237.



Synthesis and characterization of ester-bonded stationary phases for liquid chromatography



Szymon Bocian^a, Alicja Nowaczyk^b, Bogusław Buszewski^{a,*}

^a Chair of Environmental Chemistry & Bioanalytics, Faculty of Chemistry, Nicolaus Copernicus University, Gagarin 7 st., 87-100 Torun, Poland

^b Department of Organic Chemistry, Faculty of Pharmacy, Collegium Medicum in Bydgoszcz, Nicolaus Copernicus University, Jurasza 2, 85-094 Bydgoszcz, Poland

ARTICLE INFO

Article history:

Received 23 June 2014

Received in revised form

17 July 2014

Accepted 21 July 2014

Available online 21 August 2014

Keywords:

Ester bonded stationary phase

Liquid chromatography

Stationary phase characterization

Polar embedded stationary phase

ABSTRACT

The new type of stationary bonded phases for liquid chromatography with immobilized artificial membrane properties was synthesized. Based on the modification of diol-bonded silica gel the cholesterol-ester and alkyl-ester stationary phases were obtained. The structures of synthesized material were confirmed by different physico-chemical techniques such as elemental analysis, infrared spectroscopy (FTIR), ¹³C CP/MAS NMR and chromatography. Synthesized stationary phases were characterized and visualized by computer modeling that indicates the regions of potential hydrophobic and polar interactions. Synthesized material possess residual hydroxyl groups that reduce the hydrophobicity of the material and causes better stability at high water concentration. Due to surface properties these materials are became polar embedded stationary phases.

© 2014 Elsevier B.V. All rights reserved.

1. Introduction

Some of the liquid chromatographic analyses needs the application of water-rich mobile phases (more than 85% water or a buffer). In such condition the performance of hydrophobic stationary phases indicate that the bonded ligands might be collapsing. This problem could be solved by increasing of organic content in the mobile phase which should improve solvation and bring bonded ligands back to the original conformation. To avoid this procedure, which reduces the retention and selectivity of the separation, some manufacturers introduce stationary phases incorporated polar groups mixed with the original alkyl ligands (polar embedded stationary phases). Another possibility is to add some polar groups during endcapping procedure (polar end-capped stationary phases) [1]. This produces variation in the bonding.

One of the method increasing the polarity of hydrophobic adsorbent is the synthesis of *N*-acylamide stationary phases [2,3]. These types of adsorbents consist of a hydrophobic alkyl ligand (e.g., C12 or C18) bonded to aminopropyl silica with using amide bond. Such structure of the stationary phase offers better solvation and thus better stability and efficiency in water-rich mobile phases [4].

* Corresponding author. Tel.: +48 56 611 43 08; fax: +48 56 611 48 37.
E-mail address: bbusz@chem.umk.pl (B. Buszewski).

In the group of hydrophobic/hydrophilic phases the cholesterol-bonded material has to be mentioned [5,6]. The first attempt was described by Siouffi's [7]. This methodology relays on the reaction of the terminal amine group of bonded aminopropyl silica with cholesteryl chloroformate. In the same time Buszewski et al. [8], had presented independently the methodology of cholesterol bonded phase synthesis during modification of amino-propyl intermediate deposition. This material offers specific properties and it can be successfully used to separate mixtures by both chromatographic systems: reversed phase and normal-phase [9–13]. Unfortunately they are not so popular than other stationary phases.

Since the late 60's the knowledge of the silica gel modification was developed and led to the synthesis of so-called "dedicated" stationary phases. Coupling the skills with physicochemical studies the nature of the interactions of analytes with the surface of stationary phase enabled design of the new generation chemically bonded stationary phases. The molecular modeling also contributed to the development of a new generation of chromatographic packing. The consequence of making a progress in this area is the introduction of new types of stationary phases which are characterized by a variety of properties. An example can be materials mimic biological membranes. Simplified methods of such chemically bonded stationary phase are shown in Fig. 1.

In 1989, Pidgeon et al. [14] first described the stationary bonded phases for liquid chromatography that mimics the phospholipids bilayer of cell membranes. It was consisted of phospholipids analogs monolayer covalently bonded to the silica surface.

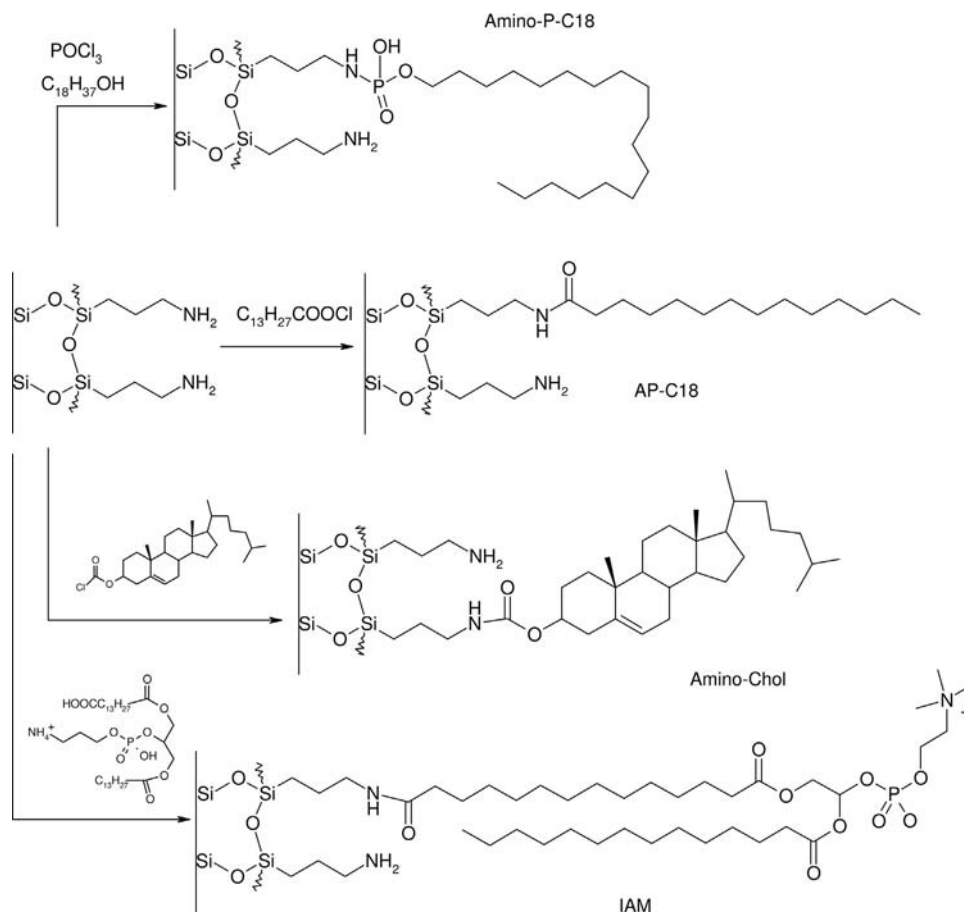


Fig. 1. Simplified methods of the chemically bonded stationary phases, which mimics the cell membrane properties.

This material was called *immobilized artificial membranes* (IAMs) [15,16]. IAM bonded phase more closely mimics the interaction of analytes with biological membranes rather than the classical octadecyl stationary phase. It is caused by combinations of possible hydrophobic, ion pairing, and hydrogen bondings [17,18].

One of the newest material, which simulate the biologic membrane is the *N,O*-dialkyl phosphoramidate stationary phase [19,20]. Physico-chemical properties of those adsorbents allow using them in separation of both hydrophobic and polar substances. Changing the length of main chain in wider range enabled to obtain chromatographic materials with different hydrophobic-polar properties.

The goal of our work was to synthesize a new generation of ester-bonded stationary phases for liquid chromatography which possess properties similar to the cell membrane. Based on the previous experiences with the synthesis of *N,O*-dialkyl phosphoramidate stationary phase, the currently prepared stationary phase was obtained during chemical modification of diol-bonded silica gel. The structure of the synthesized chemically bonded ligands was confirmed by elemental analysis, solid state NMR and FT-IR spectroscopy. The potential application of synthesized material for chromatographic analyses was presented below.

2. Experimental

2.1. Instruments

The liquid chromatograph was a Shimadzu Prominence system (Tokyo, Japan) equipped with ternary gradient pump (LC-20AD), diode array detector (SPD-M20A), an autosampler (SIL-20A), and

a column thermostat (CTO-10AS VP). Data were collected using LabSolution software.

The degree of coverage of the surface by alkylsilyl ligands (α_{RP}) was calculated on the basis of the carbon percentage determined on a Model 240 CHN analyzer (Perkin Elmer, Norwalk, USA).

Solid state NMR measurements were performed on a Bruker Avance III 700 MHz (Karlsruhe, Germany). The ^{29}Si and ^{13}C CP/MAS NMR spectra were obtained with rotation frequency 8 kHz, pulse time 2 ms, acquisition time 0.01643 s, and relaxation time 6 s. All spectra were externally referenced with liquid tetramethylsilane (TMS) and the chemical shifts (δ) were given in parts per million (ppm).

Adsorbents were packed using laboratory-made apparatus equipped with Haskel packing pump (Burbank, CA, USA) into 125×4.6 mm i.d. stainless steel columns using the slurry method. About 1.5 g of the modified silica was made into the slurry with 15 ml of chloroform and placed into the packing apparatus. Methanol has been used as a packing pressurizing solvent during the filling process. Columns were packed under a constant pressure of 40 MPa.

2.2. Materials

As a support for the synthesis the silica gel Kromasil 300 (Akzo Nobel, Bohus, Sweden) were used with particle size $5 \mu\text{m}$, and pore diameter 300 \AA .

Reagents for the stationary phase synthesis: (3-glicidoxypopyl)trimethoxysilane, dodecanoyl chloride, and cholesterol chloroformate were purchased from Alfa Aesar (Karlsruhe, Germany). Organic solvents used during synthesis: toluene, methanol and

hexane were ACS. grade, purchased from Avantor Performance Materials (Center Valley, PA, USA).

Two different mobile phase systems were used in the measurements: methanol–water and acetonitrile–water. Organic solvents (methanol and acetonitrile) were high-purity “for HPLC” gradient grade from Sigma Aldrich (St. Louis, MO, USA). Water was purified using a Milli-Q system (Millipore, El Paso, TX, USA) in our laboratory.

The standard test compounds: aniline, phenol, homologs of benzene and PAHs were obtained from Sigma-Aldrich (St. Louis, MO, USA). The concentration of tests compounds was in the range of 10–40 µg/ml. The injection volumes were in the range 2–10 µl.

2.3. Methods

Silanol activity (S_{AG}) and the hydrophobicity (H_G) of the stationary phases were determined according to the method described by Galushko [21] and commonly used for stationary phases characterization [22]. To determine these factors the analysis of aniline, phenol, benzene and toluene retention were done using a mobile phase containing 60% methanol in water. The silanol activity S_{AG} and hydrophobicity H_G can be calculated as follows using solute retention factors k :

$$S_{AG} = 1 + 3[(k_{aniline}/k_{phenol}) - 1] \quad (1)$$

$$H_G = (k_{toluene} + k_{benzene})/2 \quad (2)$$

In all methods the flow rate was 1 ml/min. Measurements were carried out at 298 K. Column dead volumes were measured using thiourea as a marker.

Computer modeling was performed using the Gaussian 03 program [23]. The visualizations were prepared using the GaussView 4.1 [24]. The starting model of the silica gel surface was taken from our previous work [25]. In the next step the Diol, Diol-Ester C12 and Diol-Chol stationary bonded phases was constructed by substitution the hydrogen atoms from the silanol groups by 1, 2, 3 and 4 diol ligands randomly grafted onto the slice of the silica gel, respectively. Further, the hydrogen atom in diol structure was substituted by alkyl and cholesterol ligands. All the molecules geometries were optimized using the molecular mechanics methods MM3 until the root mean square gradient value becomes smaller than 0.01 kcal mol⁻¹ Å⁻¹. Then the single point energy (SPE) calculations were performed at the DFT/B3LYP level of theory using the 6–31G** basis set. Later, using the surface data generated from Gaussian checkpoint files, and the GaussView 4.1 program, the distribution of charge in a molecule was calculated. To obtain a 3D plot of the MEP, the electrostatic potential cube file was calculated from total SCF density. The contour maps of the electrostatic potential were then drawn using the following parameters: the distance between the grid point of 0.02 Å, and the isovalues 0.0004. All computations were performed on a HP-6200 wx workstation. The Gaussian suite of programs calculates the electrostatic potential maps and surfaces as the distribution of the potential energy of a unit positive charge in a given molecular space, with a resolution controlled by the grid density.

2.4. Synthesis procedure

2.4.1. Diol silica gel

Before the chemical modification of bare silica gel, a sample of adsorbent was placed in a specially designed glass reactor protecting against the contact of reagents with the external environment. Silica gel was treated at 180 °C under vacuum (10⁻² Pa) for 10 h in order to remove physically adsorbed water. Then, the temperature was decreased to 90 °C and (3-glycidoxypropyl)trimethoxysilane

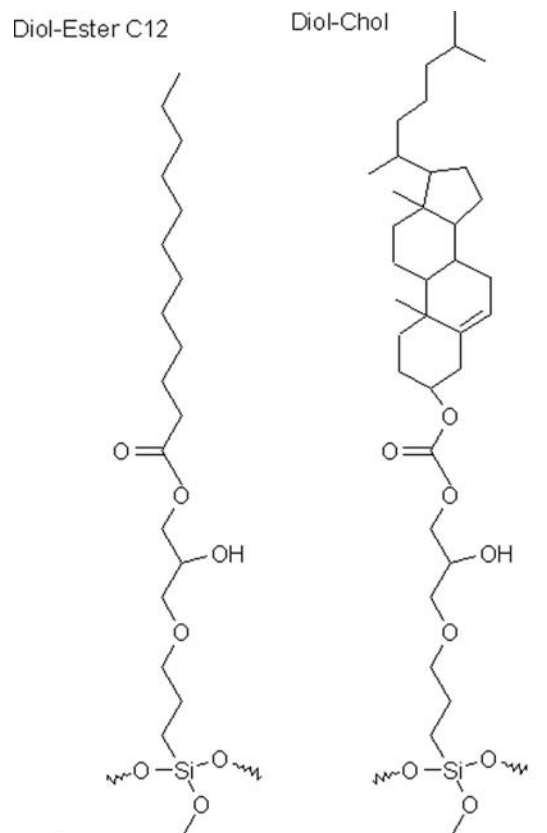


Fig. 2. Structures of synthesized stationary phases: Diol-Ester C12 and Diol-Chol.

was added. After 12 h the reaction products were washed out with toluene, methanol and hexane, and dried.

In the second step, the synthesized material was treated with 1% sulfuric acid to hydrolyze the epoxide ring. After the hydrolysis, the diol-bonded stationary phase was washed in water and methanol. Synthesized material was dried under vacuum.

2.4.2. Diol-Ester C12

The diol-bonded silica gel was placed in a glass reactor and heated up to 100 °C during 10 h. Further, the support was modified using dodecanoyl chloride in toluene solution with addition of triethylamine at 65 °C during 12 h under reflux. The reaction products were washed out with toluene, methanol and hexane. Synthesized material was dried under vacuum.

2.4.3. Diol-Chol

The diol-bonded silica gel was placed in a glass reactor and heated up to 100 °C within 10 h. Then, the support was modified by using cholesteryl chloroformate in toluene solution with addition of triethylamine at 95 °C during 12 h under reflux. The reaction products were washed out with toluene, methanol and hexane. Synthesized material was dried under vacuum. Structures of synthesized stationary phases are shown in Fig. 2.

3. Results and discussion

3.1. Elemental analysis

Synthesized adsorbents were a subject of elemental analysis. Table 1 presents results of chemical modification of the silica gel surface, i.e. content of carbon, hydrogen after each bonding reaction, determined by elemental analysis. It allows the calculation of

bonded ligands coverage density (α_{RP}) on the silica surface. Calculation was performed using Berendsen equation [26]:

$$\alpha_{RP}^I = \frac{10^6 P_C}{1200 n_C - P_C (M_1 - n_X) S_{BET}} \frac{1}{\text{mmol/m}^2} \quad (3)$$

where α_{RP}^I – coverage density [$\mu\text{mol/m}^2$], P_C – percent of carbon [%], n_C – number of carbon atoms in the ligand, M_1 – molar mass of the ligand, n_X – number of functional group in reactive group of the silane, and S_{BET} – specific surface area [m^2/g].

As it can be seen in Table 1, the amount of bonded carbon increases after the second step of the reaction. Additionally, the bonding of cholesterol molecule to diol ligand provides higher carbon deposit on the stationary phase surface. Due to the steric hindrance, the coverage of bonded cholesterol molecules is lower than the coverage density of diol ligands. However, only about 10% of diol ligands remind unbounded in the Diol-Chol stationary phase. The bonding of fatty acid (C12) to diol ligands are more effective. The coverage density of C12 chains is around 10% higher than coverage of diol ligands. It suggests that some of diol ligands created the ester bond by both hydroxyl groups.

3.2. NMR spectroscopy

The structures of the Diol, Diol-Ester C12 and Diol-Chol bonded phases were confirmed by ^{13}C and ^{29}Si cross polarization (CP) MAS-NMR spectroscopy. Fig. 3 displays the obtained ^{29}Si CP MAS NMR spectra. Both spectroscopic techniques are powerful methods for characterizing the chemically bonded stationary phases. The analysis of ^{29}Si CP/MAS NMR spectra obtained for unmodified gel show that on the silica surface three types of silanols are presented: geminal silanols (Q_2 ; $\delta = -92$ ppm), single silanols (Q_3 ; $\delta = -102$ ppm), and siloxane groups (Q_4 ; $\delta = -112$ ppm). After derivatization the intensity of signals (Q_2) and (Q_3) decrease and the intensity of signal (Q_4) increase as a result of siloxane bond

creating (see Fig. 3). After modification reaction new signals are observed. Their chemical shifts depending on the functionalities of used silanes, and they appeared at: T_3 : $\delta = -66.3$ ppm and T_2 : $\delta = -59.2$ ppm. The absence of T_1 signals at $\delta = -48$ ppm indicates a high degree of the crosslinking of ligands on the silica surface [27–31].

Carbon atoms of bonded ligands for each observed signal have been marked on the figure (see Fig. 4). The carbon atom connected to silicon gives a signal indicated by peak at $\delta = 11$ ppm.

The absence of bands at $\delta = 2.5$ ppm proved the presence of a polymeric-type of the stationary phase. The signal at $\delta = 156$ ppm corresponds to the carbon atom in the carbonyl groups and signals at $\delta = 140$ ppm and $\delta = 121$ ppm represent carbons connected by a double bond in the ligand deposition. The carbon atom connected with the hydroxyl group in the cholesterol molecule has a chemical shift of $\delta = 74$ ppm. Signals in the range of $\delta = 19$ – 57 ppm correspond to the cholesterol moiety bonded to aminoalkyl ligands. The NMR analysis confirms the presence of the expected functional groups in the structure of bonded ligands, similar to that presented earlier [9,32,33].

The ^{13}C CP/MAS NMR spectrum of Diol intermediate contains 3 signals. These signals correspond to carbon atom bonded with silicon, bonded with two carbons or bonded with carbon and oxygen atom, as it was shown in Fig. 4A.

The ^{13}C CP/MAS NMR spectrum obtained for the Diol-Chol stationary phase (Fig. 4C) confirmed the presence of cholesterol molecule and alkyl bonded ligands. In the range of chemical shift values from +15 to +60 ppm, peaks corresponding to the bonded organic moiety can be observed [34–38].

In the case of Diol Ester C12 stationary phase, the signal of alkyl carbons may be found in the range 20–35 ppm. Due to low carbon content in both phases, Diol-Chol and Diol-Ester C12 (5.2 and 3.2, respectively), the signals of carbonyl atoms are not visible in the NMR spectra. On the other hand, the NMR spectra confirm the bonding of cholesterol group and alkyl chains. Thus, the synthesized stationary phases were investigated by Fourier Transform Infrared Spectroscopy.

3.3. FTIR spectroscopy

Synthesized stationary phases were also investigated using FTIR spectroscopy. On the spectrum of diol stationary phase the weak signal, that corresponds to methylene group ($-\text{CH}_2-$) may be found at $\tilde{\nu} = 2919$ cm^{-1} and 1459 cm^{-1} . Additionally, signals that correspond to hydroxyl group may be found at $\tilde{\nu} = 3443$ cm^{-1} and

Table 1
Physico-chemical characterization of prepared stationary phases.

Property	Abbreviation	Diol	Diol-Ester C12	Diol-Chol
Carbon percentage [%]	P_C	1.023	3.237	5.244
Hydrogen percentage [%]	P_H	0.621	0.985	1.066
Coverage density [$\mu\text{mol/m}^2$]	α_{RP}	1.32	1.44	1.20

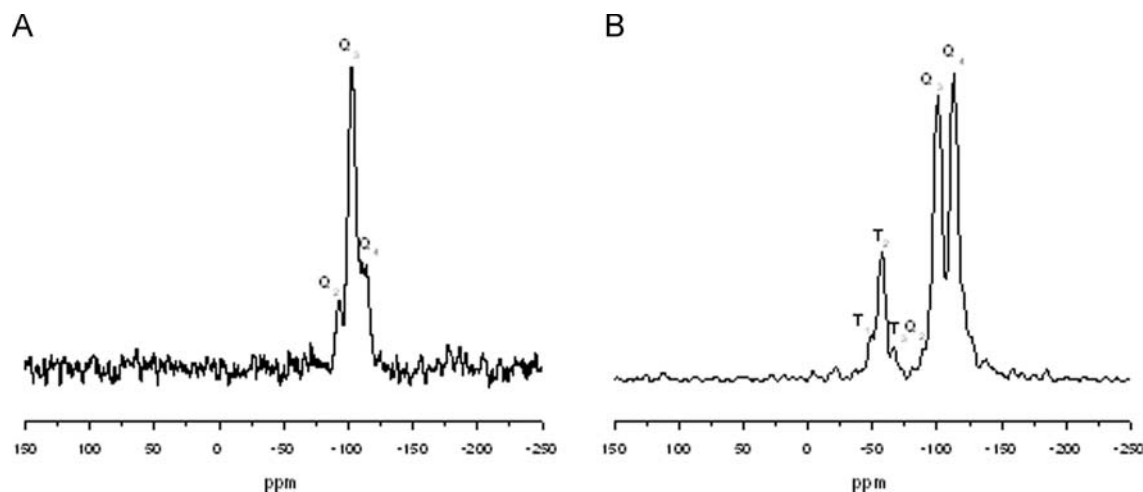


Fig. 3. ^{29}Si CP MAS NMR spectra of bare silica gel (A) and diol bonded phase (B).

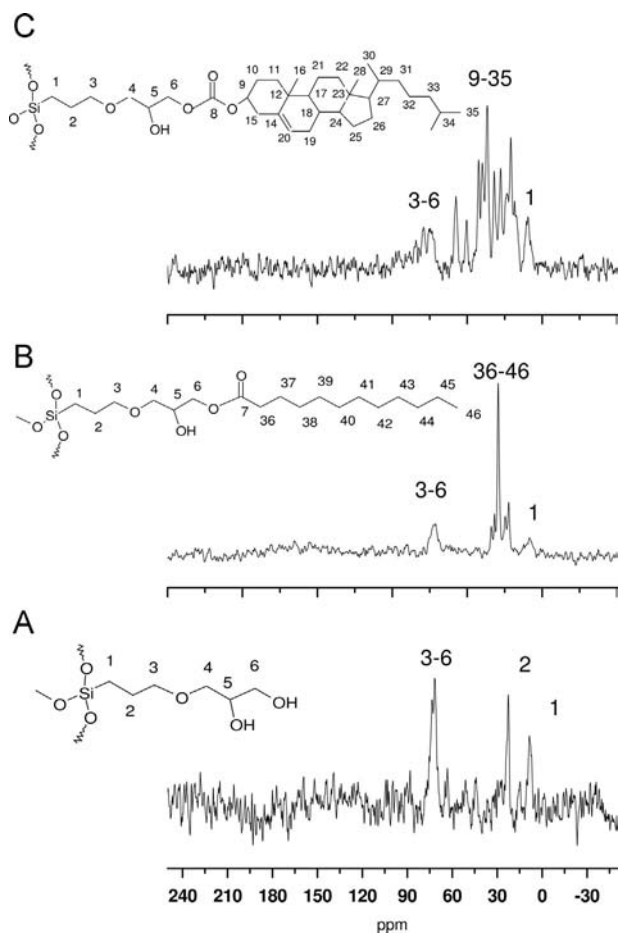


Fig. 4. ^{13}C CP MAS NMR spectra of diol (A), Diol-Ester C12 (B) and Diol-Chol (C) stationary bonded phases.

1635 cm^{-1} and signal of C–O bond at $\tilde{\nu}=1884\text{ cm}^{-1}$. It confirms, that silica gel was modified with diol ligands.

After modification of diol-bonded stationary phase, in the structures of Diol-Chol and Diol-Ester C12, the signals of methyl groups ($-\text{CH}_3$) may be observed at $\tilde{\nu}=2874$ and 2858 cm^{-1} , respectively. The signal of ester bond stretching may be found at $\tilde{\nu}=1744$ and 1727 cm^{-1} . As a result of ester bond creation, the intensity of the hydroxyl groups signal decreases for Diol-Chol (3436 cm^{-1}) and Diol-Ester C12 (3443 cm^{-1}) compared with diol stationary phase (3443 cm^{-1}). Detailed analysis of FTIR spectra is shown in Table 2.

Based on the NMR and FT-IR investigations of synthesized materials, the proposed structures of synthesized adsorbents, presented in Fig. 2, were confirmed. In both materials there are unbounded hydroxyl groups which influencing the hydrophobic/polar properties of the packing material. It has to be emphasized that the presence of ester bond in the ligand structure causes the limitation in the pH range, in which the stationary phase may be operated. Due to properties of ester bond, these materials cannot be used in the mobile phases with extreme pH.

3.4. Structural modeling

For better description of the properties of investigated stationary bonded phases, molecular modeling studies were performed. Our modeling study involves the charge distribution in the studied stationary bonded phases. A common way to visualize the distribution of charge in a molecule is a map of the electrostatic potential in the form of a 3D plot or a 2D contour plot of the

Table 2

The analysis of FT-IR spectra of synthesized materials.

Group	Type	Chemical shifts [cm^{-1}]		
		Diol	Diol-Chol	Diol-Ester C12
–OH	Stretching	3443	3436	3443
–CH ₂	Stretching	2919	2955	2930
–CH ₃	Stretching	–	2874	2858
C–C	Stretching	–	2025	2034
C–O	Stretching	1884	1889	1889
R–C–O–R'	Stretching	–	1744	1727
–OH	Bending	1635	1631	1636
–CH ₂	Bending	1459	1471	1459
–O–Si–O–	Stretching	1100	1100	1104
–O–Si–O–	Bending	805	805	805
–O–Si–O–	Bending	470	471	470

electrostatic potential distribution (MEP). Regions of the electron density surface that are more negative than others in a MEP are colored red. Regions in the MEP that are less negative (or are positive) are blue. The spectrum of color indicates the trend in charge value from most negative (red) through green and yellow (neutral) to positive (blue) [39,40].

Taking into account the molecular interaction, it would be more informative to discuss the hydrophobicity and hydrophilicity phenomena. From this point of view, if specific area is more red or blue, the more hydrophilic is the molecular fragment. Consequently colors ranging from green to yellow accounts for hydrophobic properties of the fragment.

According to the basic theory of electrostatics, the negative potentials correspond to attraction of the probe unit charge by the higher electron density in the space, while the positive potentials correspond to repulsive interactions of the probe charge with unshielded nuclear forces present in the low electron density spaces [41]. Silica gel surface, Diol intermediate, Diol-Ester C12 and Diol-Chol MEP plots are presented in Fig. 5. The color code of these maps is in the range between -0.03972 a.u. (deepest red) and 0.03972 a.u. (deepest blue). As can be seen from the MEP, regions having the negative potential are over the electronegative atom (oxygen atom), the regions having the positive potential are over the hydrogen atoms. The calculated MEP shows that the most negative electrostatic potential is concentrated around oxygen atoms. In the case of oxygen, the presence of hydrogen (diol group) results in strongly positive potential at their side shielding the effects of oxygen atoms alone. Regions having extremely positive electrostatic potential are these including H atoms near the silica gel surface (silanols), which implies their hydrophilic character. However, around the H atoms of the alkyl chain and cholesterol molecule attached to the diol group via ester bond, electrostatic potential is in the range specific for hydrophobic character. From this result, we can say that the stationary bonded phases have hydrophilic character at the vicinity of the silica surface, diol-bonded groups and hydrophobic properties starting at about the 10–13 Å above silica surface. Results of stationary phase surface modeling confirms, that such materials may become a polar embedded stationary phase. They offer both, hydrophobic and polar interaction in chromatographic system. Additionally, the hydrophilic character at the vicinity of the silica surface and ester bonds should cause better stability of these materials at high water concentration during chromatographic process.

3.5. Polarity/hydrophobicity investigation

The retention of four standard compounds (aniline, phenol, benzene and toluene) on the tested stationary phases was compared using mobile phase containing 60% methanol in water.

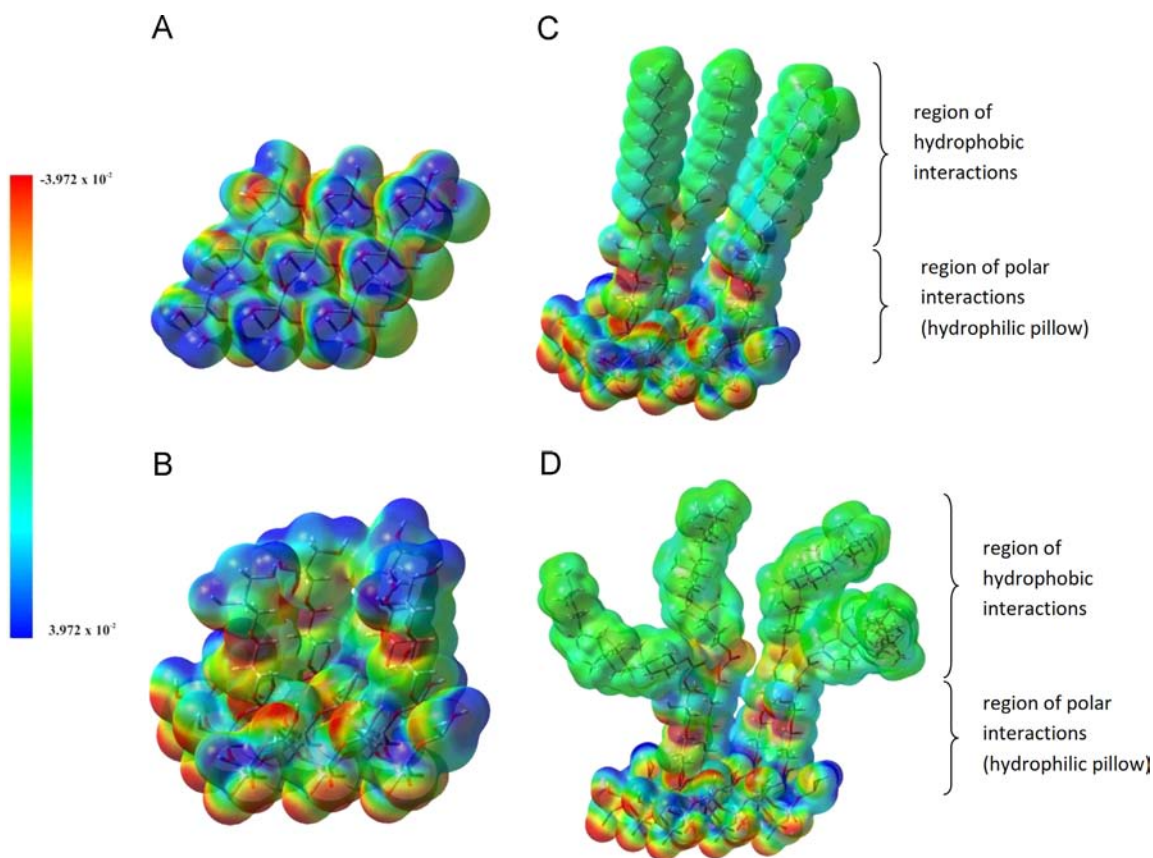


Fig. 5. Calculated electrostatic potential maps for silica gel (A), diol (B), Diol-Ester C12 (C) and Diol-Chol (D) stationary bonded phases.

Silanol activity and stationary phase hydrophobicity were calculated according to Galushko test [21]. The results are presented in Table 3. These two parameters obtained from Galushko test differentiate phenyl-bonded stationary phases.

Diol-Ester C12 and Diol-Chol stationary bonded phases exhibit specific surface properties. Due to the polar groups in the ligand structure (e.g., hydroxyl and carbonyl groups) the hydrophobicity of the adsorbent is reduced. It is observed in the comparison of Diol-Chol with Amino-Chol stationary phase, where cholesterol packing synthesized on the amine-bonded silica exhibit significantly higher hydrophobicity. On the other hand, both Diol-Ester C12 and Diol-Chol materials exhibit high silanol activity. This may be attributed not only to residual silanol interactions, but also with polar interaction of hydroxyl groups in the diol moiety. Similar result was observed for *N,O*-dialkyl phosphoramidate C18 [20]. It has to be mentioned, that despite of lower hydrophobicity synthesized stationary phases may be applied in reversed phase liquid chromatography (RP LC). This was discussed in next paragraph.

3.6. Reversed-phase retention

Both chemically bonded stationary phases, Diol-Ester C12 and Diol-Chol, were tested in RP LC conditions. As a test sample, the mixture of alkyl benzene derivatives was used. Chromatograms are shown in Fig. 6. The retention of alkyl benzene derivatives was higher on Diol-Chol stationary phase, as a result of higher hydrophobicity of this material. Less hydrophobic Diol-Ester C12 material offers lower retention.

As seen in Fig. 6 both stationary phases allow to separate test compounds with good selectivity. Detailed parameters of the separation, such as retention factor, number of theoretical plates, resolution, selectivity and tailing factor are presented in Table 4.

Table 3

Silanol activity and hydrophobicity of the investigated stationary phases.

Property	Diol-Ester C12	Diol-Chol	Amino-Chol*	<i>N,O</i> -dialkyl phosphoramidate C18*
Hydrophobicity	0.26	0.65	4.02	0.80
Silanol activity	1.46	0.87	0.50	2.24

* Data taken from the literature for the comparison [20].

As it can be seen in Table 4, prepared columns exhibit sufficient selectivity up to 8300 theoretical plates per 125 mm length column. Together with good selectivity, synthesized material provide high resolution of the test sample. For the comparison, the dependences of log *k* parameters plotted against carbon number in the alkyl chain of alkyl benzene derivatives are shown in Fig. 7.

Embedded polar groups (hydroxyl and carbonyl) in the bottom part of bonded ligands constitute a region of polar interactions, as it was indicated in Fig. 5. This polar region adsorbs preferentially water molecules. The stable solvated structure is formed, which was called “hydrophilic pillow” [2,42]. These stationary phases are more stable in MeOH–water mobile phase because of the hydrogen bonds creation than in the case of ACN–water mixture.

The alkyl chains and cholesterol molecules form hydrophobic layer over the “hydrophilic pillow” (see Fig. 5). This “hydrophilic pillow” structure causes effective shielding of residual silanols from the contact with nonpolar analytes. It has to be mentioned, that on the stationary phase surface the residual accessible silanols are present, which may be partially ionized. In the case of “hydrophilic pillow”, silanols are shielded by adsorbed water. As a result of these phenomena, in reversed-phase conditions when nonpolar solutes are analyzed, the organic chains participate in the

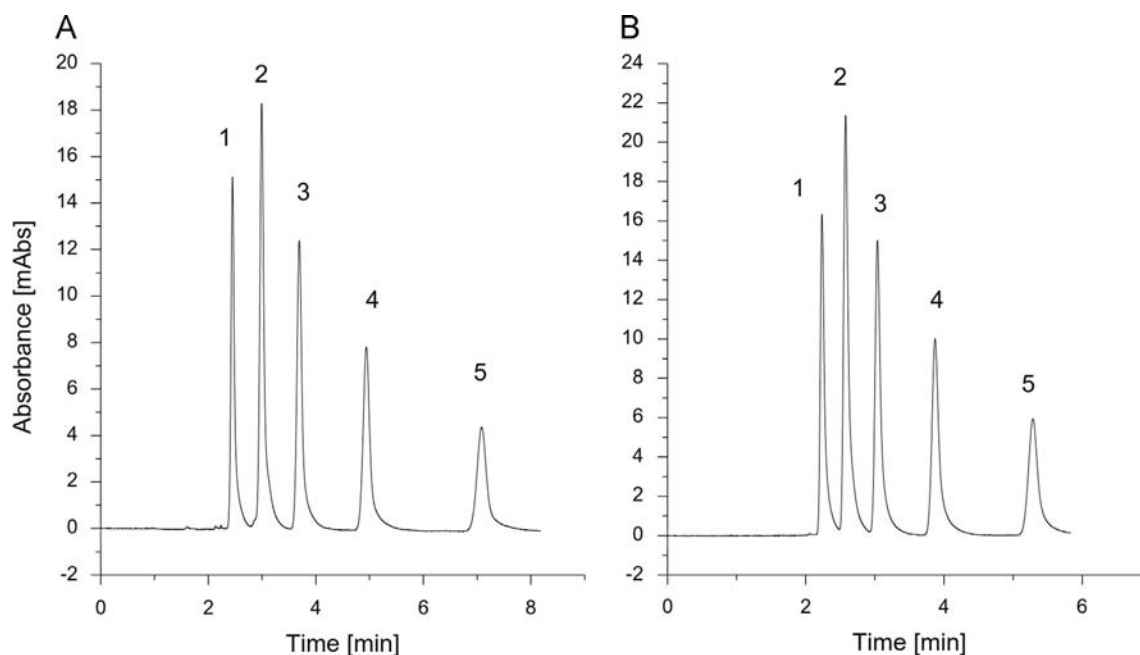


Fig. 6. Separation of alkyl benzene derivatives: benzene (1), toluene (2), ethylbenzene (3), propylbenzene (4) and butylbenzene (5) on Diol-Chol stationary phase; 60% MeOH in water (A) and Diol-Ester C12 stationary phase; 50% MeOH in water (B).

Table 4
Parameters of alkyl benzene derivatives separation on synthesized stationary phases.

Conditions	Compound	Retention factor (<i>k</i>)	Number of theoretical plates	Resolution (R_s)	Selectivity (α)	Tailing factor (10%)
Diol-Chol 60% MeOH	Benzene	0.61	7937	–	–	1.48
	Toluene	0.97	8183	4.48	1.58	1.51
	Ethylbenzene	1.43	7929	4.68	1.47	1.33
	Propylbenzene	2.24	7654	6.36	1.57	1.25
	Butylbenzene	3.65	7734	7.82	1.63	1.16
Diol-Ester C12 50% MeOH	Benzene	0.47	7564	–	–	1.64
	Toluene	0.70	7668	3.10	1.48	1.62
	Ethylbenzene	1.00	7884	3.62	1.44	1.38
	Propylbenzene	1.55	7948	5.37	1.55	1.22
	Butylbenzene	2.48	8318	6.98	1.60	1.00

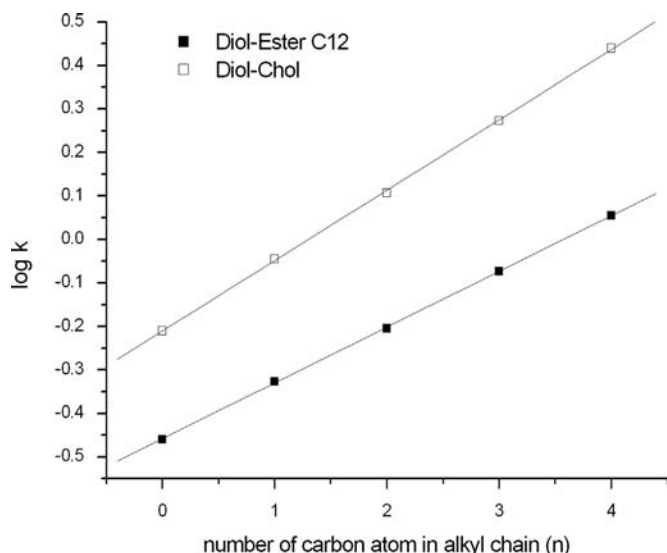


Fig. 7. Dependences of $\log k$ of alkyl benzene derivatives with different number of carbon atom in the alkyl chain. Mobile phase: 50% MeOH in water.

retention, only. The hydrophilic part is excluded from the interactions with hydrophobic solutes such as alkyl benzene homologs. These solutes do not migrate to water-rich layer. As a result, presented stationary phases work properly in RP LC systems.

Stationary phases were also tested using PAHs. Both stationary phases separates PAHs, however, the Diol-Chol material provides better selectivity which may be attributed to the presence of cholesterol molecule. The exemplary chromatograms of PAHs separation using MeOH or ACN as an organic modifiers are shown in Fig. 8.

Detailed parameters of the separation presented in Fig. 8 are listed in Table 5. In the case of PAHs separation, higher efficiency was obtained, up to 10,400 theoretical plates per 125 mm length column. Unfortunately, in tested conditions, it was impossible to separate phenantrene and anthracene in reasonable time of analysis in isocratic conditions.

4. Conclusions

The new types of stationary phases for liquid chromatography were synthesized. Obtained materials were investigated using

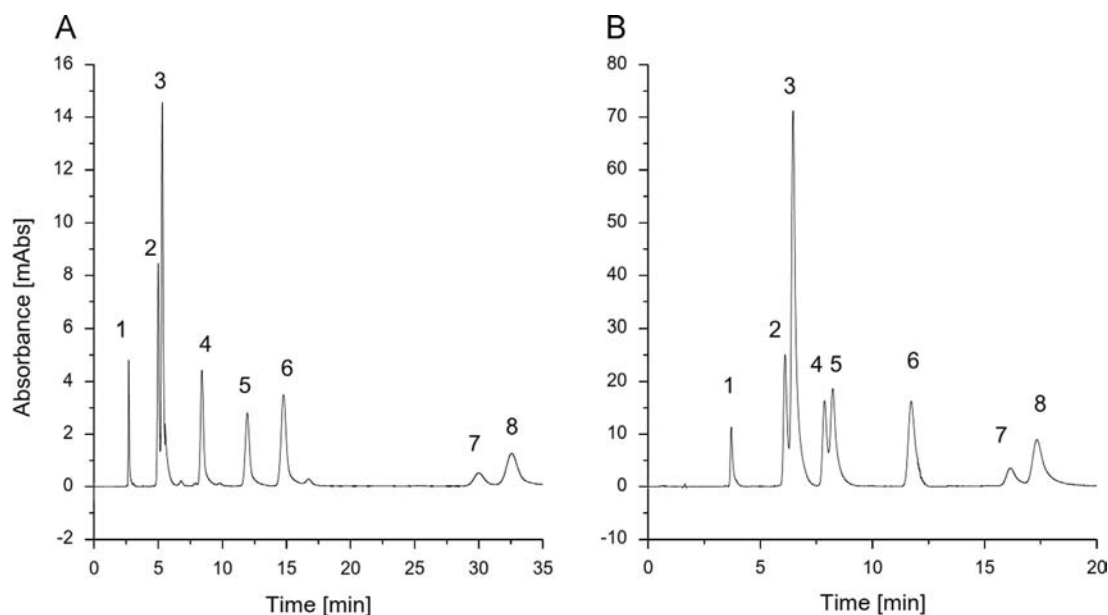


Fig. 8. Separation of PAHs: naphthalene (1), phenantrene (2), anthracene (3), pyrene (4), chrysene (5), benzo(a)anthracene (6), perylene (7) and benzo(a)pyrene (8) on Diol-Chol stationary phase (A) using 70% MeOH in water and on Diol-Ester C18 (B) using 40% ACN in water.

Table 5

Chromatographic parameters of PAHs separations.

Conditions	Compound	Retention factor (k)	Number of theoretical plates	Resolution (R_s)	Selectivity (α)	Tailing factor (10%)
Diol-Chol 70% MeOH	Naphthalene	0.78	8110	–	–	1.34
	Phenanthrene	2.29	7196	12.93	2.95	–
	Anthracene	2.50	6795	1.28	1.09	1.25
	Pyrene	4.53	6699	9.24	1.81	1.16
	Chrysene	6.86	7066	7.23	1.51	1.07
	Benzo(a)anthracene	8.72	7081	4.45	1.27	1.08
	Perylene	18.73	10,405	16.21	2.15	1.22
	Benzo(a)pyrene	20.43	7393	1.92	1.09	1.16
Diol-Ester C12 40% ACN	Naphthalene	1.44	8186	–	–	1.44
	Phenanthrene	3.02	7649	10.81	2.10	–
	Anthracene	3.25	7172	1.23	1.08	1.53
	Pyrene	4.17	7800	4.24	1.28	–
	Chrysene	4.42	6359	0.95	1.06	–
	Benzo(a)anthracene	6.72	9220	7.76	1.52	1.17
	Perylene	9.62	8227	7.36	1.43	1.24
	Benzo(a)pyrene	10.40	7221	1.56	1.08	1.47

instrumental analysis. Their structures of synthesized materials were confirmed using the IR and NMR spectroscopy. New stationary phases: Diol-Ester C12 and Diol-Chol were tested according their application in reversed-phase chromatography. In this conditions Diol-Chol exhibits higher retention of nonpolar compounds as a result of higher hydrophobicity. The structure of the bonded ligands offers specific properties of the adsorbents, such as relatively low hydrophobicity due to the presence of polar embedded groups (hydroxyl and carbonyl).

Ester groups embedded in the structure of bonded ligands and residual and hydroxyl groups constitute a layer of polar interactions. It causes the presence of “hydrophilic pillow” on the stationary bonded phase surface, which is inaccessible for non-polar solutes.

Acknowledgments

This work was supported by Ministry of Science and Higher Education, Grant no. NCN 2013/09/D/ST4/03807 for period

2014–2017. The authors thank Akzo Nobel (Bohus, Sweden) for kind donation of the Kromasil 300 silica gel used in this study.

References

- [1] J. Layne, *J. Chromatogr. A* 957 (2002) 149–164.
- [2] B. Buszewski, J. Schmid, K. Albert, E. Bayer, *J. Chromatogr.* 552 (1991) 415–427.
- [3] B. Buszewski, M. Jezierska-Switla, S. Kowalska, *J. Chromatogr. B* 792 (2003) 279–286.
- [4] B. Buszewski, M. Jaroniec, R.K. Gilpin, *J. Chromatogr. A* 668 (1994) 293–299.
- [5] S. Bocian, M.T. Matyska, J.J. Pesek, B. Buszewski, *J. Chromatogr. A* 1217 (2010) 6891–6897.
- [6] A. Catabay, C. Okumura, K. Jinno, J.J. Pesek, E. Williamsen, J.C. Fetzer, W. R. Biggs, *Chromatographia* 47 (1998) 13–20.
- [7] C. Delaurent, V. Tomao, A.M. Siouffi, *Chromatographia* 45 (1997) 355–363.
- [8] M.A. Al-Haj, P. Haber, R. Kalisz, B. Buszewski, M. Jezierska, Z. Chiltonczyk, *J. Pharm. Biomed. Anal.* 18 (1998) 721–728.
- [9] B. Buszewski, M. Jezierska, M. Welniak, R. Kalisz, *J. Chromatogr. A* 845 (1999) 433–445.
- [10] B. Buszewski, M. Jezierska, B. Ostrowska-Gumkowska, *Mater. Chem. Phys.* 72 (2001) 30–41.
- [11] J.J. Pesek, M.T. Matyska, *LC–GC N. Am.* 25 (2007) 480–490.
- [12] B. Buszewski, M. Jezierska-Switla, R. Kalisz, A. Wojtczak, K. Albert, S. Bachmann, M.T. Matyska, J.J. Pesek, *Chromatographia* 53 (2001) S204–S212.

- [13] C. Courtois, G. Pagès, S. Caldarelli, C. Delaurent, *Anal. Bioanal. Chem.* 392 (2008) 451–461.
- [14] C. Pidgeon, U. Venkataram, *Anal. Biochem.* 176 (1989) 36–47.
- [15] S. Ong, S. Cai, C. Bernal, D. Rhee, X. Qiu, C. Pidgeon, *Anal. Chem.* 66 (1994) 782–792.
- [16] X. Qiu, S. Ong, C. Bernal, D. Rhee, C. Pidgeon, *J. Org. Chem.* 59 (1994) 537–543.
- [17] A. Taillardat-Bertschinger, P.-A. Carrupt, F. Barbato, B. Testa, *J. Med. Chem.* 46 (2003) 655–665.
- [18] C. Courtois, C. Allais, T. Constantieux, J. Rodriguez, S. Caldarelli, C. Delaurent, *Anal. Bioanal. Chem.* 392 (2008) 1345–1354.
- [19] S. Bocian, A. Nowaczyk, B. Buszewski, *Anal. Bioanal. Chem.* 404 (2012) 731–740.
- [20] S. Bocian, M. Paca, B. Buszewski, *Analyst* 138 (2013) 5221–5229.
- [21] S.V. Galushko, *Chromatographia* 36 (1993) 39–42.
- [22] M. Molikova, P. Jandera, *J. Sep. Sci.* 33 (2010) 453–463.
- [23] M.J. Frisch, G.W. Trucks, H.B. Schlegel, G.E. Scuseria, M.A. Robb, J.R. Cheeseman, V.G. Zakrzewski, J.A. Montgomery, R.E. Stratmann, S. Burant, J.C. Dapprich, J.M. Millam, A.D. Daniels, K.N. Kudin, M.C. Strain, O. Farkas, J. Tomasi, V. Barone, M. Cossi, R. Cammi, B. Mennucci, C. Pomelli, C. Adamo, S. Clifford, J. Ochterski, G. A. Petersson, P.Y. Ayala, Q. Cui, K. Morokuma, D.K. Malick, A.D. Rabuck, K. Raghavachari, J.B. Foresman, J. Cioslowski, J.V. Ortiz, B.B. Stefanov, G. Liu, A. Liashenko, P. Piskorz, I. Komaromi, R. Gomperts, R.L. Martin, D.J. Fox, T. Keith, M.A. Al-Laham, C.Y. Peng, A. Nanayakkara, C. Gonzalez, M. Challacombe, P.M. W. Gill, B.G. Johnson, M.W. Chen, W. Wong, J.L. Andres, M. Head-Gordon, E.S. Replogle, J.A. Pople, *Gaussian 03, Revision D.01*, Gaussian, Inc., 2004.
- [24] GaussView, Version 4.1, Semichem, Inc., Shawnee Mission, KS, 2003.
- [25] B. Buszewski, S. Bocian, A. Nowaczyk, *J. Sep. Sci.* 33 (2010) 2060–2068.
- [26] G.E. Berendsen, L. de Galan, *J. Chromatogr.* 196 (1980) 21–37.
- [27] D.W. Sindorf, G.E. Maciel, *J. Am. Chem. Soc.* 105 (1983) 1487–1493.
- [28] B. Buszewski, M. Jezierska, M. Wehniak, D. Berek, *J. High Resolut. Chromatogr.* 21 (1998) 267–281.
- [29] K. Krupczyńska, B. Buszewski, P. Jandera, *Anal. Chem.* 76 (2004) 227A–234A.
- [30] K. Albert, *J. Sep. Sci.* 26 (2003) 215–224.
- [31] G.E. Maciel, D.W. Sindorf, *J. Am. Chem. Soc.* 102 (1980) 7606–7607.
- [32] K. Albert, E. Bayer, *J. Chromatogr.* 544 (1991) 345–370.
- [33] H. Yeman, T. Nicholson, J.J. Pesek, M. Matyska, K. Albert, *J. Sep. Sci.* 36 (2013) 173–181.
- [34] B. Buszewski, R.M. Gadzała-Kopciuch, M. Markuszewski, R. Kaliszan, *Anal. Chem.* 69 (1997) 3277–3284.
- [35] B. Buszewski, Z. Suprynowicz, P. Staszczuk, K. Albert, B. Pfeiderer, E. Bayer, *J. Chromatogr.* 499 (1990) 305–316.
- [36] J.J. Pesek, M.T. Matyska, R.J. Yu, *J. Chromatogr. A* 947 (2002) 195–203.
- [37] H.R. Ansarian, M. Derakhshan, M. Rahman, T. Sakurai, M. Takafuji, I. Taniguchi, H. Ihara, *Anal. Chim. Acta* 547 (2005) 179–187.
- [38] E. Bayer, K. Albert, J. Reiners, M. Nieder, D. Muller, *J. Chromatogr.* 264 (1983) 197–213.
- [39] A.R. Leach, *Molecular Modelling: Principles and Applications*, Prentice Hall, Englewood Cliffs, 2001.
- [40] J.B. Foresman, A. Frisch, *Exploring Chemistry with Electronic Structure Methods*, Gaussian, Inc., Pittsburg, PA, 1998.
- [41] T.W.G. Solomons, C.B. Fryhle, *Organic Chemistry*, 2004.
- [42] R. Gadzała-Kopciuch, B. Buszewski, *J. Sep. Sci.* 26 (2003) 1273–1283.



Review

Nanoparticles applied to plant science: A review



Sandra Cristina Capaldi Arruda^a, Alisson Luiz Diniz Silva^{b,c}, Rodrigo Moretto Galazzi^{b,c},
Ricardo Antunes Azevedo^a, Marco Aurélio Zezzi Arruda^{b,c,*}

^a Laboratory of Plant Biochemistry and Genetics, Department of Genetics, Escola Superior de Agricultura Luiz de Queiroz, ESALQ, USP, Piracicaba, SP 13400-970, Brazil

^b Spectrometry, Sample Preparation and Mechanisation Group, Institute of Chemistry, University of Campinas – Unicamp, P.O. Box 6154, Campinas, SP 13083-970, Brazil

^c National Institute of Science and Technology for Bioanalytics, Institute of Chemistry, University of Campinas – Unicamp, P.O. Box 6154, Campinas, SP 13083-970, Brazil

ARTICLE INFO

Article history:

Received 2 June 2014

Received in revised form

16 August 2014

Accepted 18 August 2014

Available online 24 August 2014

Keywords:

Characterization

Synthesis

Toxicity

Sensing

Phytoremediation

Analytical techniques

ABSTRACT

The present review addresses certain important aspects regarding nanoparticles and the environment, with an emphasis on plant science. The production and characterization of nanoparticles is the focus of this review, providing an idea of the range and the consolidation of these aspects in the literature, with modifications on the routes of synthesis and the application of the analytical techniques for characterization of the nanoparticles (NPs). Additionally, aspects related to the interaction between the NPs and plants, their toxicities, and the phytoremediation process, among others, are also discussed. Future trends are also presented, supplying evidence for certain possibilities regarding new research involving nanoparticles and plants.

© 2014 Elsevier B.V. All rights reserved.

Contents

1. Introduction	693
2. Characterization of the nanoparticles	694
2.1. Characterization based on separation techniques	694
2.2. Characterization based on microscopy techniques	695
2.3. Characterization based on spectrometric techniques	695
2.4. Detecting nanoparticles in plants	696
3. Nanoparticles in the plants	698
3.1. Nanoparticles promoting growth and development in plants	698
3.2. Nanoparticles and plant phytotoxicity	699
4. Phytoremediation and nanoparticles	701
5. Trends	703
6. Conclusion	703
Acknowledgments	703
References	703

1. Introduction

In nanoscience or in nanotechnology science, a particle is defined as a small object that behaves as an entire unit regarding its transport and properties. Therefore, the particle diameter is a variable used to

* Corresponding author at: Spectrometry, Sample Preparation and Mechanisation Group, Institute of Chemistry, University of Campinas – Unicamp, P.O. Box 6154, Campinas, SP 13083-970, Brazil. Tel.: +55 19 3521 3089; fax: +55 19 3521 3023.

E-mail address: zezzi@iqm.unicamp.br (M.A. Zezzi Arruda).

classify those particles. By convention, coarse particles are those that cover a range from 10,000 to 2,500 nm, fine particles are those ranging from 2,500 to 100 nm, and nanoparticles (NPs) (or ultrafine particles) are those sized from 1 to 100 nm, whether they are dispersed in gaseous, liquid or solid media [1,2]. Nanostructured materials did not first come into existence with the recent emergence of the field of nanotechnology; the natural world is abundant with examples of systems in nanoscale structures. However, we have witnessed recent advances in the synthesis and characterization tools that have fueled an escalation in the study and industrial use of nanostructured materials. NP research is currently an area of intense scientific interest driven by the desire to fabricate materials with novel and improved properties due to a wide variety of potential applications in the areas of physical, chemical, biological and health sciences and other interdisciplinary fields of science and engineering [1,3].

Recently, the use of NPs in commercial products and industrial applications has significantly increased, although understanding the interaction mechanisms at the molecular level between the NPs and the biological systems is clearly lacking [4,5]. Moreover, certain NP properties, such as the large specific surface area and its greater reactivity, have raised questions concerning its adverse effects on human and environmental health [6,7]. Regarding this possibility and with a goal to support the sustainable development of nanotechnology, it is expected that possible risks must be evaluated to elucidate all of the relevant aspects involved in the uses of the NPs. However, the information concerned about the fate of the NPs in water and soil remain limited. Certain ideas related to the involvement of the NPs in the environment have suggested that they might be bioaccumulated through the food chain and can accumulate in organisms at the top of the food chain. Corroborating this idea and considering plants as the producers in the food chain, these organisms are an important component in the ecological system and may serve as a potential pathway for the transport of the NPs and as a route for bioaccumulation into the food chain [8].

Currently, positive and negative effects of NPs on plants have been reported, and researchers have studied the effects of NPs on plant germination and growth with the goal to promote their use for agricultural applications [5]. However, certain reports have confirmed that NPs can induce phytotoxicity and have a negative effect on seed germination and growth, but simultaneously, the exclusive properties of NPs can be used to improve seed germination and crop performance [5]. Concerning the nanotoxicity, Rico et al. [9] have commented that there are no conclusive studies and that those studies involving NPs and plant toxicity are only beginning; it is also clear that this aspect requires additional research.

In this context, we believe that research related to the use, application and elucidation of the action mechanism of the NPs in plants is essential, whether developed in the environmental area or in physiology and crop production, and this review was designed to evaluate the NPs produced in this area over the last 10 years, aiming to provide a perspective on the state of the art in the use of NPs in plant science. To date, relatively little is known about the uptake, accumulation and responses to engineered NPs by plants; therefore, this review attempts to examine and note the possible phytotoxicity and/or beneficial stimulatory effects of the application of the NPs in plants.

2. Characterization of the nanoparticles

The characterization of the NPs is essential to obtain more information about their properties and their applications, focusing on toxicological studies [10]. A large variety of techniques (see Fig. 1) is used in the characterization of NPs, such as composition, morphology,

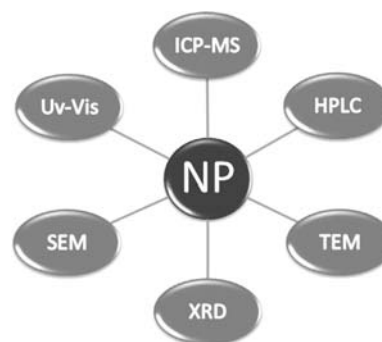


Fig. 1. Some techniques currently applied for the characterization and/or quantification of nanoparticles. SEM: scanning electron microscopy, UV-vis: UV-vis spectrophotometry, ICP-MS: inductively coupled plasma mass spectrometry, HPLC: high performance liquid chromatography, TEM: Transmission electron microscopy, XRD: X-Ray diffraction.

coating, size, among others [10–12]. UV-vis spectroscopy, Near Infrared (NIR), Fourier Transform Infrared Spectrometry (FTIR), scanning electron microscopy (SEM), transmission electron microscopy (TEM), atomic force microscopy (AFM), X-ray diffraction (XRD), High-performance liquid chromatography (HPLC) and related techniques with atomic spectrometry, such as the single particle inductively coupled plasma mass spectrometry (SP-ICP-MS) and flow field-flow fractionation inductively coupled plasma mass spectrometry (AF4-ICP-MS) are highlighted in this review. Other techniques could be used to investigate other characteristics of NPs, such as electrical conductivity, resistivity, capillary electrophoresis, among others [10,11].

The choice of the technique for NP characterization should consider the complexity of the matrix, the analyte concentration and the physico-chemical characteristics. In certain cases, separation and/or sample dilution techniques can be used to enable the characterization process. The techniques described in this review can be separated into the following three groups: separation, microscopy and spectroscopic, as has been proposed by Fabrega et al. [10].

2.1. Characterization based on separation techniques

Separation techniques are typically employed to characterize the size [13,14] and/or shape of the NPs [15,16]. The first separation techniques employed in the study of the NPs and the nanostructures are centrifugation and ultrafiltration. The separation is based on the difference in the settling time of the NPs and the porosity of the filter [11]. Centrifugation is inefficient at separating NPs with similar sizes, and co-sedimentation may occur. Furthermore, this technique is inadequate for the separation of NPs smaller than 10 nm [10,11]. Ultrafiltration is largely applied to the fractionation of samples containing different NPs [13]. However, distinguishing the aggregation of the structures of larger particles is not possible with this technique, and the separation of NPs with similar sizes is not currently possible by simple separation techniques, such as centrifugation [10,11].

HPLC is one of the most efficient separation techniques, effectively promoting the separation of small sizes (< 10 nm) of NPs. For example, Soto-Alvaredo, Montes-Bayón and Bettmer [13] using the reverse phase, have performed the speciation of NPs over a range of 10–40 nm and have differentiated the NPs from the ion route (silver), in this case. Care must be taken to ensure the efficiency of this technique because of the small interaction of the analyte with the matrix components so that the separation occurs by the interaction of the analyte with the chromatographic phases. In this technique, the identification is based on the NP size, and the differentiation requires a minimum difference of 10 nm among the NPs analysed. Furthermore, the differentiation between the

clusters and the isolated NPs was not possible using HPLC; however, it is a promising technique when used with ICP-MS [13].

Additional widespread separation techniques are gel electrophoresis and capillary electrophoresis (CE) [15–17]. One example is the work reported by Xu et al. [15] in which the separation of the Au NPs using gel electrophoresis has been accomplished. The separation of NPs occurs using their different mobilities, different loads, sizes and interactions with the matrix of each NP. Polyacrylamide gel electrophoresis (PAGE) has small pores, and the heterogeneity of the pores can be high, which may prevent the use of this technique to characterize the NPs [17]. However, the use of preparative electrophoresis with agarose gel has proven to be promising for this purpose [15].

Capillary electrophoresis also appears to be a promising technique; it features a low consumption of the sample and reagents [17] and is applicable in the separation of metal NPs, metal oxide NPs, and polymer NPs [10]. For example, in the study by Liu et al. [18], the separation of the Au NPs (5–41 nm) based on the size of the particles in solution has been performed using CE. This study has revealed that there is a linear relationship between the electrophoretic mobility and the radius of the NPs in which under the experimental conditions, the sodium dodecylsulfate can coat the NPs, reducing the interaction with the capillary wall.

Other separation or fractionation techniques involved in the characterization of the NPs are size exclusion chromatography (SEC), cross-flow ultrafiltration (CFUC), flow field-flow fractionation (AF4), among others [10,11,17]. The AF4 technique is provided in more detail because it is currently coupled with ICP-MS.

2.2. Characterization based on microscopy techniques

Microscopy is one of the most used techniques for the characterization of NPs. Microscopy is generally applied to the evaluation of size, shape and particle aggregation [10,17]. The primary advantage of these techniques is the absence of a comparison with standards because the images of the NPs are generated, and, in certain cases, three-dimensional images are produced [10]. The information is obtained on a particles-to-particles basis [11], enabling more accurate information about the NPs. However, the quantitative process becomes extremely time consuming and is dependent on the statistical tools.

Another difficulty in using microscopy techniques is related to the sample preparation. The drying process can lead to agglomeration of the NPs, causing a response that differs from the actual characteristic of the sample [10,17]. This problem may be even greater when employing a real matrix containing natural NPs and the presence of organic matter.

The SEM is applied to studies of metal NPs, because a conductive material is required to undergo this analysis [11,19]. In addition, this material must be coated with gold or graphite, and the analysis is performed under vacuum. However, this process can promote agglomeration of the NPs, leading to loss of information.

Among the microscopy techniques, the most used is TEM [10–12,17,19,20]. This technique allows the visualization of organic matter, because it is stained with heavy metals [11], allowing differentiation from a few nanometers to tens of nanometers with a high resolution along the 3D-images [10,11]. Although widely employed, TEM is time consuming because it requires many images to ensure the representativeness of the results and can be compromised by the subjectivity of the choice of regions for the photography when visualization of the entire sample is not possible using this technique [17].

AFM is a high-resolution technique (< 1 nm) that has been applied to characterize the NPs. The images are atomic topographies in which the sides are overestimated, whereas the accuracy for the height is relatively high. In the study by Hasselov et al.

[11], a comparison between the microscopy techniques has been performed, and AFM and TEM have exhibited close and accurate results, whereas SEM has exhibited a low accuracy [10,11].

2.3. Characterization based on spectrometric techniques

Characterization using spectrometric analysis techniques is the most used in the study of NPs, especially UV–vis spectrometry. UV–vis spectra provide information on particle aggregation and the average particle size [18,21]. This technique is based on the absorption of plasmons, generated by free electrons on the surface of the NP, which interact with the electromagnetic field; a higher radius of the NP causes the absorption to shift to higher wavelengths [22,23]. UV–vis spectrometry is an economical technique and is widely used to monitor the syntheses of the NPs but can also be applied as a detector for separation techniques, such as CE, AF4 and HPLC. Certain visual characteristics are also applied to the monitoring of summaries; currently, the color change caused by the change in the form of the interaction with light is an indication of the formation of NPs during the synthesis process [17,19,21]. In the study by Rajasekharreddy et al. [21], UV–vis has been used to differentiate the size of the NPs synthesized in plants. The observed results using the UV–vis technique have been confirmed by further characterization techniques.

X-ray diffraction (XRD) has a wide application in the field of nanostructures characterization. This technique provides elementary NP information and displays information about the crystalline state [11,19]. According to Hasselov et al. [11], information about the NP constitution, even when the amount of the NP element constitution is low, is possible due to the good sensitivity of this technique. Dispersive spectroscopy X-ray (EDX) has also been applied to gain elementary information about the material [10,24]. The EDX presents semi-quantitative information; however, it is possible to obtain information about each particle [10]. One elegant example is the study performed by Chen et al. [24], in which the composition of the AuNP has been determined by EDX and has been shown feasible for NPs larger than 20 nm.

The coating of the NPs is largely evaluated by techniques involving infrared radiation. Among these techniques, FTIR has been highlighted, which has primarily been applied to identify functional groups of organic compounds that coat the surface of the NPs with a stabilising action or by adsorption [25,26]. This technique was used to identify the coating of NPs synthesized by fungi. The identification has revealed that proteins reduce the metal and the coating and stabilize the formed NPs by preventing aggregation and/or oxidation [26]. In addition to the information about the shape, size and coating, quantification of the NPs is another important parameter. The quantification has been widely performed by mass spectrometry with inductively coupled plasma (ICP-MS), which presents a high sensitivity and allows multi-elemental quantification [10].

Other applications have been developed using ICP-MS, enabling not only the quantification but also the acquisition of information about the size and the size distribution of the NPs; this is possible using the technique of SP-ICP-MS or AF4-ICP-MS [27]. These techniques are promising in terms of characterization of the NPs primarily because they allow the following: (i) working with dilute solutions; (ii) faster analysis compared with microscopy analysis; (iii) simple or non-existent sample preparation; and (iv) avoidance of particle agglomeration. In addition to these advantages, these techniques also have a high sensitivity, allowing the characterization of 10 nm diameter NPs [27,28]. However, there are also certain limitations with these techniques; the most relevant are that a certain amount of statistical work for SP-ICP-MS is required and multiple analyses are necessary to be representative. For AF4-ICP-MS, the primary limitations are the high cost and the

possibility of changing the properties of the NPs during fractionation. For both of these techniques, the characterization of those NPs that have more than one metal becomes difficult [28].

Another coupling of ICP-MS with separation techniques has previously been shown in the literature and also appears promising in terms of characterization of the NPs, primarily due to the speed of the analysis.

2.4. Detecting nanoparticulates in plants

In the scientific literature, there have been many studies involving NPs and plants, providing a warning of the possible adverse effects once those materials act as transponders to specific targets inside of an organism [29], to specific organelles inside a cell [30], or are bound to a protein or RNA molecules in the cells [31]. Due to the high surface/volume ratio, the NPs are extremely reactive and catalytic [32] and may pass through the cell membranes. However, the interactions of the NPs with these systems are not well known. To better exemplify this issue, Fig. 2 illustrates possible NP dynamics in plant and soil. In this context, certain studies that have been published with this theme are discussed in this review, highlighting the analytical techniques and experimental developments employed to evaluate the possible alterations caused by exposure to NPs.

In the study by Lee et al. [33], the phytotoxicity of AgNPs in crop plants has been investigated. The plants showed a correlation between the growth efficiency and the concentration of the AgNPs once the smaller growth of the plants cultivated with AgNPs was observed. This growth inhibition is due to the absorption of the AgNPs by the plants and the presence of dissolved Ag ions, which can also be toxic. The bioavailability of the AgNPs was small in the soil, and the authors have considered that the toxicity of these NPs was reduced [34] and have evaluated the effects of the AgNPs suspension used as an antifungal and antibacterial fertiliser in rice. After application of the AgNPs, the capacity of the response of the plants was evaluated, which showed a notable change in color compared with the control plants, possible because the AgNPs were bound to the cell wall. Moreover, the plants exposed to low concentrations of AgNPs showed higher growth than the control plants, whereas at higher AgNPs concentrations, a minor growth was observed due to the alterations in the cell morphology and in the structural characteristics.

In this type of study with plant species, it is also important to evaluate the effects of ions. For example, Yin et al. [35] have evaluated the effects on seed germination and the growth of many species of plants cultivated with two different types of AgNPs. According to the authors, AgNPs caused the same or stronger effects than AgNO_3 on the growth of the plants, confirming the

high toxicity of the AgNPs. Moreover, based on their results, the authors have indicated the importance of studies using this approach to understand the interaction and transport of AgNPs and the direct and indirect effects of these NPs in the plants. In another report, the accumulation and the biological effects of SeNPs on tobacco plants cultivated with $530 \mu\text{mol L}^{-1}$ SeNPs have been evaluated [36], revealing that the roots of the tobacco plants accumulated a high concentration of Se (ca. 3000 mg kg^{-1}). Moreover, the plants were also cultivated with selenate to evaluate the total concentration and distribution of Se in the plant compared with the SeNPs. The authors have verified that selenate, in the $265\text{--}532 \mu\text{mol L}^{-1}$ concentration range, showed toxic and inhibitory effects on plant growth, and a higher quantity of total Se accumulated in the plants, whereas that of the SeNPs treatment, at the same concentrations, stimulated the germination and growth of the plants. This result may be due to the different natures of the two Se species. Additionally, the excess of selenate or selenite can also induce oxidative stress, catalyzing the oxidation of the thiols and simultaneously generating superoxides with physiologic alterations in the plant morphology [37].

Larue et al. [38] have evaluated the accumulation, uptake and effect of TiNPs in wheat. The seeds were germinated for 15 days on sand soaked with the Hoagland solution, and after germinating, each plantlet was carefully transferred to an individual vial containing a TiO_2 -NP suspension (100 mg L^{-1}). The plants were exposed to TiO_2 -NPs for 7 days for the accumulation and translocation experiments and for the investigation of the effect of the TiNPs on plant development. Ti-rich clusters were observed in the plant roots cultivated with the TiNPs, indicating the accumulation of the NPs in the wheat roots. The authors have suggested a direct interaction between the size of the TiNPs and the cell wall components. Concerning the uptake, only the TiNPs of a smaller size were detected in the wheat leaves. However, according to the authors, ICP-MS failed to detect any statistically significant differences in the Ti content in the leaves of the plants exposed to lower NPs compared with the leaves of the control plants. Finally, the authors have concluded that the accumulation of the TiNPs in the plants does not induce any oxidative stress in the leaves, indicating that these NPs do not affect wheat photosynthesis.

Studies involving the bioavailability of hematite NPs in *Arabidopsis thaliana* (*A. thaliana*) have been performed by Marusenko et al. [39]. In this study, *A. thaliana* was grown on agar media with the following 3 different Fe treatments: media amended with Fe_2O_3 NPs (Fe-NP), media amended with ethylenediaminetetraacetic acid bound to Fe (EDTA-Fe), and a control, without any Fe addition (No-Fe). To compare the Fe uptake among the plants grown in these three treatments, UV-visible spectroscopy was used to compare the chlorophyll concentration. The EDTA-Fe treatment showed higher chlorophyll absorption than the other two treatments tested when the spectra for the No-Fe and Fe-NP plants were similar and, generally, had lower absorbance than those from the EDTA-Fe treatment. These results demonstrated that No-Fe and Fe-NP treated plants had less chlorophyll than the EDTA-Fe treatment. This result is consistent with the visual observation of yellow leaves in 95% of plants in the No-Fe and Fe-NP treatments, whereas 100% of the plants in the EDTA-Fe treatment exhibited green leaves, suggesting that the Fe-NPs were not used for chlorophyll production. Another method to evaluate Fe uptake consisted of the determination of the total Fe in the plant tissue using ICP-MS. According to the results, on the 7th day, the Fe concentration for the three treatments was the highest, decreasing throughout the remainder of the experiment due to a progressive dilution of the plant-Fe with the increase of the biomass. On day 7, the EDTA-Fe treated plants contained 642 mg kg^{-1} Fe, the Fe-NP plants contained 236 mg kg^{-1} Fe, and the No-Fe plants contained 336 mg kg^{-1} Fe. Throughout the experiment, the authors have considered that the higher Fe concentrations in the plants treated with EDTA-Fe

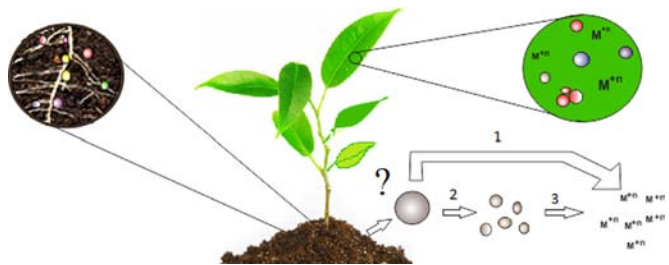


Fig. 2. Theoretical nanoparticle dynamics in plant and soil. As proposed by different authors and emphasized in this review, the behavior of NPs in plants can be evaluated under different points of view, but until now, it is not entirely clear. The figure shows some possible steps related to the NP dynamics: In (1) the NP is directly decomposed in the soil, then producing ions, which may be incorporated to plants, or “large” NPs are decomposed firstly in the soil, producing smaller NPs (2), which may be incorporated as they are, or these smaller NPs are decomposed again, forming ions (3), which may be incorporated to plants.

compared with the Fe-NP treated plants and the similar internal Fe concentrations between the No-Fe and Fe-NP treated plants confirmed that *A. thaliana* was able to take up EDTA-Fe but not Fe-NP. Due to these results, the authors have suggested that the NPs were not bioavailable.

The effect of the nanoscale Zn oxide particle (ZnO-NP) on the germination, growth and yield of peanuts has been evaluated by Prasad et al. [39]. The peanut plants were cultivated in soil with the following three different treatments: ZnO-NPs, bulk ZnSO₄ as the Zn source and a control group. The bulk Zn and ZnO-NP treatments improved the seed germination rate and shoots and roots length compared with the control, and the ZnO-NP treatment showed a higher stimulator effect in the peanut growth. In addition, the plants treated with bulk ZnSO₄ showed a smaller amount of chlorophyll and a shorter plant height compared with the ZnO-NPs. The uptake of Zn by the seeds was confirmed by the SEM-EDAX measurements. This analysis confirmed the presence of higher amounts of Zn in regions in which the C and N concentrations were higher in those seeds treated with the ZnO-NPs.

Burklew et al. [40] have evaluated the growth, development and microRNA expression of tobacco exposed to aluminum oxide NPs (Al₂O₃-NP) in agar media. This study demonstrated that Al₂O₃ had a negative effect on the growth and development of tobacco plants when the concentration of the NPs was increased. For microRNA analysis by real-time PCR (RT-PCR) and quantitative real-time PCR (qRT-PCR), the total RNA was extracted using the mirVana miRNA Isolation Kit (Ambion, Austin, TX), according to the manufacturer's standard protocol. The total RNA was then quantified, the quality was evaluated using a Nanodrop ND-1000 spectrophotometer (Nanodrop Technologies, Wilmington, DE), and the RNA samples were stored in a -80 °C freezer. The results confirmed that the Al₂O₃-NP treatment altered the expression levels of certain microRNAs in the tobacco. At higher concentrations of the NPs (0.5 and 1%), all of the microRNAs tested were up-regulated. However, at 0.1% Al₂O₃-NPs, all of the tested miRNAs were down-regulated, except for microR156, microR157, and microR172, which were up-regulated. These three microRNAs were up-regulated in response to an increase in the Al₂O₃-NPs exposure, but these changes in expression were insignificant.

In another study [42], the developmental responses of maize and cabbage exposed to AgNPs and ZnO-NPs have been evaluated along with their respective ionic salts (AgNO₃ and ZnSO₄) for comparative studies. According to the results, ionic Ag showed a higher uptake and phytotoxicity compared with the AgNPs when the average root length of the plants treated with AgNO₃ was shorter compared with the AgNPs. This fact was confirmed by the results obtained through Ag quantification in maize seedlings using ICP-MS, which showed more than a 55-fold higher Ag (as total Ag) uptake with the AgNO₃ (200 µg mL⁻¹) treatment than the baseline control. In contrast, this biouptake was 4.5-fold higher with the AgNP treatment than the control. Thus, it is evident that NPs versus ionic salt treatments showed a different potential of the metal-based NPs and their ions for developmental toxicity in agriculturally important crop plant species.

The uptake of water-dispersible CdSe/ZnS quantum dot (QD) NPs by *Arabidopsis thaliana* plants using a hydroponic culture has been investigated by Navarro et al. [43]. The total Cd/Se concentrations were determined for the exposed plants by ICP-MS. The uptake of the QDs by *A. thaliana* was compared with the uptake of free Cd²⁺ and SeO₃²⁻. These ions were to be taken up by *A. thaliana* once the membrane transporters mediated the entrance of these ions through the hydrophobic lipid bilayer. Uptake of Cd²⁺ by plants is generally mediated by cation (Ca²⁺/Fe²⁺/Mn²⁺/Zn²⁺) transporters, whereas for SeO₃²⁻, there is no evidence of uptake mediated by membrane transporters. In plants exposed to Cd and Se, the presence of these ions in the leaves indicated a certain

amount of translocation from the roots. For the QDs, uptake was only observed when the NPs were conjugated to organic nitrogen substrates, such as glycine, arginine and chitosan. According to the results, on day 7 of the exposure period, the plant cell remained impermeable to the QDs, which were neither endocytosed or transported passively/actively through the plant roots. This result is possibly due to the stability of the QDs in the suspension. It was unclear whether the oxidative stress was due to the uptake of the intact QDs or the dissolved ions.

A comparative study of the effects of TiO₂ and the Ag NPs on tomatoes cultivated in a hydroponic culture has been performed by Song et al. [44]. For both of the particles, independent of the concentration, no significant differences in the germination rates were observed. Additionally, for the TiO₂-NPs exposure, the root length and biomass were unaltered. However, the plants treated with the AgNPs exhibited significant decreases in root growth, even at the lowest (50 mg L⁻¹) concentration used, whereas those exposed to the highest concentration (5000 mg L⁻¹) failed to show significant increases in root growth throughout the experimental period. The authors have presumed that these seedlings died due to their lack of growth after six days and, consequently, set 5000 mg L⁻¹ as the limit of exposure. Moreover, the biomass of the tomato decreased with an increasing AgNP concentration, indicating that the NPs produced toxicity at low levels, and according to the ICP emission spectrometry results, the metal uptake from the AgNPs was higher than TiO₂ when the Ag concentrations in AgNP were significantly higher compared with the Ti concentrations in the TiO₂-NPs-treated plants. This difference may be due to changes in TiO₂-NPs hydrodynamic diameters and agglomeration, whereas the AgNPs showed smaller hydrodynamic diameters. The Total Antioxidant Capacity (TAC) did not significantly change among the treatments for both of the NPs. However, the superoxide dismutase (SOD) enzyme activity, which is an indicator of stress and is known to increase in plants exposed to toxic metals [45], was altered for both of the NPs, providing evidence that the NPs induced physiological stress.

The tissue level uptake and spatial distribution of the gold NPs (AuNPs) with different surface charges in rice (*Oryza sativa* L.) roots and shoots under hydroponic conditions has been investigated using laser ablation-inductively coupled plasma-mass spectrometry (LA-ICP-MS) by Koelmel et al. [46]. Freeze-dried rice shoot and root samples were washed with a deionised water, acetone, and deionised water sequence to remove any surface contaminants. When suitable solid standards for the gold determination in plant tissue were not readily available, the calibration was performed using a series of prepared gold spiked solid cellulose standards to evaluate the Au concentration distribution in the rice tissue by LA-ICP-MS. Horizontal linear laser ablation scans across the untreated control and 1.6 mg L⁻¹ of Au as the AuNPs-treated rice shoot samples in the short-term uptake experiment were evaluated employing a laser energy of 35%, a spot size of 35 mm, a repetition rate of 5 Hz, and a scan speed of 5 mm/s for the initial laser ablation experiments. According to the results, the background ¹⁹⁷Au/¹³C signal across the control rice shoot blade demonstrated a low Au background signal that was similar to the control samples. However, the AuNPs with the neutral [AuNP(0)] and negative [AuNP(-)] charge treated rice showed high ¹⁹⁷Au/¹³C signals against the control, whereas the AuNPs with the positive [AuNP(+)] charge-treated rice samples slightly increased in this shoot sample. These results showed visual evidence of the Au uptake by the rice plants, revealing that they are heterogeneously distributed in the tissue. For the short-term treatment after 5 days, the concentration of Au in the rice roots determined by LA-ICP-MS was highest in the plants treated with AuNP(+), lower in the plants treated with AuNP(0), and lowest for the plants treated with AuNP(-) for two replicate

measurements of the same rice plant root and analysed at different times. However, this pattern distribution was opposite for the rice shoots, with the AuNP(+)-treated rice having the lowest concentration of AuNP in the shoot and the AuNP(−)-treated rice having the highest concentration. These results demonstrated that rice bioaccumulates the AuNPs with the level distribution dependent on the surface charge of the NP, and the LA-ICP-MS approach might aid the biomonitoring of the interaction of the AuNPs with the plant cells.

3. Nanoparticles in the plants

An interesting review focusing on NPs in edible plants published by Rico et al. [9], commented that not all of the plants exposed to or treated with NPs will present toxicity or even any positive effects. Similarly, it is not possible to attest that no effects will be observed. These authors have suggested that proteomic, genomic, and metabolomic studies will be helpful for those researchers aiming to better understand the mechanisms involved in the interactions of the NPs with plants.

In terms of constitution, there are different types of NPs and nanomaterials that have been used in plant science, and they can be divided into carbon nanomaterials (CBNMs) and metal based nanomaterials (MBNMs). The most common NPs in the CBNMs group are fullerene (C₇₀), fullerol (C₆₀(OH)₂₀) and carbon nanotubes, and for the MBNMs group, the most common NPs are TiO₂, CeO₂, Fe₃O₄, ZnO, and AgNO₃ [9], and we can consider those NPs composed using Au, Cu and the rare earth elements.

Corroborating these ideas, we divided this part of our review into the following sections: NPs as promoters of plant growth and development and NPs as a phytotoxic agent for plant growth and development.

3.1. Nanoparticles promoting growth and development in plants

The current literature has reported the positive effects of NPs on plants. An example of NPs showing a positive effect is TiNP, and in this case, several articles [47–50] have shown that nano-sized TiO₂ can promote a positive effect on plants. Zheng et al. [47], working with spinach, have verified an enhancement of plant growth when TiO₂-NPs were administered to the seeds or when they were sprayed onto the leaves. TiO₂-NPs were shown to increase the activity of several enzymes and promote the adsorption of nitrate, which accelerated the transformation of inorganic nitrogen into organic nitrogen.

Seed priming has recently been shown to be a good alternative to increase the seed vigor, the synchronisation of germination, and the improvement of the growth of the seedlings of many crops under particularly stressful conditions [51]. An adaptation of this technique appears promising, and additional work should be performed in nano priming. For example, the use of nano-anatase on parsley seeds resulted in increases in the percentage of germination, the germination rate index, the root and shoot length, the fresh weight, the vigor index, and the chlorophyll content of the seedlings [52]. Another interesting example was the use of nano priming with biogenic NPs to increase the seedling vigor and to improve the germination percentage and the seedling growth of *Tridax procumbens* L. The results revealed that this strategy showed a positive response in triggering the anti-oxidative mechanism in germinating seeds under chilling [53].

Different types and compositions of NPs are available, and they are chosen according to the extent of their application rather than in systematic studies. In plant science, the most commonly used are the silver, titanium, zinc and gold NPs compared with others, but this does not indicate that other NPs (i.e., Yb, Cs and Cd)

cannot be used. Certain researchers have been working to better understand the effects of different types of NPs on plants. There is an agreement that the effects produced by these materials is dependent on the type of NPs, the plant species, and the plant substrate (i.e., soil, hydroponics, and culture medium), and these effects are inconsistent among the different studies. Therefore, many subjects, studies and challenges involving the biological effects of NPs remain unresolved.

To verify any positive effect of TiNP, Feizi et al. [54] have observed that the germination rate of *Salvia* improved when the seeds were exposed to 60 mg L^{−1} of bulk and nanosized TiO₂ after 21 days of seed incubation. However, the applied treatments did not have significant effects on the shoot, root and seedling elongation or the biomass. The lowest mean germination time (8.42 and 8.7 days for bulk and nanosized TiO₂, respectively) occurred with the exposure of sage seeds to 60 mg L^{−1} bulk and nanosized TiO₂, but according to the authors, higher concentrations did not improve the average germination time. Moreover, exposure of sage seeds to 60 mg L^{−1} bulk and nano TiO₂ particles led to an enhanced germination rate. In this research, the authors concluded that generally, there was a significant response of the sage seed to nanosized TiO₂. The authors believed that the research indicated a positive effect of nanosized TiO₂, leading to the possibility of a new approach to overcome problems related to seed germination in certain plant species, especially medicinal plants.

An interesting study using the magnetic properties of carbon-coated iron NPs published by González-Melendi et al. [55] shows the significant potential of NPs in nanodevices used as delivery systems applied to plants based on the principles used in medical sciences. The authors have suggested that this mechanism could be applied to a broad range of uses, particularly, to address infections. In this specific research, the hypothesis was that because NPs were attached to agrochemicals (or other substances), they could reduce the damage to other plant tissues, consequently reducing the amount of contaminants released into the environment. Therefore, to verify their hypothesis, the authors have aimed to present a number of tools for the detection and analysis of carbon-coated iron magnetic core-shell NPs, which were introduced into plants. Inside the plant, the magnetic NPs were evaluated for their concentration in selected plant tissues by magnetic field gradients. The results introduced a wide range of possibilities for the use of magnetic NPs in plant research and agronomy, primarily because NPs can be charged with different substances before their introduction within the plants, and, if necessary, the NPs can be concentrated into localized areas using magnets. In terms of detection and localization studies, the authors have suggested the use of microscopy techniques.

NPs can also be applied in studies related to environmental sciences. Due to its high sensitivity to environmental effects, the aquatic environment is an interesting study plot, because it currently represents a complete ecosystem or a complete food chain. Thus, Juhel et al. [56] have evaluated the effects of alumina NPs on the growth, morphology and photosynthesis of the aquatic plant *Lemna minor*. Lemnaceae (or duckweed) is ideally suited for the study of the development of toxicity and/or stress acclimation; these plants are commonly used for regulatory toxicity testing of chemicals and frequently used for ecotoxicological testing. In this study, the hypothesis was that aluminum oxide NPs (alumina and Al₂O₃-NP) could enhance the growth of *L. minor*. Therefore, the effects of the engineered alumina NPs on the growth, morphology and photosynthesis of this plant were analysed. This research was based on previously published results showing that alumina NPs can enhance the electron transfer efficiency of isolated photosynthetic reaction centers [57] and that if alumina NP can mediate growth enhancement, then this would constitute a “response potential”. In contrast, Juhel et al. [56] have shown that the exposure of *L. minor* for 7 days

to a constantly high level of one nanoparticle, under otherwise optimized growth conditions, is not realistic from an environmental perspective. Therefore, in this case, further research is required to explore the environmental relevance of the identified growth response. However, the advantage of controlled laboratory experiments, such as those used in this study, is that they favor basic studies about the fundamental mechanisms underlying alumina NP-mediated growth stimulation. The authors have affirmed that they have reported for the first time the stimulatory effect of alumina NPs on growth and their role in increasing the biomass accumulation of *L. minor*. Interestingly, the enhancement of the biomass accumulation was, according to the authors, proportional to the plant morphological adjustments to the alumina NPs, such as the increase in the root length, in the number of fronds per colony, and a specific gain in the photosynthetic efficiency.

Many reports in the literature have indicated that metal NPs have previously been related to an enhanced energy transfer efficiency of isolated reaction centers; therefore, in this research, the mechanism underlying the alumina-mediated enhancement of the biomass accumulation in *L. minor* has been proposed, and it is associated with the increased efficiencies of the light reactions of photosynthesis [56].

Hernandez-Viezcas et al. [58] have verified the effects of zinc oxide (ZnO) NPs (ZnO NPs) in velvet mesquite (*Prosopis juliflora-velutina*) after 15 days in hydroponics, using ZnO NPs of 10 nm and at concentrations varying from 500 to 4000 mg L⁻¹. To determine the Zn concentrations in the roots, leaves and stems, the inductively coupled plasma optical emission spectroscopy (ICP OES) technique was used. To evaluate the plant stress, the specific activity of catalase (CAT) and ascorbate peroxidase (APX) was performed, and the biotransformation of ZnO NPs and the Zn distribution in the plant tissues were determined by X-ray absorption spectroscopy (XAS) and micro X-ray fluorescence (μXRF), respectively. The results were interesting because in addition to the facts that plants absorbed Zn from the NPs and the biochemical assays revealed that ZnO produces increases in the specific activity of CAT (in the root, stem and leaves) and APX (only in the leaves), no evidence of chlorosis, necrosis, stunting or wilting, even after 30 days of treatment, were observed, suggesting that this plant presents a certain level of tolerance to ZnO NPs and to Zn released from the NPs. Using the XAS technique, the absence of ZnO NPs within the plant tissues was verified, but in terms of the chemical species, Zn was found as Zn (II), resembling the Zn(NO₃)₂ spectra. For Zn translocation studies, the use of μXRF images has led the authors to conclude that Zn was absorbed from the NPs by the roots and was not adsorbed on the root surface. This interesting research has indicated an important concept because the authors have been careful to separate the effects produced by ZnO-NPs from those related to and produced by Zn released from the NPs.

3.2. Nanoparticles and plant phytotoxicity

The mechanisms of nanotoxicity remain unknown; however, it can be assumed that they would be closely related to the chemical composition, chemical structure, particle size and surface area of the NPs. The toxicity of the NPs may be attributed to the following two different actions: (1) a chemical toxicity based on the chemical composition, e.g., the release of (toxic) ions; and (2) stress or stimuli caused by the surface, size and/or shape of the particles. It has been confirmed that the solubility of oxide NPs significantly affected the cell culture response, and other recent evidence has suggested that the nanoparticle-mediated toxicity cannot be solely explained by the release of the dissolved components of the NP [59–61].

In the environment, in plants or in animals, certain authors have compared metal toxicity with the toxicity of the NPs and have concluded that the pathways leading to toxicity differ. Therefore, an

interesting method used to evaluate the toxicity profile of the NPs is the introduction of certain parameters within the experimental tests to concurrently evaluate the dynamics of the NPs and the ions and, from there, to infer the actual condition of the toxicity.

An analysis of the literature reveals that not all of the studies have evaluated the effects of the ions released from the NPs and the effects of the NPs on plants, causing a certain level of doubt about the data interpretation. For example, in a plant culture exposed to NPs, the gains or the losses are obtained in the development, growth or productivity exclusively due to the effects of the NPs or there may be an effective participation of the primary ion. Either the NPs, the ion or both substantially contributed to the determination of the result of the experiment.

As previously mentioned, NPs can interact with their surrounding environment, and plants are essential components of all ecosystems. Thus, one can hypothesize that NPs will interact with plants, and these interactions (such as uptake and accumulation in the plant biomass) will affect their fate and transport in the environment. NPs could also adhere to plant roots and exert physical or chemical toxicity on the plants. The interaction with the microorganisms in the soil cannot be ruled out because they can positively interact with the plants [62]; this is the case for the arbuscular mycorrhizal fungi (AMF), which can form a mutualistic association with roots of many plant species [63]. Another aspect that should be considered is the soil because, depending on the soil, the bioavailability of the elements can change [64]. An increasing number of publications have recently considered the interactions of the NPs with plants, and most of these studies have focused on the potential toxicity of the NPs to plants. [65–67]

The first report of negative effects of NPs on several plants (corn, cucumber, soybean, cabbage, and carrot) at a relatively low dosage has been performed by Yang [49]. However, the authors did not consider the fact that soluble Al³⁺ can act as a potential toxic element to the root and can inhibit root growth [68]. The authors have warned that care must be taken in toxicity testing when the effects may be related to simple solubility. Lin and Xing [67] have investigated the phytotoxicity of five types of NPs (multiwalled carbon nanotubes, aluminum, alumina, zinc and zinc oxide) on the seed germination and root growth of six higher plant species. In the root elongation test, all of the plants were affected when suspended in 2000 mg L⁻¹ nano-Zn or nano-ZnO. Cañas et al. [69] have investigated the effects of functionalised and non-functionalised single-walled carbon nanotubes on the root elongation of six crop species (cabbage, carrot, cucumber, lettuce, onion, and tomato). The CNTs and the fCNTs affected the root elongation of the six crop species, but the phytotoxicity varied between the CNTs and the fCNTs, with the CNTs affecting more species. Lee et al. [33] have studied AgNPs, which were evaluated in terms of the plant phytotoxicity by applying the NPs to agar medium or to artificial soil. For the experiments, two edible crops, *Phaseolus radiatus* and *Sorgum bicolor*, were used and cultivated in agar or in artificial soil doped with AgNPs. In the agar medium, colloidal AgNPs were used, ranging from 5 to 25 nm with concentrations of 0, 5, 10, 20, and 40 mg L⁻¹. The homogeneity of the NPs was measured with a microscope because agar is a gelatinous medium. As an additional aid, the authors have verified that there were no significant differences in the pH values of the conditions adopted in both of the experiments, because the agar media exhibited a pH of 6.9 ± 0.4 and the soil media had a pH of 6.4 ± 0.2. In the soil experiment, an aqueous AgNP solution was used, which was mixed with the soil to adjust the NP gradient to 0, 100, 300, 500, 1000, and 2000 mg kg⁻¹ dry soil. Toxicity tests were performed in a glass jar test unit at a controlled temperature of 25 ± 1 °C. The data indicated that the exposure medium has an important effect on the phytotoxicity of the silver NPs. In terms of toxicity and bioavailability of the AgNPs, in the agar medium, *P. radiatus* and

S. bicolor showed an AgNPs concentration dependent-growth inhibition, and the EC50 (effective concentration that would inhibit growth by 50%) values of *P. radiatus* and *S. bicolor* were calculated as 13 and 26 mg L⁻¹, respectively. In the soil media, *P. radiatus* was not significantly affected by the impediment within the test concentration. In addition, *S. bicolor* exhibited a slightly reduced growth rate. The bioavailability and the effect of the silver ions dissolved from the AgNPs were lower in the soil than in the agar. An interesting result from this study is that the behavior of the Ag ions caused a greater toxicity in the plants grown on agar; between them, *S. bicolor* was more affected. For plants grown in artificial soil, these effects were not observed, although the levels of the Ag ions were higher than those obtained in the agar medium (the Ag⁺ in the agar and the soil samples was measured as 1.3 ± 0.0 mg L⁻¹ and 2.7 ± 0.4 mg kg⁻¹, respectively). Therefore, in addition to the higher concentrations of Ag⁺ in the artificial soil, the plants cultured under these conditions did not exhibit toxicity, which could be explained by the following three primary reasons, as proposed by the authors: (i) the apparent toxicity observed in the soil was attributable to the particle toxicity; (ii) lower rates of NP dissolution can be attributed to the reduction in the surface and a greater soil aggregation, and (iii) the agar and soil have different mechanisms for sorption of the dissolved Ag⁺ ion and the AgNPs. The findings from this study show the importance of the media effect on the toxicity of the plant NPs and confirm our previous suggestion about the importance of the type of soil used, which agrees with the authors suggestion that the application of NPs in real soil should be studied, which can be important to understand the terrestrial toxicity of NPs [33].

Clément et al. [70] have also evaluated the phytotoxicity of the NPs in daphnia and algae, rotifers and plants as model organisms, applying the TiNPs. The authors have observed that because Ti presents different chemical structures according to the medium (crystal anatase or rutile), the responses in terms of toxicity were dependent on the type of Ti structure. The results revealed that TiO₂ NPs in an anatase crystal structure are toxic in all of the tests and at high concentrations, and due to their antimicrobial properties, a significant growth of the roots was observed. It has been suggested that because the rutile form presented lipophilicity, the TiO₂ NPs can produce larger aggregates in aqueous medium, which promotes a reduced effect on biological organisms and a lower toxicity compared with the anatase form. In flax (*Linum usitatissimum* L.), a significant growth of the roots was observed, and the best concentration of the TiO₂-NPs was 100 mg L⁻¹. In the aquatic plant *Lemna minor* (used as an environmental toxicity plant indicator), Gubbins et al. [71] have observed the effects of the application of AgNPs. Contrasting data obtained by Juhel et al. [56], working with alumina NPs in *L. minor*, have shown an increase in the biomass accumulation, and the authors [71] have related the phytotoxicity of the AgNPs under modified OECD test conditions. According to Gubbins et al. [71], the results have indicated an inhibition of plant growth when these plants were exposed to AgNPs (5 mg L⁻¹) with a size ranging from 20 to 100 nm, and the phytotoxicity was more acute with a long exposure time and a linear dose–response pathway. This research corroborated the idea that the phytotoxicity of the NPs is related to the size, shape, exposure time and concentration of the NPs. Therefore, it is expected that if the aquatic environment is contaminated with NPs, then the aquatic plants could accumulate NPs and present a certain level of toxicity, thereby altering various parameters of growth and development. In terms of the AgNPs, certain authors [72,73] have argued that there are limited data reporting on the biological uptake and effects of NPs and on the biological effects of the AgNPs, although certain properties concerning nanomaterials and the nanoscale have suggested that these particles could be toxic or hazardous due to their unknown or unusual mechanism of action. This hypothesis has been widely discussed in the various reports used

in this review article, and it is clear, based on the data and results, that AgNP within the environment presents a potential risk to higher plants, therefore, to the functioning of the ecosystem [71].

Jiang et al. [74] have verified the toxicity of hydroxyapatite (HAP), which is widely used in bone reconstruction due to its similar chemical structure compared with the inorganic composition of the human bone [75]. Because of its biocompatibility, biodegradability and amenability to achieve highly controlled morphologies [76], nano-sized HPA could be extensively used as a delivery vehicle for proteins [77], antibiotics [78], drugs [79], radioisotopes [80], genes [81], antigens for vaccines [82] and anticancer medicines for human hepatocellular carcinoma cell [83], ovarian carcinoma cell [84], cervical cancer cell [85], among others. In the nanocrystallisation of HAP, the surface activity would be enhanced, and certain properties that the macro-sized HAP did not have would be revealed. Hence, a problem arose whether the HAP NPs had biotoxicity. Thus, Jiang et al. [74], considering the importance of HAP for medical proposes and the difficulty to attest to its biotoxicity, have decided to verify the type of response of mung bean plants exposed to HAP NPs to study the relationship between the biocompatibility and the biotoxicity of these NPs. The hypothesis questioned whether the HAP nanomaterials would be beneficial to the plants because the calcium ions would promote growth or whether they would be harmful because the NPs would enter into the cells, causing cytotoxicity and possibly inhibiting the growth. According to the authors, the goal of this research was to provide a preliminary perspective about the biotoxicity of the HAP nanomaterials on plant growth. In terms of biotoxicity, it was possible to verify that the mung bean sprouts were inhibited, depending on the amount of intracellular HAP NPs, and the nanostructure and Ca²⁺ concentration were considered as the primary factors causing cell apoptosis and were the reason for the observed inhibitory effect.

In another study reporting on the NP phytotoxicity, Ma et al. [86] have verified that at low concentrations of AgNPs (1 mg L⁻¹), the toxicity could be observed in seedlings of *Arabidopsis thaliana* plants. In terms of size, AgNPs ranging from 20 nm to 80 nm clearly stunted the growth, whereas the phytotoxicity was dependent on the concentration and particle size of the NPs. The root tip (the cap and columella) were observed to turn light brown when the primary roots were exposed to the AgNPs. According to the authors, this color was attributed to the adsorption of the AgNPs either itself or in conjunction with the cell wall materials or even with secondary metabolites produced by the root tips. As observed in other studies, the exact mechanism concerning the phytotoxicity remains unclear. Furthermore, the determination of the phytotoxicity of metallic NPs and their oxides is complex, primarily because of the potential dissolution of the metallic ions released from the NPs and the potential toxicity and uptake of the metallic ions [86]. This complexity becomes clear when the study on the phytotoxicity of ZnO NPs performed by Lin and Xing [67] is considered, because the data obtained on the ZnO NPs applied to *Lolium perenne* indicated that the phytotoxicity cannot be explained by the dissolution of ZnO NPs from bulk materials alone. Faisal et al. [87] have investigated the induction of phytotoxicity in tomato (*Lycopersicon esculentum*) seedling roots induced by nickel oxide NPs (NiO-NPs). To verify this hypothesis, the authors have evaluated the translocation of NiO-NPs in the root cells and the ultra-structural changes in the cell organelles, the potential of the NiO-NPs to release Ni ions and their role in intracellular ROS generation to induce mitochondrial dysfunction, the levels of oxidative stress throughout specific enzymes (CAT # 707002, GSH # 703002, SOD #706002 and LPO # 705002) and the cell cycle alterations and apoptosis/necrosis analysis. This comprehensive and elegant study has provided evidence that has advanced the understanding of the phytotoxicity mechanism of the NiO-NPs in tomato plants. By utilizing a complete pool of analyses and methodologies, which corroborate the initial hypothesis, these authors have concluded that when the tomato seeds are

exposed to a short term NiO-NPs treatment, a significant repression of root growth was observed, which caused an oxidative imbalance, confirmed by the enhancement in the levels of the antioxidant enzymes tested, leading to the manifestation of phytotoxicity. In terms of changes in the structure of the organelles induced by NiO-NPs, the ultrastructure analysis revealed the translocation of the NiO-NPs in the cell cytoplasm, characterizing changes in the structure of the organelles. In addition to the results showing an enhancement in the enzymes related to oxidative stress, the use of flow cytometry and fluorescence imaging data has suggested oxidative stress and mitochondrial dysfunction, which according to the authors, perhaps stimulated the process of apoptosis. In addition to this evidence of phytotoxicity, the increase in the caspase-3-like protease activity confirmed the potential of the NiO-NPs to trigger the intrinsic apoptotic pathway in tomato plants due to the release of the Ni ions [87]. The more general conclusion of this study has suggested that to better understand the effect of the NiO-NPs on the growth of the tomato seedling roots, it is essential to use a transdisciplinary approach.

Kumari et al. [88] have attempted to investigate the phytotoxicity of the NPs at the cytogenetic level by analysing the genotoxic effects of ZnO NPs using root cells of *Allium cepa*. As discussed in this review, the evaluation of the effects of the NPs involves a series of analytical techniques to better understand these mechanisms. In this study, the authors have used SEM and TEM to investigate the cellular morphology, the chromosomal alterations and the occurrence of a micronucleus (MN). As expected, after the bulk characterization of the ZnO NPs and ZnO (particle size for the NPs < 100 µm and the ZnO bulk < 5 µm) and after the ZnO NPs and ZnO bulk dispersion (25, 50, 75, and 100 µg mL⁻¹), the roots were subjected to treatment with these solutions, and the results indicated that the root exposure to the ZnO NPs caused cytotoxicity and genotoxicity. The cytotoxic potential of the ZnO NPs was shown to be concentration dependent, which was linked to the mitotic inhibition index. The analysis of the chromosome morphology showed a direct relationship between the increases in the number of aberrations and the increase in the concentrations of the NPs. The most common type of aberration was the stick chromosomes (i.e., a chromatid type of aberration) [89], which were observed more often at the anaphase–telophase stages. An important conclusion is that the phytotoxicity was observed at the molecular and nuclear cell level, because the occurrence of stick chromosomes might be due to the degradation or depolymerization of chromosomal DNA. In terms of the presence of a micronucleus in the root cell meristems, these structures were observed during interphase and in higher quantities at the higher ZnO NPs concentration applied (100 µg mL⁻¹). Using SEM, the NPs were shown to be transported between the cells through plasmodesmata. By comparing the toxicity of the ZnO NPs and Zn, the authors have concluded that the toxicity of the ZnO NPs was higher than the ZnO bulk, stressing that their results indicated that the toxicity of the ZnO NPs was not due to dissolved zinc ions alone. The authors have also explained these results based on the ROS (reactive oxygen species) activation. In ROS formation and release, the conversion of fatty acids to toxic lipid peroxides occurs, leading to the disruption of biological membranes [45], consequently facilitating the entrance and damage by NPs and metals, causing TBARS (thiobarbituric acid reactive species) formation, which damages the membrane permeability. This specific report has shown that by increasing the concentrations of the ZnO NPs or the ZnO bulk, higher values for the TBARS were observed.

4. Phytoremediation and nanoparticles

Due to the tremendous development of nanotechnology in recent years and the wide application of NPs in various sectors, the

risk of environmental contamination will become even more significant in the near future. Water and soil are among the probable contamination environments. However, the environmental contamination with toxic elements (including metals) or compounds (such as pesticides), among others is a reality that has already and unfortunately been established; anthropogenic activities are making the situation worse [90]. The use of NPs aggravates the problem, although the benefits of their use are immense, indicating that any processes should be carefully monitored to avoid any further contamination of the environment. The mediation of soils and aquatic environments contaminated with metals has been extensively studied using vegetable organisms in a process called phytoremediation [91,92]. Certain studies have been performed that test the possible phytoremediation of the contaminated environments with NPs. It is known that the Au, Ag, CuO, ZnO and C₆₀ NPs are readily absorbed and translocated by plant organisms either as NPs or in their ionic form [93].

Iron NPs have been studied by Bystrzejewska-Piotrowska et al. [94] in which the accumulation capacity by *Lepidium sativum* and *Pisum sativum* L. of Fe₃O₄-NP with an average size of 50 nm has been evaluated. The NPs contained ⁵⁹Fe and were determined by gamma spectrometry, serving as a placeholder for the path of the NP in organisms. The two species showed an accumulation capacity for Fe₃O₄-NP with more than 90% in the roots due to the strong adsorption (approximately 39.5 g kg⁻¹ for *Pisum sativum* L and 7.8 g kg⁻¹ for *Lepidium sativum*). This result is interesting because, when considering heavy metals accumulation by plants, the large majority of plant species tend to accumulate the metals in the root system with only a small percentage being translocated to the aboveground parts of the plants [95,96]. Therefore, it is important to establish whether a more predominant trend of the NPs accumulation is defined and whether the metal involved follows the same trend as the chemical form available in the soil or in the water.

Zhao et al. [97], studying the cultivation of *Cucumis sativus*, have observed that the plant survived when grown at levels of 400 and 800 mg kg⁻¹ of CeO₂ or ZnO NPs. The study was not targeted for phytoremediation; however, it was verified that this plant species has the capacity to accumulate zinc and cerium, with the zinc detected even in the fruit. However, the percentage of accumulation was low, not exceeding 5% in any of the cases.

Using *Zea mays* grown in soil at ZnO-NP concentrations ranging from 0 to 800 mg kg⁻¹ in the presence or absence of sodium alginate, no changes in the plant biomass was observed in the presence of sodium alginate, even for higher values of ZnO-NP in the soil [98]. The presence of alginate increases the availability of Zn in the soil. The maize plants exhibited higher Zn content in the roots and shoots after 30 days of cultivation to the highest level of cultivation (800 mg ZnO-NP kg⁻¹ in the presence of alginate), accumulating 769 mg Zn kg⁻¹ in the roots and 495 mg Zn kg⁻¹ in the shoots. However, the translocation factor was low, indicating that most of the Zn becomes stuck in the roots [98]. These previous findings have been corroborated by the work of Lin and Xing (2008) [99], studying the toxicity of ZnO-NP, which showed a lower translocation of ZnO-NP in *Lolium perenne* plants. The study also showed that the amount of zinc absorbed by the plant might have a direct correlation with the content of organic matter in the soil. The presence of Zn in the seeds was not evaluated because the cultivation period was only up to 30 days [99].

In a study by Dimkpa et al. [100], the performance of wheat in the presence of CuO-NP and ZnO-NP has been compared with the performance in the presence of CuO and ZnO of a non-nanometric size in sandy soil. Copper and zinc were shown to accumulate in the aerial parts of the wheat, indicating that the absorption of these metals was related to the presence of these elements in the soil. No differences were observed between the translocation of

the various ZnO and CuO forms, indicating that the process of absorption and translocation is not related to the shape of the metal in the soil. However, it is important to remember that these two elements are normally used by the plants; thus, they are part of the plant cell metabolism.

The TiO₂-NPs have been studied by Jacob et al. [101]. Four plant species were used in this study, two of them of dry soil (beans (*Phaseolus vulgaris*) and wheat (*Triticum aestivum*)) and two wetland plants (*Rumex crispus* and *Elodea canadensis* L). The cultivations were performed with TiO₂-NP (average size less than 25 nm) at concentrations ranging from 0 to 30 mg L⁻¹, with the exception of *Elodea canadensis* with a maximum concentration of 20 mg L⁻¹. For all of the treatments tested, no change was observed in the plant biomass. The rooted plants showed a high content of Ti in the root (4.07 mg g⁻¹), especially for wheat, and all of the plants studied showed translocation of Ti. It could also be verified that other nutrients, such as phosphorus, can compete for the absorption of Ti

in aquatic environments based on the data with *Elodea canadensis*. Thus, the plants exhibited the potential for phytoextraction of Ti originating from the TiO₂-NP. However, further studies are required to understand the absorption mechanism of Ti into the organism.

Another study also performed with TiO₂-NP but with *Cucumis sativus* L. allowed the detection of NPs in the fruits [102]. The cucumber plants were grown on sandy soil for 150 days with concentrations of TiO₂-NP (27 nm) ranging from 0 to 750 mg kg⁻¹ in the soil. The presence of NPs in the fruit indicated that the NPs might have been translocated from the soil to the fruits, without having undergone changes due to biochemical processes [102].

Certain authors have noted that plants could have a significant metal absorption and can synthesize NP after this process, which justifies further studies to understand the dynamics of the metal ions inside the plants, because they may be able to absorb and accumulate NP; certain examples are *Chilopsis linearis* for Au [103], *Brassica juncea* for Au and AgNP [104,105] and *Physalis alkekengi* L. for ZnO-NP [106].

Table 1
Effects of nanoparticles in different plant species.

Nanoparticle	Particle size (nm)	Plant	Concentration	Observed effect	Reference
Ag	5–25	<i>Phaseolus radiates</i> , <i>Sorghum bicolor</i>	0, 5, 10, 20, 40 mg L ⁻¹	Growth inhibition	[33]
Ag		<i>Oriza sativa</i>	30–60 µg mL ⁻¹	At higher concentration: affected and damaged cell wall; shoot growth more susceptible	[34]
PVP-AgNP and GA-AgNP		Wetland plants	1, 10 or 40 mg L ⁻¹	Growth reduction in GA-AgNP treatments	[35]
Se		<i>Nicotiana tabacum</i>	265–530 µmol L ⁻¹	Stimulated plant germination and growth	[36]
Ti	14–65.5	<i>Triticum aestivum</i> spp	100 mg L ⁻¹	NP accumulation in roots; no impacts on photosynthesis	[38]
Fe	22.3–67.0	<i>Arabidopsis thaliana</i>		Plants treated with FeNP presented less chlorophyll	[39]
Al		<i>Nicotiana tabacum</i>	0.1–0.5–1.0 %	MicroRNAs were up regulated in response to increase the Al ₂ O ₃ -NPs exposure	[41]
Ag and Zn		<i>Zea mays</i> ; <i>Brassica</i>	200 µg mL ⁻¹	Ag showed higher uptake and phytotoxicity in comparison to AgNPs; in contrast, the biouptake was higher in AgNP treatment than the control	[42]
Ti and Ag		<i>Lycopersicon esculentum</i>	50 mg L ⁻¹	AgNPs: significant decreases in root growth at the lowest concentration used; TiO ₂ -NPs: no alteration in root length and biomass.	[44]
Bulk and nanosized TiO ₂	21	<i>Salvia officinalis</i>	60 mg L ⁻¹	Improving germination rates	[54]
Carbon-coated FeNP		<i>Curcubita pepo</i>		Penetration and translocation of magnetic nanoparticles in whole living plants and into plant cells.	[55]
Alumina NP	20	<i>Lemma minor</i>	For bulk-alumina: 1–1000 mg L ⁻¹	Stimulatory effect of Alumina NP on growth and its role in increasing biomass accumulation	[56]
Zn	10	<i>Prosopis juliflora-velutina</i>	500–4000 mg L ⁻¹	Increasing on CAT activity in roots, stems, and leaves; APOX increased only in stems and leaves. XANES spectra demonstrated that ZnO NPs were not present in plant tissues; Zn was found as Zn(II).	[58]
Ag	20, 100	<i>Lemma minor</i>	5 µg g ⁻¹	Inhibition of plant growth was dependent of NP size and this became more acute with longer exposure time	[71]
Ag	20–80	<i>Arabidopsis thaliana</i>	1 mg L ⁻¹	Seedling toxicity	[86]
Ni	≤ 50	<i>Lycopersicon esculentum</i>	0.025–2.0 mg mL ⁻¹	Repression in root growth; changes in organelles structures	[87]
Zn	< 100	<i>Allium cepa</i>	25, 50, 75, 100 µg mL ⁻¹	Phytotoxicity at molecular and nuclear cell level; direct relation between the increase in the number of chromosomes aberrations and the NPs concentrations increasing.	[88]
Fe	50	<i>Lepidium sativum</i> and <i>Pisum sativum</i>		Both species showed a root accumulation of Fe ₃ O ₄ -NP due to its strong adsorption.	[94]
Ce or Zn		<i>Cucumis sativus</i>	400 or 800 mg kg ⁻¹	Plants survived when growing at 400 or 800 mg kg ⁻¹ of CeO ₂ or ZnO NP; plant capacity to accumulate zinc and cerium	[97]
Zn		<i>Zea mays</i>	0 to 800 mg kg ⁻¹ in presence or absence of sodium alginate	No changes in plant biomass, even for higher values of ZnO-NP in soil; the translocation factor was low, and the most of the Zn becomes stuck in the roots.	[98]
Zn		<i>Lolium perenne</i>		Lower translocation of ZnO-NP; the amount of zinc absorbed by plant may have a direct correlation with the organic matter in the soil	[99]
Ti	≤ 25	<i>Phaseolus vulgaris</i> ; <i>Triticum aestivum</i> ; <i>Rumex crispus</i> and <i>Elodea canadensis</i>	0–30 mg L ⁻¹ and 0–20 mg L ⁻¹ for <i>Elodea canadensis</i>	No change in plant biomass; rooted plants showed high content of Ti in the root; all plants showed translocation of Ti	[101]
Ti	27	<i>Cucumis sativus</i>	0–750 mg kg ⁻¹ of soil	Detection of NPs in fruits	[102]

In order to summarize some of the applications reported in this review, the Table 1 shows examples taking into account the NPs used, their sizes and concentration, the plant species and the effect observed.

5. Trends

Considering the theme of this review and the importance of the studies involving NPs in plant science, it is pertinent to comment on the recent advances in the use of nanoparticles as sensors or probes, which can be applied to several areas, including human health, chemistry, physics, plant science, biology and industries. Certain researchers have produced interesting studies over recent years, emphasizing one study by Lodeiro et al [107] in which they have noted the advantages in using the fluorescence and colourimetric properties of NPs, allowing their use as chemosensors, when the nanosystems have remarkable photophysical and photochemical properties, which can lead to a variety of applications. Similarly, Oliveira et al [108] have obtained for the first time a cysteine amino acid linked to an emissive coumarin to coat gold NP to form a chemosensor system for *in vitro* and *in vivo* use or application. In this specific case, gold NP was superior due to its application in drug delivery, imaging, and the control of protein activity, among others. In this research, to verify the new chemosensors, the authors have carefully studied those materials using certain techniques, such as elemental analysis, MALDI-TOF-MS spectrometry, infrared, X-ray crystal diffraction, among others. Therefore, in addition to the construction of the chemosensors, it was possible to obtain stable, small gold NP (AuNPs), which could allow for the construction of a more sophisticated chemosensor composed of coumarin-cysteine-AuNPs.

Although the production and characterization of the NPs and their detection in different samples are consolidated in the literature and major progress has been achieved in terms of synthesis, as shown in this section, along with analytical techniques used to accomplish these tasks, the evaluation of the consequences, such as the toxicity of these NPs in plants remains unknown. Another existing gap is related to imaging techniques for the local evaluation of the NPs in different plant tissues, enabling, for example, a real map view of their distribution in the plant cell and its compartments. The stress response to NPs is also a field that appears to be relatively simple to develop, considering the extensive number of studies on the metal stress response in plants [109]. Additional research possibilities include evaluating the effect of NP accumulation/deposition in a plant cell organelle, e.g., the mitochondria or the chloroplast.

It is also important to remember that the concentration, plant organ/tissue, length of the experiment, elemental form, plant species, and type of experimental treatment (chronic/acute) may result in distinct stress responses. Studies with other toxic metals in plants are widely available, and several biochemical, physiological and genetic aspects have been investigated [45,90,110], but the same specific responses remain scarce when NPs are concerned. Moreover, another aspect that should receive attention in future research is the effect of NPs on the plant-soil-microorganisms interaction, perhaps giving priority to studies under realistic conditions in the soil where plants are cultivated and microorganisms are present, with certain ones producing beneficial effects, whereas others compromise the plant development and the final yield [111]. The concerted action of researchers to conduct major research programs must involve a multidisciplinary approach.

For example, this review discussed a significant number of reports, but one aspect that perhaps appeared to be neglected was the use of mutants and transgenic plants, or in a broader sense, we must investigate the aspects discussed in this review, exploring

the existing genetic variability. Different genotypes for the same plant species (e.g., inbred lines, varieties, hybrids, mutants, etc.) may show completely different responses to the same NPs.

One aspect that cannot be neglected is the metal uptake and accumulation by plants that are used for animal and human consumption. This aspect involves increased concern because of the possibility of these metals, and possibly the NPs, entering the food chain with an eventual effect on human health.

This type of study would be helpful and urgent, and we urge authors working with NPs to consider this aspect so that more detailed studies on the kinetics of the uptake, accumulation and translocation of the NPs within the plant system are conducted, providing new insights into the use of NPs and their effect and toxicity on plants. Directly linked to this proposal for future studies, it is also important to remember that certain plant species are considered metal hyperaccumulators; their study and use in phytoremediation have been explored, and a significant amount of literature is available. However, the same is not true regarding NPs, and understanding the mechanism of the response of hyperaccumulator plants to NPs would be a key element in identifying mechanisms involved in stress tolerance and NP toxicity.

6. Conclusion

NPs are a reality, although this information is not wide spread or known by the general public. Although it appears that NPs occur naturally, the industrial production of these nanomaterials introduces certain scientific issues that deserve a significant amount of attention, such as production, characterization, sensing and the interaction between the NPs and the environment. It is essential to understand the diversity of the aspects involving NPs and plants if major advances in this field are to be made, for example, the interaction of the NPs with plants and the consequences of this interaction, among other fundamental issues. We attempted to provide an overview and present all of these aspects with a certain degree of detail in this review. Analytical, physiological, biological and environmental studies, among others, involving NPs and plant science are of utmost importance to gain further insight into the impact of NPs.

Acknowledgments

The authors are grateful to Fundação de Amparo a Pesquisa do Estado de São Paulo (FAPESP, São Paulo, Brazil, grant numbers 2009/54676-0, 2012/21344-7, 2013/15646-3) and the Conselho Nacional de Desenvolvimento Científico e Tecnológico (CNPq, Brasília, Brazil, grant number 150350/2013-9) for the financial support and fellowships.

References

- [1] S.K. Ghosh, T. Pal, *Chem. Rev.* 107 (2007) 4797–4862.
- [2] C. Buzea, I.I. Pacheco, K. Robbie, *Biointerphases* 2 (2007) 17–71.
- [3] R. Taylor, S. Coulombe, T. Otanicar, P. Phelan, A. Gunawan, W. Lv, G. Rosengarten, R. Prasher, T. Himanshu, *J. Appl. Physics* 113 (2013) 1–13.
- [4] R. Barrena, E. Casals, J. Colon, X. Font, A. Sanchez, V. Puentes, *Chemosphere* 75 (2009) 850–857.
- [5] L.R. Khot, S. Sankaran, J. Mari Maja, R. Ehsani, E.W. Schuster, *Crop Protection* 35 (2012) 64–70.
- [6] T. Andre Nel, L. Mädler, L. Ning, *Science* 311 (2006) 622–627.
- [7] A.D. Maynard, R.J. Aitken, T. Butz, V. Colvin, K. Donaldson, G. Oberdorster M.A. Philbert, J. Ryan, A. Seaton, V. Stone, S.S. Tinkle, L. Tran, N.J. Walker D.B. Warheit, *Nature* 444 (2006) 267–269.
- [8] H. Zhu, J. Han, J.Q. Xiao, Y. Jin, *J. Environ. Monit.* 10 (2008) 713–717.
- [9] C.M. Rico, S. Majumdar, M. Duarte-Gardea, J.R. Peralta-Videa, J.L. Gardea-Torresdey, *J. Agric. Food Chem.* 59 (2011) 3485–3498.
- [10] J. Fabrega, S.N. Luoma, C.R. Tyler, T.S. Galloway, J.R. Lead, *Environ. Int.* 37 (2011) 517–531.

- [11] M. Hasselov, J.W. Readman, J.F. Ranville, K. Tiede, *Ecotoxicology* 17 (2008) 344–361.
- [12] K.B. Narayanan, N. Sakthivel, *Adv. Colloid Interface* 169 (2011) 59–79.
- [13] J. Soto-Alvaredo, M. Montes-Bayón, J. Bettmer, *Anal. Chem.* 85 (2013) 1316–1321.
- [14] M. Palencia, B.L. Rivas, H. Valle, *J. Membr. Sci.* 455 (2014) 7–14.
- [15] X. Xu, K.K. Caswell, E. Turcker, S. Kabisatpathy, K.L. Brodhacker, W.A. Scrivens, *J. Chromatogr. A* 1167 (2007) 35–41.
- [16] N. Surugau, P.L. Urban, *J. Sep. Sci.* 32 (2009) 1889–1906.
- [17] A.I. López-Lorente, B.M. Simonet, M. Valcárcel, *Trends Anal. Chem.* 30 (2011) 58–71.
- [18] F.K. Liu, Y.Y. Lin, C.-H. Wub, *Anal. Chim. Acta* 528 (2005) 249–254.
- [19] O. Véron, J.-P. Blondeau, D. De, S. Meneses, C.A. Vignolle, *Surf. Coat. Technol.* 227 (2013) 48–57.
- [20] H. Hagendorfer, R. Kaegi, M. Parlinska, B. Sinnet, C. Ludwig, A. Ulrich, *Anal. Chem.* 84 (2012) 2678–2685.
- [21] P. Rajasekharreddy, P.U. Rani, B. Sreedhar, *J. Nanopart. Res.* 12 (2010) 1711–1721.
- [22] C.S. Seney, B.M. Gutzman, R.H. Goddard, *J. Phys. Chem. C* 113 (2008) 74–80.
- [23] M. Delay, T. Dolt, A. Woellhaf, R. Sembritzki, F.H. Frimmel, *J. Chromatogr. A* 1218 (2011) 4206–4212.
- [24] H. Chen, Y.-M. Yeh, Jian-Zhi Chen, Song-Ming Liu, B.Y. Huang, Zhi-Huei Wu, Shan-Lin Tsai, Hung-Wei Chang, Yu-Cheng Chu, C.H. Liao, *Thin Solid Films* 549 (2013) 74–78.
- [25] S. Nagarajan, K.A. Kuppusamy, *Indian J. Nanobiotechnol.* 11 (2013) 39–49.
- [26] D. Singh, V. Rathod, S. Ningangouda, J. Hiremath, A.K. Singh, J. Mathew, *Chem. Appl.* (2014) 1–8.
- [27] D.M. Mitrano, A. Barber, A. Bednar, P. Westerhoff, C.P. Higgins, J.F. Ranville, *J. Anal. At. Spectrom.* 27 (2012) 1131–1142.
- [28] A. Ulrich, S. Losert, N. Bendixen, A. Al-Kattan, H. Hagendorfer, B. Nowack, C. Adhart, J. Ebert, M. Lattuade, K. Hungerbühler, *J. Anal. At. Spectrom.* 27 (2012) 1120–1130.
- [29] M.E. Akerman, W.C. Chan, P. Laakkonen, S.N. Bhatia, E. Ruoslahti, *Proc. Natl. Acad. Sci. USA* 99 (2002) 12617–12621.
- [30] A. Hoshino, K. Fujioka, T. Oku, S. Nakamura, M. Suga, Y. Yamaguchi, K. Suzuki, M. Yasuhara, *Microbiol. Immunol.* 48 (12) (2004) 985–994.
- [31] K.G.N. Suzuki, T.K. Fujiwara, M. Edidin, A. Kusumi, *J. Cell Biol.* 177 (4) (2007) 731–742.
- [32] J. Ying, *Nanostructured Materials*, Elsevier, California, 2001.
- [33] W.-M. Lee, J.I. Kwak, Y.-J. An, *Chemosphere* 86 (2012) 491–499.
- [34] F. Mirzajani, H. Askari, S. Hamzelou, M. Farzaneh, A. Ghassempour, *Ecotoxicol. Environ. Saf.* 88 (2013) 48–54.
- [35] L. Yin, B.P. Colman, B.M. McGill, J.P. Wright, E.S. Bernhardt, *PLoS One* 7 (10) (2012) 1–7.
- [36] E. Domokos-Szabolcsy, L. Marton, A. Sztrik, B. Babka, J. Prokisch, M. Fari, *Plant Growth Regul.* 68 (2012) 525–531.
- [37] R.A. Gomes-Junior, P.L. Gratão, S.A. Gaziola, P. Mazzafera, P.J. Lea, R.A. Azevedo, *Funct. Plant Biol.* 34 (2007) 449–456.
- [38] C. Larue, J. Laurette, N. Herlin-Boime, H. Khodja, B. Fayard, A.M. Flank, F. Brisset, M. Carriere, *Sci. Total Environ.* 431 (2012) 197–208.
- [39] Y. Marusenko, J. Shipp, G.A. Hamilton, J.L.L. Morgan, M. Keebaugh, H. Hill, A. Dutta, X. Zhuo, N. Upadhyay, J. Hutchings, P. Herckes, A.D. Anbar, E. Shock, H.E. Hartnett, *Environ. Pollut.* 174 (2013) 150–156.
- [40] T.N.V.K.V. Prasad, P. Sudhakar, Y. Sreenivasulu, P. Latha, V. Munaswamy K.R. Reddy, T.S. Sreerprasad, P.R. Sajanalal, T. Pradeep, *J. Plant Nutr.* 35 (2012) 905–927.
- [41] E. Burkley, J. Ashlock, W.B. Winfrey, B. Zhang, *PLoS One* 7 (5) (2012) 1–10.
- [42] L.R. Pokhrel, B. Dubej, *Sci. Tot. Environ.* 452–453 (2013) 321–332.
- [43] D.A. Navarro, M.A. Bisson, D.S. Aga, J. Hazard. Mater. 211–212 (2012) 427–435.
- [44] U. Song, H. Jun, B. Waldman, J. Roh, Y. Kim, J. Yi, E.J. Lee, *Ecotoxicol. Environ. Saf.* 93 (2013) 60–67.
- [45] P.L. Gratão, A. Polle, P.J. Lea, R.A. Azevedo, *Funct. Plant Biol.* 32 (2005) 481–494.
- [46] J. Koelme, T. Leland, H. Wang, D. Amarasiriwardena, B. Xing, *Environ. Pollut.* 174 (2013) 222–228.
- [47] L. Zheng, F. Hong, S. Lu, C. Liu, *Biol. Trace Elem. Res.* 105 (2005) 83–91.
- [48] F. Hong, J. Zhou, C. Liu, F. Yang, C. Wu, L. Zheng, P. Yang, *Biol. Trace Elem. Res.* 104 (2005) 1–11.
- [49] F. Yang, C. Liu, F. Gao, M. Su, X. Wu, L. Zheng, F. Hong, P. Yang, *Biol. Trace Elem. Res.* 119 (2007) 77–88.
- [50] F. Gao, C. Liu, C. Qu, L. Zheng, F. Yang, M. Su, F. Hong, *Biometals* 21 (2008) 211–217.
- [51] R.F. Carvalho, F.A. Piotta, D. Schmidt, L.P. Peters, C.C. Monteiro, R.A. Azevedo, *Sci. Agric.* 68 (2011) 598–602.
- [52] E.H. Dehkourdi, M. Mosavi, *Biol. Trace Elem. Res.* 155 (2013) 283–286.
- [53] H. Bhati-Kushwaha, A. Kaur, C.P. Malik, *Indian J. Plant Sci.* 2 (2013) 54–62.
- [54] H. Feizi, S. Amirmoradi, F. Abdollahi, S.J. Pour, *Annu. Res. Res. Biol.* 3 (4) (2013) 814–824.
- [55] P. González-Melendi, R. Fernández-Pacheco, M.J. Coronado, E. Corredor P.S. Testillano, M.C. Risueño, C. Marquina, M.R. Ibarra, D. Rubiales, A. Pérez-de-Luque, *Ann. Bot.* 101 (2008) 187–195.
- [56] G. Juhel, E. Batisse, Q. Hugues, D. Daly, F.N.A.M. van Pelt, J. O'Halloran M.A.K. Jansen, *Aquat. Toxicol.* 105 (2011) 328–336.
- [57] V.A. Nadochenko, V.V. Nikandrov, A.A. Gorenberg, M.G. Karlova E.P. Lukashov, A.Yu. Semenov, N.S. Bukharina, A.N. Kostrov, E.P. Permenova, O.M. Sarkisov, *High Energy Chem.* 42 (2008) 591–593.
- [58] J.A. Hernandez-Viezcás, H. Castillo-Michel, A.D. Servin, J.R. Peralta-Videa J.L. Gardea-Torresdey, *Chem. Eng. J.* 170 (2011) 346–352.
- [59] T.J. Brunner, P. Wick, P. Manser, P. Spohn, R.N. Grass, L.K. Limbach, A. Bruiniink, W.J. Stark, *Environ. Sci. Technol.* 40 (14) (2006) 4374–4381.
- [60] W.S. Cho, M. Cho, J. Jeong, M. Choi, H.Y. Cho, B.S. Han, S.H. Kim, H.O. Kim Y.T. Lim, B.H. Chung, *Toxicol. Appl. Pharmacol.* 236 (1) (2009) 16–24.
- [61] F. Gagné, C. André, R. Skirrow, M. Gélinas, J. Auclair, G. van Aggelen, P. Turcotte, C. Gagnon, *Chemosphere* 89 (2012) 615–622.
- [62] S.A.L. Andrade, P.L. Gratão, R.A. Azevedo, A.P.D. Silveira, M.A. Schiavinato, P. Mazzafera, *Environ. Exp. Bot.* 68 (2010) 198–207.
- [63] S.A.L. Andrade, P.L. Gratão, M.A. Schiavinato, A.P.D. Silveira, R.A. Azevedo, P. Mazzafera, *Chemosphere* 75 (2009) 1363–1370.
- [64] L.C.A. Melo, L.R.F. Aleoni, G. Carvalho, R.A. Azevedo, *J. Plant Nutr. Soil Sci.* 174 (2011) 847–859.
- [65] F. Battke, K. Leopold, M. Maier, U. Schmidhalter, M. Schuster, *Plant Biol.* 10 (2009) 272–276.
- [66] S. Lin, J. Reppert, Q. Hu, J.S. Hunson, M.L. Reid, T. Ratnikova, *Small* (2009) 1128–1132.
- [67] D. Lin, B. Xing, *Environ. Pollut.* 150 (2007) 243–250.
- [68] G. Zhou, J.F. Pereira, E. Delhaize, M. Zhou, J.V. Magalhaes, P.R. Ryan, *J. Exp. Bot.* (2014) eru121v1-eru121 1–10.
- [69] J.E. Cañas, M. Long, S. Nations, R. Vadan, L. Dai, M. Luo, R. Ambikapathi E.H. Lee, D. Olszyk, *Environ. Toxicol. Chem.* 27 (2008) 1922–1931.
- [70] L. Clément, C. Hure, N. Marmier, *Chemosphere* 90 (2013) 1083–1090.
- [71] E.J. Gubbins, L.C. Batty, J.R. Lead, *Environ. Pol* 159 (2011) 1551–1559.
- [72] R.D. Handy, R. Owen, E. Valsami-Jones, *Ecotoxicology* 17 (2008) 287–314.
- [73] S.J. Klaine, P.J.J. Alvarez, G.E. Batley, T.F. Fernandes, R.D. Handy, D.Y. Lyon, S. Mahendra, M.J. McLaughlin, J.R. Lead, *Environ. Toxicol. Chem.* 27 (2008) 1825–1851.
- [74] H. Jiang, J.K. Liu, J.D. Wang, Y. Lu, M. Zhang, X.H. Yang, D.J. Hong, J. Hazard. Mater. 270 (2014) 71–81.
- [75] J. Loo, Y. Siew, S. Ho, F. Boey, J. Ma, J. Mater. Sci. Mater. Med 19 (2008) 1389–1397.
- [76] A.I. Raafat, A.A.S. Eldin, A.A. Salama, N.S. Ali, J. Appl. Polym. Sci. 138 (2013) 1697–1705.
- [77] T. Matsumoto, M. Okazaki, M. Inoue, S. Yamaguchi, T. Kusunose, T. Toyonaga, Y. Hamada, J. Takahashi, *Biomaterials* 25 (2004) 3807–3812.
- [78] S.P. Victor, T.S.S. Kumar, J. Biomed. Nanotechnol. 4 (2008) 203–209.
- [79] X.G. Cheng, L. Kuhn, *Int. J. Nanomed.* 2 (2007) 667–674.
- [80] H.T. Ong, J.S.C. Loo, F.Y.C. Boey, S.J. Russell, J. Ma, K.W. Peng, *J. Nanopart. Res.* 10 (2008) 141–150.
- [81] S. Bisht, G. Bhakta, S. Mitra, A. Mairea, *Int. J. Pharm.* 288 (2005) 157–168.
- [82] A.K. Goyal, K. Khatri, A. Mehta, B. Vaidya, S. Tiwari, R. Paliwal, S. Paliwal, *J. Biomater. Appl.* 24 (2009) 65–84.
- [83] Z.S. Liu, S.L. Tang, Z.L. Ai, *World J. Gastroenterol.* 9 (2003) 1968–1971.
- [84] L. Fu, W. Feng, Z.L. Peng, J.F. Li, Y.B. Li, *Chin. J. Biomed. Eng.* 26 (2007) 585–587.
- [85] H.J. Chae, J.M. Park, G.Y. Lee, H.R. Park, G.S. Jeong, H.M. Kim, S.K. Yoo H.R. Kim, *Am. J. Chin. Med.* 32 (2004) 103–107.
- [86] X. Ma, J.G. Lee, Y. Deng, A. Kolmakov, *Sci. Total Environ.* 408 (2010) 3053–3061.
- [87] M. Faisal, Q. Saquib, A.A. Alatar, A.A. Al-Khedhairi, A.K. Hegazy, J. Musarrat, *J. Hazard. Mater.* 250–251 (2013) 318–332.
- [88] M. Kumari, S.S. Khan, S. Pakrashi, A. Mukherjee, N. Chandrasekaran, *J. Hazard. Mater.* 190 (2011) 613–621.
- [89] H. Yi, Z. Meng, *Mutat. Res.* 537 (2003) 109–114.
- [90] P.L. Gratão, C.C. Monteiro, R.F. Carvalho, T. Tezotto, F.A. Piotta, L.E.P. Peres R.A. Azevedo, *Plant Physiol. Biochem.* 56 (2012) 79–96.
- [91] H. Ali, E. Khan, M.A. Sajad, *Chemosphere* 91 (2013) 869–881.
- [92] L.A. Souza, F.A. Piotta, R.C. Nogueiro, R.A. Azevedo, *Sci. Agric.* 70 (2013) 290–295.
- [93] J.L. Gardea-Torresdey, C.M. Rico, J.C. White, *Environ. Sci. Technol.* 48 (2014) 2526–2540.
- [94] G. Bystrzejewska-Piotrowska, M. Asztemborska, R. Stęborowski, H. Polkowska-Motrenko, B. Danko, J. Ryniewicz, *Nukleonika* 57 (3) (2012) 427–430.
- [95] A.P. Vitória, P.J. Lea, R.A. Azevedo, *Phytochemistry* 57 (2001) 701–710.
- [96] G.J.G. Pereira, S.M.G. Molina, P.J. Lea, R.A. Azevedo, *Plant Soil* 239 (2002) 123–132.
- [97] L. Zhao, Y. Sun, J.A. Hernandez-Viezcás, A.D. Servin, J. Hong, G. Niu J.R. Peralta-Videa, M. Duarte-Gardea, J.L. Gardea-Torresdey, *J. Agric. Food Chem.* 61 (2013) 11945–11951.
- [98] L. Zhao, J.A. Hernandez-Viezcás, J.R. Peralta-Videa, S. Bandyopadhyay, B. Peng, B. Munoz, A.A. Kellerce, J.L. Gardea-Torresdey, *Environ. Sci.: Processes Impacts* 15 (2013) 260–266.
- [99] D. Lin, B. Xing, *Environ. Sci. Technol.* 42 (2008) 5580–5585.
- [100] C.O. Dimkpa, J.E. McLean, D.E. Latta, E. Manango, D.W. Britton, W.P. Johnson, M.I. Boyanov, A.J. Anderson, *J. Nanopart. Res.* 14 (2012) 1125–1139.
- [101] D.L. Jacob, J.D. Borchardt, L. Navaratnam, M.L. Otte, A.N. Bezbaruah, *Int. J. Phytoremediat.* 15 (2013) 142–153.
- [102] A.D. Servin, M.I. Morales, H. Castillo-Michel, J.A. Hernandez-Viezcás, B. Munoz, L. Zhao, J.E. Nunez, J.R. Peralta-Videa, J.L. Gardea-Torresdey, *Environ. Sci. Technol.* 47 (2013) 11592–11598.
- [103] E. Rodriguez, J.G. Parsons, J.R. Peralta-Videa, G. Cruz-Jimenez, J. Romero-Gonzalez, B.E. Sanchez-Salcedo, G.B. Sauppe, M. Duarte-Gardea, J.L. Gardea-Torresdey, *Int. J. Phytoremediat.* 9 (2007) 133–147.

- [104] A.T. Marshall, R.G. Haverkamp, C.E. Davies, J.G. Parsons, J.L. Gardea-Torresdey, D. van Agterveld, *Int. J. Phytoremediat.* 9 (2007) 197–206.
- [105] I.R. Beattiew, R.G. Haverkamp, *Metallomics* 3 (2011) 628–632.
- [106] J. Qu, X. Yuan, X. Wang, P. Shao, *Environ. Pollut.* 159 (2011) 1783–1788.
- [107] C. Lodeiro, J.L. Capelo, J.C. Mejuto, E. Oliveira, H.M. Santos, B. Pedras, C. Nuñez, *Chem. Soc. Rev.* 39 (2010) 2948–2976.
- [108] E. Oliveira, C. Nuñez, B.R. Gonzalez, J.L. Capelo, C. Lodeiro, *Inorg. Chem.* 50 (2011) 8797–8807.
- [109] M.A.Z. Arruda, R.A. Azevedo, *Ann. Appl. Biol.* 155 (2009) 301–307.
- [110] C.C. Monteiro, R.F. Carvalho, P.L. Grato, G. Carvalho, T. Tezotto, L.O. Medici L.E.P. Peres, R.A. Azevedo, *Environ. Exp. Bot.* 71 (2011) 306–320.
- [111] M.N. Dourado, P.F. Martins, M.C. Quecine, F.A. Piotto, L.A. Souza, M.R. Franco, T. Tezotto, R.A. Azevedo, *Ann. Appl. Biol.* 163 (2013) 494–507.



Electrochemical biotin detection based on magnetic beads and a new magnetic flow cell for screen printed electrode



Julien Biscay, María Begoña González García, Agustín Costa García*

Department of Physical and Analytical Chemistry, Faculty of Chemistry, University of Oviedo, 33006 Oviedo, Spain

ARTICLE INFO

Article history:

Received 25 April 2014

Received in revised form

3 August 2014

Accepted 5 August 2014

Available online 27 August 2014

Keywords:

Biotin detection

Flow injection analysis

Flow cell with an integrated magnet

Screen printed electrode

Magnetic beads

ABSTRACT

The use of the first flow-cell for magnetic assays with an integrated magnet is reported here. The flow injection analysis system (FIA) is used for biotin determination. The reaction scheme is based on a one step competitive assay between free biotin and biotin labeled with horseradish peroxidase (B-HRP). The mixture of magnetic beads modified with streptavidin (Strep-MB), biotin and B-HRP is left 15 min under stirring and then a washing step is performed. After that, 100 μL of the mixture is injected and after 30 s 100 μL of 3,3',5,5'-Tetramethylbenzidine (TMB) is injected and the FIAGram is recorded applying a potential of -0.2 V . The linear range obtained is from 0.01 to 1 nM of biotin and the sensitivity is 758 nA/nM. The modification and cleaning of the electrode are performed in an easy way due to the internal magnet of the flow cell.

© 2014 Elsevier B.V. All rights reserved.

1. Introduction

Flow injection analysis (FIA) techniques have been employed to automate a wide variety of chemical and biochemical analyses since their invention in the middle of the seventies [1,2]. FIA techniques are classified into the basic mode (also named normal flow injection analysis) and different special modes as stopped flow [3,4] or reverse flow [5,6]. FIA is one of the most popular continuous flow techniques and its simplicity, and flexibility allow its application in various chemistries. Moreover the flexibility in the different created formats and designs helps its introduction in laboratories using low cost instrumentation but each one has to comply with the three cornerstones of the FIA: (i) injection of discrete and well defined volume of sample solution into a flowing carrier stream; (ii) reproducible and precise timing of the manipulation that the injected sample zone is subjected to in the system, from the point of the injection to the point of detection; and (iii) the creation of a concentration gradient of the injected sample, providing a transient, but reproducible readout of the recorded signal. The second generation of FIA including stopped flow injection [7], bead injection [8–10], sequential injection with lab on valve [11] has opened new perspectives with many analysis systems. The majority of these systems have in common the detection of the product before the equilibrium state is reached, which considerably reduces the analysis time. To overcome

shortcomings such as contamination of the surface of the detector or the lack of sensitivity, an appealing tool is used called the bead-injection analysis [12,13]. Magnetic beads (MBs) are generally used for it high surface area per volume. The ability to accommodate higher numbers of immobilized molecules helps to improve sensitivity and consequently detection limit of the assay. Another benefit is their easy manipulation with external magnets which makes it possible to perform biological reaction events away from the electrode surface [14] and reduce the complexity for sensing application. Moreover their uses minimize the matrix effect thanks to the washing procedures and faster assay kinetics that are achieved since the beads are in suspension [15]. Many articles have been published using both the advantages of magnetic beads and screen printed electrodes [16,17]; articles about FIA and its application in pharmaceutical [18,19] and biomedical analysis can be found [20] but articles on any assay using a magnetic flow cell with an integrated magnet for screen printed electrodes have not been reported.

In this paper an electrochemical biotin assay using a flow injection system which includes for the first time a flow cell for magnetic assay with an integrated magnet is described. The present strategy is based on a competition scheme where biotin and the biotin-HRP compete for the binding sites of streptavidin, which are immobilized on the magnetic beads surface. After molecular recognition, the beads are injected into the FIA system and immobilized on the electrode surface with the help of the integrated magnet of the flow cell which is exactly situated underneath the working electrode of the screen printed electrode. After the injection of the substrate, enzymatic product reduc-

* Corresponding author.

E-mail address: costa@uniovi.es (A. Costa García).

tion current is obtained, which is inversely related to biotin concentration. The electrochemical response is measured using the amperometric technique applying a constant potential. Moreover the packing of MBs on the SPCE surface also implied that the enzyme reaction product was generated very close to the electrode surface, thus allowing the steady-state to be reached rapidly (which implies faster measurements), and minimizing diffusion limitations of the electroactive species.

2. Experimental

2.1. Chemicals

Sodium hydroxide (1.064.1000) was delivered by MERCK (Spain), magnetic beads of 1 μm diameter modified with streptavidin (Dynabeads[®] MyOne[™] Streptavidin C1) (Strep-MB) (ref. 650.01) were purchased from Invitrogen, Biotinylated Horseradish Peroxidase (HRP-B) (ref. 29139) was supplied by Thermo Scientific and 3,3',5,5' tetramethylbenzidine (TMB) (ref. T0440), and Biotin (ref. B4501) were purchased from SIGMA. All chemicals were of analytical reagent grade, and the Milli-Q water used was obtained from a Millipore Direct-Q[™] 5 purification system. Stock solution of 5×10^{-6} M of B-HRP, 5×10^{-3} M of Biotin and 7×10^8 magnetic beads per mL was daily prepared in 0.1 M phosphate buffer (PB) pH 7.2 and stored at 4 °C in a refrigerator.

2.2. Apparatus and electrodes

Chronoamperometric measurements were performed using an ECO Chemie μ Autolab type II potentiostat interfaced with a Pentium 166 computer system and controlled by the Autolab GPES software version 4.8 for Windows 98. All measurements were carried out at room temperature. Screen-Printed Carbon Electrodes (ref DRP-110), an edge connector (ref. DRP-CAC), were purchased from DropSens, S.L (Oviedo, Spain). The screen-printed electrodes consist of a Carbon working (4 mm diameter), carbon auxiliary and silver pseudo reference electrodes printed on an alumina substrate. An insulating layer serves to delimit the electrochemical cell and electric contacts. The magnetic flow cell (ref. CFLWCL-MAGN) was designed and purchased from DropSens, S.L (Oviedo, Spain). It is a methacrylate wall-jet Flow-Cell for FIA, with an unscrewed open-close system which allows an easy electrode replacement. This cell is designed to obtain an inlet flow perpendicular to the electrode's surface, and an outlet flow forming a 45° angle and an O-ring which limits the volume of the electrochemical cell. The integrated magnet is a cylindrical magnet which in the upper position is situated exactly above the working electrode and permits the modified magnetic beads to fix on the surface of the electrode. When the magnet is in the lower position, the magnetic beads are eliminated from the surface of the electrode.

This new magnetic flow cell is represented in Fig. 1A. The cell is one of the parts of the flow injection analysis system which is schematically represented in Fig. 1B

The FIA system used for the detection of biotin is a 12 cylinder Perimax Spetec peristaltic pump (Spetec GmbH, Germany) which allows the 0.1 M PB pH 7.2 stream to flow through the system. Desired solutions are injected by means of a six port rotary valve, Model 1106 (Omnifit Ltd., UK) equipped with a 100 μL loop.

2.3. Assay procedure

The reaction scheme is based on a one step competitive assay between free biotin and biotin labeled with horseradish peroxidase (B-HRP). The mixture of magnetic beads modified with

streptavidin (Strep-MB), biotin and B-HRP is left for 15 min under stirring and then a washing step is performed. It consists of a re-suspension of the beads in the 0.1 M PB solution at pH 7.2 and then a separation with the magnet to remove the supernatant. This operation is repeated 3 times. The scheme of the assay is reported in Fig. 2.

2.4. Electrochemical measurement

Amperometric detection was performed applying a constant potential to the modified electrode. The carrier solution (phosphate buffer, pH 7.2) was pumped at a constant flow rate (1 mL/min) until a stable baseline was recorded. Then, the flow rate was changed to 0.5 mL/min and the magnet was moved to the upper position. Finally, 30 s after the injection of 100 μL of the sample, the flow rate was changed to 1 mL/min and then 100 μL of TMB diluted 5 times (this dilution was necessary to avoid the oxidation peak due to the TMB itself) were injected into the system and the reduction current was observed and recorded 10 s after the injection of the substrate. Finally, the magnet is moved to the lower position and for 3 min at a flow rate of 3 mL/min the carrier is pumped in order to wash the electrode surface. After the washing step another analytical run can be performed.

2.5. Real sample measurement

The methodology was tested in two pharmaceuticals with a known concentration of biotin. The first one is MEDEBIOTIN tablets (pharmaceutical 1) and second is MEDEBIOTIN vials (pharmaceutical 2). Each tablet (0.072 g) contains 5 mg of biotin, and each vial of 1 mL contains 4.6 mg of biotin. So 0.01 g of the pharmaceutical 1 was dissolved in 100 mL of the buffer. Then, an aliquot of this solution was diluted 1:50,000 times. Concerning the pharmaceutical 2, the vial was diluted in 1 L of the buffer and from this solution, a second dilution was performed (1:50,000). Finally mixtures of Strep-MB/B-HRP/Pharmaceutical were prepared and left under stirring for 15 min. Then a washing step was performed and finally the amperometric measurement was performed as explained in Section 2.4. Both samples were measured in triplicate.

3. Result and discussion

3.1. Optimization of the parameters of the flow injection analysis system

3.1.1. Flow rate

3.1.1.1. *Injection of the mixture.* The flow rate obtained when the mixture of reaction is injected in the FIA system is very important because there must be equilibrium between the pulling power of the flow carrier and the power of magnet in the flow cell that retains the magnetic beads. To carry out this study, a mixture of Strep-MB (7×10^7 magnetic beads per mL)/B-HRP (5×10^{-7} M), prepared as explained in Section 2.3 was injected at different flow rates of the carrier (0.5, 1, 1.5, 2 mL/min). Then TMB was injected and the reduction current was recorded applying a potential of -0.20 V and using a flow rate of 1 mL/min. The results obtained are summarized in Table 1. The analytical signal decreases when the flow rate increases because the number of Strep-MB fixed on the electrode surface is lower. At higher flow rates the pulling power of the flow carrier is higher than the capacity of the magnet to retain all magnetic beads on the electrode surface. In other words, the effect of cleaning is higher than the retention of the Strep-MB on the electrode surface and consequently, lower analytical signals are obtained. Thus, for further studies, a flow

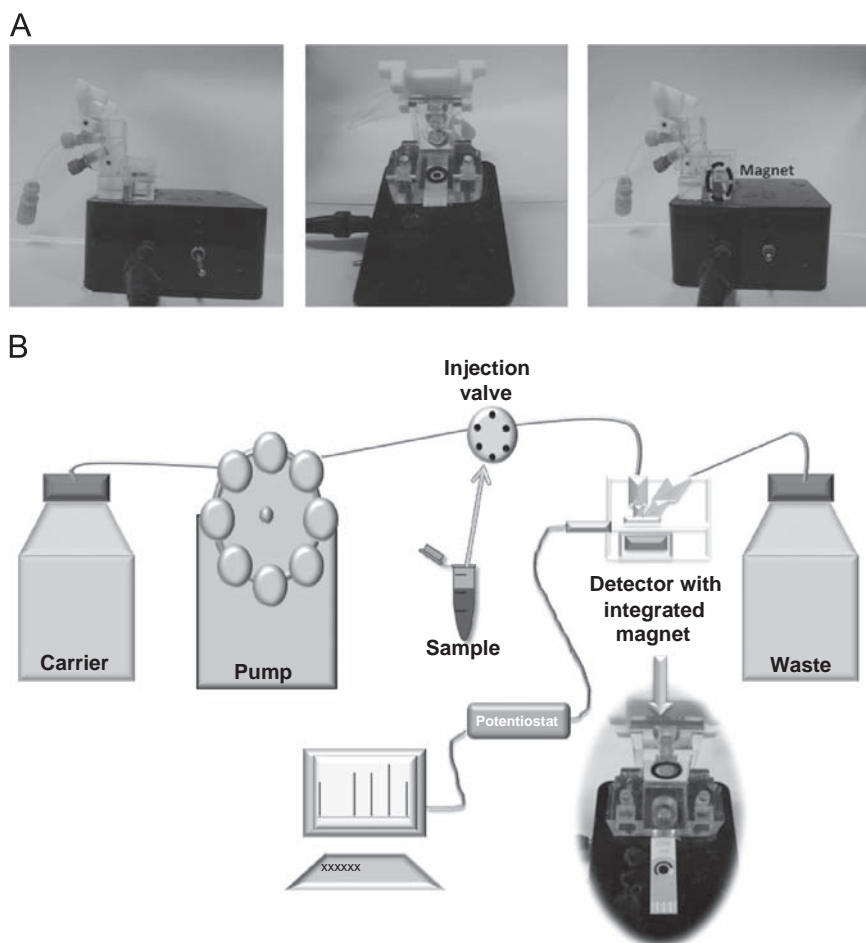


Fig. 1. (A) Images of the magnetic flow cell, with the magnet up and down. (B) Scheme of the FIA system.

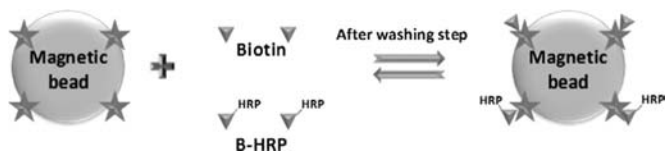


Fig. 2. Scheme of the competitive Biotin assay.

Table 1

Influence of the flow rate, during the injection of the mixture Strep-MBs/HRP-B, on the analytical response; $E_{\text{applied}} = -0.2$ V; TMB diluted 5 times; Strep-MB (7×10^7 magnetic beads per mL)/B-HRP (5×10^{-7} M). Each signal is the mean of three measurements. Flow rate 1 ml/min; Flow carrier 0.1 M phosphate buffer pH 7.2.

Flow rate (mL/min)			
0.5	1	1.5	2
(-5573 ± 64) nA	(-5100 ± 100) nA	(-2850 ± 132) nA	(-1375 ± 106) nA

rate of 0.5 mL/min, for the injection of the mixtures, where higher analytical signals were obtained, has been chosen.

3.1.1.2. Cleaning of the electrode. The influence of the flow rate on the efficiency of the washing step also has been studied. The washing step consists of placing the magnet in the lower position, so that the carrier washes the surface of the electrode sending the magnetic beads to the waste. Without magnetic field, the Strep-MBs are not retained on the electrode and the carrier can clean it.

A mixture of Strep-MB (7×10^7 magnetic beads per mL)/B-HRP (5×10^{-7} M) was prepared as explained in Section 2.3, and was injected with a flow rate of 0.5 mL/min. After the injection of the TMB and recording the reduction current at -0.20 V, a washing step is performed pumping a flow of 1, 2 and 3 mL/min (Fig. 3A, B and C, respectively) for 3 min in each case. To check the efficiency of the washing step, TMB was injected again. In the case of 1 mL/min, the washing step was totally inefficient because a similar reduction peak was observed after the second injection of TMB, whereas in the case of 2 mL/min a decrease in the intensity of the reduction peak was noted. Finally if the washing step was performed with a flow rate of 3 mL/min, the cleaning was more efficient because after the second injection of TMB, no reduction peak can be observed. All these results are summarized in Fig. 3.

To complete this study, the washing step was performed, applying a flow rate of 3 mL/min, for 1, and 2 and 3 min. The reduction peak after the second injection of TMB totally disappeared with a washing step of 3 min (data not shown). It means that the surface of the electrode is enzyme free. So for further experiments the washing step will be performed for 3 min with a flow rate of 3 mL/min.

3.2. Optimization of the parameters that affect the analytical response

3.2.1. Optimization of the applied potential

To determine the best detection potential, 40 μ L of TMB was added on a SPCE and a cyclic voltammetry was recorded between -0.40 and $+0.80$ V at scan rate of 50 mV/s. In Fig. 4A both

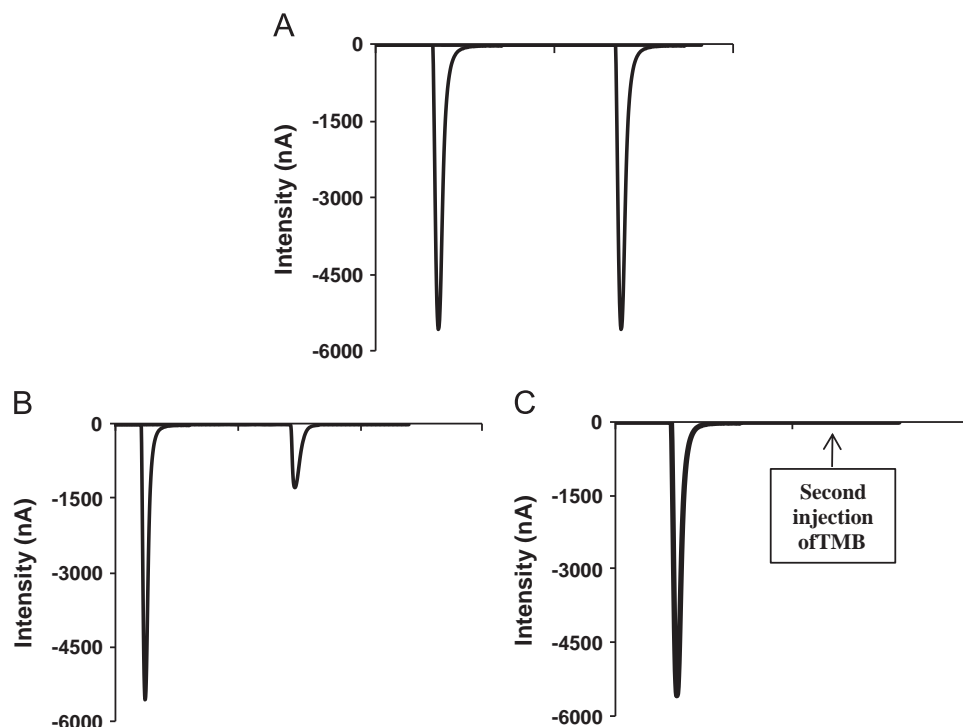


Fig. 3. Optimization of the washing flow rate; Flow rate 1 ml/min (A), 2 ml/min (B) and 3 ml/min (C). Flow carrier 0.1 M phosphate buffer pH 7.2; TMB diluted 5 times; $E_{\text{applied}} = -0.2$ V; Strep-MB (7×10^7 magnetic beads per mL)/B-HRP (5×10^{-7} M).

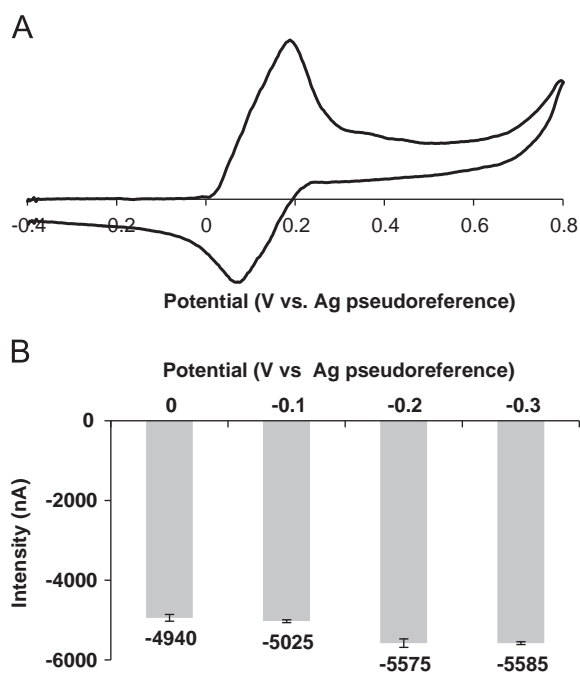


Fig. 4. (A) Cyclic voltammogram of TMB in 0.1 M phosphate buffer solution pH 7.2. $\nu = 50$ mV/s. (B) Influence of the applied potential on the analytical response; Strep-MB (7×10^7 per mL)/ B-HRP (5×10^{-7} M); TMB diluted 5 times. Each signal is the mean of three measurements. Flow rate 1 ml/min; Flow carrier 0.1 M phosphate buffer pH 7.2.

oxidation and reduction peaks of TMB are obtained between +0.00 and +0.20 V. So, a hydrodynamic curve was registered when TMB is injected into the FIA system and potentials between 0.00 and -0.30 V are applied, where the oxidation of TMB does

not occur. Previously, a mixture of Strep-MB (7×10^7 per mL)/ B-HRP (5×10^{-7} M) was prepared as explained in Section 2.3 and injected into the FIA system. The results are summarized in Fig. 4B.

The highest analytical response was obtained for -0.20 V. This potential was chosen for further studies.

3.2.2. Concentration of HRP-B

To determine the best concentration of B-HRP for the competitive assay, different mixtures of Strep-MB and HRP-B were prepared. The number of Strep-MB per mL was fixed to 7×10^7 and the concentration of B-HRP was between 5×10^{-12} and 5×10^{-8} M. The mixture was prepared as previously explained and the FIAGram was recorded applying -0.20 V as explained in Section 2.4. A linear relationship between current and B-HRP concentration in the range of 0.05 and 5 nM was obtained with a correlation coefficient of 0.9997 ($n=7$) according to the following equation:

$$I(\text{nA}) = -505.96C_{\text{B-HRP}}(\text{nM}) - 30.8$$

This result indicates that the saturation of the binding sites of Strep-MB with the enzymatic conjugate B-HRP is reached for a concentration of 5 nM. For further experiments, 5 nM has been chosen as the concentration for B-HRP. By selecting this concentration, it is insured that the maximum slope is achieved.

3.2.3. Optimization of the number of magnetic beads per mL

For the purpose to determine the best number of magnetic beads per mL, a mixture of Strep-MB/B-HRP with different number of magnetic beads per mL and a constant concentration of B-HRP were prepared. So in this study a number of magnetic beads comprised between 7×10^5 and 7×10^8 beads per mL were used and the concentration of B-HRP was 5 nM. The different mixtures were left under stirring for 15 min, and after washing, the chronoamperogram was recorded. The results are presented in

Table 2

Influence of the concentration of MBs on the analytical response; $E_{\text{applied}} = -0.2$ V; TMB diluted 5 times; B-HRP (5×10^{-9} M). Each signal is the mean of three measurements. Flow rate 1 ml/min; Flow carrier 0.1 M phosphate buffer pH 7.2.

Magnetic beads (per mL)			
7×10^8	7×10^7	7×10^6	7×10^5
(-3550 ± 50) nA	(-1336 ± 15) nA	(-546 ± 15) nA	(-133 ± 15) nA

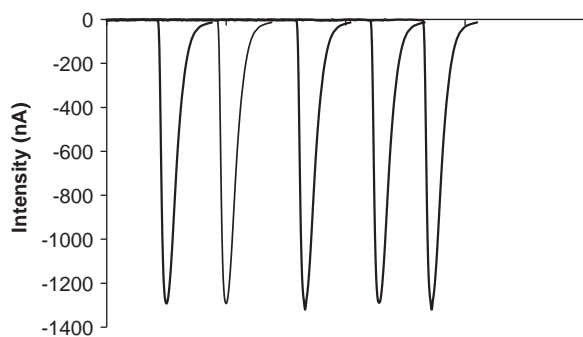


Fig. 5. Amperometric detection of TMB in the flow injection analysis system with the magnetic flow-cell; TMB diluted 5 times; $E_{\text{applied}} = -0.2$ V; Flow rate 1 ml/min; Flow carrier 0.1 M phosphate buffer pH 7.2 Strep-MB (7×10^7 magnetic beads per mL)/B-HRP (5×10^{-9} M).

Table 2 and represent the mean of 3 signals obtained with the same SPCE.

As it can be seen in **Table 2** that the analytical response increases with the number of magnetic beads. Moreover, for lower number of magnetic beads than 7×10^7 , an important decrease in the signal can be noticed. Nevertheless, in order to be economically viable, 7×10^7 magnetic beads per mL for the following experiments was selected.

3.2.4. Reproducibility

To check the reproducibility of the assay, a mixture of 7×10^7 magnetic beads per mL and 5 nM of B-HRP was prepared. After 15 min under stirring and a washing step, the mixture was injected into the FIA system. Then TMB diluted 5 times was injected and the peak current was recorded applying -0.20 V. After a washing step, the injection of the mixture and the TMB were repeated 5 times. The reduction peaks obtained are presented in **Fig. 5**. An analytical signal of -1320 ± 19 nA (RSD: 1.5%) was obtained. These results demonstrate the robustness of the electrode and the efficiency of the washing step.

3.3. Biotin assay

3.3.1. Calibration curve

The biotin assay was carried as explained in **Section 2.3**. Different mixtures of magnetic beads, B-HRP, and biotin were prepared. In each solution, the number of magnetic beads and the concentration of B-HRP were 7×10^7 per mL and 5 nM respectively, and the concentration of biotin was comprised between 5×10^{-11} and 10^{-7} M. The calibration plot is shown in **Fig. 6**.

A linear relationship between peak current and biotin concentration in the range between 0.01 and 1 nM was obtained with a correlation coefficient of 0.998 according to the following equation:

$$I(\text{nA}) = 758.8C_{\text{biotin}}(\text{nM}) - 939.6$$

The detection limit of this method was 7.5×10^{-3} nM of biotin and the reproducibility obtained was 2% ($n=3$). In comparison with other methods for biotin determination using magnetic

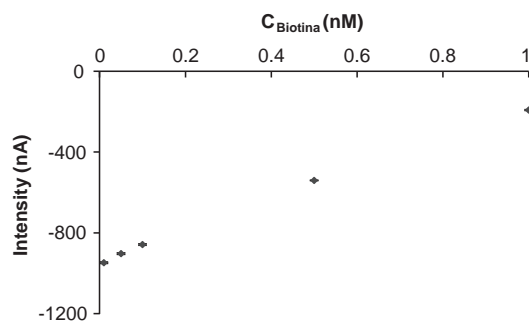


Fig. 6. Calibration curve of biotin under the optimized conditions assay. Strep-MB (7×10^7 per mL)/B-HRP (5×10^{-9} M); TMB diluted 5 times. Flow rate 1 ml/min; Flow carrier 0.1 M phosphate buffer pH 7.2. Each point is the mean of three measurements.

Table 3

Measurement of biotin in real samples. Data are given as average \pm SD ($n=3$).

Type	Reference value	Value obtained
MEDEBIOTIN (tablet)	5 mg	4.8 ± 0.3 mg
MEDEBIOTIN (vial)	4.6 mg/mL	4.5 ± 0.1 mg/mL

beads, it is probably one of the fastest methods because only 4 min are necessary to obtain one analytical response (13 analytical signals can be obtained per hour). This short analysis time is due to the extremely short enzymatic reaction time. Once the TMB is injected into the FIA system, the enzymatic reaction occurs in a very short time (few seconds) instead of minutes. The present biotin assay presents better limit of detection in comparison with other electrochemical methods for biotin determination [21–23]. Last but not least, the SPCE does not need tedious pretreatment or previous modification and the washing step only performed with the buffer does not damage the electrode surface. Moreover, the first assay using a magnetic flow cell with an integrated magnet is reported here. In the literature few articles are reported on coupling magnetic beads and flow injection analysis system. For example Krejčova et al. [24] have coupled paramagnetic particles with a flow injection analysis, but the magnetic beads are used for the isolation of the complex H5N1–CdS and are not deposited on the detector. On the other hand Pan and Yang [25] used functionalized magnetic beads for the carcinoembryonic antigen. But they used external magnet and glassy carbon electrode.

3.3.2. Application to real sample

Two pharmaceuticals with a known value of biotin have been used to validate our methods. These samples have been prepared as explained in **Section 2.5**. These two pharmaceuticals present a very high concentration of biotin, because their use is to compensate a lack of biotin in the organism; hence important dilutions have to be performed. Taking in account all the dilutions, the accuracy of the result obtained for both samples the accuracy obtained is satisfactory and the standard deviation obtained is also very good. The results are tabulated in **Table 3**.

4. Conclusion

Here, a new biotin assay using magnetic beads and a flow analysis system with the first flow cell with an integrated magnet is reported. The biotin assay described here is easy to use, cost-effective, time saving, and robust. It is obtained by a one step competitive assay and after the biological reaction a first analytical

signal can be obtained after 1 min thanks to the flow injection analysis system. This technique coupled to a new cell with an integrated magnet allows the modification and the cleaning of the electrode surface in a very easy way and much analysis can be obtained in a very short time. Moreover, it has been reported here that in order to demonstrate the viability of the method, and to validate it, a biotin assay is employed to determine biotin in two pharmaceuticals available in the market. In the future a lot of assays based on the magnetic beads and flow injection analysis can be obtained.

References

- [1] J. Ruzicka, H. Hansen, *Anal. Chim. Acta* 78 (1975) 145–157.
- [2] K.K. Stewart, G.R. Beecher, P.E. Hanc, *Anal. Biochem.* 70 (1976) 167–173.
- [3] P. Dugoa, N. Fawzya, F. Cichelloa, F. Cacciola, P. Donatob, Luigi Mondello, *J. Chromatogr. A* 1278 (2013) 46–53.
- [4] M. Maciejewska, A. Szczureka, Ł. Ochromowicz, *Sens. Actuat. B* 141 (2009) 417–423.
- [5] F.R. Mansour, N.D. Danielson, *Trends Anal. Chem.* 40 (2012) 1–14.
- [6] S. Feng, M. Zhang, Y. Huang, D. Yuann, Y. Zhu, *Talanta* 117 (2013) 456–462.
- [7] R.O. Hassan, A.T. Faizullah, *Arab. J. Chem.* 6 (2013) 393–400.
- [8] E.C. Vidotti, V.C. Almeida, C.C. Oliveira, *Talanta* 64 (2004) 993–999.
- [9] M.J. Ruedas Rama, A. Ruiz Medina, A. Molina Díaz, *J. Pharm. Biomed. Anal.* 35 (2004) 1027–1034.
- [10] Y. Yu, Y. Jiang, R. He, *Talanta* 88 (2012) 352–357.
- [11] J. Wang, E. Hansena, M. Miró, *Anal. Chim. Acta* 499 (2003) 139–147.
- [12] S.S.M.P. Vidigal, I.V. Tóth, A.O.S.S. Rangel, *Talanta* 84 (2011) 1298–1303.
- [13] K. Jitmanee, S. Kradtap Hartwell, J. Jakmunee, S. Jayasvasti, J. Ruzicka, K. Grudpan, *Talanta* 57 (2002) 187–192.
- [14] E. Palecek, M. Bartosik, *Chem. Rev.* 112 (6) (2012) 3428–3461.
- [15] F. Bettazzi, E. Hamid-Asl, C.L. Esposito, C. Quintavalle, N. Formisano, S. Laschi, S. Catuogno, M. Iaboni, G. Marrazza, M. Mascini, L. Cerchia, V. De Franciscis, G. Condorelli, I. Palchetti, *Anal. Bioanal. Chem.* 405 (2–3) (2013) 1025–1034.
- [16] A. Erdem, G. Congur, *Talanta* 118 (2014) 7–13.
- [17] R.K. Mendes, S. Laschi, D.R. Stach-Machado, L.T. Kubota, G. Marrazza, *Sens. Actuat. B* 166–167 (2012) 135–140.
- [18] K. Mervartova, Miroslav Polasek, J.M. Calatayud, *J. Pharm. Biomed. Anal.* 45 (2007) 367–381.
- [19] E. Khaled, I.A. El-Sabbagh, N.G. El-Kholly, E.Y.A. Ghahni, *Talanta* 87 (2011) 40–45.
- [20] M.F. Bergamini, A.L. Santos, N.R. Stradiotto, M.V.B. Zanoni, *J. Pharm. Biomed. Anal.* 43 (2007) 315–319.
- [21] R. Kizek, M. Masarik, K.J. Kramer, D. Potesil, M. Bailey, J.A. Howard, B. Klejdus, R. Mikelova, V. Adam, L. Trnkova, F. Jelen, *Anal. Bioanal. Chem.* 381 (2005) 1167–1178.
- [22] S. Tanaka, F. Yamamoto, K. Sugarwara, H. Nakumura, *Talanta* 44 (1997) 357–363.
- [23] J. Ho, W. Hsu, W. Liao, J. Chiu, M. Chen, H. Chang, C. Li, *Bioelectron* 26 (2010) 1021–1027.
- [24] L. Krejčová1, D. Dospivová1, M. Ryvolová, P. Kopel, D. Hynek, S. Krizkova, J. Hubalek, V. Adam, R. Kizek, *Electrophoresis* 33 (2012) 3195–3204.
- [25] J. Pan, Q. Yang, *Anal. Bioanal. Chem.* 388 (2007) 279.



Quantification of acesulfame potassium in processed foods by quantitative ^1H NMR



Takashi Ohtsuki*, Kyoko Sato, Yutaka Abe, Naoki Sugimoto, Hiroshi Akiyama

National Institute of Health Sciences, 1-18-1 Kamiyoga, Setagaya-ku, Tokyo 158-8501, Japan

ARTICLE INFO

Article history:

Received 1 July 2014

Received in revised form

1 August 2014

Accepted 2 August 2014

Available online 11 August 2014

Keywords:

Absolute quantification

Processed food

Quantitative NMR

Acesulfame potassium

ABSTRACT

Acesulfame potassium (AceK), a high-intensity and non-caloric artificial sweetener, is used in various processed foods as a food additive. In this study, we established and validated a method for determining the AceK content in various processed foods by solvent extraction and quantitative ^1H NMR, using a certified reference material as the internal standard. In the recovery test, the proposed method gave satisfactory recoveries (88.4–99.6%) and repeatabilities (0.6–5.6%) for various processed foods. The limit of quantification was confirmed as 0.13 g kg^{-1} , which was sufficiently low for the purposes of monitoring AceK levels. In the analysis of commercially processed foods containing AceK, all AceK contents determined by the proposed method were in good agreement with those obtained by a conventional method based on dialysis and HPLC. Moreover, this method can achieve rapid quantification and yields analytical data with traceability to the International System of Units (SI) without the need for an authentic analyte standard. Therefore, the proposed method is a useful and practical tool for the determination of AceK in processed foods.

© 2014 Elsevier B.V. All rights reserved.

1. Introduction

Acesulfame potassium (AceK) is a high-intensity, non-caloric artificial sweetener with a sweetening strength approximately 200 times that of sucrose. As such, AceK is consumed as a sugar substitute in order to restrict sugar intake and control blood glucose levels [1]. In addition, this compound is used as a food additive in more than 100 countries [2] due to its high stability under acidic conditions and heating. Many countries regulate the use of AceK according to specific legislation regarding food additives based on acceptable daily intake (ADI) values (0–15 mg/kg of body weight per day) established by the Joint Food and Agriculture Organization of the United Nations (FAO)/World Health Organization (WHO) Expert Committee on Food Additives (JECFA) [3]. The maximum usage level of AceK in various foods is determined by the Codex Committee. In Japan, AceK can currently be used in specific processed foods such as chewing gum, jam, ice cream, soft drink, and beverages containing *Lactobacillus*. The maximum level is set between 0.35 g kg^{-1} and 15 g kg^{-1} .

Abbreviations: AceK, Acesulfame potassium; ADI, acceptable daily intake values; CRM, certified reference material; qNMR, quantitative NMR; IS, internal standard; LOQ, limit of quantification

* Corresponding author. Tel./fax: +81 3 3700 9403.

E-mail address: ohtsuki@nihs.go.jp (T. Ohtsuki).

<http://dx.doi.org/10.1016/j.talanta.2014.08.002>

0039-9140/© 2014 Elsevier B.V. All rights reserved.

Accordingly, reliable analytical methods are necessary to monitor AceK content in processed foods and to assure regulatory compliance.

Several analytical methods have been applied in the determination of AceK in foodstuffs such as processed foods and beverages. Among them, chromatographic methods including HPLC [4–6], ion chromatography [7], and HPLC–MS/MS [8] are used most frequently in the quantification of AceK. In these chromatographic methods, an authentic standard, such as a certified reference material (CRM) with a proven identity and purity determined by metrological valid procedures, is required in order to obtain reliable analytical results.

On the other hand, quantitative NMR (qNMR) is a considerably powerful tool to quantify analytes without the need for identical standards, and is considered to be a primary ratio method [9,10]. In particular, quantification using ^1H NMR (qHNMR) is widely applied in the quantification of medicines [11,12], beverage components [13,14], and natural products in medicinal plant extracts [15–17] due to its high sensitivity and the widespread presence of ^1H nuclei in organic molecules [18]. In qHNMR, the content or concentration of the analyte is determined using the ratio between the integral values of a specific signal of the analyte to that of an internal standard (IS). The integral values of the analyte and IS are directly proportional to the number of protons per resonance line times the molar concentration of the analyte and the IS, respectively. Therefore, the absolute quantitative value of the analyte can be determined with metrological traceability to the International

System of Units (SI), if a specific CRM is used as the IS in qHNMR. Recently, qHNMR with IS, also called AQARI (accurate quantitative NMR with internal reference substance), was reported [19]. We previously demonstrated that qHNMR using an SI-traceable reference material combined with solvent extraction could be utilized to determine the absolute content of preservatives in processed foods [20,21].

In this study, we developed a novel method for the determination of AceK in processed food using solvent extraction and qHNMR. To determine the accuracy and precision, we also applied and validated the proposed method using various processed foods. Furthermore, we compared the proposed method to a conventional method based on dialysis and HPLC.

2. Materials and methods

2.1. Processed food samples

Twelve processed foods without AceK (chewing gum, red bean paste, candy, jelly, biscuits, ice cream, jam, salad dressing, vegetable pickled in soybean sauce, sherbet, a soft drink, and a beverage containing *Lactobacillus* species) and five processed foods that specified the use of AceK on the label (candy, two types of jellies, biscuits, and a soft drink) were purchased from markets in Tokyo, Japan.

2.2. Chemicals and reagents

Analytical grade AceK (purity: >98%) and 2,2-dimethyl-2-silapentane-5-sulfonate- d_6 sodium salt (DSS- d_6) (Code no. 048-31071, Lot. EPL1095, purity: $92.2 \pm 0.7\%$), the certified reference material, were obtained from Wako Pure Chemical Industries, Ltd. DMSO- d_6 and HPLC grade acetonitrile were obtained from Kanto Chemical Co., Inc. (Tokyo, Japan). Ultrapure water (purified to $18 \text{ M}\Omega \text{ cm}$) using a Millipore (Danvers, MA, USA) Milli-Q water purification system was used. All other chemicals were of analytical grade and were purchased from Kanto Chemical Co., Inc. (Tokyo, Japan) and Wako Pure Chemical Industries, Ltd. (Osaka, Japan). Hexane saturated with acetonitrile and acetonitrile saturated with hexane were prepared as follows: 500 mL of acetonitrile and 500 mL of hexane were transferred to a separating funnel and were shaken vigorously. After the upper and lower layers were completely separated, they were used as hexane saturated with acetonitrile and acetonitrile saturated with hexane, respectively. Acesulfame was prepared by the acid hydrolysis of AceK as follows: AceK (8 g) in 5% sulfuric acid (100 mL) was allowed to sit at room temperature for 15 min. Subsequently, the solution was partitioned with ethyl acetate (100 mL²) and the ethyl acetate layer was evaporated to yield acesulfame (6 g). Prepared acesulfame was completely characterized using DART-TOFMS and NMR.

2.3. Instruments

¹H NMR was measured on a JNM-ECA 600 spectrometer (JEOL Ltd., Tokyo, Japan). HPLC was performed on a Shimadzu HPLC system (LC-10A) equipped with an SPD-M10Avp diode array detector (Shimadzu Corporation, Kyoto, Japan). Homogenization was carried out using an ULTRA-TURRAX T 25 digital homogenizer (IKA Works, Wilmington, NC, USA). An XP2U (Mettler-Toledo AG, Greifensee, Switzerland) ultra-micro balance was used to weigh the analytical grade AK for qHNMR analysis, and DSS- d_6 . A ME235S (Sartorius, Bloomington, MN, USA) semi-micro balance was used to weigh the processed foods, DSS- d_6 stock solution, and DMSO- d_6 .

2.4. Pretreatment of the processed foods

2.4.1. Solvent extraction

The four processed foods (chewing gum, candy, jelly, and vegetable pickled in soy bean sauce) were cut into small pieces before weighing. Portions (5 g) of all processed foods were accurately weighed in glass centrifuge tubes. A saturated solution of sodium chloride (20 mL), 10 vol% sulfuric acid (4 mL), and diethyl ether (20 mL) were added, and the mixture was subjected to high-speed homogenization for approximately 1 min. The homogenate was centrifuged at 1500g for 5 min, and then the upper layer was transferred to a clean flask. The residue was homogenized again with 20 mL of diethyl ether and centrifuged at 1500g for 5 min. The upper layers were combined and then evaporated at 30 °C to yield the qHNMR sample.

For the biscuit, ice cream, jam, and salad dressing, 10 mL of methanol was added to the extract to remove oil components after the evaporation of the upper layer, as described above, and then the samples were centrifuged. Finally, the methanol layer was transferred to a clean flask and then evaporated to yield the qHNMR sample.

For chewing gum, 20 mL of hexane saturated acetonitrile and acetonitrile saturated hexane was added to the extract following the evaporation of the upper layer, as described above, and then the sample was centrifuged. Subsequently, the acetonitrile layer was evaporated to obtain the qHNMR sample.

2.5. Dialysis

The dialysis procedure utilized in this study was the same as described previously [4]. Briefly, the solid processed foods were cut into small pieces prior to weighing. Accurately weighed portions (20 g) of all processed foods were packed into cellulose tubes with 20 mL of 0.01 mol L⁻¹ hydrochloric acid containing 10% sodium chloride and set to glass vessel. After the total volume was adjusted to 200 mL by the addition of 0.01 mol L⁻¹ hydrochloric acid in a glass vessel, the sample was dialyzed against 0.01 mol L⁻¹ hydrochloric acid for 48 h. Then, 20 mL of dialysate and 2 mL of 0.1 mol L⁻¹ tetra-*n*-propyl ammonium bromide were transferred to a volumetric flask and the volume was adjusted to 25 mL by the addition of water. Five milliliters of the sample solution was passed through a Sep-Pak Vac C₁₈ column. After washing the column with 10 mL of water, the sample was eluted with 10 mL of 40% methanol. The obtained eluate was passed through a Bond Elut SAX column for further purification. After washing the column with 5 mL of 0.5% phosphoric acid and water, AceK was eluted with 5 mL of 0.3 mol L⁻¹ hydrochloric acid. This eluate was transferred to a volumetric flask, and the volume was adjusted to 5 mL by the addition of water. The final solution was filtered with a 0.45 μm syringe filter and used for HPLC analysis.

2.6. qHNMR measurements

2.6.1. qHNMR measurement parameters

qHNMR was measured using previously described parameters [20,21]. The data were processed using the qNMR analysis software, Alice 2 for qNMR "PURITY" (JEOL RESONANCE Ltd.). The signal integral value calculated with this software was used for quantitative analysis. The chemical shift of all data was referenced to DSS- d_6 at δ_H 0.00.

2.7. Preparation of the DSS- d_6 stock solution and determination of its concentration

The reference material, DSS- d_6 (21.91 mg), was dissolved in 100 g of DMSO- d_6 to obtain the stock solution. The concentration

of DSS- d_6 in the stock solution was calculated to be 0.202 mg g^{-1} , based on the purity of DSS- d_6 (92.2%).

2.8. qHNMR measurement of prepared acesulfame

Three samples of acesulfame (10 mg; prepared as described in Section 2.2) were accurately weighed using an ultra-micro balance. Each sample was then placed in a separate vial, and the stock solution (1 g) was added to each vial to fully dissolve the samples. Each solution was then transferred to a 5 mm (outer diameter) NMR tube (Kanto Chemical Co., Inc., Tokyo, Japan) to a height of 4 cm from the bottom of the tube and was subjected to qHNMR analysis. The purities of acesulfame were calculated using the following equation:

$$\text{Purity (\%)} = \frac{I_{\text{AF}}/H_{\text{AF}}}{I_{\text{DSS}}/H_{\text{DSS}}} \frac{M_{\text{AF}}/C_{\text{AF}}}{M_{\text{DSS}}/C_{\text{DSS}}} \times 100, \quad (1)$$

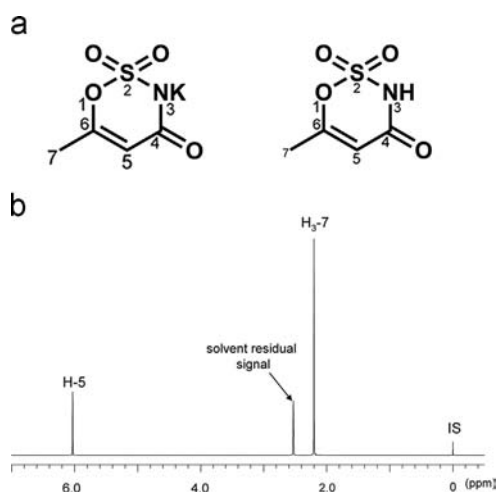


Fig. 1. Chemical structure of AceK (left) and acesulfame (right) (a) and ^1H NMR spectrum of acesulfame in $\text{DMSO-}d_6$ containing DSS- d_6 (b). IS, internal standard.

Table 1
Purity of acesulfame determined by qHNMR.

Signal (δ , ppm)	Number of protons	Purity (%) ^a	RSD (%)
2.20	3	97.8	0.1
6.04	1	97.7	0.1

^a Values represent the mean of three independent experiments.

where I_{AF} and I_{DSS} are the signal integral values for the acesulfame and DSS- d_6 , respectively. H_{AF} and H_{DSS} are the number of protons for the acesulfame and DSS- d_6 signals, respectively. M_{AF} and M_{DSS} are the molecular weights of acesulfame and DSS- d_6 , respectively. C_{AF} and C_{DSS} are the acesulfame concentration (10 mg g^{-1}) and DSS- d_6 concentration (0.202 mg g^{-1}) in the stock solution.

2.9. Recovery test

The recovery was determined by spiking acesulfame in 12 processed foods and obtaining triplicate measurements. The four levels (0.50, 1.0, 2.5, and 5.0 g kg^{-1}) of acesulfame in each processed food were close to each maximum usage levels of AceK permitted in Japan. Accordingly, these four levels were used as the high concentration levels of each food in this test. After solvent extraction of each spiked food sample, the samples were subjected to qHNMR measurements. The recoveries of each food sample were calculated using the following equation:

$$\text{Recovery (\%)} = \frac{\text{Measured concentration}}{\text{Spiked concentration}} \times 100 \quad (2)$$

$$\text{Measured concentration (g kg}^{-1}\text{)} = \frac{I_{\text{AF}}/H_{\text{AF}}}{I_{\text{DSS}}/H_{\text{DSS}}} \frac{M_{\text{AF}}/W_{\text{FD}}}{M_{\text{DSS}}/C_{\text{DSS}}} \quad (3)$$

where W_{FD} is the concentration of the food sample by weight (g g^{-1} ; 5 g food sample/1 g stock solution).

Table 2
Comparison of gravimetric and experimental values.

Gravimetric value (mg g^{-1}) ^a	δ_{H} 2.20			δ_{H} 6.04		
	Experimental value (mg g^{-1}) ^a	RSD (%) ^b	Relative error (%) ^c	Experimental value (mg g^{-1}) ^a	RSD (%) ^b	Relative error (%) ^c
0.15	0.15	0.1	-0.7	0.15	0.9	-2.0
0.30	0.30	0.1	-0.8	0.30	0.0	-0.9
0.61	0.61	0.2	-0.8	0.61	0.5	-0.8
1.2	1.2	0.2	-0.4	1.2	0.3	-0.3
2.4	2.4	0.1	-0.9	2.4	0.1	-0.7
4.9	4.9	0.3	-0.6	4.9	0.3	-0.6
9.8	9.8	0.1	0.5	9.8	0.1	0.3
20	20	0.2	0.8	20	0.2	0.1
25	25	0.2	0.3	25	0.2	0.5

^a Each gravimetric and experimental values represent the mean of three independent experiments.

^b RSD, relative standard deviation.

^c Relative error calculated with the following equation: Relative error = [(experimental value - gravimetric value)/gravimetric value] \times 100.

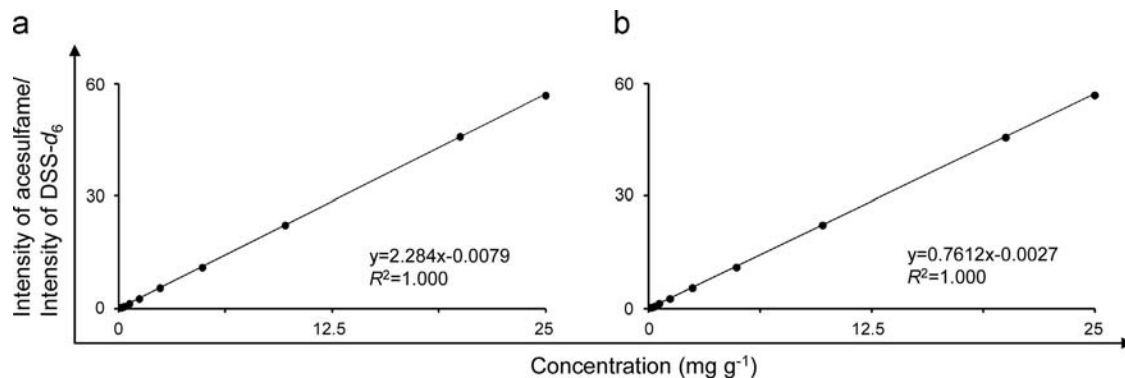


Fig. 2. Relationship between acesulfame concentration and the ratio of the integral of acesulfame:DSS- d_6 signals. (a) δ_{H} 2.20 and (b) δ_{H} 6.04.

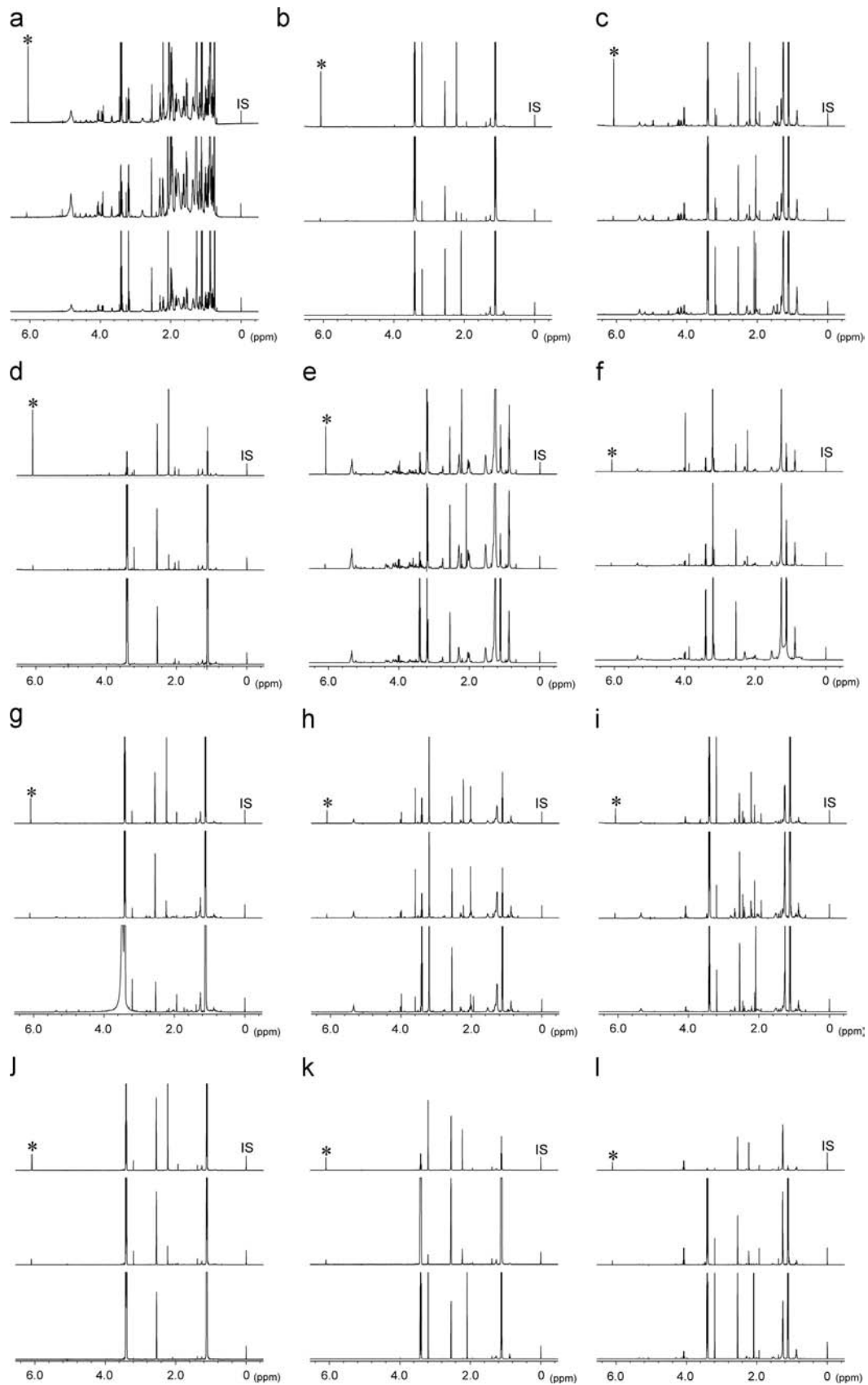


Fig. 3. ^1H NMR spectra of samples extracted from processed foods spiked with acesulfame at the high concentration level (top), 0.13 g kg^{-1} (middle), and blank (bottom). The signals marked with asterisks were used for quantification. (a) Chewing gum, (b) red bean paste, (c) candy, (d) jelly, (e) biscuit, (f) ice cream, (g) jam, (h) salad dressing, (g) vegetable pickled in soybean sauce, (h) sherbet, (i) soft drink, and (j) beverage containing *Lactobacillus* species. IS, internal standard (DSS-d_6).

2.10. qHNMR measurement of AceK in the processed foods

The extract obtained from the solvent extraction of each of the processed foods was dissolved in 1 g of stock solution and subjected to qHNMR. In qHNMR, AceK the from respective food samples was detected as acesulfame owing to the acid hydrolysis of AceK during extraction. The AceK contents of the food samples were calculated using the following equation:

$$\text{Content (g kg}^{-1}\text{)} = \frac{I_{AF}/H_{AF}}{I_{DSS}/H_{DSS}} \frac{M_{AF}/W_{FD}}{M_{DSS}/C_{DSS}} \times 1.233, \quad (4)$$

where 1.233 is the ratio of the molecular weights between AceK and acesulfame.

2.11. HPLC measurement

The sample solution obtained by dialysis was subjected to HPLC analysis at 230 nm using a Capcell pak NH₂ (4.6 mm i.d. × 250 mm, particle size 5 μm; Shiseido, Tokyo, Japan) at 40 °C and a flow rate of 1.5 mL/min with 1% phosphoric acid/acetonitrile (2:3) as the mobile phase. The AceK contents of the food samples were calculated using the following equation:

$$\text{Content (g kg}^{-1}\text{)} = \frac{C \times 200 \times 25}{1000 \times W \times 20}, \quad (5)$$

where *C* is the concentration of the acesulfame in the sample solution (μg mL⁻¹) and *W* is the weight of the sample (g).

3. Results and discussion

3.1. qHNMR measurement of acesulfame

To ensure whether qHNMR could be used for quantification of the AceK content in the processed foods, the acesulfame was first analyzed using qHNMR, because AceK was converted to acesulfame through acid hydrolysis during pre-treatment of processed foods. As shown in Fig. 1, the ¹H NMR spectrum displayed the two characteristic singlet signals of acesulfame due to a methyl group at δ_H 2.20 and an olefinic proton at δ_H 6.04, in addition to signals of DSS-*d*₆, the internal standard, at δ_H 0.00 and residual proton of DMSO-*d*₆ in the stock solution. We considered that these two signals could be applied in the qHNMR quantification of acesulfame, because these signals were well separated from other signals. Therefore, the absolute purity of acesulfame was determined from the ratio of the integrated signal intensity of each the two characteristic signals to the signal of DSS-*d*₆. The results shown in Table 1 indicate that the purities calculated using the signal of acesulfame at δ_H 2.20 were not significantly different those calculated using the signal at δ_H 6.04. These results suggested that the two signals were suitable for the accurate quantification of acesulfame.

3.2. Linearity

To determine the linearity and the measuring range of the three signals, acesulfame solutions at nine different concentrations including 0.15, 0.30, 0.61, 1.2, 2.4, 4.9, 9.8, 20, and 25 mg g⁻¹ were prepared and the calibration curves of each signal were subsequently plotted based on the linear regression analysis of the ratio of the integrated signal intensity of each signal to that of DSS-*d*₆ (*Y*) versus the concentration of acesulfame (*X*, mg mL⁻¹). As shown in Fig. 2, clear linear regressions with the coefficient of determination of 1.0 were obtained in the range of 0.15–25 mg g⁻¹ for the signal at δ_H 2.20 and 0.30–25 mg g⁻¹ for the signal at δ_H 6.04, indicating a good linear relation in the method's response.

In these concentration ranges, relative errors between the experimental values obtained using qHNMR and the gravimetric value of each signal were also less than 1%, as shown in Table 2.

3.3. Accuracy and precision of the proposed method

To develop a quantitative method for AceK in processed foods using qHNMR, the method combining extraction method for pre-treatment and subsequent qHNMR analysis was examined to determine the AceK in processed foods. Although dialysis is generally used as a conventional pre-treatment [4,22] for the quantification of AceK in processed foods, it requires 48 h to purify AceK from processed foods. To avoid this time-consuming process, we utilized solvent extraction using diethyl ether as the extraction solvent based on a previous report [20,21].

To assess the intra-day accuracy and precision of the proposed quantitative method, we performed the recovery test using the samples of 12 kinds of the processed foods spiked with known amounts of acesulfame with triplicate measurements at each level. Fig. 3 shows a representative ¹H NMR spectra of acesulfame-spiked sample extracts and blank sample extracts. In these spectra, whole or partial overlaps between the signal at δ_H 2.02 in

Table 3
Recovery of acesulfame from various processed foods.

Sample	0.13 g kg ⁻¹ Spiked		High concentration level spiked		
	Recovery (%) ^a	RSD (%) ^b	Level (g kg ⁻¹)	Recovery (%) ^a	RSD (%) ^b
Chewing gum	97.8	5.6	5.0	88.4	2.4
Red bean paste	97.7	3.0	2.5	96.5	1.3
Candy	96.7	0.6	2.5	98.2	2.4
Jelly	92.6	1.6	2.5	98.0	1.7
Biscuit	90.9	2.7	2.5	95.1	3.4
Ice cream	99.2	0.6	1.0	92.4	4.1
Jam	99.3	1.4	1.0	99.6	0.8
Salad dressing	90.4	1.1	1.0	96.8	1.7
Vegetable pickled in soybean sauce	96.5	4.8	1.0	98.6	2.7
Sherbet	97.1	1.7	1.0	98.5	1.5
Soft drink	98.2	0.9	0.50	94.6	1.5
Beverage containing <i>Lactobacillus</i> species	99.0	2.6	0.50	95.6	4.0

^a Each recovery value represents the mean of three independent experiments performed on the same day.

^b RSD, intra-day relative standard deviation.

Table 4
Inter-day recoveries, repeatability, and intermediate precisions of acesulfame in chewing gum, ice cream, and vegetable pickled in soybean sauce.

Sample	0.13 g kg ⁻¹			High concentration level spiked		
	Recovery (%) ^a	RSD _r (%) ^{b,d}	RSD _{ip} (%) ^{c,d}	Recovery (%) ^a	RSD _r (%) ^{b,d}	RSD _{ip} (%) ^{c,d}
Chewing gum	94.3	1.9	4.8	86.2	2.9	2.9
Ice cream	97.0	2.9	3.7	91.4	4.4	4.5
Vegetable pickled in soybean sauce	94.3	3.7	4.0	93.9	3.6	4.7

^a Each recovery value represents the mean of results on five different days (two trials per day).

^b RSD_r, the relative standard deviation for repeatability.

^c RSD_{ip}, the relative standard deviation for intermediate precision.

^d RSD_r and RSD_{ip} are calculated by one-way analysis of variance of the recovery values obtained on five different days.

acesulfame and those in other ingredients of the foods were observed in some samples. These overlaps considerably affected the accurate quantification of spiked acesulfame, especially at low concentrations. On the other hand, with the quantification using the signal at δ_H 6.04, the signals of other ingredients were minimal in the range of δ_H 5.8– δ_H 6.2. Therefore, we utilized the signal at δ_H 6.04 to determine the acesulfame content in all food samples. As shown in Table 3, the recoveries and RSDs of all samples spiked with the high concentration level ranged from 88.4% to 99.6% and from 0.8% to 4.1%, respectively. At a concentration of 0.13 g kg^{-1} , the recoveries were in the range of 90.4–99.2% with RSDs less than 5.6%. Consequently, the results suggested that the proposed method was reliable in the determination of AceK in processed foods.

3.4. Intermediate precision

To evaluate the intermediate precision and accuracy of the proposed method, we performed the recovery test on five different days, as described in the section entitled accuracy and precision of the proposed method. In this test, we selected three food samples (chewing gum, ice cream, and vegetable pickled in soybean sauce). As shown in Table 4, the proposed method gave precise intermediate data from all spiked samples, for which the RSD ranged from 2.9% to 4.8%. In addition, the recoveries of all samples ranged

from 86.2% to 91.7%. As such, the proposed method was highly reliable and reproducible.

3.5. Limit of quantification of the proposed method

According to previous reports [20,21], the limit of quantification (LOQ) was determined based on the accuracy (recovery), inter- and intra-day precisions (RSD) in the recovery test, and signal-to-noise (S/N) ratio of the signal for quantification. The recoveries for all samples spiked at 0.13 g kg^{-1} , the lowest spiked concentration, were larger than 90% while their intra- and inter-day precision were lower than both 6%. In terms of the S/N ratio, Malz and Jancke reported that an S/N ratio at least 150 was necessary for qHNMR measurements with uncertainty of less than 1% [23]. Additionally, we previously demonstrated that the S/N ratio for quantification should be at least 100 to precisely determine the level of some preservatives in processed foods [20,21]. In this study, the means of the S/N ratios of all samples spiked at 0.13 g kg^{-1} of acesulfame were larger than 100. These results indicate that the proposed method could efficiently determine acesulfame or salts such as AceK in processed foods at concentrations of at least 0.13 g kg^{-1} using the signal at δ_H 6.04. As such, we estimated that the LOQ of the proposed method is 0.13 g kg^{-1} in processed foods. As the maximum usage levels of AceK in processed foods are in the range of $0.35\text{--}15 \text{ g kg}^{-1}$ in Japan, the

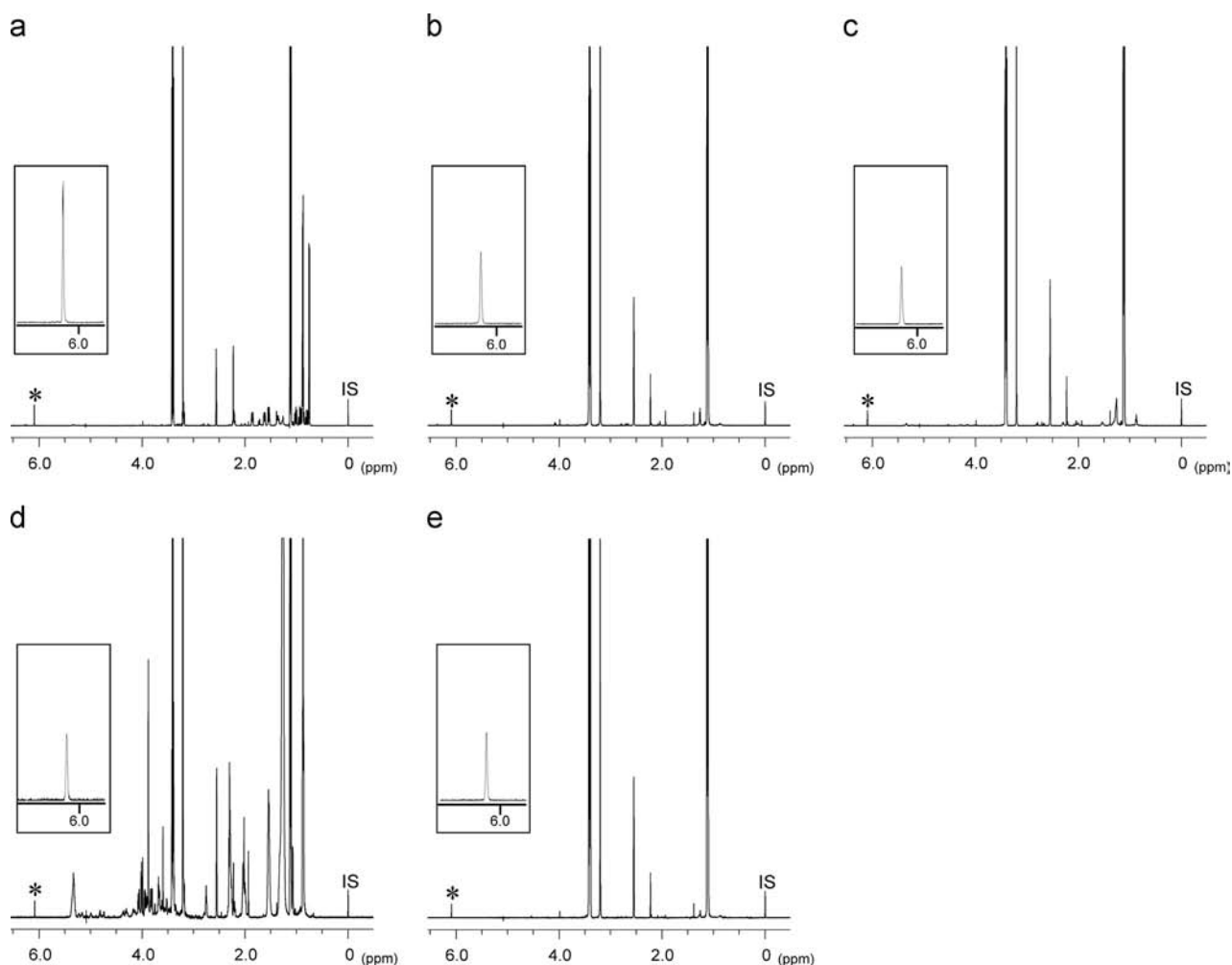


Fig. 4. ^1H NMR spectra of sample solutions from commercially produced foods containing AceK. The signals (δ_H 6.04) marked with asterisks were used for quantification. The signals at δ_H 6.04 are highlighted. (a) Candy, (b) Jelly I, (c) Jelly II, (d) biscuit, and (e) soft drink. IS, internal standard (DSS-d_6).

Table 5
Comparison of AceK contents in commercial foods determined by two methods.

Sample	Proposed method (solvent extraction/qHNMR)		Conventional method (dialysis/HPLC)	
	Content (g kg ⁻¹)	RSD (%)	Content (g kg ⁻¹)	RSD (%)
Candy	0.52	0.4	0.50	3.6
Jelly I	0.25	1.9	0.25	1.4
Jelly II	0.21	1.3	0.21	9.1
Biscuit	0.22	4.1	0.24	3.2
Soft drink	0.20	0.4	0.20	3.0

proposed method can be applied for the monitoring of AceK in processed foods for regulatory purposes.

3.6. Comparison of proposed method and conventional methods for commercial processed foods

To clarify the applicability of the proposed method for the quantification of commercial processed foods containing AceK, the method was applied using candies, jellies, biscuits, and soft drinks containing AceK and was compared with conventional methods that use a combination of dialysis and HPLC. Fig. 4 shows representative ¹H NMR spectra of the four food samples. We selected the signal at δ_H 6.04 for to determine the amount of acesulfame potassium in the processed foods, because this signal was well separated from the interference signals in all processed foods. As shown in Table 5, no significant differences between the AceK levels determined using the proposed method and those determined using the conventional method were found in any food samples by statistically evaluation ($P < 0.05$) with the *t*-test. Although, the RSDs of the proposed method with Jelly I and biscuits were slightly larger than those of the conventional method, the RSDs of all samples were lower than 9.1%. These results suggested that the proposed method was as reliable as the conventional method. Therefore, we conclude that the proposed method is suitable for the determination of AceK in various processed foods.

4. Conclusion

In this study, we developed and validated a method for the determination of AceK content in various processed foods using a combination of solvent extraction and qHNMR. Although quantification of AceK in cola beverages using ¹H NMR with an external calibration curve was previously reported [24], this report exemplifies the first use of qHNMR to determine AceK levels in various processed foods. Our study demonstrates the advantages of the proposed method including high accuracy, intra-day and inter-day precision, as well as good linearity. Compared with the conventional method, the proposed method exhibited similar capabilities in the determination of AceK in various samples, but was significantly faster in comparison to 49 h in the conventional method. The breakdown of the timeline of the conventional method includes 48 h of dialysis, 50 min of HPLC analysis

including the analysis of the standard to create the calibration curve, followed by 10 min for the determination of AceK. On the other hand, the proposed method requires an initial solvent extraction which requires 45 min, while the following qHNMR analysis accounts for 15 min, and the final determination of AceK requires 5 min. Moreover, an additional advantage of the proposed method is that absolute quantification with SI-traceability can be performed in the determination of AceK in processed foods, without the need for an authentic and identical analyte standard. As such, the proposed method is a very useful and efficient tool for determining AceK content in processed foods. In addition, this method could potentially be used as an alternative at inspection centers or quarantine laboratories to assess the suitability of usage levels and compliance with labeling provisions for quality control, and to monitor of AceK consumption for consumer safety.

Acknowledgments

This work was supported by a Grant-in-Aid for Scientific Research from the Ministry of Health, Labour, and Welfare of Japan to TO (H22-Syokuhin-Wakate-020).

References

- [1] M. Fukuda, T. Terata, K. Tsuda, M. Sugawara, N. Kitatani, Y. Seino, *Food Sci. Technol. Res.* 16 (2010) 457–466.
- [2] P. Shankar, S. Ahuja, K. Sriram, *Nutrition* 29 (2013) 1293–1299.
- [3] WHO Technical Report Series, no. 806, Evaluation of Certain Food Additives and Contaminants, Thirty-Seventh Report of the Joint FAO/WHO Expert Committee on Food Additives, 1991, pp. 20–21.
- [4] T. Moriyasu, M. Nakazato, C. Kobayashi, Y. Kikuchi, K. Hayano, Y. Tamura, *Shokuhin Eiseigaku Zasshi* 37 (1996) 91–96.
- [5] N. Dossi, S. Toniolo, S. Susmel, A. Pizzariello, G. Bontempelli, *Chromatographia* 63 (2006) 557–562.
- [6] A. Wasik, J. McCourt, M. Buchgraber, *J. Chromatogr. A* 1157 (2007) 187–196.
- [7] Y. Zhu, Y. Guo, M. Ye, F.S. James, *J. Chromatogr. A* 1085 (2005) 143–146.
- [8] H.-S. Lim, S.-K. Park, I.-S. Kwak, H.-I. Kim, J.-H. Sung, S.-J. Jang, M.-Y. Byun, S.-H. Kim, *Food Sci. Biotechnol.* 22 (2013) 233–240.
- [9] T.J. Quinn, *Metrologia* 34 (1997) 61–65.
- [10] R.J. Wells, J. Cheung, J.M. Hook, *Accredit. Qual. Assur.* 9 (2004) 450–456.
- [11] A. Zoppi, M. Linares, M. Longhi, *J. Pharm. Biomed. Anal.* 37 (2005) 627–630.
- [12] A.A. Salem, H.A. Mossa, B.N. Barsoum, *J. Pharm. Biomed. Anal.* 41 (2006) 654–661.
- [13] C. Almeida, I.F. Duarte, A. Barros, J. Rodrigues, M. Spraul, A.M. Gil, *J. Agric. Food Chem.* 54 (2006) 700–706.
- [14] F.H. Larsen, F. van den Berg, S.B. Engelsen, *J. Chemom.* 20 (2007) 198–208.
- [15] G.F. Pauli, B.U. Jaki, D.C. Lankin, *J. Nat. Prod.* 70 (2007) 589–595.
- [16] M. Paoli, A. Bighelli, V. Castola, F. Tomi, J. Casanova, *Magn. Reson. Chem.* 51 (2013) 756–761.
- [17] J. Staneva, P. Denkova, M. Todorova, L. Evstatieva, *J. Pharm. Biomed. Anal.* 54 (2011) 94–99.
- [18] T. Rundlof, M. Mathiasson, S. Bekiroglu, B. Hakkarainen, T. Bowden, T. Arvidsson, *J. Pharm. Biomed. Anal.* 52 (2010) 645–651.
- [19] M. Tahara, N. Sugimoto, T. Ohtsuki, A. Tada, H. Akiyama, Y. Goda, Y. Ikarashi, *Environ. Sci.* 27 (2014) 142–150.
- [20] T. Ohtsuki, K. Sato, N. Sugimoto, H. Akiyama, Y. Kawamura, *Talanta* 99 (2012) 342–348.
- [21] T. Ohtsuki, K. Sato, N. Frusho, H. Kubota, N. Sugimoto, H. Akiyama, *Food Chem.* 141 (2013) 1322–1327.
- [22] C. Kobayashi, M. Nakazato, H. Ushiyama, Y. Kawai, Y. Tateishi, K. Yasuda, *Shokuhin Eiseigaku Zasshi* 40 (1999) 166–171.
- [23] F. Malz, H. Jancke, *J. Pharm. Biomed. Anal.* 38 (2005) 813–823.
- [24] P. Maes, Y.B. Monakhova, T. Kuballa, H. Reusch, D.W. Lachenmeier, *J. Agric. Food Chem.* 60 (2012) 2778–2784.



Fast determination of 40 drugs in water using large volume direct injection liquid chromatography–tandem mass spectrometry



Clara Boix^a, María Ibáñez^a, Juan V. Sancho^a, Javier Rambla^b, José L. Aranda^b,
Salomé Ballester^b, Félix Hernández^{a,*}

^a Research Institute for Pesticides and Water, University Jaume I, Avda. Sos Baynat, s/n-12071 Castellón, Spain

^b Iproma S.L., Camino de la Raya, 46, 12005 Castellón, Spain

ARTICLE INFO

Article history:

Received 2 May 2014

Received in revised form

30 July 2014

Accepted 2 August 2014

Available online 11 August 2014

Keywords:

Direct injection

Illicit drugs

Pharmaceuticals

Effluent wastewater

Surface water

Liquid chromatography

Triple quadrupole mass spectrometry

ABSTRACT

This work describes a rapid analytical method based on direct sample injection of water samples for the simultaneous identification/quantification of 40 emerging compounds, including pharmaceuticals and drugs of abuse. The water samples were analyzed by ultra-high-performance liquid chromatography coupled to hybrid triple quadrupole mass spectrometer (UHPLC–MS/MS QqQ). Taking profit of the increasing sensitivity of nowadays tandem mass spectrometers, direct sample injection of large volumes has been an attractive alternative to pre-concentration steps. In this work, the developed methodology has been validated at three concentration levels (10, 100 and 1000 ng/L) in 10 different water samples of different types (5 effluent wastewater and 5 surface water samples). The majority of compounds could be satisfactory validated at these concentrations, showing good recoveries and precision. With only few exceptions, the limits of quantification (LOQs), estimated from the sample chromatogram at lowest spiked level tested, were below 3 ng/L. The method was applied to the analysis of 10 effluent wastewater and 10 surface water samples. Venlafaxine was the compound most frequently detected (80%) in surface water, followed by acetaminophen (70%). Regarding effluent wastewater, valsartan and 4-acetyl aminoantipyrine were detected in 9 out of 10 samples analyzed. These two compounds together with 4-formyl aminoantipyrine and naproxen showed the highest concentrations (> 2000 ng/L). In these cases, a dilution step was required for a correct quantification. As an additional evaluation of the method performance, the same water samples were analyzed in another laboratory by a second analytical methodology, based on on-line solid-phase-extraction coupled to LC–MS/MS (QqQ).

© 2014 Elsevier B.V. All rights reserved.

1. Introduction

The presence of human and veterinarian pharmaceuticals, as well as illegal drugs of abuse, in environmental samples has been recognized as a potential environmental threat [1,2]. These groups of contaminants are of present concern, due to their very high biological activity, psychoactive properties and still not well known effects to the aquatic environment [1,3]. After their consumption, these compounds can be excreted as the parent compound, as metabolites or as a mix of unchanged compound plus metabolites, reaching first the wastewater treatment plants (WWTPs) and finally the aquatic environment if they are not completely removed by WWTPs. The concentrations of these compounds in the environment depend on many factors, including their consumption pattern and use, the percentage of wastewater

collected and the characteristics of the processes used for wastewater treatment [4]. Recently, several works have reported the presence of drugs and metabolites in the environmental, showing concern for its unknown impact [5–7].

Current analytical methods developed for quantifying low concentration of pharmaceuticals [2,8–10] and illicit drugs [11,12] in aquatic samples, usually include pre-concentration steps, the most common being those based on solid-phase extraction (SPE). Extraction from water samples has usually been performed by off-line SPE [5,6,8,9,11], although on-line SPE-LC has also been reported as a time and cost-saving alternative thanks to its fully automation [7,13]. Large-volume injection (LVI) is an attractive approach for aqueous samples that has been applied in several works as a rapid and efficient alternative to conventional SPE [14–18]. Typically, LVI involves the direct injection of sample volumes that range from 100 to 5000 μ L versus the more conventionally injected volumes of 10–20 μ L [14]. The improvement in sensitivity comes from the injection of sample volumes larger than usual. LVI provides good reproducibility and low sample contamination as a consequence of

* Corresponding author. Tel.: +34 964 387366; fax: +34 964 387368.

E-mail address: felix.hernandez@uji.es (F. Hernández).

the minimal sample handling. Moreover, it allows to increase sample throughput at minimal cost compared to both off- and on-line SPE, because no SPE cartridges and solvents are needed [14]. Despite the injection of larger volumes, modern and sensitive instruments are commonly needed for final measurement, as the increase in injection volume does not compensate the pre-concentration factors normally reached by SPE. In addition, peak shape may be deteriorated for early eluting analytes when increasing injection volume despite the lower eluotropic strength of water sample. Moreover, only clean water is usually directly injected in the system otherwise matrix effects could not be properly compensated for. Although, we show that effluent wastewater might be considered clean water in our LVI approach.

Modern multi-class methods applied for the determination of polar pharmaceuticals or drugs of abuse are mostly based on liquid chromatography (LC). The use of UHPLC in combination with tandem mass spectrometry (MS/MS) using triple quadrupole (QqQ) [2,8,10,11,19–22] or ion trap (IT) analyzers [23–27], has made possible the development of faster and more sensitive methods. Moreover, the fact of working with short dwell times in new instruments, allows increasing the number of selected reaction monitoring (SRM) transitions acquired simultaneously per compound making possible not only quantification but also a reliable identification. Although LC–MS/MS is the technique of choice at present to analyze polar compounds in aquatic samples, the presence of pharmaceuticals in environmental samples has also been investigated by LC coupled to high resolution mass spectrometry (HRMS), using time-of-flight (TOF MS) [28–30] or Orbitrap analyzers [31–33]. HRMS analyzers have strong potential for large screening and for identification/elucidation purposes, but they show less sensitivity than state-of-the-art MS/MS instruments, making that LC–MS/MS are considered the optimum analyzers for quantification at trace level.

The goal of the present paper is to develop fast and sensitive analytical methodology combining the advantages of UHPLC–MS/MS with last-generation triple quadrupole and large-volume direct sample injection. Thus, a rapid method avoiding sample manipulation (i.e. pre-concentration and clean-up) has been developed for the determination of forty highly consumed compounds, including pharmaceuticals, drugs of abuse and some veterinary drugs, in water samples. The quantitative validation has been performed at three concentration levels (10, 100 and 1000 ng/L) in 5 surface water (SW) and 5 effluent wastewater (EWW) samples. Several isotopically-labeled internal standards have been tested for correction of expected matrix effects. In order to evaluate the applicability of the method, 20 water samples (10 SW and 10 EWW) were analyzed. The same samples were analyzed by another laboratory using a methodology based on on-line SPE–LC–MS/MS (QqQ).

2. Experimental

2.1. Reagents and chemicals

Pharmaceutical reference standards were purchased from Sigma-Aldrich (St Louis, MO, USA), LGC Promochem (London, UK), Toronto Research Chemicals (Ontario, Canada), Across Organics (Geel, Belgium), Bayer Hispania (Barcelona, Spain), Fort Dodge Veterinaria (Gerona, Spain), Vetoquinol Industrial (Madrid, Spain) and Aventis Pharma (Madrid, Spain). All reference standards presented purity higher than 93%.

Illicit drugs and metabolites studied were amphetamine, 3,4-methylenedioxymethamphetamine (MDMA or ecstasy), cocaine, cocaethylene and benzoyllecgonine. These compounds were obtained from Sigma-Aldrich (Madrid, Spain), Cerilliant (Round

Rock, TX, USA) and the National Measurement Institute (Pymble, Australia) as solutions in methanol, acetonitrile or as salt.

Standard stock solutions of each compound were prepared at 100 mg/L in methanol or acetonitrile. Intermediate solutions (10 mg/L) were prepared by dilution of the stock solution ten-fold with methanol. Mixed working solutions containing all analytes were prepared daily from intermediate solutions by appropriate dilution with water, and were used for preparation of the aqueous calibration standards and for spiking samples in the validation study.

Isotopically-labeled internal standards (ILIS) of omeprazole- d_3 , acetaminophen- d_4 , diclofenac- d_4 , valsartan- d_8 , carbamazepine 10,11-epoxide- d_{10} and salicylic acid- d_3 were from CDN Isotopes (Quebec, Canada); atorvastatin- d_5 from Toronto Research Chemicals and sulfamethoxazole- $^{13}C_6$ and trimethoprim- $^{13}C_3$ were from Cambridge Isotope Laboratories (Andover, MA, USA). Deuterated drugs of abuse were purchased from Cerilliant as solutions in methanol or acetonitrile at a concentration of 100 mg/L (amphetamine- d_6 , MDMA- d_5 , benzoylecgonine- d_3 , cocaine- d_3 and cocaethylene- d_8). A mix ILIS working solution at 100 μ g/L was prepared in MeOH and used as internal standard. All solutions were stored in amber glass bottles at $-20^\circ C$.

HPLC-grade methanol (MeOH), HPLC-grade acetonitrile (ACN), formic acid (HCOOH, content > 98%), ammonium acetate (NH_4Ac , reagent grade) and sodium hydroxide (NaOH, > 99%) were purchased from Scharlab (Barcelona, Spain). HPLC grade water was obtained from distilled water passed through a Milli-Q water purification system (Millipore, Bedford, MA, USA).

2.2. Instrumentation

UHPLC analysis were carried out with a Waters Acquity ultra-performance liquid chromatography (UPLC) system (Waters, Milford, MA, USA), equipped with a binary solvent manager and a sample manager. Chromatography separation was performed using an Acquity UPLC BEH C18 1.7 μ m particle size analytical column 100 mm \times 2.1 mm (Waters). The mobile phases used were A=H₂O and B=MeOH, both with 0.01% HCOOH and 1 mM NH_4Ac . The percentage of organic modifier (B) was changed linearly as follows: 0 min, 5%; 7 min, 90%; 8 min, 90%; 8.1 min, 5%; 10 min, 5%. The flow rate was 0.4 mL/min. The column was kept at 40 $^\circ C$ and the sample manager was maintained at 5 $^\circ C$. Analysis run time was 10 min. The sample injection volume was 100 μ L.

A Waters Acquity UPLC system was interfaced to a triple quadrupole mass spectrometer Xevo TQS (Waters) equipped with an orthogonal Z-spray electrospray ionization interface (ESI) operated in positive and negative ion mode. Cone gas as well as desolvation gas was nitrogen (Praxair, Valencia, Spain) set up 250 L/h and 1200 L/h, respectively. For operation in the MS/MS mode, collision gas was argon 99.995% (Praxair, Madrid, Spain) with a pressure of 4×10^{-3} mbar in the collision cell (0.15 mL/min). Other parameters optimized were capillary voltages 3.5 kV (ESI+) and 3.0 kV (ESI-); source temperature 150 $^\circ C$ and desolvation temperature 650 $^\circ C$. Cone voltage was selected as 10 V for all compounds, due to no variations were observed. Dwell times were automatically selected in order to obtain enough points per peak and can be decreased down to 3 ms.

All data were acquired and processed using MassLynx v 4.1 software (Waters).

2.3. Sample preparation

All water samples were centrifuged at 4500 rpm for 5 min. 1-mL surface water or effluent wastewater was spiked at 50 ng/L with the ILIS mix. 100 μ L of the sample was directly injected in the UHPLC–MS/MS system.

2.4. Validation study

Acquisition was performed in SRM mode, with the (de)protonated molecular ion of each compound chosen as precursor ion. The most abundant product ion of each target analyte was typically used for quantification and two additional product ions were used for confirmation. LC retention time was also compared with that of the reference standards (within $\pm 2.5\%$) to help to confirm the compounds detected in samples. 14 compounds were quantified using their corresponding labeled analyte as internal standard and 5 compounds were quantified using an analog IS (see Table 2). The remaining 21 compounds were quantified by external calibration using absolute responses.

The linearity of the method was studied by analyzing standard solutions in triplicate at eight concentrations, in the range from 1 to 2500 ng/L. Satisfactory linearity was assumed when the correlation coefficient (r^2) was higher than 0.99, based on relative responses (analyte peak area/ILIS peak area), except for those compounds that were quantified without ILIS (absolute response).

Method accuracy (estimated by means of analysis of spiked samples directly injected into the LC–MS/MS system) and precision (expressed as repeatability, in terms of relative standard deviation (RSD)) were evaluated in surface water and effluent wastewater, spiked at three concentrations (10, 100 and 1000 ng/L). A total of 10 different water samples were used for the method validation (5 effluent wastewater and 5 surface water samples). Quantification was made by using calibration standards in solvent and relative or absolute responses as a function of the ILIS was used or not for matrix effects correction. Recovery values between 70% and 120%, with RSD lower than 20% were considered as satisfactory. The limit of quantification (LOQ) was estimated for a signal to noise (S/N) ratio of 10 from the sample chromatograms at the lowest validation level tested, using the quantification transition. Adequate blank samples were not found for several analytes as they were present in all samples collected. In these cases, LOQ values were estimated from the chromatograms of the non-spiked “blank” samples, considering the concentration levels.

2.5. Water samples

20 water samples (10 EWWs and 10 SWs) were collected in polyethylene high-density bottles in selected sites of the Spanish Mediterranean area (Castellon and Valencia provinces). Composite EWW samples were collected from different WWTPs using primary and secondary treatment methods. Grab SW were sampled from different rivers (3), reservoirs (3) and lakes (4). All samples were taken from October to December in 2012. Samples were stored at -18°C until analysis. Before analysis, samples were thawed at room temperature.

2.6. On-line SPE LC–MS/MS Q/Q

An alternative analytical methodology was also applied following the protocol used in routine analysis by an ISO 17025 certified laboratory in Spain (IPROMA S.L.). For LC analysis, an Agilent 1200SL binary pump was coupled to a hybrid triple quadrupole/linear ion trap mass spectrometer system API3200QTRAP from Applied Biosystems–Sciex (Foster City, California, USA). On-line SPE was performed by using an Agilent 1200 pump and a Strata-X cartridge (2×20 mm, $25 \mu\text{m}$) from Phenomenex (Torrance, CA, USA). This equipment also includes a PAL autosampler (CTC Analytics, Switzerland) for automated sample injection. The injection volume to the on-line SPE was 2 mL of water, previously centrifuged at 2500 rpm for 5 min (wastewater samples were diluted 1/20). Chromatographic separation was performed on a reversed-phase column ZORBAX Eclipse XDB-C18 (50×4.6 mm,

$1.8 \mu\text{m}$) from Agilent (Palo Alto, CA, USA) maintained at 40°C . Mobile phases A and B were 0.1% formic acid in water and 0.1% formic acid in methanol, respectively. The following linear gradient was used: hold at 95%A for 4.5 min, decreased to 70%A over 4.6 min, decreased to 0%A over 6.5 min and then increased to 95% A over 10.1 min, returning to the initial conditions. The flow rate was set to $600 \mu\text{L}/\text{min}$ [34].

3. Results and discussion

In this work, 35 human and veterinary pharmaceuticals and 5 drugs of abuse were selected (Table 1). Eight pharmaceuticals were among the most widely consumed in Spain [35]. The rest of compounds were selected due to their reported presence in water samples and to their potential negative effect on living organisms of the aquatic environment. Moreover, 4 compounds corresponded to metabolites of pharmaceuticals: salicylic acid, metabolite of acetylsalicylic acid [36]; and 4-aminoantipyrine, 4-acetyl aminoantipyrine and 4-formyl aminoantipyrine, metabolites of dipyrene [37–39].

3.1. MS/MS optimization

Individual standard solutions were directly infused in the MS/MS system. The majority of the compounds (33 out of 40) were determined with ESI operating in positive ionization mode, using the protonated molecule $[\text{M}+\text{H}]^+$ as precursor ion. The 7 remaining compounds were determined in negative ionization using $[\text{M}-\text{H}]^-$ as precursor ion. The three most sensitive SRM transitions (in terms of signal-to-noise ratio) were selected for each compound. The most abundant was used for quantification (Q) whereas the other two transitions were acquired for confirmation (q_1 , q_2). The only exception was salicylic acid (only one transition), and gemfibrozil and naproxen (two transitions) because of their poor fragmentation. MS/MS parameters as well as SRM transitions and retention times are listed in Table 1. This table also shows the average (q/Q) ratios obtained from the calibration standards. The RSDs for q/Q ratios illustrate whether these ratios might be considered to be concentration dependent or not (e.g. RSD < 15% would indicate little variation of the q/Q values over the concentration range tested, from 1 to 2500 ng/L).

Three SRM transitions were acquired per compound, whereas for ILIS, only the quantification transition was monitored. Using our fast-acquisition triple quadrupole mass analyzer, dwell times as low as 3 ms per transition could be automatically set up allowing satisfactory peak shape (at least 10 points-per peak) and sensitivity for all 40 compounds investigated.

3.2. UHPLC conditions

In this work, different mobile phases (acetonitrile and methanol) with different composition (HCOOH and NH_4Ac at various concentrations) were tested. The effects of pH and ionic strength of the mobile phase on the peak shape, resolution and efficiencies were evaluated by varying the buffer concentration. Finally, a gradient consisting of water (solvent A) and MeOH (solvent B) both with 1 mM ammonium acetate and 0.01% formic acid was chosen as an appropriate mobile phase.

Initially, $10 \mu\text{L}$ were injected in the system as reference conditions. In order to further improve sensitivity, injection of increasing sample volumes was performed. On the basis of the column dimensions and the particle size (in this case, 2.1×100 mm, $1.7 \mu\text{m}$), the dead volume of the column was estimated to be $400 \mu\text{L}$. The recommended injection volume should not exceed the 10% of this dead volume, this is, $40 \mu\text{L}$. Trying to perform LVI for

Table 1
MS/MS optimized conditions for selected compounds.

Compound	ESI	T_R (min)	Precursor ion (m/z)	Q transition	C.E. (eV)	q_1 transition	C.E. (eV)	q_1/Q (RSD)	q_2 transition	C.E. (eV)	q_2/Q (RSD)
4-Acetyl aminoantipyrine	+	2.85	245.9	246 > 228	10	246 > 83	20	0.71(3)	246 > 104	20	0.38(4)
4-Aminoantipyrine	+	3.15	204.1	204 > 56	15	204 > 159	10	0.29(5)	204 > 83	15	< 0.01(5)
4-Formyl aminoantipyrine	+	2.81	232.1	232 > 83	20	232 > 104	20	0.63(4)	232 > 214	10	0.63(7)
Acetaminophen	+	1.99	152.1	152 > 110	15	152 > 65	25	0.20(5)	152 > 93	20	0.26(8)
Alprazolam	+	5.77	308.9	309 > 281	25	309 > 205	25	0.11(4)	309 > 274	25	0.21(5)
Amphetamine	+	2.81	136.2	136 > 91	15	136 > 119	10	0.43(6)	136 > 65	10	0.12(15)
Atorvastatin	+	6.68	558.9	559 > 440	20	559 > 466	15	0.20(5)	559 > 292	25	0.17(4)
Benzoyllecgonine	+	3.32	290.0	290 > 168	15	290 > 105	25	0.34(6)	290 > 92	25	< 0.01(16)
Bezafibrate	-	6.10	359.8	360 > 274	20	360 > 154	25	0.24(5)	360 > 85	15	0.07(6)
Carbamazepine	+	5.32	236.9	237 > 194	20	237 > 192	20	0.24(5)	237 > 179	25	0.08(5)
Clarithromycin	+	6.11	590.0	590 > 158	20	590 > 116	25	0.20(13)	590 > 98	25	0.06(9)
Cocaethylene	+	4.24	318.0	318 > 196	20	318 > 82	25	0.71(4)	318 > 150	25	0.18(7)
Cocaine	+	3.74	304.1	304 > 182	15	304 > 82	25	0.56(8)	304 > 105	25	0.19(9)
Diclofenac	-	6.87	294.1	294 > 250	10	294 > 214	20	0.04(3)	294 > 178	20	< 0.01(5)
Enalapril	+	4.99	376.9	377 > 234	15	377 > 117	25	0.24(4)	377 > 303	15	0.30(10)
Erythromycin	+	5.62	734.2	734 > 158	25	734 > 576	15	0.11(5)	734 > 558	15	0.03(10)
Florfenicol	-	3.32	355.7	356 > 336	10	356 > 185	20	1.00(1)	356 > 119	25	0.04(15)
Flumequine	+	5.11	261.9	262 > 244	15	262 > 202	25	0.30(9)	262 > 174	25	0.01(13)
Furaltadone	+	2.37	324.9	325 > 100	20	325 > 252	15	1.00(6)	325 > 281	10	0.77(4)
Gemfibrozil	-	7.46	248.9	249 > 121	20	249 > 127	10	0.07(10)			
Irbesartan	+	6.26	428.8	429 > 207	25	429 > 195	20	0.17(2)	429 > 180	25	0.04(4)
Levamisol	+	2.48	205.0	205 > 178	20	205 > 91	25	0.29(10)	205 > 123	25	0.43(11)
Lincomycin	+	2.89	407.0	407 > 126	20	407 > 359	15	0.07(9)	407 > 389	15	0.03(9)
Lorazepam	+	5.76	320.9	321 > 275	20	321 > 303	15	0.50(6)	321 > 229	25	0.34(8)
MDMA	+	2.90	194.0	194 > 163	10	194 > 105	20	0.34(5)	194 > 135	20	0.33(9)
Nalidixic acid	+	4.92	233.0	233 > 215	10	233 > 187	25	0.71(4)	233 > 159	25	0.19(8)
Naproxen	-	6.11	230.2	185 > 169	20	229 > 169	15	0.01(15)			
Olanzapine	+	3.25	312.9	313 > 256	20	313 > 84	20	0.56(12)	313 > 213	25	0.45(10)
Omeprazole	+	5.23	345.7	346 > 198	10	346 > 136	25	0.45(3)	346 > 151	15	0.32(4)
Oxolinic acid	+	4.24	261.9	262 > 244	15	262 > 216	25	0.13(12)	262 > 158	25	0.04(8)
Pantoprazole	+	5.18	383.9	384 > 200	10	384 > 138	25	1.10(4)	384 > 153	15	0.36(5)
Pravastatin	-	5.76	423.0	423 > 321	15	423 > 303	15	1.00(5)	423 > 101	25	0.53(11)
Roxithromycin	+	6.22	679.1	679 > 158	25	679 > 116	25	0.22(6)	679 > 98	25	0.04(16)
Salicylic acid	-	4.26	137.0	137 > 93	15						
Sulfadiazine	+	2.11	251.0	251 > 156	15	251 > 92	25	0.71(5)	251 > 108	20	0.43(2)
Sulfadoxine	+	3.44	310.9	311 > 156	15	311 > 92	25	0.42(8)	311 > 108	25	0.48(13)
Sulfamethorazole	+	3.26	253.8	254 > 92	25	254 > 156	15	1.27(7)	254 > 108	20	0.56(6)
Trimethoprim	+	2.88	291.0	291 > 123	25	291 > 230	20	1.11(7)	291 > 261	25	0.83(5)
Valsartan	+	6.27	435.8	436 > 207	25	436 > 235	15	1.12(6)	436 > 261	15	< 0.01(17)
Venlafaxine	+	4.61	278.1	278 > 58	15	278 > 260	10	0.43(5)	278 > 121	25	0.24(2)
ILIS											
Acetaminophen-d ₄	+	1.89	155.9	156 > 114	15						
Amphetamine-d ₆	+	2.79	141.7	142 > 93	15						
Atorvastatin-d ₅	+	6.67	563.9	564 > 445	20						
Benzoyllecgonine-d ₃	+	3.32	293.1	293 > 171	20						
Carbamazepine 10,11-epoxide-d ₁₀	+	4.47	263.0	263 > 190	25						
Cocaethylene-d ₈	+	4.23	326.0	326 > 204	20						
Cocaine-d ₃	+	3.74	306.9	307 > 185	20						
Diclofenac-d ₄	-	6.85	299.9	300 > 256	10						
MDMA-d ₅	+	2.90	199.0	199 > 165	10						
Omeprazole-d ₃	+	5.22	348.8	349 > 198	10						
Salicylic acid-d ₄	-	4.26	140.7	141 > 97	15						
Sulfamethoxazole- ¹³ C ₆	+	3.27	260.0	260 > 162	15						
Trimethoprim- ¹³ C ₃	+	2.87	294.1	294 > 264	18						
Valsartan-d ₈	+	6.24	443.9	444 > 207	15						

ES, electrospray ionization; T_R , retention time; MW, monoisotopic molecular weight; Q, quantification; q , confirmation; C.E., collision energy.

this system, 50 and 100 μ L were tested, obtaining satisfactory chromatographic peak shape in all cases. The best sensitivity was achieved when injecting 100 μ L. Hence, the injection of 100 μ L was selected for further validation.

3.3. Matrix effects: quantification

The high complexity and variability of the matrices in water samples (especially in wastewater samples) affected considerably the recovery values of some compounds. For almost half of the studied compounds, matrix effects resulting in ionization suppression were observed, being more important in EWW samples than in SW. Thus, acetaminophen and atorvastatin showed recoveries

between 60 and 120% in the five SW tested, but decreased down to 27–60% in EWW. A few compounds experimented ionization enhancement due to co-eluted matrix components, leading to recoveries > 100%. This was the case of levamisol, MDMA or trimethoprim. Among the different approaches proposed in the literature to remove or compensate for the matrix effects, the use of isotopically-labeled internal standards (if available) was considered the preferred option. Fourteen compounds could be corrected with their own ILIS, as they were available to our laboratory, obtaining satisfactory figures after correction, as expected. Erythromycin, levamisol, pravastatin, sulfadiazine and venlafaxine were corrected using an analog ILIS (Table 2). The selection of analog ILIS was mainly based on chemical structure

Table 2

Results of the method validation for effluent wastewater (EWW) and surface water (SW). Limit of quantification (LOQ), recovery (%) and relative standard deviation at the three validation levels studied.

Compound	SW (n=5)				EWW (n=5)				ILIS used for correction
	Recovery (RSD) (both in %)			LOQ (ng L ⁻¹)	Recovery (RSD) (both in %)			LOQ (ng L ⁻¹)	
	10 ng L ⁻¹	100 ng L ⁻¹	1000 ng L ⁻¹		10 ng L ⁻¹	100 ng L ⁻¹	1000 ng L ⁻¹		
4-Acetyl aminoantipyrine	59 (16) ^a	79 (19) ^a	72 (5) ^a	0.8	95 ^b	69 ^b	78 (14) ^a	2.0	-
4-Aminoantipyrine	95 (12) ^a	74 (14) ^a	81 (9)	0.7	110 ^b	66 ^b	97 ^b	0.4	-
4-Formyl aminoantipyrine	72 (13) ^a	105 (12) ^a	88 (4) ^a	1.9	120 ^b	68 ^b	82 (18) ^a	1.7	-
Acetaminophen	103 (17) ^a	111 (10)	107 (9)	1.1	131 (3) ^a	113 (15)	118 (7)	1.5	Acetaminophen-d ₄
Alprazolam	88 (18) ^a	79 (10)	78 (8)	0.3	81 (16) ^a	74 (9)	77 (11)	1.2	-
Amphetamine	-	96 (12)	78 (19)	6.3	-	110 (11)	107 (11)	12.5	Amphetamine-d ₆
Atorvastatin	84 (11)	85 (7)	100 (9)	0.8	92 (14)	92 (5)	109 (2)	0.8	Atorvastatin-d ₅
Benzoylcegonine	88 (18)	83 (7)	97 (10)	0.1	88 (20) ^a	80 (16)	109 (2)	0.1	Benzoylcegonine-d ₃
Bezafibrate	87 (20) ^a	83 (16)	95 (12)	1.3	82 (11) ^a	102 (24) ^a	111 (13)	2.1	-
Carbamazepine	81 (19)	65 (7)	91 (8)	0.2	77 (16) ^a	75 (15)	94 (8)	1.1	Carbamazepine 10,11-epoxide-d ₁₀
Clarithromycin	93 (4) ^a	97 (14) ^a	90 (9)	2.9	117 ^b	73 (17) ^a	81 (16)	4.1	-
Cocaehtylene	89 (12)	93 (9)	97 (9)	0.7	100 (5)	93 (5)	102 (4)	0.8	Cocaehtylene-d ₈
Cocaine	77 (19) ^a	69 (11)	111 (10)	1.0	70 (9)	88 (17)	116 (3)	1.1	Cocaine-d ₃
Diclofenac	-	82 (14) ^a	105 (5)	6.8	-	78 (17) ^a	104 (11)	7.2	Diclofenac-d ₄
Enalapril	99 (17)	88 (6)	92 (5)	0.7	109 (9)	81 (4)	94 (8)	1.8	-
Erythromycin	115 (6)	85 (15)	72 (14)	0.8	125 ^b	92 (23) ^a	94 (19)	2.1	Sulfamethoxazole- ¹³ C ₆
Florfenicol	69 (17)	91 (12)	83 (15)	2.2	97 (11)	84 (14)	109 (11)	8.6	-
Flumequine	87 (14)	87 (10)	113 (5)	0.4	90 (17)	73 (14)	97 (9)	1.2	-
Furaltadone	88 (11)	87 (10)	88 (10)	0.7	88 (16)	69 (16)	80 (17)	1.4	-
Gemfibrozil	83 (15) ^a	99 (12) ^a	92 (8)	2.3	103 ^b	92 ^b	90 (18)	1.8	-
Irbesartan	86 (16) ^a	87 (13) ^a	97 (8)	0.2	115 ^b	78 (12) ^a	99 (5)	1.0	-
Levamisol	83 (15)	95 (7)	101 (5)	0.2	87 (19) ^a	98 (16)	106 (10)	2.1	Cocaehtylene-d ₈
Lincomycin	84 (15) ^a	81 (17) ^a	104 (10)	0.1	88 (12)	78 (15)	75 (12)	0.4	-
Lorazepam	88 (14) ^a	82 (15)	86 (7)	3.1	109 (9) ^a	78 (20) ^a	94 (5)	4.5	-
MDMA	100 (10)	96 (6)	105 (8)	0.5	99 (18)	93 (2)	103 (8)	1.4	MDMA-d ₅
Nalidixic acid	93 (14)	91 (9)	114 (6)	1.8	90 (17)	75 (13)	98 (9)	2.7	-
Naproxen	77 (18) ^a	70 (7)	80 (13)	11.7	62 ^b	78 ^b	85 (13)	7.3	-
Olanzapine	-	86 (1) ^a	108 (12) ^a	0.8	-	-	156 (13)	11.6	-
Omeprazole	103 (13)	89 (8)	98 (8)	0.2	118 (24)	95 (4)	102 (2)	1.1	Omeprazole-d ₃
Oxolinic acid	96 (12)	83 (10)	86 (5)	1.8	98 (13)	70 (10)	80 (16)	2.9	-
Pantoprazole	93 (15)	99 (8)	103 (5)	0.1	93 (13)	81 (12)	105 (8)	0.8	-
Pravastatin	96 (14)	81 (13)	85 (13)	15.4	113 ^b	82 (10)	83 (8)	16.7	Diclofenac-d ₄
Roxithromycin	-	92 (4) ^a	83 (13)	5.6	-	95 (9) ^a	91 (16)	5.4	-
Salicylic acid	-	-	93 (15)	37.6	-	119 ^b	84 (8)	41.1	Salicylic acid-d ₄
Sulfadiazine	102 (16)	99 (9)	116 (8)	1.4	106 (19)	97 (7)	111 (12)	1.8	Sulfamethoxazole- ¹³ C ₆
Sulfadoxine	85 (12)	83 (11)	104 (7)	0.2	80 (18)	64 (12)	86 (16)	0.5	-
Sulfamethoxazole	96 (16) ^a	80 (10)	98 (11)	0.5	103 ^b	83 (10)	106 (7)	0.8	Sulfamethoxazole- ¹³ C ₆
Trimethoprim	83 (14)	87 (13)	93 (10)	1.8	111 ^b	81 (19)	104 (10)	2.3	Trimethoprim- ¹³ C ₃
Valsartan	74 (11)	88 (4)	98 (12)	3.8	114 ^b	98 (18) ^a	89 (14) ^a	4.2	Valsartan-d ₈
Venlafaxine	79 (21) ^a	78 (15)	102 (11)	0.2	111 ^b	88 (19) ^a	100 (6)	1.0	Atorvastatin-d ₅

^a Validation performed for n=2–4, due to the high analyte concentration found in some “blank” samples.

^b Recovery values without RSD mean (n=1).

and/or retention time similarity between analyte and ILIS, as it was expected that both were affected by similar constituents of the matrix. In particular cases, e.g. erythromycin, an ILIS eluting at different retention time and with different chemical structure (sulfamethoxazole-¹³C₆) was able to perform an efficient matrix effects correction, as previously reported by Gracia-Lor et al. [8]. The rest of the analytes were quantified using absolute response as matrix effects in the ten water samples tested were not much relevant.

3.4. Method validation

Analytical characteristics of the method were evaluated in two types of water samples: five surface water and five effluent wastewater samples, spiked at three concentration levels each (10, 100 and 1000 ng/L).

The linearity of the method was studied in the range 1–2500 ng/L for all compounds. Calibration curves showed in all

cases correlation coefficients greater than 0.99, and residuals lower than 25%.

Accuracy and precision were estimated from injection of different water samples spiked at the three concentrations indicated above. All the “blank” samples contained at least one or more target analytes. Thus, the samples were previously analyzed and those with lower drug concentration were selected as “blank” samples for method validation. Concentration of target compounds found in these “blank” samples were subtracted from the spiked samples.

The results obtained for most compounds were satisfactory at the three validation levels, with recoveries between 70 and 120% and precision (RSD) below 20% (Table 2). At the lowest level (10 ng/L) amphetamine, diclofenac, olanzapine, roxithromycin and salicylic acid could not be validated, due to their lower sensitivity. For some compounds, validation was not feasible in all the samples tested due to the high analyte concentration found in different “blank” samples (e.g. the three dipyrone metabolites or gemfibrozil). In these cases, the number of data used in validation

was less than 10 (5 SW and 5 EWW) (highlighted as ^a or ^b in Table 2).

The method presented satisfactory precision for most compounds with RSDs below 20% at the three fortification levels. Regarding LOQ, they were ≤ 3 ng/L for 32 out of 40 compounds in SW. For another 5 analytes LOQs ranged from 3 to 7 ng/L, and for the remaining 3 were slightly higher, between 12 and 38 ng/L. In EWW, 29 compounds presented LOQs ≤ 3 ng/L, 7 ranged from 3 to 9 ng/L and the remaining 4 were between 12 and 41 ng/L. According to our data, it seems that the type of water did not much affect the attainable sensitivity despite of being a direct injection method.

3.5. Analysis of water samples

To demonstrate the applicability of the method developed, 10 effluent wastewater and 10 surface water samples were analyzed. In every sequence of analysis, a calibration curve in solvent was injected at the beginning and at the end of the batch sample. Quality controls (QCs) were also included in every sequence, consisting on selected EWW and SW samples spiked with all pharmaceuticals at 100 ng/L. QC recoveries were satisfactory (in the range of 70–120%) for the majority of the compounds. However, QCs recoveries for venlafaxine (using atorvastatin- d_5 as IS) and for levamisol (using cocaethylene- d_8) were around 130%. As it has been already reported in the literature, the use of analogs IS does not always assure an efficient matrix effects correction [40,41].

Identification of positive findings was supported by evaluation of q_1/Q and q_2/Q ratios. The finding was considered as positive when retention time and at least one experimental ion-ratio were within the established tolerances [42], when compared with a reference

standard. Although the acquisition of two SRM transitions per compound together with the accordance in the retention time are normally considered sufficient for a reliable confirmation of the compound identity, in this work three transitions were acquired in order to increase the confidence of the confirmation process [40]. Using three transitions, one can minimize the possibilities of reporting false negatives when the ion ratio is not accomplished, in those cases where one of the transitions seems to be interfered. As an example, Fig. 1 shows positive findings of alprazolam, bezafibrate and sulfamethoxazole in EWW. As it can be seen, the three transitions showed a peak at the same retention time. Moreover, at least one q/Q ratio was within tolerance limits.

Tables 3 and 4 show the concentration values (ng/L) found for each compound in EWW and SW, respectively. 32 analytes were detected in the 10 EWWs analyzed, illustrating the frequent occurrence of drugs in wastewater samples and the fact that many of them are not completely removed in WWTPs. Carbamazepine, used for the treatment of epilepsy and bipolar disorder, was the compound most frequently detected, appearing in all samples analyzed. This was followed by the angiotensin II antagonist valsartan and 4-acetyl aminoantipyrine (metabolite of the analgesic dypirone), which were present in 90% of EWWs. 4-formyl aminoantipyrine (another metabolite of dypirone), the anthelmintic levamisol, the antibiotics sulfamethoxazole and trimethoprim, and the antidepressant venlafaxine appeared in 80% of EWWs. The highest concentrations corresponded to 4-acetyl aminoantipyrine (7.2 $\mu\text{g/L}$), valsartan (4.6 $\mu\text{g/L}$), 4-formyl aminoantipyrine (3.2 $\mu\text{g/L}$) and the analgesic naproxen (1.9 $\mu\text{g/L}$). In these cases, samples were diluted and re-analyzed to fit the linear range of the method.

In relation to surface water samples, up to 26 compounds were detected in the samples analyzed. All these compounds were also found in EWWs, normally at higher concentrations. Venlafaxine and

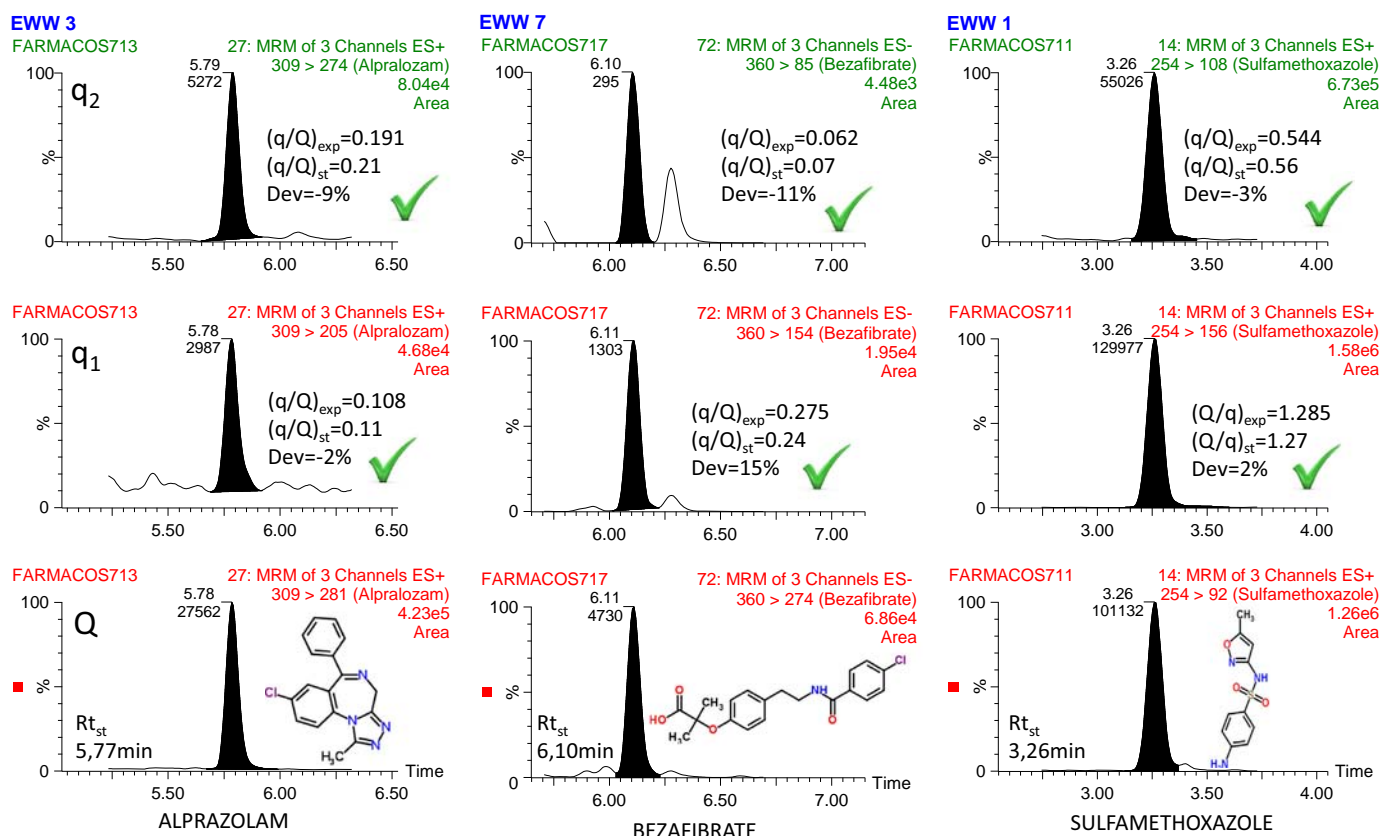


Fig. 1. UHPLC-MS/MS chromatograms detected in EWW samples.

Table 3

Summary of the results obtained for target pharmaceuticals in EWW, applying the analytical methodology described in this article. Between brackets, the concentrations obtained using the on-line SPE-LC-MS/MS alternative method.

Compound	EWW (ng/L)									
	1	2	3	4	5	6	7	8	9	10
4-Aminoantipyrine ^a	9	15	< LOQ	–	< LOQ	40	43	14	–	26
Acetaminophen ^a	–	–	–	14	–	45	< LOQ	–	8	–
Amphetamine ^a	–	21	–	–	29	–	–	–	–	–
Benzoylcegonine ^a	< LOQ	40 (48)	6	< LOQ	656 (735)	11	100 (127)	43 (54)	< LOQ	43 (50)
Clarithromycin ^a	–	14	26	–	34	< LOQ	27	15	–	–
Cocaethylene ^a	–	< LOQ	–	–	15	< LOQ	8	–	–	< LOQ
Cocaine ^a	9	< LOQ	–	< LOQ	72 (54)	12	–	12	8	24
Diclofenac ^a	–	266 (251)	884 (1115)	–	216 (313)	158 (241)	845 (1181)	300 (386)	–	212 (322)
Erythromycin ^a	13	55	–	–	37	18	49	14	–	25
Flumequine ^a	–	–	< LOQ	–	–	–	–	–	–	7
MDMA ^a	–	45	–	–	45	< LOQ	–	22	–	48
Nalidixic acid ^a	–	–	17	–	< LOQ	–	–	–	–	8
Naproxen ^a	–	42	32	–	1942 (3007)	–	515 (642)	< LOQ	–	357 (419)
Oxolinic acid ^a	–	–	–	–	–	–	–	–	–	5
Pantoprazole ^a	–	5	2	–	< LOQ	4	4	7	–	4
Sulfadiazine ^a	–	–	28	–	–	–	–	10	–	–
Sulfamethoxazole ^a	89	35	372 (308)	< LOQ	19	21	29	25	–	29
Trimethoprim ^a	15	83	9	–	75	4	13	86	–	25
Venlafaxine ^a	414 (366)	316 (282)	421 (389)	–	343 (457)	263 (314)	252 (265)	201 (208)	< LOQ	239 (260)
4-Acetyl aminoantipyrine	77	3032	253	–	7239	197	1357	2298	18	689
4-Formyl aminoantipyrine	860	1583	3425	–	3208	766	1898	1235	< LOQ	853
Alprazolam	14	11	17	–	< LOQ	12	13	10	–	12
Atorvastatin	–	7	–	–	16	–	–	–	–	< LOQ
Bezafibrate	–	29	–	–	87	10	35	16	–	53
Carbamazepine	112	52	119	3	135	64	149	54	2	90
Gemfibrozil	–	765	4	–	538	25	507	365	< LOQ	95
Irbesartan	–	531	< LOQ	–	506	404	799	266	< LOQ	484
Levamisol	44	311	155	–	150	163	768	178	–	497
Lincomycin	–	–	–	–	< LOQ	–	6	109	–	7
Lorazepam	–	52	–	–	109	58	81	46	–	74
Pravastatin	–	16	–	–	–	–	< LOQ	< LOQ	–	–
Valsartan	41	2864	54	–	4575	291	1457	246	13	399

–: not detected.

^a Compounds also analyzed by the on-line SPE LC-MS/MS methodology described in section.

acetaminophen were the compounds most frequently detected, being present in 80% and 70% of the samples, respectively. 4-acetyl, 4-formyl aminoantipyrine, cocaine and its metabolite benzoylcegonine, were present in 60% of SWs analyzed. The highest concentration corresponded to dipyrone metabolites 4-formyl (0.72 µg/L) and 4-acetyl aminoantipyrine (0.66 µg/L).

As an illustrative example, Fig. 2 shows UHPLC-MS/MS chromatograms for SW 4 (only the quantitative transition Q is shown), which was positive for 19 out of the 40 target compounds. Concentration data for this sample are shown in Table 4, where it can be seen that acetaminophen presented the highest value (480 ng/L). Four drugs of abuse (benzoylcegonine, cocaethylene, cocaine and MDMA) were also detected in the range of 7–31 ng/L. These figures reveal that licit and illicit drugs can actually reach surface water due to the incomplete removal in WWTPs.

3.5.1. On-line SPE HPLC-ESI-MS/MS

The same 20 samples were analyzed by another laboratory that applied an analytical methodology based on on-line SPE-LC coupled to triple quadrupole mass spectrometry. With this methodology, only 25 human and veterinary pharmaceuticals and drugs of abuse were included in the target method. All of them were determined with ESI operating in positive ionization mode. For confirmation, two SRM transitions at the same retention time, and the accomplishment of the *q/Q* ratios were required. Regarding quantification parameters, two internal standards were used to

correct possible deviations: diclofenac-¹³C₆ for pharmaceuticals and cocaine-d₃ for drugs of abuse. The linearity of the method was studied in the range 2–150 ng/L for all compounds. The method presented satisfactory accuracy and precision for all compounds, with recoveries values > 85% and RSDs below 13%. Regarding LOQ, they ranged from 2 to 20 ng/L for SW and from 40 to 400 ng/L for EWW. The on-line SPE-LC method was implemented in this laboratory under requirements of ISO-170025 [34].

Data obtained are also shown in Tables 3 and 4 (between brackets). Six compounds (cocaine, benzoylcegonine, diclofenac, naproxen, sulfamethoxazole and venlafaxine) were found in EWW samples, less than in the direct injection methodology (32 compounds). This was surely due to the higher LOQs obtained in the on-line procedure, due to the dilution step (1/20) applied to EWW samples prior to on-line SPE. The concentration values ranged from 0.048 to 3.1 µg/L and were in agreement with the results obtained by the direct injection approach. Regarding surface water samples, where no dilution was performed, up to 8 compounds could be detected (benzoylcegonine, cocaine, acetaminophen, clarithromycin, diclofenac, levamisol, naproxen and venlafaxine). Among them, venlafaxine was the compound most frequently detected (3 out of 10 SW analyzed), and the highest concentration found was for acetaminophen (0.65 µg/L). All concentration values obtained by this methodology were also in accordance with the results reported after direct injection analyses.

Except for the differences due to the distinct sensitivity of the two procedures, the concentrations found by both of them for the

Table 4
Summary of the results obtained for target pharmaceuticals in SW, applying the analytical methodology described in this article. Between brackets, the concentrations obtained using the on-line SPE-LC-MS/MS alternative method.

Compound	SW (ng/L)									
	1	2	3	4	5	6	7	8	9	10
Acetaminophen ^a	–	–	–	480 (654)	9	13	13	12	32 (10)	10
Benzoylcegonine ^a	< LOQ	< LOQ	18 (8)	31 (23)	6	< LOQ	< LOQ	7	6	6
Clarithromycin ^a	–	–	11	34 (45)	–	–	–	–	–	–
Cocaethylene ^a	–	–	–	7	–	–	–	–	–	–
Cocaine ^a	8	< LOQ	8	14 (8)	–	8	8	10 (5)	–	< LOQ
Diclofenac ^a	–	34 (24)	135 (99)	14	–	–	–	–	–	–
Erythromycin ^a	–	–	10	< LOQ	–	–	–	–	–	–
Flumequine ^a	3	–	–	–	–	–	–	< LOQ	–	–
Levamisol ^a	–	4	76 (44)	5	–	–	–	–	–	–
MDMA ^a	–	–	15	13	–	–	–	–	–	–
Nalidixic acid ^a	3	–	–	< LOQ	–	–	–	4	–	–
Naproxen ^a	–	–	67 (56)	114 (172)	–	–	–	–	–	–
Oxolinic acid ^a	5	–	–	–	–	–	–	–	–	< LOQ
Pantoprazole ^a	–	1	–	–	–	–	–	–	–	–
Sulfamethoxazole ^a	–	21	25	11	13	< LOQ	–	–	–	< LOQ
Trimethoprim ^a	3	–	< LOQ	5	–	–	–	–	–	–
Venlafaxine ^a	9	244 (217)	93 (61)	30 (18)	16	10	< LOQ	< LOQ	9	16
4-Acetyl aminoantipyrine	–	< LOQ	719	182	8	9	6	< LOQ	–	21
4-Formyl aminoantipyrine	–	9	663	101	33	13	–	< LOQ	–	60
Alprazolam	–	11	8	< LOQ	–	–	–	–	–	–
Carbamazepine	< LOQ	73	22	10	7	–	2	2	–	6
Gemfibrozil	–	–	105	80	–	–	–	–	–	–
Irbesartan	–	< LOQ	5	40	–	–	–	–	–	6
Lincomycin	–	12	5	1	–	–	–	–	–	–
Lorazepam	–	13	18	< LOQ	–	–	–	–	–	44
Valsartan	–	–	13	224	–	–	–	–	–	–

–: not detected.

^a Compounds also analyzed by the on-line SPE LC-MS/MS methodology described in section.

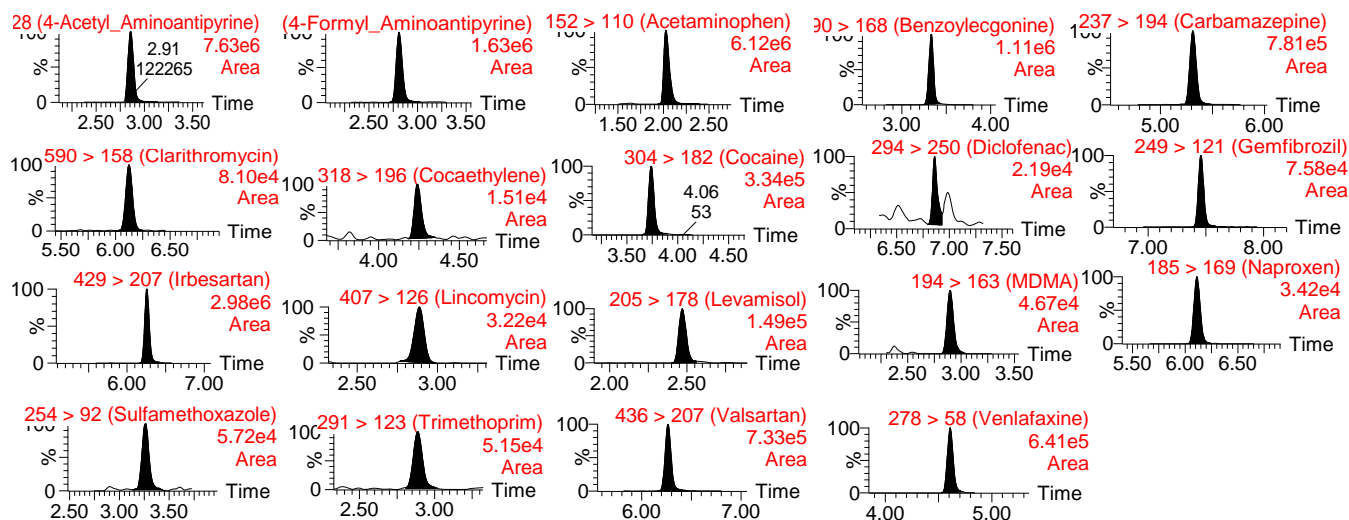


Fig. 2. UHPLC-MS/MS chromatograms (Q transition) for a surface water sample (SW 4, see Table 4) where 19 target compounds were found. Positive/negative voltage switching mode applied within the same run.

wide majority of positive samples were rather similar, supporting the applicability and reliability of our more-sensitive large-volume direct injection approach.

4. Conclusions

Analytical methodology based on UHPLC-MS/MS QqQ has been developed for the simultaneous quantification and confirmation of 40 human and veterinary pharmaceuticals and drugs of abuse in effluent wastewater and surface samples. The direct injection of water samples (100 μ L), without any previous sample treatment,

has been shown as an attractive approach as it avoids time-consuming sample preparation steps and reduces the amounts of solvents used. The determination of target compounds was performed in positive/negative voltage switching mode in a single chromatographic run of only 10 min. With a few exceptions, a highly reliable identification of the compounds was feasible thanks to the acquisition of three SRM transitions per compound and the accomplishment of the ion ratio and retention time deviations. Satisfactory accuracy and precision were obtained in recovery experiments at three concentration levels in two kinds of water matrices, EWW and SW, using 10 different samples to this aim. The LOQs were in most cases lower than 3 ng/L.

The application of this method to 10 effluent wastewater and 10 surface samples, allowed the detection of 32 and 26 compounds, respectively. Carbamazepine was the compound most frequently detect (100%) in EWW and venlafaxine (80%) in SW samples. This methodology has been proven to be an attractive and efficient approach for rapid determination of pharmaceuticals and drugs of abuse in environmental water, achieving low LOQs without the need for a preliminary pre-concentration step.

Acknowledgments

The authors are very grateful to Serveis Centrals d'Instrumentació Científica (SCIC) of University Jaume I for using the Xevo TQ5 mass spectrometer. The financial support of the Centro de Desarrollo Tecnológico Industrial (CDTI IDI-20110823/EXP00044257), of the Spanish Ministry of Education and Science (Ref CTQ2012-36189) and of Generalitat Valenciana (research group of excellence PROMETEO/2009/054; Collaborative Research on Environment and Food Safety, ISIC/2012/016) is acknowledged.

References

- [1] D. Fatta-Kassinos, S. Meric, A. Nikolaou, *Anal. Bioanal. Chem.* 399 (2011) 251–275. <http://dx.doi.org/10.1007/s00216-010-4300-9>.
- [2] I. Senta, S. Terzic, M. Ahel, *Water Res.* 47 (2013) 705–714. <http://dx.doi.org/10.1016/j.watres.2012.10.041>.
- [3] S. Castiglioni, R. Bagnati, M. Melis, D. Panawennage, P. Chiarelli, R. Fanelli, et al., *Water Res.* 45 (2011) 5141–5150. <http://dx.doi.org/10.1016/j.watres.2011.07.017>.
- [4] S. Ortiz de García, G. Pinto Pinto, P. García Encina, R. Irusta Mata, *Sci. Total Environ.* 444 (2013) 451–465. <http://dx.doi.org/10.1016/j.scitotenv.2012.11.057>.
- [5] N. Dorival-García, A. Zafra-Gómez, S. Cantarero, A. Navalón, J.L. Vilchez, *Microchem. J.* 106 (2013) 323–333. <http://dx.doi.org/10.1016/j.microc.2012.09.002>.
- [6] D.R. Baker, B. Kasprzyk-Hordern, *Sci. Total Environ.* 454–455 (2013) 442–456. <http://dx.doi.org/10.1016/j.scitotenv.2013.03.043>.
- [7] R. López-Serna, A. Jurado, E. Vázquez-Suñé, J. Carrera, M. Petrović, D. Barceló, *Environ. Pollut.* 174 (2013) 305–315. <http://dx.doi.org/10.1016/j.envpol.2012.11.022>.
- [8] E. Gracia-Lor, J.V. Sancho, F. Hernández, *J. Chromatogr. A* 1218 (2011) 2264–2275. <http://dx.doi.org/10.1016/j.chroma.2011.02.026>.
- [9] R. López-Serna, M. Petrovic, D. Barceló, *Chemosphere* 85 (2011) 1390–1399. <http://dx.doi.org/10.1016/j.chemosphere.2011.07.071>.
- [10] S. Bayen, X. Yi, E. Segovia, Z. Zhou, B.C. Kelly, *J. Chromatogr. A* 1338 (2014) 38–43. <http://dx.doi.org/10.1016/j.chroma.2014.02.034>.
- [11] L. Bijlsma, J.V. Sancho, E. Pitarch, M. Ibáñez, F. Hernández, *J. Chromatogr. A* 1216 (2009) 3078–3089. <http://www.scopus.com/inward/record.url?eid=2-s2.0-62349135470&partnerID=40&md5=ae09aefbddd73dfd6e6160b3f338cf>.
- [12] S. Castiglioni, E. Zuccato, E. Crisci, C. Chiabrando, R. Fanelli, R. Bagnati, *Anal. Chem.* 78 (2006) 8421–8429. <http://dx.doi.org/10.1021/ac061095b>.
- [13] S. Huntscha, H.P. Singer, C.S. Mc Ardell, C.E. Frank, J. Hollender, *J. Chromatogr. A* 1268 (2012) 74–83. <http://dx.doi.org/10.1016/j.chroma.2012.10.032>.
- [14] A.C. Chiaia, C. Banta-Green, J. Field, *Environ. Sci. Technol.*, 42, 20088841–8848. <http://dx.doi.org/10.1021/es802309v>.
- [15] F. Busetto, W.J. Backe, N. Bendixen, U. Maier, B. Place, W. Giger, et al., *Anal. Bioanal. Chem.* (2011) 1–12. <http://dx.doi.org/10.1007/s00216-011-5290-y>.
- [16] J.-D. Berset, R. Brenneisen, C. Mathieu, *Chemosphere* 81 (2010) 859–866. <http://dx.doi.org/10.1016/j.chemosphere.2010.08.011>.
- [17] M.M. Galera, P.P. Vázquez, M.D.M.P. Vázquez, M.D.G. García, C.F. Amate, *J. Sep. Sci.* 34 (2011) 1796–1804. <http://dx.doi.org/10.1002/jssc.201100117>.
- [18] M.J. Martínez Bueno, S. Uclés, M.D. Hernando, A.R. Fernández-Alba, *Talanta* 85 (2011) 157–166. <http://dx.doi.org/10.1016/j.talanta.2011.03.051>.
- [19] E. Zuccato, S. Castiglioni, R. Fanelli, *J. Hazard. Mater.* 122 (2005) 205–209. <http://dx.doi.org/10.1016/j.jhazmat.2005.03.001>.
- [20] A.L.N. Van Nuijs, I. Tarcornicu, W. Simons, L. Bervoets, R. Blust, P.G. Jorens, et al., *Anal. Bioanal. Chem.* 398 (2010) 2211–2222. <http://dx.doi.org/10.1007/s00216-010-4101-1>.
- [21] S. González Alonso, M. Catalá, R.R. Maroto, J.L.R. Gil, Á.G. de Miguel, Y. Valcárcel, *Environ. Int.* 36 (2010) 195–201. <http://dx.doi.org/10.1016/j.envint.2009.11.004>.
- [22] M.D. Hernando, M.J. Gómez, A. Agüera, A.R. Fernández-Alba, *Pharm. Anal.* 26 (2007) 581–594. <http://dx.doi.org/10.1016/j.trac.2007.03.005>.
- [23] R. Rosal, A. Rodríguez, J.A. Perdigón-Melón, A. Petre, E. García-Calvo, M.J. Gómez, et al., *Water Res.* 44 (2010) 578–588. <http://dx.doi.org/10.1016/j.watres.2009.07.004>.
- [24] M.A. Sousa, C. Gonçalves, E. Cunha, J. Hajšlová, M.F. Alpendurada, *Anal. Bioanal. Chem.* 399 (2011) 807–822. <http://dx.doi.org/10.1007/s00216-010-4297-0>.
- [25] Y. Valcárcel, S. González Alonso, J.L. Rodríguez-Gil, A. Gil, M. Catalá, *Chemosphere* 84 (2011) 1336–1348. <http://dx.doi.org/10.1016/j.chemosphere.2011.05.014>.
- [26] M. Gros, M. Petrovic, A. Ginebreda, D. Barceló, *Environ. Int.* 36 (2010) 15–26. <http://dx.doi.org/10.1016/j.envint.2009.09.002>.
- [27] M. Gros, S. Rodríguez-Mozaz, D. Barceló, *J. Chromatogr. A* 1248 (2012) 104–121. <http://dx.doi.org/10.1016/j.chroma.2012.05.084>.
- [28] R. Diaz, M. Ibáñez, J.V. Sancho, F. Hernández, *J. Chromatogr. A* 1276 (2013) 47–57. <http://dx.doi.org/10.1016/j.chroma.2012.12.030>.
- [29] M. José Gómez, O. Malato, I. Ferrer, A. Agüera, A.R. Fernández-Alba, *J. Environ. Monit.* 9 (2007) 719–729. <http://dx.doi.org/10.1039/b702844j>.
- [30] F. Hernández, L. Bijlsma, J.V. Sancho, R. Díaz, M. Ibáñez, *Anal. Chim. Acta* 684 (2011) 87–97. <http://dx.doi.org/10.1016/j.aca.2010.10.043>.
- [31] L. Bijlsma, E. Emke, F. Hernández, P. de Voogt, *Anal. Chim. Acta* (2013). <http://dx.doi.org/10.1016/j.aca.2013.01.010>.
- [32] C.L. Chitescu, E. Oosterink, J. de Jong, A.A.M. Linda Stolker, *Anal. Bioanal. Chem.* 403 (2012) 2997–3011. <http://dx.doi.org/10.1007/s00216-012-5888-8>.
- [33] F. Wode, C. Reilich, P. van Baar, U. Dünbier, M. Jekel, T. Reemtsma, *J. Chromatogr. A* 1270 (2012) 118–126. <http://dx.doi.org/10.1016/j.chroma.2012.10.054>.
- [34] IPROMA SOP, Determinación de fármacos y drogas en agua de consumo, continental y residual empleando SPE-on-line y HPLC-MS/MS. (http://www.msssi.gob.es/biblioPublic/publicaciones/recursos_propios/infMeDic/docs/SubgruposATCvol35n4.pdf) (accessed on March 2011).
- [35] M. Farré, M. Petrovic, D. Barceló, *Anal. Bioanal. Chem.* 387 (2007) 1203–1214. <http://dx.doi.org/10.1007/s00216-006-0936-x>.
- [36] L. Penney, C. Bergeron, B. Coates, A. Wijewickreme, *J. AOAC Int.* 88 (2005) 496–504.
- [37] H. Ergün, D.A.C. Frattarelli, J.V. Aranda, *J. Pharm. Biomed. Anal.* 35 (2004) 479–487. <http://dx.doi.org/10.1016/j.jpba.2004.02.004>.
- [38] M. Ibáñez, E. Gracia-Lor, J.V. Sancho, F. Hernández, *J. Mass Spectrom.* 47 (2012) 1040–1046.
- [39] T. Benijts, R. Dams, W. Lambert, A. De Leenheer, *J. Chromatogr. A* 1029 (2004) 153–159.
- [40] E. Gracia-Lor, J.V. Sancho, F. Hernández, *J. Chromatogr. A* 1217 (2010) 622–632. <http://dx.doi.org/10.1016/j.chroma.2009.11.090>.
- [41] European Union Decision 2002/657/EC, Off. J. Eur. Commun. L221 (2002) 8–36 (12 August 2002).



Simultaneous pharmacokinetic and pharmacodynamic analysis of 5 α -reductase inhibitors and androgens by liquid chromatography tandem mass spectrometry

Rita Upreti^a, Gregorio Naredo^b, Abdullah M.M. Faqehi^a, Katherine A. Hughes^a, Laurence H. Stewart^c, Brian R. Walker^{a,b}, Natalie Z.M. Homer^b, Ruth Andrew^{a,b,*}

^a Endocrinology, University/British Heart Foundation Centre for Cardiovascular Science, Queen's Medical Research Institute, University of Edinburgh, 47, Little France Crescent, Edinburgh EH16 4TJ, United Kingdom

^b Mass Spectrometry Core, Wellcome Trust Clinical Research Facility, Queen's Medical Research Institute, University of Edinburgh, 47, Little France Crescent, Edinburgh EH16 4TJ, United Kingdom

^c Department of Urology, NHS Lothian, Western General Hospital, Crewe Road South, Edinburgh EH4 2XU, United Kingdom

ARTICLE INFO

Article history:

Received 28 April 2014

Received in revised form

25 July 2014

Accepted 30 July 2014

Available online 14 August 2014

Keywords:

Testosterone

Dihydrotestosterone

5 α -reductase

Dutasteride

Finasteride

Liquid chromatography tandem mass spectrometry

ABSTRACT

Benign prostatic hyperplasia and prostate cancer can be treated with the 5 α -reductase inhibitors, finasteride and dutasteride, when pharmacodynamic biomarkers are useful in assessing response. A novel method was developed to measure the substrates and products of 5 α -reductases (testosterone, 5 α -dihydrotestosterone (DHT), androstenedione) and finasteride and dutasteride simultaneously by liquid chromatography tandem mass spectrometry, using an ABSciex QTRAP[®] 5500, with a Waters Acquity[™] UPLC. Analytes were extracted from serum (500 μ L) via solid-phase extraction (Oasis[®] HLB), with ¹³C₃-labelled androgens and d9-finasteride included as internal standards. Analytes were separated on a Kinetex C18 column (150 \times 3 mm, 2.6 μ m), using a gradient run of 19 min. Temporal resolution of analytes from naturally occurring isomers and mass +2 isotopomers was ensured. Protonated molecular ions were detected in atmospheric pressure chemical ionisation mode and source conditions optimised for DHT, the least abundant analyte. Multiple reaction monitoring was performed as follows: testosterone (m/z 289 \rightarrow 97), DHT (m/z 291 \rightarrow 255), androstenedione (m/z 287 \rightarrow 97), dutasteride (m/z 529 \rightarrow 461), finasteride (m/z 373 \rightarrow 317). Validation parameters (intra- and inter-assay precision and accuracy, linearity, limits of quantitation) were within acceptable ranges and biological extracts were stable for 28 days. Finally the method was employed in men treated with finasteride or dutasteride; levels of DHT were lowered by both drugs and furthermore the substrate concentrations increased.

© 2014 The Authors. Published by Elsevier B.V. This is an open access article under the CC BY license (<http://creativecommons.org/licenses/by/3.0/>).

1. Introduction

Finasteride and dutasteride, are irreversible inhibitors of 5 α -reductase isozyme(s) [1]. They were developed to decrease the conversion of testosterone to its more potent metabolite

Abbreviations: BPH, benign prostatic hyperplasia

* Corresponding author at: Endocrinology, University/British Heart Foundation Centre for Cardiovascular Science, Queen's Medical Research Institute, University of Edinburgh, 47, Little France Crescent, Edinburgh EH16 4TJ, United Kingdom. Tel.: +44 131 242 6763; fax: +44 131 242 6779.

E-mail addresses: ritaupreti@yahoo.com (R. Upreti),

g.naredo@ed.ac.uk (G. Naredo), A.M.M.Faqehi@sms.ed.ac.uk (A.M.M. Faqehi),

Katherine.Hughes@ed.ac.uk (K.A. Hughes),

laurence.stewart@nhslothian.scot.nhs.uk (L.H. Stewart),

b.walker@ed.ac.uk (B.R. Walker), n.z.m.homer@ed.ac.uk (N.Z.M. Homer),

ruth.andrew@ed.ac.uk (R. Andrew).

<http://dx.doi.org/10.1016/j.talanta.2014.07.087>

0039-9140/© 2014 The Authors. Published by Elsevier B.V. This is an open access article under the CC BY license (<http://creativecommons.org/licenses/by/3.0/>).

5 α -dihydrotestosterone (DHT) (Fig. 1) in the treatment of benign prostatic hyperplasia (BPH) and are now being proposed for use in prostate cancer [2]. In its early stages, prostate cancer is androgen-responsive and androgen ablation therapy is effective in restraining tumour growth [3]. As the disease advances, the tumour becomes "castration resistant", with changes in the responsiveness of the androgen receptor (AR) and in its associated signalling pathways. Under these circumstances, local androgen synthesis inhibitors, such as 5 α -reductase inhibitors, may be used to further lower levels of any remaining intra-tumoural androgen [4], often derived from adrenal sources. In many therapeutic settings where 5 α -reductase inhibitors are used or studied, the simultaneous assessment of pharmacodynamics and pharmacokinetics is desirable, and best achieved by measurement of steroid concentrations and drug concentrations respectively.

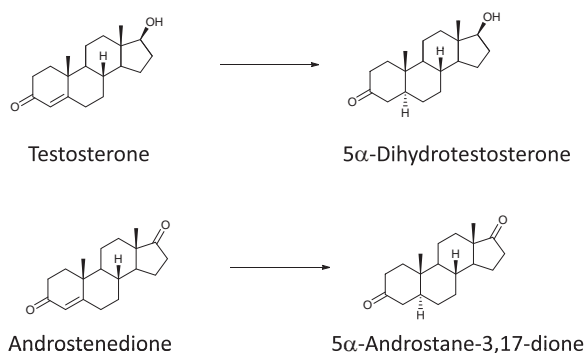


Fig. 1. Reactions catalysed by 5 α -reductases 1 and 2. 5 α -Reductases catalyse the irreversible reduction of the 4–5 double bond in the A-ring, e.g. of testosterone and androstenedione.

Finasteride, the first drug in class, is selective for 5 α -reductase type 2 [5], exerting its effects most markedly in the prostate. Dutasteride is a “dual” 5 α -reductase type 1 and 2 inhibitor [6], developed to lower the levels of DHT further, achieving \sim 94% reduction in DHT compared with \sim 70–80% suppression by finasteride [7–10]. However, by inhibiting 5 α -reductase 1, it has the potential to influence the hormonal milieu in a wider array of tissues [11], notably the liver. 5 α -Reductases metabolise not only androgens but also glucocorticoids, mineralocorticoids and progestogens. Therefore, inhibitors of 5 α -reductase isozymes, and in particular of type 1 5 α -reductase may have effects on diverse steroid hormone signalling pathways. Recent studies suggest that inhibition of 5 α -reductase type 1 in liver may adversely influence insulin sensitivity [12], predispose to fatty liver [13] and also alter stress responses [14].

Pharmacodynamic and pharmacokinetic studies of 5 α -reductases are achieved by measurement of the androgenic substrate and product, together with circulating drug concentrations. Such measures also permit assessment of treatment adherence in clinical studies. To minimise sample volume, maximise efficiency of sample processing, allow analysis without unblinding participants, and permit simultaneous pharmacodynamic and pharmacokinetic evaluation, a single assay measuring both drugs and androgen concentrations is desirable. Dutasteride [15,16] and finasteride [17–22] have been quantified previously by liquid chromatography–mass spectrometry (LC–MS), but only individually. Testosterone and androstenedione, the principle endogenous androgenic substrates of 5 α -reductase circulate in \sim 1–30 nM concentrations [23,24], and testosterone is routinely monitored by LC tandem MS (LC–MS/MS) in clinical biochemistry laboratories [25]. However, analysis of DHT presents particular challenges due to its low concentrations, especially following 5 α -reductase inhibition [8] and poor propensity to ionise. The use of LC tandem MS (LC–MS/MS) has allowed measurement of DHT in adult [24] and paediatric populations [26], overcoming the need for derivatisation with GC–MS methods [27,28], the low sensitivity and lack of mass separation with HPLC methods with ultraviolet detection [29] and the lack of specificity with immunoassays [30]. While many approaches to quantify DHT by LC–MS have also required derivatisation [31–33], this may not be possible in conjunction with simultaneous analysis of drug levels.

We developed a novel assay simultaneously measuring inhibitors (finasteride and dutasteride), substrates (testosterone, androstenedione) and product (DHT) of 5 α -reductases in human serum. The approach was evaluated in monitoring pharmacodynamic responses to 5 α -reductase inhibitors in men.

2. Materials and methods

2.1. Reagents and standards

Unless stated otherwise, chemicals (including 2,3,4- $^{13}\text{C}_3$ labelled androgens) were from Sigma-Aldrich (Dorset, UK) and all solvents were from Rathburn Chemical Ltd (Walkerburn, UK). Water and formic acid (FA) were from Fisher Scientific (Loughborough, UK). Methanol (HPLC gradient grade) was from VWR (Lutterworth, Leicestershire, UK). Finasteride was from Sternaloids (Newport, RI, USA) and dutasteride from AK Scientific (Mountain View, CA, USA). 23,23,23,24,24,24,25,25,25- $^3\text{H}_9$ -finasteride (d9-finasteride) was synthesised in-house [34]. Stock solutions were prepared at 1 and 0.01 mg/mL in methanol, and stored at -20°C . Working solutions were prepared on the day of analysis.

2.2. Biological samples

Pooled male human serum and steroid-stripped serum for the method of optimisation and validation were from TCS Biosciences (Buckingham, UK). Due to residual androstenedione and testosterone being detectable in the steroid-stripped serum, it was re-stripped before use. Dextran-coated charcoal was added to steroid-stripped serum (0.1 g/10 mL), stirred (\sim 24 h, 4°C) and removed by centrifugation (1811g, 4°C , 30 min). Stripped serum was sequentially filtered through 1.20 μm (Sartorius minisart, Sartorius AG, Göttingen, Germany) and 0.22 μm filters (Millex[®] GP filter unit, Millipore Ireland Ltd., Carrigtwohill, Ireland) until clear and aliquots frozen (-20°C) until use.

2.3. LC–MS/MS instrumentation and MS tuning

Chromatographic separation was performed on a Waters Acquity[™] UPLC (Manchester, UK) with autosampler, and detection on an ABSciex QTRAP[®] 5500 mass spectrometer (Warrington, UK), operated with Analyst[®] Software version 1.5.1. Nitrogen was the source, curtain and collision gas. Compound specific tuning (collision energy, cell exit potential and declustering potential) in positive atmospheric pressure chemical ionisation (APCI) mode was performed using methanolic solutions of steroids, internal standards and drugs. The masses of precursor ions were determined and transitions yielding the most abundant product ions selected from the eight most abundant transitions screened. MS source conditions were then optimised for DHT, the least abundant analyte; final optimised conditions were curtain gas 25 psi, collision gas low, spray voltage 5 kV, nebuliser current 3.5 μA , source temperature 500°C , and ion source gas 55 psi.

2.4. Extraction and chromatographic method

Samples were extracted via solid-phase extraction (Oasis[®] HLB, 30 μm , 30 mg (Waters, Elstree, UK)). Extraction cartridges were primed with methanol (1 mL) then water (1 mL). Samples (500 μL), enriched with internal standard (1 ng), were mixed with water (500 μL) and loaded onto primed extraction cartridges. After a wash step (50% methanol in water, 1 mL), analytes were eluted with methanol (1 mL). Eluates were dried under oxygen-free nitrogen (37°C) and reconstituted in mobile phase (30:70 methanol:water + 0.1% FA; 100 μL). Injection volume was 10 μL .

Analytes were eluted at 35°C from a Kinetex C18 column (150 \times 3 mm, 2.6 μm , Phenomenex[®], Macclesfield, UK) with a 1 min hold followed by a 9 min linear gradient from 30:70 to 80:20 (methanol:water with 0.1% FA) at a flow rate of 250 $\mu\text{L}/\text{min}$. Conditions were sustained until 16 min followed by re-equilibration.

3. Assay validation

3.1. Recovery

Recovery was calculated by expressing the mean of the integrated peak areas from extracted standards as a percentage of that of unextracted standards. This was performed in replicates of 6 using stripped serum as matrix and enriched with androstenedione (1 ng), testosterone (1 ng), DHT (10 ng), finasteride (1 ng) and dutasteride (10 ng).

3.2. Ion suppression by serum

The effect of the biological matrix (human serum) on ionisation efficiency was assessed in replicates of 6 by post-spiking extracted blank serum with all analytes in amounts corresponding to the midpoint of the standard curve (indicated by *), and responses compared with those of standards with the same amounts of analytes dissolved in mobile phase (30:70 methanol:water +0.1% FA). Blank serum sample were also analysed so amounts of endogenous analytes could be subtracted from peak areas detected in post-spiked samples.

3.3. Analyte specificity

Extracts of blank stripped and unstripped serum were analysed and checked for interferences at or close to the expected retention times for androgens and drugs and internal standards respectively. Chromatographic resolution was ensured between anticipated endogenous stereo or positional isomers, e.g., testosterone, epitestosterone and dehydroepiandrosterone (DHEA), and also between endogenous hormones and predicted mass +2 isotopomeric interferences, e.g., mass +2 testosterone and DHT. Ratios of quantifier and qualifier mass transitions were monitored for analytes all except DHT, where the ion generated by the qualifier transition was not detected in serum. Quantifier:qualifier ratios in biological samples were considered acceptable if within 20% of the mean ratio of standards.

3.4. Limits of detection (LOD) and lower limits of quantitation (LLOQ)

LOD were determined by analysing solutions prepared by serial dilution of analyte and internal standard stock solutions, with the LOD assigned to a peak area where signal:noise ratio (SNR) was ≈ 3 . LLOQ following extraction was determined by extracting analyte and internal standard from serum at amounts corresponding to $0.2 \times \text{LOD}$, $0.5 \times \text{LOD}$, LOD and $5/3 \times \text{LOD}$. The LLOQ was defined as the amount where relative standard deviation in replicates of 6 was $\leq 20\%$.

3.5. Linearity

Two standard curves were generated, one in water (for quantitation of androgens) and one in serum (for quantitation of dutasteride and finasteride), with 1 ng of each internal standard. Standard curves represented concentration ranges: testosterone (1, 2[#], 3, 5, 7.5[#], 10*, 12.5, 15[#] ng/mL), androstenedione and DHT (0.1, 0.2[#], 0.5, 1, 2^{**}, 3, 4, 5[#] ng/mL), finasteride and dutasteride (1, 2[#], 5, 10, 25^{**}, 50, 75, 100[#] ng/mL); * used to assess ion suppression, # used to assess accuracy and precision. Peak areas of each analyte and internal standard were integrated and a calibration curve constructed (peak area ratio of analyte/internal standard versus concentration of analyte). Regression lines of best fit were constructed and considered acceptable if the regression

coefficient, r , was > 0.99 . Accuracy was compared using different weightings (none, $1/x$ and $1/x^2$).

3.6. Precision and accuracy

The intra-assay accuracy and precision were determined with 3 points of the standard curve prepared in replicates of 6 (low, medium, high, indicated by # above). Precision was also determined using 6 replicates of a patient sample. The inter-assay accuracy and precision were determined from four standard curves prepared on different days. The precision was calculated as the relative standard deviation of the mean (RSD) with $\text{RSD} (\%) = \text{standard deviation}/\text{mean} \times 100$. The % accuracy was calculated as the calculated concentration/theoretical concentration $\times 100$. Injector variability was assessed by injecting (6 times) the midpoint standards (medium) of the calibration curve, and a pooled male serum sample enriched with both finasteride (10 ng/mL) and dutasteride (20 ng/mL).

3.7. Stability

Stability was assessed by reinjection of a single calibration curve and patient sample after 24 h in the auto-sampler (10 °C) and following 28 day storage (-20 °C). Acceptable storage conditions were those giving $\leq 10\%$ change in response.

3.8. Method exemplification

Drugs and steroids were quantified in serum collected from male subjects (age 20–85 years, $n=16/\text{group}$) prior to and following 90 days of treatment once daily with either dutasteride (0.5 mg, Glaxo Smith Kline Pharmaceuticals, Poznań, Poland) or finasteride (5 mg; Gedeon Richter, Budapest, Hungary). Local ethical committee approval and informed consent were obtained.

3.9. Data analysis

Assay validation data are presented as mean (RSD) and biological concentrations as mean \pm standard error of the mean. Effects of drugs on concentrations of substrates and product of 5α -reductases were tested by repeated measure ANOVAs with Fisher's post-hoc tests and associations tested by Pearson Correlation. Where appropriate, data below the limits of quantitation were imputed as $0.5 \times \text{LLOQ}$ for statistical tests.

4. Results and discussion

4.1. Mass spectrometric conditions and fragmentation of analytes

All analytes and internal standards in solution ionised to form their protonated molecular ions in both positive electrospray (ESI) and APCI modes (Table 1). Although others have previously used ESI [24], APCI was selected due to less ion suppression during steroid analysis in the biomatrix. Signal responses in post-spiked serum compared to unextracted serum were androstenedione 110.8% (1.7%), testosterone 115.3% (2.1%), DHT 109.2% (2.4%), finasteride 111.0% (0.9%), dutasteride 97.2% (3.0%). APCI typically suffers less from ion suppression due to reduced ionisation of phospholipids and other competing compounds [35].

Androgens fragmented as previously reported [24] to yield product ions incorporating the A-ring of the steroid [36] and the presence of the three ¹³C atoms was evident in the product ions of their internal standards. Finasteride, d9-finasteride and dutasteride fragmented as reported previously [15,34]. It was important to enhance the signal for DHT, the least abundant analyte with

Table 1
Mass spectral conditions for analysis of analytes and internal standards utilising atmospheric pressure chemical ionisation.

	Mass (amu)	Precursor ion (m/z)	Product ion Quan; Qual	Declustering potential (V)	Collision energy (V) Quan; Qual	Cell exit potential (V) Quan; Qual
ANALYTES						
Androstenedione	286.4	287	97; 109	56	29; 27	18; 12
Testosterone	288.4	289	97; 109	16	27; 31	14; 16
5 α -Dihydrotestosterone*	290.4	291	255; *	16	21; *	28; *
Finasteride	372.5	373	317; 305	26	27; 41	14; 28
Dutasteride	528.5	529	461; 264	161	45; 55	48; 32
Internal Standards						
¹³ C ₃ -androstenedione	289.4	290	100; 112	31	27; 39	12; 16
¹³ C ₃ -testosterone	291.4	292	100; 112	1	27; 35	4; 8
¹³ C ₃ -dihydrotestosterone*	293.4	294	258; *	61	21; *	12; *
d9-Finasteride	381.6	382	318; 314	41	33; 41	34; 36

Amu: atomic mass unit; Quan: quantifier ion; Qual: qualifier ion; V: volts. *: Qualifier ion not detected in biological matrix.

poorest ionisation efficiency, hence source conditions were optimised for this analyte. Quantifier and qualifier transitions were defined for each analyte and internal standard (Table 1); however, in the case of DHT the signal from the potential qualifier ion (m/z 291 \rightarrow 91) was not detectable in the biological matrix. The 3 α , 5 α -reduced product formed from androstenedione was included in initial screening but was not pursued into full validation. This steroid generated ions with similar intensity to DHT but, due to lower substrate concentrations, this product was present in concentrations which could not be readily detected in 500 μ L of serum.

4.2. Selection of internal standards

¹³C labelled internal standards of androgens were selected, since some deuterium labelled steroids proved unsuitable due to variable loss of stable-isotopes during sample processing or ionisation, and isotopomers labelled in the D-ring did not retain deuterium in the product ion. Loss of deuteriums (particularly when attached to the steroid A-ring), has been described by others [37–39]. ¹³C₃-Androstenedione, ¹³C₃-testosterone and ¹³C₃-DHT proved suitable for robust quantitation as described further, subject to chromatographic resolution. For example, the mass +1 isotopomer of ¹³C₃-androstenedione could interfere with quantitation of DHT.

We have previously reported the synthesis of d9-finasteride [34] and others have used d3-finasteride as the internal standard for gas chromatography–MS [40]. In all other reports of finasteride and dutasteride analysis, non-deuterated internal standards were used, with finasteride often used as the internal standard for dutasteride [15,16], and other compounds used for finasteride quantitation [18–20,29]. d9-Finasteride had sufficient structural similarity to both 5 α -reductase inhibitors for robust analysis of either drug, however synthesis of deuterated dutasteride in future may offer added benefits for precision and accuracy.

4.3. Chromatographic conditions

The potential for interference between endogenous positional isomers (testosterone and DHEA), stereoisomers (testosterone and its 17 α -epimer) and also isobaric isotopomers from naturally occurring ¹³C₂ isotopomers was noted, requiring selective chromatographic approaches. This combined approach had not been achieved previously for steroids and drugs. Reported methods for detection of individual analytes predominantly use C18 columns, though these varied in length from 50 mm [15–17] to 150 mm [19,20]. Attempts with alternative stationary phases were not

successful with all analytes. Although finasteride could be efficiently eluted with the steroids, combined analysis with dutasteride proved more challenging. Adequate peak resolution was seen with most analytes of interest using a pentafluorophenyl column, however dutasteride was not detected; with 6 fluorine atoms and an aromatic unit in the molecule, dutasteride may have a much greater affinity for the column, though π – π interactions. Greatest peak intensities for all analytes were found with a Kinetex C18 column, a porous shell column, and acceptable peak resolution with column length of 150 mm.

Acetonitrile has often been selected as the organic component of the mobile for analysis of dutasteride and finasteride [18–20], and methanol for androgens [24,41]. However, acetonitrile suppressed ionisation of all analytes and hence methanol was selected. Ionisation was improved when formic acid was added as a modifier, with 0.1% yielding maximum responses, while still retaining consistency in chromatographic separation. We did not observe the improvements in analysis of testosterone, androstenedione and finasteride reported previously following buffering formic acid with ammonium acetate [17,42]. The duration of the gradient was optimised, being the key component allowing optimal baseline separation (particularly of testosterone and epitestosterone), ultimately requiring a 19 min run. Extension of the isocratic time after the initial gradient was important to maintain peak symmetry of DHT.

4.4. Extraction

Extraction was optimised to maximise recovery of endogenous DHT from serum, while extracting both androgens and 5 α -reductase inhibitors. DHT and dutasteride proved the most challenging analytes.

Based on previously published reports, we evaluated a series of liquid-liquid extractions employing ethyl acetate:hexane (3:2, v/v, with and without NaOH (0.1 M)) and ethyl acetate (with and without saturated NaCl) with samples tested neat, mixed with water, acidified (mixed with 0.1% FA) or alkaline (mixed with 5% ammonia). Despite good recovery of testosterone and androstenedione, these approaches did not recover endogenous DHT or the 5 α -reductase inhibitors efficiently. In supported liquid extractions, pre-extraction mixing was tested with FA (1%, 0.1%), water, NH₄OH (0.1 M), and acetic acid (0.1%), and extracting solvents tested were dichloromethane, diethyl ether, ethyl acetate, hexane, methanol and acetonitrile. Supported liquid-liquid extractions proved highly variable for steroid analysis, and recoveries achieved for 5 α -reductase inhibitors were inadequate. Protein precipitation and phospholipid crash methods gave poorer recoveries and again

endogenous DHT was not detected. Solid-phase extraction had been used previously in separate assays for 5 α -reductase inhibitors [15,18] and androgens [26,43] and the reversed-phase polymeric sorbent, Oasis[®] Hydrophilic Lipophilic Balanced (HLB), was ultimately selected. This technology also allowed transfer to 96-well plate format, suitable for high-throughput processing.

Mixing serum with water prior to extraction yielded the best extraction efficiency and the composition of the wash step proved vital to decrease background noise in the DHT transition. When using only 5% methanol in the wash step, several large peaks eluted close to the retention time of DHT; these could be eliminated by washing with 50% methanol in water, followed by elution in methanol (Fig. 2A and B). Using the final methods, extraction efficiencies all exceeded 80%: androstenedione 88.7% (15.4%); testosterone 84.6% (13.4%); DHT 85.5% (14.7%); finasteride 89.6% (14.3%); dutasteride 94.5% (10.4%).

5. Assay validation

5.1. Analyte specificity

All analytes and internal standards were temporally resolved from potential isomeric and isobaric interferences. Of note, testosterone and its biologically inert epi-isomer, epitestosterone, were separated chromatographically (Fig. 2C). The highly abundant isobaric steroid DHEA was not detected in the mass transitions (both quantifier and qualifier) monitored for testosterone. At amounts used, internal standards did not give any detectable interference in the analyte transitions.

An additional consideration was the potential presence of metabolites of 5 α -reductase inhibitor drug in serum. As well as unchanged drug, dutasteride is known to have 3 major (4'-hydroxydutasteride, 1,2-dihydrodutasteride, and 6-hydroxydutasteride) and 2 minor (6,4'-dihydroxydutasteride and 15-hydroxydutasteride) metabolites detected in human serum following dosing to steady state [44]. Finasteride has two main in vivo metabolites detected in serum [45]. With different molecular weights to their parent drug, metabolites of both finasteride and dutasteride would be anticipated to give rise to different precursor ions and mass transitions and hence not be detected in the current assay.

5.2. LOD and LLOQ

Analyte limits of detection and lower limits of quantitation (Table 2) permitted analysis of anticipated concentrations of analytes in serum and were similar to those of Kulle et al. [26] for testosterone and androstenedione, although slightly poorer for DHT. The anticipated reference ranges for expected concentrations in serum in adult men are: androstenedione 0.23–2.41 ng/mL [23,46], testosterone 2.65–9.71 ng/mL and DHT 0.14–0.77 ng/mL [24], finasteride 1.8–49 ng/mL [45] and dutasteride 36 ng/mL [44]. Notably finasteride and dutasteride could be quantified accurately even in amounts with signal:noise ≤ 3 (defined as the LOD). These limits would permit analysis of most analytes (except DHT) in volumes as low as 10 μ L but to allow the incorporation of DHT, 500 μ L of serum was required.

5.3. Linearity

Standard curves were linear in the range required, and for all analytes mean r was >0.99 (SD between 0.002–0.004). Mean intercepts (SD) were: androstenedione -0.007 (0.02); testosterone 0.084 (0.31); DHT -0.011 (0.02); finasteride 0.044 (0.06);

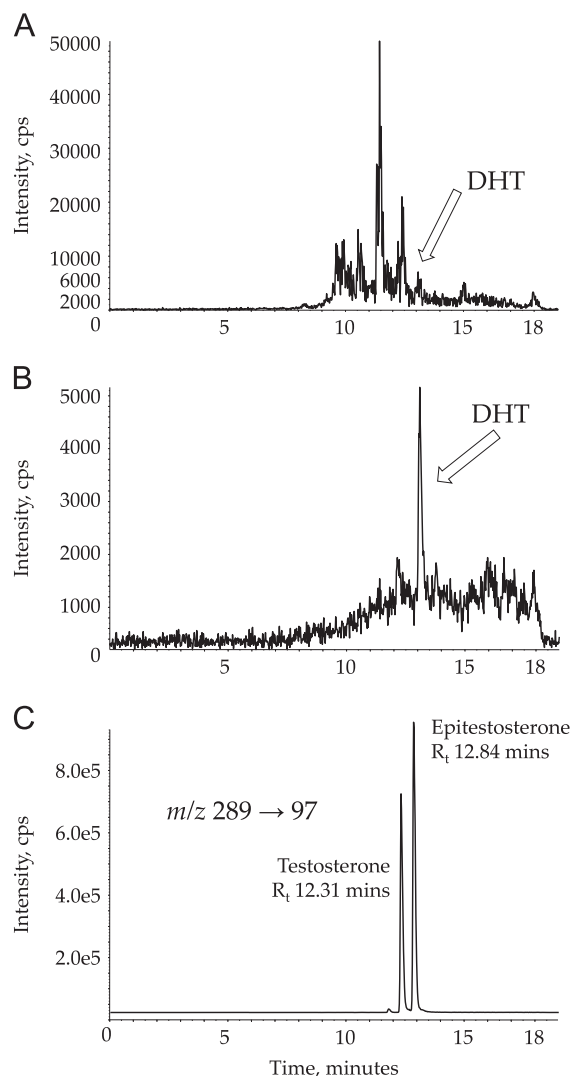


Fig. 2. Mass chromatograms demonstrating analytical challenges. Representative mass chromatograms demonstrating improvement in signal to noise in mass transition (m/z 291 \rightarrow 255) representing DHT recovered from normal male serum, following optimisation of the wash step. (A) Wash step of 5% methanol in water. (B) Wash step of 50% methanol in water. DHT, dihydrotestosterone; cps, counts per second. (C) Mass chromatogram (m/z 289 \rightarrow 97) demonstrating separation of endogenous isomers of testosterone. cps, counts per second.

Table 2

Limits of detection and lower limits of quantitation.

	Standard curve range (ng/mL)	LOD (ng/mL)	LLOQ (ng/mL)
Androstenedione	0.1–5	0.08	0.125
Testosterone	1–15	0.003	0.005
5 α -Dihydrotestosterone	0.1–5	0.13	0.21
Finasteride	1–100	0.02	0.003
Dutasteride	1–100	0.2	0.1

Abbreviations: LOD: limits of detection, LLOQ: lower limits of quantitation.

dutasteride $8.13E^{-08}$ ($2.42E^{-07}$). $1/x$ weighting was used for all analytes except DHT, where no weighting was applied.

5.4. Precision and accuracy

Intra- and inter-assay precision and accuracy of analysis are summarised in Table 3. While acceptable results were obtained for testosterone and androstenedione across the range of

Table 3
Intra-assay and inter-assay precision and accuracy.

	Target concentration (ng/mL)	Intra-assay (n=6)			Inter-assay (n=4)		
		Concentration (ng/mL): mean (SD)	Precision (% RSD)	Accuracy (%)	Concentration (ng/mL): mean (SD)	Precision (% RSD)	Accuracy (%)
Androstenedione	Low (0.2)	0.18 (0.01)	5.4	87.6	0.19 (0.02)	19.3	93.6
	Mid (2)	1.65 (0.12)	7.2	101	1.75 (0.16)	8.9	92.3
	High (5)	4.22 (0.27)	6.5	98.3	5.01 (0.59)	11.9	103.4
	Sample	0.16 (0.02)	9.9	–	0.20 (0.04)	20.1	–
Testosterone	Low (2)	1.80 (0.07)	2.8	94.4	1.88 (0.19)	10.0	94.9
	Mid (7.5)	6.50 (0.42)	5.8	101	7.29 (0.83)	11.3	100.6
	High (15)	14.40 (0.75)	4.9	100	15.28 (0.65)	4.2	103.3
	Sample	9.40 (0.61)	6.0	–	4.22 (0.21)	5.0	–
5 α -Dihydrotestosterone	Low (0.2)	0.17 (0.02)	11.8	87	0.23 (0.04)	15.5	119.5
	Mid (2)	1.70 (0.11)	6.4	90	1.83 (0.14)	7.4	100.0
	High (5)	4.11 (0.20)	4.9	103	5.00 (0.60)	12.1	105
	Sample	1.39 (0.19)	12.8	–	1.13 (0.31)	27.3	–
Finasteride	Low (2)	2.18 (0.24)	10	101	1.87 (0.30)	16.2	92.7
	Mid (25)	24.68 (1.34)	5.5	104	24.51 (2.08)	8.5	100.9
	High (100)	95.69 (6.23)	6.5	101	99.17 (4.35)	4.4	102.3
	Sample	8.45 (0.35)	4.1	–	8.96 (0.69)	7.8	–
Dutasteride	Low (2)	1.67 (0.37)	22	88.2	1.86 (0.16)	8.8	94.5
	Mid (25)	25.07 (2.40)	9.6	110	26.00 (2.60)	10.0	107.4
	High (100)	107.51 (16.06)	14.9	108	86.5 (4.40)	5.1	105
	Sample	16.25 (1.83)	11.2	–	15.05 (1.26)	8.4	–

concentrations tested, increasing inter-assay variability in DHT analysis was observed at low values, close to the LLOQ. In the case of finasteride and dutasteride, acceptable intra- and inter-assay precision and accuracy were demonstrated across the range of concentrations anticipated in clinical studies (Table 3), although in future stable-isotope labelled dutasteride might allow for lowering of the LLOQ. Acceptable reproducibility upon repeat injections of standards and samples was demonstrated with relative standard deviations between 3.1 and 5.9%.

5.5. Stability

Acceptable autosampler and extract storage stability were demonstrated for a calibration curve and patient samples, as shown in Table 4, with less than 10% decline during typical handling conditions.

5.6. Pharmacodynamic assessments in clinical samples

The assay presented was applied to a clinical research study with male volunteers studied prior to and following three months of finasteride (5 mg daily) or dutasteride (0.5 mg daily) [12]. Dutasteride and finasteride treatment resulted in a 46.5% and 47.1% suppression of DHT concentrations respectively (Fig. 3A and B). This is somewhat less than reported previously [47], but provided a robust marker of target engagement. The concentrations of dutasteride achieved would be anticipated to inhibit both isozymes of 5 α -reductase effectively. Relationships were not observed between amounts of DHT and those of dutasteride or finasteride, possibly due to maximal inhibition of the enzyme (Fig. 3C and D); doses of finasteride greater than 5 mg/day do not to achieve an increase in efficacy [48] and likewise the concentrations achieved of dutasteride were close to the maximal effect demonstrated by Gislekog et al. [49]. The reduction in DHT was accompanied by an increase in the concentrations of the enzyme substrate, testosterone, following treatment with both finasteride and dutasteride, of a similar magnitude to previously reported [50]. Androstenedione, a further

Table 4
Stability upon storage.

	Relative response after 24 h in autosampler (10 °C)	Relative response after 28 days in freezer (–20 °C)
Androstenedione	102.7%	98.3%
Testosterone	99.7%	101.0%
5 α -Dihydrotestosterone	90.0%	97.5%
Finasteride	95.3%	103.4%
Dutasteride	92.0%	92.0%

Relative response for calculated concentrations for all analytes in a single patient sample after 24 h in the autosampler (10 °C) and after 28 days in the freezer (–20 °C).

substrate also increased significantly following dutasteride treatment, with a strong trend evident with finasteride ($p=0.06$).

With pre-treatment concentrations of DHT approximately 0.8 ng/mL, it is anticipated that measurement of suppression of DHT to ~25% of its original value would be possible using this analytical approach. Levels fell below the LLOQ in more subjects receiving dutasteride than finasteride. Increased sample or injection volume, derivatisation or further advances in technology may allow extension of the pharmacodynamic range measurable.

6. Conclusions

The novel method developed was suitable for simultaneous measurement of androgens, dutasteride and finasteride from human serum, despite significant challenges in chromatographic and extraction method development. The assay requires relatively little sample volume (500 μ L), has a simple extraction method compatible with a 96-well format, and is able to quantify DHT without derivatisation, although advances in sensitivity would still be beneficial and allow quantitation of DHT and androstane-3 α ,5 α -dione in smaller volumes. Expected concentrations of all

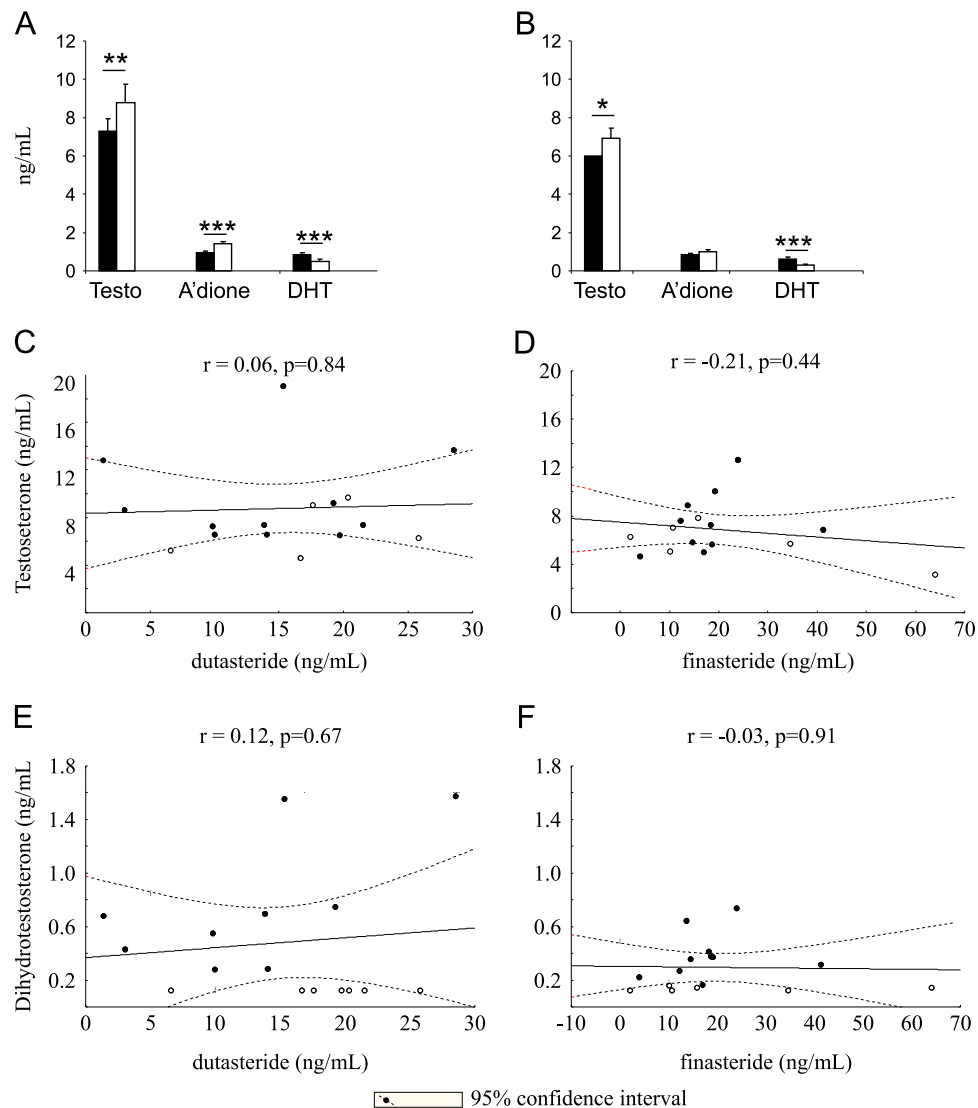


Fig. 3. (A and B) The concentrations of testosterone (Testo) and androstenedione (A'dione) were significantly increased by dutasteride and those of testosterone only by finasteride. Dihydrotestosterone (DHT) concentrations were reduced by both drugs. Data are mean \pm SEM ($n=16$), compared by repeated measure ANOVA, with Fisher's post-hoc test. Correlations were not observed between the concentrations of testosterone (C; dutasteride; D; finasteride) or DHT (E; dutasteride; F; finasteride) and those achieved of drug. Data show Pearson correlations, depicted with 95% confidence intervals. Data points (for DHT) which were recorded as less than the limit of detection were imputed at 0.125 ng/mL for statistical purposes and are represented in open circles.

analytes fell within the linear range of the standard curve in healthy men. The method is able to quantify DHT suppression to approximately 25% of normal values and can be used to detect enzyme inhibition and compliance with both 5α -reductase inhibitors. Intra- and inter-day precision and accuracy were acceptable and stability testing demonstrated the assay to be applicable to normal laboratory practice.

Acknowledgements

The authors wish to thank Sanjay Kothiyia and the Wellcome Trust Clinical Research Facility Mass Spectrometry Core for technical support and the Chief Scientist Office, Scotland, UK and the Royal Embassy of Saudi Arabia for funding this work (Grant no. CZB/4/642). RU is a recipient of a Graham Aitken Nuffield post-graduate travelling scholarship.

References

- [1] S. Aggarwal, et al., *Steroids* 75 (2) (2010) 109–153.
- [2] L.P. Nacusi, D.J. Tindall, *Nat. Rev. Urol.* 8 (7) (2011) 378–384.
- [3] J.A. Salvador, R.M. Pinto, S.M. Silvestre, *J. Steroid Biochem. Mol. Biol.* 137 (2013) 199–222.
- [4] J.L. Mohler, M.A. Titus, E.M. Wilson, *Clin. Cancer Res.* 17 (18) (2011) 5844–5849.
- [5] G.C. Tian, *J. Pharm. Sci.* 85 (1) (1996) 106–111.
- [6] S.V. Frye, *Curr. Top. Med. Chem.* 6 (5) (2006) 405–421.
- [7] P.O. Gisleskog, et al., *Clin. Pharmacol. Ther.* 64 (6) (1998) 636–647.
- [8] R.V. Clark, et al., *J. Clin. Endocrinol. Metab.* 89 (5) (2004) 2179–2184.
- [9] R. Wurzel, et al., *Prostate Cancer Prostatic Dis.* 10 (2) (2007) 149–154.
- [10] J.K. Amory, et al., *J. Clin. Endocrinol. Metab.* 92 (5) (2007) 1659–1665.
- [11] D.W. Russell, J.D. Wilson, *Annu. Rev. Biochem.* 63 (1994) 25–61.
- [12] R. Upreti, et al., *J. Clin. Endocrinol. Metab.* (2014) jc20141395.
- [13] J.K. Dowman, et al., *Endocrinology* (2013).
- [14] D.E. Livingstone, et al., *J. Endocrinol.* (2014).
- [15] N. Gomes, et al., *Chromatographia* 69 (1) (2009) 9–18.
- [16] N.V.S. Ramakrishna, et al., *J. Chromatogr. B – Anal. Technol. Biomed. Life Sci.* 809 (1) (2004) 117–124.
- [17] X. Chen, et al., *J. Chromatogr. Sci.* 46 (4) (2008) 356–361.

- [18] M.L. Constanzer, C.M. Chavez, B.K. Matuszewski, J. Chromatogr. B – Anal. Technol. Biomed. Life Sci. 658 (2) (1994) 281–287.
- [19] F.G. de Menezes, et al., *Arzneimittelforschung* 51 (2) (2001) 145–150.
- [20] F.-Q. Guo, et al., *J. Pharm. Biomed. Anal.* 43 (4) (2007) 1507–1513.
- [21] B.K. Matuszewski, M.L. Constanzer, C.M. Chavez-Eng, *Anal. Chem.* 70 (5) (1998) 882–889.
- [22] P.B. Phapale, et al., *J. Chromatogr. B – Anal. Technol. Biomed. Life Sci.* 878 (20) (2010) 1718–1723.
- [23] M.M. Kushnir, et al., *Clin. Chem.* 56 (7) (2010) 1138–1147.
- [24] S. Shiraishi, et al., *Clin. Chem.* 54 (11) (2008) 1855–1863.
- [25] M.M. Kushnir, et al., *Clin. Biochem.* 44 (1) (2011) 77–88.
- [26] A.E. Kulle, et al., *J. Clin. Endocrinol. Metab.* 95 (5) (2010) 2399–2409.
- [27] C. Legrand, et al., *J. Chromatogr. B – Anal. Technol. Biomed. Life Sci.* 663 (2) (1995) 187–192.
- [28] S.A. Wudy, et al., *Steroids* 57 (7) (1992) 319–324.
- [29] P. Ptacek, J. Macek, J. Klima, *J. Chromatogr. B – Anal. Technol. Biomed. Life Sci.* 738 (2) (2000) 305–310.
- [30] J. Taieb, et al., *Clin. Chem.* 48 (3) (2002) 583–585.
- [31] H. Licea-Perez, et al., *Steroids* 73 (6) (2008) 601–610.
- [32] K. Yamashita, et al., *Steroids* 74 (12) (2009) 920–926.
- [33] T.F. Kalthorn, et al., *Rapid Commun. Mass Spectrom.* 21 (19) (2007).
- [34] R. Upreti, et al., *J. Chromatogr. B Analyt. Technol. Biomed. Life Sci.* 930 (2013) 121–128.
- [35] O.A. Ismaiel, et al., *J. Chromatogr. B – Anal. Technol. Biomed. Life Sci.* 875 (2) (2008) 333–343.
- [36] M. Nielen, et al., *J. Chromatogr. B – Anal. Technol. Biomed. Life Sci.* 830 (1) (2006) 126–134.
- [37] E. Stokvis, H. Rosing, J.H. Beijnen, *Rapid Commun. Mass Spectrom.* 19 (3) (2005) 401–407.
- [38] C.M. Chavez-Eng, M.L. Constanzer, B.K. Matuszewski, *J. Chromatogr. B – Anal. Technol. Biomed. Life Sci.* 767 (1) (2002).
- [39] Boudreau, N., et al. Relative instability of deuterated internal standard under different pH conditions and according to deuterium atoms location. In: American Association of Pharmaceutical Scientists Annual Meeting and Exposition, 2009.
- [40] A. Guarna, et al., *J. Chromatogr. B – Anal. Technol. Biomed. Life Sci.* 674 (2) (1995) 197–204.
- [41] D.T. Harwood, D.J. Handelsman, *Clin. Chim. Acta* 409 (1-2) (2009) 78–84.
- [42] P. Macdonald, et al., *Endocr. Abstr.* 21 (2010).
- [43] K. Mitamura, et al., *Anal. Sci.* 21 (10) (2005) 1241–1244.
- [44] GlaxoSmithKline, Avodart Dutasteride, GlaxoSmithKline, United Kingdom, 2008.
- [45] Merck, Proscar Finasteride Tablets, I. Merck & Co. Whitehouse Station, NJ, USA, 1998.
- [46] NHS Lothian, Biochemistry and Haematology, Lothian University Hospitals Division, Department of Laboratory Medicine, Edinburgh, 2011–2013.
- [47] S. Gravas, M. Oelke, *World J. Urol.* 28 (1) (2010) 9–15.
- [48] J.F. Steiner, *Clin. Pharmacokinet.* 30 (1) (1996) 16–27.
- [49] P.O. Gislekog, et al., *Br. J. Clin. Pharmacol.* 47 (1) (1999) 53–58.
- [50] G.J. Gormley, et al., *J. Urol.* 167 (2 Pt 2) (2002) 1102–1107 (discussion 1108).



Determination of secondary and tertiary amines as N-nitrosamine precursors in drinking water system using ultra-fast liquid chromatography–tandem mass spectrometry

Qihua Wu^a, Honglan Shi^{a,*}, Yinfa Ma^a, Craig Adams^b, Todd Eichholz^c, Terry Timmons^c, Hua Jiang^d

^a Department of Chemistry and Environmental Res Center, Missouri University of Science and Technology, Rolla MO, USA

^b Civil and Environmental Engineering Department, Utah State University, Price UT, USA

^c Missouri Department of Natural Resources, Jefferson City MO, USA

^d City of Tulsa Water and Sewer Department, Tulsa OK, USA

ARTICLE INFO

Article history:

Received 22 May 2014

Received in revised form

1 August 2014

Accepted 3 August 2014

Available online 11 August 2014

Keywords:

N-nitrosamine

Precursors of N-nitrosamines

N-nitrosodimethylamine (NDMA)

Ultra-fast liquid chromatography–tandem mass spectrometry

Drinking water system

Disinfection by-product

ABSTRACT

N-Nitrosamines are potent mutagenic and carcinogenic emerging water disinfection by-products (DBPs). The most effective strategy to control the formation of these DBPs is minimizing their precursors from source water. Secondary and tertiary amines are dominating precursors of N-nitrosamines formation during drinking water disinfection process. Therefore, the screening and removal of these amines in source water are very essential for preventing the formation of N-nitrosamines. A rapid, simple, and sensitive ultrafast liquid chromatography–tandem mass spectrometry (UFLC-MS/MS) method has been developed in this study to determine seven amines, including dimethylamine, ethylmethylamine, diethylamine, dipropylamine, trimethylamine, 3-(dimethylaminomethyl)indole, and 4-dimethylaminoantipyrine, as major precursors of N-nitrosamines in drinking water system. No sample preparation process is needed except a simple filtration. Separation and detection can be achieved in 11 min per sample. The method detection limits of selected amines are ranging from 0.02 µg/L to 1 µg/L except EMA (5 µg/L), and good calibration linearity was achieved. The developed method was applied to determine the selected precursors in source water and drinking water samples collected from Midwest area of the United States. In most of water samples, the concentrations of selected precursors of N-nitrosamines were below their method detection limits. Dimethylamine was detected in some of water samples at the concentration up to 25.4 µg/L.

© 2014 Elsevier B.V. All rights reserved.

1. Introduction

N-Nitrosamines are a group of emerging water disinfection by-products (DBPs) that are potentially carcinogenic to humans [1] and classified as probable human carcinogens by the International Agency for Research on Cancer (IARC). United States Environmental Protection Agency (US EPA) is currently listed a group of major N-nitrosamines in Contaminant Candidate List 3 (CCL 3) [2]. N-Nitrosamines have been found to form in drinking waters system [3–8]. N-nitrosodimethylamine (NDMA) is one of the most commonly detected N-nitrosamines in drinking water system with concentrations ranging from 0 to 630 ng/L [7,9–12]. Due to the potential carcinogenic effects of N-nitrosamines, there are

increasing concerns on the control and removal of N-nitrosamines in drinking water systems.

N-nitrosamines are mainly formed in the disinfection process and distribution system [5]. Therefore, removing N-nitrosamines precursors prior to water disinfection will be the best way to minimize the N-nitrosamine formation. Several studies have shown that precursors of N-nitrosamines are compounds that contain organic nitrogen, such as natural organic matter, cationic flocculants, and anion exchange resins that are used for ion-exchange in water treatment [1,5,13–15]. Among those compounds, secondary amines such as dimethylamine (DMA), ethylmethylamine (EMA), diethylamine (DEA), and dipropylamine (DPA) are one group of the most important precursors of N-nitrosamines. It has been reported that DMA is primary precursor of NDMA, [5], and DEA, EMA, and DPA are secondary N-nitrosamines precursors that are mainly used as intermediates in the chemical and pharmaceutical industries [16]. It has also been reported that tertiary amines containing dimethylamine functional

* Corresponding author. Tel.: +1 573 341 4433.

E-mail address: honglan@mst.edu (H. Shi).

groups, such as trimethylamine (TMA), 4-dimethylaminoantipyrine (DMAP), and 3-(dimethylaminomethyl)indole (DMAI) are also precursors of N-nitrosamines (such as NDMA) during chloramination [17,18]. These amines can also be formed during the biodegradation of proteins, amino acids, and other nitrogen-containing compounds [16,17,19–21].

The formations of N-nitrosamines, especially NDMA, from DMA and other amines during chlorination and chloramination have been extensively investigated [5,8,22]. In most studies, the reaction yield of NDMA formation is very low (0.1% or less). However, the expected concentrations of DMA and other amines in source water are usually at the $\mu\text{g/L}$ level [10,11]. The formations of N-nitrosamines are still not negligible with such low reaction yield since N-nitrosamines are considered to be carcinogenic to humans even at very low ng/L level [1].

Analysis of amines is generally performed by gas chromatography (GC), liquid chromatography (LC), or ion chromatography (IC) coupled with different detectors [10,16,19–21,23–31]. However, most of these analytical methods involve time-consuming derivatization process and sometime cause poor method performance. Satcher et al. [16] developed a gas chromatography coupled with mass spectrometry (GC–MS) method for analysis of primary and secondary aliphatic amines in waste and surface water with detection limits ranging from 0.22 to 1.20 $\mu\text{g/L}$. However, sample derivatization is required to enhance the method performance and only DMA and DEA were included in this method [16]. Gao et al. [30] developed a method for the determination of primary and secondary aliphatic amines including DMA and DEA by using a HPLC with fluorescence detection. The selected amines were derivatized with a fluorescent derivatization reagent and the detection limits were in the range of 0.01 to 0.04 nM. However, the derivatization procedure takes for 25 min and the sample analysis takes 40 min.

High-performance liquid chromatography coupled with tandem mass spectrometry (HPLC–MS/MS) is a powerful and reliable analytical technique for quantitative analysis of compounds at trace levels due to its good linearity, high sensitivity, and selectivity. HPLC–MS/MS methods have been developed to determine secondary amines in various sample matrices [28,29]. Romero et al. [29] developed a method for direct analysis of biogenic and volatile amines including TMA in anchovy by using ultra-pressure (UP) LC–MS/MS. However, the limits of quantification are relatively high (25 $\mu\text{g/L}$) compared to that of the method using GC–MS. Moreover, these methods have not been applied to determine amines that are considered as major N-nitrosamine precursors in drinking water. Thus, it is very crucial to develop a method for fast and simple analysis of secondary and tertiary amines as N-nitrosamine precursors for better monitoring and control of N-nitrosamine formations in drinking water system.

This study developed a novel rapid and sensitive method for the determination of seven amines, including DMA, EMA, DEA, DPA, TMA, DMAI, and DMAP, as N-nitrosamines precursors in drinking water system by using UFLC–MS/MS. Water samples, after filtration through 0.22 μm Nylon membrane filters, were directly injected and analyzed without extraction or derivatization. Separation and detection were achieved within 11 min. The detection limits of selected amines are ranging from 0.05 to 1 $\mu\text{g/L}$, except for EMA (5 $\mu\text{g/L}$). These detection limits are comparable to derivatization–GC–MS analysis method.

2. Material and methods

2.1. Chemicals and reagents

All amines standards with purity better than 97%, DMA (dimethylamine solution 40 wt% in H_2O), TMA (trimethylamine solution 25 wt% in H_2O), DMAI, DMAP, EMA, DEA, and DPA were purchased from

Sigma-Aldrich (St. Louis, MO). All solvents (methanol, acetonitrile, etc.) are LC–MS grade which were purchased from Fisher Scientific (Fairlawn, NJ, USA). Formic acid (mass spectrometry grade) was obtained from Sigma Aldrich (St. Louis, MO). Ultrapure water was generated by a Milli-Q Advantage® A10 and Millipore Elix® water purification system (Millipore, Billerica, MA). Stock standard solutions of individual amine compounds (with concentrations at 10 mg/mL) were prepared by exact weighing of the solids or liquids and dissolution in 2 mL of MQ water or methanol (for DMAI only). The secondary stock standards mixture solutions were prepared by diluting the each individual standard stock solution to the concentrations ranging from 100 to 500 mg/L . These stock solutions were then stored in screw-capped amber glass vials at 4 °C in the dark. Working standard mixture solutions at the concentrations were prepared by appropriate dilution of the stock solutions with ultrapure water. No headspace was left for all the standard solutions.

2.2. Water sample collection and preservation

500 mL amber glass bottles with Teflon liner screw caps were used to collect water samples. Prior to use, bottles were pre-cleaned with Mill-Q water, methanol, acetone, and Mill-Q water, and then baked at 105 °C for at least 2 h. About 40 mg of sodium thiosulfate was added to each bottle to quench any residual chlorine that had been used for disinfection. To collect treated tap water samples, the water was allowed to flow from the tap without an aerator for about 5 min prior to completely filling the sample bottle, with no headspace and no overflow. To collect source water from rivers and lakes, a large pre-cleaned wide-mouth bottle or beaker was used to take the water, and then the water was carefully transferred to a sample bottle to completely fill the bottle with no headspace remaining. The water sample was filtered through a 0.22 μm Nylon filter prior to analysis.

2.3. UFLC–MS/MS analysis

A 4000Q Trap mass spectrometer (AB SCIEX, Concord, ON, CA) equipped with an Shimadzu LC–20ADXR UFLC system (Columbia, MD) was used for all analyses. The column was a Phenomenex Polar-RP C-18 column (150 \times 2.0 mm I.D., 4 μm particle size, Phenomenex, Torrance, CA). Analyst 1.5 software was used for data acquisition and quantification. Separation was achieved by a gradient elution program with eluent A (Milli-Q water with 0.1% formic acid) and eluent B (methanol with 0.1% formic acid): started from 5% B and maintained B at 5% for 2 min; increased to 70% B over 0.5 minute and increased to 100% B in 2.5 min; maintained at 100% B for 3 min, then decreased to 5% B over 0.1 minute and maintained for 3 min. The total run time was 11 min. The total flow rate was set to 0.20 ml/min and the injection volume was 15 μL . Positive electrospray ionization (ESI) with the multiple reaction monitoring (MRM) mode was used for quantification. Nitrogen gas used for curtain and collision gases was generated by a N_2 Generator (Peak scientific, Billerica, MA). The ion source temperature was set at 550 °C with an ion spray voltage of 5500 V. The nebulizer gas, auxiliary gas, and curtain gas were 50, 65, and 25 psi, respectively. The instrumental conditions and method parameters are shown in Table 1.

2.4. Quality control

During the method development, the linear range of calibration for each compound, method detection limit, reagent blank, reproducibility, spike recoveries of each compound in ultrapure water and in water matrices were all performed. During the analysis of water samples, at least one blank, two duplicated samples, and one spike sample were processed with sample preparation and

Table 1
Instrumental conditions of 4000Q Trap mass spectrometer for selected amines.

Parameters	DMA	EMA	TMA	DEA	DPA	DMAI	DMAI
CAS#	124-40-3	624-78-2	75-50-3	109-89-7	142-84-7	87-52-5	58-15-1
MRM ions (<i>m/z</i>)	46 > 31	60 > 32	60 > 44	74 > 46	102 > 43	175 > 131	232 > 113
Declustering potential (V)	61	41	6	21	41	36	51
Collision cell exit potential (V)	31	17	29	13	19	13	21
Entrance potential (V)	10	10	10	10	10	10	10
Collision energy (V)	6	3	6	4	4	24	20
Dwell time (ms)	150	150	100	100	100	50	50

UFLC-MS/MS detection for every 10 samples. These sample matrices were chosen to be representative of river and well water.

3. Results and discussion

3.1. Optimization of LC-MS/MS conditions

Seven selected amines were detected using UFLC-MS/MS. All target compounds were detected with positive ESI mode and their compound-dependent parameters (accurate ion pairs, declustering potential, collision cell exit potential, collision energy, and entrance potential) were optimized individually for maximum sensitivity. First, direct infusions of standard working solution of each amine at concentrations ranging from 0.1 to 0.5 mg/L were performed. The working solution was prepared by proper dilution of stock solution using ultrapure water and the flow rate was set to 0.60 ml/h. Then flow injection was used to optimize other ESI-MS/MS parameters, such as ion source temperature, ion spray voltage, and curtain gas pressure. The flow injection was achieved by injecting standard mixture solution of 100 µg/L of each amine at a LC operation flow rate 0.2 ml/min.

After mass spectrometer parameters were optimized, gradient elution was performed to separate the selected amines. Since the pK_a values of selected amines are all relatively high (9–11) and positive ionization mode was used, formic acid was used as additives. The optimum LC separation was obtained using 0.1% (v/v) formic acid in both lab reagent water and methanol as mobile phases. Fig. 1 shows a representative of MRM-mode UFLC-MS/MS chromatogram of the seven amines standards in reagent water. The optimized value of mobile phase flow rate was 0.2 ml/min and the injection volume was set to 15 µL. Under these conditions, good separation was achieved and all selected amines are eluted from 2.0 to 6.7 min. Co-eluting amines were monitored at different MRM ion pair transitions.

Dwell times were also optimized for each compound to obtain a sufficient number of data points across the peak while maintaining the signal intensity. The optimum values of dwell time were from 50–150 ms and at least 15 data points for each peak were obtained.

3.2. Method validation and method detection limit in different water matrix

The performance of developed method was validated by a series of tests including linearity range, spike recovery, precision, accuracy, and limits of detection/quantification in source water matrix and drinking water matrix. The linearity range of the method was obtained by analyzing various concentrations of selected amine standards in lab reagent water. By plotting the peak area vs. the concentration, linear functions were obtained for each selected amine and presented in Table 2. The linearity coefficients were all higher than 0.99 with a linearity range of 2–100 µg/L for DMA and DEA, 1–100 µg/L for TMA, 7.5–150 µg/L

for EMA, 1–75 µg/L for DPA, 0.2–75 µg/L for DMAI, and 0.1–75 µg/L for DMAP.

Spike recovery was studied to evaluate the matrix effect. Based on test results (not shown) without the quenching agent, the amine standards would react with the residual disinfectants in the water samples and yield low spike recoveries. Thus sodium thiosulfate was added into each water sample to serve as quenching agent at the concentration of 80 ppm, as it was mentioned in the sample collection procedure. By adding appropriate amount of standard solutions of the selected amines in water samples, the percent recoveries and relative standard deviations were calculated and reported in Table 2 for source water. Three different concentrations (10 µg/L, 20 µg/L, and 50 µg/L) and seven replicated samples of each concentration were performed discretely in both untreated source water and finished water. Recoveries of all selected amines in untreated source water and finished water ranged between 88.5 and 116%. Good reproducibilities for all amines were obtained with the percent relative standard deviation less than 10% mostly. Similar or better performances were obtained for reagent water.

The method detection limit (MDL) for each amine compound was determined as the lowest injected standard that gave a signal-to-noise (S/N) ratio between 3 and 5 calculated by measuring the signal peak height to averaged background noise ratio [32]. The background noise was based on the peak-to-peak baseline near the analyte peak. The MDLs for the studied amines were between 0.02 and 5 µg/L in reagent water. The precision of the UFLC-MS/MS method was evaluated by determining the relative standard deviation (RSD) of spiked samples obtained from multiple ($n=7$) replicate analyses. For analyte-free untreated source water spiked with 10 and 20 µg/L amine standards, RSD ranged from 2.12% to 13.8% (Table 2).

3.3. Occurrence of selected amines as precursors of N-nitrosamines in drinking water treatment systems

Water samples were collected from five different drinking water treatment facilities in Missouri and Oklahoma State. For the same facility, samples were taken for both untreated source water and treated drinking water in different seasons. Water samples were filtered and then analyzed using the developed method to determine the concentrations of selected amines as N-nitrosamines precursors. The results are shown in Table 3 and Table 4. To ensure precision in the screening, replicates samples (at least 20% of the total numbers of samples) were measured for each batch. Analytical accuracy for the measurements was tested by sample spike recoveries. Recoveries of selected amines in treated and untreated water ranged from 80 to 120%. The reproducibility with the percent relative standard deviation was less than 10%.

Among all the collected water samples, only DMA was detected in two facilities at concentrations up to 25.4 µg/L. The concentrations of other amine precursors of N-nitrosamines were below their MDLs. Overall the concentrations of selected amines in the source water were relatively lower compare to the occurrence data

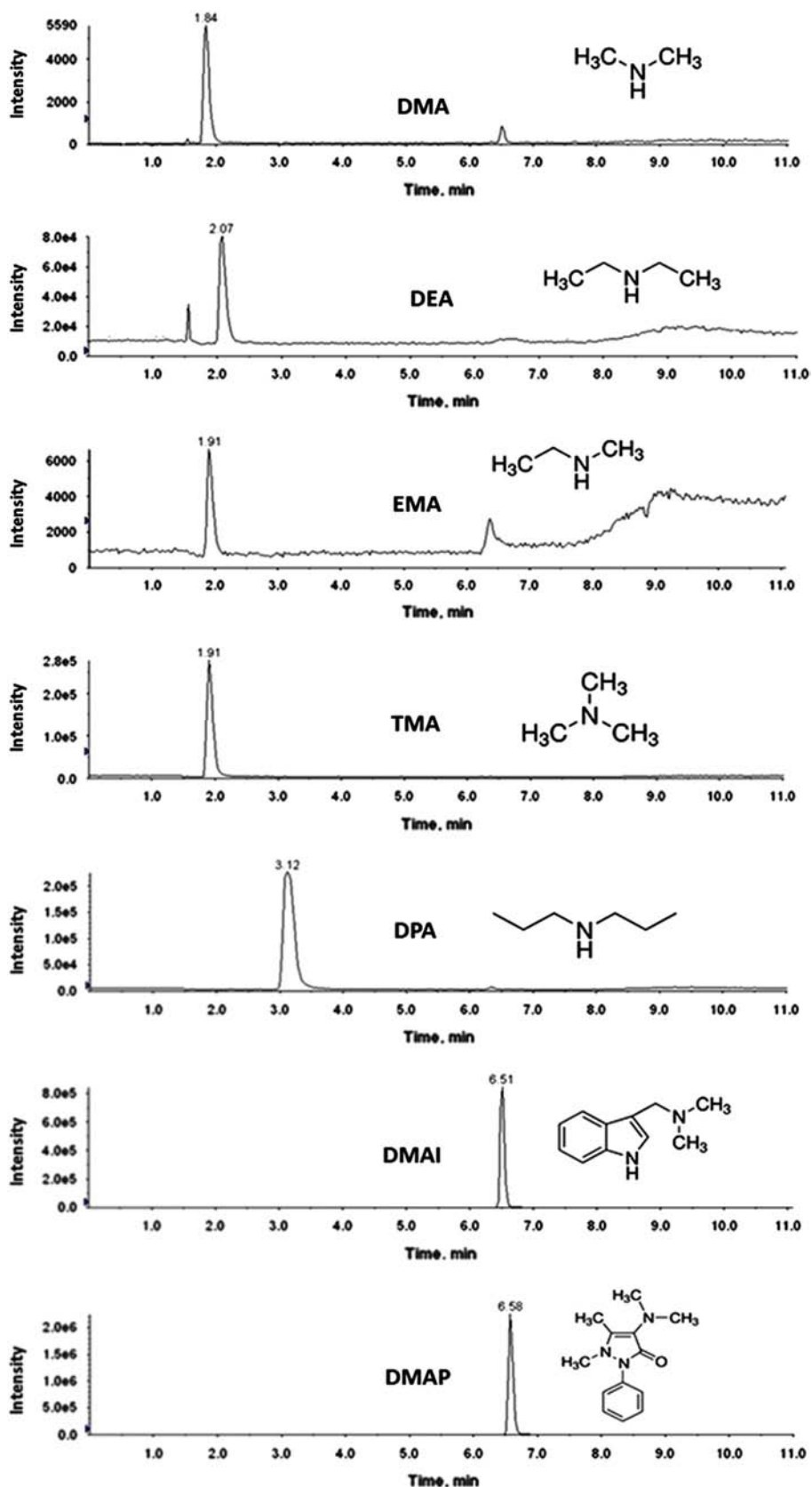


Fig. 1. The extracted-ion chromatogram (XIC) of selected amines as precursors of N-nitrosamines in reagent water.

from other publications [1,10,11]. Interestingly, higher concentrations of DMA were found in the finished water than untreated source water. As it is shown in Table 3, for facility 1 in season 2,

DMA was not detectable in the untreated source water but was found in finished water at the concentration of 1.8 $\mu\text{g/L}$. For facility 3 in season 2, DMA was detected at the concentrations of 1.2 and

Table 2
UFLC/MS/MS method performance results including method detection limit (MDL), calibration range and linearity (regression coefficient, R^2), precision (coefficient of variation, %CV), and accuracy (percent spike recovery).

Compound	MDL ($\mu\text{g/L}$)	Calibration range ($\mu\text{g/L}$)	Coefficient of Determination (R^2)	10 $\mu\text{g/L}$ spiked in untreated source water		20 $\mu\text{g/L}$ spiked in untreated source water		50 $\mu\text{g/L}$ spiked in finished water	
				CV (%)	Accuracy (%)	CV (%)	Accuracy (%)	CV (%)	Accuracy (%)
DMA	1.00	2–100	0.9996	2.12	106.0	7.78	93.0	8.99	108.0
EMA	5.00	7.5–150	0.9968	11.4	97.9	3.88	88.5	13.8	101.3
TMA	0.50	1–100	0.9997	2.82	103.0	6.01	105.5	10.2	111.9
DEA	1.00	2–100	0.9983	4.24	97.4	7.88	89.0	10.6	100.6
DPA	0.20	1–75	0.9995	5.51	101.0	2.12	97.0	7.49	92.1
DMAI	0.05	0.2–75	0.9959	3.53	116.0	4.24	103.0	12.2	95.3
DMAP	0.02	0.1–75	0.9965	4.97	108.0	6.36	96.0	4.74	95.7

Table 3
Concentrations ($\mu\text{g/L}$) of selected amines as precursors of N-nitrosamines detected in Missouri State drinking water facilities. Chlorination (gaseous chlorination or hypochlorination) was used as disinfectants for these water treatment plants.

Sample ID		DMA	EMA	TMA	DEA	DPA	DMAI	DMAP
		Concentration ($\mu\text{g/L}$)						
Facility 1 (Surface water)								
Season 1, June	Untreated source water	< 1.0	< 5.0	< 0.5	< 1.0	< 0.2	< 0.05	< 0.02
	Finished water	< 1.0	< 5.0	< 0.5	< 1.0	< 0.2	< 0.05	< 0.02
Season 2, September	Untreated source water	< 1.0	< 5.0	< 0.5	< 1.0	< 0.2	< 0.05	< 0.02
	Finished water	1.8	< 5.0	< 0.5	< 1.0	< 0.2	< 0.05	< 0.02
Facility 2 (Ground water)								
Season 1, June	Untreated source water	< 1.0	< 5.0	< 0.5	< 1.0	< 0.2	< 0.05	< 0.02
	Finished water	< 1.0	< 5.0	< 0.5	< 1.0	< 0.2	< 0.05	< 0.02
Season 2, September	Untreated source water	< 1.0	< 5.0	< 0.5	< 1.0	< 0.2	< 0.05	< 0.02
	Finished water	< 1.0	< 5.0	< 0.5	< 1.0	< 0.2	< 0.05	< 0.02
Facility 3 (Ground water)								
Season 1, June	Untreated source water	< 1.0	< 5.0	< 0.5	< 1.0	< 0.2	< 0.05	< 0.02
	Finished water	< 1.0	< 5.0	< 0.5	< 1.0	< 0.2	< 0.05	< 0.02
Season 2, September	Untreated source water	1.2	< 5.0	< 0.5	< 1.0	< 0.2	< 0.05	< 0.02
	Finished water	25.4	< 5.0	< 0.5	< 1.0	< 0.2	< 0.05	< 0.02
MDL ($\mu\text{g/L}$)		1.0	5.0	0.5	1.0	0.2	0.05	0.02

Table 4
Concentrations ($\mu\text{g/L}$) of selected amines as precursors of N-nitrosamines detected in Oklahoma State drinking water facilities. Gaseous chlorination was used for disinfection.

Sample ID		DMA	EMA	TMA	DEA	DPA	DMAI	DMAP
		Concentration ($\mu\text{g/L}$)						
Facility 1 (Surface water)								
Season 1, July	Untreated source water	< 1.0	< 5.0	< 0.5	< 1.0	< 0.2	< 0.05	< 0.02
	Finished water	< 1.0	< 5.0	< 0.5	< 1.0	< 0.2	< 0.05	< 0.02
Season 2, October	Untreated source water	< 1.0	< 5.0	< 0.5	< 1.0	< 0.2	< 0.05	< 0.02
	Finished water	< 1.0	< 5.0	< 0.5	< 1.0	< 0.2	< 0.05	< 0.02
Season 3, January	Untreated source water	< 1.0	< 5.0	< 0.5	< 1.0	< 0.2	< 0.05	< 0.02
	Finished water	< 1.0	< 5.0	< 0.5	< 1.0	< 0.2	< 0.05	< 0.02
Season 4, March	Untreated source water	< 1.0	< 5.0	< 0.5	< 1.0	< 0.2	< 0.05	< 0.02
	Finished water	< 1.0	< 5.0	< 0.5	< 1.0	< 0.2	< 0.05	< 0.02
Facility 2 (Surface water)								
Season 1, July	Untreated source water	< 1.0	< 5.0	< 0.5	< 1.0	< 0.2	< 0.05	< 0.02
	Finished water	< 1.0	< 5.0	< 0.5	< 1.0	< 0.2	< 0.05	< 0.02
Season 2, October	Untreated source water	< 1.0	< 5.0	< 0.5	< 1.0	< 0.2	< 0.05	< 0.02
	Finished water	< 1.0	< 5.0	< 0.5	< 1.0	< 0.2	< 0.05	< 0.02
Season 3, January	Untreated source water	< 1.0	< 5.0	< 0.5	< 1.0	< 0.2	< 0.05	< 0.02
	Finished water	< 1.0	< 5.0	< 0.5	< 1.0	< 0.2	< 0.05	< 0.02
Season 4, March	Untreated source water	< 1.0	< 5.0	< 0.5	< 1.0	< 0.2	< 0.05	< 0.02
	Finished water	< 1.0	< 5.0	< 0.5	< 1.0	< 0.2	< 0.05	< 0.02
MDL ($\mu\text{g/L}$)		1.0	5.0	0.5	1.0	0.2	0.05	0.02

25.4 µg/L for untreated source water and finished drinking water, respectively. These results indicate that more N-nitrosamines precursor (DMA) might be introduced to the water during the water treatment process. Two possible sources are cationic flocculants and anion exchange which are frequently used for ion-exchange during drinking water treatment processes. These materials have potentials to leach out N-nitrosamine precursors during the treatment [1,5] and need to be closely monitored.

4. Conclusion

In this study, a rapid and sensitive UFLC-MS/MS method for quantitative analysis of secondary and tertiary amines as N-nitrosamines precursors in drinking water system was developed. Separation and detection were achieved in 11 min per sample and no extraction or derivatization was necessary. Method detection limits are ranging from 0.02 to 1 µg/L, except EMA (5 µg/L). The developed method was applied to determine the selected amines in source and drinking water samples. The precursors concentrations were not detectable (< MDLs) in most water samples, but DMA was detected in some water samples at the concentration up to 25.4 µg/L. The developed method from this study will be very useful for monitoring of N-nitrosamine precursors and the control of N-nitrosamines formations in drinking water system.

Acknowledgments

This research work was supported by the Missouri Department of Natural Resources and Tulsa Metropolitan Utility Authority. The authors also thank Danielle West, Ariel Donovan, RuiPu Mu, Runmiao Xue, Kun Liu, and Yongbo Dan at Missouri University of Science and Technology, and staff at the water treatment facilities for sample collection, transport, and filtration processes.

References

- [1] S.D. Richardson, T.A. Ternes, *Anal. Chem* 83 (2011) 4614–4648.
- [2] U.S. EPA, Water: Contaminant Candidate List 3 – CCL (<http://water.epa.gov/scitech/drinkingwater/dws/ccl/cc13.cfm>).
- [3] M. Asami, M. Oya, K. Kosaka, *Sci. Total Environ* 407 (2009) 3540–3545.
- [4] J.W. Charrois, S.E. Hrudey, *Water Res* 41 (2007) 674–682.
- [5] W.A. Mitch, D.L. Sedlak, *Environ. Sci. Technol* 36 (2002) 588–595.
- [6] B. Jurado-Sánchez, E. Ballesteros, M. Gallego, *J. Sep. Sci* 33 (2010) 610–616.
- [7] Y.-Y. Zhao, J. Boyd, S.E. Hrudey, X.-F. Li, *Environ. Sci. Technol* 40 (2006) 7636–7641.
- [8] Y.-Y. Zhao, J.M. Boyd, M. Woodbeck, R.C. Andrews, F. Qin, S.E. Hrudey, X.-F. Li, *Environ. Sci. Technol* 42 (2008) 4857–4862.
- [9] J.W. Charrois, M.W. Arend, K.L. Froese, S.E. Hrudey, *Environ. Sci. Technol* 38 (2004) 4835–4841.
- [10] H. Zhang, S. Ren, J. Yu, M. Yang, *J. Environ. Sci* 24 (2012) 1885–1890.
- [11] W. Wang, S. Ren, H. Zhang, J. Yu, W. An, J. Hu, M. Yang, *Water Res* 45 (2011) 4930–4938.
- [12] U.S. EPA, United States Environmental Protection Agency Occurrence Data Accessing Unregulated Contaminant Monitoring Data. (<http://water.epa.gov/lawsregs/rulesregs/sdwa/ucmr/data.cfm>).
- [13] W.I. Kimoto, C.J. Dooley, J. Carré, W. Fiddler, *Water Res* 14 (1980) 869–876.
- [14] I. Najm, R.R. Trussell, *J. Am. Water Works Ass* 93 (2001) 92–99.
- [15] R. Shen, S.A. Andrews, *Water Res* 45 (2011) 944–952.
- [16] F. Sacher, S. Lenz, H.-J. Brauch, *J. Chromatogr. A* 764 (1997) 85–93.
- [17] H. Ohshima, T. Kawabata, *IARC Sci. Publ* (1977) 143–153.
- [18] W. Mitch, D. Sedlak, *Water Supply* 2 (2002) 191–198.
- [19] M.-K. Kim, J.-H. Mah, H.-J. Hwang, *Food Chem* 116 (2009) 87–95.
- [20] B. Ten Brink, C. Damink, H. Joosten, J. Huis In't Veld, *Int. J. Food Microbiol* 11 (1990) 73–84.
- [21] J. Pietsch, F. Sacher, W. Schmidt, H.-J. Brauch, *Water Res* 35 (2001) 3537–3544.
- [22] J. Choi, R.L. Valentine, *Environ. Sci. Technol* 37 (2003) 4871–4876.
- [23] Y.-C. Wu, S.-D. Huang, *Anal. Chem* 71 (1999) 310–318.
- [24] F. Li, H.-y. Liu, C.-h. Xue, X.-q. Xin, J. Xu, Y.-g. Chang, Y. Xue, L.-a. Yin, *J. Chromatogr. A* 1216 (2009) 5924–5926.
- [25] M.E. Erupe, A. Liberman-Martin, P.J. Silva, Q.G. Malloy, N. Yonis, D.R. Cocker III, K.L. Purvis-Roberts, *J. Chromatogr. A* 1217 (2010) 2070–2073.
- [26] C. Cháfer-Pericás, R. Herráez-Hernández, P. Campíns-Falcó, *Talanta* 66 (2005) 1139–1145.
- [27] L. Yang, Z. Chen, J. Shen, X. Liu, H. Li, Y. Han, *China Water Wastewater* 26 (2010) 93–97.
- [28] K. Verma, *Analyst* 124 (1999) 1017–1021.
- [29] R. Romero-González, M.a.I. Alarcón-Flores, J.L.M.n. Vidal, A.G. Frenich, *J. Agr. Food Chem* 60 (2012) 5324–5329.
- [30] P.-F. Gao, Z.-X. Zhang, X.-F. Guo, H. Wang, H.-S. Zhang, *Talanta* 84 (2011) 1093–1098.
- [31] E. Paleologos, M. Kontominas, *Anal. Chem* 76 (2004) 1289–1294.
- [32] D.C. Harris, *Quantitative Chemical Analysis*, eighth ed, W.H. Freeman and Company, New York (2010) 105.

Talanta

The International Journal of Pure and Applied Analytical Chemistry

Aims & Scope

Talanta provides a forum for the publication of original research papers, preliminary communications, and critical reviews in all branches of pure and applied analytical chemistry. Papers are evaluated based on established guidelines, including the fundamental nature of the study, scientific novelty, substantial improvement or advantage over existing technology or methods, and demonstrated analytical applicability. Original research papers on fundamental studies, and novel sensor and instrumentation development, are especially encouraged. Novel or improved applications in areas such as clinical and biological chemistry, environmental analysis, geochemistry, and materials science and engineering are welcome.

Analytical performance of methods should be determined, including interference and matrix effects, and methods should be validated by comparison with a standard method, or analysis of a certified reference material. The developed method should especially comprise information on selectivity, sensitivity, detection limits, accuracy, and reliability. However, applying official validation or robustness studies to a routine method or technique does not necessarily constitute novelty. Proper statistical treatment of the data should be provided. Relevant literature should be cited, including related publications by the authors, and authors should discuss how their proposed methodology compares with previously reported methods.

Since classical spectrophotometric measurements and applications (including derivative spectrophotometry), fluorimetry, solvent extraction, titrimetry, chemometrics, etc. are well established and are considered routine analytical methods, studies in such areas should demonstrate a unique and substantial advantage over presently known systems. New reagents or systems should demonstrate clear advantage, and their presentation should be comprehensive rather than generating a series of similar papers for several analytes or similar reagents. Modifications of reagents should demonstrate significant improvements. Obvious application of known chemistries or methods to established instrumental techniques are discouraged.

Application of established analytical approaches to relatively simple matrices having no major interferences, such as pharmaceutical preparations, are discouraged unless considerable improvements over other methods in the literature are demonstrated. Papers dealing with analytical data such as stability constants, pK_a values, etc. should be submitted to more specific journals, unless novel analytical methodology is demonstrated, or important analytical data are provided which could be useful in the development of analytical procedures.

Editors-in-Chief

Professor G.D. Christian, University of Washington, Department of Chemistry, 36 Bagely Hall, P.O. Box 351700, Seattle, WA 98195-1700, U.S.A.

Professor J.-M. Kauffmann, Université Libre de Bruxelles (ULB), Faculty of Pharmacy, Campus Plaine CP 205/6, Boulevard du Triomphe, B-1050 Brussels, Belgium, Fax: +32 2 650 5225, Tel: +32 2 650 5215, Email: talanta@ulb.ac.be

Associate Editors

Professor J.-H. Wang, Research Center for Analytical Sciences, Northeastern University, Box 332, Shenyang 110004, China

Professor J.L. Burguera, Los Andes University, IVAIQUIM, Faculty of Sciences, P.O. Box 542, 5101-A Mérida, Venezuela.

Dr Ian McKelvie, School of Chemistry, The University of Melbourne, Victoria 3010, Australia, Phone: +61 3 8344 6567, Email: ian.mckelvie@gmx.com.

Assistant Editors

Dr R.E. Synovec, Department of Chemistry, University of Washington, Box 351700, Seattle, WA 98195-1700, U.S.A.

Ms. Dominique (D.) Mertens, Université Libre de Bruxelles, Faculty of Pharmacy, Service de Chimie Analytique Instrumentale et, Bioélectrochimie, Campus Plaine CP 205/6, Boulevard du Triomphe - B-1050 Brussels, Belgium, Email: dmertens@ulb.ac.be, Tél : +32 (0)2 650 52 47, Fax : +32 (0)2 650 52 25

Talanta

R. Apak (Istanbul, Turkey)
E. Bakker (Auburn, AL, U.S.A.)
D. Barceló (Barcelona, Spain)
B. Birch (Luton, UK)
J.-L. Capelo-Martinez (Caparica, Portugal)
O. Chailapakul (Thailand)
D.S. Chung (Seoul, Korea)
S. Cosnier (Grenoble, France)
M. del Valle (Barcelona, Spain)
A.A. Galal (Giza, Egypt)
A.G. Gonzales (Seville, Spain)
M. Hernandez-Cordoba (Spain)
P. Hubert (Liège, Belgium)

J. Kalivas (Pocatella, ID, U.S.A.)
A.A. Karyakin (Moscow, Russia)
S. Kolev (Melbourne, Australia)
J.-M. Lin (Beijing, China)
S. Motomizu (Okayama, Japan)
R. Niessner (München, Germany)
J.A. Nobrega (São Carlos, SP, Brazil)
A.C. Olivieri (Rosario, Argentina)
S. Ozkan (Ankara, Turkey)
J.-M. Pingarron (Madrid, Spain)
M.D. Porter (Salt Lake City, UT, U.S.A.)
V. Remcho (Corvallis, OR, U.S.A.)
M. Shamsipur (Kermanshah, Iran)

Y.-H. Shao (Beijing, China)
P. Solich (Hradec Králové, Czech Republic)
D.G. Themelis (Thessaloniki, Greece)
K. Thurbide (Calgary, AB, Canada)
T. Toyo'oka (Shizuoka, Japan)
D.L. Tsalev (Sofia, Bulgaria)
B. Walczak (Katowice, Poland)
J. Wang (Tempe, AZ, U.S.A.)
J.D. Winefordner (Gainesville, FL, U.S.A.)
X.-H. Xia (Nanjing, China)
X.-P. Yan (Tianjin, China)
E.A.G. Zagatto (Piracicaba, SP, Brazil)
X. Zhang (Beijing, China)

Talanta

The International Journal of Pure and Applied Analytical Chemistry

Editors-in-Chief

Professor G.D. Christian, University of Washington, Department of Chemistry, 36 Bagely Hall, P.O. Box 351700, Seattle, WA 98195-1700, U.S.A.

Professor J.-M. Kauffmann, Université Libre de Bruxelles (ULB), Faculty of Pharmacy, Campus Plaine CP 205/6, Boulevard du Triomphe, B-1050 Brussels, Belgium, Fax: +32 2 650 5225, Tel: +32 2 650 5215, Email: talanta@ulb.ac.be

Associate Editors

Professor J.-H. Wang, Research Center for Analytical Sciences, Northeastern University, Box 332, Shenyang 110004, China

Professor J.L. Burguera, Los Andes University, IVAIQUIM, Faculty of Sciences, P.O. Box 542, 5101-A Mérida, Venezuela

Dr Ian McKelvie, School of Chemistry, The University of Melbourne, Victoria 3010, Australia, Phone: +61 3 8344 6567, Email: ian.mckelvie@gmx.com

Assistant Editors

Dr R.E. Synovec, Department of Chemistry, University of Washington, Box 351700, Seattle, WA 98195-1700, U.S.A.

Ms. Dominique (D.) Mertens, Université Libre de Bruxelles, Faculty of Pharmacy, Service de Chimie Analytique Instrumentale et, Bioélectrochimie, Campus Plaine CP 205/6, Boulevard du Triomphe - B-1050 Brussels, Belgium, Email: dmertens@ulb.ac.be, Tél : +32 (0)2 650 52 47, Fax : +32 (0)2 650 52 25

Advisory Board

Chairman: Professor J.D. Winefordner, Gainesville, FL, U.S.A.

Talanta

R. Apak (Istanbul, Turkey)
E. Bakker (Auburn, AL, U.S.A.)
D. Barceló (Barcelona, Spain)
B. Birch (Luton, UK)
J.-L. Capelo-Martinez (Caparica, Portugal)
O. Chailapakul (Thailand)
D.S. Chung (Seoul, Korea)
S. Cosnier (Grenoble, France)
M. del Valle (Barcelona, Spain)
A.A. Galal (Giza, Egypt)
A.G. Gonzales (Seville, Spain)
M. Hernandez-Cordoba (Spain)
P. Hubert (Liège, Belgium)

J. Kalivas (Pocatella, ID, U.S.A.)
A.A. Karyakin (Moscow, Russia)
S. Kolev (Melbourne, Australia)
J.-M. Lin (Beijing, China)
S. Motomizu (Okayama, Japan)
R. Niessner (München, Germany)
J.A. Nobrega (São Carlos, SP, Brazil)
A.C. Olivieri (Rosario, Argentina)
S. Ozkan (Ankara, Turkey)
J.-M. Pingarron (Madrid, Spain)
M.D. Porter (Salt Lake City, UT, U.S.A.)
V. Remcho (Corvallis, OR, U.S.A.)
M. Shamsipur (Kermanshah, Iran)

Y.-H. Shao (Beijing, China)
P. Solich (Hradec Králové, Czech Republic)
D.G. Themelis (Thessaloniki, Greece)
K. Thurbide (Calgary, AB, Canada)
T. Toyo'oka (Shizuoka, Japan)
D.L. Tsalev (Sofia, Bulgaria)
B. Walczak (Katowice, Poland)
J. Wang (Tempe, AZ, U.S.A.)
J.D. Winefordner (Gainesville, FL, U.S.A.)
X.-H. Xia (Nanjing, China)
X.-P. Yan (Tianjin, China)
E.A.G. Zagatto (Piracicaba, SP, Brazil)
X. Zhang (Beijing, China)

Volume 131(2015)



ELSEVIER

Amsterdam – Boston – London – New York – Oxford – Paris – Philadelphia – San Diego – St. Louis